Unsaturated Soil Mechanics
from Theory to Practice

Editors
Zhenghan Chen, Changfu Wei, De'an Sun & Yongfu Xu



CRC Press
Taylor & Francis Group
A BALKEMA BOOK

This page intentionally left blank

PROCEEDINGS OF THE 6TH ASIA-PACIFIC CONFERENCE ON UNSATURATED SOILS, GUILIN, CHINA, 23–26 OCTOBER 2015

Unsaturated Soil Mechanics—from Theory to Practice

Editors

Zhenghan Chen
Department of Civil Engineering, PLA Logistical Engineering University, China

Changfu Wei
College of Civil Engineering and Architecture, Guilin University of Technology, China

De'an Sun
Department of Civil Engineering, Shanghai University, China

Yongfu Xu
Department of Civil Engineering, Shanghai Jiaotong University, China

CRC Press
Taylor & Francis Group
Boca Raton London New York Leiden

CRC Press is an imprint of the
Taylor & Francis Group, an **informa** business

A BALKEMA BOOK

CRC Press/Balkema is an imprint of the Taylor & Francis Group, an informa business

© 2016 Taylor & Francis Group, London, UK

Typeset by MPS Limited, Chennai, India
Printed and bound in Great Britain by CPI Group (UK) Ltd, Croydon, CR0 4YY

All rights reserved. No part of this publication or the information contained herein may be reproduced, stored in a retrieval system, or transmitted in any form or by any means, electronic, mechanical, by photocopying, recording or otherwise, without written prior permission from the publishers.

Although all care is taken to ensure integrity and the quality of this publication and the information herein, no responsibility is assumed by the publishers nor the author for any damage to the property or persons as a result of operation or use of this publication and/or the information contained herein.

Published by: CRC Press/Balkema
P.O. Box 11320, 2301 EH Leiden, The Netherlands
e-mail: Pub.NL@taylorandfrancis.com
www.crcpress.com – www.taylorandfrancis.com

ISBN: 978-1-138-02921-7 (Hbk)
ISBN: 978-1-315-64334-2 (eBook PDF)

Unsaturated Soil Mechanics—from Theory to Practice – Chen et al. (Eds)
© 2016 Taylor & Francis Group, London, ISBN 978-1-138-02921-7

Table of contents

Preface XIII
Acknowledgements XV
Organizing Committee XVII

Invited and Keynote papers

Relationship between the laboratory SWCCs and field stress state 3
D.G. Fredlund

Tensiometer techniques for determining soil water retention curves 15
D.G. Toll, J.D. Asquith, A. Fraser, A.A. Hassan, G. Liu, S.D.N. Lourenço, J. Mendes, T. Noguchi, P. Osinski & R. Stirling

Capillary barrier as a slope protection 23
H. Rahardjo

Evolution of mesoscale structures of unsaturated expansive soil and intact loess under various stress and hydraulic paths 37
Z.H. Chen, Z.H. Yao, J.F. Guo & Q.Q. Miao

Slope stability analysis methods and application to 1 g failure model tests 53
Y. Kohgo

Investigation of mechanical and physio-chemical coupling through swelling pressure 65
Y.J. Cui

Testing of the hydro-mechanical behaviour of shales 73
L. Laloui, A. Ferrari & V. Favero

Desiccation crack depth and tensile strength in compacted soil 79
G.A. Miller, A. Hassanikhah & M. Varsei

Monotonic and cyclic shear stiffness of unsaturated soil at different temperatures 89
C.W.W. Ng, C. Zhou & J. Xu

Moisture and gas flow properties of compacted loess final covers for MSW landfills in Northwest China 103
L.T. Zhan

Experimental study on characteristics of the collapsibility of Ili loess 117
A.J. Zhang, Y.C. Xing, X.L. Hu, M.X. Guo & B. Zhang

Unsaturated soil behaviour

Microstructure

Analysis on microstructure and water retention properties of lime-treated soil 129
Y.J. Wang, Y.J. Cui, A.M. Tang, C.S. Tang & N. Benahmed

The microstructure information of natural loess in different areas, China 133
H.J. Hu, K. Zhou, Y.S. Luo, W.P. Zhao, Q. Hu & Z.Y. Zhang

Understanding the collapsible behavior of loess from microstructure information 137
P. Li, S.K. Vanapalli & T.L. Li

Microstructure change of loess soil during wet collapsing 143
X.X. Shao, H.Y. Zhang & J.W. Liu

Research on evolution of meso-structure of Q_2 loess during plastic and brittle failure in triaxial tests 147
X.W. Fang, C.N. Shen, Z.H. Chen & J. Li

Research on wetting-induced microstructure change of Q_2 loess 151
C.H. Li, X.W. Fang, C.N. Shen & Y.X. Ou

Structural damage properties of loess under loading and moistening 155
S. Shao, S.J. Shao & A.Z. Luo

The microstructure and soil-water characteristic of unsaturated loess 163
D.R. Hao, H.J. Liao, C.M. Ning & X.P. Shan

Hydraulic behaviors of unsaturated expansive soils 169
L.C. Miao, Y. Cui & H. Zeng

Discussion on cushion material strength after freezing-thawing cycle based on pore size distribution model 173
J.P. Yuan, Q.L. Wang, C.L. Han & K.B. Li

Nuclear Magnetic Resonance assay of carbon dioxide hydrate in silt 177
H.H. Tian, C.F. Wei, X.L. Xia & H. Wang

Evolution of soil water in silt soils based on NMR technique 181
P. Chen, C.F. Wei, J. Liu & W.J. Xue

Point of Zero Charge of two highly plastic expansive soils 185
B. Lin & A.B. Cerato

Stress-strain and strength characteristics

Influence of unsaturated state variables on small strain elastic behaviour 191
A.M. Hasan & S.J. Wheeler

Some remarks on the mechanical yielding of unsaturated soils 197
M. Lloret-Cabot, J.A. Pineda, D. Sheng & M.P. Cordão Neto

Deformation and yielding for intact Q_3 loess under various stress paths 205
D.F. Zhang, C.L. Chen, D.B. Yu, Y.T. Shu & P. Gao

An experimental method to study the drying-wetting behaviour of a sand 211
M. Milatz

Characterizing soil mechanical response induced by drought climate using a novel micropenetrometer 217
D.Y. Wang, C.S. Tang, S.K. Xu, K.Q. Sun, P. Wang & B. Shi

Investigating the volume change characteristics of bentonite/sand mixture under hydro-mechanical coupling condition 223
Z.G. Chen, C.S. Tang, D.Y. Wang, P. Wang, K.Q. Sun & B. Shi

Deformation characteristics and permeability of saturated bentonite-sand mixtures 229
W.J. Sun, Z.F. Wei, S.Q. Liu, C. Chen, L. Zhang & D.A. Sun

Investigation on swelling-shrinkage behavior of compacted expansive soils during wetting-drying cycles 235
N.F. Zhao, W.M. Ye, B. Chen & Y.G. Chen

Cracks' evolution characteristics of remolded expansive soils in the soaking and loading process 241
Z.H. Yao, Z.H. Chen, W. Li, L.H. Su, Q.Q. Miao & J.H. Zhang

Resilient modulus – soil suction correlations for two subgrade soils from China 247
Z. Han & S.K. Vanapalli

Wetting collapse at high degree of saturation during shearing for unsaturated sand 253
B.J. Shwan

Development of a new cyclic simple shear apparatus and test verification on loess 257
S.J. Shao, Q. Wang & S. Shao

Consolidation behavior of unsaturated Chuanxi compacted soil with soil suction control oedometer 263
D. Lu & W. Li

Experimental study of mechanical behavior of unsaturated silty clay in different loading sequences under constant water content condition 267
A.M. Rasool, K. Jiro & T. Shinya

Change in shear behavior of unsaturated volcanic coarse-grained soil due to fine particles run off 275
X.Y. Zheng, T. Ishikawa & T. Tokoro

Effect of fine grain contents on the unsaturated mechanical characteristics of embankment materials 281
B.S. Kim, Y. Takeshita, S. Kato & S.W. Park

Research on physical and mechanical properties of Xinjiang Daxigou loess 287
Z.Q. Hu, S. Lin, Z.J. Li & H.R. Li

Study on dynamic modulus and deformation characteristics of loess under bidirectional cyclic loads 293
X.D. Zhang, Y.S. Luo, P.C. Wang & L.X. Hu

Shear strength of a swelled soil examining influence of swelling boundary conditions 299
B.F. Lim & G.A. Siemens

Strength behaviors of the unsaturated silty clay based on ring shear test 305
W.J. Xue, P. Chen & C.F. Wei

Influence of matric suction on shear strength behavior of remolded unsaturated basalt residual soil 309
J. Chen, X.W. Lei, F.Z. Cheng & Q.S. Meng

Study on shear strength characteristics of the remolded laterite soil in Guilin 315
X.J. Chen, X. Huang, G.Y. Xiao, H.B. Chen & Y.L. Qi

Experimental analysis on tensile strength of unsaturated sandy clay under different initial densities and water contents 321
R.J. Che, G.Q. Cai & C.G. Zhao

Water retention and hydraulic behavior

A non-linear hysteresis model for soil-water retention behaviour 329
A.N. Zhou

Common mistakes in determination of air entry value from gravimetric water content based Soil-Water Characteristic Curve 335
A.Y. Pasha, A. Khoshghalb & N. Khalili

Non-isothermal water retention curve and volume change equation for unsaturated soils 343
A.N. Zhou, J. Li & D. Sheng

A simplified method to estimate the Soil-Water Characteristic Curve 349
Y.T. Fan & E.C. Leong

Effect of specimen preparation on water retention and deformation behaviour of unsaturated soils 355
D.A. Sun, Y. Gao & A.N. Zhou

A research of affect factor on hysteresis behavior for Soil-Water Characteristic Curve 361
J. Li & F.Y. Liu

Soil water retention of a compacted sandy clay with sub-critical water repellency 367
S.D.N. Lourenço, N. Jones, C.P. Morley, S.H. Doerr & R. Bryant

Measurement of Soil-Water Characteristic Curve of expansive soil using filter paper method 371
H. Li, L.C. Li & Z.Q. Huang

Drying-wetting Soil-Water Characteristic Curves of highly expansive soil 375
A.M. Al-Mahbashi, T.Y. Elkady & M.A. Alshamrani

Measurement of Soil-Water Characteristic Curve with a continuous pressurization method 379
S. Kato, M. Hatakeyama, H. Abe, B.S. Kim & Y. Takeshita

Hydraulic properties for soils that undergo volume change as soil suction is increased 383
F. Zhang, D.G. Fredlund & G.W. Wilson

Role of unsaturated permeability function in seepage analyses 393
A. Rahimi, H. Rahardjo & E.C. Leong

Effects of variability of unsaturated hydraulic properties on stability of residual soil slopes 401
Q. Zhai, H. Rahardjo & A. Satyanaga

Measurement of hydraulic properties of unsaturated permeable polyurethane bound asphalt materials 407
L. Renken, M. Oeser, M. Milatz & J. Grabe

Hydro-mechanical behaviour of shot-clay bentonite 413
A. Ferrari, A. Seiphoori & L. Laloui

Effect of heating to Soil-Water Characteristic Curve of compacted bentonite 419
T. Nishimura

Development of test-bed and model test for one-dimensional heat and moisture transfer in soils 425
Z.T. Zeng, Y.L. Zhao, H.B. Lu, C.F. Wei & Y. Zhang

Thermal conductivity of unsaturated mixtures of loess soil with granulated rubber 433
Z.H. Li, H.Y. Zhang & Y.M. Sheng

Laboratory study on drainage-seepage controlling of fine/coarse structure in unsaturated expansive soil slope 439
Q.H. Wu, J.F. Zhang, G.S. Zhu, H.D. Cui & X.Y. Liu

Water retention properties of unsaturated coarse-grained soils: The experimental study of the effect of Microbialy Induced Calcite Precipitation 445
R. Saffari, G. Habibagahi, E. Nikooee & A. Niazi

Effect of grain size on soil moisture evaporation process 451
S.K. Xu, C.S. Tang, K.Q. Sun & P. Wang

Osmotic suction of two highly plastic expansive soils 455
B. Lin & A.B. Cerato

Modelling

Fundamentals and constitutive modelling

Rate effects in inter-granular capillary bridges 463
Y. Zhang, D. Hanaor & Y.X. Gan

Interaction force between pore water and soil skeleton 467
L.T. Shao & X.X. Guo

Development of a hydro-thermal coupled model for unsaturated soils 473
N. An, S. Hemmati, Y.J. Cui & A.M. Tang

Nonlinear analysis of stress-strain relations of unsaturated soils 479
J.H. Zhang, Z.H. Chen, D. Chen, Q.Q. Miao & Z.H. Yao

Problems associated with determination of yield curves for unsaturated soils 487
X. Zhang

Structural and mechanical behavior of expansive soil with pore damage 491
M.S. Cheng, S.J. Wang, Y.Q. Zhang, S.H. Jiang & Z.H. Chen

Prediction of 1-D heave of a natural expansive soil slope of Zao-yang in China using the SWCC-based and water content-based models 497
H.Y. Tu & S.K. Vanapalli

Potential of surfactants for clay improvement 503
N. Jones, S.D.N. Lourenço & A. Paul

Cam-clay model applicable to unsaturated clayey sand 507
Q.Q. Miao, Z.H. Chen, Q.Q. Zhu, Z.H. Yao & J.H. Zhang

Analysis, improvement and evaluation of the generalized Soil-Water Characteristic Curve 511
Z.H. Chen & J.H. Zhang

A fractal-based Soil-Water Characteristic Curve model for deformable soils 519
A. Khoshghalb, A.Y. Pasha & N. Khalili

The formulation of the water retention curve with deformation and hysteresis 525
Q.D. Huang, C.G. Zhao & G.Q. Cai

Validity of the bimodal equations for fitting the Soil-Water Characteristic Curve behavior of cracked expansive soils 531
X. Wang & S.K. Vanapalli

A model for thermal influence on water retention curve in high suction range 537
B. Qin, Y. Lu, F.Z. Zhang & Z.H. Chen

Evaluation of Soil-Water Characteristic Curves of sand-cement mixtures 543
A.O. Al Shenawy, S.H. Al-hadama & T.Y. Elkady

Study on the absorbed suction of unsaturated soil based on the Horsfield close packing model 547
L.S. Tang, Y.L. Sun, Z.W. Deng & H.T. Sang

Effective stress for volume change of unsaturated soils 555
Y.F. Xu, Z.R. Cao, H.G. Zhu & F.F. Chu

Failure of divide-and-conquer approach in the characterization of unsaturated soils 561
X. Zhang

Reanalysis on shear strength of unsaturated soils 569
L.T. Shao, G.F. Zheng & X.X. Guo

Influence of sodium chloride on evaporation and cracking of earthen heritages 575
Y. Zhang, W.M. Ye, B. Chen & Y.G. Chen

Prediction of swelling by effective stress of bentonite in salt solution 581
G.S. Xiang, Y.F. Xu, T. Chen & H. Jiang

An elastoplastic constitutive model for chalk with considering chalk-fluid physicochemical interaction 587
T.T. Ma, C.F. Wei & X.L. Xia

An elastoplastic constitutive model for gas hydrate-bearing soils with hydrate dissociation 595
R.T. Yan & C.F. Wei

An intelligent back analysis optimization method of constitutive parameters for surrounding rock 601
Y. Zhang, B.C. Liu, Y.N. Hou & Z.T. Zeng

Predicting liquefaction of unsaturated sands using a coupled hydro-mechanical elastoplastic constitutive model 607
B. Zhang, K.K. Muraleetharan & C. Liu

Numerical modelling

Numerical modelling of swelling/shrinkage behaviour of unsaturated soils for buried pipe stress analysis 615
D. Weerasinghe, J. Kodikara & H. Bui

Numerical study on expansive soil slope stability considering the cracks and coupling effects 621
S.C. Qi & S.K. Vanapalli

A numerical model for heat and moisture migration in unsaturated freezing soil 629
J. Teng, D. Sheng, S. Liang & S. Zhang

Effective stress based numerical modelling of shallow foundations on unsaturated soil 635
Y. Tang & H.A. Taiebat

Development of a fully coupled thermo-hydro-chemical simulator for gas hydrate extraction 641
W.T. Li, C.F. Wei & T.T. Ma

Three-dimensional DEM simulation of constant-water-content triaxial tests on the unsaturated remolded loess 649
T. Li & M.J. Jiang

Simulation of particle crushing using Discrete-Element Method (DEM) 655
Y. Xi & Y.F. Xu

A new numerical method for one-dimensional compression test of crushable particles based on DEM 661
Y.D. Wang & Y. Xi

Sensitive THM coupled analysis of buffer-rock barriers for nuclear waste storage 665
Y.F. Qiao, A. Ferrari, L. Laloui & W.Q. Ding

Engineering applications and case histories

Field testing

Monitoring of a suburban environment: Soil-plant-atmosphere and clay movements 673
D.A. Cameron, S.J. Vorwerk & G. Keppel

Field monitoring of suction distribution in Coarse-Grained and Fine-Grained residual soil 679
N. Gofar, H. Rahardjo & M.L. Lee

Determining volume of failed soil mass in a landslide from satellite images 685
B.J.M. Lim, E.C. Leong & K.S. Low

Field monitoring to study the effect of rainfall on tree stability 691
N. Amalia, H. Rahardjo, T.T. Lee, E.C. Leong & Y.K. Fong

The impacts of climate change on expansive soil movements in Australia 697
X. Sun, J. Li, A.N. Zhou & G. Ren

A study on the feasibility of using centrifugal model test to simulate in-situ soaking test on loess 703
S.L. Jin, Y.C. Xing, W.Q. Zhao, A.J. Zhang & P. An

Model test on lateral earth pressure of highly expansive soil 709
S.A. Khattab, M.K. Al-Shamam & K.A. Al-Juari

Experimental study on the saturation changes of dredged fills during vertical vacuum preloading 717
J.J. Ma, J. Wang, P. Wang, Y.Q. Cai & H.T. Fu

Stress evolution in THMC GMZ-bentonite China-Mock-up for geological disposal of high level radioactive waste in China 721
Y.M. Liu, S.F. Cao, J. Wang, J.L. Xie, L.K. Ma, X.G. Zhao & L. Chen

Selection and analysis of enclosure structure of deep foundation pit in Lanzhou metro 727
N. Guo, Z.H. Chen & X.H. Yang

Design and installation of comprehensive instrumentation system of high-fill foundation in mountainous airport 733
Y.P. Zhu, X.H. Yang, Z.B. Shi, W.X. Cai & H.J. Jiang

Engineering applications

Comparisons between the measured and predicted resilient modulus of subgrade Red clay using a SWCC based model 743
W.L. Zou, J.F. Zhang, Y.L. Li, S.K. Vanapalli, H.Y. Tu & J. Zhang

Application of MPK framework to interpret volume change behavior of compacted unsaturated soils 749
A. Abeyrathne, T. Islam, J. Kodikara & H. Bui

Behaviour of pipes subjected to fault movements in unsaturated soils using spring analysis 753
D.J. Robert & K. Soga

Engineering characteristics of granite residual soils of landslide in Wuzhou, Guangxi, China 759
Z.B. Wang, K. Li, C.F. Wei & Z.Q. Xu

Cavity expansion in unsaturated silty sand exhibiting hydraulic hysteresis for three drainage conditions 765
H. Yang & A.R. Russell

Translational slip failures on slope incorporating unsaturated soil mechanics 771
W. Huang, E.C. Leong & H. Rahardjo

Investigation on the failure mechanisms of unsaturated high loess slope triggered by irrigation 777
X.T. Zhang, T.L. Li & W.H. Liu

Estimation of soil shrinkage curve 785
M. Wijaya & E.C. Leong

Effect of infiltration characteristics of soil on tree stability 791
A. Rahimi, H. Rahardjo, E.C. Leong, T.T. Lee, A.W.K. Law & Y.K. Fong

An analysis of plain strain deformation and strength characteristics of loess with vertical structure 797
Y. Zhang, S.J. Shao & L.J. Wang

Engineering properties of lead contaminated expansive soil 807
X.Q. Zhang, F.S. Zha, J.J. Liu & K.R. Cui

Feasibility investigation of a local weathered soil as final cover material for a landfill in south China 811
J. Liu, R. Chen, T.L.T. Zhan, Z.Q. Li & C.W.W. Ng

Modelling of transport and erosion of bentonite in the fracture 817
T. Chen & Y.F. Xu

Water-rock interaction for marly rocks of Badong group in the Three Gorges Reservoir Area 823
X.J. Chen, L.L. Xia, Z.Y. Zhao, Y. Song, B. Chai, J. Tong & B. Jiang

Feasibility analysis of electromagnetic field in geotechnical engineering research 829
B.X. Shi, S.S. Chen, G.R. Zhang & C. Zhou

Improvement of soil stability along rail corridors through native vegetation 835
M. Pallewattha, B. Indraratna & C. Rujikiatkamjorn

Mechanism of new anchored reinforced vegetation system for strengthening swelling rock and soil slope 839
Y. Xu, S. Xian & S. Pei

Research on the electrical resistivity of early solidified soil composing of dredged clays 845
F.Z. Cheng, X.W. Lei, Y.S. Liao, Q.S. Meng & J. Chen

The hydrological mechanism of a residual soil slope underwent deformations during rainfall 849
C.C. Fan & S.H. Liu

Comparative analysis on flexible supporting technology of different types of expansive soil cutting slope in the south and the north of China 855
H.P. Yang, J.S. Lin & J. Xiao

Effect of sodium chloride solution on adsorbed water content of clays 861
X.L. Xia, C.F. Wei, T.T. Ma & H.H. Tian

Swelling of GMZ bentonite with saline solutions and its prediction 865
L. Zhang, D.A. Sun & Y.M. Liu

Geo-Barrier System as a retaining structure 871
H. Rahardjo, Q. Zhai, A. Satyanaga, E.C. Leong, C.L. Wang & L.H. Wong

Numerical stimulation of geogrid reinforced flexible supporting treating expansive soil cut slope 877
J. Xiao, H.P. Yang & S.Y. Zhu

The effect of traffic loading to buried water mains in partially saturated soils 883
C. Randeniya, D.J. Robert & C.Q. Li

Effect of water content on long-term cyclic behaviour of railway track-bed materials 889
F. Lamas-Lopez, Y.J. Cui, J.C. Dupla, A.M. Tang, J. Canou, N. Calon & S. Costa D'Aguiar

Analogy study on surface deterioration of earthen monuments 895
Y. Chen, J.F. Wang, H.Y. Zhang & Y.X. Gai

Analysis of the failure of a polluted red clay foundation in the north Guilin karst area 899
C.M. Mu, K.L. Han & Y. Liu

Unsaturated Soil Mechanics—from Theory to Practice – Chen et al. (Eds)
© 2016 Taylor & Francis Group, London, ISBN 978-1-138-02921-7

Preface

Since the first International Conference on Unsaturated Soils, which was held in 1995, in Paris, France, remarkable advances have been achieved in the research and practice on unsaturated soil mechanics. The series of Asia-Pacific Conferences on Unsaturated Soils began in Singapore in 2000. Since then, four conferences have been held under the continued support of the Technical Committee on Unsaturated Soils (TC106) of the International Society of Soil Mechanics and Geotechnical Engineering (ISSMGE). The conferences have provided an excellent forum for researchers and practitioners in the region and beyond to present their latest developments and exchange ideas on the subjects related to unsaturated soils. As the organizers of the sixth Asia-Pacific Conference on Unsaturated Soils, we are excited to carry on this great tradition of conferences in October 23–26, 2015, in the beautiful City of Guilin, China.

In the past two decades also, the development of large-scale, complex infrastructure systems in China, such as the South-to-North Water Diversion Project, the Qinghai-Tibet Railway and interstate high-speed railway networks, have raised numerous unforeseen major technical problems related to unsaturated soils, and brought great challenges as well as opportunities to the Chinese community of unsaturated soil mechanics and engineering. Through participating and completing these significant projects, our community has achieved full breadth and expertise to tackle problems with economic, social, political, scientific and engineering dimensions. Such achievements have greatly fostered the development of unsaturated soil mechanics in China, attracting more and more attention from all over the world.

This proceedings collects more than 140 technical papers, including 10 invited and keynote lectures, from fourteen countries or districts in the Asia-Pacific region and beyond. In particular, the first Asia-Pacific distinguished lecture, which will be launched in this conference, is also included. The contributions address the fundamental behavior of unsaturated soils, containing all the invited and keynote lectures, and present theoretical and numerical modeling and engineering applications. The topics of concern span the full spectrum from theory to practice, with strong relevance to the problems in the region and beyond such as collapse/swelling, freezing/thawing, desiccation shrinkage, rainfall-induced slope failure, contaminant transport, shale gas extraction and so on, largely representing the latest development of unsaturated soil mechanics.

The conference is held under the auspice of TC106 of ISSMGE and the Chinese Society of Soil Mechanics and Geotechnical Engineering. We wish to thank all the individuals and parties involved, in particular the participants, and the sponsors for their support and/or attendance. Our thanks are also given to the Guilin University of Technology, the State Key Laboratory of Geomechanics and Geotechnical Engineering, and Institute of Rock and Soil Mechanics, Chinese Academy of Sciences for their continued support.

Z.H. Chen, C.F. Wei, D.A. Sun & Y.F. Xu
June 30, 2015

This page intentionally left blank

Unsaturated Soil Mechanics—from Theory to Practice – Chen et al. (Eds)
© 2016 Taylor & Francis Group, London, ISBN 978-1-138-02921-7

Acknowledgements

The editors are grateful to the following individuals who helped review the manuscripts of the proceedings:

Yujun Cui	Ecole des ponts ParisTech (ENPC), France
Mingjing Jiang	Tongji University, China
Lingwei Kong	Institute of Rock and Soil Mechanics, CAS, China
Fengyin Liu	Xi'an University of Technology, China
Charles W.W. Ng	Hongkong University of Science and Technology, China
Bing Qin	PLA Logistic Engineering University, China
De'an Sun	Shanghai University, China
Chaosheng Tang	Nanjing University, China
Yongfu Xu	Shanghai Jiaotong University, China
Weimin Ye	Tongji University, China
Changfu Wei	Institute of Rock and Soil Mechanics, CAS, China
Chenggang Zhao	Beijing Jiaotong University, China
Liangtong Zhan	Zhejiang University, China
Lulu Zhang	Shanghai Jiaotong University, China

This page intentionally left blank

Unsaturated Soil Mechanics—from Theory to Practice – Chen et al. (Eds)
© 2016 Taylor & Francis Group, London, ISBN 978-1-138-02921-7

Organizing Committee

Chairman

Zhenghan Chen Xuejun Chen

Technical secretary

Changfu Wei Yongfu Xu Haibo Lv Xiangwei Fang

Committee

Lingwei Kong	Wei Ma	Yichuan Xin	Wei Zhang
Shengjun Shao	Ju Wang	Mingjing Jiang	Zhanlin Cheng
Chenggang Zhao	Lanmin Wang	De'an Sun	Yongli Xie
Xuefeng Huang	Xiaohong Bai	Houjian Liu	Linchang Miao
Weimin Ye	Zhangjian Xu	Longtan Shao	Yasheng Luo
Yanpeng Zhu	Yuemiao Liu	Heping Yang	Guolin Yang
Mingxin Zheng	Fengyin Liu	Liansheng Tang	Xinrong Liu
Bo Liang	Huimin Ma	Jianbing Peng	Hongjian Liao
Weilie Zou	Yongqiang Zheng	Guisheng Ma	Jilin Qi

Local Advisory Committee

Zuyu Chen	Yuanming Lai	Dingyi Xie
Chenggang Bao	Zongze Yin	Qinglin Xie
Jianmin Zhang	Xiating Feng	Benzhen Zhu
Jianping Han		

International Advisory Committee

H. Rahardjo, Singapore	B. Huat, Malaysia
A. Ridley, UK	Y. Kohgo, Japan
D. Toll, UK	D. Sheng, Australia
S. Houston, USA	G.A. Miller, USA
S. Vanapalli, Canada	P. Delage, France
A. Gens, Spain	D.G. Fredlund, Canada
C.W.W. Ng, China	C.H. Benson, USA
Z.H. Chen, China	K.K. Muraleetharan, USA
S. Wheeler, UK	A. Iizuka, Japan
E.E. Alonso, Spain	N. Khalili, Australia
N. Lu, USA	L. Hoyos, USA
K. Kawai, Japan	S.M. Rao, India
W. Mairaing, Thailand	T.T. Soon, Singapore
Y.J. Cui, Thailand	L. Laloui, Switzerland
F. Zhang, Japan	J. Li, Australia
L.M. Zhang, China	X. Zhang, USA
J. Chu, USA	A. Jotisankasa, Thailand

This page intentionally left blank

Invited and Keynote papers

This page intentionally left blank

Unsaturated Soil Mechanics—from Theory to Practice – Chen et al. (Eds)
© 2016 Taylor & Francis Group, London, ISBN 978-1-138-02921-7

Relationship between the laboratory SWCCs and field stress state

D.G. Fredlund
Golder Associates Ltd., Saskatoon, SK, Canada

ABSTRACT: The SWCC has played a dominant role in arriving at acceptable engineered solutions for unsaturated soils. This paper describes unique SWCC attributes for three types of soils; namely, a.) silt soils, b.) sand soils, and c.) clay soils. The saturation of each soil type can be subdivided into three zones; namely, i.) the capillary (or boundary effect) zone, ii.) the two phase (or transitional) zone, and iii.) the residual (or dry) zone. Unsaturated soil properties can be estimated for all three types of soils but the manner in which the theory is applied in the field can be quite different depending upon the soil type. The paper focuses on bridging the gap between the laboratory measurement of the SWCC and the application of unsaturated soil mechanics in engineering practice.

1 INTRODUCTION

Unsaturated soil mechanics has now developed to the point where the geometry of most geotechnical engineering problems embraces both the saturated and unsaturated portions of the soil profile. The saturated soil properties must be known in order to perform an analysis or the numerical modeling of a geotechnical engineering problem. The properties for the unsaturated soils portion are generally estimated based on the laboratory measurement of the Soil-Water Characteristic Curve, SWCC, (also called the Water Retention Curve [WRC]).

There are three pillars associated with the development of sound engineering practices for saturated-unsaturated soil systems (Fredlund, 2009). The pillars can be labeled as: i.) laboratory testing of the soil, ii.) numerical modeling of the problem within the context of a boundary-value problem, and iii.) establishment and adherence to sound engineering protocols as shown in Figure 1.

The measurement of the (drying) soil-water characteristic curve, SWCC has risen above all other constitutive relations as the pre-eminent information required for the application of unsaturated soil mechanics. The SWCC, in combination with the saturated soil properties, has made it possible for geotechnical engineers to numerically model the saturated and unsaturated soil zones as a combined continuum. Numerical modeling can generally be reduced to the solution of (nonlinear) Partial Differential Equations (i.e., PDEs) regardless of the type of physical process being simulated. The word 'nonlinear' is used because, in general, the PDEs being solved become nonlinear whenever unsaturated soil properties are involved.

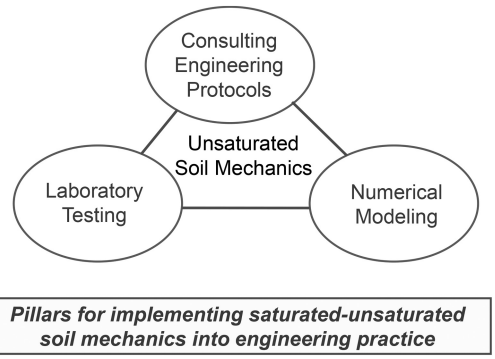


Figure 1. The three main pillars of an applied science for unsaturated soil mechanics.

The establishment of widely accepted engineering practice protocols has occurred over a period of time as unsaturated soil theories have been gradually incorporated into engineering practice. Geotechnical engineering practices have embraced unsaturated soil mechanics principles and theories. It would appear that the application of unsaturated soil mechanics theories is now at the point where unsaturated soils protocols are being generally accepted in engineering practice. In other words, all three pillars for the implementation of saturated-unsaturated soil mechanics are firmly in-place.

While there have been great strides made in the application of unsaturated soil mechanics, the rapid development of unsaturated soil mechanics has led to some careless practices, particularly with respect

to the application of laboratory measurements and the numerical analysis of field problems. The problems, in part, may be due to a lack of continuity between laboratory research studies and the verification of unsaturated soil mechanics theories in the field. There is need to re-visit the interpretation of laboratory test results and their application to field problems.

This paper is based on experiences where unsaturated soil mechanics has been applied in engineering practice. In most cases, the SWCC has played a dominant role in arriving at an acceptable engineered solution. The paper attempts to bridge the gap between research studies on unsaturated soils and the application of unsaturated soil mechanics in engineering practice.

The objectives of this paper are to: i.) describe the unique Soil-Water Characteristic Curve, SWCC, attributes for three types of soil; namely, a.) silt soils, b.) sand soils, and c.) clay soils, and: ii.) to describe the relationship between the laboratory SWCC and field stress state conditions. The computational procedures that can be used to estimate various unsaturated soil property functions associated with various physical processes are considered to be outside the scope of this paper.

2 ATTRIBUTES OF THE DRYING SOIL-WATER CHARACTERISTIC CURVE

The SWCC has become the key to the implementation of unsaturated soil mechanics into engineering practice (Fredlund, 2009). The SWCC is a hysteretic constitutive relationship between the amount of water in the soil and the suction applied to the soil. While the SWCC is hysteretic in character, it is the 'drying' branch that has become the basic relationship measured in engineering practice (Figure 2). The 'drying' branch has also become the branch from which all other relations and hysteretic effects are generally estimated.

Unsaturated soil behavior is strongly influenced by the degree of saturation of the soil. There are two basic variables that must be known on the (drying) SWCC curve; namely, the: i.) air-entry value, AEV, and ii.) residual conditions (i.e., residual suction, ψ_r, and residual water content). The AEV and residual conditions provide the engineering with the main information required for the determination of all unsaturated soil properties. The AEV and residual conditions divide unsaturated soil behavior into three zones; namely, the 'capillary' or the 'boundary effect' zone; the 'transitional' or 'two phase' zone; and the 'residual' or 'dry' zone. A sigmoidal type curve on a semi-logarithmic plot represents a unimodal curve that is typical of many soils.

There are several empirical equations that have been proposed to represent the unimodal SWCC (e.g., van Genuchten, 1980; Fredlund and Xing, 1994).

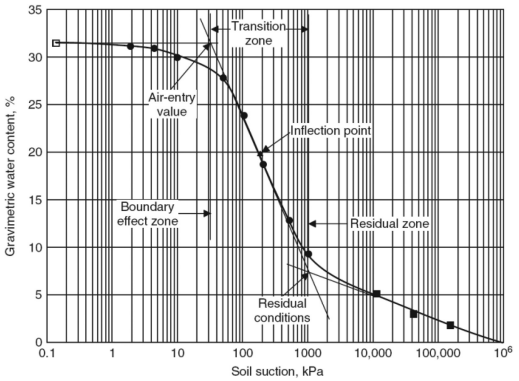


Figure 2. The basic features of the drying SWCC.

The Fredlund-Xing (1994) equation shown as Eq. [1] will be used in this paper to illustrate the linkage between laboratory testing of unsaturated soils and the application of unsaturated soil theories in engineering practice.

$$w(\psi) = C(\psi)\frac{w_s}{\left\{ln\left[e + \left(\psi/a_f\right)^{n_f}\right]\right\}^{m_f}} \quad [1]$$

where:

$w(\psi)$ = water content at any soil suction, ψ

e = irrational constant equal to 2.71828 used when taking the natural logarithm,

a_f = fitting parameter indicating the inflection point that bears a relationship to, and is greater than the air-entry value,

n_f = fitting parameter related to the rate of desaturation,

m_f = fitting parameter related to the curvature near residual conditions, and

$C(\psi)$ = correction factor directing the SWCC to 10^6 kPa at zero water content, and is written as,

$$C(\psi) = 1 - \frac{ln\left(1 + \psi/\psi_r\right)}{ln\left(1 + 10^6/\psi_r\right)} \quad [2]$$

ψ_r = estimated residual suction for the soil.

The Fredlund-Xing (1994) equation allows for the best-fit of unimodal soil data from an extremely low suction to an upper limiting suction value of 1,000,000 kPa. There are three primary fitting parameters in the Fredlund-Xing (1994) that influence on the shape of the SWCC (a_f, n_f, and m_f). Figure 3 shows the effect on the SWCC of changing the a_f variable. The a_f variable can be used to laterally shift the inflection point. The ordinate of the SWCC is represented in terms of normalized water content (i.e., any gravimetric water content divided by the saturation gravimetric water content).

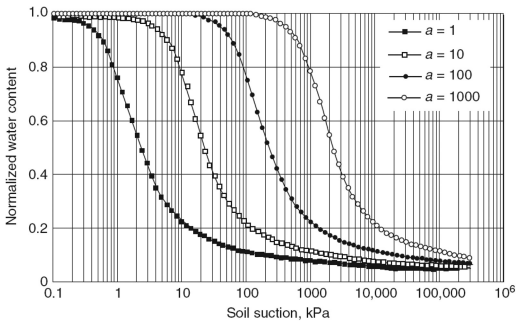


Figure 3. The effect of the "af" variable in the Fredlund-Xing (1994) equation for the SWCC.

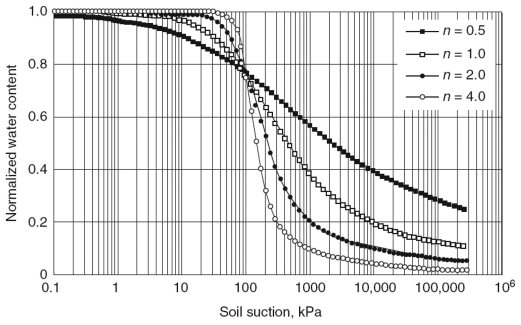


Figure 4. The effect of the "nf" variable in the Fredlund-Xing (1994) equation for the SWCC.

The n_f variable changes steepness of the desaturation of the SWCC. Figure 4 shows the effect of changing the n_f variable while a_f is held at 100. The third variable m_f, provides increased flexibility in controlling the shape of the SWCC. A correction factor, $C(\psi)$, ensures that the SWCC ends at zero water content at a suction of 1,000,000 kPa.

3 LABORATORY TESTING PROCEDURES FOR MEASURING THE SWCC

The SWCC has been somewhat arbitrarily subdivided into a 'low suction' range and a 'high suction' range with the arbitrary subdivision set at approximately 1,500 kPa. Suctions in the 'low suction' range are assumed to be predominantly 'matric suction' and suctions in the 'high suction' range are assumed to be predominantly 'total suction'. At first, this may seem somewhat 'strange' and paradoxical way to arbitrarily change from matric suction to total suction on the suction scale. However, upon closer examination it has been quite possible to accommodate this 'scale change' since some engineering problems are predominantly

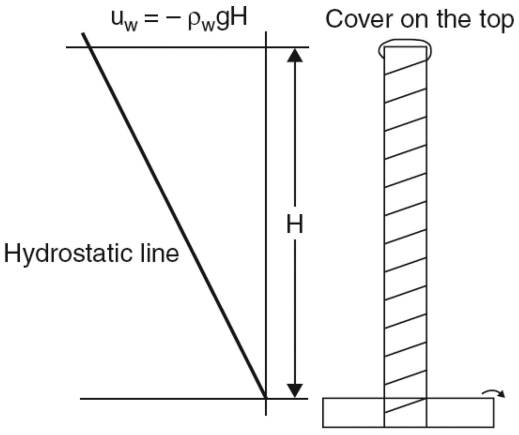


Figure 5. Short column test on sand soil for the measurement of the SWCCs.

in the 'low suction' range while other engineering problems are in the 'high suction' range.

Numerous laboratory test procedures have been proposed for the measurement of the SWCC. However, this paper briefly comments on the test procedures that have become most dominant in geotechnical engineering; namely, i.) column tests, ii.) pressure plate apparatuses, and iii.) vapor pressure equilibrium.

3.1 *Short laboratory column tests*

Short laboratory column tests with a height in the order of 1 to 2 meters and a diameter of 10 to 15 cm have been found to be practical for measuring the SWCC on sand soils, (Yang et al., 2004). Sand is first placed into the column at the desired density (Figure 5). The pore-water pressures in the soil column can then be allowed to achieve an equilibrium state through control of the upper or lower boundary condition. For example, water can be allowed access to the soil column from the base of the column. After a few days, the pore-water pressures will have reached a state of hydrostatic equilibrium and a measurement of the water content at various distances above the base of the column will allow the determination of the 'wetting' SWCC. The lowest matric suction for which the gravimetric water content can be measured is about 0.1 kPa. It is also possible to measure the saturated water content corresponding to zero suction.

Providing access of water to the top of the soil column for a period of time, followed by allowing drain-down from the column, allows for the determination of the 'drying' SWCC. It is also possible to apply a controlled moisture flux at the top of the column and thereby provide a direct measurement of the SWCC and the unsaturated coefficient of permeability of the soil. It will also be necessary to measure matric suction at one or more points near the mid-point of the column.

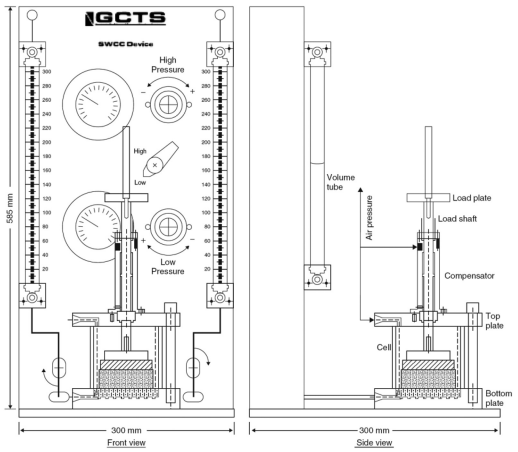


Figure 6. GCTS pressure plate apparatus designed to apply matric suctions up to 1,500 kPa.



Figure 7. Chilled-mirror device (WP4-T) to measure the total suction on small soil specimens.

3.2 *Pressure plate apparatuses*

A wide range of pressure plate apparatuses have been designed and built for measuring the SWCC. These apparatuses utilize the axis-translation concept and are designed to operate over a particular matric suction range. The apparatuses range from the original Tempe cell (for suctions up to 100 kPa), to the Pore Pressure Extractors (for suctions up to 1,500 kPa). Many of these apparatuses were developed for the agriculture industry and were marketed by SoilMoisture Equipment Corporation, Santa Barbara, California. These apparatuses have served well for measuring the water storage capacity of soils in connection with plant growth.

The equipment requirements within geotechnical engineering have differed somewhat from those in the agriculture industry. It is not surprising that a number of new pressure plate apparatuses have been developed to better serve the needs of the geotechnical engineering profession. Figure 6 shows the pressure plate apparatus marketed by GCTS, Tempe, Arizona.

The GCTS pressure plate apparatus allows for the independent control of the total stress (under K_o loading), the pore-air pressure and the pore-water pressure (Fredlund et al., 2012). Matric suctions as low as 0.5 kPa can be applied through use of a hanging column device. At the same time, suctions as high as 1,500 kPa can be applied to the soil specimen. The high air-entry ceramic disk in the base plate of the apparatus can be changed for better accuracy over particular matric suction ranges. The water volume change and overall volume change are independently measured as long as the soil sample does not pull away from the sides of the soil specimen ring. It is also possible to measure air diffusion and separate the volume of diffused air from the volume of water moving in or out of the soil specimen.

Other pressure plate apparatuses have also been designed and are being marketed in various countries.

3.3 *Vapor pressure equalization (Chilled-mirror device)*

The Lord Kelvin thermodynamic equilibrium equation, in conjunction with a vapor pressure equalization chamber, can be used to create a vapor pressure environment where the soil can come to equilibrium. Various vapor pressure environments can be achieved using a variety of vacuum desiccators. However, in recent years it has become more common to make use of a chilled-mirror device such as the WP4-T from Decagon Devices Inc., (Figure 7). The WP4-T device has commonly been used in the total suction range between 1,000 kPa and 1,000,000 kPa. While there have been recent claims that it is possible to extend the measurement range below 1000 kPa, these claims do not appear to have been verified to-date.

It is also possible to use thermocouple psychrometers and filter paper to measure total suctions in the high suction range. However, the chilled-mirror technique has rapidly become the preferred device of choice.

4 THE "IDEAL" MATERIAL FOR UNSATURATED SOIL RESEARCH AND RELATING THEORY TO FIELD CONDITIONS

The range of soil suctions of interest in geotechnical engineering extends over about 8 orders of magnitude (i.e., from 0.01 to 1 million kPa). The wide range of suctions gives rise to the need for more than one suction measurement system. In other words, the laboratory testing of a sand soil is quite different from the testing of a clay soil. As an example, the air-entry values for soils can range from being less than 0.1 kPa for coarse sand to being greater than 3,000 kPa for clay soils. It should not come as a surprise that not all soils are equally as easy to test in the laboratory.

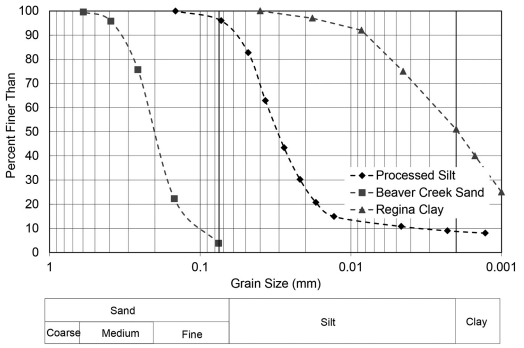


Figure 8. Grain-size distribution curves for three soils tested.

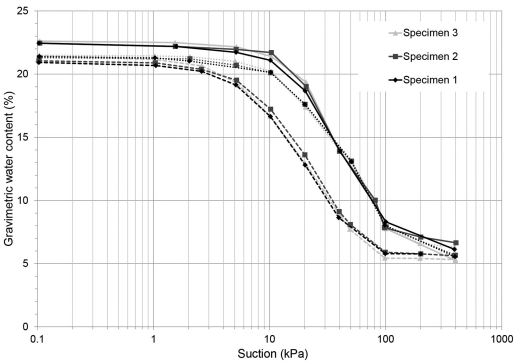


Figure 9. Wetting and drying curves expressed in terms of gravimetric water content for three specimens of Processed Silt.

Laboratory testing of unsaturated soils is undertaken to; i.) test constitutive soil relations for their uniqueness, and to; ii.) establish laboratory testing protocols that can be used when using numerical modeling to solve practical geotechnical engineering problems. While these two purposes are somewhat inter-related, they are also designed to meet the independent needs of research and practical engineering applications.

Three soils have been selected for comparison purposes (Pham, 2002; Fredlund, 1964). The grain-size distribution curves for the three soils are shown in Figure 8. The median particle sizes of each of the materials are separated by approximately one order of magnitude. Later in this paper it will be shown that the engineering behavior can vary widely than might be anticipated from the grain-size distribution curves.

The ability to reliable laboratory tests on unsaturated soils depends to a large extent on the ability to test materials over a particular range of the stress state variables. The stress state variables of interest in engineering practice are: i.) net normal stress, ($[\sigma - u_a]$ where σ represents the total stress and u_a represents pore-air pressure), and ii.) soil suction, particularly matric suction, ($[u_a - u_w]$ where u_w represents pore-water pressure). The use of high air-entry pressure plates along with the axis-translation technique give rise to a preferred range of stresses for laboratory testing.

For those who have undertaken extensive laboratory testing it is discovered that it is difficult to control matric suctions lower than about 1 kPa. At the same time, it would likely be agreed that it is hard to control matric suctions much higher 500 kPa. These practical limitations influence the type of material that should be used in laboratory testing programs for the verification of constitutive behavior of unsaturated soils.

4.1 *Features of a silt soil SWCC*

The ideal soil for studying unsaturated soil behavior is a silt sized material in light of the limitations with respect to laboratory testing. The material should be of relatively low compressibility and testing of the material should start from an initially slurry state. Matric suctions should then be applied and the material should go through the air-entry state and the residual state within the range of the testing apparatus. Just such a material (i.e., Processed silt) was tested by Pham (2002). Figure 9 shows the results of three soil-water characteristic curves that were measured on Processed silt.

Each soil specimen was subjected to an initial applied suction of 0.1 kPa with suctions increasing to 400 kPa. This is referred to as the 'initial drying curve' of the SWCC. Each soil specimen was then unloaded by reducing the suction back to 0.1 kPa and this curve is referred to as the 'main wetting curve' of the SWCC. The soil specimen was once again subjected to increased suctions up to 400 kPa and this curve is referred to as the 'main drying curve' of the SWCC.

There are several observations that can be made from these results. First, the results from the three independent tests gave almost identical results. Second, the air-entry value and the residual suctions were well within the laboratory testing range. Third, the wetting SWCC was essentially parallel to the drying SWCC and the lateral shift between the two curves was 37.6%. Fourth, there was a slight difference between the 'initial drying curve' and the 'main drying curve', which was due to air entrapped as a result of the soil being subjected to drying and wetting.

The Processed silt is a low compressibility material and as a result the material experienced almost no volume change when it was subjected to matric suctions up to 400 kPa. It is possible to also plot the laboratory test results in terms of degree of saturation or volumetric water content with the result that SWCCs retain the same values for the air-entry value and the residual suction. Figure 10 shows the data for the Processed silt plotted in terms of degree of saturation. As a result the amount of water in the soil takes on a dimensionless scale between 0 and 100% (or 0.0 and 1.0).

Figure 11 provides an interpretation of the laboratory test results and Table 1 summarizes the fitting parameters associated with the Fredlund-Xing (1994)

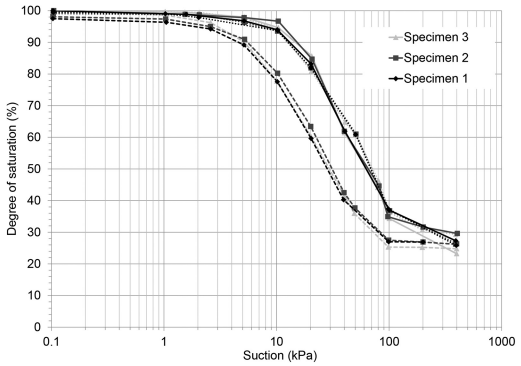


Figure 10. Wetting and drying curves expressed in terms of degree of saturated for three specimens of Processed Silt.

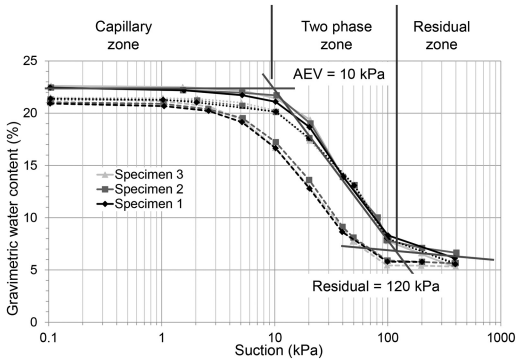


Figure 11. Graphical constructions to interpret the features of the drying and wetting curves for specimens of Processed Silt.

SWCC fitting equation. The results show that the air-entry value is approximately 10 kPa for all three specimens. The same is true regardless of whether the 'initial drying curve' is used or the 'main drying curve' is used. Likewise, the residual suction from the three soil specimens was approximately 120 kPa. The fitting parameters for the Fredlund-Xing (1994) equation are also similar for the 'initial drying curve' and the 'main drying curve'. The main difference in the fitting parameters is for the a_f value which changes from approximately 21 kPa for the drying curves to 8 kPa for the wetting curve (see Table 1).

The air-entry value and the residual suction value provide the three primary subdivisions that are required for understanding unsaturated soil behavior; namely, the capillary zone, the two phase zone and the residual zone. The results indicate that the Processed silt will behave essentially as a saturated soil in the capillary zone. The Processed silt will behave essentially as a two phase material (i.e., air and water in the pores), when the matric suctions range between 10 kPa and 120 kPa. And the Processed silt will behave essentially as a dry material when matric suctions exceed 120 kPa.

Table 1. SWCC parameters for Processed silt fitted with Fredlund-Xing (1994) equation.

Curve	a_f	n_f	m_f	AEV (drying) kPa	Residual suction, kPa (drying)
Initial drying	20.5	2.71	0.64	10	120
Main drying	21.1	2.04	0.72	10	120
Main wetting	8.1	2.38	0.62		

Hysteresis Shift = 37.6% of a log cycle

Those are broad generalizations taken from the drying SWCC. These generalizations do not take hysteresis effects into consideration; however, the interpretation of the laboratory test results allows the geotechnical engineer to develop a general conceptualization of how the material is likely to behave. Hysteretic effects and its significance in the application of unsaturated soil theories are briefly discussed later in the paper.

It is important to now extend the general conceptualizations from the laboratory test results to equilibrium stress states in the field.

4.2 *Linkage of the Soil-Water Characteristic Curve, SWCC, to the field application of unsaturated soil mechanics*

Let us transfer the laboratory test results on the Processed silt to field conditions. Let us assume that the silt strata is quite thick (e.g., more than 16 meters). Let us also assume that the silt material was originally saturated with the water table at ground surface. In other words, the field conditions are assumed to be similar to the laboratory test conditions used for the SWCC tests. Let us also assume that over a period of time the groundwater table is gradually lowered to a depth of 16 meters.

4.3 *Interpretation for silt soil conditions*

As the groundwater table is gradually lowered, it is assumed that the net moisture flux at the ground surface is essentially zero. In other words, evaporation from the ground surface is essentially equal to precipitation. Consequently, a hydrostatic equilibrium condition is maintained between the groundwater table and the pore-water stress state between the groundwater table and the ground surface as shown in Figure 12.

Let us now suppose that the groundwater table is at a depth of 16 meters at the time that the deposit was sampled and tested in the laboratory. The equilibrium matric suction profile can be added to the depth axis as shown in Figure 13. Let us also assume that the geotechnical engineer took the soil sample for testing from a depth of 8 meters. If it was possible to measure the *in situ* matric suction on the sample, it should be 80 kPa according to the hydrostatic equilibrium condition. However, the sample will be taken to

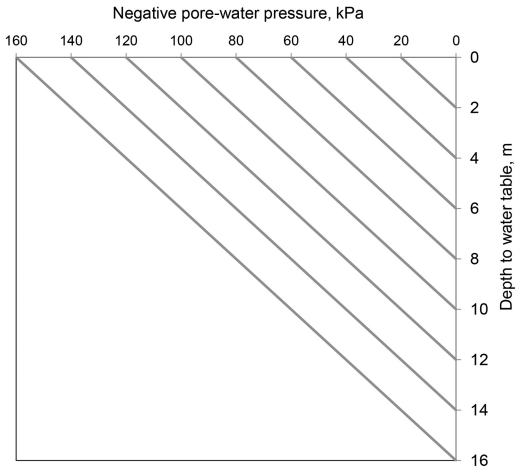


Figure 12. Hydrostatic equilibrium conditions in the field.

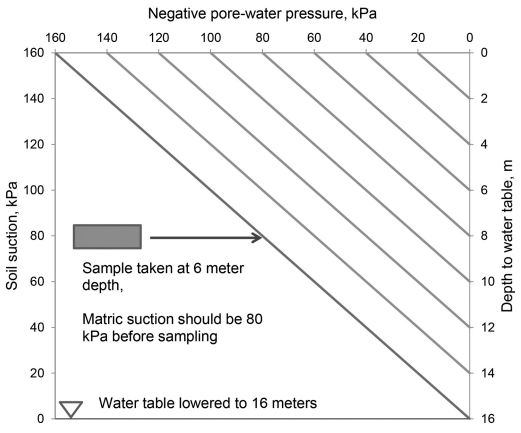


Figure 13. Hydrostatic equilibrium conditions as water table is lowered to 16 meters.

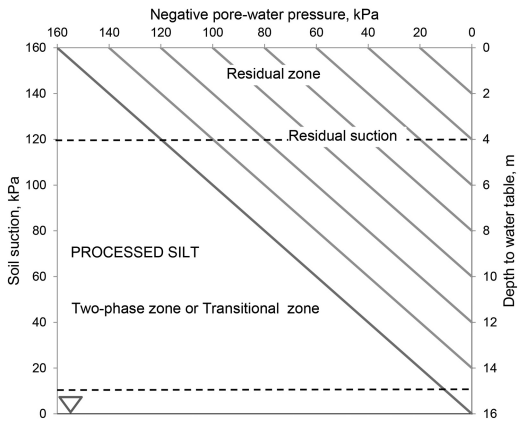


Figure 14. Drying Processed silt soil to an initial equilibrium condition in the field with the water table at 16 meters.

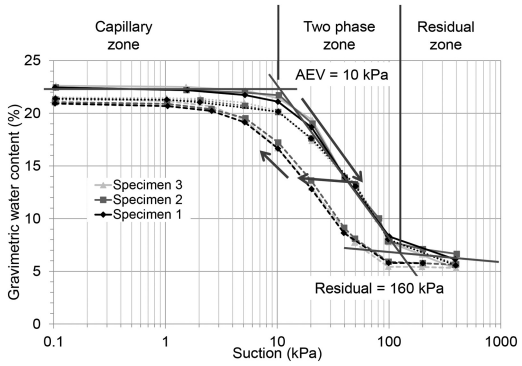


Figure 15. Subsequent wetting and incorporating hydraulic hysteresis into unsaturated soil behavior.

the laboratory where it will be given access to water and the matric suction in the soil specimen will go to zero.

The information from the laboratory SWCC test on the Processed silt can now be transferred to the hydrostatic equilibrium plot of field conditions as shown in Figure 14. The capillary zone can be seen to extend for a distance of 1 meter above the groundwater table. The residual suction is encountered at a depth of 4 meters. In other words, the top 4 meters near ground surface will be in a dry (or residual) soil state. There will be about 11 meters of soil in the transitional or two phase zone.

The geotechnical engineer must be able to take the laboratory test results that are plotted on a logarithmic scale in terms of matric suction and transfer them to field conditions which will be interpreted on an arithmetic scale. The transfer of scales from the laboratory to the field can be deceptive but it is important for the geotechnical engineer to be aware of the zone of unsaturation that is applicable to the problem at-hand.

The information transfer between the laboratory and the *in situ* conditions has been restricted to monotonic stress state conditions (i.e., a gradual increase in matric suction with time). Let us now suppose that the groundwater table begins to rise over a period of time. Figure 15 shows how the stress state will move from the drying curve, across along a scanning curve to the wetting bounding curve.

Upon wetting, the soil first undergoes a slight increase in water content as the matric suction may change quite substantially. The effect of cycles of drying and wetting are of considerable interest in geotechnical engineering, particularly with regard to near-ground-surface features such as soil cover designs. While some attention has been paid to the effects of hysteresis on engineering designs, it still remains an area needing further research. Further discussion on hysteresis is outside the scope of this paper.

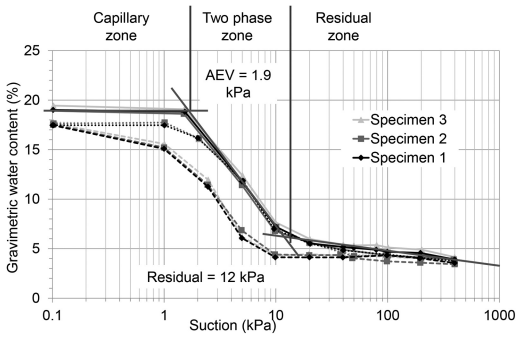


Figure 16. Relating unsaturated soil behavior of Beaver Creek sand to field stress states.

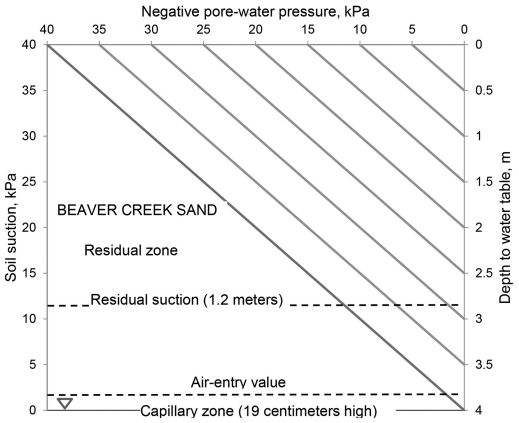


Figure 17. Drying Beaver Creek sand to an initial equilibrium condition in the field with the water table at 4 meters.

Table 2. SWCC parameters for Beaver Creek sand fitted with Fredlund-Xing (1994).

Curve	a_f	n_f	m_f	AEV (drying) kPa	Residual suction, kPa (drying)
Initial drying	3.18	5.27	0.52	1.9	12.
Main drying	2.82	3.52	0.55	1.9	12.
Main wetting	1.23	3.20	0.59		

– Hysteresis Shift = 34.7% of a log cycle

4.4 *Interpretation for sand soil SWCC*

Let us now consider the case of the Beaver Creek sand for which the grain-size distribution was shown in Figure 8. The SWCC laboratory results for three specimens of Beaver Creek sand are shown in Figure 16. The following observations can be made: i.) the test results from the three specimens tested are closely reproducible, ii.) the air-entry value determined from either the initial drying curve or the main drying curve is approximately 1.9 kPa, iii.) the residual suction for the sand is approximately 12 kPa, and iv.) the lateral shift (or hysteresis) between the drying curve and the wetting curve is 34.7%. Table 2 shows the best-fit parameters corresponding to the Fredlund-Xing (1994) equation.

The information from the SWCC can now be transferred to the *in situ* stress conditions. Let us assume that the soil stratigraphy consists of sand from ground surface to a depth greater than 5 meters. Let us also assume that the water table has gradually been reduced from ground surface to a depth of 4 meters.

The key variables associated with the SWCC can now be transferred to hydrostatic pore-water pressure conditions in the field as shown in Figure 17. The air-entry value suggested that the capillary zone above the water table is only about 19 cm and residual suction is reached at a distance of about 1.2 meters above the water table. Placing the key parameters from the SWCC onto the stratigraphy in the field assists the geotechnical engineer in understanding the type of unsaturated soil behavior that can be anticipated. The results show that the soil behaves in a saturated manner for only 19 cm above the water table and then behaves as a two phase unsaturated soil. The portion of the soil profile that is 1.2 meters above the water table behaves essentially as a dry soil provided there is no significant infiltration at the ground surface. It should be noted that the upper portion of the soil profile will began to behave as a two phase system as water is allowed to infiltrate from the ground surface.

Comparing the SWCCs for sand and silt to field stress state conditions amplifies the significant difference between sand and silt behavior in the field. The sand soil has a much smaller capillary zone than the silt. The silt has a considerable zone where two phase unsaturated soil mechanics applies in comparison to the sand profile. The sand may have a large portion of the profile where the soil behaves essentially as a dry soil. The emphasis has been on the stress state transfer from a logarithmic scale on the SWCC to field conditions.

4.5 *Interpretation of a clay soil SWCC (Regina clay)*

Consideration will now be given to the interpretation of the SWCC measured on a clay soil. Let us once again assume that the clay is prepared as a slurry material for which the SWCC can then be measured. The basic SWCC measured in the laboratory involves the measurement of gravimetric water content versus soil suction (Fredlund, 1964). The clay material will undergo considerable volume change as soil suction is applied. Consequently, the assumption of 'no volume change as suction is changed' cannot be applied to the clay soil. It is also necessary to measure the

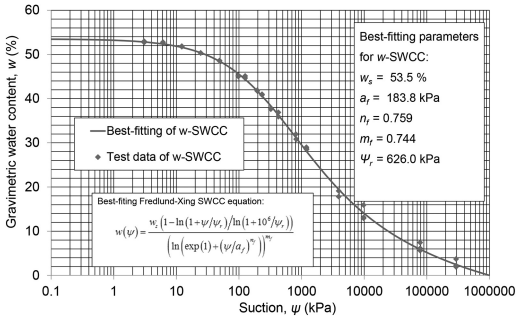


Figure 18. Drying SWCC for Regina clay measured in terms of gravimetric water content versus suction.

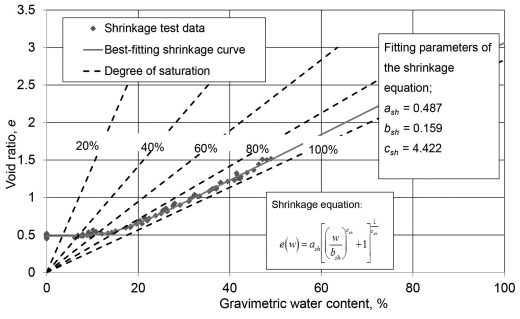


Figure 19. Shrinkage curve for Regina clay (i.e., void ratio versus gravimetric water content).

shrinkage curve for Regina clay in order that the various volume-mass relationships can be computed with respect to changes in soil suction.

Regina clay has 50% clay size particles. The liquid limit is 75% and the plastic limit is 25%. Regina clay is classified as highly plastic, calcium montmorillonite clay (Fredlund, 1964).

Figure 18 presents the gravimetric water content versus soil suction relationship for the initial drying curve. The effect of hysteresis was not studied for Regina clay. The water content versus suction relationship depicts the usual S-shaped curve; however, the air-entry value for the soil cannot be determined from this graph. The true air-entry value for the soil must represent the point where the soil begins to desaturate and must be identified on the degree of saturation versus suction relationship.

The Fredlund-Xing (1994) equation (i.e., Equation [1]), can be best-fit to the data measured for the gravimetric water content versus soil suction. The fitting parameters are: $a_f = 184$ kPa, $n_f = 0.759$, and $m_f = 0.744$.

The shrinkage curve for Regina clay is shown in Figure 19 and it represents the relationship for the change in volume (i.e., void ratio) as gravimetric water content changes during the drying process (Fredlund and Zhang, 2013). The suction in the soil is increased during the drying process. The actual suction in the soil does not need to be measured; however, the relationship between volume change and water content change can be used to compute other volume-mass relationships.

A shrinkage curve equation has been proposed by M. Fredlund, (2002) to best-fit the void ratio versus water content drying curve.

$$e(w) = a_{sh}\left(\left(\frac{w}{b_{sh}}\right)^{c_{sh}} + 1\right)^{1/c_{sh}} \qquad [3]$$

where: a_{sh} = the minimum void ratio upon complete drying, b_{sh} = slope of the drying curve, and c_{sh} = the sharpness of curvature as the soil desaturates. The best-fit parameters for the shrinkage curve on Regina clay are: $a_{sh} = 0.487$, $b_{sh} = 0.159$, and $c_{sh} = 4.42$.

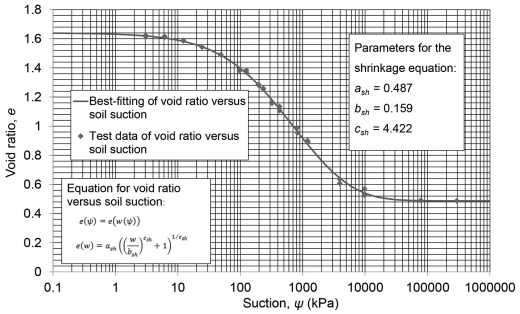


Figure 20. Drying curve expressed in terms of void ratio versus soil suction for specimens of Regina clay.

The best-fit equations for the gravimetric water content SWCC and the shrinkage curve can be combined to give the relationship between void ratio and soil suction as shown in Eq. [4].

$$e(\psi) = e(w(\psi)) \qquad [4]$$

Figure 20 presents the void ratio versus soil suction. The results indicate that volume change continues to occur well into the high soil suction range.

It is also possible to calculate the degree of saturation versus soil suction in accordance with Eq. [5]

$$S(\psi) = \frac{G_s w(\psi)}{e(w(\psi))} \qquad [5]$$

The computed degree of saturation versus soil suction curve is shown in Figure 21. The degree of saturation SWCC can be used to show the various zones of saturation. The air-entry value is shown to occur at a suction of approximately 3,000 kPa. The results suggest that the soil should behave essentially as a saturated soil until a suction of about 3,000 kPa is reached. The residual suction for Regina clay is difficult to ascertain but should be in the order of 300,000 kPa. Therefore, the 'two phase' zone for Regina clay would range between suctions of 3,000 kPa and 300,000 kPa.

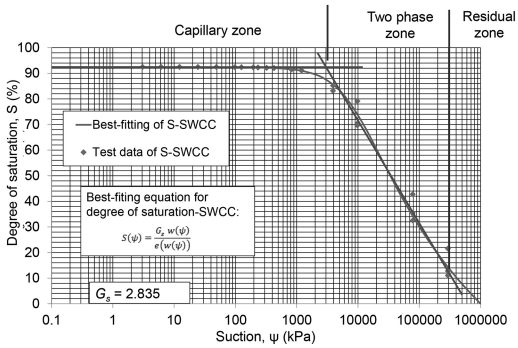


Figure 21. Drying curve expressed in terms of degree of saturation versus soil suction for specimens of Regina clay.

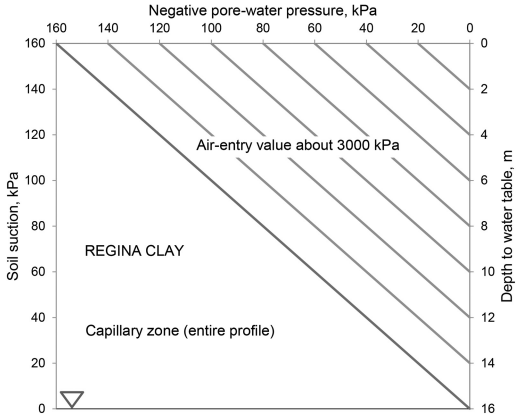


Figure 22. Drying Regina clay to an initial equilibrium condition in the field with the water table at 16 meters.

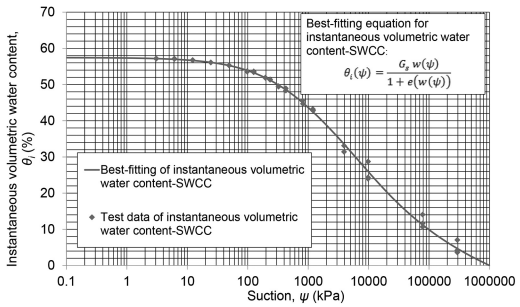


Figure 23. Drying curve expressed in terms of volumetric water content versus soil suction for specimens of Regina clay.

The effects of stress history (i.e., subsequent wetting and drying cycles) and possible cracking of the soil makes the constitutive relations associated with Regina clay extremely complex. The intent of the paper is not to sort out all these complexities of clay behavior but rather to show distinct difference between clay behavior and 'silt and sand' soil behavior.

The interpretation of the Regina clay (S-SWCC) can be placed onto the field stress state diagram (Figure 22). The transfer of drying conditions to the field stress state diagram shows that a 16 meter layer of Regina clay with a water table at 16 meters will remain in the 'capillary zone'. As such it should remain saturated unless excessive drying occurs at the ground surface. This does not mean; however, that changes in total stress and changes in pore-water pressure will have the same effect on soil behavior changes in total stresses. Changes in total stresses are generally due to self-weight consolidation or applied vertical loads whereas changes in suction are isotropic.

There is another difference that needs to be noted when dealing with compressible clay soils. The difference is related to modeling water storage. The formulations of transient seepage problems are usually presented in terms of chances in volumetric water content as soil suction changes. Therefore it is necessary to also be able to compute a relationship between the water storage modulus and suction. Volumetric water contents can be computed using Eq. [6].

$$\theta(\psi) = \frac{G_s w(\psi)}{1 + e(w(\psi))} \qquad [6]$$

Figure 23 shows the volumetric water content versus soil suction for the drying curve for Regina clay. The differentiation of volumetric water content with respect to soil suction gives the water storage modulus required for transient seepage modeling.

The SWCCs for silt, sand and clays show that the three soil types may need to be applied in quite different manners when being applied to *in situ* or field conditions. The differences can be visualized, in part, by transferring the main parameters of the laboratory measured SWCC onto a field hydrostatic pore-water pressure diagram.

5 OBSERVATIONS RELATED TO THE INTERPRETATION OF THE SWCC

1. The primary relationship to measure for an unsaturated soil is the drying SWCC from a zero suction value to a maximum soil suction of 1,000,000 kPa.
2. Entrapped air between the initial drying curve and the main drying curve does not appear to significantly influence the determination of the air-entry value of a soil.
3. Engineering practice has focused on obtaining as accurate an indication as possible of the drying SWCC. The wetting SWCC is most commonly estimated.
4. The gravimetric water content SWCC can be used for the estimation of unsaturated soil properties when the soil being tested is essentially incompressible with respect to suction changes.

5. A shrinkage curve needs to be measured and the degree of saturation SWCC must be computed when the soil is compressible with respect to changes in suction.
6. The air-entry value and the residual suction are the two primary variables required when applying unsaturated soil mechanics theories in engineering practice. These two variables define the extent of the capillary zone (boundary effect zone), the two phase zone (or transitional zone), and the residual zone (or dry).
7. The air-entry value and the residual suction can be compared to *in situ* hydrostatic pore-water pressure conditions in order to assist in making the transition from the laboratory test to field conditions.
8. The zones of desaturation can be applied to the field stratigraphy to determine the relative significance of each zone of saturation.
9. Sand, silt and clay soils respond quite differently with regard to the application of unsaturated soil mechanics. Silt soils are preferable for verifying unsaturated soil mechanics theories in the laboratory.
10. Hysteresis effects are often not measured in engineering applications and it is necessary for the geotechnical engineering to make an appropriate assumption with regard to an adequate simulation of drying and wetting effects.

5.1 *Consideration of other unsaturated materials encountered in engineering practice*

The SWCC appears to be the primary information required by the geotechnical engineer when applying unsaturated soil mechanics in engineering practice. However, there is still numerous issues related to unsaturated soil behavior that needs to be studied through detailed research studies. There are challenges related to applying unsaturated soil mechanics to certain classes of soils. Some of these soils are listed below.

1. Compacted soils have an artificially imposed stress state or matric suction. The soil structure is different in that it has a more open-structure created by the compaction process. The SWCC may exhibit bimodal behavior because of the initial draining of the larger pore sizes.
2. Swelling soils are sampled in the field and have initial matric suction. A soil specimen is prepared and then the matric suction which is released prior to commencing the measurement of the SWCC. There needs to be further studies related to the most appropriate testing protocol that should be used when testing expansive soils. The interpretation and application of the laboratory results in engineering practice needs to be clarified.
3. Collapsible soil testing protocol and procedures for the application of the measured SWCC need to be better understood.
4. The SWCC for residual soils needs to be studied in greater detail.
5. Cracked soils tends to give rise to a more complex SWCC; one that may be bimodal in character (Zhang et al., 2003).
6. Heap leach materials are known to generally have a bimodal SWCC. However, there has been little research on how the bimodal SWCC should be used to estimate unsaturated soil properties and how the results should be applied in engineering practice.

The use of the SWCC in unsaturated soil mechanics has been a topic receiving extensive attention at research conferences in recent years. There has been awareness that the measured SWCC serves a significant role when attempting to apply unsaturated soil mechanics theories in engineering practice. At the same time, it has become apparent that different soils have substantially different SWCCs. The various SWCCs must be interpreted with attention given to generating the protocols that produce the most accurate application of unsaturated soil mechanics theories. Stated another way, greater attention must be given to engineering practice procedures that render the most benefit with respect to the problem at-hand.

LIST OF REFERENCES

Fredlund, D.G. (1964). Comparison of soil suction and one-dimensional consolidation characteristics of a highly plastic clay. Technical Paper No. 245, National Research Council of Canada, Division of Building Research, Ottawa, ON.

Fredlund, D.G. (2009). Paradigm shifts to facilitate the practice of unsaturated soil mechanics, Proceedings of the 4th Asia-Pacific Conference on Unsaturated Soils, Newcastle, Australia, November 23–25, Vol. 1, pp. 599–611.

Fredlund, D.G., and Xing, A. (1994). Equations for the soil-water characteristic curve, Canadian Geotechnical Journal, 31(4), pp. 521–532.

Fredlund, D.G. and Zhang, F. (2013). Combination of shrinkage curve and soil-water characteristic curves for soils that undergo volume change as soil suction is increased, Proceedings of the 18th International Conference on Soil Mechanics and Geotechnical Engineering, Paris, France, September 2–6.

Fredlund, D.G., Rahardjo, H., and Fredlund, M.D. (2012). Unsaturated Soil Mechanics in Engineering Practice, John Wiley & Sons, New York, N.Y., 926 p.

Pham, H.Q. (2002). An engineering model of hysteresis for soil-water characteristic curves, M.Sc. thesis, University of Saskatchewan, Saskatoon, SK, 190 p.

Van Genuchten, M.T. (1980). A closed-form equation for predicting the hydraulic conductivity of unsaturated soils, Journal of Soil Science Society of America, Vol. 44, pp. 892–898.

Yang, H., Rahardjo, H., Leong, E.C., and Fredlund, D.G. (2004). Factors affecting drying and wetting soil-water characteristic curves of sandy soils, Canadian Geotechnical Journal, Vol. 41, No. 5, pp. 908–920.

Zhang, L.M., Li, J.H., and Fredlund, D.G. (2010). Hydraulic conductivity function for unsaturated cracked soil, Proceedings of the Fifth International Conference on Unsaturated Soils, Barcelona, Taylor & Francis Group, London, Vol. 2, pp. 993–999.

This page intentionally left blank

Unsaturated Soil Mechanics—from Theory to Practice – Chen et al. (Eds)
© 2016 Taylor & Francis Group, London, ISBN 978-1-138-02921-7

Tensiometer techniques for determining soil water retention curves

D.G. Toll & J.D. Asquith
School of Engineering and Computing Sciences, Durham University, Durham, UK

A. Fraser, A.A. Hassan, G. Liu, S.D.N. Lourenço, J. Mendes,
T. Noguchi & P. Osinski
formerly School of Engineering and Computing Sciences, Durham University, Durham, UK

R. Stirling
School of Civil Engineering and Geosciences, Newcastle University, Newcastle Upon Tyne, UK

ABSTRACT: The water retention behaviour of soils is an essential aspect of understanding the unsaturated behaviour of soil materials. This paper looks at a relatively new method of measurement for soil water retention curves, using high capacity tensiometers. New equipment for carrying out continuous measurements of water content, suction and volume change is described. The results are compared with traditional pressure plate measurements, as well as filter paper and chilled mirror hygrometer tests. It has been suggested that tensiometer measurements and pressure plate data give different results. This is confirmed by the larger data set provided here. It is found that the differences between the techniques can be explained by different volumetric responses.

1 INTRODUCTION

The water retention behaviour of soils is an essential aspect of understanding the unsaturated behaviour of soil materials (Fredlund, 2002). It represents the relationship between suction and water content (which can be gravimetric or volumetric) or may be represented in terms of degree of saturation. It is an essential piece of information for modelling unsaturated flow in soils and is used in the estimation of the permeability function (e.g. Brooks & Corey, 1964; van Genuchten, 1980). It can also be used in the interpretation of shear strength (Vanapalli et al., 1996).

This paper looks at a relatively new method of measurement for soil water retention curves, using high capacity tensiometers. The results are compared with traditional pressure plate measurements, using axis translation techniques. Other results from filter paper tests and chilled mirror hygrometer are also reported. It has been suggested that tensiometer measurements and pressure plate data give different results (Toll et al., 2013). A larger data set is provided here to investigate this suggestion and to help explain any differences.

Results are presented for a sandy clay fill material which have been obtained as part of an investigation of the impacts of climate on infrastructure slopes (iSmart: www.ismartproject.org). Water retention curves are required for modelling soil atmosphere interactions (Toll et al., 2014), which is an essential part of the iSmart project.

2 SOIL WATER RETENTION BEHAVIOUR

A typical water retention curve (in terms of volumetric water content) is shown in Figure 1. This relationship has also been called the Soil Water Characteristic Curve (SWCC). However, since the relationship is highly dependent on other factors, such as void ratio, it cannot be properly referred to as a "characteristic" and

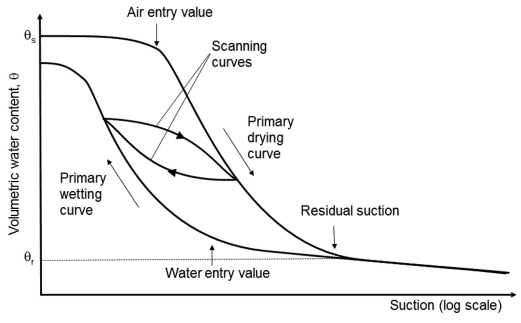


Figure 1. Typical Soil Water Retention Curve (after Toll, 2012).

hence the term Soil Water Retention Curve (SWRC) is preferred.

If the soil starts from a saturated state (at the saturated water content, θ_s) and is then subject to drying, it will follow the *Primary Drying Curve*. As suction increases, the largest pores will reach their limiting value of suction, and they will start to desaturate. The suction at which this starts to occur, when air enters the soil, is known as the *Air Entry Value*. Beyond the air entry value, the soil will reduce in water content as finer and finer pores progressively desaturate. At a value of suction known as the *Residual Suction* (with a corresponding residual water content, θ_r) the SWRC may flatten and much smaller changes in volumetric water content result from an increase in suction. It is suggested that within the residual zone, beyond the residual suction, water is held as adsorbed water on clay particles (McQueen and Miller, 1974) rather than as capillary water held by menisci. To achieve zero water content (equivalent to an oven dried condition) requires a suction of the order of 170 MPa (pF 6.25) (McKeen, 1992) or 1 GPa (pF 7) (Fredlund and Xing, 1994).

On wetting from an oven dried state, the soil will follow the *Primary Wetting Curve* (Figure 1). At a point known as the *Water Entry Value*, a significant increase in water content occurs as more pores start to fill. When the suction is reduced to zero, the final volumetric water content may be lower than the initial saturated value, θ_s, either due to air bubbles remaining trapped within the soil, or as a result of irrecoverable shrinkage of the soil.

The primary drying and wetting curves define an envelope of possible states within which the soil can exist. If drying is halted partway down the primary drying curve and wetting is started, the soil will follow an intermediate *Scanning Curve*, that is flatter than the primary wetting curve, until the primary wetting curve is reached. Similarly, if wetting is halted partway up the primary wetting curve and drying is started, the soil will follow another Scanning Curve, that is flatter than the primary drying curve, until the primary drying curve is reached.

3 MEASURING SWRCS USING HIGH CAPACITY TENSIOMETERS

An important advance has been in the determination of the Soil Water Retention Curves (SWRCs) with high suction tensiometers. The major advantage is that drying can be imposed naturally, where negative pore water pressures are created (Toll et al., 2013). In the axis translation technique (as used in the pressure plate), desaturation is induced by artificially imposed an elevated air pressure. In this scenario, the pore water pressure is always positive and desaturation can only occur by air entry at the boundaries of the sample. However, in natural drying, internal pores can desaturate by cavitation when the pore water pressure becomes highly negative.

Using the tensiometer technique, suction can be measured in samples either dried continuously while exposed to the atmosphere (continuous procedure) or by drying in stages (stage procedure). The same technique can be used for wetting, where water is added in a slow, controlled way. In the stage procedure, the specimen is sealed and allowed to equalise internally after each period of drying or wetting. Both approaches are quicker than traditional methods for obtaining SWRCs (e.g. pressure plate). For example, Lourenço (2008) reports that tests carried out using a tensiometer by continuous drying took 2 days, stage drying less than 7 days, whereas a pressure plate test on the same material took 7 weeks to perform.

Cunningham (2000), Boso et al. (2003), Toker et al. (2004), Teixeira and Marinho (2006), Lourenço et al (2007; 2012; 2015) have determined SWRCs, using high suction tensiometers to measure suction and an electronic balance to record water content. Boso et al. (2003) presented a comparison between SWRCs obtained by stage and continuous drying for samples of reconstituted clayey silt. The evaporation rate during continuous drying was slowed down by wrapping the sample in a porous geotextile. The results revealed no differences between the SWRCs using the two procedures. Cunningham (2000) investigated the influence of the evaporation rate on the measured SWRC for continuously dried samples of reconstituted silty clay. Similar results were obtained suggesting that the evaporation rate had little or no influence on the resulting soil water retention curve.

Lourenço et al. (2007) also compared SWRCs for a sandy clay determined by means of high suction tensiometers following both stage and continuous drying. The SWRCs obtained by continuous drying showed higher suctions (by as much as 200kPa) than the SWRCs obtained by stage drying at the same water content (equivalent to higher water contents at the same suction). These results were initially explained by the lack of suction equalization throughout the sample due to: (i) the fast evaporation rate controlled by the low relative humidity inside the laboratory, (ii) the limited surface area of the sample exposed to the atmosphere, (iii) the fact that the measurements of suction were conducted on the exposed sample surface and (iv) possible additional errors introduced by the experimental set-up (e.g. errors in the measurement of the sample mass due to the weight and stiffness of the tensiometer cable).

Toll et al. (2013) reported a small number of measurements (by Lourenço, 2008 and Tarantino et al., 2011) comparing tensiometer and pressure plate data. They showed that the axis translation tests show higher water contents than those measured by natural drying using tensiometer measurements. They explained these differences in water content as being consistent with the fact that the axis translation technique (used in the pressure plate) prevents cavitation from occurring within the soil and desaturation only occurs by air entry from the sample boundaries. This seemed a feasible explanation to explain the higher water contents

observed in pressure plate tests compared with tensiometer measurements.

4 TEST PROCEDURES FOR SOIL WATER RETENTION CURVES

4.1 *Material tested*

The soil used in this study was a glacial till (Durham Lower Boulder Clay) obtained from fill material used in the construction of an experimental embankment constructed in North East England (Hughes et al., 2009) that is being investigated as part of the iSmart project (www.ismartproject.org). The material was prepared by sieving through a 2.8 mm sieve to remove the larger particles to reduce the variation in properties (Mendes, 2011). The sieved material comprised 30% sand, 35% silt and 35% clay, i.e., a sandy clay soil. The Liquid Limit was 43.3% and the Plastic Limit was 23.7%, resulting in a Plasticity Index of 19.6. The particle density is 2.66 Mg/m^3.

Specimens for testing were prepared by compaction into a 100 mm diameter mould using the equivalent compactive effort of the standard Proctor test (BS light compaction, BS 1377-4, 1990). Samples were compacted wet of optimum at a water content of 24%. This resulted in specimens close to saturation (degree of saturation, $S_r > 95\%$). From the larger compacted samples, smaller specimens were cut according to the requirements for each technique as follows.

Specimens having a diameter of 75 mm and a thickness of 20 mm were trimmed from the 100 mm diameter compacted samples for testing in the tensiometer and pressure plate equipment.

For filter paper tests, samples of 100 mm diameter and 25 mm thickness were air dried until they reached the desired gravimetric water contents. The samples were then trimmed to a diameter of 55mm diameter and 20 mm thickness before testing.



Figure 2. View of equipment for tensiometer-based SWRC measurement, showing the frame sitting on the electronic balance and connected to the data-logging system.

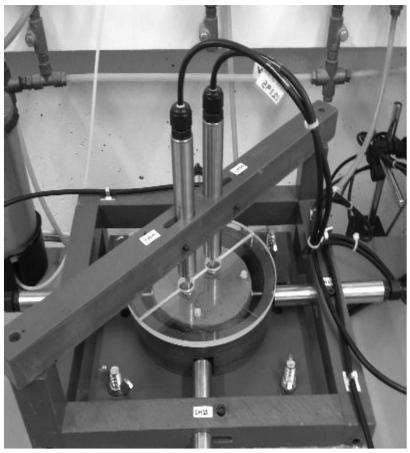


Figure 3. PVC frame holding six LVDTs to measure volume change.

4.2 *Tensiometer test method*

The tensiometer SWRC test procedure has been developed from that used by Lourenço et al. (2007; 2011). Subsequent modifications by Noguchi et al. (2012) and Liu et al. (2015) have improved the procedure, in particular adding the capability for continuous volume change readings. Prior to this, volumetric measurements were obtained by measuring the sample diameter and height using a Vernier micrometer.

The experimental apparatus (Liu et al., 2015) allows continuous measurements of water content, suction and volume change. The apparatus was made up of a PVC frame (shown in Figure 2) placed on an electronic balance to determine the change in sample weight and hence water content (as used by Lourenço et al., 2011).

For volume change measurements, four displacement transducers were installed through the four outside beams of the frame to measure radial displacement of the specimen and two more displacement transducers were fitted through the upper beam to measure axial displacement (change in height) (Figure 3). Volume change of the specimen could then be calculated from the radial and axial deformations.

A high suction tensiometer developed at Durham University (Lourenço et al., 2006; Toll et al., 2013) was used to measure suction. These devices have been used for direct measurement of suction as large as 2000 kPa. The tensiometer was fitted through a hole in the support plate, with a tight fitting rubber O-ring to secure it in place. All transducers were connected to a real-time data acquisition system (Toll, 1999).

All the cables of the transducers and the tensiometer were fixed and supported by retort stands to minimize the influence of cable stiffness on the mass measurement (Lourenco, 2008). Results by Liu et al. (2015) showed that the apparent mass change due to the cables was less than 0.25g. In the latest version of the equipment, wireless data logging has been adopted

to eliminate the problem of cable stiffness (Asquith, unpublished).

4.3 *Pressure Plate method*

The pressure plate device used was a modified version of the commercial 15 bar equipment supplied by Soil Moisture Corp. of Santa Barbara, California, USA. The original single high air entry value (HAEV) porous ceramic plate of 1500 kPa was replaced by 4 independent plates enabling multi sample testing (Vaquero, 2007). The conventional burette was replaced by independent volume gauges (one volume gauge for each plate). The volume gauges allow back pressure to be applied underneath the HAEV porous ceramic plate, which can be beneficial in preventing dissolved air coming out of solution. The volume gauges were connected to a data acquisition system to observe the equilibration of water flow from the soil samples.

The highest suction imposed was 1100 kPa, using an air pressure of 1310 kPa and a water pressure of 210 kPa. The equalisation of a soil sample was assumed to be reached when the volume change read by the gauge was less than 0.35 cc/day, which was the expected air diffusion rate (a property of the porous ceramic plate). However, mass measurements were used to determine the water content after equilibrium was observed, to avoid potential errors in the volumetric measurements due to air diffusion.

4.4 *Filter Paper method*

The method for the filter paper technique was adapted from Bulut et al. (2001). Two soil discs (55 mm diameter and 20 mm thickness) at the same water content were used for one measurement.

Three Whatman 42 filter papers (middle one for measuring the matric suction and outer ones for protecting the measuring filter paper from soil contamination) were placed on top of a disc sample and another disc sample was placed on top of the filter papers in intimate contact. The two disc samples with filter papers in between were taped together with electrical tape and placed in a glass jar. The lid was taped and the glass jar was then wrapped in four layers of plastic film (cling film) and finally coated in paraffin wax, so that no exchange of air was possible. The soil within the jar was allowed to equalise in a water bath at 25°C for a period of 14 days, which was found to be the upper limit of equalisation period (Leong et al., 2002). Three measurement sets were prepared for each soil water content. After equalisation, the mass of the filter paper and soil samples was then measured to an accuracy of 0.0001 g, as swiftly as possible. The filter paper and soil samples were then oven-dried for determination of the water content. The water content of the filter paper was calculated and a corresponding suction was determined using van Genuchten's (1980) calibration equation. This calibration was found by Noguchi et al (2012) to give the best match to other direct measurements.

4.5 *Chilled Mirror Dewpoint method*

A Decagon Devices WP4 was used to measure suction within the range 0 to 300 MPa with a resolution of 0.1 MPa. This method determines the relative humidity of the air above a sample in a closed chamber where at temperature equilibrium, relative humidity is a direct measurement of water potential (Decagon Devices Inc., 2015).

Samples were statically compacted to a diameter of 38 mm and height 8 mm. They were dried to required masses corresponding to a range of water contents (Stirling & Hen-Jones, 2015). On achieving the desired mass, the sample was then divided. A portion was placed into the drawer of the WP4, after being left to reach temperature equilibrium with the device for no less than 15 min. The remaining portion was used for bulk density determination. By weighing in air and in a non-wetting fluid of known density, the bulk density of the sample was deduced. This enabled the calculation of volumetric water content and the degree of saturation to be determined from the bulk density of the soil at known gravimetric water content.

5 SOIL WATER RETENTION CURVES FOR A SANDY CLAY

The results obtained by the authors of the paper have been compiled in Figures 4–6. These include pressure plate, stage drying and continuous drying by Lourenço (2008); pressure plate, stage drying, continuous drying and filter paper by Noguchi (2009); pressure plate, stage drying and continuous drying tests by Fraser (2014); continuous drying tests by Osinski (2014); continuous drying tests by Asquith (unpublished); dewpoint hygrometer tests by Stirling and Hen-Jones (2015).

Figure 4 shows the data plotted as gravimetric water content against suction. Gravimetric water content is the measure usually used by geotechnical engineers in practice.

The data from the different methods generally show reasonable agreement. The continuous drying tests define a relatively tight band of data. The filter paper tests and the dewpoint hygrometer tests show reasonable agreement in the higher suction range (1,000–10,000 kPa). The dotted line in the figure is probably representative of the primary drying curve for this soil.

Specimens that were prepared at a lower water content than the saturated water of 25% follow slightly flatter curves (equivalent to scanning curves) that merge with the other data at higher water contents.

The lower suction range (up to 2000 kPa) is shown at an expanded scale in Figure 5. It can be seen in Figure 5 that the pressure plate data plots above the results from tensiometer measurements, particularly in the region 20–400 kPa. This agrees with the observations of Toll et al. (2013) that the axis translation tests show higher water contents than those measured by natural drying using tensiometer measurements. An explanation put forward by Toll et al. (2013) was that cavitation

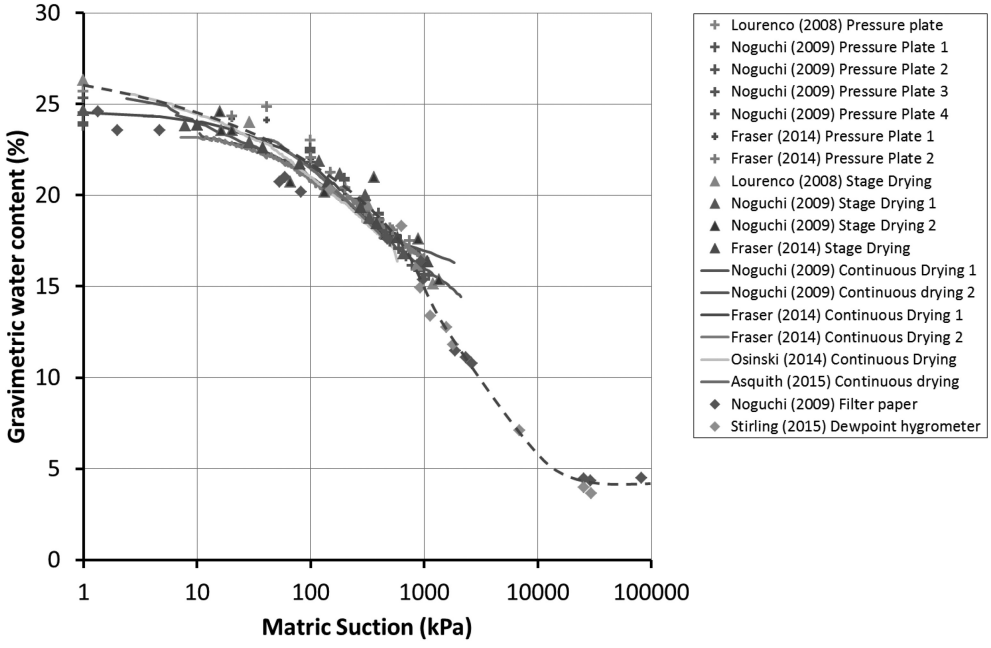


Figure 4. Soil water retention curves expressed in terms of gravimetric water content.

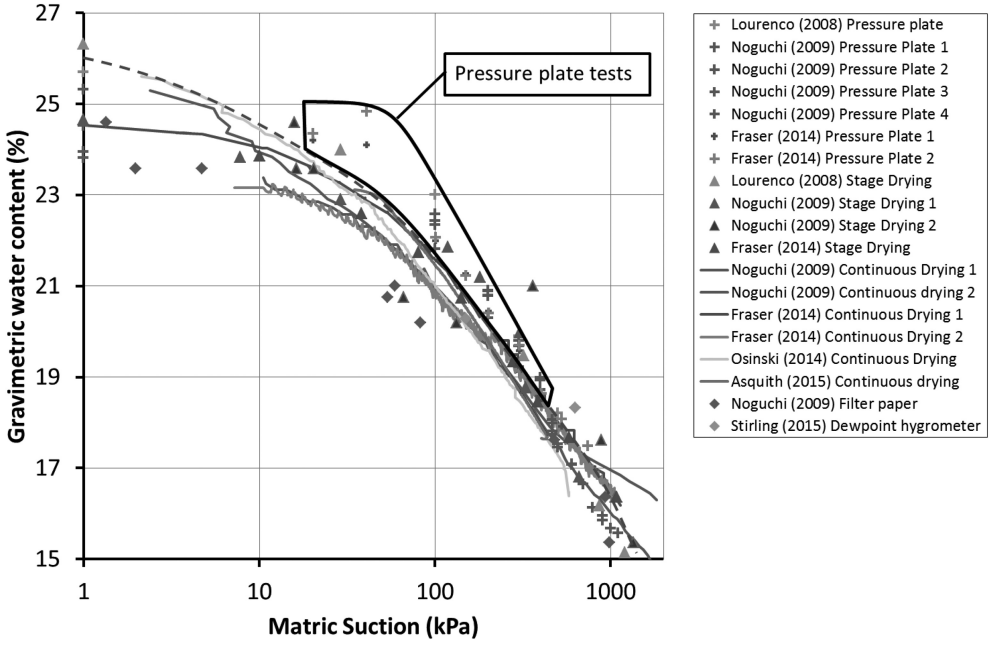


Figure 5. Soil water retention curves expressed in terms of gravimetric water content (lower suction range).

was prevented in the pressure plate tests (using axis translation) whereas cavitation could take place during natural drying. However, cavitation would not be expected to occur at suctions less than 100 kPa.

The impression given by the gravimetric water content plot is that the tensiometer tests are desaturating at lower suctions than the pressure plate tests, since the water contents are lower. However, it has to be remembered that gravimetric water content change can be due to volume change (shrinkage) as well as due to desaturation. The data is therefore plotted in terms of degree of saturation in Figure 6. This shows that, in fact, the pressure plate tests desaturate at lower suctions than the tensiometer test. The trend of pressure plate results

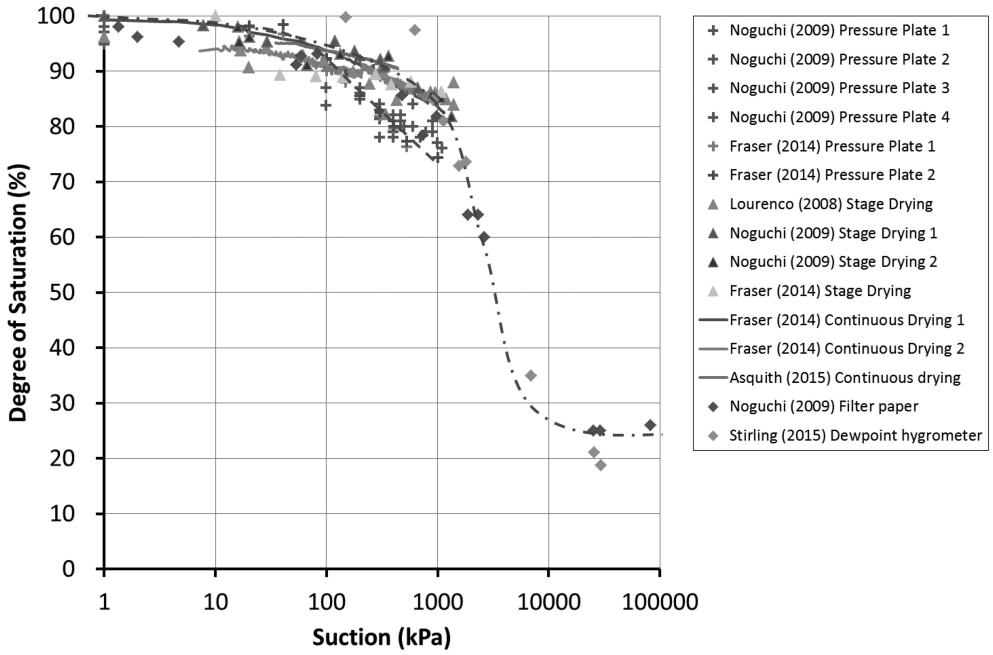


Figure 6. Soil water retention curves expressed in terms of degree of saturation.

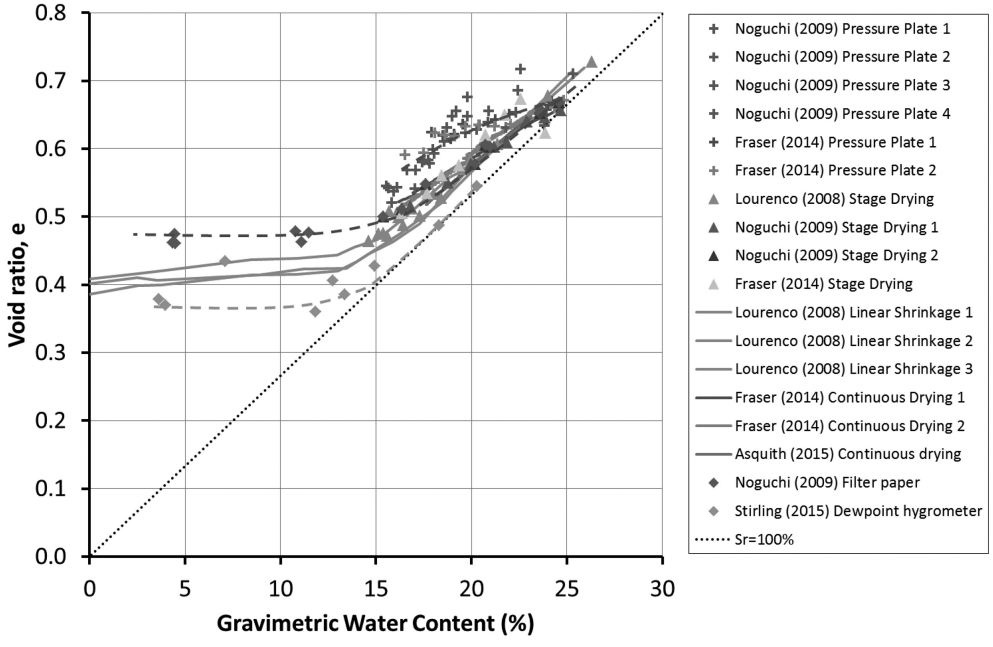


Figure 7. Shrinkage paths observed during SWRC testing.

(indicated by the short-dotted line) indicates a separation at around 80 kPa from the paths followed by the tensiometers (indicated by the chain-dotted line).

To understand these differences in degree of saturation, it is important to consider the volume changes during drying. Figure 7 shows the data plotted as conventional shrinkage curves, in the form of void ratio against gravimetric water content. Also shown are the results of 3 linear shrinkage tests carried out by Lourenço (2008) indicating a shrinkage limit around 13–14%.

Figure 7 shows that the tensiometer tests follow a similar path over the range of water contents from 25% down to 15%. They tend to track down close to the

$S_r = 100\%$ line, like the linear shrinkage tests. However, the pressure plate tests show a different shrinkage path, where they move away from the saturation line at water contents below 23%. They demonstrate less shrinkage than the other tests.

It is also interesting to see that the filter paper tests and the dewpoint hygrometer tests, where drying was continued below 15%, show a similar pattern to the linear shrinkage tests, but reach different ultimate void ratios below the shrinkage limit.

These results demonstrate the importance of obtaining volumetric measurements as part of the determination of the soil water retention curves. Having equipment that can provide continuous volume change readings is a therefore advantageous.

6 CONCLUSIONS

New equipment has been developed for measurement of soil water retention curves, using a high capacity tensiometer. It provides continuous measurements of water content (from an electronic balance), suction (from a high suction tensiometer) and volume change (using LVDTs to measure changes in diameter and height).

A large data set of soil water retention measurements have been made on a sandy clay fill material, the material used in the construction of an instrumented embankment to investigate climate impacts on infrastructure slopes.

The results are compared with traditional pressure plate measurements, filter paper tests and chilled mirror hygrometer tests. It is confirmed that tensiometers measurements and pressure plate data give different results, as has been previously observed. The differences between the techniques can be explained by different volumetric responses. The pressure plate tests show different shrinkage paths, resulting in less volume change. This is reflected in significant differences in the degrees of saturation attained at the same suction. The pressure plate tests tend to show higher gravimetric water contents than the tensiometer measurements, but lower degrees of saturation.

The results demonstrate the importance of obtaining volumetric measurements as part of the determination of the soil water retention curves. The equipment described here provides a great advantage in allowing the determination of continuous volume change readings.

REFERENCES

Boso, M., Romero, E. & Tarantino, A. 2003. The use of different suction measurement techniques to determine water retention curves, *Unsaturated soils: Experimental studies,* (ed. Schanz T), Berlin: Springer-Verlag, 171–181.

British Standards Institute (1990), BS1377: *Methods of test for Soils of civil engineering purposes,* BSI, Milton Keynes.

Brooks, R.H., & Corey, A.T. 1964. Hydraulic properties of porous media, *Hydrology Papers, No. 3,* Colorado State University, Fort Collins, Colorado.

Cunningham, M.R. 2000. The mechanical behaviour of a reconstituted unsaturated soil, *PhD Thesis, Imperial College of Science, Technology and Medicine, London*.

Decagon Devices Inc. 2015. WP4C water potential meter. http://www.decagon.com/products/soils/benchtop-instruments/wp4c-water-potential-meter/. Accessed 19 May 2015.

Fraser, A. 2014. Water retention behaviour of soils, *MEng Final Year Project Report, Durham University*.

Fredlund, D.G. 2002. Use of the soil-water characteristic curve in the implementation of unsaturated soil mechanics. *Proc. . Third Int. Conf. on Unsaturated Soils, UNSAT 2002, Recife, Brazil*. (eds. J.F.T. Juca, T.M.P. de Campos, and F.A.M. Marinho. London: Taylor and Francis, Vol. 3, pp. 887–902.

Fredlund, D.G., and Xing, A. 1994. Equations for the soil-water characteristic curve. *Canadian Geotechnical Journal*, 31, 4: 521–532.

Hughes, P.N., Glendinning, S., Mendes, J., Parkin, G., Toll, D.G., Gallipoli, D., Miller, P. 2009. Full-scale testing to assess climate effects on embankments. *Special Issue of Engineering Sustainability: Proc. Institution of Civil Engineers*, 162, 2, pp. 67–79.

Leong, E. C., He, L., and Rahardjo, H. 2002. Factors Affecting the Filter Paper Method for Total and Matric Suction Measurements. *Geotechnical Testing Journal,* 25, 3, pp 321–332.

Liu, G., Toll, D.G., Kong, L. & Asquith, J.D. 2015. Matric suction and volume characteristics of compacted clay soil under drying and wetting cycles, *submitted to ASTM Geotechnical Testing Journal*.

Lourenço, S.D.N. 2008. Suction Measurements and Water Retention in Unsaturated Soils, *PhD Thesis, Durham University*. Available online: http://etheses.dur.ac.uk/1331/.

Lourenço, S.D.N., Gallipoli, D., Toll, D.G. and Evans, F.D. 2006. Development of a Commercial Tensiometer for Triaxial Testing of Unsaturated Soils, *Proc. 4th International Conference on Unsaturated Soils, Phoenix, USA, Geotechnical Special Publication No. 147*, Reston: ASCE, Vol.2, pp. 1875–1886.

Lourenço, S.D.N., Gallipoli, D., Toll, D.G., Evans, F.D. & Medero, G.M. 2007. Determination of the Soil Water Retention Curve with Tensiometers, in *Experimental Unsaturated Soil Mechanics*, (ed. T. Schanz), Springer, pp. 95–102.

Lourenço, S.D.N., Gallipoli, D., Toll, D.G., Augarde, C.E. & Evans, F. 2011. A new procedure for the determination of the Soil Water Retention Curves by continuous drying using high suction tensiometers. *Canadian Geotechnical Journal*, 48, 2, pp. 327–335.

Lourenço, S.D.N., Jones, N., Morley, C., Doerr, S.H. & Bryant, R. 2015. Hysteresis in the soil water retention of a sand–clay mixture with contact angles lower than ninety degrees, Vadose Zone Journal, doi:10.2136/vzj2014.07.0088.

McKeen, R.G. 1992. A model for predicting expansive soil behaviour, *Proc. 7th Int. Conf. on Expansive Soils, Dallas*, Vol. 1, pp. 1–6.

McQueen, I.S. and Miller, R.F. 1974. Approximating soil moisture characteristics from limited data: empirical evidence and tentative model. *Water Resources Research*, 10, pp. 521–527.

Mendes, J. 2011. Assessment of the impact of climate change on an instrumented embankment: an unsaturated soil

mechanics approach. *PhD Thesis, Durham University*. Available online: http://etheses.dur.ac.uk/612/.

Noguchi, T. 2009. Comparison of Major Suction Measurement Techniques Used to Determine the Soil Water Retention Curves, *MEng Final Year Project Report, Durham University*.

Noguchi, T., Mendes J. & Toll, D.G. 2012. Comparison of soil water retention curves obtained by filter paper, high capacity suction probe and pressure plate, *Proc. 5th Asia-Pacific Conference on Unsaturated Soils, Pataya, Thailand*, pp. 368–373.

Osinski, P. 2015., Soil Water Retention Curves for BIONICS soil, *Short Term Scientific Mission Report, EU COST Action TU1202*.

Stirling, R. & Hen-Jones, R. 2015. Investigating geotechnical/geophysical relationships in unsaturated glacial till, *Short Term Scientific Mission Report, EU COST Action TU1202*.

Tarantino, A., Gallipoli, D., Augarde, C.E., De Gennaro, V., Gomez, R., Laloui, L., Mancuso, C., McCloskey, G., Munoz, J., Pereira, J-M., Peron, H., Pisoni, G., Romero, E., Raveendiraraj, A., Rojas, J.C., Toll, D.G., Tombolato, S. & Wheeler, S. 2011. Benchmark of experimental techniques for measuring and controlling suction. *Symposium in Print on Partial Saturation in Compacted Soils, Géotechnique* 61, 4, pp. 303–312.

Toker N., Germaine J., Sjoblom K., Culligan P. 2004. A new technique for rapid measurement of continuous soil moisture characteristic curves, *Géotechnique*, 54, 3, 179–186.

Toll, D.G. 1999. A data acquisition and control system for geotechnical testing, in *Computing Developments in Civil and Structural Engineering* (eds. B. Kumar and B.H.V. Topping), Edinburgh: Civil-Comp Press, pp 237–242.

Toll, D.G. 2012. The behaviour of unsaturated soils. *Chapter 5 in A Handbook of Tropical Residual Soil Engineering*, (eds. Huat, B.B.K., Toll, D.G. & Prasad, A.) London: Taylor and Francis, ISBN: 9780415457316.

Toll, D.G., Lourenço, S.D.N. and Mendes, J. 2013. Advances in suction measurements using high suction tensiometers, *Engineering Geology*, 165, pp 29–37.

Toll, D.G., Md. Rahim, M.S., Karthikeyan, M. & Tsaparas, I. 2014. Soil atmosphere interactions for analysing slopes in tropical soils, *Proc. Int. Conf. IACMAG, Kyoto Japan* (eds. F. Oka, A. Murakami, R. Uzuoka), London: Taylor & Francis (CRC Press).

van Genuchten, M.Th., 1980. A closed-form equation for predicting the hydraulic conductivity of unsaturated soils, Soil Sci. Soc. Am. J., 44, 892–898.

Vanapalli, S.K., Fredlund, D.G., Pufahl, D.E. & Clifton, A.W. 1996. Model for the prediction of shear strength with respect to soil suction. *Canadian Geotechnical Journal*, 33, 3, pp. 379–392.

Vaquero, J.L. 2007. Soil suction measurement using the pressure plate technique within the MUSE network, *Project re-port, Durham University*.

Unsaturated Soil Mechanics—from Theory to Practice – Chen et al. (Eds)
© 2016 Taylor & Francis Group, London, ISBN 978-1-138-02921-7

Capillary barrier as a slope protection

H. Rahardjo
School of Civil and Environmental Engineering, Nanyang Technological University, Singapore

ABSTRACT: A capillary barrier is a two-layer system of distinct hydraulic properties that is used as a cover system. The distinct hydraulic properties prevent water infiltration into the soil below the capillary barrier system by utilizing unsaturated soil mechanics principles. This paper illustrates the research and application of the capillary barrier system as a slope cover to prevent rainfall-induced slope failures. The mechanics and performance of Capillary Barrier System (CBS) as a slope protection have been investigated through laboratory tests, numerical analyses and field tests at Nanyang Technological University (NTU), Singapore. Several slopes protected by CBS have been constructed and fully instrumented. The results of this study on CBS illustrate good performance of CBS as a slope protection against rainfall-induced slope failures. In addition, the use of recycled materials as capillary barrier materials have been studied and found to be feasible. An improved system using Dual Capillary Barrier (DCB) has been developed and shown to be more superior to the Single Capillary Barrier (SCB). A retaining wall system incorporating capillary barrier principles, named GeoBarrier System (GBS) has also been developed for its use in underground basement carpark. This study on capillary barrier system (single and dual) and geobarrier system for slope protection and retaining wall exemplifies the application of unsaturated soil mechanics to engineering practice.

1 INTRODUCTION

In recent decades, many parts of the world are experiencing more rainy days with higher rainfalls over a shorter time scale due to climate change (IPCC, 2013). The increase in the rainfall amount may exacerbate slope failures in tropical countries like Singapore where many slope failures during rainfall have already been experienced (Chatterjea, 1989; Toll et al., 1999; Rahardjo et al., 2001). Most of the slope failures were observed in the residual soil with a steep slope angle (Krahn et al., 1989; Ng et al., 2008; Rahardjo et al., 2012a). The steep residual soil slopes are usually associated with a thick unsaturated zone above the groundwater table (Figure 1). The negative pore-water pressure above the groundwater table contributes additional shear strength to the unsaturated soil. As water infiltrates into the slope, pore-water pressure in the slope increases (matric suction decreases), and the additional shear strength due to matric suction will decrease or even disappear, causing the slope to be more susceptible to failure. Evaporation and transpiration will restore the loss of matric suction in the slope and this climatic variation occurs at all times (Rahardjo et al., 2013a). To protect slopes against the possibility of rainfall-induced slope failures, preventive measures are necessary.

Various slope protection methods have been developed and used in geotechnical engineering practice. Broms and Wong (1991) classified the preventive and remedial measures of slopes into three categories: (i) geometric methods, (ii) chemical and mechanical methods and (iii) hydrological methods. Geometric methods involve the modification of the geometry of the slope to increase its stability. Chemical and mechanical methods include strengthening the soil mass within the slope by adding chemical or mechanical matters (grouting, cement column, soil nailing, geosynthetics). Hydrological methods include controlling the slope surface and soil water condition

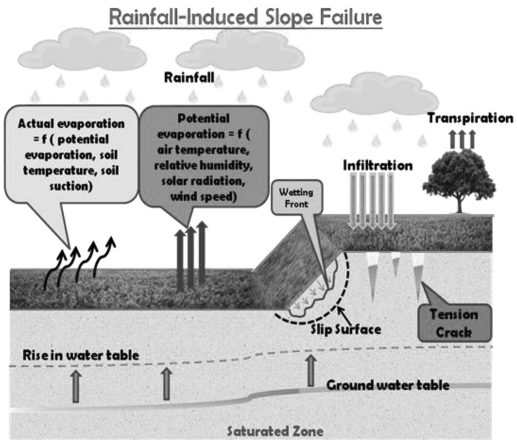


Figure 1. Mechanism of rainfall-induced slope failures.

by preventing or minimizing water infiltration into the slope (i.e., maintaining the negative pore-water pressure or matric suction of the soil slope). Modification to the slope's geometry is not always feasible in urban areas like Singapore due to the space constraint. A chemical or mechanical method is usually expensive and may not be always suitable for preventing rainfall-induced slope failures.

Previous research works indicated that hydrological method or commonly called soil cover is the best method to be used for slope protection (Yanful et al., 1999; Tami et al., 2004a; Yang et al., 2006; Rahardjo et al., 2013b). The most common and widely used soil cover is a low-permeability compacted soil. However, this soil cover was observed to be susceptible to deterioration, especially in arid and semiarid areas. The compacted soil may experience crack, subsidence, root and animal intrusions (Suter et al., 1993). Therefore, capillary barrier system is commonly used as soil cover to minimize water infiltration into the waste materials (landfill) (Morris and Stormont, 1998; Stormont and Anderson, 1999; Morii et al., 2013). Up to now, limited study has been carried out on the application of capillary barriers for slope protection against rainfall-induced slope failure due mainly to the much higher slope angles compared to landfill covers. A comprehensive research programme on the performance of capillary barrier system as a slope protection measure since 1999 is ongoing at Nanyang Technological University (NTU). In this paper, the results of laboratory tests, numerical analyses and field instrumentation are presented. In addition, the enhancements of capillary barrier system, dual capillary barrier system and geobarrier system are also illustrated.

2 CAPILLARY BARRIER SYSTEM

A capillary barrier is commonly defined as a non-cohesive cover system consisting of a fine-grained soil overlying a coarse-grained soil (Figure 2). The difference in particle sizes of the fine-grained and the coarse-grained layers results in the difference in the hydraulic properties (i.e. soil-water characteristic curve and permeability function) of the soils across the interface of the fine-grained and the coarse-grained layers. A negative pore-water pressure at the interface under unsaturated condition results in the lower permeability of the coarse-grained layer as compared to that of the fine-grained layer. The low permeability of the coarse-grained layer limits the downward movement of water and holds the infiltrating water in the fine-grained layer to be released through lateral diversion, evaporation and transpiration. Capillary barriers can be found in both natural and engineered forms. Natural capillary barriers occur in both small and large scales. Kueper and Frind (1991) and Miyazaki (1988) observed that the contrasting hydraulic properties of fine and coarse grains create small-scale capillary barriers that greatly affect the flow paths of contaminants and water infiltration. Montazer and Wilson (1984)

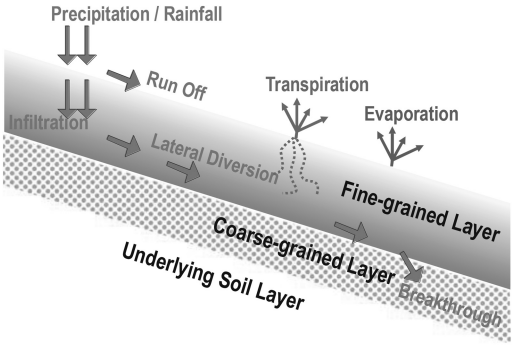


Figure 2. Capillary barrier system.

found large-scale natural capillary barriers in the geological formations at Yucca Mountain, Nevada which consist of tilted layers of welded and non-welded tuffs. This system diverted water infiltration from the waste repository at Yucca Mountain. Chai (2008) observed that the natural formation of residual soil at a certain location in Malaysia has a lower permeability as compared to that of deeper depths. As a result, a large-scale natural capillary barrier is developed and these conditions prevent rainwater from infiltrating into the deeper layers and consequently, the shear strength of the soil slope can be maintained.

Engineered capillary barriers can be constructed in various forms, ranging from the most common and simple design of two layers of soils with different particle sizes, to a more complex design that includes multiple layers of fine-grained and coarse-grained layers to achieve a specific requirement (Morris and Stormont, 1998). In the simple design of a capillary barrier, the fine-grained layer does not only serve as a lateral diversion medium, but also as a rooting medium and a water storage medium. Numerous research works have been conducted to investigate the performances of capillary barrier systems for different applications, through laboratory experiments (Harnas et al., 2014; Huang et al., 2011; Krisdani et al., 2005; Miyazaki, 1990; Stormont and Anderson, 1999; Tami et al., 2004b; Tidwell et al., 2003; Yang et al., 2006;), numerical analyses (Aubertin et al., 2006; Bussiere et al., 2003; Harnas et al., 2013; Morris and Stormont, 1999; Oldenburg & Pruess, 1993; Ong, 2002; Rahardjo et al., 2009; Sugiyama et al., 2014; Takayama et al., 2014) or field studies (Kampf et al., 2003; Khire et al., 1999; Krisdani et al., 2010; Morii et al., 2013; Rahardjo et al., 2012a; Rahardjo et al., 2012b, 2013b; Sakamoto et al., 2011, Sun et al., 2010; Weeks et al., 2004; Yanful et al., 2006).

3 MECHANICS OF CAPILLARY BARRIER

A capillary barrier system (CBS) relies on the contrast in unsaturated permeability between the fine-grained layer and the coarse-grained layer that impedes downward movement of infiltrating water. As long as a

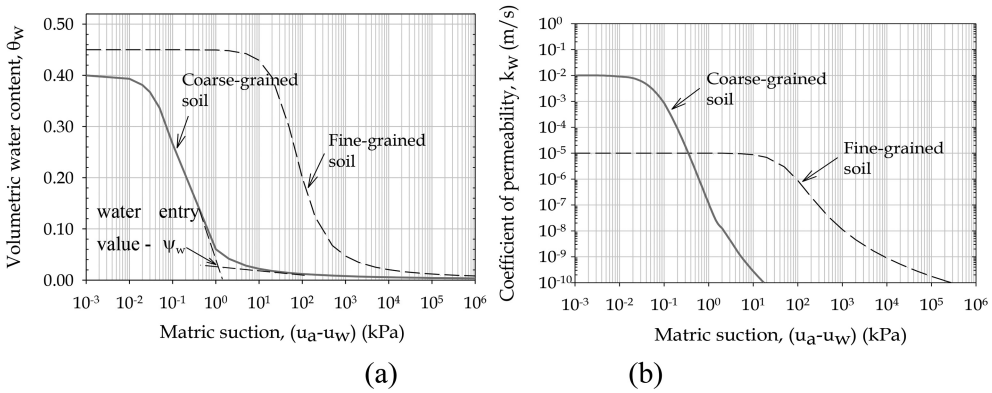


Figure 3. (a) Soil-water characteristic curves and (b) permeability functions of CBS.

CBS remains unsaturated, water can only flow along the fine-grained layer and it will not be able to penetrate the coarse-grained layer (Stormont and Anderson, 1999). Figures 3a and 3b show typical soil-water characteristic curves and permeability functions of CBS materials, respectively. At high matric suction values, the coefficient of permeability of the coarse-grained layer is much lower than that of the fine-grained layer (Figure 3b). In this case, rainwater will not flow into the coarse-grained layer, but will be stored or diverted laterally through the fine-grained layer. As the infiltration process continues, the volumetric water content of the fine-grained layer increases and the coefficient of permeability of the fine-grained layer also increases. However, when the infiltrating water reaches the fine-coarse interface, the matric suction of the coarse-grained layer will decrease. When the water-entry value, ψ_w of the coarse-grained soil (Figure 3a) is reached, the coefficient of permeability of the coarse-grained layer will start to increase rapidly and water will start to flow into the coarse-grained layer. Under this condition, there will be no barrier effect from the coarse-grained layer and CBS is no longer effective in preventing downward water movement.

Several laboratory tests have been carried out at NTU to study the water flow through soil layers in CBS. Yang et al. (2004) constructed soil columns to study the infiltration of water through soil layers in CBS. The infiltration tests were performed using several combinations of CBS materials, such as fine sand overlying medium sand, medium sand overlying gravelly sand, fine sand overlying gravelly sand and silty sand overlying gravelly sand. It was concluded that a saturated coefficient permeability ratio of 2 to 3 orders of magnitude between the fine-grained and the coarse-grained layers was generally effective to produce a capillary barrier effect. Yang et al. (2004) also suggested that the minimum thickness of the coarse-grained layer required in a CBS is approximately equal to the residual matric suction head of the coarse-grained layer, which is also close to the water-entry value of the coarse-grained layer. A coarse-grained layer which is thicker than the minimum thickness may not increase the barrier effect, while a coarse-grained layer which is thinner than the minimum thickness will reduce the barrier effect. Indrawan et al. (2006) investigated the use of different soil mixtures as fine-grained layers in CBS. The experimental results indicated that a soil mixture of 75% residual soil and 25% medium sand was effective in maintaining matric suctions during the wetting process.

Krisdani et al. (2006) conducted a one-dimensional (1-D) laboratory test (Figure 4) to investigate the infiltration characteristics through a capillary barrier system and the storage of the fine-grained layer. The performance of CBS constructed using different materials (i.e. geosynthetic material and gravelly sand) as coarse-grained layer was also studied. The Soil-Water Characteristic Curve (SWCC) and permeability function of materials used in CBS are presented in Figure 5. The experimental results showed that the capillary barrier effect existed in both capillary barrier columns with geosynthetic material and gravelly sand as the coarse-grained layer (Figure 6). Krisdani et al. (2006) concluded that the recovery of water storage of the CBS is mainly controlled by the lateral diversion flow and the evapotranspiration process.

Tami et al. (2004b) investigated the potential use of CBS as a slope stabilization technique by limiting infiltration into a soil slope. An infiltration box of 2.45 m in length, 2 m in height and 0.4 m in width was used to construct the laboratory capillary barrier model (Figure 7). Three combinations of materials consisting of 0.2 m thick fine sand overlying 0.2 m thick gravelly sand, 0.4 m thick fine sand overlying 0.2 m thick gravelly sand and 0.2 m thick silty sand overlying 0.2 m thick gravelly sand were investigated. The Soil-Water Characteristic Curves (SWCC) and permeability functions of the materials used in CBS are presented in Figure 8. The inclination angle of the CBS model was 30°. The experimental results (Figure 9) showed that no breakthrough into the coarse-grained layer was observed during Test I (rainfall tests of 4.9 mm/h for 9 hours) and Test II (rainfall tests of 5.8 mm/h for 6 hours). These results indicated that

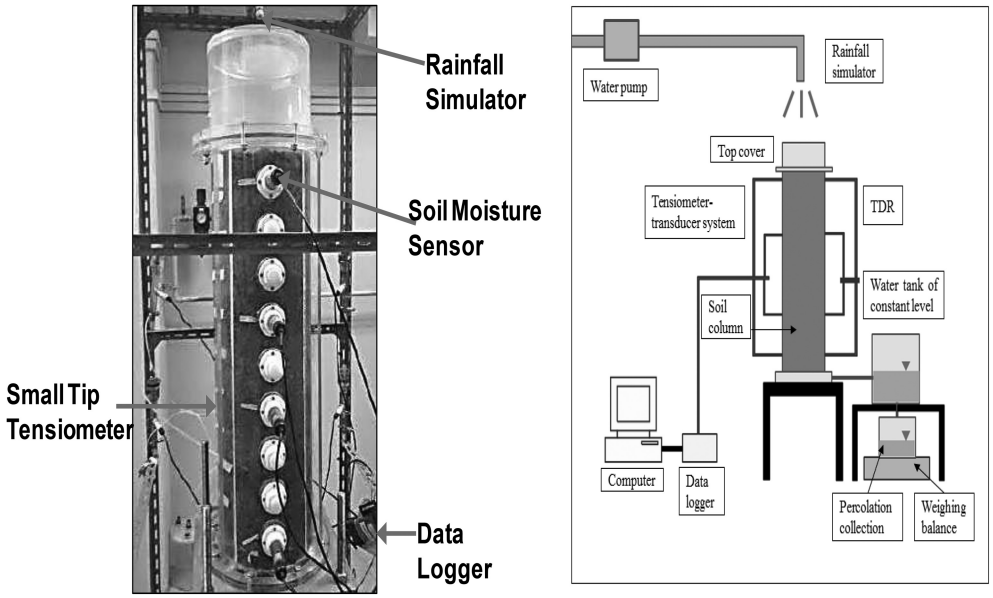


Figure 4. Infiltration column for 1-D infiltration test of CBS.

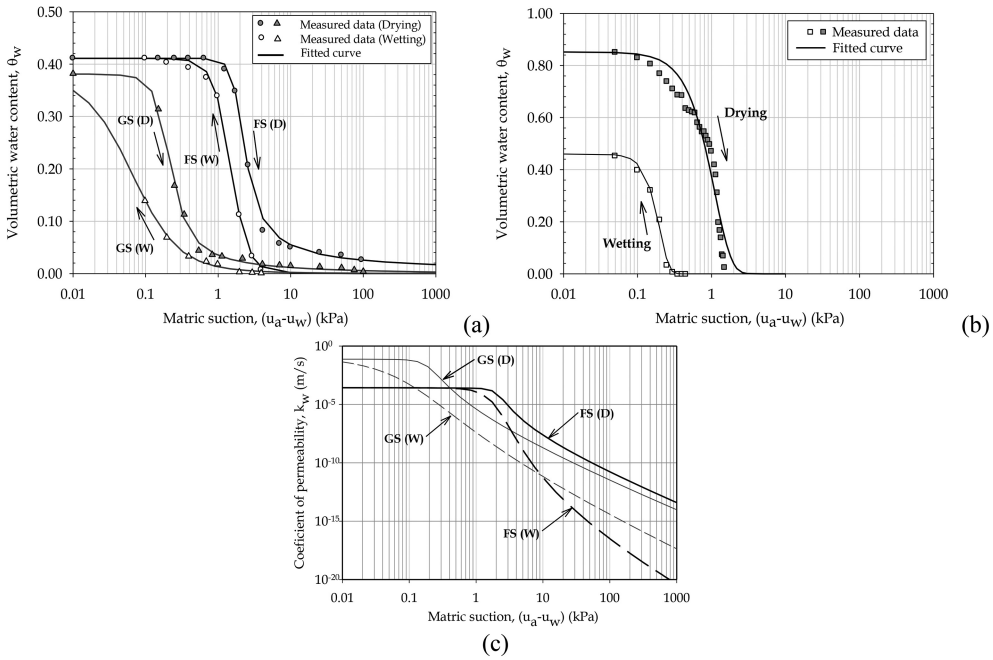


Figure 5. (a) Soil-Water Characteristic Curves of Gravelly Sand (GS) and fine sand (FS) (b) Geotextile-water characteristic curves of the geosynthetic material (c) permeability functions of GS and FS during drying (D) and wetting (W) process (Krisdani et al., 2006).

CBS has high potential application as a slope stabilization measure against rainfall-induced slope failures.

The CBS materials must be selected properly with careful consideration of the controlling parameters of the materials in order to design an effective CBS. Rahardjo et al. (2007a) carried out a parametric study to obtain the controlling parameters of the CBS materials. The results show that there are three controlling parameters that must be considered in selecting the CBS materials, which are: the ratio between the water-entry value of the fine-grained layers and the coarse-grained layers (ψ_w-ratio), the water-entry value of

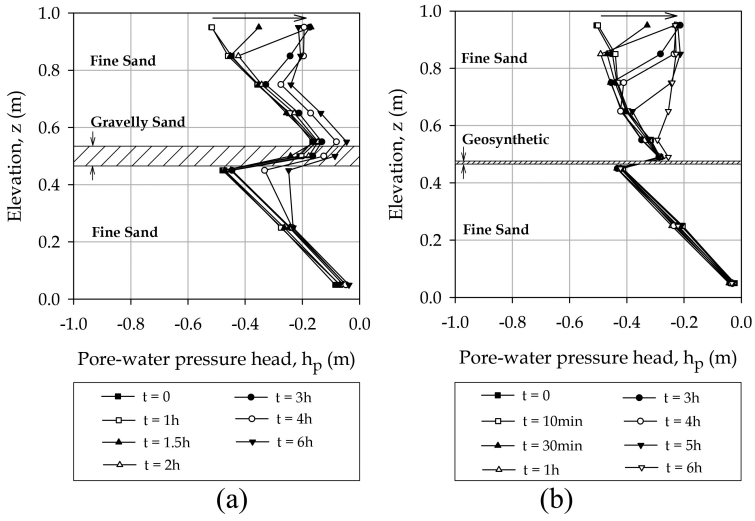


Figure 6. Pore-water pressure head profiles of fine sand overlying (a) gravelly sand and (b) geosynthetic material within CBS during rainfall (Krisdani et al., 2006).

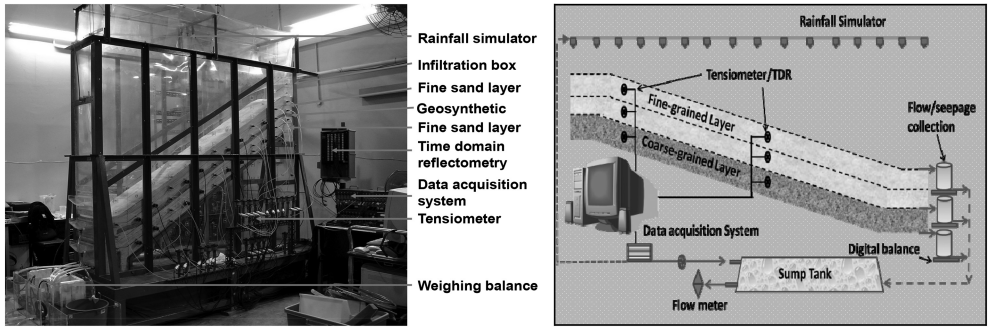


Figure 7. 2-D infiltration box of capillary barrier system.

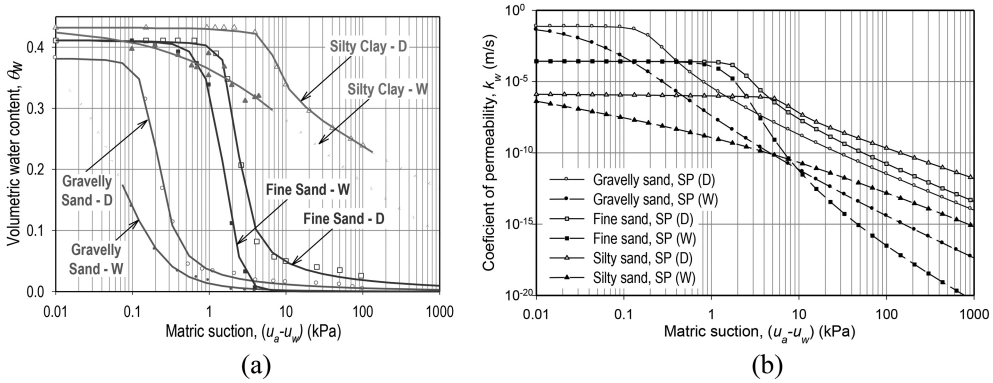


Figure 8. (a) Soil-water characteristic curves and (b) permeability functions of materials used in 2-D infiltration test (Tami et al., 2004b).

the coarse-grained layer and the saturated coefficient permeability of the fine-grained layer.

Rahardjo et al. (2007a) concluded that the minimum ψ_w-ratio should be 10 to create the barrier effect between the fine-grained layer and the coarse-grained layer and to minimize the infiltration of water into the coarse-grained layer. The coarse-grained layer must have a low water-entry value (preferably less than 1 kPa) in order to maintain the effectiveness of the CBS for a longer period of time. The saturated coefficient

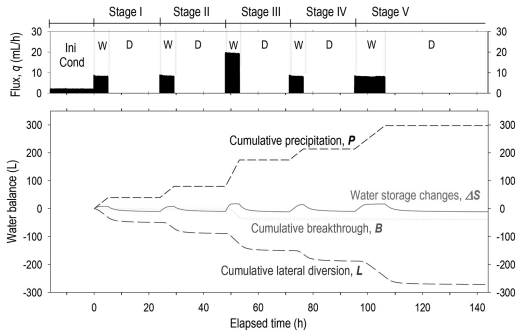


Figure 9. Water balance observed in 2-D infiltration tests of fine sand (40 cm thickness) over gravelly sand (20 cm thickness) (Notes: W = wetting, D = drying) (Tami et al., 2004b).

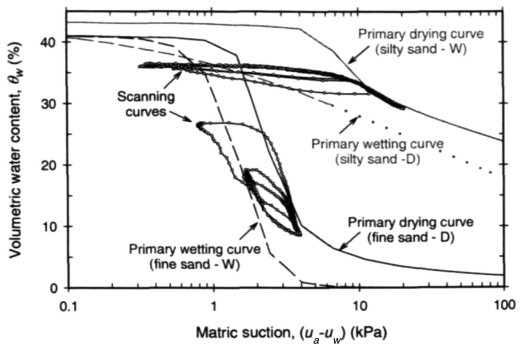


Figure 10. Comparison of scanning curves measured on silty sand and fine sand (Notes: D = drying and W = wetting) (Tami et al., 2007).

permeability of the fine-grained layer should not be too low (preferably higher than 10^{-5} m/s) to allow water to flow out from the fine-grained layer by lateral diversion and as a result, the CBS remains effective.

In addition to the three controlling parameters, Tami et al. (2007) concluded that the fines content within fine-grained layers also affect the effectiveness of the CBS. The fine-grained layer should have low fines content so that the SWCC of the soil for the fine-grained layer will be steep and the soil is able to drain a large amount of water during a rainfall as shown by the scanning curves of SWCC in Figure 10. As a result, the storage capacity of the fine-grained layer is increased rapidly after the rain stops. In addition, the use of soils with low fines content as the fine-grained layer prevents the development of cracks in the upper layer of CBS, especially during dry period when matric suctions are high.

4 CONSTRUCTION AND INSTRUMENTATION OF CAPILLARY BARRIER

CBSs were constructed and instrumented at three different locations in Singapore, Bedok, Ang Mo Kio and

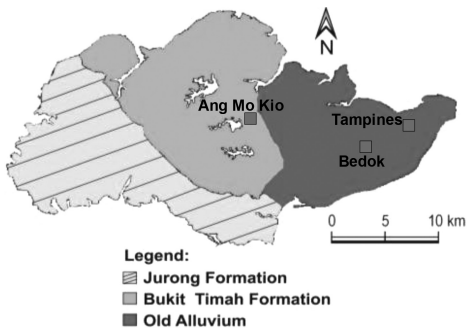


Figure 11. Location of slopes with capillary barrier system in Singapore.

Tampines (Figure 11). Rahardjo et al. (2007b) investigated the performance of CBS as a slope cover for minimizing rainwater infiltration into a cut slope in residual soil from Old Alluvium at Bedok that experienced a shallow slip failure. CBS was constructed using 10 cm thick fine sand as the fine-grained layer contained within a 20 cm thick geocell and placed above the geosynthetic material as the coarse-grained layer (Figure 12). Several tensiometers were installed within the CBS area to investigate the performance of the CBS during and after rainfall (Figure 12). The results showed that the CBS constructed in the repaired slope at Bedok was able to reduce the infiltrating rainwater and to maintain the negative pore-water pressure in the slope down to 2.1 m depth from the ground surface. Therefore, CBS can be used to repair a slope and maintain the stability of the slope against rainfall-induced slope failure.

Rahardjo et al. (2012b) constructed a CBS on a residual soil slope from Bukit Timah Granite at Ang Mo Kio (Figure 11) that had experienced numerous rainfall-induced slope failures in the past. The CBS was built using 20 cm thick fine sand as the fine-grained layer and placed above 20 cm thick granite chips as the coarse-grained layer (Figure 13). Both fine sand and granite chips were contained within a 20 cm thick cellular confinement system. The total area of the slope covered with a capillary barrier system was approximately 140 m^2. The slope had a total height of 8 m, a slope angle of 37° at the toe of the slope and 33° at the 5 m height of the repaired area.

Laboratory test results indicated that the specific gravity, liquid limit, and plastic limit range of the residual soil were in the range of 2.64–2.68, 53–66%, and 36–38%, respectively (Rahardjo et al., 2012b). The slope consisted of silty sand and silt with moderate to high plasticity (sand-silt) with a unit weight of 13.52 kN/m^3, an effective cohesion of 8 kPa, an effective friction angle of 33°, and a ϕ^b angle of 25°. The fine-grained layer was compacted to a relative density (D_r) between 70–90%, or to the required dry density (ρ_d) of 1.56 Mg/m^3. The coarse-grained layer was compacted to a relative density (D_r) between 70–90%, or to the required dry density (ρ_d) of 1.65 Mg/m^3. The

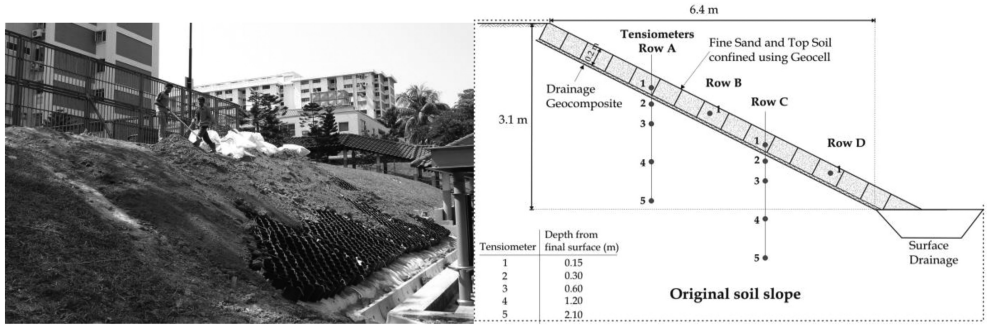


Figure 12. Construction and field instrumentation of CBS in Bedok (Rahardjo et al., 2012a).

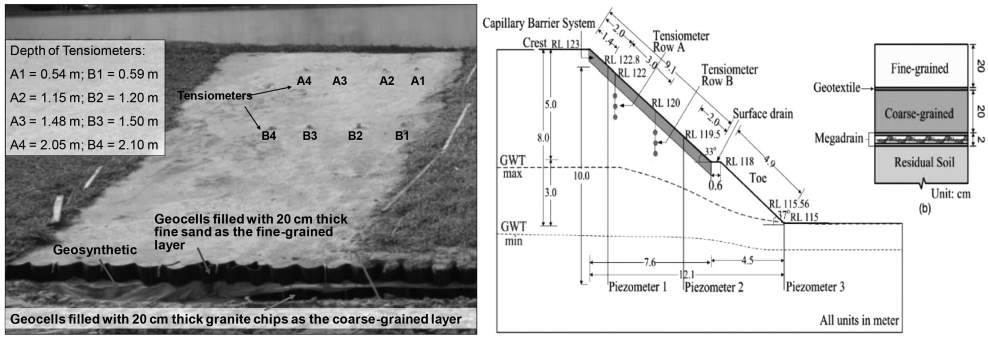


Figure 13. Construction and field instrumentation of CBS in Ang Mo Kio (Rahardjo et al., 2012b).

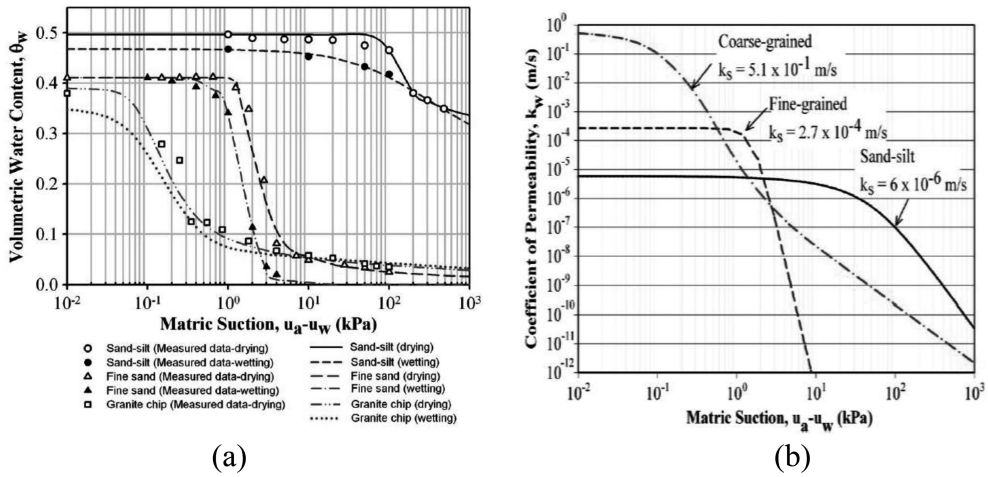


Figure 14. (a) SWCCs and (b) permeability functions of CBS materials and residual soil from Bukit Timah Granite (Rahardjo et al., 2012b).

SWCCs and permeability functions of CBS materials and residual soil from Bukit Timah Granite are presented in Figure 14.

Tensiometers and piezometers were installed within the slope with and without CBS at Ang Mo Kio. The monitoring results as shown in Figure 15 demonstrate that pore-water pressures under the slope with CBS were able to maintain negative values of pore-water pressures (matric suction) under rainfall conditions. The negative pore-water pressure contributed to the shear strength of the soil, resulting in the slopes to be less susceptible to failure. On the other hand, the pore-water pressure under the original slope was easily affected by the rainfall infiltration. Figure 15 illustrates that the pore-water pressures under the original slope followed the rise and fall of rainwater infiltration.

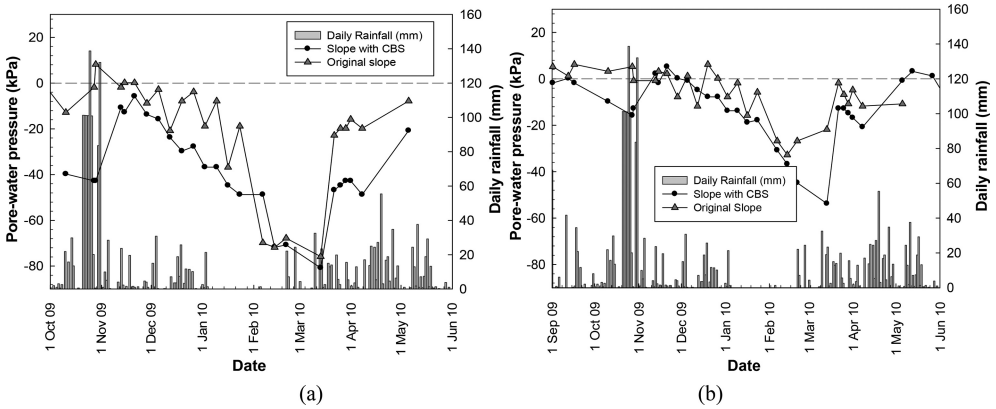


Figure 15. Pore-water pressure variations of slope with and without CBS at Ang Mo Kio observed from tensiometers at (a) Row A and (b) Row B.

Pore-water pressures under the original slope were higher than pore-water pressures under the slope with CBS when rainfall occurred.

In Singapore, about 2 million ton of wastes from construction and demolition are generated. For sustainable development, recycling and reuse of these wastes are important. Therefore, Rahardjo et al. (2013b) constructed a CBS with recycled concrete aggregates (RCA) as the coarse-grained layer. In addition, a CBS with Secudrain as the coarse-grained layer was also constructed. Both CBSs were constructed at the residual soil slope in Old Alluvium at Tampines (Figure 11) using fine sand as the fine-grained layer. The slope had a height of 8.2 m, a length of 22.6 m, and a slope angle of 20°. The area of the slope covered with the CBS was about 40 m^2 in the middle section of the slope (Figure 16). The investigated slope consisted of two different layers of residual soil.

Laboratory test results indicated that the specific gravity, water content and dry density range of the residual soil are 2.61–2.66, 16.8%–25.8%, 1.31 Mg/m^3–1.73 Mg/m^3, respectively. The slope consisted of sandy materials with effective cohesion varying from 2 to 5 kPa, effective friction angle varying from 29° to 37°, and ϕ^b angle varying from 20° to 27°. The fine-grained layer was compacted to a relative density (D_r) between 70–90%, or to the required dry density (ρ_d) of 1.58 Mg/m^3.The coarse-grained layer was compacted to a relative density (D_r) between 70–90%, or to the required dry density (ρ_d) of 1.53 Mg/m^3. The SWCCs and permeability functions of CBS materials and residual soil from Old Alluvium are presented in Figures 17 and 18, respectively.

Several instruments were installed in the CBS slope and the original slope at Tampines to investigate the effectiveness of the capillary barrier system in minimizing rainwater infiltration and improving stability of the slope. Four tensiometers at different depths (0.6 m, 1.2 m, 1.5 m and 2 m) were installed in the middle of the CBS slope. Three piezometers were installed near

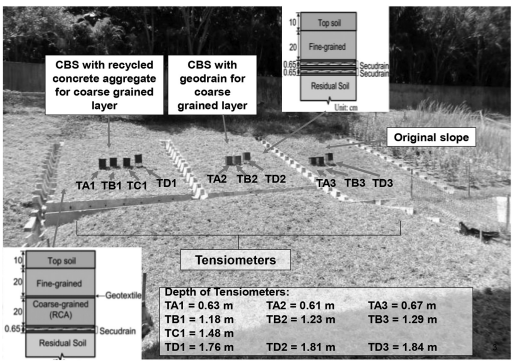
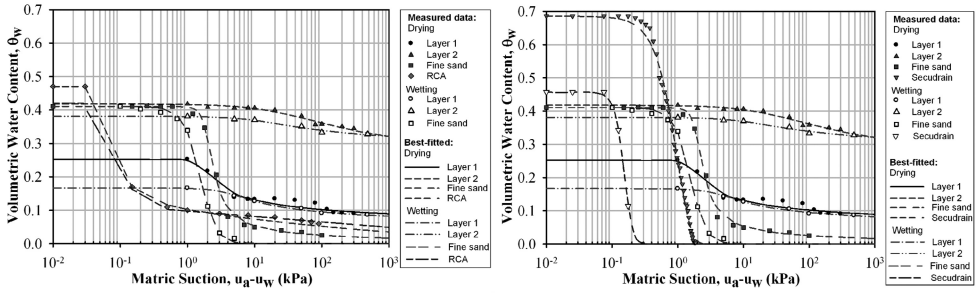


Figure 16. Construction of capillary barrier system in Tampines.

the crest, in the middle and near the toe of the original slope to observe the variation of groundwater table location during dry and wet periods. A rainfall gauge was installed at the crest of the original slope to obtain the rainfall data. All instruments were connected to a data acquisition system to monitor the instruments' readings continuously during dry and wet periods. The monitoring results of tensiometers showed that the negative pore-water pressures during rainfall were relatively constant at the CBS slope as compared with those in the original slope (Figure 19). In addition, the negative pore-water pressures in the CBS slope were higher than those in the original slope. It showed that the CBS was effective to minimize the infiltration of rainwater into deeper layers of the slope at Tampines. The results also showed that the recycled concrete aggregates can be used to replace gravel as a coarse-grained layer in CBS.

Slope stability analyses were carried out by incorporating the pore-water pressures measured on 30 July 2010 to obtain the variation in factor of safety of slope at Tampines using Bishop's simplified method



(a) (b)

Figure 17. SWCCs of residual soil from Old Alluvium and materials for CBS with (a) RCA and (b) Secudrain as coarse-grained layer (Rahardjo et al., 2013b).

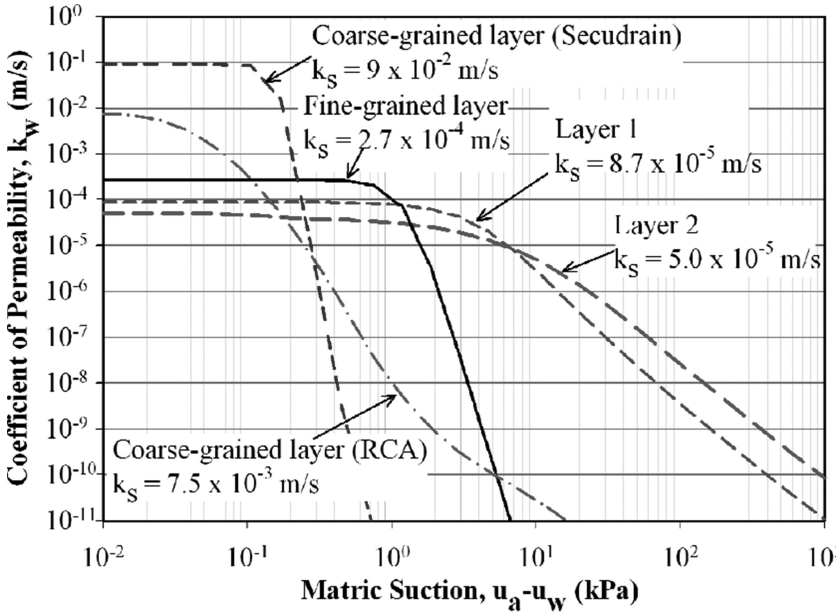
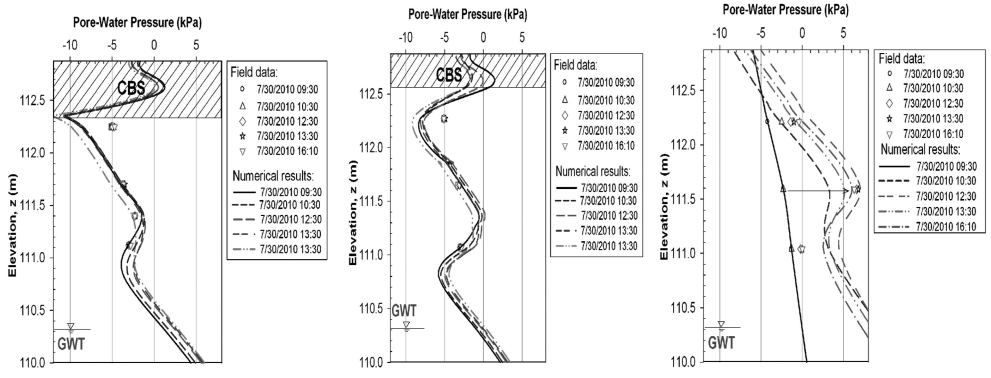


Figure 18. Permeability functions of residual soil from Old Alluvium and materials for CBS (Rahardjo et al., 2013b).



(a) (b) (c)

Figure 19. Pore-water pressure profiles of slopes (a) with CBS using RCA as coarse-grained layer, (b) with CBS using Secudrain as coarse-grained layer and (c) without CBS (Rahardjo et al., 2013b).

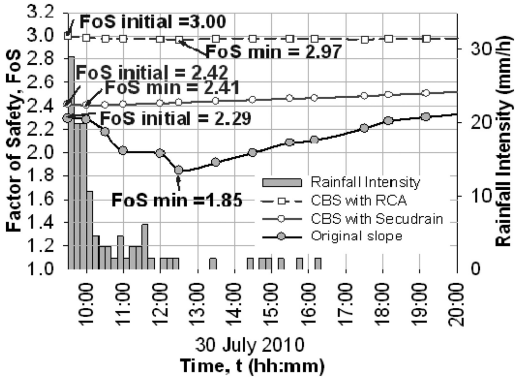


Figure 20. Factor of safety variations for slopes with and without CBS during and after rainfall (Rahardjo et al., 2013b).

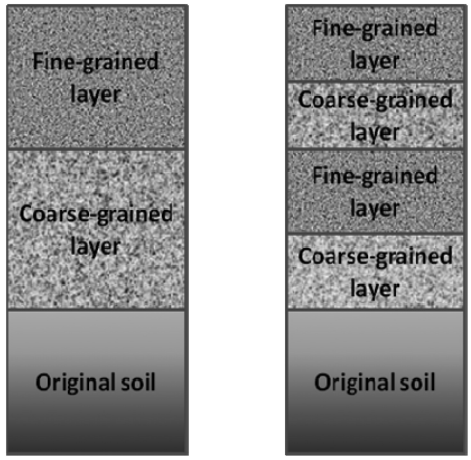


Figure 21. Cross sections of dual capillary barrier system.

of slices. Figure 20 indicates that the factor of safety of slope with CBS can be maintained constant during rainfall. The analyses show the good performance of both slopes covered with the CBS during rainfall as compared to the original slope, illustrating the benefits of a capillary barrier system as part of a slope protection.

5 DEVELOPMENT OF DUAL CAPILLARY BARRIER (DCB) SYSTEM

Harnas et al. (2014) developed a new system, called Dual Capillary Barrier (DCB) to increase water storage of the capillary barrier and therefore, increase the lateral diversion of the capillary barrier. A DCB consists of two stacks of CBS (SCB or Single Capillary Barrier) as shown in Figure 21. The advantages of a DCB over SCB can be illustrated using comparisons of typical pore-water pressure profiles and volumetric water contents at initial and breakthrough conditions presented in Figures 22a and 22b, respectively (Rahardjo et al., 2013c). For SCB, at breakthrough condition, the pore-water pressure at the bottom of the fine grained layer is similar to the water-entry value of the coarse-grained layer. The pore-water pressure decreases linearly (45°) with increasing height of the fine-grained layer. For DCB, similar principle applies to the pore-water pressure at the bottom and throughout the height of the fine-grained layers at breakthrough condition. The pore-water pressure at the upper coarse-grained layer is assumed to be constant as represented by a vertical line with a value similar to the water-entry value of the coarse-grained layer. The storage capacity of SCB and DCB is calculated by measuring the area bounded by the volumetric water content profile at the initial condition and the volumetric water content profile at breakthrough condition. The typical storage capacity of DCB can be observed to be higher than the storage capacity of SCB as shown in Figure 22b.

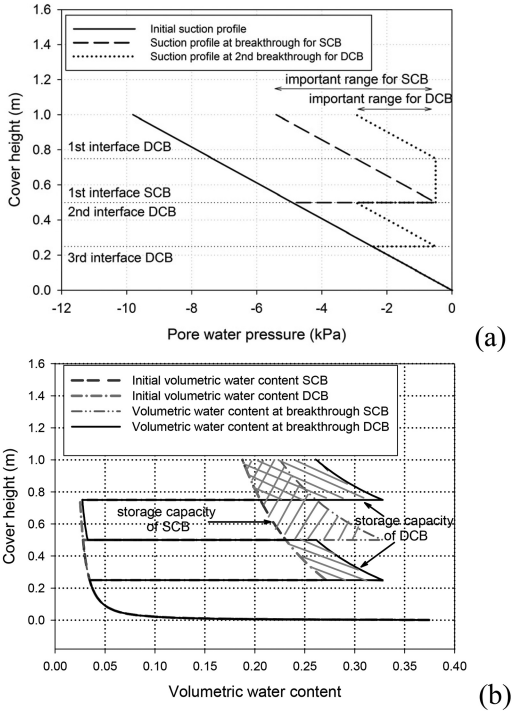


Figure 22. Theory of (a) pore-water pressure and (b) volumetric water content for DCB system at initial and breakthrough conditions (Rahardjo et al., 2013c).

A DCB column was constructed in the laboratory using Fine Recycled Asphalt (FRA) as the fine-grained layer and Coarse Recycled Asphalt (CRA) as the coarse-grained layer in the laboratory. The Water Characteristic Curves (WCC) and permeability functions of FRA and CRA are presented in Figure 23. One-dimensional (1-D) infiltration test was carried out

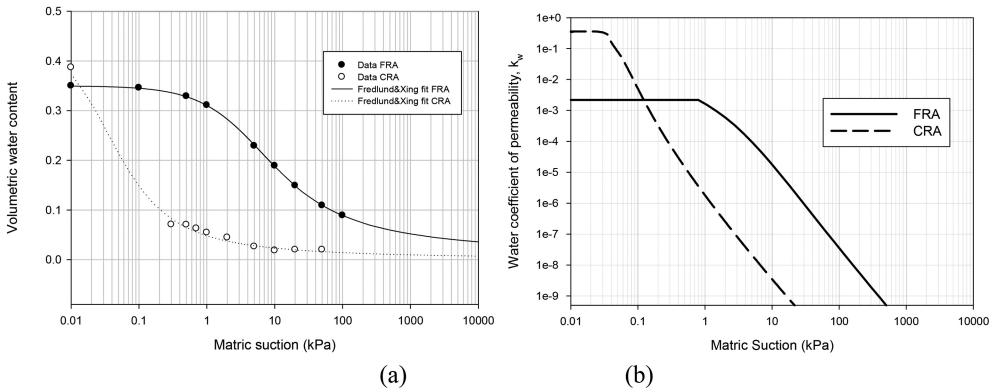


Figure 23. (a) WCCs and (b) permeability functions of FRA and CRA (Harnas et al., 2014).

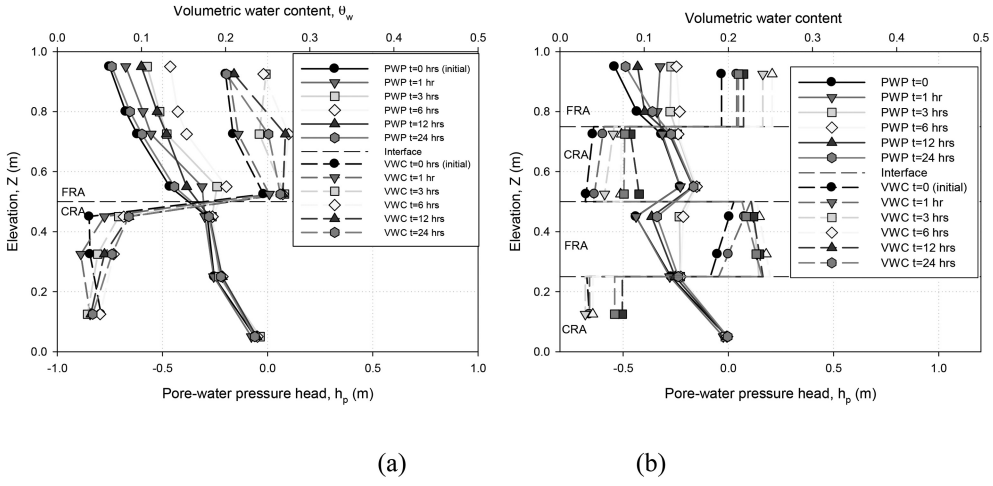


Figure 24. Pore-water pressure profiles and volumetric water contents of (a) SCB and (b) DCB during rainfall (Harnas et al., 2014).

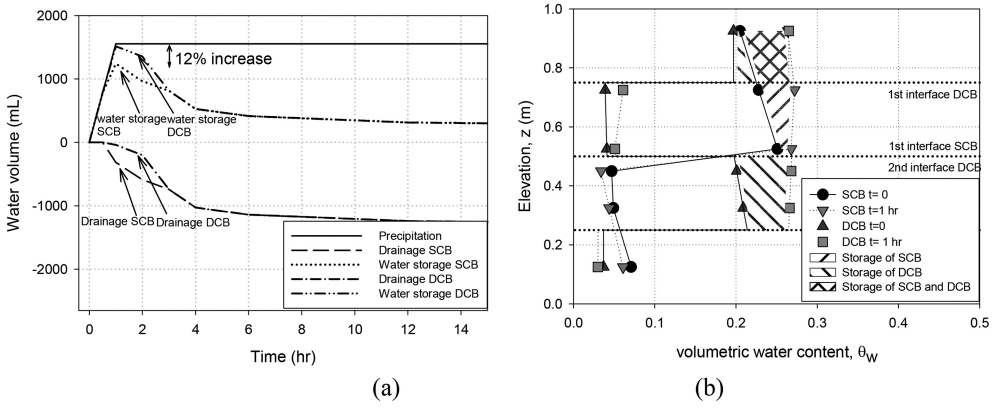


Figure 25. Comparison of (a) water balance and (b) water storage of SCB and DCB (Rahardjo et al., 2013c).

to study the performance of DCB as compared to SCB. The pore-water pressure profiles and volumetric water contents during rainfall are presented in Figures 24a and 24b, for SCB and DCB, respectively. The comparison of water storage and water balance of SCB and DCB are presented in Figure 25. The results indicated that DCB was able to increase the water storage by about 12% as compared to that of

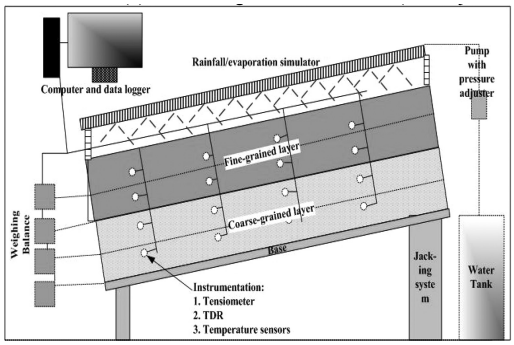


Figure 26. Schematic diagram of infiltration box for the investigation of lateral diversion capacity of DCB.

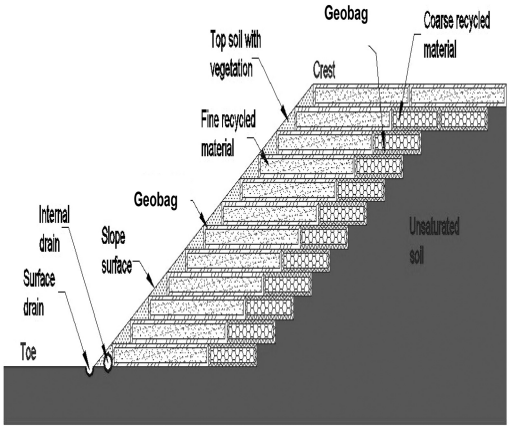


Figure 27. Schematic diagram of geobarrier system.

SCB. The increase in water storage of a DCB compared to SCB could create an increase in the lateral diversion of DCB. The lateral diversion capacity of DCB is currently being investigated in NTU using an infiltration box illustrated in Figure 26.

6 DEVELOPMENT OF GEOBARRIER SYSTEM

To create more usable space, steep slopes in urban cities become a necessity. Besides the conventional retaining wall for steep slopes, current research work at NTU investigates the possibility of combining CBS and geobag, called GeoBarrier System (GBS), to prevent rainwater infiltration, improve slope stability and to act as a retaining wall (Figure 27). The GBS can be deployed to optimise the design of underground structures for multi-level basement car parks (Figure 28) and undulating terrains in Singapore town including slope improvement works. Prior to implementation of GBS, a pilot study is being carried out by constructing GBS at a residual soil slope in Bukit Timah Granite, Singapore (Figure 29). Comprehensive instruments including weather station will be installed within GBS

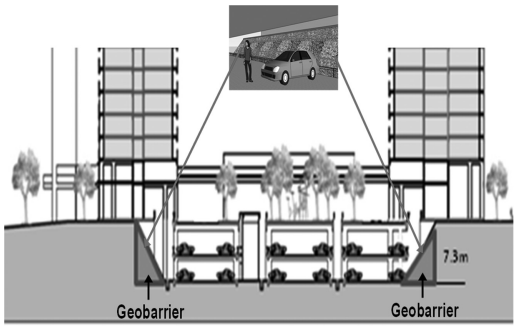


Figure 28. Wall-free multi-level basement carpark.

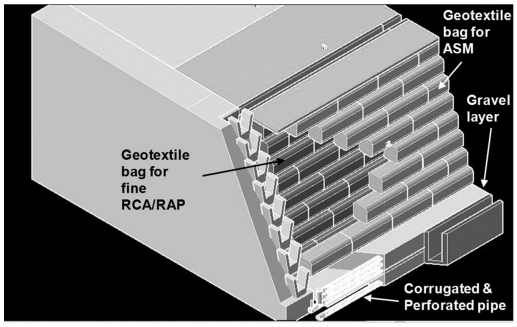


Figure 29. Geobarrier system to be constructed at residual soil slope in Bukit Timah Granite on Orchard Boulevard (Note: ASM: Approved soil mixture).

to assess the performance of GBS in minimizing rainwater infiltration into the underlying residual soil and in maintaining the stability of steep slope during and after rainfall. GBS is environmental friendly as it uses recyclable materials and does not use steel or concrete. It is a cost effective green system that reduces carbon footprint when compared to a reinforced concrete retaining wall. The surface material of GBS can also be vegetated to blend in with the surrounding environment. Flexibility of the GBS enables it to accommodate creep and long term differential ground settlements.

7 CONCLUSIONS

The mechanics and performance of Capillary Barrier System (CBS) as slope protection have been investigated through laboratory tests, numerical analyses and field tests over a period of more than a decade at Nanyang Technological University, Singapore. Three CBS have been constructed and fully instrumented in three different locations in Singapore. The results of this study on CBS illustrate good performance of CBS as a slope protection against rainfall-induced slope failures.

The controlling parameters for designing capillary barrier system have been identified through this study. In addition, the use of recycled materials as capillary

barrier materials have been studied and found to be feasible. An improved system using Dual Capillary Barrier (DCB) has been developed and shown to be more superior to the Single Capillary Barrier (SCB). A retaining wall system incorporating capillary barrier principles, named GeoBarrier System (GBS) has also been developed for its use in underground basement carpark. This study on capillary barrier system (single and dual) and geobarrier system for slope protection and retaining wall exemplifies the application of unsaturated soil mechanics to engineering practice.

ACKNOWLEDGEMENT

The author is grateful to the following organizations and persons who have contributed to this study. The supports received from Nanyang Technological University, Ministry of Education, Housing & Development Board, Ministry of National Development are greatly acknowledged. The study was accomplished mainly through the research works of the PhD students under the author's supervision, Dr. Denny Tami, Dr. Henry Krisdani, Dr. Alfrendo Satyanaga, Dr. Fakhrur Rozy Harnas and his Master students, Dr. Yang Hong, Dr. IGB Indrawan and Mr. Hua Chai Juay. The supports received from Prof. Leong Eng Choon and Prof. D.G. Fredlund, Dr. Johnny Wong Liang Heng and Mr. Ng Yew Song are greatly acknowledged with special mention goes to Mr. Wang Chien Looi who is a strong supporter for the application of unsaturated soil mechanics into engineering practice.

REFERENCES

Aubertin, M., Cifuentes, E., Apithy, S.A., Bussiere, B., Molson, J., Chapuis, R.P. & Maqsoud, A. 2006. An investigation of factors that influence the water diversion capacity of inclined covers with capillary barrier effects. *In Proceeding of the fourth international conference on unsaturated soils, 2–6 April 2006, Carefree, Arizona*.

Broms, B.B. & Wong, K.S. 1991. Landslides, *in Foundation Engineering Handbook*, VanNorstand Reinhold, New York, pp. 410–446.

Bussiere, B., Aubertin, M., & Chapuis, R.P. 2003. The behaviour of inclined covers as oxygen barriers. *Canadian Geotechnical Journal* 40(3): 512–535.

Chai, P.S. 2008. *Capillary barrier effect on the response of residual slope to rainfall infiltration*, Master Thesis, University Teknologi Malaysia. Malaysia

Chatterjea, K. 1989. *Observations on the fluvial and slope processes in Singapore and their impact on the urban environment*, PhD Thesis, National University of Singapore. Singapore.

Harnas, F.R., Rahardjo, H. & Wang, J.Y. 2013. Design of Landfill Cover using Construction and Demolition Waste: Material Characterization and Numerical Modelling. *In Proceedings of 18th Southeast Asian Geotechnical & Inaugural AGSSEA Conference, 29–31 May 2013, Singapore*

Harnas, F., H. Rahardjo, E.C. Leong & J.-Y. Wang. 2014. An Experimental Study on Dual Capillary Barrier using Recycled Asphalt Pavement Materials. *Canadian Geotechnical Journal* 51(10): 1165–1177.

Huang, M., Barbour, S., Elshorbaggy, A.A., Zettl, J.D & Si, B. 2011. Infiltration and drainage processes in multilayered coarse soils. *Canadian Journal of Soil Science* 91: 77–81.

Indrawan, I.G.B., Rahardjo, H. & Leong, E.C. 2006. Effects of Coarse-Grained Materials on Properties of Residuals Soil. *Journal of Engineering Geology* 82(3): 154–164.

Intergovernmental Panel on Climate Change (IPCC). 2013. *Climate Change: The Physical Science Basis. Contribution of Working Group I to the Fifth Assessment Report of the Intergovernmental Panel on Climate Change*. Final draft underlying scientific-technical assessment. Stockholm, Sweden. 205 pp.

Kampf, M., Holfelder, T., & Montenegro, H. 2003. Identification and paramaterization of flow processes in capillary barriers. *Water Resources Research* 39(10).

Khire, M., Benson, C., & Bosscher, P. 1999. Capillary Barriers in Semi-Arid and Arid Climates: Field Data & Model Predictions Made with UNSAT-H. *Journal of Geotechnical and Geoenvironmental Engineering* 125(8): 518–527.

Kueper, B.H. & Frind, E.O. 1991. Two phase flow in heterogeneous porous media. *Water Resources* 27: 1059–1070

Krahn, J., Fredlund, D.G. & Klassen, M.J. 1989. Effect of soil suction on slope stability at Notch Hill. *Canadian Geotechnical Journal* 26: 269–278.

Krisdani, H., Rahardjo H. & Leong, E.C. 2005. Behaviour of Capillary Barrier System Constructed using Residual Soil. *In Proceeding of Geo-Frontiers Conference on Innovative Barriers and Barrier Materials*, Austin, Texas, USA, 24–26 January, pp. 1–15.

Krisdani, H., Rahardjo, H. & Leong, E.C. 2006. Experimental Study of 1-D Capillary Barrier Model using Geosynthetic Material as the Coarse-Grained Layer. *In Proceedings of 4th International Conference on Unsaturated Soils. Geo Institute. Phoenix, Arizona, U.S.A.*, 2–5 April, pp. 1683–1694

Krisdani, H., Rahardjo, H. & Leong, E.C. 2010. Application of Geosynthetic Material as a Coarse-grained Layer in Capillary Barriers. Special Issue on Unsaturated Geosynthetics. *Geosynthetics International Journal* 17(5): 323–331.

Miyazaki, T. 1988. Water flow in unsaturated soil in layered slopes. *Journal hydrology* 102:201–214.

Miyazaki, T. 1990. Visualization of refraction water flow in layered soils. *Soil Science* 149:317–319.

Montazer, P. & Wilson, W.E. 1984. Conceptual hydrological model of flow in the unsaturated zone, Yucca Mountain, Nevada, *U.S. Geological Survey Water Resources Investigation Report No. 84-4345*. 55pp.

Morii, T., Suzuki, T., Kawai, T., Kobayashi, K. & Matsumoto, K. 2013. Performance of Capillary Barrier System included in test shallow land waste repository. *Bulletin Faculty Agriculture Niigata University* 65(2):179–186.

Morris, C.E. & Stormont, J.C. 1998. Evaluation of Numerical Simulations of Capillary Barrier field tests. *Geotechnical and Geological Engineering* 16: 201–213.

Morris C.E. & Stormont J.C. 1999. Parametric study of unsaturated drainage layers in a capillary barrier. *Journal of Geotechnical and Geoenvironmental Engineering* 125:1057–1065.

Ng, C.W.W., Springman, S.M. & Alonso E.E. 2008. Monitoring the Performance of Unsaturated Soil Slopes. *Geotechnical and Geological Engineering* 26(6): 799–816.

Oldenburg, C.M. & Pruess, K. 1993. On numerical modeling of capillary barriers. *Water Resources Research* 29: 1045–1056.

Ong, T.H. 2002. Rainfall-induced slope failures: controlling factors and mitigation with capillary barriers. *Master of Engineering Thesis, School of Civil And Environmental Engineering, Nanyang Technological University, Singapore*.

Rahardjo, H., Li, X.W., Toll, D.G & Leong, E.C. 2001. The effect of antecedent rainfall on slope stability. *Journal of Geotechnical and Geological Engineering, special Issue on Unsaturated and Collapsible Soils* 19: 371–399.

Rahardjo, H., Ong, T.H., Rezaur, R.B. & Leong, E.C. 2007a. Factors Controlling Instability of Homogeneous Soil Slopes under Rainfall Loading. *ASCE Journal of Geotechnical and Geoenvironmental Engineering*. 133(12): 1532–1543.

Rahardjo, H., Satyanaga, A. & Leong, E.C. 2007b. Characteristics of Pore-Water Pressure Response in Slopes During Rainfall. *Proceedings of 3rd Asian Conference on Unsaturated Soils. Nanjing, China, 21–23 April, 493–498.*

Rahardjo, H., Rezaur, R.B. & Leong, E.C. 2009. Mechanism of rainfall-induces slope failures in tropical regions, *In Proceedings of the First Italian Workshop on Landslides (IWL): Rainfall-induced landslides: Mechanisms, Monitoring Techniques and Nowcasting Models for Early Warning Systems. Dipartimento Di Ingegneria Civile, Seconda Universita di Napoli, Naples 1:31–42.*

Rahardjo, H., Satyanaga, A. & Leong, E.C. 2012a. Unsaturated Soil Mechanics for Slope Stabilization. *Geotechnical Engineering, Southeast Asian Geotechnical Journal* 43(1) 48–58.

Rahardjo, H., Santoso, V.A., Leong, E.C., Ng., Y.S. & Hua, C.J. 2012b. Performance of an Instrumented Slope Covered by a Capillary Barrier System. *ASCE Journal of Geotechnical and Geoenvironmental Engineering* 138(4): 481–490.

Rahardjo, H., Satyanaga, A. & Leong, E.C. 2013a. Effects of Flux Boundary Conditions on Pore-water Pressure Distribution in Slope. *Journal of Engineering Geology, Special Issue on Unsaturated Soils: Theory and Applications* 165:133–142.

Rahardjo, H., Santoso, V.A., Leong, E.C., Ng, Y.S., Tam, C.P.H. & Satyanaga, A. 2013b. Use of Recycled Crushed Concrete and Secudrain in Capillary Barrier for Slope Stabilization. *Canadian Geotechnical Journal* 50: 1–12.

Rahardjo, H., Satyanaga, A., Harnas, F.R., Wang, J.Y. & Leong, E.C. 2013c. Capillary Barrier System for Landfill Capping. *Proceedings of Coupled Phenomena in Environmental Geotechnics (CPEG), a TC 215 Symposium, 1–3 July 2013, Torino, Italy*

Sakamoto, A., Nishigaki, M. & Yokota, S. 2011. Study of capillary barriers that use industrial byproducts. *Journal of the Japan Society of Material Cycles and Waste Management* 22(3):190–200.

Stormont, J.C. & Anderson, C.E. 1999, Capillary Barrier Effect from Underlying Coarse Soil Layer, *Journal of Geotechnical and Geoenvironmental Engineering ASCE* 125(8): 39–51.

Sugiyama, Y., Nomura, S., Kawai, K. & Mimura, M. 2014. Numerical evaluation for performance of a capillary barrier system. *In Proceedings of the International Conference on Unsaturated Soil, 2–4 July 2014, Sydney, Australia*.

Suter, G.W., Luxmoore, R.J. & Smith, E.D. 1993. Compacted soil barriers at abandoned landfill sites are likely to fail in the long term, *Journal Environmental Quality* 22(2): 217–226.

Sun, J., Yuen, S.T.S. & Fourier, A.B. 2010. The effect of using a geotextile in a monolithic (evapotranspiration) alternative landfill cover on the resulting water balance. *Waste Management*, 3: 2074–2083.

Takayama, Y., Ikuta, Y., Iizuka, A., Kawai, K., Taki, T., Sakao, R. & Ichikawa, Y. 2014. Numerical evaluation of multiple soil barrier system preventing water infiltration. *In Proceedings of the international conference on Unsaturated Soil, 2–4 July 2014, Sydney, Australia.*

Tami, D., Rahardjo, H., Leong, E.C. & Fredlund, D.G. 2004a. Design and Laboratory Verification of a Physical Model of Sloping Capillary Barrier. *Canadian Geotechnical Journal*, 41(5): 814–830.

Tami, D., Rahardjo, H., Leong, E.C. & Fredlund, D.G. 2004b. A Physical Model for Sloping Capillary Barriers. *Geotechnical Testing Journal*, 27(2): 173–183.

Tami, D., Rahardjo, H. & Leong, E.C 2007. Characteristics of Scanning Curves of Two Soils. *Soils and Foundations*, 47(1): 97–109

Tidwell, V.C., Glass, R.J., Chocas, C., Barker, G. & Orear, L. 2003. Visualization experiment to investigate capillary barrier performance in the context of a yucca mountain emplacement drift. *Journal of Contaminant Hydrology* 62(63): 287–301.

Toll, D.G., Rahardjo, H. & Leong, E.C. 1999. Landslides in Singapore. *In Proc. 2nd International Conference on Landslides, Slope Stability and the Safety of Infra-Structures, Singapore, July 27–28*, pp. 269–276.

Weeks, S.W., Sander, G.C., Braddock, R.D. & Matthews, C.J. 2004. Saturated and unsaturated water flow in inclined porous media. *Environmental Modeling & Assessment* 9:91–102.

Yanful, E.K., Simms, P.H., Rowe, R.K. & Stratford, G. 1999. Monitoring and Experimental Soil Waste Cover near London, Ontario, Canada. *Geotechnical and Geological Engineering* 17: 65–84.

Yanful, E.K., Mousavi, S.M. & Desouza, L.-P. 2006. A numerical study of soil cover performance. *Journal of Environmental Management* 81: 72–92.

Yang, H., Rahardjo, H., Wibawa, B. & Leong, E.C. 2004. A soil column apparatus for laboratory infiltration study. *Geotechnical Testing Journal* 27(4): 347–355.

Yang, H., Rahardjo, H. & Leong, E.C. 2006. Behaviour of Unsaturated Layered Soil Columns during Infiltration. *ASCE Journal of Hydrologic Engineering* 11(4), 329–337.

Unsaturated Soil Mechanics—from Theory to Practice – Chen et al. (Eds)
© 2016 Taylor & Francis Group, London, ISBN 978-1-138-02921-7

Evolution of mesoscale structures of unsaturated expansive soil and intact loess under various stress and hydraulic paths

Z.H. Chen
Department of Civil Engineering, Logistical Engineering University, Chongqing, China;
Jointly, Civil Engineering College, Guiilin Technology University, Guilin, China

Z.H. Yao
Engineering College, Air Force Engineering University, Xi'an, China

J.F Guo & Q.Q. Miao
Department of Civil Engineering, Logistical Engineering University, Chongqing, China

ABSTRACT: The evolution of the mesoscale structures of unsaturated expansive soil and loess was investigated using a CT-triaxial apparatus. The expansive soil was sampled from two different sites located in the canal slope of the Middle Line Engineering of Transfer Water from South to North in China. The loess samples, including Q_3 and Q_2 loess, were obtained from the sites of 11# Pumping Station in Lanzhou, Ningxia, and the site of Pucheng Power in Shaanxi province, respectively. Total 59 simples of expansive soil dividing into eight groups of CT-triaxial tests with controlled suction and net cell pressure were conducted under the conditions of loading, laterally unloading, constant net mean stress and wetting-drying circle, respectively. Total 49 simples of intact loess (Q_3 and Q_2) dividing into eight groups of CT-triaxial tests were carried out with controlled suction and net mean stress under the conditions of loading, laterally unloading and wetting, respectively. A number of CT images and CT data of the meso-structural evolution of the samples were obtained. A method for determining the yield stress was suggested. Some regularity of holes and cracks developing or closing in samples was discovered. It is shown that the macro-behaviors of soils are closely related to their meso-structural variations. For expansive soil, fissures initiate and grow during loading or during wetting-drying circles, and the yielding stress decreases as the soil damage continues. For intact loess, the holes and fissures in samples become smaller and smaller and even disappear during loading or during inundation, depending on the stress state, and the original structure of the loess can be changed, while a new homogeneous structure can be formed during wetting. Empirical equations were developed, based on the mean and standard deviation of CT data, to describe the evolution of the mesocale structures of the expansive soil and loess during loading and wetting-drying cycles or collapse process, respectively. Using these evolution equations, damage-elastoplasticity constitutive models for intact expansive soil and intact loess are developed and applied to the analysis of the deformation and stability of an expansive soil slope during excavation and rain infiltration-evaporation circles. The collapse deformation and the change of water content of an in-situ test of loess in Lanzhou are simulated under the wetting condition. This research demonstrates that the CT technology can be used to quantitatively characterize the evolution of the meso-structures of soils.

1 INTRODUCTION

Each type of soils, such as collapsible loess and expansive soil, has its own special macro-, meso-, micro-structures. The mechanical properties of soils are related to their interior factors (i.e., mineralogical composition and structure) and the outer factors (i.e., loading and environmental changes). For example, the strength of collapsible loess and expansive soil are very high during the dry seasons. However, the strength will decrease drastically when they are inundation. In addition, the two kinds of soils show opposite deformations during wetting, i.e., loess occurs collapse while expansive soil appears swelling. The two opposite phenomena can only be explained by their internal reasons. In 1994 the first author of the paper pointed out that constitutive relations of the special soils are related with their special micro-structure (Chen 1994). The characteristics and evolution laws of soil structure are important to establish their constitutive models. The structure of soil is divided into three levbels: macro, meso and micro. Macro-phenomenon is the outer manifestation of soil's inner structure while meso- and micro-structure show the mechanism and nature of the macro phenomenon.

Since 2000, a series of researches have been conducted on the meso-structure analysis of loess and expansive soil using the CT-triaxial apparatus by the

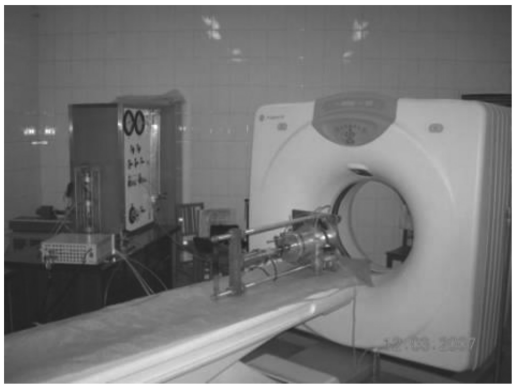


Figure 1. CT-triaxial apparatus research workstation.

authors (Chen et al. 2001, 2007, 2009, Lu et al. 2002a, b, Wei 2007, Zhu & Chen 2008, 2009, Fang et al. 2008a, b, 2010, 2011, Yao et al. 2010a, b, Li et al. 2010a, b, Wang et al. 2012a, b, 2013). In this paper, the meso-structure and evolution laws of expansive soil and loess under the loading and moisture changes were systematically investigated firstly; Then, the evolution laws were used to set up the damage-elasto-plasticity constitutive models and corresponding consolidation models for expansive soil and loess, respectively; Finally, the deformation and stability of a expansive soil slope are analyzed during excavation and rain infiltration- evaporation circles, and the collapse deformation and the change of water content of an in-situ test in Lanzhou are simulated during wetting.

2 EXPERIMENTAL EQUIPMENT

In recent years, great effort has been paid to study meso-structures and constitutive relations of special soils such as loess and expansive soil, by the authors. The matching of computerized tomography with triaxial test apparatus for unsaturated soils in 2001 was a good start (Chen et al. 2001). In 2004, a multifunctional triaxial apparatus of unsaturated soil combining with CT machine developed successfully (Chen et al. 2007), and over 30 of stress path tests on saturated soil, unsaturated soil and special soils can be conducted with the equipment. A triaxial apparatus to study wet-collapse and wet-swelling was developed (Zhu & Chen 2008) in 2005, and a GDS pressure-volume controller is used to control the hydraulic head and inundation capacity. The measuring accuracy of hydraulic pressure is 1 kPa and the measuring accuracy of inundation capacity is 1 mm. At last, the CT-triaxial apparatus research workstation (Wei 2007) was established in 2006 as shown in Figure 1. The CT machine made by GE is a spiral scanner type of Prospeed AL. Its spatial resolution is 0.38 mm and its density resolution is 0.3% (3 Hu). The technical details of the CT scanner are shown in table 1. All CT images are reconstructed by the GE system.

Table 1. The technical parameters of the CT scanner.

Voltage/ kv	Current/ mA	Time/ s	Thickness/ mm	Spatial resolution/ mm
120	165	3	3	0.38

The CT-triaxial apparatus not only can control suction, accurately measure deformation and inundation capacity, but also can dynamically nondestructively observe the meso-structural evolutions of the samples. It is a powerful tool to study the internal structure of soils.

3 GETTING STARTED

Crack is one of important structural feature, which influences the mechanical properties of expansive soil. In order to discover the characteristics of the crack evolution of expansive soil, 8 groups of tests including 59 samples were conducted (Table 2). The expansive soil samples were drawn from two sites located in the canal slope of the Middle Line of Transfer Water from South to North in China. The size of samples was 39.1 mm in diameter and 80 mm in height. These tests were CT-triaxial tests in loading and wet-dry circles. A total of 666 CT images and a number of CT data of the test samples were obtained.

3.1 *The characteristics of structure damage evolution of intact expansive soil during loading*

Fifteen CT-triaxial drained tests of undisturbed expansive soils with net cell pressure and suction controlled were conducted (see table 2, No.① and ③). The initial conditions and test parameters of samples are shown in table 3. However, only the data of sample 2# are listed since space is limited.

The scanning cross-sections which were marked 1 and 2 located at 1/3H and 2/3H from the top of specimen. Each sample was scanned 6 times and the scanning pictures were marked as a, b, c, d, e and f successively. 1a, 1b, 1c, 1d, 1e and 1f were corresponding to the cross-section of 1/3H (Figure 2). The CT images of sample 2# clearly illustrate that the structures of the samples change obviously from initial deformation to failure and several cracks gradually developed.

The test results of the samples indicate crack evolution rules. 1) The initial damage of structure of undisturbed expansive soil is distinct and heterogeneous in space. 2) Shear makes an obvious development of structure damage (which is from fissure development to several crack connection). 3) Both suction and cell pressure affect damage evolution. The higher the cell pressure or suction is, the lower the damage degree

Table 2. CT-triaxial tests performed for expansive soil.

Soil site	Sample	Number of test group (according to test condition and stress path)	test number	Image	Test time
Nanyang	Intact	① shear with suction = C & net cell pressure = C	6	72	2000
	Remold	② first stage: 5 of wet-dry circles at free state	12	66	
		second stage: shear with suction = C & net cell pressure = C	10	120	
Taocha	Intact	③ shear with suction = C & net cell pressure = C	9	82	2006
		④ shear with suction = C & net mean stress = C	3	20	
		⑤ shear with suction = C & axial stress = C, net lateral pressure decrease	3	18	
	Remold	⑥ first stage: 5 times of wet-dry circles at free state	4	48	2008
		second stage: soaking with net mean stress = C/deviatoric stress = C		92	
		⑦ first stage: 0–4 of wet-dry circles to cause different degree of damage	6	108	2009
		second stage: hydrostastic compression step by step			
		⑧ samples with through holes (different distribution),	6	100	2010
		Shear with suction = C & net cell pressure = C			
Total			59	726	

Table 3. Initial conditions and test parameters of sample 2#.

Initial conditions		Scanning sequence	Deviator tress/kPa	Deviator strain/%
Dry density ρ_d/g.cm^{-3}	1.68	a	0	0.00
		b	153	0.95
Water content w/%	22.1	c	302	3.30
Void ratio e	0.63	d	283	5.38
Matric suction s/kPa	100	e	238	8.19
Net cell pressure p/kPa	50	f	211	11.24

of sample will be. 4) The formation of fracture plane of undisturbed soil has several characteristics as follows: a) Inevitability: preexisting fissures, or weakness planes or large cavity, which are the weak areas of samples, easily extend to fracture plane (dash line in Figure 2). b) Randomness: there are no signs before fracture plane forming, however, fissure occurs with shear and develops to fracture plane (dash line in Figure 2). c) Correlation: new fracture plane grows due to other fracture planes (dash lines and ④ in Figure 2).

Taking the mean value of CT data of undisturbed samples as the base value, a damage variable can be defined as the relative difference of base value and the mean value of CT data in the process of tests. Damage evolution equation can be obtained through analysis on test date:

$$D_1 = D_0 + \exp\left(\frac{p_0}{p}\varepsilon_s^{s/p_{atm}}\right) - 1 \quad (1)$$

where D_0 is the initial value of damage variable, ε_s is deviator strain, s is suction, p_{atm} is atmospheric pressure, p and p_0 are spherical stress and pre-consolidation pressure, respectively.

Equation (1) can reflect the influence of deviator stress, pre-consolidation pressure, suction and initial damage degree on expansive soil in the process of shear. It is convenient to use equation (1) in constitutive relationship because of its simple style and a few of parameters involved.

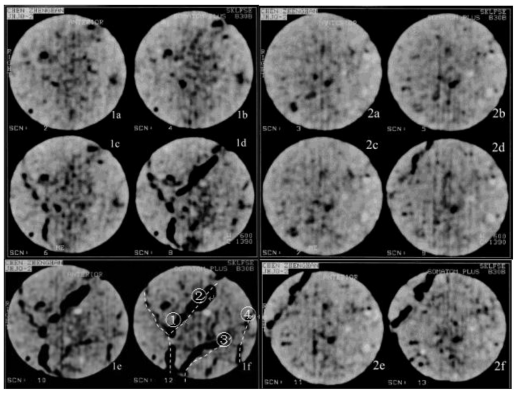


Figure 2. Scanning images during triaxial shear test of sample 2# of intact expansive soil.

3.2 *Characteristics of structure damage evolution of remolded expansive soil in the process of wet-dry circles*

Twelve wet-dry cycle tests of remolded expansive soils were carried out. Each sample went through 5 wet-dry circles (see table 2, No.②). The sizes and the scanning cross-sections of the samples were as same as in section 3.1. However, the scanning pictures were marked as a0∼a5 and b0 ∼ b5, successively, were corresponding to the cross section of 1/3H and 2/3H from

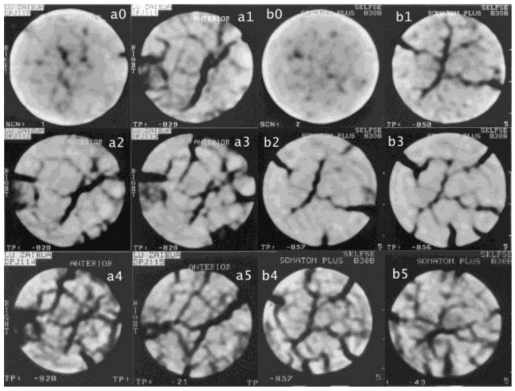


Figure 3. Scanning images through 5 times of wet-dry Circle of sample 5# of remolded expansive soil.

the top of specimen, respectively. The picture marked as a0 and b0 associated with the initial state of the specimen. A total of 66 CT images were obtained.

Let H and SD denote the mean value and the standard deviation of CT data of a scanning section, respectively. The results of the tests show that H decrease and SD augment as the times of wet-dry circles increase. The images show that the cracks initiate and extend continuously. At last, the crannies becomes connectivity each other as shown in Figure 3.

Taking the CT data corresponding to the initial state of specimen as the base value, a damage variable D_2 can be defined as the relative difference of base value and the value of CT data in the process of wet-dry circles tests.

The damage values related to various volumetric strains in wet-dry circle tests are show in Figure 4. Through curve-fitting, the damage evolution equation upon the wet-dry circle test is:

$$D_2 = \exp(A\varepsilon_v) \tag{2}$$

where A is a soil parameter, and ε_V is volumetric strain. It is obviously that the damage evolution equation is in good agreement with the experiments.

3.3 *Characteristics of structure damage evolution of intact expansive soil during net lateral pressure decreasing*

In order to simulate the case of slope excavation, three tests under the conditions of axial stress keeping constant whereas net lateral pressure decreasing for intact expansive soil simples were carried out (see table 2, No.⑤). The size and the scanning cross-sections of the samples were as same as in section 3.2. The suctions of the three simples were controlled to 100, 150 and 200 kPa, respectively. The initial net cell pressures of the tests were 200 kPa. It is found that failure for the three simples takes place when axial strains are less 1%. However, two cracks took shape (Figure 5). This result shows that slope excavation would induce fissures and landslide.

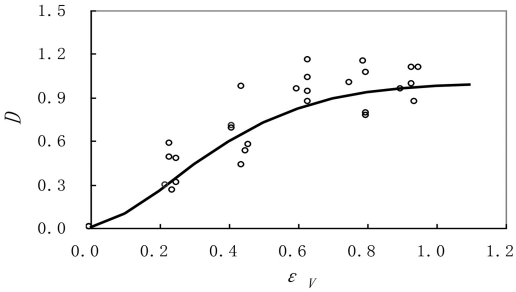


Figure 4. The damage values vs. volumetric strains of samples in the process of wet-dry circles tests.

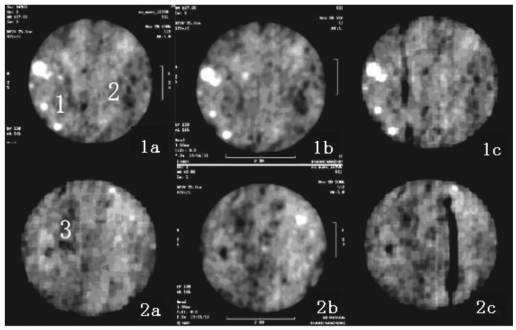


Figure 5. Scanning images during net cell pressure decreasing test of intact expansive soil.

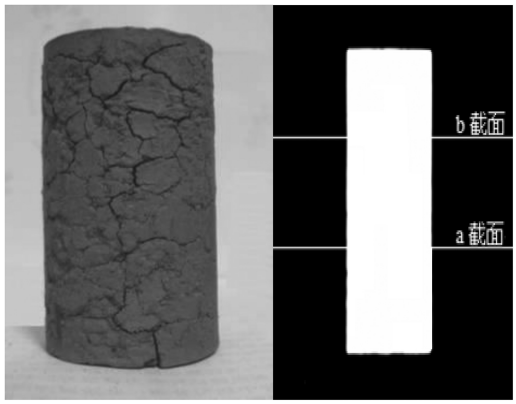


Figure 6. Photo of sample 3# after 3 wet-dry cycles (left) and scanning locations (right).

3.4 *Influence of structure damage to the yielding of remolded expansive soil*

In order to investigate the effect of structure damage to yield stress, 6 of hydrostastic compression tests with suction controlled were carried out (see table 2, No.⑦). Samples were undergone through 0–4 of drying-wetting cycles to make certain damage of their structure before test (see Figure 6). Test scheme and initial state index of 6 samples are shown in Table 4. The sizes of the samples were as same as in section 3 and the scanning cross-sections is shown in Figure 6.

Table 4. State parameters of samples and test scheme for test No.⑦ in table 2.

Sample number	Dry density	Water content	Degree of saturation	Suction	Wet-dry cycles
	$g \cdot cm^{-3}$	%	%	kPa	times
0#	1.500	26.55	88.39	0	0
1#	1.637	21.63	88.39	50	1
2#	1.586	23.32	88.29	50	2
3#	1.569	24.05	88.73	50	3
4#	1.506	26.44	88.67	50	4
5#	1.505	26.34	88.33	100	4

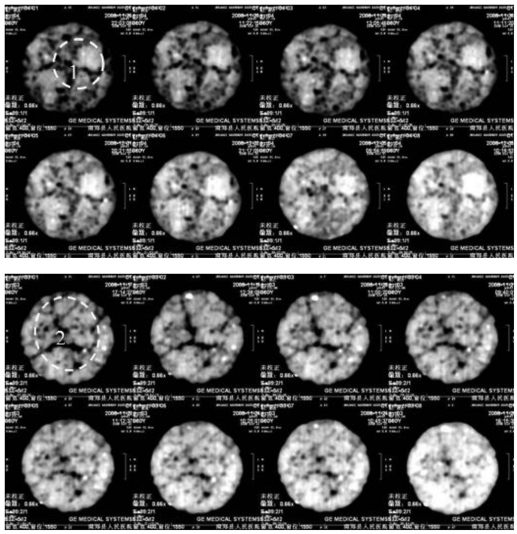


Figure 7. CT images of sample 4# at different loading state.

Every sample undergone 9 times scanning, which correspond to net mean stress reaching at 0, 25, 50, 75, 100, 150, 200, 250 and 350 kPa. Net mean stress is equal to 0 kPa represents the initial state of each sample before loading. A total of 108 CT scanning images were acquired.

Figure 7 shows CT images of sample 4# in different loading state. It is obvious that cracks and fissures in the sample close gradually as loading.

Figure 8 shows relationship between specific volume and net mean stress. There is a turn point on each curve in Figure 8. The stress of the turn point can be taken as yielding stress. Yielding stresses can also be determined with the help of CT data as shown in Figure 9(a) and Figure 9(b).

The yielding stresses of 5 samples are arranged in Table 5. It can be seen that the more drying-wetting cycle, the less the value of yielding stress. In other words, yielding stress decreases as the degree of damage increase.

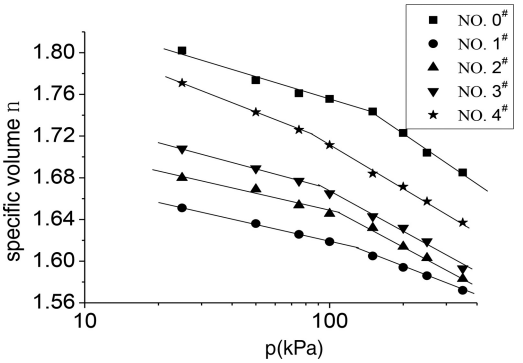
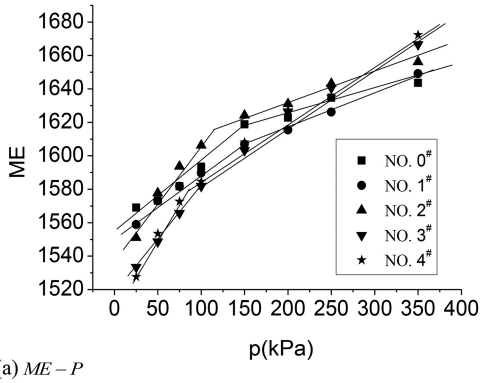
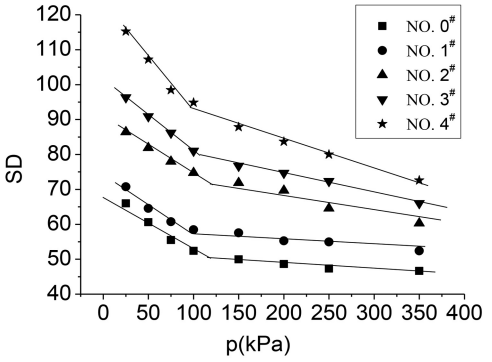


Figure 8. Relationship of $v - \lg p$ of samples.



(a) $ME - P$



(b) $SD - P$

Figure 9. Net hydrostatic pressure p vs. ME and SD.

A parameter, m_p, is proposed to reflect the structural change of sample during loading as follows:

$$m_p = \frac{ME - ME_i}{ME_f - ME_i} \tag{3}$$

where ME_i, ME_f and ME are the CT numbers before loading, at failure and at any time during loading process, respectively. Figure 10 shows the relationship

Table 5. Yielding stress of samples.

Samples number	Yielding stress (1)	(2)	(3)	Average value
0#	150.34	153.78	139.93	148.01
1#	134.58	145.94	122.35	134.29
2#	116.61	125.28	109.49	116.95
3#	94.25	100.75	91.97	95.73
4#	62.14	66.12	62.11	63.46

Yielding stress determined from: (1) Figure 8; (2) Figure 9(a); (3) Figure 9(b), (c)

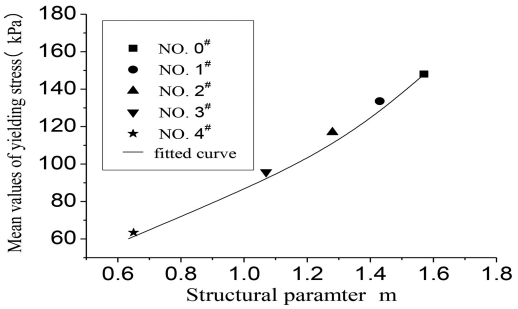


Figure 10. Relationship of yielding stress and parameter m.

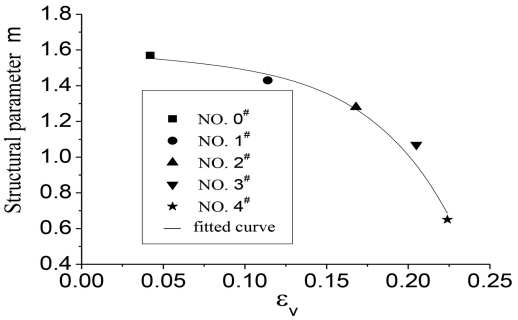


Figure 11. Relationship of ε_v vs. parameter m.

curve of yielding stress vs. structure parameter m. The curve in Figure 10 can be fitted with the following equation

$$p_0 = p_{0i}\exp(m - m_{0i}) \tag{4}$$

where p_{0i} and m_{0i} are the yielding stress and structure parameter of the sample without undergoing dry-wet cycles (i.e., simple $0^{\#}$ in table 4).

The relationship of m vs. ε_v is shown in Figure 10 and can be described by the following equation:

$$m = m_{0i} - \exp(a + b\varepsilon_v) \tag{5}$$

where a and b are the constant.

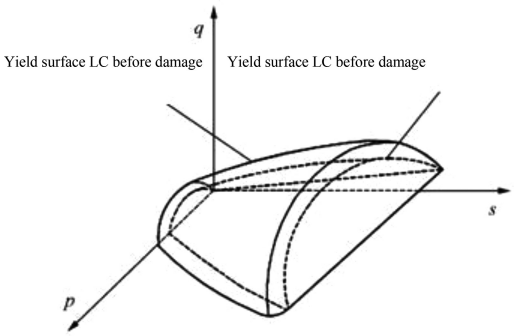


Figure 12. Configuration of yielding surface after damage.

Substituting Eq. (5) into Eq. (4), a modified mode of BExM proposed by Gens & Alons (1992) is gained as follows

$$f_1(p,q,s) \equiv q^2 - M^2(p + p_s)[p_{0i}\exp(-\exp(a + b\varepsilon_v)) - p] \tag{6}$$

Eq. (6) links the macroscopic volumetric strain to yield stress, and provides a convenience for engineering application.

Figure 12 shows configuration of yielding surface after damage. It can be seen that yield surface would shrink as structure damage increases.

3.5 *Structure evolution of remolded expansive soil during triaxial soaking test after wet-dry cycles*

For purpose of study the evolution of fissure and crack during triaxial soaking test, 4 tests of remolded expansive soil were conducted. The tests consisted of two stages. Firstly, the samples were undergone through 3 wet-dry circles to produce fissures and cracks, and then CT- triaxial soaking tests were carried out (see Table 2, No.⑥). In the first stage, the scanning cross-sections were as same as in Figure 6, and 6 times scanning were taken for each section. However, in the second stage, 5 scanning cross-sections, labeled as a, b, c, d and e corresponding to 1/6, 2/6, 3/6, 4/6 and 5/6 of height of simple from the bottom of the sample, were selected for each sample as shown in Figure 13, and scanning conducted when the soaking water was 0, 5, 10, 15, and 20 g for each section. Table 6 shows the initial index and stress state of the 4 simples.

Figure 14 shows the parts of scanning images of simple 4#, and Figure 15 is the scanning images of cross-sectional b of sample 1#. It is evident that cracks tend to close as soaking water. In other words, the structure of soil is repaired. However, the degree of crack close depending on the stress state and the amount of soaking water.

A parameter m is suggested to describe the degree of structure repair of soil during soaking, i.e.,

$$m = \frac{ME - ME_i}{ME_f - ME_i} \tag{7}$$

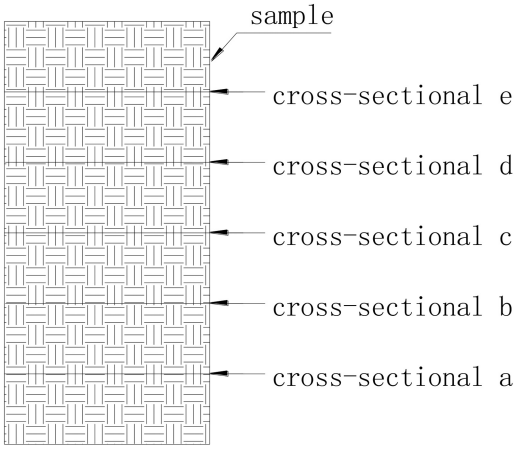


Figure 13. Scanning cross-sections for triaxial soaking test.

Table 6. Initial index and stress state of the samples before soaking.

Sample number	Dry density	Water content	Ambient pressure	Devitor stress
	g·cm^{-3}	%	kPa	kPa
#1	1.78	4.74	50	50
#2	1.79	4.61	50	100
#3	1.77	4.70	100	50
#4	1.76	4.66	100	100

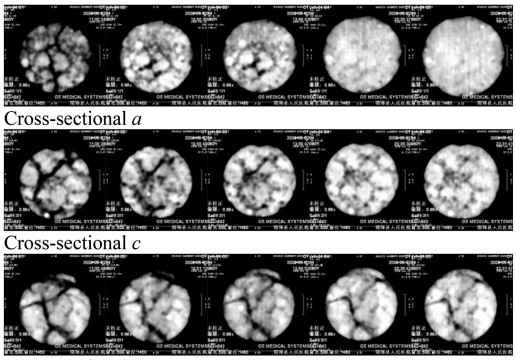


Figure 14. CT images of cross-sections a, c and e of sample 4# corresponding to the amount of soaking water.

where, ME_i is the CT value corresponding to the end of the third wet-dry cycle, ME_f is the CT value when the cracks close completely during triaxial soaking test, ME is the CT scanning number in the wetting process at any time.

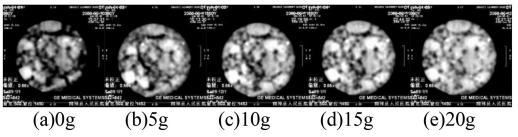


Figure 15. CT images of cross-sectional b of sample 1# corresponding to the amount of soaking water.

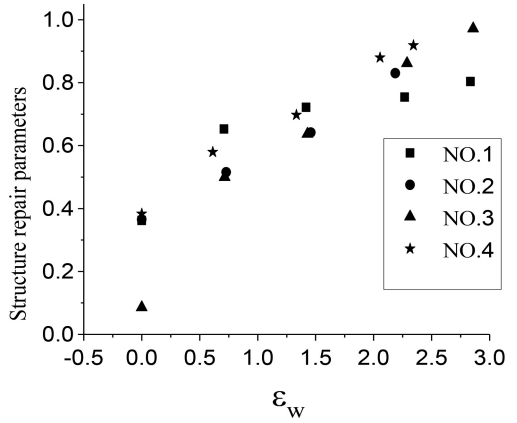


Figure 16. The relationship of m vs. ε_w.

In addition, a dimensionless parameter about water content change is defined as

$$\varepsilon_w = (w - w_0) / w_0 \tag{8}$$

where, w_0 is initial water content, w is water content during soaking test at any time.

Figure 16 shows the test data in $m - \varepsilon_w$ coordinate frame and the relationship of m and ε_w can be fitted as follows

$$m = m_0 + \exp[\frac{p}{q + p_{atm}}(a\varepsilon_w)] - 1 \tag{9}$$

where, m_0 is the initial value of structural repair parameter, p net mean stress, q deviatoric stress, p_{atm} atmospheric pressure, a is a test parameter and a equals to 0.32 with the help of multiple regression method.

Equation (9) is the evolution rule of structural repair which reflects the influence of net mean stress and deviator stress as well as water content on crack enclose.

Figure 17 shows the relationship between fitted and measured structural repair parameter of the 4 samples.

3.6 *The effect of damage location on the mechanical behaviors of remolded expansive soil*

For the sake of exploration the effect of damage location on the mechanical behavior of expansive soil, a series of triaxial shear tests were carried out (see table 2, No.⑧). 5 remolded samples were labeled as

simple A, B, C, D and E, respectively (Figure 18). The initial damage of each simple are demonstrated as follows. There is no damage in simple A. Simple B has a through hole with 3 mm diameter which locates in the centre symmetric axis of the simple. A through hole with 6 mm diameter in simple C locates in the centre symmetric axis of the simple. There is a through hole with 6 mm diameter in simple D, however, it deviates 9.8 mm from the centre symmetric axis of the simple. There are 4 through holes with 3 mm diameter in simple E, and they are random distribution (Figure 19). The areas of holes of simple B, C and D are equal.

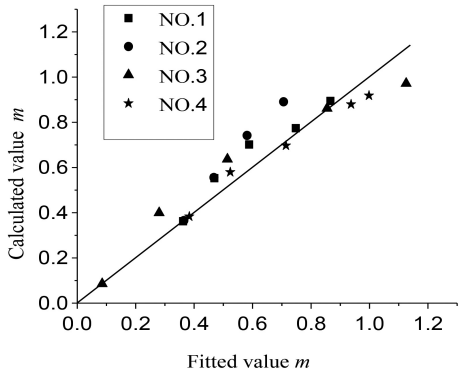


Figure 17. Comparing the calculated value with measuring value.

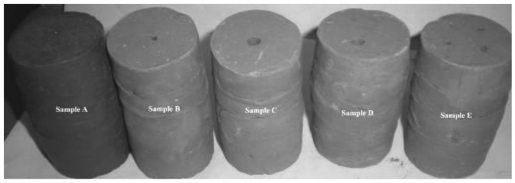


Figure 18. Photographs of samples after tests.

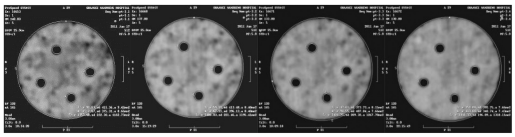


Figure 19. CT images of the section e of sample E.

The initial dry density of samples is 1.55 g/cm^3. 100 kPa of net cell pressure and 50 kPa of suction were maintained for each simple during test. 5 scanning cross-sections of each sample were as same as in Figure 13. Each section were scanned 4 times which correspond to axial strain reaching at 0%, 5%, 10% and 15% (Figure 19).

It is found that the curves of deviator stress vs. axial strain of simple C, D and E are approximately coincidence. In other words, the degree of damage only depends on the total area of holes instead of their distribution.

4 STRUCTURE EVOLUTION OF LOESS

Loess distributes widely in the North China and it covers an area of 440,000 km^2. The main body of loess in china mantles hills and plateaus around the famous Loess Plateau (with an area of 273,000 km^2) of the middle reaches of the Yellow River Valley. Engineering problems and geological disasters like collapse, dilapidation, landslide and earthquake were encountered frequently, and all these were caused by the unique composition and structure of loess, et al.

Collapsibility is the most important feature of loess. However, collapsibility depends on the meso-structure of loess. In order to discover the characteristics of the meso-structure evolution of loess, 8 groups of CT-triaxial tests including 49 samples of Q_3 loess and Q_2 loess were conducted (Table 7). The samples of

Table 7. CT-triaxial tests performed for loess.

Soil site	Soil	Number of test group (according to test condition and stress path)	Test number	Image	Test time
11# Pumping Station In Ningxia	Intact Q_3	① First stage: suction = C, net cell pressure = C, deviator stress = C Second stage: wetting until suction equals to zero Third stage: deviator increase with net cell pressure = C	6	273	2007
Pucheng Power station In Shaanxi	Intact Q_2	② shear with suction = C & net cell pressure = C	8	84	2008
		③ shear with water content = C & cell pressure = C	4	42	
		④ wetting until saturated with cell pressure = C & deviator stress = C	4	124	
Lanzhou Technology University	Intact Q_3	⑤ First stage: suction = C & net cell pressure = C Second stage: axial stress = C & net lateral pressure decrease	12	168	2009–2010
		⑥ First stage: suction = C & net cell pressure = C Second stage: wetting until suction equals to zero	9	90	
		⑦ First stage: suction = C & net cell pressure = C Second stage: wetting until suction equals to zero Third stage: axial stress = C & lateral pressure decrease	3	24	
		⑧ First stage: suction = C & axial stress = C, Second stage: net lateral pressure decrease to a target value Third stage: wetting until suction equals to zero	3	42	
Total			49	847	

Q_3 loess were drawn from two sites located in 11# Pumping Station in Ningxia province and Lanzhou Technology University, China. The samples of Q_2 loess were drawn from the sites located in Pucheng Power Station of Shaanxi province, China. A total of 847 CT images and a number of CT data were obtained.

4.1 *The structure evolution of Q_3 loess during loading and collapsing*

The samples are undisturbed Q_3 loess drawn from the site of 11# pumping station in Ningxia province. Six tests were conducted (see table 7, No.①). The size of samples was 39.1 mm in diameter and 80 mm in height. The initial conditions and test parameters of the samples are shown in table 8. Each sample was scanned 6 sections (Figure 20), and each section was scanned from 6 to 8 times. The scanning pictures were marked as a, b, c, d, e, f, g and h corresponding to a section in successive scanning. A total of 273 CT images were obtained.

4.1.1 *Analysis of CT images and deformation of samples during loading*

Figure 21 shows the Scanning images of 5th section of sample 3# of Q_3 loess during loading. The scanning pictures were marked as a, b, c, d, e, f, g and h corresponding to the initial state, the end of consolidation, and deviator stress (q) equal to 25, 50, 75, 100, 150 and 200 kPa of the 5th section (Table 9). H and SD in table 9 are the mean value and the standard deviation of CT data of the 5th section.

It is clear from Figure 21 and Table 9 that consolidation has significant effect on the meso-structure of sample, and there is no evident change in the meso-structure of sample 3# before deviator stress less than 150 kPa. In addition, the defect region (black part in Figure 21) not vanishes completely at the end of loading.

4.1.2 *The relationship of meso-structure evolution and macro-mechanical reaction during collapse*

The CT-triaxial collapse tests of Q_3 loess have been done under various mass of inundation. The initial conditions and test parameters of sample 4# are shown

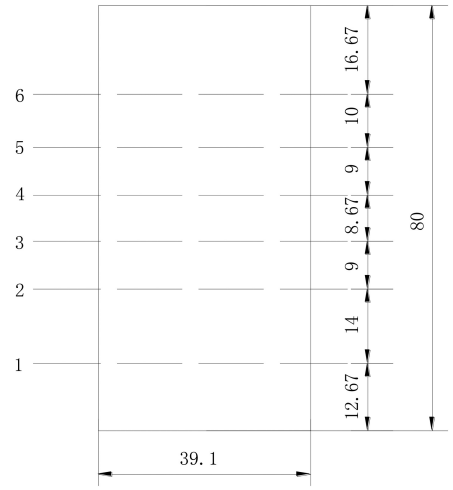


Figure 20. Scanning position (length unit: mm).

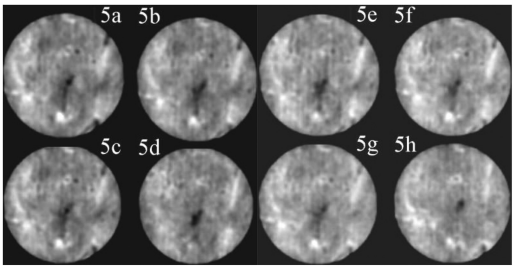


Figure 21. Scanning images of 5th section of sample 3# of Q_3 loess during loading.

Table 9. CT data and stress state of sample 3# during loading.

Stress state	Scan sequence	5th Section H	5th Section SD
Initial state	a	821.1	49.4
End of consolidation	b	854.6	44.7
25 kPa	c	856.5	44.7
50 kPa	d	852.7	41.4
75 kPa	e	854.1	42.6
100 kPa	f	854.0	41.7
150 kPa	g	887.0	45.9
200 kPa	h	927.2	43.4

Table 8. Initial physical parameters and stress states of samples before soaking.

No. of sample	Initial dry density ρ_d/g.cm^{-3}	Initial water content w/%	Void ratio e	Net cell pressure $(\sigma_3 - u_a)$/kPa	Matric suction s/kPa	Deviator stress q/kPa	Water pressure during soak/kPa
1#	1.31	11.0	1.08	100	150	0	4
2#	1.31	11.0	1.08	200	150	0	12
3#	1.32	11.0	1.04	100	150	200	14
4#	1.32	11.0	1.05	100	250	0	12
5#	1.31	11.0	1.06	100	150	100	14
6#	1.30	11.0	1.08	100	150	250	14

Table 10. Test data of during soaking of sample 4#.

Sample state	Scan sequence	Volume strain ε_v/%	Deviator strain ε_s/%
Initial state	a	0	0
End of consolidation	b	1.6	0
Soak water 7.656 g	c	0.54	0
Soak water 16.481 g	d	2.09	0
Soak water 22.169 g	e	3.19	0
Soak water 28.921 g	f	4.27	0
Soak water 36.605 g	g	4.45	0
Soak water 62.042 g	h	4.79	0

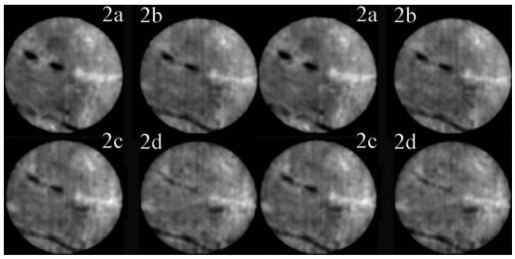


Figure 22. Scanning images during triaxial collapse of 2nd section of sample 4# of intact Q_3 loess.

in table 10. The scan images of CT-triaxial inundation tests of Q_3 are show in Figure 22 and 23. From the CT images, the following understanding can be summarized.

1) For certain stress state, the original structure of the loess is damaged during collapse and a new stable homogeneous structure is formed simultaneously. In the CT images, the fissures and the cavity in the undisturbed loess samples shrink gradually, even disappear at last.

2) Either spherical stress or shear stress can lead to collapse including volume strain and shear strain. The 1#, 2# and 4# samples (Table 8) are in hydrostatic state of stress, and their collapsible volume strains are 4.3%, 1.27% and 4.79%, respectively. It can be seen that the structure of 4# sample occurs a substantial change from an non-homogeneous (even with cracks) to a quite homogeneous state. For example, from Figure 22-2b to Figure 22-2c, the mean value of the CT data increases from 829.06 to 983.26 with an increment of 154.2. However, from Figure 22-2f to Figure 22-2g and from Figure 23-3f to Figure 23-3g, the mean values of the CT data change only in the fractional part.

The above two opinions proposed by the first author of the paper in 1986 firstly (Chen & Liu 1986a,b), and now are proved by the CT images, which give the visual evidence to the structure changes of the loess in the process of collapse. These two characteristics of collapse also show that collapse is different from shear failure, in other words, shear deformation during collapse process of loess is generally limited and taking

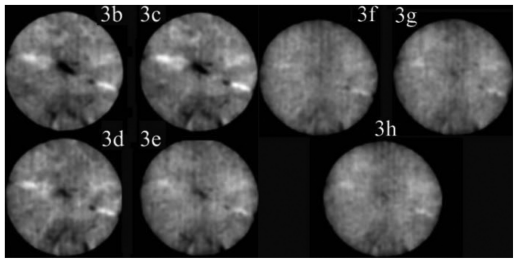


Figure 23. Scanning images during triaxial collapse of 3rd section of sample 4# of intact Q_3 loess.

the M-C criteria as initial collapse condition is unreasonable, which was pointed out by the first author of the paper (Chen & Liu 1986b) in 1986.

4.1.3 *Structure evolution equation of Q_3 loess in the processes of loading and collapse*

The loess sample before experiment is treated as the one with no structural damage, and its corresponding CT mean value is H_i. The sample whose original structure is destroyed completely by shear after saturation is treated as the one with entirely structural damage (no structural strength), and its CT mean value denotes by H_f. A structure parameter of a loess sample is defined as follows:

$$m_1 = \frac{H_f - H}{H_f - H_i} \tag{10}$$

where, H is the mean value of CT data in each section of the sample at a particular moment. When the original structure of the samples does not be damaged, $H = H_i$, $m_1 = 1$. While the structures of samples are completely destroyed, $H = H_f$, $m_1 = 0$.

The structure damage variable of intact Q_3 loess during loading only (i.e., before wetting) is defined as:

$$D_1 = \frac{m_{1c} - m_{1\sigma}}{m_{1o}} \tag{11}$$

where m_{1c} is the cstructure parameter at the beginning of the damage of the structure, $m_{1\sigma}$ is the structure parameter corresponding to the stress σ, and m_{1o} is the initial structure parameter of the sample.

Structure damage variable D_1 of the sample is related to the volume strain (excluding the part of volume strain before damage) and deviator strain (excluding the part of deviator strain before damage) (Figure 24). Using the method of dual linear regression, the following damage evolution equation is obtained:

$$D_1 = A_1 \langle \varepsilon_v - \varepsilon_{vc} \rangle + A_2 \langle \varepsilon_s - \varepsilon_{sc} \rangle \tag{12}$$

$$\langle \varepsilon_v - \varepsilon_{vc} \rangle = \begin{cases} 0 & (\varepsilon_v \le \varepsilon_{vc}) \\ \varepsilon_v - \varepsilon_{vc} & (\varepsilon_v > \varepsilon_{vc}) \end{cases} \tag{13}$$

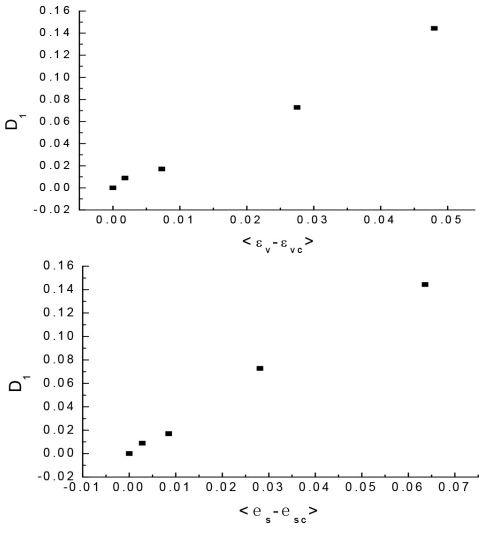


Figure 24. D_1 VS. $\langle \varepsilon_v - \varepsilon_{vc} \rangle$ and D_1 VS. $\langle \varepsilon_s - \varepsilon_{sc} \rangle$ (3# sample).

$$\left\langle \varepsilon_s - \varepsilon_{sc} \right\rangle = \begin{cases} 0 & (\varepsilon_s \le \varepsilon_{sc}) \\ \varepsilon_s - \varepsilon_{sc} & (\varepsilon_s > \varepsilon_{sc}) \end{cases} \tag{14}$$

where ε_{vc} and ε_{sc} are volume strain and deviator strain threshold respectively when the structure of the loess begins to be obviously damaged. A_1 and A_2 are the soil parameters.

Similarly, the structure damage variable of Q_3 loess in the process of collapse under certain stress state is defined as follows:

$$D_2 = \frac{m_{1\sigma} - m_{1\sigma w}}{m_{1o}} \tag{15}$$

where $m_{1\sigma w}$ is the structure parameter of the sample in the process of collapse at any moment.

Through analyzing the relationship of structure damage variable D_2 with collapse volume strain ε_v^{sh} and collapse deviator strain ε_s^{sh} as well as normalized volume moisture content $(\theta - \theta_\sigma)/(\theta_s - \theta_\sigma)$ (Figure 25), MATLAB provides a fitting function for the non-linear fitting, and the damage evolution equation is obtained as follows:

$$D_2 = 1 - \exp\left[-\left(A_3 \varepsilon_v^{sh} + A_4 \varepsilon_s^{sh} + A_5 \right) \frac{\theta - \theta_\sigma}{\theta_s - \theta_\sigma} \right] \tag{16}$$

where A_3, A_4, A_5 are parameters of soil.

4.1.4 *Determining yield stress of intact loess with the help of CT scanning data*

Figure 26 shows the relations of CT number vs. stress of two scanning sections of 3# simple Q_3 loess during shear (Table 8). It can be seen that there is a characteristic point at each curve. The CT numbers of pre- and post- the point change significantly, which means that the point is yield point. Thus, a method to determine yield point is proposed with the help of CT scanning data.

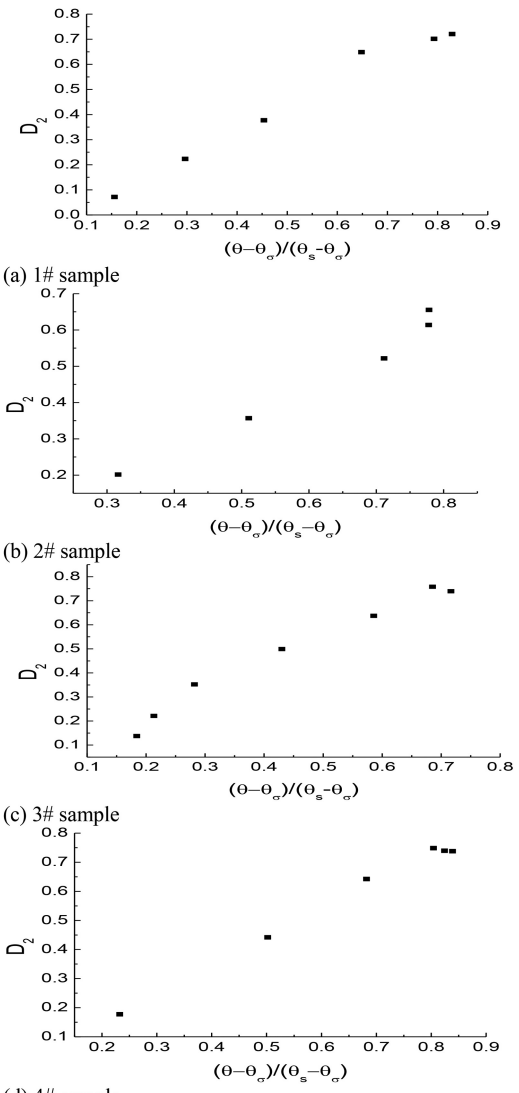


Figure 25. D_2 vs. normalized volumetric water content.

4.2 *The structure evolution of Q_2 loess during loading*

Figure 27 shows the CT images of 4# simple of Q_2 loess during shear with Suction = 300 kPa and net confined stress = 100 kPa net confined stress = 100 kPa. It is obvious that a major of cracks close and the sample becomes dense and harden.

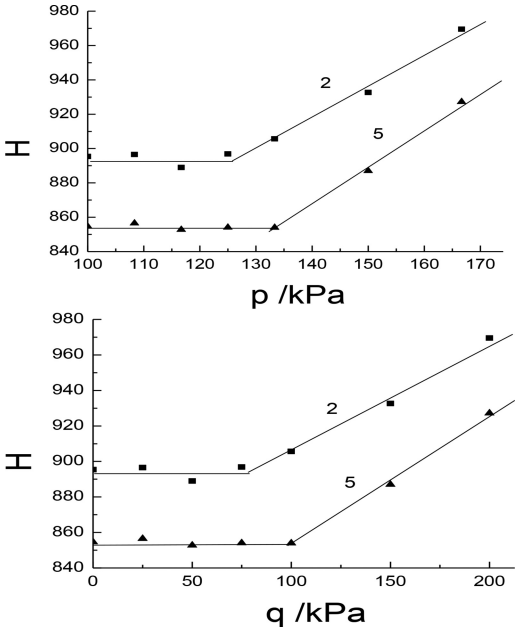


Figure 26. CT number vs. stress of two scanning sections of 3# simple Q_3 loess during shear.

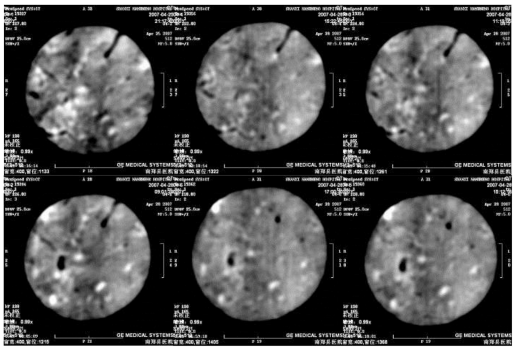


Figure 27. CT number vs. stress of two scanning sections of 3# simple Q_2 loess.

Figure 28 shows the CT images of 8# simple of Q_2 loess with water content = 4.78% and consolidation stress = 50 kPa during shear. Sample becomes softening and cracks developing.

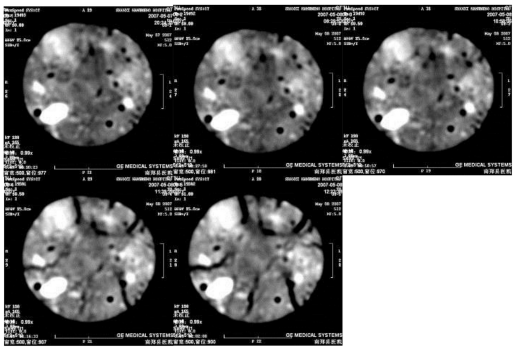
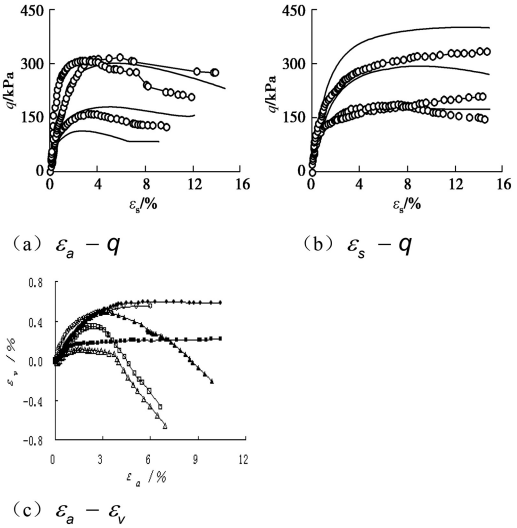


Figure 28. CT images of 8# simple of Q_2 loess with water content CT images of 8# simple of Q_2 loess with constant water content.



(a) $\varepsilon_a - q$ (b) $\varepsilon_s - q$

(c) $\varepsilon_a - \varepsilon_v$

Figure 29. Comparison of model prediction with test stress-strain curves of intact expansive soil.

5 APPLICATIONS

5.1 *Elasto-plastic damage model of undisturbed expansive soil and its application*

There are two ways to found the elasto-plastic damage model. The first method introduced in section 3.4 and a modified mode of BExM is given by equation (6). The second method is using theory of composite damage (or disturbed state concept) (Desai et al. 1997) which takes the soil as a process transforming gradually from the undisturbed soil to a complete damage soil and the soil deformation is described by a composite material that is built by a certain proportion of undisturbed soil and damage soil. Accordingly, Lu Zaihua etc. (2003) established a elasto-plastic damage model of undisturbed expansive soil, which includes 3 aspects of stress-strain relationships for describe the deformations of intact soil and complete damage soil as well as the damage evolution laws described by equations (1) and (2), respectively. Among them, the model for intact parts is using the incremental nonlinear model of unsaturated soil which is put forward by the first author (Chen et al. 1999) of the paper, and the model for change of water content is using the generalized soil water characteristic curve proposed by the first author (Chen 1999, Huang et al. 2000, Fang et al. 2004) of the paper, too.

From the shear stress–strain curve of undisturbed expansive soils located in Nanyang city (Figure 29),

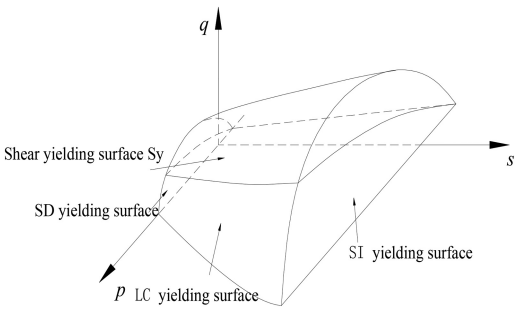


Figure 30. Yield surfaces of intact expansive soil.

dilatancy phenomenon is obvious under low confining pressure. BExM model uses the elliptic yield surface of modified Cambridge model which is suitable for the soil with the characteristics of volume reduction when shear. In order to make up for its shortcomings, the parabolic shear yield surface (SY) proposed by Yin Zongze is leaded into BExM model. Thus, the elasto-plastic damage model of undisturbed expansive soil consists of 4 yield surfaces (Lu et al. 2001): SI, SD, LC and SY, and their space shapes are shown in Figure 30.

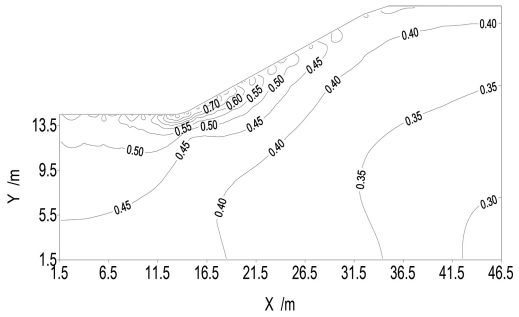
The triaxial shear test results with 6 soil samples from Nanyang city were used to validate the plastic damage model preliminarily, the model predictions with test stress-strain curves are approximately agreement (Figure 29).

Lu Zaihua combined above elasto-plastic damage model of undisturbed expansive soil with the consolidation theory of unsaturated soils proposed by the first author (Chen 1993, Chen et al. 1993) of the paper, the consolidation model of undisturbed expansive soil is got and a program UESEPDC is designed (Lu 2001, Lu et al. 2006). The program includes 33 sub programs.

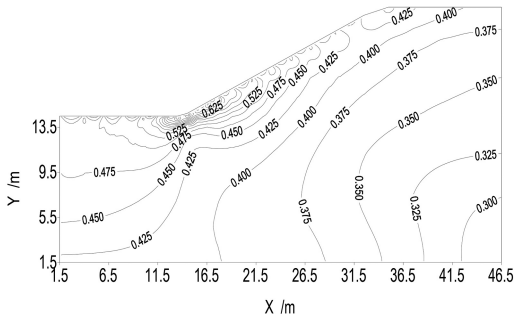
Using the program UESEPDC, a slope of expansive soil during rainfall and evaporation circles is simulated, and the fields of stress, displacement, pore water pressure, pore air pressure, degree of damage and plastic zone are obtained (Lu 2001, Lu et al. 2006, Chen et al. 2008a, b) (see Figure 31 and 32). It is obvious that the numerical analysis results reproduce the phenomenon of the shallow landslide of expansive soil slope.

5.2 *Elasto-plastic damage model of intact loess and its application*

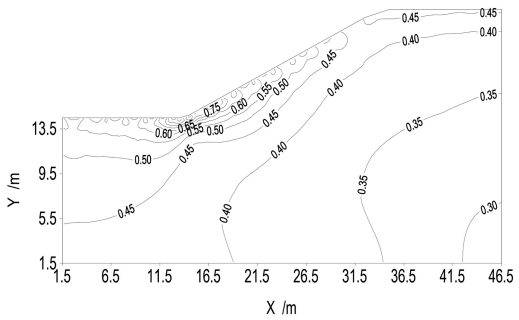
Combining above damage evolution laws of loess described by equations (12) and (16) with Barcelona model (Alonso et al. 1990), a elasto-plasticity damage model for intact Q_3 loess is obtained by Zhu Yuanqing (2008), Li Jiagui (2010) and Yao Zhihua (2012). Further, Yao Zhihua (2012) combined the elasto-plastic damage model of intact loess with the consolidation theory of unsaturated soils proposed by the first author



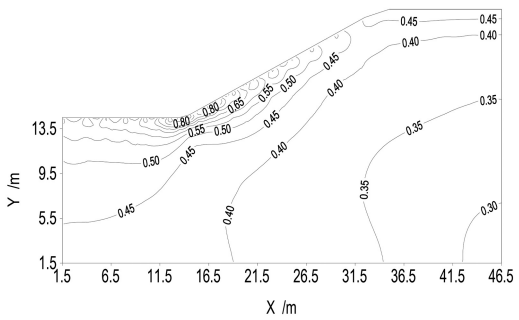
a. After the first circle



b. After the second circle



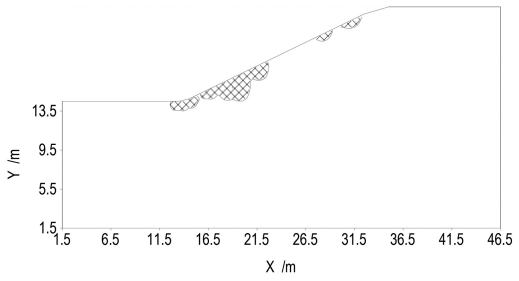
c. After the third circle



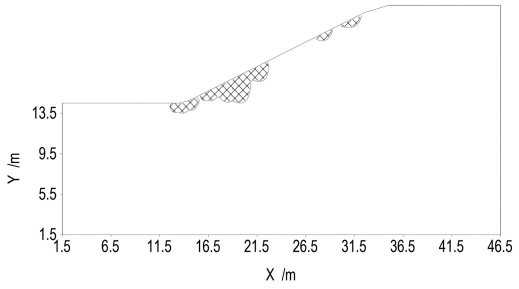
d. After the forth circle

Figure 31. Degree of damage of expansive slope during rainfall and evaporation circles.

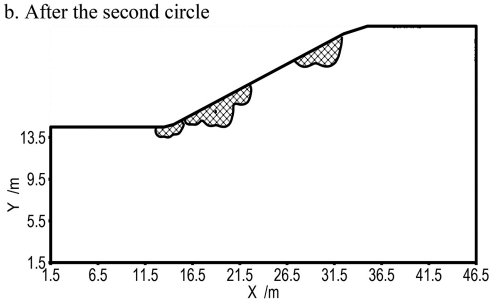
(Chen 1993, Chen et al. 1993) of the paper, the consolidation model for loess is got and a program ULEPDSC is designed. The program includes 26 sub-programs and 3 input files.



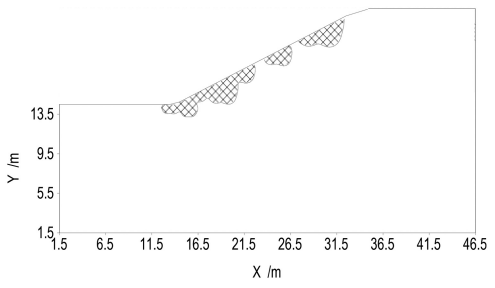
a. After the first circle



b. After the second circle



c. After the third circle



d. After the forth circle

Figure 32. Plastic zone of expansive slope during rainfall and evaporation circles.

Using the program ULEPDSC, a large scale in-situ immersion test (Yao et al. 2012) in Lanzhou are simulated. The wet front position, the volumetric water content, pore water pressure, pore air pressure, horizontal displacement, vertical displacement are obtained during immersion process, which coincided with the results of the immersion test (Fig. 33 and 34).

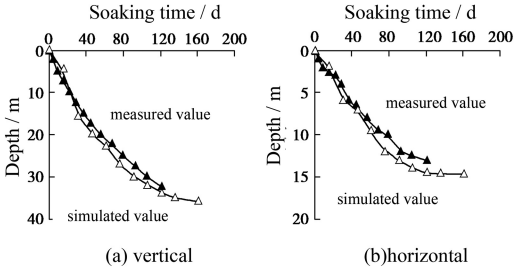
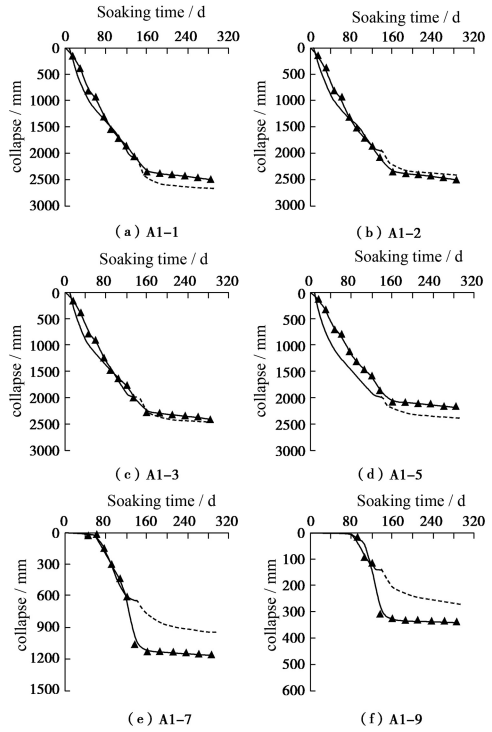


Figure 33. Comparison of measured and computed positions of horizontal and vertical wetting front.



(Triangles represent computation value, full line represents the test data during immersion, dash line represents test data after immersion)

Figure 34. Comparison of measured and computed total collapses on surface points.

6 CONCLUSION

(1) The macro-scale behaviors of the soil samples are closely related with their meso-structural evolutions.
(2) Fissures sprout and grow during loading or during wet-dry circles for undisturbed expansive soil and remolded expansive soil.
(3) The original structure of the loess is damaged and a new homogeneous structure is formed during wetting and for certain stress state. The holes and fissures of intact loess may become gradually

small even disappear during loading or inundation depending on stress state of soil.

(4) Based on CT data, the definitions of the structure damage variable of the loess and expansive soil are given. The structural damage evolution equations of two kinds of soils are obtained in various test conditions.

(5) CT technology gives the visual evidence to the structure changes of soils, and makes a solid test foundation to establish the damage evolution equation and structure constitutive model of soils.

ACKNOWLEDGEMENT

This work has been supported by the National Natural Science Foundation of China (Grant No. 10372115, 10672182, 11072265 & 11272353).

REFERENCES

Alonso, E.E., Gens A. & Josa A. A constitutive model for partially saturated soils [J]. Géotechnique, 1990, 40(3): 405–430.

Chen, Z.H. & Z.D. Liu. 1986a. Mechanism on collapse deformation of loess. Chinese Journal of Geotechnical Engineering, 8(2): 1–12. (in Chinese)

Chen, Z.H. & Z.D. Liu. 1986b. Some problems on collapsibility of loess. Chinese Journal of Civil Engineering, 19(3): 62–69. (in Chinese)

Chen, Z.H., S.G.Sun, X.W. Fang e tal. 2007. Development and application of multifunction triaxial apparatus. Journal of Logistical Engineering University, 23(4): 1–5. (in Chinese)

Chen, Z.H. 1994. New development in research of unsaturated soils. Sino-Canadian Symposium on Unsaturated/Expansive soils, June, 145–152.

Chen, Z.H., Fang, X.W., et al. The meso-structures and their evolution characteristics of expansive soil and loess [J]. Geomechanics, 2009, 30(1): 1–11. (in Chinese)

Chen, Z.H., Lu, Z.H., Guo, J.F., Fang, X.W., Zhou, H.Q. Theoretical model and numerical analysis on unsaturated expansive soil slope during digging and climate change courses (II)–Numerical analysis [A]. Proc. 12th IACMAG Conference, 1–6 October, 2008b, Kala Academy, Panjim, Goa, India, 618–630.

Chen, Z.H., Lu Zai-hua, Guo J.f, Fang X.W., Zhou H.Q. Theoretical model and numerical analysis on unsaturated expansive soil slope during digging and climate change courses (I)–Elasto-plasticity-damage constitutive relationship and consolidation model [A]. Proc. 12th IACMAG Conference, 1–6 October, 2008a, Kala Academy, Panjim, Goa, India, 2222–2231.

Chen, Z.H., Xie, D.Y., Liu, Z.D. Consolidation theory of unsaturated soil based on the theory of mixture (I) [J]. Applied Mathematics and Mechanics (English Edition), 1993, 14(2): 137–150.

Chen, Z.H., Z.H., Lu & Y.B. Pu, 2001. The matching of computerized tomography with triaxial test apparatus for unsaturated soils. Chinese Journal of Geotechnical Engineering 23(4): 387–392. (in Chinese)

Chen, Z.H., Zhou, H.Q., D.G. Fredlund. Nonlinear model for unsaturated soils and it s application [J]. Chinese Journal of Geotechnical Engineering, 1999, 21(5): 603–608. (in Chinese)

Chen, Z.H., Consolidation theory of unsaturated soil based on the theory of mixture (II) [J]. Applied Mathematics and Mechanics (English Edition), 1993, 14 (8): 721–733.

Chen, Z.H. 1999. Deformation, strength, yield and moisture change of a remolded unsaturated loess. Chinese Journal of Geotechnical Engineering, 21(1): 82–90. (in Chinese)

Desai, C.S., Shao, C., Park, I.J. Disturbed state model of cyclic behavior of soils and interface in dynamic soils structure interaction [C]// In: 9th Int. Conf. Computer Methods and Advances in Geomechanics. Wunhan, 1997, Vol. I: 31–42.

Fang, X.W., C.N. Shen, Z.H. Chen, et al. 2011. Triaxial wetting tests of intact Q2 loess by computed tomography, Chinese Journal of Civil Engineering, 44(10): 98–106. (in Chinese)

Fang, X.W., Chen, Z.H., Shen, C.N. A study on effect of shear on soil-water characteristic curve of an unsaturated soil [J]. Rock and Soil Mechanics, 2004, 25(9), 1451–1454. (in Chinese)

Fang, X.W., Chen, Z.H., Shen, C.Q., et al. Analysis on meso-structure evolution of unsaturated natural Q2 loess during yield hardening [J]. Chinese Journal of civil Engineering, 2008a, 30(7): 1044–1050. (in Chinese)

Fang, X.W., Chen, Z.H., Shen, C.Q., et al. meso-testing research on structure damage evolution of natural Q2 loess [J]. Chinese Journal of Hydraulic Engineering, 2008b, 39(8): 940–946. (in Chinese)

Fang, X.W., Shen, C.N., Chen, Z.H., et al. Quantitative study of meso-structure evolution of intact Q2 loess during triaxial shear test [J]. Rock and Soil Mechanics, 2010, 31(1): 27–31. (in Chinese)

Gens, A. & E.E. Alonso, 1992, A framework for the behaviour of unsaturated expansive clays, Canadian Geotechnique Journal, 29: 1013–1032.

Huang, H., Chen, Z.H, Li, G. A study on yield locus of unsaturated soils on p-s plane and soil-water characteristic curve [J]. Rock and Soil Mechanics, 2000, 21(4): 316–321. (in Chinese)

Li, J.G., Chen, Z.H., Huang, X.F, et al. CT-triaxial shear tests on the meso-structure evolution and strength of unsaturated loess Q3 during unloading confining pressure [J]. Rock and Soil Mechanics, 2010a, 31(4): 1084–1091. (in Chinese)

Li, J.G. Active soil pressure of unsaturated intact loess in Q3 considering the meso-structure evolution under lateral unloading conditions [D]. PhD thesis: Logistic engineering university. 2010.9. (in Chinese)

Li, J.G., Chen, Z.H., Huang, X.F. CT-triaxial Test for collapsibility of undisturbed Q3 loess [J]. Chinese Journal of Rock Mechanics and Engineering, 2010b, 29(6): 1288–1296. (in Chinese)

Lu, Z.H. 2001. Elasto-plasticity-damage constitutive model of unsaturated expansive soil and applications on multi-field coupling numerical analysis for Soil Slope. Chongqing: Ph. D. dissertation, Logistical Engineering University. (in Chinese)

Lu, Z.H. & Chen Z.H. An elastoplastic damage constitutive model of unsaturated undisturbed expansive soil [J]. Chinese Journal of Geotechnical Engineering, 2003, 25(4): 422–426. (in Chinese)

Lu, Z.H., Chen Z.H., Cao J.D. A study on the strength and deformation characteristics and the constitutive model of natural expansive soils [J]. Rock and Soil Mechanics, 2001, 22(3): 339–342. (in Chinese)

Lu, Z.H., Chen, Z.H, Pu, Y.P. Study on damage evolution of natural expansive soil with computerized tomography during triaxial shear test [J]. Journal of Hydraulic Engineering, 2002a, 6: 106–112. (in Chinese)

Lu, Z.H., Chen, Z.H., Fang, X.W. et al. Structural damage model of unsaturated expansive soil and its application in multi-field couple analysis on expansive soil slope [J]. Applied Mathematics and Mechanics (English Edition), 2006, 27(7): 891–900.

Lu, Z.H., Chen, Z.H., Pu, Y.P. A CT study on the crack evolution of expansive soil during drying and wetting cycles [J]. Rock and Soil Mechanics, 2002b, 23(4): 417–422. (in Chinese)

Wang, S.J., X. Li & Z. H. Chen. Study on three dimensional reconstruction of macro/meso-structure evolution of expansive soil with CT-triaxial apparatus. Applied Mechanics and Materials, 2012b, 238:422–426.

Wang, S.J., Y. Han, X. Li, L.C. Shi, Y. Q. Zhang & Z. H. Chen. Study of strength and deformation of cylindrical hole damaged expansive soil by CT test. Rock and Soil Mechanics, 2013, 34(10): 2763–2768. (in Chinese).

Wang, S.J., Z. H. Chen, X. Li. Peng Zhen, Yuan Jun. Pore-damage evolution and mechanical properties of remolded soil by CT-triaxial test. Transactions of the Chinese Society Agricultural Engineering, 2012a, 28(7): 103–108. (in Chinese)

Wei, X.W. 2007. On wet-swelling deformation and characteristics of structure evolution of expansive soil. Chongqing: Master Degree Dissertation, Logistical Engineering University. (in Chinese)

Yao, Z.H., Chen, Z.H., Huang, X.F et al. Influence of structural damage on yielding characteristics of expansive soils [J]. Chinese Journal of Rock Mechanics and Engineering, 2010b, 29(7): 1503–1512. (in Chinese)

Yao, Z.H., Chen, Z.H., Zhu, Y.Q., et al. Meso-structural change of remolded expansive soils during wetting-drying cycles and triaxial soaking tests [J]. Chinese Journal of Geotechnical Engineering, 2010a, 32(1): 68–76. (in Chinese)

Yao, Z.H., Huang, X.F., Chen, Z.H., et al. Comprehensive soaking tests on self-weight collapse loess with heavy section in Lanzhou region [J]. Chinese Journal of Geotechnical Engineering, 2012, 34(1): 65–74. (in Chinese)

Yao, Z.H., Water-air migration, mechanical characteristics and foundation collapse deformation of self-weight collapse loess with heavy section [D]. Chongqing: Logistic Engineering University. 2012. (in Chinese)

Zhu, Y. Q. & Z. H. Chen. 2008. A new method of studying collapsibility of loess, Chinese Journal of Geotechnical Engineering, 30(4): 524–528. (in Chinese)

Zhu, Y. Q. & Z. H. Chen. Experimental study on dynamic evolution of meso-structure of intact Q3 loess during loading and collapse using CT and triaxial apparatus [J]. Chinese Journal of civil Engineering, 2009, 31(8): 1219–1228. (in Chinese)

Zhu, Y. Q. Constitutive model of undisturbed collapsible loess based on meso-structure change [D]. Chongqing: Logistic Engineering University, 2008. (in Chinese)

Unsaturated Soil Mechanics—from Theory to Practice – Chen et al. (Eds)
© 2016 Taylor & Francis Group, London, ISBN 978-1-138-02921-7

Slope stability analysis methods and application to 1 g failure model tests

Y. Kohgo
Tokyo University of Agriculture and Technology, Tokyo, Japan

ABSTRACT: In this paper we present slope stability analysis methods based on saturated and unsaturated consolidation analysis methods and its application to 1g failure model tests. At the first part we reviewed the methods and constitutive equations coupled with the methods. In the constitutive equations, two important conditions, which should be satisfied to simulate behavior of unsaturated soils, are described. They are (1) to consider two suction effects and (2) to consider saturation conditions. At the second part, we present an application of a saturated and unsaturated consolidation analysis method coupled with an elastoplastic model for unsaturated soils, which satisfies the conditions (Code name: GEOCUP), to the slope stability problem. It has a potential to be the most powerful design tool for evaluating slope stabilities. A series of 1G slope failure model tests, which consisted of a shallow surface sand layer on a relatively hard foundation, were simulated. The simulation results were well consistent with the typical test results

1 INTRODUCTION

Global warming is one of the most concern things. The global warming may induce not only larger-sized typhoons but also a lot of local heavy rainfalls. According to reports of JMA (Japan Meteorological Agency 2009), the mean annual event times of rainfalls with over 50 mm/hr intensity for every ten years in Japan are 160 in 1976–1987, 177 in 1988–1997 and 233 in 1998–2007 and the event times gradually increase. The main sediment disasters in Japan are listed in Table 1. Over several 10s peoples are killed or missed every year. The annual mean damage for the last 10 years due to typhoons and heavy rainfalls comes up about US $ 6 billion.

Under the situations it is very important to investigate the stability of slopes due to heavy rainfalls. In the investigation of stability of slopes, we have some warning procedures. Most of the procedures are empirically established only by correlations between rainfall intensity and the slope-failure frequency. Though the soil water index proposed by Okada et al. (2001) includes information of soil water infiltrated, no information of the mechanical data of soils is taken into account in the procedure.

Some groups conduct 1 g level (Orense et al. 2004, Tohari et al. 2007, Tokoro et al. 2012) or centrifuge slope model tests (Tanaka et al. 2009, Kohgo et al. 2011). In analytical research works, some methods in which saturated and unsaturated seepage analysis method was combined with limit equilibrium method (Fredlund & Rahardjo 1993), rigid-plastic analysis method (Shimada et al. 1999), or elasto-plastic analysis method (Nobuoka et al. 2009) are proposed. Saturated and unsaturated consolidation analysis methods, which seem to be the most powerful tool for the analysis of slope stabilities, are going to be applied.

Table 1. Main sediment disasters in Japan.

Year	Prefecture	Cause	Num. of victims
2003	Kumamoto	SRF*	19
2004	Mie, Tokushima, Kagawa, Ehime	Typhoon 21	17
2004	Nagano, Toyama, Gifu, Hyogo, Kyoto, Okayama, Kagawa, Ehime	Typhoon 23	27
2005	Kagoshima, Miyazaki, Oita, Yamaguchi	Typhoon 14	22
2006	Nagano etc.	Torrential rain	20
2009	Yamaguchi etc.	Torrential rain	21
2011	Wakayama etc.	Typhoon 12	62
2012	Kumamoto etc.	Torrential rain	23
2013	Tokyo etc.	Typhoon 26	40
2014	Hiroshima	Torrential rain	74

*Seasonal Rain Front

In this paper, the consolidation analysis methods applying to the slope stabilities are at first mentioned and our application of a consolidation analysis method to a series of 1 g rainfall model tests, which had a shallow surface loose sand layer on a relatively hard foundation and can be often seen in natural slopes, is presented. We will discuss the performance of the method.

2 CONSOLIDATION ANALYSIS METHODS

2.1 *Classifications of consolidation analysis methods*

We will try to classify consolidation analysis methods, which are applied to stabilities of embankments and natural slopes, according to Kohgo's definitions (Kohgo, 2003).

He classified the methods into two on the base of the field equations used. The first is the method where the force equilibrium for whole soil mass and the mass conservation of pore water equations are adopted as field equations under the assumption that pore air pressure is always equal to the atmospheric pressure. Hereafter, we call this method Method I. The field equations are expressed as follows in weak forms,

$$-\int_V \sigma_{ij}\delta\varepsilon_{ij}^{*}dV+\int_V \gamma F_i\delta u_i^{*}dV+\int_{S_2}\bar{T}_i\delta u_i^{*}dS=0, \quad (1)$$

$$\int_V S_r\dot{\varepsilon}_{ii}\delta u_w^{*}dV-\int_V v_i^{w}\delta u_{w,i}^{*}dV +\int_V n\dot{S}_r\delta u_w^{*}dV+\int_{S_4}\bar{Q}^{w}\delta u_w^{*}dS=0, \quad (2)$$

where σ_{ij} = stress tensor; γ = unit weight of soil mass; F_i = body force unit vector; δu_i^{*} = virtual displacement vector; $\delta\varepsilon_{ij}^{*}$ = virtual strain tensor; S_r = degree of saturation; δu_w^{*} = virtual pore water pressure; v_i^{w} = relative displacement velocity vector of water with respect to the soil skeleton; n = porosity; V = total volume of the mass considered; a superposed dot denotes differentiation with respect to time and subscripts after comma denote spatial differentiation.

Boundary conditions concerned with Equations (1) and (2) are as follows.

$$u_i=\bar{u}_i \qquad \text{on } S_1, \quad (3)$$

$$\bar{T}_i=\sigma_{ij}n_j \qquad \text{on } S_2, \quad (4)$$

$$u_w=\bar{u}_w \qquad \text{on } S_3, \quad (5)$$

$$\bar{Q}^{w}=v_i^{w}n_i \qquad \text{on } S_4, \quad (6)$$

where $\bar{u}_i$ = displacement vector given on the boundary S_1; $\bar{T}_i$ = traction vector given on the boundary S_2; $\bar{u}_w$ = pore water pressure given on the boundary S_3; $\bar{Q}^{w}$ = water flux given on the boundary S_4; and n_i = unit vector normal to boundary.

The second method (Method II) is the method where the mass conservation equation of pore air is moreover added to Equations (1) and (2). The equation is as follows.

$$\int_V\left(1-S_r+h_sS_r\right)\dot{\varepsilon}_{ii}\delta u_a^{*}dV+\int_V\left(1-h_s\right)n\dot{S}_r\delta u_a^{*}dV -\int_V v_i^{a}\delta u_{a,i}^{*}dV-\int_V h_sv_i^{w}\delta u_{a,i}^{*}dV +\int_{S_6}\bar{Q}^{a}\delta u_a^{*}dS+\int_{S_4}h_s\bar{Q}^{w}\delta u_a^{*}dS=0, \quad (7)$$

where h_s = Henry's coefficient of solubility; δu_a^{*} = virtual pore air pressure; and v_i^{a} = relative displacement velocity vector of air with respect to the soil skeleton.

Boundary conditions for Equation (7) are as follows.

$$u_a=\bar{u}_a \qquad \text{on } S_5, \quad (8)$$

$$\bar{Q}^{a}=v_i^{a}n_i \qquad \text{on } S_6, \quad (9)$$

where $\bar{u}a$ = pore air pressure given on the boundary S_5; and $\bar{Q}^{a}$ = air flux given on the boundary S_6. Supposing S total area of the boundary, the following equation is valid.

$$S=S_1+S_2=S_3+S_4=S_5+S_6. \quad (10)$$

The Method I is subdivided into two according to consideration of unsaturated ranges. In the first category (hereafter called Method I-1), full saturation and insular air saturation, in which air only exists as air bubbles, conditions are only taken into account. Then, the left hand third term in Equation (2) may be evaluated on the base of the assumption that pores of soils are filled with a single compressive fluid. The term means the compressibility of the fluid. Therefore this method only deals with a kind of saturated soils.

The second category (hereafter called Method I-2) is the method in which the full saturation and the unsaturation until very low degree of saturation conditions are taken into account. Generally, the function integrated in the left hand third term in Equation (2); $n\dot{S}r$ is rewritten as,

$$n\dot{S}_r=n\frac{\partial S_r}{\partial t}=n\frac{\partial S_r}{\partial s}\frac{\partial s}{\partial t}=-n\frac{\partial S_r}{\partial s}\dot{u}_w. \quad (11)$$

Then, the left hand third term in Equation (2) should be evaluated from soil water retention curves. The term means the gradients of the soil water retention curves $\partial Sr/\partial Ss$, (s = suction). In the Method I-2, you should choose the soil water retention model that can express saturation and unsaturation until low degree of saturation conditions. The most suitable one is Tangential model proposed by the author (Kohgo 1995, Kohgo 2008). In this method, unknown variables are deformations and pore water pressure. The solution is easier than that of Method II. The Method I can hardly be applied to a problem, in which air within soils is trapped and the pressure increases due to infiltration of water.

In the Method II, the condition in the left hand second term of Equation (7) is similar to that in the left hand third term in Equation (2) as it was just discussed. In this method, unknown variables are deformations, pore water and air pressures.

2.2 *Constitutive equations*

In this section, constitutive equations only mean stress-strain relationships of soils. The constitutive equations may be mainly divided into two according to stress concepts. They are the models based on stress variable method (Alonso et al. 1990) and those based

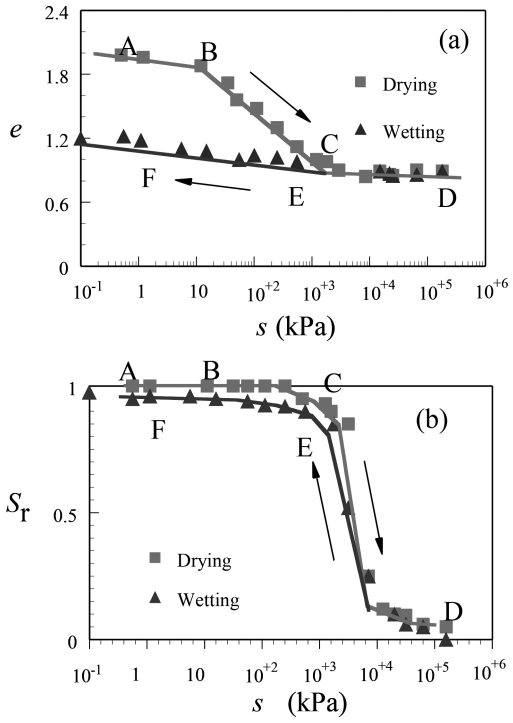


Figure 1. A typical volume change behavior due to suction (data from Fleureau et al. 1993).

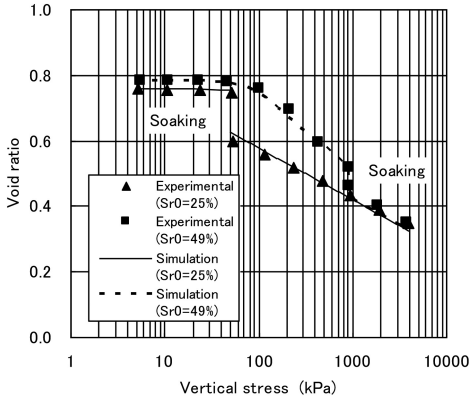


Figure 2. Oedometer test results with saturation collapse and their simulations. (S_{r0}: Initial degree of saturation).

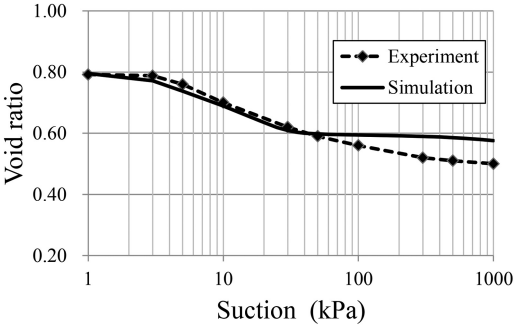


Figure 3. Consolidation test result of Yellow soil due to suction.

on effective stress method (Kohgo et al. 1993a, b). The effective stress concept in unsaturated soils has been discussed. The ultimate understanding is given by Kohgo (2003). You may also use the effective stress concept in the unsaturated soil mechanics field. When you adopt this concept, you should consider another suction effect. The most important point in modelling of constitutive equations namely is to take two suction effects into account. The effects are (1) an increase in suction increases effective stresses, and (2) an increase in suction enhances yield stresses and affects resistance to plastic deformations. The effect (1) comes from the effect that pore water acts as a neutral stress and this is a similar manner as that Terzaghi (1936) pointed out. The effect (2) comes from the capillary forces that act at the grain contact points. The capillary forces are attractive and act like a water-soluble glue.

Another important point is to consider soil water retention conditions. If the suction is smaller than the air entry value of the soil s_e, the mechanical behavior may be regarded as that of saturation soils. Then Terzaghi's effective stress concept is valid. If the suction is larger than s_e, the two suction effects described above should be considered. One method to express these phenomena is to formulate the suction effects as functions of effective suction shown in Equation (16).

If these two important points should be taken into account, we may explain the typical experimental behavior of unsaturated soils. The behavior is that 1) the volume change behavior shown in Figure 1 (Fleureau et al. 1993) expresses in order elasticity, elastoplasticity and elasticity as suction increases, 2) collapse due to wetting (a typical example shown in Figure 2), and 3) both shear strength and yield stress increase with an increase in suction. The behavior 1) is especially very interesting. In the experimental test shown in Figure 1, as the suction is smaller than s_e until point C shown in this figure, the behavior is similar to that of the saturated soil. The behavior of this part changes from elasticity to elastoplasticity. If the second important point described above is taken into account, we can explain the behavior because the behavior is regarded as the saturated one. If you consider the first important point, the later part after point C at which the suction is larger than s_e, can also be explained. At the region, the yield stress may become farther larger than the current stress point.

Kohgo et al. (1999) and Kohgo et al. (2007) showed the simulation results of the behavior 1) to 3). The results are shown in Figures 2, 3 and 4. Unfortunately, there is small number of models that satisfy the conditions described above except our models (Kohgo et al. 1993(a), (b), Kohgo 2007).

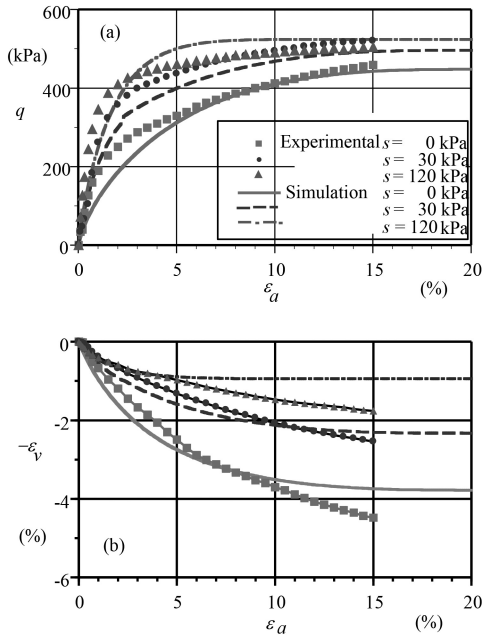


Figure 4. Triaxial compression tests and their simulation results for an unsaturated silt.

3 SLOPE MODEL TESTS DUE TO RAINFALL

In this chapter, I would like to present the results of 1 g slope failure tests due to rainfalls. The slope model consists of a shallow surface sand layer on a relatively hard foundation with a 45 degrees slope.

3.1 *Procedure of model tests*

The model slopes used in this series of tests are shown in Figure 5. The model consisted of two materials: Kasumigaura sand for the surface layer and DL clay for the hard foundation of the slope. The physical properties of each material are shown in Table 2. The grading curves are shown in Figure 6. The soil slope models were constructed in a steel soil box with a transparent glass surface in the front of the box. The dimensions of the model slopes were 122 cm in height (including the 100 cm height DL clay and the 22 cm height Kasumigaura sand), 42 cm in crest width, 70 cm in depth, and 162 cm in base length. The slope gradient was 45 degrees. At first, the base foundation was constructed by compacting DL clay in the maximum dry density (compaction ratio = 100%) and the water content w = about 17%. The thickness of each DL clay layer after construction was 5 cm and, finally, it consisted of 20 layers. After the construction of DL clay layer the sand layer was laid on the DL clay. Three different densities of the sand layer were employed: $D_r = 0\%$, 25%, and 50% with the same water content w = about 10%. The rolled thickness of each sand layer was 4 cm. The 23 rolled layers needed to be constructed. The initial conditions of models are

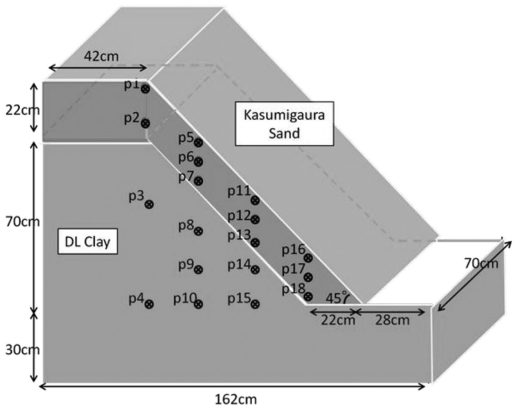


Figure 5. Model slope used in the tests.

Table 2. Physical properties of soils used in the tests.

Materials		DL Clay	Kasumigaura Sand
Density of soil particle (g/cm^3)	ρ_s	2.653	2.692
Consistency		NP	NP
Maximum dry density (g/cm^3)	ρ_{dmax}	1.538	1.664
Minimum dry density (g/cm^3)	ρ_{dmin}		1.358
Optimum water content (%)	w_{opt}	21.3	16.2
Maximum particle size (mm)	d_{max}	0.039	0.760
Coefficient of permeability (m/s)	k_s	6.68×10^{-7}	1.25×10^{-4}

shown in Table 3. In order to drain infiltration water, a U-shaped pipe drain covered with a non-woven textile was inserted at the most downstream and base of the DL clay layer. Three rainfall intensities $I = 25$, 50 and 100 mm/hr were employed in these cases. During the tests, pore water pressures and displacements were measured. The pore water pressures were monitored with 18 pore water pressure (PWP) transducers (Capacity = 100 kPa). Each transducer was connected to each ceramic chip with a thin tube filled with de-aired water. The air entry values of the ceramic chips were about 100 kPa. The ceramic chips were saturated with de-aired water under a vacuum. The 18 ceramic chips were installed into the soil slopes. The installed positions (P1–P18) are shown in Figure 5 and the level of each ceramic chip was the same as that of each associated transducer mounted on the outside board of the soil box. To measure the deformations of the slopes, pictures were taken through the transparent glass of the soil box with a digital camera. The displacements were calculated by using Particle Image Velocity (PIV) analysis method (White et al., 2003).

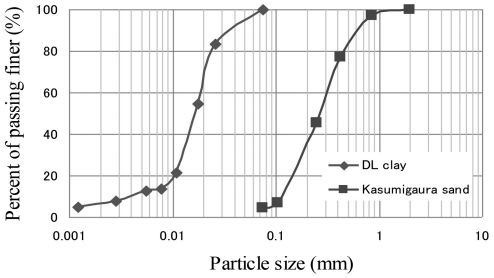


Figure 6. Grading curves of soils used in the tests.

Table 3. Initial conditions of model slopes.

Case	Rainfall intensity I (mm/hr)	Relative density D_r (%)	Water content w (%)	Degree of saturation S_r (%)
1	25	0	10.6	28.7
2	25	25	10.0	30.2
3	25	50	9.8	32.9
4	50	0	11.0	29.8
5	50	25	10.0	30.2
6	50	50	10.0	33.6
7	100	0	12.9	34.9
8	100	25	10.0	30.2
9	100	50	9.8	32.9

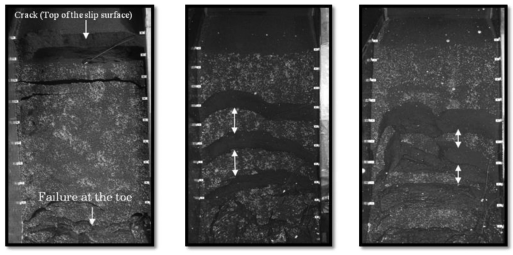
3.2 *Test results*

In the model tests, failures occurred in all cases. In this paper, we will only mention the influence of different densities of the sand layers. Figures 7 and 8 show situations of the slope failures of the models with the same rainfall intensity $I = 50$ mm/hr taken from diagonally above the slopes and taken through the transparent glass of the soil box, respectively. In Case 4, a small failure started at the toe of the slope. After the failure areas reached to a level of the slope, a clear and large but shallow slope failure was observed (see Figures 7(a) and 8(a)). It was a typical surface failure.

On the other hand, in Case 5, a small failure occurred at the toes of the slopes and the sequential small failures progressed to the upper parts of the slopes. The failures were a typical progressive failure and no clear and large slip surface appeared (see Figure 7(b) and 8(b)). The similar failure can be seen in Case 6 but widths of the sequential small failures in Case 5 were larger than those in Case 6 shown in Figures 7(c) and 8(c).

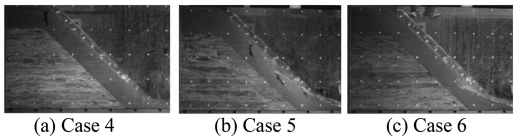
Figure 9 shows the total displacement vectors for Cases 4, 5 and 6. The displacements were only measured within the sand layer. Elapsed time t shown in the following figures expresses time that measured from the commencement of rainfall. Directions of the displacements were clearly different in each case.

In Case 4 at $t = 81$ minutes, the displacements occurred along the slope and the large displacements



(a) Case 4 (b) Case 5 (c) Case 6

Figure 7. Birds eye views of the slope models after failures.



(a) Case 4 (b) Case 5 (c) Case 6

Figure 8. Cross sections of the slope models after failures.

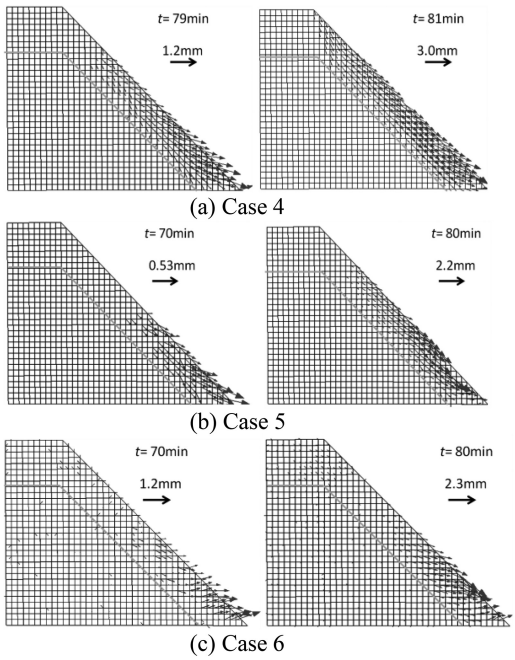
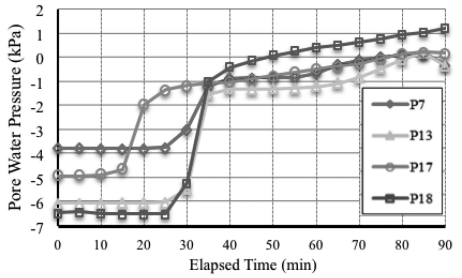


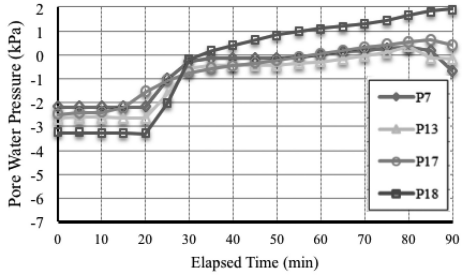
Figure 9. Displacement vectors obtained from the model tests.

were measured in the almost whole area of the sand layer. The maximum value of the displacements was measured at slightly upper part of the toe and it was 3.0 mm just before the failure at $t = 79$ minutes and reached finally 18.0 mm after the surface failure at $t = 81$ minutes.

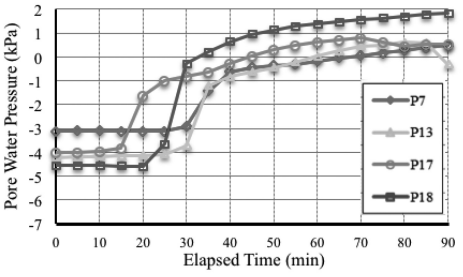
Meanwhile horizontal displacements were dominant in Case 6 and the sand mass moved horizontally (see Figure 9(c)). The behavior may be closely related to the sequential small failures occurred in this case. In Case 5, the sand mass moved intermediate direction



(a) Case 4



(b) Case 5



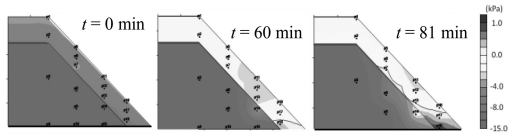
(c) Case 6

Figure 10. Relationship between PWP values and elapsed times measured at P7, P13, P17 and P18.

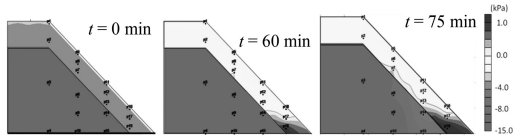
between Cases 4 and 6. The deformed areas reached to more upper parts of the sand layer than that in Case 6.

Figure 10 shows relationship between PWP values and elapsed times. In Case 4, the first failure started from the toe of the slope at $t = 68$ minutes. It was found from Figure 10(a) that the PWP of P18 at $t = 68$ minutes was only positive and others were slightly negative. The same results could be seen in Cases 5 and 6. The places near P18 at which PWP values were positive were almost consistent with the small failure regions. Thus the failures started from the regions with positive PWP values. Now supposing that the elapsed time, at which a PWP value reaches zero, is defined as effective time t_e. The t_e values at P 18 in Cases 5 and 6 were the same 32 minutes and they were faster than that in Case 4; $t_e = 50$ minutes. The effective times at P7, P13 and P17 were respectively 78, 81 and 78 minutes in Case 4, 57, 72 and 57 minutes in Case 5, and 68, 59 and 45 minutes in Case 6. The effective times almost increase as the rainfall intensities decrease.

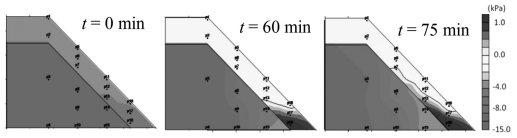
Figure 11 shows distributions of PWP values. The initial PWP values expressed negative and those of



(a) Case 4



(b) Case 5



(c) Case 6

Figure 11. Distributions of PWP values.

the DL clay layer reached around -20 kPa. As little changes of PWP values within DL clay layer during the tests, the rainwater could not infiltrate into the layer. After the rainwater infiltrated into the sand layer, then encountered the DL clay layer and might flow down along the boundary between the sand and DL clay layers. Such situations could be seen in Figures 11(a) at $t = 81$ minutes, 11(b) at $t = 75$ minutes and 11(c) at $t = 75$ minutes.

Comparing Figures 11(a), 11(b) and 11(c) at the same elapsed time $t = 60$ minutes, there was a clear seepage surface in Case 6 and the surface appeared on a relatively high level portion of the slope surface. Meanwhile the seepage surface in Case 4 did not appear on the slope surface. The seepage surface in Case 5 also appeared on the slope surface but the level was lower than that in Case 6.

At the saturation parts, the permeability of the sand in Case 6 was smaller than that in Case 4, since the density of the sand in Case 6 was higher than that in Case 4. Then the water infiltrated in Case 6 might not be sufficiently drained and accumulate at the toe. The situations shown in Figure 11 at $t =$ around 80 minutes may appear by the mechanism described above.

4 SIMULATIONS OF THE MODEL TESTS

4.1 *Simulation procedures*

Unknown variables in these equations are displacements of soil skeleton and pore water pressures. The field equations (1) and (2) are used and introduced to the discrete system using the finite element method and the solution procedure based on the modified Newton-Raphson method is adopted (Kohgo et al. 1995, 2010).

We have to take into account material nonlinear properties: stress-strain relationship, permeability, and

soil water retention curves, to conduct consolidation analysis. We adopted an elastoplastic model with two suction effects as stress-strain relationship (Kohgo et al. 1993b, 2007). The two suction effects described in previous section are taken into account. In suction effect (1), the effective stress equations can be expressed as Equations (12) to (14);

$$\sigma' = \sigma - u_{eq}, \tag{12}$$

$$u_{eq} = u_a - s, \qquad (s \le s_e) \tag{13}$$

$$u_{eq} = u_a - \left(s_e + \frac{a_e}{s^* + a_e} s^* \right), \qquad (s > s_e) \tag{14}$$

where σ' = effective stress; σ = total stress; and a_e = a material parameter. Suction s and effective suction s^* are defined as follows:

$$s = u_a - u_w, \tag{15}$$

$$s^* = \langle s - s_e \rangle. \tag{16}$$

where u_a = pore air pressure; u_w = pore water pressure; s_e = air entry suction; and the brackets $< >$ denote a Heaviside function: the operation $< z > = 0$ at $z < 0$ and $< z > = z$ at $z \ge 0$.

The suction effect (2) may be formulated by evaluating the state surface, which defines elastoplastic volume change behavior in unsaturated soils (Kohgo et al. 1993a). The state surface can be plotted in the space with the axes: effective mean stress p', effective suction s^*, and void ratio e. The shapes of state surfaces depend on types of soils. Here, they are postulated to be as Equations (17)–(19).

$$e = -\lambda^* \log(-p') + \Gamma^*, \tag{17}$$

$$\lambda^* = \lambda + \frac{\lambda^*_{f1} s^*}{s^* + a_1^*}, \tag{18}$$

$$\Gamma^* = e^0_{01} + \frac{(\Gamma - e^0_{01})\lambda^*}{\lambda}. \tag{19}$$

where $\lambda = \lambda^*$ at saturation; $\Gamma = \Gamma^*$ at saturation; λ^* = slopes of $e - \log(-p')$ curves in the elastoplastic range; Γ^* = void ratios of $e - \log(-p')$ curves in the elastoplastic range at $-p' =$ unit; and λ^*_{f1}, a^*_1, e^0_{01} = material parameters. These two suction effects were introduce to a generalized elastoplastic model in which the critical state concept, Mohr-Coulomb model combined with Cap model and subloading surface concept were employed. More details can be found in the reference (Kohgo et al. 2007).

Soil water retention curves were modeled by the equations that were formulated by insuring continuities of the tangential slope c of soil water retention curves. The model is therefore designated as the Tangential model (Kohgo 1995, 2008).

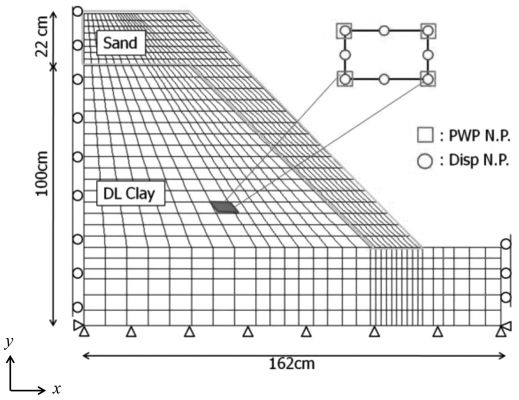


Figure 12. Finite element mesh and boundary conditions.

The permeability is considerably influenced by deformations and changes of the degree of saturation of soil. Therefore, the permeability property was assumed to be a function of void ratio e and degree of saturation S_r as follows.

$$k = k_s \cdot E_p \cdot H_p, \tag{20}$$

$$E_p = \frac{1 + e_0}{1 + e} \left(\frac{e}{e_0} \right)^{n_p}, \tag{21}$$

$$H_p = \left(\frac{S_r - S_{rf}}{S_{re} - S_{rf}} \right)^{m_p}. \tag{22}$$

where k_s = the permeability at saturation; m_p and n_p = material parameters; e_0 = initial void ratio; S_{rf} = residual degree of saturation; and S_{re} = degree of saturation at air entry.

In the elastic range, the elastic moduli were assumed to be functions of p' and J_2 as follows:

$$K = \frac{-2.3(1 + e_0)}{\kappa} p' + K_i, \tag{23}$$

$$G = G_i + \gamma_J \sqrt{J_2} - \gamma_p p'. \tag{24}$$

where K = bulk modulus, G = shear modulus; κ = slope of $e - \log(-p')$ curve in the elastic range; J_2 = the second deviator stress invariant; and K_i, G_i, γ_J and γ_p = material parameters.

4.2 *Simulation results*

In this analysis, a plane strain condition is supposed. The finite element mesh and boundary conditions are shown in Figure 12. Pore water pressures on the surfaces of the slope and the foundation were assumed to maintain negative or zero (seepage condition) during Construction stage and the amounts of flux associated with prescribed rainfall intensities were applied on them during Rainfall stage. The base was rigid and

impervious and the both sides of the model were fixed in only x direction and impervious. The parameters used are shown in Tables 4 and 5.

The simulations were conducted for all cases. Simulation results are shown in Figures 13–17. Figure 13 shows comparison of experiment and simulation results of PWP distributions in Case 5; $I = 50$ mm/hr, and $D_r = 25\%$. At $t = 0$ minute in both cases relatively small negative PWP values appeared at the shoulder of the slope. As the region of the simulation was larger than experimental one, whole distributions were almost the same. At $t =$ around 30 minutes the similarities became higher and at around 50 minutes positive PWP values appeared at the toe of the slope in both cases. The area with positive PWP (saturated area) values was restricted in the sand layer and the stability of the slope rapidly lost after that. In the saturated area a small failure started. Thus saturation induced the failure.

Figure 14 shows distributions of PWP at each elapsed time t in Case 5. The PWP values mainly changed within the sand layer and the PWP values were mainly accumulated at the toe of the slope. The

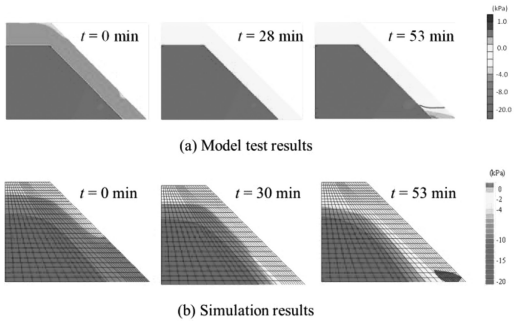


Figure 13. Comparison of experiment and simulation results of PWP distributions in Case 5.

Table 4. Parameters for Kasumigaura sand.

Elasticity		Plasticity		State surface	
κ	0.0079	α_h	1.0×10^4	λ	0.042
K_i (kPa)	50	ϕ'	30.0 deg.	Γ	0.915
G_i (kPa)	77	ϕ'_{cs}	33.4 deg.	e^0_{01}	0.760
γ_J	0.0	R	1.7	λ^*_{f1}	0.037
γ_p	80.0			a^*_1 (kPa)	2.8
Effective stress		**Permeability**		**SWR****	
a_e (kPa)	15.0	k_s (m/min)	7.5×10^{-3}	S_{re}	0.920
s_e (kPa)	0.50	m_p	1.3	S_{rm}	0.350
		n_p	3.0	S_{rf}	0.150
				s_m (kPa)	2.9
				s_f (kPa)	10.0
				c_m	6.0×10^{-1}
				c_f	8.0×10^{-4}

**SWR = Soil Water Retention

Table 5. Parameters for DL clay.

Elasticity		Plasticity		State surface	
κ	0.020	α_h	5.0×10^4	λ	0.152
K_i (kPa)	0.1	ϕ'	26.2 deg.	Γ	1.306
G_i (kPa)	0.1	ϕ'_{cs}	32.0 deg.	e^0_{01}	0.508
γ_J	0.0	R	1.0	λ^*_{f1}	0.044
γ_p	70.0			a^*_1 (kPa)	17.4
Effective stress		**Permeability**		**SWR****	
a_e (kPa)	33.3	k_s (m/min)	4.0×10^{-5}	S_{re}	0.990
s_e (kPa)	10.0	m_p	3.0	S_{rm}	0.600
		n_p	3.0	S_{rf}	0.160
				s_m (kPa)	13.0
				s_f (kPa)	120.0
				c_m	1.0×10^{-2}
				c_f	9.0×10^{-4}

**SWR = Soil Water Retention

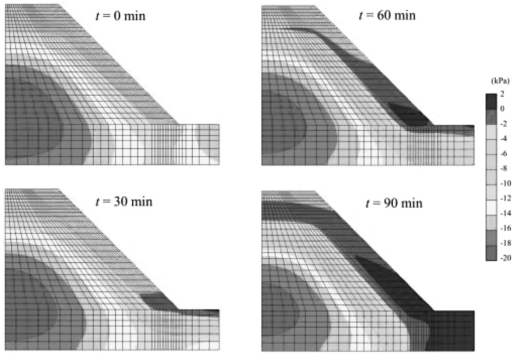


Figure 14. Distributions of PWP at each elapsed time t in Case 5.

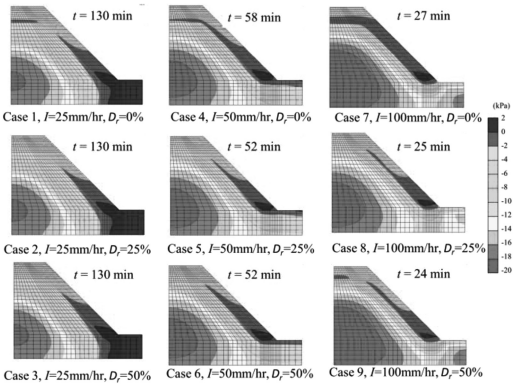


Figure 15. PWP distributions at the starting times of the first slope failures in all cases.

saturated area started at the toe and progressed to the upper part with time and unstableness of the slope rapidly advanced with the expansion of the saturated parts. The situations of the expansion of saturation part can be seen at $t = 60$ and 90 minutes.

Figure 15 shows the simulation results of PWP distributions at the starting times of the first slope failures in all cases. In all cases the saturation within the sand layer near the toe of the slope were calculated. In Cases 1, 2 and 3 with the same $I = 25$ mm/hr, the failures occurred at the same time 130 minutes. The saturated parts appeared within the DL clay base on the front of the slope and the sand layer near the toe of the slope. Meanwhile in Cases 4, 5 and 6 with $I = 50$ mm/hr, the failure started at $t = 58$, 52 and 52 minutes, respectively. The positive PWP values were calculated only within the sand layer near the toe of the slope. In Cases 7, 8 and 9 with $I = 100$ mm/hr, the failure times were $t = 27$, 25 and 24 minutes, respectively. The saturated parts within the sand layer near the toe of the slope were restricted in the very small areas. Thus the area of saturated parts and the occurrence times of the first failure were affected by the intensities of rainfalls. The case with the lower rainfall intensity took the more times in initiation of failures and had the wider saturation

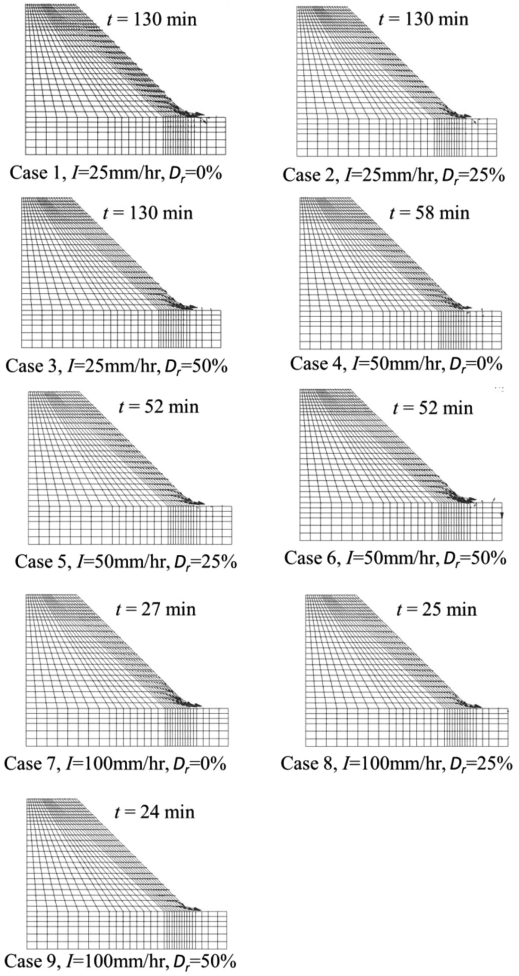


Figure 16. The displacement vectors at the starting times of the first slope failures in all cases.

areas. The influence of the difference of the relative densities D_r of the sand layer was relatively small.

Figure 16 shows the displacement vectors at the starting times of the first slope failures in all cases. In all cases, the large vector values were calculated within the sand layer near the toe of the slope. The directions of the vectors at the toe of the slope were almost the same and faced to the front of the slopes. In Case 1, the relatively large values of the vectors were calculated within the almost whole sand layer, but in other cases the values only concentrated at the toe.

Figure 17 shows the simulation results of shear strain contours in Cases 4, 5 and 6. Those cases had the same rainfall intensity I but the different relative densities D_r of the sand layers. In all cases the parts, at which large amounts of shear strains were calculated, only existed within the sand layers. In Case 4, larger shear strains appeared at the toe of the slope, within the part the first failure might occur and the

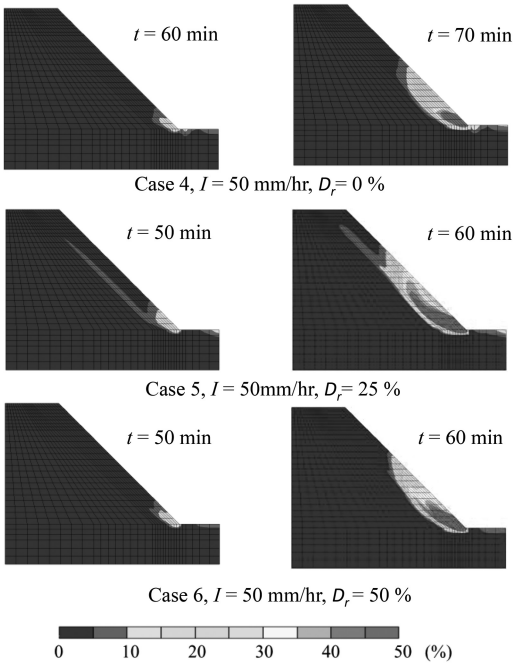


Figure 17. The simulation results of shear strain contours in Cases 4, 5 and 6.

part did not extend to the upper part of the slope comparing other cases. Meanwhile in Cases 5 and 6, at first the part with larger strains appeared at the toe of the slope, which was the same situation as Case 2, but during only 10 minutes the part extended to upper parts and larger ranges become unstable. Progressive failures might occur in the parts. However the property that the failure patterns depend on D_r values, which can be seen in experimental tests (see Figures 7 and 8), might be not clearly calculated.

5 CONCLUSIONS

In this paper we present slope stability analysis methods based on saturated and unsaturated consolidation analysis methods and its application to 1g failure model tests. At the first part we reviewed the methods and constitutive equations coupled with the method. The methods were classified into two on the base of field equations used. We discussed the important point in the use of the equations. That is the condition in choosing soil water retention models. These models should express saturation and unsaturation until low degree of saturation conditions.

In the constitutive equations, we pointed out two important points: (i) to take two suction effects into account and (ii) to consider soil water retention conditions. The two suction effects are (1) an increase in suction increases effective stresses, and (2) an increase in suction enhances yield stresses and affects resistance to plastic deformations. In the point (ii), the mechanical behavior changes at the air entry suction. If the suction is smaller than the air entry value of the soil s_e, the mechanical behavior may be regarded as that of saturation soils. If the suction is larger than s_e, the two suction effects described above should be considered.

At the second part, we present an application saturated and unsaturated consolidation analysis method coupled with an elastoplastic model for unsaturated soils, which satisfies the conditions (Code name: GEOCUP), to the slope stability problem. It has a potential to be the most powerful design tool for evaluating slope stabilities. A series of 1G slope failure model tests, which consisted of a shallow surface sand layer on a relatively hard foundation, are simulated. We obtained following conclusions from the experiment tests:

(E1) Failures occurred in all cases. In Case 3 ($D_r = 0$ %), the sand mass moved along the slope and a clear, large but shallow failure finally occurred. It was a typical surface failure,

(E2) The horizontal deformations of the sand mass were dominant in Case 5 ($D_r = 50$ %). After the first slip surface appeared at the toe of the slope, in sequence the slip surfaces appeared and they progressed to the upper parts of the slope. The failure was a typical progressive failure,

(E3) The sand mass moved to intermediate direction between Cases 3 and 5 in Case 4 ($D_r = 25\%$). However other failure processes were similar to those of Case 5. In Cases 4 and 5, these failures occurred within the area at which PWP values became positive,

(E4) PWP values rose up faster with an increase in the relative densities of the sand subsurface layers. The PWP values in Case 3 had been keeping negative values for a long time,

(E5) There was a clear seepage surface in Case 5 and the surface appeared on a relatively high level portion of the slope surface. Meanwhile the seepage surface in Case 3 did not appear on the slope surface. The seepage surface in Case 4 also appeared on the slope surface but the level was lower than that in Case 5.

We could obtain the following results from the simulations:

(S1) Negative pore water pressures dissipated from the toes of the slopes and the saturated zones progressed to upper parts of the slopes,

(S2) Large deformations were only accumulated in the sand layer,

(S3) The failures started from the saturated toes and the failure zones progressed upper parts of the sand layer.

(S4) The difference of failure patterns due to the differences of D_r values might be clearly calculated,

(S5) These situations mentioned above were consistent with the experimental results. Therefore this consolidation analysis method is suitable for analyzing problems of slope stabilities due to rainfalls.

Finally we would like to appreciate my students and staffs of National Institute for Rural Engineering, Tsukuba, Japan for their helps and contributions to this series of experimental model tests. The research presented herein was supported by the Japan Society for the Promotion of Science (JSPS) (the grant No. was 23580327).

REFERENCES

Alonso, E.E., Gens, A. & Josa, A. 1990. A constitutive model for partially saturated soils. *Geotechnique* 40(3): 405–430.

Fleureau, J.M., Kheirbek-Saoud, S., Soemitro, R. and Taibi, S. 1993. Behavior of clayey soils on drying–wetting paths. *Can. Geotech. J.* 30: 287–296.

Fredlund, D.G. & Rahardjo, H. 1993. *Mechanics for unsaturated soils*, John Wiley & Sons: 321–345.

Japan Meteorological Agency 2009. *Watching report of meteorological changes 2009 Chapter 1*: 29–30.

Kohgo, Y. 1995. A consolidation analysis method for unsaturated soils coupled with an elastoplastic model. *Proc. 1st Int. Conf. Unsaturated Soils*: 1085–1093.

Kohgo, Y. 2003. Review of constitutive models for unsaturated soils and initial-boundary value analyses, *Proceedings of the 2nd Asian Conference on Unsaturated Soils*: 21–40.

Kohgo, Y. 2008. A hysteresis model of soil water retention curves based on bounding surface concept, *Soils and Foundations* 48(5): 633–640.

Kohgo, Y., Asano, I. & Hayashida, Y. 2007. An elastoplastic model for unsaturated rockfills and its simulations of laboratory tests, *Soils and Foundations* 47(5): 919–929.

Kohgo, Y., Horpibulsuk, S. & Tamrakar, S.B. 1999. Simulation of volume change behavior of yellow soil sampled from Khon Kaen City in Northeast Thailand. *Eleventh Asian Regional Conference on Soil Mechanics and Geotechnical Engineering*: 141–144.

Kohgo, Y., Nakano, M. & Miyazaki, T. 1993a. Theoretical aspects of constitutive modeling for unsaturated soils, *Soils and Foundations* 33(4): 49–63.

Kohgo, Y., Nakano, M. & Miyazaki, T. 1993b. Verification of the generalized elastoplastic model for unsaturated soils, *Soils and Foundations* 33(4): 64–73.

Kohgo, Y., Tokoro, N., Togari, A. & Shimamura, M. 2011. Simulation of behavior of a slope model with a shallow subsurface sand layer due to rainfall. *Proc. 5th Asian Pacific Conference on Unsaturated Soils*: 741–746.

Kohgo, Y., Takahashi, A. & Suzuki, T. 2010. Centrifuge model tests of a rockfill dam and simulation using consolidation analysis method. *Soils and Foundations* 50(2): 227–244.

Nobuoka, T., Ugai, K., Wakai, A. & Fei, C. 2009. A study of the slope stability prediction in considering unsteady rain and unsaturated character of soil, *J. Civil Eng. C* 65(1): 29–40.

Okada, K., Makihara, Y., Shinpo, A., Kunitsugu, M. & Saito, K. 2001. Soil water index, *Tenki* 48(5): 349–356.

Orense, R. P., Shimoma, S., Maeda, K. & Towhata, I. 2004. Instrumented model slope failure due to water seepage, *J. Natural Disaster Science* 26(1): 15–26.

Shimada, K., Morii, T., Fujii, H. & Nishimura, S. 1999. Slope stability analysis considering reduction of shear strength of unsaturated soil due to rain infiltration, *Trans. of JSIDRE*, No. 204: 93–98.

Tanaka, H., Kudoh, Y. & Kaneko, H. 2009. Slope stability consisting of two different layers caused by rainfall, *Prediction and simulation methods for geohazard mitigation*, CRC Press, CD-ROM.

Terzaghi, K. 1936. The shearing resistance of saturated soil and the angle between the plane of shear. *Proc. 1st Int. Conf. Soil Mech. Found. Eng.* Vol. 1 Harvard, Mass.: 54–56.

Tohari, A., Nishigaki, M. & Komatsu, M. 2007. Laboratory experiments on initiation of rainfall-induced slope failure with moisture content measurements, *J. Geotechnical and Geoenvironmental Eng.* 133(5): 575–587.

Tokoro, N., Tanikawa, K., Saito, H., Kohgo, Y. & Hori, T. 2012. On 1G slope failure model tests due to rainfalls–Difference of failure patterns due to difference of densities of a subsurface sand layer – *Proc. 2nd Advances in Transportation Geotechnics*: 755–760.

White, D.J., Take, W.A. & Bolton, M.D. 2003. Soil deformation measurement using particle image velocimetry (PIV) and photogrammetry, *Geotechnique* 53(7): 619–631.

This page intentionally left blank

Unsaturated Soil Mechanics—from Theory to Practice – Chen et al. (Eds)
© 2016 Taylor & Francis Group, London, ISBN 978-1-138-02921-7

Investigation of mechanical and physio-chemical coupling through swelling pressure

Y.J. Cui
Ecole des Ponts ParisTech, Laboratoire Navier/CERMES, Cité Descartes, Champs-sur-Marne, Marne-la-Vallée Cedex 2, France

ABSTRACT: Oedometer tests were carried out on natural stiff clays with loading/unloading/reloading. Common unloading/reloading loops were identified. Further examination of the unloading or reloading curves shows that each path can be satisfactorily considered as bi-linear with a small and a large slopes separated by a threshold vertical stress. There is a good relationship between the threshold stress and the void ratio just before the unloading or reloading. Further examination showed that this threshold stress corresponds to the swelling pressure of soil. It can be then deduced that the unloading/reloading loops are rather due to the competition between the mechanical and physico-chemical effects on soil microstructure changes than the viscosity effect as commonly admitted.

1 INTRODUCTION

The swelling pressure of a soil is commonly defined as the stress under which no volume change occurs upon wetting. According to this definition, swelling takes place when wetting a soil under a stress lower than the swelling pressure, while collapse takes place when wetting the soil under a stress higher than the swelling pressure. Various methods can be used for determining soil swelling pressure (see Figure 1). The "constant-volume" method (path OA) is based on the use of a relatively rigid cell with total pressure measurement. The final value of pressure after stabilisation is the swelling pressure of soil. For the "zero-swell" method (path OBB'), the equipment employed is a conventional oedometer (Basma et al., 1995; Nagaraj et al., 2009). Firstly, a low initial load (0.1 MPa for example) is applied on the specimen prior to water flooding. As the specimen wets up it attempts to swell. When the swell exceeds a certain value (0.1% for instance), additional pressure is added in small increment to bring the volume of soil specimen back to its initial value (Basma et al., 1995; Attom et al., 2001). This operation is repeated until the specimen ceases to swell. The swelling pressure is defined as the stress under which no more swelling occurs. The "swell-consolidation" method (path OCC') consists of re-saturating the soil under a low pressure (0.1 MPa for example). After swell completion, standard consolidation test is performed. The pressure required to bring the soil specimen back to its initial void ratio is considered as the swelling pressure (Basma et al., 1995; Agus, 2005).

The soil swelling pressure depends on several factors: i) the soil nature – the more plastic the soil the higher the swelling pressure; ii) the initial suction or initial water content – the drier the soil the higher the swelling pressure; iii) the soil density – the denser the soil the higher the swelling pressure; iv) the microstructure of soil – the swelling pressure is strongly related to the orientation of clay particles, and different swelling pressure value can be obtained for different directions with different particle orientations. Soil pore water salinity also affects the swelling pressure value if different water is used in the test.

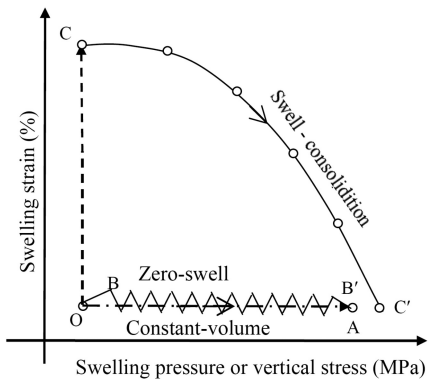


Figure 1. Methods for swelling pressure determination (Wang et al. 2012).

Wang et al. (2012) showed that the swelling pressure depends solely on the final dry density of soil. They investigated different bentonite-based materials such as MX80, FoCa7 (Imbert et al., 2006), FEBEX (Villar et al., 2002) and Kunigel V1 (Dixon et al., 1996), and

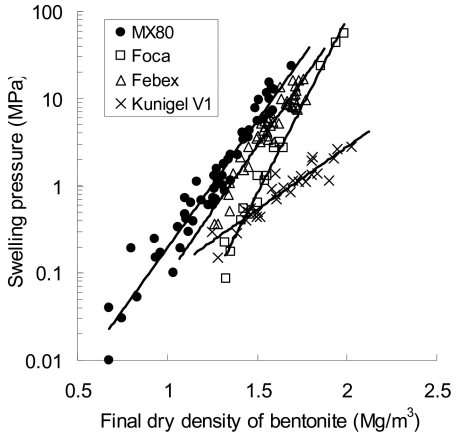


Figure 2. Swelling pressure versus final dry density of bentonite (Wang et al. 2012).

Table 1. Montmorillonite content and external cations type of several bentonites.

Bentonite	Montmorillonite Content (%)	Type
MX 80	75–90	Na
FEBEX	92	Ca
FoCa	50 Beidellite 50 Kaollite	Ca
Kunigel V1	48	Na

observed that for each bentonite, there is a unique relationship between the swelling pressure and the final dry density of bentonite (see Figure 2).

The different relationships can be related to the different clay natures (i.e. montmorillonite, beidellite and saponite, etc.), the different montmorillonite contents and the different exchangeable cation types (i.e. calcium or sodium), as shown in Table 1. In general, the swelling capacity of sodium bentonite is higher than that of calcium bentonite; with the same type of exchangeable cations, a larger montmorillonite content leads to a higher swelling pressure.

It appears then that for a given soil, the final density of soil defines its swelling pressure. As the soil density can evolves for both saturated and unsaturated soils with water intake, the swelling pressure evolves too for both soils. This implies that the identified relationship between swelling pressure and final density should be independent of the soil state, saturated or unsaturated, at which the final density is reached. In other words, the notion of swelling pressure should be also applicable for saturated soils.

On the other hand, it is well known that the soil compression curves show unloading/reloading loops. These loops have been commonly explained by the soil viscosity effect: clayey soils have larger loops because of their relatively higher viscosity, and sandy soils have narrow loops because of their low viscosity, silty soils being in between. When investigating the compressibility of a soil, these loops are often ignored and an average slope is usually considered in the calculation of soil volume change. Obviously, this practice is relatively easy for sandy soils and silty soils, but difficult for clayey soils and even impossible for expansive soils.

From a fundamental point of view, explaining the unloading/reloading loops by viscosity effect seems too simplistic and unclear. Further study on the involved mechanisms is needed based on the swelling patterns of clayey soils.

This aspect was investigated by Cui et al. (2013) through oedometer tests with several unloading/reloading cycles on natural stiff clays, Ypresian clays (YPClay). The results were analysed based on the competition between the mechanical effect and physico-chemical effect occurring during unloading or reloading. A new mechanism related to the soil swelling pressure was proposed, that is consistent with the aforementioned unique relationship between swelling pressure and soil final density. This mechanism was verified by the results from the oedometer tests on other natural stiff clays such as Boom Clay and London clay.

2 MATERIALS AND METHODS

The materials studied are cores sampled from Ypresian formation at four different depths, namely YPClay43 from 330.14 m–330.23 m depth, YPClay64 from 351.20 m–351.29 m depth, YPClay73 from 361.30 m–361.34 m depth, and YPClay 95 from 382.35 m–382.44 m depth. Their clay mineralogy and physical properties are shown in Table 2 and Table 3, respectively. The four depths have comparable clay fractions (between 48 and 59%) as well as similar smectite contents (between 26 and 34%), suggesting similar physical properties in terms of plasticity. However, the value of plasticity index I_P (see Table 3) show a much lower plasticity for YPClay43 as compared to the three other depths. YPClay43 has also the lowest liquid limit ($w_L = 75$) and the highest carbonates content $CaCO_3$ (10.16%), its other parameters (specific gravity G_s, initial water content w_0, initial void ratio e_0) being similar to that of other depths. It is possible that the high carbonates content of YPClay43 gives rise a lower level of plasticity as indicated by its value of *PI* in Table 3. The chemical composition of pore water is presented in Table 4.

Oedometer tests were performed on soil samples of 50 mm diameter and 20 mm height by hand-trimming from cores that have 1000 mm length and 100 mm diameter. After installing soil sample in the oedometer cell, step loading up to the in situ vertical effective stress (up to point A in Figure 3a) was carried out without contact with water in order to avoid any swelling which would affect the initial soil microstructure (Delage et al., 2007; Cui et al., 2009, Deng et al.,

Table 2. Mineralogy of YPClay (Vandenberghe et al., 2011).

Mineral Depth (m)	YPClay43 330.14–330.23	YPClay64 351.20–351.29	YPClay73 361.30–361.34	YPClay95 382.35–382.44
Clay (% wt)	54	48	57	59
Illite	5	4	5	6
Kaolinite	2	5	3	3
Smectite	32	26	33	34
Illite/Smectite	12	10	12	13
Chlorite/others	3	3	4	3
Non-clay (% wt)	46	52	43	41
Quartz	32	36	31	27
K-feldspar	6	7	6	7
Plagioclase	6	6	5	3
Others	2	3	1	4

Table 3. Physical properties of YPClay.

Soil	G_s (-)	w_L (-)	I_p (-)	w_0 (%)	e_0	Sr_0 (%)	CaCO3 (%)
YPClay43	2.78	75	42	26	0.81	89	10.16
YPClay64	2.79	114	80	26	0.79	92	1.38
YPClay73	2.80	137	101	31	0.94	93	0.88
YPClay95	2.80	132	88	30	0.95	87	3.82

2011a, b, c). Note that the in situ vertical effective stresses (σ'_{v0}) were estimated by taking an average density of the overlying soils equal to 1.9 Mg/m^3 (van Marcke and Laenen, 2005) with an underground water level assumed to be at the ground surface. For convenience, σ'_{v0} was rounded to 3.2 MPa for all the four depths. The degree of saturation at point A, calculated using the initial degree of saturation (see S_{r0} in Table 3) and the volume change recorded, was found to be 100% for all the samples tested.

Under σ'_{v0}, the bottom porous stone and the drainage tubes were saturated with the in situ synthetic water that has the same chemical composition (see Table 4) as the field pore water (A–B). Afterwards, step unloading to 0.125 MPa (B–C), reloading up to 16 MPa (C–D), unloading again to 0.125 MPa (D–E), reloading up to 32 MPa (E–F) and finally unloading to 0.125 MPa (F–G) were conducted. The stabilization of volume change was considered as achieved when the vertical strain rate is lower than 5×10^{-4}/8 h (AFNOR, 1995, 2005).

3 EXPERIMENTAL RESULTS

Figure 1 shows the compression curve for the four depths. For YPClay43 (Figure 3a), YPClay64 (Figure 3b) and YPClay73 (Figure 3c), two full unloading/reloading cycles and one extra single unloading were applied, while for YPClay95 (Figure 3d), only one full cycle and one extra single unloading were applied. Figure 3a shows that the application of the in situ vertical effective stress (3.2 MPa) led the soil sample to point A. When saturating the bottom porous stone and the drainage tubes, a negligible volume change (A to B) was observed, confirming that the sample was fully saturated. Upon unloading from B to C, a nearly bi-linear curve was observed: when the stress was higher than a threshold stress σ_{s1} the slope was small, and when the stress was lower than σ_{s1} the slope is significantly larger. Upon reloading from C to D, a tri-linear curve was identified. Below the stress at point B, a nearly bi-linear curve was again observed, with a small slope below a threshold stress σ_{s4} and a larger slope beyond σ_{s4}. Further loading beyond point B gave rise to a larger slope, certainly related to the plastic volume changes. Examination of the unloading/reloading curve B-C-B shows a hysteretic loop. The same phenomenon can be observed when unloading the sample from D to E and reloading the sample from E to F: there is a nearly bi-linear curve from D to E with a small slope beyond a threshold stress σ_{s2} and larger slope below σ_{s2}, there is also a nearly bi-linear curve from E to D with a threshold stress σ_{s5}, and when the stress is beyond point D, the slope is increased because of the plastic volume change. The unloading from F to G confirmed the bi-linearity of the curve with a threshold stress σ_{s3}. Comparison of the unloading slopes shows that both the small slope and large slope were increasing with the maximum stress applied prior to unloading.

The same observation can be made on the results from the tests on the other three depths (YPClay64 – Figure 3b, YPClay73 – Figure 3c and YPClay95 – Figure 3d). There are also more or less well defined bi-linear curves for both unloading and reloading paths with threshold stresses.

It must be mentioned that the bi-linearity observed in this study should be considered as a particular case because for most clayey soils, non-linear curves are often observed. It is likely that there is relatively well defined bi-linearity for natural stiff clays like the studied YPClay. Basically, the shape of the curves depends on both the soil nature and soil microstructure.

Table 4. Chemical composition of pore water YPClay (after van Marcke and Laenen, 2005).

Ion	Min (mg/L)	Max (mg/L)	Min (10^{-3} M)	Max (10^{-3} M)
Na+	4160.0	7459.0	180.87	324.30
K+	94.3	919.0	2.42	23.56
Ca2+	226.0	808.1	5.65	20.20
Mg2+	83.0	418.0	3.46	17.42
Fe	0.2	13.9	0.00	0.25
CI−	6069.0	13540.0	170.96	381.41
S042−	226.4	6535.0	2.36	68.07
HC03−	24.4	274.5	0.40	4.50

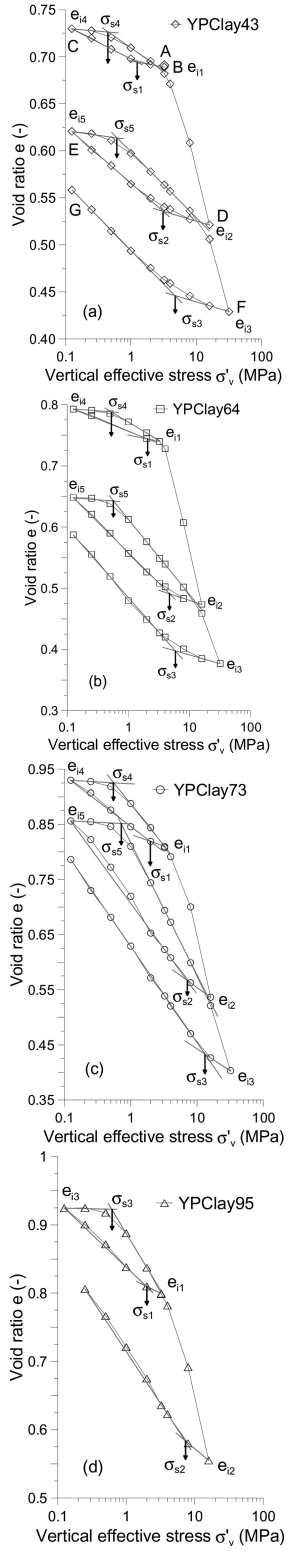


Figure 3. Oedometer tests with unloading/reloading on YPClay.

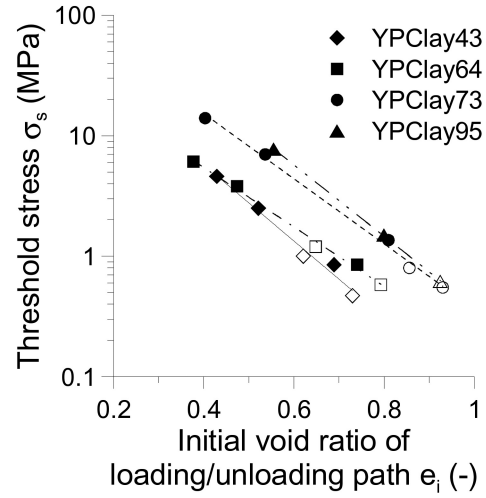


Figure 4. Swelling stress versus the void ratio just before unloading or reloading for YPClay – Closed symbols are for unloading path, open symbols for loading path.

To further analyse the results, in Figure 4, the values of threshold stress in Figure 3 for each depth are presented as a function of the void ratio just before each unloading or reloading (σ_{s1} with e_{i1}; σ_{s2} with e_{i2}; σ_{s3} with e_{i3}; σ_{s4} with e_{i4}; σ_{s5} with e_{i5}). A good linear relationship is obtained in a semi-logarithmic plane for all the four depths. In order to verify this observation, some results from oedometer tests on stiff Boom Clay from the Essen site are collected from the literature, and shown in Figure 5. It is observed that the variations of swelling pressure with the initial void ratio before unloading or reloading for Boom Clay at different depths (cores numbered Ess75, Ess83, Ess96, Ess104 and Ess112) show also good linear relationships. Obviously, the relationship between $\sigma_s$and e_i is soil nature and microstructure dependent: the slope and the position of lines are different for different soils.

Figure 6 shows the results obtained on the basis of the data reported by Gasparre and Coop (2008) on London clay at Healthrow Airport Terminal 5. It involves six samples from different depths: 7 m (C7), 10 m (B10), 25 m (B25), 28 m (B28), 36 m (A36) and 51 m (A51). Note that letters A, B, C are the names of three lithological units among the five main ones in the London Basin (King, 1981). Again, a good linear relationship is observed for all samples with unloading/reloading.

4 INTERPRETATION AND DISCUSSION

Delage and Lefebvre (1984) showed that when compressing a clayey soil in oedometer, macro-pore collapse occurs first during loading path under stresses higher than the preconsolidation pressure or yield stress of soil, leading to irrecoverable volume changes; this process results in microstructure changes characterized by more and more orientated particles.

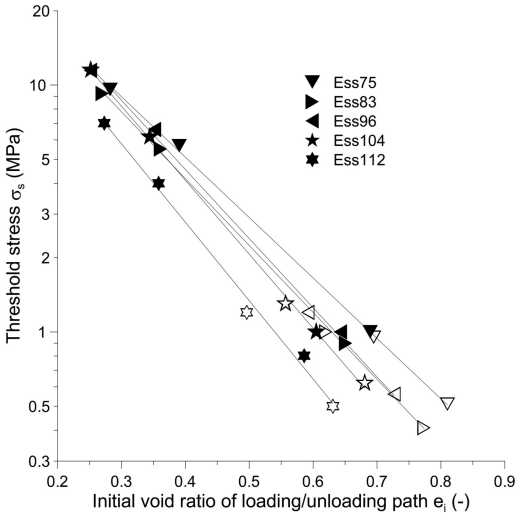


Figure 5. Swelling stress versus the void ratio just before unloading or reloading for Boom Clay from the Essen site – Closed symbols are for unloading path, open symbols for loading path.

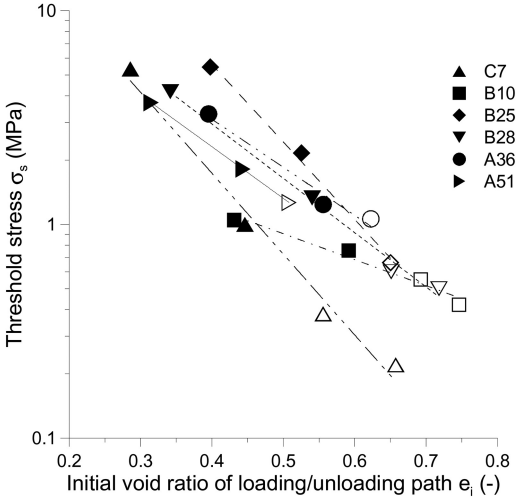


Figure 6. Swelling stress versus the void ratio just before unloading or reloading for London clay. – Closed symbols are for unloading path, open symbols for loading path.

As Le et al. (2011) indicated, with a more orientated microstructure the physico-chemical interaction between clay particles and adsorbed water is enhanced. Indeed, Olson and Mesri (1970) pointed out that the competition between the mechanical effect and physico-chemical effect on soil volume change behaviour depends strongly on the particles geometric arrangement defined by the contact angle between particles: the mechanical effect is more pronounced when the contact angle is large, and on the contrary, the physico-chemical effect becomes dominant when the particles are more parallel with a small contact angle. Thereby, upon mechanical loading in oedometer the contact angle is decreasing, leading to the increase of the physico-chemical effect.

Basically, the increase of physico-chemical effect due to loading can be well evidenced during unloading: the more oriented particles undergo higher repulsion forces and thus show more significant swell: the unloading curve could have a much greater slope than the initial loading slope before the preconsolidation pressure is reached, and the void ratio after full unloading could even be higher than the initial void ratio. Examination of the unloading slopes in Figure 3 confirms this reasoning: the unloading slope is indeed increasing with increasing yield stress.

The description above shows that when unloading from the previous maximum stress (commonly termed as yield stress), the compression behaviour is mainly governed by the competition between the physico-chemical effect and mechanical effect. When the external stress is higher than the repulsive force related to the soil particles-water interaction (physico-chemical effect), low swelling volume change occurs; otherwise, higher swelling volume change can be expected. Similarly, upon reloading, when the external stress is lower than a certain value, there is no significant change of the microstructure created during the previous unloading. On the contrary, when the external stress becomes higher, the mechanical effect becomes dominant giving rise to larger volume change corresponding to the collapse of the microstructure created previously during unloading. This conceptual description implies that it is possible to determine a characteristic stress that separates the zone with prevailing physico-chemical effect from the zone with prevailing mechanical effect. It is indeed what is observed in Figure 3 with the threshold stresses. Upon unloading, when the vertical stress is higher than the threshold stress σ_s, the volume change is characterized by the mechanical rebound; however, in the lower stress range the volume change is characterized by the physico-chemical swelling.

Furthermore, if we admit that the physico-chemical effect mentioned above corresponds to the matric suction as we do commonly for expansive soils (saturated or unsaturated), the threshold stress identified should correspond to the swelling pressure. To verify this reasoning, the swelling pressure of Boom Clay from the Mol site determined by Horseman et al. (1987) from zero-swell tests are compared with the threshold stress/initial void ratio relationship determined by Horseman et al. (1987) and determined from oedometer test on a core namely BM101 (Figure 7). A good agreement is obtained, confirming that the threshold stresses determined in this study are indeed the swelling pressures.

In fact, the small mechanical rebound upon unloading implies an insignificant microstructure change, i.e., the microstructure pattern remains rather orientated with dominated face-to-face particle contacts (see Figure 8). Note that the description of different particles contacts using patterns of face-to-face, face-to-edge etc. was done by several authors as Sides and

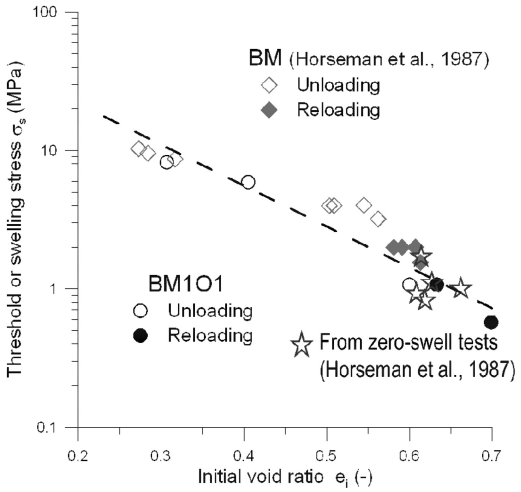


Figure 7. Swelling pressure versus void ratio for Boom Clay from the Mol site.

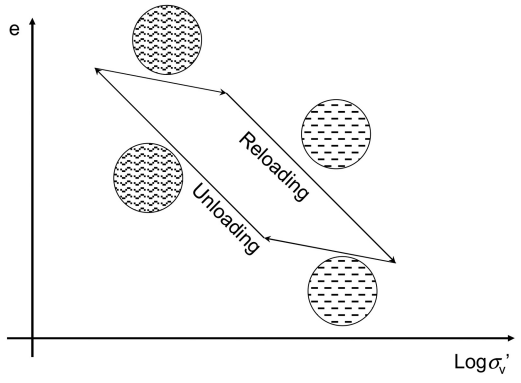


Figure 8. Representation of microstructure changes during unloading/reloading.

Barden (1970), Collins and Mc Gown (1974), van Olphen (1977) and Mitchell and Soga (2005), and the interpretation given here remains qualitative and should be verified by further studies. When the external stress is lower than the threshold stress or swelling pressure σ_s, the prevailing physico-chemical effect leads to a significant microstructure change characterized by formation of more and more face-to-edge particle contacts. This microstructure change corresponds to a larger soil swelling. Following this concept, the threshold stress or swelling pressure σ_s separates the zone with insignificant microstructure change from the zone with significant microstructure change. The increase of this swelling pressure with loading ($\sigma_{s1} < \sigma_{s2} < \sigma_{s3}$) observed in Figure 3 is also consistent with the common results of unsaturated expansive soils: a higher stress causes lower void ratio or higher density, increasing the swelling pressure (Villar et al., 2008; Siemens et al., 2009; Wang et al., 2012).

The reasoning above applies also for the reloading path. When the external stress is lower than the swelling pressure, the matric suction related to the physico-chemical effect is high enough to balance the effect of external stress, and the soil microstructure changes insignificantly (with the face-to-edge particles preserved). As a result, the slope of the compression curve is small. By contrast, when the external stress is higher than the swelling pressure, the mechanical effect becomes dominant and larger volume change occurs by collapse of large-pores (the particles arrangement tends towards face-to-face type), leading to a larger slope of the compression curve.

Note that the model proposed for microstructure changes during unloading/reloading is totally conceptual. It should be confirmed by experimental evidence in further studies implying appropriate techniques for microstructure observation at clay particles scale and upon mechanical unloading/reloading. Theoretically, the more plastic the soil is (high smectite content, high plasticity index I_P, large methylene blue value, etc.), the more the microstructure changes from face-to-face pattern to face-to-edge pattern can be expected.

As indicated before, the swelling pressure is not the same for the unloading and reloading: the value is related to the void ratio before unloading or reloading. Figures 4–7 show that there is a linear relationship between the swelling pressure and the void ratio before unloading or reloading in a semi-logarithmic plane for natural stiff clays as YPClay, Boom Clay and London clay, although this relationship is soil nature dependent. This is consistent with the results from the tests on unsaturated expansive soils, thereby bring another evidence for the identified threshold stress as swelling pressure. Note that for other soils there is not necessarily bi-linear unloading/reloading curves and in that case it is difficult to determine the relationship between the swelling pressure and void ratio before unloading or reloading. However, it is believed that the conceptual model developed in this study would be still applicable.

5 CONCLUSION

Recent studies prove that for a given soil, the final dry density is the only factor defining the swelling pressure of soil. Basically, this phenomenon is true for unsaturated soils, and it should be also true for initially saturated soils having matric suction related to the physic-chemical integration between clay particles and adsorbed water. As this soil matric suction effect can be fully reflected during unloading/reloading process, it seems possible to investigate the soil density change under the combined effect of mechanical load and physico-chemical interaction, and then to further identify the soil swelling behaviour.

To verify this concept, oedometer tests were carried out with loading/unloading/reloading on natural stiff clays, Ypresian clays (YPClay), from different

depths. The unloading/reloading loops of compression curves of YPClay were explained by the competition between the mechanical and physico-chemical effects. Upon unloading, when the applied stress is higher than a threshold stress, the mechanical effect is dominant and only small mechanical rebound is observed; by contrast, when the applied stress is lower than the threshold stress, physico-chemical effect becomes dominant, giving rise to soil swelling with a larger slope. Upon reloading, when the applied stress is lower than another threshold stress, the microstructure is more or less preserved thank to the contribution of the soil matric suction, leading to a small volume change; on the contrary, when the applied stress is higher than this threshold stress, the mechanical effect prevails and larger volume change occurs by collapse of large-pores. There is a good linear relationship between the threshold stress and the void ratio just before unloading or reloading. The results of Boom clay from the Essen site and of London clay confirm these findings. Further examination on Boom Clay from the Mol site shows the threshold stress identified in the unloading/reloading loops corresponds to the soil swelling pressure, and the good relationship between the threshold stress and void ratio corresponds totally to the relationship between the swelling pressure and final density for unsaturated soils. It can be then concluded that the unloading/reloading loop is rather due to the competition between the mechanical and physico-chemical effects than the viscosity effect as commonly admitted.

ACKNOWLEDGEMENTS

The author would like to address his great thanks to his co-workers from both Ecole des Ponts ParisTech (Dr Nguyen Xuan Phu, Dr Wang Qiong, Dr Tang Anh Minh) and the European Underground Research Infrastructure for Disposal of nuclear waste in Clay Environment – Euridice (Dr Li Xiangling).

REFERENCES

AFNOR, 1995. Sols : reconnaissance et essais: essai de gonflement à l'oedomètre, détermination des déformations par chargement de plusieurs éprouvettes. XP P 94–091.

AFNOR, 2005. Geotechnical investigating and testing, Laboratory testing of soils, Part 5: Incremental loading Oedometer test. XP CEN ISO/TS 17892-5.

Agus, S., 2005. An Experimental study on hydro-mechanical characteristics of compacted bentonite-sand mixtures. PhD thesis. Bauhaus-University Weimar, Germany.

Attom, M., Abu-Zreig, M., Obaidat, M., 2001. Changes in clay swelling and shear strength properties with different sample preparation techniques. *Geotechnical Testing Journal, ASTM*, 24, 157–163.

Basma, A.A., Al-Homoud, A.S., Husein, A., 1995. Laboratory assessment of swelling pressure of expansive soils. *Applied Clay Science* 9 (5), 355–368.

Collins, K., Mc Gown, A., 1974. The form and function of microfabric features in a variety of natural soils. Géotechnique 24 (2), 223–254.

Cui Y.J., Nguyen X.P., Tang A.M., Li X.L. 2013. An insight into the unloading/reloading loops on the compression curve of natural stiff clays. *Applied Clay Science* 83–84, 343–348.

Cui, Y.J., Le, T.T., Tang, A.M., Delage, P., Li X.L., 2009. Investigating the time dependent behaviour of Boom clay under thermo-mechanical loading. *Géotechnique* 59 (4), 319–329.

Delage, P., Lefebvre, G., 1984. Study of the structure of a sensitive Champlain clay and of its evolution during consolidation. *Canadian Geotechnical Journal* 21 (1), 21–35.

Delage, P., Le, T.T., Tang, A.M., Cui, Y.J., Li, X.L., 2007. Suction and in-situ stresses of deep Boom clay samples. *Géotechnique* 57 (1), 239–244.

Deng, Y.F., Tang, A.M., Cui, Y.J., Nguyen, X.P., Li, X.L., Wouters, L., 2011a. Laboratory Hydro-mechanical Characterisation of Boom Clay at Essen and Mol. *Physics and Chemistry of the Earth* 36 (17–18), 1878–1890.

Deng, Y.F., Tang, A.M., Cui, Y.J., Li, X.L., 2011b. A study on the hydraulic conductivity of Boom clay. *Canadian Geotechnical Journal* 48, 1461–1470.

Deng, Y.F., Cui, Y.J., Tang, A.M., Nguyen, X.P., Li, X.L., Van Geet M., 2011c. Investigating the pore-water chemistry effects on the volume change behaviour of Boom clay. Physics and Chemistry of the Earth 36 (17–18), 1905–1912.

Dixon, D.A., Gray, M.N., Graham, J., 1996. Swelling and hydraulic properties of bentonites from Japan, Canada and USA. *Proceedings of the second International Congress on Environmental Geotechnics*, Osaka, Japan, pages 5–8.

Gasparre, A., Coop, M.R., 2008. Quantification of the effects of structure on the compression of a stiff clay. *Canadian Geotechnical Journal* 45 (9), 1324–1334.

Horseman, S.T., Winter, M.G., Entwistle, D.C., 1987. Geotechnical characterization of Boom clay in relation to the disposal of radioactive waste. Commission of the European Communities, EUR 10987, p. 87.

Imbert, C., and Villar, M.V., 2006. Hydro-mechanical response of a bentonite pellets-powder mixture upon infiltration. *Applied Clay Science*, 32 (3–4):197–209.

King, C., 1981. The stratigraphy of the London Basin and associated deposits. Tertiary Research Special Paper 6, Backhuys, Rotterdam, the Nerthelands.

Le, T.T., Cui, Y.J., Munoz, J.J., Delage, P., Tang, A.M., Li, X., 2011. Studying the stress-suction coupling in soils using an oedometer equipped with a high capacity tensiometer. *Front. Archit. Civ. Eng. China* 5 (2), 160–170.

Mitchell, J.K., Soga, K., 2005. Fundamentals of soil behavior. John Wiley & Sons Inc.

Nagaraj, H.B., Munnas, M.M., Sridharan, A., 2009. Critical Evaluation of Determining Swelling Pressure by Swell-Load Method and Constant Volume Method. *Geotechnical Testing Journal, ASTM*, 32, 305–314.

Olson, R.O., Mesri, G., 1970. Mechanisms controlling compressibility of clays. *Journal of Soil Mechanics and Foundation Division, Proceeding of the American Society of Civil Engineers*, SM6, pp. 1863–1878.

Sides, G., Barden, L., 1970. The microstructure of dispersed and flocculated samples of kaolinite, illite and montmorillonite. *Canadian Geotechnical Journal* 8, 391–399.

Siemens, G., Blatz, J.A., 2009. Evaluation of the influence of boundary confinement on the behaviour of unsaturated swelling clay soils. *Canadian Geotechnical Journal* 46 (3), 339–356.

van Olphen, H., 1977. An Introduction to Clay Colloid Chemistry, second ed. Wiley Interscience, New York.

Vandenberghe N., 2011. Qualitative & quantitative mineralogical analyses on the Ypresian clay. Report of Applied Geology & Mineralogy Group of K. U. Leuven to NIRAS-ONDRAF.

van Marcke, Ph., Laenen, B. 2005. The Ypresian clays as possible host rock for radioactive waste disposal: an evaluation. Report of Belgian agency for radioactive waste and enriched fissile materials, p. 149.

Villar, M.V., 2002. Thermo-hydro-mechanical characterisation of a bentonite from Cabo de Gata. A study applied to the use of bentonite as sealing material in high level radioactive waste repositories. Publicación Técnica ENRESA 01/2002, Madrid, 258 p.

Villar, M.V., Lloret, A., 2008. Influence of dry density and water content on the swelling of a compacted bentonite. *Applied Clay Science* 39 (1–2), 38–49.

Wang, Q., Tang, A.M., Cui, Y.J., Delage, P., Gatmiri, B., 2012. Experimental study on the swelling behaviour of bentonite/claystone mixture. *Engineering Geology* 124, 59–66.

Unsaturated Soil Mechanics—from Theory to Practice – Chen et al. (Eds)
© 2016 Taylor & Francis Group, London, ISBN 978-1-138-02921-7

Testing of the hydro-mechanical behaviour of shales

L. Laloui, A. Ferrari & V. Favero
Swiss federal Institute of Technology, Lausanne, EPFL, Switzerland

ABSTRACT: Shales are among the most commonly considered geomaterials in current energy-related geomechanical investigations, as they are involved in engineering applications such as the unconventional extraction of natural gas, CO_2 sequestration and nuclear waste geological storage. A deep understanding of their hydro-mechanical behaviour is of primary significance for such applications. In this paper selected results on the water retention behaviour and on the high pressure oedometric compression behaviour of shales are presented.

1 INTRODUCTION

The geomechanical behaviour of shales is quickly becoming one of the most important issues in modern geomechanics, largely driven by the geological storage of nuclear waste, the extraction of shale gas and the sequestration of CO_2.

In the context of such engineering applications, a deep understanding of the hydro-mechanical behaviour of shales is of primary significance. The mechanical properties and the permeability are of primary importance in determining the production capacity of shale gas reservoirs.

Water retention mechanisms play a major role in fluid trapping due to the capillary forces present in low permeability formations or in the resaturation of the shale formation after ventilation, as in the case of deep geological repositories. Wetting and drying episodes have significant impacts on shale volumetric behaviour: swelling/shrinkage of shales may be caused by changes in suction or variations in the degree of saturation; additionally, significant swelling pressures may develop when volumetric expansion upon wetting is prevented.

In this paper selected results on the water retention behaviour and on the high pressure oedometric compression behaviour of shales are presented.

2 TESTED MATERIALS

Results from three shales are presented. Two of the considered shales come from a deep geothermal well near the village of Schlattingen in the Molasse Basin in Northern Switzerland; one belongs to the Opalinus Clay formation and one to the so-called "Brown Dogger" formation. The third shale considered is the Opalinus Clay which comes from the Mont Terri Underground Rock Laboratory (URL) in Northern Switzerland. The Opalinus Clay from Schlattingen (OPA-deep) is the deepest shale formation considered in this study (depth of 837.44–891.25 m); it consists mainly of claystone with a carbonate content of 10–20% and a quartz content in the range of 15–32%. The "Brown Dogger" from Schlattingen (BD-deep) was extracted at a depth of 766.67–807.44 m and consists of silty to clay-rich marls with 30–50% carbonates and 20–25% quartz. The Opalinus Clay from the Mont Terri URL (OPA-shallow) from the shaly facies consists of dark grey silty, calcarerous shales with a typical content of 25–30% carbonate, 5–10% quartz and 10–15% biodetritus. Index properties for the tested core samples are summarized in Table 1, which reports the average particle density (ρ_s), the bulk density (ρ), the gravimetric water content (w), the void ratio (e), the degree of saturation (S_r) and the Atterberg limits (the liquid limit w_L and the plastic limit w_P). The OPA-deep cores present two different densities; the most superficial cores, indicated as OPA-deep', have a higher void ratio and water content compared to the deepest samples (OPA-deep"). Mineralogical analysis of the cores showed that the OPA-deep with higher porosity presents reduced quartz content (approximately 17%) with respect to the denser cores (typical value about 28%); also they have slightly higher Atterberg limits.

Grain size distributions were obtained using an ad-hoc procedure that included material crashing, particle dispersion and sedimentation analysis (Ferrari & Laloui, 2012), and it results in approximately: 4% sand, 62% silt, 34% clay for OPA-shallow; 21% sand, 57% silt, 22% clay for OPA-deep; 20% sand, 61% silt, 19% clay for BD-deep.

The porosity network has been analysed, in terms of Pore Size Density (PSD) functions, by means of Mercury Intrusion Porosimetry (MIP) technique. Unimodal PSD functions were found for all the tested shales, showing pore modes at approximately 20 nm for the OPA-shallow and BD-deep and at 8 nm for the OPA-deep'.

Table 1. Geotechnical characteristics of the tested shales.

Shale	Depth m	ρ_s Mg/m^3	ρ Mg/m^3	w %	e –	S_r %	w_L %	w_P %
OPA-shallow	~300	2.74	2.46	6.9	0.21	92	38	23
BD-deep	767–807	2.75	2.52–2.56	2.7–4.4	0.09–0.12	69–99	25–33	10–23
OPA-deep′	837–838	2.74	2.49	4.3–4.9	0.14–0.15	80–94	36–39	22–25
OPA-deep″	855–891	2.71	2.54–2.55	3.3–3.6	0.09–0.11	93–96	29–33	19–22

Synthetic waters were used in the experiments in order to recreate the in-situ pore water compositions for the cores that were extracted at Mont Terri (Pearson, 1998) and at the Schlattingen site (Mäder, 1998). The osmotic suction of these synthetic waters was measured by a WP4c dew-point psychrometer (Leong et al., 2003; Cardoso et al., 2007) and resulted in values of 1.2 MPa for the Mont Terri synthetic water (OPA-shallow) and 0.98 MPa for the Schlattingen synthetic water (BD-deep and OPA-deep) (Ferrari et al., 2014).

Water retention behaviour of all the presented shales was investigated. 1D volumetric behaviour at high stresses was also investigated for two of them: OPA-shallow and BD-deep.

3 WATER RETENTION BEHAVIOUR INVESTIGATION: EXPERIMENTAL TECHNIQUE

The developed experimental technique for determining shale retention behaviour is based on the direct control of the water content and the subsequent measurement of the total suction (Ferrari et al., 2014). Different hydraulic paths are considered in order to analyse the response of the material in wetting and drying episodes. The following sections describe the specimen preparation technique, the water content control, the suction measurement and the volume change detection.

3.1 *Specimen preparation and water content control*

The specimens for water retention investigation are obtained from a shale core: slices of approximately 7–8 mm in height are cut with a diamond saw without using water (to preserve the initial condition), and they are immediately divided into smaller specimens with lateral sizes of approximately 20 mm. Three specimens are tested to obtain the initial condition in terms of water content, void ratio and total suction. Firstly, the main wetting and drying paths are sought; to this aim the material is initially brought to a dry state or to a "zero-matric-suction" state, respectively. The dry state is obtained by placing the specimens in silica gel desiccators and leaving them to dry for approximately three weeks (applied total suction of approximately 300 MPa) until no significant weight changes can be detected. The "zero-matric-suction" condition is achieved by placing the specimens in a sealed-glass jar, within which a relative humidity of 100% is imposed; the specimens are wrapped in filter paper and rest on porous stones immersed in water. Synthetic water, corresponding to the in-situ water composition, is used in order to preserve the initial osmotic suction of the material. The specimens were hence wetted by capillarity action, allowing for volume changes.

The weight evolution over time is monitored to assess the equilibrium, and the process is stopped once no further evolution is observed (usually in three weeks). Once equilibration is achieved, the main wetting and drying paths can be determined. To obtain the main drying path, the equalized specimens are air-dried under laboratory-controlled conditions ($T = 22°C$, $RH \approx 45\%$, equivalent total suction of about 110 MPa) or placed in a desiccator with silica gel for the driest states. During the drying, the weight of the specimens is monitored using a precision balance (0.001 g), and the process is stopped once the target water content is reached. The specimens are then packed hermetically for three days to allow for internal redistribution of the water content. The procedure to obtain the main wetting path consists of the addition of a target amount of water on the surface of the specimen with a syringe. Synthetic water is used to ensure that the osmotic suction component is preserved. Each specimen is placed in a hermetic container for three days to allow for the internal redistribution of the water.

3.2 *Suction and volume measurements*

The total suction of each specimen is measured using the dewpoint psychrometer. The psychrometer gives indirect measure of the total suction of a sample by reading the relative humidity established by the sample in a closed environment.

The total suction is then obtained by the psychrometric law (Fredlund & Rahardjo, 1993) which relates the Relative Humidity (RH) and the absolute temperature (T) to the total suction:

$$\psi = -\frac{\rho_w RT}{M_w} \ln(\mathrm{RH}) \tag{1}$$

where R is the universal gas constant and ρ_w and M_w are the density and the molecular mass of water, respectively.

When the retention properties are sought in terms of degree of saturation, the measurement of the volume change upon water content evolution is required. This determination allows for the quantification of shale swelling/shrinkage behaviour related to suction changes under unstressed conditions. In this case, the specimen volume is measured just after the measurement of the total suction with a destructive technique.

The method adopted for the volume measurement is based on a fluid displacement technique using a pycnometer filled with kerdane. Kerdane was selected for its immiscibility with water and its ability to invade the air-filled pore spaces of the surface without affecting the soil structure (Peron et al. 2007).

4 VOLUMETRIC BEHAVIOUR OF SHALES AT HIGH CONFINING STRESSES

4.1 *Experimental device and techniques*

In order to analyse the hydro-mechanical behaviour of the shales at high stresses, a multi-purpose oedometric cell was developed (Ferrari & Laloui, 2012). The layout of the apparatus is shown in Figure 1.

The cell is designed to hold cylindrical specimens (12.5 mm in height and 35 mm in diameter). The oedometer cell is inserted into a rigid stainless steel frame. The loading ram is positioned in the lower part of the system to prevent the specimen from being loaded before the test starts. The vertical load is applied by a hydraulic jack connected to a pressure/ volume controller.

The relationship between the controller pressure and the vertical stress on the specimen was assessed through a calibration step, which took into account the friction developed within the system (Salager et al. 2010). The maximum vertical stress that can be imposed on the specimen is 100 MPa.

The volumetric strains are measured by three LVDTs (with a resolution of 1 μm), which are fixed to the frame and are in contact with the loading ram. Two pressure/volume controllers are used to control the pore water pressure at the bottom and top bases (up to 2 MPa) and to measure the volume changes of the pore water.

An ad-hoc procedure was developed (Ferrari et al., 2013) and systematically applied to obtain the specimens for the oedometric tests.

The high pressure oedometric tests were performed on two of the presented shales: OPA-shallow and BD-deep.

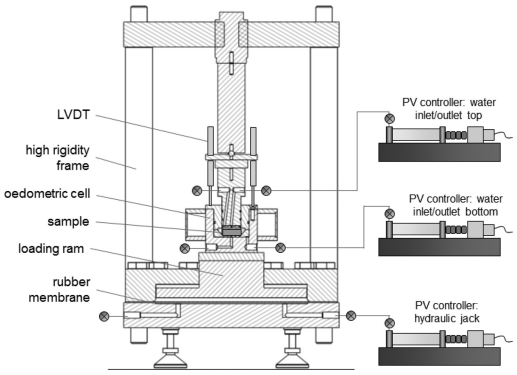


Figure 1. High-pressure oedometric cell used to perform tests on shales in saturated conditions (Ferrari & Laloui, 2012).

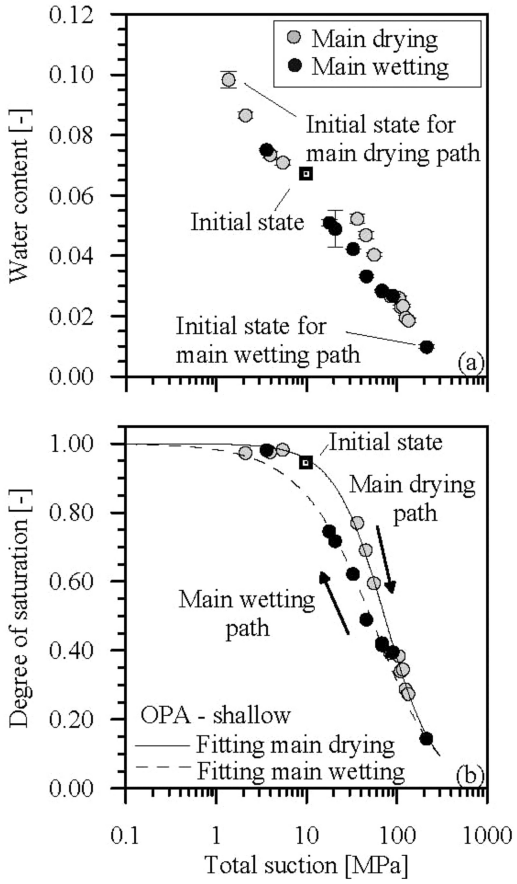


Figure 2. Water retention behaviour of the OPA-shallow shale in terms of water content (a) and degree of saturation (b) as a function of the total suction.

5 EXPERIMENTAL RESULTS

5.1 *Main drying and wetting paths*

The main wetting and drying paths obtained for the OPA-shallow are shown in Figure 2. The evolution of the water content with the total suction is shown in Figure 2a; each point of the curve represents an average value of three specimens, which were brought to the same target water content value; their standard deviation is also represented. The initial condition

corresponds to a water content of 6.7%. For the specimens equalized to the "zero matric suction" state, the measured total suction was 1.4 MPa, which is in good agreement with the osmotic suction of the synthetic water used for this initial wetting. The points obtained by the controlled drying procedure describe a progressive increase in total suction along with a reduction in water content; the driest state obtained with this procedure corresponds to a water content of 1.9% and a measured total suction of 134 MPa. This drying path tends to the residual condition that was achieved in the desiccator (w = 1.0%, suction = 213 MPa), when the initial state for the main wetting path was sought.

The retention curves in terms of the degree of saturation were obtained by combining the volume evolution and the water content along the wetting and drying paths. The results have been fitted with a Van Genuchten's type (Van Genuchten, 1980) expression:

$$S_r = \left(1 + \left(\frac{\Psi}{P}\right)^n\right)^{(-\lambda)} \tag{2}$$

where P, n and λ are the fitting parameters; the fitting values obtained by the least square method are reported in Table 2.

The initial state for the OPA-shallow corresponds to a degree of saturation of 95%; this value seems to confirm the fact that the material is reported to be close to saturation in situ; in addition, the initial state is found to be located along the main drying path as a consequence of the coring process and the exposure to the atmosphere before preservation.

The main drying path allows for the identification of the maximum total suction value that the material can sustain without significant changes in the degree of saturation (air entry value, ψ_e).

For the OPA-shallow, this value is 11 MPa (taken as the total suction corresponding to 95% of the degree of saturation), and the corresponding void ratio is 0.19. The material shows a hysteretic behaviour which is significant for total suction values lower than 100 MPa (Fig. 2b).

Similar behaviours were obtained for OPA-deep and BD-deep. The initial states correspond to a water content of 3.2% for both the BD-deep and OPA-deep' shale samples.

For the BD-deep and OPA-deep' specimens that were equalized to the "zero matric suction" state, the measured total suction was 1.2 MPa, which is in good agreement with the osmotic suction of the synthetic water. The initial conditions correspond to a degree of saturation of 80% for BD-deep and 54% for OPA-deep'. The registered low initial degree of saturation for OPA-deep' is attributed to a non-perfect preservation of the core used in the investigation.

The tested shales reveal that very limited changes in the gravimetric water content are required to undergo complete cycles of wetting and drying, expecially for the deeper shales.

Table 2. Values of the fitting parameters for water retention behaviour.

	n		P		λ	
	–		MPa		–	
Shale	w	d	w	d	w	d
OPA-shallow	0.98	1.53	110.13	78.17	1.80	1.08

w = wetting; d = drying

5.2 *Void ratio changes*

For all the tested specimens the volume determination was carried out after the total suction measurments. The obtained results are depicted in Figure 3 in terms of void ratio versus total suction. Significant swelling/shrinkage behaviour was observed with suction variation.

The values of the void ratio obtained for the lowest measured suction are in very good agreement with the results of free swelling tests (also shown in Fig. 3) carried out with the same synthetic water used for determining the water retention curves.

The shrinkage limits (assumed to be defined by $\Delta e/\Delta\psi < 0.1\%$) were identified at suction value of approximately 10 MPa for OPA-shallow and 14 MPa for BD-deep and OPA-deep', and they were found to be approximately 4.1% for the BD-deep and 6.4% and for the OPA-shallow and OPA-deep'.

The void ratio evolution with suction was fitted with the following incremental expression:

$$\dot{e} = -\frac{\dot{\Psi}}{K_{ref}}\left(\frac{\Psi_{ref}}{\Psi}\right)^m \left(1 + e_0\right) \tag{3}$$

in which K_{ref}, ψ_{ref} and m are the fitting parameters and e_0 is a reference void ratio. The values of the

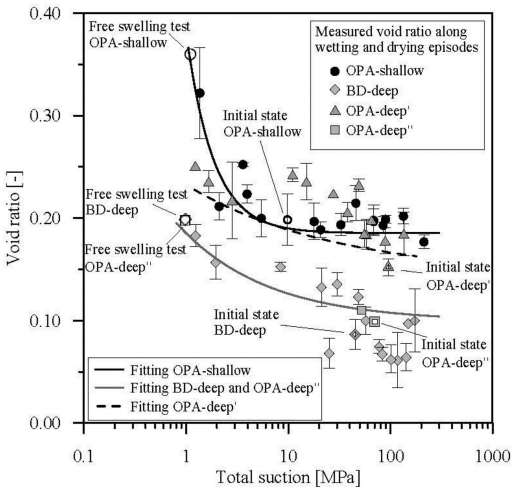


Figure 3. Void ratio evolution as a function of the total suction.

parameters obtained by the least square method are reported in Table 3. Only few results were collected on OPA-deep", due to the limited quantity of available material, and are also shown in Figure 3. The collected points align well with the trend registered for the BD-deep shale. The analysis of the volumetric response to suction changes allows for the quantification of the swelling potential for the tested shales. The measured volumetric deformations associated with the complete wetting of the material, starting from the driest condition, were 12.3%, 11.4% and 8.6%, for OPA-shallow, BD-deep and OPA-deep, respectively.

Table 3. Values of fitting parameters for volumetric behaviour.

Shale	K_{ref} MPa	ψ_{ref} MPa	m –	e_0 –
OPA-shallow	14.66	1.62	2.63	0.31
BD-deep	29.00	1.03	1.50	0.20
OPA-deep′	45.00	0.98	1.30	0.22

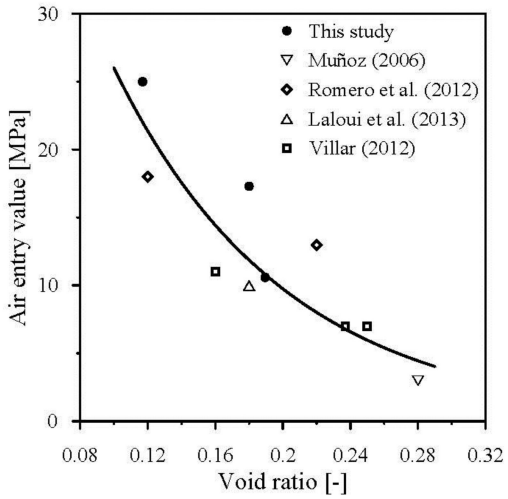


Figure 4. Air entry value as a function of the void ratio for Opalinus Clay Shale (Ferrari et al., 2014).

The highest swelling potential was observed for OPA-shallow; this behaviour can be explained by the higher clay content of this shale compared to the deep shales; in addition, greater depth and diagenetic processes, which result in a higher degree of cementation, might be responsible for the lower swelling potential of the deepest shales.

The collected results on the retention properties of the tested shales provide information on the effects of the void ratio on the air entry value.

Figure 4 depicts the total suction and the void ratio at which the shales started to desaturate along the main drying paths.

The results are supplemented with other available data from the literature for the Opalinus Clay. A unique exponential evolution function is proposed, and it captures the observed trend well (Ferrari et al., 2014):

$$\Psi_e\left[MPa\right] = 69.39 \cdot \exp\left(-9.82 \cdot e\right) \tag{4}$$

5.3 *High pressure oedometric tests results*

The high pressure oedometric tests were performed by incremental loading and attained a maximum vertical stress equal to 30 MPa and 100 MPa for the OPA-shallow and the BD-deep, respectively. The high level of applied vertical stress was required to observe the transition from the over- to the normally-consolidated state of each material. The specimens were initially saturated in isochoric conditions, by applying a back pressure in the range of 20–50 kPa, and the developed swelling pressure was measured. Afterward, two loading-unloading cycles were performed in steps and in drained condition, allowing for the complete dissipation of the excess pore water pressure generated by the oedometric compression. Synthetic waters aiming to reproduce the in-situ pore water composition were used throughout the tests.

Figure 5 depicts the total settlements of the OPA-shallow and the BD-deep, respectively, which are measured at the end of each loading step and corrected in light of the deformation of the apparatus. The results are presented in terms of volumetric strain versus vertical effective stress.

Figure 5 also depicts the volumetric strain relative to the end of the primary consolidation. The

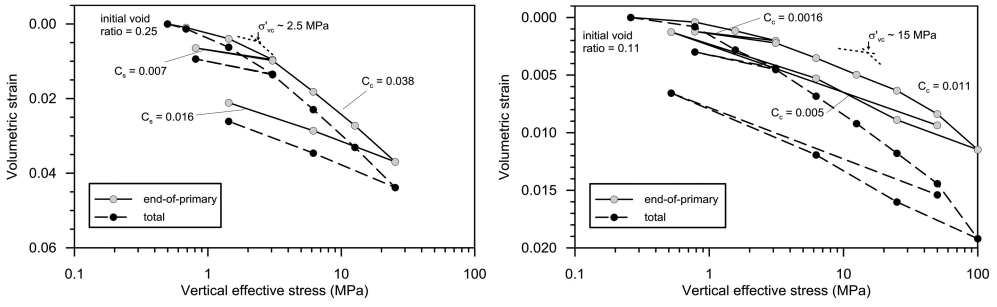


Figure 5. Results of the oedometric test: on the left OPA-shallow, on the right BD-deep (Ferrari & Laloui, 2012).

difference between the total and the end-of-primary strains is associated with the secondary consolidation component. The average computed coefficients of secondary compression were 0.0006 for the OPA-shallow and 0.0004 for the BD-deep. The end-of-primary strains are used to compute the compression and the swelling indexes and to assess the vertical effective yield stresses.

6 SUMMARY AND CONCLUSIONS

This paper summarized selected results on the water retention behaviour and on the high-pressure oedometric compression behaviour of shales.

Results from samples of different shale types, such as Opalinus Clay and Brown Dogger, have been presented. Testing different shale types allowed for the possibility to capture the important features of their mechanical and retention behaviour. This information is highly relevant when considering that these materials are host rock candidates for the deep geological disposal of high-level nuclear waste. As a consequence, retention capacity will be a fundamental component during the ventilation (drying) and resaturation (wetting) phases of the repository.

The presented technique for the water retention analysis of shales is capable of capturing the important features of the retention behaviour, such as the hysteresis domain and the air entry value. The assessment of the volume change due to suction variation has allowed (i) expressing the retention behaviour in terms of degree of saturation, (ii) capturing the main drying and wetting paths, and (iii) highlighting the significant changes in porosity undergone by the shales along wetting and drying hydraulic episodes.

Results from high-pressure oedometric tests on shales were summarized. Attainment of a vertical effective stress in the range of 30–100 MPa was needed to measure the vertical yield stress.

REFERENCES

Cardoso, R., Romero, E., Lima, A., Ferrari, A. 2007. A comparative study of soil suction measurement using two different high-range psychrometers. In: Schanz T, editor. *2nd Int. Conf. on Mech. of Unsat. Soils, Weimar, Germany*. Berlin: Springer-Verlag :79–93.

Ferrari, A. & Laloui, L. 2012. Advances in the testing of the hydro-mechanical behaviour of shales. In *Multiphysical Testing of Soils and Shales:* 57–68. Springer Berlin Heidelberg.

Ferrari, A., Favero, V., Manca, D., Laloui, L. 2013. Volumetric behavior and consolidation of shales at high confining stresses. In Proceedings of the *47th US Rock Mechanics/Geomechanics Symposium* (No. EPFL-CONF-187353).

Ferrari, A., Favero, V., Marschall, P., Laloui, L. 2014. Experimental analysis of the water retention behaviour of shales. *International Journal of Rock Mechanics and Mining Sciences*, 72: 61–70.

Fredlund DG, Rahardjo H., 1993. *Soil Mechanics for Unsaturated Soils*. John Wiley and Sons.

Laloui, L., Salager, S., Rizzi, M., 2013. Retention behaviour of natural clayey materials at different temperatures. *Acta Geotechnica*; 8(5):537–546.

Leong, E.C., Tripathy, S., Rahardjo, H. 2003. Total suction measurement of unsaturated soils with a device using the chilled-mirror dew point technique. *Géotechnique*; 53(2):173–182.

Mäder, U. 1998. Recipe and preparation of a simplified artificial pore water for Opalinus Clay and Brown Dogger. *NAGRA AN*: 11–159.

Muñoz, J.J. 2006. Thermo-hydro-mechanical analysis of soft rock, application to a large scale heating test and large scale ventilation test. *PhD thesis*, Universitat Politècnica de Catalunya, Barcelona.

Pearson, F.J. 1998. Opalinus Clay experimental water: A1 Type, Version 980318. *PSI Internal report TM-44-98-07*, Paul Scherrer Institut, Villigen PSI, Switzerland.

Peron, H., Hueckel, T., Laloui, L. 2007. An improved volume measurement for determining soil water retention curves. *Geotechnical Testing Journal* 30(1): 1–8.

Romero, E., Senger, R., Marschall, P. 2012. Air Injection Laboratory Experiments on Opalinus Clay. Experimental techniques, Results and Analyses. *3rd EAGE Shale Workshop*, Barcelona.

Salager, S., Ferrari, A., Laloui, L. 2010. New experimental tools for the characterization of highly overconsolidated clayey materials in unsaturated conditions. In L. Laloui, editor, *Mechanics of unsaturated geomaterials*: 113–126. John Wiley & sons.

Van Genuchten, M.T. 1980. A closed-form equation for predicting the hydraulic conductivity of unsaturated soils. *Soil science society of America journal*, 44(5): 892–898.

Villar, M.V., Romero, F.J. 2012. Opalinus Clay 2 – phase flow parameters. *FORGE report* D5 14 37.

Unsaturated Soil Mechanics—from Theory to Practice – Chen et al. (Eds)
© 2016 Taylor & Francis Group, London, ISBN 978-1-138-02921-7

Desiccation crack depth and tensile strength in compacted soil

G.A. Miller, A. Hassanikhah & M. Varsei
University of Oklahoma, Norman, OK, USA

ABSTRACT: Considering desiccation cracks is important in the stability analysis of earthen slopes subjected to drying and wetting climatic events. To incorporate desiccation cracks into the analysis requires knowledge of the expected depth and distribution of cracks. In this paper, a simple method for estimating the depth of desiccation cracking in compacted soil based on elastic theory is presented, and an innovative method for determining tensile strength of desiccating soils is discussed. Measured tensile strengths compared favorably to predicted strengths based on a Mohr-Coulomb model that incorporates a microstructurally based effective stress to account for differences in macropore and micropore degrees of saturation. Predicted crack depths were reasonable compared to field observations, but predictions can vary depending on estimated soil parameters. An example of a preliminary approach to slope stability analysis incorporating desiccation cracks is presented.

1 INTRODUCTION

In many places, dry and wet weather cycles lead to desiccation of fine-grained soils. In places prone to long drying periods, extensive desiccation can occur with cracks reaching depths of a few meters or more in high plasticity soils (Morris et al. 1992). These cracks can be problematic for natural and engineered clayey soils, such as Compacted Clay Liners (CCLs) and embankment fill. In embankment and cut slopes, desiccation cracks allow runoff from subsequent rainfall events to rapidly penetrate the soil profile and compromise the stability. Resulting slope failures in cut slopes and embankments are a pervasive and costly problem along infrastructure corridors in many areas of the world.

Impacts of climate change are likely to exacerbate problems caused by desiccation cracking because for many parts of the world and the USA, climate "model simulations suggest there will be a tendency towards more intense rain and snow events separated by longer periods without precipitation" (AMS Council 2012). Impacts of desiccation cracking on slope stability will become increasingly important to consider; however, there are currently no widely accepted or publicized approaches to the problem. This was partly the motivation for the research discussed in this paper.

Research presented in this paper is part of a larger project focused on studying mechanisms causing slope failure at two instrumented test sites containing clayey soils and where desiccation cracking was observed during dry periods. Instrumentation included weather monitoring instruments and soil moisture sensors, while laboratory testing involved establishing soil water characteristic curves, unsaturated and saturated strength, hydraulic conductivity, and other engineering properties. In addition, a new device was developed to determine the tensile strength of desiccating compacted soil. A primary goal of the research is to evaluate the slope stability considering the effects of wetting and drying cycles and the role of desiccation cracking in the variation of moisture contents within the slope. The focus of this paper is on the development of a simple method for estimating the depth of desiccation cracks, laboratory determination of the tensile strength and a model for estimating the tensile strength.

2 BACKGROUND

2.1 *Desiccation cracking and laboratory determination of tensile strength*

Tensile strength plays an integral role in predicting crack initiation in numerical modeling and crack depth prediction. Mechanical modeling of desiccation cracking in soils may employ an approach based on tensile stress failure or fracture mechanics (Kodikara and Costa 2013). According to Kodikara and Costa (2013), important studies that fall in the first category, for example, include work by Morris et al. (1992), Kodikara and Choi (2006), Peron et al. (2009), and Amarasiri et al. (2010). Work falling into the fracture mechanics based approaches includes Lachenbruch (1961), Morris et al. (1992), Ayad et al. (1997) and Amarasiri and Kodikara (2011). Whether the tensile stress failure approach or fracture mechanics approach to predicting desiccation behavior is taken, models in both categories require tensile strength as an input. Thus, understanding soil tensile behavior during desiccation is critically important.

Methods for estimating tensile strength from experimental measurements generally fall into two

categories encompassing direct and indirect techniques. Indirect techniques (e.g. Konrad and Ayad 1997, Harrison et al. 1994) include for example, soil beam flexure tests, fracture measurements in notched specimens, and a relatively new approach that uses an unconfined penetration device (Kim et al. 2012). Direct measurement methods (e.g. Nahlawi et al. 2004, Tamrakar et al. 2005, Vesga 2009) involve measurement of stresses as a soil specimen is failed in direct tension.

While these methods are innovative and useful, they do not account for two aspects of tensile failure in desiccating soils. First, the tensile strength is determined at essentially constant water content conditions. This is not consistent with the desiccation process of natural and compacted soils that start at one water content and fail at another during drying. Second, during desiccation, tensile stresses are produced by drying under increasing suction when the soil is restrained. On the other hand, in direct and indirect tensile strength tests, the tensile stresses are produced by external loading under constant suction. Since, behavior of soils is known to be stress-path dependent, there is an unanswered question as to how much difference would result, if any, in tensile strengths measured using different stress paths. More recently, ring-shaped samples with constraint on the interior edge have been used (Costa and Kodikara 2012) to estimate tensile strength of desiccating soils using a fracture mechanics approach. While this innovative approach overcomes these issues, it is not a direct measurement technique in that it requires back analysis to determine the tensile strength and the ring does not allow for direct measurement of the entire stress field, which in this case is highly nonlinear. The novel first generation tensile strength apparatus described in this paper was designed to permit direct measurement of the uniaxial tensile strength during desiccation.

2.2 *Predicting desiccation crack depths*

Morris et al. (1992) developed analytical solutions for predicting desiccation crack depths using three approaches, based on 1) theory of elasticity, 2) transition between tensile and shear failure, and 3) linear elastic fracture mechanics. They presented some limited field evidence showing that the tensile failure approach provided reasonable predictions of desiccation crack depth. They developed their equations for the specific case of modeling mine tailings deposited as a slurry. Assumptions made in the development of the equations for crack depth are suitable for normally consolidated soils that start out in a saturated state. In addition, the suction profiles assumed were either constant or linearly decreasing from the ground surface.

As pointed out by Miller et al. (1998), the analytical solutions of Morris et al. (1992) have limited applicability in situations involving layered soils, deep water tables, nonlinear suction profiles and anisotropic properties. However, the case of compacted embankments is reasonably simulated assuming a homogenous profile. As a starting point, the method presented in this paper builds on the elastic theory approach of Morris et al. (1992) by modifying the analytical solutions to account for suction changes and stress conditions in compacted, unsaturated soil while incorporating a number of simplifying assumptions. The formulation is given in Section 3 and uses an estimate of the tensile strength of the soil determined from the unique device developed by the authors to determine the tensile strength during desiccation under approximated uniaxial stress conditions.

3 A SIMPLE MODEL FOR PREDICTING DESICCATION CRACK DEPTH

3.1 *Formulation for Determining Desiccation Crack Depth based on Elastic Theory*

Following on the work of Morris et al. (1992), a simple preliminary approach for predicting desiccation crack depth in compacted soil was developed. The equation for predicting crack depth based on elastic theory involves the following simplifying assumptions:

1) The crack depth corresponds to a point below the ground surface where the final horizontal stress equals the tensile strength of the soil.
2) Depth of cracks is based on a formulation for a horizontal ground surface. As a starting point for analyzing slopes, it will be assumed the depth of cracks measured normal to face of the slope will be similar to the depth of cracks for a horizontal surface.
3) Cracks form in one direction along a linear plane.
4) The crack has zero thickness and vertical stress remains constant at the bottom of the crack.
5) Horizontal stress at a given depth is the same in all directions up to the point of cracking.
6) Pore air pressures remain at atmospheric pressure (zero gage pressure).
7) The horizontal strain is zero up to the point of cracking.
8) The soil behaves as a linear elastic material up to the point of cracking.

Based on the equations presented by Fredlund and Rahardjo (1993), the incremental elastic equation for strain in a horizontal direction for isotropic unsaturated soil can be written as follows:

$$\varepsilon_x = \frac{\Delta(\sigma_x - u_a)}{E} - \frac{\mu}{E}\left(\Delta\sigma_y + \Delta\sigma_z - 2\Delta u_a\right) + \frac{\Delta(u_a - u_w)}{H} \quad (1)$$

where, $\varepsilon_x =$ is taken as strain normal to the long axis of the crack prior to cracking, $\Delta(\sigma_i - u_a)$ is the change in net normal stress in the x, y, and z (vertical) directions, u_a is the air pressure, u_w is water pressure, $\Delta(u_a - u_w)$ is the change in matric suction, and E and H are the elastic moduli with respect to net normal stress and suction.

Incorporating the assumptions, $\varepsilon_x = 0$, $\Delta u_a = 0$, $u_a = 0$, $\Delta\sigma_z = 0$ and $\Delta\sigma_x = \Delta\sigma_y$; Equation 1 simplifies to:

$$\Delta\sigma_x = \frac{E}{H(1-\mu)}\Delta(u_a - u_w) \tag{2}$$

The initial horizontal stress, σ_{xo} is equal to $K_o\sigma_{vo} = K_o\gamma z_c$, and the final horizontal stress, σ_{xf}, is assumed to be equal to the tensile strength of the soil, σ_t; thus, $\Delta\sigma_x = K_o\gamma z_c - \sigma_t$. The vertical total stress is σ_{vo}, γ is the total unit weight, K_o is the ratio of the horizontal to vertical total stress before desiccation, and z_c is the depth of cracking. Substituting these expressions into Equation 2 leads to an expression for the desiccation crack depth:

$$z_c = \frac{E}{K_o\gamma H(1-\mu)}\Delta(u_a - u_w) + \frac{\sigma_t}{K_o\gamma} \tag{3}$$

3.2 *Application and sensitivity of the model*

The preliminary approach presented was applied based on observations made at a field test site containing a compacted soil embankment. The embankment fill was composed of moderately plastic soil in which desiccation cracks were observed to develop over the face of the slope. The test site was instrumented with weather monitoring stations and soil moisture sensors with data recorded over a period of about two years. During the recording period the embankment was subjected to drought conditions during which desiccation cracks were observed in the slope face. Following drought conditions a period of wetting led to a shallow seated failure in the slope. It was estimated that the failure surface was roughly 2 m below the surface of the slope at its deepest location.

To predict desiccation crack depths, the compacted embankment soil was assumed to have initial conditions corresponding to the maximum dry unit weight and optimum water content. The corresponding initial suction, $(u_a - u_w)_o$, was determined from the drying Soil Water Characteristic Curve (SWCC) for similarly compacted soil. To estimate the final suction, volumetric moisture content measurements from instrumentation at the field test site were analyzed to determine the maximum changes in suction that occurred during a two-year monitoring period. Based on this analysis it was estimated that the maximum change in suction during a drying event at a measurement depth of 1.8 m was likely in range of 100 to 200 kPa. For the initial analysis, the final suction, $(u_a - u_w)_f$, was taken at 150 kPa lower than the initial suction. Thus, the change in suction associated with Equation 4 is $\Delta(u_a - u_w) = (u_a - u_w)_o - (u_a - u_w)_f = 150$ kPa.

Initial lateral stresses are unknown; however, since compacted cohesive soils can experience lateral stress ratios approaching unity or greater (e.g. Duncan and Seed 1986), as a first approximation, a value of 1.0 was selected. A Poisson's ratio of 0.35 and E/H ratio of 0.3 were selected as a starting point based on work of Morris et al. (1992) and suggestions in Fredlund and Rahardjo (1993). The tensile strength of the soil was determined by direct measurement while the soil was undergoing desiccation from an initial condition corresponding to the initial conditions of the embankment soil. The method for determining tensile strength is discussed in greater detail in Section 4.

Table 1. Embankment soil properties.

PI	18
LL	38
%Sand	11
%Silt	49
%Clay Size	40
γ_{dmax}, kN/m^3	17.3
w_{opt}, %	18
USCS	CL
k_{sat}, cm/sec	6.42×10^{-7}

Table 2. Model parameters for Equation 4.

Parameter	Value	Determined by:
E/H	0.3	estimated
μ	0.35	estimated
K_o	1	estimated
σ_{tu}, kPa	−17	measured
σ_t, kPa	−27	calculated
$\Delta(u_a - u_w)$, kPa	150	measured w, field and lab and SWCC

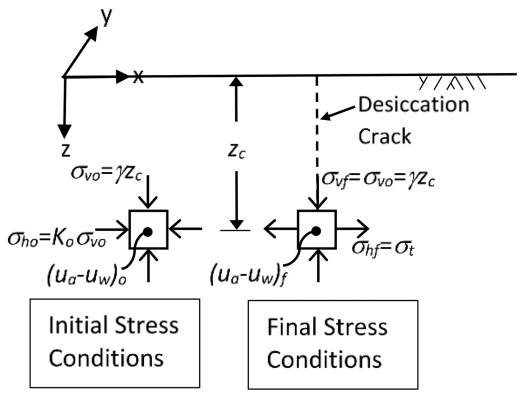


Figure 1. Schematic of assumed stress conditions in desiccating compacted soil.

Embankment soil properties are summarized in Table 1 and parameters used with Equation 3 are summarized in Table 2. A schematic of assumed initial and final stress conditions during development of a desiccation crack are shown in Figure 1. Estimated crack depths based on Equation 4 are relatively sensitive to the selected values of Poisson's ratio (μ), modulus ratio (E/H), lateral stress ratio (K_o), and change in suction,

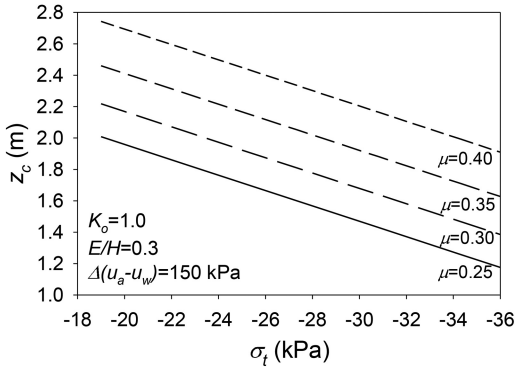


Figure 2. Crack depth vs. tensile strength for varying Poisson's ratio.

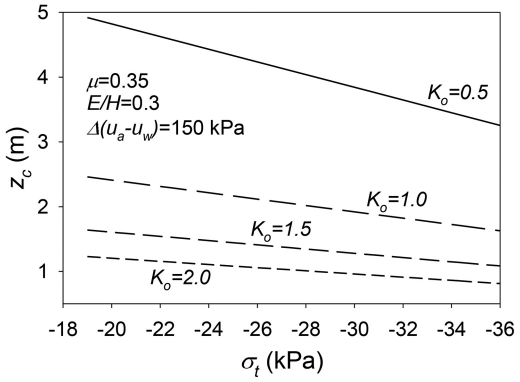


Figure 3. Crack depth vs. tensile strength for varying lateral earth pressure ratio.

$\Delta(u_a - u_w)$ as shown in Figures 2 to 5. For the parameters used in Table 1, the estimated depth of desiccation cracks using Equation 3 is 2.0 m, which is similar to the estimated depth of the failure surface observed at the embankment test site. It is postulated that the desiccation cracks facilitate significant wetting and softening in the soil down to the depth of cracking during significant wetting events that follow a drying event, resulting in sliding of this weakened upper layer.

3.3 *Cracking depth based on field suction estimates*

Based on field observations at sites in Australia, Morris et al. (1992) suggested that desiccation cracks generally occur within the active zone of a soil profile. This is consistent with Equation 3 in that only values of z_c greater than zero are valid and this only occurs when $\Delta(u_a - u_w)$ is greater than some critical value with $z_c = 0$. Rearranging Equation 3, it is possible to solve for the change in suction needed to produce cracking at a given depth:

$$\Delta(u_a - u_w) = \left(z_c - \frac{\sigma_t}{K_o \gamma} \right) \frac{K_o \gamma H (1 - \mu)}{E} \qquad (4)$$

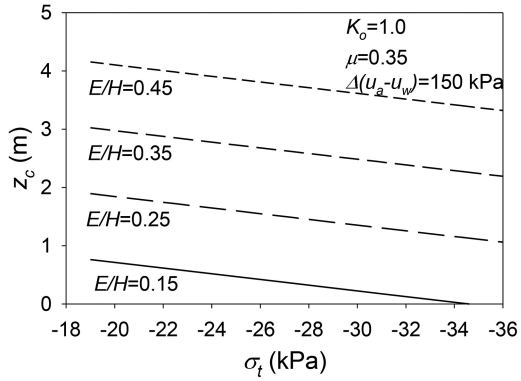


Figure 4. Crack depth vs. tensile strength for varying modulus ratio.

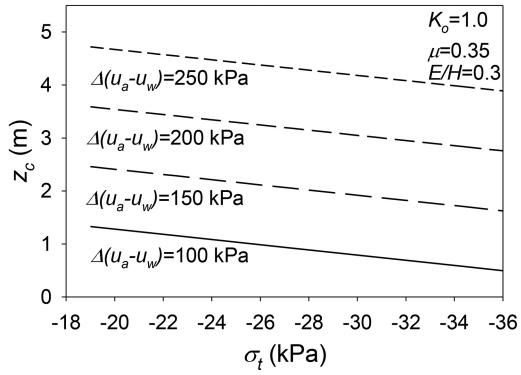


Figure 5. Crack depth vs. tensile strength forvarying matric suction change.

Equation 4 provides a more useful estimation of depth of cracking as demonstrated in Figure 6. In Figure 6 the estimated changes in suctions at various depths based on extreme values of moisture content determined at the embankment site and the SWCC are shown. The bottom of the active zone is the point where the estimated change in suction is zero; this point is at a depth of 2.3 m and was extrapolated from the previous two measurement depths (0.9 and 1.8 m). Superimposed on the profile of estimated field changes in suction are lines showing the changes in suction required to produce cracking at various depths based on Equation 4. The "best estimate" line is based on model parameters in Table 2. The ±25% lines were obtained by increasing and/or decreasing the model parameters in Table 2 (not including $\Delta(u_a - u_w)$ which was calculated in Equation 4) by 25% such that the lowest and highest values of predicted changes in suction resulted. The purpose of this was to show the range of predicted crack depths that might result due to uncertainty in estimating model parameters. Crack depths are estimated by the intersection of the line of measured suction changes with theoretical lines relating suction change to crack depth. Based on the field

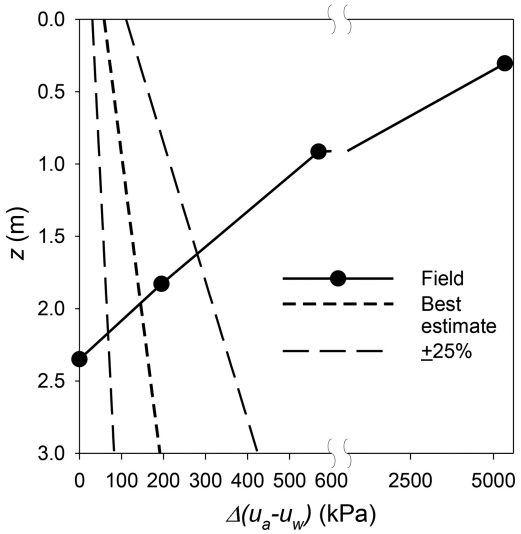


Figure 6. Change is suction based on extreme variations in field measured water contents andtheoretical change in suction to produce cracking.

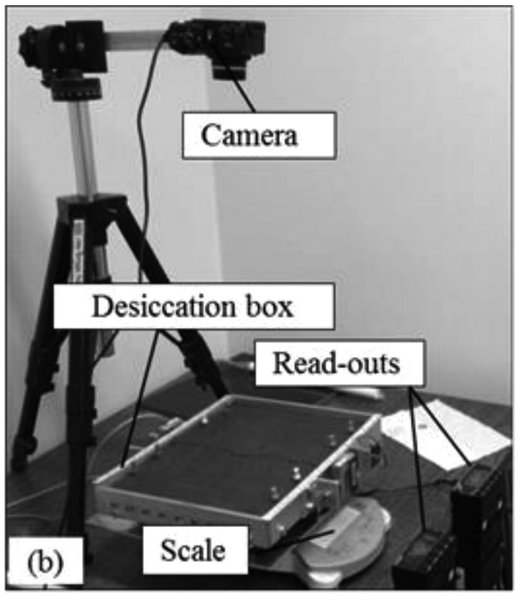


Figure 7. Photograph of desiccation box apparatus.

estimates of suction changes shown, the range of estimated crack depths considering uncertainty in model parameters is 1.7 to 2.2 m with the best estimate at about 2.0 m. From a practical point of view, this range of cracks depths seems reasonable especially considering the significant variation of model parameters. Subsequent analyses, of seepage processes for example, can use a range of predicted crack depths and spacing to determine the impact of desiccation cracks on suction profiles. In addition, although not shown in Figure 6, different field estimates of suction change can also be investigated based on soil-climate modeling results and/or to account for uncertainty in field determined suction values due to extreme weather conditions different from those encountered during field monitoring.

4 MEASUREMENT AND MODELING OF TENSILE STRENGTH DURING DESICCATION

A unique device developed at the University of Oklahoma was used to measure the approximate uniaxial tensile strength of a compacted soil during desiccation. A brief description is provided here and details of the device and testing procedure can be found elsewhere (Varsei et al. 2014). A picture of the first generation apparatus is shown in Figure 7. The desiccation box (l = 305 mm, w = 254 mm), consists of two halves slightly separated by a thin gap and connected by two load cells along the sides. Soil is compacted into a single thin layer (12.7 mm) to the target moisture content and density, covered and placed into a humidity room overnight. The soil is compacted on overlapping Teflon sheets placed in the bottom of the box to minimize base restraint and screws passing through the ends of the box are embedded in the soil to provide end restraint. To begin testing, the load cells are connected and the soil is placed on a laboratory bench where the relative humidity is such that the soil desiccates. As the soil dries, tensile stresses build up in the soil and the forces generated are registered by the load cells. The desiccation box rests upon a digital scale so that moisture losses can be determined. A camera above the system records the readout from the scale and load cells over time and captures images of the developing crack. The maximum load cell readings are used to calculate the tensile strength. It is assumed that the maximum load corresponds to an intact condition just prior to crack initiation and the average tensile stress in the soil bed is equal to the load divided by the cross-sectional area of the soil perpendicular to the direction of loading. Plots of force and water content versus time are shown for selected test results in Figure 8, and in Figure 9 tensile strengths are shown for the embankment soil at different initial water contents and dry unit weights (γ_{dmax}, $0.95\gamma_{dmax}$ and $0.84\gamma_{dmax}$). With regard to Figure 9, note that for higher unit weights (γ_{dmax}, $0.95\gamma_{dmax}$), difficulties in compacting soil to the target density precluded the determination of tensile strengths for higher water contents.

As shown in Figures 8 and 9, soils compacted at lower water contents are more brittle than at higher water contents. Also, the uniaxial tensile strength tends to increase with increasing dry unit weight and increasing compaction water content up to a point, after which it decreases. The effective degree of saturation described by Alonso et al. (2010) provides an explanation for these observations as well as a basis for modeling and predicting tensile strength from SWCC and shear strength data.

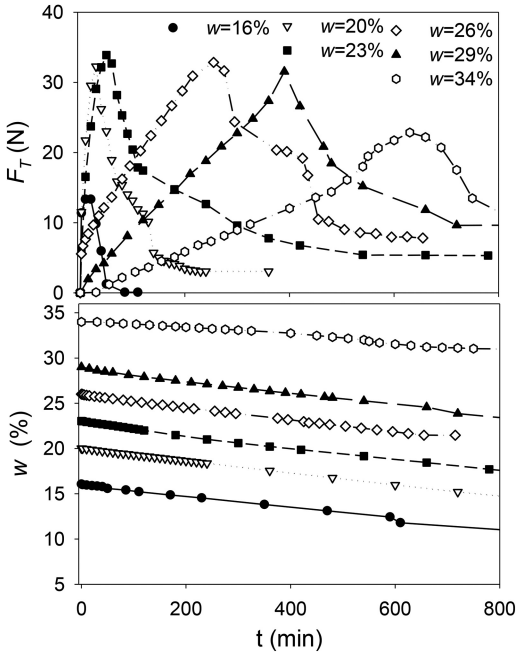


Figure 8. Results of desiccation box tests for soil compacted to about $\gamma_d = 14.5$ kN/m^3. Note the sample at $w = 34\%$ was close to $\gamma_d = 13.5$ kN/m^3.

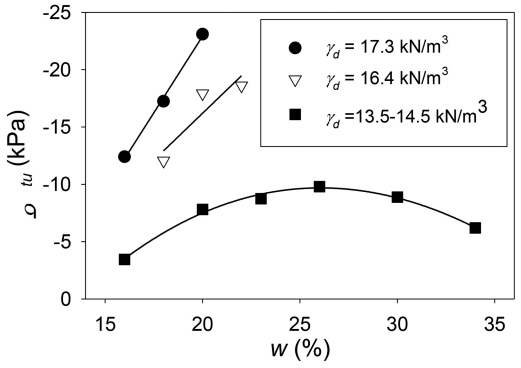


Figure 9. Uniaxial tensile strength determined from desiccation box tests.

4.1 *Modeling and predicting tensile strength*

The relationships between water content, dry density and tensile strength shown in Figure 9 can be explained using a dual porosity model that describes the contribution of water associated with macropores and micropores in the soil, as discussed by Alonso et al. (2010). In developing a microstructurally based effective stress for unsaturated soil, it was postulated that water in the macropores dominates soil behavior relative to matric suction and that this water essentially defines the "effective degree of saturation". In compacted clayey soils, dual porosity structures are expected, especially at water contents less than optimum due to formation of clods (large particles or clumps). Macropores exist between the larger clods while the micropores are found within clods. As the compaction water content increases in soil, the structure evolves from larger to smaller macropores as macroparticles (clods) sizes get smaller. Also, the saturation level of increasingly smaller macropores gets larger with increases in compaction water content. The increase in saturation of the macropores increases the interfacial area between macroparticles (clods) and water, which equates to higher interparticle forces due to a given suction. However, at the same time the compaction water content is increasing the suction is decreasing. Thus, there are two opposing factors that influence the effective stress and tensile strength in compacted soils: increasing effective degree of saturation tends to increase effective stress and improve strength while decreasing suction tends to diminish effective stress and strength. At lower water contents changes in effective degree of saturation are dominant leading to increasing strength with increasing water content, but at higher water contents the decreases in suction are dominant leading to decreases in strength with continued increases in compaction water content.

The effective degree of saturation is a measure of the degree to which the macropores in a dual porosity structure are filled with water. In this model, it is assumed that water volume held within micropores remains constant. In developing the equation for effective degree of saturation, the degree of saturation (as ordinarily defined) is separated into the macroscopic and microscopic degrees of saturation. The macroscopic degree of saturation (S_r^M) is associated with the water occupied in relatively large open pores, where the capillary forces govern the effective stress. The microscopic degree of saturation (S_r^m) is associated with the small pores in which physico-chemical bonds exists between the water and soil particles. These contributions are expressed in the following equation:

$$S_r = S_r^m + S_r^M \tag{5}$$

where S_r is ordinary degree of saturation (i.e. volume of water divided by volume of voids). Effective degree of saturation is thus defined as:

$$S_r^e = \frac{S_r - S_r^m}{1 - S_r^m}$$

$$\text{for } S_r > S_r^m \text{ and } S_r^e = 0 \text{ for } S_r \le S_r^m \tag{6}$$

Equation 6 varies from 0 when there is no water in the macropores ($S_r \le S_r^m$) to 1 when the soil is saturated. Because the distinction between micropores and macropores in soil is not clear, and because Equation 6 discounts the contribution of water in the soil when ($S_r \le S_r^m$), Alonso et al. (2010) proposed an alternative equation. It is continuous for all values of S_r from 0 to 1 and provides a smooth transition at the point where $S_r = S_r^m$, while still retaining some essential features of Equation 6 (see Alonso et al. (2010) for more discussion). The proposed equation is:

$$S_r^e = (S_r)^\alpha \tag{7}$$

where α ($\alpha \geq 1$) is a material parameter. The α parameter is 1 for soils with uniform pore size distributions, such as for sands, and considerably larger for soils that develop distinct macropore and micropore structures, such as compacted clays.

Incorporating the effective degree of saturation, a general equation for effective stress based on the model proposed by Alonso et al. (2010) is:

$$\sigma' = \sigma - u_a + S_r^e(u_a - u_w) \tag{8}$$

where σ' is the effective stress, σ is total stress, u_a is pore air pressure, u_w is pore water pressure, and $u_a - u_w$ represents matric suction. Note, this is similar to the Bishop (1959) effective stress equation with the Bishop χ factor equal to S_r^e.

Incorporating this effective stress into the Mohr-Coulomb strength equation gives:

$$\tau = c' + (\sigma - u_a)\tan\phi' + S_r^e(u_a - u_w)\tan\phi' \tag{9}$$

where τ is the shear strength on some plane, c′ is the effective stress cohesion intercept, and ϕ' is the effective stress friction angle. Equation 9 can be rearranged such that:

$$\tau = c + (\sigma - u_a)\tan\phi' \tag{10}$$

and

$$c = c' + S_r^e(u_a - u_w)\tan\phi' \tag{11}$$

The cohesion, c, represents the intercept when net normal stress equals zero in the net normal stress-shear stress plane as shown in Figure 10. Under uniaxial tension with the major principal net normal stress equal to zero, the tensile strength (σ_{tu}) is equal to the minor principal net normal stress at failure as shown in Figure 10. The equation for the tensile strength is given by:

$$\sigma_{tu} = -\frac{2c\cos\phi'}{1+\sin\phi'} \tag{12}$$

or

$$\sigma_{tu} = -\frac{2c\cos\phi' + 2S_r^e(u_a - u_w)\tan\phi'\cos\phi'}{1+\sin\phi'} \tag{13}$$

Note that the tensile strength under isotropic tension (σ_{ti}) can be determined from the intercept at shear stress equal zero as indicated on Figure 9. This formulation for tensile strength based on a Mohr-Coulomb model is similar to that given by others (e.g. Lu et al. 2009, Lakshmikantha et al. 2012).

Equation 13 was used to provide theoretical estimates of tensile strength and compared to the results obtained from the desiccation experiments. As shown in Figure 11, the best match between theoretical and measured tensile strengths was obtained using an

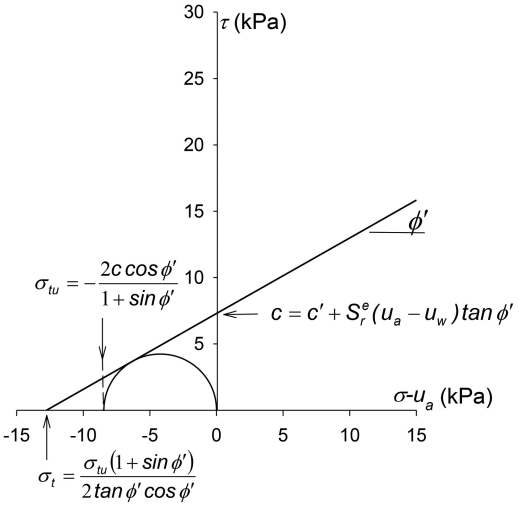


Figure 10. Tensile strength for uniaxial and isotropicloading defined relative to the Mohr-Coulomb failure envelope.

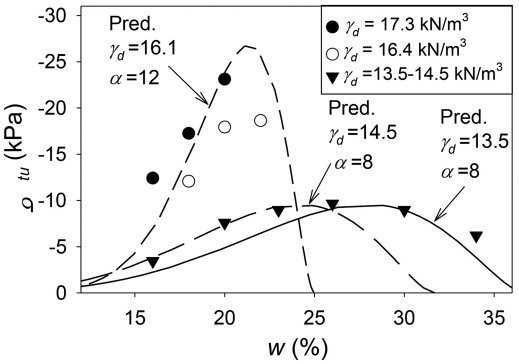


Figure 11. Comparison of measured and predictedtensile strength.

effective degree of saturation (Equation 7) with α equal to 8 and 12, for low and high unit weight soil, respectively. Note that values of total suction (ψ) from the SWCC in Figure 12 were substituted for matric suction in Equation 13 along with corresponding effective degrees of saturation.

Contrary to granular soils where the pores mostly consists of free water and α approaches 1, for fine-grained soils that contains significant amounts of micropore and macropore structure, the difference between the apparent and effective degree of saturation can be significant as shown in the middle graph of Figure 12. The lower graph of Figure 12 indicates that the contribution of suction is relatively insignficant until the degree of saturation, S_r, exceeds about 0.3 and 0.5 for α of 8 and 12, respectively. This corresponds to the point at which the effective degree of saturation, S_r^e, rises from close to zero as capillary water begins filling the macropores while suction is very high. The combined contribution of suction and effective degree of saturation shown in the lower graph of Figure 12

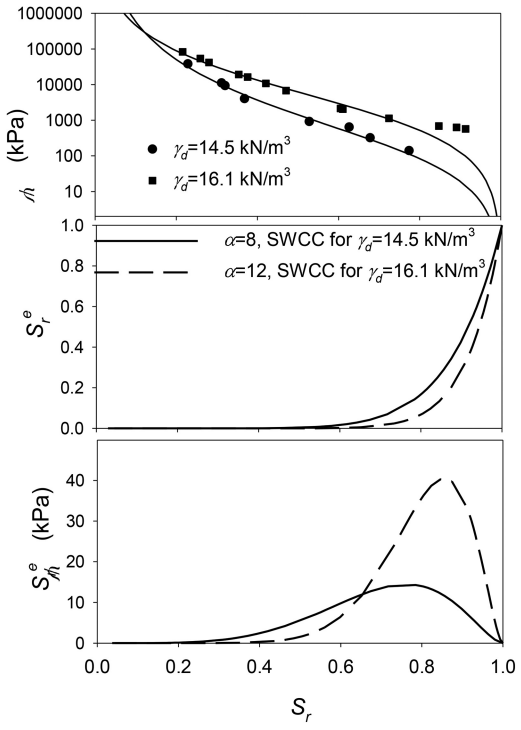


Figure 12. Relationships between suction, effectivedegree of saturation and degree of saturation.

indicates the maximum suction contribution occurs at a degree of saturation between 75% and 85% for α between 8 and 12.

The predicted tensile strengths shown in Figure 11 were calculated using strength parameters obtained from unsaturated and saturated direct shear tests, which provided ϕ' and c' values of 29.7° and 7.7 kPa for the embankment soil. The effective stress cohesion intercept, c', was assumed to be zero in the embankment soil, as this provided the best predictions of tensile strength. The SWCC data in Figure 12 was obtained from drying tests on compacted samples. After saturating the samples, they were allowed to dry during which sample weights were determined and corresponding suctions were measured using a chilled mirror hygrometer device. One issue that needs to be addressed is the volume change that occurs when compacted samples are wetted and dried during SWCC testing as this will affect the calculated degrees of saturation. While the authors are continuing to look deeper at some of the issues associated with measurement techniques and various assumptions employed in this research, the preliminary comparison of predicted and measured tensile strength shown in Figure 11, indicates that the model utilizing the microstructurally based effective stress of Alonso et al. (2010) holds promise for compacted soils. Further, the favorable comparison between measured and predicted tensile strengths provides some validation of the experimental method.

Stress conditions in the soil bed approximate a uniaxial stress condition whereby the major principal total stress at failure is zero and the minor principal stress is equal to the uniaxial tensile strength (σ_{tu}), as shown in Figure 10. To estimate the tensile strength corresponding to isotropic loading (σ_t), the expression shown in Figure 10 can be used if the effective stress friction angle of the soil (ϕ') is known, given as:

$$\sigma_t = \sigma_{tu} \frac{1 + \sin\phi'}{2\tan\phi'\cos\phi'} \tag{14}$$

For the purpose of estimating crack depths the tensile strength corresponding to isotropic loading was computed using Equation 14.

5 SUMMARY AND CONCLUSIONS

A simple formulation for predicting depth of desiccation cracks in compacted soils was presented. The method is based on the theory of elasticity incorporating estimates of tensile strength and expected changes in suction and stress conditions during drying. The method is particularly useful when the depth for the active zone and expected suction changes are well defined. Compared to field observations from an embankment test site and general observations from the literature, predicted depths of desiccation cracks seem reasonable.

Tensile strengths were determined from laboratory desiccation box tests under approximate uniaxial conditions. The unique testing device allows for determination of tensile strength of compacted soil during drying. Theoretical estimates of tensile strength using a microstructural representation of effective stress and a Mohr-Coulomb strength model compared favorably to the measured tensile strengths. Unsaturated strength parameters from suction-controlled direct shear tests and experimentally determined soil water characteristic curves were used as input to the models.

While the model for predicting crack depths involves many assumptions requiring further investigation, it provides a reasonable practical framework to predict crack depths for use in other analyses such as unsaturated seepage. The authors have done some preliminary seepage analyses of cracked and uncracked slopes considering a cracked layer with enhanced hydraulic conductivity and a thickness equal to the predicted depth of cracking. Suction profiles are then imported into unsaturated slope stability analyses. Results thus far are encouraging in comparison to actual slope failures at the embankment test site; yet, there is much additional research needed to enhance and validate methods used.

ACKNOWLEDGEMENTS

The authors are grateful for the support of the Oklahoma Department of Transportation and the

Oklahoma Transportation Center for funding this research. In addition, the authors thank Michael Schmitz for his invaluable design and fabrication skills.

REFERENCES

Alonso, E. E., Pereira, J. M., Vaunat, J., and Olivella, S. 2010. A microstructurally based effective stress for unsaturated soils. *Géotechnique*, 60(12), 913–925.

Amarasiri, A., Kodikara, J., and Costa, S. 2010. Numerical Modelling of Desiccation Cracking. *International Journal for Numerical and Analytical Methods in Geomechanics,* 48: 336–340.

Amarasiri, A. and Kodikara, J. 2011. Use of Material Interfaces in DEM to Simulate Soil Fracture Propagation in Mode I Cracking. *International Journal of Geomechanics*, 11(4): 314–322.

American Meteorological Society (AMS). 2012. Climate Change – An Information Statement of the American Meteorological Society. Adopted by AMS Council 20 August 2012, www.ametsoc.org/policy/2012climate change.html.

Ayad, R., Konrad, J.M., and Soulié, M. 1997. Desiccation of a sensitive clay: application of the model CRACK. *Canadian Geotechnical Journal*, 34: 943–951.

Costa, S. and Kodikara, J. 2010. Evaluation of J integral for clay soils using a new ring test. *Geotechnical Testing Journal*, 35(6):1–9.

Duncan, J.M. and Seed, R.B. 1986. Compaction-induced earth pressures under Ko-conditions. *Journal of Geotechnical Engineering, 112(1):1–22.*

Fredlund, D.G. and Rahardjo, H. 1993. Soil Mechanics for Unsaturated Soils. John Wiley and Sons.

Harrison, J.A., Hardin, B.O., Mahboub, K. 1994. Fracture toughness of compacted cohesive soils using ring test. *Journal of Geotechnical Engineering*, 120(5): 872–891.

Kim, T.H., Kim Ta., H., and Kang, G.C. 2012. Factors influencing crack induced tensile strength of compacted soil. *Journal of Materials in Civil Engineering*, 24(3), 315–320.

Kodikara, J.K., and Choi, X. 2006. A simplified analytical model for desiccation cracking of clay layers in laboratory tests. In: Miller, G.A., Zapata, C.E., Houston, S.L., Fredlund, D.G. (eds.), *Proc. Fourth International Conference on Unsaturated Soils*, ASCE Geotechnical Special Publication 147, 2: 2558–2567.

Kodikara, J.K. and Costa, S. 2013. Desiccation Cracking in Clayey Soils: Mechanisms and Modelling. L. Laloui and A. Ferrari (Eds.): *Multiphysical Testing of Soils and Shales*, SSGG, Springer-Verlag Berlin Heidelberg, pp. 21–32.

Konrad, J. M., and Ayad, R. 1997. An idealized framework for the analysis of cohesive soils undergoing desiccation. *Canadian Geotechnical Journal*, 34(4), 477–488.

Lachenbruch, A.H. 1961. Depth and spacing of tension cracks. *J. Geophysical Research*, 66(12): 4273–4292.

Lakshmikantha, M.R., Prat, P.C., and Ladesma, A. 2006. An experimental study of cracking mechanisms in drying soils. *Proc. 5th International Conference on Environmental Geotechnics*, Thomas Telford, London, pp. 533–540.

Lu, N., Kim, T., Sture, S., and Likos, W. 2009. Tensile Strength of Unsaturated Sand. *J. Eng. Mech.*, 135(12), 1410–1419.

Miller, C.J., Mi, H., and Yesiller, N. 1998. Experimental analysis of desiccation crack propagation in clay liners. *Journal of the American Water Resources Association*, 34(3):677–686.

Morris, P.H., Graham, J., and Williams, D.J. 1992. Cracking in drying soils. *Canada Geotechnical Journal,* 29(2): 263–277.

Nahlawi, H. 2004. Behavior of reactive soil during desiccation. Masters Thesis, Monash University, Australia.

Peron, H., Hueckel, T., Laloui, L., and Hu, L.B. 2009. Fundamentals of desiccation cracking of fine grained soils: experimental characterisation and mechanisms identification. *Canadian Geotechnical Journal*, 46: 1177–1201.

Tamrakar, S., Mitachi, T., Toyosawa, Y., and Itoh, K. 2005. Development of a New Soil Tensile Strength Test Apparatus. *Site Characterization and Modeling*: 1–10. doi: 10.1061/40785(164)26.

Varsei, M., Bourasset, C. M., and Miller, G. A. 2014. Laboratory Investigation of Desiccation Cracking. ASCE. *In Geo-Congress 2014 – Geo-characterization and Modeling for Sustainability:* 4076–4083.

Vesga, L. F. (2009). Direct tensile-shear test (DTS) on unsaturated kaolinite clay. *Geotechnical Testing Journal*, 32(5): 397–409.

This page intentionally left blank

Unsaturated Soil Mechanics—from Theory to Practice – Chen et al. (Eds)
© 2016 Taylor & Francis Group, London, ISBN 978-1-138-02921-7

Monotonic and cyclic shear stiffness of unsaturated soil at different temperatures

C.W.W. Ng & C. Zhou
The Hong Kong University of Science and Technology, Hong Kong Special Administrative Region, China

J. Xu
Hohai University, Nanjing, China

ABSTRACT: Shear stiffness of soil is one of the most important geotechnical parameters for predicting ground movements and monotonic and cyclic responses of many earth structures. In this keynote, a newly developed temperature and suction controlled cyclic triaxle apparatus is introduced. Measured results of anisotropic shear modulus at very small strains, shear modulus degradation curve at small strains and resilient modulus under cyclic loads at various suctions and temperatures are analyzed and reported. Semi-empirical state-dependent equations for anisotropic shear modulus and resilient modulus of unsaturated soil are proposed.

1 INTRODUCTION

It is well recognized that the stress-strain behavior of soil is highly non-linear and soil stiffness may decay with an increase in strain by orders of magnitude (Jardine et al. 1984). Fig. 1 shows an idealized degradation curve of soil stiffness with strain, with typical strain ranges encountered in engineering structures and measured in laboratory testing (Atkinson and Sallfors 1991; Mair 1993). Atkinson and Sallfors (1991) defined three strain ranges: very small strains (less than 0.001%), small strains (between 0.001% and 1%) and large strains (larger than 1%). It is clear that typical strains encountered in engineering structures are in the small strain range. An understanding of soil behaviour at small strains is thus essential for predicting ground movements and the performance of many earth structures and energy foundations under working conditions.

In many parts of the world, soils at and near the Earth's surface are often unsaturated and subjected to daily variations of water content (suction) and temperature (McCartney and Khosravi 2013). Many theoretical and experimental studies have illustrated that unsaturated soil behaviour is strongly affected by suction and temperature (Romero et al. 2003; François and Laloui 2008; Tang et al. 2008; Uchaipichat and Khalili 2009). Most of these studies, however, focused on soil behaviour at strains larger than 1%. Small strain behaviour of unsaturated soil, especially at different temperatures, is not fully understood.

On the other hand, soils in many earth structures (e.g., pavement) are subjected to cyclic loads. Resilient

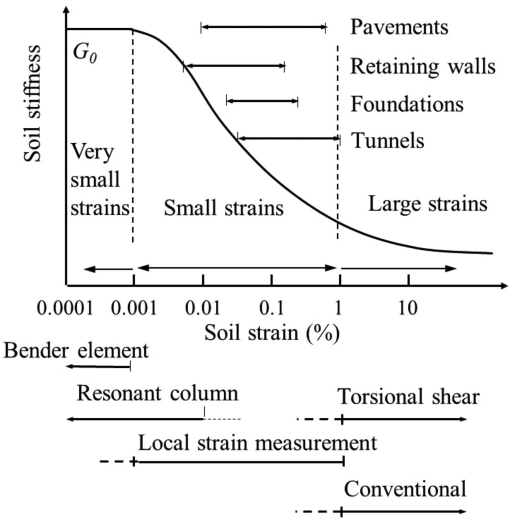


Figure 1. Typical stiffness-strain relationship of soil encountered in engineering structures and measurable ranges.

modulus M_R, defined by Seed et al. (1962) as the ratio of repeated deviator stress to recoverable axial strain in a cyclic triaxial test, is widely used as a stiffness parameter of soil under cyclic loads. By testing soil specimens compacted at different water contents, some previous researchers reported that M_R of an unsaturated soil significantly depends on water content (Seed et al. 1962; Sivakumar et al. 2013). However,

soil suction was rarely measured or controlled in these previous tests. More importantly, as far as the authors are aware, there is no study of thermal effects on cyclic soil behavior.

By using a new temperature and suction controlled cyclic triaxial apparatus, monotonic and cyclic shear stiffness of an unsaturated soil at various suctions and temperatures are investigated. In particular, anisotropic shear modulus at very small strains, shear modulus degradation curve at small strains, resilient modulus under cyclic loads are measured and analyzed. Semi-empirical state-dependent equations for anisotropic shear modulus and resilient modulus of unsaturated soil are proposed. It should be noted that the contents of this keynote are mainly based on and extracted from Ng et al. (2009), Ng and Zhou (2014) and Zhou et al. (2015).

2 THEORETICAL CONSIDERATIONS OF UNSATURATED SOIL STIFFNESS

2.1 *State-dependent anisotropic shear modulus*

Previous researchers (Roesler 1979) found that the velocity of a shear wave propagating in a completely dry or saturated soil depends on the principal stresses in the plane of shear (i.e., stresses in the directions of wave propagation and particle motion), but it is independent of the stress normal to the plane of shear. Effects of the two principal stresses in the plane of shear on shear wave velocity are found to be similar (Bellotti et al. 1996). In addition to principal stresses, void ratio also has an effect on shear wave velocity. Based on these findings, Ng and Leung (2007) proposed a semi-empirical equation for the relationship between shear wave velocity and the state of a saturated soil:

$$v_{s(ij)} = C_{ij} f(e) p_r^{-n} (\sigma_i' \times \sigma_j')^{n/2} \tag{1}$$

where C_{ij} is a constant reflecting the inherent soil properties in the ij plane, with dimension m/s; $f(e)$ is a void ratio function relating shear wave velocity to void ratio; p_r is a reference pressure taken as 1 kPa for simplicity; n is an empirical stress exponent; σ_i' and σ_j' are effective principal stresses in the direction of wave propagation and particle motion, respectively.

With the development of unsaturated soil mechanics, various constitutive variables have been proposed to describe the behaviour of unsaturated soils (Gens 2010). Based on the thermodynamic theory, Houlsby (1997) showed that a complete description of unsaturated soil behaviour requires at least two stress state variables. Keeping the interpretation of experimental data rigorous yet simple, this keynote adopts the most commonly used two independent constitutive variables (Jennings and Burland 1962), namely net normal stress ($\sigma - u_a$) and matric suction ($u_a - u_w$), where σ, u_a, u_w are total normal stress, pore air pressure and pore water pressure, respectively. Based on these two independent stress state variables, Ng and Yung (2008) proposed the following expression to capture the velocity of shear waves travelling in unsaturated soil:

$$v_{s(ij)} = C_{ij} f(e) \left[\frac{(\sigma_i - u_a)}{p_r} \times \frac{(\sigma_j - u_a)}{p_r}\right]^{\frac{n}{2}} \left[1 + \frac{(u_a - u_w)}{p_r}\right]^b \tag{2}$$

where b is an empirical exponent reflecting the influence of matric suction on shear wave velocity. This equation allows a smooth transition between unsaturated and saturated states. When soil is saturated (i.e., $u_a - u_w = 0$), Eq. (2) reduces to Eq. (1).

The shear wave velocity for a homogeneous cross-anisotropic elastic continuum with a symmetrical vertical axis subjected to principal stresses in the horizontal and vertical directions is expressed by the following equation:

$$v_{s(ij)} = \sqrt{G_{0(ij)} / \rho} \tag{3}$$

where ρ is bulk density of the medium and $G_{0(ij)}$ is elastic shear modulus in the ij plane. If a specimen is homogeneous and cross-anisotropic, shear modulus of an unsaturated soil, $G_{0(ij)}$, can be obtained from Eq.s (2) and (3) and expressed as follows (Ng and Yung 2008):

$$G_{0(ij)} = C_{ij}^2 F(e) \left[\frac{(\sigma_i - u_a)}{p_r} \times \frac{(\sigma_j - u_a)}{p_r}\right]^n \left[1 + \frac{(u_a - u_w)}{p_r}\right]^{2b} \tag{4}$$

where $F(e)$ is void ratio function describing effects of void ratio on shear modulus.

2.2 *Degree of stiffness anisotropy*

If the degree of stiffness anisotropy of a soil is expressed in terms of the ratio of shear modulus in the horizontal plane ($G_{0(hh)}$) to that in the vertical plane ($G_{0(hv)}$), by making use of Eq. (4), the degree of stiffness anisotropy of an unsaturated soil can be expressed as follows (Ng and Yung 2008):

$$\frac{G_{0(hh)}}{G_{0(hv)}} = \left(\frac{v_{s(hh)}}{v_{s(hv)}}\right)^2 = \frac{C_{hh}^2}{C_{hv}^2} \left[\frac{(\sigma_h - u_a)}{(\sigma_v - u_a)}\right]^n \tag{5}$$

It can be seen from Eq. (5) that the degree of stiffness anisotropy of an unsaturated soil depends on inherent material properties, C_{hh}^2/C_{hv}^2, and the ratio of net normal stresses in the horizontal and vertical directions, $(\sigma_h - u_a)/(\sigma_v - u_a)$. However, the degree of stiffness anisotropy appears to be independent of soil suction. If a soil is subjected to isotropic stress condition, this equation can be further simplified:

$$\frac{G_{0(hh)}}{G_{0(hv)}} = \left(\frac{v_{s(hh)}}{v_{s(hv)}}\right)^2 = \frac{C_{hh}^2}{C_{hv}^2} \tag{6}$$

Eq. (6) suggests that under isotropic stress state, the degree of stiffness anisotropy expressed in terms of $G_{0(hh)}/G_{0(hv)}$ only depends on inherent anisotropic material properties.

2.3 *Resilient modulus under cyclic loads*

Many equations have been proposed to predict M_R in pavement engineering. One of the most widely used formulations is as follows (Uzan 1985):

$$M_R = a_r\left(\frac{\sigma_1+\sigma_2+\sigma_3}{p_{atm}}\right)^{b_r}\left(\frac{q_{cyc}}{p_{atm}}\right)^{c_r} \quad (7)$$

where σ_1, σ_2 and σ_3 are principal total stresses; q_{cyc} is cyclic shear stress, defined as the amplitude of change in deviator stress during cyclic loading-unloading; p_{atm} is atmospheric pressure and parameters a_r, b_r and c_r are regression coefficients. Clearly, Eq. (7) cannot completely describe M_R of an unsaturated soil since it does not consider suction effects.

On the other hand, following its definition, M_R can be considered to be equivalent to secant Young's modulus of a material (Brown et al. 1987). For an isotropic elastic material, Young's modulus is linked to shear modulus G by the formulation of $E = 2G\ (1+\nu)$, where ν is Poisson's ratio. It may be reasonable to assume that suction affects shear modulus and resilient modulus in a similar manner qualitatively. Referring to Eq. (4), it is logical to revise Eq. (7) and propose a new equation for M_R of an unsaturated soil as follows:

$$M_R = M_0\left(\frac{p}{p_r}\right)^{k_1}\left(1+\frac{q_{cyc}}{p_r}\right)^{k_2}\left(1+\frac{u_a-u_w}{p}\right)^{k_3} \quad (8)$$

where p is net mean stress; parameters k_1, k_2 and k_3 are regression exponents. The term M_0 denotes M_R at the reference stress state when $p-u_a=p_r$, $q_{cyc}=p_r$ and $u_a-u_w=0$. This equation empirically incorporates the effects of a number of factors such as microstructure and void ratio on M_0, which is equivalent to C_{ij} and $F(e)$ in Eq. (4). The term $(p/p_r)^{k1}$ quantifies the influence of net mean stress on M_R. The term $(1+q_{cyc}/p_r)^{k2}$ reflects the variations of M_R with cyclic stress. The term $(1+(u_a-u_w)/p)^{k3}$ considers suction effects on M_R.

The above state-dependent equations, for predicting anisotropic shear modulus at very small strains (Eq. (4)), degree of stiffness anisotropy (Eq. (6)) and resilient modulus (Eq. (8)), were verified in Ng and Yung (2008) and Ng et al. (2013) at the isothermal condition. To predict soil stiffness at various temperatures, soil parameters in these equations may be temperature dependent. In the current keynote, these equations are used to interpret experimental results, whenever appropriate.

3 TESING APPARATUS AND MEASURIGN DEVICES

Fig. 2 shows the schematic diagram of a new temperature and suction controlled cyclic triaxial apparatus

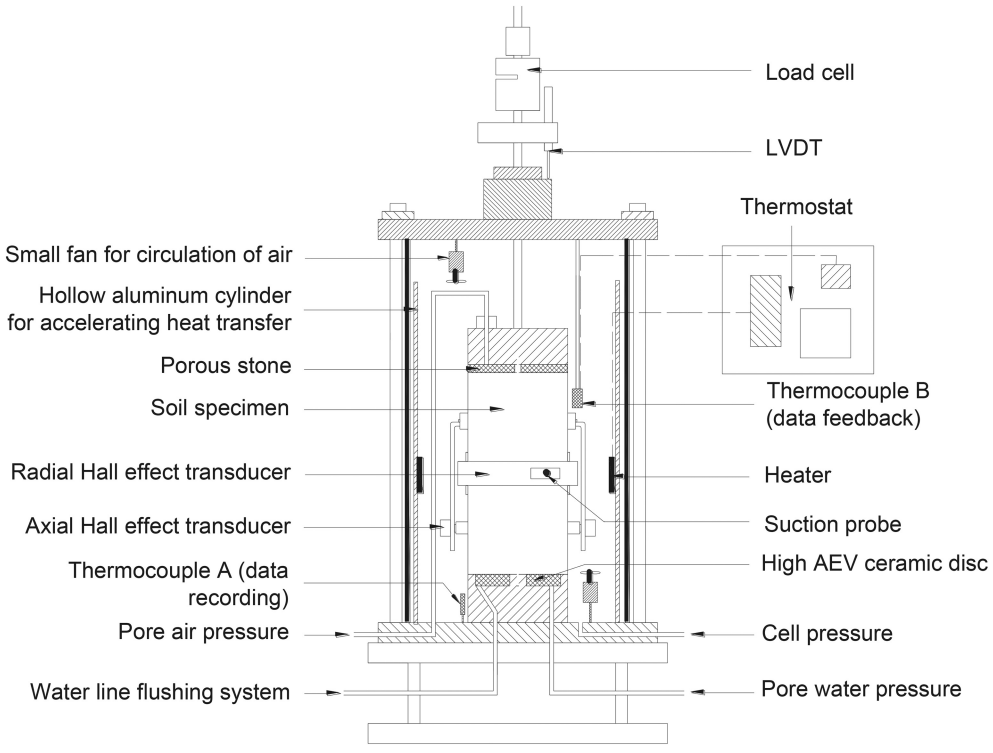


Figure 2. A new temperature and suction controlled cyclic triaxial apparatus for testing unsaturated soils.

for testing unsaturated soils (Ng and Zhou 2014). The system consists of a triaxial cell, four independent pressure controllers, five transducers and a computer. The four pressure controllers are capable of controlling axial stress (σ_a), cell pressure (σ_r), pore air pressure (u_a) and pore water pressure (u_w) independently. The five transducers consist of an external load cell for measuring axial force, a linear variable differential transformer (LVDT) for measuring axial displacement externally and three pressure transducers for monitoring cell pressure (σ_r), pore air pressure (u_a) and pore water pressure (u_w). This triaxial system is controlled by a closed-loop feedback scheme. It can be used to apply both static and cyclic loads. To measure water volume change of a soil specimen, a vertical tube is connected to the pedestal to determine the amount of water flowing in or out of the soil specimen. This is achieved by measuring the height of the water column by a sensitive differential pressure transducer inside the tube. In addition, this triaxial apparatus is equipped with a shear-wave velocity measurement system, a set of local Hall-effect strain transducers and a high capacity suction probe.

3.1 *Suction control*

The new system adopted the axis-translation technique (Hilf 1956) to control soil suction ($u_a - u_w$) by applying u_a and u_w independently. u_a was controlled through a coarse low air-entry value (AEV) corundum disk placed on top of a soil specimen, whereas u_w was controlled through a saturated high AEV (300 kPa) ceramic disk sealed to the base pedestal of the triaxial apparatus. The conventional pedestal of the triaxial cell was modified to incorporate both a high AEV ceramic disk and a bender element. In addition, a spiral-shaped drainage groove of 3 mm wide and 3 mm deep connected to the water drainage system was carved in the base pedestal. It serves as a water channel for flushing air bubbles that may be trapped or accumulated beneath the ceramic disk as a result of air diffusion during long periods of unsaturated soil testing. Diffused air was removed by flushing de-aerated water along the spiral-shaped drainage groove beneath the ceramic disk once every 24 hours throughout a test.

3.2 *Temperature control*

To apply thermal loads, a heating system was added to the triaxial apparatus. The heating system consisted of a thermostat, a heater and thermocouple A. As shown in Fig. 2, the heater and thermocouple A were installed inside the triaxial cell. Both of them were connected to the thermostat, forming a closed-loop control and feedback system. During a test, the thermostat adjusted the heater output based on the feedback from thermocouple A. When the dissipating energy and the heater output were balanced, the air temperature inside the triaxial cell reached equilibrium. It is reasonable to assume that the soil temperature is equal to the air temperature in the triaxial cell at equilibrium state. Depending on the target temperature, 1–3 hours were required to achieve thermal equilibrium.

To enhance the uniformity of temperature inside the triaxial cell, two small fans and a hollow aluminum cylinder were installed in the triaxial cell. The fan improved air circulation, while the aluminum cylinder enhances heat transfer because of its high thermal conductivity. To check the uniformity of temperature, two thermocouples (A and B) were installed at different locations inside the triaxial cell. They measured air temperature at a distance of about 5 mm from the soil specimen. When thermal equalization was reached, the readings of the two thermocouples were almost identical. They remained fairly constant with a maximum fluctuation of ±0.5°C.

3.3 *Shear wave velocity measurement*

The shear wave velocity measurement system consisted of bender elements, a function generator, a power amplifier, a multi-channel filter, an oscilloscope and a computer. The arrangement of bender elements on each specimen is shown in Fig. 3(a). Three pairs of bender elements were installed on each specimen to measure shear wave velocities in different planes. Thus, very small strain shear moduli in different planes can be determined. A pair of bender elements was inserted into the top and bottom platens to measure the velocity of vertically transmitted shear wave with horizontal polarization, $v_{s(vh)}$. A pair of bender element probes was developed and inserted into the mid-height of each specimen to measure velocities of horizontally transmitted shear waves with vertical and horizontal polarization, $v_{s(hv)}$ and $v_{s(hh)}$. Each bender element probe consisted of two pieces of bender elements in a T-shaped assembly, as shown in Fig. 3(b).

The input signal consisted of a single sinusoidal pulse with a frequency of 2 to 15 kHz. The range of frequency was selected to obtain a clear signal and to minimize the near field effect (Sanchez-Salinero et al. 1986). The velocity of a shear wave propagating in soils in the direction of the wave propagation, *i*, and

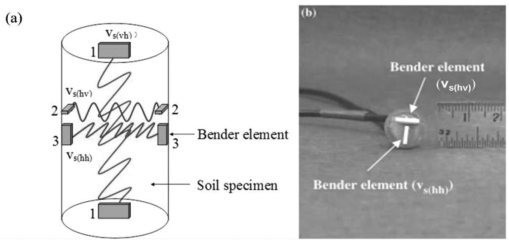


Figure 3. Details of bender element (a) Arrangement of bender elements; (b) Horizontal bender element probe at the mid-height of specimen.

particle motion, j, can be calculated from the following equation:

$$v_{s(ij)} = \frac{L_i}{t_{ij}} \tag{9}$$

where L_i is travel distance and t_{ij} is travelling time of the shear wave propagating over the distance L_i.

3.4 *Local strain and pore pressure measurements*

In order to avoid possible errors in the conventional external measurements of axial strain using a LVDT, such as seating, alignment, bedding and compliance errors (Jardine et al. 1984), Hall-effect transducers (Clayton et al. 1989) were adopted to measure local strains at center portion of each soil specimen. As shown in Fig. 2, the Hall effect transducers measured local soil deformation at the mid-height of each specimen. One of these Hall effect transducers was used to measure radial deformation, while the other two were used to measure axial deformation independently. After calibration, the resolution and accuracy of each Hall effect transducer were about 1 and 3 μm respectively, corresponding to vertical strains of about 0.001% and 0.003% (Ng and Xu 2012). As expected, axial strain obtained using an LVDT (external device) was generally larger than that obtained using a Hall effect transducer (local device). This is because the former method measures the overall deformation of a soil specimen together with various experimental errors as illustrated above, whereas the latter records the actual displacement of the soil specimen. For greater reliability, axial strain measured using Hall effect transducers was used and reported in this study.

Since the Hall effect transducers measured local deformation at the mid-height of a specimen, it was sensible to measure pore water pressure also at this level. A suction probe was employed to monitor pore water pressure at the mid-height of a specimen during cyclic loading-unloading, although a conventional pore water pressure transducer was still used to measure pore water pressure at the bottom. For unsaturated soil testing, pore water pressure measured at the mid-height also provided guidance for suction equalization. The suction probe was modified from a Druck PDCR-81 miniature pore water pressure transducer by replacing the low AEV ceramic tip with a high AEV ceramic tip (500 kPa) (Ng and Xu 2012). Thus it was able to measure negative pore water pressure of up to 480 kPa, close to the AEV of the ceramic tip.

Considering that the Hall effect transducers and the suction probe were exposed to elevated temperatures, they were carefully calibrated in a temperature-controlled oven at three temperatures (20, 40 and 60°C). At each temperature, they were calibrated under both loading and unloading conditions. It was found that the suction probe and Hall effect transducer are both sufficiently temperature compensated in the temperature range from 20 to 60°C. The thermal insensitivity of these transducers ensures accurate measurement of pore water pressure and soil deformation during thermal loading.

4 SOIL SPECIMEN PREPARATIN

4.1 *Soil tested*

The soil tested in the study is a yellowish-brown completely decomposed coarse ash tuff (CDT), commonly found in Hong Kong and often used as construction materials. Fig. 4 shows the particle size distribution of CDT as determined by sieve and hydrometer analyses (BSI 1990). The physical properties of CDT are summarized in Table 1. Following the Unified Soil Classification System (ASTM 2006), CDT is classified as silt (ML).

Fig. 5 shows two stress-dependent water retention curves (WRCs) of CDT, measured by Ng and Xu (2012) using a triaxial pressure plate system. Two identically prepared triaxial specimens were subjected to

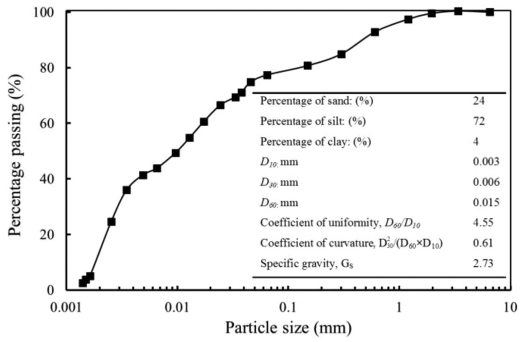


Figure 4. Particle size distribution of completely decomposed tuff (CDT).

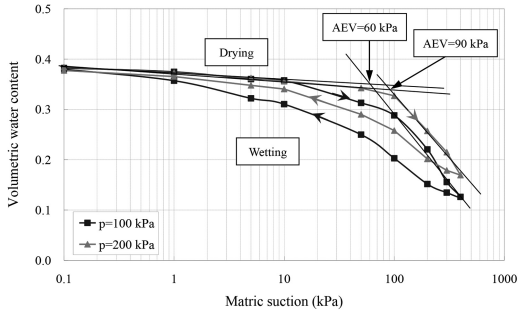


Figure 5. Stress-dependent water retention curves of compacted CDT.

Table 1. Index properties of CDT.

Index test	Measured value
Standard compaction tests	
Maximum dry density: (kg/m^3)	1760
Optimum water content: (%)	16.3
Atterberg limits	
Liquid limit: (%)	43
Plastic limit: (%)	29
Plasticity index: (%)	14

a drying and wetting cycle under net mean stresses of 100 and 200 kPa. Total volume change and water volume changes of each specimen were measured by a double-cell measurement system and a ballast tube, respectively. It can be seen from the figure that soil WRC is dependent on stress level. The specimen subjected to a higher net mean stress tends to possess a higher AEV. The AEVs are estimated to be 60 and 90 kPa at net mean stresses of 100 and 200 kPa, respectively. In addition, the specimen subjected to net mean stress of 200 kPa shows a slightly lower desorption rate than the one under net mean stress of 100 kPa. The above observations are probably because that soil specimen under higher net mean stress has a smaller average pore-size distribution and thus a better water retention ability (Ng and Pang 2000).

4.2 *Specimen preparation*

Each triaxial specimen, 76 mm in diameter and 152 mm in height, was compacted at initial water content of about 16.3% and dry density of about 1760 kg/m^3. In order to produce a uniform specimen, the specimen was compacted in 10 layers. After the completion of compaction, the height and diameter dimensions of the specimen were measured by a caliper (readable to 0.01 mm) and a PI tape (readable to 0.01 mm), respectively. The average initial suction of the specimens after compaction is 95 kPa as measured by a high capacity suction probe. The variations of measured initial suction among different height of each specimen and the variations of measured initial suction among different specimens are all less than ±2 kPa.

5 TEST PROGRAM AND PROCEDURES

Three series of tests were carried out on compacted CDT specimens. The objective of the first series of tests was to study anisotropic shear modulus at very small strains. The second series of tests were conducted to investigate shear modulus degradation curve at small strains. The purpose of the third series of tests was to study resilient modulus under cyclic loading and unloading.

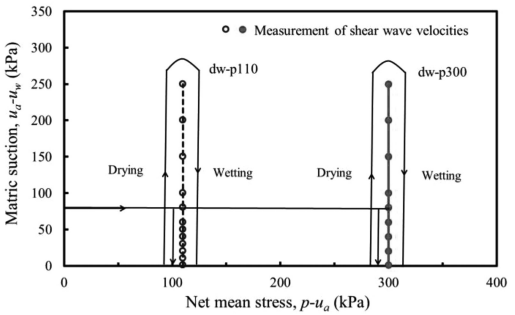


Figure 6. Stress paths of dying-wetting tests under constant isotropic net stresses.

5.1 *Series A: tests for investigating anisotropic shear moduli at very small strains*

To study anisotropic shear moduli of unsaturated soil during drying-wetting, two dying-wetting tests (series A) were carried out at two different isotropic net stresses. Fig. 6 shows the stress paths of the two tests. Desired net mean stresses of 110 and 300 kPa were firstly applied to specimens (dw-p100 and dw-p300), which were then brought to zero suction at constant net mean stress for suction equalization. The purpose of applying a suction equalization state was to ensure that soil moisture has reached its equilibrium state, when pore air pressure and pore water pressure were equal to predefined values throughout a specimen. This stage was considered to be completed when the rate of water content change was less than 0.04% per day (Sivakumar 1993), which corresponded to a water flow of about 0.5 cm^3 per day. This equalization criterion was used in all series of tests in this study. Once a specimen was equalized at its predefined stress and suction level, shear wave velocities ($v_{s(vh)}$, $v_{s(hv)}$ and $v_{s(hh)}$) were measured, and then suction was increased to the next desired value. Upon completion of the drying phase at a suction of 250 kPa, wetting phase began. When soil suction was decreased to zero, the wetting phase was completed. The drying-wetting tests consisted of a sequence of equalization stages. Shear wave velocities ($v_{s(vh)}$, $v_{s(hv)}$ and $v_{s(hh)}$) were measured at the end of each equalization stage, as shown by dots in the figure. More details of this series of tests were given by Ng et al. (2009).

5.2 *Series B: tests for measuring shear modulus reduction at small strains under monotonic loading*

To investigate suction and thermal effects on shear modulus reduction at small strains, four suction- and temperature-controlled triaxial tests (series B) were carried out. Each test consisted of four stages: isotropic compression, suction equalization, thermal equalization and shearing. Fig. 7 shows the thermo- hydro-mechanical paths of all tests at the first three stages. After compaction and set-up in the apparatus, initial

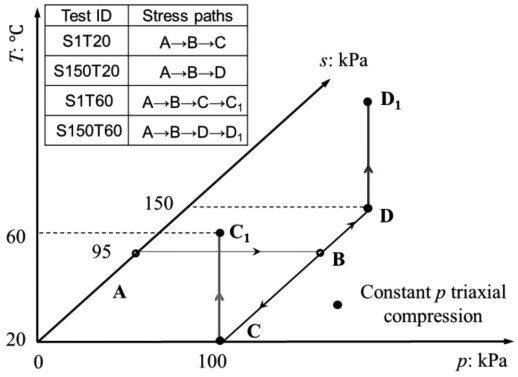


Figure 7. Stress paths of suction and temperature controlled constant p compression tests.

state of each specimen was controlled at point A. During the compression stage, the net confining pressure of each specimen was directly increased from 0 to 100 kPa at constant water content condition. Then, soil specimens in tests S1T20 and S1T60 were wetted from initial suction (95 kPa) to 1 kPa. Soil specimens in tests S150T20 and S150T60 were dried from 95 kPa to 150 kPa. The third stage was the application of thermal loading. For the two tests carried out at room temperature (20°C) (S1T20 and S150T20), it was unnecessary to change soil temperature. For the tests carried out at higher temperature (60°C) (S1T60 and S150T60), the soil specimens were heated to 60°C. After that, soil specimens were sheared at constant mean net stress (p), suction and temperature to determine the decay in shear modulus with increasing strain. The choice of a constant p stress path was operated to eliminate coupling effects of dp and dq on shear modulus (Atkinson and Sallfors 1991; Ng et al. 2000). The deviator stress was increased at a rate of 3 kPa per hour, slow enough to generate excess pore water pressures lower than ±2 kPa during shearing. More details of this series of tests were given by Zhou et al. (2015).

5.3 *Series C: tests for determining resilient modulus under cyclic loads*

To investigate cyclic behavior of unsaturated soil, nine suction- and temperature-controlled cyclic triaxial tests (series C) were carried out at three suctions of 60, 30 and 0 kPa. At each suction level, three tests were carried out at different temperatures of 20, 40 and 60°C. Similar to tests in Series B, each test in this series consisted of four stages: isotropic compression, suction equalization, thermal equalization and shearing. Fig. 8 shows stress paths of all tests at the first three stages. The purposes of these three stages were to control the stress, suction and temperature of soil specimen, respectively. After equalization of stress, suction and temperature, each specimen was subjected to cyclic loading and unloading at constant temperature and water content. Cyclic deviator stress in haversine form was applied, while net confining

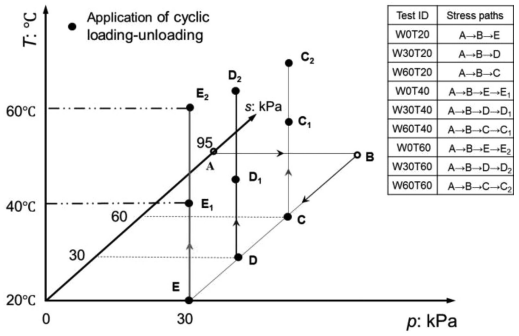


Figure 8. Stress paths of suction and temperature controlled cyclic triaxial tests.

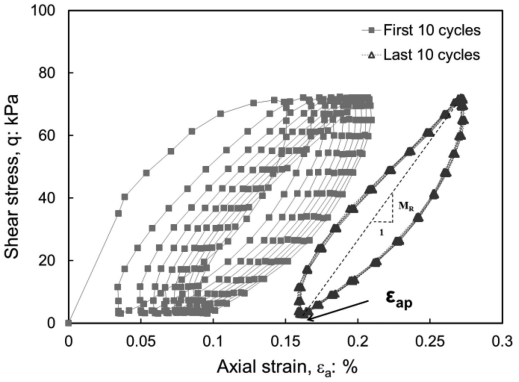


Figure 9. Typical stress-strain relationship of unsaturated soil in a 100-cycle tests.

pressure was maintained constant at 30 kPa. Four levels of cyclic stress (30, 40, 55 and 70 kPa) were applied to each specimen in succession, with 100 cycles at each cyclic stress.

Fig. 9 shows the typical stress-strain relationship of unsaturated soil measured during a 100-cycle triaxial test. For clarity, only the first and last 10 cycles are presented in the figure. During the first 10 cycles, soil plastic strain accumulates with increasing number of cycles. During the last 10 cycles, there is no obvious additional accumulation of plastic strain, implying that the soil specimen has reached a stable reversible response. From soil stress-strain relationship at the stable state, resilient modulus of soil at each stress, suction and temperature condition is calculated and reported in this keynote. More details of this series of tests were given by Ng and Zhou (2014).

6 INTERPRETATIONS OF EXPERIMENTAL RESULTS

6.1 *Anisotropic shear modulus at very small strains*

Fig. 10 shows variations of $G_{0(vh)}$, $G_{0(hv)}$ and $G_{0(hh)}$ with suction measured from two drying-wetting tests

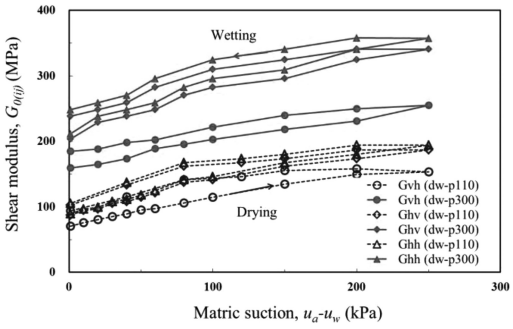


Figure 10. Variations of shear moduli with matric suction during drying-wetting tests.

(series A). It can be seen that $G_{0(vh)}$, $G_{0(hv)}$ and $G_{0(hh)}$ increase with an increase in suction following a similar trend during the drying path. Similar results that G_0 of unsaturated soil increases with increasing suction have been reported by Mancuso et al. (2002) in their measurements of single G_0 values. The beneficial effects of suction on very small strain shear modulus arise from at least three possible reasons:

(1) As it is well known, the average skeleton stress (σ*) of unsaturated soils may be expressed as:

$$\sigma^* = \sigma_{ij}^t - u_a + S_r(u_a - u_w) \tag{10}$$

where σ_{ij}^t is total stress, and S_r is degree of saturation. The average skeleton stress expresses the stress transferred through soil skeleton (Wheeler et al. 2003). In the suction range considered, the value of $S_r(u_a - u_w)$ increases with increasing suction and leads to stiffening of the soil skeleton.

(2) Pore water may be classified as bulk water and meniscus water (Wheeler et al. 2003). Similar to net stress, u_w in bulk water affects both normal and tangent forces between soil particles, as captured by Eq. (10). On the contrary, u_w in the meniscus water affects only normal forces at particle contacts, providing additional bonding forces at particle contacts and stabilizing the soil skeleton. This stabilization effect is not captured by Eq. (10). The normal force induced by meniscus water between two spherical particles can be expressed as (Ng and Zhou 2014):

$$\Delta N = \frac{\pi T_s^2}{(u_a - u_w)} \frac{\left(\sqrt{9 + 8R(u_a - u_w)/T_s} - 3\right)\left(\sqrt{9 + 8R(u_a - u_w)/T_s} + 1\right)}{4} \tag{11}$$

where T_s is air-water surface tension coefficient; R is radius of spherical particle. According to this equation, ΔN is larger at higher $(u_a - u_w)$. Furthermore, Fig. 5 shows that S_r greatly decreases as suction increases. The number of menisci, which is related to $(1 - S_r)$ (Gallipoli et al. 2003), is thus expected to increase with an increase in suction. As suction increases, both the stabilization effect exerted by ΔN and the number of menisci become more significant and therefore soil skeleton behaves stiffer.

(3) An increase in suction induces the volume shrinkage of soil specimen (Ng and Pang 2000). Due to higher density, shear modulus measured at higher suctions is larger.

Due to these reasons, the measured shear moduli, $G_{0(vh)}$, $G_{0(hv)}$ and $G_{0(hh)}$, all increase with increasing suction at a given net mean stress. Furthermore, the observed increase in shear moduli with an increase in suction is captured by the term $[1 + (u_a - u_w)/p_r]^{2b}$ in Eq. (4).

After drying to a suction of 250 kPa, soil specimen is subjected to a wetting process. Similar to WRCs (see Fig. 5), there is a hysteresis between the drying and wetting stiffness curves showing variations of shear moduli with matric suction. At any given suction, the shear moduli measured during wetting are consistently higher than those obtained during drying. Since the induced axial and radial strains of each soil specimen are relatively small (less than $\pm 0.3\%$), total volume change is not significant. The shear modulus hysteresis may be because that the water content on the wetting curve is lower than that on the desorption curve at the same suction. Given a lower water content, the number of water meniscus is larger and therefore its stiffening effects are more significant.

6.2 *Stiffness anisotropy at very small strains*

The degree of stiffness anisotropy is expressed in terms of the ratio of shear modulus in the horizontal plane ($G_{0(hh)}$) to that in the vertical plane ($G_{0(hv)}$ or $G_{0(vh)}$) in this keynote. In a homogeneous cross-anisotropic elastic continuum, $G_{0(vh)}$ should be equal to $G_{0(hv)}$. However, a discrepancy between measured $G_{0(vh)}$ and $G_{0(hv)}$ is observed, as illustrated in Figs 10. This discrepancy may be attributed to the following four reasons (Ng et al. 2009). Firstly, soil specimen was actually not a homogeneous cross-anisotropic elastic continuum. Due to the preferred orientation of particles in the horizontal direction, a horizontally transmitted shear wave travels through fewer particle contacts per unit distance than does a vertically transmitted shear wave and this results in $v_{s(hv)}$ being higher than $v_{s(vh)}$ (Jardine et al. 1999). Secondly, transmitting frequencies used by the horizontally mounted bender element probes ($v_{s(hh)}$ and $v_{s(hv)}$) were higher than those used by the platen-mounted bender elements ($v_{s(vh)}$) (Pennington et al. 2001). Thirdly, bender element embedded in the base pedestal probably deflected more than the horizontally mounted bender elements did inside the probe and hence resulted in a lower $v_{s(vh)}$ (Pennington et al. 2001). Fourthly, platen end effects on stiffness measurements could be another cause of the discrepancy (Germaine and Ladd 1988). To eliminate the differences in frequency and boundary effects, $G_{0(hh)}$ and $G_{0(hv)}$ reported in Fig. 10 were chosen for calculating degree of stiffness anisotropy. This is because

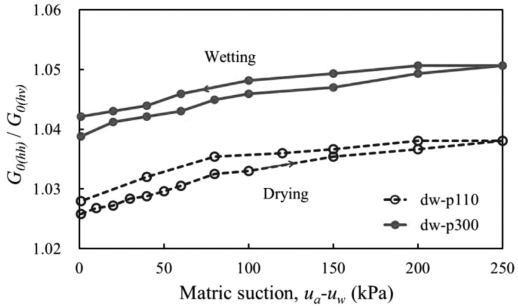


Figure 11. The relationship between degree of stiffness anisotropy and matric suction during drying-wetting tests.

that $G_{0(hh)}$ and $G_{0(hv)}$ were generated by the same bender element probe and they had the same frequency, travelling path and boundary conditions (Pennington et al. 2001).

Fig. 11 shows the relationship between degree of stiffness anisotropy, $G_{0(hh)}/G_{0(hv)}$, and suction for the two drying-wetting tests. At net mean stresses of 110 and 300 kPa, variations of degree of stiffness anisotropy with soil suction follow a similar trend. Although the magnitudes of the increase in $G_{0(hh)}/G_{0(hv)}$ with an increase in matric suction are very small, there is a clear trend showing that the degree of stiffness anisotropy increases with increasing matric suction. Moreover, $G_{0(hh)}/G_{0(hv)}$ value at net mean stress of 300 kPa is consistently higher than that at net mean stress of 110 kPa. These observations illustrate that stiffness anisotropy is more significant at higher matric suction and higher net mean stress. There is a hysteresis between the drying and wetting stiffness curves showing the variations of stiffness anisotropy with matric suction. The changing rates of stiffness anisotropy and the sizes of hysteresis loops at two different net mean stresses are almost the same.

According to Eq. (6), the observed stiffness anisotropy should be attributed to the inherent anisotropy (C_2^{hh}/C_2^{hv}) induced in the tested soil during specimen preparation. However, the observed stiffness anisotropy may not be solely caused by the inherent anisotropy induced during specimen preparation. This is because the specimens have undergone isotropic compression and suction equalization, as illustrated in Fig. 6. On the other hand, although the magnitudes of increase in $G_{0(hh)}/G_{0(hv)}$ are not large, there is a clear trend showing that $G_{0(hh)}/G_{0(hv)}$ of CDT increases with an increase in suction but at a reducing rate at a given net mean stress. The measured results seem to be consistent with theoretical work by Li (2003) who demonstrated that variations of suction could induce anisotropic strains under isotropic stresses.

6.3 *Shear modulus reduction at small strains*

Fig. 12(a) shows the stress-strain relations of unsaturated CDT measured through suction and temperature controlled constant p triaxial compression tests

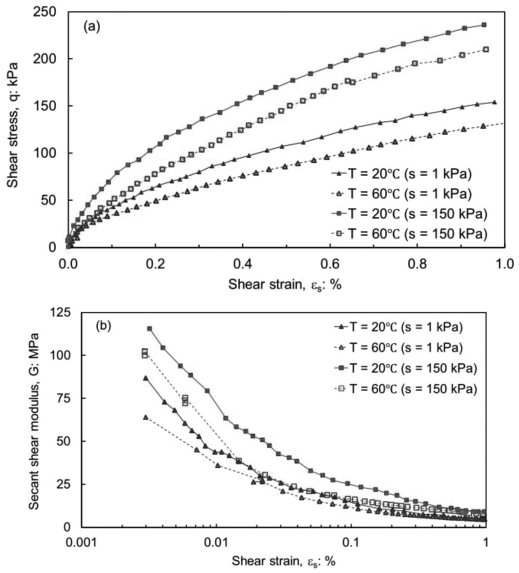


Figure 12. Effects of matric suction on (a) stress–strain relationship; (b) shear modulus degradation curve.

(series B). As expected, the deviator stress of all specimens increases non-linearly with increasing strain. At the same deviator stress, soil specimen at higher suction is affected by consistently smaller strain than that at lower suction. This is because the shear stiffness of unsaturated soil increases with increasing suction, as illustrated in Fig. 10.

From the slope of stress-strain curve, secant shear moduli (G) at different strains are determined and presented in Fig. 12(b). As strain increases from 0.003% to 1%, measured G values of all specimens greatly reduce, but they remain always greater at higher suction. On the other hand, it is clearly revealed in the figure that measured G is consistently smaller at 60°C than that at 20°C at a given suction. Furthermore, when mobilized shear strain is 0.003%, thermal effect on G is more significant at suction of 1 kPa (reduction of about 30% as soil temperature increases from 20 to 60°C) than that at 150 kPa (reduction of about 15%). At some other strains (for example, 0.03%), however, thermal effect on G seems less significant at suction of 1 kPa (reduction of about 15%) than that at 150 kPa (reduction of about 30%). The observed reduction of G with increasing temperature may be attributed to temperature dependency of T_s in Eqn (11), which is equal to 72.8 and 66.2 mN/m at 20°C and 60°C respectively (Ng and Menzies 2007). The decrease in T_s with increasing temperature would affect both the retention ability of the soil (Romero et al. 2003), causing a reduction of S_r and σ^*, and the inter-granular extra stress induced by the meniscus water (see Eqs (10) and (11)). More discussion on thermal effects at various suctions is given later. The observed behaviour can be also explained by thermo-plasticity theory. As a matter of fact, thermo-mechanical models for unsaturated soil (e.g. François and Laloui (2008)) suggest that yield

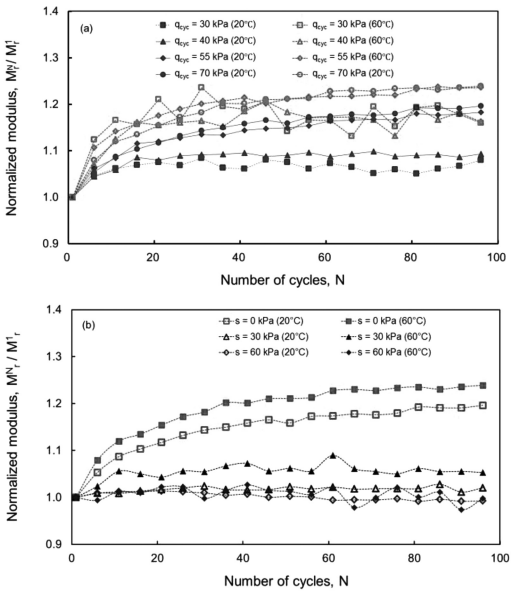


Figure 13. Effects of number of cycles on resilient modulus: (a) at zero suction; (b) at suctions of 0, 30 and 60 kPa.

stress and OCR decreases as an over-consolidated soil is heated at constant stress. Given a smaller OCR, soil response would be softer during shearing.

6.4 *Effects of number of cycles on resilient modulus*

Fig. 13(a) shows the relationship between M_r^N/M_r^1 and N at zero suction, where M_r^1 and M_r^N are resilient moduli measured from the first and Nth cycles of cyclic triaxial tests (series C) respectively. At 20°C, the ratio M_r^N/M_r^1 increases consistently with increasing N. The rate of increase is highly dependent on cyclic stress. At cyclic stresses of 30 and 40 kPa, M_R^N/M_R^1 increases by 10% during the first 20 cycles. There is no obvious change during the subsequent cycles. At cyclic stress of 55 and 70 kPa, M_r^N/M_r^1 increases continuously with N. With 100 cycles, the increase in M_R^N/M_R^1 is up to 20%. Thus, the influence of N on M_r^N/M_r^1 is more significant at higher cyclic stress. This is because the accumulated contractive volumetric strain during cyclic loading-unloading increases with an increase in cyclic stress at an increasing rate. The measured contractive volumetric strain is only 0.03% and 0.04% at cyclic stresses of 30 and 40 kPa, but increases to 0.09% and 0.25% under cyclic stress of 55 and 70 kPa. Due to larger contractive volumetric strain, densification effect on M_R is more significant at a higher cyclic stress.

On the other hand, soil response at 60°C is qualitatively similar to that at 20°C. However, the increase in M_r^N/M_r^1 with N is larger at 60°C than at 20°C. At cyclic stresses of 30 and 40 kPa, M_r^N/M_r^1 is larger at 60°C than at 20°C by about 10%. At cyclic stresses of 55 and 70 kPa, M_r^N/M_r^1 is larger at 60°C than at 20°C by only about 5%. More discussion on the suction and thermal effects on resilient modulus are given later.

Fig. 13(b) shows the relationship between M_r^N/M_r^1 and N at cyclic stress of 70 kPa for different suction and temperature conditions. At 20°C, M_r^N/M_r^1 increases with N by up to 20% at zero suction, but it remains almost constant at suctions of 30 and 60 kPa. This is because plastic deformation is much smaller at suctions of 30 and 60 kPa than at zero suction. On the other hand, as temperature increases from 20 to 60°C, the change in M_r^N/M_r^1 is less than 5%. Compared to suction effect, thermal effects on M_r^N/M_r^1 are not so obvious at the given cyclic stress.

It is well illustrated in Fig. 13 that M_r^N/M_r^1 generally achieves a constant value within 100 cycles of loading and unloading. This is consistent with the observations from Fig. 9 that soil response is almost reversible during the last 10 cycles. Following AASHTO (2003) standard for testing resilient modulus, M_R during the last five cycles were determined for each condition of stress, suction and temperature.

6.5 *Effects of temperature on resilient modulus*

Fig. 14(a) shows the influence of temperature on M_R at zero suction. As soil temperature increases from 20 to 60°C, M_R increases by about 5% at lower cyclic stress (30 and 40 kPa) but decreases by about 5% at higher cyclic stress (55 and 70 kPa). The two different responses may be due to the fact that temperature could affect M_R through different mechanisms. On the one hand, the electrical force between soil particles becomes relevant for fine-grained soil. Based on DLVO double layer theory (Israelachvili 2011), electric repulsive forces between soil particles increase as temperature increases. This would reduce interparticle forces and hence a decrease in soil stiffness (Santamarina et al. 2001). On the other hand, as illustrated in Fig. 13(a), the increase in M_r^N/M_r^1 with the number of cycles is larger at 60°C than at 20°C by about 5%. This suggests that effects of soil densification on M_R are more significant at higher temperature. These two mechanisms appear to produce opposite effects on M_R. Furthermore, Fig. 13(a) reveals that thermal effects on M_r^N/M_r^1 are dependent on cyclic stress. At cyclic stresses of 30 and 40 kPa, M_r^N/M_r^1 is larger at 60°C than at 20°C by about 10%. At cyclic stresses of 55 and 70 kPa, M_r^N/M_r^1 is larger at 60°C than at 20°C by only about 5%. Therefore, at lower cyclic stress (30 and 40 kPa), the second mechanism is more significant. It is therefore that measured M_R increases with increasing temperature. At higher cyclic stress (55 and 70 kPa), the second mechanism is relatively less important. Soil behaviour is likely dominated by the first mechanism and in this case measured M_R decreases as soil temperature increases.

Figs 14 (b) and (c) show thermal effects on M_R at suctions of 30 and 60 kPa, respectively. At these two suctions, M_R measured at 60°C is smaller than that

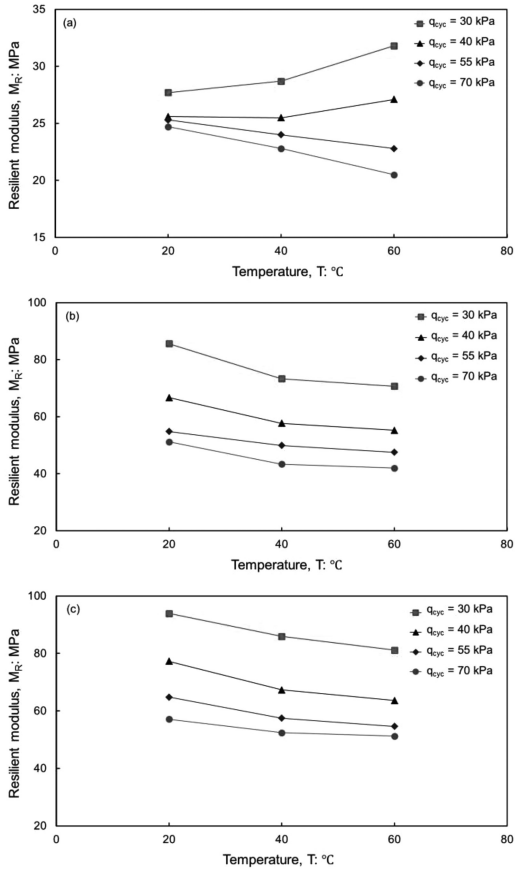


Figure 14. Thermal effects on Young's modulus at suctions of: (a) 0 kPa; (b) 30 kPa; (c) 60 kPa.

measured at 20°C by up to 20 MPa. Compared to thermal effects on M_R at zero suction (see Fig. 14(a)), thermal effects on M_R are more significant at suctions of 30 and 60 kPa than at zero suction. Through a series of suction- and temperature-controlled triaxial tests on a compacted unsaturated silt, Uchaipichat and Khalili (2009) observed that for over- consolidated soil, the yield surface shrinks with an increase in temperature. Moreover, the size of the yield surface is more sensitive to temperature at higher matric suction. The observations from their study and the current one suggest that thermal effects on mechanical behaviour are more significant at unsaturated state than at saturated state. This may be attributed to the temperature dependency of air-water surface tension T_s. The values of T_s at temperatures of 20, 40 and 60°C are 72.8, 69.6 and 66.2 *mN/m*, respectively (Ng and Menzies 2007). A decrease in surface tension affects unsaturated soil behaviour in at least two ways. Firstly, as temperature increases, the water retention ability of unsaturated soil slightly decreases and hence the degree of saturation at a given suction becomes smaller (Romero et al. 2003). A reduction in the degree of saturation would induce a decrease

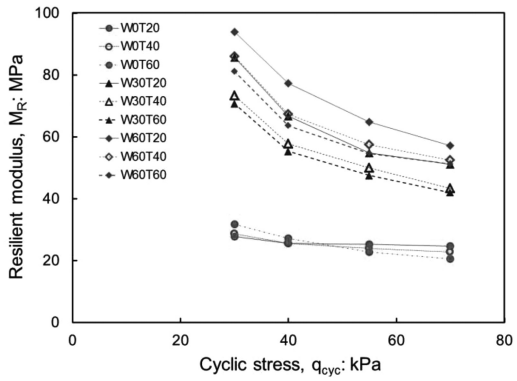


Figure 15. Influence of cyclic stress on resilient modulus during cyclic triaxial tests.

of Bishop's stress, as illustrated by Eq. (10). Secondly, Eq. (11) suggests that normal forces induced by meniscus water decrease with decreasing surface tension. For these two reasons, the contribution of suction to soil stiffness may be reduced due to thermal loading. Thermal effects on the mechanical behaviour of unsaturated soil would be more significant at unsaturated state.

6.6 *Influence of suction and cyclic stress on resilient modulus*

Fig. 15 shows the influence of cyclic stress on M_R at various suctions and temperatures. It is revealed in the figure that the influence of q_{cyc} on M_R can be classified into two types. As q_{cyc} increases from 30 to 70 kPa, M_R is almost constant at zero suction, but it decreases by about 40% at suctions of 30 and 60 kPa.

The reduction of M_R with increasing q_{cyc} is related to the strain dependency of soil stiffness. As illustrated in Fig. 12, soil stiffness decreases with an increase in strain level. Furthermore, reversible axial strain (ε_a^r) under cyclic loads can be calculated using the following equation:

$$\varepsilon_a^r = q_{cyc} / M_R \tag{12}$$

According to Eq. (12), ε_a^r during the last 10 cycles in each test can be estimated from M_R and q_{cyc}. For instance, when cyclic stress increases from 30 to 70 kPa at zero suction and 20°C, ε_a^r increases from 0.1% to 0.3%. An increase in strain level induces a decrease in M_R.

The fact that reduction of M_R is more significant at suctions of 30 and 60 kPa suggests that the degree of non-linearity of soil stress-strain behaviour depends on suction. This is because as discussed above, for the four levels of q_{cyc}, ε_a^r at zero suction ranges from 0.1% and 0.3%. Similarly, ε_a^r at suctions of 30 and 60 kPa is in the range from 0.03% to 0.15%. Furthermore, it is illustrated in Fig. 11 that the degradation rate of soil stiffness with strain is slightly affected by suction. At suctions up to 150 kPa, the stiffness degradation rate

is consistently larger in the strain range from 0.03% to 0.15% than that in the strain range from 0.1% to 0.3%. Therefore, the rate of decrease of M_R with q_{cyc} is much larger at suctions of 30 and 60 kPa than at zero suction.

It is also clearly illustrated in Fig. 14 that M_R are significantly affected by soil suction. For example, at q_{cyc} of 30 kPa and temperature of 20°C, M_R more than doubles when s increases from 0 to 30 kPa. Then when s further increases from 30 to 60 kPa, M_R increases by only about 10%. The observed increase of M_R with an increase in suction is well captured by the term $(1 + (u_a - u_w)/p)^{k3}$ in Eq. (8).

7 SUMMARY AND CONCLUSIONS

In this keynote, the development of a new temperature and suction controlled cyclic triaxial apparatus was introduced and described. Measured results of shear stiffness of an unsaturated compacted silt subjected to both monotonic and cyclic loads were reported. Semi-empirical state-dependent equations were proposed to capture effects of net stress, matric suction and void ratio on anisotropic shear moduli at very small strains and resilient modulus under cyclic loading-unloading. Based on derived equations and experimental data, some key conclusions are summarized as follows:

1. From wetting and drying tests at different net stresses, measured very small strain shear moduli, $G_{0(vh)}$, $G_{0(hv)}$ and $G_{0(hh)}$, consistently increase with an increase in suction at a given net stress, as predicted by the proposed state-dependent equations. The observed contribution of suction to soil stiffness is mainly attributed to an increase of the average skeleton stress and inter-particle normal forces. Consequently, an increase of suction would stabilize and stiffen soil skeleton.
2. At a given suction, there is a hysteresis between the drying and wetting stiffness. At the same suction, the shear moduli measured during wetting are consistently higher than those obtained during drying. The shear modulus hysteresis is possibly attributed to water content on the adsorption path is lower than that on the desorption path.
3. It is evident that the degree of stiffness anisotropy $G_{0(hh)}/G_{0(hv)}$ increases with an increase in soil suction but at a decreasing rate. At the same suction, $G_{0(hh)}/G_{0(hv)}$measured along the wetting path are larger than that along the drying path.
4. From constant p triaxial compression tests at different temperatures, it is found that over the strain range from 0.003% to 1%, monotonic shear stiffness is slightly smaller at higher temperature. This is likely to be due to the reduction of the air-water surface tension with an increase of temperature, weakening the average skeleton stress and the stabilization effects on soil skeleton.
5. From cyclic triaxial tests, each unsaturated specimen tested reached a stable reversible response within 100 cycles. At zero suction, the ratio between resilient modulus of the Nth cycle and the resilient modulus of first cycle M_r^N/M_r^1 increases with number of cycles N because of soil densification under cyclic loads. There is a threshold cyclic stress below which M_r^N/M_r^1 increases with N by about 10%, while M_r^N/M_r^1 increases by about 20% above the threshold. At suctions of 30 and 60 kPa, however, the influence of N on M_r^N/M_r^1 is minor due to negligible volumetric plastic strain. On the other hand, thermal effect on M_r^N/M_r^1 is also very minor.
6. Measured resilient modulus M_R at the stable state (i.e., $N = 100$) under cyclic loads is significantly affected by soil suction. At a given temperature, M_R increases by more than twofold when suction increases from 0 to 60 kPa. On the other hand, thermal effects on M_R of the silt under cyclic loads are more significant at suctions of 60 and 30 kPa than that at zero suction. At zero suction, as soil temperature increases from 20 to 60°C, M_R changes by about 5%. At suctions of 60 and 30 kPa, given the same change of soil temperature, M_R decreases by about 20%. The observed thermal effects on soil stiffness imply that any design based on parameters measured at room temperature would underestimate soil deformation, when soil temperature in the field is significantly higher than room temperature.

ACKNOWLEDGEMENTS

The authors would like to acknowledge financial support from the Research Grants Council (RGC) of the HKSAR (grant no. GRF 617213) and from HKUST (grant no. FP204). The Specialized Research Fund for the Doctoral Program of Higher Education (grant no.s M-HKUST603/13 and 20130094140001) administered by the RGC and the National Science Foundation of China (grant no. 51378178) are also gratefully acknowledged. Moreover, the research grant 2012CB719805 provided by the Ministry of Science and Technology of the People's Republic of China through the National Basic Research Program (973 project) is gratefully acknowledged. In addition, the authors would like to thank the Research Grants Council of the Hong Kong Special Administrative Region for supporting the research grant HKUST6/CRF/12R.

REFERENCES

AASHTO 2003. Standard method of test for determining the resilient modulus of soils and aggregate materials. American Association of State Highway and State Highway Officials, Washington, D.C.

ASTM 2006. Standard practice for classification of soils for engineering purposes (unified soil classification system). American Society of Testing and Materials, West Conshohocken.

Atkinson, J.H., and Sallfors, G. 1991. Experimental determination of stress-strain-time characteristics in laboratory

and in situ tests. Proceedings of the 10th ECSMFE, Florence, Italy, 3: 915–956.
Bellotti, R., Jamiolkowski, M., LoPresti, D.C.F., and ONeill, D.A. 1996. Anisotropy of small strain stiffness in Ticino sand. Géotechnique, 46(1): 115–131.
Brown, S.F., Loach, S.C., and O'Reilly, M.P. 1987. Repeated loading of fine grained soils. Pavement Design and Maintenance Division, Highways Group, Transport and Road Research Laboratory, Crowthorne, Berkshire.
BSI 1990. Methods of test for soils for civil engineering purposes. British Standards Institution, London.
Clayton, C., Khatrush, S., Bica, A., and Siddique, A. 1989. Hall effect sensors in geotechnical instrumentation. Geotechnical Testing Journal, 12(1): 69–76.
François, B., and Laloui, L. 2008. ACMEG-TS: A constitutive model for unsaturated soils under non-isothermal conditions. International Journal for Numerical and Analytical Methods in Geomechanics, 32(16): 1955–1988.
Gallipoli, D., Gens, A., Sharma, R., and Vaunat, J. 2003. An elasto-plastic model for unsaturated soil incorporating the effects of suction and degree of saturation on mechanical behaviour. Géotechnique, 53(1): 123–135.
Gens, A. 2010. Soil-environment interactions in geotechnical engineering. Géotechnique, 60(1): 3–74.
Germaine, J.T., and Ladd, C.C. 1988. Triaxial testing of saturated cohesive soils. Advanced triaxial testing of soil and rock. ASTM STP, 977: 421–459.
Hilf, J.W. 1956. An investigation of pore water pressure in compacted cohesive soils. Technical Memo 654, Denver: US Bureau of Reclamation.
Houlsby, G.T. 1997. The work input to an unsaturated granular material. Géotechnique, 47(1): 193–196.
Israelachvili, J.N. 2011. Intermolecular and surface forces: revised third edition. Academic press.
Jardine, R., Kuwano, R., Zdravkovic, L., and Thornton, C. 1999. Some fundamental aspects of the pre-failure behaviour of granular soils. Proc. Int. Symp. on Pre-failure Deformation of Geomaterials, 2: 1077–1111.
Jardine, R.J., Symes, M.J., and Burland, J.B. 1984. The measurement of soil stiffness in the triaxial apparatus. Géotechnique, 34(3): 323–340.
Jennings, J.E., and Burland, J.B. 1962. Limitations to the use of effective stresses in partly saturated soils. Géotechnique, 12(2): 125–144.
Li, X.S. 2003. Effective stress in unsaturated soil: a microstructural analysis (vol 53, pg 273, 2003). Géotechnique, 53(9): 844–844.
Mair, R.J. 1993. Unwin Memorial Lecture 1992 Developments in Geotechnical Engineering Research – Application to Tunnels and Deep Excavations. Proceedings of the Institution of Civil Engineers-Civil Engineering, 97(1): 27–41.
Mancuso, C., Vassallo, R., and d'Onofrio, A. 2002. Small strain behavior of a silty sand in controlled-suction resonant column – torsional shear tests. Canadian Geotechnical Journal, 39(1): 22–31.
McCartney, J.S., and Khosravi, A. 2013. Field monitoring system for suction and temperature profiles under pavements. Journal of Performance of Constructed Facilities, 27(6): 818–825.
Ng, C.W.W., and Pang, Y.W. 2000. Experimental investigations of the soil-water characteristics of a volcanic soil. Canadian Geotechnical Journal, 37(6): 1252–1264.
Ng, C.W.W., and Leung, E.H.Y. 2007. Determination of shear-wave velocities and shear moduli of completely decomposed tuff. Journal of Geotechnical and Geoenvironmental Engineering, ASCE, 133(6): 630–640.
Ng, C.W.W., and Menzies, B.K. 2007. Advanced unsaturated soil mechanics and engineering. Taylor & Francis, London and New York.
Ng, C.W.W., and Yung, S.Y. 2008. Determination of the anisotropic shear stiffness of an unsaturated decomposed soil. Géotechnique, 58(1): 23–35.
Ng, C.W.W., and Xu, J. 2012. Effects of current suction ratio and recent suction history on small-strain behaviour of an unsaturated soil. Canadian Geotechnical Journal, 49(2): 226–243.
Ng, C.W.W., and Zhou, C. 2014. Cyclic behaviour of an unsaturated silt at various suctions and temperatures. Géotechnique, 64(9): 709–720.
Ng, C.W.W., Pun, W., and Pang, R.P. 2000. Small strain stiffness of natural granitic saprolite in Hong Kong. Journal of Geotechnical and Geoenvironmental Engineering, ASCE, 126(9): 819–833.
Ng, C.W.W., Xu, J., and Yung, S.Y. 2009. Effects of wetting-drying and stress ratio on anisotropic stiffness of an unsaturated soil at very small strains. Canadian Geotechnical Journal, 46(9): 1062–1076.
Ng, C.W.W., Zhou, C., Yuan, Q., and Xu, J. 2013. Resilient modulus of unsaturated subgrade soil: experimental and theoretical investigations. Canadian Geotechnical Journal, 50(2): 223–232.
Pennington, D.S., Nash, D.F.T., and Lings, M.L. 2001. Horizontally mounted bender elements for measuring anisotropic shear moduli in triaxial clay specimens. Geotechnical Testing Journal, 24(2): 133–144.
Roesler, S.K. 1979. Anisotropic shear modulus due to stress anisotropy. Journal of the Geotechnical Engineering Division, 105(7): 871–880.
Romero, E., Gens, A., and Lloret, A. 2003. Suction effects on a compacted clay under non-isothermal conditions. Géotechnique, 53(1): 65–81.
Sanchez-Salinero, I., Roesset, J.M., Stokoe, I., and Kenneth, H. 1986. Analytical studies of body wave propagation and attenuation, DTIC Document.
Santamarina, J.C., A., K.K., and A., F.M. 2001. Soils and waves : particulate materials behavior, characterization and process monitoring. J. Wiley & Sons, Chichester; New York.
Seed, H.B., Chan, C.K., and Lee, C.E. 1962. Resilience characteristics of subgrade soils and their relation to fatigue failures in asphalt pavements. *In* Proceedings of the international conference on structural design of asphalt pavements, Ann Arbor, Michigan1962, pp. 611–636.
Sivakumar, V. 1993. A critical state framework for unsaturated soilPhd thesis, University of Sheffield.
Sivakumar, V., Kodikara, J., O'Hagan, R., Hughes, D., Cairns, P., and Mckinley, J.D. 2013. Effects of confining pressure and water content on performance of unsaturated compacted clay under repeated loading. Géotechnique, 63(8): 628–640.
Tang, A.M., Cui, Y.J., and Barnel, N. 2008. Thermo-mechanical behaviour of a compacted swelling clay. Géotechnique, 58(1): 45–54.
Uchaipichat, A., and Khalili, N. 2009. Experimental investigation of thermo- hydro- mechanical behaviour of an unsaturated silt. Géotechnique, 59(4): 339–353.
Uzan, J. 1985. Characterization of granular material. Transportation Research Record, 1022: 52–59.
Wheeler, S.J., Sharma, R.S., and Buisson, M.S.R. 2003. Coupling of hydraulic hysteresis and stress-strain behaviour in unsaturated soils. Géotechnique, 53(1): 41–54.
Zhou, C., Ng, C.W.W., and Xu, J. 2015. Effects of temperature and suction on secant shear modulus of unsaturated soil. Accepted by Géotechnique Letters.

This page intentionally left blank

Unsaturated Soil Mechanics—from Theory to Practice – Chen et al. (Eds)
© 2016 Taylor & Francis Group, London, ISBN 978-1-138-02921-7

Moisture and gas flow properties of compacted loess final covers for MSW landfills in Northwest China

Liang-tong Zhan
MOE Key of Laboratory of Soft Soils and Geoenvironmental Engineering, Zhejiang University, Hangzhou, China

ABSTRACT: In the northwest of China, loess is widely distributed, and the climate is mainly arid and semiarid. The use of loess as an alternative earthen final cover material is promising. However, the understanding on the performance of a compacted loess final cover is far from adequate. This paper will focus on the research on moisture and gas flow properties of loess as a cover material. Firstly, the distribution of loess and the climate condition in northwest China are reviewed. Then the multi-scale study program, including soil element tests, soil column tests and a full-scale testing facility at Xi'an landfill, is presented. The current findings from the laboratory and field study on the moisture and gas flow properties of the compacted loess are discussed with an emphasis on the scale effect. At last, the paper presents a preliminary numerical evaluation of the loess cover performance with respect to limiting water percolation and gas emission. The study demonstrates that the compacted loess final cover underlain by a gravel layer, having a considerable water storage capacity and relatively low conductivity for water and gas flow, is likely to perform well in the northwest China.

1 INTRODUCTION

Loess and loess-like deposits cover about 10% of the Earth's land surface, mainly distributed in temperate zones and the semi-arid zones. The thickest and most extensive loess area is located in the Chinese Loess Plateau, which is situated in northwest China. The climate in northwest China, being dominated by a continental monsoon climate, is mainly arid or semi-arid. In the cities of this region, nearly 100% of Municipal Solid Wastes (MSWs) are disposed at landfills. Loess has became a requisite material for landfill operation. It is generally used as for daily cover and interim cover for controlling odor and vectors and limiting the ingress of water. On the basis of two decades' research and practice, the use of loess (i.e., a fine grained soil) as an alternative earthen final cover material is promising in the northwest China with a non-humid climate condition. However, the research towards this direction is far from adequate.

Currently there are generally two types of alternative earthen final covers: monolithic and capillary barrier. A monolithic cover use a single layer of fine-grained non-swelling soil to retain water until it is either transpired through vegetation or evaporated from the soil surface. A capillary barrier cover consists of a fine grained soil layer underlain by a coarser-grained material layer (e.g., gravel). The difference in the unsaturated hydraulic properties between the two layers can form a capillary break at the interface, which allows the upper fine grained layer to retain more water than a monolithic cover with an indentical thickness. When the soil materials are available locally, the earthen final covers have advantage over the regulatory-described composite covers with respect to economic and technical aspects, especially in the long term performance (Albright et al. 2002; Zhan et al., 2014a).

Since 1990s, European and American researches have been doing theoretical and experimental studies on the hydrological performance of earthen final covers. One of the most famous research projects was the Alternative Cover Assessment Project (ACAP) organized by the EPA in USA (Albrigth et al. 2002; Bolen et al. 2001). Under the ACAP, twenty-seven full-scale lysimeter test facilities were established at 12 landfill sites located in 8 states with different climate conditions. The field study involved 15 earthen final covers, including 9 monolithic covers and 6 capillary barrier covers. Monitoring data was collected for a long term period to demonstrate the cover performance as well as to calibrate the existing numerical models. Most of the current study and field evidences demonstrated that the earthen final covers perform well at limiting deep percolation of water in arid, semi-arid areas and in some cases semi-humid areas of the North American.

As compared with the study on the hydrological performance of earthen final covers, the investigation on landfill gas (LFG) emission from earthen final covers is far from adequate. Recently, the role of soil covers in the mitigation of odor and methane gas emission has been drawn attention. In addition, the fate of vegetation at the landfill environment and its effect on the cover performance are not fully understood. Actually,

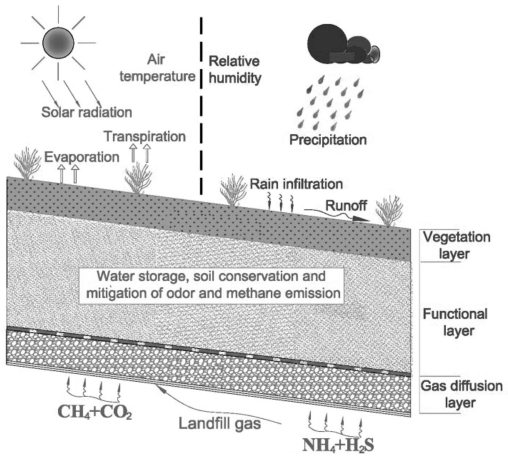


Figure 1. Soil-plant-atmospheric interaction of an earthen final cover for MSW landfills.

the earthen final cover with vegetation is a soil-plant-atmospheric interaction system (Fig. 1). Further understanding of the cover performance should be based on a multi-field coupled framework involving moisture flow, gas flow, heat flow, biochemical aspects and so on. This paper will focus on the research on moisture and gas flow properties of loess as a cover material, including the multi-scale study program, the current finding from the laboratory and field study and the preliminary evaluation of the loess cover performance with respect to limiting water percolation and gas emission.

2 LOESS DISTRIBUTION AND CLIMATE CONDITION IN NORTHWEST CHINA

2.1 *Loess distribution and category*

Loess and loess-like deposits cover about 10% of the Earth's land surface, mainly distributed in temperate zones and the semi-arid zones close to desert margins (30°–55° N and 30°–40°S) (Liu et al. 1985). The thickest and most extensive loess area is located in the Chinese Loess Plateau, which is situated in north China. Fig. 2 shows the distribution of loess in China. Chinese loess covers a total area of 6.4×10^5 km^2, mainly distributed in the Loess Plateau (with an area of 4.4×10^5 km^2). The Loess Plateau, with an elevation of 1200–1600 m above sea level, is located in the upper and middle reaches of the Yellow River, has a loess cover with thickness largely ranging from 30 to 80 m. In general, the maximum thickness of the loess deposits in the central and southern parts of the Loess Plateau can up to 180 m (Liu et al. 1998).

As shown in Fig. 2, the loess deposits are transported from the desert basins in northern and northwestern China by winds and accumulated on the Loess Plateau since the beginning of the Quaternary (Liu et al. 1985). The dust particles of the desert basins are transported

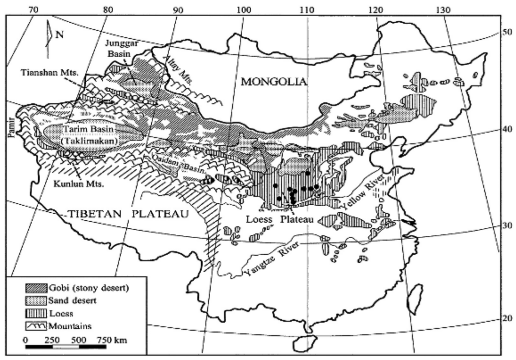


Figure 2. The distribution of loess in China (Sun et al.2002).

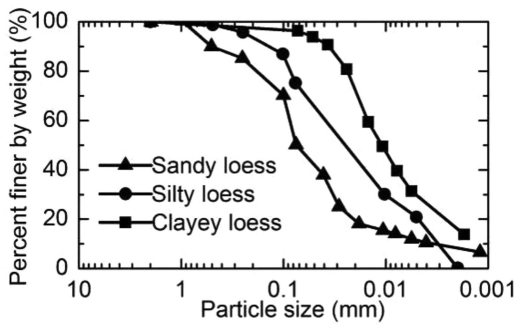


Figure 3. Particle size distribution curves of 3 types of loesses.

to high altitude by updrafts, enter westerly circulation system, drift towards eastern and southeastern China, and are deposited on the area to the east of 100°E, i.e., the Loess Plateau. Then due to biochemical weathering, the deposited dust particles form loess. The loess deposits in China compose complete Quaternary sequences, namely, all the strata from Q_1 to Q_4 are found.

Typical loess units are characterized by a yellowish color, uniform texture, a massive and porous structure, significant vertical joints and stratification, high carbonate contents and collapsibility (Liu et al. 1998). The Loess in Northwest China can be divided into three categories, i.e., sandy, silty and clayey Loesses. The particle size of Loess shows an increasing trend from southeast to northwest. Fig. 3 shows particle size distribution curves for the three categories of loess, i.e., sandy, silty and clayey Loesses. It can be seen that the dominant particles are silty particles ($0.075 \sim 0.002$ mm) with a percentage greater than 50%. The percentage is less than 40% for both sand particles and clay particles.

2.2 *Climate condition*

Dominated by a continental monsoon climate, northwestern China, with a low annual precipitation, is under the control of arid or semi-arid climate. The

Table 1. Climate parameters for the three representative cities during the latest 50 years.

Parameters	Yinchuan (North*)	Lanzhou (Middle*)	Xi'an (Southeast*)
	Arid	Semi-arid	Semi-humid
P/PET	0.2 ~ 0.5	0.5 ~ 0.8	0.5 ~ 1.0
P (mm)	200	350	500
PET (mm)	1100	600 ~ 800	600 ~ 700

*Location in the Loess Plateau

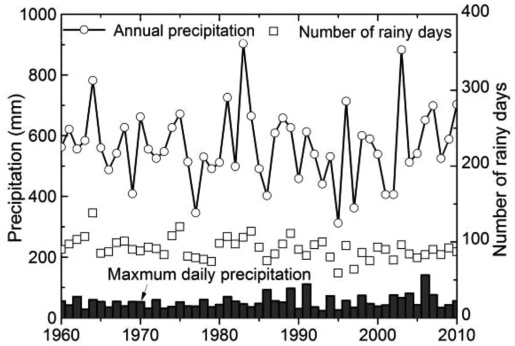


Figure 4. Annual Precipitation in Xi'an from 1960 to 2010.

average annual precipitation gradually decreases from the south-east to the north-west, concentrated in a few months for the year (Ding et al. 2001). In most regions of the Loess Plateau, the average annual rainfall ranges from 300 mm in the northwest to 650 mm in the southeast, but the relevant mean annual evaporation varies from 623.8 to 1254.0 mm (Chen et al. 2008). In summer, the Loess Plateau is under the control of the warm-humid southeast summer monsoon of tropical/subtropical origin, leading to abundant precipitation. Due to the strengthening of the monsoon, most of the annual rainfall is concentrated in July, August and September. In winter, the cold-dry northwest winter monsoon of sub-arctic origin prevails across the region.

As the landfills are usually located in urban areas, three representative cities in northwest China are selected to present the climate condition. They are: Yinchuan of Ningxia Province (arid climate), Lanzhou of Gansu Province (semi-arid climate) and Xi'an of Shanxi Province (semi-humid climate). Table 1 shows the magnitude of annual precipitation (P), potential evaporation (PET), and humid index (P/PET) for the three representative cities. The data was based on the statistics of meteorological data records from 1960 to 2010.

Fig. 4 shows the distribution of annual precipitation in Xi'an for the latest fifty years (1960 to 2010). The data statistics indicate that the average value of annual precipitation during the latest 50 years is 566.9 mm with the maximum value of annual precipitation at

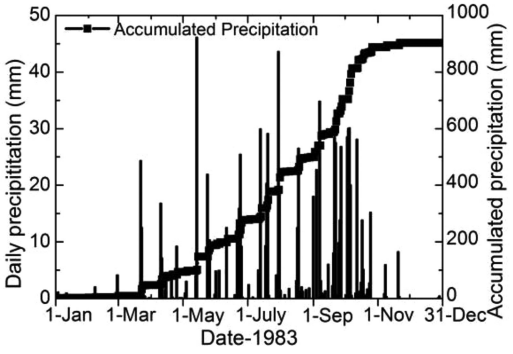


Figure 5. Distribution of precipitation for the wettest year of Xi'an (1983).

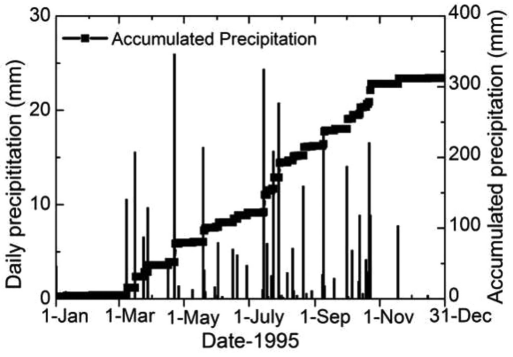


Figure 6. Distribution of precipitation for the driest year of Xi'an (1995).

903.2 mm in 1983. The average number of annual precipitation days is 92. Fig. 5 and Fig. 6 show the distribution of daily precipitation in 1983 (the wettest year) and 1995 (the driest year) in Xi'an, respectively. The data indicates that the annual precipitation is not uniformly distributed in the year. There is more rainfall in the summer from May to September while little in December, January and February. It should be noted that the rainy season in this region coincides with the plant growing period.

3 MULTI-SCALE STUDY PROGRAM

With a financial support from the National Basic Research Program of China ("973" Project, grant number 2012CB719805), a multi-scale study program has been established to investigate the performance of loess final covers for MSW landfills in northwest China. Soil element tests were performed in lab to measure water retention curves, water and gas permeability of a re-compacted loess. Water infiltration tests and gas permeation tests were carried out on loess soil columns to measure the dependency of water and gas permeability on soil moisture content. A loess final cover

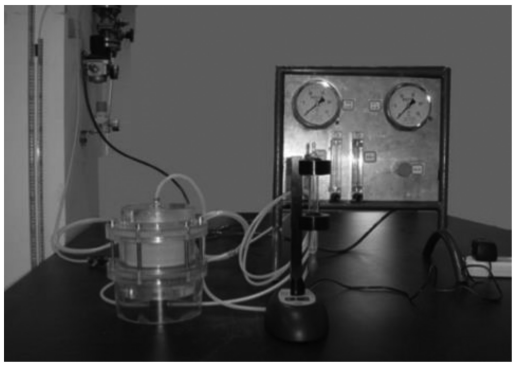


Figure 7. Testing device for measuring gas permeability.

testing facility with an area of 600 m^2 was constructed at the Xi'an landfill of MSWs, rainfall simulation tests and gas injection tests were carried out to measure the in-situ water and gas permeability of the loess. The testing facility was well instrumented for a long-term monitoring of the performance of the loess final cover for limiting both water percolation and LFG emission. It was the first testing facility established in China for studying the performance of an earthen final cover.

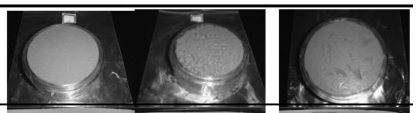
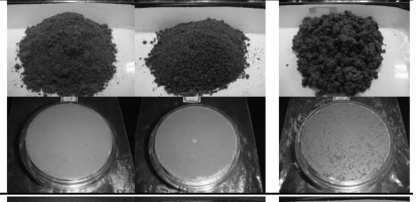
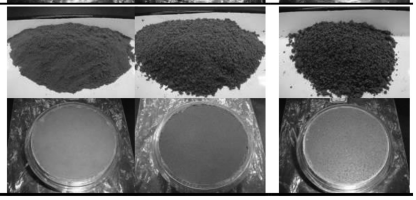
3.1 *Laboratory measurement of moisture and gas flow properties*

Ten tons of loess samples were taken to laboratory from the side slope of the Xi'an landfill. The loess samples belonged to the strata of Q_2 to Q_3, and both intact and disturbed samples were taken. This paper focuses on the study on the disturbed samples of the Q_3 stratum. The loess consists of 5% gravel-size calcareous concretion, 3% sand, 82% silt, and 10% clay. The liquid limit and plasticity index are 36.7 and 22%, respectively. The loess can be described as a clayey loess. The maximum dry density determined from a compaction test is 1.70 Mg/m^3, being corresponding to an optimum water content of 19.5%. For the laboratory study, the gravel-size calcic concretion was removed by passing the loess sample through 2 mm sieve. Soil specimens were prepared by compacting the sieved sample statically to the prescribed dry density (i.e., 1.35–1.60 Mg/m^3) at various values of water content (i.e., 0–24.0%).

Water retention curves of the compacted loess specimens were measured by using a 15-bar pressure plate extractor. The specimens were compacted to three different values of dry density (i.e., 1.35, 1.45 and 1.60 Mg/m^3), and then saturated under a constant volume condition. Both drying and wetting curves were measured within the suction range of 0–1500 kPa. Saturated permeability of the compacted loess specimens were measured by following the falling head method.

Gas permeability of the compacted loess specimens was measured by the purposely-designed gas permeation device (see Fig. 7). The specimen size was 100 mm in diameter and 50 mm in height. Experiments

Table 2. Photos of soil samples and specimens prepared at different compaction water contents.

Mixing way No.	*w*=15.0%	*w*=19.3%	*w*=24.0%
1			
2			
3			

were carried out to investigate the influence of clod size, compaction water content, and post-compaction water content on the gas permeability of the compacted loess (Zhan et al. 2014b). To achieve different clod sizes (see Table. 2), three methods of soil and water mixing were used. The first way involved pouring water into the oven-dried soil samples before mixing, resulting in a relatively large clod size at high water contents (e.g., 15.0%, 19.3%, and 24.0%). The second way involved spraying water over the soil samples before mixing. In the third way, water was sprayed over the soils samples step by step. Between each step, the soil samples were mixed thoroughly with the added water and any large aggregated soil lumps were broken up as small as possible with a pestle. Therefore, the smallest clod size at high water contents was obtained using the third way. To investigate the influence of post-compaction water content on gas permeability, the initial soil structure for the compacted specimens should be identical. To achieve this requirement, the post-compaction water content was changed using the osmotic technique.

3.2 *Soil column tests on moisture and gas flow behavior*

To investigate the moisture and gas flow behavior in the loess final covers, a soil column testing apparatus was developed in the laboratory (see Fig. 8). The soil column housed in 4–5 sections of Perspex cylinders was 200 mm in diameter and 800–1000 mm in height. A flux of gas mixture (e.g., 50% methane and 50% carbon dioxide) can be applied at the bottom of soil column by using a couple of mass flow controllers.

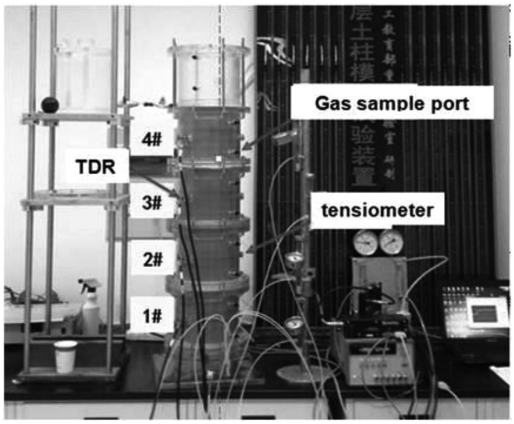


Figure 8. Soil column testing device for a loess cover.



Figure 9. Location of full scale testing facility for loess final cover at Xi'an landfill.

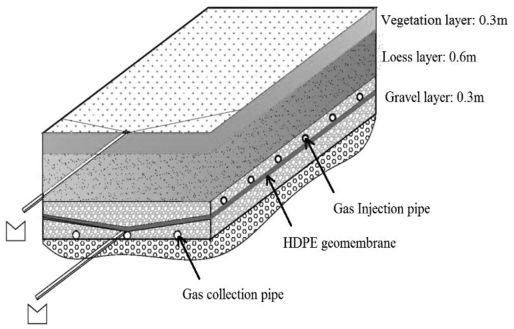


Figure 10. Profile of loess final cover within a pan-type lysimeter.

A water ponding can be applied on the top of soil column by using a Mariotte bottle. At the middle height of each section (200 mm long), there were a TDR probe and tensiometer installed for measuring the change in moisture content and soil suction. In addition, two ports were set at the same elevation for gas sampling and gas pressure measurement. The port for gas pressure measurement was connected to a U-tube, where the gas pressure was measured. A soap film flowmeter was used to measure gas overflow rate from the top of soil column.

With the above testing apparatus, a loess soil column with a thickness of 800 mm was set up to simulate a loess final cover unit, which consisted of 300 mm top soil ($\rho_d = 1.3$ Mg/m^3) and 500 mm water storage layer ($\rho_d = 1.45$ Mg/m^3). Instantaneous profile method was implemented on the soil column to measure the change in water coefficient of permeability with soil suction. Gas permeation tests were carried out on the soil column under constant water content condition and water infiltration condition. For the latter condition, the loess soil column was subjected to a gas flux of 8 ml/min (i.e., 1:1 methane and carbon dioxide mixture) at the bottom and a water ponding of 3 cm on the top, and the coupled process of rainwater infiltration and gas upward flow in the soil column was investigated.

3.3 *Full scale testing facility at Xi'an landfill of MSWs*

The site of Xi'an landfill is located in the Jiangchun loess gulch, being 16 km east of Xi'an city. The landfill was put into operation in 1994 and has disposed of over 20 million tons of MSWs. At present, the landfill, covering an area of 1100 ha, accepts all the MSWs generated in Xi'an city (about 6500 tons per day). The landfill consists of a number of filled platforms that are set back at an embankment slope of 3H/1V and 10 m in height. The landfill slope has reached a height of 90 m. An area of 30 m long by 20 m wide was selected on the 8th embankment slope to construct the loess final cover testing facility (see Fig. 9). The current slope inclination is 3.4H/1V. The fill age of the waste layer under the facility was between 3 and 5 years as of the facility construction time (i.e., November, 2013).

The loess final cover testing facility was constructed in a way similar to the test sections of the Alternative Cover Assessment Project (ACAP) in USA, with the exception of the components for gas testing and monitoring. The main feature of all ACAP test sections was a large (10×20 m) instrumented pan-type lysimeter used for direct measurement of surface runoff (R), soil water storage (S), and percolation (P) from a full-depth cover profile. A detailed description of the construction of each ACAP test section can be found in Bolen et al. (2001). The lysimeter size in this study is 24 m long and 10 m wide. A buffer area 5 m wide was set around the perimeter of lysimeter to reduce boundary effects. The base and sidewalls of the lysimeter were lined with polyethylene geomembrane to create an independent hydrological unit for easy analyses of water and gas balance. The cover profile above the base geomembrane was comprised of geotextile protection layer, 300 mm thick gravel layer, geotextile separation layer, 600 mm thick storage layer of compacted loess ($\rho_d = 1.45$ Mg/m^3) and 300 mm thick vegetative layer of compacted loess ($\rho_d = 1.35$ Mg/m^3) (see Fig. 10). It is anticipated that capillary barrier effect will be

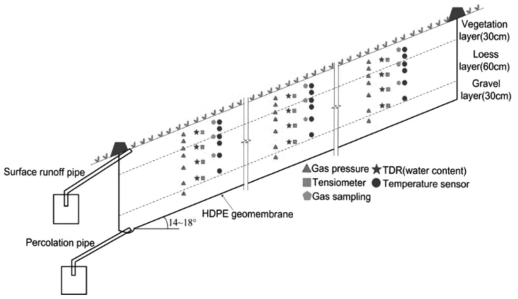


Figure 11. Instrumentation at the full scale testing facility.

formed at the interface of the compacted loess and the gravel layer (5–20 mm in particle size). Perforated PPR pipe lines were installed in the gravel layer and connected to the ground surface so that gas can be pumped to the base of the cover profile. The profile under the base geomembrane was comprised of geotextile protection layer, 300 mm thick gravel layer (30–50 mm in particle size) , geotextile separation layer and waste layers. Perforated PE pipe lines were installed in the gravel layer for a collection of landfill gas.

Artificial rainfall simulation was implemented by using a purposely-designed sprinkler system for the test site. The sprinkler system comprised a pump, a main water-supply line, six groups of distribution tubes and twenty-seven sprinkler heads. The sprinkler heads were arranged in such a way that a relatively uniform rainfall could be produced. The artificial rainfall intensity applied in this study was approximately 3.0 mm/hr. Gas permeation tests were performed by pumping air or landfill gas to the bottom gravel layer via the pre-installed PPR pipe lines. Air pumping was implemented by using a high-capacity air compressor. Landfill gas supply was provided by the landfill gas collection from the waste layers under the testing facility.

Instruments were installed at the test section to continuously monitor soil conditions (water content, temperature, pore-gas and pore-water pressures), water and gas flows, and meteorological conditions. Time domain reflectometer probes (TDRs), thermal sensors and jet filled tensiometers were used to measure soil moisture, temperature and negative pore-water pressure, respectively. The pore gas pressure was measured by a pressure meter which was connected to a gravel bag installed at the desired depth by a pipe line. These sensors were installed in three nests in the test section (see Fig. 11). Each nest contained 21 probes placed at various depths. Meteorological conditions were measured by a weather station installed at the site, and the measurements include wind speed, wind direction, solar radiation, air temperature, relative humidity, and precipitation.

The construction and installation activities of the facility consisted of several tasks including removal of interim cover, lysimeter installation, soil placement and compaction, instrumentation, installing flow

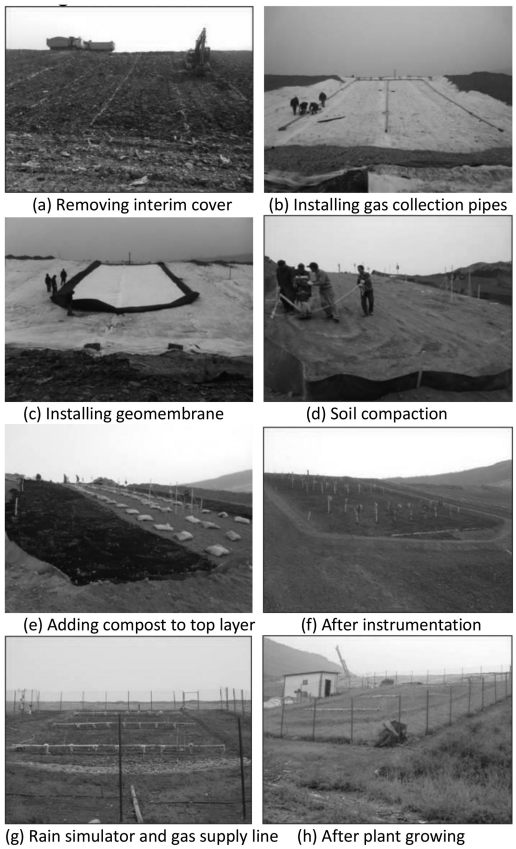


Figure 12. Construction process of the testing facility.

monitoring system, setting up rainfall simulator and gas pumping system (see Fig. 12). Most of the construction procedures followed the experiences of ACAP (Bolen et al., 2001). During the soil placement and compaction, disturbed and undisturbed soil samples were collected from each layer and shipped to the laboratory for testing. Field quality assurance activities were performed in accordance with the relevant standards. The QA activities included testing geomembrane seams, control of compaction density and moisture content, calibration of monitoring instruments, and leak testing of collection basins.

3.4 *Numerical study on the performance of loess final covers*

In addition to laboratory and field study, numerical modeling has served as an important tool in the design and performance evaluation of earthen final covers, especially for the assessment of long-term performance during the service life over several decades. In order to provide an adequate representation of real performance, numerical modeling should be closely linked to the data collection from laboratory and field.

One of main objectives of the ACAP was to evaluate the capabilities and limitations of the existing computer codes in modeling of hydrological performance of earthen final covers. Several codes including HELP, UNSAT-H, EPIC, HYDRUS, VADOSE/W etc. have been evaluated by comparing the model prediction with the water balance data collected from the sites with different climate conditions (Albright et al. 2002; Bohnhoff et al., 2009). The ACAP report suggested that the Richard's Equation-based codes (e.g., UNSAT-H, VADOSE/W) were better able to capture the performance of earthen final covers under both arid and humid conditions than the simple water balance codes (HELP, EPIC). The success of numerical modeling also depends on a proper incorporation of meteorological data, soil parameters and vegetation parameters. All the current computer codes (UNSAT-H, HYDRUS, VADOSE/W, LEACHM) are weak in the modeling of the evapotranspiration behavior (Bohnhoff et al., 2009). In this paper, the computer code of VADOSE/W was used to carry out a preliminary evaluation on the hydrological response of the loess final cover to the wettest year (1983) recorded in Xi'an. In addition, the computer code of AIR/W was used to evaluation landfill gas emission from the loess final cover during the driest year (1995) recorded in Xi'an.

4 MOISTURE AND GAS FLOW PREPERTIES OF COMPACTED CLAYEY LOESS

4.1 *Water retention property*

Soil Water Characteristic Curve (SWCC), also known as water retention curve, describes the relationship between moisture content and soil suction in unsaturated soils. SWCC is a significant curve to quantify the water storage capacity of a soil. Fig. 13 shows the laboratory measurement of drying and wetting SWCCs for the compacted clayey loess ($\rho_d = 1.45\,Mg/m^3$), which were best fitted using the van Genuchten equation. According to the best fitting SWCCs, the air-entry value for the compacted loess was 13.4 kPa, the saturated water content θ_s was about 48%, the field capacity θ_c being corresponding to a suction of 33 kPa and the water content θ_r at the wilting point (i.e., a suction of 1500 kPa) were approximately 32% ~ 37% and 10% ~ 15%, respectively. A significant hysteresis existed between the drying and wetting curves, and the moisture content near zero suction on the wetting curve was about 10% lower than that on the drying curve. The available water storage capacity, being defined as the difference of θ_c and θ_r, was 20% for the compacted clayey loess. It meant that 1 m thick compacted loess layer could retain 200 mm rain water without percolation. The compacted clayey loess is a good water storage material for the use in landfill covers in Northwest China.

Fig. 14 shows a comparison between the field measurements of water content versus suction relationship and the laboratory SWCCs for the compacted clayey loess ($\rho_d = 1.45\,Mg/m^3$). The field data were recorded during the wet season of 2014 by the TDRs and jet filled tensiometers installed in the field testing facility at Xi'an landfill. It can be seen that almost all the data points from field measurement were below the drying curve of laboratory measurement. Although the field data points were relatively scatter, the median line was close to the wetting curve of laboratory measurement. This was because a wetting hydrological process prevailed in the field monitoring period. The SWCCs representing the field condition were obtained by adjusting the van Genuchten model parameters of the laboratory SWCCs in accordance with the field measurements. As shown in the Fig. 14, the deduced SWCCs for field study were different from the laboratory SWCCs with respect to the slope and hysteresis of SWCC. The scale effect on the water retention property of compacted loess should be further investigated.

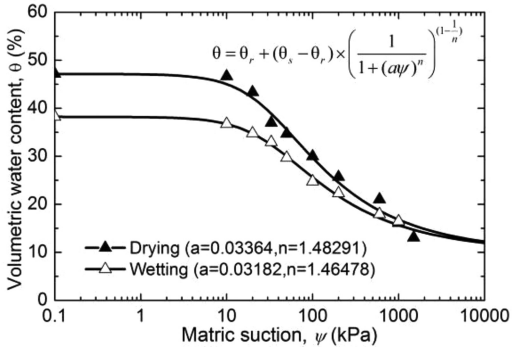


Figure 13. SWCC of the compacted clayey loess ($\rho_d = 1.45\,Mg/m^3$).

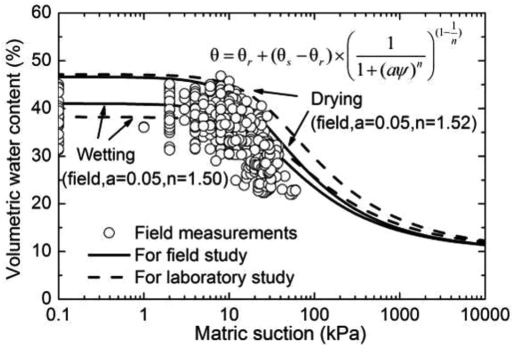


Figure 14. Comparison of field and laboratory data of SWCCs for the compacted clayey loess.

4.2 *Hydraulic conductivity*

Hydraulic conductivity is another important parameter for evaluating the performance of loess final covers.

Table 3. Comparison of saturated permeability between laboratory and field measurements.

Testing scale		ρ_d (Mg/m^3)	k_{sat} (m/s)
Laboratory	Soil element	1.30	5.0×10^{-7}
	Soil element	1.45	$1.0 \sim 1.8 \times 10^{-7}$
Field	Extreme rainfall simulation test	1.30	$5.0 \sim 8.3 \times 10^{-7}$
	Double-ring infiltration tests	1.45	$1.8 \sim 2.0 \times 10^{-7}$

Table 3 shows the comparison of saturated permeability measured in the field and laboratory for the compacted loess. The field measurement was obtained from the extreme rainfall simulation test on the field testing facility. On the basis of the applied rainfall intensity and the measurement of runoff, the infiltration rate into the top loess layer ($\rho_d = 1.30$ Mg/m^3) was determined and the saturated permeability was assumed to be equal to the steady infiltration rate. The deduced field values of saturated permeability for the compacted loess ($\rho_d = 1.30$ Mg/m^3) were in between 5.0×10^{-7} m/s and 8.3×10^{-7} m/s, being slightly greater than the measurement in the laboratory. For the compacted loess layer with a dry density of 1.45 Mg/m^3, double-ring infiltration tests were conducted at the buffer area of the field testing facility. The measured infiltration rate curve showed a decreasing trend with the infiltration time, and tended towards a steady infiltration rate. Being equal to the steady infiltration rate, the field value of saturated permeability for the compacted loess ($\rho_d = 1.45$ Mg/m^3) was 1.8–2.0 $\times 10^{-7}$ m/s. The values measured in the laboratory was 1.0–1.8 $\times 10^{-7}$ m/s. The above comparison between field and laboratory measurements indicated that the scale effect for the saturated permeability of the compacted loess was not significant. The measurements of saturated permeability indicated that the compacted clayey loess was a low permeable material, being able to limit water ingression.

Fig. 15 shows a comparison between the laboratory and field measurements of unsaturated hydraulic conductivities for the compacted clayey loess ($\rho_d = 1.45$ Mg/m^3). The laboratory measurements were obtained from the instantaneous profile method implemented on the soil column of compacted loess. The instantaneous profiles of water content and soil suction were measured by the TDR probes and tensiometers installed at different elevations of the soil column which was subjected to a water ponding of 50 mm on the top. Due to the limiting range of tensiometer measurement, only the hydraulic conductivity within the suction range of 0–85 kPa was measured. The field data points of unsaturated hydraulic conductivity were also obtained from the instantaneous profiles of water content and soil suction recorded in the field testing facility during the extreme rainfall simulation test. The water flow in the loess final

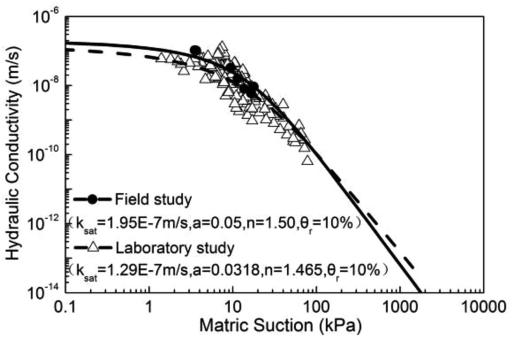


Figure 15. Changes of unsaturated hydraulic conductivity with suction for the compacted clayey loess ($\rho_d = 1.45$ Mg/m^3).

cover was assumed to be one-dimensionally perpendicular to the sloping surface. It can be seen that the field data points were reasonably consistent with the laboratory measurements. The unsaturated hydraulic conductivity curves shown in Fig. 15 were predicted from the measured saturated permeability (Table 3) and the best-fitted wetting curve of SWCC (Fig. 13 and 14) by using the van Genuchten-Mualem Model. The predicted unsaturated hydraulic conductivity curves for both the field and laboratory study agreed well with the corresponding measurements. The unsaturated hydraulic conductivity decreased significantly with the increasing suction. When the suction was increased from 0 to 50 kPa, the unsaturated hydraulic conductivity decreased to the order of 10^{-9} m/s, becoming relatively impermeable to water.

4.3 *Gas permeability*

Gas permeability is a key parameter for evaluating the performance of earthen final cover with respect to limiting LFG emission. For a compacted fine-grained soil, the gas permeability is controlled by both the soil structure and the gas-filled porosity. Fig. 16 shows the laboratory measurements of gas permeability on the compacted loess specimens ($\rho_d = 1.45$ Mg/m^3) prepared by using three different soil-water mixing methods. The specimen preparation methods and the used experimental apparatus refer to Zhan et al. 2014b. The different mixing methods produced different clod sizes in the compacted specimens (Table 2), and resulted in a significant influence on the gas permeability, especially at the high degree of saturation. When the degree of saturation was greater than 30%, the change of gas permeability with degree of saturation significantly depended on the soil-water mixing way. For a given degree of saturation, the influence of clod size and soil structure on gas permeability could be up to three orders of magnitude. This finding is different from the previous studies (Hamamoto et al. 2011), which generally neglect the effect of the clod size on the gas permeability. When the degree of saturation was

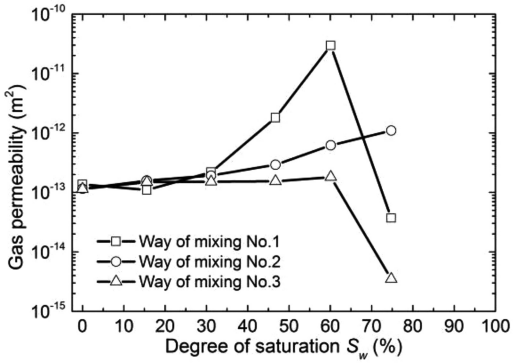


Figure 16. Relationship between gas permeability and degree of saturation for the compacted specimens prepared using different mixing methods.

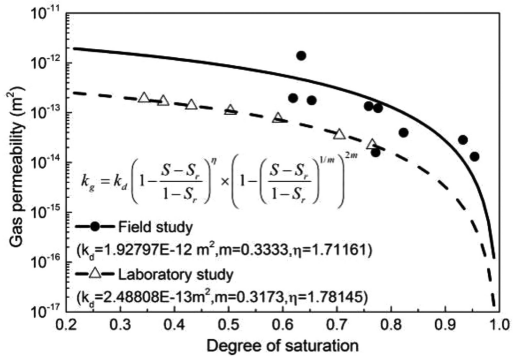


Figure 17. Comparison of gas permeability versus saturation degree curve between laboratory and field study.

below 30%, it was not easy to produce a clod, and the gas permeability did not depend on the way of soil-water mixing.

Fig. 17 shows a comparison between the laboratory and field measurements of gas permeability for the compacted loess ($\rho_d = 1.45\ Mg/m^3$). The laboratory measurement was performed on the compacted loess specimens with the same soil structure initially, resulted from the same soil-water mixing way and the same compaction water content (i.e., 13%). The degree of saturation was changed after compaction by using the osmotic technique. Thus, the relationship between gas permeability and degree of saturation shown in Fig. 17 is free of the influence from soil structure. The field data points were obtained from the gas permeation tests at the field testing facility at Xi'an landfill. The field data points of gas permeability were relatively scatter, and the mean value was about one order of magnitude greater than the laboratory measurement. The difference was believed to be related to the difference in soil structure. The compacted loess in the field consisted of more clods, being relatively non-uniform.

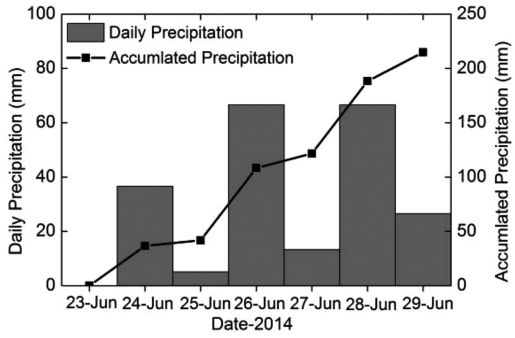


Figure 18. Daily and accumulated precipitation applied during the extreme rainfall simulation test.

The gas permeability versus saturation degree curves shown in Fig. 17 were predicted by using the van Genuchten model. The prediction for the laboratory study was based on the best-fitted wetting curve of SWCC (Fig. 13) and the gas permeability was measured on the nearly dry specimen. The prediction for the field study was based on the best-fitted wetting curve of SWCC (Fig. 14) and the field measurements of gas permeability. The gas permeability curves for both field and laboratory study firstly showed a gentle decrease with the increasing saturation, and then a significant decrease when the degree of saturation was greater than 85%. The behavior implies that when rainfall infiltration results in a high saturation in the compacted loess final cover, its gas permeability will drop significantly, and a build-up of gas pressure is likely to occur at the base of the final cover.

5 PERFORMANCE EVALUATION OF LOESS FINAL COVERS AT XI'AN LANDFILL

5.1 *Hydrological response to extreme rainfall*

As mentioned previously, extreme rainfall simulation test was carried out on the field testing facility to determine the maximum capacity available for water storage for the compacted loess final cover underlain by the gravel layer. Fig. 18 shows the distribution of precipitation applied during the extreme rainfall period from 24th to 29th in June 2014. The artificial rainfall intensity applied by the sprinkler system was maintained at a constant value of 3.0 mm/h. As a result of the variation in rainfall duration, the daily precipitation was not uniformly distributed in the six days. The daily precipitation on June 24th, 26th and 28th was greater than those on the other three days. The accumulated precipitation sprinkling on the final cover reached a value of 214.8 mm, being 1/3 of the average value of annual precipitation in Xi'an.

The hydrological responses of the loess final cover to the simulated rainfall were recorded by the flow

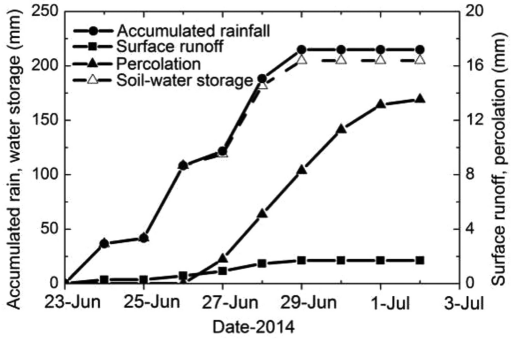


Figure 19. Water balance data for the cover profile being subjected to extreme rainfall simulation test.

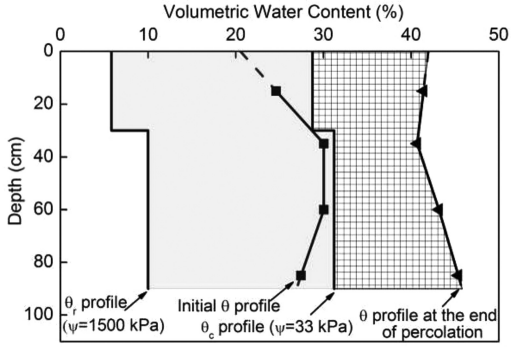


Figure 20. Change of volumetric water content profiles.

monitoring system and the instrumentation installed at the testing facility. Fig. 19 shows the key components of water balance data including surface runoff, deep percolation, and water storage during the period from June 23rd to July 2nd. The total amount of evaporation during the simulated rainfall periods was estimated to be 40-50 mm based on the measured evaporation potential. Thus, the infiltration rate into the final cover was equal to the difference between the applied rain intensity and the measured runoff. The water storage in the cover profile was equal to the difference between the infiltration and the measured deep percolation. It can be seen that the surface runoff was insignificant, and the accumulated amount was about 2 mm, being 1% of the total precipitation. It meant most of rainfall infiltrated into the cover system. Deep percolation was not measured until the fourth day of rainfall (i.e., on June 27th). The delayed percolation was attributed to the water storage capacity of the compacted loess layer, which was further enhanced by the capillary barrier effect at the loess/gravel interface. The total amount of deep percolation collected at the completion of flux was 13.5 mm, being equal to 6.5% of the total precipitation applied on the cover system. With the water balance data, the amount of water stored in the cover system during the rainfall period can be determined as 140–150 mm.

Fig. 20 shows the change of volumetric water content profiles recorded by the TDRs installed at different depths. It should be noted that the initial water content prior to the simulated rainfall was greater than that corresponding to the wilting point (i.e., a suction of 1500 kPa). The amount of water storage in the cover system prior to the simulated rainfall can be calculated from the difference between the initial water content profile and the profile corresponding to the wilting point. With a consideration of the pretest water storage, the maximum capacity available for water storage for the cover system was determined as 304.9 mm. The water storage capacity for the single layer of loess with the same thickness (900 mm) was estimated as 196.1 mm. A comparison of these two values indicated that the capillary barrier effect at the loess/gravel interface resulted in an increase in water storage capacity by 55.5%.

5.2 *Numerical evaluation of water percolation in the wettest year*

The objective of this section is to use the computer code of VADOSE/W to evaluate the potential percolation through the loess final cover during the wettest year (1983), which was recorded in Xi'an between 1960 and 2010. The final cover profile used for the numerical modeling was similar to that constructed in the field testing facility, i.e., a compacted loess layer underlain by a gravel layer. The required thickness of the compacted loess layer was determined as 1.3 m by following the water balance method proposed by Khire et al. (2000). The determination was based on the wettest year's meteorological data, the wetting SWCC of the compacted loess and the water entry value of the gravel. Details of the calculation can be found in Zhan et al. (2014c). The thickness of the underlying gravel layer was set as 0.3 m.

5.2.1 *Numerical model*

1-D model of a soil column consisting of the cover profile was set up by using the computer code of VADOSE/W. VADOSE/W, developed by GEO-SLOPE International Ltd., is a commonly used computer code for simulating the hydrological response of earthen final covers to the change in atmospheric condition. The computer code must be run with simultaneous coupled heat and water flow. The water mass transfer equation is derived from the Richards equation for transient flow in unsaturated soils with adaptations for vapor flow. The heat transfer equation is a standard Fourier equation for conductive heat transfer with modifications for the inclusion of vapor transfer and convective heat transfer due to flowing water. VADOSE/W can be used into run in 1D or two-dimensional (2D) models. VADOSE/W uses the finite element method to solve the boundary-value problem. The spatial-and-temporal discretization used in

the simulation was set so as to limit mass balance error and achieve numerical convergence.

5.2.2 *Hydraulic and thermal properties of soil materials*

Solving the numerical model requires an input of the hydraulic and thermal properties for the compacted loess and the gravel. The wetting curve of SWCC for field study shown in Fig. 14 and the hydraulic conductivity curve for field study shown in Fig. 15 were input. Both the two curves were calibrated with the field measurements obtained at the testing facility. The thermal properties for the compacted loess reported by Wang (2007), including the volumetric specific heat capacity curve and the thermal conductivity curve, were input into the numerical model. The hydraulic and thermal properties of the gravel reported by Zhan et al. (2014a) and Jia (2010) were used.

5.2.3 *Boundary and initial conditions*

The upper boundary condition of the 1-D model was the soil-atmospheric conditions in the wettest year of 1983 in Xi'an, which were represented by meteorological data and vegetation parameters. The daily-based meteorological data set of 1983 in Xi'an obtained from China Meteorological Data Sharing Service System was input into the model. The one-year data set included maximum and minimum temperature, maximum and minimum relative humidity, average wind speed, and daily precipitation. The daily precipitation was assumed to be distributed in a Sinusoidal form within the second half day (i.e., 12:00 to 24:00 pm) according to most of rainfall patterns recorded in Xi'an (Wang et al. 2013). The total precipitation in the year was 903 mm. With the meteorological data set, the data of solar radiation in each day was predicted by the VADOSE/W by considering the latitude of Xi'an (i.e., 34.18°).

The vegetation parameters input into the model included leaf area index (LAI), root depth and plant moisture limiting function. The vegetation growing season in Xi'an was between March 1 and November 1). The peak value of LAI for the vegetation on the loess final cover was assumed as 1. The change of LAI with time is shown in Fig. 21. The maximum root depth was assumed as 0.3 m. VADOSE/W assumes that the root density is triangular, which means that the root density at the ground surface is the greatest. A plant limiting function was used to relate transpiration rate to water availability, and its detailed description can be found from Bohnhoff et al. (2009).

A unit hydraulic gradient condition was used for the bottom boundary condition in the model. The initial volumetric water content of the compacted loess layer was set as 30%, being corresponding to the average value of soil suctions measured in the first month of 2015 (i.e., 39 kPa). The initial volumetric water content of the gravel layer was set as 0.3% (i.e., residual point), being corresponding to a suction of 10 kPa. The initial temperature of the cover profile was set as 5° according to the average value of field measurements in the first month of 2015. To be simple, all the initial conditions were assumed to keep unchanged with the depth.

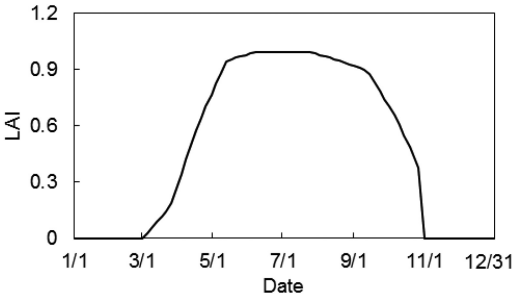


Figure 21. Change of leaf area index (LAI) with time for the vegetation in Xi'an.

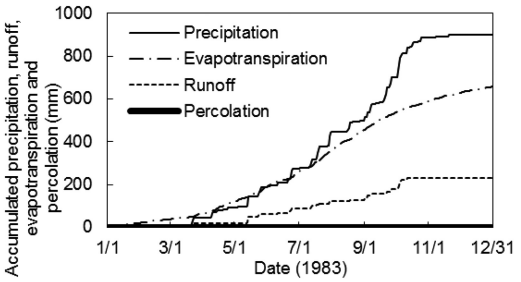


Figure 22. Prediction of water balance quantities for the loess final cover in the wettest year.

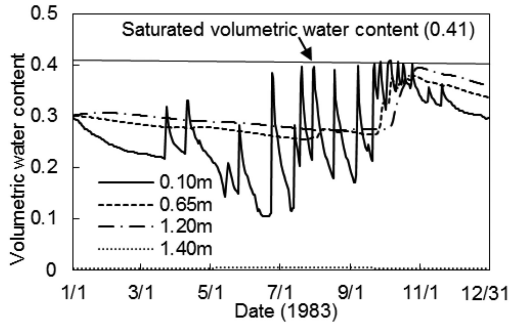


Figure 23. Changes of volumetric water content with time at different depths in the cover profile.

5.2.4 *Simulation results and analysis*

Fig. 22 shows the changes of four primary water balance quantities, including precipitation, runoff, evapotranspiration, and percolation, during the wettest year of 1983 in Xi'an. Fig. 23 shows the predicted changes of volumetric water content with time at different

depths in the cover profile (i.e., 1.3 m compacted loess underlain by 0.3 m gravel). As shown in Fig. 22, during the first five months of dry seasons, the accumulated evapotranspiration was always greater than the accumulated precipitation. As a result, the volumetric water content at depths of 0.65 m and 1.2 m kept decreasing with time. The occasional rainfalls only resulted in an increase in water content at the shallow depth (e.g., 0.1 m).

During the wet season in between May 15 and November 1, the total precipitation was 740 mm, accounting for 82 percent of the annual precipitation. The runoff appeared in May and became significant as a result of frequent and intense rainfall events occurred. It was found that the evapotranspiration was also significant during this period. This was because wet soil condition, high atmospheric temperature and plant growing coincided in the same period. The soil-atmospheric behavior is favorable for limiting deep percolation through the earthen final cover. As shown in Fig. 23, the volumetric water content at the depths of 0.65 m and 1.2 m increased significantly in September and October, but both of them kept well below the saturated line. There was no increase in the volumetric water content at the depth of 1.4 m, indicating no ingress of water into the gravel layer.

During the last two months of the year, the climate became dry and cold, and the hydrological response of the loess final cover was similar to that during the first five months. The predicted values of cumulative evapotranspiration and cumulative runoff were 656 mm and 231 mm, respectively, and their summation was 887 mm, being close to the total precipitation (903 mm). No deep percolation was predicted in the wettest year in Xi'an. The numerical simulation indicated that the capillary barrier cover, consisting of 1.3 m compacted loess layer underlain by 0.3 m gravel layer, would have a good performance in the semi-humid regions of northwest China. The performance will be further validated by the accumulation of field monitoring data collected at the testing facility.

5.3 *Numerical evaluation of gas emission in the driest year*

The objective of this section is to use the computer code of AIR/W to evaluate the landfill gas emission from the loess final cover during the driest year (1995), which was recorded in Xi'an between 1960 and 2010. The total precipitation in 1995 was 312 mm, being 1/3 of that for the wettest year. The final cover profile considered here was kept the same as the one used in the previous section.

5.3.1 *Numerical model and input parameters*

The gas flow in an earthen final cover is significantly influence by the soil moisture condition, which depends on soil-atmospheric condition. So numerical modeling of gas flow must be run with simultaneous coupled water flow (Zhan et al. 2015a). For this purpose, the module of AIR/W developed by GEO-SLOPE International Ltd. was used to evaluate the gas emission potential. The coupled gas and water conservation of mass equations considered in the computer code of AIR/W can be found in the software manual. In the governing equation, pore gas pressure was not assumed to be atmospheric. In this study, the AIR/W module was solved for the isothermal case. The same 1D model of cover profile as that used in VADOSE/W was established using AIR/W.

In addition to the hydraulic properties input into VADOSE/W, the gas permeability curves for the compacted loess and the gravel were required for running AIR/W. The gas permeability curve for field study shown in Fig. 17 was input for the compacted loess layer. The gas permeability curve for the gravel layer was predicted using the van Genuchten model on the basis of the dry gas permeability (1.56×10^{-2} m/s) and the SWCC of the gravel (Zhan et al. 2014a).

5.3.2 *Boundary and initial conditions*

The upper boundary condition for water phase was determined from the water balance data of the cover model simulated by using VADOSE/W. The one-year meteorological data set of 1995 was input into the model, and all the other parameters were kept the same as those used previously. The predictions of precipitation, runoff and evapotranspiration in every day of 1995 were obtained. The daily net infiltration, being equal to the daily precipitation minus the daily runoff and daily evapotranspiration, was input to AIR/W as the upper boundary condition of the model. The bottom boundary condition was kept as a unit hydraulic gradient condition.

For the gas phase flow, the upper boundary condition of the cover model was set as a gas pressure preview condition, in which the gas pressure preview value was set as 2 kPa, i.e., the air entry value (AEV) of the loess. The lower boundary condition was set as a constant gas pressure of 0.75 kPa, which is the limiting pressure at the bottom of landfill cover suggested by the China standard of CJJ112-2007. The initial values of volumetric water content for the compacted loess and the gravel were set as 30% and 0.3%, respectively. The initial gas pressure profile was obtained by running a steady state analysis with the upper boundary and the lower boundary being set as 0kPa (atmospheric pressure) and 0.75 kPa, respectively. AIR/W also uses the finite element method and the spatial-and-temporal discretization used in the simulation was kept the same as that used in VADOSE/W previously.

5.3.3 *Simulation results and analysis*

The simulation results for the model of cover profile (i.e., 1.3 m compacted loess layer underlain by 0.3 m gravel layer) were presented in terms of gas pressure distribution and gas emission rate. Fig. 24 shows the distribution of pore gas pressure at different depths in the cover profile. Fig. 25 shows the daily gas emission rate and the accumulated gas emission from the cover surface. It can be seen from Fig. 24 and Fig. 25

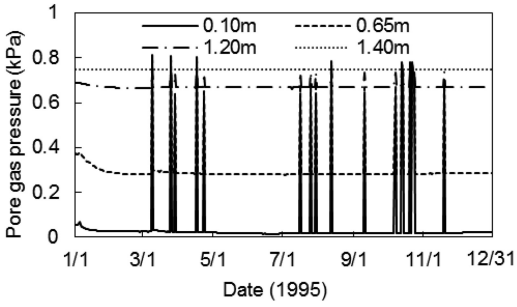


Figure 24. Changes of pore gas pressure with time at different depths in the loess cover.

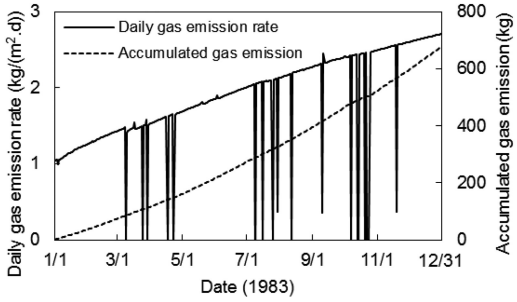


Figure 25. Prediction of daily gas emission rate and accumulated gas emission from the loess cover.

that the pore gas pressures and the daily gas emission rate were sensitive to the rainfall events (see Fig. 6). Pulses of gas pressure were observed on the days with net infiltration, especially at the shallow depths. Correspondingly, temporary decrease in the daily gas emission rate was observed on the rainy days. The response is related to that fact that rainfall infiltration resulted in an increase in soil moisture content and a decrease in gas permeability. During the first two months of 1995, evaporation prevailed on the cover system, and a continuous decrease in pore gas pressure was observed at depth of 0.1 m, 0.65 m and 1.2 m. The daily and accumulated values of gas emission rate kept increasing.

During the wet season in between March and November in 1995, the total precipitation was 299 mm, accounting for 96 percent of the annual precipitation of 1995 (i.e., 312 mm). The predicted values of evapotranspiration and runoff were 262 mm and 111 mm, respectively. The sum of evapotranspiration and runoff during the wet season, being 473 mm, was greater than the total precipitation. So the cover profile overall experienced a drying process with the exception of the rainy days. As a result, the predicted value of daily gas emission rate kept increasing during the days without rainfall, and the accumulated gas emission rate also increased significantly during the wet season.

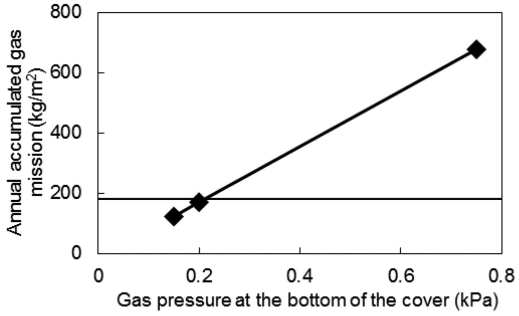


Figure 26. Relationship between predicted annual gas emission and executing gas pressure at the bottom of the cover.

The prediction of accumulated gas emission at the end of 1995 was 678 kg/m^2, which was significantly greater than the limiting value of annual gas emission suggested in the Australia standard (i.e., 164 kg/m^2). It should be noted that the prediction was obtained by assuming the gas pressure at the bottom of the cover system was kept at 0.75 kPa, i.e., the limiting pressure suggested by the China standard of CJJ112-2007. The actual gas pressure, depending on the gas production rate of the underlying waste layers, is generally lower than the limiting value. Fig. 26 shows the change in the predicted annual gas emission with the executing gas pressure under the cover system. When the executing gas pressure was controlled below 0.2 kPa, the predicted annual gas emission rate from the loess final cover could meet the requirement in the Australia standard.

Engineering measures should be taken to reduce the landfill gas emission from the earthen final cover. There are two approaches for this purpose. One is to control the gas pressure under the final cover by active collection of landfill gas at the gas diffusion layer. This measure would be necessary at most of MSW landfills in China, at which gas collection efficiency are generally low due to the wet condition of waste piles (Zhan et al. 2015b). Another approach is to use a bio-cover with a methane oxidation capability to mitigate the methane gas emission. When the landfill gas diffuses through the bio-cover with aerobic methanotrophic bacteria, part of the methane constituents will be oxidized by the oxygen diffused from the atmospheric to the cover profile. Many studies have been conducted to investigate the methane oxidation capability of earthen final covers (Scheutz et al. 2009). Yang et al. (2015) carried out batch tests to measure the methane oxidation capability of the clayey loess with an addition of compost. The measured methane oxidation capacity for the loess containing 3.0% compost was 10–15 μg $CH_4/(g \cdot h)$. On the basis of the measurement, 3.0% compost by weight was added to the loess material for constructing the top 300 mm vegetation layer in the field testing facility at the Xi'an landfill. It is anticipated that the cover system will function as a bio-cover to mitigate the methane gas emission.

6 SUMMARY

On the basis of the multi-scale experimental study on the moisture and gas flow properties of the compacted clayey loess and the preliminary performance evaluation of the loess final cover, the following findings are drawn:

(1) The compacted clayey loess had a considerable water storage capacity and a relatively low hydraulic conductivity. The soil did not exhibit a significant scale effect in the water retention characteristic and the hydraulic conductivity.
(2) The influence of clod size and soil structure on gas permeability could be up to three orders of magnitude. The field measurements of gas permeability were about one order of magnitude greater than the laboratory measurements.
(3) No water percolation was predicted for the compacted loess layer (1.3 m) underlain by a gravel layer (0.3 m) in the wettest year of Xi'an. The capillary barrier effect at the loess/gravel interface resulted in an increase in water storage capacity by 55%.
(4) The predicted annual LFG emission from the compacted loess final cover in the driest year of Xi'an was likely to be greater than the limiting value suggested by the Australia standard. The excessive LFG emission could be drawn down by controlling the gas pressure under the final cover via active collection of LFG.

ACKNOWLEDGEMENT

The author acknowledges the financial support from the National Basic Research Program of China (grant no. 2012CB719805), the support from Prof. Chen Yunmin and Prof. Charles W W Ng and the assistance from the postgraduate students.

REFERENCES

Albright, W.H., and Glendon, W.G. 2002. Alternative Cover Assessment Project (ACAP) Phase I Report.

Bohnhoff, G.L., Ogorzalek, A.S., Benson, C.H., Shackelford C.D., and Apiwantragoon, P. 2009. Field Data and Water-Balance Predictions for a Monolithic Cover in a Semiarid Climate. Journal of Geotechnical and Geoenvironmental Engineering 135(3): 333–348.

Bolen, M.M., Roesler, A.C., Benson, C.H., and Albright, W.H. 2001. Alternative cover assessment program: Phase II report. Geo-Engineering Report.

Chen, H., Shao, M., and Li, Y. 2008. The characteristics of soil water cycle and water balance on steep grassland under natural and simulated rainfall conditions in the Loess Plateau of China. Journal of hydrology 360(1): 242–251.

Ding, Y.H., and Wang, S.R. 2001. The climate and ecological environment in northwest China. Bei Jing: Weather Publisher.203pp.

Hamamoto, S., Moldrup, P., Kawamoto, K., Wickramarachchi, P.N., Nagamori, M., and Komatsu, T. 2011. Extreme compaction effects on gas transport parameters and estimated climate gas exchange for a landfill final cover soil. Journal of Geotechnical and Geoenvironmental Engineering 137(7): 653–662.

Jia, G.W. 2010. Study on the water transport in the landfill earthen final cover and its controlling method. Ph.D. Thesis, Zhejiang University, Hangzhou, China.

Khire, M.V., Benson, C.H., and Bosscher, P.J., 2000. Capillary barriers: Design variables and water balance. Journal of Geotechnical and Geoenvironmental Engineering 126(8): 695–708.

Liu, T.S., and Ding, Z. 1998. Chinese loess and the paleomonsoon. Annual review of earth and planetary sciences 26(1): 111–145.

Liu, T.S. 1985. Loess and environment. Beijing: Science. 482 pp. (In Chinese)

Scheutz, C., Kjeldsen, P., Bogner, J.E., Visscher, D.A., Gebert, J., Hilger, H.A., H, H.M., and Spokas, K. 2009. Microbial methane oxidation processes and technologies for mitigation of landfill gas emissions. Waste Management & Research 27(5): 409–455.

Sun J. 2002. Earth and Planetary Science Letters. Plateau 203(3): 845-859.

Wang, Z.L., Li, X.Y., and Yang, A.Q. 2013. Analysis of Precipitation Characteristics of the Fifteen Periods on the Loess Plateau of Shanxi Province. Research of Soil and Water Conservation 20(5): 176–179. (in Chinese)

Wang, T.H., Liu, Z.C., and Lu, J. 2007. Experimental study on coefficient of thermal conductivity and specific volume heat of loess. Rock and Soil Mechanics 28(4): 655–658. (in Chinese)

Yang, Y.B., Zhan, L.T., Chen, Y.M., and Shi, W. 2015. Methane oxidation capacity of landfill cover loess and its impact factors. China Environmental Science 35(2): 484–492.

Zhan, L.T., Qiu, Q.W., Yang, Y.B. 2015a. Soil column tests and numerical simulation of moisture and gas coupled flow in an unsaturated loess cover. Submitted to Chinese Journal of Geotechnical Engineering.

Zhan, L.T., Xu, X.B., and Chen, Y.M. 2015b. Dependence of Gas Collection Efficiency on Leachate Level at Wet Municipal Solid Waste Landfills and Its Improvement Methods in China. Journal of Geotechnical and Geoenvironmental Engineering.

Zhan, T.L., Li, H., and Jia, G.W. 2014a. Physical and numerical study of lateral diversion by three-layer inclined capillary barrier covers under humid climatic conditions. Canadian Geotechnical Journal 51(12): 1438–1448.

Zhan, T.L., Yang, Y.B., Chen, R., Ng, C. W. W., and Chen, Y. M. 2014b. Influence of clod size and water content on gas permeability of a compacted loess. Canadian Geotechnical Journal 51(12): 1468–1474.

Zhan, L.T., Jiao, W.G., Kong, L.G., and Chen, Y.H. 2014c. Feasibility analysis of using loess as soil cover material for landfills in Northwest China and its analysis of design thickness. Rock and Soil Mechanics 35(12): 3361–3369.

Unsaturated Soil Mechanics—from Theory to Practice – Chen et al. (Eds)
© 2016 Taylor & Francis Group, London, ISBN 978-1-138-02921-7

Experimental study on characteristics of the collapsibility of Ili loess

A.J. Zhang
Northwest A&F University, Yangling, Shaanxi, China

Y.C. Xing
China Institute of Water resources and Hydropower Research, Beijing, China

X.L. Hu
Engineering Quality Inspection Centre, Administration of Xinjiang Ili River Basin Development and Construction, Ili, Xinjiang, China

M.X. Guo & B. Zhang
Northwest A&F University, Yangling, Shaanxi, China

ABSTRACT: Due to the wide distribution of the loess in China, the regional differences of loess has been the focus of attention, but less attention has been paid to Xinjiang loess. In this research, based on a channel engineering, it is proved by the large amount geological survey and indoor test that Xinjiang Ili loess is typical eolian loess. Its thickness is large and has a uniform texture. There is no paleosol layer and the deposition process has not been influenced by hot and humid climate. Salinity, especially the calcium carbonate, has not been through the leaching effect of the rain. Its micro-structure is extremely unstable. The density, moisture content and saturation are low, while the dissolved salt content is high. In the meantime, the intensity is not low. This is significantly different from the loess in the Loess Plateau. From the collapsibility test and the field immersion test, this study provides strong evidence that the collapsibility of Xinjiang Ili loess is quite strong, the maximum collapsibility coefficient reachs 0.18 ($p = 200$ kPa). After the immersion of the trial pit, the settlement has started quite early and developed quickly. The maximum settlement reaches a large value of 3.69 m. By comparing the measured and calculated amount of collapsibility, the correction factor of the Ili loess should be in the range of 1.0–1.5. It is suggested to entitle the loess in Xinjiang Ili valley Tekes River level IV terrace with "Ili loess" as a typical sample of eolian loess.

1 INTRODUCTION

Loess is a typical category of soil that deposited in the dry environment of the quaternary geochronology. It has unique features, such as large porosity, incomplete consolidation and water sensibility. Especially for collapsible loess, sudden additional settlements may happen under self-weight or other forces when it is immersed in the water or in saturated condition. This process is usually entitled as collapse deformation, which will severely endanger the engineering construction in the area. Thus collapse is one of the must-face problems, such as channel engineering, in which the building is designed for water transportation.

In literature, the research has primarily focused on the loess collapsibility in the Loess Plateau, which is divided into seven areas according to the collapse intensity (GB 50025-2004). The I area is in Longxi in Gansu province, II area between Gansu Longdong, Northern Shaanxi and West of Shanxi, III area in the middle of Shaanxi province, IV area between Northern parts of Shanxi and Hebei province, V area in Henan province, VI and VII in other fringe parts (GB 50025-2004). Based on plenty of experimental studies and indoor tests on each area, the area correction factors ($\beta 0$) for the calculation of field collapse settlement for different regions, are 1.50 for area I, 1.20 for area II, 0.9 for area III, and 0.5 for other areas. However, they are mainly studied according to the experiments in low terrace of the loess regions. Of note, less attention has been paid to the loess in Xinjiang Uygur Autonomous Region (Xinjiang in short).

In the study reported by Shao et al. (2015), they have summarized that: in recent years, with the rapid development of infrastructure construction in loess regions, construction projects has moved from low terrace of the loess regions to loess tableland and high terrace areas, and extends to the border regions such as Xinjiang. Loess foundation is no longer a foundation that involve limited thickness of collapsible loess under self-weight and additional structural stress in low terrace regions, but a foundation that

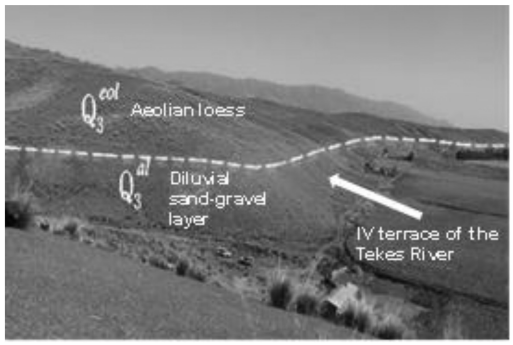
increasingly face with big thickness of collapsible loess and other specific problems. The past understanding of the collapsibility and intensity stability of loess foundation is already unable to satisfy the need of practical projects, which brings great challenge to the geotechnical engineering practice. The collapsibility in a particular area with big thickness of loess has become an urgent technical problem in geotechnical engineering.

The Ili valley in Xinjiang locates in northwest of China, border with Kazakhstan, is the only region affected by the Atlantic Ocean climate. The east, south and north, three sides of the valley, are surrounded by Tian Shan Mountain. The west and south sides of the mountain are higher than the east and north sides. The highest peak is Tomur at 7443 m. The Tian Shan Mountain mainly consists of Poluokenu, Nalati and Keguqin etc. There is also a Wusun mountain in the middle of Ili valley, which runs west-east at 200–3500 m. Wusun Mountain divided the valley into two regions: the Ili River diluvial-alluvial Plain and the Zhaosu-Tekes basin. The Ili valley is shaped in triangle with a wide west and narrow east. The length from west to east is around 170 km. The multi-year average precipitation in the valley is 417.6 mm and its 600 mm in the mountain area. The amount of precipitation is more abundant than other parts of Xinjiang. The annual average temperature is 10.4°C. The main river is Ili River. It runs in from Kazakhstan at southwest, and runs out into Kazakhstan again at northeast after going around the valley. The upper stream of the river called Tekes River and its main tributaries are Akyazi, Kukesu and Gonnes. Ili River starts from the junction of Gonnes and Tekes. The main tributary is Kashi River. There is collapsible loess distributed at all terrace levels of Tekes River (most in VI level terrace), which is in the south of the valley. In addition, there is collapsible loess distributed in the diluvial plain area as well, which locates in the north of the Ili River. From the geological origin of view, there were intense glacial activities before the middle Pleistocene in the area, which formed a large thickness of sand-gravel moraine and diluvial sand-gravel layer. During the late Pleistocene, a long period of dry and cold weather condition formed a large-scale loess deposition. The whole process of deposition was basically not affected by the hot and humid climate. Furthermore, there was no strong role of water after the deposition, due to less rain and good prevention of rainwater infiltration by vegetation on the soil surface. Thus, unlike the loess in Loess Plateau, where exists multi-layer ancient soil and the sequence of old-new accumulation, the Ili loess need to be paid special attention to.

In this paper, a significant amount of indoor tests and field immersion tests were conducted based on a large channel engineering project. Detailed research work was carried out on the Ili loess, which reveals its basic characteristics, particularly how its collapsibility is changing. This research will provide technical support to the evaluation and treatment of the collapsibility of large thickness self-weight Ili loess.



(a) The surrounding landscape



(b) The basic stratigraphic distribution

Figure 1. Basic geomorphic and stratigraphic distribution of the tested area.

2 BASIC CHARACTERISTIC TEST OF ILI LOESS

The tested area locates in the IV terrace of the Tekes River, and is surrounded by the finest local pasture.

It's soil hilly geomorphology and contains two layers of quaternary geochronology, which corresponding to the Q_3^{eol} Aeolian loess and Q_3 glacial and diluvial sand-gravel layer. The maximum thickness of the collapsible loess is 30 m. The basic geomorphic and stratigraphic distribution of the tested area is shown in Figure 1.

Five exploratory wells were digged by the way of artificial excavation, with the maximum depth of 30 m. They are numbered as TK1, TK2, TK3, TK1-1 and TK2-1. After digging, it is found that there are 40 cm humus (black and contains a lot of grassroots), and 30 m loess (white-yellow, homogeneous and exists large pores). However, there is no presence of ancient soil. It is dry and maintains small water content in the first 23 m of the sample. The water content increases afterwards. Above 10 m depth of the sample, grassroots can be found occasionally, however none exists below 10m. No groundwater was found in the exploration depth. In order to ensure the reliability of the test results, multi-unit parallel test was used to conduct the physical and mechanical tests of loess.

2.1 *Material composition*

The composition of loess means its mineral composition, and mainly consists of all kinds of minerals and their content. The mineral composition of the soil directly determines its physical, mechanical and chemical properties. The minerals in loess are generally divided into several categories, such as granular material, clay minerals, salts, pore water and pore gas etc. Sometimes, there is humus, grassroots and fossils (like snail's shell) exist as well. Different minerals play different roles in loess. Granular material, mainly includes quartz, feldspar and other debris, is the main component of the soil. Clay minerals are montmorillonite, illite, chlorite, kaolinite and water mica etc. They usually have a large surface area and are wrapped around the granular materials with particle size under 0.005mm, which determines the sensitivity of soil to water. Since montmorillonite consists of upper and lower silicon-oxygen tetrahedron and alumina-oxygen octahedron in the middle of the composition, the weak link between crystal layers makes the binding force small and easy to produce lattice substitution. Thus inflation will happen when water intrusion occurs. Illite and kaolinite with different lattice structures show less expansion properties in water. Salts are divided into types: soluble salts, poorly soluble salts and insoluble salts. The soluble salts are mainly composed of positive ions like Ca^{2+}, Mg^{2+} and negative ions like CI^{-}, $CO3^{2-}$, which caused the unstable cementation in loess. The poorly soluble salts mainly are gypsum with a slightly stronger water stability performance. However, the insoluble salts are mainly composed of carbonate (primarily $CaCO_3$) and play critical cementation role in loess. It is the primary component which determines the degree of cementation between granular materials.

The following conclusions are made according to the test results from X-ray diffraction, scanning electron microscopic measurement and ion determination methods.

(1) The granular materials of Ili loess are quartz, calcite and albite, with the corresponding contents of 26.1%–29.4%, 16.4%–22.6% and 12.6–21.6% respectively. The average content of the granular materials is about 49% of the total weight.
(2) The clay minerals are illite, chlorite, kaolinite and illite- montmorillonite mixture. The illite has the maximum content of 17.1%–19.7%, followed by 7.3%–9.5% content of chlorite, 3.0%–3.5% content of kaolinite and 0.0%–0.6% content of montmorillonite. The average content of clay minerals accounted for about 31% by weight. The expansion is unlikely to happen even when the water intrusion occurs, due to the high content of illite. However, the material basis for collapse exists.
(3) Several results are made through 216 tests. The soluble salts in Ili loess mainly consist of Ca and Mg positive ions and CI and CO3 negative ions, with the maximum content of 19.2 g/kg. The upper and lower average contents are 7.53 g/kg and 2.18 g/kg. The mean value is 4.48 g/kg, which is quite different with the content in the middle of Shaanxi province (1–2 g/kg). According to "Code for Investigation of Geotechnical Engineering" (GB50021-2001), it should be classified as saline soil when the soluble salts has a content greater than 0.3% (3 g/kg) and the soil has engineering characteristics such as soluble depression, salt expansion and corrosion etc. Thus the Ili loess can be considered as saline soil because of the high content of soluble salts.
(4) The poorly soluble salts are mainly gypsum, with a consistent content with other regions. The average content is 11.45 g/kg. The insoluble carbonate has an average content of 174.8 g/kg, which is slightly larger than the loess in Loess Plateau.
(5) The tests also indicate that there is few difference of mineral composition between samples with different depths, which in turn implies that the Ili loess has a same soil condition and uniform texture

2.2 *Microscopic structure*

From the microstructure point of view, three aspects of particle morphology, connection type and arrangement, are the primary features that affect soil properties. Table 1 summaries the basic microstructure properties of Ili loess by scanning electron microscope (SEM) method. Figure 2 shows two example images of SEM. It can be seen that the particles are grainy and there is no existence of clot particles. The connections between particles are mainly point contact with little surface contact. In addition, undisturbed soil samples at different depths show an aerial structure form, with some individual exceptions. The observations indicate that the Ili loess has the characteristics of point contact, aerial structure form and few cementations, which lead to a highly unstable structure and exhibit strong potential collapsibility.

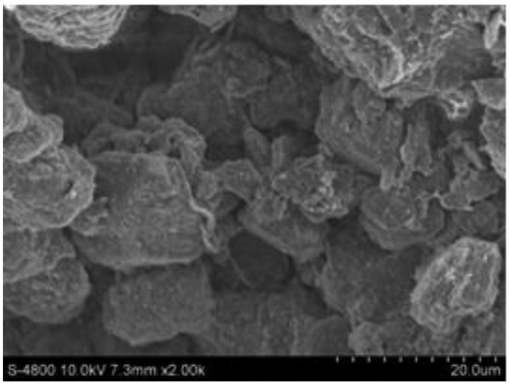
2.3 *Physical property*

The following results are obtained from 71 grain size distribution tests. The contents of coarse-grain, silt, clay, colloidal grain are 0.5%–13.8%, 63.7%–84.5%, 19.2%–34.5%, and 7%–13.5% respectively. Thus the Ili loess belongs to low liquid limit clay (CL). The silt content based property is consistent with the general characteristics of loess. Figure 3 shows the grain composition of Ili loess. It can be seen that the distribution of grain contents is narrow, which verifies the uniformity of Ili loess.

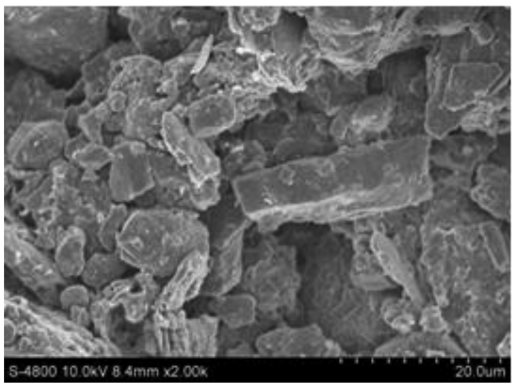
Figure 4 shows the distribution of water content and dry density at different depths. It is shown that both the natural water content and dry density of Ili loess is small. The water content is stable at around 8.7%. The average dry density within 8 m is 1.22 g/cm^3, its 1.37 g/cm^3 between 8–22 m and its 1.29 g/cm^3 for the rest.

Table 1. The basic microstructure properties of Ili loess.

Sample depth (m)	Microstructure			
	Particle shape	Connection	Arrangement	Potential collapsibility
3.5–4.0	grainy	point contact	aerial form	strong
11.5–12.0	grainy	point contact	aerial form	strong
19.5–20.0	grainy	point contact	inlaid form	median
29.5–30.0	grainy	point contact	aerial form	strong



(a) Sample 2



(b) Sample 4

Figure 2. Two example images of SEM.

2.4 *Mechanical property*

From the tests, the permeability coefficient of Ili loess is measured as 0.9×10^{-4}–2×10^{-4} cm. This value varies little at different depths. The average coefficient of compressibility at natural conditions is 0.12 MPa^{-1}, and its 1.04 MPa^{-1} at saturated condition, which belongs to high compressive soil. From the e-log p curve, Ili loess is normally consolidated soil without ultra-consolidation pressure, which is different from the loess in Loess Plateau with over-consolidation and under-compaction.

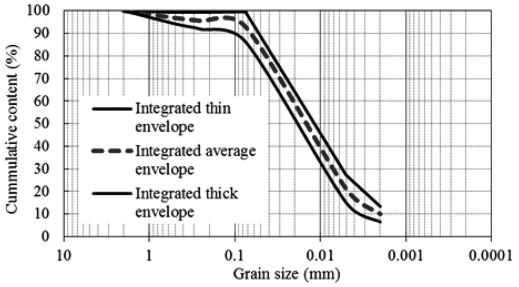


Figure 3. The grain composition of Ili loess.

According to the triaxial consolidated-undrained shear tests, the average intensity indexes of total stress under saturation are c of 4.0 kPa and ϕ of 20.6°. The average intensity indexes of effective stress are c' of 13.9 kPa and ϕ' of 24.8°. The average intensity indexes of total stress of unsaturated consolidated-undrained test are c of 40.8 kPa and ϕ of 23.3°. The unsaturated Fredlund intensity parameters are $c' = 25.5$ kPa, $\phi_b = 12.4°$, and $\phi' = 23.0°$. The experimental results show that, despite the low density, the intensity of Ili loess is strong no matter under natural condition or saturated condition, especially the internal friction angle is high.

3 THE INDOOR COLLAPSIBILITY TEST OF ILI LOESS

3.1 *Variation of collapsible coefficient with depth*

Figure 5 shows the variation of collapsible coefficient with depth at different external pressures through batches of compression test (including both single and double line methods). Figure 5(a) and (b) indicate that, when the external pressure is small (p = 50 and 100 kPa) the collapsible coefficient at shallow layers is larger than deep layers. However, for large pressure conditions in Figure 5(c) and (d), one can notice that the collapsible coefficient is relatively large both at shallow and deep layers. The maximum coefficient reached 0.18 at p = 200 kPa, which implies that the Ili loess has strong collapsibility.

3.2 *Variation of collapsible coefficient with external pressure*

The water film transfer method is adopted to obtain different samples with different water content (starting from natural state). Then the samples are used for collapsibility test to determine the collapsible coefficient. In this way, the influence of water content to the collapsibility of the undisturbed loess is obtained. The results are shown in Figure 6. The relationship between collapsible coefficient and the external pressure appears to be hump shape ("increasing-peak-decreasing" pattern). A later peak of collapsible

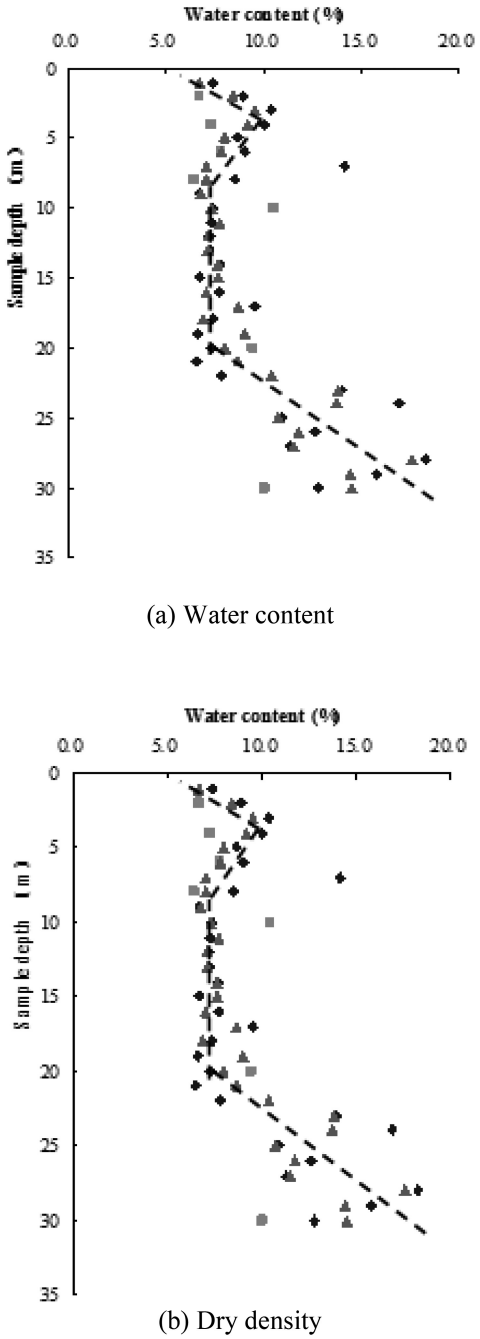


Figure 4. The distribution of water content and dry density at different depths.

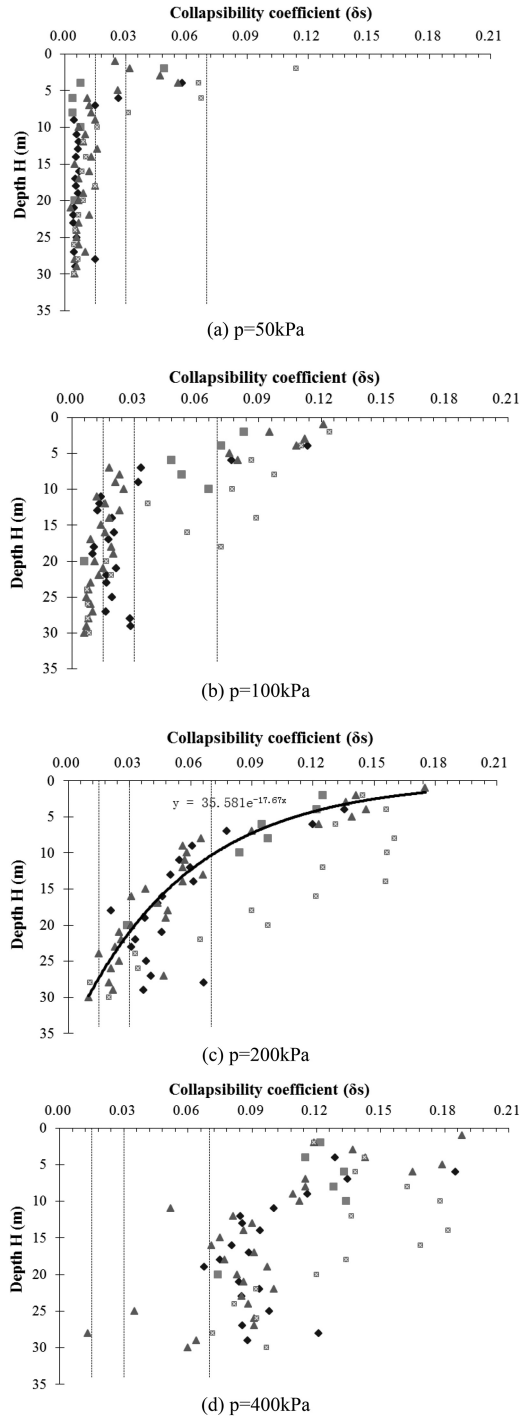


Figure 5. The variation of collapsible coefficient with depth at different pressures.

coefficient is observed for the drier samples. On the contrary, wetter samples have an earlier peak. However, for each pressure condition, there always is peak and it's not constant increasing with the external pressure. The reason is the relationship between the collapse deformation, compressive deformation and total deformation. The total deformation is the sum of the collapse deformation and the compressive deformation. It always increases as the increment of pressure. The collapse deformation accounts for larger proportion at low pressure condition. Therefore it has a

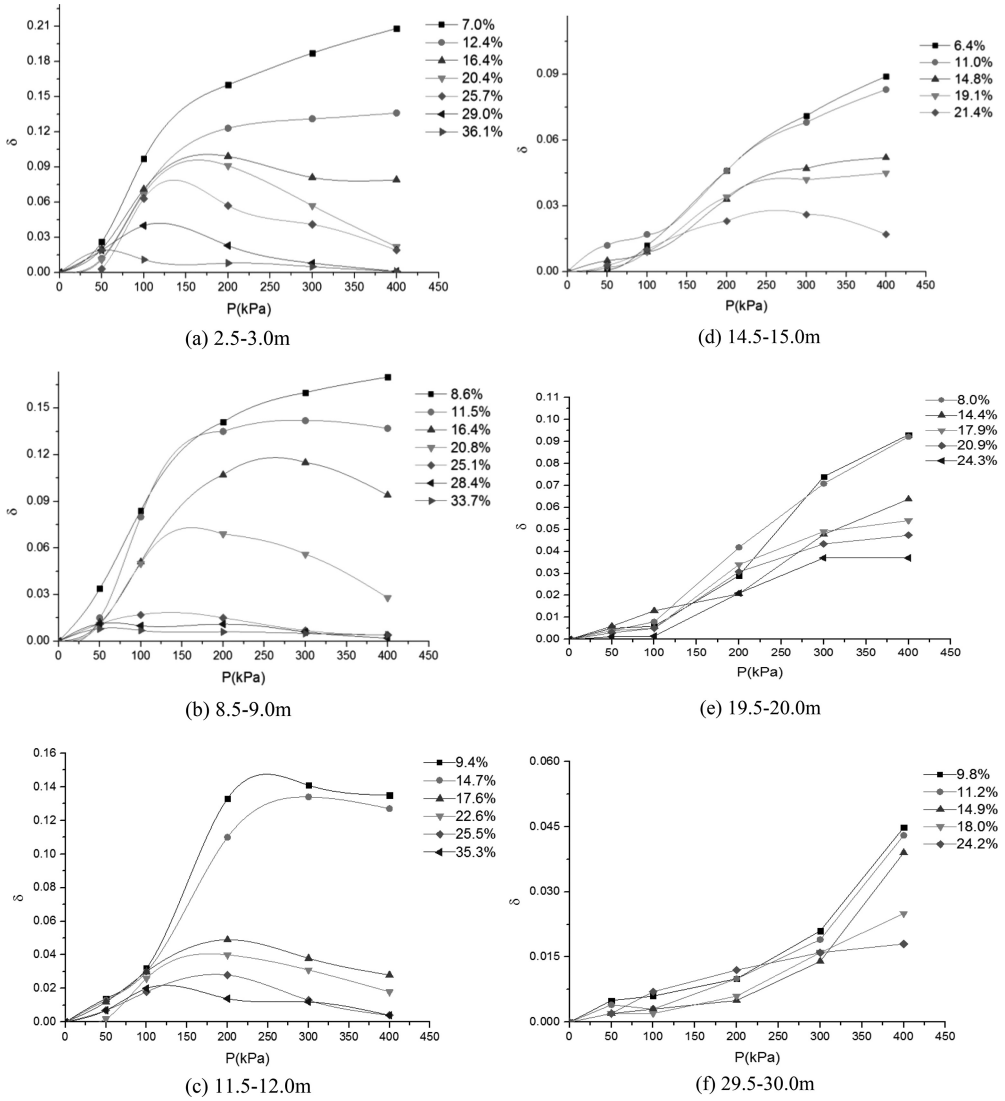


Figure 6. Variation of collapsible coefficient with external pressure at different water content.

same trend with pressure. However, when the pressure exceeds the peak value and continuously increases, although the total deformation is still increasing, the compressive deformation gradually taking the primary proportion which makes the collapse deformation reduced.

3.3 *Variation of collapsible coefficient with water content*

Figure 7 shows the variation of collapsible coefficient with water content. It can be seen that, despite the change of external pressure, collapsible coefficient is always reducing as the increasing of water content. In the meanwhile, the reducing gradient is small at low pressures and large at high pressures.

4 FIELD IMMERSION TEST OF ILI LOESS

The field immersion test is the most intuitive and effective way of studying the collapse of loess foundation. In this research, large field immersion tests were conducted to investigate the applicability of pre-immersing method on loess foundation. The collapse deformation was also measured. The tested immersing pit is a circular with the diameter of 30 m. There is a protective layer of sand and gravel on top (0.1 m). 20 m deep injection ϕ130 holes in 2/3 area are constructed to accelerate the immersion of water. The water is irrigated from 1 km away to the test field by channels. The construction of water storage forebay, pumping stations, water pipelines, high level pool and water gate etc. supplies the water into the test field. There are

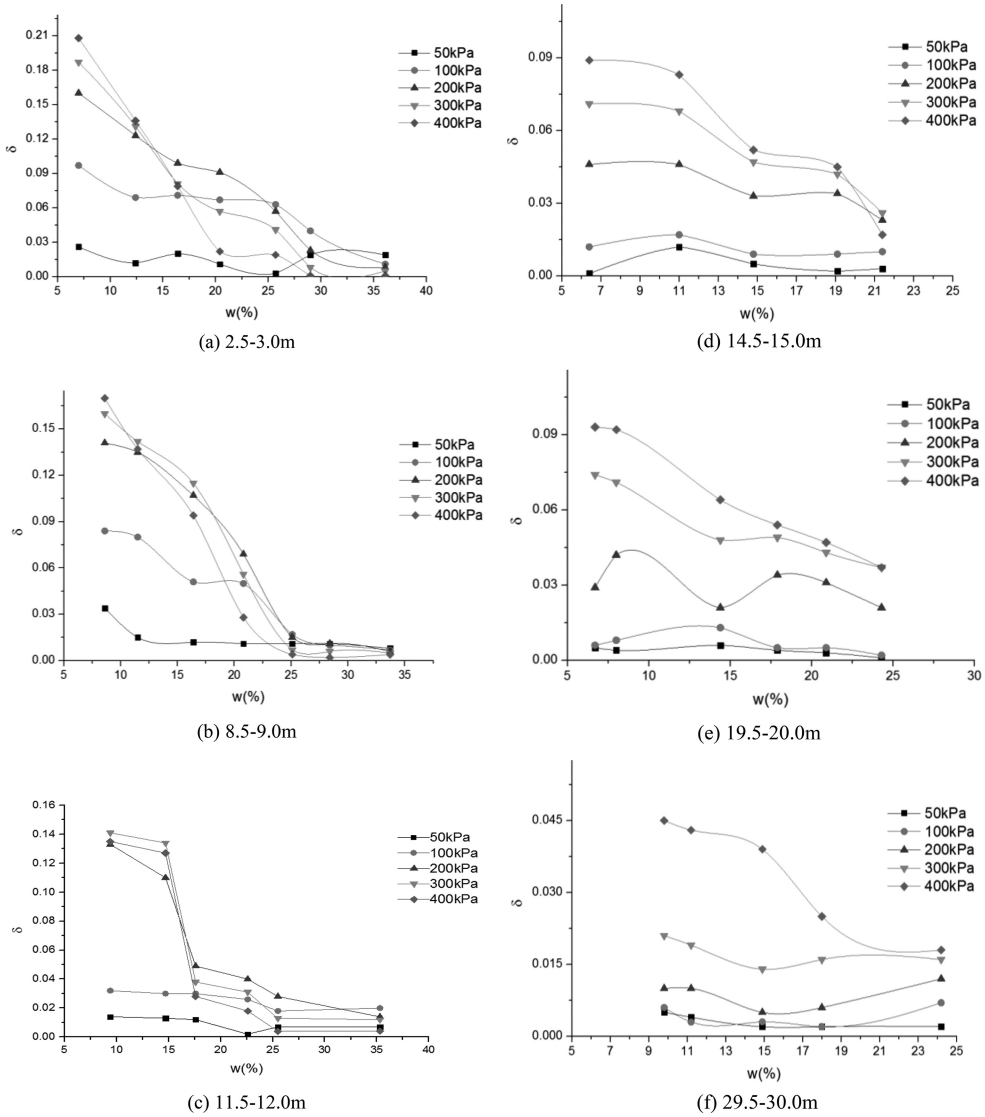


Figure 7. Variation of collapsible coefficient with water content at different pressures.

four types of observation points: surface deformation, soil moisture, deep subsidence and layered settlement. They are used to monitor the surface deformation, layered settlement and water moisture changes during the immersing process. Surface deformation observation points are distributed in 30° intervals and have a total number of 35. There are five different deep subsidence observation points and seven layered settlement observation points. Both strong magnetic ring and ordinary magnetic ring at different depths are used for circular magnetic observation points. It's 14 and 45 in total for strong and ordinary magnetic rings. Four exploratory wells are distributed for soil moisture observation at a distance of 12.5m and 14m to the centre of the circle. 32 TDR-3 soil moisture sensors are buried at different depths. The basic information for immersion test is shown in Figure 8.

The start date of immersion test is 16th August 2013 and the test ended on 10th April 2014 with a total of 190 days. During the early injection, water was flowing into the holes, causing partial collapse nearby. After 2 hours, two injection holes were collapsed at the orifices. 7 hours of injection caused 1/3 of the whole area collapse near the injection area.

The maximum settlement already exceeded 1m. When the content of injected water reached 2000 m^3, the collapse area reached 60% of the whole area. There were mainly two settlements happened, with a maximum diameter of 8 m and maximum depth of 2 m. In the meantime, test pit and its border appeared circular



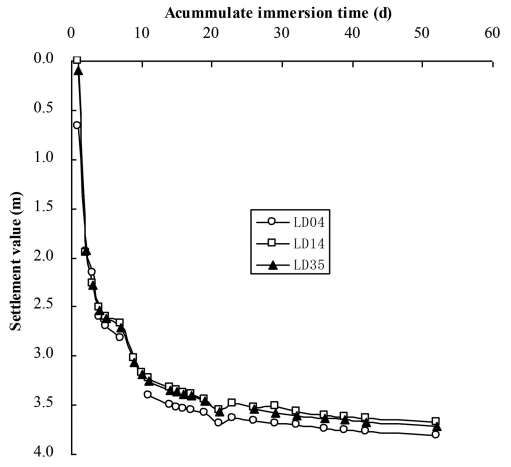
Figure 8. The basic information for immersion test.



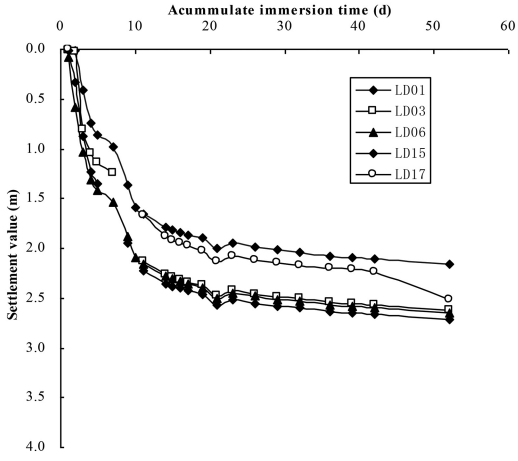
Figure 9. The pit after stopping the injection.

cracks with unequal spacing. When the injection water reached around 2900 m^3, the two settlements continuously expanded and the collapse area was nearly 80% of the pit. The collapse almost developed to the border of the pit. The cracks in the pit appeared as ladder shape settlements and were constantly staggered and broke through. The largest settlement then reached nearly 3 m. The pit kept constantly collapse afterwards. The continuous development of circular cracks caused serious dislocation with a maximum value of 1 m. The maximum crack width reached 0.6 m. The pot-like bottom of the pit after settlement was formed. The surface became a compacted layer due to the precipitation and accumulation of soluble salts. Figure 9 shows the pit after stopping the injection. From the deformed morphology point of view, the soil of the test region is very sensitive to water with severe deformation and large collapse. This indicates that the loess has a large collapsibility under self-weight and has very poor ability of anti-erosion and disintegration.

There are two clear settlement areas happened in the pit after the immersion of water. The first one has a large deformation and locates near the injection holes. The second one has a slightly smaller settlement. Figure 10 shows the variation of maximum settlement value with time at the two places. It can be seen that



(a) The first settlement area



(b) The second settlement area

Figure 10. The variation of maximum settlement value with time at the two settlement areas.

both of the settlements happened quickly and largely at an early stage. The first area has a maximum settlement of 3.69 m only after 21 days of water injection, and the second area has a maximum value of 2.56 m. However, the settlement in the first area was not only caused by its self-weight, but also the contributions from erosion and disintegration near the injection holes. Thus, the self-weight collapsible amount from the experiment is in the range of 2.56–3.69 m.

Table 2 calculates the self-weight collapsible amount through the method in the code [1], in which the collapsibility coefficient was obtained by indoor experiments. The self-weight collapsible amount was calculated with three different regional indexes (0.5, 1.0 and 1.5 respectively). From the table, the conclusion agrees well that this test area is IV self-weight collapsible ground. At the same time, it is incorrect that Ili loess belongs to “other regions” in the code

Table 2. Summary of self-weight collapsible amount.

No.	Method	Self-weight collapsible amount (mm)	Total collapsible amount (mm)	Collapsibility level
1	Code with $\beta 0 = 0.5$	1070.3	2219.3	IV
2	Code with $\beta 0 = 1.0$	2140.5	2711.3	IV
3	Code with $\beta 0 = 1.5$	3210.8	3203.3	IV
4	The field immersion test value	2560–3690		IV

with the regional index of 0.5. More accurate value should be 1.0 to 1.5.

5 CONCLUSIONS

(1) The Ili loess in Xinjiang has a large thickness, uniform texture and no existence of ancient soil layer. The soil does not change significantly with depth. Without the influence of hot and humid climate, its salinity, particularly calcium carbonate, has not been leached by rainwater. The characteristics of point contact, aerial structure form and few cementations, lead to a highly unstable structure. The density, water content and saturation are all low. But the content of soluble minerals is high. The Ili loess belongs to normal-consolidated and under-compaction soil. The Ili loess could be considered as typical eolian loess. Thus deep and throughout research on it could potentially unveil the deposition history of loess.

(2) The collapsibility of Ili loess is strong with a maximum coefficient value of 0.18 (P = 200 kPa). The hump shape with a peak value is found for the relationship between collapsible coefficient and the pressure. The pressure is bigger corresponding to the peak coefficient of the drier samples. On the contrary, the pressure is smaller when the peak coefficient is reached for wetter samples. Therefore, it is efficient to reduce the collapse by adjusting pressure value to avoid the corresponding one at peak coefficient. The collapsible coefficient is related to four main factors: external pressure, initial water content, dry density and initial collapse pressure. It reduces as the increase of initial water content and becomes zero when the saturation is 80% or above. The collapse reduces greatly (even stops) when the dry density reaches certain value. Thus another effective way to reduce the collapse is increasing the dry density. The collapse deformation does not vary according to first apply load or immerse in water. Thus the collapsibility is irrelevant to the sequence of applying load and immerse in water. The collapse of loess is an irreversible process. After collapse in water (under certain pressure), there is no further collapse by dehumidifying and humidifying process (assume the pressure is constant). The collapse value will only increase if the pressure is increased.

(3) The field immersion test shows that both of the settlements happened quickly and largely at an early stage, with a maximum value of 3.69m. The comparison of field test results with calculations from the code shows that the correct regional index should be 1.0–1.5.

(4) It is suggested that the Ili loess in the IV terrace of the Tekes River in Ili valley in Xinjiang should be studied separately as typical eolian loess and named as “Ili loess”.

ACKNOWLEDGEMENTS

The research is funded by NSFC (No. 51279171).

REFERENCES

Aijun Zhang & Yichuan Xing. The collapsible characteristics of unsaturated loess during humidifying process. Research and Engineering of collapsible loess, Yusheng Luo, Guolie Wang. Beijing: China Architecture and Building Press, 2001: 123–126.

Baojian Liu. Test and Theoretical Analysis about the Process of Settlement of Highway Subgrade. Xi’an: Xi’an University of Technology, 2005.

Baojian Liu, Yongli Xie & Youcheng Yu. In-situ testing study on infiltration in unsaturated loess. Chinese Journal of Rock Mechanics and Engineering, 2014, 23 (24): 4156–4160.

Dingyi Xie. Exploration of some new tendencies in research of loess soil mechanics. Chinese Journal of Geotechnical Engineering, 2001, 23 (1): 3–13.

GB 50025-2004. Code for building construction in collapsible loess zone. 2004. (GB50025-2004).

Guolie Wang. Engineering treatment regulations of thick collapsible loess ground in Gansu Province. Lanzhou: Gansu Province Institute of Civil Engineering and Architecture, Technical and Professional Commission, 2008.

Hongjin Qian, Yusheng Luo et al. Collapsible loess foundation. Beijing: China Architecture and Building Press, 1985.

Minzhen Liu. Collapsible loess of intermittent water immersion test. Chinese Journal of Geotechnical Engineering, 1985, 7 (1): 47–54.

Shengjun Shao, Jun Li, Guoliang Li, Guohua Deng, Jiwen Zhang, Yang Liu & Shuai Shao. Evaluation method for self-weight collapsible deformation of large thickness loess foundation. Chinese Journal of Geotechnical Engineering, 2015, 37 (6): 965–978.

Sumin Zhang & Jianguo Zheng. Collapsible loess (Q3) of humidification deformation characteristics. Chinese Journal of Geotechnical Engineering, 1990, 12 (4): 12–31.

Xuefeng Huang. Zhenghan Chen, Shuang Ha, Saiguang Xue, Shuxun Sun, Yiming Xu, Xueju Jin & Yuanqing Zhu. Large area field immersion tests on characteristics of deformation of self weight collapse loess under

overburden pressure. Chinese Journal of Geotechnical Engineering, 2006, 28 (3): 382–389.
Zhihua Yao, Xuefeng Huang, Zhenghan Chen & Jianhua Zhang. Comprehensive soaking tests on self-weight collapse loess with heavy section in Lanzhou region. Chinese Journal of Geotechnical Engineering, 2012, 34 (1): 65–74.
Zhihua Yao, Xuefeng Huang, Zhenghan Chen, Xiangwei Fang, Qiangqiang Miao & Jiangshui Zhang. New recognition of collapsibility evaluation and remnant collapse of loess. Rock and Soil Mechanics, 2014, 35 (4): 998–1006.
Zhujiang Shen & Zaiqiang Hu. Binary medium model for loess. Journal of Hydraulic Engineering, 2003, 25 (7): 1–6.
Zudian Liu. Loess Mechanics and Engineering. Shaanxi Science and Technology Press, 1997.

Unsaturated soil behaviour

Microstructure

This page intentionally left blank

Unsaturated Soil Mechanics—from Theory to Practice – Chen et al. (Eds)
© 2016 Taylor & Francis Group, London, ISBN 978-1-138-02921-7

Analysis on microstructure and water retention properties of lime-treated soil

Y.J. Wang, Y.J. Cui, A.M. Tang & C.S. Tang
Ecole des Ponts ParisTech, U.R. Navier/CERMES, Cité Descartes, Champs–sur–Marne, Marne–la–Vallée, Cedex 2, France

N. Benahmed
IRSTEA Aix en Provence, Unité de Recherche Ouvrages Hydrauliques, Aix en Provence Cedex 5, France

ABSTRACT: Lime treatment can improve the workability and mechanical behaviour of soil. It has been proved as an effective soil improvement technique and widely applied in geo-engineering fields. In this paper, the effect of lime treatment on compacted soil microstructure and water retention ability was investigated. Mercury Intrusion Porosimetry (MIP) tests were carried out on both untreated and lime-treated silty soil compacted dry of optimum and cured for different days. Both the untreated and treated samples present typical bimodal pore size distribution characteristics. The addition of lime gave rise to changes in microstructure, which significantly depended on curing time. Water retention curves of lime-treated soil were also determined by WP4 dewpoint PotentiaMeter. The obtained data illustrated that water retention capacity of lime-treated soil increased slightly with increasing curing time. Moreover, a good agreement was observed with the results obtained through the MIP data.

1 INTRODUCTION

Lime treatment is an effective soil improvement technique which induces modifications of geotechnical properties and mechanical behaviors of soil, such as grain size distribution, plasticity, shear strength, shear modulus and compressive strength (Bell 1996; Russo 2005; Consoli et al. 2009; Tang et al. 2011). The addition of lime into soil immediately induces the cation exchange, followed by the flocculation process. Pozzolanic reactions which significantly contribute to the strength gain by bonding the soil particles together are time dependent, and could last several years or even longer (Little 1999).

The efficiency of lime treatment is influenced by soil aggregates size, lime content, mixing method and curing conditions. Different behaviours of lime-treated soil in the field conditions with respect to that in the laboratory conditions were reported. Generally, the loss of efficiency of lime treatment in the field was attributed to the climate changes and the aggregates size effect (Bozbey & Guler 2006; Kavak & Akyarh 2007; Cuisinier & Deneele 2008; Tang et al. 2011). Tang et al. (2011) showed that the shear modulus of lime-treated soil decreased with the increasing maximum aggregates size, and the sample prepared by larger aggregates were quite sensitive to the wetting/drying cycles simulating the climate changes.

Microstructure changes of soil resulted from the addition of lime are analyzed in several studies, using the Mercury Intrusion Porosimetry (MIP). Cuisinier et al. (2011) found that a new small pores class was formed in the compacted soil after lime treatment. Metelkova et al. (2012) analyzed the effect of lime percentage on the pore space evaluations of a lime-treated compacted loess, noticing that the macroporosity increased with lime percentage due to flocculation, and 2% of lime was sufficient for pozzolanic reactions. Russo & Modoni (2013) stated that the time dependent microstructure of lime-treated silt was largely related to the initial moulding water content.

As for the unsaturated soil, water retention property is strongly related to its hydro-mechanical behaviours. It was reported that lime treatment could modify the water retention capacity of soil due to the series of reactions between soil particles and lime (Russo 2005; Khattab & Al-Taie 2006; Tedesco 2007). However, the curing time effect on the water retention ability of lime-treated soil can be easily interfered by the test duration.

In this study, microstructure investigation of lime-treated soil based on MIP tests was performed in consideration of large aggregates size ($D_{max} = 5$ mm). Water retention capacity of treated soil was determined by both MIP prediction model and WP4 suction measurement with shorter test duration.

2 MATERIALS AND METHODS

A natural soil from Héricourt, France, is chosen in this experimental investigation. It contains a silt/clay fraction ($\leq$0.08 mm) of about 57%. The geotechnical properties of this soil are presented in Table 1.

Table 1. Geotechnical properties of the natural soil.

	G_s	w_L (%)	w_P (%)	I_P(%)
Natural soil	2.7	51	28	23

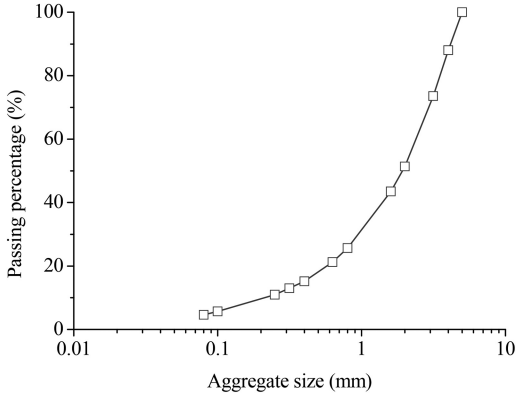


Figure 1. Aggregate size distribution of natural soil with $D_{\max} = 5$ mm.

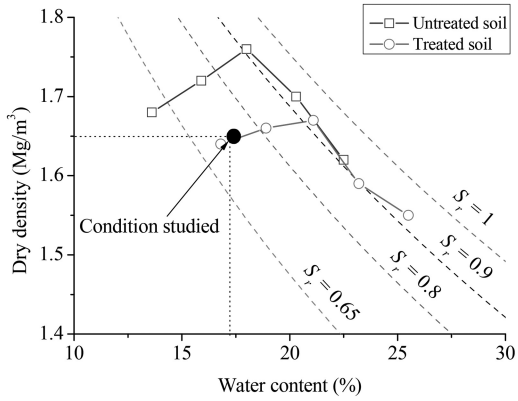


Figure 2. Normal proctor curves of untreated soil and 2% lime-treated soil.

The soil was first air-dried, ground and then passed through the target sieve ($D_{max} = 5$ mm). Its aggregate size distribution after sieving is shown in Figure 1.

Quicklime was used. Its CaO content is around 97.3%. 100% of this quicklime could pass through the 2 mm sieve and about 82.7% passed through the 80 μm sieve.

The natural soil after sieving ($D_{\max} = 5$ mm) was first mixed with 2% lime (calculated by the dry weight of dry soil), then humidified to a target water content. After thoroughly mixing, 1 hour of mellowing period was allowed before compaction. According to the Normal Proctor Curve of 2% lime-treated soil given in Figure 2, the soil state considered is on the dry side of optimum (dry density $\rho_d = 1.65$ Mg/m^3 and corresponding water content $w = 17\%$).

The compacted lime-treated samples were well preserved and cured for different days ($t = 1$, 7 and 28 days). Then, each sample was freeze-dried in liquid nitrogen (Delage & Pellerin 1984) before it was subjected to Mercury Intrusion Porosimetry (MIP) test. Autopore IV 9500 mercury intrusion porosimetry was used to analyze the microstructure of lime-treated soil. Both low-pressure and high-pressure systems (around 3.5 kPa to 230 MPa) were applied, corresponding to the entrance pore diameter ranging from 355 μm to 0.006 μm. The mercury intrusion process is quite similar with the drying path of the water retention curve (Prapaharan et al. 1985; Romero et al. 1999). Romero et al. (1999) proposed a method to predict the water retention curve by a MIP model considering the residual water content which is related to adsorbed water.

Samples used for the tests to determine the water retention curve were cut into several small pieces at curing time of $t = 7$ and 28 days in order to shorten the total test duration which might interfere with the curing time effect. Each small sample was air-dried at a different time interval. Then, it was well packed and stored for 12 h to ensure a good water homogenization before suction measurement. Suction was determined by WP4 dewpoint PotentiaMeter. The latter can measure the suction rapidly, employing a chilled mirror dew-point method. Immediately after the suction measurement, sample was oven-dried to determine the corresponding water content.

3 RESULTS

As shown in Figure 3, the pore size distribution curves of both untreated soil and lime-treated soil had a bi-modal characteristic, with a population of larger inter-aggregate pores (macro-pores) and a population of smaller intra-aggregate pores (micro-pores). For the untreated soil, the modal size of inter-aggregate pores was about 72.75 μm and that of intra-aggregate pores was about 0.39 μm. The addition of lime shifted the modal size of both inter-aggregate and intra-aggregate pores into smaller values (29.87 μm and 0.83 μm, respectively) at a short curing time of $t = 1$ day. With increasing curing time, these two values continuously decreased. Specifically, the peak value of inter-aggregate pores was 26.73 μm at curing time of $t = 7$ days, while it decreased to 21.40 μm at curing time of $t = 28$ days. More obviously, the peak value of intra-aggregate pores decreased to 0.18 μm ($t = 7$ days) and 0.12 μm ($t = 28$ days), respectively. At curing times of $t = 7$ and 28 days, a decrease of the frequency of the relatively larger inter-aggregate pores (d ranged from 35 to 330 μm) with an increase of the frequency of the relatively smaller pores (d ranged from 6.5 to 23 μm) was detected for the lime-treated soil. Similar phenomenon was observed in the population of intra-aggregate pores: at curing time of $t = 28$ days, a dramatic increase of the frequency of the smaller intra-aggregate pores (d ranged from 0.01

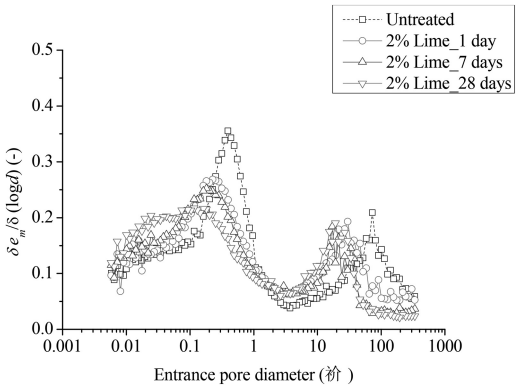


Figure 3. Pore size distribution curves of untreated soil and 2% lime-treated soil.

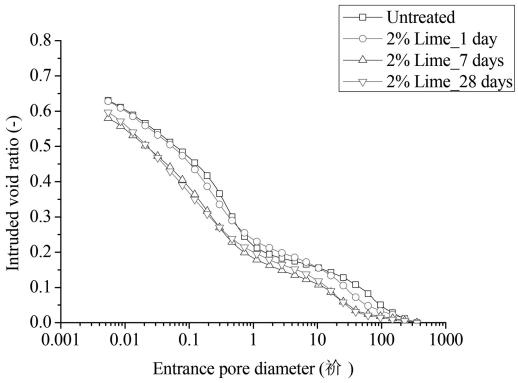


Figure 4. Cumulative intruded void ratio curves of untreated soil and 2% lime-treated soil.

to 0.1 μm) and a relevant decrease of the frequency of the larger intra-aggregate pores were detected.

According to the cumulative intruded void ratio curves as presented in Figure 4, the addition of lime immediately caused a slight decrease in the porosity of the treated soil, compared with that of untreated soil. The intrusion decreased gradually during the longer curing time.

Water retention curves of both untreated soil and treated soil deduced from MIP data were presented in Figure 5 in comparison with the results obtained by WP4 tests. Generally, it was observed a good agreement between the predicted results with the test data. Compared with the water retention curve of untreated soil, lime-treated soil had a relatively higher water retention ability, which was revealed by both the two different methods. Afterwards, its water retention ability was improved gradually with the increase of curing time. The difference between the two results was also diminished in a longer curing term ($t = 28$ days).

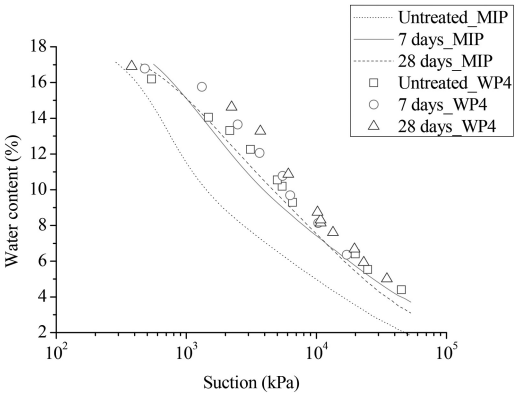


Figure 5. Water retention curves of untreated soil and 2% lime-treated soil.

4 DISCUSSION

The pore size distribution of untreated soil compacted dry of optimum was detected as a bi-modal characteristic with both inter-aggregate pores and intra-aggregate pores. The addition of lime did not modify this curve shape but decrease the peak values of both populations of pores. At the curing time of $t = 1$ day, an immediate decrease of peak values due to the lime and the corresponding reaction products filling in both the inter-aggregate pores and intra-aggregate pores was observed. At curing time of $t = 7$ days, these two classes of pores became smaller, which is attributed to more cementitious compounds. For a longer curing period ($t = 28$ days), higher frequency of smaller intra-aggregate pores was detected while that of inter-aggregate pores was less modified. For samples compacted dry of optimum, intra-aggregate pores were presumably saturated, and inter-aggregate pores were filled with air, leaving some discontinuous water phase inside (Delage et al. 1996; Alonso et al. 1987). Sufficient water in the smaller pores kept the pozzolanic reactions continuing while the reactions in the inter-aggregate pores were suspended. This result was consistent with the results of Russo and Modoni (2013).

The cumulative intruded curves in Figure 4 illustrated that porosity of lime-treated soil decreased slightly during curing time. It was mainly due to the cementitious compounds filling the pores. Furthermore, these products could also form bonds between particles, with trapping some larger pores.

Both MIP predicted results and WP4 tested data denoted that the water retention capacity of soil was increased by lime-treatment. Similar phenomenon was observed by other studies (Russo 2005; Tedesco 2007; Cecconi & Russo 2008). The increase of water retention capacity induced by lime addition was related to the decreased sizes of both inter-aggregate pores and intra-aggregate pores. At the longer curing time, the cementitious compounds could also reduce the interconnection between pores. More constricted pores

would result in an improvement of water retention capacity of treated soil.

5 CONCLUSION

MIP test and water retention curve measurement on both lime-treated soil and untreated soil compacted dry of optimum were performed. The effect of curing time on microstructure and water retention property of soil was analyzed. The following conclusions can be drawn:

- Lime treatment has modified the pore size distribution of soil immediately. With increasing curing time, the modal sizes of both inter-aggregate pores and intra-aggregate pores were shifted to the smaller values. At a relative longer curing time, high frequency of smaller intra-aggregate pores was detected.
- The porosity of lime-treated soil decreased during curing. It can be attributed to the cementitious compounds filling in the pores, which reduced the interconnectivity between pores.
- The good agreement between the predicted suction results given by MIP model and the experimental data obtained by WP4 shows that MIP is an effective technique to evaluate soil water retention capacity with short test duration.

ACKNOWLEDGEMENTS

The authors wish to acknowledge the support of the European Commission via the Marie Curie IRSES project GREAT – Geotechnical and geological Responses to climate change: Exchanging Approaches and Technologies on a world-wide scale (FP7-PEOPLE-2013-IRSES- 612665). The financial support of the China Scholarship Council (CSC) is also greatly acknowledged.

REFERENCES

Alonso E.E., Gens A., Hight D.W., 1987. Special problem soils-General report, IX ECSMFE, Dublin, (3): 1087–1146.

Bell, F.G., 1996. Lime stabilization of clay minerals and soils, Engineering Geology, 42(4): 223–237.

Bozbey, I. & Guler, E., 2006. Laboratory and field testing for utilization of an excavated soil as landfill liner material, Waste Management, 2006, 26(11): 1277–1286.

Cecconi, M. & Russo, G., 2008. Prediction of soil-water retention properties of a lime stabilised compacted silt, Unsaturated Soils: Advance in Geo-Engineering-Toll et al. (eds), Taylor & Francis Group, London, ISBN 978-0-415-47692-8: 271–276.

Consoli, N.C., Lopes, L.S. & Heineck, K.S., 2009. Key parameters for the strength control of lime stabilized soils, Journal of materials in Civil Engineering, 21(5): 210–216.

Cuisinier, O., Auriol, J.C., Le Borgne, T. & Deneele, D., 2011. Microstructure and hydraulic conductivity of a compacted lime-treated soil, Engineering Geology, 123(3): 187–193.

Cuisinier, O. & Deneele, D., 2008. impact of cyclic wetting and drying on the swelling properties of a lime-treated expansive clay, Jourées Nationales de Géotechnique et de Géologie de l'Ingénieur JNGG'08, Nantes, 18–20.

Delage, P. & Pellerin, F.M., 1984. Influence de la lyophilisation sur la structure d'une argile sensible du Québec, Clay Minerals, 19(2): 151–160.

Delage, P., Audiguier, M., Cui, Y. J. & Howat, M., 1996. Microstructure of a compacted silt, Canadian Geotechnical Journal, 33(1): 150–158.

Kavak, A. & Akyarh, A., 2007. A field application for lime stabilization, Environmental Geology, 51(6): 987–997.

Khattab, S.A.A. & Al-Taie, L.K.I., 2006. Soil-water characteristic curves (SWCC) for lime treated expansive soil from Mosul City, In Unsaturated Soils, 1671–1682.

Little, D.N., 1999. Evaluation of structural properties of lime stabilized soils and aggregates, Vol 1: Summary of Findings Prepared for the National Lime Association.

Metelkova, Z., Bohac, J., Prikryl, R. & Sedlarova, I., 2012. Maturation of loess treated with variable lime admixture: Pore space textural evolution and related phase changes, Applied Clay Science, 61:37–43.

Prapaharan, S., Altschaeffl, A. G. & Dempsey, B. J., 1985. Moisture curve of compacted clay: mercury intrusion method, Journal of Geotechnical Engineering, 111(9): 1139–1143.

Romero, E., Gens, A. & Lloret, A., 1999. Water permeability, water retention and microstructure of unsaturated compacted Boom clay, Engineering Geology, 54(1): 117–127.

Russo, G., 2005. Water retention curves of lime stabilised soil, Advanced Experimental Unsaturated Soil Mechanics, Taylor & Francis, London, 391–396.

Russo, G. & Modoni, G., 2013. Fabric changes induced by lime addition on a compacted alluvial soil, Géotechnique Letters, 3: 93–97.

Tang, A., Vu, M. & Cui, Y., 2011. Effects of the maximum grain size and cyclic wetting/drying on the stiffness of a lime-treated clayey soil, Géotechnique, 61: 421–429.

Tedesco, D.V., 2007. Hydro-mechanical behaviour of lime-stabilised soils, PhD Thesis, University of Cassino, Italy.

Unsaturated Soil Mechanics—from Theory to Practice – Chen et al. (Eds)
© 2016 Taylor & Francis Group, London, ISBN 978-1-138-02921-7

The microstructure information of natural loess in different areas, China

H.J. Hu, K. Zhou, Y.S. Luo & W.P. Zhao
College of Water Resources and Architectural Engineering, Northwest A&F University, Yangling, Shaanxi, China

Q. Hu & Z.Y. Zhang
College of Information Engineering, Northwest A&F University, Yangling, Shaanxi, China

ABSTRACT: The scan electron microscope photos of natural loess in three cities were analyzed to study the difference of microstructure. The objects of the particles or pores were obtained by manual drawing and compiled program and the size and direction of each object were obtained by image analysis software. The quantitative parameters reflecting size, shape, and directional arrangement of particles or pores were calculated by the above parameters. Results showed that the median diameter of particle in Xi'an and that of pores in Lanzhou is the smallest, and the shape of particles in Lanzhou and that of pores in Yuncheng is the most similar to strip. The direction of particles and pores arrange uniformly in space. The median pore diameters obtained by manual drawing and compiled program are near to each other. This lay a basis for using compiled program to obtain objects, which can overcome the time-consuming of manual drawing.

1 INTRODUCTION

Natural loess is an unsaturated and structured soil. The macro mechanical properties of loess such as the soil water retention curve, the collapsibility, the strength etc. are closely related to its microstructure. Liu (1963) published monograph about structure and material composition of Chinese loess, the purpose of which is to provide reference for the study on the engineering properties of loess. Wang & Lin (1990) summed up many years of work, published monograph about micro structure and physical mechanical properties of Loess China, which provided the reference for the prediction and evaluation of loess engineering properties of using loess microstructure. The two books pay great attention to the scale and shape of particles or pores, and the distribution of cementing materials $CaCO_3$, but the statistics quantitative parameters were not given. The pore size distribution was first given by Lei (1980), who used mercury intrusion porosimetry. Hu et al. (1995) used a quantitative description method to analysis the Scan Electron Microscope (SEM) photos of clay and gave the quantitative description of the micro structure of clay. Wang (2010) applied vacuum on the natural loess and injected resin, then polished, obtained section, and applied SEM, obtained clear pictures of micro structure, which overcomes the drawback that the obtained microstructure is not at the same level or depth. According to the SEM photos obtained by Wang (2010), quantitative analysis of particles and pores are given in this paper.

2 THE EXTRACTION METHOD OF MICROSTRUCTURE INFORMATION

According to scan electron microscope photos of loesses from Lanzhou, Xi'an and Yuncheng obtained by Wang M (2010), the boundary of grain and pore are drawn by AutoCAD and each object is separated in order that the close objects are not judged as one object, then the objects are filled with white and imported to the image processing software (Image-pro-plus IPP6.0). The size and shape quantitative parameters of particle and pore, such as the length of the major axis, minor axis length, area and the direction of the long axis angle, are obtained. According to these parameters, the average diameter, shape factor, abundance, circumscribed circle roundness, directional probability entropy are calculated in Excel.

The median diameter D_{50} of particles or pores is calculated according to equation (1).

$$D_{50} = D_m + \frac{0.5\sum_{i=1}^{n} D_i^3 - \sum_{j=1}^{m} D_j^3}{\sum_{k=1}^{m+1} D_k^3 - \sum_{j=1}^{m} D_j^3}(D_{m+1} - D_m) \quad (1)$$

Where $D_i = (L_{\mathrm{li}} + L_{\mathrm{si}})/2$, L_{li} is the length of the major axis of the particle and L_{si} is the length of the minor axial of the particle. The volume of particles or pores larger than D_{m+1} exceeds the 50% of total volume of particles or pores and the volume of particles or pores

larger than D_m is less than the 50% of total volume of particles or pores.

The shape coefficient K is calculated according to equation (2).

$$K = (\sum_{i=1}^{n} K_i)/n \tag{2}$$

Where $K_i = 2L_{si}/(L_{li} + L_{si})$.

The shape factor C is calculated according to equation (3).

$$C = (\sum_{i=1}^{n} C_i)/n \tag{3}$$

Where $C_i = L_{\mathrm{si}}/L_{\mathrm{li}}$

The circumcircle roundness R is calculated according to equation (4).

$$R = (\sum_{i=1}^{n} R_i)/n \tag{4}$$

The orientation probability entropy is calculated according to equation (5). When the directional probability entropy is close to 1, it indicates the major axises of particles are arranged disorderly, namely nearly isotropic.

$$H_m = -\sum_{i=1}^{l} F_i(\alpha)\log_l F_i(\alpha) \tag{5}$$

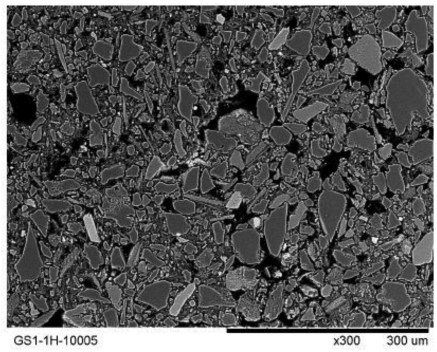
Where $F_i(\alpha) = m_i/M \times 100\%$, M is the total number of particles, mi is the number of particles in the i location, l is the total numbers of location for 360°.

The above parameters express the size, shape and arrangement of particle or pore. The mean diameter represents the size of particle or pore. The shape coefficient, abundance, circumscribed circle roundness and perimeter circularity indicate the circular characteristics of particles or pores. The long axis directional probability entropy reflects the arrangement of particles or pores.

3 MICROSTRUCTURE INFORMATION OF NATURAL LOESS FROM DIFFERENT AREAS

3.1 *Microstructure information of particles*

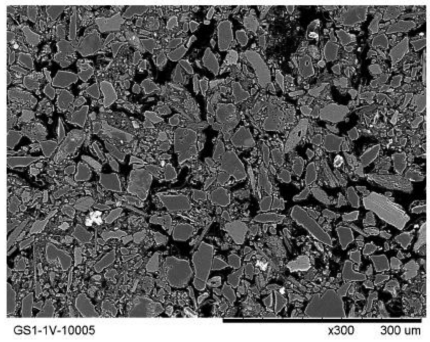
The horizontal and vertical SEM photos of Lanzhou loess with the depth of 2m and manual drawing of particles boundaries are shown in Figure 1. Widen the distance between particles, fill the color and import these AutoCAD photos into IPP software to obtain the parameter of each particle, and then obtain the average value. The quantitative parameters are obtained as shown in table 1. The median particle diameter of Lanzhou loess is the largest, Yuncheng loess is second, Xi'an is minimum. The particle shape of Yuncheng



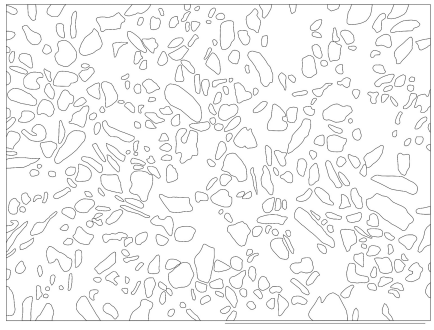
(a)The horizontal section photo of SEM



(b)The horizontal section photo of manual drawing



(c)The vertical section photo of SEM



(d)The vertical section photo of manual drawing

Figure 1. The scan electron microscope photos and manual drawing photos of Lanzhou loess particles.

Table 1. The comparison of particle miscroparameters of natural loess in different areas.

The region	The direction	D_{50} /um	K	C	R	Hm
Lan	Horizontal	19.92	0.733	0.599	0.656	0.985
zhou	Vertical	24.58	0.728	0.594	0.665	0.988
	Average	22.25	0.730	0.596	0.660	0.987
Xi'an	Horizontal	10.62	0.741	0.609	0.660	0.985
	Vertical	11.46	0.731	0.592	0.657	0.984
	Average	11.04	0.736	0.601	0.659	0.984
Yun	Horizontal	17.37	0.757	0.626	0.672	0.977
cheng	Vertical	20.83	0.753	0.621	0.669	0.992
	Average	19.10	0.755	0.624	0.671	0.985

loess is the most simiar to circular and that of Lanzhou loess is the least similar to circular, proving that the corners of Lanzhou loess particles are more obvious. About the orientation of particles, the difference of directional probability entropy among the three loesses is not large and all are close to 1, which indicates that the arrangement of particles is nearly isotropic.

3.2 *The microstructure information of pores*

The pore boundary is drawn by Autocad as shown in Figure 2. The distance of each pore is widened, then imported into IPP software and pore parameters are obtained. The obtained average quantitative parameters are shown in table 2. The median pore diameter of Lanzhou loess is smaller than the Xi'an. On the pore shape, the pores in Xi'an loess are more similar to the circular than the pores in Lanzhou loess. On the orientation of pores, the difference of directional probability entropy among the two loesses is not large and the values are close to 1, which indicates that the arrangement of pores is nearly isotropic.

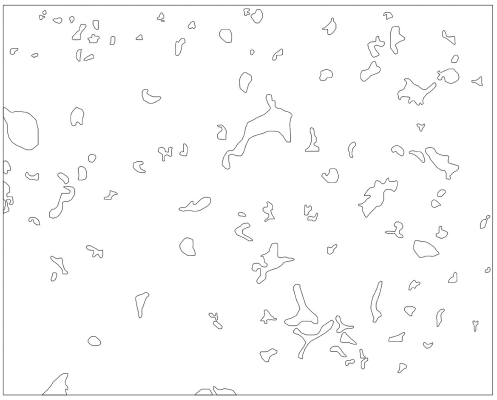
3.3 *The microstructure difference between particle and pore*

Comparing Tables 1 and 2, it can be obtained that the median particle diameter is near or smaller to the median pore diameter. The particles and pores in three regions arrange uniformly in space.

3.4 *The comparison of pore microstructures obtained by manual drawing and compiled program*

The pore structures obtained by the compiled program are shown in Figure 3. The obtained average quantitative parameters are shown in Table 3.

Comparing Table 2 with Table 3, it can be obtained that the results obtained by two methods are near to each other at the median pore diameter, which demonstrate that the reasonability of compiled program. The median pore diameter of Lanzhou loess is smallest



(a) The horizontal section



(b) The vertical section

Figure 2. The manual drawing photos of Lanzhou loess pores.

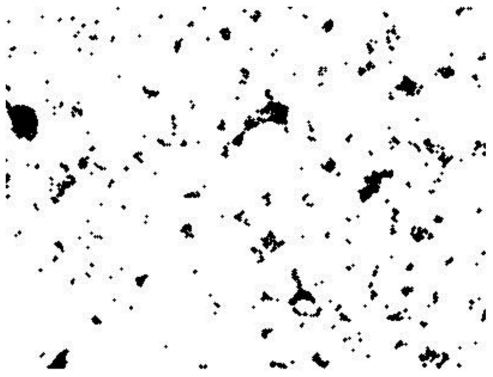
Table 2. The comparison of pore parameters of natural loess in different areas.

The region	The direction	D_{50} /um	K	C	R	Hm
Lan	Horizontal	38.58	0.718	0.579	0.597	0.963
zhou	Vertical	37.54	0.667	0.521	0.537	0.968
	Average	38.06	0.693	0.550	0.567	0.966
Xi'an	Horizontal	68.92	0.746	0.611	0.657	0.963
	Vertical	83.22	0.728	0.588	0.618	0.972
	Average	76.07	0.737	0.599	0.638	0.968

and the pore shape of Yuncheng loess is the most similar to the strip. At the arrangement, there are some differences. The authors think the results obtained by compiled program are more reasonable.

4 CONCLUSION

The scan electron microscope photos of Lanzhou loess, Xi'an loess and Yuncheng loess are analyzed



(a) The horizontal section



(b) The vertical section

Figure 3. The pore structure of Lanzhou loess obtained by the compiled program.

Table 3. The pore parameters of natural loess obtained by the complied program.

The region	The direction	D_{50} /um	*K*	*C*	*R*	*Hm*
Lan	Horizontal	31.96	0.835	0.745	0.755	0.825
zhou	Vertical	30.85	0.801	0.703	0.704	0.842
	Average	31.41	0.818	0.724	0.730	0.834
Xi'an	Horizontal	76.22	0.828	0.736	0.738	0.796
	Vertical	80.00	0.815	0.719	0.713	0.844
	Average	78.11	0.822	0.728	0.726	0.820
Yun	Horizontal	60.34	0.781	0.67	0.667	0.894
cheng	Vertical	47.85	0.776	0.665	0.656	0.977
	Average	54.10	0.779	0.668	0.662	0.936

and the quantitative microstructure parameters of loess particle and pore are obtained. The main conclusions are shown as follows.

(1) The Lanzhou loess has the largest median particle diameter, and Xi'an loess has the smallest median particle diameter. The particle shape of Yuncheng loess is the most near to circular and that of Lanzhou loess is the least near to circular. Grain orientation arrangements are nearly isotropic for three loesses.

(2) The median pore diameter of Lanzhou loess is smallest and the pore shape of Yuncheng loess is the most similar to the strip.

(3) Comparing the particle and pore information, the median diameter of the particles is near to or less than the median pore diameter.

(4) The pore microstructures obtained by manual drawing and compiled drawing are similar, which lay a basis for using compiled program to obtain the objects in SEM photo, which can overcome the time-consuming of manual drawing.

ACKNOWLEDGEMENTS

The research was supported by the National Natural Science Foundation of China with grant No. 51409220, the Start-up Research Fund for the Doctor of the Northwest A&F University with grant No. 2013BSJJ097, Chinese Universities Scientific Fund with grant No. 2014YB049. These supports are greatly appreciated.

REFERENCES

Hu, R.L., Li, X.Q., Guan, G.L. et al. 1995. The research on the quantitative microstructure model and engineering geology characters of clay. Beijing: geological publishing house.

Lei, X.Y. 1984. Characteristics of pore distribution of loess around Xi'an. Hydrogeology & Engineering Geology, 4: 34–37.

Liu, D.S. 1966. The material component and structure of loess. Beijing: Science Press,

Wang, Y.Y. & Lin, Z.G. 1990. The physical-mechanical properties and structure characters of Chinese loess. Beijing: Science Press,

Wang, M. 2010. Study on structure of collapsible loess in China [Ph. D thesis]. Taiyuan: Taiyuan University of Technology.

Unsaturated Soil Mechanics—from Theory to Practice – Chen et al. (Eds)
© 2016 Taylor & Francis Group, London, ISBN 978-1-138-02921-7

Understanding the collapsible behavior of loess from microstructure information

P. Li
Department of Civil Engineering, University of Ottawa, Ottawa, ON, Canada
School of Geological Engineering and Geomatics, Chang'an University, Xi'an, Shaanxi, China

S.K. Vanapalli
Department of Civil Engineering, University of Ottawa, Ottawa, ON, Canada

T.L. Li
School of Geological Engineering and Geomatics, Chang'an University, Xi'an, Shaanxi, China

ABSTRACT: Recent advancements in microstructure observation technologies have significantly contributed towards rational characterization of the collapse behaviour of loess soils. In this paper, microstructure characteristics of collapsible loess are summarized taking account of the following four factors; particle pattern, contact relation, pore form and bonding material. The summarized research suggests that all the four factors are dependent on each other. The two dominant factors that control the collapse behaviour of loess are pore form and bonding material. In other words, spaced pores and clay bonds that are respectively related to the pore form and bonding material of collapsible soils are two key parameters that significantly influence their collapsibility behaviour. All four factors should however be fundamentally understood for comprehensive estimation of the collapse behaviour of loess soils.

1 INTRODUCTION

Loess soils cover about 10% and 6.6% of the total land area of the world and China, respectively. In China, loess soils are widely distributed on Loess Plateau that mainly covers six provinces; namely, Gansu, Shaanxi, Shanxi, Henan, Ningxia and Qinghai. Since loess soils are mostly transported by wind and deposited in arid or semi-arid regions, they are found in a state of unsaturated condition. Loess soils typically collapse when there is an increase in their natural water content which contributes to a sudden decrease in soil volume under a practically unchanged vertical stress, making loess a problematic soil. Studies show that during the period from 1974 to 1975, a total of 1505 buildings were damaged and 80 km-long underground pipeline ruptured in collapsible loess soil deposits of China (Sun, 2013). The total collapse settlement in Heifangtai, China induced by irrigation for more than 40 years has been measured to be about 6 m (Sun, 2013). Self-weight collapse settlements of loess soils in cities of Lanzhou, Guyuan, Huayin and Lingbao in China measured by field water immersion tests were 2.65, 2.15, 0.95 and 0.48 m, respectively (Huang, 2006).

Various empirical relationships have been proposed in the literature to estimate collapse behavior of loess soils from their physical properties such as dry density or void ratio (Zorlu, 2009; Adnan, 1992). However, these relationships were not found to be valid in many scenarios for successful use in practice. This may be attributed to soils exhibiting different microstructure characteristics in spite of having similar physical properties. For example, a loess soil with few large pores may have the same void ratio or density as another loess soil with many small pores.

The genesis of explaining the collapse behavior based on how loess behavior is influenced due to capillary stresses, soluble salts, colloids shortage, electrostatic attraction and under compaction is referred to as traditional interpretation in this paper. During the last few decades with the advancement in observation technologies such as Scanning Electronic Microscope (SEM) and digital microscope, microstructure of loess have been used as a tool for interpreting collapse behaviour of loess soils (Xu, 2009; Yang, 1988). The microstructure of collapsible soils can be interpreted taking account of four factors that influence the microstructure; namely, particle pattern, contact relation, pore form and bonding material. The summarized research suggests that all the four factors that influence the microstructure are dependent on each other; however, pore form and bonding material may be suggested as the two dominant factors that control collapse behaviour of loess soil deposits. More specifically, spaced pores which are larger than surrounding soil particles and clay bonds at particle

contacts have a significant influence on the collapsibility. The comprehensive behaviour of collapsible loess soil however cannot be fundamentally characterized based on a single factor. The influence of all the four structural factors should be investigated for a rational interpretation of collapse behaviour of loess soils.

2 TRADITIONAL INTERPRETATION OF COLLAPSE BEHAVIOR OF LOESS SOILS

2.1 *Capillary stress*

Sandy soils that are typically in a state of unsaturated condition exhibit apparent cohesion because particles are pulled together due to the contribution of capillary stresses (Terzaghi, 1943). However, sandy soils collapse on soaking due to loss of contribution from capillary stresses. Capillary stress influence has been used as a tool in the interpretation for collapsibility of unsaturated loess soils. Although it is observed that soil particles either spread or gather with the expansion or shrinkage of water film in soil pores (Gao, 1979), capillary stress approach was unsatisfactory to explain why identical loess soil samples show different collapse behaviors when they are treated with different liquids such as water or other saline solutions (Guo, 1958).

2.2 *Soluble salts*

Soluble salts in crystal or microcrystalline states are believed to act as bonding materials among particles in unsaturated loess soils. These salts are expected to dissolve as soil moisture increases to some degree contributing to a decrease in the bonding strength and leading to the collapse of loess soils (Guan, 1986; Houston, 1988). This interpretation however was found to be invalid because soluble salts are in a dissolved state in pore water even when the moisture content is as low as 8% (Tan, 1988). The total content of soluble salts is also found to be less than 0.1%, typically, in loess soils. Yang (1988) measured several soluble salts content in loess soils of various regions from China are summarized in Table 1.

2.3 *Shortage of colloids*

Some researchers suggest that collapse is a result of short of colloids or clay particles (i.e. clay content is less than 10%). If a loess soil has more clay particles, it may expand instead of collapse on inundation. Some scholars identified the colloids as montmorillonite and hydromica, or suggested minimum clay content. However, this interpretation also fails to explain why Lanzhou loess soil, which has a high content of illite hydromica, exhibits serious collapsibility (Gao, 1979).

2.4 *Electrostatic attraction*

An increase in the water content in soil pores leads to decrease in bonding strength of electrostatic attraction on the surface of clay particles or due to Van der Waals' forces among particles (Gao, 1979). Kraev (1971) suggested that limited montmorillonite presence at loess soil particle contacts would swell and loosen the primary loose structure on soaking, which contributes to collapse in loess soils. However, some experimental results on non-collapsible loess soils were not supportive of this explanation (Han, 2012).

2.5 *Under compaction*

Collapsibility of loess soils has been conventionally attributed to their loose structure; for this reason, it is logical to attribute collapsibility to the characteristic of under compaction (Sergeev, 1986). This interpretation has been widely accepted in the literature as it alleviates the use of complicated mechanisms to explain collapse phenomenon (Feda, 1966). However, loess samples that are initially consolidated under a high vertical stress and then provided with access to water in oedometer tests still exhibit collapse behavior.

The above traditional interpretations based on physical mechanics have significantly contributed towards better understanding collapsible behavior; however, they were found to be unsatisfactory for universally explaining for all loess soils.

3 UNDERSTANDING COLLAPSIBILITY OF LOESS SOILS FROM MICROSTRUCTURE

Recent advances in observation technologies that include binocular loupe, polarization microscope, digital microscope and scanning electronic microscope (SEM) have been found to be valuable tools for understanding of loess soil microstructure and their relationship with the collapse behavior of loess soils.

In this paper, microstructure of loess soils is analyzed in terms of four different factors; namely:

(i) particle pattern, (ii) contact relation, (iii) pore form, and (iv) bonding material. These four factors are dependent on each other; however, the microstructure of loess soils can be better explained taking account of the influence of all four factors.

3.1 *Particle pattern*

It is widely agreed that loess soils are composed of particles that are typically in the size range 10–60 μm, of which particles larger than 20 μm account for about 75% of the total solid constituents (Tan, 1988). Primary minerals coated by clay film, cemented by microcrystalline calcium carbonate form aggregates, both coated primary minerals and aggregates are regarded as skeleton particles of the loess soil structure. Fig.1 summarizes the formation process of aggregates in loess soils (modified after Gao, 1980a). Aggregates with higher plasticity exhibit blunt sensitivity to changes in moisture content than primary minerals.

Table 1. The contents of soluble salts in loess soils from various regions of China (Yang, 1988).

Solubility		$NaHCO_3$ 9.6	$Na_2SO_4 \cdot 10H_2O$ 19.4	KCl 34.0	NaCl 36.0	$MgSO_4 \cdot 7H_2O$ 35.5	$MgCl_2$ 54.5	Total amount (%)
Location	Zanhuang, Hebei	0.001	0.005	0.001	0.001	0.000	0.000	0.009
	Taiyuan, Shanxi	0.000	0.036	0.001	0.000	0.004	0.003	0.044
	Linfen, Taiyuan	0.000	0.068	0.002	0.002	0.000	0.000	0.072
	Luochuan, Shaanxi	0.012	0.027	0.001	0.001	0.000	0.000	0.041
	Tianshui, Gansu	0.003	0.038	0.001	0.004	0.000	0.000	0.046
	Dingxi, Gansu	0.000	0.073	0.002	0.000	0.018	0.003	0.096



Figure 1. Particle patterns in loess soils: (*a*) primary mineral; (*b*) primary mineral coated by clay film; (*c*) aggregate (modified after Gao, 1980a).

On the other hand, skeleton particles of loess soils were simply defined as particles ranging from 5 to 250 μm. Particles that are larger than 10 μm are called coarse and those smaller than 10 μm are considered as fine (Lei, 1983, 1987). Yang (1988) defined skeleton particles as those larger than 10 μm, which account for more than 70% of the total solid mass, while those smaller than 2 μm act as bonding materials, constituting 10 ∼ 15%. Particles between 2 and 10 μm are typically filling materials among skeleton particles. Yuan (2007) divided particles in loess soils into sand ($60 < d < 2000$ μm), silt ($2 < d < 60$ μm) and clay ($d < 2$ μm). Silts-dominant deposits are more favorable for the formation of large pores, which contribute to collapse behavior of loess soils. There is however optimum clay content that contributes to collapsibility to the largest extent. Handy (1973) provided detailed information with respect to clay content for identifying collapsible soils from non-collapsible soils; he stated that an increase in clay content contributes to a decrease in collapse.

Most classifications for particle pattern in loess soils are based on grain size and origin. However, classification is also based on particle shape, such as block, grain and flake (Krinsley, 1973), which can be easily understood. Primary minerals- dominant deposits are more sensitive to wetting and loading than aggregate deposits. In general, more the aggregates, weaker would be the collapsibility of loess (Gao, 1980a, 1980b).

3.2 *Contact relation*

Collapsible soil particles contact is typically point to point, point to side or face to face. The contact relations between these particles are basically of two types, namely point-contact relation and face-cementation relation depending on the amount of bonds at contacts (Gao, 1980). As for point-contact relation, there are only a few microcrystalline calcium carbonates and clay minerals at the contact aside from clay and calcium carbonate film on the particle surface. However, face-cementation relation not only has larger contact area but there is a concentration of calcium carbonate and clay minerals at the contact. Generally, two contact relations coexist in a loess soil with different proportions; contact relation variation is similarly consistent with variation in terms of climate condition (Gao, 1980; Guan, 1989). The point-contact relation is more common in primary minerals-dominant soils and have large pores/void ratio; which likely collapse on soaking, while the opposite is true for face-cementation relation.

Contact relations in loess soils have been recognized as brackety, interlocking and dispersed contact taking account of pore form and bonding material state (Lei, 1983, 1987). He described the brackety contact as the contact relation among particles surrounding brackety pores; interlocking contact results from interlocking arrangement of particles which is observed in conventional soils and dispersed contact is in a state that soil particles are separated by thick clay and calcium carbonate bonds.

3.3 *Pore form*

Different particle patterns and contact relations result in different pore forms; which include spaced pores, interparticle pores and intraparticle pores, as well as macro pores (Gao, 1980a). Macro pores usually include root holes, wormholes and holes attributed to rodents. These pores typically extend to a long distance and the root hole walls are typically cemented firmly by secondary calcium carbonate. For this reason, macro pores have negligible effect on collapsible behavior of loess soils (Gao, 1980a; Lei, 1983).

Spaced pores are typically associated with loose deposition or spaced arrangement of particles, and characterized by the size much larger than surrounding particles (Yang, 1988). Spaced structure contributes to favorable spatial conditions that facilitate loess soils collapse. In addition, spaced structure also contributes to a critical state condition with the bonding strength equal to the gravitational potential of overhanging soil

particles. As loess soil gets wet bonding strength weakens and overhanging particles fall into spaced pores and collapse. In many scenarios, interparticle pores resulted from interlocking arrangement of soil particles are commonly seen in any kind of soils, these pores are arguably and experimentally proved to play a negligible role in controlling collapse behavior (Reznik, 2007). Usually spaced pores coexist with interparticle pores in loess soils, while the former may be dominant in soils in the shallow and arid regions (Gao, 1980a, 1980b). However, converse characteristic is observed loess soils of humid regions, which typically extend to great depths. Lei (1983, 1987) classified soil pores into original pores, such as interparticle pores (brackety pores and interlocking pores) and intraparticle pores, secondary pores (root holes, wormholes, rodent holes, joints, fissures and Karst caves). Schematic diagrams of the first two types of pores are shown in Figure 2. The characteristics of all types of pores, as well as their influence on the collapse behavior are summarized in Table 2.

Yang (1988) found pores that are smaller than 54 μm account for 97% of the total void volume from microstructure observation of loess soils deposited in different geological ages and positions. Although pores that are larger than 54 μm have a high failure rate, they were found to make little contribution to the space condition for collapse or particle rearrangement. However, pores smaller than 54 μm contribute to 80% space for collapse based on the comparison in the proportion of every pore group before and after collapse.

Zhao (1994, 1997) argued that classifications for soil pores mislead spaced pores with brackety pores. Brackety pores are different from spaced pores not only in size but also with respect to their influence on the collapsibility. Both spaced and brackety pores are formed by abnormal arrangement of coarse particles with point-contact relation. Spaced pores are typically larger than surrounding particles (i.e. >20 μm). Spaced pores of 20 to 80 μm size contribute to heavy collapse, while brackety pores, ranging from 8 to 20 μm, contribute to medium to weak collapse. As soil collapses, spaced pores may convert into brackety pores, which is the reason why loess soils usually collapse more than once. For this reason, all brackety pores and most of spaced pores fall into the pore group of smaller than 54 μm as per Yang (1988). Table 3 shows the characteristics of each type of pores and the corresponding collapsibility level (modified after Zhao, 1994).

Assallay (1997) divided soil pores into small, medium, large and giant pores, among which only large pores make a contribution to wetting-induced collapse.

Classifications for soil pores as summarized in this paper are more fundamental in nature and well defined for rational explanation of collapse behavior of loess. These classifications suggest that pores with different size and form have different influence on collapsibility of loess. For this reason, void ratio, which is not based on size and form of the pore, cannot be used as an index for estimating the collapsibility of loess soils. This behavior also explains why relationships between collapsibility coefficient and void ratio for collapsible loess soils in different regions show completely different trends.

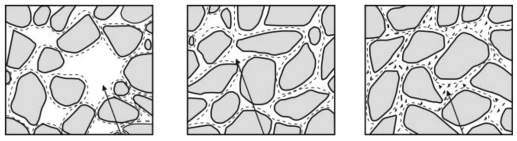


Figure 2. Original pores in loess: (a) brackety pores; (b) interlocking pores; (c) intraparticle pores (the closed gray spaces represent soil particles, Lei, 1987).

From the above discussions it is clear that large pores (i.e. spaced pores and brackety pores) have a major influence on collapse behavior of loess.

Information of each size group pores before and after collapse provides better definitions of soil pores which are required for collapse to occur (Yang, 1988). More studies in this direction would be useful as they may further contribute to better understanding of collapsibility of loess soils.

3.4 *Bonding material*

Bonding in loess soils can be attributed to several sources, such as suction, surface friction and colloids bonding. The influence of bonding material is introduced in this section assuming that other bonding strength sources are the same in an unsaturated soil.

Gao (1980a, 1980b) stated that different states of calcium carbonate show different functions; however, only microcrystalline calcium carbonate contributes to cementing particles together and affects the collapsibility of loess. For this reason, the total amount of calcium carbonate in soil cannot be regarded as an index to estimate collapse behavior. Cabrera (1973) highlighted the long- and short-range bonding effects. Calcium carbonate bonding may be either long- or short-range bonding depending on the amount of calcium carbonate bonds. It is the short-range bonding that has far worsening effect on the collapsibility of loess.

It is unreasonable to attribute collapse to leaching of calcium carbonate on inundation because calcium carbonate leaching is certainly a slow process that requires many cycles of wetting and drying. On the other hand, if the soil structure is believed to fail at the points of contacts where there are no calcium carbonate bonds, then the initial expansion phenomenon before collapse cannot be reasonably explained, which is typically observed in laboratory tests when soil is initially subjected to wetting. This reasoning suggests that other non-water-stable materials contribute to bonding strength in unsaturated condition except for calcium carbonate.

Table 2. Characteristics of all types of pores in loess soils (modified after Lei, 1987).

Type			Size (radius, um)	Characteristics	Reaction to pressure	Influence on collapsibility
Secondary	Root holes		large pores	Dense walls	Depend on whether the pore walls are cemented by $CaCO_3$ or not	
	Wormholes		>16	Loose walls		
	Mouse holes			Large, fragile		
	Joints & fissures			Closed, rough edges		
	Karst caves			Closed, radial, irregular, smooth walls		
Original	Interparticle	Brackety pores	Mediate pores 16 ~ 4	Spaced pores of Gao (1980a, 1980b) classification	Sensible	Significant
		Interlocking pores	Small pores 4 ~ 1	Interparticle pores of Gao (1980a, 1980b) classification	Relatively slow	Insignificant
	Intraparticle pores		Micropores < 1	Numerous, irregular distribution	Slow	Extremely insignificant

Table 3. Combinations of pores and corresponding collapsibility levels (modified after Zhao, 1994).

Collapsibility level	Non-collapse	Weak collapse	Mediate collapse	Strong collapse	Extremely strong collapse
Dominant pore type	Brackety and interlocking pores	Brackety pores	Brackety pores	Brackety pores and spaced pores	Spaced pores
collapsibility coefficient	< 0.015	0.015 ~ 0.04	0.04 ~ 0.07	0.07 ~ 0.10	>0.10
Changes in pores	Unobvious	Unobvious decrease in brackety pores	Obvious decrease in brackety pores and spaced pores	Obvious decrease in spaced pores and part of brackety pores	Obvious decrease in spaced pores

Yang (1988) divided bonding materials into water-stable and non-water-stable materials. The former includes calcium carbonate, calcium sulfate, iron oxide, iron hydroxide, water-stable secondary mica and secondary zeolite, which have been found to be the same before and after collapse. Non-water-stable bonding materials include soluble salts, clay particles and secondary mica. Since contents of both soluble salts and secondary mica are typically less than 0.1% in loess soils, clay bonding has a significant contribution to decrease of bonding strength on inundation.

Guo (1958) found that the total collapse settlements in hot water, NaCl and $CaCl_2$ solution respectively show a gradually decreasing trend. He suggested that salt dissolution weakens bonding strength and induces collapse, while $CaCO_3$ was considered soluble. According to Barden (1973), clay is a dominant bonding agent although calcium carbonate bonding is important.

In summary, bonding can be attributed to: (i) soluble salts, (ii) calcium carbonate, and (iii) clay particles in loess soils. The decrease or loss of bonding strength has been recognized as one of the factors that contribute to collapse of loess in the literature. The effect of soluble salts however has been denied as discussed earlier in this paper. However, it is unclear whether the decrease of ion concentration reduces bonding strength. On the other hand, if loess soil particles are only cemented by clay particles, collapse deformation on inundation should exhibit a degree of plasticity instead of a sudden volume decrease. Therefore, a combination of calcium carbonate and clay minerals should be realized as the key bonding materials that control the collapsibility of loess.

As per the discussions summarized, collapse behavior of loess is influenced by all four structural factors; which are more or less dependent of each other. For example, spaced pores and point-contact always reinforce each other. From the mutual relations among four factors and the final representations of the soil structure based on the summarized analyses, pore form and bonding material can be suggested as two dominant factors that control the collapse behavior of loess soils. In other words, spaced pores and clay bonds are required for collapse to occur on inundation. The comprehensive behavior of collapsible soils cannot be fundamentally characterized based on any single factor for a rational interpretation of collapse behavior of loess soils need investigations on all four structural factors.

4 SUMMARY

Microstructure observation technologies have significantly contributed towards better understanding

of structural factors that contribute to the collapse behaviour of loess soils during the last two decades The microstructure of collapsible loess soils can be summarized considering four structural factors; namely, particle pattern, contact relation, pore form and bonding material. All these four factors are more or less dependent on each other. However, pore form and bonding material should be recognized as the two key factors that have more influence compared to the other factors. The classification for soil pores is becoming more clear, well defined, and favorable for analysis of the collapsibility. Bonding materials have been recognized as soluble salts, calcium carbonate and clay minerals in loess soils from the literature. However, a combination of calcium carbonate and clay minerals should be suggested as the main bonding materials with a greater degree of confidence. For rational interpretation of collapse behavior of loess soils, the influence of all the four structural factors however should be investigated.

ACKNOWLEDGEMENTS

The first author gratefully acknowledges her appreciation to the Chinese Scholarship Council, which funded her Joint PhD research program. The second author thanks the support from NSERC for his research programs. The third author thanks the Chinese Ministry of Science and Technology for supporting his research program (2014CB744701).

REFERENCES

Assallay, A.M., Rogers, C.D.F. & Smalley, I.J. 1997. Formation and collapse of metastable particle packings and open structures in loess deposits. *Engineering Geology* 48:101–115.

Barden, L., Mcgown, A. & Collins, K. 1973. The collapse mechanism in partly saturated soil. *Engineering Geology* 7:49–60.

Basma, A.A. & Tuncer E.R. 1992. Evaluation and control of collapsible soils. *Journal of Geotechnical Engineering* 118(10):1941–1504.

Cabrera, J.G. & Smalley, I.J. 1973. Quickclays as products of glacial action: a new approach to their nature, geology distribution and geotechnical properties. *Engineering Geology* 7:11–133.

Feda, J. 1966. Structural stability of subsident loess soil from Praha-Dejvice. *Engineering Geology* 1: 201–219.

Gao, G.R. 1979. Study of the microstructures and the collapse mechanism in loess soil from Lanzhou. *Journal of Lanzhou University* (6):123–134.

Gao, G.R. 1980a. The microstructures of loess in China. *Chinese Science Bulletin* (20):945–948.

Gao, G.R. 1980b. Classification for microstructure of loess and its collapsibility. *Chinese Science* (12):1203–1212.

Guan, W.Z. 1986. On soluble salts and the mechanism of loess collapsibility. *Journal of Guilin College Geology* 6(3):271–278. *Coal Engineering* (10):154–155.

Guan W.Z. 1989. The collapse types and characteristics of loess in Xi'an and Lanzhou. *Journal of Guilin College Geology* 9(1):74–80.

Guo, J.Y. 1958. Study on the reasons for collapse. *Hydrogeology & Engineering Geology* (4):7–11.

Han, H.D. 2012. Characteristics of non-collapsible loess soils.

Handy, R.L. 1973. Collapsible loess in Lowa. *Soil Science Society of America Proceedings* 37:281–284.

Huang, X.F., Chen, Z.H. & Ha, S.. 2006. Large area field immersion tests on characteristics of deformation of self weight collapse loess under overburden pressure. *Chinese Journal of Geotechnical Engineering* 28(3):382–389.

Huston, S.L., Houston, W.N. & Spadola, D.J. 1988. Prediction of field collapse of soils due to wetting. *Journal of Geotechnical Engineering* 114(1):40–58.

Kraev, V.F. 1971. On subsidence of loess soils of the Ukraine. *Pbl. Int. Assoc. Hydrol. Sci. Land Subsidence*, *Tokyo Symp*. 1:321–324.

Krinsley, D.H. & Smalley, I.J. 1973. Shape and nature of small sedimentary quartz particles. *Science* 180:1277–1279.

Lei, X.Y. 1983. Type of the loess microtextures in Xi'an district. *Journal of Northwest University* (4):56–65.

Lei, X.Y. 1987. Pore types of loess soils in China and its collapsibility. *Chinese Science* (*B section*) (12):1310–1316.

Reznik, Y.M. 2007. Influence of physical properties on deformation characteristics of collapsible soils. *Engineering Geology* 92:27–37.

Sergeev, E.M. & Komissarova, N.N. 1986. Genesis and postgenetic changes of loess rocks. *Loess Rocks of the USSR*, *Nedra Moscow*:4–27.

Sun, P.P., Zhang, M.S. & Zhu, L.F.. 2013. Typical case study of loess collapse and discussion on related problems. *Geological Bulletin of China* 32(6):847–851.

Tan, T. 1988. Fundamental properties of loess from northwestern China. *Engineering Geology* 25:103–122.

Terzaghi, K. 1943. *Theoretical soil mechanics*, New York: John Wiley & Sons.

Xu, L., Dai F.C. & Jin Y.L. 2009. Discussion on the mechanism of loess collapsibility from the perspective of unsaturated soil mechanics theory. *Hydrogeology and Engineering Geology* (4):62–65.

Yang, Y.L. 1988. Study on collapsible mechanism of loess soils. *Chinese Science (B section)* (7):756–766.

Zhao, J.B. & Chen, Y. 1994. Study on pores and collapsibility of loess. *Journal of Engineering Geology* 2(2):77–83.

Zhao, J.B., Yue, Y.L. & Chen, Y. 1997. Collapsibility of loess and its origin. *Journal of Geomechanics* 3(4):62–68.

Zorlu, K. & Kasapoglu K.E. 2009. Determination of geomechanical properties and collapse potential of a caliche by in situ and laboratory tests. *Environmental Geology* 56:1449–1459.

Unsaturated Soil Mechanics—from Theory to Practice – Chen et al. (Eds)
© 2016 Taylor & Francis Group, London, ISBN 978-1-138-02921-7

Microstructure change of loess soil during wet collapsing

X.X. Shao
School of Civil Engineering and Mechanics, Lanzhou University, China

H.Y. Zhang
Key Laboratory of Mechanics on Disaster and Environment in Western China of Ministry of Education, Lanzhou University, China

J.W. Liu
School of Civil Engineering and Mechanics, Lanzhou University, China

ABSTRACT: Loess soil is a problematic soil which exhibits collapse property when saturated with water. This paper tends to provide direct evidence quantitatively describing the microstructure change in loess soil during different stages of collapse. Malan loess soil (Q_3) was sampled and compacted to various densities to poses different collapsibilities. Elevated volumes of water were added to the specimens with the same density to establish the correlation between wetting deformation and saturation degree. All specimens were tested by Scanning Electron Microscope (SEM) and Mercury Intrusion Porosimetry (MIP) to investigate the microsturcture change during different collapsing stages. Test results indicate that under certain pressure the void ratio of loess soils specimens, even though with different initial densities, decreases exponentially with the increase of saturation degree, and finally become to be almost the same. The specimens with lower density are characterized by a microstructure that most of pores size is greater than that of the particles size, and the adjustment of these big pores during wetting is responsible for the strong collapsibility

1 INTRODUCTION

Loess soil is characterized as its initial structure that can be destroyed when saturated with water at a certain pressure. Collapsible loess is widely distributed in South America, North America, Eastern Europe and Central Asia. The collapse of loess may cause geologic hazards such as landslide, avalanche, land collapse, crack, inclination and even structure failure.

Metastable structure is a key factor to the collapse ability of loess soil. Gao (1980) dealt with the result of SEM and soil test, and reported that the collapsibility of loess was due to its microstructure instability. Pu (2000) analyzed the CT images of loess specimens, and concluded that loess is collapsed when its skeleton was destroyed after water penetration. Sha & Chen (2006) studied microstructure of loess with different compaction after collapse, and reported that the existence of micropore and medium pore was the mainly responsible for the loess collapse. SEM has the advantage of revealing the soil microstructure by its intuitionistic image. Moreover, MIP can quantitatively identify the pore diameter of loess soil ranges from a few nanometer up to several hundreds of micrometer Therefore, this research use SEM and MIP techniques to investigate the microstructure change of the loess specimens is saturated with elevated water, so to reveal the dynamic change of collapse deformation with different dry densities from the viewpoint of unsaturated soil mechanics. In addition, a quantitative description to the change of particle size and pore size distribution before and after the collapse was provided.

2 MATERIALS AND METHODS

2.1 *Materials*

The loess soil used in this study is Malan(Q_3) loess with a yellowish brown colour, and in wet and dense condition, obtained from Gaolan Mountain in Lanzhou City, China. The physical properties of soil are shown in Table 1. Loess soil was static-compacted at a water content of 9% to different densities such as 1.30, 1.40, 1.50 g/cm^3 for collapsibility test.

2.2 *Wetting deformation test*

Wetting deformation tests were performed in a WG triple high pressure oedometer apparatus in accordance with standard GB/T50123-1999 except the water addition. Specimens were cut into Φ61.8 mm $\times$ 20 mm ring, first load press was applied, and elevated volumes of distilled water was added to the specimens. After 12 h, second load pressure was added until the final pressure of 900 kPa. When the

Table 1. Physical properties of loess soil.

Specific gravity	Natural water content (%)	Natural dry content ($g \cdot cm^{-3}$)	Plastic limit (%)	Liquid limit (%)	Soil classification
2.72	9.00	1.59	18.09	27.08	silt

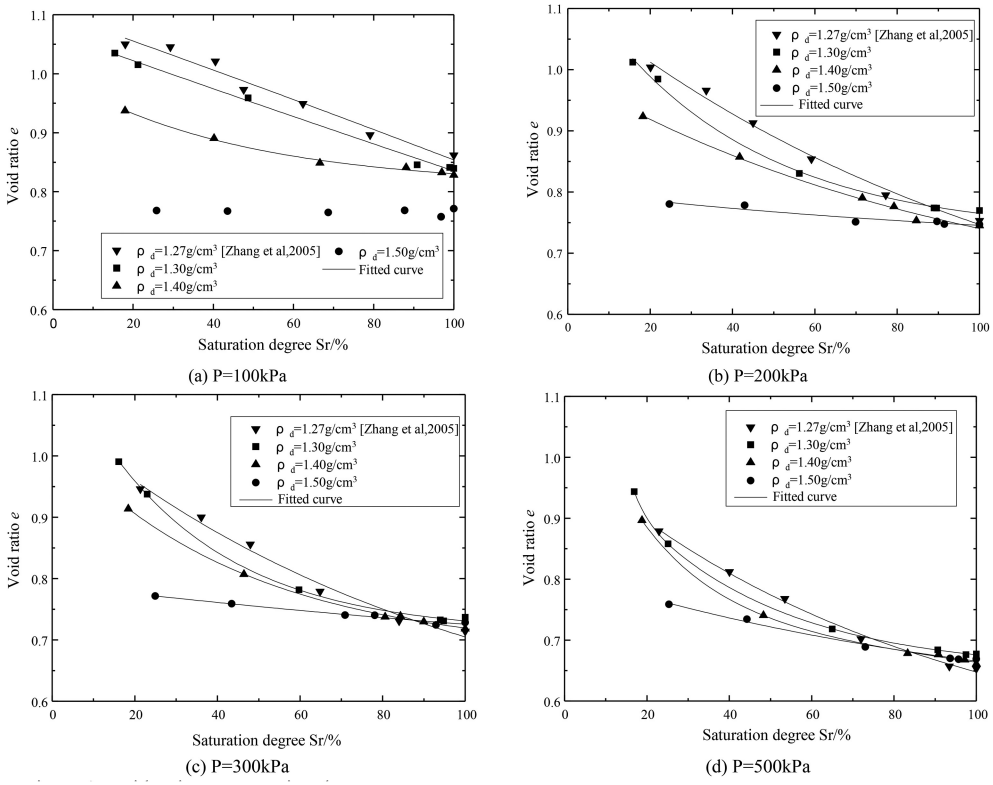


Figure 1. Void ratio vs. saturation degree.

dialgauge reading did not change for 24 h, the total deformation of each specimen was recorded to establish the correlation between wetting deformation and saturation degree.

2.3 *Wetting deformation test*

All specimens after collapse test were investigated by SEM (Hitachi, SU-1500) and MIP (Quantachrome, PM-60) to study the microstructure change during different collapsing stages. As a preparation, specimens were cut into cubes less than 1 cm^3 for maximize heat transfer and then dehydrated by freeze dryer (FD-2A).

Four SEM photos with clear image of particles and pores for each specimen were selected, for quantitative statistics by the ImageJ software package to study the particle size variation during the collapsing procedure. SEM images were quantitative statistics by ImageJ in two steps: First, the threshold was determined and binary images were obtained; second, the profile of particle was segmented manually and the corresponding particle area was extracted. Then, particle size distributions of loess soil after wetting deformation test were obtained form the value of particle area. The quantitative change in micro-porosity diameter of loess soil during collapsing was reported by MIP test result.

3 RESULTS AND DISCUSSION

3.1 *Relationship between wetting deformation and saturation degree*

Figure 1 shows the relationship between saturation degree and void ratio for loess soil with various initial dry densities under different pressure. The data for loess with dry densities of 1.30, 1.40 and 1.50 g/cm^3 obtained in this study and for dry density of 1.27 g/cm^3 have been published in literature (Zhang et al., 2005).

Table 2. Regression parameters for void ratio and saturation degree (%).

Dry density ($g \cdot cm^{-3}$)	Pressure (kPa)	a	b	c	d	f	R^2
1.27	100	−1.55	−1271.05	−1.56	−1311.12	4.21	0.9140
1.30	100	0.10	45.40	0.10	45.40	0.81	0.9776
1.40	100	0.01	25.10	0.04	24.10	0.77	0.9719
1.50	100	–	–	–	–	–	–
1.27	200	0.31	113.29	0.31	113.30	0.49	0.9575
1.30	200	0.21	39.04	0.21	39.04	0.73	0.9891
1.40	200	0.20	98.12	0.20	98.13	0.60	0.9673
1.50	200	0.07	29.39	0.07	29.39	0.74	0.9360
1.27	300	0.28	96.45	0.28	96.46	0.51	0.9340
1.30	300	0.23	31.52	0.23	31.52	0.71	0.9959
1.40	300	0.18	46.29	0.18	46.29	0.68	0.9965
1.50	300	0.07	54.56	0.07	54.56	0.70	0.9463
1.27	500	0.26	84.83	0.26	84.83	0.49	0.9843
1.30	500	8.76	3.09	0.41	36.38	0.65	0.9996
1.40	500	69.88	2.02	0.45	19.17	69.13	0.9967
1.50	500	0.12	107.72	0.12	107.72	0.57	0.9660

Generally, at the same vertical pressure, the void ratio of specimen decrease with the increase of saturation degree.

Figure 1a shows that under 100 kPa vertical pressure, the specimens with low-dry density (1.27, 1.30, 1.40 g/cm^3) have larger void ratio initially before wetted, and the void ratio decrease rapidly with increase in saturation. The void ratio for low-dry density specimens approaches to a value, almost the same (0.828∼0.866) when fully saturated. With respect to the high-density specimen (1.50 g/cm^3), the void ratio almost keep the same with the increase of saturation degree. Fig.1b shows the result of specimens under 200 kPa vertical pressure. Where the low-dry density specimens (1.27, 1.30, 1.40 g/cm^3) express a wetting deformation similar to that under 100 kPa pressure. Specifically, the void ratio decreases with increasing saturation degree, and tend to be equal at fully saturated condition, such as 0.756. With the increase of saturation degree, the high-dry density specimen deform slightly, and the final void ratio gradually decrease to 0.747, much closer to the average void ratio(0.756) of low-dry density collapsed specimens.

Under high vertical pressure such as the case of P = 300, 400 kPa as shown in Figures 1c and 1d, the void ratio of low-density specimens decrease more rapidly with the increase of the saturation degree, and finally approaches the void ratio of the specimens with high-dry density (1.50 g/cm^3) when fully saturated. Fig. 1 shows that the void ratio decreases exponential with the increase of saturation degree (%), with a relationship function:

$$e = a \cdot \exp(-S_r / b) + c \cdot \exp(-S_r / d) + f \quad (1)$$

Where e is void ratio; S_r is saturation (0%≤ Sr≤100%); and a, b, c, d, f are fitting parameters of regression equation. Specific fitting parameters for various initial dry densities under different pressures are listed in Table 2.

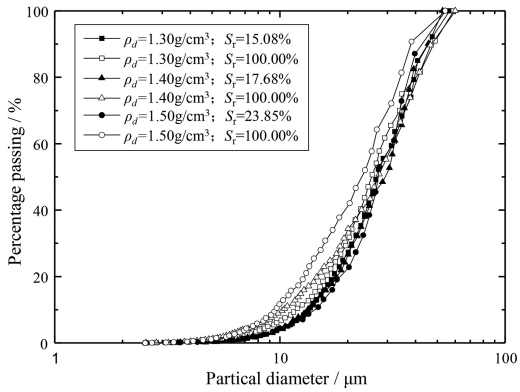


Figure 2. Particle size distribution of loess specimens before and after collapse.

3.2 *Microstructure change of loess soil during wetting collapsing*

Figure 2 shows the particle size distribution of loess specimen of various dry densities before and after collapse. It can be found from Figure 2 that two curves of 1.30 g/cm^3 dry density tend to coincidence. With the increasing of dry density (1.40, 1.50 g/cm^3), the particle size distributions of specimen before and after collapse are tend to be different. This means that there is no change in particle size of collapsible loess (1.30 g/cm^3) during the process of wetting collapse. But for loess with very little collapsibility, during the process of loading and wetting, the pressure act directly on the particle and the particle strength decreased by water immersion. Therefore, some of particles were broken instead of loess's inner structure adjustment.

The pores of loess soil can be divided into four classes according to its pore size (Lei 1987): Large pore ($d > 32\,\mu m$), Medium pore ($8 < d \leq 32\mu m$),

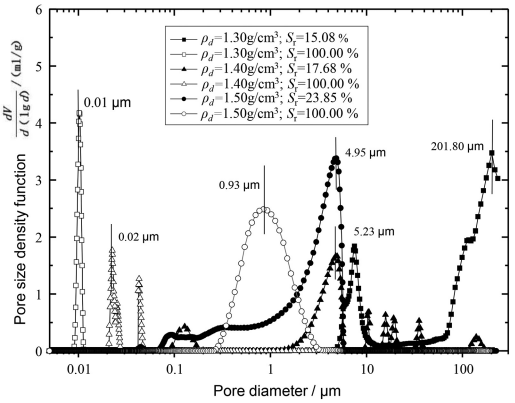


Figure 3. Pore size distribution of loess specimens before and after collapse.

Small pore ($2 < d \leq 8\,\mu m$) and Micropore ($d \leq 2\mu m$). Figure 3 shows the pore size distribution of specimens with various dry densities before and after collapse. Before collapse, the pore size distribution curves for loess soils with dry densities of 1.30g, 1.40 and 1.50 have a multiple-porosity structure, as indicated by a typical pore diameter around 201.80 μm, 5.23 μm, 4.95 μm, respectively. However, the pore size distribution curves for the same loess soils after collapse have a single-porosity structure, corresponding to a typical pore diameter around 0.01 μm, 0.02 μm and 0.93 μm, respectively.

Figure 3 provides two insights about the pore size change during loess soil collapse. Firstly, wetting collapse derivates from pore structure damage instead of particle size change. Loess collapse is directly corresponded to the decrease in pore size as well as void ratio. Secondly, all pores with different size are contributed to loess collapse. Loess soil before collapse has a pore size distribution characterized with two peaks. After wetting collapse, this distribution becomes to one peak. This means that all the original pores, where larger or smaller, become even smaller at a saturated, collapsed condition. Figure 3 also provides information about remaining pore as affected by the initial pore size. For instance, with increasing densities, from 1.30 to 1.50 g/cm^3, the specimens have a typical pore size as 201.80, 5.23 and 4.95 μm, respectively. At wet collapsed condition, the corresponding specimens have a typical pore size as 0.01, 0.02 and 0.93 μm, respectively. This indicates that loess soil with a much looser structure tends to be collapsed thoroughly.

4 CONCLUSIONS

(1) Under different pressures, the void ratio of loess specimens, with various initial densities, decrease exponentially with the increase of saturation degree, and finally tend to be equal.
(2) The particle size distribution of loess soil has little change during the process of wetting collapse, while the pore structure damage is responsible for the collapse.
(3) Loess soil with low density is characterized with much more macrospores and high collapsibility, and tends to be collapsed to condition with much smaller pores remained.

ACKNOWLEDGEMENT

The present work has been sponsored by the Foundation of Key Laboratory of Mechanics on Disaster and Environment in Western China (Lanzhou University), Ministry of Education (No. 201405).

REFERENCES

Ahmed, S., Lovell, C.W. & Diamond, S. 1974 Pore sizes and strength of compacted clay. Journal of the Geotechnical Engineering Division. 100(4): 407–425.

Gao, G.R. 1980. Microstructure classification of loess and collapsibility. Science China (Series A) (12): 1203–1208.

Lei, X.Y. 1987 Pore type of loess in china and collapsibility. Science China (Series B) (12): 48–54.

Pu, Y.B., Chen, W.Y. & Liao, Q.R. 2000. Research on CT structure changing for damping process of loess in longdong. Chinese Journal of Geotechnical Engineering 22(1): 49–54.

Sha, A.M. & Chen, K.S. 2006 Relationship between collapsibility and microstructure of compacted loess. Journal of Chang'an University, 2006, 26(4): 1–4.

Zhang, M.H., Xie, Y.L. & Liu, B.J. 2005 Characteristics of collapsibility coefficient curves of loess during moistening and demoistening process. Rock and Soil Mechanics 26(09): 1363–1368 (in Chinese).

Unsaturated Soil Mechanics—from Theory to Practice – Chen et al. (Eds)
© 2016 Taylor & Francis Group, London, ISBN 978-1-138-02921-7

Research on evolution of meso-structure of Q_2 loess during plastic and brittle failure in triaxial tests

X.W. Fang
Department of Civil Engineering, Logistical Engineering University, Chongqing, China

C.N. Shen
Chongqing University of Science and Technology, Chongqing, China

Z.H. Chen & J. Li
Department of Civil Engineering, Logistical Engineering University, Chongqing, China

ABSTRACT: A series of triaxial shear tests on unsaturated undisturbed Q_2 loess were conducted using CT-multifunction triaxial apparatus. The distinct CT images and detailed CT data during the evolution of meso-structure were obtained nondestructively. It is shown that some structure damages such as pore, flow, ginger nut, etc. exist in undisturbed Q_2 loess. The initial structure of Q_2 loess is inhomogeneous. The CT data is prominently affected by ginger nut. The meso-structure evolution of plastic failure deformation for undisturbed Q_2 loess can be divided into three stages, i.e., slightly dense stage, stage of slight adjustment of structure, and rapidly dense stage. The meso-structure evolution of brittle failure deformation for undisturbed Q_2 loess can be divided into four stages, i.e. slightly dense stage, initial damage stage, rapid damage development stage, and steady damage development stage. The mechanical properties of macrostructure can be properly explained by the characters of meso-structure evolution.

1 INTRODUCTION

Loess, territorial and special, is widely distributed on earth. It occupies an area of 640.000 square kilometers which is of 6.6 percent of Chinese area. Loess is mainly distributed over the Yellow River drainage area. All sorts of problems of loess are found in the infrastructure construction, ecological environment protection and national defense during the development of western regions. Previous studies mainly focus on Q_3 loess, while less involved in Q_2 loess. Future studies of Q_2 loess's mechanical and engineering properties have great engineering practical value.

Many experiment studies show that undisturbed loess is structural soil. The stress-strain curves of loess are usually presented as 3 types and 5 forms, namely brittle failure (including strong soften and weak soften), plastic failure (including strong harden and weak harden) and ideal plastic failure. During the triaxial shear test, the evolution of meso-structure is distinct with different failure forms, especially for the type of brittle failure and plastic failure. Their evolution features of internal structure are totally different during the process of shear deformation. In this paper, the triaxial shear tests of Q_2 loess were conducted, for the brittle failure and the plastic failure. The evolution of internal meso-structure during shearing was future studied, which provided theoretical basis to study the mechanical properties of loess.

2 EXPERIMENT INTRODUCTION

2.1 *Specimen preparation*

The undisturbed Q_2 loess used in this study collected from the depth of 16 to 16.2 m of Pucheng electric power plant, Shanxi province, China. Because of the low initial water content (4%–6%) and high initial suction value, water membrane transfer method was used to unite the initial water content to the 18% after the soil was cut in plate. The quantity of water injected are close to 20g and if injected at one time, the sample would expand, so injection of water were carried out by using medical uniform 5 ml syringe injection, 12 hours at each time, two times in total. After water injection, samples should be turned every 12 hours a time, and put in the moisturizing pot in order to make the water evenly distributed. Figure 1 shows the two undisturbed loess samples.

2.2 *Laboratory equipment*

Chen and Lu (2001) developed a modified triaxial apparatus utilizing CT to observe internal structure of specimens. Recently Chen et al. (2007) and Fang (2008) further improved the apparatus named as CT-multi-function triaxial apparatus for soil, and established a CT-triaxial work station (Fig. 2). The CT machine is Prospeed AI horizontal spiral

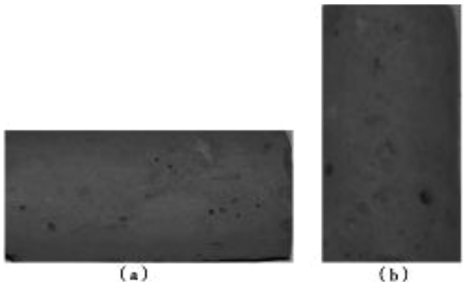


Figure 1. Specimen of undisturbed Q_2 loess.



Figure 2. CT-triaxial work station of Logistical Engineering University.

scanning machine produced by GE Corporation. This CT machine has many advanced features such as scanning quickly, high resolution ratio, good image quality, low energy consumption and intellective.

2.3 *Test procedures*

A series of triaxial shear tests on unsaturated undisturbed Q_2 loess were conducted using the improved CT-multi-function triaxial apparatus. The evolution of internal structure during triaxial tests was studied by CT scanning. Firstly the specimens were consolidated at constant pressure, and then were sheared at the rate of 0.0167 mm/min. Two sections (Section 1 and section 2 which located one-third and two-thirds of height for each specimen) of specimens were scanned before consolidation and during shearing.

3 THE STRESS-STRAIN CURVES

Figure 3 shows the stress-strain curves of triaxial shear tests. The figure indicated that 8 specimens with constant suction experienced plastic failure, while specimens with constant water content (high suction) experienced brittle failure. The stress-strain curve develops from soften type to harden and ideal plastic type with the decrease of suction and the increase of cell pressure.

Figure 3 (a)~(c) show the curves with same suction and different net cell pressure. With the increase of net cell pressure, the stress-strain curves develop from ideal plastic type to strong harden type. Figure 3 (d) shows the results when controlling the water content.

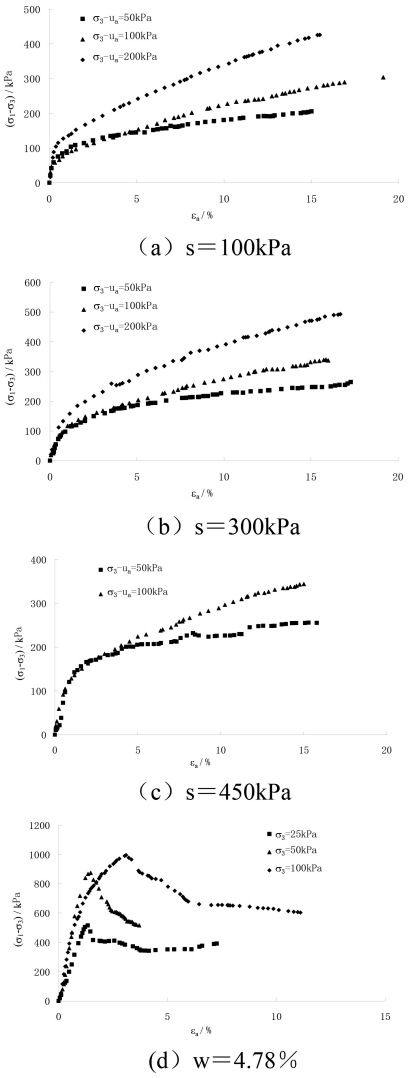


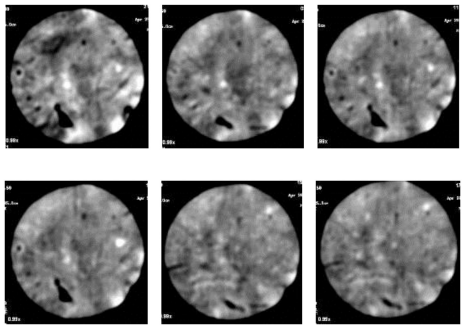
Figure 3. Relationship of deviator stress and axial strain.

The curves were obviously divided into 3 stages, that are stage 1(stress increase as strain increase), stage 2(stress decrease as strain increase) and stage 3(stress stay constant as strain increase).

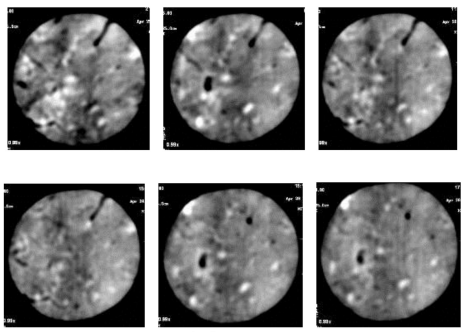
4 CT IMAGES AND EVOLUTION OF MESO-STRUCTURE

According to the laws of CT images, the grayscales of CT images are closely related to corresponding density of Q_2 loess. The black zone of images represent low density of Q_2 loess (i.e. pore, flow), and the white zone represents high density of Q_2 loess (i.e. ginger nut).

6～7 scanning were conducted during tests for each specimen. Each scanning, for one section, CT-number (denoted by ME) and standard deviation of CT-number (denoted by SD) was obtained. ME reflects mean density of all matter of scanning sections and SD reflects

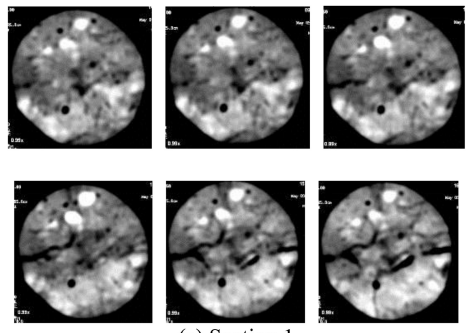


(a) Section 1

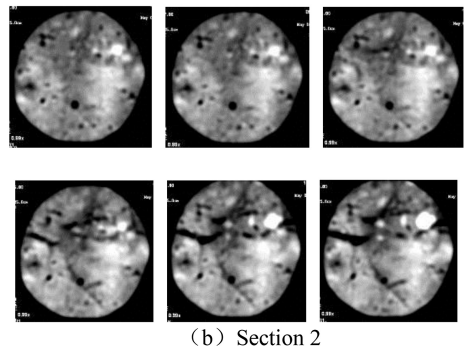


(b) Section 2

Figure 4. Scanned CT images of the plastic failure specimens during testing ($s = 300$ kPa, $\sigma_3 - u_a$, 100 kPa).



(a) Section 1



(b) Section 2

Figure 5. Scanned CT images of the brittle failure specimens during testing ($w = 4.78\%$, σ_3, 100 kPa).

the variation of density. Fig. 4 and Fig. 5 show representative scanned CT images of plastic failure and brittle failure specimens during testing.

4.1 *The initial characters of loess*

From Figures 1, 4, 5, the damages of Q_2 loess were obviously consisting of lots of pore, flow and ginger nut, etc. The differences of ME (between 974.46 ~ 1228.43) and SD (94.19 ~ 248.03) were obvious. The two specimens which ME exceeded 1200 had ginger nut of high density.SD of two specimens were also high. ME and SD of the two sections of the same specimen were quite different. High density zone, low density zone, irregular shape pore, flow and ginger nut, etc appeared randomly. Therefore, the initial structures showed anisotropy of undisturbed loess and the influence of ginger nut on ME and SD was obvious.

4.2 *Evolution of meso-structure for plastic failure specimens*

(1) Consolidation stage. Changes of CT images and CT data (ME and SD) showed variations due to the both effect of suction and net cell pressure. If only considering the effects of net cell pressure, the specimens would be contractive and homogeneous, corresponding to the increasing ME and the decreasing SD. If only considering the effects of suction, the ME would decrease and SD would increase because a portion of water (ME = 0) draining out of specimens were filled up by air (ME = −1000). Therefore, the changes of ME and SD reflected the influences of both suction and net cell pressure. For the three specimens with low suction (equal to 100 kPa), ME increased and SD decreased due to dominant effect of net cell pressure. The changes of the ME and SD, especially the latter one were greater with the increase in net cell pressure. The strength and deformation modules of soils increased with the increase in consolidation net cell pressure. This was explained from the perspective of evolution of meso-structure. At constant suction of 300 kPa, ME decreased when net cell pressure was 50 kPa, while increased when net cell pressure was 100 kPa and 200 kPa. At constant suction of 300 kPa, SD decreased significantly with the increase in net cell pressure. When suction was equal to 450 kPa, ME decreased but SD was almost unchanged because of low net cell pressure of 50 kPa. From consolidation stage, one could see that ME was properly used to describe the evolution of structure during drained triaxial shear tests at constant suction and constant net cell pressure.

(2) Yield stage. The 2nd to 3rd scanning was taken as the yield stage which the deviatoric stress increased rapidly and the deviatoric strain increased slowly. In this stage, the changes of CT images weren't obvious. The density of soils

increased and the difference decreased. In this stage, the stress increased rapidly and the strain increased slowly before yield were explained from greater slope of ME versus deviatoric strain and small slope of ME versus deviatoric stress. SD decreased generally with the increase in deviatoric strain and stress. Therefore, ME was also properly used to reflect the changes of structure in the yield stage.

(3) Hardening stage. The 3rd to last scanning image was taken as hardening stage in which the deviator stress increased rapidly. In this stage, the density of soils increased and the variations of the density decreased corresponding to the increasing ME and the decreasing SD. From CT images, the flaws and cracks were compressed. Most pores were destroyed and compressed, even disappeared; but small portion of pores which distributed isolated area (such as specimens 1# and 6#)or the around of high density zone such as ginger nut(such as specimen 7#) almost unchanged. The sectional area increased gradually during test. From Figures 2, 3, the changes of ME and SD versus deviator strain and deviator stress in the hardening stage were different from those in the yield stage. Yield stress could be determined according to the difference of ME versus deviator stress of deviator strain, especially the former one in the yield and hardening stage. ME versus deviator stress curves can be approximated by two straight lines and the intersection of the two lines can be taken as the yield stress.

4.3 *Evolution of meso-structure for brittle failure specimens*

From Figure 5, the evolution of meso-structure for brittle failure specimens would be divided into four stages.

(1) Consolidation stage. With the low cell pressure, the loess specimens were consolidated slightly and the uneven degree decreased, the corresponding ME increased slightly and SD decreased.

(2) Before peak stress stage. Fig.3 (d) showed the peak stresses of specimens were 516, 874 and 996 kPa, and the corresponding axial strain were 1.34%, 1.48% and 3.1%. The 2nd and 3rd scanning of each specimen can be concluded into this stage, undergoing a process of contraction and dilatancy stages. Some of the flaws and cracks were expanded, which means the failure begun. In local area, the specimens were compressed and became even, ME increased and SD decreased. Then, with the volume of specimens increasing, ME began to decrease and SD began to increase. From CT images, the changes were not obvious and the specimens were not damage at this stage.

(3) Softening stage. The deviator stress decreased rapidly and the volume of specimens increased rapidly after the peak value. This stage continues until the fourth or fifth scanning. ME decreased obviously and SD increased. The formation of shear rupture surface would be seen in the image, the shape and quantity of shear surface were different since the initial state and cell pressure were different

(4) Residual strength stage. ME continued to decrease and SD increase. The shear rupture surface expanded and connected.

5 CONCLUSIONS

(1) The damages of Q_2 loess are obvious including lots of pore, flow and ginger nut, etc. The initial structures show anisotropy of undisturbed loess and the influence of ginger nut on ME and SD is obvious.

(2) The meso-structure evolution of plastic failure deformation for undisturbed Q_2 loess could be divided into three stages, i.e., slightly dense stage (consolidation stage), stage of slight adjust-ment of structure (yield stage), and rapidly dense stage (hardening stage).

(3) The meso-structure evolution of brittle failure deformation for undisturbed Q_2 loess could be divided into four stages, i.e. slightly dense stage (consolidation stage), initial damage stage (before peak stress stage), rapid damage development stage (softening stage), and steady damage development stage (residual strength stage).

(4) The mechanical properties of macrostructure can be properly explained by the characters of meso-structure evolution.

ACKNOWLEDGEMENTS

This work was financially supported by the National Natural Science Foundation of China (No.11272354, 51479208).

REFERENCES

Chen Zheng-han et al. 2001. The matching of computerized tomography with triaxial test apparatus for unsaturated soil. *Chinese Journal of Geotechnical Engineering* 23(4): 387–392.

Chen Zheng-han et al. 2007. Development and application of multi-function triaxial apparatus for soil. *Journal of Logistical Engineering University* 23(4): 1–5.

Desrues J. et al. 1996. Void ratio evolution inside shear bands in triaxial sand specimens studied by computed tomgraphy. *Geotechnique* 46(3): 529–546.

Fang Xiang-wei. 2008. *Study on microstructure, meso-structure and mechanics properties of Q_2 loess*. Chongqing : China.

Finno R. J. et al. 1997. Shear bands in plane strain compression of loose sand. *Geotechnique* 47(1): 149–165.

Otani J. et al. 2000. Application of X-ray CT method for characterization of failure in soil. *Soils and Foundations* 40(2): 111–118.

Unsaturated Soil Mechanics—from Theory to Practice – Chen et al. (Eds)
© 2016 Taylor & Francis Group, London, ISBN 978-1-138-02921-7

Research on wetting-induced microstructure change of Q_2 loess

C.H. Li & X.W. Fang
Department of Civil Engineering, Logistical Engineering University, Chongqing, China

C.N. Shen
Chongqing University of Science and Technology, Chongqing, China

Y.X. Ou
Department of Civil Engineering, Logistical Engineering University, Chongqing, China

ABSTRACT: Microstructure change of Q_2 loess due to wetting is studied in this paper. Samples were wetted to different degrees of saturation by applying suction change as the confining pressure held constant. SESM technique was used to observe the wetting-induced microstructure changes. Photographs obtained were processed and microstructure features as inter-aggregate pore size distribution were analyzed. It could be seen that, as Q_2 loess is wetted, pores of sizes ranging from 10 to 20 μm become dominant. Volume of pores of larger pore sizes decreases and volume of pores of sizes ranging from 10 to 20 μm increases. And changes in size of pore and aggregate are correlated, expansion of aggregates, due to absorption of water, lead to decrease in size of the pores, while collapse of aggregate structure also makes pore sizes smaller.

1 INTRODUCTION

Researches on structural change of Q_2 loess due to wetting are often carried out on micro scale or meso scale. CT was used to study structural variation of Q_2 loess during wetting on a meso scale (Fang et al. 2008). CT images and related data are used to describe its meso-structure variation when wetted. As for microstructure study, features that well indicate structural variation due to wetting depends on the soil studied, different microstructure features are adopted for different soil. Some microstructure features of Q_2 loess are presented in Fang's thesis (Fang et al. 2014). In this paper, microstructure variation of Q_2 loess due to wetting is studied by ESEM technique (Romero & Simms 2008). The undisturbed loess studied is from Pucheng, Shanxi Province, China.

2 ESEM TEST SCHEME

Suction in unsaturated soil is closely related to water content, and their relation is shown by SWCC, which is a constitutive equation for unsaturated soil. Theoretically, wetting of soil can be taken as variation of suction in soil. In the following test, Q_2 loess will be wetted and loaded along a simple loading-wetting path, and its microstructure variation will be studied. The simple loading-wetting path adopted in the test, as shown in Fig. 1, is, in nature, wetting under constant pressure. And different degrees of saturation are achieved by suction change.

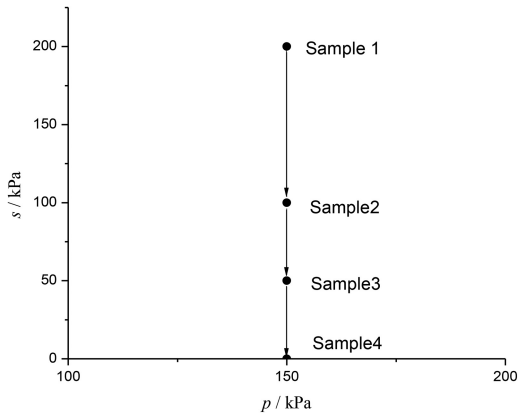


Figure 1. Wetting-loading path adopted in research on microstructure of Q2 loess.

ESEM technique was used to observe structural variation of Q_2 loess due to wetting; pictures taken are processed via software specified for picture analysis. Microstructure features are analyzed and wetting-induced structural variation is observed.

Process for preparation of Q_2 loess samples of different degrees of saturation are listed as follows:

(1) Unsaturated isotropic consolidation. Samples were consolidated under net pressure p of 15 kPa and suction of 200 kPa. As consolidation ended, samples would be wetted to preset degree of saturation by applying suction change.



Figure 2. ESEM test samples.

(2) Wetting under constant pressure. Pressure was held constant at the end of consolidation, and then samples were wetted. In unsaturated triaxial cell, samples were wetted from bottom. To ensure fully saturation, sufficient time was needed for wetting. And suction change is applied as samples were wetted saturated. Suction change defines the degree of saturation to be achieved, suction applied are $s_1 = 200\,\text{kPa}$, $s_2 = 100\,\text{kPa}$, $s_3 = 50\,\text{kPa}$, $s_4 = 0\,\text{kPa}$ for the four test series.

Microstructure variation are induced by wetting, different degree of saturation corresponds to different variation of microstructure induced by wetting.

3 ESEM TEST SAMPLE PREPARATION

ESEM technique is a direct way to observe microstructure of Q_2 loess; lots of pictures are obtained in preparation for further analysis. Magnifications adopted in this test was 3000, 1500, 1000, 500, 200 and 100.

When four series of Q_2 loess samples of different degrees of saturation were prepared, a cubic of $2 \times 1.5 \times 1.5\,\text{cm}^3$ was cut from a loess sample, a total of 4 ESEM test samples were prepared for each test series. ESEM test samples are shown in Fig. 2.

ESEM test samples were broken into halves before ESEM test. Samples to be tested were wrapped in tin leaf and placed under the electron microscope. The apparatus used and the samples under observation are shown below.

4 ESEM TEST RESULTS AND THE PICTURE PROCESSING

Analysis of ESEM test results were carried out by a software named Scion Image, which can be used for picture processing and other purposes. Microstructural feature as pore size distribution, grain size distribution can be obtained via picture processing of this software. And these microstructure features will be further analyzed to indicate structural variation due to wetting.

Size of intra-aggregate pores are less than $0.1\,\mu m$, these are the pores that could not be observed in the ESEM photographs. Therefore pore sizes collected from ESEM photographs are those of intra-aggregate pores. And pore size distribution curves do not resemble those obtained through MIP technique which is bimodal for soil consisted of aggregates. However loss

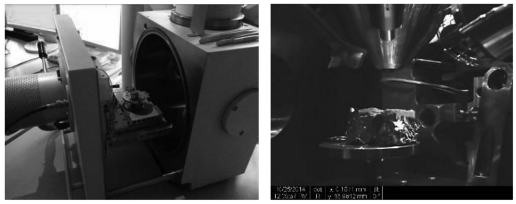


Figure 3. ESEM test of Q2 loess samples.

of information on intra-aggregate pores is not of significance for those pores will remain their volume during loading and wetting. It could be concluded that wetting-induced microstructure change are not associated with intra-aggregate pores, variation of inter-aggregate pore size distribution with wetting shows microstructure fabric change.

Typical ESEM photographs of Q_2 loess wetted to different degree of saturation are listed in Figure 4.

5 WETTING-INDUCED MICROSTRUCTRAL CHANGE OF Q2 LOESS

5.1 *Inter-aggregate Pore Size Distribution*

As mentioned above, microstructure change due to wetting could be described by variation of inter-aggregate pore size distribution, which can be obtained from ESEM photographs. Photographs of Q_2 loess wetted to different degree of saturation were processed and statistical information on inter-aggregate pore size was collected.

Figure 4 shows intra-aggregate pore size distribution at $s_1 = 200\,\text{kPa}$, and such statistical information when $s_2 = 100\,\text{kPa}$, $s_3 = 50\,\text{kPa}$, $s_4 = 0\,\text{kPa}$ could be obtained in the same way. Seen from Fig. 5, inter-aggregate pores are mostly consisted of pores with size less than $20\,\mu m$. The same goes for cases of $s_2 = 100\,\text{kPa}$, $s_3 = 50\,\text{kPa}$, $s_4 = 0\,\text{kPa}$.

Inter-aggregate size pore distribution were compared between $s_1 = 200\,\text{kPa}$, $s_2 = 100\,\text{kPa}$, $s_3 = 50\,\text{kPa}$, and $s_4 = 0\,\text{kPa}$, as shown in Fig.6. It is obvious that inter-aggregate pore size distribution varies as the loess is wetted from $s_1 = 200\,\text{kPa}$ to $s_4 = 0\,\text{kPa}$.

As Q_2 loess is wetted enormously, volume of pores with larger pore sizes decreases and volume of pores of sizes ranging from 10 to $20\,\mu m$ increases. This could be interpreted: as soil is wetted from $s_1 = 200\,\text{kPa}$ to $s_4 = 0\,\text{kPa}$ pores of sizes ranging from 10 to $20\,\mu m$ will become dominant. Zhao & Chen (1994) pointed out that pores of sizes ranging from 20 to $80\,\mu m$ are responsible for enormous collapse, while those with sizes ranging from 8 to $20\,\mu m$ are responsible for moderate collapse. It should be noted that Q_2 loess mostly consisted of pores of sizes less than $20\,\mu m$ will induce moderate collapse, as is seen in engineering practice.

Wang (2010) says $20\,\mu m$ is a threshold size, loess containing pores with their sizes larger than it is likely to collapse enormously. Such conclusion is drawn through lots of statistical surveys.

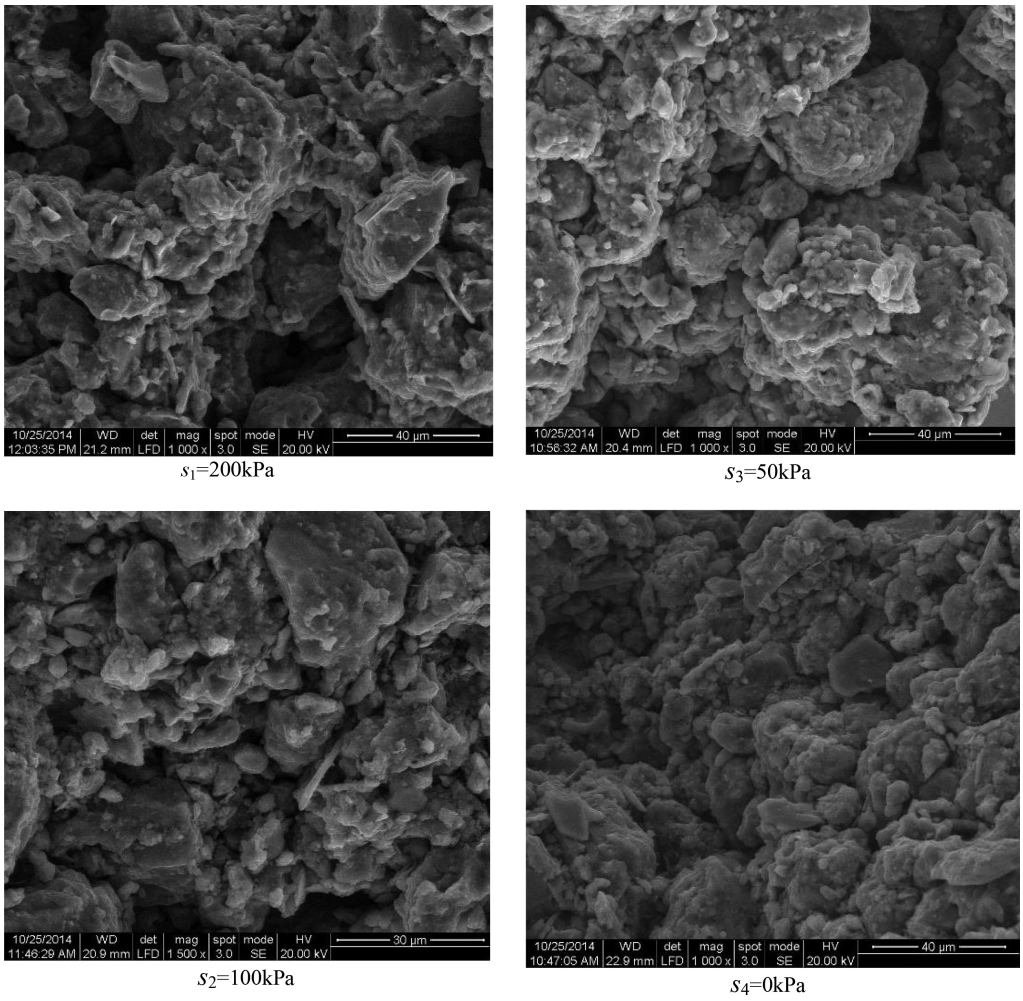


Figure 4. ESEM photographs of Q2 loess wetted to different degree of saturation.

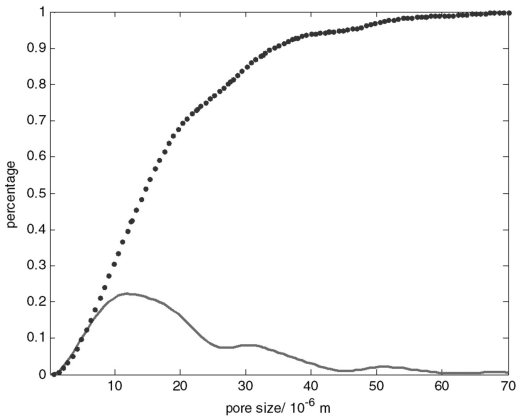


Figure 5. ESEM test of Q2 loess samples.

Wetting of Q_2 loess makes volume of larger pores diminish, eliminating its collapse potential, however, such potential could not be reduced enormously for pores that lead to moderate collapse remain large part of its pore size distribution.

5.2 *Change of aggregate size*

Size of aggregates could also be obtained via picture processing of ESEM photographs. Aggregate size distribution of Q_2 loess at $s_1 = 200$ kPa is shown in Figure 7.

Figure 8 shows wetting-induced change in aggregate size distribution as loess is wetted from $s_1 = 200$ kPa to $s_4 = 0$ kPa. It could be seen as wetting advances, number of aggregates of larger size increases, for aggregate absorbs water and becomes

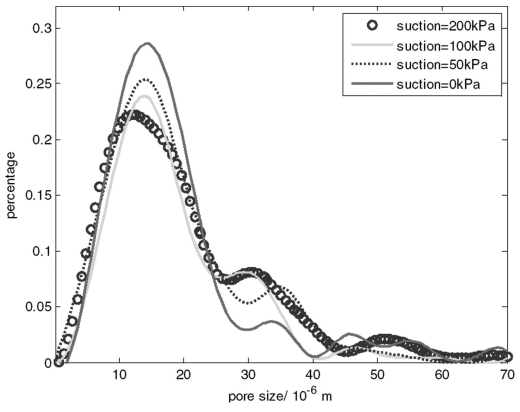


Figure 6. Wetting-induced change in inter-aggregate pore size distribution.

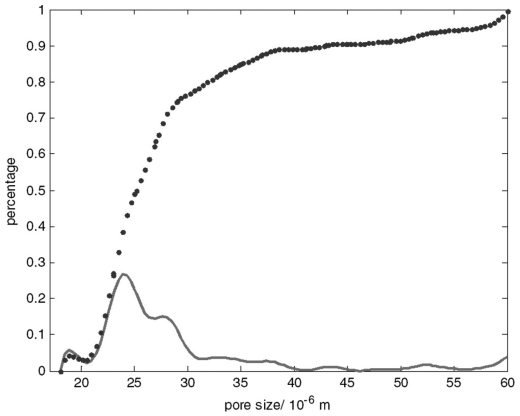


Figure 7. Aggregate size distribution at $s_1 = 200$ kPa.

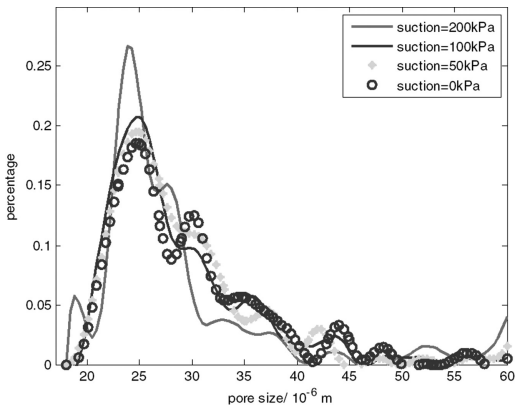


Figure 8. Wetting-induced change in aggregate size distribution.

larger. Note that changes in size of pore and aggregate are correlated, for expansion of aggregate lead to decrease in size of the pores, while collapse of aggregate structure also makes pore sizes smaller.

6 CONCLUSION

Q_2 loess samples were wetted to different degrees of saturation by applying suction change as the confining pressure held constant. SESM technique was used to observe the microstructure change due to wetting. Photographs obtained were processed and microstructure features as inter-aggregate pore size distribution were analyzed.

(1) As Q_2 loess is wetted, Pores of sizes ranging from 10 to 20 μm become dominant. Volume of pores of larger pore sizes decreases and volume of pores of sizes ranging from 10 to 20 μm increases.
(2) Changes in size of pore and aggregate are correlated, expansion of aggregates, due to absorption of water, lead to decrease in size of the pores, while collapse of aggregate structure also makes pore sizes smaller.

ACKNOWLEDGEMENTS

This work was financially supported by the National Natural Science Foundation of China (No.11272354, 51479208).

REFERENCES

Fang Xiangwei et al. 2011. Triaxial wetting tests of intact Q_2 loess by computed tomography. *China Civil Engineering Journal* 44(10): 100–106.

Fang Xiangwei et al. 2014. Research on microstructure of remolded Q_2 loess. *Chinese Journal of Underground Space and Engineering* 10(6): 1231–1236.

Romero, E. & Simms, P. 2008. Microstructure investigations in unsaturated soils. a review with special attention to mercury intrusion porosimetry and environmental scanning electron microscopy. *Geotech. Geol* 26(6): 705–772.

Wang Mei. 2010. *Study on structure of collapsible loess in China*. Taiyuan: China.

Zhao Jingbo & Chen Yun. 1994. Study on pores and collapsibility of loess. *Journal of Engineering Geology* 2(2): 76–83.

Unsaturated Soil Mechanics—from Theory to Practice – Chen et al. (Eds)
© 2016 Taylor & Francis Group, London, ISBN 978-1-138-02921-7

Structural damage properties of loess under loading and moistening

S. Shao, S.J. Shao & A.Z. Luo
Institute of Geo-engineering, Xi'an University of Technology, Xi'an, China

ABSTRACT: The stress-strain relationship of intact loess with different water contents was obtained by the triaxial tests. According to the difference among stress-strain curves of loess with different humidity, the loess structural damage caused by the moistening, consolidation and shearing was explored by the initial tangential modulus changing with increasing of water content and strain. When the secondary structure of damaged loess was developed under moistening, shearing and consolidation, the stress-strain curves is in hyperbola. The damaged structure is corresponding to the different stress-strain states in the process of shearing deformation, in which the whole development process are revealed. The structure variation of intact loess is derived from the action of loading and moistening. Meanwhile, this paper proposed the structural damage property parameters of the intact structure damage development law that can completely be applied to evaluate the collapsible loess under the varying conditions of water content fields and stress fields; and they are used to establish the stress-strain equation for the structural loess.

1 INTRODUCTION

Loess is a special soil with the structural property. The structural property of loess shows that maintaining its structure stabilization capacity before the structural variety is not damaged and the structural changeability is loss of stabilization capacity after the structure failure (Xie, 2001). The changes of stress state and water content of loess caused by external loading and humidity increase will occur simultaneously in the loess mass, in which the stress state and humidity are the functions of time and space. Generally, because the stress increase is likely to cause the variations of soil structure, and water content increase is likely to make soil structure connection weaken that soil displays, the damage variations of soil structure was developed by the inter-coupling of loading and water submerging within soil body. Further, the structure variation results in the deformation and strength characteristics changing in various kinds of mechanical effects (Liu, 1996). Because of the structural properties of collapse loess increasing the capacity, the structural behavior is in correspondence with a certain stress state and water content. Accordingly, both can change simultaneously or either of one will change; and soil grain arrangement within soil body and colloidal state can change, the micro-structural change can cause the changes of macro-mechanical behaviors in the loess. It is just the loess strong structural behaviors that make loess soil be very sensitive to water content and stress condition changes so that moistening and loading processes are also the process of loess original structure damage and softening (Shao, 2004). The most of existing non-linear constitutive models or elastic-plastic models can only describe the process of deformation change, or modify the existing models with an aim at structural soil behaviors without considering the structural damage evolution laws caused by moistening and loading. Accordingly, it is hard for them to reflect the real mechanical characteristics of structural soil and stress-strain changing laws (Xie et al., 1999; Shao et al., 2004; Shen, 1993). To summarize the above description, this paper deals with the intact loess deformation characteristics acted by moistening and loading under the conditions of tri-axial tests, discusses the damage evolution laws of structural loess under the conditions of moistening, iso-directional compress and moistening and shearing stress, and seeks for a parameter which is able to reflect intact structure damage evolution law of the collapsible loess in an overall way under the varying conditions of water content field and stress field, and establishes the stress-strain equation based on the structural damage parameters.

2 STRUCTURAL DAMAGE BEHAVIORS OF LOESS UNDER THE TRI-AXIAL SHEARING

On the whole, the people analyze damage behaviors of the loess in view of damage properties of the mechanical composite materials, that is, the stress borne by the damage loess with a certain trait can be shared by the intact loess and completed damage loess in terms of a certain proportion, and the same deformation occur on the intact loess and completed damage loess. Based

on this hypothesis, the stress sharing can be described as follows:

$$\{\sigma\} = (1-\omega)\{\sigma_i\} + \omega\{\sigma_d\} \quad (1)$$

where, σ_i and σ_d are the intact loess and complete damage loess sharing stress; ω is the damage ratio. Owing to the intact loess and complete damage loess having the same deformation, which is actual deformation of the damage loess, thus, the following equation can be derived:

$$E = (1-\omega)E_i + \omega E_d \quad (2)$$

where, E, E_i and E_d are the whole magnitude modulus and sharing stress of the intact loess and complete damage loess respectively. If the whole magnitude modulus of the damage loess can be decided, the damage parameter can be obtained.

Based on the viewpoint that moistening and loading can cause damage, the damage parameters of loess, being able to reflect the loess structural damage changes under moistening and consolidation pressure, are established by the changing law between the initial tangent modulus and consolidation pressure and water content. However, the structural damage changes can occur in the shearing process. The certain damage loess with different humidity under consolidation pressure is not only different of the initial shearing modulus, but also different of the whole magnitude modulus (the cutting modulus) in the shearing process. The modulus changing measured by the test can also reflect the damage changes of soil structure in shearing process. It can be seen that loading damage should be further distinguished into the consolidation damage and shearing damage in order to reflect the structure changes in the shearing process, and both can cause the structure damage coupled with moistening.

As to the normal consolidation soil, its structure appears newborn all the time in the process of consolidation and shearing, the stress-strain relation can be expressed as follows:

$$\sigma_1 - \sigma_3 = \frac{\varepsilon_1}{a + b\varepsilon_1} \quad (3)$$

where, a and b are soil feature parameters, the reciprocal of a is the initial tangent modulus, which mainly reflects the effect of compressive hardening caused by the consolidation pressure, the reciprocal of b is the approximation value of stress-strain curve, which reflect the shearing strength of soil maintaining the structure unchanging. However, under the action coupling with consolidation pressure and moistening, there is not only the compressible hardening of loess under compressing, but also the softening of the structural damage. Under the effect coupling with shearing and moistening, there is not only shearing contraction hardening of loess, but also the softening of the shear damage. That is to say, the parameter a not only relates to the initial consolidation pressure, but also to the changes of water content. At the same time, because the structure strength continues to change, the shearing strength reflected by b continues to change in the shearing process. If soil structure is no change in the shearing deformation process, b value is fixed, the shearing stress-strain relationship of loess with a certain structure, being similar to the saturated normal consolidated soil, can still be described by the hyperbola pattern. The structural changes can be described by the hyperbola relation with different b values in the shearing process. Namely, a value reflects the moistening-compressing damage caused by moistening and consolidation pressure; b value is a changing quantity with the shearing deformation, reflecting that moistening-shearing damage caused by the moistening and shearing pressure. Supposing that when shearing starts, the approximation value of the fitting hyperbola is b0, and damaged, the approximation value of the fitting hyperbola is b_R , the varying laws of b value reflect the changes of shearing strength on different structures soil body in the sharing process. Basing on the variation of b value with shearing deformation, the stress-strain curves can be divided into the hardening and softening type.

Based on the above analysis, when the initial water content and consolidation pressure are fixed, a value is constant in Eq. (3), stress and strain state can be determined by corresponding to b value in the shearing deformation process, but b value varies with the strain development. When $b_0 < b_R$, this indicates that the anti-shearing strength of loess under the shearing initial structural conditions is larger than under the strain failure structural conditions so that the corresponding stress-strain curve can be judged to fall into the softening type curve. When $b_0 > b_R$, this indicates that the anti-shearing strength of loess under the shearing initial structural conditions is smaller than under the strain secondary structural conditions so that the stress-strain curve can be judged to belong to the hardening type curve. It can be seen that the process of moistening and loading is the successively damaging variation process in the soil body structure. Whether the stress-strain curves are the hardening or softening types, they can be expressed by a family of hyperbolas drawn by a value determined with the initial water content and consolidation stress and b value varying between b_0 and b_R. Therefore, based on the tri-axial shearing testing results of loess with different humidity, if the parameters, which are a, b_0 and b_R, varying laws of structural loess, can be obtained, the secant modulus of structural loess in the different damages state in Eq. (2) can be derived. Therefore, the equation can be derived from Eq. (3):

$$E = \frac{(\sigma_1 - \sigma_3)}{\varepsilon_1} = \frac{1}{(a + b\varepsilon_1)} \quad (4)$$

here, E is the secant modulus corresponding ideal hyperbola with a certain b value under a certain structural condition in actual strain states, it reflects the degrees of consolidation pressure, humidity and

damaging failures as well as the effect of shearing deformation development, which can be described and expressed by the following Eq.

$$E = F(\sigma_{3c}, w, \omega, \varepsilon_1) \tag{5}$$

It can be seen from Eq. (5) that when the modulus is obtained under any certain consolidation pressure, humidity and strain state, the damage parameters for loess under the complete damage states can be decided based on Eq. (2) by the modulus corresponding to the intact loess .

3 ANALYSIS OF TRIAXIAL TESTING RESULTS OF LOESS

3.1 *Results of tri-Axial shearing tests*

All experiments of Xi'an Q_3 loess, its dry density being 1.30 g/cm3, were conducted by triaxial test equipment under consolidation drainage condition. To reflect the action of consolidation pressure upon loess structure, range of consolidation pressure is 100–300 kPa. To reflect the effect of humidity upon structural property of loess, range of water content of samples is 3.1%, 6%, 10%, 14%, 22% and 26%.

Test results shown in Fig.1 indicate that although Q_3 loess is loose in density, and good in porosity development, its humidity (water content) is so small ($w = 3.1\%$) that its structural property is apparent, and the stress-strain curves appear to be softening pattern. With the increase of consolidation pressure (100 kPa–300 kPa), the compressing-hardening feature is enhanced, and the softening feature of stress-strain curves is weakened. When water content increased, the compressing-hardening feature will become more prominence with an increase of consolidation pressure. Meanwhile, with the enhancement of compressing-hardening feature and the secondary structure, the stress-strain relationship appears gradually to be weak softening type in the shearing process. When water content and consolidation pressure are high, the intact structure is damaged to great extent, but the secondary structure develop and shearing contraction enhances under consolidation; and in the shearing process, the stress-strain curves gradually develop from the weak hardening type into strong hardening type. Obviously, when water content is low, consolidation pressure can bring weak damage to the intact structure, and the intact structure can display the apparent changes in the shearing process, there are obvious peak values and residual strength. When water content increase, the coupling of moistening and consolidation pressure will enhance the damage of intact structure, but the varying of intact structure will reduce in the shearing process, and the compressing-hardening and the secondary structure feature can gradually enhance. In addition, it can be seen from Figs that consolidation pressure has greater effect upon the residual stress, with consolidation pressure increasing, the residual

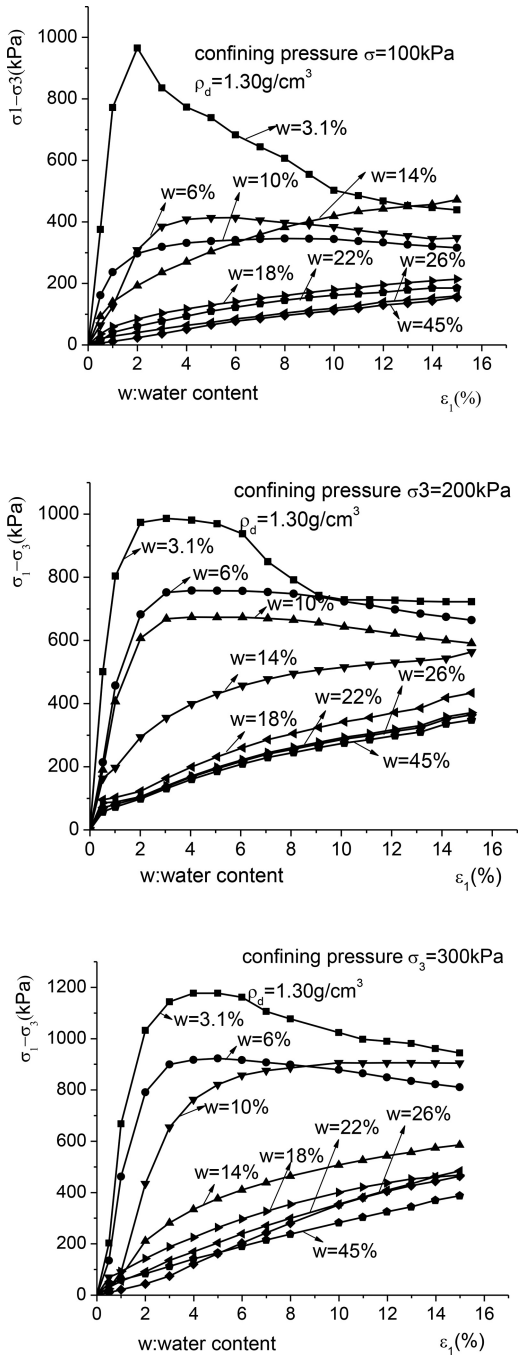


Figure 1. The stress-strain curve of the same initial consolidation pressure.

stress increases, this indicates that increasing the consolidation pressure can improve soil residual strength under the same conditions of water content in the shearing process.

3.2 *Varying law of the initial tangent modulus*

By analyzing different humidity and stress-strain curves under the different conditions of water content and consolidation pressure, the varying laws of the initial tangent modulus can be obtained, as shown in Fig. 2. It can be seen that the initial tangent modulus decreases with an increase in water content in the structural damaging evolution process of collapsible loess, this illustrates that changes of water content (humidity) is one of the most important factors that structural damage changes. Meanwhile, with an increase in consolidation pressure, the initial tangent modulus represent a descending tendency, this indicates that structure feature of the collapsible loess weakened with an increase in consolidation pressure. That is, the changes of the initial stress can also yield the same damage to the structure of the loess. This is the obvious features that intact loess is different from of remodel loess. When water content increases to a certain extent, the initial modulus has tended to the horizon or level line with the variation of initial consolidation pressure, it is illustrated that soil structural properties have released fully by moistening at this time. With an increase of water content, shearing contract features become more and more apparent.

The varying laws of the initial tangent modulus with water content increasing indicate that loess structure gradually suffers from damage under the coupling action of moistening and consolidation, and structural damage caused by moistening and compressing develops gradually so that the secondary structure and compressing hardening are gradually enhanced, thus, the initial tangent modulus reduce gradually, and tend to a certain fixed value in the end. Moistening can dissolve parts of colloids and salt base, and make sucking connection loss its function at the same time. The wedging function of water membrane renders all the expansion and contraction potential energy released and damages the solid-chemical bounding linkage among grains as a result of accelerating the damage of loess structure. Consolidation pressure has had a certain effect upon loess structure. With initial stress field increasing, the damage of loess structure increases gradually.

In analyzing the relation curves among the initial tangent modulus and water content as well as consolidation pressure, they can be expressed by the following equation:

$$E_i^w = K_w Pa e^{-n_w} \tag{6}$$

When the range of consolidation pressure is within 100 kPa–300 kPa, *Kw* is within 692.11–1860.64, n_w is within 9.1–12.0

The relation of initial tangent modulus with consolidation pressure can be expressed by the following equation:

$$E_i^\sigma = K_\sigma Pa\left(\frac{\sigma_{3c}}{Pa}\right)^{-n_\sigma} \tag{7}$$

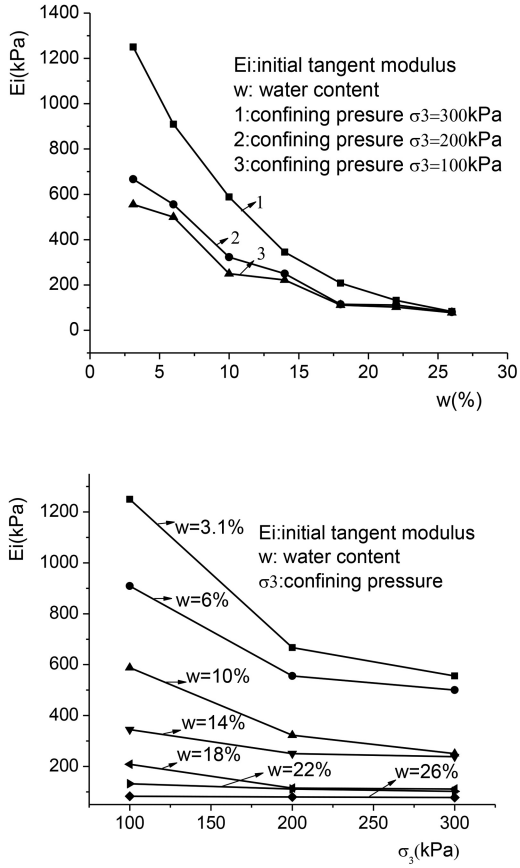


Figure 2. The curve of initial tangent modulus and water content and consolidation pressure.

where, when the range of water content is within 3.1%–26%, *K* is within 82.8–1215.3, n_σ is within 0.571–0.7563.

In considering comprehensively the effect of water content and consolidation pressure, the following comprehensively-unified equation is present:

$$E_i^{w\sigma} = KPa\left(\frac{\sigma_{3c}}{Pa}\right)^{-n_\sigma} \cdot e^{-n_w \cdot w} \tag{8}$$

In this paper, modulus number *K* is suggested to take 1863.1; n_σ is suggested to take 0.7563, and $n_w = -0.03096\,\sigma_{3c} + 14.6997$. the varying laws of initial tangent modulus are determined, that is, a value in Eq.(2) is derived.

3.3 *Varying laws of b value*

Under the conditions of consolidation stress and humidity, when a value is decided, b value can be obtained in terms of Eq.(2) under different shearing stress states. As to the softening type curves, the changing laws of b value with the axial strain is shown in

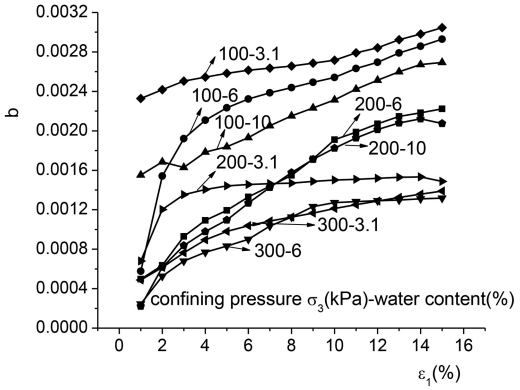


Figure 3. The curve between b and axis strain of softening stress-strain curves.

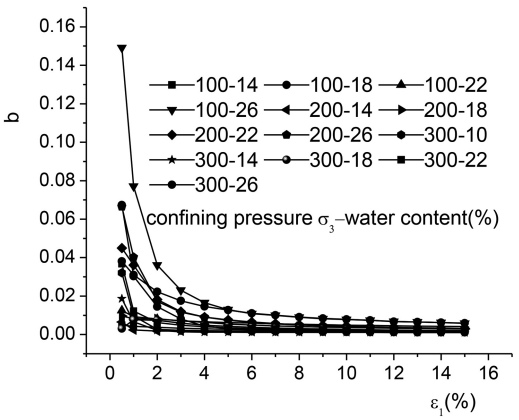


Figure 4. The curve between *b* and axis strain of hardening stress-strain curves.

Fig.3. This paper suggests the following power function equations to describe the changing laws of the softening type curves:

$$b = A_1 \varepsilon^{B_1} \tag{9}$$

Where, A_1, B_1 are the test parameters; and they are related to the initial consolidation pressures and water contents.

A vast number of test data show that the initial structure damage is protruding and the secondary structure growth is more apparent than the intact structure with the enhancement in the coupling of both initial consolidation pressures and moistening, so that the stress-strain relation curve shows the hardening features. But, soil body still has suffered from structural damage in the shearing process. As to the hardening type curves, its changing laws of b value with axial strain is shown in Fig.4. Also, this paper suggests that the power function is used to describe the varying regulations of the damage development of the hardening type curves in the following:

$$b = A_2 \varepsilon^{-B_2} \tag{10}$$

where, A_2, B_2 are the test parameters. They are also related to the initial consolidation pressures and water contents.

It can be seen that the hardening type curve of structural collapsible loess can not be simply considered as the ideal hyperbola, but the ideal hyperbola used to study the hardening type hyperbola of structural collapsible loess is great difference.

3.4 *The judging whether softening or hardening type curves*

Since there are different changing laws of b value on the softening type curves and hardening type curves, it is necessary to make different judging to the *b* value. Through taking consider the properties of the

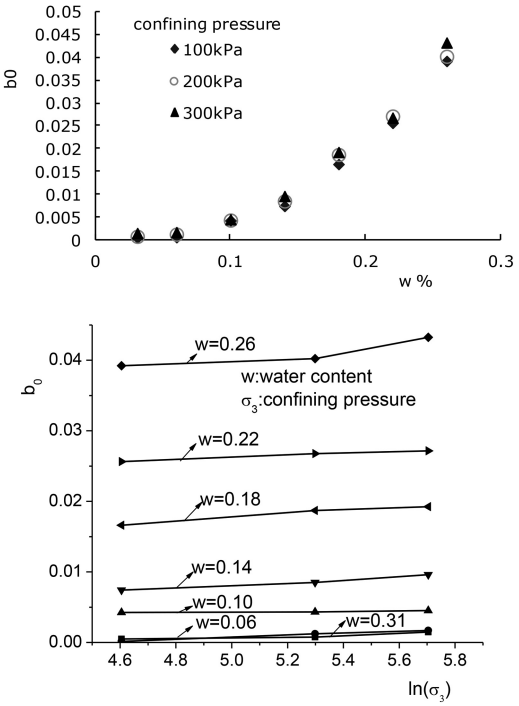


Figure 5. The relationship between b_o and water content and consolidation confining pressure.

stress-strain relationship curves under the same consolidation pressure and water content in the shearing process, the curves , given the b value, can be determined under the *a* value. Where, b_o is the *b* value of the initial shearing damage in the shearing process; b_R is the corresponding damage state b value when strain reaches the damage, the relationship curves with b_o and b_R under different consolidation pressures and water contents are shown in Figures 5 and 6.

Based on the above curve features, b_o and b_R can be described using the following function equations:

$$b_o = A_o e^{-B_o w} + C_o \ln(\sigma_{3c}) + D_o \tag{11}$$

$$b_R = A_R e^{-B_R w} + C_R \ln(\sigma_{3c}) + D_R \tag{12}$$

where, $A_o, B_o, C_o, A_R, B_R, C_R, D_R$ are the testing parameters, which can be determined by the conventional tri-axial tests.

4 THE DAMAGE CHANGING LAWS OF LOESS UNDER LOADING AND MOISTENING

4.1 *Definition for Damage Ratio*

In terms of above descriptions, under the coupling of loading and moistening, structural loess damage process includes not only the effect of compressing-moistening damage to soil structure for consolidation pressures and moistening, but also the moistening-shearing damage effect for moistening shearing damage. It includes not only the damage of intact structure, but also the growth of secondary structure. The damage of intact structure and growth of secondary structure are always accompanied in the process of consolidation and shearing deformation under some given moistening conditions. Accordingly, the structure damage parameters defining must reflect compressing-moistening damage and shearing-moistening damage as well as the growth of secondary structure. Based on Eq.(2), damage ratio can be described by the difference values among the initial tangent modulus of the undamaged intact loess and some strain corresponding to damage loess secant modulus, and the difference value ratio among the intact loess initial tangent modulus and corresponding to the complete damage secant modulus. As following:

$$\omega = \frac{E_i - (E)_{\varepsilon_1}}{E_i - (E_d)_{\varepsilon_1}} \tag{13}$$

Where, *Ei* is the initial tangent modulus of intact loess; $(E)_{\varepsilon 1}$ is the secant modulus of damage loess under some strain condition; $(Ed)_{\varepsilon 1}$ is the secant modulus of complete damage loess under the same strain condition. Eq.(4) can be used to determine modulus: parameter a can reflect the moistening damage of intact structure and the growth effect of the secondary structure, and parameter b can reflect the shearing-moistening damage of intact structure and the growth effect of secondary structure.

4.2 *Changing Laws of the Modulus*

Owing to the different of compressing-moistening damage of intact structure and the growth of secondary structure in the compressing deformation process, and the different of shearing-moistening damage of intact structure and the growth of secondary structure in the shearing deformation process, the shearing stress-strain curves appear to be the different softening type or hardening type curves. They can be differentiated by the changing laws of b value determined by the hyperbola relationship under different shearing states, and they can be also determined by comparing the initial b_o with the damage strain state b_R in the shearing process.

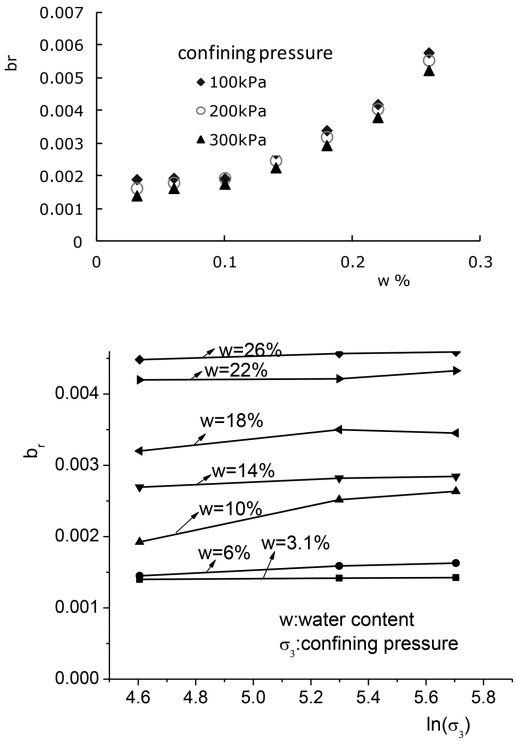


Figure 6. The relationship between b_R and water content and consolidation pressure.

The secant modulus equation of softening type curves should be as follows:

$$E = \frac{1}{1/\{KPa(\frac{\sigma_{3c}}{Pa})^{-n_\sigma} e^{-n_w w}\} + A_1 \varepsilon_1^{B_1+1}} \tag{14}$$

The secant modulus equation of hardening type curves should be as follows:

$$E = \frac{1}{1/\{KPa(\frac{\sigma_{3c}}{Pa})^{-n_\sigma} e^{-n_w w}\} + A_2 \varepsilon_1^{-B_2+1}} \tag{15}$$

4.3 *Damage Ratio and Stress-Strain Equation*

When the damage ratio is determined in terms of Eq.(13), the secant modulus of the intact loess and the complete damage loess are needed. In this paper, based on the test results of the stress-strain under the conditions of different water contents (3.0–26%) and

consolidation pressures (100–300 kPa) and the hyperbola distribution of different structural states reflected in the shearing process, when water content is 3.0% and consolidation pressure is 100 kPa, the moisture pressure is the minimum and the initial tangent modulus is the maximum and b_0 value is the minimum; when water content is 26.0% and consolidation pressure is 100 kPa, the moisture pressure is the maximum and the initial tangent modulus is the minimum and b_0 value is the maximum. Accordingly, the initial hyperbola of the initial shearing-moistening damage states can be served as stress-strain curves of the intact loess and stress-strain curves of the completed damage loess. Respectively, the complete loess is defined under the conditions of that water content is 26.0%, and consolidation pressure is 300 kPa.

The modulus of intact loess is as follows:

$$E_i = 1863.1Pa \cdot e^{-11.61w} \tag{16}$$

The modulus of complete damage loess is as follows:

$$E_d = \frac{1}{1/(1863.1Pa \cdot e^{-11.61\times 0.26}) + A_2\varepsilon^{B_2+1}} \tag{17}$$

Based on Eq.(13), (14), (15), the damage ratios can be determined respectively in the process of softening and hardening type shearing deformation, that is, when $b_0 < b_R$, the damage ratio is as follows:

$$\omega = \frac{e^{-11.61w} - \dfrac{e^{-11.61w}}{1+1863.1Pa \cdot e^{-11.61w} \cdot A_1\varepsilon^{B_1+1}}}{e^{-11.61\cdot 26} - \dfrac{e^{-11.61\times 0.26}}{1+1863.1Pa \cdot e^{-11.61\times 0.26} \cdot A_2\varepsilon^{B_2+1}}} \tag{18}$$

When $b_0 > b_R$, the damage ratio is as follows:

$$\omega = \frac{e^{-11.61w} - \dfrac{e^{-11.61w}}{1+1863.1Pa \cdot e^{-11.61w} \cdot A_2\varepsilon^{B_2+1}}}{e^{-11.61\cdot 26} - \dfrac{e^{-11.61\times 0.26}}{1+1863.1Pa \cdot e^{-11.61\times 0.26} \cdot A_2\varepsilon^{B_2+1}}} \tag{19}$$

And then, in terms of the view of composite materials in the damage mechanics, based on Eq. (1), the stress-strain equation can be described as the increment equation:

$$\begin{aligned}\{\Delta\sigma\} &= (1-\omega)[D_i]\{\Delta\varepsilon\} \\ &+ \omega[D_d]\{\Delta\varepsilon\} - (\{\sigma_i\} - \{\sigma_d\})\Delta\omega\end{aligned} \tag{20}$$

where, $[D_i]$ and $[D_d]$ are the intact loess and damage loess tangent radial matrix respectively. Application of the above equation, the actual deformation process of the collapsible loess can be obtained under loading and moistening process.

5 CONCLUSIONS

(1) Under coupling of loading and moistening, loess structure appears to be a damaging and forming process that intact structure is destroyed and secondary structure is developed. In the process of consolidation and shearing deformation of loess tested by triaxial apparatus, there are the damage of intact structure and formation of secondary structure caused by compressing-moistening as well as the shearing-moistening.

(2) The degrees are different of compressing-moistening damage of intact and the growth of the secondary structure, and the shearing stress-strain curves are different. Supposing when the stress-strain curves without structural changes in the shearing process, are the ideal hyperbola variations, the changing of loess structure can be revealed by the different hyperbola distribution determined by the actual shearing stress-strain states in the shearing process.

(3) Based on the changing of the hyperbola distribution that can reflect different structural in the shearing process, the stress-strain curves under the different humidity and consolidation pressure can be classified into the softening and hardening types. The former indicates that the compressing-moistening damage is smaller, but the structural variation is obvious in moistening-shearing process; the latter indicates that the compressing-moistening pressure damage is projected, and the growth of secondary structure is apparent in the shearing moistening process.

(4) Based on the viewpoint of composite materials in the damage mechanics, it is suggested that the changing of the damage ratio between compressing-moistening damage and shearing-moistening damage should be taken into consideration, so that the corresponding stress-strain equation is established, which is able to reflect the changing of loess structural damage in the loading and moistening process.

REFERENCES

Liu Z D. 1996, Loess Mechanical Engineering. Shaanxi Provincial Sci-Tech Press, Shanghai.

Shao S J. 2004, Damage Evolution Behavior of Collapsible Loess. Chinese Journal of Rock Mechanics and Engineering, 23(24): 4161–4165.

Shao S J, Zhou F F and Long J J. 2004, Intact Loess Structural Behavior and Its Quantitative Parameter. Chinese Journal of Geotechnical Engineering, 26(4): 531–536.

Shen Z J. 1993, An Elastic-plastic Damage Model for Cement Clays. Chinese Journal of Geotechnical Engineering, 15(3): 21–28.

Xie D Y. 2001, New Progress of Loess Mechanics in China. Chinese Journal of Geotechnical Engineering, 23(1): 1–13.

Xie D Y, Qi J L. 1999, A New Approach on Loess Structural Behaviors and Its Quantitative Parameters. Chinese Journal of Geotechnical Engineering, 20(2): 6511–6516.

This page intentionally left blank

Unsaturated Soil Mechanics—from Theory to Practice – Chen et al. (Eds)
© 2016 Taylor & Francis Group, London, ISBN 978-1-138-02921-7

The microstructure and soil-water characteristic of unsaturated loess

D.R. Hao & H.J. Liao
Department of Civil Engineering, Xi'an Jiaotong University, Xi'an, China

C.M. Ning
Department of Capital Construction, Xi'an Jiaotong University, Xi'an, China

X.P. Shan
Beris Engineering and Research Corporation, Qingdao, China

ABSTRACT: Studying the effect of pore structure on matric suction is of great significance in theory and application. A series of indoor experimental studies has been done using Xi'an remolded loess by Pressure Plate Extractor in this paper. Firstly, soil-water characteristic curves considering different initial water contents and sand contents were obtained, air entry values were determined and influences of initial water content and sand content on soil-water characteristic curves were analyzed. Then, based on the pore size determination method, the effect of pore structure on matric suction was analyzed. The results show that with the increase of initial water content, the pore structure tends to be compact, and make the drying rate slow and water absorbing capacity strong; with the increase of sand content, the pore structure tends to be loose, and make the drying rate quick and water absorbing capacity weak. Microstructure of soils illustrates that matric suction is influenced by the pore size distribution of soil. Thus from the micro view, the research of physical environment effect on matric suction is of practical significance.

1 INTRODUCTION

Matric suction perhaps is the most widely used index in dealing with physical phenomena in unsaturated soil. This variable governs or influences flow phenomena, stress phenomena, deformation phenomena, etc. Soil-water characteristic curve is used to describe the relation between matric suction and moisture state and reflects the internal mechanisms of unsaturated soil. In recent years, many researchers including Black (1962), Mitchell & Avalle (1984), Vanapalli & Fredlund (1999), Miller (2002), Zhou (2005), Liu (2011) have studied the influences, such as density, water content, and particle size distribution on matric suction of unsaturated soil and suggested that each of these factors influences air entry value, the dying rate and other indexes of the soil-water characteristic curve. While in essence, each of these factors makes change of pore structure, then leads to the change of soil-water characteristic curve. Matric suction is considered a variable that closely connects to pore structure of unsaturated soil. Thus, the study on the effect of pore size distribution on matric suction considering different possible physical environment of unsaturated soil is of great significance to the application of unsaturated soil mechanics in engineering practice.

Table 1. Physical properties of soil samples.

w(%)	ρ(g/cm^3)	w_L(%)	w_p(%)	I_p
4.40	1.687	32.9	20.0	12.9

2 LOESS SAMPLES AND TEST CONDITIONS

2.1 *Physical properties of soil*

Soil samples are taken from the north slope of Bailu Table l and (34° 16′ 9″ N, 109° 3′ 51″ E), in Xi'an City, Shaanxi Province, Western China. The liquid limit and plastic limit were 32.9% and 20.0% separately measured by SYS digital determinator. According to grain size distribution curve of soil samples, the percentage of soil by weight of which particle size that less than 0.075 mm is 47.1%. The physical properties are shown in Table 1. Based on *Code for Design of Building Foundation* (GB50007- 2011) and *Soil Engineering Classification Criterion* (GB/T50145-2007), the soil samples are regarded as silty sand loess.

2.2 *Device and test conditions*

Pressure Plate Extractor 5bar (1600 type) and 15bar (1500F1 type) produced by Soil moisture Equipment

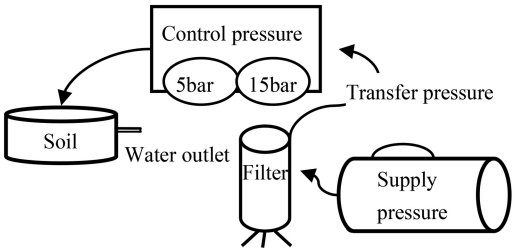


Figure 1. Diagram of Pressure Plate Extractor.

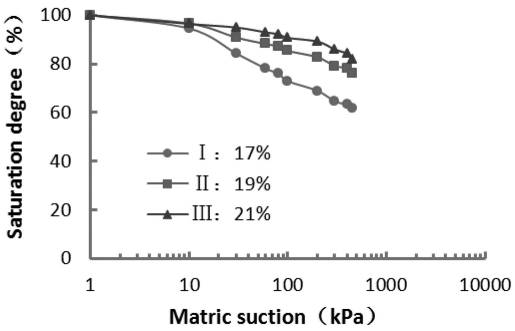


Figure 2. SWCC with different initial water contents.

Corporation of USA is used in the experiment. It consists of three parts, which are pressure device, extractor, and drainage system, as shown in Figure 1.

In order to study the influence of initial water content on matric suction of unsaturated soil, three groups of samples are prepared by controlling the number of light compaction as 60 and the dry densities of the samples are all 1.585 g/cm^3. Three groups I, II, III of soil are made with the initial water content as 17%, 19%, 21% respectively.

In order to study the influence of particle size distribution on matric suction of unsaturated soil, three groups of samples IV, V, VI are prepared by controlling the sand content as 20%, 40%, 60% respectively. The dry densities and initial water content are 1.585 g/cm^3 and 19% separately.

Air pressures are given by stepwise loading method as 0.1bar, 0.3bar, 0.6bar, 0.8bar, 1bar, 2bar, 3bar, 4bar and 5bar.

3 INVESTIGATION OF TEST RESULTS

3.1 *Effect of initial water content on SWCC*

The soil-water characteristic curve is shown in Figure 2 considering three different initial water contents. It can be seen that when the initial water content is smaller, the change of saturation degree is larger with matric suction increases. In other word, the drying rate of the sample with smaller initial water content is faster and the water absorbing capacity is weaker.

Table 2. Air entry value of the samples with different initial water contents.

Sample number	I	II	III
Initial water content	17%	19%	21%
Air entry value (kPa)	4.5	4.9	5.4

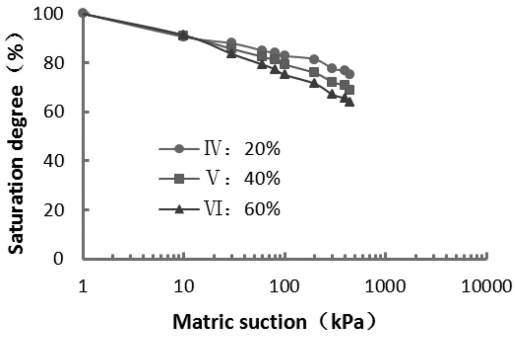


Figure 3. SWCC with different initial sand contents.

Table 3. Air entry value of the samples with different sand contents.

Sample number	IV	V	VI
Sand content	20%	40%	60%
Air entry value (kPa)	5.9	3.1	1.9

By the definition of air entry values based on the test results, the values are determined in Table 2. It can be seen that the sample with higher initial water content has larger air entry value.

3.2 *Effect of sand content on SWCC*

The soil-water characteristic curve is shown in Figure 3 considering three different sand contents. It shows that when the sand content is smaller, the change of saturation degree is smaller with matric suction increases. In other word, the drying rate of the sample with smaller initial water content is slower and the water absorbing capacity is stronger.

The air entry values of the samples are showed in Table 3. It can be seen that the sample with higher sand content has smaller air entry value.

It can be seen from the experiments that matric suction is closely related to the micro state of pore structure. The physical environment changes, such as initial water content and sand content, can influence the change of pore structure, and further make the change of matric suction. The impact of pore structure on matric suction will be discussed in the following.

4 ANALYSIS OF THE IMPACT OF PORE STRUCTURE ON MATRIC SUCTION

4.1 *Calculation theory of pore size distribution*

William Thomson established the relation between matric suction and pore size in 1871. The Kelvin formula was proposed as follows.

$$r_k = -\frac{2T_s v_w}{RT\ln(\mathrm{RH})} = \frac{2T_s}{u_a - u_w} \tag{1}$$

where r_k is pore size (um); T_s is surface tension (J/m^2); v_w is partial molar volume of water vapor (m^3/mol); R is universal gas constant (J/(mol · K)); T is thermodynamic temperature (K); RH is relative humidity of pore water vapor (%);$u_a - u_w$ is matric suction (kPa).

The accurate size of pore r_p^i is composed of Kelvin pore size r_k^i and water film thickness t^i:

$$r_p^i = r_k^i + t^i \tag{2}$$

Halsey Equation can be used to evaluate the water film thickness t^i.

$$t^i = \tau\left[-\frac{5}{\ln(\mathrm{RH}^i)}\right]^{1/3} \tag{3}$$

where t^i is the water film thickness adhering to soil particles when the relative humidity is in the i step increment; τ is effective diameter of adsorbate molecule.

When the relative humidity or matric suction is in the i step increment, the variation of pore volume ΔV_p^i filled by gas or water per mass soil can be defined as:

$$\Delta V_p^i = \frac{\Delta w^i}{\rho_w} \tag{4}$$

Mass water content Δw^i in the equation (4) can be determined by the pressure plate extractor test.

Combined with equations (1), (2), (3), the pore size can be calculated. The pore volume per mass soil of each size can be determined by equation (4).

4.2 *Calculation and discussion*

4.2.1 *Pore size distribution with different water contents*

Based on the experiment results, the relation between mass water content and matric suction of the samples with different initial water contents are showed in Figure 4.

It can be seen that during the dying process, mass water content decrease fast then tend to smooth with the increase of matric suction. When the mass water content is the same, the sample with high initial water content has large matric suction. Under the same number of light compaction, the sample with high initial water content has strong water absorbing ability.

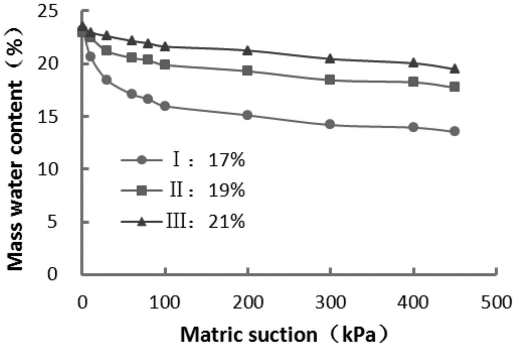


Figure 4. SWCC with different initial water contents.

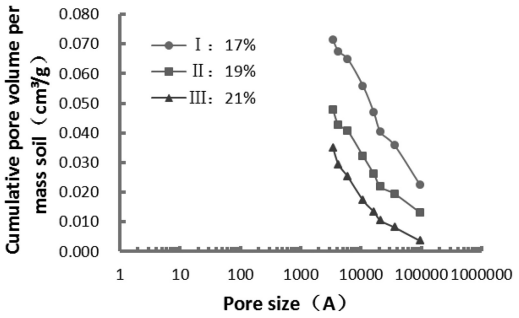


Figure 5. Pore size distribution curve of the samples with different initial water contents. (1 μm = 10000A).

Table 4. Percentage of pore volume distribution of the samples with different initial water contents.

Initial water content	Percentage of pore volume (%)		
	Pore size (<1 μm)	Pore size (1~4 μm)	Pore size (4~16 μm)
17%	22.53	46.48	30.99
19%	32.61	39.13	28.26
21%	50.00	38.89	11.11

From Figure 4, pore size distribution of the samples with different initial water contents are showed in Figure 5.

From Figure 5, with the same dry density, cumulative pore volumes per mass soil of the samples are different. The samples with initial water content 17%, 19%, 21% have cumulative pore volumes per mass soil 0.071 m^3/g, 0.048 m^3/g, 0.035 m^3/g respectively. With the increase of initial water content, cumulative pore volumes tend to decrease.

Percentage of pore volume distribution of the samples with different initial water contents is analyzed from Figure 5, showed in Table 4.

As shown in Table 4, for the sample with initial water content 17%, there are more big pore (size 4~16 μm) among the soil particles. The pore volumes of different

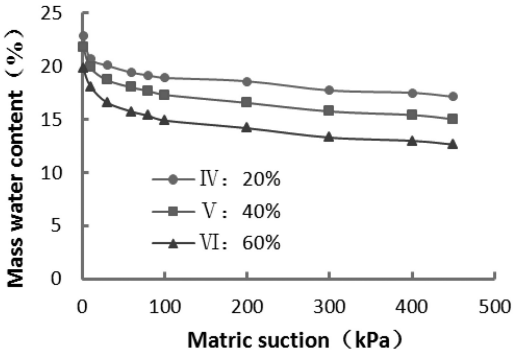


Figure 6. SWCC with different sand contents.

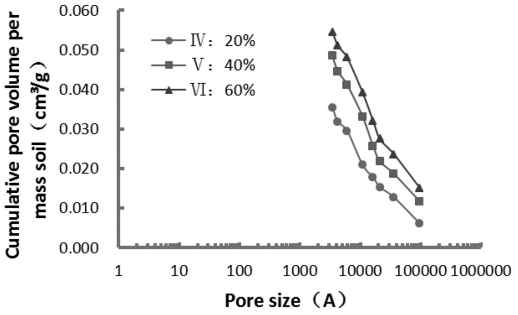


Figure 7. Pore size distribution curve of the samples with different sand contents. (1 μm = 10000A).

size are quite large. For the sample with initial water content 21%, the sizes of pore are quite small and even, and the pores are compact. Therefore, within a given range, the air entry value will be larger and dying rate will be slower with the increase of initial water content.

4.2.2 *Pore size distribution with different sand contents*

Based on the experiment results, the relation between mass water content and matric suction of the samples with different sand content are showed in Figure 6.

It can be seen in Figure 6 that, during the dying process, mass water content decrease fast at smaller matric suction then tend to smooth with the increase of matric suction. When mass water content is the same, the sample with small sand content has large matric suction. Under the same number of light compaction and initial water content, the sample with small sand content has strong water absorbing ability.

From Figure 6, Pore size distribution of the samples with different sand content is showed in Figure 7.

From Figure 7, with the same dry density and initial water content, cumulative pore volumes per mass soil of the samples are different. The samples with sand content 20%, 40%, 60% have cumulative pore volumes per mass soil 0.035 m^3/g, 0.048 m^3/g, 0.055 m^3/g respectively. With the increase of sand content, cumulative pore size volumes tend to increase.

Table 5. Percentage of pore volume distribution of the samples with different sand contents.

Sand content	Percentage of pore volume (%)		
	Pore size (<1 μm)	Pore size (1~4 μm)	Pore size (4~16 μm)
20%	41.67	41.67	16.67
40%	30.61	44.90	24.49
60%	27.78	44.44	27.78

Percentage of pore volume distribution of the samples with different sand content is analyzed from Figure 7, showed in Table 5.

As shown in Table 5, with the sand content increase, there are more big pores (pore size 4~16 μm), and the pore volume of different size are quite large. Thus when the sand content of the sample increase to 60%, the dying rate is quicker and water absorbing ability is weaker compared with the small sand content. When the sand content decreases to 20%, the small pores take large place of the pore structure, making the soil compact. Thus the sample with small sand content has slower dying rate and the water absorbing ability is stronger.

5 CONCLUSIONS

Based on the pressure plate extractor experiment considering the effect of initial water content and sand content on matric suction, some conclusions can be drawn as follows:

With initial water content increase, the pore structure changes from less compact state to compact state. At a given range, the drying rate is slower and water absorbing capacity is stronger with initial water content increase.

The different sand content directly changes the soil particle structures. With the sand content increase, the pore structure change from compact state to less compact state. At a given range, the drying rate is faster and water absorbing capacity is weaker with initial sand content increase.

For a certain unsaturated soil, the micro structure of pore has close relation with physical environment around, such as the initial water content and soil particle composition. The soil-water characteristic curve reflects the pore structure of the soil mass. Therefore, from the micro view, the research of physical environment effect on matric suction is of practical significance.

ACKNOWLEDGMENTS

This paper is funded by the national natural science foundation of China (51279155, 41172276), which is gratefully acknowledged.

REFERENCES

Black W.P.M. A method of estimating the California bearing ratio of cohesive soils from plasticity data. Geotechnique, 1962,12(4):271–282.

Liu Feng-yin, Zhang zhao, etal. Effects of initial density and dying-wetting cycle on soil water characteristic curve of unsaturated loess. Rock and Soil Mechanics, 2011, 32(Supp.2):132–136.

Mitchell P.W., Avalle D.L. A technique to predict expansive soil movements. Proc., 5th Int. Conf. on Expansive Soils, Adelaide, 1984:124–130.

Miller C J. Impact of soil type and compaction conditions on soil water characteristic. Journal of Geotechnical and Geoenvironmental Engineering, ASCE, 2002, 128(9):733–742.

The ministry of Water Resources of the People's Republic of China (2008): GB/T 50145-2007 *Soil Engineering Classification Criterion*. Beijing: China Planning Press.

The ministry of Construction of People's Republic of China (2012): GB 50007–2011 *Code for Design of Building Foundation*. Beijing: China Architecture & Building Press.

Vanapalli S.K., Fredlund D.G., Pufahl D.E. The influence of soil structure and stress history on the soil-water characteristics of a compacted till [J]. Geotechnique. 1999, 49(2):143–159.

X. P. Shan, H. J. Liao, et al. Study on Soil-Water Characteristic Curve of Unsaturated Loess. The Fifth China-Japan Geotechnical Engineering Conference.

Zhou Jian, Yu Jian-lin. Influences affecting the soil-water characteristic curve. Zhejing University Science, 2005, 6A(8):797–804.

This page intentionally left blank

Unsaturated Soil Mechanics—from Theory to Practice – Chen et al. (Eds)
© 2016 Taylor & Francis Group, London, ISBN 978-1-138-02921-7

Hydraulic behaviors of unsaturated expansive soils

L.C. Miao, Y. Cui & H. Zeng
School of Transportation, Southeast University, Nanjing, China

ABSTRACT: Hydraulic behaviors of unsaturated soils not only depend on soil type, but are relative of structure, density, stress, drying state, wetting state, etc. This study includes: the first, considering the real stress state of soil masses in the field, we designed the new equipment to measure the soil-water characteristic curve and soil-water characteristic curves of the Guangxi expansive soil were measured under different vertical pressures; the second, the mercury porosimetry method was used to determine the distribution of various open pore diameters for drying and wetting Guangxi expansive soil samples; final, the meso-structure characteristics were studied for different initial degree of saturation of Guangxi expansive soils during shear test.

1 INTRODUCTION

Expansive soils are the most problematic soil in arid and semi-arid regions and are generally defined as clay soils containing swelling minerals, such as montmorillonite and illite. The increase of moisture content in expansive soils will cause swelling, while the decrease of moisture content induces the shrinkage. The more water is absorbed, the more the soil volume increase. Expansive soils also shrink when they dry out which may also result in cracks in expansive soils. The cycles of shrinkage and swelling of expansive soils can cause the great amounts of volume changes. This kind of the volume change of the expansive soil results in structural damage, especially in lightweight structures such as embankments, sidewalks, driveways, basement floors, pipelines and foundations, etc. Serious damages of structures induced by expansive soil volume change cost several billions of dollars annually in expansive soil regions in over the world (Nelson and Miller 1992).

When expansive soils absorb great amount of water, heave of expansive soils will be induced. Jennings and Knight (1957) first proposed to predict the heave of expansive soils using oedometer tests. Burland (1962) developed a method using the slope of the rebound portion of the consolidation-swell curve to determine the heave of expansive soil. Fredlund and Rahardjo (1993) set up the theoretical framework to predict the heave of expansive soils considering soil suction. Fredlund (1983), Fredlund and Rahardjo (1993) proposed a formula of the heave prediction equation for oedometer tests. Nelson et al. (1998) presented a method of estimating the index parameter using test results from commercial soil testing laboratories. In the paper, we focus on hydraulic characteristics, micro-structure of unsaturated expansive soils.

2 SWCC OF THE EXPANSIVE SOIL

The soil-water characteristic curves of Guangxi expansive soils are measured using a pressure plate made by Soil-moisture Equipment Corporation of Canada. The specimens were prepared by the static compaction. The physical properties of Guangxi expansive soils are listed in Tables 1. The soil mineralogy is summarized in Tables 3. The compacted samples were saturated with assistance of vacuum. Three dry densities of samples were prepared at, 1.42 g/cm^3, 1.48 g/cm^3 and 1.54 g/cm^3, respectively.

The SWCCs for Guangxi expansive soils are shown in Figures 1. The air entry value of the soil–water characteristic curve increases as dry density of the soil sample increases. The residual water content point is essentially stable for different dry density samples. The key values of the SWCC are summarized in Table 3. Figure 1 shows that the slope of the soil-water characteristic curves between the air entry value point and residual water content increases.

The SWCC behaviors are related to the pore structure, pore size and pore connectivity point will be steeper in slope as the dry density.

In other hand, the influence of the stress state is studied for the soil–water characteristic curve of the expansive soil. Figure 2 is the soil–water characteristic curve of the different pre-load the Guangxi expansive soil specimen in total suction range. Figure 2 illustrates that the hysteresis potential is decreased as the pre-load increases.

Table 1. Physical indexes of Guangxi expansive soils.

G_S	w_L (%)	w_P (%)	I_p (%)	Free swell (%)	Gradation (%) >0.05 mm	0.05–0.005 mm	<0.005 mm
2.70	61.4	30.3	31.1	45.0	10.6	39.5	49.9

Table 2. Mineral composition of Guangxi expansive soils.

Smectite	Illite	Quartz	Feldspar	Other
8–10%	15–25%	20–30%	5–10%	15–20%

Table 3. The key values of SWCCs of Guangxi expansive soil.

Dry density, g/cm^3	1.42	1.48	1.54
Air entry value (kPa)	10.0	33.0	45.0
Residual water content (%)	6.35	6.66	6.92

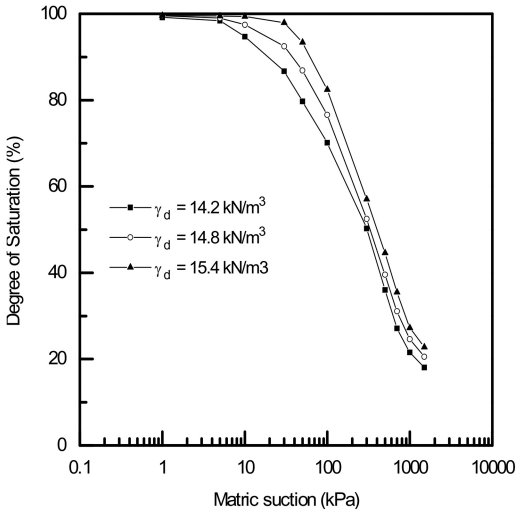


Figure 1. Soil-water characteristic curves for various dry densities of Guangxi expansive soils.

3 MICRO-STRUCTURE FEATURE OF THE EXPANSIVE SOIL

The mercury porosimetry method was used to determine the distribution of pore diameters. The technique is based on the principles of capillarity governing liquid penetration into small pores. Assuming cylindrical soil pores, pore radius can be calculated by equation (1) for an applied pressure P (Delage & Lefebvre, 1984).

$$r = \frac{2T_s \cos\alpha}{P} \quad (1)$$

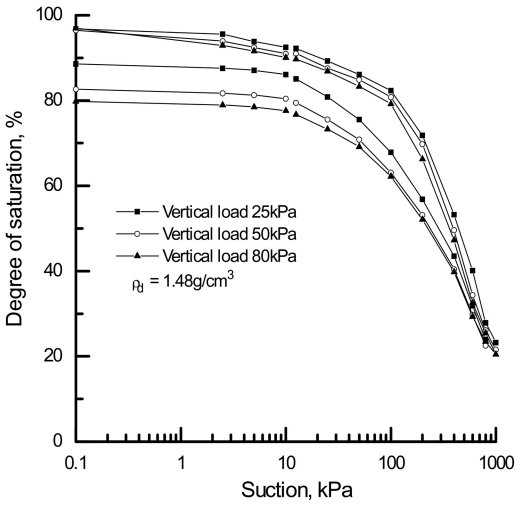


Figure 2. Effect of vertical loading for SWCC.

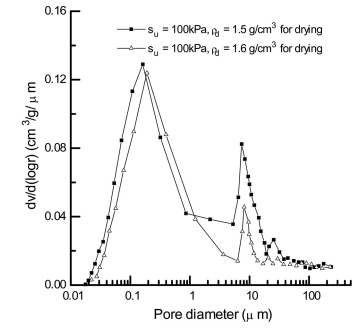
where r is the soil pore radius; T_s is the surface tension, $T_s = 0.480$ N/m; α is the contact angle between soil particle and mercury = 140°; P is the pressure of mercury intrusion. The influence of different mechanical, hydraulic (wetting and drying) and chemical (pore water concentration changes) stress paths on the pore-size distribution (PSD) of compacted FEBEX bentonite have been analyzed by Musso et al. (2003).

Mercury intrusion tests on Guangxi expansive soil samples for different wetting and drying path and stress states with varying dry densities 1.5 g/cm^3 and 1.6 g/cm^3 are performed. Fig. 3 shows the results of the mercury intrusion tests on the two dry densities of Guangxi expansive soils. Figure 3(a) shows the results of the mercury intrusion tests on the two dry densities of Guangxi expansive soils drying branch at $S_u = 100$ kPa. Figure 3(b) lists the results of the mercury intrusion tests on the two dry densities of Guangxi expansive soils wetting branch at $S_u = 100$ kPa. Figure 3(c) shows the results of the mercury intrusion tests on the two different suctions of Guangxi expansive soils drying branch for $\rho_d = 1.5$ g/cm^3. Figure 3(d) shows the different mercury intrusion curves of Guangxi expansive soils for drying and wetting branches at different suctions. The results of the mercury intrusion tests show that: (1) the pore size distribution curves of Guangxi expansive soils appear the double porosity features of micropores and macropores; (2) the micropores is basically steady and the macropores vary with dry density of soil samples; (3) the micropores and macropores present obvious different between drying path and wetting path.

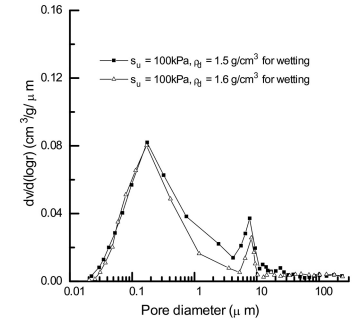
4 CONCLUSIONS

The conclusions from this study are summarized as follows:

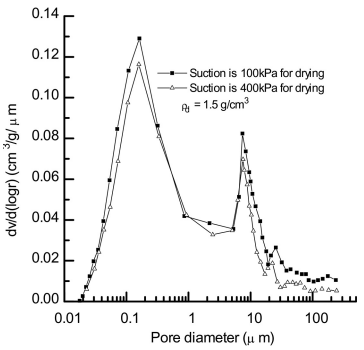
(1) The shapes of soil-water characteristic curves depend on dry density, pore size, pore structure



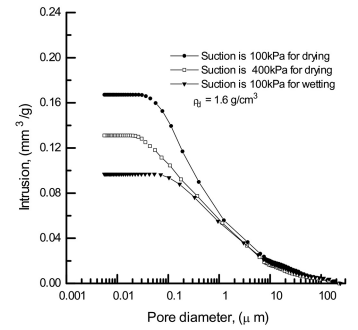
(a)



(b)



(c)



(d)

Figure 3. MIP's results for drying path, wetting path at different density and suctions.

and stress state. The hysteresis loop of SWCC is decreased as the pre-load increases.

(2) The mercury intrusion tests for Guangxi expansive soils present that the pore size distribution curves are bimodal curves, which shows the double porosity features (the micropores and macropores). Also the micropores is steady and the macropores vary with the initial dry density of soil samples.

(3) The pore size distribution are relative with mechanical (loading), hydraulic (wetting and drying) and stress paths.

ACKNOWLEDGMENT

This work was carried out as part of the projects No. 51278099 of National Natural Science Fund of China (NSFC).

REFERENCES

Burland, J.B. (1962). "The Estimation of Field Effective Stresses and the Prediction of Total Heave Using a Revised Method of Analyzing the Double Oedometer Test." *The Civil Engineer in South Africa. Tran*. South African Institute of Civil Engineering. July.

Delage, P. (2007). Microstructures features in the behaviour of engineered barrier for nuclear waste disposal. In: Schanz, T. (Ed.), *Experimental Unsaturated Soil Mechanics*, Springer, Weimar, pp. 11–32.

Dif, A.F. & Blumel, W.F. (1991). Expansive soils with cyclic drying and wetting. ASTM, *Geotechnical Testing Journal*, 14(1): 96–102.

Fredlund, M. D. (1998). "Unsaturated seepage modeling made easy." *Geotech. News*, June, 52–59.

Fredlund, D.G. and Rahardjo, H. (1993). "Soil Mechanics for Unsaturated Soils." *John Wiley & Sons, Inc.*, New York.

Jennings, J. E. B. & Burland, J. B. (1962). Limitations to the use of effective stresses in partly saturated soils. *Géotechnique*, 12(1): 125–144.

Nelson, J.D. & Miller, D.J. (1992). "Expansive Soils. Problems and Practice in Foundation and Pavement Engineering." *John Wiley and Sons*, New York.

This page intentionally left blank

Unsaturated Soil Mechanics—from Theory to Practice – Chen et al. (Eds)
© 2016 Taylor & Francis Group, London, ISBN 978-1-138-02921-7

Discussion on cushion material strength after freezing-thawing cycle based on pore size distribution model

J.P. Yuan, Q.L. Wang & C.L. Han
Key Laboratory of Ministry of Education for Geomechanics and Embankment Engineering, Geotechnical Research Institute of Hohai University, Nanjing, Jiangsu, China

K.B. Li
Shen Kan Qinhuangdao Engineering & Technology Corporation of MCC, Qinhuangdao, Hebei, China

ABSTRACT: Studies have shown that the frost heaving deformation of cushion material varies with its gradation. A pore distribution model and Pore Distribution Index (PDI) has been used to successfully analyse the relationship between the frost heaving deformation and the micro-structure characteristics of cushion material. For further understanding the impaction mechanism of gradation on shear strength for cushion material and the validation of proposed pore distribution model and pore distribution index, a series of laboratory shearing tests are carried out. Cushion material samples are prepared of different gradation after one freezing-thawing cycle with the same initial moisture content and void ratio. Direct shear apparatus are used to obtain the shear strength for 5 groups of samples. Test results show that along with PDI increasing, the friction angle decreases first and then increases; while the cohesion increases first and then decreases. The shear strength shows linear relationship with PDI under different normal pressure. The gradients of $\tau_f \sim$ PDI lines decrease when normal pressure increases. As normal pressure increasing, the tendency of $\tau_f \sim$ PDI line changes from slight increasing to slight decreasing. Based on pore distribution model, the impaction mechanism of gradation on shear strength for cushion material is discussed.

1 INTRODUCTION

With the development of China's Western Campaign, foundation engineering construction in the permafrost area is bound to increase. Especially in the field of hydraulic engineering, the Concrete Face Rock-Fill Dams (CFRD) have been widely built for its good adaptability under different geological and climate conditions. The construction of CFRD can use local materials and be finished in a relatively short period of time. Furthermore, CFRD has the advantages of safe operation and easy maintenance. However, in cold regions the cushion material may cause frost heaving deformation, which leads to damages of cracking, uplifting or leakage. In addition, after freezing-thawing cycles, the strength of cushion material may decrease, triggering the shear displacement between concrete face and cushion material, which increases the risk of dam failure. To ensure the safety of CFRD in cold areas, it's necessary to get better understanding on the strength variation of cushion material after freezing-thawing cycles.

Previous studies have proved that gradation is one of the key factors for cushion material, which has close relationships with its permeability (Liu 2001), the frost heaving deformation (Dang 1995, Yu et al. 2010) and the shear strength (Liu et al. 2011). Laboratory tests have shown that the frost heaving deformation of cushion material varies with its gradation (Wang & Yue 2013). A pore distribution model has been proposed by Yuan et al. (2014) to study the mechanism of frost heaving deformation on cushion material. The proposed Pore Distribution Index (PDI) has been used to successfully analyze the relationship between the frost heaving deformation and the micro-structure characteristics of cushion material.

For further understanding the impaction mechanism of gradation on shear strength for cushion material and the validation of proposed pore distribution model and pore distribution index, a series of laboratory shearing tests are carried out in this paper. The PDI based on gradation design criteria for cushion material is discussed.

2 PORE DISTRIBUTION MODEL AND PORE DISTRIBUTON INDEX

The pore distribution model proposed by Yuan et al. (2014) is based on following hypotheses:

(1) Soil particles are ideal spheres;
(2) The distribution for all particles in different sizes is completely uniform;

(3) All the particles in one gradation group have the same size, which is the arithmetic average value of minimum and maximum of particle sizes in this group;
(4) For arbitrary position, the void ratio of soil remains constant, i.e. the pore distribution is uniform.

Based on pore distribution model, a Pore Distribution Index (PDI) has been introduced, which is given by following equation:

$$\mathrm{PDI} = \sum \lg\left(\frac{d_0}{d}\right) \lg n \tag{1}$$

where n = the quantity of equivalent pore in one grain group; d = the equivalent pore diameter of one group; d_0 = the critical equivalent pore diameter.

According to the definition of PDI, the more fine content (particle smaller than 0.075 mm in diameter), the more micro-pores, and the greater PDI; and on the contrary, the more coarse content (particle larger than 5 mm in diameter), the more macro-pores, and the smaller pore distribution index.

3 LABORATORY SHEAR TEST

3.1 *Testing material*

The testing material, a kind of semi-permeable aggregate, consists of silty clay, granite and quartz sand. The main physical properties are listed in Table 1. Its gradation curve is shown in Figure 1. According to the study (Guan 1993), there's no moisture migration effect on this soil during freezing-thawing cycles.

Table 1. Basic physical properties of cushion aterial.

Void ratio e	Water content ω/%	Permeability coefficient K/cm · s^{-1}	Specific gravity ρ_s
0.34	9	7.26×10^{-4}	2.68

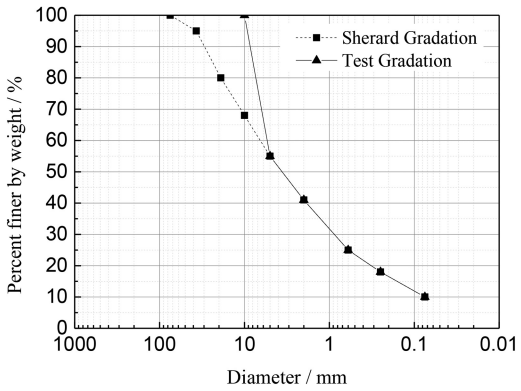


Figure 1. Particle distribution curve for testing material and reduced scale material referencing Sherard gradation.

As the size limitation of testing apparatus, equivalent replacement method is adopted to reduce the scale of test material, referencing Sherard Gradation (SL237-1999). The maximum particle diameter of reduced scale material is 10 mm.

3.2 *Samples preparation*

Tests samples are compacted into 61.8 mm in diameter, 20 mm in height. 5 different gradations groups of samples are prepared with same initial moisture content (9%) and same void ratio (0.34). In each group, there are 4 samples. The difference from each other in same group is the percentage in one fraction. Tests samples are labeled according to the fraction size with A, B, C and D indexing different percentage in the fraction (Table 2). Testing data for each sample are obtained from 6 parallel tests.

Compacted samples are conducted for one freeing-thawing cycle before shearing test. During freezing process, samples are put into an automatically temperature controlled refrigerator within modified oedometer containers, which restrict the heave deformation into vertical direction. The freezing temperature is 20 ± 2°C. After 5 hours freezing process, the samples are taken out from refrigerator into a thermostat for 5 hours with temperature at -20 ± 2°C.

3.3 *Direct shear test*

Test samples after one freezing-thawing cycle are tested on direct shear apparatus produced by Nanjing Factory of Soil Instrument. Shearing rate is 1.2 mm/min, and the applied vertical loads are 25,

Table 2. Gradation information of samples.

Gradation Groups	Samples No.	The percent finer than given sieve size/% 0.075 mm	0.025 mm	0.6 mm	2 mm	5 mm	10 mm
I	0.075-A	4	18	25	41	55	100
	0.075-B	7					
	0.075-C	10					
	0.075-D	13					
II	0.25-A	10	12	25	41	55	100
	0.25-B		15				
	0.25-C		18				
	0.25-D		21				
III	0.6-A	10	18	19	41	55	100
	0.6-B			22			
	0.6-C			25			
	0.6-D			28			
IV	2-A	10	18	25	35	55	100
	2-B				38		
	2-C				41		
	2-D				44		
V	5-A	10	18	25	41	49	100
	5-B					52	
	5-C					55	
	5-D					58	

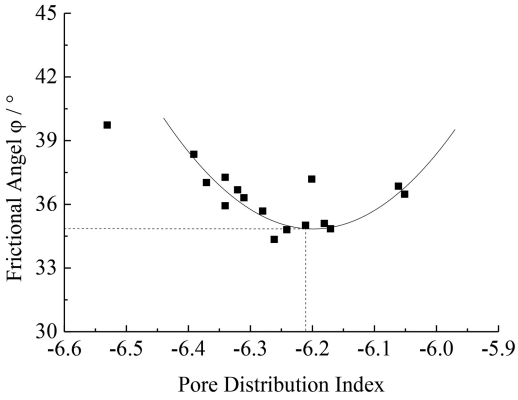


Figure 2. The curve for frictional angel vs. PDI.

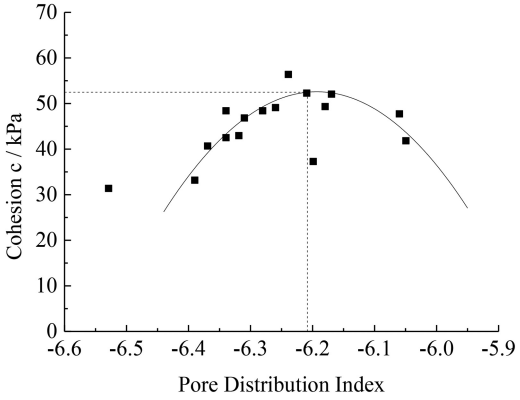


Figure 3. The curve for cohesion vs. PDI.

50, 100, 200, 400 kPa. At the strain-hardening behavior, the shear strength is obtained according to shear displacement at 4 mm.

4 TEST RESULTS AND DISCUSSION

4.1 *Strength parameter and PDI*

Figure 2 shows the curve for friction angle φ varies with Pore Distribution Index (PDI), which is an opening up parabola. There is a trough where minimum friction angle is 34.6°, and PDI is −6.21 correspondingly. It seems that friction angle rises after the first drop as PDI increasing.

The curve for cohesion c varies with pore distribution index shows a downward opening parabola (Fig. 3). The maximum of cohesion at the peak is 52.5 kPa and corresponding PDI is −6.21 (same as the trough point for $\varphi \sim$ PDI curve). As PDI increasing, cohesion decreases after the first rise.

When PDI is relatively small (Fig. 4a), the particles interlocking structure introduces mostly macropores. It's difficult for particles to move when shearing, which results in relatively high friction angle. Meanwhile, relatively less contact points results in relatively low cohesion.

As PDI increasing gradually, middle size particles and mesopores increase (Fig. 4b). The particle's dislocation becomes relatively easier, then the friction angle decreases. At the same time, the number of contact points increase gradually, which leads to cohesion increasing accordingly.

When PDI is relatively high, the macropores and mesopores are turned into micropores (Fig. 4c). More fine grains make higher roughness for shear plane, which results in higher friction angle. Under this situation, macropores and mesopores are turned into micropores, and fine particles clusters appear. The fine particles clusters act as individual particles in larger size, which turns the whole aggregate into "double-layer structure". The number of "real" contact points (between clusters) decreases, which induces declination of cohesion.

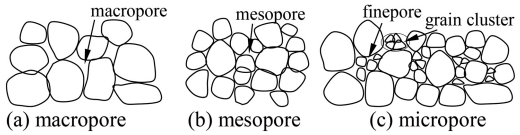


Figure 4. Diagram of pore distribution for different particle distribution condition.

4.2 *Strength and PDI*

As we can see, as PDI changes, the friction angle and cohesion change on two contrary directions. So, what is the relationship between shear strength and PDI? Figure 5 shows the curves for shear strength τ_f vs. PDI for the samples with different gradation and under different normal pressure. It shows a linear relationship of $\tau_f \sim$ PDI for each normal pressure condition. Furthermore, it can be noticed that the tendency of $\tau_f \sim$ PDI line changes as vertical pressure changes. When vertical pressure is relatively low (25, 50 kPa), the shear strength slightly increases along with the increasing of PDI. But for higher vertical pressure (200, 400 kPa), the shear strength declines slightly when PDI increases. And for vertical pressure of 100 kPa, the $\tau_f \sim$ PDI line remains almost horizontally.

Defining the gradient of $\tau_f \sim$ PDI line as k_{PDI}.

$$k_{\mathrm{PDI}} = \frac{\Delta \tau_f}{\Delta \mathrm{PDI}} \tag{2}$$

Then plot the relationship of k_{PDI} vs. normal pressure (Fig. 6). It can be obviously found that k_{PDI} decreases nonlinearly as normal pressure increases, which can be expressed in following empirical formula.

$$k_{\mathrm{PDI}} = k_0 + \alpha e^{-\frac{\sigma_n - \sigma_0}{\beta}} \tag{3}$$

where, $k_0 = -103.9$; $\alpha = 120.0$; $\beta = 245.8$; $\sigma_0 = 40.4$.

As we can see, for the guarantee of required strength, the gradation of smaller PDI should be

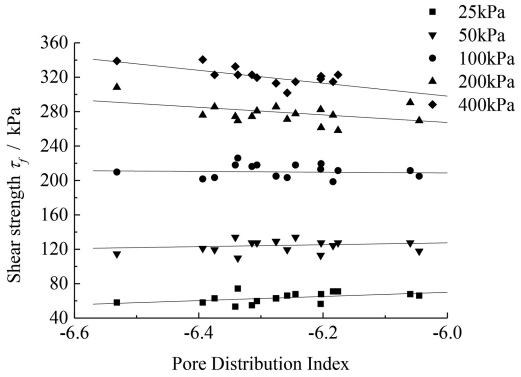


Figure 5. Shear strength varies with PDI under different normal pressure.

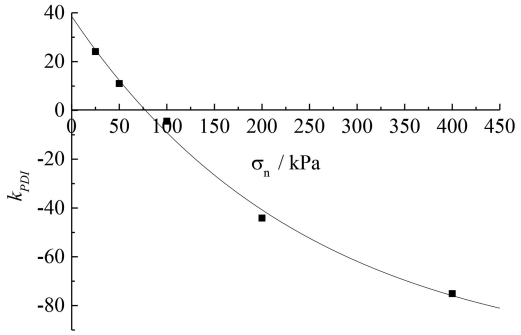


Figure 6. Gradients of $\tau_f \sim$ PDI line k_{PDI} under different normal pressure.

adopted when under higher vertical load; however, when vertical load is relatively low, the gradation of higher PDI is the better choice.

5 CONCLUSIONS

Based on proposed pore distribution model, analyses are carried out on the series of laboratory shearing tests results. The main conclusions are as follows:

(1) It shows PDI has a close relationship with the shear strength of cushion material after one freezing-thawing cycle. As PDI increasing, friction angle rises after the first drop, and there is a valley on $\varphi \sim$ PDI curve; while cohesion decreases after the first rise, c ~ PDI curve shows a peak.

(2) The shear strength of cushion material after one freezing-thawing cycle shows linear relationship with PDI under different normal pressure. As normal pressure increasing, the tendency of $\tau_f \sim$ PDI line changes from slight increasing to slight decreasing. The gradients of $\tau_f \sim$ PDI lines decrease nonlinearly when normal pressure increases.

(3) The impaction of gradation on shear strength for cushion material is the interacting combination of particles and clusters. As PDI increases, macropores turn into mesopores and micropores gradually. "Double-layer structure" appears when PDI is greater than a certain value.

ACKNOWLEDGEMENTS

This research was sponsored by "the National Natural Science Foundation of China" (Grant No. 51378008) and the Fundamental Research Funds for the Central Universities (B15020060).

REFERENCES

Andersland, O.B. & Landanyi, B. 2004. *Frozen ground engineering*. New Jersey: John Wiley & Sons, Inc.

Dang, L.W. 1995. The cushion material design of the concrete face rock-fill dam in cold area. *Chinese Journal of Water resources and Hydropower Engineering* (4): 11–13.

Guan, Z.C. 1993. Some technological problems of the design of concrete face rock-fill dam in cold region. *Chinese Journal of Water Resources and Hydropower Northeast China* (11): 2–7.

Liu, J. 2001. Experimental study of optimum gradation of crushed stone cushion for concrete-face rock-fill dam. *Chinese Journal of Hydro-Science and Engineering* (4): 1–7.

Liu, M.C., Gao, Y.F. & Liu, H.L. 2011. Effect of particle breakage on strength and deformation of modeled rock-fills. *Chinese Journal of Geotechnical Engineering* 33(11): 1691–1699.

Sherard, J.L., Dunnigan, L.P. & Talbot, J R. 1984. Basic properties of sand and gravel filters. *Journal of Geotechnical Engineering* 110(6): 684–700.

Wang, T.L. & Yue, Z.R. 2013. Influence of fines content on frost heaving properties of coarse grained soil. *Chinese Journal of Rock and Soil Mechanics* 34(2): 359–364.

Yu, L.L., Xu, X.Y. & Li, P.F. 2010. Frost-heaving property of bedding materials of face rock-fill dam. *Chinese Journal of Building Materials* 13(3): 347–351.

Yuan, J.P., Li, K.B. & He, J.X. 2014. Discussion on frost heave deformation of cushion material based on pore distribution model. *Chinese Journal of Rock and Soil Mechanics* 35(8): 2179–2183.

Unsaturated Soil Mechanics—from Theory to Practice – Chen et al. (Eds)
© 2016 Taylor & Francis Group, London, ISBN 978-1-138-02921-7

Nuclear Magnetic Resonance assay of carbon dioxide hydrate in silt

Huihui Tian, Changfu Wei & Xiaolong Xia
State Key laboratory of Geomechanics and Geotechnical Engineering, Institute of Rock and Soil Mechnnics, Chinese Academy of Sciences, Wuhan, Hubei, P.R. China

Hui Wang
College of civil engineering and architecture, Guilin University of Technology, Guilin, Guangxi, China

ABSTRACT: Proton Nuclear Magnetic Resonance (NMR) is a rapid, quantitative and nondestructive measurement that can provide a wealth of information about the fluids in oils- and water-saturated rock and soil. It is potentially useful for quantifying pore size control of hydrate formation and dissociation. In this paper, NMR of liquid water was used to indirectly detect and assay carbon dioxide hydrate in earth material. The results indicate that hydrate in smaller pores dissociates first and then the hydrate in larger pores and hydrate saturation is calculated with NMR data.

1 INTRODUCTION

Gas hydrates have crystalline structures, which involve a lattice made up of hydrogen-bonded water molecules with guest gas molecules occluded. The guest gases, which are normally low-molecular-weight gases such as carbon dioxide, hydrogen sulfide, sulfur dioxide, and some other gases including nitrogen and light hydrocarbons, react with water under low temperature-high pressure conditions. The types of gases and formation conditions determine which of three known distinct crystal structures I, II and H the lattice are. Works on hydrates was only of academic interest from the first discovery and document of natural gas hydrates by Sir Humphrey Davy in 1811 (Sloan & Koh, 2008). Ever since the hydrate was found in bulk by blocking oil and natural gas pipelines in industry, more and more laboratory work was done on the thermodynamics and kinetics of gas hydrates (Shuqiang Gao et al., 2009, M.M. Mooijer-wan den Heuvel et al., 2002). But these researches were limited to the hydrates prepared from pure water and in a few cases from water containing inhibitors such as salts, molecule sieves and alcohols under bulk condition.

The explosive investigations were stimulated by the discovery of natural gas hydrate deposits in many permafrost regions and beneath deep oceans as a potential clean fuel (Boswell, 2007, Collett et al., 2015). Simultaneously the hydrates formed in pores can strongly change the mechanic properties of sediments and the dissociation of hydrates induced by small disturbance in ambient environmental condition (aroused by human activities or climate change) could trigger various geological hazards and environmental issues (Grozic & Ghinassian, 2010). In recent years, considerable attention has been directed to (1) resulting gas hydrate accumulation, (2) identifying and predicting natural and induced environmental and climate impacts of natural gas hydrate, (3) analyzing the natural gas hydrate role as a geohazard.

Now our understanding of natural gas hydrate in nature and their potential role as an energy resource, a geohazard, or as an agent of global climate change is growing and evolving, but is also known with certainty that laboratory have contributed greatly to our understanding of hydrate and will continue to be a critical source of the information needed to advance our understanding of natural gas hydrate. Handa (1992), smith (2002a, 2002b), wilder (2001), Kneafsey (2007) and Uchida (1999, 2002) reported phase equilibrium conditions for carbon dioxide, methane and propane hydrates in porous media of nominal radii in nm-scale and analysis the results based on modified statistical thermodynamic model suggested by Henry et al. (1999) to model hydrate formation in porous media. Experiments data matched model well.

However, measurements of hydrate equilibrium conditions in natural porous media in the laboratory are limited. From the limited information available in these studies, it is impossible to draw any conclusions on the thermodynamic and kinetic stability of gas hydrates in restricted geometries. To provide more experimental data for modeling, and to gain a better understanding of this complex system, experiments are performed to investigate the properties of hydrate in silt which is more closer to natural sediments hydrates located. In this work, the partially water-saturated silt sample is contained in a PEEK pressure vessel. Since the hydrate relaxation occurs within the dead time of measurement, NMR is used

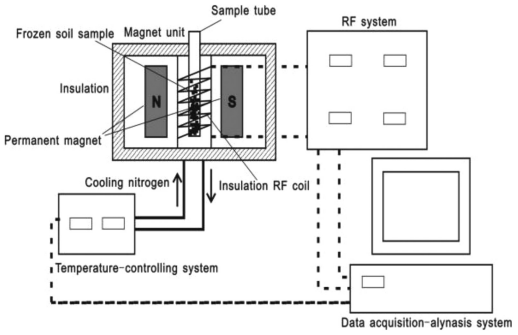


Figure 1. Schematic of the 22 MHz MiniMR setup.

to determine the content and distribution of liquid water in sample for each equilibrium point. The tests are performed to (1) primary observe the changes of water content and distribution occurring in response to hydrate dissociation, (2) calculate hydrate saturation by NMR data.

2 EXPERIMENTAL METHODS

Carbon dioxide with minimum purity of 99.9% was obtained from Wuhan xiangyun. Distilled degasses water was used to prepare sample in cylindrical bottle ($V = 10\,cm^3$, $h = 2\,cm$) with silt was obtained in Huanghe river and washed before experiment. Silt properties are presented in Table 1. The NMR setup used in the experiments is a 22 MHz MiniMR developed jointly by the Institute of Rock and Soil Mechanics, Chinese Academy of Sciences, and Niumag Corporation, Suzhou, Jiangsu Province, China. As schematically shown in Fig. 1, the system consists of a sample tube, magnet unit, RF system, temperature-controlling system and data acquisition-analysis system. To generate a stable magnetic field, the temperature of the magnet unit is set to be 32°C, within a variation of ±0.01°C. The silt sample is cooled in a cold bath. The temperature-controlling unit has an accuracy of 0.1°C. The transversal relaxation time T_2 of hydrate is about 10 μs, which is one-order smaller than the dead time of the NMR device (about 80 μs), so that the NMR signal only comes from the liquid water in the sample.

A high-pressure cell about 19 ml in volume constructed using PEEK which has low themal conductivity, high strength and nearly no signal NMR signal. The cylindrical bottle made by PTEE (has the similar physical properties with PEEK) was filled by 15 gram silt with 15% water content in weight in three layers and 3 gram water was added to sample additionally to saturate the sample. The cell was evacuated for 30 min to remove air. Due to the hysteresis for hydrate growing, the P-T condition at hydrate dissociation is a more accurate representation of the true equilibrium condition than the one of hydrate at growth.

We choose CO_2 as the guest gas in our experiments for the reason that the CO_2 hydrate yields the same crystal structure I as the CH_4 hydrate, but at much lower pressure (for the same temperature). The minimum temperature is −5°C for our experiment, CO_2 hydrate begin to dissociate at 2.1 MPa.

Table 1. Description of silt.

Particle size range/mm	≥0.075	0.075∼0.05	0.05∼0.005	≤0.005
Sizes distribution/%	34.5	30.5	35	0

Equilibrium pressures were obtained for the dissociation of carbon dioxide hydrate in sample at various temperatures. Before hydrate dissociation, the hydrate was fully formed in sample at −5°C and, to prevent the pore ice formation, the temperature of sample was increased to 1°C. The dissociation of carbon dioxide hydrate in confined small pores started at 1°C and the equilibrium pressures were measured by the gradual temperature increase method. During the experiment, the saturated samples were cooled in the cold bath, and the temperature was slowly decreased step by step. After each temperature was applied, sufficient time was left for the sample to reach equilibrium which was verified by the pressure to reach an appropriate level. Then the samples were moved into the NMR sample tube, in which the sample was isolated from the environment and NMR measurement was conducted. This was continued until all the hydrate dissociated. The temperature raised by about 0.5–1.0°C each step and the whole test usually finished within 3 to 5 days. The measured NMR data were analyzed using an inversion procedure based on the Fourier transformation. Temperature measurements were made with a platinum resistance thermometer with a resolution of ±0.01°C. The pressure measurements were made with a 150 atm full-scale pressure gauge with a resolution of ±2.5 atm.

3 RESULTS AND DISCUSSION

3.1 *Decomposition characteristic of carbon dioxide hydrate in silt*

Figure 2 shows the hydrate bearing silt sample after hydrate formation. A fissure is observed across the sample and it is speculated that may be caused by water migration during hydrate formation. When the sample cooled, hydrate crystals first formed in the macro pores where the water potential was large, sucking water from the surrounding water saturated pores into the macro pores. Carbon dioxide hydrate indicated by white crystal disseminated evenly in silt sample. In hydrate research, documenting and analyzing the hydrate formation process from the microscopic point of view in sediments is practically important. To this end, Fig. 3 depicts distribution curves of the relaxation time T_2 for sample at different temperatures during the hydrate dissociation. In general, the amplitude of the

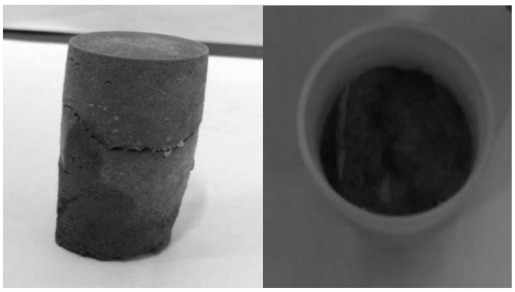


Figure 2. Photographs of carbon dioxide hydrate bearing sample.

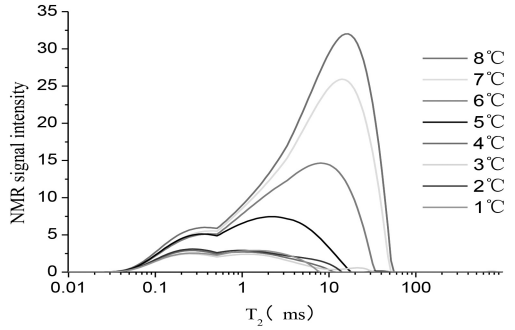


Figure 3. T2 distribution curves during hydrate dissociation.

NMR relaxation curve provides information about the fluid content in porous media, while the T_2 is used for the characterization of water in soils with

$$\frac{1}{T_2} \approx \frac{\rho_2 A}{V} = \rho_2 \frac{F}{R} \tag{1}$$

Here, we can associate the longer relaxation times with water between the aggregates and in large pore space and the shorter times with water held in smaller intra-aggregate pores. So T_2 distribution curves may shed insights into the variation of pore water content and distribution in the soils during hydrate dissociation process. Fig. 3 shows that hydrate in silt is not sensitive to temperature below 4°C during dissociation process, because fluid water content and dissociation kept basically constant. As temperature slowly increased, the T_2 distribution curves recorded at temperature higher than 4°C yield bimodal distributions and exhibit overall trend that hydrate in smaller pores dissociated first and then the hydrate in larger pores, which in turn made the bimodal distribution more apparent. These phenomena can be explained by referring to the energy status of the pore water. Indeed, compared to the free pore water or the pore water in larger pores, the bound water and the water in smaller pores has lower activity due to stronger capillary and adsorption effect. Hence, dissociation is prone to occur in smaller pores, whereas formation takes place in larger pores first.

Table 2. Hydrate equilibrium conditions for hydrate in silt calculated with NMR data.

T/K	P/MPa	S_h
274.15	2.1	0.85098
275.15	2.1	0.85694
276.15	2.1	0.87994
277.15	2.05	0.87274
278.15	2.2	0.72018
279.15	2.5	0.47132

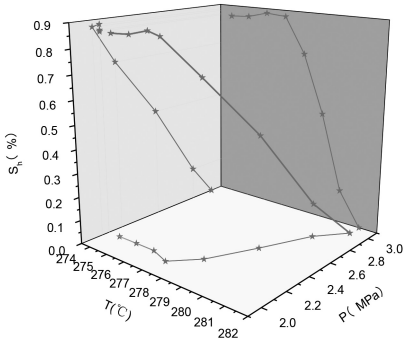


Figure 4. A three-dimensional P-T-S_h curve associated with carbon dioxide hydrate in silt.

3.2 *Carbon dioxide hydrate equilibrium conditions in silt*

Amplitude of the NMR relaxation curve which can be simplified as NMR signal (P) provides information about the fluid content in porous media but can not directly sense the presence of hydrate. So when the hydrate exists in silt, there would be NMR signal deficit between silt sample without hydrate and that with hydrate and the difference gives directly the amount of hydrate present in silt sample. Clearly, variables NMR signal P and hydrate saturation S_h are very well correlated to each other, which can be characterized using a linear equation, i.e., $P = \alpha S_h - \beta$, α and β are fitting parameters, and the S_h calculated are listed in Table 2.

The curve in Fig. 4 demonstrates that the hydrate equilibrium pressure observed as the result of hydrate decomposition from a porous medium are a function of hydrate saturation S_h as well as temperature. As a result two-dimensional P-T curve associated with hydrate equilibrium in the bulk becomes a three-dimensional curve that lies on a P-T-S_h surface when one considers hydrate dissociation in porous medium.

4 CONCLUSIONS

NMR techniques were employed to investigate carbon dioxide hydrate dissociation to improve the understanding of clathrate hydrate mechanisms and it has been demonstrated that NMR techniques could be adapted to experiments on soil containing hydrate.

It was found that that hydrate in smaller pores dissociated first and then the hydrate in larger pores, which could be explained by referring to the energy status of the pore water. Because compared to the free pore water or the pore water in larger pores, the bound water and the water in smaller pores has lower activity due to stronger capillary and adsorption effect. Simultaneously, hydrate saturation was calculated with NMR data and some preliminary test results were presented.

ACKNOWLEDGEMENT

This research was supported by the National Natural Science Foundation of China through grants 11372078 and the Guangxi Natural Science Foundation through grants 2012GXNSFGA060001, and the Major Projects of Guangxi Natural Science Foundation through grants 2012GXNSFEA053002.

REFERENCES

Boswell, R., Resource potential of methane hydrate coming into focus [J]. *Journal of Petroleum Science and Engineering*, 2007, 56: 9–13.

Collett, T., Bahk, J., Baker, R., Boswell, B., Divins, D., Frye, M., Goldberg, D., Husebo, J., Koh, M., Malone, M., Morell, M., Myers, G., Shipp, C. and Torres, M., Methane hydrates in nature-current knowledge and challenges [J]. *Journal of Chemical and Engineering Data*, 2015, 60: 319–329.

Grozic, J.L.H. and Ghiassian, H., Undrained shear strength of methane hydrate-bearing sand: preliminary laboratory results [C]. Proceedings 6th Canadian permafrost conference and 63rd Canadian geotechnical conference, Calgary. 2010: 459–466.

Handa, Y.P. and Stupin, D.Y. Thermodynamic properties and dissociation characteristics of methane and propane hydrates in 70-.ANG.-radius silica gel pores. 1992. 8599–8603.

Henry, P., Thomas, M. and Ben Clennell, M., Formation of natural gas hydrates in marine sediments 2. Thermodynamic calculations of stability conditions in porous sediments. *Journal of Geophysical Research-Solid Earth*, 1999, 104(B10): 23005–23022.

Kneafsey, T.J., Tomutsa, L., Moridis, G.J., Seol, Y., Freifeld, B.M., Taylor, C.E. and Gupta, A., Methane hydrate formation and dissociation in a partially saturated core-scale sand sample [J], *Journal of Petroleum Science and Engineering*, 2007, 56: 108–126.

Mooijer-van den Heuvel, M.M., Witteman, R. and Peters, C.J., Gas hydrate phase equilibria for propane in the presence of additive components [J], Fluid Phase Equilib. 193 (2002) 245–259.

Shuqiang Gao, Walter G Chapman, Waylon House. Aplication of low field NMR T2 measurements to clathrate hydrates [J], *Journal of Magnetic Resonance*, 197 (2009) 208–212.

Sloan, E.D., Koh, C.A., Clathrate hydrate of natural gases (Third Edition). CRC Press. Taylor & Francis Group, 2008.

Smith, D.H., Wilder, J.W. and Seshadri, K., Methane hydrate equilibria in silica gels with broad pore-size distributions. *Aiche Journal*, 2002a. 48(2): 393–400.

Smith, D.H., Wilder, J.W. and Seshadri, K., Thermodynamics of carbon dioxide hydrate formation in media with broad pore-size distributions. Environmental Science & Technology, 2002b. 36(23): 5192–5198.

Uchida, T., Ebinuma, T. and Ishizaki, T., Dissociation condition measurements of methane hydrate in confined small pores of porous glass. *Journal of Physical Chemistry B*, 1999. 103(18): 3659–3662.

Uchida, T., Ebinuma, T., et al., Effects of pore sizes on dissociation temperatures and pressures of methane, carbon dioxide, and propane hydrates in porous media. *Journal of Physical Chemistry B*, 2002. 106(4): 820–826.

Wilder, J.W., Seshadri, K. and Smith, D.H., Resolving apparent contradictions in equilibrium measurements for clathrate hydrates in porous media. *Journal of Physical Chemistry B*, 2001. 105(41): 9970–9972.

Unsaturated Soil Mechanics—from Theory to Practice – Chen et al. (Eds)
© 2016 Taylor & Francis Group, London, ISBN 978-1-138-02921-7

Evolution of soil water in silt soils based on NMR technique

P. Chen, C.F. Wei & J. Liu
State Key Laboratory of Geomechanics and Geotechnical Engineering, Institute of Rock and Soil Mechanics, Chinese Academy of Sciences, Wuhan, China

W.J. Xue
School of Civil Engineering and Architecture, Wuhan University of Technology, Wuhan, China

ABSTRACT: The content and distribution of soil water is important for evaluating the deformation and strength properties of unsaturated soils. In this paper Nuclear Magnetic Resonance (NMR) technique was adopted to determine and monitor the evolution of soil water in silts after the equilibrium state reached at each matric suction step. The experiment results show that the distribution curves of transverse relaxation times T_2 gradually move left and down with the increment of matric suction. The evolution process of pore water can be clearly explained by the distribution curves of T_2 from the micro-scale. The NMR signal of soil water is linearly correlated with the degree of saturation of silt soils. Hence, the NMR method can be used to measure the change of water content and doesn't perturb the samples. Furthermore, the measuring range of pore water by the NMR technique is much larger than the residual degree of saturation.

1 INTRODUCTION

Soil-water retention is significantly influence the mechanical response of soils, such as shear strength and compression properties (Vanapalli et al., 1999). In addition, the soil-water retention curve is also necessary to analyze the seepage process and stability of earth slopes under precipitation conditions and changes of water table (Chen et al., 2014).

Due to the importance of the soil-water retention curve, many different methods are developed to measure the curve (Lu and Likos, 2004). Axis translation technique is usually adopted in the laboratory to obtain the soil-water retention curves, such as pressure plate method. The empirical models were also developed based on the measured data in order to predict the change of soil-water in soils. However, these models were obtained by fitting the experimental data or based on the capillary tube assumption. The physical mechanics is little given by the type model. And some parameters in the model are not clear explained physically. In fact, the soil-water retention curve tightly relates to the size, the distribution and their connection of the pores in soils in micro-scale (Mitchell & Soga, 2005). The pore size and the distribution of the pores are usually explored by the microscope analysis method. Furthermore, it's very helpful to explain the mechanics of soil-water retentions in macro-scale by obtained the change of pore water in the soils from the micro-scale technique.

Nuclear magnetic resonance transverse relaxation technique (NMR) is adopted in the geotechnical engineering for micro-scale analysis of soils (Tyrologou et al., 2005). The effectiveness of the measured method has been verified for the porosity measurement of porous media (Gallegos & Smith, 1988). Recently, the technique has been adopted to obtain the change of soil-water in sand soils (Tian et al., 2014). However, the method has not been applied to measure the content and distribution of pore water in fine grained soils, such as silt or clay. And the relationship has not been given between the signal of NMR and degree of saturation.

The aim of this paper is to explore the suitability of the NMR method to determine the content and distribution of pore water in fine grained soil and develop a nondestructive method for soil-water retention curve. Firstly, the soil-water retention curve of fine grained soil is measured by the pressure plate method. Then, the pore water in the same sample is measured by the NMR method. A quantitative relationship between the signal of NMR and degree of saturation will be developed. Lastly, a new measured method for the soil-water retention curve of fine grained soil can be verified based on the results of pressure plate.

2 MATERIAL AND EXPERIMENTAL METHOD

2.1 *Physical characteristics of tested material*

The physical experiments for the tested soils have been done in the laboratory and the results have been given in the Table 1. The distribution curve of soil particles is given in Figure 1.

Table 1. The physical characteristics of tested soils.

Soil types	Low plasticity silt
Initial water content	12.0%
Specific gravity	2.73
Plastic limit	15.5
Liquid limit	27.5

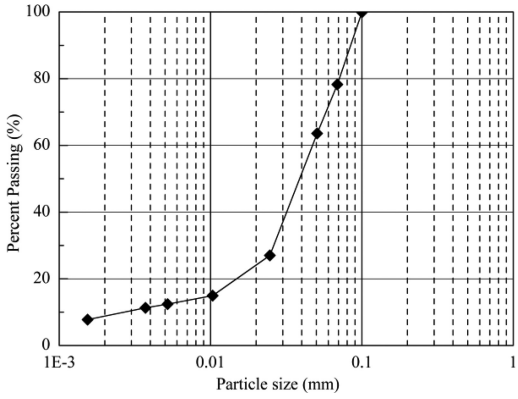


Figure 1. Particle-size distribution curves for the tested soil.

2.2 *Experimental method*

The silt specimens with different dry densities are used in the experiment. The dry densities of the silt samples are 1.45 g/cm^3, 1.60 g/cm^3, 1.75 g/cm^3. And the corresponding porosity are respectively. The specimens of 45 mm in diameter and 20 mm in height are prepared by the static press method. The initial mass water contents of different samples are all the same, equal to 12%. At beginning, these samples are saturated with distilled water after vacuum seeding about 3–5 h. The samples are taken out and put into the magnetic field of the Nuclear Magnetic Resonance system (NMR) after it is maintained submerged about 24 h. The detailed method for measuring the T_2 distribution curves was given in literature (Tian et al., 2014). These samples are put into the pressure plate and the first matric suction is applied after the NMR experiment. These samples will be taken out from the plate and measured by the NMR when the soil-water state reaches at one matric suction step. The distribution of transverse relaxation times T_2 will be obtained at the matric suction. These samples are again put into the plate. And another matric suction step will be applied. The experimental process will be repeated step by step. The selected matric suction steps are 0-5-10-20-40-60-80-120-160-200-260 kPa respectively.

3 RESULTS

3.1 *Soil-water retention curve*

The soil-water retention curve of different soil samples are measured by the pressure plate, given in Figure 2.

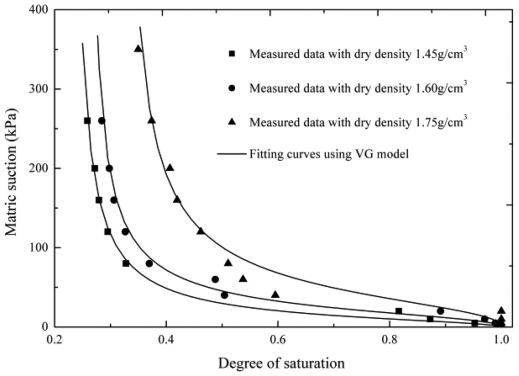


Figure 2. Soil-water retention curves of silt samples.

Table 2. The parameters of VG-model for the samples with different dry density.

Dry density (g/cm^3)	α	n	S_r^{irr}
1.45	0.0887	2.00	0.226
1.60	0.0497	2.28	0.259
1.75	0.0260	2.32	0.320

The VG-model is adopted to predict the soil-water retention curve (Van Genuchten, 1980). The equation is given as follows,

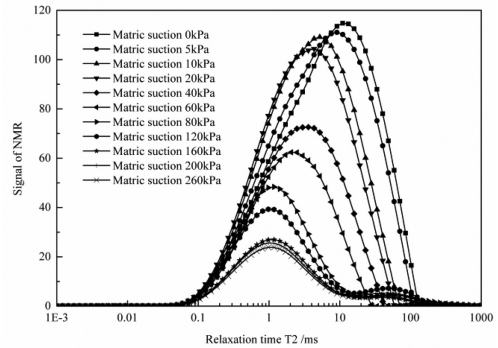
$$S_r = S_r^{irr} + (1 - S_r^{irr})\left[\frac{1}{1+(\alpha s_c)^n}\right]^{(1-\frac{1}{n})} \quad (1)$$

where S_r is the degree of saturation of water; s_c is the matric suction; α is the parameter related the air entry value; n is a shape parameter; S_r^{irr} is the residual degree of saturation.

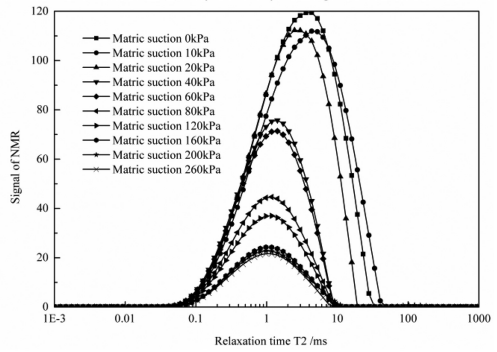
The parameters of the model are shown in Table 2. From Figure 2, the air entry value of different dry density samples is 5 kPa (1.45 g/cm^3), 10 kPa (1.60 g/cm^3) and 20 kPa (1.75 g/cm^3), respectively. The residual degree of saturation increases with the increasement of dry density of samples. The effect of dry density is small on the slope of soil-water retention curves. The shape of the soil-water retention curves can be divided into four stages, from the saturation state to initial drainage (lower than the air entry value), fast drainage stage (between air entry value and 60 kPa), slowly drainage stage (60–160 kPa) and little drainage stage (large than 160 kPa).

3.2 *Experimental results from NMR*

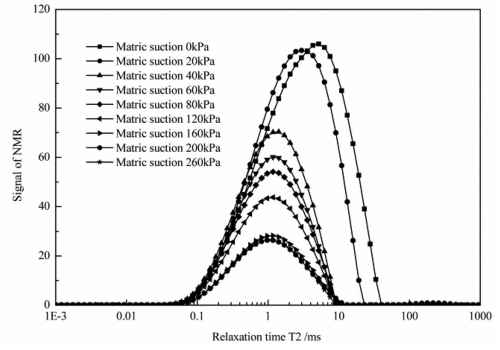
The distribution curves of transverse relaxation times T_2 of different samples from the NMR experiment are shown in Figure 3. There are four stages based on the distribution curves T_2 of different samples from Figure 3. (1) The first stage: the signal of NMR falls off corresponding the range of T_2 (10–100 ms) under



(a)Dry density 1.45g/cm^3



(b)Dry density 1.60g/cm^3



(c) Dry density 1.75g/cm^3

Figure 3. T_2 distribution curves of the silt samples with different dry densities at different matric suction steps.

the matric suction 0–20 kPa. And the signal of NMR increases with the range of T_2 (0.02–10 ms). The location of pore water in the soils relates to the value of T_2. The size of pores in which the pore water exists is large when the value of T_2 is large. The change of the distribution curves T_2 show that the pore water in the large pores is drained and the one in the small pores is increased with the increasement of matric suction. The similar results are obtained in the literature (Bird et al., 2005, Tian et al., 2014). (2) The second stage: the range of matric suction is in 20–60 kPa. The signal of NMR with the range of T_2 10–100 ms decreases to zero when matric suction gradually increases. The change shows that the pore water in the large pores has been exhausted. The peak value of distribution curves of T_2 decreases. And the curve shrinks to the left. The results show that some of pore water in the small pores is also expelled. (3) The range of matric suction is in 60–160 kPa is the third stage. The range of T_2 keeps constant. And the area of the curves only becomes diminished. The tendency of the distribution curves shows that pore water in all the small pores is drained simultaneously at each matric suction step. (4) The fourth stage is that matric suction is larger than 160 kPa. The change of signal of NMR is very small. The pore water is hardly drained when the residual degree of saturation reaches at the stage. Furthermore, the comparison of the distribution curves of T_2 for different dry densities shows that the proportion of the large pores decreases with the increasement of dry density. The proportion of the small pores increases with the increasement of dry density. Hence, the pore water is expelled hardly with the high dry density, seen in Table 2.

3.3 *The relationship of signal of NMR and the degree of saturation of soils*

The experimental results have verified that the peak value of FID and the area enclosed by the distribution curves of T_2 and the T_2 axis can be used to characterize the content of pore water in porous media (Black and Tice, 1989, Tian et al., 2014). The relationship of the peak value P of FID and the degree of saturation S_r is given in Figure 4 based on the experimental data of different soil samples. The linear equation is adopted to fit the tested data. The correlation between the measured data and fitting curves is well. The linear equations and correlation coefficient are given in the Table 3. The water content can be obtained by measuring the peak value P of FID directly and the sample is not damaged. The linear correlation between the area A_N of the distribution curves of T_2 and S_r is better than the ones between P and S_r for the silt soils with three different dry densities, seen in Figure 5 and Table 3. The relation between A_N and S_r is recommended for obtaining the water content in soils based on the NMR technique when the desired precision is high. It is worth noting that S_r is not equal to zero when the signal of NMR (P or A_N) is disappeared based on the linear equations. Hence, a little water in the pores of one soil has not signal of NMR. The content of pore water increases with the increment of the dry density of silts. This can be explained that the sample with the large dry density has more small pores, in which the adsorption effect on pore water is much stronger than the one in a sample with small dry density. And the water content is much lower than the residual degree of saturation. Some pore water is hardly drained by the axis translation technique adopted in the experiments. Other method need to be adopted in order to decrease the degree of saturation, such as salt solution method. Furthermore, the test method can be used for measuring the content of adsorbed water for considering the film flow.

Table 3. The fitting equations and correlation coefficients and between NMR signal and S_r.

Soil samples	Fitting equations	R^2
$\rho_d = 1.45$ g/cm^3	$P = 2418.2\ Sr - 29.26$	0.9871
	$A_N = 2669.5\ Sr - 146.25$	0.9939
$\rho_d = 1.60$ g/cm^3	$P = 2047.6\ Sr - 71.11$	0.9904
	$A_N = 2357.1\ Sr - 199.89$	0.9918
$\rho_d = 1.75$ g/cm^3	$P = 2007.9\ Sr - 210.33$	0.9876
	$A_N = 2349.5\ Sr - 425.37$	0.9935

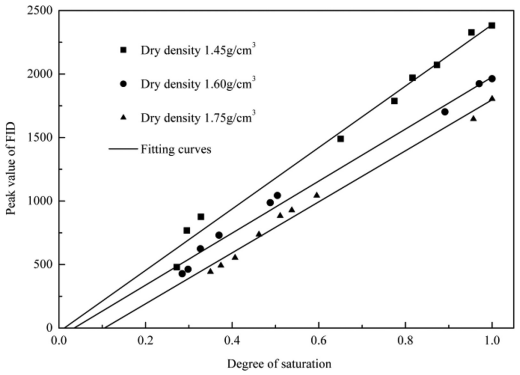


Figure 4. The relationship of the peak value P of FID with degree of saturation S_r of silt samples with different dry densities.

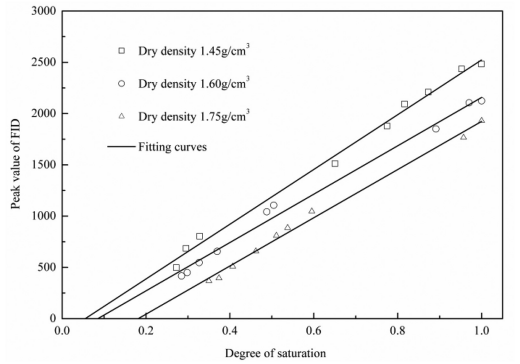


Figure 5. The relationship of the area A_N of T_2 distribution curves with the degree of saturation S_r of silt samples with different dry densities.

4 CONCLUSION

NMR method can be used to measure the content and distribution of pore water in silty soils.

The linear correlation of the peak value P of FID, and the area A_N of the distribution curves of T_2 and the degree of saturation S_r are both well. But the linear relation between A_N and S_r is recommended to predict the water content by the signal of NMR of silt samples with different dry densities if the desired precision of measuring the water content is high.

The content of soil water which has no signal of NMR in pores increases with the increment of the dry density of silts. The results show that the adsorption effect on pore water in soils with the large dry density is much stronger than the one in the soil with small dry density. The lowest water content from the NMR technique is much lower than the residual degree of saturation.

ACKNOWLEDGEMENTS

This research was supported by the National Natural Science Foundation of China through grants # 11302243 and 51239010, and the Natural Science Foundation of Guangxi through grant # 2012GXNSFGA060001.

REFERENCES

Bird, N.R.A., Preston, A.R., Randall, E.W., Whalley, W.R. & Whitmore, A.P. 2005. Measurement of the size distribution of water-filled pores at different matric potentials by stray field nuclear magnetic resonance. *European Journal of Soil Science,* 56, 135–143.

Black, P.B. & Tice, A.R. 1989. Comparison of soil freezing curve and soil-water curve data for windsor sandy loam. *Water Resources Research,* 25, 2205–2210.

Chen, P., Wei, C.F. & Ma, T.T. 2014. An analytical model of soil-water characteristics with considering the effect of air entrapment. *Int. J. Geomech.,* DOI: 10.1061/(ASCE)GM.1943-5622.0000462, online.

Gallegos, D.P. & Smith, D.M. 1988. A NMR technique for the analysis of pore structure: determination of continuous pore size distributions. *Journal of Colloid and Interface Science,* 122, 143–153.

Lu, N. & Likos, W.J. 2004. Unsaturated soil mechanics. *Wiley, New York.*

Mitchell, J.K. & Soga, K. 2005. Fundamentals of soil behavior. *New York: John Wiley & Sons*.

Tian, H.H., Wei, C.F., Wei, H.Z., Yan, R.T. & Chen, P. 2014. An NMR-Based Analysis of Soil-Water Characteristics. *Applied Magnetic Resonance,* 45, 49–61.

Tyrologou, P., Dudeney, A.W.L. & Grattoni, C.A. 2005. Evolution of porosity in geotechnical composites. *Magnetic Resonance Imaging,* 23, 765–768.

Van Genuchten, M.T. 1980. A closed-form equation for predicting the hydraulic conductivity of unsaturated soils. *Soil Science Society of America Journal,* 44, 892–898.

Vanapalli, S.K., Fredlund, D.G. & Pufahl, D.E. 1999. The influence of soil structure and stress history on the soil-water characteristics of a compacted till. *Geotechnique,* 49, 143–159.

Unsaturated Soil Mechanics—from Theory to Practice – Chen et al. (Eds)
© 2016 Taylor & Francis Group, London, ISBN 978-1-138-02921-7

Point of Zero Charge of two highly plastic expansive soils

B. Lin
State Key Laboratory of Petroleum Resources and Prospecting, China University of Petroleum, Beijing, China

A.B. Cerato
School of Civil Engineering and Environmental Sciences, University of Oklahoma, Norman, OK, USA

ABSTRACT: The physicochemical characteristics have profound influences on the hydraulic and mechanical responses of highly plastic expansive soils. A distinct feature to characterize how the neighboring clay particles would interact with each other is the Point of Zero Charge, or PZC, of a clayey sample. This study investigated the PZC of two highly plastic expansive soils through laboratory efforts. The point of zero net charge, or PZNC, was used to represent the PZC instead, owing to its physical soundness and experimental accessibility. It was found that neither of the soils demonstrated a clear cross point between the cation exchange capacity (CEC) and Anion Exchange Capacity (AEC) curves against the pH. In consequence, the PZC of the soils could only be qualitatively estimated. The major reason behind this phenomenon lies in the existence of multi-type clay minerals that possess different PZC values in a natural clayey sample.

1 INTRODUCTION

The Point of Zero Charge (PZC) of a clay particle determines the charge type and strength at its faces and edges, when the particle is subjected to a specific pH environment (Zelazny et al. 1996, Sposito 1998). Therefore, the pH value of a pure clay sample sheds light on how the particles are being charged and interacting with each other on a micro-scale. This microscopic performance has profound influences on the microstructure and subsequently the mechanical responses of clayey soils. For example, Wang and Siu (2006a & b) examined the impact of pH on the structural characteristics and mechanical behavior of a pure kaolinite sample. However, the PZC of a natural clayey soil was rarely explored, impeding the attempts to predict its macroscopic behavior from a physical (microscopic) point of view. In this regard, the PZC of two field-collected, highly plastic expansive soils was investigated.

2 GEOTECHNICAL AND PHYSICOCHEMICAL PROPERTIES

Investigations were conducted on two soils; one with slight swelling potential, named Carnisaw, and a highly expansive soil, named Eagle Ford. The former was collected from Le Flore, Oklahoma and the latter was retrieved in Irving, Texas. Carnisaw soil is red brown residual silt with high plasticity, weathered from shale of Pennsylvania age. Eagle Ford soil is yellowish/tan highly plastic clay weathered from fossiliferous clayey shale with sandy shale lenses. The field samples were processed through a No. 10 U.S. sieve prior to laboratory experiments in order to remove occasional coarse sands or gravels. Table 1 lists their geotechnical and physicochemical properties. Common geotechnical tests were performed following ASTM standards (ASTM 2011). The specific surface area (SSA, total) was obtained following the

EGME (Ethylene Glycol Monoethyl Ether) surface area determination method (Cerato & Lutenegger 2002). The Cation Exchange Capacity (CEC) data

Table 1. Physical properties of Carnisaw and Eagle Ford soils.

Soil property	Carnisaw	Eagle Ford
% passing No. 200 sieve	84	100
Clay size fraction (% $<2\,\mu m$)	51	66
Specific gravity, G_s	2.8	2.7
Liquid limit, LL	59	92
Plastic limit, PL	32	35
Plasticity index, PI	27	57
Optimum moisture content, w_{opt} (%)	26.2	27.1
Maximum dry unit weight, γ_{dmax} (kN/m^3)	15.9	14.2
Percent of free swell, s (%)	2.3	12.7
Swell pressure, p_s (kPa)	75	263
Specific surface area, SSA (m^2/g)	107.5	213.5
Cation exchange capacity, CEC (meq/100 g)	27.3	49.6
USCS classification	MH	CH

were measured from the 1 N ammonium acetate (CH3COONH4) extraction method (Rhoades 1982).

3 IMPACT OF POINT OF ZERO CHARGE ON CLAY PARTICLE INERATION

The investigation on the interparticle physicochemical forces involved the Point of Zero Charge (PZC) analysis. Several types of points of zero charge exist. They are derived from different molecular models of surface charge, each corresponding to a specific physical meaning through a particular lab test (Sposito 1998). The Point of Zero Net Charge (PZNC) is defined as the pH value at which the intrinsic surface charge, σ_{in}, is zero. The PZNC was suggested as the PZC that is most experimentally accessible and conceptually versatile (Zelazny et al. 1996). Therefore the PZNC is referred to as PZC in this article. An expression of σ_{in} at point of zero net charge gives

$$\sigma_{in} \equiv \sigma_o + \sigma_H = 0 \quad (1)$$

where σ_{in} represents the surface charge density of the adsorbent structure (of a clay particle); σ_o is the net permanent surface charge density or structural charge density owing to isomorphous substitution being independent of pH or ionic strength; σ_H is the net proton surface charge density originating from complex protons on hydroxyl groups and varies with pH and ionic strength (Sposito 1992 & 1998). When the pH value of the electrolyte surrounding a clay particle falls below the PZC of the related clay mineralogy, the edge of the particle tends to hold positive charge due to migration of the surrounding protons to oxygen ions in the hydroxyls at the aluminum edge sites of the octahedral sheet. On the other hand, a pH above PZC produces negative charges on the edge sites, as the relatively high pH provokes breaking of hydrogen bonds in hydroxyl groups and exposes the negatively charged oxygen ions.

The net total particle surface charge density, σ_p, is given as

$$\sigma_p \equiv \sigma_{in} + \sigma_S = - \sigma_d \quad (2)$$

where σ_s is the stern layer surface charge density, which is a combination of inner-sphere and outer-sphere complex charge densities; σ_d is the surface charge density of diffused ion swarms or diffuse double layer (DDL). It is worth noting that even though DDL encompasses both the charged surface and diffuse layer, the term DDL is frequently used in lieu of the latter. Obviously, σ_p is balanced by σ_d in order to maintain electrical neutrality. By combining the electric effect of the stern layer with that of the DDL, two simplified conceptual models describing the clay particle associations at different pH conditions relative to the PZC are constructed and illustrated in Fig. 1. It should be noted that the conceptual models in Fig. 1 are relevant for a pure clay sample, which has only one type of clay mineral. In the first model the interparticle interaction is dominated by Coulombic electrostatic force while in the second, the forces are principally DDL repulsion and, to a lesser extent, van der Waals force.

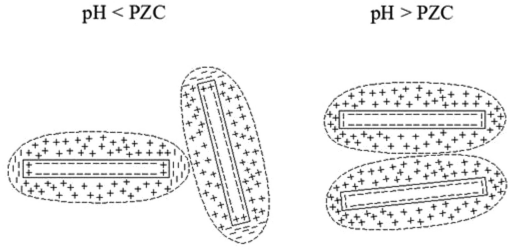


Figure 1. Interaction of clay particles at different pH values.

4 EXPERIMENTAL SETUP

The PZC tests on Carnisaw and Eagle Ford were performed following a procedure developed and improved by several researchers (Schofield 1949, van Raij & Peech 1972, Wada & Okamura 1977, Marsh et al. 1987), with details provided by Zelazny et al. (1996) and briefly introduced here. For each soil, 5 g (oven-dried weight) of air-dried soil, passing a No. 10 U.S. sieve, was placed into each of ten, 100 mL pre-weighed centrifuge tubes. 50 mL of 1 M KCl was added and then the sample tubes were shaken for 1 hour in a reciprocal shaker. The suspensions were then centrifuged to discard the supernatant and further washed five times with 50 mL of 0.01 M KCl. At the final washing, the pH values of the suspensions were adjusted by adding 1 M KOH or HCl to cover a range of about 2 ~ 11. The suspensions were centrifuged and the supernatants were transferred to labeled bottles for K^+ and Cl^- determination. The tubes, plus residues, were weighed to determine entrained solutions. The residues were washed four times with 20 mL of 0.5 M $NaNO_3$ to displace the adsorbed K^+ and Cl^-, while all the centrifuged solutions were decanted into labeled bottles and analyzed for K^+ and Cl^- concentrations again. The concentration of K^+ was determined by atomic emission spectrometry and that of Cl^- was by the colorimetric mercuric thiocyanate method (ASTM 2011). The obtained variations of CEC and AEC (anion exchange capacity) with pH are presented in Figures 2 and 3 for Carnisaw and Eagle Ford, respectively. The CEC values determined from the CH_3COONH_4 extraction method (Rhode 1982) are also shown for the comparison purpose. Only one data point is achieved by using the CH_3COONH_4 extraction method, however, because this method tests a soil at its intrinsic pH.

5 RESULTS AND DISCUSSION

As observed in Figures 2 and 3, CEC increases while AEC decreases as a function of pH in either Carnisaw or Eagle Ford, as a larger pH environment favors negative charging of clay particles and subsequent

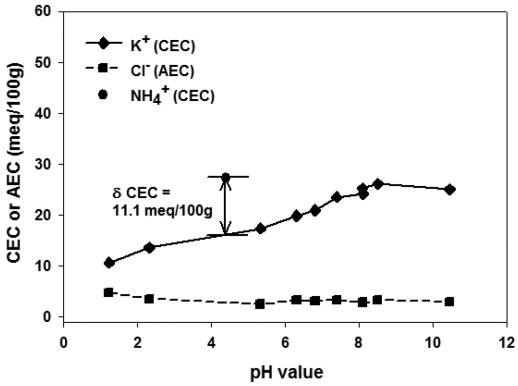


Figure 2. PZC test result of the Carnisaw soil.

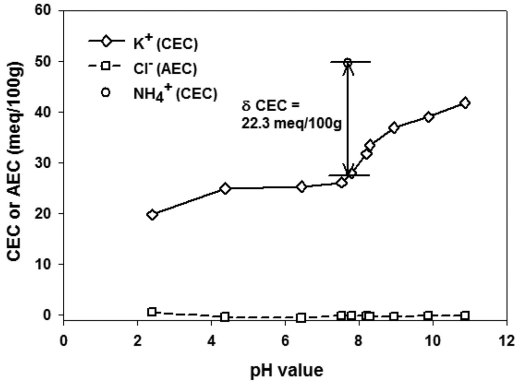


Figure 3. PZC test result of the Eagle Ford soil.

attraction of more positive charges in the vicinity to the particle surface, which is also implied by Figure 1.

According to Eq. (2) and by ignoring the term σ_s (assuming that the effect of stern layer has been integrated into that of DDL), the condition of PZC as $\sigma_{in} = 0$ requires that CEC equals AEC. Unfortunately, the intersection of CEC and AEC curves, as shown in Figures 2 and 3, cannot be identified, even though the two curves show a tendency to converge. This is partly because difficulty was encountered in controlling the pH of the suspension when the pH was lower than 2.0, where the reading fluctuated substantially with no tendency to stabilize. The other reason why the CEC and AEC curves do not intersect may lie in the possibility that the entrained adsorbed Cl^- was not adequately retrieved after the final washing with $NaNO_3$, therefore giving low measured AEC magnitudes. Nevertheless, it is safe to say that PZC < 2 holds for both soils given the tendency of convergence of the curves at low pH values. Another interesting observation is the over-prediction of CEC using CH_3COONH_4 (or similarly, NH_4NO_3) as the extraction solution, the method widely used for the determination of CEC for fine-grained soils. This is because NH_4^+ can displace fixed K^+, giving rise to overestimated CEC values for soils containing mica and vermiculite (Zelazny et al. 1996), such as Carnisaw (Table 1). Eagle Ford, on the other hand, may perhaps contain mica-like minerals that were not readily detected by X-ray diffraction.

It should be noted that the PZC values attained represent the entire soil sample on average. Unlike the PZC of a homogeneous clay sample, like pure kaolinite, that functions as the determining factor in fabric formation (Wang and Siu 2006a & b), the value of a heterogeneous sample plays more of a qualitative role in impacting the sample structure; namely, the greater the pH of a sample relative to its PZC, the closer the structure resembles the second model in Fig. 1. Therefore it can be postulated that Carnisaw (pH = 4.4, Table 1) may form an edge-face and edge-edge flocculated structure, whereas the structure of Eagle Ford (pH = 7.7, Table 1) may display a laminar fabric with more substantial development of face-face particle association. The edge-edge association (not given in Fig. 1) can be viewed as the case when two particles of distinct mineral composition have their edge sides bonded to each other because one is negatively charged and the other is positively charged at their edges (particles from both models shown in Fig. 1) at an identical pH. Further evidence in support of the arguments above can be referred to the direct microstructural observations provided by Lin and Cerato (2014).

6 CONCLUSIONS

In this study the PZC of two highly plastic expansive soils was investigated. The PZC was used to analyze the interparticle electrostatic bonding or repulsion through the medium known as DDL. For natural samples composed of mixed minerals, the corresponding PZC is not as determinative in such an analysis as that for a pure clay sample like kaolinite, because interaction could occur between the particles of different mineralogical makeup. As such, it can only be qualitatively argued that a lower pH enhances edge-face particle association; such an argument could be verified by direct observation on microstructure. The ammonium replacement method, instead of using sodium nitrate as the extraction fluid, resulted in significant overestimation of CEC for natural samples containing vermiculite or mica, owing to the displacement of the fixed potassium ions by ammonium ions.

ACKNOWLEDGEMENTS

We would like to express our gratitude to the U.S. National Science Foundation (Grant No. 0746980), and the National Natural Science Foundation of China (Grants No. 51404281, 51325402, 51490650, 51174217 and 51234006) for their financial supports. Our research was also supported by the Foundation of State Key Laboratory of Petroleum Resources and Prospecting (Grant No. PRP/indep-4-1309) and the

Science Foundation of China University of Petroleum, Beijing (Grant No. 2462013YJRC037).

REFERENCES

ASTM. 2011. 2011 Annual Book of ASTM Standards. Volume 04.08 Soil and Rock (I): D420-D5876 and Vol. 4.09 Soil and Rock (II): D5877 – latest. West Conshohocken, Pennsylvania.

Cerato, A.B. & Lutenegger, A.J. 2002. Determination of surface area of fine-grained soils by the ethylene (EGME) method. *Geotech. Test. J.*, 25(3), 315–321.

Lin, B. & Cerato, A.B. 2014. Application of SEM and ESEM in microstructural investigation of shale-weathered expansive soils along swelling-shrinkage cycles, *Eng. Geol.*, 177, 66–74.

Marsh, K.B., Tillman, R.W. & Syers, J.K. 1987. Charge relationships of sulfate sorption by soils. *Soil Sci. Soc. Am. J.*, 51, 318–323.

Rhoades, J.D. 1982. Cation exchange capacity. In: Page AL et al. (eds) Methods of soil analysis, agronomy 9, 2nd edn. American Society of Agronomy, Madison, 159–165.

Schofield, R.K. 1949. Effect of pH on electric charges carried by clay particles. *J. Soil Sci.*, 1, 1–8.

Sposito, G. 1992. "Characterization of particle surface charge." In J. Buffle and H.P. van Leeuwen (ed.) Environmental particles. Lewis Publ., Boca Raton, FL, vol. 1, 291–314.

Sposito, G. 1998. On points of zero charge. *Environ. Sci. Tech.*, 32(19), 2815–2819.

van Raij, B. & Peech, M. 1972. Electrochemical properties of some Oxisols and Alfisols of the Tropics. *Soil Sci. Soc. Am. Proc.*, 36, 587–593.

Wada, K. & Okamura, Y. 1977. Measurements of exchange capacities and hydrolysis as a means of characterizing cation and anion retentions by soils. Proc. Int. Seminar on Soil Environ. and Fertility Management in intensive agriculture, Tokyo, Oct 10–14, 811–815.

Wang, Y.H. & Sui, W.K. 2006a. Structure characteristics and mechanical properties of kaolinite soils. I. Surface charge and structural characterization. *Can. Geotech. J.*, 43, 587–600.

Wang, Y.H. & Sui, W.K. 2006b. Structure characteristics and mechanical properties of kaolinite soils. II. Effects of structure on mechanical properties. *Can. Geotech. J.*, 43, 601–617.

Zelazny, L.W., He, L. & Vanwormhoudt, A. 1996. Charge analysis of soils and anion exchange. In Methods of Soil Analysis, Part 3. Chemical Methods—SSSA Book Series no. 5, 1231–1253.

Stress-strain and strength characteristics

This page intentionally left blank

Unsaturated Soil Mechanics—from Theory to Practice – Chen et al. (Eds)
© 2016 Taylor & Francis Group, London, ISBN 978-1-138-02921-7

Influence of unsaturated state variables on small strain elastic behaviour

A.M. Hasan & S.J. Wheeler
University of Glasgow, UK

ABSTRACT: Bender/extender element testing of unsaturated compacted speswhite kaolin samples was used to investigate the influences of mean net stress $\bar{p}$, suction s, specific volume v and degree of saturation S_r on shear and compression wave velocities, V_s and V_p, and hence on small strain elastic values of undrained shear modulus and undrained constrained modulus. Testing was performed in a suction-controlled triaxial cell and involved combinations of isotropic loading and unloading stages and wetting and drying stages, in an attempt to isolate the influence of each unsaturated state variable. The results showed that increases of V_s are caused by increases of $\bar{p}$ and decreases of v. Combined increases of s and decreases of S_r during drying also lead to increases of V_s, and conversely combined decreases of s and increases of S_r during wetting lead to decreases of V_s. Separating the effects of changes of s and S_r on V_s was not possible, because the evidence on the influence of a change of S_r at constant s was contradictory. Increases of V_p are caused by increases of $\bar{p}$ and S_r and decreases of v, whereas the influence of a change of s at constant S_r is unclear.

1 INTRODUCTION

Combined bender/extender elements (Lings & Greening, 2001) provide measurements of shear wave velocity V_s and compression wave velocity V_p, which can be used to determine small strain elastic values of undrained shear modulus G_u and undrained constrained modulus M_u respectively:

$$G_u = \rho V_s^2 \tag{1}$$

$$M_u = \rho V_p^2 \tag{2}$$

where ρ is the bulk density. The undrained constrained modulus M_u in (2) is related to the undrained bulk modulus K_u and shear modulus G_u by:

$$M_u = K_u + 4G_u/3 \tag{3}$$

For a given soil, the values of G_u and M_u, and hence V_s and V_p, will vary with soil state. Under saturated conditions and isotropic stress states, the soil state is fully defined by the values of mean effective stress p' and specific volume v (or void ratio $e = v - 1$). Various empirical expressions have been proposed relating small strain elastic shear modulus ($G_u = G'$ for saturated conditions) to p' and e for saturated soils under isotropic stress states, see for example Viggiani & Atkinson (1995). Given that bulk density ρ can be expressed solely as a function of v for a specific soil under saturated conditions, this means that shear wave velocity V_s for a specific soil under saturated conditions and isotropic stress states is solely a function of p' and v:

$$V_s = f(p', v) \tag{4}$$

Under saturated conditions, the value of undrained constrained modulus M_u (see (3)) is dominated by the value of K_u, because this is much larger than G_u. The value of K_u is, in turn, controlled almost entirely by the bulk modulus of water K_w (a constant), the bulk modulus of the soil particles K_s (a constant for a given soil) and the value of v. Hence, the compression wave velocity V_p for a specific soil under saturated conditions is solely a function of v:

$$V_p = f(v) \tag{5}$$

For a soil under unsaturated conditions, net stresses and matric suction s are often selected as appropriate stress state variables (other combinations of stress state variables are possible), and both specific volume v and degree of saturation S_r are additional independent state variables. Hence, for a specific soil under unsaturated conditions and isotropic stress states, the most general proposal is that both shear wave velocity V_s and compression wave velocity V_p will depend upon the values of $\bar{p}$, s, v and S_r, where $\bar{p}$ is mean net stress:

$$V_s = f(\bar{p}, s, v, S_r) \tag{6}$$

$$V_p = f(\bar{p}, s, v, S_r) \tag{7}$$

Authors such as Ng & Yung (2008) and Sawangsuriya et al. (2009) have examined the variation of V_s or G_u under unsaturated conditions, including the roles of some of the state variables in (6). Similarly, Alramahi et al. (2008) and Eseller-Bayat et al. (2013) have examined the influence of some of the state variables in

(7) on the variation of V_p or M_u under unsaturated conditions. These previous experimental studies have, however, generally not been able to entirely separate the roles of the different state variables. For example, they do not show whether dependency on both s and S_r is required in expressions for V_s and V_p under unsaturated conditions, or whether it is sufficient to include only one of these two state variables. This is relevant, because hysteresis in the water retention behaviour means that there is not a unique relationship between s and S_r for a given soil (Wheeler et al. 2003).

The objective of the work described in this paper was to explore more fully the roles of the state variables $\overline{p}$, s, v and S_r on the variation of V_s and V_p under unsaturated conditions, by performing bender/extender element testing during isotropic stress paths involving combinations of loading, unloading, wetting and drying.

2 TEST PROGRAMME

2.1 *Sample preparation*

Three unsaturated samples of speswhite kaolin clay (LL = 68%, PL = 36%) were prepared by compaction at a water content of 25% (4% dry of the optimum from the standard Proctor compaction test). An isotropic form of static compaction was used (Al-Sharrad 2013). The uncompacted soil mix was sealed within a large cylindrical rubber membrane and then subjected to an isotropic compaction stress of 390 kPa in a triaxial cell. A smaller, 50 mm diameter, 100 mm height, triaxial test sample was then cored from the larger body of soil. Samples were subsequently tested in a suction-controlled triaxial cell fitted with bender/extender elements.

2.2 *Bender element testing*

Shear wave velocity V_s and compression wave velocity V_p were measured using two pairs of bender/extender elements. Both pairs transmitted horizontally across the sample, at the sample mid-height, giving two independent measurements of the horizontal compression wave velocity V_{ph}. One pair was aligned to give shear waves of vertical polarization and the other was aligned to give shear waves of horizontal polarization, providing measurements of shear wave velocities V_{shv} and V_{shh} respectively (where the second and third subscripts represent the transmission direction and polarization direction respectively).

Transmitter bender/extender elements were excited by a single sinusoidal pulse, using a frequency of 20 kHz for shear waves and 35 kHz for compression waves, corresponding to wavelengths of approximately 10 mm in both cases. These frequencies conformed to the recommendation of Leong et al. (2005) that wavelengths should be less than 30% of the transmission path length and preliminary tests (Hasan & Wheeler, in press) indicated that they provided reliable and consistent values of wave velocity.

Values of wave velocity were calculated from the tip-to-tip distance between transmitter and receiver bender elements and the measured travel time. Travel time was determined from transmitted and received signals, using a peak-to-first-peak method in the time domain. Preliminary tests (Hasan & Wheeler, in press) investigated four possible methods for determining travel time (using both time and frequency domains) and concluded that the selected method was the most reliable.

2.3 *Stress paths*

Figure 1 shows the stress paths followed in Tests A, B and C. In all three tests the as-compacted suction was approximately 650 kPa (point X in Fig. 1). After mounting in the triaxial cell, a mean net stress of 10 kPa was applied (point Y in Fig. 1) and then samples were wetted to a suction of 300 kPa (points A_1, B_1 and C_1).

Test A involved isotropic loading ($A_1 - A_2$) at constant suction ($s = 300$ kPa) to $\overline{p} = 300$ kPa, followed by isotropic unloading ($A_2 - A_3$) to $\overline{p} = 10$ kPa. Test B involved a wetting-drying cycle ($B_1 - B_2 - B_3$) at $\overline{p} = 10$ kPa to a minimum suction of 50 kPa, followed by isotropic loading-unloading ($B_3 - B_4 - B_5$) at $s = 300$ kPa. Finally, Test C involved isotropic loading ($C_1 - C_2$) at $s = 300$ kPa to $\overline{p} = 100$ kPa, followed by a wetting-drying cycle ($C_2 - C_3 - C_4$) at $\overline{p} = 100$ kPa to a minimum suction of 50 kPa and then isotropic loading and unloading ($C_4 - C_5 - C_6$) at $s = 300$ kPa.

Loading and unloading stages were performed by increasing or decreasing $\overline{p}$ at a fixed rate of 2 kPa/hour, whereas wetting and drying stages were performed by applying a rapid change of s to the sample boundary and then waiting until inflow or outflow of water reached an appropriately low rate. Bender/extender element (BEE) tests were performed at intervals throughout each test (see Fig. 1).

The purpose of the wetting-drying cycles in Tests B and C was to ensure that during subsequent isotropic loading and unloading the values of S_r were different for samples A, B and C (due to hysteresis in the retention behaviour), even though the suction value was identical at 300 kPa in all three cases. For sample C the wetting was expected to produce collapse compression, whereas collapse compression was not expected in the wetting performed in Test B, so that the subsequent loading stages of Tests B and C were expected to be at different values of v.

3 TEST RESULTS

3.1 *Variation of specific volume v*

Figure 2 shows the variation of v for all three tests. The two data points at the end of each isotropic loading stage represent the start and end of a 24 hour rest period. There were small differences in the measured initial values of v for the three samples (after

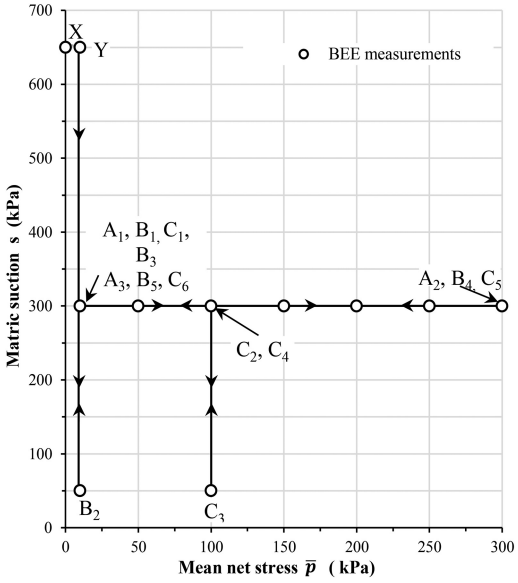


Figure 1. Stress paths for Tests A, B and C.

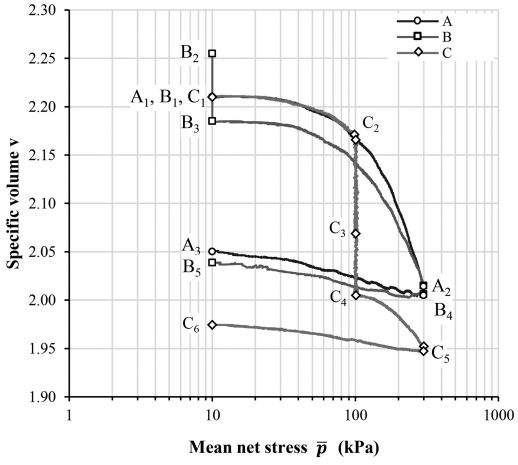


Figure 2. Variation of specific volume.

initial wetting to $s = 300$ kPa). Investigation over a large number of tests suggested that this was mainly attributable to small errors in measurements of initial sample volume rather than to variability between samples. Results were therefore adjusted so that initial values of v were identical for all three samples (see A_1, B_1 and C_1 in Fig. 2).

The variation of v during Test A (see Fig. 2) showed, as expected, significant irreversible compression during the isotropic loading-unloading cycle ($A_1 - A_2 - A_3$), with the suggestion of yielding during loading.

During Test B, swelling was observed during the wetting stage ($B_1 - B_2$) (see Fig. 2), with no indication of any wetting-induced collapse compression. This was followed by shrinkage during the drying stage

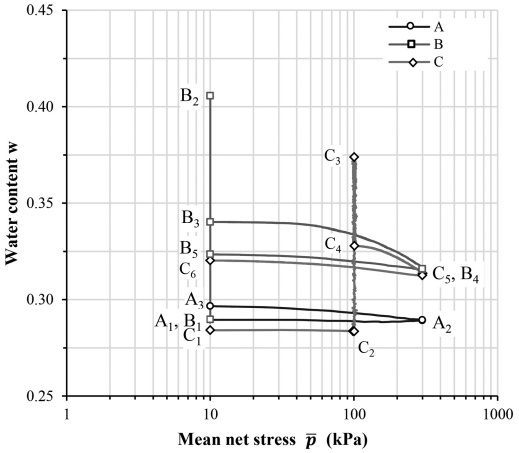


Figure 3. Variation of water content.

($B_2 - B_3$), with a net reduction of v over the wetting-drying cycle ($B_1 - B_2 - B_3$). During the subsequent isotropic loading stage ($B_3 - B_4$) the compression curve gradually converged with the curve from Test A, and during subsequent unloading ($B_4 - B_5$) the variation of v was very similar to Test A.

For Test C, Figure 2 shows that the variation of v during the initial loading ($C_1 - C_2$) was, as expected, almost identical to that from Test A. The subsequent wetting stage ($C_2 - C_3$) produced significant reduction of v (collapse compression), and this was followed by further shrinkage in the drying stage ($C_3 - C_4$). The final isotropic loading ($C_4 - C_5$) and unloading ($C_5 - C_6$) stages produced irreversible compression, with the suggestion of yielding during loading. By the end of the loading stage ($C_4 - C_5$) the compression curve had not fully converged with the curves from Tests A and B, and the final value of v after unloading to C_6 was still significantly lower than in Tests A and B.

3.2 *Variation of degree of saturation S_r*

Figure 3 shows the measured variations of water content w for the three samples, and Figure 4 shows the corresponding variations of degree of saturation S_r, calculated by combining the measurements of v and w from Figures 2 and 3. The initial values of S_r shown in Figure 4 for the three samples (at A_1, B_1 and C_1) were all very similar.

The variation of S_r during Test A (see Fig. 4) showed significant irreversible increase of S_r during the loading-unloading cycle ($A_1 - A_2 - A_3$), with the suggestion of yielding during the loading stage.

In Test B there was significant net increase of S_r during the wetting-drying cycle ($B_1 - B_2 - B_3$), as a consequence of hysteresis in the water retention behaviour, so that the value of S_r at the start of the subsequent loading stage was higher than in Test A (compare B_3 and A_1 in Fig. 4). By the end of the loading stages (B_4 and A_2 in Fig. 4) the difference between the

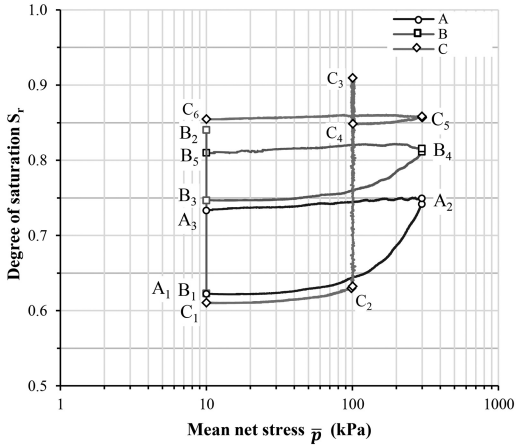


Figure 4. Variation of degree of saturation.

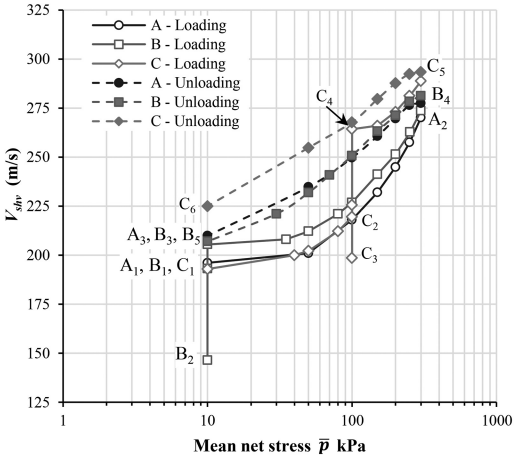


Figure 5. Shear wave velocity V_{shv}.

values of S_r in Tests B and A had reduced, and this difference in S_r then remained almost unchanged during the final unloading stages ($A_2 - A_3$ and $B_4 - B_5$).

In Test C the variation of S_r (see Fig. 4) during the first loading stage ($C_1 - C_2$) was very similar to that in Test A, as expected. A large increase of S_r occurred during the wetting stage ($C_2 - C_3$), with a smaller reduction of S_r during the subsequent drying stage ($C_3 - C_4$), as a consequence of hysteresis in the water retention behaviour. Little further change of S_r occurred during the final loading stage ($C_4 - C_5$) and unloading stage ($C_5 - C_6$), and the value of S_r remained higher than in Tests A and B.

3.3 *Influence on shear wave velocity V_s*

Figures 5 and 6 show the variations of shear wave velocities V_{shv} and V_{shh} for all three samples. Comparison of Figures 5 and 6 shows that the values of V_{shv} and V_{shh} were always very similar, confirming that the isotropic compaction procedure and subsequent isotropic stress history resulted in soil samples with isotropic properties.

Results from Test A in Figures 5 and 6 show that the shear wave velocity V_s increased during the loading stage ($A_1 - A_2$), as $\overline{p}$ increased, s remained constant, v decreased (Fig. 2) and S_r increased (Fig. 4). During this loading stage $A_1 - A_2$, the variation of V_s shown in Figs. 5 and 6 followed a qualitatively similar form to the variations of v and S_r shown in Figures 2 and 4 respectively, suggesting that changes to one or both of these state variables may have contributed significantly to the variation of V_s. Established experience for saturated soils (see (4)) suggests that the increase of $\overline{p}$ and the decrease of v would both have contributed to the increase of V_s during loading stage $A_1 - A_2$, whereas previous experience gives little indication of whether the increase of S_r (at constant s) could also have contributed to the increase of V_s or instead could have partially offset the effects of the changes to $\overline{p}$ and v.

Comparing values of V_s from the unloading stage ($A_2 - A_3$) of Test A, with corresponding values of V_s at the same values of $\overline{p}$ in the previous loading stage ($A_1 - A_2$) (i.e. at the same values of $\overline{p}$ and s, but different values of v and S_r), it is clear that the lower values of v and higher values of S_r in the unloading stage have led to higher values of V_s than in the loading stage. Again, lower values of v contributing to higher values of V_s is consistent with existing experience for saturated soils, but it is unclear whether this has been enhanced or partially offset by the influence of the higher values of S_r.

Inspection of Figures 5 and 6 shows that a significant decrease of V_s occurred during the wetting stage ($B_1 - B_2$) of Test B. This decrease of V_s can be partially attributed to the increase of v during the wetting stage (Fig. 2), but this increase of v was relatively small and it is therefore likely that the combined decrease of s and increase of S_r (Fig. 4) during the wetting stage also contributed to the significant decrease of V_s. It is not, however, possible to separate the influences of the decrease of s and the increase of S_r. The value of V_s at the end of the drying stage ($B_2 - B_3$) was higher than at the start of the wetting-drying cycle (compare B_3 and B_1 in Figs. 5 and 6). This is consistent with the net reduction of v over the wetting-drying cycle (Fig. 2), but it is not clear whether the net increase of S_r over the wetting-drying cycle also contributed to the increase of V_s or partially offset the effect of the decrease in v.

During the isotropic loading stage ($B_3 - B_4$) of Test B, values of V_s were initially slightly higher than within Test A, but by the end of the loading stage and during subsequent unloading ($B_4 - B_5$) the values of V_s were very similar to those from Test A (see Figs. 5 and 6). This pattern of behaviour is entirely consistent with the difference of v between Tests A and B at the start of loading and the gradual erasure of this difference as loading progressed (see Fig. 2). The fact that values of V_s were very similar during the unloading stages of Tests $A$and B, when values of v were very similar but values of S_r were significantly different

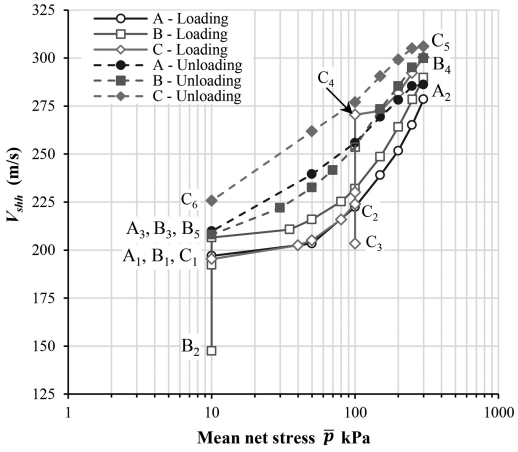


Figure 6. Shear wave velocity V_{shh}.

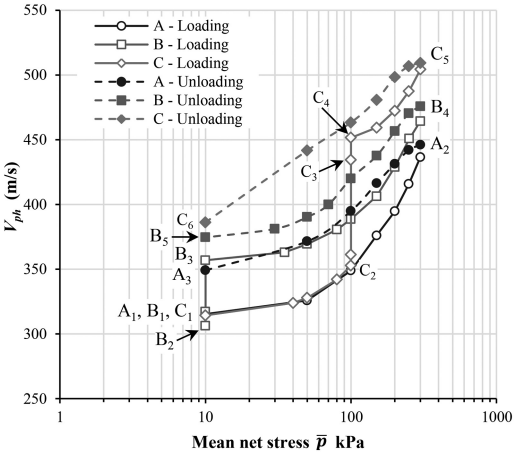


Figure 7. Compression wave velocity V_{ph}.

(see Fig. 4), suggests that the change of S_r (at constant s) had relatively little influence on the value of V_s.

A noteworthy point from Test B is that the value of V_s at the end of the loading-unloading cycle was very similar to the value measured at the beginning of the cycle (compare B_5 and B_3 in Figs. 5 and 6), despite the fact that the value of v was substantially lower at the end of the cycle than at the beginning (see Fig. 2). This reduction of v would have been expected to produce a significant increase of V_s, so the fact that V_s was almost unchanged at the end of the loading-unloading cycle suggests that the influence of the decrease of v must have been offset by the influence of the increase of S_r between B_3 and B_5 (see Fig. 4). This suggestion, that an increase of S_r (at constant s) could lead to a decrease of V_s, is contradictory to the suggestion arising from the comparison of Tests $A$and B, that an increase of S_r has little effect on V_s (see previous paragraph).

In Test C, the variation of V_s during the initial loading stage ($C_1 - C_2$) was, as expected, very similar to that observed in Test A (see Figs. 5 and 6).

During the wetting stage ($C_2 - C_3$) of Test C, there was a decrease in the value of V_s, suggesting that the combined influence of the decrease of s and increase of S_r (tending to produce a decrease of V_s) was stronger than the influence of the decrease of v (which would be expected to produce an increase of V_s). The drying stage ($C_3 - C_4$) then produced a large increase of V_s, consistent with the fact that the decrease of v (Fig. 2) would be expected to produce an increase of V_s and so would the combined influence of the increase of s and the decrease of S_r (Fig. 4). The value of V_s at the end (C_4) of the wetting-drying cycle was significantly greater than the value at the beginning (C_2) (see Figs. 5 and 6), consistent with the net decrease of v over the cycle, with the influence of the net increase of S_r (at constant s) being unclear.

At the end of the final isotropic unloading stage of Test C, the value of V_s was higher than in Tests A and B (compare C_6 with A_3 and B_5 in Figs. 5 and 6). This is consistent with the lower final value of v in Test C (see Fig. 2), and it is unclear whether this was enhanced or partially offset by the higher value of S_r (see Fig. 4).

Further contradictory evidence on the influence of a change of S_r (at constant s) on the value of V_s emerges from comparing other points within Test C with appropriate points in Tests A and B. For example, the value of V_s at C_4 is noticeably higher than at $\bar{p} = 100$ kPa within unloading stages $A_2 - A_3$ and $B_4 - B_5$, and it seems unlikely that this can be attributed solely to a slightly lower value of v (see Fig. 2). This suggests that the higher value of S_r at C_4 (see Fig. 4) may also have contributed to the higher value of V_s i.e. a suggestion that an increase of S_r (at constant s) leads to an increase of V_s, whereas previous suggestions were either that an increase of S_r (at constant s) has little effect on V_s or leads to a decrease of V_s.

3.4 *Influence on compression wave velocity V_p*

Figure 7 shows the variation of compression wave velocity V_{ph} for all three samples. The two independent measurements of V_{ph}, from the two bender/extender element pairs, were always very consistent, and each data point shown in Figure 7 is the average of the two measurements.

Space limitations preclude a full exposition of the interpretation of the results for V_p shown in Figure 7, but the results suggest that increases of V_p are caused by increases of $\bar{p}$, decreases of v and increases of S_r, whereas the separate influence of a change of s (at constant S_r) is unclear. Note that a combined decrease of s and increase of S_r (wetting) produces an increase of V_p, whereas it produces a decrease of V_s.

Simple illustrations of the influences of v and S_r on compression wave velocity V_p are given by considering the wetting-drying cycles in Tests B and C. During the wetting stage ($B_1 - B_2$) of Test B, there was a small decrease in the value of V_p, because the effect of the increase of v was partially offset by the effects of the increase of S_r. In the wetting stage ($C_2 - C_3$) of Test C,

there was a large increase of V_p, caused by a combination of the decrease of v and the increase of S_r. Further small increase of V_p occurred during the subsequent drying stage ($C_3 - C_4$) of Test C, suggesting that the influence of the decrease of v outweighed the influence of the decrease of S_r. In both Tests B and C there was significant net increase of V_p over the wetting-drying cycle ($B_1 - B_2 - B_3$ and $C_1 - C_2 - C_3$), because of the net decrease of v and net increase of S_r over the cycle.

4 CONCLUSIONS

Bender/extender element test results suggest that, for a soil under unsaturated conditions and isotropic stress states, increases of shear wave velocity V_s are caused by increases of $\overline{p}$ and decreases of v. Combined increases of s and decreases of S_r during drying also lead to increases of V_s, whereas combined decreases of s and increases of S_r during wetting lead to decreases of V_s. The experimental evidence on the separate influences of s and S_r on V_s is, however, contradictory, so that it is unclear whether an increase of S_r at constant s leads to a decrease or increase of V_s or to no significant effect on V_s. The experimental results also suggest that increases of compression wave velocity V_p are caused by increases of $\overline{p}$, decreases of v and increases of S_r, but the separate influence of a change of s (at constant S_r) is unclear.

Given the contradictory evidence on the separate influences of s and S_r on V_s, when interpreted in a framework employing $\overline{p}$, s, v and S_r as unsaturated state variables, it may be useful to examine whether interpretation in terms of alternative unsaturated stress state parameters (such as the mean Bishop's stress p^* employed in the constitutive framework of Wheeler et al. (2003)) would be advantageous. This might also mean that it would be easier to establish explicit expressions describing the variations of V_s and V_p with unsaturated state variables, if this alternative approach resulted in the formulation of expressions for V_s and V_p involving fewer variables.

REFERENCES

Alramahi, B., Alshibli, K.A., Fratta, D., & Trautwein S., 2008. A suction-control apparatus for the measurement of P and S wave velocity in Soils. *Geotechnical Testing Journal*, 31(1): 12–23.

Al-Sharrad, M.A. 2013. Evolving anisotropy in unsaturated soils: experimental investigation and constitutive modeling. *PhD thesis, University of Glasgow, UK*.

Eseller-Bayat, E., Gokyer, S., Yegian, M.K., Deniz, R.O. & Alshawabkeh, A. (2013). Bender elements and bending disks for measurement of shear and compression wave velocities in large fully and partially saturated sand specimens. *Geotechnical Testing Journal*, 36(2): 1–8.

Hasan, A.M. & Wheeler, S.J., in press. Measuring travel time in bender/extender element test. *16th European conference on Soil Mechanics and Geotechnical Engineering*, Edinburgh, UK, accepted.

Leong, E.C., Yeo, S.H. & Rahardjo, H. 2005. Measuring shear wave velocity using bender elements. *Geotechnical Testing Journal*, 28(5):488–498.

Lings, M.L. & Greening, P.D. 2001. A novel bender/extender element for testing. *Géotechnique*, 51(8): 713–717.

Ng, C.W.W. & Yung, S.Y., 2008. Determination of the anisotropic shear stiffness of an unsaturated decomposed soil. *Géotechnique*, 58(1): 23–35.

Sawangsuriya, A., Edil, T.B., & Bosscher, P.J., 2009. Modulus-Suction-Moisture Relationship for Compacted Soils in Postcompaction State. *Journal of Geotechnical and Geoenvironmental Engineering*, 135(10): 1390–1403.

Viggiani, G. & Atkinson, J.H., 1995. Interpretation of bender element tests. *Géotechnique*, 45(1): 149–154.

Wheeler, S.J. Sharma, R.S. & Buisson, M.S.R., 2003. Coupling of hydraulic hysteresis and stress–strain behaviour in unsaturated soils. *Géotechnique*, 53(1): 41–54.

Unsaturated Soil Mechanics—from Theory to Practice – Chen et al. (Eds)
© 2016 Taylor & Francis Group, London, ISBN 978-1-138-02921-7

Some remarks on the mechanical yielding of unsaturated soils

M. Lloret-Cabot, J.A. Pineda & D. Sheng
The University of Newcastle, Newcastle, Australia

M.P. Cordão Neto
The University of Brasilia, Brasilia, Brazil

ABSTRACT: This paper discusses the model predictions of a series of conventional isotropic loading stress paths, at different values of constant suction, obtained from the simulations of three existing constitutive models for unsaturated soils. The well-known Barcelona Basic Model (BBM) is used as a reference point of the analysis, whereas two more recent models, involving both predictions of degree of saturation, are included in the discussion to expand and complement the research. In addition to the comments on the effects of suction on mechanical yielding and associated normal compression lines, the paper discusses some of the influences that the predicted elasto-plastic volumetric behaviour (due to mechanical yielding) has on the water retention behaviour (degree of saturation variations) during the conventional isotropic loading paths considered.

1 INTRODUCTION

The use of well-established constitutive models represents a useful tool of research, not only to explore further the capabilities of the constitutive model itself, but mainly to understand better, fundamental features of behaviour that are underlying the formulation of the model.

This paper presents a discussion on the model predictions of a set of conventional isotropic stress paths at constant suction using three existing constitutive models for unsaturated soils. The starting point is the Barcelona Basic Model (BBM) proposed by Alonso, Gens and Josa in 1990. The constitutive model proposed by Wheeler et al. (2003) and the constitutive model proposed by Sheng et al. (2008) (referred to as the SFG model) are the other two models employed. In order to include predictions of degree of saturation, the BBM and SFG models are combined with the coupled relationships for the water retention behaviour proposed in Sheng & Zhou (2011). The formulation of the Wheeler et al. (2003) model accounts already for predictions of degree of saturation.

2 CONSTITUTIVE MODELS

The three constitutive models used in this paper are only briefly introduced in this section. Full descriptions of their formulations can be found elsewhere (e.g. Alonso et al., 1990; Wheeler et al., 2003 and Sheng et al., 2008). The two models using the same pair of constitutive (or stress state) variables are presented first (i.e. BBM and SFG) followed by the Wheeler et al. (2003) model. All three models are only presented for isotropic stress states.

2.1 *The Barcelona Basic Model (Alonso et al. 1990)*

For isotropic stress states, the BBM uses the mean net stress $\bar{p}$ and (matric) suction s defined as:

$$\bar{p} = p - u_a \tag{1}$$

$$s = u_a - u_w \tag{2}$$

where p is the mean total stress, u_a is the pore air pressure and u_w is the pore water pressure.

Elastic volumetric behaviour is associated with changes in $\bar{p}$ and s according to:

$$dv^e = -\kappa \frac{d\bar{p}}{\bar{p}} - \kappa_s \frac{ds}{(s + p_{at})} \tag{3}$$

where v is the specific volume, κ is an elastic swelling index giving the gradient of constant suction unloading/re-loading lines in the v:ln $\bar{p}$ plane, κ_s is a second elastic swelling index to account for the influence of suction in (elastic) volumetric behaviour and p_{at} is the atmospheric pressure.

Isotropic loadings at constant suction involving elasto-plastic variations of v, define a series of normal compression lines in the v:ln $\bar{p}$ plane of the form:

$$v = N(s) - \lambda(s) \ln \frac{\bar{p}}{\bar{p}^c} \tag{4}$$

where $\overline{p}^c$ is a reference value of mean net stress (associated with the intercept $N(s)$) and $\lambda(s)$ is the gradient of a normal compression line at suction s. $\lambda(s)$ varies with suction according to:

$$\lambda(s) = \lambda(0)\left[(1-r)\exp(-\beta s) + r\right] \tag{5}$$

where $\lambda(0)$ is the gradient of the normal compression line at zero suction, whereas r and β are two soil parameters.

Alonso et al. (1990) assumed that r was less than 1 which implies that $\lambda(s)$ decreases with increasing suction in accordance with the experimental data provided by, amongst others, Maswoswe (1985), Josa (1988) and Vicol (1990). Conversely, Wheeler et al. (2002) demonstrated that values of r greater than 1 could also be considered within the BBM formulation to predict increases of $\lambda(s)$ with increasing suction, in accordance with the experimental results presented in Wheeler and Sivakumar (1995), Sivakumar and Wheeler (2000), amongst others. Any of the two alternatives ($r < 1$ and $r > 1$) has important implications on the predicted normal compression lines and, therefore, on how the model predicts collapse compression behaviour upon wetting (Wheeler and Karube, 1996).

Combining (3) and (4) an expression defining how the isotropic yield stress varies with suction (linking plastic compression during loading and plastic compression during wetting to the same process of inter-particle or inter-aggregate slippage) can be obtained:

$$\frac{\overline{p}_0(s)}{\overline{p}^c} = \left(\frac{\overline{p}_0^*}{\overline{p}^c}\right)^{\frac{\lambda(0)-\kappa}{\lambda(s)-\kappa}} \tag{6}$$

where $\overline{p}_0(s)$ defines the yield net stress as a function of s and $\overline{p}_0^*$ is the pre-consolidation net stress at zero suction (see Figure 1).

2.2 *SFG model (Sheng et al., 2008)*

Sheng et al. (2008) proposed a constitutive model for unsaturated soils that, for isotropic stress states, employs the same constitutive variables used in the BBM ($\overline{p}$ and s). Similarly to the BBM, elastic volumetric behaviour is associated with changes in $\overline{p}$ and s, but now including an influence of suction on the second swelling index (see Equations 7 and 8). In addition, the SFG model assumes a double logarithmic approach similar to that used for saturated soils (see Butterfield, 1979):

$$\frac{dv^e}{v} = -\kappa_{vp}\frac{d\overline{p}}{\overline{p}+s} - \kappa_{vs}\frac{ds}{(\overline{p}+s)} \tag{7}$$

where,

$$\kappa_{vs} = \begin{cases} \kappa_{vp} & s < s_{sa} \\ \kappa_{vp}\dfrac{s_{sa}}{s} & s \geq s_{sa} \end{cases} \tag{8}$$

where s_{sa} is the saturation suction and corresponds to value of suction at which the soil reaches saturation (i.e. $S_r = 1$), κ_{vp} is an elastic swelling index related to changes in $\overline{p}$ and κ_{vs} is a second elastic swelling index related to changes in s.

For isotropic loadings at constant suction, the elasto-plastic variations of specific volume lie on a normal compression line of the form:

$$\ln v = \ln N - \lambda_{vp}\ln\frac{\overline{p}+s_i}{\overline{p}_i+s_i} \tag{9}$$

where λ_{vp} is the gradient of the saturated normal compression line, $\overline{p}_i$ is a reference value of mean net stress (associated with the intercept $\ln N$) and s_i is the (constant) value of suction.

For compacted soils, the SFG model proposes the following expression of the LC yield curve:

$$\overline{p}_{yn}(s) = \begin{cases} \overline{p}_{yn0} - s & s < s_{sa} \\ \dfrac{\overline{p}_{yn0}}{\overline{p}_{y0}}\left(\overline{p}_{y0} + s - s_{sa} - s_{sa}\ln\dfrac{s}{s_{sa}}\right) - s & s \geq s_{sa} \end{cases} \tag{10}$$

where $\overline{p}_{yn0}$ is the pre-consolidation pressure at zero suction and $\overline{p}_{y0}$ is a soil parameter (see Figure 2).

2.3 *Coupled relationships to describe variations of degree of saturation (Sheng and Zhou, 2011)*

Predictions of degree of saturation for the BBM and SFG models will be provided by the relationships proposed in Sheng & Zhou (2011). More specifically, for stress paths involving decreases of suction on a main wetting curve (with no plastic changes of volumetric strains) as well as for isotropic loadings at constant s, the variations of S_r will be described by:

$$dS_r = -\lambda_{ws}\frac{ds}{s} + \frac{S_r}{n}(1-S_r)^m\, d\varepsilon_{vol} \tag{11}$$

where the scalar m is a fitting parameter and λ_{ws} is the gradient of a main wetting curve in the retention plane S_r: $\ln s$.

2.4 *Wheeler et al. (2003) model*

For isotropic stress states the model of Wheeler et al. (2003) is expressed in terms of the mean Bishop's stress p^* and modified suction s^*:

$$p^* = p - \left(S_r u_w + (1-S_r)u_a\right) = \overline{p} + S_r s \tag{12}$$

$$s^* = (u_a - u_w)n \tag{13}$$

where n is the porosity.

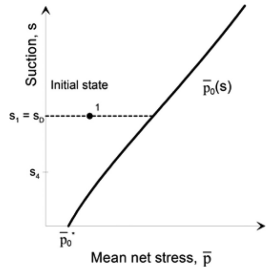


Figure 1. Loading Collapse yield curve for the BBM (Alonso et al., 1990) for $r > 1$.

Elastic volumetric behaviour is associated with changes of mean Bishop's stress through:

$$dv^e = -\kappa \frac{dp^*}{p^*} \tag{14}$$

where κ is an elastic swelling index giving the gradient of elastic swelling lines in the v:lnp^* plane.

The elastic variations of degree of saturation are associated with changes of modified suction:

$$dS_r^e = -\kappa_s \frac{ds^*}{s^*} \tag{15}$$

where κ_s is the gradient of a scanning curve in the S_r:ln s^* plane.

Plastic variations of specific volume and degree of saturation are, respectively, given by (Wheeler et al., 2003):

$$dv^p = -\frac{(\lambda - \kappa)}{(1 - k_1 k_2)} \left(\frac{dp_0^*}{p_0^*} - k_1 \frac{ds_\beta^*}{s_\beta^*} \right) \tag{16}$$

$$dS_r^p = -\frac{(\lambda_s - \kappa_s)}{(1 - k_1 k_2)} \left(\frac{ds_\beta^*}{s_\beta^*} - k_2 \frac{dp_0^*}{p_0^*} \right) \tag{17}$$

where k_1 and k_2 are two coupling parameters, p_0^* is a soil parameter (i.e. Bishop's pre-consolidation pressure) that defines the position of the LC (Figure 3) whereas s_β^* can be s_I^* or s_D^* defining, respectively, the locations of the SI (Suction Increase) and SD (Suction Decrease) yield curves (Figure 3).

The expressions of the three yield curves for isotropic stress states are:

$$LC : p^* - p_0^* = 0 \tag{18}$$

$$SI : s^* - s_I^* = 0 \tag{19}$$

$$SD : s_D^* - s^* = 0 \tag{20}$$

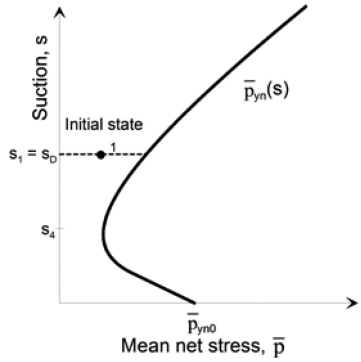


Figure 2. Loading Collapse yield curve for the SFG model (Sheng et al., 2008).

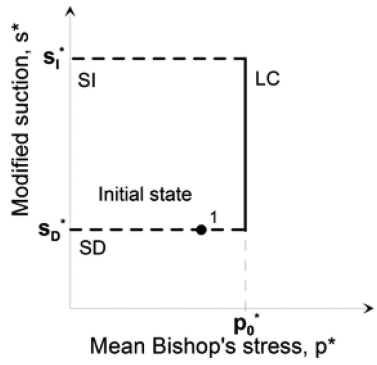


Figure 3. Loading Collapse, Suction Decrease and Suction Increase yield curves for the Wheeler et al., (2003) model.

3 DISCUSSION

Model predictions are discussed in this section using four isotropic loading paths performed at four different values of suction s_1, s_2, s_3 and s_4, varying the mean net stress from $\bar{p}_1$ to $\bar{p}_5$ (Figure 4). All simulations start at the same initial state 1 ($\bar{p}_1, s_1, e_1, S_{r1}$) which is assumed to be on the main wetting curve (see Figures 1–3). Consequently, the isotropic stress paths carried out at a lower value of suction than the initial one, s_1, involve, before loading, a prior isotropic wetting at a constant mean net stress $\bar{p}_1$ varying suction from s_1 to the corresponding value s_2, s_3 or s_4 (see the heavier dashed line in Figure 4). Assuming the initial state of the simulations on the main wetting curve is a reasonable assumption when modelling stress paths of compacted materials performed at much lower values of suctions than the as-compacted suction (see Lloret-Cabot et al., 2013).

The selected model parameter values for each of the models correspond to the experimental data on compacted speswhite kaolin tested by Sivakumar (1993). Using this experimental data, Lloret-Cabot et al. (2014a) suggested a set of parameter values for the SFG and Wheeler et al. (2003) models. In order to be consistent with the soil parameters used for the

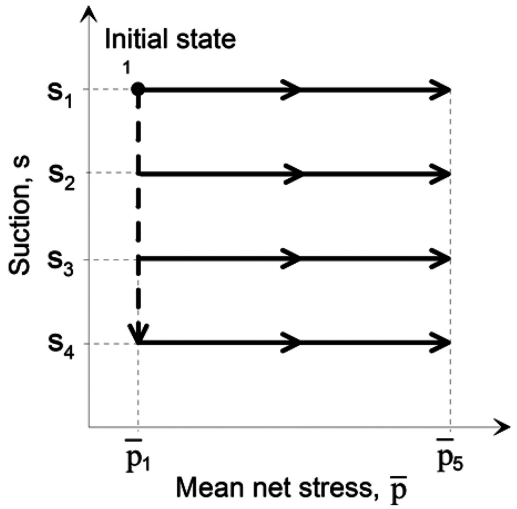


Figure 4. Stress paths considered in the simulations.

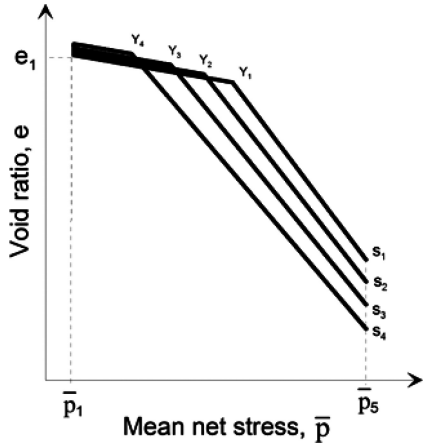


Figure 5. BBM predictions for void ratio against mean net stress (horizontal axis in log scale).

SFG and Wheeler et al. (2003) models, the simulations of the BBM correspond to the model parameter values suggested by Gallipoli et al. (2010) for the same soil and using the same set of experimental data.

3.1 *Isotropic loading paths at constant suction: volumetric behaviour*

Figures 5, 6 and 7 show, respectively, the results of the simulations for the BBM, the SFG and the Wheeler et al. (2003) models, for variations of e against $\overline{p}$ during the investigated isotropic loadings at constant s together with the initial wetting at constant $\overline{p}$ for tests at suction s_2, s_3 and s_4.

The overall predictions of e with $\overline{p}$ showed in the figures are qualitatively similar in the three models, although only in the BBM the predicted normal compression lines correspond to straight lines when plotted

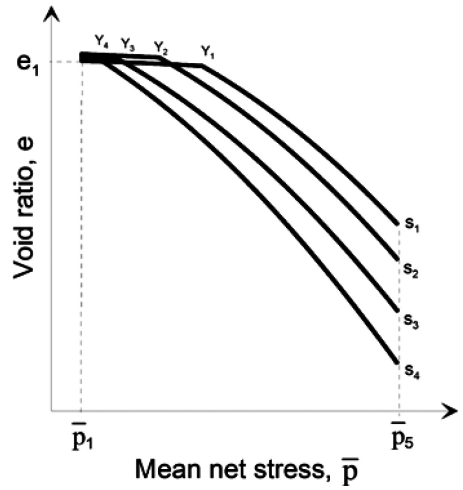


Figure 6. SFG model predictions for void ratio against mean net stress (horizontal axis in log scale).

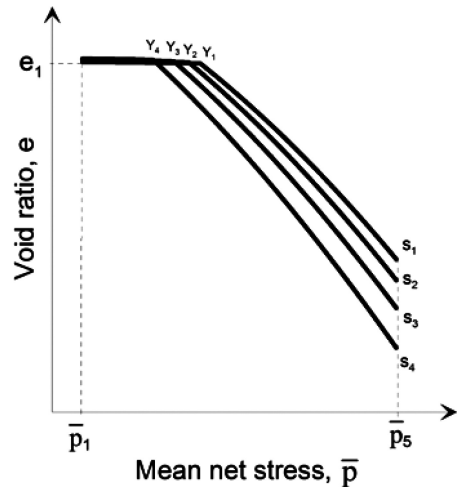


Figure 7. Wheeler et al. (2003) model predictions for void ratio against mean net stress (horizontal axis in log scale).

in the e:ln $\overline{p}$ plane. Note that the axes scales are the same for the three figures, and their corresponding labels have been intentionally omitted to give more generality to the discussion. Particularly interesting, is the similarity observed in the values of the mean net stress at which the corresponding model LC curve is reached (see points Y in each figure).

Conversely, the shape of the normal compression lines and also the distance between them varies considerably in the three model predictions (see Figures 5–7). In particular, the (straight) BBM normal compression lines tend to converge at high values of $\overline{p}$ as a consequence of considering $r > 1$, which results in $\lambda(s)$ increasing with increasing suction (see Figure 5). In contrast, the normal compression lines for the SFG and Wheeler et al. (2003) models diverge with increasing

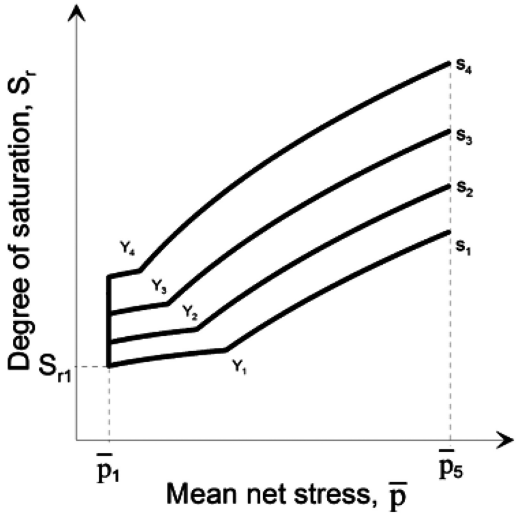


Figure 8. BBM predictions for degree of saturation against mean net stress.

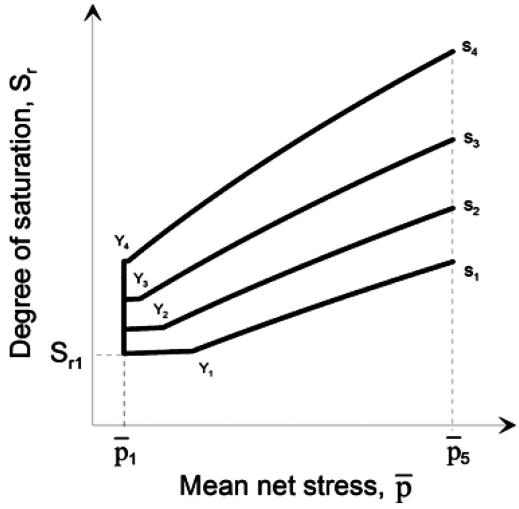


Figure 9. SFG model predictions for degree of saturation against mean net stress.

$\bar{p}$ (see Figures 6 and 7). Such divergence is somewhat in disagreement with a number of experimental data reported in the literature (see for instance, Sun et al. 2007). Indeed, as stated in Wheeler et al. (2002): "*for many soils, the complete picture, if examined over a sufficiently wide range of* $\bar{p}$*, is probably that the normal compression lines for different values of suction initially diverge with increasing* $\bar{p}$ *and then subsequently converge at higher values of* $\bar{p}$". The simulations presented here, however, involve only a limited range of $\bar{p}$ (fully saturation does not occur) and the soil response described in Wheeler et al. (2002) is not apparent. Other research showing simulations that involved larger amounts of loading, demonstrated that such behaviour may also be predicted with the SFG and Wheeler et al. (2003) models (see, respectively, Sheng et al., 2008 and Raveendiraraj, 2011).

3.2 *Isotropic loading paths at constant suction: retention behaviour*

Figures 8, 9 and 10 show, respectively, the results of the simulations for the BBM, the SFG and the Wheeler et al. (2003) models, for variations of S_r against mean net stress during the isotropic loadings (again, the same axes scale is used in all three figures).

The overall predictions of S_r with $\bar{p}$ plotted are qualitatively similar in the three models. This was likely to occur for the BBM and SFG models (as both account the influence of volumetric strains on water retention behaviour in an equivalent way) but not for the Wheeler et al. (2003) model which explicitly account for the influence of mechanical behaviour on degree of saturation in its coupled formulation.

For the BBM and the SFG models, the predictions of S_r during the initial wetting at constant $\bar{p}$ are essentially controlled by the gradient λ_{ws} of the main wetting

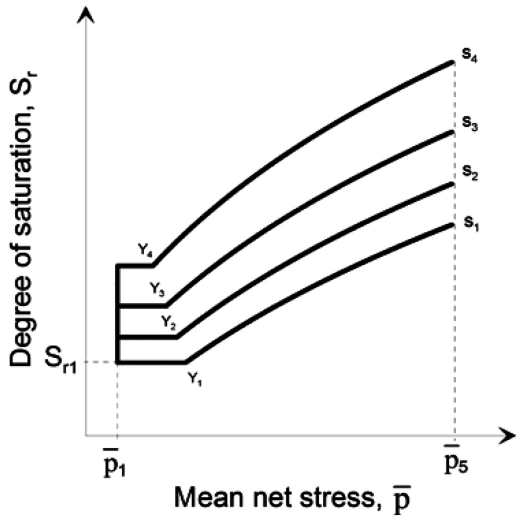


Figure 10. Wheeler et al. (2003) model predictions for degree of saturation against mean net stress.

curve (which is assumed to be the same in the two models).

During the isotropic loadings, the three models predict an initial small increment of degree of saturation. For the BBM and SFG models this increase of S_r is directly associated with elastic volumetric strains (compression) as a consequence of the increase in mean net (see Equation 12). Similarly, in the Wheeler et al. (2003) model, the increase of $\bar{p}$ (and, hence, of p^*) causes a small (elastic) decrease in n reducing, very slightly, s^* during loading which results in yielding on the SD curve.

Once the LC yield curve is reached (see points Y in Figures 5–10) large reductions of e are predicted (see Figures 5–7) causing a substantial increase in S_r. For

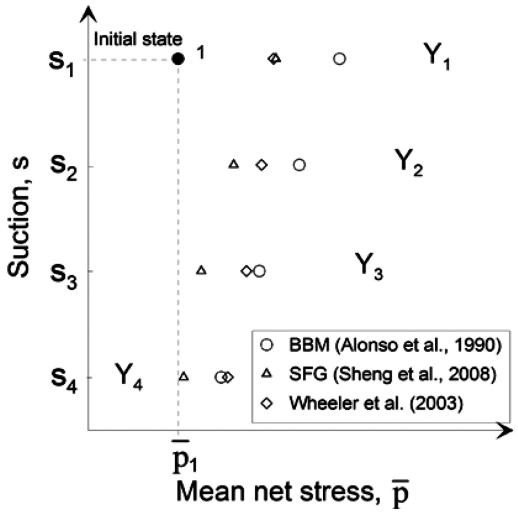


Figure 11. Mechanical yielding points for each of the models.

the BBM and SFG models, this increase of S_r is solely related to the increase of (total) volumetric stains (see Equation 13) whereas the large increase of S_r predicted by the Wheeler et al. (2003) model arises from the combination of several components. From points Y onwards, the model predicts simultaneous yielding on LC and SD yield curves. Yielding on LC results in predictions of large plastic compression (Figure 7) which produce both, a significant reduction of s^* (as the porosity reduces) and a coupled upward movement of the SD curve (essentially controlled by the coupling parameter k_2). Together, these result in predictions of significant yielding on the SD yield curve, and hence large increases of S_r after the yield point (Figure 10).

3.3 *Mechanical yielding points*

It is interesting to plot together the values of mean net stress at which each model reaches its corresponding LC curve for each value of suction. These results are presented in Figure 11 in the s: $\bar{p}$ plane. Inspection of this figure shows that all models predict an increase of the mechanical yield stress with suction. For the BBM and SFG models, this pattern of behaviour is rather obvious when looking at the shape of the LC yield curve assumed (see Figures 1 and 2). However, this feature is not entirely apparent when looking at the LC yield curve assumed in the Wheeler et al. (2003) model (see Figure 3) and is explained as follows.

In the Wheeler et al. (2003) model, yielding on the SD yield curve is associated with filling of voids with water causing plastic changes of degree of saturation. This means that the additional stabilising effect provided by meniscus water bridges is being reduced making slippage at the contacts more likely and, hence, decreasing the stability of the soil skeleton against mechanical yielding (see Lloret et al. 2014b). This is represented in the model by a coupled inward movement of the LC yield curve when yielding on the SD curve alone occurs (which is essentially controlled by the coupling parameter k_1). Hence, as the initial state is on the SD curve and yielding on this yield curve occurs throughout any of the initial wettings from s_1 to s_2, s_3 or s_4, the values of mean Bishop's stress at which the LC yield curve is reached decrease with decreasing suction and, as a consequence, also the corresponding values of mean net stress (see Figure 11). Interestingly, Figure 11 provides additional support to the view that a good representation of observed unsaturated soil behaviour can be achieved by models that adopt quite different assumptions.

4 CONCLUSIONS

Model predictions for the normal compression lines at different values of suction are investigated using three existing constitutive models for unsaturated soils. As expected, all three models predict an increase of the mechanical yield stress with increasing suction and this is demonstrated with a series of isotropic loading stress paths at constant s.

For the two models in which the variations of degree of saturation are not fully considered within their formulation, the coupled relationships proposed in Sheng and Zhou (2011) can be easily incorporated to predict water retention behaviour during the set of isotropic stress paths investigated involving loading and wetting. Incorporation of such relationships into the BBM and the SFG models provides similar results to the predictions of S_r given by the Wheeler et al. (2003) model, which explicitly incorporates S_r in its formulation.

The qualitative conclusions discussed in the paper should apply generally to any simple loading paths, but specific quantitative comparisons (e.g. which of the 3 models predict the highest and lowest values of yield stress) will depend upon the particular loading path followed, the previous stress history of the soil and the parameter values selected for each of the 3 models.

AKNOWLEDGEMENTS

Fruitful discussions with Prof. S.J. Wheeler are gratefully acknowledged. The research has benefited from a *New staff grant* (**G1301107**) from the University of Newcastle (Australia).

REFERENCES

Alonso, E.E., Gens, A. & Josa, A. 1990. A constitutive model for partially saturated soils. *Géotechnique,* 40(3): 405–430.

Butterfield, R.A. 1979. Natural law of soils (and advance on e-log p'). *Géotechnique,* 29: 469–480.

Gallipoli, D., D'Onza, F. & Wheeler, S.J. 2010. A sequential method for selecting parameters values in the Barcelona

basic model. *Canadian Geotechnical Journal,* 47: 1175–1186.

Josa, A. 1988. *Un modelo elastoplástico para suelos no saturados*. PhD Thesis. Universitat Politècnica de Catalunya, Barcelona.

Lloret, M. 2011. *Numerical Modelling of Coupled Behaviour in Unsaturated Soils*. PhD Thesis. University of Strathclyde and University of Glasgow, UK.

Lloret-Cabot, M., Sánchez, M. & Wheeler, S.J. 2013. Formulation of a three-dimensional constitutive model for unsaturated soils incorporating mechanical-water retention couplings. *International Journal for Numerical and Analytical Methods in Geomechanics*, 37: 3008–3035.

Lloret-Cabot, M., Wheeler, S.J., Sánchez, M. 2014b. Unification of plastic compression in a coupled mechanical and water retention model for unsaturated soils. *Canadian Geotechnical Journal*, 51(12): 1488–1493.

Lloret-Cabot, M., Wheeler, S.J., Pineda, J.A, Sheng, D. & Gens, A. 2014a. Relative performance of two unsaturated soil models using different constitutive variables. *Canadian Geotechnical Journal*, 51(12): 1423–1437.

Maswoswe, J. 1985. *Stress path for a compacted soil during collapse due to wetting*. PhD Thesis. Imperial College, London.

Raveendiraraj, A. 2009. C*oupling of mechanical behaviour and water retention behaviour in unsaturated soils*. PhD Thesis, University of Glasgow, UK.

Roscoe, K.H. & Burland, J.B. 1968. *On the generalised stress-strain behavior of wet clay*. Engineering Plasticity (eds Heyman J & Leckie FA), Cambridge University Press, Cambridge: 535–609.

Sheng, D., Fredlund, D.G., & Gens, A. 2008. A new modelling approach for unsaturated soils using independent stress variables. *Canadian Geotechnical Journal*, 45: 511–534.

Sheng, D. & Zhou, A. 2011. Coupling hydraulic with mechanical models for unsaturated Soils. *Canadian Geotechnical Journal,* 48: 826–840.

Sivakumar, V. 1993. *A critical state framework for unsaturated soil*. PhD Thesis, University of Sheffield, UK.

Sivakumar, V. & Wheeler, S.J. 2000. Influence of compaction procedure on the mechanical behaviour of an unsaturated compacted clay. Part 1: Wetting and isotropic compression. *Géotechnique,* 50(4): 359–368.

Sun, D.A, Sheng, D. & Xu, Y.F. 2007. Collapse behaviour of unsaturated compacted soil with different initial densities. *Canadian Geotechnical Journal*, 44(6): 673–686.

Vicol, T. 1990. *Comportement hydraulique et mécanique d'un limón non saturé. Application a la modelisation*. PhD Thesis, École Nationale des Ponts et Chaussées, Paris.

Wheeler, S.J. & Karube, D. 1996. Constitutive modelling. In: *Unsaturated Soils* (E.E. Alonso & P. Delage, eds.). Rotterdam: Balkema, (3): 1323–1356.

Wheeler, S.J. & Sivakumar, V. 1995. An elasto-plastic critical state framework for unsaturated soil. *Geotechnique*, 45(1): 35–53.

Wheeler, S.J., Gallipoli, D. & Karstunen, M. 2002. Comments on use of the Barcelona basic model for unsaturated soils. *International Journal for Numerical and Analytical Methods in Geomechanics,* 26(15): 1561–1571.

Wheeler, S.J., Sharma, R.S. & Buisson, M.S.R. 2003. Coupling of hydraulic hysteresis and stress-strain behaviour in unsaturated soils. *Géotechnique,* 53(1): 41–54.

This page intentionally left blank

Unsaturated Soil Mechanics—from Theory to Practice – Chen et al. (Eds)
© 2016 Taylor & Francis Group, London, ISBN 978-1-138-02921-7

Deformation and yielding for intact Q_3 loess under various stress paths

D.F. Zhang, C.L. Chen, D.B. Yu & Y.T. Shu
Institute of Geotechnical Engineering, Xi'an University of Technology, Shaanxi Province, Xi'an, China
Shaanxi Provincial Key Laboratory of Loess Mechanics and Engineering,
Xi'an University of Technology, Xi'an, China

P. Gao
CCTEG XI'AN Research Institute, Xi'an, China

ABSTRACT: A series tests of isotropic and constant stress ratio triaxial compression as well as drain triaxial shear were performed with different controlled suctions on intact loess. The influences of the suction, stress ratio and net confining pressure on volume deformation and yielding were investigated. The models described the relation of void ratio versus the net mean stress under various stress paths, and the shapes of yield curves on the deviator stress versus the net mean stress plane were proposed. The results showed that during isotropic and constant stress ratio triaxial compression, the net mean yield stress and the index of compressibility after yielding increased consistently with suction for a certain stress ratio, and these firstly increased and then decreased with the increase of stress ratio for a certain suction. The yield stresses and volume deformation were related to the suction and net confining pressure during triaxial shear, and different from isotropic and constant stress ratio triaxial compression. The shapes of the initial and subsequent yield curves on the deviator stress versus the mean net stress plane were near-elliptical and skewed about K_{0s} line of saturated soil. The expansion of the yielding was apparently an isotropic effect of the suction or stress during hardening.

1 INTRODUCTION

Based on isotropic reconstituted clay deformation, the researchers at Cambridge University proposed the elliptical yield curves centered on the isotropic axis (Roscoe, Schofield & Wroth, 1958). However, the researchers had disagreements on yielding of unsaturated soil. Alonso (1990) and Wheeler (1995) assumed that the yield curves at constant suction s were identical to that of the modified Cam-Clay model. The expansion of the yield curves occurred with suctions increasing (Zakaria, 1995). Maatouk (1995) found that the shapes of the yield curves for unsaturated silty soil were very different from the elliptic shape centered on the isotropic axis given by the modified Cam-Clay model used with the aim of simplicity by Alonso (1990), and the deviator yield stress increased more rapidly than the spherical yield stress. Cui (1996) investigated the yield locus of compacted silts, showing that the typical shape of yield curves was more or less elliptic centered on K_0 line in the stress space. As the suction increased, the expansion of the yield curve occurred without any rotation of the axis. The studies by Chen (1999) and Chen (2014) showed that the yield curves of the reconstituted and intact unsaturated loess were different from those given by Alonso (1990) or Maatouk (1995). Thus, experimental works are still needed to further study the yielding of unsaturated soil. In previous work, the more attention for yielding was paid to the remolded unsaturated soil and less intact soil. Chen (2014) studied the shapes of yield curves for intact Q_3 loess without the yield points below K_0 line. In addition, the investigations on the deformation behaviors for intact loess under different stress paths remained relatively scarce.

The aim of the paper was to study the deformation and yielding for intact Q_3 loess. A series of tests were performed including isotropic and constant stress ratio triaxial compression as well as triaxial shear under different controlled suctions.

2 MATERIALS AND METHODS

2.1 *Soil samples*

The physical properties of unsaturated intact Q_3 loess are given in Table 1. Triaxial specimens, 39.1 mm in diameter and 80 mm in height, were prepared by the

Table 1. Physical properties of intact loess.

Specific gravity, G_s	Water content, w_0/%	Dry density, ρ_{d0}/(g · cm^{-3})	Void ratio, e_0	Liquid limit, w_L/%	Plastic limit, w_P/%
2.70	15.2	1.26	1.143	30.0	19.5

special triaxial cutting apparatus. To reduce the influence of dry density, the controlled deviations are less than 0.03 g/cm^3.

2.2 *Testing program*

The three stress paths triaxial tests were performed in order to study the deformation and yielding for the unsaturated intact loess:

(a) Isotropic compression (CI) tests with step loading net confining pressures σ_3 up to 600 kPa under controlled suctions.
(b) Constant stress ratio compression (CR) tests under controlled suctions, and with stress ratios η ($=q/p$) of 0.15, 0.35, 0.62, 0.90, the corresponding ratio K ($=\sigma_3/\sigma_1$) were 0.86, 0.72, 0.56 (equal to K_{0s} of saturated soil, $K_{0s} = 1 - \sin\varphi' = 0.56$, $\varphi' = 26°$), 0.44. Where $q = \sigma_1 - \sigma_3$, $p = (\sigma_1 + 2\sigma_3)/3$, σ_1 and σ_3 were net axial stress and net confining pressure respectively.
(c) Triaxial shear (CD) tests under controlled suctions and net confining pressures, and with the net confining pressures σ_3 of 50, 100, 200, 400 kPa.

In the above three types of tests, suctions s were controlled at 0, 50, 100 and 200 kPa. In addition, the constant stress ratio compression under $s = 0$ was also performed at $\eta = 1.1$ ($K = 0.37$). Due to limited instrument bearing capacity, the maximum net confining pressure of 600 kPa was adjusted to 500 kPa at suction $s = 200$ kPa.

2.3 *Testing methods*

Suction of the sample at the natural water content ($w_0 = 15.2\%$) was 125 kPa. The measured water contents of the sample were 14.0, 17.0, 21.8 and 42.3% (saturated water content) respectively corresponding to suctions of 200, 100, 50 and 0 kPa under null stress. To save suction balance time, the natural sample was wetted or dried to the water content corresponding to the controlled-suction before the tests.

The triaxial apparatus used in this study was developed by Letry Testing Maching Co. Ltd. and Institute of Geotechnical Engineering, Xi'an University of Technology, China. The apparatus were modified for unsaturated soil testing (Chen, 2014). The desired suction was balanced by the axis translation method under a net confining pressure of 5 kPa (in order to make rubber membrane cling to the sample). That is, the applied air pressure u_a was equal to the desired suction s, and the drain valve opened ($u_w = 0$) until the water volume exchanges achieved stabilization. The isotropic and constant stress ratio compression tests were performed with step loading net confining pressures σ_3 up to 600 kPa ($\sigma_3 = 12.5$, 25, 50, 100, 200, 300, 400, 600 kPa). During each step, the pressure was maintained until to achieve stabilization of both sample volume changes and water exchanges. For the drained triaxial shear tests, when the stabilization condition had been achieved under the applied pressure σ_3 and controlled suction s, shear was performed at a strain rate of 0.004 mm/min under constant σ_3 and s. The stabilization criterions were the sample volume changes and water exchanges were less than 0.012 cm^3 over an interval of 2 h.

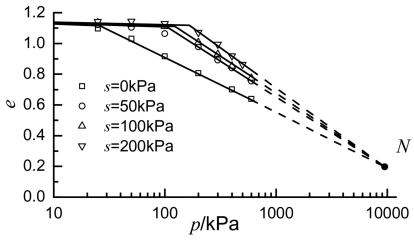


Figure 1. e–ln p curves from isotropic compression tests.

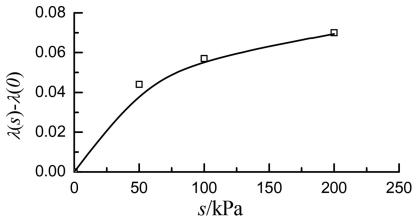


Figure 2. Relationship between $\lambda(s)$–$\lambda(0)$ and s.

3 DEFORMATION BEHAVIOURS

3.1 *Isotropic compression tests*

Figure 1 shows the relationships between void ratio and net mean stress ($e - \ln p$) at various suctions. It can be seen that the void ratio decreases with the increase of net mean stress. The $e - \ln p$ curves are approximately composed of two intersecting lines. The intersections points are the isotropic compression yield stress p_y. The slope κ of the elastic segment seems reasonably independent of suction. The slope $\lambda(s)$ and p_y of the plastic segment are dependent on suction, which increase with suction. The relationship between $\lambda(s) - \lambda(0)$ and s is shown in Figure 2, which can be described by hyperbolic function. The quantity $\lambda(s)$ is represented as:

$$\lambda(s) = \lambda(0) + s/(a + bs) \tag{1}$$

where $\lambda(0)$ is the slope of the normal compression line of saturated soil in the $e - \ln p$ plane and a, b are intercept and slope of $s/(\lambda(s) - \lambda(0)) \sim s$ curve respectively. For the soil tested, $a = 618.3$, $b = 11.3$.

The normal compression lines (NCLs) for different suctions gather to a point N (e_n, p_n) under the higher net mean stress (Figure 1), where the void ratio e_n is roughly equal to 17% of the initial void ratio. That is to say, the influence of suction on compressive deformation is slight as net mean stress is higher, which is similar to the test results that the $e - \ln p$ curves for the disturbed samples intersect at a point under a

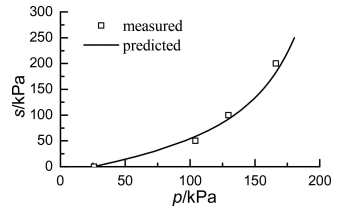


Figure 3. Isotropic loading collapse yield curves.

higher pressure, where the void ratio is roughly equal to 42% of the initial void ratio (Schmertmann, 1955). In addition, it is confirmed the assumption that no collapse for unsaturated soil occurs at the state of point N, which is proposed by Sun (2000). Thus, the equation for the shape of the loading-collapse (LC) yield curve is derived by the use of Sun's (2000) method. The $e-\ln p$ curves at a certain suction s and $s=0$ intersect at point N, which can be used to determine the p_{n}.

$$p_{\mathrm{n}} = p_i e^{(e_i(0)-e_i(s))/(\lambda(0)-\lambda(s))} \tag{2}$$

where p_{i} is the reference net mean stress, $e_{\mathrm{i}}(0)$ and $e_{\mathrm{i}}(s)$ are respectively void ratio of NCLs of saturated soil and unsaturated soil at $p=p_{\mathrm{i}}$. And,

$$\left.\begin{aligned} e_n &= e_0 - \kappa \ln p^*_{y0} - \lambda(0)\ln(p_n / p^*_{y0}) \\ e_n &= e_0 - \kappa \ln p_y - \lambda(s)\ln(p_n / p_y) \end{aligned}\right\} \tag{3}$$

From Equation (3) we have:

$$\big(\lambda(s)\text{-}\kappa\big)\ln(p_n / p_y) = \big(\lambda(0)\text{-}\kappa\big)\ln(p_n / p^*_{y0}) \tag{4}$$

Substituting Equation (1) and (2) into Equation (4) and solving for p_{y} gives

$$p_y = p_n \left(p^*_{y0} / p_n\right)^{\frac{\lambda(0)-\kappa}{\lambda(0)+s/(a+bs)-\kappa}} \tag{5}$$

where $p*_{\mathrm{y0}}$ and p_{y} are the yield stress for saturated soil and unsaturated soil respectively. p_{n} is determined by Equation (2) or graphic method (the corresponding stress at void ratio $e_{\mathrm{n}}=0.17e_0$). Equation (5) is similar to the equation proposed by Sun (2000). Nonetheless, the expressions of abscissa axis p and relationship between λ(s) and λ(0) are different. Figure 3 shows measured and predicted LC yield curves. It can be observed that the yield stresses estimated by using Equation (5) are in accord with those measured approximatively.

3.2 *Constant stress ratio compression tests*

The typical relationships between void ratio and net mean stress ($e-\ln p$) performed in Figure 4. It can be seen that the net mean stress and deviator stress cause compression deformation. The void ratio decreases with the net mean stress increasing. The $e-\ln p$ curves

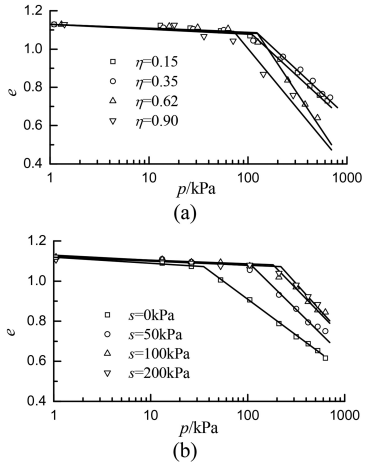


Figure 4. Constant stress ratio compression test results (a) various stress ratios at $s=50$ kPa and (b) various suctions at $\eta=0.15$.

exhibit two approximately linear segments. The intersections of the two linear segments define anisotropic compression yield stress p_{ya}. This behavior is similar to that observed under isotropic compression conditions.

The typical $e-\ln p$ curves at $s=50$ kPa and various stress ratios of Figure 4(a) demonstrate that slope κ in the elastic zone seems reasonably independent of the stress ratio, whereas the slope $\lambda_{\mathrm{a}}(s)$ in the plastic zone and yield stress p_{ya} are different at various stress ratios. As a result that the corresponding void ratios for the same net mean stress are significantly different. It is indicates that the stress-strain relationship is closely related to stress paths. Similar behavior is obtained for soft clays (Zeng, 2012).

The typical $e-\ln p$ curves at $\eta=0.15$ and various suction of Figure 4(b) show that slope κ in the elastic zone seems reasonably independent of the suction, whereas the slope $\lambda_{\mathrm{a}}(s)$ in the plastic zone and yield stress p_{ya} are different at various suctions.

The $p_{\mathrm{ya}}-\eta$ and $\lambda_{\mathrm{a}}(s)-\eta$ curves at different suctions are shown in Figure 5. The p_{ya} and $\lambda_{\mathrm{a}}(s)$ increase firstly and then decrease with stress ratio increasing for the same suction, which are larger than those in isotropic compression ($\eta=0$). The stress ratios η of turning points are all equal to 0.62 ($K=K_{0\mathrm{s}}=0.56$) at various suctions. The results of Zeng (2012) indicate the same tendency for the soft clay.

The representative relationships between volumetric strain ε_{v} and axial strain ε_1 at $s=50$ kPa and various stress ratios are presented in Figure 6(a). It can be seen that ε_{v} increases nonlinearly at first, then increases linearly with the increase of ε_1. The $\Delta\varepsilon_{\mathrm{v}}/\Delta\varepsilon_1$ ratios of linear segments at various suctions are shown in Figure 6(b) as a function of K. The $\Delta\varepsilon_1/\Delta\varepsilon_{\mathrm{v}}$ ratios increase linearly with stress ratios K. The stress ratio K at $\Delta\varepsilon_1/\Delta\varepsilon_{\mathrm{v}}=1$ is coefficient of static earth pressure K_0. The K_0 at $s=200$, 100, 50 and 0 kPa are 0.51, 0.52, 0.53 and 0.58 respectively, and K_0 at $s=0$ kPa is approximately equal to $K_{0\mathrm{s}}$ (=0.56) calculated as

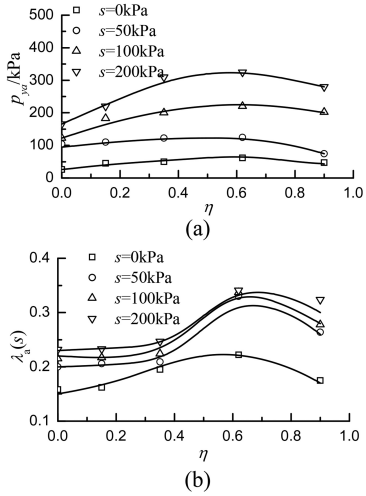


Figure 5. Effect of stress ratio on the soil parameters (a) $p_{ya}-\eta$; (b) $\lambda_a(s)-\eta$.

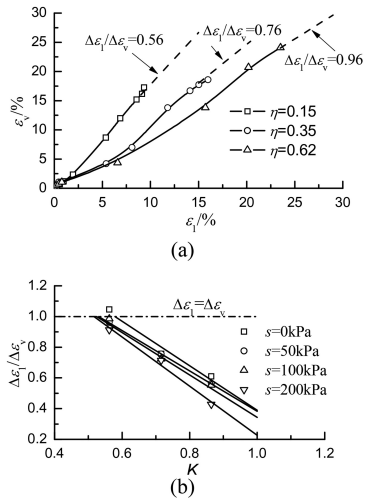


Figure 6. Results for constant stress ratio compression tests (a) $\varepsilon_v-\varepsilon_1$ for $s=50$ kPa; (b) $\Delta\varepsilon_v/\Delta\varepsilon_1-K$.

$(1-\sin\varphi')$. It shows that the K_0 decreases with the suction increasing. The results of unsaturated silty soil discussed by Maatouk (1995) indicate the same tendency.

3.3 *Triaxial shear tests*

The typical $e-\ln p$ curves during the triaxial shear and critical state ($\varepsilon_1=15\%$ as failure criterion) are shown in Figure 7. The isotropic compression lines (ICLs) are also plotted in Figure 7. The $e-\ln p$ curves in saturated state of Figure 7(a) show rapid decline in line at various σ_3. These in unsaturated state of Figure 7(b) are approximately composed of intersecting lines at various σ_3. The stresses of intersections points

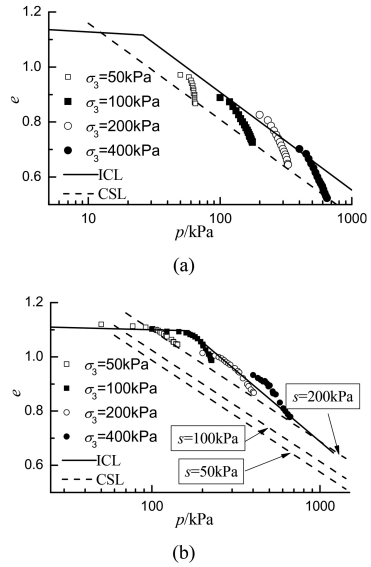


Figure 7. $e-\ln p$ curves from triaxial shear tests: (a) $s=0$ kPa; (b) $s=200$ kPa.

are defined the net mean yield stress p_{ys} and the deviator yield stress q_{ys} $(=3(p_{ys}-\sigma_3))$. The curves coincide with isotropic compression lines before yielding, and deviate that after yielding for $\sigma_3<p_y$. The specimens have yielded prior to shear for $\sigma_3>p_y$, so that the curves deviate isotropic compression lines before and after yielding.

As shown in Table 2, the slope $\lambda_s(s)$ post-yield and p_{ys} $(\sigma_3<p_y)$ increase consistently with σ_3 at constant suctions. p_{ys} increases and $\lambda_s(s)$ decreases with the suction increasing at constant σ_3. $\lambda_s(s)$ is larger than that in constant stress ratio compression with the exception of the $\eta=0.62$ compression tests at $s=50$ and 100 kPa.

The critical state lines (CSLs) on the void ratio versus the net mean stress plane ($e-\ln p$) at various suctions of Figure 7 are nearly lines. The slope of CSL (Figure 7(a)) in saturated state (=0.152) is parallel with the normal compression line (NCL). The slopes of CSLs in unsaturated state (Figure 7(b)) are approximately all equal to 0.178. These are greater than those of saturated soil (0.152) and less than the slopes of NCLs in unsaturated state. Consequently, the CSLs are not parallel with the NCLs for unsaturated intact loess. That is different from Cam-Clay model (Roscoe, Schofield & Wroth, 1958).

4 YIELD BEHAVIOUR

The yield curves and the K_{0s} line on the deviator stress versus the mean net stress (q–p) plane are plotted in Figure 8. The initial yield curves are plotted in Figure 8(a), for suctions of 0, 50, 100 and 200 kPa, with the results of shear tests at $p_y>\sigma_3$, isotropic and constant

Table 2. Soil parameters for traixial shear tests.

	$s=0$ kPa		$s=50$ kPa		$s=100$ kPa		$s=200$ kPa	
σ_3/ kPa	λ_s (s)	p_{ys}/ kPa	λ_s (s)	p_{ys}/ kPa	λ_s (s)	p_{ys}/ kPa	λ_s (s)	p_{ys}/ kPa
50	0.300	/	0.262	75	0.227	88	0.220	106
100	0.322	/	0.264	117	0.255	153	0.249	184
200	0.405	/	0.289	/	0.286	/	0.256	/
400	0.416	/	0.374	/	0.367	/	0.345	/

stress ratio compression tests. For certain plastic volumetric strain ε_{vp}, the typical subsequent yield curves at various suctions s are shown in Figure 8(b). For certain suction s, the typical extended subsequent yield curves used as a hardening parameter ε_{vp} are shown in Figure 8(c).

The initial (Figure 8(a)) and subsequent (Figure 8(b)) yield curves induced from constant stress ratio compression tests for saturated intact loess are near-elliptical centered on K_{0s} line in the stress space. It is different from the elliptical yield curves centered on the isotropic axis by the modified Cam-Clay model. This is because that the saturated intact loess has a clear anisotropy induced the vertical and horizontal to the consolidation pressure range in the natural process of deposition of soil. Thus, the stress-strain behaviors of saturated intact loess can not be directly described by the modified Cam-Clay model.

The initial yield stress point induced from shear tests basically coincides with constant stress ratio compression tests ($\eta=0.35$) for $s=50$ kPa (Figure 8(a)). It is indicated that the initial yield points under different stress paths are located in the same initial yield curve. That is the influence of stress path on the yield curves can be not taken into account.

The initial and subsequent yield points have good regularity for unsaturated intact loess. The shapes of the initial (Figure 8(a)) and subsequent (Figure 8(b)) yield curves are near-elliptical and skewed about K_{0s} line. This skewed shape of the yield curves has also been observed by other researchers (e.g. Cui, 1996) for unsaturated compacted silt. So, the elliptical yield curves proposed by Alonso (1990) and Wheeler (1995) cannot be directly applied to the unsaturated intact loess. Moreover, it confirms the Chen's (2014) inference on the distribution of yield points in the following K_{0s} line area.

As suction increases, the expansion of the yield curve occurs without any rotation of the axis for certain plastic volumetric strain ε_{vp} (Figure 8(a), (b)), showing apparently an isotropic effect of the suction during hardening. The results of unsaturated compacted silt discussed by Cui (1996) indicate the same tendency.

When the plastic volumetric strain ε_{vp} increase consistently with the stress, the expansion of the yield curve (Figure 8(c)) occurs without any rotation of the axis for certain suction, showing apparently an isotropic effect of the stress during hardening. It indicates the same tendency for natural plastic clay discussed by Graham (1983).

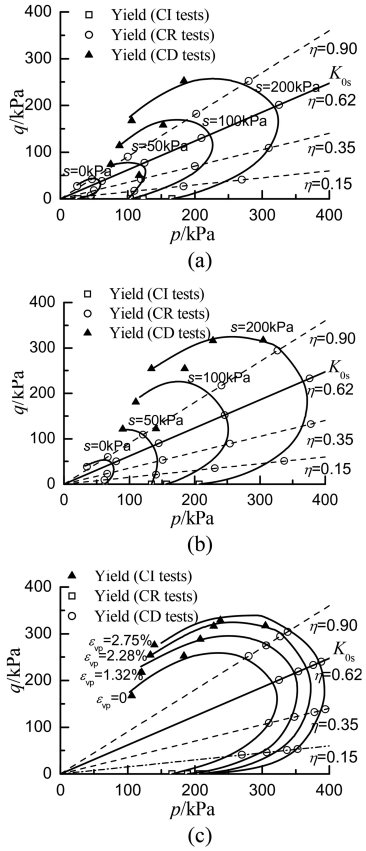


Figure 8. Experimental determination of yield curves: (a) $\varepsilon_{vp}=0$ at various suction; (b) $\varepsilon_{vp}=2.28\%$ at various suction; (c) $s=200$ kPa at various ε_{vp}.

5 CONCLUSION

(1) The yield stress and the index of compressibility post-yield increase consistently with suction during isotropic compression. Based on the inference that compression curves converge at the larger net mean stress for various suctions, the equation of LC curve is proposed.

(2) The volume deformation is closely related to suction and stress path during constant stress ratio compression. The yield stress and the index of compressibility post-yield increase consistently with suction at constant stress ratio, and increase firstly and then decreased when the stress ratio increases at certain suction.

(3) The volume deformation depends on suction and net confining pressure during triaxial shear. Except it coincidence with volume deformation of isotropic compression before yielding as net

confining stress is less than isotropic compression yield stress, and is different from that of isotropic and constant stress ratio triaxial compression under the others conditions. The yield stress increases consistently with the suction and net confining pressure. The $e - \ln p$ critical state lines (CSLs) at various suctions are not parallel with the NCLs.

(4) The shapes of the initial and subsequent yield curves on the deviator stress versus the mean net stress (q–p) plane are near-elliptical and skewed about K_{0s} line. The expansion of the yield curve is apparently an isotropic effect of the suction or stress during hardening.

Results of this study provide an experimental basis for the establishment of elasto-plastic model on unsaturated intact loess.

6 NOTATION

e	void ratio
$e_i(0)$	void ratio of the normal compression lines of saturated soil at $p = p_i$.
$e_i(s)$	void ratio of the normal compression lines of unsaturated soil at $p = p_i$.
σ_3	net confining pressure
σ_1	net axial stress
p	net mean stress $(\sigma_1 + 2\sigma_3)/3$
q	deviator stress $\sigma_1 - \sigma_3$
p_i	reference net mean stress
p_y	net mean yield stress during isotropic compression
p_{ya}	net mean yield stress during anisotropic compression
p_{ys}	net mean yield stress during shearing
q_{ys}	net deviatoric yield stress during shear
s	matrix suction $u_a - u_w$
u_a	air pressure
u_w	pore water pressure
$\lambda(0)$	stiffness parameter of saturated soil during isotropic compression
$\lambda(s)$	stiffness parameter of unsaturated soil during iso tropic compression
$\lambda_a(s)$	stiffness parameter of unsaturated soil during anisotropic compression
$\lambda_s(s)$	stiffness parameter of unsaturated soil during shear
κ	stiffness parameter in the pre-yield range
η	stress ratio q/p
K	stress ratio σ_3/σ_1
K_0	coefficient of static earth pressure
K_{0s}	coefficient of static earth pressure of saturated soil
ε_1	axial strain
ε_v	volumetric strain
ε_{vp}	plastic volumetric strain

ACKNOWLEDGEMENTS

The present study was supported by the National Basic Research Program of China (973 Program) with Grant No. 2011CD403305, by the National Natural Science Foundation of China with Grant No. 50878183, by the Key Laboratory Program of Department of Education of Shaanxi Province of China with Grant No. 14JS063, and by the Characteristics Research Program of Xi'an University of Technology 2012 annual with Grant No.118-211302. The authors are grateful to Dr Wang Song-he (Xi'an University of Technology) for helpful discussions.

REFERENCES

Alonso E, Gens A, Josa A. A constitutive model for partially saturated soils. *Geotechnique*, 1990, 40(3): 405–430.

Chen C L, Zhang D F, Dong Y Z, et al. Suction and mechanical behaviours of unsaturated intact loess from constant water content triaxial tests. *Chinese Journal of Geotechnical Engineering*, 2014, 36(7): 1195–1202.

Chen Z H. Deformation, strength, yield and moisture change of a remolded unsaturated loess. *Chinese Journal of Geotechnical Engineering*, 1999, 21(1): 82–90.

Cui Y J, Delage P. Yielding and plastic behaviour of an unsaturated compacted. *Geotechnique*, 1996, 46(2): 291–311.

Graham J, Noonan M L, Lew K V. Yield states and stress-strain relationships in a natural plastic clay. *Canadian Geotechnical Journal*, 1983, 20(3): 502–516.

Maatouk A, Leroueil S, Rochelle P. Yielding and Critical state of a collapsible unsaturated silty soil. *Geotechnique*, 1995, 45(3): 465–477.

Roscoe K H, Schofield A N & Wroth C P. On the yielding of soils. *Geotechnique*, 1958, 8(1): 22–53.

Sun D A, Matsuoka H, Yao Y P, et al. An elsato-plastic model for unsaturated soil in three-dimensional stresses. *Soils and Foundations*, 2000, 40(3): 17–28.

Wheeler S J, Sivakumar V. An elasto-plastic critical state framework for unsaturated soil[J]. *Geotechnique*, 1995, 45(1): 35–53.

Schmertmann J H. The undisturbed consolidation behavior of clay. *Journal of Geotechnical and Geoenvironmental Engineering*, ASCE, 1955, 120: 1201–1233.

Zakaria I, Wheeler S J, Anderson W F. Yielding of unsaturated compated kaolin. *ALONSO E E. DELAGE P. eds. Unsaturated soils. Proceeding of the First International Conference on Unsaturated Soils*. Rotterdam: Balkema. 1995: 223–228.

Zeng L L, Hong Z S, Liu S Y, et al. Experimental study on different compression behaviors of natural clays caused by various stress paths. *Chinese Journal of Geotechnical Engineering*, 2012, 34(7): 1250–1255.

Unsaturated Soil Mechanics—from Theory to Practice – Chen et al. (Eds)
© 2016 Taylor & Francis Group, London, ISBN 978-1-138-02921-7

An experimental method to study the drying-wetting behaviour of a sand

M. Milatz
Institute of Geotechnical Engineering and Construction Management,
Hamburg University of Technology (TUHH), Germany

ABSTRACT: The Soil-Water Characteristic Curve (SWCC) is a basic function of unsaturated soil behaviour. It is essential for the understanding of effective stress in unsaturated soils and for unsaturated flow behaviour. Therefore, the experimental determination of the SWCC is an important issue of research. This task is often time consuming and in many cases, using standard test methods, only the main branches for either drying or wetting can be determined. For some types of soil however, the SWCC encounters rigorous hysteretic behaviour, which is of importance when cyclic flow occurs. Therefore, also test data on hydraulic hysteresis and the scanning curves is needed. In this paper an experimental method is presented, which allows to determine the SWCC of a coarse grained soil in a transient way, taking hysteresis into account.

The method applies a flow of water volume to a small soil specimen, subjected to atmospheric air pressure at the top. This allows to prescribe monotonic or cyclic drying or wetting paths in the degree of saturation–suction space. While the degree of saturation can be calculated from the prescribed water outflow, the soil suction is simultaneously measured on top of the specimen using a miniature tensiometer. As a result of the test the SWCC can be obtained as well as different scanning paths and their slope $\delta S_r/\delta s$, which is especially important for the development of hydraulic hysteresis models.

1 INTRODUCTION

The soil-water characteristic curve can be seen as a principal relationship for understanding and describing the mechanical and hydraulic behaviour of unsaturated soils. The knowledge of the curve allows to assess the influence of capillarity on shear strength by introducing an effective stress principle for unsaturated soils (Bishop 1959, Fredlund et al. 1978, Lu and Likos 2006, Lu et al. 2010) and equally delivers a basis for modelling unsaturated hydraulic conductivity (Mualem 1976, van Genuchten 1980).

Unfortunately, the hydraulic behaviour described by the SWCC is very complex due to several phaenomena of the liquid-solid interface at the micromechanical scale. Different contact angles for wetting and drying of the soil as well as different pore sizes create the hysteretic nature of the soil-water characteristic curve with its main drying and main wetting paths and the scanning paths (Bear 1979, Bear and Cheng 2010). The latter represent the hydraulic memory of a soil, which accounts for the hydraulic paths being a function of the wetting and drying history and which makes the modelling of the hydraulic behaviour under cyclic hydraulic loading very complicated. In many representations and models the hysteresis is treated as a closed circle for the main drying and wetting paths when full saturation is reached. In reality however, the behaviour is further influenced by the occlusion of air bubbles, evoking open hysteresis paths, which also hinders an easy modelling approach.

Different models have been proposed by several authors to model the complicated hysteretic nature of soil-water characteristic curve numerically. A comparison of different models is given in (Jaynes 1984), hightlighting four different models proposed amongst others by Hanks et al. (1969), Dane and Wierenga (1975) and Mualem and Miller (1979). The proposed models are often implemented to numerical algorithms, such as the finite difference method, to model one dimensional seepage under drying and wetting conditions. Jaynes (1984) comes to the conclusion that the so-called linear method, which describes the scanning path as a linear branch between the main drying and main wetting curves, appears to be favourable compared to other methods. A reason for this is the fact, that linear scanning curves cannot overlap at cyclic changes in suction and predict erroneous pumping effects. Newer numerical research on the hysteretic behaviour of the SWCC has been undertaken by Yang et al. (2011) who modelled cyclic drying and wetting of an unsaturated soil column using finite differences with the assumption of linear scanning curves. A method to calculate non-linear scanning curves with a smooth transition between the main branches of the SWCC has been presented by Li (2005). Similar to previous methods an algorithm has to decide, whether the current increment of degree saturation corresponds to drying or wetting. A new attempt to overcome this, has been made by Fuentes and Triantafyllidis (2013) who propose a rate-dependent "hypoplastic" formulation for the modelling of a hysteretic soil-water

characteristic curve. By describing the main drying and wetting paths in a rate-formulation using the time derivatives of suction and degree of saturation $\dot{s}$ and $\dot{S}_r$ the whole soil-water characteristic curve can be described by a closed equation, because the direction of moisture transport is naturally incorporated in the algebraic sign of $\dot{s}$. A smooth transition of the non-linear scanning curves with the main drying and wetting paths is managed with the help of an interpolation function, taking different forms for drying or wetting scanning paths.

To the knowledge of the authors, the data basis of hysteretic drying-wetting paths of the soil-water characteristic curve is not that pronounced as it should be for deriving mathematical models. This may be a consequence of the challenge of measuring hydraulic paths under cyclic drying-wetting boundary conditions. Due to a reduced hydraulic permeability, the testing procedure may last very long, also depending on the type of soil. Many methods have been presented for determining the soil-water characteristic curve in the laboratory and some of the methods have been standardised (ASTM D 6836-02(2008)e2 2008). Conventional methods are the hanging water column method, the axis translation method or vacuum methods (Vanapalli et al. 2008). A common principle in the testing methods is to control suction and to simultaneously capture the change of degree of saturation or volumetric water content by measuring the pore water outflow of the soil specimen. Thus not all methods are suitable to determine drying and wetting in the same test.

In order to investigate the hydraulic behaviour of relatively coarse soils, such as sands, for cyclic hydraulic paths, a method is proposed which aims at determining the soil-water characteristic curve the other way round: In the method a sand specimen is cyclically dried and wetted by extracting and injecting a defined pore water volume, while matric suction is measured as a reaction to the imposed changes in specimen degree of saturation. The method is used to investigate the character of the scanning curves of a sand. Open questions are the slope of the scanning curves, which could be used in modelling, or the question, whether the drying-wetting paths are dependent on the rate of the degree of saturation $\dot{S}_r$ which has already been considered by Schubert (1982).

2 PROPOSAL OF A VOLUME CONTROLLED METHOD

In this section a new method will be presented that allows to investigate the drying-wetting behaviour of a coarse grained soil by prescribing changes of S_r within a small sand specimen. Contrary to other methods, such as the pressure plate apparatus, suction s is not controlled, but can develop according to the change in S_r and therefore must be measured.

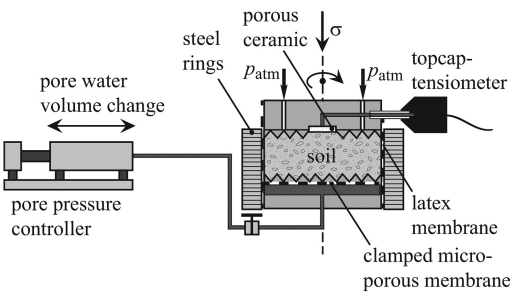


Figure 1. Test set-up for the determination of hydraulic paths of the SWCC by applying a pore water volume change.

2.1 *Test set-up*

The test set-up allows to impose a pore water volume change on small soil specimens by using a pore water pressure controller (GDS instruments, UK). The cylindrical soil specimens can be submitted to vertical stress σ within the loading frame of a simple shear apparatus which has been presented by Milatz and Grabe (2015). The specimen is horizontally restrained by a stack of steel rings which allow to assume K_0-conditions. For the measurement of matric suction the topcap-tensiometer presented in Milatz and Grabe (2014) and Milatz and Grabe (2015) is used. The specimen top is connected to the atmosphere through vent holes. Therefore, pore air pressures u_a are assumed to be negative and matric suction is composed of negative pore water pressures $s = -u_w$. A drawing of the test set-up and its technical components is represented in Figure 1.

The topcap-tensiometer consists of a laboratory tensiometer of type T5, manufactured by UMS GmbH, Munich, Germany. The tensiometer is screwed into the loading topcap of the simple shear apparatus. The tensiometer body as well as the embedded ceramic plate and water channel are filled with deaired water and connect the specimen pore water phase with the pressure transducer of the tensiometer. The laboratory tensiometer can measure pore water pressure in the range of ± 100 kPa with an accuracy of 0.5 kPa according to the manufacturer.

The pressure controller is able to resolve a volume change of 1 mm^3 and can be used to ramp or cycle the water volume using a computer controlled keypad. This feature allows to impose linear or cyclic flux boundary conditions to the base of the specimen in order to specify the degree of saturation.

Instead of using a common porous ceramic plate at the bottom of the specimen a microporous membrane, as proposed by Nishimura et al. (2012), can be clamped into the base plate below the specimen. This procedure allows to reduce the outflow impedance, when a volume change of pore water is imposed and therefore makes the data-aquisition of transient suction and degree of saturation paths possible. In the tests a microporous membrane with pore diameter of 0.8 µm and mean Air Entry Value (AEV) of 83 kPa, manufactured by PALL corp., is used. This low AEV

Table 1. Selected soil parameters of CTB-sand.

ρ_s (kg/m^3)	e_{min} (–)	e_{max} (–)	d_{10} (mm)	d_{max} (mm)	U (–)
2650	0.41	0.86	0.16	2.0	2.4

ρ_s: grain density, e_{min}: min. void ratio.
e_{max}: max. void ratio.
d_{10}: grain diameter at 10% passing.
d_{max}: max. grain diameter, U: uniformity index.

Table 2. Parameters of the Van Genuchten model.

hydr. state	α (1/kPa)	n (–)	S_m (–)	S_{res} (–)
drying	0.287	5.814	1.0	0.144
wetting	0.566	4.664	0.863	0.144

S_e: effective degree of saturation (–).
S_m: max. degree of saturation (–).
S_{res}: residual degree of saturation (–).

is sufficient for the investigated sand, bringing about a high permeability of the interface between specimen and dewatering system.

2.2 *Investigated soil*

The tested soil is a medium sand with low portions of fine and coarse sand from the river Elbe at Hamburg, in the north of Germany. It is of sedimentary origin and widely used in construction and backfilling of quay walls at the Port of Hamburg. It was collected at Container Terminal Burchardkai (CTB) and is therefore referred to as "CTB-sand" throughout this paper. An overview of selected soil parameters is given in Table 1. The soil-water characteristic curve of CTB-sand shows low capillary behaviour with an AEV of 2.5 to 3 kPa. Test data for a drying path and a consecutive rewetting path has been obtained for a sand specimen with an initial void ratio of $e = 0.5$ via an ordinary pressure plate test and by applying a vacuum control method (Milatz 2013). The experimental data is plotted together with approximations using the Van Genuchten model (van Genuchten 1980) according to equations 1 and 2 in Figure 2. The applied model parameters are represented in Table 2. The reduced S_r at rewetting due to occluded air bubbles can be modelled with the help of a maximum degree of saturation S_m. Setting $S_m = 1$ results in a perfectly closed hysteresis of the main drying and wetting path at $S_r = 1$, illustrated in Figure 2 as a dotted line.

$$S_e = \frac{1}{(1+(\alpha s)^n)^m}, \quad m = 1 - \frac{1}{n} \tag{1}$$

$$S_r = (S_m - S_{res})S_e + S_{res} \tag{2}$$

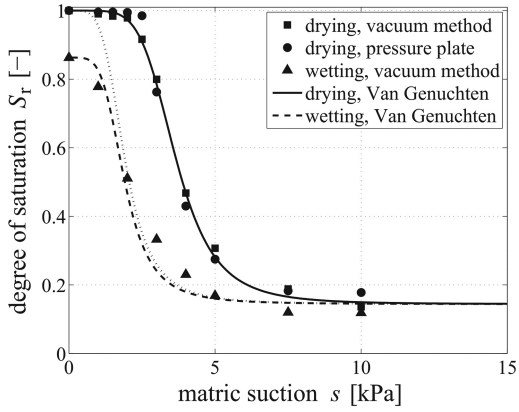


Figure 2. Test results for the main drying and rewetting behaviour of CTB-sand versus calculated curves using the Van Genuchten model.

2.3 *Specimen preparation and test conditions*

Before a hydraulic test can start, the filter membrane as well as the dewatering system must be saturated with deaired water. This is done by immersing all components in a basin with deaired water and then placing it in a vacuum container. After evacuating the container for some time and flushing the connections of the dewatering system with deaired water from the pore pressure controller, the microporous filtermembrane is clamped to the base plate, still submerged in the water basin. When the latex membrane, illustrated in Figure 1 has been pulled over the stack of steel rings fixed by a ring holder, the sand specimen can be filled into the designated specimen volume. The sand is carefully gushed into the cavity, which is already filled with deaired water, in order to achieve an initially saturated specimen. The specimen with a diameter of 50 mm is then compacted to an initial specimen height of 17.9 mm, equivalent to an initial void ratio of $e = 0.5$, using a vibrating table. With the dewatering tube already connected to the pore pressure controller, the specimen is finally placed in the loading frame of the simple shear apparatus, the ceramic of the topcap-tensiometer is wetted, any surplus of water at the topcap is removed and the topcap is lowered onto the specimen top. For this purpose a slow computer-controlled docking procedure with a target contact stress of $\sigma = 10$ kPa is applied. When contact between topcap and specimen top is reached, the vertical stress is slowly increased to $\sigma = 50$ kPa. During this initial loading step, no vertical water drainage is allowed. The specimen settlements are measured using a linear variable differential transformer (LVDT) during the whole test. A photograph of the soil specimen ready for hydraulic testing is depicted in Figure 3.

Finally, the hydraulic testing can begin by applying different pore water volume changes ΔV_w with the pressure controller, which are summarised in Table 3. A negative algebraic sign of ΔV_w indicates an extraction of pore water causing drying of the specimen.

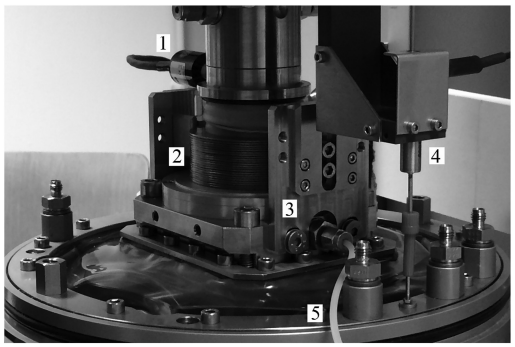


Figure 3. Detail of sand specimen and measurement devices in the simple shear apparatus: 1: Topcap-tensiometer, 2: Specimen within steel rings, 3: Membrane and ring holder, 4: LVDT, 5: Dewatering tube connected to pressure controller.

Table 3. Hydraulic steps in the volume-controlled cyclic drying-wetting test.

Step	hydraulic condition	ΔV_w (mm^3)	Δt (s)
①	first drying	−8211	1800
②	first wetting	+8211	1800
③	second drying	−5865	1286
④	3 cycles wetting-drying	±1173	1029
⑤	final wetting	+5865	1286

ΔV_w: imposed pore water volume change.
Δt: time interval.

The first two test steps represent a first drying and rewetting of the sand specimen in order to investigate, whether a closed main hysteresis loop is obtained. The specimen is drained and then rewetted by imposing a volume change of $\Delta V_w = 8211\,\text{mm}^3$ in 1800 s. This results in a volume change rate of $\frac{\Delta V_w}{\Delta t} = 4.56\,\text{mm}^3/\text{s}$. In the third step the degree of saturation is reduced with the same drainage rate and then a cyclic sinusoidal volume change amplitude $\Delta V_w = \pm 1173\,\text{mm}^3$ is imposed in step 4. The pore water volume is cycled into and out of the specimen for three cycles with an averaged constant rate of $\frac{\Delta V_w}{\Delta t} = 4.56\,\text{mm}^3/\text{s}$ as in the initial steps. Of course, in reality, the rate follows a cosine-like distribution due to the sinusoidal excitation. In the final step 5 the total volume change is reduced to zero, theoretically leaving the specimen in a saturated state again.

3 RESULTS

In this section first results of a hydraulic test on dense CTB-sand will be presented. The applied total pore water volume as well as specimen void ratio calculated from recorded settlements is represented in Figure 4 for the hydraulic steps 1 to 5.

It can be seen that the wetting seems to cause a decrease of void ratio due to pronounced settlements when $S_r = 1$ is approached. For the calculation of S_r,

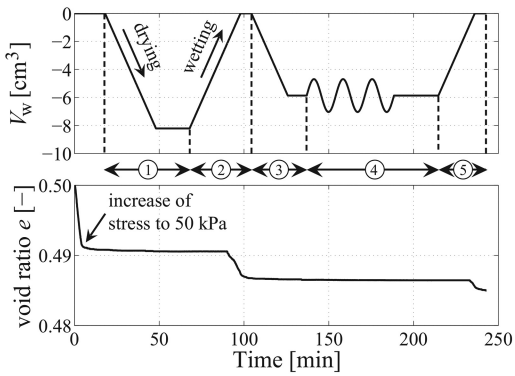


Figure 4. Applied pore water volume change and void ratio calculated from specimen settlement versus test time.

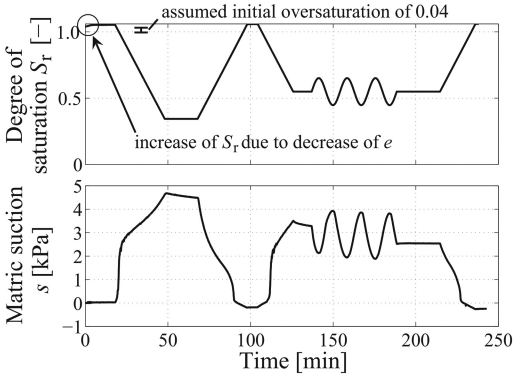


Figure 5. Degree of saturation calculated from pore water volume change and measured matric suction versus test time.

equation 3 is used, taking pore water volume change ΔV_w, void ratio e, specimen volume V and a correction term ΔS_r into account.

$$S_r = 1 + \frac{\Delta V_w}{\frac{e}{1+e} V} + \Delta S_r \tag{3}$$

The obtained degree of saturation as well as matric suction, measured with the topcap-tensiometer, are represented in Figure 5 versus test time. Due to the initial compression and decrease of e at saturated conditions the outflow data causes the calculated S_r to rise above 1. Furthermore, in the first dewatering stage a decrease in degree of saturation was noticed causing a nonlinear increase in matric suction below the AEV of the sand. As this behaviour is interpreted as an initial oversaturation due to excess water on top of the specimen and adhering to the topcap-tensiometer ceramic disc and topcap itself, the saturation data was corrected by an excess saturation of $\Delta S_r = 0.04$, increasing the initial degree of saturation to circa 1.05. This correction due to the problem that an initially saturated state can only be assumed, gives very reasonal data for the

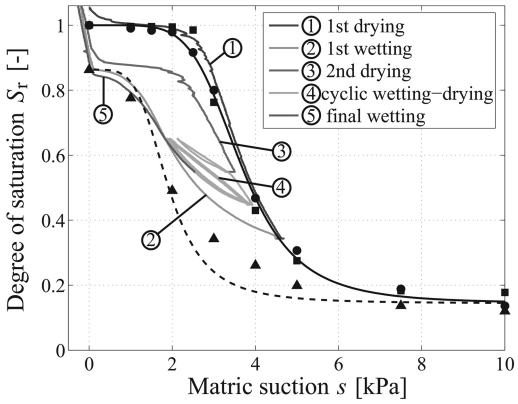


Figure 6. Obtained soil-water characteristic curve for the different imposed hydraulic paths.

first drying branch of the obtained SWCC, illustrated in Figure 6, as compared to data already presented in Figure 2. It can be seen that the AEV is very well predicted by the volume change and tensiometer data.

In the hydraulic step 2 a rewetting-scanning path from $S_r = 0.34$ to 0.86 is obtained which perfectly fits to the rewetting path from Figure 2 with a vacuum method leading to a similar S_m. Obviously, the rewetting leads to enclosed air, causing $S_m < 1$. However, in the volume-controlled test the water pressure controller forces the pore water through the specimen again and it rises above its top as can be deduced from the negative suction (hydrostatic water pressure) measured by the topcap-tensiometer in Figure 6. In the following second drying path (hydraulic step 3) $S_r = 0.55$ is reached in a drying scanning-curve that resembles the main drying-curve. Both drying curves show oscillations in the tensiometer data which may be due to imperfections in the hydraulic contact of the saturated ceramic disc and the soil water phase as already described in Milatz and Grabe (2015).

In step 4 the cyclic volume change creates three cycles of wetting-drying-scanning paths in the range $S_r = 0.55 \pm 0.1$. The first cycle shows a deviation from the two following scanning cycles which look very similar to each other and show only slight non-linear behaviour. A close-up view with each scanning cycle separated in a subplot is represented in Figure 7.

For these cyclic scanning loops a mean linear slope $\delta S_r / \delta s = -0.1$ can be calculated as represented in Figure 7 as black linear functions. This quasi-linear slope may be a justification for hysteresis models which consider scanning paths to be linear.

The final wetting in step 5 causes matric suction to decrease again and allows to deduce a maximum saturation $S_m = 0.85$ for vanishing matric suction which is below $S_m = 0.86$ for the second wetting-scanning path in hydraulic step 2. This decrease in S_m after excessive hydraulic drying-wetting cycles shows that the occlusion of air bubbles may increase due to cyclic pumping effects.

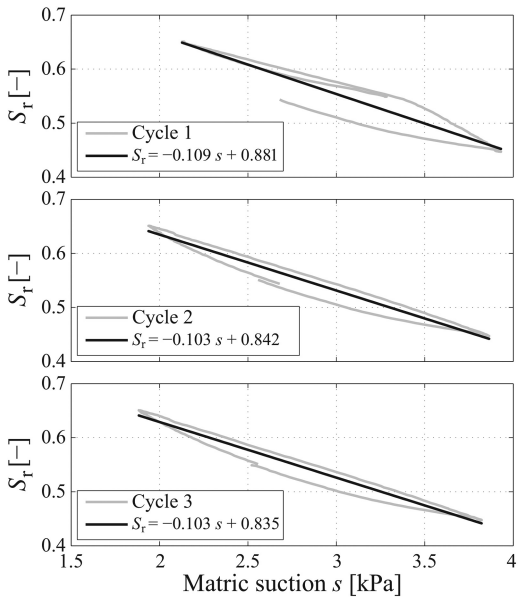


Figure 7. Separated scanning-paths in cyclic test step 4 versus linear approximation functions.

4 DISCUSSION AND OUTLOOK

In this paper a volume-controlled hydraulic method has been presented that allows to obtain drying-wetting paths of the soil-water characteristic curve in a short time period for a medium sand. The presented data of measured matric suction using a tensiometer and of degree of saturation calculated from the imposed pore water outflow volumes show a good agreement to the SWCC obtained from conventional methods.

Nevertheless, the presented method may suffer from errors, caused by the initial assumption of full saturation. Other saturation-related errors may be due to the fact that the degree of saturation calculated from outflow data is only a state variable that is averaged over the specimen volume. The specimen volume is, however, small due to a low specimen height, in the presented test. Other errors may occur due to erroneous tensiometer measurements at low degree of saturation. In the case of granular soils, the hydraulic contact between ceramic disc and soil water phase may be lost on drying. Therefore, it is believed that the presented method may be limited to a certain saturation range. This leads to further considerations about the applicability of the method to other soils. In the case of finer soils with a very low hydraulic conductivity the method could be problematic, when higher flow velocities are imposed.

Improvements to the presented method could be obtained by applying a modified topcap-tensiometer with a pointed ceramic tip that can pierce into the soil in order to ensure better hydraulic contact.

In further tests these unanswered issues will be addressed and the drying and wetting velocities $\dot{V}_w$

and $\dot{S}_r$ will be varied in order to investigate their influence on the different hydraulic paths of the soil-water characteristic curve. By directly controlling the degree of saturation, more data on the complicated hydraulic behaviour could be obtained to enlarge the data basis for hydraulic models.

REFERENCES

ASTM D 6836-02(2008)e2 (2008). *Standard test methods for determination of the soil water characteristic curve for desorption using a hanging column, pressure extractor, mirror hygrometer, and/or centrifuge.* ASTM International.

Bear, J. (1979). *Hydraulics of groundwater*. New York: Mc Graw-Hill (Mc Graw-Hill Series in Water Resources and Environmental Eng.).

Bear, J. & A. H.-D. Cheng (2010). *Modeling groundwater flow and contaminant transport*. Springer.

Bishop, A. W. (1959). The principle of effective stress. *Teknisk Ukeblad 106* (39), 859–863.

Dane, J. H. & P. J. Wierenga (1975). Effect of hysteresis on the prediction of infiltration, redistribution and drainage of water in a layered soil. *Journal of Hydrology 25*, 229–242.

Fredlund, D. G., N. R. Morgenstern, & R. A. Widger (1978). The shear strength of unsaturated soils. *Canadian Geotechnical Journal 15*, 313–321.

Fuentes, W. & T. Triantafyllidis (2013). Hydro-mechanical hypoplastic models for unsaturated soils under isotropic stress conditions. *Computers and Geotechnics 51*, 72–82.

Hanks, R. J., A. Klute, & E. Besler (1969). A numeric model for estimating infiltration, distribution, drainage and evaporation of water from soil. *Water Resources Research 5*, 1064–1069.

Jaynes, D. B. (1984). Comparison of soil-water hysteresis models. *Journal of Hydrology 75*, 287–299.

Li, X. S. (2005). Modelling of hysteresis response for arbitrary wetting/drying paths. *Computers and Geotechnics 32*, 133–137.

Lu, N., J. W. Godt, & D. T. Wu (2010). A closed-form equation for effective stress in unsaturated soil. *Water Resources Research 46*.

Lu, N. & W. J. Likos (2006). Suction stress characteristic curve for unsaturated soil. *Journal of Geotechnical and Environmental Engineering 132* (2), 131–142.

Milatz, M. (2013). On the control of low negative water pressures in laboratory tests on unsaturated sand. In *Proc. of 5th International Young Geotechnical Engineers' Conference (iYGEC)*, pp. 55–58.

Milatz, M. & J. Grabe (2014, 2–4 July 2014). Triaxial and simple shear tests on unsaturated sand specimens with negative pore water pressures. In *Proc. of 6th International Conference on Unsaturated Soils (UNSAT 2014), 2–4 July 2014, Sydney, Australia*, Volume 2, pp. 1631–1637.

Milatz, M. & J. Grabe (2015). A new simple shear apparatus and testing method for unsaturated sands. *Geotechnical Testing Journal 38*, 9–22.

Mualem, Y. (1976). A new model for predicting the hydraulic conductivity of unsaturated porous media. *Water Resources Research 12*, 593–622.

Mualem, Y. & E. E. Miller (1979). A hysteresis model based on an explicit domain-dependence function. *Soil Science Society of America Journal 43*, 1067–1073.

Nishimura, T., J. Koseki, D. G. Fredlund, & H. Rahardjo (2012). Microporous membrane technology for measurement of soil-water characteristic curve. *Geotechnical Testing Journal 35* (1), 1–8.

Schubert, H. (1982). *Kapillarität in porösen Feststoffsystemen*. Springer Verlag.

van Genuchten, M. T. (1980). A closed-form equation for predicting the hydraulic conductivity of unsaturated soils. *Soil Science Society of America Journal 44* (5), 892–898.

Vanapalli, S. K., M. V. Nicotera, & R. S. Sharma (2008). Axis translation and negative water column techniques for suction control. *Geotechnical and Geological Engineering 26* (6), 645–660.

Yang, C., D. Sheng, & J. P. Carter (2011). Hysteretic seepage analysis in unsaturated soil covers. In *Proc. of 5th Asia-Pacific Conference on Unsaturated Soils (AP–UNSAT 2011)*, Volume 2, Kasetsart University, Pattaya, Thailand, pp. 541–546.

Unsaturated Soil Mechanics—from Theory to Practice – Chen et al. (Eds)
© 2016 Taylor & Francis Group, London, ISBN 978-1-138-02921-7

Characterizing soil mechanical response induced by drought climate using a novel micropenetrometer

D.Y. Wang, C.S. Tang, S.K. Xu, K.Q. Sun, P. Wang & B. Shi
School of Earth Sciences and Engineering, Nanjing University, Nanjing, China

ABSTRACT: As natural soil is subjected to drought climate, desiccation cracking can occur due to water loss by evaporation. The presence of cracks is the result of soil tensile failure induced by the development of suction and tensile stress during drying. Revealing the evolution characteristics of the mechanical parameters of soil under drought climate is highly significant to the evaluation of soil engineering performance. In the present work, a novel micropenetrometer was developed to detect soil internal mechanical response by referring to the measured penetration resistance (R_p). A series of penetration tests were conducted on initial saturated slurry which was subjected to continuous drying by simulating drought climate in laboratory. It has been found that the developed micropenetrometer provides an effective tool to quantitatively evaluate the mechanical behaviour of clayey soil during the drying process with advantages of simple operation, high precision and a wide range of moisture content, etc. In the high moisture content range ($w \geq 20.93\%$), the profile R_p of specimen remained stable and its spatial difference was very small during the continuously drying process. As water evaporation proceeded, the water moisture of soil continually decreased ($w < 20.93\%$) and the spatial difference of soil penetration resistance became more evident. With the increase of penetration depth, the R_p decreased and gradually became stable. The R_p increased exponentially with the decrease of average moisture content, which can be contributed to the increment of soil suction, the enhancement of interaction force among soil particles and the increment of the soil particle connections due to the shrinkage of soil.

1 INTRODUCTION

It is well known that the desiccation cracking is likely to occur on soil as subjected to drought climate. Cracking is the result of soil tensile failure induced by the development of suction and tensile stress during drying. Generally, the overall macro mechanical behaviour of the soilis largely determined by soil internal mechanical strength especially the micro structure strength between soil particles/aggregates. Many engineering problems are directly or indirectly related to the weakening of soil internal mechanical strength caused by the variation of hydraulic or mechanical boundary conditions. Thus, better understand the internal mechanical behaviour of soil during drought climate is essential for the mitigation of the possible geotechnical and geological problems related to climate loading.

The soil internal strength has been widely studied in the field of agronomy (Weaich 1992, Motavalli 2003, Lapen et al. 2004, Kılıç et al. 2004, Júnior et al. 2006, Bachmann et al. 2006). In these investigations, the cone penetrometer was used to assess soil physical restrictions in clay soils for crop growth (Motavalli 2003, Lapen et al. 2004, Kılıç et al. 2004, Júnior et al. 2006). The easy obtainable penetration resistance (R_p) data were also used to evaluate the compaction state by Bachmann et al. (2006). In practical engineering applications, the cone penetration test (CPT) is widely accepted as an easy, rapid and relatively economical field test method to investigate the mechanical behavior in soil profile (Elbanna and Witney, 1987, Lunne et al., 1976, Shin and Kim, 2011, Low et al., 2010). However, the corresponding apparatuses are of large size and cannot be used to evaluate the mechanical behaviour of soil from a microscopic view, and it also cannot be used in laboratorial test.

In this investigation, a novel micropenetrometer was developed to detect soil internal mechanical response induced by drought climate. A series of penetration tests were conducted on an initially saturated specimen which was subjected to continuous drying. Based on the obtained penetration resistance, the penetration stress characteristic curve was established over a broad range of water content.

2 MATERIAL AND METHOD

2.1 *Material*

Xiashu Soil taken from Nanjing was used in this investigation. The physical properties of the soil are list in Table 1. The mineralogical composition of Xiashu soil was analyzed by X-ray diffraction which showed that the clay minerals are dominated byillite.

Table 1. Physical properties of Xiashu Soil.

Specific gravity	Liquid limit	Plastic limit	Plasticity index	Clay (<2μm)
2.73	36.5%	19.5%	17.6	22%

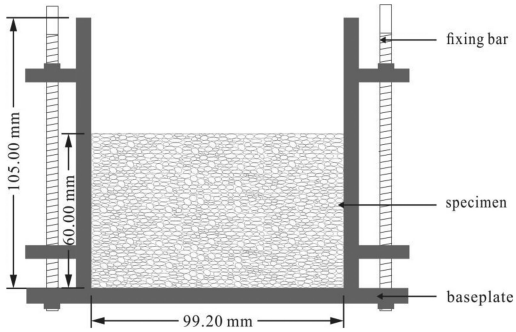


Figure 1. Schematic diagram of the stainless steel container.

2.2 *Specimen preparation*

The collected Xiashu soil was air-dried ($w = 7.3\%$), crushed to pass through a 2 mm sieve and mixed with distilled water to prepare a fully saturated slurry. The slurry was thoroughly mixed by stick until all the aggregates have been completely dispersed. After that, desired quantity of slurry was poured into stainless steel containers, which is 105 mm in height and 99.2 mm in inner diameter, as the schematic drawing shown in Fig. 1. Three long fixing bars (two visible in Fig. 1) were used to fix the base plate. The container with slurry was then placed on a vibration device for 5 minutes to remove entrapped air bubbles in the slurry. They were sealed with plastic membrane for at least 48 hours to allow slurry deposition. The final settled slurry thickness was about 60 mm.

2.3 *Apparatus*

In order to quantitatively evaluate the soil internal mechanical strength during drying, a specific micropenetrometer was developed. The schematic diagram of the micropenetrometer is presented in Fig. 2. This micropenetrometer mainly consists of three systems: load and displacement controlling and measuring system (control box, control panel, load transducer and displacement transducer), platen positioning system (platen and position adjuster), and data collecting system (data logger and computer). The soil sample with the container is placed on the platen. A penetration probe is connected to the load transducer (with a capacity of 100 N and a resolution of 0.01 N), and fixed on the center of the crossbeam of the load frame. A displacement transducer with a capacity of 50 mm and a resolution of 0.01 mm is mounted on the platen. The load frame is driven by a motor that can apply constant displacement rate during the penetration test.

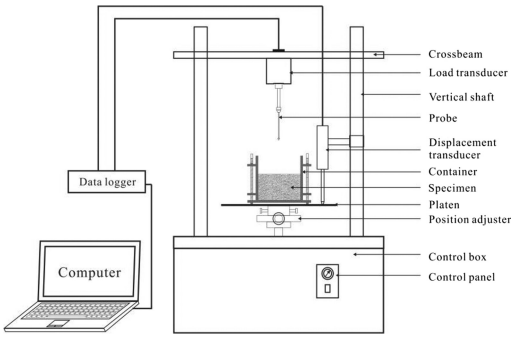


Figure 2. Schematic diagram of the micropenetrometer.

In order to eliminate the side friction between probe and soil matrix during penetration process, a special mini-probe with enlarged head was designed (Fig. 3). The probe has a length of 60 mm. The cone at the probe head has an apex angle of 60°, and the base diameter is 2.0 mm which is slightly larger than the rod (1.5 mm in diameter). As the schematic drawing shown in Fig. 3, during the penetration test, the measured force of the load transducer actually equals to the tip resistance of the probe. The measured displacement corresponds to the actual penetration depth (d_p). Generally, when the probe penetrates into a soil vertically at a constant rate, the higher the soil mechanical strength, the greater the measured R_p will be, and vice versa. The resistance caused by soil particles/aggregates is therefore considered as an indicator of soil inner mechanical strength (Liu et al., 2006, Gu et al., 2013, Wang et al., 2014). According to the obtained R_p and d_p, the penetration curve (R_p versus d_p) can be plotted. Hence, the variation of mechanical strength along soil profile would be characterized.

2.4 *Test procedures*

After the specimen was prepared, it was subjected to continuous drying. The penetration tests were performed during drying. The test started from the initial slurry state. During drying, the specimens were placed in an oven with constant temperature of 50°C, and moved to the platen of load frame to perform penetration test at different intervals (as seen in Fig. 4). After the weight of the specimens reached stabilization, the drying path was stopped.

It should be noted that, during penetration test, a porous metal cover was placed on the top surface of specimens to prevent soil moisture evaporation. In the metal cover, as shown in Fig. 5, many small holes (3 mm in diameter) were drilled for positioning the penetration points. The penetration positions were carefully selected and marked in the center area of the specimens (about 15–20 mm far from the boundary). In this investigation, the distance between each neighboring penetration point was ensured larger than 20 mm, namely 10 times higher than the diameter of the penetration cone (i.e. 2 mm). This distance

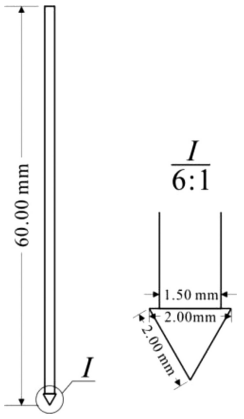


Figure 3. Schematic diagram of the mini-probe.

is assumed to be enough to eliminate the possible impaction of neighboring penetration points. In order to reduce moisture evaporation, only one hole in the top cover was open for penetration, and the others were sealed by adhesive tape during the test. The penetration rate was controlled to be constant at 5 mm/min. After each penetration, the weight of the specimen was measured by a balance (accuracy of 0.01 g), it was used to back-calculate the corresponding average water content (w_a) after the test. According to the measured R_p and effective cross-sectional area (A_e) of the probe, the corresponding apparent penetration stress (λ_s) can be calculated and used to describe the mechanical strength of soil, defined as follows:

$$\lambda_s = \frac{R_p}{A_e} \tag{1}$$

where λ_s is the penetration stress (MPa), R_p is the penetration resistance (N), A_e is the effective cross-sectional area of the probe (mm^2). In this paper, the effective cross-sectional area of the probe is 3.14 mm^2.

3 RESULTS AND DISCUSSION

The typical penetration curves (R_p versus d_p) of the slurry specimen at different average water contents w_a are plotted in Figure 6. As can be seen, the moisture of the specimen varies in a broad range from initial high value of about 42.66% to a low value of about 11.64%. All the curves show similar pattern at the initial stage of the penetration test ($d_p < 3$ mm), namely the R_p increases with increasing d_p before a peak value is reached. This phenomenon can be attributed to the conical probe head used in this investigation. Before the conical probe head was fully penetrated into soil, the contact area between probe and soil gradually increased with increasing d_p, and the corresponding resistance therefore also increased.

For simplicity and clarity, only the penetration data after $d_p \geq 3$ mm will be plotted for analysis in the following sections, as shown in Fig. 7. Moreover, The R_p

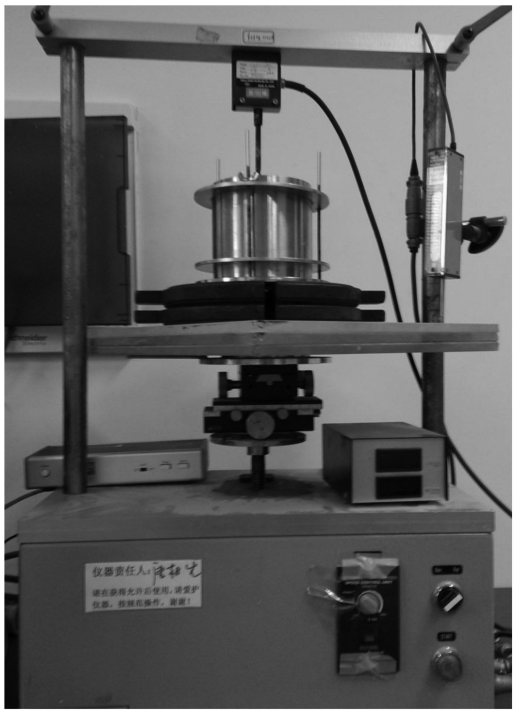


Figure 4. Photo of penetration test.

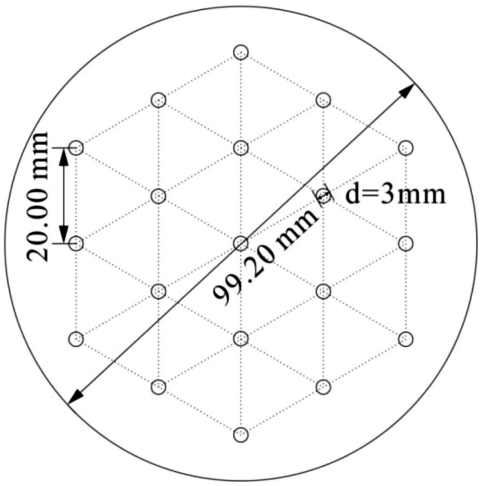


Figure 5. Schematic diagram of the porous metal cover (Top view of the top cover).

at specific depth (5, 10, 15, 20, 25, 30 and 35 mm) with decreasing w_a is also plotted for analysis. As can be seen, the overall R_p is very small at higher w_a range (i.e. 42.66%–20.93%). The R_p generally remains constant with increasing d_p, indicating that the internal strength of the specimen are relatively uniform in the profile. With continuous drying, the overall R_p increases lightly from about 1 to 10 Nas the w_a decreases from

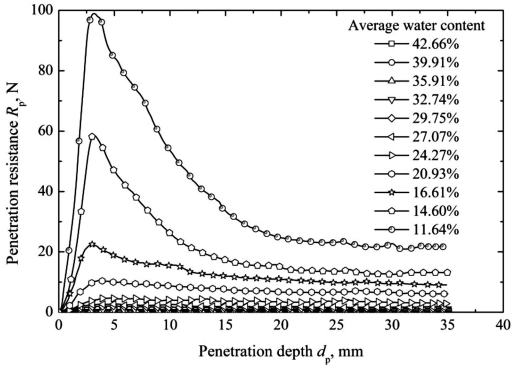


Figure 6. The typical penetration curves of the slurry specimen.

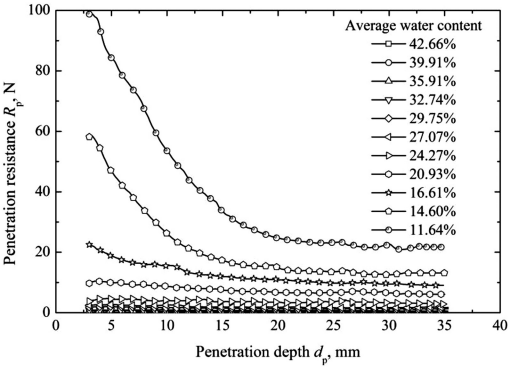


Figure 7. The typical penetration curves($d_p \geq 3$ mm) of the slurry specimen.

42.66% to 20.93%. However, as the w_a reaches relative lower range (i.e. 16.61%–11.64%), the penetration curves are much different from that observed at higher w_a range. The R_p increases quickly at shallow depth and decreases exponentially with increasing d_p. Fig. 9 shows the change of $\Delta R_{p(w)}/R_{p(20.93\%)}$ with d_p. As can be seen, at 5 mm depth, the R_p increases by 743% from approximately 10 to 84 N as w_a decreases from 20.93% to 11.64%. At 15 mm depth, the R_p increases by 347% from approximately 7.5 to 33.6 N as w_a decreases from 20.93% to 11.64%. However, at deep depth (20/25/30/35 mm depth), the R_p increases by 249% as w_a decreases from 20.93% to 11.64%. It indicates that drying results in significant increase in soil strength as well as heterogeneous distribution of internal strength in profile. The profile strength in upper soil layer is always higher than that in lower soil layer.

Fig. 10 shows penetration stress characteristics curve, namely the change of the average penetration stress (λ_{as}) with w_a during drying, which is determined by the equation (1) and Fig. 7. As can be seen, with decreasing w_a during drying, the λ_{as} generally increases exponentially. At water content of 42.66%, the λ_{as} is only about 20 kPa. As w_a decreases to 11.64%, the λ_{as} increases significantly to about 12153 kPa. It can also be seen that the increase rate of during drying is relative low at high water content range (i.e. 42.66%–24.27%). After that, a slight decrease of w_a can result in an obvious increase of λ_{as}.

Generally, the internal strength of soil depends on the bonding force between soil particles/aggregates, which includes various inter-particle/aggregate forces such as (1) van der Waals forces, (2) electrical double layer repulsion or attraction, (3) cementation due to solute precipitation, (4) capillary stress due to the negative pore water pressure, and (5) capillary stress due to the surface tension of liquid (Lu and Likos, 2006, Lu et al., 2007). When the probe penetrates into a soil vertically at a constant rate, the higher the soil mechanical strength, the greater the measured R_p will be, and vice versa. Upon drying, soil water evaporation plays an important role, which could result in the development of suction recognized as one of the

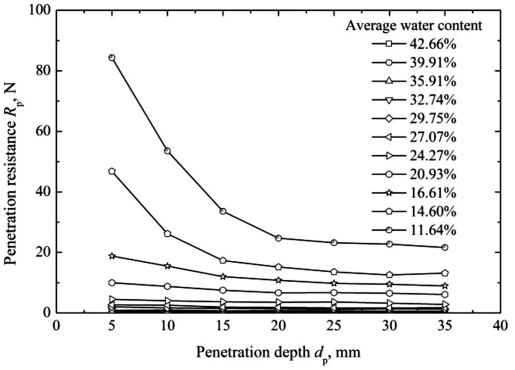


Figure 8. Change of R_p at specific depth.

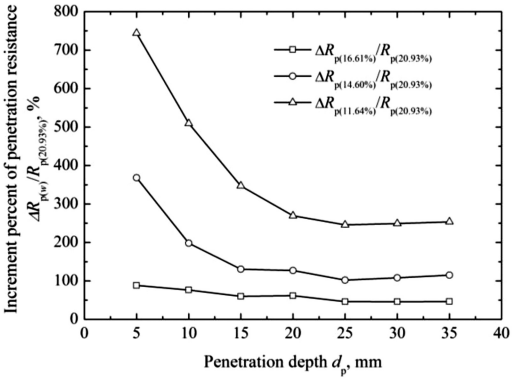


Figure 9. Change of $\Delta R_{p(w)}/R_{p(20.93\%)}$ and d_p atrelative lower w_a range (16.61%–11.64%).

important parameters to analyze the evolution of soil mechanical strength. For this reason, the discussion on the obtained results and the development of internal strength during drying will be mainly concentrated on soil moisture aspects.

As an initially saturated slurry specimen is subjected to drying, water evaporation of soil would always begin from the soil surface firstly, which is due

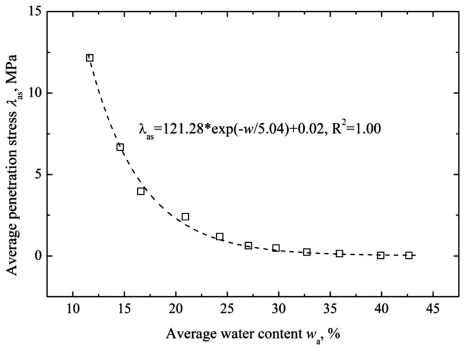


Figure 10. Change of λ_{as} with w_a during drying.

to the moisture vapor face (the soil-air interface) of soil and the free water face both located in the soil surface. At higher w_a range (i.e. 42.66%–20.93%), there are enough water supplied to the moisture vapor face. As water evaporation proceeds, the moisture of the entire specimen decreases and the spatial difference of moisture is very small. Therefore, the mechanical strength of slurry specimen section remains stable. During this stage, the hydration film among soil particles of slurry specimen becomes thicker and thicker and the volume shrinkage occurs, which results in the increment of the interaction force among soil particles and the soil particle connections. These factors can induce the increase of the R_p. In addition, the moisture in deeply seated pores is drawn to the surface by capillary forces, which forms capillary water columns. Menisci exists among soil particles in the top layer of the specimen. With the increase of capillary suction in the top layer, the soil mechanical strength in the top layer increases obviously, resulted in the increase of the R_p in the top layer. As water evaporation proceeds, the soil water content is continually diminishing. During this stage (i.e. 16.61%–11.64%), the entire specimen is in anunsaturated state, and the Drawn water cannot meet the requirement of water evaporation. Menisci exists among soil particles in the entire specimen, and the moisture of deep soil evaporation transfers from capillary to diffusion mode. The moisture of the top layer evaporates faster than that of the deep layer, and soil suction of the top layer increases faster than that of deep layer. At the last, soil moisture distribution and soil suction in profile becomes non-uniform. With increasing soil suction among soil particles, the soil mechanical strength in the top layer increases obviously, resulting in the increase of R_p in the top layer. In addition, the decrease of pore ratio and the increment of the soil particle joint connection due to the shrinkage deformation of soil will also contribute to enhancing mechanical strength of clayey soil.

4 CONCLUSIONS

A novel micropenetrometer was developed, and it was applied to quantitatively characterize the profile mechanical response of a clayey soil as subjected to drought climate. The following conclusion can be drawn:

(1) The developed micropenetrometeroffers an effective method to quantitatively evaluate the mechanical behaviour of clayey soil during the drying process with advantages of simple operation, high precision and a wide range of moisture content, etc.
(2) In the high moisture content range ($w \geq 20.93\%$), the R_p of specimen section remained stable and its spatial difference was very small during the continuously drying process.
(3) As water evaporation proceeded, the water moisture of soil continually decreased ($w < 20.93\%$) and the spatial difference of soil penetration resistance became more evident. With the increase of penetration depth, the R_p decreased and gradually became stable.
(4) Based on the measured penetration resistance, the penetration stress characteristic curve was established over a broad range of water content. Generally, the penetration stress increased exponentially with the decrease of average moisture content, which can be contributed to the increment of soil suction, the enhancement of interaction force among soil particles and the increment of the soil particle connections due to the shrinkage of soil.

It should be noted that this paper only presents the preliminary results we obtained during drying process. More detailed experiments are necessary in order to further confirm the drawn tentative conclusions.

ACKNOWLEDGEMENTS

This work was supported by the National Science Foundation of China for Excellent Young Scholars (Grant No. 41322019), Key Project of National Natural Science Foundation of China (Grant No. 41230636), and National Basic Research Program of China (973 Program, Grant No. 2011CB710605) and Natural Science Foundation of Jiangsu Province (Grant No. BK2011339). The authors want to address their thanks to X.W. Luo at Nanjing University for his help to conduct the tests.

REFERENCES

Bachmann, J., Contreras, K., Hartge, K. H. & Macdonald, R. 2006. Comparison of soil strength data obtained in situ with penetrometer and with vane shear test. *Soil and Tillage Research,* 87, 112–118.

Elbanna, E. B. & Witney, B. D. 1987. Cone penetration resistance equation as a function of the clay ratio, soil moisture content and specific weight. *Journal of Terramechanics,* 24, 41–56.

Gu, K., Tang, C., Shi, B., Hong, J. & Jin, F. 2013. A study of the effect of temperature on the structural strength of a clayey

soil using a micropenetrometer. *Bulletin of Engineering Geology and the Environment,* 73, 747–758.

Júnior, V. V., Carvalho, M. P., Dafonte, J., Freddi, O. S., Vidal Vázquez, E. & Ingaramo, O. E. 2006. Spatial variability of soil water content and mechanical resistance of Brazilian ferralsol. *Soil and Tillage Research,* 85, 166–177.

Kılıç, K., Özgöz, E. & Akbaş, F. 2004. Assessment of spatial variability in penetration resistance as related to some soil physical properties of two fluvents in Turkey. *Soil and Tillage Research,* 76, 1–11.

Lapen, D. R., Topp, G. C., Edwards, M. E., Gregorich, E. G. & Curnoe, W. E. 2004. Combination cone penetration resistance/water content instrumentation to evaluate cone penetration–water content relationships in tillage research. *Soil and Tillage Research,* 79, 51–62.

Liu, Z. B., Shi, B. & Sheng, D. C. 2006. A micropenetrometer for detecting structural strength inside soft soils. *Geotechnical Testing Journal,* 29, 443–450.

Low, H. E., Lunne, T., Andersen, K. H., Sjursen, M. A., Li, X. & Randolph, M. F. 2010. Estimation of intact and remoulded undrained shear strengths from penetration tests in soft clays. *Géotechnique,* 60, 843–859.

Lu, N. & Likos, W. J. 2006. Suction stress characteristic curve for unsaturated soil. *Journal of Geotechnical and Geoenvironmental Engineering,* 132, 131–142.

Lu, N., Wu, B. L. & Tan, C. P. 2007. Tensile strength characteristics of unsaturated sands. *Journal of Geotechnical and Geoenvironmental Engineering,* 133, 144–154.

Lunne, T., Eide, O. & Ruiter, J. 1976. Correlations between cone resistance and vane shear strength in some Scandinavian soft to medium stiff clays. *Canadian Geotechnical Journal,* 13, 430–441.

Motavalli, P. 2003. Use of soil cone penetrometers to detect the effects of compaction and organic amendments in claypan soils. *Soil and Tillage Research,* 74, 103–114.

Shin, Y. J. & Kim, D. 2011. Assessment of undrained shear strength based on Cone Penetration Test (CPT) for clayey soils. *KSCE Journal of Civil Engineering,* 15, 1161–1166.

Wang, D. Y., Tang, C. S., Li, J. & Shi, B. 2014. Super miniature penetration test on structural strength of clayey soil during evaporation. *Journal of Engineering Geology,* 22, 818–823. (in Chinese)

Weaich, K. 1992. Use of a penetration resistance characteristic to predict soil strength development during drying. *Soil and Tillage Research,* 25, 149–166.

Unsaturated Soil Mechanics—from Theory to Practice – Chen et al. (Eds)
© 2016 Taylor & Francis Group, London, ISBN 978-1-138-02921-7

Investigating the volume change characteristics of bentonite/sand mixture under hydro-mechanical coupling condition

Z.G. Chen, C.S. Tang, D.Y. Wang, P. Wang, K.Q. Sun & B. Shi
School of Earth Sciences and Engineering, Nanjing University, Nanjing, China

ABSTRACT: Understanding the volume change characteristics of bentonite/sand mixture as an optional buffer/backfill material under coupling hydro-mechanical condition is highly significant for evaluating the long-term safety of the repository. In this investigation, six groups of bentonite/sand mixtures were prepared with different contents of quartz sand, i.e. 0%, 10%, 20%, 30%, 40% and 50%. The mixtures were subjected to uniaxial compression (to a final dry density of 1.7 Mg/m^3) and saturation (under 0.2 MPa vertical pressure) in sequence. The volume change behaviour and the effect of sand content were analyzed. It is found that: (1) The compression behaviour of mixture significantly depends on sand content, saturation state and density. As the mixture is unsaturated and at relative low dry density ($\rho_d < 1.7$ g/cm^3), the compression index decreases linearly with increasing sand content. However, as the mixture is saturated and at relative high dry density ($\rho_d > 1.7$ g/cm^3), the compression index of mixture is independent of sand content, and the corresponding value is much less than that at unsaturated and loose state. (2) The final swelling strain of the mixture decreases exponentially with increasing sand content. As the sand content in the mixture is higher than 40%, volume collapse occurs during saturation, and collapse extent is enhanced by increasing sand content. (3) The observed volume change characteristics of the mixture under different hydro-mechanical conditions or at different sand contents are mainly related to the distribution of bentonite and sand in the mixture, and their dominant effect on soil skeleton. Generally, the higher sand content and higher density, the volume change behaviour the mixture is more conditioned by sand.

1 INTRODUCTION

With the rapid development of nuclear energy, a lot of HLW (high-level radioactive) waste has been produced. In China, the generation rate of HLW in 2020 will reach 1 000 t per year (Cui et al., 2006). Therefore, the safe disposal of HLW has become an urgent issue, and it is necessary to find an appropriate and reasonable engineering solution.

After many years research on HLW disposal, the concept of deep geological disposal is widely accepted. That is, burying the HLW to underground stable formation at 500–1000 m. Engineering barrier is an indispensable component in the design and construction of geological disposal repository. Therefore, the overall performance of buffer/backfill material largely determines the safety and function of the repository. Especially in a multi-field coupled (temperature field, water potential field, stress field and the chemical field) complex conditions, physical and chemical properties of the engineered barrier materials possibly changes over time, thus affecting the long-term safe operation of the repository system. For this reason, many research institutions have carried out extensive studies on the geotechnical behavior of engineered barrier (Ye et al., 2010, Cuisinier et al., 2005, Hoffmann et al., 2007). Now, compacted bentonite or bentonite-sand mixture are widely recognized as the potential buffer/backfill material mainly because of its high content of montmorillonite, low permeability, high adsorption and better mechanical properties (Pusch, 1979).

The main mechanism of engineered barriers is that buffer/backfill material which filled between surrounding rock and waste tank will plug the internal gap of media and fully isolate nuclear waste from external environment in its swelling process. Hence, the buffer/backfill material is required to meet strict expansion characteristics. For the deformation requirements, many researchers carried out swelling tests by controlling load and suction in order to understand the mechanism of swelling deformation. Increasing axial load and sand content significantly inhibits swelling deformation, and the initial water content has little effect on the final deformation, but it has an obvious effect on the swelling rate (Liu et al. 2001, Wang & Liu 2000). Ye et al. (2007) established a relationship between bentonite swelling deformation and suction under the unsaturated condition, and the swelling mechanisms were discussed based on microstructure observation. In addition, some researchers also studied the influence of initial compaction conditions, pore solution and suction on swelling behavior (Qin et al. 2008, Baille et al. 2010). For the swelling pressure,

Table 1. The basic physical property indexes of bentonite.

Gravity *Gs*	Water content *w*/%	Liquid limit w_l/%	Plastic limit w_p/%	Plastic index I_p	Maximum dry density ρ_d/(g/cm^3)	Montmorillonite content/%
2.71	9.26	153.3	33.3	120	1.69	85.3

numerous researches have also been down in the past decades. For instance, Liu & Wang (2002) found that swelling pressure is mainly affected by the dry density. Generally, the swelling pressure increases with increasing dry density. This is consistent with other researchers such as Ye et al. (2007) and Sun et al. (2009). In addition, Ma et al. (2010) and Tang et al. (2012) found that the property of pore water, boundary conditions and test methods are crucial factor affecting the swelling pressure. Furthermore, Komine & Ogata (1996), and Liu et al. (2013) established a mathematical model to predict swelling pressure.

In this paper, a series of oedometer tests were conducted on bentonite/sand mixture to investigate the compression and swelling behavior. The effect of sand content on the volumetric deformation was analyzed.

2 MATERIAL AND METHOD

2.1 *Materials*

In this paper, artificial standards quartz sand was adopted, and its basic properties are described as follows: diameter of 0.5–1.0 mm, silica content of 99.45% and the relative density of 2.65. The bentonite in this test is commercial calcium bentonite, and its physical and mechanical characteristics are shown in Table 1.

2.2 *Specimen preparation*

First of all, dry the sand and bentonite respectively in the oven at 105°C for 24 hours. Then 6 groups of mixtures with different content of sand from 0% to 50% (mass content) have been prepared. The weight of mixture is calculated according to target dry density of 1.7 g/cm^3, a thickness of 10 mm and diameter of 39.1 mm in order to weigh and pour the mixture into a mold (Fig. 1) for pre-compaction. The initial parameters of each sample are shown in Table 2.

2.3 *Test procedures*

The pre-compacted specimen was subjected to uniaxial compression and saturation sequentially, and deformation characteristics under each stress path were real-time monitored. The presupposed test path is shown in Fig. 2, and specific test steps are introduced as follows:

(1) Put the prepared specimen with the mould on a three-combination oedometer for the uniaxial compression test which includes 12 grades of load: 0.2 MPa, 0.23 MPa, 0.262 MPa, 0.325 MPa, 0.450 MPa, 0.700 MPa, 0.949 MPa, 1.199 MPa, 2.199 MPa, 4.198 MPa, 8.197 MPa and 10.196 MPa. Keep 1 hour for each load. As shown in Fig. 1, the mould is T-shaped for purpose of that their continued compression deformation will be limited after the samples are compacted to target dry density.

(2) After the graded compression tests, compress all the specimens to a dry density of 1.70 g/cm^3 with a height of 10 mm. Then soak the specimen in water for the swelling test with a load of 0.2 MPa. Stop this process until the deformation of the specimen is less than 0.1% within 24 hours.

Table 2. Initial parameter of specimens.

Sample No.	Sand content/ %	Initial dry density/ g/cm^3	Initial height/ mm	Specimen diameter/ mm
T0	0	1.15	14.84	39.1
T1	10	1.15	14.84	39.1
T2	20	1.15	14.84	39.1
T3	30	1.15	14.84	39.1
T4	40	1.40	12.15	39.1
T5	50	1.40	12.15	39.1

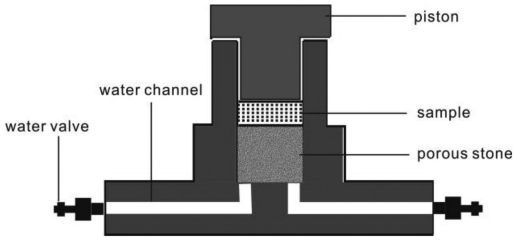


Figure 1. The mould in this test.

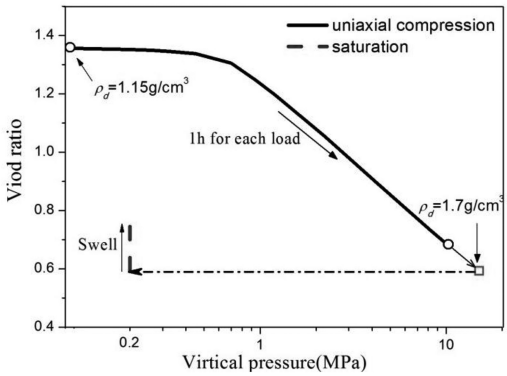
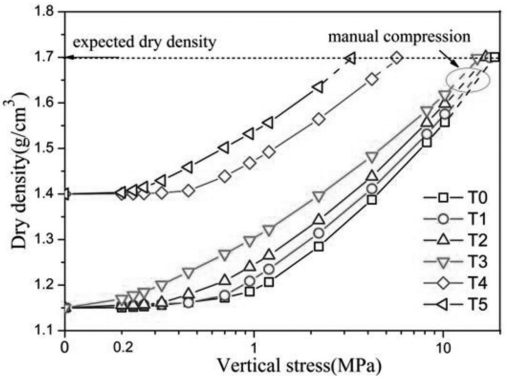
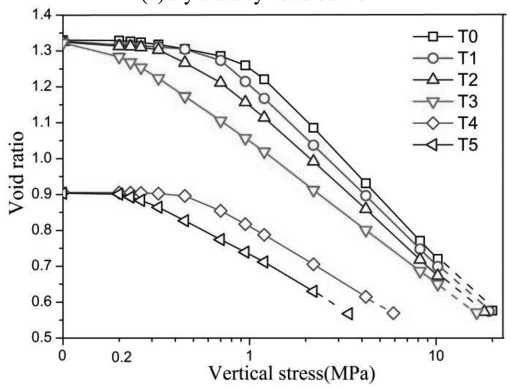


Figure 2. Stress path of the test.



(a)dry density-load curve



(b)void ratio-load curve

Figure 3. Compression curve of the sample.

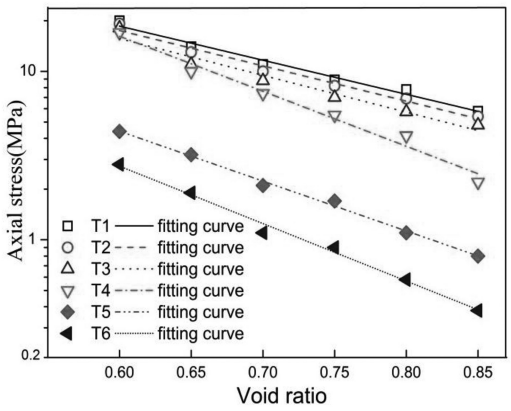


Figure 4. The relationship between the axial stress and void ratio.

3 TEST RESULTS

3.1 *Uniaxial compression*

Compression curves are shown in Fig. 3. The dry density-load curve (Fig. 3(a)) shows that with the increase of axial load, the dry density of the specimen increases, while the void ratio decreases, and the bentonite/sand mixture changes from loose to a dense compacted system. For specimens with different sand content, the variations of dry density with load show different characteristics: specimens (T0–T3) with low sand content didn't reach the target dry density (1.7 g/cm^3) after complete loading procedure, while specimens (T4–T5) with high sand content reached the target dry density when it was subjected to the eleventh (8.197 MPa) and the tenth load (4.198 MPa) respectively.

Under the same load condition, the final dry density specimen can achieve increases with increase of the sand content, in other words, when the sample is expected to be compacted to the same dry density, the required load decreases with the sand content increases. For instance, when the specimens were compacted to the dry density of 1.5 g/cm^3, the requisite load for T0 was about 7.5 MPa, while the requisite load for T5 was 0.65 MPa. The former is 11.5 times of the latter. This enormous difference of load is explained that compressibility of bentonite/sand mixture becomes easier when the sand was added to the bentonite. It means that additives can significantly save compression energy and reduce project costs.

Another distinction can be found by comparing void ratio-load curve is that the degree of change in void ratio varies widely through the same loading stage. For example, through the first five loads, void ratio of T0 reduced by about 4% to T5 of about 11%. This difference is mainly due to the different pore structure produced by different proportions and over-consolidation caused in the early pre-compaction process. On the other hand, compared to the same void ratio under axial stress in different specimens (Fig. 4), it is found that with the increase of the degree of compaction, the extent of axial stress difference decreases. Especially for specimens T0–T3 with low sand content, the axial stress in the void ratio of 0.6 becomes corresponding closer.

Compression index of different samples is calculated by obtaining the slope of the straight line on e–lg p curve, and there is an equation of the relationship between compression index C_c and sand content α after fitting previous results.

$$C_c = 0.55 - 0.00557 * \alpha \quad (1)$$

3.2 *Saturation*

After the end of uniaxial compression, the sample was compressed to the identical dry density of 1.7 g/cm^3. The saturation was begun with an axial load of 0.2 MPa and the same hydraulic height, while the swelling deformation was recorded by the electronical dial indicator.

The relationship between swelling strain and time is shown in Fig. 6(a). As shown in the swelling curve, the deformation of the sample increases with time increasing and eventually stabilized. No matter at what stage,

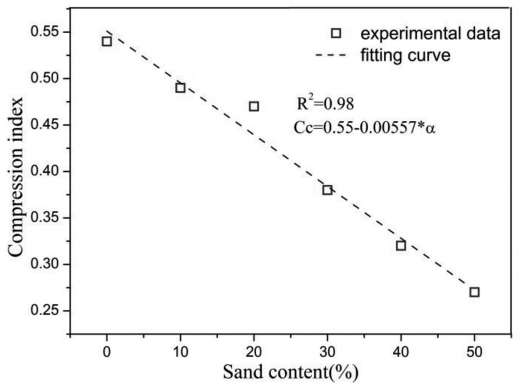
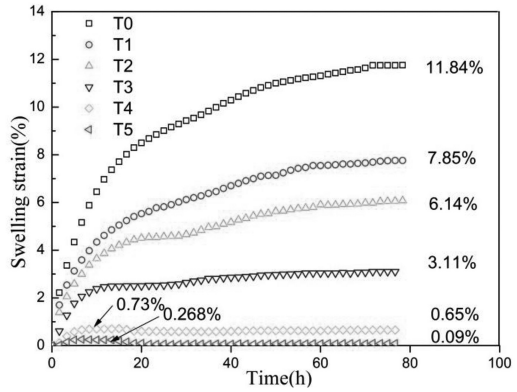
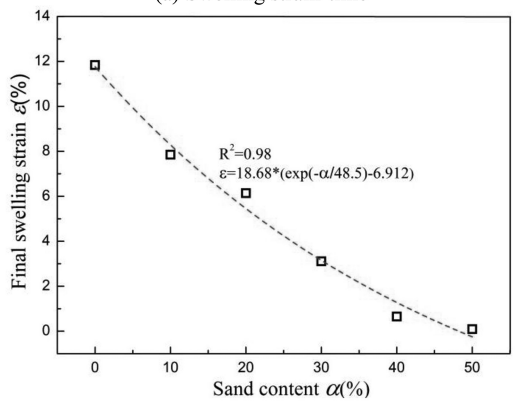


Figure 5. The relationship between compression index and sand content.



(a) Swelling strain-time



(b) Final strain-sand content

Figure 6. Volume change in the process of swelling.

the swelling strain of samples with low sand content is always higher than that with high sand content, and the final swelling strain decreases exponentially with quartz sand content (Fig. 6(b)). There is significant difference in the final swelling strain of different sand content, for instance, the final swelling of T0 and T5 were 11.84% and 0.09% respectively, but the former is 130 times higher than the latter. In addition, from the swelling curve can also be found that swelling deformation can be divided into three stages, i.e., rapid swelling phase, slow deformation phase and stable phase. For swelling curve of T1, in the initial 20 h the curve is steeper, indicating a faster rate of expansion at this time. Then between 20–70 h, the curve is gradually gentle, indicating that the rate of expansion slowed down. After 70 h, the curve is smooth and steady, and finally the sample trend to stabilize. Moreover, with the increasing content of quartz sand, the time required for sample to stabilization gradually reduced.

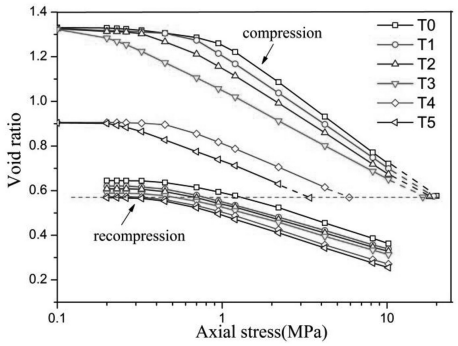
Besides, swelling curves of T0–T3 and T4–T5 indicate distinct characteristics. Specifically, the former swelling curves increase monotonically, but the latter first increases reaching a peak, then decreases. This phenomenon indicates the occurrence of a structural collapse during the swelling process. This paper introduced the "collapse rate of structure" to describe this phenomenon, which is defined as the ratio of the difference between the peak and the final steady swelling strain and the peak swelling strain, expressed as a percentage. For instance, peaks welling strain of T4 is 0.73%, and the final swelling strainis 0.65%, so the collapse rate of structure calculated by aforesaid parameters is 11.0%. Otherwise, peak swelling strain and the final swelling strain of T5 are 0.27% and 0.09% respectively, and the collapse rate of structure is about 66.7%. The results indicate that the higher sand content, the more remarkable structure collapsed during the saturation.

4 DISCUSSION

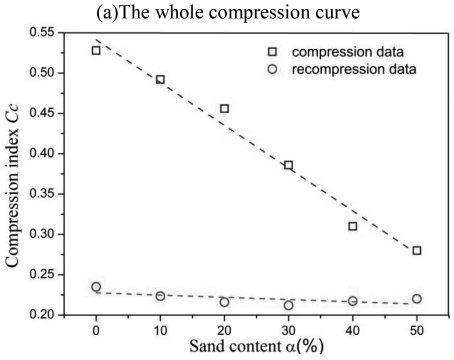
4.1 *The comparison of compression behaviour*

Fig. 7(a) shows the compression curve. The compression indices of the first compression and recompression can be drawn from the slope of line segment on compression curves (Fig. 7(b)). It is worth noting that this recompression was accomplished after saturation in order to compare two compression indices. The compression indices of the first compression are all bigger than recompression due to that the soil became denser after the first compression and its compressibility sharply declined. In the first compression, compression indices decreased linearly with increasing sand content, while in recompression, compression indices basically stabilized among 0.20 and 0.25 and were independent of sand content.

The main reason is that soil was completely dry in the first compression. Under the circumstance, its compressibility was mainly interrelated with pore structure and grain size distribution. As a result, the decrease of pore diameter caused by grain rearrangement led to macroscopically decrease of volume. As stated before, with the increase of sand content, the internal skeleton of soil gradually transformed from bentonite skeleton to quartz sand skeleton, and the occurrence of relative displacement needed grains



(a)The whole compression curve



(b) Comparison of compression index

Figure 7. Comparison of two compression index.

to overcome more resistance, so the resistance to deformation increased. Therefore, compression index decreases linearly with increasing sand content. The second compression occurred after soil was saturated and completed swelling, so the compressibility of soil is not only related to the pore structure, but also relates to its characteristics of drainage.

When soil is under saturation state, the volume change is caused by compression comes from drainage of pore water. After swelling, the volume of T0 increased by 11.84% and the volume increase of T5 could be ignored with the increase of less than 0.1%. Theoretically, T0 has greater compressibility than T5, however, their compression indices of recompression are 0.235 and 0.227 which differs slightly as was illustrated in Fig. 7. There are two main reasons. First, the density of soil was high after the first compression. In terms of T0, hydrophilic montmorillonite mineral absorbed a large amount of bound water under saturation state, so it had strong water-holding capacity. With the decreasing of pore diameter, seepage channels were blocked, which makes it difficult for pore water to drain off, so the compressibility decreased. Secondly, T5 contains a large percentage of quartz sand, and its volume barely changed during saturation. Consequently, quartz sand skeleton led the compression deformation of the sample. Its compressibility is almost as low as before.

4.2 *Characteristics of swelling strain variation*

During saturation (under 0.2 MPa vertical pressure), the characteristics of swelling strain-time curve is different from other samples (Fig. 6(a)), which means volume collapse occurs during saturation. Generally speaking, volume collapse easily occurs when samples have low dry density or are under high vertical pressure. The main reason is that there are relatively big pores in samples or attachment force among grains is lowered through saturation and the structure of soil is softened, so the skeleton can not stand further loading and compression deformation occurs. The reason why T4 and T5 collapsed is that they contain a large percentage of sand. Among sand grains, there are bigger pores where bentonite lies and is swelled with water. Restraint of sand grain skeleton on swelling deformation creates swelling pressure whose effect is similar to the increasing of pore water pressure. Consequently, effective stress among sand grains decreases, and friction reduces. Therefore, volume collapse occurs under loading, and grains are rearranged to more stable condition.

Swelling of sample T0–T3 can be clearly divided into three stages, that is rapid swelling phase, slow deformation phase and stability phase. More than 70% of swelling strain occurs in the phase of rapid swelling. With the swelling in progress, water content of samples increases while internal suction and moister absorption capacity decreases. The hydration rate of montmorillonite drops with the decrease of moister absorption capacity of pores. Additionally, montmorillonite mineral at the bottom will form a hydration film due to that saturation starts from the bottom. The film blocks channels of pore water and samples' permeability decreases, which explains why the hydration rate of the top of the soil declines. This is also a significant factor that causes three phases of swelling.

Besides, phases of swelling deformation are also related to micro-structure adjustment during saturation. Normally, there are pores of three different sizes in bentonite/sand mixture, that is big pores among sand grain, medium pores among bentonite aggregate and small pores among clay mineral. Moister will soak into big pores first during saturation. Aggregate disintegrates and break up into small grains to fill big pores rapidly. The volume gains a lot after disintegration of aggregate, so swelling deformation develops fast. Then hydration mostly occurs within small bentonite grains, so deformation and its effect on structure are confined to relatively small scale. Swelling deformation of later stage is generally the hydration of a large amount of small grains which lasts until all soil grains complete hydration.

5 CONCLUSIONS

(1) The compression deformation characteristics of bentonite/sand mixture are significantly affected by sand content, saturation state, density and so on. As the mixture is unsaturated and at relative

low dry density ($\rho_d < 1.7$ g/cm^3), the compression index decreases linearly with increasing sand content. As the mixture is saturated and at relative high dry density ($\rho_d > 1.7$ g/cm^3), the compression index of mixture is independent of sand content, and the corresponding value is much less than that at unsaturated and loose state.

(2) Sand content significantly affects swelling deformation and final swelling strain. In this paper, as the sand content in the mixture is higher than 40%, volume collapse occurs during saturation, and collapse extent is enhanced by increasing sand content.

(3) Swelling deformation of bentonite/sand mixture has three phases. In the first phase, swelling strain increases rapidly, then gradually decreases and stabilizes in the final phase.

REFERENCES

Agus, S.S. & Schanz, T. 2008. A method for predicting swelling pressure of compacted bentonites. *ActaGeotechnica* 3:125–127.

Baille, W., Tripathy, S. & Schanz, T. 2010. Swelling pressures and one-dimensional compressibility behaviour of bentonite at large pressures. *Applied Clay Science* 48(3): 324–333.

Cuisinier, O. & Masrouri, F. 2005. Hydro-mechanical behavior of a compacted swelling soil over a wide suction range. *Engineering Geology*, 81: 204–212.

Cui, S.L., Zhang, H.Y. & Zhang, M. 2012. Swelling characteristics of compacted GMZ bentonite–sand mixtures as a buffer/backfill material in China *Engineering Geology,* 141: 65–73.

Dixon, D.A., Graham, J. & Gray, M.N. 1999. Hydraulic conductivity of clays in confined tests under low hydraulic gradients. *Canadian Geotechnical Journal* 36(5): 815–825.

Hoffmann, C., Alonso, E.E. & Romero, E. 2007. Hydro-mechanical behavior of bentonite pellet mixtures. *Physics and Chemistry of the Earth*, 32: 832–849.

Komine, H. & Ogata, N. 1996. Prediction for swelling characteristics of compacted bentonite *Canadian Geotechnical Journal,* 33(1): 11–22.

Liu, L. 2013. Prediction of swelling pressures of different types of bentonite in dilute solutions. *Colloids and Surfaces A: Physicochemical and Engineering Aspects,* 434: 303–318.

Liu, Q.S. & Wang, Z.J. 2002. Influence factors of sand-bentonite mixtures on the swelling pressure *Journal of Rock Mechanics and Engineering,* 21(7):1054–1058.

Liu, Y.M. & Chen, Z.R. 2001. The feasibility of GMZ bentonite inner Mongolia as a backfill material for high-level radioactive waste repository. *Journal of minerals*, 21 (3): 541–543.

Liu, Y.M., Xu, G.Q. & Liu, S.F. 2001. Study on compactibility and swelling property of buffer/backfilI material for HLW repository. *Uranium geology*, 17(1): 44–47.

Qin, B., Chen, Z.H. & Liu, Y.M. 2008. Swelling-shrinkage behaviour of Gaomiaozi bentonite. *Journal of Geotechnique Engineering* 30(7): 1005–1010.

Sun, D.A., Cui, H.B. & Sun, W.J. 2009. Swelling of compacted sand-bentonite mixtures. *Applied Clay Science* 43: 485–492.

Tang, C.S., Cui, Y.J. & Tang, A.-M. 2010. Remodeling COx mudstone in saturation during the evolution of the stress-strain. *Geotechnical Engineering* 32(8):1166–1171.

Xu, Y.F., Sun, D.A. & Dong, P. 2003. A vestigation in swelling characteristics of bentonite-sand mixture. *Journal of rock mechanics and engineering* 22 (3): 451–455.

Ye, W.M., Lai, X.L. & Wang, Q. 2014. An experimental investigation on the secondary compression of unsaturated GMZ01 bentonite. *Applied Clay Science* 21: 223–245

Ye, W.M., Chen, Y.G. & Chen, B. 2010. Advances on the knowledge of the buffer/backfill properties of heavily-compacted GMZ bentonite. *Engineering Geology*, 116(1): 12–20.

Zhang, H.Y., Cui, S.L. & Liu, J.S. 2010. Experimental study of swelling pressure of compacted bentonite-sand mixture. *Rock and Soil Mechanics* 31(10): 3087–3090.

Unsaturated Soil Mechanics—from Theory to Practice – Chen et al. (Eds)
© 2016 Taylor & Francis Group, London, ISBN 978-1-138-02921-7

Deformation characteristics and permeability of saturated bentonite-sand mixtures

W.J. Sun, Z.F. Wei, S.Q. Liu, C. Chen, L. Zhang & D.A. Sun
Department of Civil Engineering, Shanghai University, Shanghai, China

ABSTRACT: A series of one-dimensional consolidation tests by using oedometer were conducted on saturated compacted Gaomiaozi (GMZ) sodium bentonite-sand mixture. The permeability coefficient was calculated by Terzaghi's one-dimensional consolidation theory after the consolidation coefficient is obtained by the square root of time method. The indirect method derived from consolidation theory is feasible to calculate the permeability coefficient of low permeability clay like saturated bentonite. The test results show that the calculated permeability coefficient decreases with increasing vertical stress in elastoplastic stage, and they show the linear relationship in double logarithmic plot. Moreover, void ratio is a key parameter of permeability, and the calculated permeability coefficient decreases linearly with decreasing void ratio in semi-logarithmic plot for mixtures with the same sand mixing ratio. In addition, the relationships between permeability coefficient and void ratio under constant sand mixing ratio are shifted towards higher permeability with increasing sand mixing ratio. The montmorillonite void ratio is adopted in order to predict the permeability of saturated bentonite-sand mixture with different sand mixing ratios. The experimental data obtained from above indirect method and other permeability test data published in public illustrate that the permeability coefficient and montmorillonite void ratio presents a linear relationship in double-logarithmic plots for mixtures with a low sand mixing ratio. According to the above linear relationship, the saturated permeability of different types of bentonite-sand mixtures can be determined for a given initial dry density.

1 INTRODUCTION

Bentonite with a main component of montmorillonite is planned for using as a matrix material of engineered barrier in deep geological disposal system because of its high swelling property, low hydraulic conductivity, good self-sealing capacity, and excellent radionuclide sorption property, and etc.

Adding a certain proportion of the quartz sand to bentonite can efficiently enhance the compression performance, the thermal conductivity and material strength properties. Simultaneously, it can also improve the long-term stability and reduce the cost of the project (Chapuis, 1990; Kenney et al., 1992; Chen et al., 2010), and etc. Moreover, such bentonite-sand mixture has fewer amounts of swelling upon wetting and shrinkage upon drying than pure bentonite under the same dry density, which can avoid the destruction to repository itself by excessive swelling strain or swelling pressure and the reduction of the sealing function of barriers.

However, adding sand to bentonite can induce changes of permeability of engineered barrier or impervious barrier. Research has shown that under specific sand mixing ratio and dry density, the permeability coefficient of compacted bentonite-sand mixture may be lower than that of pure bentonite, and the more significant influence of sand properties on the permeability of mixtures will be with increasing the sand mixing ratio (Yong et al., 1986).

As the groundwater resets after construction of the disposal, the bentonite-sand mixtures reach a saturated state gradually due to wetting. Therefore, in performance assessment exercises concerning the long term behaviour of waste repositories it is a usual assumption to consider fully saturated bentonite-sand mixtures (Hoffman et al., 2007). The hydraulic property of bentonite-sand mixtures will change due to the variation of the microstructure during swelling (Komine, 2004) Whether the saturated hydraulic conductivity can satisfy the requirements of low permeability and make restrictions on nuclide migration or not is the premise to ensure the long-term safety of geological disposal repository. Therefore, in order to make long term evaluations on deep geological disposal project, it's of great significance to perform saturated permeability tests on the bentonite-sand mixtures with different sand mixing ratios and put forward the corresponding prediction model.

So far, a number of studies have been taken on the permeability and its model prediction of bentonite-sand mixtures by many researchers (e.g., Chapuis,

Table 1. Main physical indexes of GMZ-07 sodium bentonite and sand.

GMZ-07 Na bentonite	β (%)	G_s	w_L (%)	w_P (%)	I_P
	71	2.76	125	30	95
Sand	G_s'	D_{50} (mm)	C_u		
	2.65	0.34	1.97		

Note: β is montmorillonite content, G_s is specific density of bentonite, w_L is liquid limit, w_P is plastic limit, I_P is plastic index, G_s' is specific density of sand, D_{50} is average diameter, C_u is uniformity coefficient.

1990; Hoffman et al., 2007; Komine, 2008; Shirazi et al., 2010; Ye et al., 2010; Zhang et al., 2012; Tripathi, 2013; Sun et al., 2014).

Due to low permeability of high expansive soils such as bentonite, it is difficult and inaccurate to measure the saturated permeability coefficient of bentonite-sand mixtures by conventional falling head method. Therefore, a series of one-dimensional consolidation tests were conducted on saturated GMZ07 sodium bentonite-sand mixtures to study the deformation behaviour, meanwhile, the permeability coefficient was calculated using indirect methods derived from consolidation theory to study the permeability of bentonite-sand mixtures Moreover, a prediction model of permeability coefficient of mixtures with a low sand mixing ratio is preliminarily established to prepare for the permeability coefficient of bentonite-sand mixtures with various sand mixing ratios. Simultaneously, the study can provide experimental data and theoretical references for determining the content of sand needed for bentonite-sand mixtures used in deep geological disposal systems and waste landfill sites.

2 TESTING PROGRAM

2.1 *Testing materials*

GMZ-07 sodium bentonite and Fujian standard sand are used in the tests. The main mineral component of the bentonite is montmorillonite with the content about 71%, and associated minerals are some quartz, feldspar, calcite, very small amounts of kaolinite and illite in mass. The main physical indexes of GMZ-07 sodium bentonite and Fujian sand are listed in Table 1. The deionized water is used during the tests to minimize the influence of ion exchange as the bentonite has a very high cation exchange capacity. The bentonite and sand were firstly dried in the oven under 105°C for about 12 h before use.

2.2 *Testing method and procedure*

The pure bentonite or the bentonitesand mixtures with different sand mixing ratios in mass (0%, 30%, 50%, 70% and 80%) were compacted under the same initial dry densities of 1.5 g/cm^3 in consolidation rings. The ring's inner diameter is 61.8 mm and height is 20 mm. The specimen height is 1.5 mm, smaller than the ring's height in order to prevent the specimen expansion from the ring when swelling upon water uptake at low vertical pressure.

The specimen was carried out one-dimensional swelling deformation tests due to wetting. After swelling tests, compression tests on saturated specimens were conducted to study the deformation characteristics of saturated bentonite. Because of the low permeability of bentonite, it is difficult and inaccurate to measure the permeability conductivity of saturated bentonite by usual falling head method. Therefore, the saturated permeability coefficient was calculated by Terzaghi's one-dimensional consolidation theory after the consolidation coefficient was obtained by the square root of time method,

$$c_v = \frac{0.848\bar{h}^2}{t_{90}} \tag{1}$$

where c_v is the vertical consolidation coefficient (cm^2/s); $\bar{h}$ is the average drainage path length, and equal to half the average of initial height and final height at one vertical stress (cm); t_{90} is the value of time at degree of consolidation equal to 90%.

According to Terzaghi's one-dimensional consolidation theory, the saturated permeability conductivity can be calculated by the following relation:

$$k = c_v m_v \gamma_w \tag{2}$$

where k is the coefficient of permeability (cm/s); m_v is the coefficient of volume compressibility (m^2/kN); γ_w is the unit weight of water, $\gamma_w = 9.8$ kN/m^3. The indirect method derived from consolidation theory is feasible and suitable for the permeability coefficient measurement of low permeable saturated clays (Shirazi et al., 2010; Sun et al., 2014).

3 TEST RESULTS AND DISCUSSIONS

3.1 *Compression deformation characteristics of saturated GMZ sodium bentonite and sand mixtures*

After swelling tests, compression tests on five saturated specimens (No. 1 No. 5) were conducted. The sand mixing ratio, vertical stress during water uptake, initial dry density, void ratio after saturation and loading paths in compression test are listed in Table 2.

Except for the compression tests, swelling pressure tests and swelling deformation tests under different vertical stress (100, 200, 400, 800, 1600, 2475 kPa) were also conducted on several pure bentonite specimens with the initial dry density of 1.5 g/cm^3. The number corresponding to these swelling tests is No. 10, as shown in Table 2.

Table 2. Test parameters of specimens.

No.	α (%)	σ_v (kPa)	ρ_{d0} (g/cm^3)	e	*Remarks*
1	0	25	1.5	1.73	*Loading paths* (kPa)
2	30	25	1.5	1.16	50-100-200-400-800-
3	50	25	1.5	0.98	1600
4	70	12.5	1.5	0.83	
5	80	12.5	1.5	0.72	
6	0	–	1.5	–	*Swelling tests*

Note: α is sand mixing ratio; σ_v is vertical stress during water uptake; ρ_{d0} is initial dry density; e is void ratio after saturation

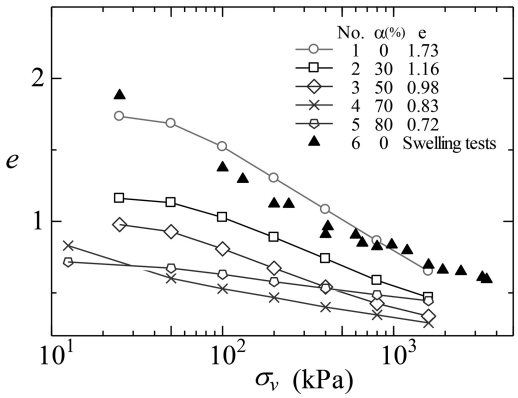


Figure 1. e vs. log σ_v relation for saturated GMZ sodium bentonite and sand mixtures.

Figure 1 shows the relationship between void ratio and permeability coefficient in semi-logarithmic plot of saturated GMZ sodium bentonite-sand mixtures with different sand mixing ratio. It can be seen that the void ratio decreases with the increase of sand mixing ratio, that is to say, the larger sand mixing ratio of soil specimen is, the easier soil specimen to be compacted. And when the sand mixing ratio reaches 80%, the void ratios are larger than those of No. 3 and No. 4 specimens at the higher stress. Simultaneously, the compression index decreases gradually with the increase of sand mixing ratio, which indicates that the influence of sand particles among the mixture becomes more significant. The main reason for the phenomenon is that the property of sand makes greater influence on the compression characteristics of mixtures with increasing sand mixing ratio, and the compression deformation is mainly resulted from the deformation of the sand skeleton.

In addition, two kinds of stress path tests were conducted on pure bentonite specimens, as shown in Table 2, No. 1 specimen was firstly immersed under low stress of 25 kPa, after swelling the vertical stress was loaded step by step. Meanwhile, the swelling pressure tests and swelling deformation tests were conducted on several specimens of No. 6. It can be seen from Figure 1 that the relations between void ratio and vertical stress of specimens experiencing two kinds of

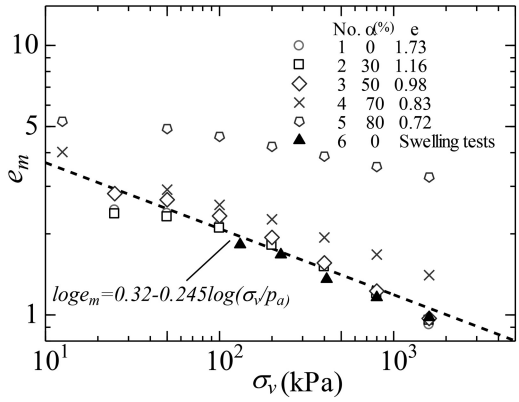


Figure 2. log e_m vs. log σ_v relationship for saturated GMZ sodium bentonite and sand mixtures.

stress path are almost similar, which illustrates that the change of pore is independent on the loading path.

Sun et al. (2009) introduced the concept of montmorillonite void ratio e_m to analyze the swelling characteristics of bentonite-sand mixtures. e_m can be defined as the ratio of water volume at saturation V_w to the volume of montmorillonite V_m,

$$e_m = \frac{V_w}{V_m} = \frac{m_w}{m_m} \cdot \frac{\rho_m}{\rho_w} \tag{3}$$

where V_w is the volume of water, V_m the volume of montmorillonite, ρ_w the density of water, ρ_m the grain density of montmorillonite, m_w is the water mass of saturated specimen after wetting, m_m the mass of montmorillonite.

The montmorillonite void ratio characterizes the amount of water absorbed by montmorillonite per unit volume after swelling reaches a stable state. The swelling tests revealed that the maximum amount of water absorbed by montmorillonite per unit volume was constant under a certain stress after the swelling reached a stable state. Moreover, it was independent of the initial dry density and the initial content of water or sand.

The relationship between the montmorillonite void ratio e_m and the vertical stress σ_v of pure bentonite and bentonite mixed with a low sand mixing ratio was a unique straight line in a double logarithmic plot, and the corresponding equation can be represented as follows:

$$\log e_m = a - b\log(\sigma_v / p_a) \tag{4}$$

where p_a is atmospheric pressure in kPa; σ_v is vertical stress in kPa; and a and b are the material parameters that can be determined from the swelling deformation tests under two different vertical stresses; and where a and b vary with types of bentonite. For GMZ sodium bentonite, $a = 0.32$ and $b = 0.245$ (Sun and Sun, 2012).

Figure 2 shows the relationship between the montmorillonite void ratio e_m and the vertical stress σ_v of

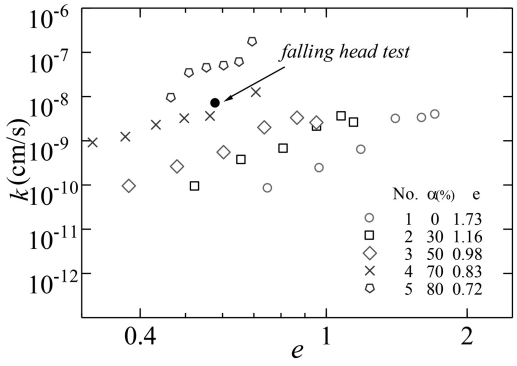


Figure 3. log e vs. log k relation for saturated GMZ sodium bentonite-sand mixture.

GMZ sodium bentonite-sand mixtures with different sand mixing ratios. The dotted line in the figure is the unique linear $e_m - \sigma_v$ relationship, that is, $\log e_m = 0.32 - 0.245 \log (\sigma_v / p_a)$. It can be seen that the test results No. 1, No. 2 and No. 3 specimens with the relative lower sand mixing ratio are in good agreement with the prediction line. While for the mixture with a 70% sand mixing ratio, the $e_m - \sigma_v$ linear relationship was satisfied at the lower vertical stress, but it did not follow the line any more when the vertical stress was beyond the certain value where a sand skeleton would form. And also for the mixture with a sand mixing ratio of 80%, the values of e_m were not at the line at the very beginning. Therefore, it can be concluded that a sand skeleton would form when the stress is more than the 'starting deviation stress' and the e_m value would deviate from the line. Moreover, the higher the sand mixing ratio in the mixture, the smaller the vertical stress at which deviation begins.

3.2 *Permeability of saturated GMZ sodium bentonite and sand mixtures*

The permeability coefficient can be obtained by the indirect method derived from consolidation theory mentioned in section 2.2 and it can be calculated by Eq. (2). In Eq. (2), the coefficient of volume compressibility m_v is expressed as $\Delta\varepsilon/\Delta p$, where $\Delta\varepsilon$ is the variation in volume strain under increment of vertical stress Δp. Therefore, the calculated permeability coefficient is the value under geometric mean of previous vertical stress and current vertical stress. Therefore, the calculated permeability coefficient is the value under 70.7, 141.4, 282.8, 565.7, 1131.4 kPa separately, corresponding to the vertical stresses in compression curves of 50, 100, 200, 400, 800, 1600 kPa in Figure 1. Moreover, the void ratio is also the value under geometric mean vertical stress.

Void ratio plays a leading role on permeability (Nishida et al., 1971; Shirazi et al., 2010; Zhang et al., 2012). Figure 3 shows the relationship between void ratio and saturated permeability coefficient in double logarithmic plot of bentonite-sand mixtures with different sand mixing ratios of 0%, 30%, 50%, 70% and 80% respectively. It can be seen that saturated permeability coefficient decreases with the decrease of void ratio under the same sand mixing ratio and they show a linear relationship in the double logarithmic coordinates, moreover, the saturated permeability coefficient decreases with the decrease of sand mixing ratio under the same void ratio.

For bentonite-sand mixtures with a high sand mixing ratio, the hydrated bentonite particles occupy the space between the sand particles and then swell to fill the void space. As the sand mixing ratio decreases, the content of bentonite increases, and the thickness of bentonite around the sand particles will increase, leading to more void spaces being filled with bentonite, and less space of water seepage (Abichou et al., 2002). Hence, the permeability coefficient of mixtures with a lower sand mixing ratio is lower under the same void ratio.

For the purpose of verification, the falling head permeability tests were conducted on the compacted specimen with sand mixing ratio of 70%, initial water content of 18% and initial void ratio of 0.58. The measured permeability of the specimen with void ratio of 0.58 is 7.0×10^{-9} cm/s, and the value is marked in Figure 3 by "•". It can be seen that experimental result using the falling head method is close to the calculated result of specimen with the same sand mixing ratio using the indirect method derived from consolidation theory. The comparison testifies that the indirect method is feasible and suitable to calculate the saturated permeability coefficient of low permeable clays.

In Figure 3, the vertical stresses corresponding to 6 data points of each mixture with certain sand mixing ratio were 35.3, 70.7, 141.4, 282.8, 565.7, 1131.4 kPa respectively according to the descend order of permeability coefficient. It can be seen that the permeability coefficients of mixtures with the lower mixing ratio (No. 1, No. 2 and No. 3) are almost similar under the same vertical stress even if the void ratios of mixture with different sand mixing ratios show great difference.

Accordingly, the relationship between saturated permeability coefficient and vertical stress is drawn in double logarithmic coordinates ($\log k - \log \sigma_v$) to mixtures with different sand mixing ratios, as shown in Fig. 4. It can be seen that for mixtures with lower sand mixing ratio saturated permeability coefficients of mixtures with different sand mixing ratios are almost similar under same vertical stress and they decrease linearly with the increase of vertical stress in log-log plot, which can be expressed as:

$$\log k = -8.54 - 1.51(\log \sigma_v / p_a) \tag{5}$$

While, with the increasing of sand mixing ratio, $k - \sigma_v$ relationship will not obey the line, as No. 4 specimen's relationship shown in Figure 4.

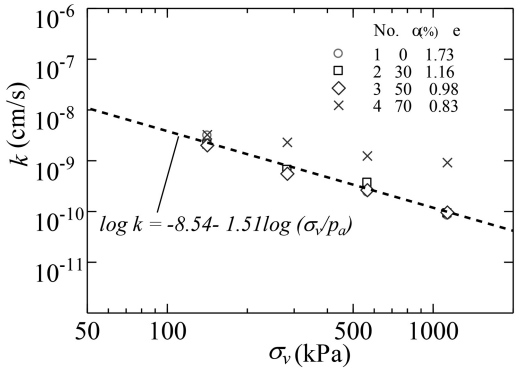


Figure 4. Relationship between saturated pemeability coefficient and vertical stress of GMZ sodium bentonite and sand mixtures.

3.3 *Normalization analysis of saturated permeability coefficient for bentonite-sand mixtures with different sand mixing ratios*

In an ideal sand-bentonite mixture, hydrated bentonite completely and uniformly fills all the pore spaces between sand particles, and permeant flows only through the hydrated bentonite. The sand particles are assumed to act as impervious inclusions (Kenney et al. 1992). The montmorillonite void ratio is the variable of saturated state, which is characterized as the amount of water absorbed by montmorillonite per unit volume after swelling reaches a stable state. Moreover, void ratio plays a leading role on permeability. Therefore, the montmorillonite void ratio is adopted to predict the permeability of saturated bentonite-sand mixtures with different sand mixing ratios.

Shirazi et al. (2010) conducted a series of one-dimensional consolidation tests on slurry Kunigel bentonite-sand mixtures with low sand mixing ratios, and calculated the permeability coefficient by indirect method derived from consolidation theory. Figure 5 (a) shows the $\log e$ vs. $\log k$ relationship of slurry mixtures, it can be seen that the permeability coefficient decreases with the decrease of sand mixing ratio, asunder the same void ratio. The montmorillonite void ratio can be obtained corresponding to void ratio in Figure 5(a), hence the $\log e_m$ vs. $\log k$ relationship of slurry mixtures can be obtained, as shown in Figure 5(b). It can be seen that the permeability coefficient and montmorillonite void ratio present the linear relationship in double-logarithmic plots.

The ideal sand-bentonite mixture in Kenney et al. (1992) refers to the mixture with a low sand mixing ratio. At this time, the permeability coefficient appears to be controlled by the permeability coefficient of bentonite. According to the above linear relationship, the saturated permeability of Kunigel bentonite and bentonite-sand mixtures with the low sand mixing ratio can be determined corresponding to a given initial dry density.

The relationship between montmorillonite void ratio and saturated permeability coefficient is drawn

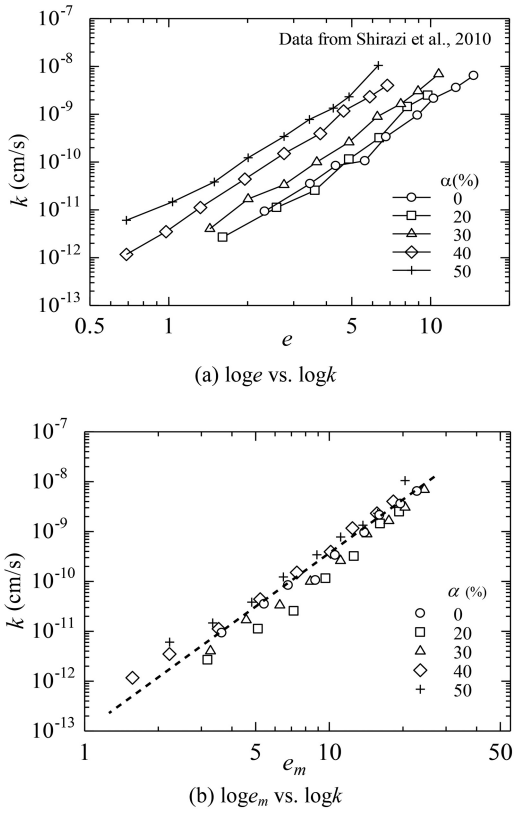


Figure 5. The relationship between permeability coefficient and deformation for slurry Kunigel bentonite-sand mixtures with low sand mixing ratios.

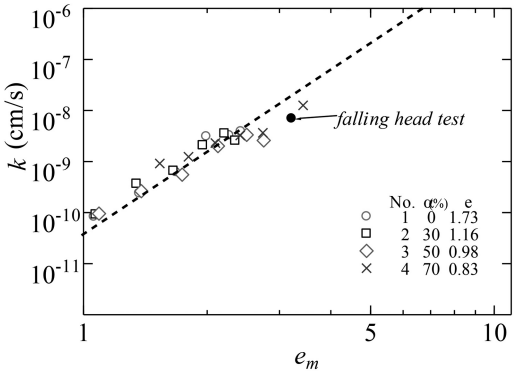


Figure 6. $\log e_m$ vs. $\log k$ relationship for saturated GMZ sodium bentonite-sand mixture.

in double logarithmic coordinates ($\log e_m - \log k$) to mixtures with different sand mixing ratios, as shown in Fig. 6. It can be seen that saturated permeability coefficients of mixtures with different sand mixing ratios are almost similar under same montmorillonite void ratio. That is to say, the relationship between the montmorillonite void ratio and the saturated permeability coefficient of bentonite-sand mixtures with low sand

mixing ratio is satisfied with the linear $\log e_m - \log k$ relationship, and the saturated permeability can be predicted according to the line.

4 CONCLUSIONS

A series of one-dimensional compression tests were conducted on saturated compacted GMZ-07 sodium bentonite-sand mixtures, and the deformation behaviour of saturated bentonite-sand mixtures are analyzed. Simultaneously, the permeability coefficients were obtained by the indirect method derived from consolidation theory and permeability of bentonite-sand mixtures were studied. The main conclusions are listed as follows:

1) The void ratio decreases with increasing the sand mixing ratio under the same vertical stress, and the compression index decreases gradually with increasing the sand mixing ratio.
2) For pure bentonite and bentonite-sand mixtures with a low sand mixing ratio, the relationship between montmorillonite void ratio and vertical stress can be represented as a unique line in a double logarithmic plots, however, for mixtures with a high sand mixing ratio, the above relationship deviates from the line when the stress is larger than the 'starting deviation stress'. Moreover, the higher the content of sand in the mixture, the smaller the vertical stress at which deviation began.
3) Void ratio plays a leading role on permeability, the saturated permeability coefficient decreases linearly with the decrease of void ratio in the double logarithmic coordinates for mixtures with the same sand mixing ratio, and the permeability coefficient decreases with the decrease of sand mixing ratio under the same void ratio.
4) The permeability coefficient versus montmorillonite void ratio presented the linear relationship in double-logarithmic plots and the saturated permeability coefficient can be determined for mixture with a given initial dry density.

ACKNOWLEGEMENTS

The authors appreciate the financial support of the National Sciences Foundation of China (Grant No. 41102163) and the Open Research Fund of State Key Laboratory of Geomechanics and Geotechnical Engineering, Institute of Rock and Soil Mechanics, Chinese Academy of Sciences (Grant No. Z013008).

REFERENCES

Abichou, T., Benson, C.H., Edil, T.B. 2002. Micro-structure and hydraulic conductivity of simulated sand-bentonite mixtures. *Clays and Clay Minerals*, 50(5): 537–545.

Chapuis, R.P. 1990. Sand-bentonite liners: Predicting permeability from laboratory test. *Canadian Geotechnical Journal*, 27(1): 47–57.

Chen, Y.G., Ye, W.M., Wang, Q., Chen, B. 2010. Influence factors of sand-bentonite mixtures on hydraulic conductivity. *Journal of Engineering Geology*, 18(3): 357–362.

Hoffman, C., Alonso, E.E., Romero, E. 2007. Hydro-mechanical behaviour of bentonite pellet mixtures. Physics and Chemistry of the Earth, 32: 832–849.

Kenney, T., Vanveen, W., Swallow, M., Sungaila, M. 1992. Hydraulic conductivity of compacted bentonite-sand mixtures. *Canadian Geotechnical Journal,* 29(3): 364–374.

Komine, H. 2004. Simplified evaluation on hydraulic conductivities of sand-bentonite mixture backfill. *Applied Clay Science*, 26(1–4): 13–19.

Komine, H. 2008. Theoretical equations on hydraulic conductivities of bentonite-based buffer and backfill for underground disposal of radioactive wastes. *Journal of Geotechnical and Geoenvironmental Engineering*, 134(4): 497–508.

Nishida, Y., Koike, H., Nakagawa, S. 1971. Coefficient of permeability of highly plastic clays. *Proceedings of 4th Budapest Conference on Soil Mechanics and Foundation Engineering*: 219–224.

Shirazi, S.M., Kazama, H., Salman, F.A., et al. 2010. Permeability and swelling characteristics of bentonite. *International Journal of the Physical Sciences*, 5(11): 1647–1659.

Sun, D.A., Cui, H.B., Sun, W.J. 2009. Swelling of compacted sand–bentonite mixtures. *Applied Clay Science*, 43(3): 485–492.

Sun, W.J., Liu, S.Q., Sun, D.A., et al. Swelling characteristics and permeability of bentonite[C]. Unsaturated Soils: Research and Applications – Proc 6th International Conference on Unsaturated Soils, UNSAT 2014, 2: 1211–1217.

Sun, W.J., Sun, D.A. 2012. Comparison of swelling characteristics between Gaomiaozi Ca-bentonite and Na-bentonite, 4th International Conference on Problematic Soils: 243–250. Wuhan, 2012.9.21-23.

Tripathi, K.K. 2013. Hydraulic Conductivity Prediction of Saturated Sand-Bentonite Mixtures. *Geotechnical Geological*, 31: 581–591.

Ye, W.M., Chen, Y.G., Chen, B., et al. 2010. Advances on the knowledge of the buffer/backfill properties of heavily-compacted GMZ bentonite. *Engineering Geology*, 116: 12–20.

Yong, R.N., Boonsinsuk, P., Wong, G. 1986. Formulation of backfill material for a nuclear fuel waste disposal vault. *Canadian Geotechnical Journal*, 23: 216–228.

Zhang, M., Zhang, H.Y., Cui, S.L., et al. 2012. Engineering properties of GMZ bentonite-sand as buffer/backfilling material for high-level waste disposal. *European Journal of Environmental and Civil Engineering*. 16(10): 1216–1237.

Unsaturated Soil Mechanics—from Theory to Practice – Chen et al. (Eds)
© 2016 Taylor & Francis Group, London, ISBN 978-1-138-02921-7

Investigation on swelling-shrinkage behavior of compacted expansive soils during wetting-drying cycles

N.F. Zhao
Key Laboratory of Geotechnical and Underground Engineering of Ministry of Education, Tongji University, Shanghai, China

W.M. Ye, B. Chen & Y.G. Chen
Key Laboratory of Geotechnical and Underground Engineering of Ministry of Education, Tongji University, Shanghai, China
United Research Center for Urban Environment and Sustainable Development, the Ministry of Education, Shanghai, China

ABSTRACT: Geotechnical problems induced by the effects of wetting-drying cycles related to the seasonal climate or environmental variations are widely spread in the expansive clay areas. Based on the double-structure properties, volumetric behavior of compacted expansive soils was discussed and corresponding influence factors were analyzed. The SI and SD suction yield lines were introduced and corresponding hardening law was built. Then, under the framework of the BBM model, a new constitutive model was developed for the description of the elastic and plastic deformation during the wetting and drying processes. Verifications have been conducted using some tests results from literature. Results show that the constitutive model proposed in this work has less parameters and high accuracy.

1 INTRODUCTION

Problems including heave-subsidence (related to the seasonal climate or environmental variations) induced deflections of building foundations in the expansive clay areas (Chen 1988), as well as the cyclic volumetric change, cracking and even invalidation of compacted bentonite based artificial barrier system in a deep geological repository (Alonso et al. 2005; Alonso et al. 2011; Ye et al. 2011) etc. Related to wetting-drying processes commonly exist in geotechnical fields. Therefore, investigation on the swelling-shrinkage behavior of compacted expansive clay subjected to the drying-wetting cycles has great theoretical and practical significances.

Following this concept, for estimation of the swelling-shrinkage behavior of expansive clay, lots of laboratory tests have been conducted. Most of these tests can be clarified into two main categories, alternately soaked-dried tests (Basma et al. 1996; Tripathy et al. 2002) and cyclic suction-controlled tests (Alonso et al. 2005; Airò Farulla et al. 2010). Alternately soaked and dried tests are mainly conducted for simulating extreme and severe environmental conditions, while cyclic suction-controlled tests are conducted for describing moderate environmental conditions. The following consensuses can be drawn from both of the two categories of tests: (1) The magnitude of swelling deformation increases with the increase of water moisture or the decrease of suction. Conversely, the magnitude of shrinkage deformation increases with the decrease of water moisture or the increase of suction. (2) The difference between swelling and shrinkage deformation of expansive clay under wetting-drying cycles reaches its maximum value in the first cycle, then, it decreases with the increase of the wetting-drying cycles. (3) Before the equilibrium state, the current accumulated (total) deformation is expansion or shrinkage depends on soil properties, initial conditions, vertical load or confining pressure, etc. (4) The soil deformation will reach an equilibrium state after experiencing several wetting-drying cycles.

Based on experimental results, some constitutive models for expansive clay were proposed by many researchers. The BExM model proposed by Gens and Alonso (1992), Alonso et al. (1999) and Alonso et al. (2005) for expansive clay has been received wide acceptance. Under the framework of this model, Alonso et al (2011), Gens et al. (2011), developed models with consideration of coupling effects of thermal, mechanical and hydraulic behavior. The BExM model was based on the consideration of two structure levels of expansive clays: the micro-structural level at which swelling of active minerals takes place, and the micro-structural level responsible for major structural rearrangement (Alonso et al. 1999). The BExM model includes definitions of behavior of

the macro-structural level, behavior of the micro-structural level and mechanical coupling between the two structural levels. The macro-structural volumetric strain was calculated by the BBM model, which was developed by Alonso et al. (1990) for description of lower plasticity unsaturated soils. The micro-structural volumetric strain was calculated by the porous media non-linear elastic theory or the double layer theory. The coupling deformation was calculated by two coupling functions (fI and fD) defined by Alonso et al. (1999). However, double-structure models are burdened with complexity and parameters about macro-structural and micro-structural deformation that are difficult to obtain (Wang & Wei 2014). On one hand, the micro-structural level deformation is so difficult to observe through conventional tests and some micro-structure parameters have to be assumed. On the other hand, the two coupling functions are also difficult to be determined. Therefore, the application of the BExM model was seriously limited because of its complexity and difficulty in obtaining of parameters.

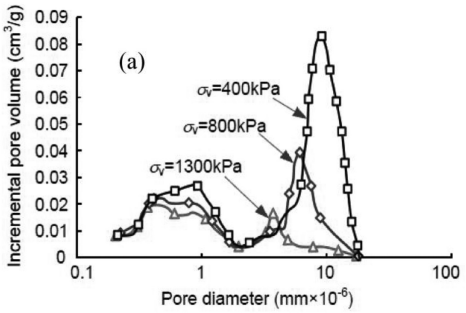
Due to the problems mentioned above, the framework of double-structure model could be simplified by assuming that the role of macroporosity in swelling of dense compacted soils could be neglected (Cui et al. 2002; Koliji et al. 2008). Following this concept, they developed a global mechanical model based on the microstructure of the soil. However, with consideration of the role of macroporosity, a practical constitutive model was proposed for compacted expansive clays by Wang and Wei (2014), which has less parameters with definite physical significances. Unfortunately, both the analyzing procedure of the swelling-shrinking deformation and the determination of model parameters during drying-wetting cycles are all relatively complicated. Furthermore, this model has not been verified for simulating more complex drying-wetting cyclic path.

Based on the analyses of the swelling-shrinkage behavior of expansive clay under cyclic wetting-drying processes and their main influencing factors, a model was proposed under the framework of the BBM model. The SI and SD suction yield lines were introduced for describing elastic and plastic deformation under the wetting and drying processes. A new hardening law of SI and SD suction yield lines was proposed. Using the tests results from three articles, verifications have been conducted. Results showed that the proposed model has less parameters and high accuracy.

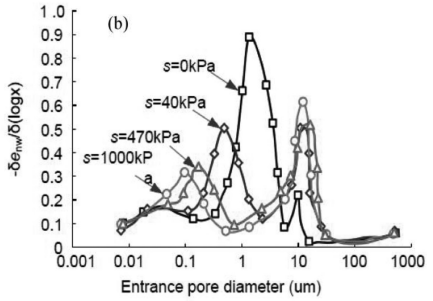
2 SWELLING-SHRINKAGE BEHAVIOR

2.1 *Influence of the net stress and suction on the structure of expansive soils*

Expansive clay has two distinct structures, i.e. micro-structure and macro-structure, its deformation depends on the net stress and suction experienced (Alonso et al. 1990; Alonso et al. 1992). Under constant suctions, the volume change on the macro-structure level could be affected by the net stress,



(a) Pore size distribution of compacted soil after static compaction to different static pressures (Sivakumar et al. 2006).



(b) Development of pore size distribution of compacted London clay with wetting (Monroy et al. 2010)

Figure 1. Pore size distribution of compacted clay.

while that on the micro-structure level would almost not (Fig. 1b) (Sivakumar et al. 2006). Therefore, the influence of the net stress on the micro-structural level could be neglected. However, under the constant net stress, the volume change both on the macro-structure level and the micro-structural level could be affected by suction (see Fig. 1a) (Monroy et al. 2010). Distribution of the macroporosity and the microporosity changes obviously with decreasing suction, which leads to the double porosity structure faded to a single one. Therefore, suction effects on micro-structure and micro-structure of the test soil should be concerned. The electron microscope scanning test results show that the deformation of aggregate on the micro-structure level has almost reversibility (Airò Farulla et al. 2010). However, on the macrostructure level, some aggregates will break into smaller aggregates due to the swelling on wetting procedure (Katti et al. 2001), while some aggregates will converge due to the shrinkage on drying procedure. The break or converging of the soil aggregates will induce the slipping and reorientation of soil particles and result in the plastic deformation (Prashant & Penumadu, 2007). As the wetting-drying cyclic progress continues, the number of soil aggregates decreases and the double porosity structure of compacted expansive clay fades (Ye et al. 2011). Consequently, the plastic deformation of the expansive clay decreases as the wetting-drying cycles increase.

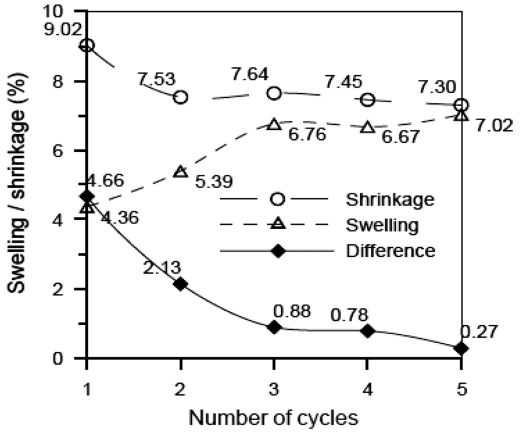


Figure 2. Evolution of swelling and shrinkage with the number of controlled-suction cycles ($\sigma_v = 196$ kPa). (Alonso et al. 2005).

Therefore, the effects of the net stress would govern the macro-structure level deformation, while the effects of suction would govern the deformation both on the macro-structure level and micro-structure level. On the micro-structure level, suction induces elastic strain; while on the macro-structure level, suction induces not only elastic strain, but also plastic strain. Following this concept, in this work, suction induced deformation is considered as the elastic deformation and the plastic ones.

2.2 *Volumetric changes on drying and wetting procedures*

Measured typical evolution of swelling and shrinkage deformation under the controlled-suction cycles under $\sigma_v = 196$ kPa was presented in Fig. 2 (Alonso et al. 2005). Fig. 2 clearly shows that the shrinkage deformation is larger than the swelling one in each cycle, while the difference decreases as the cycles increase. After experienced five drying and wetting cycles, the soil tended towards an "elastic" (reversible) state.

It also means that the SI and SD yield lines exist in the p-s stress space during the drying-wetting cycles, the SI yield line is activated as suction increases during the drying procedure, the SD yield line is activated as suction decreases during wetting procedure. It will be seen from this that the evolution law of SI controls the shrinkage elastic strain and plastic strain with suction increases, the evolution law of SI controls the wetting elastic strain and plastic strain with suction decrease.

3 A CONSTITUTIVE MODEL FOR EXPANSIVE SOILS SUBJECTED TO WETTING AND DRYING CYCLES

3.1 *Elastic and plastic strain*

The volumetric strain is composed of swelling strain and shrinkage strain, which includes the elastic swelling strain and the plastic swelling strain, the elastic shrinkage strain and the plastic shrinkage strain, respectively (Eq (1)).

$$\begin{cases} \varepsilon_{v-} = \varepsilon_{v-}^{e} + \varepsilon_{v-}^{p} \\ \varepsilon_{v+} = \varepsilon_{v+}^{e} + \varepsilon_{v+}^{p} \end{cases} \tag{1}$$

Here, ε_{v-} is the total swelling strain, ε_{v-}^{e} is the elastic swelling strain, ε_{v-}^{p} is the plastic swelling strain; ε_{v+} is the total plastic strain, ε_{v+}^{e} is the elastic shrinkage strain, ε_{v+}^{p} is the plastic shrinkage strain. Positive sign represents the shrinkage strains and the negative sign represents swelling strains.

Referred to the volumetric expression of the BBM model, equations in Eqs (2) and (3) were proposed in this work for the calculation of the increments of elastic or plastic deformations

$$\begin{cases} d\varepsilon_{vs-}^{e} = \dfrac{\kappa_s}{v}\dfrac{ds}{(s + p_{at})} \\ d\varepsilon_{vs-}^{p} = \dfrac{\lambda_{s-} - \kappa_s}{v}\dfrac{ds_{I0}}{(s_{I0} + p_{at})} \end{cases} \tag{2}$$

$$\begin{cases} d\varepsilon_{vs+}^{e} = \dfrac{\kappa_s}{v}\dfrac{ds}{(s + p_{at})} \\ d\varepsilon_{vs+}^{p} = \dfrac{\lambda_{s+} - \kappa_s}{v}\dfrac{ds_{D0}}{(s_{D0} + p_{at})} \end{cases} \tag{3}$$

Here, parameters $d\varepsilon_{vs-}^{e}$ and $d\varepsilon_{vs-}^{p}$ are the elastic swelling strain and the plastic swelling strain, respectively. Parameters $d\varepsilon_{vs+}^{e}$ and $d\varepsilon_{vs+}^{p}$ are the elastic shrinkage strain and the plastic shrinkage strain, respectively. Parameters s_{I0} and s_{D0} are the initial yield stresses, respectively. Parameter κ_s is the elastic compression coefficient or the rebound coefficient induced by suction changes. Parameters λ_{s-} and λ_{s+} are the plastic coefficients corresponding to the drying or wetting processes, respectively. Parameter p_{at} is the air pressure.

3.2 *The framework of this model*

(1) yield function

The yield lines of SI and SD in the e-p-s stress space can be expressed as

$$\begin{cases} f_D = s_D \\ f_I = s_I \end{cases} \tag{4}$$

Here, S_I and S_D are the initial suction yield stresses.

3.3 *The hardening rule*

The initial yield curves of SI and SD for unsaturated expansive clay depend on the initial suction state. During the drying or wetting processes, the yield curves of SI and SD will move along the drying or wetting path

correspondingly and their locations in the p-s stress space can be determined by the next formulations:

$$\begin{cases} de_{-} = \kappa \ln\left(\dfrac{s_0}{s_1}\right) + \left(\lambda_{s-} - \kappa\right) \ln\left(\dfrac{s_2 + p_{at}}{s_0}\right) \\ de_{+} = \kappa \ln\left(\dfrac{s_0}{s_2 + p_{at}}\right) + \left(\lambda_{s+} - \kappa\right) \ln\left(\dfrac{s_1}{s_0}\right) \end{cases} \tag{5}$$

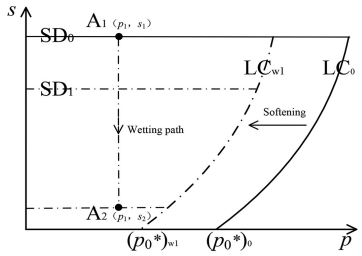
Where, parameter s_1 and s_2 are the maximum and minimum suction values settled for the wetting-drying (suction-controlled) cyclic tests, respectively. Parameter s_0 is the yield suction of the soil after experiencing the wetting/drying process. The other parameters are the similar to that mentioned above.

The working mechanism of the hardening rule was given schematically in Fig. 3. At the beginning of the cyclic suction-controlled tests, the specimen was consolidated at a constant net stress (p_1) and controlled to an initial suction (s_1) (Fig. 3(a)). Then the specimen was suction-controlled from A1 to A2. Correspondingly, according to the new hardening rules, the suction decrease yield line moves from SD_0 to SD_1 (Fig. 3(b)). After that, the first drying procedure was suction controlled from A2 to A1 with the initial suction increase yield line moved from SI_0 to SI_1 (Fig. 3(a)). And then, the second wetting procedure was suction-controlled from A1 to A2, as shown in Fig. 3(c). During which, the reversible volumetric strain was recorded when the suction decreased from the point A1 to A3 and the irreversible volumetric strain was observed for the suction decreasing from the point A3 to A2. This process was followed by the second drying procedure with suction increased from A2 to A1 and the initial suction-increasing yield curve moved from SI_1 to SI_2, as shown in Fig. 3(d). During which, when the specimen was suction-controlled from A2 to A1, the reversible volumetric strains was recorded for suction increased from A2 to A4 and the irreversible volumetric strain was obtained, when suction changed from A4 to A1. After experiencing several wetting and drying cycles, the volumetric deformation on wetting-drying process becomes approximate reversible as depicted in Fig. 3(e).

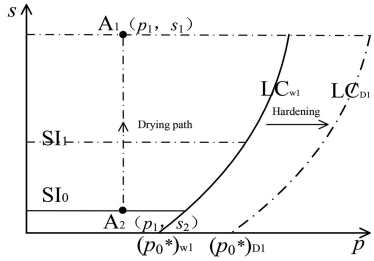
Therefore, the volumetric deformation on wetting-drying process of the specimen can be described by the variations of SI or SD yielding lines (Fig. 3). This indicates that the model proposed in this work can describe the volumetric change behavior of expansive clay under wetting-drying courses.

3.4 *Parameters determination*

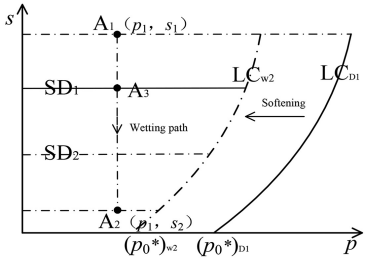
There are 9 parameters for computing the swelling-shrinkage strain in proposed model in this work. Addition to the parameters of the BBM model, parameters related to the suction variations and the SI or SD yield line should be determined. The elastic deformation coefficient (κs) could be determined using the equilibrium (final) stage of the specimen experienced several drying-wetting cycles. The plastic shrinkage



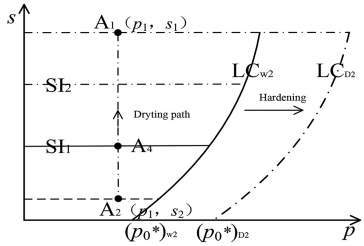
(a) Evolution of the yield lines in the first wetting process



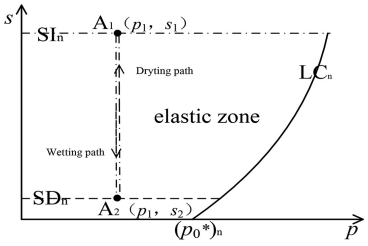
(b) Evolution of the yield lines in the first drying process



(c) Evolution of the yield lines in the second wetting process

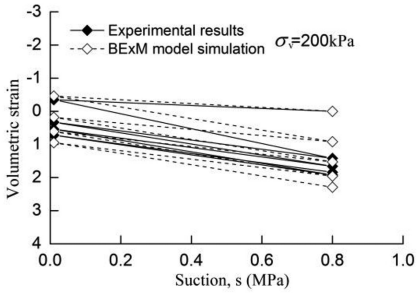


(d) Evolution of the yield lines in the second drying process

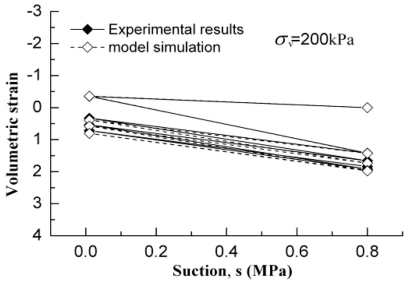


(e) Evolution of the yield lines experiencing wetting and drying processes

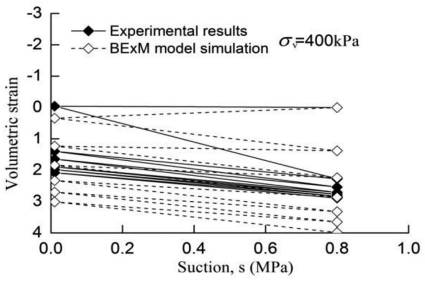
Figure 3. Schematic mechanism of the proposed hardening law.



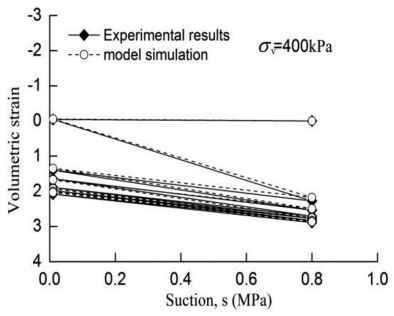
a. Comparison of results calculated by the BExM model to the measured ones (σ_v=200kPa)



b. Comparison between the results of the proposed model and the measured ones (σ_v=200kPa)



c. Comparison of results calculated by the BExM model to the measured ones (σ_v=400kPa)



d. Comparison of results calculated by the BExM model to the measured ones (σ_v=400kPa)

Figure 4. Simulation of the test results (Airò Farulla et al. 2010).

Table 1. Parameters of proposed model.

Model	Parameter	Airò Farulla et al. 2010
BBM	σ_v*/kPa	400
	p^c/kPa	180
	$\lambda(0)$	0.083
	κ	0.03
	β/MPa^{-1}	2.08
	r	0.751
The proposed model	λ_{SI}	0.0002–0.01
	λ_{SD}	0.008–0.01
	κ_s	0.003–0.01

deformation coefficient (λsi) could be determined by the first drying path. The plastic swelling deformation coefficient (λsd) could be obtained from the first wetting path. These parameters are not a constant, which are closely related to the initial dry density and the net stress.

4 MODEL VERIFICATION

For verification of the model proposed in this work, results of cyclic wetting and drying tests of expansive clays reported by Airò Farulla et al. (2010) were simulated. Meanwhile, the calculated results were also compared to that predicted by the BExM model. Airò Farulla et al. (2010) reported the results of cyclic suction-controlled tests on a kaolinitic–illitic clay. For the properties of the clay tested, the liquid limit is 58%, the plasticity index is 30% and the specific gravity is 2.78.

For preparation of the specimen, the compacted specimen was suction-controlled to an initial suction of 800 kPa. Then, the cyclic-suction controlled procedure of 10 kPa to 800 kPa was applied under the vertical net stresses 100 and 200 kPa, respectively. All the vertical net stresses applied are lower than the preconsolidation stress of the soil at its saturated state (650 kPa).

Results simulated by the model proposed in this work and the BExM model were presented and compared to the measured ones in Fig. 4. Figs. 4(a)∼4(b) show that results of the two test (tested under the vertical net stresses 200 and 400 kPa), the results simulated by the model proposed in this work could fit better to the measured ones than the BExM model did.

5 CONCLUSION

The swelling-shrinkage volumetric strains of the compacted expansive soils under the wetting-drying cycles were discussed and the main influencing factors were briefly analyzed. Based on this, a constitutive model was proposed under the framework of the BBM model. Some main conclusions can be drawn as follows.

Based the swelling-shrinkage behavior of the expansive clay under cyclic wetting-drying processes, the total volumetric deformation was divided into the elastic and the plastic ones. The plastic deformation was only recorded at the macro-structural level, while the elastic deformation was observed both at macro- and micro-structural levels.

The SI and SD suction yield lines were introduced and corresponding hardening law was built. Based on these, a new constitutive model was developed for the description of the elastic and plastic deformation during the wetting and drying processes.

Verification results show that the constitutive model proposed in this work has less parameters and high accuracy.

REFERENCES

Airò Farulla, C., Ferrari, A., and Romero, E. 2010. Volume change behaviour of a compacted scaly clay during cyclic suction changes. Canadian Geotechnical Journal, 47(6): 688–703.

Alonso, E.E., Gens, A., and Josa, A. 1990. A constitutive model for partially saturated soils. Géotechnique, 40(3): 405–430.

Alonso, E.E., Vaunat, J., and Gens, A. 1999. Modelling the mechanical behaviour of expansive clays. Engineering Geology, 54: 173–183.

Alonso, E.E., Romero, E., Hoffmann, C., and García-Escudero, E. 2005. Expansive bentonite-sand mixtures in cyclic controlled-suction drying and wetting. Engineering Geology, 81: 213–226.

Alonso, E.E., Romero, E., and Hoffmann, C. 2011. Hydromechanical behaviour of compacted granular expansive mixtures: experimental and constitutive study. Géotechnique, 61(4): 329–344.

Basma, A.A., Al-Homoud, A.S., Husein Malkawi, A.I., and Al-Bashabsheh, M.A. 1996. Swelling-shrinkage behavior of natural expansive clays. Applied Clay Science, 11(2): 211–227.

Cui, Y.J., Yahia-Aissa, M., and Delage, P. 2002. A model for the volume change behavior of heavily compacted swelling clays. Engineering Geology, 64: 233–250.

Gen, A., and Alonso, E.E. 1992. A framework for the behavior of unsaturated expansive clays. Canadian Geotechnical Journal, 29(6): 1013–1032.

Gens, A., Valleján, B., Sánchez, M., Imbert, C., Villar, M.V., and Van Geet, M. 2011. Hydromechanical behaviour of a heterogeneous compacted soil: experimental observations and modelling. Géotechnique, 61(5): 367–386.

Katti, D.R., and Shanmugasundaram, V. 2001. Influence of swelling on the microstructure of expansive clays. Canadian Geotechnical Journal, 38 (1): 175–182.

Koliji, A., Vulliet, L., and Laloui, L. 2008. New basis for the constitutive modelling of aggregated soils. Acta Geotechnica, 3(1): 61–69.

Monroy, R., Zdravkovic, L., and Ridley, A. 2010. Evolution of microstructure in compacted London clay during wetting and loading. Géotechnique, 60(2): 105–119.

Nowamooz, H., and Masrouri, F. 2010. Influence of suction cycles on the soil fabric of compacted swelling soil. Comptes Rendus Geoscience, 342: 901–910.

Nowamooz, H., Mrad, M., Abdallah, A., and Masrouri, F. 2009. Experimental and numerical studies of the hydrome-chanical behaviour of a natural unsaturated swelling soil. Canadian Geotechnical Journal, 46(4): 393–410.

Prashant, A., Penumadu, D. 2007. Effect of micro fabric on mechanical behavior of kaolin clay using cubical true triaxial testing. ASCE Journal of Geotechnical and Geoenvironmental Engineering, 133(4): 433–444.

Sivakumar, V., Tan, W.C., Murray, E.J., and McKinley, J.D. 2006. Wetting, drying and compression characteristics of compacted clay. Géotechnique, 56(1): 57–62.

Tripathy, S., Subba Rao, K.S., and Fredlund, D.G. 2002. Water content-void ratio swell-shrink paths of compacted expansive soils. Canadian Geotechnical Journal, 39(4): 938–959.

Wang Gang, Wei Xing. 2014. Modeling swelling- shrinkage behavior of compacted expansive soils during wetting-drying cycles. Canadian Geotechnical Journal, 47(6): 688–703.

Ye, W.M., N.C. Borrell, J.Y. Zhu, B. Chen, Y.G. Chen. 2014. Advances on the investigation of the hydraulic behaviour of compacted GMZ bentonite. Engineering Geology, 169: 41–49.

Ye, W.M., Wan M., Chen B. 2011. Micro-Structural behaviors of densely compacted GMZ01 bentonite under drying/wetting cycles. Chinese Journal of Geotechnical Engineering. 33(8): 1173–1177 (in Chinese).

Unsaturated Soil Mechanics—from Theory to Practice – Chen et al. (Eds)
© 2016 Taylor & Francis Group, London, ISBN 978-1-138-02921-7

Cracks' evolution characteristics of remolded expansive soils in the soaking and loading process

Z.H. Yao
Engineering College, Air Force Engineering University, Xi'an, China

Z.H. Chen
Department of Civil Engineering, Logistical Engineering University, Chongqing, China
Civil Engineering College, Guilin Technology University, Guilin, China

W. Li & L.H. Su
Engineering College, Air Force Engineering University, Xi'an, China

Q.Q. Miao & J.H. Zhang
Department of Civil Engineering Logistical Engineering University, Chongqing, China

ABSTRACT: In order to research the characteristics of cracks' evolution of remolded expansive soils, the tests of wetting and drying cycles were firstly carried out with remolded expansive soil in free state, then the triaxial soaking tests under certain confining pressure and deviatoric stress and hydrostatic compression tests controlled certain suction were done by using of CT (Computer Tomography) technology to get meso-structural changes on cracks. The test results indicate that both wetting and drying cycles induce the production and closure of the cracks. In the triaxial soaking tests, the cracks tend to close, and the closure degree relates with the stress state. The volume changes is formed from three distinct phases which decreases firstly, then increases rapidly because of swell effect, and lastly decreases with the expansive pressure releasing and modulus reducing. During the hydrostatic compression process, the cracks of expansive soil, only the effect of external load would evolve for void with the growths of load, but don't close entirely. Under the impact of both water and external load, the cracks closure level is better than that only external load. Water is the key point to infect the production and closure of cracks, more attention would give for water producing effects on expansive soil projects.

1 INTRODUCTION

The expansive soil has the properties of being cracking swell-shrink and over-consolidation. Expansive soil is a typical kind of unsaturated soil with significant structural characteristics which influences the deformation and yield of the soil. The swell-shrink characteristic is the important inherent factor inducing cracks. Most failures of expansive soil projects are water-linked, and the cracks have provided an easy path for the water infiltration (Bao 2004, Wang et al. 2005) There are quite a few literatures focusing on the study of cracks caused by wetting and drying cycle. Using the CT technology, Lu et al. (2002) studied the evolution of cracks of Nanyang (in China) remolded expansive soil after several drying-wetting cycles, but did not study and analyze the evolution path of cracks of the soil samples in the process of soaking. Liu et al. (1994) and Yuan (2003) carried out the soaking test on expansive soil, but they did not deal with the evolution process of cracks after soaking. Lei et al. (2005) pointed out that, under certain confining pressure, the cracks of (Ankang city, in China) expansive soil would gradually grow, develop and finally cut through. However, they could not make the quantitative analysis of the evolution of cracks because of only one sample.

Using the CT as a tool, this paper makes a real-time observation on the meso-scale evolution of cracks during the wetting and drying cycle, and performs a series of triaxial soaking tests on the expansive soil with cracks created by the wetting and drying cycles, so as to study the behavior of the crack of expansive soil in the process of soaking and make a quantitative analysis. In order to understand the structural evolution of expansive soils to its constitutive relationship, hydrostatic compression test controlled suction was carried out with CT-triaxial apparatus for remolded expansive soil which was suffered multi-drying-wetting cycles in advance to form certain degree of damage of soil structure. The characteristics of cracks influenced by external load were researched from meso-scale.

Compared with soaking and loading procure, cracks evolution of remolded expansive soils would be learned from meso-scale on the condition of water



Figure 1. CT-triaxial apparatus of Logistical Engineering University.

and load. This paper' results would provide some test basis for cracks' evolution characteristics of remolded expansive soils.

2 EXPERIMENTAL PROCEDURE

2.1 *Sample preparation and test equipment*

The expansive soil used for test was derived from the channel slope of South-to-North water diversion project at Taocha, Henan province, China. The diameter and height of remolded sample are 3.91 mm and 80 mm respectively. The initial index of the samples are listed as follows: specific density d_s is 2.71, dry density ρ_d is 1.55 g/cm^3, water content w is 24.70%, saturation ratio S_r is 88.58%, and void ratio e is 0.76. The test was carried out in Logistical Engineering University (see Fig. 1).

The test system consists of a CT machine, a multifunctional triaxial apparatus of unsaturated soil invented and upgraded by Chen (2001, 2007) and a soaking facility created by Zhu (2008). The loading procedure is controlled by a stepping motor, which also decides the shear rate. The soaking adverse pressure and water amount are regulated by a GDS pressure-volume controller.

2.2 *Test scheme*

There are 4 samples in triaxial soaking test and one sample in hydrostatic compression test. All the tests include two stages. Firstly, the prepared samples go through wetting and drying cycle, in order to produce the initial cracks, and then CT-triaxial soaking tests are carried out. The CT number ME and variance SD can be obtained and ME and SD respectively represent average density and density diversity of soil samples.

2.2.1 *Wetting and drying cycles*

The samples were firstly dried for 24 hours in a thermostat drier, and then the initial degree of saturation were controlled at the same value (88.58%) using the Water Film Diversion Method. Subsequently, the humidified samples were placed in a moist jug for 72 hours. During this period, the samples were overturned every 24 hours, so that the moisture would get a homogeneous distribution.

Table 1. Initial parameters and stress states of the sample before soaking.

Sample number	Dry density g/cm^3	Water content %	Ambient pressure kPa	Deviator stress kPa
1#	1.78	4.74	50	50
2#	1.79	4.61	50	100
3#	1.77	4.70	100	50
4#	1.76	4.66	100	100

Taking the end of the humidification period as the initial state, the first wetting and drying cycle was ended when the first drying process was finished. And the following humidification and dehydration of the sample was noted as the second wetting and drying cycle, by analogy. In light of the test requirements and the developments of the cracks, 3 wetting and drying cycles and 6 scanning procedures were carried out, so the development and closure of the cracks inside the sample can be seen clearly.

2.2.2 *Triaxial soaking test*

When three cycles of wetting and drying were finished, the development of the cracks can be observed obviously, and then the triaxial soaking test was conducted. Initial parameters and stress state of the sample are shown in Table 1.

Before soaking, the sample was consolidated under a controlled ambient pressure. The stabilized criterion for the volumetric change of sample is no more than 0.006 cm^3 within 2 hours, and the water discharge less than 0.006 cm^3 per hour.

After consolidation, the deviator stress was applied until the required value. In this period, the stabilized criterion for axial displacement is no more than 0.01 mm per hour and no more than 0.006 cm^3 within 2 hours for volumetric change of sample. The shear rate is 0.0167 mm/min.

A standard GDS volume/ pressure controller is used in soaking stage. The rated pressure and volume of the controller are 2 MPa and 1000 cm^3 .The degree of accuracy is 1 kPa in the measurement of pressure, and 1 mm^3 in the measurement of soaking water. Soaking at a constant head can be achieved using this controller which also regulates the pressure to control the speed of soaking (Zhu et al. 2008).

2.2.3 *Hydrostatic compression test*

The sample was firstly undergone through multi-drying-wetting cycle in order to damage the samples' structure. Sample was dried by electric oven with controlling temperature 35°C about one day. After being dried, an amount of water was added to the samples in order to control the degree of saturation remains its initial value, 88.58%. Samples surface appeared cracks during drying-wetting cycles as shown in Figure 3. A hydrostatic compression test with controlled suction

Table 2. State parameter of samples and test scheme.

Sample number	Volume cm^3	Dry density g/cm^3	Void ratio	Water content %	Degree of Saturation %	Suction kPa	Cycle frequency times
$5^{\#}$	92.05	1.57	0.74	24.05	88.58	50	4

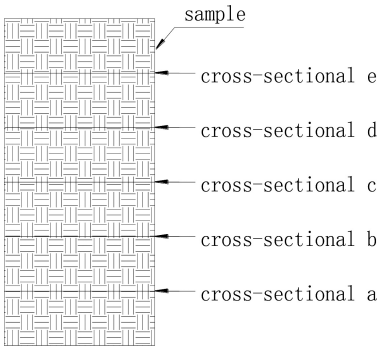


Figure 2. Image of CT scanning position.

50 kPa was carried out for one sample. State parameter of samples and test scheme are shown in Table 2.

2.3 *CT scanning*

2.3.1 *Scanning of the samples in wetting and drying cycles*

The proper window width and window level are needed to analysis the scanned images (Cai et al. 1996). Window width is a chosen span of CT numbers when displaying the scanned images. Materials, according to its density, are divided into 16 levels (grayscale) within that chosen span, from light to dark. And window level is an average number between the upper and lower limit of the CT numbers. Sine different materials have different CT numbers, it is better to choose material's CT number as the centre of the span for scanning, so that the subtle differences can be observed. And the centre of the span is called window level. The brightness of the scanned images is affected by the window level, because the scanned images look light when the window level is low and dark when it is high. So different tests need for different window levels, in response to different vision requirements (vide infra).

However, different window width and window level do not affect the data of CT scanning. Based on the former experience, the window width of the scanned images in wetting and drying cycles is set 400 generally, and the window level is usually set 1600.

Set the central line of the sample as the zero point of scanning, and then scan the section at the third point and two-third point of the sample (see Fig. 2, cross sectional b and d), thus the CT number ME and variance SD can be obtained. Each sample was scanned for 6 times, and 48 scanned images were acquired. Followings are the parameters used for scanning: the voltage strength is 120 kV, current strength is 165 mA, scanning duration is 3 s, scanned thickness is 3 mm and amplification coefficient is 5.

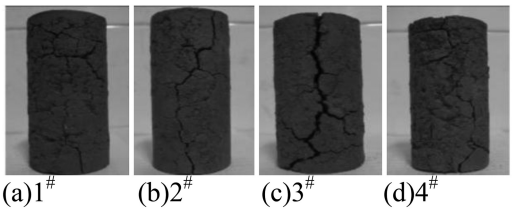


Figure 3. Sample photographs after being dried for three times.

2.3.2 *Scanning of the CT-triaxial soaking test and hydrostatic compression tests*

Parameters of CT scanning in the soaking test are the same as those in wetting and drying cycles. When the consolidation and loading of deviator stress get stable, scan the sample and take it as the initial state. When the soaking water was 5, 10, 15, and 20 g (sample No.4 gets 17 g), scanned the sample respectively, and 5 sections were scanned every time. These sections are labeled as a, b, c, d and e (see Fig. 2), the heights of them are 13.5, 26.5, 40.0, 53.5 and 66.5 mm from the bottom of the sample.

Every sample undergone 9 times scanning totally in the process of hydrostatic compression tests, which correspond to net mean stress 0, 25, 50, 75, 100, 150, 200, 250 and 350 kPa. 0 kPa represents the initial state of each sample before loading. In the process of hydrostatic compression tests only cross-sectional b and d were scanned by CT.

3 ANALYSIS OF TEST RESULTS

3.1 *Sample change in wet – dry cycles*

Figure 3 shows the photos of four samples after three wet – dry cycles. Lots of cracks appear in the sample surface (especially Fig. 3a). Figures 4 and 5 are the CT images of sample NO.1 and NO.3. Two figures show drying procedures can lead to the generation and closing up of sample cracks, and during wetting procedure, small cracks closes, large cracks expands. In drying process, small cracks expand, and large cracks would become narrow.

3.2 *Analysis of CT scan data during wetting – drying cycles*

The relationship between CT scan data and scan frequency is shown in Figure 6. The curve of ME values takes on the shape "M" (see Fig. 6a) because of the process of wetting-drying cycles. The curve of SD values arises slowly before the fourth scanning (see Fig. 6b), but the first peak point appears in the fifth scanning, which reflects the quick development of cracks and

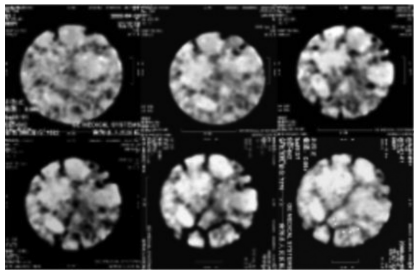


Figure 4. CT images of 1/3 height of sample No.1 from downward.

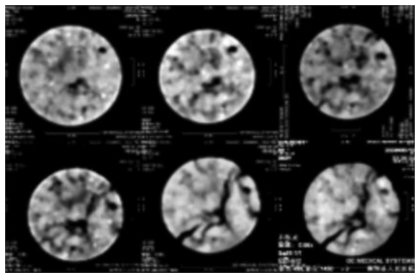
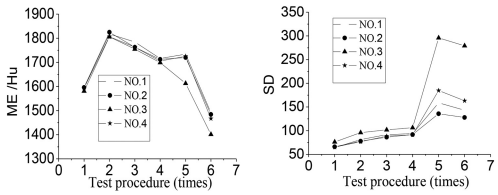


Figure 5. CT images of 1/3 height of sample No.2 from bottom.



(a)ME (b)SD

Figure 6. Relationship between scanning data and test procedure in wetting and drying cycles.



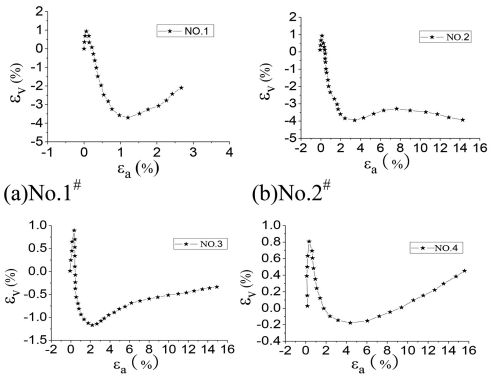
(a)No.1# (b)No.2# (c)No. 3# (d)No.4#

Figure 7. Photographs of samples after soaking test.

the decrease of homogeneity of specimens, during the second wetting procedure.

3.3 *Macroscopic and mesoscopic response of samples in CT-triaxial test*

Figure 7 shows the images of four samples after triaxial test. Due to lesser confining pressure and deviatoric stress, sample NO.1 don't appear damage after being saturated. Sample NO.2 takes place shear damage,



(a)No.1# (b)No.2#

(c)No. 3# (d)No.4#

Figure 8. Relationships between ε_v and ε_a during soaking test.

and don't come to saturated state, and its axial strain increases suddenly and rises to 14.4% when water amount is equal to 17 g. This phenomenon is due to low confining pressure and large deviator stress. There is a swelling phenomenon at the bottom of two samples NO.3 and NO.4 which are not similar to others due to the large deviator stress (see Fig. 7c and Fig. 7d).

The relationship between volumetric strain ε_v and axial strain ε_a is shown in Figure 8. The negative value of volumetric strain stands for swelling. The curve (see Fig. 8) can be divided into three stages: firstly, the sample volume decreases since the surface layer of sample become wet and the modulus of surface layer get low, so that the cracks located in surface layer of specimen is narrow down; secondly the sample volume increases because water infiltrates into the interior of sample and the major of expansive pressure appears; and thirdly the sample volume decreases once again due to the release of expansive pressure.

Xie (2007) researched three-dimensional expansive pressure of remolded expansive soil from the same site, the dry density of samples 1.7 g/cm^3, water content 9.85%, vertical expansive pressure is 402 kPa , and horizontal expansive pressure gets close to 300 kPa. Generally speaking, expansive pressure would increase when water content decreases and dry density reduces. The dry density and water content of the samples in this study are greater but less than that researched by Xie et al. (2007), thus, the expansive pressure would be great; it is just the reason about expansive phenomenon. (The expansive pressure surpasses 300 kPa, with the ambient pressure is equal to 100 kPa).

Due to the space limitation of the paper, CT images of sample No.4 are only shown in Figure 9. Every cross-sectional CT images in the first scanning procedure, shows there are lots of cracks which help water penetrate into samples. When soaking amount reaches up to 5 g, cracks at the bottom of sample enclose, there are only some little caverns in inner sample. The cracks at the top of samples only become narrow. When soaking amount increases continuously, crack width and

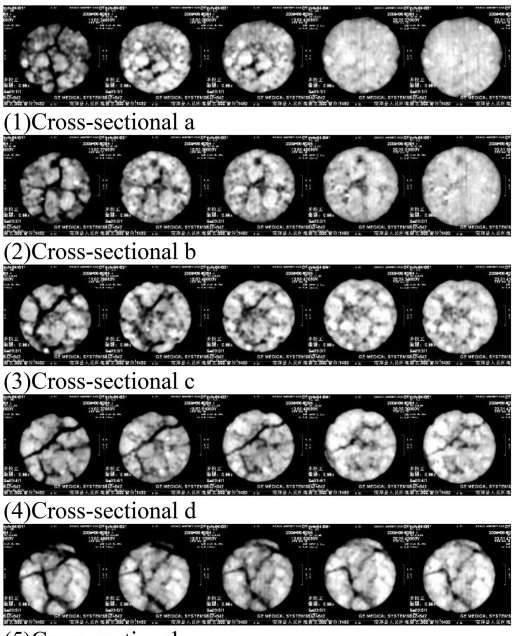


Figure 9. CT images of five cross-sections of sample No.4 in different water supplies.

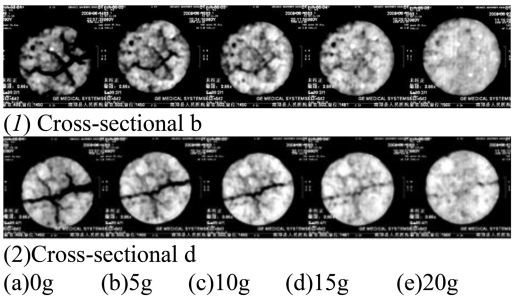
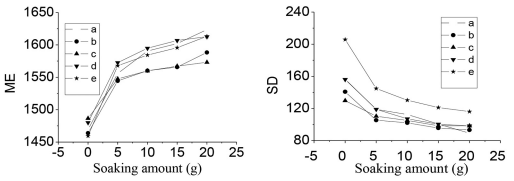


Figure 10. CT images of cross-sectional b of sample No.3 in different water supplies.

cavern size also reduce. Soaking amount comes to 15 g, the black area of cross-sectional a and b change largely into white area. However, the cracks of cross-sectional d and e don't totally close when test finishes. All in all, the cracks widths of remolded expansive soil firstly become narrow, and then evolve to little cavern, and disappear lastly.

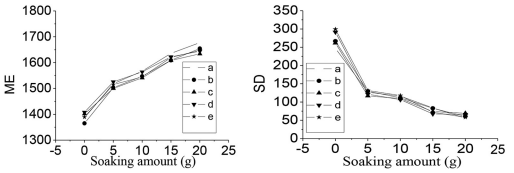
To sum up, the cracks in different position would tend to close. This result is contrary to Lei' researches (2005) which showed cracks of intact expansive soil would enlarge during CT triaxial soaking test.

Five images of cross sectional b and d of sample No.3 in different water supplies shown in Figure 10. Cracks and caverns don't close completely after at the end of test due to the low confining pressure. Therefore



(a)ME (b)SD

Figure 11. Variation of No.1 scanning data with soaking amount.



(a)ME (b)SD

Figure 12. Variation of No.3 scanning data with soaking amount.

different stress state would influence the closure and evolution of sample cracks and caverns.

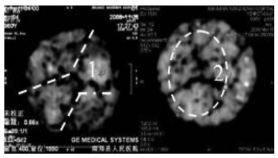
3.4 *Scanning data during soaking test*

Figures 11 and 12 show the curve of ME and SD with soaking amount of sample No.1 and No.3 respectively. Two curves indicate ME and SD values would respectively increase and decrease with the soaking amount augmentation.

Figure 11 shows that the CT number ME and variance SD undergo greater decrease after the soaking amount surpass 5 g. At section c, d and e, the increase of ME and the decrease of SD tend to be stable, after the soaking amounts surpass 15 g. when it comes to section a and b, the increase of ME and the decrease of SD tend to be more obvious than those of other sections, mainly because the water content of the tow sections are higher than that of other sections, which leads to the change of the scan data. The initial heterogeneity of specimen No.3 is not obvious, as shown in Figure 12. When the test was ended, the CT number ME and variance SD of the five sections are close to each other, implicating the benign closure of cracks and the homogeneity of density. The test curves are in regular shape, because of the higher ambient pressure and the longer soaking process.

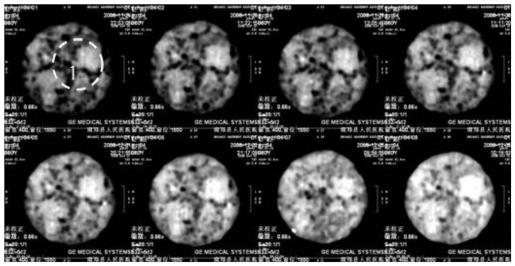
3.5 *CT scanning images*

Figure 13 shows the CT photos of sample number 5 before loading. Because the sample undergone through 4 times drying-wetting cycles, cracks and fissures appear in inner sample. Figure 14 shows CT images of sample No.4 in different loading state. The first scanning image shows that large cracks close to a certain extent by comparison to Figure 13. When load

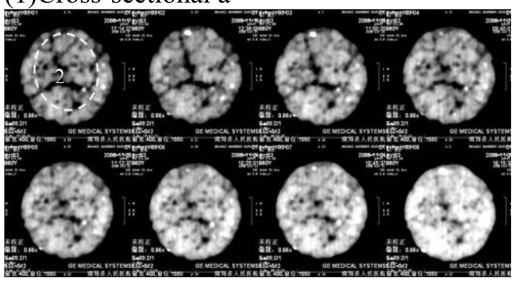


(1)Cross-sectional a (2)Cross-sectional b

Figure 13. CT images of sample No.5 before loading.



(1)Cross-sectional a



(2)Cross-sectional b

Figure 14. CT images of sample No.5# in different loading state.

is 150 kPa, most of lager cracks evolve little carven because samples get yielding in high mean net stress. All in all, Cracks and fissures of sample will gradually close along with loading.

Compared by soaking test, the cracks of expansive soil during only the effect of external load, would evolve for void with the growths of load, but don't close entirely. Under the impact of both water and external load, the cracks closure level is better than that only external load. Water is the key point to infect the production and closure of cracks, more attention would give for water producing effects on expansive soil projects.

4 CONCLUSIONS

In unconfined condition, wetting and drying procedures can lead to the generation and closing up of sample cracks. During wetting procedure, small cracks will close, and large cracks will expand. In drying process, small cracks will expand, and large cracks become narrow.

In the action of water, the sample cracks would be close gradually, and the closure degree of sample crack is closely related to stress state. The sample volume change can be divided into three stages: firstly, the volume decreases, then increases due to expansive action, and thirdly decreases once again because of the release of expansive pressure and reduction of modulus.

The cracks of expansive soil, only the effect of external loading, would evolve for void with the growths of load, but don't close entirely. Under the impact of both water and external load, the cracks closure level is better than that only external load. Water is the key point to infect the production and closure of cracks, more attention would give for water producing effects on expansive soil projects.

REFERENCES

Bao, C. G. 2004. Fissuring property study of expansive soils. Theory and practice of expansive soil treatment technology. *Beijing: China communications press*, 24–35.

Cao, D. Q. & Cai, Z. N. 1996. CT Diagnostics of Body. Beijing: *people Military medical publish*.

Chen, Z. H., Lu, Z. H. & Pu, Y. B. 2001. The matching of computerized tomography with triaxial test apparatus for unsaturated soils. *Chinese Journal of Geotechnical Engineering*, 23(4): 387–392.

Chen, Z. H., Sun, S. G. & Fang, X. W. et al. 2007. Development and application of multi-function triaxial apparatus for soil. *Journal of Logistical Engineering University*, 23(4): 34–38.

Lei, S. Y. & Xu, Y. 2005. Microscopic analysis of triaxial soaking process in original expansive soils. *Journal of Lanzhou University of Technology*, 31(1): 119–112.

Liu, Z. D. & Wang, Y. 1994. Study on triaxial deformation of expansive soils soaked in water. *Journal of Wuhan University of Hydr. & Elec. Eng*. 27(12): 616–621.

Lu, Z. H., Chen, Z. H., & Pu, Y. B. 2002. A CT study on the crack evolution of expansive soil during drying and wetting cycles. *Rock and Soil Mechanics*, 23(4): 417–422.

Wang, G. L., Chen, S. S. & Xu, G. M. 2005. Centrifuge model test on stability of expansive soil slope under alternation between drying and wetting. *Hydro-science And Engineering*, 4(12): 6–10.

Xie, D. Y. & Qi, J. L. 1999. Soil structure characteristics and new approach in research on its quantitative parameter. *Chinese Journal of Geotechnical Engineering*, 21(6): 651–656.

Xie, Y., Chen, Z. H. & Sun, S. G. et al. 2007. Test research on three-dimensional swelling pressure of remolded expansive clay. *Rocks and Soil Mechanics*, 28(8): 1636–1642.

Yuan, J. P. 2003. A conceptual model for the fissure in unsaturated expansive soil: an research of slope stability of expansive soil. *Nanjing: Hohai University*.

Zhu, Y. Q. & Chen, Z. H. 2008. A new method of studying collapsibility of loess. *Chinese Journal of Geotechnical Engineering*, 30(4): 524–528.

Unsaturated Soil Mechanics—from Theory to Practice – Chen et al. (Eds)
© 2016 Taylor & Francis Group, London, ISBN 978-1-138-02921-7

Resilient modulus – soil suction correlations for two subgrade soils from China

Z. Han & S.K. Vanapalli
Department of Civil Engineering, University of Ottawa, Ottawa, Canada

ABSTRACT: In recent years, determination and prediction of the resilient modulus (M_R) – soil suction (s) correlations have been encouraged worldwide for reliable pavement designs extending mechanistic design methods taking account the influence of environmental factors. In this study, the constitutive model proposed by Han & Vanapalli (2015a) is extended to predict the non-linear $M_R - s$ correlations for two different subgrade soils from China. This constitutive model is formed with only one constant model parameter that does not need calibration. In addition, all information required for using this model can be determined using conventional laboratory testing equipment. There is good agreement between the measurements and the predictions of the $M_R - s$ correlations for the two soils investigated. The model introduced in this paper is simple and can be used in the prediction of the $M_R - s$ correlations for compacted cohesive subgrade soils for the rational design of pavements.

1 INTRODUCTION

The in-service mileage of highway network by the end of year 2013 exceeded 100 thousand kilometers in China. Annual new construction, maintenance and rehabilitation costs associated with this network in China are estimated to be approximately several hundreds of billions of RMB (MOT 2013). Significant savings associated with the rehabilitation costs are possible by implementing rational pavement design methods which offer better resistance against the deterioration of the pavement structure that typically arise from the influence of environmental factors such as the moisture regime and the temperature fluctuations.

One approach for investigating the influence of moisture regime on the pavement behavior is to characterize the variation of pavement design parameters with respect to moisture regime changes extending mechanistic methods. There are several research studies in the literature that provide correlations between the resilient modulus (M_R), which is the key parameter used in the mechanistic pavement design methods, and the moisture contents information (e.g., degree of saturation S_r, volumetric water content θ, or gravimetric water content w) for different pavement base course and subgrade soils (Li & Selig 1994, Drumm et al. 1997, Khoury et al. 2011). The M_R – moisture content correlations are generally described using empirical equations which however are soil-type dependent and hence have limitations in the rational characterization of the M_R (Heath et al. 2004, Ng et al. 2013).

Several recent studies suggested relating the M_R with soil suction (s) using constitutive models to reasonably describe and predict the influence of moisture regime. Such approaches also have received considerable research attention in China, in recent years (e.g., Xie et al. 2001, Yang et al. 2006, Qiu et al. 2011, Liu et al. 2013, Zhang 2013, Ng et al. 2013). Comprehensive summary of constitutive models proposed for predicting the $M_R - s$ correlations are available in Han & Vanapalli (2015b).

In this paper, the variation of M_R with respect to s for two subgrade soils from China is predicted using a recently proposed constitutive model (Han & Vanapalli 2015a). The $M_R - s$ relationship can be predicted using this model with the information of the M_R at saturation condition (M_{RSAT}), the M_R and s at optimum moisture content condition (M_{ROPT} and s_{OPT}), and the Soil-Water Characteristic Curve (SWCC). The model is formulated using a single parameter which is a constant value for all cohesive subgrade soils. Reasonably good predictions are achieved for both the soils investigated in this study. The constitutive model is simple as it only requires information (e.g., M_{RSAT}, M_{ROPT}, s_{OPT} and SWCC) that can be determined using conventional testing equipment. Due to these reasons, the proposed model is a promising tool for the rational design of pavements to resist the deteriorations that arise from environmental factors.

2 THOERETICAL CONSIDERATIONS

2.1 *Succinct review of current constitutive models for the M_R*

The M_R is the elastic modulus of soils that have been subjected to large number of cyclic loadings.

Similar to other types of elastic moduli which are stress-dependent, the M_R in conventional soil mechanics is also described using different relationships to the applied stress levels in the literature. Equation 1 (recommended by the MEPDG 2004) represents the general formulation of constitutive models proposed in the literature for describing the dependency of the M_R on the applied confining stress (i.e., bulk stress, θ_b) and cyclic shearing stress (i.e., octahedral shear stress, τ_{oct}).

$$M_R = k_1 p_a \left(\frac{\theta_b}{p_a}\right)^{k_2} \left(\frac{\tau_{oct}}{p_a} + 1\right)^{k_3} \quad (1)$$

where p_a is atmosphere pressure (i.e., 101.3 kPa); k_1, k_2 and k_3 are model parameters.

The soil suction in the presently used constitutive models is either incorporated into the externally applied stresses extending Bishop's effective stress concept for unsaturated soils (e.g., Yang et al. 2006; Liang et al. 2008, see Equation 2 for example; Zhang 2013) or is formulated as an independent term into the stress dependent models (Khoury et al. 2009, see Equation 3 for example; Cary & Zapata 2011; Ng et al. 2013). Both approaches are widely used to provide reasonable predictions for $M_R - s$ correlations of different soil types. More discussions on this topic are provided in Han & Vanapalli (2015b).

$$M_R = k_4 p_a \left(\frac{\theta_b + \chi s}{p_a}\right)^{k_5} \left(1 + \frac{\tau_{oct}}{p_a}\right)^{k_6} \quad (2)$$

$$M_R = k_7 p_a \left(\frac{\theta_b}{p_a}\right)^{k_8} \left(k_{10} + \frac{\tau_{oct}}{p_a}\right)^{k_9} + k_{11} s^{k_{12}} \quad (3)$$

where k_4 through k_{12} are model parameters, χ is Bishop's effective stress parameter.

Three common concerns regarding the current constitutive models for $M_R - s$ correlations are:

i) Suitable model parameters (e.g., k_4 through k_6 and χ in Equation 2, k_7 through k_{12} in Equation 3) are required for providing good fit between the measured and predicted M_R values. Extensive experimental data however is required for the calibration of these model parameters;
ii) For the same constitutive model, the model parameters calibrated for one soil may not be suitable for other soils;
iii) M_{ROPT} values are typically determined in the conventional pavement design practice to calibrate the k_1, k_2 and k_3 values in Equation 1. This is because pavement soils are generally compacted at optimum moisture content to achieve favorable mechanical properties. Information on the M_{ROPT} however could not be directly used to predict the $M_R - s$ correlations in most of the currently used constitutive models.

2.2 *A new model for $M_R - s$ correlations*

Han & Vanapalli (2015a) proposed a constitutive model to predict the $M_R - s$ correlations for compacted cohesive subgrade soils. The model when represented in a normalized form requires only one fitting parameter ξ (see Equation 4).

$$\frac{M_R - M_{RSAT}}{M_{ROPT} - M_{RSAT}} = \frac{s}{s_{OPT}} \left(\frac{w}{w_{OPT}}\right)^{\xi} \quad (4)$$

where w is the gravimetric water content. In this equation, the M_{ROPT} and M_{RSAT} can be predicted using any conventional stress-dependent models such as Equation 1. The M_{RSAT} is found to be less sensitive to applied stress levels in comparison with the M_R at higher soil suction values. For this reason, the M_{RSAT} can be considered as a constant value irrespective of the applied stress levels without introducing significant errors in the predictions for cohesive subgrade soils (Han & Vanapalli 2015a).The model parameter ξ is suggested equal to 2.0 for all cohesive subgrade soils. This value has been successfully used to provide reasonable predictions for 11 different subgrade soils collected from different locations and tested using different techniques to determine the M_R (Han & Vanapalli 2015b). The s_{OPT} can be measured using simple techniques such as the filter paper method or pressure plate method. The w corresponding to different s can be estimated using the SWCC models such as one proposed by Fredlund & Xing (1994) (Equation 5).

$$\frac{w}{w_{SAT}} = \left\{1 / \ln\left[2.718 + \left(\frac{s}{a}\right)^n\right]\right\}^m \quad (5)$$

where w_{sat} is the saturation gravimetric water content; a, n, and m are model parameters. Substituting Equation 5 and $\xi = 2.0$ into Equation 4 yields Equation 6.

$$\frac{M_R - M_{RSAT}}{M_{ROPT} - M_{RSAT}} = \frac{s}{s_{OPT}} \left\{\frac{\ln[2.718 + (s_{OPT}/a)^n]}{\ln[2.718 + (s/a)^n]}\right\}^{2m} \quad (6)$$

Equation 1 is used to predict the M_{ROPT} considering the influence of applies stress while M_{RSAT} is assumed to be a constant in Equation 6. The prediction of the $M_R - s$ correlations in this study is based on Equation 6 using the information of M_{ROPT}, M_{RSAT}, s_{OPT} and the SWCC.

3 MODEL VALIDATIONS

3.1 *Soils and their SWCC*

Experimental data derived from two subgrade soils found in China (a Red clay tested by Zhang 2013, noted as Soil A; and a clayey soil tested by Liu et al. 2013, noted as Soil B) are used in this study. The properties and other details of these two soils are summarized in Table 1.

Table 1. Properties and other details of the two soils used in this study.

Details	Soil A	Soil B
ρ_{dmax} (kg/m^3)	1502	1652
w_{OPT} (%)	30	18.5
w_L (%)	84.1	48.4
I_p (%)	45.2	24.8
RC (%)	96	96
AASHTO[1]	A-7-5	A-7-6
USCS[2]	MH	CL
M_R testing protocol	AASHTO T292-91	NCHRP 1-28A
Applied stress levels (kPa)	$\sigma_c = 15, 30, 45, 60$; $\sigma_d = 35, 55, 75, 105$	$\sigma_c = 30$; $\sigma_d = 30, 55, 75, 105$

Notations: ρ_{dmax} = maximum dry density, w_L = liquid limit, I_p = plasticity index, RC = relative compaction, σ_c = confining stress, σ_d = cyclic deviator stress.
Note: Soils classified according to [1]AASHTO M-145, and [2]ASTM D2487-11, unified soil classification system.

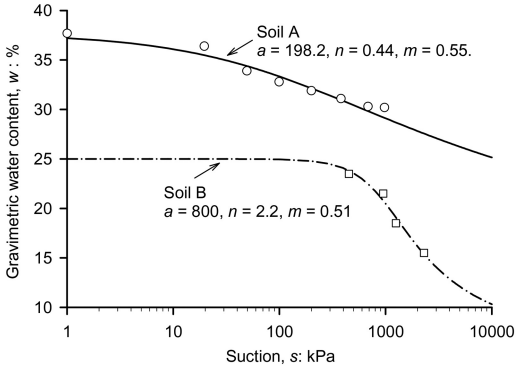


Figure 1. SWCC of the two soils used in this study.

Both soil A and soil B specimens were compacted at different moisture contents (w_{OPT}, $w_{OPT}+4\%$, $w_{OPT}+6\%$ for soil A; $w_{OPT}-3\%$, w_{OPT}, $w_{OPT}+3\%$, $w_{OPT}+5\%$ for soil B) and then subjected to the cyclic loading tests under various stress levels to determine the M_R values.

Soil suction values of soil A specimens were determined from its SWCC referencing to different compaction moisture contents (Zhang 2013) while soil suction values of soil B specimens were measured after the cyclic loading tests using filter paper method (Liu et al. 2013). Figure 1 shows the measured SWCC (symbols) and the fitted SWCC using Equation 5 (lines) for soil A and soil B. The values of the parameters used in Equation 5 (i.e., a, n, and m) are also shown in Figure 1.

3.2 M_{ROPT} and M_{RSAT}

The M_{ROPT} of soil A and soil B are predicted using Equation 1. The model parameter values used in Equation 1 for soil A and soil B are summarized in Table 2 along with the corresponding coefficient of determination (R^2) values.

Table 2. Model parameters in Equation 1 for predicting M_{ROPT}.

Parameters	k_1	k_2	k_3	R^2
Soil A	1816	0.143	−1.174	0.87
Soil B	1560	−0.957	0.8	0.99

Note: M_R, θ_b, and τ_{oct} are in kPa.

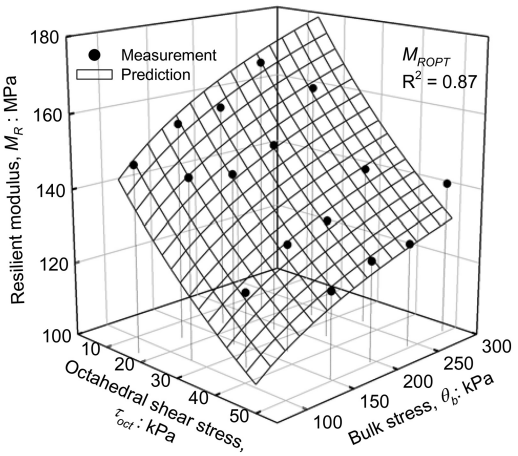


Figure 2. Measured and predicted M_{ROPT} of soil A.

Figure 2 shows, in the $M_R - \theta_b - \tau_{oct}$ space, the comparisons between the predicted M_{ROPT} of soil A and the measurements reported by Zhang (2013). The measured M_R is non-linear with respect to both θ_b and τ_{oct}. Equation 1 extends a smooth surface in the $M_R - \theta_b - \tau_{oct}$ space and well simulates the measured behavior of the M_{ROPT}.

The M_{RSAT} values for soils A and soil B are assumed to be 70 MPa and 40 MPa respectively as the measured M_{RSAT} values were not reported for soil A and soil B (Liu et al. 2013, Zhang 2013). The assumed values are found suitable for use in Equation 6 to provide reasonable predictions. More discussions about the M_{RSAT} is available in the next section.

3.3 *Comparisons between the measurements and predictions on the $M_R - s$ correlations*

Figure 3 shows, in the $M_R - \sigma_d - s$ space, the comparisons between the measured M_R of soil A and the predictions by Equation 6 under different σ_c levels. It can be observed from Figure 3 that the measured variation of the M_R with respect to the s is influenced by both σ_c and σ_d. The assumed $M_{RSAT} = 70$ MPa is close to the measured M_R values at lower soil suction levels. Using this M_{RSAT} value along with the: (i) M_{ROPT} predicted by Equation 1 (see Table 2 and Figure 2); (ii) SWCC predicted by Equation 5 (see Figure 1), Equation 6 predicts different smooth surfaces in the

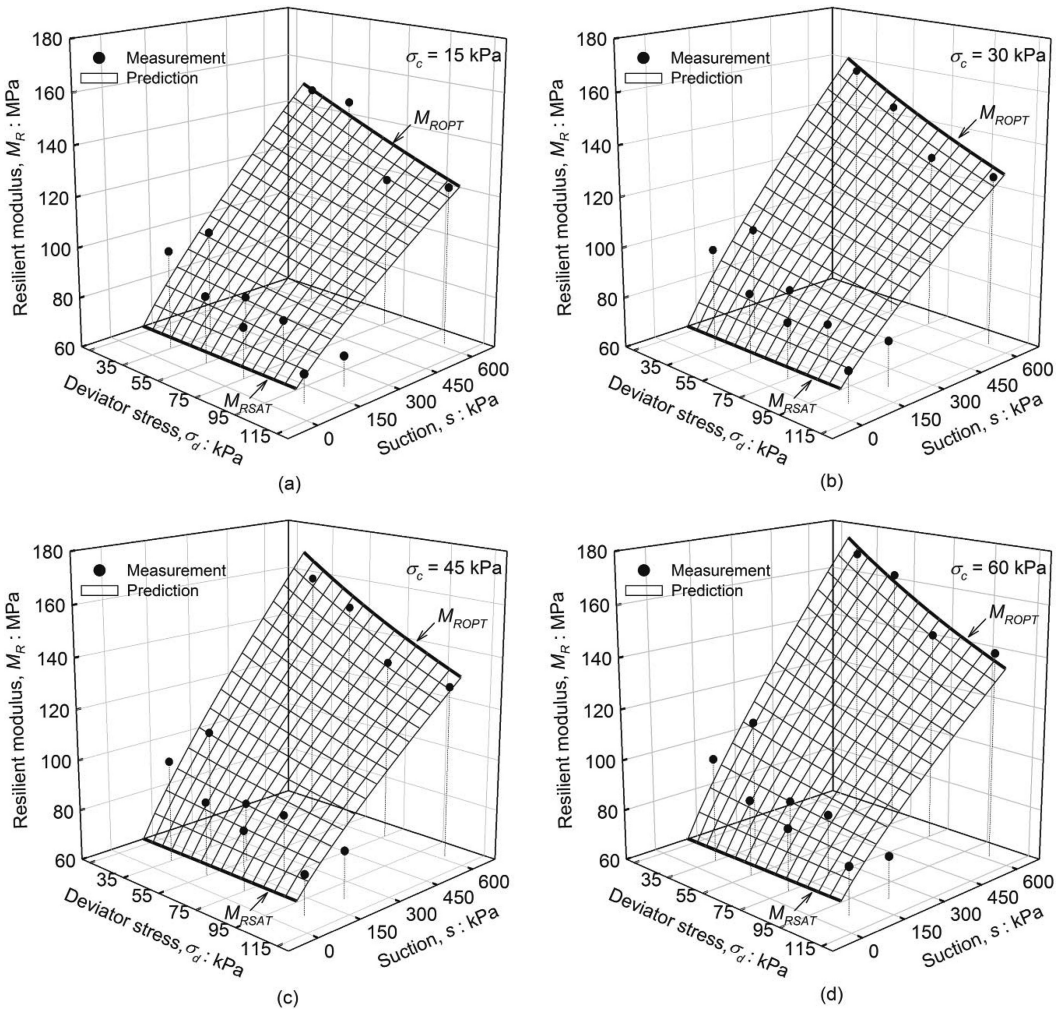


Figure 3. Comparisons between the measurements and predictions for soil A at confining stresses of (a) 15 kPa, (b) 30 kPa, (c) 45 kPa and (d) 60 kPa.

$M_R - \sigma_d - s$ space corresponding to different σ_c levels and well captures the variation of the M_R with both soil suction and applied stress levels.

Reasonably good predictions are also achieved for soil B as shown in Figure 4 using $M_{RSAT} = 40$ MPa and the predicted M_{ROPT} and SWCC from Equation 1 and Equation 5, respectively.

Figure 5 shows the overall comparisons between the measured M_R of soil A and soil B, and the predictions provided by the model introduced in this paper. The two soils chosen in this study are significantly different with respect to their properties (see Table 1) as well as the SWCC (see Figure 1). The M_R values are also determined using different testing protocols over different soil suction ranges (AASHTO T292-91 for soil A over soil suction range of 50 to 650 kPa, NCHRP 1-28A for soil B over soil suction range of 400 to 2500 kPa). Predictions with high R^2 values are achieved for both soils.

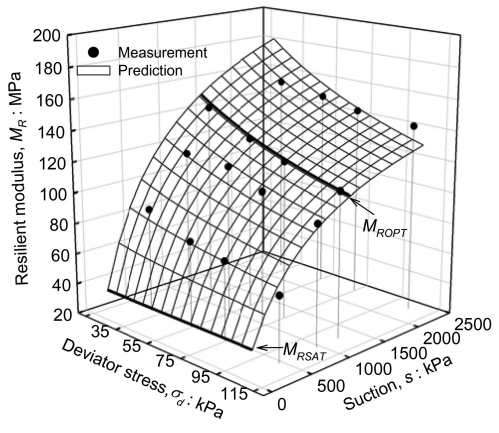


Figure 4. Comparisons between the measurements and predictions for soil B at confining stress of 30 kPa.

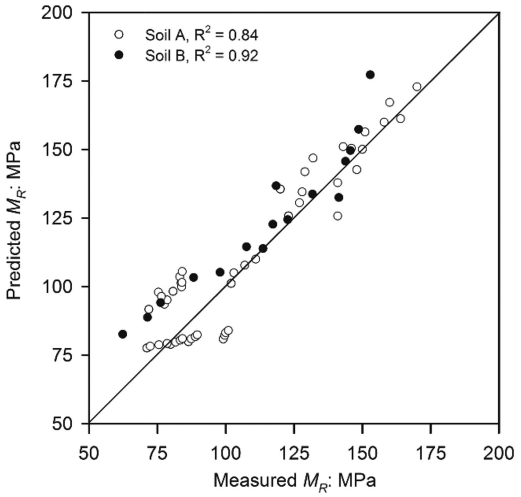


Figure 5. Comparisons between the measurements and predictions for soil A and soil B.

It should be noted that only the measured M_{ROPT} values are used to calibrate Equation 1 which is further used in Equation 6. Other measured M_R values are not used in any regression analysis to determine model parameter values.

4 SUMMARY AND CONCLUSIONS

A new constitutive model proposed by Han & Vanapalli (2005a) is used in this paper for predicting the resilient modulus – soil suction correlations. The model requires the following information:

i) M_{ROPT} and M_{RSAT} which could be predicted using conventional stress-dependent models; the M_{RSAT} also can be simplified as a constant value regardless of applied stresses;
ii) Soil-Water Characteristic Curve (SWCC);
iii) s_{OPT} which could be measured using simple techniques or estimated from the SWCC.

Experimental data on the M_R derived from two different subgrade soils from China using different testing techniques are used in this paper to verify the performance of the model. It has been shown that the model is capable of providing reasonable predictions for both the soils investigated in this paper taking account the influence of the applied stress levels and soil suction.

The model proposed by Han & Vanapalli (2005a) is simple for use in practice as it allows the direct use of M_{RSAT} and M_{ROPT} which can be determined using conventional testing equipment. In addition other required information such as the SWCC and s_{OPT} can be easily measured using simple equipment such as pressure plate and filter paper. The model uses a constant fitting parameter $\xi = 2.0$ which alleviates the need for extensive experimental data to calibrate model parameters.

The model can also be combined with other simple techniques for predicting the $M_R - s$ correlations. For example, the SWCC required by the model can be estimated using the one-point method proposed by Catana et al. (2006). This one-point method estimates the entire SWCC using one point measurement of the $w - s$ relationship and the I_p of soils which further simplifies the determination of the SWCC. The introduced model combined with one-point method for the SWCC has been successfully applied to predict the SWCC and $M_R - s$ correlations for several subgrade soils from China (Han et al. 2015).

REFERENCES

AASHTO. 1992. Designation T292-91: *Standard Method of Test for Resilient Modulus of Subgrade Soils and Untreated Base/Sub-Base Materials*. American Association of State Highway and Transportation Officials. Washington, D.C.

AASHTO. 2008. Designation M-145: *Classification of Soil and Soil-Aggregate Mixtures for Highway Construction*. American Association of State Highway and Transportation Officials. Washington, D.C.

ARA, Inc., ERES Consultants Division. 2004. *Guide for Mechanistic – Empirical Design of New and Rehabilitated Pavement Structures*. Final report, NCHRP Project 1-37A. Transportation Research Board, Washington, D.C.

Cary, C.E., & Zapata, C.E. 2011. Resilient modulus for unsaturated unbound materials. *Road Materials and Pavement Design*, 12(3): 615–638.

Catana, M.C., Vanapalli, S.K., & Garga, V.K. 2006. The water retention characteristics of compacted clays. *Proc. 4th Int. Conf. on Unsaturated Soils*, Carefree, USA, 1348–1359.

Drumm, E.C., Reeves, J.S., Madgett, M.R., & Trolinger, W.D. 1997. Subgrade resilient modulus correction for saturation effects. *ASCE J. Geotech. Geoenviron. Eng.*, 123(7): 663–670.

Fredlund, D.G., & Xing, A. 1994. Equations for the soil-water characteristic curve. *Can. Geotech. J.*, 31(4): 521–532.

Han, Z., & Vanapalli, S.K. 2015a. Model for predicting the resilient modulus of unsaturated subgrade soil using the soil-water characteristic curve. *Can. Geotech. J.*, doi: 10.1139/cgj-2014-0339.

Han, Z., & Vanapalli, S.K. 2015b. State-of-the-Art: Prediction of resilient modulus of unsaturated subgrade soils. *ASCE Int. J. Geomech*. (Accepted for publication)

Han, Z., Mihambanou, B., & Vanapalli, S.K. 2015. Two-step approach for estimating the resilient modulus of pavement subgrade taking account the influence of moisture regime. *In 2015 ASCE Airfield & Highway Pavement Conf.*, Miami, USA.

Heath, A.C., Pestana, J.M., Harvey, J.T., & Bejerano, M.O. 2004. Normalizing behavior of unsaturated granular pavement materials. *ASCE J. Geotech. Geoenviron. Eng.*, 130(9): 896–904.

Khoury, N.N., Brooks, R., & Khoury, C.N. 2009. Environmental influences on the engineering behavior of unsaturated undisturbed subgrade soils: effect of soil suctions on resilient modulus. *Int. J. Geotech. Eng.*, 3(2): 303–311.

Khoury, N., Brooks, R., Khoury, C., & Yada, D. 2011. Modeling resilient modulus hysteretic behavior with moisture variation. *ASCE Int. J. Geomech.*, 12(5): 519–527.

Li, D., & Selig, E.T. 1994. Resilient modulus for fine-grained subgrade soils. *ASCE J. Geotech. Eng.*, 120(6), 939–957.

Liang, R.Y., Rabab'ah, S., & Khasawneh, M. 2008. Predicting moisture-dependent resilient modulus of cohesive soils using soil suction concept. *ASCE J. Transp. Eng.*, 134(1): 34–40.

Liu, W., Li, Z., Dong, C., & Liu, Z. 2013. Study on prediction model of dynamic resilient modulus of cohesive subgrade soils considering under different moisture. *Hwy. Eng.*, 38(6): 6–9. (In Chinese)

Ministry of Transportation of People's Republic of China (MOT). http://www.moc.gov.cn/

Ng, C.W.W., Zhou, C., Yuan, Q., & Xu, J. 2013. Resilient modulus of unsaturated subgrade soil: experimental and theoretical investigations. *Can. Geotech. J.*, 50(2): 223–232.

Qiu, X., Qian, J., & Zhang, S. 2011. Research on prediction model of dynamic resilient modulus of subgrade soil based on matric suction. *Hydrogeol. & Eng. Geol*. 38(3): 49–53. (In Chinese)

Witczak, M.W. 2003. NCHRP 1-28A: *Harmonized Test Method for Laboratory Determination of Resilient Modulus for Flexible Pavement Design*. Final Report. TRB, National Research Council, Washington, D.C.

Xie, H., Wu, H., & Ling, J. 2001. Influence of moisture content and suction on modulus of pavement subgrade. *Chinese J. Hwy. Transp.* 14, 19–21. (In Chinese)

Yang, S.R., Kung, J.H.S., Huang, W.H., & Lin, H.D. 2006. Resilient modulus of unsaturated cohesive subgrade soils. *Chinese J. Geotech. Eng.*, 28(2): 225–229. (In Chinese)

Zhang, J. 2013. *Experimental Study on Modulus of Resilience and Residual Strain of Unsaturated Red Clay Subgrade under Traffic Loading*. Master Thesis, Wuhan University, China. (In Chinese)

Unsaturated Soil Mechanics—from Theory to Practice – Chen et al. (Eds)
© 2016 Taylor & Francis Group, London, ISBN 978-1-138-02921-7

Wetting collapse at high degree of saturation during shearing for unsaturated sand

B.J. Shwan
Department of Civil and Structural Engineering, University of Sheffield, Sheffield, UK

ABSTRACT: Wetting collapse at a high degree of saturation was investigated by performing a series of drained unsaturated direct shear tests on the fine sand. The degree of saturation of the sample at different stages during the test was monitored. Wetting collapse was observed where the response is punctuated by a sudden loss of strength and volume followed by rapid recovery of strength. After this, further repeated sudden losses of strength were observed but without significant loss of volume. The sudden volume loss was most evident for the samples with highest saturation. Dry and saturated samples generally displayed continuous oscillations in strength, with no collapse. Results showed that up to 67% of the volume change could be lost during the sudden change, typically post peak. It is hypothesised that this behaviour is due to increase of the degree of saturation (reduction in suction) and the availability of the space between the voids.

1 INTRODUCTION

Wetting collapse is a sudden, large deformation behaviour of unsaturated soils Nuth (2009) and it highly depends on the applied mechanical stress and the stress history Buisson & Wheeler (2000). This behaviour is caused by the reduction in suction upon inundation Matyas & Radhakrishna (1968), Escario & Saez (1986), Cox (1978), Lloret & Alonso (1980), and Blanchfield & Anderson (2000). Near the saturation, a large reduction in volume can occur and this is the case for clay soils Alonso et al. (1990) and for coarse-grained soil Blanchfield & Anderson (2000).

When the granular soils are compacted well, the collapse will be limited due to small space accessibility.

This work is, therefore, devoted to the behaviour of the wetting collapse for the unsaturated sand at a high degree of saturation by performing a series of drained constant rate of strain direct shear tests at different normal stresses and applied suctions. The factors affecting this behaviour are explained and therefore, a simple hypothesis is proposed.

2 EXPERIMENTAL WORK

2.1 *Soil properties*

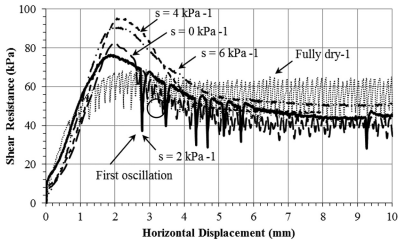
The soil used in this study was fine sand designated as Fraction D available from the David Ball Group, UK. The physical properties and the shear strength parameters for the sand are shown in Table 1.

Table 1. Physical properties and shear strength parameters for the test sand.

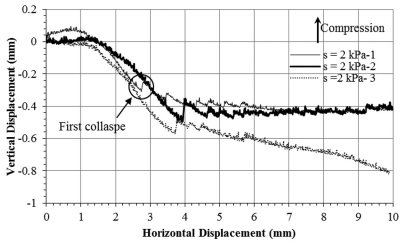
Physical properties	
G_s	2.65
γ_{dry} kN/m^3	15.30
γ_{sat} kN/m^3	19.33
Void ratio, e	0.699
Coefficient of uniformity, *cu*	1.529
Coefficient of curvature, *cv*	1.095
Particle size range mm	0.075–0.3
e_{min}	0.538
e_{max}	0.871
Relative density %	52
Shear strength parameters	
c_{dry} kPa	13.45
ϕ_{dry} degree	44.1

2.2 *Modified direct shear apparatus*

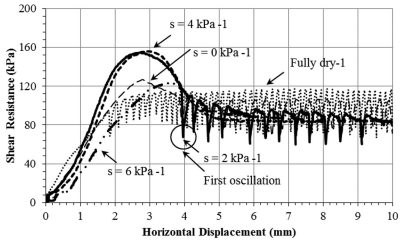
A modified circular direct shear box with a diameter of 80 mm was designed with the following additional features over standard laboratory shear boxes: (i) a High Air Entry Disk (HAED) of 1 bar in the bottom half of the shear box, (ii) grooves at the bottom half of the shear box to form a water reservoir underneath the HAED, (iii) influent and effluent ports in the bottom half of the box to allow saturation of the groove channel during test initialization and connection to a burette (iv) a burette to allow application of a hanging water column for applying and controlling suction. (v) a camera installed in front of the burette to capture the water level in the burette at different stages during the test. The degree of saturation, therefore, can be calculated accordingly. The sample preparation



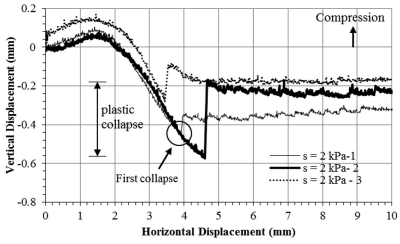
(a) Shear resistance versus horizontal displacement for σ = 50 kPa-1.



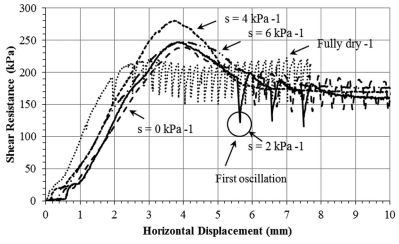
(b) Vertical displacement versus horizontal displacement at *s* = 2 kPa for three repeat tests at σ = 50 kPa.



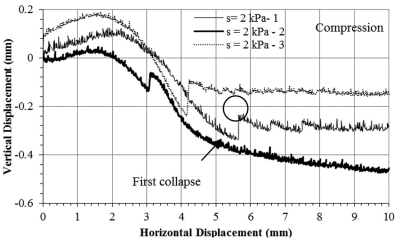
(c) Shear resistance versus horizontal displacement for σ = 100 kPa-1.



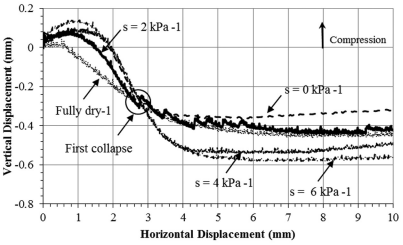
(d) Vertical displacement versus horizontal displacement at *s* = 2 kPa for three repeat tests at σ = 100 kPa.



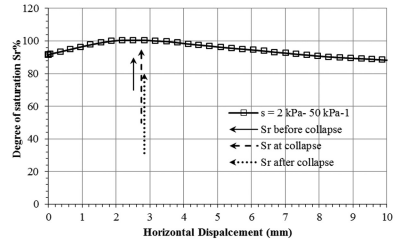
(e) Shear resistance versus horizontal displacement for σ = 200 kPa-1.



(f) Vertical displacement versus horizontal displacement at *s* = 2 kPa for three repeat tests at σ = 200 kPa.



(g) Vertical displacement versus horizontal displacement for σ = 50 kPa-1 and different applied suctions.



(h) Degree of saturation versus horizontal displacement for *s* = 2 kPa and σ = 50 kPa-1.

Figure 1. Direct shear results.

and suction application using the Hanging Column Technique (HCT) are given by Shwan & Smith (2015).

3 RESULTS

A series of drained unsaturated direct shear tests were conducted at different vertical stresses of 50, 100 and 200 kPa and at a range of applied suctions, *s* (dry, 0, 2, 4 and 6 kPa). At each normal stress and applied suction, three repeat tests were conducted and named as 1, 2 and 3, respectively within the figure's legend.

Figures 1a, c and e show shear resistance versus horizontal displacement for the first repeat test for the three applied normal stresses. The shearing rate of the dry, saturated and unsaturated samples were 0.0096, 0.048 and 0.0096 mm/min, respectively.

Unsaturated samples exhibit higher shear resistance compared to the dry and fully saturated cases. Fully dry, saturated and samples of $s = 2$ kPa show a sudden loss of strength (oscillation-circled in Figs. 1a, c and e) then followed by rapid recovery. Other repeat tests (test 2 and 3) demonstrated closely similar behaviour. Figure 1g shows the corresponding vertical displacement versus horizontal displacement of the different applied suctions for $\sigma = 50\ \text{kPa}^{-1}$ where collapse behaviour happened only for the case when $s = 2$ kPa (circled in Fig. 1g). The collapse behaviour was observed for the

Table 2. Degree of saturation at initial and at the wetting collapse for $s = 2$ kPa.

σ kPa	S_{ri} %	S_{rp} %	Wetting collapse %
50-1	91.5	100.4	16
50-2	90.4	96.2	24.3
50-3	89.9	91.6	15
100-1	90.8	101	21.1
100-2	90	96	67.7
100-3	88.9	106.8	65.2
200-1	90.2	111.2	26.9
200-2	89.8	100.1	45.4
200-3	89	113.8	61.7

other repeat tests (1, 2 and 3) at the different applied normal stresses for $s = 2$ kPa as shown in Figures 1b, d and f (the Figs. presented in this manner in order to be easier for the reader to match the first oscillation with the first collapse). The $s = 2$ kPa is close to the air-entry value of the sand used (2.3 kPa). More details about the Soil Water Characteristic Curve (SWCC) of the sand is given by Shwan & Smith (2014).

4 WETTING COLLAPSE AT HIGH DEGREE OF SATURATION

Referring back to Figures 1b, d and f for all cases at $s = 2$ kPa, collapse coincides with the first oscillation of the shear resistance (i.e. see Fig. 1a, oscillation happened at horizontal displacement = 2.74 mm for $s = 2$ kPa^{-1} which coincides with collapse at the same horizontal displacement for $s = 2$ kPa^{-1} in Fig. 1b – circled in the Figs.). This sudden decrease in volume is a wetting plastic deformation change as an irreversible rearrangement of the particles happened.

A huge volume change occurred at a high degree of saturation or near fully saturated case. The hypotheses to explain this behaviour is due, firstly increase of degree of saturation and hence decrease of effective stress and secondly due to availability of the space between the particles. Further details are discussed below.

To further support the first reason of the wetting collapse, Table 2 is presented.

For $s = 2$ kPa, the initial S_{ri} were between (88.9–91.4) % for the three repeat tests. S_{ri} value is calculated by knowing the amount of water expelled from the sample during application of the suction (before shearing). Here the volume of the sample is constant and the initial void ratio is known (e = 0.699 – see Table 1). An increase of the degree of saturation at the plastic collapse S_{rp} can be seen during the shearing (see Table 2). Values of S_{rp} are obtained by performing linear interpolation of the two S_r values before and after the collapse (see Fig. 1h). The values of the S_r before and after the collapse were obtained by knowing the amount of water expelled or imbibed by the sample during the shearing. Here the volume of the sample and void ratio are calculated based on one installed vertical LVDT reading at the corresponding stage of the shearing (before or after the collapse). This is an estimation of the volume and interprets why values of S_{rp} higher than 100% are obtained (see Table 2). Note that for all the cases, the collapse happened at a time not in a match with the time of capturing the water level in the burette by the camera. This is why the interpolation was performed. The errors are expected to be small by using the interpolation for the S_{rp} as the maximum difference between S_r before and after the collapse was 1.5%.

Table 2 shows that up to 67.7 % of the volume change (wetting collapse %) could be lost during the sudden change, typically post peak. The wetting col lapse % in Table 2 was calculated as a percentage between the vertical displacement just before and at the collapse.

Unsaturated samples prepared at $s = 4$ ($S_{ri} = 24$–36%) and $s = 6$ kPa ($S_{ri} = 15$–22%) did not show wetting collapse (see Fig. 1g) indicating the dominance of the high degree of saturation on this behaviour.

The degree of collapse highly depends on the availability of the space between the particles which is the second reason of this behaviour.

In other words, the collapse is significantly affected by the interlocking position for the particles. Fully saturated samples (in spite of their high S_{ri}) did not show any wetting collapse (see Fig. 1g – $s = 0$ kPa^{-1}) because of unavailability of the space between the particles.

The wetting collapse is, therefore, a function of both high degree of saturation and availability of the space between the particles.

5 CONCLUSIONS

The wetting collapse of the unsaturated sand was investigated by performing a series of the drained constant rate of strain direct shear tests while monitoring the degree of saturation. The following conclusions are demonstrated:

1. The wetting collapse occurred at a high degree of saturation at suction near the air entry value of the sand used in this study.
2. The wetting collapse is an irrecoverable plastic deformation in which huge reduction in volume change can be observed. This behaviour has nothing to do with the ultimate resistance of the soil as it is post-peak behaviour.
3. It is hypothesised that the wetting collapse is due to the high degree of saturation and the availability of the space between the particles.

REFERENCES

Alonso, E. E., Gens, A. & Josa, A. 1990. A constitutive model for partially saturated soils. Geotechnique 3, 405–430.

Blanchfield, R. & Anderson, W. 2000. Wetting collapse in opencast coalmine backfill. Proceedings of the ICE-Geotechnical Engineering, 143, 139–149.

Buisson, M. & Wheeler, S. 2000. Inclusion of hydraulic hysteresis in a new elastoplastic framework for unsaturated soils. Experimental evidence and theoretical approaches in unsaturated soils, 109–119.

Cox, D. W. 1978. Volume change of compacted clay fill. Proceedings, Institution of civil engineers conference on clay fills, P.P 79–86 London.

Escario, V. & Saez, J. 1986. The strength of partly saturated soils. Geotechnique, 36, 453–456.

Lloret, A. & Alonso, E. 1980. Consolidation of unsaturated soils including swelling and collapse behaviour. Geotechnique, 30, 449–477.

Matyas, E. L. & Radhakrishna, H. 1968. Volume change characteristics of partially saturated soils. Geotechnique, 18, 432–448.

Nuth, M. 2009. Constitutive modelling of unsaturated soils with hydro-geomechanical couplyings. PhD thesis, École Polytechnique Federale De Lausanne, France.

Shwan, B. J. & Smith, C. C. 2014. Application of limit analysis in unsaturated soils: numerical and experimental study of bearing capacity. In Unsaturated Soils: Research and Applications – Proceedings of the 6th International Conference on Unsaturated Soils, UNSAT 2014 Sydney, Australia.

Shwan, B. J. & Smith, C. C. 2015. Investigation of the shear strength of unsaturated sand using a modified direct shear apparatus. VXI ECSMGE (In press). Edinburgh.

Unsaturated Soil Mechanics—from Theory to Practice – Chen et al. (Eds)
© 2016 Taylor & Francis Group, London, ISBN 978-1-138-02921-7

Development of a new cyclic simple shear apparatus and test verification on loess

S.J. Shao, Q. Wang & S. Shao
Institute of Geotechnical Engineering, Xi'an University of Technology, Xi'an, China

ABSTRACT: A new cyclic simple shear apparatus was recently developed at the Institute of Geotechnical Engineering, Xi'an University of Technology, China and is described in this paper. It has a cubical hinged pressure cell and is driven by three hydraulic-servo-motors. The ingenious pressure cell is composed of four rigid plates installed at the upside, downside, left and right sides of a cubical specimen, as well as two groups of mutually paralleled vertical hinge bars assembled forward and behind the specimen. Both of the right and left plates are hinged to the bottom plate. The top plate in company with the top ends of vertical plate and hinge bars are restricted along the horizontal direction but can move freely along the vertical direction. This pressure cell overcomes the limitations of previous simple shear apparatuses such as non-uniform stress and strain, specific shear plane, and size effect. The capabilities of this apparatus are demonstrated with a series of cyclic simple shear tests on loess specimens under different strain amplitudes.

1 INTRODUCTION

Dynamic soil properties are mainly evaluated using cyclic triaxial compression, cyclic simple shear, cyclic torsion shear, and shaking table tests at laboratory. The advantages and limits of each of these tests have been summarized by Bhatia et al. (1985) and Saada et al. (1982). The cyclic triaxial compression test is used more extensively than the cyclic simple shear test today. However, the cyclic simple shear test comes closest to approximate the field conditions during earthquake loadings, which is generally accepted by researchers. The present simple shear apparatus can be classified into two sorts, one with cylindrical specimen and the other with square specimen.

The first cylindrical simple shear device was devised by Kjellman (1951). The simple is enclosed with a rubber membrane reinforced on the outside by aluminium rings which prevent lateral strain. Roscoe (1953) and Sowers (1963) pointed out that some lateral deformation may generate between the aluminium rings so the lateral stresses will be not indeterminate. Also, the shear stresses across a horizontal circular cross section are not uniform because the stresses must be tangential to the circular boundary unless the vertical walls of the device transmit vertical shear stresses to the sample. Bjerrum and Landva (1966) devised an improved version of the Kjellman (1951) device in their studies of simple shear in clays. The improved device employs a sample 80 mm in diameter and 10 mm high, which is surrounded by a spiral wire reinforced membrane. The stress concentrations are quite local at the edges of the sample and about 70% of the sample is subject to reasonably uniform stress conditions, reported by Lucks et al. (1972).

Roscoe (1953) developed a rectangular specimen type that utilizes four metal plates, which were hinged at edges, to apply simple shear strain to a sample 60 mm square in plan and approximately 22 mm high. For this type, shear strain is more uniform then the cylindrical type, but the contract relations between any two adjacent plates, and the boundary condition of sample are not explicit. Beside, the sealing and water pressure measurement are hard to implement. Thus, Roscoe (1967) improved the old version with contact stress transducers which were used to measure the induced boundary stresses. The Roscoe type modified for repeated loading has been used by many investigators e.g. Peacock and seed (1968), Finn et al. (1971), and Seed and Peacock (1971) in their studies on liquefaction potential.

This paper reports a new rectangular type of cyclic simple shear apparatus that was recently developed in the Xi'an University of Technology, and analyzed the testing results of loess under different conditions. The device is featured with the upper loading plate that is not hinged with anyone of the lateral confining plates. The upper loading plate is restricted with a top cap, thus can move along the vertical direction rather than horizontal direction. The top end of the lateral confining plates is coupled with two steel rollers at angle, whose motion is limited along vertical path and can rotate freely. Following this, the contract between lateral confining plate and top plate can be considered as equivalent hinge. The more important improvement is the top plate can move along vertical direction freely thus conduct vertical load and displacement. This device could simulate various field loading conditions under pure shear strain, especially for earthquake load. It can be used to investigate dynamic stress-strain

relations under drainage and un-drainage condition, damping ratio, seismic settlement, and liquefaction.

2 THE APPARATUS

The cyclic triaxial device consists of the following components: a pressure cell, a stress application system, and a measurement and control system. A brief description of these components is provided below.

2.1 *Pressure cell*

Similar to the construction of Roscoe (1953) type, the pressure cell of this one also has four square rigid plates for surrounding a cubical space. However, the four square rigid plates of the Roscoe (1953) type are hinged end to end, while for this type both vertical plates are hinged to bottom plate not to top plate. The top view of the pressure cell is shown in Figure 1(a). It can be seen from Figure 1(a) that a cubical cell is composed of three rigid plates at left, right and bottom sides, two groups of paralleled link arms at the both front and behind faces, besides a rigid plate at top side that is not displayed in this figure. Both ends of the link arms are hinged to two cross beams, which are restricted to a base frame along slide guide with roller bearing. A definite gap is set up between any two adjacent link arms so as to ensure the link arm is able to rotate with respect to the cross beam. The rotation of link arms as well as the vertical movement of the cross beam are consistent with the rotation between left/right plates and bottom plate. The linkage mechanism is shown from Figure 1(b) that both right and left rigid plates are fixed to a groove steel with four screws, respectively; the groove steel is hinged to the four cross beams at corners; the rotation of link arms thus works following the rotation between the vertical and bottom plates; the bottom plate is installed to a rolling base plate which can linearly move back and forth.

Then, the cubical space as shown in Figure 1(a) is the pressure cell for specimen that is enclosed with four rigid plates and two groups of paralleled link arms. It also can be seen from Figures 1(b) that the vertical and bottom sides of pressure cell are hinged to each other and fixed to the base frame and the rolling base. However, the top side for pressure cell is not hinged to them. The top rigid plate is installed to a loading ram. The loading ram is confined with a top cap which is fixed to the base frame with six screws. The top cap could restrict the loading ram and top rigid plate to move along the vertical direction.

3 STRESS APPLICATION SYSTEM

The pressure cell as depicted above is suitable for a cubic specimen with side length of 70 cm. The specimen is firstly put into a custom-made membrane mold and then set into the pressure cell. The faces of specimen cling to internal face of pressure cell so that the pressure cell could provide lateral confining conditions. Correspondingly, the simple shear test on cubic specimen under lateral confining conditions need two loading systems, one along the vertical direction for vertical loads and the other along the horizontal direction providing shear force, as shown in Figure 2.

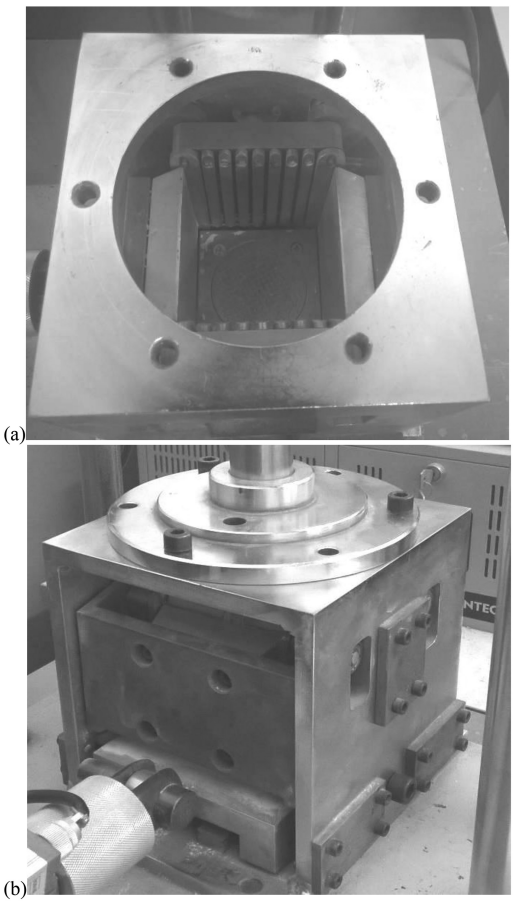


Figure 1. (a) Top view and (b) end view of pressure cell.

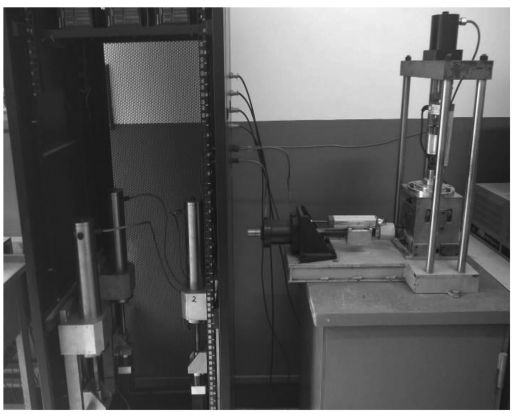


Figure 2. General view of the cyclic simple shear apparatus.

The vertical directional loading system exerts force on the upper face of specimen along the vertical direction. Figure 2 exhibits that a hydraulic cylinder is screwed to the reaction frame. The hydraulic cylinder is connected to another one which is directly driven by a step-servo motor, and its piston is screwed to a load transducer. The load transducer and the loading ram are linked with a adjustable attachment that consists of three segments. The three segments are connected with a steel bolt and a screwed cap, with which the three segments can adjust the interval between the load transducer and the loading ram along the vertical direction. Moreover, the adjustable attachment as well as the loading transducer and the loading ram can be taken apart from the reaction frame. These detachable parts are convenient for the installation and un-installation of soil specimen.

The horizontal directional loading system applies push as well as pull forces to the rolling base along one dimensional horizontal direction. It can be seen from Figure 3 that the horizontal piston-cylinder is connected with two hydraulic cylinders. Correspondingly, one provides horizontal push force and the other exerts horizontal pull force. Hence, the rolling base can move back and forth under the push-pull forces. At the same time, the rolling base drives the bottom rigid plate making a horizontal reciprocating motion, which drives the other parts of pressure cell rotating. The connection between the horizontal loading piston rod and rolling base is the same as that along the vertical direction. However, the horizontal connection does not need reinstallation once the initial position of rolling base was adjusted well and the horizontal displacement and pressure transducers were fixed.

3.1 *Measurement and control systems*

The automatic measurements of deformation and pressure and the control systems mainly consist of transducer, data acquisition system and control cabinet. Two groups of load and displacement transducers are set up for measuring the vertical and horizontal directional stress and displacement. Each of them are installed to the piston rods along the horizontal and vertical directions, as shown in Figure 2. The vertical directional load transducer is used to measure the stress acting on the upper surface of specimen, while the horizontal directional load transducer is utilized to record the shear stress loading paralleled to the bottom face of specimen.

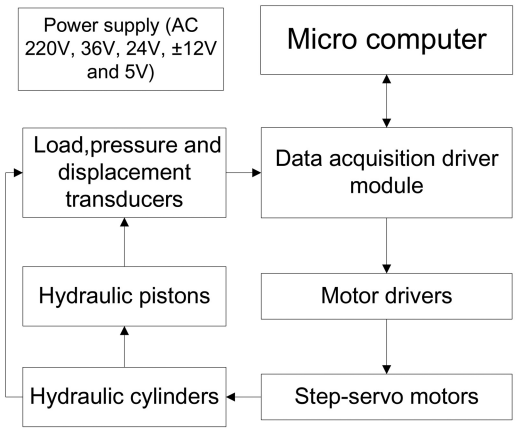


Figure 3. Control diagram of cyclic simple shear apparatus.

Both the pressure and deformation in both vertical and horizontal directions are fed back to microcomputer in real time, and thus microcomputer could control stress application and strain developing in predetermined paths. The control diagram of this process is illustrated in Figure 3 and can be finished automatically in such orders: (1) transducer measures stress or stain; (2) stress or strain translates to voltage messages through resistance strain gage; (3) electrical signal of voltage is amplified and fed back to microcomputer; (4) inverse feedback runs in microcomputer; and (5) message of feedback is sent back to control step-servo motor.

4 TESTING PERFORMANCE OF THE CYCLIC SIMPLE SHEAR APPARATUS

The cyclic simple shear apparatus could perform three kinds of geotechnical tests on soils or loess deposits, i.e., consolidation test, slow simple shear test, and cyclic simple shear test. The consolidation test can be performed with such input options as horizontal load, vertical load, and consolidation time. The slow simple shear test can be conducted under different vertical loads and horizontal strain rates, and its off-test can be controlled with a predetermined horizontal displacement. Comparatively, the cyclic simple shear test is able to be carried out with such controlling parameters as vertical load, adjusting period of step-servo motors, amplitude of horizontal strain, period of cyclic load, types of cyclic load, etc.

A large number of historical earthquake investigations show that earthquake damages on loess such as seismic subsidence, landslip and liquefaction have been a main risk for loess area. Accordingly, many researchers i.e., Zhang (1986 and 1990), Wang (2000) and Xu (2006) worked on the earthquake damages of loess and achieved a lot of developments. However, all of these studies were carried out on the basis of the dynamic triaxial tests, even through the dynamic triaxial apparatus is not the best approach to simulate the site effect of earthquake load. Considering the stress waves in level ground conditions, the most approximate simulation is based on a shear wave which propagates vertically in the soil, even though the propagation of seismic waves is actually more complex than that. The main advantage of cyclic simple shear tests is that the shear plane is horizontal compared to triaxial tests. Thus, the stress conditions of cyclic simple shear tests are closer to in situ conditions under earthquake. Here a series of tests are performed on undisturbed loess specimens for verifying the performance of the

Table 1. Physical parameters of loess specimens.

Embedded Depth m	Dry density g/cm^3	Pore ratio	Natural water content %	Plasticity index
4	1.228	1.198	3.74	8.73
16	1.296	1.084	12.39	8.37
20	1.338	1.018	12.23	8.44

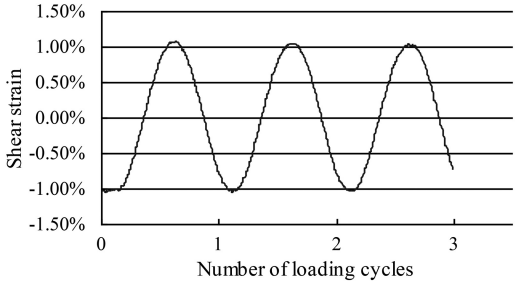


Figure 4. Time history of shear strain.

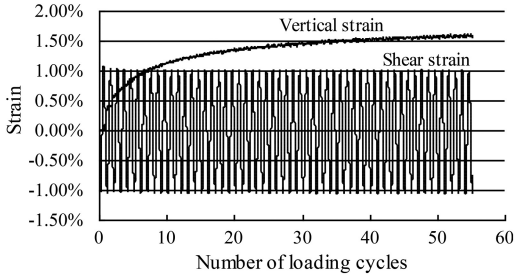


Figure 5. Time histories of both shear and vertical strains.

cyclic simple shear apparatus as well as the seismic subsidence behaviors of loess. The loess specimens were sampled from Dingxi metropolitan area of Gansu province with the embedded depths of 4, 16 and 20 m. Their basic physical parameters are listed in Table 1. Table 1 shows that the loess deposits have relative larger pore ratio and smaller plasticity index, which are representative physical parameters of typical silt loess with large pores or structural skeleton.

Cyclic simple shear tests were conducted on loess specimens using the strain-controlled cyclic loading with uniform strain amplitude and under different water contents, vertical stresses and strain amplitudes. Figure 4 displays the loading history of uniform strain amplitude of 1% versus the number of loading cycles. The loading history processes along a perfect sinusoidal curve which is predefined by the control program of this apparatus. This obviously demonstrates the sensitive measurement and the reliable loading control of apparatus. Figure 5 exhibits the developing process of vertical strain for the loess specimen of embedded depth = 20 m under the cyclic loading with uniform strain amplitude. It can be seen from Figure 5 that the vertical strain increases rapidly at the

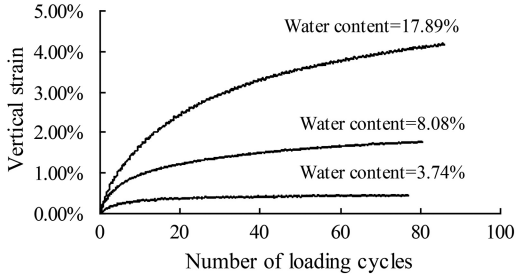


Figure 6. Vertical strain versus the number of loading cycles for loess specimen under different water contents.

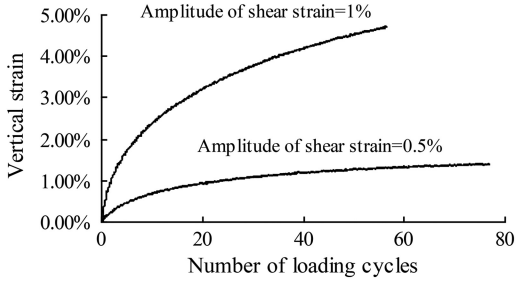


Figure 7. Time history of vertical strain under different amplitudes of shear strain.

early stage of loading process and most of final vertical stain has been accumulated. The following cyclic loading does not produce significant increment of vertical strain. This laboratory phenomenon is mainly because of the structure with large pores and weak linkage between soil particles. The collapse of structure will happen once the weak linkages are destroyed by cyclic loading. Then, the divorced soil particles would fill in the pores of loess. The collapse companied with the filling could lead to the rapid settlement of loess site, that is the formation cause of seismic subsidence of loess.

The major loading conditions for vertical strain include two aspects of loading conditions and physical properties. The loading conditions depend on dynamic loads, i.e., shaking number, loading mode, predominant period and peak of acceleration, while the physical properties of loess involves density, void ratio, water content and micro-structure etc. Figure 6 show the vertical strain versus the number of loading cycles of loess specimens (embedded depth = 4 m) under different water contents. It is clear that the magnitude of vertical strain is larger with larger water content; and that the increment speed is also larger at the initial stage of vertical strain for loess under larger water content than that under smaller water content, on account of the damage effect of water on loess structure. Figure 7 illustrates the influence of amplitude of uniform strain on vertical strain. Vertical strain is not obvious under smaller amplitude of strain and does not increase anymore after a certain loading cycles. However, the vertical strain increases significantly under larger strain amplitude than smaller one.

5 CONCLUSIONS

A new type of cyclic simple shear apparatus was developed by S. J. Shao et al. in the the Institute of Geotechnical Engineering, Xi'an University of Technology, China. The apparatus has a cubical hinged pressure cell that is composed of four rigid plates each installed at the upside, downside, left and right sides of a cubical specimen, as well as two groups of mutually paralleled vertical hinge bars assembled forward and behind the specimen. The device is featured with the upper loading plate that is not hinged with anyone of the lateral confining plates but restricted with a top cap. The more important improvement is the top plate can move along vertical direction freely rather than horizontal direction thus conduct vertical load and displacement. This pressure cell overcomes the limitations of previous simple shear apparatuses such as non-uniform stress and strain, specific shear plane, and size effect.

Test results on undisturbed loess specimens with different water contents, vertical loads and amplitudes of shear strain show that: (1) the apparatus has a reliable control system and a sensitive measurement system; (2) relationships between vertical strain, shear strain and the number of loading cycles could reveal the formation process of seismic subsidence of loess; and (3) vertical strain of loess become larger with larger water content and amplitude of shear strain.

ACKNOWLEDGEMENTS

This research was financially supported by the National Natural Science Foundation of China (No. 41272320).

REFERENCES

Bhatia, S., Schwab, J. & Ishibashi, I. 1985. Cyclic Simple Shear, Torsional Shear, and Triacial — A Comparative Study, In the V. Khosla (eds), *Advances in the Art of Testing Soils under Cyclic Conditions*, *Detroit, 24 October 1985*. Virginia: Amer Society of Civil Engineers.

Bjerrum, L. & Landva, A. 1966. Direct Simple Shear Tests on Norwegian Quick Clay. *Geotechnique* 16(1): 1–20.

Finn, W. D. L., Pickering, D. J. & Bransby, P. L. 1971. Sand Liquefaction in Triaxial and Simple Shear Tests. *Journal of the Soil Mechanics and Foundations* Division. 97(No. SM4): 639–659.

Kjellman, W. 1951. Testing of Shear Strength of Clay in Sweden, *Geotechnique* 2: 225–232.

Lucks, A. S., Christian, J. T. & Gregg, E. B., et al. 1972. Stress conditions in NGI simple shear test. *Journal of the Soil Mechanics and Foundations* Division 98(SM1): Paper 8618.

Peacock, W. H. & Seed, H. B. 1968. Sand liquefaction under cyclic loading simple shear conditions. *Journal of the soil Mechanics and Foundations* Division 94(No. SM3): 689–708.

Roscoe, K. H., Bassett, R. H. & Cole, E. R. L. 1967. Principal axes observed during simple shear of a sand. *Proceedings of the Geotechnical Conference, Oslo, 21–24 February 1976.* Oslo: Norwegian Geotechnical institute.

Roscoe, K. H. 1953. An Apparatus for the Application of Simple Shear to Soil Samples Proceedings, *Third International Conference on Soil Mechanics and Foundation Conference Engineering, Switzerland 16–27 August 1953*. Zurich: Organizing Committee.

Seed, H. B. & Peacock, W. H. 1971. Test Procedures for Measuring Soil Liquefaction Characteristics. *Journal of the Soil Mechanics and Foundation* Division, 97(No. SM8): 1099–1119.

Saada, A. S., Fries, G. & Ker, C. C., 1982. An Evaluation of Laboratory Testing Techniques in Soil Mechanics. *Soils Found* 23(2): 381–395.

Sowers, G. F. 1963. Strength Testing of Soils. *Laboratory Shear Testing of Soil*, A. S. T. M. Special Technical Publication (No. 361): 3–21.

Wang, L. M., Yuan, Z. X., & Wang, J. et al. 2000. Laboratory Study of Effect of Dry Density on Seismic Settlement of Compacted Loess. *Earthquake Engineering and Earthquake Vibration* 20(1): 75–80.

Xu, S. H., Wang, L. M. & Yuan, Z. X. 2006. Study on Initial Judging Criterions of Loess Seismic Subsidence. *Northwest Seismological Journal* 28(2): 140–143.

Zhang, Z. Z. & Duan, R. W. 1986. Discussion on Seismic Subsidence of Loess Sites in The Northwest of China during Earthquakes. In V. Cotecchia (eds), *Proceedings of the International Symposium on Engineering Geology Problems in Seismic Areas*, *Bari, 13–19 April 1986*. Bari: Istituto.

Zhang, Z. Z., Duan, R. W. & Wang, L. M. 1990. Judgment and Predication of Seismic Subsidence of Loess. *The third conference of nation soil dynamics symposium, Shanghai, 22–25 June 1990*. Shanghai: Tongji University Press.

This page intentionally left blank

Unsaturated Soil Mechanics—from Theory to Practice – Chen et al. (Eds)
© 2016 Taylor & Francis Group, London, ISBN 978-1-138-02921-7

Consolidation behavior of unsaturated Chuanxi compacted soil with soil suction control oedometer

D. Lu & W. Li
School of Civil Engineering, Southwest Jiaotong University, Chengdu, P. R. China

ABSTRACT: Compacted soil has been used widely in geotechnical engineering. In the construction of highway embankments, earth dams, and many other engineering structures, loose soils must be compacted to increase their unit weights. In the present work, soil suction were controlled for three kinds of soil samples and the compressibility of the compacted remolded soil, especially the variation of compaction mechanical parameters with soil density and soil suction, was studied under the coupling action of water (suction)-stress (additional stress) in order to predict the rules of the volumetric strain of the Chuanxi compacted soil structure (roadbed, slope, earth dam, etc) under different climatic hydrologic conditions.

1 INTRODUCTION

The soil compaction quality directly affects their operation situation of various fill structures such as railway subgrade, highway subgrade and earth dam etc. The remolded compacted soil belongs to unsaturated soil after transportation operation (Fredlund & Rahardjo 1993). Thus, it's necessary to study compression properties of the compacted soil whose natural void is normally large under different water-stress coupling conditions. The soil one-dimensional compressibility (i.e. consolidation behavior) is expressed by two parameters in soil mechanic: compression index and preconsolidation stress. The compressibility of unsaturated soil has been researched widely in recent years. The research result of the soils whose physical properties are similar to the compacted soil shows that: preconsolidation stress decreases with the increase of water content (Alexandrou & Earl 1998, Défossez et al. 2003, Imhoff et al. 2004, Mosaddeghi et al. 2006). For compression index, some results show that it decreases with the increase of water content (Zhang et al. 1997, Défossez et al. 2003), while another researches show that the variation of water content has no significant effect on the compression index (Larson et al. 1980, O'Sullivan 1992, Smith et al. 1997, Arvidsson & Keller 2004, Imhoff et al. 2004, Mosaddeghi et al. 2006). It is noteworthy that all of these researches study the soil compressibility by controlling water content rather than soil suction. Soil structure would be variable with the increase of saturation degree during the compression process, which causes the changes in compression index and preconsolidation stress. Therefore, it is not accurate enough to reflect the relationship between soil moisture condition and compressibility by controlling water content. Suction-control technique which can maintain constant water content is the only method to solve this problem. Suction is rightly the cause of the change in water content. The relationship between suction and water content is equivalent to the relationship between stress and strain. It is possible to analyze the compressibility of compacted soil through suction-control instead of moisture-control in compression experiment. This technique has been used widely in clay and other soils with large density. Some results show the compression index decreases with the increase of soil suction (Alonso et al. 1990, Cui & Delage 1996, Chen et al. 1999, Rampino et al. 2000, Mancuso et al. 2002, Romero et al. 2003), while another results show the compression index increases with suction (Adams & Wulfsohn 1998, Kogho et al. 2001, Wang et al. 2002, Futai & Amleida 2005) and the proconsolidation stress increases with suction also (Cui & Delage 1996, Alexandrou & Earl 1998, Défossez et al. 2003, Imhoff et al. 2004, Mosaddeghi et al. 2006). There are various reasons for these differences such as the differences in soil structure (type of soil) and initial conditions (initial density, initial suction and suction range etc.). The research on compression properties of Chuanxi mixed soil, which is a major compacted soil used in geotechnical fill structures such as railway and highway subgrades in the west of Sichuan province, with soil suction control has not been carried out currently in China.

In this paper, the consolidation behavior of Chuanxi unsaturated mixed soil, in particular the change in compression modulus, was analyzed under different hydrologic conditions (soil suction), initial conditions (density) and stress conditions (additional stress).

2 METHODS AND MATERIALS

2.1 *Test equipment*

The used test equipment was strain-controlled direct shear apparatus which can be used for consolidation test and direct shear test of unsaturated soil. The applied vertical maximum stress can reach 800 kPa. The air entry value of ceramic plate is 500 kPa (i.e. the maximum value of controlled suctions).

2.2 *Soil samples preparation*

The soil was humidified by pulverization to reach the controlled initial water content of 10% (dry state). Then, three kinds of mixed soil samples could be prepared by compaction in the cell to reach 61.8 mm in diameter and 40 mm in height.

2.3 *Test program*

Compression tests were separately conducted to three kinds of mixed soil with different initial void ratios ($e_0 = 0.7$, 0.9 and 1.1) and controlled suctions ($s = 50$, 100, 200, and 400 kPa). Consolidation test were carried out under stepwise loading with applied vertical stress sequentially 50 kPa, 100 kPa, 200 kPa, 400 kPa and 800 kPa. The vertical displacements of soil samples were recorded successively in order of time. The stable standard of vertical deformation for each stress step is less than 0.004 mm/h.

3 RESULTS AND DISCUSSION

3.1 *Change in void ratio*

Based on the test data, according to three kinds of mixed soil samples at different initial void ratios and suctions conditions, the consolidation curves (e-lg p) are shown in Figure 1, which presents the change in void ratio during the loading process for two types of soil. Figure 2 indicates the e-lg p curves of three types of soil with the same initial void ratio $e_0 = 0.7$ and the same soil matric suction ($s = 50$ or 200 kPa). The other curves under different void ratios and suction values are not shown in this paper because of their similar form.

Figures 1a and 1b show that with greater the suction, the upper curve indicates a slower decrease in void ratio under the same initial void ratio. In other words, the greater soil suctions, under the same loading process, the value of the settlement decreases with that of the compressibility of the soil. This shows that with the increase of suction, soil resistance could be strengthened. This is mainly because as the water content decreases (i.e. the suction increases), the water-air interface tension gradually increases, resulting in an additional contact force between soil particles. Therefore, the soil resistance has been enhanced. The soil suction is a key parameter affecting the consolidation behavior of mixed soil. Moreover, the smaller

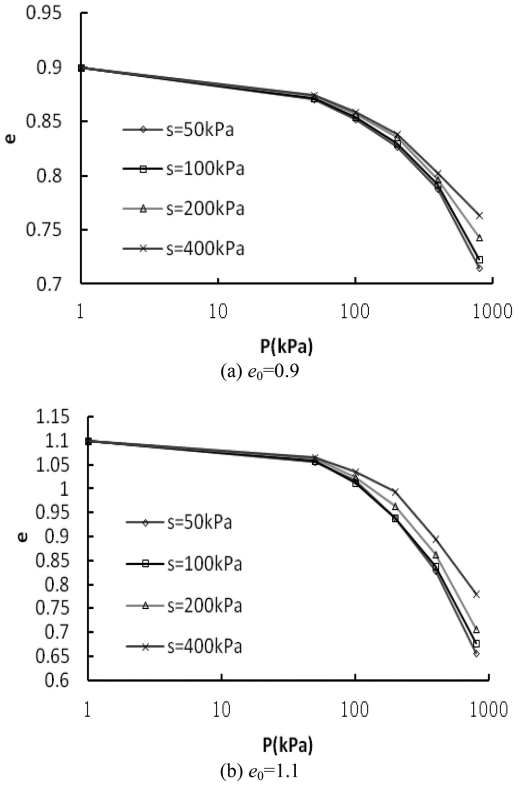
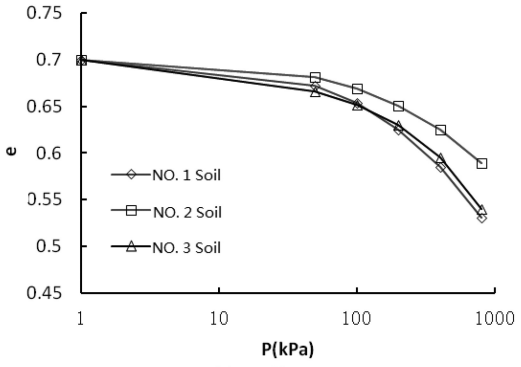


Figure 1. Consolidation curves (e-lg p) modified with suction for soil I (a) and soil II (b) under different initial void ratio ($e_0 = 0.9$ and 1.1).

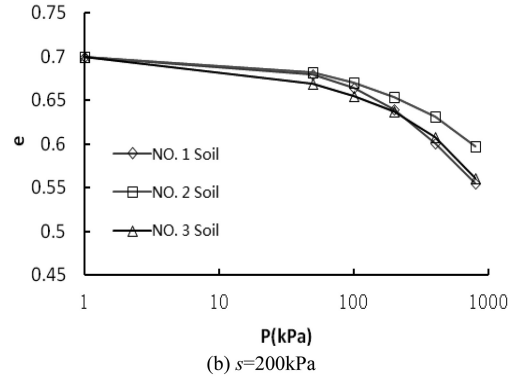
the initial void ratio, the smaller change in void ratio. Therefore, it's shown that the initial void ratio is also an important factor that affects mixed soil consolidation behaviors.

As can be seen in Figure 2, there is a little difference between three soils at the beginning. In the second stage of consolidation, with the same suction, the curve slope of soil II should be smaller than the other two soils. This may be because three soil samples contain different content of quartz and K feldspar minerals (soil I 41%-42%, soil II 72%-80%, soil III 43%-50%) and similar clay minerals content. Clay minerals can form the cementation between soil particles. In the first stage, clay minerals content determines the shape of the curves. While in the second stage, starting from $p = 100$ kPa, soil resistance is provided by coarse particles. Soil II has the maximum content of high strength minerals and then a smaller slope in consolidation curve. The results show that the soil mineral composition, content and particle size distribution are important factors influencing mixed soil consolidation behavior.

As can be seen in Figure 2, there is a little difference between three soils at the beginning. In the second stage of consolidation, with the same suction, the curve slope of soil II should be smaller than the other two soils. This may be because three soil samples contain



(a) s=50kPa



(b) s=200kPa

Figure 2. Consolidation curves (e-lg$p$) of three kinds of mixed soil with the same initial void ratio ($e_0 = 0.7$) and suction ($s = 50$ or 200 kPa).

different content of quartz and K feldspar minerals (soil I 41%-42%, soil II 72%-80%, soil III 43%-50%) and similar clay minerals content. Clay minerals can form the cementation between soil particles. In the first stage, clay minerals content determines the shape of the curves. While in the second stage, starting from $p = 100$ kPa, soil resistance is provided by coarse particles. Soil II has the maximum content of high strength minerals and then a smaller slope in consolidation curve. The results show that the soil mineral composition, content and particle size distribution are important factors influencing mixed soil consolidation behavior.

Cui (2011) carried out the consolidation tests with suction control on Guangxi expansive soil under the similar conditions ($e_0 = 0.9$, $s = 200$ kPa, $p = 800$ kPa), while the variation in void ratio for expansive soil is much smaller than the mixed soil. The main reason for this difference may be that the fine particles content of three kinds of mixed soil is far less than Guangxi expansive soils. Due to the higher soil fines content, under the same suction, the more intergranular liquid content is, the more suction-affected area will be, thus leading to a rise in soil resistance. It can be inferred that fines content is also an important factor affecting the consolidation behaviors of unsaturated mixed soil.

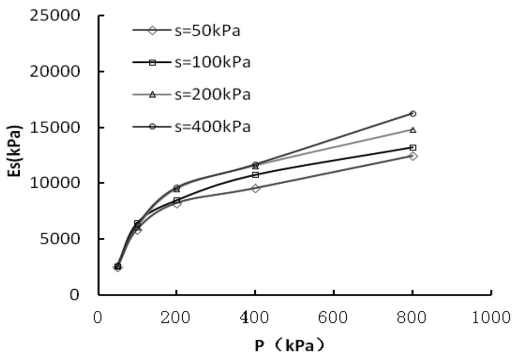


Figure 3. Change in compression modulus with soil suction for soil III with $e_0 = 0.7$.

Table 1. Change in compression modulus for three kinds of mixed soil ($e_0 = 0.7$, $s = 50$ kPa).

	Compression modulus: Es		
Vertical stress: p kPa	Soil I MPa	Soil II MPa	Soil III MPa
50	3.1	4.5	2.4
100	4.7	6.8	5.8
200	5.8	9.1	8.2
400	8.7	13.7	9.5
800	12.3	18.7	12.4

3.2 *Change in compression modulus*

Figure 3 shows the change of compression modulus with soil suction and applied vertical stress for soil III with $e_0 = 0.7$. The other curves under different void ratio sand suction values are not shown in this paper because of their similar form. The compression modulus increased with soil suction. That's mainly because the larger suction, the more likely the contractile skin (water-air interface) serves to improve soil strength. However, the change of some points at the beginning is contrary to this conclusion, which may be related to the lower load and unstable contact between piston and soil sample. In different soil samples, the increase of compression modulus varies (Table 1), because three kinds of soil contain different content of quartz, K feldspar and clay minerals.

4 CONCLUSIONS

In this paper, consolidation behaviors of three unsaturated mixed soils have been studied with different initial void ratios and controlled suctions.

The compression modulus increases with the suction and the loads for the same soil. It increases with the decrease of the initial void ratio. Soil II has a large resistance and a maximum compression modulus. The results show that the consolidation behaviors of

unsaturated mixed soil could be affected principally by initial void ratio, soil suction, mineral composition and fines content.

ACKNOWLEDGEMENTS

This paper was supported by the Open Project Program of National Engineering Laboratory for Technology of Geological Disaster Prevention in Land Transportation.

REFERENCES

Adams, A. & Wulfsohn, D. 1998. Critical-state behaviour of an agricultural soil. *Journal Agricultural Engineering Research* 70: 345–354.

Alexandrou, A. & Earl, R. 1998. The relationship among the pre-compaction stress, volumetric water content and initial bulk density of soil. *Journal Agricultural Engineering Research* 71: 75–80.

Alonso, E.E., Gens, A. & Josa, A. 1990. A constitutive model for partially saturated soils. *Géotechnique* 40: 405–430.

Arvidsson, J. & Keller, T. 2004. Soil precompression stress: I. A survey of Swedish arable soils. *Soil & Tillage Research* 77: 85–95.

Chen, Z.H., Fredlund, D.G. & Julian, K.M.G. 1999. Overall volume change, water volume change, and yield associated with an unsaturated compacted loess. *Canadian Geotechnical Journal* 36: 321–329.

Cui, Y.J. & Delage, P. 1996. Yielding and plastic behaviour of an unsaturated compacted silt. *Géotechnique* 46: 291–311.

Cui, Y. & Miao, L.C. 2011. Testing study of permeability characteristics of unsaturated compacted expansive soils, *Rock and Soil Mechanics* 32(7): 2007–2012.

Défossez, P., Richard, G., Boizard, H. & O'Sullivan, M. 2003. Modelling change in soil compaction due to traffic as function of soil water content. *Geoderma* 116: 89–105.

Fredlund, D.G. & Rahardjo, H. 1993. *Soil mechanics for unsaturated soils*. New York: John Wiley & Sons, Inc.

Futai, M.M. & Almeida, M.S.S. 2005. An experimental investigation of the mechanical behaviour of an unsaturated gneiss residual soil. *Géotechnique* 55: 201–213.

Imhoff, S., Da Saliva, A.P. & Fallow, D. 2004. Susceptibility to compaction, load support capacity and soil compressibility of Hapludox. *Soil Science Society of America Journal* 68: 17–24.

Kogho, Y., Asano, I. & Tagashira, H. 2001. Modelling of state surfaces of unsaturated soils. In K. Adachi & M. Fukue (eds), *Clay Science for engineering*: 467–474. Rotterdam: Balkema.

Larson, W.E., Gupta, S.C. & Useche, R.A. 1980. Compression of agricultural soils from eight soil orders. *Soil Science Society of America Journal* 44: 450–457.

Mancuso, C., Vassallo, R. & d'Onofrio, A. 2002. Small strain behavior of a silty sand in controlled-suction resonant column-torsional shear tests. *Canadian Geotechnical Journal* 39: 22–31.

Mosaddeghi, M.R., Hemmat, A., Hajabbasi, M.A., Vafaeian, M. & Alexandrou, A. 2006. Plate sinkage versus confined compression tests fir In Situ soil compressibility studies. *Biosystems Engineering* 93: 325–334.

O'Sullivan, M.F. 1992. Uniaxial compaction effects on soil physical properties in relation to soil type and cultivation. *Soil & Tillage Research* 24: 257–269.

Rampino, C., Mancuso, C. & Vinale, F. 2000. Experimental behaviour and modelling of an unsaturated compacted soil. *Canadian Geotechnical Journal* 37: 748–763.

Romero, E., Gens, A. & Lloret, A. 2003. Suction effects on a compacted clay under non-isothermal conditions. *Géotechnique* 53: 65–81.

Smith, C.W., Johnston, M.A. & Lorentz, S. 1997. Assessing the compaction susceptibility of South African forestry soils. II. Soil properties affecting compactibility and compressibility. *Soil & Tillage Research* 43: 335–354.

Wang, Q., Pufahl, D.E. & Fredlund, D.G. 2002. A study of critical state on an unsaturated silty soil. *Canadian Geotechnical Journal* 39: 213–218.

Zhang, H., Hartge, K.H. & Ringe, H. 1997. Effectiveness of organic matter incorporation in reducing soil compactibility. *Soil Science Society of America Journal* 61: 239–245.

Unsaturated Soil Mechanics—from Theory to Practice – Chen et al. (Eds)
© 2016 Taylor & Francis Group, London, ISBN 978-1-138-02921-7

Experimental study of mechanical behavior of unsaturated silty clay in different loading sequences under constant water content condition

A.M. Rasool, K. Jiro & T. Shinya
Saitama University, Japan

ABSTRACT: Constant water content tests correspond to a field condition in which the rate of loading is much higher than the rate at which the pore water is able to drain out of the unsaturated soil. In order to study mechanical behavior of unsaturated soil a series of constant water content tests was performed in this study. Soil specimens were tested under isotropic loading-unloading, monotonic and cyclic loads. In this research, different loading sequences were applied to study effects of stress history on change in void ratio and suction, and on shear characteristics of unsaturated soil.

1 INTRODUCTION

The suction dependency of the mechanical behavior of unsaturated soil has been discussed by several researchers e.g., Fredlund et al., 1978; Cui & Delage, 1996; Toyota et al., 2003; Geiser et al., 2006). However, many of studies were conducted under drained conditions for both the pore air and the pore water, i.e., constant suction conditions, or undrained conditions for only the pore water and drained conditions for the pore air, due to the difficulty of measuring or controlling the air pressure. Nishimatsu et al. (2004), Kodaka et al. (2006), and Oka et al. (2010) conducted triaxial tests under fully undrained conditions, namely, constant water and constant air shearing tests, and discussed the importance of air pressure on the mechanical behavior of unsaturated silty soil. In practice, drained conditions for water and air cannot always be attained; for example, the increase in air pressure in a river embankment during the seepage. Therefore, it is necessary to investigate the unsaturated soil behavior under fully undrained conditions by measuring both the pore air pressure and the pore water pressure. For dynamic behavior, many researchers have considered the liquefaction resistance of partially saturated soil, and have reported that degree of saturation has a significant effect on the behavior during cyclic loading (e.g., Yoshimi et al. 1989; Tsukamoto et al., 2002; Okamura and Soga, 2006; Sawada et al., 2006). Neither pore air nor pore water can efficiently flow out from the soil skeleton during earthquakes. Hence, the behavior of the pore air pressure is also considered to play an important role during dynamic loading as well as during monotonic loading. However, there are few studies in which changes in air pressure have been investigated. Yabuki et al. (2007) conducted cyclic triaxial tests of unsaturated silt under fully undrained conditions, and measured the changes in pore air pressure and pore water pressure separately. Unno et al. (2008) performed cyclic tests on unsaturated sand with low levels of suction, in which the pore air pressure as well as the pore water pressure were measured.Rojas and Mancuso (2009) reported that the effect of the strain rate on the soil behavior during shear tests under drained conditions appears to be negligible when the level of strain rate is 0.25–2.5%/h for the tested silty sand. Oka et al. (2010) conducted monotonic triaxial tests with different strain rates for unsaturated compacted silt, and showed that the strain rate affected the stress-strain relations and the stress paths for the fully undrained tests. The effect of the loading rate during cyclic loading has been examined for saturated soils by several researchers (e.g., Yamamoto & Hyodo, 2000). They showed that the cyclic strength of saturated clayey soil is higher with a higher loading rate, i.e., with higher frequency. As for unsaturated soils, Nishimura and Koseki (2009) have recently showed frequency dependent behavior of unsaturated silty soil under undrained conditions. However, there are still many uncertainties on the rate dependent behavior of unsaturated soils especially under fully undrained conditions. In the present study, a series of monotonic and cyclic load tests under undrained conditions has been conducted on silty soil. The effect of stress history on change in void ratio and suction and on shear characteristics of unsaturated soil was studied in this research.

2 STATE BOUNDARY SURFACE

2.1 *Saturated soils*

The basic equation for the state boundary surface for the ordinary Cam clay, a model for saturated soil is

$$\frac{q'}{M_{p'}} + \left(\frac{\lambda}{\lambda - k}\right) ln\, p' - \left(\frac{\Gamma - v}{\lambda - k}\right) = 1 \qquad (1)$$

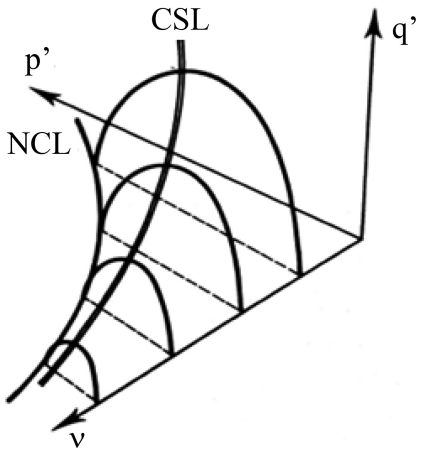


Figure 1. State boundary surface saturated soils.

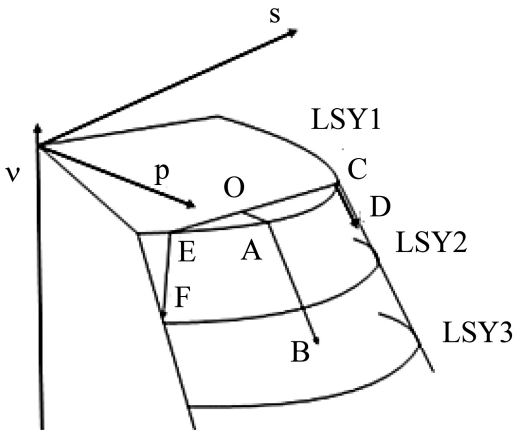


Figure 2. Schematic plots of the corresponding plastic hardening surface in p–s–ν space.

This defines the state boundary surface shown in Figure 1 surface meets ν : p′ plane along isotropic normal compression line where $q' = 0$ and $\nu = N - \lambda \ln p'$ hence, substituting into Equation 1.

$$N - \Gamma = \lambda - k \tag{2}$$

The curve shown in Figure 1 are constant volume sections and undrained stress paths. The equation for an undrained stress path can be obtained from Equation 1 with $\nu = \Gamma - \lambda \ln p'_c$, where p'_c is the stress at the intersection of the constant volume section and the critical state line and is

$$\frac{q'}{M_{p'}} + \left(\frac{\lambda}{\lambda - k}\right) ln - \left(\frac{p'}{p_c}\right) = 1 \tag{3}$$

A yield curve is the intersection of an elastic wall given by $\nu = \nu_k - k \ln p'$ with the state boundary surface. At the critical state line the specific volume is ν_c and the mean stress is p'_c. Eliminating ν and ν_k, the equation for the yield curve is

$$\frac{q'}{M_{p'}} + ln \left(\frac{p'}{p_c}\right) = 1 \tag{4}$$

2.2 *Unsaturated soils*

The difficulty with using a single equivalent effective stress to explain unsaturated soil behavior has resulted in the adoption of two stress-state variables. Matyas and Radhakrishna (1968) proposed the concept of state surfaces to relate void ratio and degree of saturation with net normal stress, p, and matric suction, s, and used them to explain unsaturated soil behavior. Wheeler and Karube (1996) envisioned that "there is an inextricable link between the form of the normal compression lines in the ν : p plane and the shape of the loading–collapse (LC) yield curve as it expands in the s : p plane" and pointed out that "in developing an elasto-plastic model, it is therefore only necessary to define either the changing shape of the yield curve as it expands or the form of the normal compression lines for different values of suction." Delage and Graham (1996) sketched a three-dimensional image of the elastic and elasto-plastic volume change of the BBM in the p–s–ν space. Under isotropic stress conditions, the state boundary surface comprised an elastic surface and a plastic hardening surface as shown in Figure 2. The sharp discontinuity at the intersection between the suction increase (SI) and LC yield curves was considered unlikely in natural material, and a smooth transition was sketched, essentially making the LC and SI curves a single-yield curve. Gens (1996) and Wheeler et al.(2003), however, considered that the point at the intersection between the SI and LC yield curves could be favorably used to link the irrecoverable structural changes that occur either by loading or by wetting when the soil is subjected to applied stress that is sufficiently high. Blatz and Graham (2000) plotted a three dimensional volume state boundary surface of their model in the p–s–ν space.

In case of unsaturated soils, besides void ratio, moisture content is also a parameter. In order to draw similar state boundary surface, as the first step of test series, the stress history has been changed and it is tried to achieve same moisture content with different stress histories and shear behavior with different void ratio is studied as in Figure 3.

3 DESCRIPTION OF TEST DEVICE

Figure 4 gives a schematic diagram of the testing device for cylindrical specimens 50 mm in diameter and 100 mm in height. In order to separate the routes for the measurement and the control of the pore air pressure and the pore water pressure, a membrane and a PTFE (polytetrafluoroethylene, known as Teflon) sheet were used. The PTFE sheet was placed on the top

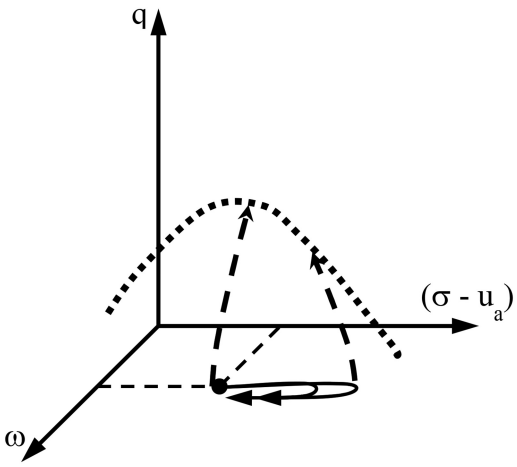


Figure 3. State boundary surface unsaturated soils.

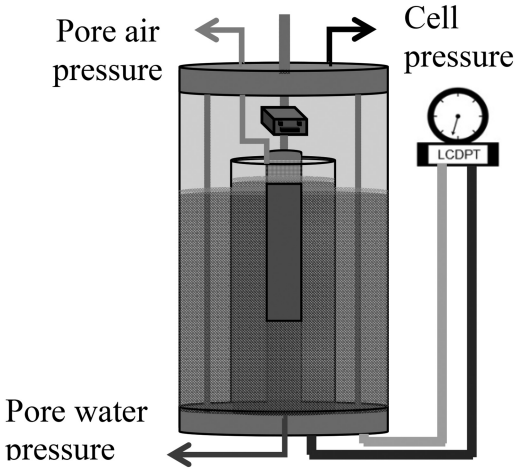


Figure 4. Schematic diagram of triaxial cell.

of the specimen to cut off the flow of water and to measure the air pressure. The membrane filter was installed in the lower pedestal to cut off the flow of air and to measure the water pressure. The thin membrane filter with pores of 0.45 mm has air entry value of 420 kPa. For undrained tests, no pore water was allowed to flow out in both the isotropic consolidation and monotonic shearing process. The salient feature of this triaxial apparatus is that both pore air and water pressures can be measured separately. Pore air pressure transducer was installed in the top cap and connected to air regulator in order to give continuously supply of the air throughout the test. In addition to this, solenoid valve was also installed in the air drainage line inside the top cap. The change in volume of specimen during the triaxial tests was measured as the change in the water level in the inner cell by LCDPT. Both monotonic loading tests and cyclic loading tests were conducted under strain-controlled conditions. The vertical load of the soil specimen was measured by the inner load cell.

Table 1. Specimens preparation.

	Without Layer		In Layer	
Height	ω(%)	ρ(g/cm^3)	ω(%)	ρ(g/cm^3)
2 cm	21.27	1.305	20.60	1.296
2 cm	21.09	1.291	20.64	1.295
2 cm	20.87	1.285	20.77	1.294
2 cm	20.49	1.285	20.54	1.295
2 cm	20.26	1.262	20.42	1.297

Table 2. Initial properties of specimens.

Specimen	SP:1	SP:2/1	SP:4/1	SP:1/CS	SP:2/1/CC
Ht. (cm)	9.96	9.96	9.96	9.96	9.96
Dia. (cm)	4.94	4.94	4.94	4.94	4.94
ω (%)	25.30	25.28	25.20	25.00	25.20
ρ (g/cm^3)	1.29	1.29	1.30	1.30	1.30
S_r (%)	64.30	64.26	64.18	64.03	64.37

All instruments were connected with dynamic strain amplifiers which were then connected to A/D board and finally to PC.

3.1 *Sample preparation*

The silty soil known as "DL clay" in Japan was tested in this study. The soil density is 2.635 g/cm^3 and the liquid limit is non-plastic. The main reason of using this clay is that it has low degree of saturation and high initial suction as compared to the kaolin clay. Initially two soil specimens, each having height 10 cm and diameter 5 cm, were prepared with same density in order to check homogeneity of specimen along its length, first specimen was prepared by putting whole soil inside mold and compacted statically while other specimen was prepared by putting soil in layer of 2 cm as shown in Table 1, both specimen were then cut in 2 cm slices density, moisture content of each layer was calculated, which showed specimen prepared in layers was more homogenous throughout its height than other specimen.

Therefore, the specimens used in this study were prepared by putting soil in layer of 2 cm and compacting statically in order to get homogenous sample. The soil was mixed well with water to make up the water content of approximately 25.30%, and statically compacted in layers in a special apparatus with a hydraulic jack in order to obtain homogeneity. The specimens were compacted statically to achieve a dry density of around 1.30 g/cm^3. The initial properties of all specimens are listed in Table 2 and it can be seen that all specimen have almost same properties.

4 TEST PROCEDURE

In this research five compacted unsaturated soil specimens with almost same properties were prepared

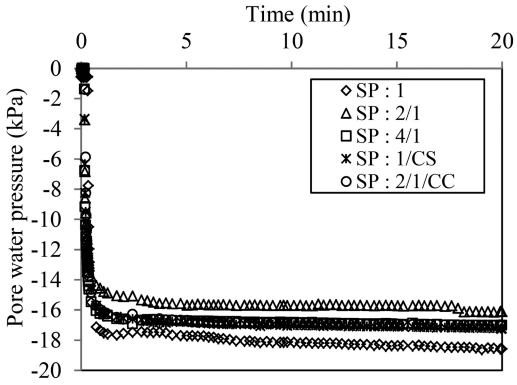


Figure 5. Initial suction of specimens.

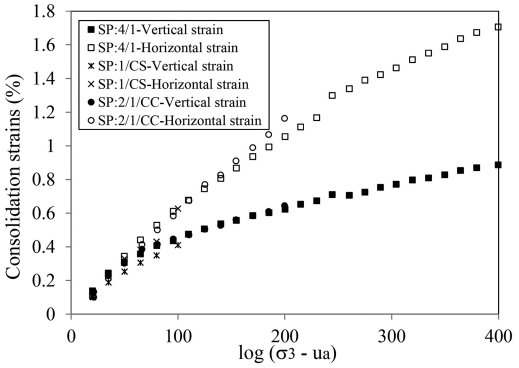


Figure 6. Effect of isotropic loading on specimen.

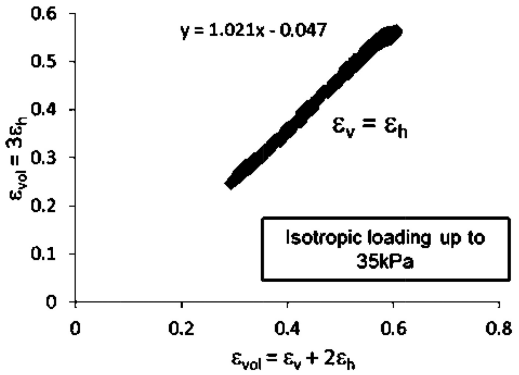


Figure 7. Loading up to 35 kPa.

using DL clay. Specimen "SP : 1" was consolidated isotropically under net pressure of 100 kPa and shared monotonically, specimen "SP : 2/1" was consolidated under net pressure of 200 kPa then unloaded to 100 kPa and sheared monotonically, specimen "SP : 4/1" was consolidated under net pressure of 400 kPa then unloaded to 100 kPa and sheared monotonically Specimen "SP : 1/CS" was consolidated under net pressure of 100 kPa then a small cyclic deviatoric stress of $\Delta q = \pm 20$ kPa was applied just before monotonic shearing Specimen "SP : 2/1/CC" was consolidated under net pressure of 200 kPa and sheared monotonically after isotropic unloading/reloading cycles. The net pressure was increased in 5, 10, 15 kPa steps with a time interval of one hour for each loading or unloading phase whereas last confining pressure was left overnight before shearing.

5 EXPERIMENTAL RESULTS

5.1 *Initial suction*

It is clear that initial suction influences the behavior of unsaturated soil. However, the suction depends on pore-water distribution and degree of saturation. Figure 5 shows the variation of the monitored values of initial suction with time of statically compacted specimens with degree of saturation approximately 64% when they were set in the triaxial apparatus. Due to almost same values of degree of saturation for all specimens, it generally look that initial suction stabilizes after 20 min and all curves converged to an initial suction of about 15–17 kPa. The less time in stabilizing is due to use of thin membrane filter having air entry value of 420 kPa.

5.2 *Effect of stress history*

In isotropic loading stage, stresses in three directions are equal i.e. ($d\sigma_x = d\sigma_y = d\sigma_z = d\sigma_3$) and no shear stress is developed. It is supposed that soil will undergo equal deformations in all direction when subjected to an equal all around pressure or isotropic pressure. The pre-consolidation pressure during the static compaction was kept approximately 100 kPa on all specimens. During isotropic consolidation the isotropic load applied on specimens were 100, 200 and 400 kPa which was increased in steps of 5, 10, 15 kPa with a time interval of one hour for each loading and unloading stage as shown in Figure 6.

5.3 *Effect of isotropic loading/reloading*

It was observed that the vertical strain of specimen was almost equal to horizontal strain i.e. $\varepsilon_v = \varepsilon_h$ up to 100 kPa. Therefore, specimens behave almost isotropically when loaded up to 100 kPa. However, anisotropy was observed when loaded beyond 100 kPa due to over-consolidation load as shown in Figure 6. Beyond 100 kPa the vertical strain of specimens was less than horizontal strain i.e. $\varepsilon_v < \varepsilon_h$. Isotropic behavior of soil was also observed during loading and unloading phase as shown in Figures 7 and 8. In order to check the isotropic behavior during loading and unloading phase $\varepsilon_{vol} = 3\varepsilon_h$ is plotted against $\varepsilon_{vol} = \varepsilon_v + 2\varepsilon_h$. It was observed that specimen behave isotropically when loaded up to 100 kPa i.e. up to pre-consolidation pressure, anisotropy was observed when specimen was loaded up to 200 kPa, unloaded to 100 kPa.

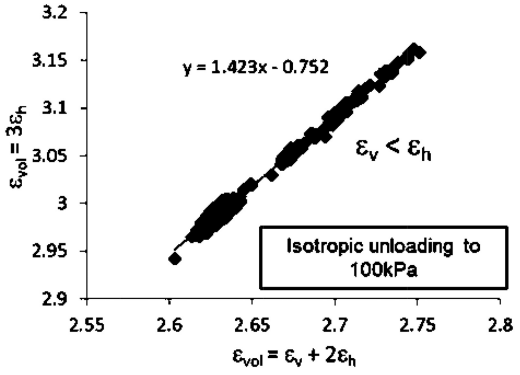


Figure 8. Unloading to 100 kPa.

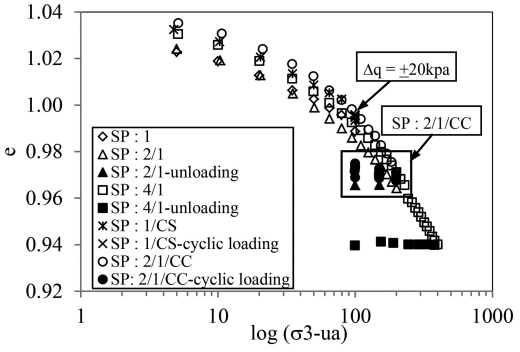


Figure 9. Effect of net stress on void ratio.

5.4 *Change of void ratio with net stress*

Unsaturated soils are characterized by the presence of an air phase, a water phase and an air-water interface in the voids The void changes with increase or decrease in load resulting in change in characteristics of the unsaturated soil. The change of void ratio with change of net pressure in undrained condition was observed in this research. It was noticed that void ratio decreases with increase in net pressure for all the specimens during the loading phase as shown in Figure 9. No significant change in void ratio was observed in specimens when simply unloaded from 200 kPa to 100 kPa and 400 kPa to 100 kPa. A little more decrease in void ratio was observed in SP : 2/1/CC when isotropic unloading/reloading cycles were applied as shown in Figure 10. It was also observed that due to application of deviatoric stress cycles of $\Delta q = \pm 20$ kPa in the case of SP : 1/CS, there was just a little decrease in void ratio because of small value of cyclic deviatoric stress.

5.5 *Effect of net stress on degree of saturation*

As change of void ratio changes degree of saturation, the water-retention curve will be affected during loading and unloading of net stresses. Figure 11 shows the effect of change in degree of saturation on suction. With the increase in net stress, the void ratio decrease, degree of saturation increases and pore water pressure

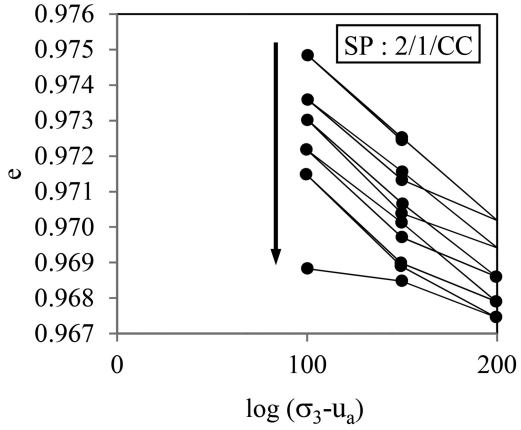


Figure 10. Effect of unloading/reloading on void ratio on specimen SP: 2/1/CC.

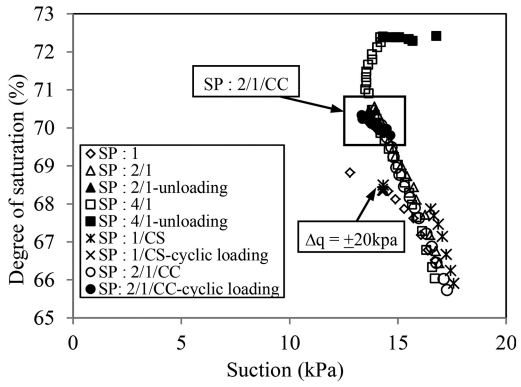


Figure 11. Effect of degree of saturation on suction.

increases. Due to increase in pore water pressure, suction decreases. Therefore it is noted that suction decreases with increase in degree of saturation during the loading phase for all the tests and increase during unloading phase for test SP : 4/1. In SP : 2/1/CC, as a result of decrease in void ratio due to cyclic consolidation, the degree of saturation increased during unloading/reloading cycles. In SP : 1/CS test, suction and degree of saturation remained almost constant for cyclic deviatoric stress application as shown in Figure 12.

5.6 *Effect of axial strain on suction*

Effect of axial strain on suction was studied during monotonic shearing. It was observed that suction increased with increase in axial strain for almost all the specimens as shown in Figure 13. The suction increased with decrease in pore water pressure during monotonic shearing.

5.7 *Effect of monotonic and cyclic load*

Most of the experimental investigations conducted on unsaturated soil have been performed under a constant air pressure. In the present study, silty soil was sheared

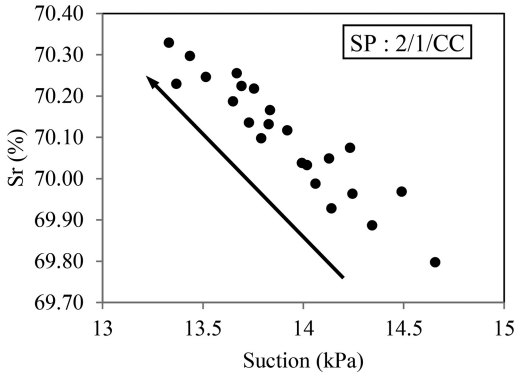


Figure 12. Effect of loading/reloading on degree of saturation.

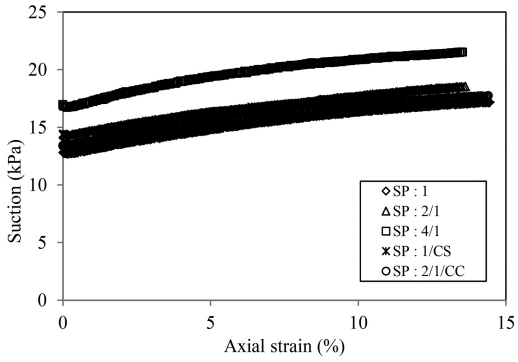


Figure 13. Effect of axial strain on suction.

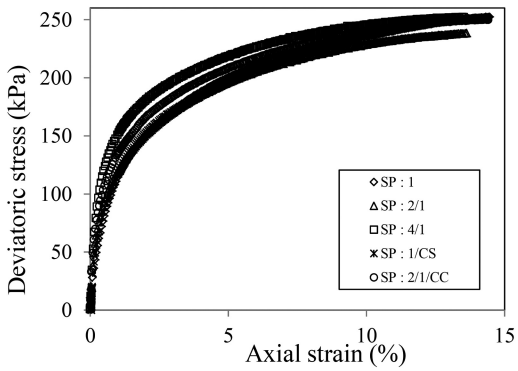


Figure 14. Effect of monotonic loading.

without drainage of both air and water. A small cyclic deviatoric stress of $\pm$20 kPa was given to specimen SP : 1/CS just before monotonic shearing, whereas all other specimens were subjected to monotonic shear right after isotropic consolidation. Change in axial strain with cyclic deviator stress application in SP : 1/CS is shown in Figure 15 and other monotonic shear test results in Figure 14. SP : 1/CS specimen showed gradual increase in the axial strain up to 0.05% after 20 cycles. As suction and net pressure was almost

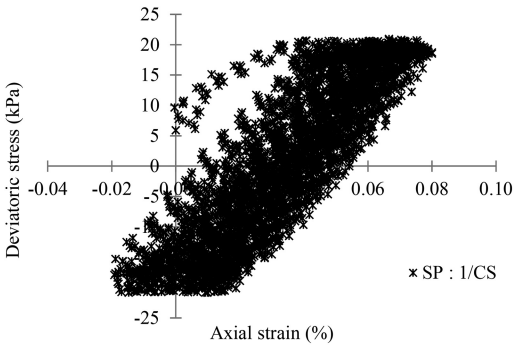


Figure 15. Effect of cyclic deviatoric stress.

the same for all specimens, they showed almost same behavior. However, the SP : 4/1 specimen showed the highest stiffness among others probably due to the highest maximum past pressure of 400 kPa. The SP : 2/1/CC specimen also showed higher stiffness owing to the less void ratio caused by isotropic unloading/reloading cycles. It was also noted that, for all the specimens, suction increased due to decrease in pore water and dilatant behavior with increase in axial strain.

6 CONCLUSIONS

A series of tests on DL clay shows that suction decreases with increase in degree of saturation as void ratio decreases with increase in net pressure. Unloading does not affect void ratio or degree of saturation whereas cyclic consolidation results in a little decrease in void ratio and increase in degree of saturation. Unsaturated soils behave isotropically under isotropic loading at low net pressure. Axial strain increases as a result of cyclic deviatoric stress. Suction increases with increase in axial strain during monotonic shearing. Finally mechanical behavior of DL clay is not affected significantly by loading sequences incorporated in this study.

REFERENCES

Kimoto, S. and Oka, F. (2011): Monotonic and cyclic behavior of unsaturated sandy soil under drained and fully undrained conditions, Soils and Foundation 51, 663–681.

Oka, F., Kodaka, T., Suzuki, H., Kim, Y., Nishimatsu, N. and Kimoto, S. (2010): Experimental study on the behavior of unsaturated compacted silt under triaxial compression, Soil and Foundation 50, 695–700.

Jonggil Chae, Byeongsu Kim, Seong Park, and Shoji Kato (2009): Effect of suction on unconfined compressive strength in partly saturated soils, KSCE Journal of Civil Engineering 4, 281–290.

Rojas, J. C. and Mancuso, C. (2009): Effect of loading rate on the behavior of unsaturated soils, Proc. 17th Int. Conference on Soil Mechanics and Geotechnical Engineering, 761–764.

Unno, T., Kazama, M., Uzuoka, R. and Sento, N. (2008): Liquefaction of unsaturated sand considering the pore air pressure and volume compressibility of soil particle skelton, Soil and foundation 48, 87–99.

Yabuki, T., Oka, F., Kimoto, S., Higo, Y. and Watanabe, T. (2007): Mechanical behavior of unsaturated silt under cyclic loading, Proc. 42nd Annual meeting of JGS, Nagoya, 771–772.

Sawada, S., Tsukamoto, Y. and Ishihara, K. (2006): Residual deformation characteristics of partially saturated sand soils subjected to seismic excitation, Soil Dynamics and Earthquake Engineering, 26, 175–182.

Okamura, M. and Soga, Y. (2006): Effect of pore fluid compressibility on liquefaction resistance of partially saturated sand, Soils and Foundations, 46(5), 695–700.

Wheeler, S.J., Sharma, R.S., and Buisson, M.S.R. (2003): Coupling of hydraulic hysteresis and stress–strain behaviour in unsaturated soils. Géotechnique, 53(1): 41–54. Doi:10.1680/geot.2003.53.1.41

Geiser, F., Laloui, L. and Vulliet, L. (2000): On the volume measurement in unsaturated triaxial test, Proc. Conf. Unsaturated Soils for Asia, Unsat-Asia, Balkema, Rotterdam, 669–674.

Blatz, J. and Graham, J. (2000): A system for controlled suction in triaxial tests. Géotechnique, 50(4), 465–469.

Fredlund, D.G. (2000): Historical developments and milestones in unsaturated soil mechanics. Proc. Conf. Unsaturated Soils for Asia Unsat-Asia 2000, 53–68, Singapore, Balkema, Rotterdam.

Yamamoto, Y. and Hyodo, M. (2000): The effect on cyclic shear characteristics of clays, Journal of Geotechnical Engineering, Japan Society of Civil Engineering, No. 645, III-50, 63–76.

Delage, P. & Graham, J. (1996): Mechanical behaviour of unsaturated soils. Proc. 1st Int. Conf on Unsaturated Soils UNSAT' 95 3, 1223–1256, Paris, Balkema, Rotterdam.

Gens, A. (1996): Consitutive modeling: Application to compacted soils . Proc. 1st Int. Conf on Unsaturated Soils UNSAT' 95, Paris 3, 1179–1200.

Cui, Y.J. and Delage, P. (1996): Yielding and plastic behaviour of an unsaturated compacted silt, Géotechnique 46, 291–311.

Wheeler, S. and Karube, D. (1995): Constitutive behaviour. Proc. 1st Int. Conf on Unsaturated Soils UNSAT'95 3, 1323–1356, Paris, Balkema, Rotterdam.

Cui, Y.J., Delage, P. and Sultan, N. (1995): An elasto-plastic model for compacted soils. Proc. 1st Int. Conf. on Unsaturated Soils UNSAT'95 2, 703–709, Paris, Balkema, Rotterdam.

Fredlund, D.G. and Rahardjo, H. (1993): Soil Mechanics for Unsaturated Soils, John Wiley and Sons Inc.

Yoshimi, Y., Tanaka, K. and Tokimatsu, K. (1989): Liquefaction resistance of partially saturated sand, Soils and Foundations, 29(3), 157–162.

Fredlund, D.G., Morgenstern, N.R., and Widger, R.A. (1978): The shear strength of unsaturated soils, Canadian Geotechnical Journal, 15, 313–321.

Fredlund, D.G., Morgenstern, N.R. and Widger, R.A. (1978): The shear strength of unsaturated soils. Canadian Geotechnical Journal 15(3), 313–321.

Matyas, E.L. and Radhakrishna, H.S. (1968): Volume change characteristics of partially saturated soil. Géotechnique, 18, 432–448.

This page intentionally left blank

Unsaturated Soil Mechanics—from Theory to Practice – Chen et al. (Eds)
© 2016 Taylor & Francis Group, London, ISBN 978-1-138-02921-7

Change in shear behavior of unsaturated volcanic coarse-grained soil due to fine particles run off

X.Y. Zheng
Graduate School of Engineering, Hokkaido University, Sapporo, Japan

T. Ishikawa
Faculty of Engineering, Hokkaido University, Sapporo, Japan

T. Tokoro
Department of Civil Engineering, Tomakomai National College of Technology, Tomakomai, Japan

ABSTRACT: Slope failures or landslides on soil ground formed by volcanic soils occur frequently in Hokkaido, Japan. The objective of this paper is to examine the effect of fine particles run off on the shear strength of volcanic coarse-grained soils under unsaturated condition. An unsaturated triaxial apparatus was used and a series of monotonic triaxial compression tests for a crushable volcanic coarse-grained soil from which fine particles have been partially removed previously were performed under various degree of saturation. By comparing test results to the previous research, it has been known that the shortage in fine particles have a strong effect on the shear strength of volcanic coarse-grained soil in both saturated and unsaturated conditions. With fine particles run off, the shear strength decreased sharply as if it has suffered a deterioration process.

1 INTRODUCTION

Volcanic coarse-grained soils are very common in Japan. They are generated due to frequently occurred volcanic activities since the quaternary period. Volcanic coarse-grained soils also widely spread over more than 40% of the area of the Hokkaido Island, the most northern island of Japan. Because of their advantages of lightweight and relatively good stability, these soils have been generally used as construction material, particularly, in foundations or man-made earth structures (embankments and cut slopes, etc.).

According to previous researches, volcanic coarse-grained soils showed quite different behavior from other soils, such as sands or clays. The most distinctive feature of them is so-called crushability. Particles crushing can even happen at relatively low stress state such as shallow ground layer, which leads to a degradation in static and dynamic deformation-strength characteristics (Sahaphol & Miura 2005). Therefore, volcanic coarse-grained soils have been classified as "problematic soils" since the 1980s (Miura & Yagi 2003).

In recent years, geotechnical disasters, like slope failures at cut slope or landslides at natural slopes, usually occur during the snow-melting season in Hokkaido. It has been considered that these slope failures are caused by an increasing degree of saturation due to the melting water and the particles crushing induced by freeze-thaw action (Ishikawa & Miura 2011).

In addition to the previous research findings, there might be another reason for the above mentioned disasters which is fine particles run off. Nowadays due to climate change extremely heavy rain is very common in the snow melting season During that period, a large amount of rainfall together with snow melting water permeated into the ground simultaneously. Then fine particles contained in ground formed by volcanic coarse-grained soil will be carried out of soil structure by permeated water. This change in the fine content should cause some differences in the shear behavior. Some researchers have investigated the effect of fine particles on shear behavior (e.g. Sterpi 2003). They developed a seepage erosion model and evaluated the effect of fines on shear behavior of sand and gravel mixture. However, they just removed the fines simply by reconstituting the soil through sieving before triaxial compression test. The structure of reconstituted soil specimen may be different from one that is natural formed.

The main purpose of this paper is to examine the influences of absence of fine particles on the shear behavior of volcanic coarse-grained soil under both saturated and unsaturated conditions. In order to attain the objective, a series of monotonic triaxial compression tests for crushable volcanic coarse-grained soil from which fine particles have been removed previously were performed under various degree of saturation by using an unsaturated triaxial apparatus. The results are then compared with previous research findings (Ishikawa et al. 2010) in which the shear

Table 1. Index properties of test material.

Sample name	Kashiwabara volcanic soil
ρ_s (g/cm^3)	2.34
$\rho_{d\,max}$ (g/cm^3)	0.623
$\rho_{d\,min}$ (g/cm^3)	0.462
D_{50} (mm)	1.25
F_c (ϕ75 μm) (%)	1.94

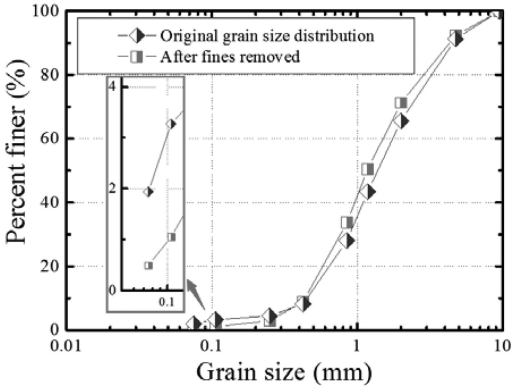


Figure 1. Grain size distribution of Kashiwabara volcanic soil.

behavior of volcanic coarse-grained soil has been tested without removal of fine particles.

2 METHODOLOGY

2.1 *Test materials*

The tested soil material is called Kashiwabara volcanic soil, which was sampled from natural deposits formed by the eruption of Shikotsu caldera 31,000–34,000 years ago in Hokkaido area. The index properties and the grain size distribution curves of the Kashiwabara volcanic soil are shown in Table 1 and Figure 1 respectively.

As shown in Table 1 and Figure 1, the soil has a fine content of about 1.9%. Especially the low value of dry density is also shown in the samples because its constituent particles are very porous. This special characteristic leads to extremely high crushability of soil particles.

2.2 *Test apparatus*

A schematic diagram and a photo of the triaxial apparatus for unsaturated soil are shown in Figure 2. The monotonic triaxial compression tests were performed using this apparatus by employing axis translation technique (Hilf 1956) along with pressure membrane method.

Prescribed matric suction was achieved by controlling pore air pressure (u_a) and pore water pressure (u_w) separately during testing. Instead of ceramic

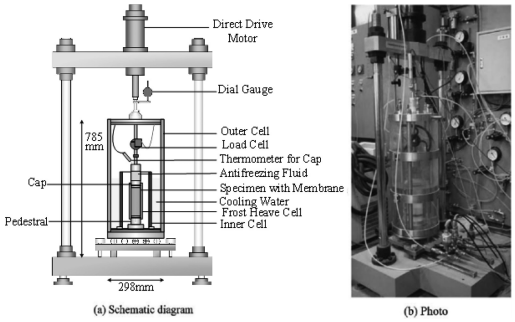


Figure 2. Schematic diagram and photo of triaxial apparatus.

disk, pore water pressure was exerted to specimens through a hydrophilic acrylic copolymer membrane filter (Versapor membrane filter, Air Entry Value, AEV = 110 kPa) which was attached to the water plumbing path. Meanwhile the pore air pressure was applied through a hydrophobic polyflon filter on the top of the specimen. Furthermore triaxial compression test under saturated condition could be performed just by removing the Versapor membrane and the polyflon filter.

The axial loading to a soil specimen could be applied through a Direct Drive Motor, DDM. The axial stress (σ_a) was measured by using a load cell installed inside the triaxial cell, and the axial strain (ε_a) was measured by an external displacement transducer. The volumetric strain (ε_v) and the volume of drainage (ΔV_w) were measured through differential pressure transducers attached to pedestal and double tube burette respectively.

2.3 *Preparation of test specimen*

In this research, soil with particle size smaller than 75 μm, is referred to as fines according to the Unified Soil Classification System (ASTM 2000) and American Association of State Highway and Transportation Officials (AASHTO 1986) classification systems. All specimens were prepared as follows. At first, a special mold as illustrated in Figure 3 was made for removing fines. Inside the mold, an ASTM 200 (D = 0.075 mm) metal wire mesh was attached to ensure only fines would be carried out of the specimen.

Then cylindrical specimens with initial 70 mm diameter and 170 mm height were made by falling oven dried test material into above mentioned mold with the air-pluviation method (Fig. 4). The initial dry density (ρ_0) could be adjusted by simply changing the falling height of test material to keep the dry density after consolidation (ρ_{dc}) similar to previous research (Ishikawa et al. 2010) which is about 0.52 g/cm^3. A fluctuation in dry density within ±5% would be accepted. According to JGS 0520, to ensure the experiment accuracy, the ratio between maximum particle diameter and specimen diameter should be less than 5. Hence, soil particles with grain size greater

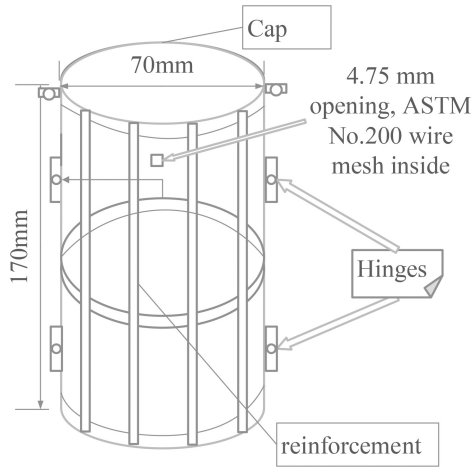


Figure 3. Mold for fines removal.

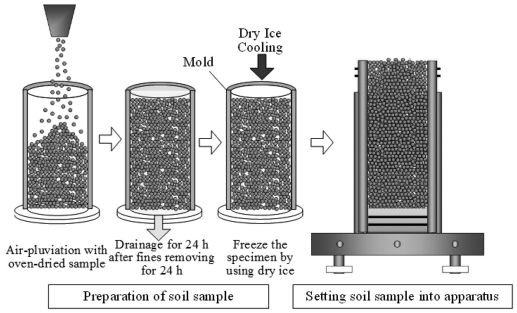


Figure 4. Preparation of soil specimen.

than 9.5 mm contained in original soil were previously screened out. After the mold was fully filled with test material, a cap made of stainless steel was mounted on to prevent sample loss.

Afterwards, together with soil specimen the mold has been put into an acrylic tank. An upward seepage flow induced by hydraulic head of 1 m (Fig. 5) was then applied. 1 m hydraulic head was necessary to ensure fine particles were fully removed for simulating the mechanism of fine particle runoff which happens in real ground under heavy rain condition during snow melting period. Several pre-tests have proved that as shown in grain size distribution curves on Figure 1, 24 hours water flushing would cause the fine content decreasing a lot to an almost constant value of about 0.5%. The mold was, then, taken out of the tank. The soil specimen was dewatered by gravity at a room temperature of about 20°C for 24 hours to ensure the degree of saturation is low enough to avoid strength loss caused by followed dry ice freezing process (JGS0520 2000).

Because volcanic coarse-grained soil is a kind of cohesionless material, it can barely keep its cylindrical shape without mold's support. So dry ice was used to freeze the soil specimen to keep its shape.

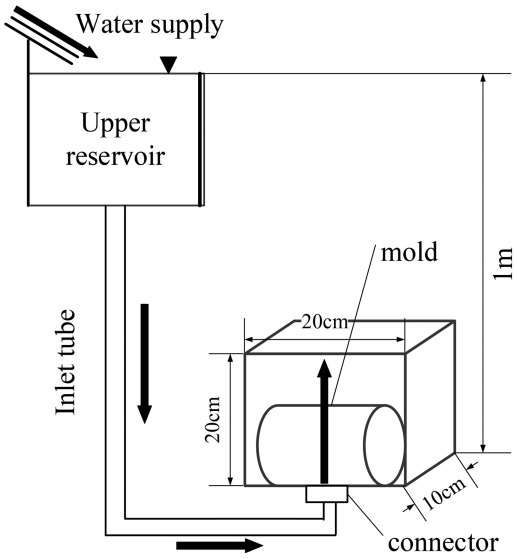


Figure 5. Fines removing method.

3 EXPERIMENTAL PROGRAMS

3.1 *Consolidation process*

Monotonic triaxial compression tests were conducted after specimen preparation. At the beginning, every frozen specimen was set into pressure cell under a cell pressure of 20 kPa for unfreezing at least 2 hours.

After unfreezing process, the consolidation process would start. For saturated condition, soil specimen was saturated by using double vacuuming method (Ampadu & Tatsuoka 1993) which extracted the pore air from the top of the specimen by giving a negative air pressure. Meanwhile de-aired water was supplied from the bottom of the specimen. After that, a back pressure up to 200 kPa was applied to make sure that the B value would excess 0.96. When the soil specimen was fully saturated, the isotropic consolidation would continue in fully drained condition under a preset effective confining pressure (σ'_c) of 49 kPa which has been achieved by applying a cell pressure (σ_c) of 249 kPa and pore water pressure (u_w) of 200 kPa till there were no changes in axial displacement or in drainage volume.

For unsaturated conditions, the quasi-saturated soil specimen would be isotropically consolidated under a preset net normal stress (σ_{net}) of 49 kPa which achieved by applying a cell pressure (σ_c) of 249 kPa and both pore air pressure (u_a) and pore water pressure (u_w) of 200 kPa in fully drained condition till there were not any changes in axial displacement or drainage volume. After that, matric suction ($s = u_a - u_w$) had been given to the soil specimen by decreasing pore water pressure to a targeted value while keeping the pore air pressure constant until the drainage was stopped or the drainage speed was less than 0.01 ml/min. For comparing to the previous research (Ishikawa et al. 2010), the matric suctions were set at

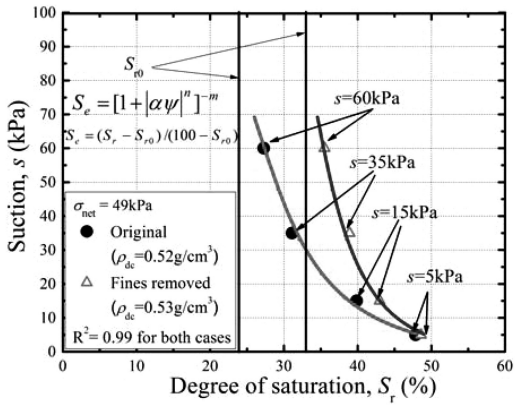


Figure 6. Matric suction, s versus degree of saturation, S_r.

5 kPa, 15 kPa, 35 kPa and 60 kPa which were related to the degree of saturation (S_r) of approximately 48.6%, 43%, 38.9% and 35.5% respectively.

3.2 *Shear process*

After consolidation process, holding other parameters constant, soil specimen was sheared continuously by using the DDM to apply an axial deviator stress (q) under fully drained condition (CD test). The shear velocity for Kashiwabara volcanic soil was set to 0.2%/min for comparing to previous research (Ishikawa et al. 2010). The shear process was finished after reaching the axial strain (ε_a) of 25%.

4 RESULTS AND DISCUSSIONS

4.1 *Effect of fines run off on SWCC*

Figure 6 shows the matric suction against degree of saturation for both soil samples with original grain size distribution and those without fines in triaxial compression tests under various matric suctions. This relationship could be seen as part of soil-water characteristic curves, SWCCs, during the drying process with a net normal stress, σ_{net}, of 49 kPa, although it is not the result from SWCC test.

In low matric suction range, degree of saturation decreases fast with increasing matric suction. As matric suction gets close to a value of 60 kPa, degree of saturation becomes, however, hard to change. It gets closer and closer to a certain value, which is called residual degree of saturation, S_{r0}. The value of S_{r0} is about 24% for soil with original grain size distribution and about 33% for soil without fine content. Each residual degree of saturation was derived as shown in Figure 6. Both blue and red lines are the fitted curves for experiment plots indicated by van Genuchten model (van Genuchten 1980). Each of these curves gradually approaches to residual degree of saturation in x-direction. It seems there was a right shift in soil-water characteristic curve after fines had been removed. The reason for the right shift is considered as follows. Hypothetically, because the coarse-grained particles are very porous, there are many opening intra-particle voids on the surface of constituent particles (Nakata & Miura 2007). Without fines clogging the voids in where water tends to be stored, the water retentivity of soil has increased. This shift causes a relatively large residual degree of saturation and consequently a different parameter χ (more details are discussed in the next section). Table 2 shows calculated magnitudes of χ at different matric suctions by using Karube's model (Karube et al. 1996) for both soil specimens with original grain size distribution and those without fines.

Table 2. Magnitudes of χ under different conditions.

	Fines removed		Original grain size distribution	
s	S_r %	χ	S_r %	χ
5	48.6	0.233	47.9	0.314
15	43.0	0.149	39.9	0.209
35	38.9	0.088	31.1	0.093
60	35.5	0.037	27.2	0.043

From Table 2, it is clear that the magnitude of χ would decrease when fines were removed. As discussed in the following section, smaller χ value causes smaller suction stress, and then it results less increment in shear strength which is attributed to the matric suction. This phenomenon may give another viewpoint to explain the degradation in shear behavior after fine particles were removed.

It is not all clear, however, why such right shift in SWCC would generate when fines were removed. It looks like further research should be performed.

4.2 *Shear behavior change due to fines run off*

Figure 7 shows the relationship between axial deviator stress (q), volumetric strain (ε_v), and axial strain (ε_a) during CD test under various unsaturated conditions (different matric suctions). The CD test data of Kashiwabara volcanic soil (with original grain size distribution) which had been obtained from previous research (Ishikawa et al. 2010) also showed up in these figures as a comparison to the current research to explain the effect of fine particles run off.

From Figure 7, it can be observed that volumetric strain increases with increasing axial strain (strain hardening). When axial strain reaches about 15%, the increment in volumetric strain, trends to stop and starts turning to drop (strain softening) as axial strain increases continuously, just similar to the behavior of dense sands and over consolidated clays. It is also worth to notice that the volumetric changes in both soil samples (with and without fines content) tend to be the same even there was a huge difference in shear strength.

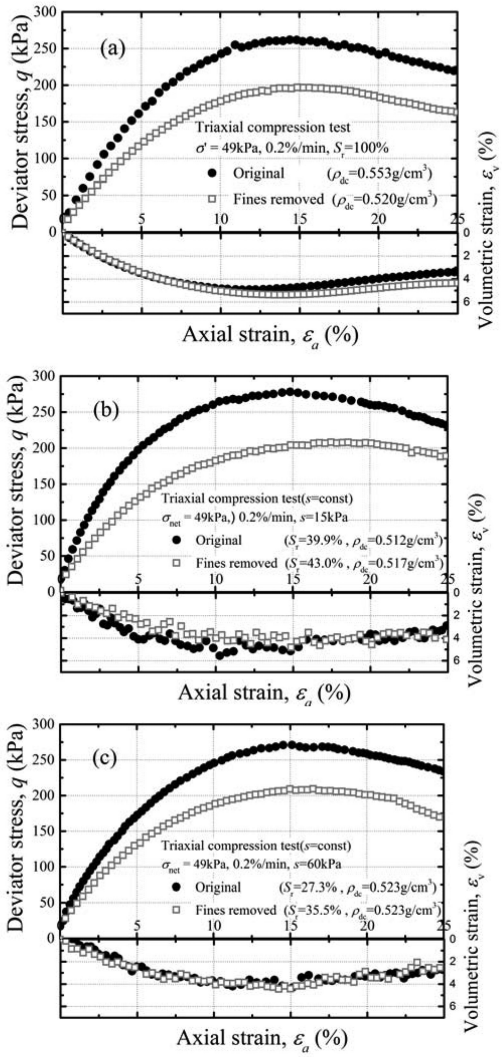


Figure 7. Shear behavior of Kashiwabara volcanic soil under saturated condition (a) and unsaturated condition (b), (c).

From these figures, it can also be observed that there is a big change in the shear strength between volcanic coarse-grained soils with and without fine content. It seems that soil will undergo degradation in shear strength regardless of matric suction when the fines are removed. Figure 8 shows the peak strength of each soil specimen under different unsaturated conditions against matric suction. For each matric suction, the shear strength of soil samples in which fines were removed has decreased sharply. Since there was almost no distinct change in the density after consolidation between specimens with original grain size distribution and those without fines, it could say that the effect of fine particles run off on the density after consolidation could be neglected. It is considered that the fine content plays a cushion role between angled

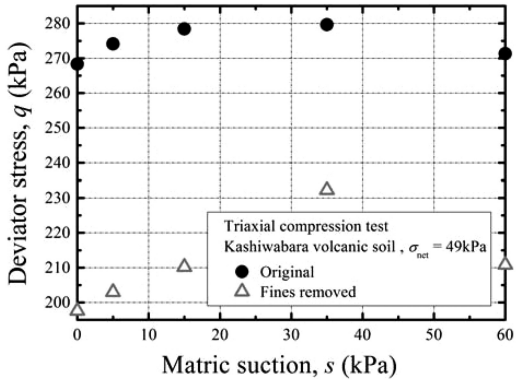


Figure 8. Peak strength versus matric suction.

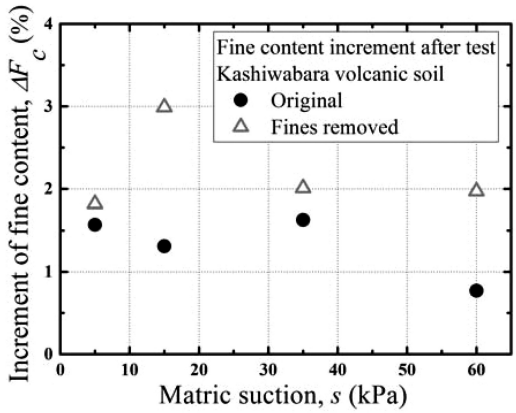


Figure 9. Increment of fine content after shear process under different matric suctions.

granular particles. Fines filled the void around bigger particle making bigger particles fully contacted. Without fine particles, bigger coarse-grained particles may contact others with its sharp angle. This imperfect contact could make soil particles more crushable and then leads to a lower shear strength. Figure 9 shows the increment of fine content after shear process. Specimens without fine particles tend to have greater increment in fine content which means particle crushed more than did those with original grain size distribution. Hence fine content in the volcanic coarse-grained soil has a crucial effect on the shear strength. Besides, while looking at each branch of these two data sets in Figure 8, it could also be found that the shear strength increases with increasing matric suction in low suction range. Conversely, once matric suction exceeds a specific value the shear strength will get dropped.

It could be thought that this phenomenon is caused by rapid decrease in parameter χ. According to Bishop's theory:

$$\sigma' = (\sigma - u_a) + \chi(u_a - u_w) \quad (1)$$

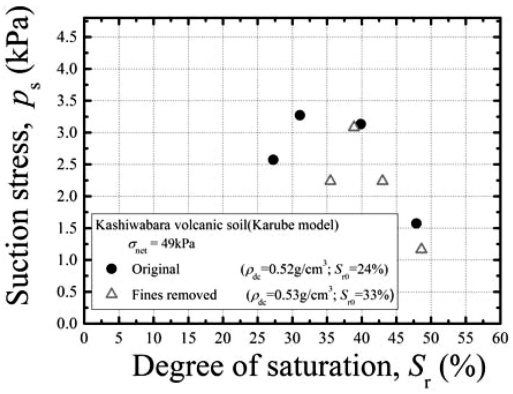


Figure 10. Suction stress, p_S versus degree of saturation, S_r.

where σ' is effective stress; χ is a parameter related to the degree of saturation and ranging from 0 to 1; $\chi(u_a - u_w)$ is suction stress, p_s.

There are many methods suggested by researchers around the world to evaluate the magnitude of parameter χ. In this study model shown in Equation 2 (Karube et al. 1996) would be used for evaluating the magnitude of parameter χ.

$$\chi = \frac{S_r - S_{r0}}{100 - S_{r0}} \tag{2}$$

where S_{r0} is called residual degree of saturation.

In general, the later part of Equation 1 $\chi(u_a - u_w)$ takes credit for strengthening in shear strength. However, the strengthening effect will not exist for every case. In Equation 2, it should be noted that the closer the degree of saturation approaches the residual degree of saturation the smaller the χ will be. Then it leads to less attributable to matric suction caused increment in shear strength. In the case of volcanic coarse-grained soil, it directly causes the drop in shear strength at matric suction of 60 kPa. By assuming residual degree of saturation is 24% for specimens with original grain size distribution and 33% for those from which fines have been removed, suction stress could be calculated. Just as Figure 10 illustrates, at the first, suction stress will increase when matric suction increases. Then it begins turning down after reaches the peak.

5 CONCLUSIONS

The findings obtained from this research can be summarized as below:

1. The fine content plays an important role in affecting shear behavior of volcanic coarse-grained soil.
2. Degradation in shear strength will generate when fine particles are carried out of soil structure.
3. Fine particles give effects to soil-water characteristic curve which in turn affects shear strength of volcanic coarse-grained soil.

The research findings indicate that fine content has a strong influence on the shear characteristic of a crushable volcanic coarse-grained soil in both saturated and unsaturated conditions even the content of fines does not take much big proportion. Nonetheless, there are still a lot of investigations should be made such as analyzing the influence of fines run off on soil-water characteristic curve in more detail and finding if there is a better way to evaluate the magnitude of parameter χ for volcanic coarse-grained soil.

ACKNOWLEDGEMENTS

This research was supported in part by Grant-in-Aid for Scientific Research (B) (23360201) from Japan Society for the Promotion of Science (JSPS) KAKENHI.

REFERENCES

Ampadu, S. K. & Tatsuoka, F. 1993. Effect of setting method on the behavior of clays in triaxial compression from saturation to undrained shear. *Soils and Foundations* 33(2): 14–34.

Hilf, J. W. 1956. An investigation of pore-water pressure in compacted cohesive soils. *Technical Memorandum* 654. Washington D.C.: US Bureau of Reclamation.

Ishikawa, T., Miura, S. & Ito, K. 2010. Influence of freeze-thaw action on mechanical behavior of unsaturated crushable volcanic soil. In Eduardo Alonso & Antonio Gens (eds.), *The Fifth International Conference on Unsaturated Soils*; *Proc. Intern. Conf., Barcelona, 6–8 September* 2010. 549–554. CRC Press/Balkema.

Ishikawa, T. & Miura, S. 2011. Influence of freeze-thaw action on deformation-strength characteristics and particle crushability of volcanic coarse-grained soils. *Soils and Foundations* 51(5): 785–799.

Karube, D., Kato, S., Hamada, K. & Honda, M. 1996. The relationship between the mechanical behavior and the state of pore water in unsaturated soil. *Journal of JSCE* 535(III-34): 83–92.

Miura, S. & Yagi, K. 2003. Mechanical behavior and particle crushing of volcanic coarse-grained soils in Japan. In Tan et al. (eds), *Characterization and Engineering Properties of Natural Soils*; *Proc. Intern. Workshop, Singapore*, *2–4 December 2002*. 1169–1203. Lisse, Swets and Zeitlinger.

Nakata, T. & Miura, S. 2007. Change in void structure due to particle breakage of volcanic coarse grained soil and its evaluation. *Journal of Geotechnical Engineering* 63(1): 224–236.

Sahaphol, T. & Miura, S. 2005. Shear moduli of volcanic soils. *Soil Dyn. Earthquake Eng* 25(2): 157–165.

Sterpi, D. 2003. Effects of the erosion and transport of fine particles due to seepage flow. *International Journal of Geomechanics* 3: 111–122.

van Genuchten, M. Th. 1980. A closed-form equation for predicting the hydraulic conductivity of unsaturated soils. *Soil Science Society of America Journal* 44(5): 892–898.

Yagi, K. & Miura, S. 2004. Evaluation of mechanical characteristics for crushable volcanic soil ground. *Journal of Geotechnical Engineering* 757(III-66): 221–234.

Unsaturated Soil Mechanics—from Theory to Practice – Chen et al. (Eds)
© 2016 Taylor & Francis Group, London, ISBN 978-1-138-02921-7

Effect of fine grain contents on the unsaturated mechanical characteristics of embankment materials

B.S. Kim & Y. Takeshita
Graduate School of Environmental and Life Science, Okayama University, Okayama, Japan

S. Kato
Department of Civil Engineering, Kobe University, Kobe, Japan

S.W. Park
Department of Civil & Environmental Engineering, Dankook University, Yongin, Korea

ABSTRACT: In order to evaluate the safety of an embankment under unsaturated state against the infiltration of a heavy rain, the quantitative evaluation on the mechanical characteristics of embankment materials needs. In particular, this study concentrated on the fine grain content (under sieve #200) closely related to the decrement of shear strength due to the infiltration at a rainfall because the embankment is composed of soil materials involving fine and gravel grains. Thus, a series of the constant water content compression tests in this study are performed using a decomposed granite soil of the embankment. Through these results, the shear behavior on the fine grain contents from 10% to 40% is examined through the effect of the suction according to the degree of saturation. Here, the suction value is derived by the SSM (Suction stress – SWRC Method). It is expected that the effect of the fine grain contents on the unsaturated mechanical characteristics of embankment materials could be clarified through these results.

1 INTRODUCTION

The geotechnical strength of an embankment of a river comprised of gravel, sand, silt, and clay is affected the infiltration and the erosion at rainfall. The huge losses of both life and property due to the collapse of the embankment so far have accumulated. It is generally that the decrement of the effective stress, that is, the soil shear strength on the potential failure surface is caused by the increase of the pore water pressure and seepage due the rainfall (Terzaghi 1950; Sidle and Swanston 1982; Sitar et al., 1992; Anderson and Sitar 1995) and then is triggered the collapse of the embankment (Ng and Shi 1998; Rahardjo and Leong 1997; Kim et al. 2004). In particular, because the embankment over the water level of the river is under an unsaturated condition, it should be considered on the decrease of the suction due to the seepage and the rise of the water level of the river at rainfall affects the soil shear strength (Lumb 1975; Rahardjo et al. 1995; Ng and Shi 1998; Fourie et al. 1999).

On the other hand, the fine grain content (F_c) which is defined as a percentage of soils passing No. 200 (75 μm) sieve is a very important factor for the shear strength of the embankment. The fine grain content also has a significant impact on the mobility of rainfall-induced landslides (Wang and Sassa 2003). Although embankment materials below the fine grain content (F_c) of 50% has been suggested with other factors such as the compaction and the maximum particle size etc. in Japan, the unsaturated mechanical characteristics on the fine grain content should be examined so that the embankment material could be selected for the stability of the embankment under unsaturated state.

The relationships of the suction, degree of saturation, and suction stress according to the fine grain content (F_c) of 10%, 25%, and 40% in this study are examined. Thus, it is expected that the effect of the fine grain contents on the unsaturated mechanical characteristics of the embankment material could be clarified through these results.

2 THEORETICAL BACKGROUND

2.1 *Shear strength and suction stress for unsaturated soils*

Many studies have been carried out in order to examine the shear strength and deformation behaviors for unsaturated soil based on the extended Mohr-Coulomb criterion for saturated soil (e.g., Fredlund and Morgenstern, 1977; Fredlund et al., 1978; Vanapalli et al., 1996; Khalili and Khabbaz, 1998; Gens et al., 2006). Several studies have attempted to explain effectively the increment of the shear strength, that is, the

apparent cohesion (Δc) due to the matric suction in unsaturated soil like Eq. (1).

$$\tau = c' + (\sigma_{net} - u_a)\tan\phi' + \Delta c \quad (1)$$

where τ = the shear strength on the failure plane; σ = normal stress; u_a = pore air pressure; c' = the effective cohesion; and ϕ' = the effective angle of internal friction.

In particular, Fredlund et al. (1978) proposed a shear strength equation for unsaturated soils in which two independent stress state variables are used. This equation is an extended Mohr-Coulomb failure equation as follows in Eq. (2). Vanapalli et al. (1996) proposed Eq. (3) on the shear strength for unsaturated soils considering the degree of saturation based on the Eq. (2).

$$\tau = c' + (\sigma - u_a)\tan\phi' + (u_a - u_w)\tan\phi^b \quad (2)$$

$$\tau = c' + (\sigma - u_a)\tan\phi' + [(\frac{S_r - S_{r0}}{1 - S_{r0}}) \times s] \times (\tan\phi') \quad (3)$$

where u_w = pore water pressure; ϕ^b = angle indicating the rate of change in shear strength relative to changes in matric suction ($s = u_a - u_w$); S_r = degree of saturation; and S_{r0} = residual degree of saturation.

On the other hand, in order to estimate the effects of suction and soil water, Karube et al. (1996) proposed the suction stress given by the next equation.

$$p_s = \frac{S_r - S_{r0}}{1 - S_{r0}} \times s \quad (3)$$

Karube et al. (1996, 2001) reported that the stress states at the maximum compression state in the triaxial test for the unsaturated clay specimen were arranged uniquely in the relationship of ($p_{net} + p_s$) for q'. Here, the net mean principal stress, p_{net}, and the effective deviator stress, q'. These test results show that a critical state exists for unsaturated soil, and that the concept of suction stress can be applied to the result of a triaxial test for unsaturated soil under a high confining pressure. As another approach of the suction stress, Lu and Likos (2006) introduced an expression for the intergranular stress in unsaturated soil considering the microscopic interparticle force and stress analyses. They reported that the suction stress can be conceptualized as the result of interparticle physicochemical stresses attributable to cementation, van der Waals attraction etc.

2.2 *Suction stress-SWRC Method (SSM)*

Kim et al. (2010) proposed the Suction stress-SWRC Method (SSM) in order to estimate the suction and the suction stress based on the SWRC (Soil Water Retention Curve) in the direct shear tests using the suction plate method under the condition of constant pore air-water pressure for the specimen. Although the pressure plate method is used in a direct shear test apparatus, adopting the suction value as a test condition that is the same as that at the failure plane cannot be ensured because of the characteristic (i.e., opening between the shear boxes) of the direct shear test. As a result, the peak shear strength of the unsaturated state agreed with the failure line of the saturated state through the application of the suction stress.

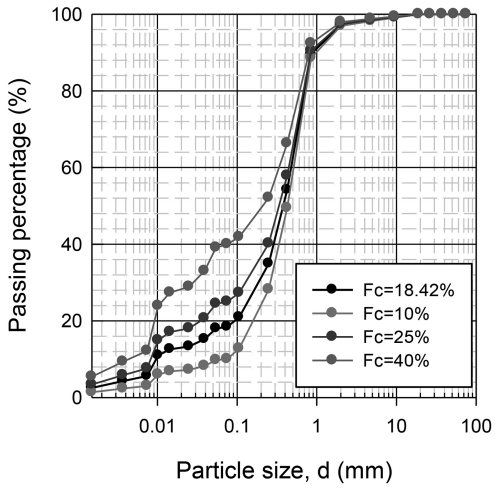


Figure 1. The grain size distribution curve according to the fine grain content (F_c).

As a subsequent study, Kim et al. (2013) also examined the application of suction stress on the results of the direct shear test under constant volume condition for unsaturated soil. It was found that the stress paths for unsaturated soil agreed well with the maximum volumetric compression point (M.C.P.) line, which was obtained under saturation and constant pressure conditions, through applying the suction stress in the (σ_{net}, τ) plane. Thus, the suction value obtained by the SSM on the failure plane could be estimated from the SWRC with the degree of saturation of a specimen. This result showed that a unique relation exists between the saturated and unsaturated states with the suction stress, and also showed the applicability of the SSM. Furthermore, it has been studied that the SSM can be applied to the results of not only the direct shear test, but also the triaxial test and the unconfined compression test.

3 TESTING PROGRAM

3.1 *Soil sample*

The soil sample used in this study is a decomposed granite soil, so called Masado in Japan, which has the soil particle density of 25.8 kN/m^3, the liquid limit of N.P, and the plastic limit of 24.6%. The maximum dry density and the optimum water content are 1.88 g/cm^3 and 131%, respectively. The percentage passing No. 200 (75 μm) sieve of Masado, that is, the fine grain content (F_c) is 18.4% and the soil type under the Unified Soil Classification System (USCS) classification is SM. Figure 1 shows the grain size distribution curve

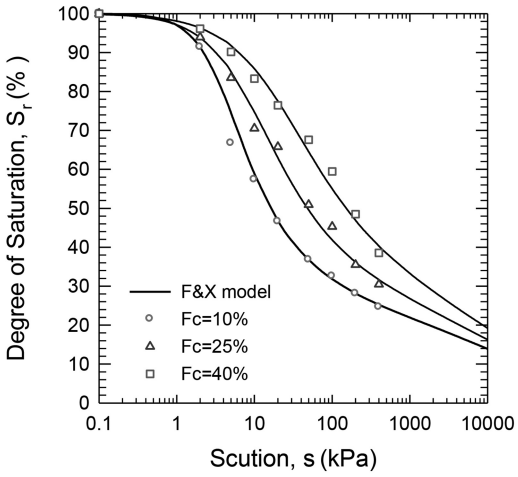


Figure 2. The soil water characteristic curves on $F_c = 10\%$, 25% and 40%.

Table 1. Fitting parametersat the SWCCs.

	Fitting parameters		
F_c (%)	a	n	m
10	3.20	1.72	0.64
25	6.00	1.19	0.70
40	14.20	0.98	0.73

according to the fine grain content (F_c). Each soil samples were made by using itself.

In order to establish the relationship between the soil water moisture and the suction, the soil-water characteristic test for the drying process was carried out under a one dimensional consolidation state. The specimen size used was 60.0 mm in diameter and 10.0 mm in height, and the specimen was prepared using the static compaction method under 90% of the maximum dry density. The SWCCs on $F_c = 10\%$, 25% and 40% shows in Fig. 2. The fitting parameters of a, n, and m in the Fredlund and Xing's model (1994) were summarized in Table 1.

3.2 *Testing method*

The specimens for the CWCC test were composed of three layers by the static compaction under various initial degrees of saturation, and 90% of the maximum dry density. The size of the specimen was 50 mm in diameter and 100 mm in height. The initial condition of the specimens according to the fine grain content (F_c) is summarized in Table 2.

Figure 3 shows a sketch of the testing apparatus used in this study. After the specimen was set on the pedestal of the cell, it was covered with a rubber membrane and a loading cap, and then sealed with O-rings. The cell was filled with water. During the shear process, the amount of the cell water drainage was measured with a difference pressure transducer that was connected to

Table 2. Initial condition of the specimens.

F_c (%)	ρ_{di} (g/cm^3)	S_{ri} (%)	S_{rf} (%)	p_s(kPa)
10	1.699	49.73	47.52	9.50
	1.696	60.85	53.35	7.36
	1.706	68.14	63.30	5.13
	1.704	78.57	73.06	3.87
25	1.699	50.18	48.14	27.20
	1.695	61.21	52.43	21.08
	1.692	71.83	66.47	10.83
	1.670	78.05	75.71	7.12
40	1.707	48.60	46.89	96.59
	1.701	65.10	63.60	34.22
	1.692	72.09	69.00	25.25
	1.679	82.35	76.56	16.69

Note: ρ_{di}: initial dry density, w_i: initial water content, S_{ri} & S_{rf}: degree of saturation at initial & failure, and p_s: suction stress.

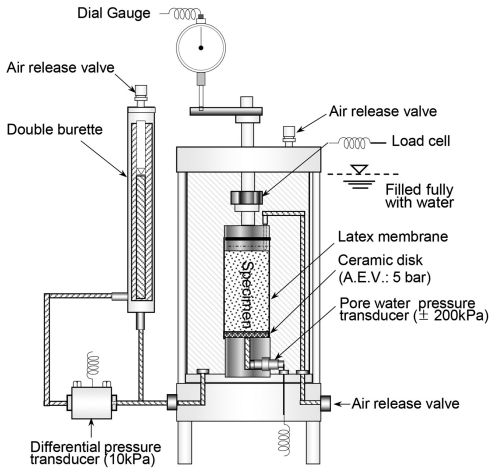


Figure 3. The testing apparatus used in this study.

the inside of the cell. The volume change of the specimen was calculated by correcting the amount of the cell water drainage for the piston penetration into the cell during shearing. A ceramic disk, whose air entry value was 500 kPa, was sealed into the pedestal of the cell to measure the pore-water pressure of specimen. A porous metal plate was set in the loading cap. The shear process was started with the shearing rate of 0.1% per minutes. The horizontal and vertical displacements, and the volume change were automatically measured during shearing.

4 TEST RESULTS AND DISCUSSIONS

4.1 *Shear strength and dilatancy according to the fine grain content*

The CWCC tests of 12 patterns according to the degree of saturation of 50% to 80%, and the fine grain content (F_c) of 10%, 25%, and 40% were performed. Figure 4

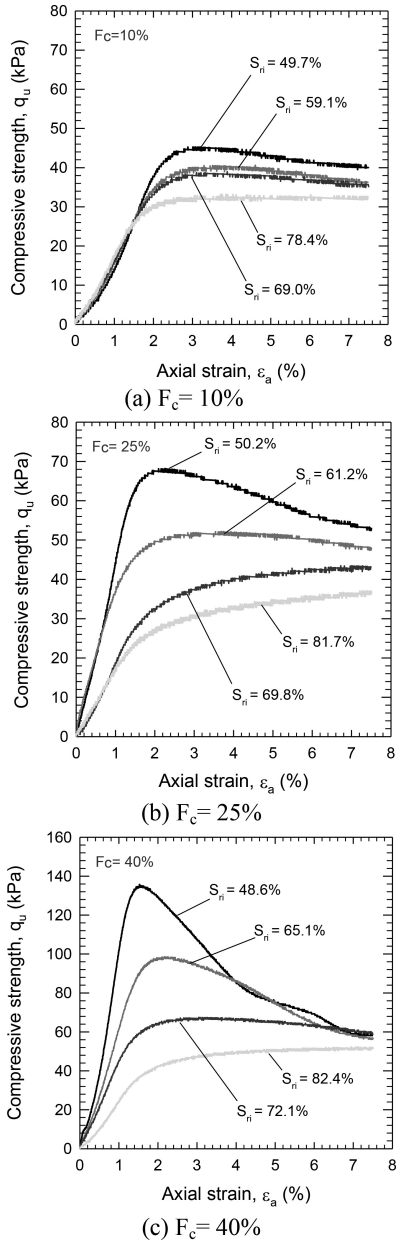


Figure 4. Relationship of the axial strain (ε_a) and the compressive strength (q_u).

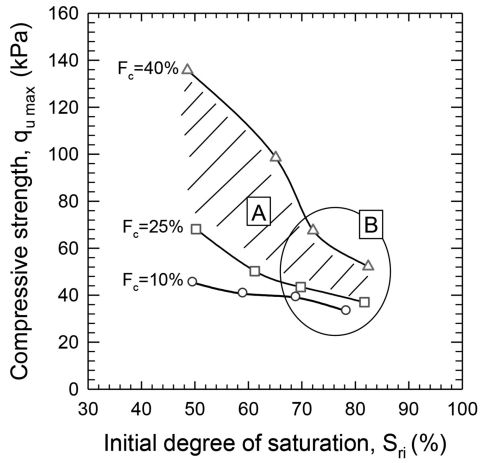


Figure 5. Relationship of the peak compressive strengths and the initial degree of saturation according to the fine grain content.

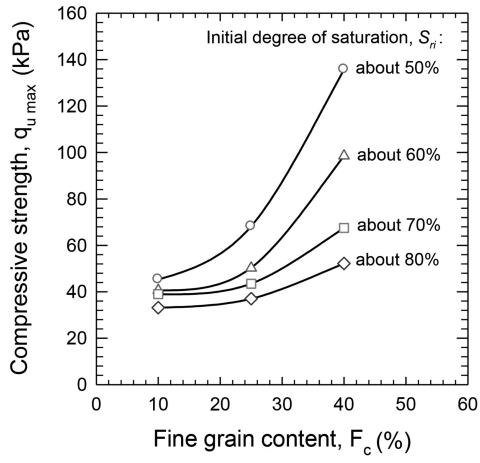


Figure 6. Relationship of the peak compressive strengths and F_c according to the initial degree of saturation.

shows the relationship of the axial strain (ε_a) and the compressive strength (q_u). Figure 5 shows the relationship of the peak compressive strengths and the initial degree of saturation according to the fine grain content. It could be observed that as the initial degree of saturation (S_{ri}) is decreases, the compressive strength increases regardless of the fine grain content. In particular, at the initial degree of saturation (S_{ri}) of 50%, the unconfined compression strengths increase sharply, and reach more quickly the peak value. Figure 6 shows the relationship of the peak compressive strengths and the fine grain content according to the initial degree of saturation. It was found that under the condition of the fine grain content from 10% to 40%, as the fine grain content increases, the peak compressive strength ($q_{u\ max}$) increases.

Figure 7 shows the relationship of the axial strain (ε_a) and the volumetric strain (ε_v). All of the results shows the dilative behavior after the compressive behavior. In the case of the fine grain content (F_c) of 10%, the magnitude of volumetric strain (ε_v) is below -6% and those behaviors are similar to each other regardless of that of $S_{ri} = 81.7\%$. It is observed that the volumetric behaviors of $F_c = 25\%$ and $F_c = 40\%$ are below -8%, and have a wide difference due to the degree of saturation, that is, the suction. In particular, it is found that the dilatancy of $F_c = 40\%$ at the same degree of saturation condition is larger than

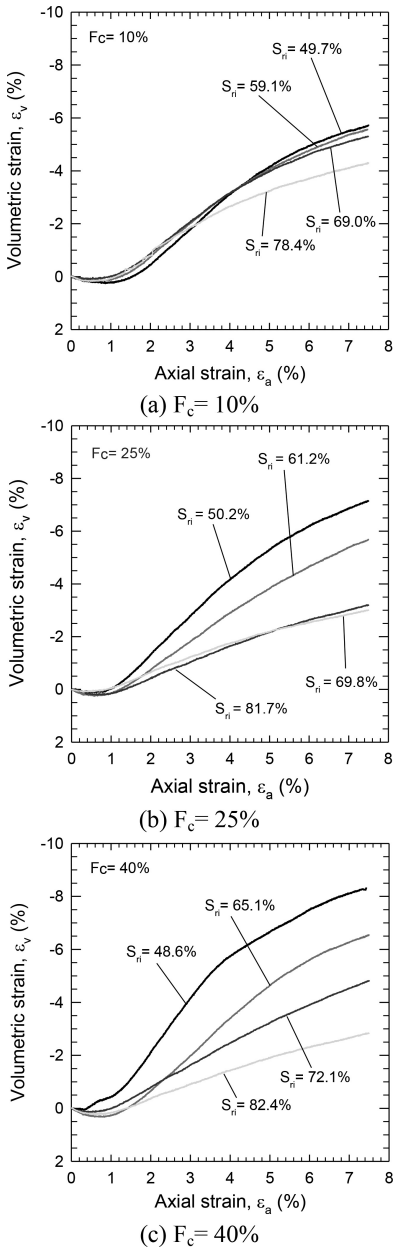


Figure 7. Relationship of the axial strain (ε_a) and the volumetric strain (ε_v).

that of $F_c = 25\%$ due to the effect of the fine grain content (F_c).

As shown in Fig. 5, it was observed that the deference of the compressive strengths between $F_c = 10\%$ and $F_c = 25\%$ according to S_{ri} is smaller compared to those of $F_c = 40\%$. In the case of $F_c = 10\%$, there is no the increase of the compressive strength according to the degree of saturation. In the case of $F_c = 25\%$, the compressive strengths are similar to those of $F_c = 10\%$ at $S_{ri} = 70\%$ and 80%. The area A between $F_c = 25\%$ and $F_c = 40\%$ means the increase of the compressive strengths due to the effect of the fine grain content. This could be understood that the effect of the suction for the compressive strength due to the fine grain content over $F_c = 25\%$ is maximized.

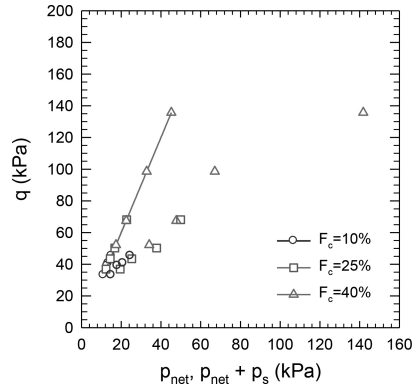


Figure 8. Application of the suction stress using the SSM.

On the other hand, it needs an enough time so that the embankment is saturated by the infiltration and the erosion with the rise of the water revel of the river at the rainfall. Thus, the embankment should have the enough strength against the collapse at the range (area B) of the high degree of saturation of 70% and 80% by the descent of the water revel of the river after the rainfall. As shown in Fig. 5, at the range of the high degree of saturation of 70% and 80%, the compressive strengths at $F_c = 40\%$ are about 1.5 times larger than those of $F_c = 10\%$ and $F_c = 25\%$. From these results, at the range between $F_c = 10\%$ and $F_c = 40\%$ in this study, it can be said that the material of the embankment over $F_c = 25\%$ contributes to the safety of the embankment with the maximization of the effect of the suction.

From these results, it could be understood in this study that because the increment of the fine grain content (F_c) is corresponded to the increment of the suction, the soil over $F_c = 25\%$ has a decided advantage as a material of the embankment.

4.2 *Application of suction stress (p_s) using SSM*

The suction values (s^*) of the results of the CWCC tests according to the fine grain content (F_c) were derived using the SSM based on the degree of saturation at failure so that the effect of the suction on the shear strength was evaluated. Here, s^* means the value obtained from the SSM. It could be obtained that the suction values base of $S_{rf} = 80\%$ on the SWCC results of $F_c = 10\%$, 25%, 40% using the SSM are 4.0 kPa, 7.1 kPa, and 16.7 kPa, respectively. Thus, it was understood that the deference of the peak compressive strengths between $F_c = 25\%$ and 40% is caused by the effect of the suction.

Figure 8 shows the result of the application of the suction stress (cf. Eq. (3); $p_s = [(S_r - S_{r0})/(1 - S_{r0})] \times s^*$) using the SSM in ($p_{net}$ & $p_{net} + p_s$, q) plane.

Here, the residual degree of saturation (S_{r0}) is zero. It is observed that these results for unsaturated soils were moved as much as the confining stress due to the suction. This result could be understood that the relationship of the shear strengths between saturated and unsaturated soils at failure can be explained through the application of the suction stress (p_s) as an equivalent confining stress.

5 CONCLUSION

Based on test results presented in this study, the following conclusions can be drawn:

(1) It could be observed that as the initial degree of saturation (S_{ri}) is decreases, the compressive strength increases regardless of the fine grain content. In particular, at the initial degree of saturation (S_{ri}) of 50%, the unconfined compression strengths increase sharply, and reach more quickly the peak value.
(2) This could be understood that the increase of the dilatancy due to the suction is larger than the decrease of the dilatancy due to the increase of the fine grain content.
(3) The area A between $F_c = 25\%$ and $F_c = 40\%$ means the increase of the compressive strengths due to the effect of the fine grain content. This could be understood that the effect of the suction for the compressive strength due to the fine grain content over $F_c = 25\%$ is maximized, and the soil over $F_c = 25\%$ has a decided advantage as a material of the embankment.
(4) The results of the application of the suction stress using the SSM in (p_{net} & $p_{net} + p_s$, q) plane were examined. It could be understood that the relationship of the shear strengths between saturated and unsaturated soils at failure can be explained through the application of the suction stress (p_s) as an equivalent confining stress.

REFERENCES

Anderson, S.A. and Sitar, N. 1995. Analysis of rainfall-induced debris flow. *Journal of Geotechnical Engineering, ASCE*, Vol. 121, No. 7: 544–552.

Fourie A.B., Rowe D., and Blight G.E. 1999. The effect of infiltration on the stability of the slopes of a dry ash dump. *Géotechnique*, Vol. 49, No. 1: 1–13.

Fredlund, D.G., Morgenstern, N.R., and Widger, R.A. 1978. The shear strength of unsaturated soils. *Canadian Geotechincal Journal*. Vol. 15, No. 3: 313–321.

Fredlund, D.G., Morgenstern, N.R., and Widger, R.A. 1978. The shear strength of unsaturated soils. *Canadian Geotechincal Journal*, Vol. 15, No. 3: 313–321.

Fredlund, D.G., and Xing, A. 1994. Equations for the Soil-Water Characteristic Curve. *Canadian Geotechnical journal*, Vol. 31, No. 4: 521–532.

Gens, A., Sanchez, M., and Sheng, D. 2006. On constitutive modeling of unsaturated soils. *Acta Geotechnica*. Vol. 1: 137–147.

Karube, D., Kato, S., Hamada, K., and Honda, M. 1996. The relationship between the mechanical behavior and the state of pore-water in unsaturated soil. *Geotechnical Engineering Journal, JSCE.* Vol. 535(III-34): 83–92. (In Japanese)

Karube, D., and Kawai, K. 2001. The role of pore water in the mechanical behaviour of unsaturated soils. *Geotech. Geological Eng*. Vol. 19: 211–241.

Khalili, N., and Khabbaz, M. H. 1998. A unique relationship for χ for the determination of the shear strength of unsaturated soils. *Geotechnique*. Vol. 48, No. 5: 681–687.

Kim, B.S., Shibuya, S., Park, S.W., and Kato, S. 2010. Application of suction stress for estimating unsaturated shear strength of soils using direct shear testing under low confining pressure. *Canadian Geotechnical Journal*. Vol. 47, No. 9: 955–970.

Kim, B.S., Shibuya, S., Park, S.W., and Kato, S. 2013. Suction stress and its application on unsaturated direct shear test under constant volume condition. *Engineering Geology*, Vol. 155: 10–18.

Kim, J., Jeong, S., Park, S., and Sharma, J. 2004. Influence of rainfall-induced wetting on the stability of slopes in weathered soils. *Engineering Geology*, Vol. 75, No. 3–4: 251–262.

Krahn, J., Fredlund, D.G., and Klassen, M.J. 1989. Effect of soil suction on slope stability at Notch Hill. *Canadian Geotechnical Journal*, Vol. 26, No. 2: 269–278.

Lambe, P.C. (1996). Residual soils. In: special report 247. Landslides: investigation and mitigation. *Washington DC: TRB, National Research Council*: 507–524.

Lu, N., and Likos, W.J. 2006. Suction stress characteristic curve for unsaturated soil. *J. Geotech. Geoenviron. Eng*. Vol. 132, No. 2: 131–142.

Lumb, P. 1975. Slope failures in Hong Kong, *Quarterly Journal of Engineering Geology and Hydrogeoloy*, Vol. 8: 31–65.

Ng, C.W.W., and Shi, Q. 1998. A numerical investigation of the stability of unsaturated soil slopes subjected to transient seepage. *Computers and Geotechnics*, Vol. 22, No. 1: 1–28.

Rahardjo, H., Lim, T.T., and Chang, M.F., Fredlund D.G. 1995. Shear-strength characteristics of a residual soil. *Canadian Geotechnical Journal*, Vol. 32: 60–77.

Rahardjo, H. and Leong, E.C. 1997. Soil-water Characteristic Curves and Flux Boundary Problems, Unsaturated Soil Engineering. *Practice-Geotechnical Special Publication*, Vol. 68: 88–112.

Sidle, R.C. and Swanston, D.N. 1982. Analysis of a small debris slide in coastal Alaska. *Canadian Geotechnical Journal*, Vol. 19: 167–174.

Sitar, N., Anderson, S.A., and Johnson, K.A. 1992. Conditions leading to the initiation of rainfall-induced debris flows. *Geotech. Eng. Div. Specialty Conf.: Stability and Perf. Of Slopes and Embankments-II. ASCE, New York, NY: 834–839.*

Terzaghi, K. 1950. Mechanism of landslides. In: Paige, S. (Ed), Application of Geology to Engineering Practice (Berkey Volume). *Geological Society of America, New York*: 83–123.

Vanapalli, S.K., Fredlund, D.G., Pufahl, M.D. and Clifton, A.W. 1996. Model for prediction of shear strength with respect to soil suction, *Canadian Geotechnical Journal*, Vol. 33, No. 3: 379–392.

Wang, G., and Sassa, K. 2003. Pore-pressure generation and movement of rainfall-induced landslides: effects of grain size and fine-particle content. *Engineering Geology*, Vol. 69, No. 1–2: 109–125.

Unsaturated Soil Mechanics—from Theory to Practice – Chen et al. (Eds)
© 2016 Taylor & Francis Group, London, ISBN 978-1-138-02921-7

Research on physical and mechanical properties of Xinjiang Daxigou loess

Z.Q. Hu, S. Lin, Z.J. Li & H.R. Li
School of Civil Engineering and Architecture, Xi'an University of Technology, Xi'an, China

ABSTRACT: The dam technology, dam methods of embankment dam is closely with the dam soil, and therefore must be studied physical and mechanical properties of soil material. In this paper, with the study of Xinjiang Daxigou dam soil, compaction characteristics, compression characteristics, strength properties, wetting deformation characteristics were analyzed. The results showed that: compaction work has great impact on the dry density, but the extent must be noted when increasing compaction to improve the compaction degree. Soil compaction has great impact on the compression characteristics, Compression coefficient rapidly decreased as the pressure increases, inflection point can be saw when the pressure reaches a certain level. Compression modulus increases with the increasing pressure and compaction degree. Water content and void ratio indicators have a certain function with strength index. Duncan – Chang model parameters present certain regularity as the change of moisture content and compaction, and the compaction degree has a great influence on parameters. Stress level has a significant influence on wetting deformation, and it is closely related to the compaction degree.

1 INTRODUCTION

The material of embankment dam is local earth-rock material, and it is closely related to the dam technology, dam methods of embankment dam and the local dam soil. It is necessary to study the physical and mechanical properties of soil. The compaction characteristics, strength properties, wetting deformation characteristics and other physical and mechanical properties of the soil are important factors about the security and stability of embankment dam.

Because of the special geographical and climate environment, Xinjiang loess is different from other regions loess. Zhou (1963) first studied the Xinjiang loess, he thinks that the loess in Xinjiang is closely related to glaciers and local drought environment. After the 1980s, Su et al. (1991), Zhang et al. (1985), Teng (1986) and other people studied the loess of northern Xinjiang, and they think that the formation of the loess of northern Xinjiang is similar to the Malan loess. Since the 1990s, many scholars do the further work in Xinjiang loess (Gao & Liu, 1990; Zhao et al., 1993; Zhao, 1997), they think that most of the loess of northern Xinjiang is the product of the early dry cold climate environment. After 21st century, the research of Xinjiang loess is expanded to the whole Xinjiang region (Yu & Wen, 1994; Fang et al., 2002), which involves micro-structure (Shi et al., 2007; Ye & Jin, 1998; Ye, 2001), paleomagnetic and ancient climate (Ye et al., 2003). Even so, the study of the physical and mechanical characteristics of loess in Xinjiang is less.

With the study of Xinjiang Daxigou dam soil, through configuring the reshaping of the different degree of compaction loess, the compaction characteristics, compression characteristics, strength properties, wetting deformation characteristics were analyzed.

2 THE TEST SOILS AND TEST METHODS

2.1 *Test soils*

The test soil is taken from T2 soil yard of Xinjiang Urumqi river Daxigou dam engineering, which is located in IV level terrace. The soil, between the non-dispersion soil and the dispersion soil, belong to the expansive clay, is the eolian loess. And the basic physical properties are shown in Table 1.

2.2 *Test methods*

According to the maximum dry density of 0.88, 0.90, 0.92, 0.95, 0.98 times, meaning the dry density are 1.61 g/cm^3, 1.65 g/cm^3, 1.68 g/cm^3, 1.74 g/cm^3, 1.79 g/cm^3, which are for the various physical and mechanical properties tests, and the tests are performed according to the soil testing standard.

"Standard of soil test method".

(1) Preparation of soil: preparation water content is 13.8% (the optimal water content), nature dry dehumidification and humidifying water transfer membrane methods are used to make saturated specimen.
(2) Compaction test: the DJS-3 standard light portable compaction instrument was used, and seven kinds of design scheme was designed. The experimental scheme shown in Table 2.

Table 1. The basic physical properties indexes of Daxigou loess.

Percentage of Particle size (%)									Compaction 25 N (power is 592.2 kJ/m^3)		
>0.075 mm	0.075–0.005 mm	<0.005 mm	Non-uniform coefficient Cu	Curvature coefficient Cc	d_{50} (mm)	Plastic limit ωp (%)	Liquid limitω L (%)	Plastic index Ip	Optimal water content (%)	Maximum dry density (g/cm^3)	Permeability coefficient
2.7	70.32	26.98	8.33	1.33	0.011	19.8	27.4	7.6	14.5	1.8	2.5×10^{-5}

Table 2. Compaction test program.

Compaction times	5	10	15	20	25	35	45
Power of compaction kJ/m^3	118.4	236.9	355.3	473.8	592.2	829.1	1066.0

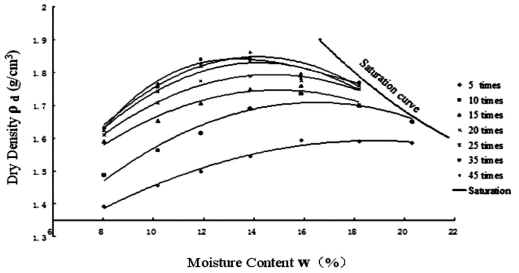


Figure 1. Compaction curves under different compaction times.

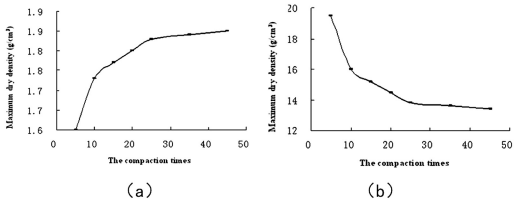


Figure 2. Curves of compaction times between maximum dry density and optimum moisture content.

(3) Compression test: Control the optimal water content, 13.8%, when preparing different compaction degree of the remolded sample. Step by step in testing the vertical pressure, respectively read peer pressure dial indicator reading.
(4) Triaxial test: It's mainly doing consolidation drained triaxial shear tests. The triaxial shear apparatus which is manufactured by Nanjing electric power automation equipment factory is used, and shear ratio is 0.016 mm/min, consolidation stress ratio K_c is 1.0, consolidation confining pressure is 100, 200, 300, 400 kPa, water content is 9.2%, 13.8% (the optimal water content), 17.2%, and saturated water content respectively. The pressure chamber is circumscribed, the value shear is measured by dial gauge which is connected to the pressure chamber.

The compaction curve of different compaction power is shown in Figure 1. The relation of the compaction times with the maximum dry density and optimum water content is shown in Figure 2.

3 THE TEST RESULTS AND ANALYSIS

3.1 *Research of the soil compaction characteristics*

Figures 1 and 2 show that compaction power has a great influence on dry density. The maximum dry density increases with increasing of compaction power, but the optimum water content reduce gradually. The increment of maximum dry density reduces gradually with increasing of compaction power. The maximum dry density does not unlimited increase with the increasing of compaction work after the compaction power reaching a certain value. From the safe and economic consideration, the most reasonable compaction times are 25 times. This is consistent to the fitted relationship of the compaction function and maximum dry density by Blotz with the method of least squares. Through increasing the compaction to improve the degree of compaction must be to pay attention to the problem of "degree", the increasing of compaction power will lead to reduce of optimum water content. The optimal water content is 14.5% when the each layers has 20 hits, The optimal water content is 13.8% when teach layers has 25 hits. When the hit times increases to 45 times, the optimal water content reduce to 13.4%. Therefore the attention should be paid to control water content in practical engineering.

3.2 *Research on the soil compression characteristics*

The parameters of Duncan-Chang E-μ model was solved, and the various rulers of parameters with the changes of the compaction degree and water content was analyzed.

Figure 3 shows that the pore ratio decreases rapidly with the confining pressure increasing at the lower

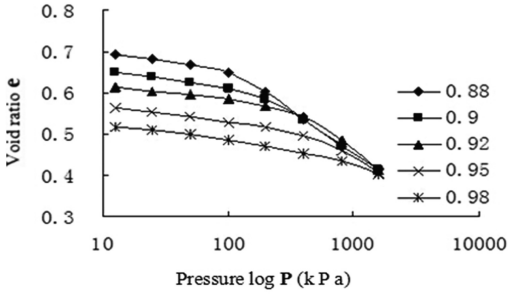


Figure 3. *e*–lg *p* curves of different compaction degree.

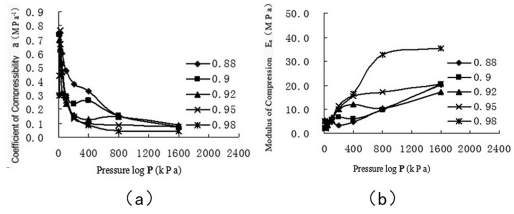


Figure 4. A-P and Es-P curves of different compaction degree.

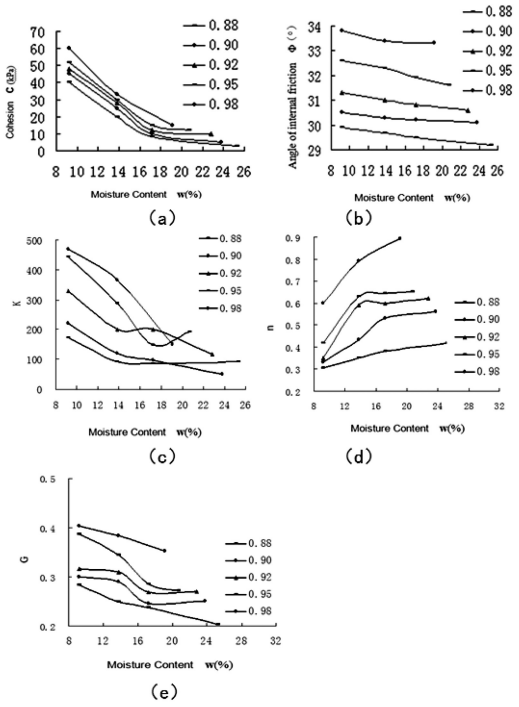


Figure 5. Duncan-Chang E-μ model parameters with the water content.

pressure. The smaller of the compaction degree, the faster of the increasing speed of the pore ration, this is because the soil is more likely to be compaction at the lower compaction degree. The compression curve fell more and more slowly with pressure increasing.

The *e*-lg *p* curve can be divided into three phases obviously. Firstly, the internal structure of soil has not been damaged obviously, and the compression curves keep a steady state. Secondly, the internal structure of soil is damaging and secondary structure gradually formed, and compression curve shows nonlinear obviously. Thirdly, the internal structure of soil was completely damaged, the compression curve shows linear change. The yield stress increases gradually with the increase of degree of compaction. For example, when the compaction degree is 0.88, the yield pressure is about 100 kPa. When the compaction degree is 0.98, the yield pressure is about 800 kPa. We can obtain the compression coefficient and compression modulus Es and draw the relationship curve with the overlying pressure. As shown in figure 4.

Figure 4 (a) shows that the compression coefficient reduce rapidly with the increasing of pressure at the same compaction degree, when the pressure reaches a certain degree the turning points appeared, then the compression coefficient reduce slowly with the increasing of pressure.

Figure 4 (b) shows that the compression modulus Es increases with the increasing of pressure, and shows that linear increase with the compaction degree at the small compaction degree, the increase speed slow down gradualy when the compaction degree increase to a certain value, and the inflation point appears.

3.3 *Research on the soil static strength characteristics*

The parameters of Duncan-Chang E-μ model was solved, and the various rulers of parameters with the changes of the compaction degree and water content was analyzed. The curves of parameters with the changes of compaction degree and water content are shown in Figures 5 and 6 respectively.

Figures 5 (a) and (b) show that the soil shear strength has an obvious correlation with the water content, the shear strength is smaller with the higher water content. This is because that the increase of water content will cause soil in the matrix suction decreases, and the matrix suction of unsaturated soil is characterized by the negative pore water pressure generally. The increase of water content will make Daxigou loess wetting and the strength of the soil reduce.

The influence of water content on the cohesive force is more obvious than the internal friction angle. For example, As compaction degree is 0.88, the water content increased from 9.2% to 13.8%, the cohesive force rapidly reduced from 40 kPa to 20 kPa, and internal friction Angle relegated from 29.9° to 29.7°, the reduction is small.

We can find that the relationship of water content and the cohesive force approximate a quadratic function by formula fitting, and with the internal friction Angle approximate linear relationship. The pore ratio and strength accord with been indexes function relation. Considering the mutual influence of both

water content and degree of compaction, the effective stress strength index formula of Daxigou loess were deduced.

$$C = a\omega^2 + b\omega + ce^n + f(e,\omega) + d$$
$$\phi = a'\omega + b'e^n + f'(e,\omega) + c' \quad (1)$$

where e, ω—pore ratio, water content; a, b, c, n—the test constant related to the C; and a', b', c'—the test constant related to the ϕ.

The Duncan-Chang model other parameters show some regularity with the changes of water content and compaction degree. k decreases with the increasing of water content under the same compaction degree, increases with the increasing of water content, opposite to the k. R_f changes little with water content (Calculation can take its average). F and D with the changes of water content are not obvious.

K, n, R_f, C, ϕ, G are all increase with increasing of compaction degree under the same water content, F and D with the changes of compaction degree are not obvious. This means that the tangent modulus of elasticity Et and volume deformation modulus Bt increases quickly with the increasing of dry density, so in the engineering construction to strictly control the degree of compaction and related indicators. So we must strictly control the related indexes, such as compaction degree in engineering construction.

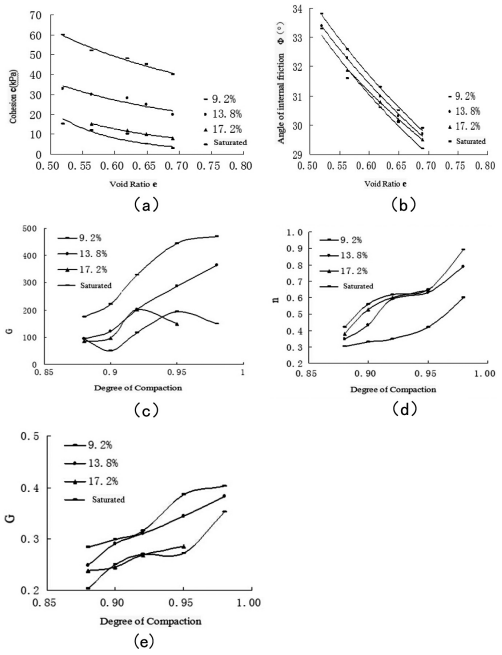


Figure 6. Duncan-Chang E-μ model parameters with the compaction degree.

3.4 *The influence of stress level on wetting deformation*

3.5 *The relation of stress level and volume strain*

We can regard the gap of primary stress with 15% axial strain as $(\sigma_1 - \sigma_3)_f$ when the stress-strain curve is the hardening type curve, we can regard the max of $(\sigma_1 - \sigma_3)$ as $(\sigma_1 - \sigma_3)_f$ when the stress-strain curve is the softening type curve. We can obtain any primary stress gap corresponding to the stress level $D_L = (\sigma_1 - \sigma_3)/(\sigma_1 - \sigma_3)_f$. To stress level D_L as the X axis, shear strain ε_v for the Y axis built coordinate system, drawing the curves between the stress level and the volume strain under different confining pressure.

As the stress levels – volume strain curves of different degree of compaction with confining pressure 200 kPa for an example (Fig. 9), we can get the following conclusions.

(1) The volume strain increased with the increasing of stress level. When the stress level is lower, the volume strain increases slowly, when the stress level increases to a certain value, with the increasing of stress level the speed of shear strain increases is faster, and appears inflection point. With the increasing of confining pressure, the inflection point turns left and the critical stress level decreases under the same initial water content.

(2) The volume strain increases with the increasing of the initial water content, under the same confining pressure the same stress level. The influence of initial water for volume shear is more apparently when the water content is small at the lower Confining pressure, but the curve has been almost coincide when the water content close to the

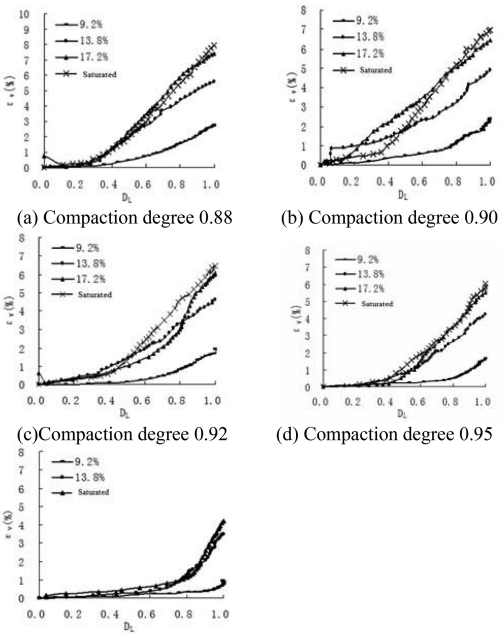
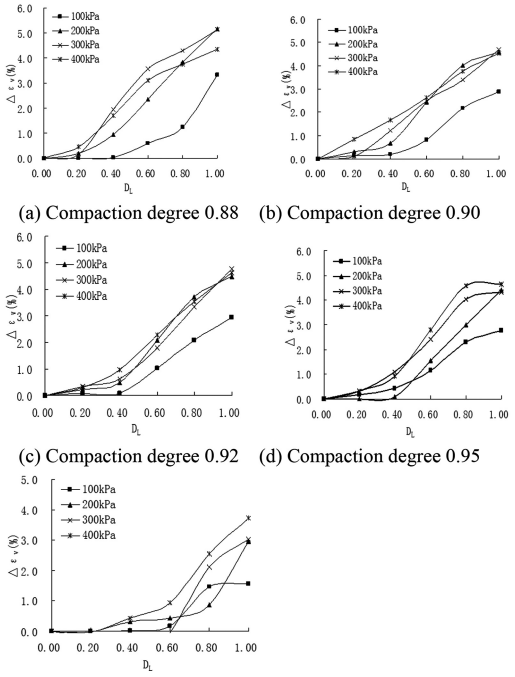


Figure 7. Stress levels – body strain curves of 200 kPa Confining pressure.

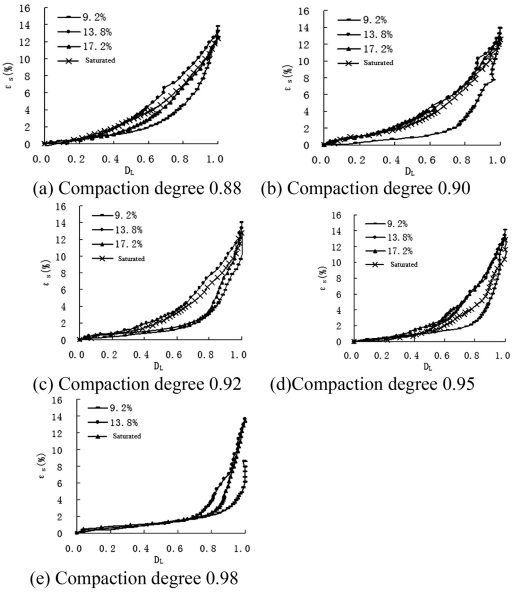


(a) Compaction degree 0.88 (b) Compaction degree 0.90

(c) Compaction degree 0.92 (d) Compaction degree 0.95

(e) Compaction degree 0.98

Figure 8. D_L–$\Delta\varepsilon_v$ curves of different compaction degree.



(a) Compaction degree 0.88 (b) Compaction degree 0.90

(c) Compaction degree 0.92 (d)Compaction degree 0.95

(e) Compaction degree 0.98

Figure 9. Stress level – shear strain curves of 200 kPa Confining pressure.

saturated water content. This shows that water content change on the influence of the curve relative to the smaller confining pressure has been weakened under low water content, the higher water content is opposite.

We can find the volume strain when the water content is 9.2%, saturated water content and the stress level is 0, 0.2, 0.4, 0.6, 0.8, 1 respectively. Also we can obtain the gap of volume strain $\Delta\varepsilon_v = \varepsilon_v - \varepsilon_{v9.2}$ under the same stress level D_L. To stress level D_L as the X axis, the gap of volume strain $\Delta\varepsilon_v$ for the Y axis built the curve of $D_L - \Delta\varepsilon_v$, as shown in Figure 8.

The Figure 8 shows that, under the same compaction degree, $\Delta\varepsilon_v$ increases with the increasing of stress level. Under the lower stress level, $\Delta\varepsilon_v$ increases more slowly, after the stress level increases to a certain value, $\Delta\varepsilon_v$ increases rapidly and the inflection point appears, and all of the inflection point is close under different compaction degree, about $D_L = 0.6$. The volume strain $\Delta\varepsilon_v$ has an increased trend with the increasing of confining pressure.

3.6 *The relation of stress level and shear strain*

To stress level D_L as the X axis, volume strain $\varepsilon_s = \varepsilon_1 - \varepsilon_v/3$ for the Y axis built coordinate system, drawing the curve between the stress level and the shear strain under different confining pressure.

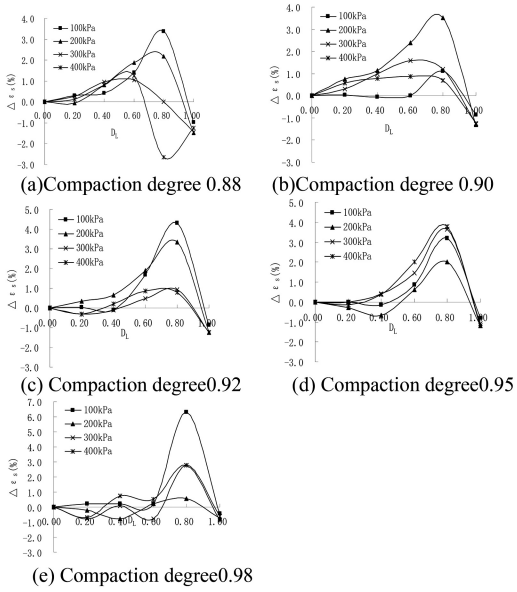
As the stress levels – shear strain curve of different degree of compaction with confining pressure 200 kPa for an example (Fig. 9), we can get the following conclusions.

(1) The shear strain increased with the increasing of stress level. When the stress level is lower, the shear strain increases slowly, when the stress level increases to a certain value, with the increasing of stress level the speed of shear strain increases is more faster, so there is a transition region. With the increasing of confining pressure, the transition region turns left and the critical stress level decreases until it is not obvious at the same initial water content.

(2) The shear strain increases with the increasing of the initial water content, under the same confining pressure the same stress level. The influence of initial water for volume shear is more apparently when the water content is small at the lower confining pressure, but the curve has been almost coincide when the water content close to the saturated water content. The curve shows more uniform with the change of water content at high confining pressure.

(3) The shear strain has a normalized tendency with the increasing of stress level under the same confining pressure and different initial water content. When the stress level reaches to 1, the gap of the shear strain under different initial water content is smaller.

We can find the shear strain when the water content is 9.2%, saturated water content and the stress level is 0, 0.2, 0.4, 0.6, 0.8, 1 respectively. Also we can obtain the gap of shear strain $\Delta\varepsilon_s = \varepsilon_s - \varepsilon_{s9.2}$ under the same stress level D_L. To stress level D_L as the X axis, the



(a)Compaction degree 0.88 (b)Compaction degree 0.90

(c) Compaction degree0.92 (d) Compaction degree0.95

(e) Compaction degree0.98

Figure 10. $D_L - \Delta\varepsilon_s$ curves of different compaction degree.

gap of shear strain $\Delta\varepsilon_s$ as the Y axis, the curves of $D_L - \Delta\varepsilon_s$ was shown in Fig. 10.

The Figure 10 shows that $\Delta\varepsilon_s$ has an increasing trend with the increasing of confining pressure under the same degree of compaction. Under the same water content, the greater the degree of compaction, the greater the $\Delta\varepsilon_s$. When the stress level is low, $\Delta\varepsilon_s$ increases more slowly. When the degree of compaction is large, $\Delta\varepsilon_s$ shows ups and downs, fluctuating around 0. After the stress level arrived at a certain level, $\Delta\varepsilon_s$ increasing rapidly. When $D_L = 0.8$, $\Delta\varepsilon_s$ is maximum, when $D_L > 0.8$, $\Delta\varepsilon_s$ reduced quickly to negative.

4 CONCLUSIONS

(1) The compaction work has a great influence on the dry density, 25 times is the most reasonable compaction times considering the safe and economic consideration. The increasing of compaction function will lead to the optimal water content decreases, so more attention must be paid to control water content in practical engineering.

(2) The soil compaction degree has a great influence on compression. Firstly, the compression coefficient reduce rapidly with the increasing of pressure, when the pressure reaches a certain degree the turning points appeared, compression modulus Es increases with the increasing of pressure and degree of compaction.

(3) The relationship of water content and the cohesive force approximate a quadratic function, and with the internal friction Angle approximate linear relationship. The pore ratio and strength accord with been indexes function relation. Considering the mutual influence of both water content and degree of compaction, the effective stress strength index formula of Daxigou loess were deduced.

(4) The parameters of Duncan-Chang mode shows some regularity with the change of water content and degree of compaction. And the degree of compaction has a great influence on the parameters of Duncan-Chang mode, so we must strictly control the related indexes such as compaction degree in engineering construction.

(5) The stress level has a significant effect on wetting deformation, and the influence degree is closely related to the degree of compaction.

REFERENCES

Fang X., Shi Z., Yang S., Li J., Jiang P. 2002. Tianshan loess and GuErBanTongGuTe desert development and drying of northern xinjiang. Science bulletin 47(7), 540–545.

Gao C., Liu J., 1990. The research of Urumqi river basin loess. Quaternary Sciences 3, 251–260.

Shi Z., Dong M., Fang X., 2007. The characteristics of later pleistocene loess-paleosol magnetic susceptibility in Yili Bason. Journal of Lanzhou University (Natural Sciences) 43(2), 7–10.

Su H., Wen Q., 1991. The quaternary sedimentary geochemical characteristics in northern Xinjiang. Geochimica1, 56–63.

Teng Z., 1986. Some of the characteristics of loess and its forming conditions in Xinjiang preliminary understanding. Journal of northwest university (natural science edition) 16(1), 69–76.

Ye W., 2001. Study on Magnetic Susceptibility of Loess and Paleosol Sequences in Westerly Region of Xinjiang. Journal of desert research 21(4), 514–520.

Ye W., Jin H., 1998. Depositional features and material sources of loess in Yili region, Xinjiang. Arid Land Geography 21(4), 1–8.

Ye W., Sang C., Zhao X., 2003. Spatial-Temporal Distribution of Loess and Source of Dust in Xinjiang. Journal of desert research 23(5), 514–520.

Yu S., Wen Q., 1994. The geochemical features of rare earth elements in xinjiang region on the loess. Arid Land Geography 17(2), 75–82.

Zhang H., Wen H., 1985. New findings in the study of loess in Xinjiang. The geological knowledge 8, 19–20.

Zhao X., 1997. Kerry ya river mineral assemblage characteristics of loess and environmental significance. Arid Land Geography 20(3).

Zhao X., Maimai T., Liu J., Luo J., 1993. Since middle of late pleistocene kerry river basin in the loess sedimentary characteristics and environment evolution. Arid Land Geography 18(1).

Zhou T., 1963. Quaternary continental sedimentary main types of Xinjiang and its relationship with landform climate development. ACTA Geographica Sinica 29(2), 109–129.

Unsaturated Soil Mechanics—from Theory to Practice – Chen et al. (Eds)
© 2016 Taylor & Francis Group, London, ISBN 978-1-138-02921-7

Study on dynamic modulus and deformation characteristics of loess under bidirectional cyclic loads

X.D. Zhang, Y.S. Luo, P.C. Wang & L.X. Hu
College of Water Resources and Architectural Engineering, Northwest A and F University, Yangling, Shanxi, China

ABSTRACT: Phase difference has certain effects on dynamic shear modulus of loess. With $\varphi = 180°$ as the tuning point, dynamic shear modulus of loess decreases first and then increases with rise of phase difference, and when phase difference is 180°, dynamic shear modulus decreases to the lowest level, while increasing of radial vibration amplitude significantly reduces initial dynamic shear modulus of loess. When phase difference is less than 180°, increase of phase difference accelerates the development of shear strain, and when phase difference is greater than 180°, the development of dynamic shear strain slows down with increase of phase difference. By calculating transformation, it is found that dynamic tensile & compressive load quickens the increasing of dynamic shear strain, and when the dynamic tensile & compressive and shear loads change simultaneously, change in dynamic shear load has much more prominent impact on the development of dynamic shear strain.

1 INTRODUCTION

People began to carry out further research on dynamic characteristics of soil under seismic loads because of the Alaska earthquake in America and the Niigata earthquake in Japan which happened in 1964 (Xie 2011). At present, when scholars simulate the seismic loads using dynamic triaxial apparatus, the majority follow the method proposed by Seed (Seed & Lee 1966, Seed & Pcacock 1971, Seed & Idriss 1971). Based on the suggestion of Seed, the seismic loads can be simply simulated by dynamic shear load, and it is considered that the earthquake damage mainly caused by dynamic shear load. When an earth occurs, seismic waves propagating from the source to the ground include transverse waves (S-waves) and longitudinal waves (P-waves), and the transverse waves produce shear dynamic load whereas the longitudinal waves produce tensile & compressive dynamic load, consequently, under the effects of these two dynamic loads, horizontal shear vibration and vertical tensile & compressive vibration occur simultaneously in loess. With considering the high decay rate of longitudinal waves when it propagates (Gu et al. 2012), simulating method adopted by Seed is reasonable when a earthquake with deep earthquake source or small earthquake magnitude occurs, but it is not suitable for the occurrence of earthquakes with shallow source or large magnitude. The city epicentral earthquake is usually with shallow source and large earthquake magnitude, and a large number of buildings in the city epicentral earthquake are destroyed with overlarge vertical deformation due to the effects of tensile & compressive dynamic load, such as the Tangshan earthquake in 1976 (Wang et al. 2010), the San Salvador earthquake in 1986 (Bommer et al. 2001), and the Japan's Kobe earthquake in 1995 (Zhou et al. 2011). When we do the research on dynamic characteristics of soil, in order to make the dynamic stress state much closer to the actual seismic condition, both the shear dynamic load and tensile & compressive dynamic load should be applied on the test sample. By this way, much more accurate dynamic parameters of soil can be obtained and provided for geotechnical seismic design. Many scholars have carried out the research on dynamic characteristics of soil under the condition of axial tensile & compressive and torsional shear coupling (Kabilamany & Ishihara 1991, Trandafir & Sassa 2004). However, the research under the bidirectional dynamic loads with two-way dynamic triaxial apparatus is uncommon, and Wang et al. (1996), Cai et al. (2008) have done some primary research.

Loess is one kind of typical regional special soil, in China, it's distributed in arid or semi-arid areas where the earthquakes with large magnitude occur frequently. Therefore, researching the dynamic characteristics of loess under the tensile & compressive dynamic load and shear dynamic load coupling is necessary. Presently, very few people do the research on dynamic characteristics of loess under bidirectional dynamic loads. So, in this paper, the dynamic shear modulus and shear strain properties of loess under bidirectional dynamic loads are explored, and the effects of radial vibration amplitude and phase difference on the dynamic shear modulus and dynamic shear strain are mainly analyzed, which is helpful for geotechnical seismic design in loess region.

Table 1. Testing programs.

Consolidation style	σ_{3c} kPa	q_{ds} kPa	σ_{dhm} kPa	φ °
Isotropic consolidation	200, 300	10	20, 40, 60	0, 45, 90, 135, 180, 225, 270, 315, 360

*In table 1, σ_{3c}, q_{ds}, σ_{dhm}, φ are confinig pressure, initial cyclic deviator stress, radial vibration amplitude and phase difference respectively

2 THE TEST METHOD

The specific testing programs are shown in the table 1. In the testing programs, cyclic deviator stress is the difference between axial dynamic load and radial dynamic load, i.e. $q_d = \sigma_{dv} - \sigma_{dh}$. The initial cyclic deviator stress is the difference between initial axial vibration amplitude and radial vibration amplitude, i.e. $q_{ds} = \sigma_{dvms} - \sigma_{dhm}$. In tests, consolidation pressure is put onto soil samples firstly and the consolidation starts. Consolidation process is finished with axial deformation of samples during 30 minutes is less then 0.01 mm. After consolidation, bidirectional vibration starts with applying both axial dynamic loads and radial dynamic loads on samples. Both the vibration wave types of axial and radial loads are sine waves with frequency of 1 Hz. The axial dynamic loads are applied level-by-level, and the vibration amplitude increases gradually with the increasing rate of 5 kPa, while the radial vibration amplitude is a constant. Under each level of load, the sample vibrates 5 times until the axial dynamic deformation is larger than 5%. Stress diagram of sample under bidirectional dynamic loads is shown in Figure 1.

In Figure 1, σ_{dv} and σ_{dh} are axial and radial dynamic loads respectively, and σ_{1c} and σ_{3c} are axial and radial confining pressure respectively. From the Figure 1, it can be seen that there are both tensile & compressive dynamic load (σ_{d45}) and shear dynamic load (τ_{d45}) on the shear surface with angle of 45° of soil sample. How to calculate σ_{d45} and τ_{d45} is shown by Formula 1 and Formula 2 respectively.

$$\sigma_{d45} = \sigma_{3c} + (\sigma_{dv} + \sigma_{dh})/2 \quad (1)$$

$$\tau_{d45} = (\sigma_{dv} - \sigma_{dh})/2 \quad (2)$$

The dynamic elastic module of loess is calculated by using the stress-strain hysteresis loop (as shown in Fig. 2), and the calculation formula is shown in formula 3. Using the formula 4 and formula 5, the dynamic shear modulus (G_d) and dynamic shear strain (γ_d) can be obtained by converting from dynamic elastic modulus (E_d) and dynamic strain (ε_d).

$$E_d = (q_{d\max} - q_{d\min})/(\varepsilon_{d\max} - \varepsilon_{d\min}) \quad (3)$$

$$G_d = E_d/2(1+\mu) \quad (4)$$

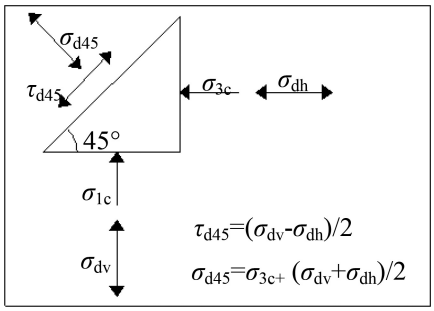


Figure 1. Stress diagram of sample under bidirectional dynamic loads.

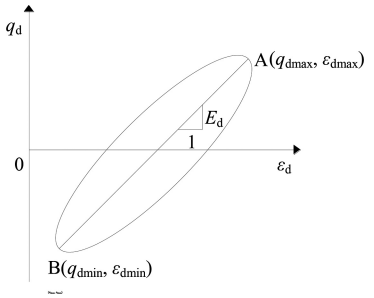


Figure 2. Calculation of dynamic elastic modulus.

$$\gamma_d = \varepsilon_d(1+\mu) \quad (5)$$

In formula 3, q_{dmax} and q_{dmin} are the maximum deviator stress and minimum deviator stress in each cycle, and ε_{dmax} and ε_{dmin} are the maximum dynamic strain and minimum dynamic strain in each cycle. In formula 4 and formula 5, μ is the Poisson ratio, we choose 0.4 as the value of Poisson ratio because the testing material is clay with low liquid limit.

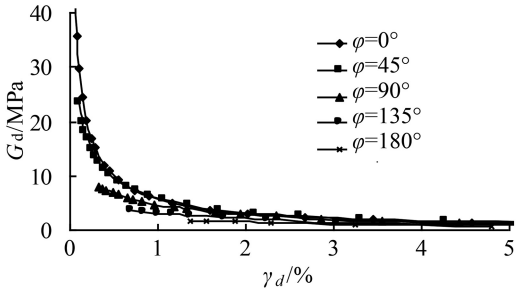
3 ANALYSIS OF TEST RESULTS

3.1 *Effects of phase difference on dynamic shear modulus of loess*

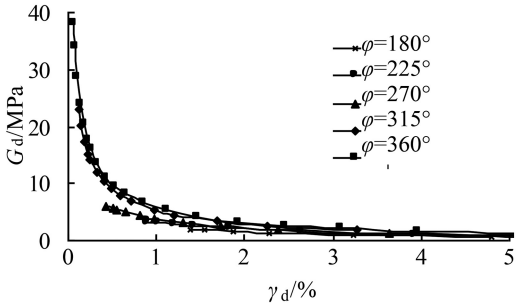
The $G_d \sim \gamma_d$ curves of loess under different phase difference and a certain radial dynamic loads were shown in Figure 3, from which we can find that the $G_d \sim \gamma_d$ curves reach the lowest level with the 180° of phase difference, and the dynamic shear modulus decreases with the phase difference rising from 0° to 180°, while the value of dynamic shear modulus increases moderately with the increasing of phase difference from 180° to 360°. At the meantime, the shear strain increases dramatically and the dynamic shear modulus would decay in a small extent under the effect of initial dynamic stress when the phase difference is 180°.

The relation curve between $1/G_d$ and γ_d is linear, and it could be indicated that:

$$1/G_d = a + b\gamma_d \quad (6)$$



(a) σ_{3c}=200kPa, σ_{dhm}=40kPa



(b) σ_{3c}=200kPa, σ_{dhm}=40kPa

Figure 3. Relationship between dynamic shear modulus and dynamic shear strain.

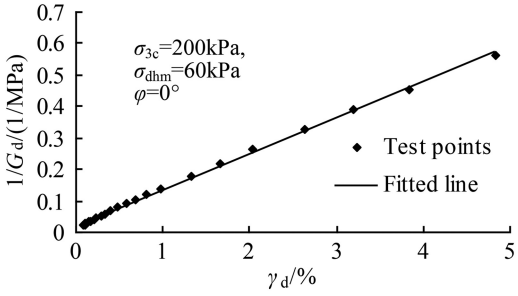


Figure 4. Relationship between $1/G_d$ and γ_d of loess measured by test.

In formula 6, G_d and γ_d stand for dynamic shear modulus and dynamic shear strain respectively, and a, b stand for intercept and slope of relation line between $1/G_d$ and γ_d respectively. The measured relation line between $1/G_d$ and γ_d was shown in Figure 4. It can be easily found that when $\gamma_d = 0$, the $1/G_0 = a$, and the initial dynamic shear modulus could be calculated by the intercept of $1/G_d \sim \gamma_d$ relation line, i.e. $G_0 = 1/a$. In order to study the influence of dynamic shear modulus of loess by phase difference under low strain, the relation of $1/G_d \sim \gamma_d$ was used to calculate the G_0.

Figure 5 shows the curves between phase difference and initial dynamic shear modulus of loess under the confining pressure of 200 kPa, and it tells that the affection of initial dynamic shear modulus by phase difference changes is opposite before and after the

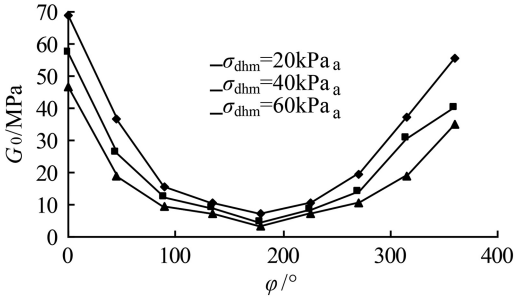


Figure 5. Relationship between initial dynamic shear modulus and phase difference.

Table 2. Comparison of initial dynamic shear modulus under $\varphi = 0°$ and $\varphi = 180°$.

σ_{dhm} kPa	$G_{0\ (\varphi=0°)}$ MPa	$G_{0\ (\varphi=180°)}$ MPa	$G_{0(\varphi=180°)}/G_{0(\varphi=0°)}$	η
20	68.8	7.4	10.77%	89.23%
40	57.1	4.5	7.89%	92.11%
60	46.9	3.2	6.79%	93.21%

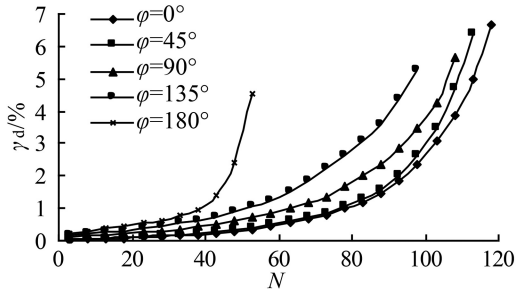
*In table 2, $G_{0\ (\varphi=0°)}$ and $G_{0\ (\varphi=180°)}$ are initial dynamic shear modulus under phase difference of 0° and 180° respectively, η is decay rate of initial dynamic shear modulus.

turning point of 180° (φ). When $\varphi < 180°$, the initial dynamic shear modulus (G_0) decreases with the increasing of phase difference, and it declines sharply when the phase difference is between 0° and 90°, while the dumpling speed is relatively slow when the phase difference is between 90° and 180°. When $\varphi > 180°$, the initial dynamic shear modulus increases with the rise of phase difference, and the relationship of increasing speed and dumping speed between 0° and 180° resembles symmetrically.

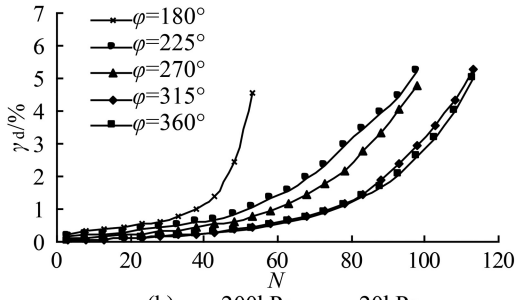
Table 2 shows the comparison results of initial dynamic shear modulus of loess under 200 kPa of confining pressure when the phase difference are 0° and 180°. It can be found that, when $\sigma_{dhm} = 20$ kPa, the value of initial dynamic shear modulus under $\varphi = 180°$ only accounts for 10.77% of that under $\varphi = 0°$, which decreases nearly by 90%, and the decay rate increases with increasing of radial dynamic amplitude.

3.2 *The dynamic shear strain of loess under bidirectional cyclic loads coupling*

Figure 6 shows the curves between dynamic shear strain and cyclic numbers, from which we can see that, dynamic shear strain increases fastest when the phase difference is 180°, and development law of dynamic shear strain with rise of cyclic number shows opposite trend before and after the turning point of 180°. When the phase difference is less than 180°, increasing of phase difference accelerates the development of dynamic shear strain, while the developing speed

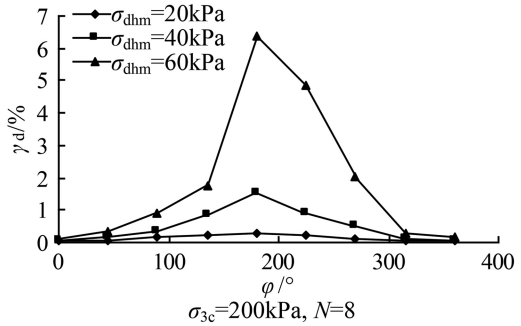


(a) σ_{3c}=200kPa, σ_{dhm}=20kPa



(b) σ_{3c}=200kPa, σ_{dhm}=20kPa

Figure 6. Relationship between dynamic shear strain and cycle numbers.



σ_{3c}=200kPa, N=8

Figure 7. Relationship between dynamic shear strain and phase difference.

of dynamic shear strain slows down with rise of phase difference from 0° to 180°.

Figure 7 shows how dynamic shear strain change with phase difference and radial vibration amplitude under the confining pressure of 200 kPa and cyclic number of 8 times. It indicates that, the change law of dynamic shear strain with phase difference and radial vibration amplitude is the same as that showed in Figure 6, and it is clear that the stress combination with $\sigma_{dhm} = 60$ kPa and $\varphi = 180°$ is the most unfavorable combination for loess to resist shear deformation. The dynamic shear strain under the stress combination ($\sigma_{dhm} = 60$ kPa and $\varphi = 180°$) is 20.9 times and 46.4 times as high as that under stress combination ($\sigma_{dhm} = 20$ kPa and $\varphi = 180°$) and stress combination ($\sigma_{dhm} = 60$ kPa and $\varphi = 0°$) respectively.

Table 3. Effects of tensile & compressive and shear dynamic loads on dynamic deformation of loess.

Factors		σ_{d45}	τ_{d45}	Develpoment of γ_d
Rise of φ	0°～180°	Decrease	Increase	Accelerated
	180°～360°	Increase	Decrease	Slowed down
Rise of σ_{dhm}		Increase	Constant	Accelerated

*In table 3, σ_{d45} and τ_{d45} are tensile & compressive and shear dynamic loads on shear surface of specimen respectively.

3.3 *Effects of tensile & compressive dynamic loads coupling on dynamic deformation of loess*

The calculation formulas of axial and radial dynamic loads are shown in formula (7) and formula (8) respectively. Substitutig formula (7) and (8) into formula (1) and (2), the calculation formulas of σ_{d45} and τ_{d45} can be obtained. By calculating, the changing laws of σ_{d45} and τ_{d45} are obtained, and so the effects of σ_{d45} and τ_{d45} coupling on dynamic deformation are, which are shown in table 3.

$$\sigma_{dv} = \sigma_{3c} + \sigma_{dvm}(\sin 2\pi t + \varphi) \tag{7}$$

$$\sigma_{dh} = \sigma_{dhm} \sin 2\pi t \tag{8}$$

From Table 3, it can be seen that, with shear dynamic load keeping constant, development of shear strain of loess gets faster with increasing of tensile & compressive load, which tells that the application of tensile & compressive dynamic load plays a role of accelerating the development of dynamic shear strain. When the tensile & compressive and shear dynamic loads change simultaneously, development of shear strain accelerates with increasing of dynamic shear load and slows down with decrease of it, no matter tensile & compressive dynamic load increases or not. That is to say, under the coupling of tensile & compressive and shear dynamic loads, shear dynamic load has the much more significant effects on dynamic shear strain.

4 CONCLUSIONS

By applying axial and radial loads on the triaxial specimen simultaneously and using the stress on 45° surface of specimen to simulate the seismic tensile & compressive and shear dynamic loads, the characteristics of dynamic shear modulus and dynamic shear strain of loess are explored, and the preliminary conclusions are shown as follows:

(1) Phase difference has certain effects on dynamic shear modulus of loess. The dynamic shear modulus decreases with the phase difference rising from 0 to 180°, while the value of dynamic shear modulus increases moderately with increasing of phase difference from 180° to 360°, and when the phase difference is 180°, the dynamic shear modulus of loess decreases to the lowest level.

(2) Phase difference has significant impact on initial dynamic shear modulus of loess. With $\sigma_{dhm} = 20$ kPa, the initial dynamic shear modulus under $\varphi = 180°$ accounts for only 10.77 percent of that under $\varphi = 0°$, which attenuates nearly 90%. The attenuation rate of the initial dynamic shear modulus shows an upward trend with rise of radial vibration amplitude.
(3) Phase difference and radial vibration amplitude both affect the development of dynamic shear strain of loess obviously. When the phase difference is less than 180°, increasing of phase difference accelerates the development of shear strain, while the development of dynamic shear strain slows down with the increase of phase difference when it is greater than 180°. Also, the development of dynamic shear strain accelerates with increasing of radial vibration amplitude.
(4) Application of dynamic tensile & compressive load quickens the development of dynamic shear strain, and when tensile & compressive and shear dynamic loads change simultaneously, dynamic shear load has much more prominent effects on development of dynamic shear strain.

REFERENCES

Bommer, J.J., Georgallides G. & Tromans I. J. 2001. Is there near-field for small-to-moderate magnitude earthquakes?. *Journal of Earthquake Engineering* 5(3):395–423.

Cai, Y.Q., Wang, J. & Hai, J. 2008. Study on strength and deformation behaviors of soft clay under bidirectional exciting cyclic loading. *Chinese Journal of Rock Mechanics and Engineering* 27(3):495–504.

Gu, C., Cai, Y.Q. & Wang, J. 2012. Coupling effects of P-waves and S-waves based on cyclic triaxial tests with cyclic confininf pressure. *Chinese Journal of Geotechnical Engineering* 34(10):1903–1909.

Kabilamany, K. & Ishihara, K. 1991. Cyclic behavior of sand by the multiple shear mechanism model. *Soil Dynamics and Earthquake Engineering* 10(2):97–101.

Seed, H.B. & Lee, K.L. 1966. Liquefaction of saturated sand during cyclic loading. *Journal of the Soil Mechanics and Foundation Division*, ASCE 92(6):105–134.

Seed, H.B. & Peacock, W.H. 1971. Test procedures for measuring soil liquefaction characteristics. *Journal of the Soil Mechanics and Foundation Division*, ASCE, 97(8):1099–1119.

Seed, H.B. & Idriss, I.M. 1971. Simplified procedure for evaluating soil liquefaction potential. *Journal of the Soil Mechanics and Foundation Division*, ASCE 97(9):1249–1273.

Trandafir, A.C. & Sassa, K. 2004. Undrained cyclic shear response evaluation of sand based on undrained monotonic ring shear tests. *Soil Dynamics and Earthquake Engineering*, 24(11):781–787.

Wang, J., Cai, Y.Q., Ding, G.Y. & Pan, X.D. 2010. Experimental research on characteristics of dynamic modulus and damping ratio of saturated soft clay under bidirectional exciting cyclic loading. *Chinese Journal of Rock Mechanics and Engineering* 29(2):423–432.

Wang, H.J., Shen, R.F. & Ma, Q.G. 1996. Dynamic strength of soil under multi-direction loading. *Journal of Tsinghua University (Sci & Tech)* 36(4):93–98.

Xie, D.Y. 2011. Soil dynamics. Beijing: Higher Education Press.

Zhou, J., Bai, B. & Xu, J.P. 2001. Theory and calculation of soil dynamics. Beijing: China Architecture and Building Press.

This page intentionally left blank

Unsaturated Soil Mechanics—from Theory to Practice – Chen et al. (Eds)
© 2016 Taylor & Francis Group, London, ISBN 978-1-138-02921-7

Shear strength of a swelled soil examining influence of swelling boundary conditions

B.F. Lim & G.A. Siemens
GeoEngineering Centre at Queen's-RMC, Royal Military College of Canada, Kingston, Canada

ABSTRACT: Damage caused by swelling soils is measured in billions of dollars every year. Swelling capacity is realized by a combination of volumetric expansion and/or swelling-induced stresses. Following swelling the shear strength characteristics of the swelled soil is also of interest. The shear strength and stiffness characteristics are measured by subjecting expansive soil specimens to controlled swelling conditions followed by axial compression in a modified triaxial apparatus. The results show that rigid swelling boundary conditions cause a higher stress state and density following swelling and a corresponding higher strength and stiffness.

1 INTRODUCTION

Damage to infrastructure caused by swelling soils is measured in billions of dollars every year. Damage is caused by excessive deformations as well as swelling-induced stresses on infrastructure constructed in swelling soil. A retaining wall constructed with swelling soil backfill is illustrated in Figure 1a. As the soil swells, the soil at point 'A' will swell under a Constant Mean Stress (CMS) condition, while the soil next to the retaining wall (point 'B') will swell under confined conditions due to the vicinity of the retaining wall. Siemens and Blatz (2009) considered the influence of boundary conditions on swelling behavior and formulated the concept of the Swell Equilibrium Limit (SEL) as illustrated in Figure 1b. Starting at the same initial state (open box on Figure 1b) the soil swells along a CMS or Constant Volume (CV) swell paths to the SEL.

Numerous researchers have studied the response of swelling soils to wetting and drying conditions in the laboratory and constitutive models exist for modeling swelling behavior. However, the shear strength of swelling soil after swelling is less studied. Al-Mhaidib and Al-Shamrani (2006) performed swelling tests in a triaxial cell under constant cell pressure conditions (CMS). The test methodology allowed for a pre-determined quantity of axial swelling followed by shearing. Domitrović and Kovačević (2013) performed shearing tests in a direct shear apparatus.

The SEL framework is a unifying framework for swelling soil that may be extended for shear strength. Consider a new foundation constructed near the retaining wall (Figure 1a). Swelled soil at points 'A' and 'B' will now be subjected to additional shear stresses from the new foundation construction. Traditionally

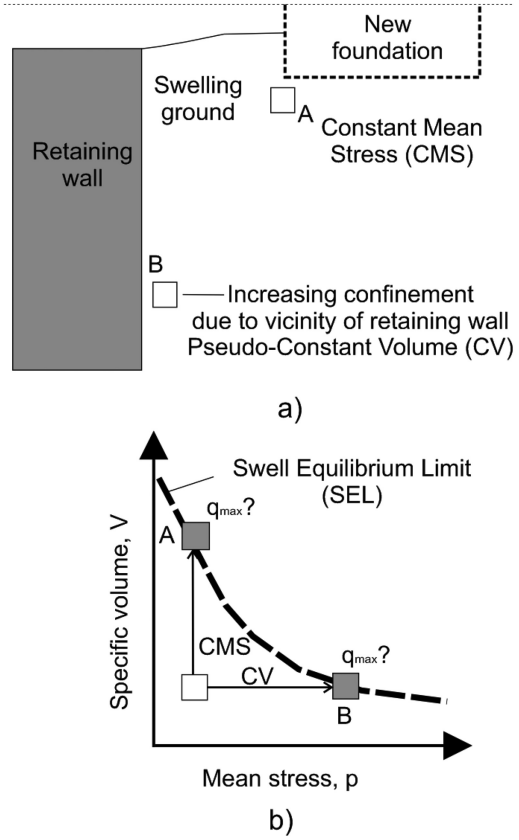


Figure 1. a) Retaining wall constructed in swelling soil illustrating Swell Equilibrium Limit (SEL) and b) V-p paths for Constant Mean Stress and Constant Volume.

swelling soil tests are performed in oedometer cell, which has been beneficial for studying compressibility of swelling soils. Few studies have been performed in laboratory apparatuses that allow for measurement of shear strength and stiffness following swelling.

Siemens and Blatz (2007) reported a triaxial apparatus that allowed for control of boundary conditions during swell tests. A similar apparatus is used in this study to perform swelling tests under controlled boundary conditions followed measurement of the shear strength of the swelled soils. The results indicate the swell path significantly affects the shear strength of the soil.

2 MATERIALS AND METHODS

2.1 *Lake Agassiz clay*

The soil tested in this study was taken from Southern Manitoba, Canada. The local geology is glacially dominated with a glacial till overlain by a swelling clay layer, which ranges from 12 m to 15 m in thickness (Baracos and Graham 1983). The area is well known for foundation issues due to the swelling nature of the soil (Siemens and Blatz 2008). The soil has a liquid limit, plastic limit, and plasticity index of 85, 34 and 51, respectively, and is classified as a high plasticity clay using the Unified Soil Classification System (USCS). The soil consists of 74% clay- and 20% silt-sized particles (Lim 2014). Swelling test specimens are compacted to target optimum dry density and water content, which was measured to be 1.62 Mg/m^3 and 20% respectively.

2.2 *Specimen preparation*

A complete description of specimen preparation and test procedure can be found in Lim (2014), which follows from Siemens and Blatz (2007). In order to facilitate efficient saturation, the cylindrical specimen is wrapped with a layer of nonwoven geotextile as shown in Figure 2a. The geotextile is connected hydraulically to the bottom and top filter stones and surrounds the specimen. The geotextile acts as a conduit allowing water to infiltrate the specimen from the perimeter, which makes the test axi-symmetric and shortens the saturation path length. A total of four rectangle cut-outs are indicated in Figure 2a. Figure 2b is a photograph of a swelling test specimen installed in the modified triaxial apparatus. These cut-outs are included to allow for direct contact of the radial Linear Variable Displacement Transducers (LVDTs) contact points to measure radial deformations of the specimen. Hydraulic connection at the cut-out locations is maintained with a filter paper wrap around the middle of the specimen (Figure 2a).

2.3 *Test methodology*

A swelling test is performed on a cylindrical specimen under pre-determined boundary conditions using a modified triaxial apparatus. The three stages of a swelling-shearing test are:

1) isotropic compression,
2) swelling under controlled boundary conditions, and
3) shearing.

For the swelling phase, the pre-determined boundary condition is defined in mean stress – volume swell path (Figure 1b). A Constant Mean Stress (CMS) stress-volume path is performed by holding cell pressure constant when the specimen is given access to water. The swell path moves vertically upward parallel with the y-axis in a V-p plot (Figure 1b). A CMS test measures the maximum swelling potential



a)



b)

Figure 2. a) Photograph of triaxial specimen displaying nonwoven geotextile and filter paper wrap and b) installed triaxial specimen showing radial LVDTs located at cut-out location.

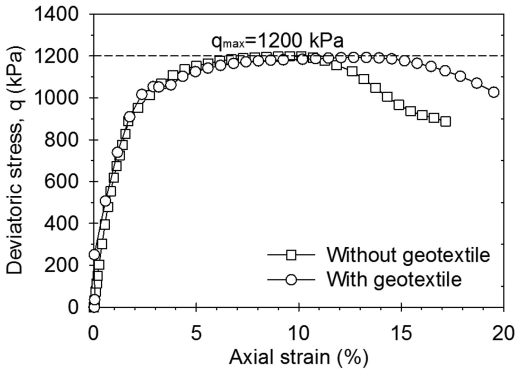


Figure 3. Impact of nonwoven geotextile wrap on stress-strain behaviour.

of the soil at the initial stress. In a second scenario, a Constant Volume (CV) test, the initial volume of the specimen is kept constant by increasing confining pressure. The confining pressure is increased to counteract the swelling capacity of the soil after. The stress path followed by a CV test moves horizontally parallel with the x-axis in a V-p plot (Figure 1b). When the swelling phase is completed, the test continues with shearing by engaging the compression machine motor and applying a constant axial strain rate to the specimen.

2.3.1 *Impact of geotextile wrap on measured stress-strain response*

The test methodology reported by Siemens and Blatz (2007) includes a geotextile wrap to surround the perimeter of the cylindrical specimen. For swelling tests, the impact of the geotextile wrap was minimal. To determine the impact of the geotextile on the stress-strain response, two tests were performed, one with the geotextile wrap and one without. The tests used Bearpaw clay compacted to a targeted condition of 1.74 Mg/m^3 initial dry density and 15% of water content. The as-compacted specimen was compressed at 200 kPa cell pressure and overnight. Subsequently, a shearing test was activated at a constant strain rate of 0.0021 mm/min (20% strain in 6.6 days). The stress-strain curves from the specimen installed with geotextile and without geotextile are plotted in Figure 3. Both curves are remarkably similar including initial stiffness and maximum shear strength. The strain-softening behaviour of the two specimens was slightly different with the geotextile-wrapped specimen remaining at its peak shear strength approximately 3% more axial strain than the specimen without geotextile wrap. Comparing the two test results indicates the geotextile wrap has only nominal effect on the stress-strain behaviour of the tests.

3 RESULTS

The test results summarized in this paper are a subset of a larger test matrix aimed at assessing the Swell

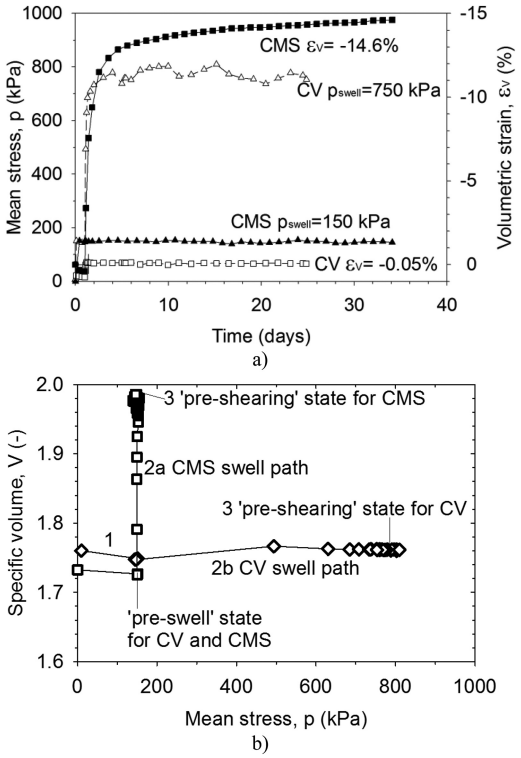


Figure 4. Triaxial swelling test results for CMS and CV tests plotted as a) mean stress (p) and volumetric strain (ε_V) versus time and b) specific volume versus mean stress indicating 1 – isotropic compression, 2a – CMS swell path, 2b – CV swell path, and 3 – 'pre-shearing' state.

Equilibrium Limit of the Lake Agassiz clay and the strength and yield envelope of the swelled soil.

3.1 *Swelling test results*

Select results for the CMS and CV swelling tests are plotted in Figure 4 as specific volume versus mean stress (V-p). The CMS specimen was prepared to the target density and moisture content, wrapped with filter paper and nonwoven geotextile (Figure 2a) and built into the triaxial apparatus (Figure 2b). Stage 1 of the test was isotropic compression of 150 kPa, which lasted 24 hours (Figure 4a). The triaxial swelling test was initiated by opening the back pressure line to allow water to infiltrate the specimen. The back pressure was maintained constant at 100 kPa throughout the swelling stage. The specimen swelled (negative volumetric strain in Figure 4a) to over −12% volumetric strain from time = 2–4 days and then a slower swelling rate was observed for the remainder of the test. In V-p space (Figure 4b) the specimen swells vertically to equilibrate with the new moisture regime. Cell pressure and back pressure were held constant at 150 kPa and 100 kPa respectively. At the end of the swelling stage (detailed results not

shown), the specimen swelled to 14.5% volumetric strain (V = 1.99) and took on 62.9 mL of water.

The CV test was initiated to the same target dry density and moisture content. The specimen was prepared in a nominally identical manner, installed and brought to 150 kPa mean stress in the modified triaxial apparatus. Following isotropic compression a CV swelling test was initiated by supplying 100 kPa back pressure (Figure 4a). The mean stress (cell pressure) was raised in order to maintain the 'pre-swelling' volume of the specimen. From time = 2–4 days, the cell pressure was raised to 750 kPa and then was held constant for the remainder of the CV swelling test. In V-p space (Figure 4b) the swelling path (2b) is horizontal until the specimen comes into equilibrium with the moisture and stress regime. At the end of the test the specimen is at volumetric strain −0.05% (V = 1.76), a mean stress of 750 kPa, and had taken on 24.5 mL of water.

3.2 *Shearing test results*

The 'pre-shearing' stress and volume states of the CMS and CV specimens are significantly different (Figure 4a and 4b). To determine the impact of the swelling conditions on the shear strength, stage three of the test was axial compression at a rate of 0.0021 mm/min (20% axial strain in 6.6 days). Back pressure was maintained at 100 kPa during shearing and the drainage lines left open. Volume was measured using local LVDTs connected radially and axially to the specimen (Figure 2b).

The stress-strain curves of CMS 150 and CV 150 were plotted in deviator stress (q) versus axial strain in Figure 5 and the results are summarized in Table 1.

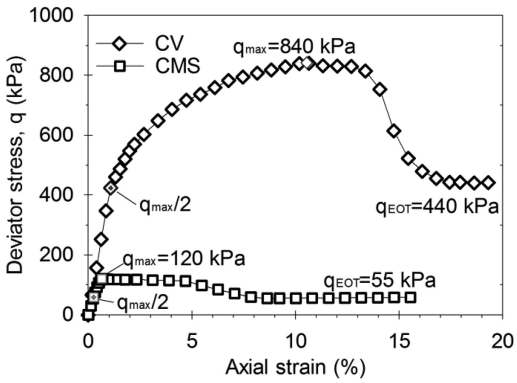


Figure 5. Shear test results for CMS and CV tests plotted as deviator stress versus axial strain.

Qualitatively the stress-strain curves appear similar with an initially high stiffness, a portion with constant maximum shear strength followed by strain softening to a end of test value.

The CV specimen stress-strain curve (plotted with open squares) began with a steep slope and then levelled off gradually until it reached the maximum deviator stress, which was measured at 840 kPa. The corresponding axial strain was 10.5% when the shear strength was at its peak. Then, the specimen experienced strain-softening after axial strain of 14% and the strength dropped to its end of test value of 440 kPa.

The strength behavior of CMS specimen (plotted with open circles in Figure 5) is different from CV. Quantitatively the strength of CMS 150 is significantly lower than the CV strength. The maximum shear strength of CMS 150 was measured at only 120 kPa. The curve began with a steep slope until it reached the peak value of 120 kPa at axial strain of 0.6%. Then, the curve levelled off followed by strain-softening from 5–10% axial strain. The end of test strength was measured at 55 kPa.

Stiffness variation of the CV and CMS tests was evaluated at half the maximum deviator stress ($q_{max}/2$ highlighted on Figure 5). The secant modulus was evaluated at this point and is summarized in Table 1 as 39.0 MPa and 23.1 MPa for the CV and CMS test respectively. Similar to the shear strength, the stiffness of the CMS is lower than the CV test.

4 SUMMARY

Swelling behavior of expansive soils depends on boundary conditions, which can range from constant stress to constant volume (Siemens & Blatz 2009). Shear strength of swelled soils is also of interest (Al-Mhaidib and Al-Shamrani 2006; Domitrović and Kovačević 2013) and the stress-strain characteristics are have been shown to depend on the boundary conditions and resulting 'pre-shearing' stress and volume states. Comparing the two tests shows the CMS specimen swells to a higher volume while at a lower stress compared to the CV. The CV specimen swells against a rigid boundary and is at a higher stress and lower volume prior to shearing. From an unsaturated perspective, the specimens are both at a high saturation, so the influence of matric suction on the shear strength is considered minimal.

The shear test results on post-swelling specimen highlights the impact of boundary conditions on the shear strength of expansive soil. From shear strength analysis, strength resistance in post-CV test is higher

Table 1. Shear test results summary.

Test	'Pre-shearing' mean stress (kPa)	'Pre-shearing' specific volume (−)	Maximum deviator stress, q_{max} (kPa)	Secant stiffness at $q_{max}/2$ (MPa)	End of Test (EOT) deviator stress, q_{EOT} (kPa)
CMS	150	1.99	840	23.1	55
CV	750	1.76	120	39.0	440

than the post-CMS test. Higher shear strength and stiffness is achieved in CV test because higher density of the soil particles following CV swelling. Taking the CMS test as the base value, the increase of strength in from CV swelling is seven-times (7) stronger with only a 5-fold higher mean stress. The stiffness increase observed also coincided with the boundary conditions with the CV test having higher value.

Swelling soils experience different boundary conditions depending on the stress levels and the constraint of soil movement in the ground. The control of boundary condition at swelling soil plays an influential role in swelling-induced stresses, swelling magnitude and post-swelled strength behaviour. Under the SEL unifying framework, the CMS specimen represents a soil that is free to expand to its maximum volume potential while the CV specimen satisfies its swelling potential in swelling-induced stress. The result of the post-swelling shear test shows that higher strength and stiffness is achieved when the soil boundary condition is constrained. The post-swelling shearing test result provides important information of the shear strength behaviour of the soil. This finding gives the designer a better insight of the actual behaviour of swelling soil which may be overlooked by a conventional strength test.

REFERENCES

Al-Mhaidib, A.I. and Al-Shamrani, M.A. 2006. *Influence of swell on shear strength of expansive soils*. In Proceedings of Advances in Unsaturated Soil, Seepage, and Environmental Geotechnics: 160–165 [doi: 10.1061/40860(192)16]

Baracos, A. and Graham, J. 1981. Landslide problems in Winnipeg. *Canadian Geotechnical Journal* (18): 390–401.

Crawford, C. B. 1964. Some characteristics of Winnipeg clay. *Canadian Geotechnical Journal* 1(4): 227–35.

Domitrović, D. and Kovačević, Z.B. 2013. The relationship between swelling and shear strength properties of bentonites. In Proceedings of the 18th International Conference on Soil Mechanics and Geotechnical Engineering, Paris 2013, 291–222.

Graham, J., Noonan, M.L. and Lwe, K.V. 1983. Yield states and stress-strain relationships in a natural plastic clay. *Canadian Geotechnical Journal* (20): 502–16.

Lim, B. F. 2015. Advanced testing and a numerical tool for swell equilibrium limit of expansive soils. PhD thesis., Department of Civil Engineering, Royal Military College of Canada, Kingston, ON.

Siemens, G.A. and Blatz, J.A. 2007. A triaxial apparatus for applying liquid infiltration with controlled boundary conditions and internal suction measurement. *Journal of Geotechnical and Geoenvironmental Engineering*. 133(6): 748–752 [doi: 10.1061/(ASCE)1090-0241].

Siemens, G.A. and Blatz, J.A. 2008. *Numerical modelling of shallow foundations on swelling clay soil using the swelling equilibrium limit*. 1st European Conference on Unsaturated Soils (E-UNSAT), Durham, United Kingdom, 2–5 July 2008, 855–860.

Siemens, G.A. and Blatz, J.A. 2009. Evaluation of the influence of boundary confinement on the behaviour of unsaturated swelling clay soils. *Canadian Geotechnical Journal* (46): 339–56 [doi: 10.1139/T08-125].

Vanapalli, S. K, Fredlund, D. G., Pufahl, D.E., Clifton, A.W. 1996. *Model for the Prediction of Shear Strength with Respect to Soil Suction*. Canadian Geotechnical Journal, (33): 379–392.

This page intentionally left blank

Unsaturated Soil Mechanics—from Theory to Practice – Chen et al. (Eds)
© 2016 Taylor & Francis Group, London, ISBN 978-1-138-02921-7

Strength behaviors of the unsaturated silty clay based on ring shear test

Wenjiao Xue
State Key Laboratory of Geomechanics and Geotechnical Engineering, Institute of Rock and Soil Mechanics, Chinese Academy of Sciences, Wuhan, Hubei, P. R. China
Jointly School of Civil Engineering and Architecture, Wuhan University of Technology, Wuhan, Hubei, P. R. China

Pan Chen & Changfu Wei
State Key Laboratory of Geomechanics and Geotechnical Engineering, Institute of Rock and Soil Mechanics, Chinese Academy of Sciences, Wuhan, Hubei, P. R. China

ABSTRACT: The strength behavior of unsaturated soils is important to evaluate the stability of slopes underwent the change of water content. The shear strength behavior of silty clay with different dry densities and water contents was explored by ring shear tests. The experimental results show that the shear strength of the silty clay decreases with the increment of water content at the same dry density. The change of shear strength of clayey soils with a low dry density shows the behavior of the normal consolidation soil. The one with the high dry density shows the behavior of the overconsolidation soil. The overconsolidation effect falls off when water content increases. The cohesion and friction angle of the soils decreases with the increment of water content. The effect of water content on the parameters of shear strength is greater than the one from the dry density when water content is more than 18%.

Keywords: Shear strength; Ring shear test; Silty clay; Dry density; Water content

1 INTRODUCTION

The hydraulic and strength characteristics of unsaturated soils have been recently gained widespread attention from researchers and as well as from practicing engineers, i.e., rainfall induced landslides, embankments, and soil bearing capacity (Jotisankasa and Mairaing, 2010, Rahardjo et al., 2010, Zhu and Anderson, 1998). It is needed to obtain the shear strength of soils accurately for evaluating the stability of geotechnical materials.

In order to explore the strength behavior of unsaturated soils, abundant experiments have been conducted by shear tests (Likos et al., 2010, Jiang et al., 2006). The results showed that the strength of unsaturated soils was significantly affected by the water content, dry density of soils and stress state (Adekalu et al., 2007, Dong et al., 2012, Kayadelen et al., 2007). The effect of water content on the strength characteristics of unsaturated soils has been researched and many strength models have been developed (Bishop et al., 1971, Fredlund et al., 1978, Chen et al., 2013). However, most of the research results were based on the experimental data from the direct shear test. There are some drawbacks to measure the strength of soils by the direct shear test (Han et al., 2014). Recently, a ring shear test method was adopted to measure the shear strength of saturated and unsaturated soils (Hoyos et al., 2014, Li and Aydin, 2013). The shear surface is unchanged and the sample is continuously sheared in one direction for any angular rotation in the ring shear test. The new method is very suitable to measure the shear strength behavior of soils from the landslide prone area (Jotisankasa and Mairaing, 2010, Li and Aydin, 2013).

In this paper, consolidation drained shear tests are conducted by the ring shear apparatus to explore the effect of the water content and initial void ratio on the strength behavior of silty clays. The strength behaviors of silty clays are analyzed based on the experimental results.

2 MATERIAL AND METHOD

The remolded silty clay is chosen in the experiments. The physical characteristics of tested soil are given in Table 1. The ring shear apparatus (DTA-138) is used

Table 1. Physical property of the tested soil.

Soil types	Silty clay
Air-dry water content (%)	5.1
Specific gravity	2.74
Plastic limit	36.2
Liquid limit	19.4

Table 2. Chosen samples with different water contents and dry densities.

Water content (%)	Dry density (g/cm^3)
12	1.40
	1.60
	1.80
18	1.40
	1.60
	1.80
24	1.40
	1.60
	1.80

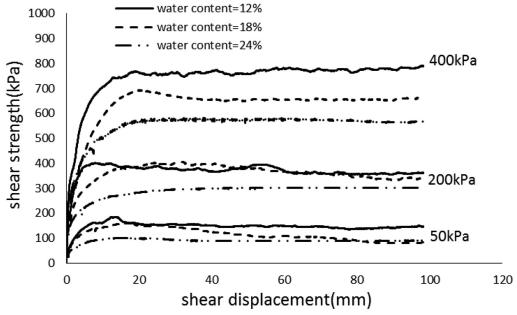
to measure the shear strength of soils by consolidation drained shear tests. The external diameter and inner diameter of the shear box are 150 and 100 mm, respectively. The height of the box is 20 mm.

A series samples with different initial water content and dry densities are prepared by the static pressure method. Before the shear test, all the samples are saturated by the distilled water after the air in the soils pumped out by a vacuum pump. The chosen water content and dry densities are given in Table 2. The applied normal stresses on the soil samples are 50, 200 and 400 kPa, respectively. There are 27 silty clay samples are used in the shear tests. The shear speed is 0.36°/min and the shear displacement is 90°.

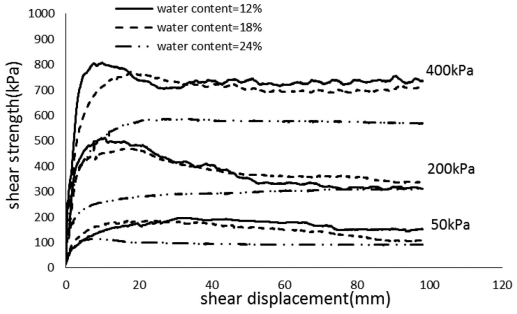
3 RESULTS

The shear stress-displacement curves of samples with different water contents and dry densities are given in Figure 1. The results show that shear strength decreases with the increment of water content at the same dry density. The main reason is that suction stress in the specimen decreases when the water content increases (Lu et al., 2010). Compared with the samples at high dry density, the softening behavior of soils is not distinct with low dry density (1.40 g/cm^3). That is, the shear strength characteristic of the soils with a low dry density shows the behavior of the normal consolidation soil. However, the decrement of the shear strength is large in the soils with higher dry densities (1.60 g/cm^3 and 1.80 g/cm^3). The tendency of shear strength of the soils with a higher dry density shows the behavior of the overconsolidation soil. The overconsolidation effect falls off when the water content increases. The softening effect is much remarkable when the water content is lower.

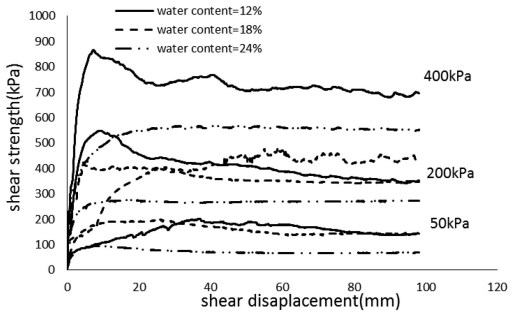
The shear strength envelopes for the peak strength of silty clay soils at different dry densities are given in Figure 2. The effect of water content on peak strength can be observed from Figure 2. The Mohr-Coulomb criterion is used to obtain the parameters of shear strength. The linear relationship between normal stress and shear strength is well with the correlation coefficients $R = 0.956$–1.000. The results show that the



(a) Dry density of 1.40 g/cm^3



(b) Dry density of 1.60 g/cm^3

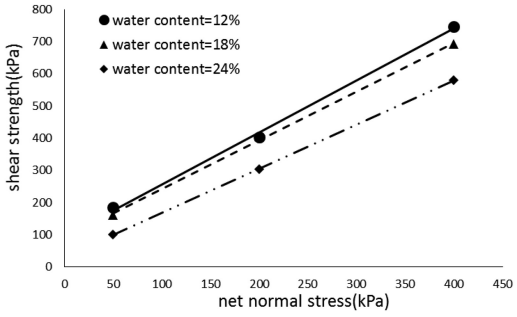


(c) Dry density of 1.80 g/cm^3

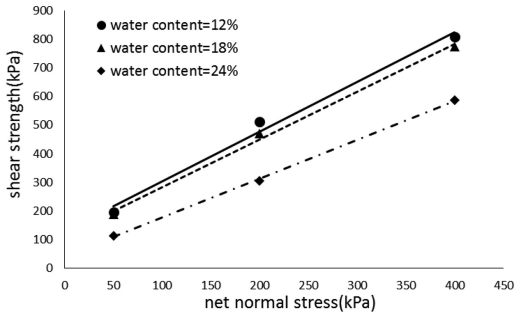
Figure 1. Results of ring shear tests.

peak strength of soils increases with the increment of dry density. The peak strength of soils decreases with increment of water content.

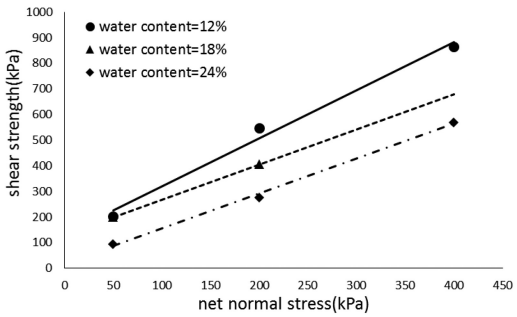
Figure 3 shows the effect of water content on the cohesion and inner friction angle, respectively. The cohesion is greatly influenced by the water content, shown as Figure 3(a). The main reason is that the tendency indicates that the increment in water content leads to the decrement of suction stress in the clayey samples. Hence, the cohesion of clayed soils decreases. The effect of the dry density on the cohesion is large at the low water content. Figure 3(b) shows that the change of the inner friction angle slightly decreases with the increment of water content at dry densities 1.40 and 1.60 g/cm^3. There is larger decrement of the inner friction angle when the change of water content is 12% to 18% at dry density 1.80 g/cm^3. It is worth noting that the inner friction angle is nearly coincident



(a) Dry density of 1.40



(b) Dry density of 1.60



(c) Dry density of 1.80

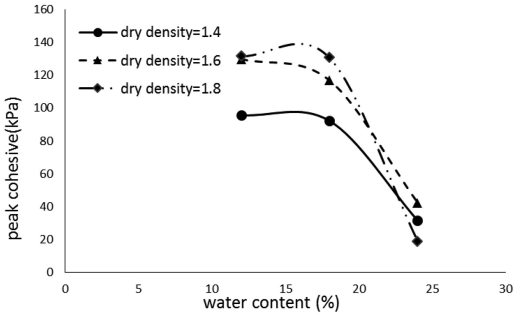
Figure 2. Shear strength failure envelopes.

at the water content of 24% though the dry density of clayed soil is different. The results also show that the inner friction angle is largely affected by the dry density at low water content. However, the inner friction angle is almost the same when the water content is equal to 24%.

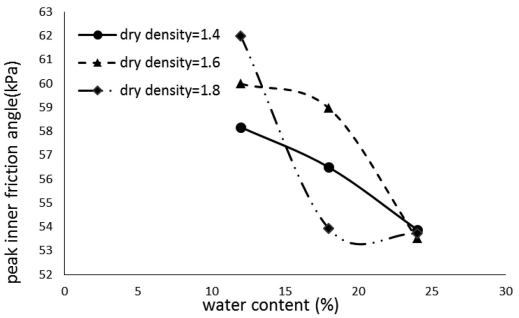
4 CONCLUSION

The tested results were obtained from a series of ring shear tests performed on statically compacted specimens of silty clays with different water content and dry densities. Some conclusions could be drawn.

The results showed that peak shear strength decreased with the increment of water content at the same dry density. The change of shear strength of the samples with a low dry density showed the behavior of the normal consolidation soil. The one with high dry density showed the behavior of the overconsolidation soil. The softening effect fell off when the water content increased.



(a) Cohesion *vs* water content



(b) Inner friction angle *vs* water content

Figure 3. The relationship between the cohesion, inner friction angle and water content, dry densities.

The cohesion was greatly influenced by the water content. The effect of the dry density on the cohesion is larger at the range of low water content. The inner friction angle decreased slightly with the increment of water content.

ACKNOWLEDGEMENT

This research was supported by the National Natural Science Foundation of China through grants # 11302243, 11372078 and the Guangxi Natural Science foundation through grants 2012GXNSFGA060001.

REFERENCES

Adekalu, K. O., Okunade, D. A. & Osunbitan, J. A. 2007. Estimating trafficability of three Nigerian agricultural soils from shear strength-density-moisture relations. *International Agrophysics,* 21, 1–5.

Bishop, A. W., Green, G. E., Garga, V. K., Andresen, A. & Brown, J. D. 1971. A new ring shear apparatus and its application to the measurement of residual strength. *Geotechnique,* 21, 273–328.

Chen, P., Wei., C. F., Liu, J. & Ma, T. T. 2013. Strength theory model of unsaturated soils with suction stress concept. *J. Appl. Math.,* 2013, 1–10, ID 756854.

Dong, Q., Liu, L. & Hou, L. 2012. Influence of Matric Suction on Shear Strength Behavior of Unsaturated Silty Sand. *In:* Du, X. L., Zheng, J. J., Yan, W. M., Li, Y. & Zhang, J. W. (eds.) *Trends in Civil Engineering, Pts 1–4.*

Fredlund, D. G., Morgenstern, N. R. & Widger, R. A. 1978. The shear strength of unsaturated soils. *Can. Geotech. J.,* 15, 313–321.

Han, T., Dhodapkar, S. & Gong, T. 2014. Impact of Different Shear Rates on Flow Functions Measured by a Ring Shear Tester. *Particulate Science and Technology,* 32, 366–370.

Hoyos, L. R., Velosa, C. L. & Puppala, A. J. 2014. Residual shear strength of unsaturated soils via suction-controlled ring shear testing. *Engineering Geology,* 172, 1–11.

Jiang, G., Noonan, M. J. & Ratecliffe, T. J. 2006. Effects of soil matric suction on retention and percolation of Bacillus subtilis in intact soil cores. *Water Air and Soil Pollution,* 177, 211–226.

Jotisankasa, A. & Mairaing, W. 2010. Suction-Monitored Direct Shear Testing of Residual Soils from Landslide-Prone Areas. *Journal of Geotechnical and Geoenvironmental Engineering,* 136, 533–537.

Kayadelen, C., Tekinsoy, M. A. & Taskiran, T. 2007. Influence of matric suction on shear strength behavior of a residual clayey soil. *Environmental Geology,* 53, 891–901.

Li, Y. R. & Aydin, A. 2013. Shear zone structures and stress fluctuations in large ring shear tests. *Engineering Geology,* 167, 6–13.

Likos, W. J., Wayllace, A., Godt, J. & Lu, N. 2010. Modified Direct Shear Apparatus for Unsaturated Sands at Low Suction and Stress. *Geotechnical Testing Journal,* 33, 286–298.

Lu, N., Godt, J. W. & Wu, D. T. 2010. A closed-form equation for effective stress in unsaturated soil. *Water Resources Research,* 46.

Rahardjo, H., Nio, A. S., Leong, E. C. & Song, N. Y. 2010. Effects of Groundwater Table Position and Soil Properties on Stability of Slope during Rainfall. *Journal of Geotechnical and Geoenvironmental Engineering,* 136, 1555–1564.

Zhu, J. H. & Anderson, S. A. 1998. Determination of shear strength of Hawaiian residual soil subjected to rainfall-induced landslides. *Geotechnique,* 48, 73–82.

Unsaturated Soil Mechanics—from Theory to Practice – Chen et al. (Eds)
© 2016 Taylor & Francis Group, London, ISBN 978-1-138-02921-7

Influence of matric suction on shear strength behavior of remolded unsaturated basalt residual soil

J. Chen
Wuhan University of Science and Technology, Wuhan, China
Zhongkai University of Agriculture and Engineering, Guangzhou, China

X.W. Lei & F.Z. Cheng
Wuhan University of Science and Technology, Wuhan, China

Q.S. Meng
Key Laboratory of Rock and Soil Mechanics, Chinese Academy of Sciences, Wuhan, China

ABSTRACT: The red-brown basalt residual soils which are on the surface of slopes in the northwest of Guizhou were taken as the research objects in this paper. Shear strength behavior of unsaturated soils under different water content and dry density conditions are determined though the unconsolidated-drained test, the relationships between soil-water characteristic curve and shear strength behavior are compared though integrating the former research results. The relationships between shear strength and water content about the unsaturated basalt residual soil are explored under different dry density conditions. Then the influence of matric suction on shear strength behavior about unsaturated basalt residual soils is revealed. This paper will provide a basis for the subsequent studies on the slope stability analysis.

1 INTRODUCTION

There are a large number of different weathered basalt residual soils distributed in the highway slopes of Yunnan and Guizhou. The stability of the slope largely depends on the shear strength of the red-brown soils which covered the surface. It is not consistent with actual if the saturated soil shear strength indexes which based on the traditional soil mechanics are used in the slope stability analysis. Based on the unsaturated soil mechanics, there are four parts forming the strength of unsaturated soil: the effective cohesion, friction between particles, matric suction and osmotic suction. Therefore the research focus is the contributions about matric suction to the strength characteristics of unsaturated soils. In practical engineering, unsaturated soils are often divided into two kinds of common soils: one is instability or "activity" zone, another is stability zone. Stability zone is in the deep area of the whole unsaturated soils, the distribution of matric suction is stable, while the instability or "activity" zone, which close to the surface, the distribution of matric suction is influenced by seasonal variation and changed with time (Lu 2012). Therefore, it is necessary to study the influence of matric suction on shear strength behavior of basalt residual soils in this paper.

2 TEST METHOD AND RESULTS

2.1 *Soil samples*

In this paper, the soil samples are taken from two slopes which in Hezhang section from Bijie to Weining highway in Guizhou. The soil can be divided into three types according to the degree of weathering: red-brown soil, yellow-brown soil and dark-brown soil. The red-brown soil, the strongest weathering one which located in the surface of the slope is chosen as the soil samples. The soil is clay, loose and dry in surface, moist and blocky close to the bottom, easily scattered or by water erosion. The particle is tiny but strong, the particle size is gradually increased from surface to the downward (Wang 2012, Yu 2012). They both took samples on the site and tested the basic physical properties though indoor soil tests: the natural density $\rho = 1.71$–2.01 g/cm^3, the water content $w = 30.1\%$–48%, particle proportion $G_s = 2.76$, natural void ratio $e_0 = 0.548$, liquid limit $w_l = 74.2\%$, plastic limit $w_p = 41.1\%$, Plastic limit index $I_p = 33.1$ (Yu 2012)

2.2 *Matric suction measurement*

Matric suction of unsaturated soil is related to the water content has been the accepted view, matric

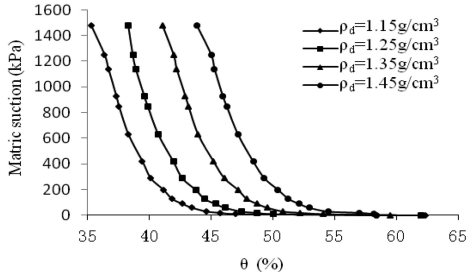


Figure 1. Relationship between matric suction and volumetric water content (Yu 2012).

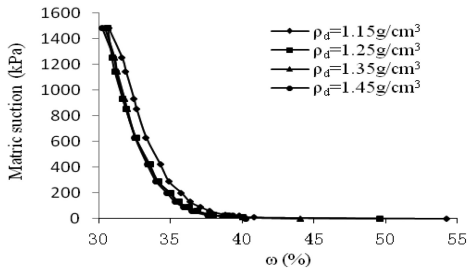


Figure 2. Relationship between matric suction and mass water content.

suction changed along with water content, relationship between water content and matric suction is defined as the soil-water characteristic curve. The curve reflects the relationship between the energy of the water and the number of the water in the soil, the curve cannot be got by theoretical analysis according to the basic properties, and it can only be determined by experiment (Liu 2009). At present, there are mainly three kinds of instruments used to test the matric suction of unsaturated soil: three triaxial meter for unsaturated soils, direct shear meter for unsaturated soils, pressure plate meter. Yu (2012) measured the soil-water characteristic curve during desorption process by the USA SOIL MOISTREU integrated pressure plate meter. The matric suction is in the range of 10 kPa to 1480 kPa. He chose 5 bar and 10 bar clay plate according to the soil properties, made remolded samples at initial water content of 30.1% and dry density of 1.15 g/cm^3, 1.25 g/cm^3, 1.35 g/cm^3, 1.45 g/cm^3, respectively.

Yu (2012) obtained the relationship between the matric suction and volumetric water content in Figure 1. The relationship of matric suction and mass water content is obtained in Figure 2, according to the calculation formula of volumetric water content $\theta = w\rho_d/\rho_w$.

From the test, we can see the results consistent with the general theory. The matric suction of the red-brown basalt residual soil decreased with the increased volumetric water content, and a limit volumetric water content is exist. The matric suction is very sensitive to the change of the volumetric water content when the volumetric water content is less than this value, it

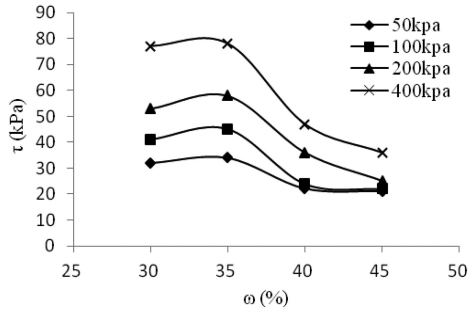


Figure 3. Relationship between shear strength and water content when $\rho_d = 1.15$.

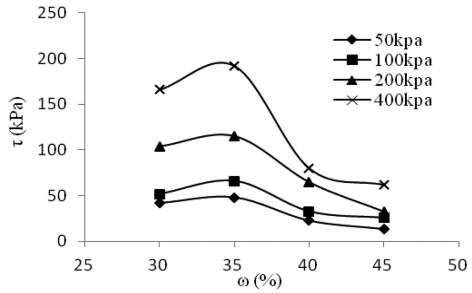


Figure 4. Relationship between shear strength and water content when $\rho_d = 1.25$.

reduced greatly with the increased volumetric water content.

While the sensitivity of matric suction on the change of volumetric water content decreased when the volumetric water content is higher than the limit value, the matric suction decreased slowly with the increased volumetric water content. At the same time, dry density has a significant influence on soil-water characteristic curve, the larger dry density soil has the larger residual water content, the variation of matric suction and mass water content is similar.

2.3 *Direct shear test and results*

In order to investigate the relationship between shear strength and water characteristic curve, and reflected the relationship between shear strength index and dry density of basalt residual soil. The mass water content of the soil samples in the direct shear test is 30.1%, dry density is 1.15 g/cm^3, 1.25 g/cm^3, 1.35 g/cm^3. Dried, hammered and sieved residual soils are respectively arranged into several groups of different dry density remolded soil samples. The unconsolidated-drained test worked on the vertical pressure of 50 kPa, 100 kPa, 200 kPa, 400 kPa, the shear rate is 0.8 mm/min. The shear strength index c, φ about different dry density about unsaturated residual soil are solved through analysis of the test results.

According to direct shear test, the relationship between total stress strength, apparent cohesion and apparent internal friction angle and water content on different dry density are shown in Figures 3–7.

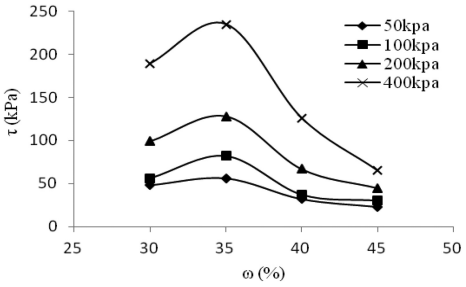


Figure 5. Relationship between shear strength and water content when $\rho_d = 1.35$.

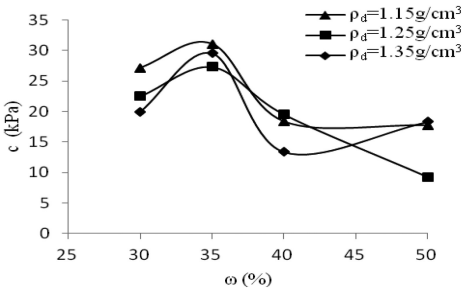


Figure 6. Relationship between apparent cohesion and water content.

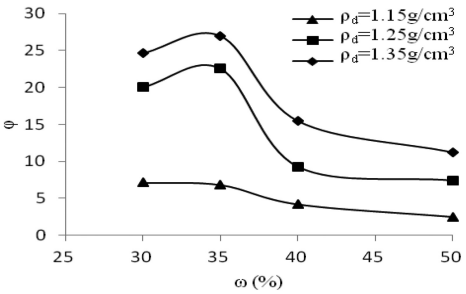


Figure 7. Relationship between apparent internal friction angle and water content.

From Figures 3–5, the total stress strength shows a nonlinear rise, decline and then stable gradually with the change of water content, the dry density did not affect this trend, it only influence the shear strength. The apparent internal friction angle changed relatively slowly with water content when the dry density is lower, and the change is similar with shear strength when the dry density is higher, see Figure 7. The nonlinear change of the apparent cohesion with the water content is obviously, but the dry density influences this trend, see Figure 6.

The unconsolidated-drained test can furthest reduce the variation of matric suction which caused by soil compression and water discharge during the consolidation and shear process. Therefore, the shear strength of unsaturated soil obtained in this test is total stress strength which implies matric suction, shear strength index is apparent cohesion and apparent internal friction angle which implies matric suction too (Yan et al. 2011).

3 RELATIONSHIP BETWEEN SHEAR STRENGTH INDEX AND MATRIC SUCTION

The influence of matric suction on shear strength behavior about unsaturated basalt residual soils is still not clear though the research of this aspect has been carried out widely. Firstly, the existing studies on different type of unsaturated soils about the influence of matric suction on shear strength index c, φ is not consistent. Lin et al. (2007) chose silty sand, sandy silt and silty clay, discussed the relationship of matric suction and shear strength of compacted soil through the pressure plate test and direct shear test. He pointed out that the matric suction has great influence on apparent cohesion and apparent internal friction angle. Hu et al. (2005) considered that in the experimental range the cohesion of undisturbed loess increases linearly with matric suction, which has little effect on the effective internal friction angle (Dang & Li 1996). Yan et al. (2011) also considered that the effect of matric suction on the shear strength of unsaturated remolded loess was mainly reflected in the apparent cohesion, while the effect can ignored on internal friction angle. Though the research of unsaturated silty clay which taken from the Xiaolangdi Dam Huang et al. (2007) showed that the effect of matric suction on apparent internal friction angle is very small, but great on apparent cohesion. Chen et al. (2012) researched the unsat- urated granite residual soil from Xiamen. She showed that the effect of matric suction on the shear strength was mainly reflected in the apparent cohesion, while for the apparent internal friction angle, some influence only showed in low range of the matric suction. Secondly, the contribution of matric suction to shear strength also appeared two results: linear and nonlinear. Escario and Juca showed that the shear strength of unsaturated clayey sand increased gradually when the matric suction is less than 1000 kPa, but the growth rate decreased gradually (Escario & Juca 1989). Farouk A et al. (2004) had a similar conclusion though the study of unsaturated siliceous sand. Farouk et al. (2004), Huang et al. (2007), Lin et al. (2007), Meng et al. (2007) and some other scholars showed that the shear strength parameters of unsaturated silty clay, silty sand, sandy silt and silty clay are not constant, they decreased with the increased matric suction. Hu et al. (2005), Cheng et al. (2008) showed that the shear strength parameters of unsaturated undisturbed loess and swelling soil are near constant when the matric suction is less than a certain value.

3.1 *Relationship between shear strength and matric suction*

For the red-brown unsaturated basalt residual soil, the soil-water characteristic curve and the relationship between shear strength and water content are contrasted. The relationship between shear strength

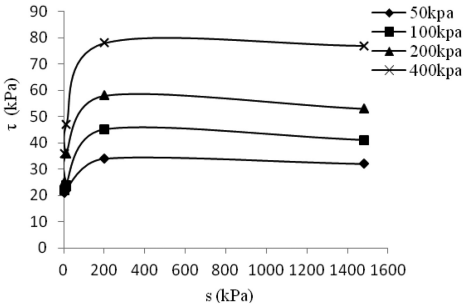


Figure 8. Relationships between shear strength and matric suction when $\rho_d = 1.15$.

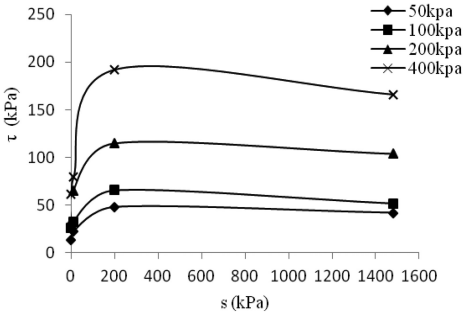


Figure 9. Relationships between shear strength and matric suction when $\rho_d = 1.25$.

and matric suction of different dry density soil under different normal stress are shown in Figures 8–10.

From Figures 8–10, the relationships between shear strength and matric suction of each unsaturated residual soil samples are almost identical under different normal stress. That is, for different dry density soils which under a constant vertical pressure, the shear strength increase significantly with the increased matric suction when matric suction are in 0–200 kPa, the shear strength change a little with the increased matric suction when matric suction are in 200–1500 kPa. This is verified that the shear strength of unsaturated soils implies the influence of matric suction. On the other hand, it shows that the shear strength of red-brown unsaturated basalt residual soil enhanced by the matric suction in a certain range, but the contribution to shear strength becomes small with the increased matric suction.

Fredlund shear strength theory of unsaturated soil is a two-variable strength formula which based on Mohr-Coulomb failure criterion and set up by test (Fredlund et al. 1978). See Formula 1. Two independent stress state variables: the net stress and the matric suction are used to study the shear strength of unsaturated soil.

$$\tau_f = c' + (\sigma_n - u_a)\tan\varphi' + (u_a - u_w)\tan\varphi^b \quad (1)$$

where c' and φ' are both effective shear strength index of unsaturated soil. They can be determined by routine shear strength test, they did not change with the matric suction. tan φ^b is the growth rate of shear strength with

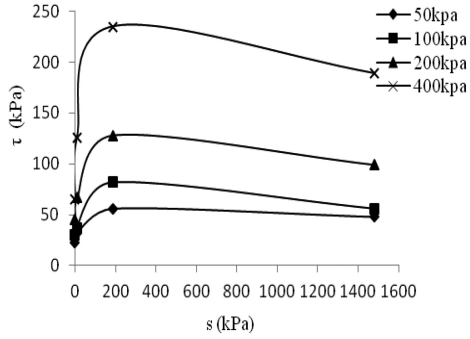


Figure 10. Relationship between shear strength and matric suction when $\rho_d = 1.35$.

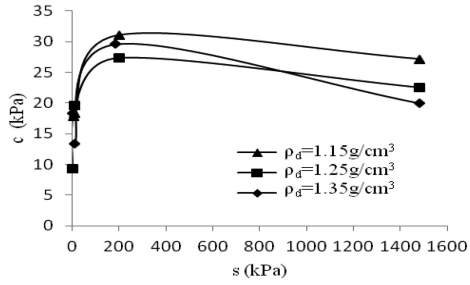


Figure 11. Relationship between apparent cohesion and matric suction.

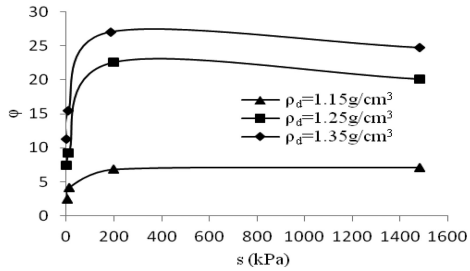


Figure 12. Relationships between apparent internal friction angle and matric suction.

increased matric suction ($u_a - u_w$) (Zhao et al. 2008), φ^b is the inclination of the relati- onship between shear strength and matric suction.

From Figure 8–10, they showed that in the case of a constant vertical pressure, φ^b decrease sharply with the increased matric suction when the matric suction is in 0–200 kPa, The influence of matric suction on shear strength is weakened when the matric suction is more than 200 kPa, the curve tend to be gentle, the value tend to be stable.

3.2 *Relationships between apparent cohesion, apparent internal friction angle and matric suction*

Figure 11–12 are the other reflects about shear strength and matric suction. The apparent cohesion of each

soil samples increase greatly with the increased matric suction when the matric suction is in 0–200 kPa, The apparent internal friction angle increase slowly with the increased matric suction only when the dry density is 1.15 g/cm^3, the apparent internal friction angle just increase greatly with the increased matric suction about the rest dry density soil samples. The apparent cohesion decreases slightly with the increased matric suction when the matric suction is in 200–1500 kPa. The apparent internal friction angles are almost unchanged and approximate to be a certain value with the increased matric suction.

The test shows that, the matric suction has significant influence on apparent cohesion when the dry density is lower, but the influence is weaker on apparent internal friction angle. With the increase of dry density, the influence of matric suction on apparent cohesion and apparent internal friction angle are both obvious.

4 CONCLUSION

The red-brown basalt residual soils which are on the surface of slopes in the northwest of Guizhou province were taken as the research objects in this paper. The relationships between mass water content and shear strength index are studied though the unconsolidated-drained test. The relationships between matric suction and shear strength index are analyzed though contrasting with the former research results. The following conclusions are obtained:

1. In the unconsolidated-drained test, the total stress strengths are different when the dry densities of soil samples are different, but the trend is consistent with the water content, showing a characteristics of non-linear rise, drop and gradually stable. The apparent internal friction angle changed relatively slowly with water content when the dry density is lower, and the change is similar with shear strength when the dry density is higher. The nonlinear variation of apparent cohesion about different dry density soil samples with water content is obvious, but the dry density influences this trend.
2. The relationships between shear strength and matric suction of each unsaturated residual soil samples are almost identical under different normal stress. This is verified that the shear strength of unsaturated soils implies the influence of matric suction. On the other hand, it shows that the shear strength of red-brown unsaturated basalt residual soil enhanced by the matric suction in a certain range, but the contribution to shear strength becomes small with the increased matric suction.
3. In the case of a constant vertical pressure, φ^b decrease sharply with the increased matric suction when the matric suction is in 0–200 kPa, the influence of matric suction on shear strength is weakened when the matric suction is more than 200 kPa, the curve tend to be gentle, the value tend to be stable.
4. When the matric suction is in 0–200 kPa, the matric suction has significant influence on apparent cohesion when the dry density is lower, but the influence is weaker on apparent internal friction angle. With the increase of dry density, the influence of matric suction on apparent cohesion and apparent internal friction angle are both obvious.

REFERENCES

Chen, D.X., Ni, J., Zhang, M.X. et al., 2012. Experimental Study on the Shear Strength of Unsaturated Residual Soils in Xiamen. *Journal of Xiamen University*, 51(5):877–881.

Chen, J.B., Hao, H.Y. & Lu, F.W., 2008. The Strength Characteristic of Unsaturated Expansive Soils. *Soil Engineering and Foundation,* 22(6):76–80.

Dang, J.Q. & Li, J., 1996. The effect of water content on the strength of unsaturated loess. *Journal of Northwest University of Agriculture,* 24(1):57–60.

Escario, V. & Juca, J., 1989. Shear and deformation of partly saturated soils. *Proceedings of the 12nd International Conference on Soil Mechanics and Foundation Engineering*: 43–46. Rio de Janeiro.

Farouk, A., Lamboj, L. & Kos, J., 2004. Influence of matric suction on the shear strength behavior of unsaturated sand. *Czech Technical University Publishing House*, 44:11–16.

Fredlund, D.G., 1978. The shear strength of unsaturated soils. *Canadian Geotechnical Journal,* 15(3):313–321.

Huang, Z.Q., Liu, X.T., Liu, F.S. et al., 2007. Test study on the effect of matric suction on the 1# landslide in Xiaolangdi Dam reservoir. *China Water Transport,* 7(7):123–125.

Hu, S.X., Zhou, X.D. & Chen, Z.H., 2005. Test study on strength character of unsaturated and undisturbed loess. *Rock and Soil Mechanics,* 26(4):660 –672

Lu, N., 2012. *Unsaturated Soil Mechanics*. Beijing: Higher Education Press.

Liu, X.W., Chang, L.J. & Hu, X.R., 2009. Experimental research of matric suction with water content and dry density of unsaturated laterite. *Rock and Soil Mechanics,* 30(11):3302–3306.

Lin, H.Z., Li, G.X., Yu, Y.Z. et al., 2007. Influence of matric suction on shear strength behavior of unsaturated soils. *Rock and Soil Mechanics,* 28(9):1931–1936

Meng CJ., 2009. Analysis on unsaturated and clayey foundation bearing capacity in consideration of suction. *Sugared Engineering,* 5:141–142.

Meng, Q.L., Yao, H.L. & Qiu, L.F., 2001. The contribution of matric suction to shear strength of unsaturated soils. *Rock and Soil Mechanics,* 22(4):423–431.

Wang, C.S., 2012. Testing Study on Engineering Mechanical Properties of Basalt Residual Soil in Guizhou. *Wuhan University of Science and Technology.*

Wang, C.S., Lei, X.W., Meng, Q.S. et al., 2012. Testing study on strength of red-brown soil of weathered basalt soil in Guizhou. *Geotechnical Investigation and Surveying*, 40(1):12–15.

Yu, P., 2012. Research and analysis on water character of basalt residual soil in Guizhou. *Tianjin Institute of Urban Construction.*

Yan, Y.J., Wen, B.P. & Ji, B.X., 2011. Contribution of matric suction to shear strength of unsaturated remolded loess soils. *Journal of Engineering Geology*, 19(6):865–874.

Zhao, H.L., Ma, Y.L. & Niu, H.K., 2001. Discussion on Research Method of Shear Strength of Unsaturated Soil. *Geotechnical Engineering Technique*, 3:142–145.

This page intentionally left blank

Unsaturated Soil Mechanics—from Theory to Practice – Chen et al. (Eds)
© 2016 Taylor & Francis Group, London, ISBN 978-1-138-02921-7

Study on shear strength characteristics of the remolded laterite soil in Guilin

X.J. Chen, X. Huang & G.Y. Xiao
Guilin University of Technology, Guilin, China

H.B. Chen
North China University of Technology, Beijing, China

Y.L. Qi
China Nonferrous Metals, Changsha, Survey and Design Institute Co. Ltd., Changsha, China

ABSTRACT: To investigate the shear strength characteristics of the remolded laterite soil in Guilin, a series of triaxial tests were conducted to study the influences of the dry density and moisture content of the remolded laterite soil on the shear strength. The experimental results show that the strengths of remolded saturated laterite soil and unsaturated one are quite different under the same optimum moisture content. The relationship of cohesion and internal friction angle with the dry density of the remolded unsaturated laterite soil can be represented by a convex quadratic polynomial function. However, the concave quadratic polynomial curve needs to describe the relation of the cohesion and internal friction angle with the dry density of the remolded saturated laterite soil.

1 INTRODUCTION

As one type of special soil, laterite soil is widely distributed in the central and western regions of China. It has many special engineering properties which are significantly different from other types of soil, especially in physical, mechanical and hydrological properties etc.

Currently, many scholars have studied the strength characteristics of soils under different conditions. Miller (2002) studied the soil water characteristic curves of various types of soils under different compactive effort and water content. In view of the laterite soil in Guangxi, Zhao et al. (2003, 2004) and others carried out systematic work on the mechanical index, swelling shrinkage properties and pore size distribution at different stages of dehydration of undisturbed laterite soil in Guangxi by different experimental methods. Fu et al. (2013) measured dehydrated soil-water characteristic curve of the Guilin laterite soil used the pressure plate extractor. In this paper, combined with previous experimental studies (Wei et al. 2004, Wei, et al. 2005), the unconsolidated undrained triaxial shear tests will be conducted on saturated and unsaturated remolded laterite soil with different dry densities. Based on the results from the triaxial test, the relation among dry density, water content and shear strength of laterite soil in Guilin is developed. The mechanic and hydrological characteristics are analyzed (Tan et al. 2011, Chen et al. 2014).

2 MATERIAL AND METHOD

The residual laterite soil from one site of Diecai district in Guilin is chosen as the tested samples. The basic physical indexes are shown in Table 1.

The shear strength of remolded laterite samples under different dry densities are tested. Automatic saturated soil triaxial apparatus (28-T0401/AC) is adopted from Nanjing Soil Instrument Co. Ltd. The diameter and height of the sample are 39.1 mm and 80 mm, respectively. Due to the maximum dry density and optimum moisture content of the laterite soil is about 1.55 g/cm^3 and 30%, respectively. The maximum dry density of 1.55 g/cm^3 is chosen for preparing the tested soils. Meawhile, a large numbers of parallel tests are performed. The remolded soil samples are prepared according to the Standard for soil test method (GB/T50123-1999) of China. Because of the

Table 1. The basic physical indexes of laterite soil.

Name of indexes	value
Natural water content ω (%)	34.91
Unit weight γ (kN/m^3)	18.3
Void ratio e	1.07
Compression modulus E_s (MPa)	8.50
Liquid limit ω_L (%)	63
Plasticity index I_p	24.9
Liquid index L_p	−0.12

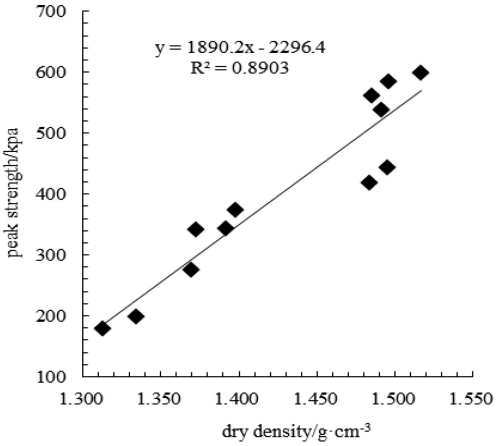


Figure 1. Relation of the peak of shear strength and dry densities of remodeling unsaturated laterite soil.

maximum dry density corresponding to the optimal moisture content is 1.55 g·cm^{-3}, select dry density 1.32, 1.39, 1.46, 15.3 g·cm^{-3} as compaction control standard, the corresponding standard triaxial test sample mass are 163, 172, 182, 188 g, among them, the sample of 163 g is compacted of four layers, the others are compacted of five, six, seven layers in order. Satiate the samples of compacted laterite soil, then conduct triaxial undrained shear test. According to different forms of damage, choose different failure criteria, and when the peak occurs, choose the deviatoric stress of shear peak as failure criteria, and when the peak does not appears, choose the deviatoric stress of 15% axial strain as failure criteria. (Chen et al. 2013, Liu 2008, Yuan 2003), and the five different confining pressure σ_3 is chosen, e.g. l00, 150, 200, 250, 300 kPa, respectively.

3 ANALYSIS OF TEST RESULTS

3.1 *Relation between the shear peak and dry density of remolded unsaturated laterite soil*

The relationship between the peak of shear strength and dry density under different confining pressure is given in Figure 1. The individual discrete points with large deviations from the experimental data have been eliminated. A linear fitting equation is used to fit the experimental data in Fig. 1. The values of the parameters in Eq. (1) is given in Table 2.

$$(\sigma_1 - \sigma_2)_{\max} = a\rho_d + b \tag{1}$$

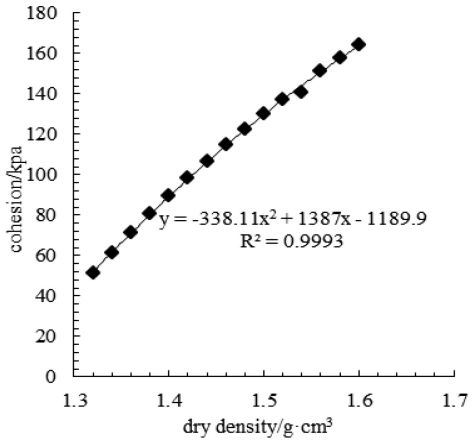
3.2 *Relation of the parameters of shear strength and dry densities of remodeling unsaturated laterite soil*

According to the peak value of shear strength fitting Eq. (1), the shear strength is calculated under different confining pressures and dry densities. The value of cohesion and internal friction angle is obtained based on the criteria of Mohr-Coulomb under various dry density ($\rho_d = 1.3$–1.6 g/cm^3). The quadratic polynomial function is adopted to fit the data, given in Eqs. (2) and (3), respectively. The fitting curves are shown in Fig. 2.

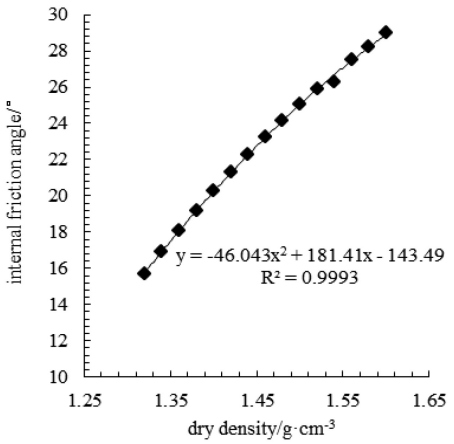
$$c = a_1\rho_d^2 + b_1\rho_d + c_1 \tag{2}$$

Table 2. Parameters from fitting the relations the peak of shear strength and dry density.

Parameters	Confining pressure σ_3 (kPa)			
	$\sigma_3 = 100$	$\sigma_3 = 150$	$\sigma_3 = 200$	$\sigma_3 = 250$
a	1890.2	2127.2	2429.4	2458.1
b	−2296.4	−2538.7	−2932.6	−2927.8



(a) Cohesion and dry density



(b) Internal friction angle and dry density

Figure 2. Relationship between the shear strength and dry density of unsaturated laterite soil.

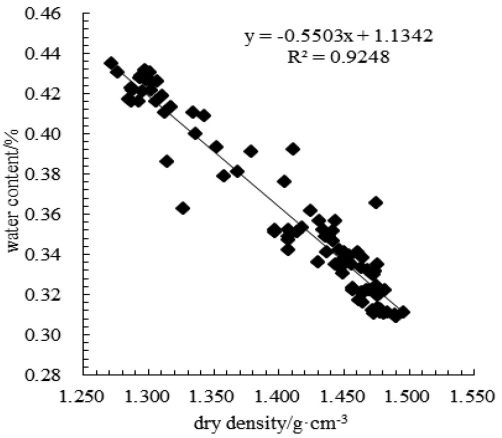


Figure 3. Relationship of dry density and moisture content of saturated remodeling laterite soil.

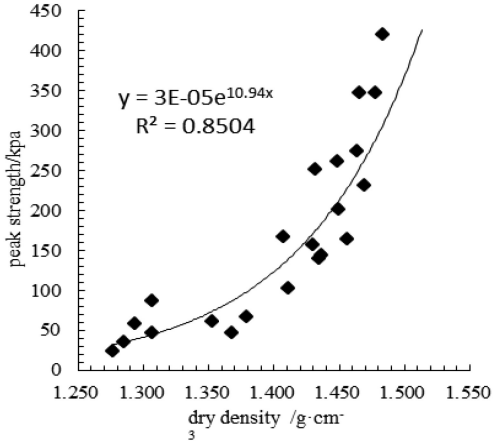


Figure 4. Relationship of shear strength and dry density of saturated laterite soil.

$$\varphi = a_2\rho_d^2 + b_2\rho_d + c_2 \tag{3}$$

The fitting parameters for cohesion are $a_1 = -338.11$, $b_1 = 1387$, $c_1 = -1189.9$. and the fitting parameters for internal friction angle are $a_2 = -46.043$, $b_2 = 181.4$, $c_2 = -143.49$.

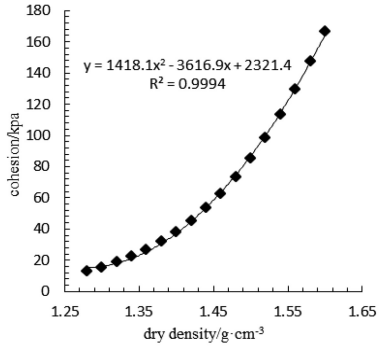
3.3 *Relation between the shear peak and dry density of the remolded saturated laterite soil*

The relationship of dry density and water content of remolded saturated soils is given in Figure 3. A linear relationship between water content and dry density was observed ($\omega = -0.5503\rho_d + 1.1342$, $1.25 < \rho_d < 1.55$) from the Figure.

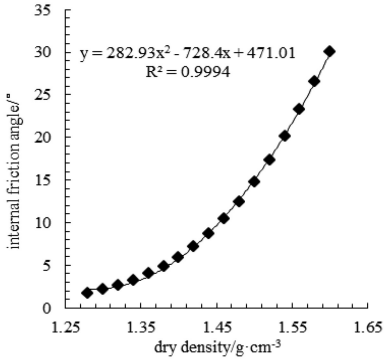
The measured data and fitting curve of shear strength and dry density of saturated remolded laterite soil under confining pressure 100 kPa are both given in Figure 4. An exponential relation Eq. (4) is adopted for fitting the measured data, and the parameters are given in Table 3.

Table 3. The fitting parameters of Eq. (4).

	Confining pressure σ_3 (kPa)				
Parameters	$\sigma_3 = 100$	$\sigma_3 = 150$	$\sigma_3 = 200$	$\sigma_3 = 250$	$\sigma_3 = 300$
$a \times 10^{-4}$	0.3	1	4	1	1
b	10.94	10.00	9.15	10.11	10.19



(a) Relationship between cohesion and dry density



(b) Relationship between internal friction angle and dry density

Figure 5. The relationship between the parameters of shear strength and dry density of saturated laterite soil.

$$(\sigma_1 - \sigma_2)_{\max} = ae^b \tag{4}$$

3.4 *Relathion of the parameters of shear strength and dry density of saturated laterite soil*

The change of cohesion and internal friction angle with dry density is given in Figure 5 under the range of dry density $\rho_d = 1.25$–1.6 g/cm^3. Eqs. (2) and (3) are also used to fitting the data. The fitting curves are shown in Figure 5. The fitting parameters for cohesion are $a_3 = 1418.1$, $b_3 = -3616.9$, $c_3 = 2321.4$, and the fitting parameters for of the internal friction angle is $a_4 = 282.93$, $b_4 = -728.4$, $c_4 = 471.01$.

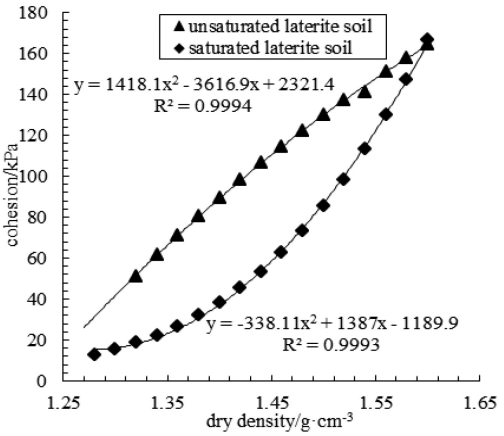


Figure 6. Relationship between cohesion and dry density.

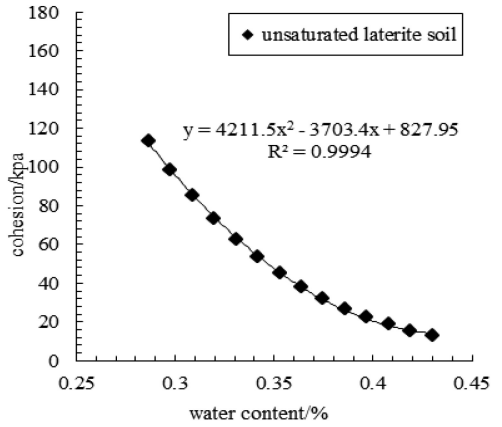


Figure 7. Relationship between cohesion and water content.

4 DISCUSSION

4.1 *Relationship between the cohesion and dry density, moisture content*

The strength changes of unsaturated and saturated remolded laterite soils were compared, seen in Figure 6. The cohesions of unsaturated laterite soil were convex quadratic polynomial increment with the dry density. However, cohesions of saturated laterite soil follow the concave quadratic polynomial curve with the dry density (Li 1997).

The difference of cohesions between unsaturated and saturated clay reached the maximum value at the dry density about 1.41 g/cm^3. The two curves intersected at the point with the dry density reaching 1.60 g/cm^3. Moreover, the intersection was just the point in which the samples have the maximum dry density. The change and fitting curve of cohesion and water content are both shown in Figure 7. The cohesions decrease with the increase of the water content. And the attenuation curve can be presented by a quadratic polynomial relation. The results also show that the change of water content have significant

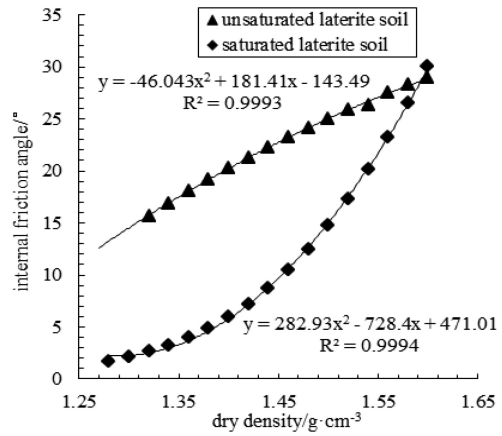


Figure 8. Relationship between internal friction angle and dry density.

influence on the decrease of the cohesions in soils. Especially, the maximum attenuation of the cohesion was about 80% when the change of water content ranges from 30% to 41%. However, when the water content is larger than 43%, which approaches fully saturation, the fluctuations of the cohesion were not obvious and almost stabilized. The mechanics can be explained as follows: the cementation materials of laterite soil are mainly iron, aluminum, etc. The crystalline goethite and cementation coexist in the laterite soils during the air drying process. When the water content of the air dried laterite soil increases, a part of the water-stable crystalline free iron oxide could be converted into cementation iron. Furthermore, the cementation irons are able to cement to form certain cohesion (Kong et al. 1993). Meanwhile, Fu et al. (2013) used the van Genuchten model to analyze the soil-water characteristic curve of the laterite soil in Guilin. The increase of water content leads to the increase of matric suction. The matric suction contributes a lot to the cohesion of the remolded unsaturated laterite soil (NIE et al. 2009). The experimental results show that the cohesion of the unsaturated laterite soil is high when the water content ranges from 30% to 41%.

4.2 *Relationship between the internal friction angle and dry density, moisture content*

Figure 8 shows that the relation of internal friction angle and dry density of the remolded unsaturated laterite soil can be described by a progressive increased trend with a convex quadratic polynomial function. However, the internal friction angle of the one shows a progressive increase of concave quadratic polynomial.

The difference of cohesions reaches the maximum value when the dry density was near 1.35 g/cm^3. The two fitting curves are also intersected when the dry density of the sample was 1.60 g/cm^3, which is just the maximum dry density of the laterite soil. The water content also has significant influence on the internal

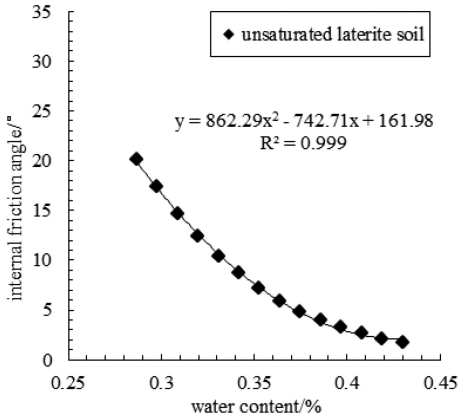


Figure 9. Relationship between internal friction angle and water content.

friction angle of the soil. The friction angle can be almost negligible when the clay is at a high water content. However, there was a substantial increase of the internal friction angle with the decrease of water content at the low range of water content (Bi et al. 2005). A part of the free iron oxide which is in cementation state forms grain group structure. Comparing with the crystalline form, there was big difference in the shape, size of single particles and cumularspharolith structure. The free iron oxide in crystalline state forms an envelope on the external surface of cumularspharolith, which will increase the surface roughness and occlusion degree among cumularspharolith in soils. Hence, the internal friction angle increases. As the water content was within a certain range, crystalline cumularspharolith structure is in certain water stability (Ma et al. 2007). The friction angle changed slowly when the water content changed from 35% to 43%, seen in Fig. 9. As the water content increased, the occlusion degree of crystalline cumularspharolith structure was gradually reduced under the lubrication action of water and the pore structure gradually increasing, which was macroscopically reflected by the reduced internal friction angle.

5 CONCLUSION

The shear strength increased linearly with the dry density of the unsaturated remolded laterite soil compacted at optimum moisture content under various confining pressures. The cohesion and internal friction angle of remolded unsaturated laterite soil were in a progressive increase relationship of convex quadratic polynomial with the dry density.

The relation between dry density and water content of saturated remolded laterite soil was linear. The cohesion and internal friction angle were both in a progressive increase of concave quadratic polynomial with the increase of the dry density of the remolded saturated laterite soil.

Under the same optimum moisture content, the remarkable difference of the strengths of remolded saturated laterite soil and the one of unsaturated laterite soil is shown from the measured data. The maximum difference of the cohesive force and internal friction angle comes out in the samples with the dry density 1.41 g/cm^3 and 1.35 g/cm^3, respectively.

ACKNOWLEDGEMENT

This work was supported by the National Natural Science Fund of China (No. 41262011), Key Laboratory Program of Guangxi Geotechnical Mechanics and Engineering (No. 11-kf-02 & No. 11-CX-01 & No. 12-A-01-02).

REFERENCES

Bi Qingta, Jiang Guoping, Ding Shuyun. 2005. Water content influence on the shearing strength of red clay. [J]. *Earth and environmen*t. 33(3) (in Chinese).

Chen Xuejun, Qi Yunlai, Lu Lixia, et al., 2013. Impact of Different Preparation Methods on the Optimum Moisture Content and Maximun Dry Density of Guilin Laterite soil. *Safety and Environmental Engineering*, 20(5), 136–139 (in Chinese).

Chen Zhenhan, 2014. On basic theories of unsaturated soils and special soils [J]. *Chinese Journal of Geotechnical Engineering* (02):202–271 (in Chinese).

Fu Xinhui, Wei Changfu, Yan Rong-tao, et al., 2013. Research on strength characteristics of unsaturated laterite soil, *Journal of Guilin University of Technology*, 33(3), 488–492 (in Chinese).

Kong Lingwei, Luo Hongxi, 1993. Effect of the Conversion in Form of Free Iron Oxide on the Engineering Property of the Laterite soil. *Rock and Soil Mechanics*, 14(4), 25–39 (in Chinese).

Liu Guangming, 2008. Analysis to Triaxial Shearing Test of Clay. Harbin Engineerning University (in Chinese).

Li jingyang, 1997. Mechanical strength of residual laterite in guizhou [J]. *Fournal of Guizhou University of Technology*, 26(2): 73–78 (in Chinese).

Ma Lin, Wang Qing, Yuan Guohong, 2007. Expermi ental study on function of free iron oxide in red soil. *Journal of Harbin University of Commerce (Natural Sciences Edition)*, 1, 57–61 (in Chinese).

Miller C. J., 2002. Impact of soil type and compaction conditions on soil water characteristic. *Journal of Geotechnical and Geoenvironmental Engineering, ASCE,* 128 (9), 733–742.

Ng C. W. W., Pang Y W., 2000. Influence of stress state on soil-water charateristics and slope stability. *Journal of Geotechnical and Geoenvironmental Engineering,* 126(2), 157–166.

Nie Qingke, Li Peipei, Wang Yinghu, et al., 2009. Mechanical characteristics of red clay under triaxial impact loading [J]. *Chinese Journal of Geotechnical Engineering* (02):202–271 (in Chinese).

Tan Yun-zhi, Kong Ling-wei, 2011. Guo Ai-guo, et al., 2011. Experimental study on wetting deformation of compacted laterite [J]. *Chinese Journal of Geotechnical Engineering,* 33(3):484–489 (in Chinese).

Wei Fu-cai, 2005. Material Compositions and Engineering Geological Properites of Guilin Red Soil. [J]. *Journal of*

Jiangxi Normal University (Natural science), 29(5):460–464 (in Chinese).

Wei Shihong, Liao Yiling, Qin Gang, et al., 2006. On Overconsolidation Properties, Low Degree of Density, and Characteristics of Deformation of Laterite soil in Qianzhong Area [J]. *Journal of Guizhou University of Technology*, 35(4), 9–12 (in Chinese).

Yuan Juyun, 2003. Earth engineering testing and principle [M]. Shanghai, Tongji University Press (in Chinese).

Zhao Ying-wen, Kong Ling-wei, Guo Ai-guo, et al., 2003. Mechanical behaviors and water-sensitive properties of intact Guangxi laterite [J]. *Rock and Soil Mechanics*, 24(4), 568–572 (in Chinese).

Zhao Yingwen, Kong Lingwei, Guo Ai-guo, et al., 2004. Strength properties and swelling-shrinkage behaviors of compacted lateritic clay in Guangxi [J]. *Rock and Soil Mechanics*, 25(3), 370–373 (in Chinese).

Unsaturated Soil Mechanics—from Theory to Practice – Chen et al. (Eds)
© 2016 Taylor & Francis Group, London, ISBN 978-1-138-02921-7

Experimental analysis on tensile strength of unsaturated sandy clay under different initial densities and water contents

R.J. Che & G.Q. Cai
School of Civil Engineering, Beijing Jiaotong University, Beijing, China

C.G. Zhao
College of Civil Engineering and Architecture, Guilin University of Technology, Guilin, China

ABSTRACT: This paper presents a reasonable and effective method of measuring tensile strength directly on compacted soil samples. The soil used in this test was sandy clay, which were taken from Chengdu, China. The adapted experimental device based on the shear box for the measurement of the tensile strength is presented. The purpose of this experiment is to predict the changing law of tensile strength with initial dry density and water content. Some results may be discovered: (1) When initial dry density keeps constant, the measured tensile strength generally increases with increasing water content, reach a peak value, after the peak, tensile strength decreases with increasing water content: (2) When water content keeps constant, with initial dry density increased, the specimen will be more dense, which leads to larger value of tensile strength. From test results and analysis, it shows that initial dry density and water content make great influence on tensile strength.

1 INTRODUCTION

Tensile strength of granular media is often used as an indication for a material's capability to sustain an external tensile stress without breaking. In most cases, it is generally assumed that soil materials exhibit only shear strength and insignificant or no tensile strength and cohesion. With recently increasing interest in unsaturated soils, a number of researchers have drawn attention to the importance of tensile strength. In recent years, due to limitation of the existing test methods, it had been reported that only a few tests could determine tensile strength in unsaturated soils. There are various hypotheses on tensile strength which still not be proved.

Because tensile strength generally varies with dry density and water content, its magnitude could be on the order of several kPa for sands or several hundreds of kPa for clays. It may have considerable impacts on the stability of dams, reservoirs, landfills and so on. Many scientists and researchers have done great experiments which prove that tensile strength in unsaturated soils is considerable. Several methods for testing tensile strength of soils have been used in the literature. Most recently, experiment works have been carried out on unsaturated soils with high water content using a specifically designed apparatus based on a conventional direct shear test ring, in which the tensile load is applied by a conventional motor. In this test, one-half of the specimen mold is kept fixed, while the other part is free to move longitudinally. As reported by Trabelsi (2010), this test equipment can measure the direct tensile stress-displacement characteristics. Tarmrakar *et al*. (2005) proposed a direct tensile apparatus to measure the tensile strength on saturated and unsaturated soils. Lakshmikantha *et al.* (2008) proposed a similar testing technique that is based on direct tension. Gary and Graham (2000) suggested a simple new testing method by which specimens are essentially broken under applied tensile force instead of compression loads. Nahlawi (2013) presented a new method for testing direct tensile strength of unsaturated soils, guided by a method developed for concrete testing (Hannant *et al*. 1999). Lu *et al*. (2005) developed a direct tensile strength apparatus to accurately measure the tensile strength characteristics of unsaturated sands, this equipment is simple in principle, accurate in measurement, and reliable in obtaining repeatable tensile strength, its basic idea is to use the weight generated by tilting a sample to split it.

In this paper, the tensile strength with initial dry density and water content is tested using a new developed apparatus. Two types of experiment are presented: (1) measurements of tensile strength of soil samples at different water contents, prepared at making an effort to keep constant soil dry density; (2) measurements of tensile strength of soil samples at different initial dry density, prepared making an effort to keep constant water content. The results and some conclusions are obtained after the laboratory tests.

2 TEST APPARATUS

As shown in Figure 1, tensile test apparatus consists of horizontal platform upon which apparatus molds

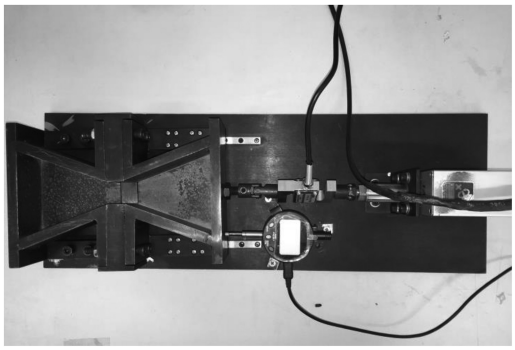


Figure 1. Plan view of new designed tensile strength apparatus for soil specimens.

having two halves: fixed mold and movable mold. The inner shape of this mold is trapezoidal, which holds the specimen. Two molds are screwed together before staring the experiments. One mold of the apparatus is fixed to the horizontal platform while the other mold can move freely on the horizontal platform. In order to reduce the friction between platform and movable mold, linear sliding roller is placed necessarily here. During the test, movable mold is pulled away in horizontal direction until the soil sample in molds fails in tension with apparent tensile crack appearing at the middle of the sample where two halves of the mold is attached. Load cell between the movable mold and motor rod measures the tensile load. This tensile load divided by the area of the tensile crack, gets the tensile stress. The two molds have the same size, whose top edge is 2.6 cm, bottom edge is 9.6 cm, and the height is 9.6 cm. The minimum width at the constricted section of this mold is 2.6 cm and the depth is 5.2 cm. The total volume of these two molds is appropriately 636.06 cm^3. Before every tension test, the volume and dry density were known, the soils' weight needed for the test could be calculated from above parameters.

3 MATERIALS AND SAMPLE PREPARATION

3.1 *Materials*

This paper presents reasonable results obtained for sandy clay which comes from the construction site in Chengdu, China. It is crushed, subangular, well-graded and silica. Its grain size ranges from 0.075 mm to 0.25 mm. Grain size distribution curve and properties for this kind of soil are shown in Figure 2 and Table 1.

3.2 *Specimen preparation*

Specimens for the tension testing were prepared under constant dry density (1.2 g/cm^3), but water content of every specimen is different (10%, 12%, 14%, 16%, 18%). While keeping dry density constant, compacted specimens were prepared by directly and statically compressing the prerequisite amount of soil kept

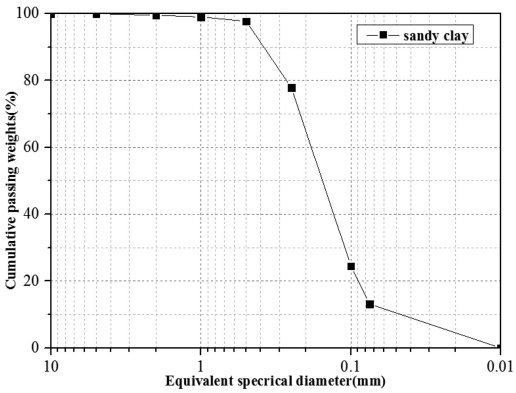


Figure 2. Grain size distribution curves of sandy clay.

Table 1. Properties for the sandy clay in the test.

Materials	ρ_d (g/cm^3)	ω_p (%)	ω_L (%)	I_P
Sandy clay	1.2	6.6	25.3	18.7

within the tensile mold of the apparatus, using some special compaction tools. Because the height of each mold is 5.2 cm, in order to obtain more accurate results, each specimen would be compacted in 5 layers using a special hammer to achieve predetermined dry density. After compacting each layer, shaving the surface is necessary and essential step. After compaction, the mold with the specimen was kept at an environment with 22°C temperature and more appropriate relative humidity until starting test.

4 INSTALLATION AND SETUP

After compaction of soils and getting a smooth top surface, the mold equipment was carefully turned upside down and was placed on the testing rigid frame. One mold was fixed to the rigid frame and the other, which places on the linear rollers, was attached to the electromotor via a load cell. The load cell was placed between the movable mold and motor shaft, which can measure and transfer the tensile force to computer. The displacement grating rested on movable mold can measure and record specimen's displacement around every moment during the test, then transferred these data to the computer as form of Excel. The screws which were earlier fixed to prevent the movement of movable mold of the apparatus are un-screwed. The side inserts were removed without inducing any restraint to tensile loading. The soil specimen was finally ready for testing, as shown in Figure 3. It should be very slow and careful during the sample installation and setup without making big disturbance, especially to the gap between the molds. This is very important for the accuracy of measured tensile strength. It is proved that the designed apparatus is useful and necessary for this high-precision tension test.

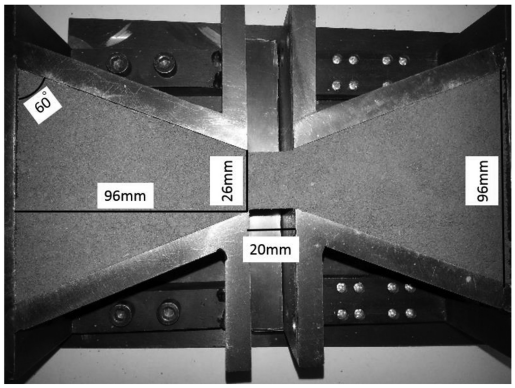


Figure 3. The specimen ready for the direct tensile test.

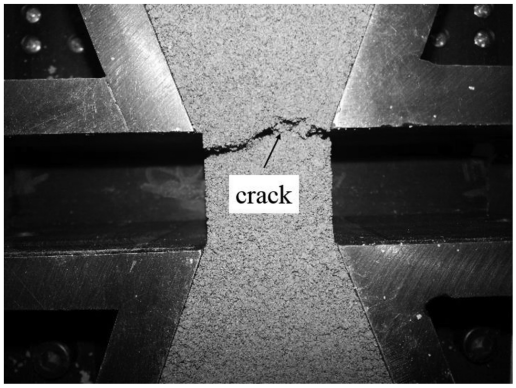


Figure 4. Plan view of the specimen after tension failure.

5 TESTING PROCEDURE

The tests were conducted at a constant tensile displacement rate of 0.5 mm/min on the movable mold. It can slide freely and horizontally to apply a tensile force to the middle part of specimen. As apparent crack expected, the displacement speed was quite slow (0.5 mm/min) to permit readings of loads and displacements having enough time to transfer to computer as form of Excel. Readings was collected at 0.25 s intervals until failure of specimen. When the apparent crack occurred in the neck part of Specimen, it is considered that whole test could be finished. However, readings of loads and displacement would continue to change after crack occurred. During this moment, some new phenomena was found, which is helpful to final discussion and analysis. After completing the test, the mold was removed from the apparatus, and the specimen weighed immediately. Before and after the test, water content of the specimen was measured.

6 RESULTS AND DISCUSSIONS

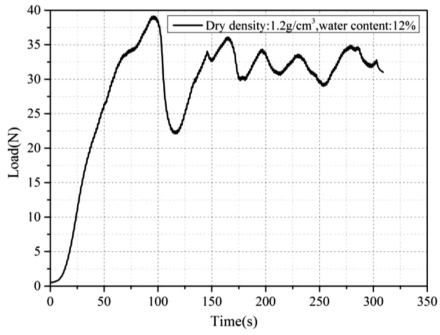
In all 15 tests, the failure of tested specimens occurred approximately vertically and cracking developed rapidly throughout the full length of the failure section at the specimen neck. As intended, the dry density was reasonably constant for specimens compacted within the molds. Taking two specimens as example, its dry density and water content are 1.2 g/cm^3 (1.4 g/cm^3) and 12%, respectively. The results are stated in four diagrams: (a) load-displacement curve; (b) load-time curve; (c) displacement-time curve; (d) stress-strain curve, as shown in Figure 5 and Figure 6. From above curves, it is clearly indicated that the tensile force vibrated with increasing displacements and times. The displacement increased with increasing times and tensile stress had the same tendency with tensile strength. Figure 5(d) and 6(d) shows that the first peak value maybe the tensile strength of soils that is on different dry densities and water contents. It can be seen from Figure 7 and Figure 8 that the tensile strength of soils with dry density of 1.4 g/cm^3 is larger than that with dry density of 1.2 g/cm^3 on the same water content. From above phenomenon, it can be concluded that larger dry density makes the specimen denser, which lead to larger values of tensile strength on the same water content. When initial dry density keeps constant, the measured tensile strength generally increases with increasing water content, reach a peak value, after the peak, tensile strength decreases with increasing water content. The appearance of value of tensile strength indicates that with combined effect of optimum moisture content and maximum dry density, the tensile strength will reach the peak value. The tensile strengths of these two dry densities are shown in Table 2 and Table 3.

7 THE MECHANISMS FOR TEST RESULTS

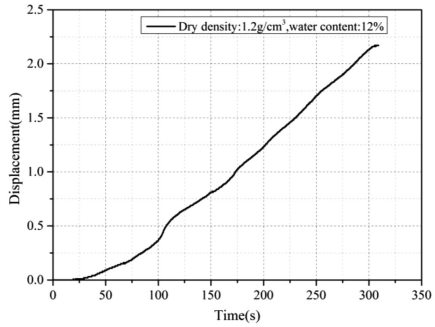
From above test results, some discussions would be finally obtained after analyzing these test data. Furthermore, based on these discussions, there are some mechanism interpretations that can explain the test results of unsaturated sandy clay, which could be stated as follows:

(1) When water content keeps constant, with increasing of dry density, the pores between soil particles would be narrowed, the contact areas between soil particles could be increased, the adhesions and molecular forces between the particles of clay minerals would be increased; At the same time, the concentration of clay and cements would also be increased, the resulting reinforced cohesion would also be increased simultaneously. So, when water content keeps constant, the tensile strength of soils would be increased with increasing dry density.

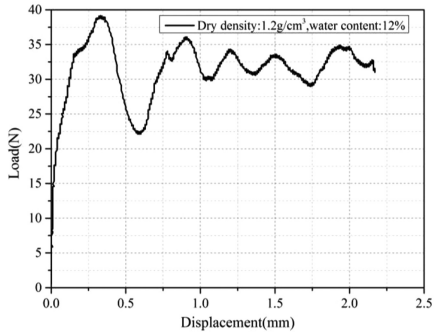
(2) When dry density keeps constant, within initially certain range, with increasing of water content, adsorption forces between soil particles and pore water are gradually increasing, the water in the soil belongs to strong bound water, then the tensile strength of soils will gradually increase with the increasing of adsorption; After reaching the



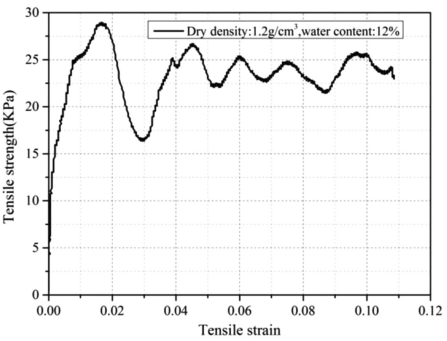
(a) Load-time changing curve



(b) Displacement-time changing curve

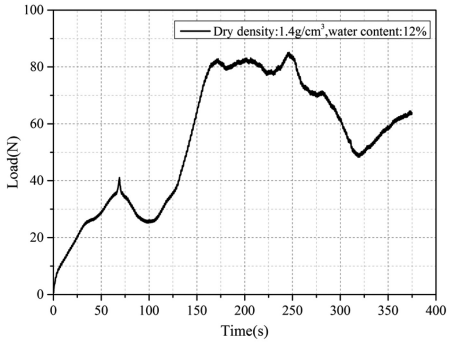


(c) Load-displacement changing curve

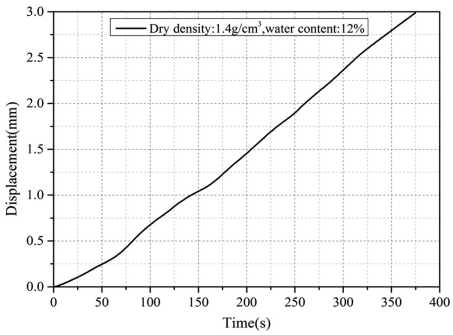


(d) Tensile stress-strain changing curve

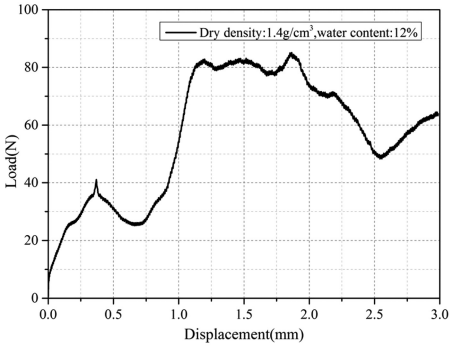
Figure 5. The changing curves drawn by processed data of unsaturated sandy clay of tensile strength experiments (ρ_d: 1.2 g/cm^3).



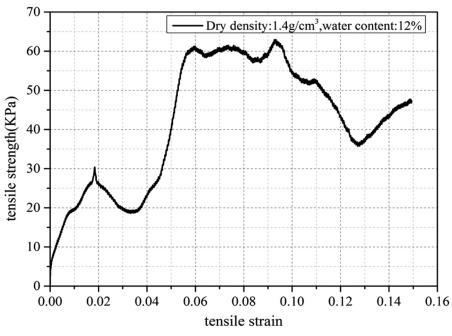
(a) Load-time changing curve



(b) Displacement-time changing curve



(c) Load-displacement changing curve



(d) Tensile stress-strain changing curve

Figure 6. The changing curves drawn by processed data of unsaturated sandy clay of tensile strength experiments (ρ_d: 1.4 g/cm^3).

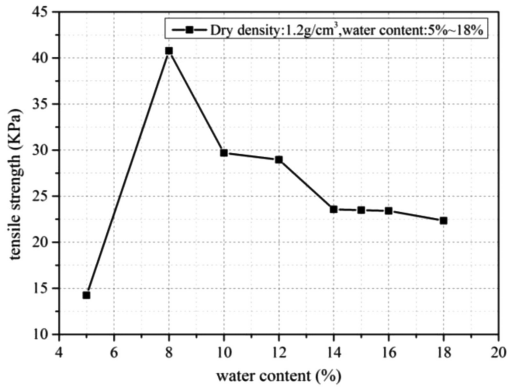


Figure 7. Tensile strength-water content changing curve with the dry density of 1.2 g/cm^3.

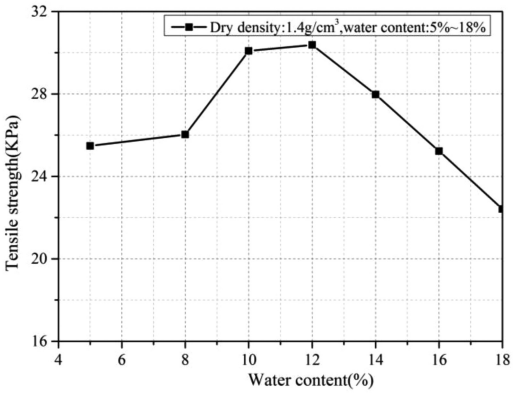


Figure 8. Tensile strength-water content changing curve with initial dry density of 1.4 g/cm^3.

Table 2. Water content and tensile strength for sandy clay in dry density of 1.2 g/cm^3.

Test number	Dry density (g/cm^3)	Water content (%)	Tensile strength (kPa)
1	1.2	5	14.24
2		8	40.78
3		10	29.69
4		12	28.96
5		14	23.55
6		15	23.47
7		16	23.40
8		18	22.33

peak value of tensile strength, with the increasing of water content, the pores between soil particles remain unchanged, but some soluble or medium dissolved salt cement is dissolved by excess water, the concentration of clay and cement is greatly reduced, the resulting reinforced cohesion will be decreased, then the water film between soil particles will be thickened, the adhesive force and molecular force between soil particles will be weakened finally. So within certain range of water content, the tensile strength decreases with the increasing of water content.

Table 3. Water content and tensile strength for sandy clay in dry density of 1.4 g/cm^3.

Test number	Dry density (g/cm^3)	Water content (%)	Tensile strength (kPa)
1	1.4	5	25.48
2		8	26.03
3		10	30.09
4		12	30.38
5		14	27.97
6		16	18.41
7		18	22.41

8 CONCLUSIONS

From the tests conducted for unsaturated sandy clay under different initial dry densities and water contents, the following conclusions can be concluded:

(1) When initial dry density keeps constant, the measured tensile strength generally increases with increasing water content, reach a peak value, after the peak, tensile strength decreases with increasing water content.
(2) When initial dry density keeps constant, the appearance of value of tensile strength indicates that with combined effect of optimum moisture content and maximum dry density, the tensile strength will reach the peak value.
(3) When water content keeps constant, with initial dry density increases, which means the specimen will be denser, leading to a larger value of tensile strength.
(4) From test results and analysis, it shows that initial dry density and water content make great influence on tensile strength.

ACKNOWLEDGMENTS

The financial support from the Fundamental Research Funds for the Central Universities (2015JBM068, 2015RC019) and the National Natural Science Foundation of China (51208031, 51478145) are grateful acknowledged.

REFERENCES

Heibrock G, Zeh R M, Witt K J. Tensile strength of compacted clays. Unsaturated soils: Experimental studies. Springer Berlin Heidelberg, 2005: 395–412.

Ibarra S Y, McKyes E, Broughton R S. Measurement of tensile strength of unsaturated sandy loam soil. Soil and Tillage research, 2005, 81(1): 15–23.

Kim T H, Hwang C. Modeling of tensile strength on moist granular earth material at low water content. Engineering Geology, 2003, 69(3): 233–244.

Kim T H, Sture S. Capillary-induced tensile strength in unsaturated sands. Canadian Geotechnical Journal, 2008, 45(5): 726–737.

Lakshmikantha M R, Prat P C, Ledesma A. Experimental evidence of size effect in soil cracking. Canadian Geotechnical Journal, 2012, 49(3): 264–284.

Lu N, Kim T H, Sture S, et al. Tensile strength of unsaturated sand. Journal of engineering mechanics, 2009, 135(12): 1410–1419.

Lu N, Wu B, Tan C P. Tensile Strength Characteristics of Unsaturated Sands [J]. Journal of Geotechnical & Geoenvironmental Engineering, 2007, 133(2):144–154.

Nahlawi H, Chakrabarti S, Kodikara J. A direct tensile strength testing method for unsaturated geomaterials. Geotechnical Testing Journal, 2004, 27(4): 356–361.

Péron H, Hueckel T, Laloui L, et al. Fundamentals of desiccation cracking of fine-grained soils: experimental characterisation and mechanisms identification. Canadian Geotechnical Journal, 2009, 46(10): 1177–1201.

Rifai S M, Miller C J. Theoretical assessment of increased tensile strength of fibrous soil undergoing desiccation. Journal of Geotechnical and Geoenvironmental Engineering, 2009, 135(12): 1857–1862.

Tamrakar S B, Mitachi T, Toyosawa Y. Measurement of soil tensile strength and factors affecting its measurements. Soils and Foundations, 2007, 47(5): 911–918.

Tamrakar S B, Mitachi T, Toyosawa Y. Factors affecting tensile strength measurement and modified tensile strength measuring apparatus for Soil. Experimental Unsaturated Soil Mechanics. Springer Berlin Heidelberg, 2007: 207–218.

Tang G X, Graham J. A method for testing tensile strength in unsaturated soils. Geotechnical Testing Journal ASTM, 2000, 23(3): 377–382.

Trabelsi H, Jamei M, Guiras H, et al. Some investigations about the tensile strength and the desiccation process of unsaturated clay. EPJ Web of Conferences. EDP Sciences, 2010, 6: 12005.

Trabelsi H, Jamei M, Zenzri H, et al. Crack patterns in clayey soils: Experiments and modeling. International Journal for Numerical and Analytical Methods in Geomechanics, 2012, 36(11): 1410–1433.

Vesga L F. Direct tensile-shear test (DTS) on unsaturated kaolinite clay. ASTM geotechnical testing journal, 2009, 32(5): 397–409.

Water retention and hydraulic behavior

This page intentionally left blank

Unsaturated Soil Mechanics—from Theory to Practice – Chen et al. (Eds)
© 2016 Taylor & Francis Group, London, ISBN 978-1-138-02921-7

A non-linear hysteresis model for soil-water retention behaviour

A.N. Zhou
School of Civil, Environmental and Chemical Engineering, Royal Melbourne Institute of Technology (RMIT), Melbourne, Australia

ABSTRACT: Hysteresis is common in soil-water phenomena, and the soil-water retention relationship is not a one-to-one relationship between the effective degree of saturation and the matric suction. Existing theoretical soil-water retention models are usually derived by applying a capillary law that does not depend on the contact angle to the cumulative distribution function of soil pores. These theoretical models usually contain equations only for the main drying and wetting branches, so additional empirical scanning laws are needed to model hysteresis behaviour between these branches. This paper proposes a contact angle-dependent model in incremental form to reproduce soil-water hysteresis behaviour. The change in suction during scanning wetting and drying processes leads to a change in both the effective degree of saturation and the liquid-solid contact angle. An allocation proportion function is proposed to divide suction increments into two parts, one of which is allocated to the change in the effective degree of saturation and the other consumed by changing the contact angle. The proposed hysteresis model contains only four parameters that can be conveniently calibrated by the main drying branch and a scanning wetting curve. Test results are included to validate the proposed hysteresis model.

1 INTRODUCTION

The Soil-Water Characteristic Curve (SWCC) is defined as the relationship between the effective degree of saturation S_e (or degree of saturation, S_r) and the matric suction s (or soil-water potential ψ). The effective degree of saturation can be defined as follows:

$$S_e = \frac{S_r - S_r^{res}}{1 - S_r^{res}} \tag{1}$$

where $S_r \geq S_r^{res}$ and S_r^{res} is the residual degree of saturation and is a constant, irrespective of the applied suction or mechanical loads. The soil-water characteristic curve is also called the soil moisture characteristic curve or the soil-water retention curve. A soil's SWCC can usually give an indication of its hydraulic properties and has various applications in soil physics and soil mechanics. The SWCC is widely used to predict hydraulic conductivity, soil water storage, field capacity and soil aggregate stability in agricultural engineering (Brady, 1999). It is also commonly employed in estimating the permeability, shear strength and stress-strain relationships of unsaturated soils (Sheng, 2011).

When it was first introduced, the equations of a SWCC were usually obtained through the curve-fitting method for given experimental data and referred to as empirical SWCC equations (such as in Brooks and Corey, 1964; van Genuchten, 1980, etc.). Later, SWCC equations could be derived theoretically based on the soil pore size distribution obtained from probability density functions (e.g., Fredlund and Xing, 1994; Zhang and Chen, 2005) or from iterating fractal functions (e.g., Tyler and Wheatcraft, 1990; Gimenez *et al.*, 1997). These theoretical methods were also used to reveal the physical backgrounds of existing empirical SWCC equations. For example, Tyler and Wheatcraft (1990) derived Brooks and Corey's equation (Brooks and Corey, 1964) through a two-dimensional fractal function (Sierpinski carpet). The theoretical derivation indicated that the exponential fitting index in Brooks and Corey's equation was dependent on the fractal dimension related to the pore size distribution. These empirical and theoretical SWCC equations can be used to produce a one-to-one soil-water retention relationship between the effective degree of saturation and the suction. However, the soil-water retention relationship for soils is not unique and hydraulic hysteresis is common in soil-water phenomena.

In soil physics, hydraulic hysteresis behaviour is qualitatively attributed to several factors such as the ink-bottle effect resulting from non-uniformity in the shape and size of interconnected pores and the different liquid-solid contact angles for advancing and receding water menisci. However, those explanations are rarely applied to quantitative predictions of soil-water hysteresis behaviour. In unsaturated soil mechanics, the hysteresis behaviour is quantitatively described by a linear scanning curve (e.g., Vaunat *et al.*, 2000; Wheeler *et al.*, 2003; Sheng *et al.*, 2008) through the analogy with elastoplasticity from early research. However, the linear scanning curve does not usually provide satisfactory predictions of hydraulic hysteresis

behaviour, especially within the domain bounded by the main wetting and drying curves. Several non-linear models reproducing the hydraulic hysteresis were recently presented that were more capable of simulating smooth hysteresis behaviour between the main wetting and drying branches than linear models. Some of these models are found in Li (2005), Pedroso *et al.* (2008), Muraleetharan *et al.* (2009), Pedroso and Williams (2010), Zhou *et al.* (2012a). Nevertheless, these non-linear methods describing hydraulic hysteresis behaviour within the domain bounded by the main wetting and drying curves are based mainly on data-fitting methodology and are usually phenomenological in nature.

This paper presents a new SWCC equation in the incremental form based on the contact angle-dependent capillary law. Suction increments (ds) are divided into two parts, one ((1– k)ds) that contributes to the change in the effective degree of saturation and another (kds) that is consumed by changing the liquid-solid contact angle, where k is a function that indicates the allocation proportion of ds. A simple non-linear equation is then proposed to specify the allocation proportion function (k), which further controls the soil-water hysteresis behaviour. This allocation proportion function is then integrated into van Genuchten's model, which is adopted as the main drying branch in this study. It should be noted that other empirical and theoretical SWCC models can also be used as the main drying branch as alternatives to van Genuchten's model. Finally, a number of test results on soil-water hysteresis behaviour are included to validate the proposed SWCC equation.

2 CONTACT ANGLE VARIATION

The contact angle is the angle at which a liquid or vapour interface meets a solid surface. A single liquid solid system has a spectrum of equilibrium contact angles, and the variation in contact angle is referred to as the contact angle hysteresis in chemical sciences. The maximum and minimum contact angles are called the advancing contact angle (θ_A) and receding contact angle (θ_R), respectively. The advancing and receding contact angles can be generated by several methods, such as the tilting plate method. As the surface of the tilting plate is inclined, gravity causes the contact angle on the downhill side to increase, while the contact angle on the uphill side decreases, as seen in Figure 1a, and this change generates the advancing and receding contact angles, respectively. The adding/removing volume method is another way to generate advancing and receding contact angles. When volume is added to the drop in maximum volume permitted without increasing the three-phase line, the maximum possible contact angle is referred to as the advancing angle (see Figure 1b). When the maximum volume that can be removed without reducing the three-phase line is reached, the resulting contact angle is the receding angle (see Figure 1b).

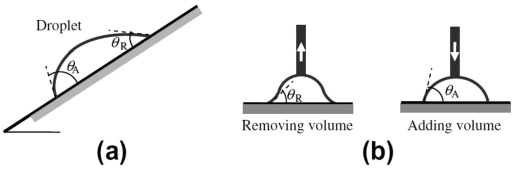


Figure 1. Experimental methods for generating advancing and receding contact angles: (a) tilting plate method and (b) adding/removing volume method.

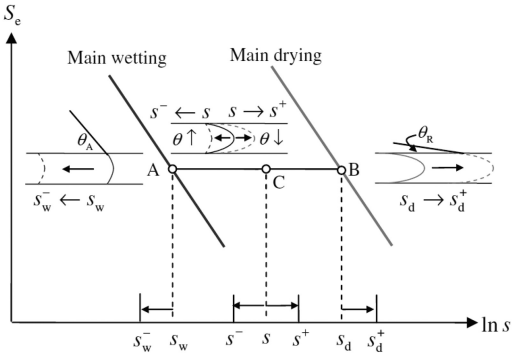


Figure 2. Variation of contact angle in different drying/wetting conditions.

Under different drying and wetting conditions, the contact angle is not always a constant but may vary between advancing and receding contact angles. During the drying process along the main drying branch (e.g., drying from point A, s_d to s_d^+; see Figure 2), which is similar to the process of removing volume mentioned above, the contact angle remains a receding contact angle (θ_R) during drying. During the main wetting process (e.g., wetting from point B, s_w to s_w^-; see Figure 2), which is similar to the process of adding volume mentioned above, the contact angle remains an advancing contact angle (θ_A) during wetting. The contact angle is not a constant, except in the main drying and wetting conditions. For the transitional states, such as scanning drying/wetting processes at point C ($s^- \leftarrow s$ or $s \rightarrow s^+$), the contact angle remains between the receding contact angle and the advancing contact angle and its value continues to change during the drying/wetting process until the state point moves to the main drying or wetting branches. For the transitional states, as shown in Figure 2, the contact angle (θ) decreases when the suction increases and increases when the suction decreases. However, the variation in contact angle is commonly omitted from the data and the capillary law, which is independent of contact angle, is predominantly adopted in deriving theoretical SWCC equations, such as in Tyler and Wheatcraft (1990) and Fredlund and Xing (1994). Neglecting the contact angle variation is one of the main reasons for the incapability of the previous SWCC models to predict hydraulic hysteresis behaviour.

3 CONTACT ANGLE-DEPENDENT HYSTERESIS MODEL

The effective degree of saturation can be derived from the cumulative distribution function of soil pores $F(r)$. $F(r)$ is a function of the total volume of pores that are greater than any arbitrary pore radius (r) and can be integrated from the pore size distribution function $f(r)$. The arbitrary pore radius (r) is called the threshold radius. If pores greater than the threshold radius are dewatered by applying matric suction, the effective degree of saturation is given by:

$$S_e = 1 - F(r) = 1 - \int_r^{r_{max}} f(r)\mathrm{d}r \tag{2}$$

The key relationship connecting the cumulative distribution function of soil pores with soil-water retention behaviour is the capillary law, which can be expressed as follows:

$$s = \frac{2\sigma^{lg}\cos\theta}{r} \Leftrightarrow r = \frac{2\sigma^{lg}\cos\theta}{s} \tag{3}$$

where σ^{lg} is the liquid gas interfacial tension and θ is the liquid-solid contact angle, which is usually treated as a constant in the existing models. Based on equations (2) and (3), the suction of an arbitrary point (such as point C in Figure 2) can be written as:

$$s = \frac{2\sigma^{lg}\cos\theta}{F^{-1}(1-S_e)} \tag{4}$$

where $F^{-1}(1 - S_e)$ is the inverse function of F with regard to variable '$1 - S_e$'. This equation demonstrates that variation of the contact angle can cause the variation of suction and vice versa under a constant effective degree of saturation. For the main drying branch ($\theta = \theta_R$) we obtain $s_d = 2\sigma^{lg}\cos\theta_R / F^{-1}(1 - S_e)$. Under an effective degree of saturation, the ratio between the arbitrary suction (s) and the suction on the drying branch (s_d) is written as:

$$s = \frac{\cos\theta}{\cos\theta_R} s_d \tag{5}$$

where s_d can be obtained from any theoretical SWCC equation, such as that in Tyler and Wheatcraft (1990) or Fredlund and Xing (1994). Because some empirical SWCC equations can be derived theoretically from equations (2) and (3), these SWCC models could also be employed to determine s_d. Van Genuchten's equation, which can be obtained by the above theoretical approach assuming a suitable pore size distribution function (Fredlund and Xing, 1994), is used here as an example (other SWCC equations are also applicable):

$$s_d = a_d\left(S_e^{n/(1-n)} - 1\right)^{1/n} \tag{6}$$

where n is a parameter related to the pore size distribution in van Genuchten's equation and a_d is a parameter related to the air entry value. Substituting equation (6) into (5) yields:

$$S_e = \left[1 + \left(\frac{s\cos\theta_R}{a_d\cos\theta}\right)^n\right]^{-1+1/n} \tag{7}$$

This equation shows that the effective degree of saturation is related to both the suction level (s) and the contact angle (θ). Equation (7) cannot be employed to predict hysteresis behaviour directly because soil-water hysteresis is a path-dependent process that requires incremental formulations. The increment of S_e can be derived from equation (7) by assuming θ is not a constant and the variation in the contact angle ($\mathrm{d}\theta$) is also caused by the suction change ($\mathrm{d}s$):

$$\begin{aligned}\mathrm{d}S_e &= \frac{\partial S_e}{\partial s}\mathrm{d}s + \frac{\partial S_e}{\partial \theta}\mathrm{d}\theta = \frac{\partial S_e}{\partial s}\mathrm{d}s + \frac{\partial S_e}{\partial \theta}\frac{\mathrm{d}\theta}{\mathrm{d}s}\mathrm{d}s, \\ &= \frac{1-n}{s}\left[1 + \left(\frac{s\cos\theta_R}{a_d\cos\theta}\right)^n\right]^{(1-2n)/n}\left(\frac{s\cos\theta_R}{a_d\cos\theta}\right)^n\left(1 + s\tan\theta\frac{\mathrm{d}\theta}{\mathrm{d}s}\right)\mathrm{d}s\end{aligned} \tag{8}$$

The contact angle is constant in the main drying and wetting branches ($\theta = \theta_R$ or θ_A, $\mathrm{d}\theta/\mathrm{d}s = 0$), so the given suction increment ($\mathrm{d}s$) fully contributes to the change in the effective degree of saturation ($\mathrm{d}S_e$) because the term $(1 + s\tan\theta(\mathrm{d}\theta/\mathrm{d}s))$ is equal to 1. However, the term $(1 + s\tan\theta(\mathrm{d}\theta/\mathrm{d}s))$ in front of $\mathrm{d}s$ is not always equal to 1 in the general conditions indicated in equation (8). The sign of $\mathrm{d}\theta/\mathrm{d}s$ is negative during the scanning wetting/drying processes; that is, $\mathrm{d}\theta > 0$ if $\mathrm{d}s < 0$ or $\mathrm{d}\theta < 0$ if $\mathrm{d}s > 0$ (see Figure 2). Therefore, the term $(1 + s\tan\theta\ (\mathrm{d}\theta/\mathrm{d}s))$ is less than 1 for the scanning wetting/drying processes. Equation (8) indicates that for a given suction change ($\mathrm{d}s$), only a portion of the change (i.e., $(1 + s\tan\theta(\mathrm{d}\theta/\mathrm{d}s))\mathrm{d}s$) contributes to the change in the effective degree of saturation and the rest is consumed by the contact angle alteration in the scanning wetting/drying process. If the entire suction increment ($\mathrm{d}s$) is allocated to the contact angle alteration, the scanning curve is a flat line, which implies no change in the effective degree of saturation has occurred:

$$\frac{\mathrm{d}\theta}{\mathrm{d}s} = -\left|\frac{\mathrm{d}\theta}{\mathrm{d}s}\right|_{max} = -\frac{1}{s\tan\theta} \qquad (\mathrm{d}S_e = 0) \tag{9}$$

The maximum absolute value of $\mathrm{d}\theta/\mathrm{d}s$ that is equal to $1/s\tan\theta$ can be achieved only when $\mathrm{d}S_e$ is set to the minimum (i.e., 0). Under real conditions, the change in contact angle ($\mathrm{d}\theta$) and effective degree of saturation ($\mathrm{d}S_e$) are considered to occur synchronously to some extent, which implies that the absolute value of $\mathrm{d}\theta/\mathrm{d}s$ should be less than the maximum value. We could use a general function k to quantify the allocation proportion for the suction increment that further affects the

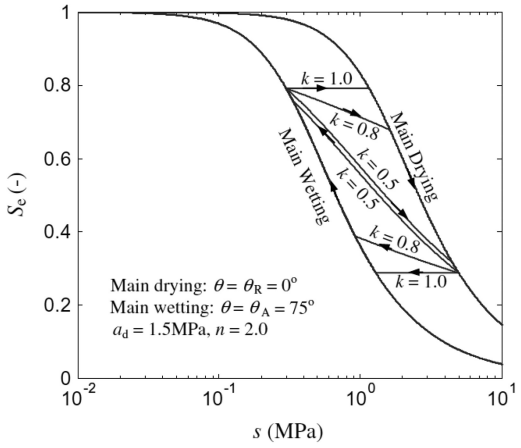


Figure 3. Predicted scanning curves when k is set to a constant.

hysteresis pattern of a soil. In general, $\mathrm{d}\theta/\mathrm{d}s$ can be written as:

$$\frac{\mathrm{d}\theta}{\mathrm{d}s} = -k\left|\frac{\mathrm{d}\theta}{\mathrm{d}s}\right|_{\max} = -\frac{k}{s\tan\theta},\quad 0 \le k \le 1 \tag{10}$$

k is always equal to zero in the main wetting and drying because the contact angle stays constant (θ_A or θ_R). If k is set as a constant for the scanning wetting and drying, the resultant scanning curve is almost linear (see the predicted scanning curves with different values of k in Figure 3). Test results presented by Muraleetharan *et al.* (2009) showed that the linear scanning law was acceptable but not accurate enough, especially for hydro-mechanical coupling constitutive models that employ the effective degree of saturation as an additional constitutive variable (such as Zhou *et al.*, 2012a; Zhou *et al.*, 2012b).

Special conditions should be taken into account to generate the specific formulation for function k when reproducing non-linear hysteresis behaviour. The contact angle is constant in the main drying and wetting branches, which means k must be zero. k varies from 1 to 0 in a scanning drying process (from turning point A to merging point B, see Figure 4) during which the contact angle alters from θ_A (point A) to θ_R (point B). At the beginning of the scanning drying process (see turning point A in Figure 4), the value of k jumps from 0 (for point A^-, which is still on the main wetting branch) to 1 (for point A^+, which is on the scanning drying curve). k is set to 1 for point A^+ to indicate that the change in the contact angle occurs prior to the change in degree of saturation at the turning point. In other words, a suction increment at the turning point is fully allocated to the contact angle alternation. Such a discontinuity in the value of k for point A reflects the fact that this point is a turning point where the suction path changes (i.e., $\mathrm{d}s$ changes from negative to positive and the suction path is not smooth at the turning point). However, the value of θ at point A is still continuous,

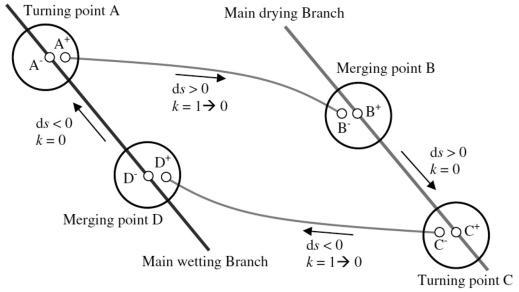


Figure 4. Turning and merging points on SWCCs.

and θ is equal to θ_A for both A^+ and A, so the predicted water retention curve at turning point A is continuous but not smooth. At the end of the scanning drying process (see merging point B in Figure 4), k is set to 0 to reflect the fact that the change in contact angle is completed when the scanning curve touches the main drying curve. The value of k (=0) and θ (=θ_R) remains the same for both B^- and B^+ because $\mathrm{d}s$ is still positive (i.e., the suction path is smooth) at the merging point. Therefore, the predicted water retention curve at merging point B is continuous and smooth. In a scanning wetting process (from point C to D in Figure 4) that alters the contact angle from θ_R to θ_A, k again varies from 1 to 0 in a similar manner. The predicted water retention curve is continuous but not smooth at turning point C and both continuous and smooth at merging point D.

The non-linear equation that satisfies the above conditions can be represented as:

$$k = \begin{cases} \left(\dfrac{\cos\theta - \cos\theta_R}{\cos\theta_A - \cos\theta_R}\right)^b & \mathrm{d}s > 0 \\ \left(\dfrac{\cos\theta_A - \cos\theta}{\cos\theta_A - \cos\theta_R}\right)^b & \mathrm{d}s < 0 \end{cases} \tag{11}$$

where parameter b ($0 < b < 1$) is adopted to control the curvature of the $\cos\theta$–k relationship. Equation (11) is not unique for function k, but is perhaps one of the simplest options for representing it. The initial value of θ can be determined using equation (7) for a known (s, S_e) at the initial state. The evolution law for θ is defined with equation (10). Based on equations (8), (10) and (11), the change in the effective degree of saturation for an arbitrary point (s, S_e) can be written as:

$$\mathrm{d}S_e = \frac{n-1}{s} S_e^{1/(1-n)}\left(S_e^{n/(n-1)} - 1\right)(1-k)\,\mathrm{d}s \tag{12}$$

Equation (12) indicates that $(1-k)\mathrm{d}s$ contributes to the change in degree of saturation for a suction increment ($\mathrm{d}s$), but the rest ($k\mathrm{d}s$) is consumed by the contact angle alteration. The value of k jumps from 0 to 1 at the turning points, which matches the suction path change. However, the entire θ–s relationship and the entire S_e–s relationship are still continuous.

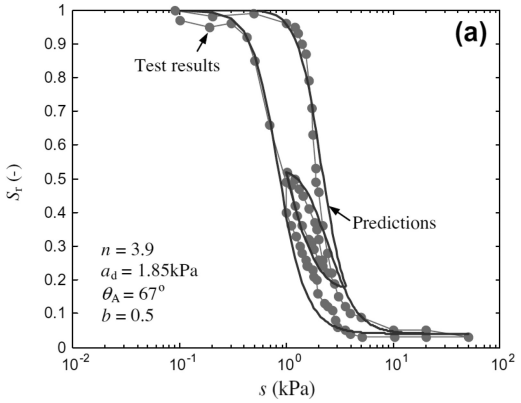


Figure 5. Hysteresis behaviour of Houston sand (data after Lins *et al.*, 2007): test results and model predictions.

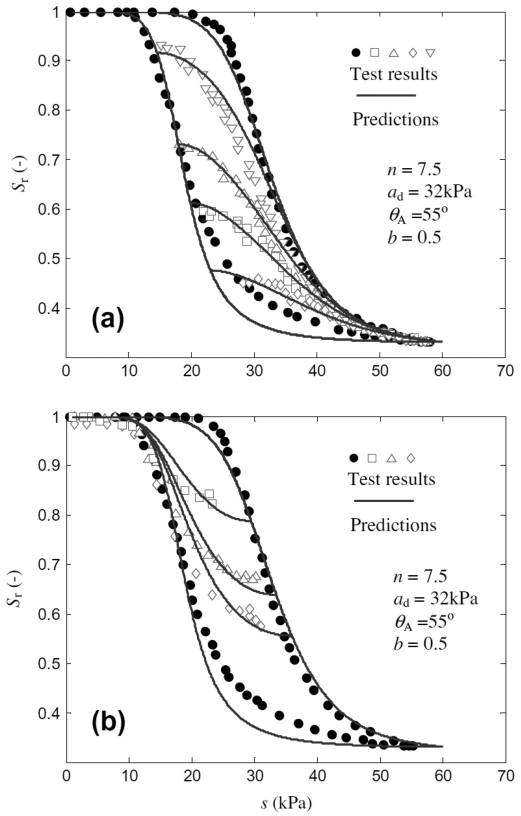


Figure 6. Test results and model predictions for the hysteresis behaviour of sand (data after Gillham *et al.*, 1976): (a) scanning drying tests and (b) scanning wetting tests.

4 EXPERIMENTAL VALIDATION

Lin *et al.* (2007) conducted a water retention test on Houston sand to reveal the hysteresis behaviour of this course granular soil. The test results and model predictions are plotted with 4 parameters in Figure 5.

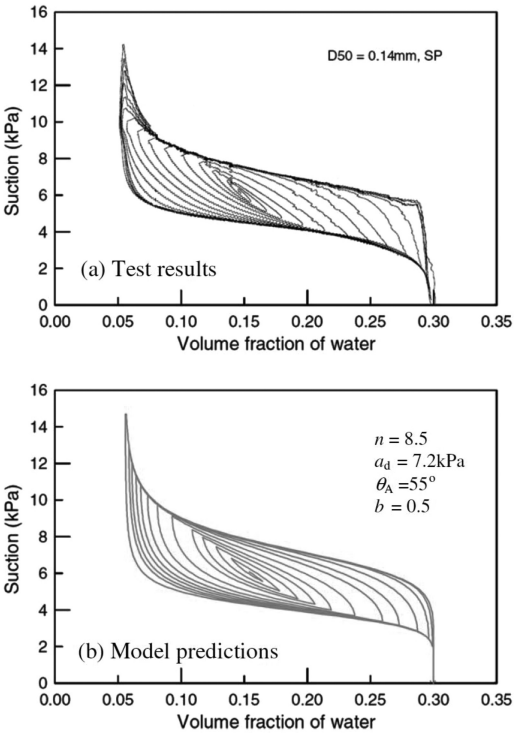


Figure 7. Hydraulic hysteresis loops for Berkley springs sand (data after Muraleetharan *et al.*, 2009): (a) test results and (b) model predictions.

Comparison of the model predictions with the experimental data indicates that the proposed hysteresis model is capable of reproducing non-linear water retention behaviour for Houston sand.

A series of scanning drying and wetting test results obtained by Gillham *et al.* (1976) are employed in this paper to validate the proposed hysteresis model. The black dots in Figure 6 stand for the observed main drying and wetting boundaries taken from Gillham *et al.* (1976). Figure 6a and Figure 6b show the scanning drying test results and scanning wetting test results, respectively. The parameters for scanning wetting and drying are the same and indicated in Figure 6. The prediction curves calculated by the proposed hysteresis model are plotted against test results in Figure 6, which shows that the predictions and observations are in good agreement with each other.

Muraleetharan *et al.* (2009) presented test results on the water retention behaviour of poorly graded Berkley springs sand (US F-95), which are expressed in the suction space and volume fraction of water (n^w). The volume fraction of water (i.e., the volumetric water content) at the fully saturated state is 0.3. Given that the residual degree of saturation is 0.17, the volume fraction of water can be calculated from the effective degree of saturation using $n^w = 0.3 \times (S_e(1 - 0.17) + 0.17)$. The test results are replotted in Figure 7a and the model predictions and parameters

are presented in Figure 7b. This comparison demonstrates that the predicted hysteresis loops agree with the observed results, which confirms the ability of the proposed model to reproduce the hydraulic hysteresis behaviour of Berkley springs sand.

5 CONCLUSIONS

In traditional theoretical methods, the capillary law, which does not depend on contact angle, is usually applied directly to the cumulative distribution function of soil pores to derive the mathematical equations of soil-water characteristic curves (SWCCs). However, the hysteresis behaviour of soil-water phenomena is commonly neglected because the contact angle is assumed to be constant for simplicity.

This paper presented a new contact angle-dependent model to interpret the hydraulic hysteresis behaviour of unsaturated soils. In the proposed model, a suction increment is divided into two parts, one that leads to a change in the effective degree of saturation and another that is consumed by the change in the liquid-solid contact angle. Soil-water hysteresis behaviour is controlled by an allocation proportion function that governs the division of the suction increment.

The proposed contact angle-dependent model, which employs van Genuchten's equation to define the main drying branch, contains only 4 parameters. These 4 parameters are physically meaningful and can be conveniently calibrated using the main drying branch and an arbitrary scanning wetting curve. The predictions made by the proposed model agree with experimental observations of the hydraulic hysteresis behaviour of unsaturated soils in the literature. More details can be found in Zhou (2013).

REFERENCES

Brady, N. C. (1999). The Nature and Properties of Soils (12th ed.). Prentice-Hall, Upper Saddle River, New Jewery.

Brooks, R., and Corey, A. (1964). Hydraulic properties of porous media. Hydrology Paper, No. 3, Colorado State University, Fort Collins, Colorado.

Fredlund, D. G., and Xing, A. (1994). Equations for the soil-water characteristic curve. Canadian Geotechnical Journal, 31(3): 521–532.

Gillham, R. W., Klute, A., and Heerman, D. F. (1976). Hydraulic properties of a porous medium: Measurement and empirical representation. Soil Sci Soc Am J, 40: 203–207.

Gimenez, D., Perfect, E., Rawls, W. J., and Pachepsky, Y. (1997). Fractal models for predicting soil hydraulic properties: a review. Engineering Geology, 48(3–4): 161–183.

Li, X. S. (2005). Modelling of hysteresis response for arbitrary wetting/drying paths. Computers and Geotechnics, 32(2): 133–137.

Lins, Y., Zou, Y., and Schanz, T. (2007). Physical modeling of SWCC for granular materials. Theoretical and numerical unsaturated soil mechanics, Weimer pp. 61–74. Germany: Springer.

Muraleetharan, K. K., Liu, C., Wei, C., Kibbey, T. C. G., and Chen, L. (2009). An elastoplatic framework for coupling hydraulic and mechanical behavior of unsaturated soils. International Journal of Plasticity, 25(3): 473–490.

Pedroso, D. M., Sheng, D., and Zhao, J. (2008). The concept of reference curves for constitutive modelling in soil mechanics. Computers and Geotechnics, 36(1): 149–165.

Pedroso, D. M., and Williams, D. J. (2010). A novel approach for modelling soil-water characteristic curves with hysteresis. Computers and Geotechnics, 37(3): 374–380.

Sheng, D. (2011). Review of fundamental principles in modelling unsaturated soil behaviour. Computers and Geotechnics, 38: 757–776.

Sheng, D., Fredlund, D. G., and Gens, A. (2008). A new modelling approach for unsaturated soils using independent stress variables. Canadian Geotechnical Journal, 45(4): 511–534.

Tyler, S. W., and Wheatcraft, S. W. (1990). Fractal processes in soil water retention. Water Resour. Res., 26(5): 1047–1054.

van Genuchten, M. T. (1980). A closed-form equation for predicting the hydraulic conductivity of unsaturated soils. Soil Science Society of America Journal, 44: 892–898.

Vaunat, J., Romero, E., and Jommi, C. (2000). An elastoplastic hydromechanical model for unsaturated soils. Experimental evidence and theoretical approaches in unsaturated soils. Proceedings of international workshop on unsaturated soil, (A. Tarantino and C. Mancuso, eds.) pp. 121–138. Rotterdam: Balkema.

Wheeler, S. J., Sharma, R. S., and Buisson, M. S. R. (2003). Coupling of hydraulic hysteresis and stress-strain behaviour in unsaturated soils. Geotechnique, 53(1): 41–54.

Zhang, L. M., and Chen, Q. (2005). Predicting bimodal soil-water characteristic curves. Journal of Geotechnical and Geoenviromental Engineering, ASCE, 131(5): 666–670.

Zhou, A. N. (2013). A contact angle-dependent hysteresis model for soil–water retention behaviour. Computers and Geotechnics, 49: 36–42.

Zhou, A. N., Sheng, D., Sloan, S. W., and Gens, A. (2012a). Interpretation of unsaturated soil behaviour in the stress-saturation space, I: Volume change and water retention behaviours. Computers and Geotechnics, 43: 178–187.

Zhou, A. N., Sheng, D., Sloan, S. W., and Gens, A. (2012b). Interpretation of unsaturated soil behaviour in the stress-saturation space, II: Constitutive relationships and validations. Computers and Geotechnics, 43: 111–123.

Unsaturated Soil Mechanics—from Theory to Practice – Chen et al. (Eds)
© 2016 Taylor & Francis Group, London, ISBN 978-1-138-02921-7

Common mistakes in determination of air entry value from gravimetric water content based Soil-Water Characteristic Curve

A.Y. Pasha, A. Khoshghalb & N. Khalili
School of Civil and Environmental Engineering, The University of New South Wales, Sydney, Australia

ABSTRACT: Pitfalls in the common approaches to obtaining the Air Entry Value (AEV) from Soil-Water Characteristic Curves (SWCCs) are discussed and the typical mistakes made in the literature are highlighted. A consistent graphical approach for the determination of AEV based on an understanding of the effects of stress history and volume change on gravimetric water retention behaviour is presented. The robustness and application of the approach are demonstrated using experimental data from the literature.

1 INTRODUCTION

The Soil-Water Characteristic Curve (SWCC) is one of the most fundamental relationships in the mechanics of unsaturated soils that is used in the calculations relating to deformation (Matyas and Radhakrishna 1968), shear strength (Fredlund et al. 1978), effective stress (Khalili and Khabbaz 1998), multiphase flow and transport (Abriola and Pinder 1985), water retention (Brooks and Corey 1964), drainage (Hillel 1980), and appears explicitly in the constitutive formulations of pore-air and pore-water, satisfying pore-phase volume change compatibility for a change in suction (Khalili et al. 2008). Indeed, more research effort has been devoted to the quantification and characterisation of water retention behaviour in soils than any other topic in the mechanics of unsaturated porous media.

Corresponding to the suction at the transition point between saturated and unsaturated states in a SWCC plot, air entry value (AEV, shown as s_{ae} in mathematical equations) is a key unsaturated soil parameter which serves as a pivotal input in many constitutive relationships relating to the mechanics of unsaturated soils.

Numerous approaches have been proposed for the interpretation of AEV from the experimental SWCC data (Fredlund and Xing 1994; Vanapalli et al. 1998; Zhai and Rahardjo 2012). However, they have invariably been based on the assumption of soil non-deformability, neglecting the complexities arising from the volume change and stress history dependency of the water retention behaviour in unsaturated soils. In deformable materials, SWCC can assume very different shapes, even for a single soil type, depending on the volume change-suction relationship and stress history of the soil (Ng and Pang 2000; Vanapalli et al. 1999). Ignoring such dependencies can lead to gross misinterpretation of SWCC data and extraction of soil parameters that are markedly in error.

In this paper, different forms of SWCC corresponding to different soil stress histories are discussed and mathematical expressions for gravimetric water content versus suction, in both saturated and unsaturated regions, are developed for each case. Difficulties and misinterpretations frequently encountered in the literature in dealing with SWCC are examined using several numerical examples. A simple methodology is proposed for the evaluation of AEV from gravimetric water content based SWCC for deformable soils, without the need for the soil volume change data with suction. The application and appropriateness of the approach are demonstrated using an extensive array of experimental test data from the literature. It is shown that the proposed approach can be applied to a range of soil data with different initial condition, volume change behaviour and stress history.

2 COMMON APPROACHES TO DETERMINATION OF AEV FROM EXPERIMENTAL DATA

The AEV is most commonly determined graphically from the experimental SWCC data plotted in a semi-logarithmic (semi-log) plane. It is typically taken as the suction corresponding to the intersection point of two straight lines: the first line is representative of the saturated zone of SWCC, i.e. the data points at which the air phase has not invaded the pores; and the second line is represented by the desaturation zone when connected pathways of air phase are formed across the pores. The second line is usually drawn as a tangent passing through the inflection point of SWCC. For constructing the first line, depending on the data reduction approach adopted (i.e. SWCC based on degree of saturation, SWCC-*S*, gravimetric water content, SWCC-*w*, or volumetric water content,

SWCC-θ), a horizontal line asymptotic to SWCC-S at zero suction (e.g. Sillers et al. 2001b), or a sloping line tangent to SWCC-w and SWCC-θ at zero suction (e.g. Khalili and Khabbaz 1998; Khalili et al. 2004; Pham and Fredlund 2008) have been used. The reason behind the sloping saturated line in SWCC-w and SWCC-θ plots is that in deformable soils, prior to the air phase entering the pore space, some of the water in the pores will be expelled due to the change in the stress state of the soil. However, in SWCC-S the degree of saturation remains constant and equal to unity while the soil is saturated, and therefore the first line is drawn horizontally. Some investigators have incorrectly extended this observation to water content based soil-water characteristic curves, requiring that saturated zone in SWCC-w and SWCC-θ is also represented by a horizontal line. This approach ignores the deformation of the soil with suction; i.e. during the testing, and can lead to AEVs that are several orders of magnitude in error. Examples of such deficiency have been highlighted by Zargarbashi and Khalili (2012) in relation to the work of Guan et al. (2010).

The problem of using a horizontal, instead of a sloping, line for constructing the saturated portion of SWCC-w or SWCC-θ, is in fact a special case of a more fundamental problem in evaluating AEV from SWCC-w or SWCC-θ. In many cases, the common graphical approaches for determining AEV, irrespective of using a horizontal or a sloping line; i.e. to represent the first part of SWCC-w, can lead to erroneous evaluations of AEVs for deformable soils.

Many researchers in soil science as well as geotechnical engineering consider the first break in the drying branch of SWCC-w or SWCC-θ as an indication of the point of air entry (e.g. Vanapalli et al. 1998; Fredlund and Xing 1994; Fredlund et al. 2001; Zhai and Rahardjo 2012). For a non-deformable medium, this statement is entirely correct. However, it may not be true for deformable soils depending on the mechanical properties of the soil, the value of air entry (AEV), the pore size distribution index of the soil, and the stress history of the soil.

3 EFFECT OF STRESS HISTORY ON SWCC-W FOR DEFORMABLE SOILS

To demonstrate the impact of stress history on the water content versus suction response of deformable soils, a series of numerical examples are presented for an elemental volume of a soil with mechanical properties κ, λ and p'_c; κ is the slope of the unloading-reloading line in $v \sim \ln p'$ plane, where v is the specific volume and p' is the mean effective stress; λ is the slope of normal compression line (NCL) in the $v \sim \ln p'$ plane; and p'_c is the preconsolidation pressure of the soil. The general cases in which the water retention test is performed at a net mean stress (p_{net}) will be discussed. In this context, the water retention response of the soil is assumed to follow Brooks and Corey model represented by:

$$S_{eff} = \left(\frac{s_{ae}}{s}\right)^{\lambda_p} \tag{1}$$

where

$$S_{eff} = \frac{S_r - S_{res}}{1 - S_{res}} \tag{2}$$

is the effective degree of saturation; S_r is the total degree of saturation; S_{res} is the residual degree of saturation; and λ_p is the pore size distribution index of the soil.

Three stress states: i) normally consolidated, ii) overconsolidated with $p'_c < p_{net} + s_{ae}$ and, iii) overconsolidated with $p'_c > p_{net} + s_{ae}$ are considered, reflective of the various stress histories of a soil. Effective stress is used for the quantification of the volume change of soil due to a change in suction, expressed as (Bishop 1959):

$$\sigma' = (\sigma - u_a) + \chi(u_a - u_w) \tag{3}$$

in which σ' is the effective stress; σ is the total stress; u_a and u_w are the pore air and pore water pressures, respectively; and $\sigma - u_a$ is the net stress, σ_{net}. $u_a - u_w = s$ is the matric suction, and χ is the effective stress parameter, determined in this work using the relationship proposed by Khalili and Khabbaz (1998).

3.1 *Normally consolidated soil or soil prepared from slurry*

Soils with the externally applied stress equal to the preconsolidation pressure, p'_c, (but less than the AEV) or soils prepared from a slurry, behave as Normally Consolidated (NC) in the saturated zone of the SWCC ($s \leq s_{ae}$). In such soils, the initial part of SWCC$-w$ curve, in a semi-log plane, can be approximated with a single line having a slope corresponding to the slope of the normal compression line, λ, as the volume of water lost during this stage is equal to the decrease in the volume of the voids. After the start of desaturation, the change of water content with suction in the SWCC-w plot is controlled primarily by the pore size distribution of the soil. The suction at the intersection of these two parts of SWCC-w is regarded as AEV.

In this case, the total form of SWCC-w is derived as:

$$w = \begin{cases} w_0 - \dfrac{2.3\lambda}{G_s}\log\left(\dfrac{s + p_{net}}{s_0 + p_{net}}\right) & ;\ s < s_{ae} \quad (4a) \\ w_{ae}\left((1 - S_{res})\left(\dfrac{s_{ae}}{s}\right)^{\lambda_p} + S_{res}\right) & ;\ s > s_{ae} \quad (4b) \end{cases}$$

In Equation (4), G_s is the specific gravity of solid grains, and w_{ae} is the gravimetric water content at AEV, calculated as

$$w_{ae} = w_0 - \frac{2.3\lambda}{G_s}\log\left(\frac{s_{ae} + p_{net}}{s_0 + p_{net}}\right) \tag{4c}$$

where w_0 is the reference water content at the reference reference stress state, $s_0 + p_{net}$. Also note that since Equation (4) is derived for normally consolidated soils, hence $p_{net} = p'_c$ in this equation.

A graphical representation of Equation (4), in terms of water content versus $s + p_{net}$, for the case of $p_{net} = p'_c \neq 0$, is given in Figure 1. The SWCC contains two separate parts in this case, a linear part where the soil remains saturated and behaves as a normally consolidated soil followed by a non-linear part where the soil is desaturated. Note that in the cases where $p_{net} = p'_c \neq 0$, the saturated part of the SWCC-w will appear as a line only when the data is plotted versus $s + p_{net}$ instead of pure suction as shown in Figure 1. It is evident from Figure 1 that using the common procedure of drawing a horizontal line or a straight line through the initial data points, and a best fit through the rest of the data to determine AEV (shown by long and short dashed lines) can lead to gross miscalculations of AEV. The true AEV is the value of suction corresponding to the intersection of the two straight lines representing the steeply inclined saturated section of the response and the tangent to the initial portion of the desaturation response. The task of correctly identifying AEV becomes further exacerbated when the slopes of the lines before and after AEV are of similar magnitude as depicted in Figure 1b.

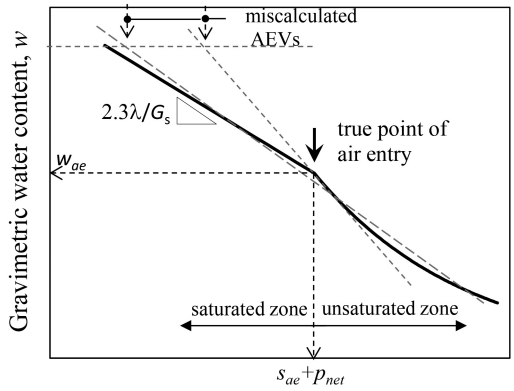


Figure 1. Schematic SWCCs for normally consolidated soils or soils with $p_{net} = p'_c$ presented in terms of water content with possible miscalculated AEVs, with (a) different, and (b) similar, slopes before and after the point of air entry.

3.2 *Overconsolidated soil* $p'_c < p_{net} + s_{ae}$

For the case of overconsolidated soils where $p'_c < p_{net} + s_{ae}$, the total form of SWCC-w in a semi-log plane can in turn be derived as follows:

For $s + p_{net} < p'_c < s_{ae} + p_{net}$:

$$w = w_0 - \frac{2.3\kappa}{G_s}\log\left(\frac{s+p_{net}}{s_0+p_{net}}\right); \quad (5a)$$

for $p'_c < s + p_{net} < s_{ae} + p_{net}$:

$$w = w_0 - \frac{2.3\kappa}{G_s}\log\left(\frac{p'_c}{s_0+p_{net}}\right) - \frac{2.3\lambda}{G_s}\log\left(\frac{s+p_{net}}{p'_c}\right) \quad (5b)$$

and for $p'_c < s_{ae} + p_{net} < s + p_{net}$:

$$w = w_0 - \frac{2.3\kappa}{G_s}\log\left(\frac{p'_c}{s_0+p_{net}}\right) - \frac{2.3\lambda}{G_s}\log\left(\frac{s+p_{net}}{p'_c}\right) \quad (5c)$$

in which

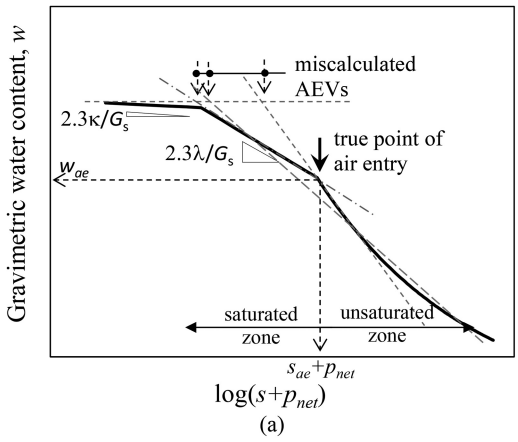
$$w_{ae} = w_0 - \frac{2.3\kappa}{G_s}\log\left(\frac{p'_c}{s_0+p_{net}}\right) - \frac{2.3\lambda}{G_s}\log\left(\frac{s_{ae}+p_{net}}{p'_c}\right) \quad (5d)$$

The graphical representation of Equations (5), in terms of water content versus $s + p_{net}$, is given in Figure 2. Again, it is evident that using the usual approaches to determination of AEV from SWCC-$w$may lead to gross miscalculations. Of particular interest in this case is that the preconsolidation pressure, p'_c, is directly reflected in SWCC-w as a break point at the value of suction equal to $p'_c - p_{net}$ (first break point in Figure 2). At this break point, the soil is still saturated, and the stress state of the soil has merely changed from overconsolidated to normally consolidated. In the literature, this break point is often taken, by mistake, as the point of air entry for the soil.

3.3 *Overconsolidated soil* $p'_c > p_{net} + s_{ae}$

For the case of overconsolidated soils where $p'_c > p_{net} + s_{ae}$, the total form of SWCC-w in semi-log plane can be derived as:

$$w = \begin{cases} w_0 - \dfrac{2.3\kappa}{G_s}\log\left(\dfrac{s+p_{net}}{s_0+p_{net}}\right) & ; s < s_{ae} \quad (6a) \\ w_{ae}\left((1-S_{res})\left(\dfrac{s_{ae}}{s}\right)^{\lambda_p} + S_{res}\right) & ; s > s_{ae} \quad (6b) \end{cases}$$



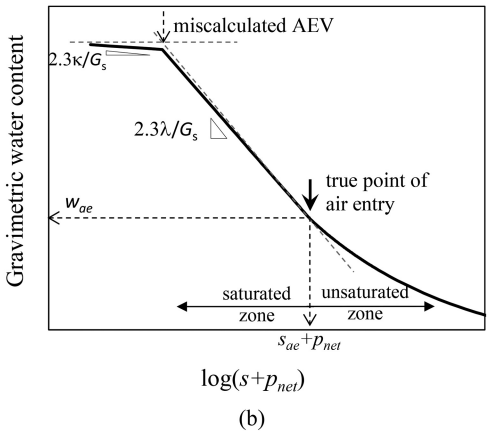


Figure 2. Schematic SWCCs for overconsolidated soils with $p_c' < p_{net} + s_{ae}$ presented in terms of water content with possible miscalculated AEVs, with (a) different, and (b) similar, slopes before and after the point of air entry.

where

$$w_{ae} = w_0 - \frac{2.3\lambda}{G_s}\log\left(\frac{s_{ae}+p_{net}}{s_0+p_{net}}\right) \quad (6c)$$

A schematic representation of SWCC-*w* for overconsolidated soils with $p_c' > p_{net} + s_{ae}$, is presented in Figure 3. As shown, the evaluation of AEV is less prone to error in this case compared to normally consolidated and/or overconsolidated soils with $p_c' < p_{net} + s_{ae}$.

For overconsolidated soils with $p_c' > p_{net} + s_{ae}$, the soil volume change during application of suction is small, and the preconsolidation pressure of the soil does not feature in SWCC-*w* response of the soil. More precisely, SWCC-*w* will only show a single break point, corresponding to the point of air entry. In this case, the slope of the saturated portion of the curve is dependent upon the slope of unloading-reloading curve in $v \sim lnp$ plane, k, and the common approach of defining AEV at the intersection of the two straight portions of the water retention response will yield an accurate estimation of AEV. Note that in the general case of non-zero net mean stress, in order to calculate

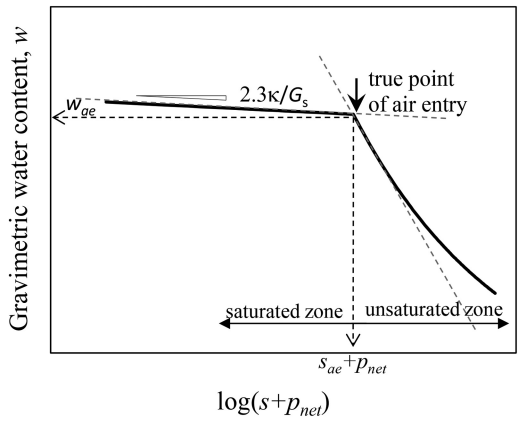


Figure 3. Schematic SWCC for overconsolidated soils with $p_c' > p_{net} + s_{ae}$ presented in terms of water content.

the AEV the value of the horizontal axis at the point of air entry should be reduced by p_{net}.

4 PROPOSED METHOD FOR DETERMINATION OF AEV FROM SWCC-W

From the examples provided, it is evident that the suction corresponding to AEV may not always coincide with a clear break point in a SWCC-*w* plotted in a semi-log plane. In fact, in some cases, more than one break may also be identified in the SWCC−*w* plot for a soil. These cases have been proven to be difficult to handle in the literature as the existing approaches for determination of AEV from SWCC data can lead to erroneous estimations.

In order to minimize error in the determination of AEV, particularly for the cases highlighted above, it is suggested that the gravimetric water content data are plotted versus $s + p_{net}$ (suction plus net mean stress) on the semi-log scale and versus s (suction) on the log-log scale, in the same graph. A secondary vertical axis within the same range of values used for the primary axis may be adopted for this purpose; e.g. see Figure 4 for the previously discussed case of overconsolidated soils with $p_c' < p_{net} + s_{ae}$. As shown, plotting data in the two mentioned scales has the following advantages: 1) According to the existing SWCC models and based on numerous experimental data, by plotting SWCC in a log-log scale, the unsaturated part of the response may be represented by a straight line, with a slope related to the pore size distribution index of the soil, λ_p. Therefore, in the log-log scale the unsaturated part of the response can be readily distinguished by a linear behaviour. On the other hand, in the semi-log plane it is the saturated part of the curve that is identified by a linear or bilinear behaviour depending on the soil stress history. Hence, the two curves are complementary, and when drawn together on a single graph results in an easier identification of AEV. In this approach, the AEV is identified as the point

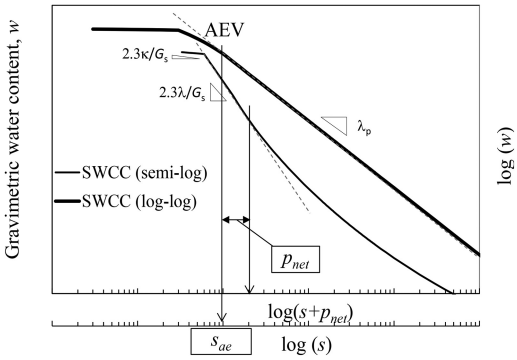


Figure 4. Schematic SWCC for overconsolidated soils with $p'_c < p_{net} + s_{ae}$ presented in terms of gravimetric water content in both semi-log and log-log scales (for $s_{res} = 0$) along with the proposed method to determine AEV.

where the saturated data deviate from the straight line drawn to the unsaturated part of the plot on the log-log scale. Also on the semi-log scale, the unsaturated data deviate from the line drawn through the saturated part of the plot at the air entry point where the AEV can be calculated by subtracting p_{net} from the value of the horizontal coordinate at the separation point on the semi-log plot. The two curves should yield the same values air entry suction which can be regarded as the AEV of the soil. The slopes of the above-mentioned linear parts also have clear physical meanings, and can be utilised to calculate soil parameters for the purposes of constitutive modelling; 2) Drawing two plots with two different scales in the same graph also minimizes the possibility of missing or misrepresenting the location of the point of air entry when the slopes of the SWCC-w graph before and after AEV are similar (see Figure 4). Even if the break may not be detectable on one or both of the plots, it will be possible to determine the AEV by locating the suction value at which data depart from linear/bilinear responses on both plots.

For the case of overconsolidated soils with $p'_c < p_{net} + s_{ae}$ (Figure 4), the first break in the SWCC-w plot corresponds to the preconsolidation pressure of the soil and must not be taken as AEV. For these soils, the air entry will occur at a greater suction which may or may not appear as a distinct break in the SWCC-w graph, plotted on a semi-log plane. As such, in an overconsolidated soil, if two break points appear in the SWCC-w graph, the first point is likely to be due to the preconsolidation pressure of the soil, and only the second break point may be related to AEV. The most difficult SWCC-w graphs to interpret are those in which the soil is overconsolidated but it contains only a single break point as shown in Figure 4. In such cases, without a knowledge of the preconsolidation pressure of the soil, or adopting the two scale plotting approach proposed, it will be very difficult if not impossible to identify the point of air entry and in all likelihood the sudden change in the slope of SWCC-w will be taken as AEV, which may not be correct. Despite this, none of the existing mathematical expressions presented in the literature for modelling SWCC-w take this potential source of error into account and consider the first change in the slope of SWCC-w as AEV, irrespective of the stress history of the soil (e.g. Fredlund and Xing 1994; Pham and Fredlund 2008; van Genuchten 1980).

Another advantage of the method proposed is that it essentially eliminates the need for measuring the volume change of the sample during SWCC test. Correct estimation of AEV is possible by simply plotting SWCC$-w$ on two semi-log and log-log scales and identifying the linear parts of each plot. Provided due attention is given to the possibility of having a bilinear response in the initial part of the semi-log graph, AEV can be estimated with limited or no data on the stress history of the sample or volume change of the sample during the test. Such estimation of AEV will not be possible using the common semi-log plots of SWCC$-w$ data. At this point it is important to note that AEV is not a unique property of soil and it varies with volume change, stress history, the way a sample is prepared, etc. Therefore, discussions in this paper pertain only to the determination of AEV for a given soil with a given stress history, void ratio, structure and fabric.

5 EXPERIMENTAL VALIDATION

In this section, the application of the proposed method to determine AEV and other soil parameters from SWCC data is investigated using the experimental data for three different categories of soils discussed in previous sections.

The first data taken from Fredlund and Houston (2013), pertains to a SWCC test on the highly plastic Regina Clay prepared from slurry and preconsolidated under a very small load prior to SWCC testing which falls in the category of normally consolidated soils as described previously. The test was performed on drying path of SWCC at zero net mean stress ($p_{net} = 0$).

The experimental SWCC-w data are presented in Figure 5, plotted both in semi-log and log-log planes. Two linear parts in the curves are identified: one representing the saturated region on the semi-log plot, and the other representing the unsaturated region on the log-log plot. The point of departure from linear behaviour in each of the plots is identified as the AEV of the soil with $s_{ae} = 4000$ kPa. The slopes of the two straight lines in Figure 5a can also be used to calculate: $\lambda = 0.249$, and $\lambda_p = 0.43$. Figure 5b confirms that the estimated AEV agrees very well with AEV obtained from SWCC-S data. Also notice that the form of SWCC-S remains unaffected by the stress history as the influence of volume change during testing is included in the data reduction of the water retention test results. This again confirms that when volume change data during testing is available, the most appropriate form of presentation of water retention results is SWCC-S.

The second data is related to a SWCC test on a soil mixture of 20% pure Speswhite kaolin, 10% London

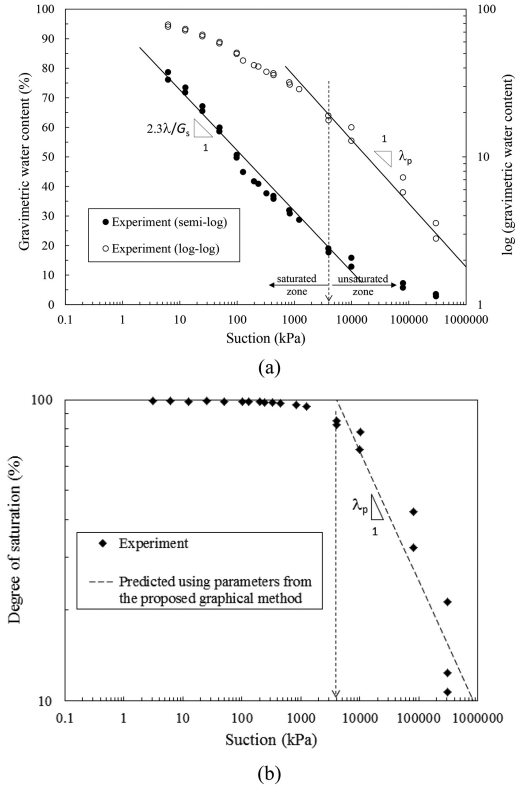


Figure 5. Drying path SWCC of normally consolidated Regina clay at zero net mean stress: (a) Experimental data in SWCC-*w* space along with the proposed graphical method to obtain parameters and (b) Experimental data in SWCC-*S* space along with the predicted curve using the parameters from the graphical method (Data after Fredlund and Houston 2013).

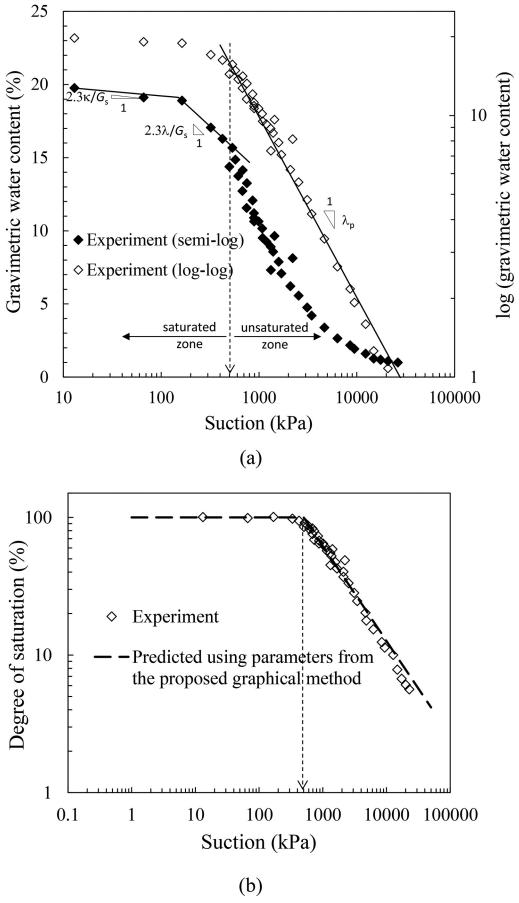


Figure 6. Drying path SWCC of a clay-silt mixture at zero net mean stress: (a) Experimental data in SWCC-*w* space along with the proposed graphical method to obtain parameters and (b) Experimental data in SWCC-*S* space along with the predicted curve using the parameters from the graphical method (Data after Cunningham et al. 2003).

clay and 70% HPF4 silica silt reported by Cunningham et al. (2003). The reconstituted sample was prepared in oedometer to a vertical effective stress of 200 kPa before the SWCC test and hence it falls in the category of overconsolidated soils. Finally, the third test have been performed by the authors on a mixture of 65% Sydney sand and 35% Kaolin clay. This sample was prepared from slurry and was preconsolidated to a high vertical stress of 400 kPa in oedometer prior to the water retention test. The test was performed on drying path at zero net mean stress ($p_{net} = 0$).

Figure 6a presents the drying path SWCC-*w* of the soil using both semi-log and log-log scales according to the proposed method. Two pronounced breaks are identified in the semi-log plot. The first one, at a lower suction, is due to the preconsolidation of the soil, and the second one, at a higher suction, is attributed to the AEV, which is estimated as 500 kPa. Using the proposed graphical technique, a bilinear curve is fitted to the experimental points prior to AEV on the semi-log plot in Figure 6a, representing the soil behaviour in the saturated zone. Another line is drawn through the experimental data on the log-log plot, representing the response in the unsaturated zone. Once again, the point of deviation from the linear behaviour in both plots is defined as the air entry point (Figure 6a). Other model parameters obtained from the data are: $\kappa = 0.007$; $\lambda = 0.07$; and $\lambda_p = 0.69$. It is noted that the first break occurs at a suction value of 150 kPa, which is slightly lower than the vertical preconsolidation pressure of the sample (i.e. 200 kPa). This is due to the difference between the isotropic preconsolidation pressure, captured during suction loading, and that corresponding to oedometric consolidation obtained from the one-dimensional loading of the sample. Similar to the previous examples, the same AEV and λ_p are obtained from SWCC-*S* data as shown in Figure 6b.

The third example is related to Thu et al. (2007) data on coarse kaolin classified as high plasticity silt (MH). The sample was compacted at maximum dry density and optimum water content and then subjected to a net confining stress of 100 kPa. The SWCC was performed on the sample without removing the stress.

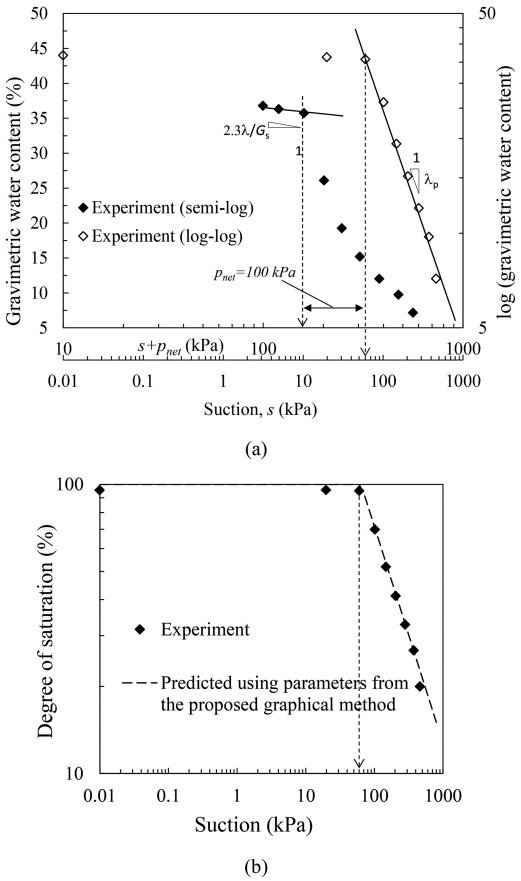


Figure 7. Drying path SWCC of a compacted silt at 100 kPa net mean stress: (a) Experimental data in SWCC-*w* space along with the proposed graphical method to obtain parameters and (b) Experimental data in SWCC-*S* space along with the predicted curve using the parameters from the graphical method (Data after Thu et al. 2007).

The experimental SWCC-*w* for this sample is plotted in Figure 7a in both log-log and semi-log scales according to the proposed method. A single break point is observed in the semi-log and log-log SWCC-*w* plots with the corresponding suction value less than 100 kPa from both curves. The slope of the linear part before this break point in the semi-log plot is very low and around the re-compression index, κ, of reported for the soil. This soil falls under the category of overconsolidated soils with $p_c' > p_{net} + s_{ae}$ which is due mainly to the sample preparation method described above. The proposed method yields an AEV of 60 kPa, and also a λ_p of 0.74 which is consistent with the experimental SWCC-*S* as shown in Figure 7b.

6 CONCLUSIONS

Pitfalls in the interpretation of water content based SWCC and evaluation of AEV are discussed. Different forms of SWCC-*w* corresponding to different stress histories are examined. It is shown that extreme caution should be exercised in the interpretation of water retention data presented in terms of gravimetric water content versus suction. Specifically, it has been shown that methodologies which do not take into account the stress history of soil may yield grossly erroneous estimations of AEV. Where volume change data are measured; i.e. during the water retention test, the SWCC should be presented in terms of degree of saturation versus suction for the correct estimation of AEV. For cases in which volume change is not measured, a simple graphical technique is proposed for the evaluation of AEV from the SWCC data presented in terms of gravimetric water content. The validity and application of the model are demonstrated using experimental data from the literature.

REFERENCES

Abriola, L.M., and Pinder, G.F. 1985. A multiphase approach to the modeling of porous media contamination by organic compounds. 1. Equation development. Water resources research, 21(1): 11–18.

Bishop, A.W. 1959. The principle of effective stress

Brooks, R.H., and Corey, A.T. 1964. Hydraulic properties of porous media. Hydrology Papers, Colorado State University(March).

Cunningham, M.R., Ridley, A.M., Dineen, K., and Burland, J.B. 2003. The mechanical behaviour of a reconstituted unsaturated silty clay. Géotechnique, 53(2): 183–194.

Fredlund, D., Morgenstern, N., and Widger, R. 1978. The shear strength of unsaturated soils. Canadian Geotechnical Journal, 15(3): 313–321.

Fredlund, D.G., and Xing, A. 1994. Equations for the soil-water characteristic curve. Canadian Geotechnical Journal, 31(4): 521–532.

Fredlund, D.G., and Houston, S.L. 2013. Interpretation of soil-water characteristic curves when volume change occurs as soil suction is changed. In Advances in Unsaturated Soils, CRC Press. pp. 15–31.

Guan, G., Rahardjo, H., and Choon, L. 2010. Shear Strength Equations for Unsaturated Soil under Drying and Wetting. Journal of Geotechnical and Geoenvironmental Engineering, 136(4): 594–606.

Hillel, D. 1980. Fundamentals of soil physics. Academic Press, Inc.(London) Ltd.

Khalili, N., and Khabbaz, M.H. 1998. A unique relationship for χ for the determination of the shear strength of unsaturated soils. Géotechnique, 48(5): 681–687.

Khalili, N., Geiser, F., and Blight, G.E. 2004. Effective stress in unsaturated soils: Review with new evidence. International Journal of Geomechanics, 4(2): 115–126.

Khalili, N., Habte, M.A., and Zargarbashi, S. 2008. A fully coupled flow deformation model for cyclic analysis of unsaturated soils including hydraulic and mechanical hystereses. Computers and Geotechnics, 35(6): 872–889.

Matyas, E.L., and Radhakrishna, H.S. 1968. Volume Change Characteristics of Partially Saturated Soils. Géotechnique, 18: 432–448.

Ng, C., and Pang, Y. 2000. Influence of Stress State on Soil-Water Characteristics and Slope Stability. Journal of Geotechnical and Geoenvironmental Engineering, 126(2): 157–166.

Pham, H.Q., and Fredlund, D.G. 2008. Equations for the entire soil-water characteristic curve of a volume change soil. Canadian Geotechnical Journal, 45(4): 443–453.

Sillers, W.S., Fredlund, D.G., and Zakerzaheh, N. 2001b. Mathematical attributes of some soil-water characteristic curve models. Geotechnical and Geological Engineering, 19(3–4): 243–283.

Thu, T.M., Rahardjo, H., and Leong, E.C. 2007. Soil-water characteristic curve and consolidation behavior for a compacted silt. Canadian Geotechnical Journal, 44(3): 266–275.

van Genuchten, M.T. 1980. A closed-form equation for predicting the hydraulic conductivity of unsaturated soils. Soil Science Society of America Journal, 44(5): 892–898.

Vanapalli, S., Sillers, W., and Fredlund, M. The meaning and relevance of residual state to unsaturated soils. In 51st Canadian Geotechnical Conference, Edmonton, Alberta, October 4–7, 1998.

Vanapalli, S., Fredlund, D., and Pufahl, D. 1999. The influence of soil structure and stress history on the soil–water characteristics of a compacted till. Géotechnique, 49(2): 143–159.

Zargarbashi, S., and Khalili, N. 2012. Discussion of "Shear Strength Equations for Unsaturated Soil under Drying and Wetting" by Goh Shin Guan, Harianto Rahardjo, and Leong Eng Choon. Journal of Geotechnical and Geoenvironmental Engineering, 137(12): 1310–1313.

Zhai, Q., and Rahardjo, H. 2012. Determination of soil-water characteristic curve variables. Computers and Geotechnics, 42: 37–43.

Unsaturated Soil Mechanics—from Theory to Practice – Chen et al. (Eds)
© 2016 Taylor & Francis Group, London, ISBN 978-1-138-02921-7

Non-isothermal water retention curve and volume change equation for unsaturated soils

A.N. Zhou & J. Li
School of Civil, Environmental and Chemical Engineering, Royal Melbourne Institute of Technology (RMIT), Melbourne, Australia

D. Sheng
Centre for Geotechnical and Materials Modelling, School of Engineering, The University of Newcastle, NSW, Australia

ABSTRACT: This study presents a simple approach to model the effect of temperature on the Soil-Water Retention Curves (SWRCs) of deformable soils and takes into consideration the following two aspects: (1) the effect of temperature on the liquid–gas interfacial tension and (2) temperature-induced deformation of the soil skeleton. The first aspect, the temperature effect, can be modelled using an equation proposed by Grant and Salehzadeh, but the second aspect is generally neglected in the literature. To quantify the thermo-hydro-mechanical (THM) deformation of unsaturated soils (i.e., the second aspect mentioned above), a simple volume change equation, referred to as the non-isothermal SFG volumetric equation, is proposed on the basis of the original SFG framework. A three-dimensional THM yield surface in the space of net mean stress, suction and temperature is presented here. The proposed volume change equation is integrated into the non-isothermal SWRC by means of a simple hydro-mechanical coupling law. A number of experimental results reported in the literature are employed to confirm the validity of the proposed non-isothermal SFG volume change equation and the non-isothermal SWRC equation.

1 INTRODUCTION

In this study, an alternative approach to describing thermal effects on SWRCs for deformable soils is presented. The thermal effect (dT) is separated into two parts: the effect on the liquid–gas interfacial tension ($\partial\sigma^{lg}/\partial T$) and the effect on the thermal deformation ($\partial e/\partial T$), both of which affect the soil–water retention behaviour (dS_e), as shown in Figure 1. The thermal deformation ($\partial e/\partial T$) is quantified by the proposed volume change equation (i.e., the non-isothermal SFG model). The non-isothermal SFG model is then integrated into the proposed SWRC equation via the coupling method presented in Sheng and Zhou (2011). This study is organised as follows. The first part of the paper addresses the quantification of thermal effects on SWRCs and proposes a new equation for the saturation variation caused by temperature change, which involves the temperature-induced volume change and the hydraulic response coupled with it. In the second part of the paper, a non-isothermal SFG volumetric model based on the SFG framework (Sheng *et al.*, 2008) is proposed to quantify the temperature-induced volume change under an arbitrary suction and net stress. The third part of the paper presents a numerical study of the proposed non-isothermal SWRC equation into which the non-isothermal SFG volume change equation is embedded. In the final part of the paper, the proposed non-isothermal SFG volumetric model and non-isothermal SWRC equation are validated against experimental data.

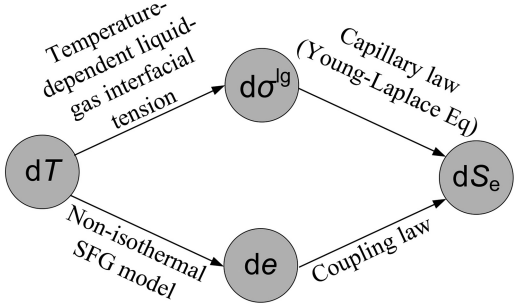


Figure 1. Scheme to model thermal effects on SWRCs of deformable soils.

2 INTERPRETING THERMAL EFFECTS ON WATER RETENTION BEHAVIOUR

2.1 *Saturation variation for undeformable soil due to temperature change*

The effective degree of saturation (S_e) of a soil under a given suction can be theoretically derived based on

the normalised cumulative distribution function of soil pores, $F(r)$, which ranges between 0 and 1. $F(r)$ stands for the fraction of the volume of pores that are greater than an arbitrary pore radius (r) to the total volume of pores. $F(r)$ can be integrated from the renormalised pore size distribution function, $\bar{f}(r)$, by assuming that the pore network of a soil has a simple geometric configuration. It should be noted that $\bar{f}(r)$ does not include the micropores whose pore water cannot be desorbed by drying. If pores greater than an arbitrary pore radius are dewatered by applying a matric suction, the effective degree of saturation is given by

$$S_e = 1 - F(r) = 1 - \int_r^{r_{max}} \bar{f}(r)\mathrm{d}r \tag{1}$$

where r is an arbitrary pore radius. The key relationship to connect the normalised cumulative distribution function of soil pores with the soil–water retention behaviour is the capillary law (i.e., the Young–Laplace equation in Figure 1), which can be expressed as follows:

$$s = \frac{2\sigma^{lg}\cos\theta}{r} = \frac{2\sigma^{lg}}{r} \tag{2}$$

where s is the matric suction, which is equal to the capillary pressure; σ^{lg} is the liquid–gas interfacial tension; and θ is the liquid–solid contact angle, which is usually treated as zero for simplicity Combining equations (2) and (1), we can derive the relationship between the effective degree of saturation and suction (i.e., SWRC). However, in practice, the laboratory method to determine the pore size distribution function of a soil (e.g., the mercury intrusion method) is still relatively complicated. Therefore, the soil–water retention behaviour is usually measured by a phenomenological method, i.e., through suction-controlled drying/wetting tests. However, equations (1) and (2) still reveal the important interrelationship among the effective degree of saturation, the pore radius and distribution, the liquid–gas interfacial tension and the matric suction in theory. Let us assume that van Genuchten's equation represents soil–water retention behaviour under conventional laboratory conditions (i.e., no temperature change, suction-relevant deformation only), i.e.,

$$S_e = \frac{S_r - S_r^{res}}{1 - S_r^{res}} = \left(1 + (s/a)^n\right)^{-m} \tag{3}$$

where S_r^{res} is the residual degree of saturation and a, n, and m are three fitting parameters related to the pore size distribution. The normalised cumulative distribution function, $F_0(r)$, of soil pores corresponding to van Genuchten's SWRC equation at laboratory temperature T_0 can be derived by combining equations (1), (2) and (3):

$$F_0(r) = 1 - \left(1 + \left(\frac{2\sigma_0^{lg}}{a}\frac{1}{r}\right)^n\right)^{-m} \tag{4}$$

where σ_0^{lg} is the liquid–gas interfacial tension at temperature T_0. The soil is assumed to be undeformable with temperature change, which implies that all soil pores are unchanged at different temperatures, i.e., $F(r) = F_0(r)$, where $F(r)$ is the normalised cumulative distribution function at an arbitrary temperature. Temperature change only affects the liquid–gas interfacial tension term in the capillary law, i.e., $r = 2\sigma_T^{lg}/s$ at temperature T. The effective degree of saturation at temperature T can be written as

$$S_e = 1 - F(r) = \left(1 + \left(\frac{2\sigma_0^{lg}}{a}\frac{s}{2\sigma_T^{lg}}\right)^n\right)^{-m} \tag{5}$$

where σ_T^{lg} is the liquid–gas interfacial tension at temperature T. Philip and de Vries (1957) presented a linear function to qualify the thermal effect on the liquid–gas interfacial tension, i.e.:

$$\sigma_T^{lg} = a' + b'T \tag{6}$$

where a' and b' are two fitting parameters. Grant and Salehzadeh (1996) calibrated the values of parameters a' and b', which can be set to 0.1177 ($\mathrm{Nm^{-1}}$) and -0.0001535 ($\mathrm{Nm^{-1}K^{-1}}$) for the pure water and air interface. Substituting equation (6) into equation (5) yields

$$S_e = 1 - F(r) = \left(1 + \left(\frac{\beta' + T_0}{\beta' + T}\frac{s}{a}\right)^n\right)^{-m} \tag{7}$$

where $\beta' = a'/b' = -766.7K$. Equation (7) was first proposed by Grant and Salehzadeh (1996) to model the thermal effect on soil–water retention behaviour. The pore size distribution of the soil is assumed to be unchanged in deriving the equation above. That is, $F(r)$ is assumed to remain unchanged with changes in temperature (the expression of $F(r)$ and all fitting parameters a, n, and m are assumed to be independent of temperature.).

2.2 *Saturation variation due to volume change*

Soil, however, is deformable, and temperature change may lead to either elastic or elastoplastic soil deformation. Sheng and Zhou (2011) proposed an incremental relationship between the effective degree of saturation (S_e) and the void ratio (e) to model the change in the soil–water retention behaviour due to volume change (i.e., the coupling law in Figure 1):

$$\mathrm{d}S_e = \left(\frac{S_e}{e}(1 - S_e)^{\zeta}\right)\mathrm{d}e \tag{8}$$

where e is the void ratio; ζ is a fitting parameter for hydro-mechanical coupling, the calibration method and detailed discussion of which can be found in Sheng and Zhou (2011); and de is the void ratio change due

to external factors such as stress and temperature. Suction change can also induce volume change, but this volume change is incorporated into SWRC equations in the process of determining fitting parameters via laboratory tests. A gross approximation of the value of this parameter for silty clay and silt is in the range of 0.05 to 0.25, based on a number of experimental results (see Zhou *et al*. 2012). In this study, the value of the parameter ζ is set to 0.1.

2.3 *Saturation variation for deformable soil due to temperature change*

The temperature-induced saturation change under an arbitrary suction can therefore be attributed to the following two aspects: (1) the variation in S_e due to gas–liquid interfacial tension change at different temperatures and (2) the variation in S_e due to thermal volume change. This interpretation can be formularised as follows:

$$\mathrm{d}S_\mathrm{e} = \left(\frac{\partial S_\mathrm{e}}{\partial \sigma^{\mathrm{lg}}} \frac{\partial \sigma^{\mathrm{lg}}}{\partial T} + \frac{\partial S_\mathrm{e}}{\partial e} \frac{\partial e}{\partial T} \right) \mathrm{d}T \tag{9}$$

where

$$\begin{cases} \dfrac{\partial S_\mathrm{e}}{\partial \sigma^{\mathrm{lg}}} = mn \dfrac{S_\mathrm{e}\left(1 - S_\mathrm{e}^{1/m}\right)}{a' + b'T} \\ \dfrac{\partial \sigma^{\mathrm{lg}}}{\partial T} = b', \ \dfrac{\partial S_\mathrm{e}}{\partial e} = \dfrac{S_\mathrm{e}}{e}(1 - S_\mathrm{e})^{\zeta} \end{cases} \tag{10}$$

Substituting Eq. (10) into Eq. (9) yields

$$\mathrm{d}S_\mathrm{e} = \left(mn \frac{S_\mathrm{e}(1 - S_\mathrm{e}^{1/m})}{\beta' + T} + \frac{S_\mathrm{e}}{e}(1 - S_\mathrm{e})^{\zeta} \frac{\partial e}{\partial T} \right) \mathrm{d}T \tag{11}$$

The initial value of the effective degree of saturation (S_e^0) can be found from the reference SWRC equation (i.e., SWRC at the reference temperature T_0; see equation (3)). Once the reference SWRC is determined, the saturation variation at an arbitrary suction due to temperature change (i.e., $T - T_0$) can be determined via equation (11). The SWRC at an arbitrary temperature (T) can be determined by applying equation (11) to the entire suction range, i.e.,

$$S_\mathrm{e} = S_\mathrm{e}^0 + \int_{T_0}^{T} \mathrm{d}S_\mathrm{e} \tag{12}$$

In equation (11), the term $\partial e/\partial T$ is still unspecified. This term stands for the thermal deformation (i.e., the variation in the void ratio due to temperature change), which should be known a priori before equation (11) is applied. The thermal deformation ($\partial e/\partial T$) that is related to the net stress, suction and temperature can be specified through the non-isothermal SFG model presented in the next section. If $\partial e/\partial T$ is set to zero, the proposed model reduces to Grant and Salehzadeh's model.

3 THERMAL DEFORMATION OF UNSATURATED SOILS

In this section, the volume change equation of the SFG model (Sheng *et al.*, 2008) is extended from isothermal to non-isothermal states to capture the temperature effect on the volume change of unsaturated soils. This proposed volume change equation (i.e., the non-isothermal SFG model) can be used to specify the term $\partial e/\partial T$ in equation (11).

3.1 *SFG Volume change equation under an isothermal conditions: a brief review*

The SFG framework (Sheng *et al.*, 2008) employs net stress and suction as two fundamental constitutive variables. The key equation of the SFG framework is a volume change model (referred to herein as the original or isothermal SFG model). Zhou and Sheng (2009) provided a systematic experimental validation of the SFG framework, including its volume change equation, yield surfaces and shear strength criterion. The SFG volume change equation is presented as follows:

$$\mathrm{d}v = -\frac{\lambda_{\mathrm{vp}}}{\bar{p} + s}\mathrm{d}\bar{p} - \frac{\lambda_{\mathrm{vs}}}{\bar{p} + s}\mathrm{d}s \tag{13}$$

where v is the specific volume ($=1 + e$), $\bar{p}$ is the net mean stress ($=p - u_\mathrm{a}$, where p is the total mean stress), λ_{vp} is the elastoplastic compression index related to the increase in the net mean stress, and λ_{vs} is the elastoplastic compression index related to the increase in suction, expressed as follows:

$$\lambda_{\mathrm{vs}} = \begin{cases} \lambda_{\mathrm{vp}} & s \le s_{\mathrm{sa}} \\ \lambda_{\mathrm{vp}} \dfrac{s_{\mathrm{sa}}}{s} & s > s_{\mathrm{sa}} \end{cases} \tag{14}$$

where s_{sa} is the maximum suction at which the soil can remain fully saturated. In practice, for simplicity, this term can be considered equal to the air entry value (s_e). Equations (13) and (14) can only be applied to the elastoplastic response of a soil. With respect to elastic deformation ($\mathrm{d}v^\mathrm{e}$), the elastic compression index (κ_{vp}) should be used in place of the elastoplastic compression index (λ_{vp}) in equations (13) and (14).

In the SFG framework, the yield surface can be derived based on the volume change equation, i.e., equation (13). For unsaturated soils, the relationship between the yield stress ($\bar{p}_0$) at zero suction (i.e., the intersection between the yield surface and the axis of net mean stress) and the current yield stress ($\bar{p}$) at an arbitrary suction level (s) can be written as follows:

$$\begin{cases} \bar{p} = \bar{p}_0 - s \ \ (\text{if } s < s_{\mathrm{sa}}) \\ \bar{p} = \bar{p}_0 - s_{\mathrm{sa}} - s_{\mathrm{sa}} \ln \dfrac{s}{s_{\mathrm{sa}}} \ \ (\text{if } s \ge s_{\mathrm{sa}}) \end{cases} \tag{15}$$

where $\bar{p}$ is the current yield stress under suction s and $\bar{p}_0$ is the preconsolidation pressure when $s = 0$.

This yield surface can be applied to describe the drying process (increasing s) under constant net stresses ($\bar{p} = const$). Sheng *et al.* (2008) addressed the fact that loading of an unsaturated soil can change the shape of the yield surface, which can be used to interpret the loading–collapse behaviour of an unsaturated soil. For an unsaturated soil, loading under constant suction ($\bar{p} \to \bar{p}_n$) leads to a new yield surface (i.e., the loading–collapse surface):

$$\begin{cases} \bar{p}_n = \bar{p}_{n0} - s \quad (\text{if } s < s_{sa}) \\ \bar{p}_n = \dfrac{\bar{p}_{n0}}{\bar{p}_0}\left(\bar{p}_0 + s - s_{sa} - s_{sa}\ln\dfrac{s}{s_{sa}}\right) - s \quad (\text{if } s \geq s_{sa}) \end{cases} \tag{16}$$

where $\bar{p}_{n0}$ is the new yield stress at zero suction for the yield surface after loading. When $\bar{p}_{n0} = \bar{p}_0$, equation (15) is identical to equation (16). A typical loading process on an unsaturated soil sample can be described by Eqs (15) and (16), as shown in Figure 2.

Drying from the initial state (from A_0 to Y in Figure 2) leads to expansion of the yield surface from A_0B_0 to AB. In terms of the drying process, the shape of the yield surface remains unchanged (i.e., equation (15)). The loading under unsaturated states (from Y to Y′) will move and reshape the yield surface (the AB surface) to a new yield surface (the A′B′ surface) that indicates the collapse potential if wetting occurs. The elastoplastic volumetric strain ($d\varepsilon_v^p$) can be expressed via the yield stress at zero suction ($\bar{p}_{x0} = \bar{p}_0$ or $\bar{p}_{n0}$ subject to drying or loading) which obeys the conventional stress–strain relationship for saturated soils:

$$d\varepsilon_v^p = \frac{\lambda_{vp} - \kappa_{vp}}{1+e}\frac{d\bar{p}_{x0}}{\bar{p}_{x0}} \tag{17}$$

where $\bar{p}_{x0} = \bar{p}_0$ and $d\bar{p}_{x0} = d\bar{p}_0$ when equation (15) applies for the drying process (A_0Y) and $\bar{p}_{x0} = \bar{p}_{n0}$ and $d\bar{p}_{x0} = d\bar{p}_{n0}$ when equation (16) applies for the loading process (YY′). More details about SFG model for isothermal conditions can be found in Sheng *et al.* (2008).

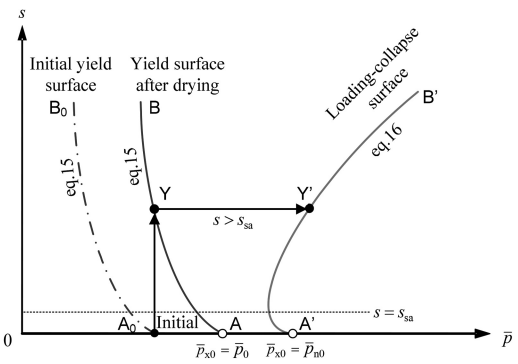


Figure 2. SFG yield surface in isothermal conditions.

3.2 *SFG Volume change equation under non-isothermal conditions*

Analogous to the conventional elastoplasticity method in terms of stress, the following two simple equations are proposed to describe elastic and plastic responses due to temperature change (Yao & Zhou, 2013):

$$d\varepsilon_v^e = \frac{\kappa^T}{1+e}dT,\ d\varepsilon_v^p = \frac{\lambda^T - \kappa^T}{1+e}dT \tag{18}$$

where κ^T is the elastic compression index due to temperature change and λ^T is the elastoplastic compression index due to temperature change. Equation (18) can be used to quantify the term $\partial e/\partial T$ if the yield surface is determined. The thermal deformation appears to be independent of the stress and suction. However, the thermal-induced yielding (yield surface) is related to the temperature, stress and suction, as can be shown by incorporating equation (18) into the original SFG model.

Under non-isothermal conditions, the plastic volumetric strain can be obtained by combining equations (17) and (18):

$$d\varepsilon_v^p = \frac{\lambda_{vp} - \kappa_{vp}}{1+e}\frac{d\bar{p}_{x0}}{\bar{p}_{x0}} + \frac{\lambda^T - \kappa^T}{1+e}dT \tag{19}$$

The yield stress $\bar{p}_{x0}$ can be determined from equation (15) or equation (16), based on the isothermal SFG framework dependent on different drying/loading paths. The elastic volumetric strain for the non-isothermal SFG model can be expressed as follows:

$$d\varepsilon_v^e = \frac{\kappa_{vp}}{1+e}\frac{d\bar{p}}{\bar{p}+s} + \frac{\kappa_{vs}}{1+e}\frac{ds}{\bar{p}+s} + \frac{\kappa^T}{1+e}dT \tag{20}$$

If we set the plastic volumetric strain increment in equation (19) to zero, the yield surface in the plane of the net mean stress ($\bar{p}_{x0}$) at zero suction and temperature (T) can be represented as follows:

$$\bar{p}_{x0}^T = \bar{p}_{x0}^{T_0}\exp\left[-\frac{\lambda^T - \kappa^T}{\lambda_{vp} - \kappa_{vp}}(T - T_0)\right] \tag{21}$$

where $\bar{p}_{x0}^T$ is the yield stress at zero suction and temperature T and $\bar{p}_{x0}^{T_0}$ is the yield stress at zero suction and the reference temperature (T_0). Substituting equation (21) into equation (15), the yield surface in the space of $\bar{p} - s - T$ can be written as follows:

$$\bar{p} = \begin{cases} \bar{p}_0^{T_0}\exp\left[-\dfrac{\lambda^T - \kappa^T}{\lambda_{vp} - \kappa_{vp}}(T - T_0)\right] - s, \ (\text{if } s < s_{sa}) \\ \bar{p}_0^{T_0}\exp\left[-\dfrac{\lambda^T - \kappa^T}{\lambda_{vp} - \kappa_{vp}}(T - T_0)\right] - s_{sa} - s_{sa}\ln\dfrac{s}{s_{sa}}, \ (\text{if } s \geq s_{sa}) \end{cases}$$

where $\bar{p}$ is the yield stress at s and T and $\bar{p}_0^{T_0}$ is the preconsolidation pressure (at zero suction) at the reference temperature (T_0). Following the isothermal SFG

model, mechanical loading ($\overline{p} \to \overline{p}_n$) from the above yield surface leads to the loading–collapse yield surface in the non-isothermal condition (i.e., substituting equation (21) into equation (16)):

$$\overline{p} = \begin{cases} \overline{p}_{n0}^{T_0} \exp\left[-\dfrac{\lambda^T - \kappa^T}{\lambda_{vp} - \kappa_{vp}}\left(T - T_0\right)\right] - s, \ (\text{if } s < s_{sa}) \\ \dfrac{\overline{p}_{n0}^{T_0}}{\overline{p}_0^{T_0}}\left\{\overline{p}_0^{T_0} \exp\left[-\dfrac{\lambda^T - \kappa^T}{\lambda_{vp} - \kappa_{vp}}\left(T - T_0\right)\right] + s - s_{sa} - s_{sa} \ln\dfrac{s}{s_{sa}}\right\} - s, \ (\text{if } s \geq s_{sa}) \end{cases} \tag{23}$$

where $\overline{p}_{n0}^{T_0}$ is the new yield stress at zero suction for the new yield surface after loading under the reference temperature (T_0). Equations (22) and (23) represent the yield surface of the non-isothermal SFG model.

4 EXPERIMENTAL VALIDATIONS

4.1 *Experimental validations of the non-isothermal volume change model*

Uchaipichat (2005) presented a series of non-isothermal suction-controlled compression tests of an unsaturated silt obtained in the Bourke region in Australia. The confining pressure varies from 50 kPa to 500 kPa. Tests were carried out at three different temperature levels: 25°C, 40°C, and 60°C. The suction of samples was set to four different levels for each temperature level: 0, 10 kPa, 100 kPa and 300 kPa. The air entry value (s_e) is estimated to be approximately 20 kPa. The values of the parameters λ^T and κ^T are calibrated to 2.37×10^{-4}(1/°C) and -5.53×10^{-5}(1/°C), respectively.

A compression test at the reference temperature (i.e., room temperature of 25°C) on a fully saturated specimen ($s = 0$) is employed to calibrate the elasto-plastic and elastic compression indices due to the net stress change, as shown in Figure 3a. The values of the compression parameters $\lambda_{vp}$and κ_{vp} are calibrated to 0.09 and 0.008, respectively. At the reference temperature and fully saturated conditions, the pre-consolidation pressure is calibrated to be 200 kPa (i.e. $\overline{p}_0^{T_0} = 200$ kPa). All the predictions for different suction levels and different temperatures are conducted based on the non-isothermal SFG model, i.e., equations (19), (20) and (22). Comparisons between the measured results (data from Uchaipichat, 2005) and predictions for different temperatures and different suctions are shown in Figure 3 (T= 25°C), Figure 4 (T = 40°C), and Figure 5 (T = 60°C). The initial yield stresses predicted by Eq.(22) at different suction levels and temperatures are indicated in each figure. The comparisons between model predictions and test results indicate that the proposed non-isothermal SFG model is capable of predicting: (1) the reduction in yield stress (in terms of net stress) with increasing suction and temperature and (2) the volume change behaviour due to mechanical loading at various temperatures and suction levels.

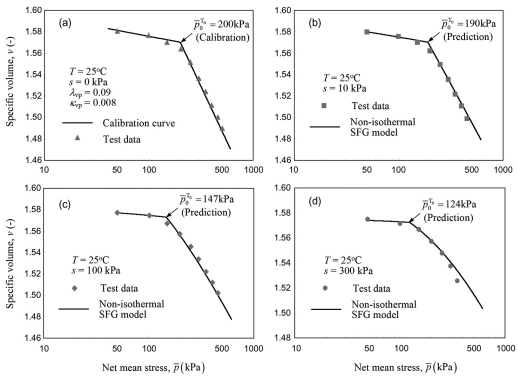


Figure 3. Comparison between measured results for Bourke silt (25°C) and predictions under different suctions (data after Uchaipichat, 2005). (a) $s = 0$ (for calibration), (b) $s = 10$ kPa, (c) $s = 100$ kPa and (d) $s = 300$ kPa.

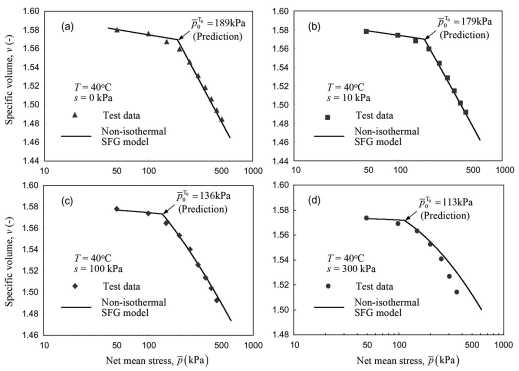


Figure 4. Comparison between measured results for Bourke silt (40°C) and predictions under different suctions (data after Uchaipichat, 2005). (a) $s = 0$, (b) $s = 10$ kPa, (c) $s = 100$ kPa and (d) $s = 300$ kPa.

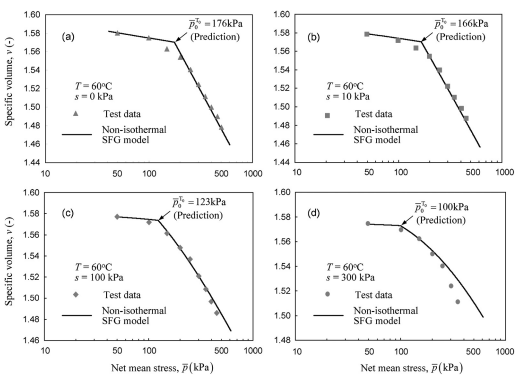


Figure 5. Comparison between measured results for Bourke silt (60°C) and predictions under different suctions (data after Uchaipichat, 2005). (a) $s = 0$, (b) $s = 10$ kPa, (c) $s = 100$ kPa and (d) $s = 300$ kPa.

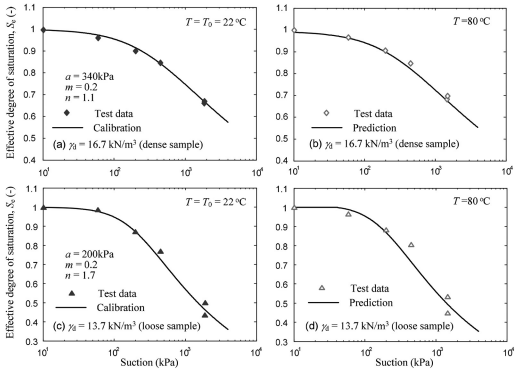


Figure 6. Experimental branches of SWRCs of Boom clay with different initial dry unit weights and calculated curves under different temperatures. (a) dense specimen $\gamma_d = 16.7\,\text{kN/m}^3$ at 22°C, (b) dense specimen $\gamma_d = 16.7\,\text{kN/m}^3$ at 80°C, (c) loose specimen $\gamma_d = 13.7\,\text{kN/m}^3$ at 22°C, (d) loose specimen $\gamma_d = 13.7\,\text{kN/m}^3$ at 80°C (data after Romero *et al.*, 2003).

4.2 *Experimental validations on non-isothermal SWRC equation*

A series of experimental studies (Romero *et al.*, 2003) was conducted on unsaturated Boom clay under non-isothermal conditions for the purposes of constructing engineering barriers for storage and disposal of high-level nuclear water. The Boom clay, obtained from Mol, Belgium, contains 20–30% kaolinite, 20–30% illite and 10–20% smectite. Experimental specimens were prepared at two different dry unit weights ($\gamma_d = 13.7\,\text{kN/m}^3$ and $16.7\,\text{kN/m}^3$) and at two different temperatures (22°C and 80°C). The wetting branch of the SWRCs for the loose specimen ($\gamma_d = 13.7\,\text{kN/m}^3$, $e = 0.932$) was carried out under a constant vertical net stress of 1.2 MPa, and that for the dense specimen ($\gamma_d = 16.7\,\text{kN/m}^3$, $e = 0.591$) was carried out under a constant vertical net stress of 0.085 MPa. Heating for the loose specimen under a high vertical net stress leads to elastoplastic compression because the initial state point is located on the yield surface, but heating for the dense specimen under a low vertical stress leads to elastic swelling only. Equation (18) is adopted to calculate the thermal deformation and determine the value of the term $\partial e/\partial T$ in equation (11). $\lambda^T = 3.65 \times 10^{-4}$ (1/°C), and $\kappa^T = -9.11 \times 10^{-5}$ (1/°C). All the hydraulic parameters are estimated from the SWRCs at a reference temperature of 22°C (see Figure 6a and Figure 6c). The parameter for hydro-mechanical coupling (ζ) is assumed to be 0.1, as mentioned above.

The test results for both the dense and loose specimens at the reference temperature (22°C) are replotted in Figure 6a ($\gamma_d = 16.7\,\text{kN/m}^3$) and Figure 6c ($\gamma_d = 13.7\,\text{kN/m}^3$). The isothermal van Genuchten equation is employed here to fit the test data (see fitting curves in Figure 6a and Figure 6c) and calibrate the hydraulic parameters. The predictions for both the dense and loose specimens at the high temperature (80°C) are performed via the proposed non-isothermal SWRC equation (i.e., equation (11)). Comparisons between the predicted and measured results are shown in Figure 6b ($\gamma_d = 16.7\,\text{kN/m}^3$) and Figure 6d ($\gamma_d = 13.7\,\text{kN/m}^3$). From the comparisons, we can conclude that the proposed non-isothermal SWRC equation can predict the water retention behaviour at different temperatures well.

5 CONCLUSIONS

A non-isothermal SWRC equation that takes into consideration two effects of temperature change is presented in this study. The first thermal effect on SWRC is the change in the liquid–gas interfacial tension due to temperature change. The second thermal effect is the thermal deformation that further affects the SWRC. To determine the thermal deformation in unsaturated soils, the original isothermal SFG model is extended to non-isothermal conditions. Both the non-isothermal SFG model and non-isothermal SWRC equation are validated against experimental data. More details can be found in Zhou, *et al*. (2014).

REFERENCES

Grant, S. A., and Salehzadeh, A. (1996). Calculation of temperature effects on wetting coefficients of porous solids and their capillary pressure functions. *Water Resour. Res.*, **32**(2): 261–270.

Philip, J. R., and de Vries, D. A. (1957). Moisture movement in porous materials under temperature gradient. *Transactions American Geophysical Union*, **38**: 222–232.

Romero, E., Gens, A., and Lloret, A. (2003). Suction effects on a compacted clay under non-isothermal conditions. *Geotechnique*, **53**(1): 65–81.

Sheng, D., Fredlund, D. G., and Gens, A. (2008). A new modelling approach for unsaturated soils using independent stress variables. *Canadian Geotechnical Journal*, **45**(4): 511–534.

Sheng, D., and Zhou, A. N. (2011). Coupling hydraulic with mechanical models for unsaturated soils. *Canadian Geotechnical Journal* **48**(5): 826–840.

Uchaipichat, A. (2005). *Experimental investigation and constitutive modelling of thermo-hydro-mechanical coupling in unsaturated soils*, PhD Thesis, UNSW, Sydney, Australia.

Yao, Y. P., and Zhou, A. N. (2013). Non-isothermal unified hardening model: a thermo-elastoplastic model for clays. *Geotechnique* **63**(15): 1328–1345.

Zhou, A. N., and Sheng, D. (2009). Yield stress, volume change and shear strength behaviour of unsaturated soils: Validation of the SFG model. *Canadian Geotechnical Journal*, **46**(9): 1034–1045.

Zhou, A. N., Sheng, D., and Carter, J. P. (2012). Modelling the effect of initial density on soil-water characteristic curves. *Geotechnique* **62**(8): 669–680.

Zhou, A. N., Sheng, D., and Li, J. (2014). Modelling water retention and volume change behaviours of unsaturated soils in non-isothermal conditions. *Computers and Geotechnics*, **55**: 1–13.

Unsaturated Soil Mechanics—from Theory to Practice – Chen et al. (Eds)
© 2016 Taylor & Francis Group, London, ISBN 978-1-138-02921-7

A simplified method to estimate the Soil-Water Characteristic Curve

Y.T. Fan & E.C. Leong
School of Civil & Environmental Engineering, Nanyang Technological University, Singapore

ABSTRACT: The Soil-Water Characteristic Curve (SWCC) is an important property for unsaturated soils. The SWCC expresses the relationship between water content and suction. It can be used to estimate the permeability function and shear strength of unsaturated soil. However, the test duration to obtain the SWCC is very long. Hence, many methods have been developed to estimate the SWCC. To-date, it appears that the most reliable method to estimate the SWCC requires at least one SWCC measurement point. The objective of this paper is to evaluate one such method for soil types ranging from sand to clay. The evaluation showed that the method is reliable for most soils. For the cases where the method gives less reliable estimate of the SWCC, the reasons were investigated and recommendations were provided for the improvement of the method.

1 INTRODUCTION

Soil-Water Characteristic Curve (SWCC) of a soil can be used to determine a number of unsaturated soil properties, such as shear strength, coefficient of permeability and coefficient of water volume change. However, the test duration to obtain the SWCC is very long. Research has focused on the development of indirect methods to estimate the SWCC from the index properties of the soils. This indirect method is less time-consuming, simpler, and more economical.

Indirect methods to estimate the SWCC include Catana et al. (2006), Houston et al. (2006) and Chin et al. (2010). To-date, it appears that Chin et al. (2010) is simpler and performs better than existing one-point methods. The objective of this paper is to evaluate Chin et al. (2010) method to estimate SWCC for soil types ranging from sand to clay.

2 CHIN ET AL. (2010) METHOD

Chin et al. (2010) method estimates the SWCC using one SWCC measurement point and basic index properties. Parameters of Fredlund and Xing (1994) SWCC equation were correlated with the basic properties. The Fredlund and Xing (1994) SWCC equation is given as:

$$\theta_w = C(\psi)\frac{\theta_s}{\left\{\ln\left[e+\left(\frac{\psi}{a}\right)^n\right]\right\}^m} \quad (1a)$$

$$\text{where } C(\psi) = \left[1-\frac{\ln\left(1+\frac{\psi}{\psi_r}\right)}{\ln\left(1+\frac{1{,}000{,}000}{\psi_r}\right)}\right] \quad (1b)$$

where θ_w is volumetric water content; ψ is matric suction; θ_s is saturated volumetric water content; e is the natural number (i.e., 2.718281); a, n, m are curve-fitting parameters; and ψ_r is matric suction corresponding to the residual volumetric water content, θ_r.

In this SWCC estimation method, the soils are divided into two categories according to the grain-size distribution. The two categories are fine-grained soils, which are defined as soils with $P_{200} \geq 30\%$, and coarse-grained soils, which are defined as soils with $P_{200} < 30\%$. The way of defining "fine-grained soils" and "coarse-grained soils" is different from the definitions in the Unified Soil Classification System (USCS). The correlations between basic properties and parameters of Fredlund and Xing SWCC equation for both fine-grained soils and coarse-grained soils are presented below.

2.1 *Fine-grained soils ($P_{200} \geq 30\%$)*

Adjustable variable x is introduced to allow the SWCC to pass through or come close to the measured SWCC point. The SWCC parameters for fine-grained soils are given below:

$$a = -2.4(x) + 722 \quad \text{(kPa)} \quad (2a)$$

Table 1. Fine-grained soils ($P_{200} \geq 30\%$) for evaluation.

Reference	Sample	USCS
Johari et al. (2011)	1, 4, 6, 7, 8, 9	ML
	2, 3, 10, 12, 13, 14	CL
	5, 11	CL-ML
Rahardjo et al. (2011)	M1, M2, M3	GM-MH
	RS	MH
Mohammadi (2012)	a, b, c, d, e, f	–
Puppala et al. (2006)	DFW, Arlington	CL
Song et al. (2011)	Silt	–
Liu et al. (2012)	K-8, Sasaguri, Takeda	–

$$n = 0.07(x)^{0.4} \quad (2b)$$

$$m = 0.015(x)^{0.7} \quad (2c)$$

$$\psi_r = 914e^{[-0.002(x)]} \text{ (kPa)} \quad (2d)$$

2.2 *Coarse-grained soils ($P_{200} < 30\%$)*

Adjustable variable x is introduced to allow the SWCC to pass through or come close to the measured SWCC point. The SWCC parameters for coarse-grained soils are given below:

$$a = 0.53(D_{50})^{-0.96} \text{ (kPa)} \quad (3a)$$

$$n = x \quad (3b)$$

$$m = -0.23\ln(x) + 1.13 \quad (3c)$$

$$\psi_r = 100 \text{ (kPa)} \quad (3d)$$

2.3 *Selection of SWCC measurement point*

The selection of the SWCC measurement point is important in this SWCC estimation method. Chin et al. (2010) recommended that a matric suction of 500 kPa be used for fine-grained soils (100 kPa shall be used when 500 kPa is not available) and 10 kPa be used for coarse-grained soils.

3 METHOD AND MATERIALS

To evaluate Chin et al. (2010) SWCC estimation method, a total of 60 soils was collated from published literature with 30 soils each of fine-grained ($P_{200} \geq 30\%$) and coarse-grained ($P_{200} < 30\%$) soils. Details of the soils collated are summarized in Tables 1 and 2.

The following procedures were adopted for the evaluation:

1) The experimental data of SWCC for each of the soils were extracted from the literature and digitized.
2) Equation 1 and either Equation 2 or 3 were employed to estimate the SWCC.

Table 2. Coarse-grained soils ($P_{200} < 30\%$) for evaluation.

Reference	Sample	D_{50} (mm)
Smettem and Gregory (1996)	EB10	0.3122
	EB20	0.3168
	D10	0.4224
	D20	0.4006
	D30	0.3840
	D50	0.3660
	D90	0.3546
	WH10	0.3082
	WH20	0.3341
	WH30	0.3178
	WH50	0.3139
Jauhiainen (2004)	11CTA	0.4221
	11CTB1	0.4142
	11CTB2	0.4300
	11CTC	0.4021
	21VTB1	0.1471
	21VTB2	0.1413
	21VTC	0.1785
	22VTC	0.1587
	111MTA	0.4187
	111MTB1	0.4185
	111MTB2	0.4276
	111MTC	0.4260
	121MTA	0.1752
	121MTB1	0.1907
	211CTA	0.2763
	211CTB1	0.2622
	211CTB2	0.2743
	211CTC	0.2488
	231MTA	0.2603

3) Using one of the SWCC measurement points (500 kPa for fine-grained soil or 10 kPa for coarse-grained soils), the variable x in Equation 2 or 3 was adjusted so that the estimated SWCC passes through or comes close to the SWCC measurement point. The adjustment was made using the Solver routine provided in Microsoft Excel and minimizing the squared error $(\theta_i - \theta_{i(est)})^2$ for the SWCC measurement point.
4) The goodness of fit of the estimated SWCC and the experimental SWCC data was quantified by the sum of squared error (SSE), which is given as follows:

$$SSE = \sum_{i=1}^{N} (\theta_i - \theta_{i(est)})^2 \quad (4)$$

4 RESULTS & DISCUSSIONS

Tables 3 and 4 present the x, a, n, m, ψ_r, SE (at the point of measurement) and SSE for fine-grained and coarse-grained soils, respectively. From Tables 3 and 4, it can be seen that the variations of SSE are quite small, which implies that Chin et al. (2010) method to estimate SWCC is reliable for most of the soils. Out of the 60 soils, the estimated SWCCs for four fine-grained soils (a, Silt, K-8 and Sasaguri) and four

Table 3. Parameters x, a, n, m, ψ_r, SE and SSE for fine-grained soils.

Sample	x	a (kPa)	n	m	ψ_r	SE	SSE
1	288.14	30.47	0.67	0.79	513.65	5.40E-26	0.0030
2	274.86	62.33	0.66	0.76	527.48	6.13E-27	0.0084
3	255.91	107.81	0.64	0.73	547.85	7.10E-28	0.0075
4	267.42	80.18	0.65	0.75	535.38	3.27E-25	0.0089
5	267.03	81.13	0.65	0.75	535.80	6.24E-26	0.0007
6	288.54	29.51	0.67	0.79	513.25	7.36E-26	0.0040
7	291.22	23.06	0.68	0.80	510.50	1.80E-25	0.0017
8	294.18	15.97	0.68	0.80	507.49	2.01E-23	0.0071
9	284.18	39.96	0.67	0.78	517.74	2.38E-26	0.0035
10	263.85	88.75	0.65	0.74	539.22	1.24E-26	0.0057
11	255.56	108.67	0.64	0.73	548.24	2.62E-26	0.0040
12	267.65	79.63	0.65	0.75	535.14	1.87E-29	0.0016
13	243.60	137.35	0.63	0.70	561.51	3.41E-15	0.0086
14	279.57	51.04	0.67	0.77	522.54	8.79E-27	0.0042
M1	285.20	37.52	0.67	0.78	516.68	8.05E-25	0.0066
M2	274.93	62.17	0.66	0.76	527.41	4.02E-27	0.0042
M3	276.55	58.28	0.66	0.77	525.70	6.21E-29	0.0043
RS	253.44	113.74	0.64	0.72	550.57	5.31E-28	0.0026
a	300.82	0.03	0.69	0.81	500.79	2.01E-17	0.3554
b	294.17	16.00	0.68	0.80	507.50	8.29E-23	0.0065
c	297.41	8.20	0.68	0.81	504.21	1.78E-24	0.0045
d	298.58	5.40	0.68	0.81	503.04	1.15E-28	0.0043
e	254.70	110.71	0.64	0.72	549.18	3.75E-22	0.0051
f	263.88	88.69	0.65	0.74	539.19	2.10E-29	0.0006
DFW	182.95	282.91	0.56	0.58	633.92	6.41E-28	0.0008
Arlington	190.25	265.39	0.57	0.59	624.73	1.11E-30	0.0015
Silt	300.79	0.11	0.69	0.81	500.83	1.27E-19	0.3441
K-8	300.46	0.89	0.69	0.81	501.15	1.05E-20	0.1527
Sasaguri	297.00	9.20	0.68	0.81	504.63	2.69E-23	0.0181
Takeda	296.80	9.69	0.68	0.81	504.84	2.73E-25	0.0042

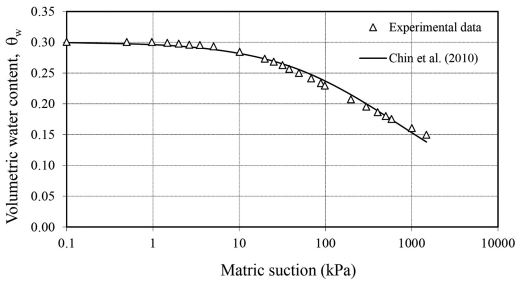


Figure 1. SWCC estimation for fine-grained soil sample f.

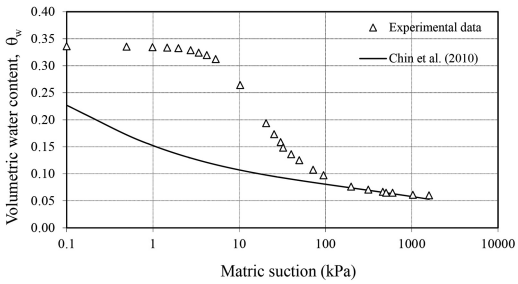


Figure 2. SWCC estimation for fine-grained soil sample a.

Table 4. Parameters x, a, n, m, ψ_r, SE and SSE for coarse-grained soils.

Sample	x	a (kPa)	n	m	ψ_r	SE	SSE
EB10	1.42	1.62	1.42	1.05	100	2.72E-24	0.0087
EB20	2.06	1.60	2.06	0.96	100	2.65E-16	0.0033
D10	1.78	1.21	1.78	1.00	100	1.47E-23	0.0081
D20	2.44	1.28	2.44	0.93	100	5.23E-18	0.0028
D30	2.47	1.33	2.47	0.92	100	1.70E-16	0.0031
D50	2.09	1.39	2.09	0.96	100	1.46E-14	0.0037
D90	1.84	1.43	1.84	0.99	100	6.31E-19	0.0040
WH10	1.77	1.64	1.77	1.00	100	9.63E-23	0.0064
WH20	1.25	1.52	1.25	1.08	100	5.07E-26	0.0084
WH30	1.08	1.59	1.08	1.11	100	3.45E-21	0.0097
WH50	0.85	1.61	0.85	1.17	100	1.66E-17	0.0153
11CTA	1.34	1.21	1.34	1.06	100	5.29E-23	0.0012
11CTB1	0.95	1.24	0.95	1.14	100	2.44E-19	0.0009
11CTB2	1.76	1.19	1.76	1.00	100	4.46E-22	0.0087
11CTC	8.12	1.27	8.12	0.65	100	4.69E-04	0.0135
21VTB1	2.21	3.34	2.21	0.95	100	2.58E-19	0.0016
21VTB2	1.78	3.47	1.78	1.00	100	7.05E-15	0.0054
21VTC	10.30	2.77	10.30	0.59	100	1.32E-03	0.0056
22VTC	2.98	3.10	2.98	0.88	100	1.66E-24	0.0082
111MTA	1.04	1.22	1.04	1.12	100	4.62E-19	0.0094
111MTB1	1.29	1.22	1.29	1.07	100	1.07E-19	0.0046
111MTB2	1.34	1.20	1.34	1.06	100	6.79E-23	0.0030
111MTC	8.01	1.20	8.01	0.65	100	2.52E-04	0.0228
121MTA	1.55	2.82	1.55	1.03	100	5.60E-19	0.0048
121MTB1	1.05	2.60	1.05	1.12	100	6.18E-18	0.0315
211CTA	1.49	1.82	1.49	1.04	100	4.96E-22	0.0022
211CTB1	1.56	1.92	1.56	1.03	100	2.35E-18	0.0102
211CTB2	2.23	1.83	2.23	0.95	100	4.75E-15	0.0089
211CTC	9.22	2.01	9.22	0.62	100	3.70E-04	0.0198
231MTA	0.85	1.93	0.85	1.17	100	7.56E-25	0.0149

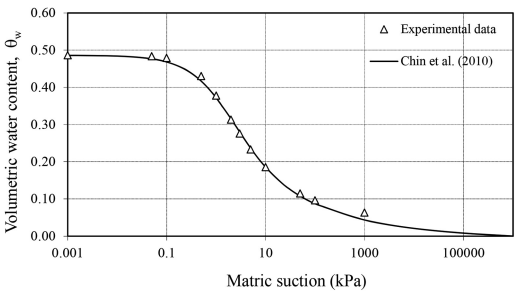


Figure 3. SWCC estimation for coarse-grained soil sample 11CTB1.

Table 5. Re-estimation of SWCC for fine-grained soil samples a, Silt, K-8 and Sasaguri.

Sample	x	Exponent of n	SE	SSE
a	297.35	0.556	3.16E-20	0.0014
Silt	294.68	0.600	3.32E-04	0.0041
K-8	290.38	0.600	2.80E-04	0.0032
Sasaguri	300.23	0.300	4.26E-05	0.0082

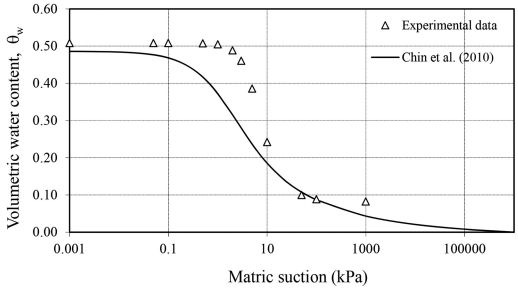


Figure 4. SWCC estimation for coarse-grained soil sample 121MTB1.

Table 6. Re-estimation of SWCC for coarse grained soil samples WH50, 111MTC, 121MTB1 and 211CTC.

Sample	x	n	SE	SSE
WH50	26.33	3.96	6.84E-04	0.0028
111MTC	2.94	5.27	3.01E-16	0.0166
121MTB1	24.93	4.81	1.01E-13	0.0155
211CTC	10.82	15.00	2.32E-04	0.0316

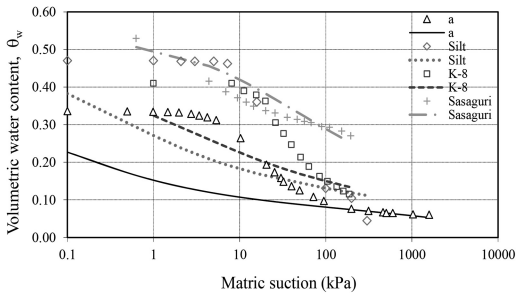


Figure 5. SWCC estimation for fine-grained soil samples in Table 5 using one-point measurement at matric suction of 500 kPa.

coarse-grained soils (WH50, 111MTC, 121MTB1 and 211CTC) were relatively poor. Figures 1–4 show typical good and poor estimation cases for fine-grained (Figures 1 and 2) and coarse-grained soils (Figures 3 and 4).

To improve the estimated SWCC, it is recommended to use two SWCC measurement points instead (at 20 kPa and 500 kPa for fine-grained soils, and 2 kPa and 10 kPa for coarse-grained soils). In addition, for fine-grained soil it is also necessary to adjust the exponent of n (constrained between 0.3 and 0.6) in Equation 2b together with x. For coarse-grained soils, the value of n is constrained to be between 0.5 and 15. Using this method, the SWCCs for the soil samples a, Silt, K-8, Sasaguri, WH50, 111MTC, 121MTB1 and 211CTC were re-estimated and the results are presented in Table 5 and Table 6. Comparing the SSEs in Tables 5 and 6 with the corresponding SSEs in Tables 3 and 4, it can be seen that the SSEs have improved except for sample 221CTC. Figures 5 and 6, and 7 and 8 (markers –

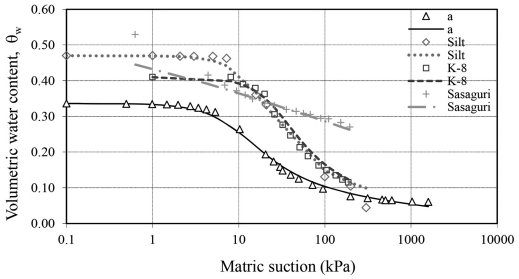


Figure 6. SWCC estimation for fine-grained soil samples in Table 5 using two-point measurement at matric suctions of 20 kPa and 500 kPa.

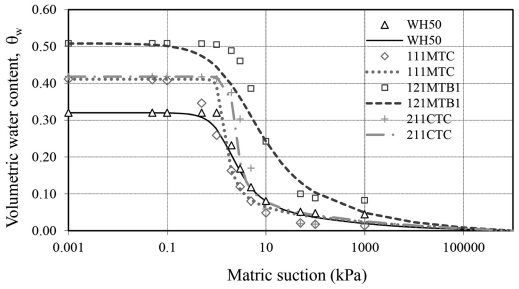


Figure 7. SWCC estimation for coarse-grained soil samples in Table 6 using one-point measurement at matric suction 10 kPa.

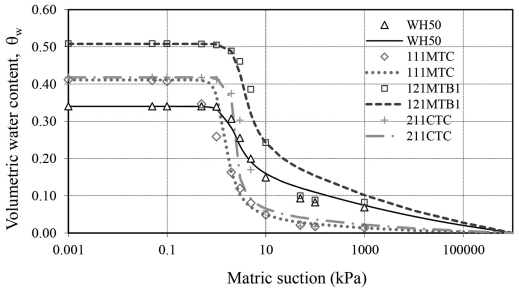


Figure 8. SWCC estimation for coarse-grained soil samples in Table 6 using two-point measurement at matric suction 2 kPa and 10 kPa.

experimental SWCC data; lines – estimated SWCC) present the comparison of using one-point measurement and two-point measurement for the soil samples in Tables 5 and 6, respectively. Figures 6 and 8 clearly show the improvement in the estimation of the SWCC with the two-point measurement.

5 CONCLUSION

The results showed that Chin et al. (2010) estimation method for SWCC using one-point measurement is reliable for most soils. It can be used to obtain a preliminary estimate of the SWCC.

To improve the SWCC estimation, it is recommended that two measurement points be used at 20 and 500 kPa, and 2 and 10 kPa matric suctions for fine-grained soils and coarse-grained soils, respectively. It is also necessary to adjust the exponent of n (constrained between 0.3 and 0.6) in Equation 2b together with x for fine-grained soils so that the estimated SWCC passes through the two SWCC measurement points. For the coarse-grained soils, the variable x and hence n in Equation 3 need to be constrained to be between 0.5 to 15. The modified method was shown to give a better estimate of the SWCC.

ACKNOWLEDGEMENT

We wish to acknowledgement the funding for this project from Nanyang Technological University under the Undergraduate Research Experience on Campus (URECA) programme.

REFERENCES

Catana, M.C., Vanapalli, S.K., & Garga, V.K. 2006. The water retention characteristics of compacted clays. In *Proceedings of the 4th International Conference on Unsaturated Soils*, Carefree, Arizona, USA, 2–6 April 2006. Vol. 2, pp. 1348–1359.

Chin, K.B., Leong, E.C., & Rahardjo, H. 2010. A simplified method to estimate the soil-water characteristic curve. *Canadian Geotechnical Journal*, 47(12): 1382–1400. doi:10.1139/T10-033

Houston, W.N., Dye, H.B., Zapata, C.E., Perera, Y.Y., & Harraz, A. 2006. Determination of SWCC using one point measurement and standard curves. In *Proceedings of the 4th International Conference on Unsaturated Soils*, Carefree, Arizona, USA, 2–6 April 2006. Vol. 2, pp. 1482–1493.

Jauhiainen, M. 2004. Relationship of particle size distribution curve, soil water retention curve and unsaturated hydraulic conductivity and their implications on water balance of forested and agricultural hillslopes. *Ph.D. dissertation*, Helsinki University of Technology, Finland.

Johari, A., Habibagahi, G., & Ghahramani, A. 2011. Prediction of SWCC using artificial intelligent systems: A comparative study. *Scientia Iranica*, 18(5): 1002–1008.

Liu, Q., Yasufuku, N., Omine, K., & Hazarika, H. 2012. Technical note: Automatic soil water retention test system with volume change measurement for sandy and silty soils. *Soils and Foundations*, 52(2):368–380.

Mohammadi, M., & Meskini-Vishkaee, F. 2013. Predicting soil moisture characteristic curves from continuous particle-size distribution data. *Pedosphere*, 23(1): 70–80.

Puppala, A. J., Punthutaecha, K., & Vanapalli, S. K. 2006. Soil-water characteristic curves of stabilized expansive soils. *Journal Of Geotechnical And Geoenvironmental Engineering*, 132(6): 736–751.

Rahardjo, H., Satyanaga, A., D'Amore, G. A., & Leong, E.C. 2012. Soil–water characteristic curves of gap-graded soils. *Engineering Geology*, 125: 102–107.

Smettem, K.R.J., & Gregory, P.J. 1996. The relation between soil water retention and particle size distribution parameters for some predominantly sandy Western Australia soils. *Australian Journal of Soil Research*, 34(5): 695–708.

Song, Y., Hwang, W., Jung, S., & Kim, T. 2011. A comparative study of suction stress between sand and silt under unsaturated conditions. *Engineering Geology*, 124: 90–97.

This page intentionally left blank

Unsaturated Soil Mechanics—from Theory to Practice – Chen et al. (Eds)
© 2016 Taylor & Francis Group, London, ISBN 978-1-138-02921-7

Effect of specimen preparation on water retention and deformation behaviour of unsaturated soils

D.A. Sun & Y. Gao
Department of Civil Engineering, Shanghai University, Shanghai, China

A.N. Zhou
School of Civil, Environmental and Chemical Engineering, Royal Melbourne Institute of Technology (RMIT), Melbourne, Australia

ABSTRACT: A series of water retention and mechanical tests and Mercury Intrusion Porosimetry (MIP) on unsaturated compacted and reconstituted specimens of a non-expansive clay, were performed to investigate effect of the specimen preparation on the water retention behaviour and its pore-size distribution, as well as investigate effect of suction on mechanical behaviour. The experimental results indicate that the air-entry value of the reconstituted specimen is higher than that of compacted specimen with the same void ratio. This is because the reconstituted specimen exhibits a unimodal pore-size distribution and its pore-size has a uniform distribution from the results of MIP tests. The soil-water characteristic curves and residual water content of two differently prepared specimens are almost the same in the high suction region. Secondly, the void ratio of reconstituted specimen decreased with increasing the suction under the isotropic net stress of 20 kPa, while the void ratio of compacted specimen shows a little change during the same suction equilibrium process.

1 INTRODUCTION

Soils partially saturated with water are referred to as unsaturated soils or partially saturated soils. Most soils involved in infrastructure construction and agriculture engineering are found in partially saturated conditions, especially in the area where semi-arid and arid climates prevail. Soil's unsaturation can be generally attributed to the following two main reasons: natural environment and human activities. For example, in the semi-arid and arid environments where the ground water level is several meters below the ground surface level, and soils in the vadose zone are naturally unsaturated. On the other hand, unsaturated soils can be very common in the compaction process. The fill materials from soil borrow pits are artificially mixed with water to achieve the optimum water content from the dry side and then compacted to the target dry unit weight. The soils after compaction are still unsaturated since the optimum water content is usually lower than the saturated water content.

Engineering behaviour of a soil becomes outstandingly complicated once it is unsaturated. Changes in degree of saturation and suction, which can be caused either by evaporation and infiltration in natural environment or by artificial adjustment of water content, alter all mechanical and hydraulic properties of a soil. For example, unsaturated soils can experience distinctive volume change (collapse or swelling) and shear strength alteration upon the variation in degree of saturation and suction even under the constant stress level. Infrastructure that founded on unsaturated soils can be severely damaged because of huge changes on volume and strength.

Once a soil changes from saturated state to unsaturated states, some existing soil mechanics principles developed for saturated soils would be no longer valid for unsaturated soils. In light of this, a great deal of research efforts have been paid to dealing with engineering problems associated with unsaturated soils following the pioneering work by (Alonso et al. 1990). In the past two decades, a great deal of experimental studies were conducted to investigate the mechanical and hydro-mechanical behaviour of unsaturated soils, and a number of constitutive models were proposed to interpret and simulate the observed behaviour. It is noted that the existing constitutive models are almost exclusively established through and validated by the experimental results from the compacted specimens. With regard to the compacted specimens, the soil is usually oven-dried, smashed and then sieved to dry soil powder first. After that, the dry soil powder is mixed with sprayed water to set initial water content to the target magnitude. The wet soil then statically or dynamically compacted to a dry unit weight (or void ratio). Aggregates of fine-grained soil particles are formed when the dry soil powder is moistened (Tarantino and de Col 2008). In general, neither static nor dynamic compaction is able to remove the particle aggregates (Tarantino 2011; Tarantino 2011; Tarantino

& de Col 2008). According to the test results from the Mercury Intrusion Porosimetry (MIP), this sampling method leads to at least two populations of pores (i.e. inter-aggregate pores) and intra-aggregate pores. The average size of the inter-aggregate pores, which are the pores among the aggregates, is usually much larger than that of the intra-aggregate pores, which are the pores within the aggregates. However, the inter-aggregate pores, which are not as stable as the intra-aggregate pores, can be removed by either wetting or high pressure.

On the other hand, unsaturated soil sample can be prepared by drying saturated reconstituted soil samples, which may be better to represent natural unsaturated soils due to lowering of the ground water level or uplifting of the ground level. Compared with compacted samples, in terms of pore-size distribution, reconstituted samples usually contain a single population of pore-sizes and exhibit a mono-modal pore distribution. With respect to the constitutive modelling, the reconstituted sample seems more basic because (1) the stress history is relatively clear during sample preparation and (2) other influence factors such as soil structure (i.e. aggregation) have been removed during sampling. In addition, the modified Cam-clay model that was originally designed for interpreting the mechanical behaviour of reconstituted saturated soils is commonly employed as the platform to develop constitutive models for unsaturated soils. Therefore, the experimental studies on unsaturated samples prepared from reconstituted soil should more coincide with the common approach for developing constitutive models (Zhou & Sheng 2009). However, compaction is the dominant sampling method in the practice of experimental study and the test results from unsaturated reconstituted soil samples (Cunningham et al. 2003; Jennings & Burland 1962; Jotisankasa 2005; Monroy 2005; Tarantino & de Col 2008) are still limited in the literature.

As remarked by Tarantino (2011), the comparison study between compacted and reconstituted unsaturated soils can lead to (1) a better understanding of the role of microstructure in soil's hydro-mechanical behaviour, and (2) a rethink on whether the current modelling approach mainly based on compacted soil data can still be applicable for reconstituted unsaturated soils. Through a series of laboratory tests such as isotropic compression and drying, this technical paper presents a systematic comparative study to investigate effects of sampling methods (compaction/reconstitution) on hydro-mechanical behaviour of unsaturated soils. During the sampling, the initial states (such as initial void ratio, initial suction, etc.) are strictly controlled to be the same for different sampling methods, to ensure validity of the comparison.

2 MATERIAL AND TESTING PROCEDURE

A series of laboratory experimental programs, including (1) water retention tests with deformation measurement, and (2) suction-controlled isotropic compression tests, were designed with the main objective of investigating the hydro-mechanical behaviour of unsaturated soil samples made via either the compaction or reconstitution method.

2.1 *Material and specimen preparation*

The soil used in this study is referred to as Pearl clay, which has a liquid limit of 49% and a plasticity index of 27%. The soil is composed of about 50% clay and about 50% silt. The clay mineralogy compositions, determined using X-ray diffraction test, include quartz, pyrophyllite, and kaolinite in the dominant order. There is little expansive clay mineral in Pearl clay.

The size of specimens for investigating the mechanical behaviour via triaxial/isotropic compression tests is set to 38 mm in diameter and 76 mm in height. Specimens were prepared via either the compaction method or reconstitution method, which are referred to as compacted specimens and reconstituted specimens, respectively. Compacted specimens were prepared by compaction in a mould at water content of about 26%, which is obtained by spraying water over the dry powdered Pearl clay uniformly. Specimens were compacted in five layers, with each layer statically compacted at the blow number of 15 per layer using a 12 mm diameter plunger. The vertical stress compaction stress is dependent on the force applying on the plunger, which can be used to set different initial densities. The reconstituted specimens were prepared as follows. The powdered Pearl clay was thoroughly mixed with water at a water content of about 100% to form a slurry state, and then the slurry soil was consolidated one-dimensionally with the vertical pressure of 49 kPa. The size of consolidation cell is 100 mm in diameter and 150 mm in height. After the consolidation was completed (i.e., the vertical deformation was stable), the soil was taken out from the consolidation cell via a jacking equipment. The water content after the consolidation is about 43% and the degree of saturation is about 100%. The specimen for tests can be obtained from a consolidated reconstituted soil sample by a 38 mm diameter cutting tube (100 mm in height). The remaining sample was stored in desiccator with covering double films to keep water content constant. The initial stress and suction of the compacted specimens and reconstituted specimens are adjusted by the suction controlled apparatus.

2.2 *Test procedure*

To obtain the water retention behaviour of the soil in a wide range of suction, two techniques of suction control were used. In the lower suctions ranging from 1 kPa to 1500 kPa, the axis translation technique was adopted in the pressure plate device, i.e., the Pressure Plate Method (PPM). For the higher suctions ranging from 3 MPa to 367 MPa, the suction was applied by

Table 1. Saturated salt solution and corresponding suction (20°C).

Saturated salt solutions	RH%	Total suction (MPa)
LiBr	6.6	367.54
$MgCl_2$	33.1	149.51
NaBr	59.1	71.12
KI	69.9	48.42
NaCl	75.5	38.00
KCl	85.1	21.82
KNO_3	94.6	7.48
K_2SO_4	97.6	3.29

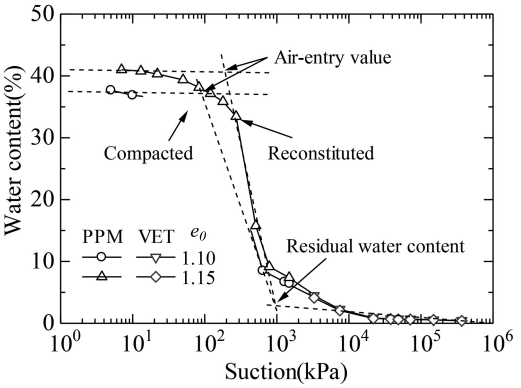


Figure 1. SWCC of differently prepared specimens during drying.

means of the Vapour Equilibrium Technique (VET) in desiccators.

A pressure plate device was used for measuring the Soil-Water Characteristic Curve (SWCC), which is equipped with 15 bar High Air Entry (HAE) ceramic disc and 1.5 MPa pressurizer. It is designed based on the axis translation technique, which directly controls suction by increasing air pressure while maintaining pore-water pressure in the specimens equal to atmospheric pressure. The HAE ceramic plate is placed in the pressure cell. The bottom of the HAE ceramic disc is sealed with rubber and the water beneath the ceramic disc is connected to the outside water volume tube.

The specimens, together with the stainless steel cutting rings, were placed on the HAE ceramic disc in the pressure cell. The tests were performed with an increase in suction from 0 kPa to 1500 kPa by several steps. When the water and the deformation of the specimen reach the equilibrium, the test proceeds to the next suction level. The change in water drainage from the soil specimen is recorded during the testing. Finally, the water content corresponding to specified suction can be calculated from the change in the amount of water in the specimen and final water content of the soil specimen.

The Vapor Equilibrium Technique (VET) is commonly employed to control high suctions in testing of unsaturated soils (Delage et al. 1998). VET uses a chemical solution such as saturated salt solution to generate constant total suction conditions in a closed space (such as a sealed container). The potential of the chemical solution forces the water potential in the closed space and that in soil samples to reach equilibrium. Greenspan (1977) collected reference data for the relative humidity of the saturated salt solutions, as shown in Table 1. One of the drawbacks of this technique is that the equilibration time can be very long (up to several months) due to the excessive slowness of the vapor transfers.

Two specimens with 61.8 mm diameter and 20 mm height were prepared for the drying tests, respectively, using VET. The samples for the drying test were prepared by cutting the saturated specimen into eight pieces. Two pieces of them were put into a temperature controlled sealed desiccator on the top of saturated salt solution for two months to reach equilibrium. One piece is used to measure the water content and another is used to measure the volume of irregular soil sample according to the Archimedes' principle.

3 TEST RESULTS AND DISCUSSIONS

3.1 *Effect of specimen preparation method on water retention behaviour*

Figure 1 shows the measured water retention behaviour with the changes in water content (w) versus suction (s) in the drying tests on saturated compacted and reconstituted specimens by using two methods (i.e., pressure plate method and vapor equilibrium technique). Figure 1 show that the air-entry values of the compacted and reconstituted specimens are about 100 kPa and 200 kPa, respectively. The residual water content of compacted and reconstituted specimens is almost the same (about 4%). For the suction value lower than the residual suction value (about 950 kPa), the SWCC of reconstituted specimen is located at the right side of that of compacted one. Interestingly, for suction values higher than the residual suction value, the relationships between water content and degree of saturation versus suction can be considered as unique and specimen preparation method or soil structure no longer affects the SWCC.

3.2 *Effect of specimen preparation method on pore-size distribution*

The soil water characteristics of compacted soils depend on several factors such as soil type, soil structure and stress states, etc. For the same type of soil, the soil structure is an important factor to affect the SWCC and it can be simply represented by the pore-size distribution (PSD), which can be determined by the mercury intrusion porosimetry (MIP) tests.

The MIP tests are used to evaluate the pore-size distribution of powder and bulk materials with open and inter-connected pore structures. An assumption

Table 2. Samples for MIP tests.

Test No.	Initial void ratio e_0	Void ratio e_a before MIP	Sample preparation method
CF	1.15	1.15	Compacted, and freeze-dried
SF	1.15	1.10	Compacted, saturated and freeze-dried
RF	1.14	1.14	Reconstituted and freeze-dried
RA	1.16	1.04	Reconstituted and air-dried

Note: e_a is void ratio after drying

is made that cylindrical flow channels with a radius r exist in soils, and the pores with smaller than the radius r are intruded by mercury under an applied pressure. The unique relationship between the intrusion pressure and equivalent pore diameter was established by Washburn (1921).

$$p(d) = \frac{-4T_s \cos\theta}{d} \tag{1}$$

where d is the pore diameter, T_S is the surface tension of the mercury, θ is the contact angle, and $p(d)$ is the applied pressure.

Using the air-drying method to dehydrate the wet soil samples for the MIP test may cause the varying degrees of volumetric shrinkage strain on soil samples (Sasanian & Newson, 2013). The pore-size distribution of air-dried specimens is similar to those of specimens subjected to the high suction. Therefore, compacted and reconstituted specimens with different sample preparation methods were prepared for the MIP tests, as listed in Table 2. The MIP apparatus used in this study was the Micromeritics AutoPore IV with a maximum intrusion pressure of 413.7 MPa.

Figure 2 presents the PSDs of compacted and reconstituted samples (i.e., CF, SF, RA and RF). The total cumulative volume value of sample RA is smaller than that of sample RF, as shown in Figure 2a. This is mainly because the air-drying method to dehydrate the wet soil samples for MIP test causes volumetric shrinkage. Distinct bimodal PSD features can be seen for unsaturated compacted sample (i.e., CF), whereas only weak bimodal PSD features are present for the saturated compacted sample (i.e., SF) in Figure 2b. The log-differential pore volumes of unsaturated and saturated compacted samples are similar to a diameter of 2 um, as shown in Figure 2b. This is considered to be the boundary between the intra-aggregate pores and the inter-aggregate pores. The reconstituted samples (i.e., RF and RA) exhibit unimodal PSD with peak roughly between 0.1and 2 μm in Figure 2c. Therefore, the compacted samples contain two types of pore (i.e., the intra-aggregate pores and inter-aggregate pores), while the reconstituted samples contain only one type of pore (i.e., the intra-aggregate pores).

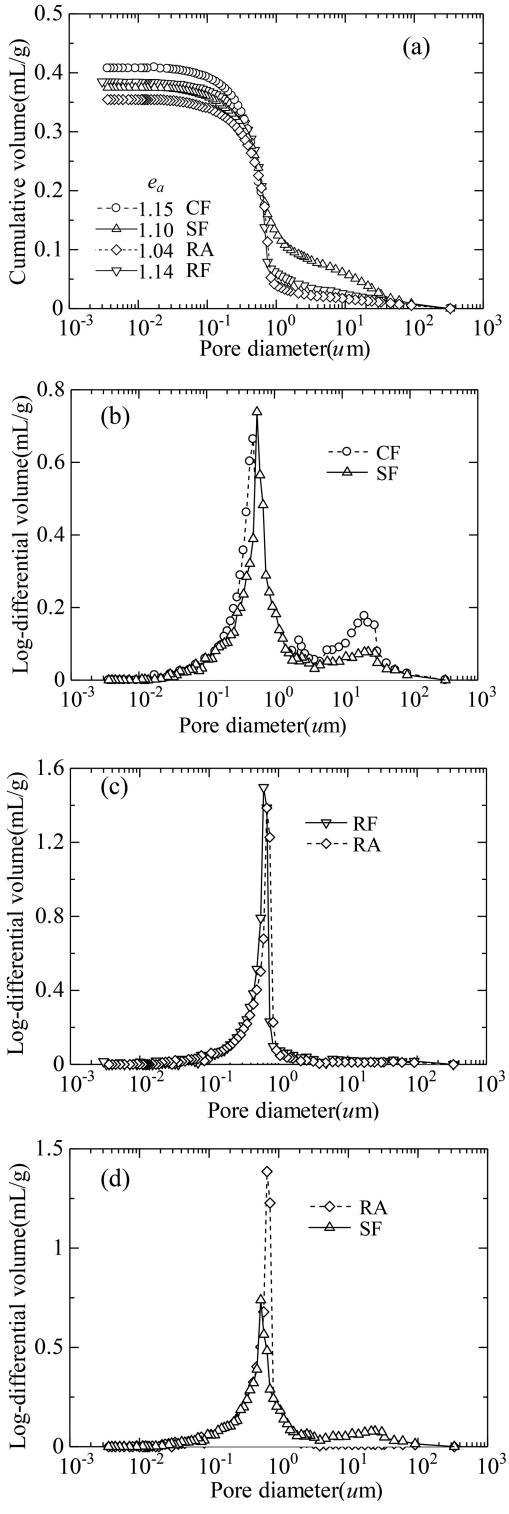


Figure 2. The pore-size distribution of compacted and reconstituted samples: (a) cumulative distribution, (b) (c) and (d) log-differential pore-size distribution.

Let us assume that cylindrical flow channels with a diameter d exists in the soil, and the key relationship connecting the cumulative distribution curve of the pore size with soil-water characteristics is the capillary law, which can be expressed as follows:

$$s = \frac{4\sigma \cos\theta_w}{d} \tag{2}$$

where σ is the liquid gas interfacial tension of 0.072 N/m at 25° (Fredlund & Rahardjo, 1993) and θ_w is the liquid-solid contact angle, which is treated as zero in calculating. If the pore diameter $d = 0.3$ um, the suction value 960 kPa is obtained by Eq. (2).

Figure 2d shows that the diameters of almost all remaining pores in reconstituted sample RA are roughly smaller than 2 μm, while there are some pores with diameters higher than 2 μm left in sample SF. When the pore diameter smaller than 0.3 um, the PDSs of the samples (i.e., CF, SF, RA and RF) almost coincide with each other. It is capable of explaining why the SWCC of reconstituted specimen is located at the right side of that of compacted one in the low suction range, and specimen preparation method or soil structure no longer affects the SWCC in the high suction range under the same initial void ratio, as shown in Figure 1.

3.3 *Effect of specimen preparation method on suction- controlled isotropic compression features*

Figure 3 shows the mean net stress versus void ratio relationship for reconstituted specimens by increasing up to different suction ($s = 0$, 150, 250, 350 and 450 kPa) under mean net stress of 20 kPa and isotropic compression under different constant suctions. It can be seen that the void ratio of reconstituted specimens decreases obviously with increasing the suction under mean net stress of 20 kPa. When the suction keep a constant, the void ratio of specimens decreases with the increasing the mean net stress. The void ratio of specimens changes slightly with increasing the mean net stress under the suctions of 350 kPa and 450 kPa.

These deformation characteristics can be explained by the elastoplastic model for unsaturated soils by Sheng et al. (2008), as shown in Figure 4. The initial state of reconstituted specimens in the plane of mean net stress versus suction is point A or close to A point in Figure 4. When the suction increase, the suction path will push up the 45° line of the yield curve for reconstituted clay just like line *a* to line *b* in Figure 4 and the plastic volume change will take place. Once the suction is sufficiently high and the soil become unsaturated, increasing suction is likely less effective in causing plastic volume change, and the yield curve should drift away from the 45° line (like lines *c* and *d* in Fig. 4). In Figure 3, the void ratio of reconstituted specimens changes little with increasing the suction from 350 kPa to 450 kPa under mean net stress of 20 kPa. Because the yield curve drift away from the 45° line and its

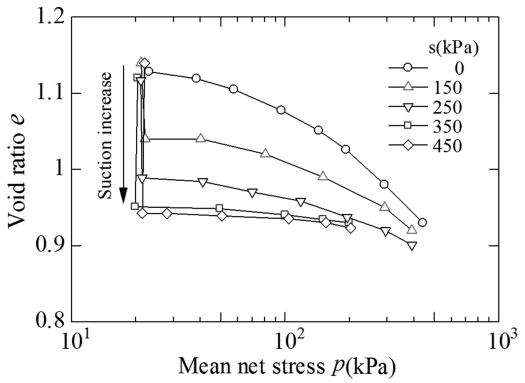


Figure 3. Results of suction equalization and compression tests on reconstituted specimens.

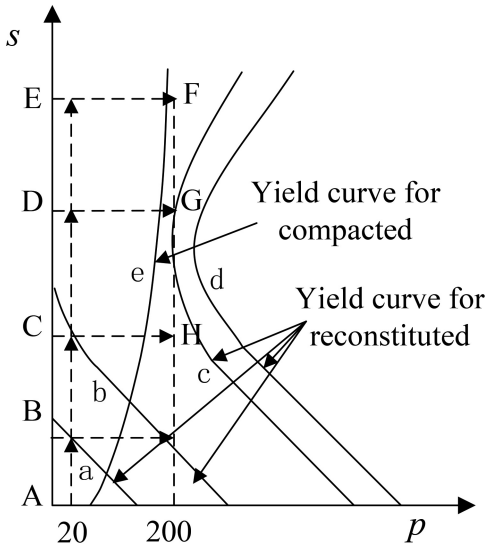


Figure 4. Yield curve for unsaturated reconstituted and compacted soils.

stress path DE inside the elastic region, as shown in Figure 4. The void ratio of specimens changes slightly with increasing the mean net stress under constant suctions of 350 kPa and 450 kPa in Figure 3. The reason is that the stress paths of specimens (DG and EF in Fig. 4) are inside the elastic region.

Figure 5 shows the mean net stress versus void ratio relationship for reconstituted and compacted specimens tested under application of suction from their initial suction to 150 kPa under mean net stress of 20 kPa and isotropic compression from 20 kPa to about 400 kPa under constant suction of 150 kPa. It can be seen that the void ratio decreases slightly for compacted specimens and decreases largely with increasing the suction from the initial suction up to 150 kPa under mean net stress of 20 kPa. The deformation behavior of compacted specimens is different

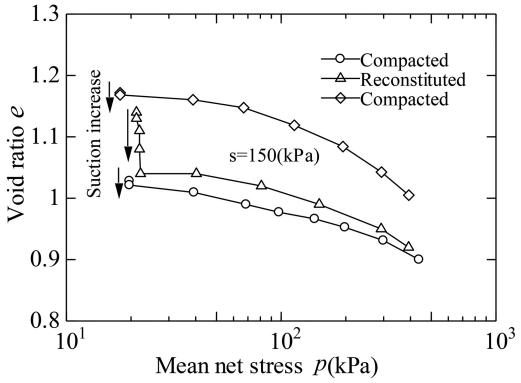


Figure 5. Results of suction equalization and compression tests on reconstituted and compacted specimens.

from that of reconstituted specimens during the suction equilibrium, because the initial suction of compacted specimen is about 120 kPa and the stress path is inside the elastic region for compacted soils (the yield locus is curve *e* in Fig. 4) and the initial suction of compacted specimen is about 30 kPa and the stress path goes across the yield loci for reconstituted soils (the yield locus are curves *a* and *b* in Fig. 4).

4 CONCLUSIONS

A series of the hydro-mechanical behaviour tests were performed on compacted and reconstituted specimens of Pearl clay, together with the MIP tests to probe the microstructures of the soil. The following conclusions can be obtained from this study:

(1) The water retention test results on Pearl clay show that the SWCC of reconstituted specimen is located at the right side of that of compacted one in the suction range smaller than the residual suction, and the effect of specimen preparation method no longer has influence in the suction range larger than the residual suction under the same initial void ratio. This result can be also explained by the difference in the pore-size distribution of the two specimens.

(2) The void ratio of reconstituted specimen decreased with increasing the suction value under the isotropic net stress of 20 kPa, while the void ratio of compacted specimen shows a little change during the same suction equilibrium process.

ACKNOWLEDGEMENT

The authors express their gratitude for the grants provided by the National Natural Science Foundation of China (No.11272194).

REFERENCES

Alonso E E, Gens A & Josa A. 1990. A constitutive model for partially saturated soils. *Géotechnique* 40(3): 405–430.

Cunningham M R, Ridley A M, Dineen K & Burland J B. 2003. The mechanical behaviour of a reconstituted unsaturated silty clay. *Géotechnique* 53(2): 183–194.

Delage, P., Howat, M., Cui, Y.J. 1998. The relationship between suction and swelling properties in a heavily compacted unsaturated clay. *Engineering Geology*, 50(1–2): 31–48.

Fredlund D G & Rahardjo H. Soil mechanics for unsaturated soils, John Wiley & Sons, Inc., 1993.

Greenspan L. 1977. Humidity fixed points of binary saturated aqueous solutions. *Journal of Research of the National Bureau of Standards*, 81(1): 89–96.

Hilf J W. 1956. An investigation of pore water pressure in compacted cohesive soils. US Department of Interior, Bureau of Reclamation.

Jennings J E B & Burland J B. 1962. Limitations to the use of effective stresses in partly saturated soils. *Géotechnique* 12(2): 125–144.

Jotisankasa A. 2005. Collapse behaviour of a compacted silty clay. Imperial College London, London.

Monroy R. 2005. The influence of load and suction changes on the volumetric behaviour of compacted London clay. Imperial College London, London, UK.

Sasanian S & Newson T A. 2013. Use of mercury intrusion porosimetry for microstructural investigation of reconstituted clays at high water contents. *Engineering Geology*, 158: 15–22.

Sheng D C, Fredlund D G & Gens A. 2008. A new modeling approach for unsaturated soils using independent stress variables, Canadian Geotechnical Journal, 45(2): 511–534.

Tarantino A. 2011. Unsaturated soils: Compacted versus reconstituted states. In *Unsaturated Soils*. Edited by E.E. Alonso and A. Gens. CRC Press, Barcelona, Spain. pp. 113–136.

Tarantino A, & de Co, E. 2008. Compaction behaviour of clay. *Géotechnique* 58(3): 119–214.

Washburn E W. 1921. Note on a method of determining the distribution of pore sizes in a porous material. *Proc. of the National Academy of Sciences of the USA*, 7 (4): 115–116.

Zhou A N & Sheng D. 2009. Yield stress, volume change and shear strength behaviour of unsaturated soils: Validation of the SFG model. *Canadian Geotechnical Journal* 46(9): 1034–1045.

Unsaturated Soil Mechanics—from Theory to Practice – Chen et al. (Eds)
© 2016 Taylor & Francis Group, London, ISBN 978-1-138-02921-7

A research of affect factor on hysteresis behavior for Soil-Water Characteristic Curve

J. Li
Institute of Geotechnical Engineering, Xi'an University of Technology, Xi'an, China
School of Civil Engineering and Architecture, Shaanxi University of Technology, Hanzhong, China

F.Y. Liu
Institute of Geotechnical Engineering, Xi'an University of Technology, Xi'an, China

ABSTRACT: Soil-Water Characteristic Curve (SWCC) has been widely used in geotechnical engineering, and plays a significant role in unsaturated soil mechanics, so the research of SWCC will become the key of unsaturated soil. A test is carried out by GCTS SWCC device for soil-water characteristic curve for different initial dry densities, drying-wetting cycles and different stress conditions. It is calculated that the hysteresis degrees of soil during various measurement conditions, using the concept has proposed hysteretic degrees. The effect factors on the hysteresis characteristics of SWCC are analyzed. The causes of such factors are discussed theoretically. It shows that hysteresis characteristic of soil-water characteristic curve can be traced to the change of the pore volume and these results will be more favourable guidance on unsaturated soil properties.

1 INTRODUCTION

Soil-Water Characteristic Curve is great significance, and it acts like compression curve in saturated soil mechanics. However, the study is less that hysteretic behavior of soil-water characteristic curve, due to the impact on test equipment and time of cycle. We will study on the influence of hysteretic behavior of unsaturated soil factors, combine the concept of unsaturated soils has been proposed hysteretic degree through experimental, theoretically cause of these factors qualitative analysis to better understanding of unsaturated related to the nature of the soil.

Soil-Water Characteristic Curve (SWCC) can reveal good water retention properties of unsaturated soils, which shows the relationship between soil moisture in the soil and water phase, that is matrix suction and volume or weight of moisture or water content. It has an effect on unsaturated soil shear strength, deformation and permeability characteristics. Research on soil-water characteristic curve, has been widely developed in the formula described (Gardner 1958, Van 1980, Huang 1994, Fredlund 1994, Kosugi 1994), hysteresis simulation (Li 2005, Pham 2005, Nuth 2008, Mualem 2009, Min 2010), aspects compaction conditions (Vanapalli 1999, Miller 2002), temperature (Sugii 2002, Romero 2001, Imbert 2005) and hysteresis characteristics. Among them, it is a wet cycle that the soil-water characteristic curve of hysteretic behavior in the event of changes in the soil, due to various factors leading to its characteristic hysteresis phenomena occurs. Currently, the study of factors affecting such properties include pore size effect, the bottleneck effect, the contact angle, wet and dry cycles, stress history, initial water content, dry density, structural, etc. In describing soil hysteretic characteristics, the hysteresis loop area is widely used to characterize soil hysteretic behavior. Hysteresis loop area refers to the increase or decrease in wet soil-water characteristic curve surrounded by the hysteresis loop area, which describes the absolute size of the hysteresis loop, can reflect to some extent the different bodies unearthed in the process of changes in the wet the absolute size of the aqueous state. But because on the one hand laborious measuring hysteresis curve, completing a group of test data need several months, on the other hand calculating hysteresis loop area is affected by the SWCC expression, and some may be integral, some easy points or not integration, resulting in relatively few scholars study on hysteretic behavior, which makes the soil-water characteristic curve qualitatively reveal hysteresis characteristics law becomes hard. Therefore, Liu (2011) proposed the concept of hysteresis degree. "Hysteresis degree" to reflect the concept of volumetric water content within a certain range, SWCC hysteretic behavior proportion, its ability to be able to characterize the occurrence of hysteresis. In order to better reveal the SWCC hysteretic characteristics related factors, we have some experimental study that the hysteretic characteristics under certain conditions.

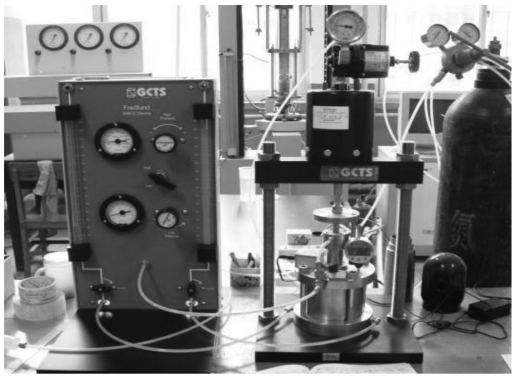


Figure 1. The device of GCTS-type SWCC.

2 TRIAL-RELATED CONDITIONS

2.1 *Test instruments and test methods*

A GCTS-SWCC instrument developed by Prof. Fredlund and GCTS Company is used to conduct the test, as shown in Fig.1. The instrument is capable of measuring a certain net normal stress state under continuous soil-water characteristic curve, using the ceramic plate that high intake values by epoxy adhesive qualities set in the ring, this collar and clay plate embedded in the base of the concave tank, the inner wall by O-ring seal, engraved with a group of snake bottom slot for scour clay plate attached to the bottom of the bubble. The moisture content of the sample can be calculated by reading the two body variants tube displacement, the body becomes the smallest scale tubes are 1 mm, the test may be one of them as the body becomes tube (as left tube), the other as a loss correction pipe (tube at right), both at the same time to avoid errors generated when the double tube readings, but also consider the impact of the loss of water (Zhang 2013). The specific test operations and balance standard matric suction can be found in Zhou (2010) and Liu (2010) studies. Zhou (2010) test operation includes pre-loaded sample processing clay plates, sample loading and sealing the pressure chamber, the handling of the water after sample loading, testing and treatment, before the test needs to be evacuated specimen sample after the demolition of the sample gas saturation, and erase saturation attached to the surface of the water film-like, and then weighed quality, and calculate the saturation moisture content. Balancing test matrix suction drainage standards for the amount of change within 24 hours, whichever is less than 0.1 ml (Liu 2010).

2.2 *Sample*

Soil samples taken from Qujiang campus loess of Xi'an University of Technology, high sample and diameter of 3.13×7.13 cm, preparation of initial water content is 18%, for a cylindrical sample remoulded, Sample preparation method according to the literature of Liu (2010). Samples taken from the literature Hong Kong volcanic soil of $20 \times 20 \times 20$ cm cube-like remoulded (Charles 2000).Their main indicators of physical and mechanical properties as shown in Table 1.

2.3 *Test methods*

Due to the long test cycle of SWCC, this paper documents provided test data and laboratory test data made to measure SWCC tests mainly from the following aspects, in order to calculate the hysteresis values, revealing different conditions of SWCC lag of return characteristics.

(1) volcanic soil remodeling samples of Hong Kong without pressure wet cycle test different initial dry density, as shown in Table 2; (2) Xi'an loess and Hong Kong volcanic soil wet and dry cycle test several times, as shown in Table 3; (3) with initial dry density of 1.47 g/cm3 remodeling Hong Kong volcanic soil samples and undisturbed samples were (0 kPa, 40 kPa, 80 kPa) of wet and dry cycles under different stress test, as shown in Table 4.

3 TEST RESULTS AND DISCUSSION

3.1 *Hysteresis characteristics of soil-water characteristic curve under different initial dry densities*

Hong Kong volcanic soil research data cited Professor Wu Hongwei(Liu 2010), the hysteresis curve and fitting curve shown in Figure 2, by hysteresis curve calculated values as shown in Table 5, and relationship between the dry density and hysteresis degrees curve shown in Figure 3.

From Figure 2 hysteresis curve morphological point of view, the larger the sample dry density, hysteresis curve surrounded by the hysteresis loop area is significantly smaller than the dry density of small samples; Figure 3 shows the relationship between the graph view, dry density of the sample, the smaller the degree of hysteresis. The reason is that, as the sample initial dry density increases, the soil pore volume decreases, matric suction increases, the permeability decreases, the residual volumetric water content is reduced, the soil-water characteristic curve of hysteretic behavior weakened, hysteresis value decreases.

3.2 *Drying-wetting Cycles on the influence of soil-water characteristic curve hysteresis characteristics*

Figure 4 shows a sample that test curve and fitting curve that twice Xi'an loess and three times Hong Kong volcanic soil drying-wetting cycles soil water characteristic curve, its hysteresis value of hysteresis curve is calculated as shown in Table 6.

From experimental hysteresis curve, whether loess or volcanic soil, the hysteresis loop area decreases

Table 1. Index perties of Xi'an loess and Volcanic soil.

Soil type name	Specific Gravity	Plasticity index	Liquid limit water content /%	Plastic limit moisture /%	ptimum water content /%	Maximum dry density /g/cm^3
Xi'an loess	2.72	13.3	30.9	17.6	13.4	1.78
Volcanic soil	2.62	22	55.4	33.4	22	1.603

Table 2. The drying-wetting cycle test of volcanic soil specimens with different initial dry densities.

Sample No.	Sample Type	Test types	The maximum suction applied /kPa	Sample initial dry density /g/cm^3
CDV—R1 (C)	Remodeling Sample	No pressure drying-wetting cycle	400	1.47
CDV—R2 (C)	Remodeling Sample	No pressure drying-wetting cycle	200	1.50
CDV—R3 (C)	Remodeling Sample	No pressure drying-wetting cycle	200	1.53

Table 3. The test program of loess and volcanic soil with repeatedly drying-wetting cycle.

Sample No	Saturation mode	Sample initial dry density g/cm^3	Sample Type	Wet and dry cycles	The maximum suction /kPa
WH—1.39	Saturated flooding	1.39	No pressure drying-wetting cycle	2	800
CDV—R1(C)—1.47	Pumping saturation	1.47	No pressure drying-wetting cycle	3	400

Note: The saturation table WH-1.39 sample water saturation after only reached about 80 percent, and did not completely saturated.

Table 4. Drying-wetting cycle test of remolded and natural volcanic soils under different stress conditions.

Sample No	Sample Type	Test types	Applied stress/ kPa	The maximum suction applied/kPa	Sample initial dry density/ g/cm^3
CDV—R1 (C) (0 kPa)	Remodeling Sample	No pressure drying-wetting cycle	0	400	1.47
CDV—R2 (C) (40 kPa)	Remodeling Sample	Pressure drying-wetting cycle	40	200	1.47
CDV—R3 (C) (80 kPa)	Remodeling Sample	Pressure drying-wetting cycle	80	200	1.47
CDV—N1 (C) (0 kPa)	Undisturbed samples	No pressure drying-wetting cycle	0	100	1.47
CDV—N2 (C) (40 kPa)	Undisturbed samples	Pressure drying-wetting cycle	40	200	1.47
CDV—N3 (C) (80 kPa)	Undisturbed samples	Pressure drying-wetting cycle	80	200	1.47

Note: The table "R" representative sample remodeling, "N" on behalf of undisturbed samples; initial dry density of 1.47 g/cm3 void ratio corresponding to 0.782.

with drying-wetting cycles increases, the calculated value of each hysteresis also reflects this trend. The reason is that, with the increase drying-wetting cycles, resulting in a sample void residual bubbles continue to prevent water continues to enter the pores, so that the amount of bubbles within the sample stabilized, thus further weaken the influence of drying-wetting cycles generated, SWCC cause hysteretic behavior continues to weaken, the hysteresis values decreasing trend weakened.

3.3 *Effects of stress on soil-water characteristic curve of hysteretic characteristics*

Data cited hysteresis curve in this section are undisturbed natural volcanic soil sample data and reshape, based on data drawn hysteresis curve of natural or remodeling volcanic soil under different stress, it be shown in Figure 5. Their hysteresis degrees calculation results in Table 7. Relationship curve of Hysteresis degree and stress condition are shown in Figure 6.

Hysteresis curve cited the experimental point of view, whether remoulded samples or natural samples, hysteresis loop area is increase as stress decrease. The calculated degree of each hysteresis also reflects this trend. The reason is that the stress increase the dry density of the sample, the pore volume decreases, the difference of soil water content decreases, the adsorption of water in the pores of the soil increased, resulting in reduced hysteresis characteristics, hysteresis value decreases.

As can be seen, it may be effected by the dry density, drying-wetting cycles and variations of vertical stress, it due to changes void volume of soil. For researching it, we summarized the stress under the

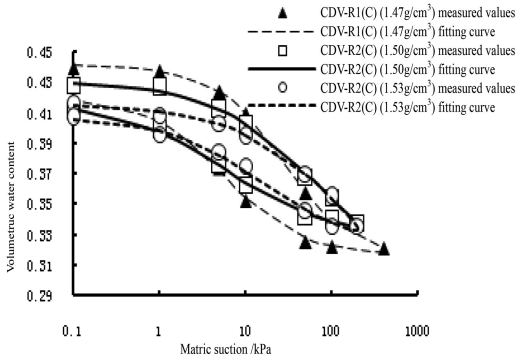


Figure 2. The measured and best fitted drying-wetting cycle SWCCs of volcanic soil specimens with different initial densities.

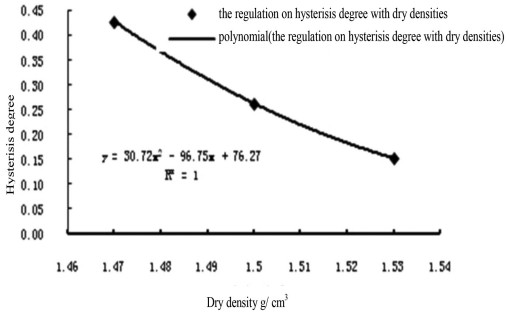
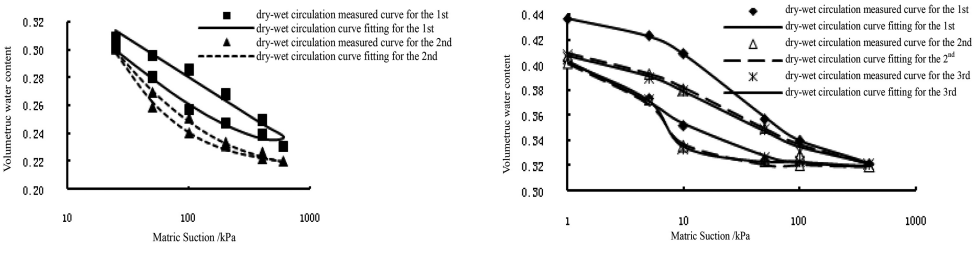


Figure 3. The regulation on hysterisis degree with different dry densities of volcanic soil.

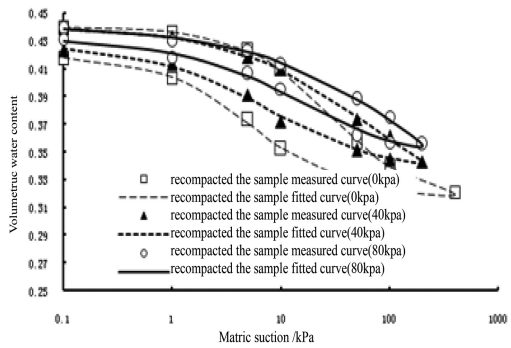
Table 5. Summarization of the hysterisis degree of volcanic soil with different initial densities.

Sample No	Residual volumetric water content	Saturated volumetric water content	Residuals	$\Delta\theta_{max}$/ Corresponding suction	Hysteresis degree
CDV-R1(C)	0.3120	0.4408	5.69×10^{-6}	0.05492/9 kPa	0.4264
CDV-R2(C)	0.2844	0.4311	1.59×10^{-5}	0.03827/9.2 kPa	0.2609
CDV-R3(C)	0.2468	0.4153	1.16×10^{-5}	0.02646/23 kPa	0.1570

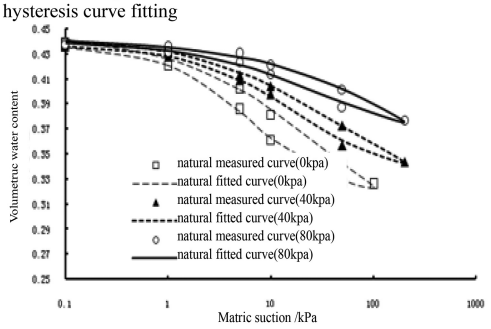


(a) drying-wetting loess 2nd cycle test fitting curves and graphs (b) three times volcanic soil wet cycle test fitting curves and graphs

Figure 4. The measured and best-fitted repeated drying-wetting cycle SWCCs of loess and volcanic soil.



(a) Remodeling test volcanic soil under different stress and hysteresis curve fitting



(b) Undisturbed volcanic soil under different stress test and hysteresis curve fitting

Figure 5. The measured and best-fitted drying-wetting cycle SWCCs of remodeling and natural volcanic soil with different stress conditions.

condition of different dry density and the pore ratio and the degree of hysteresis curve hysteresis of their value, it is shown in table 8. So we are to draw sample void ratio and its corresponding curve hysteresis is worth relation curve, as shown in Figure 7. It can see that the soil dry density changes caused by the change of void ratio on the hysteretic effect results are much smaller than the remoulded, undisturbed soil stress changes caused by the pore ratio on the hysteretic degrees. For remake sample and undisturbed sample, stress decreases, and pore ratio increases, the hysteresis of the corresponding hysteresis curve of the degree of value also increase, but from the point of the curve slope of as shown in figure 7, undisturbed sample decreasing degree is much less than remaking sample, hysteresis degree value is far less than the remake sample. The reason is that the same sample of

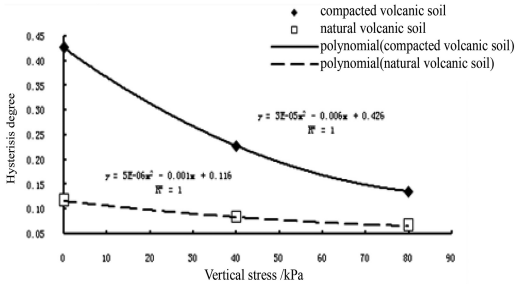


Figure 6. The regulation on hysterisis degree with stress compacted and natural volcanic soils.

Table 6. Summarization of the hysterisis degree of loess and volcanic soil after repeatedly drying-wetting cycle tests.

	Loess drying-wetting cycles		Volcanic soil drying-wetting cycles		
Project	1	2	1	2	3
Residual volumetric water content	0.0677	0.2105	0.3120	0.3081	0.3068
Saturated volumetric water content	0.4880	0.3997	0.4408	0.4188	0.4163
Residuals	2.12×10^{-5}	1.41×10^{-5}	5.66×10^{-6}	6.01×10^{-5}	4.23×10^{-5}
$\Delta\theta_{max}$/Corresponding suctionkPa	0.01937/95	0.00845/68	0.05492/9	0.04640/14	0.04577/12
Hysteresis degree	0.0461	0.0446	0.4264	0.4192	0.4180
Reduce the magnitude of hysteresis values	/	3.25%	/	1.67%	0.29%

Table 7. Summarization of the hysterisis degree of compacted and natural volcanic soil in different stress conditions

Sample No.	Residual volumetric water content	Saturated volumetric water content	Residuals	$\Delta\theta_{max}$/ Corresponding suction	Hysteresis degree
CDV-R1(C)	0.3120	0.4408	5.69×10^{-6}	0.05492/9 kPa	0.4264
CDV-R2(M)	0.2941	0.4412	8.08×10^{-6}	0.03348/12.3 kPa	0.2276
CDV-R3(M)	0.2655	0.4410	1.14×10^{-5}	0.02370/24 kPa	0.1351
CDV-N1(C)	0.2494	0.4487	4.35×10^{-5}	0.02319/14 kPa	0.1164
CDV-N2(M)	0.3044	0.4435	1.82×10^{-5}	0.01164/31 kPa	0.0837
CDV-N3(M)	0.2773	0.4417	9.61×10^{-6}	0.01082/35 kPa	0.0658

Note: The table “R” representative sample remodeling, “N” on behalf of undisturbed samples.

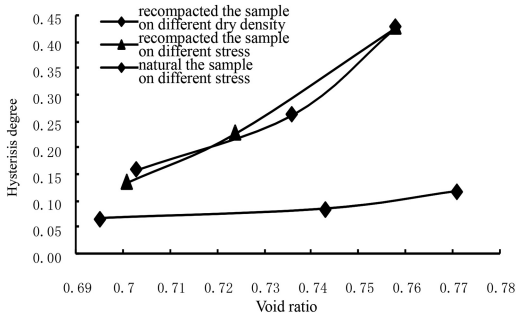


Figure 7. Influence of void ratio on the hysterisis degree of conditions of different soil specimens.

structural effect on the soil-water characteristics have weakened, lead to the undisturbed sample hysteresis curve hysteresis value than the remake sample, and the hysteresis value decreases with increasing stress of trend will be less than remaking sample.

4 CONCLUSION

Factors affecting soil-water characteristic curve hysteresis characteristics is too many, in this paper, the initial dry density, drying-wetting cycle times and vertical stress under the soil-water characteristic curve of unsaturated soil was tested, and curve fitting, with the result of the experiment by using hysteresis value of the hysteresis characteristics of soil in the characterization, discussed the related factors influencing the hysteresis degree value. The results showed that the dry density changes caused by void ratio changes cause hysteresis degree value of the effects of changes in the results are much smaller than the influence of stress; Void ratio changes for the remoulded soil-water characteristic curve hysteresis characteristics is greater than the influence of undisturbed soil influence on it, they can be summed up in the influence of soil samples porosity ratio on the hysteretic characteristics of soil-water characteristic curve. But how to reference in the constitutive equation and considering the void ratio change under the action of the hysteretic characteristics of study will need to be in the follow-up work.

REFERENCES

Charles W W Ng and Y W Pang. Experimental investigations of the soil-water characteristics of a volcanic soil. Canadian Geotechnical Journal, 37: 1252–1264, 2000.

Fredlund D G, Xing A. Equations for the soil-water characteristic curve. Canadian Geotechnical Journal, 1994, 31(4): 521–532.

Kosugi K. Three-parameter lognormal distribution model for soil water retention. Water Resource Research, 1994, 30(4): 891–901.

Gardner W R. Some steady-state solutions of the unsaturated moisture flow equation with application to evaporation from a water table. Soil Science, 1958, 85(4): 228–232.

Huang S Y. Evaluation and laboratory measurement of the coefficient of permeability in deformable, unsaturated soils. Saskatoon, Canada: University of Saskatchewan, 1994.

Imbert C, Olchitzky E, Lassabatère T, et al. Evaluation of a thermal criterion for an engineered barrier system. Engineering Geology, 2005, 81(3): 269–283.

Liu Fengyin, Zhang Zhao, Zhou Dong, etc. Effects of initial density and drying-wetting cycle on soil-water characteristic curve of unsaturated loess. Rock and Soil Mechanics, 2011, 32 (S): 132–136.

Liu Fengyin, Zhang Zhao, Zhou Dong, et al. Debugging of GCTS-Type SWCC device and analysis of the corresponding technical indexes. Journal of Xi'an University of Technology, 2010, 26(3): 320–325.

Li X S. Modeling of hysteresis response for arbitrary wetting/drying paths[J]. Computers and Geotechnics, 2005, 32(2): 133–137.

Miller C J, Yesiller N, Yaldo K, et al. Impact of soil type and compaction conditions on soil-water characteristic. Journal of Geotechnical and Geoenvironmental Engineering, 2002, 128(9): 733–742.

Min T K, Huy P T. A soil-water hysteresis model for unsaturated sands based on fuzzy set plasticity theory. KSCE Journal of Civil Engineering, 2010, 14(2): 165–172.

Mualem Y, Beriozkin A. General scaling rules of the hysteretic water retention function based on Mualem's domain theory[J]. European Journal of Soil Science, 2009, 60(4): 652–661.

Nuth M, Laloui L. Advances in modeling hysteretic water retention curve in deformable soils. Computers and Geotechnics, 2008, 35(6): 835–844.

Pham H Q, Fredlund D G, Barbour S L. A study of hysteresis models for soil-water characteristic curves. Canadian Geotechnical Journal, 2005, 42(6): 1548–1568.

Romero E, Gens A, Lloret A. Temperature effects on the hydraulic behaviour of an unsaturated clay. Geotechnical and Geological Engineering, 2001, 19(3–4): 311–332.

Sugii T, Yamada K, Kondou T. Relationship between soil-water characteristic curve and void ratio, Proceedings of the 3rd International Conference on Unsaturated Soils. Recife, Brazil: Swets and Zeitlinger, 2002, Vol. 1: 209–214.

Van Genuchten M Th. A closed-form equation for predicting the hydraulic conductivity of unsaturated soils. Soil Science Society of America Journal, 1980, 44(5): 892–898.

Vanapalli S K, Pufahl D E, Fredlund D G. The influence of soil structure and stress history on the soil-water characteristics of a compacted till. Geotechnique, 1999, 49(2): 143–159.

Zhang Zhao, Liu Fengyin, Zhao Xuguang, ect. A soil-water characteristic curve model considering void ratio variation with stress. Shuli Xuebao, 2013, 44(5): 578–585.

Zhou Dong. Investigation of stress state-dependent soil-water characteristic curve and permibility behavior for unsaturated soil. Xi'an: Xi'an University of Technology. 2010.

Unsaturated Soil Mechanics—from Theory to Practice – Chen et al. (Eds)
© 2016 Taylor & Francis Group, London, ISBN 978-1-138-02921-7

Soil water retention of a compacted sandy clay with sub-critical water repellency

S.D.N. Lourenço
The University of Hong Kong, Hong Kong SAR, China

N. Jones & C.P. Morley
Cardiff University, UK

S.H. Doerr & R. Bryant
Swansea University, UK

ABSTRACT: Soil water retention curves are usually obtained on the assumption that soils are wettable. While this is true at high water contents, where pores are filled by water or a film of water covers the particles, it is less likely for drier states, where the adhesion of water menisci to the surface of the particles is controlled by the material chemistry and surface roughness, the presence of organic matter and the soil water content. Here, we present suction, water content and wettability measurements for model samples following drying paths. A comparison is done for a model material (sandy clay) in an initially wettable and sub-critical water repellent state ($<90°$). Wettability was manipulated by treatment with organic acids which mimic the chemistry of natural water repellent substances. Suction was measured with a high suction tensiometer and wettability via contact angles by the sessile droplet method. The results revealed lower water retention and greater contact angles for the water repellent samples.

1 INTRODUCTION

Soil Water Retention Curves (SWRC) are usually obtained on the assumption that soils are wettable i.e. water menisci with zero degrees contact angles. The contact angles of the water menisci against the soil particles quantify wettability. While this may be correct at high water contents, it is less likely for drier states, where the adhesion of water menisci to the surface of the particles is controlled by the material chemistry and surface roughness, the presence of organic matter and the soil water content. In nature, soil water repellency is induced by water-repellent substances of organic origin, such as natural waxes in forest soils and substances that result from vegetation fires (Doerr et al., 2006). When these soils are wetted, water menisci with contact angles $>90°$ or a threshold value are formed and water does not infiltrate. In slopes water repellency induces debris flows, which have been documented to occur after wildfires (Moody & Ebel, 2014). Following the soil science terminology, which will be used here, wettable soils have contact angles of 0°, sub-critical water-repellent soils $<90°$ and water-repellent soils $>90°$. According to Young-Laplace equation, a contact angle of 90° marks the theoretical threshold for attraction or repulsion between two particles or infiltration to occur or not in granular media. This study focus on wettability conditions 0°–90°, or sub-critical water repellent conditions, where the occurrence of slight water repellency is more likely.

The drying paths of SWRCs were obtained for a wettable and sub-critical water repellent sandy clay mixture by measuring directly the soil water content, suction and wettability. For suction, a new high suction tensiometer (Lourenço et al., 2008) was used. Wettability was via contact angles by the sessile drop method (Bachmann et al., 2000). The same material was used in wettable and water repellent conditions. Water repellency was induced by substances of similar chemistry to those in nature. Model granular materials were used to minimize sample variability and facilitate the measurements and clayey soils because the effect of wettability is poorly understood on these materials.

2 MATERIALS AND METHODS

2.1 Manipulation of soil wettability

To induce sub-critical water repellency (contact angles $<90°$) the procedure detailed next was followed:

a) The medium-sand sand and clay (Speswhite kaolin) were oven-dried at 105°C to remove any residual water content. The treatment was conducted in 300 g portions.
b) After drying, stearic acid (3.48 g) and octadecane (3.12 g) were added to 150 g of sand and 150 g of

clay and mixed with a solvent (400 ml of chloroform) in a flask which was then placed on a water bath in a rotary evaporator and allowed to mix for 24 hours. The use of stearic acid ($C_{17}H_{35}CO_2H$) and octadecane ($C_{18}H_{38}$) closely simulate the chemistry of natural water repellent substances (Morley et al., 2005). These quantities (3.48 g stearic and 3.12 g octadecane) were found to produce contact angles in the vicinity of 90° in the treated, air-dried samples.

c) After mixing for 24 h in the rotary evaporator the chloroform was evaporated by raising the temperature to approximately 70°C. The sample was then collected from the flask and stored until further use.

d) To compact the samples, the sand and clay (treated or untreated) were mixed at the optimum water content of 17%, left to equilibrate for 24 h, and compacted following the British Standard for the laboratory testing soils (BS1377, 1990). This produced a cylindrical sample of approximately 1000 cm^3, bulk density 1.97 Mg/m^3, void ratio 0.57 and degree of saturation 80% for both the wettable and water repellent samples.

2.2 *Measurement of matric suction*

Suction was measured with a high suction tensiometer (Ridley & Burland, 1993), manufactured at Cardiff University, with a 1500 kPa air-entry value ceramic stone (Figure 1). High suctions are possible to maintain as long as (1) the stone and reservoir are fully saturated, usually requiring pressurization up to 4 MPa, (2) suction is below the air-entry value of the stone, the maximum commercially available is 1500 kPa, and (3) the dimensions of the inner reservoir are kept as small as possible (at the micron-level) (Take and Bolton, 2003). The tensiometer used in this research measured up to 1000 kPa, its suction at cavitation.

The tensiometer was pressurized to the range 2–3 MPa, and the measurement range tested by leaving the stone to dry to the atmosphere. The tensiometer was saturated, if suction at cavitation reached 1000 kPa. If not, the instrument was placed back in the pressure vessel and repressurized. No calibration in the negative range was conducted. The calibration from the positive range was extended to the negative range.

Suction was measured at constant water content conditions by smearing the stone against the soil and waiting for equilibrium. For drier samples, the stone was covered on thin film of water to force the contact with the soil. For accuracy, measurements were conducted by two separate tensiometers. Prior to the measurements, the tensiometer was removed from the vessel and left in free water for 2 to 3 days to allow the metal body to recover from the pressure vessel confinement (the pressure readings would creep up or down immediately after removal).

2.3 *Measurement of apparent contact angles*

The compacted sample was placed directly in the goniometer stage (Kruss GmbH, Germany), and a sessile water drop of approximately 10 μL dropped at the surface in a different area from where suction was measured. A video was recorded, and the contact angle measured for the first image of the 10 μL drop that allowed the air-water-solid interface to be identified (Bachmann et al., 2000). Given that the wettability of the clay-sand mixture is rather high, with the drop spreading laterally as soon as it touches the sample surface, each video frame was analyzed (sampling rate = 25 frames per second) until the air-water interface was visible and the contact angle measurable, usually in less than 1 s. The average contact angle was computed from five contact angle measurements.

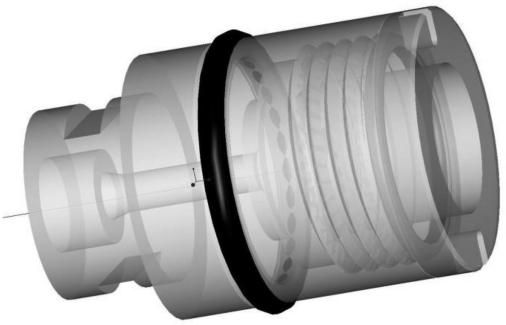


Figure 1. The high suction tensiometer used (diameter = 14mm; length = 22mm) (Drawing: Xiangwei Wang).

2.4 *Procedure to obtain the main drying path*

To determine the drying path, the compacted samples (near full saturation) were dried to the atmosphere in steps of approximately 200 kPa suction until the desired level of suction and until a maximum of 1000 kPa. When it reached the target value, the sample was wrapped in layers of cling film and left to equilibrate for 24 h to ensure redistribution of water between the sample boundaries and the core. After equilibration, measurements of suction, mass (for the gravimetric water content) and contact angles were taken.

A new sample was used for each measurement, since each contact angle measurements involve wetting the sample with a small drop. Therefore, all samples were subjected to the same drying history and both the contact angle and tensiometer measurements were conducted in different areas across the surface of the samples.

3 RESULTS AND DISCUSSION

3.1 *Drying Soil Water Retention Curves*

Figure 2 shows suction as a function of the gravimetric water content for the wettable and water repellent samples. Immediately after compaction suction was approximately 80 kPa for all samples, corresponding to a degree of saturation of 80 %. Figure 2 shows the water repellent sample positioned below the wettable

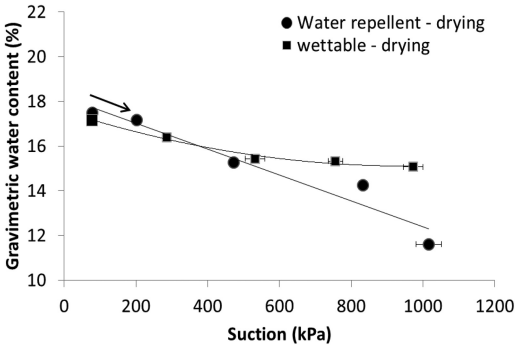


Figure 2. Relations between suction and gravimetric water content for a wettable and water repellent sample under a drying path.

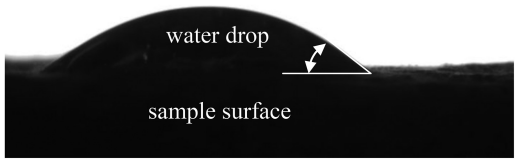


Figure 3. Contact angles (annotated) for the wettable sample at 1000 kPa suction, as measured by the sessile drop method (drop diameter ~10mm).

sample for suctions higher than 400 kPa, indicating that the water repellent samples retained less water than the wettable samples when dried for the same suction range. For the wettable samples, an increase of suction to 1000 kPa required a decrease in the gravimetric water content by 1.4%, while for the water repellent samples the gravimetric water content decrease was 5.9%.

Figure 3 and 4 show the contact angles for the wettable and water repellent samples, respectively. The contact angles were measured on the wet internal part of the drop, on the left and right side and averaged. The smooth surface of the clayey sample allows the edges of the drop to be identified, which is a challenge when conducting these measurements in sands. However, given that the contact angles represent a measurement done in dynamic conditions obtained during the first miliseconds of the water drop resting on the surface of the sample, the standard deviation reached ±25.1° at around 1000 kPa suction.

Figure 5 shows the relation between the apparent contact angles and suction for the wettable and water repellent samples. The plot shows increasing and higher contact angles for the water repellent soil. For the wettable samples, the increase in the contact angles was from 13° to 26°. The contact angles around 20° are comparable to other minerals: mica (10°), dolomite (5.6–7.6°), quartz (30°) (Bryant et al., 2006; Gence, 2006; Fisher & Lark, 1980). For the water repellent samples the contact angles increased from 47.7° to 87.1° (both at 1000 kPa). The relation between contact angles and suction was linear for both soils.

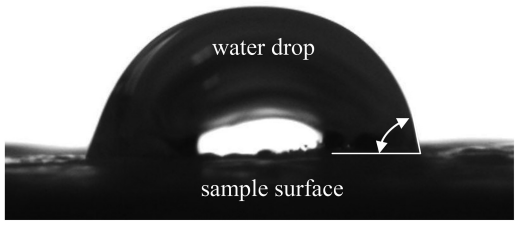


Figure 4. Contact angles (annotated) for the water repellent sample at 1000 kPa suction, as measured by the sessile drop method (drop diameter ~10 mm).

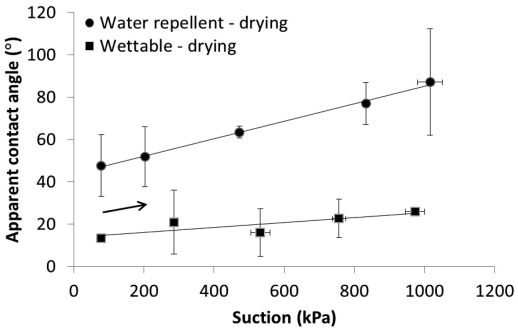


Figure 5. Relations between suction and apparent contact angles for a wettable and water repellent sample under drying path.

4 CONCLUSIONS

Soil water repellency is a soil condition that develops in certain soils as they dry. Direct measurements of suction with high suction tensiometers, wettability via contact angles with a goniometer and gravimetric water content revealed lower water retention for the water repellent materials following drying paths. Their inability to hold water is due to the increased contact angles (or reduced wettability).

ACKNOWLEDGEMENTS

This research was funded by Engineering and Physical Sciences Research Council (UK) (EP/008756/1) and the Royal Society (UK) (RG090044). Dr. Xiangwei Wang (School of Engineering – Cardiff University now at Aviation and Aerospace – Rolls-Royce) manufactured the high suction tensiometers.

REFERENCES

Bachmann, J., R. Horton, R.R. van der Ploeg & S. Woche. 2000. Modified sessile drop method for assessing initial soil-water contact angle of sandy soil. *Soil Sci. Soc. Am. J.* (64): 564–567

Bryant, E. M., Bowman, R. S. & Buckley, J. S. 2006. Wetting alteration of mica surfaces with polyethoxylated amine surfactants. *J. Petrol. Sci. Engng 52* (2–4): 244–252

Doerr, S.H., R.A. Shakesby, L.W. Dekker & C.J. Ritsema. 2006. Occurrence, prediction and hydrological effects of water repellency amongst major soil and land use types in a humid temperate climate. *Eur. J. Soil Sci.* (57): 741–754

Fisher, L. R. & Lark, P. D. 1980. The effect of adsorbed water vapour on liquid water flow in Pyrex glass capillary tubes. *J. Colloid Interface Sci.* 76 (1): 251–253.

Gence, N. 2006. Wetting behavior of magnesite and dolomite surfaces. *App. Surf. Sci.* 252 (10): 3744–3750

Lourenço, S.D.N., D. Gallipoli, D. Toll, C. Augarde, F.Evans & G. Medero. 2008. Calibrations of a high suction tensiometer. *Géotechnique* 58(8): 659–668

Moody, J.A. & Ebel, B. 2014. Infiltration and runoff generation processes in fire-affected soils. *Hydrol. Processes* (38): 3432–3453

Morley, C.P., K.A. Mainwaring, S.H. Doerr, P. Douglas, C.T. Llewellyn & L.W. Dekker. 2005, Organic compounds at different depths in a sandy soil and their role in water repellency. *Aust. J. Soil Res.* (43): 239–249

Ridley, A., and J. Burland. 1993. A new instrument for the measurement of soil moisture suction. *Géotechnique*, 43(2): 321–324

Unsaturated Soil Mechanics—from Theory to Practice – Chen et al. (Eds)
© 2016 Taylor & Francis Group, London, ISBN 978-1-138-02921-7

Measurement of Soil-Water Characteristic Curve of expansive soil using filter paper method

H. Li
Institute of Resources and Environment, North China Institute of Water Conservancy and Hydroelectric Power, Zhengzhou, China

L.C. Li
Guilin University of Technology, Guilin, China

Z.Q. Huang
Institute of Resources and Environment, North China Institute of Water Conservancy and Hydroelectric Power, Zhengzhou, China

ABSTRACT: The change in matric suction can significantly influence the stability of a soil slope. Through a soil water characteristic curve the matric suction can be determined provided the water content is given. In this paper the filter paper method is adopted to measure the soil water characteristic curves of an unsaturated expansive soil, including the initial drying curve, the main wetting curve and second-order scanning curves. Based on the experimental data, the internal variables-based capillary hysteretic model is calibrated and introduced to simulate the hysteretic soil-water characteristics of the expansive soil, showing good agreements between simulated and measured results.

1 INTRODUCTION

Soil Water Characteristic Curve (SWCC) is the relationship between the matric suction and the water content in the soil (Huang, 2008, 2009). SWCC is the most important part for unsaturated soil research. Vanapalli (1996) studied the relationship between SWCC and the strength of unsaturated soil and found that SWCC has great influence on the strength of unsaturated soil. Fredlund (1996, 1997) studied SWCC and found that the coefficient of permeability, shear strength and other factors could be obtained from SWCC. There are many kinds of methods to measure matric suction for unsaturated soil, such as 8 presure plate method, filter paper method, tensiometer method, thermal sensor method and so on. Filter paper method is used to measure the matric suction for unsaturated expansive soil in this paper.

Matric suction and water content do not have one-to-one correspondence during the wetting path and the drying path for unsaturated expansive soil. It shows that there is a hydraulic hysteresis characteristic of SWCC. Wei Changfu has suggested a Capillary Hysteresis Internal Variable Model (CHIVM) to solve this problem. Matric suction of a arbitrary change hydraulic path can be detected by using CHIVM. The hydraulic hysteresis is simulated and campared with the test result.

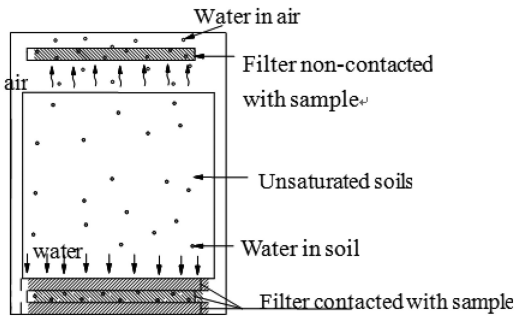


Figure 1. The principle diagram of the filter paper method.

2 METHOD AND MATERIAL

2.1 *Measurement principles*

If the filter direct contacts with the soil and moisture balance can be gained, the salt dissolved in water would move to the filter paper, so the result we got is the matric suction for the soil. If the filter doesn't direct contact with the soil, there is a one-to-one correspondence between the water content of the filter paper and the total suction. Fig. 1 is the principle figure for the test.

Table 1. Physical and mechanical indices of soil samples.

Liquid Limit WL/%	Plastic Limit WP/%	Plastic Index IP IP	Free swelling Ratio %
43	22	21	50

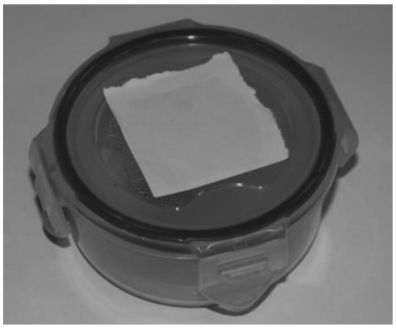


Figure 2. Sealed Container.

2.2 Material and procedure

Expansive soil, according to "the expansion of land area building technical specifications" category, from the Middle Route of South-to-north Water Diversion Project in Nanyang are used as samples. The basic physical parameters are shown in Table 1. According to "the expansion of land area building technical specifications" category, experiments are carried out to test the soil for the low expansion of expansive soil.

As a porous filter media material, the filter paper's moisture sensitivity is high. Material uniformity, absorption rate, stagnant water capacity and other characteristics of different models have a greater difference. Whatman No.42 filter paper is used for the test. The rate of a given relation is as shown in the following formula (1) (2).

$$\text{Lg}\psi = 2.909\text{-}0.0229\omega_f \ (\omega_f \geq 47) \quad (1)$$

$$\text{Lg}\psi = 4.945\text{-}0.0673\omega_f \ (\omega_f \leq 47) \quad (2)$$

LockLock box is used as a sealing device which is shown in Figure 2. The Lock lock box is placed into an oven temperature box (0°–100°). The accuracy of measuring balance is 0.0001 g.

2.3 *Test method*

The initial drying curve, the main wetting curve and the second grade scanning curve of the expansive soil are tested by using filter paper method. The water content of the prepared soil samples is 25%. Produce 26 ring-knife samples. 10 samples are used to test the initial drying curve, 10 samples are for main wetting curve and 6 samples are for second grade scanning curve. The prepared sample was placed in a room where the temperature is 15°, so that the samples are dried naturally to simulate a drying path. A watering can is used to spray the surface of the samples to simulate natural rainfall to simulate the wetting path. Measure the moisture content during wetting and drying process from time to time. Take samples with different moisture content to be loaded.

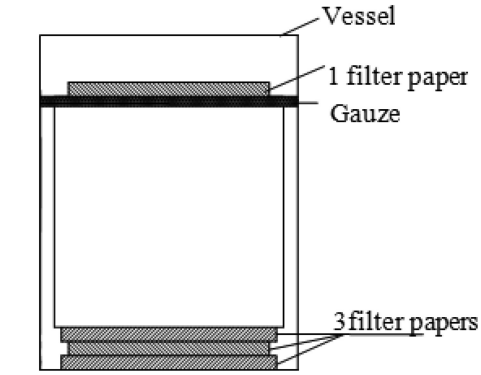


Figure 3. Schematic Diagram of the Filter Paper Method.

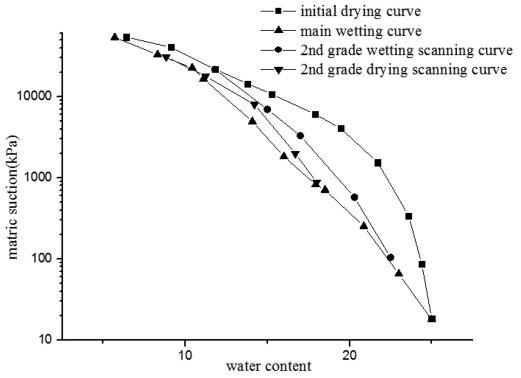


Figure 4. SWCC for expansive soil.

Put the filter paper into a drying oven for about 16 hours to ensure its water content was zero. Measure the paper's mass. Put three dried filter papers onto the bottom of the ring-knife. Put the sample and the filter papers in to a sealed box. Then put a gauze net on the top of the soil sample, as shown in Fig. 3.

Place the samples into an isothermal humidistat. Adjust the temperature to 15° for about 10 days to ensure exchange equilibrium between the sample and the water filter. Then remove the middle one of the three filter papers and measure the mass of the paper. Then dry the paper by using a drying oven and measure the dried mass of the paper. Then calculate the water content of the balanced paper.

3 RESULTS AND ANALYSIS

3.1 *Soil-water characteristic curve*

Based on the moisture content of the filter paper measured by the test, and formulas (1) and (2), the matric

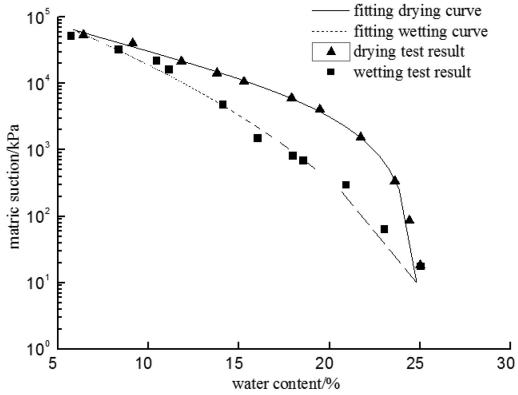


Figure 5. Fitting Chart for the SWCC.

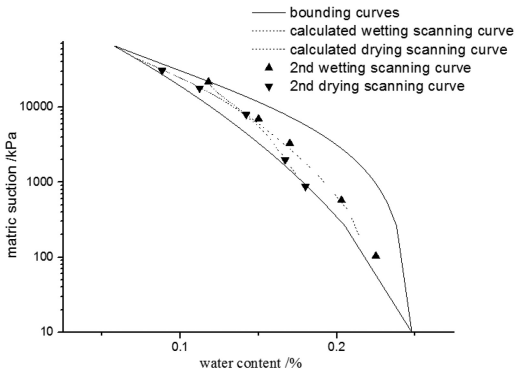


Figure 6. Simulation Results of the Capillary Hysteresis Internal Variable Model.

suction corresponding to different moisture content can be calculated and the soil-water characteristic curve can be gained (Bai, 2011, Wu 2013), as shown in Fig. 4. As can be seen from Figure 4, the filter paper method-based soil water characteristic curve and the pressure plate meter-based curve are basically the same. For unsaturated expansive soil, the soil-water characteristic curves measured using the filter paper method are inexpensive and easy for large-scale range, applicability and high accuracy data. This method can be used as an effective method for measuring the class of unsaturated soil.

3.2 *Fitting of SWCC*

Firstly, the Fredlund proposed model is used to fit on the soil water characteristic curve of expansive soil SWCC that is measured by filter paper method.

$$\theta = \frac{\theta_{sat} + \theta_{irr}(P_c / b)^d}{1 + (P_c / b)^d} \tag{3}$$

Wherein, b and d are model parameters which could be gained by fitting the experimental data. θ_{sat} is saturated water content, θ_{irr} is residual moisture content. Origin software is used to fit the dehumidification and moisture curves. Wherein, in order to obtain better fitting results, θ_{sat} is greater than the saturated water content of the sample and θ_{irr} is less than the residual moisture content of the sample, as shown in fig. 5. Drying curve fitting result is: $b = 1.25537E12$, $d = 0.144$, $\theta_{sat} = 0.337$, $\theta_{irr} = -3.072$. Wetting curve fitting result is: $b = 37995$, $d = 0.695$, $\theta_{sat} = 0.248$, $\theta_{irr} = 0.072$.

3.3 *Scanning curve by using capillary hysteresis internal variable model*

The capillary hysteresis internal variable model is used to simulate the soil-water characteristic relationship in which the water content of the soil sample is changed arbitrarily while the initial drying curve and the main wetting curve are given, as shown in Fig. 6.

In Fig. 6, points B0-B3 are the second grade drying scanning curve, which are located in the main wetting curve. Points A0–A3 are the second grade wetting scanning curve, which are located in initial drying curve. Curve CD is the calculating result of second grade drying scanning curve by using the capillary hysteresis internal variable model. Curve A0E is the calculating result of the second grade wetting scanning curve. Fig. 6 shows that the scanning curves are in conformity better off the measured results calculated. It is obvious that the capillary hysteresis internal variable model can be used to simulate arbitrary changes of any class scanning curve of soil-water characteristic curve of unsaturated expansive soil.

4 CONCLUSIONS

1. Using filter paper method to measure soil water characteristic curve of unsaturated expansive soil is simple and widely applicable. But the operation has a high requirement.
2. The filter paper method to measure soil water characteristic curve can be used to fit the simulating model proposed by D. G. Fredlund. The fitting results are in good agreement with the experimental data.
3. The capillary hysteresis internal variable model can be well applied in unsaturated expansive soil. The calculating result is consistent with the measured value.

ACKNOWLEDGEMENTS

This work is financially supported by the Plan for Scientific Innovation Talents of Henan Province, Natural Science Foundation of China (41202246) and Key Technological Research Project of Henan Province.

REFERENCES

Zhiquan Huang, Linfeng Wu, Anming Wang. Stability analysis of expansive soil slope based on in-situ shear test, *Rock and Soil Mechanics*, 2008, 29(7): 1764–1768.

Zhiquan Huang, Xianting Chen, Tong Jiang. Experimental study of strength characteristics of unsaturated soil of landslide l# in Xiaolangdi Reservoir, *Rock and Soil Mechanics*, 2009, 30(3): 640–644.

Fredlund D, Rahardjo H. soil mechanics for unsaturated soils. Beijing: China Building Industry Press, 1997, 256–278.

Vanapalli S, Fredlund DG, Pufahl DE. The relationship between the soil-water characteristic curve and the unsaturated shear strength of a compacted glacial till. *Geotechnical Testing Journal*, 1996, 19: 259–268.

Fredlund DG, Xing A, Fredlund MD. The relationship of the unsaturated soil shear to the soil-water characteristic curve. *Canadian Geotechnical Journal*, 1996, 33(3): 440–448.

Fredlund D, Xing A, Huang S. Predicting the permeability function for unsaturated soils using the soil-water characteristic curve. *Canadian Geotechnical Journal*, 1994, 31(4): 533–546.

Zhiquan Huang, Sijing Wang, Synergetic-bifurcated prediction model of slope occurrence and its application, *Science in China, Ser. E*, 2003, 46: 69–77.

Zhiquan Huang, K. Tim Law, Handong Liu. Tong Jiang. The chaotic characteristics of landslide evolution: a case study of Xintan landslide. *Environmental Geolog,* 2009, 56(8): 1585–1591.

Xuedong Zhang, Chenggang Zhao, Yan Liu. Simulation and hysteresis model for soil-water characteristic curves. *Journal of engineering geology*, 2010, 18(6): 920–925.

Jinru Cheng, Manxi Jin. Suctioncalibrationfor filterpaper. *Rock and Soil Mechanics*, 2002, 23(6): 800–802.

Zhao Wang, Jinxin Yang, Juanjuan Kuang. Application of filter paper method in field measurement of matric suction. *Chinese Journal of Geotechnical Engineering*. 2003, 25(4): 405–408.

Fuping Bai, Sihong Liu, Jiao Yuan. Calibration test for total suction wetting curve of filter paper. *Rock and Soil Mechanics*, 2011, 32(8): 2336–2340.

Dean Sun, Junran Zhang, Haibo Lv. Soil-water characteristic curve of Nanyang expansive soil in full suction range. *Rock and Soil Mechanics*, 2013, 34(7).

Junhua Wu, Junping Yuan, Song Yang. Experimental study on SWCC of expansive soil with cracks using filter paper method [J]. *Advances in Science and Technology of Water Resources*, 2013, 33(5): 61–64.

Wei C, Dewoolkar MM. Formulation of capillary hysteresis with internal state variables. *Water Resources Research*, 2006, 42(7).

Unsaturated Soil Mechanics—from Theory to Practice – Chen et al. (Eds)
© 2016 Taylor & Francis Group, London, ISBN 978-1-138-02921-7

Drying-wetting Soil-Water Characteristic Curves of highly expansive soil

A.M. Al-Mahbashi
Eng. Abdullah Bugshan Research Chair in Expansive Soils, Department of Civil Engineering, College of Engineering, King Saud University, Riyadh, Saudi Arabia

T.Y. Elkady
Eng. Abdullah Bugshan Research Chair in Expansive Soils, Department of Civil Engineering, College of Engineering, King Saud University, Riyadh, Saudi Arabia
Department of Public Work, Cairo University, Egypt

M.A. Alshamrani
Eng. Abdullah Bugshan Research Chair in Expansive Soils, Department of Civil Engineering, College of Engineering, King Saud University, Riyadh, Saudi Arabia

ABSTRACT: Numerous studies conducted on different soils had focused on evaluating the drying Soil-Water Characteristic Curve (SWCC); however, in some applications measurement of wetting soil-water characteristic curve is equally important. SWCC determination for expansive soils provides an additional challenge due to volume changes that samples undergo due to change in water content. This paper aims to present the results of an experimental program developed to investigate the SWCC of a highly expansive soil under wetting and drying cycle. SWCC determination was carried out using axis translation technique. In addition, the effects of sample saturation procedures on SWCC were investigated by considering two saturation methods: free swell and preload method under optimum and dry of optimum water content conditions. The results revealed that saturation procedures had a significant effect on drying SWCC (mostly represented in saturated water content and air-entry value). At high suction (i.e., >0.4 MPa), the effect of saturation method and initial molding conditions tend to diminish. Significant hysteresis has been noticed between drying and wetting soil-water characteristic curves due to air entrapped inside soil pores during drying path and inelastic volume changes during drying and wetting SWCC path. Effect of saturation procedures was more pronounced in the case of drying-SWCC, whereas in the wetting path the difference was less markable.

1 INTRODUCTION

Soil-Water Characteristic Curve (SWCC) is an important hydraulic property which represents the relationship between water content (i.e., volumetric water content (θ), gravimetric water content (w), or degree of saturation (S)) and soil suction. The soil-water characteristic curve describes the ability of soil to retain (or hold) water at different suctions.

Air-Entry Value (AEV), residual water content (w_r) and saturated water (w_{sat}) content represent main parameters of the SWCC. The value of suction where the water content begins to drop quickly during the drying process (or in which air starts entering largest pores) is called air-entry value (AEV). The residual water content is the point in the curve where the change in water content is insignificantly affected by increase in suction. All these characteristics are important parameters that describe the unsaturated soil behavior. Behavior of unsaturated soil is a function of the amount of water occupied in its pores. SWCC depicted the variation of soil suction and water inside the soil pores so, it reflects pores size and its distribution in the soil and considered as a key parameter in interpreting unsaturated soil behavior (Nowamooz & Masrouri 2010, Amaral et al 2013, Casini et al 2013).

Numerous models have been proposed to predict unsaturated behavior of soil such as hydraulic conductivity, shear strength, and volume change using SWCC (Leong & Rahardjo 1997, Barbour 1998). These models are valuable in reducing of time and costs required in direct measurement of unsaturated soil properties. Depending on the type of geotechnical application, the drying or wetting curve should be selected.

Based on SWCC measurement procedure, two types of SWCC may arise; namely, drying (or desorption) curve and wetting (or adsorption) curve. The drying curve depicts the changes in water content with increase in soil suction (desorption or drying process), while the wetting curve shows the corresponding changes of water content along with reduction in soil

suction (adsorption or wetting process). Drying and wetting SWCCs are different curves with different characteristics (Agus & Shanz 2006). In general, water content of soil sample during drying path is greater than that obtained for this sample during wetting path at same value of suction.

Recently, several studies have been conducted to investigate the hysteresis of drying-wetting SWCCs of expansive soil (Li 2005, Bennett et al. 2012, Wang et al. 2013, Zhang et al. 2013). Pham et al. (1994) stated that differences between drying-wetting path of SWCCs are attributed to: i) plastic deformation of the soil; and ii) air entrapped during the drying process. Ke et al. (2013) noted that saturated water content and residual water content are changing during drying-wetting path which indicate changes in soil retention properties. Substantial difference in water content at zero suction between drying and wetting SWCC was observed (Likos et al. 2013). Pham et al. (2003) concluded that fully saturated condition is not reached during the determination of wetting SWCC following the evaluation of the drying SWCC because of air entrapped in soil pores during drying process.

This study aims to evaluate the drying and wetting SWCCs of highly expansive soil. Furthermore, the effect of saturation procedures on the drying-SWCC for samples with different molding conditions (i.e., optimum and dry-of-optimum) was investigated.

2 MATERIAL USED

The expansive clay was taken from an excavated test pit of depth 2–3 m below ground surface in Al-Qatif city which is located in the Eastern Province of Saudi Arabia. The city is 20 km North of Al-Dammam city the main port in the province (latitude 26°56′N and longitude 50°01′E). For the current study, clay samples were crushed in laboratory after air drying and sieved using sieve No 40.

Tests were conducted to perform a full geotechnical characterization of expansive clay according to American Society of Testing and Materials (ASTM). Geotechnical characterization included Atterberg limits (ASTM D 4318-2000), standard proctor compaction, grain size distribution tests (ASTM D 422-2002) and one dimensional oedometer tests (D 2435 – 04) to assess swelling characteristics of Al-Qatif clay. A summary of geotechnical characterization data for the tested soil is presented in Table 1.

3 EXPERMINTAL WORK

Determination of the dry and wetting SWCC were conducted using Fredlund SWC device. This device operates on the principle of axis translation using a high entry value ceramic disc. Furthermore, the device has a capability to follow different stress conditions and measuring both drying and wetting path of SWCC. More information regarding device instruction and testing procedures is provided by Pham et al. (2004), Padilla (2006), and Al-Mahbashi (2014).

Table 1. technical characteristics of Al-Qatifclay.

Value	Test
Specific Gravity, G_s	2.71–2.77
Liquid Limit, w_L (%)	160–170
Plastic Limit, w_P (%)	60
Shrinkage Limit (%)	11–15
Plasticity Index (%)	100–110
Classification	(CH)
OMC and MDD	(36% and 1.21 gm/cm^3)
Unified soil swelling potential (ASTM D4546-03)	17–26%
Swelling pressure (kPa)	450–600
Passing #200 (%)	95
Clay percentage (%)	72

Remolded samples were prepared with dry density and water content obtained from compaction curve (Table. 1). Soil samples were statically com-pacted into a test ring to final dimensions of 50 mm diameter and 16 mm height using a hand operated hydraulic jack.

For the determination of the drying SWCC, soil samples were saturated at the beginning of the test using an oedometer cell to monitor vertical strain during saturation. In this study, the saturation pro-cess, of soil samples were performed using two methods; namely; free swell (FS) and preload method (PL). For the free swell saturation procedure, the compacted sample was placed in an oedometer cell where it was inundated with distilled water under a small stress of 7 kPa. Samples were allowed to swell until reaching swell strain equilibrium (approximately after 24 hours). In the preload method, the sample was allowed to swell freely under small stress of 7 kPa to reach vertical strain equilibrium and then gradually loaded to return to its initial height.

After saturation, the sample was transferred to the Fredlund SWC device and placed carefully in the center of ceramic disk with ensuring good contact between the base of sample and the ceramic disc. In the drying path, the suction values were increased gradually up to 1400 kPa, while in the wetting path suction increments reversed to around 1 kPa. Increment of suction was applied by adjusting the air pressure regulator until desired suction is reached.

The equilibrium under each applied suction increment was considered attained when there was no change in the water level (in the water tubes fixed on the device) for 24 hr. For the determination of sample water content at suction equilibrium, device cell was dismantled and the weight of soil sample with ring was recorded as expeditiously as possible.

4 RESULTS AND DISCUSSION

4.1 *Effect of saturation procedures*

The effect of saturation procedures (i.e., FS and PL) on the drying SWCC of expansive clay compacted

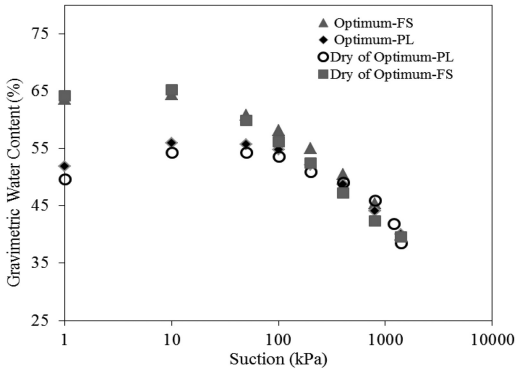


Figure 1. Effect of saturation procedures on SWCC.

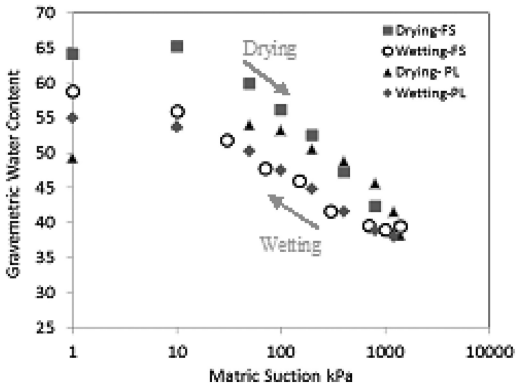


Figure 2. Drying-wetting SWCC of highly expansive soil.

at optimum and dry of optimum moisture content is evaluated in Figure 1. From Figure 1, it is observed that saturation procedure had a significant effect on SWCC shape. Saturated water content (w_{sat}) for sample prepared using the Preloading Method (PL) was less than that obtained for sample prepared using Free Swell method (FS). In addition, AEV for sample saturated under preload condition was greater than AEV for sample saturated under free swell condition. This is attributed to the reduction in soil voids associated with sample-loading during saturation process. Increase in AEV also indicates low rate of desaturation or, in other words, increase in water retention capacity. In conclusion, saturation procedures had a significant effect on SWCC of highly expansive soil in suction range less than 400 kPa (reflected in a decrease in saturated water content and increase of AEV for sample saturated with preload method). At high suction (greater than 400 kPa) the SWCC seemed to be independent of saturation procedures as shown in Fig 1. Furthermore, the effect of initial molding water content (optimum and dry of optimum) is less significant for both FS and PL samples. Slight decrease in retention capacity was noticed for sample compacted at dry of optimum moisture content (i.e., 32%).

4.2 *Drying-Wetting Soil-Water Characteristic Curves*

The drying and wetting SWCCs for highly expansive soil compacted at dry of optimum condition are presented in Fig 2. This figure also shows the effect of sample saturation procedure on the shape of drying and wetting SWCC. From Fig. 2, it is observed that SWCCs of FS-sample experience hysteresis due to drying and wetting cycle. The difference between drying and wetting SWCC decreases with increase of soil suction. Saturated water content and air-entry value for drying path are greater than their values for wetting path. These characteristics can be attributed to air entrapment in soil pores during the drying process. In addition, inelastic volume changes that took place during drying and wetting of expansive soils (Zhang

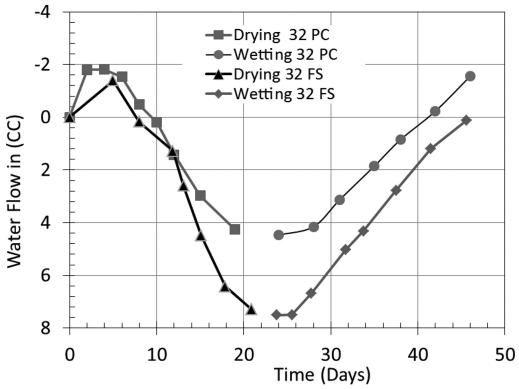


Figure 3. Water flow during drying-wetting process.

et al. 2013) will contribute to changes in the desorption and absorption characteristics of soil. Fig 2 also depicts the drying and wetting SWCCs of PL-sample. These curves also show hysteresis. Wetting curve tend to merge back to the drying curve in the low suction range (i.e., less than 50 kPa).. This is attributed to rebound of volume change (more than initial volume at drying path) in PL-sample associated with wetting process.

Figure 3 depicts water flow (desorbed and absorbed) with time for both samples during drying and wetting SWCC test. From Fig. 3, it is apparent that the rate of water desaturation is greater in the FS-sample than PL-sample. Stress applied on PL-sample during saturation caused a reduction of soil pores (void ratio) which in turn reduce the desaturation rate in PL-sample. Furthermore, saturation procedures had a more pronounced effect on the drying-path than the wetting-path. The wetting path for both FS and PL-samples showed insignificant differences with the exception of saturated water content, there is a notable difference. This could be attributed to the shrinkage mechanism associated with soil drying (in both samples) which in turn diminishes the effect of saturation procedures (pre load) on soil pores in the wetting path.

The slopes of re-saturation of both samples in wetting process were almost parallel (Fig. 3). This clearly substantiated the previous statement.

5 CONCLUSION

The following conclusions can be derived from this study:

- Saturation procedures had a significant effect on drying SWCC of highly expansive soil. This effect was reflected as a decrease in saturated water content, decrease in desaturation rate and increase of AEV for sample saturated with preload method.
- At high suction levels (greater than 400 kPa) the SWCC not to be affected by saturation procedures.
- Significant difference was observed between drying and wetting soil water characteristic curve, this difference mostly presented in w_{sat} and AEV. Curve slope also slightly changed during drying and wetting. These hysteresis are due to air entrapped during drying process and inelastic of volume change associated with drying and wetting SWCCs.
- Effect of saturation procedures (FS and PL) was more pronounced in drying-SWCC. Shrinkage mechanism associate with drying stage diminishes the effect of saturation procedures. When sample were wetted-path there is no significant effect deduced in wetting-SWCC.

ACKNOWLEDGMENT

The authors acknowledge that this research was financially supported by King Saud University, Vice Deanship of Research Chairs.

REFERENCES

Agus, S. S., & Schanz, T. (2006). Drying, wetting, and suction characteristic curves of a bentonite-sand mixture. In Unsaturated Soils 2006 (pp. 1405–1414). ASCE.

Al-Mahbashi, A. M. 2014. Soil-Water Characteristic Curves of Treated and Untreated Highly Expansive Soil Subjected to Different Stresses, MSc Thesis, King Saud University, Ri-yadh, Saudi Arabia.

Amaral, M. F., Viana da Fonseca A., Romero E., Arroyo M. (2013) A practical method for suction estimation in unsaturated soil testing" Advances in Unsaturated Soils: Proc. of 1st Pan American Conference on Unsaturated Soils, Cartagena, Colombia, 20–22 February: 185–189.

ASTM D 422 (2002). Standard Test Method for Particle-Size Analysis of Soils,Vol. 4.08. D-18 Committee on Soils and Rocks.West Conshohocken, PA.

ASTM D 4318 (2000). Standard Test Methods for Liquid Limit, Plastic Limit, and Plasticity Index of Soils, Vol. 4.08. D-18 Committee on Soils and Rocks.West Conshohocken, PA.

ASTM D 4546 (2003). Standard Test Methods for One-Dimensional Swell or Collapse of Cohesive Soils, Vol. 4.08.D-18 Committee on Soils and Rocks.West Conshohocken, PA.

ASTM D 2435 (2003). Standard Test Methods for One-Dimensional Consolidation Properties of Soils Using Incremental Loading, Vol. 4.08.D-18 Committee on Soils and Rocks.West Conshohocken, PA.

Barbour, S. L., 1998. Nineteenth Canadian Geotechnical Collo-quium: The soil-water characteristic curve: a historical per-spective. Canadian Geotechnical Journal, 35(5), 873–894.

Bennett, C. L., Tripathy, S., & Thomas, H. R. (2012). Wetting Characteristics of Compacted Bentonites at Large Applied Suctions. In Unsaturated Soils: Research and Applications (pp. 229–234). Springer Berlin Heidelberg.

Casini F., Vaunat J., Romero E., Desideri A. (2013). Progressive emergence of double porosity in a silt during compaction. Advances in Unsaturated Soils: Proc. of 1st Pan American Conference on Unsaturated Soils, Cartagena, Colombia, 20–22 February: 425–430.

Ke, K. Y., Tan, Y. C., Chen, C. H., & Lin, H. T. (2013). Char-acterizing the hydraulic properties of unsaturated sand con-sidering various porosities and drying – wetting paths of the retention curve. Hydrological Processes, 27(4), 592–604

Leong E. C., and Rahardjo H. (1997). "Review of soil-water characteristic curve equations." J. Geotech. Geoenviron. Eng. 123(12) 1106–1117.

Li, X. S. (2005). Modelling of hysteresis response for arbitrary wetting/drying paths. Computers and Geotechnics, 32(2), 133–137.

Likos, W. J., Lu, N., & Godt, J. W. (2013). Hysteresis and Un-certainty in Soil Water-Retention Curve Parameters. Journal of Geotechnical and Geoenvironmental Engineering, 140(4).

Nowamooz H., Masrouri F. (2010). Relationship between soil fabric and suction cycles in compacted swelling soils. Engi-neering Geology. 114: 444–455.

Padilla, J., Perera, Y., Houston, W., Perez, N., and Fredlund, D. (2006). Quantification of air diffusion through high airentry ceramic disks.Proccedings of the 4th Int. Conf. on Unsatu-rated Soils, 1852–1863, Arizona, USA.

Pham, H. Q., Fredlund, D. G., & Bandy, J. T. (1994). USE OF THE GCTS APPARATUS FOR THE MEASUREMENT OF SOIL-WATER CHARACTERISTIC CURVES. Evaluation, 2.

Pham, H. Q., Fredlund, D. G., & Barbour, S. L. (2003). A prac-tical hysteresis model for the soil-water characteristic curve for soils with negligible volume change. Géotechnique, 53(2), 293–298.

Wang, M. W., Qin, S., & Li, J. (2013). Soil-water characteristics of lime-treated expansive clays in Hefei. Applied Me-chanics and Materials, 256, 558–562.

Zhang, R., Zheng, J. L., & Ng, C. W. W. (2013). Experimental study on stress-dependent soil water characteristic curve of a recompacted expansive soil. Applied Mechanics and Materials, 256, 283–286.

Unsaturated Soil Mechanics—from Theory to Practice – Chen et al. (Eds)
© 2016 Taylor & Francis Group, London, ISBN 978-1-138-02921-7

Measurement of Soil-Water Characteristic Curve with a continuous pressurization method

S. Kato
Kobe University, Kobe, Japan

M. Hatakeyama
Oyo Corporation, Tokyo, Japan

H. Abe
Institute for Unsaturated soils, Nagano, Japan

B.S. Kim & Y. Takeshita
Okayama University, Okayama, Japan

ABSTRACT: In order to measure the Soil-Water Characteristic Curve (SWCC), a continuous pressurization method is presented (Hatakeyama et al., 2015). In this method, the air pressure for the specimen is continuously increased for an air pressure chamber, in which a small pore water measurement devise is equipped inside the specimen. For the specimen, the suction is defined as a difference between the air pressure applied and the pore water pressure measured. The soil moisture is measured with the water displacement through the ceramic disk equipped in the pedestal of the pressure chamber. In this method, SWCCs for a soil specimen in drying and wetting process are measured in two or three days. It is found that soil moisture characteristic curves in drying and wetting processes obtained by new testing apparatus were in acceptable agreement with those obtained by conventional test apparatus. It was also verified that the testing time of retentively test with continuous pressurizing method is notably shorter than that of with conventional test method. In this paper, the measured results for several soil are shown, and the applicability of this method is examined.

1 INTRODUCTION

Soil-Water Characteristic Curve (SWCC) is an important property which effects on the mechanical property of unsaturated soil. As well known, it shows hysteresis between drying and wetting process. In the early stage of study for unsaturated soil, it was measured with the soil column test or the suction plate method in which an equilibrium state for soil water is attained. The seepage property is estimated through the obtained SWCC based on the some theoretical background.

Among the mechanical properties of unsaturated soil, the increase of cohesion with suction is one of the important theme for researchers and engineers who has a concern for unsaturated soil. Fredlund et al. (1978) firstly pointed out the relationship between the increases of cohesion with increase of suction in general style. Vanapalli et al. (1996) and Karube et al. (1996) shows a similar equation which estimate of the increase of cohesion with the soil moisture and the suction. After that, many researchers tried to explain the relationship between the increase of the cohesion and the suction. Kato et al. (2003) and Lu et al. (2010) show the relationship between them through the SWCC. Therefore, The SWCC is a key to study the mechanical properties of unsaturated soil.

In order to measure the SWCC for one soil, the time to be need for the measurement is a problem. Usually in the suction plate method, it takes about one month to measure SWCC for one cycle of drying and wetting process. Therefore, some un-equilibrium test methods have been proposed, but they can be used only for the drying process.

In this paper, Continuous Pressurization Method (Hatakeyama et al., 2015) is introduced. In this method, the air pressure for the specimen is continuously increased for the suction plate chamber in which a small pore water measurement devise is equipped inside the specimen. The adaptability of this method for a several soil is also examined.

2 TEST APPRATUS AND TEST PROCEDURE

2.1 *Test apparatus used*

Figure 1 shows a sketch of the new apparatus used. The cylinder specimen of 60 mm in diameter and 40 mm

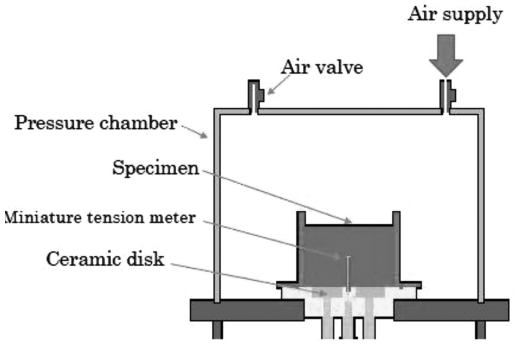


Figure 1. A sketch of test apparatus used.

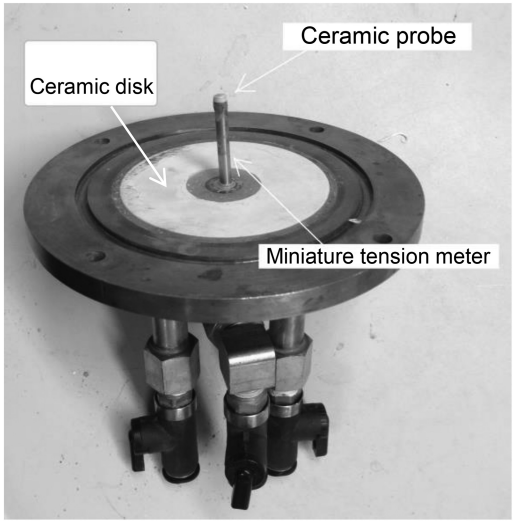


Figure 2. Pedestal of pressure chamber.

in height is placed in the mold which is set in a pressure chamber. The pedestal of the chamber equips a ceramic disk (AEV = 500 kPa) placed on the bottom of the specimen and a miniature tension meter as shown in Fig. 2.

In this study, two types of the ceramic disk were used for the miniature tension meter. One is the high flow type with AEV = 100 kPa, and its saturated hydraulic conductivity is 8.6×10^{-6} cm/sec. The other is the standard type with AEV = 300 kPa, and its saturated hydraulic conductivity is 2.5×10^{-7} cm/sec.

2.2 *Soil sample and test procedure*

In order to measure the water displacement from the specimen, the weight measuring device was connected to the drainage line from the ceramic disk.

A sample was compacted inside the mold statically to attain the dry density of test condition. Then, the compacted sample was saturated with the inundation,

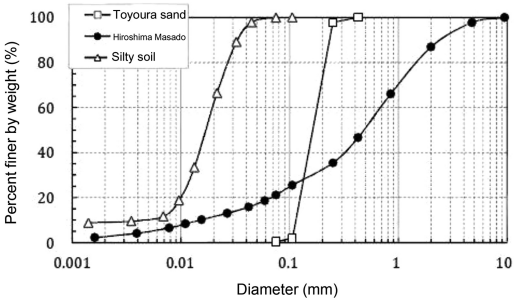


Figure 3. Particle distribution curve of soil sample (Hatakeyama et al., 2015).

and then it was set on the pedestal. Before this procedure, a hole is drilled in the specimen to penetrate the miniature tension meter.

After setting the chamber, the test was started. An air pressure was increased and decreased for the chamber with a constant pressure increment. During this process, the air pressure inside the chamber was measured, and the pore water pressure inside the specimen was measured with the miniature tension meter. The soil water displacement was also monitored with the weighing device for the drainage from the specimen.

The suction for the specimen was decided as the pressure difference between the air pressure and the pore water pressure, and the soil moisture was calculated from the soil water displacement and the initial condition. Three kinds of sample were used. The distribution curves are shown in Fig. 3. Toyoura sand is the standard sand used in Japan with the density of soil particle is 2.64 g/cm^3. Hirosima masado is a decomposed granite soil obtained from Hiroshima Pref. with the density of soil particle is 2.61 g/cm^3. The other is a silty soil that is made artificially from a mother rock with the density of soil particle is 2.65 g/cm^3 and often used for unsaturated soil test in Japan.

3 TEST RESULT AND DISCUSSION

3.1 *Effect of increment of air pressure for SWCC*

In this test method, it is important to decide an appropriate increment of an air pressure, because it effects on the testing time and the reliability of the SWCC measured. In order to examine the influence of increment of the air pressure, Hatakeyama et al. (2015) carried out the SWCC test for the three samples with the Continuous Pressurization Method. An example of test result for Hiroshima Masado which contains fine particle is shown in Fig. 4. The test was carried out three kinds of the air pressure increment. From this result, it was found that the SWCCs of 0.003 kPa/min and 0.1 kPa/min is similar. The test results for other two sample showed a similar tendency. Therefore, in order to carry our one test in a several days, the air pressure increment of 0.1 kPa/min was chosen for the test.

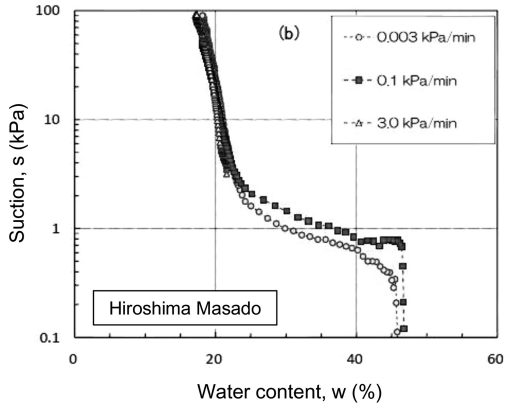


Figure 4. Comparison of SWCC obtained under different air pressure speed (Hatakeyama et al., 2015).

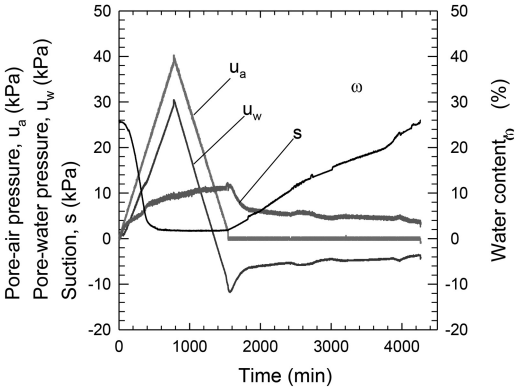


Figure 5. Test result of u_a, u_w and water content with AEV = 300 kPa.

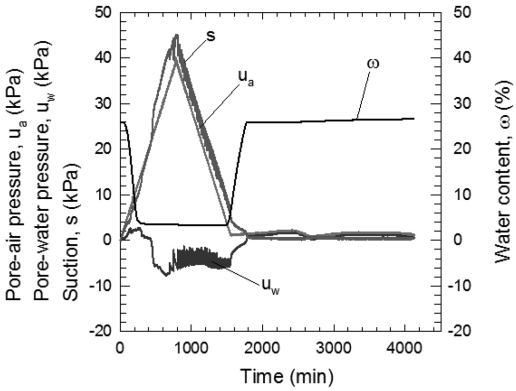


Figure 6. Test result of u_a, u_w and water content with AEV = 100 kPa.

3.2 *Test result of Toyoura sand*

Figure 5 shows the relationship of elapsed time with the air pressure supplied, the pore water pressure measured and the water displacement from the specimen for the test result of Toyoura sand with the miniature tension meter of AEV = 300 kPa. Figure 6 shows the similar relationship for the test result of Toyoura sand with the miniature tension meter of AEV = 100 kPa. In Fig. 5, the air pressure was increased linearly to 40 kPa and then decreased to 0 kPa. The pore water pressure increased and decreased with the change of air pressure. It should be noted that the suction increased continually to the end of this process. This means that the drying curve of SWCC is obtained from this part. After the air pressure equaled to zero value, the pore water pressure increased from the negative value. During this process, the suction value decreased and the wetting curve of SWCC was measured. The soil moisture decreased during the drying process, and the increased in the wetting process. Figure 6 shows the similar test result for the case of AEV = 100 kPa. In this case, the change of pore water is different from that observed in Fig. 5. It decreased for the negative value with the increase of the air pressure, and during the decrease of the air pressure, it increased to zero value. The suction value increased to 40 kPa, which is higher value than the result in Fig. 5.

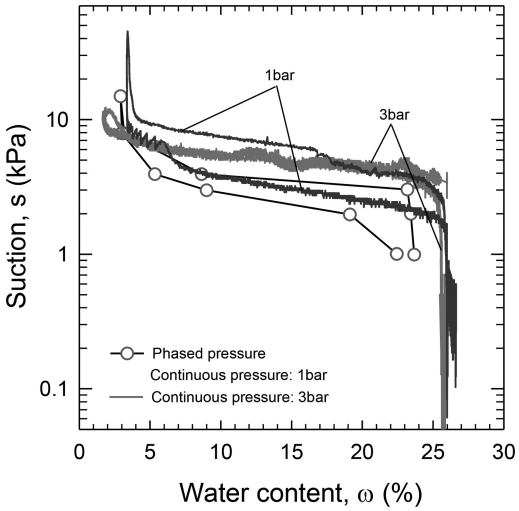


Figure 7. Comparison of SWCCs for Toyoura sand.

Figure 7 shows the comparison of SWCCs obtained with the SWCC measured with the suction plate method (Hatakeyama et al. 2015). It is found that the SWCC obtained shows similar tendency with that measured with the suction plate method.

3.3 *Test results for the other soil*

Hatakeyama et al. (2015) applied the continuous pressurization method for the specimens of silty soil and Hirosima Masado. The test results are shown in Figs. 8 and 9, respectively. The pore water increased non-linearly with increase of the air pressure. Then it decreased non-linearly to the negative value. The suction value increased till the intermediate part of the air pressure decreasing process, and then decreased to zero value. It should be noted that the drying

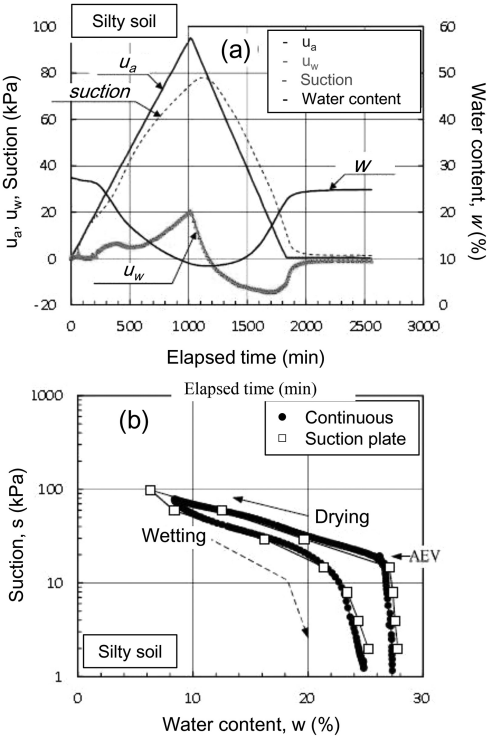


Figure 8. Test result of Silty soil (Hatakeyama et al., 2015).

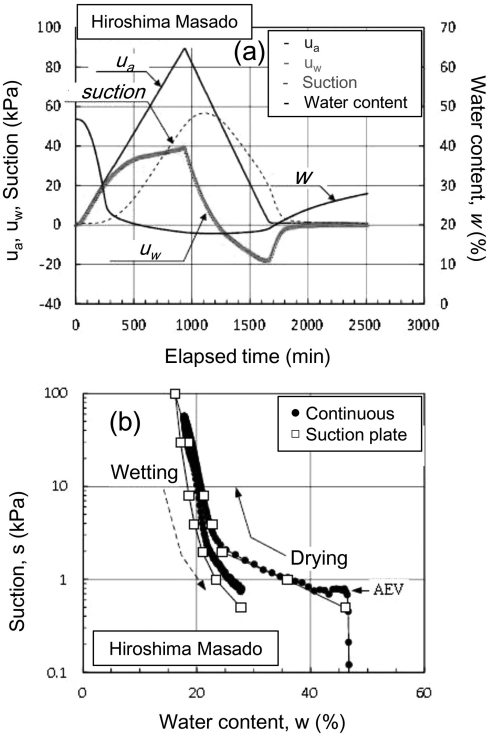


Figure 9. Test result of Hiroshima Masado (Hatakeyama et al., 2015).

and wetting processes finished in two days which is remarkably shorter than that for the suction plate method. Figures 8(b) and 9(b) show the comparision of the SWCC measured with those obtained by the suction plate method. It is found that the SWCC measured agrees well with those obtained by the suction plate method.

From these test results, it is concluded that the Continuous Pressurization Method is applicable for the sand to the silty soil specimen, and it measures the SWCC in shorter time than the suction plate method.

4 CONCLUDING REMARKS

The Continuous Pressurization Method was introduced, and its applicability was examined for three kinds of soil sample. The pore water pressure changed differently for the increasing and decreasing processes of the air pressure continuously increased according to the soil sample. The comparison of the SWCC obtained showed a good agreement with that obtained with the suction plate method. These test results shows an applicability of this method for the sand to silty soil specimen. It is found that the Continuous Pressurization Method can measure the SWCC in shorter time than the suction plate method.

REFERENCES

Fredlund et al. 1978, The shear strength of un-saturated soils, Can. Geotech. J., 15(3), 313–321.

Hatakeyama et al. 2015, Development of Water Retention Test Apparatus According to the Continuous Pressurization Method, Oyo Technical Report, No34, 23–54.

Karube et al. 1996, The relationship between shearing characteristics and the composition of pore-water in unsaturated soil, J. Geo. Eng., JSCE, 575, 49–58. (in Japanese)

Kato et al. 2003, Effects of suction on behavior of unsaturated sand in triaxial test, Pro. 2nd Asian Conf. on Unsaturated soils, UNSAT-ASIA, Osaka, Japan, 247–252.

Lu et al. 2010, A closed–form equation for effective stress in unsaturated soil, Water Resources Research, 46(5), 1–14.

Vanappali et al. 1996, Model for prediction of shear strength with respect to soil suction, Can. Geotech. J., 33(3), 379–392.

Unsaturated Soil Mechanics—from Theory to Practice – Chen et al. (Eds)
© 2016 Taylor & Francis Group, London, ISBN 978-1-138-02921-7

Hydraulic properties for soils that undergo volume change as soil suction is increased

F. Zhang
University of Alberta, Edmonton, Alberta, Canada

D.G. Fredlund
Golder Associates Ltd., Saskatoon, Saskatchewan, Canada

G.W. Wilson
University of Alberta, Edmonton, Alberta, Canada

ABSTRACT: The coefficient of permeability function and the water storage function are two hydraulic property functions required for numerical modeling of transient seepage problems. Methodologies presently available for the estimation of the unsaturated coefficient of permeability are based on an assumption that no volume change occurs as soil suction is changed. This assumption is generally valid when dealing with sands or silts. However, the estimation techniques need to be revised when predicting the hydraulic properties for soils that undergo significant volume change as soil suction changes, (e.g. slurry Regina clay). This paper is to investigate the hydraulic properties for soils that undergo volume change as soil suction is increased during a drying process. The revised methodology considers both the influence of void ratio change and degree of saturation change in an uncoupled manner. The influence of varying amounts of void ratio change is also discussed.

1 INTRODUCTION

Unsaturated soil mechanics plays an important role in geotechnical engineering practice involving unsaturated soils, such as foundation design for buildings constructed on unsaturated expansive soils, design of a highway built on unsaturated compacted soils. The success of the implementation of unsaturated soil mechanics into geotechnical engineering practice depends largely on the advancement of numerical computing techniques and the appropriate mathematical description of constitutive relationships. Advanced numerical computing techniques make it possible to solve the mathematical problems that are complex and highly nonlinear. Advanced numerical computing techniques require the input of appropriate mathematical constitutive relationships that characterizes the system being simulated. The unsaturated soils problems may involve volume-mass constitutive relationships, shear strength constitutive relationships and hydraulic conductivity constitutive relationships (Fredlund 2000).

Proper unsaturated soil property functions are required for numerical modeling of geotechnical engineering problems such as transient seepage problems and contaminant transport problems. Geotechnical engineering problems such as seepage from tailings and mine waste can be reduced to the solution of one or more partial differential equations. Each partial differential equation contains material properties that are either constants or mathematical functions. The material properties must be provided in order to obtain reasonable results. Most computer software for modeling unsaturated soils involves the solution of a partial differential equation (e.g. SVOffice 2009, GeoStudio 2012, etc.). The correctness of the numerical modeling results depends largely on the accuracy of the input of the material properties. This paper is dedicated to the study of hydraulic properties for the water phase.

The coefficient of permeability function and the water storage function are two hydraulic property functions required when modeling seepage through unsaturated soils. Considerable research has been directed towards the estimation of the coefficient of permeability function. The study of the coefficient of permeability for a soil can be categorized as the saturated coefficient of permeability and the unsaturated coefficient of permeability. Saturated coefficient of permeability for most soils is a constant that is measured experimentally. For a saturated soil that changes volume, the saturated coefficient of permeability becomes a function of the changing void ratio (Taylor 1948, Chapuis 2012). For unsaturated soils, there are four categories of models used for the estimation of unsaturated coefficient of permeability functions (Fredlund et al. 2012); namely, i.)

empirical models, ii.) statistical models, iii.) correlation models and iv.) regression models. Empirical models and statistical models appear to be most extensively used in geotechnical engineering. The methods presently found in the research literature for estimating the unsaturated coefficient of permeability function are based on an assumption that no volume change occurs as soil suction is changed, considering only the influence of changes in the degree of saturation. Van Genuchten-Burdine equation (van Genuchten 1980), van Genuchten-Mualem equation (van Genuchten 1980) and Fredlund, Xing and Huang permeability function (Fredlund et al. 1994) are three well-known unsaturated permeability functions. These conventional methods produce reasonable estimations for the coefficient of permeability functions for unsaturated soils with no volume changes. Initially slurry Regina clay has been found to be a soil that undergoes significant volume change as soil suction is increased during a drying process. In other words, a conventional unsaturated coefficient of permeability function cannot mathematically describe the coefficient of permeability function of Regina clay that undergoes both desaturation and volume change during the drying process. Both the void ratio and the degree of saturation must be considered when estimating the coefficient of permeability function for a drying soil that undergoes volume change such as Regina clay.

This paper presents a methodology for the estimation of the coefficient of permeability function for soils that undergo volume change as soil suction is changed (e.g. slurry Regina clay). Both void ratio and the degree of saturation are taken into account as two influencing factors. Experimental data for Regina clay are used to illustrate and explain the new estimation method. The research study shows how volume change can influence the permeability function for a drying soil.

2 REVISED THEORY FOR THE COEFFICIENT OF PERMEABILITY FUNCTION

Degree of saturation and void ratio are two controlling volume-mass properties that influence the coefficient of permeability of a soil. The coefficient of permeability at a particular soil suction during a drying process, is the product of the relative coefficient of permeability and the saturated coefficient of permeability corresponding to the void ratio of the soil.

$$k(\psi) = k_r(\psi) \times k_s(\psi) \tag{1}$$

where, $k(\psi)$ = coefficient of permeability at a particular suction of ψ; $k_r(\psi)$ = relative coefficient of permeability at a suction of ψ; $k_s(\psi)$ = reference saturated coefficient of permeability at a soil suction of ψ.

Reference saturated coefficient of permeability is defined to be a function of soil suction. Reference saturated coefficient of permeability is the saturated coefficient of permeability corresponding to the void ratio of the soil at a particular soil suction. In other words, the material at a particular skeletal structure (or void ratio) has a particular saturated coefficient of permeability which is the reference saturated coefficient of permeability in Eq. (1).

2.1 *Shrinkage curve and Soil-Water Characteristic Curve (SWCC)*

A shrinkage curve defines the relationship between the void ratio and the gravimetric water content. Fredlund et al. (2002) proposed a shrinkage curve equation that provides a mathematical description of the shrinkage curve. The shrinkage curve equation is shown as Eq. (2).

$$e(w) = a_{sh}\left[\left(\frac{w}{b_{sh}}\right)^{c_{sh}} + 1\right]^{\frac{1}{c_{sh}}} \tag{2}$$

where: a_{sh} = the minimum void ratio, e_{min}; a_{sh}/b_{sh} = slope of the line of tangency; c_{sh} = curvature of the shrinkage curve; w = gravimetric water content.

The soil-water characteristic curve, SWCC, presents the relationship between the amount of water in a soil and various applied soil suctions. There are four designations of water content commonly used to define the amount of water in a soil, namely, gravimetric water content, w, volumetric water content, θ (where the volume of water is referenced to the original total volume of the soil specimen), instantaneous volumetric water content, θ_i (where the volume of water is referenced to the instantaneous total volume of the soil specimen), and degree of saturation, S. With each designation of the amount of water in the soil, there is a particular form of the SWCC. As a result, it can be said that there are four different forms of SWCC, namely, gravimetric water content-SWCC (w-SWCC), volumetric water content-SWCC (θ-SWCC), instantaneous volumetric water content-SWCC (θ_i-SWCC), and degree of saturation-SWCC (S-SWCC).

The equation for the gravimetric water content-SWCC, w-SWCC (Fredlund & Xing 1994) can be written as shown in Eq. (3).

$$w(\psi) = \frac{w_s\left(1 - \ln\left(1 + \psi/\psi_r\right)/\ln\left(1 + 10^6/\psi_r\right)\right)}{\left(\ln\left(\exp(1) + \left(\psi/a_f\right)^{n_f}\right)\right)^{m_f}} \tag{3}$$

where: ψ = soil suction; a_f, n_f, m_f, and ψ_r = mathematical fitting parameters; w_s = initial saturated gravimetric water content; $w(\psi)$ = gravimetric water content at a designed soil suction of ψ.

Equations for other forms of SWCC (θ-SWCC, θ_i-SWCC, S-SWCC) can be obtained by combining of Eq. (2) and Eq. (3) based on basic volume-mass relationships.

For soils that do not undergo volume change as soil suction changes, all four SWCCs provide the same information to the geotechnical engineer when estimating other unsaturated soil property functions. However, for a soil that undergoes volume change as soil suction is increased in a drying process, w-SWCC, θ_i-SWCC and S-SWCC are different from one another. It should be noted that S-SWCC must be used for the estimation of the relative coefficient of permeability function, while θ_i-SWCC should be used for the estimation of the water storage function in all cases (Fredlund and Zhang 2013, Zhang and Fredlund 2014).

2.2 *Consideration of the void ratio*

Void ratio is one of the two main factors that govern the coefficient of permeability of a material that undergoes volume change as soil suction is increased. Void ratio affects reference saturated coefficient of permeability in Eq. (1).

The saturated coefficient of permeability of a saturated soil depends on the pore sizes and the pore distribution or arrangement within the soil (Chapuis 2012). A change in the void ratio changes the pore sizes and the pore distribution, thus influencing the saturated coefficient of permeability of the soil. A number of research studies have been undertaken on the saturated coefficient of permeability as a function of void ratio for saturated soils that undergo volume change (Chapuis 2012). Eq. (4) (Taylor 1948) has been found to mathematically describe the relationship between experimentally measured saturated coefficient of permeability, k_{sat} and void ratio, e.

$$k_{sat}(e) = \frac{10^{-11} C e^{x}}{1+e} \tag{4}$$

where: k_{sat} = saturated coefficient of permeability; e = void ratio; C, x = fitting parameters.

Void ratio is changing with soil suction during a drying process when the material undergoes volume change as soil suction is increased (Fredlund et al. 2011). This means the reference saturated coefficient of permeability is changing with soil suction as void ratio is changing. The relationship between the void ratio and the soil suction can be determined by combining the shrinkage equation (Fredlund et al. 2002), Eq. (2) and the mathematical equation for the gravimetric water content-SWCC, w-SWCC (Fredlund & Xing 1994), Eq. (3). Then the reference saturated coefficient of permeability can be obtained by substituting the equation for the relationship of void ratio versus soil suction into the saturated coefficient of permeability function, Eq. (4). The change in the reference saturated coefficient of permeability is the result of a change in void ratio during the drying process as soil suction increases. The reference saturated coefficient of permeability reflects the influence of the void ratio on the coefficient of permeability for a soil that undergoes volume change as soil suction changes.

2.3 *Consideration of the degree of saturation*

Degree of saturation is another factor that influences the coefficient of permeability of a material. Degree of saturation influences the relative coefficient of permeability, $k_r(\psi)$ in Eq. (1). Changes in the degree of saturation change the tortuosity of the flow path within the porous media, thus affecting the relative coefficient of permeability.

The relative coefficient of permeability of a material is a function of soil suction reflecting the influence of the degree of saturation on the coefficient of permeability. Considerable research has been done on the estimation of the relative coefficient of permeability in unsaturated soil mechanics. The relative coefficient of permeability is primarily determined by the pore-size distribution (Brooks & Corey 1964), of a soil and its estimation is generally based on the soil-water characteristic curve. The Fredlund et al. (1994) permeability function is one of those commonly used unsaturated permeability functions. The relative permeability function (Fredlund et al. 1994)) takes the following form:

$$k_r(\psi) = \frac{\int_{\ln(\psi)}^{b} \frac{\theta(e^y) - \theta(\psi)}{e^y} \theta'(e^y)\, dy}{\int_{\ln(\psi_{aev})}^{b} \frac{\theta(e^y) - \theta(\psi_{aev})}{e^y} \theta'(e^y)\, dy} \tag{5}$$

where: $b = \ln(1000000)$; y = a dummy variable of integration representing the logarithm of soil suction.

It should be noted that S-SWCC must be used in Eq. (5) for the estimation of the relative coefficient of permeability function with the air-entry value, AEV as the lower limit of integration. The effect of the lower limit of integration on the calculation of the permeability function is studied in detail by Zhang and Fredlund (2015).

The product of the reference saturated coefficient of permeability and the relative coefficient of permeability function generates the actual permeability function that considers both of the influence of void ratio change and degree of saturation change for a soil that undergoes volume change as soil suction is increased.

3 APPLICATION OF THE REVISED THEORY TO REGINA CLAY

3.1 *Presentation of the experimental data*

Initially slurry Regina clay is a material that undergoes large volume changes as soil suction is increased. Experimental data from Fredlund (1964) is presented and interpreted using the proposed theory for the estimation of the permeability function.

Regina clay had a liquid limit of 75%, a plastic limit of 25% and contained 50% clay size particles. The material is prepared at a water content slightly above

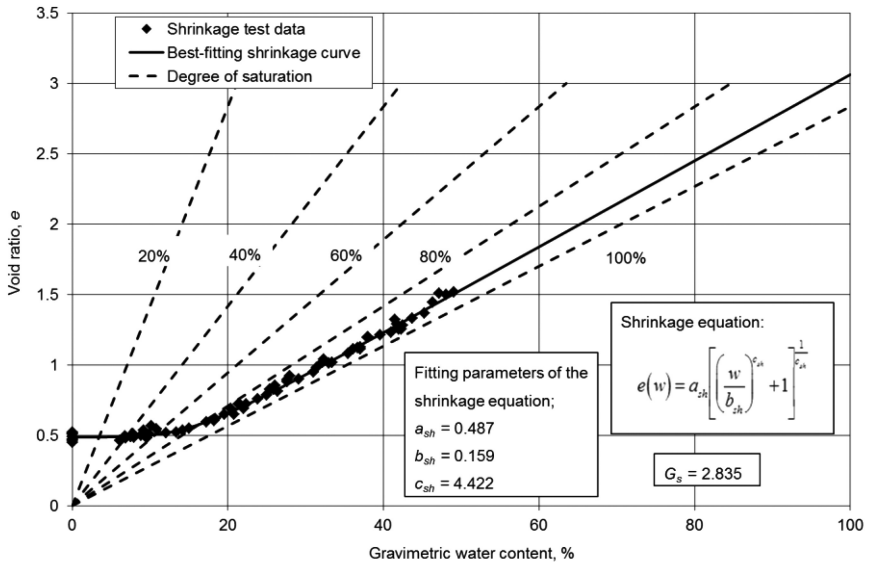


Figure 1. Shrinkage curve of Regina clay.

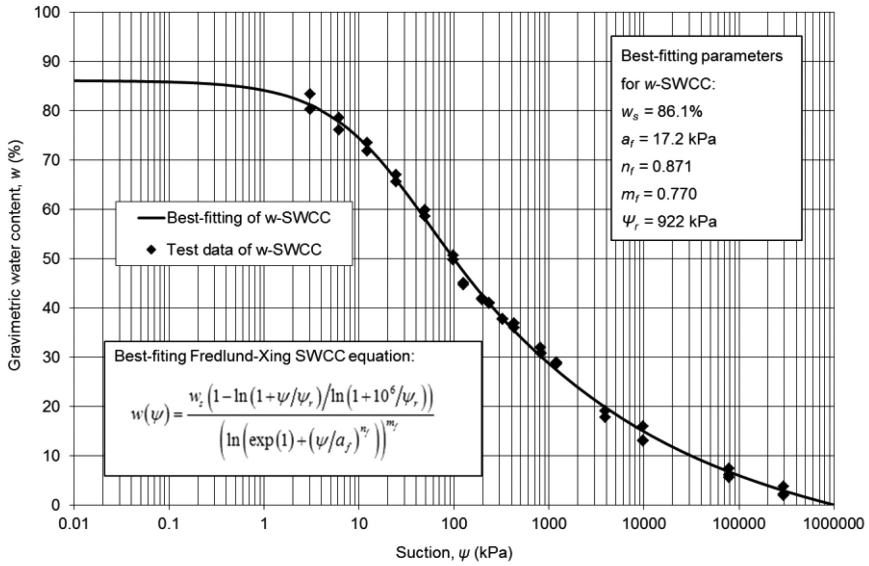


Figure 2. Gravimetric water content versus soil suction.

the liquid limit and then subjected to various consolidation pressures under one-dimensional loading. After the applied load was removed, the soil specimens were subjected to a series of matric suction values. High suction values (in excess of 1500 kPa) were applied through equalization in a constant relative humidity environment.

Shrinkage curves and soil-water characteristic curves were measured on Regina clay. The shrinkage curve of Regina clay is shown in Figure 1. The void ratio of Regina clay decreases with the gravimetric water content as water evaporates from the soil. The best-fitting parameters of the shrinkage curve are $a_{sh} = 0.487$, $b_{sh} = 0.159$, and $c_{sh} = 4.422$. The specific gravity of Regina clay is 2.835. Figure 2 shows the gravimetric water content, w, plotted versus soil suction for Regina clay that was initially preloaded to 6.125 kPa. The gravimetric water content soil-water characteristic curve, w-SWCC was best-fitted with Fredlund and Xing (1994) equation, (i.e. Eq. (3)). The best-fitting parameters are $a_f = 17.2$ kPa, $n_f = 0.871$, $m_f = 0.770$, and $\psi_r = 922$ kPa. The initial gravimetric water content was 86.10%. The w-SWCC was used in conjunction with the shrinkage curve to calculate other forms of the SWCC. The volume-mass properties versus soil suction were used to interpret

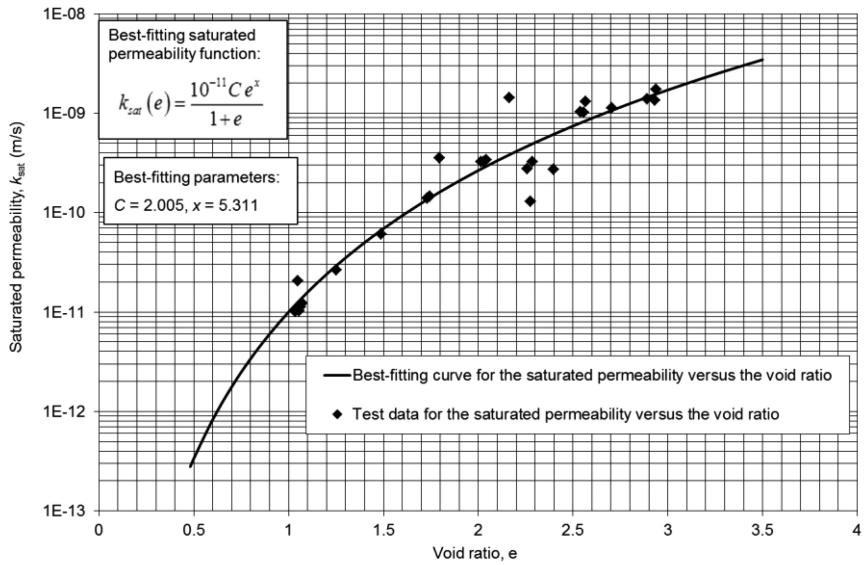


Figure 3. Measured data and its best-fitting for the relationship of the saturated permeability versus void ratio for Regina clay.

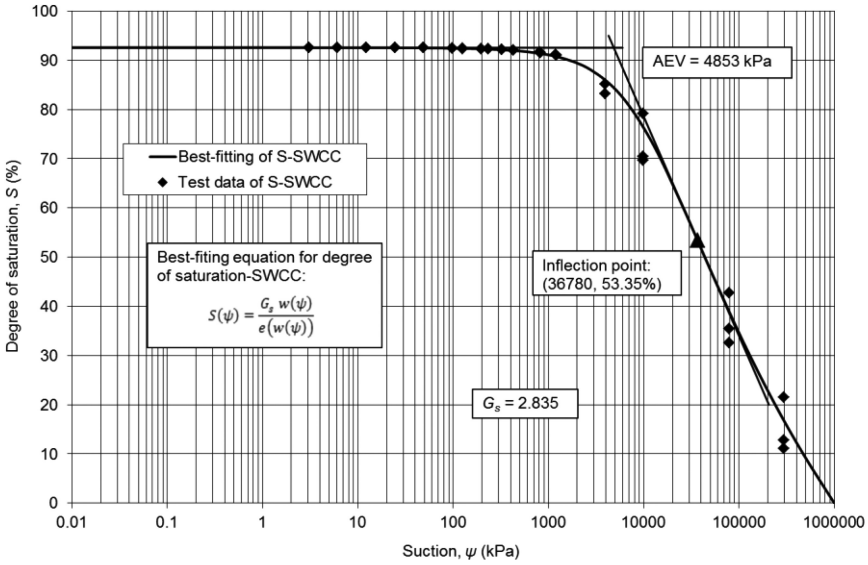


Figure 4. Measured data and its best-fitting of the *S*-SWCC for Regina clay.

the SWCC results. The "true" air-entry value, AEV was determined (Vanapalli et al. (1998)) and the relative permeability function was computed using the Fredlund et al. (1994) estimation theory.

The experimental data for the relationship of the saturated coefficient of permeability versus the void ratio were also obtained for Regina clay. The experimental data were best-fitted by Eq. (4). Figure 3 shows the measured data and the best-fitting curve for the relationship of the saturated permeability versus the void ratio for Regina clay. The fitting parameters are $C = 2.005$ and $x = 5.311$.

The shrinkage curve, the *w*-SWCC and the curve of the saturated coefficient of permeability versus the void ratio were used to estimate the appropriate permeability function for Regina clay.

3.2 *Interpretation of the experimental data*

The gravimetric water content-SWCC, *w*-SWCC was combined with the shrinkage curve to obtain other forms of SWCC. The resulting plot of the degree of saturation-SWCC, *S*-SWCC is presented in Figure 4. The "true" air-entry value (AEV) for a material that

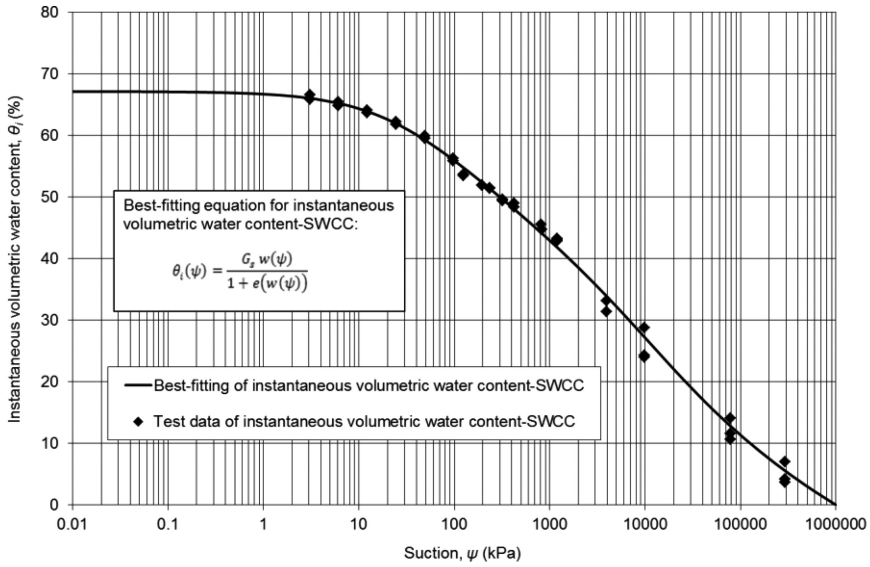


Figure 5. Measured data and its best-fitting of the θ_i-SWCC for Regina clay.

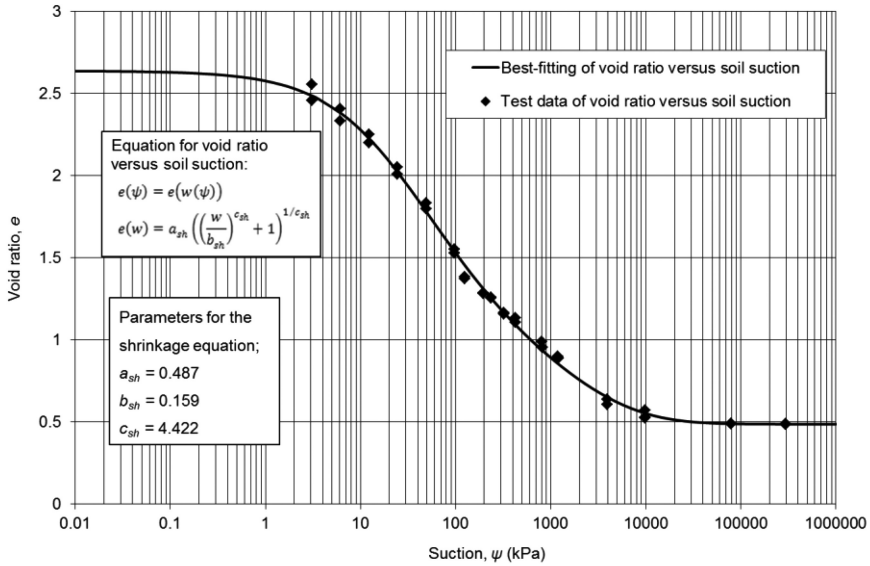


Figure 6. Measured data and its fitting for the relationship of void ratio versus soil suction for Regina clay.

undergoes volume change as soil suction is changed is obtained from the *S*-SWCC of the soil. Using the graphical construction method suggested by Vanapalli et al. (1998), the "true" AEV was interpreted from the *S*-SWCC (see Fig. 4) as 4853 kPa. The plot of θ_i-SWCC is shown in Figure 5. The θ_i-SWCC is the correct form of SWCC that should be used for the estimation of the water storage function. The θ_i-SWCC can be used for the water storage function in all cases, regardless of whether or not volume change takes place.

The relationship between void ratio and soil suction is obtained by combining the *w*-SWCC and the shrinkage curve. The plot of void ratio versus soil suction is shown in Figure 6. The void ratio decreases from 2.661 to 0.624 when the soil suction increases from 0 to its AEV of 4853 kPa. The void ratio at the AEV of 4853 kPa is 0.624 for Regina clay preloaded to 6.125 kPa. Regina clay experiences significant volume change before the soil suction reaches its AEV during its drying process. Comparing to the volume change experienced before the AEV, the volume change of the specimen is relatively small and insignificant after the soil suction exceeds the AEV.

As void ratio changes with soil suction, the reference saturated coefficient of permeability changes

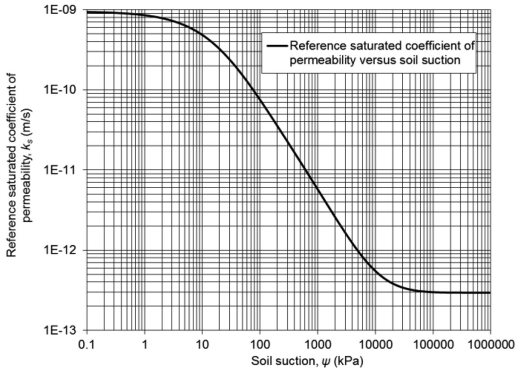


Figure 7. Reference saturated coefficient of permeability versus soil suction for Regina clay.

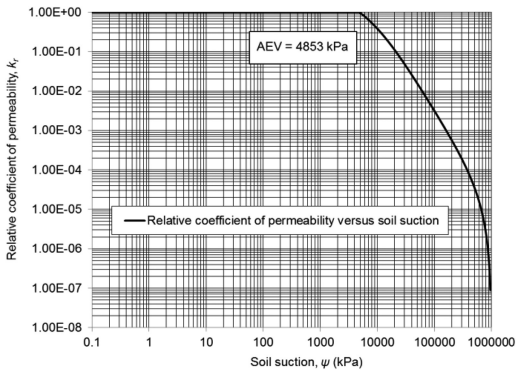


Figure 8. Relative coefficient of permeability versus soil suction for Regina clay.

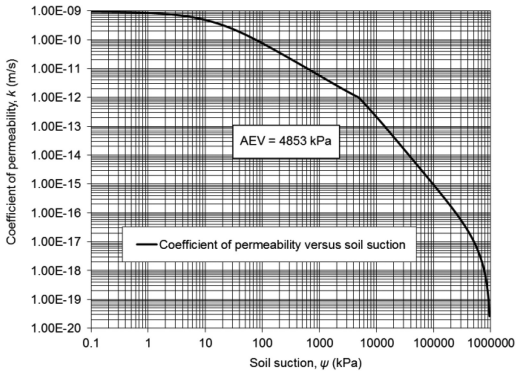


Figure 9. Coefficient of permeability versus soil suction for Regina clay.

with soil suction during the drying process of Regina clay. The reference saturated coefficient of permeability is a function of soil suction. It is the saturated coefficient of permeability corresponding to the void ratio at a particular soil suction during the drying process. The curve of the reference saturated coefficient of permeability versus soil suction for Regina clay is shown in Figure 7.

The curve of the relative coefficient of permeability versus soil suction for Regina clay is presented in Figure 8. Figure 8 shows that the relative coefficient of permeability remains 1.0 until the soil suction approaches the AEV of the soil. When the AEV is surpassed, desaturation starts and the relative coefficient of permeability reduces from 1.0 towards zero. The correct curve for the relative coefficient of permeability versus soil suction is obtained from *S*-SWCC with AEV as the lower limit of integration for the integral in the denominator of Eq. (5). After having the relative coefficient of permeability function, $k_r(\psi)$ shown in Figure 8 and the reference saturated coefficient of permeability function, $k_s(\psi)$ shown in Figure 7, the coefficient of permeability function, $k(\psi)$ can be obtained by multiplying the relative coefficient of permeability function, $k_r(\psi)$ with the referenced saturated coefficient of permeability function, $k_s(\psi)$ according to Eq. (1). The coefficient of permeability versus soil suction for Regina clay is presented in Figure 9.

4 INFLUENCE OF THE VOLUME CHANGE

Three hypothesized soils are studied in a comparative manner to investigate the influence of the volume on the estimation of the coefficient of permeability for a soil, namely Soil #1, Soil #2, and Soil #3. Figure 10 shows the different shrinkage curves for the three hypothesized soils. The fitting parameters for Soil #1 are $a_{sh} = 0.981$, $b_{sh} = 0.37$, and $c_{sh} = 500$. The fitting parameters for Soil #2 are $a_{sh} = 0.7$, $b_{sh} = 0.264$, and $c_{sh} = 6$. The fitting parameters for Soil #3 are $a_{sh} = 0.48$, $b_{sh} = 0.181$, and $c_{sh} = 6$. These three hypothesized soils share the same *w*-SWCC as shown in Figure 11. The fitting parameters for Fredlund & Xing (1994) equation are $a_f = 10$ kPa, $n_f = 2.0$, $m_f = 1.0$, and $\psi_r = 100$ kPa. The initial gravimetric water content is 37.0%. However, these three hypothesized soils undergo different amounts of volume change as soil suction is increased during a drying process as Figure 12 reveals. Soil #1 represents a soil that has no volume change as soil suction is increased. Soil #2 is a typical soil that experiences some volume change during the drying process. Soil #3 is the soil that would have the most volume change.

Figure 13 shows the three different *S*-SWCCs for the three hypothesized soils that undergo different amounts of volume change. *S*-SWCC is the SWCC that should be used to determine the AEV, thus three AEVs obtained for the three soils are different. The AEV for Soil #1 is 5.10 kPa, for Soil #2 10.06 kPa, for Soil #3 17.11 kPa.

S-SWCC is also the correct form of SWCC that should be used to estimate the relative coefficient of permeability function with Eq. (5). Figure 14 presents the relative coefficient of permeability curves for the three hypothesized soils. The change of volume causes the change of the *S*-SWCC, thus changing the AEV and the relative coefficient of permeability function. The soil with more volume change has a higher relative

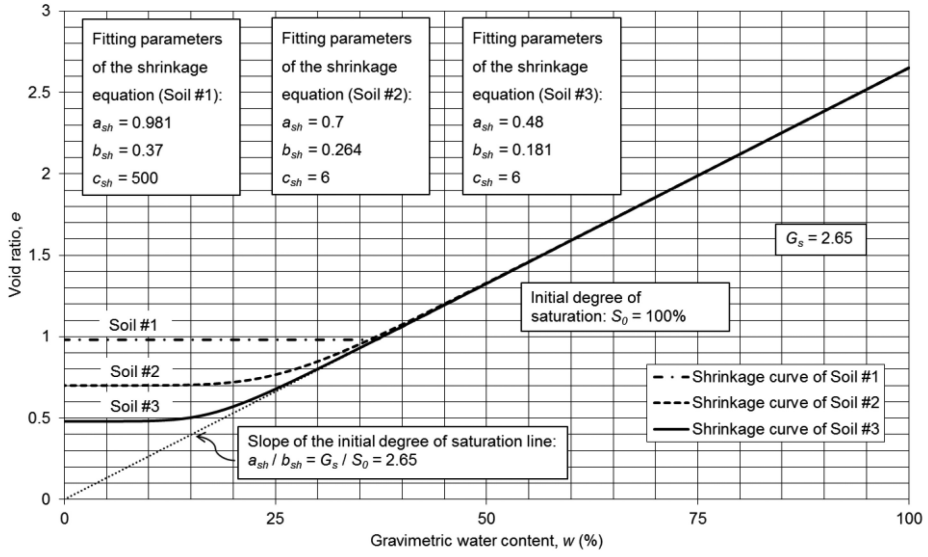


Figure 10. Shrinkage curves for the three hypothesized soils.

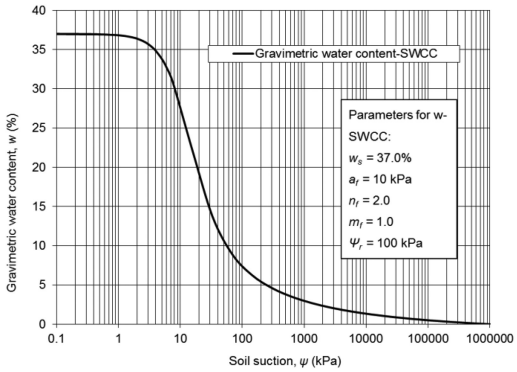


Figure 11. *w*-SWCC for the three hypothesized soils.

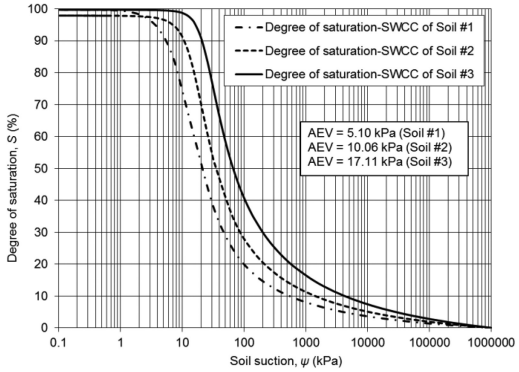


Figure 13. *S*-SWCC for the three hypothesized soils.

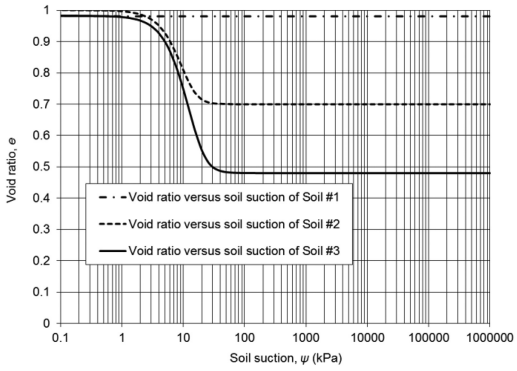


Figure 12. The change of the void ratio with soil suction for the three hypothesized soils.

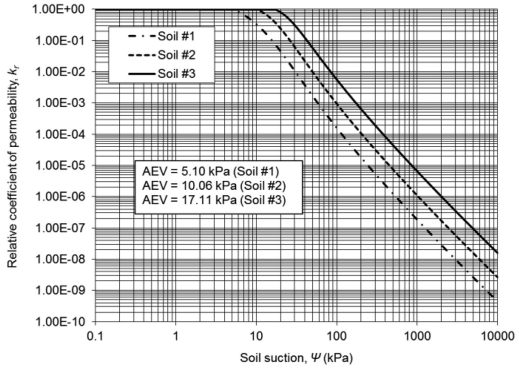


Figure 14. The relative coefficient of permeability versus soil suction for the three hypothesized soils.

coefficient of permeability at particular soil suction if *w*-SWCC is the same as Figure 14 reveals.

Assume that all these three hypothesized soils have a value of 3.0 for the *C* parameter in Eq. (4) for the curve of saturated permeability versus void ratio. And assume the three hypothesized soils have the same saturated permeability at the void ratio of 0.981. Figure 15

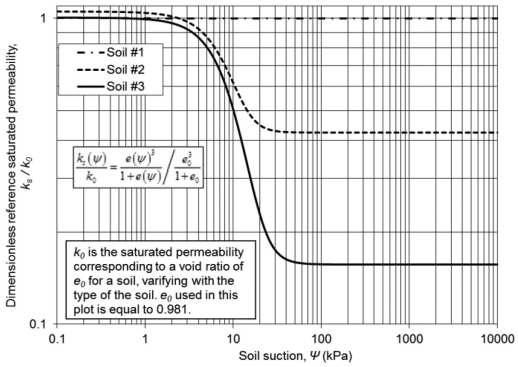


Figure 15. The dimensionless reference saturated coefficient of permeability versus soil suction for the three hypothesized soils.

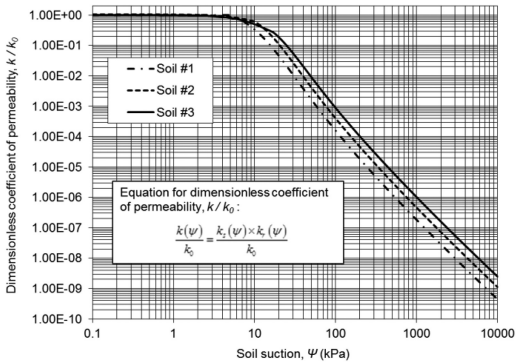


Figure 16. The dimensionless coefficient of permeability versus soil suction for the three hypothesized soils.

shows the dimensionless reference saturated coefficient of permeability curves for the three hypothesized soils. The dimensionless reference saturated coefficient of permeability curve shown in Figure 15 is the reference saturated coefficient of permeability function referenced to the reference saturated coefficient of permeability at the void ratio of 0.981. The results in Figure 15 show that the reference saturated coefficient of permeability of Soil #1 remains the same during the drying process since the Soil #1 doesn't change volume. The reference saturated coefficient of permeability of Soil #2 changes 0.5 orders of magnitude in value. Soil #3 has a change of 0.8 orders of magnitude in the reference saturated coefficient of permeability for it has the most volume change of these three soils. The decrease in the void ratio as soil suction is increased reduces the reference saturated coefficient of permeability.

Figure 16 shows the dimensionless coefficient of permeability versus soil suction for the three hypothesized soils. As analyzed above, the change in volume during a drying process reduces the reference saturated coefficient of permeability, but increases the relative coefficient of permeability. The combined impact shown in Figure 16 is an increase in the coefficient of permeability due to the change of volume as soil suction is increased.

5 CONCLUSIONS

The degree of saturation and the void ratio are two factors that govern the coefficient of permeability for a particular soil. Conventional methodologies for estimating unsaturated coefficient of permeability only take into account of the degree of saturation based on an assumption of no volume change during the drying process, while saturated soil mechanics limits to the cases of saturated soils investigating the relationship between the saturated permeability and the void ratio. This paper presents a revised theory considering both the degree of saturation and the void ratio for the estimation of the coefficient of permeability for soils that undergo volume change as soil suction is increased, such as Regina clay. The coefficient of permeability function proposed in this paper consists of two main components, namely, the reference saturated coefficient of permeability function and the relative coefficient of permeability function. The coefficient of permeability function is the result of the multiplication between the reference saturated coefficient of permeability function and the relative coefficient of permeability function. The reference saturated coefficient of permeability function is controlled by the void ratio as soil suction changes. The relative coefficient of permeability function is greatly influenced by the degree of saturation and must be determined from *S*-SWCC using the AEV as the lower limit of integration. The experimental data for Regina clay is used for the illustration of the proposed theory. A study concerning the influence of the volume change on the coefficient of permeability function reveals that the change of volume during a drying process causes changes in both *S*-SWCC and the curve of void ratio versus soil suction. The decrease in volume during the drying process reduces the reference saturated coefficient of permeability, but increases the relative coefficient of permeability. The combined impact is an increase in the coefficient of permeability due to the decrease of volume as soil suction is increased. Though the apparent influence is not significant in the case of this comparative study, it is important to realize the complicated mechanisms behind.

REFERENCES

Chapuis, R. P. 2012. Predicting the saturated hydraulic conductivity of soils: a review. *Bull.Eng.Geol.Env.*71(3): 401–434.

Brooks, R. H. & Corey, A. T. 1964. Hydraulic properties of porous media. *Hydrology Papers*. Colorado State University, (March).

Zhang, F. and Fredlund, D. G. 2015. "Examination of the estimation of relative permeability for unsaturated soils". *Canadian Geotechnical Journal*.

Zhang, F., Fredlund, D. G., Wilson, G. W., and Sedgwick, A. 2014. "Determination of the permeability function for drying oil sands tailings undergoing volume change and desaturation". *Proceedings of the 4th International Oil Sands Tailings Conference, Banff, A.B. 2014*.

Fredund, D. G., and Zhang, F. 2013. "Combination of shrinkage curve and soil-water characteristic curves for soils that undergo volume change as soil suction is increased". *Proceedings of the 18th International Conference on Soil Mechanics and Geotechnical Engineering, Paris 2013*.

Fredlund, D. G. 1964. *Comparison of soil suction and one-dimensional consolidation characteristics of a highly plastic clay*. The University of Alberta.

Fredlund, D. G. & Xing, A. 1994. Equations for the soil-water characteristic curve. *Canadian Geotechnical Journal* 31(4): 521–532.

Fredlund, D., Xing, A. & Huang, S. 1994. Predicting the permeability function for unsaturated soils using the soil-water characteristic curve. *Canadian Geotechnical Journal* 31(4): 533–546.

Fredlund, D. G., Stone, J., Stianson, J. & Sedgwick, A. 2011. Determination of water storage and permeability functions for oil sands tailings. *Tailings and Mine Waste 2011*. Vancouver, Canada.

Fredlund, D. G., Rahardjo, H., & Fredlund, M. D. 2012. *Unsaturated soil mechanics in engineering practice*. John Wiley & Sons.

Fredlund, M. D. 2000. *The role of unsaturated soil property functions in the practice of unsaturated soil mechanics*. The University of Saskatchewan.

Fredlund, M. D., Wilson, G. W. & Fredlund, D. G. 2002. Representation and estimation of the shrinkage curve. *Proc., 3rd Int. Conf. on Unsaturated Soils*. UNSAT 2002.

Taylor, D. W. 1948. *Fundamentals of soil mechanics*. J. Wiley & Sons; London: Chapman & Hall.

Van Genuchten, M. T. 1980. A closed-form equation for predicting the hydraulic conductivity of unsaturated soils. *Soil Sci. Soc. Am. J.* 44(5): 892–898.

Vanapalli, S.K., Sillers, W.S. & Fredlund, M.D. 1998. The meaning and relevance of residual state to unsaturated soils. *Proceedings of the Fifty-First Canadian Geotechnical Conference*. Edmonton, AB.

Unsaturated Soil Mechanics—from Theory to Practice – Chen et al. (Eds)
© 2016 Taylor & Francis Group, London, ISBN 978-1-138-02921-7

Role of unsaturated permeability function in seepage analyses

A. Rahimi, H. Rahardjo & E.C. Leong
Nanyang Technological University, Singapore

ABSTRACT: Unsaturated permeability function is the key parameter in seepage analyses. The unsaturated permeability function is often estimated from Soil-Water Characteristic Curve (SWCC) by means of estimation models. However, different estimation models result in different unsaturated permeability functions. In this paper, the effect of using different unsaturated permeability functions, as estimated by the different models, on seepage analyses is presented. The different unsaturated permeability functions can affect the results of seepage analyses which in turn may affect the design of earth structures. In this study, a column of residual soil was subjected to typical rainfall conditions in Singapore through numerical modelling. The results of the analyses show that infiltration characteristics of the residual soil column were noticeably affected when different unsaturated permeability functions were used for the same soil.

1 INTRODUCTION

Unsaturated permeability function is the key parameter in seepage analyses. The hydraulic properties of soil (soil-water characteristic curve, saturated permeability and unsaturated permeability) have been shown to significantly affect the results of transient seepage analyses and stability of slopes subjected to rainfall (Rahardjo et al., 2007; Rahimi et al., 2010a; Rahimi et al., 2010b). The unsaturated permeability function is often estimated from SWCC by means of estimation models. The SWCC of a soil is usually measured in the laboratory and best-fitted using a best-fit SWCC equation. A relative permeability equation is then used to integrate the best-fitted SWCC. The result of this process is the unsaturated permeability function of the soil. A generalized unsaturated permeability function can be expressed as follows (Rahimi, 2015):

$$k_w(\psi) = k_s \left[\int_{\psi(\theta_{wL})}^{\psi(\theta_w)} f(\psi) f'(\psi) d\psi \Big/ \int_{\psi(\theta_{wL})}^{\psi(\theta_s)} f(\psi) f'(\psi) d\psi \right]^d \quad (1)$$

where, $k_w(\psi)$ is the unsaturated permeability function as a function of suction; k_s is the saturated permeability; $f(\psi)$ is SWCC function; $\psi(\theta_{wL})$ is a parameter which varies for different models. However, different estimation models result in different unsaturated permeability functions (Mualem, 1986). The study by Rahimi et al. (2015, 2014) investigated the factors which cause the variation between all the estimated unsaturated permeability functions by various models. It was found that the measured SWCC data range, followed by best-fit SWCC equation and relative permeability equations were the most important factors causing this variation. Even though studies showed that hydraulic properties of soil significantly affect the results of seepage analyses, there is a lack of knowledge on the effect of the different unsaturated permeability functions on seepage analyses. Therefore, the objective of this paper is to quantify the effect of the identified parameters (i.e., measured SWCC data range, best-fit SWCC equation and relative permeability equation) of the unsaturated permeability functions on seepage analyses.

2 METHODOLOGY

In order to investigate the effect of the identified parameters (i.e., measured SWCC data range, best-fit SWCC equation and relative permeability equation) of the unsaturated permeability functions on seepage analyses, three estimation models namely, FCM, FMM and VMM, $m = 1 - 1/n$ (Rahimi, 2015) are selected as the unsaturated permeability estimation models. FCM estimation model is the combination of Fredlund and Xing (1994) SWCC equation with Childs and Collis-George (1950) relative permeability equation, FMM estimation model is the combination of Fredlund and Xing (1994) SWCC equation with Mualem (1976) relative permeability equation and VMM, $m = 1 - 1/n$ estimation model is the combination of van Genuchten (1980) SWCC equation with Mualem (1976) relative permeability equation. The measured SWCC data of a residual soil, collected from a construction site at a depth of 3 to 4 m from the ground surface, at Bukit Timah Road, Singapore (Rahardjo et al., 2012) was used to perform the seepage analyses. In practice, SWCC is generally measured in the laboratory over a limited suction range due to the

Table 1. Five different cases.

Case	SWCC	Relative permeability	k_w
A	[1]F&X (1994)-DR1	[3]CCG (1950)	FCM-DR1
B	F&X (1994)-DR2	CCG (1950)	FCM-DR2
C	[2]VG (1980)-DR1	CCG (1950)	VCM, $m = 1 - 1/n$ – DR1
D	VG (1980)-DR2	CCG (1950)	VCM, $m = 1 - 1/n$ – DR2
E	F&X (1994)-DR2	[4]M (1976)	FMM-DR2

1: Fredlund and Xing (1994); 2: van Genuchten (1980), $m = 1 - 1/n$; 3: Childs and Collis-George (1950); 4: Mualem (1976).

Table 2. Three different scenarios for study the effecting parameters, measured SWCC data ranges, best-fit SWCC equation and relative permeability equation.

Effecting parameter	Compared cases	Scenario
Measured SWCC data range	A & B C & D	1
Best-fit SWCC equation	B & D	2
Relative permeability equation	B & E	3

cost and time constraints. For this Residual Soil (RS), SWCC was measured over a wide suction range of up to 1500 kPa suction. However, two different cases were assumed. First, it was assumed that the measured SWCC data were only available up to 100 kPa (i.e., the measured data beyond 100 kPa was omitted) and the measured SWCC data up to 100 kPa (i.e., DR1) were best-fitted using the two best-fit SWCC equations of Fredlund and Xing (1994) and van Genuchten (1980). The best-fitted SWCCs were then used for estimation of unsaturated permeability functions by FCM and VMM, $m = 1 - 1/n$ model. Second, it was assumed that the measured SWCC data were available up to 1500 kPa (i.e., all the measured SWCC data) and all the measured SWCC data up to 1500 kPa (i.e., DR2) were best-fitted using the two best-fit SWCC equations of Fredlund and Xing (1994) and van Genuchten (1980). The best-fitted SWCCs were then used for estimation of unsaturated permeability functions by FCM, VCM, $m = 1 - 1/n$ and FMM model by DR2. Therefore, five different cases, namely A, B, C, D and E were obtained to investigate the role of unsaturated permeability functions in seepage analyses as shown in Table 1.

All the five cases were compared according to Table 2. The effect of measured SWCC data range was investigated by comparing cases A and B and cases C and D and it was named as scenario 1 as shown in Table 2. The best-fitted SWCCs and unsaturated permeability functions of scenario 1 are shown in Fig. 1.

The effect of best-fit SWCC equation was investigated by comparing cases B and D and it was named as scenario 2 as shown in Table 2. The best-fitted SWCCs and unsaturated permeability functions of scenario 2 are shown in Fig. 2. The effect of relative permeability equation was investigated by comparing cases B and E and it was named as scenario 3 as shown in Table 2. The best-fitted SWCCs and unsaturated permeability functions of scenario 3 are shown in Fig. 3.

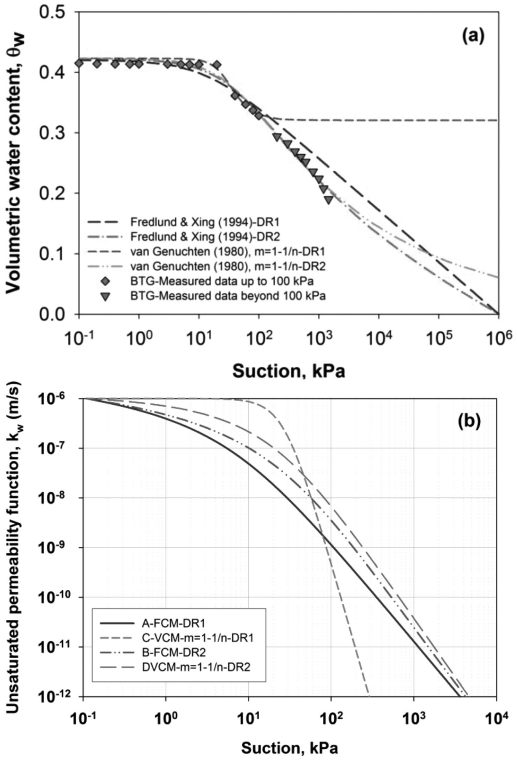


Figure 1. Soil hydraulic properties used in numerical modelling for scenario 1: (a) soil-water characteristic curve, (b) unsaturated permeability function.

3 NUMERICAL MODELING

Seepage analyses were conducted using a numerical model of a homogenous soil column using SEEP/W (Geo-slope International, 2012) software. The soil column of 5 m height and 0.5 m width was subjected to rainfall intensity equal to the saturated permeability of the soil for a duration of 24 hours (see Fig. 4).

The infiltration process of the rainwater into the soil column was conducted using a saturated-unsaturated, finite element seepage analysis. A value of 1×10^{-6} (m/s) was assumed for the saturated permeability of soil which is a typical value for residual soils of Singapore (Rahardjo et al., 2007). The soil column finite element mesh consisted of 3250 elements as shown in Fig. 4b. The boundary and initial conditions applied to the soil column are also shown in Fig. 4. A boundary flux, q, equal to rainfall intensity, I_r, was applied to the surface of the soil column. The nodal flux, Q, equal to zero was applied along the sides of the soil column to simulate no flow zone. The water table was assumed

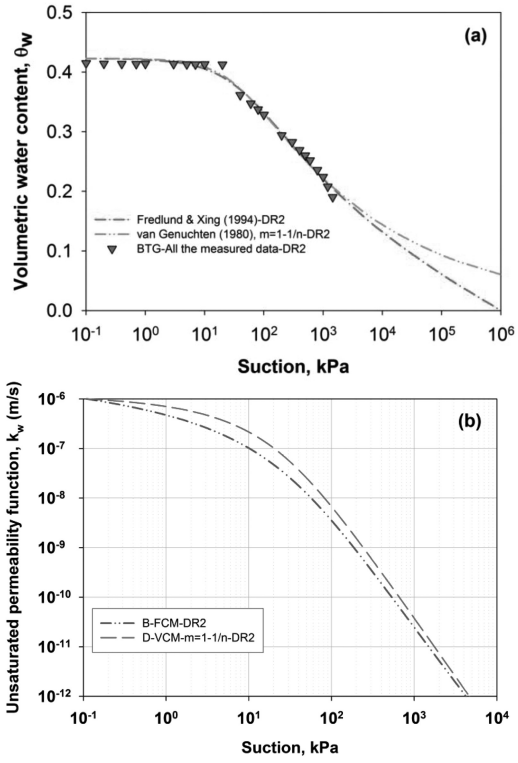


Figure 2. Soil hydraulic properties used in numerical modelling for scenario 2: (a) soil-water characteristic curve, (b) unsaturated permeability function.

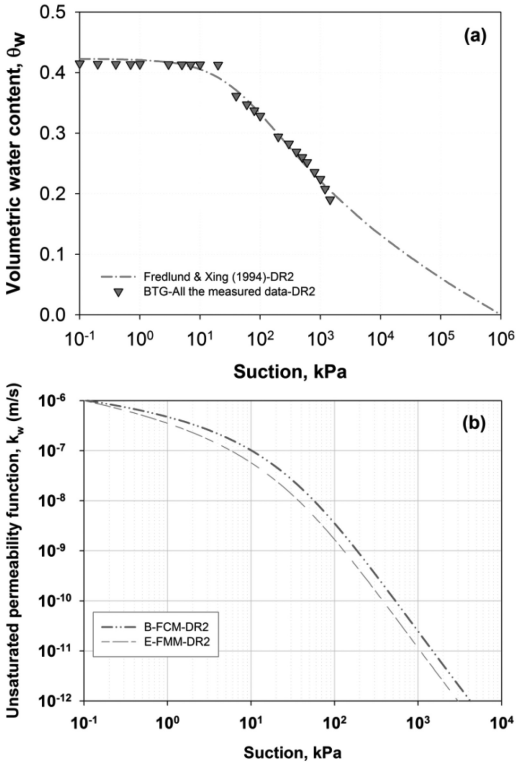


Figure 3. Soil hydraulic properties used in numerical modelling for scenario 3: (a) soil-water characteristic curve, (b) unsaturated permeability function.

to be at the bottom of the soil column. The SWCC and unsaturated permeability function of the soil column were assigned for each of the five cases of A, B, C, D and E according to Table 1.

The water-flow governing equation used in the software for solving a one-dimensional transient seepage analyses is as follows:

$$m_w^2 \gamma_w \frac{\partial h_w}{\partial t} = \frac{\partial}{\partial y}\left(-k_{wy}\frac{\partial h_w}{\partial y}\right) + q \tag{2}$$

where m_w^2 = slope of soil-water characteristic curve; γ_w = unit weight of water; h_w = hydraulic head or total head; t = time; k_{wy} = coefficient of permeability with respect to water as a function of matric suction in y-direction; and q = applied flux at the boundary. The numerical analyses were performed for all the five cases of A, B, C, D and E and the results were compared according to the three different scenarios shown in Table 2.

4 RESULTS AND DISSCUSSION

Two different parameters namely, normalized depth of wetting front, D'_{WF}, and matric suction reduction, R_M, were defined according to Equations 3 and 4 to compare and characterize the responses of the soil column for scenarios 1, 2 and 3.

$$D'_{WF} = \frac{D_{WF}}{H} \tag{3}$$

where D'_{WF} is normalized depth of wetting front; D_{WF} is depth of wetting front and H is height of the column.

$$R_M(\%) = ABS\left[\frac{PWP - PWP_i}{PWP_i}\right]100 \tag{4}$$

where R_M is the matric suction reduction; PWP is the pore-water pressure at any time step and PWP_i is the initial pore-water pressure. Depth of wetting front, D_{WF}, was defined as the depth from the soil surface over which the degree of saturation has changed due to water infiltration (Rahardjo et al., 2010).

4.1 *Effect of measured SWCC data range*

As explained earlier, the effect of measured SWCC data range on seepage analyses was investigated by comparing the results of cases A-FCM-DR1 and B-FCM-DR2 with the same best-fit SWCC and relative permeability equations and two different measured SWCC data ranges. In addition, the results

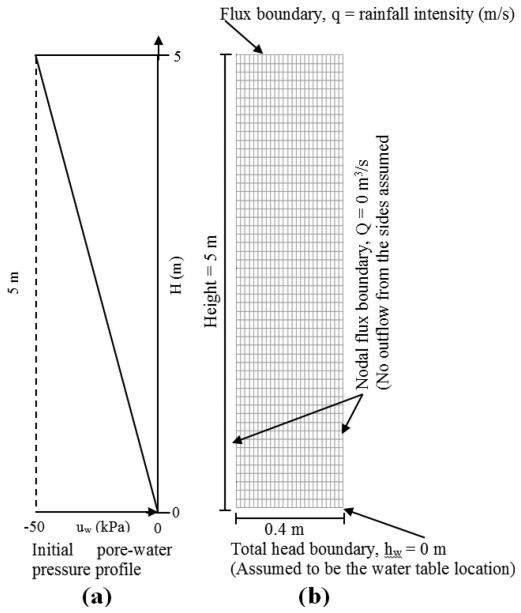


Figure 4. Finite element model and initial condition for the homogeneous soil column: (a) initial condition, (b) mesh and boundary condition (Figure not to scale).

of cases C-VCM, $m = 1 - 1/n$-DR1 and D-VCM, $m = 1 - 1/n$-DR2 with the same best-fit SWCC and relative permeability equations and two different measured SWCC data ranges were compared. The matric suction reduction, R_M, versus height, H, for cases A, B, C and D are shown in Fig. 5 and the normalized depth of wetting front, D'_{FW}, versus time for all the four cases of A, B, C and D are shown in Fig. 6. Fig. 5 shows that for all the four cases, the matric suction decreased with time as the rainfall continued. After rainfall stopped (i.e., at $t = 24$ h), the matric suction increased in the upper part of the soil column but decreased in the lower part of the soil column. This behaviour shows that the rainwater infiltrated into the lower part of the soil column even after the rainfall has ceased.

Comparison between A-FCM-DR1 (see Fig. 5a) and B-FCM-DR2 (see Fig. 5b) shows that the matric suction reduction and matric suction recovery was at a slightly higher rate for case B. This characteristic was reflected in the deeper normalized depth of wetting front, D'_{FW}, for B (i.e., 0.488) as compared to A (i.e., 0.584) as shown in Fig. 6. This shows that using different measured SWCC data ranges resulted in different SWCC and k_w (see Fig. 1) and in turn, in different matric suction profiles before and after rainfall. However, as shown in Figure 5, in both of the cases, A and B, the maximum matric suction reduction was about 100% (at $t = 8$ h). Comparison between C-VCM, $m = 1 - 1/n$-DR1 (see Fig. 5c) and D-VCM, $m = 1 - 1/n$-DR2 (see Fig. 5d) shows that the matric suction reduction profile was at a significantly higher rate for C-VCM, $m = 1 - 1/n$-DR1. However, the

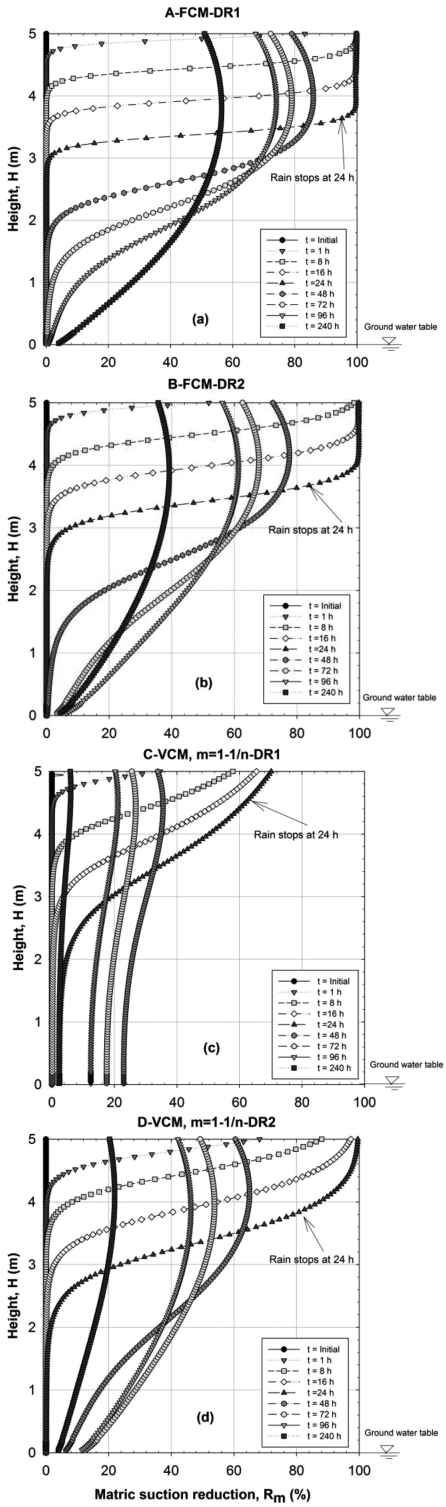


Figure 5. Matric suction reduction profiles-effect of measured data range: (a) A-FCM-DR1 (b) B-FCM-DR2 (c) C-VCM, $m = 1 - 1/n$-DR1 (d) D-VCM, $m = 1 - 1/n$-DR2.

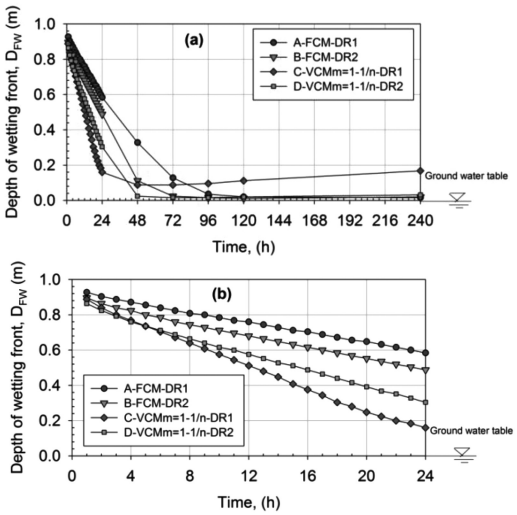


Figure 6. Normalized depth of wetting front-effect of measured SWCC data range.

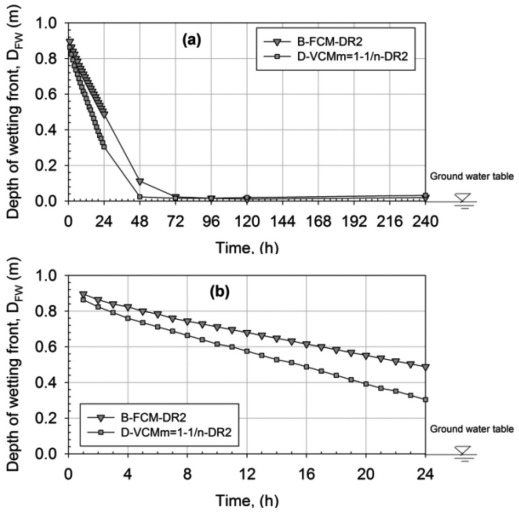


Figure 7. Normalized depth of wetting front-effect of SWCC equation.

maximum matric suction reduction was about 70% for case C (at t = 24 h) as compared to 100% for case D.

The higher k_w of case C as compared to that of case D caused the higher infiltration rate for the case C. Therefore, the rainwater infiltrated faster into the lower part of the soil column and caused reduction of matric suction in the lower part of the soil column. While the reduction of matric suction in the upper part of the column did not reach 100% as compared to that of case D. This characteristic was reflected in the deeper normalized depth of wetting front, D'_{FW}, for C (i.e., 0.16) as compared to D (i.e., 0.304) as shown in Fig. 6. In general, it can be concluded that the effect of measured SWCC data range used to best-fit the SWCC and estimate the unsaturated permeability function had a significant effect on the seepage analyses results.

As shown in Fig. 6, D'_{FW}, at t = 24 h was deeper for B (i.e., 0.488) as compared to A (i.e., 0.584). In addition, D'_{FW}, was deeper for C (i.e., 0.16) as compared to D (i.e., 0.304). Therefore, the difference between C and D was larger than the difference between A and B. This characteristic shows that VCM, m = 1 − 1/n model has higher sensitivity then the FCM model to the measured SWCC data ranges. In the other words, Fredlund and Xing (1994) SWCC equation was less sensitive to the measured SWCC data ranges.

4.2 *Effect of best-fit SWCC equation*

The effect of best-fit SWCC equation on seepage analyses was investigated by comparing the results of cases B-FCM-DR2 and D-VCM, m = 1 − 1/n-DR2 with the different best-fit SWCC, but the same relative permeability equations and the same measured SWCC data ranges (see Fig. 2).

The matric suction reduction, R_M, versus height, H, for cases B and D are shown in Fig. 5. The figure shows that for both of the cases, the matric suction reduced with time as the rainfall continued. After rainfall stopped (i.e., at t = 24 h), the matric suction increased in the upper part of the soil column but the matric suction decreased in the lower part of the soil column. Comparison between B-FCM-DR2 (see Fig. 5b) and D-VCM, m = 1 − 1/n-DR2 (see Fig. 5d) shows that the matric suction reduction and matric suction recovery was at a higher rate for case D. Case B reached the maximum matric suction reduction of 100% at t = 8 h, while Case D reached the maximum matric suction reduction of 100% at t = 24 h. This was due to the higher unsaturated permeability of case D as compared to that of case B even when the same relative permeability equation and the same measured SWCC data range were used in the development of both models. Therefore, selection of the best-fit SWCC equation plays an important role when conducting seepage analyses.

The normalized depth of wetting front, D'_{FW}, versus time for cases B and D is shown in Fig. 7. As shown in the figure, D'_{FW}, at t = 24 h was deeper for case D (i.e., 0.304) as compared to case B (i.e., 0.488). This shows that the best-fit SWCC equation can significantly affect the results of seepage analyses.

4.3 *Effect of relative permeability equation*

The effect of relative permeability equation on seepage analyses was investigated by comparing the results of cases B-FCM-DR2 and E-FMM-DR2 with the different relative permeability equations, but same best-fit SWCC and the same measured SWCC data ranges (see Fig. 3). The matric suction reduction, R_M, versus height, H, for cases B and E are shown in Fig. 8. The figure shows that for both cases, the matric suction decreased with time as the rainfall continued. After the rainfall stopped (i.e., at t = 24 h), the matric suction increased in the upper part of the soil column but

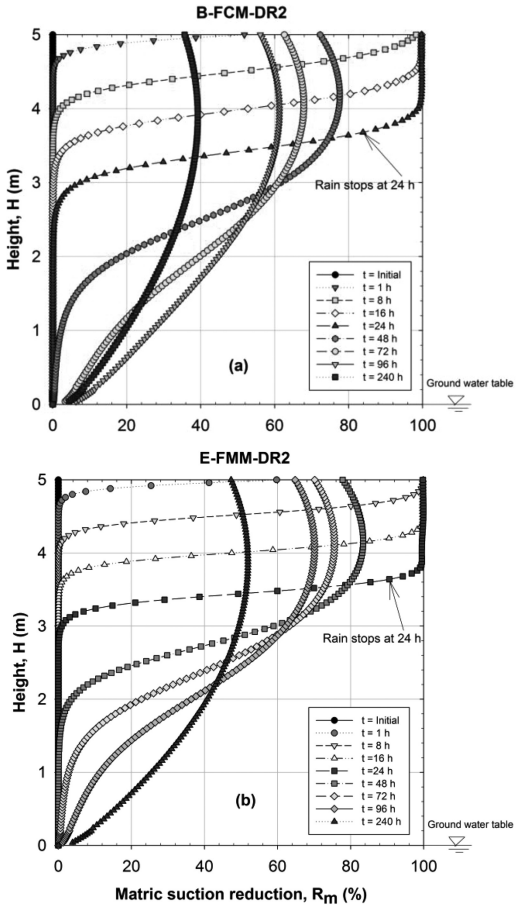


Figure 8. Matric suction reduction profiles-effect of relative permeability equation: (a) B-FCM-DR2, (b) E-FMM-DR2.

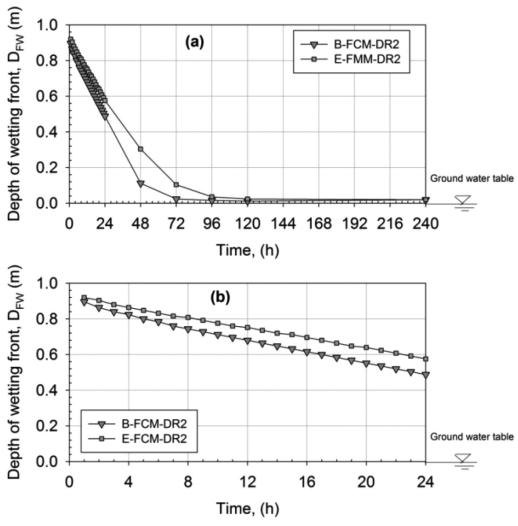


Figure 9. Normalized depth of wetting front-effect of relative permeability equation.

the matric suction decreased in the lower part of the soil column.

Comparison between B-FCM-DR2 (see Fig. 8a) and E-FMM-DR2 (see Fig. 8b) shows that the matric suction reduction and matric suction recovery were more or less the same for both of the cases. Cases B and E reached the maximum matric suction reduction of 100% at t = 8 h. The normalized depth of wetting front, D'_{FW}, versus time for the cases B and E is shown in Fig. 9. As shown in Fig. 9, D'_{FW}, was slightly deeper for case B (i.e., 0.488) as compared to case E (i.e., 0.576). If the difference between D'_{FW} of cases B and E (i.e., effect of relative permeability equation) is compared to that of B and D (i.e., effect of best-fit SWCC equation), it can be seen that the effect of best-fit SWCC equation is more important than the effect of the relative permeability equation.

5 CONCLUSIONS

Based on seepage analyses of a residual soil column subjected to 24 h rainfall of 1×10^{-6} m/s, it was found that the measured SWCC data range noticeably affected the results. The effect was more significant for van Genuchten (1980), m = 1 − 1/n based models. The effect of best-fit SWCC equation was more important than the effect of relative permeability equation on the seepage analysis results.

ACKNOWLEDGEMENT

The first author is a recipient of the SINGA scholarship.

REFERENCES

Childs, E.C. and Collis-George, N. 1950. The permeability of porous materials. Proceedings of the Royal Society of London, Series A (Mathematical and Physical Sciences) 201, 392–404.

Fredlund, D. G. and Xing, A. 1994. Equations for the soil-water characteristic curve. Canadian Geotechnical Journal, 31(4): 521–532.

Geo-slope International, (2012). SEEP/W for finite element seepage analysis, user's guide, Calgary, Alta., Canada.

Harianto Rahardjo, Alfrendo Satyanaga, Gabriele AR D'Amore, Eng-Choon Leong Soil–water characteristic curves of gap-graded soils. Engineering Geology, 125: 102–107.

Mualem, Y. 1986. Hydraulic conductivity of unsaturated soils: predictions and formulas Methods of soil analysis, part 1, physical and mineralogical methods (2nd edition), American Society of Agronomy, Agronomy Monographs 9(1) 5.

Rahardjo, H., Ong, T. H., Rezaur, R. B. and Leong, E. C. 2007. Factors controlling instability of homogeneous soil slopes under rainfall. Journal Geotechnical and Geoenvironmental Engineering., 133(12): 1532–1543.

Rahardjo, H., TH Ong, RB Rezaur, E. C., Leong, Delwyn G Fredlund, (2010) Response parameters for characterization of infiltration. Environmental Earth Sciences 60(7): 1369–1380.

Rahimi, A., Rahardjo, H., and Leong, E.C. 2010. Effect of antecedent rainfall patterns on rainfall-induced slope failure. Journal of Geotechnical and Geoenvironmental Engineering, 137(5): 483–491.

Rahimi, A., Rahardjo, H., and Leong, E.C. 2010. Effect of hydraulic properties of soil on rainfall-induced slope failure. Engineering Geology, 114(3): 135–143.

Rahimi, A., Rahardjo, H., and Leong, E.C. 2015. Effect of range of soil–water characteristic curve measurements on estimation of permeability function. Engineering Geology, 185: 96–104.

Rahimi, A., Rahardjo, H., and Leong, E.C. 2014. Underlying parameters affecting estimation of unsaturated permeability of soils. In Proceedings of the Unsaturated Soils: Research & Applications, Sydney, July 2014. pp. 1073–1077.

Rahimi, A., 2015. Parameters affecting estimation of unsaturated permeability of soils. PhD Thesis, Nanyang Technological University, Singapore.

van Genuchten, M. T. 1980. Closed-form equation for predicting the hydraulic conductivity of unsaturated soils. Soil Science Society of America Journal, 44(5): 892–898.

This page intentionally left blank

Unsaturated Soil Mechanics—from Theory to Practice – Chen et al. (Eds)
© 2016 Taylor & Francis Group, London, ISBN 978-1-138-02921-7

Effects of variability of unsaturated hydraulic properties on stability of residual soil slopes

Q. Zhai, H. Rahardjo & A. Satyanaga
School of Civil and Environmental Engineering, Nanyang Technological University, Singapore

ABSTRACT: Matric suction plays an important role in stability of residual soil slopes against rainfall. Changes in matric suction during rainfall are controlled by infiltration characteristics of the soil. Both Soil-Water Characteristic Curve (SWCC) and unsaturated permeability function (k_w function) have significant effects on the infiltration characteristics of the soil. The matric suction in the soil can be computed using the governing flow equation with input of SWCC and k_w function. The variability in unsaturated soil properties such as SWCC and k_w function will result in uncertainties in the computed matric suction in the soil during rainfall. Consequently, uncertainty in matric suction will affect the computed Factor Of Safety (FOS) for slope stability. In this study, confidence limits of SWCC and k_w function of residual soils derived from Bukit Timah granite in Singapore are computed using the experimental data from published literatures. The variability in the computed matric suction and FOS as a result of uncertainty in SWCC and k_w function is presented by analyzing a typical slope with constant boundary conditions and varying soil properties (i.e. SWCC and k_w function). The effects of variability in SWCC and k_w function on the infiltration and slope stability are discussed in this paper.

1 INTRODUCTION

Rainfall-induced slope failure is common in tropical areas (Tan et al. 1987, Brand 1992, Gasmo et al. 2000, and Tsaparas et al. 2002). Infiltrated rainwater will decrease the suction in the soil and therefore, reduce the factor of safety of the slopes. Researchers (Anderson 1983; Brand 1992; Ching et al. 1984; Franks 1999; Gasmo et al. 2000; Rahardjo et al. 2005, 2006, 2007, 2010, 2011) have studied and observed that rainwater infiltration is the major factor for rainfall-induced slope failure. In other words, stability of many slopes is dependent on the rainwater infiltration. On the other hand, the SWCC and k_w function control the infiltration characteristics of the soil. Therefore, the unsaturated hydraulic properties of soil have significant effects on rainfall-induced slope stability.

Residual soils were developed or weathered from their underlying parent materials and had the same general chemistry as those parent materials. The weathering of the parent materials took the forms of physical weathering (disintegrating), chemical weathering (decomposition) and chemical transformation. Therefore, the properties of residual soil could vary a lot due to the variability of parent materials and the forms of weathering. The variability in unsaturated hydraulic properties of residual soil was investigated and discussed in this paper. The effect of the variability in unsaturated hydraulic properties on the slope stability was presented and discussed through numerical analyses using software of Seep/W and Slope/W.

2 LITERATURE REVIEW

Soil-Water Characteristic Curve (SWCC) and permeability function are the two major hydraulic properties of unsaturated soil that have significant effects on infiltration characteristics of the soil. SWCC defines the relationship between the amount of water in the soil and the suction in the soil. Leong and Rahardjo (1997) presented that Fredlund and Xing (1994) equation as illustrated in equation (1) performed best as compared with other different forms of best fit equation and it could be used for a wide range of soil for representation of the SWCC. Zhai and Rahardjo (2012a, 2012b) suggested that there were only three fitting parameters in Fredlund and Xing (1994), and C_r in the equation was an input value and not a fitting parameter.

$$\theta = C(\psi)\frac{\theta_s}{\left\{\ln\left[e+\left(\frac{\psi}{a}\right)^n\right]\right\}^m} = \left[1-\frac{\ln\left(1+\frac{\psi}{C_r}\right)}{\ln\left(1+\frac{10^6}{C_r}\right)}\right]\frac{\theta_s}{\left\{\ln\left[e+\left(\frac{\psi}{a}\right)^n\right]\right\}^m} \quad (1)$$

where,

a, n, m: fitting parameters;

C_r: parameter related to residual suction that can be selected as $C_r = 1500$ kPa for most cases.

θ_s: saturated volumetric water content.

Permeability function defines the relationship between coefficient of permeability for unsaturated soil and the suction in the soil. Permeability function of unsaturated soil is normally computed from SWCC (i.e. indirect method) instead of direct measurement since the direct measurement is much more time consuming and costly. Mualem (1986) categorized these prediction models into three groups: empirical, macroscopic, and statistical model. Leong and Rahardjo (1997) suggested that the statistical model was most rigorous and provided most accurate results. Fredlund and Rahardjo (1993) introduced the Kunze et al. (1968) equation as the method for the indirect computation of permeability function of unsaturated soil.

Rahardjo et al. (2010) studied three response parameters (i.e. the depth of wetting front, the matric suction reduction depth and the sectional infiltration rate) for characterization of rainwater infiltration. Rahimi et al. (2010) conducted a parametric study on the effect of hydraulic properties of soil on the rainfall induced slope failure. Dye et al. (2011) discussed the effect of uncertainty in SWCC on the moisture flow in the soil. Rahardjo et al. (2012) presented the variability of residual soil properties including plastic limit (PL), liquid limit (LL), effective cohesion of soil (c'), effective angle of internal friction (ϕ'), grain size distribution (GSD), and Soil-Water Characteristic Curve (SWCC) in Singapore. Zhai and Rahardjo (2013) proposed a statistical method for quantification of variability in SWCC.

3 THEORY

The method as presented by Zhai and Rahardjo (2013) for estimation of confidence limits of best fitted SWCC from measured experimental data is discussed in this paper. The theories of water flow in unsaturated soil and shear strength of unsaturated soil are also presented in this section.

3.1 *Confidence limits of best fitted SWCC.*

Zhai and Rahardjo (2013) proposed the equations for determination of confidence limits of best fitted SWCC as follows:

$$\text{when } 0 < \psi < a_{max},\ \theta_{upper} = C(\psi)\frac{\theta_s}{\left\{\ln\left[e+\left(\frac{\psi}{a_{max}}\right)^{n_{max}}\right]\right\}^{m_{min}}}$$

$$\text{when } \psi > a_{max},\ \theta_{upper} = C(\psi)\frac{\theta_s}{\left\{\ln\left[e+\left(\frac{\psi}{a_{max}}\right)^{n_{min}}\right]\right\}^{m_{min}}}$$

$$\text{when } 0 < \psi < a_{min},\ \theta_{lower} = C(\psi)\frac{\theta_s}{\left\{\ln\left[e+\left(\frac{\psi}{a_{min}}\right)^{n_{min}}\right]\right\}^{m_{max}}}$$

$$\text{when } \psi > a_{max},\ \theta_{lower} = C(\psi)\frac{\theta_s}{\left\{\ln\left[e+\left(\frac{\psi}{a_{min}}\right)^{n_{max}}\right]\right\}^{m_{min}}}$$

------- (2) (3)

where,

$$a_{max} = a + t_{\alpha/2}\sqrt{Var(a)} \qquad a_{min} = a - t_{\alpha/2}\sqrt{Var(a)}$$
$$n_{max} = n + t_{\alpha/2}\sqrt{Var(n)} \qquad n_{min} = n - t_{\alpha/2}\sqrt{Var(n)}$$
$$m_{max} = m + t_{\alpha/2}\sqrt{Var(m)} \qquad m_{min} = m - t_{\alpha/2}\sqrt{Var(m)}$$

a, n and m are fitting parameters.

3.2 *Differential equation for water flow in unsaturated soil*

Seep/W was formulated on the basis that water flows through both saturated and unsaturated soil follows Darcy's law. Darcy's law was modified by Richard for unsaturated soil and the governing differential equation used in the software of Seep/W for solving a transient and two dimensional seepage analyses is illustrated as follows:

$$\frac{\partial}{\partial x}\left(k_x\frac{\partial H}{\partial x}\right)+\frac{\partial}{\partial y}\left(k_y\frac{\partial H}{\partial y}\right)+Q = m_w\gamma_w\frac{\partial H}{\partial t}$$

------ (4)

where,

H = total head;

k_x, k_y = coefficient of permeability in x and y directions;

m_w = the slope of storage curve;

γ_w = the unit weight of water;

Q = applied boundary flux.

3.3 *Shear strength of unsaturated soil*

Fredlund et al. (1978) introduced the equation of shear strength for unsaturated soil using two independent stress variables. The shear strength equation for unsaturated soil is illustrated in equation (4) as follows:

$$\tau = c' + (\sigma - u_a)\tan\phi' + (u_a - u_w)\tan\phi^b$$

------ (5)

where,

τ = the shear strength of unsaturated oil;

σ = total normal stress;

u_a = air-pressure;

ϕ' = effective angle of internal friction;

c' = effective cohesion of soil;

$u_a - u_w$ = suction in the soil;

ϕ^b = angle indicating the rate of increase in shear strength relative to the matric suction.

Table 1. Soil properties of residual soil from Bukit Timah granite in Singapore.

Soil	USCS	k_s (m/s)	G_s	LL (%)	PL (%)	Sand (%)	Fine (%)	Reference
SLR-la	SM	2.50E-08	2.6	108	47	61	39	Agus et al. 2001, 2005
SLR-lb	SM	7.36E-08	2.61	64	34	72	28	Agus et al. 2001, 2005
SLR-lc	SM	2.88E-07	2.55	60	35	75	25	Agus et al. 2001, 2005
SLR-2a	MH	2.78E-08	2.6	105	47	38	62	Agus et al. 2001, 2005
SLR-2b	MH	3.00E-08	2.61	116	48	38	62	Agus et al. 2001, 2005
SLR-2c	CH	1.36E-08	2.55	61	36	43	57	Agus et al. 2001, 2005
YS-1	MH	7.27E-08	2.61	54	33	44	56	Agus et al. 2001, 2005
YS-b	MH	4.80E-07	2.53	68	49	32	68	Agus et al. 2001, 2005
LA-a	SC	9.51E-07	2.53	48	37	66	34	Agus et al. 2001, 2005
LA-b	SM	5.37E-08	2.6	97	38	72	28	Agus et al. 2001, 2005
LA-c	SM	1.86E-08	2.54	61	4	62	38	Agus et al. 2001, 2005
LA-d	SM	3.57E-08	2.6	97	38	75	25	Agus et al. 2001, 2005
MR1	SM	6.00E-06	2.66	52	31	53	46	Rahardjo et al. 2011
MK2	MH	3.30E-05	2.58	54	39	40	60	Rahardjo et al. 2011
SS	MH	2.20E-06	2.59	48	27	61	38.9	Tami et al. 2007
TR1	CH	3.19E-08	2.59	71	34	27	73	Rahardjo et al. 2012
TR2	MH	5.65E-05	2.66	51	29	30	70	Rahardjo et al. 2012
BBA1	CL	5.27E-09	2.82	31	20	43	54	Rahardjo et al. 2012
BBA2	CL	8.28E-08	2.64	34	20	20	80	Rahardjo et al. 2012
BB1	MH	1.20E-08	2.65	55	32	3	97	Rahardjo et al. 2012
BB2	SM	2.15E-08	2.71	49	30	51	49	Rahardjo et al. 2012
AMK1	SM	8.52E-06	2.54	56	38	58	42	Rahardjo et al. 2012
AMK2	SM	3.96E-06	2.58	58	36	53	47	Rahardjo et al. 2012
AMA	MH	2.52E-07	2.7	54	29	29	70	Rahardjo et al. 2012
TWL	MH	5.60E-06	2.66	72	45	5	95	Rahardjo et al. 2012

4 UNSATURATED HYDRAULIC PROPERTIES OF RESIDUAL SOIL FROM BUKIT TIMAH GRANITE IN SINGAPORE

A total of twenty five sets of data for residual soil from Bukit Timah granite as collected from published literatures are investigated for their variability in unsaturated hydraulic properties of soil. The soil properties of the twenty five sets of data are summarized in Table 1. The variability in SWCC and permeability function of residual soil from Bukit Timah Granite is determined using both box-plot method and equations from Zhai and Rahardjo (2013) as illustrated in Figures 1 and 2.

Figures 1 and 2 indicate that the variability in SWCC and permeability function as determined using Zhai and Rahardjo (2013) equations agree with that determined using the box-plot method. Figures 1 and 2 also indicate that median is not located at the center of the box meaning the degree of saturation, S, and $\log(k_w)$ follow a biased distribution.

5 SIMULATION FOR SEEPAGE AND SLOPE STABILITY ANALYSES

Two-dimensional seepage analyses were carried out using a numerical model as illustrated in Figure 3. The slope height, H_s, was selected to be 10 meters, the slope angle, α, was selected to be 45 degrees and the initial depth of ground water table, H_w, was selected to be 2 meters below the toe of the slope, based on a typical ground water table position in Singapore. The distance between the slope and the side of the slope model was set to three times the height of the slope and Q, equal to

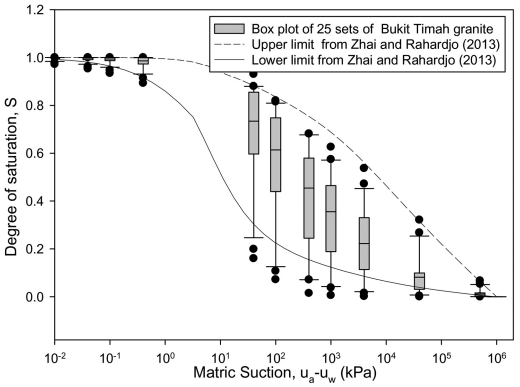


Figure 1. Variability in SWCC for residual soil from Bukit Timah granite.

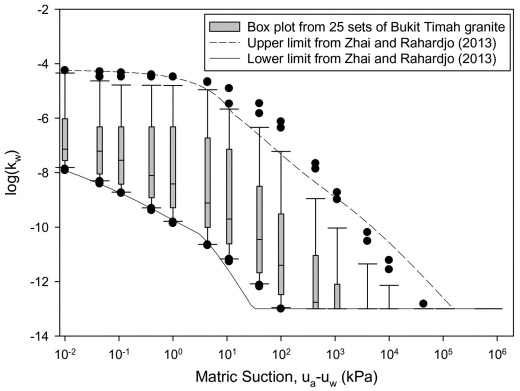


Figure 2. Variability in computed permeability function for residual soil from Bukit Timah granite.

zero with potential seepage review was assigned to the bottom and along the sides of the slope model above the groundwater table. The constant total head, h_w, on each side was applied as the boundary along the sides of the slope model below the groundwater table. The rainfall with intensity of 22 mm/hour and a duration of 24 hours was applied to the slope surface as a flux boundary, q. Ponding was not allowed to occur at the slope surface. In other words, the excess rainfall at the slope surface was removed as run-off. Rahardjo et al. 2007 concluded that slope geometry (i.e. slope angle and slope height) and initial depth of water table had secondary effects on the stability of the slope. Therefore, slopes with the same geometry and initial water table were adopted for simulation. Three types of soils (i.e. soils with the best fitted SWCC named as Soil A, soil with upper limit of SWCC named as Soil B and soil with lower limit of SWCC named as Soil C) were assigned to a single layer of soil. To make the analysis results to be comparable, $k_s = 6 \times 10^{-6}$ m/s, which is within the range of saturated coefficient of permeability for the residual soil from Bukit Timah granite as illustrated in Figures 2, was assigned to the three types soils. The permeability functions of the three types of

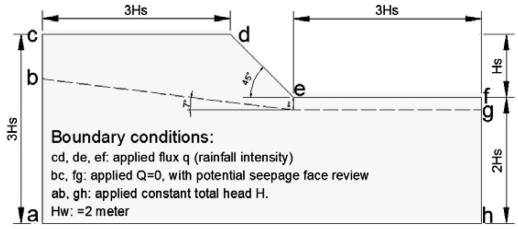


Figure 3. Slope geometry and boundary condition of residual soil.

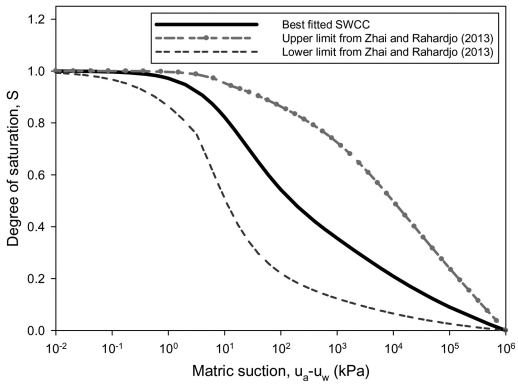


Figure 4. Best fitted SWCC and confidence limits for residual soil from Bukit Timah granite.

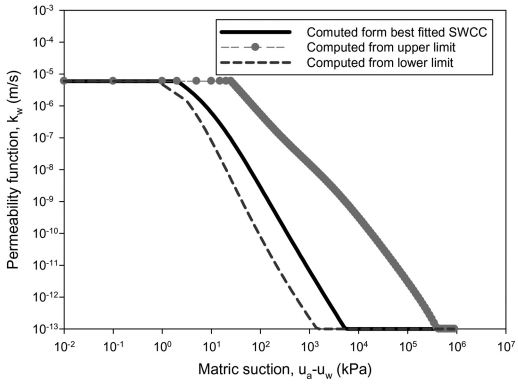


Figure 5. Computed permeability functions for residual soil from Bukit Timah granite.

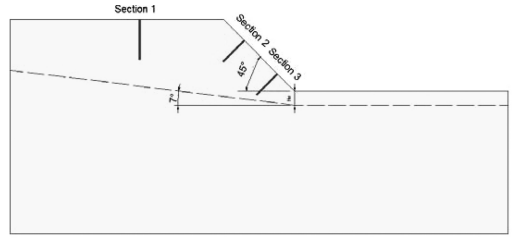


Figure 6. Sections for monitoring of PWP.

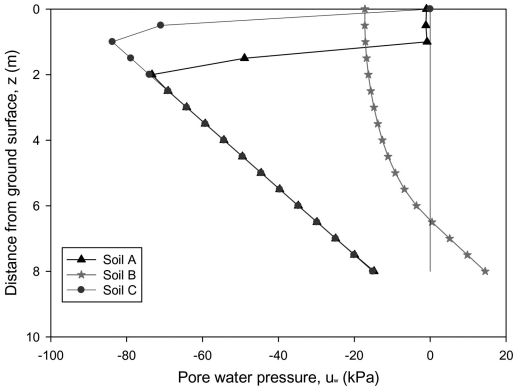


Figure 7. Pore-water pressure profiles on section 1 after 24 hours rainfall.

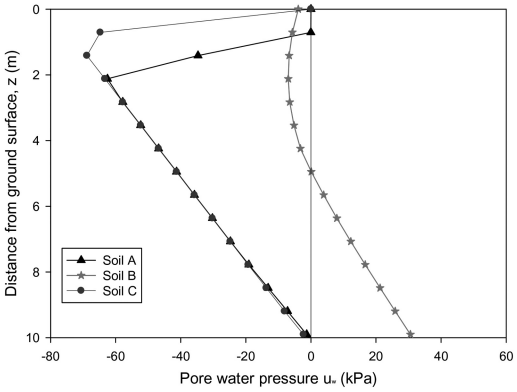


Figure 8. Pore-water pressure profiles on section 2 after 24 hours rainfall.

soil were computed from their respective SWCC using the statistical method. The SWCCs and permeability functions used in the simulation model are illustrated in Figures 4 and 5, respectively.

As the effects of shear strength parameters on slope stability were not studied in this paper, an effective cohesion $c' = 12\,\text{kPa}$ and an effective friction angle $\phi' = 33°$, which are within the range as presented by Rahardjo et al. 2012, were assigned to these three types of soil for slope stability analyses. The angle indicating the rate of increase in shear strength relative to the matric suction $\phi^b = 0.5\,\phi'$ was used in this study.

6 RESULTS AND DISCUSSIONS

Pore-water pressures (PWP) on three sections as shown in Figure 6 were computed using Seep/W are illustrated in Figures 7 to 9.

Figures 7 to 9 indicate that pore-water pressures in Soil B is higher than that in the Soil A and C after 24 hours of rainfall. In other words, Soil B can be most easily infiltrated by rainwater while Soil C can be most difficult to be infiltrated by rainwater. The wetting front in Soil B is much deeper than that in Soil A and C.

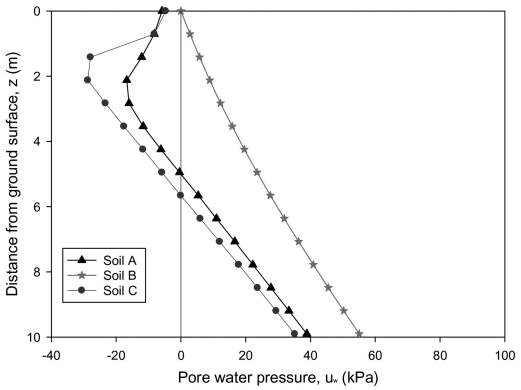


Figure 9. Pore-water pressure profiles on section 3 after 24 hours rainfall.

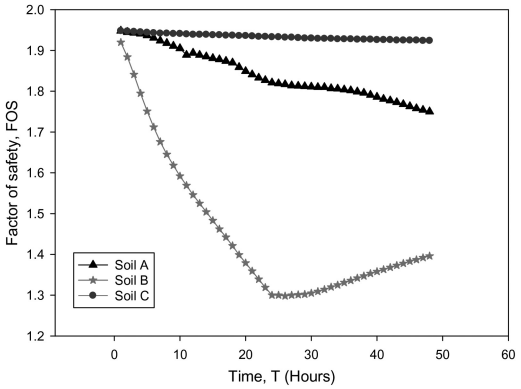


Figure 10. Computed FOS for the slope with residual soil from Bukit Timah granite.

Stability analyses in this study were performed by incorporating the pore-water pressure from seepage analyses into Slope/W. The variation in factor of safety obtained from three cases of slope stability analyses were calculated using Bishop's simplified method of slices. The computed factors of safety (FOS) were illustrated in Figure 10.

Figure 10 indicates that the effect of variability in SWCC and k_w function on slope stability is significant. As shown in Figure 10, the FOS can drop by 30% if upper limit of SWCC instead of best fitted SWCC is adopted for simulation. Figure 10 suggests it is conservative to adopt upper confidence limit of SWCC for simulation of rainwater infiltration.

7 CONCLUSIONS

Twenty-five sets of data consisting of SWCCs and saturated coefficients of permeability for residual soil from Bukit Timah granite in Singapore are used for the investigation of its variability with respect to the unsaturated hydraulic properties of the soil. The computed variability in SWCC and permeability function as obtained using Zhai and Rahardjo (2013) equation agrees with that determined using the box-plot method. The degree of saturation, S, and $\log(k_w)$ are found to follow a biased distribution as observed from the box-plot results. The results of analyses indicate that the soil with upper limit of SWCC is most easily infiltrated by rainwater and most sensitive to slope instability during rainfall. The wetting front in the soil with upper limit of SWCC is much deeper than that in the soils with best fitted SWCC and lower limit of SWCC.

REFERENCES

Anderson, M. G. (1983) "*Prediction of soil suction for slope in Hong Kong.*" Geotechnical Control Office, Hong Kong, GCO publication, 1 (84), 243.

Brand, E. W. (1992) "*Slope instability in tropical areas.*" Proc. of the 6th Int. Symposium on Landslides, Christchurch, New Zealand, 3, 2031–2051.

Ching, R. K. H., Sweeney, D. J. and Fredlund, D. G. (1984) "*Increase in factor of safety due to soil suction for two Hong Kong slopes.*" Proc. of the 4th Int. Symposium on Landslides, Toronto, Canada, 617–623.

Dye H.B., Houston S.L. and Welfert B.D (2011) "*Influence of Unsaturated Soil Properties Uncertainty on Moisture Flow Modeling.*" Geotech Geol Eng 29 (161–169).

Franks, C. A. M. (1999) "*Characteristics of some rainfall-induced landslides on natural slopes.*" Lantau Island, Hong Kong, Quarterly J. of Eng. Geology, 32, 247–259.

Fredlund, D. G. Morgenstern, N. R. and Widger, R. (1978) "*The shear strength of unsaturated soil.*" Canadian Geotechnical Journal, August, Vol. 15, No. 3, pp. 313–321.

Fredlund, D.G. and Xing, A. (1994) "Equations for the soil-water characteristic curve." Canadian Geotechnical Journal, 31(3): 521–532.

Gasmo, J. M., Rahardjo, H. and Leong, E. C. (2000) "Infiltration effects on stability of residual soil slope." Computers and Geotechnics 26, 145–165.

Kunze, R.J., Uehara, G., and Graham, K (1968) "*Factors important in the calculation of hydraulic conductivity.*" Proc., Soil Sci. Soc. of Am., 32, 760–765.

Leong, E.C. and Rahardjo H. (1997) "*Review of soil-water characteristic curve equations.*" J. Geotech. Geoeniron. Eng 123(12), 1106–1117.

Mualem. Y (1986) "*Hydraulic conductivity of unsaturated soils: prediction and formulas.*" Methods of soil analysis. Part 1, Physical and mineralogical methods. 2nd Ed., Agronomy. A. Klute ed., Am Soc of Agronomy, Inc., and Soil Sci. Soc. of Am., Inc., Madison, Wis., 799–823.

Rahardjo, H., T.T. Lee, E.C. Leong and R.B. Rezaur (2005). "*Response of a Residual Soil Slope to Rainfall*". Canadian Geotechnical Journal, April, Vol. 42, No. 2, pp. 340–351.

Rahardjo, H., Lee, T. T., Leong, E. C. and Rezaur, R. B. (2006) "*Reply to Discussion by Londono A. C. on "Respsonse of a residual soil slope to rainfall." by Rahardjo, H., Lee, T. T., Leong, E. C. and Rezaur, R. B. [Can. Geotech. J., 42: 340–351 (2005)].*" Can Geotech. J., 43, 979–984.

Rahardjo, H., Ong, T. H., Rezaur, R.B. and Leong, E. C. (2007) "*Factors controlling instability of homogeneous soil slopes under rainfall loading.*" ASCE J. of Geotechnical and Geoenvironmental Eng. 133 (12), 1532–1543.

Rahardjo, H., Ong, T. H., Rezaur, R.B., Leong, E. C. and Fredlund, D. G. (2010) "*Response parameters for*

characterization of infiltration." Environmental Earth Science, 60(7), 1369–1380.

Rahardjo, H., Santoso, V. A., Leong, E. C., Ng, Y. S. and Hua, C. J. (2011) "*Numerical analysis and monitoring performance of residual soil slopes.*" Soils and Foundations Vol. 51, No. 3, 471–482.

Rahardjo, H., A. Satyanaga, E.C. Leong and Y.S. Ng (2012). "*Variability of Residual Soil Properties*". Journal of Engineering Geology, June, Vol. 141–142, No. 124–140.

Rahardjo, H., Satyanaga, A. and Leong E. C. (2013) "*Effect of flux boundary condition on pore-water pressure distribution in slope.*" Engineering Geology 165, 133–142.

Rahimi, A. Rahardjo, H. and Leong, E.C. (2010) "*Effect of hydraulic properties of soil on rainfall-induced slope failure.*" Engineering Geology 114, 135–143.

Tan, S. B., Tan, S. L., Lim, T. L. and Yang, K. S. (1987) "*Landslides problems and their control in Singpoare.*" Proc. 9th Southeast Asian Geotechnical Conf., Bangkok, 1:25–1:36.

Tsaparas, I., Rahardjo, H., Toll, D.G. and Leong, E. C. (2002) "*Controlling parameters for rainfall-induced landslides.*" Computer and Geotechnics, 29(1), 1–27.

Zhai Q., Rahardjo H. (2012a) "*Determination of soil–water characteristic curve variables.*" Comput Geotech 2012; 42:37–43.

Zhai Q., Rahardjo H. (2012b) "*Reply to the discussion by Bellia et al. on "Determination of soil–water characteristic curve variables" by Zhai Q, Rahardjo H. Comput Geotech 2012; 42:37–43*" Comput Geotech Volume 45, Pages 151–152.

Zhai Q., Rahardjo H. (2013) "*Quantification of uncertainty in soil-water characteristic curve associated with fitting parameters*" Engineering Geology 163, 144–152.

Unsaturated Soil Mechanics—from Theory to Practice – Chen et al. (Eds)
© 2016 Taylor & Francis Group, London, ISBN 978-1-138-02921-7

Measurement of hydraulic properties of unsaturated permeable polyurethane bound asphalt materials

L. Renken & M. Oeser
Institute of Highway Engineering, RWTH Aachen University, Germany

M. Milatz & J. Grabe
Institute of Geotechnical Engineering and Construction Management, Hamburg University of Technology (TUHH), Germany

ABSTRACT: In order to reduce the far reaching consequences of surface sealing, the use of permeable pavements is increasingly gaining importance especially with regard to sparing the natural resources, groundwater, soil and the climate. Permeable Polyurethane (PU) bound asphalt pavements are currently the most effective high-tech construction method for environmentally friendly transport infrastructures and modern waste water management. Because of the enhanced permeability of such pavements, the design of the sub-construction requires specific attention. An unexplored approach is to install the permeable pavements directly on the unbound subsoil, in order to drain the accumulated water completely. The infiltration of the rainwater through the construction leads to an increased water supply in the subsoil. However, the hydro-mechanical interaction of the porous PU-asphalt structure and the subsoil is still unknown. To gain primary insights into this mechanism the hydraulic properties of different PU-bound asphalt mixtures are analyzed focusing on the Soil-Water Characteristic Curve (SWCC) and the hydraulic conductivity. The air entry value of highly porous structures is estimated to be quite low, leading to challenges when measuring small-scale suction. In this paper first results of laboratory tests are presented.

1 INTRODUCTION

With regard to the high loads and increasing maintenance requirements for road pavements, the demand for efficient and sustainable material concepts with a high stability and an enduring functionality increases. Furthermore, the progressing development of urban areas and strong industrial activity have led to a significant expansion of sealed areas in human settlements and the transport infrastructure in Europe and other developed parts of the world. Sealed surfaces substantially reduce the natural retention capacity of an area. Impacts can be observed in a change of the natural water runoff and consequentially an interference with the natural hydrological cycle. In order to reduce the far reaching consequences of surface sealing, the use of permeable pavements is increasingly gaining importance, especially with regard to sparing the natural resources, groundwater, soil and the climate. The use of permeable pavements for infrastructure, particularly the utilization of porous asphalt constitutes a constructive approach to solving the aforementioned problems. To drain accruing surface water quickly the infiltration of the precipitation through the layers is necessary. The improved drainage performance of the pavement significantly increases groundwater replenishment and can lead to an improved hydraulic supply of the surrounding flora.

A void-rich design of pavement constructions for traffic areas, in particular through the use of porous asphalts, is currently the most effective structurally feasible "high-tech" construction method. Due to the void content of Porous Asphalt (22 vol% to 28 vol%) a major contribution to noise reduction can also be achieved. The water permeability also contributes to increased traffic safety due to the reduction of water spray and the reduced risk of aquaplaning.

Although conventional Porous Asphalts (PA) have been optimized and further developed in terms of adhesive properties and durability within the last years, their applicability remains restricted due to their limited lifetime resulting from the high susceptibility to grain ravelling (loss of aggregates), caused by mechanical shear stresses. Under high mechanical shear stress, failure of the adhesion can occur in the monolithic adhesive structure, resulting in a shift of the particle skeleton. Furthermore, the binder exhibits an increased susceptibility to aging which is due to its largely accessible surfaces. Generally, PA-surfaces have a shorter life span than conventional road pavements (Renken et al. 2010).

As part of past research and development project FE07.0264/2012/ARB (2012) a completely new and innovatively bound permeable material concept was developed. Initial research by Renken and Oeser (2014), Renken (2014), Renken et al. (2015), Schacht

et al. (2011) and Schacht et al. (2014) has shown, that the synthetic binder polyurethane is suitable for a full substitution of other binders. Such permeable pavements based on polyurethane are a promising innovative approach for the development of a feasible solution. Research by Renken and Oeser (2014) showed that a porous structure (high permeability) in combination with a high material strength can be achieved throughout the complete service temperature range. Moreover, a high resistance to permanent deformation, crack formation as well as sufficient fatigue resistance was exhibited.

Because of the enhanced permeability of the porous PU-asphalt, the design of the sub-construction requires specific attention. The infiltration of rainwater through the construction leads to an increased water supply in the underlying layers. However, this is in conflict with construction engineering standards. Hence, specific demands to safeguard the construction are required. In Oeser et al. (2012) hydraulic and mechanical properties of materials for base courses were examined. According to this the subgrade must offer sufficient permeability in consideration of the water conditions at hand.

Due to the infiltration of rainwater and the upward movement of groundwater from the base layer or subsoil, the porous pavement structure as well as its base layer are frequently in an unsaturated state. Therefore, the hydraulic and mechanical behavior may be influenced by capillary effects. Questions remain, concerning the importance of these effects on the hydraulic performance of the pavement which is supposed to facilitate drainage even under high infiltration conditions caused by heavy rain. Furthermore, the passage of vehicles may have an effect on the pore-air and pore-water pressures and thus influence the capillary pressure within the pavement which has been shown by Grabe and Milatz (2014). Pressure changes may lead to pumping effects within the pavement, evoking moisture transport and under bad conditions suffusion effects of smaller particles and dirt from the pavement into the pore space, thus clogging the porous structure. In the presence of capillary water or occluding particles the initial favorable drainage properties and noise reduction may be weakened.

In order to assess the described effects in further research projects, in a first step, the importance of capillary effects in innovative PA-mixtures will be investigated in this paper. For this purpose, different PU-bound asphalt mixtures were manufactured in the laboratory of the *Institute of Highway Engineering at RWTH Aachen University*, Germany. The specimens are manufactured by using different grading curves and grain sizes which leads to a variation of the porosity n.

The hydraulic conductivity in the saturated state is quite high as a result of large pores; this makes the determination of the soil-water characteristic curve a challenge. A pressure plate extractor is used in combination with an air pressure controller with a fine resolution to measure the dewatering paths of the SWCC of the asphalt specimens. The tests are performed in the soil laboratory at the *Institute of Geotechnical Engineering and Construction Management at Hamburg University of Technology (TUHH)*, Germany. The first results of the tests performed so far show limited capillary effects. Nevertheless, the complex structure of the new asphalt mixtures, bound and coated by a very smooth layer of polyurethane, shows some interesting effects, which will be described and discussed in this paper.

2 LABORATORY TESTS ON POROUS PU-ASPHALT

2.1 *Polyurethane-bound systems*

Polyurethane is a multifunctional material and consists primarily of the two components polyol and isocyanate. Polyurethane may be produced in an oleochemical process using oils from plants. The main focus in the development of oleochemical polyurethanes is on the production of the polyol component. Polyols are organic compounds with polyvalent alcohols, the hydroxyl groups. The production is based on natural oils and fats which mainly consist of triglycerides and glycerol esters from saturated and unsaturated fatty acids. This means that such polyurethanes consist of up to 50% renewable raw materials and the final product can be classified as environmentally sustainable (Evertz and Petersen 2007).

In the production of PU-bound material systems, the material components are mixed together in a manner that the PU-binder completely coats the specific surface area of the used aggregates, which are permanently bonded at the contact points after hardening, to form a monolithic, three-dimensional and stable structure. One can work with a relatively low binder content, as a thin coating of the mineral surface is sufficient to attain adequate material strength. The binder content is defined as $B = 6$ wt% based on experience. Consequently, the binder content is determined by the selected grading curve and the surface area of the aggregates respectively. The exact binder content can be calculated iteratively or analytically according to Arand (1978) or Oeser (2010) and depends on the specific surface area. The processing time (pot life) at room temperature (20°C) of the mixture is around 35 min. Subsequently the manufactured mixtures were placed in the molds and compacted by means of a hand roller. After a hardening time of 24 h the samples can be removed from the molds and the core samples can be prepared. Hereinafter the dimensions of the completed samples were measured and the density and the void content were calculated. A photograph of the three PU-asphalt specimens worked on in this paper is depicted in figure 1 and their properties are summarized in table 1.

Contrary to other coarsely grained porous media such as sands the particles within the porous PU-bound asphalt matrix are partially bound and completely coated by the PU binder, which creates special

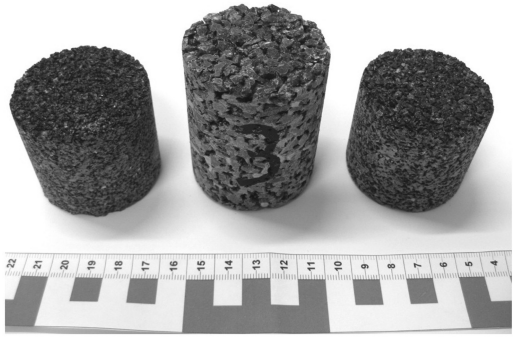


Figure 1. Cylindrical PU-asphalt specimens used in the hydraulic laboratory tests. From left to right: P1, P3, P2.

Table 1. Parameters of the polyurethane-bound asphalt mixtures.

		Asphalt specimen		
Parameter	Unit	P1	P2	P3
spec. diameter d	mm	50	50	50
spec. height h	mm	44.9	43.5	61.0
porosity n	–	0.306	0.325	0.361
density ρ	kg/m^3	1.715	1.683	1.666
min. grain diam. $d_{\min}$	mm	0.063	0.25	0.063
max. grain diam. $d_{\max}$	mm	2.0	2.0	5.0
filler content f	wt%	–	–	3.1

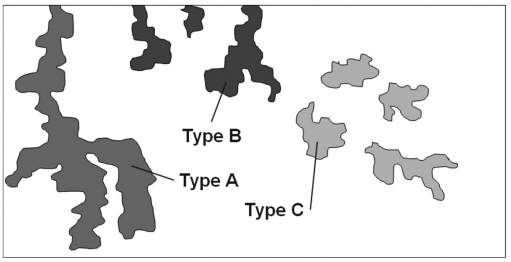


Figure 2. Schematic view of different pore structures.

pore geometries and a very smooth particle surface. According to Lin (1993) pores can be classified into three different types, which are represented in figure 2. For a good hydraulic performance type A – and type B-pores are the most influential. These types were described as "effective voids", because they can absorb water and drain into underlying layers. Void Type C does not influence the permeability significantly. A detailed view of the pore distribution of a porous PU-asphalt specimen with a porosity of $n = 0.361$ is represented in figure 3.

2.2 *Determination of saturated hydraulic conductivity*

The determination of saturated hydraulic conductivity was conducted using the permeability test in the vertical direction according to FGSV (2009) on a

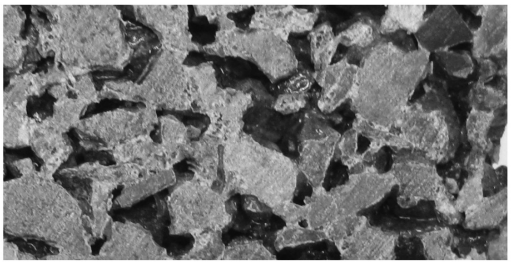


Figure 3. Detailed view of a diamond sawn porous PU-asphalt surface ($n = 0.361$). The detail size is approx. 40×20 mm.

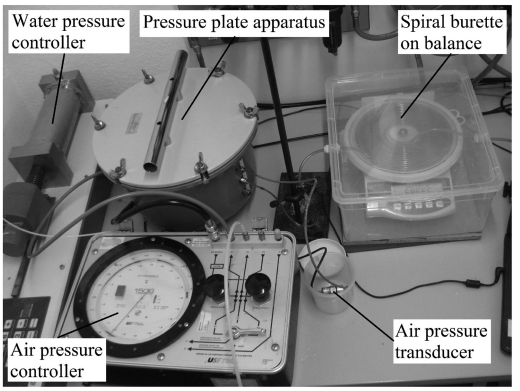


Figure 4. Test set-up for the determination of the SWCC of PU-asphalt specimens using a pressure plate apparatus.

cylindrical specimen ($d = 100$ mm and $h = 60$ mm). The aim of these investigations is to determine the coefficient of permeability k_f in the vertical direction. In the test water flows through a saturated specimen vertically at a constant effective hydrostatic head of 300 mm in a defined time. The specimen sides are made impermeable by sealing. The coefficient of permeability $k_{f,v}$ in the vertical direction can be calculated from the resulting water outflow Q_v.

2.3 *Determination of soil-water characteristics*

In order to investigate the dewatering behaviour of the PU-bound porous asphalt mixtures, the specimens are tested in the pressure plate apparatus. To take into account the expected low air entry suctions, an air pressure controller with a fine resolution is applied. The chamber air pressure is measured with an air pressure transducer (Type Kyowa PGM-02KG) connected to the pressure plate apparatus. This transducer type has a pressure range of ± 20 kPa and has already been used by Sako et al. (2011) to measure low air pressure changes in an unsaturated weathered granite soil caused by rain infiltration.

Due to the quick desaturation of the porous asphalt matrix a burette was thought to be unfavorable to measure the outflow volume. Therefore, a gravimetric method is used, to measure the water volume outflow and continuously log the data to a computer.

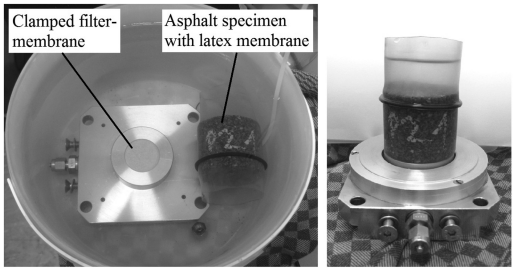


Figure 5. Saturated base pedestal with clamped filter membrane and asphalt specimen immersed in a water bath (left) and mounted specimen after specimen preparation (right).

The method has already been used in combination with simple shear tests on unsaturated sand specimens (Milatz and Grabe 2015). The method uses an encased laboratory scale (resolution of 0.01 g) with a spiral shaped burette placed on the weighing plate. The drained water volume flows into the burette and the weight change is logged to a computer. The specimen top and level of the spiral shaped burette are kept at the same height during the dewatering tests in order to minimize an initial gravity flow out of the specimen. The whole test set-up with all described components is depicted in figure 4. As porous ceramic disks are known to impede the flow in drainage tests of unsaturated soils, a special base pedestal has been devised which allows to use microporous membranes as an interface as proposed by Nishimura et al. (2012). These filter-membranes have a moderate air entry value (AEV) and allow for an increased drainage velocity due to their small thickness of $2.29 \cdot 10^{-4}$ m. Filter-membranes with a pore diameter of 0.8 µm and an average AEV of 83 kPa (PALL corp.) were used. The base pedestal has also been used in the simple shear tests mentioned above.

The base pedestal as well as the filter-membranes are placed in a vacuum chamber to remove air voids in the drainage system and are then flushed with deaired water using the water pressure controller represented in figure 4. The filtermembranes are then fixed with a cover plate and an o-ring seal under air free conditions while being immersed in a water container. The asphalt specimens are also saturated by submersing them in deaired water and deairing them in a vacuum container. Finally, a latex membrane is pulled over the specimens and they are placed on the saturated base pedestal, still covered by deaired water. The base pedestal with a clamped filter-membrane as well as a detail of the mounted specimen before being placed in the pressure plate apparatus are represented in figure 5. The initially saturated asphalt specimens are dewatered by imposing incrementally increasing air pressure steps. The continuous outflow data as well as the air pressure measurements allow for the calculation of the SWCC from equilibrium data points. The current degree of saturation S_r can be calculated from the pore water

Table 2. Saturated coefficients of permeability $k_{f,v}$.

		Asphalt specimen		
Parameter	Unit	P1	P2	P3
$k_{f,v}$	10^{-4} m/s	2.79	5.53	47.6

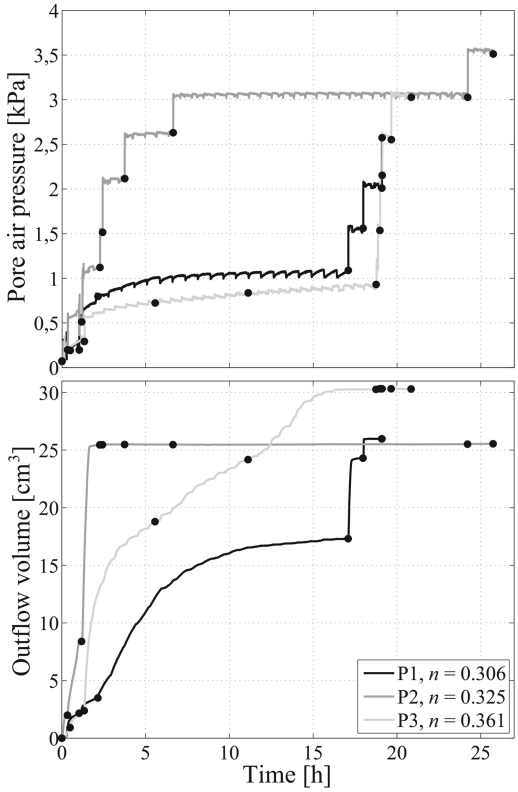


Figure 6. Results of dewatering tests: Applied pore air steps (top) and resulting pore water outflow (bottom) vs. test time.

outflow volume ΔV_w and the specimen pore volume nV using equation 1.

$$S_r = 1 - \Delta S_r = 1 - \frac{\Delta V_w}{nV} \tag{1}$$

3 RESULTS

The obtained results for the saturated hydraulic conductivity of the three tested specimens are summarized in table 2. The permeability tests performed at RWTH Aachen University by Renken and Oeser (2014) and Renken et al. (2015) show a high hydraulic conductivity of all investigated samples. All variants are to be classified as “highly permeable” according to DIN 18130-1:1998-05 (1998). Sample P3 shows the significantly highest value, despite of a porosity comparable to the other specimens. This indicates that the pore

Table 3. Hydraulic parameters.

Parameter	Unit	Asphalt specimen		
		P1	P2	P3
α	1/kPa	1.11	2.00	1.92
n	–	6.0	5.5	5.0
S_{res}	–	0.037	0.080	0.299
$S_{r,ovendry}$	–	0.241	0.179	0.140

structure is the most important parameter influencing the permeability of porous systems. Particularly the size and the geometry of the pores as well as the distribution of pores substantially influence the permeability. The requirement for a classification as permeable according to FGSV (2009) using the criterion $k_{f,v} \geq 5.4 \cdot 10^{-5}$ m/s is obtained by all variants. Due to these large conductivities in the order of magnitude comparable to very coarse sand, the porous PU-asphalt mixtures tend towards gravity flow with obviously very low capillary effects. Nevertheless, since the structure of the PU-bound asphalt matrix may evoke special effects, the specimens were tested for their SWCC with the procedure presented above. Figure 6 shows a plot of the imposed air pressure steps compared to the resulting pore water outflow over time for the three tested specimens. The chosen equilibrium data points for plotting the SWCC are also shown in the same figure. It can be seen that the specimens start to desaturate at very low air pressures between 0.3 and 0.7 kPa. As a result of the low pressure level the data points of the applied air pressures show oscillations which may also be a consequence of the control process. Furthermore, the applied pressure had to be observed regularly as it showed a slight increase over time which can be ascribed to control problems at the low pressure level. The calculated equilibrium data points which allow for the deduction of the drying branch of the SWCC for the asphalt specimens are demonstrated in figure 7 for the asphalt specimens. The data points are plotted together with curves computed with the model of van Genuchten (1980) for the effective degree of saturation S_e according to equation 2.

$$S_e = \frac{1}{(1+(\alpha s)^n)^m}, \quad m = 1 - \frac{1}{n} \tag{2}$$

The parameters n and p_e are empirical constants needed to relate the effective degree of saturation S_e to matric suction s. The degree of saturation S_r is then computed using the residual degree of saturation S_{res} in the relation given by equation 3.

$$S_r = S_e(1 - S_{res}) + S_{res} \tag{3}$$

The parameters for the van Genuchten model are shown in table 3. In addition the final degrees of saturation calculated from the oven dried specimen $S_{r,ovendry}$ are presented. The residual degree of saturation has

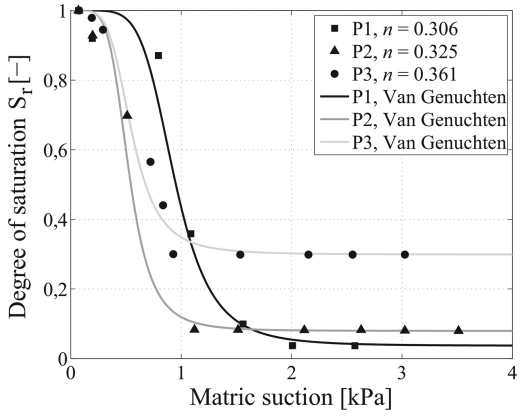


Figure 7. Obtained data points describing the drying path of the SWCC of porous PU-asphalt specimens compared to curves computed with the model of van Genuchten (1980).

been selected as the final value of degree of saturation calculated from the outflow. The data points demonstrate that the dewatering behaviour is characterized by very low air entry values between 0.3 and 0.5 kPa. The different porosities seem to influence the water retention behaviour. In addition to the fast dewatering at low capillary pressures, an abrupt end of the water outflow can be noticed for all specimens, resulting in the sharp bend in the saturation change for capillary pressures higher than 1 kPa for specimens P3 and P2 and 2 kPa for specimen P1. When S_r is calculated from the initially saturated state and the outflow data, this stop of drainage results in a very high residual degree of saturation for specimen P3. The comparison of S_{res} and $S_{r,ovendry}$ in table 3 shows that the residual degrees of saturation calculated from the initially saturated specimen and the outflow data are lower in two of three cases compared to the degrees of saturation obtained from oven drying. In all cases the difference between the values is quite high.

4 DISCUSSION AND OUTLOOK

In this paper measuring the hydraulic performance of polyurethane-bound porous asphalt materials with a focus on capillary effects was attempted. Although the obtained data allowed for the determination of a drying path of the SWCC for the specimens confirming the assumed low capillarity, some irregularities are noticeable in the results and will be discussed hereinafter.

The deviation of the residual degrees of saturation obtained from predicting calculations and from the oven dried specimens at the end of the tests may result from several factors. First, errors in the determination of the gravimetric water content may result either from specimen drainage at its removal from the base plate or from additional water adhering to the specimen. Second, the low S_{res}-values calculated from outflow data, may indicate that specimens P1 and P2

were over-saturated in the beginning of the test, leading to a surplus of water, flowing through and out of the specimen. Third, a higher final degree of saturation calculated from the outflow data in the case of P3 may result from errors in the predicting calculations of S_r and the assumption of initially saturated pore spaces. The errors occur when the last assumption is not true. This consideration leads to the idea that there may be enclosed pores (type C), enclosed by PU-binder within the specimens as described by Lin (1993) as well as the fact that the geometry of the pores and their distribution substantially influence the permeability (hydraulic performance). These ineffective pores would contribute to the pore volume of the specimen but not to the volume open to pore water.

In addition to the totally enclosed pore space, semi-open pore space ("dead ends") can be conceived. This equally neutral pore space would entrap pore water irrespective of capillary effects, prohibiting it from draining in the vertical direction due to pore air pressure. This could represent an explanation for the relatively high residual water contents obtained from the oven dried specimens in table 3. The incorporation of a corrected water accessible porosity $n^* = n - n_{\text{closed}} - n_{\text{dead end}}$ in the predicting calculations of the degree of saturation from outflow data (equation 1), would lead to lower calculated residual saturations which may come closer to the final degrees of saturation obtained from the oven dried specimens.

On the whole, the presented results show, that capillary effects in PU-bound porous asphalt are very low and seem to be neglibible. However, the observed effects may influence the drainage behaviour of a real pavement. The observed fast desaturation due to air pressures, leads to the assumption that small changes in air pressure, induced by passing traffic, can lead to high saturation changes in a real pavement. This fact, together with the observed high residual water contents is important for ensuring the driving comfort as it is influenced by surface spray during rain events. Moreover, the water retention behaviour may influence the noise reduction effects mentioned above as a function of S_r.

To further describe the water retention behaviour and the special features occurring in a partially enclosed pore space, more tests are needed. As an alternative to the pressure plate apparatus, the hanging water column method (Vanapalli et al. 2008) could be used to impose even finer suction steps. Furthermore, an analysis of the effective pore geometries and connectivities would be helpful to assess the corrected pore space open to pore water.

REFERENCES

Arand, W. (1978). Zur Bestimmung der Korngrößenverteilung von Mineralstoffen. *Bitumen* (2), 50–57.

DIN 18130-1:1998-05 (1998). *Soil – investigation and testing; Determination of the coefficient of water permeability – Part 1: Laboratory tests.* Deutsches Institut für Normung e.V. (DIN).

Evertz, T. & K. Petersen (2007). Neue Wege bei der Verfestigung von Deckwerken. *Wasser und Abfall 6*.

FE 07.0264/2012/ARB (2012). Simulation-based development of new road construction materials and innovative manufacturing and installation methods. *r&d project BMVi*.

FGSV (2009). *Merkblatt für versickerungsfähige Verkehrsflächen*. FGSV-Verlag.

Grabe, J. & M. Milatz (2014). The change of matric suction due to heavy vehicle crossing. In *Proc. of 6th International Conference on Unsaturated Soils (UNSAT 2014), 2–4 July 2014, Sydney, Australia*, Volume 2, pp. 1431–1437.

Lin, S.-J. (1993). *Steuerung des Hohlraumgehaltes von Dränasphalt im Hinblick auf die Optimierung seiner bautechnischen Eigenschaften*. Ph. D. thesis, Universität Fridericiana zu Karlsruhe (TH).

Milatz, M. & J. Grabe (2015). A new simple shear apparatus and testing method for unsaturated sands. *Geotechnical Testing Journal 38*, 9–22.

Nishimura, T., J. Koseki, D. G. Fredlund, & H. Rahardjo (2012). Microporous membrane technology for measurement of soil-water characteristic curve. *Geotechnical Testing Journal 35 (1)*, 1–8.

Oeser, M. (2010). Nichtlineare numerische Simulationsmodelle für Verkehrswegebefestigungen. Habilitation, Schriftenreihe Professur für Straßenbau, no. 18.

Oeser, M., P. Hovagimian, & U. Kabitzke (2012). Hydraulic and mechanical properties of porous cement-stabilised materials for base courses of picps. *International Journal of Pavement Engineering 13*, 68–79.

Renken, L. (2014). Potential innovativer, wasserdurchlässiger Materialien für Verkehrsflächen. In *Aachener Straßenbau- und Verkehrstage (ASVT)*, Aachen.

Renken, L. & M. Oeser (2014). Innovative Material Concepts? Application Potentials and Characterization of Synthetic Road Pavements. In *Aachener Mitteilungen, no. 62, Proc. 3rd. China-Europe Workshop on Functional Pavement.*

Renken, L., M. Simon, & M. Oeser (2015). Development of Permeable Block Pavements based on Polyurethane. In *Proc. of 11th Int. Conference on Concrete Block Pavements (ICCBP 2015)*, Dresden.

Renken, P., M. Wistuba, J. Grönninger, & K. Schindler (2010). Adhäsion von Bitumen am Gestein. *Forschung Straßenbau und Straßenverkehrstechnik 1043*.

Sako, K., T. Danjo, R. Fukagawa, & H. H. Bui (2011). Measurement of pore-water and pore-air pressure in un-saturated soil. In *Proc. of 5th Asia-Pacific Conference on Unsaturated Soils (AP-UNSAT 2011)*, Volume 1, Kasetsart University, Pattaya, Thailand, pp. 443–448.

Schacht, A., C. Busen, M. Munk, & M. Oeser (2014). Application of a porous interlayer for road temperature control. In *PIARC XIVth International Winter Road Congress*, Andorra.

Schacht, A., D. Wang, & B. Steinauer (2011). Un-tersuchung der Kornausbrüche bei poro-elastischen Fahrbahnbelägen mit dem Aachener-Ravelling-Tester (ARTe). *Bauingenieur* 4(86).

van Genuchten, M. T. (1980). A closed-form equation for predicting the hydraulic conductivity of unsaturated soils. *Soil Science Society of America Journal 44 (5)*, 892–898.

Vanapalli, S. K., M. V. Nicotera, & R. S. Sharma (2008). Axis translation and negative water column techniques for suction control. *Geotechnical and Geological Engineering 26 (6)*, 645–660.

Unsaturated Soil Mechanics—from Theory to Practice – Chen et al. (Eds)
© 2016 Taylor & Francis Group, London, ISBN 978-1-138-02921-7

Hydro-mechanical behaviour of shot-clay bentonite

A. Ferrari, A. Seiphoori & L. Laloui
Swiss federal Institute of Technology, Lausanne, EPFL, Switzerland

ABSTRACT: Experimental tests were conducted to characterise the hydro-mechanical behaviour of shot-clay MX-80 bentonite. Granular bentonite was mixed continuously with water and shot on the walls of a tunnel section at the Grimsel Underground Research Laboratory (URL), in Switzerland. The shot-clay was placed to create a layer of bentonite in direct contact with the host rock to avoid preferential water and/or gas flow along the tunnel wall. Samples for an experimental programme were collected during the shooting. Results from an experiment, conducted under controlled total suction to analyse the hydro-mechanical behaviour of the material, are shown.

1 INTRODUCTION

Engineered Gas Transport Systems (EGTS) are used to limit gas overpressures in the backfilled underground structures of nuclear waste repositories to acceptable levels without compromising the radionuclide retention capacity of the engineered barrier system (EBS) (Nagra, 2008). The main design elements of an EGTS are (i) specially designed backfill materials for the emplacement caverns, characterised by high porosity and high compressive strength, and (ii) gas-permeable tunnel seals consisting of sand/bentonite (S/B) mixtures with bentonite contents of 20% to 30%.

Technological gaps may generate preferential flow paths within the S/B mixture (Wang et al., 2013). Hence a bentonite ring with a target hydraulic conductivity of at least 1E-12 m/s, corresponding to a dry density of the bentonite of approximately 1.4 Mg/m^3, had to be emplaced around the S/B seal on order to avoid preferential water and/or gas flow along the tunnel wall. The first solution assessed was "shot-claying", which used mixing MX-80 granular bentonite with water (volumetric water-to-bentonite ratio of 3 to 11.7), feeding the mixture into a hydraulic pump and shooting the mixture onto the tunnel wall.

In the experiments summarized in the present study, after the layer of emplacing the bentonite on a tunnel wall, the layer was subjected to several hydro-mechanical processes, some of which resulted from the experimental emplacement and others of which were tested in the lab to assess their potential to optimise the final dry density of the bentonite ring after full saturation (Ferrari et al., 2014). The laboratory tests primarily assessed the impact of a ventilation phase immediately following shot-claying and the compaction due to the emplacement of the S/B seal inside the bentonite ring. The material was characterised in terms of its index properties, microstructural features, swelling potential and water retention capacity. A comprehensive stress path was designed, and a controlled-suction test was carried out to assess the probable hydro-mechanical response of the material during the various expected phases of environmental conditions in the repository.

2 TESTED MATERIAL

2.1 *Sampling procedure and index properties*

Laboratory tests were carried out on material samples collected on site during the emplacement of the shot-clay. After the emplacement of the first bentonite layer, the shooting was suspended to allow the installation of several cylindrical steel tubes (with diameters of 9.5 cm and heights of 12 cm), that were pushed approximately 1 cm into the bentonite layer.

The mixture of bentonite and water was then shot directly into the sampling tubes (Fig. 1a), and eventually, the cylinders were extracted, trimmed (Fig. 1b), sealed and transported to the laboratory.

MX-80 bentonite was used for the shot-clay experiment. It contains 85% Na-smectite clay, which has a specific area of 523 m^2/g (Plötze & Weber, 2007) and confers the high swelling capacity. The index properties of the shot-clay MX-80 bentonite were determined in the laboratory. A pycnometer was used to measure specific gravity that results to be $G_s = 2.74$. Kerdane was used, rather than water, because its non-polarity prevents the development of diffuse double layers. A liquid limit $w_l = 4.30$ was measured using the fall cone penetration technique (BSI, 1990; Wood, 1985) and a plastic limit $w_p = 0.65$ was determined in accordance with ASTM D4318. The samples that were extracted immediately from the shot layer and sealed had an average water content of 0.39. Instead the samples that

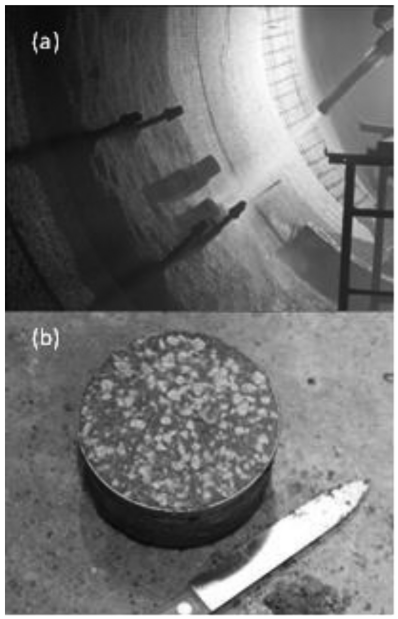


Figure 1. Shot-clay MX-80 bentonite: (a) shooting of the mixture of water and bentonite into the tubes; (b) extracted sample tube.

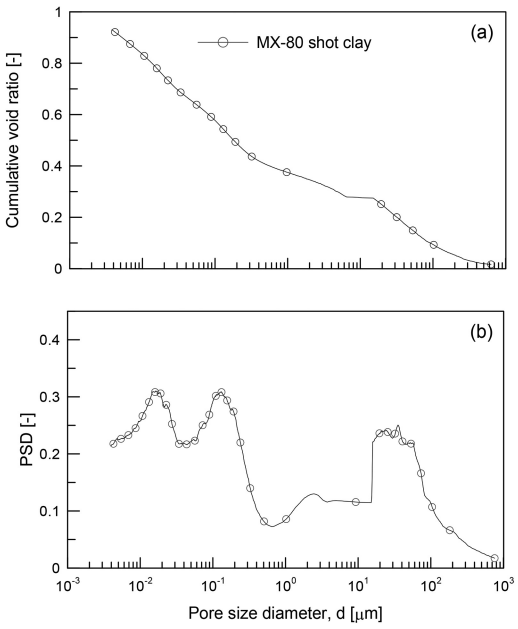


Figure 2. Results of the MIP test on a sample of MX-80 shot-clay bentonite: cumulative void ratio (a), and pore size density function (PSD) vs. pore size diameter (b).

were exposed to the site conditions for approximately 30 minutes before the tubes were sealed had $w = 0.32$.

Determination of the grain size distribution of the granular bentonite (apparent grain size distribution) was performed by sieving the bentonite grains at their hygroscopic water content. The analysis revealed a sand-sized fraction of 60% and a gravel-sized fraction of 30%. The bulk density and the dry density were in the ranges of 1.58–1.63 Mg/m^3 and 1.14–1.17 Mg/m^3, respectively. The average void ratio was 1.4. Complementary density measurements were performed on samples cored out from the bentonite layer after the shot-clay was completed and the results were in the same range of those obtained for the samples collected in the tubes installed before the shooting.

The initial total suction was measured using a chilled-mirror a WP4c dew-point psychrometer (Decagon Device Inc., 2002; Leong et al., 2003; Cardoso et al. 2007). The device measures the total suction using the psychrometric law, which relates the water potential of the material to the relative humidity established in the measuring chamber in which the specimen is placed. Initial total suction values of 4 MPa and 6 MPa were measured for the samples at water contents of 0.38 and 0.32, respectively.

2.2 *Microstructural features*

Mercury Intrusion Porosimetry (MIP) was used to determine the Pore Size Density (PSD) function of a sample of shot-clay. A cubic specimen approximately 5 mm in size was cut and freeze-dried to remove the pore water. The MIP test was carried out using a Thermo Electron Corporation porosimeter attained a maximum intrusion pressure of 400 MPa (corresponding to an entrance pore size diameter of approximately 4 nm). The pressure was changed incrementally, and the intruded volume was measured continuously. Figure 2 shows the cumulative intrusion void ratio (e_{HG}) and the pore size density function ($PSD = -\Delta e_{HG}/\Delta(\log d)$) versus the entrance pore diameter (d).

The difference between the cumulative void ratio and the void ratio measured on the samples (0.45) is associated with the inter-lamellar bentonite porosity that cannot be accessed by the mercury and with the largest pores on the sample surface being filled by the mercury before the intrusion process starts. A multimodal pore size density function was obtained and is shown in Figure 2b. A peak with a modal value of approximately 20 nm is observed, common also in compacted granular bentonites, and is associated with the intra-aggregate porosity, i.e. the pores between the bentonite particles within the aggregates (e.g. Romero et al., 2011). Pore sizes in the range of 4×10^{-2} to 10 μm correspond to inter-aggregate and intra-bentonite-grain pores. Pore sizes larger than 10 μm correspond to inter-bentonite-grains pores and represent the macro-pores in the shot-clay bentonite.

3 EXPERIMENTAL PROGRAMME

The behaviour of the shot-clay MX-80 bentonite was assessed through a comprehensive laboratory campaign (Ferrari et al., 2014). The aim of the tests was

to analyse the response of the material to the environmental conditions expected in the repository from emplacement through full saturation. The material's swelling potential, water retention behaviour and volumetric response under hydro-mechanical loading were analysed on specimens cored out from the tube samples collected on site. Distilled water was used in all of the experiments.

3.1 *Swelling behaviour*

The swelling potential of the shot-clay MX-80 bentonite was evaluated by the means of constrained and free swelling tests, performed on specimens 1.88 cm in height and 7.53 cm in diameter. Each specimen was placed in a rigid-confined steel cell, resting on a porous disk connected to a water inlet. The upper part of the specimen was in contact with a coarse porous stone, and a flushing line was connected to the upper part of the cell. The cell containing the specimen was inserted into a rigid frame to ensure constant-volume conditions. The specimen was taken to the laboratory and placed in the test apparatus as soon as possible, in order to capture any swelling associated with the homogenisation of the water content in the material after the shooting, and in this phase no access to water was provided. A load cell (with an accuracy of 10 kPa with respect to the area of the specimen) was placed between the top cap and the frame to measure the swelling pressure. An initial total vertical stress of 80 kPa was applied to ensure good contact of the various parts of the apparatus. The specimen was then inundated with water, and the swelling pressure was continuously monitored until it stabilised.

The free swelling test was carried out by saturating the specimen and measuring the vertical heave with an LVDT system. A constant pore water pressure of 10 kPa was applied to the lower base of the specimen, and the flushing line on the top was opened periodically to ensure the evacuation of air from the top of the cell during the rising of the wetting front.

3.2 *Water retention behaviour*

The water retention curve for the main drying path was analysed using a controlled air drying process in which the total suction was measured with the dew-point psychrometer. Several specimens were cored from one sample using a special holder that could be positioned directly in the device for the suction measurement. After the initial water content and total suction of the sample were determined, a drying path was initiated in each specimen by air-drying in a controlled way, under laboratory-controlled conditions ($T = 22°C$, $RH = 40\%$). During the drying the evolution of the water content was monitored for each specimen by continuously weighing the sample holder and the process was stopped once each specimen reached its target water content value. The sample holder was then sealed, and the sample was cured for 2–3 days to allow for the redistribution of the water within the specimen. The total suction of the specimen was then measured using the WP4c psychrometer, then the volume of the specimen was measured, and the water content was determined by oven-drying. Detailed information on the analysis of the water retention behaviour of compacted granular MX80bentonite can be found in Seiphoori et al. (2014).

3.3 *Controlled-suction hydro-mechanical tests*

A controlled-suction hydro-mechanical test was carried out to measure the volume change and water content variation in the material over the range of environmental conditions expected in the repository. An ad hoc experimental setup was arranged (Ferrari et al., 2014). The cell holds a sample with a diameter of 7.53 cm and a height of 1.88 cm. The vertical load is controlled by a level arm system and it is assumed to be representative of the in situ stress conditions. The vertical displacement is measured by an LVDT installed on the top the cell. The computed vertical strains in the cell are equivalent to the radial strains of the shot-clay in the tunnel. The total suction is controlled using the vapour equilibrium technique. The pore water potential of the material is represented by the migration of water molecules through the vapour phase, relative to a reference system of a known water potential, until equilibrium is achieved (Romero, 2001). At the end of the equalisation phase, the pore water and the vapour phase have the same potential. Through this equality and by assuming that the water vapour obeys the ideal gas law, it is possible to express the total suction of the material ψ as (Fredlund & Rahardjo, 1993):

$$\psi = -\frac{\rho_w RT}{M_w} \ln(RH) \tag{1}$$

where R is the universal gas constant and ρ_w and M_w are the density and the molecular mass of water, respectively, RH is the relative humidity of the closed system in which the specimen is placed and T is the absolute temperature.

Variably saturated NaCl solutions and a saturated $Mg(NO_3)$ solution were used to control the relative humidity and hence the total suction of the reference system. Romero (2001) and Witteveen et al. (2013) provided the relationship between the solution concentration and the applied suction. Figure 3 shows the applied stress path, chosen on the range of environmental conditions that the shot-clay material is expected to experience in the evolution of the repository. In the initial state (point A), the specimen was placed in the cell and equalised to a total suction of 6 MPa using a 1.3 M NaCl solution. This suction was the value measured in the sample immediately following the shooting. A vertical stress of 8 kPa was applied to ensure good contact between the specimen and the loading system.

The vertical load was increased to 67 kPa to simulate an initial compaction of the material (path A–B)

to reproduce the emplacement of the buffer material (such as bentonite blocks) in the repository.

A drying path (B–C) was applied to reflect the ventilation phase of the repository, during which the material will be exposed to the relative humidity of the tunnel. A suction of 87 MPa was applied using a saturated $Mg(NO_3)$ solution, corresponding to a relative humidity of 50% at the laboratory temperature, which was the average relative humidity at the Grimsel URL.

A loading path (C–D) was then applied increasing the vertical stress to 249 kPa at a constant total suction of 87 MPa, in order to reproduce the development of the swelling pressure in the buffer material when it is wetted through the vapour phase.

The path D–E reflected the wetting of the material upon water vapour uptake from the surrounding host rock. The wetting was performed using a saturated NaCl solution, resulting in a total suction of 37 MPa (corresponding to a relative humidity of 75%). During this phase, the volume was kept constant to reflect the presence of the buffer material. The axial strain was limited to the range of ±0.25% by increasing the vertical stress in small steps, to prevent swelling of the material. This process was repeated until the specimen did not exhibit any further tendency to swell.

Eventually, the specimen was flooded with distilled water (path E–F) to measure the maximum swelling potential associated with the full saturation of the material. To accomplish this operation, the cell was removed from the loading system and installed in a highly rigid frame equipped with a load cell. An initial vertical stress equal to the swelling pressure obtained at the end of path D–E was applied.

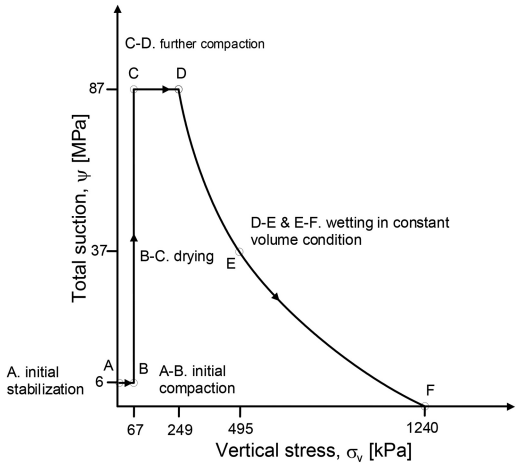


Figure 3. Stress path implemented for the investigation of the hydro-mechanical behaviour of the shot-clay MX-80 bentonite.

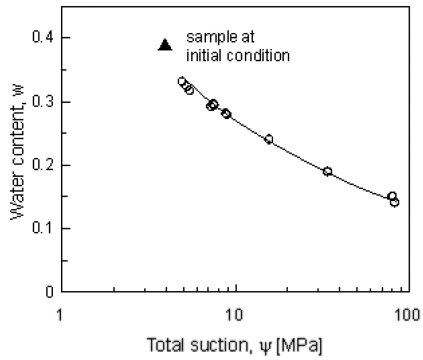


Figure 4. Water retention behaviour of shot-clay MX-80 bentonite in terms of water content vs. total suction.

4 TEST RESULTS

4.1 *Swelling and water retention behaviour*

The result of the constrained swelling test shows that the initial homogenisation of the water content after the shooting did not produce any appreciable swelling pressure. A maximum swelling pressure of 990 kPa was observed 10 days after the cell was flooded under constant-volume conditions. The result of the free swelling test, in terms of the axial strain and water content evolution over time, shows that a final swelling strain of 324% and a final water content of 280% (corresponding to a calculated degree of saturation of 99%) were reached after approximately 64 days. The water retention behaviour of shot-clay MX-80 bentonite along a drying path is depicted in Figure 4 in terms of water content versus the total suction. The initial condition measured on the whole sample from which the specimens were extracted is also reported. A residual degree of saturation of approximately 40% (water content of 0.15) was obtained. The measured void ratio of the specimens was initially higher than the sample void ratio. This difference is attributable to the rebound of the material during the specimen extraction. In general the water retention behaviou

4.2 *Hydro-mechanical behaviour*

Figure 5 depicts the equilibrium states in the planes of total suction vs. vertical stress, axial strain vs. vertical stress, total suction vs. water content and axial strain vs. water content. During the initial equalisation phase (A), no significant deformation of the specimen was recorded, and only limited wetting was observed.

This wetting is attributed to initial drying of the specimen during the cell installation. The water content reached (34%) is consistent with the water retention curve. The loading path (A–B) at constant total suction caused an axial strain of approximately 1% without any expulsion of water. The following drying step (B–C) took 33 days to reach equilibrium and resulted in significant shrinkage of the material (9%) and a reduction of the water content to 14.2%, consistent with the water retention curve (Fig. 4). At this stage, the cell was opened to assess the loss of lateral contact with the oedometric ring and the formation of drying cracks. Lateral shrinkage of approximately 4% in radial strain was calculated by analysing the

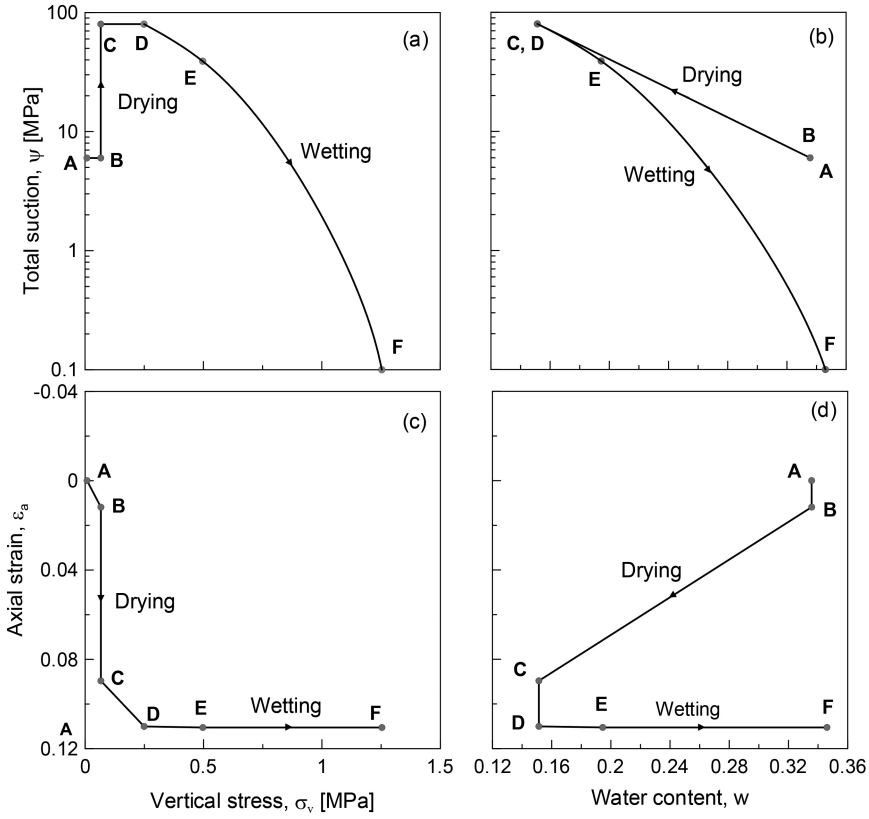


Figure 5. Results of the controlled-suction hydro-mechanical test.

images collected. Interestingly, the creation of drying cracks was also observed on site, three to four days after the shooting. A loading path was applied by increasing the vertical stress to 249 kPa (C–D) while maintaining constant total suction. As a result, the axial strain increased up to 11% while the water content increased slightly. The wetting path D–E, which was applied using an unsaturated NaCl solution in the vapour phase, resulted in an increase of the water content to approximately 0.20, while the variation in the axial strain was maintained in the range of ±0.25%. A swelling pressure of 495 kPa was measured during that intermediate saturation step. The cell was also opened for visual observation after this path. The specimen swelled due to water vapour uptake, reversing the lateral shrinkage around the perimeter that occurred during the drying procedure along path B–C. The cracks observed earlier in the centre of the sample were only partially healed and were still clearly observed.

The flooding of the specimen (path E–F) at constant volume led to the development of a final swelling pressure of 1,250 kPa after approximately 6 days. The cell was finally dismantled and the full homogenisation of the specimen was observed due to saturation. A final water content of 0.41 (corresponding to a computed final degree of saturation of 99%) was measured.

The experimental results were compared with the results of complementary tests performed on compacted samples of granular MX-80 bentonite with a similar apparent grain size distribution, prepared at various dry densities (Seiphoori, 2014) and it was observed that the shot-clay emplacement technique does not change the overall behaviour of the granular MX-80 bentonite, except that the low initial dry density leads to reduced swelling capacity and a reduced air entry value and an increasing tendency to form drying cracks, compared to the compacted MX-80 bentonite (Ferrari et al., 2014).

5 CONCLUSIONS

Information on the hydro-mechanical behaviour of the material under various loading conditions were obtained by the presented experimental programme.

The most severe changes in strain and water content were associated with drying during the ventilation phase. The test highlighted the tendency of the material to crack during the drying step at a relative humidity of 50%, which is typical for GTS in the winter. The shot-clay bentonite showed, however, good self-sealing properties once full saturation was attained.

The formation of drying cracks at the imposed relative humidity could be a consequence of the low emplacement dry density (Kleppe & Olson, 1985; Péron et al., 2009).

The dry density achieved with the shot-clay technique was lower than the target value. In order to reach a higher dry density, the method could be improved by optimising the original granular bentonite material and reducing the amount of water added during shot-claying (Koch, 2002; Teodori, 2012). The shot-clay emplacement technique was capable of providing a homogeneous layer of bentonite along the entire section of the tunnel; such layer would not be realizable by simply pouring the granular bentonite (Ferrari et al., 2014). The laboratory test results show that the final density (after full saturation under constrained conditions) can be improved considerably by ventilating the tunnel at 50% RH, but the results also show that post-compaction of the material has little impact on the final density. Overall, the shot-clay technique has high potential to achieve the final dry density of 1.4 Mg/m^3 in MX-80 bentonite, which was the target density in this experiment. However, the shot-clay application of the bentonite on the tunnel surface, which permits free swelling, may be more limited than the application into a closed volume, as performed by Dixon et al. (2011), because in that case, the early swelling of the material is limited by the confined volume of the backfilled void space.

REFERENCES

BS 1377-2: 1990. Methods of test for soils for civil engineering purposes: Classification tests (Atterberg Limit), *British Standard Institution* (BSI).

Cardoso, R., Romero, E., Lima, A., Ferrari, A. 2007. A comparative study of soil suction measurement using two different high-range psycrometers. In: Schanz, T. (ed.) *2nd Int. Conf. on Mech. of Unsat. Soils*, Weimar, Germany: 79–93. Berlin: Springer.

Decagon Device Inc., 2002. *Dewpoint PotentiaMeter: Operators Manual,*Version 2.1.

Dixon D., Sandén T., Jonsson, E. & Hansen, J. 2011. Backfilling of deposition tunnels: Use of bentonite pellets. *Clay Technology AB, Swedish Nuclear Fuel and Waste Management*: 11–44.

Ferrari, A., Seiphoori, A., Rüedi, J., & Laloui, L. 2014. Shot-clay MX-80 bentonite: An assessment of the hydro-mechanical behaviour. *Engineering Geology*, 173: 10–18.

Fredlund DG, Rahardjo H., 1993. *Soil Mechanics for Unsaturated Soils*. John Wiley and Sons.

Kleppe, J.H., & Olson, R.E. 1985. Desiccation cracking of soil barriers. *Hydraulic barriers in soil and rock*, ASTM STP874, ASTM Philadelphia: 263–275.

Koch, D. 2002. Bentonites as a basic material for technical base liners and site encapsulation cut-off walls. *Applied clay science* 21(1): 1–11.

Leong, E.C., Tripathy, S., Rahardjo, H. 2003. Total suction measurement of unsaturated soils with a device using the chilled-mirror dew point technique. *Géotechnique* 53(2): 173–182.

Nagra, 2008. Effects of post-disposal gas generation in a repository for low- and intermediate-level waste sited in the Opalinus Clay of Northern Switzerland. *Technical Report* Nagra, Wettingen, Switzerland.

Péron, H., Hueckel, T., Laloui, L., & Hu, L. 2009. Fundamentals of desiccation cracking of fine-grained soils: experimental characterisation and mechanisms identification. *Canadian Geotechnical Journal* 46(10): 1177–1201.

Plötze, M. & Weber, H.P. 2007. ESDRED: Emplacement tests with granular bentonite MX-80. Laboratory results from ETH Zürich. *Nagra Working Report* NAB 07–24. Nagra, Wettinge

Romero, E. 2001. Controlled suction techniques. 4º *Simpósio Brasileiro de Solos Nâo Saturados*. W.Y.Y. Gehling & F. Schnaid (eds.). Porto Alegre, Brasil: 535–542.

Romero, E., Della Vecchia, G., & Jommi, C. 2011. An insight into the water retention properties of compacted clayey soils. *Géotechnique* 61(4): 313–328.

Seiphoori, A. 2014. Thermo-Hydro-Mechanical characterization and modelling of the behaviour of MX-80 granular bentonite. *PhD Thesis. EPFL*.

Seiphoori, A., Ferrari, A., & Laloui, L. 2014. Water retention behaviour and microstructural evolution of MX-80 granular bentonite during wetting and drying episodes, Geotechnique, 64(9), 721–734.

Teodori, S., Rueedi, J., Spillmann, T., Reinhold, M., Trick, T., Keller, M., Steiner, P., Isler, S., Gräfe, K., Garcia-Sineriz, J.L., Palacios Jimenez, B., Jacobs, F., Maurer, H.R., Tisato, N., Marelli, S., Ferrari, A., Manca, D., Seiphoori, A., 2012. NAB 12-58, GAST (Gas-Permeable Seal Test), Pre-testing Report. *NAGRA technical report.*

Wang, Q., Minh Tang, A., Cui, Y.J., Delage, P., Barnichon, J.D., Ye, W.M., 2013. The effects of technological voids on the hydro-mechanical behaviour of compacted bentonite–sand mixture. *Soils and Foundations* 53 (No. 2), 232–245.

Witteveen, P., Ferrari, A., & Laloui, L. 2013. An experimental and constitutive investigation on the chemo-mechanical behaviour of a clay. *Géotechnique* 63(3): 244–255.

Wood, D.M. 1985. Some fall-cone tests. *Géotechnique* 35(1): 64–68.

Unsaturated Soil Mechanics—from Theory to Practice – Chen et al. (Eds)
© 2016 Taylor & Francis Group, London, ISBN 978-1-138-02921-7

Effect of heating to Soil-Water Characteristic Curve of compacted bentonite

T. Nishimura
Ashikaga Institute of Technology, Japan

ABSTRACT: Radioactive waste was widely produced, and was classified as following: Low Level Waste (LLW), Medium or Intermediate Level Waste (MLW – ILW) and High Level Waste (HLW). Geological disposal facility is designed correspond to each radioactivity level that safety assessment regard to repository facilities is different for natural barrier and engineered barrier. The waste disposal for HLW is constructed most deep under-ground, have been implemented with high strict deign management. The engineered barrier consisted of compacted bentonite surround the canister containing the vitrificated high level waste, maintain steady condition in natural host rock. This study investigates volume deformation of compacted bentonite due to different relative humidity environment, and various temperatures were controlled. The soil-water characteristic curves were measured for a bentonite subjected to hydration effort and heating activity. Other soil materials such as kaolin and sand were used compare to compacted bentonite, the results describe significant difference on water retention activity.

1 INTRODUCTION

1.1 *Back ground*

Atomic power plant supply enough electrical power to industrial activity or human life that must be administer under strict surveillance. Simultaneously, the radioactive waste have been produced from atomic plant that geo-environment should establish the radioactive waste management. Also, the elimination of radioactive waste is closely associated with other manner such as natural disintegration of the unstable nuclei, medical activity. These waste was widely produced, and was classified as following: Low Level Waste (LLW), Medium or Intermediate Level Waste (MLW – ILW) and High Level Waste (HLW). Geological disposal facility is designed correspond to each radioactivity level that safety assessment regard to repository facilities is different for natural barrier and engineered barrier (Delage, 2013). The waste disposal for HLW is constructed most deep underground, have been implemented with high strict deign management (Hywel et al., 2014). The engineered barrier consisted of compacted bentonite surround the canister containing the vitrificated high level waste, maintain steady condition in natural host rock. Compacted bentonite which has typical couple problem associated to Thermal – Hydration – Mechanical (THM). Suggested a couple THM formulation modelling can be predict basically phenomena for engineered barrier. However, throughout the compacted bentonite transform from unsaturated condition to saturated condition due to seepage with so long-time, the micro-macro structures have interaction, and affect to mechanical properties. During the hydro-transformation at micro-macro structure, the vitrification in the canister produce high heating that the temperature approach to 100 degrees. At least, its process causes to occur uncertainly of compacted bentonite, and more experimental researches are required to obtain correctly understand and performance assessment for safety engineered barrier.

1.2 *Purpose of this study*

This study investigates volume deformation of compacted bentonite due to different relative humidity environment, and various temperatures were controlled. The soil-water characteristic curves were measured for a bentonite subjected to hydration effort and heating activity. Its temperature had a range from 20 degrees to 60 degree through SWCC test. Other soil materials such as kaolin and sand were used compare to a bentonite, the results describe a significant difference on water retention activity. Particularly, the deformation of compacted bentonite with elapsed time depended to temperature that was related to change the thickness of contract skin. The expansion deformation described first with highly heating. At most high temperature, the surface of compacted bentonite specimen had damage which indicated crack like a pattern of conjoined hexagons. This study evidences problems of compacted bentonite subjected to complex THM solutions.

2 TEST PROCEDURE

2.1 *Soil materials*

Sodium bentonite, a kaolin and a sand were used for this test program. The kaolin and sand were prepared

Table 1. Chemical contents in a bentonite used for this test program.

Symbol	Percentage %
SiO_2	69.7
TiO_2	0.14
Al_2O_3	15.8
Fe_2O_3	1.69
MgO	2.19
CaO	2.00
Na_2O	2.04
K_2O	0.24

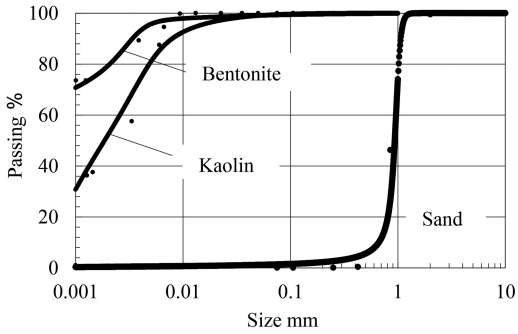


Figure 1. Grain size distribution for three different soil materials.

Table 2. Summary of fine contents for soil materials used in this test.

	Bentonite	Kaolin	Sand
Fine content %	100	99.1	1.3
Silt content %	4.4	18.3	0.8
Clay content %	95.6	80.8	0.5

to compare in soil-water characteristic curve of the bentonite. The seven different chemical components in the bentonite are shown in Table 1.

Grain size distribution were measure by the method for particle size distribution of soils (JIS A 1204:2009). The grain size distribution curves for all materials obtained from test are shown as Fig. 1.

The black symbol dot express as measured value, all curved lines are plotted following the data sets. Each materials described unique distribution curves. Particularly, bentonite and kaolin have highly fine content. The analysis of size distribution is shown in Table 2 that its data sets are distinguished as a fine content, a silt content and a clay content. The bentonite had most high clay content, which was more than 95%.

2.2 *Suction control for SWCC test*

This study measured soil-water characteristic curve at high suction ranges (i.e. more than suction of 1000 kPa). The high suction was controlled directly using vapor pressure technique which was more than 2.8 MPa corresponding to RH 98%. Delage et al. (1998) described some salt solution and the suction under different temperature. Also, the Test method for water retentively for soils (JGS 0151-2009) defined measurement method of water retention of soils with several testing methods. The test specification include vapor pressure technique with some salt solutions. This test required some salt solutions to apply high suction at range from 2.8 MPa to 296 MPa that it was applicable to a range from 98% to 11% in humidity. The salt solution used in SWCC test was summarized in Table 3. The suction values in Table 2 are the application of temperature of twenty degrees. Delage et al. (1998) described that influence of temperature on suction remained by salt solutions was extremely small changes. It was suitable for performance of SWCC test under different temperatures, and suction values defined in Table 3 used to establish the soil-water characteristic curve.

Table 3. Summary of salt solutions used for vapor pressure technique.

Salt	Symbol	RH %	Suction MPa
Potassium Sulfate	K_2SO_4	98	2.83
Potassium Nitrate	KNO_3	95	6.94
Ammonium Dihydrogenphosphate	$NH_4H_2PO_4$	93.1	9.8
Sodium Chloride	NaCl	75	39
Magnesium Nitrate	$Mg(NO_3)_2 \cdot 6H_2O$	54	83.4
Magnesium Chloride	$MgCl_2 \cdot 6H_2O$	33	148
Lithium Chloride	Licl	11	296



Figure 2. Suction control by vapor pressure technique.

2.3 *SWCC test for a powder bentonite*

The soil specimens had two different types, and one was powder condition, other one was compacted condition. The powder specimens mean no compaction. The glass containers were used for SWCC test which had the volume of 0.5 liter in capacity. All powder materials (i.e. bentonite, kaolin and sand) were storage in the container with the required salt solutions. Subsequently, the container was made airtight for remaining constant humidity (i.e. constant suction). All glass container put in the temperature control equipment. The

required temperatures were controlled from twenty degrees to sixty degrees. An initial weight of specimens had generally 10 g, and an initial water content water content was generally 6%.

For one required suction value, the test was proceeded at least one month. Firstly, all specimens were applied a suction of 2.83 MPa corresponding to a relative humidity of 98%. After the specimen had equilibrium with the suction, the replacement of salt solutions changed suction value in the container. The humidity was decreased, and the dry process was employed. The suction was 296 MPa at end of SWCC test which correspond to the humidity of 11%. Figure 2 shows the glass container in the temperature equipment.

2.4 *Measurement of deformation for a compacted bentonite*

The volume changes were measured for compacted bentonite with the different suctions and different temperature. All specimens were statically compacted. The initial sample was a height of 2 cm, and a diameter of 6 cm. The initial conditions were following; water content was 6.0% and dry density was 1.60 g/cm3. All compacted specimens were placed in the glass desiccator, and controlled humidity value was 98% at beginning. On the way of test, some determined numbers for specimens were measured using a vernier caliper such as a diameter, height and weight. This test was performed in the two different humidity, namely, 98% and 33%.

3 TEST RESULTS

3.1 *Changing of water content with elapsed days*

The changes of water content for powder bentonite were measured in humidity of 98% at twenty degrees, and increasing of water content with days were described in Fig. 3. The black circle symbol mean the powder bentonite that other data sets express the various compacted bentonites. The change of water content measured by Nishimura and Koseki (2014) is described in Fig. 3. The water content rapidly increased at beginning of test in humidity of 98% except compacted bentonite with a height of 10 cm. The lateral face of compacted bentonite with a height of 10 cm was covered in order to prevent the destruction. It caused to occur the smoothly increment of water content compare with the compacted bentonite having a height of 2 cm. All bentonite specimens eventually approached to generally same water content value.

3.2 *SWCC for powder bentonite*

All powder specimens described relationship between suction and water content on logarithmic scale as Figs. 4 to 6. All data sets included the different temperatures, and suction rages had from 2.83 MPa to 296 MPa. The

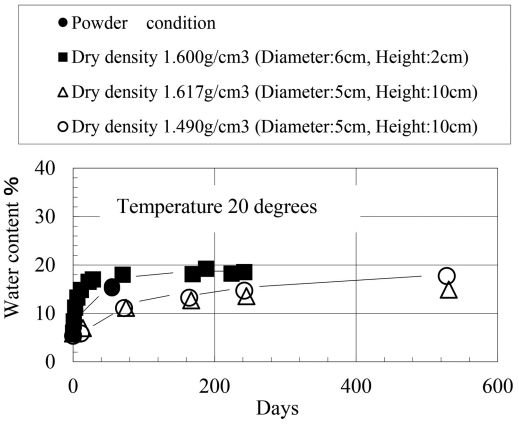


Figure 3. Change of water content under RH 98% with days.

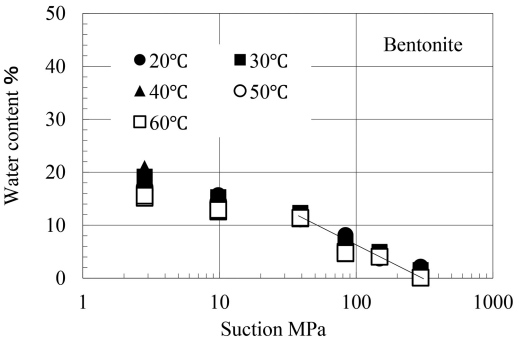


Figure 4. SWCC of bentonite under different temperatures.

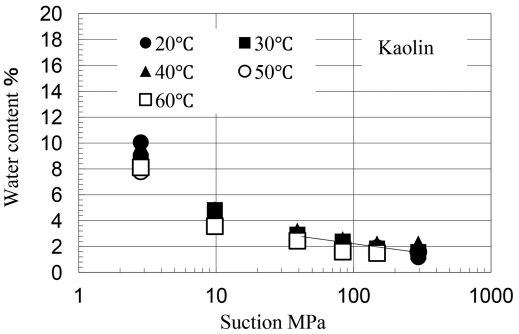


Figure 5. SWCC of kaolin under different temperatures.

suction ranges correspond to 98% to 11% in humidity. The SWCC test was commenced with suction of 2.8 MPa, and the water contents both bentonite and kaolin increased than each initial water content. The increment of bentonite was so large that was over 15%. It caused that initial suction of bentonite was larger than suction of 2.83 MPa in humidity of 98%. In case of sand, water content decreased, and its value was less than an initial water content.

Measured water contents of all specimens decreased with increasing of suction (i.e. decreasing of

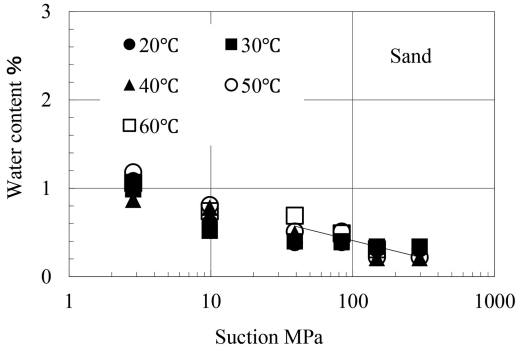


Figure 6. SWCC of sand under different temperatures.

Table 4. Summary of defined slope from each SWCCs.

	Bentonite	Kaolin	Sand
Slope	2.36	0.17	0.12

humidity). The bentonite indicated smoothly reduction till suction was 39 MPa. The water content remained 12% at least. At process of drying, effect of increasing of suction was appeared, the reduction was established clearly.

The great elimination of soil moisture was indicated for kaolin and sand due to decreasing of humidity. The remaining soil moisture of sand was absolutely small, and it was negligible. On the suction range was from 39 MPa to 296 MPa, relationship between water content and suction was possible to make straight line on logarithmic scale that defined the different slope of line on drying portion. Each slope was summarized in Table 4. The bentonite was highly slope value, and sand was lowest slope. The slope of bentonite had a fourteen times compare to that of kaolin that described highly water retention activity. At limited high suction rages, difference between kaolin and sand was small regard to slope.

3.3 *Influence of temperature on water retention for bentonite*

The soil-water characteristic curves assessing effort of temperature was considered with based on experimental data sets. It was difficult to find the influence of temperature from soil-water characteristics curves. Once again, the influence of temperature on water retention activity for each materials was investigated through relationship between water content and temperature as shown in Figs. 7 to 9. The water content having equilibrium with determined whole suctions were plotted against temperatures. There were some scatter in the result, when kaolin was applied the suction of 2.83 MPa. All three different materials evidenced similar tendency that the water content remained constant under one fixed suction even if

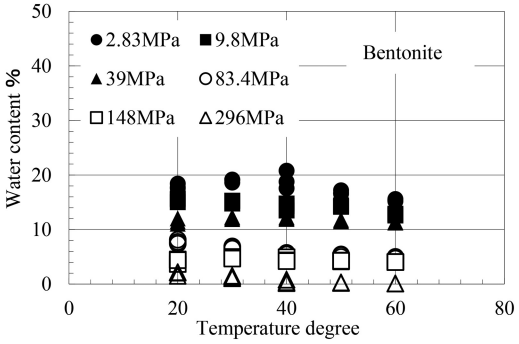


Figure 7. Relationship between temperature and water content for bentonite.

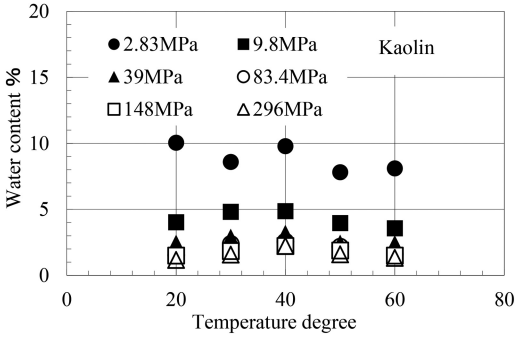


Figure 8. Relationship between temperature and water content for kaolin.

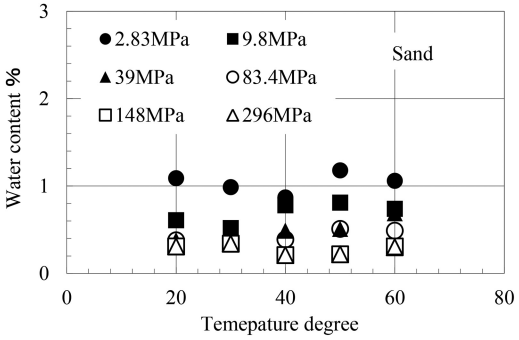


Figure 9. Relationship between temperature and water content for sand.

the temperature of materials increased. It was realized obviously that the changes of water content depended on suction, and the effort of temperature was indistinct. These behavior was observed regardless of fine content.

3.4 *Deformation of compacted bentonite under high relative humidity*

The compacted bentonite was applied the change of suction due to change of humidity, and both volume change and water content were measured with elapsed

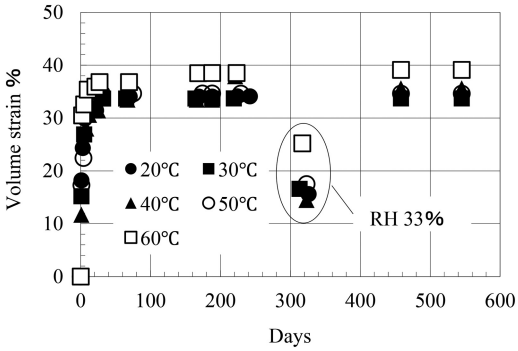


Figure 10. Volume change of compacted bentonite with days.

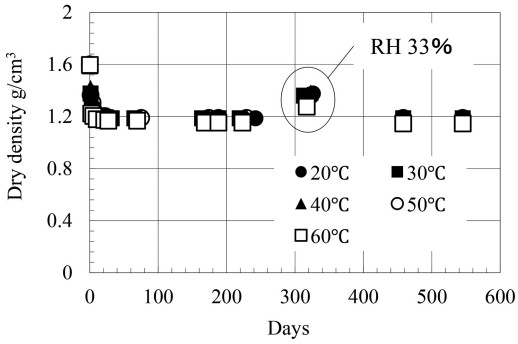


Figure 11. Change of dry density of compacted bentonite with days.

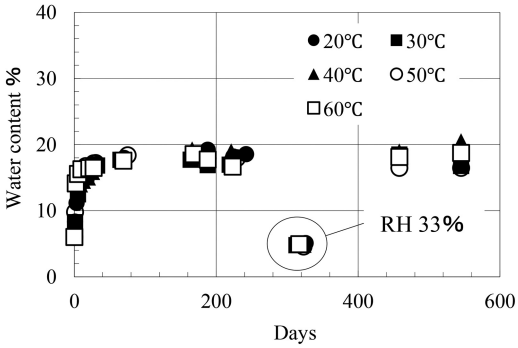


Figure 12. Change of water content of compacted bentonite with days.

days. Figure 10 showed the volume deformation with days. At beginning of humidity of 98%, the volume expansion rapidly increased regardless of temperature. The specimen of sixty degrees indicated large changes compare to other temperatures. The volume strain of 35% was measured a period of forty days. Subsequently, the rate of volume strain was approached to be slightly, and eventually the volume strain was steady. Accordingly, the dry density of specimens were decreased as shown in Fig. 11. Many cracks on the top surface of compacted bentonite were observed directly

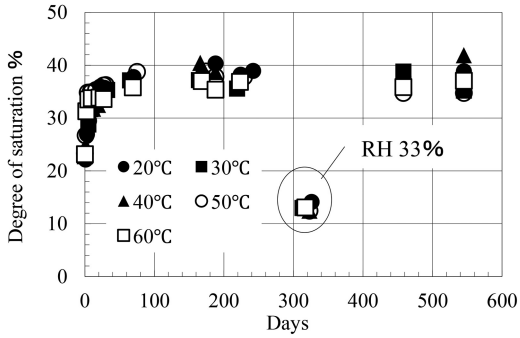


Figure 13. Change of degree of saturation of compacted bentonite with days.

which were mostly occupied in hexagon or honeycomb pattern. There were irregular cracks on lateral surface.

Increasing of water content occurred at same times as volume expansion as above mentioned. The change of water content in the equilibrium process with the humidity of 98% was showed in Fig. 12. The behavior of water content was similar to that of volume change with days. In addition, the behavior of degree of saturation was showed in Fig. 13. Degree of saturation was calculated with expansion volume strain and increment of water content together, and the changes were showed in Fig. 13. Consequently, the degree of saturation approached to over 35% compared to initial value.

After the specimens were equilibrium with the humidity of 98%, the humidity was decreased from 98% to 33% to measure the deformation due to the effort of drying. All specimens occurred shrinkages regardless of temperatures. The reduction of volume strain was not enough to achieve initial volume, and the plastic deformation remained in the specimen. Also, the remaining deformation was large at temperature of sixty degrees.

The water contents at humidity of 33% approached to initial water content which had similar regardless of temperature. The dry densities increased, and degree of saturations were decreased. Particularly, degree of saturations of all specimens were lower than that of initial specimens.

Once again, wetting process was performed to specimens in the humidity of 98%. The expansive deformations were measured, and the dry densities decreased due to increasing of humidity (i.e. decreasing of suction). Increment of water content coincided with volume expansion, and degree of saturation increase together. At end of equilibrium with the humidity of 98% through the humidity of 33%, each physical properties such as dry densities, water contents and degree of saturations were similar to them of the humidity was 33%. Also, it was not find out the influence of temperature on deformation and soil moisture retention activity of compacted bentonite.

Figure 14 shows the upper surface of compacted bentonite when elapsed days was 188 days. The cracks

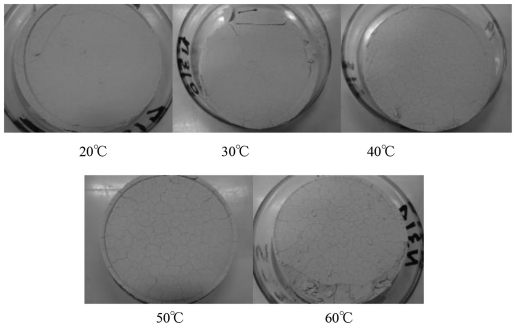


Figure 14. Observations of compacted bentonite at 188 days under RH 98%.

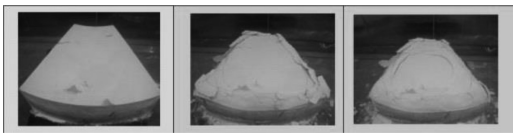


Figure 15. Occurrence of cracks of compacted block bentonite.

were observed for all temperatures which its formations were honeycomb pattern or hexagon. Particularly, the sixty degree induced the upward growth of cracks, the increasing of temperature affected to the development of cracks. As like to the deformation of compacted bentonite was coincident with the report by NUMO (2010). Figure 15 shows the serious deformation transition induced by environment changes, namely, highly temperature and highly humidity. Such as deformation as this, the mechanical properties of compacted bentonite remove into uncertainly behavior in the future.

4 CONCLUSIONS

This study investigated the soil-water characteristic curves of a bentonite subjected to change of temperature, and measured volume deformation of compacted bentonite due to different relative humidity environment.

(1) The bentonite had highly water retention activity compare to the kaolin, and the soil-water characteristic curve of bentonite was significant difference to both kaolin and sand.
(2) It was realized obviously that the decrement of water content depend on suction that the influence of temperature was indistinct.
(3) The compacted bentonite described volume deformation due to change of the humidity. Many cracks such as hexagon or honeycomb pattern occurred in the compacted bentonite subjected to highly humidity.

ACKNOWLEDGMENTS

This study was encouraged by Research Aid Found from Ashikaga Institute Technology.

REFERENCES

Delage, P., Howat, M.D. and Cui, Y.J. 1998. The relationship between suction and swelling properties in a heavily compacted unsaturated clay, *Engineering Geology*, 50, 31–48.

Delage, P. 2013. On the thermal impact on the excavation damaged zone around deep radioactive waste disposal, *Journal of Rock Mechanics and Geotechnical Engineering*, Vol. 5, 179–190.

Hywel, R. Thomas., Philip J. Vardon, and Peter J. Cleall. 2014. Three-dimensional behaviour of a prototype radioactive waste repository in fractured granitic rock, *Canadian Geotechnical Journal*, Vol. 51, 246–259.

Nishimura, T. and Koseki, J. 2014. Deformation of compacted bentonite due to changes in relative humidity, *Proceedings of the Sixth International Conference on Unsaturated Soils, UNSAT2014*, 923–928.

Nuclear Waste Management Organization of Japan (NUMO). 2010. Chapter 6 Technologies for design, construction, operation and closure of the repository, Safety of the Geological Disposal Project 2010, Safe Geological Disposal Based on Reliable Technologies, NUMO-TR-11-01, 6-1∼6-140.

Unsaturated Soil Mechanics—from Theory to Practice – Chen et al. (Eds)
© 2016 Taylor & Francis Group, London, ISBN 978-1-138-02921-7

Development of test-bed and model test for one-dimensional heat and moisture transfer in soils

Z.T. Zeng, Y.L. Zhao, H.B. Lu, C.F. Wei & Y. Zhang
Guangxi Key Laboratory of New Energy and Building Energy Saving (Guilin University of Technology), Guilin, Guangxi Province, China

ABSTRACT: The process of soil heat and moisture transfer is a focus of attention in environmental geotechnical engineering. In this paper, a test-bed was developed for simulating soil one-dimensional heat and moisture transfer process. Then, soil heat and moisture effects under the impact of the temperature gradient and moisture gradient were discussed, and the interactions between moisture migration and heat transfer were verified. On these bases, the further analysis of soil heat and moisture transfer mechanism was presented. The results are shown: (1) The developed test-bed has the properties of simple operation and accurate temperature controlling, which can be effectively used for simulating soil one-dimensional heat and moisture transfer effect. (2) The rate of heat transfer is very slow in testing soil column and the soil adjacent the heat source has the maximum temperature gradient; with the distance away from heat source increasing, the soil temperature decreases rapidly; the temperature influence range is wider with the larger temperature difference between the hot and cold sides. Compared with initial water content and dry density of soil, the temperature difference between the hot and cold sides is the major factor of affecting the temperature field in the testing soil column. (3) After being heated, the water content distribution curve of testing soil column is in turn divided into three segments that are the temperature difference diffuser, the common diffuser and the undisturbed segment.

1 INTRODUCTION

As a porous media, soils generally are made from solid, liquid and gas tri-phase matters such as soil grain, water and air, which often occur migration movements under the joint action of a variety of transport mechanism in soils due to atmospheric environment impacts (Zhao, 1997). In natural environment, the heat and moisture transfer process of soils is controlled by a variety of influencing factors such as soils temperature, pressure, type, porosity and the relative content of liquid phase and gas phase in soils et al (Milly, 1984; Xia, 1995; Hans, 2004; Liu, 2005; Li, 2007). Therefore, it is a complex process with energy exchange and material flow under the interaction of above mentioned factors and becomes a focus of attention in environmental geotechnical engineering. At present, a lot of theoretical researches and models (Hart, 1986; Chen, 1993; Liu, 1996; Chen, 1998; Ji, 2011; Zhao, 2013) have been made for the heat and moisture migration process by domestic and foreign scholars, but it is found that the theory researches have not been closely enough linked with practical engineering due to the lack of specific experimental verification. For example, the current research results not only failed to afford adequate basic test data, but also could not provide a reliable practical foundation for the widespread application of theoretical models. Obviously, it is necessary to research and develop a soil test device which can be simulated one-dimensional heat and moisture transfer process in order to study the heat and moisture migration effect in soils under the combined action of temperature gradients and moisture gradients.

Based on the above mentioned purpose, this paper has developed a test-bed for simulating one-dimensional heat and moisture transfer in soils. Though model tests for three types of soils, This article discusses soil heat and moisture effect under the impact of the temperature gradient and the moisture gradient and verifies the interaction between moisture migration and heat transfer. The results can provide basic experimental data for improving the theoretical models of heat and moisture transfer in soils.

2 ONE-DIMENSIONIONAL HEAT AND MOISTURE TRANSFER TEST-BED FOR SOILS

The one-dimensional heat and moisture transfer test-bed was made from a constant temperature heating system and a testing soil column, which was shown as Figure 1. During the tests, the testing tank was filled with red clay, silty clay and fine sand. The red clay and silty clay were taken from the ground source heat pump test site, and the sand was often used as building materials. When one end of the soil column was being heated by the copper heating tank, the changes

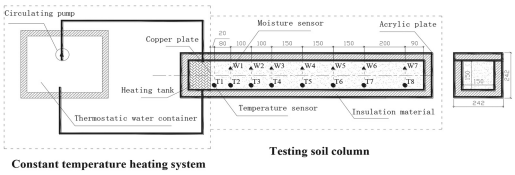
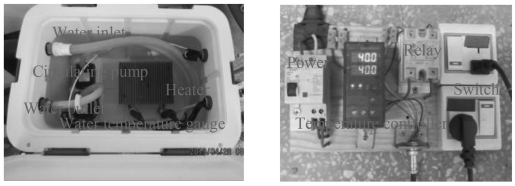


Figure 1. System diagram of test device.



a) Heating section b) Control section

Figure 2. Constant temperature heating system.

of temperature and water content of soil in different positions of the soil column were measured with the embedded sensors.

2.1 *Constant temperature heating system*

A thermostatic water container was made to provide a stable constant temperature heat. The body was a 20 L incubator, in which there were an electric heater, a water temperature gauge and two circulating pumps, and out of which there were a relay, a temperature controller and a power, which is shown as Figure 2.

Heater: It was working with two electric heaters, the power of which was 800 W for each. A fin was attached on the upper, which can expand the heating scope of the heater and make the heat diffusion more uniform.

Circulating pump: Two submersible pumps were used to water circulation in the test process, which one was for internal water of the thermostatic water container to make the water temperature more uniform (called as "internal cycle"), the other was for the water circulation between the thermostatic water container and the heating tank (called as "external cycle"). Due to small system resistance, both cycles used JY-PG 150 submersible from Jiyin company of Hongzhou, maximum head of which was 1.6 m and the maximum flow rate was 800 L/h.

Temperature controller: HP-613 PID temperature controller was used to control the calefaction heat quantity of electric heater. Measured results showed that the temperature fluctuations of the water inside the container were within 0.1°C, which can be met the test requirements.

Heating tank: It can be filled into the heating section of soil test chamber, which was shown as Figure 3. In common metallic materials, copper was a good choice for processing materials because of its high conductivity, good plasticity and medium price.

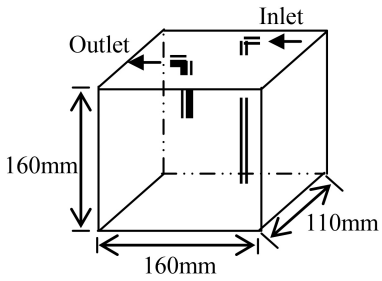
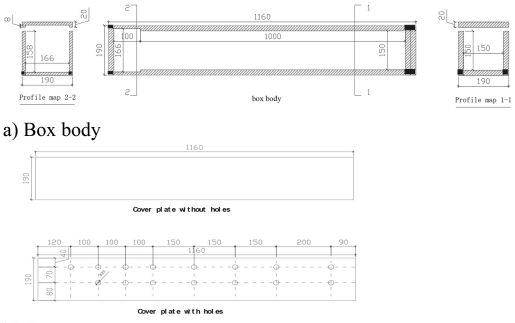


Figure 3. Schematic diagram of heating tank.



a) Box body

b) Covers

Figure 4. Design drawing of soil testing chamber.

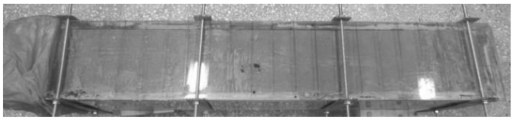


Figure 5. Testing soil column.

2.2 *Soil testing chamber*

Soil testing chamber was made by 2 cm thickness acrylic plate, which can insulate both water and heat. The length of the box was 1160 mm, and the inner section size was 150 mm × 150 mm. It can be divided into two sections. The left section was the constant temperature heating system, the length of which was 120 mm and the inner section size was 166 mm × 166 mm. The right section was the soil testing column, the length of which was 1000 mm and the inner section size was 150 mm × 150 mm. In order to facilitate to make the soil column and installing the sensors, the chamber was designed with a removable cover (as showed in Figure 4). The cover with holes was used for installing sensors in test, and another without holes was for filling soils to prevent soil leakage. Finished testing soil column was shown as Figure 5.

2.3 *Measurement section*

Temperature measurement: The soil temperature were measured by PT100 platinum resistance thermometers (JMT-36C), and their accuracy were 0.1°C. Each thermometer had been calibrated exactly before test,

and the temperature data were manual collected with a JMZX-7000 integrated testing instrument.

Water content measurement: Soil moisture was classified into volumetric water content (θ) and mass water content (ω). For the continuity and effectiveness of the test results, θ was automatically measured with MiniTrase moisture test apparatus produced by Soil-moisture Equipment Corp during the heating test process. After test, some soils around the sensors were taken out for determining ω by drying weighing method in order to obtain the final state of moisture migration in the soil column.

Flow measurement: The flow of circulating water was measured by a portable ultrasonic flow meter. The measurement results showed that the circulating water flow rate remained substantially constant, and the average value was 150 L/h.

3 ONE-DIMENSIONAL HEAT AND MOISTURE TRANSFER MODEL TEST FOR SOILS

3.1 *Test programs and processes*

(1) Test content

Test soils were red clay, silty clay and fine sand, and the specific test conditions were as follows. (Heating time was 12h)

red clay: ①-1-(T_s=40℃,ρ_d=1.4g/cm^3,ω_0=20%);
①-2-(T_s=40℃,ρ_d=1.4g/cm^3,ω_0=25%);
①-3-(T_s=40℃,ρ_d=1.4g/cm^3,ω_0=30%);
②-1-(T_s=40℃,ω_0=25%,ρ_d=1.3g/cm^3);
②-2-(T_s=40℃,ω_0=25%,ρ_d=1.4g/cm^3);
②-3-(T_s=40℃,ω_0=25%,ρ_d=1.5g/cm^3);
③-1-(ρ_d=1.4g/cm^3,ω_0=25%,T_s=30℃);
③-2-(ρ_d=1.4g/cm^3,ω_0=25%,T_s=40℃);
③-3-(ρ_d=1.4g/cm^3,ω_0=25%,T_s=50℃).

silty clay: ①-1-(T_s=40℃,ρ_d =1.5g/cm^3,ω_0=10%);
①-2-(T_s=40℃,ρ_d =1.5g/cm^3,ω_0=15%);
①-3-(T_s=40℃,ρ_d =1.5g/cm^3,ω_0=20%);
②-1-(T_s=40℃,ω_0=15%,ρ_d =1.4g/cm^3);
②-2-(T_s=40℃,ω_0=15%,ρ_d =1.5g/cm^3);
②-3-(T_s=40℃,ω_0=15%,ρ_d =1.6g/cm^3);
③-1-(ρ_d=1.5g/cm^3,ω_0=15%,T_s =30℃);
③-2-(ρ_d=1.5g/cm^3,ω_0=15%,T_s =40℃);
③-3-(ρ_d=1.5g/cm^3,ω_0=15%,T_s =50℃).

fine sand: ①-1-(T_s=40℃,ρ_d=1.5g/cm^3,ω_0=10%);
①-2-(T_s=40℃,ρ_d=1.5g/cm^3,ω_0=14.2%);
②-1-(T_s=40℃,ω_0=10%,ρ_d=1.4g/cm^3);
②-2-(T_s=40℃,ω_0=10%,ρ_d=1.5g/cm^3);
③-1-(ρ_d=1.5g/cm^3,ω_0=10%,T_s=40℃);
③-2-(ρ_d=1.5g/cm^3,ω_0=10%,T_s=50℃).

(2) Test process

Taking the first condition-① of red clay for example, the test process was shown as follows.

① Preparing soils: The red clay was prepared by mixing dried, crushed red clay particles passing through a sieve with 5 mm aperture with distilled water at a water content 20% for 24 hours under constant temperature ($T_r = 22°C$), so that soil temperature and moisture were of uniform distribution.

② Making samples: The soil column was compacted at a dry density 1.4 g/cm^3 with a 5cm height layer.

③ Installing sensors: After 8 temperature sensors and 7 moisture sensors were successively installed in the appointed location, the heating tank was put in the testing chamber to make close contact with the soil column with the other end doing the strict closure insulation. Then, Closed the cover and sealed all the holes on it to prevent heat and moisture loss from the hole.

④ Seal standing: The testing chamber was sealed with glass cement to make the testing soil column completely cut off with outside air. To strengthen the insulation effect, a layer of 30 mm thick PVC/NBR rubber insulation materials was wrapped in the outside of the testing chamber. Then let the soil column standing for 24 hours, so that soil temperature and moisture were of uniform distribution.

⑤ Setting heating source's temperature: The operation process was as following: starting the temperature controller and heater—setting temperature to 40°C—starting internal circulation pump—preparing in the constant temperature state.

⑥ Starting test: Firstly, started the external circulation pump to make the best start; then, collected and recorded the temperature and moisture changes in soil column; Finally, measured the circulating water flow with a portable ultrasonic flow meter after the water flow was stable.

⑦ Finishing test: The test was continuing until the soil column had been heating for 12 hours, followed by removal of the insulation material, cover, thermostatic heating tank, sensors. Then some soils around the sensors were taken out to measure the mass water content by drying weighing method. Finally, soil column samples were excavated to clean the chamber.

⑧ Testing of soil with water content 25%: Changing the soil water content of 25%, the test was repeated as the steps ①～⑦.

⑨ Testing of soil with water content 30%: Changing the soil water content of 30%, the test was repeated as the steps ①～⑦.

3.2 *Test results and analysis*

Whole tests were conducted in a laboratory with stable temperature 22°C to ensure the initial temperature of the soil column maintained constant. For good insulation measures during tests, the soil column had been little affected by external environment and the temperature of the cold end was keeping the initial temperature all the time.

(1) Soil column temperature change results and analysis

① Effect of the heat source temperature T_s

Figure 6 shows the temperature distribution test results of three soil columns (red clay, silty clay and fine sand) being heated for 12 hours with different

heating source temperatures T_s. Thus, the influence of temperature on the heat source temperature distribution within the soil column is essentially the same. That is to say, the closer soils is to the heat source, the greater the temperature gradient is in the soil; With distance from heat source increasing, the soil temperature decreases rapidly; After red clay, silty clay, fine sand is in turn far away from the heating source at different distance 0.5 m, 0.6 m, 0.7 m, there is only a little change in their temperature. Comparing the test curves of soils with different heating source temperatures, it is shown that the temperature gradient in the soil is large due to the high heating source temperature and the influence scope of temperature change will also increase accordingly. In Figure 6-a, the temperature influence scopes of red clay column are successively the distance away from the heating source with 0.45 m, 0.50 m, 0.60 m when the temperature of the heating source is 30°C, 40°C, 50°C.

It is also a fact from the figure 6 that the scopes of thermal diffusion of red clay, silty clay, fine sand are respectively 0.5 m, 0.6 m, 0.7 m, thus the heat transfer capacity of above mentioned three soils are in the following orders: fine sand > silty clay > red clay. The reason is perhaps that the heat transferring speed of fine sand is the fastest for its biggest thermal conductivity and thermal diffusivity among the three soils. Similarly, the red clay has the smallest thermal conductivity and thermal diffusivity, so its transferring speed of heat is the slowest. While transferring speed of heat of silty clay is between the above two soils because of its middle thermal conductivity and thermal diffusivity. On the other hand, red clay has the biggest value of specific heat capacity, which makes the heat be easily accumulated in the vicinity of the heated end. To some extent, it has further influenced the heat transfer capacity of red clay.

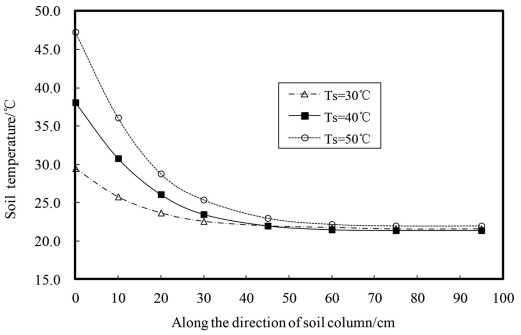
② Effect of the initial water content ω_0

Figure 7 shows the temperature distribution test results of three soil columns (red clay, silty clay and fine sand) being heated for 12 hours with different initial water contents ω_0.

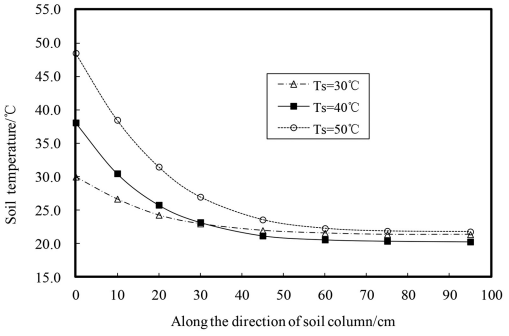
Thus, the influence of the initial moisture content on the soil temperature field distribution is essentially the same. The soil with bigger initial moisture content usually has the bigger thermal conductivity and volumetric specific heat capacity, which makes the heat be accumulated easily. Therefore, the soil temperature of the same position in the soil column is likewise higher. On the contrary, the soil with smaller initial moisture content usually has the smaller thermal conductivity and volumetric specific heat capacity, which does not make the heat be accumulated easily. Therefore, the soil temperature of the same position in the soil column is likewise lower. At the same time, compared with the influence degree of different heat source temperatures, the initial water content has less influence effect on the soil temperature field distributions.

③ Effect of the dry density ρ_d

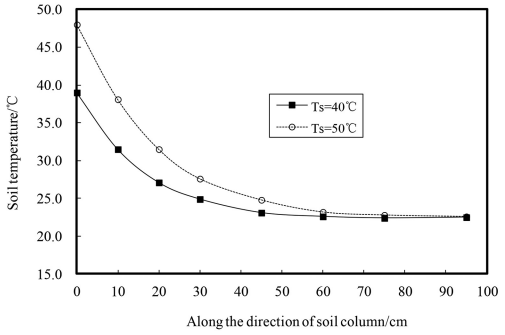
Figure 8 shows the temperature distribution test results of three soil columns (red clay, silty clay and fine sand) being heated for 12 hours with different dry densities ρ_d. Thus, the influence of the dry density on the soil temperature field distribution is essentially the same. The soil with bigger dry density usually has the bigger thermal conductivity and volumetric specific heat capacity, which makes the heat be accumulated easily. Therefore, the soil temperature of the same position in the soil column is likewise higher. On the contrary, the soil with smaller dry density usually has the smaller thermal conductivity and volumetric specific heat capacity, which does not make the heat be accumulated easily. Therefore, the soil temperature of the same position in the soil column is likewise lower. At the same time, compared with the influence degree



a) Red clay

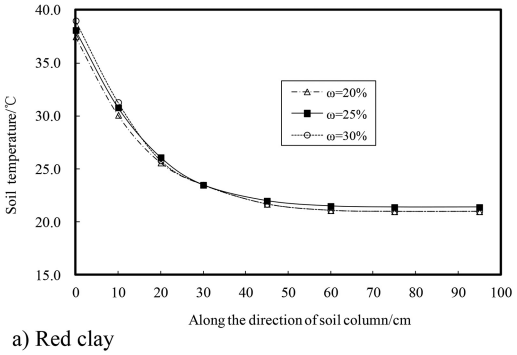


b) Silty clay

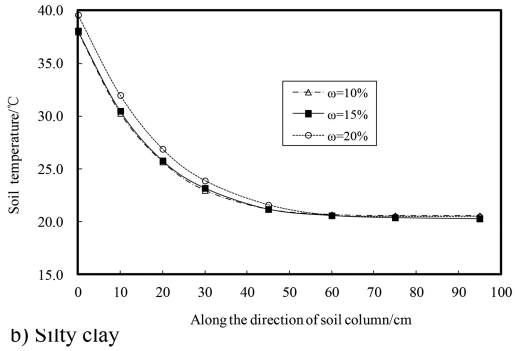


c) Fine sand

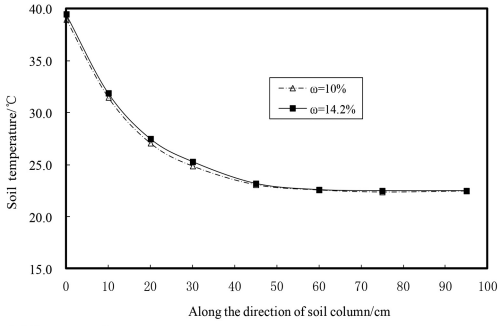
Figure 6. The impact of source temperature on soil temperature distribution.



a) Red clay

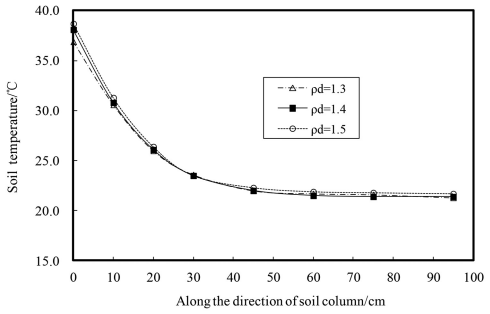


b) Silty clay

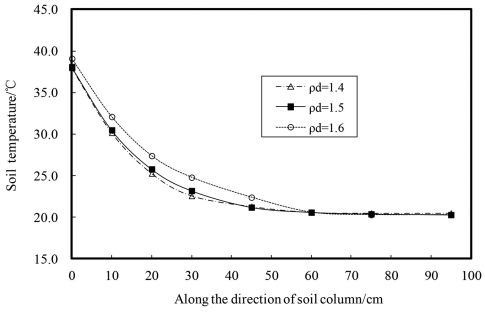


c) Fine sand

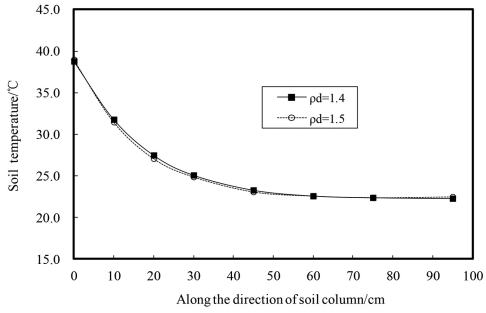
Figure 7. The impact of initial water content on soil temperature distribution.



a) Red clay



b) Silty clay



c) Fine sand

Figure 8. The impact of initial water content on soil temperature distribution.

of different heat source temperatures, the dry density has less influence effect on the soil temperature field distributions.

(2) Soil column moisture migration results and analysis

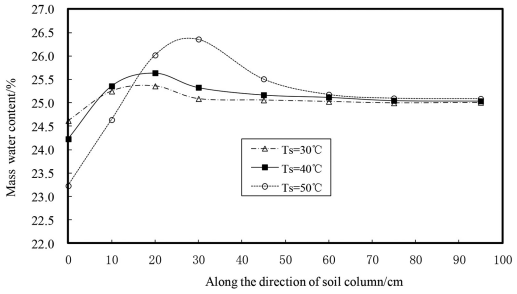
Figure 9 shows the water content distribution test results of three soil columns (red clay, silty clay and fine sand) being heated for 12 hours with different heating source temperatures Ts. It is a fact that the water content of soil near a heat source side are showing a significant downward trend and the water content of soil in the region with a distance 20–30 cm away from the heating end is significantly higher than the initial value to inform a peak here. The reason is that the moisture of the heating end starts migration out with the driving action of a temperature gradient and informs an aggregation for a peak. After the peak value, soil moisture content decreases gradually and eventually is close to the initial value.

According to its variety track, the water content curve of the soil column from figure 9 is divided into three segments that are the temperature difference diffuser, the common diffuser and the undisturbed segment.

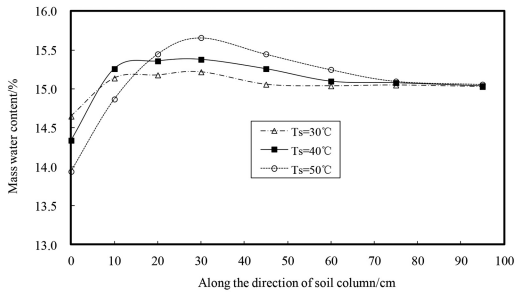
① The temperature difference diffuser

A typical feature of this section is that the changing direction of soil moisture is opposite to that of temperature gradients of soil column.

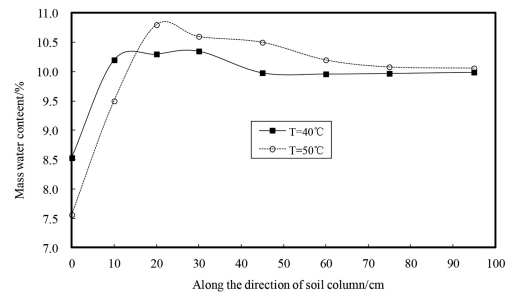
The left end of the soil column, to which the heating part is close has the maximum temperature gradients and the strongest water diffusion (referred to as "temperature difference force") which caused by the



a) Red clay



b) Silty clay



c) Fine sand

Figure 9. The impact of source temperature on soil water content distribution.

former. With the distance increasing, the temperature differences decrease gradually, and the temperature difference power thereupon decreases. Therefore, the water diffusion caused by the temperature gradients gradually weakens from left to right.

At the initial time, the moisture and temperature of soils in each part of the soil column are distributed evenly, so the moisture gradients and temperature gradients both are zeroes. After the temperature differences of soils near the heating end existing, the temperature gradients drive the moisture migrating to the right direction, which make the soil water content decreasing. Therefore, there are moisture gradients (referred to as "moisture differences force") which drive the soil moisture migrating from right to left.

From the above analysis, it is known that the direction of moisture migration which caused by the temperature differences force is opposite to that of moisture differences force in this section, but the former is far higher than the latter. In all, the moisture in the soil column is migrated to the right end and the soil water content of the left end decreases. With distance increasing, both forces show gradually decreasing trends, but the rate of the former is bigger than the latter. The two forces reach a temporary equilibrium at a little far away from the heating end (about 20–30 cm). As the temperature differences force is still bigger than the moisture differences force, the migrated moisture constantly accumulates to make the soil water content to reach a peak value, which is bigger than the initial water content value.

② The common diffuser

The gradients of temperature and moisture have the same changing direction in this section. Along with the direction of the hot end to the cold end, both are shown that the values of the left end are big but the values of the right are few. With the common action of both above forces, the soil moisture is migrating from the hot end to the cold end. However, the migration rate of soil moisture is very slow due to the values of both the diffusing force are small.

③ The undisturbed segment

Due to the distance far away from the heat source, the moisture migration effect has little influence on the soil water content, which is still kept an initial value.

4 CONCLUSION

(1) The developed test-bed has the properties such as clear principle, simple operation, good thermal insulation and accurate temperature controlling, which can be effectively used for simulating soil one-dimensional heat and moisture transfer effect.

(2) The rate of heat transfer is very slow in the testing soil column and the soil near the heat source has the maximum temperature gradient; with distance away from heat source increasing, the soil temperature decreases rapidly; the temperature influence range is wider with the larger temperature difference between the hot and cold sides. Compared with initial water content and dry density of soil, the temperature difference between the hot and cold sides is the major factor of affecting the temperature field in testing soil column.

ACKNOWLEDGMENT

This research has been supported by National Natural Science Foundation of China (Grant No. 41272358, 51409051), Natural Science Foundation of Guangxi Province of China (Grant No. 2013GXNSFBA019233) and Natural Science Foundation of Guangxi Province under an "innovative research team" project (Grant No. 2012GXNSFGA060001).

REFERENCES

Chen S.X. & Chen S.Y. (1993). Numerical modeling of coupled heat and moisture transfer in unsaturated soil. Rock and Soil Mechanics, 14(2):41–52.

Chen Z.Q., Shi M.H. & Yu W.P. (1998). Non-equilibrium thermodynamics method of heat and moisture transport properties in unsaturated soil. ACTA PEDOLOGICA SINICA, 35(2):218–226.

Hart D.P. & Couvillion R. (1986). Earth coupled heat transfer. Publication of the National Water Well Association.

Janssen H., Carmeliet J. & Hens H. (2004). The influence of soil moisture transfer on building heat loss via the ground. Building and Environment, 39(7): 825–836.

Ji H.Y. (2011). Study on heat and moisture transfer at high-temperature in wet soil. Tianjin: Hebei University of Technology.

Li H.X., Xia Z.Q. & Ma G.H. (2007). Effect of water content variation on soil temperature process and water exchange. Journal of Hohai University (Natural Sciences), 35(2):172–175.

Liu B.C., Liu W. & Peng S.W. (2005). Study of heat and moisture transfer in soil with a dry surface layer. International Journal of Heat and Mass Transfer, 48(21): 4579–4589.

Liu W., Wang C.Q. & Yang J.B., et al. (1996). A general mathematical model for heat and moisture transfer in unsaturated porous media. Journal of Huazhong University of Science and Technology, 24(1):8–11.

Milly P.C.D. (1984). A simulation analysis of thermal effects on evaporation from soil. Water Resources Research, 20(8):1087–1098.

Xia Z.Q., Guo B.F. & Jiang H.G., et al. (1995). Effects of temperature variation on soil water movement and water exchange between soil water and phreatic water. Advances in Water Science, 6 (Special Issue):15–22.

Zhao X.X., Liu W. & Li Y.P., et al.(1997). On the motion of water, moisture and heat in soil. Journal of Huazhong of Science and Technology, 25(5):5–7.

Zhao Y.L., Zeng Z.T. & Lu H.B., et al. (2013). Review and prospect of heat and moisture migration mechanism and mechanical behavior of soil in shallow geothermal energy exploitation. Journal of Engineering Geology, 21(2): 222–227.

This page intentionally left blank

Unsaturated Soil Mechanics—from Theory to Practice – Chen et al. (Eds)
© 2016 Taylor & Francis Group, London, ISBN 978-1-138-02921-7

Thermal conductivity of unsaturated mixtures of loess soil with granulated rubber

Z.H. Li
Northwest University for Nationalities, China

H.Y. Zhang & Y.M. Sheng
Key Laboratory of Mechanics on West Disaster & Environment, DOE Lanzhou University, China

ABSTRACT: Addition of rubber pellet to loess soil can improve the mechanical and thermal property of loess, providing a potential utilization in road foundation against frost heave. This paper reports the results of thermal conductivity test on unsaturated Granulated Rubber and Loess soil Mixtures (GRLM) compacted at various densities and moisture contents by Hot Disk Thermal Constants Analyzer. Test results show that the thermal conductivity of GRLM decreases with increasing rubber content, and increases with increasing moisture content and compacted effort at rubber content less than 20%. A theoretical model is established to describe the conductive heat flow through unsaturated GRLM with modification of four-phase composition to solid mixtures of rubber pellets and mineral particles. The model function is verified to be reasonable for practical application by the good correlation between predicted and measured thermal conductivities.

1 INTRODUCTION

China has been the most productive nation of scrap tires since 2012 which generated approximately 280 million scrap tires in that year (Zhu et al. 2014). Some of the scrap tires are recycled such as tire-derived fuel for energy generation, remanufactured tires, highway crash barriers, low-grade rubber products, etc. There is still a large amount waste tires were illegally or improperly disposed of. Many researchers have been undertaking over thirty years in studying the possibilities of using tire shreds or whole tires as lightweight materials in civil engineering. The researchers indicated that tire shreds possess some potential properties compared to natural soils, such as high durability, high strength, thermal insulation capacity, and can be successfully used as reinforced earth fill (Foose et al. 1993, Garga et al. 2000), asphalt modifier (Shuler et al. 1993), leachate drainage layer (Duffy et al. 1995, Reddy et al. 1998), lightweight fill (Humphrey et al. 1992, Tweedie et al. 1998, Masad et al. 1996), construction of civil engineering (Moo-Young et al. 2003, Edeskär 2006, Zornberg et al. 2004).

To avoid pure scrap tires spontaneously combustion, the application of tire shreds used in civil engineering as lightweight fill are mixed with mineral soils such as sand, silt, clay and so on. (Masad et al. 1996, Youwei et al. 2003, Zornberg et al. 2004, Lee et al. 1999, Bernal et al. 1996, Ghazavi et al. 2004, Li et al. 2012).

Loess is usually used as backfill materials of embankment in west north of China. The physical and mechanical properties of Loess and tire shreds mixtures have been studied (Li et al. 2010, 2011 and 2012). The research shows that the granulated rubber and loess mixtures (GRLM) can be compacted when the rubber content of weight is less than 50% under standard effort (600 kN-m/m^3), and find the optimum rubber content leading the highest strength of mixtures is 30% and 40% at Proctor compaction energy and modified Proctor energy respectively. Thermal properties has significant relation to engineering applications such as ground heat exchangers, high voltage power cables (Abdel, et al. 1981), underground pipelines (Slegel et al. 1977), nuclear waste vaults (Gera et al. 1996), frost heave damage of culvert, mitigation techniques in permafrost degradation (M-lepage et al. 2012) et al. Most of the research works done on the thermal properties focused on pure shredded tires (Shao, et al. 1995, Humphrey, et al. 1997, Hoor, et al. 2011) which are commonly used as thermal insulators in landfill liners, beneath roadways et al.

The objective of this paper is to present a method to measure the thermal conductivity of unsaturated GRLM using transient plane source (TPS) method. The effect of the rubber content, water content, and compaction effort on the thermal conductivity of GRLM has also been discussed. The effective thermal conductivity of unsaturated GRLM was estimated by an enhanced series-parallel model and Maxwell model of conduction heat flow through a unit cell of mixtures.

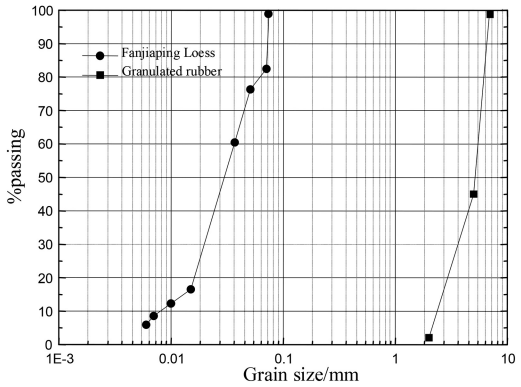


Figure 1. Gradation curves of materials.

Table 1. Physical properties of materials.

Properties	Loess (silt)		Granulated rubber
	Mean	Range	
Water content (%)	7.76	5.00–10.00	0.8–1.17
Density (g/cm^3)	1.43	1.39–1.48	
Dry density (g/cm^3)	1.32	1.30–1.35	
Specific gravity (–)	2.70	2.70–2.71	1.17
Liquid limit (%)	25.7	24.8–27.0	
Plastic limit (%)	18.7	18.3–19.3	
Plastic index (–)	7.0	6.50–6.90	

2 MATERIALS AND METHODS

2.1 *Materials*

Materials used for this study were as same as used in the mechanical tests performed by Li et al. (2009, 2010, 2011) (Table 1 and Fig. 1).

Specimens were prepared using loess and granulated rubber without steel belts. Thermal properties of pure loess, pure granulated rubber and mixtures of these two materials (X = 10, 20, 30, 40, and 50% rubber content by weight) were tested. The specimens were compacted in the modified ring cell under different compaction effort to gain target unit weight.

Loess was locally obtained from high terrace, formation of Quaternary outcropping in the Lan Zhou basin in northwest China. The tire shreds were cut into controlled cube sizes to achieve side of around 5 mm with wires removed. According to ASTM D 6270-98 the tire shreds were named as granulated rubber. Table 1 summarizes the physical properties of loess and granulated rubber, and Figure 1 shows grain size distributions for them.

2.2 *Equipment*

Hot Disk Thermal constants Analyzer was used in this investigation to test specimens using Transient Plane Source (TPS) method, which is convenient technology for the study of heat transfer. The method is based on the use of a transiently heated plane sensor, which consists of an electrically conducting pattern in the shape of a double spiral, which has been etched out of a thin metal (Nickel) foil. This spiral is sandwiched between two thin sheets of an insulating material. The Hot Disk sensor is used as a heat source and as a dynamic temperature sensor with the accuracy over the whole range of Thermal Conductivity (0.005 $Wm^{-1}K^{-1}$ to 500 $Wm^{-1}K^{-1}$) is within +/−5% and the reproducibility is within +/−2%.

2.3 *Specimens preparation*

The GRLM were prepared by combing granulated rubber according designed rubber content and water content with loess uniformly. The specimens were compacted to the desired density and water content in the ring with 79.8 mm internal diameter, 20 mm height with a metal hammer under standard Proctor energy (600 kN-m/m^3) and modified effort to achieve total volume corresponding to the designed density. Two same samples were used to clamp the probe for each testing.

3 RESULTS AND DISCUSSION

3.1 *Effect of rubber content on the thermal conductivity*

Figure 2 illustrates the variation of rubber content versus thermal conductivity for specimens compacted under Standard Procter energy. The results indicate that for a given compaction level, as the rubber content increases the thermal conductivity decreases. The thermal conductivity of the loose granulated rubber without compaction is 0.26 $Wm^{-1}K^{-1}$, which value is slightly higher than the range of laboratory studies from 0.19–0.232 $Wm^{-1}K^{-1}$ (Shao & Zorling (1995), Humphrey et al. (1997a)). Soil thermal properties are depended on the density, particle, pore microstructure, mineralogy, and moisture content (e.g., Farouki 1981). GRLM is four-phase composite material in which some of natural soil solid is replaced by granulated rubber and the "soil" fabric is changing with the rubber content (Fig. 3).

When rubber content is less than 20% (by weight), granulated rubber do not contact each other and is floating in the matrix of loess. The thermal properties of GRLM which rubber content is less than 20% are significantly controlled by unsaturated loess system which consists of matrix (loess) density, particle and pore microstructure, mineralogy, and water content. When rubber content is more than 30% (by weight) rubber particles contact each other and fine particles of loess fill the pore spaces densely between the rubber solids. When the rubber contents is exceed 40% (by weight), it is difficult for matrix to fill the pore space densely, and the thermal properties are more like

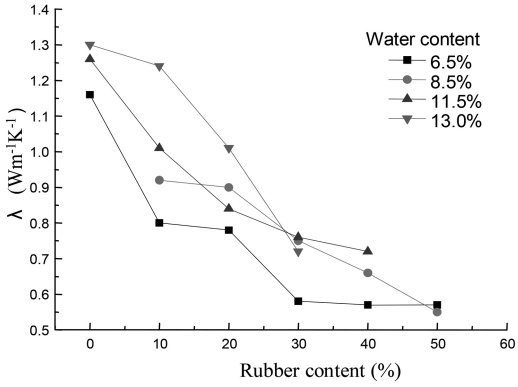


Figure 2. Thermal conductivity vs. rubber content.

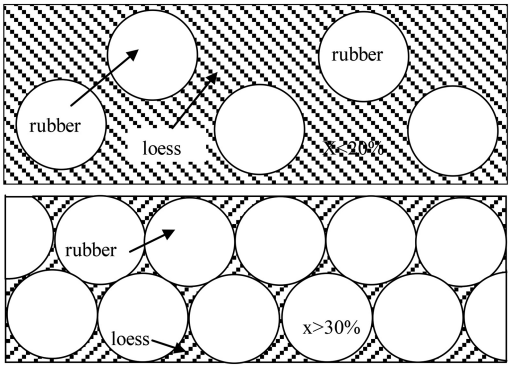


Figure 3. Schematic diagram of the fabric for GRLM at different rubber content.

pure granulated rubbers which are minor influenced by stress, water content and tire shred size.

3.2 *Effect of water content*

Figure 4 shows the relationship between thermal conductivity and water content, illustrating that when granulated rubber content is less than 20%, the thermal conductivity increases as water content increases.

When the rubber content exceeds 40%, the water content has a minor influence on the thermal conductivity due to the high draining capacity of granulated rubber at high water content and showing properties like coarse soil without cohesion. The lack of testing data for high rubber content and high water content of GRLM is due to difficulty of preparing samples using Hot Disk TPS2500s.

3.3 *Effect of compaction effort on thermal conductivity*

Figure 5 illustrates the compaction effort versus the thermal conductivity. The GRLM dry density of low rubber content (<20% by weight) increase as compaction effort increasing. While the thermal conductivity increases as compaction effort increases.

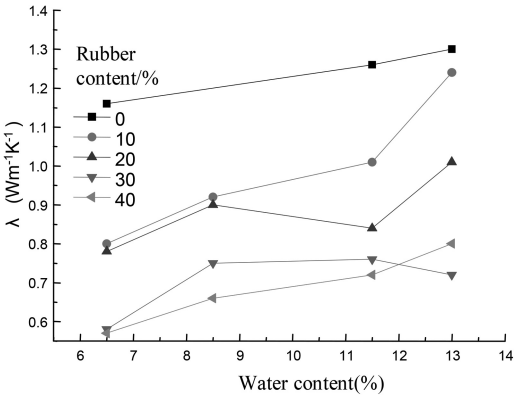


Figure 4. Thermal conductivity vs. water content.

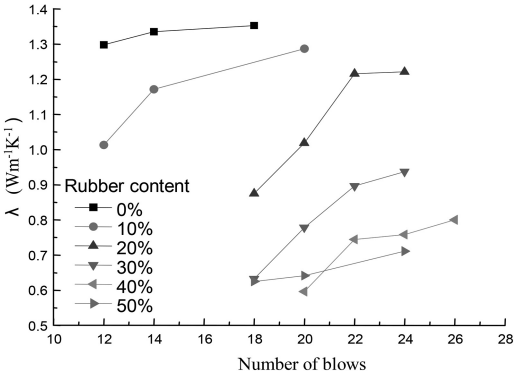


Figure 5. Thermal conductivity vs. number of blows.

The rubber solids do not contact each other just "floating" in fine soil when rubber content of GRLM is lower and the mixtures can be compacted density with increasing effort at optimum water content. The rubber solid are the skeleton of mixtures when rubber content is more than 30%, and the elastic solid absorbed apart of compaction energy under high compaction effort. As a result the density of the GRLM at high rubber content has no significant increasing.

4 MODELING OF GRLM CONDUCTIVITY

Modeling soil thermal conductivity is not easy to implement because of the enormous structural complexity of unsaturated porous systems and difficulty of taking account into both heat and mass transfer. In measuring soil thermal properties, the principle of equipment is based on the classical theory of heat flow transfer in solids. When application of these manners to unsaturated soils brings about numerous not including phenomenon, such as porous capillary system,

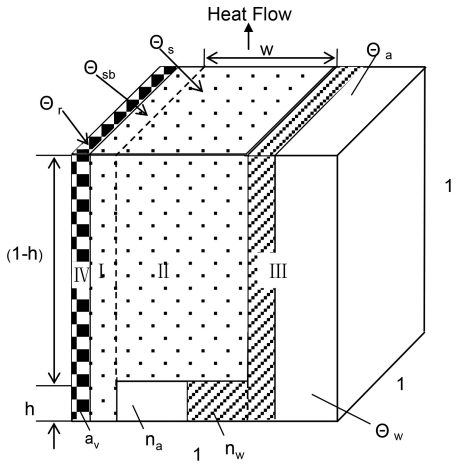


Figure 6. Partitioned GRLM cubic cell of rubber content <20% by weight.

simultaneous heat and water flow combined with latent heat effects.

Woodside & Messmer (1960) adapted the model of estimating the electrical conductivity of granular materials to develop the model for heat flow estimating in two-phase porous media at full dryness and saturation. Farouki (1986) upgraded the model at full saturation to unsaturated soils by introducing an additional term. Kasubuchi (1982) examined a series-parallel model applied to three-phase porous systems. Vodek (2012) gave a new model of unsaturated soil which was calibrated using experimental thermal conductivity data of five soils of different texture (coarse, medium, and fine).

The condition of adding granulated rubber into natural soil can be divided into two soil fabrics: one is granulated rubber floating in matrix soil without contact each other (model 1); the other is granulated rubber solid contacting each other and natural soil fit the pore space (Fig. 3) (model 2). The model of unsaturated GRLM is four-phase porous systems, e.g. rubber solid, natural soil solid, water, and air. First, the GRLM model assumes one-dimensional conductive heat flow through the elementary cubic cell of unsaturated GRLM. Second, the GRLM model assumes water is contained only in the pores of the natural soils due to little water absorbability of rubber solid. Third, the heat flow is split along four independent paths each adiabatically insulated on the sides (Fig. 6) for first fabric (x < 20% by weight). For model 2 the heat flow through the elementary cubic cell of unsaturated GRLM is along a series arrangement path of unsaturated loess and dry granulated rubber (Fig. 7) when rubber content is more than 30% (by weight), and the model can use Mexwell (1954) equation (Eq. 8).

When heat flows along separate paths in parallel orientation of GRLM cubic cell, the model 1 can be expressed by the following:

Model 1:

$$\lambda_{mix} = \lambda_r a_v + \lambda_s \Theta_{sb} + \frac{A^2}{B+C} + D + E \quad (1)$$

$$A^2 = (1 - n - \Theta_{sb} - a_v + n_{wm})^2 \quad (2)$$

$$B = \frac{1 - n - \Theta_{sb} - a_v}{\lambda_s} \quad (3)$$

$$C = \frac{n_{wm}}{\lambda_w \exp(1 - S_r^{-X}) + \lambda_a [1 - \exp(1 - S_r^{-X})]} \quad (4)$$

$$D = \lambda_w [n S_r - n_{wm} \exp(1 - S_r^{-X})] \quad (5)$$

$$E = \lambda_a [n(1 - S_r) - n_{wm} [1 - \exp(1 - S_r^{-X})]] \quad (6)$$

$$a_v = \frac{x(0.01w + 1) G_{ss}}{0.01x(0.01w + 1)(G_{ss} - G_{st}) + G_{st}} \quad (7)$$

Model 2:

$$\lambda_{mix} = \frac{\lambda_r [2\lambda_r + \lambda_u - 2n(\lambda_u - \lambda_r)]}{2\lambda_u + \lambda_r + n(\lambda_u - \lambda_r)} \quad (8)$$

where λ_{mix} is the thermal conductivity of GRLM for different fabric, λ_r is the thermal conductivity of rubber solid, a_v is the rubber content by volume which can be gained from equation 7, λ_s is the thermal conductivity of loess solid, λ_u is the thermal conductivity of unsaturated loess gained form the literature of Vodek (2012), Θ_{sb} is a continuous path through loess solid contacts which is a fitted value, n is porosity, n_{wm} is miniscule pores filled with fluid and also is a fitted value, λ_w and λ_a are the thermal conductivity of water and air at the testing temperature respectively, S_r is the saturation of GRLM, X is the miniscule pore water retention factor that is dependent on loess texture and more details can reference the literature of Vodek (2012), x is rubber content by weight, w is water content, G_{ss} and G_{st} are the specific gravity of loess solid and granulated rubber respectively.

The performance of model 1 and model 2 were evaluated with respect to experimental data (λ_{exp}) using the root-mean-squared error (RMSE):

$$RMSE = \sqrt{\frac{1}{N} \sum_{1}^{N} (\lambda_{exp} - \lambda_{pre})^2} \quad (9)$$

where λ_{pre} is the predicted data by either Equation 1 or Equation 8, and N is the total number of sample data. The predicted data and their corresponding RMSE for the two models are listed in Table 2 and Table 3.

For GRLM, model 1 of low rubber content has slightly better predictions than model 2 for high rubber content. However, the accuracy of the thermal conductivity prediction is restrictive of many factors, e.g. dispersions of testing data for high rubber content samples, testing method suitability, and test methods accuracy of some important parameters (λ_{u-dry}, λ_{u-sat}, Θ_{sb}, n_{wm}, X, λ_s).

Table 2. Performance of model 1.

Soil code	a_v (%)	S_r (%)	n (–)	λ_{pre} ($Wm^{-1}K^{-1}$)	λ_{exp}
c1w1	22.57	56.61	33.61	1.15	1.29
c1w2	22.42	49.89	34.75	1.08	1.01
c1w3	22.04	37.83	36.39	0.96	0.92
c1w4	21.36	21.40	37.11	0.74	0.80
c1w5	22.83	66.16	32.66	1.22	1.31
c1p1	22.42	50.06	34.77	1.08	1.01
c1p2	22.35	50.50	33.73	1.11	1.17
c1p3	22.65	46.39	38.98	0.97	1.03
c1p4	22.44	50.22	34.87	1.08	1.03
c2w1	39.73	52.47	30.66	0.79	0.84
c2w2	38.58	32.85	30.92	0.69	0.98
c2w3	38.96	33.38	34.43	0.65	0.86
c2w4	38.23	24.83	32.84	0.61	0.80
c2w5	40.55	64.80	31.09	0.81	1.01
c1w1	22.57	56.61	33.61	1.15	1.29

RMSE = 0.14
Note: $\lambda_s = 3.92\,W_m^{-1}K^{-1}$, $n_{wm} = 0.078$, $\Theta_{sb} = 0.021$ (Tarnawski, et al. 2010)

Table 3. Performance of model 2.

Soil code	a_v (%)	S_r (%)	n (–)	λ_{pre} ($Wm^{-1}K^{-1}$)	λ_{exp}
c3w1	45.40	45.40	32.62	0.89	0.72
c3w4	33.06	33.06	27.81	0.81	0.58
c3p1	50.40	50.40	28.07	0.93	0.70
c4w2	38.23	38.23	29.88	0.92	0.72
c4p1	51.05	51.05	25.41	0.98	0.78
c4p3	36.12	36.12	30.69	0.84	0.74
c5w2	30.75	30.75	27.97	0.93	0.57
RMSE = 0.23		$\lambda_r = 0.19$ ($Wm^{-1}K^{-1}$)			

5 CONCLUSIONS

This study prevents a convenient Transient Plane Source (TPS) method to measure the thermal conductivity of unsaturated Granulated Rubber and Loess Mixtures (GRLM). The effects of rubber content, water content, and compaction energy on the thermal conductivity have been investigated. The salient conclusions that can be drawn from this investigation are as follows:

1. The thermal conductivity decreased as the rubber content increased. This is due to the low thermal conductivity of granulated rubber; and
2. The thermal conductivity increased as water content increased. When the rubber content exceeds 40%, the water content has a minor influence on the thermal conductivity due to the high draining capacity of granulated rubber.
3. The thermal conductivity of low rubber content GRLM increased as compaction effort increased. For High rubber content (>40%), the increasing trend was not obvious after some compaction energy. This is due to elastic of rubber solids which reduced the effect compaction energy.

More importantly, two composite models have been introduced in this study to predict the thermal conductivity of unsaturated GRLM. It is expressed in terms of thermal conductivity and volume content of each GRLM phase and some fitted parameters to form four-phase porous system. The proposed models have been validated using the thermal conductivity test results in this study. The Predictions of the proposed model agreed with the measured results. More study need to perform on the thermal conductivity of loess solids and fitted parameters.

REFERENCES

Abdel-Hadi, O.N., & Mitchell, J.K. 1981. Coupled heat and water flows around buried cables. J. Geotech. Engrg Div., 107(11), 1461–1487.

Bernal, A. 1996. Laboratory study on the use of tire shreds and rubber-sand in backfills and reinforced soil applications. Ph.D. Thesis, the University of Purdue.

Duffy, D.P., 1995. Using Tire Chips as a Leachate Drainage Layer. Waste Age, September, pp. 113–122.

Edeskär, T. 2006, Use of tire shreds in civil engineering applications technical and environmental properties, Ph.D. Thesis, Luleå University of Technology, Luleå (In Swedish).

Farouki, O.T. 1986. Thermal Properties of Soils (Trans Tech Publication, Zurich).

Foose, G.J. 1993. Shear Strength of Sand Reinforced with Shredded Waste Tires. *MS Thesis*, Department of Civil and Environmental Engineering, University of Wisconsin, Madison.

Garga, V.K. & O'Shaughnessy V. 2000. Tire-reinforced earth fill. Part 1: Construction of a test fill, performance, and retaining wall design. Can Geotech. J. 37:75–96.

Gera, F., Hueckel, T. & Peano, A. 1996. Critical issues in modeling of the long-term hydro-thermal performance of natural clay barriers. Planet. Space Sci., 52, 91–99.

Ghazavi, M. 2004. Shear strength characteristics of sand-mixed with granular rubber. Geotechnical and Geological Engineering, 22:401–416.

Hoor, A., Rowe, R. K. & F. ASCE. 2011. Application of Thermal Insulation in Landfill Liners. Geo-Frontiers ASCE 2011. 1034–1045.

Humphrey, D.N. & Manion, W.P. 1992. Properties of Tire Chips for Lightweight Fill. Grouting, Soil Improvement and Geosynthetics, Vol. 2, Geotechnical Special Publication No. 30, ASCE, 1344–1355.

Humphery, D. N., Chen, L. H. & Eaton, R. A. 1997. Laboratory and field measurement of the thermal conductivity of tire chips for use as sub grade insulation. Transportation Research Board, 76th Annual Meeting, Washington D.C.

Kasubuchi, T. & Natl, B. 1982. Inst. Agric. Sci. Ser. B33, 1

Lee, J.H., Salgado, R., Bernal, A. and Lovell, C.W. 1999. Shredded Tires and Rubber- Sand as Lightweight Backfill. Journal of Geotechnical and Geoenvironmental Engineering, February, pp. 132–141.

Li, Z.H. & Zhang, H.Y. 2012. Shear strength properties of granulated rubber and loess mixtures. Rock and Soil Mechanics. Vol. 32, No. 10, 3013–3019 (in Chinese).

Li, Z.H. & Zhang, H.Y. 2010. Compaction properties of granulated rubber and loess mixtures. Rock and Soil Mechanics. Vol. 31, No. 12, 3715–3720 (in Chinese).

Li, Z.H. & Zhang, H.Y. 2011. Compression properties of granulated rubber-loess mixtures as fill materials. Applied Mechanics and Materials. Vols. 71–78, 673–676.

Masad, E., Taha, R., Ho, C. & Papagiannakis, T. 1996 Engineering Properties of Tire/Soil Mixtures as a Lightweight Fill Material. Geotechnical Testing Journal, ASTM, Vol. 19, No. 3, 297–304.

Maxwell, J.C. 1954. A treaties on Electricity and Magnetism. 3rd edition. New York: Dover.

M-Lepage J. & Dore G. 2012. Thermal effectiveness of the mitigation techniques tested at Beaver Creek Experimental road site based on a heat balance analysis (Yukon Canada). Cold Regions Engineering: Sustainable Infrastructure Development in a Changing Cold Environment ASCE 2012. 42–51.

Moo-Young, H., Sellasie, K., Zeroka, D. & Sabnis, G. 2003. Physical and chemical properties of recycled tire shreds for use in construction. J. Environmental Engineering, 129(10), 921–929.

Reddy, K.R. & Saichek, R.E. 1998. Characterization and Performance Assessment of Shredded Scrap Tires as Leachate Drainage Material in Landfills. Proceedings of the Fourteenth International Conference on Solid Waste Technology and Management, Philadelphia, PA.

Shuler, S. & Estakhri, C. 1993. Recycled tire rubber as an asphalt modifier. Use of waste materials in hot-mix asphalt, ASTM STP 1193, H. Fred Waller, ed, American Society for Testing and Materials, Philadelphia, pp. 39–68.

Shao, J. & Zarling, J. P. 1995. Thermal conductivity of recycled tire rubber to be used as insulating fill beneath roadways. Alaska Department of Transportation and Public Facilities. Report No. SPR-UAF-9309A.

Slegel, D.L. & Davis, L.R. 1977. Transient heat and mass transfer in soils in the vicinity of heated porous pipes. J. Heat Transfer, 99, 541–621.

Tarnawski, V.R., Momose T., Leong, W.H. & Wagner, B. 2010. in Proceedings of ASTM-ATI-UIT 2010 Conference, Vol. II, p. 969.

Tweedie, J.J., Humphrey, D.N. & Sanford, T.C. 1998c Full-Scale Field Trials of Tire Shreds as Lightweight Retaining Wall Backfill Under At-Rest Conditions. Transportation Research Record 1619, Transportation Research Board, National Research Council, Washington, D.C., 64–71.

Vlodek, R. Tarnawski, Leong, W.H. 2012. A series-parallel model for estimating the thermal conductivity of unsaturated soils. Int J Thermophys 33:1191–1218.

Woodside, J.H. & Messmer, J. 1960. Molecular effects in heat conduction through porous rocks. Journal of Geophysical Research Vol. 65, No. 10, 3481–3485.

Youwai, S. & Bergado, D.T. 2003. Strength and Deformation Characteristics of Shredded Rubber Tire-Sand Mixtures. Canadian Geotechnical Journal, Vol. 40, No. 2, 254–264.

Zhu, B.Z., Cheng, G., Wang, Y. & Xu, M.L. 2014. Review of recycling utilization for waste tire in China. J. Guangzhou chemical industry, Vol. 42, No. 9, 11–12.

Zornberg, J.G., Cabral, A., & Viratjandr, C. 2004. Behavior of tire shred-soil mixtures. Canadian Geotechnical Journal, 41(2), 227–241.

Unsaturated Soil Mechanics—from Theory to Practice – Chen et al. (Eds)
© 2016 Taylor & Francis Group, London, ISBN 978-1-138-02921-7

Laboratory study on drainage-seepage controlling of fine/coarse structure in unsaturated expansive soil slope

Q.H. Wu
Key Laboratory of Geotechnical Mechanics and Engineering of Ministry of Water Resources, Changjiang River Scientific Research Institute, Wuhan, China
Three Gorges Research Center for geo-hazard, Ministry of Education, China University of Geosciences, Wuhan, China

J.F. Zhang, G.S. Zhu, H.D. Cui & X.Y. Liu
Key Laboratory of Geotechnical Mechanics and Engineering of Ministry of Water Resources, Changjiang River Scientific Research Institute, Wuhan, China

ABSTRACT: Drainage-seepage controlling of expansive soil slope is one of important scientific problems for the safety of south-to-north water transfer project in China. A dual structure of capillary barrier, i.e., a cover system commonly consisting of a relatively fine soil layer over a relatively coarse soil layer, was introduced. The aim of this article was to investigate how the particle size and grain grading of the coarse soil affected the capillary barrier effect. Therefore, six trials (the particle sizes decreased from scheme 1 to scheme 6) were conducted. The results showed that preferential flow was more obviously in coarse soil with larger particle size and poorer grain size distribution. Steady drainage efficiencies referring to the ratio of steady drainage intensity to the rainfall intensity, were 91%, 80%, 86%, 100%, 100% and 97%, respectively. Therefore, the capillary barrier effect could be controlled by both the particle size and grain size distribution.

1 INTRODUCTION

The cracks formed in expansive soil during the process of the dry-wet cycle, which resulted in rainfall infiltrating rapidly soil, and lower mechanical strength. The south-to-north water transfer middle project has a length of 1400km, 340km of which was in expansive soil zone. The excavation of expansive soil slope could make complete structure and strong stability of expansive soil be exposed to atmosphere if no protect measures, which was easy to induce shallow slide. As early as in 1969, 13 large expansive soil landslides happened in the project of Yin Dan project, and high cost for the slope treatment (Guo et al., 2008). Therefore, in order to ensure the safe operation of the channel of south-to-north water transfer project, expansive soil slope stability is one of the most critical technical problems. A dual structure (hereinafter referred to as CB, Capillary Barrier), i.e., fine/coarse soil structure, was suggested to deal with drainage and seepage of the expansive soil slope, although the materials of cement panel and geotextile were generally used to deal with the drainage problem successfully, but the service life was short and ecological function was poor.

Yang et al. (2004) investigated the CB effect of fine/coarse structures in three soil columns under rainfall, the results showed that the coarse grain layer could prevent effectively water across the boundary layer, and larger particle sizes of the coarse soil for the stronger hindering effect. Kämpf et al. (2003) found that only a small amount of water flowed out when the rainfall intensity was smaller, while preferential flow appeared in the coarse soil for the stronger rainfall. Using dyeing tracer technology, Tidwell et al. (2003) observed directly the soil water transfer process of the CB under rainfall. Tami et al. (2004) studied the CB effect under the condition of different rainfall intensities and duration, implied that the CB effect was controlled by the soil water-holding capacity of the upper fine soil when the rainfall intensity was stronger. Parent and Cabral (2006) investigated the effect of the thickness of the fine soil and lithology structure of CB on the CB effect by simulation method, the results showed that the effect of sand/gravel structure was best.

Zhang et al. (Zhang et al., 2009; Zhang, 1998) analyzed theoretically the advantages and shortages of the traditional techniques, such as concrete slab and geomembrane covering, modified soil and no expansive soil replacing. And the CB structure was suggested to solve the problem of expansive soil landslide of south-to-north water transfer project, since which has the both ecological and drainage-seepage controlling functions. Shi et al. (2004) investigated the effect of sand layer in the middle of clay column on moisture movement, the results revealed that the sand layer

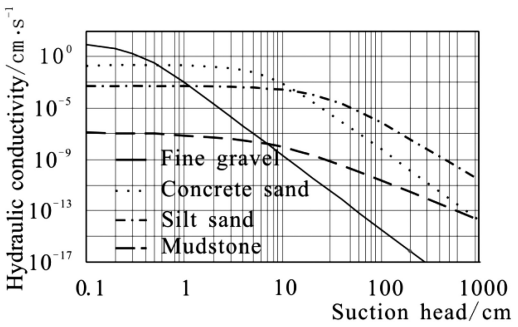


Figure 1. Hydraulic conductivity vs. suction for several soil medium.

hindered soil capillary from rising, and decreased its migration rate. Qin et al. (2010) focused on the thickness and slope angle of CB, the research revealed that the CB effect was stronger with larger thicknesses and slope angles, but was weaker with higher rainfall intensity. However, Deng et al. (2012) found that rainfall could infiltrate into the coarse soil layer when rainfall intensity was larger than the maximum drainage capacity of fine layer, and the CB effect could be improved by increase the rainfall intensity.

In this paper, the influence of particle size and grain size distribution on the drainage and seepage efficiency of CB was investigated, applying Brilliant Blue FCF (C.I. 42090) dye tracer. The results of the study could be applied directly to the expansive soil slope of the south-to-north water transfer project as well as to nuclear waste and landfill pollutants anti-seepage treatment, etc.

2 MATERIALS AND METHODS

2.1 *Test principle*

Soil hydraulic conductivity increased exponentially with decreasing soil suction, increased degree of which was greater with larger soil particle size, shown in Figure 1. The dual-structure was defined by fine/coarse structure, i.e., fine soil was on the top of the coarse soil. In theory, the unsaturated hydraulic conductivity of the fine soil was larger than the coarse soil when the suction head was higher than the critical head (i.e., it is the suction head when hydraulic conductivities of fine and coarse soil are equal), therefore, the coarse could prevent the rainfall from infiltrating.

2.2 *Physical model*

The physical model was a rectangular, mainly composed of soil column, rainfall system and drainage system, shown in Figure 2. In order to observe directly the process of soil water transfer, the material of model was chosen as organic glass, and the Brilliant Blue FCF (C.I. 42090) dye tracer was added to the rainfall. The sizes of rectangular and rainfall system were 20 cm (long) × 16 cm (wide) × 20 cm (high) and

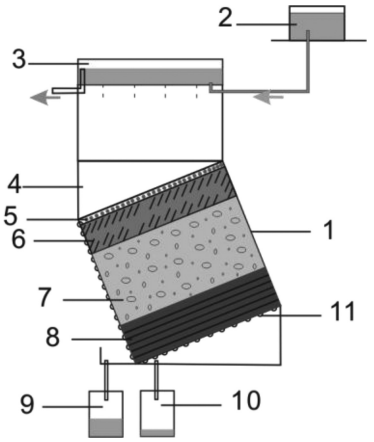


Figure 2. Physical mode.
1-soil column 2-water supply system 3-rainfall simulator 4-wedge (slope degree 22°) 5-gravel layer 6-fine soil 7-coarse soil 8- slope soil 9-collecting system for left face 10-collection system for the bottom 11-porous plate.

20 cm (long) × 16 cm (wide) × 16 cm (high), respectively. The bottom and left face which were made of porous plate were both freely seepage boundaries, and the boundary at the top was opened to atmosphere for rainfall. The other sides were all impermeable boundary.

2.3 *Soil sampling and filling*

The fine soil, coarse soil and slope soil were all collected in Nanyang city of Henan province. The soil particle composition and physical parameters were shown in table 1. The all soil sample needed to be air-dried for15 days, then sieved. There were 6 types of coarse soil. All samples were filled in the physical model according to their dry bulk densities, and compacted manually per 2cm height of soil. The initial mass water content of the fine soil, coarse soil and slope soil were 10%, 3% and 10%, respectively.

2.4 *Test scheme*

Six test schemes were designed as shown in Table 2. The rainfall intensity was all 3.60×10^{-4} cm/s, and no runoff formed on the soil surface. The infiltration processes were photographed by a digital camera. The drainage at the left face and seepage at the bottom were both collected by two beakers.

3 RESULTS AND DISCUSSION

The infiltrated patterns were influenced by both the grain size and grain grading of the coarse soil. The soil water transport pattern could Brilliant Blue FCF (C.I. 42090) dye with a characters of easily dissolvable and no-adsorptive, which could be obtained by shooting

Table 1. Soil particle composition and physical parameters.

Sample	Soil type	Particle distribution/% 10–20 mm	5–10 mm	2–5 mm	1–2 mm	0.075–1.0 mm	0.005–0.075 mm	<0.005 mm	Dry bulk density/ ($g \cdot cm^{-3}$)	Saturated hydraulic conductivity/ ($cm \cdot s^{-1}$)
Fine soil	Sandy loam	–	–	–	–	54.6	40.7	4.3	1.55	5.16×10^{-4}
Coarse soil 1		27	73	–	–	–	–	–	1.70	1.77
Coarse soil 2	Fine gravel	10	50	40	–	–	–	–	1.70	1.34
Coarse soil 3		–	50	50	–	–	–	–	1.70	1.59
Coarse soil 4		–	25	50	25	–	–	–	1.70	1.39
Coarse soil 5		–	–	50	25	25	–	–	1.70	0.29
Coarse soil 6	Gravel sand	–	–	25	50	25	–	–	1.70	0.15
Slope soil	Clay	–	–	1.6	1.5	9.9	55.4	31.6	1.60	5.3×10^{-6}

Table 2. Test scheme.

Test scheme	Rainfall intensity ($\times 10^{-4}$cm/s)	Rainfall duration (min)	Initial mass water content (−)
1	3.50	380	
2	3.50	302	Fine soil was 10%
3	3.50	300	
4	3.50	340	Coarse soil were 3%
5	3.50	320	Slope soil was 10%
6	3.50	380	

photos at representative times, shown in Figure 3 (for scheme 4) and Figure 4 (for scheme 6).

3.1 *Dyeing Characters*

Scheme 1

(1) The fine soil: The drainage started 30min after the beginning of the rainfall. After rainfall, the soil was excavated. We found that the soil moisture content was low, showing a fine drainage effect. (2) The coarse soil: The preferential flow developed highly. At 160 min, the rainfall flowed out from the interface of coarse soil and slope soil, named by C-P interface. When the rainfall was over, the drainage finished simultaneously. The soil moisture content was very high in the region of 3 cm depth over the C-P interface when the rain stopped. (3) The slope soil: 1 cm thickness of soil was dyed completely, and soil water content was very high. At the bottom of the soil column, some water drops formed, but no-continue water flow. In all, the drainage and seepage effect of scheme 1 was poor.

Scheme 2

(1) The fine soil: The drainage happened during 112 min to 172 min after the beginning of the rainfall, but the flow rate was very low. (2) The coarse soil: The soil water movement pattern was preferential flow. At 85 min, the rainfall flowed out from the C-P interface. The drainage process continued for 40min after rainfall. (3) The slope soil: At 268 min, some water drops formed at the bottom of the soil column, but no water flow developed. 0.5 cm–1 cm depth of soil was dyed completely under the C-P interface. In all, the drainage and seepage effect of scheme 2 was also poor.

Scheme 3

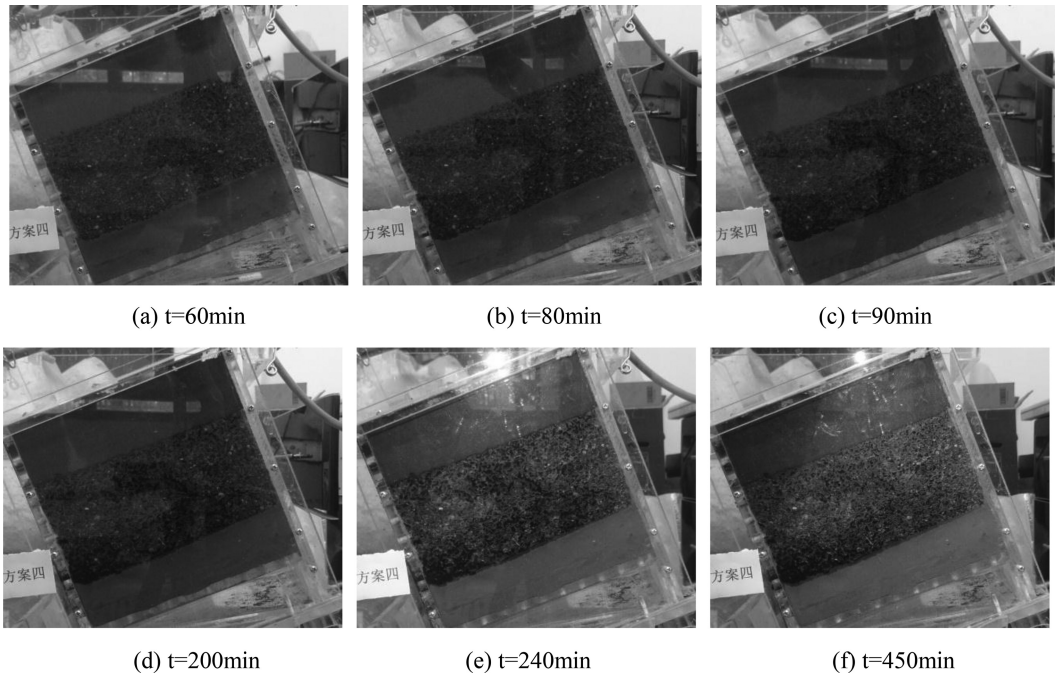
(1) The fine soil: The drainage happened during 44 min to 60 min after the beginning of the rainfall, but the flow rate was very low. (2) The coarse soil: The preferential flow developed. At 66 min, two preferential paths formed at 5 cm apart from the left side, and rainfall infiltrated quickly into the C-P interface. Then the soil was saturated, and soil water started to drain. After rainfall, 90% of the coarse soil was dyed, and the drainage process continued for 40 min. (3) The slope soil: No water drops formed at the bottom. Only 0.5 cm thickness of soil was dyed under the C-P interface. Overall, the drainage and seepage effect was better than the scheme 1 and scheme 2.

Scheme 4

(1) The fine soil: At the left boundary, only some water drops formed at 50min after the beginning of the rainfall, but no continual water flow. (2) The coarse soil: At 80 min, two preferential paths formed at 2 cm and at 10 cm apart from the left side, respectively, and rainfall infiltrated quickly into the C-P interface. Over the C-P interface, 0.2–0.4 cm depth of dyed water formed, where soil water started to drain. At 200 min, the dyed regions of the coarse soil layer were completely continuous, implying that a continuous horizontal flow field appeared where the rainfall could be drained rapidly and effectively. After rainfall, 95% of the coarse soil was dyed, and the drainage process continued for 110 min. About 4 cm depth over the C-P interface, the soil was saturated. (3) The slope soil: No water flowed out from the bottom. Only 0.2–0.4 cm depth of soil was dyed under the C-P interface. Overall, the drainage and seepage effect was good.

Scheme 5

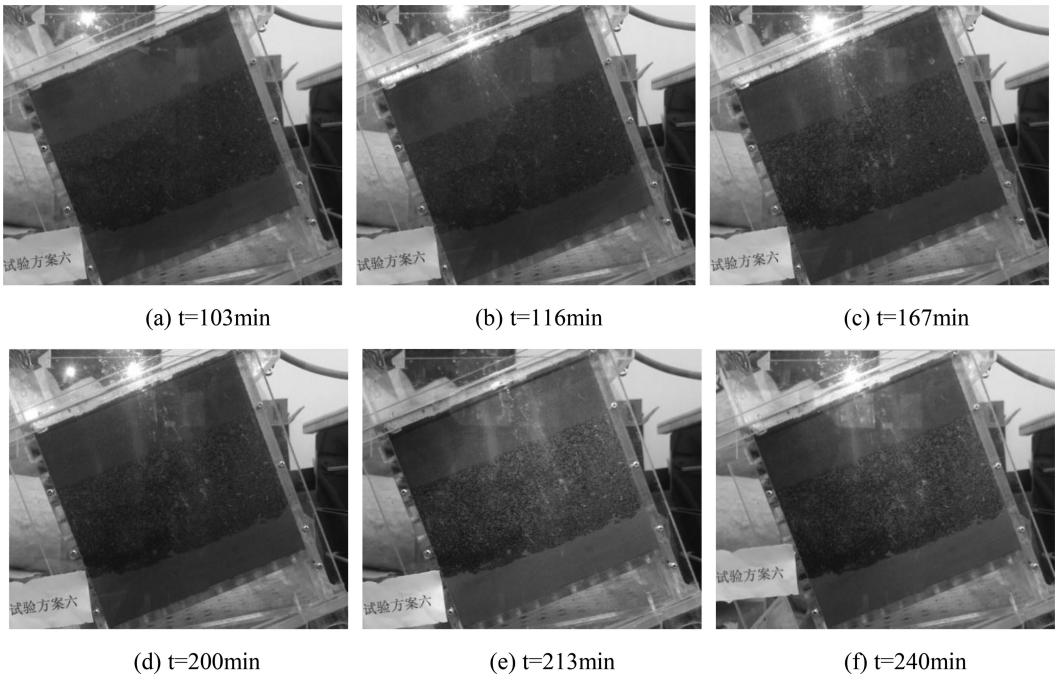
(1) The fine soil: No water drained out. (2) The coarse soil: At 80 min, the rainfall infiltrated uniformly into the C-P interface, and no preferential flow appeared. The uniform-continuous-horizontal seepage field started to form, which accelerated rainfall



(a) t=60min (b) t=80min (c) t=90min

(d) t=200min (e) t=240min (f) t=450min

Figure 3. The soil water transport matter of the test scheme 4 at representative times.



(a) t=103min (b) t=116min (c) t=167min

(d) t=200min (e) t=213min (f) t=240min

Figure 4. The soil water transport matter of the test scheme 6 at representative times.

drainage horizontally. No water flowed out from the interface until at 110 min. At 280 min, the coarse soil was dyed completely. (3) The slope soil: No water flowed out from the bottom. Only 0.1–0.2 cm thickness of soil was dyed under the C-P interface. Overall, the drainage and seepage effect was better than scheme 4.

Scheme 6

The characteristics of soil water transport in the three types of soils were the same as the

Table 3. Evaluated results of drainage-seepage controlling for the 6 test schemes.

Scheme	Rainfall intensity (10^{-4}cm/s)	Initial drainage time (min)	Continued drainage time after rainfall (min)	Stable drainage intensity (10^{-4}cm/s)	Stable drainage effect(%)	Total drainage effect(%)
1	3.50	24	0	0.32	91	43
2	3.50	85	40	0.28	80	56
3	3.50	44	40	0.30	86	69
4	3.50	60	110	0.35	100	79
5	3.50	87	80	0.35	100	71
6	3.50	112	–	0.34	97	–

scheme 5. According to the 6 test schemes, the drainage and seepage effect of the scheme 6 was best.

3.2 *Analysis of Drainage and Seepage Controlling*

The drainage intensity increased gradually, and reaches a stable value after some time. Then it would decrease gradually when the rainfall was over. Two parameters, i.e., stable drainage efficiency and comprehensive drainage efficiency, were applied to evaluate the drainage-seepage controlling effect, and the evaluated results were shown in Table 3. Stable drainage efficiency referred to the ratio of stable drainage intensity to the rainfall intensity, while comprehensive drainage efficiency referred to the ratio of the whole drainage volume, containing rainfall and no-rainfall periods, to the rainfall volume. The stable drainage efficiencies of the six schemes were 91%, 80%, 86%, 100%, 100% and 97%, respectively. Comparing the results of scheme 1 and scheme 2, the preferential flow of the coarse soil with a greater grain size was more obviously, resulting in that the rainfall would infiltrate quickly into the coarse soil and flowed out. Therefore, the stable drainage efficiency of the dual structure for scheme 1 was larger than scheme 2. As the particle size became smaller, and grain grading was better, the porosities were smaller resulting in an uniform-continuous-horizontal seepage field and higher stable drainage efficiencies, e.g., the stable drainage efficiencies of the schemes of 4, 5 and 6 were closed to the rainfall intensity. The comprehensive drainage efficiencies of scheme 1, 2, 3, 4 and 5 were 43%, 56%, 69%, 79% and 71%, respectively. The parameter increased firstly with smaller grain size and poorer grain grading, and then decreased.

The drainage-seepage ability of the fine/coarse soils was controlled mainly by the particle size and distribution of the coarse. Bigger particle size and poorer grain grading could induce easily the preferential flow phenomena, accelerating the rainfall infiltrating into the coarse soil and reaching at the C-P interface, which resulted in a poor drainage-seepage controlling. The main reasons: (1) Although the rainfall could infiltrate quickly into the coarse soil layer from the interface of fine soil and coarse soil since the preferential flow developed, the seepage paths were all nearly vertical direction and independence each other. Therefore, it was difficult for rainfall to move laterally in the coarse soil. Almost rainfall infiltrated into the C-P interface by the preferential paths, which increased the risk that rainfall infiltrated into the slope soil. (2) The particle size of the schemes 4, 5 and 6, were smaller than the schemes 1 and 2. Although the initial drainage time was longer, few preferential paths developed, and an uniform- continuous-horizontal seepage field could form. Then most of rainfall quickly flowed laterally, and only a litter water was infiltrated into the slope soil.

In all, the drainage and seepage efficiencies of the schemes 4, 5 and 6 were high, and could be chosen to protect the slope from rainfall infiltrating. However, the comprehensive drainage efficiency of the scheme 4 was highest. In addition, 25% of fine soil with a particle size region of 0.075–1.0 mm was added into both the schemes 5 and 6, which would increase the cost of material. Therefore, the scheme 4 was suggested as the best scheme to prevent the rainfall from infiltrating into the slope soil.

4 CONCLUSIONS

The dry-wet cycle of expansive soil could result in fissures when expansive soil was exposed to atmosphere. Therefore, it was necessary to deal with the expansive soil slope in south-to-north water transfer project water supply project in China. Six test schemes were carried out to investigate the drainage-seepage controlling of a fine/coarse soils structure, using the Brilliant Blue FCF (C.I. 42090) dye tracer. Coarse soils with larger particle size and poorer grain grading could develop easily preferential flow which decreased the drainage efficiency and increased the risk that rainfall infiltrated into the slope soil. The stable drainage efficiency for the schemes 1, 2, 3, 4, 5 and 6 were 91%, 80%, 86%, 100%, 100% and 97%, respectively, while the comprehensive drainage efficiencies (except the scheme 6) were 43%, 56%, 69%, 79% and 71%, respectively. Considering the cost of material, the scheme 4 was the best choice to protect the expansive soil slope. The research results could be applied directly to the expansive soil side slope and seepage controlling of slopes in projects. In fact, the texture of the fine soil and rainfall pattern (e.g., rainfall intensity and rainfall time

and frequency) could influence the drainage-seepage effect of the dual structure. Also, the model scale was also a problem to find a prefect dual structure.

ACKNOWLEDGMENTS

This study was supported by the National Nature Science Funds of China (41402213 and 51279016), Open Fund of Institute of Hydrogeology and Environmental Geology, CAGS (KF201503), and Open Fund of Three Gorges Research Center for Geo-hazard, Ministry of Education, China University of Geosciences (TGRC201403), and Fund of Foreign Student Science and Technology Activities Project, Ministry of Personnel. PRC (2014). Thanks for all members who participated in field work and offered helpful advice for this study.

REFERENCES

Deng, L.H., Zhang, L.T., Chen, Y.M., et al. 2012. Model tests on capillary-barrier cover with unsaturated drainage layer. *Chinese Journal of Geotechnical Engineering* 34(1):75–80(in Chinese).

Guo, X., Li, Q.Y., Cheng, Z.L., et al. 2008. Geotechnical research in the middle route of south-to-north water transfer project. *South-to-North Water Transfers and Water Science & Technology* 16(1):35–37(in Chinese).

Kämpf, M., Holfelder, T. & Montenegro, H. 2003. Identification and parameterization of flow processes in artificial capillary barriers. *Water Resource Research* 39(10): 21–29.

Parent, S.É., Cabral, A. 2006. Design of inclined covers with capillary barrier effect. *Geotechnical & Geological Engineering* 24(3):689–710.

Qian, T.W., Huo, L.J. & Zhao, D.Y. 2010. Laboratory investigation into factors affecting performance of capillary barrier system in unsaturated soil. *Water Air Soil Pollut* 206:295–306.

Shi, W.J., Wang, Z.R., Shen, B., et al. 2004. Soil capillary water upward movement from sand layered soil column. *Journal of Soil Water Conservation* (6):167–170.

Tami, D., Rahardjo, H., Leong, E.C., et al. 2004. A physical model for sloping capillary barriers. *Geotechnical Testing Journal* 27(32):GTJ11431-272.

Tidwell, V., Glass, R., Chocas, C., et al. 2003. Visualization experiment to investigate capillary barrier performance in the context of a Yucca Mountain Emplacement Drift. *Journal Contam Hydrology* 62(3):287–301.

Yang, H., Rahardjo, H., Leong, E.C., et al. 2004. A study of infiltration on three sand capillary barriers. *Canadian Geotechnical Journal* 41:629–643.

Zhang, J.F. 1988. On the variation of specific yield in response to uniform fall of water table in stratified porous media. *Journal of Hydraulic Engineering* (8):9–17.

Zhang, J.F., Liu, X.M., Jiao, J.J. 2009. A protection scheme of double layers with drainage function for expansive soil slopes by canal. *Journal of Yangtze River Scientific Research Institute* 26(11):37–41.

Unsaturated Soil Mechanics—from Theory to Practice – Chen et al. (Eds)
© 2016 Taylor & Francis Group, London, ISBN 978-1-138-02921-7

Water retention properties of unsaturated coarse-grained soils: The experimental study of the effect of Microbialy Induced Calcite Precipitation

R. Saffari & G. Habibagahi
Department of Civil and Environmental Engineering of Shiraz University, Shiraz University, Shiraz, Iran

E. Nikooee
Department of Earth Sciences, Utrecht University, The Netherlands

A. Niazi
Biotechnology research institute, Shiraz University, Shiraz, Iran

ABSTRACT: The soil water retention curve is one of most fundamental characteristics of unsaturated soils. The soil water retention curve indicates the amount of moisture content of the soil with respect to different values of soil suction. Shear strength, permeability coefficient, and volume change of unsaturated soils are closely related to the soil water retention curve. Therefore, determination of this curve is essential for understanding of the hydraulic and mechanical characteristics of unsaturated soils. Soil improvement is one of the key subjects of geotechnical engineering. In fact, the very first step in understanding the efficiency of various soil-improvement methods for unsaturated soils, is by no doubt, investigating their influences on the soil water retention properties. In recent years, in order to improve the soil mechanical characteristics, a new soil improvement technique (i.e., biological soil stabilization) has been developed which is more compatible with the environment. This technique is based on the so-called Microbially Induced Calcite Precipitation (MICP). In this study, the influence of MICP on the retention properties of an unsaturated coarse-grained soil sample has been explored using pressure plate apparatus experiment. The results of this study revealed that by increasing the amount of bacterial solution, the retention properties of soil samples are considerably affected. The soil water retention alterations are mainly manifested in the change in air entry value of the retention curve as a result of the change in bacterial concentration.

1 INTRODUCTION

1.1 *Soil water retention curve: its place in unsaturated soil mechanics*

The unsaturated soil mechanics was born to scientifically and methodologically answer questions concerning the hydraulic and mechanical behavior of unsaturated soils. In order to describe the behavior of such complex multiphase media, saturation of wetting phase and suction have long been recognized as two important pillars and necessary elements of any constitutive modeling framework for modeling unsaturated soil behavior. The relationship describing the connection of these two variables, known as soil water retention curve, also called Soil-Water Characteristic Curve (SWCC), is, therefore, an important characteristic of these media based on which various formulations for the other mechanical and hydraulic parameters of unsaturated soils have been proposed in the literature (Fredlund & Rahardjo, 1993; Fredlund et al.,1994; Fredlund et al., 1996; Vanapalli & Fredlund, 2000, and Khalili & Khabbaz 1998 among many others).

1.2 *Soil water retention curve: the effect of mechanical, hydraulic and environmental loading*

In order to apply the proposed relationships in the literature for different projects and different practical conditions, thus, one needs to be aware of the effects of the mechanical loading, hydraulic conditions as well as environmental loading (bio-chemical factors) on the soil water retention curves. It is known that the temperature change can alter the retention properties of the unsaturated soils (see for instance Grant & Salehzadeh, 1996; Bachmann et al. 2002, Grant 2003, and Zhou et al. 2014). The retention properties of the same unsaturated soil but at different net stress states are also dissimilar. To model temperature and net stress dependence of the soil retention properties, various experimental, theoretical, and numerical studies have been performed in the literature (see for instance, Ng et al. 2000, Romero et al. 2001, Nuth & Laloui, 2008, Tarantino, 2009, Uchaipichat & Khalili 2009, Salager et al. 2011, Khaksar et al. 2011, Rostami et al. 2013, Tavakoli Dastjerdi et al. 2014). But another group of the important environmental factors

which has not yet been well explored is the effect of microorganisms on the retention properties of unsaturated soils. Such issue (the effect of bio-chemical factors involved therein on the retention properties of unsaturated soil) is of considerable importance in a number of engineering applications, an outstanding example of which is the biological soil improvement techniques. These techniques utilize either the local soil ecosystem and in situ microorganisms (endogenous microorganisms) or the exogenous ones (external sources of non-pathogenic microorganisms) and rely on different bio-chemical processes such as microbial induced calcite precipitation, and subsequent changes in the soil micro-fabric such as bio-clogging and bio-cementation.

The soil biological improvement has successfully been applied for different purposes ranging from increasing shear strength of coarse-grained soils, mitigating the liquefaction potential and reducing internal erosion susceptibility (Al Qabany, 2011; Montoya et al., 2012, 2013; De Jong et al. 2013; Jiang et al. 2014, Kavazanjian & O'Donnell, 2015) to reducing the swelling and collapse potential in fine-grained problematic soils (Sadjadi et al. 2014, Morales et al. 2014, Nikeghbal et al. 2015). But for the reason that soil liquefaction can also happen in unsaturated soils (Liu & Muraleetharan 2012), and swelling and collapsible soil undergo dramatic volume changes mainly in their unsaturated state, therefore, the first step to understand and simulate the biologically improved fine grained and coarse grained soils involved in such applications is to understand the effect of biological stabilization on such soils in unsaturated state. Hence, understanding the alterations of the soil water retention curves under biological stabilization is an important key to move forward.

Up to authors' knowledge, the effect of bio-geo-chemical processes and factors involved in biological soil improvement techniques on soil fabric (micro- and macro-fabric) and subsequently on the retention properties of unsaturated soils has not yet been comprehensively studied in the literature. Therefore in this study, as the first step for this purpose, the effect of biological soil improvement on the water retention properties of coarse-grained soil samples has been studied and main parameters of the soil water retention curve which are affected by the microbial soil stabilization have been referred to. Moreover, the potential contributing mechanisms have been described. Finally concluding remarks have been made and further research directions have been described.

2 MATERIALS AND METHODS

2.1 *Sample preparation and experimental procedure*

Based on the results from the sieve analysis (and based on ASTM2487 standards) and following the Unified Soil Classification System (USCS) the prepared soil sample is designated as sand. In order to investigate the effect of biological treatment on the retention properties of unsaturated soils, soil samples were treated with the solutions of Bacillus Sphaericus Bacteria which is one of the known active microorganisms commonly used in microbial induced calcite precipitation. Lyophilized ampules of Bacillus Sphaericus Bacteria under strain name of PTCC 1487 were obtained from Iranian Organization of Scientific Research (IROST). Ingredients of the culture media which was used to cultivate bacteria are described in the Table 1. The ingredients of culture media except Urea were poured into distilled water and the resulting solution was autoclaved for 20 minutes at 120 C. Urea was then added by means of a filter paper (with opening size of 0.22 micrometer).

Table 1. Culture medium composition.

Components of liquid culture media	Amount (gr/lit)
Sodium bicarbonate	2.12
Nutrient broth	3
Ammonium chloride	10
Yeast extract	20
Urea	10

Here, we focus on the effect of bacterial concentration of the solution on the change in the retention properties of unsaturated soils. To measure/quantify the bacterial concentration of the solution, usually, the optical density of the solution is measured by the photo-spectrometer. In this study in order to obtain the optical density of the solution, the following procedure was followed: The system was calibrated with the culture media without bacteria to obtain the reference number (i.e., the number shown by the system for culture media was considered as the basis number). Then, the optical density measurement of the bacterial solution was performed with regard to the basis value. In order to determine the required time for the growth of bacteria, the bacterial growth rate curve was obtained. The growth rate curve is a curve based on which the required time for arriving at a certain optical density can be found. The growth rate curve obtained in this study for bacillus Sphaericus is presented in Figure 1.

To prepare the soil samples, the samples were kept in closed-lid containers which were able to preserve the moisture constantly for 24 hours. After 24 hours, wet soils were then statically compacted. The compaction rate was set to 2 mm per minute. The compacted and treated samples were then kept in zipped plastic containers for 4 days. After 4 days, the soil water retention curves of the treated and control samples were obtained by means of a pressure plate apparatus.

3 RESULTS AND DISCUSSION

3.1 *The obtained soil water retention curves*

The obtained soil water retention curves have been presented in figure 2. The Van Genuchten (VG) parameters obtained from fitting the VG formula to the

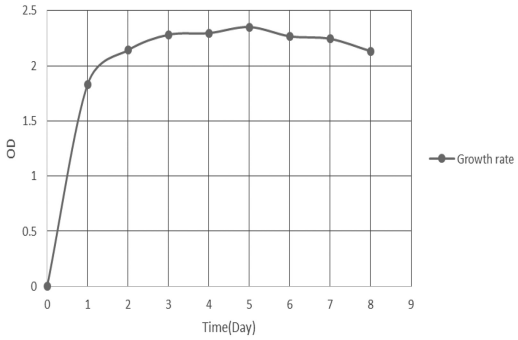


Figure 1. Growth rate diagram for the bacillus sphaericus used in this study (od in vertical axis stands for optical density, a measure of bacterial concentration).

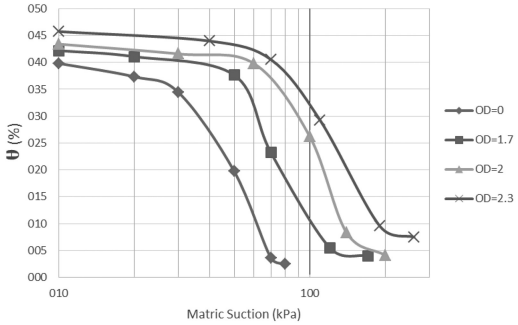


Figure 2. Soil water retention curves of coarse-grained samples mixed with treatment solution 12%.

curves have been presented in table 2. The VG formula reads as:

$$\theta = \theta_r + \frac{(\theta_s - \theta_r)}{\left[1 + (\alpha \mathrm{h})^n\right]^m} \quad (1)$$

Where θ is water content, h is matric suction, r denotes the residual and s specifies the saturated state, respectively. α, n, and m are Van Genuchten parameters.

Van Genuchten parameters have been presented in Table 2.

3.2 *The role of different bio-chemical mechanisms, and the effect of bacterial concentration*

The variation of α-parameter of Van Genuchten which is closely related to the air entry value of soil is depicted in figure 3. As it can be seen by increasing the bacterial concentration, α-parameter decreases. We attribute this change to the change in soil micro-fabric. The microbial-induced calcite precipitation results in the so-called bio-clogging and bio-cementation which eventually lead to the alteration of the soil porous network, and finally, an increase in the air entry value. The soil porous network is composed of pores and throats which connect the adjacent pores (Rostami et al. 2013). The drainage process is mainly controlled

Table 2. Van Genuchten parameters obtained for the biologically treated sand at various bacterial concentrations.

OD	0	1.70	2.0	2.30
α	0.021	0.015	0.01	0.009
n	6.320	6.343	6.731	4.573
θ_r	0	3.743	2.988	4.943
θ_s	37.860	41.660	41.950	44.760

by the size of the throats. It can, hence, be deduced that the size of throats has considerably been influenced by the microbially induced calcite precipitation. Throats are smaller than pores and therefore, their morphology, size and shape can be more prone to alteration by the bio-clogging and bio-cementation. The observed change in the drying retention curves in general, and in the air entry value in particular confirms this expectation. The higher the bacterial concentration is, the more pronounced the bio-clogging and bio-cementation effects, the higher the throat size change, and consequently, the higher the air entry value would become. Furthermore as Table 2 reveals, the residual water content has also been increased by increasing the bacterial concentration. Such an increase in the residual water content can be attributed to an increase in the number of fully clogged throats as a result of an increase in amount of precipitated crystals. An increase in the number of fully clogged throats in the soil porous network leads to more water entrapment (more disconnected and entrapped water clusters) at higher suction values and eventually, an increase in the residual water content. Moreover, an increase in the saturated water content is observed. There are two bio-chemical mechanisms which control saturated water content. In fact, generation of different gaseous chemical components like CO_2, and nitrogen during the involved chemical reactions and generation of bio-film and bio clogging can affect the porous structure and water content in two different ways. The net effect of the two and the competition between the two can result in either an increase or a decrease in saturated water content. Here, an increase in saturated water content has been observed. Further experiments are required to make a better evaluation of these alterations in the water retention curves and to clearly understand the role of the aforementioned mechanisms.

3.3 *The importance of soil type*

An important issue which needs to be discussed here is the role of soil type. As it can be seen in figure 1, in this study an increase in bacterial concentration resulted in a continuous (monotonic) increase of air entry values (a decrease in α-parameter as revealed by Figure 3) and continuous upward movement of soil water retention curve (i.e., continuous increase of suction value associated with each saturation level, Figure 2). We should note that this observation may not hold for fine-grained soil samples where the complex interplay of bio-

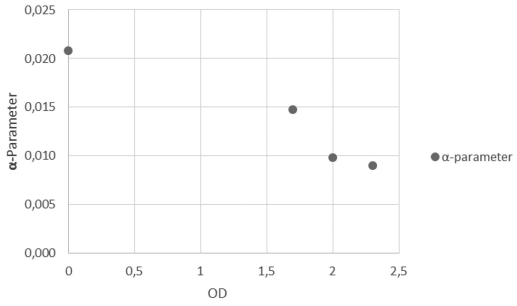


Figure 3. α-parameter of Van Genuchten versus bacterial concentration.

geo-chemical factors and the soil micro- and macro-fabric both should be considered. Here, the only influential factor on the retention properties of the considered soil sample is supposed to be the effect of microorganisms on the pore size distribution, and in a general term, on the porous structure of the soil. Whereas in fine grained-soils, many more possible interactions should be considered such as the effect of microorganisms on the soil micro-fabric, interlayer cations, and so forth. Accordingly, a simple monotonic trend (a monotonic increase in air entry value with the bacterial concentration) may not occur as observed in this study. This, of course, needs to be further elucidated in course of future experiments on fine-grained soils to explore the change in retention properties of finer grained soils as influenced by the microbial induced calcite precipitation and the difference in the response of coarse- and fine-grained soils to such bio-chemical alterations has to be determined carefully.

4 CONCLUDING REMARKS AND FUTURE RESEARCH DIRECTIONS

In this study, the effect of bacillus sphaericus on the water retention properties of unsaturated coarse-grained soil samples has been studied. The results revealed that the major influence of the bacillus sphaericus on the retention proprieties of unsaturated soils is increasing the air entry value of soils. It is hypothesized that the bacterial induced calcite precipitation results in an increase in the number of pores of smaller radii which contribute to the saturation level associated with each suction value. This phenomenon eventually results in an upward movement of soil water retention curves and an increase in the air entry values. In addition to that, the change in the throat size and the number of the fully clogged throats of the soil porous network are also postulated as two possible mechanisms behind the observed changes in the air entry value and residual water content of the soil, respectively. It seems that the saturated water content is mainly controlled by the competition between bio-gas generation and the bio-clogging and bio-cementation processes and the net physical effect of the two.

Supplementary experiments such as Mercury Intrusion Porosimetry (MICP) are, therefore, recommended to assess the pore size distribution of biologically treated soils and to further explore such alterations. Cautionary remarks were given not to generalize these results to fine-grained soils where the complex chemical interaction of soil pore fluid cations with the clay platelets can be of major contribution and can change the observed trend at various bacterial concentrations. To make further progress on this topic, pore fluid chemistry tests, biogas measurement and analysis of micro-fabric of the treated soils samples are the subject of ongoing work by the authors. A detailed analysis of the dependency of the observed trends on the soil type can, moreover, be considered as the suggested research direction for future studies on this topic.

REFERENCES

Al Qabany, A. 2011. *Microbial carbonate precipitation in soils*. Doctoral dissertation, University of Cambridge, UK.

Bachmann, J., Horton, R., Grant, S. A., & Van der Ploeg, R. R. 2002. Temperature dependence of water retention curves for wettable and water-repellent soils. *Soil Science Society of America Journal* 66(1): 44–52.

Bachmann, J., & van der Ploeg, R. R. 2002. A review on recent developments in soil water retention theory: interfacial tension and temperature effects. *Journal of Plant Nutrition and Soil Science* 165(4): 468–478.

De Jong, J.T., Soga, K.S., Kavazanjian, E., Burns, S., Van Paassen, L.A., Al Quabany, A., Aydilek, A., Bang, S.S., Burbank, M., Caslake, L.F., Chen, C.Y., Cheng, X., Chu, J., Ciurli, S., Esnault-Filet, A., Fauriel, S., Hamdan, N., Hata, T., Inagaki, Y., Jefferis, S., Kuo, M., Laloui, L., Larrahondo, J., Manning, D.A.C., Martinez, B., Montoya, B.M., Nelson, D.C., Palomino, A., Renforth, P., Santamarina, J.C., Seagren, E.A., Tanyu, B., Tsesarsky, M., Weaver, T. 2013. Biogeochemical processes and geotechnical applications: progress, opportunities and challenges. *Geotechnique*, 63(4): 287–301.

Fredlund, D. G., Xing, A., & Huang, S. 1994. Predicting the permeability function for unsaturated soils using the soil-water characteristic curve. *Canadian Geotechnical Journal* 31(4): 533–546.

Fredlund, D. G., Xing, A., Fredlund, M. D., & Barbour, S. L. 1996. The relationship of the unsaturated soil shear to the soil-water characteristic curve: *Canadian Geotechnical Journal* 33(3): 440–448.

Grant, S. A. & Salehzadeh, A. 1996. Calculation of temperature effects on wetting coefficients of porous solids and their capillary pressure functions. *Water Resources Research* 32(2): 261–270.

Grant, S. A. 2003. Extension of a temperature effects model for capillary pressure saturation relations. *Water resources research* 39(1), SBH-1.

Fredlund, D. G., & Rahardjo, H. 1993. *Soil mechanics for unsaturated soils*. John Wiley & Sons.

Jiang, N., Soga, K., and Dawoud, O. 2014. Experimental Study of the Mitigation of Soil Internal Erosion by Microbially Induced Calcite Precipitation. *Proceedings of Geo-Congress 2014*: 1586–1595. doi: 10.1061/9780784413272.155

Kavazanjian, E., Jr. and O'Donnell, S. 2015. Mitigation of Earthquake-Induced Liquefaction via Microbial Denitrification: A Two-Phase Process. *IFCEE 2015 Proceedings*: 2286–2295. doi: 10.1061/9780784479087.212

Khaksar, H., Habibagahi, G., and Nikooee, E. 2013. SWRC Modeling in Unsaturated Soils: A Pore Network Approach. *Poromechanics V Proceedings*: 1570–1579. doi: 10.1061/9780784412992.186

Khalili, N., & Khabbaz, M. H. 1998. A unique relationship of chi for the determination of the shear strength of unsaturated soils. *Geotechnique* 48(5): 681–687.

Liu, C. & Muraleetharan, K. 2012. Numerical Study on Effects of Initial State on Liquefaction of Unsaturated Soils. *Proceedings of GeoCongress 2012*: 2432–2441.doi: 10.1061/9780784412121.249

Montoya, B. M., DeJong, J. T. & Boulanger, R. W. 2013. Dynamic response of liquefiable sand improved by microbial-induced calcite precipitation. *Géotechnique* 63(4): 302–312.

Montoya, B., DeJong, J., Boulanger, R., Wilson, D., Gerhard, R., Ganchenko, A., and Chou, J. 2012. Liquefaction Mitigation Using Microbial Induced Calcite Precipitation. *Proceedings of GeoCongress* 2012: 1918–1927. doi: 10.1061/9780784412121.197

Morales, L., Romero, E., Jommi, C., Garzón, E., & Giménez, A. 2014. Feasibility of a soft biological improvement of natural soils used in compacted linear earth construction. *Acta Geotechnica* 10(1): 157–171.

Ng, C. W., & Pang, Y. W. 2000. Influence of stress state on soil-water characteristics and slope stability. *Journal of geotechnical and geoenvironmental engineering* 126(2): 157–166.

Nikeghbal, A. Nikooee, E., Habibagahi G., and Niazi, A. 2015. Stabilization of collapsible soils: A biological technique. 13–17 September 2015, Edinburgh, *Proceedings of 16th European Conference of Soil Mechanics and Foundation Eng. (ECSMGE), accepted for inclusion and publication*.

Nuth, M., & Laloui, L. 2008. Advances in modelling hysteretic water retention curve in deformable soils. *Computers and Geotechnics* 35(6): 835–844.

Romero, E., Gens, A., & Lloret, A. 2001. Temperature effects on the hydraulic behaviour of an unsaturated clay. Geotechnical & Geological Engineering, 19(3–4), 311–332.

Rostami, A., Habibagahi, G., Ajdari, M., & Nikooee, E. 2013. Pore Network Investigation on Hysteresis Phenomena and Influence of Stress State on the SWRC. *International Journal of Geomechanics* (in press). doi: 10.1061/(ASCE)GM.1943-5622.0000315

Sadjadi, M., Nikooee, E., and Habibagahi, G. 2014. Biological treatment of swelling soils using microbial calcite precipitation. *Unsaturated Soils: Research & Applications:* 917–922.

Salager, S., Rizzi, M., & Laloui, L. 2011. An innovative device for determining the soil water retention curve under high suction at different temperatures. *Acta Geotechnica*: 6(3): 135–142.

Tarantino, A. 2009. A water retention model for deformable soils. *Géotechnique* 59(9): 751–762.

Tavakoli Dastjerdi, M. H., Habibagahi, G., & Nikooee, E. 2014. Effect of confining stress on soil water retention curve and its impact on the shear strength of unsaturated soils. *Vadose Zone Journal* 13(5). doi:10.2136/vzj2013.05.0094

Uchaipichat, A., & Khalili, N. 2009. Experimental investigation of thermo-hydro-mechanical behaviour of an unsaturated silt. *Geotechnique* 59(4): 339–353.

Vanapalli, S. K., & Fredlund, D. G. 2000. Comparison of different procedures to predict unsaturated soil shear strength. *Geotechnical Special Publication*: 195–209.

Zhou, A. N., Sheng, D., & Li, J. 2014. Modelling water retention and volume change behaviours of unsaturated soils in non-isothermal conditions. *Computers and Geotechnics* 55: 1–13.

This page intentionally left blank

Unsaturated Soil Mechanics—from Theory to Practice – Chen et al. (Eds)
© 2016 Taylor & Francis Group, London, ISBN 978-1-138-02921-7

Effect of grain size on soil moisture evaporation process

S.K. Xu, C.S. Tang, K.Q. Sun & P. Wang
School of Earth Sciences and Engineering, Nanjing University, Nanjing, China

ABSTRACT: Soil moisture evaporation is one of the main processes of soil-atmosphere interactions. It has an important impact on the engineering properties of soil. It is also a direct cause of many engineering and geo-environmental problems. In this investigation, laboratory evaporation tests were carried out on sands to study the influence of grain size on soil moisture evaporation process. Three groups of initially saturated specimens were prepared with different grain sizes, i.e. S1 with grain size ranges from 0.2 to 0.5 mm; S2 with grain size ranges from 0.5 to 1 mm; S3 with grain size ranges from 2 to 3 mm. The specimens were allowed to dry under room temperature. An identical pan contained pure water was also placed in the room which provided the reference for the potential evaporation. During dry, the water loss was monitored at the same intervals and used to calculate the corresponding actual evaporation rate. The results show that the soil moisture evaporation process can be divided into three stages: constant rate stage, falling rate stage, and residual stage. The evaporation process was significantly influenced by grain size. Generally, the coarser sand showed higher evaporation rate than that of finer sand even at the same water content condition. The duration of constant evaporation stage decreased with decreasing grain size.

1 INTRODUCTION

Soil moisture evaporation is one of the main processes of soil-atmosphere interactions. It has an important impact on the engineering properties of soil. It is also a direct cause of many engineering and geo-environmental problems. Over the past few decades, scholars around the world carried out extensive researches to understand soil moisture evaporation process. For example, Camillo et al. (1983) developed a model of the upper soil and lower atmosphere boundary layer for using with remotely sensed data, which includes soil surface energy and moisture balances. Kondo et al. (1990) developed a soil model for estimating the evaporation from a bare soil, which adopts a parameter represents the resistance to the diffusion of vapor in the surface soil layer; Fredlund and Xing (1994) proposed a general equation for the soil-water characteristic curve based on the pore-size distribution of the soil; Wilson et al. (1994) presented a soil-atmosphere model for predicting the rate of evaporation from soil surfaces, which is based on the Dalton-type equation for evaporation from a surface into the atmosphere; Kayyal (1995) studied the development of shrinkage cracks during evaporation and the factors influencing evaporation rate; Wilson et al. (1997) studied the effect of soil suction on evaporative fluxes from soil surfaces and determined a relationship between the actual evaporation rate and total suction; Yamanaka et al. (1997) examined the effects of atmospheric conditions on soil evaporation in the wind tunnel tests under different atmospheric conditions; Snyder et al. (2000) and Ventura et al. (2006) presented a modal that used a daily mean evapotranspiration ET_0 rate to estimate evaporation for constant rate stage, and also used daily mean ET_0 and a soil hydraulic β factor to estimate evaporation for falling rate stage. Yang and Yanful (2002) studied the interactions of evaporation and drainage in cover soils under different water table conditions, utilizing an evaporation test system consisting of an evaporation column and a water supply/drainage system. The results showed that the water table depression had less effect on the low permeability soil than on the high permeability soils. Komatsu (2002) developed a function between the evaporation efficiency and the characteristic volume fraction θ_c of water. Aydin et al. (2005) proposed a simplified model using matric potential for estimating actual evaporation from bare soil. Cui et al. (2008) presented various methods for quantification of evapotranspiration, especially energy balance approaches and the fundamental aspects of evapotranspiration. Cui et al. (2008&2013) used a miniature tensiometer to monitor the field soil suction and develop a large scale environmental chamber to investigate soil-atmosphere interaction. Ta (2009) studied the impact of crack on soil evaporation, and developed a model which considers cracks; Xue and Akae (2010) developed a maximum surface temperature model (MSTM) to study the effect of soil water content and salinity on daily evaporation from soil column. Song et al. (2010) studied the effects of surface soil mixed with sand on water infiltration and evaporation in laboratory. Tang et al. (2011) summarized the impact of various factors

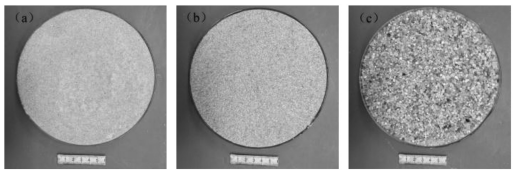


Figure 1. Photos of specimens placed in evaporation pans. (a) Fine sand specimen. (b) Medium sand specimen. (c) Coarse sand specimen.

on soil water evaporation process and analyzed the internal mechanism and soil characteristics for each stage.

Overall, soil moisture evaporation is a very complex scientific problem. It is influenced by lots of factors, which include external environmental conditions (temperature, relative humidity, solar radiation, wind speed, etc.) and soil properties (mineral composition, suction, particle size, water content, dry density, etc.). In this investigation, laboratory evaporation tests were carried out on sands to study the influence of grain size on soil moisture evaporation process.

2 MATERIALS AND METHODS

Three kinds of sands with different grain sizes were used in this test. Relatively three groups of initially saturated specimens were prepared, i.e. S1 with grain size ranges from 0.2 to 0.5 mm (fine sand); S2 with grain size ranges from 0.5 to 1 mm (medium sand); S3 with grain size ranges from 2 to 3 mm (coarse sand). Specimens were placed in evaporation pans like Kondo (1992) did.

The sands are 2.5 cm thick in the pans which have a diameter of 150 mm (Figure 1). Moisture in the sands can only evaporate from the surface. Three parallel specimens were prepared for each test group, so as to reduce experimental error. The specimens were allowed to dry under room temperature which was controlled by air-conditioner (temperature of 20°C, relative humidity of 40%). An identical evaporation pan contained pure water was also placed in the room. It was used to provide the reference for the potential evaporation. During drying, the water losses of specimens were monitored at the same interval and used to calculate the corresponding actual evaporation rate. Weight of each specimen was measured by an electronic balance (accuracy of 0.01 g) every hour.

3 RESULT AND DISCUSSION

The actual rate of evaporation (*Ea*) was calculated for each specimen, and the potential evaporation (*Ep*) for pure water specimen. After drying, the final water content was measured for each specimen.

Figure 2 shows the ratio of *Ea*/*Ep* versus time for each group of specimens. The results show that the soil moisture evaporation process can be divided into three

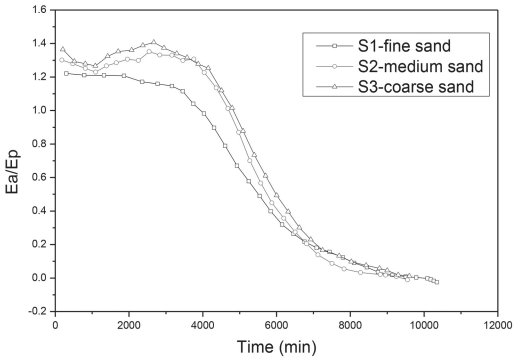


Figure 2. The ratio of actual evaporation and potential evaporation, *Ea*/*Ep*, versus drying time for sands with various grain sizes.

stages as we all known before, i.e. constant rate stage, falling rate stage and residual stage. It can be seen that the ratio in the constant rate stage is greater than 1.0. Wilson (1997) supposed the deviation can be attributed to slight variations in the aerodynamic resistance in the air spaces above the water and soil evaporation pans, as well as the surface temperatures at the time of the tests. However, it is a common phenomenon for sand specimen. Figure 2 shows that coarse sand has a greatest ratio of 1.35 approximately, followed by medium sand, and finally fine sand. It can be deduced that the reason is the capillarity between sand particles, which cannot be used for free water. In the constant rate stage, the flux of water moves in the capillary liquid water form. It results that the decrease of moisture in sand specimens is more than that of pure water. Moreover, moisture is adsorbed on the surface of sand particles, and the interface of moisture and air became an irregular one which has a greater area. Sands with greater grain size have larger pores and interface of moisture and air, which leads a greater evaporation rate.

The evaporation rate begins to decrease first for the fine sand, second for medium sand, latest for coarse sand, which means moisture evaporation enter into falling rate stage. In other words, the duration of constant evaporation stage decreased with decreasing grain size. However, it is not only influenced by particle size, but also influenced by the initial water content. Moisture in the upper layer of specimens is evaporated and it appears a dry layer. The moisture under the evaporation interface transfers in capillary liquid water form, while the moisture in the dry layer flows in the vapor forms. The evaporation becomes weaker with time going, and the falling rate stage ends. Finally, the evaporation rate of specimens is close to zero in the residual stage, because there is no more water in the specimens can be supplied for evaporation. There is only water vapor transporting by molecular diffusion from soil pore to the soil surface for the residual stage.

Figure 3 shows the ratio of *Ea*/*Ep* versus water content for each group of sands during dry. For specimens with high water content, the evaporation rate remains stable. The decline of evaporation rate happens when

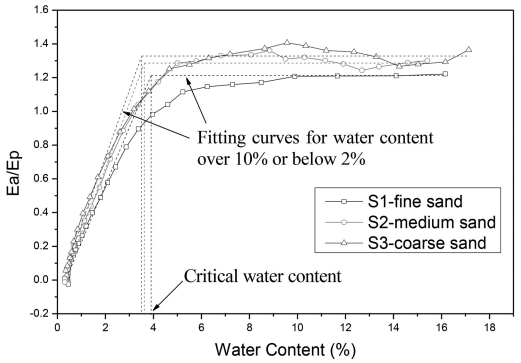


Figure 3. The ratio of actual evaporation and potential evaporation, *Ea*/*Ep*, versus water content for sands with various grain sizes.

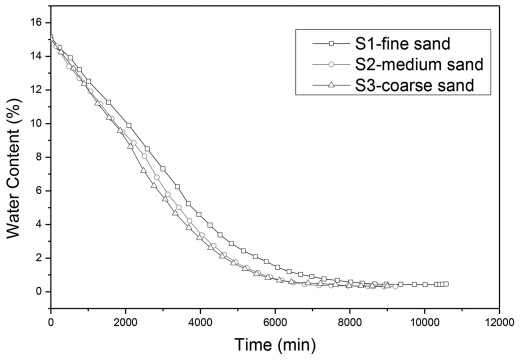


Figure 4. Water content versus time for fine sand, medium sand, and coarse sand.

water content reach a critical value. It can be seen that the critical water content of coarse sand is about 3.5%, which is slightly less than that of medium sand (3.6%) and fine sand (3.9%). Moreover, the *Ea*/*Ep* decreases down to 1 first for the fine sand, second for the medium sand, and finally for the coarse sand. The evaporation rate of medium sand is always between fine sand and coarse sand during drying. It can be concluded that the evaporation process was significantly influenced by grain size under the same conditions. Soil with more coarse grains has higher evaporation rate than soil with more fine grains.

In Figure 3, it shows that three groups of specimens have a final water content of about 0.3%. It also can be seen that the evaporation rate of sands in residual stage fluctuates around 0 from figure 2. It suggests that the flux of water vapor transports by molecular diffusion from sand to the air is equal to that transports from air to sand in residual stage.

Figure 4 shows the water content versus time for sands with various grain sizes. Three groups of sands start with the same water content of 15% and then water content of sands decline constantly during drying. For constant rate stage, water content declines as a linear curve which means the rate of evaporation is constant. Water content for fine sand declines little slower than that for medium sand and coarse sand, which is influenced by grain and pore size. For falling rate stage, Specimens change from saturated to unsaturated. Soil water transfers in both forms of capillary liquid water and the vapor diffusion. Vapor pressure gradient between pore gas and air decreases, and suction increases for each group of sands (Fredlund and Xing, 1964; Wilson et al., 1997). The rate of evaporation also reduces with the decrease of water content. When the interface of evaporation become deep enough and vapor pressure gradient get greater and suction become larger, the evaporation enters into residual stage at last. For residual stage, the curves of water content turn to a horizontal line, and water content falls to a residual value.

4 CONCLUSION

Soil moisture evaporation process can be divided into three stages: constant rate stage, falling rate stage, and residual stage. For constant rate stage, the flux of water moves in the capillary liquid water form. The evaporation rate is mainly controlled by meteorological environment, and remains a relatively constant value. For the falling rate stage, specimens become saturated and it appears a dry layer in the upper layer of each specimen. Soil water transfers in both forms of capillary liquid water and vapor diffusion. Vapor pressure gradient decreases and suction increases rapidly, which makes the rate of evaporation have a slower decreasing fall. For the residual stage, water content of specimens fall to a low residual value. Water vapor transports by molecular diffusion from soil pore to the soil surface.

Finally, it can be concluded that the evaporation process was significantly influenced by grain size. Generally, the coarser sand showed higher evaporation rate than that of finer sand even at the same water content condition. The duration of constant evaporation stage decreased with decreasing grain size. The critical water content at the transition point from constant rate stage to falling rate stage decreased with increasing grain size.

ACKNOWLEDGEMENTS

This work was supported by the National Science Foundation of China for Excellent Young Scholars (Grant No. 41322019), Key Project of National Natural Science Foundation of China (Grant No. 41230636). The authors also wish to acknowledge the support of the European Commission via the Marie Curie IRSES project GREAT-Geotechnical and geological Responses to climate change: Exchanging Approaches and Technologies on a world-wide scale (FP7-PEOPLE-2013- IRSES-612665).

REFERENCES

Aydin, M., Yang, S.L., Kurt, N. & Yano, T. 2005. Test of a simple model for estimating evaporation from bare soils in different environments. *Ecological Modelling* 182(1): 91–105.

Camillo, P.J., Gurney, R.J. & Schmugge, T.J. 1983. A soil and atmospheric boundary layer model for evapotranspiration and soil moisture studies. *Water Resources Research* 19(2): 371–380.

Cui, Y.J., Tang, A.M. Mantho, A.T. & De Laure, E. 2008. Monitoring field soil suction using a miniature tensiometer. *Geotechnical Testing Journal* 31(1): 95–100.

Cui, Y.J., Ta, A.N., Hemmati, S., Tang, A.M. & Gatmiri, B. 2013. Experimental and numerical investigation of soil-atmosphere interaction. *Engineering Geology* 165: 20–28.

Cui, Y.J. & Zornberg, J.G. 2008.Water balance and evapotranspiration monitoring in geotechnical and geoenvironmental engineering. *Geotechnical and Geological Engineering* 26(6): 783–798.

Fredlund, D.G. & Xing, A. 1994. Equations for the soil-water characteristic curve. *Canadian Geotechnical Journal* 31(3): 521–532.

Kayyal, M.K. 1995. Effect of the moisture evaporative stages on the development of shrinkage cracks in soil. *In Proceedings of First International Conference on Unsaturated Soils*: 373–379.

Komatsu, T.S. 2006. Toward a robust phenomenological expression of evaporation efficiency for unsaturated soil surfaces. *Journal of Applied Meteorology* 42(9): 1330–1334.

Kondo, J., Saigusa, N. & Sato, T. 1990. A parameterization of evaporation from bare soil surfaces. *Journal of Applied Meteorology* 29(5): 385–389.

Kondo, J. Saigusa, N. & Sato, T. 1992. A model and experimengtal study of evaporation from bare-soil surfaces. *Journal of Applied Meteorology* 31(3): 304–312.

Snyder, R.L., Bali, K., Ventura, F. & Gomez-MacPherson, H. 2000. Estimating evaporation from bare or nearly bare soil. *Journal of Irrigation and Drainage Engineering* 126(6): 399–403.

Song, R.Q., Chu, G.X., Ye, J., et al. 2010. Effects of surface soil mixed with sand on water infiltration and evaporation in laboratory. *Transactions of the CSAE* 26(*Supp*.1): 109–114. (in Chinese)

Ta, A.N. 2009. Etude de l'interaction soil-atmosphere en chamber environmentale. *Paris: Ecole des Ponts Paristech*.

Tang, C.S., Shi, B. & Gu, K. 2011. Experimental investigation on soil water evaporation process during drying. *Journal of Engineering Geology* 19(5): 1–7. (in Chinese)

Ventura, F., Snyder, R.L. & Bali, K.M. 2006. Estimating evaporation from bare soil using soil moisture data. *Journal of Irrigation and Drainage Engineering* 132(2): 153–158.

Wilson, G.W., Fredlund, D.G. & Barbour, S.L. 1994. Coupled soil-atmosphere modelling for soil evaporation. *Canadian Geotechnical Journal* 31(2): 151–161.

Wilson, G.W., Fredlund, D.G. & Barbour S L. 1997. The effect of soil suction on evaporative fluxes from soil surface. *Canadian Geotechnical Journal* 34: 145–155.

Xue, Z. & Akae, T. 2010. Effect of soil water content and salinity on daily evaporation from soil column. *Journal of American Science* 6(8): 576–580.

Yamanka, T., Takeda, A. & Sugita F. 1997. A modified surface-resistance approach for representing bare-soil evaporation: wind tunnel experiments under various atmospheric condition. *Water Resources Research* 33(9): 2117–2128.

Yang, M. & Yanful, E.K. 2002. Water balance during evaporation and drainage in cover soils under different water table conditions. *Advances in Environmental Research* 6(4): 505–521.

Unsaturated Soil Mechanics—from Theory to Practice – Chen et al. (Eds)
© 2016 Taylor & Francis Group, London, ISBN 978-1-138-02921-7

Osmotic suction of two highly plastic expansive soils

B. Lin
State Key Laboratory of Petroleum Resources and Prospecting, China University of Petroleum, Beijing, China

A.B. Cerato
School of Civil Engineering and Environmental Sciences, University of Oklahoma, Norman, OK, USA

ABSTRACT: The investigation of hydromechanical behavior of unsaturated expansive soil depends on accurate determination of the Soil-Water Characteristic Curves (SWCCs). This research studies the characteristic curves of two highly clayey expansive soils initially compacted at optimum moisture content (w_{opt}) and maximum dry density (γ_{dmax}), starting from their fully expanded states. Pressure plate and dewpoint potentiameter (WP4) tests were performed to achieve the drying paths. Comparisons were made between the drying paths from the two types of tests to deduce osmotic suction. The attained osmotic suction values exhibit either an increase or decrease with increasing water content, depending on soil type.

1 INTRODUCTION

The hydromechanical behavior of unsaturated expansive soils is highly dependent on their SWCCs. Common laboratory methods of measuring SWCCs of plastic soils include pressure plate (or membrane) tests (Tinjum et al. 1997; Miller et al. 2002; Leong et al. 2003; Wang and Benson 2004; Agus & Schanz, 2006; Puppala et al. 2006) with a measuring range of matric suction up to 1500 kPa, and chilled mirror hygrometer tests (Leong et al. 2003; Wang and Benson, 2004; Thakur et al., 2005; Agus & Schanz, 2006; Sreedeep & Singh, 2006; Thakur et al. 2006; Birle et al. 2008; Agus et al. 2010), also named dew-point potentiameter tests, with a total suction range of 0∼300 MPa.

Total suction, ψ, is the sum of the matric suction, ψ_m and the osmotic suction, ψ_o (Fredlund & Rahardjo, 1993). The regular practice of determining osmotic suction involves measuring electrical conductivity of extracted pore water by using a pore fluid squeezer (Fredlund & Rahardjo, 1993) and using an empirical relation to deduce osmotic suction based on a correlation curve developed by USDA (1950). This type of squeezer is scarce and not readily accessible; moreover, a great error is highly probable in the determination from the extracted pore water (Leong et al. 2003), regarding the significant osmotic pressure (Mitchell & Soga 2005) that the squeezing piston has to overcome to extract the pore water. In past studies, due to measurement difficulties, osmotic suction was usually assumed constant with the change of water content and omitted in deriving SWCCs for which total suction is taken as a substitute for matric suction. The influence of osmotic suction on the soil mechanical behavior is small compared to that of matric suction; however, osmotic suction may dominate the total suction measurement, resulting in the use of total suction as a proxy for matric suction problematic (Miller & Nelson, 2006). Osmotic suction can be measured as the difference of magnitude in between total suction measured from a dew point potentiameter (WP4, also known as chilled mirror hygrometer), and matric suction obtained from the null type axis-translation technique (Leong et al. 2003; Sreedeep & Singh, 2006). Leong et al. (2003) tested on two residual soils (both are classified as elastic silt (MH, according to Unified Soil Classification System (USCS)) with plasticity index (PI) = 14 and 17) and found osmotic suctions of 92-1400 kPa, depending on water content. Sreedeep and Singh (2006) discovered an osmotic suction of 6200–9800 kPa of a MH soil (PI = 24), also varying with water content. This research investigated the matric suction values of two expansive soils of various plasticity (classified as elastic silt (MH) and fat clay (CH), according to USCS) using pressure plate tests in the range of 1 ∼ 1000 kPa, and then the total suction magnitudes using dewpoint potentiameter measurements in the range of 0 ∼ 100 MPa.

The model of Fredlund and Xing (1994) was used here to relate suction to water content:

$$w = w_s\left[1 - \frac{\ln(1+\psi/\psi_r)}{\ln(1+10^6/\psi_r)}\right]\left[\frac{1}{\{\ln[e+(\psi/\alpha)^n]\}^m}\right] \quad (1)$$

where w is the gravimetric water content; w_s is the gravimetric water content at saturation; ψ represents the suction (kPa); ψ_r is the suction at residual water content; α is the optimized parameter related to air-entry suction; e is the base of natural logarithm; and n,

Table 1. Geotechnical and physical properties of Carnisaw and Eagle Ford soils.

Soil property	Carnisaw	Eagle Ford
% passing No.200 sieve	84	100
Clay size fraction (% <2 μm)	51	66
Specific gravity, G_s	2.8	2.7
Liquid limit, LL	59	92
Plastic limit, PL	32	35
Plasticity index, PI	27	57
Optimum moisture content, w_{opt} (%)	26.2	27.1
Maximum dry unit weight, γ_{dmax} (kN/m^3)	15.9	14.2
Percent of free swell, s (%)	2.3	12.7
Swell pressure, p_s (kPa)	75	263
Specific surface area, SSA (m^2/g)	107.5	213.5
Cation exchange capacity, CEC (meq/100 g)	27.3	49.6
USCS classification	MH	CH

m are the model parameters reflecting the pore size distribution and the shape of the SWCC at high suction. Gravimetric water content, instead of volumetric water content, is used in this study due to significant soil volumetric change and cracking during the WP4 test.

2 EXPERIMENTAL PROGRAM

2.1 *Materials*

Experiments were conducted on two natural expansive soils: Carnisaw soil with slight swelling potential, and Eagle Ford soil with significant swelling capacity. The Carnisaw and Eagle Ford samples were collected from Le Flore, Oklahoma, and Irving, Texas, respectively. Carnisaw soil is red brown residual silt with high plasticity, weathered from shale of Pennsylvania age. Eagle Ford soil is yellowish/tan highly plastic clay weathered from fossiliferous clayey shale with sandy shale lenses. X-ray diffraction studies show that both soils contain clay minerals including montmorillonite/vermiculite, kaolinite, illite, and traces of palygorskite. Some geotechnical and physical properties of the soils are summarized in Table 1.

The percent of swell (under a surcharge load of 1 kPa) and the swell pressure were determined by method A of ASTM D4546 (ASTM 2011). The total specific surface area (SSA) values were obtained following the (Ethylene Glycol Monoethyl Ether) EGME surface area determination method (Cerato & Lutenegger 2002). The cation exchange capacity (CEC) and the pH were achieved in using a 1 N ammonium acetate extraction method (Rhoades 1982).

When testing the drying path (in terms of gravimetric water content) of clayey soils using a dewpoint potentiameter (WP4), the influence of initial compaction dry density is negligible at the suction values greater than 1000 kPa (Thakur et al. 2005; Thakur et al. 2006; Birle et al. 2008). However, suction has been shown to increase with compaction effort as determined in the pressure plate apparatus with a measurement suction range below 1000 kPa (Miller et al. 2002). In order to compare results from the two types of tests, soil samples for both tests were prepared in the same manner, in that all specimens were initially compacted at w_{opt} and γ_{dmax} (determined by standard proctor test ASTM D698 (2011)), using volume based compaction.

2.2 *Pressure plate tests*

The SWCC was determined in a 15-bar pressure plate extractor manufactured by Soilmoisture Equipment, Corp, following the drying path approach according to ASTM D6836 – 02(2008)e2 (2011). Pressure plates with measurement limits of 100 kPa, 300 kPa, 500 kPa and 1500 kPa were used. The flow of water from the soil specimens into burettes were monitored in intervals of 24 hours until stabilized after suction was imposed. Each soil sample was compacted in 5 layers in a 63 mm diameter by 132 mm length steel mold, using a 24.4 N steel hammer. The compacted sample was then trimmed into four 51.3 mm in diameter and 10.2 mm thick specimens and placed in rubber rings. Each specimen was sandwiched between two porous stones and immersed in de-aired, de-ionized water contained in an ice chamber in a 100% humidity room and allowed to imbibe water for a period of 72 hours. After 72 hours, the degree of saturation for all the specimens was estimated at more than 96% from volume-mass calculation. The porous stones were then removed and the samples were placed, ensuring good contact, on the pressure plates. Details of test apparatus and process can be referred to Lin and Cerato (2012 & 2013).

2.3 *Dewpoint potentiameter tests*

The dewpoint potentiameter test was carried out using a WP4-T model manufactured by Decagon Devices, Inc, which is an upgraded WP4 model with the additional function of "user-selectable" internal temperature control. The WP4-T potentiameter was calibrated periodically with a standard 0.5 KCl liquid. Each soil sample was first mixed with de-ionized water and compacted in 5 layers with a 16 mm diameter, 5.8 N cylindrical stainless steel rod into a 36.5 mm in inner diameter and 100 mm in length stainless steel tube. After being cured for one day, the compacted sample was extruded from the tube using a solid wooden cylinder, carefully cut and placed in five stainless steel cups with a dimension of 10 mm in depth, 36.5 mm in inner diameter and 1.5 mm wall thickness, with the aid of a sharp knife and a wire hacksaw. A thin spatula was used to trim and smooth the surface of the soil specimen inside the cup so that the final specimen thickness reached approximately 5 mm as required by the

Table 2. Soil water characteristic curve fit parameters.

Parameter	Carnisaw	Eagle Ford
α (kPa)	80	110
n	1.30	2.70
m	0.10	0.14
ψ_r (kPa)	8000	6000
R^2	0.99	0.93

WP4-T manual that the specimen thickness should be less than half of cup depth to avoid contamination of the chamber.

A filter paper and porous stone were placed on top of the soil specimen in each half-filled cup to prevent soil loss to the water. These half-filled cups were then placed in a desiccator filled with de-aired and de-ionized water, located in a humidity room for 72 hours. The degree of saturation was estimated to be more than 98% after imbibing water. Afterwards, the specimens were air dried for approximately 20 ~ 35 minutes and sealed for 3–4 hours for moisture homogenization, and then placed in the sample equalization area on the top surface of the WP4-T for additional 2 hours for further temperature and moisture equilibrium. After this process the temperature of the specimen was within 0.1°C difference of the WP4-T chamber temperature (set at 25°C). This procedure was found adequate for moisture equalization throughout the soil specimen as the suction measured following this procedure matched well the magnitude obtained after the 24 hour sealing period suggested by Agus and Schanz (2006), with the difference falling within the device accuracy. The equalized specimen was then tested in the WP4-T chamber after which the specimen weight was immediately recorded. The above process was repeated for the next water content measurement. At the end of the drying process, the specimens were oven dried from which the gravimetric water content corresponding to each measured suction value was back-calculated.

3 RESULTS AND DISCUSSION

The pressure plate and WP4 results of Carnisaw and Eagle Ford soils are presented in Fig. 1 together with the fitted curves for the pressure plate test results only. The water content at a matric suction of 1 kPa was taken as the saturated water content. Non-linear regression analyses were performed in a *MATHEMATICA* software platform to determine the best-fit model parameters. The fit parameters for the drying paths obtained from the pressure plate tests soils are listed in Table 2.

The study of osmotic suction can be carried out by comparing the results of the pressure plate (or membrane) and the WP4 tests (Sreedeep & Singh 2006). Comparisons were made between data points having the water contents within the same range. The fit

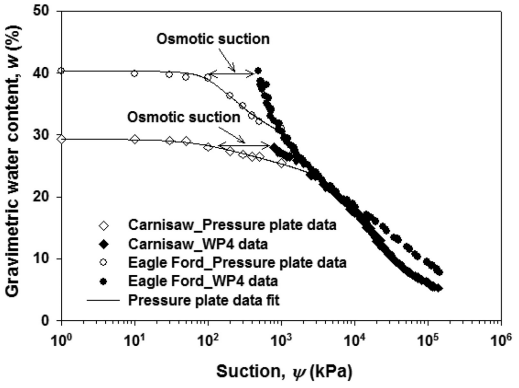


Figure 1. SWCCs from the pressure plate and WP4 tests.

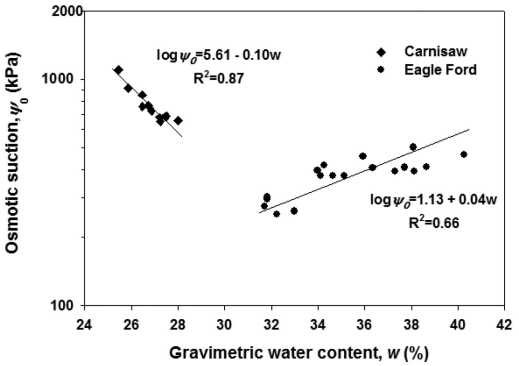


Figure 2. Osmotic suction vs. gravimetric water content.

curves are used for describing the pressure plate test results. The osmotic suction is deduced as the difference between the total suction of each WP4 data point and the matric suction of the point on the fit curve which shares the same water content value (Fig. 1). The changes of the obtained osmotic suction with increasing water content are presented in Figure 2 for both soils.

While the trends of osmotic suction with water content change shown in Fig. 1 look similar, because of the log scale, they are in fact opposite for both soil samples. It can be observed that the osmotic suction of Carnisaw soil is higher at lower water contents (Fig. 2). The same trend was discovered by Sreedeep and Singh (2006) in comparing the results of the pressure membrane test and the WP4 test of one soil also classified as MH. It was argued that such a trend could be attributed to the higher concentration of solutes in pore fluid at a lower water content resulting in higher osmotic suction (Sreedeep & Singh, 2006). However, Eagle Ford soil shows the reverse trend as osmotic suction decreases with decreasing water content (Fig. 2). At the same time, the measured osmotic suction magnitudes of Eagle Ford are much lower than those of Carnisaw. These phenomena may be due to the fact that Eagle Ford, as a CH type soil, has much higher plasticity than Carnisaw resulting in a more significant formation

of the diffuse double layer. The diffuse double layer forms around clay particles as the negatively charged particle surface and the diffuse ion swarm in the adjacent phase (Mitchell & Soga 2005). Osmotic suction mainly depends on pore fluid chemistry in the macropores of the soils. For sand, silt and some lean clay in which the diffuse double layer effect is none or less significant, most water in the soil exist as free bulk fluid in macropores. In this case, osmotic suction can be viewed as surface tension at the interface between pure water and salt solution (Miller & Nelson, 2006). However, in highly plastic soils (e.g., Eagle Ford) where most water exists in the form of bound water in the diffuse double layer when the soils are relatively dry (at low water contents), there is no adequate bulk water available for salt dissolution to generate osmotic suction. As the water content is increased, the volume of the bulk fluid expands and the chemical ions previously bounded on clay particle surface or contained in diffuse double layer begin to diffuse into the bulk fluid. Therefore, a larger proportion of free water adsorbed by Eagle Ford was first consumed in development of the diffuse double layer, which generates osmotic suction only when there is sufficient bulk fluid available in the macropores for dissolving salts.

In Figure 1, the pressure plate test data of Carnisaw show a clear tendency to converge with the WP4 test data when the suction value increases higher than 1000 kPa. The comparison between the pressure plate and the WP4 test data of a MH soil by Sreedeep and Singh (2006) also shows such a tendency. Meanwhile, the similar convergence occurs at a suction value close to 1000 kPa for Eagle Ford. Thus, it can be safely postulated that the pressure plate and the WP4 data would converge when the suction rises higher than 1000 kPa, regardless of the trend type of osmotic suction with the change of water content. In other words, although Carnisaw shows a trend of increase of osmotic suction with decreasing water content (Fig. 2), it may be decreasing at a higher suction range since the data from the two types of test tend to converge. At the same time, the trend of osmotic suction with water content of Eagle Ford (Fig. 2) illustrates such a convergence phenomenon. The assessment of osmotic suction, as well as the development of its magnitude with water content change, still needs further research.

4 CONCLUSIONS

Suction versus gravimetric water content results of two expansive soils were obtained from measurements using both pressure plate tests and WP4 tests. The SWCCs were obtained from non-linear regression using the Fredlund and Xing (1994) model. Osmotic suction was determined from the difference of total and matric suction measured from the WP4 and the pressure plate tests, respectively.

Osmotic suction either increases or decreases with an increase in water content depending on the soil type. Higher concentration of salt solutes in the pore fluid of Carnisaw soil may result in an increase of osmotic suction with decreasing water content. On the other hand, for Eagle Ford which is highly plastic clay, a significant amount of water may be consumed by the development of diffuse double layer and therefore, osmotic suction can only develop at high water contents. Also, caution must be employed in substituting total suction for matric suction at the low suction range (<1000 kPa), especially when dealing with highly plastic soils.

ACKNOWLEDGEMENTS

We would like to express our gratitude to the U.S. National Science Foundation (Grant No. 0746980), and the National Natural Science Foundation of China (Grants No. 51404281, 51325402, 51490650, 51174217 and 51234006) for their financial supports. Our research was also supported by the Foundation of State Key Laboratory of Petroleum Resources and Prospecting (Grant No. PRP/indep-4-1309) and the Science Foundation of China University of Petroleum, Beijing (Grant No. 2462013YJRC037).

REFERENCES

Agus, S.S. & Schanz, T. 2006. Drying, wetting, and suction characteristic curves of a bentonite-sand mixture. *Unsaturated Soils 2006*, ASCE, Carefree, Arizona, April 2–6, 2006, 1405–1414.

Agus, S.S., Schanz, T. & Fredlund, D.G. 2010. Measurements of suction versus water content for bentonite-sand mixtures. *Can. Geotech. J.*, 47, 583–594.

ASTM. 2011. 2011 *Annual Book of ASTM Standards*. Volume 04.08 Soil and Rock (I): D420-D5876 and Volume 4.09 Soil and Rock (II): D5877 – latest. West Conshohocken, Pennsylvania.

Birle, E., Heyer, D. & Vogt, N. 2008. Influence of the initial water content and dry density on the soil-water retention curve and the shrinkage behavior of a compacted clay. *Acta Geotech.*, 3, 191–200.

Cerato, A.B. & Lutenegger AJ 2002. Determination of surface area of fine-grained soils by the ethylene (EGME) method. *ASTM Geotech. Test. J.*, 25(3):315–321.

Fredlund, D.G. & Rahardjo, H. 1993. Soil mechanics for unsaturated soils. John Wiley and Sons, INC., New York, 517p.

Fredlund, D.G. & Xing, A. 1994. Equations for the soil-water characteristic curve. *Can. Geotech. J.*, 31, 521–532.

Leong, E.C., Tripathy, S. & Rahardjo, H. 2003. Total suction measurement of unsaturated soils with a device using the chilled-mirror dew-point technique. *Geotechnique*, 53(2), 173–182.

Lin, B. & Cerato, A.B. 2012. Investigation on soil-water characteristic curves of untreated and stabilized highly clayey expansive soils. *Geotech. Geol. Eng.*, 30, 803–812.

Lin, B. & Cerato, A.B. 2013. Hysteretic soil water characteristics and cyclic swell-shrink paths of compacted expansive soils. *Bull. Eng. Geol. Eng.*, 72 (1), 61–70.

Mitchell, J.K. & Soga, K. 2005. Fundamentals of Soil Behavior. 3rd Edition. John Wiley and Sons, Inc. New Jersey. 577p.

Miller, C.J., Yesiller, N., Yaldo, K. & Merayyan, S. 2002. Impact of soil type and compaction conditions on

soil water characteristic. *J. Geotech. Geoenviron. Eng.*, 128(9), 733–742.
Miller, D.J. & Nelson, J.D. 2006. Osmotic suction in unsaturated soil mechanics. *Unsaturated Soils 2006*, ASCE, Carefree, Arizona, April 2–6, 2006, 1382–1393.
Puppala, A.J., Punthutaecha, K. & Vanapalli, S.K. 2006. Soil-water characteristic curves of stabilized expansive soils. *J. Geotech. Geoenviron. Eng.*, 132(6), 736–750.
Rhoades, J.D. 1982. Cation exchange capacity. In: Page AL (ed) Methods of soil analysis. Agronomy 9, 2nd edn. American Society of Agronomy, Madison, pp 159–165.
Sreedeep, S. & Singh, D.N. 2006. Methodology for determination of osmotic suction of soils. *Geotech. Geol. Eng.*, 24, 1469–1479.
Thakur, V.K.S., Sreedeep, S., Singh, D.N. 2005. Parameters affecting soil-water characteristic curves of fine-grained soils. *J. Geotech. Geoenviron. Eng.*, 131(4), 521–524.
Thakur, V.K.S., Sreedeep, S., Singh, D.N. 2006. Laboratory investigations on extremely high suction measurements for fine-grained soils. *Geotech. Geol. Eng.*, 24, 565–578.
Tinjum, J.M., Benson, C.H., Blotz, L.R. 1997. Soil-water characteristic curves for compacted clays. *J. Geotech. Geoenviron. Eng.*, 123(11), 1060–1069.
USDA 1950. Diagnosis and improvement of saline and alkali soils. USDA Agricultural Handbook No. 60. Untied States Department of Agriculture.
Wang, X. & Benson, C. 2004, Leak-Free Pressure Plate Extractor for Measuring the Soil-Water Characteristic Curve, *Geotech. Test. J.*, 27(2), 1–10.

This page intentionally left blank

Modelling

Fundamentals and constitutive modelling

This page intentionally left blank

Unsaturated Soil Mechanics—from Theory to Practice – Chen et al. (Eds)
© 2016 Taylor & Francis Group, London, ISBN 978-1-138-02921-7

Rate effects in inter-granular capillary bridges

Y. Zhang, D. Hanaor & Y.X. Gan
School of Civil Engineering, The University of Sydney, NSW, Australia

ABSTRACT: Water retention curves, describing the relationships between the degree of saturation and matric suction, are important to hydro-mechanical properties in unsaturated soils. Matric suction is usually used to describe the ability of soil to absorb water in applications such as dam soil infiltration or rainfall infiltration, and plays a significant role in calculating slope stability and landslide risks. In unsaturated soil mechanics, matric suction is also known as capillary pressure and depends on wetting angles of pore fluid on the surfaces of soil grains. In this paper, we experimentally investigate the behavior of an individual capillary interaction between two solid substrates connected by a liquid bridge. We applied various relative velocities between the two surfaces and measured the change of capillary force as a function of relative displacement. A clear rate-dependent force-displacement relationship was found during the separation of the two surfaces, while for approaching surfaces no observable difference was identified within the range of testing speeds. Under the same environmental conditions and liquid drop volume, it was found that faster plate movement yields larger observed capillary forces. Furthermore, we implemented "pause" stages after moving the upper plate to specified positions at a given speed. When the upper plate was stationary, the capillary force decreased gradually before reaching a certain value over time. When the upper plate resumed movement at another speed, the force-distance curve was found to join the curve of the new speed rather than the original trajectory. These phenomena indicate that time and rate effects indeed play a significant role in capillary forces.

1 INTRODUCTION

It is widely known that rainfall plays a significant role in landslide stability. A large amount of statistical data has shown that most landslides occur during or after a significant rainfall event [1]. Such phenomena are very common in Asian areas such as Japan, Hong Kong and parts of China. In the field of soil mechanics researchers are increasingly aware that under conditions of rainfall and infiltration, occurrences of soil landslides have a close relationship with seepage in unsaturated soils [2].

Water infiltration brings about a reduction in matric suction in unsaturated soils, which results in a decrease of soils' shear strength. The decrease of matric suction along a potential slip surface in a soil results in the reduction of slope stability [3]–[4]. The relationship between matric suction of soil and the water content is called the soil water characteristic curve (SWCC) [5]. Several water retention curve models have been proposed in this field recently. A numerical model of water flow and its retention hysteresis was developed with the aid of discrete element method (DEM) techniques [6] and has been effectively employed to describe the capillary interactions at different conditions of water saturation. The shape of hysteresis under different degree of saturation shows that the scanning curves are determined by the dynamics of contact angles. In the transition between drainage and wetting, the distribution of local contact angles determines water retention relations between water potential and saturation. The larger the saturation range is, the larger the hysteresis scanning area it will be.

The fist theory of capillary forces acting at microscopic scales was established by Young [7] and Laplace [8]. On the basis of this foundation, numerous researchers have focused on the studies of capillary forces in the range of contexts involving different geometries, environmental conditions or materials. However, previous research results have primarily focused on the modeling of capillary condensation. Only few studies have focused on the effect of external factors in giving rise to hysteresis type phenomena. Recently, some research groups have experimentally demonstrated the effect of contact angle hysteresis on capillary forces arising from a drop of water between two plates [9]. According to their research results, capillary forces changes under different contact angles. Moreover, the significance of displacement rate on the behavior of capillary interactions between approaching or receding surfaces remains unclear and merits further clarification.

The aim of this study is to explore the force-separation behavior during the approach and separation of surfaces at different velocities. Specifically, we focus on the controlling of the displacement speeds of two glass plates connected by a liquid bridge to facilitate an improved understanding of capillary interactions as described in the following sections.

2 THEORY

2.1 *The Young-Laplace equation*

The aim of this work is to experimentally shed light on the impact of displacement rate on the hysteresis behavior of capillary forces arising from liquid bridges.

We assume the volume V of a liquid bridge remains constant during each of our experiments. Contact angles are further assumed to be equal, such that $\theta = \theta_1 = \theta_2$ as shown in Figure 1. The capillary force mainly depends on the distance D between two substrates, the surface tension γ_{lv} of the liquid-vapor interface, volume V and contact angle θ. If the length scale, as given by $s = (3V/4\pi)^{1/3}$ is small compared to the capillary length $l_{cap} = (\gamma_{lv}/g\Delta_\rho)^{1/2}$, where g is gravitational acceleration and $\Delta\rho$ is the difference between the liquid and vapor densities, then the influence of gravity is considered to be negligible. In the case of water, the value of l_{cap} is determined to be 2.7 mm, which indicates that for $V \ll 0.082$ ml, gravitational contributions can be neglected. The volume of liquid bridges in the present work (0.01 ml) complies with this criterion and thus gravitational contributions can be neglected.

The capillary force is the sum of forces arising from the surface tension ($F_{tension}$) and Laplace pressure ($F_{laplace}$) as (F_{total})

$$F_{total} = F_{tension} + F_{laplace} = 2\pi r_N \gamma + \pi {r_N}^2 \Delta_p \qquad (1)$$

where r_N is the radius of the bridge neck and γ the surface tension of the liquid. The pressure difference, Δ_p was calculated by the numerical integration of the Laplace-Young equation. The equation may be written in the following form

$$\Delta_p = \gamma_{lv}\left(\frac{1}{R_1} + \frac{1}{R_2}\right) \qquad (2)$$

where R_1 and R_2 are the principal radii of curvature.

2.2 *Definition of the problem*

Capillary liquid bridges are most commonly considered in conditions of static equilibrium. Taking the example of a drop of oil (o) in water (w) (Figure 2). If the o/w interface is displaced radially by an amount dR, the work done by the pressure and capillary force can be written as:

$$\delta W = -p_o dV_o - p_w dV_w + \gamma_{ow} dA \qquad (3)$$

where $dV_o = 4\pi R^2 dR = -dV_w$, and $dA = 8\pi R dR$ are respectively the increase in volume and surface of the drop, p_o and p_w are the pressures in the oil and water, and γ_{ow} is the interfacial tension between oil and water. When the condition is under mechanical equilibrium $\delta W = 0$, which leads to the relationship

$$\Delta p = p_o - p_w = \frac{2\gamma_{ow}}{R} \qquad (4)$$

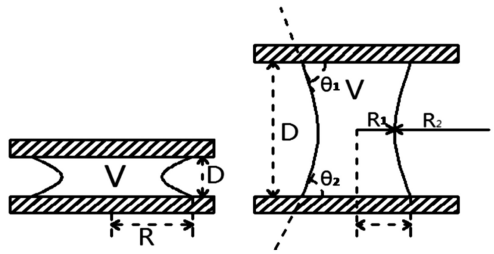


Figure 1. Illustration of a liquid bridge with volume V between two parallel substrates with contact angle θ_1 and θ_2.

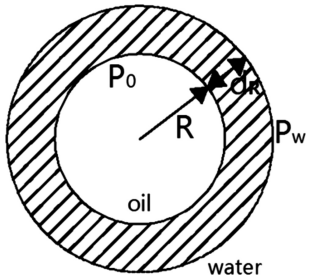


Figure 2. A drop of oil in water.

However, in reality, most cases do not involve static equilibrium conditions owing to changes in external factors. Hence, the work done by the external pressure is larger than 0, which means $\Delta p < \frac{2\gamma_{ow}}{R}$. Following this, the capillary force that exists between two substrates is expected to change with varying external controlling factors.

In this paper, we change only the velocity of the substrates during movement while maintaining other factors constant. We wish to find out the relationship between capillary forces and displacement rates.

3 EXPERIMENTAL SET-UP

In our experiments, an advanced goniometer system is set up as shown in Figure 3. This system includes an illumination source, a high-speed camera and a stage. It operates on an anti-vibration honeycomb platform with mounting holes. Between the illumination source and the camera we placed an electronic analytical balance to record capillary forces with an accuracy of 100 μN. We fixed a cleaned and dried glass microscope slide substrate on a stage mounted on the balance with the upper substrate held in place by a fixture mounted to a vertical translation stage, shown in the inset of Figure 3. The displacement speed of the stage was controlled to give approaching and receding velocities between the substrates

A micrometer syringe was used to control the volume of the drop introduced between the substrates with an accuracy of 0.001 ml. At the start of the experimental procedure, water was dropped on the surface of the lower substrate. Moving the upper surface downwards into contact with the droplet then formed a liquid

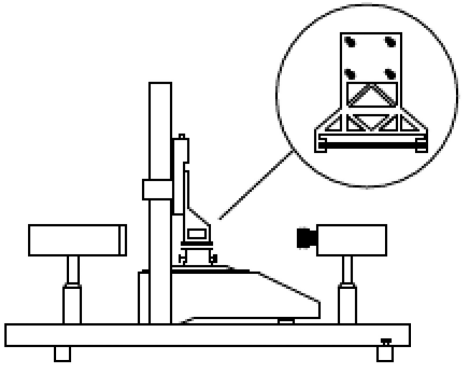


Figure 3. Schematics of the advanced goniometer system. The magnified window shows the balance component.



Figure 4. Images of capillary bridge between two substrates during experiment.

bridge. Subsequently the capillary force displacement behavior was studied by the movement of the upper substrate with simultaneous data acquisition from the analytical balance. Meanwhile, the camera in conjunction recorded substrate displacement and bridge shape with image processing software (DROPimage Advanced).

4 RESULTS AND DISCUSSIONS

Images of the liquid bridges produced in the present work at various stages of substrate displacement are shown in Figure 4.

4.1 *Measurement of Capillary Forces with two moving parallel plates*

Figure 5 shows the representative force-separation curves for a capillary bridge experiment between two cleaned glass substrates. The volume of the drop is 0.01 ml, the initial separation of the two parallel substrates is 0.4 mm. The x axis corresponds to the distance between two parallel substrates and the y axis indicates the capillary force arising from the capillary bridges. The lines in the image are the mean values and each displacement speed was repeated three times. The green line shows results obtained from the speed of 0.01 mm/s and the blue line shows the 0.02 mm/s. The black one was at the speed of 0.05 mm/s.

In this experiment, the capillary force-separation hysteresis is clearly evident. In this capillary bridge, the forces for both the approaching and receding phases are attractive for separation values of 0.4–2 mm. As the capillary bridge didn't break during

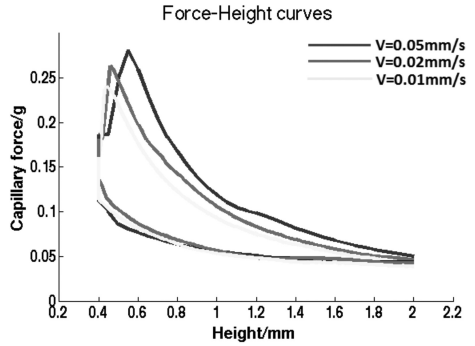


Figure 5. Capillary force-separation curves under speed of 0.05 mm/s, 0.02 mm/s and 0.01 mm/s.

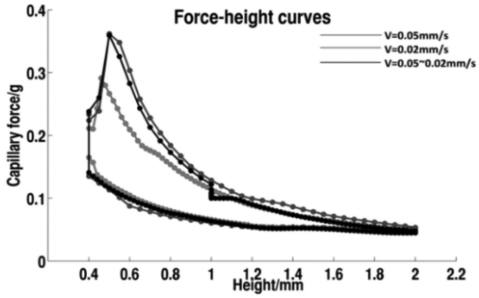


Figure 6. Force-separation curves under different speeds.

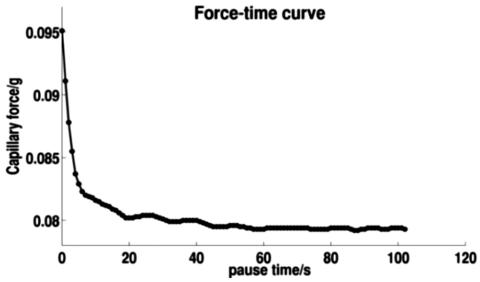


Figure 7. Force-time curve.

the separation stage, the force didn't exhibit any sudden drops. The plot of the capillary force during the approaching and recession stages can form a closed area. More importantly, the capillary force increases when substrate displacement takes place at a faster rate. However, during the approach of the substrates the rate dependence of the capillary force is not clearly observed.

4.2 *Measurement of Capillary Forces when parallel plates suspend*

In order to verify the existence of rate effects, we examined the effects of interrupting the movement of the upper substrate. The results are shown in Figure 6–11.

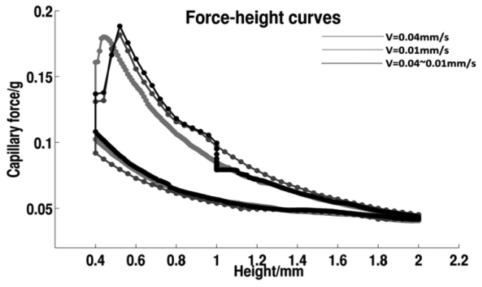


Figure 8. Force-separation curves under different speeds.

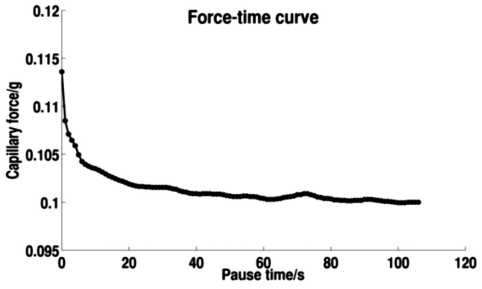


Figure 9. Force-time curve.

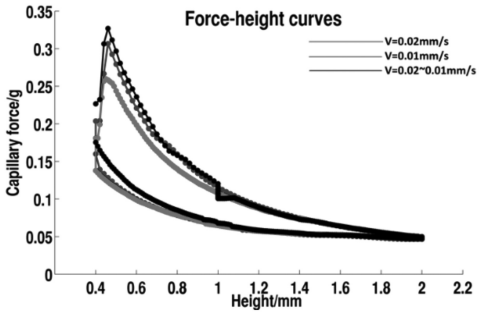


Figure 10. Force-separation curves under different speeds.

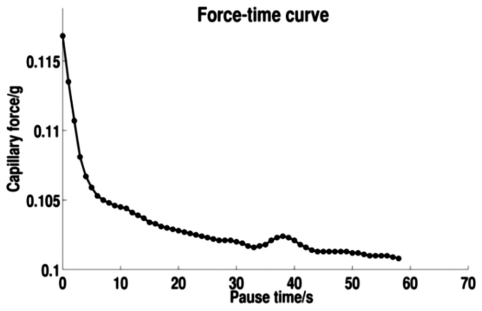


Figure 11. Force-time curve.

Figures 6, 8 and 10 show the capillary force-separation curves for conditions of varied displacement speeds. We selected two different speeds and after an initial displacement at the first selected rate we interrupted the movement of the upper substrate for a pause of about 100s before recommencing movement at the second rate. As a result, we found that the capillary force decreased during the stationary phase, and subsequent to the recommencement of motion converged with the force displacement curve of the second rate.

5 CONCLUSION

We constructed and carried out experiments to explore how capillary force changes with the displacement velocity between two substrates during receding and approaching motion. Owing to the short duration of the experiments, the influence of temperature and humidity on the evaporation rate of the droplets can be ignored. We thus assume that the volume of the drop is constant during the whole experiments. Experimental results have shown that the capillary force-separation curves for capillary bridges exhibit hysteresis under different speed conditions. The hysteresis of the force-separation curve is directly related to the speed of substrates. But the change of velocity only influences the upper branch of the hysteresis curve (during the receding phase) and has little influence on the lower branch (during decreasing substrate displacement). For higher displacement rates, the capillary force is found to increase. Furthermore, the capillary force diminishes with times exhibiting an initially sharp decrease before converging to a constant value.

REFERENCES

[1] Yuan-yuan, Y. & Hong-wei, H. 2005. Landslide hazard probability analysis for Sichuan province using landslide inventory.Chinese Journal of Rock Mechanics and Engineering. Vol. 24, Supp. 2.

[2] Yeh, H.F., Chen, J.F. & Lee, C.H. 2004. Application of a water budget model to evaluate rainfall recharge and slope stability. J. Chin. Inst. Environ. Eng., 14(4), 227–237.

[3] Hsin-Fu Yeh, Chen-Chang Lee & Cheng-Haw Lee. 2008. A rainfall-infiltration model for unsaturated soil slope stability.

[4] Rahardjo, H., Leong, E.C & Rezaur, R.B. 2002. Studies of rainfall-induced slope failures.Proceedings of the National Seminar, Slope. Bandung, Indonesia. 15–29.

[5] Fredlund, D.G. 1995. Prediction of unsaturated soil functions using the soil-water characteristic curve. Bengt B. Broms Symposium in Geotechnical Engineering. 13–16, Singapore.

[6] Yixiang, G., Maggi, F., Buscarnera, G. & Einav, I. 2013. A particle-water based model for water retention hysteresis. Geotechnnique Latters 3, 152–161.

[7] Young, T. 1805. An essay on the cohesion of fluids. Soc. Lond. 95, 65–97.

[8] Laplace, P. S. 1805. Sur L' Action Capillaire. In Dixieme Livre du Traite de Mecanique Celeste Paris, 1805–1806; pp. 1–65.

[9] De Souza, E. J., Gao, L., McCarthy, T. J., Arzt, E. & Crosby, A. J. 2008. Effect of contact angle hysteresis on the measurement of capillary forces.Langmuir, 24, 1391–1396.

Unsaturated Soil Mechanics—from Theory to Practice – Chen et al. (Eds)
© 2016 Taylor & Francis Group, London, ISBN 978-1-138-02921-7

Interaction force between pore water and soil skeleton

L.T. Shao & X.X. Guo
State Key Laboratory of Structural Analysis for Industrial Equipment, Dalian University of Technology, Dalian, Liaoning, China
Department of Engineering Mechanics, Dalian University of Technology, Dalian, Liaoning, China

ABSTRACT: According to the equilibrium differential equation of pore water, the expression of interaction force between pore water and soil skeleton is derived, which shows the relationship between the interaction force and pore water pressure. And then the expressions of seepage force for both saturated and unsaturated soils are discussed. For a saturated soil, the seepage force is the interaction force between pore water and soil skeleton. It differs from the conventional expression by a factor of porosity n. Therefore, it is inferred that the definition or expression of the conventional seepage force needs to be modified. Similarly, the expression of seepage force for an unsaturated soil is the same as that for a saturated soil. But the coefficient of the expression is volumetric water content, namely the porosity with respect to the water content instead of porosity n. For an unsaturated soil, in addition to the seepage force caused by the movement of pore water relative to soil skeleton, the change of the water content, namely the gradient of water content may also lead to the interaction force. It indicates that not only pore water movement, but also the change of the distribution of water content will contribute to the interaction force between soil skeleton and pore water. From the derivation process, it has also been found that, for a horizontal soil layer in a static equilibrium state, i.e., under the condition of constant temperature, constant humidity and no water movement, the distribution of the water content along the height of the soil layer above ground water level indicates the intrinsic relationship between matric potential and water content, namely the soil-water characteristic curve, which suggests a simple method to obtain the soil water characteristic curve. Besides, the paper also illustrates the physical significance of Darcy's law, and gives the theoretical formula of the coefficient of permeability for an unsaturated soil.

1 INTRODUCTION

Seepage problem is a common problem in many engineering problems. When a hydrogeologist predicts the tendency of the underground water level and the migration of pollutants, when an oil expert calculates the movement of three-phase interface (water, oil and gas), when the physiologist studies the microcirculation of blood, they all need to solve the seepage problem.

The concept of seepage force and its simplified formula were put forward by Terzaghi (1943). In soil mechanics, seepage force is generally defined as the force acting on pore water caused by the movement of pore water relative to soil skeleton in a unit volume of soil. The seepage force is a kind of body force, the dimension is the same as that of the unit weight of water, and the direction is consistent with that of the seepage. On the issues of seepage force (Chen, 2008; Chen, 1998; Gong, 1996; Chen, 1994) and its application to stability calculation of landslide, is the issue of academic debate for many years. Because the experts and scholars had different understandings of seepage force, so that academic reference for seepage force is still very sensitive and has doubts.

Darcy's law (Darcy, 1856; Neuman, 1977) is a test law based on the permeability test of saturated soil, and is lack of clear theoretical basis. When solving the seepage problem of unsaturated soil, the general method is to directly promote Darcy's law to the unsaturated soil. Measuring the permeability coefficient of unsaturated soil is very time-consuming. So a lot of experience or semi-experience formulas of permeability coefficient of unsaturated soil were put forward, such as Brooks-Corey model (Brooks, 1964), Gardner model (Gardner, 1970) and Van-Genuchten model (Van, 1980), and so on. So far, a theory formula of the permeability coefficient of unsaturated soils has still not been proposed.

In this paper, the expressions of seepage force for both saturated and unsaturated soils are derived by the equilibrium differential equation of pore water. For a saturated soil, the seepage force is the interaction force between pore water and soil skeleton. It differs from the conventional expression by a factor of porosity n. For an unsaturated soil, this expression is the same as that for a saturated soil. But the coefficient of the expression is volumetric water content, namely the porosity with respect to the water content instead

of porosity n. The seepage force for an unsaturated soil includes two parts: one caused by the movement of pore water relative to soil skeleton, the other caused by the change of the water content, namely the gradient of water content. It indicates that not only pore water movement, but also the change of the distribution of water content will contribute to the interaction force between soil skeleton and pore water. In addition, a simple method to obtain the soil water characteristic curve is suggested through the distribution of the water content along the height of the soil layer above ground water level. At last, according to the equilibrium differential equation of pore water, the physical significance of Darcy's law is illustrated, and the theoretical formula of the coefficient of permeability for an unsaturated soil is derived.

2 SEEPAGE FORCE FOR SATURATED SOIL

In almost all of the soil mechanics textbook, the seepage force for a saturated soil is given by

$$\boldsymbol{J} = \gamma_w \boldsymbol{i} \tag{1}$$

In which J is the seepage force (vector), γ_w is the unit weight of water, and i is the seepage gradient (vector) also known as the water potential gradient.

For a saturated soil, take the free bodies to carry out internal force analysis for the soil skeleton and pore water respectively by introducing interaction force between pore water and soil skeleton (Shao, 2011; Shao, 2014). The equilibrium differential equation of pore water can be written as (take the z direction as an example)

$$n\frac{\partial u_w}{\partial z} + f_z + n\gamma_w = 0 \tag{2}$$

In which u_w is the pore water pressure, n is the porosity, f_z is the interaction force between soil skeleton and pore water. $H = u_w/\gamma_w + z$, H is the total water head, z is the position water head.

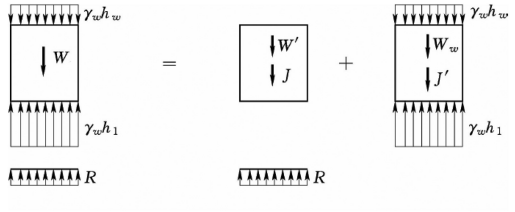
So equation (2) can be further written as

$$n\gamma_w \frac{\partial H}{\partial z} + f_z = 0 \tag{3}$$

In which $i_z = \frac{\partial H}{\partial z}$, the interaction force acting on the pore water between soil skeleton and pore water can be deduced

$$f_z = -n\gamma_w i_z \tag{4}$$

Formula (4) represents the force acting on the pore water from the soil skeleton in the unit volume of soil, as the pore water flows. Because in the unit volume of soil, the seepage force acting on the soil skeleton and the interaction force acting on the pore water are equal in magnitude but opposite in direction, the seepage force can be written as



(a)Soil body (b)Soil skeleton (c)Pore water

Figure 1. Two types of free body considering the seepage force.

$$\boldsymbol{f} = n\gamma_w \boldsymbol{i} \tag{5}$$

In which H is the total water head, u_w is the pore water pressure, z is the position head, f is the interaction force between soil skeleton and pore water, namely seepage force (vector), n is the porosity, γ_w is the unit weight of water, i is the water potential gradient (vector).

Since J and f represent the same meaning, why the expression of f does differ from that of J by a factor of porosity n? Because in the soil mechanics textbook, the definition of J is the seepage force in a unit volume of pore water not in the pore water of a unit volume of soil.

In the soil mechanics textbook, generally take a free body of pore water in a vertical or inclined direction to carry on an equilibrium analysis in order to obtain the expression of the seepage force (Chen, 1998).

Considering equilibrium condition of the pore water free body (Fig. 1), the seepage force can be written as

$$j = j' = \gamma_w i \tag{6}$$

If we confirm that the seepage force is the seepage force acting on soil skeleton from pore water in the unit volume of soil body, namely, the seepage force acting on pore water from skeleton soil in the unit volume of soil body, and note that is the pore water in the unit volume of soil body, rather than in the unit volume of pore water, then the forces analysis of pore water free body of the above soil column (Fig. 1) can be derived as follows.

(1) The gravity of the pore water, that is, the weight of the pore water in the soil column.

$$W_w = \gamma_w V_v = n\gamma_w V = n\gamma_w L \tag{7}$$

(2) Boundary water pressure on the upper and down face of water column are $\gamma_w n h_w$ and $\gamma_w n h_1$ respectively (When the area of soil column is equal to 1, the area of pore water is equal to n).

(3) Resistance acting on the pore water from the soil particles in the soil column, it and seepage force

are equal in magnitude but opposite in direction. j' is the resistance acting on the pore water from the soil particles in a unit volume soil, then the total resistance is $J' = j'L = J$, in the vertical downward direction.

Considering equilibrium condition of the pore water free body (Fig. (1c)), we can get

$$n\gamma_w h_w + W_w + J' = n\gamma_w h_1 \tag{8}$$

$$n\gamma_w h_w + nL\gamma_w + j'L = n\gamma_w h_1 \tag{9}$$

$$j' = \frac{n\gamma_w \left(h_1 - h_w - L\right)}{L} = \frac{n\gamma_w \Delta h}{L} = n\gamma_w i \tag{10}$$

So the seepage force can be written as $j = j' = n\gamma_w i$, which is the same result as that by applying equilibrium differential equation of pore water.

Of course, if we define that the seepage force is the penetration resistance acting on the unit volume of pore water, then the expression of seepage force can be rewritten as

$$\boldsymbol{j} = \boldsymbol{j}' = \gamma_w \boldsymbol{i} \tag{11}$$

If j represents the penetration resistance acting on the unit volume of pore water, and f represents the penetration resistance acting on pore water in the unit volume of soil, then the relationship between j and f satisfies the following formula

$$\boldsymbol{f} = n\boldsymbol{j} \tag{12}$$

According to the condition that seepage force acting on the same cross section is the same, the relationship between j and f can also be obtained.

$\because f \cdot A = j \cdot A_w$ and $A_w = n \cdot A$(A is cross section area)

$\therefore f \cdot A = j \cdot A_w = j \cdot n \cdot A$

Namely $f = j \cdot n$.

There is a problem in the above discussions, should the reaction force of buoyancy force of soil particle be included in the weight of pore water? Under the condition of static equilibrium, the gravity of pore water causes the change of the pressure, and the effect of the pressure produces the buoyancy force of soil skeleton, whose value is equal to the weight of the water displaced by soil skeleton. The so called reaction force of buoyancy force of soil particle is in fact the water pressure, which changes neither the weight of the water nor water pressure. No matter how the interaction between pore water and soil skeleton is, pore water pressure on the surface of pore water free body is still pore water pressure. As a result, taking pore water as the analysis object, its gravity should not contain the reaction force of buoyancy force of soil particle.

3 SEEPAGE FORCE FOR UNSATURATED SOIL

The seepage problem for unsaturated soil includes the seepage of pore water and pore gas. The seepage force produced by pore water and pore gas are referred to as the seepage force for unsaturated soil. As in saturated soil, the seepage force of pore water for unsaturated soil is defined as the seepage force acting on soil skeleton from pore water in a unit volume of soil body, and the seepage force of pore gas for unsaturated soil is defined as the seepage force acting on soil skeleton from pore gas in a unit volume of soil body. They are respectively equal to the seepage resistance acting on pore water and pore gas from soil skeleton in a unit volume of soil body. According to this definition, we still refer to equilibrium differential equation to derive the seepage force of unsaturated soil.

3.1 *Uniform water content*

Take the interaction force between pore water and soil skeleton as an example. Assuming that water content of soil is even, the equilibrium differential equations of pore water for an unsaturated soil can be written as (Shao, 2014)

$$n_w \frac{\partial u_w}{\partial z} + f_{swz} + n_w \gamma_w = 0 \tag{13}$$

In which n_w is the porosity with respect to the water content instead of porosity n in equation (2).

The pore water pressure in an unsaturated soil is negative, which can be expressed as soil water potential in soil physics and soil water dynamics. For open air, the pore gas pressure and solute potential can be ignored, the total water potential (water head) can be expressed by

$$H = \frac{u_w}{\gamma_w} + z \tag{14}$$

In which u_w/γ_w is the suction head, z is the position head. Then, substitute equation (14) into equation (13), the seepage force of unsaturated soil can be get under the condition of uniform water content.

$$\boldsymbol{f} = n_w \gamma_w \boldsymbol{i} \tag{15}$$

In which f represents the interaction force caused by relative movement between soil skeleton and pore water, namely the seepage force (vector). n_w is the porosity with respect to the water content instead of porosity n in equation (2), namely volumetric water content. γ_w is the unit weight of water. i is the gradient of water potential (vector).

As we can see, under the condition of uniform water content, the expression of seepage force for an unsaturated soil is the same as that for a saturated soil. But the coefficient of the expression is volumetric water content, namely the porosity with respect to the water content instead of porosity n.

3.2 *Uneven water content*

Formula (15) expresses the interaction force caused by relative movement between soil skeleton and pore water under the condition of uniform water content. Generally, water content in unsaturated soil is uneven. The equilibrium differential equations (13) of pore water for an unsaturated soil can be rewritten as

$$n_w \frac{\partial u_w}{\partial z} + u_w \frac{\partial n_w}{\partial z} + f_{swz} + n_w \gamma_w = 0 \tag{16}$$

Furthermore, the interaction force between soil skeleton and pore water can be obtained, its expression is

$$f_z = n_w \gamma_w i_z + u_w \frac{\partial n_w}{\partial z} \tag{17}$$

As you can see, for an unsaturated soil, in addition to the seepage force ($n_w \gamma_w i_z$) caused by the movement of pore water relative to soil skeleton, the change of the water content, namely the gradient of water content may also lead to the interaction force ($u_w \frac{\partial n_w}{\partial z}$). It indicates that not only pore water movement, but also the change of the distribution of water content will contribute to the interaction force between soil skeleton and pore water.

The interaction force corresponding to the change of the distribution of water content performances as the holding role and is essentially caused by the surface tension. However, the seepage force is caused by the movement of pore water relative to soil skeleton. Under the condition of laminar flow, it is proportional to the permeability velocity (the relative movement velocity of pore fluid relative to soil skeleton). When there is no relative movement between soil skeleton and pore fluid, namely there is no seepage, there is no seepage force. According to the equilibrium differential equation, for an unsaturated soil in a static equilibrium state, there also exits the interaction force between soil skeleton and pore fluid caused by the change of water content. The explanation is as follows.

As we know, under the condition of constant temperature and no water movement, pore water pressure in a soil layer has a linear distribution along the height z, the soil water potential of each point in the soil layer is equal, as shown in figure 2 (Shao, 2014). Take the free water surface in the soil layer as a standard reference plane and take pure free water state in the plane as a standard reference state, namely soil water potential of point "O" is equal to zero. So below the free water surface, the sum of gravitational potential and pressure potential of pore water is equal to zero, and above the free water surface, the sum of matric potential and gravitational potential of pore water is equal to zero. Therefore, for a horizontal soil layer in a static equilibrium state, matric potential is equal to negative gravitational potential. The distribution of the water content along the height of the soil layer above ground water level indicates the intrinsic relationship between matric potential and water content, namely the soil-water characteristic curve, which suggests a simple method to obtain the soil water characteristic curve.

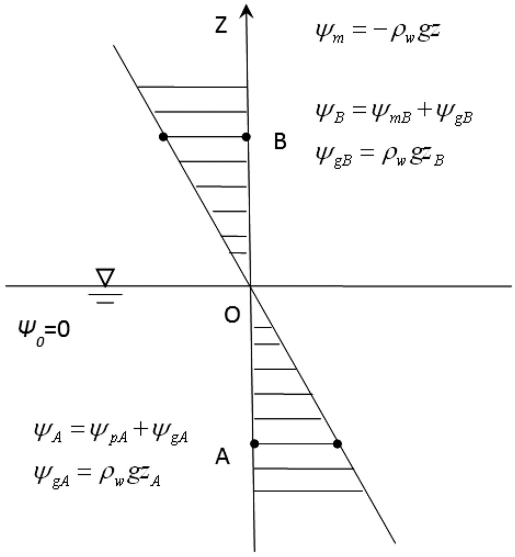


Figure 2. Distribution of pore water pressure in a soil layer under the condition of constant temperature and no water movement.

Substituting the distribution formula of pore water pressure into the equilibrium differential equation (13) of pore water, the interaction force between soil skeleton and pore water in a saturated soil layer and an unsaturated soil layer under the condition of static equilibrium can be obtained. The interaction forces are written as f_{sw0x} and f_{sw0z} in the x axis direction and Z axis direction respectively.

For a saturated soil layer,

$$f_{sw0x} = f_{sw0z} = 0 \tag{18}$$

For an unsaturated soil layer,

$$f_{sw0x} = \gamma_w n_e \frac{\partial S_{e0}}{\partial z} z_0 \; ; \quad f_{sw0z} = \gamma_w n_e \frac{\partial S_{e0}}{\partial x} z_0 \tag{19}$$

In which n_e is the effective porosity, $n_e = n - n_r$, n_r is the porosity of the residual water, S_{e0} is the effective saturation degree in a hydrostatic equilibrium state.

It can be seen that, for a saturated soil layer under the condition of static equilibrium, the interaction force between soil skeleton and pore water is equal to zero, and for an unsaturated soil layer, the change of water content shows the change of holding force, if there is a change in holding force in the pore water free body, the interaction force between soil skeleton and pore water is not equal to zero.

Therefore, it is suggested that the definition of seepage force should not contain the interaction force caused by the change of water content. So, in the case of uneven distribution of water content, the interaction force between soil skeleton and pore water is not equal to the seepage force, it also contains the interaction force corresponding to the change of water content.

4 DARCY'S LAW AND THEORETICAL FORMULA OF THE COEFFICIENT OF PERMEABILITY FOR AN UNSATURATED SOIL

4.1 *Darcy's law*

In hydraulics, the flow patterns are laminar flow and turbulent flow. For laminar seepage in a homogeneous saturated soil, it is reasonable to assume that the resistance of the pore fluid flow is in proportion to the seepage velocity, i.e.,

$$f_{wsi} = a_i \frac{v_i}{n} \tag{20}$$

where V_i is flow velocity of pore water, f_{wsi} is the interaction force between soil skeleton and pore water, a_i is the resistance coefficient for unit volume of pore water in laminar seepage.

By introducing the total water head function, $H = z + u_w/\gamma_w$, substituting the total water head function and equation (20) into equation (2) yields

$$v_i = -k_i J_i \tag{21}$$

where $J_i = H_{,i}$ and $k_i = \frac{n^2\gamma_w}{a_i}$.

Equation (21) is the seepage motion equation of pore water in a saturated soil. It reflects the relationship between the seepage velocity of pore water and the seepage gradient (water potential gradient), namely, the seepage velocity of pore water in a saturated soil is in proportion to seepage gradient. Equation (21) is the expression of Darcy's law. This means that, Darcy's law can be derived from the equilibrium differential equation of pore water assuming that the resistance of the pore water flow is in proportion to its velocity. In other words, Darcy's law proves that the resistance of the pore water flow in a saturated soil is proportional to the velocity of seepage flow. The formula of Darcy's law is just a simplified form of the momentum balance equation of laminar flow in a saturated soil. In a word, Darcy's law represents the linear proportional relationship between the resistance of the pore water flow and the flow velocity. The significance of Darcy's law is that it givens the relationship between the seepage velocity of pore water and hydraulic gradient from the macroscopic point of view. It is the basic physical relationship of the motion of pore water without having to pay attention to the interaction force between soil skeleton and pore water from the mesoscopic point of view.

4.2 *Theoretical formula of the coefficient of permeability for an unsaturated soil*

When pore water flows through unsaturated soil, it is also subjected to a flowing resistance, namely the interaction force between soil skeleton and pore water caused by the relative movement of soil skeleton and the flowing pore water. The flow of pore water in an unsaturated soil will not be in a turbulent state, be in laminar seepage. Similar to a saturated soil, for laminar seepage, the resistance of pore water flow is proportional to the velocity of seepage flow, can be written as:

$$f'_{swx} = a'_x \frac{v_x}{n_{ew}} \quad ; \quad f'_{swx} = a'_z \frac{v_z}{n_{ew}} \tag{22}$$

In which f'_{swx} and f'_{swz} are the components of the interaction force owing to water flowing, a'_x and a'_z are the factors of the interaction force in an unsaturated soil. $n_{ew} = n_w - n_r$, which denotes the effective porosity of water.

Thus the total interaction force between pore water and soil skeleton can be obtained by adding equation (22) and equation (19), i.e.,

$$f_{swx} = a'_x \frac{v_x}{n_{ew}} + \gamma_w n_e \frac{\partial S_{e0}}{\partial x} z_0 \tag{23}$$

$$f_{swz} = a'_z \frac{v_z}{n_{ew}} + \gamma_w n_e \frac{\partial S_{e0}}{\partial z} z_0 \tag{24}$$

Ignoring the interaction force between pore water and pore gas, and substituting the expression (23) and (24) of the interaction force between pore water and soil skeleton into the equilibrium differential equation (13) of pore water for an unsaturated soil, we can obtain

$$v_x = -k_x \left[\frac{\partial (S_e H)}{\partial x} - z \frac{\partial S_e}{\partial x} + z_0 \frac{\partial S_{e0}}{\partial x} \right] \tag{25}$$

$$v_z = -k_z \left[\frac{\partial (S_e H)}{\partial z} - z \frac{\partial S_e}{\partial z} + z_0 \frac{\partial S_{e0}}{\partial z} \right] \tag{26}$$

In which $k_x = n_e^2 \rho_w g/\alpha'_x, k_z = n_e^2 \rho_w g/\alpha'_z, S_e = n_{ew}/n_e = (S - S_r)/(1 - S_r)$.

Furthermore, it can be written as

$$v_x = -k_{ux} \frac{\partial H}{\partial x} \tag{27}$$

$$v_z = -k_{uz} \frac{\partial H}{\partial z} \tag{28}$$

So we can obtain that

$$k_u = k \left[S_e + (H - z) \frac{\partial S_e}{\partial H} + z_0 \frac{\partial S_{e0}}{\partial H} \right] \tag{29}$$

In which k_u is the permeability coefficient for an unsaturated soil (function), k is a parameter related to the interaction coefficient between pore water and soil skeleton, with the same physical significance as the permeability coefficient for a saturated soil.

For an unsaturated soil, the expression of motion equation for pore water given by formula (27) and formula (28) is the same as the existing equation, but it

is derived from the equilibrium differential equation of pore water, in which the expression of permeability coefficient is a theoretical formula. It can avoid using empirical or semi-empirical formula of permeability coefficient for an unsaturated soil, and also can avoid the trouble of the measurement of permeability coefficient. It is of great significance for solving seepage problem of an unsaturated soil.

5 CONCLUSION

According to the equilibrium differential equation of pore water, the expressions of seepage force for both saturated and unsaturated soils were discussed. The following conclusions can be obtained.

(1) For a saturated soil, the seepage force is the interaction force between pore water and soil skeleton. It differs from the conventional expression by a factor of porosity n. Therefore, it is inferred that the definition or expression of the conventional seepage force needs to be modified.
(2) For an unsaturated soil, the expression of seepage force is the same as that for a saturated soil. But the coefficient of the expression is the porosity with respect to the water content instead of porosity n. The seepage force includes two parts, one caused by the movement of pore water relative to soil skeleton, and the other caused by the change of the water content, namely the gradient of water content.
(3) For a horizontal soil layer in a static equilibrium state, i.e., under the condition of constant temperature, constant humidity and no water movement, the distribution of the water content along the height of the soil layer above ground water level is the soil-water characteristic curve.
(4) The theoretical formula of the coefficient of permeability for an unsaturated soil is deduced, which shows the relationship between permeability coefficient, saturation and soil water potential.

ACKNOWLEDGEMENTS

This research was supported financially by the National Natural Science Foundation of China (No. 51479023).

REFERENCES

Brooks, R. H., Corey, A. T. (1964) "Hydraulic properties of porous media". Hydrology Paper, Vol. 3, No. 3, pp. 1–27.
Chen, J. M. (2008) "The definition and argument of seepage force in soil", Geotechnical Engineering World, Vol. 11, No. 10, pp. 22–24.
Gong, X. N. (1996) "Advanced soil mechanics", Zhejiang university press.
Chen, X. Z. (1998) "Soil mechanics and foundation", Tsinghua university press.
Chen, Z. Y. (1994) "Soil mechanics", Tsinghua university press.
Darcy, H. (1856) "Les Fontaines Publiques de la Ville de Dijon". Paris: Victor Dalmont.
Gardner, W. R., Hillel, D., Benyamini, Y. (1970) "Post-irrigation movement of soil water: Redistribution". Water Resources Research, Vol. 6, No. 3, pp. 851–861.
Neuman, S. P. (1977) "Theoretical derivation of Darcy's law". Acta Mechanica, Vol.25, pp. 153–170.
Shao, L. T. (2011) "Skeleton stress equation for saturated soils". Chinese Journal of Geotechnical Engineering, Vol. 33, No. 12, pp. 1833–1837.
Shao, L. T. & Guo, X. X. (2014) "New explanation of the effective stress". Beijing: China Waterpower Press.
Terzaghi, K. (1943) "Theoretical Soil Mechanics", John Wiley & Sons, Inc.
Van, G. M. T. (1980) "A closed-form equation for predicting the hydraulic conductivity of unsaturated soils". Soil Science Society of America Journal, Vol. 44, No. 5, pp. 892–898.

Unsaturated Soil Mechanics—from Theory to Practice – Chen et al. (Eds)
© 2016 Taylor & Francis Group, London, ISBN 978-1-138-02921-7

Development of a hydro-thermal coupled model for unsaturated soils

N. An
Laboratoire Navier/CERMES, Ecole des Ponts ParisTech, France

S. Hemmati
IFSTTAR – French Institute of Science and Technology for Transport, Development and Networks, France

Y.J. Cui & A.M. Tang
Laboratoire Navier/CERMES, Ecole des Ponts ParisTech, France

ABSTRACT: A hydro-thermal coupled model for unsaturated soil is presented, which takes moisture and heat transfers into consideration. A finite-element method by FreeFem++ is developed, allowing the spatial and temporal matric suction and temperature changes to be described. The volumetric water content, hydraulic conductivity and thermal conductivity are expressed as a function of the key variable – soil matric suction. Some other parameters are related to another key variable – soil temperature. Comparison between the numerical result and testing data shows the relevance of this coupled model provided that suitable boundary conditions and soil parameters are considered. This hydro-thermal coupled model can be used for predicting the change of matric suction (volumetric water content) and temperature in unsaturated soils and applied for investigating the interaction between unsaturated soil and atmosphere.

1 BACKGROUND

In order to study the interaction between unsaturated soil and atmosphere, the evaporation (or infiltration) and soil state need to be considered at the same time. Lots of experimental works and theoretical formulas have been developed. Smith (1943), Phillip & de Vries (1957), Luikov (1975) and Blight (1997) introduced theoretical and applied models to describe the moisture movement in unsaturated porous media. Wilson (1990, 1994) put forward the coupled model of heat and mass transfers in unsaturated soils, and conducted the column drying test to evaluate the model. But most of their works focused on the evaporation theory and experimental work. Regarding the simulation work, Wilson (1994), Cui et al. (2005, 2010) did simulation work about the interaction between unsaturated soil and atmospheree based on finite difference method. Thomas et al. (1980, 1987, 1991, 1995, 2012) studied the temperature and capillary potential variations in unsaturated soils based on a coupled model. They also added volume change and chemical effect into the coupled model. Jahangir (2012) developed another fully coupled numerical model taking liquid flow, air flow and heat flow into consideration. In his paper, only temperature changes were studied, and the water flow under the influence of temperature was not analysed. Hemmati et al. (2012) analysed the interaction between unsaturated soil and atmosphere, obtaining soil water content variations and the induced settlements.

Numerical works on the temperature variation at soil surface were scarce. With the interaction happening at the soil surface, heat transfer and mass transfer influenced each other at the same time. It means that evaporation and infiltration can lead to changes of soil temperature. In this paper, a new fully coupled hydro-thermal model was proposed for simulating the behaviour of unsaturated soil by considering the soil-atmosphere interaction. Additionally, with the column drying test conducted by Wilson (1990), this hydro-thermal coupled model was evaluated.

2 THEORY

In a non-isothermal unsaturated soil, solid grains, water liquid and air are the three basic phases which may change simultaneously. Especially, the vapor flow and liquid flow in the region near soil surface significantly influence the soil moisture content and its distribution because of evaporation/infiltration. In order

to build the fully coupled model, some assumptions are made:

- The solid phase is assumed to be a continuous medium, and no volume change occurs.
- The water phase is considered to be a continuous pore-water as two parts: liquid flow and vapor flow.
- The air pressure keeps as a constant, thus air flow will not be considered in the simulation.

2.1 *Moisture transfer*

During moisture transfer, both liquid flow and vapor flow exist as:

$$q = q_l + q_v \tag{1}$$

With Darcy's law, the liquid transfer is expressed by an equation relating the total potential to the vector liquid flux density:

$$q_l = -K_w \rho_l (\nabla \varphi + \nabla z) \tag{2}$$

Generally, the pore vapor flux is considered to be caused by two effects, one is the bulk flow of the pore air, and another one is under molecular diffusion.

The mass flux of the pore vapor due to molecular diffusion can be expressed by Fick's law. Without considering the pore air flow effect, the total mass flux of the pore vapor is expressed as (Philip 1957):

$$q_v = -D_{atm} \alpha \beta \nabla \rho_v \tag{3}$$

The vapor density can be described in a local equilibrium state which exists between the liquid and vapor phases as:

$$\rho_v = \rho_0 \exp(\varphi g M_w / RT) \tag{4}$$

$$\begin{aligned} q_v &= -D_{atm} \alpha \beta \left(\frac{\rho_0 h g M_W}{RT} \nabla \varphi + h \frac{\partial \rho_0}{\partial T} \nabla T \right) \\ &= -\rho_l \left(\frac{D_{atm} \alpha \beta \rho_0 h g M_W}{RT \rho_l} \nabla \varphi + \frac{D_{atm} \alpha \beta h}{\rho_l} \frac{\partial \rho_0}{\partial T} \nabla T \right) \\ &= -\rho_l \left(D_{\varphi v} \nabla \varphi + D_{Tv} \nabla T \right) \end{aligned} \tag{5}$$

The liquid mass conservation equation is expressed as:

$$\frac{\partial w}{\partial t} = -\nabla q \tag{6}$$

w is the moisture content (kg/m^3), which can be determined by combining the vapor part and the liquid part:

$$w = \theta \rho_l + (\eta - \theta) \rho_v \tag{7}$$

Thus, the govern equations can be written as:

$$C_{\varphi T} \frac{\partial T}{\partial t} + C_{\varphi} \frac{\partial \varphi}{\partial t} = \nabla \cdot \left[K_{\varphi T} \nabla T \right] + \nabla \cdot \left[K_{\varphi} \nabla \varphi \right] + \rho_l \nabla K_w$$

where,

$$C_{\varphi} = (\rho_l - \rho_v) \frac{\partial \theta}{\partial \varphi} + (\eta - \theta) \frac{\rho_0 h g M_W}{RT}$$

$$C_{\varphi T} = -(\eta - \theta) \frac{\rho_0 \varphi g M_W h}{RT^2}$$

$$K_{\varphi T} = \rho_l D_{Tv}$$

$$K_{\varphi} = \rho_l D_{\varphi v} + K_W \rho_l$$

$$D_{\varphi v} = \frac{D_{atm} \alpha \beta \rho_0 h g M_W}{RT \rho_l}$$

$$D_{Tv} = \frac{D_{atm} \alpha \beta h}{\rho_l} \frac{\partial \rho_0}{\partial T} \tag{8}$$

2.2 *Heat transfer*

Because of the low temperature gradients, the heat transfer in unsaturated soils is mainly by conduction and convection process. Generally, the thermal conduction is in accordance with Fourier's law. We take the conduction process simply into consideration for the heat flow analysis.

The heat energy flux per unit area can be written based on Fourier's law as:

$$Q = -\lambda \nabla T + L_v (q_l + q_v) \tag{9}$$

Also, the conservation equation of heat energy is written as:

$$\frac{\partial (CT)}{\partial t} = -\nabla \cdot Q \tag{10}$$

Thus, the govern equation of heat flow is:

$$C_T \frac{\partial T}{\partial t} + C_{T\varphi} \frac{\partial \varphi}{\partial t} = \nabla \cdot \left[K_T \nabla T \right] + \nabla \cdot \left[K_{T\varphi} \nabla \varphi \right] + L_V \rho_l \nabla K_w$$

where,

$$C_T = \rho_s c_{ps} (1 - \eta) + \rho_l c_{pl} \theta + \rho_v c_{pv} (\eta - \theta) + \rho_a c_{pa} (\eta - \theta)$$

$$\lambda = (1 - \eta) k_s + \theta k_w + (\eta - \theta) k_v + (\eta - \theta) k_a$$

$$C_{T\varphi} = T \frac{\partial C}{\partial \varphi} = T \frac{\partial C}{\partial \theta} \frac{\partial \theta}{\partial \varphi} = T (\rho_l c_{pl} - \rho_v c_{pv} - \rho_a c_{pa}) \frac{\partial \theta}{\partial \varphi}$$

$$K_T = \lambda + L_v \rho_l D_{Tv}$$

$$K_{T\varphi} = L_v (\rho_l K_w + \rho_l D_{\varphi v}) \tag{11}$$

2.3 *FEM-Weak forms*

In order to calculate these two governing equations with finite element method in FreeFem++, some transformations are required to be conducted.

With the assumptions for the boundary conditions:

$$\begin{aligned} -K_w\frac{\partial \Phi}{\partial n} &= L_{vn} \\ \lambda\frac{\partial T}{\partial n} &= T_{vn} \end{aligned} \tag{12}$$

For liquid flow, its weak form is written as follows:

$$\begin{aligned} &\int_\Omega N_r\left(C_{\varphi T}\frac{\partial T}{\partial t}+C_\varphi\frac{\partial \varphi}{\partial t}\right)d\Omega-\int_\tau N_r K_{\varphi T}T_{vn}d\tau \\ &+\int_\Omega K_{\varphi T}\nabla N_r\nabla T d\Omega+\int_\tau N_r\frac{K_\varphi}{K_w}L_{vn}d\tau \\ &+\int_\Omega K_\varphi\nabla N_r d\Omega+\int_\Omega N_r\nabla K_\varphi d\Omega \\ &+\int_\Omega K_\varphi\nabla N_r\nabla\varphi d\Omega-\int_\Omega N_r\rho_l\nabla K_w d\Omega=0 \end{aligned} \tag{13}$$

For heat flow, it is as follows:

$$\begin{aligned} &\int_\Omega N_s\left(C_T\frac{\partial T}{\partial t}+C_{T\varphi}\frac{\partial \varphi}{\partial t}\right)d\Omega-\int_\tau N_s K_T T_{vn}d\tau \\ &+\int_\Omega K_T\nabla N_s\nabla T d\Omega+\int_\tau N_s\frac{K_{T\varphi}}{K_w}L_{vn}d\tau \\ &+\int_\Omega K_{T\varphi}\nabla N_s d\Omega+\int_\Omega N_s\nabla K_{T\varphi}d\Omega \\ &+\int_\Omega K_{T\varphi}\nabla N_s\nabla\varphi d\Omega-\int_\Omega N_s L_v\rho_l\nabla K_w d\Omega=0 \end{aligned} \tag{14}$$

3 EVALUATION

A column drying test was conducted by Wilson (1994), which shows the temperature and water content change in the soil by evaporation. It was chosen to evaluate the developed coupled model. The column was filled with saturated Beaver Creek sand initially. After draining to get a hydrostatic situation, it was sealed at the base and at the circumference. The surface of column was allowed to evaporate freely. The temperature and the volumetric water content changes were recorded by thermocouples at different depths. The laboratory air temperature was controlled at 38°C and the relative humidity was kept as 10% for 35 days. The details about this column drying test are shown in Figure1 and Figure 2.

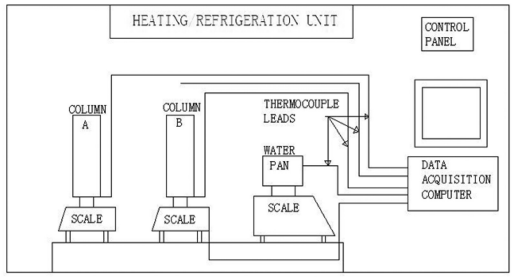


Figure 1. Column drying test by Wilson (1990).

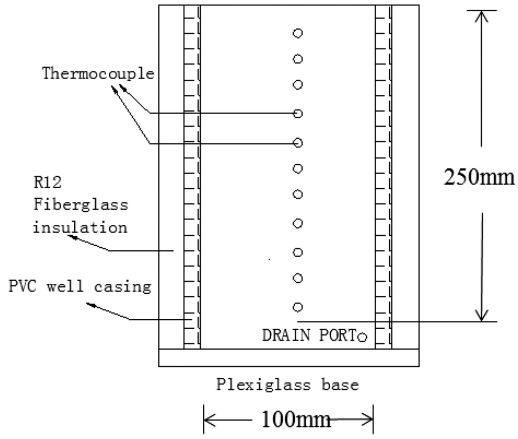


Figure 2. Details about the column drying test by Wilson (1990).

3.1 *Determination of parameters*

For the Beaver Creek sand used in the column drying test, we need to use its soil water retention curve, hydraulic conductivity curve and thermal conductivity for the numerical calculation. These curves are shown in Figures 3–5 respectively.

Based on the parameters selected by Cui et al. (2005), some modifications were made. The soil water retention curve was expressed as:

$$\theta=\frac{\theta_{ws}-\theta_r}{1+\left\{1+\left[\left(\theta_{ws}-\theta_r\right)/\left(\theta_{w1}-\theta_r\right)-1\right]\right\}\left(\varphi/\varphi_1\right)^\xi}+\theta_r \tag{15}$$

where, $\theta_{ws}=0.45$; $\theta_{w1}=0.2$; $\xi=1.98$; $\psi_1=6$ kPa.

Its hydraulic conductivity is calculated by:

$$K=\frac{K_s}{1+\left[\left(K_s/K_{w1}\right)-1\right]\left(\varphi/\varphi_1\right)^\xi} \tag{16}$$

where, $K_s=3.9\text{e-}6$ m/s; $K_{w1}=9.63\text{e-}8$ m/s; $\psi_1=2$ kPa; $\xi=3$.

When soil temperature changes in the range of 30°C–38°C, this formula is applied for calculating the soil thermal conductivity:

$$\lambda=4.44\cdot\theta+1 \tag{17}$$

3.2 *Numerical results and analysis*

The simulation results about temperature and volumetric water content in the first day are shown in Figures 6–7.

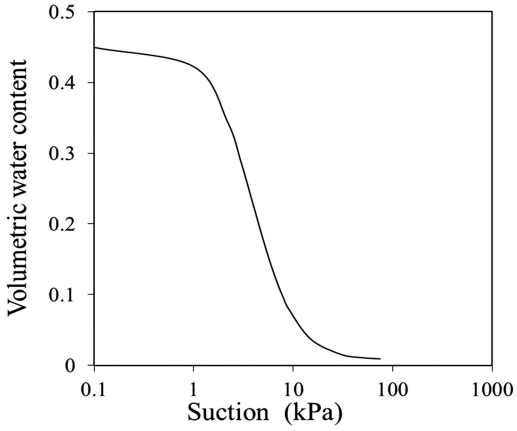


Figure 3. Soil water retention curve for Beaver Creek sand.

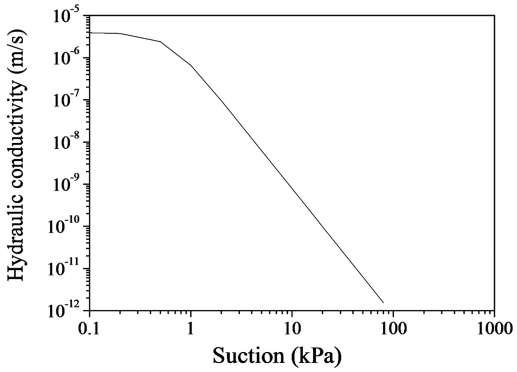


Figure 4. Hydraulic conductivity curve for Beaver Creek sand.

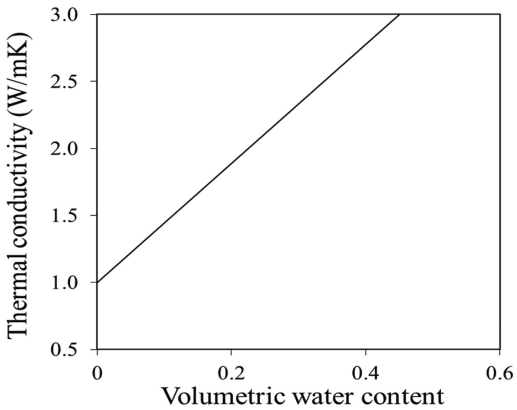


Figure 5. Thermal conductivity curve for Beaver Creek sand.

For the temperature change in Figure 6, the numerical results are nearly consistent with the test data. The bottom temperature ($h = 0$ m) keeps almost constant over time. With the increase of soil height, the temperature decreases more rapidly, which is the result of

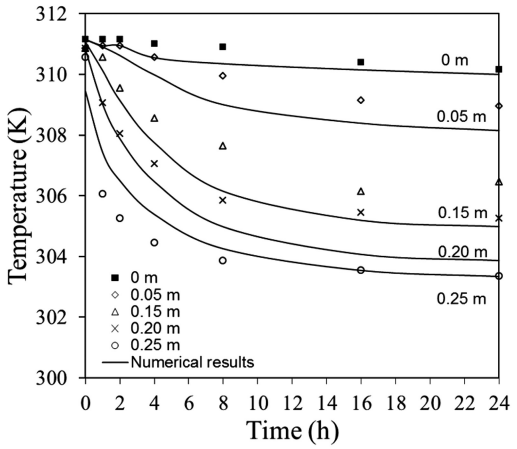


Figure 6. Comparison between numerical results and column drying test data of temperature change as time at different heights.

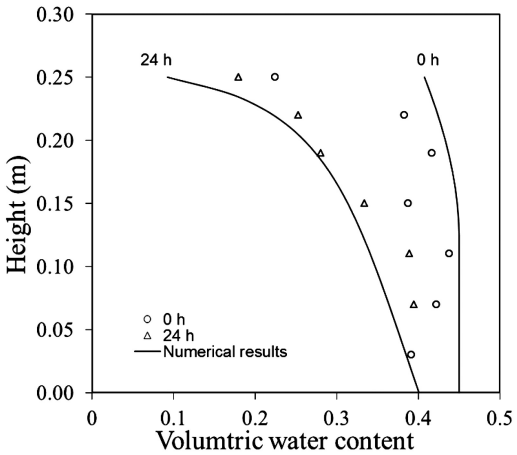


Figure 7. Comparison between numerical results and column drying test data about soil volumetric water content distribution.

surface water evaporation. As evaporation is an energy consuming process, the temperature of the whole soil column goes down. The soil surface is significantly influenced by the evaporation, and it is therefore the lowest. However, the temperature distribution in the middle location of the column shows a little larger discrepancy. This shows that even though insulation materials were set around the column, as the test going on, the soil inside was unavoidably influenced by the ambient air temperature. Therefore, the real soil temperature in the middle of column is a little larger than the calculation result.

In Figure 7, as time changes, the total water content of the soil column decreases and the water content in the region near soil surface decreases rapidly. We can see that the result of the initial situation and the first day by numerical calculation and test data are

consistent even though no enough data were provided for this stage.

A satisfactory correspondence is obtained between the computation and the measurement, showing that this coupled model is relevant when suitable parameters are chosen and real boundary conditions are considered. Therefore, it can be used for further numerical analyses.

4 CONCLUSIONS

In this study, a coupled hydro-thermal model of unsaturated soil was proposed which considers the matric suction and temperature of unsaturated soil. After defining the two control equations, they were rewritten and transferred to weak forms in order to be applied in FreeFem++. By setting appropriate boundary conditions, the change of temperature and suction of unsaturated soil can be correctly determined. Then, this coupled model was evaluated by simulating a column drying test conducted by Wilson (1990). The numerical result and the testing data are found consistent, showing the performance of the model.

Besides, during the interaction between unsaturated soil and atmosphere, the energy balance and the mass balance decide the boundary conditions, which are iterated variables during calculation. They are changing based on the real situation of atmosphere environment and unsaturated soil in the whole process. More research work about the physical phenomenon and mechanisms need to be done for further comprehension about this interaction process.

ACKNOWLEDGEMENTS

The authors wish to acknowledge the support of the European Commission by the Marie Curie IRSES project GREAT – Geotechnical and geological Responses to climate change: Exchanging Approaches and Technologies on a world-wide scale (FP7-PEOPLE-2013-IRSES- 612665).

5 NOTATIONS

C Volumetric heat capacity of the soil (J/m^{3}K)
$C_{T\psi}$ Volumetric isothermal capacity of the structure (J/m^{3}K)
C_T Volumetric thermal capacity of the structure (J/m^{3}K)
$C_{\psi T}$ Volumetric thermal capacity of moisture (kg/m^{3}K)
C_ψ Volumetric isothermal capacity of moisture (kg/m^3 K)
c_{pl} Specific heat capacity of water liquid (J/kg K)
c_{ps} Specific heat capacity of structure (J/kg K)
c_{pv} Specific heat capacity of pore vapor (J/kg K)
c_{pa} Specific heat capacity of air (J/kg K)
D_{atm} Molecular diffusivity of vapor in the air (m^2/s)
K_T Thermal soil structure diffusivity (W/m K)
$K_{T\psi}$ Isothermal soil structure diffusivity (W/m)
$K_{\psi T}$ Thermal moisture diffusivity (m^2/s K)
K_ψ Isothermal moisture diffusivity (m^2/s)
D_{Tv} Thermal vapor diffusivity (m^2/s K)
$D_{\psi v}$ Isothermal vapor diffusivity (m^2/s)
K Unsaturated hydraulic conductivity (m/s)
K_s Saturated hydraulic conductivity (m/s)
K_{w1} Unsaturated hydraulic conductivity at a suction ψ_1 (m/s)
L_v Latent heat of vaporization (J/kg)
P_a Pore dry air pressure (Pa)
Q Heat flux per unit area (W/m^2)
q Density of moisture flow rate (kg/m^{3}s)
q_l Density of liquid flow rate (kg/m^{3}s)
q_v Density of vapor flow rate (kg/m^{3}s)
L_{vn} Surface liquid flow (m/s)
T_{vn} Surfce heat source flow (W/m^2)
RH Relative humidity
R Universal gas constant (J/molK)
T Absolute temperature (K)
S Degree of saturation (%)
w Moisture content (kg/m^3)
z Elevation head (m)
α Tortuosity factor for soil
β Cross-sectional area of the soil that is available] for vapor flow
ϕ Soil porosity
θ Volumetric water content
θ_{ws} Saturated volumetric water content
θ_{w1} Volumetric water content at a suction ψ_1
ψ Matric suction head (m)
ψ_1 Matric suction head corresponding θ_{wl} (m)
λ Unsaturated thermal conductivity (W/mK)
λ_s Thermal conductivity of soil (W/m K)
λ_w Thermal conductivity of water (W/m K)
λ_v Thermal conductivity of vapor (W/m K)
λ_a Thermal conductivity of air (W/m K)
ρ_0 Density of saturated water vapor (kg/m^3)
ρ_v Vapor density (kg/m^3)
ζ Coefficient of proportionality

REFERENCES

Blight, G.E. 1997. Interaction between the atmosphere and the earth. Géotechnique 47(4): 715–767.

Cui, Y.J., Lu, Y.F., Delage, P., Riffard, M. 2005. Field simulation of in situ water content and temperature changes due to ground-atmospheric interactions. Géotechnique 55(7): 557–567.

Cui, Y.J., Gao, Y.B., Ferber, V. 2010. Simulating the water content and temperature changes in an experimental embankment using meteorological data. Engineering Geology 114: 456–471.

Hemmati, S., Gatmiri, B., Cui, Y.J., Vincent, M. 2012. Thermo-hydro-mechanical modelling of soil settlements induced by soil-vegetation-atmosphere interactions. Engineering Geology 139–140: 1–16.

Jahagir, M.H., Sadrnejad, S.A. 2012. A new coupled heat, moirture and air transfer model in unsaturated soil. Journal of Mechanical Science and Technology 26(11): 3661–3672.

Luikov, A.V. 1975. Systems of differential equations of heat and mass transfer in capillary-porous bodies, International Journal of Heat and Mass Transfer 18: l–14.
Philip, J.R., De Vries, D.A. 1957. Moisture movement in porous media under temperature gradients, Transactions American Geophysical Union 38: 222–232.
Smith, W.O. 1943. Thermal transfer of moisture in soils, Transactions American Geophysical Union 24: 511–523.
Thomas, H.R., Morgan, K., Lewis, R.W. 1980. A fully non-linear analysis of heat and mass transfer problems in porous bodies. International Journal for Numerical Methods in Engineering 15(9): 1381–1393.
Thomas, H.R. 1987. Non-linear analysis of heat and moisture transfer in unsaturated soil: Journal of Engineering Mechanics 113(8): 1163–1180.
Thomas, H.R., Li, C. 1991. Parallel computing solution of coupled flow processes in soil. Journal of Computing in Civil Engineering 5(4): 428–443.
Thomas, H.R., He, Y. 1995. Analysis of coupled heat, moisture and air transfer in a deformable unsaturated soil. Géotechnique 45(4): 677–689.
Thomas, H.R., Sedighi, M., Vardon, P.J. 2012. Diffusive reactive transport of multicomponent chemicals under coupled thermal, hydraulic, chemical and mechanical conditions. Geotechnical and Geological Engineering 30: 841–857.
Wilson, G.W. 1990. Soil evaporative fluxes for geotechnical engineering problems. PhD dissertation, University of Saskatchewan, Saskatoon.
Wilson, G.W., Fredlund, D.G., Barbour, S.L. 1994. Coupled soil-atmosphere modeling for soil evaporation. Canadian Geotechnical Journal 31(1): 151–161.

Unsaturated Soil Mechanics—from Theory to Practice – Chen et al. (Eds)
© 2016 Taylor & Francis Group, London, ISBN 978-1-138-02921-7

Nonlinear analysis of stress-strain relations of unsaturated soils

J.H. Zhang, Z.H. Chen, D. Chen & Q.Q. Miao
Logistical Engineering University, Chongqing, China

Z.H. Yao
Air Force Engineering University, Xi'an, China

ABSTRACT: The $E-\mu$ nonlinear model and its improved models are not applicable to soils with strain-softening behavior and obvious dilatancy. In order to overcome the disadvantages of the above models, the rate of Poisson's ratio is proposed, and it is found that, under triaxial shearing, the tangent modulus of unsaturated soils and the rate of Poisson's ratio decay exponentially with the axial strain. Based on this law, a non-linear model describing the stress-strain relationships of unsaturated soils is proposed, which can reflect both the strain-hardening and strain-softening behavior of unsaturated soils, and also can describe the stress-strain characteristics of unsaturated soils under various stress paths. The influencing factors of model parameters are analyzed. Besides the dilatancy of unsaturated soil specimens, the relationship between attenuation of tangent modulus and yielding of unsaturated soil specimens is discussed.

1 INTRODUCTION

Most soils in practical engineering are unsaturated soils, which are different from saturated soils. Chen et al. (1999) presented a nonlinear model of unsaturated soils, which can be seen as the improvement of $E-\mu$ model for saturated soils proposed by Duncan & Chang (1970). Ling et al. (2008) considered the effect of moisture content on the strength and deformation of unsaturated soils, and presented another improved $E-\mu$ model. Due to the limitation of its mathematical form, the $E-\mu$ hyperbolic model and its improved models can not reflect the strain-softening behavior and obvious dilatancy of soils.

In order to overcome the disadvantages of the $E-\mu$ models, Gitau et al. (2006) proposed an exponential model, and Wang et al. (2010) proposed a composite exponential-hyperbolic model for stress-strain curve of seashore soft soil.

Based on triaxial shearing tests, this paper presents a new nonlinear model of unsaturated soils. The soil used in the tests was collected from the slope bank at Anyang district of Henan province in China. The detailed information about the tests was introduced by Zhang et al. (2011).

2 MODEL ESTABLISHMENT

2.1 *Description of tangent modulus*

Figure 1 shows the variation of tangent modulus with axial strain of the soil specimens from the slope bank at Anyang district under triaxial shearing tests. It is found that the tangent modulus decays exponentially with the axial strain, which can be described as:

$$E_t = \frac{\partial(\sigma_1-\sigma_3)}{\partial\varepsilon_a} = E_i\left[(1-r_1)\exp(-\beta_1\varepsilon_a)+r_1\right] \tag{1}$$

where E_t is tangent modulus; $(\sigma_1-\sigma_3)$ and ε_a are deviatoric stress and axial strain, respectively; E_i is the initial tangent modulus (the tangent modulus at $\varepsilon_a=0$); β_1 is the attenuation index of modulus (the larger β_1 is, the faster tangent modulus decays with the axial strain); r_1 is the tangent modulus ratio, $r_1=E_t(\varepsilon_a\to\infty)/E_i$.

The comparison of Equation (1) and test data are shown in Figure 1, from which it can be seen that Equation (1) is in good agreement with test data.

2.2 *Description of deviatoric stress-axial strain relations*

Integral of Equation (1) in the interval $[0, \varepsilon_a]$ arrives at:

$$\sigma_1-\sigma_3 = \frac{E_i}{\beta_1}\left[(1-r_1)(1-\exp(-\beta_1\varepsilon_a))+r_1\beta_1\varepsilon_a\right] \tag{2}$$

The comparison of Equation (2) and test data is shown in Figure 2, from which it can be seen that Equation (2) agrees well with test data.

2.3 *Description of tangent Poisson's ratio*

The rate of Poisson's ratio is proposed as:

$$\dot{\mu}_t = \frac{\partial\mu_t}{\partial\varepsilon_a} \tag{3}$$

where $\dot{\mu}_t$ is the rate of Poisson's ratio, μ_t is tangent Poisson's ratio, $\mu_t=\partial(-\varepsilon_r)/\partial\varepsilon_a$. The radial strain ε_r

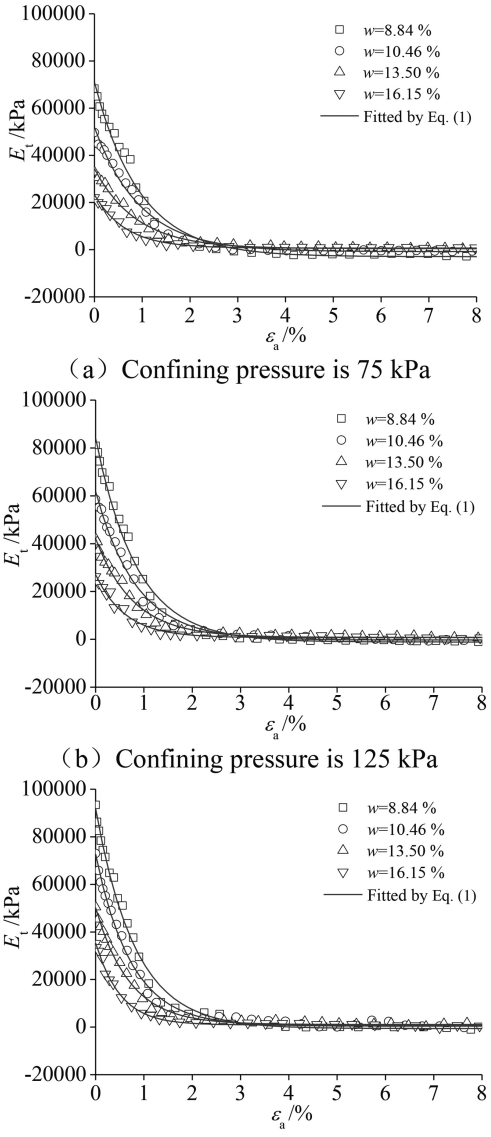


Figure 1. Variation of tangent modulus with axial strain.

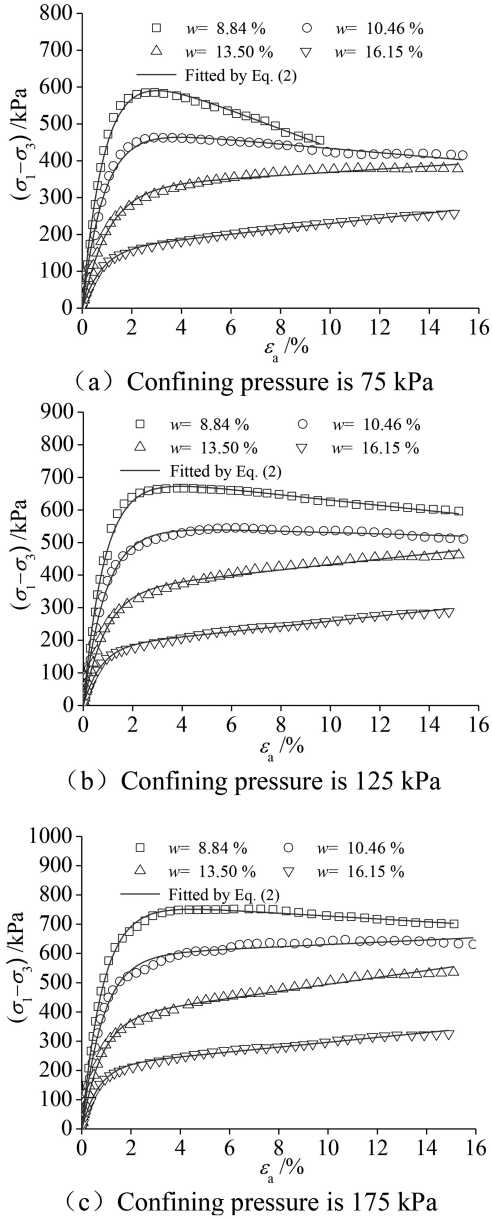


Figure 2. Variation of deviator stress with axial strain.

have opposite signs to axial strain ε_a when the soil specimens are under compression.

Analysis of the test data show that, $\dot{\mu}_t$ decays exponentially with ε_a, which can be expressed as:

$$\dot{\mu}_t = \lambda \exp(-\beta_2 \varepsilon_a) \tag{4}$$

where λ is a fitting parameter decided by tests; β_2 is the attenuation index of rate of Poisson's ratio. The larger β_2 is, the faster Poisson's ratio rate decays with the axial strain.

The comparison of Equation (4) and test data are shown in Figure 3, from which it can be seen Equation (4) and test data show good agreement.

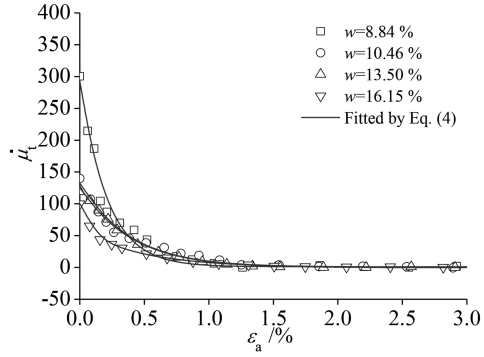
Integral of Equation (4) in the interval [0, ε_a] arrives at:

$$\mu_t = \frac{\lambda}{\beta_2}\left[1-\exp(-\beta_2 \varepsilon_a)\right] + \mu_i \tag{5}$$

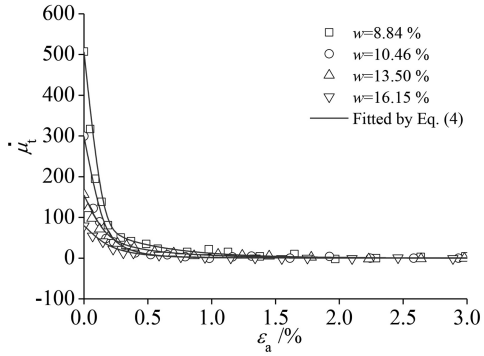
where μ_i is the initial tangent Poisson's ratio, $\mu_i = \mu_t(\varepsilon_a \to 0)$.

To get clear on the meaning of λ, let $\varepsilon_a \to \infty$ in Equation (5). Therefore, $\mu_t(\varepsilon_a \to \infty) = \lambda/\beta_2 + \mu_i$, and then:

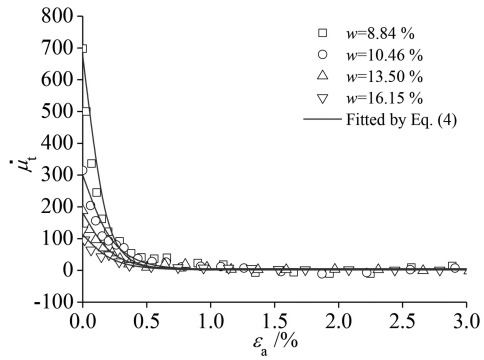
$$\lambda = \beta_2\left[\mu_{tu} - \mu_i\right] = \beta_2 \mu_i \left(r_2 - 1\right) \tag{6}$$



（a）Confining pressure is 75 kPa



（b）Confining pressure is 125 kPa



（c）Confining pressure is 175 kPa

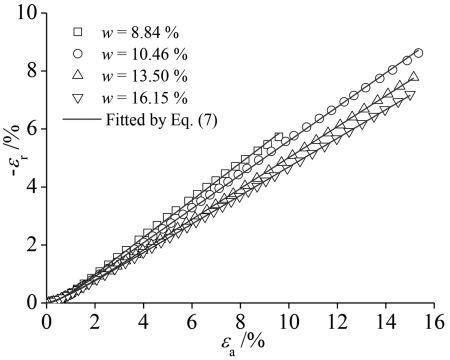
Figure 3. Variation of Poisson's ratio rate with axial strain.

where μ_{tu} is ultimate tangent Poisson's ratio, $\mu_{tu} = \mu_t$ ($\varepsilon_{a\to\infty}$); r_2 is the ratio between μ_{tu} and μ_i, $r_2 = \mu_{tu}/\mu_i$.

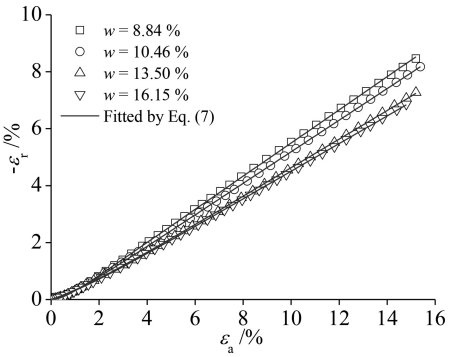
2.4 *Description of radial strain-axial strain relations*

Substituting Equation (6) into Equation (5) and then integral of Equation (5) in the interval [0, ε_a] arrives at:

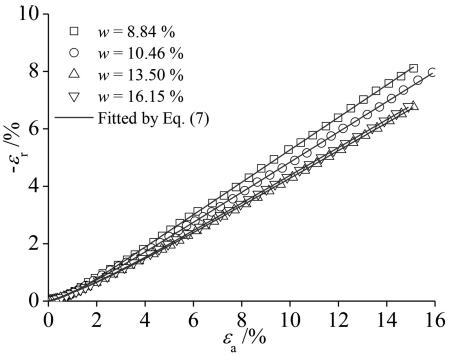
$$-\varepsilon_r = \frac{\mu_i}{\beta_2}\left[(1-r_2)\left(1-\exp(-\beta_2\varepsilon_a)\right)+r_2\beta_2\varepsilon_a\right] \tag{7}$$



（a）Confining pressure is 75 kPa



（b）Confining pressure is 125 kPa



（c）Confining pressure is 175 kPa

Figure 4. Variation of negative radial strain with axial strain.

The comparison of Equation (7) and test data are shown in Figure 4, from which it can be seen Equation (7) is well coincident with test data.

2.5 *Summary of the model*

The proposed nonlinear model has four equations as follows:

$$\left.\begin{aligned} E_t &= a_1\beta_1\exp(-\beta_1\varepsilon_a)+b_1 \\ \mu_t &= a_2\beta_2[1-\exp(-\beta_2\varepsilon_a)]+\mu_i \\ \sigma_1-\sigma_3 &= a_1[1-\exp(-\beta_1\varepsilon_a)]+b_1\varepsilon_a \\ -\varepsilon_r &= a_2[1-\exp(-\beta_2\varepsilon_a)]+b_2\varepsilon_a \end{aligned}\right\} \tag{8}$$

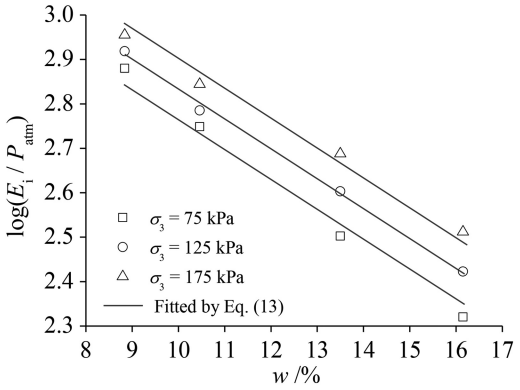


Figure 5. Variation of $\log(E_i/P_{atm})$ with w and σ_3.

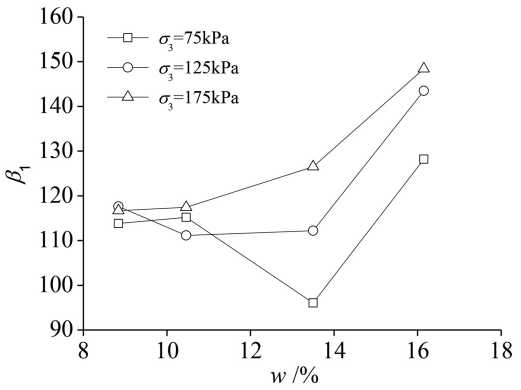


Figure 6. Variations of β_1 with moisture content and cell pressure.

where $a_1 = E_i(1-r_1)/\beta_1$, $b_1 = E_i r_1$, $a_2 = \mu_i(1-r_2)/\beta_2$, $b_2 = \mu_i r_2$.

This model has six parameters, i.e., E_i, r_1, β_1, μ_i, r_2 and β_2. From Equation (8) it can be seen, under triaxial compression, when the model parameters are determined, the tangent modulus (E_t), the tangent Poisson's ratio (μ_t), the deviatoric stress ($\sigma_1 - \sigma_3$) and the radial strain (ε_r) are only related with the axial strain (ε_a).

3 DETERMINATION AND ANALYSIS OF MODEL PARAMETERS

The determination of model parameters can be performed with triaxial shearing tests and fitting to test data using Equation (8). It must be pointed out that, the values of model parameters varied with soil classification, density, moisture content (or saturation degree), drainage condition and stress state, etc. To illustrate the determination method of model parameters and analyze the main influencing factors of them, test data from Zhang et al. (2011) are used. When determining the model parameters, all the coefficients of determination (R^2) exceed 0.95 and residual scatterplots appear unordered, showing the values of model parameters are reliable.

3.1 *Analysis of influencing factors of E_i*

Variation of E_i with w and σ_3 in triaxial undrained test is shown in Figure 5, in which the data can be described as follows:

$$\log(E_i/P_{atm}) = m + n_1 w + n_2(\sigma_3/P_{atm}), \quad R^2 = 0.9875 \qquad (9)$$

where P_{atm} is the value of standard atmospheric pressure; m stands for the value of $\log(E_i/P_{atm})$ of dry soil under confining pressure 0 kPa, $m = 3.338$; $n_1 = -6.759$ and $n_2 = 0.137$, which indicates that E_i decrease with water content and increase with confining pressure.

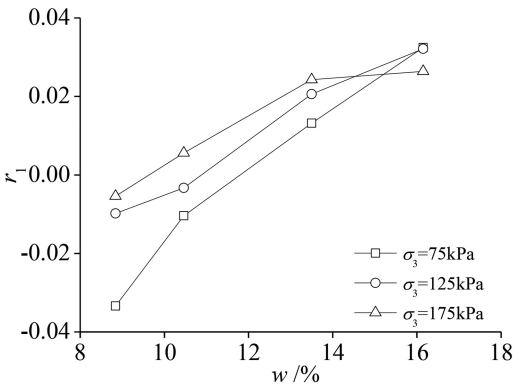


Figure 7. Variation of r_1 with moisture content and cell pressure.

3.2 *Analysis of influencing factors of β_1*

Variation of β_1 with w and σ_3 in triaxial undrained test is shown in Figure 6. In general, under the same confining pressure, β_1 gets to its minimum value when the moisture content approaches the optimum moisture content (12.32%). That is because under the optimum moisture content the soil particles are tightly bound to each other.

3.3 *Analysis of influencing factors of r_1*

As stated previously, the value of β_1 reflects the reduction rate of tangent modulus, while the value of r_1 mirrors the extent of modulus reduction. Variation of r_1 with w and σ_3 is shown in Figure 7. In general, r_1 increases with σ_3 and w. That is, the larger confining pressure and higher moisture result in less reduction of tangent modulus.

3.4 *Analysis of influencing factors of μ_i*

Variation of μ_i with w and σ_3 is shown in Figure 8, from which it can be seen that, under the same confining pressure, μ_i gets to its maximum value when

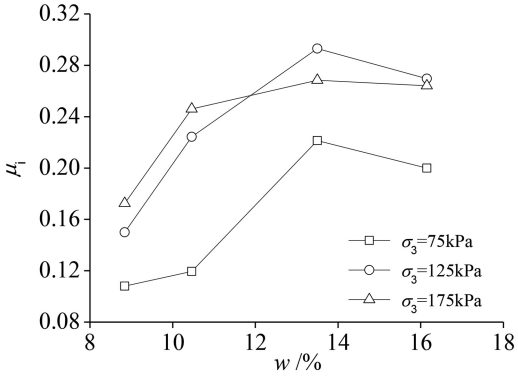


Figure 8. Variation of μ_i with moisture content and cell pressure.

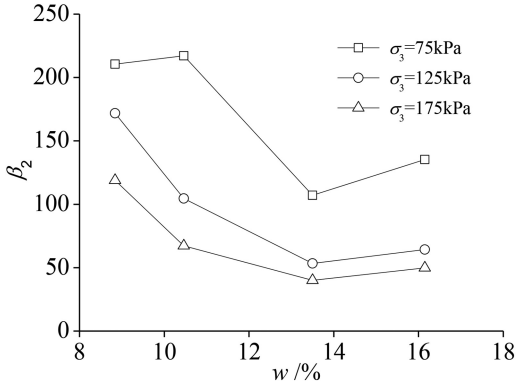


Figure 9. Variation of β_2 with moisture content and cell pressure.

the moisture content approaches the optimum moisture content. However, there is no obvious rule in variation of μ_i with the confining pressure.

3.5 *Analysis of influencing factors of β_2*

Variation of β_2 with w and σ_3 is shown in Figure 9. Under the same moisture content, β_2 increases with the confining pressure, showing that the tangent Poisson's ratio increases slowly under high confining pressure. On the other hand, under the same confining pressure, β_2 gets to its minimum value when the moisture content approaches the optimum moisture content.

3.6 *Analysis of influencing factors of r_2*

As shown in Figure 10, under the same confining pressure, r_2 gets to its minimum value when the moisture content approaches the optimum moisture content. On the other hand, r_2 decreases with the increasing confining pressure.

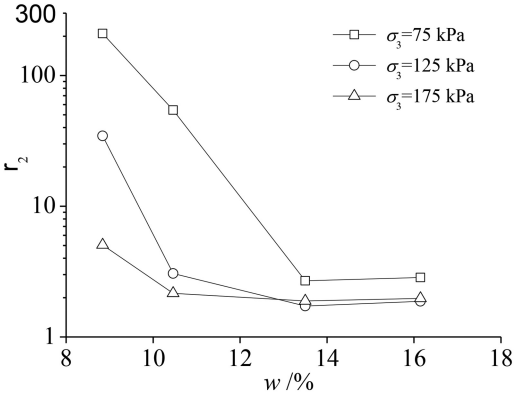


Figure 10. Variation of r_2 with moisture content and cell pressure.

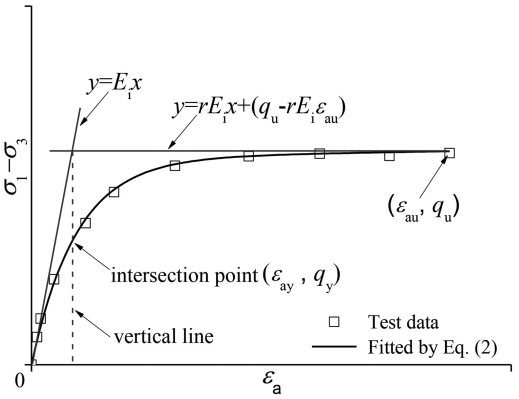


Figure 11. Determination of yielding strain and deviator stress.

4 DISCUSSION

4.1 *Relationship between the attenuation of tangent modulus and yielding of soil specimen*

Analysis of test data show that, there exists relationship between attenuation rate of tangent modulus and yielding speed of soil specimen. Methods for describing the yielding of soil specimens can be found from Alonso et al. (1990) and Chen et al. (1999), and the method proposed by Chen et al. (1999) is used in this paper to determine the axial strain of soil specimen at yielding. As shown in Figure 11, ε_{ay} and q_y are the axial strain and deviatoric stress of soil specimen at yielding, respectively. ε_{au} and q_u are the axial strain and deviatoric stress of soil specimen at the end of the test, respectively.

After ε_{ay} is determined, curves drawn using each pair of ε_{ay} and the corresponding β_1 is shown in Figure 12, from which it can be seen, β_1 decreases

monotonously with increasing ε_{ay}, and the relationship between ε_{ay} and β_1 can be expressed by $\beta_1 = 1/\varepsilon_{ay}$.

4.2 *Relationship between tangent modulus ratio and ultimate tangent Poisson's ratio*

From Figure 2 and Figure 4 it can be seen, when moisture content and confining pressure are low, the $(\sigma_1 - \sigma_3) \sim \varepsilon_a$ relation curve shows strain-softening shape (see Figure 2), and correspondingly the location of $-\varepsilon_r \sim \varepsilon_a$ relation curve is high and the linear segment of it shows a large slope (see Figure 4).

On the one hand, according to the definition of r_1, when $r_1 < 0$, the $(\sigma_1 - \sigma_3) \sim \varepsilon_a$ curves show strain-softening shape; when $r_1 > 0$, the $(\sigma_1 - \sigma_3) \sim \varepsilon_a$ curves show strain-hardening shape. On the other hand, as stated previously, μ_{tu} stands for the ultimate tangent Poisson's ratio, $\mu_{tu} = r_2 \mu_i$.

Relationship between r_1 and μ_{tu} is shown in Figure 13, from which it can be seen that r_1 decreases approximately linearly with the increasing of μ_{tu}. That is, with the increase of the ultimate tangent Poisson's ratio, the shape of the $(\sigma_1 - \sigma_3) \sim \varepsilon_a$ curve will turn from strain-hardening to strain-softening.

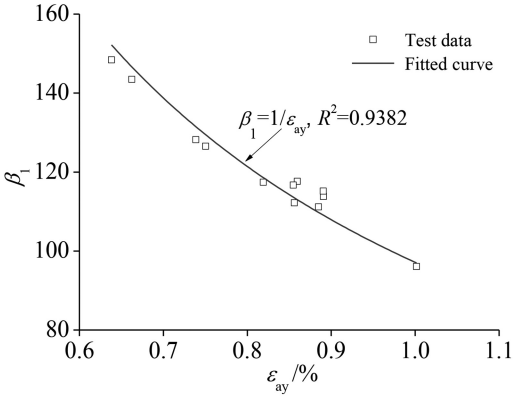


Figure 12. Relationships between β_1 and ε_{ay}.

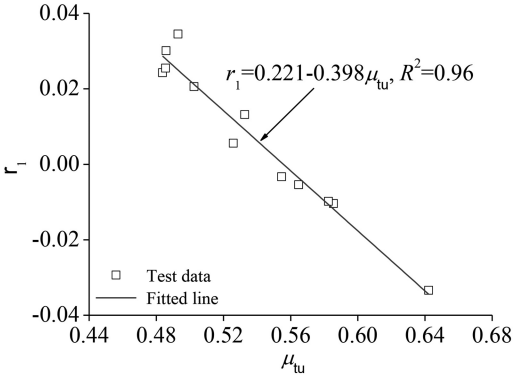


Figure 13. Relationships between r_1 and μ_{tu}.

The ultimate tangent Poisson's ratios of several specimens exceed 0.5 due to dilatancy of soil specimens, which is explained as follows.

In the Conventional triaxial shear tests:

$$-\varepsilon_r = -(\varepsilon_v - \varepsilon_a)/2 \tag{10}$$

where ε_v stands for the volumetric strain of soil specimen.

Take the derivative of the two sides of Equation (10) with respect to ε_a, then:

$$\mu_t = \frac{\partial(-\varepsilon_r)}{\partial \varepsilon_a} = \frac{1}{2}\left[-\frac{\partial \varepsilon_v}{\partial \varepsilon_a} + 1\right] \tag{11}$$

$$2(\mu_t - 0.5) = -\frac{\partial \varepsilon_v}{\partial \varepsilon_a} \tag{12}$$

From Equation (12) it can be seen, when μ_t exceeds 0.5, $\partial\varepsilon_v/\partial\varepsilon_a$ will be less than 0, that is, dilatancy of the soil specimen occurs.

5 MODEL APPLICATION

The proposed model will be used and meanwhile be verified as follows in simulating the triaxial tests of unsaturated soils.

5.1 *Simulation of stress-strain relations of unsaturated soils in consolidated drained triaxial shear tests*

The triaxial compression test data of weathered residual granite soil used in this section are from Kim et al. (2010), and the soil specimens have the dry density of 1.70 g/cm^3, initial moisture content of 11.6%, and matric suction of 50 kPa.

The effectiveness of the proposed model in fitting test data is shown in Figure 14, from which it can be seen that the proposed model matches well with test data. The values of model parameters are listed in Table 1.

5.2 *Simulation of stress-strain relations of unsaturated soils in consolidated undrained triaxial shear tests*

The test data are from Kim et al. (2010), and the soil properties in this section are the same as those in section 5.1.

The effectiveness of the proposed model in fitting test data is shown in Figure 15, from which it can be seen that the proposed model shows good agreement with test data. The values of model parameters are listed in Table 1.

6 CONCLUSION

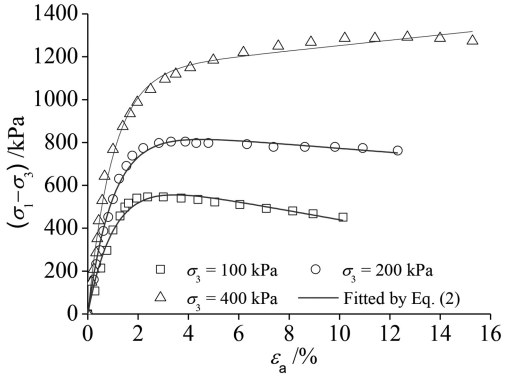
The triaxial compression test data of unsaturated soils are analyzed in this paper. The rate of Poisson's ratio and a model to describe the stress-strain relationships of unsaturated soils are proposed. Main conclusions of analysis are as follows:

(1) It is found that both the tangent modulus and the rate of Poisson's ratio decay exponentially with axial strain, which can be expressed by Equation (1) and Equation (4), respectively. And Equation (2) can describe the behaviors both the strain-hardening and strain-softening curves.

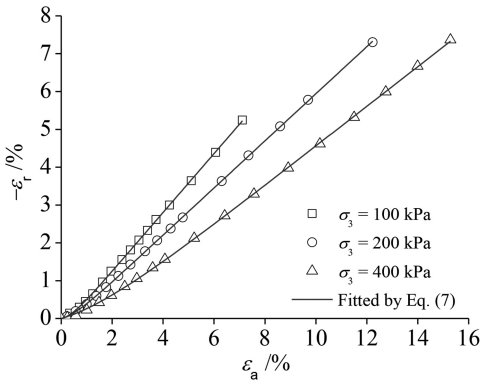
(2) Tangent modulus ratio (r_1) decreases approximately linearly with the increasing ultimate tangent Poisson's ratio (μ_{tu}). With the increase of μ_{tu}, the shape of the deviatoric stress-axial strain curves will turn from strain-hardening shape to strain-softening shape due to dilatancy of soil specimens.

(3) There exists approximate reciprocal relationship between the attenuation index of modulus (β_1) and the axial strain of soil specimen at yielding (ε_{ay}).

(4) The proposed model can describe the stress-strain relationships of unsaturated soils under various stress paths.

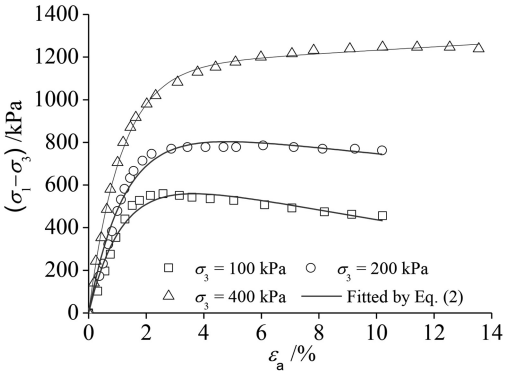


(a) Deviatoric stress-axial strain relations

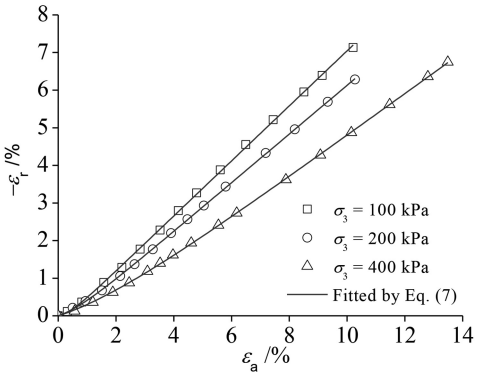


(b) Negative radial strain-axial strain relations

Figure 14. Description of data of consolidated drained shearing.



(a) Deviatoric stress-axial strain relations



(b) Negative radial strain-axial strain relations

Figure 15. Description of test data of consolidated undrained shearing.

Table 1. Results of verification of proposed model using test data from Kim et al. (2010).

Test conditions	σ_3/kPa	E_i/MPa	β_1	r_1	μ_i	β_2	r_2	R^2
Consolidated drained shear	100	62.24	99.11	−0.034	0.100	220.25	7.80	0.98
	200	86.24	100.75	−0.011	0.148	165.37	4.21	0.99
	400	117.62	103.19	0.011	0.191	48.54	2.75	0.99
Consolidated undrained shear	100	56.99	88.40	−0.041	0.139	216.57	5.25	0.97
	200	71.79	82.44	−0.020	0.256	113.09	2.53	0.98
	400	104.52	89.93	0.008	0.244	41.28	2.27	0.99

It must be pointed that the model proposed in this paper is based on triaxial loading tests. And the applicability of this model to triaxial unloading tests remains to be proven.

REFERENCES

Alonso, E. E., Gens, A. and Josa, A. A. 1990. Constitutive model for partially saturated soils. *Geotechnique* 40(3): 405–430.

Chen, Z. H. 1999. Deformation, strength, yield and moisture change of a remolded unsaturated loess. *Chinese Journal of Geotechnical Engineering* 21(1): 82–90.

Chen, Z. H. & Zhou, H. Q. 1999. Nonlinear model for unsaturated soils and its application. *Chinese Journal of Geotechnical Engineering* 21(5): 603–608.

Duncan, J. M. & Chang, C. Y. 1970. Nonlinear analysis of stress and strain in soils. *Journal of the Soil Mechanics and Foundations Division, ASCE* 96(5): 1629–1653.

Gitau, A. N., Gumbe, L. O. and Biamah, E. K. 2006. Influence of soil water on stress-strain behaviour of a compacting soil in semi-arid Kenya. *Soil & Tillage Research* 89: 144–154.

Kim, C. K. & Kim T. H. 2010. Behavior of unsaturated weathered residual granite soil with initial water contents. *Engineering Geology* 113(1): 1–10.

Ling, H., Yin, Z. Z. and Cai, Z. Y. 2008. Experimental study on stress-water content-Strain relationship of unsaturated soil. *Rock and Soil Mechanics* 29(3): 651–655.

Wang, W., Song, X. J., Ling, H., Lu, T. H. and Zhou, G. W. 2010. Composite exponential-hyperbolic model for stress-strain curve of seashore soft soil. *Chinese Journal of Geotechnical Engineering* 32(9): 1455–1459.

Zhang, J. H., Chen, Z. H., Miao, Q. Q., Sun, S. G. and Yao, Z. H. 2011. Strength Tests on the Remolded Cohesive Soil of the Bank Slope at Anyang District. *Journal of Logistical Engineering University* 27(5): 1–6.

Unsaturated Soil Mechanics—from Theory to Practice – Chen et al. (Eds)
© 2016 Taylor & Francis Group, London, ISBN 978-1-138-02921-7

Problems associated with determination of yield curves for unsaturated soils

X. Zhang
College of Civil Engineering and Architecture, Wuhan Polytechnic University, Wuhan, China
Department of Civil and Environmental Engineering, University of Alaska Fairbanks, Fairbanks, USA

ABSTRACT: In the development of an elasto-plastic framework for unsaturated soils, it is necessary to determine the shape of the yield curve. Accordingly, correct determination of shapes of yield curves is of significant importance. Existing methods rely on use of a series of specimens with "identical" stress history to determine the initial shape of yield curve. Preparation of such specimens requires thoughtful preparation, careful instrumentation, and lengthy equilibrium time, which makes identical specimens very difficult to obtain. As a result, the yield curve obtained through the existing methods could be misleading. This paper discussed the problems associated with the determination of yield curve for unsaturated soils.

1 INTRODUCTION

Attention is increasingly paid to the elasto-plastic behavior of unsaturated soils. Alonso et al. (1990) proposed the first elasto-plastic model for unsaturated soils, which was later referred to as the Barcelona Basic Model (BBM). Since then a great number of elasto-plastic models have been proposed (Alonso & Gens 1992; Alonso et al. 1994; 1999; Cui & Delage 1996; Wheeler & Sivakumar 1996; Vaunat et al. 2000; Gallipoli et al. 2003; Sheng et al. 2004; Wheeler 1996; Wheeler et al. 2003; Thu et al. 2007). Although these models used different experimental curves for the unsaturated soil behavior and were presented in different stress spaces, they included a yield curve or multiple yield curves which separated the elastic region from the elasto-plastic region under isotropic conditions and largely fell in the same framework of BBM.

During the development of elasto-plastic model for an unsaturated soil, it is necessary to determine the shape of yield curve. The shape of yield curve cates the beginning of the irrecoverable volume changes and is closely related to unsaturated soil behavior. An approach which is capable, effective, and simple to correctly determine the shape of yield curves becomes more and more critical.

2 EXISTING METHODS

Methods for determining the shape of yield curve for unsaturated soils were proposed by many researchers (Alonso et al. 1990; Delage & Graham 1996; Gens 1996; Wheeler & Karube 1996; Cui & Delage 1996; Thu et al. 2007). It was extensively accepted that the shape of the LC yield curve can be independently determined either from loading tests under constant suction or from wetting tests under constant applied stress (Alonso et al. 1990; Alonso & Gens 1992; Alonso et al. 1994; 1999; Delage & Graham 1996; Gens 1996; Wheeler & Karube 1996; Cui and Delage 1996; Wheeler & Sivakumar 1996; Vaunat et al. 2000; Robles & Elorza 2002; Gallipoli et al. 2003; Sheng et al. 2004; Wheeler 1996; Wheeler et al. 2003; Thu et al. 2007). Figure 1 illustrates in a schematic way the relationship between these two types of stress paths. Figure 1a shows a soil specimen being loaded from A, yielding at B and compressing plastically with volumetric hardening to C under constant suction ($s = s_1$). The corresponding specific volume v versus lnp behavior is curve ABC in Figure 1b. AB is a reloading straight line with a slope of κ in the elastic zone, BC is a virgin compression line with a slope of $\lambda(s_1)$ in the plastic zone, and B is a yield point determined by Casagrande's method (Casagrande 1936). The change in stiffness is defined as yielding and now well-established experimentally (Delage & Graham 1996). Usually κ is assumed to be constant during loading and unloading while λ is a function of suction (Alonso et al. 1990; Alonso & Gens 1992; Alonso et al. 1994; 1999; Delage & Graham 1996; Gens 1996; Wheeler & Karube 1996; Cui & Delage 1996; Wheeler & Sivakumar 1996; Vaunat et al. 2000; Robles and Elorza 2002; Gallipoli et al. 2003; Sheng et al. 2004; Wheeler 1996). At least another two tests (stress path DEF and GHI in Figure 1a) are needed to obtain the initial shape of the LC yield curve HEB. The associated compression behaviors are curves DEF and GHI in Figure 1b. The line joining H, E, and B represents the loading yield curve corresponding to the outer limit of states of stress and suction lower than had been previously experienced. The curve joining U, V, and W in Figure 1(a) represents a subsequent loading yield line produced by plastic hardening from H to U, from E to V, or from B to W.

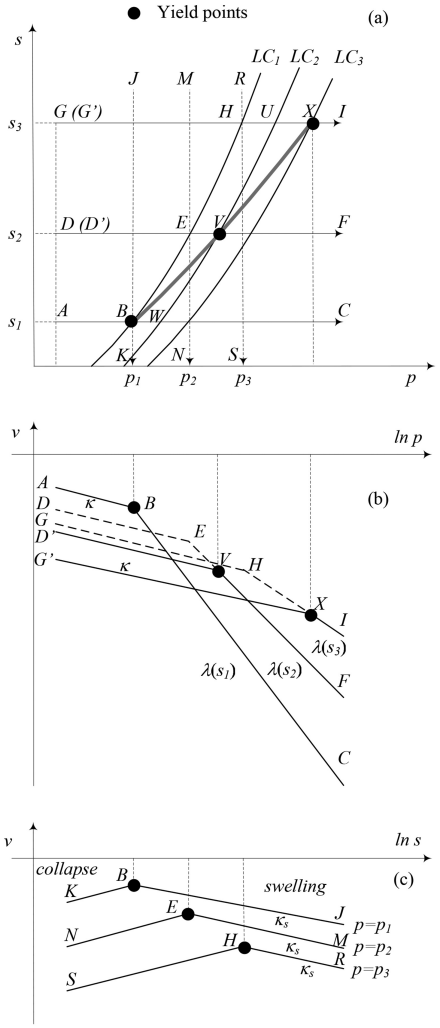


Figure 1. Methods to determine the shape of LC yield curve. (a) Stress paths, (b) *v-lnp* curves for constant suction tests, (c) *v-lns* curves for wetting tests.

Figures 1a and 1c also show stress paths and the changes in the specific volume (from J to B to K, from M to E to N, and from R to H to S) when wetting tests under constant applied stress are used to determine the shape of the LC yield curve. These tests require soil specimens with relatively high initial suctions. The soil will swell in the elastic zone (from J to B, from M to E, and from R to H) and collapse in the elasto-plastic zone (from B to K, from E to N, and from H to S) during wetting. In practice, such tests were rarely used due to the difficulties in measuring suction under significant volume changes during collapse.

For the SI yield curve, only one drying test under constant applied load was needed in the BBM, since the SI yield curve was assumed to be horizontal (Alonso et al. 1990). For shapes other than a straight line as shown in Figure 2, Thu et al. (2007) conducted multiple drying tests under constant applied stress to

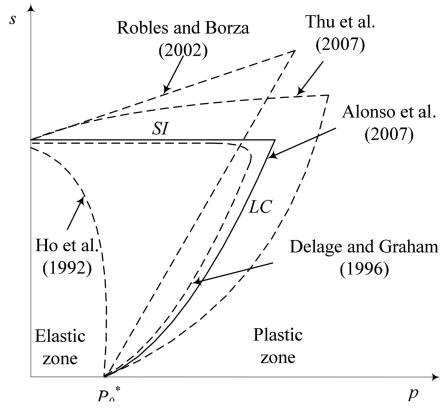


Figure 2. LC and SI yield curves on the $s-p$ plane by different researchers.

determine the shape of the SI yield curve (shown in Figure 2). Figure 2 also shows yield curves determined by other researchers (Ho et al. 1992; Delage & Graham 1996; Robles and Elorza 2002; Thu et al. 2007) using the same approach.

3 POTENTIAL PROBLEMS

Although the above methods are straightforward and theoretically well-established, it is difficult to implement them correctly in the laboratory. To obtain soil specimens with identical stress histories so that all the specimens can reach the same LC and SI yield curves, it requires 1) thoughtful preparation of specimens so that their initial states such as the net normal stress, suction, and specific volume are known; and 2) careful instrumentation and lengthy equilibrium time. However, it is only theoretically possible because loading, drying, and wetting can cause soil to yield and the positions of the LC and SI yield curves to change. Numerous researchers reported that carefully prepared "identical specimens" had different yield points when the soil specimens were tested following exactly the same stress paths (Wheeler & Sivakumar 1995; Rampino et al. 2000; Blatz & Graham 2003). For soil specimens with different stress histories, their positions of LC and SI yield curves will be different. Use of the above methods will then lead to misleading results. Using Figure 3 as an example, three soil specimens are assumed to be used for isotropic loading tests under constant suctions s_1, s_2, and s_3. The stress histories for these three soil specimens are different due to the fact that the preparation processes are not perfectly identical, which are represented by different locations of the LC yield curves LC_1, LC_2, and LC_3, respectively in Figure 3a. The corresponding *v-lnp* curves are ABC, D'VF and G'XI in Figure 3b, which are similar to those in Figure 1b. According to the method as described above, curve BVX, made up of three yield points B, V, and X, will be considered as a yield curve. However, it is not the correct yield curve

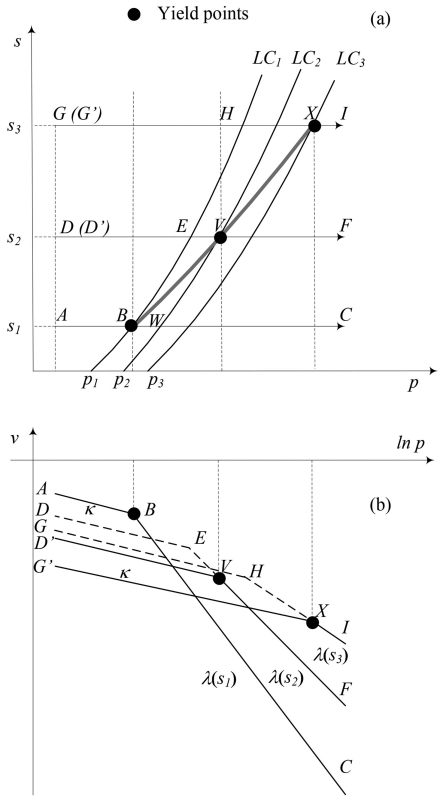


Figure 3. Possible problems associated with existing method.

because these three yield points B, V, and X actually belong to three different yield curves LC_1, LC_2, and LC_3, respectively. In addition, dotted lines in Figure 3) show the *v-lnp* curves ABC, DEF and GHI when the three specimens have identical stress histories, that is, these three soil specimens have the same yield curve BEH (LC_1). Because their patterns are very similar, one can easily miscalculate the shape of the LC yield curve. It is noted that there are many other possibilities of the relative positions of the LC_1, LC_2, and LC_3, and use of the existing methods can result in LC yield curves with shapes significantly different from either BVX or BEH.

In addition, even if identical specimens can be obtained, soil may have different stress history due to improper experimental design. This is mainly caused by the fact that the initial positions of the LC and SI yield curves are unknown before the soil specimens are tested.

Assuming a soil has shapes of LC and SI yield curves (Fig. 4) as those proposed by Alonso et al. (1990), three soil specimens are carefully prepared and have identical initial conditions (point A in Fig. 4) and stress history (represented by LC_1 and SI_1 with P_0^* of the preconsolidation stress). In order to determine the shape of the SI1 curve according to Thu et al.'s method (2007), one has to load the soil specimens to

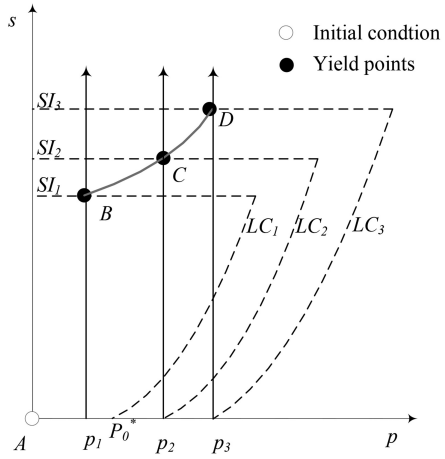


Figure 4. Possible changes in stress histories before testing.

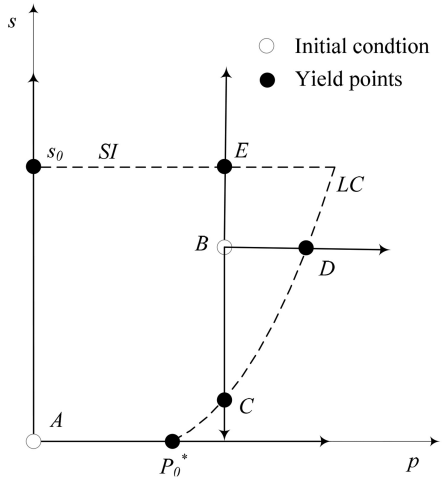


Figure 5. Preliminary counter-measures to overcome the problem associated with the exiting methods.

different confining stresses p_1, p_2, and p_3. Under most conditions, the initial position of the LC_1 yield curve is unknown. It is possible that the designed loading stresses, say p_2 and p3, are set to be greater than P_0^*. Thus it can lead to soil yielding and change of the locations of the LC and SI yield curve from LC_1-SI_1 to LC_2-SI_2 and LC_3-SI_3 in Figure 4. According to the approach in Thu et al. (2007), three yield points, B, C, and D will be obtained and curve BCD is considered as a SI yield curve. Again, it is however not correct because B, C, and D belong to different SI yield curves.

4 POSSIBLE SOLUTION

It is suggested that before any method is used, some trial tests be performed to determine the initial position of the LC and SI yield curves. For example, for the soil specimens with initial condition of point A (Fig. 4b), an

isotropic consolidation test at $s = 0$ and a drying test at constant load $p = 0$ should be performed to determine the preconsolidation stress P_0^* and yield suction s_0. For the soil specimens with initial condition of point B in Figure 5, three tests, a wetting test along stress path BC, a loading test under constant suction along stress path BD, and a drying test along stress path BE are needed to determine the range of the elastic zone CDE.

However, the trial test paths in Figure 5 can only solve the problem illustrated in Figure 4, but not those shown in Figures 3a and 3b. Furthermore, at present there is no method available for the determination of the evolution the LC and SI yield curves during yielding. It is therefore important to develop a simple and theoretically solid method for the correct determination of LC and SI yield curves and their evolutions during yielding.

5 CONCLUSIONS

Yield curve is an important component in the development of elasto-plastic models for unsaturated soils. Yield curve separates the elastic and plastic zones and determines the beginning of the irrecoverable volume changes. In the development of an elasto-plastic framework for unsaturated soils, it is critical to correctly determine the shape of the yield curve. Existing methods rely on use of a series of specimens with "identical" stress history to determine the initial shape of yield curve. Preparation of such specimens requires thoughtful preparation, careful instrumentation, and lengthy equilibrium time, which makes identical specimens very difficult to obtain. As a result, the yield curve obtained through the existing methods could be misleading. This paper discussed the problems associated with the determination of yield curve for unsaturated soils. Some preliminary counter-measures are proposed to overcome the problem associated with the exiting methods.

ACKNOWLEDGEMENT

This research was supported by the "100 Gifted People Plan of Hubei Province, China."

REFERENCES

Alonso, E. E., Gens, A., and Josa, A. (1990). "A Constitutive Model for Partially Saturated Soils." Geotechnique, 40(3), pp. 405–430.

Alonso, E. E., Vaunat, J., and Gens, A. (1999). "Modeling the Mechanical Behavior of Expansive Clays." Engineering Geology, 54(1–2), pp. 173–183.

Blatz, J. A., and Graham, J. (2003). "Elastic-plastic Modeling of Unsaturated Soil Using Results from a New Triaxial Test with Controlled Suction." Geotechnique, 53(1), pp. 113–122.

Casagrande, A. (1936). "The Determination of the preconsolidation Load and its Practical Significance." In Proceedings of the 1st International Conference on Soil Mechanics and Foundation Engineering, Cambridge, Mass. A.A. Balkema, Rotterdam, The Netherlands. Vol. 3, pp. 60–64.

Cui, Y. J. and Delage, P. (1996). "Yielding and Plastic Behaviour of an Unsaturated Compacted Silt." Geotechnique, 46(2), pp. 291–311.

Delage, P. and Graham, I. (1996). "State of the Art Report-Understanding the Behavior of Unsaturated Soils Requires Reliable conceptual models." Proceedings of 1st International Conference on Unsaturated Soils, Paris; 3, pp. 1223–1256.

Fredlund, D. G. and Rahardjo, H. (1993). Soil Mechanics for Unsaturated Soils. John Wiley and Sons, New York.

Gallipoli, D., Wheeler, S. J., and Karstunen, M. (2003). "Modeling the Variation of Degree of Saturation in a Deformable Unsaturated Soil." Geotechnique, 53(1), pp. 105–112.

Gens, A. (1995). "Constitutive Modelling: Application to Compacted Soil." Proceedings of 1st International Conference on Unsaturated Soils, Paris; 3, pp. 1179–1200.

Ho, D.Y.F., Fredlund, D. G., and Rahardjo, H. (1992). "Volume Change Indices during Loading and Unloading of an Unsaturated Soil." Canadian Geotechnical Journal, 29, pp. 195–217.

Lloret, A. and Alonso, E. E. (1980). "Consolidation of unsaturated soils including swelling and collapse behavior." Geotechnique, 30(4), pp. 449–477.

Matyas, E.L. and Radhakrishna, H. S. (1968). "Volume change characteristics of partially saturated soils." Geotechnique, 18(4), pp. 432–448.

Rampino, C., Mancuso, C., and Vinale, F. (2000). "Experimental behaviour and modelling of an unsaturated compacted soil." Canadian Geotechnical Journal, 37: 748–763.

Robles, J., and Elorza, F. J. (2002). "A Triaxial Constitutive Model for Unsaturated Soils." In Environmental geomechanics. Edited by Laurent Vulliet, Lyesse Laloui, and Bernard Schrefler. EPFL Press, Lausanne, Switzerland. pp. 207–213.

Sheng, D., Sloan, S. W., and Gens, A. (2004). "A Constitutive Model for Unsaturated Soils: Thermomechanical and Computational Aspects." Computational Mechanics, 33(6), pp. 453–465.

Thu, T. M., Rahardjo, H., and Leong, E. C. (2007). "Soil-water Characteristic Curve and Consolidation Behavior for a Compacted Silt." Canadian Geotechnical Journal, 44(3), pp. 266–275.

Vaunat, J., Romero, E., and Jommi, C. (2000). "An Elasto-plastic Hydro-mechanical Model for Unsaturated Soils." Experimental evidence and theoretic approaches in unsaturated soils (Eds. Tarantino, A. and Mancuso, C.), Rotterdam: Balkema, pp. 121–138.

Wheeler, S. J. (1996). "Inclusion of Specific Water Volume within an Elasto-plastic Model for Unsaturated Soils." Canadian Geotech. J. 33, pp. 42–57.

Wheeler, S. J. and Karube, D. (1996). "State of the Art Report-Constitutive Modeling." Proceedings of 1st International Conference on Unsaturated Soils, Paris; 3, pp. 1323–1356.

Wheeler, S. J. and Sivakumar, V. (1995). "An Elasto-plastic Critical State Framework for Unsaturated Soil." Geotechnique, 45(1), pp. 35–53.

Wheeler, S. J., Sharma, R. S., and Buisson, M. S. R. (2003). "Coupling of Hydraulic Hysteresis and Stress-strain Behavior in Unsaturated Soils." Geotechnique, 53(1), pp. 41–54.

Unsaturated Soil Mechanics—from Theory to Practice – Chen et al. (Eds)
© 2016 Taylor & Francis Group, London, ISBN 978-1-138-02921-7

Structural and mechanical behavior of expansive soil with pore damage

M.S. Cheng, S.J. Wang, Y.Q. Zhang & S.H. Jiang
College of Engineering and Technology, Southwest University, Chongqing, China

Z.H. Chen
Department of Architectural Engineering, Logistical Engineering University of PLA, Chongqing, China

ABSTRACT: To probe into the structural evolution and relevant mechanical characteristics of cylindrical pored damage of expansive soils, novel CT-triaxial consolidated drained tests were conducted. Results indicate that the strength of specimens weaken dramatically by the pore damage, when the pore size is larger, it's easier to be failure. The cross-section area of pore decreases with the increasing of net confining pressure under controlled-suction states. Under the same net confining pressure, when the suction is larger, the reduction of cross-section pore area is more obvious. Furthermore, the increments of ME value enhances gradually when the net confining pressure changed from 50 kPa to 200 kPa. It means that the specimens become denser when the confining pressure value getting higher. Correspondingly, the decrements magnitude of SD value increases gradually when the net confining pressure was changed from 50 kPa to 200 kPa. The structure of the specimens become homogenized during the tests.

1 INTRODUCTION

As a special unsaturated geological soil with multi-cranny and remarkable expand-shrink property, expansive soils is widely distributed in the world (Shi et al. 2002), so many geotechnical infrastruc-tures resting on this unsaturated ground involves a wide range of deformations(Hamid et al. 2009, Miao et al. 2007), while constructions are dominated by the foundation stability behavior, that poses much geotechnical hazards on engineering structures, causing billions of dollars loses in numerous regions in the world every year (Yitagesu et al. 2008, Zhang et al. 2009, Shamrani et al. 2010). Fissure is an important structural characteristic of expansive soil, which has great influence on its mechanical properties. There is various primitive and secondary cleavages in expansive soils, evolving with the changing of environment conditions (Schaffer et al. 2008, Wang et al. 2011), which makes the mecha-nical behavior even more complex. It's noteworthy that the harm is long lasting and concealing. It requires an adequate estimation of initial damage, structural evolution and mechanical behavior.

Much work has been devoted to research expansive soils, mainly concentrated on the classification of expansive soils, the fissures and strength properties under loading. Abundant achie-vements were obtained via triaxial apparatus and direct shear devices with remould specimens without initial damage (Hamid et al. 2009, Wang et al. 2011). However, both natural and compacted soils exists a particular internal soil initial structural damage, these conventional techniques mentioned above can only achieve external evolution information. There are limited perspectives available to explain the structural evolution when it is naturally or mechanically damaged internal.

X-ray computed tomography (CT) is a non-invasive and non-disturbed technique applied in medical fields initially, which was introduced by Hounsfield in 1973 (Hounsfield 1973). It was firstly used in soil science by Petrovic in soil bulk density analysis (Petrovic et al. 1982). Soon, many achieve ments were acquired on macroscopic and mesos-copic scale of expansive soil about fissures using CT technology (Lu et al. 2004, Dang 2005a, b, Tippkotter 2009, Yao et al. 2010, Wang et al. 2011, Ying et al. 2012, Chen 2014), such as the defining of integrity and damage degree, damage location and criterion of rock and soil based on CT number. Ying et al. (2012) investigated the influences of fissures on slope stability of expansive soil, demonstrated the reason why soil reinforcement method is effective mainly lies in its fissures developing were controlled. Yao (2009) studied expansive soil fissures developing, yield stress characteristics with initial damaged remolded under loading by wetting-drying cycles and triaxial immersion tests, quantita-tive equations were proposed with yield stress and structural parameters to generalize the Barcelona expansive soil model to a wider condition with structure damages.

Here, a CT apparatus supported with unsaturated soil triaxial machine was applied, and the internal structure changing process of unsaturated undisturbed expansive soil was observed and measured dynamically, non-destructively and real- timely during triaxial shear tests and wetting-drying cycle tests by Chen's team (Lu 2004, Yao et al. 2010, Wang et al. 2011).

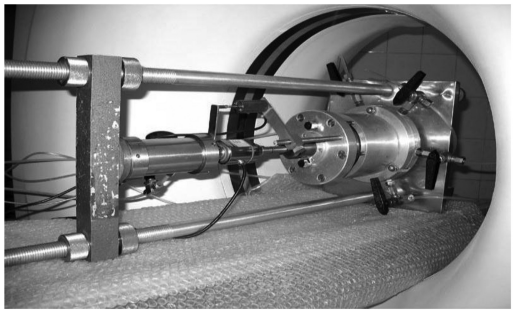


Figure 1. Multifunctional CT-triaxial apparatus.

Fruitfully, clear CT images and relevant data of internal structural damage evolution of soil specimens were obtained, and the correspon-ding damage evolution equation was proposed. In this paper, artificial pore-damage remolded expansive soils were made, then CT-triaxial tests were performed at given confining pressure and suction. Throughout the shear processing, specimens were scanned by CT programmatically. The macroscopic and mesoscopic structural evolution law and mechanical behavior of expansive soil with different initial damage were analyzed.

2 MATERIAL AND EQUIPMENT

2.1 *X-ray CT-triaxial testing apparatus*

As previously noted, compared with other measuring technologies, X-ray computed tomography has such advantages that the material internal structure evolution could be observed dynamically, non-disturbedly and quantitatively in the loading tests process. It could be available to create three-dimensional images on the basis of different thin layers' information of the object, providing with a large detection area and high resolution images (Yin et al. 2012), which contains quantitative information of deformation, damage and fissures. Chen (2008) modified an unsaturated triaxial apparatus combined with CT to get a CT-triaxial apparatus, which performs fully advantages of the two in observing materials inside microstructures. Shown in Figure 1.

Each material point was obtained by CT apparatus, whose absorption coefficient μ in a specific cross section was converted into CT number according the equation: $\mathrm{CT}_n = 1000 \times (\mu_m - \mu_w)/\mu_w$. Where, CT_n is the X-ray absorption strength of some point of some material, μ_m is X-ray absorption coefficient of this material, μ_w is water's X-ray absorption coefficient. The density of a material was assessed by X-ray diffraction, which could be calculated by its CT number, according to the all CT number of a selected area in the section, the general CT value of ME and at a certain confidence level SD value were recorded by CT apparatus. ME represents the average density of the all point in the selected area. SD value reflects the uneven degree of density of all matter in some designated area scanned, which suggests the structural strength of the region indirectly.

Table 1. Initial state parameters of specimens.

D_r	ρ g/cm^3	ω %	S_r mm	Pore diameter
2.73	1.70	20.0	89.5	No. 1 ~ 6 are 8 mm; No. 7 is 2 mm; No. 8 is non-pore

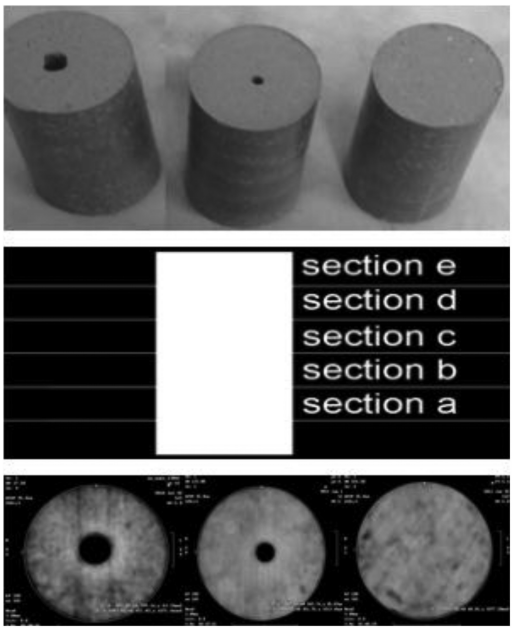


Figure 2. Specimens, scanning section schematic and corresponding CT images (From left to right, the diam is 8mm, 2mm and non-pore).

2.2 *Specimens preparation*

Eight different aperture artificial cylindrical pored damage expansive soils were prepared in a brief introduction:

The soil tested in the experiment was taken from the site known as the *Central Line Project of South-to-North Water Diversion* in Taocha, China. It was crushed it to pass 1 mm sieve and mixed with distilled water at rated water moisture. Then it was compacted in a brass cylinder in five layers. The volume of each sample was consistent (diam = 39.1 mm and height = 80 mm). Before the specimens were took out from the sleeve, different size of vertical pore were made with different diameter hollow-metal bars. Initial state parameters and diameter of specimens are shown in table 1. Different initial vertical cylindrical-pore damaged specimens, scanning section schematic and relevant CT scanning photographs are presented in Figure 2.

Table 2. Different suction and net confining pressure scheme of triaxial shear test.

Sample number	σ_3-u_a	Suction
No. 1	50	100
No. 2	100	100
No. 3	200	100
No. 4	50	200
No. 5	100	200
No. 6	200	200
No. 7	200	100
No. 8	200	100

2.3 *Experimental scheme*

Eight specimens prepared previous were performed consolidated drained triaxial shear tests under rated net confining pressure and suction condition (shown in table 2).

Before testing, specimens were consolidated in an oedometer cell of triaxial apparatus till the draining and deformation is stable under a constant pressure and suction. The stability indicator is that its volumetric strain and drainage are less than 0.063 cm and 0.012 cm every two hours respectively, and the shear strain rate was set to 0.0167 mm/min. Then the experiments were performed immediately. Particularly, the specimens were scanned to reach CT information by triaxial CT apparatus at the stage of axial strain are 0%, 5%, 10%, 15%. Five sections (1/6 *h*, 1/3 *h*, 1/2 *h*, 2/3 *h*, 5/6 *h*, where *h is* the height of the sample) of the soil column were scanned at one stage throughout the tests, shown in Figure 2.

3 STRUCTURAL EVOLUTION

3.1 *CT images analysis*

Throughout the tests, 140 CT scanning photographs were achieved. Because of the limited space, this paper just chooses typically specimen of No. 1 (diam = 8 mm, $\sigma_3 - u_a = 50$ kPa, suction = 100 kPa) to dis-cuss, so as to afford a theoretical and visual basis for structural evolution behavior of the specimens. Presented in Figure 3, from left to right, the axial strain is 0%, 5%, 10%, 15% respectively; from bottom to top, the cross section scanned is from section a to section e. For the same cross-section position scanned, it could be observed that differences in pore area behavior are most the same. That indicating the evolution is relatively homoge-neous. With the increasing of axial strain, the pore area decreases, and the soil is compacted.

3.2 *Cylindrical-pore area and axial strain*

As shown in Figure 4, during the test, the cylindrical pore area declines gradually with axial deformation increasing. As scheme designed previously, No. 1, No. 2, No. 3 specimens' curve were under the same

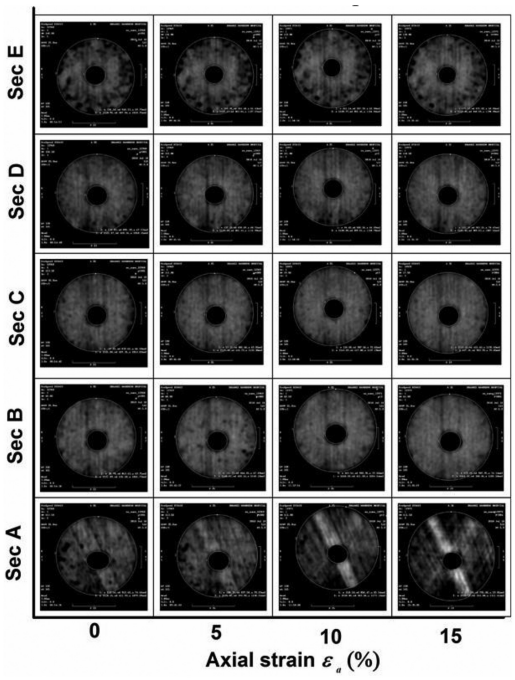


Figure 3. Deformation and structural evolution CT photographs of No. 1 specimen.

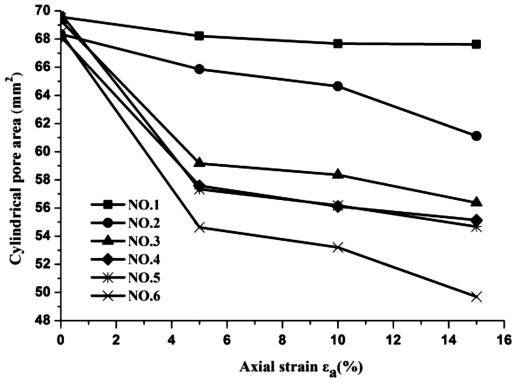
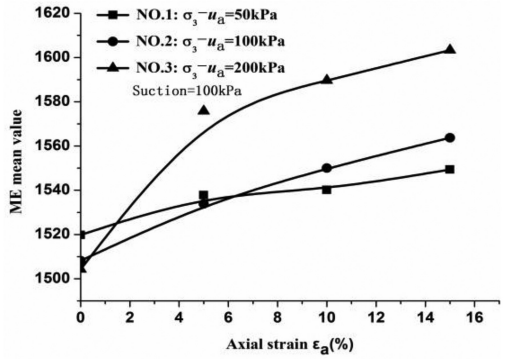


Figure 4. Pore area behavior observed vary with axial strain.

suction of 100 kPa but at different net confining pressure (50 kPa, 100 kPa, 200 kPa). Overall, the trend is obvious, when net confining pressure gets greater, the cylindrical pore area of sample reduces more. The same regularity are also presented in No. 4, No. 5, No. 6. Compared No. 1 with No. 4, No. 2 with No. 5, No. 3 with No. 6, it could be observed that cylindrical-pore area curve reduces greatly when the suction controlled higher.

3.3 *ME value and axial strain*

From Figure 5, it's obvious that when the axial raises, the ME value goes up correspondingly, which indicates



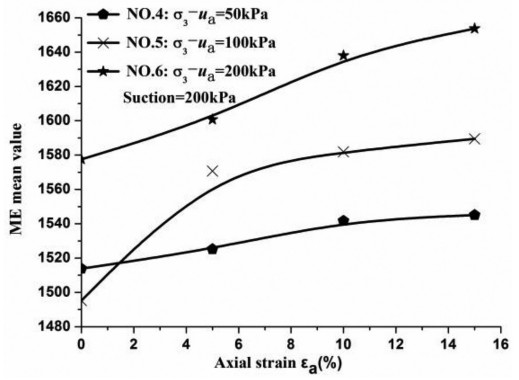
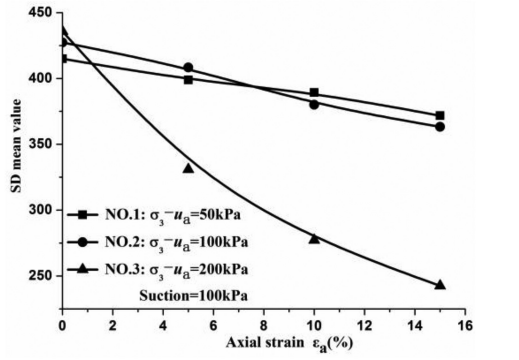


Figure 5. ME value vary with axial strain.



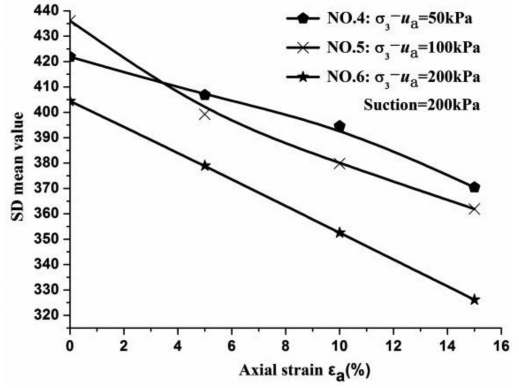


Figure 6. SD value vary with axial strain.

the average density increased during the shear process. From the trend of gradient increasing of ME value, conclusions could be made that under a controlled rated suction, the greater the net confining pressure is, the magnitude of ME value increases more.

3.4 *SD value and axial strain*

As plotted in Figure 6. Collectively, when the axial strain increases, while the SD value decreases. Generally, when pressure increasing, the internal pores, fissures shrinks gradually. The uneven degree of scanning section decreased. Consequently, the soil column was compacted. Variations in SD curve shows that under the same suction, when net confining pressure is greater, the SD value undergoes a great amplitude decrease, which shows net confining pressure has a significant effect on SD value.

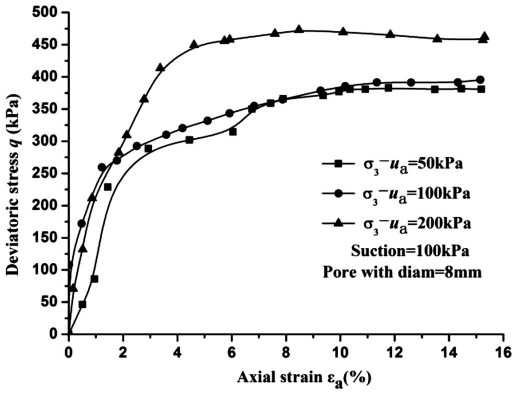


Figure 7. Deviatoric stress—axial strain behavior of No. 1 ~ 3 at suction = 100 kPa.

4 STRENGTH CHARACTERISTICS

4.1 *Deviatoric stress-axial strain relationship at the same initial damage*

Figure 7 presents the relationship between deviatoric stress and axial strain under the condition of damage-pore size 8 mm, suction-controlled 100 kPa, the net confining pressure of No. 1, No. 2, No. 3 is 50 kPa, 100 kPa and 200 kPa respectively. Obviously, we can observe that with the increasing of axial loading, axial strain and deviatoric stress also increased. At the beginning of axial strain increasing, the deviatoric stress change range of No. 1 is relatively larger, then its growth gets slower. Ultimately, when the axial strain increases to 11%, it appears a stable variation which is 375 kPa. Specimen 2 and 3 (net confining pressure is 100 and 200 kPa respectively) manifest a similar changing law. Compared No. 1 with No. 2, when the

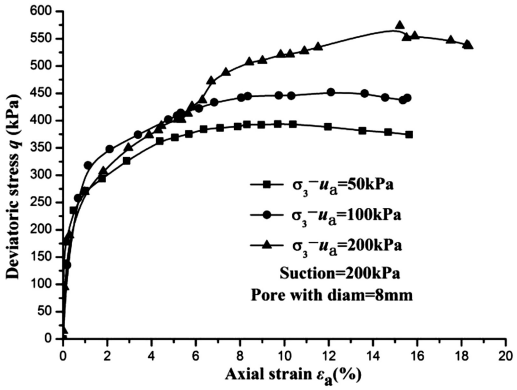


Figure 8. Deviatoric stress-axial strain behavior of No. 1 ~ 3 at suction = 200 kPa.

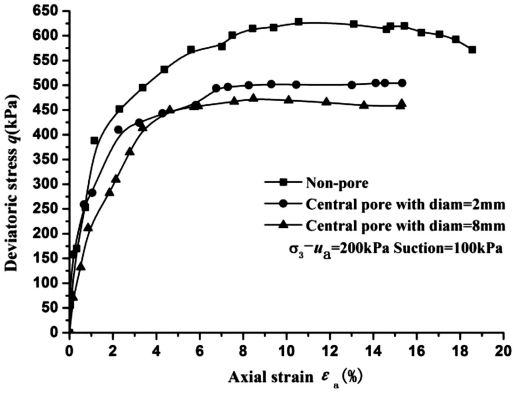


Figure 9. Variation of deviatoric stress with axial strain of different diameter pore specimens.

axial strain over 2%, specimen 3 shows a higher deviatoric stress. What's more, No. 3 reaches to a stable variation stage earlier at 6% axial strain, while No. 1 and No. 2 at 11%.

On the contrary, Figure 8 shows the relationship between axial strain and deviatoric stress of No. 4, No. 5, No. 6 specimens. The test conditions is that pore size at 8 mm, suction is 200 kPa, and the net confining pressure is 50 kPa, 100 kPa, 200 kPa respectively. The general regularity of Figure.8 is just like Figure 7. That is, the axial strain gets higher, so does the deviatoric stress. Dissimilarly, when the axial increases from 0% to 6%, the deviatoric stress undergoes a rapid changing rate. Initially, at the beginning of load increasing, the deviatoric stress changes sharply, the greater the suction is, so the deviatoric stress changes to higher value more quickly.

Compared Figures 7 & 8, it's obviously that along with the axial stress increasing, deviatoric stress gets higher. As pictures noted, the early growth relatively faster, when the axial strain curve reaches at a specified amount, then becomes stable, specimens presents a plastic collapse. Under the same initial damage state, the suction kept the same, when the net confining pressure gets greater, a higher deviatoric stress value is required to turn the specimen damaged. Besides, under the same net confining pressure, when the suction gets greater, the deviatoric stress shows a higher change rang level. That is to say, suction has a relatively prominently influence on sample failure than the net confining pressure.

4.2 *Deviatoric stress—axial strain relationship at different initial damage extent*

Figure 9 describes the relationship between devia-toric stress and axial strain at different damaged aperture specimens under suction 100 kPa and the net confining pressure of 200 kPa. In this figure, deviatoric stress goes up with the increasing of axial strain. At the same axial strain, non-pore specimens' deviatoric stress are the largest, next the 2 mm pore specimen, the 8 mm pore damaged specimens are the least, that is because different size of specimens' internal cylindrical pore lead to various structural damage morphology. Due to the stress transfer characteristics of soil was affected by structural damage, the greater the amount of structural damage is, the deviatoric stress varies more slower with the axial strain changing, and it's more easier to be destroyed.

5 CONCLUSIONS

The structural evolution and mechanical behavior of remolded expansive soil with different cylindrical pore-damage conditions were investigated by CT – triaxial apparatus test. Results shows that:

1). In the controlled suction and net confining pressure experiments, when suction at a constant value, the decreasing range of cylindrical pore area gets larger with the increasing of net confining pressure. When net confining pressure controlled the same, the reduction velocity of cylindrical pore area gets faster along with the increasing of suction.
2). Six cylindrical pore-damaged specimens show that ME value of every specimen scanned by CT increased while the SD value reduced relatively during the tests. When the deviatoric stress reaches at 350 kPa, the ME and SD value change dramatically. That illustrates that the soil column was compressed and the structure tend to be more homogeneous in the shearing stage. The ME value growing amplitude increases while the SD decreasing rang added under the same suction.
3). Cylindrical pore-damage of specimen has an obvious weaken effect on the strength of the expansive soil. Different aperture of pore-damaged specimens have a disparate yield strength and deformation characteristics. That is, the aperture size has a great influence on yield strength and deformation.

The results could gain some valuable insight into the internal evolution and mechanical behavior, and make

some sense in the further study of destruction mechanism of roadbed, slope, etc. at expansive soil areas. And the method can also be borrowed into laboratory tests where to explore the influence of soil pore, crack and fissures forming and developing on the mechanical properties leading by environ-ment changing.

ACKNOWLEDGMENT

This study was supported by the Natural Science Foundation of China (NSFC) under grants 10902091 and 51208078. The authors are grateful to the NSFC for the financial support. M.S. Cheng would also like to acknowledge the financial support provided by the Fundamental Research Funds for the Central Universities under grants XDJK2013C042 and XDJK2013C042.

REFERENCES

Chen, Z.H. 2014. On basic theories of unsaturated soils and special soil. *Chinese Journal of Geotechnical Engineering* 36(2): 201–272.

Dang, F.N. 2005a. Damage-fracture evolution theory of rock and soil (I): damage-fracture space. *Rock and Soil Mechanics* 26(4): 513–519.

Dang, F.N. 2005b. Damage-fracture evolution theory of rock and soil (II): physical state indexes and divisional damage-fracture theory. *Rock and Soil Mechanics* 26(5): 673–679.

Hamid, T. & Miller, G. 2009. Shear strength of unsaturated soil interfaces. *Can Geotech J* 46(5): 595–606.

Hounsfield, G.N. 1973. Computerized transverse axial scanning (tomography). 1. Description of system. *Br. J. Radiol* 46:1016–1022.

Lu, Z.H., Chen, Z.H., Pu, Y.B. 2004. Quantitative analysis on damage evolution of intact expansive soil during triaxial shearing tes. *Chinese Journal of Rock Mechanics and Engineering* 23(9): 1428–1432.

Miao, L.C., Houston, S.L., Cui, Y., et al. 2007. Relationship between soil structure mechanical behavior for an expansive unsaturated clay. *Can Geotech J* 44(2): 126–137.

Petrovic, A.M., Siebert, J. E., Rieke, P. E. 1982. Soil bulk density analysis in three dimensions by computed tomographic scanning. *Soil Sci. Soc. Am. J.* 46, No. 3, 445–450.

Shi, B., Jiang, H.T., Liu, Z.B., et al. 2002. Engineering geological characteristics of expansive soils in China. *Engineering Geology* 67(1–2): 63–71.

Shamrani, M., Mutaz, E., Puppala, A., & Dafalla, M. 2010. Characterization of Problematic Expansive Soils from Mineralogical and Swell Characterization Studies. *GeoFlorida* 2010: 793–802. American Society of Civil Engineers.

Schaffer, B., Stauber, M., Mueller, T.L., et al. 2008. Soil and macro-pores under uniaxial compression. I. Mechanical stability of repacked soil and deformation of different types of macro-pores. *Geoderma* 146: 183–191.

Schaffer, B., Mueller, T.L., Stauber, M., et al. 2008. Soil and macro-pores under uniaxial compression. II. Morphometric analysis of macro-pore stability in undisturbed and repacked soil. *Geoderma* 146: 175–182.

Tippkotter, R., Eickhorst, T., Taubner, H., et al.2009. Detection of soil water in macropores of undisturbed soil using microfocus X-ray tube computerized tomography (mCT). *Soil Till. Res.* 105, 12–20.

Wang, S.J., Sun, S.J., Chen, Z.H., et al. 2011. Triaxial shear test of pore-damaged remolded Expansive soil. *Journal of Southwest University (Natural Science Edition)* 33(3): 128–132.

Wang, S.J., Chen, Z.H., Li, X., et al. 2011. Experimental study on pore-damage evolution of remolded soil. *Journal of Southwest University (Natural Science Edition)* 33(3): 128–132.

Yitagesu, F.A., Van, D.M., Van, D.W., et al. 2008. Spectroscopy to characterize expansive soils. *IEEE International Geoscience & Remote Sensing Symposium*: 1250–1254.

Yin, Z.Z., Yuan, J.P., Wei, J., et al. 2012. Influences of fissures on slope stability of expansive soil. *Chinese Journal of Geotechnical Engineering*, 34(12): 2–5.

Yao, Z.H., Chen, Z.H., Zhu, Y.Q., et al. 2010. Meso-structural change of remolded expansive soils during wetting-drying cycles and triaxial soaking tests. *Chinese Journal of Geotechnical Engineering* 32(1): 68–76.

Zhang, L. & Zhang, Z.S. 2009. Swelling Test of Expansive Soil in Xi'an-Ankang Railway. *International conference on transportation engineering* 2632–2637. Reston Va, American Society of Civil Engineers.

Unsaturated Soil Mechanics—from Theory to Practice – Chen et al. (Eds)
© 2016 Taylor & Francis Group, London, ISBN 978-1-138-02921-7

Prediction of 1-D heave of a natural expansive soil slope of Zao-yang in China using the SWCC-based and water content-based models

H.Y. Tu & S.K. Vanapalli
University of Ottawa, Ottawa, Ontario, Canada

ABSTRACT: Various empirical and experimental methods are available in the literature; respectively, for the estimation and determination of swelling pressure for expansive soils. Empirical methods are only valid for expansive soils for which they have been proposed. Experimental methods on the other hand are expensive, cumbersome and time-consuming for use in conventional geotechnical engineering practice. To overcome the above limitations, two models have been proposed in the recent literature for predicting the swelling pressure. One of these models uses the Soil-Water Characteristic Curve (SWCC) as a tool and the other is a water content-based model. Both these models are respectively used in the present study to predict the variation of swelling pressure with respect to initial soil suction and/or water content for the natural expansive soil at Zao-yang location in China. The predicted swelling pressure is then used to estimate the ground heave at the same site with an equation proposed by the authors of this paper. This equation has been proposed by modifying Fredlund (1983) equation to estimate the 1-D heave of unsaturated expansive soils. These techniques have been combined and extended in the present study for predicting the evolution of ground heave taking account of artificial rainfall in the numerical analyses. The predicted variations of ground heave using the two models are then compared with the monitored data of the investigated natural expansive soil slope. There is a reasonable comparison between the measured ground heave at Zao-yang using the SWCC model and predicted values; however, the water content based model over estimates the ground heave.

1 INTRODUCTION

The methods used for ground heave prediction of expansive soils can be classified as: (i) empirical methods, (ii) soil suction methods, and (iii) oedometer methods. Empirical methods are based on investigations performed on local or limited number of soils and hence are not universally valid. Soil suction methods are considered to be reasonable and reliable for the estimation of the ground heave; however, the effect of in-situ effective stress is not considered (Nelson & Miller 2012). The oedometer tests are commonly used to measure the swelling pressure and swelling index values. These values are conventionally used to estimate the heave of expansive soils. The oedometer tests are time consuming to perform, the testing results are less reproducible, and the correction procedures on the semi-logarithmic scale are prone to errors. For these reasons, there is a need for reliable yet simple techniques for determining or estimating heave behavior of expansive soils.

Recently, a Soil-Water Characteristic Curve (SWCC) based model was proposed by Vanapalli et al. (2014) to predict the variation of swelling pressure, p_s for natural expansive soils with respect to soil suction. In addition, the water content-based model proposed by Vanapalli & Lu (2012) is modified and used in the present study to predict the variation of swelling pressure with respect to changes in the water content.

The swelling index, C_s is estimated by modifying a relationship which was expressed as a function of plasticity, I_p proposed by Vanapalli & Lu (2012). The predicted swelling pressure, p_{sp} and the estimated swelling index, C_{se} are then used for estimation of the 1-D heave for unsaturated expansive soils. This is achieved by employing modified Fredlund (1983) equation (Vanapalli et al. 2014). Fredlund (1983) equation is widely used for estimating the potential 1-D heave of expansive soils at saturation condition.

In this paper, both these models are extended for predicting the evolution of ground heave taking account of the artificial rainfall on a case study in Zao-yang, China. Commercial software (VADOSE/W), is used for estimating the changes in suction and water content in the expansive soil profile due to the artificial rainfall. The SWCC-based model provides a reasonable yet conservative estimation compared with the measured data. The water content-based model on

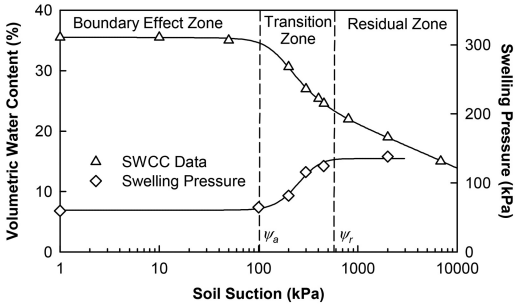


Figure 1. Typical relationship between the SWCC and the swelling pressure variation with respect to soil suction (after Pedarla et al. 2012).

the other hand overestimates the ground heave. However, both the models are promising for use in practice for predicting the 1-D heave with respect to time for expansive soils.

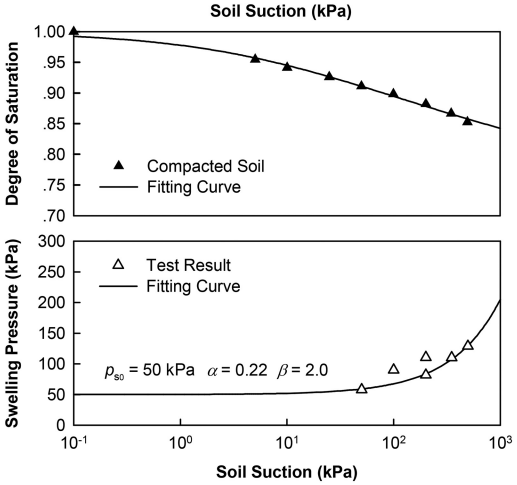


Figure 2. The SWCCs and the swelling pressure variations with respect to soil suction for natural Zao-yang expansive soils.

2 SWEELING PRESSURE PREDICTION

2.1 *SWCC-based swelling pressure prediction model*

2.1.1 *Proposed model*

Vanapalli et al. (2014) proposed a model (Eq. 1) to predict the variation of swelling pressure of expansive soils with respect to suction. Equation 1 was developed based on an understanding that there is a distinct relationship between the swelling pressure and the SWCC. This relationship can be illustrated using the test results of Pedarla et al. (2012) (see Fig. 1); the major features can be described as below:

(i) Swelling pressure increases with increasing soil suction;
(ii) Swelling pressure versus soil suction relationship is nonlinear and is typically an S-shape plot across boundary effect zone, transition zone and residual zone of the SWCC;
(iii) Swelling pressure is relatively constant for the suction values less than the air-entry value, ψ_a (i.e. in the boundary effect zone);
(iv) Swelling pressure increases at a rapid rate in the transition zone (i.e., from ψ_a to ψ_r) with respect to soil suction;
(v) Rate of swelling pressure increment in the residual zone (i.e. suction value is greater than ψ_r) decreases with respect to soil suction.

Gens & Alonso (1992), Kassiff & Shalom (1971) and Blight (1965) studies show expansive soils exhibit swelling pressure even at saturated condition. These observations are consistent with the results shown in Figure 1, which demonstrates a well-defined intercept of swelling pressure-axis at saturation condition. Vanapalli et al. (2014) termed this portion of swelling pressure (i.e. intercept) as p_{s0} and suggested this value would be approximately 50 kPa for natural expansive soils.

Vanapalli et al. (2014) proposed swelling pressure prediction model for natural expansive soils, using the SWCC as a tool (Eq. 1).

$$p_s = p_{s0} + \alpha \cdot \psi_i \cdot \left(\frac{S}{100}\right)^{\beta} \quad (1)$$

where, p_s = swelling pressure, p_{s0} = interception value on swelling pressure-axis at zero suction value, ψ_i = initial soil suction, α and β = fitting parameters, S = degree of saturation.

2.1.2 *Fitting parameters, α and β for the model*

A constant value of 2 was found suitable for use as the β value in the proposed model (Vanapalli et al. 2014). This value has also been found to be suitable for predicting the variation of modulus of elasticity and resilient modulus with respect to soil suction for fine-grained soils (Oh et al. 2009; Adem and Vanapalli 2014; Han and Vanapalli 2015).

Zhan et al. (2007) conducted a series of free swell (FS) tests on Zao-yang expansive soils on various soil specimens to determine swelling pressure. The variation of swelling pressure with respect to initial soil suction was measured for both natural and compacted soil specimens (Fig. 2).

Based on the measured data, regression analysis is performed to determine the fitting parameter, α for the natural Zao-yang expansive soils. A scientific data analysis graphing software (SigmaPlot) is used to conduct the regression analysis, which results in α value of 0.22 (see Figure 2).

2.2 *Water content-based swelling pressure prediction model*

2.2.1 *Proposed model*

Vanapalli & Lu (2012) suggested water content based semi-empirical model (see Eq. 3) extending research studies of Fredlund (1983) and Hamberg & Nelson (1984) for predicting the swelling pressure (Eq. 4). This model alleviates the need for measurements of soil suction in the field. In this model, a constant value of the suction modulus ratio, C_w is used for soils with a plasticity index, I_p greater than 30 (Eq. 3) (Vanapalli & Lu 2012). The swelling index, C_s can however be estimated from the I_p value using a recently proposed empirical equation (Eq. 5) (Vanapalli et al. 2014).

$$C_s \frac{h}{1+e_i} \log p_s' \propto C_w \frac{h}{1+e_i}\left(w_f - w_i\right) \tag{2}$$

$$\log(K \cdot p_s') = \frac{C_w \cdot \Delta w}{C_s} \tag{3}$$

where,

$$C_w = 0.024 \tag{4}$$

$$C_s = 0.188/[1+\mathrm{e}^{(44.526-I_p)/15.636}] \tag{5}$$

where, C_s = swelling index, C_w = suction modulus ratio, p_s' = corrected swelling pressure, h = thickness of ith layer, e_i = initial void ratio, w_f = saturated water content, w_i = initial water content, K = fitting parameter, I_p = plasticity index.

Equation 2 suggests that there is a relationship between the term of ($\log p_s'$) and the term of ($C_w \cdot \Delta w / C_s$). However, in the prediction model (Eq. 3) proposed by Vanapalli & Lu (2012), the fitting parameter, K is located inside the logarithmic term (i.e. [$\log (K \cdot p_s')$]) rather than between the two terms. To mitigate this limitation, the present study proposes a modified prediction model (Eq. 6) using a fitting parameter, λ.

$$\log(p_s') = \frac{C_w \cdot (w_f - w_i)}{C_s \cdot \lambda} \tag{6}$$

where, λ is the fitting parameter.

2.2.2 *Fitting parameter, λ for the model*

Zhan et al. (2007) performed FS tests on various natural soil specimens to determine swelling pressure of Zao-yang expansive soil. From Figure 2, it can be observed that the swelling pressures were measured at five different initial suction values within the range from 50 to 500 kPa. The corresponding initial water content (w_i) of these soil specimens can be back-calculated from the wetting curve of the SWCCs of natural Zao-yang expansive soil (Fig. 3). In addition, the saturated water content, w_f can be determined as

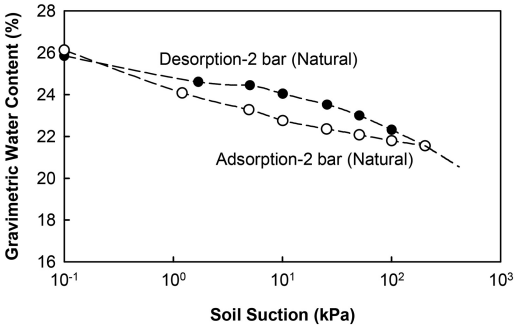


Figure 3. The SWCCs in terms of gravimetric water contend for natural Zao-yang expansive soils (modified after Zhan et al. 2007).

26% from Figure 3. The information of ($w_f - w_i$) values can hence be determined for each of the specimens from the above information. Regression analysis is performed using these data, resulting in a λ value of 0.96 for natural Zao-yang expansive soils.

As there is a logarithmic term in Equation 6, the swelling pressure prediction is rather sensitive to the water content values. Figure 1 suggests that the variation of initial water content in the residual zone contributes to insignificant changes on the swelling pressure. Hence, the proposed water content-based model (Eq. 6) is only applicable for the soils with w_i value greater than the residual water content, w_r. The w_r value of natural Zao-yang expansive soil is approximately 21% from the SWCCs (Fig. 3).

3 GROUND HEAVE PREDICTION

Fredlund (1983) proposed an equation for estimating the heave in expansive soils (Eq. 7) using corrected swelling pressure, p_s'.

$$\Delta h = h \frac{C_s}{1+e_0} \log\left(\frac{p_f}{p_s'}\right) \tag{7}$$

where, h is the thickness of soil layer, C_s is swelling index, e_0 is initial void ratio, p_s' is corrected swelling pressure, p_f ($=\sigma_y + \Delta\sigma_y - u_{wf}$) is final stress state, (σ_y is total overburden pressure, $\Delta\sigma_y$ is the change in total stress, u_{wf} is pore-water pressure), and Δh is the heave of the soil layer.

However, the testing procedures for obtaining swelling pressure and swelling index are rather cumbersome and also time-consuming. The p_s' value of undisturbed specimen is less reproducible since the p_s' value is estimated on a logarithm scale and sensitive to the correction procedures. Furthermore, assumptions are required with respect to the final stress state, which is rather subjective. Besides, the accuracy of ground heave estimation using Equation 7 depends on assumption related to the final stress state. Expansive soils

are typically assumed to attain fully saturated condition (i.e., final pore-water pressure, u_{wf} is zero) for estimating heave. For such a scenario, Equation 7 estimates the potential (maximum) heave of the expansive soil.

Natural expansive soils are typically in a state of unsaturated condition and rarely reach fully saturated condition. Vanapalli et al. (2014) proposed an equation set (Eqs 8, 9) to estimate the heave of an unsaturated expansive soil at different wetting stages.

$$\begin{cases} \Delta h = \Delta h_i - \Delta h_w \\ \quad = C_s h\left[\dfrac{\log(p_0/p_{si})}{1+e_i} - \dfrac{\log(p_0/p_{sw})}{1+e_w}\right] \end{cases} \quad (8)$$

$$\Delta h = \frac{e_i - e_w}{1+e_i} h \quad (9)$$

where, e_i is void ratio of initial condition, e_w is void ratio of subsequent wetting condition, p_{si} is swelling pressure of the soil at initial condition, p_{sw} is swelling pressure of the soil at subsequent wetting condition, p_0 ($=\sigma_y + \Delta\sigma_y$) is overburden pressure, Δh_i is the maximum potential heave at initial condition, and Δh_w is the maximum potential heave at a subsequent wetting condition, Δh is the heave in the expansive soil from initial condition to the subsequent wetting condition.

4 CASE STUDY INFORMATION OF AN EXPANSIVE SOIL SLOPE AT ZAO-YANG, CHINA

The natural expansive soil slope discussed in the present study was located about 230 km north-west of Wuhan and about 100 km south of the intake canal for the South-to-North Water Transfer Project (SNWTP) in Nanyang, Henan, China (Ng et al. 2003). The soil at this location constitutes of yellow-brown clay, in which the predominant clay minerals are montmorillonite and illite. The top layer of this soil was desiccated and had an abundance of cracks.

Ng et al. (2003) conducted two artificial rainfall infiltration tests during the one-month monitoring period (from August 13 to September 12, 2001). Prior to the rainfall simulation, three rows of instrumentation (R1, R2, R3) were placed at different positions of the slope to measure the water content, soil suction, and ground movements (horizontal and vertical). The focus of the study is related to the estimation of the ground heave at the top of the slope (R1), where the evolution of water content and soil suction during the monitoring duration was recorded in the literature. Figure 4a and Figure 5 summarize the soil suction and water content profiles at different stages during the infiltration test. The depth of the active zone can be considered to be about 2 m, since the changes of water content (or soil suction) below this depth is insignificant. Furthermore, the soil suction is approximately zero by the end of the monitoring period at this depth, suggesting, saturated condition was achieved.

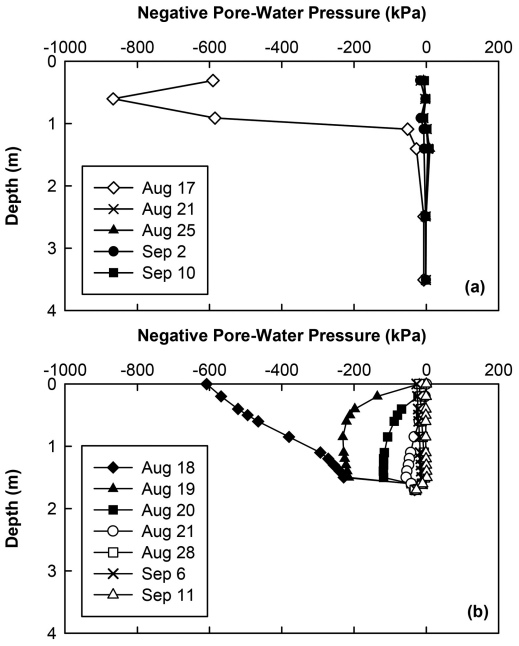


Figure 4. The profiles for negative pore-water pressure: (a) in-situ measurement (after Ng et al. 2003), (b) prediction using VADOSE/W.

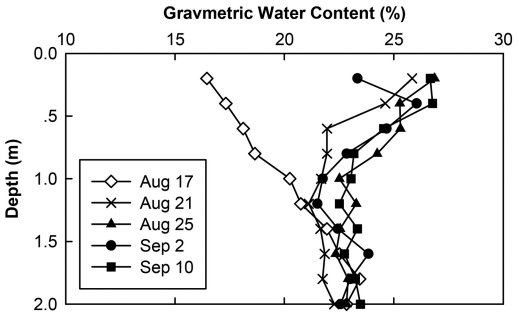


Figure 5. The in-situ measurement on water content (after Ng et al. 2003).

5 CASE STUDY ANALYSES USING PROPOSED METHODS

5.1 *Ground heave prediction using the SWCC-based model*

There was limited investigation on the water content and soil suction within the top 0.3 m depth (see Fig. 4). In this zone, the soil had some vegetation and grass with its roots and also it was highly fissured. For this reason, the soil above this depth was assumed to be non-expansive in the present case study. Based on the initial soil suction profile recorded in Figure 4a,

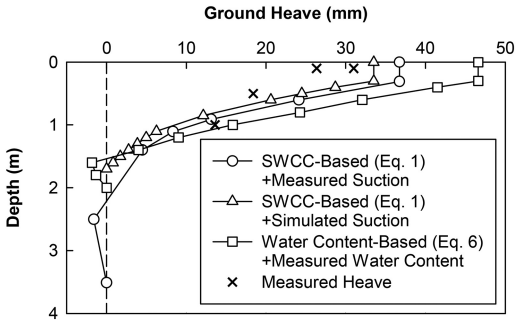


Figure 6. The predicted variation of maximum potential heave with respect to depth.

the potential heave at the top of the slope can be predicted using the proposed swelling pressure prediction model (Eq. 1) along with the Fredlund (1983) equation (Eq. 7). The values of required model parameters ($\alpha = 0.22$, and $\beta = 2.0$) for Zao-yang expansive soil has been established in previous sections. Figure 6 presents the comparison between the predicted potential (maximum) heave and the measured final heave.

The evolution of the ground heave with respect to climate change (or time) is of significant interest in engineering practice. The information of the variation of soil suction with respect to climate change is required to estimate the swelling pressure and ground heave using the proposed techniques. The commercial software, VADOSE/W has been used as a tool in the present study to predict the variation of matric suction with respect to climate changes.

The response of Zao-yang slope to the climate change is modelled using VADOSE/W (2012). After establishing the slope model (Fig. 7), two rainfall simulations were performed on the slope model in accordance with the in-situ artificial infiltration testing processes (Ng et al. 2003).

The initial condition of pore-water pressure is defined using a spatial function available in the software. This spatial function can be used to generate consistent matric suction profiles for the entire slope based on the field data. The original field data of matric suction values (Fig. 4a) were measured at R1, R2, R3 within the depth of 4.0 m (Ng et al. 2003).

The climate data of Wuhan city has been summarized by Adem (2015). Together with the rainfall intensity, it has been applied on the slope surface as the climate boundary. The hydraulic boundaries of both left and right sides of the slope model are defined as flux = 0 m/day. These hydraulic boundaries are assigned from the depth of 2 m (i.e., below the shallow layers).

The simulated variation of suction with respect to time at R1 is shown in Figure 4b, which demonstrates a reasonably good agreement with the measured data (Fig. 4a). The simulated variation illustrates how suction gradually changes during the early stages of the infiltration (from Aug 18 to 22 of 2003). The results

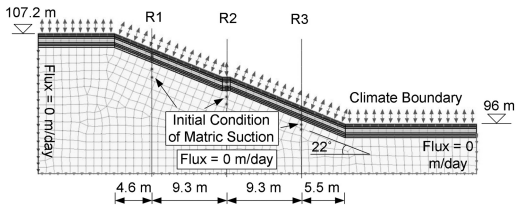


Figure 7. The established numerical model.

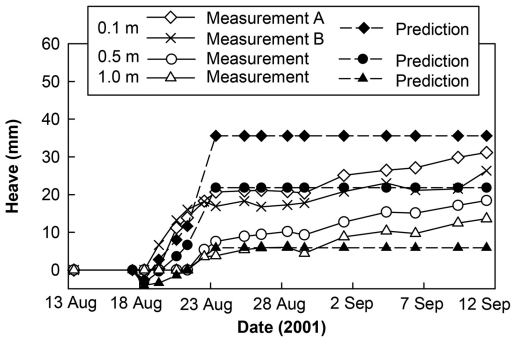


Figure 8. The predicted variation of ground heave with respect to time using the SWCC-based model.

of suction simulation establish the required information in the prediction of ground heave with respect to time using the proposed SWCC-based swelling pressure prediction model (Eq. 1) and the modified Fredlund equation (Eq. 8). Figure 8 summarizes the measured and predicted variation of ground heave at R1 using SWCC-based model. There is a reasonable comparison between the measured and predicted values; the predicted values are however are higher than the measured values.

5.2 *Ground heave prediction using the water content-based model*

The information about the variation of water content with respect to time is summarized in Figure 5. This information can be used in the modified Fredlund model (Eq. 8) and the proposed water content-based model (Eq. 6). The model parameter, $\lambda = 0.96$ established for Zao-yang expansive soil is used in the present prediction analysis. The prediction is based on an assumption that the decrease of initial water content beyond the residual water content will not result in further increase in the swelling pressure (or swell potential). The results of both the predicted potential heave and the predicted time-process suggest an over-estimation of heave in comparison to the measurements (see Fig. 6 and Fig. 9).

6 DISCUSSION AND CONCLUSIONS

Numerical simulation is undertaken in the present study to predict the evolution of matric suction for

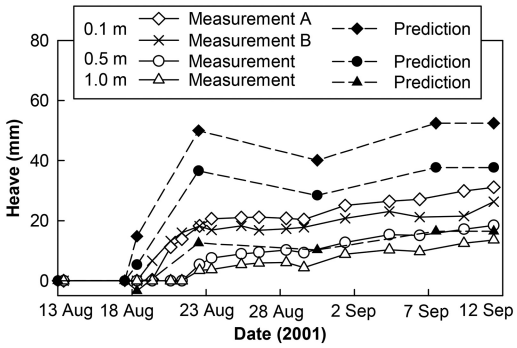


Figure 9. The predicted variation of ground heaves with respect to time using the water content-based model.

the natural expansive soil slope located at Zao-yang taking account of the influence of artificial rainfall. After establishing the simulation results on matric suction, both of the SWCC-based model and water content-based model are used to predict the variation of swelling pressure (swell potential) of the soil with respect to the change of climate factors (or time). This information is used to predict the evolution of ground heave in expansive soil, which is of considerable interest in engineering practice.

The application of the SWCC-based swelling pressure prediction model (Eq. 1), the swelling index prediction equation (Eq. 6), along with the modified Fredlund equation (Eq. 8) (Vanapalli et al. 2014) provide a reasonable ground heave estimation with the measured values. There is however certain limitation for the water content-based model (Eq. 6). The predicted results are sensitive to the change of the $(w_f - w_i)$ term. The prediction using water content-based model is based on an assumption that the decrease of w_i beyond w_r results in insignificant changes on the swelling pressure.

The SWCC-based model results in a reasonable estimation on the ground heave of the Zao-yang slope. However, the water content-based model overestimates ground heave values for the present case study.

REFERENCES

Adem, H.H. & Vanapalli, S.K. 2014. Elasticity moduli of expansive soils from dimensional analysis. *Geotechnical Research*, 1(2): 60–72.

Adem, H.H. 2015. *Modulus of elasticity based method for estimating the vertical movement of natural unsaturated expansive soils*. Ph.D. Thesis, University of Ottawa, Ottawa, Canada.

Blight, G.E. 1965. The time-rate of heave of structures on expansive clays. In *Moisture equilibria and moisture changes in soils beneath covered areas*, G.D. Aitchison (eds), Butterworths, Sydney.

Fredlund, D.G. 1983. Prediction of ground movements in swelling clays. *Proceedings of the 31st Annual Soil Mechanics and Found Engineering Conference, University of Minnesota, Minneapolis, 1983.*

Gens, A. & Alonso, E.E. 1992. A framework for the behaviour of unsaturated expansive clays. *Canadian Geotechnical Journal*, 29(6), 1013–1032.

Geo-Slope. 2012. GEO-STUDIO VADOSE/W Software Package. Version 8.14. Calgary, Alberta.

Hamberg, D.J. & Nelson, J.D. 1984. Prediction of floor slab heave. *Proceedings of the 5th International Conference on Expansive Soils, Adelaide, South Australia.*

Han, Z. & Vanapalli, S.K. 2015. Model for predicting the resilient modulus of unsaturated subgrade soil using the soil-water characteristic curve. *Canadian Geotechnical Journal*, accepted for publication.

Kassiff, G. & Shalom, A.B. 1971. Experimental relationship between swell pressure and suction. *Géotechnique*, 21(3): 249–255.

Nelson, J.D. & Miller, D.J. 1992. *Expansive Soils: Problems and Practice in Foundation and Pavement Engineering*. John Wiley and Sons, Inc., New York.

Ng, C.W.W., Zhan, L.T., Fredlund, D.G. & Gong, B.W. 2003. Performance of an unsaturated expansive soil slope subjected to artificial rainfall infiltration. *Géotechnique*, 53(2): 143–157.

Oh, W.T., Vanapalli, S.K. & Puppala, A.J. 2009. Semi-empirical model for the prediction of modulus of elasticity for unsaturated soils. *Canadian Geotechnical Journal*, 46(8): 903–914.

Pedarla A., Puppala, A.J., Hoyos L.R., Vanapalli S.K. & Zapata, C. 2012. SWRC modelling framework for evaluating volume change behavior of expansive Soils. *Proceeding of E-UNSAT 2012, Napoli, Italy, June 2012.*

Vanapalli, S.K. & Oh, W.T. 2010. A model for predicting the modulus of elasticity of unsaturated soils using the soil-water characteristic curve. *International Journal of Geotechnical Engineering*, 4(4): 425–433.

Vanapalli, S.K. & Lu, L. 2012. A state-of-the art review of 1-D heave prediction methods for expansive soils. *International Journal of Geotechnical Engineering*, 6(1): 15–41.

Vanapalli, S.K., Tu, H. & Oh, W.T. 2014. Soil-water characteristic curve based methods for predicting the swelling pressure and ground heave in expansive soils. Keynote Address, *Indian Geotechnical Conference, IGC-2014, Kakinada, India*.

Zhan, L.T., Chen, P. & Ng, C.W.W. 2007. Effect of suction change on water content and total volume of an expansive clay. *Journal of Zhejiang University (SCIENCE A)*, 8(5): 699–706.

Unsaturated Soil Mechanics—from Theory to Practice – Chen et al. (Eds)
© 2016 Taylor & Francis Group, London, ISBN 978-1-138-02921-7

Potential of surfactants for clay improvement

N. Jones
Amey Geotechnics, UK

S.D.N. Lourenço
Department of Civil Engineering, The University of Hong Kong, Hong Kong SAR, China

A. Paul
School of Chemistry, Cardiff University, UK

ABSTRACT: The paper presents an experimental study on the behaviour of unsaturated soils with surfactant solutions. Suction measurements by means of high suction tensiometers, compaction tests and the Atterberg limits were conducted in mixtures of sand and kaolin, with and without surfactant solutions. The results revealed a prominent effect on suction, but to a lesser extent on the Atterberg limits and compaction behavior (the maximum dry density). This research represents an exploratory study on the potential of surfactants to improve the mechanical properties of soils.

1 INTRODUCTION

1.1 *Surfactants*

Surfactants are molecules which consist of one polar, hydrophilic head group (water-loving) and one non-polar, hydrophobic tail group (water-hating). Surfactants have an affinity for a surface, forming into an orientated monolayer at the interface and reducing the interfacial tension. When the surface has no more room for surfactant molecules they begin to self-associate and form aggregates inside the bulk of the liquid (micelles). Micelles typically contain between 20–100 surfactant molecules. The concentration of surfactants, at which micelles begin to form, is defined as the critical micelle concentration (CMC). The CMC depends on surfactant type/chemistry and other conditions of the solution such as temperature (Rosen, 1989).

The chemical affinity of a surfactant with a given clay soil and the levels of adsorption achieved depends on the basic structure of the surfactant. Surfactants are classified into three groups according to the nature of the hydrophilic portion of the molecule after dissociation in an aqueous solution: (1) anionic surfactants (negatively charged head group); (2) cationic surfactants (positively charged head group); (3) nonionic surfactants (non-charged) (Rosen, 1989).

Surfactants can be absorbed to clays. Sanchez-Martin et al. (2008) found that polar surfactant adsorption towards clays would stabilize, whereas non-ionic surfactant adsorption (including Triton X-100) would continue to increase above the CMC. Sanchez-Martin et al. (2008) also found cationic surfactants to be the most adsorbent across a variety of clay soil types. Wang et al. (1999) studied cationic surfactants and their adsorption behaviour with kaolinite and found that once the surfactant CMC had been reached, adsorption levels would level off, suggesting that micelle formation can interrupt further adsorption. Instead, the highest adsorption levels occurred at concentrations just below the CMC. Another property influencing the adsorption potential of surfactants is the chain length of surfactant tail groups and the chain structure within these groups. Clay surface charge distribution is sensitive to changes in chain lengths. Single chained cationic surfactants, for example, have shown a significantly greater adsorption potential towards kaolinite in comparison with double chained cationics at similar concentrations (Wang et al., 1999).

Surfactants control surface tension. Surface tension is the measure of the cohesive energy present at an interface. It is possible to describe the situation as having a line tension, which can be quantified as the force per unit length acting on an imaginary line drawn in the surface. For liquid water, at room temperature, the surface tension is 72 mNm^{-1}. Surface tension is important for matric suction in unsaturated soils because matric suction depends, not only, on the radii of small water menisci at the interparticle contacts but also on the surface tension, where a reduction in surface tension reduces suction. Since matric suction is a key variable controlling unsaturated soil behavior, being able to regulate suction via surface tension offers a series of new opportunities to use surfactants as additives for ground improvement.

1.2 *Surfactants and soil behaviour*

There is a lack of research specifically into the effects of surfactants on the engineering properties of soils. Among the relevant literature, it has been shown that surfactants can influence fluid density and viscosity, thus speeding up or slowing down the apparent hydraulic conductivities of soils (Lee et al, 2002). Depending on the properties and concentration of a surfactant used and clay interlayer electrostatics, Akbulut et al. (2012) revealed that surfactants can cause both flocculation and dispersion of clay particles. For example, cationic surfactants CTAC and QEFA were found to produce a dramatic change in clay plasticity. Within the effect of surfactants on soil compaction, Berney et al. (2003) assessed the influence of a wetting agent on compaction, and found that the soil with the surfactant solution achieved a higher maximum dry density at the optimum water content than the sample only with water. The Authors justified it based on a reduction of suction. However, no evidence was provided. More recently, Gluck (2010) concluded that the observed changes in the maximum dry density on various compacted granular samples with and without a commercial detergent were within possible experimental error.

In order to test the potential benefits of surfactants for ground improvement, such as an increase in maximum dry density during compaction, their effects on various soils and properties were tested in the laboratory. The remit in this study is to investigate the effect Merpol A, a non-ionic surfactant, on some soil parameters (consistency, compaction and suction) on different compositions of kaolin and sandy soils at concentrations of 0.05% and 1.0%. The composition of kaolin to sand ranged from 100:0, to 50:50 and 25:75, respectively.

2 MATERIALS AND METHODS

2.1 *Consistency and compaction tests*

The surfactant solution used was Merpol A. It is described as a nonionic, polyethylene glycol phosphate ester, non-foaming wetting agent (Sigma-Aldrich, 2010). A surface tension of 26 mN/m^{-1} at 0.1% aqueous volume, and critical micelle concentration of 0.005% is provided in the product specification.

All tests were conducted with samples of Speswhite kaolin (100% kaolin) and mixtures of sand and kaolin at ratios of 50% kaolin: 50% sand and 25% kaolin: 75% sand, at surfactant concentrations of 0.05% and 1%, both above the critical micelle concentration. Prior to all tests, both the sand and clay were oven-dried.

To determine the consistency behavior, the liquid limit (LL) was obtained following the Cone Penetrometer Method (BS1377:Part 2:1990:4.3) with LL corresponding to a penetration of 20 mm while the plastic limit (PL) also followed BS1377 with PL obtained for a water content of a thread of soil that crumbles at 3 mm.

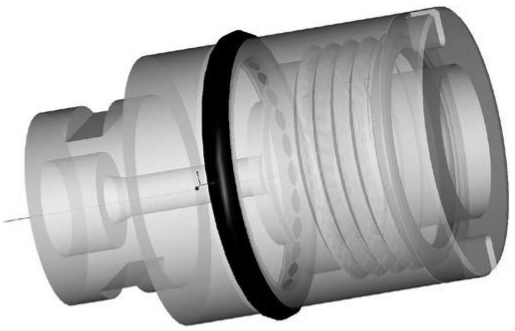


Figure 1. The high suction tensiometer used (diameter = 14 mm; length = 22 mm).

To determine the compaction behavior, testing followed BS1377, with dynamic compaction in three layers at increasing water contents. Selected compacted samples were kept in the compaction mold with the bottom and upper surfaces sealed with paraffin wax for suction measurement.

2.2 *Measurement of matric suction*

Suction was measured with a high suction tensiometer (Ridley & Burland, 1993), manufactured at Cardiff University, with a 1500 kPa air-entry value ceramic stone (Figure 1). The tensiometer used in this research measured up to 1000 kPa, its suction at cavitation.

The tensiometer was pressurized to the range 2–3 MPa, and the measurement range tested by leaving the stone to dry to the atmosphere. The tensiometer was considered saturated, if suction at cavitation reached 1000 kPa. If not, the instrument was placed back in the pressure vessel and repressurized. No calibration in the negative range was conducted. The calibration from the positive range was extended to the negative range.

Suction was measured at constant water content conditions by smearing the stone against the soil and waiting for equilibrium. For drier samples, the stone was covered on thin film of water to force the contact with the soil. For accuracy, measurements were conducted by two separate tensiometers. Prior to the measurements, the tensiometer was removed from the vessel and left in free water for 2 to 3 days to allow the metal body to recover from the pressure vessel confinement.

3 RESULTS AND DISCUSSION

3.1 *Consistency behaviour*

Figure 2a and 2b show the effect of surfactant concentration on the plastic and liquid limit, respectively. The increasing concentration of surfactant, from 0% to 1%, increased the plastic limit for the three soil mixtures. For the kaolin sample, the plastic limit increased from 35.1% to 42.6% while for the 25% kaolin sample,

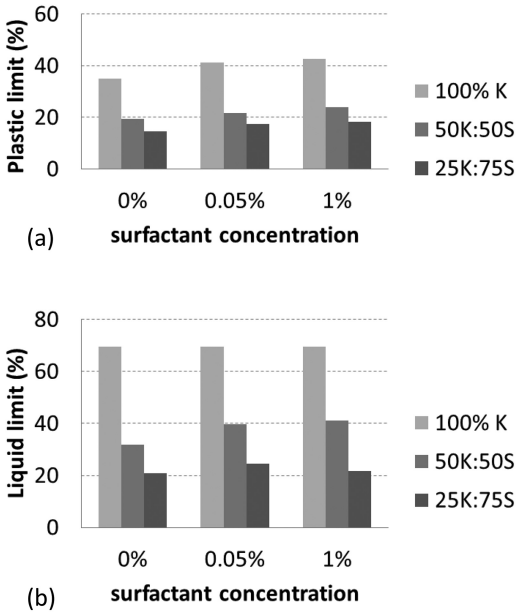


Figure 2. Effect of the surfactant concentration in the consistency behavior of three soil mixtures (K = kaolin, S = sand). (a) Plastic limit; (b) Liquid limit.

the increase was from 14.5% to 18.2%. For the liquid limit, the results were not conclusive, with LL remaining unchanged for the kaolin sample, increasing for the 50% kaolin sample and increasing and decreasing for the 25% kaolin sample.

3.2 *Compaction behavior*

Figures 3a, 3b and 3c show the compaction curves at different surfactant concentrations (0%, 0.05%, 1%) for 10% kaolin, 50% kaolin and 25% kaolin, respectively. Figure 3a, for kaolin, shows tests at two further concentrations at 0.1% and 4.5%. The compaction curves revealed no particular trend, with the curves superimposing for the 50% and 25% kaolin samples. Differences in the maximum dry density and optimum water content between the three figures are due to the material, rather than surfactant concentration. The only exception is for the kaolin samples, where the maximum dry density dropped by 0.05 Mg/m^3 for the samples prepared at higher surfactant concentrations (1% and 4.5%). This finding contradicts the results by Berney et al. (2003) where the maximum dry density was increased with the surfactants.

3.3 *Suction behaviour*

Figure 4a shows suction against the surfactant concentration for a 50:50 sample at 10% and 15% water content. At 10% water content, there was a reduction of 235 kPa by adding 0.05% surfactant and 800 kPa when adding 1% surfactant solution. At 15% water content, the reduction in suction was smaller because of the higher water content.

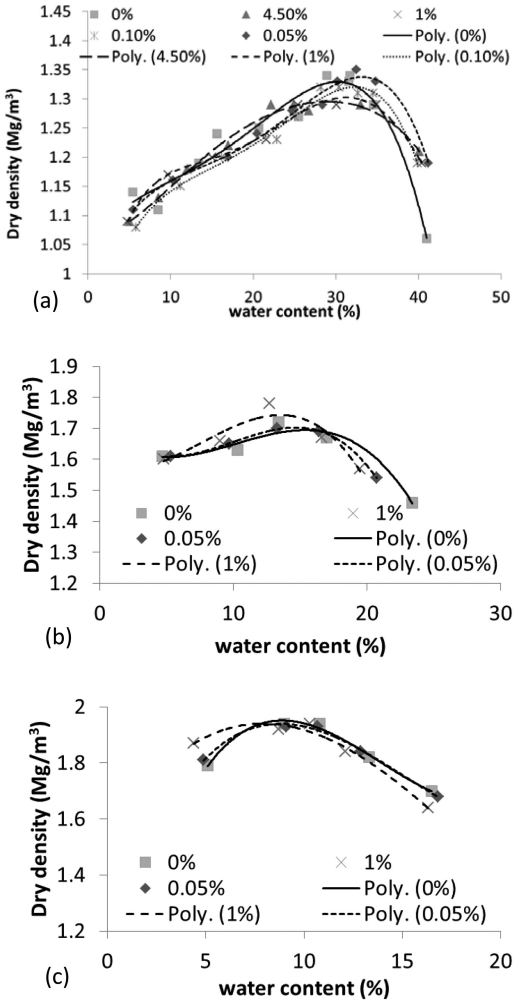


Figure 3. Compaction curves at different surfactant concentrations for (a) 100% kaolin, (b) 50% kaolin: 50% sand, (c) 25% kaolin: 75% sand.

Figure 4b shows suction against the surfactant concentration for a 75:25 sample at 5% and 10% water content. The results are similar to Figure 2, except that given the higher sand content, the water content was smaller (5%) to achieve high suctions (1000 kPa for the sample without surfactant).

These results confirm that the surfactants reduce suction, possibly linked to a reduction in the surface tension.

3.4 *Summary*

This preliminary study revealed no discerning trends in common between the three sets of results (consistency, compaction and suction), suggesting that the surfactants have specific effects in certain soil properties. The presence of surfactants had an effect in the plastic limits and suction behaviour, but was inconclusive

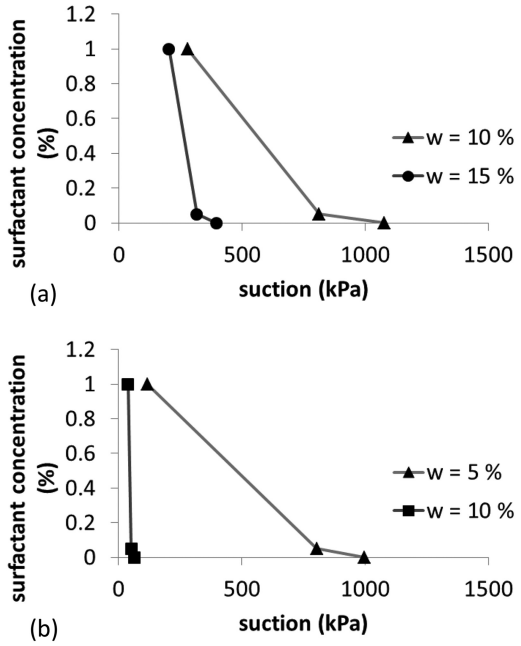


Figure 4. Effect of surfactant concentration on suction for (a) 50% kaolin: 50% sand, and (b) 25% kaolin: 75% sand.

in the compaction behaviour and liquid limit. Increasing surfactant concentrations decreased suction and increased the plastic limits. A reduction in the maximum dry density did occur but only at high surfactant concentrations.

The compaction results revealed that the explanation proposed by Berney et al. (2003) whereby the maximum dry density is increased due to a reduction in suction does not hold for all soils and conditions. The maximum dry density changed little even when suction was reduced by 80% at 1% surfactant concentration.

This study also revealed that the CMC, an important property of surfactants, does not act as a threshold in the soil behavior. If it did, soil properties would not change for concentrations higher than the CMC. But, as shown for all datasets, increasing concentrations past the CMC had an effect on suction, plastic limit and compaction. This suggests that surfactant molecules populate, not only the air-water interfaces decreasing surface tension, but may be absorbing to the clay particles and forming micelles in the liquid phase. Therefore the interplay between the three, may affect soil behavior.

4 CONCLUSIONS

The paper presents an experimental study on the behavior of unsaturated soils with surfactant solutions. Suction measurements by means of high suction tensiometers, compaction tests and the Atterberg limits were conducted in mixtures of sand and kaolin, with and without surfactant solutions. Compaction showed a decrease in the maximum dry density for the 100% kaolin sample at higher surfactant concentrations. The change in the maximum dry density data between the different concentrations was negligible or inconclusive. Plastic limits grew significantly with increasing surfactant concentration. Suction consistently reduced with increasing surfactant concentrations, even past the CMC, which suggests that surface tension cannot be the only mechanism responsible for decreasing suction. Other factors, such as the absorption of surfactant molecules to the clay particles and micelle formation in the pore water may also affect soil behaviour.

REFERENCES

Akbulut, Z., Kurt, N. & S. Arasan, 2012. Surfactant modified clays' consistency limits and contact angles. *Earth Sciences Resource Journal*, 16 (2):13–19.

Berney, E., Peters, J., Newman, K. & D. Smith. 2003. Effect of surfactants on dry-side compaction of silty sand. *Transportation Research Record: Journal of the Transportation Research Board*, 1819:57–62.

Gluck, O. (2010). The Effect of surfactants as soil compaction aids. MSc. Dissertation, Cardiff University, pp. 117.

Lee, D.-H., Cody, R.D., Kim, D.-J. & S. Choi. 2002. Effect of soil texture on surfactant-based remediation of hydrophobic organic-contaminated soil, *Environment International*, 27:681–688.

Ridley, A., and J., Burland. 1993. A new instrument for the measurement of soil moisture suction. *Géotechnique*, 43(2):321–324.

Rosen, M.J. 1989. Surfactants and interfacial phenomena, 2nd edition, John Wiley & Sons Inc.

Sánchez-Martín, M.J., Dorado, M.C., del Hoyo, C. & M.S. Rodríguez-Cruz, 2008. Influence of clay mineral structure and surfactant nature on the adsorption capacity of surfactants by clays. *Journal of Hazardous Materials* 150:115–123.

Wang, J., Han, B., Dai, M., Yan, H., Li, Z. & R.K. Thomas. 1999. Effects of chain length and structure of cationic surfactants on the adsorption onto Na-Kaolinite. *Journal of Colloid and Interface Science* 213:596–601.

Unsaturated Soil Mechanics—from Theory to Practice – Chen et al. (Eds)
© 2016 Taylor & Francis Group, London, ISBN 978-1-138-02921-7

Cam-clay model applicable to unsaturated clayey sand

Q.Q. Miao
Chongqing Communications Research and Design Institute, Chongqing, China

Z.H. Chen
Department of Civil Engineering, Logistical Engineering University, Chongqing, China

Q.Q. Zhu
College of Chemical Engineering, Northwest Minority University, Lanzhou, China

Z.H. Yao
Engineering College, Air Force Engineering University, Xi'an, China

J.H. Zhang
Department of Civil Engineering, Logistical Engineering University, Chongqing, China

ABSTRACT: To study the mechanical behavior of unsaturated clayey sand, a series of triaxial shear tests were carried out under different suctions of 0, 50, 100 and 200 kPa and different confining pressures of 100, 200 and 300 kPa. The Cam-clay model that can calculate volumetric strain of saturated soil was used to predict the unsaturated soil behavior. The calculated model parameters were got to compare with the actual measured data. Under the condition of smaller suction and low confining pressure for unsaturated clayey sand, Cam-clay model could better simulate the strength and deformation characteristics of unsaturated clayey sand. The relationship curves of axial strain and volumetric strain substantially decrease shape body. But under high confining pressure and larger suction, the Cam-clay model is hard to reflect the dilatancy characteristics of unsaturated clayey sand. This shows further that the Cam-clay model can reflect obviously body shrinkage characteristics and the reaction of the sandy soil dilatancy is poor.

1 INTRODUCTION

Research on elasto-plastic constitutive model for unsaturated soil (Alonso et al. 1990, Karube 1989, Toll 1990, Wheeler 1992, Chen et al. 1999, etc.) was built on the basis of Cam-clay model, which is a common research in saturated soil. The main difference between saturated soil and unsaturated soil is how to consider the effect of suction. The saturated soil of Cam-clay model is extended to unsaturated soil, the key is to increase the suction variables. This paper, based on the results of a serial of tests on clayey sand, tries to put the modified Cam-clay into unsaturated soil.

2 THE CAM-CLAY MODEL INTRODUCTION

Elastic strain increment can be obtained by Hooke's law (Matsuoka & Sun 2006).

$$d\varepsilon_{ij}^{e}=\frac{1+v}{E}d(\sigma_{ij}-u_a)-\frac{v}{E}d\sigma_{mm}\delta_{ij} \tag{1}$$

where, $d\sigma_{mm}=p=(\sigma_1+\sigma_2+\sigma_3)/3-u_a$, E is the elastic modulus of soil, v is Poisson's ratio, which is equal to 0.35.

$$d\varepsilon_{v}^{e}=\frac{3(1-2v)}{E}dp \tag{2}$$

$$\Delta e=e-e_0=-\lambda\ln\frac{p_x}{p_0} \tag{3}$$

$$\varepsilon_v=\frac{-\Delta e}{1+e_0}=\frac{\lambda}{1+e_0}\ln\frac{p_x}{p_0} \tag{4}$$

$$\varepsilon_v^{e}=\frac{k}{1+e_0}\ln\frac{p_x}{p_0} \tag{5}$$

$$\varepsilon_v^{p}=\varepsilon_v-\varepsilon_v^{e}=\frac{\lambda-k}{1+e_0}\ln\frac{p_x}{p_0} \tag{6}$$

ε_v^{e} and ε_v^{p} are the elastic and plastic strain.
Equation (5) can be rewritten

$$d\varepsilon_{v}^{e}=\frac{k}{1+e_0}\frac{dp}{p} \tag{7}$$

Combining Equations (2) and (7) gives

$$E = \frac{3(1-2v)(1+e_0)}{k} p \tag{8}$$

where, e is void ratio, λ, k, M are Cam-clay model parameters.

The plastic yield function of the Cam-clay model is

$$f = \frac{\lambda - k}{1+e_0} \ln \frac{p}{p_0} + \frac{\lambda - k}{1+e_0} \ln(1 + \frac{q^2}{M^2 p^2}) - \varepsilon_v^p = 0 \tag{9}$$

On the condition of consistency, it can be obtained

$$df = \frac{\partial f}{\partial p} dp + \frac{\partial f}{\partial q} dq + \frac{\partial f}{\partial \varepsilon_v^p} d\varepsilon_v^p = 0 \tag{10}$$

$$d\varepsilon_v^p = d\varepsilon_1^p + d\varepsilon_2^p + d\varepsilon_3^p = \Lambda \frac{\partial f}{\partial \sigma_{ii}} \tag{11}$$

From Eq. (10) and (11), Eq. (12) can be got

$$\Lambda = -\frac{(\partial f / \partial p)dp + (\partial f / \partial q)dq}{(\partial f / \partial \varepsilon_v^p)(\partial f / \partial \sigma_{ii})} \tag{12}$$

$$\frac{\partial f}{\partial \sigma_{ij}} = \frac{\partial f}{\partial p}\frac{\partial p}{\partial \sigma_{ij}} + \frac{\partial f}{\partial q}\frac{\partial q}{\partial \sigma_{ij}} \tag{13}$$

From Eq (9),

$$\begin{aligned} \frac{\partial f}{\partial p} &= \frac{\lambda - k}{1+e_0}\frac{1}{p} + \frac{\lambda - k}{1+e_0}\frac{1}{1+(q^2/(M^2p^2))} \times (-2)\frac{q^2}{M^2} \times \frac{1}{p^3} \\ &= \frac{\lambda - k}{1+e_0 p}\frac{1}{p}\frac{M^2p^2 - q^2}{M^2p^2 + q^2} \end{aligned} \tag{14}$$

$$\frac{\partial f}{\partial q} = \frac{\lambda - k}{1+e_0}\frac{M^2p^2}{M^2p^2+q^2} \times \frac{2q}{M^2p^2} = \frac{\lambda - k}{1+e_0}\frac{2q}{M^2p^2+q^2} \tag{15}$$

$$\frac{\partial p}{\partial \sigma_{ij}} = \frac{\delta_{ij}}{3} \tag{16}$$

$$q = \sqrt{\frac{3}{2}(\sigma_{ij} - p\delta_{ij})(\sigma_{ij} - p\delta_{ij})} \tag{17}$$

$$\frac{\partial q}{\partial \sigma_{ij}} = \sqrt{\frac{3}{2}}\frac{(\partial(\sigma_{kl} - p\delta_{kl})/\partial\sigma_{ij})(\sigma_{kl} - p\delta_{kl}) \times 2}{2\sqrt{(\sigma_{mn} - p\delta_{mn})(\sigma_{mn} - p\delta_{mn})}} = \frac{3(\sigma_{ij} - p\delta_{ij})}{2q} \tag{18}$$

$$\frac{\partial f}{\partial \sigma_{ij}} = \frac{\lambda - k}{1+e_0}(\frac{M^2p^2 - q^2}{M^2p^2+q^2}\frac{\delta_{ij}}{3p} + \frac{3(\sigma_{ij} - p\delta_{ij})}{M^2p^2+q^2}) \tag{19}$$

According to Eq. (12), the following equations can be got

$$\Lambda = dp + \frac{2pq}{M^2p^2 - q^2} dq \tag{20}$$

$$d\varepsilon_{ij}^p = \Lambda \frac{\partial f}{\partial \sigma_{ij}} = \frac{\lambda - k}{1+e_0}(\frac{M^2p^2 - q^2}{M^2p^2+q^2}\frac{\delta_{ij}}{3p} + \frac{3(\sigma_{ij} - p\delta_{ij})}{M^2p^2+q^2})(dp + \frac{2pq}{M^2p^2+q^2}) \tag{21}$$

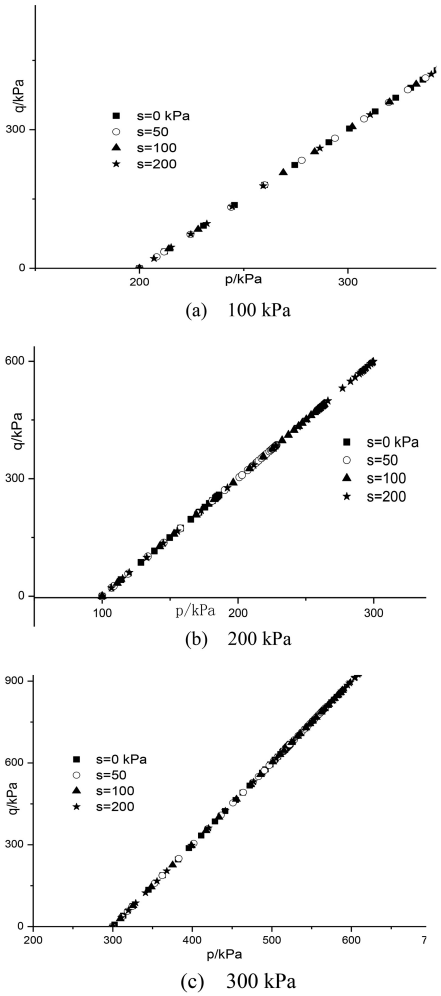


Figure 1. $p-q$ relation in drained triaxial test under different confining pressures.

$$d\varepsilon_v^p = \frac{\lambda - k}{1+e_0}\frac{1}{p}\frac{M^2p^2 - q^2}{M^2p^2+q^2}(dp + \frac{2pq}{M^2p^2 - q^2} dq) \tag{22}$$

From the above derivation, it can be calculated volume change of triaxial soil samples.

This paper extends the application of saturated soil Cam-clay model calculation to unsaturated soil, it only takes $p = (\sigma_1 + \sigma_2 + \sigma_3)/3 - u_a$ to replace $p = (\sigma_1 + \sigma_2 + \sigma_3)/3$. e_0 is the initial void ratio of unsaturated soil in every compression curve corresponding to different suction. λ and k represent the slope of compression curves and rebound curves in different suction. E is confirmed by Equation (8).

3 MODEL PREDICTION AND TEST RESULTS

Figure 1 was the relationship between p and q of 3 groups on condition under different suctions. Fig. 1(a), (b) and (c) show that under the condition of same

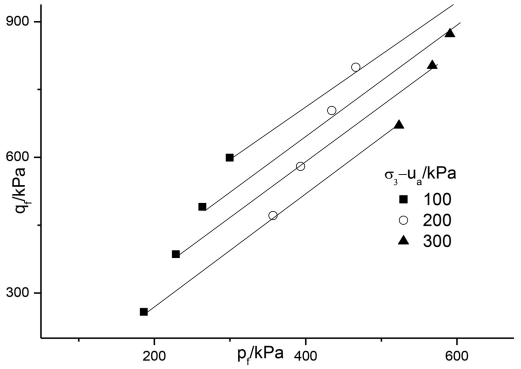


Figure 2. Critical state in $q-p$ plane.

confining pressure, different suction, 4 soil samples in p-q plane, the relationship between p and q is a linear in shearing process, it shows $\eta = q/p = const$, shear stress q and net mean stress p increases ratio are always consistent with the increase of suction. But with the increase of confining pressure, the slopes of the 3 lines were almost close to each other. It means that the strength of soil samples grow with the increase of confining pressure.

Figure 2 shows critical point drawn in the plane of the12 triaxial shear tests about shear stress and net mean stress. The suctions of four lines from top to bottom respectively are 200 kPa, 100 kPa, 50 kPa and 0 kPa. Figure 2 shows the slope that four straight lines are almost the same. The same suction in the critical state and different net confining pressure, q_f/p_f of the sample is a constant. The same net confining pressure and different suction critical failure state, q_f/p_f of the sample is also a constant. We can see from Figure 2, the same net confining pressure, the greater the suction, the bigger failure point of the shear strength. That is to say that the soil resistance shear ability is stronger. When the same suction, the greater the net confining pressure, the stronger failure shear strength.

Figure 3 shows $q/p-\varepsilon_s$ and $\varepsilon_v-\varepsilon_s$ relationship at different suctions. Figure 4 is for the Cam-clay model to calculate the 3 group that 12 specimens drained triaxial shear test between the predicted and test data comparison. Solid icon is for $q/p-\varepsilon_s$, and hollow for model prediction. Solid icon is the relationship of $\varepsilon_v-\varepsilon_s$, hollow is for model prediction. The 12 samples of 4 different groups unsaturated clayey sand drained triaxial shear test under different suctions, different confining pressure and 4 different suction triaxial isotropic tests were carried out. The Cam-clay model parameters of unsaturated clayey sand are listed in Tables 1 and 2. From Figures 1 and 2 and Table 1, it shows that the mean value of M was 1.5647.

The calculated by the model of $q/p-\varepsilon_a$ and $\varepsilon_v-\varepsilon_a$ compared with the test that unsaturated clayey sand strength and deformation characteristics of simulation model can be applied to Cam-clay model Curves of axial strain and volumetric strain present contraction shape in the low confining and low suction. But the

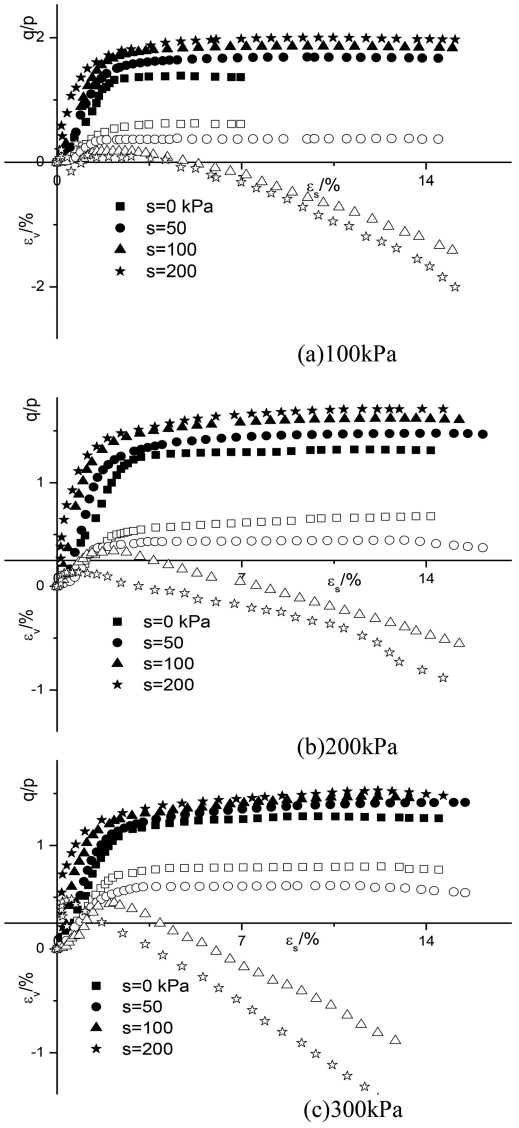


Figure 3. $q/p-\varepsilon_s$ and $\varepsilon_v-\varepsilon_s$ relations under different confining pressures.

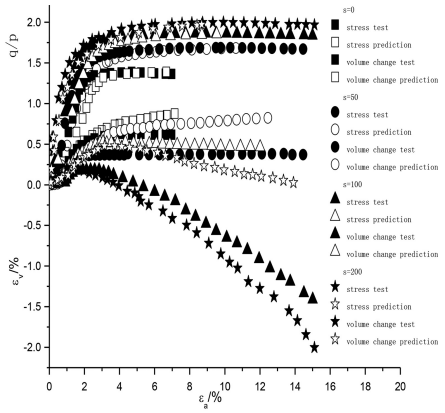
Table 1. Value of M under drained triaxial tests.

Suction (kPa)	0	50	100	200	Average Confining pressure (kPa)
100	1.3861	1.6875	1.8613	1.9991	1.7335
200	1.3191	1.4745	1.6191	1.7133	1.5315
300	1.2806	1.4140	1.4769	1.5451	1.4291
Average	1.3286	1.5253	1.6524	1.7525	1.5647

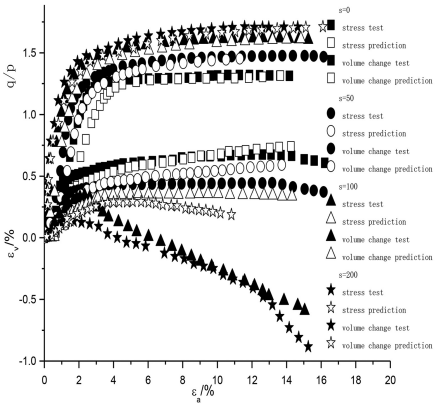
Cam-clay model is hard to reflect the dilatancy characteristics of unsaturated clayey sand, under higher confining pressure and larger suction. This shows further the Cam-clay model reflects the shrinkage

Table 2. Value of λ, k under drained triaxial tests.

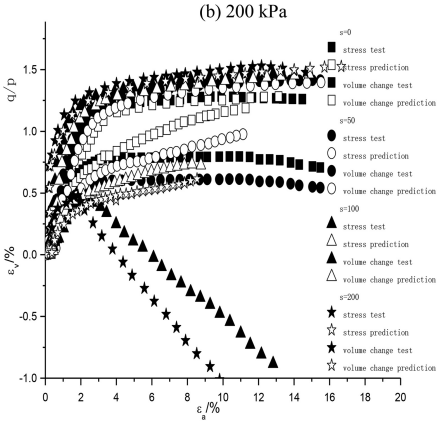
Suction (kPa)	0	50	100	200
0	1.3861	1.6875	1.8613	1.9991
200	1.3191	1.4745	1.6191	1.7133
300	1.2806	1.414	1.4769	1.5451



(a) 100 kPa



(b) 200 kPa



(c)300kPa

Figure 4. Test result versus prediction of Cam-clay model under different confining pressures.

characteristics significantly, but to reflect dilatancy of sandy soil poorly.

4 CONCLUSION

With a serial of triaxial tests on unsaturated clayey sand, the modified Cam-clay model for saturated soils was extended to unsaturated soils. Conclusions are drawn as follows:

(1) Under the different suction and same confining pressure, the relationship between p and q present a linear in shearing process.
(2) The same net confining pressure, the greater the suction, the bigger failure point of the shear strength. The soil resistance shear ability is stronger. When the same suction, the greater the net confining pressure, the stronger failure shear strength.
(3) In the low confining and low suction, unsaturated clayey sand strength and deformation characteristics of simulation model can be applied to Cam-clay model. Curves of axial strain and volumetric strain present contraction shape, but under higher confining pressure and larger suction, the Cam-clay model is hard to reflect the dilatancy characteristics of unsaturated clayey sand.

ACKNOWLEDGEMENTS

This work was financially supported by 53 batch China postdoctoral science foundation funded project and the Fundamental Research Funds for the Central Universities.

REFERENCES

Alonso E. E., et al. 1990. A Constitutive Model for Partialy Saturated Soil. Geotechnique, 40(3):405–430.

Alonso E. E., et al. 1992. A Framework for the Behaviour of unsaturated expansive clays. Can. Geotech. J., 29: 1013–1032.

Chen Z.H., Zhou H.Q., Fredlund D. G. 1999. Nonlinear model for unsaturated soils and it s application. Chinese Journal of Geotechnical Engineering, 21(5): 603–608.

Karube D. 1989. Yie1d Functions of Unsaturated Soil. Proc 12nd CSMFE, 1:615–618.

Matsuoka H., Sun D.A. 2006. The SMP concept-based 3D constitutive Models for Geomaterials, London: Taylor & Francis.

Toll D. G. 1990. A framework of unsaturated behaviour. Geotechnique, 40(1):31–44.

Wheeler S. J., et al. 1992. Development and application of a critical state model for unsaturated soil. Proc. Worth Memorial Symposium on Predictive soil Mechanics, Oxford: 558–572.

Unsaturated Soil Mechanics—from Theory to Practice – Chen et al. (Eds)
© 2016 Taylor & Francis Group, London, ISBN 978-1-138-02921-7

Analysis, improvement and evaluation of the generalized Soil-Water Characteristic Curve

Z.H. Chen & J.H. Zhang
Logistical Engineering University, Chongqing, China

ABSTRACT: The expression of generalized soil-water characteristic curve (GSWCC for short) which includes the net mean stress and deviator stress was proposed by the authors in 2004. In order to analyze and evaluate the influence of stress state and stress path on GSWCC, three groups of tests were conducted for 26 unsaturated remolded soil samples using a triaxial apparatus. The first group of tests are triaxial shrinking tests during which both deviator stress and net mean stress retain constants whereas matric suction increases; The second group of tests are triaxial hydrostatic compression tests during which both deviator stress and matric suction keep constants whereas net mean stress augments; The third group of tests are triaxial shear tests during which both net mean stress and matric suction maintain constants whereas deviator stress enlarges. The research results show that both stress state and stress path have significant effects on GSWCC; There are coupling effects of stress state variables on GSWCC, so that a modified expression of GSWCC is proposed; The predicted results by using the modified expression show good agreement with the test data and are much better than those predicted by adopting the expression of GSWCC. However, the expression of GSWCC is quite useful if relative errors of the predictions and test data are limited in 10%.

1 INTRODUCTION

The soil-water characteristic curve, namely SWCC, reflects the water retaining characteristics of unsaturated soils. And it is one of the fundamental constitutive relations of unsaturated soils (Fredlund et al. 1993). Recent researches reveal that, the SWCC is affected greatly by the density (Zhou et al. 2005; Zhang et al. 2010), particle size distribution (Stoicescu et al. 2005; Aung et al. 2010), mineral composition (Lu et al. 2005) and wet-dry path (Pham et al. 2005; Tuk et al. 2010).

However, the traditional SWCC only reflects the relations between moisture content (or saturation degree) and matric suction of soils. Through a series of experiments on the remoulded unsaturated loess, Chen et al. (1999) and Huang et al. (2000) found the relations between moisture content and net mean stress, and presented the concept of generalized SWCC (or GSWCC for short) and established the expression of GSWCC, which takes in to account the effect of both matric suction and net mean stress. Fang et al. (2004) carried out the consolidated drained triaxial compression tests on the remoulded unsaturated loess with the net mean stress and matric suction being constant, investigated the effect of shearing on the discharge of water, and built up the expression of GSWCC which could further reflect variation of moisture content with matric suction, net mean stress and deviator stress. The expression of GSWCC is as follows:

$$w = w_0 - ap - b\ln(\frac{s + p_{atm}}{p_{atm}}) - cq \tag{1}$$

where w_0 and w stand for the initial moisture content and certain moisture content with regard to the stress state, respectively. The symbols p, s and q represent the net mean stress, matric suction and deviator stress, respectively. The parameters a, b and c can be determined by tests, and p_{atm} stands for the value of standard atmospheric pressure. In the condition of triaxial stress state, p, s and q are defined as follows:

$$p = \frac{\sigma_1 + 2\sigma_3}{3} - u_a \tag{2}$$

$$s = u_a - u_w \tag{3}$$

$$q = \sigma_1 - \sigma_3 \tag{4}$$

where σ_1, σ_3 are the major and minor principal stress, respectively, and u_a and u_w are the pore air pressure and pore water pressure, respectively.

In the past, when studying $w - s$ and $w - p$ relations, the deviator stress (q) was fixed at zero, ignoring the effect of q on $w - s$ and $w - p$ relations, and when studying the $w - q$ relations, the mean net stress (p) was fixed at certain value, neglecting the influence of different p on $w - q$ relations. To make improvement, this paper tries to get a closer look at the effect of stress state and stress path on the water discharge through a series of tests.

The volumetric strain of water (ε_w) is defined by the ratio of the volume water variation (ΔV_w) to the initial

Table 1. Comparison between measured values and corrected values of the water discharge.

Description of the testing conditions			Measured value/cm^3	Corrected value/cm^3	Relative error (%)
Triaxial Shrinking tests	$q_0 = 0$	$p_0 = 50$	4.44	4.33	2.54
		$p_0 = 100$	4.89	4.47	9.40
		$p_0 = 200$	6.02	5.69	5.80
	$q_0 = 100$	$p_0 = 50$	4.09	3.79	7.92
		$p_0 = 100$	3.90	3.75	4.00
		$p_0 = 200$	4.96	4.78	3.77
	$q_0 = 200$	$p_0 = 100$	3.32	3.11	6.75
		$p_0 = 200$	3.98	3.67	8.45
Isotropic compression tests	$q_0 = 0$	$s_0 = 50$	3.46	3.26	6.13
		$s_0 = 100$	3.99	3.88	2.84
		$s_0 = 200$	5.67	5.22	8.62
	$q_0 = 100$	$s_0 = 50$	3.02	2.75	9.82
		$s_0 = 100$	3.88	3.57	8.68
		$s_0 = 200$	5.01	4.69	6.82
	$q_0 = 200$	$s_0 = 50$	2.34	2.17	7.83
		$s_0 = 100$	3.49	3.46	0.87
		$s_0 = 200$	4.39	4.30	2.09
P-fixed consolidated drained shear tests	$p_0 = 100$	$s_0 = 50$	1.50	1.38	8.70
		$s_0 = 100$	2.58	2.43	6.17
		$s_0 = 200$	3.36	3.15	6.67
	$p_0 = 200$	$s_0 = 50$	2.31	2.15	7.44
		$s_0 = 100$	3.25	3.04	6.91
		$s_0 = 200$	3.78	3.64	3.85
	$p_0 = 300$	$s_0 = 50$	3.54	3.46	2.31
		$s_0 = 100$	3.99	3.81	4.72
		$s_0 = 200$	4.75	4.58	3.71

volume of soil sample (V_0). And ε_w is linked with w through the following expression:

$$w = w_0 - \frac{1+e_0}{d_s}\varepsilon_w \tag{5}$$

where e_0 and d_s represent the initial void ratio and specific density of samples, respectively.

2 METHOD

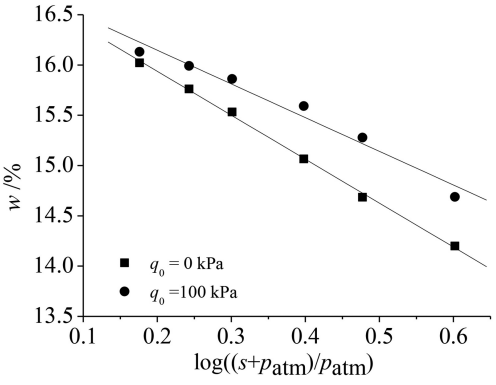
2.1 *Test apparatus and the preparation of soil samples*

The test apparatus is the triaxial apparatus for testing unsaturated soils of Logistical Engineering University. The soil used in the tests was collected from the slope bank at Anyang district of Henan province in China. Before the tests, the soil with the gravimetric initial moisture content 16.72% were remolded in a mold to be cylindrical samples, which are 39.10 mm in diameter and 80.00 mm high. And the initial dry density is 1.80 g/cm^3.

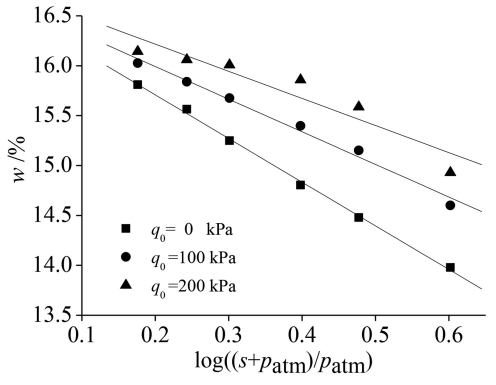
2.2 *Testing program*

The tests were divided in three groups. In the first group, the deviator stress and net mean stress held constant with the matric suction adding by several loading steps. In the second group, the deviator stress and the matric suction held constant with the net mean stress adding by several loading steps. And in the third group, the matric suction and net mean stress held constant with the deviator stress adding step-by-step. That is, in each group, there was only one independent variable. There were 26 tests in all, and the testing program is listed in Table 1, in which the subscript "0" of the symbols p_0, q_0 and s_0 indicates that these values being constant during the tests. Under each stress level, the equilibrium of the water variation was determined by the criterion that the volume change of the sample within 2 hours is less than 0.0063 cm^3 and the amount of water discharge is less than 0.012 cm^3.

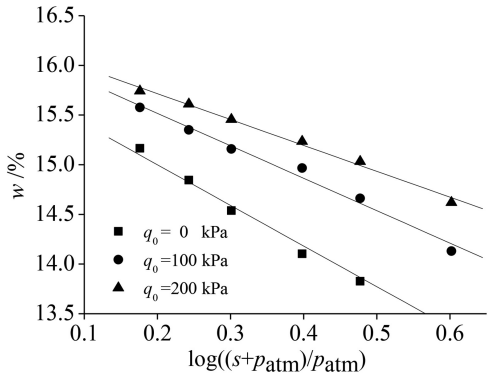
Note that a single test lasted several hours and there existed deviation of the measuring system of water discharge, the measured water discharge should be corrected. Therefore, after each test, the soil sample was weighed and then compared with initial weight of the sample, and the difference is the actual value of total water discharge, which was then subtracted from the measured total water discharge, and the result was divided by the time duration of this test and then distributed to the measured values of the water discharge in each loading step according to its time duration. The measured values and corrected values are listed in Table 1. Although the measured values and corrected values are close, the corrected values are used in the following analysis.



（a） p_0 =50 kPa



（b） p_0 =100 kPa



（c） p_0 =200 kPa

Figure 1. The $w-\log((s+p_{atm})/p_{atm})$ relations of triaxial Shrinking tests.

3 ANALYSIS OF WATER VARIATION

The increment form of water variation can be described as:

$$d\varepsilon_w = \frac{ds}{H_{wt}} + \frac{dp}{K_{wpt}} + \frac{dq}{K_{wqt}} \tag{6}$$

Table 2. Results of triaxial shrinking tests.

	$q_0 = 0$ kPa		$q_0 = 100$ kPa		$q_0 = 200$ kPa	
s_0/kPa	$\beta(p)$	$\lambda w(p)$	$\beta(p)$	$\lambda w(p)$	$\beta(p)$	$\lambda w(p)$
50	−0.44	0.79	−0.34	0.60	–	–
100	−0.44	0.79	−0.33	0.59	−0.27	0.49
200	−0.41	0.74	−0.33	0.59	−0.26	0.47
Mean value	−0.43	0.77	−0.33	0.059	−0.27	0.48

where

$$\left.\begin{aligned} H_{wt} &= \ln 10\frac{s+p_{atm}}{\lambda_w(p)} \\ K_{wpt} &= -\frac{1+e_0}{d_s\beta(s)} \\ K_{wqt} &= -\frac{1+e_0}{d_s\alpha(s)} \end{aligned}\right\}$$

and H_{wt}, K_{wpt} and K_{wqt} denote three tangent bulk modulus of water, which are related to net mean stress, matric suction and deviator stress, respectively. And the measurement of the three parameters are introduced by Chen et al. (1999) and Fang et al. (2004). In the previous researches, the parameters $\beta(s)$, $\alpha(s)$, $\lambda_w(p)$, K_{wpt} and K_{wqt} were considered as constants.

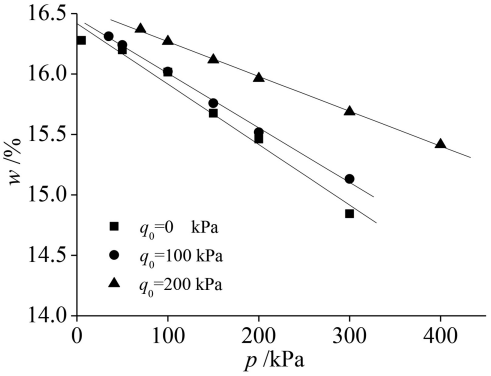
3.1 *Water variation of triaxial shrinking tests*

The $w-\log((s+p_{atm})/p_{atm})$ relations of triaxial shrinking tests are shown in Figure 1, from which it can be seen that the moisture content increase with the matric suction and there exists nearly linear relations between w and $\log((s+p_{atm})/p_{atm})$, which can be fitted by a straight line using the method of least square. The slope of the fitted line can be denoted as $\beta(p)$. Under the same net mean stress, the fitted lines with larger deviator stress are higher than other ones with lower deviator stress. The reason is that the deviator stress leads to the dilatation and the increase of void ratio, which further results in the rise of water retention holding capacity of the soil samples.

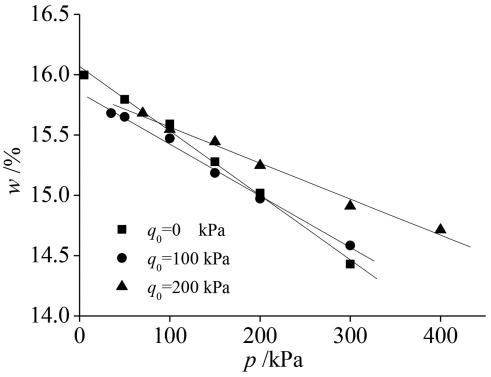
The values of $\beta(p)$ and $\lambda_w(p)$ are listed in Table 2, where $\lambda w(p) = -d_s\beta(p)/(1+e_0)$. From Table 2 it can be seen that when the deviator stress is constant, the values of $\lambda_w(p)$ under different matric suctions are close to each other, thus the mean value of them is considered as the value of $\lambda_w(p)$ under this deviator stress. And the relations between the value of $\lambda_w(p)$ and deviator stress can be described using the Equation (7).

$$\lambda_w(p) = a_2 + b_2 q_0 \tag{7}$$

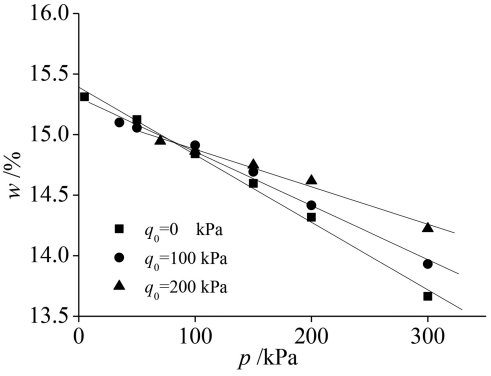
where a_2 equals 0.076, standing for the value of $\lambda_w(p)$ at 0 kPa deviator stress; and b_2 equals -0.00015 kPa^{-1}, which indicates that the value of $\lambda_w(p)$ decrease with the increasing deviator stress.



（a） s_0 =50 kPa

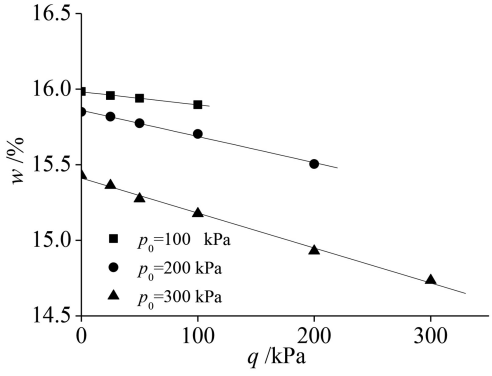


（b） s_0 =100 kPa

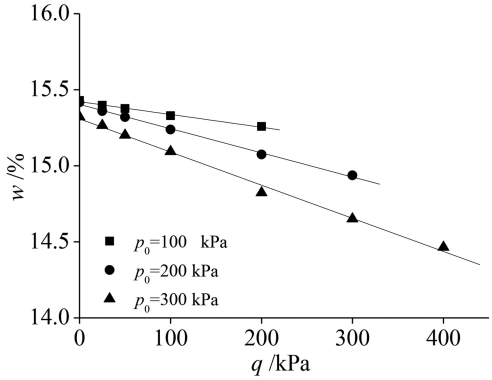


（c） s_0 =200 kPa

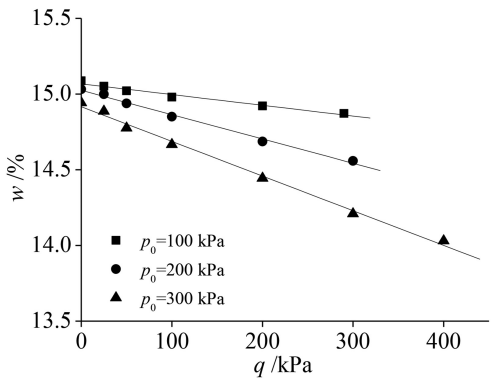
Figure 2. The $w-p$ relations of isotropic compression tests.



（a） s_0 =50 kPa



（b） s_0 =100 kPa



（c） s_0 =200 kPa

Figure 3. The $w-q$ relations of P-fixed consolidated drained shear tests.

Table 3. Results of triaxial isotropic compression tests.

	$q_0=0$ kPa		$q_0=100$ kPa		$q_0=200$ kPa	
s_0/kPa	$\beta(s)/\times10^{-5}$ kPa^{-1}	$K_{wpt}/\times10^4$ kPa	$\beta(s)/\times10^{-5}$ kPa^{-1}	$K_{wpt}/\times10^4$ kPa	$\beta(s)/\times10^{-5}$ kPa^{-1}	$K_{wpt}/\times10^4$ kPa
50	−501	111	−452	123	−288	193
100	−534	104	−428	1.30	−298	186
200	−558	0.99	−445	125	−309	1.80
Mean value	−531	105	−442	126	−298	186

Table 4. Results of triaxial p-fixed consolidated drained shear tests under different controlled net mean stresses.

	$p_0 = 100$ kPa		$p_0 = 200$ kPa		$p_0 = 300$ kPa	
s_0/kPa	$\alpha(s)/\times 10^{-6}$ kPa^{-1}	$K_{wqt}/\times 10^4$ kPa	$\alpha(s)/\times 10^{-6}$ kPa^{-1}	$K_{wqt}/\times 10^4$ kPa	$\alpha(s)/\times 10^{-6}$ kPa^{-1}	$K_{wqt}/\times 10^4$ kPa
50	−8.62	6.44	−173	3.21	−231	2.40
100	−8.40	6.61	−159	3.49	−218	2.55
200	−7.10	7.82	−161	3.45	−229	2.43
Mean value	−8.04	6.96	−164	3.39	−226	2.46

Table 5. Fitted parameters of Equation (14) and Equation (15).

a_1/kPa	a_2	a_3/kPa	b_1	b_2/kPa^{-1}	b_3
9800.70	0.76	87700	40.77	−0.00015	−225

3.2 *Water variation of isotropic compression tests*

Figure 2 describes the $w - p$ relations of isotropic compression tests. From Figure 2, it can be seen that the moisture content of samples decrease with the increasing net mean stress. And there exists nearly linear relations between w and p under different matric suctions and deviator stresses. And the slope of the fitted $w - p$ lines is denoted as $\beta(s)$. Under the same matric suction, the $w - p$ lines with larger deviator stress are higher than other ones. The reason for this is mentioned in section 3.1.

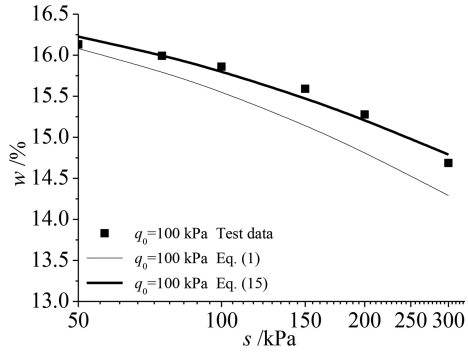
The values of $\beta(s)$ and the tangent bulk modulus (K_{wpt}) that is related to net mean stress are listed in Table 3, which reveals that at the same deviator stress, the values of K_{wpt} at different matric suctions are close. Therefore, the mean value of K_{wpt} under different matric suctions is considered as the value of K_{wpt} related to this deviator stress. And the relations between the value of K_{wpt} and deviator stress can be fitted using the Equation (8).

$$K_{wpt} = a_1 + b_1 q_0 \tag{8}$$

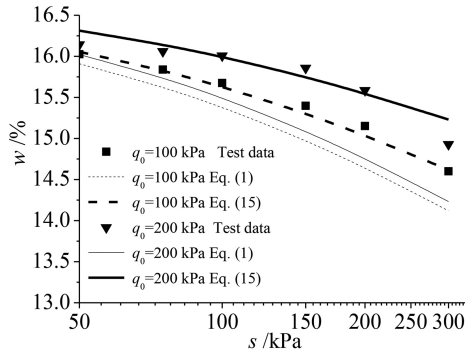
where a_1 equals 9800.70 kPa, denoting the value of K_{wpt} at the deviator stress 0 kPa; and b_1 equals 40.77, indicating the increasing trend of K_{wpt} with rising deviator stress.

3.3 *Water variation of triaxial P-fixed consolidated drained shear tests*

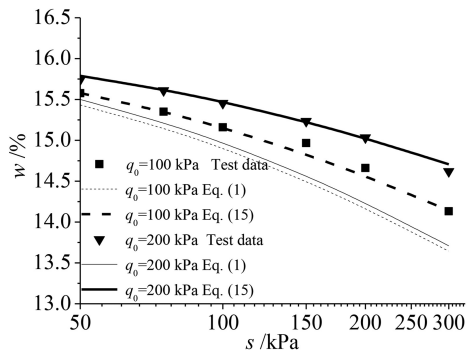
Figure 3 describes the $w - q$ relations of p-fixed consolidated drained shear tests. From Figure 3, it can be found that there exists a nearly linear relation between w and q under different matric suctions and net mean stresses. And the slope of the fitted $w - q$ lines is denoted as $\alpha(s)$. At the same matric suction, the $w - q$ lines with larger deviator stress are lower than other



(a) p_0 =50 kPa



(b) p_0 =100 kPa



(c) p_0 =200 kPa

Figure 4. The $w - s$ relations in triaxial shrinking tests.

ones, because lager net mean stresses result in higher degree of compression and more water discharge of soil samples.

The values of $\alpha(s)$ and the tangent bulk modulus (K_{wqt}) that is related to deviator stress are listed in Table 4, which demonstrates that at the same net mean stress, matric suction only has a slight effect on the values of K_{wqt}. Therefore, the mean value of K_{wqt} under different matric suctions is considered as the value of K_{wqt} related to this net mean stress.

And the relations between the value of K_{wqt} and net mean stress can be fitted using the Equation (9).

$$K_{wqt} = a_3 + b_3 p_0 \tag{9}$$

where a_3 equals 87700 kPa, standing for the value of K_{wqt} at 0 kPa net mean stress; and b_3 equals – 225, which indicates that the value of K_{wqt} decrease with the increasing net mean stress.

3.4 *Refinement of GSWCC expression*

From Equations (7)–(9), the values of K_{wpt} and $\lambda_w(p)$ are related to deviator stresses, and values of K_{wqt} are related to net mean stresses. Therefore, the new symbols $\overline{K}_{wpt}$, $\overline{H}_{wt}$ and $\overline{K}_{wqt}$ are used to denote the tangent bulk modulus linked with net mean stress, matric suction and deviator stress, respectively. And their expressions are as follows based on Equations (7)–(9):

$$\overline{K}_{wpt} = a_1 + b_1 q_0 \tag{10}$$

$$\overline{H}_{wt} = \ln 10 \frac{s + p_{atm}}{\overline{\lambda}_w(p)} = \ln 10 \frac{s + p_{atm}}{a_2 + b_2 q_0} \tag{11}$$

$$\overline{K}_{wqt} = a_3 + b_3 p_0 \tag{12}$$

Accordingly, the increment form of water variation can be described as:

$$d\varepsilon_w = \frac{dp}{\overline{K}_{wpt}} + \frac{ds}{\overline{H}_{wt}} + \frac{dq}{\overline{K}_{wqt}} \tag{13}$$

Substituting Equations (10)–(11) into Equation (12) and then integral of the equation leads to:

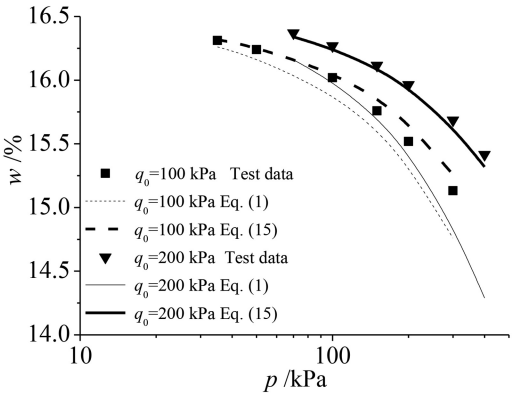
$$\varepsilon_w = \frac{p}{a_1 + b_1 q_0} + \frac{a_2 + b_2 q_0}{\ln 10} \ln\left(\frac{s + p_{atm}}{p_{atm}}\right) + \frac{q}{a_3 + b_3 p_0} \tag{14}$$

And substituting Equation (14) into Equation (5) arrives at:

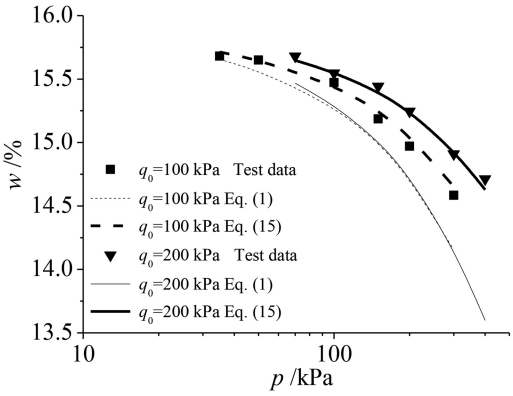
$$w = w_0 - \bar{a} p - \bar{b} \ln\left(\frac{s + p_{atm}}{p_{atm}}\right) - \bar{c} q \tag{15}$$

which is the expression of modified GSWCC, where $\bar{a} = \frac{1 + e_0}{d_s(a_1 + b_1 q_0)}$, $\bar{b} = \frac{(1 + e_0)(a_2 + b_2 q_0)}{d_s \ln 10}$ and $\bar{c} = \frac{1 + e_0}{d_s(a_3 + b_3 p_0)}$. And parameters a_1, a_2, a_3, b_1, b_2 and b_3 are all related to soils properties, and they are summarized in Table 5.

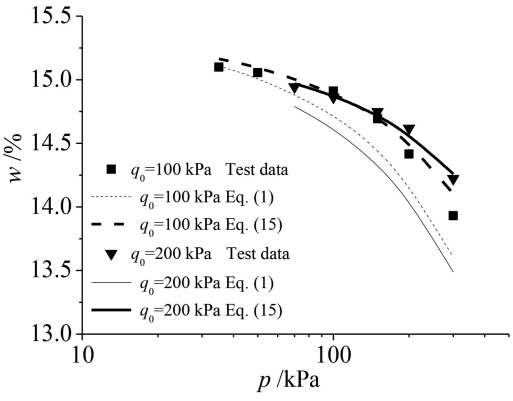
Equations (14)–(15) reflect the cross effect of net mean stress and deviator stress and also reveals the cross effect of deviator stress and matric suction on the water retention capacity of soil samples. Therefore, these two equations are considered as the refinement of Equation (1). And Equations (14)–(15) may be termed



(a) s_0 =50 kPa



(b) s_0 =100 kPa



(c) s_0 =200 kPa

Figure 5. The $w - p$ relations in the triaxial isotropic compression tests.

Table 6. The comparison of test data with Equation (1) and Equation (15).

Stress path of test	Amount of test data	Relative error between test data and calculated value using Equation (1)			Relative error between test data and calculated value using Equation (15)		
		Maximum value	Percentage of points with relative error below 5%	Percentage of points with relative error below 1%	Maximum value	Percentage of points with relative error below 5%	Percentage of points with relative error below 1%
Shrinking tests	48	6.23%	46/95.83%	21/43.75%	2.01%	48/100%	45/93.75%
Isotropic compression tests	53	7.58%	48/90.57%	24/45.28%	1.24%	53/100%	50/94.34%
P-fixed consolidated drained shear tests	50	3.90%	50/100%	37/74.00%	1.76%	50/100%	46/92%

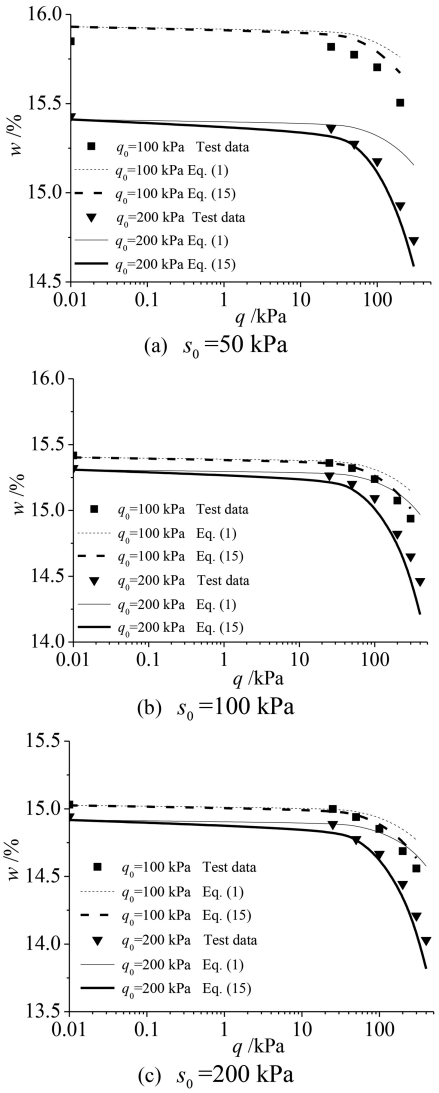


Figure 6. The $w-q$ relations in the*P*-fixed consolidated drained shear tests.

as modified generalized SWCC (or MGSWCC for short).

The comparison of test data with calculated moisture contents using the expression of GSWCC (Eq. (1)) and expression of MGSWCC (Eq. (15)) of the all 26 tests under different stress path are laid out in Figures 4, 5 and 6 and Table 6, from which it can be found that the calculated moisture contents using the expression of MGSWCC (Eq. (15)) are in better agreement with the test data than those using Equation (1). Also, it should be noted that if the relative error is allowed to be within 10%, there is no need to revise the expression of GSWCC.

4 CONCLUSION

(1) Both stress state and stress path have significant effects on GSWCC, and there are coupling effects of stress state variables on GSWCC, so that a modified expression of GSWCC is proposed.
(2) The predicted results by using the modified expression show good agreement with the test data and are much better than those predicted by adopting the expression of GSWCC. However, the expression of GSWCC is quite useful if relative errors of the predictions and test data are limited in 10%.

ACKNOWLEDGEMENTS

The study is supported by the National Natural Science Foundation of China (11272353).

REFERENCES

Fredlund, D. G., Rahardio, H. 1993. *Soil mechanics for unsaturated soils.* New York: Wiley & hissons.

Zhou, J. & Yu, J. L. 2005. Influences affecting the soil-water characteristic curve. *Journal of Zhejiang University* 6A(8): 797–804.

Zhang, X. D., Zhao, C. G. , Cai, G. Q. and Liu, Y. 2010. Research on influence of soil density on soil-water

characteristic curve. *Rock and Soil Mechanics* 31(5): 1463–1468.

Stoicescu, J. F. , Haug, M. D. and Fredlund, D. G. 1996. The soil-water characteristics and pore-size distribution of a sand-bentonite mixture. *Proceedings of the 49th Canadian Geotechnical Conference* 2: 721–728.

Aung, K. K. , Rahardjo, H. , Leong, E. C. and Toll, D. G. 2001. Relationship between porosimetry measurement and soil-water characteristic curve for an unsaturated residual soil. *Geotechnical and Geological Engineering* 19: 401–416.

Lu, Y. F., Chen, G. F., Luo, X. Q. and Cui, Y. J. 2008. Study of soil-water characteristical curve and its influential factors. *Rock and Soil Mechanics* 29(9): 2481–2486.

Pham, H. Q. , Fredlund, D. G. and Barbour, S. L. 2005. A study of hysteresis models for soil-water characteristic curves. *Canadian Geotechnical Journal* 42(6): 1548–1568.

Tuk, K. M. & Phan, T. H. 2010. A Soil-Water Hysteresis Model for Unsaturated Sands Based on Fuzzy Set Plasticity Theory. *KSCE Journal of Civil Engineering* 14(2): 165–172.

Chen, Z. H. , Zhou, H. Q. and Fredlund, D. G. 1999. Nonlinear model for unsaturated soils and its application. *Chinese Journal of Geotechnical Engineering* 21(5): 603–608.

Huang, H. & Chen, Z. H. 2000. A study On yield locus of unsaturated soils on p-s plane and soil-water characteristic curve. *Rock and Soil Mechanics* 21(4): 316–321.

Fang, X. W., Chen, Z. H. and Shen, C. N. 2004. Tests with Controlled Net Mean Stress Equaling Constant of an Remolded Unsaturated Loess. *Journal of Chongqing University* 27(9): 124–127.

Fang, X. W., Chen, Z. H., Shen, C. N. and Sun, S. G. 2004. A study on effect of shear on soil-water characteristic curve of an unsaturated soil. *Rock and Soil Mechanics* 25(9): 1451–1454.

Chen, Z. H., Xie, D. Y. and Wang, Y. S. 1993. Experimental Studies of Laws of Fluid Motion, Suction and Pore Pressures in Unsaturated Soil. *Chinese Journal of Geotechnical Engineering* 15(3): 9–20. Chen, Z. H. 1999. Deformation, strength, yield and moisture change of a remolded unsaturated loess. *Chinese Journal of Geotechnical Engineering* 21(1): 82–90.

Unsaturated Soil Mechanics—from Theory to Practice – Chen et al. (Eds)
© 2016 Taylor & Francis Group, London, ISBN 978-1-138-02921-7

A fractal-based Soil-Water Characteristic Curve model for deformable soils

A. Khoshghalb, A.Y. Pasha & N. Khalili
School of Civil and Environmental Engineering, UNSW Australia, Sydney, Australia

ABSTRACT: A fractal-based model for the Soil-Water Characteristic Curve (SWCC) in a deformable unsaturated soil is presented. Assuming fractal structure for soil and incorporating the dependency of pore shape and volume on void ratio using Eshelby's classical theory for load-deformation of a single elastic ellipsoidal void embedded in an infinite isotropic elastic matrix, variation of the SWCC with void ratio is quantified. The applicability of the model to two sets of experimental data from the literature is investigated. It is shown that the predictions of the volume change dependency of the SWCC are in good agreement with the published data.

1 INTRODUCTION

The Soil-Water Characteristic Curve (SWCC) is frequently defined as a plot of volumetric water content, degree of saturation or gravimetric water content versus matric suction. It is one of the fundamental relationships in the mechanics of unsaturated soils, and is universally used as input to constitutive models as well as developing empirical correlations for strength, deformation and hydraulic properties of unsaturated soils.

In recent years, significant contributions to mathematical representation of SWCC have been made using the fractal approach, in which particle size distribution, pore volume and pore surface are assumed to obey fractal scaling (e.g. see Giménez et al. 1997; Tyler and Wheatcraft 1989; Perfect and Kay 1995; Bird et al. 2000; Hunt and Gee 2002; Perfect 2005; Russell 2010; Russell and Buzzi 2012; Russell 2014). Fractal-based SWCCs are particularly attractive as they establish a link between SWCC and soil microstructure. However, many of the contributions made to date rely on the assumption that the fractal dimension of pore size distribution (PSD) remains independent of the void ratio (e.g. see Bird et al. 2000; Russell and Buzzi 2012), irrespective of the overwhelming laboratory test data showing that a change in soil volume can lead to a change in PSD, and therefore its fractal dimension (e.g. see Simms and Yanful 2005, Li and Zhang 2009). Indeed, to rectify this deficiency, some of the void ratio dependent SWCC models that assume a constant pore size distribution index (PSDI), incorporate a correction function for large suctions to indirectly accommodate for the variation of the PSDI with void ratio (Hu et al. 2013).

In this paper, a fractal based model is presented for the volume change dependency of SWCC for unsaturated soils. Double porosity and hydraulic hysteresis are ignored for the sake of simplicity. Deformation of a single ellipsoidal void embedded in an infinite isotropic elastic matrix under remotely applied stress is used to approximate change in pore shape with loading (Eshelby 1957). Mathematical expressions are derived for the evolution of PSD fractal dimension, air entry suction and pore shape with void ratio. Particular attention is given to the conservation of solid mass, conservation of pore surface, and fractal scale of pore and grain size distributions. The model is verified using two experimental data sets from the literature.

2 FRACTAL DESCRIPTION OF A SOIL

In this section, the mathematics of fractal distribution of particle and pore sizes in a soil is detailed. The fractal microstructure is taken to be representative of the soil structure at any instant during a loading or deformation event (e.g. see Katz and Thompson, 1985; Krohn and Thompson, 1986 and Crawford et al., 1993). Both pore space and solid space are taken as fractals in the pore/particle size range of interest. The pore structure is recognized with a single fractal dimension.

Assuming continuous PSD over a range of pore sizes (r), between r_{min} and r_{min}, in which and are the smallest and largest pores respectively, the probability density function ($W(r)$) of pore radius r is written as (Hunt 2001)

$$W(r) = Ar^{-D_p-1} \tag{1}$$

where D_p is the fractal dimension of PSD and A is the normalisation coefficient. S and D_p are assumed

as functions of void ratio. The total volume of pores having radius larger than ($r_{min} < r < r_{max}$) is then

$$V_{p_{>r}} = \int_r^{r_{max}} \left(\Lambda_p r^3\right) A r^{-D_p-1} dr = \frac{\Lambda_p A}{3-D_p}\left({r_{max}}^{3-D_p} - r^{3-D_p}\right) \quad (2)$$

where Λ_p is a dimensionless pore shape parameter taking a value of $4\pi/3$ for sphere. The total pore volume is therefore

$$V_p = \frac{\Lambda_p A}{3-D_p}\left({r_{max}}^{3-D_p} - {r_{min}}^{3-D_p}\right) = \frac{\Lambda_p A}{3-D_p} {r_{max}}^{3-D_p}\left(1 - R^{D_p-3}\right) \quad (3)$$

where $R = r_{max}/r_{min}$. Similarly, the total surface area of pores having radius larger than r becomes

$$S_{p_{>r}} = \int_r^{r_{max}} \left(\Gamma_p r^2\right) A r^{-D_p-1} dr = \frac{\Gamma_p A}{2-D_p}\left({r_{max}}^{2-D_p} - r^{2-D_p}\right) \quad (4)$$

where Γ_p is a dimensionless shape parameter corresponding to the surface area of the pores. The total pore surface area is then

$$S_p = \frac{\Gamma_p A}{2-D_p}\left({r_{max}}^{2-D_p} - {r_{min}}^{2-D_p}\right) = \frac{\Gamma_p A}{2-D_p} {r_{max}}^{2-D_p}\left(1 - R^{D_p-2}\right) \quad (5)$$

In a fractal soil, the distribution of particle sizes can also be represented with a similar fractal description albeit with different normalisation parameters, shape parameters and fractal dimensions. For a fractal description of a soil to be valid, R must be adequately large – at least in the order of 10^2 following Yu and Li (2001) recommendations – and a log–log representation of the particle size distribution (percentage passing vs. particle size) should produce approximately a straight line. Several investigators (Feng et al. 2004; Katz and Thompson 1985; Krohn and Thompson 1986; Malcai et al. 1997) found that R is often in the range of 10^2 to 10^4 in real porous media. Theoretical justification (Bittelli et al. 1999; Turcotte 1986) as well as experimental evidences (Sahimi 2011) also shows the relevance of fractal soil assumptions.

In soils, different pore size distributions can result from a single particle size distribution. Therefore, the particle size and pore size distributions must be characterized using different fractal dimensions (Russell 2010; Yu et al. 2009). Assuming no particle crushing occurs, the fractal dimension of particle size distribution is constant, while the fractal dimension of PSD is taken to be void ratio dependent.

3 SWCC MODEL

Theoretical expression for a SWCC must have some association with characteristics of the pore sizes (Russell 2010). If complications due to difference between drying and wetting paths and also osmotic and phisyo-chemical effects are neglected, and it is assumed that hydraulic accessibility of any pore does not depend on smaller pores (Perfect 1997), it can be assumed that as suction increases, the larger pores empty while the smaller pores remain saturated (Hunt 2001). Then, when pores with radius larger than $\hat{r}$ ($r_{min} \le \hat{r} \le r_{max}$) are emptied, the saturation ratio can be calculated as

$$S_r = \frac{\int_{r_{min}}^{\hat{r}} (\Lambda_p r^3) A r^{-D_p-1} dr}{\int_{r_{min}}^{r_{max}} (\Lambda_p r^3) A r^{-D_p-1} dr} = \frac{\hat{r}^{3-D_p} - {r_{min}}^{3-D_p}}{{r_{max}}^{3-D_p} - {r_{min}}^{3-D_p}} = \frac{\left(\frac{\hat{r}}{r_{max}}\right)^{3-D_p} - R^{D_p-3}}{1-R^{D_p-3}} \quad (6)$$

Now, according to the Young-Laplace equation, the suction required to empty a pore is inversely proportional to the radius of the draining pore throat, which in turn is related to the radius of the pore ($s \propto 1/r$,), hence from (6) we have

$$S_r = \frac{\left(\frac{s_a}{s}\right)^{3-D_p} - R^{D_p-3}}{1-R^{D_p-3}} \qquad s \ge s_a \quad (7)$$

where s_a is the suction required to drain the largest pores (corresponding to r_{max}) or the air entry value (AEV). Notice that due to complete emptying of the pore at s corresponding to r, the residual degree of saturation cannot be captured using the present model.

4 VOID RATIO EFFECTS

Variation of the SWCC when the soil undergoes hydraulic and/or mechanical loading induced volume change is quantified in this section for a soil with a known reference SWCC. Soils with the same void ratio but different structures are treated as entirely different soils with different reference SWCC for the purpose of this modelling.

4.1 *Pore size distribution fractal dimension*

A change in the soil void ratio alters the PSD and hence R, resulting in a change in PSD fractal dimension. To capture this phenomenon, we use (3), to obtain the total volume of solids as

$$V_s = \frac{\Lambda_p A\, {r_{max}}^{3-D_p}}{(3-D_p)e}\left(1 - R^{D_p-3}\right) \quad (8)$$

where e is the void ratio.

In addition, in an assembly of soil grains packed to a given porosity, the radius of the typical largest grain that may be inserted in the pores (maximum pore size) is directly proportional to the void ratio raised to the power of fractal dimension of the PSD ($r_{max} \propto e^{\alpha D_S}$) (Dodds and Weitz 2002, 2003). α is the grain shape

factor which assumes a value of one for circular particles and a value greater than one for other shapes. Now, from (5) and (8), we can write

$$S_p \propto \frac{\Gamma_p A}{2-D_p} e^{\alpha D_s (2-D_p)} (1 - R^{D_p - 2}) \tag{9}$$

$$V_s \propto \frac{\Lambda_p A\, e^{\alpha D_s (3-D_p)}}{(3-D_p)e} (1 - R^{D_p - 3}) \tag{10}$$

For no particle crushing, particle surface area remains constant as e varies. If the sum of the contact areas between particles is assumed negligible compared to the overall particle surface area, pore surface area must also remain constant as e varies (Russell 2010). Furthermore, assuming solid compressibility is negligible, solid volume is also constant. From these constraints, we have

$$\frac{d}{de}\left(\frac{S_p}{V_s}\right) = \frac{d}{de}\left(\frac{\Gamma_p}{\Lambda_p} \cdot \frac{3-D_p}{2-D_p} e^{1-\alpha D_s} \frac{1-R^{D_p-2}}{1-R^{D_p-3}}\right) = 0 \tag{11}$$

in which Γ_p/Λ_p is a dimensionless parameter reflecting the shape of the pores. Considering a spheroidal representation of the pores, taking $\lambda = r_1/r_2$ as the pore aspect ratio (the radius of pores in the two horizontal directions is taken to be the same), and using Berli and Or (2006) model for pore shape evolution with stress in an elastic homogenous media, the variation of λ with void ratio for oblate pore shapes ($\lambda < 1$) is captured as (for details of the derivations see Khoshghalb et al. (2014))

$$F = \Gamma_p/\Lambda_p \propto \left[1 + 2\lambda_0^{1.6} EXP\left(1.6\beta(e - e_0)\right)\right]^{1/1.6} \tag{12}$$

where e_0 is the initial void ratio, and λ_0 is the initial pore aspect ratio. β is defined

$$\beta = \frac{f_1 - f_2}{(1+2k)(1-2\nu)} \tag{13}$$

where ν is the Poisson's ratio of the soil, k is the ratio of the horizontal to vertical stresses, and f_1 and f_2 are known functions of pore geometry, elastic properties of the medium and stress field (see Berli and Or, 2006). Substituting (12) into (11) yields

$$\frac{d}{de}\left(\frac{S_p}{V_s}\right) = \frac{d}{de}\left(e^{1-\alpha D_s}\left[1 + 2\lambda_0^{1.6} EXP\left(1.6\beta(e - e_0)\right)\right]^{1/1.6} \frac{3-D_p}{2-D_p} \frac{1-R^{D_p-2}}{1-R^{D_p-3}}\right) = 0 \tag{14}$$

On the other hand, according to Katz and Thompson (1985), in a fractal porous medium showing self-similarity over 3 to 4 orders of magnitude, we have

$$R = [1 + 1/e]^{1/(3-D_p)} \tag{15}$$

Combining (14) and (15), the variation of fractal dimension of PSD in terms of change in void ratio is quantified as (see Khoshghalb et al. (2015))

$$\frac{dD_p}{de} = \left\{ \frac{1-\alpha D_s}{e} + \frac{2\beta\lambda_0^{1.6} EXP\left(1.6\beta(e-e_0)\right)}{1+2\lambda_0^{1.6} EXP\left(1.6\beta(e-e_0)\right)} + \frac{1-(1+1/e)^{\frac{1}{3-D_p}}}{(1+e)\left[1-(1+1/e)^{\frac{1}{3-D_p}-1}\right]} + \frac{(1+1/e)^{\frac{1}{3-D_p}-1}}{e(1+e)(3-D_p)\left[1-(1+1/e)^{\frac{1}{3-D_p}-1}\right]} \right\} \times \left\{ \frac{ln(1+1/e)\times\left[(1+1/e)^{\frac{1}{3-D_p}-1}\right]}{(3-D_p)^2\times\left[1-(1+1/e)^{\frac{1}{3-D_p}-1}\right]} - \frac{1}{(2-D_p)(3-D_p)} \right\}^{-1} \tag{16}$$

4.2 *Air entry value*

To capture the change in AEV with volume change, according to Young-Laplace equation we have $S_a = B/r_{max}$ or $S_a r_{max} = B$, where B is a constant related to the air water interface tension. Taking $r_{max} \propto e^{\alpha D_S}$, we then have

$$\frac{d}{de}(e^{\alpha D_s} s_a) = 0 \tag{17}$$

which leads to a simple expression for the variation of AEV with void ratio,

$$\frac{ds_a}{de} = -\frac{\alpha D_s s_a}{e} \tag{18}$$

It is interesting to note that very similar relationships have been established by Masin (2010) and Khoshghalb and Khalili (2013) for the variation of AEV with void ratio through invoking the existence of elastic and plastic potentials for unsaturated soils.

4.3 *Soil-Water Characteristic Curve*

The variation of SWCC with void ratio can now be captured by substituting (15) into (7)

$$S_r = (1 + e)\left(\frac{s_a}{s}\right)^{3-D_p} - e \qquad s \geq s_a \tag{19}$$

and through the use of (16) and (18) for quantifying the variation of D_p and AEV with void ratio, respectively.

5 VALIDATION

5.1 *Evolution of SWCC with void ratio*

Salager et al. (2013) performed a series of SWCC tests on a clayey silty sand, compacted to different initial dry

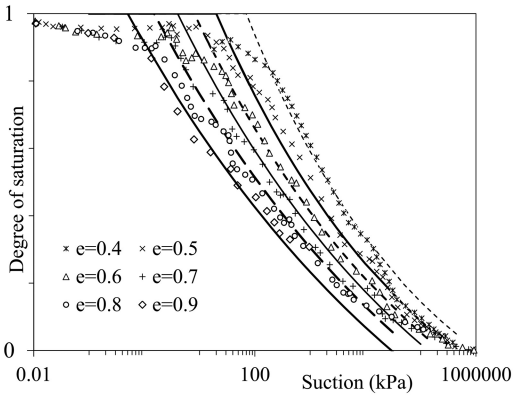


Figure 1. Constant volume SWCCs, and best fits using equation (19), for the data of Salager et al. (2013).

densities. The changes in the degree of saturation at different void ratios with suction were reported. These data were used in this study to construct constant volume SWCCs of the soil as shown in Figure 1. The parameters D_p and S_a were obtained by fitting equation (19) to the experimental SWCCs.

Figure 2 show predictions of evolution of D_p and S_a versus e using (18), taking constant volume SWCC at $e = 0.60$ as the reference SWCC. The calibrated model parameters were: $D_p = 2.905$, $S_a = 8$ kPa, $\lambda_0 = 3$, $k = 0.5$, $\alpha = 1.4$ and $\rho = 0.3$. $D_s = 2.65$ was obtained from the particle size distribution curve of the soil. Very good agreement with the experimental data is obtained, considering the experimental error associated with unsaturated soil tests. A better fit to the experimental data could have been achieved by fine-tuning the model parameters, but this was intentionally avoided.

5.2 *Change of degree of saturation with void ratio under constant suction*

The change of the degree of saturation with void ratio at constant-suction triaxial test performed by Casini (2008) on a sample of silty soil, and reported in D'Onza et al. (2011), is simulated in this section for further model verification. The sample was made by compaction at 13% water content and was subjected to an equalisation suction of 200 kPa, a confining cell pressure of 20 kPa and a deviatoric stress of 15 kPa. The sample was then subjected to a constant suction anisotropic loading with the ratio of deviator stress to mean net stress kept at 0.75.

The calibrated SWCC parameters at the reference void ratio of $e = 0.8$ were $D_p = 2.76$, and the air-expulsion value, $S_{ex} = 5$ kPa according to D'Onza et al. (2011). The air-expulsion value was used here as the triaxial loading test was along the main wetting branch of the SWCC considering the sample preparation reported. Using the particle size distribution curve of the soil, the fractal dimension of soil grains

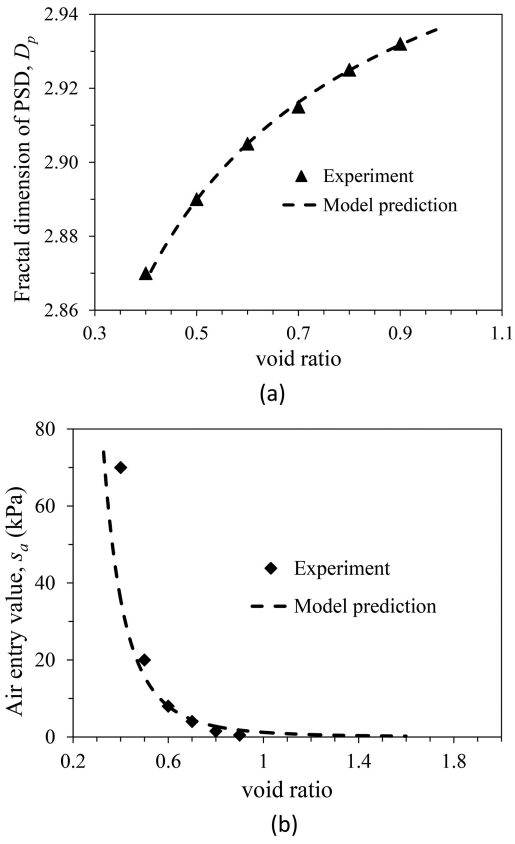


Figure 2. Evolution of: (a). fractal dimension of PSD, D_p, and (b). AEV, S_a, with void ratio for clayey silty sand. Experimental data are extracted form Salager et al. (2013).

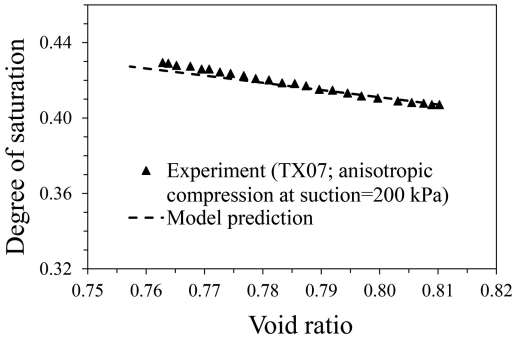


Figure 3. Measured and predicted variation of degree of saturation with void ratio in constant-suction triaxial compression path on Jossigny silt.

was calibrated as $D_s = 2.4$. Other parameters used in the simulations were: $\alpha = 1.1$, $\lambda_0 = 0.3$, $\rho = 0.3$, and $k = 0.75$. The model prediction in terms of variation of degree of saturation with void ratio is shown in Figure 3. A very good agreement is obtained with the

experimental data, which demonstrates the capability of the model in capturing the change of degree of saturation with void ratio at constant-suction loading path.

6 CONCLUSIONS

A fractal based model for SWCC was developed taking into account volume change effects. Different fractal dimensions are used for pore and grain size distributions. Assuming no particle crushing, the fractal dimension of particle size distribution is assumed constant, whereas that of PSD is taken to be void ratio dependent. Particle and pore property restrictions were exploited to determine the volume change dependency of the SWCC parameters in terms of soil's pore and particle properties. The application of the model to two test data sets from the literature is examined. Good agreement is obtained between experimental data and model predictions in all cases considered.

ACKNOWLEDGEMENT

This paper is a reduced version of the paper published in *Géotechnique*, 2015, vol. 65, no. 2, pp. 141-146. The authors wish to thank A/Prof Adrian Russell for his helpful suggestions and valuable comments on the manuscript.

REFERENCES

Berli, M., and Or, D. (2006). Deformation of pores in viscoplastic soil material. International Journal of Geomechanics, 6(2): 108–118.

Bird, N.R.A., Perrier, E., and Rieu, M. (2000). The water retention function for a model of soil structure with pore and solid fractal distributions. European Journal of Soil Science, 51(1): 55–63.

Bittelli, M., Campbell, G.S., and Flury, M. 1999. Characterization of particle-size distribution in soils with a fragmentation model. Soil Science Society of America Journal, 63(4): 782–788.

Casini, F. (2008). Effetti del grado di saturazione sul comportamento meccanico di un limo. PhD thesis. Universita' degli Studi di Roma 'La Sapienza', Rome.

Crawford, J. W., Ritz, K., and Young, I. M. (1993). Quantification of fungal morphology, gaseous transport and microbial dynamics in soil: an integrated framework utilising fractal geometry. Geoderma, 56(1): 157–172.

Dodds, P.S., and Weitz, J.S. (2002). Packing-limited growth. Physical Review E – Statistical, Nonlinear, and Soft Matter Physics, 65(5): 056108/056101-056108/056106.

Dodds, P. S. and J. S. Weitz (2003). Packing-limited growth of irregular objects. Physical Review E – Statistical, Nonlinear, and Soft Matter Physics 67(1 2): 161171–161177.

D'Onza, F., Gallipoli, D., Wheeler, S., et al. (2011). Benchmark of constitutive models for unsaturated soils. Géotechnique, 61(4): 283–302.

Eshelby, J.D. (1957). The Determination of the Elastic Field of an Ellipsoidal Inclusion, and Related Problems. Proceedings of the Royal Society of London. Series A. Mathematical and Physical Sciences, 241(1226): 376–396.

Feng, Y., Yu, B., Zou, M., and Zhang, D. 2004. A generalized model for the effective thermal conductivity of porous media based on self-similarity. Journal of Physics D: Applied Physics, **37**(21): 3030–3040.

Giménez, D., Perfect, E., Rawls, W.J., and Pachepsky, Y. (1997). Fractal models for predicting soil hydraulic properties: A review. Engineering Geology, 48(3–4): 161–183.

Hu, R., Chen, Y.F., Liu, H.H., and Zhou, C.B. (2013). A water retention curve and unsaturated hydraulic conductivity model for deformable soils: Consideration of the change in pore-size distribution. Geotechnique, 63(16): 1389–1405.

Hunt, A.G. (2001). Applications of percolation theory to porous media with distributed local conductances. Advances in Water Resources, 24(3–4): 279–307.

Hunt, A.G., and Gee, G.W. (2002). Application of critical path analysis to fractal porous media: Comparison with examples from the Hanford site. Advances in Water Resources, 25(2): 129–146.

Katz, A.J., and Thompson, A.H. (1985). Fractal sandstone pores: Implications for conductivity and pore formation. Physical Review Letters, 54(12): 1325–1328.

Khoshghalb, A. and Khalili, N. (2013). A meshfree method for fully coupled analysis of flow and deformation in unsaturated porous media. International Journal for Numerical and Analytical Methods in Geomechanics, 37(7): 716–743.

Khoshghalb, A., A. Y. Pasha, and N. Khalili (2015) A fractal model for volume change dependency of the water retention curve. Géotechnique 65, 141–146.

Krohn, C. E., and Thompson, A. H. (1986). Fractal sandstone pores: automated measurements using scanning-electron-microscope images. Physical Review B, 33(9), 6366.

Li, X., and Zhang, L.M. (2009). Characterization of dual-structure pore-size distribution of soil. Canadian Geotechnical Journal, 46(2): 129–141.

Malcai, O., Lidar, D.A., Biham, O., and Avnir, D. 1997. Scaling range and cutoffs in empirical fractals. Physical Review E – Statistical Physics, Plasmas, Fluids, and Related Interdisciplinary Topics, 56(3 SUPPL. A): 2817–2828.

Perfect, E. (1997). Fractal models for the fragmentation of rocks and soils: A review. Engineering Geology, 48(3–4): 185–198.

Perfect, E. (2005). Modeling the primary drainage curve of prefractal porous media. Vadose Zone Journal, 4(4): 959–966.

Perfect, E., and Kay, B.D. (1995). Applications of fractals in soil and tillage research: A review. Soil and Tillage Research, 36(1–2): 1–20.

Russell, A.R. (2010). Water retention characteristics of soils with double porosity. European Journal of Soil Science, 61(3): 412–424.

Russell, A.R. (2014) How water retention in fractal soils depends on particle and pore sizes, shapes, volumes and surface areas. Geotechnique 64, 379–390.

Russell, A.R., and Buzzi, O. (2012). A fractal basis for soil-water characteristics curves with hydraulic hysteresis. Geotechnique, 62(3): 269–274.

Sahimi, M. 2011. Flow and Transport in Porous Media and Fractured Rock: From Classical Methods to Modern Approaches: Second Edition.

Salager, S., Nuth, M., Ferrari, A., and Laloui, L. (2013). Investigation into water retention behaviour of deformable soils. Canadian Geotechnical Journal, 50(2): 200–208.

Simms, P. H., and Yanful, E. K. (2005). A pore-network model for hydromechanical coupling in unsaturated compacted clayey soils. Canadian Geotechnical Journal, 42(2): 499–514.

Turcotte, D.L. 1986. Fractals and fragmentation. Journal of Geophysical Research, 91(B2): 1921–1926.

Tyler, S.W., and Wheatcraft, S.W. (1989). Application of fractal mathematics to soil water retention estimation. Soil Science Society of America Journal, 53(4): 987–996.

Yu, B., and Li, J. 2001. Some fractal characters of porous media. Fractals, 9(3): 365–372.

Yu, B., Cai, J., and Zou, M. (2009). On the physical properties of apparent two-phase fractal porous media. Vadose Zone Journal, 8(1): 177–186.

Unsaturated Soil Mechanics—from Theory to Practice – Chen et al. (Eds)
© 2016 Taylor & Francis Group, London, ISBN 978-1-138-02921-7

The formulation of the water retention curve with deformation and hysteresis

Q.D. Huang
Beijing Jiao-tong University, Beijing, China

C.G. Zhao
Beijing Jiao-tong University, Beijing, China
Guilin University of Technology, Guilin, China

G.Q. Cai
Beijing Jiao-tong University, Beijing, China

ABSTRACT: A thermodynamically consistent SWCC framework is proposed for modeling the hysteresis of capillarity and the effect of deformation in unsaturated soil. It is derived from the second law of thermodynamics that: capillary hysteresis and plastic deformation is an intrinsic dissipation; the suction is not only related to the changes of fluid phases, but also controlled by the deformation of solid phase; the changes of solid phase and fluid phase are coupling. Capillary hysteresis and the effects of solid deformation are demonstrated at microscopic scale. By virtue of the notion of the bounding surface plasticity, a model of SWCC is developed, which adds only two parameters. Finally, the model predictions are compared with experimental measurements found in the previous literature, showing that the new model is capable of describing the capillary hysteretic phenomena and the effects of soil deformation in a variety of unsaturated soils.

1 INTRODUCTION

A Soil-Water Characteristic Curve (SWCC) which represents the relationship between the degree of saturation (S_r) and matric suction, is the key to figure out the fluid-solid coupling, the shear strength and strain, and the contaminant transport in unsaturated soil. Therefore SWCC is a subject of great interest in geotechnical engineering practice. SWCC has been widely studied during the past several decades, focusing on (1) fitting equation, (2) influence of soil compaction conditions, (3) modeling of hysteresis, and (4) influence of temperature.

Experimental evidences show that: the deformation and compaction conditions of unsaturated soils have a great influence on SWCC; the deformation and compaction of unsaturated soils are changed with matrix suction. It is called mechanical and hydro-mechanical coupling. Although several models of SWCC are proposed, the coupling phenomena cannot be simulated by most of the existing models. Therefore, the evolution of elastic-plastic volumetric strain should be considered when modeling drying-wetting circle of SWCC. There are some series of constitutive models which take volumetric strain into account:

(1) Relating void ratio, air entry value and initial density to parameters of SWCC. Gallipoli modified the parameters in van Genuchten equation and related them with strain. Nuth and Laloui (2008) extracted a new intrinsic outline for the retention curve from data, which were equivalent to zero deformation retention tests and qualified the dependency of the physical parameter air entry value upon void ratio. Zhou et al. (2012) proposed a method based on the intrinsic constraints between the degree of saturation and the void ratio for a three-phase mixture. The difference caused by water in macroscopic pores and microscopic pores was taken into account in the model.
(2) Considering the pore size distribution function. Based on the capillary model and Childs' (1950) statistical assumption, Zhang found a motion law of the point on a SWCC in the situation of density variation. Hu assumed that the pore size distribution characteristics of the pore size distribution are not significantly altered. A water retention curve (WRC) model contained seven parameters was formulated. The model could characterize the effects of soil deformation on WRC by the change of pore size distribution.
(3) Based on experiment data, Mbonimpa et al. (2006) using the experimental data extended MK model to describe and predict the WRC of deformable clayey soils by introducing the volumetric shrinkage curve. Salager et al. (2010) introduced an experimental method to determine the soil-water retention surface (SWRS) which was established in the space void ratio-suction – water content and

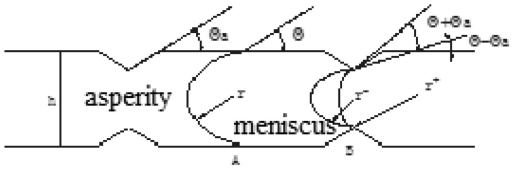


Figure 1. A fluid-fluid meniscus moving through a pore channel with small roughness.

applied to a clayey silty sand. Taratino (2009) presented an experimental study on water retention behavior of two reconstituted soil and two compacted soils. Based on these findings, a void-ratio dependent water retention model for main drying and main wetting behavior had been formulated.

Most of the aforementioned models have found applications in simulating two-phase flow in unsaturated porous media. Despite their merits, these models were not explicitly derived from first principles. Wei viewed capillary hysteresis as an intrinsic dissipation mechanism, which can be characterized by a set of internal state variables. By virtue of the bounding surface plasticity, a model of capillary hysteresis was developed. Based on Wei's work, a new model is derived from the law of thermodynamics by taking the influences of soil deformation on SWCC into account. Only two additional parameters are introduced, which can be conveniently calibrated by mean of conventional water retention tests.

2 THEORETICAL FRAMEWORK

2.1 *Microscopic motivation*

From the pore-scale mechanism, the capillary hysteresis can be explained by the contact-line hysteresis.

As illustrated in Figure 1, in equilibrium condition the contact line located at B, and the contact angle of solid wall and asperity are denoted by Θ and Θ_a respectively. If the capillary pressure is changed slightly, the curvature of meniscus will change and the meniscus will not migrate from B to another asperity until the changes of exceeds a certain range, which is given by

$$\frac{2\sigma\cos(\Theta+\Theta_a)}{h} \le p_c \le \begin{cases} 2\sigma\cos(\Theta-\Theta_a)/h & \Theta \ge \Theta_a \\ 2\sigma/h & \Theta < \Theta_a \end{cases} \tag{1}$$

where σ is the surface tension and h the diameter of the pore channel.

The contact-line hysteresis model assumes that the pores in the unsaturated soil are incompressible and the changes of the local capillary have no influences on the pore, which are inconsistent with experimental data. In this paper the diameter of the pore channel h is considered as a variable which is related with the volumetric strain. According to Equation (1), the macroscopic capillary pressure is defined by:

$$F(P_c,T,\varepsilon_v^p,\xi_k) = |P_c - \delta(\varepsilon_v^p,\xi_k)| - \kappa(\varepsilon_v^p,\xi_k) \le 0 \tag{2}$$

where T is absolute temperature, P_c is called capillary press or matrix suction, $\delta(\varepsilon_v^p, \xi_k)$ and $\kappa(\varepsilon_v^p, \xi_k)$ are the positive function of ε_v^p and ξ_k, which represent kinematic harden and isotropic harden. ε_v^p and ξ_k represent plastic volumetric strain and internal variable.

When condition $F < 0$ is satisfied, the contact line is remaining fixed, only the curvature of meniscus is changed. That is, ε_v^p and ξ_k do not vary with P_c and the region defined by the condition is $F < 0$ is the recoverable zone. If P_c is changed so that the condition (2) is violated, the menisci will migrate to a new asperity which could satisfied conditions (2), in other words, ε_v^p and change with P_c. The process is irreversible and time-dependent, but in this paper we assume the process is time-independent. That is, in time-independent process, once an alteration in P_c is applied, menisci can migrate to a new asperity at which the attain equilibrium instantly. In time-independent process, the state of the porous medium defined by P_c, ε_v^p and ξ_k, must remain on the boundary, so that:

$$F(P_c,T,\varepsilon_v^p,\xi_k) = 0 \tag{3}$$

2.2 *Evolution equations of internal variables and hardening effects*

Now supposed that P_c is composed of two contributions:

$$\dot{P}_c = \dot{P}_c^s + \dot{P}_c^f \tag{4}$$

where $\dot{P}_c^s$ and $\dot{P}_c^f$ are the change of capillary press due to the variation of solid phase and fluid phase respectively. It is different from Wei, not only the variation of the irreversible volumetric moisture content θ_l will trigger loading process, but also the plastic strain:

$$\begin{cases} \dot{\varepsilon}_v^p = m < L_s > \\ \dot{\theta}_l = r_k < L_f > \end{cases} \tag{5}$$

where $L_\alpha(\alpha = s, w, n)$ is loading function, m and r_k are the direction of $\dot{\varepsilon}_v^p$ and $\dot{\theta}_l$.

Follow the procedure which was proposed by Wei, the following equation can be obtained:

$$\begin{cases} \dot{P}_c^f = -K_p^f \dot{\theta}_l \\ \dot{P}_c^s = -K_p^f \dot{\varepsilon}_v^p \end{cases} \tag{6}$$

where $K_p^s = -m(\partial f/\partial\varepsilon_v^p)$ and $K_p^f = -r_k(\partial f/\partial\xi_k)$.

According (6), $-K_p^f$ is the slope the scanning curve on the $\theta_l \sim P_c^f$ plane at the current capillary pressure, and $-K_p^s$ is the slope of the scanning curve on the $\varepsilon_v^p \sim P_c^s$ plane.

In loading process, $\delta(\varepsilon_v^p, \xi_k)$ and $\kappa(\varepsilon_v^p, \xi_k)$ decide the position and size of the recoverable zone. We need to introduce several additional internal variables to characterize the hardening effect. For convenience, the

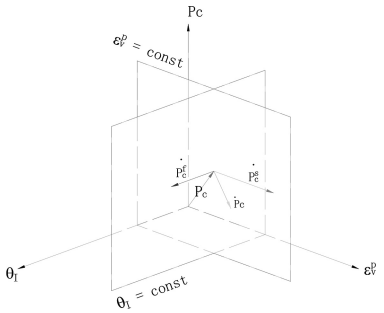


Figure 2. The illustration of the components of $\dot{P}_c$.

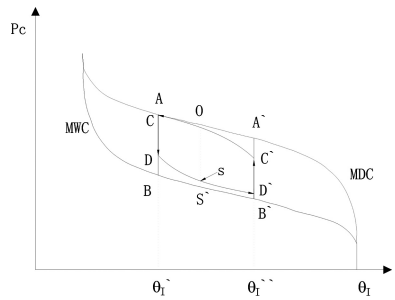


Figure 3. A conceptual model of capillary hysteresis.

cumulative irreversible moisture content and cumulative plastic volumetric strain which are defined by $\overline{\theta_I} = \int_0^t |\theta_I|\, dt$ and $\overline{\varepsilon_v^p} = \int_0^t |\varepsilon_v^p|\, dt$ are chosen as hardening variables.

Now Equation (4) can be rewritten as follows:

$$\dot{P}_c = \dot{P}_c^s + \dot{P}_c^f = \hat{n}_s (H_\delta^s + H_\kappa^s)\dot{\overline{\varepsilon_v^p}} + \hat{n}_f (H_\delta^f + H_\kappa^f)\dot{\overline{\theta_I}} \tag{7}$$

where

$$H_\delta^s = \partial\delta(\overline{\theta_I}, \overline{\varepsilon_v^p}) / \partial\overline{\varepsilon_v^p} \quad , \quad H_\kappa^s = \partial\kappa(\overline{\theta_I}, \overline{\varepsilon_v^p}) / \partial\overline{\varepsilon_v^p} \quad ,$$

$$H_\delta^f = \partial\delta(\overline{\theta_I}, \overline{\varepsilon_v^p}) / \partial\overline{\theta_I} \quad , \quad H_\kappa^f = \partial\kappa(\overline{\theta_I}, \overline{\varepsilon_v^p}) / \partial\overline{\theta_I} \quad ,$$

$\hat{n}_s = sign[P_c - \delta_s(\varepsilon_v^p, \xi_k)]$ and $\hat{n}_f = sign[P_c - \delta_f(\varepsilon_v^p, \xi_k)]$.

2.3 *Capillary hysteresis and concepts of the bounding surface plasticity*

In wetting/drying circle, the relation between matrix suction and the degree of saturation is not unique, that is called hysteresis phenomenon. Tsiampous et al. (2013) pointed out the hysteresis phenomenon also existed between strain and matrix suction. In the following section, we will use the bounding surface plastic to construct a hysteresis model which contains the influence of volumetric strain.

In this paper, the bounding surface is composed of the main wetting surface and the main drying surface in the $(P_c, \varepsilon_v^p, \theta_I)$ space. According Equation (4), the change of capillary press P_c equals P_c^f plus P_c^s which can be calculated in the (θ_I, P_c^f) plane and (ε_v^p, P_c^s) plane respectively as illustrated in Figure 2.

The bounding surface can be expressed as:

$$F(P_c, \varepsilon_v^p, \xi_k) = | P_c - \overline{\delta}(\varepsilon_v^p, \xi_k) | - \overline{\kappa}(\varepsilon_v^p, \xi_k) = 0 \tag{8}$$

where $\overline{\delta}(\varepsilon_v^p, \xi_k)$ and $\overline{\kappa}(\varepsilon_v^p, \xi_k)$ are two variables which characterize the hardening of the bounding zone. Now considering equation (7), we suppose that:

$$\begin{cases} F_s(P_c, \varepsilon_v^p, \xi_k) = | P_c^s - \overline{\delta_s}(\varepsilon_v^p, \xi_k) | - \overline{\kappa_s}(\varepsilon_v^p, \xi_k) = 0 \\ F_f(P_c, \varepsilon_v^p, \xi_k) = | P_c^f - \overline{\delta_f}(\varepsilon_v^p, \xi_k) | - \overline{\kappa_f}(\varepsilon_v^p, \xi_k) = 0 \end{cases} \tag{9}$$

Hence, similar to Equations (5), one can derive:

$$\begin{cases} L_s = \dfrac{1}{K_p^s} \hat{n}_s \dot{P}_c^s = \dfrac{1}{\overline{K_p^s}} \hat{\overline{n}}_s \dot{\overline{P_c^s}} \\ L_f = \dfrac{1}{K_p^f} \hat{n}_f \dot{P}_c^f = \dfrac{1}{\overline{K_p^f}} \hat{\overline{n}}_f \dot{\overline{P_c^f}} \end{cases} \tag{10}$$

Where $\overline{K_p^s} = -m(\partial F / \partial \varepsilon_v^p)$, $\overline{K_p^f} = -r_k(\partial F / \partial \xi_k)$, $\hat{\overline{n}}_s = sign[\overline{P_c^s} - \overline{\delta}_s(\varepsilon_v^p, \xi_k)]$ and $\hat{\overline{n}}_f = sign[\overline{P_c^f} - \overline{\delta}_f(\varepsilon_v^p, \xi_k)]$.

$\overline{P_c^s}$ and $\overline{P_c^f}$ are the capillary pressure at the projection on the boundary. The image point is the projection of the current position of the material state from a projection center onto the boundary loop. The projection center is different due to different assumptions and different hardening laws. The notions of projection center and image point are illustrated in Figure 3. The current state is located at S. In this paper the point O is chosen as the projection center for scanning curve DD', corresponding mapping point is S'. The projection center is not fixed but moving along AA' when the current state point S changes from D to D'. As illustrated in Figure 3 the slope of scanning curve must be larger than the slope of the boundary at the same value of x-axis, and the scanning curve asymptotically approaches the main boundary. Hence it is proposed that:

$$\begin{cases} K_p^s = \hat{K}_s(\overline{K_p^s}, P_c^s, |\boldsymbol{\varphi}|, \eta, \varepsilon_v^p) \geq \overline{K_p^s} \\ K_p^f = \hat{K}_f(\overline{K_p^f}, P_c^f, |\boldsymbol{\varphi}|, \eta, \xi_k) \geq \overline{K_p^s} \end{cases}$$

and

$$\begin{cases} K_p^s = \hat{K}_s(\overline{K_p^s}, P_c^s, 0, \eta, \varepsilon_v^p) = \overline{K_p^s} \\ K_p^f = \hat{K}_f(\overline{K_p^f}, P_c^f, 0, \eta, \xi_k) = \overline{K_p^s} \end{cases} \tag{11}$$

where $\boldsymbol{\varphi}$ which is defined by:

$$|\boldsymbol{\varphi}| = | P_c(\varepsilon_v^p, \xi_k) - \overline{P_c}(\varepsilon_v^p, \overline{\xi_k}) | \tag{12}$$

is the distance between the current capillary pressure on the scanning curve and the mapping one on the

boundary. η is the capillary pressure at the projection center.

It is necessary to identify the recoverable zone for the mathematical completion. The liner elastic relation is assumed, so that:

$$\dot{P}_c = \dot{P}_c^s + \dot{P}_c^f = -\mu_s(\dot{\varepsilon}_v - \dot{\varepsilon}_v^p) - \mu_f(\dot{\theta} - \dot{\theta}_I) \tag{13}$$

Introducing (10) and (13), we can derive:

$$-\dot{\theta} = [\frac{1}{\mu_f} + \frac{H(L_f)}{K_p^f}]\dot{P}_c^f \tag{14}$$

$$-\dot{\varepsilon}_v = [\frac{1}{\mu_s} + \frac{H(L_s)}{K_p^s}]\dot{P}_c^s \tag{15}$$

Equation (10) can be rewritten as:

$$\begin{cases} L_s = \dfrac{1}{K_p^s}\hat{n}_s\dot{P}_c^s = \dfrac{-\mu_s}{K_p^s + \mu_s}\hat{n}_s\dot{\varepsilon}_v \\ L_f = \dfrac{1}{K_p^f}\hat{n}_f\dot{P}_c^f = \dfrac{-\mu_f}{K_p^f + \mu_f}\hat{n}_f\dot{\theta} \end{cases} \tag{16}$$

3 A SIMPLIFIED MODEL OF CAPILLARY HYSTERESIS

There are numerous empirical models which take the influence of volumetric strain into consideration, have been proposed to represent the boundary surface. For convenience, Tarantino's equation is adopted:

$$(S_r)_{d,w} = \{1 + [(\frac{e}{a_{d,w}})^{1/b_{d,w}} s]^{n_{d,w}}\}^{-b_{d,w}/n_{d,w}} \tag{17}$$

where subscripts "d" and "w" represent drying and wetting, respectively. a, b and n are the material constants.

In the following, we consider a simple situation, where the recoverable zone is ignored such that it becomes a point, resulting:

$$\varepsilon_v = \varepsilon_v^p \tag{18}$$

$$\theta = \theta_I \tag{19}$$

Introducing Equations (14) and (15), one can obtain:

$$-\dot{\varepsilon}_v = \frac{H(L_s)}{K_p^s}\dot{P}_c^s \tag{20}$$

$$-\dot{\theta} = \frac{H(L_f)}{K_p^f}\dot{P}_c^f \tag{21}$$

The void ratio could be directly obtained from laboratory experiments, so that the volumetric strain was replaced by void ratio, using the following equation:

$$\dot{\varepsilon}_v^p = \dot{\varepsilon}_v = \dot{n} = \frac{1}{(1+e)^2}\dot{e} \tag{22}$$

The main drying/wetting curve in the (θ_I, P_c^f) plane can be simplified into the following form:

$$\begin{cases} F_{WT}^f(P_c, \theta) = -P_c^f + \kappa_{WT}^f(\theta) \\ F_{DR}^f(P_c, \theta) = P_c^f - \kappa_{DR}^f(\theta) \end{cases} \tag{23}$$

Where $\bar{\delta}_f(\theta) = \frac{1}{2}[\kappa_{WT}^f(\theta) + \kappa_{DR}^f(\theta)]$

$\bar{\kappa}_f(\theta) = \frac{1}{2}[\kappa_{DR}^f(\theta) - \kappa_{WT}^f(\theta)]$

According to the Equation (11), $\hat{K}_p^f$ is proposed that:

$$\hat{K}_p^f(P_c, |\boldsymbol{\varphi}|, \eta_0, \theta) = \bar{K}_p^f(\theta) + \frac{c_f |\boldsymbol{\varphi}|}{r_f - |\boldsymbol{\varphi}|} \tag{24}$$

where $r_f = |\eta_0 - \overline{P_c^f}| = \kappa_{DR}^f(\theta) - \kappa_{WT}^f(\theta)$ is the current size of bounding surface in the (θ_I, P_c^f) plane, and c_f is pressure-like parameter.

Similarly, in the (e, P_c^s) plane, the bounding surface is:

$$\begin{cases} F_{WT}^s(P_c, e) = -P_c^s + \kappa_{WT}^s(\mathrm{e}) \\ F_{DR}^s(P_c, e) = P_c^s - \kappa_{DR}^s(\mathrm{e}) \end{cases} \tag{25}$$

Where $\bar{\delta}_s(e) = \frac{1}{2}[\kappa_{WT}^s(e) + \kappa_{DR}^s(e)]$ and

$\bar{\kappa}_s(e) = \frac{1}{2}[\kappa_{DR}^s(e) - \kappa_{WT}^s(e)]$

The plastic modulus $\hat{K}_p^s$ can be casted into the following form:

$$\hat{K}_p^s(P_c, |\boldsymbol{\varphi}|, \eta_0, e) = \bar{K}_p^s(\theta) + \frac{c_s |\boldsymbol{\varphi}|}{r_s - |\boldsymbol{\varphi}|} \tag{26}$$

where $r_s = |\eta_0 - \overline{P_c^s}| = \kappa_{DR}^s(e) - \kappa_{WT}^s(e)$ is the current size of bounding surface in the (e, P_c^s) plane, and c_s is pressure-like parameter.

4 APPLICATION

In this section, the proposed model is validated through comparing the model prediction with the experimental data obtained from the previous literature. The experimental data involves main drying/wetting process, wetting and drying circle and complicated stress path.

The first set of experimental data was obtained from Sun et al. (2007). Figure 4(a) and 4(b) show the SWCC for an unsaturated specimen compacted at initial void ratios of $e_0 = 1.08$ and $e_0 = 1.08$ respectively. Figure 5a was obtained by decreasing the matric suction from 196 to 2 kPa (segment AB), increasing the suction from 2 to 490 kPa (segment BC), and then decreasing the suction from 490 to 2 kPa (segment CD) under a constant isotropic net stress of 20 kPa. Figure 4b is obtained by changing the suction under a constant isotropic net stress of 20 kPa. Frist, the specimens was

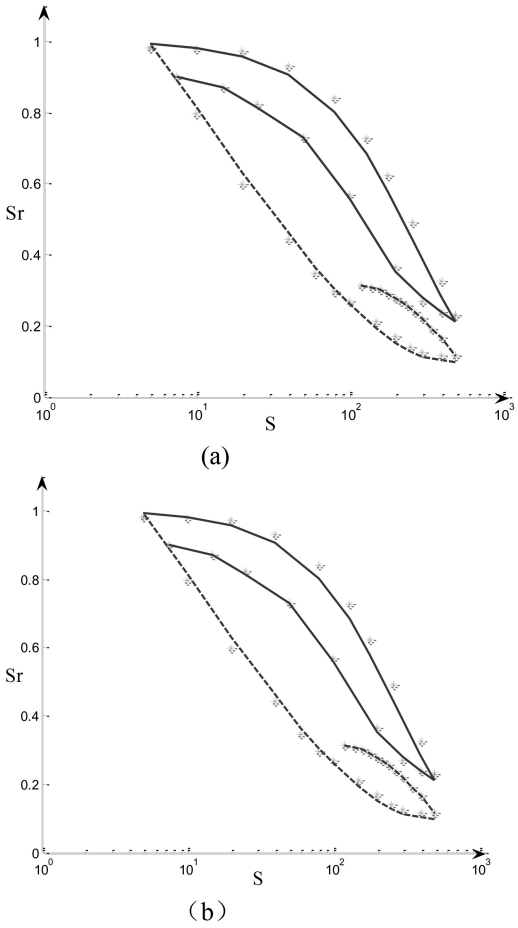


Figure 4. Wetting-drying cycles performed on Pearl clay compacted at different void ratios under isotropic net stress of 20 kPa. (a) $e_0 = 1.08$; and (b) $e_0 = 1.78$.

dried by increasing the imposed suction from 98 to 490 kPa (AB), wetted by decreasing the suction from 490 to 5 kPa (BC), dried by increasing the suction from 5 to 490 kPa (CD), and finally wetted by decreasing the suction from 490 to 7 kPa (DE). The dot line in Figure 4a and 4b are used to compute the parameters of main bounding surface and scanning curves. The solid line that was computed by the hysteresis model, fitted the experimental date very well. The corresponding material properties are summarized in Table 1 (Pearl clay).

A series of scanning wetting and drying test results obtained by Gillham et al. (1976) are employed in this paper to validate the proposed hysteresis model as illustrated in Figure 5(a) and 5(b). Employing the parameters of Colorado dune sand are summarized in the Table 1. It is worth mentioning that, there is no data of volumetric strain so that for the convenient, the initial void ratio is assumed to 1. Figure 5 show that the hysteresis was accurately simulated and it is adequate to reproduce the experimentally observed behavior through the hysteresis model. The differences

Table 1. Summary of material parameters.

	a_d	b_d	n_d	a_w
Ball clay	9834936	2.8	1.29	773
Sand soil	2751734	4.5	13.8	897
Silica sand	256.7	1.3	7.51	5.51
	b_w	n_w	c_s	c_f
Ball clay	1.4	0.74	28.5	100
Sand soil	2.5	7.61	–	51.5
Silica sand	0.59	6.15	–	225

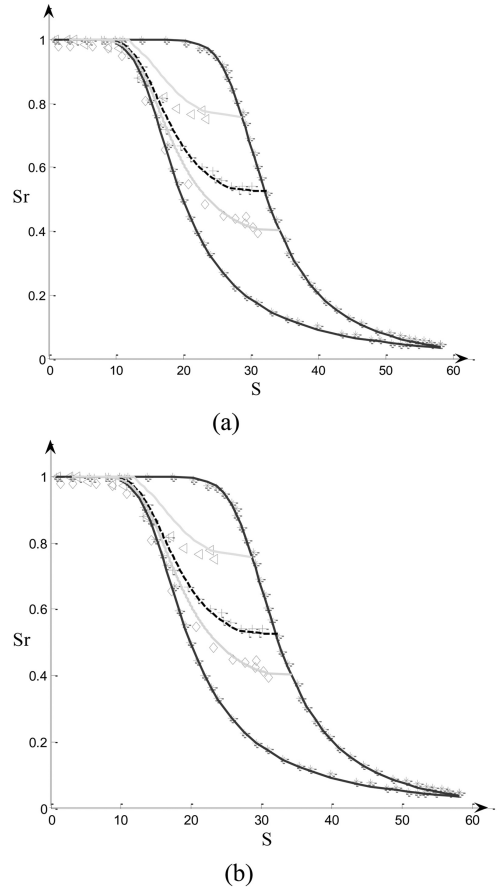


Figure 5. Test results and model predictions for the hysteresis behavior of sand: (a) scanning drying tests and (b) scanning wetting tests.

between the predict results and the experimental data could be negligible.

Huang et al. (2004) performed a laboratory experiment to establish the series of hysteresis scanning curves. White silica sand with grain diameters between 0.074–0.297 mm was compacted using a high-speed vibrator. The packed sand had a bull density of 1.68 g/cm^3 and a porosity of 0.36. The parameters were list in the Table 1. As showed in Figure 6, the hysteresis

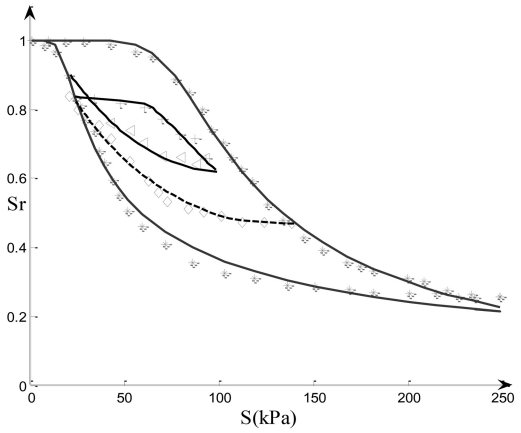


Figure 6. Test results and model predictions for the scanning curves of silica sand.

model accurately stimulates the main wetting/drying curves, primary wetting/drying curves and secondary wetting/drying curves.

5 CONCLUDING REMARKS

This study explains the influence of volumetric strain on the capillary hysteresis from the pore-scale mechanism. A novel model that can be used to simulate the effect on the capillary hysteresis is derived. By the theory of bounding surface plasticity, the proposed model adds only two parameters which can be conveniently calibrated by laboratory experiments. The results predicted by the proposed model match the experimental observations very well, and reproduce the wetting and drying circle adequately.

ACKNOWLEDGMENTS

The financial support from the National Natural Science Foundation of China (51478135, 51208031) and the Fundamental Research Funds for the Central Universities (2015JBM068, 2015RC019) are gratefully acknowledged.

REFERENCES

Brooks, R.H., and Corey, A.T. 1964. Hydraulic properties of porous medium. Civil Engineering Department, Colorado State University, Fort Collins, Colo. Hydrology Paper No. 3.

Dafalias, Y.F., and Popov, E.P. 1986. Bounding surface plasticity I: Mathematical foundation and hypoplasticity, Journal of Engineering Mechanics, 112: 967–987.

Fredlund, D.G., and Xing, A. 1994. Equations for the soil-water characteristic curve. Canadian Geotechnical Journal, 31(4): 521–532.

Gallipoli D. A hysteretic soil-water retention model accounting for cyclic variations of suction and void ratio. Géotechnique, 2012, 62(7): 605–616.

Gillham, R.W., Klute, A., Heerman, D.F. 1976. Hydraulic properties of a porous medium: measurement and empirical representation. Soil Sci Soc Am J; 40: 203–7.

Hassanizadeh, S.M., Gray W.G. 1990. Mechanics and thermodynamics of multiphase flow in porous media including interphase boundaries, Advanced Water Resource, 13(4), 169–186.

Huang, H.C., Tan, Y.C., Liu, C.W., Chen, C.H. 2004. A novel hysteresis model in unsaturated soil. Hydrological Processes, 19(8): 1653–1665.

Li, X.S. 2005. Modelling of hysteresis response for arbitrary wetting/drying paths. Computers and Geotechnics, 32: 133–137.

Mbonimpa, M., Maqsoud A., Bussière, B. 2006. Predictive Model for the Water Retention Curve of Deformable Clayey Soils. Journal of Geotechnical and Geoenvironmental Engineering, 132(9): 1121–1132.

Nuth, M., Laloui, L. 2008. Advances in modelling hysteretic water retention curve in deformable soils. Computers and Geotechnics, 35(6): 835–844.

Pride, S.R., Flekkøy, E.G. 1999. Two-phase flow through porousmedia in the fixed-contact-line regime, Phys. Rev. E, 60(4): 4285–4299.

Romero, E., Gens, A., Lloret, A. 2001. Temperature effect on the hydraulic behaviour of an unsaturated clay. Geotechnical and Geological Engineering, 19(3/4): 311–332.

Salager, S., El Youssoufi, M.S., Saix, C. 2010. Definition and experimental determination of a soil-water retention surface. Canadian Geotechnical Journal, 2010, 47(6): 609–622.

Salager, S., Jamin, F., El Youssoufi, M.S., Saix, C. 2006. Influence de la tempe'rature sur la courbe de re'tention d'eau de milieux poreux. Comptes Rendus Me'canique, 334(6): 393–398.

Sugii, T., Yamada, K., Kondou, T. 2002. Relationship between soil-water characteristic curve and void ratio. In Proceedings of the 3rd International Conference on Unsaturated Soils, Recife, Brazil, 10–13 March 2002. Edited by J.F.T. Juco, T.M.P. DeCampas, and F.A.M. Marinho. Swets and Zeitlinger, Rotterdam, the Netherlands. Vol. 1, pp. 209–214.

Sun, D.A., Sheng, D.C., Cui, H.B., Sloan, S.W. 2007. A density-dependent elastoplastic hydro-mechanical model for unsaturated compacted soils, International Journal for Numerical and Analytical Methods in Geomechanics, 31(11): 1257–1279.

Tarantino A. 2009. A water retention model for deformable soil. Géotechnique, 59(9): 751–762.

Tarantino, A., Tombolato, S. 2005. Coupling of hydraulic and mechanical behavior in unsaturated compacted clay. Géotechnique, 55(4): 307–317.

Tsiampousi, L. Zdravkovic, Potts D. M. 2013. A three-dimensional hysteretic soil-water retention curve. Géotechnique 63(2): 155–164.

Vanapalli, S.K., Fredlund, D.G., Pufahl, D.E. 1999. The influence of soil structure and stress history on the soil-water characteristics of a compacted till. Géotechnique, 49(2): 143–159.

Wei, C.F., Dewoolkar, M.M. 2006. Formulation of capillary with internal state variables. Water Resource Research, 2006, 42:W07405.

Zhang, X.D., Zhao, C.G., Liu, Y., et al. 2011. Modeling study of the relationship between deformation and water retention curve [J]. China Civil Engineering Journal, 2011, 44(7): 119–126.

Zhou, A.N., Sheng, D.C., Li, J. 2012. Modelling the effect of initial density on soil-water characteristic curves. Géotechnique, 62(8): 669–680.

Unsaturated Soil Mechanics—from Theory to Practice – Chen et al. (Eds)
© 2016 Taylor & Francis Group, London, ISBN 978-1-138-02921-7

Validity of the bimodal equations for fitting the Soil-Water Characteristic Curve behavior of cracked expansive soils

X. Wang & S.K. Vanapalli
University of Ottawa, Ottawa, Ontario, Canada

ABSTRACT: In this study, five equations from the literature proposed for different soils by various investigators for fitting the bimodal Soil-Water Characteristic Curve (SWCC) are summarized into two categories; namely, physical and mathematical theory based equations. The former type of equations is based on soil grain size or pore size distributions and the later from the mathematical features of the bimodal SWCC. The physical theory based equations provide a reasonable explanation to the SWCC behavior using the capillary law for different types of soils. The mathematical theory based equations however are more convenient to be incorporated into numerical modeling studies. In this study, the validity of these five bimodal equations was examined using a measured bimodal SWCC of an expansive soil. The results from the study presented in the paper suggest that both types of equations are capable of fitting the SWCC data for unsaturated expansive soils, although some minor deviations occur. The mathematical equations, however, are more advantageous for unsaturated expansive soils than the physical theory based equations in terms of better fitting accuracy.

1 INTRODUCTION

Geotechnical infrastructure, such as foundations, retaining walls, slopes, canals and cuts, are constructed in or with expansive soils in many regions of the world. Many of these structures pose problems due to the swell and shrink behavior of expansive soils. For example, cracks in expansive soils have a considerable effect on the slope instability (Baker 1981, Lee et al. 1990, Chowdhury & Zhang 1991, Yao & Sun 2001) as well as dam failures (Sherard 1987a,b, Talbot & Deal 1993) under various infiltration conditions. Most cracks in expansive soils are desiccation cracks resulting from loss of water associated with evaporation. These cracks can provide preferential pathways for water flow during infiltration, which significantly increases the hydraulic conductivity of the soil mass (Sivakumar & Wheeler 2000, Dane & Klute 1977).

The soil-water characteristic curve (SWCC) is defined as the relationship between the water content and soil suction. The SWCC provides valuable information about the water retention or water storage ability of an unsaturated soil within its soil structure (i.e. macro and micro pores). Fundamental information can be gathered from a SWCC to predict unsaturated soil properties, such as the coefficient of permeability (Fredlund et al. 1994) and the shear strength (Vanapalli et al. 1996). The SWCC has been widely used as a tool in geotechnical software during the past two decades for seepage and stability analyses of engineering structures (GEO-SLOPE International Ltd. 2008, Zhou at al. 1998; Sheng et al. 2008a, b).

Determination of SWCC in the laboratory can be time-consuming and expensive. For example, a time period of 6 weeks or longer is required for determination of the SWCC in the laboratory for an expansive soil. For this reason, several researchers focused on the estimation of the unimodal SWCC using the basic properties of soil, and the well-known Fredlund & Xing (1994) equation. In this equation, three fitting parameters, i.e. a, n and m (a is closely related to the air-entry value, n controls the slope of the curve, and m is associated with the residual suction) were introduced to estimate the SWCC using the method of least squares. However, they are not independently related to shape features of the unimodal SWCC (Gitarana & Fredlund 2004). For this reason, the bimodal equations proposed based on Fredlund & Xing (1994) equation will have the same limitation. To overcome this limitation, additional information may be derived from the grain-size distribution (GSD), pore-size distribution (PSD) or void ratio of soil, to provide specific physical meaning to the fitting parameters of the bimodal equations.

There is another type of estimation method based on mathematical analysis. In this method, all the chosen fitting parameters, i.e. the air-entry value, the residual suction, the residual degree of saturation, and the parameter that controls the sharpness of the curvatures, have clear physical meanings (Gitarana & Fredlund 2004).

With an increasing number of models in the literature using the SWCC as a tool in recent years to propose semi-empirical models for prediction of

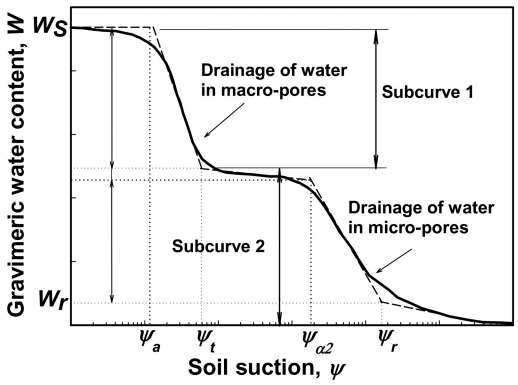


Figure 1. Conceptual bimodal soil water characteristic curve (modified after Li et al. 2014).

unsaturated soil properties and in numerical modeling studies and for practical applications, their versatility along with accuracy have become important issues. A typical unimodal SWCC has a single segment of the sigmoidal curve, which can well represent one set of pore system with different pore-size distribution patterns, such as the Fredlund & Xing (1994) equation. However, experimental results from the literature highlight that certain types of soils, such as the gap graded sols, fine-grained soils compacted at dry of optimum conditions and expansive soils, may exhibit bimodal SWCC. The bimodal nature of a soil can be mainly attributed to the soil structure consisting of both the macro and micro pores. Figure 1 shows a conceptual bimodal SWCC.

2 EQUATIONS OF BIMODAL SWCCS

2.1 *Capillary theory with SWCC*

Capillary theory has been used as a tool for interpreting the mechanics of unsaturated soils. The capillary law states that matric suction has an inverse relationship with the radius of curvature of the air-water interface. Studies by several investigators show that the radius of curvature has a significant influence on the water storage capacity of unsaturated soils (Fredlund & Rahardjo 1993, Gallipoli et al. 2003, Lu & Likos 2006). Alternatively, it can be stated that the pores within soils is similar to a bundle capillary tubes that have an important role in contributing to water storage capacity. Significant research has been undertaken during the last four decades to study the unimodal SWCC. Most of the unimodal equations proposed in the literature are based on the capillary law which also highlight the shape of the SWCC is strongly dependent of the PSD of the soil (Fredlund & Xing 1994).

Similarly, for a dual or multi-structural soil mass, capillary theory can also be extended to derive suitable fitting equations for the SWCC. It can be inferred that two or more levels of soil structures would result in distinct capillary forces in comparison with only one set of pore structure observed corresponding to the unimodal SWCC. Furthermore, more recent experiments have shown that a unimodal SWCC would be insufficient to determine variant capillary forces within the pores. Thus, an accurate description of capillary force (or bimodal SWCC) with respect to the soil particle or pore size distribution is important for understanding the water storage capacity of unsaturated soils with a dual or multi-structure. In the present study, five different bimodal SWCC equations from the literature are summarized below.

2.2 *Bimodal equations*

2.2.1 *Physical theory based equations*

Burger & Shackelford (2001a) bimodal equation based on Fredlund & Xing (1994) equation

Burger & Shackelford (2001b) obtained several SWCCs of sand–pelletized diatomaceous earth mixtures with the microscopic (intrapellet) and macroscopic (interpellet) porosity using Tempe cell, pressure plate and filter paper testing method, and found that the SWCC data is bimodal in nature. Burger & Shackelford (2001a) suggested that the data can be fitted based on existing unimodal SWCC using piecewise function (i.e. two unimodal SWCCs connected by a junction point) as given below:

$$\theta = \begin{cases} C(\psi) = \dfrac{\theta_j}{\left\{\ln\left[e + \left(\dfrac{\psi}{a'}\right)^{n'}\right]\right\}^{m'}}; & \psi_j < \psi \\ C(\psi) = \dfrac{\theta_s}{\left\{\ln\left[e + \left(\dfrac{\psi}{a}\right)^{n}\right]\right\}^{m}}; & \psi \le \psi_j \end{cases} \quad (1)$$

where $C(\psi)$ is correcting function, given by

$$C(\psi) = \begin{cases} C(\psi) = 1 - \dfrac{\ln\left[1 + \left(\dfrac{\psi}{\psi'_r}\right)\right]}{\ln\left[1 + \left(\dfrac{10^6}{\psi'_r}\right)\right]}; & \psi_j < \psi \\ C(\psi) = 1 - \dfrac{\ln\left[1 + \left(\dfrac{\psi}{\psi_r}\right)\right]}{\ln\left[1 + \left(\dfrac{10^6}{\psi_r}\right)\right]}; & \psi \le \psi_j \end{cases} \quad (2)$$

where θ is volumetric water content, θ_j is the junction volumetric water content, θ_r is the residual volumetric water content, θ_s is the saturated volumetric water content, ψ is soil suction, ψ_j is the soil suction at the junction point, ψ_r and ψ'_r is the residual soil suctions for macroscopic, microscopic portions of data, e is base of natural logarithm, a, m and n are the fitting parameters for macroscopic portion of data, a', m' and n' are the fitting parameters for microscopic portion of data.

Zhang & Chen (2005) bimodal equation

Zhang & Chen (2005) present a theoretical continuum method for determination of the SWCC for soil with a bimodal or multimodal pore-size distribution. Based on the capillary law, the water content in a multimodal soil is equal to the sum of water stored in each pore series of the soil. Therefore, the bimodal or multimodal SWCCs can be obtained by combining the unimodal SWCCs for all components of the soil corresponding to the pore series weighted by the respective volumetric percentages (i.e. Eq. 3).

$$\theta(\psi) = p_l n_{pl}\left[1-\frac{\ln\left(1+\frac{\psi}{\psi_{rl}}\right)}{\ln\left(1+\frac{10^6}{\psi_{rl}}\right)}\right]\left\{\frac{1}{\ln\left[e+\left(\frac{\psi}{a_l}\right)^{nl}\right]}\right\}^{ml} + p_s n_{ps}\left[1-\frac{\ln\left(1+\frac{\psi}{\psi_{rs}}\right)}{\ln\left(1+\frac{10^6}{\psi_{rs}}\right)}\right]\left\{\frac{1}{\ln\left[e+\left(\frac{\psi}{a_s}\right)^{ns}\right]}\right\}^{ms} \quad (3)$$

$\theta_s = \theta_{sl} + \theta_{ss}$;
$\theta_{sl} = p_l n_{pl}$;
$\theta_{ss} = p_s n_{ps}$;

where e is the base of natural logarithm, ψ_r is soil suction in the residual condition, a, m and n are three parameters of the SWCC function, subscripts l and s represent the large-pore series component and the small-pore series component, respectively.

Satyanaga et al. (2013) bimodal equation

Since the parameters of several bimodal equations are not related to the physical properties of the soil, Satyanaga *et al.* (2013) developed Eq. (4) to fit SWCC of soils with bimodal characteristics. The parameters adopted in their model were closely related to the physical properties of the soil and variables of the SWCC.

$$\theta_w = \left(1-\frac{\ln\left(1+\frac{\psi}{\psi_r}\right)}{\ln\left(1+\frac{10^6}{\psi_r}\right)}\right)\left[\begin{array}{l}\theta_r \\ +\left(\theta_{s1}-\theta_{s2}\right)\left(1-erfc\frac{\ln\left(\frac{\psi_{a1}-\psi}{\psi_{a1}-\psi_{m1}}\right)}{s1}\right) \\ +\left(\theta_{s2}-\theta_r\right)\left(1-erfc\frac{\ln\left(\frac{\psi_{a1}-\psi}{\psi_{a1}-\psi_{m1}}\right)}{s1}\right)\end{array}\right] \quad (4)$$

where θ_w is the calculated volumetric water content, θ_s is the saturated volumetric water content (measured in the laboratory), ψ is the matric suction under consideration, ψ_a represents the air-entry value of soil, ψ_m represents the matric suction at the inflection point of SWCC and s represents the geometric standard deviation of SWCC,

$$s = \left(\theta_{s2}\right)\exp\sqrt{\frac{\sum_{i=1}^{n}\left(\ln\frac{\psi_i}{\mu}\right)}{n}} \quad (5)$$

where μ is the geometric mean of matric suction

$$\mu = \sqrt[n]{\psi_1\psi_2\cdots\psi_n}$$

where θ_r represents the residual volumetric water content, ψ_r represents the matric suction corresponding to residual volumetric water content, *erfc* is the complimentary error function, can be calculated as

$$erfc = \int_{-\infty}^{X}\frac{1}{\sqrt{2\pi}}\exp\left(-\frac{x^2}{2}\right)dx \quad (6)$$

Li et al. (2014) bimodal equation

Another bimodal SWCC equation is proposed by Li et al. (2014) considering dual-porosity structure (i.e. Eq. (7)). This SWCC model is capable of fitting the SWCCs for soils varying from gravel to silt.

$$w(\psi) = \lambda\left(\frac{w_s}{\lambda+1}-w_r\right)\frac{\sqrt{\psi_t\psi_a}^{n/\log(\psi_t/\psi_a)}}{\psi^{n/\log(\psi_t/\psi_a)}+\sqrt{\psi_t\psi_a}^{n/\log(\psi_t/\psi_a)}} + \left(\frac{w_s}{\lambda+1}-w_r\right)\frac{(l\psi_t)^m}{\psi^m+(l\psi_t)^m} + \lambda w_r \times\frac{\sqrt{\psi_r\psi_{a2}}^{n/\log(\psi_r/\psi_{a2})}}{\psi^{n/\log(\psi_r/\psi_{a2})}+\sqrt{\psi_r\psi_{a2}}^{n/\log(\psi_t/\psi_{a2})}} + w_r\frac{(l\psi_r)^m}{\psi^m+(l\psi_r)^m} \quad (7)$$

where λ is the ratio of the mass content of bulk water to that of water lens, it can be calculated as the ratio $(w_s - w_r)/w_r$, w_s is saturated water content, w_r is residual water content (i.e. mass content of water-lens stored in micro-pores of soil), w_b is mass content of bulky water, ψ_a is air-entry value of a unimodal SWCC, or the first air-entry value of a bimodal or multimodal SWCC, ψ_r is suction corresponding to the residual water content of a unimodal SWCC, or the second residual suction of a bimodal SWCC, w_{b1} is mass content of bulky water stored in macro-pores, w_{l1} is mass content of water lens stored in macro-pores, w_{b2} is the mass content of bulky water stored in micro-pores, ψ_{a2} is the air entry value for water stored in micro-pores, ψ_t is the residual suction for water stored in macro-pores.

Mathematical theory based equations

Gitarana & Fredlund (2004) bimodal equation

In the model proposed by Gitarana & Fredlund (2004) for fitting bimodal SWCC, the fitting parameters have been related to well-defined soil properties or features of the curve. Specifically, the shape characteristics were described by a series of parameters (i.e. hyperbole

rotation angle, aperture angle tangent, and desaturation slope). These parameters were in turn used to represent the parameters with physical meaning that can be determined from the SWCC curve data. The parameters include the air-entry value, the residual suction, the residual degree of saturation, and a parameter that controls the sharpness of the curvatures. The physical implication of the soil parameters has been discussed for different soil types in their work, and a unique relation between suction and degree of saturation was determined. This equation is summarized below:

$$S = \frac{S_1 - S_2}{1 + \left(\psi / \sqrt{\psi_{b1}\psi_{res1}}\right)^{d1}} + \frac{S_2 - S_3}{1 + \left(\psi / \sqrt{\psi_{res1}\psi_{b2}}\right)^{d2}} + \frac{S_3 - S_4}{1 + \left(\psi / \sqrt{\psi_{b2}\psi_{res2}}\right)^{d2}} + S_4 \quad (8)$$

$$S_i = \frac{\tan\theta_i\left(1 + r_i^2\right)\ln\left(\psi / \psi_i^a\right)}{\left(1 - r_i^2\tan^2\theta_i\right)} + (-1)^i \times \frac{\left(1 + \tan^2\theta_i\right)}{\left(1 - r_i^2\tan^2\theta_i\right)}\sqrt{r_i^2\ln^2\left(\psi / \psi_i^a\right) + \frac{a^2\left(1 + \tan^2\theta_i\right)}{\left(1 - r_i^2\tan^2\theta_i\right)}} + S_i^a \quad (9)$$

where $i = 1, 2, 3, 4$, $\theta_i = -(\lambda_{i-1} + \lambda_i)/2$, is hyperbolas rotation angles, $r_i = \tan[(\lambda_{i-1} - \lambda_i)/2]$, is aperture angles tangents, $\lambda_0 = 0$, $\lambda_i = \arctan\{(S_i^a - S_{i+1}^a)/[\ln(\psi_{i+1}^a / \psi_i^a)]\}$, is desaturation slopes, $S_1^a = 1$, $S_2^a = S_{res1}$, $S_3^a = S_b$, $S_4^a = S_{res2}$, $S_5^a = 0$, $\psi_1^a = \psi_b$, $\psi_2^a = \psi_{res1}$, $\psi_3^a = \psi_{b2}$, $\psi_4^a = \psi_{res2}$, $\psi_5^a = 10^6$, $d_j = 2\exp[1/\ln(\psi_{j+1}^a / \psi_j^a)]$, is weighting factors, $j = 1, 2, 3$.

The five bimodal equations summarized above are proposed for soils with dual porosity. Cracks in soils can also be considered as another level of pores, as their sizes are essentially larger than that of pores within soil matrix. The effectiveness of these five bimodal equations in the interpretation of the water storage of a cracked expansive soil is examined in the following section.

3 COMPARISON AND FITTING RESULTS

A dual-porosity model was presented by Burger & Shackelford (2001a) using Fredlund and Xing (1994) equation to fit a bimodal SWCC. In their work, two unimodal functions have been combined separately to cover the full range of suction data (i.e. 0 to 10^6 kPa). Between the two unimodal curves, a junction point was defined, where the suction value is ψ_j and the corresponding volumetric water content is θ_j. At such point, the macroscopic porosity appears to have been completely desaturated, and the microscopic porosity begins to desaturate (Burger & Shackeford 2001a). Then, the data for suction greater or less than ψ_j are fitted separately using the unimodal SWCC function. Each set of data generates one set of fitting parameters (six in total), to fit the bimodal SWCC. In this method, determining the junction point is believed to be the most crucial step. However, the accuracy of junction point, which is generally difficult to determine, would considerably influence the fitting results.

Zhang & Chen (2005) proposed an equation by using pore size distribution function, also based on the Fredlund and Xing (1994) unimodal SWCC. For bimodal equation, two unimodal functions have been superimposed to cover the full range of suction data. Furthermore, they proposed a theoretical continuum method to predict SWCC when soil has multimodal pore-size distribution. According to the capillary law, the water content in a multimodal is equal to the sum of water stored in each pore series in the soil (Zhang & Chen 2005). Similarly, it is recognized that bimodal or multimodal SWCCs can be obtained by combining the unimodal SWCC for all components of the soil corresponding to the each pore series (Zhang & Chen 2005). However, no junction point needs to be determined in their equation. In other words, bimodal equation turns to a single function rather than the piecewise function.

Although Zhang & Chen (2005) indicated that their equation performed better among other SWCC equations, the parameters in their equation are not related to the physical properties of soil and the variables of SWCC (Satyanaga et al. 2013). A bimodal SWCC or a bimodal permeability function originates from a dual-porosity structure, and this dual-porosity property is governed by the coarse grains and the fine grains in soil (Zhang & Li 2010). Therefore, bimodal pore-size distribution could be derived for a soil with the bimodal GSD. Satyanaga et al. (2013) and Li et al. (2014) developed bimodal SWCC equations using the GSD data of soil. In both these equations, the parameters are associated with physical properties and hence valuable for physical interpretation for soils ranging from gravel to silt. This model generates from the bimodal GSD curve, since they used the gap-graded soil. Notably, Li et al. (2014) model fits both the bimodal SWCCs for gap-graded soil and unimodal SWCCs for well-graded soil reasonably well.

The above models are classified as the physical theory based equations, while there is another category of equations which belongs to the mathematical theory. To be more precise, Gitirana & Fredlund (2004) model has a theoretical basis, and it is established by considering the shape features of SWCC based on both mathematical analysis and statistical assessment. In this model, three parameters were introduced for defining the salient feature of the curve. By using those parameters the relationship between suction and degree of saturation can be reasonably well represented. This method will benefit from the use of an equation whose parameters are independent of each other and also have clear physical meaning (Gitirana & Fredlund 2004).

All the five equations were developed to cover the entire range of soil suction (i.e. 0 to 10^6 kPa) and were used for different types of soils. To examine their effectiveness for cracked expansive soils, the SWCC data measured by Ito & Azam (2011) on a cracked expansive soil from Regina is used for fitting using the

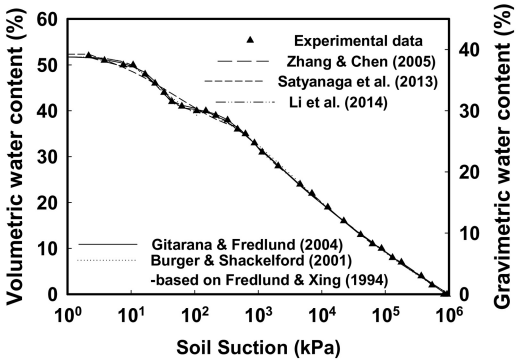


Figure 2. Fitting results of five bimodal equations used in the present study with the experimental results.

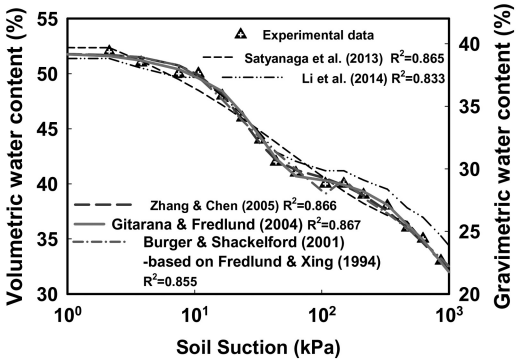


Figure 3. Fitting results of five bimodal equations (A portion of picture of Figure 2 is zoomed to highlight the differences in fitting curves).

five bimodal equations summarized in this paper. The fitting results are presented in Figure 2 and 3. There are two vertical axes in Figure 2 (the left-hand side axis is volumetric water content, and the right-hand side axis is gravimetric water content). All bimodal equations are expressed in terms of volumetric water content, except for Li et al. (2014) equation, which uses gravimetric water content. While the experimental data from Ito & Azam (2011) was in terms of volumetric water content, a conversion according to the basic volume-mass relation was made from volumetric water content into gravimetric water content to examine Li et al. (2014) equation. Since the curves in Figure 2 are close to each other, a zoomed picture (Figure 3) has been provided for clearly highlighting the differences associated with different equation fits for the suction range from 1 to 1000 kPa along with the correlation coefficient R^2 values. From the results summarized in Figures 2 and 3, all the five bimodal equations can fit experimental data of Regina clay from Canada reasonably well. More precisely, Zhang & Chen (2005) equation ($R^2 = 0.866$) and Gitirana & Fredlund (2004) equation ($R^2 = 0.867$) have the best-fitting results (short dotted line with blue color and solid-line curve with red color, respectively). Burger and Shackelford (2001) equation (dotted line with green color) also results in a relatively well fitted curve ($R^2 = 0.855$), but the experimental data has to be divided into two sets and fit separately using this method. For this reason, it is difficult to find the inflection point properly using this equation. By using Li et al. (2014) equation, a smooth but not precise curve can be obtained, since the equation was derived from a simplified theoretical model using the information of GSD ($R^2 = 0.833$). Satyanaga et al. (2013) equation provides reasonably high correlation coefficient ($R^2 = 0.866$) in spite of this equation has been originally developed for gap-graded soils.

4 SUMMARY

The SWCC has a strong relationship with soil structure. For expansive soils, once cracks emerge, soil structure changes remarkably from a relatively homogeneous nature into a differential one, e.g. dual-porosity system. Notably, structure of expansive soil can change due to development of cracks under the effect of cyclic drying and wetting process (i.e. cyclic suction loading). For this reason, it is necessary to use bimodal or even multimodal SWCC in analyzing geotechnical problems related to unsaturated expansive soils.

Five bimodal equations proposed for different soils with dual porosity from the literature are summarized in this paper. Experimental data of an unsaturated cracked expansive soil from Regina, Canada was used to verify the applicability of five different bimodal equations from the literature summarized in this paper. Results show that Zhang & Chen (2005) and Gitarana & Fredlund (2004) equations have better fitting performance. However, effects of volume change, hysteresis, and cyclic loading, which are significant in expansive soils, were not considered in all the five bimodal SWCCs discussed in this paper. Therefore, to reliably predict the SWCC of expansive soils, an equation that takes into consideration of these factors should receive further research efforts.

ACKNOWLEDGMENTS

The authors thank Shunchao Qi, PhD graduate student for his valuable contributions and editing this paper. The first author gratefully acknowledges and appreciates the China Scholarship Council and the University of Ottawa, Canada for funding her PhD research program. The second author thanks the support from NSERC, Canada for his research programs.

REFERENCES

Baker, R. 1981. Tensile strength, tension cracks, and stability of slopes. *Soils and Foundations*. 21(2): 1–17.

Burger, C.A. & Shackelford, C.D. 2001a. Soil-water characteristic curves and dual porosity of sand-diatomaceous

earth mixtures. *Journal of Geotechnical and Geoenvironmental engineering*. 127(9): 790–800.

Burger, C.A. & Shackelford, C.D. 2001b. Evaluating dual porosity of pelletized diatomaceous earth using bimodal soil-water characteristic curve functions. *Can. Geotech. J*. 38(1): 53–66.

Chowdhury, R.N. & Zhang, S. 1991. Tension cracks and slope failure. In Proceedings of the International Conference: Slope Stability Engineering, Developments and Applications. Thomas Telford, London. pp: 27–32.

Dane, J.H. & Klute, A. 1977. Salt effects on the hydraulic properties of a swelling soil. *Soil Sci Soc Am J*. 41(1): 1043–1049.

Fredlund, D.G. & Rahardjo, H. (1993). Soil mechanics for unsaturated soils. John Wiley & Sons. pp: 67–69.

Fredlund, D.G. & Xing, A.Q. 1994. Equations for the soil–water characteristic curve. *Can Geotech J*. 31(4): 521–32.

Gallipoli, D., Gens, A., Sharma, R., & Vaunat, J. 2003. An elasto-plastic model for unsaturated soil incorporating the effects of suction and degree of saturation on mechanical behaviour. *Géotechnique*. 53(1): 123–136.

GEO-SLOPE International Ltd. 2008. Stability modeling with Slope/W. 2007 Version [computer program]. GEO-SLOPE International Ltd., Calgary, Alta.

Gitirana, G.D. & Fredlund. D.G. 2004. Soil–water characteristic curve equation with independent properties. *Geotech Geoenviron Eng J*. 130(2):209–12.

Ito, M. & Azam, S. 2013. Engineering properties of a vertisolic expansive soil deposit. *Engineering Geology*. 152(1): 10–16.

Lee, D.H., Sheu, C. & Juang, C.H. 1990. Development of a slope failure potential map using fuzzy sets. Proc. NAFIPS-90, Toronto, Canada. 1:109–112.

Li X., J.H. Li & L.M. Zhang. 2014. Predicting bimodal soil–water characteristic curves and permeability functions using physically based parameters, *Computers and Geotechnics.* 57: 85–96.

Lu, N., Lechman, J., & Miller, K.T. 2008. Experimental verification of capillary force and water retention between uneven-sized spheres. *Journal of engineering mechanics*. 134(5): 385–395.

Lu, N., & Likos, W.J. 2006. Suction stress characteristic curve for unsaturated soil. *Journal of Geotechnical and Geoenvironmental Engineering*. 132(2): 131–142.

Satyanaga, A., Rahardjo H, Leong E.C. & Wang J.Y. 2013. Water characteristic curve of soil with bimodal grain-size distribution. *Comput Geotech*. 48: 51–61.

Sheng, D.C., Fredlund, D.G., & Gens, A. 2008a. A new modelling approach for unsaturated soils using independent stress variables. *Canadian Geotechnical Journal.* 45(4): 511–534.

Sheng D.C., Gens A. & Fredlund D.G. 2008b. Unsaturated soils: from constitutive modelling to numerical algorithms. *Comput Geotech*. 35(6): 810–24.

Sherard, J.L. 1987a. Lessons from the Teton Dam failure. *Engineering Geology*. 24(1): 239–256.

Sherard, J.L. 1987b. Embankment dam cracking. In Embankment-dam engineering. John Wiley & Sons, Inc., New York. Casagrande volume. pp: 271–353.

Sivakumar, V. & Wheeler, S.J. 2000. Influence of compaction procedure on the mechanical behavior of an unsaturated compacted clay. Part 1: Wetting and isotropic compression. *Géotechnique*. 50(4): 359–368.

Talbot, J.R. & Deal, C.E. 1993. Rehabilitation of cracked embankment dams. In Geotechnical Practice in Dam Rehabilitation: Proceedings of the Specialty Conference, Raleigh, N.C., 25–28 April 1993. *Geotechnical Special Publication* No. 35. Edited by L.R. Anderson. American Society of Civil Engineers, Reston, Va. pp: 267–283.

Vanapalli, S.K., Fredlund, D.G., Pufahl, D.E. & Clifton, A.W. 1996. Model for the prediction of shear strength with respect to soil suction. *Can Geotech J*. 33(3): 379–392.

Yao, Y.P., & Sun, D.A. 2001. Closure to 'Application of Lade's criterion to Cam-Clay model. J. *Eng. Mech*. 127(1): 631–633.

Zhang, L.M. & Chen, Q. 2005. Predicting bimodal soil-water characteristic curves. *Journal of Geotechnical and Geoenviron- mental Engineering*. 131(5): 666–670.

Zhang, L.M. & Li, X. 2010. Micro-porosity structure of coarse granular soils. *Journal of Geotechnical and Geoenvironmental Engineering*. 136(10): 1425–1436.

Zhou, C.B., Ye, Z.T. & Xiong, W.L. 1998. A study on unsaturated hydraulic conductivity of rock joints. *Chinese Journal of Hydraulic Engineering*. 3: 22–26 (In Chinese).

Unsaturated Soil Mechanics—from Theory to Practice – Chen et al. (Eds)
© 2016 Taylor & Francis Group, London, ISBN 978-1-138-02921-7

A model for thermal influence on water retention curve in high suction range

B. Qin
Logistical Engineering University, Chongqing, China
Fundamental Science on Nuclear Wastes and Environmental Safety Laboratory, Mianyang, China

Y. Lu, F.Z. Zhang & Z.H. Chen
Logistical Engineering University, Chongqing, China

ABSTRACT: The thermal influence on water retention curve in the high suction range was investigated theoretically. According to the thermodynamics of sorption and the Le Chatelier's principle, water adsorption by soil was always an exothermic process, and it was an inevitable phenomenon that the water retention capacity in the high suction range reduced with increasing temperature. Assuming that the adsorption heat was independent on temperature and the water retention curves at different temperature were parallel, a model was established to describe the thermal influence on the water retention curve. Comparisons were made between the model predictions and the test results in literatures. Good agreements of those comparisons showed that the model had the capability to cover the full suction range.

1 INTRODUCTION

The temperature influence on water retention curves received attentions as early as the 1950s. In the early experimental research, the temperature influence on water retention curves were generally investigated on sands or silts in low suction range, and in most case suction values were not high than 100 kPa (e.g. Gardner 1955, Wilkinson & Klute 1962, Chahal 1965, Haridasan & Jensen 1972, Hopmans & Dane 1986, Nimmo & Miller 1986, She & Sleep 1998). With the growing use of high plasticity clays as the engineered barriers for radioactive waste isolation, the temperature influence on water retention curve in high suction range were studied in recent years on several high plasticity clays, including Boom clay (Romero et al. 2001), FoCa7 clay (Imbert et al. 2005), MX-80 bentonite (Tang & Cui 2005, Jacinto et al. 2009), FEBEX bentonite (Lloret et al. 2004) and GMZ bentonite (Ye et al. 2009, Qin et al. 2012). Some consistent results in low and high suction range were obtained about the temperature influence on water retention curves. The water retention capacity generally decreases with increasing temperature, and water retention curves at different temperatures are approximately parallel to each other when plotted in the semi-log coordinate with suction in logarithmic form (e.g. Grant & Salehzadeh 1996, Romero et al. 2001, Bachmann & van der Ploeg 2002, Imbert et al. 2005, Tang & Cui 2005, Salager et al. 2010, Qin et al. 2012).

Most of available models for the temperature influence on water retention curves were established on the basis of the conventional capillary model. Based on the Young – Laplace equation, Philip and de Vries (1957) firstly proposed a model to predict the variation of suction with temperature at constant volumetric water content by considering the temperature influence on surface tension of pure free water. It was then found that the Philip – de Vries model usually underestimated the temperature influence on water retention curves. To overcome the underestimation, several mechanisms were successively incorporated to models, including: the influence of entrapped air in soil water (Peck 1960, Chahal 1965, Hopmans & Dane 1986), the influence of solute on surface tension of soil water (Hopmans & Dane 1986, Nimmo & Miller 1986), the influence of isolated water packets (Liu & Dane 1993), the influence of temperature on contact angle of the water-air interface (Grant & Salehzadeh 1996, She & Sleep 1998), the influence of thermal expansion of soil water (Salager et al. 2010), etc. Some of the capillary-based models were also been used to analyse the temperature influence of water retention curve in high suction range (e.g. Tang & Cui 2005, Jacinto et al. 2009, Salager et al. 2010). However, it should be noted that the water retention mechanism in low and high suction range is different, with capillary effect in macropores for low suctions and surface sorption effect in micropores for high suctions. It is necessary to consider the mechanism of surface sorption when modeling the temperature influence of water retention curves in high suction range. Nonetheless, Little effort has been devoted to the topic (Jacinto et al. 2011, Qin et al. 2012).

In this paper, a model are proposed based on the thermodynamics of sorption to describe the temperature influence on water retention curve in high suction range. The model is then applied to the experimental

results of several high plasticity clays to validate its capability. Comparison between the model and typical capillary-based models is finally presented.

2 MODEL FORMULATION

The soil suction for water retention curve in high suction range commonly refers to the "total suction", rather than the "matric suction" in low suction range. The total suction can be defined in terms of the partial vapour pressure of soil water by the following thermodynamic relationship (Fredlund & Rahardjo 1993):

$$\Psi = -\frac{RT\rho_w}{M_w}\ln\left(\frac{p_v}{p_{vs}}\right) \tag{1}$$

where Ψ = total suction; R = universal gas constant; T = absolute temperature; ρ_w = water density; M_w = molecular mass of water; p_v = partial vapour pressure of soil water; and p_{vs} = saturated vapour pressure of pure free water at the same temperature.

In high suction range, water vapour can be directly absorbed on the mineral surface of soil. When the high suction equilibrium is reached, the phase equilibrium between water vapour and absorbed water is also established. From the point of view of adsorption science, the water retention in high suctions can regarded as a process of gas-phase adsorption.

When water vapour is absorbed on the mineral surface, the freedom of the motion of water molecule reduces from three dimensional motion in gas phase to two dimensional motion around the mineral surface. This reduction of the degree of freedom indicates the entropy of water decreases after absorbed on the mineral surface, i.e. the adsorption entropy of water vapour on soil is negative. The adsorption heat of water vapour on soil can be calculated in terms of the adsorption entropy using the following thermodynamic relationship (Hu 2007):

$$\Delta H = T\Delta S \tag{2}$$

where ΔH = adsorption heat (positive for an endothermic process); and ΔS = adsorption entropy. For the adsorption of water vapour on soil, $\Delta S < 0$ and $T > 0$, thus $\Delta H < 0$, i.e. the adsorption of water vapour on soil is an exothermic process. According to the Le Chatelier's principle, the increase of temperature spontaneously suppresses the forward of an exothermic process. Therefore, the adsorption of water vapour on soil will definitely be restrained when the temperature increases, i.e. the water retention capability in high suction will definitely reduce with the increase of temperature. Available experimental results consist with the thermodynamic interpretation.

Applying the Clausius-Clapeyron Equation in thermodynamics (Hu 2007) to the adsorption of water vapour on soil, we have:

$$\left.\frac{\partial p_v}{\partial T}\right|_{dw=0} = -\frac{\Delta H_m p_v}{RT^2} \tag{3}$$

where ΔH_m = differential adsorption heat of water vapour on soil (different from the integral adsorption heat). The left side of the above equation refers to the variation of the partial vapour pressure of soil water p_v with temperature at constant water content, and the variation can be related to the differential adsorption heat ΔH_m according to the equation. Analogously, applying the Clausius-Clapeyron Equation to the gas-liquid phase transition of pure free water, we have:

$$\frac{\mathrm{d}p_{vs}}{\mathrm{d}T} = -\frac{\Delta H_m^{sat} p_{vs}}{RT^2} \tag{4}$$

where ΔH_m^{sat} = differential condensation heat of pure free water. The saturated vapour pressure of pure free water p_{vs} mainly depends on the temperature, and the dependence can be related to the differential condensation heat ΔH_m^{sat} by Equation 4.

For Equation 1, we can take the partial derivative of the suction Ψ with respect to the temperature T at constant water content. This yields:

$$\left.\frac{\partial \Psi}{\partial T}\right|_{dw=0} = \frac{\Psi}{T} + \frac{\Psi}{\ln\left(p_v/p_{vs}\right)}\left(\frac{1}{p_v}\left.\frac{\partial p_v}{\partial T}\right|_{dw=0} - \frac{1}{p_{vs}}\frac{\mathrm{d}p_{vs}}{\mathrm{d}T}\right) \tag{5}$$

The left side of the above equation refers to the variation of suction with temperature at constant water content, and by the equation it can be related to the variation of the partial vapour pressure p_v with temperature at constant water content and the variation of saturated vapour pressure p_{vs} with temperature. Thus, substituting Equation 3 and 4 into Equation 5, we have:

$$T\left.\frac{\partial \Psi}{\partial T}\right|_{dw=0} = \Psi + \frac{\rho_w}{M_w}\left(\Delta H_m - \Delta H_m^{sat}\right) \tag{6}$$

The temperature effects on ρ_w, ΔH_m and ΔH_m^{sat} that appeared on the right side of the above equation are generally not remarkable in the temperature range of geotechnical and geoenvironmental engineering (Dean 1999, Hu 2007, Jacinto et al. 2011). If we assume that ρ_w, ΔH_m and ΔH_m^{sat} are independent of temperature, then the right side of Equation 6 becomes to depend only on the suction Ψ, i.e.,

$$T\left.\frac{\partial \Psi}{\partial T}\right|_{dw=0} = f\left(\Psi\right) \tag{7}$$

where $f(\Psi)$ is an arbitrary function of Ψ.

As mentioned in the INTRODUCTION, experimental results commonly show that water retention curves at different temperatures are approximately parallel to each other when plotted in the semi-log coordinate with suction in logarithmic form. This can yield the following equation:

$$\frac{1}{\Psi}\left.\frac{\partial \Psi}{\partial T}\right|_{dw=0} = g\left(T\right) \tag{8}$$

where $g(T)$ is an arbitrary function of T. The left side of Equation 7 refers to the variation of Ψ in logarithmic scale with temperature at constant water content, and it is independent of the suction Ψ due to the parallelism of water retention curves at different temperatures in the semi-log coordinate.

Combining Equation 7 and 8, we have:

$$\frac{1}{\Psi} f(\Psi) = T \cdot g(T) \tag{9}$$

The left side of the above equation only depends on the suction Ψ, while the right side only depends on the temperature T. If the equation can hold, the left and right side must equal to a same constant, i.e.,

$$\frac{1}{\Psi} f(\Psi) = T \cdot g(T) = \xi \tag{10}$$

where ξ is a constant. Substituting Equation 10 into Equation 7 or 8, we have:

$$\frac{1}{\Psi} \frac{\partial \Psi}{\partial T}\bigg|_{dw=0} = \frac{\xi}{T} \tag{11}$$

which exactly is a model for the temperature influence on water retention curve in high suction range, and can describe the variation of total suction with temperature at constant water content using a single parameter ξ. Integrating Equation 11, we have:

$$\left(\frac{\Psi_i}{\Psi_0}\right) = \left(\frac{T_i}{T_0}\right)^{\xi} \tag{12}$$

where T_0 = reference temperature; T_i = current temperature; Ψ_0 = total suction for a given water content at the reference temperature; Ψ_i = total suction for the same given water content at the current temperature.

If we know the function of water retention curve at the reference temperature, which can be expressed in general form as follows:

$$w_{T_0} = w_0(\Psi) \tag{13}$$

then the water retention curve at the current temperature can be easily determined by substituting Equation 12 into Equation 13, i.e.,

$$w_T = w_0\left[\Psi\left(T_0/T\right)^{\xi}\right] \tag{14}$$

As discussed above, the water retention capability reduces with the increase of temperature, which means at constant water content the suction decreases with the increase of temperature. Hence, the parameter ξ in Equation 11 or 12 must be negative. As shown in Figure 1, the value of Ψ/Ψ_0 decreases more rapidly at larger absolute value of the parameter ξ, i.e. the temperature influence on the water retention curve is more notable at larger absolute value of the parameter ξ.

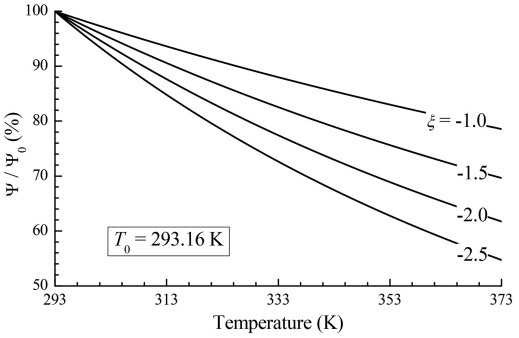


Figure 1. Variation of Ψ/Ψ_0 with temperature at different values of ξ.

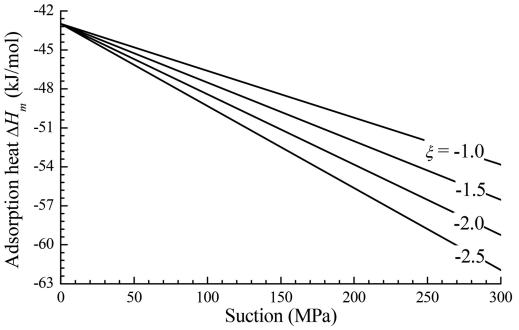


Figure 2. Variation of adsorption heat ΔH_m with suction at different values of ξ.

The parameter ξ is relevant to the adsorption heat of water vapour on soil. By substituting Equation 11 into Equation 6, the adsorption heat ΔH_m can be expressed in terms of the parameter ξ as follows:

$$\Delta H_m = \frac{(\xi - 1) M_w \Psi}{\rho_w} + \Delta H_m^{sat} \tag{15}$$

Because of the heat taken positive for an endothermic process, ΔH_m and ΔH_m^{sat} in the above equation both are of negative values. Under the same suction, the absolute value of the adsorption heat ΔH_m is higher for larger absolute value of the parameter ξ, as shown in Figure 2. Taking into account the relationship between the parameter ξ and the temperature dependence of water retention curve, it can be inferred that, if the temperature influence on water retention curve in high suction range is more notable, more heat will be released for the transition from water vapour to the absorbed water on soil.

In the thermo-hydro-mechanical analysis of the engineered barriers for radioactive waste isolation, the heat of phase transition between water vapour and the absorbed liquid water is generally incorporated as a heat source that can affect the temperature distribution (Qin et al. 2010). The heat actually is the adsorption heat ΔH_m in this paper. In literature, the heat is commonly considered to equal to the condensation heat or

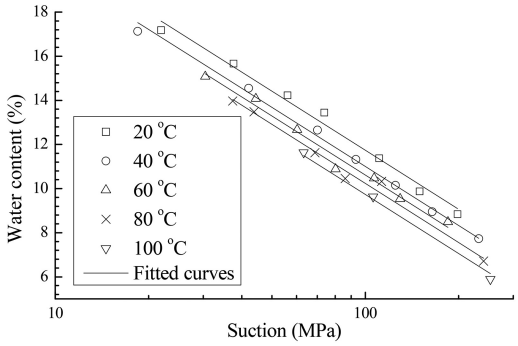


Figure 3. Test results of the water retention curves of GMZ bentonite at different temperatures.

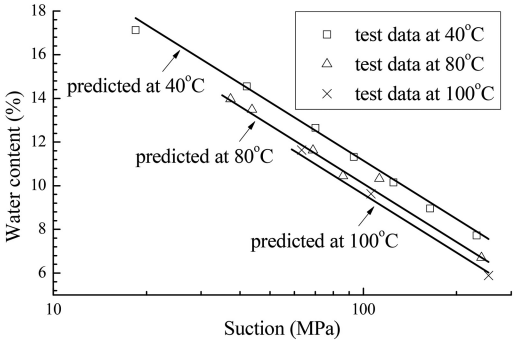


Figure 4. Comparison between measured and predicted results of GMZ bentonite.

the evaporation heat of pure free water, ignoring the effect of suction on the heat. According to Equation 15, when $\Psi = 0$ corresponding to the state of pure free water, $\Delta H_m = \Delta H_m^{sat}$. When the suction Ψ increases, the absolute value of ΔH_m grows as shown in Figure 2, i.e., more heat in the transition between water vapour and the absorbed water is involved at higher suctions. This is consist with the fact that the soil-water interaction is stronger at high suctions.

3 MODEL VERIFICATION

3.1 *Model verification on GMZ bentonite*

GMZ bentonite is the Chinese candidate buffer/backfill material for the geological disposal of high level radioactive waste. It is a natural Na-bentonite with a high content of montmorillonite more than 70%. Using the vapour equilibrium technique to control high suction, Qin et al. (2012) studied the water retention curves of GMZ bentonite at 20, 40, 60, 80 and 100°C (see Figure 3). Select 20°C as the reference temperature, and the water retention curve at 20°C can be fitted by:

$$w_{20} = a_0 \ln \Psi + c_0 \tag{16}$$

where $a_0 = -3.86$; and $c_0 = 29.51$. Combining Equations 14 and 16, the water retention curves at other temperatures can be expressed by:

$$w_T = a_0 \ln \Psi - a_0 \xi \ln\left(T/T_0\right) + c_0 \tag{17}$$

The parameter ξ can be obtained by fitting the water retention curve at any another temperature according to Equation 17. Here, the test data at 60°C is used, and $\xi = -2.27$. Then, the water retention curve at 40, 80 and 100°C can be predicted using Equation 17 with $\xi = -2.27$. As shown in Figure 4, the prediction results are in good agreement with the test results.

3.2 *Model verification on MX-80 bentonite*

MX-80 bentonite is a commercial Na-bentonite from Wyoming, with the content of montmorillonite ranging from 65% to 82%. By directly measuring the total suction at different water content using capacitive humidity sensor, Jacinto et al. (2009) studied the water retention curve of MX-80 bentonite at 40, 60, 80 and 100°C. Only the test results at dry density of 1.75 g/cm^3 are analysed here. The obtained water retention curves of the MX-80 bentonite of 1.75 g/cm^3 at 40 and 100°C can be fitted using the following equations, respectively:

$$w_{40} = -7.45 \ln \Psi + 44.50 \tag{18}$$

$$w_{100} = -7.45 \ln \Psi + 41.45 \tag{19}$$

Selecting 40°C as the reference temperature and combing the Equations 17, 18 and 19, we can obtain $\xi = -2.33$. Utilizing Equations 17 and 18 and inserting $\xi = -2.33$, the water retention curves at 60 and 80°C can be predicted as shown in Figure 5, which agree well with the test data.

Based on the same test results, the integral adsorption heats of water on the MX-80 bentonite at different water contents were analysed by Jacinto et al. (2011) using solution thermodynamics (see Figure 6). If we integrate Equation 6 under constant water content and insert Equation 12, the integral adsorption heat of water on soil $\Delta_I H_m$ can be related to the parameter ξ by the following expression:

$$\Delta_I H_m = -\frac{M_w}{\rho_w} \frac{\Delta\left[\dfrac{\Psi_0}{T}\left(\dfrac{T}{T_0}\right)^{\xi}\right]}{\Delta\left(\dfrac{1}{T}\right)} + \Delta_I H_m^{sat} \tag{20}$$

where $\Delta_I H_m^{sat}$ = integral condensation heat of pure free water. By substituting $\xi = -2.33$ into the above equation and relating Ψ_0 in the above equation to water content according to Equation 18, the integral adsorption heat of water on MX-80 bentonite can be predicted in terms of water content. As shown in Figure 6, the prediction is also in good agreement with the result of Jacinto et al. (2011).

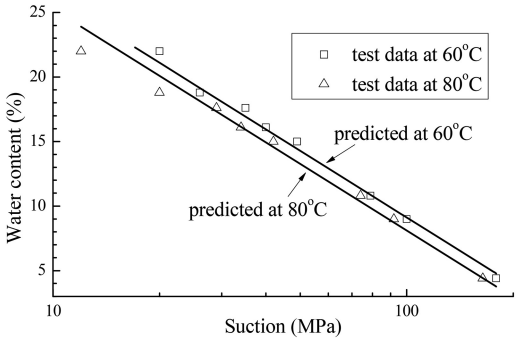


Figure 5. Comparison between measured and predicted results of MX-80 bentonite.

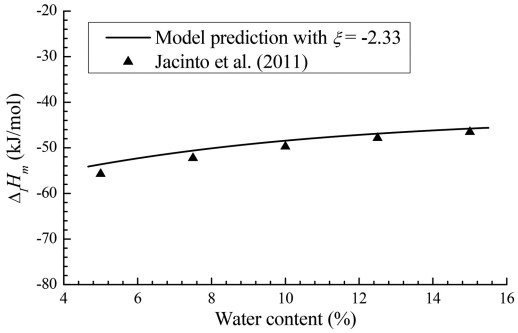


Figure 6. Comparison of adsorption heat between reported by Jacinto et al. (2011) and model predictions.

4 COMPARISON WITH CAPILLARY-BASED MODELS

The Philip – de Vries model (1957) and the Grant – Salehzadeh (1996) are the most widely used capillary-based models for the temperature influence on water retention curve. In the Philip – de Vries model, only the thermal effect on surface tension of pure free water is considered, and it can be expressed as:

$$\frac{\varphi_i}{\varphi_0} = \frac{\sigma_{sT}}{\sigma_{s0}} \tag{21}$$

where ϕ_0 = matric suction for a given volumetric water content at the reference temperature; ϕ_i = matric suction for the same given volumetric water content at the current temperature; σ_{s0} = surface tension at the reference temperature; and σ_{sT} = surface tension at the current temperature.

The Grant – Salehzadeh model can be given in the following form:

$$\frac{\varphi_i}{\varphi_0} = \frac{\beta + T_i}{\beta + T_0} \tag{22}$$

where the parameter β can reflect the thermal effect on the contact angle.

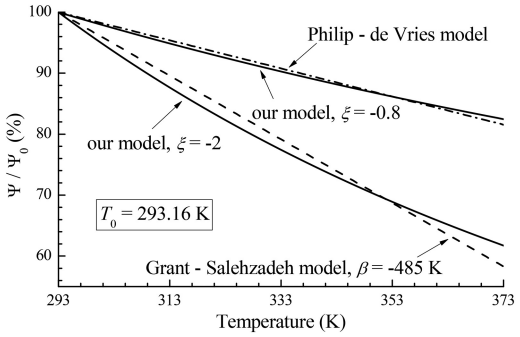


Figure 7. Variations of Ψ/Ψ_0 with temperature corresponding to different models.

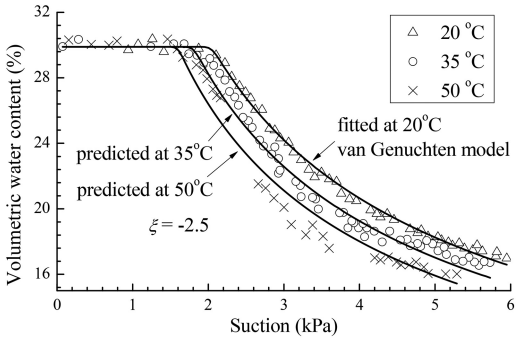


Figure 8. Comparison between measured and predicted results in the low suction range for Plainfield sand.

Obviously, the physical meaning of our model is different from the above two capillary-based models. Our model is established based on the adsorption of water on soil surface, not on the conventional capillary model. In the strict sense, our model applies only to the change of total suction with temperature in high suction range at constant gravimetric water content, while the two capillary-based models apply only to the change of matric suction with temperature in low suction range at constant volumetric water content.

Comparison of our model with the capillary-based models can be made from the perspective of mathematics, without taking the physical meanings into account, and neglecting the distinction between the constant gravimetric and volumetric water content and the distinction between total and matric suction. The values of Ψ/Ψ_0 (or ϕ/ϕ_0) corresponding to different models are compared in Figure 7. When $\xi = -0.8$, our model gives similar results to the Philip – de Vries model. If the parameters ξ and β are set to compatible values, e.g. $\xi = -2$ and $\beta = -485$ K in Figure 7, similar results can be also obtained by our model and the Grant – Salehzadeh model. Therefore, in the mathematical sense the application of our model to the low suction range is acceptable, without considering the physical basis of model.

The application of our model to the low matric suction range is conducted using the result of Plainfield

sand (Nimmo & Miller 1986). Select 20°C as the reference temperature, and the water retention curve at 20°C can be fitted using the van Genuchten model (1980). Substituting the fitted function at 20°C and $\xi = -2.5$ into Equation 14, gives the prediction of water retention curves at 35 and 50°C. As shown in Figure 8, the prediction still agrees well with the experimental result.

5 CONCLUSIONS

Based on the adsorption of water on soil, it is point out that the water retention capability in high suction definitely reduces with the increase of temperature, and a model for the temperature influence on water retention curve in high suction range is proposed. Only a single parameter is contained that can be related to the adsorption heat of water on soil. The capability of the model is validated using experimental data on GMZ bentonite and MX-80 bentonite, and it is also shown that the model can be applied to the low suction without considering the physical meanings.

ACKNOWLEDGEMENT

This work was supported by the National Natural Science Foundation of China (Nos. 11272353) and the Foundation of Fundamental Science on Nuclear Wastes and Environmental Safety Laboratory (Nos. 13zxnk03).

REFERENCES

Chahal, R.S. 1965. Effect of temperature and trapped air on matric suction. *Soil Science* 100(4): 262–266.

Dean, J. 1999. *A. Lange's handbook of chemistry, 15th edition*. New York: McGraw-Hill.

Fredlund, D.G. & Raharajo, H. 1993. *Soil mechanics for unsaturated soil*. New York: John Wiley & Sons, Inc.

Gardner, R. 1955. Relation of temperature to moisture tension of soil. *Soil Science* 79: 257–265.

Grant, S.A. & Salehzadeh, A. 1996. Calculation of temperature effects on wetting coefficients of porous solids and their capillary pressure functions. *Water Resources Research* 32(2): 261–270.

Haridasan, M. & Jensen, R.D. 1972. Effect of temperature on pressure head-water content relationship and conductivity of two soils. *Soil Science Society of America Journal* 36(5): 703–708.

Hopmans, J.W. & Dane, J.H. 1986. Temperature dependence of soil water retention curves. *Soil Science Society of America Journal* 50: 562–567.

Hu, Y. 2007. *Physical Chemistry*. Beijing: Higher Education Press. (in Chinese).

Imbert, C., Olchitzky, E., Lassabatère, T., et al. 2005. Evaluation of a thermal criterion for an engineered barrier system. *Engineering Geology* 81: 269–283.

Jacinto, A.C., Villar, M.V., Gómez-Espina, R., et al. 2009. Adaptation of the van Genuchten expression to the effects of temperature and density for compacted bentonites. *Applied Clay Science* 42: 575–582.

Jacinto, A.C., Ledesma, A., Villar, M.V., et al. 2011. Influence of temperature on the water retention capacity of soils analysis using solution thermodynamics. In Alonso, E. & Gens, A. (eds), *Proceedings of the 5th International Conference on Unsaturated Soils*: 555–560. London: Taylor & Francis Group.

Lange, N.A. 1961. *Handbook of chemistry, 10th edition*. New York: McGraw-Hill.

Liu, H.H. & Dane, J.H. 1993. Reconciliation between measured and theoretical temperature effects on soil water retention curves. *Soil Science Society of America Journal* 57: 1202–1207.

Lloret, A., Romero, E., Villar, M.V. 2004. *FEBEX II Project: Final report on thermo-hydro-mechanical laboratory tests*. Madrid: Publicación Técnica ENRESA.

Nimmo, J.R. & Miller, E.E. 1986. The temperature dependence of isothermal moisture vs. potential characteristics of soils. *Soil Science Society of America Journal* 50: 1105–1113.

Peck, A.J. 1960. Change of moisture tension with temperature and air pressure: theoretical. *Soil Science* 89(6): 303–310.

Philip, J.R. & De Vries, D.A. 1957. Moisture movement in porous materials under temperature gradients. *Transaction, American Geophysical Union* 38(2): 222–232.

Qin, B., Chen, Z.H., Fang, Z.D., et al. 2010. Analysis of coupled thermo-hydro-mechanical behavior of unsaturated soils based on theory of mixtures I. *Applied Mathematics and Mechanics (English Edition)* 31(12): 1561–1576.

Qin, B., Chen, Z.H., Sun, F.X., et al. 2012. Temperature effect on water retention curve in high suction range and its modeling based on thermodynamics of sorption. *Chinese Journal of Geotechnical Engineering* 34(10): 1877–1886.

Romero, E., Gens, A., Lloret, A. 2001. Temperature effects on the hydraulic behaviour of an unsaturated clay. *Geotechnical and Geological Engineering* 19: 311–332.

Salager, S., El Youssoufi, M.S., Saix, C. 2010. Effect of temperature on water retention phenomena in deformable soils: theoretical and experimental aspects. *European Journal of Soil Science* 61: 97–107.

She, H.Y. & Sleep, B.E. 1998. The effect of temperature on capillary pressure-saturation relationships for air-water and perchloroethylene-water systems. *Water Resources Research* 34(10): 2587–2597.

Tang, A.M. & Cui, Y.J. 2005. Controlling suction by the vapour equilibrium technique at different temperatures and its application in determining the water retention properties of MX80 clay. *Canadian Geotechnical Journal* 42: 287–296.

van Genuchten, M. Th. 1980. A closed form equation predicting the hydraulic conductivity of unsaturated soils. *Soil Science Society of America Journal* 44: 892–898.

Wilkinson, G.E. & Klute, A. 1962. The temperature effect on the equilibrium energy status of water held by porous media. *Soil Science Society of America Journal* 26(4): 326–329.

Ye, W.M., Wan, M., Chen, B., et al. 2009. Effect of temperature on soil-water characteristics and hysteresis of compacted Gaomiaozi bentonite. *J. Cent. South Univ. Technol.* 16: 821–826.

Unsaturated Soil Mechanics—from Theory to Practice – Chen et al. (Eds)
© 2016 Taylor & Francis Group, London, ISBN 978-1-138-02921-7

Evaluation of Soil-Water Characteristic Curves of sand-cement mixtures

A.O. Al Shenawy & S.H. Al-hadama
Civil Engineering Department, King Saud University, Riyadh, Saudi Arabia

T.Y. Elkady
Engineering Abdullah Bugshan Research Chair in Expansive Soils, Civil Engineering Department, King Saud University, Riyadh, Saudi Arabia
Public Works Department, Faculty of Engineering, Cairo University, Giza, Egypt

ABSTRACT: Sand-cement mixtures are typically used as subgrade for pavement and in embankment construction. In these applications, mixtures are typically unsaturated. Soil water characteristic curve is considered as a useful tool to understand the unsaturated behavior of these mixtures and provide information on the pore size distribution. This study aims at evaluating the dry soil water characteristic curves (SWCC) of soil-cement mixtures. The effect of cement content (3%, 6%, 9%, and 12% by dry weight of sand) and curing period (7 and 28 days) on the parameters of soil water characteristic curves were demonstrated. Test was performed using axis translation technique for suctions levels up to 1500 kPa. Test results revealed that the cement content had a significant effect on the air entry value and saturation water content; while had a negligible effect on the residual water content. In addition, the curing period had a negligible effect on SWCC parameters for cement content less than 6 %. As the cement content increases beyond 6%, the effect of curing period was more pronounced.

1 INTRODUCTION

Compacted soil-cement mixtures have been successfully used in many geotechnical applications such as subgrade for pavement, embankment construction and slope protection (Porbaha et al. 1998; Consoli et al. 2009a, 2009b, 2010). The addition of cement to soil causes the development of bonds between soil grains resulting in increase in shear strength and high resistance to wet and dry cycles. In the field, the soil-cement layer is generally unsaturated. Furthermore, these layers may undergo changes in moisture content due to exposure to climatic conditions (e.g., rain, temperature) or operational conditions (e.g. fluctuations in water levels in channel slope protection application). For this reason, better interpretation of the hydraulic and mechanical behavior of sand-cement mixtures can be performed using principles of unsaturated soil mechanics.

In the framework of unsaturated soil mechanics, soil suction is considered as one of the stress state variables that control the behavior of expansive soils. The SWCC defines the relationship between soil suction and water content (whether gravimetric, volumetric or degree of saturation). Engineering properties of unsaturated soil such as hydraulic conductivity and shear strength parameters were proved to be related to soil suction which in turn is related to soil water characteristic curve (SWCC) (Van Genuchten 1980; Fredlund et al. 1993, 1995, 2000; Vanapalli et al. 1996a,1996b; Barbour 1998). In spite of the above notion, limited research was conducted to evaluate the SWCC of cement stabilized soils (Kererat 2012; Hoyos et al. 2007).

This study aims at evaluating the drying soil water characteristic curves (SWCC) of sand-cement mixtures using pressure plate extraction test. Parameters investigated included cement content (3%, 6%, 9%, and 12% by dry weight of sand) and curing period (7 and 28) days.

2 MATERIALS AND METHODS

This section provides information on materials and equipment used in this study. Furthermore, testing procedures conducted to evaluate the SWCC of sand-cement mixtures were described.

2.1 *Material used*

The sand used in this study was obtained from Thumama area located at a distance of 60 km to north of the city of Riyadh, the capital of Saudi Arabia. The grain size distribution of the sand is shown in Figure 1. A summary of geotechnical properties are shown in Table 1. This sand is classified as poorly-graded sand (SP) according to the Unified Soil Classification System (ASTM D 2487-06).

Ordinary Portland cement (OPC – type-I) manufactured locally was used as the cementing agent in the

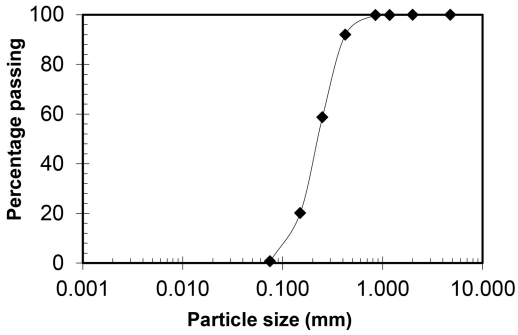


Figure 1. Grain-size distribution curve of sand.

Table 1. Geotechnical characteristics of sand.

Property	Value
D_{50} (mm)	0.22
Gravel %	0
Sand %	99.25
Passing sieve #200, %	0.75
Specific gravity	2.61
Uniformity coefficient	2.36
Coefficient of curvature	1.26
Classification Poorly graded sand (SP)	

study. The specific gravity of the cement grains was 3.12.

2.2 *Specimen preparation*

The weight of cement corresponding to the target cement content was added to the dry sand and hand mixed to obtain a homogeneous mixture. Target moisture content was then added to the mixture and mixed thoroughly to ensure uniform distribution of water. The mixture was immediately transferred to specially designed ring in order to statically compact the specimens to target dry unit weight with final dimensions of 63.5 mm in diameter and 16 mm high. The target dry unit weight and moisture content correspond to the maximum dry unit weight and optimum moisture content evaluated using standard compaction effort determined in accordance with ASTM D 698 (2002). Figure 2 shows the Compaction curves of different sand-cement mixtures as a function of cement content.

The compacted specimens with the ring are wrapped using plastic film and cured for 7 and 28 days in humid environment of relative humidity greater than 95%. At the end of the curing period, Specimens transferred to pressure plate device for SWCC evaluation.

2.3 *Soil water characteristic curves*

The drying curve of the SWCCs of sand-cement mixtures were evaluated using a pressure plate apparatus (axis translation technique). The ceramic disk and prepared specimens were subjected to saturation by

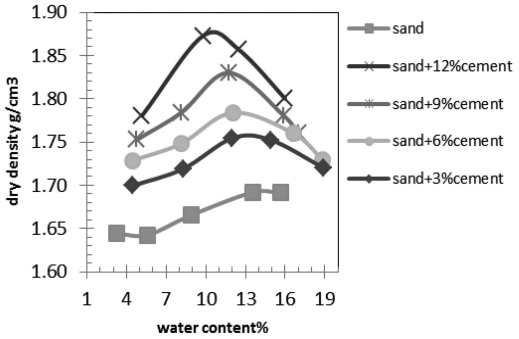


Figure 2. Compaction curves of different sand-cement mixture.

submerging in water. The saturated specimens are placed on the air-entry ceramic disk with high air entry value of 1.5 MPa in air pressure chamber. Air pressure (suction) was applied in accordance with (ASTM D 6836-02 Method C). Each suction increment was applied until equilibrium is reached. Equilibrium under each suction level was assumed to be attained when no water was observed to exit the pressure plate. After each suction application, the weight of the specimen was recorded.

After reaching equilibrium under maximum applied suction (i.e., 1.4 MPa), the specimens were oven dried for 24 hours at a temperature of 110°C for final water content determination. Water content at each suction increment was back calculated using final water content and the weight of specimen recorded after equilibrium.

3 RESULTS AND DISCUSSION

3.1 *Effect of cement content*

Figures 3 and 4 show the SWCC of sand and sand-cement mixtures; respectively. From these Figures, it is observed that the SWCC underwent significant change in shape and parameters. Comparison between Figures 4 and 3 revealed that the gravimetric water content at saturation decreased as the percentage of cement increased. For 3% cement, the gravimetric water content at saturation decreased by about 32% and 30% for 7 and 28 days curing periods; respectively, while at 12% cement, it decreased by 37% and 52% for 7 and 28 days curing period; respectively. The reduction in gravimetric water content with cement content is attributed to reduction in mixture pores size due to cement filling the pores of the sand grains and development of stronger bonds with sand particles.

Table 2 indicates that the air-entry value and residual suction were increased with increase in cement content. The boundary effect zone (between w_{sat} and air entry value) and transition zone (between the air entry value and residual water content) were enlarged. This could be attributed to the addition of cement to soil and it's above stated effects on the soil structure.

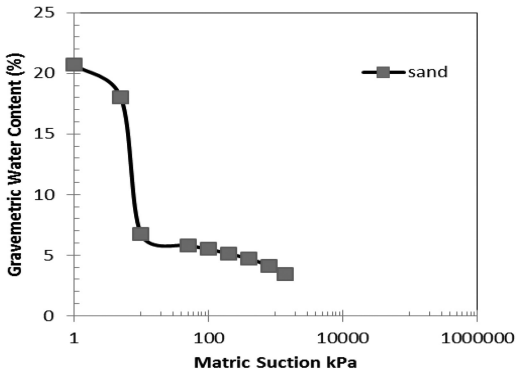


Figure 3. Soil water characteristic curves of sand.

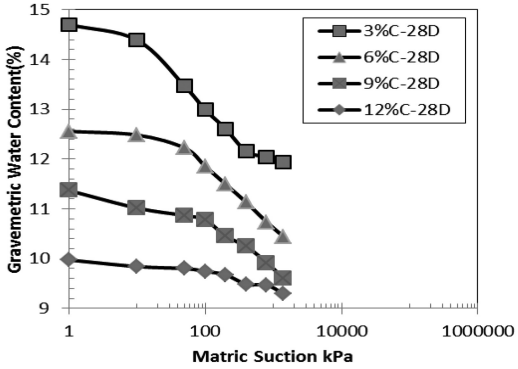


Figure 4. Soil water characteristic curves for sand-cement mixtures after 28 days curing.

Table 2. SWCC parameters for sand and sand cement mixtures.

Cement content	Curing time days	Air entry parameter w_{sat}* (%)	Air entry parameter Ψa* (KPa)	Residual parameter Wr* (%)	Residual parameter Ψr* (KPa)
Untreated	–	20.71	4	5.5	10
3%	7	14.01	9	11.5	400
	28	14.5	14	12	400
6%	7	13.7	23	11.9	500
	28	12.6	32	–	>1400
9%	7	13.3	28	11.9	600
	28	11.4	180	–	>1400
12%	7	13	50	12	600
	28	9.9	320	–	>1400

*w_{sat}: gravimetric saturation water content, Ψa: Suction corresponding to the air entry value, Wr: Residual water content, Ψr: Suction corresponding to the residual water content.

3.2 *Effect of curing period*

From Figures 5 through 8, it is observed that the as the curing period increases, the shape of the SWCCs changes. In other words, the air entry value increases

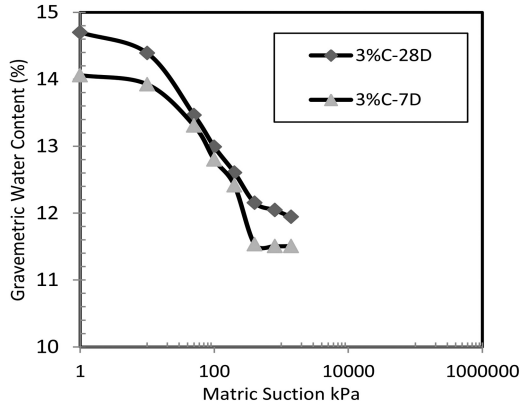


Figure 5. Effect of curing time on SWCC of sand cement mixture at 3% cement.

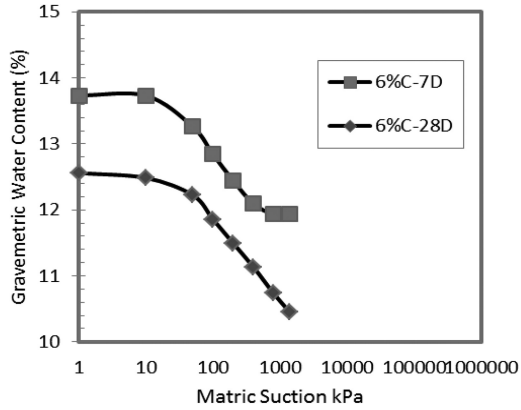


Figure 6. Effect of curing time on SWCC of sand cement mixture at 6% cement.

and the saturation water content increases. These changes are more pronounced for sand-cement mixtures with cement content equal to or greater than 6%. This is attributed to the hardening of the soil structure and decreasing of pores. Also, it was noted that there is a enlargement of SWCCs in boundary effect and transition zones with increase in curing time.

4 CONCLUSIONS

From the results of this study, the following conclusions can be summarized:

- The gravimetric water content at saturation for the sand cement mixture decreased with the increase in cement content and curing time.
- Air-entry value and residual suction increased with increase in cement content and curing time this effect was more pronounced when cement content is equal than or equal to 6% In addition, the boundary effect and transition zones were enlarged.
- The cement content had a negligible effect on the residual water content.

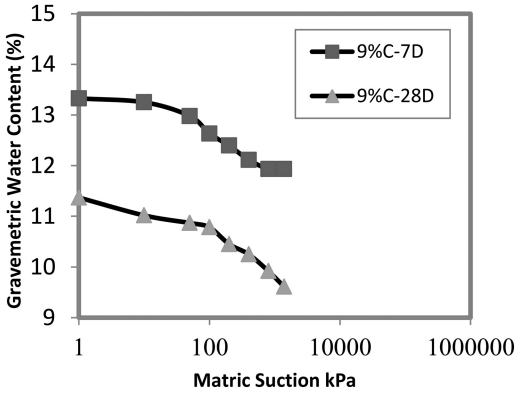


Figure 7. Effect of curing time on SWCC of sand cement mixture at 9% cement.

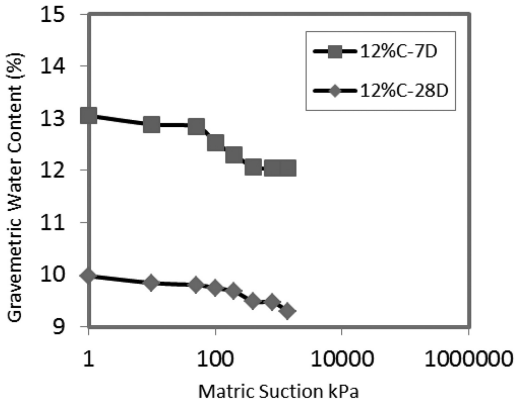


Figure 8. Effect of curing time on SWCC of sand cement mixture at 12% cement.

- The curing time had a significant effect on the trends of SWCC and their parameters for cement content greater than 6%.

REFERENCES

American Society for Testing and Materials (ASTM), (2002), "Standard Test Methods for Determination of the Soil Water Characteristic Curve for Desorption Using a Hanging Column, Pressure Extractor, Chilled Mirror Hygrometer, and/or Centrifuge1," Designation: D 6836 – 02, Annual Book of ASTM Standards, Vol. 4.08, D-18 *Committee on Soils and Rock, West Conshohocken, PA*, 1–19.

ASTM D698, (2002) Standard Test Methods Standard Test Methods for Laboratory Compaction Characteristics of Soil Using Standard Effort (12 400 ft lbf/ft^3 (600 kN m/m^3), Vol. 15.09, *Annual book of ASTM Standards, West Conshohocken, PA*.

ASTM, (2006a) "Standard classification of soils for engineering purposes." D 2487-06, *Philadelphia.*

Barbour, S. L. (1998). Nineteenth Canadian Geotechnical Colloquium: The soil-water characteristic curve: a historical perspective.*Canadian Geotechnical Journal*, 35(5), 873–894.

Consoli, N. C., Cruz, R. C., Floss, M. F., & Festugato, L. (2010). Parameters controlling tensile and compressive strength of artificially cemented sand. *Journal of geotechnical and geoenvironmental engineering,* 136(5), 759–763.

Consoli, N. C., Rosa, F. D., & Fonini, A. (2009a). Plate load tests on cemented soil layers overlaying weaker soil. *Journal of Geotechnical and Geoenvironmental Engineering*, 135(12), 1846–1856.

Consoli, N. C., Viana da Fonseca, A., Cruz, R. C., & Heineck, K. S. (2009b). Fundamental parameters for the stiffness and strength control of artificially cemented sand. *Journal of Geotechnical and geo-environmental Engineering*, 135(9), 1347–1353.

Fredlund, D. G., & Rahardjo, H. (1993). Soil mechanics for unsaturated soils. *John Wiley & Sons*.

Fredlund, D. G., Vanapalli, S. K., Xing, A., & Pufahl, D. E. (1995). Predicting the shear strength function for unsaturated soils using the soil-water characteristic curve. *In First International Conference on Unsaturated Soils, Paris, France*, pp. 6–8.

Fredlund, M. D., Fredlund, D. G., & Wilson, G. W. (2000). An equation to represent grain-size distribution. *Canadian Geotechnical Journal*, 37(4), 817–827.

Hoyos, L.R., Thudi, H.R., Puppala, A.J. (2007). Soil-water retention properties of cement treated clay. In: Proceedings of Sessions of Geo-Denver. *Congress: Problematic Soils and Rocks and In Situ characterization, Geotechnical Special Publication.* vol. 162, pp. 4–11.

Kererat, C. (2012) Test study on soil water characteristic curve (SWCC) of sandy soil-cement-bentonite mixtures. *International Science, Social Science, Engineering and Energy Conference*, 607–615.

Porbaha, A., Tanaka, H., & Kobayashi, M. (1998). State of the art in deep mixing technology: *part II. Applications. Proceedings of the ICE-Ground Improvement*, 2(3), 125–139.

Van Genuchten, M. T. (1980). A closed-form equation for predicting the hydraulic conductivity of unsaturated soils. *Soil science society of America journal*, 44(5), 892–898.

Vanapalli, S. K., Fredlund, D. G., & Pufahl, D. E. (1996a). The relationship between the soil-water characteristic curve and the unsaturated shear strength of a compacted glacial till. *Geotechnical Testing Journal*, 19, 259–268.

Vanapalli, S. K., Fredlund, D. G., Pufahl, D. E. & Clifton, A. W.(1996b). "Model for the prediction of shear strength with respect to soil suction." *Canadian Geotechnical Journal*, 33, 379–392.

Unsaturated Soil Mechanics—from Theory to Practice – Chen et al. (Eds)
© 2016 Taylor & Francis Group, London, ISBN 978-1-138-02921-7

Study on the absorbed suction of unsaturated soil based on the Horsfield close packing model

L.S. Tang
Guangdong Province Key Laboratory of Geological Processes and Mineral Resources, Guangzhou, Guangdong, China

Y.L. Sun, Z.W. Deng & H.T. Sang
Sun Yat-Sen University, Guangzhou, Guangdong, China

ABSTRACT: Based on the accumulation model, the intergranular suction theory of unsaturated soil is well developed with the typical accumulation of equal-sized particles, however, the studies on the unsaturated soil of unequal-sized particles don't receive much attention. In this paper, with the fractal theory, through the theoretical derivation, the expression of absorbed suction for the unequal-sized particles in Horsfield close packing is built. A series of tests are carried out to verify the theoretical calculation formula, and the tests results show that the established theoretical calculation formulas can reflect the main characteristics of the absorbed suction. With the water content increasing, the absorbed suction first increases and then decreases, near the optimum water content, the absorbed suction is largest, which successfully explain that the strength of unsaturated soil first increases and then decreases in a certain range of water content with the water content increasing. The relationship between the absorbed suction and dry density shows that the absorbed suction increases in the low water content and decreases in the high water content with the dry density increasing.

1 INTRODUCTION

Nowadays, most intergranular suction theories are based on the typical accumulation of equal particles, (Orr et al., 1975; De & Rigole, 1982; Lian et al., 1993; Rabinovich et al., 2005; Megias & Gauckler, 2010) studied the capillary force of the liquid bridge between two equal smooth sphere particles, (Gröger et al., 2003; Molenkamp & Nezomi, 2003) studied the capillary force of the liquid bridge between two equal coarse sphere particles. (Tang & Wang, 2000) established the concept of absorbed suction, (Zhang et al., 2012) carried on the systematic studies on the absorbed suction between the equal particles, he deduced the quantitative calculation formula of the absorbed suction in the six-party close packing, the quartet loose accumulation and any accumulation conditions. The above studies are based on the equal-sized particles accumulation way. However, the studies on the unsaturated soil of unequal-sized particles don't receive much attention.

Actually the soil particles are often unequal, even the equal particles are rare. And aimed at the unequal particles studies, there are not more researches only based on two different sizes sphere particles (Mehrotra & Sastry, 1980, 1985), even there are few researches based on more different sizes sphere particles. Therefore, it is necessary to study the absorbed suction based on close packing way of unequal particle diameters.

In this paper, based on the Horsfield close packing model of Powders mechanics and Foundation Engineering, with the fractal theory, through the theoretical derivation, the absorbed suction expression of unequal-sized particles in Horsfield close packing is built. A series of tests are carried out to verify the theoretical calculation formula, and the tests results showed that the established theoretical calculation formula can reflect the main characteristics of the absorbed suction. The research will make theoretical calculation formula for the absorbed suction of unsaturated soil to be more accord with the actual situation of soil.

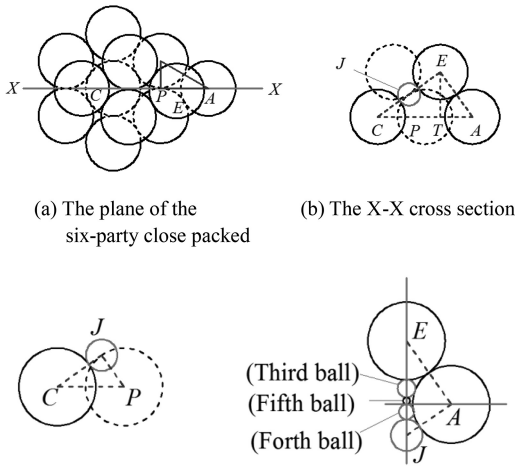
2 TYPICAL PACKING MODEL OF UNEQUAL PARTICLE DIAMETERS

2.1 *Horsfield close packing model*

In the Horsfield close packed model (Willett et al., 2000), the particles are assumed as sphere. The first ball radius R_1 are accumulated in the six-party closest way, which forms the main frame shown in Figure 1(a), the porosity n of the system is 25.94%. Figure 1(a) shows that the shape and size between the particles gap are regular and there are two forms including four angles holes surrounded by six balls and triangle holes surrounded by four balls. Assuming the basic uniform ball as the first ball (radius is R_1), filling as large as the

third ball (radius is R_3) in the four angles holes, filling as large as the second ball (radius is R_2) in the triangle holes, showing in Figure 1(b, c), it is calculated that $R_2 = 0.414\,R_1, R_3 = 0.225\,R_1$. Fill the forth ball (radius is R_4) and fifth ball (radius is R_5) in the gap between the second ball and third ball, showing in Figure 1(b, c, d), it is calculated that $R_4 = 0.177\ R_1$, $R_3 = 0.116\ R_1$. In accordance with this filling way, finally the remnants gap is filled with the minimum equal radius balls in the six-party close packing form. The Horsfield close packed way is formed, which is shown in Figure 1, the packed parameters are shown in Table 1.

According to the powders mechanics, foundation engineering and crystal mineralogy, the contact points number between single particle and other particles around are characterized by the particle coordination number Nc. The coordination number Nc is concerned with the packed way and the arrangement of the soil particles. According to the packed properties of the Horsfield model and the contact points of the various spheres, the average coordination number of model can be obtained, $\overline{N}_c = 18.6$.



(a) The plane of the six-party close packed

(b) The X-X cross section

(c) The left of the X-X cross section

(d) The right of the X-X cross section

Figure 1. Schematic of Horsfield Stacking Model.

2.2 *The fractal coefficient of Horsfield packing*

In 1975, the French scientist named Mandelbrot put forward the concept of fractal, which was used to study the chaotic phenomena and behaviors of the nature. Soil is composed with a series of soil particles. The particle composition can be expressed with the theory of fractal dimension (Fredlund & Morgenstem, 1996). The fractal dimension of the particle radius distribution is greater, which explains that the content of the fine particles is higher, the coarse particles content is lower. The fractal dimension of the particle radius distribution is lower, which explains that the content of fine particles is lower, the content of the coarse particles is higher. According to the existing literatures (NG et al., 2003; Tao & Zhang, 2009), the particles composition can be characterized by the fractal dimension, where the particles radius are greater than R, the probability distribution satisfies the following formula:

$$P(\geq R) = \int_R^{\infty} p(R)dR = kR^{-D} \tag{1}$$

where R is particle radius, $P(\geq R)$ is the probability that the particle radius is greater than R, $p(R)$ is the distribution density function of the particles radius, k is the proportionality coefficient, D is the fractal dimension.

The fractal dimension D can be calculated based on the distribution density function and the soil test results of the particle size analysis. In double logarithmic coordinates, the accumulation line $lgm(R)$-$lg(R)$ of the particles size analysis exists a straight line segment, which suggests that the soil particle size distribution possesses the fractal structure (Fredlund & Morgenstem, 1996). The fractal dimension can be determined with the following formulas:

$$D = 3 - b \tag{2}$$

$$b = \frac{\lg m(R_1) - \lg m(R_2)}{\lg R_1 - \lg R_2} \tag{3}$$

where b is the slope of line segment of the particles accumulation line in the double logarithmic coordinates, $lgm(R_1)$, $lgm(R_2)$ are respectively the particles accumulation percentage where the particles diameter are respectively less than R_1 and R_2.

Table 1. Structure of Horsfield stacking model.

Sequence	Radius	No.	Deposition rate	Porosity n	Contact points N_{ij}
First ball	R_1	8	74.1	25.9	$N_{11} = 20$
Second ball	$R_2 = 0.414R_1$	1	79.3	20.7	$N_{21} = 6$
Third ball	$R_3 = 0.225R_1$	2	81.0	19.0	$N_{31} = 8$
Forth ball	$R_4 = 0.177R_1$	8	84.2	15.8	$N_{41} = 26$, $N_{42} = 6$
Fifth ball	$R_5 = 0.116R_1$	8	85.1	14.9	$N_{53} = 8$, $N_{54} = 24$
……	minimum	maximum	96.1	3.9	……

Notes: The "minimum" and "maximum" are relative concepts, however, it is difficult to achieve close packed in reality. So in this article, it is only calculated to the fifth ball.

2.3 *Contact points per unit area*

Taking the unit volume of the soil as the research object, the soil particle is assumed as sphere. The total number of the particles is N_0, so the particle number of the certain particles diameter range dR is $p(R)dR \cdot N_0$, the volume V_R of the single particle is $\pi r^3/6$, so the volume dV_s of $p(R)dR \cdot N_0$ particles is calculated as follows:

$$dV_s = \frac{1}{6}\pi R^3 \cdot N_0 \cdot p(R)dR \tag{4}$$

Integral to R, assuming $R_{min} = \alpha R_{\max}$, the total particles volume of the unit volume can be obtained:

$$V_s = \frac{\pi N_0 kD}{6(3-D)}(1-\alpha^{3-D})R_{\max}^{3-D} \tag{5}$$

where $R_{\max}$ and $R_{\min}$ are respectively the maximum and minimum value of the soil particle size.

Based on the three phase index conversion relation of the soil mechanics, the volume of the solid soil particles V_s can be expressed by porosity n for the unit volume soil:

$$V_s = 1 \cdot (1-n) = (1-n) \tag{6}$$

Combining with formulas (5) and (6), the total number N_0 of the particles in the unit volume of soil can be obtained:

$$N_0 = \frac{6(1-n)(3-D)}{\pi D R_{\min}^D (R_{\max}^{3-D} - R_{\min}^{3-D})} \tag{7}$$

Particle coordination number N_c characterizes the particle contact points between the unit particle and the other particles around. Particle coordination number N_c is related with the accumulation and arrangement of the soil particles. For the unit volume soil, the total contact number of soil particles is defined as N_{sum}. So N_{sum} is the product of the total particles number N_0 per unit volume and the average coordination number N_c. Since each contact point is possessed by two particles

$$N_{sum} = \frac{1}{2} N_0 \cdot N_c = \frac{3(1-n)(3-D)}{\pi D R_{\min}^D (R_{\max}^{3-D} - R_{\min}^{3-D})} \cdot N_c \tag{8}$$

For the unit volume of soil, the surface area of the $p(R)dR \cdot N_0$ particles which radius are r is calculated as follows:

$$dS_s = N_0 \cdot p(r) \cdot \pi r^2 dS \tag{9}$$

Integral to r, the total particles surface area in the unit volume soil can be obtained:

$$S_s = \frac{\pi N_0 D}{(2-D)} R_{\min}^D (R_{\max}^{2-D} - R_{\min}^{2-D}) \tag{10}$$

Therefore, the contact points of the soil particles in the unit surface area can be obtained:

$$N_{sum}^s = \frac{N_{sum}}{S_s} = \frac{(2-D)}{2\pi D R_{\min}^D (R_{\max}^{2-D} - R_{\min}^{2-D})} \cdot N_c \tag{11}$$

The particles contact points in unit surface area multiplying the reduction factor α, the number of the particles contact points on the on the projection area can be obtained:

$$N_a = \alpha N_{sum}^s \tag{12}$$

3 THEORETICAL DERIVATION OF THE ABSORBED SUCTION

3.1 *Theoretical derivation of the micro absorbed suction*

Due to the wetting effect of the moisture, the absorbed suction is the suction between the soil particles, which are the components of the surface tension of the gas-liquid interface in the direction of the soil particles attachment. The suction leads to the compressive stress existing between the soil particles. Double particles model is shown as Figure 2, where R_1 is the large particle radius, R_2 is the small particle radius, θ is the contact angle, r_1 is the curvature radius of the curved liquid surface of the gas lateral, φ_1 is the unsaturated angle of the large particle, φ_2 is the unsaturated angle of the small particle, T_s is the surface tension.

The surface tension can be decomposed into the grain direction and the vertical direction. According to the micro absorbed suctions functioning in two different soil particles are balance forces, the formula can be calculated as follows:

$$T_s \sin(\theta + \varphi_1) \cdot 2\pi r_1 = T_s \sin(\theta + \varphi_2) \cdot 2\pi r_2 \tag{13}$$

The tensile stress generated by the liquid membrane surface tension between the soil particles can be obtained as follows:

$$F_s = T_s[\pi R_1 \sin\varphi_1 \sin(\theta + \varphi_1) + \pi R_2 \sin\varphi_2 \sin(\theta + \varphi_2)] \tag{14}$$

According to the literature, the tensile stress generated by the liquid membrane surface tension between the soil particles can be averaged on the area $(\pi r_1^2 + \pi r_2^2)/2$, the micro absorbed suction can be obtained as follows:

$$p_s = 2T_s \frac{R_1 \sin\varphi_1 \sin(\theta + \varphi_1) + R_2 \sin\varphi_2 \sin(\theta + \varphi_2)}{(R_1 \sin\varphi_1)^2 + (R_2 \sin\varphi_2)^2} \tag{15}$$

According to Figure 2, the relationship of the two particle radius ratio can be obtained as follows:

$$\frac{R_1}{R_2} = \frac{\sin\varphi_1 \sin(\theta + \varphi_1)}{\sin\varphi_2 \sin(\theta + \varphi_2)} \tag{16}$$

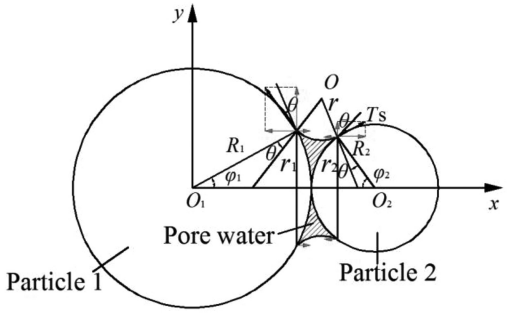


Figure 2. Model of contiguous unequal-sized spheres.

Table 2. The quantitative relation between micro absorbed suction, the particle radius and the saturated angle.

R_1, R_2/m	φ_1 (°)	φ_2 (°)	P_s (Pa)
$R_1 = 0.001$ m	5.00	7.83	1592.11
$R_2 = 0.0005$ m	10.00	15.14	757.04
$R_1/R_2 = 2$	15.00	22.53	476.61
	20.00	30.15	334.11
	25.00	38.16	246.05
	27.00	41.53	184.36
$R_1 = 0.0001$ m	5.00	7.83	6559.49
$R_2 = 0.00005$ m	10.00	15.14	3119.02
$R_1/R_2 = 2$	15.00	22.53	1963.62
	20.00	30.15	1376.54
	25.00	38.16	1013.71
	27.00	41.53	759.56
$R_1 = 0.00001$ m	5.00	7.83	13103.07
$R_2 = 0.000005$ m	10.00	15.14	6230.47
$R_1/R_2 = 2$	15.00	22.53	3922.48
	20.00	30.15	2749.75
	25.00	38.16	2024.96
	27.00	41.53	1517.28

Formula (16) shows that micro absorbed suction is the relation function between the saturated angle φ, the particle radius R and the contact angle θ. With the iterative calculation method, assuming the contact angle θ is 5°, particle radius ratio $R_1/R_2 = 2$, $T_s = 72.7 \times 10^{-3}$ N/m, the relationship between micro absorbed suction of the particles, the particle size and the saturated angle will be discussed. The calculation results are shown in Table 2.

The calculated results of the relationship between micro absorbed suction of the particles, the particle size and the saturated angle are shown in Figure 3. When the particle diameter ratio is equal, the micro absorbed suction is inversely proportional to the radius of particle size, the particle radius is larger, the micro absorbed suction is smaller. When the particle radius is smaller, the micro absorbed suction is larger. With the saturated Angle φ_1 increasing, the micro absorbed suction monotone decreases. When the saturated Angle is smaller, the curve slope is bigger. When the saturated Angle reaches a certain value, the micro absorbed suction tends to zero, which corresponds to the particle radius $R_1 = 0.001$ m, $R_2 = 0.0005$ m. The micro

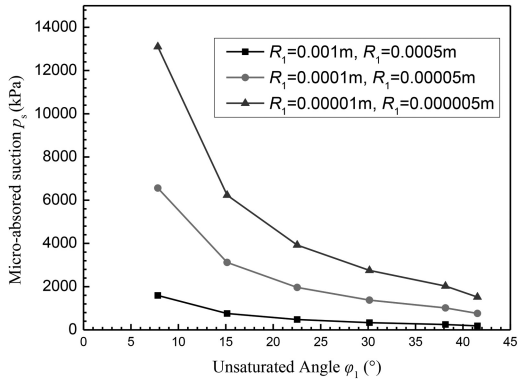


Figure 3. The relationship between the micro absorbed suction and unsaturated angle.

absorbed suction reduces to 0, the saturated Angle φ_1 is 24.39°, φ_2 is 41.53°, which are the larger saturated Angles in this condition. With the soil particle radius decreasing, the maximum saturated Angle of soil tends to increase.

3.2 *Theoretical derivation of the absorbed suction*

The micro absorbed suction p_s between the different size particles can be obtained by formula (15). The micro absorbed suction between the i ball and j ball can be expressed as $p_{s(ij)}$, the average micro absorbed suction can be calculated as follows:

$$\overline{p_s} = \frac{\sum p_{s(ij)} \cdot N_{ij}}{\sum N_{ij}} \tag{17}$$

where i, j are 1, 2, 3, 4, 5.

The particle contact points of unit cross-sectional area multiplying the average micro absorbed suction of the particle contact points, the absorbed suction can be calculated as follows:

$$S_a = \alpha N_{sum}^s \overline{p_s} = N_a \cdot \overline{p_s} \tag{18}$$

where the dimension of F_{ps} is Newton (N), $N_a = \alpha N_{sum}^5$ is the contact number per unit area, the dimension is (m^{-2}), α is reduction coefficient, the dimension of S_a is (N/m^{-2}).

3.3 *The relationship between microscopic and macroscopic physical quantities*

According to the soil conversion relationship of the three-phase index, the saturability S_r is a derivative of the water content and dry density. If the water content is certain, the saturability must correspond to the density. If the dry density is certain, the saturability must correspond to the water content. In addition, from the perspective of the saturability definition, it is the ratio of the pore water volume and the total pore volume,

which is a no dimensional variable. However, the saturability cannot characterize the variables of the soil physical properties. Meanwhile, the water content is directly related to the soil quality, its physical meaning is so clear that it is the representation of the basic physical properties of the soil. Therefore, in this paper, the influence factors of the absorbed suction only be discussed about the water content and the dry density.

(1) The relationship between the water content and the micro physical quantities

The water content w and the proportion of the particles can be respectively calculated by the following formulas:

$$w = M_w / M_s = \rho_w V_w / \rho_s V_s \tag{19}$$

$$G = \rho_s / \rho_w = M_s / \rho_w V_s \tag{20}$$

where M_w is the water mass of the soil, M_s is the particles mass of the soil, ρ_s is the density of the solid soil particles, ρ_w is the water density, combining with formula (19) and (20), the water volume of the soil can be obtained:

$$V_w = G \cdot w \cdot V_s \tag{21}$$

Combining with formula (5) and (21), the formula (21) can be written as follows:

$$V_w = \frac{\pi G w N_0 k D}{6(3-D)}(1-\alpha^{3-D})R_{\max}^{3-D} \tag{22}$$

Combining with formula (8) and (22), the water volume V_w of the soil divided the total number of contact points N_{sum}, the average volume of the water ring between any two particles can be calculated:

$$V_0 = \frac{V_w}{N_{sum}} = \frac{2\pi G w N_0 k D}{3(3-D)N_c}(1-\alpha^{3-D})R_{\max}^{3-D} \tag{23}$$

According to Figure 2, the water ring volume can be obtained:

$$V_0 = V_1 - V_2 - V_3 \tag{24}$$

$$V_1 = \frac{1}{2}\pi[(R_1 \cdot \sin\varphi_1)^2 + (R_2 \cdot \sin\varphi_2)^2] \cdot (R_1 + R_2 - R_1 \cdot \cos\varphi_1 - R_2 \cdot \cos\varphi_2) \tag{25}$$

$$V_2 = \frac{\pi R_1^3}{3}[1 + (2 - \cos\varphi_1)^3 - 3(1 - \cos\varphi_1)] \tag{26}$$

$$V_3 = \frac{\pi R_2^3}{3}[1 + (2 - \cos\varphi_2)^3 - 3(1 - \cos\varphi_2)] \tag{27}$$

where V_1 is the volume between r_1 and r_2 in Figure 2, V_2 is the segment volume of particle 1, V_3 is the segment volume of particle 2.

Combining with formula (23) and (24), the relationships between water content w, particle proportion G and saturated angle φ_1 and φ_2 of the Macro-physical quantities will be obtained.

(2) The relationship between dry density and the Macro-physical quantities

According to the soil conversion relationship of the three-phase index, the relationship between the dry density ρ_d, void ratio e and soil particles proportion G is shown as follows:

$$\rho_d = G \cdot \rho_w / (1 + e) \tag{28}$$

Combining with formula (21) and (23), the average volume of the water ring between any two particles can be calculated:

$$V_0 = \frac{2\pi\rho_d(1+e)wN_0kD}{3(3-D)\rho_w N_c}(1-\alpha^{3-D})R_{\max}^{3-D} \tag{29}$$

Combining with formula (24) and (29), the relationship between dry density ρ_d, void ratio e, water content w, particle proportion G and saturated angle φ_1 and φ_2 of the Macro-physical quantities will be obtained.

4 EXPERIMENT

4.1 *The fractal coefficient of soil samples*

The soil samples were fine sand soil sample which were sampled from construction site in Guangzhou. The nonuniform coefficient C_u was 2.06, the coefficient of curvature C_c was 0.84, the relative density of the soil was 2.72, the initial water content was 24.3%, the coarse sand (2–0.5 mm) was accounted for 5.1%, the medium sand (0.5–0.25 mm) was accounted for 11.6%, the fine sand (0.25–0.075 mm) was accounted for 73.4%, the fine sand (<0.75 mm) was accounted for 9.9%. The original soil were dried, cracked, sieved with the 0.1 mm grade sieve, and then processed into loose soil samples respectively. The samples were encapsulated with the two layers-plastic bags, and then they were put in the constant temperature moisture to make the water in the bags to migrate adequately and mix evenly. According to experimental results, the largest diameter of the particles was 0.2 mm, $R_{\max} = 2 \times 10^{-4}$ m. However, the minimum size of the particles cannot be measured by the sizing assay test. Researches had shown that the particles of which diameter were less than 1.0×10^{-6} m exist in the suspension in the form of colloid. Therefore, we regarded colloid particle size limit as the minimum particle size, $R_{\min} = 1.0 \times 10^{-6}$ m. Fractal coefficient D can be obtained by the sizing assay test.

According to the microscopic parameters of the soil samples in Table 3, the total number N_0 of the particles per unit volume can be obtained by the formula (7), the contact points per unit area N_{sum}^s can be obtained by the formula (9). According to the above assumptions, the soil were packed in accordance with the close packing model of Horsfield, so the average coordination number $\overline{N_c}$ of the model was 18.6, the parameters of the soil samples and the calculation results are shown in Table 3.

Table 3. The soil sample parameters and the calculation results.

No.	D	N (%)	R_{max} (m)	R_{min} (m)	N_0	N^s_{sum}
1	2.8512	38.7	2×10^{-4}	1×10^{-6}	1.81×10^{19}	2.710×10^{11}
2	2.8243	40.2	2×10^{-4}	1×10^{-6}	1.50×10^{19}	2.144×10^{11}
3	2.8314	46.3	2×10^{-4}	1×10^{-6}	1.06×10^{19}	2.281×10^{11}
4	2.7821	32.3	2×10^{-4}	1×10^{-6}	1.33×10^{19}	1.485×10^{11}
5	2.8125	45.6	2×10^{-4}	1×10^{-6}	1.28×10^{19}	1.935×10^{11}
6	2.8122	45.3	2×10^{-4}	1×10^{-6}	1.27×10^{19}	1.930×10^{11}
7	2.8159	46.3	2×10^{-4}	1×10^{-6}	1.28×10^{19}	1.993×10^{11}
8	2.7953	42.2	2×10^{-4}	1×10^{-6}	1.23×10^{19}	1.666×10^{11}
9	2.7865	40.6	2×10^{-4}	1×10^{-6}	1.20×10^{19}	1.543×10^{11}
AVG		41.8				1.918×10^{11}

4.2 *Absorbed suction tests*

Zhang[9] tested the unsaturated soil absorbed suction of equal diameter particles with the hygrother- mograph. Combined with formula (15), the computation expression of absorbed suction in Horsfield close packing of the unequal particles and the relative humidity can be obtained as follows:

$$S_a = 2T_s \frac{R_1 \sin\varphi_1 \sin(\theta+\varphi_1) + R_2 \sin\varphi_2 \sin(\theta+\varphi_2)}{(R_1\sin\varphi_1)^2 + (R_2\sin\varphi_2)^2} \cdot (RT\rho_w / M_w)\ln(p/p^0) \tag{30}$$

where R is molar gas constant, p_s is micro absorbed suction, T is absolute temperature, p is the vapour pressure of the meniscus corresponding to T, p^0 is the vapour pressure of the flat surface corresponding to T, V is the liquid gram-molecular volume, ρ_w is the water density, M_w is the water gram-molecular weight.

For a given unsaturated soil, the temperature was invariable, the contact angle θ, molar gas constant R ($8.314\text{J}\cdot\text{mol}^{-1}\cdot\text{K}^{-1}$), water density ρ_w, the water gram-molecular weight M_w (18.016 g/mol) were all constants. $T = t + 273.13$, the unit is K, t was the centigrade temperature. Therefore, for the given unsaturated soil, if the water content w was known, the saturated angle φ_1 and φ_2 can be calculated with formula (23) and (24). Taking the relative humidity p/p^0 which were tested by the hygrothermograph into formula (30), the absorbed suction can be obtained.

Processing the soil samples with the water content $w = 2\%, 4\%, 6\%, 8\%, 10\%, 12\%, 14\%, 16\%, 18\%$, the soil samples were divided into nine groups, the tests results are shown in Table 4. Taking the parameters into formula (30), the results are shown in Figure 3. Processing the soil samples with the dry density ρ_d were respectively 1.41 g/cm^3, 1.59 g/cm^3, 1.80 g/cm^3, 2.00 g/cm^3, the soil samples were divided into four groups, the tests results are shown in Table 5. Taking the parameters into formula (30), the results are shown in Figure 3.

Table 4. The test parameters corresponding to water content.

w/%	φ_1/(°)	φ_2/(°)	t/°C	p/p^0
2	21.03	24.23	25.3	97.1
4	24.20	37.32	25.2	98.3
6	27.24	29.11	25.4	98.5
8	30.33	32.44	25.1	99.2
12	33.26	35.72	25.2	99.6
14	36.11	38.12	25.3	99.4
16	38.22	41.52	25.2	99.5
18	41.22	44.56	25.3	99.6

Table 5. The tests parameters corresponding to dry density.

$\rho^{-3}_{d/g\cdot cm}$	e	φ_1/(°)	φ_2/(°)	t/°C	p/p^0
1.41	0.91	24.03	27.23	25.3	96.1
1.59	0.70	27.20	30.32	25.2	97.3
1.80	0.51	30.24	33.11	25.4	97.5
2.00	0.35	34.33	37.44	25.1	98.2

4.3 *Discussion*

(1) The relationship between absorbed suction and water content

Figure 4 shows that the absorbed suction presents first increasing then decreasing until to zero with the water content increasing. To express conveniently, in this article, the water content corresponding to the maximum absorbed suction is expressed as w_1, and the water content corresponding to the zero absorbed suction is expressed as w_2.

When the water content changes between w_0 and the critical value w_1, the micro absorbed suction effect area is that the suction concentrates on the left parietal of the particle. Although the micro absorbed suction decreases constantly, the total micro absorbed suction function area of the particles increases all the way, so the absorbed suction will increase gradually with

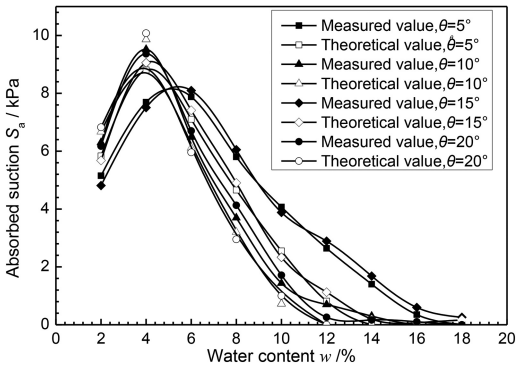


Figure 4. The relationship between the absorbed suction and water content.

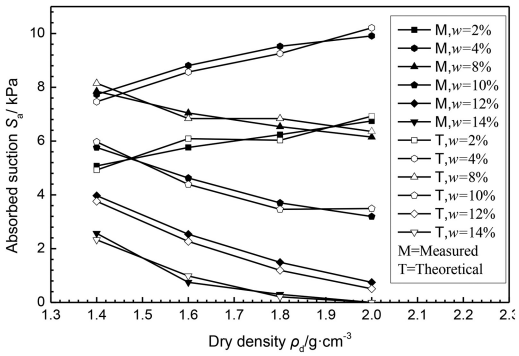


Figure 5. The relationship between the absorbed suction and water content.

the combination. When the water content reaches the critical value w_1, the micro absorbed suction function area is equal to the hemisphere projection area of the particle, at the moment, the total projection area of the particles is maximum, the absorbed suction is also maximum. With the water content furtherly increasing, the total micro absorbed suction function area is more than the left hemisphere projection area, the function area appearing on the right hemisphere is more negative, which will be offset with the equal function area of the left hemisphere. So the absorbed suction will reduce gradually until the water content reaches the critical value w_2, and both the left and right hemisphere are wetting, the soil closely reach the saturated state, the absorbed suction becomes into zero.

The variation characteristics of the absorbed suction can well explain the strength behavior of the unsaturated soil in real life, for example, the silt is dry or soaking in the water, its strength is very small. But when the saturability of the silt turns from 0 to 1, the silt strength will present that it gradually increases and then decreases until to a certain value (The structure suction exist in the soil, although the absorbed suction is 0, but the strength is not 0). The reason of this phenomenon is that when the soil moisture is lower, the wetting function makes the interaction force between particles increase, with the soil moisture becomes larger, the overall effect of the surface tension makes part of absorbed suction function cancel out, the interaction force weakens to zero or becomes neutral force until all the particles infiltration are soaked. Thus, the study on the strength behavior of the soil should consider the structure suction effect.

(2) The relationship between absorbed suction and dry density

Figure 5 shows that the absorbed suction increases with the dry density increasing in the low water content, the absorbed suction decreases with the dry density increasing in the high water content.

The causes of this phenomenon are that the particles number per unit volume increases with the dry density increasing in the low water content, the contact points of the particles increases, but as a result of the limitation of particle accumulation (The maximum coordination number is 12), the total function area of the micro absorbed suction is S_p which is always less than half the projection area, so the absorbed suction increases. When the water content is higher than the critical value w_1 (In this article, the corresponding critical value is near 4%∼6%). With the dry density increasing, the particle number per unit volume increases, which causes the saturated Angle and invasion area of the particles increase. The total function area is more than half the projection area, which causes suction decreasing. Especially when the dry density is highest, the small amplitude increasing of the water content will reaches the critical value of the water content w_2 corresponding to the this density, the absorbed suction decreases to zero.

5 CONCLUSION

In this paper, based on the Horsfield close packing model of the Powders mechanics and the Foundation Engineering, with the fractal theory and the theoretical derivation, the absorbed suction expression of the unequal-sized particles in the Horsfield close packing is built. A series of tests are carried out to verify the theoretical calculation formula, and the conclusions are obtained as follows:

(1) For the given unsaturated soil, there is a determined relationship between the absorbed suction and the water content. And there is a limitation water ratio. When the water content of soil is less than the limitation water ratio, with the water content increasing, the absorbed suction increases. When the water content of the soil is higher than the limitation water ratio, the absorbed suction decreases with the water content increasing. The study successfully explains that the strength of unsaturated soil first increases and then decreases in a certain range of water content with the water content increasing.

(2) For the given unsaturated soil, there is also a determined relationship between absorbed suction and dry density. With the dry density increasing,

the absorbed suction increases in the low water content and decreases in the high water content.

(3) The established theoretical calculation formula can reflect the main characteristics of the absorbed suction, but the actual error still exists, the possible reason is that the accumulation way of the soil particles is not like the close packing actually, and this research need to be furtherly studied.

ACKNOWLEDGEMENTS

The research work was supported by the National Natural Science Foundation of China (Grant No. 40872205), the Specialized Research Fund for the Doctoral Program of Higher Education (No. 20120171110031), the Guangdong Natural Science Foundation (No. 07003738), and the Science and Technology Planning Project of Guangdong Province, China (No. 2008B030303009).

REFERENCES

De Bisschop F. R. & Rigole, W. J. 1982. A physical model for liquid capillary bridges between adsorptive solid spheres: the nodoid of plateau. *Journal of Colloid and Interface Science* 88(1):117–128.

Fredlund, D. G. & Morgenstem, N. R. 1996. Constitutive relations for volume change in Unsaturated soils. *Can. Geoth. Jour* 13(3):261–276.

Gröger, T., Tuzun, U., Heyes, D. M. 2003. Modelling and measuring of cohesion in wet granular materials. *Powder Technology* 133(1):203–215.

Lian, G. P., Thornton, C., Adams, M. J. 1993. A theoretical study of the liquid bridge forces between two rigid spherical bodies. *Journal of Colloid and Interface Science* 161(1):138–147.

Megias-Alguacil, D. & Gauckler, L. J. 2010. Analysis of the capillary forces between two small solid spheres binded by a convex liquid bridge. *Powder Technology* 198(5):211–218.

Molenkamp, F. & Nezomi, A. H. 2003. Interactions between two rough spheres, water bridge and water vapour. *Geotechnique* 53(2):255–264.

Mehrotra, V. P. & Sastry, K. V. 1980. Pendular bond strength between unequal-sized spherical particles. *Powder Technology* 25(2):203–214.

Mehrotra, V. P. & Sastry, K. V. 1985. A novel method for the calculation of pendular bond characteristics between unequal-sized particles. *Powder Technology* 41(3):259–263.

NG.CWW, Zhan, L. T., Bao, C. G., et al. 2003. Performance of an unsaturated expansive soil slope subjected to artificial rainfall infiltration. *Geotechnique* 53(2):143–157.

Orr, F. M., Scriven, L. E., Rivas, A. P. 1975. Pendular rings between solids: Meniscus properties and capillary force. *Journal of Fluid Mechanics* 67:723–742.

Rabinovich, Y. L., Esayanur, M. S., Moudqil, B. M. 2005. Capillary forces between two sphere with a fixed volume liquid bridge: Theory and experiment. *Langmuir* 21(24): 10992–10997.

Tang, L. S. & Wang, S. J. 2000. Absorbed suction and principle of effective stress in unsaturated soils. *Chinese Journal of Geotechnical Engineering* 22(1):83–88.

Tao, G. L. & Zhang, J. R. 2009. Fractal theory and its applications in geotechnical engineering. *Sciencepaper Online* 4(7):493–497.

Willett, C. D., Adams, M. J., Johnson, S. A., et al. 2000. Capillary bridges between two spherical bodies. *Langmuir* 16(24):9396–9405.

Zhang, P. C., Tang, L. S., Deng, Z. W., Jiang, L. Q. 2012. Quantitative relationship between wet suction and water content of unsaturated soils. *Chinese Journal of Geotechnical Engineering* 34(8):1453–1457.

Unsaturated Soil Mechanics—from Theory to Practice – Chen et al. (Eds)
© 2016 Taylor & Francis Group, London, ISBN 978-1-138-02921-7

Effective stress for volume change of unsaturated soils

Y.F. Xu, Z.R. Cao, H.G. Zhu & F.F. Chu
Department of Civil Engineering, Shanghai Jiao Tong University, Shanghai, China
Institute of Geotechnical Engineering, Wentian College, Maanshan, P.R. China

ABSTRACT: This paper aims to express the e-p^e relationship using a unique curve by incorporating matric suction and osmotic suction into the effective stress. Based on the analysis of the equilibrium of the solid particles, it was possible to establish an analytical expression for the Bishops parameter χ from soil pore structure. A conceptual model is proposed to explain the influence of osmotic suction on the volume change of clays in a quantitative way. A new formula for effective stress is proposed as $p^e = p + p_\pi$ incorporating with matric suction (u_s) and osmotic suction (π), and $p_\pi = (u_s/u_{se})^{D\text{-}3}u_s$ and $p_\pi = (p/\pi)^{D\text{-}2}\pi$. It is shown that quantitative predictions of volume change in unsaturated soils can be made using the effective stress concept.

1 INTRODUCTION

Defined as "… that function of the total stress and pore pressure which controls the mechanical effects of a change in stress ..." (Bishop & Blight 1963), the effective stress sits exclusively in the solid skeleton of the soil (Terzaghi 1936). In essence, the effective stress is the macroscopic stress of the solid skeleton. The effective stress principle is probably the single most fundamental contribution in the field of soil mechanics. Without the advent of the effective stress principle, many of the significant achievements of solid mechanics–such as elastoplasticity, viscoplasticity, wave propagation, and numerical methods–could not be extended to soil engineering problems (Khalili et al. 2004). Bishop (1959) presented the effective stress for unsaturated soils.

$$p^e = (p - u_a) + \chi u_s \tag{1}$$

where p is the normal stress, u_a is pore air pressure, u_s is matric suction, $u_s = u_a - u_w$, u_w is pore water pressure, χ is effective stress parameter, attaining a value of 1 for saturated soils and zero for dry soils. However, Jennings & Burland (1962) questioned the validity of the effective stress principle in unsaturated soils arguing that it cannot explain the collapse phenomenon upon wetting. They conducted a series of consolidation tests on several unsaturated soils, and showed that upon flooding with suction reducing, all samples collapsed, rather than expanding as is implied by the effective stress principle. As was shown in recent years by several investigators, plastic deformations such as collapse can be readily described within an effective stress framework by defining the yield surface as a function of suction (Bolzon et al. 1996). It should be noted that even in saturated soils, plastic deformations such as dilation and/or collapse cannot be explained in terms of effective stresses alone without invoking an appropriate plasticity model. Another limitation of the effective stress principle, which is often cited in the literature, is that there is no unique relationship between χ and the degree of saturation. In fact, Khalili & Khabbaz (1998) recently showed that a unique effective stress equation was obtained for most soils. Chen et al. (1994) gave the effective stress parameter from the compressibility of unsaturated soils $\chi = K^n/K^{Sn}$, here K^n and K^{Sn} are the bulk modulus of granular skeleton with porosity of n and Sn, respectively, S is the degree of saturation. Sun et al. (2008) proposed that for granular materials and degrees of saturation over 50%, parameter χ may adopt the value of the degree of saturation S, that is to say, $\chi = S$. In this way, the simplified version of Bishop's equation appeared. Experiments on stiffness and shear strength evolution with suction suggest that the proportion of suction contributing to the effective stress is often much smaller than predicted by the term 'suction times degree of saturation' generally used in effective stress expressions of the Bishop type (Alonso et al. 2010).

The mechanical behavior may be strongly influenced by physicochemical effects when salt concentrated pore fluids are introduced to clays (Di Maio et al. 2004, Rao & Thyagaraj 2007). A great number of experimental studies dealing with the chemical effects on the swelling behavior of clays are available in literature (Ye et al. 2014). A strong volume change occurs as a result of osmotic consolidation during the clay samples were exposed to the solutions, and the effect of the NaCl solution shows to be reversible by exposing the sample to distilled water. Increase in pore-water salt concentration weakens the diffuse double layer repulsion forces that reduce the compressibility and swell potentials of the clay specimens (Calvello et al.

2005). Thus, the relationships between volume change and vertical overburden pressure are different curves for clays in salt solution with different concentration (Studds et al. 1998). The volume change behaviour of clays is controlled by the effective stress, in which the osmotic suction should be incorporated (Barbour & Fredlund, 1989). Rao & Thyagaraj (2007) proposed that the total net vertical stress (p) experienced by compacted clay specimens exposed to an increase in pore fluid osmotic suction, and represented as follow

$$p = (\sigma - u_w) + p_\pi \tag{2}$$

where σ is normal stress, u_w is pore water pressure, p_π is the pore fluid osmotic suction component, $p_\pi = \alpha\pi$, here π is osmotic suction, α is a empirical constant, and $0 < \alpha < 1.0$. However, Rao & Thyagaraj (2007) did not give the method to determine the value of α. Because part of the effective stress in clay is derived from net inter-particle repulsive forces seated in diffuse double layers around clay aggregations, the applicability of the concept of effective stress has at this stage been restricted to conditions of constant volume, constant chemistry, and constant temperature (Graham et al. 1992). Existing studies on volume changes in clays from changes in pore-water salinity have not examined the influence of variations in pore-water salt concentration on pore-fluid osmotic suction. The role of pore-fluid osmotic suction in the volume change behaviour of clays is not well understood. Up to the present, a comprehensive theoretical description of the combined influence of osmotic suction on the volume change behavior of clays has been lacking.

In this paper, on the basis of the fractal model for the pore-size distribution and the clay surface, effective stress is proposed by incorporating with matric suction and osmotic suction. The volume change behaviour is expressed by a unique curve using the proposed effective stress of unsaturated soils with different matric suction or in salt solution with different concentration. The comparing results of experiments in literature show the proposed effective stress offers good approach to express the volume change of unsaturated soils by a unique curve.

2 SURFACE FRACTAL DIMENSION

The surface fractal dimension serves to characterize its surface roughness or irregularities. The magnitude of the surface fractal dimension is relevant to many important physico-chemical processes namely adsorption, surface diffusion and catalysis. Avnir & Jaroniec (1989) proposed a convenient method to determine the surface fractal dimension from the nitrogen adsorption. Similarly with the adsorption isotherm equation, the correlation of the water volume absorbed by clays to the vapour pressure is given by

$$V_w / V_c = k[\ln(P/P_0)]^{D_s-3} \tag{3}$$

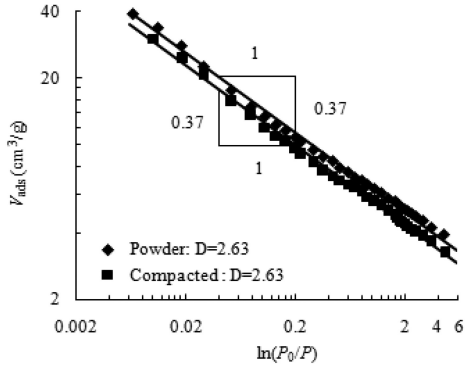


Figure 1. Surface fractal dimension from nitrogen adsorption.

where D_s is the surface fractal dimension, V_w is the water volume absorbed by clays, V_c is the volume of clays, P is the partial water vapour pressure in equilibrium with clays at some water content w and temperature T and P_0 is the equilibrium water vapour pressure of pure water at temperature T.

The nitrogen adsorption isotherms of Tsukinuno bentonite were analysed according to Eq. (3) and the results were shown in Figure 1. The surface fractal dimension was calculated using Eq. (3). The range used to estimate the surface fractal dimension was the global adsorption process ($p/p_0 = 0.01 - 0.99$), and the value of R^2 for all samples was above 0.99. The surface fractal dimension of both the powder and compacted samples was 2.63.

3 SOIL-WATER CHARACTERISTICS

For fractal pore-size distribution, a power-law existing between the measurement (r) and the pore phase

$$N(A, r) = Cr^{-D} \tag{4}$$

When the volumetric water content is less than its residual value, the pore-water is tightly absorbed by soil particle and cannot move freely and seen as a part of soil particles. The contribution of the filled pores with radius $r \to r + dr$ to the water content is given by $d\Lambda = N4\pi r^2 dr / V_T$, where Λ is the relative volumetric water content, and $\Lambda = \theta - \theta_r$, θ and θ_r are the actual and residual volumetric water content, respectively. The residual volumetric water content is the volumetric water content at which the effectiveness of matric suction to cause further removal of water requires vapour migration. Combining Eqs. (4) with the Young-Laplace equation, the soil-water characteristic curve (SWCs) is obtained as follows

$$S_e = (u_s / u_{se})^{D-3} \tag{5}$$

where S_e is the effective degree of saturation, and $S_e = \Lambda / \Lambda_s$, u_{se} is the air-entry value, $u_{se} = 2\sigma\cos\alpha / R$, R is the maximum radius of soil pores.

Figure 2 shows the soil pore-size distribution obtained from mercury intrusion porosimetry (Watabe et al. 2000). It is obtained that the fractal dimensions of the pore-size distribution of S-02, S-03 and S-04 are 2.66, 2.63 and 2.51, respectively. The maximum radium of the soil pores of S-02, S-03 and S-04 are 0.125 mm, 0.06 mm and 0.006 mm, respectively. According to the Young-Laplace equation, the air-entry values of S-02, S-03 and S-04 are 12.5 kPa, 2.5 kPa and 25 kPa, respectively.

The soil-water characteristic curves are predicted using Eq. (5) for the soils of S-02, S-03 and S-04. The air-entry value and fractal dimension of S-02, S-03 and S-04 are obtained from Figure 2. Predictions of Eq. (5) show in good accord with the experiments of the soil-water characteristic curves in Figure 3.

4 EFFECTIVE STRESS INCORPORATING MATRIC SUCTION

According the fractal model for the pore-size distribution, Xu (2004), Xu & Cao (2014) gave the stress parameter χ and is rewritten as

$$\chi = S_e \tag{6}$$

Substituting Eq. (6) into Eq. (1), effective stress is expressed as (Xu & Cao 2014)

$$p^e = (p - u_a) + (u_s / u_{se})^{D-3} u_s \tag{7}$$

The fractal dimension spans a large range from 1.0 to 3.0 obtained from the mercury intrusion tests.

The linear of $e - \ln p^e$ ($de = -\lambda d(\ln p^e)$) curves as a description of the change of volume of a soil skeleton with variations in vertical effective stress (p^e) has some physically unaccepted shortcoming (Butterfield 1979, Hashiguchi 1995). Xu et al. (2003, 2004) and Xu & Xia (2006) presented a theoretical relationship between the void ratio of clay and vertical effective stress (p^e), which is written as

$$e_c = V_w / V_c = K p^{D_s - 3} \tag{8}$$

where e_c is the void ratio of clay, V_w is the water volume, V_c is the clay volume, D_s is the surface fractal dimension. The surface fractal dimension can be substituted in value by the fractal dimension of pore-size distribution.

Lloret et al. (2005) gave the relationship between pore diameter and intruded pore volume for compacted bentonite at the dry density of 1.72 g/cm^3. Micrograph obtained using an environmental scanning electron microscope shows the bimodal distribution of pore sizes are readily apparent. That is say, the soil pores contains inter-aggregate voids and intra-aggregate voids. The compression characteristics are correlated tightly with the inter-aggregate voids. The relationship between pore diameter and intruded pore volume of inter-aggregate voids can be described by

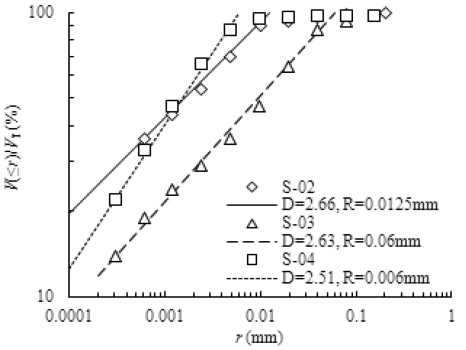


Figure 2. Fractal model for the pore-size distribution.

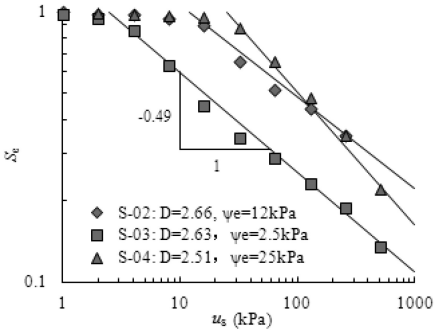


Figure 3. Experiments vs. prediction of SWCs.

fractal theory in Figure 4. The fractal dimension of the inter-aggregate voids of inter-aggregate voids is 2.85. The prediction of the soil-water characteristic curve was compared with the experimental data in Figure 5. It is found that the prediction of Eq. (5) was in accord with the experimental data of soil-water characteristic curve. The air-entry value and the residual water content are 3 kPa and 0 used in the prediction of the soil-water characteristic curve. Oedometer tests with suction control were performed for compacted bentonite by Lloret et al. (2005). Samples were compacted statically to a dry density of 1.70 ± 0.02 g/cm^3 with the material at hygroscopic water content. Compression curves of unsaturated soil with different matric suction and under different vertical stress were given by Lloret et al. (2005). Compression curves deviates from each other for the sample with different matric suction in e-log$p$ plane and that for the sample under different vertical stress in e-logu_s plane. The vertical effective stress can be calculated from matric suction and vertical stress using Eq. (7), in which $u_a = 0$. Compression curve of unsaturated soil with different matric suction and under different vertical stress was plotted in e-logp^e plane, and shown in Figure 4. Compression curve of unsaturated soil with different matric suction and under different vertical stress is nearly one line in Figure 6. That is to say, the vertical effective stress expressed in Eq. (7) is more effectively described the compression curve of unsaturated soil than vertical stress and matric suction.

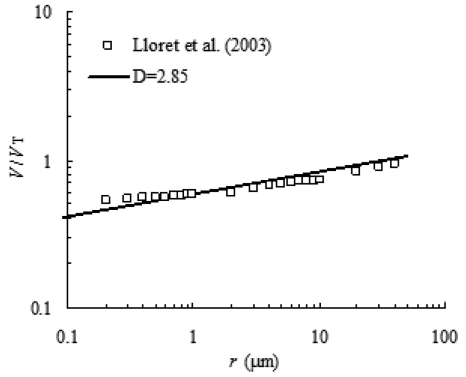


Figure 4. Fractal dimension of the soil pore-size distribution.

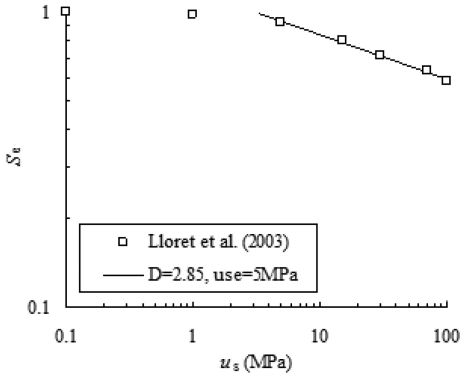


Figure 5. Comparison between experiments and prediction of the soil-water characteristic curve.

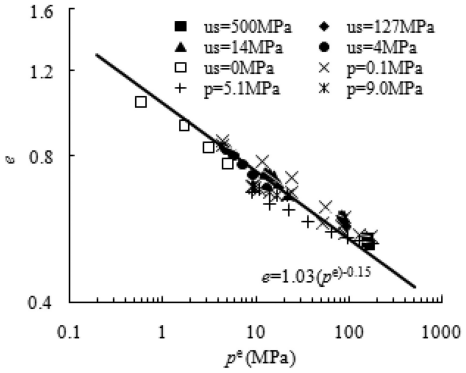


Figure 6. The relation of log$e$-logp^{e}.

5 EFFECTIVE STRESS INCORPORATING OSMOTIC SUCTION

Fundamentally, osmotic suction arises as a result of a reduction in the chemical potential of the pore water in clays due to the presence of dissolved salt in the pore-fluid. Dissolved salt may originate either from exchangeable ions in the interlayer pore space of clay minerals or from the free pore-fluid. The nature of osmotic suction can be described by the schematic shown as Figure 7a. Here, pure water is shown in contact with a salt solution through clays, a semi-permeable membrane, i.e., clays are permeable to water molecules but not to the dissolved salt. The dissolved salts decrease the chemical potential of the salt solution by an amount dependent on its concentration (Iwata et al. 1995). Thus, a gradient in chemical potential is developed that causes water to flow from the pure water into the salt solution through clays. Equilibrium is reached when the induced hydrostatic pressure becomes large enough to balance the osmotic suction tending to cause the water flow. The osmotic suction is described by the van't Hoff equation (Sposito 1981):

$$\pi = \nu RTm\phi \tag{9}$$

where π is the osmotic suction, ν is the valence of the interlayer cation, R is the universal gas constant, T is absolute temperature in Kelvin, m is the molar concentration of the salt solution, ϕ is the osmotic coefficient, $\phi = (\rho_{\mathrm{w}}/\nu M_{\mathrm{w}})\ln(P/P_0)$, M_{w} is the molecular weight of water, ρ_{w} is the unit weight water.

Consider two clay aggregate layers shown in Figure 7b. The parallel aggregate layers of an expanding clay mineral are separated by the interlayer pore space. Interlayer cations reside in the interlayer pore space to balance the negative charge of the clay surface. If we assume that no external stress is applied to the clay aggregates, that the clay aggregate layers are perfectly parallel. The net interaction stress acts on the clay particles is osmotic suction. The osmotic stress equivalent to the osmotic suction, which acts on the clay aggregates, can be written as

$$p_{\pi}L^2 = \pi(L/l)^{D_{\mathrm{s}}}l^2 \tag{10}$$

$$p_{\pi} = \pi(L/l)^{D_{\mathrm{s}}-2} \tag{11}$$

where p_{π} is the osmotic stress, π is the osmotic suction, L is the pore scale within the clay aggregates, l is the pore scale within the clay particles, D_{s} is the surface fractal dimension of the clay aggregates.

Equation (11) is the translation of the osmotic stress from the osmotic suction. The osmotic stress can be applied to the effective stress to express the volume change. In clay-water system, the water volume absorbed within the pore volume of the clay aggregates under the vertical pressure is given by

$$V_{\mathrm{w}}^{\mathrm{L}}/V_{\mathrm{m}} = \beta p^{D_{\mathrm{s}}\text{-}3} \tag{12}$$

where $V_{\mathrm{w}}^{\mathrm{L}} = LS = fL^{3\text{-}D_{\mathrm{s}}}$, here f is a shape factor, S is the pore surface area of clay aggregates, and can be written as $S = fL^{2\text{-}D_{\mathrm{s}}}$, p is the vertical overburden pressure. The vertical overburden pressure must be supported by the osmotic suction of clays (Mollins et al. 1996). Thus, the water volume absorbed within the pore volume of the clay particles under the osmotic suction is given by

$$V_{\mathrm{w}}^{\mathrm{l}}/V_{\mathrm{m}} = \beta\pi^{D_{\mathrm{s}}\text{-}3} \tag{13}$$

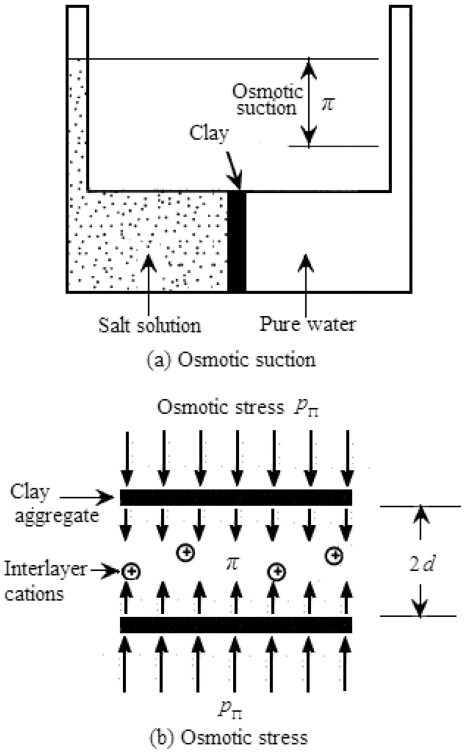


Figure 7. Schematic diagram for osmotic swelling.

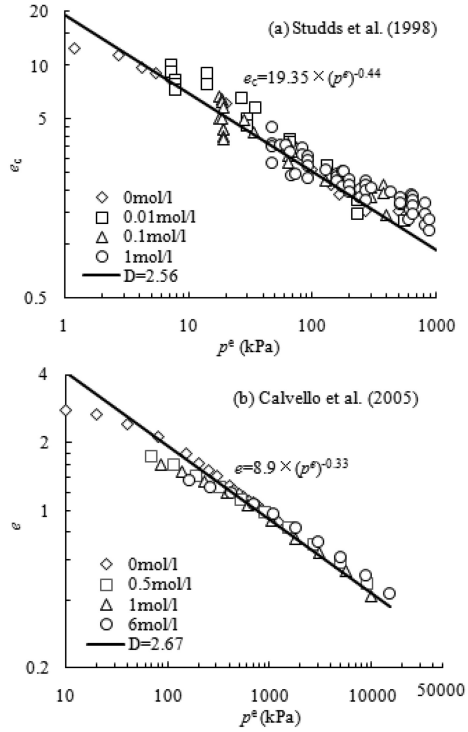


Figure 8. Relationship between void ratio and effective stress.

where $V_w^l = ls = fl^{3-D_s}$, s is the pore surface area of clay particles, $s = fl^{2-D_s}$. Combining Eq. (12) with Eq. (13), it is obtained as follow

$$\frac{V_w^L}{V_w^l} = \left(\frac{L}{l}\right)^{3-D_s} = \left(\frac{p}{\pi}\right)^{D_s-3} \tag{14}$$

Combining Eq. (14) and Eq. (11), the osmotic stress can be expressed as (Xu et al. 2014)

$$p_\pi = \pi(p/\pi)^{D_s-2} \tag{15}$$

Thus, the effective stress can be written as

$$p^e = p + p_\pi = p + \pi(p/\pi)^{D_s-2} \tag{16}$$

In Eq. (16), the effective stress can be calculated using the surface fractal dimension. The surface fractal dimension can be determined from the swelling tests using Eq. (8).

Studds et al. (1998) measured the swelling deformation of Wyoming bentonite with distilled water and various salt solution concentrations (0.01, 0.1 and 1 mol/l). The surface fractal dimension of Wyoming bentonite can be determined using Eq. (8) according to the experimental data of swelling deformation in distilled water. The surface fractal dimension determined from swelling deformation in distilled water is 2.56. Osmotic suction is calculated from Eq. (9). The effective stress is calculated from Eq. (16) using the overburden pressure and osmotic suction. The relationship between the void ratio of clay and effective stress is shown in Figure 8a. In Figure 8a, e_c is the void ratio of clay, $e_c = V_w/V_c$, here V_w is the volume of water, V_c is the volume of clay. It can be seen from Figure 8a that the $e_c p^e$ curve of Wyoming bentonite can be expressed by a unique curve in log-log plot for clays in various salt solution concentrations. From this point, the proposed effective stress is validated to express the volume change of Wyoming bentonite.

The relationship between the void ratio and the void ratio of clay is given by

$$e = Ce_c \tag{17}$$

where e is the void ratio, C is the content of clay, e_c is the void ratio of clay. Thus, the general compression curves of clays satisfy with the relationship of Eq. (8), and can be analyzed using Eq. (8).

Calvello et al. (2005) gave the compression curves of the Bisaccia clay. Compression curves of the Bisaccia clay were evaluated by means of oedometer tests. The Bisaccia clay specimens were powdered and tested dry and reconstituted with distilled water and salt solutions at various concentrations. The surface fractal dimension the Bisaccia clay is determined using Eq. (8) from the experimental data of compression curves in distilled water. The surface fractal dimension the Bisaccia clay is 2.67. Osmotic suction is calculated

from Eq. (9) using the salt concentration. The effective stress is calculated from Eq. (16) using the overburden pressure and osmotic suction. The relationship between the void ratio and effective stress is shown in Figure 8b. It can be seen from Figure 8b that the ep^e curve of Bisaccia clay can be expressed by a unique curve in log-log plot.

6 CONCLUSIONS

A fractal representation for the effective stress principle is established. The effective stress principle requires two parameters, the fractal dimension D and the air-entry value u_{se}, which can be obtained both from the pore-size distribution and the soil-water retention curve. The application of the effective stress principle to unsaturated soils is examined using a comprehensive set of shear strength and volumetric change data. Good agreement is obtained between the measured and predicted values in all cases. This has a significant simplifying effect on the constitutive modeling of unsaturated soils. The effective stress expression deduced from fractal model gives highlight to some features of the shear strength and volume change of unsaturated soils.

ACKNOWLEDGEMENTS

The National Nature Science Foundation of China (Grant Nos. 41272318 and 41472251) is acknowledged for its financial support.

REFERENCES

Alonso, E.E. Pereira, J.-M. Vaunat, J. & et al. 2010. A microstructurally-based effective stress for unsaturated soils. *Géotechnique* 60 (12): 913–925.

Avnir, D. & Jaroniec, M. 1989. An isotherm equation for adsorption on fractal surfaces of heterogeneous porous materials. *Langmuir* 5: 1431–1433.

Bishop, A.W. 1959. The principle of effective stress. *Teknisk Ukeblad* 106: 859–863.

Bishop, A.W. & Blight, G.E. 1963. Some aspects of effective stress in saturated and unsaturated soils. *Geotechnique* 13: 177–197.

Bolzon, G. Schrefler, B.A. & Zienkiewicz, O.C. 1996. Elastoplastic soil constitutive laws generalised to partially saturated states. *Geotechnique* 46(2): 270–289.

Calvello, M. Lasco, M. Vassallo, R. & et al. 2005. Compressibility and residual shear strength of smectitic clays: influence of pore aqueous solutions and organic solvents. *Rivista Italiana Di Geotecnica* 1: 34–46.

Chen, Z.H. Xie, D.Y. & Wang, Y.S. 1994. Effective stress in unsaturated soils. *Chinese Geotechnical Engineering* 16(3): 62–69.

Di Maio, C. Santoli, L. & Schiavone, P. 2004. Volume change behaviour of clays: the influence of mineral composition, pore fluid composition and stress state. *Mech. of Materials* 36: 435–451.

Graham, J. Oswell, J.M. & Gray, M.N. 1992. The effective stress concept in saturated sand-clay buffer. *Can. Geotech. J.* 29: 1033–1044.

Iwata, S. Tabuchi, T. & Warkentin, B.P.1995. *Soil-water Interactions: Mechanisms and Applications, 2nd ed, Marcel Dekker Inc.,* New York.

Jennings, J.E.B. & Burland, J.B. 1962. Limitations to the use of effective stresses in unsaturated soils. *Geotechnique* 12: 125–144.

Khalili, N. & Khabbaz, M.H. 1998. A unique relationship for x for the determination of shear strength of unsaturated soils. *Geotechnique* 48(5): 681–688.

Khalili, N. Geiser, F. & Blight, G.E. 2004. Effective stress in unsaturated soils: Review with new evidence. *International Journal of Geomechanics* 4(2): 115–126.

Lloret, A. Villar, M.V. Sanchez, M. & et al. 2003. Mechanical behavior of heavily compacted bentonite under high suction changes. *Geotechnique* 53(1): 27–40.

Rao, S.M. & Thyagaraj, T. 2007. Swell-compression behaviour of compacted clays under chemical gradients. *Can. Geotech. J.* 44: 520–532.

Sposito, G. 1981. The thermodynamic of soil solution. *Oxford Clarendon Press.* London.

Studds, P.G. Stewart, D.I. & Cousens, T.W. 1998. The effects of salt solutions on the properties of bentonite-sand mixtures. *Clay Miner.* 33: 651–661.

Sun, D.A. Sheng, D.C. & Li, X. 2008. Elastoplastic prediction of hydro-mechanical behaviour of unsaturated soils under undrained conditions. *Computers and Geotechnics* 35: 845.

Terzaghi, K. 1936. The shear resistance of unsaturated soil. *Proc. 1st Int. Conf. on Soil Mechanics and Foundation Engrg, Harvard Printing Office, Cambridge, Mass.,* 54–56.

Tripathy, S. Bag, R. & Thomas, H.R. 2013. Effect of Stern-layer on the compressibility behaviour of bentonites. *Acta Geotechnica.* doi: 10.1007/s11440-013-0222-y.

Watabe, Y. Leroueil, S. & Le Bihan, J.-P. 2000. Influence of compacted conditions on pore-size distribution and saturated hydraulic conductivity of a glacial till. *Can Geotech. J.* 37:1184–1192.

Xu, Y.F. 2004. Fractal approach to unsaturated shear strength, *J of Geotech & Geoenvir Engrg,* ASCE 3: 264–274.

Xu, Y.F. Matsuoka, H. & Sun, D.A. 2003. Swelling characteristics of fractal-textured bentonite and its mixtures. *Applied Clay Science* 22: 197–209.

Xu, Y.F. Sun, D.A. & Yao, Y.P. 2004. Surface fractal dimension of bentonite and its application to determination of swelling properties. *Chaos, Solitons & Fractals* 19(2): 347.

Xu, Y.F. & Xia, X.H. 2006. Fractal model for virgin compression of pure clays. *Mechanics Research Communications* 33: 206–216.

Xu, Y.F. & Cao, L. 2014. Fractal representation of effective stress of unsaturated soils. *Inter J Geomech. http://dx.doi.org/10.1061/(ASCE)*GM.1943-5622.0000446.

Xu, Y.F., Xiang, G.S. & Jiang, H. 2014. Role of osmotic suction in volume change of clays in salt solution. *Appl Clay Sci.* http://dx.doi.org/10.1016/j.clay.2014.09.006.

Ye, W.M. Zhang, F. Chen, B. & et al. 2014. Effects of salt solutions on the hydro-mechanical behavior of compacted GMZ01 bentonite, *Environ Earth Sci* 72: 2621–2630.

Unsaturated Soil Mechanics—from Theory to Practice – Chen et al. (Eds)
© 2016 Taylor & Francis Group, London, ISBN 978-1-138-02921-7

Failure of divide-and-conquer approach in the characterization of unsaturated soils

X. Zhang
College of Civil Engineering and Architecture, Wuhan Polytechnic University, Wuhan, China
Department of Civil and Environmental Engineering, University of Alaska Fairbanks, Fairbanks, USA

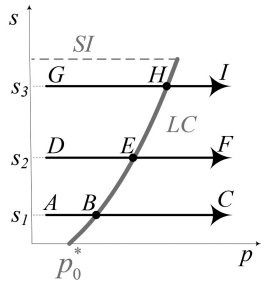
ABSTRACT: Suction-controlled triaxial (SCTX) tests are considered to allow researchers to investigate influences of individual variables on unsaturated soils under specified stress path with controls of stresses, pore water and air pressures. In the past fifty years, SCTX testing method has been established as a standard approach to characterize constitutive behavior for unsaturated soils. Most important concepts for modern unsaturated soil mechanics were developed upon results from the SCTX tests. Among these, one of the most important contributions in the constitutive modeling of elasto-plastic behavior for unsaturated soils is the Barcelona Basic Model (BBM) proposed by Alonso et al. (1990). The BBM successfully explained many features of unsaturated soils and received extensive acceptance. The BBM has now been considered as a canon of unsaturated soil mechanics and all existing elasto-plastic models are variants of the BBM. This study however indicates that the SCTX tests in fact cannot correctly produce the results needed for constitutive modelling purposes.

1 INTRODUCTION

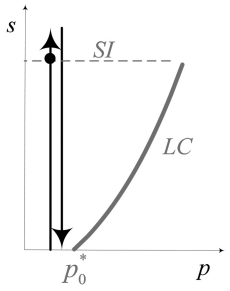
Bishop and Donald (1961) developed the first suction controlled triaxial (SCTX) testing apparatus for unsaturated soils. Compared with conventional triaxial testing apparatus for saturated soils, two adaptations were made: (1) use of the axis translation method (Hilf 1956) to control soil suction and (2) adoption of double-wall system to measure the volume change for unsaturated soils. The SCTX testing apparatus allows researchers to separately control the stress, air and pore water pressures and eliminate the complicated coupling effects and investigate unsaturated soils under specified or "controlled" stress paths. Normally stress path controlled consolidated drained tests are performed to characterize unsaturated soils. The stress paths are often designed based upon a well-established Divide-and Conquer approach in many scientific studies: when a process is influenced by several parameters and their influences are coupled together, to examine the influence of each individual parameter, one has to conduct tests which involve keeping all the influencing parameters constant except for the target parameter.

Figures 1a through 1c show the typical stress paths (straight lines with arrows) proposed by Alonso et al. (1990) to determine characterize unsaturated soils, which are consolidated drained isotropic compression tests, soil water characteristic curve tests, and consolidated drained triaxial shear tests, respectively. In such tests, only one stress variable, either p (Fig.1a) or s (Fig.1b) or shear stress q (Fig.1c), is changed, while the other stress variables remain unchanged in order to eliminate the coupling effects between different stress variables and make the test results easy to analyze.

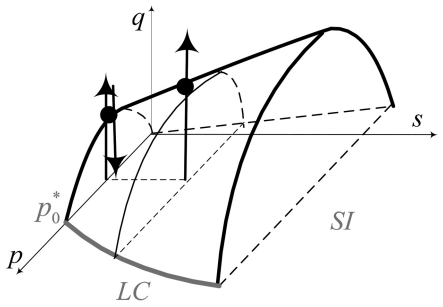
Since the late 1950s and 1960s, intense experimental work has been performed using the SCTX testing apparatus (e.g. Bishop et al. 1960; 1963; Jenning and Burland 1962; Matyas and Radhakrishna 1968; Fredlund and Morgenstern 1976; 1977; Sivakumar 1993; Sharma 1998; Rampino et al. 2000; Thu et al. 2007). Now the SCTX testing method has been established as a standard method for characterizing unsaturated soils for the constitutive modeling purpose (Delage 2002). All existing theories for modern unsaturated soil mechanics have been developed upon results from the SCTX tests(Bishop et al. 1961; 1963; Aitchison and Donald 1956; Aitchison 1961; Jenning and Burland 1962; Bishop et al. 1963; Matyas and Radhakrishna 1968; Fredlund and Morgenstern 1977; Fredlund and Rahardjo 1993; Alonso et al. 1987; 1990; Wheeler 1996 Cui and Delage 1996; Bolzon et al. 1996; Gens 1996; Wheeler and Sivakumar 1995; Wheeler 1996; Wheeler et al. 2003; Dangla et al.1997; Vaunat et al. 2000; Geiser et al. 2000; Vaunat et al. 2000; Khalili and Loret 2001; Wheeler et al. 2003, Gallipoli et al. 2003a, 2003b; Sheng et al. 2003a; 2003b; 2004; 2008a and 2008b; Tamagnini 2004; Vassallo et al. 2007; Costa and Alonso 2009). Among all the theoretic developments, one of the most important contributions was the first elasto-plastic model proposed by Alonso et al. (1990), which is later called the Barcelona Basic Model (BBM) (Alonso et al. 1999). The most important feature of the BBM was the introduction of a loading-collapse (LC) yield curve



(a) Isotropic Compression Test



(b) Soil Water Characteristic Curve Tests



(c) Triaxial Shearing Tests

Figure 1. Typical Stress Paths Used to Characterize Unsaturated Soils.

(Delage and Graham 1995; Gens 1995; Wheeler and Karube 1995) in the *p-s* plane on which the yield stress increases with the increase of suction as shown in Figs.1a and 1b. The model was then extended to triaxial stress states by assuming elliptical yield curves at constant suctions in the *q-p-s* stress space as shown in Fig. 1c.

The BBM was proposed based on results from the SCTX tests for unsaturated soils (Alonso et al. 1987; 1990). The BBM successfully explained many features of unsaturated soils. Until now, the original paper by Alonso et al. (1990) has been cited for more than 1,500 times, indicating that it has received extensive acceptance. Since 1990s many elasto-plastic models have been developed. Review of the elasto-plastic models for unsaturated soils can be found in Delage and

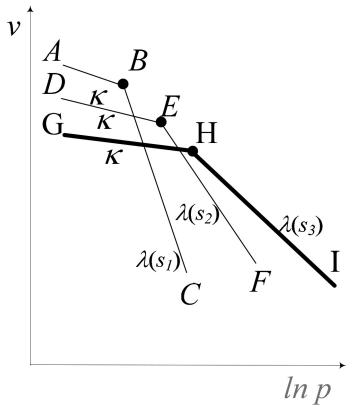


Figure 2. Typical Test Results for Stress Paths as Shown in Figure 1a.

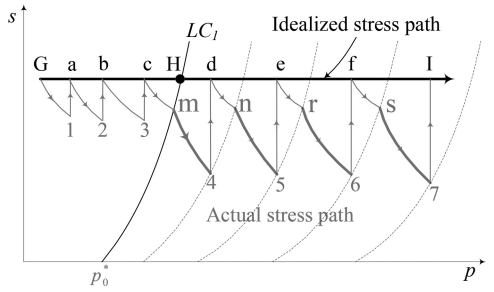
Graham (1996), Gens (1996), Wheeler and Karube (1996), Vanuat (2005), Gens et al.(2006), Wheeler (2006), Gens (2008), Sheng & Fredlund (2008), Sheng et al. (2008c), Gens (2009), Cui & Sun (2009), Gens (2010), and Sheng (2010). Sheng et al. (2004) concluded that, from the elasto-plastic theory point of view, all existing elasto-plastic models have a similar framework and can be considered variants of the BBM. Gens et al. (2006) also considered that most existing elasto-plastic models kept the same core of basic assumptions in the BBM, and sought to improve some of the limitations in the BBM.

The following discussions however suggest that the SCTX testing method is inconsistent with the BBM. If the BBM is correct, then the SCTX tests cannot be used to correctly characterize elasto-plastic behavior for unsaturated soils. In other words, it seems that the Divide-and-Conquer Approach fails in the characterization of unsaturated soils.

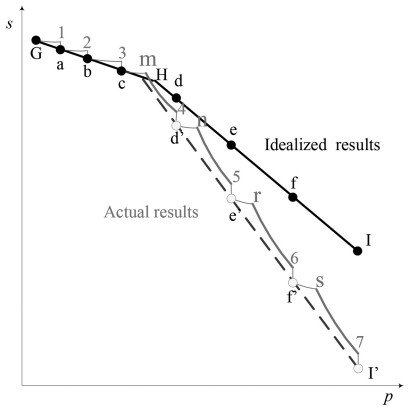
2 PROBLEM ASSOCIATED WITH STEP LOADING

Using SCTX isotropic compression tests in Fig. 1a as an example, Fig. 2 shows typical results proposed in the BBM (Alonso et al. 1990) for the idealized, horizontal constant suction stress paths such as ABC, DEF, and GHI as shown in Fig. 2a. B, E, and H are yielding points and BC, EF, and HI are virgin compression lines. If ABC, DEF, and GHI are the theoretical or "true" results for the stress paths as shown in Fig. 1a, then the following discussions indicate that suction controlled triaxial tests cannot correctly produce the needed results.

As shown in Figure 3a, the idealized stress path for an SCTX isotropic compression test of GHI in Figure 1a is GabcHdefI while its actual stress path is G1a2b3cm4dn5er6fs7I. The initial stress state of the soil specimen is point G. To reach a target new stress level at the same suction level such as point a, a load



(a) "Idealized" versus actual stress paths



(b) "Idealized" versus actual test results

Figure 3. Analysis of an SCTX Isotropic Compression Test under Step Loading.

is applied to the soil specimen. As a result, soil suction will decrease under undrained loading (G → 1). The undrained loading stress path is a reflection of the coupling effect between the hydraulic and mechanical behavior of the unsaturated soil. In order to "control" stress path (or "control suction"), one has to let the excess pore water pressure dissipate under constant stress in order to bring soil to the original suction level (1 → a in Fig. 3a). Usually, a soil sample will be isotropically consolidated to several preselected values of p such as 1–7 in Fig. 3a and the applied load should be large enough to obtain sufficient points in both the elastic (G, a, b, and c) and plastic (d, e, f, and I) zones as shown in Fig. 3b.

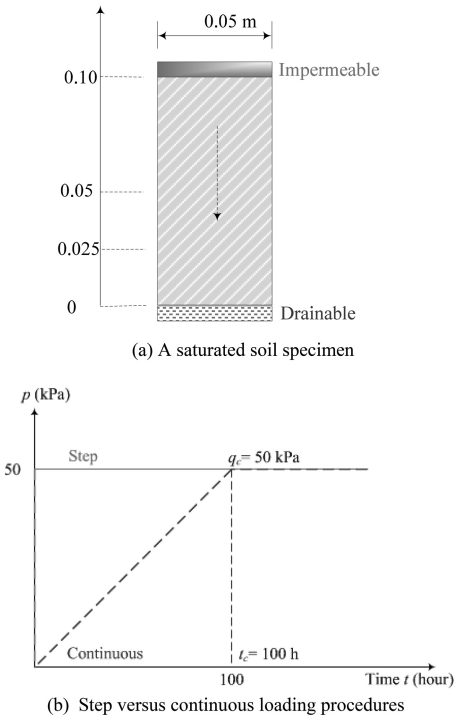
In the elastic zone, the soil behavior is stress path independent and results (specific volumes for points G, a, b, and c in Fig. 3b) from both the idealized (G → a → b → c) and actual (G → 1 → a → 2 → b → 3 → c) stress paths will be the same. In the plastic zone, unlike saturated soils, an unsaturated soil can plastically yield due to undrained loading (m → 4). Once the yield point m in Fig. 3a is reached, further increase in load will push the yield curve from LC_1 to a new position LC_2 passing point 4. The following dissipation of excess pore water pressure (increasing suction under constant stress p as represented by 4 → d) is an unloading process away from LC_2 according to the BBM. For the same stress states of d in Fig.3a, specific volume obtained by following the idealized stress path c → H → d, which represents the virgin states (d in Fig. 3b), is larger than that obtained by following the actual stress path c → m → 4 → d, which is in the new elastic zone (d' in Fig. 3b). The soil yields at the point m, with a yield stress lower than the yield stress at point H for the idealized stress path c → H → d. Similar discussions can be made for the stress paths d → n → 5 → e, e → r → 6 → f, and f → s → 7 → I. On the actual stress path, soil yields during undrained loadings of m → 4, n → 5, r → 6, and s → 7, while on the rest of the whole actual stress path, soil is the elastic zone.

In an SCTX test, very often only soil responses at the end of the each consolidation process are recorded for the constitutive modeling purpose such as points G, a, b, c, d', e', f', and I' in Fig. 3b. By doing so, an implicit assumption is used that the soil behavior is stress-path independent. However, all these points are in the elastic zone. Points d', e', f', and I' are a collection of elastic behavior of the soils with different preconsolidation stresses (or yielding histories) and are always lower than the results from the idealized stress path. They cannot provide any information regarding the plastic behavior (d, e, f, and I as shown in Fig. 3b) needed for the constitutive modeling purpose.

3 PROBLEM ASSOCIATED WITH STEP LOADING

The loading procedure of the actual stress path as shown in Fig. 3a is called step loading (Cui and Delage 1996). Another loading procedure called continuous loading procedure becomes increasingly popular in recent years in which load is continuously applied at a very small rate while holding constant both pore water pressure and air pressure (control suction). On reaching the target value of p, a sufficient rest period was allowed to ensure complete dissipation of any excess pore water pressure (Wheeler and Sivakumar 1995; Cui and Delage 1996). The difference between the two loading procedures is that excess pore water pressure generated under continuous loading is smaller than that generated under step loading, due to the extra time for excess pore water pressure dissipation (Cui and Delage 1996). The discussions in the following sections however suggest the obtained results are even more controversial.

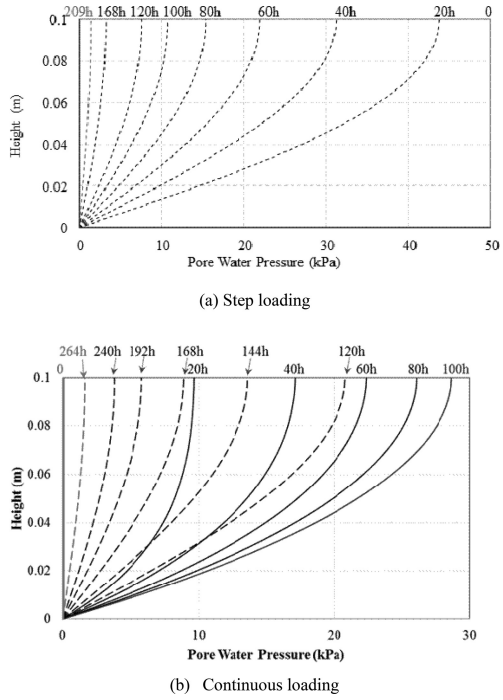
An example calculation can be used to demonstrate the differences in the two loading procedures. To keep the discussion simple, an isotropic compression test on a saturated soil specimen is used as shown in Fig. 4a. The soil specimen is assumed to be 50 mm in diameter and 100 mm in height with a single-sided drainage at the bottom of the soil specimen. The coefficient of consolidation of the soil is a constant of



(a) A saturated soil specimen

(b) Step versus continuous loading procedures

Figure 4. Step and continuous loadings on a saturated soil specimen.



(a) Step loading

(b) Continuous loading

Figure 5. Pore pressure distributions during step and continuous loadings.

2×10^{-8} m^2/s. Two different loading procedures are used as shown in Fig. 4b: one is a step loading in which the isotropic stress of 50 kPa is applied suddenly, and the other is a continuous loading with at a constant rate of 0.5 kPa/hour until an isotropic stress of 50 kPa is reached. Both loadings are maintained constant after the load applications are complete.

The pore water pressure distributions in the soil specimen at different times during step and continuous loadings are calculated using Terzaghi's one-dimensional consolidation theory and Olson's theoretic solution for time-dependent loading (Olson 1977), which are presented in Figures 5a and 5b, respectively. As can be seen in Figure 5a, during the step loading, the excess pore water pressure in the soil specimen uniformly increases to 50 kPa at the instant of load application $t = 0$. The pore water pressure is then decreased gradually due to drainage with time. It takes about 209 hours (8.7 days) for the soil to reach a degree of consolidation of 98%. The corresponding average residual excess pore water pressure is 1 kPa. It is assumed that from the viewpoint of experiment, the excess pore water pressure has been completely dissipated.

For continuous loading, as shown in Figure 5b, initially at time t = 0, the excess pore water pressure in the soil is nearly zero since the applied load is very small. With an increase in the time, the applied stress increases. The pore water pressure in the soil also increases. Its magnitude depends upon a combination of two reverse processes: increase in the pore water pressure due to the applied load and decrease in pore water pressure due to water drainage. For example, at time of 40 h, the total isotropic stress applied is 20 kPa. Due to the dissipation of excess pore water pressure, the maximum pore water pressure in the soil is only 17.12 kPa, which is at the top of the soil specimen due to the longest drainage path. The pore water pressure at t = 40 h decreases with height due to the smaller drainage path and reaches zero near the bottom of the soil specimen. Similar process continues until the applied load reaches 50 kPa (increases in pore water pressure represented by solid lines in Figure 5b), followed by a pore water pressure dissipation process (represented by dotted lines in Figure 5b). It takes about 264 hours (11 days) for the soil to reach a degree of consolidation of 98%.

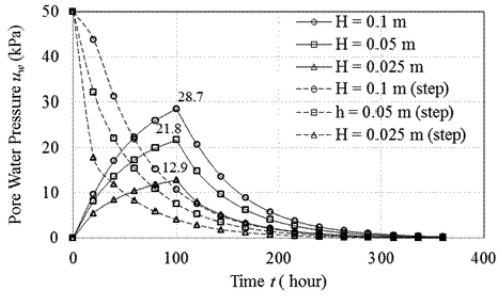
The following conclusions can be obtained from Figure 5b: (1). It takes longer time for continuous loading to reach the same degree of consolidation of 98%; (2). Before the degree of consolidation reaches 98% (t < 264 h), soil specimen in either step or continuous loading cannot be considered as a representative elementary volume (REV) since the pore water pressure distribution is not uniform.

Although the calculation is made for a saturated soil specimen, it is expected that the test results for unsaturated soils will follow similar patterns. Consequently, a third conclusion is expected for unsaturated soil specimen: continuous loading can potentially cause

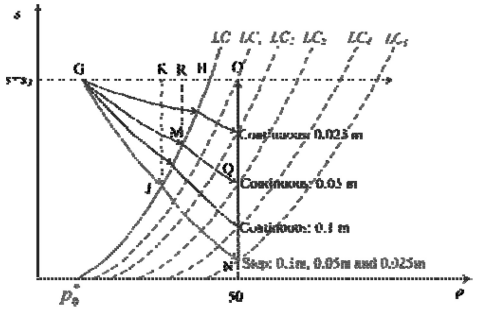
a homogenous specimen into a nonhomogeneous soil. This can be demonstrated by Figure 6. Figure 6a compares the pore water pressure variations with time at three different heights of 0.1 m, 0.05 m, and 0.025 m from bottom of the soil specimen for the two different loading processes. For step loading, the pore water pressures the maximum of 50 kPa uniformly at the instant of load application, and then decrease with time at different speeds due to different lengths of drainage path. For continuous loading, the excess pore water pressures start from zero, increases to maximum at the end of load application process, and then decrease with time. The maximum excess pore water pressures are different at different heights. This difference might not have effect on saturated soils. However, if the soil specimen is unsaturated, the situation is quite different as shown in Figure 6b. Figure 6b schematically illustrates the stress paths for an isotropic compression SCTX for an unsaturated soil with step and continuous loadings. The initial condition of the soil is at point G in Figure 6b with a preconsolidation stress of p_0^*. The associated yield curve is LC. During the step loading, the isotropic stress is applied instantaneously to the soil, causing the soil suction in the soil uniformly decrease from G to J to N, where J is the yield point. During this process, the stress states in the soil at different heights are all the same and the stress history changes in exactly the same way. Soil specimen can be considered as REV during this process. From point N to O is a process for the excess suction to dissipate. The pattern of suction distributions will be similar to those as shown in Figure 5a for saturated soils. During this process, the suction in the soil is not uniform, so it is a boundary-value problem and the soil specimen cannot be considered as REV. Only when all the excess pore water pressure is dissipated and stress states in the soil all reach point O, the soil can be considered as a REV again. As discussed previously, point O is a stress state in the elastic zone. So the final position of the yield curve is LC_5.

During continuous loading, the stress is applied slowly and the soil is allowed to drain. Consequently, the decreases in suction in the soil specimen are smaller than that during the step loading. This is the main reason why continuous loading is considered superior to step loading. However, the suction in the soil is not uniform with height during continuous loading. The larger the height, the longer the drainage path and the larger decreases in the soil suction are. The pattern of suction changes is similar to that in Figure 5b. The soil suction changes reach its peak when the load application is completed and excess pore water pressure dissipates with time at constant load along line QO. Since the maximum suction decreases are different for soil at different heights, the changes in stress histories for soil at different heights are also different.

Soil at the top of the specimen (H = 0.1 m) experiences the largest suction decrease and the corresponding yield curve is pushed to the furthest position of LC_4. Soil in the middle of the specimen has a new yield curve position of LC_3. Soil at the bottom of the



(a) Pore water pressure variations with times at different heights



(b) Yield curves for soil at different heights

Figure 6. Stress History Changes Caused by Continuous Loadings.

specimen is always at drained condition, so the stress path is G → H → O, and the yield curve is moved to LC_1. As discussed previously, the dissipation of excess pore water pressure is an unloading process, so it will not change the locations of yield curves. Consequently, when the excess pore water pressure in the soil specimen is completed during continuous loading, the stress histories of the soil vary from LC_1 (bottom of the specimen) to LC_4 (top of the specimen). The soil at the top of the specimen is expected to have the largest deformation (or collapse) and be the densest. The soil at the middle of the specimen will have less deformation and less denser. The soil at the bottom of the soil specimen will be compressed the least. In other words, a soil with identical stress history everywhere (or homogeneous) will have different stress histories along its height (nonhomogeneous) after a continuous loading SCTX test. As a result, the soil after a continuous loading cannot be used as a REV even if the soil has the same stress state everywhere. If the soil specimen is not a REV, the results cannot be used for constitutive modeling purposes. The test results obtained from a continuous loading process are averaged values of non-uniform soils in elastic zones with different stress histories. They cannot provide any information regarding the plastic behavior (d, e, f, and I as shown in Fig. 3b) needed for the constitutive modeling purpose.

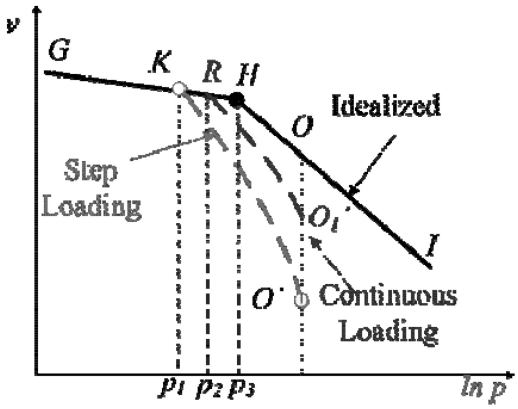


Figure 7. Schematic plot of effects of loading procedure on sctx test results.

Under continuous loadings, all the actual stress paths are closer to the idealized stress path (Fig. 6b). This means that on average the soil in the continuous loading experienced less suction reduction (and collapse) than the soil in the step loading. Consequently, the result obtained from continuous loading process O_1' has higher specific volume than those from the step loading O′, while the "true" result is point O as shown in Figure 7. Also, since the suction reduction is smaller, on average the soil in the continuous loading yields at larger stresses (represented by point R in Figure 6b and 7) than the soil in the step loading(represented by point K in Figure 6b and 7). The theoretic yield point is point H in Figure 6b and 7. Analyses in Figures 6 and 7 are consistent with the suction-controlled isotropic compression test results reported by Cui and Delage (1996), which manifested that the specific volumes under continuous loadings are much higher than those under step loadings for the same *p* and *s* on the virgin compression lines.

4 CONCLUSIONS

SCTX testing method has been established as a standard approach to characterize constitutive behavior for unsaturated soils. Most important concepts for modern unsaturated soil mechanics were developed upon results from the SCTX tests. Among these, one of the most important contributions in the constitutive modeling of elasto-plastic behavior for unsaturated soils is the Barcelona Basic Model (BBM) proposed by Alonso et al. (1990). The BBM successfully explained many features of unsaturated soils and received extensive acceptance. The SCTX tests are designed based upon the Divide-and Conquer Approach in which an implicit assumption is used: soil behavior is stress-path independent. However, it is well-established that unsaturated soil behavior is elasto-plastic and stress-path dependent. Consequently, SCTX tests, at its current version, are not suitable for characterizing behavior for unsaturated soils. The BBM is not compatible with the SCTX upon which the model is developed.

Continuous loading has been with increasing popularity as an alternative to the step loading in the SCTX tests. It is found in this paper that results obtained from continuous loading is more controversial compared with those obtained from step loading. Continuous loading can make a homogeneous soil into nonhomogeneous. Consequently, the soil specimen cannot be viewed as a REV and the obtained results are not suitable for constitutive modelling purpose. It also takes longer time to run a SCTX test with continuous loading procedure. Analyses in this paper indicate that both the specific volume and yield stresses are underestimated during an SCTX test.

ACKNOWLEDGEMENT

This research was supported by the "100 Gifted People Plan of Hubei Province, China."

REFERENCES

Alonso, E. E., Gens, A., and Gehling, W. Y. Y. (1994). "Elasto-plastic model for unsaturated expansive soils." Numerical models in geotechnical engineering. Balkema, 11–18.

Alonso, E. E., Gens, A., and Josa, A. (1990). "A constitutive model for partially saturated soils." Geotechnique, 40(3), 405–430.

Alonso, E. E., Vaunat, J., and Gens, A. (1999). "Modeling the mechanical behavior of expansive clays." Engineering Geology, 54(1–2), 173–183.

Bishop, A. W., Alpan, I., Blight, G. E., and Donald, I. B. (1960). "Factors controlling the shear strength of partly saturated cohesive soil." In: Proc., ASCE Research Conf. on Shear Strength of Cohesive Soils, Univ. of Colorado, Boulder, CO, pp. 503–532.

Bishop, A. W., and Blight, G. E. (1963). "Some aspects of effective stress in saturated and unsaturated soils." Geotechnique, 13(3), 177–197.

Bishop, A. W., and Donald, I. B. (1961). "The experimental study of partly saturated soil in the triaxial apparatus." In: Proc., 5th Int. Conf. Soil Mech., 1, 13–21.

Blatz, J. A., and Graham, J. (2003). "Elastic-plastic modeling of unsaturated soil using results from a new triaxial test with controlled suction." Geotechnique, 53(1), 113–122.

Bolzon, G., Schrefler, B. A., and Zienkiewicz, O. C. (1996). "Elastoplastic soil constitutive laws generalised to partially saturated states." Geotechnique, 46, 279–289.

Costa, L. M., and Alonso, E. E. (2009). "Predicting the Behavior of an Earth and Rockfill Dam under Construction." Journal of Geotechnical & Geoenvironmental Engineering, Vol. 135, (Issue 7), pp 851—862.

Cui, Y. J., and Delage, P. (1996). "Yielding and plastic behaviour of an unsaturated compacted silt." Geotechnique, 46(2), 291–311.

Dakshanamurthy, V., Fredlund, D. G., and Rahardjo, H. (1984). "Coupled three-dimensional consolidation theory of unsaturated porous media." Preprint of Papers: 5th Int. Conf. Expansive Soils, Institute of Engineers, Adelaide, South Australia, May, pp. 99–104.

Dangla, O. L., Malinsky, L., and Coussy, O. (1997). "Plasticity and imbibition-drainage curves for unsaturated soils: a unified approach." In: 6th international conference on numerical models in geomechanics, Montreal. Balkema, Rotterdam, pp 141–146.

Das (2008). Advanced Soil Mechanics. 3rd Edition. Taylor & Francis Group.

Delage, P (2002). "Experimental unsaturated soil mechanics." Proc. 3rd Int. Conf. on Unsaturated Soils, UNSAT, (3) 973-996, Juca JFT, De Campos TMP, Marino FAM, Recife, Brazil, Balkema.

Delage, P., and Graham, I. (1995). "State of the art report-understanding the behavior of unsaturated soils requires reliable conceptual models." In: Proc. of 1st International Conference on Unsaturated Soils, Paris, 3, pp. 1323–1256.

D'onza, F., Gallipoli, D., Wheeler, S., Casini, F., Vaunat, J., Khalili, N., Laloui, L., Mancuso, C., Masin, d., Nuth, M., Pereira, J. M. and Vassallo, R. (2011). "Benchmark of constitutive models for unsaturated soils." Geotechnique 61, No. 4, 283–302.

Fredlund, D. G., and Rahardjo, H. (1993). Soil Mechanics for Unsaturated Soils. New York: John Wiley and Sons.

Gallipoli, D., Gens, A., Sharma, R., and Vaunat, J. (2003). "An elastoplastic model for unsaturated soil incorporating the effects of suction and degree of saturation on mechanical behaviour." Geotechnique, 53, 123–135.

Gallipoli, D., Wheeler, S. J., and Karstunen, M. (2003). "Modeling the variation of degree of saturation in a deformable unsaturated soil." Geotechnique, 53(1), 105–112.

Geiser, F., Laloui, L., and Vulliet, L. (2000). "Modelling the behaviour of unsaturated silt." In: Experimental Evidence and Theoretical Approaches in Unsaturated Soils. Rotterdam: Balkema, pp. 155–175.

Gens, A. (1995). "Constitutive modelling: Application to compacted soil." In: Proc. of 1st International Conference on Unsaturated Soils, Paris, 3, pp. 1179–1200.

Gens, A., and Alonso, E. E. (1992). "A framework for the behavior of unsaturated expansive clays." Canadian Geotechnical Journal, 29, 1013–1032.

Gens, A., and Olivella, S. (2001). "THM phenomena in saturated and unsaturated porous media." Revue franc¸aise de ge'nie civil 5, 693–717.

Gens, A., Sánchez, M., and Sheng, D. (2006). "On constitutive modelling of unsaturated soils." Acta Geotechnica, 1(3), 137–147.

Hilf, J. W. (1956). "An Investigation of Pore-Water Pressure in Compacted Cohesive Soils." Ph.D. dissertation, Technical Memorandum No. 654, U.S. Department of the Interior, Bureau of Reclamation, Design and Construction Division, Denver, Colorado.

Jennings, J. E., and Burland, J. B. (1962). "Limitations to the use of effective stresses in partly saturated soils." Geotechnique, 12(2), 125–144.

Jommi, C. (2000). "Remarks on the constitutive modelling of unsaturated soils." In: Experimental Evidence and Theoretical Approaches in Unsaturated Soils. Rotterdam: Balkema, pp. 139–153.

Khalili, N., Geiser, F., and Blight, G. E. (2004). "Effective stress in unsaturated soils: review with new evidence." International Journal of Geomechanics, ASCE. Vol. 4, No. 2, 115–126

Lloret, A., and Alonso, E. E. (1980). "Consolidation of unsaturated soils including swelling and collapse behavior." Geotechnique, 30(4), 449–477.

Macari, E. J., Arduino, P., and Hoyos, L. R. (2003). "Constitutive modeling of unsaturated soil behavior under axisymmetric stress states using a stress/suction-controlled cubical test cell." International Journal of Plasticity, 19(10), 1481–1515.

Matyas, E. L., and Radhakrishna, H. S. (1968). "Volume change characteristics of partially saturated soils." Geotechnique, 18, 432–448.

Olivella, S., Carrera, J., Gens, A., and Alonso, E. E. (1994). "Nonisothermal multiphase flow of brine and gas through saline media." Transp. Porous. Media, 15, 271–293.

Olivella, S., Gens, A., Carrera, J., and Alonso, E. E. (1996). "Numerical Formulation for a Simulator (CODE_BRIGHT) for the Coupled Analysis of Saline Media." Engineering Computations, 13(7), 87–112.

Olson, R.E. (1977). "Consolidation Under Time-Dependent Loading." Journal of Geotechnical Engineering Division, ASCE, Vol. 103, No. GT1, pp. 55–60.

Rampino, C., Mancuso, C., and Vinale, F. (2000). "Experimental behaviour and modelling of an unsaturated compacted soil." Canadian Geotechnical Journal, 37: 748–763.

Sanchez, M., Gens, A., Guimaraes, L. D. N, and Olivella, S. (2005) "A double structure generalized plasticity model for expansive materials." Int. J. Numer. Anal. Meth. Geomech., 29, 751–787.

Sharma, R. S. (1998). "Mechanical behaviour of unsaturated highly expansive clays." D.Phil. thesis, University of Oxford, UK.

Sheng, D., Fredlund, D. G., and Gens, A. (2008) "A new modelling approach for unsaturated soils using independent stress variables." Canad. Geotech. J., 45(4), 511–34.

Sheng, D., Sloan, S. W., and Gens, A. (2004). "A Constitutive model for unsaturated soils: thermomechanical and computational aspects." Computational Mechanics, 33(6), 453–465.

Sheng, D., Sloan, S. W., Gens. A., and Smith, D. W. (2003a). "Finite element formulation and algorithms for unsaturated soils. Part I: theory." Int. J. Numer. Anal. Meth. Geomech., 27, 745–765.

Sheng, D., Smith, D. W., Sloan, S. W., and Gens, A. (2003b). "Finite element formulation and algorithms for unsaturated soils. Part II: verification and application." Int. J. Numer. Anal. Meth. Geomech., 27, 767–790.

Sivakumar, V. (1993). "A critical state framework for unsaturated soil." Ph.D. Thesis, University of Oxford.

Sun, D. A., Sheng, D. C., Xiang, L., and Sloan, S.W. (2008). "Elastoplastic prediction of hydro-mechanical behaviour of unsaturated soils under undrained conditions." Computers and Geotechnics: 35: 845–852.

Tamagnini, R. (2004). "An extended Cam-clay model for unsaturated soils with hydraulic hysteresis." Geotechnique, 54, 223–228.

Thu, T. M, Rahardjo, H., and Leong, E. C. (2007). "Soil-water Characteristic Curve and Consolidation Behavior for a Compacted Silt." Canadian Geotechnical Journal, 44(3), pp. 266–275.

Vaunat, J. (2005). "Elastoplastic framework to model unsaturated materials." 1 st. MUSE School "Fundamentals of Unsaturated Soils". Barcelona, Spain, 1–2 June 2005. http://muse.dur.ac.uk/.

Vaunat, J., Romero, E, and Jommi, C. (2000). "An elastoplastic hydro-mechanical model for unsaturated soils." In: Experimental Evidence and Theoretical Approaches in Unsaturated Soils. Rotterdam: Balkema, 121–138.

Wheeler, S. J. (1996). "Inclusion of specific water volume within an elastoplastic model for unsaturated soil." Can. Geotech. J., 33, 42–57.

Wheeler, S. J., and Karube, D. (1995). "State of the art report-constitutive modeling." In: Proc. of 1st

International Conference on Unsaturated Soils, Paris, 3, pp. 1323–1356.
Wheeler, S. J., and Sivakumar, V. (1995). “An elasto-plastic critical state framework for unsaturated soil.” Geotechnique, 45(1), 35–53.
Wheeler, S. J., Gallipoli, D., and Karstunen, M. (2002). “Comments on use of the Barcelona Basic Model for unsaturated soils.” Int. J. Numer. Anal. Meth. Geomech., 26, 1561–1571.
Wheeler, S. J., Sharma, R. S., and Buisson, M. S. R. (2003). “Coupling of hydraulic hysteresis and stress–strain behaviour in unsaturated soils.” Geotechnique, 53, 41–54.

Unsaturated Soil Mechanics—from Theory to Practice – Chen et al. (Eds)
© 2016 Taylor & Francis Group, London, ISBN 978-1-138-02921-7

Reanalysis on shear strength of unsaturated soils

L.T. Shao, G.F. Zheng & X.X. Guo
State Key Laboratory of Structural Analysis for Industrial Equipment, Dalian University of Technology, Dalian, Liaoning, China
Department of Engineering Mechanics, Dalian University of Technology, Dalian, Liaoning, China

ABSTRACT: This paper aims to study the shear strength of unsaturated soils based on the data available in published literatures. The relationship between the Soil Water Characteristic Curve (SWCC) and shear behavior of unsaturated soils is investigated, and it shows a nonlinear increase of shear strength with respect to soil suction. The SWCC combined with saturated shear strength parameters are used to predict the unsaturated shear strength using the proposed effective stress for unsaturated soils. A series of data from direct shear and triaxial tests performed on unsaturated soils validates the effective stress as the quantitative predictions of shear strength show a good agreement with experimental results, and a unified shear strength equation with effective stress for saturated and unsaturated soils is proposed by extending the Mohr-Coulomb shear strength criteria.

1 INTRODUCTION

Research on unsaturated soils basically follows such a process: some empirical theory, which was referenced on the concept of effective stress for saturated soils, was put forward based on the experimental results to explaining the mechanical behavior of unsaturated soils (Bao 1998; Zhao 2013). So the study on unsaturated soils is from a view of phenomenological method with no rigorous theoretical analysis.

The shear strength occupied an important position in unsaturated soils as the determination of shear strength is of fundamental importance for a large number of geotechnical problems, therefore the establishment of the shear strength theory has always been a hot research field. Generally, there are two approaches to determining the shear strength of unsaturated soils: the stress state variables framework (Fredlund et al. 1978), and the single effective stress framework (Bishop 1959). Discussion on shear strength was always existed in unsaturated soil mechanics, but after years of experiments and theoretical analysis, some common conclusions can be advanced as follows:

(a) The contribution of matric suction generally results in an increase in shear strength of unsaturated soils (Fredlund et al. 1996; Escario & Saez 1986; Vanapalli et al. 1996; Fredlund & Rahardjo 1993), but the increase in shear strength cannot continue indefinitely with the increasing suction.
(b) Experimental results show a nonlinear relationship between shear strength and the matric suction (Escario & Seaz 1986, Vanapalli et al. 1996, Cunningham et al. 2003, Gan et al. 1988). The shear strength increases rapidly at low suctions and then the increasing tendency decreases at high suction levels.
(c) Both an increase in confining pressure and matric suction could result in higher shear strength. However, the strength is more sensitive to the change of confining pressure.

In this paper, effective stress principle to unsaturated soils was briefly reviewed based on the previous work to derive the effective stress equation of unsaturated soils from the perspective of continuum mechanics (Shao 2012). The physical meaning of the effective stress of a soil was defined to be the soil skeleton stress due to external forces excluding pore fluid pressure. Then a shear strength criteria for unsaturated soils has been proposed based on the effective stress principle and it came to a conclusion that the shear strength of an unsaturated soil is determined by the effective stress (Shao 2014). Then the shear strength equation was compared to its counterpart described above. It was similar in form to the Bishop's single effective stress framework, i.e., the parameter χ related to the degree of saturation can be substituted by effective degree of saturation S_e, and it was the same with its counterpart which was developed by Vanapalli (1996) in the form of stress state variables.

It's acknowledged that the shear strength of an unsaturated soil is a function of matric suction. So in this paper, the relationship between SWCC and the shear strength, as well as the nonlinearity of shear strength with respect to matirc suction was discussed in detail. Then some attempts have been made to predict the shear strength of unsaturated soils using the proposed shear strength criteria based on the data available in literatures. Data from suction controlled direct

shear and triaxial tests (constant suction or constant water content) in the literature was found to be consistent with observed experimental results. So it proposed an equation for the shear strength of an unsaturated soil using the SWCC and the shear strength parameters of the saturated soils. It can be seen that the equation provides satisfactory predictions for unsaturated soils.

2 THE STRESS STATE AND SHEAR STRENGTH FOR UNSATURATED SOILS

Because of the successful application of the effective stress principle for saturated soils, many people have attempted to extend the principle to cover the case of unsaturated soils. Earlier research on the shear strength of unsaturated soils involved the concept of effective stress, and several equations have been developed for evaluating the shear strength of unsaturated soils (Crony et al., 1958; Aitchison, 1961; Jennings, 1961; Bishop, 1959; Bishop & Blight, 1963). Among those equations, the most representative is due to Bishop (1959).

$$\tau = c^{'} + [(\sigma - u_a) + \chi(u_a - u_w)]\tan\phi^{'} \tag{1}$$

where c' and ϕ' are saturated effective strength parameters, and χ is a parameter depending on degree of saturation, soil type and hysteresis effects due to wetting, drying and stress path.

As a representative of Bishop's equation, Khalili (1998) proposed a substitution of parameter χ based on regression analysis of experimental data from literatures.

$$\chi = \frac{\tau - \tau_0}{(u_a - u_w)\tan\phi^{'}} = \left[\frac{(u_a - u_w)}{(u_a - u_w)_b}\right]^{-0.55} \tag{2}$$

in which τ and τ_0 are the shear strength of unsaturated soils and its counterpart of saturated soils, respectively, $(u_a - u_w)_b$ refers to the air entry value of the soil. It makes use of the air entry value to determine the parameter χ, and an empirical shear strength model is proposed in terms of χ and saturated shear strength parameters.

The advantage of the Bishop form of shear strength criteria is that the complete characterization of the soil strength requires matching of a single effective stress concept. However, some researchers demonstrated that this equation did not account for the collapse behavior (volumetric compression under suction reduction) of many soils (Blight, 1965; Aitchison, 1967) and they believed that the variables used for description of a stress should be independent of the material properties but χ is related to the degree of saturation.

As a consequence of the limitations and difficulties regarding the use of Bishop's equation, there has been a tendency to use the stress state variables to describe unsaturated soil behavior. Fredlund et al. (1978) proposed that the shear strength of an unsaturated soils depending on the two independent stress

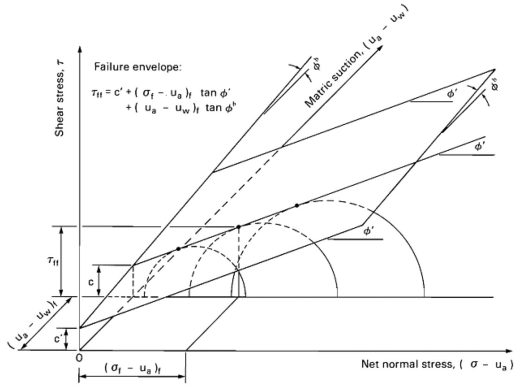


Figure 1. Extended Mohr-Coulomb failure envelop for unsaturated soils (from Gan et al. 1988).

variables: the net normal stress $(\sigma - u_a)$ and matric suction $(u_a - u_w)$, and the shear strength is evaluated as:

$$\tau = c^{'} + (\sigma - u_a)\tan\phi^{'} + (u_a - u_w)\tan\phi^{b} \tag{3}$$

where c' and ϕ' are saturated effective strength parameters, and ϕ^b is the angle of internal friction with respect to matric suction. Equation (3) defines the shear strength criteria for unsaturated soils, which is called the extended Mohr-Coulomb failure envelope (Fig. 1).

Figure 1 indicated that the shear strength envelop for unsaturated soils was characterized by a plane surface, where both ϕ' and ϕ^b were assumed to be constant. Further experimental evidence showed that the relationship between shear strength and matric suction was nonlinear and there is a consensus that ϕ^b is not constant (Escario & Saez, 1986; Gan et. al, 1988). It was believed that $\phi^b = \phi'$ for matric suction lower than the soil air-entry value, then ϕ^b decreases as the suction increases (Feuerhaemel 2006).

A great improvement of understanding on the behavior of unsaturated soils has been made and most of the constitutive models developed for unsaturated soils were based on the two independent stress stats variables (Alonso et al., 1990; Fredlund & Rahardjo, 1993; Cui & Delage, 1996). However, the determination of the parameter ϕ^b related to matric suction requires elaborate testing and costly laboratory facilities and that is beyond of many laboratory conditions.

Shao (2014) derived the effective stress for unsaturated soils on the basis of continuum mechanics by taking each phase (soil skeleton, pore air and pore water) of an unsaturated soil as independent research target. Then equilibrium equations of each phase were established by carrying out internal force analysis, and the residual water content was regarded as a part of soil skeleton, in this way the effective stress equation for unsaturated soils was obtained as follows:

$$\sigma^{'} = \sigma - u_a + S_e(u_a - u_w) = \sigma - u_a + \left(\frac{S - S_r}{1 - S_r}\right)(u_a - u_w) \tag{4}$$

where S and S_r are degree of saturation and residual degree of saturation respectively, $S_e = (S - S_r)/(1 - S_r) = (\theta - \theta_r)/(\theta_s - \theta_r)$ is the effective saturation that refers to the saturation excluding residual water content. When the soil is saturated ($S_e = 1$), the equation becomes the Terzaghi's effective stress for saturated soils. It proved that the effective stress is the soil skeleton stress due to external forces excluding pore fluid pressure. It's acknowledged that the strength and deformation of a soil is the strength and deformation of the soil skeleton. Therefore, when effect of pore fluid pressure on the strength and deformation of a soil can be ignored, changes in shear strength and deformation of a soil are due exclusively to the change of effective stress.

As the concept of effective stress was introduced to the Mohr-Coulomb criteria, the shear strength criteria for unsaturated soils in terms of single effective stress can be obtained.

$$\tau = c' + [\sigma' - u_a + S_e(u_a - u_w)]\tan\phi' \tag{5}$$

The equation was same with the shear strength formulation developed by Vanapalli (1996) based on the experimental data analysis, but Vanapalli didn't recognize that the expression in the bracket of the equation described above represents the effective stress for unsaturated soils, and he insisted that the shear strength for an unsaturated soil shouldn't be determined by a single stress state variable as it should be characterized in the framework of stress state variables.

However, a conclusion can be advanced as a unified shear strength criteria (Eq. 5) was developed either in single effective stress approach or in stress state variables approach, and it is not only applicable to unsaturated soils, but also suitable for saturated soils ($S_e = 1$).

The shear strength criteria described above is based on the assumption that the parameters c' and ϕ' are independent of soil suction or degree of saturation. Actual soils may not satisfy this assumption (Drumright 1989; Escario & Juca, 1989), but for most of the geotechnical engineering practice, the value of c' and ϕ' can be assumed to be constant for a suction range of 0–600 kPa (Khalili, 1998; Vanapalli, 1996).

3 DATA REVIEW FROM LITERATURES

The shear strength contribution due to matric suction can be mathematically expressed as:

$$\tau_m = S_e(u_a - u_w)\tan\phi' \tag{6}$$

It can be predicted using the soil-water characteristic curve since the SWCC defines the relationship between water content and matric suction. Moreover, the residual water content θ_r, or the residual degree of saturation S_r, can be determined from the SWCC.

To determine an analytical prediction on the shear strength, it is necessary to introduce a mathematical equation to represent the SWCC (Brooks and Corey 1964; Van Genuchten 1980; Fredlund and Xing 1994). Van Genuchten (1980) provided an empirical model to define the SWCC. The relevant parameters should be determined by nonlinear regression analysis.

$$S_e = \frac{\theta - \theta_r}{\theta_s - \theta_r} = \left[\frac{1}{1 + (\alpha_v \psi)^{n_v}}\right]^{m_v} \tag{7}$$

where

S_e is effective degree of saturation;
θ is volumetric water content;
θ_s is saturated volumetric water content;
θ_r is residual volumetric water content;
α_v is the parameter related to air entry value;
n_v, m_v are soil parameters;
ψ is matric suction.

Experimental study on the shear strength of unsaturated soils with respect to matric suction basically follows such approaches: Suction controlled tests using a direct shear apparatus (case data 1) or triaxial testing apparatus (case data 2) in which the soil suction was usually controlled to be constant using the axis-translation technique during the shear process, or the water content was kept constant (case data 3) during the test and then effect of varying water content on shear strength was studied. To investigate the correlation between the predicted and measured values of shear strength of unsaturated soils, several examples from the literatures were analyzed. Special attention was paid to the non-linearity of the shear strength with respect to matric suction.

3.1 *Case data 1 (Suction-controlled direct shear test)*

Zhan (2006) conducted suction-controlled direct shear tests (different suctions with the same net normal stress of 50 kPa) on compacted unsaturated expansive clay ($\rho_d = 1.56$ g/cm^3; optimum water content, 20.5%) from South-to-North Transfer Canal. The SWCC (Fig. 2) of the soil was measured using of a pressure plate extractor, and the residual water content for the clay was established using the Van Genuchten's model, which yielded value of 24.2%, or 53.7% for the residual degree of saturation. The air entry value of the compacted clay is about 24.3 kPa. Direct shear tests on saturated samples reported an effective friction angle $\phi' = 24°$ and a zero effective cohesion.

Figure 3 shows the measured shear strength data and the predictions based on the unified shear strength equation. A good fit of the predicted curve was found to the measured shear strength data. The correlation coefficient, R^2 between the predicted and measured strength is 0.91 with the maximum error of 8.4% when the suction is 100 kPa. Both the predicted and measured strength exhibited a nonlinear increase as the matric suction increase, and slope of the failure envelop commenced at a same value of ϕ' (i.e.,

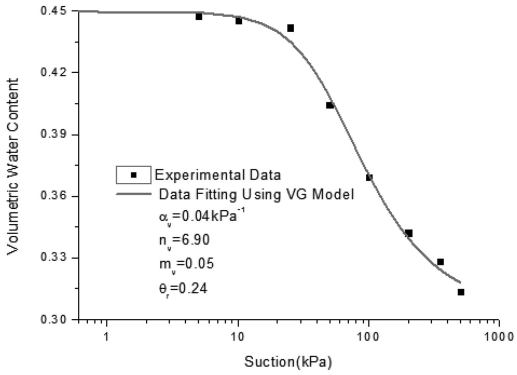


Figure 2. SWCC for a compacted clay (after Zhan 2006).

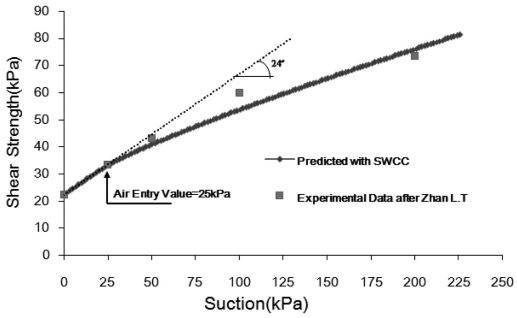


Figure 3. Comparison between predicted and measured unsaturated shear strength for a compacted soil.

24°) when the matric suction lowers than the air entry value of 24.2 kPa then decrease slightly as the suction increases. But the trend of nonlinear increase was not obvious as expected. This may be attributed to the linear increase of suction which offsets the nonlinear decrease of S_e as the suction increases from 25 kPa to 225 kPa.

3.2 *Case data 2 (Suction-controlled triaxial test)*

A similar analysis was conducted using the triaxial test reported by Khalili (2004) on many undisturbed soil samples ($w_L = 25\%$; $w_P = 19\%$; $\rho_d = 1.91$ g/cm^3) from the south junction area of Hume Dam, Australia. The saturated tests were carried out using conventional triaxial testing equipment. The effective friction angle $\phi' = 30°$ and effective cohesion $c' = 5$ kPa were reported. The unsaturated tests were carried out using a Bishop-Wesley hydraulic triaxial cell on a net normal stress of 200 kPa with different suction. The SWCC of the soil (Fig. 4) and the model fitting parameters showed that air entry value is 211.42 kPa and residual water content is 7.3%, or 43.8% for the degree of saturation.

There is a good correlation between the predicted and measured values of the maximum deviatoric stress for this kind of soil (Fig. 5). The correlation coefficient, R^2 between the predicted and measured strength

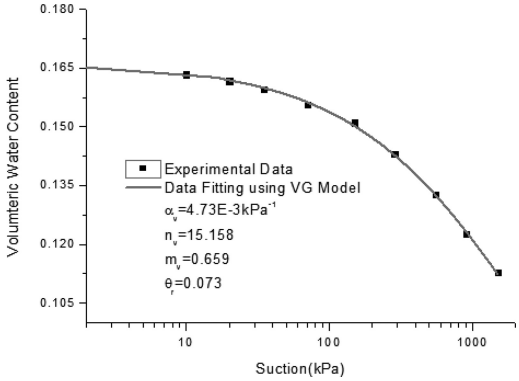


Figure 4. Soil-Water Characteristic Curve (from Khalili, 2004).

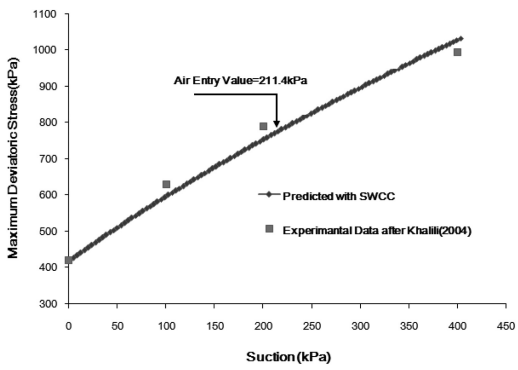


Figure 5. Comparison between predicted and measured maximum deviatoric stress.

is 0.981 with maximum error of 5.1% when the suction is 400 kPa.

The failure envelop didn't exhibit an obvious change as it was shown in Figure 3 when the suction is increased beyond the air entry value. It can be seen from the SWCC that the soil desaturates at low suction levels below the air entry value (i.e., 211.4 kPa). So the smooth transition of the SWCC nearby the air entry value can be interpreted to that phenomenon. It does not have an impact on the applicability of the shear strength criteria.

3.3 *Case data 3 (Constant water content triaxial test)*

A final example was provided by Miao L.C. (2007) who tested an expansive clay soil from Nanning, China. ($G_s = 2.7$, $W_L = 61.4\%$, $W_p = 30.3\%$, $\rho_d = 1.48$ g/cm^3 Free Swelling 45%) by drained triaxial test (different initial degree of saturation with the same confining pressure of 100 kPa). It should be noted that the soil specimens were prepared from a slurry condition. The test result showed that there is a very small change of the degree of saturation for the specimens during the shear indicating a small change of water content. Hence, the case was used as

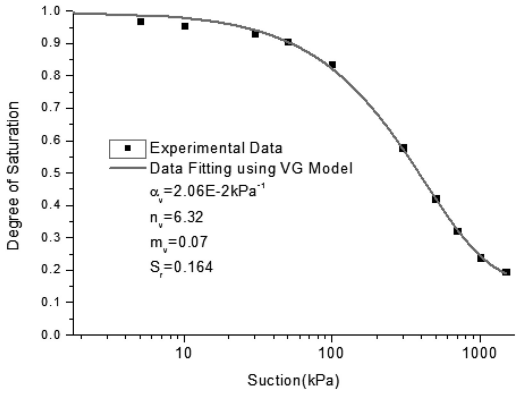


Figure 6. SWCC for Nanning expansive clay (from Miao, 2015).

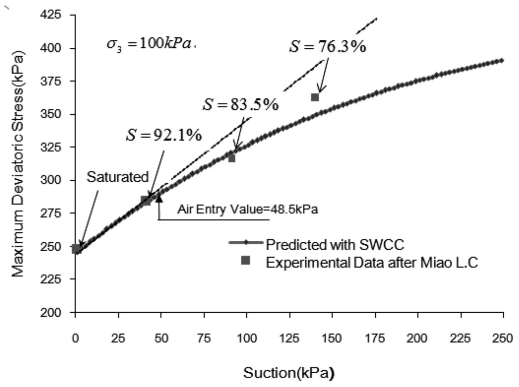


Figure 7. Comparison between predicted and measured strength for Nanning expansive clay.

an example of constant water content triaxial test. The effective friction angle $\phi' = 19.8°$ and cohesion intercept $c' = 50$ kPa was reported by saturated triaxial test. Miao L.C. (2015) showed SWCC of the compacted expansive clay (Fig. 6) which was approximated by the Van Genuchten model and it indicated that the air entry value and residual degree of saturation was 97.1 kPa and 16.4% respectively.

A good match also can be seen between the predicted strength with SWCC and the experimental results (Fig. 7). The correlation coefficient, R^2 between the predicted and measured strength is 0.952 with the maximum error of 6.4% when the degree of the saturation was 76.3%. The agreement is satisfactory.

All the predictions of shear strength using saturated soil parameters c' and ϕ' show great linear correlation with respect to effective stress for all experimental suction range, and the Mohr-Coulomb shear strength criteria can be extended to unsaturated soils.

A typical relationship between the shear strength and the matric suction can be seen by Figures 3 and 7. There is a linear increase in the shear strength with respect to matric suction, and the angle of the failure envelop is same with the effective angle of internal friction ϕ' as the soil is saturated for suction lowers than the air entry value. Then the increase in suction leads to a relatively small increase of shear strength as the increase tendency gradually flattens. The effective degree of saturation can be accounted for the nonlinear relationship between the shear strength and soil suction as the soil desaturates with a decrease in effective degree of saturation.

4 CONCLUSIONS AND PROSPECT

The unified shear strength criteria, which is applicable both for saturated and unsaturated soils, was developed based on the concept of effective stress.

The shear strength equation made use of the soil-water characteristic curve and the saturated shear strength parameters. Effective degree of saturation is account for the nonlinear relationship between the shear strength and soil suction due to the nonlinear relationship between the water content and matric suction. Data from the literature proved that predictions of shear strength with effective stress show good agreement with experimental results.

This has an important significance to the prediction of shear strength for unsaturated soils, but it needs further investigation on the applicability of the effective stress to explain the volumetric behavior of unsaturated soils.

ACKNOWLEDGMENTS

This work was carried out as a part of project No. 51479023, which is supported by the National Natural Science Fund of China. The authors are very grateful to the National Natural Science Fund of China for the financial support conceded to this research work. The helpful work provided by Zhan L.T., Khalili N. and Miao L.C. was also acknowledged.

REFERENCES

Aitchison, G.D. 1961. Relationship of mois ture and effective stress functions in unsaturated soils. *Proceeding of Conference on Pore Pressure and Suction in Soils, London,* 47–52.

Aitchison, G.D. 1967. Separate roles of site investigation, quanti-fication of soil properties and selection of operational environment in the determination of foundation design on expansive soils. *Proc. 3rd Asian Regional Conf. Soil Mech. Found. Engng, Haifa, Israel*, 3, 72–77.

Alonso, E.E., Gens, A. and Josa, A. 1990. A constitutive model for partially saturated soils. *Geotechnique*, 40(3): 405–430.

Bao C.G. 1986. The stress-strain relationship and strength characteristics for unsaturated soils (in Chinese). *Chinese Journal of Geotechnical Engineering*. 8, No. 1, 26–31.

Bishop, A.W. 1959. The principle of effective stress. *Tek, Ukebl*. 106, No. 39, 859–863.

Bishop, A.W. and Blight, G.E. 1963. Some aspects of effective stress in saturated and partially saturated soils. *Géotechnique*, 13(3): 177–197.

Blight, G. 1965. A study of effective stresses for volume change. *In Moisture equilibria and moisture changes in soils beneath covered areas* (ed. G. D. Aitchison), pp. 259–269. Sydney: Butterworths.

Brooks R.H. Corey A.T., 1964. Hydraulic properities of porous media. *Colorado State University Hydrology Paper, Fort Collins*, 27(3).

Crony, D., Coleman, J.D. and Black, W.P.M. 1958. Studies of the movement and distribution of water in soil in relation to highway design and performance. *HRB Spc. Report, Washington D.C.* 40:226–252.

Cui, Y.J. and Delage, P. 1996. Yielding and plastic be haviour of an unsaturated compacted silt. *Géotechnique*, 46(2): 291–311.

Cunningham M.R., Ridley A.M., Dineen K., Burland J.B. 2003. The mechanical behavior of a reconstituted unsaturated silty caly. *Geotechnique*. 53(2):183–194.

Drumright, E.E. 1989. The contribution of matric suction to the shear strength of unsaturated soils. *Ph.D. thesis, Colorado State University*, Fort Collins.

Escario V., Juca J. 1989. Strength and deformation of partly saturated soils, *Proceedings of the 12th International Conference on Soil Mechanics and Foundation Engineering, Rio de Janerio*, Vol. 3, pp. 43–46.

Escario V. and Saez J. 1986. The shear strength of partly saturated soils. *Geotechnique*. 36(3):453–456.

Gan J.K.M., Fredlund D.G., Rahardjo H. 1988. Determination of the shear strength parameters of an unsaturated soil using the direct shear test. *Canadian Geotechnical Journal,* 25(3):500–510.

Feuerharmel C., Pereira A., Gehling W.Y.Y., Bica A.V.D. 2006. Determination of the shear strength of two unsaturated colluvium soils using the direct shear test. *Unsaturated Soils.* 4(3):1181–1190.

Fredlund D.G., Morgenstern, N.R., amd Widger, R.A. 1978. The shear strength of unsaturated soils. *Canadian Geotechnical Journal*. 15:313–321.

Fredlund D.G., Xing A. 1994. Equations for the soil-water characteristic curve, *Canadian Geotechnical Journal*, 31:521–532.

Fredlund, D.G., Xing A., Fredlund M.D., Barbour S.L. 1996. The relationship of unsaturated soil shear strength to the soil-water characteristic curve, *Canadian Geotechnical Journal,* 33:440–448.

Fredlund D.G., Rahardjo H. 1993. Soil mechanics for unsaturated soils. *Weily*, New York.

Jennings, J.E.B. 1961. A revised effective stress law for use in the prediction of the behavior of unsaturated soils. *Pore Pressure and Suction in Soils. London*, 26-30.

Khalili N., Khabbaz M.H. 1998. A unique relationship for the determination of the shear strength of unsaturated soils. *Geotechnique* 48(5):681–687

Khalili N., Geiser F., Blight G.E. 2004. Effective stress in unsaturated soil: review with new evidence. *International Journal of Geomechanics*. 4(2): 115–126.

Miao L.C., Houston S.L., Cui Y., Yuan J.P. 2007. Relationship between soil structure and mechanical behavior for an expansive unsaturated clay. *Canadian Geotechnical Journal*, 44:126–137.

Miao L.C., Cui Y.J., Cui. Y. 2015. Hydromechanical behavior of unsaturated soils. *Journal of Materials in Civil Engineerings*.

Shao L.T. 2012. Research and exploration of soil mechanics (in Chinese). *Science Press*, Beijing.

Shao L.T., Zheng G.F., Guo X.X. 2014. Principle of Effective Stress for Unsaturated Soils. *Proceeding of the sixth international conference of unsaturated soils-Unsaturated Soils: Research & Applications 2014. Sydney*, 1317–1323.

Vanapalli S.K., Fredlund D.G., Pufahl D.E., Clifton A.W. 1996. Model for the prediction of shear strength with respect to soil suction, *Canadian Geotechnical Journal*. 33:379–392.

Van Genuchten M.Th. 1980. A closed-form equation of predicting the hydraulic conductivity of unsaturated soils. *Soil Science Society of American Journal*, 44:892–898.

Zhao C.G., Li J., Liu Y., et al. 2013. Discussion on several basic problems of unsaturatedsoil mechanics (in Chinese). *Rock and Soil Mechanics*. 34(7):1825–1831.

Zhan L.T., Charles W.W.Ng. 2006. Shear strength characteristics of an unsaturated expansive clay. *Canadian Geotechnical Journal* 43:751–763.

Unsaturated Soil Mechanics—from Theory to Practice – Chen et al. (Eds)
© 2016 Taylor & Francis Group, London, ISBN 978-1-138-02921-7

Influence of sodium chloride on evaporation and cracking of earthen heritages

Y. Zhang
Key Laboratory of Geotechnical and Underground Engineering, The Ministry of Education, Tongji University, Shanghai, China

W.M. Ye, B. Chen & Y.G. Chen
Key Laboratory of Geotechnical and Underground Engineering, The Ministry of Education, Tongji University, Shanghai, China
United Research Center for Urban Environment and Sustainable Development, The Ministry of Education, Shanghai, China

ABSTRACT: In the ancient City of Jiaohe, many earthen heritages with high NaCl content suffer the deterioration of cracked surface crusts. To investigate the effect of NaCl on crusting and cracking, desiccation tests were conducted in laboratory on three saturated slurry specimens with different salt contents (0%, 2% and 5%). The results reveal that NaCl enhanced the water retention ability of soil. With increasing salt content, time needed for specimens to reach equilibrium with the environment increased, and the durations of the initial stage and the falling stage of the evaporation process also changed. A smoother and flatter evaporation rate curve was observed in specimen with higher salt content. Image analysis was employed for evaluating the development of drying cracks during the test. Geometric parameters including CIF, the number of intersections and segments and total crack length were analyzed. All parameters decreased in higher salt content specimens, indicating a more extensive cracking in salt-free soil.

1 INTRODUCTION

Cracked surface crust is one of the most extensive and severe pathologies on salt-laden monuments in the Ancient City of Jiaohe (Zhao et al. 2003). Crusting originates from occasional concentrated heavy rainfall in summer season. The shallow surface of the remaining earthen walls can be fully saturated to form flowing slurry and then turns into strongly cracked crust during subsequent intense evaporation (Li et al. 2011). Cracks can destroy the original integrity of wall surfaces and further accelerate the deterioration by providing preferential paths for the deeper and faster movement of water, solutes and gas (Zhang et al. 2009).

Desiccation cracks exert great influences on the properties of surface as well as the underlying soil mass (Arnold et al. 2005), making the geometric characteristics of crack networks critical. Image analysis is an effective technique for the accurate quantification of the crack morphology in recent years (Lakshmikantha et al. 2009). In addition to the crack intensity factor (CIF), crack width and length, average aggregate area, the number of crack segments and intersections are also widely used to describe the extent of surface cracking (Tang et al. 2008). Compared to other influencing factors, fewer researches were conducted to investigate the impact of pore solution chemistry on the initiation and propagation dynamics of crack network as well as its final pattern (Gebrenegus et al. 2011, Hallett & Newson 2005, Panayiotopoulos & Leinas 2009). DeCarlo & Shokri (2014) found that in rectangular column specimen with lower salinity, the crack network extensively developed near the surface of specimen and a high crack fraction rapidly drops to low or zero values with increased depth. In comparison, high salt concentration leads to a more centralized network, with a lower overall cracking magnitude and a smoother crack fraction distribution along the height. Though the crack initiation is much slower in high salinity specimens, the network reaches stabilization very soon because of its high propagation rate.

Desiccation cracks occur in case that the drying shrinkage is restrained by frictional boundary and the resulted stress exceeds the tensile strength of the material. During this process, water content and the corresponding suction (negative pore water pressure) in unsaturated soil strongly determine the extent and rate of this mechanical failure (Yessiler et al. 2000). When water loses to the atmosphere from soil mass, a balance tries to reach between the evaporation and the interior moisture transport towards the exposed surface. This usually leads to spatial moisture gradients as well as a very complicated stress field distribution (Puppala et al. 2011). Tang et al. (2008, 2011a)

proposed that different crack patterns induced by various soil layer thicknesses and ambient conditions such as temperature and wetting-drying cycles are attributed to their influences on the evaporation process. In this sense, soil cracking can be regarded as a dynamic response to the complex interaction among soil, water and the environment.

The present paper reports the impacts of sodium chloride, one of the most common soluble salts in the local earthen heritages (Shao et al. 2013), on evaporation and resulting crack pattern of soil taken from Jiaohe. Desiccation tests were conducted on initially saturated slurries with different salt contents in controlled condition. During the whole drying period, moisture loss from the soil was continuously monitored to assess the evaporation rate (R_e). In addition, development of surface cracking was also recorded by a digital camera. The geometric characteristics of the crack pattern including CIF, total crack length, number of segments and intersections were quantitatively analyzed with the help of image analysis technique. Differences were compared to study the influences of various NaCl contents on the cracking mechanisms.

2 EXPERIMENTAL PROCEDURE

2.1 *Material characterization and desalination*

Because of the significant values of Jiaohe, it is not allowed to collect soil sample directly from the earthen heritages themselves. Therefore, soil dug from the site with similar properties to the heritages was used as a substitutive testing material. The tested soil is composed of 4.4% sand, 79.4% silt and 16.2% clay. Mineral compositions are mainly quartz, albite, orthoclase, clinochlore and calcite, with few expansive clay minerals. The basic soil properties are: specific gravity of 2.70, liquid limit of 30%, plastic limit of 19% and plastic index of 11, which is classified as CL in USCS.

For avoiding the influence of contained sodium chloride and other salts, the original soil sample was pretreated for desalination. The original soil blocks were firstly crushed into powder and mixed with deionized water in a mass ratio of 1:5 in a bucket. Then, after 30min stirring for the sufficient dissolution of salts, the soil sludge was left for soil particles to settle down until the solution became clear. After measuring the electrical conductivity, the supernatant was removed with a syringe. The same amount of deionized water was added back subsequently and the suspension was stirred again for further dissolution of residual salt remained in the soil. This process was repeated three times until the electrical conductivity of supernatant dropped to 117.3 us/cm from 543 us/cm.

The desalinated soil sample was dried in an oven at 105°C until its weight reached constant. Then, the dried sample was crushed into powder again and sieved with a 2 mm sieve. The particle size of the soil becomes smaller after salt removal (Fig. 1).

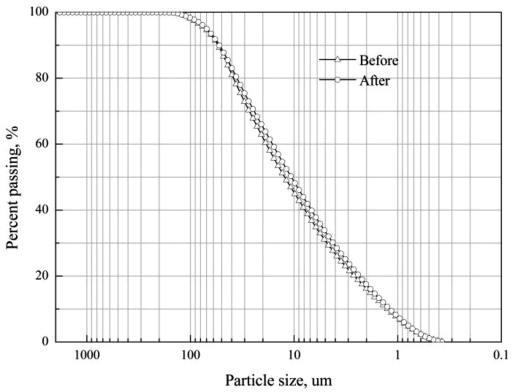


Figure 1. Particle size distribution of Jiaohe soil before and after desalination.

Table 1. Designed desiccation tests.

	Dry soil mass	NaCl content
Specimen	g	%
C0	240	0
C2	240	2
C5	240	5

2.2 *Test methods*

Three desiccation tests listed in Table 1 were conducted. Specimens for the experimentation were prepared separately with reproducible method as follows. The pretreated soil powder was weighed (240 g) and mixed with deionized water to a designed gravimetric water content of 45%. NaCl was added to designed contents of 0%, 2% and 5% of soil mass, respectively. The mixture was sealed in a plastic bag for 48 hours to ensure a homogeneous distribution of both water and salt. In oversaturated slurry, virgin mechanical state can be obtained avoiding the formation of any initial soil structures.

The slurry in equilibrium was poured into a 30 mm high, 200 mm × 200 mm square-shaped glass container. The container was vibrated sufficiently for 2min in order to remove the entrapped air bubbles in the slurry. Then the container with slurry was placed in the temperature-controlled laboratory ($T = 22 \pm 1°C$) for evaporation. The masses of the specimens were monitored regularly using an electronic balance with an accuracy of 0.01 g. Based on this, the evolution of gravimetric water content and the evaporation rate (R_e) with drying time was determined. In the meantime, crack patterns on the surfaces of the specimens were monitored with a digital camera. Photographs were used for the image analysis of the crack geometric characteristics. The salt NaCl used in this test is of analytical grade, corresponding to purity above 99.5%.

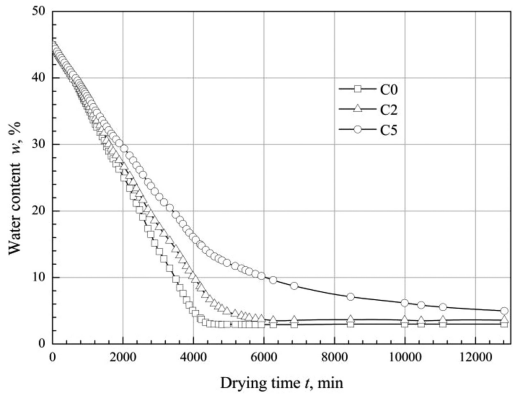


Figure 2. Water content variation of specimens with time.

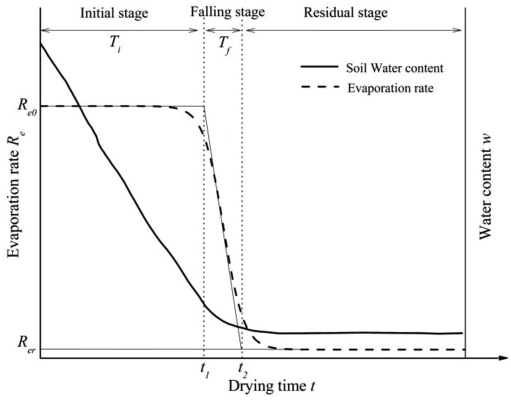


Figure 3. Definition of three stages of soil water evaporation process.

3 RESULTS AND DISCUSSION

3.1 *Evaporation*

Measured evolution of water content (m_w/m_s) with drying time for specimens C0, C2 and C5 are presented in Figure 2. It indicates that at the beginning of drying, water contents of specimens decrease linearly with time. As the evaporation continues, however, the decreasing rate slows down until the water content becomes a stabilized value. Time needed for specimen to reach its final equilibrium water content is dependent on the salt content. For specimen C0, it takes about 5480 min, which increases to about 6300 min for specimen C2 and more than 12000 min for C5. Moreover, as the salt content increases, the corresponding residual water content increases from 2.99% to 3.58% and 4.86% by mass for C0, C2 and C5, respectively. This observation may due to the fact that, as one of the hygroscopic salts, sodium chloride tends to absorb moisture from ambient air, thus enhancing the water retention ability of porous materials with increasing salt content (Franzen & Mirwald 2009).

For analyzing the entire soil desiccation process, an evolution curve of evaporation rate (R_e), here defined as the first derivative of the water content with respect to time, is presented in Figure 3. Characteristic parameters for describing the shape of R_e curve are also illustrated. Based on the variation of R_e value, initial stage, falling stage and residual stage are defined accordingly as stated by Qiu & Ben-Asher (2010). Tang et al. (2011b) also proposed that soil evaporation is typically a multiphase process which is closely related to the soil-water interaction in microscale. During the initial stage of desiccation T_i ($t < t_1$), water evaporates at a constant rate R_{e0}, accompanied by an almost linear decrease of water content. This phenomenon may attribute to the water evaporation from the exposed surface of specimen at early drying period. Under the saturated state, capillary water from the inner parts can meet the demand of vaporization on soil surface. As the drying continues ($t_1 < t < t_2$), the soil becomes unsaturated during T_f and the desaturation process as well as the moisture movement is mainly controlled by the soil structure. The velocity of liquid transfer in the soil is getting slower and at the same time, moisture begins to escape to the atmosphere in the form of vapor diffusion, both leading to a gradual falling of evaporation rate. Finally, when an equilibrium between the soil and the atmosphere is almost reached ($t > t_2$), evaporation rate stabilizes at R_{er} in the residual evaporation stage.

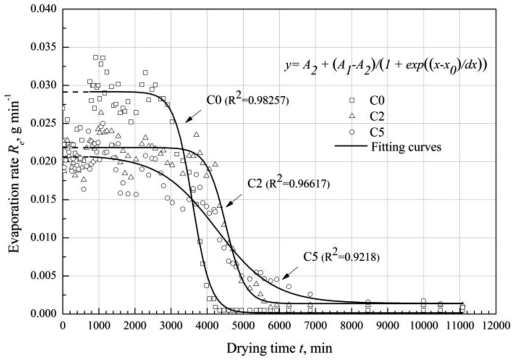


Figure 4. Evaporation rate variation of specimens with time.

Calculated water evaporation rates (g min^{-1}) of three tested specimens are illustrated with respect to drying time in Figure 4. A good correlation is shown between the obtained data and the corresponding sigmoidal fitting curves (solid lines). Figure 4 clearly indicates that the R_e curve becomes smoother and flatter with increasing sodium chloride content. As the salt content increases, the variation range of evaporation rate of the specimen decreases. When salt content increases from 0% to 2%, the reduction in R_e variation range is more significant than that of salt content changing from 2% to 5%.

For a qualitative assessment of the evaporation rate curves of three specimens influenced by NaCl, characteristic parameters including R_{e0}, R_{er}, T_i and T_f are determined and compared in Table 2. It shows that

Table 2. Characteristic parameters of R_e curves.

Characteristic parameters	C0	C2	C5
R_{e0} (10^{-2} g min^{-1})	2.92	2.19	2.09
R_{er} (10^{-4} g min^{-1})	1.41	13.6	14.0
T_i (min)	3093	3997	2690
T_f (min)	1011	1056	3165

Table 3. Geometric characteristics of cracks.

Parameters	C0	C2	C5
CIF (%)	8.78	6.38	6.36
Intersection number	235	210	175
Segment number	169	143	116
Total crack length	41170	38949	34671

the constant evaporation rate (R_{e0}) in the initial stage decreases from 0.0292 g min^{-1} for C0 without sodium chloride to 0.0219 g min^{-1} by adding 2% NaCl (C2). However, only a very small reduction of 0.001 g min^{-1} is shown for an increase of salt content from 2% (C2) to 5% (C5). Decrease of the initial evaporation rate with increasing salt content was also observed by Abou Najm et al. (2012) in a soil with NaCl solution of 3.5% content by mass. Residual evaporation rates (R_{er}) of three specimens are all approaching but not equal to zero. This reveals that vapor diffusion from the soil to the environment still exists in the residual stage. Table 2 also shows that the values of T_i and T_f of each specimen, which represent the duration of the initial and falling evaporation stages, are significantly influenced by the NaCl content. The initial stage duration (T_i) of C2 is the longest while that of specimen C5 is the shortest one. Meanwhile, with increasing content of sodium chloride, the duration of the falling stage is prolonged especially for specimen with 5% NaCl. Value of T_f for C5 is 3165 min and it is almost twice more than that of C0 and C2. During the falling stage, the evaporation rate experiences a gradual decrease. Furthermore, the decreasing rates of R_e are much slower in the specimens containing salt, which proves their enhanced water retention ability under the same environment as mentioned before.

It is commonly recognized that, evaporation rate is proportional to the difference between the ambient vapor pressure and the equilibrium vapor pressure of the evaporating liquid. For specimens with more NaCl, the pore water activity is depressed which contributes to a reduced number of water molecules escaping into the air (Abou Najm et al. 2012). Therefore, for C2 and C5 with higher salt contents, lower vapor pressures are formed above the surfaces of the specimens, resulting in a lower initial driving force for evaporation. With a continuous moisture loss from the specimens, the concentrations of pore solution in C2 and C5 keep increasing. Hence, correspondingly, the water activity is decreasing. This may be attributed to the more and more slow decreasing rate of R_e in the falling stage when salt content increases. Meanwhile, during desiccation, transmission of pore water to the evaporating surface is a key issue as well. Increasing content of NaCl induces the increase of viscosity and density of the pore liquids (Lide, 2003). Abou Najm et al. (2012) considered that higher viscosity and density of the pore solutions slow down the movement of fluid in the soil thus lower the evaporation rate. For specimens in the present work, the thickness of slurry is small, which is less than 5 mm. Therefore, the impacts induced by variations of pore solution properties on R_e may not be very significant. However, higher concentration of pore fluid leads to more extensive crystallization of NaCl in soil specimen during drying. Crystals that accumulate in the pore channels can influence the transmission of both pore fluid and vapor to the evaporation surface (Rodriguez-Navarro & Doehne 1999), resulting in the reduction of immediate surface porosity and consequently a decrease in evaporation rate.

Once the saturated flowing slurry is formed especially on earthen heritages with higher salt content after rainfall, lower evaporation rate and correspondingly a longer desiccation time might induce sufficient interaction between soil particles and the pore solution. Leaching and dissolution of minerals and the subsequent salt crystallization are possible to damage the soil structure in combination, exacerbating the deterioration of earthen heritages.

3.2 *Cracking morphology*

The photographs of the final crack networks on the surfaces of specimens with different salt contents are presented in Figure 5. It visually shows that at the end of experiment, the surface color of the specimen with higher salt content is darker than the lower ones, which may indicate that more residual water is retained by the soil.

Geometric parameters of the stabilized crack patterns of the specimens were measured using image analysis technique (Tang et al. 2008) as listed in Table 3. CIF (crack intensity factor) is defined as the ratio of cracking area to the total surface area of a drying soil mass (Yesiller et al. 2000). It decreases from 8.78% for C0 to a very similar value for C2 and C5. The decreasing trend in cracking area with increase of NaCl content is in consistent with test results reported by Gebrenegus et al. (2011) and Panayiotopoulos & Leinas (2009). Table 3 also indicates that the number of intersections and segments as well as the total crack length decrease with increasing salt content.

The evolution of crack patterns of C0 and C2 with drying time was presented in Figure 6. It can be seen that cracks often start from edges of the specimens because of the relatively weak adhesion between the glass wall and the soil. Moreover, the initiation time of cracking in slurry containing NaCl is postponed due to the lower evaporation rate. During the evaporation, primary cracks develop first dividing the soil mass into blocks. As time elapses, the secondary even

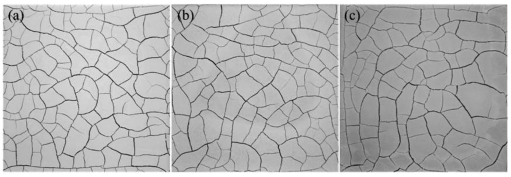


Figure 5. Final crack networks on the surface of specimens with different salt contents for (a) C0, (b) C2 and (c) C5.

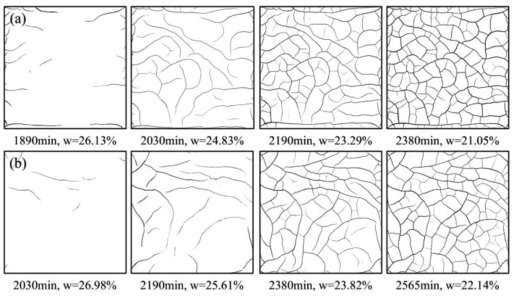


Figure 6. Evolution of crack networks on the surface of (a) C0 and (b) C2 with time and decrease of water content.

tertiary cracks progress slowly and cut the intact aggregates into numerous smaller clods (Tang et al. 2011b). After the total crack length increases to its maximum value, the widening of cracks follows. The crack networks are regarded as full developed when both the crack length and width stop increasing to reach a stable state. Figure 6 indicates the crack pattern of C0 stabilizes at a gravimetric water content of 21.05%. It takes nearly 500 min for the full development of crack network since initiation. This process is much longer for specimens with higher salt contents.

CIF values in Table 3 shows that, as the NaCl content increases, the total cracking area of Jiaohe soil decreases. Tang et al. (2011b) mentioned that the drying shrinkage of soil specimen is contributed by two fractions including vertical subsidence and lateral cracks. At the initial stage of drying, vertical subsidence, which is known as the non-cracking shrinkage, dominates the soil deformation. When the cracks initiate and evolve, the decrease in layer thickness almost stops. Literature shows that the concentration of pore fluid can exert significant impact on the microstructure of soil, especially the fine-grained one (Zhu et al. 2013). As the sodium chloride content increases, the thickness of the double diffusion layer (DDL) of clay minerals decreases which breaks down the initial voluminous structure of soil particles. As a result, subsidence of saturated slurry contributes mainly to the total shrinkage volume for specimen with a higher salt content. Correspondingly, less lateral deformation is produced leading to lower cracking area (DeCarlo & Shokri 2014). The reduction of CIF in this test clearly depends on the variation of salt content. It seems that 2% is a critical value of sodium chloride content for influencing the cracking behavior of Jiaohe soil. The number of intersections and segments as well as the total crack length all decrease with increasing salt content (Table 3). Possible explanation to this phenomenon might be the expanded channels for the solution transfer induced by DDL compression in the specimens with NaCl (Shirazi et al. 2011). Considering the increased solution permeability and the lower evaporation rate in specimens with higher salinity, a relatively uniform pore water distribution can be ensured in soil and the locally concentrated stress resulted from suction for crack initiation can be avoided. On another side, the tensile strength nearby the soil surface may also be improved by salt crystallization and cementation (Chen et al. 2014).

It seems that the cracking extent of surface crusts on earthen heritages is mitigated by sodium chloride accumulating nearby the surface zone. Hence, relatively integral surface crusts on the walls may be hard to be exfoliated and the underlying soil mass can be also protected from environmental factors. However, Cui et al. (2012) found that when exposed to wetting-drying cycles, the microstructure of soil with higher salt content was damaged more severely. This resulted in much lower mechanical strengths and resistance to wind-blown sand of the soil. Therefore, over a long period of time, surface crusts with higher salt contents on earthen heritages are probably more vulnerable to further deterioration.

4 CONCLUSIONS

Desiccation tests were conducted on initial saturated slurry specimens with 0%, 2% and 5% of NaCl. Sodium chloride exerts great impacts on the process of evaporation. With increasing salt content, the constant evaporation rate decreases accompanied by the variations in duration of the initial stage among specimens. Besides, time needed for specimen to reach equilibrium with the atmosphere also increases significantly and correspondingly, the residual water content increases as well. The evaporation rate curve becomes smoother and flatter as NaCl content increases, indicating a much slower moisture loss in specimens with higher salinity.

Image analysis of crack patterns reveals that, geometric characteristics of cracking including CIF, the number of intersections and segments and the total crack length decrease with increasing salt content. The crack initiation and propagation is mainly governed by the total water loss, the evaporation rate (R_e) variation, the pore water transmission and redistribution etc., which are all influenced by NaCl content.

The current paper proposed some preliminary results about the impacts of soluble salt (NaCl) on evaporation and cracking of Jiaohe soil. Considering the intricate mechanisms of desiccation cracking, more comprehensive investigations are needed with respect to the coupling effects of hydraulic, mechanical and chemical factors on soil properties.

REFERENCES

Abou Najm, M., Jesiek, J., Mohtar, R.H., Lura, P., Sant, G. 2012. Assessing the role of the pore solution concentration on horizontal deformations in an unsaturated soil specimen during drying. *Geoderma* 187: 31–40.

Arnold, J.G., Potter, K.N., King, K.W., Allen, P.M. 2005. Estimation of soil cracking and the effect on surface runoff in a Texas Blackland Prairie watershed. *Hydrological Processes* 19(3): 589–603.

Chen, W.W., Lv, H.M., Cui, K., Wu, G.P. 2014. Influence on strength of site soils about chlorine and sulfate salt in dry environment. *Journal of Engineering Geology* 22(Suppl.): 333–338.

Cui, K., Chen, W.W., Kuang, J., Wang, X.D., Han, W.F. 2012. Effect of deterioration of earthen ruin with joint function of salinized and alternating wet and dry in arid and semi-arid regions. *Journal of Central South University (Science and Technology)* 43(6): 2378–2384.

DeCarlo, K.F. & Shokri, N. 2014. Salinity effects of cracking morphology and dynamics in 3-D desiccating clays. *Water Resource Research* 50(4): 3052–3072.

Franzen, C. & Mirwald, P.W. 2009. Moisture sorption behavior of salt mixtures in porous stone. *Chemie Der Erde-Geochemistry* 69(1): 91–98.

Gebrenegus, T., Ghezzehei, T.A., Tuller, M. 2011. Physico-chemical controls on initiation and evolution of desiccation cracks in sand-bentonite mixtures: X-ray CT imaging and stochastic modeling. *Journal of Contaminant Hydrology* 126(1–2): 100–112.

Hallett, P.D. & Newson, T.A. 2005. Describing soil crack formation using elastic-plastic fracture mechanics. *European Journal of Soil Science* 56(1): 31–38.

Lakshmikantha, M.R., Prat, P.C., Ledesma, A. 2009. Image analysis for the quantification of a developing crack network on a drying soil. *Geotechnical Testing Journal* 32(6): 505–515.

Li, L., Shao, M.S., Wang, S.J., Li, Z.X. 2011. Preservation of earthen heritage sites on the Silk Road, northwest China from the impact of the environment. *Environmental Earth Sciences* 64(6): 1625–1639.

Lide, D.R. 2003–2004. *Handbook of chemistry and physics*. Boca Raton: CRC Press.

Panayiotopoulos, K.P. & Leinas, D. 2009. Influence of aggregate size, electrolyte concentration, and sodium adsorption ratio on crack parameters of a vertisol. *Communications in Soil Science and Plant Analysis* 40(11–12): 1712–1721.

Puppala, A.J., Manosuthkij, T., Nazarian, S., Hoyos, L.R. 2011. Threshold moisture content and matric suction potentials in expansive clays prior to initiation of cracking in pavements. *Canadian Geotechnical Journal* 48(4): 519–531.

Qiu, G.Y. & Ben-Asher, J. 2010. Experimental determination of soil evaporation stages with soil surface temperature. *Soil Science Society of America Journal* 74(1): 13–22.

Rodriguez-Navarro, C. & Doehne, E. 1999. Salt weathering: influence of evaporation rate, supersaturation and crystallization pattern. *Earth Surface Processes and Landforms* 24(3): 191–209.

Shao, M.S., Li, L., Wang, S.J., Wang, E.Z., Li, Z.X. 2013. Deterioration mechanisms of building materials of Jiaohe ruins in China. *Journal of Cultural Heritage* 14(1): 38–44.

Shirazi, S.M., Kuwano, J., Kazama, H., Wiwat, S., Ismail, Z. 2011. Response to swelling and permeability of bentonite using saline solution for nuclear waste disposal. *Disaster Advances* 4(1): 41–47.

Tang, C.S., Shi, B., Liu, C., Zhao, L.Z., Wang, B.J. 2008. Influencing factors of geometrical structure of surface shrinkage cracks in clayey soils. *Engineering Geology* 101(3–4): 204–217.

Tang, C.S., Cui, Y.J., Shi, B., Tang, A.M., Liu, C. 2011a. Desiccation and cracking behavior of clay layer from slurry state under wetting-drying cycles. *Geoderma* 166(1): 111–118.

Tang, C.S., Shi, B., Liu, C., Suo, W.B., Gao, L. 2011b. Experimental characterization of shrinkage and desiccation cracking in thin clay layer. *Applied Clay Science* 52(1–2): 69–77.

Yesiller, N., Miller, C.J., Inci, G., Yaldo, K. 2000. Desiccation and cracking behavior of three compacted landfill liner soils. *Engineering Geology* 57(1–2): 105–121.

Zhang, H.Y., Liu, P., Wang, J.F., Wang, X.D. 2009. Generation and detachment of surface crust on ancient earthen architectures. *Rock and Soil Mechanics* 30(7): 1883–1891.

Zhao, H.Y., Li, Z.X., Han, W.F., Wang, X.D., Chen, W.W. 2003. Main diseases and their causes of earthen ruins in arid region of northwestern China. *Chinese Journal of Rock Mechanics and Engineering* 22(Suppl. 2th): 2875–2880.

Zhu, C.M., Ye, W.M., Chen, Y.G., Chen, B., Cui, Y.J. 2013. Influence of salt solutions on the swelling pressure and hydraulic conductivity of compacted GMZ01 bentonite. *Engineering Geology* 166: 74–80.

Unsaturated Soil Mechanics—from Theory to Practice – Chen et al. (Eds)
© 2016 Taylor & Francis Group, London, ISBN 978-1-138-02921-7

Prediction of swelling by effective stress of bentonite in salt solution

G.S. Xiang, Y.F. Xu, T. Chen & H. Jiang
Department of Civil Engineering, Shanghai Jiao Tong University, Shanghai, China

ABSTRACT: The swelling deformation of compacted bentonite in salt solution can be expressed by surface fractal model using a unique e_m-p curve in the form of $e_m = Kp^{Ds-3}$. In this fractal model, the effective stress (p) on bentonite particles in salt solution is expressed as $p = \sigma + \pi \cdot (\sigma/\pi)^{Ds-2}$, incorporating with osmotic suction (π) and vertical pressure (σ). The coefficient K in the fractal model is calculated from the parameters of diffuse double layer (DDL) model in the osmotic swelling phase, as the effective stress is generally regarded as equal to vertical pressure in distilled water, and the excellent performance of DDL model in osmotic swelling phase. It is wonderful to express the swelling deformation of bentonite in salt solution by fractal model using the effective stress p and the calculated coefficient K, and is validated by swelling deformation tests of a commercial bentonite in laboratory and the Wyoming bentonite (MX80) conducted in literature. Distilled water and NaCl solution with different concentration were used as inundation solution in these tests. There is a great agreement between the estimation value and the experimental data of swelling deformation in distilled water and salt solution with various concentrations.

1 INTRODUCTION

Compacted bentonite has been proposed as suitable buffer/backfill materials for construction of the artificial barrier in the deep geological repository for disposal of high-level radioactive nuclear waste (HLW) in many countries (Radhakrishna et al. 1989; Komine & Ogata 1996; Ye et al. 2014). Thanks to its low hydraulic conductivity, high swelling capacity and adequate mechanical resistance, the compacted bentonite formed barrier can effectively restrict the movement of radionuclides released from the canister. The swelling deformation of compacted bentonite is usually expressed by the curve of e_m-p, where e_m is the void ratio of montmorillonite after swollen, p is the vertical overburden pressure applied in swelling deformation tests. Xu et al. (2003, 2014) theoretically and experimentally pointed out the relationship can be expressed by surface fractal model. It is suggesting the fractal model has excellent ability in prediction of swelling deformation for compacted bentonite immersed in distilled water.

Actually, compacted bentonite is usually found in salt solutions, where it is used as barrier system in nuclear waste repositories or liners in landfills. The mechanical behavior of compacted bentonite may be strongly influenced by physicochemical effects of the salt solution. A great number of experimental studies about the salt solution effects on the swelling behavior of bentonite are available in literature (Ye et al. 2014). Alawaji (1999) illustrated that swell potential, swell time and swelling pressure decreases with the increase of chemical concentrations for bentonites and mixtures. Kaufhold & Dohrmann (2010) applied salt solution on bentonite and proposed a model to explain the correlation between collapsed interlayers and layer charge density. Barbour & Fredlund (1989) studied the effect of NaCl with different concentration on sand-bentonite mixtures, and proposed a constitutive model based on the effective stress and the osmotic pressure as state parameters. Maio et al. (2004) have shown that on exposure to concentrated salt solutions, pore fluid of saturated clays flow out in response to chemical concentration gradients. The osmotic flow out of the specimen decreases the pore-water pressure, leading to an increase in effective stress and subsequent volume decrease. The volume change behavior of clays is controlled by the effective stress, in which the osmotic suction should be incorporated. The salt concentration increase favors an increase in osmotic suction of pore water, and then induces a reduction in swell potential of the compacted clay specimens. Rao & Thyagaraj (2007) pointed out the effect on swell potential values of an increase in osmotic suction of pore fluid is similar to that of an increase in total vertical pressure. The increase in osmotic suction in pore water acts as an additional effective stress component that favors the reduction in swell potential of the compacted clay specimens at a total vertical pressure to swell pressure ratio of less than unity. The total net vertical stress (p) experienced by compacted clay specimens exposed to an increase in pore fluid osmotic suction can be represented as $p = \sigma + \alpha\pi$, where σ is vertical pressure, π is the osmotic suction of pore water, α is a empirical constant, and $0 < \alpha < 1.0$. Then, basis on the fractal analyses of the structure and morphology of bentonite

Table 1. Typical physical properties of commercial bentonite and MX-80 bentonite.

Physical parameters	Commercial	MX-80
Specific gravity	2.69 g/cm^3	2.76 g/cm^3
Liquid limit	110%	407%
Plastic limit	24%	48%
Plasticity index	86	359
Content of montmorilloite	52%	75%
Cation exchange capacity	0.384 mEq/g	0.760 mEq/g

*The physical properties of MX-80 bentonite were referenced from Studds et al. (1998).

particles, Xu et al. (2014) proposed a formula for the effective stress on bentonite particles, the formula is expressed as $p = \sigma + \pi(\sigma/\pi)^{D_s-2}$. It is found the volume change behavior of clays can be expressed by a unique e_m-p curve using the proposed effective stress in salt solution.

In this paper, a modified fractal model was introduced to calculate the swelling deformation of bentonite in salt solution. In this calculation model, the coefficient K is calculated by DDL theory in distilled water at osmotic swelling phase, and the effective stress is proposed by incorporating with the osmotic suction. There is a great agreement between the estimations of swelling deformation by the modified fractal model and experimental data in laboratory, this fractal model offers a good approach to estimate the swelling characteristics for compacted bentonite in salt solution.

2 MATERIALS AND METHODS

A commercial bentonite from China and the Wyoming bentonite (MX-80) from American were chosen as the study bentonites, the typical physical properties of the bentonites were listed in Table 1.

The N_2 adsorption–desorption isotherms of the bentonite samples were measured using an ASAP 2010 M + C accelerated surface area and porosimetry analyser (Micromerity). The samples were placed in a test tube and de-aired for 12 h at 105°C under flowing nitrogen. Vapour pressure equilibrium in the sample cell was established as nitrogen is adsorbed or desorbed. The volumes of N_2 adsorption or desorption were measured by admitting or removing a given quantity of N_2 at the temperature of 77 K.

In Figure 1, it shows the nitrogen adsorption- desorption isotherms measured on the examined bentonite samples. Frenkel-Halsey-Hill (FHH) equation was used to calculate the fractal dimension. The nitrogen adsorption isotherms analyzed according to the FHH equation was shown in Figure 2, The D_s values of commercial bentonite and Wyoming bentonite are measured as 2.66 and 2.65, respectively. The adsorption isotherms of MX-80 bentonite was obtained from Celies et al. (1996).

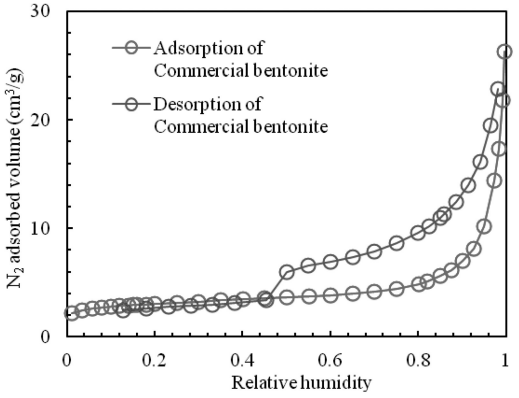


Figure 1. Nitrogen adsorption isotherms of the examined bentonite samples.

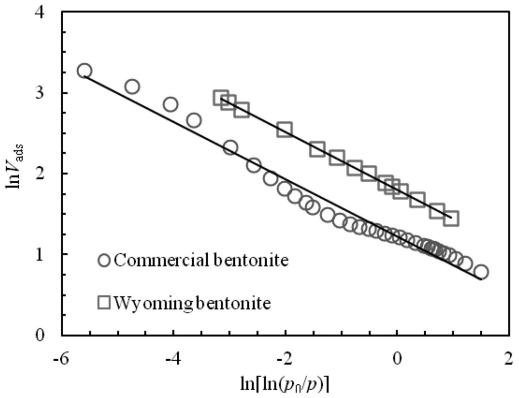


Figure 2. Analyses of FHH equation on N_2 adsorption isotherms of MX-80 and commercial bentonite.

Five vertical pressure were applied in swelling deformation tests, they were 12.5 kPa, 25 kPa, 50 kPa, 100 kPa and 200 kPa. Distilled water and 0.1M (mol/L), 0.3M, 0.6M and 1.0M NaCl solution were used as the external solution. The initial dry density of the bentonite samples was controlled around 1.7 g/cm^3.

In Figure 3, It is shown the final swelling strain of compacted bentonite specimens in NaCl solution with different concentration. It is seen there is an inverse correlation between the swelling strain and the concentration of external solution in swelling deformation tests under same vertical overburden pressure. It means the salt solution reduces the swelling deformation of compacted bentonite.

3 DETERMINATION OF COEFFICIENT K

Bentonites will swell when it in contact with a source of water or saline solutions, and the swelling process accounts primarily for two phases: crystalline swelling and osmotic swelling (Madsen & Müller 1989; Yong 1999; Laird 2006; Saiyouri et al. 2000; Ferrage et al.

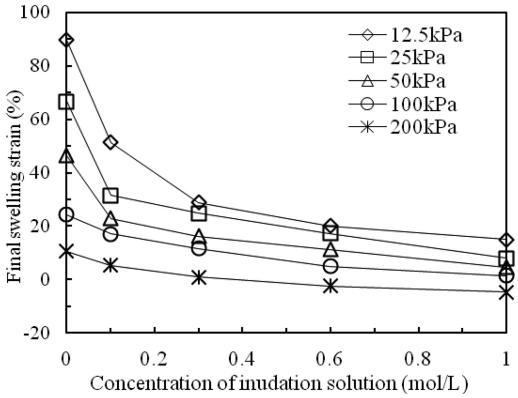


Figure 3. Swelling deformation in NaCl solution with different concentration.

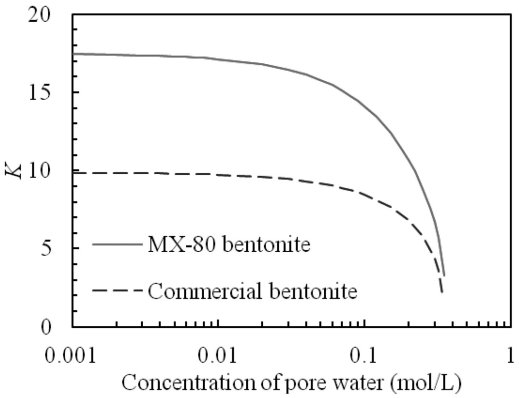


Figure 4. Relationship between the calculated value of K and the concentration of pore water.

2005). Crystalline swelling is a process whereby less than 4 discrete layers of water molecules are intercalated between the unit layers of montmorillonite, and throughout the bentonite-water system there exists a definite hydration structure to the water. Upon further ingress of water, the hydrated cations dissociate, then, from the outer surfaces of the montmorillonite particles into the interparticle pores, to form the diffuse electrical double layers. On the analysis of swelling mechanism of bentonite, DDL model was proved to be suitable for describing osmotic swelling but not for crystalline swelling.

Surface fractal model was found to be excellent in describing osmotic swelling and crystalline swelling. Xu et al. (2003, 2014) considered the correlation between the void ratio of e_m and the effective stress p can be expressed as:

$$e_{\mathrm{m}}=Kp^{D_s-3} \tag{1}$$

where K is the swelling coefficient of bentonite, $e_m = e/C = V_w/V_m$, is the void ratio of montmorillonite, and the C is the content of montmorillonite, V_{m} is the volume of montmorillonite, V_{w} is the water volume adsorbed by montmorillonite at full saturation; p is the effective stress. According to this fractal correlation, the swelling deformation of compacted bentonite will be estimated.

In distilled water, the effective stress on bentonite particles is generally considered as the vertical pressure σ applied in swelling tests. The coefficient K in fractal model is calculated based on the assumption that the fractal equation should be equivalent to DDL model in the osmotic swelling phase. The pair value of vertical pressure σ and void ratio of montmorillonite e_{m} can be calculated by DDL model when the key parameter d is given.

There is a value interval for d, as the DDL model works well in the osmotic swelling phase, which occurs after the crystalline swelling has fully taken place and the diffuse double layers have developed within the interlayer space. The lower limit of d is given by

$$d \geq \frac{t+R_{\mathrm{ion}}}{t} d_{\mathrm{m}} + R_{\mathrm{ion}} \tag{2}$$

where t is, R_{ion} is the nonhydrated radius of exchangeable cations between two layers fixed distance, d_{m} is a weighted average distance of separation. It is approximated by $d = 1.0$ nm and 1.5 nm for Commercial bentonite and Wyoming bentonite, respectively.

The values of the parameters of DDL model and exchangeable cations are available from previous studies in literature (Liu 2013; Komine et al. 2009). The calculation of DDL model is dependent on the concentration of pore water. Figure 4 shows the relationship between the coefficient K calculated by DDL model and the salt concentration of pore water, it can be found in the range of the salt concentration of pore water less than 100 mol/m^3, the value of K is almost constant and has a weak dependence on n_0. But when the salt concentration is above 0.1 mol/L, coefficient K decreases rapidly.

Bolt (1956) showed by experiment that the concentration of ions in pore water of natural clays was in the order of 10 mol/m^3. Komine & Ogata (1996) found the ion concentration of water around the compacted bentonite in the swelling pressure test is approximately 0.020–0.04 mol/L. In the swelling deformation tests, the external solution is distilled water, the concentration decreases as the volume of bentonite increases by water absorption. Therefore, it is approximated that the ion concentration of pore water n_0 is equal to 0.01 mol/L. The coefficient K in the surface fractal model for Commercial bentonite and MX-80 is 9.73 and 17.62, respectively.

4 EFFECTIVE STRESS OF BENTONITE IN SALT SOLUTION

In distilled water, the effective stress p on bentonite particles is generally regarded as the vertical pressure

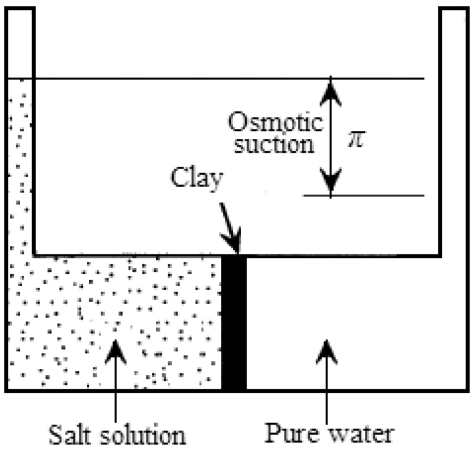


Figure 5. Principle of osmotic suction in clay-water-solution system.

σ. But, in salt solution, the effective stress p should be taken the effects of osmotic suction into consideration. Fundamentally, osmotic suction is due to the presence of dissolved salt in the pore-fluid. The nature of osmotic suction can be described by the schematic (Fig. 5). Here, pure water is shown in contact with a salt solution through clays, a semi-permeable membrane, i.e., clays are permeable to water molecules but not to the dissolved salt. The dissolved salts decrease the chemical potential of the salt solution by an amount dependent on its concentration. Thus, a gradient in chemical potential is developed that causes water to flow from the pure water into the salt solution through clays. Equilibrium is reached when the induced hydrostatic pressure becomes large enough to balance the osmotic suction tending to cause the water flow.

When bentonite is immersed in salt solution, the diffusion of dissolved salt into the clay causes the increase in concentration of pore water. The increase in osmotic suction in pore water acts as an additional effective stress component that favors the reduction in swell potential of the compacted clay specimens.

The effective stress on bentonite particles in salt solution is expressed as (Xu et al. 2014)

$$p = \sigma + \pi \left(\frac{\sigma}{\pi} \right)^{D_s - 2} \tag{3}$$

The osmotic suction π is described by the van't Hoff equation

$$\pi = \nu RTm\phi \tag{4}$$

where ν is the valence of the interlayer cation, R is the universal gas constant (J/mol·K); T is absolute temperature in Kelvin (K), m is the molar concentration of the salt solution (mol/kg), ϕ is the osmotic coefficient. Colin et al. (1985) measured the osmotic coefficient ϕ for NaCl solution with different concentration at different temperature.

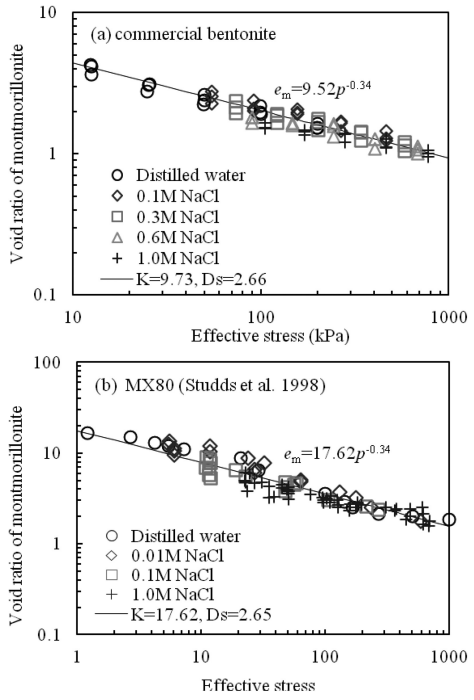


Figure 6. Relationship between void ratio of montmorillonite and effective stress for (a) commercial bentonite, (b) MX-80 studied by Studds et al. (1998).

According to Equation 3, effective stress of compacted bentonite in salt solution is obtained. The surface fractal dimension of commercial bentonite D_s measured by nitrogen adsorption is 2.66, and the coefficient K is 9.73 calculated by DDL model. Estimated value of swelling deformation by effective stress in salt solution was compared with the experimental tests of commercial bentonite (Figure 6a). A good agreement is seen between the estimations and the experimental data. It means the swelling deformation of commercial bentonite in both distilled water and NaCl solution with different concentration can be expressed by the unique curve.

Validation of the fractal model is also manifested by the unique expression of *e-p* curve for MX-80 bentonite. Studds et al. (1998) conducted the swelling deformation tests of this bentonite with distilled water and various salt solution concentrations (0.01, 0.1 and 1M) NaCl solution. The surface fractal dimension determined from nitrogen adsorption isotherm is 2.65, coefficient K was calculated as 17.62 and the effective stress is calculated using the Equation 3. A good agreement is also seen between the estimations and the experimental data as shown in Figure 6b.

5 CONCLUSION

Fractal model was used to estimate the swelling deformation of bentonite. The void ratio of montmorillonite

in salt solution is expressed as $e_m = Kp^{D_s - 3}$. In this fractal model, the coefficient K was estimated by combining the DDL model and surface fractal model in the osmotic swelling phase with the effective stress equals to overburden pressure in distilled water. This is a great agreement between the estimations of surface fractal model and experimental results.

The effective stress in salt solution is proposed incorporating with osmotic suction. The osmotic suction is calculated from the van't Hoff equation. The swelling deformation of bentonites can be expressed by the fractal model using the effective stress. This is validated by the experimental data of commercial bentonite and Wyoming bentonite in concentrated NaCl solution and distilled water. The fractal model offers a new method to express the swelling deformation for compacted bentonite in salt solution.

ACKNOWLEDGEMENTS

The National Nature Science Foundation of China (Grant No. 41272318 and 41472251) is acknowledged for its financial support. State Key Laboratory of Ocean Engineering is also acknowledged.

REFERENCES

Alawaji, H.A., 1999. Swell and compressibility characteristics of sand–bentonite mixtures inundated with liquids. *Applied Clay Science,* 15: 411–430.

Barbour, S., Fredlund, D., 1989. Mechanisms of osmotic flow and volume change in clay soils, *Canadian Geotechnical Journal,* 26(4): 551–562.

Bolt G.H., 1956. Physico-chemical analysis of the compressibility of pure clay. *Geotechnique,* 6(2): 86–93.

Celies, R., Cornejo, J., Hermosin, M.C., 1996. Surface fractal dimensions of synthetic clay-hydrous iron oxide associations from nitrogen adsorption isotherms and mercury porosimetry. *Clay Minerals,* 31: 355–363.

Colin, E., Clarke, W., Glew, D.N., 1985. Evaluation of the thermodynamic functions for aqueous sodium chloride from equilibrium and calorimetric measurements below 154°C. J. *Physical and Chemical Reference Data.* 14: 489–610.

Ferrage, E., Lanson, B., Sakharov, B.A., Drits, V.A., 2005. Investigation of smectite hydration properties by modeling experimental X-ray diffraction patterns: Part I. Montmorillonite hydration properties. *Am. Mineral,* 90: 1358–1374.

Kaufhold, S., Dohrmann, R., 2010. Stability of bentonites in salt solutions: II. Potassium chloride solution – Initial step of illitization? Applied Clay Science, 49(3): 98–107.

Komine, H., Ogata, N., 1996. Prediction for swelling characteristics of compacted bentonite. *Canadian Geotechnical Journal,* 33: 11–22.

Komine, H., Yasuhara, K., Murakami, S., 2009. Swelling characteristics of bentonites in artificial seawater. *Canadian Geotechnical Journal,* 46: 177–189.

Laird, D.A., 2006. Influence of layer charge on swelling of smectites. *Applied Clay Science,* 34: 74–87.

Liu, L.C., 2013. Prediction of swelling pressures of different types of bentonite in dilute solutions. *Colloids and Surfaces A: Physicochemical and Engineering Aspects,* 434: 303–318.

Madsen, F.T., Müller-Vonmoos, M., 1989. The swelling behaviour of clays. *Applied Clay Science,* 4(2): 143–156.

Maio, C.D., Santoli, L., Schiavone, P., 2004. Volume change behaviour of clays: the influence of mineral composition, pore fluid composition and stress state. *Mechanics of Materials,* 36: 435–451.

Radhakrishna, H.S., Chan, H.T., Crawford, A.M., Lau, K.C. 1989 Thermal and physical properties of candidate buffer-backfill materials for a nuclear fuel waste disposal vault. *Canadian Geotechnical Journal,* 26(4): 629–639.

Rao, S.M., Thyagaraj T., 2007. Swell-compression behaviour of compacted clays under chemical gradients. *Canadian Geotechnical Journal,* 44(5): 520–532.

Saiyouri, N., Hicher, P.Y., Tessier, D., 2000. Microstructural approach and transfer water modeling in highly compacted unsaturated swelling clays. *Mechanics of Cohesive-frictional Materials,* 5(1): 41–60.

Studds, P.G., Stewart, D.I., Cousens, T.W., 1998. The effects of salt solutions on the properties of bentonite-sand mixtures. *Clay Minerals,* 33: 651–661.

Xu, Y.F., Matsuoka, H., Sun, D.A., 2003. Swelling characteristics of fractal-textured bentonite and its mixtures. *Applied Clay Science* 22(4): 197–209.

Xu, Y.F., Xiang, G.S., Jiang, H., Chen, T., Chu, F.F., 2014. Role of osmotic suction in volume change of clays in salt solution. *Applied Clay Science,* 101: 354–361.

Ye, W.M., Zhang, F., Chen, B., Chen, Y.G., Wang, Q., Cui, Y.J., 2014. Effects of salt solutions on the hydro-mechanical behavior of compacted GMZ01 bentonite. *Environmental Earth Sciences*, 72, 2621–2630.

Yong, R.N., 1999. Overview of modeling of clay microstructure and interactions for prediction of waste isolation barrier performance, *Engineering Geology* 54: 83–91.

This page intentionally left blank

Unsaturated Soil Mechanics—from Theory to Practice – Chen et al. (Eds)
© 2016 Taylor & Francis Group, London, ISBN 978-1-138-02921-7

An elastoplastic constitutive model for chalk with considering chalk-fluid physicochemical interaction

Tiantian Ma
State Key Laboratory of Geomechanics and Geotechnical Engineering, Institute of Rock and Soil Mechanics, Chinese Academy of Sciences, Wuhan, Hubei, China

Changfu Wei
College of Civil and Architectural Engineering, Guilin University of Technology, Guilin, Guangxi, China

Xiaolong Xia
State Key Laboratory of Geomechanics and Geotechnical Engineering, Institute of Rock and Soil Mechanics, Chinese Academy of Sciences, Wuhan, Hubei, China

ABSTRACT: Chalk is composed of multispecies electrically charged, and the behavior is sensitive to the saturating fluid. There is pronounced physicochemical interaction between the solid particle and fluid, rendering the chalk shows strong chemo-mechanical coupling effect and complex mechanical behavior. An elastoplastic model of chalk saturated with different fluids was developed based on the modified Cam-clay model, which could be effectively used to address the chemo-mechanical behavior. In this model, the generalized osmotic pressure was introduced to represent the microscopic physicochemical stress. Based on the generalized osmotic pressure, the intergranular stress equation is formulated that can effectively account for the physicochemical effect. The generalized osmotic pressure was treated as another hardening variable, and the hardening law of the yielding pressure was given. Compared with the experimental results, the model is capable of addressing the water weakening effect of the chalk.

1 INTRODUCTION

In North Sea chalk reservoir, water injection was an important method to repressurize the reservoir. This method has proved to have a great potential for improving oil recovery. However, when water replaces oil in chalks, it has caused enhanced reservoir compaction and seabed subsidence. Chalk is an important reservoir rocks in the southern part of North Sea. It was observed that the seawater has a pronounced weakening effect on chalks (Homand & Shao 2000).

Chalk is a kind of carbonate rock, and mainly built up of the fragments of calcite skeletons, originated from planktonic algae called coccolithophorids (Risnes et al. 2003). This gives the chalk material a rather open structure and high porosity (40%∼50%) The chalk has a negative surface charge, the surface area about 2 m^2/g, similar to the clay. The purely biogenic chalk surface is reactive, and this is probably the main reason why the mechanical properties depend strongly on the types of saturating fluid.

For more than 30 years, the mechanical behavior of chalk has received considerable attention, and an extended experimental testing has been performed to investigate the interaction between water and chalk (Delage et al. 1996, Hellmann et al. 2002a, Risnes et al. 2000, 2003, Risnes & Flaageng 1999, Piau & Maury 1994). Experimental studies showed that water-saturated chalk is mechanically weaker than dry or oil-saturated chalk (Duperret et al. 2005). When the chalk exposed to water, the strain was increased (Newman 1983, Schroeder et al. 1998, Risnes et al. 2005, Heggheim et al. 2005, Madland et al. 2006). It was concluded that the Young's and bulk moduli, pore collapse yield stress, and cohesive intercept decreased with the increase of the saturation, while the Poisson's ratio, plastic volumetric hardening modulus and friction angle are more or less constant (Papamichos et al. 1997, Talesnick et al. 2001).

To clarify the basis mechanism of chalk, the EC Research Program ***Pasachalk*** has been conducted. The research showed that the influence of water on pure high porosity chalk is similar to that on partially saturated soils (Delage et al. 1996). Capillary forces have been proposed by several researchers as the main mechanism of water weakening of chalks to explain the reduction in the strength of chalk with increasing water saturation (Papamichos et al. 1997, Andersen et al. 1992, Delage et al. 1996, Risnes et al. 2003, 2005). Capillary pressure is known to induce

an apparent cohesion between chalk grains. When the water is injected into the chalk, the capillary menisci collapses and the chalk becomes weaker.

More recently, many constitutive models were developed by considering of the capillary pressure effects (Piau & Maury 1994, Scroeder et al. 1998). Papamichos et al. (1997) considered that the elastic parameters and the yield surface are suction dependent Furthermore, Homand & Shao (2000) described the collapse behavior by assuming a stress jump (additional stress) between the oil-saturated state and the water-saturated one. Based the Barcelona Basic Model (BBM) (Alonso et al. 1990) of unsaturated soils, many constitutive laws were developed, in which the change of size of shear and pore collapse yield surface depend on suction, defined as the difference between oil pressure and water pressure (Gennaro et al. 2003, Collin et al. 2002).

But such effects can only partly explain the experimental observations. Risnes & Flaageng (1999) used miscible fluids, and capillary forces could be eliminated. The experimental results has revealed that methanol saturated chalk was considerably stronger than the one saturated by water. They considered the changes in mechanical properties as the repulsive forces generated by dipole-dipole interactions between the very narrow grain contact areas. Moreover, Risnes et al. (2003) observed a linear trend between reduction in water activity and the corresponding increase in strength based on brines at high salinities and glycol–water solutions. Thus, water activity appeared to be a key parameter for the water weakening mechanism. They also pointed out that the degree of weakening depends on the strength of adsorption of fluid molecules onto the calcite surface. The basic mechanism behind this effect seems to be related to the added pressure on the grains, caused by attraction of water molecules to the chalk surface.

The concept of the partially saturated soil mechanics could not adequately explain the reduction severely in the strength of chalk. The basic mechanisms behind the chalk-water interaction have also existed disagreements. Due to the fixed charge, the intermolecular forces resulting from rock–fluid interactions will affect mechanical behavior of chalk. Hiorth et al. (2010) calculated the surface charge and the resulting disjoining pressure for different aqueous solutions. The overlap of this negatively charged layer exerts a disjoining pressure which accounts for the stability of the water film between chalk and fluid interfaces and eventually makes the core much water wetter.

In this paper, a chemical-mechanical coupling constitutive model for chalk is presented which could address the water weakening effect. The generalized osmosis pressure was introduced to characterize the micro physicochemical interaction between the pore fluid and chalk, which provides the better understanding of the mechanisms involved in chalk-water interaction. Further, the intergranular stress was formulated, which could consider the Donnan osmosis effects, capillarity and adsorption.

2 THEORETICAL FORMULATION

2.1 *Intergranular stress*

Wei (2014) established a theoretical framework for modeling the chemo-mechanical behavior of multiphase porous media, which can address skeletal deformation, fluid flow, heat conduction, solute diffusion, chemical reaction, and phase transition in a consistent and systematic way. He introduced the concept of equilibrium solution, and pointed out that the water pressure measured by a conventional transducer can be significantly different from the true pore water pressure. The general expression is derived for the electrochemical potential of a fluid species with explicitly accounting for the effects of osmosis, capillarity, and adsorption. Based on the equilibrium properties of porous media, the composition of pore water pressure is identified,

$$p^l = p^l_{\mathrm{W}} + \Pi \tag{1}$$

where p^l is the true pore water pressure and p^l_{W} is the equilibrium solution pressure (i.e. measured pressure). Π is the generalized osmotic pressure, stemming from the physicochemical interactions among different bulk phases, including electrostatic forces, van der Waals attraction, double-layer repulsion, and so on, given by

$$\Pi = \Pi_{\mathrm{D}} - \rho_{\oplus}^{l_{\mathrm{H_2O}}} \Omega^l \tag{2}$$

where Π_{D} is Donnan osmotic pressure, $\Pi_{\mathrm{D}} = \frac{RT\rho_{\oplus}^{l_{\mathrm{H_2O}}}}{\mathrm{M_{H_2O}}} \ln\left(\frac{a_A^{l_{\mathrm{H_2O}}}}{a^{l_{\mathrm{H_2O}}}}\right)$: R is the universal gas constant; T is the Kevin temperature; $\rho_{\oplus}^{l_{\mathrm{H_2O}}}$ is the mass density of water at the pure state, which is assumed to be constant; $\mathrm{M_{H_2O}}$ is the molar mass of water; $a_A^{l_{\mathrm{H_2O}}}$, $a^{l_{\mathrm{H_2O}}}$ are the activity of the water in equilibrium solution and soil respectively, which are functions of T, p^l and molar fraction $m^{l_{\mathrm{H_2O}}}$. Ω^l is the surface energy potential, which is considered as a part of the free energy potential of the pore fluid. And the pore fluid is subjected to the surface forces, fully specified as a function of on T and n_l only; n_l is the volume fraction of soil water.

Due to the electrically charged nature of chalk, the equilibrium solution in the conventional transducer is different from the pore water in chalk because the concentration of the two fluids is different due to the existence of the semipermeable membrane effect This phenomenon is usually called Donnan's effect (Mitchell & Soga 2005), which can be attributed to the existence of the fixed charges in the porous media. The phenomenon induced the Donnan osmotic pressure Π_{D}, shown in Equation (2). The surface energy Ω^l can be determined by the soil water characteristic curve. At full saturation, Ω^l_0 can be assumed as zero.

Based on the concept of true pore pressure, explicit formulas are developed for the intergranular stress,

with consideration of physicochemical effects (Wei 2014),

$$\boldsymbol{\sigma}' = \boldsymbol{\sigma} + p^g \mathbf{1} - n^l \left(s_{\mathrm{M}} - \Pi\right)\mathbf{1} \tag{3}$$

where $\boldsymbol{\sigma}$ is the total stress tensor; p^g is the gas pressure; s_{M} is the matric suction, $s_{\mathrm{M}} = p^g - p^l_{\mathrm{W}}$. At full saturation, $\boldsymbol{\sigma}' = \boldsymbol{\sigma} + p^l_{\mathrm{W}}\mathbf{1} + \Pi\mathbf{1}$; Ω^l_0 is zero, and $\Pi = \Pi_{\mathrm{D}}$.

When the chalk is saturated with the oil, there is not Donnan effect and $\Pi_{\mathrm{D}} = 0$. So the intergranular stress of water-saturated chalk is smaller than the one of oil-saturated chalk. It can also explain that this weakening effect increases with increase of temperature.

2.2 *Yielding and hardening*

As mentioned, chalk rocks present a particular mechanical behavior which is at intermediate state between a rock and a soil. The chalk has two independent mechanical properties: plastic pore collapse and plastic shear strain. With the two types of failure modes chalks may mechanically be described by a Mohr-Coulomb type failure criterion with an end cap.

The stress-strain relationship is developed by generalizing the modified Cam-Clay model, in which the yield function is given by

$$f = q^2 + M^2\left(p' + c/M\right)\left(p' - p_c\right) \tag{4}$$

where M is the slope of critical state line; p_c is the preconsolidation pressure, which is a function of plastic volumetric strain ε^p_v. c is the cohesion, the shear strength with zero normal stress on the shear plane. For accounting for the physicochemical effect on the chalk, the generalized osmosis pressure is introduced as another hardening variable. It is suggested herein that, in general, one can assume

$$p_c = p_{c0}\exp\left(\frac{\upsilon\varepsilon^p_v}{\lambda - \kappa}\right)\cdot\exp\left(-\beta\Pi\right) \tag{5}$$

where p_{c0} is the initial preconsolidation pressure of chalk saturated with oil ($\Pi_{\mathrm{D}} = 0$); υ is the specific volume, $\upsilon = 1 + e$, e the void ratio. λ, κ are the slopes of the normal consolidation line and the unloading-reloading line on the $\upsilon - \ln p'$ plane of chalk, respectively β is the hardening parameter associated with the physicochemical effect.

The yield surface is moving with the evolution of the internal hardening variable p_c, which is characterized in terms of the double-hardening mechanism in (5). Using the intergranular stress, the critical state line of chalk saturated with different fluids are same, simply given by $q = Mp' + c$

Figure 1 illustrated the yield surface and critical state line of chalk saturated with water and soltrol respectively, in which p (x-axis) represents the tradition effective mean pressure, i.e., the total mean pressure minus the measured pore pressure p^l_w. Therefore, there is the difference of apparent cohesion between the chalk saturated with water and soltrol. When the intergranular mean pressure was introduced $p' = p - \Pi$, the critical state lines coincide into the same one.

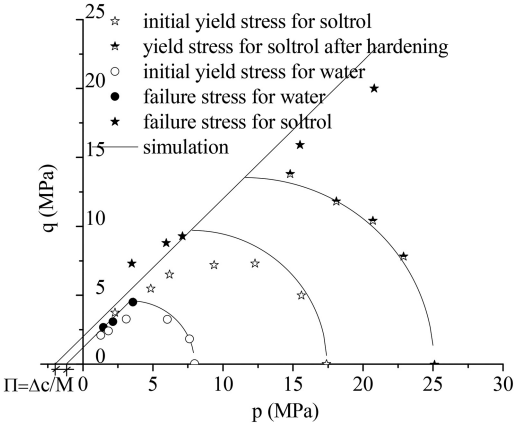


Figure 1. Yield and failure surfaces of chalk respectively in soltrol and water saturated samples.

2.3 *Elastoplastic stress-strain relation*

As in the original modified Cam-Clay model, the increments of elastic volumetric strain and deviatoric strain are defined as

$$d\varepsilon^e_v = \frac{\kappa dp'}{\upsilon p'};\quad d\varepsilon^e_q = \frac{dq}{3G} \tag{6}$$

where G is the shear modulus.

An associated flow rule is adopted herein: thus the plastic potential coincides with the yield function. The incremental plastic volumetric and deviatoric strains are given by

$$d\varepsilon^p_v = d\lambda\frac{\partial f}{\partial p'};\quad d\varepsilon^p_q = d\lambda\frac{\partial f}{\partial q} \tag{8}$$

where $d\lambda$ is the plastic multiplier that can be determined based on the consistency condition.

This model can simulate the experimental observations of chalk. For example, the methanol saturated chalk is considerably stronger than the one water saturated. The water weakening effect to some extent is a reversible effect.

2.4 *Evaluation of constitutive parameters*

The proposed model adopts the intergranular stress as stress state variable. Therefore, the parameters for the chalk saturated with different fluids are the same, which are independent of the saturating fluid. Compared with the modified Cam clay model, the new model for chalk needs two additional parameters, c and β. The original parameters can be determined in the same way as that for the modified Cam-clay model. c can be determined by the intersection of the critical

Table 1. Model parameters for chalk.

λ	κ	G (MPa)	p_{c0} (MPa)	β	Π (MPa)	c (MPa)	M
0.16	0.003	1500	17.4	0.94	0.8	2.0	1.0

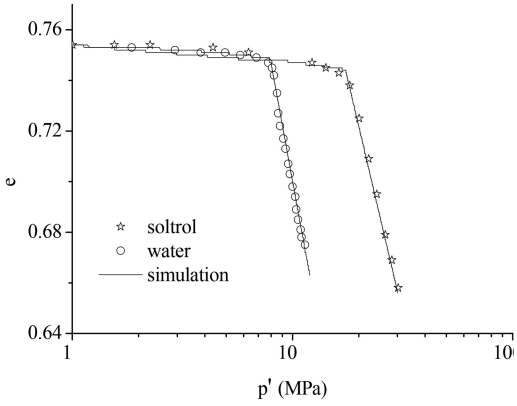


Figure 2. Comparisons of the experimental results between water and soltrol saturated chalk samples in hydrostatic compression tests.

state line of chalk saturated with oil ($\Pi_D = 0$) with q axis. β can be determined by fitting the experimental results from the relation between the preconsolidation pressure and Donnan osmosis pressure.

The Donnan osmosis pressure is a function of temperature, fixed charge of chalk and pore solution concentration. It is hard to calculate accurately though Equation (2). However, the difference between the "apparent cohesion" of chalk saturated with oil and water is induced by the Donnan osmosis pressure. So it can be determined through $\Pi = \Delta c/M$, shown in Fig. 1.

3 MODEL PERFORMANCE

The experimental results in Homand & Shao (2000a) are used to validate the proposed model. The parameters are calibrated based on the experimental results, shown as Table 1.

In Figure 2, the simulations of two hydrostatic compression tests respectively performed on "oil saturated" and "water saturated" samples are shown. If the material is deformed hydrostatically beyond the elastic limit, it will apparently enter into a strain hardening process. From the experimental results, it can be observed that the value of λ, κ are same for chalk saturated with water and soltrol. The good correlation between numerical and experimental data indicates that the weakening effect of water on plastic pore collapse of chalk is well described.

In Figures 3 to 17, two series of Triaxial compression tests with different confining pressures,

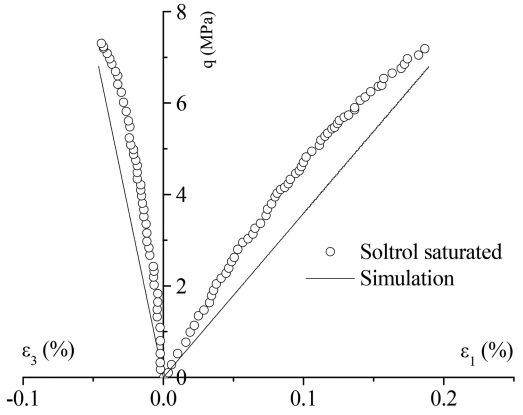


Figure 3. Stress strain curves obtained in triaxial compression test with 1 MPa confining pressure on soltrol saturated samples.

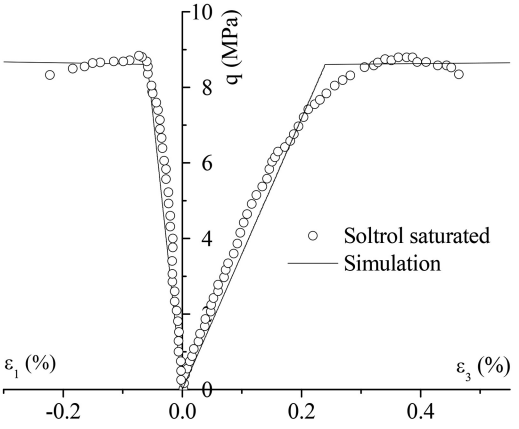


Figure 4. Stress strain curves obtained in triaxial compression test with 3 MPa confining pressure on soltrol saturated samples.

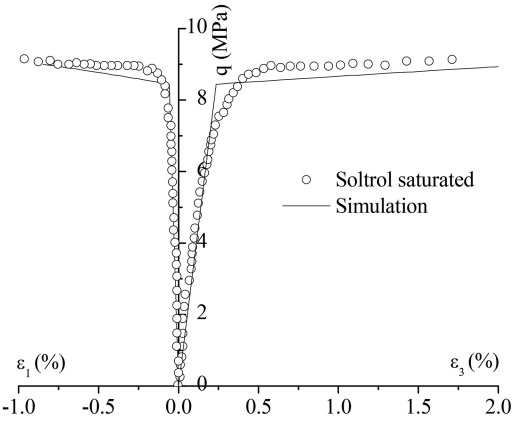


Figure 5. Stress strain curves obtained in triaxial compression test with 4 MPa confining pressure on soltrol saturated samples.

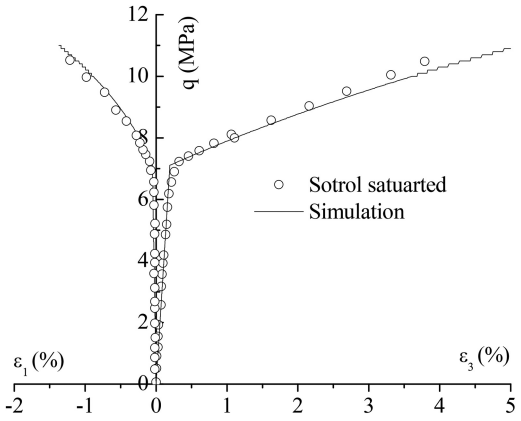


Figure 6. Stress strain curves obtained in triaxial compression test with 7 MPa confining pressure on soltrol saturated samples.

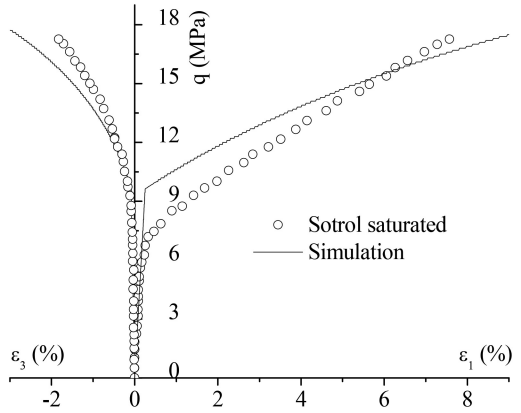


Figure 7. Stress strain curves obtained in triaxial compression test with 10 MPa confining pressure on soltrol saturated samples.

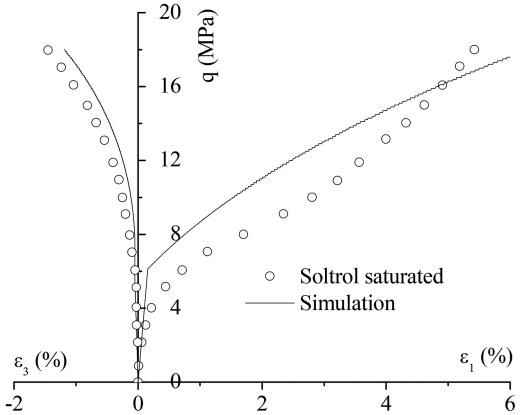


Figure 8. Stress strain curves obtained in triaxial compression test with 14 MPa confining pressure on soltrol saturated samples.

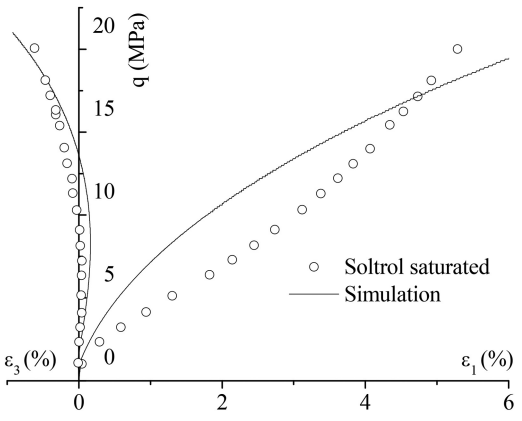


Figure 9. Stress strain curves obtained in triaxial compression test with 17 MPa confining pressure on soltrol saturated samples.

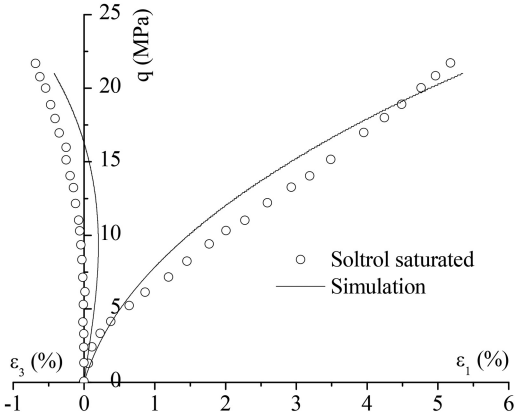


Figure 10. Stress strain curves obtained in triaxial compression test with 20 MPa confining pressure on soltrol saturated samples.

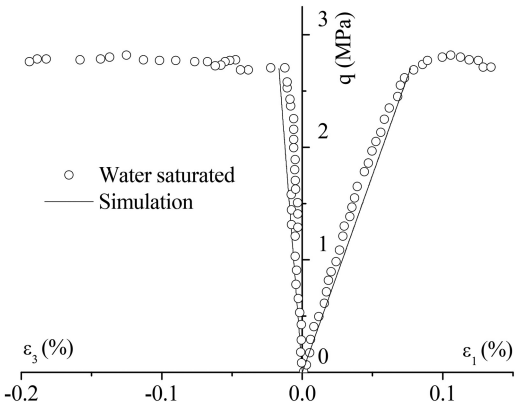


Figure 11. Stress strain curves obtained in triaxial compression test with 0.5 MPa confining pressure on water saturated samples.

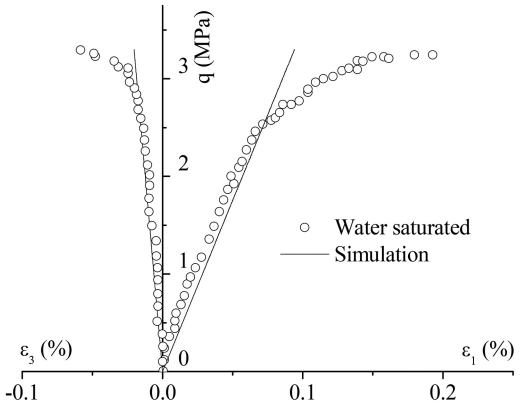


Figure 12. Stress strain curves obtained in triaxial compression test with 1.0 MPa confining pressure on water saturated samples.

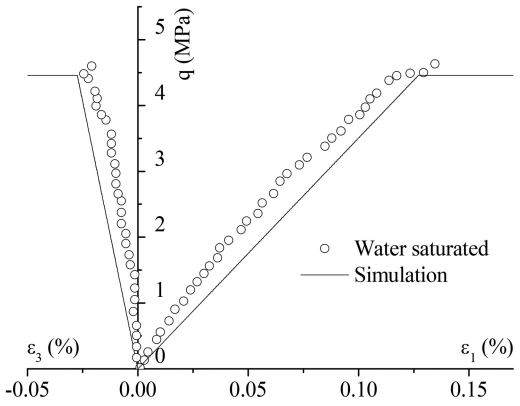


Figure 13. Stress strain curves obtained in triaxial compression test with 2.0 MPa confining pressure on water saturated samples.

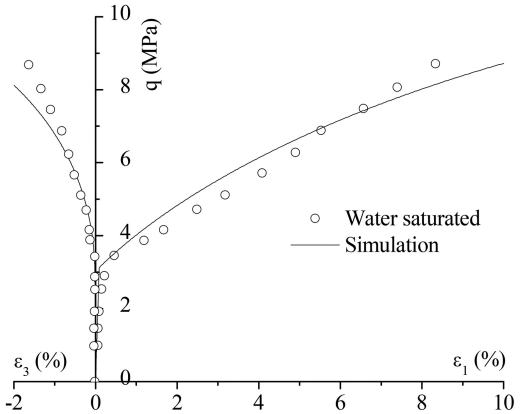


Figure 14. Stress strain curves obtained in triaxial compression test with 5.0 MPa confining pressure on water saturated samples.

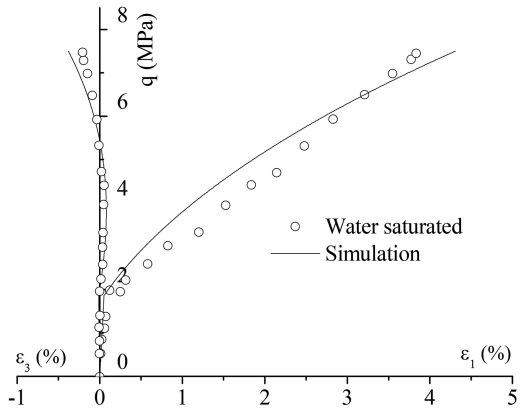


Figure 15. Stress strain curves obtained in triaxial compression test with 7.0 MPa confining pressure on water saturated samples.

respectively in water and oil saturated conditions, are simulated by using the proposed elastoplastic model.

Comparison with the experimental results shows that the proposed model is able to describe the basic mechanical behavior of porous rocks, both in "oil" and "water" saturation conditions.

4 CONCLUSIONS

An elastoplastic chemical-mechanical constitutive model was developed in the paper. The generalized osmosis pressure was introduced to characterize the micro physicochemical effects between the saturated fluids and chalk. Hence, the formulated intergranular stress could consider the mechanical and chemical effects in a consistent and systematic way.

The proposed model introduced the generalized osmosis pressure into the hardening function as independent variable to characterize the physicochemical effects on the yielding pressure. Comparison with the experimental results showed that the model is able to reproduce qualitatively and quantitatively the observed basic phenomena. Further validation tests are still necessary to get an overall appreciation of the performance of the model.

ACKNOWLEDGMENTS

The research was supported by the Natural Science Foundation of China (Grant no. 11372078) and the Guangxi Natural Science Foundation through grants 2012GXNSFGA060001, and the Major Projects of Guangxi Natural Science Foundation through grants 2012GXNSFEA053002.

REFERENCES

Alonso, E.E., Gens, A., Josa, A. 1990. A constitutive model for partially saturated soils. *Geotechnique* 40(3): 405–430.

Andersen, M.A., Foged, N., Pedersen, H.F. 1992. The rate-type compaction of a weak North Sea chalk. In J.R. Tillerson & W.R. Wawersik (eds), *Proceeding of 33rd US Rock Mechanics Symposium, Balkema, 3–5 June 1992.* Santa Fe, NewMexico.

Collin, F., Cui, Y.J., Schroeder, C., Charlier, R. 2002. Mechanical behaviour of Lixhe chalk partly saturated by oil and water: experiment and modelling. *International Journal for Numerical and Analytical Methods in Geomechanics* 26(9): 897–924.

Delage, P., Schroeder, C., Cui, Y.J. 1996. Subsidence and capillary effects in chalks. *Proc. Eurock'96 Prediction and performance on rock mechanics and rock engineering, Turin,* 1291–1298. Rotterdam: Balkema.

Duperret, A., Taibi, S., Mortimore, R.N., Daigneault, M. 2005. Effect of groundwater and sea weathering cycles on the strength of chalk rock from unstable coastal cliffs of NW France. *Engineering Geology* 78(3–4): 321–343.

Gennaro, V.D., Delage, P., Cui, Y.J., Schroeder, Ch., Collin, F. 2003. Time-dependent behaviour of oil reservoir chalk: a multiphase approach. *Soils and Foundations* 43(4): 131–148.

Heggheim, T., Madland, M., Risnes, R., Austad, T. 2005. A chemical induced enhanced weakening of chalk by seawater. *Journal of Petroleum Science and Engineering* 46(3): 171–184.

Hellmann, R., Renders, P.J., Gratier, J.P., Guiguet, R. 2002a. Experimental pressure solution compaction of chalk in aqueous solutions. Part 1. Deformation behavior and chemistry. In R. Hellmann & S.A. Wood (eds), *Water-Rock Interactions, Ore Deposits, and Environmental Geochemistry.* A Tribute to David A. Crerar; The Geochemical Society, Special Publication No 7: 129–152.

Hiorth, A., Cathles, L., Madland, M. 2010. The impact of pore water chemistry on carbonate surface charge and oil wettability. *Transport in Porous Media* 85(1): 1–21.

Homand, S., Shao, J.F. 2000. Mechanical behaviour of a porous chalk and water/chalk interaction part i: experimental study. *Oil & Gas Science and Technology – Rev IFP* 55(6): 591–598.

Homand, S., Shao, J.F. 2000. Mechanical behaviour of a porous chalk and water/chalk interaction part ii: numerical modelling. *Oil & Gas Science and Technology – Rev IFP* 55(6): 599–609.

Madland, M.V., Finsnes, A., Alkafadgi, A., Risnes, R., Austad, T. 2006. The influence of CO_2 gas and carbonate water on the mechanical stability of chalk. *Journal of Petroleum Science and Engineering* 51(3): 149–168.

Mitchell, J.K., Soga, K. 2005. *Fundamentals of soil behavior*. New York: John Wiley & Sons.

Newman, G.H. 1983. The effect of water chemistry on the laboratory compression and permeability characteristics of some North Sea chalks. *Journal of Petroleum Technology* 35(5): 976–980.

Papamichos, E., Brignoli, M., Santarelli, F. 1997. An experimental and theoretical study of a partially saturated collapsible rock. *Mechanics of Cohesive – frictional Materials* 2(3): 251–278.

Piau J., Maury V. 1994. Mechanical effects of water injection on chalk reservoirs. *Proc. Eurock'94, SPE/ISRM Int. Conf., Delft,* 819–828.

Risnes, R., Berg, T., Furuvald, A., et al. 2000. Tensional failure and solid-fluid interactions in high porosity chalk. *Proc. 4th North American Rock Mechanics Symposium*: 205–212 Rotterdam: Balkema.

Risnes, R., Flaageng, O. 1999. Mechanical properties of chalk with emphasis on chalk-fluid interactions and micromechanical aspects. *Oil & Gas Science and Technology* 54(6): 751–758.

Risnes, R., Haghighi, H., Korsnes, R.I, Natvik, O. 2003. Chalk-fluid interactions with glycol and brines. *Tectonophysics* 370(1–4): 213–226.

Risnes, R., Madland, M., Hole, M., Kwabiah, N.K. 2005. Water weakening of chalk-Mechanical effects of water-glycol mixtures. *Journal of Petroleum Science and Engineering* 48(1): 21–36.

Schroeder, C., Bois, A.P., Maury, V., Halle, G. 1998. *Water/chalk (or collapsible soil) interaction: Part II. Results of tests performed in laboratory on Lixhe chalk to calibrate water/chalk models.* Trondheim, Eurock '98.

Talesnick, M., Hatzor, Y., Tsesarsky, M. 2001. The elastic deformability and strength of a high porosity, anisotropic chalk. *International Journal of Rock Mechanics and Mining Sciences* 38(4): 543–555.

Wei, C.F. 2014. A theoretical framework for modeling the chemomechanical behavior of unsaturated soils. *Vadose Zone Journal* 13(9): 1–21.

This page intentionally left blank

Unsaturated Soil Mechanics—from Theory to Practice – Chen et al. (Eds)
© 2016 Taylor & Francis Group, London, ISBN 978-1-138-02921-7

An elastoplastic constitutive model for gas hydrate-bearing soils with hydrate dissociation

Rongtao Yan & Changfu Wei
College of Civil Engineering and Architecture, Guilin University of Technology, Guilin, China

ABSTRACT: An elastoplastic model is developed for gas hydrate-bearing soils within the framework of the modified Cam clay model. A modified effective stress formulation is introduced, and a new yield function is proposed which can describe well the enhanced stiffness, strength and dilatancy with the increment of the hydrate saturation. The bonding stress is introduced into the yield function as an additional hardening parameter to address the effect of the hydrate saturation. To describe the soil dilatancy, a flow rule is introduced, which depends upon the bonding stress and the stress ratio. It is demonstrated that the proposed model captures the main features of the behavior of gas hydrate-bearing soils including the enhanced stiffness, strength, dilatancy and strain softening during the shearing process, and is capable of describing the behavior of GHBS under hydrate dissociation.

1 INTRODUCTION

Gas hydrate is a crystalline solid that consists of natural gas and hydrogen-bonded water molecules, which is formed at low temperature and high pressure. Therefore, gas hydrate usually exists in deep water sediment with many continental margins and permafrost regions. As one of potential sources of energy, it has triggered numerous researchers to study the physical, chemical and mechanical characteristics of Gas Hydrate-Bearing Sediment (GHBS) in the past two decades. Two methods generally accepted to feasible for exploitation of gas hydrate is depressurization and thermal injection. However, these human activities maybe destabilize the hydrate-bearing soil layers, which could trigger potentially huge landslides and soil failures (Sloan, 2004). Hence, it is critical to properly characterize the responses of gas hydrate-bearing soils (GHBS) to the mechanical and hydrate dissociation (Sloan, 2004, Sultan et al., 2004).

Recently, various constitutive models for GHBS were proposed to simulate the deformation of GHBS under the mechanical loading. With the experimental results of tri-axial compression tests, a variable-compliance-type constitutive model for the gas hydrate-bearing Toyoura sand was developed by Miyazaki et al. (2008). In the framework of critical state model, Sultan & Garziglia (2011) developed an elasto-plastic constitutive model, which could capture the some key features of GHBS, such as enhanced stiffness, strength, soften and dilatancy. Recently, based on the assumption that the variation of the microelement strength follows the Weibull's distribution, Wu et al. (2013) developed a statistical damage constitutive model for hydrate-bearing soils. Clearly, the above models could predict the major mechanical characteristics of GHBS. Nevertheless, they didn't take the hydrate dissociation into account.

In this paper, we aim to develop a constitutive model with considering the hydrate dissociation loading with the foundation of above models. As is well known, the mechanical responses of GHBS are akin to those of the bonded and structured clay. Introducing the concept of structural stress, Liu & Carter (2002) developed a structured Cam clay model by modifying the formulation of effective stresses. The structure stress decreases as the clay structure breaks, and accordingly the yield surface shrinks. Within the framework of the Cam clay model, Suebsuk et al. (2010) developed a generalized critical state model for destructured, naturally structured and artificially structured clay. Going through a similar approach, with introducing the bonding stress into the yield function, the yield surface would enlarge as a result of the hydrate bonding. As the hydrate was damaged and dissociated, yield stress would decrease and yield surface shrank, which could be used to describe the mechanical responses of GHBS under the mechanical loading and hydrate dissociation.

In this paper, the works are arranged as following: Firstly, the effective stress for GHBS is modified to take the bonding stress into account, and the strength formula is modified for GHBS. Secondly, the yield function is deduced with considering the bonding effect of hydrate in the framework of critical state soil mechanics. In addition, a non-associated flow rule is adopted with the bonding stress as state variable. Finally, the proposed constitutive model is verified by previous tri-axial tests results, and can be applied to simulate and analyze the mechanical responses of GHBS subjected by the hydrate dissociation.

2 THEORETICAL FORMULATION

The soils under consideration are viewed as continua which consist of solid skeleton (s) and gas hydrate (h). In addition, it is assumed herein that, 1) gas hydrate in the pores is considered as a part of the solid skeleton; 2) the critical friction angle is regardless of hydrate saturation and occurrence morphology. Clearly, assumption 2) is motivated by the experimental observations, which illustrate that the critical internal friction angle at larger shear strain varies insignificantly with the hydrate saturation (Sultan et al., 2011; Masui et al., 2008; Yan et al., 2012; Waite et al., 2009).

2.1 *The effective stress and strength formula for GHBS*

With assumption 1), the solid composite consist of the gas hydrate and soil skeleton. So it is reasonable to consider the water pressure and bonding stress in analyzing the effective stress for GHBS. According to the views of Mitchel & Soga (2005) about the intergranular stress that is synonymous with the effective stress, we should take the bonding effect of hydrate on the mechanical characteristics into account. Therefore, the classical effective stress should be modified for GHBS:

$$\sigma' = \sigma - u_w \mathrm{I} + p_b \mathrm{I} \tag{1}$$

where p_b is the bonding stress. In the hydrate-bearing sediment, p_b is the function of the saturation of hydrate S_h and occurrence morphology. When the morphology is similar, p_b has a higher value at the higher saturation of hydrate, and vice versa. Certainly, in the process of mechanical loading on the GHBS and hydrate dissociation, the structure may collapses, which leads to the diminishing of bonding stress, p_b. I is the unit tensor.

Based on the modified effective stress, the mean effective stress and the stress ratio are represented:

$$p^* = p - u_w + p_b = p' + p_b \tag{2}$$

$$\eta^* = q / p^* = q/(p' + p_b) \tag{3}$$

where p^* is the modified mean effective pressure, p' is the classical mean effective pressure for saturated soil, $p' = p - u_w$. The modified mean effective pressure p^* is the sum of classical mean effective pressure p' and bonding stress, p_b. In Equation (3), η^* is the modified stress ratio, and q is the effective deviator stress, equal to the subtraction of axial stress and confining stress, $q = \sigma_1 - \sigma_3$.

When $\eta^* = M$, q is the strength of GHBS and expressed as follows,

$$q = M(p' + p_b) \tag{4}$$

Clearly, Equation (4) is the strength formula for GHBS. If the bonding stress p_b can be calculated, the strength will be worked out.

2.2 *Yield surface and hardening disciplines*

According to the experimental results from the previous works (Masui et al., 2005, 2008; Yan et al., 2012; Yun et al., 2007), it is clear that hydrate bonding can increase the yield stress. The additional hardening parameter p_m is elected to the yield function, which is able to enlarge the yield surface. In addition, considering the capability of resisting tension for GHBS, a yield function for GHBS is proposed as follows,

$$f = (p' + p_b)(p' - p_c - p_m) + q^2 / M^2 \tag{5}$$

In Equation (5), p_b is the tensile strength from the bonding of hydrate; p_c is the partial yield stress of resisting compression related to the deformation of soil skeleton; p_m is the partial yield stress of resisting compression related to the hydrate bonding: $p_m = k_s \cdot p_b$, where k_s is a model parameter.

According to the mechanical characteristics of GHBS, the hardening rule for the conventional cam clay model has to be modified to describe the hardening evolution of GHBS sample. Hence, the hardening rule for GHBS sample is modified and expressed as follows:

$$dp_c = \frac{(1+e)p_c[d\varepsilon_v^p + M[1-\exp(-\xi \cdot p_b)]d\varepsilon_s^p]}{\lambda_h - \kappa_h} \tag{6}$$

In equation (6), e represents the void ratio of hydrate-bearing sediments; κ_h is the gradient of unloading or swelling line of the hydrate-bearing sediments, and λ_h is the plastic compressibility coefficient of GHBS. ξ is a model parameter same to Equation (12).

As a result of the bonding of hydrates to soils, κ_h is assumed to be a function of hydrate saturation S_h:

$$\kappa_h = \kappa_0 \cdot e^{\zeta \cdot S_h} \tag{7}$$

where κ_0 is the gradient of unloading or swelling line for soils without hydrates; ζ is a model parameter which can be acquired by fitting the test data.

λ_h is the plastic compressibility coefficient of GHBS, and Sultan & Garziglia (2011) have suggested an expression:

$$\lambda_h = \lambda_0[1-(1-\frac{\lambda_1}{\lambda_0})(1-\exp(-\beta \cdot S_h))] \tag{8}$$

where λ_0 is the plastic compressibility coefficient of soils without hydrates; λ_1 is the plastic compressibility coefficient of hydrate phase and equal to 0.00147; β defines the slope of the change of the compressibility with the hydrate saturation, and the effect of β on the curves of $\lambda_h - S_h$ is illustrated in Fig. 1.

According to the above description, the hydrate formed in the pores between soil particles could cement the soil sample. Clearly, the extent of cementation on the soil sample is related to the previous

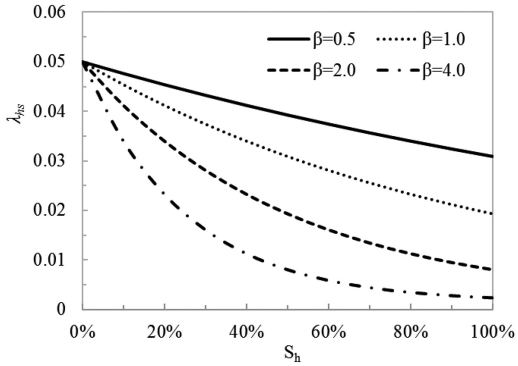


Figure 1. λ_h is a function of hydrate saturation S_h for four different values of β.

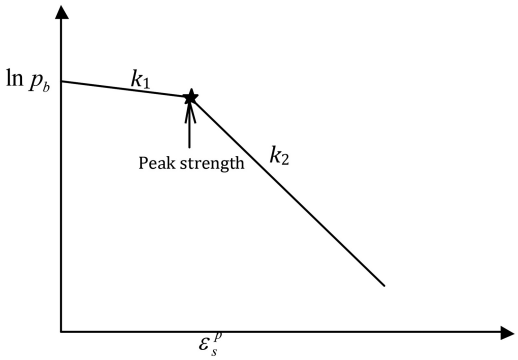


Figure 2. Schematic diagram of reduction in p_b subject to plastic deformation.

structure of sample and hydrate saturation. However, there are scarce experiment researches about the previous structure. Herein, we propose an expression to determine the initial bonding stress p_{bi}, justly considering the hydrate saturation S_h:

$$p_{bi} = m \cdot (S_h)^n \tag{9}$$

where m and n are model parameters, which can be acquired by fitting the curve of the $p_{bi} - S_h$.

As it is known, mechanical loading and hydrate dissociation could decrease the bonding stress, and a simple formula to express the decementation of GHBS is proposed,

$$dp_b = -\rho_s \cdot p_b \cdot d\varepsilon_s^p + mn(S_h)^{n-1} dS_h \tag{10}$$

where ρ_s is a model parameter representing the effect of the plastic deviatoric strain ε_s^p on the cementation stress p_b. Generally, ρ_s have two different values during the whole mechanical loading procedure. The first one corresponds to the local damage of hydrate before the peak strength, and the second one corresponds to the whole collapse after the peak strength. ρ_s could be set to be equal to k_1 or k_2, which is shown in Fig. 2.

2.3 *Flow rule*

Flow rule is used to plot the direction of plastic strain, and can be expressed by dilatancy, plastic strains ratio,

$$d = d\varepsilon_v^p \big/ d\varepsilon_s^p \tag{11}$$

The fundamental issue in determining the flow rule is to describe the dilatancy d correctly. For the GHBS, the dilatancy function in which the variable is only the modified stress ratio is not enough to describe the dilatancy behaviors. Because the dilatancy function d is an intrinsic essence, the soils show different dilatancy behaviors with different inter-structure (Li and Dafalias, 2000). Therefore, the dilatancy function d should contain not only stress ratio η, but also the internal state of material, and we can express it as follows:

$$d(\eta^*, p_b) = M \cdot \exp(-\xi \cdot p_b) - \eta^* \tag{12}$$

where ξ is a model parameter, representing the influence degree of p_b on the dilatancy d. It is worth to point out that the dilatancy function d can be retrograded to that for cam clay when there is no hydrate in soil.

2.4 *Plastic strain*

According to the yield function, the consistency equation is acquired:

$$\begin{aligned} df &= \frac{\partial f}{\partial p}dp + \frac{\partial f}{\partial q}dq + \frac{\partial f}{\partial p_c}dp_c + \frac{\partial f}{\partial p_b}dp_b + \frac{\partial f}{\partial p_m}dp_m \\ &= \frac{\partial f}{\partial p}dp + \frac{\partial f}{\partial q}dq + \frac{\partial f}{\partial p_c}dp_c + (\frac{\partial f}{\partial p_b} + k_s\frac{\partial f}{\partial p_m})dp_b = 0 \end{aligned} \tag{13}$$

Combined with the hardening discipline and flow rule, we can obtain the plastic strain:

$$d\varepsilon_s^p = -\frac{1}{A}[\frac{\partial f}{\partial p}dp + \frac{\partial f}{\partial q}dq + (\frac{\partial f}{\partial p_b} + k_s\frac{\partial f}{\partial p_m})\frac{\partial p_b}{\partial S_h}dS_h] \tag{14}$$

$$d\varepsilon_v^p = d\varepsilon_s^p \cdot d(\eta^*, p_b) \tag{15}$$

where,

$$\begin{aligned} A = &\frac{\partial f}{\partial p_c} \cdot \frac{\partial p_c}{\partial \varepsilon_v^p} \cdot d(\eta'', p_b) + \frac{\partial f}{\partial p_c} \cdot \frac{\partial p_c}{\partial \varepsilon_s^p} \\ &+ (\frac{\partial f}{\partial p_b} + k_s\frac{\partial f}{\partial p_m}) \cdot \frac{\partial p_b}{\partial \varepsilon_s^p} \end{aligned} \tag{16}$$

2.5 *Elastic behavior*

According to the elastic and plastic theory, only elastic deformation occurs for the stress excursions within yield boundary. Here, the elastic behavior obeys Hooke's law:

$$d\varepsilon_v^e = \frac{\kappa_h}{(1+e)p'}dp' - \frac{\kappa_h \cdot \ln p}{(1+e)} \cdot \zeta dS_h \tag{17}$$

Table 1. Model parameters of GHBS model for GHBS (Masui et al., 2005).

Variables	Values	Units	Variables	Values	Units
e	0.65	–	n	0.6	–
λ_0	0.02	–	M	1.07	–
κ_0	0.012	–	ξ	0.42	MPa^{-1}
β	2.0	–	k_1	0.1	–
ζ	−1.4	–	k_2	5.0	–
ν	0.15	–	k_s	1.0	–
m	8.0	MPa			

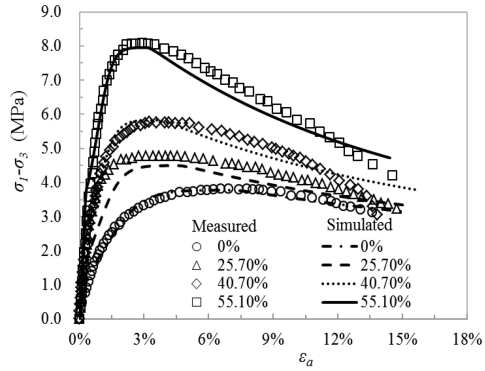
$$d\varepsilon_s^e = \frac{dq}{3G} = \frac{2(1+\nu)\kappa_h}{9(1-2\nu)vp}dq - \frac{2(1+\nu)\kappa_h}{9(1-2\nu)vp}\cdot\zeta dS_h \qquad (18)$$

where parameter ν is the Poisson's ratio and independent of hydrate (Masui et al., 2005, 2007, 2008).

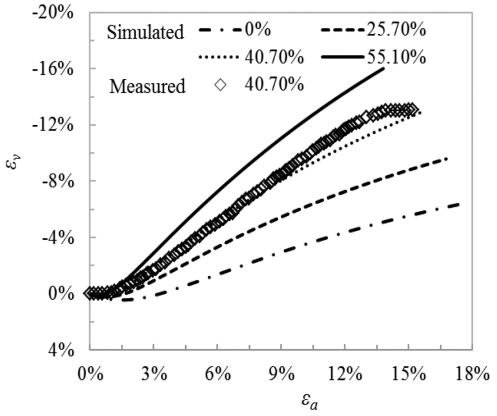
3 MODEL VERIFICATION AND PERFORMANCE

3.1 *Validation of model*

The proposed constitutive model was coded in FORTRAN, and was verified using the triaxial drained tests performed by previous investigators (Masui et al., 2005). Figure 3 shows the comparison between the model simulation and the triaxial experimental data on the samples of type B with different saturation of hydrate with 1 MPa confining pressure under drained condition. The parameters adopted by the model are summarized in Table 1. It is clearly that the model can reflect well the impacts of hydrate bonding on the mechanical characteristics for GHBS. As shown in Figure 3, the samples with the hydrate exhibit more enhancements in stiffness, strength and dilatancy with higher hydrate saturation.



(a) Deviatoric stress-axial strain



(b) Volumetric strain-axial strain

Figure 3. Comparisons of experimental and simulated results for the triaxial compressing test under drained condition (Masui et al., 2005).

3.2 *Deformation due to the hydrate dissociation*

In natural environment, hydrate dissociation maybe induce the soil deformation under the constant overlying loading, which may lead to the ground subsidence at large scale. In this section, deformations of GHBS subjected to hydrate dissociation are simulated. There are two cases elected to analyze the deformation characteristics due to the hydrate dissociation. The first case is for the isotropic stress condition, at which the sample is subjected to the constant isotropic stress condition and deforms during the hydrate dissociation; the second case is a tri-axial stress condition, at which the sample also generates strain owing to the hydrate dissociation. Clearly, the second case is probably more close to the real condition.

3.2.1 *The first case: Isotropic stress condition*

Figure 4 shows the deformation of the sample with hydrate saturation of 50% under 1.0 MPa, 2.0 MPa, 3.0 MPa mean pressures due to the hydrate dissociation. To analyze the effect of hydrate dissociation on the strain for GHBS, some model parameters are assumed according to the previous experiments and

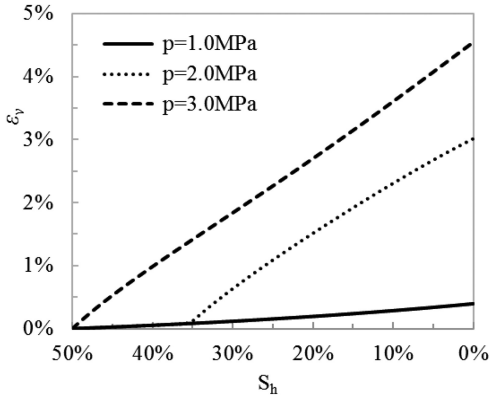


Figure 4. Deformation of GHBS ($S_h = 50\%$) under different isotropic mean pressures subjected to hydrate dissociation.

Table 2. Model parameters of GHBS model for GHBS (Masui et al., 2005).

Variables	Values	Units	Variables	Values	Units
e	0.8	–	n	2	–
λ_0	0.08	–	M	1.4	–
κ_0	0.0122	–	ξ	0.2	MPa^{-1}
β	2.0	–	k_1	0.1	–
ζ	−1.8	–	k_2	5.0	–
ν	0.15	–	k_s	1.0	–
m	8.0	MPa			

simulation examples, listing in Table 2. In addition, the pre-consolidation pressure is set to be 1 MPa. It is evident that the samples exhibit volume shrinkage during the hydrate dissociation procedure. It is because that as the hydrate dissociation, the additional effective stress carried by hydrate is transferred to the soil skeleton. From Figure 4, we also found that shrinking extents under different isotropic mean pressures are very different. At 1 MPa mean pressure, volume strain increases from 0 at hydrate saturation 50% to 0.4% at hydrate saturation 0. However, it is distinctive different that when the mean pressure is 3 MPa, the volume strain is about 4.5% at the time of hydrate dissociation finished. Such big deformation differences can be attributed to the strain characteristics under different mean pressures. When the mean pressure is 1 MPa, the stress state is inside of yield surface even when the bonding stress is zero. In other words, the volume strain is elastic. For the sample under 3 MPa mean pressure, it not only generates elastic volume strain but also plastic volume strain from the beginning to the end of the hydrate dissociation. For the 2 MPa mean pressure, the sample subjected to the hydrate dissociation exhibits elastic volume strain from the starting point to 35% hydrate saturation, and then exhibits plastic volume strain.

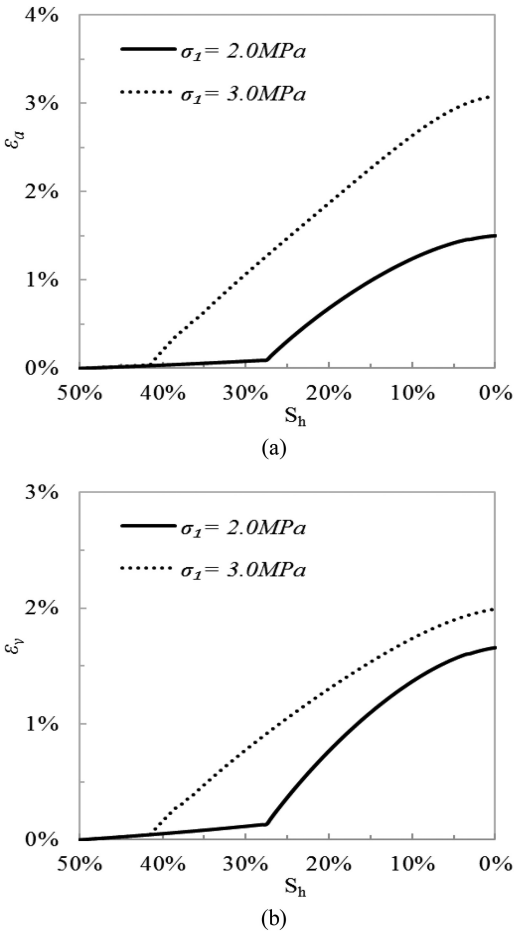


Figure 5. Deformation of GHBS ($S_h = 50\%$) subjected to the hydrate dissociation under different triaxial stress condition.

3.2.2 *The second case: Triaxial stress condition*

Figure 5 and Figure 6 shows the deformation characteristic of GHBS with hydrate saturation 50% and 35% during the hydrate dissociation under different tri-axial stress condition. The model parameters are identical to the first case, listed in Table 2. Both of pre-consolidation pressure and confining pressure are 1 MPa.

In this section, the axial stresses of 1.5 MPa and 2.2 MPa for 35% hydrate saturation, 2.0 MPa and 3.0 MPa for 50% hydrate saturation are considered. Clearly, axial strains for all cases increase and volumes shrink as a result of the hydrate dissociation. Similar to the isotropic cases, soil skeletons bear more additional effective stress with the decrease of the bonding stress, causing the soil particles compacting. With the comparing for different axial stresses, it is found that axial strains and volume strains are more distinctive for higher axial stress. In addition, due to the difference for relative position of the stress state point to the yield surface, the deformation can also be split into two steps akin to the isotropic stress case.

4 CONCLUSIONS

In this paper, based on the analysis of mechanical characteristics for gas hydrate-bearing sediments, a modified effective stress formula and strength formula are proposed for GHBS. In the framework of the critical state model, an elastoplastic model is developed for gas hydrate-bearing sediment, considering hydrate dissociation. In the proposed constitutive model, an additional hardening parameter of the bonding stress is introduced into the yield function to take the hydrate dissociation and hydrate damage into account. Moreover, in order to describe the dilatancy of samples during shearing, the flow rule is assumed to be a function of the bonding stress and the stress ratio, instead of the single parameter of stress ratio, which can reflect

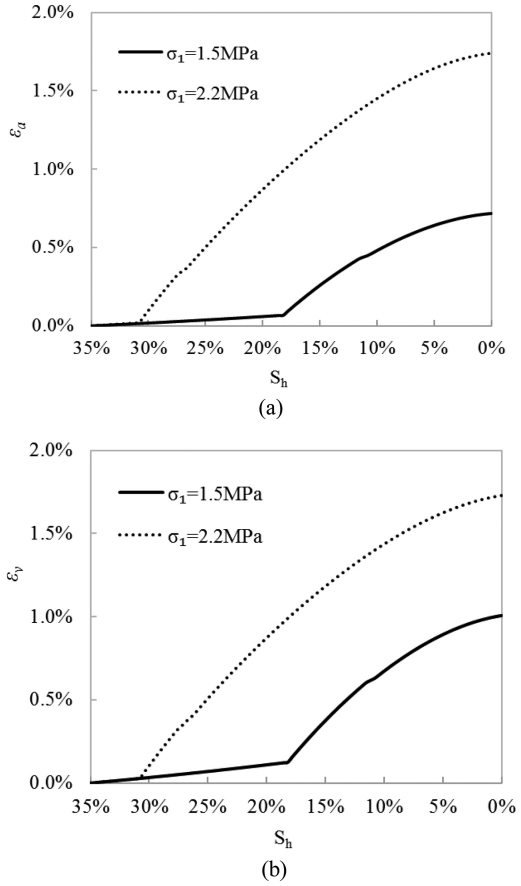


Figure 6. Deformation of GHBS ($S_h = 35\%$) subjected to the hydrate dissociation under different triaxial stress condition.

the direction of plastic strain increment more realistically. Finally, it is demonstrated that the proposed model can reflect the key characteristics including deformation, dilatancy and strain softening perfectly, and has the capability to describe the behavior of GHBS by comparing the prediction with the experimental data about the stress-strain behaviors of GHBS in triaxial tests. Besides, some performances are carried out to analyze the deformation of GHBS due to the hydrate dissociation under isotropic and tri-axial stress condition, which demonstrates that the model has the capability to describe the behavior of GHBS subjected to the hydrate dissociation.

ACKNOWLEDGEMENT

This research was supported by the National Science Foundation of China through grant NO.51309055 and the Guangxi Natural Science foundation through grants NO.2014GXNSFBA 118236 and 2012GXNSFGA060001.

REFERENCES

Li, X.S., Dafalias, Y.F., 2000. Dilatancy for cohesionless soils. *Geotechniaque*, 50, No.4, 449–460.

Liu, M.D., Carter, J.P., 2002. A structured Cam Clay model. *Canadian Geotechnical Journal,* 39: 1313–32.

Masui, A., Haneda, H., Ogata, Y., Aoki, K., 2005. Effects of methane hydrate formation on shear strength of synthetic methane hydrate sediments. *Proceeding of the fifteenth international offshore and polar engineering conference* seoul, Korea, June 19–24.

Masui, A., Haneda, H., Ogata, Y., Aoki, K., 2007. Mechanical properties of sandy sediment containing marine gas hydrates in deep sea offshore Japan. *7th ISOPE Ocean Mining and Gas Hydrates Symposium, 1–6 July, Lisbon, Portugal, International Society Offshore& Polar Engineers.*

Masui, A., Miyazaki, K., Haneda, H., Ogata, Y., Aoki, K., 2008. Mechanical characte- ristics of Natural and artificial gas Hydrate bearing sediments. *Proceedings of the 6*th International Conference on Gas Hydrate (ICGH 2008), Vancouver, British Columbia, Canada, July 6–10.

Mitchell, J.K., Soga, K., 2005. Fundamentals of Soil Behavior. John Wiley & Sons, Press. 173–194.

Miyazaki, K., Masui, A., Haneda, H., Ogata, Y., Aoki, K., Yamaguchi, T., 2008, Variable-Compliance-Type Constitutive model for methane hydrate bearing sediment. *Proceedings of the 6th International conference on Gas Hydrates (ICGH 2008)*, Vancouver, British Columbia, Canada, July 6–10.

Sloan, E.D., 2004. Introductory overview: Hydrate knowledge development. *American Mineralogist*, 89(8–9): 1155–1161.

Suebsuk, J., Horpibulsuk, S., Liu, M.D., 2010. Modified Structured Cam Clay: A generalised critical state model for destructured, naturally structured and artificially structured clays, *Computers and Geotechnics*, 37: 956–968.

Sultan, N., Cochonat, P., Foucher, J.P., Mienert, J., 2004. Effect of gas hydrates melting on seafloor slope instability. *Marine Geology*, 213(1–4): 379–401.

Sultan, N., Garziglia, S., 2011, Geomechanical Constitutive modelling of Gas-Hydrate- Bearing sediments. *Proceedings of the 7th international conference on Gas hydrates (ICGH, 2011)*, Edinburgh, Scotland, United Kingdom, July 17–21.

Waite, W.F., Santamarina, J.C., Cortes, D.D., Dugan, B., Espinoza, D.N., Germaine, J., Jang, J., Jung, J.W., Kneafsey, T.J., Shin, H., Soga, K., Winter, W.J., Yun, T.S., 2009. Physical properties of Hydrate-bearing sediments, *Reviews of Geophysics*, 47, Rg4003.

Wu Er-lin, Wei chang-fu, Wei Hou-zhen, Yan Rong-tao., 2013, A statistical damage constitutive model of hydrate-bearing sediments. *Chinese Rock and soil mechanics*, 34(1): 60–66.

Yan, R.T., Wei, C.F., Wei, H.Z., Tian, H.H., Wu, E.L., 2012., Effect of hydrate formation on mechanical strength of hydrate-bearing sand, *Chinese Journal of Geotechnical Engineering*, 34(7): 1234–1240.

Yun, T.S., Santamarina, J.C., Ruppel, C., 2007. Mechanical properties of sand, silt, and clay containing tetrahydrofuran hydrate. *Journal of Geophysical Research-Solid Earth* 112(B04106).

Unsaturated Soil Mechanics—from Theory to Practice – Chen et al. (Eds)
© 2016 Taylor & Francis Group, London, ISBN 978-1-138-02921-7

An intelligent back analysis optimization method of constitutive parameters for surrounding rock

Y. Zhang & B.C. Liu
Guangxi Key Laboratory of Geomechanics and Geotechnical Engineering, Guilin, China

Y.N. Hou & Z.T. Zeng
College of Civil and Architecture Engineering for Guilin University of Technology, Guilin, China

ABSTRACT: Determination of the constitutive parameter is important for theoretical analysis and numerical simulation. Due to the complicated behavior of the rock mass, it is difficult for traditional methods to solve this problem. Back analysis method based on stochastic global optimization is proved to be feasible. However, stochastic global optimization technology for back analysis of the constitutive parameters is cost- and efficiency-ineffective. To solve the problem, a novel hybrid optimization algorithm based on Particle Swarm Optimization (PSO) and Gaussian Process (GP) is proposed. In this algorithm, GP is used as an inexpensive fitness function calculation surrogate and a powerful tool to predict global optimum solution for accelerating the local search of PSO. Combined with FLAC^{3D}, a new back analysis optimization method called PSO-GP-FLAC^{3D} is developed for the constitutive parameters of surrounding rock. The numerical simulation of a tunnel engineering show that the method is feasible to reduce remarkably computational time for solving problem of back analysis based on numerical calculation.

1 INTRODUCTION

The rock in nature is cut into both continuous and discontinuous body by all kinds of geologic structural feature such as faults, joints and fracture zone. This is a complex material with loose body, plane of weakness and continuum. How to determine the constitutive parameters for such a complex engineering materials becomes a bottleneck problem during the theoretical analysis and numerical simulation.

In the last few decades, back analysis methods are widely used to solve the problem. However, many cases of back analysis involve objective optimization functions of multimodal, highly non-linear, with steep and flat regions and irregularities. In order to obtain reasonable constitutive parameters, it is necessary to find the optimal solution in the objective optimization function that is a typical global optimization problem. It is proved that stochastic search methods can solve multimodal optimization problem, such as genetic algorithms (GA) (Bunnag et al. 2005, Xing et al. 2006), differential evolution (Ali et al. 2012), particle swarm optimization (Behrang et al. 2011, Mathew 2012) and ant colony optimization (Toksari 2009, Leung et al. 2010). These methods evaluate the objective function in a random sample of points from the search space and subsequently manipulate the sample. Thus, they require thousands of fitness evaluations in order to determine the best sample. However, this computational burden cannot be afforded for constitutive parameters back analysis, because the fitness evaluations of which include large scale finite element method analysis. The cost of a single finite element fitness evaluation is in the order of hours of supercomputer time. Hence there is a considerable need to develop efficient method for multimodal optimization.

It has been proved useful to build surrogate models for the computationally expensive analysis and to use it for the purpose of carrying out optimization (Jin et al. 2002, Yew et al. 2003). In recent years, a number of surrogate-assisted methods have been proposed for solving this problem, such as, a hybrid GA algorithm consisting of support vector machine method (Yang et al. 2012), and a cellular particle swarm optimization that combines cellular automata with particle swarm optimization (Shi et al. 2011).However, there are still some dilemmas for these methods. Hereunder are (a) to the surrogate models, the accuracy of regression is low and the adaptability is weak for polynomial response surface. It is always difficult to find an appropriate network topology and the optimum hyperparameters for artificial neural network (ANN); (b) to strategies for optimization, surrogates should be used together with the real fitness function for learning samples. Then the surrogate models such as polynomial response surface or ANN are established by learning samples to take the place of real fitness function. However, this optimization strategy is very dependent

on learning samples that are determined before optimization, which remains unchanged during the whole optimized process. If the learning samples are not representative or deviated from the optimal value, the prediction accuracy is so bad that the searching accuracy is reduced and it will be easy to fall into local optimum solution.

In this paper, Gaussian process (GP) surrogate-assisted PSO algorithm is proposed. Combined with FLAC^{3D}, a new back analysis optimization method called PSO-GP-FLAC^{3D} is developed. Compared to GA and other stochastic search methods, PSO has characters of simple computation and rapid convergence capability. Compared to ANN, GP has the main advantage of simplicity, in which no network size or topology must be chosen. Beside that, GP owns a theoretical framework for obtaining the optimum hyperparameters self-adaptively. Furthermore, in order to solve the dilemma (b), the method of dynamically update training datasets is used to sort datasets and replace the worst dataset during iterative process.

2 PSO-GP-FLAC^{3D} BACK ANALYSIS OPTIMIZATION METHOD

2.1 *General*

In order to reduce the total number of real fitness evaluation, an optimization procedure based on PSO is proposed, using GP as an inexpensive model of the objection function. PSO is used to generate randomly control variables treated as random solution. Then the fitness of the solution can be obtained by FLAC^{3D} evaluation. The random solution and corresponding fitness is treated as a sample. After collection of some samples, a GP model is constructed for the given dataset. Once the trained model is obtained, the model can be used directly instead of FLAC^{3D} to forecast more adaptive control variables. PSO will generate new generation as the new random solution based on the zone. Finally, the current best solution is evaluated on FLAC^{3D}, which can be added to the training dataset instead of the worst particle. If the fitness is unsuccessful, a new loop starts until the required minimal solution is found.

2.2 *Fitness approximation with GP*

In this method, GP is used as the approximation of the fitness function, which can be capable to handle elegantly the uncertainty about the real fitness function, especially the noisy training data. A detailed description for GP is given in references (Seeger 2004). A brief introduction of GP is provided.

GP is a collection of random variables, any finite set of which has a joint Gaussian distribution and is completely specified by its mean function $m(\boldsymbol{x})$ and the covariance function $k(\boldsymbol{x}, \boldsymbol{x}')$:

$$f(\boldsymbol{x}) \sim GP(m(\boldsymbol{x}), k(\boldsymbol{x}, \boldsymbol{x}')) \tag{1}$$

There is a training set $\boldsymbol{D}$ of m observations, $\boldsymbol{D} = \{(\boldsymbol{x}_i, y_i) | i = 1, \ldots m\}$, where $\boldsymbol{x}$ denotes an input vector and y denotes a scalar output or target. The column vector inputs for all m cases are aggregated in the $\boldsymbol{D} \times m$ design matrix $\boldsymbol{X}$, and the targets are collected in the vector $\boldsymbol{y}$.

The goal of Bayesian forecasting is to compute the distribution $p(y_* | \boldsymbol{x}_*, D)$ of output y^* given a test input $\boldsymbol{x}^*$ and a set of training points $\boldsymbol{D}$. Using Bayesian rule, the posterior distribution for the Gaussian process outputs y^* can be obtained. By conditioning on the observed targets in the training set, the predictive distribution is Gaussian:

$$y_* | \boldsymbol{x}_*, \boldsymbol{X}, \boldsymbol{y} \sim N(\hat{y}(\boldsymbol{x}_*), \hat{\sigma}(\boldsymbol{x}_*)) \tag{2}$$

where the mean and variance are given by:

$$\hat{y}(\boldsymbol{x}_*) = \boldsymbol{k}_*^T (\boldsymbol{K} + \sigma_n^2 \boldsymbol{I})^{-1} \boldsymbol{y} \tag{3}$$

$$\hat{\sigma}^2(\boldsymbol{x}_*) = k(\boldsymbol{x}_*, \boldsymbol{x}_*) - \boldsymbol{k}_*^T (\boldsymbol{K} + \sigma_n^2 \boldsymbol{I})^{-1} \boldsymbol{k}_*^T \tag{4}$$

where a compact form of the notation setting for matrix of the covariance functions are: $\boldsymbol{k}_* = \boldsymbol{K}(\boldsymbol{X}, \boldsymbol{x}_*)$, $\boldsymbol{K} = \boldsymbol{K}(\boldsymbol{X}, \boldsymbol{X})$, σ_n^2 is the unknown variance of the Gaussian noise.

In this method, the first two generations particles have been evaluated by FLAC^{3D}, and the trained GP model can be established. Once the GP model is obtained, the fitness value is evaluated using the trained GP model instead of FLAC^{3D}. It is implemented as the following: firstly, it makes full use of the first two generations particle information to construct the training datasets. Next, GP is used to learn the training datasets and establish preliminarily nonlinear mapping relationship between the decision variables and fitness values. Finally, the trained GP model is used to evaluate the fitness instead of FLAC^{3D}. Through this measure, the number of FLAC^{3D} evaluation for PSO is clearly reduced.

2.3 *Dynamically update the training datasets*

To avoid the dependence of the algorithm on initial learning samples too much and to improve the approximation quality of GP model, the measure of dynamically update training datasets is used that can realize by the following two ways: (a) without wasting one time evaluation to the true fitness of the smallest particles of fitness from cycled generation particles, the individual information of this particle is served as the new knowledge source to update the training datasets instead of the worst particle's information; (b) when going to the outer cycle, a new generation particles is produced in outer particle swarm structure based on the optimal particles from inner fitness evaluating by FLAC^{3D}, then all the samples with real fitness are ranked from small to large according to real fitness and the same number particles as original training datasets are selected from the rank to build new training datasets.

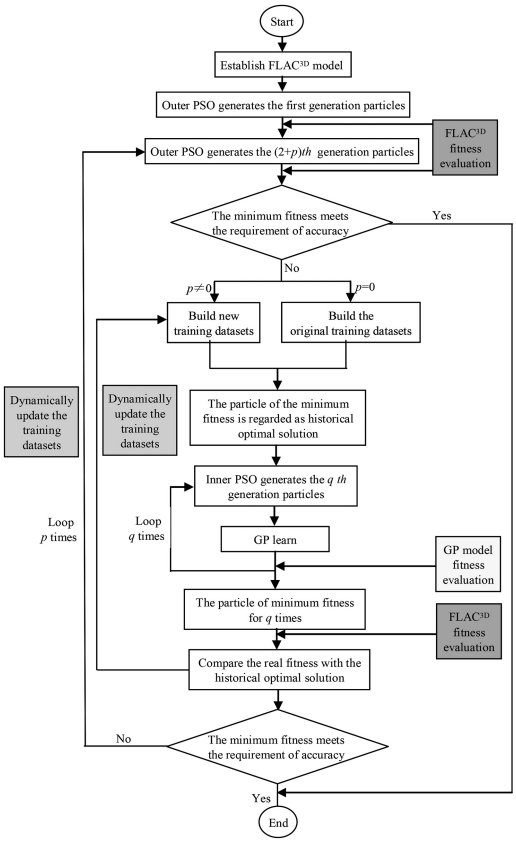


Figure 1. The structure schematic of PSO-GP-FLAC^{3D} method.

Finally, the new training datasets is learned by GP machine learning method. Maintaining training datasets capacity in the same level and enhancing the quality of training datasets can continuously improve the predictive power of GP model and the precision in the iteration process.

2.4 *The implementary provisions*

The structure of the proposed method is given in Figure 1. Its frame mainly consists of two cycles. The cycle depending on "*p*" is called outer cycle and the maximum number of outer cycle is *p*. The cycle depending on "*q*" is called inner cycle and the maximum number of inner cycle is *q*. Meanwhile, the initial values for *p* and *q* both are zero. Specific implementation steps are shown as follows:

Step 1: Establish the numerical calculation model for tunnel using FLAC^{3D}. A certain kind of the constitutive model of rock mass is chosen and the parameters of the model are regarded as the decision variables. Select the monitoring points and monitoring time. Establish the fitness function based on Equation 5.

$$\min f(\boldsymbol{x}) = \sum_{i=1}^{n}\sum_{t=1}^{m}[d_{it}(\boldsymbol{x}) - \overline{d}_{it}]^2 \tag{5}$$

where, $f(\boldsymbol{x})$ is the objective function. $\boldsymbol{x}$ is the decision variables. m is the total monitoring time. n are the total monitoring points. d_{it} is the computational displacement for the i monitoring point at t moment. $\overline{d}_{it}$ is the geodesic displacement for the i monitoring point at t moment.

The constraint is presented by Equation 6.

$$a \leqslant \boldsymbol{x} \leqslant b \tag{6}$$

where constants a and b are the upper limit and lower limit for decision variables, respectively.

Step 2: Determine the dimension of PSO according to the number of the decision variables. The first and the $(2+p)th$ generation particles of outer cycle are randomly initialized as the random solutions in accordance with the particle swarm rules[17]:

$$\left.\begin{aligned} v_{id} &= wv_{id} + c_1 r_1 (p_{id} - x_{id}) + c_2 r_2 (p_{gd} - x_{id}) \\ x_{id} &= x_{id} + v_{id} \end{aligned}\right\} \tag{7}$$

where v_{id} is a velocity vector; x_{id} is a position vector. p_{id} represents the best ever position of particle i, and its fitness is *pbest*. p_{gd} corresponds to the global best position in the swarm up to iteration d, and its fitness is *gbest*. The parameters r_1 and r_2 are two random values, uniformly distributed in [0, 1]. The parameters c_1 and c_2 are set to the acceleration constants, usually $c_1 = c_2 = [1.8, 2]$. The parameter w is the inertia weight which controls the influence of previous velocity on the new velocity. Inertia weight w can be determined by Equation 8.

$$w = w_{\max} - \frac{w_{\max} - w_{\min}}{t_{\max}} t \tag{8}$$

where t is the current iteration step; $t_{\max}$ is the maximum iteration step. $w_{\max}$ is the maximum inertia weight; $w_{\min}$ is the minimum inertia weight. Usually, $w_{\max} = 0.9$, $w_{\min} = 0.4$.

The random solutions are imported FLAC^{3D} for fitness evaluation. If the minimum fitness meets the requirement of accuracy, the algorithm is stopped. The particle of the minimum fitness is the optimal solution. Otherwise, the particle and its fitness are regarded as the information of itself. The particle of the minimum fitness is regarded as the historical optimal solution. The original training datasets is built based on the information of two generations particles.

Step 3: The method goes into the inner cycle. According to PSO rules, it can produce q generation particles of inner cycle. The nonlinear mapping relationship between the decision variables and function values is established by GP machine learning method through studying the training datasets. And then the learned GP model replacing FLAC^{3D} is used to evaluate the fitness. By circulating, the particle of minimum fitness for q times is found, that is chosen as the optimal solution based on GP predictive value.

Step 4: It is considered that there must be certain errors between the predictive value of the optimal solution and real solution. So the particle corresponding to

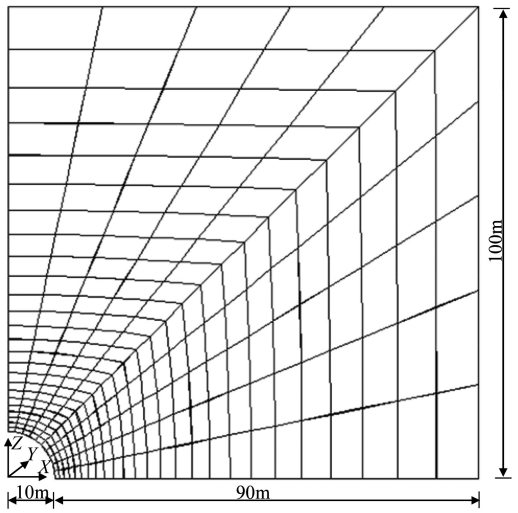


Figure 2. The mesh of tunnel.

the optimal solution is put into FLAC^{3D} to obtain the real fitness. Compared the real fitness just obtained with the historical optimal solution *gbest*, the optimal solution of current iteration step is smaller. This particle replaces the worst one in the training datasets.

Step 5: Judge the precision of the current optimal solution. If the precision satisfies the requirement of accuracy, the method is stopped. Otherwise, the $(2 + p)th$ generation particles of outer cycle are produced and evaluated by FLAC^{3D}. Then all the samples with real fitness are ranked from small to large according to real fitness and the same number particles as original training datasets are selected from the rank to build new training datasets. Finally, the program goes back to Step 3.

In order to implement the method proposed above, a MATLAB based program was developed.

3 EXPERIMENTAL RESULTS AND DISCUSSION

To analyze the performance of the method, simulations were performed about a tunnel. The proposed method was compared to the standard PSO method by evaluating precision and efficiency. The mesh of 1/4 tunnel is shown in Figure 2. The diameter of the tunnel is 20 meter. The surrounding rocks along the x and z directions are all 90 meters. The thickness of the surrounding rock along the y direction is 1 meter. The lithological character is homogeneous and the initial stress of surrounding rock is $\sigma_x = \sigma_y = \sigma_z = 30$ MPa. The constitutive model adopts the classical viscoelasticity—Viscous Model. The model has three parameters, including poisson ratio μ, elasticity modulus E and viscosity coefficient η. So PSO is three dimensional. As an example, three monitoring points a, b and c are selected at 30°, 45° and 60° along the toroidal

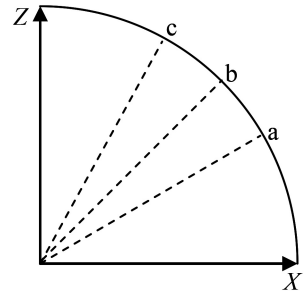


Figure 3. Monitoring points of tunnel.

Table 1. Comparison between the two methods.

	PSO-FLAC^{3D}			PSO-GP-FLAC^{3D}		
Method	μ	E	η	μ	E	η
Results of back analysis	0.19	2.01	9.83	0.19	2.01	10.2
Assumed real parameters	0.20	2.00	10.0	0.20	2.00	10.0
The relative errors/%	4.50	0.93	1.71	3.00	0.60	2.33
Times of fitness evaluation	690			206		
Computing time/s	14770			4410		

coordinate that are shown in Figure 3. The real parameters of the constitutive model are assumed to be $\mu = 0.2$, $E = 2.0$ GPa, $\eta = 10$ GPa · d. The total monitoring time is 10 days. The objective function or called fitness function can be referenced to Equation 5, where, $m = 10$d, $n = 3$, the search interval for decision variables are $0.1 \le \mu \le 0.5$, $1.0\,\text{GPa} \le E \le 5.0\,\text{GPa}$, $8.0\,\text{GPa} \cdot \text{d} \le \eta \le 12.0\,\text{GPa} \cdot \text{d}$.

The requirement of accuracy is $f < 1 \times 10^{-4}$. The parameters of PSO are dimension (D), population size (N), the maximum number of iterations (p) that is the total number of cycle for PSO-GP, maximum velocity of particle ($\boldsymbol{v}_{\max}$), and the acceleration constants (c_1 and c_2). The configuration settings of PSO used for performing the experiments are described as follows: $D = 3$, $N = 30$, $\boldsymbol{v}_{\max} = [0.01, 0.01, 0.01]$, $c_1 = c_2 = 2$, $p = 500$. The parameters of PSO for PSO-GP are the same as the standard PSO. The other parameter for PSO-GP is $q = 10$. The initial hyper-parameters of GP are $\ln \boldsymbol{l} = [-1,-1,-1]$, $\ln \sigma_f = -1$, $\sigma_n = 1 \times 10^{-6}$.

To make this a fair comparison, the two methods run independently 5 times. The final times of fitness evaluation are the average times. The results are shown in Table 1, from which it can be seen that the relative errors for the two methods are acceptable. The total number of the real fitness evaluation using PSO-GP-FLAC^{3D} and PSO-FLAC^{3D} are 206 and 690 respectively. The proposed method has a significant advantage on cost compared with the original method, which is nearly 3.4 times lower than PSO. In order to

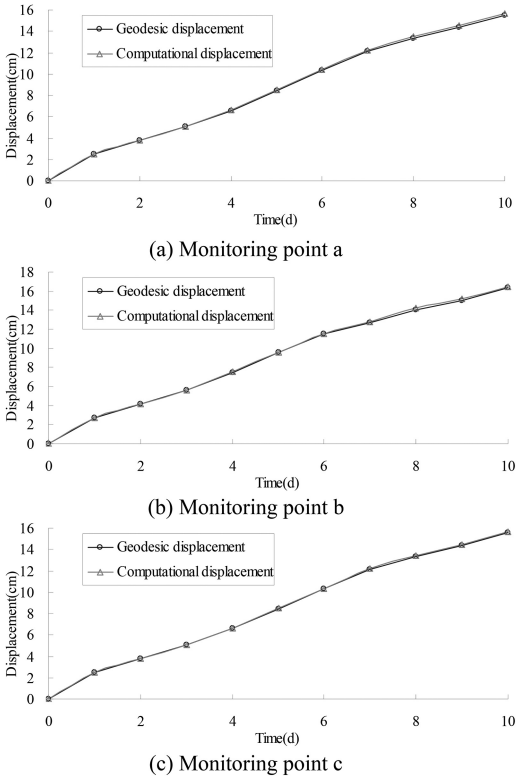


Figure 4. Comparison between computational displacement and geodesic displacement of monitoring points.

give a visualized and detailed comparison of the precision of PSO-GP-FLAC^{3D}, the comparison between the computational displacement and geodesic displacement for three monitoring points is shown in Figure 4. The computational displacement curve agrees well with the geodesic one.

4 CONCLUSIONS

In this paper, a novel back analysis optimization method based on PSO-GP algorithm and FLAC^{3D} is proposed for getting the constitutive parameters of surrounding rock. PSO is treated as an optimization technique to build the main structure and GP is used to predict the fitness instead of some evaluation using FLAC^{3D}. The results of a numerical example show that the proposed method is feasible. Compared to PSO, the proposed method has the merits of high precision and high computational efficiency. In addition, it can overcome the shortcomings that the traditional optimization back analysis method is easy to fall into local optimum or overly dependent on initial learning samples. The proposed method will be suited to other constitutive models.

ACKNOWLEDGEMENTS

The research was supported by the National Natural Science Foundation of China (51409051) and the Natural Science Foundation of Guangxi under an "innovative research team" project (2012GXNSFGA060001). The authors would like to thank the Natural Science Foundation of Guangxi (2014GXNSFBA118256), Colleges of Guangxi scientific research project (YB2014156, 2013LX051) and Scientific Research Allowance of Guilin University of Technology (002401003413).

REFERENCES

Ali, W.M. & Hegazy, Z.S. 2012. An alternative differential evolution algorithm for global optimization. *Journal of Advanced Research* 3(2): 149–165.

Behrang, M.A. & Assareh, E. 2011. New sunshine-based models for predicting global solar radiation using PSO (particle swarm optimization) technique. *Energy* 36(5): 3036–3049.

Bunnag, D. & Sun, D. 2005. Genetic algorithm for constrained global optimization in continuous variables. *Applied Mathematics and Computation* 171(1): 604–636.

Jin, Y.C. & Olhofer, M. 2002. A Framework for evolutionary optimization with approximate fitness functions. *IEEE Transactions on Evolutionary Computation* 6(5): 481–494.

Leung, C.W. & Wong, E.L. 2010. Integrated process planning and scheduling by an agent-based ant colony optimization. *Computers & Industrial Engineering* 59(1): 166–180.

Mathew, M.N. 2012. A new gradient based particle swarm optimization algorithm for accurate computation of global minimum. *Applied Soft Computing* 12(1): 353–359.

Seeger, M. 2004. Gaussian processes for machine learning. *International Journal of Neural System* 14(2): 69–106.

Shi, Y. & Liu, H.C. 2011. Cellular particle swarm optimization. *Information Sciences* 181(20): 4460–4493.

Toksari, M.D. 2009. Minimizing the multimodal functions with ant colony optimization approach. *Expert Systems with Applications* 36(3): 6030–6035.

Xing, L.N. & Chen, Y.W. 2006. An intelligent genetic algorithm designed for global optimization of multi-minima functions. *Applied Mathematics and Computation* 178(2): 355–371.

Yang, C.X. & Zhang, X.W. 2012. Estimation of amplification effect of mining-induced blast vibration on surrounding structures using a hybrid GA-SVM. *Disaster Advances* 5(4): 1113–1117.

Yew, S.O. & Prasanth, B.N. 2003. Evolutionary optimization of computationally expensive problems via surrogate modeling. *AIAA Journal* 41(4): 687–696.

This page intentionally left blank

Unsaturated Soil Mechanics—from Theory to Practice – Chen et al. (Eds)
© 2016 Taylor & Francis Group, London, ISBN 978-1-138-02921-7

Predicting liquefaction of unsaturated sands using a coupled hydro-mechanical elastoplastic constitutive model

B. Zhang, K.K. Muraleetharan & C. Liu
University of Oklahoma, Norman, Oklahoma, USA

ABSTRACT: In geotechnical earthquake engineering practice, liquefaction is only considered in saturated soils. The occurrence of liquefaction has, however, recently been observed in unsaturated sands in the laboratory and field. This paper examines the capabilities of a coupled hydro-mechanical elastoplastic constitutive model for predicting the liquefaction behavior in unsaturated sands. This model is based on the critical state soil mechanics and bounding surface plasticity framework and incorporates a hysteretic model for Soil Water Characteristic Curves (SWCCs) and coupling mechanisms between SWCCs and the stress-strain behavior of the solid skeleton. The model is utilized to simulate a series of undrained cyclic tests on Toyoura Sand at various initial conditions (degree of saturation and effective confining pressure). Comparisons between the measured and predicted number of cycles to cause initial liquefaction of unsaturated sands are provided. The results show that model prediction of liquefaction potential of unsaturated sands provides a satisfactory agreement with test results at different initial conditions.

1 INTRODUCTION

Soil liquefaction is a phenomenon in which large pore pressures develop during cyclic loading of granular soils and consequent softening of these soils. During an earthquake, a saturated soil loses shearing resistance or develops excessive strains due to the pore water pressure buildup, resulting in slope failures, foundation damage, lateral spreading and settlement. In geotechnical earthquake engineering practice, liquefaction is only considered in saturated soils and 100% degree of saturation is an essential prerequisite for liquefaction. Unsaturated granular soils are considered to be not susceptible to liquefaction. The phenomenon of liquefaction in saturated soils has been observed in the past during moderate and large earthquakes, such as in 1999 Chi-Chi (Taiwan) and 1964 Niigata (Japan) earthquakes. Numerous efforts have been made to understand the mechanism of liquefaction and develop methods for evaluating the liquefaction potential of saturated soils (Seed & Idriss 1971, Seed et al. 1985, Youd et al. 2001). Recent laboratory tests have, however, shown that not only saturated granular soils, but also the unsaturated granular soils can liquefy (Sherif et al. 1977, Yoshimi et al. 1989). Liquefaction in unsaturated soils has also been observed in the field (Hsu et al. 1995, Uzuoka et al. 2005). Laboratory tests have shown that even a small decrease in degree of saturation can result in a significant increase in liquefaction resistance of unsaturated sands (Chaney 1978, Yoshimi et al. 1989). In fact, making a saturated sand deposit into an unsaturated deposit by injecting air has been considered as a soil remediation measure to reduce the liquefaction potential (Okamura & Teraoka 2005, Yegian et al. 2007). Although extensive work has been done to study the liquefaction behavior of unsaturated sands in the laboratory, relatively few numerical studies have been carried out to investigate the liquefaction potential of unsaturated sands under different initial conditions. Since unsaturated soils are commonly encountered in natural soil deposit above the ground water table, it is especially important to systematically study the liquefaction potential of unsaturated sands.

The relationship between water content and soil suction called the Soil Water Characteristic Curves (SWCCs) plays an important role in describing the behavior of unsaturated soils. Experimental studies have shown that the SWCCs exhibit hysteresis during wetting and drying cycles. Furthermore, the SWCCs (hydro-) and stress-strain (mechanical) behavior of unsaturated soils are coupled. Following the model developed by Manzari & Dafalias (1997) and Taiebat & Dafalias (2008), Liu & Muraleetharan (2012a, b) developed a fully coupled hydro-mechanical elastoplastic constitutive model to simulate the monotonic and cyclic behavior of unsaturated sands and silts in the general stress space. The formulation of this model is based on the bounding surface plasticity within the critical state soil mechanics framework. In this study, the above-mentioned model is utilized to simulate a series of undrained stress-controlled cyclic tests on Toyoura sand under different initial conditions (degree of saturation and confining pressure). The comparisons between the measured and predicted number of cycles to cause

initial liquefaction are then provided. The main objective of the study presented in this paper is to investigate the constitutive model's capability for predicting the liquefaction potential of unsaturated sands at different initial conditions.

2 CONSTITUTIVE MODEL

For the model, the intergranular stress (or effective stress) is described as follows (Bishop 1959):

$$\boldsymbol{\sigma}' = \left(\boldsymbol{\sigma} - p_a \mathbf{I}\right) + \chi s_c \mathbf{I} \tag{1}$$

$$s_c = p_a - p_w \tag{2}$$

where $\boldsymbol{\sigma}'$ is the intergranular stress tensor, which becomes effective stress of saturated soils when matric suction is zero, $\boldsymbol{\sigma}$ is the total stress tensor, p_a is the pore air pressure, χ is Bishop's parameter, which is defined as the volume fraction of water (volumetric water content), n_w, in this study (Wei & Muraleetharan 2002a, b), s_c is matric suction, p_w is pore water pressure and $\mathbf{I}$ is the second-order unit tensor.

The model is formulated by developing three surfaces in the general stress space, namely the bounding surface (BS), critical surface (CS) and dilatancy surface (DS). These surfaces correspond to the bounding (or peak), dilatancy (or phase transfer), and critical stress ratios. The constitutive model has the following special features: 1) a hysteresis model for SWCCs based on the bounding surface plasticity concept; 2) coupling mechanisms between SWCCs and the stress-strain behavior of the solid skeleton; 3) hysteresis in the stress-strain response of the solid skeleton. The model uses intergranular stress and matric suction as stress variables and soil skeleton strains and volumetric water content as strain variables to capture the above described hysteresis and couplings. The bounding surface plasticity concept was incorporated into the hydro-mechanical behaviors in order to simulate the unsaturated sand behavior under both monotonic and cyclic loading conditions. A yield surface with a closed cap-like shape at the tip was also adapted. More details of the constitutive model can be found in Liu & Muraleetharan (2012a, b).

3 MODEL PARAMETERS AND SIMULATIONS

A set of 32 parameters are used to define the model in the general stress space. The parameters and their physical meanings are given in Table 1. Most of the model parameters can be easily calibrated from conventional triaxial compression (TC) and triaxial extension (TE) tests, while some of them have to be determined using a trial-and-error procedure. In order to evaluate the model's capability to simulate the cyclic behavior under different initial conditions, a set of laboratory test data on Toyoura sand was utilized.

Toyoura sand is a fine clean sand with a specific gravity $G_s = 2.65$ and mean particle size $D_{50} = 0.17$ mm. The minimum and maximum void ratios are $e_{min} = 0.6$ and $e_{max} = 0.97$, respectively. Results of monotonic and cyclic triaxial tests performed on unsaturated and saturated Toyoura sand can be found in the literature (Verdugo & Ishihara 1996, Unno et al. 2008). A single drying SWCC provided for Toyoura sand at $D_r = 60\%$ (Unno et al. 2008) is used as the drying bounding curve and the other SWCCs parameters are assumed. The SWCCs parameters for unsaturated Toyoura sand at $D_r = 40\%$ is assumed to be the same as those at $D_r = 60\%$. The calibration details for Toyoura sand can be found in Liu & Muraleetharan (2012b).

Okamura & Soga (2006) studied the factors that influence the liquefaction resistance of unsaturated

Table 1. Model Parameters for Toyoura sand*.

Elastic parameters	
Low-strain bulk modulus, K_0 (MPa)	20
Low-strain shear modulus, G_0 (MPa)	10
Bulk modulus exponent, b_1	0.5
Shear modulus exponent, d_1	0.5
Critical state parameters	
Location of critical state line in $e - p'$ space, e_{cr}	0.935
λ	0.019
ξ	0.7
Critical state stress ratio in TC, M_c^c	1.29
Critical state stress ratio in TE, M_e^c	1.29
State dependence parameters	
Effect of ψ on the position of BS in TC, k_c^b	0.5
Effect of ψ on the position of DS in TC, k_c^d	3.0
Effect of ψ on the position of BS in TE, k_e^b	2.0
Effect of ψ on the position of DS in TE, k_e^d	0.07
Hardening parameters	
Evolution of kinematic hardening, h_0	500
Radius of yield surface, m	0.40
Evolution of isotropic hardening due to ε_v^p, c_m	0.0
Effective confining stress at the tip of yield surface, I_0 (kPa)	5000
Power exponent, β	20
Evolution of isotropic hardening due to n_w^p, c_v	0.5
ϖ	10
Evolution of the bounding suctions duo to ε_v^p, ζ	10
Dilatancy parameters	
Dilatancy constant, B_0	0.5
Fabric parameters	
Evolution of fabric tensor, c_f	100
Limit size of fabric tensor, F_{max}	100
SWCCs parameters	
Location of bounding wetting curve in $n_w - s_c$ space, b_2	2.3
d_2	1.05
Location of bounding drying curve in $n_w - s_c$ space, b_3	4.0
d_3	1.3
Capillary elastic modulus, Γ^e (kPa)	−100
Hardening shape parameter, H	7.0
Saturated volumetric water content, n_{ws}	0.95
Residual volumetric water content, n_{wr}	0.03

*ψ – state parameter; ε_v^p – plastic volumetric strain of soil skeleton; n_w^p – irrecoverable volumetric water content change.

Table 2. Testing conditions for undrained tests on Toyoura sand.

Relative density D_r (%)	Degree of saturation S_r (%)	Effective confining pressure p' 0 (kPa)	Deviatoric stress $q*$ (kPa)
40	98	95.5	41, 45, 50
		46.5	18, 21, 24
	90	46.5	60, 65, 70

*In the constitutive model simulation, the value range of deviatoric stress is $\pm q$.

Toyoura sand through a series of undrained stress-controlled tiraxial tests. These test specimens had approximately the same relative densities ($D_r = 39$–43%), but different degrees of saturation ($S_r = 70\%$, 80%, 90%, 96%, 98% and 100%) and initial effective confining pressures (19.6 kPa, 49 kPa and 98 kPa). A Bishop's type effective stress $\sigma' = (\sigma - p_a \mathrm{I}) + \chi s_c \mathrm{I}$ was also adopted by Okamura & Soga (2006), but χ was defined as unity in their work. The effective stress used by Okamura & Soga (2006) was converted to the intergranular stress defined in this paper (Equation 1), i.e. the values of 49 kPa and 98 kPa were converted to 46.5 kPa and 95.5 kPa, respectively. In this research the predicted results are compared with undrained stress-controlled cyclic tests results at different degrees of saturation (90%, 98%) and initial effective confining pressures (46.5 kPa, 95.5 kPa) for Toyoura sand at 40% relative density. The testing conditions are shown in Table 2.

In all the model simulations, the initial suction is obtained using the given degree of saturation on the drying boundary curve. In laboratory triaxial tests, cyclic stress ratio (CSR) is defined as the ratio of one half of applied deviatoric stress, q, to initial effective confining pressure, p'_0, i.e. CSR $= q/2p'_0$. q is defined as $q = \sigma_1 - \sigma_3$ and p' is defined as $p' = (\sigma'_1 + 2\sigma'_3)/3$, where σ_1 and σ_3 are total principle stresses and σ'_1 and σ'_3 are principle intergranular stresses given by Equation 1. The initial liquefaction of unsaturated Toyoura sand is defined following the reference (Okamura & Soga 2006) on the basis of a soil specimen deforming to 5% double amplitude (DA) axial strain.

4 RESULTS AND DISCUSSION

Figure 1 shows typical model simulations for an undrained stress-controlled triaxial test on unsaturated Toyoura sand at $D_r = 40\%$, $S_r = 98\%$, $p'_0 = 95.5$ kPa, and $q = \pm 41$ kPa. The initial matric suction is 4.67 kPa. It can be observed that both pore water pressure and pore air pressures increase with the number of cycles. The matric suction becomes nearly zero at about 21st cycles at which point the effective confining pressure also becomes zero. When the effective confining pressure becomes zero, the axial strain starts to increase significantly.

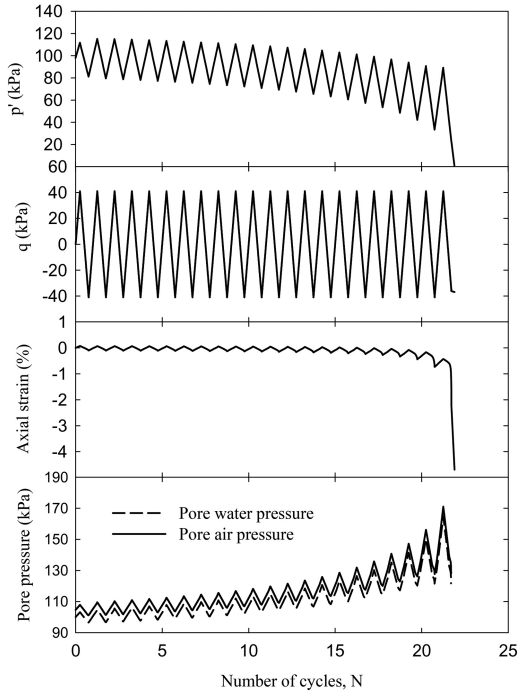


Figure 1. Predicted result of an undrained stress-controlled triaxial test on unsaturated Toyoura sand at $D_r = 40\%$, $S_r = 98\%$, $p'_0 = 95.5$ kPa and $q = \pm 41$ kPa.

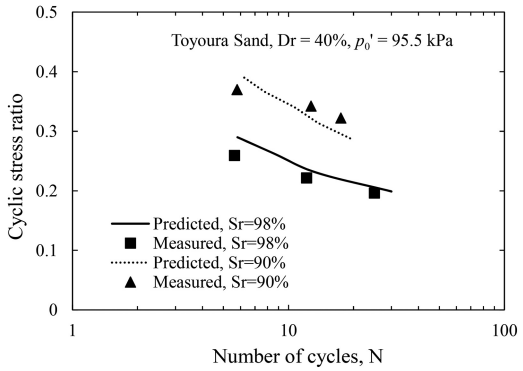


Figure 2. Comparisons between the measured and predicted number of cycles to cause liquefaction for undrained stress-controlled cyclic tests on unsaturated Toyoura sand at $D_r = 40\%$, $p'_0 = 95.5$ kPa, and $S_r = 98\%$, 90% (measured results are after Okamura & Soga 2006).

Predicted and measured number of cycles to cause liquefaction (double amplitude axial strain = 5%) for undrained stress-controlled cyclic tests on unsaturated Toyoura sand at $D_r = 40\%$ and $p'_0 = 95.5$ kPa under two degrees of saturation of $S_r = 90\%$, 98% are compared in Figure 2. The CSR values for the laboratory tests results were recalculated according to the definition of intergranular stress used in this paper. It can be observed from Figure 2 that a good match is obtained between the predicted and measured results

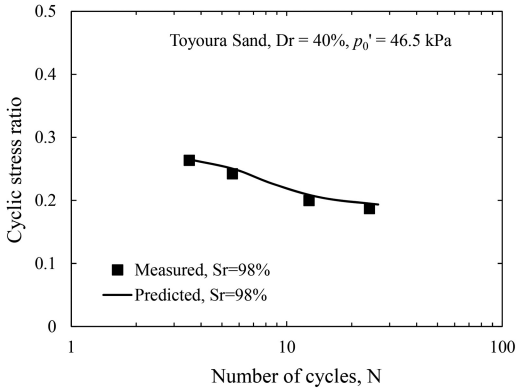


Figure 3. Comparison between the measured and predicted number of cycles to cause liquefaction for undrained stress-controlled cyclic tests on unsaturated Toyoura sand at $D_r = 40\%$ and $S_r = 98\%$ under various cyclic stress ratios (measured results are after Okamura & Soga 2006).

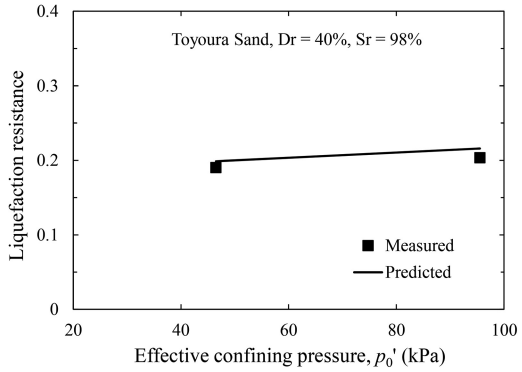


Figure 4. Comparison between the measured and predicted liquefaction resistance for undrained stress-controlled cyclic tests on unsaturated Toyoura sand at $D_r = 40\%$, and $S_r = 98\%$ under effective confining pressures of 46.5 kPa and 95.5 kPa (measured results are after Okamura & Soga 2006).

when $S_r = 98\%$ at low CSR, while there is a small discrepancy at high CSR. For the sand at $S_r = 90\%$, although there are about 2 cycles difference between the measured and predicted results, in general the model predicts the number of cycles to cause liquefaction well. The results clearly demonstrate the capabilities of this model to capture the liquefaction potential of unsaturated sands at various degrees of saturation. Furthermore, it is obvious that the liquefaction potential is influenced by the degree of saturation, i.e. lower the degree of saturation, lower the liquefaction potential of unsaturated sands.

Comparisons between the predicted and measured number of cycles to cause liquefaction for undrained stress-controlled cyclic tests on unsaturated Toyoura sand at $D_r = 40\%$, $p_0' = 46.5$ kPa and $S_r = 98\%$ under cyclic stress ratios of 0.18, 0.19, 0.23 and 0.25 are shown in Figure 3. It can be deduced from Figure 3 that the predicted number of cycles to cause liquefaction under both high and low CSRs at low effective confining pressures compares quite well with the measured ones. In order to evaluate the ability of model to predict the effect of effective confining pressure on the liquefaction potential of unsaturated sands, the liquefaction resistance is defined as the CSR to cause 5% double amplitude axial strain in 20 cycles. From Figures 2–3, the liquefaction resistances of unsaturated Toyoura sands at $D_r = 40\%$ and $S_r = 98\%$ are obtained and plotted in Figure 4. The overall performance of the model on predicting the liquefaction resistance of unsaturated sands under different effective confining pressure is satisfactory. It is of interest to note that the increase in effective confining pressure results in more resistant to liquefaction.

5 CONCLUSIONS

In this paper, the capability of a coupled elastoplastic constitutive model for predicting the cyclic behavior of unsaturated sands is investigated through comparisons between the model simulations and a series of undrained cyclic tests results on unsaturated Toyoura sand. Based on the comparisons, the following conclusions can be reached.

1) The model's ability to predict the number of cycles to cause liquefaction for unsaturated sands is generally satisfactory.
2) The liquefaction potential of unsaturated sands is influenced by the degree of saturation and effective confining pressure. A decrease in degree of saturation reduces the liquefaction potential of unsaturated sands. The liquefaction potential also decreases with an increase in effective confining pressure.

REFERENCES

Arulmoli, K., Muraleetharan, K. K., Hossain, M. M. & Fruth, L. S. 1992. VELACS: Verification of liquefaction analyses by centrifuge studies laboratory testing program: soil data report. Irvine, California, Earth Technology Corporation.

Bishop, A. W. (1959). The principles of effective stress, Tek. Ukel.

Chaney, R. C. (1978). "Saturation effects on the cyclic strength of sands." *Proceeding of ASCE Special Conference on Earthquake Engineering and Soil Dynamic*s, New York, 342–359.

Hsu, J. R. C., Jeng, D. S., & Lee, C. P. 1995. Oscillatory soil response and liquefaction in an unsaturated layered seabed. *International Journal for Numerical and Analytical Methods in Geomechanics*, 19(12), 825–849.

Liu, C. & Muraleetharan, K. K. 2012a. Coupled hydromechanical elastoplastic constitutive model for unsaturated sands and silts. I: formulation. *International Journal of Geomechanics*, 12, 239–247.

Liu, C. & Muraleetharan, K. K. 2012b. Coupled hydromechanical elastoplastic constitutive model for unsaturated sands and silts. II: integration, calibration, and validation. *International Journal of Geomechanics*, 12, 248–259.

Manzari, M. T. & Dafalias, Y. F. 1997. A critical state two-surface plasticity model for sands. *Géotechnique,* 47(2), 255–272.

Okamura, M. & Soga, Y. 2006. Effects of pore fluid compressibility on liquefaction resistance of partially saturated sand *Soils and Foundations*, 46, 695–700.

Okamura, M., & Teraoka, T. 2005. Shaking table tests to investigate soil desaturation as a liquefaction countermeasure. *Proceeding of Seismic Performance and Simulation of Pile Foundations in Liquefied and Laterally Spreading Ground* (GSP 145), R. W. Boulanger and K. Tokimatsu, ed., ASCE, Reston, VA, 282–293.

Seed, H. B., & Idriss, I. M. 1971. Simplified Procedure for Evaluating Soil Liquefaction Potential. *Journal of the Soil Mechanics and Foundations Division*, ASCE, Vol. 97, No. SM9, pp. 1249–1273.

Seed, H. B., Tokimatsu, K., Harder, L. F., & Chung, R. M. 1985. Influence of SPT Procedures in Soil Liquefaction Evaluations *Journal of Geotechnical Engineering*, ASCE, 111(12), 1425–1445.

Sherif, M. A., Tsuchiya, C., & Ishibashi, I. 1977. Saturation effects on initial soil liquefaction. *Journal of the Geotechnical Engineering Division*, 103(8), 914–917.

Taiebat, M. & Dafalias, Y. F. 2008. SANISAND: Simple anisotropic sand plasticity model. *International Journal for Numerical and Analytical Methods in Geomechanics,* 32, 915–948.

Unno, T., Kazama, M., Uzuoka, R. & Sento, N. 2008. Liquefaction of unsaturated sand considering the pore air pressure and volume compressibility of the soil particle skelton. *Soils and Foundations,* 48, 87–99.

Uzuoka, R., Sento, N., Kazama, M. & Unno, T. 2005. Landslides during the earthquakes on May 26 and July 26, 2003 in Miyagi, Japan. *Soils and foundations,* 45, 149–163.

Verdugo, R., & Ishihara, K. 1996. The steady state of sandy soils. *Soils and Foundations*, 36(2), 81–91.

Wei, C., & Muraleetharan, K. K. 2002a. A continuum theory of porous media saturated by multiple immiscible fluids: I. Linear poroelasticity. *International Journal of Engineering Science*, 40(16), 1807–1833.

Wei, C., & Muraleetharan, K. K. 2002b. A continuum theory of porous media saturated by multiple immiscible fluids: II. Lagrangian description and variational structure. *International Journal of Engineering Science*, 40(16), 1835–1854.

Yegian, M., Eseller-Bayat, E., Alshawabkeh, A., & Ali, S. 2007. Induced-partial saturation for liquefaction mitigation: Experimental investigation. *Journal of Geotechnical and Geoenvironmental Engineering*, 133(4): 372–380.

Yoshimi, Y., Tanaka, K. & Tokimatsu, K. 1989. Liquefaction resiatance of a partially saturated sand. *Soils and Foundations* 29(3): 157–162.

Youd, T., Idriss, I., Andrus, R., Arango, I., Castro, G., Christian, J., Dobby, R., Finn, W., Harder, L., Hynes, M., Ishihara, K., Koester, J., Liao, S., Marcuson, W., Martin, G., Mitchell, J., Moriwaki, Y., Power, M., Robertson, P., Seed, R. & Stokoe, K. 2001. Liquefaction Resistance of Soils: Summary Report from the 1996 NCEER and 1998 NCEER/NSF Workshops on Evaluation of Liquefaction Resistance of Soils. *Journal of Geotechnical and Geoenvironmental Engineering*, 127: 817–833.

This page intentionally left blank

Numerical modelling

This page intentionally left blank

Unsaturated Soil Mechanics—from Theory to Practice – Chen et al. (Eds)
© 2016 Taylor & Francis Group, London, ISBN 978-1-138-02921-7

Numerical modelling of swelling/shrinkage behaviour of unsaturated soils for buried pipe stress analysis

D. Weerasinghe, J. Kodikara & H. Bui
Monash University, Melbourne, Victoria, Australia

ABSTRACT: The behavior of unsaturated, surficial soil layer of the earth is more complex than saturated sublayers. Depending on the mineralogy, some soils show significant volume changes (swell and shrink) with varying moisture contents, which is known as soil reactivity. Since most of the sub structures such as pipes, shallow foundations and basements etc. are buried in this surficial soil layer, consideration of these complex behaviors is essential for sustainable designs of structures. Since computer based Finite Element Analyses (FEA) is the most common analysing tool in many engineering design problems, it is interesting to investigate the applicability of common commercial FEA software packages to address these complex situations. This paper presents an analysis of moisture governed swell/shrink behavior of unsaturated soils as an application in pipe stress analysis to quantify stresses coming to pipes from reactive soil movements.

1 INTRODUCTION

The surficial soil layer of the earth is the subject of many geotechnical engineering applications. Except for deep constructions like tunnels and pile systems, all infrastructures, including shallow foundations, roads, pipelines and basements, are built on this soil layer. Therefore, the behaviour of this surficial soil layer is crucial for the sustainability of infrastructures. When the water table is a few meters below the ground surface (as in many places), this layer remains unsaturated for most of the time. Unlike saturated soils, the presence of two non-wetting fluids (i.e. water and air) makes the behaviour of unsaturated soils complicated and challenging for geotechnical designs and constructions. Further, direct contact with the atmosphere can make this behaviour more problematic. For example, situations such as moisture-governed swelling/shrinkage, collapse under excessive wetting, desiccation cracks etc., may severely affect structures on those soils. Therefore, a full understanding of the problematic behaviours of unsaturated surficial soil and a powerful analytical method are required for designs as well as for condition assessments of infrastructures in this surficial soil layer. Since computer-based numerical methods are the quickest and most widely used analytical approaches nowadays, the use of computer programs to analyse these scenarios has become very common. This paper focuses on the numerical modelling of one of the problematic behaviours, soil reactivity.

Reactive soils (also known as expansive or swelling soils) are soils that show significant volume changes as a result of the change of water content. This reactivity is a function of some soil properties and the amount of soil moisture variation. Cameron and Walsh (1984) found that the mineral and chemical composition of the soil, particle size distribution and soil profile are the major soil properties associated with soil reactivity. In practice, higher reactivities are experienced in clayey soils with minerals like montmorillonite and bentonite. Swelling of such soil is categorised into two types by Barshad (1955): intramicellar swelling, which involves the expansion of the crystal lattice itself, as found in montmorillonite and in some of the hydrous mica clay minerals; and intermicellar swelling, which involves an increase in volume due to the adsorption of water molecules between individual clay particles. This swelling mechanism is identified by Terzaghi (1931) as either mechanical (due to deformation of platy clay particles under suction loading/unloading), or physicochemical (due to water attraction by negatively-charged clay minerals). The presence of these minerals and the potential swell of a given soil can be identified using several laboratory tests. For example, free swelling tests, linear shrinkage tests, swell pressure tests and the indirect use of the plasticity index are commonly used.

However, the severity of the potential swell of a given soil is dependent on the amount of moisture variation that the soil experiences and its intensity. Even though the soil is highly reactive, if the soil moisture is constant throughout the year, no effect would be observed in the soil. On the other hand, an area which consists of reactive soils and experiences regular soil moisture variations (due to climate changes) can be very problematic. Melbourne, Australia is a typical example of such areas.

Much land in the Melbourne metropolitan area, especially the western part, has been recognised as reactive soil zones with considerable swelling/shrinkage (Chan 2013; Gould 2011; Peck et al. 1992). Most of the soils in this area have been identified as basaltic clays with reactive properties by Peck et al. (1992). These soils are categorised as H (highly reactive clay) and E (extremely reactive) in AS2870 for building/footing design purposes. Chan (2013) observed 15 to 20 mm ground movements in this area for seasonal soil moisture variations over three consecutive years (2008–2010). This behaviour has created a number of problems for infrastructures in this area. Cracks in walls, floors, road pavements and pipes are reported frequently in these areas. Among these problems, the effect on buried pipelines has been widely highlighted in the past few decades.

Statistically, about 4000 pipe failures are reported yearly in Melbourne (Chan 2013; Gould 2011), which has become a big challenge for all water utilities. Further analyses by Chan (2013) and Gould (2011) have shown that considerably higher percentages of these failures occur in reactive soil zones. The number of failures varies with the seasonal climate changes in a consistent pattern, which shows a peak every summer. These observations and field monitoring data have led researchers to conclude that the effect of soil reactivity is a major reason for pipe failures in this area. These observations have confirmed that the pipe moves upwards and downwards with the soil and this creates some stresses on the pipe. When the stresses surpass the strength, failure occurs. Lack of a mechanism to identify these stresses prior to failure makes these failures unpredictable and this creates many management difficulties for water utilities.

This paper presents a mechanistic approach to quantify the stresses on buried pipes due to soil reactivity subject to climate influence (moisture change), as a part of the development of a pipe failure prediction database. The behaviour of a reactive soil block with a pipe segment is numerically simulated using the finite element method.

2 LITERATURE REVIEW

Some attempts to numerically simulate the behaviour of pipes in reactive soils have been reported. For example, Rajeev and Kodikara (2011) modelled a 2 m long pipe segment buried in reactive soil using a three-dimensional finite deference continuum program, FLAC^{3D}. Reactivity of the soil was simulated by assuming a linear relationship between the volumetric shrinkage of the soil ($\Delta\varepsilon_{sh}$) and the gravimetric water content change (Δw), while the soil was modelled as a nonlinear material that obeys the Mohr–Coulomb failure criterion. The total volume change of the soil was assumed to be only due to moisture variation and the effect of net stress change was ignored. Interaction between the pipe and soil was assumed to be complete no-slip contact. The results of this model showed good agreement with the experimental observations of Chan (2008).

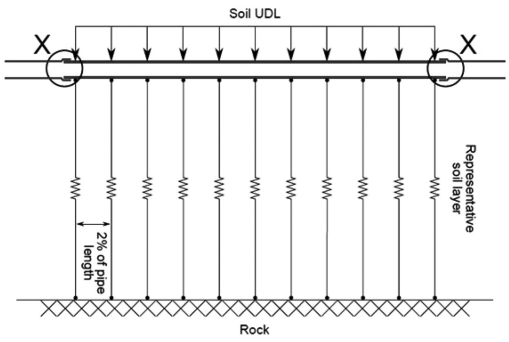


Figure 1. Winkler model by Gould (2011).

Gould (2011) modelled a 20 m long pipe segment using the two-dimensional Winkler spring approach to simulate the field behaviour of an instrumented pipe segment at Altona North, Victoria, Australia. In this model, the pipe and soil were considered as a beam and a set of springs respectively (Figure 1). The constitutive behaviour of the model is based on the void ratio – net stress – moisture content surface derived for environmentally stabilized soils by Gould et al. (2011). The effect of stress change is also incorporated in this model, as the total volume change (change of void ratio) of the soil is defined as a function of change in both stress and moisture content. Stiffness of springs was derived according to soil elastic properties and the geometric factors of the problem (pipe diameter, shape and depth influence factor). The model was developed using the OpenSEES software package.

Results of the simulation of observed moisture variation at Altona North showed that deformation estimations closely followed the field observations, whereas the pipe stresses were overestimated. However, it is clear that the stresses and deformation along the pipe are heavily affected by the boundary conditions.

Both these approaches are based on user-defined subroutines and special knowledge is required of programming languages. In addition, both approaches incorporate a number of simplifications of physical representations of pipe and soil, which may be significant for the simulation of practical problems.

3 UNSATURATED SOIL MODEL

The soil-pipe system is modelled as a three-dimensional finite element (FE) model in the general purpose FEA software Abaqus (Abaqus/CAE 6.13). A soil block and a pipe segment are the major components of this model. Reactivity of the soil is modelled as an elastic porous medium with moisture swelling properties. The selection of an elastic model can be justified, as elastic volume changes are expected for soils which have undergone a number of

wet-dry cycles, known as environmentally stabilized soils (Gould et al. 2011).

3.1 *Modelling of soil reactivity*

A porous medium is treated as a mixture of solid matter, voids that contain liquid and gas, and entrapped liquid attached to the solid matter. The mechanical behaviour of the porous medium consists of the responses of the liquid and solid matter to local pressure and of the response of the overall material to effective stress (Abaqus 6.13 documentation, theory guide). Responses of solids and liquids to local pressure can be neglected if they are incompressible. This is a reasonable assumption for soil grains and water. If the thermal volume change and the fluid entrapment are also negligible, the total volume change of the porous medium due to a known moisture change is reduced to two components (Equation 1).

$$\varepsilon_T = \varepsilon_{eff} + \varepsilon_{ms} \quad (1)$$

where, ε_T is total volumetric strain, ε_{eff} is the volumetric strain due to the change of effective stress in the soil skeleton, and ε_{ms} is the volumetric strain component due to moisture swelling. Bishop's effective stress equation (Bishop 1959) is used to compute the effective stress change to calculate ε_{eff}. In this equation, the Chi parameter (χ) is assumed as the degree of saturation (S_r) and the air pressure is zero everywhere. Then the volumetric strain is then determined using the elastic coefficient 'κ' as given in Equation 2.

$$\varepsilon_{eff} = \kappa /(1+e_0) \ln (p / p_0) \quad (2)$$

where, e_0 is the initial void ratio and p and p_0 are current and initial mean effective stresses ($\Sigma\sigma_{ii}/3$) respectively.

The second part of the total volumetric strain, the moisture swelling strain (ε_{ms}), must be defined separately as a function of the degree of saturation (S_r).

The characteristic variation of the negative pore water pressure ($-u_w$) (matric suction) with the water content can be defined as a sorption curve. Then the drying and wetting or the increasing and decreasing soil moisture contents can be defined as a change of pore water pressure. For this analysis, element type is selected with an extra degree of freedom of pore pressure.

3.2 *Soil-pipe interaction*

Since pipes have different mechanical properties, the interaction between the soil and the pipe surface must be defined as a contact interaction. This interaction is important in this problem, as the changes in soil body transfer to the pipe through this interaction. Interaction can be defined as normal and tangential contact between the pipe's surface and the soil. A compression only (surface separation under tension) normal contact and a frictional tangential contact are assumed to be a rational contact simulation for this problem. Frictional properties can be defined with a friction coefficient and an adhesion.

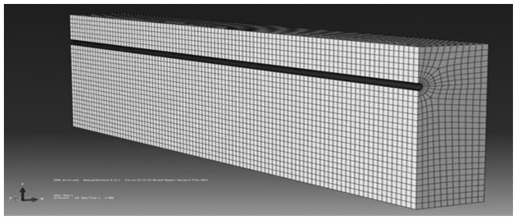


Figure 2. FE model.

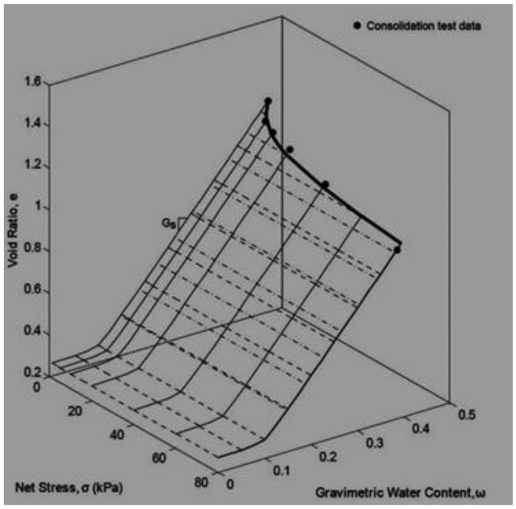


Figure 3. Environmentally stabilized soil surface for Altona North (Gould 2011).

4 SOIL-PIPE PROBLEM ANALYSIS

The instrumented pipe segment at Altona North in western Melbourne (Chan 2013; Gould 2011) was modelled to test and verify the behaviour of the above-mentioned soil model and the interaction properties. The same pipe was modelled using the wrinkle model by Gould (2011). The pipe segment is 20 m long and buried at a depth of 800 mm and located parallel to the road in the adjacent nature strip, between two concrete driveways. The same geometry was selected for analysis and only half was modelled, assuming a symmetric problem (Figure 2). The depth of the soil block was selected as the depth to the rock at this site, which is 2 m as stated by Chan (2013).

4.1 *Soil properties*

The moisture swelling curve (ε_{ms} vs S_r), the soil water characteristic curve ($-U_w$ vs S_r) and the elastic coefficient (κ) are the basic soil properties required for the model. The moisture swelling curve was derived from the environmentally stabilized soil surface (Figure 3), determined for Altona North soil by Gould (2011).

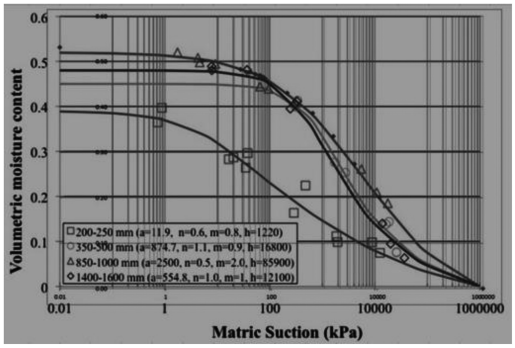


Figure 4. Soil water characteristic curves for Altona North (Chan 2013).

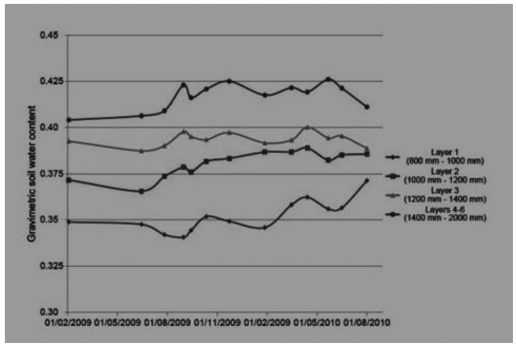


Figure 5. Measured moisture variations at Altona North (Gould 2011).

Table 1. Pipe properties.

Outer Diameter	126 mm
Wall Thickness	8 mm
Young's Modulus	150 GPa
Poisson's Ratio	0.2
Friction Coefficient with soil	0.35

The void ratio (e) vs moisture content (w) line for the average soil overburden pressure was selected from that surface and the terms rearranged to obtain total volumetric strain vs. degree of saturation curve. Then the strain change due to effective stress change (ε_{eff}) was deducted to determine the moisture swelling curve (ε_{ms} vs S_r). The soil water characteristic curves for different depths of this site were determined by Chan (2013) and the curve for the average depth was selected for this analysis (Figure 4). The elastic coefficient (κ) was assumed to be 0.05, which is a reasonable value for clayey soils.

4.2 *Pipe properties*

The cross-section and mechanical properties of the pipe are shown in Table 1.

These values are based on the values used by Gould (2011) for the Winkler model and some typical values for cast iron.

4.3 *Boundary conditions*

Boundary conditions were assigned as fixed for the bottom and side surfaces of the soil block, except for the symmetric side. Fixed boundary conditions for the sides were determined by assuming that adjacent soil masses under the concrete driveways are not supporting the soil movement in the nature strip. The pipe segment was also fixed from two ends by assuming the same conditions. The bottom of the soil is fixed because it rests on the bedrock.

4.4 *Moisture changes*

Moisture change was applied to the model as a suction change. The soil water characteristic curve in Figure 4 was used to convert moisture changes into suction changes. A measured moisture variation at the Altona North site (Figure 5) was used for this analysis, as the same variation was used for the Winkler model by Gould (2011). From this moisture variation, the wettest and the driest points were selected for the analysis to determine the results for two extreme situations.

a) soil drying b) soil wetting

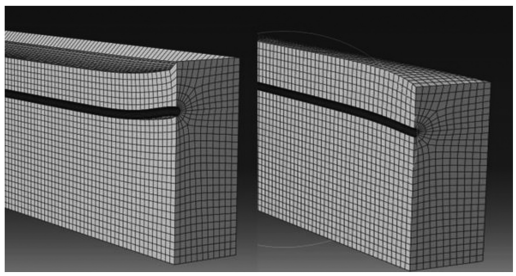


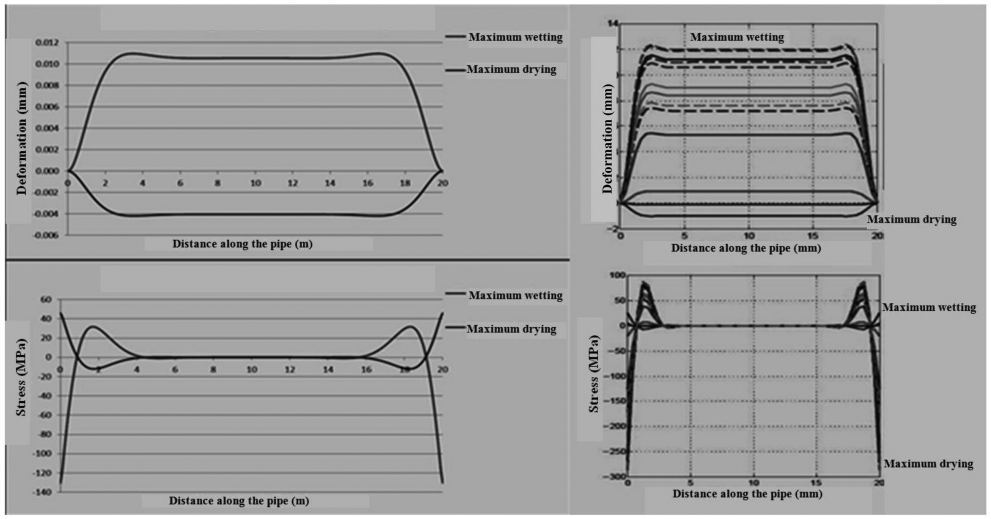
Figure 6. Deformation results of FE model.

4.5 *Analysis method*

The method of analysis selected was steady-state soil analysis and the predetermined pore water pressure (or suction, since air pressure is zero) change was applied as the external change (like external load) to the model. This type of soil analysis is only compatible with elements with pore pressure degree of freedom and computes the deformation with respect to the initial condition of the soil. Initial condition is defined in terms of void ratio (e_0), pore pressure (U_{w0}), saturation (S_{r0}) and initial effective stress field. In this analysis, this was taken as the starting position of the moisture variation curve shown in Figure 5.

5 RESULTS AND DISCUSSION

Vertical deformation of the pipe and longitudinal stress of the pipe crown are the major results of this analysis. Vertical pipe movement is upwards for increasing moisture (wetting) and downwards for decreasing moisture (drying), as shown in Figure 6.



(a)FE model (b) Wrinkle model (Gould 2011)

Figure 7. Results comparison (values are shown in Table 2).

Table 2. Results of FE and Winkler model (Gould 2011).

	Maximum vertical displacement of pipe		Max. longitudinal stress at the pipe crown	
	FE model	Winkler model	FE model	Winkler model
For maximum wetting	11 mm (upwards)	12 mm (upwards)	130 MPa (comp.)	300 MPa (comp.)
For maximum drying	4 mm (downwards)	1 mm (downwards)	45 MPa (tens.)	25 MPa (tens.)

When these results are compared with the results of the Winkler model used by Gould (2011), good agreement is seen between deformation values, while there is some disagreement for stress values with the FE model. This comparison is shown in Figure 7 and Table 2.

It should be noted that only the maximum drying and wetting profiles of the Winkler models results are compared with the results of the FE model.

However, the measured stress values of the in situ pipe for the same moisture variation period are in the range of 20–40 MPa (Chan 2013). Although both models overestimate stresses, this comparison shows that the stress estimation in the FE model is closer to the field measurements. More refinement in boundary conditions is necessary to approximate field conditions better.

6 CONCLUSION

The procedure followed in this analysis appears to be a less complicated method to simulate swelling/shrinkage behaviour of unsaturated soils. The pipe problem analysed in this paper confirms that the model is capable of producing reasonable stress and deformation results for a given moisture change. However, more attention is required for the boundary conditions of the model, because the fixed boundary condition seems like the major reason for overestimating stresses. The inclusion of soil plasticity and experimentally-identified soil pipe interaction properties can be expected to improve the results.

ACKNOWLEDGMENTS

The authors are grateful for the financial and in-kind support provided by the Smart Water Fund, Melbourne Water, City West Water Ltd., South East Water Ltd, and Yarra Valley Water.

REFERENCES

Abaqus theory guide. http://lic-abaqus.eng.monash.edu.au: 2080/v6.13/books/stm/default.htm

AS2870 2011. Residential slabs and footings. Sydney, Australia: Standards Association of Australia.

Barshad, I. (1955). Adsorptive and swelling properties of clay-water system, Proceedings of 1st National Conference on Clays and Clay Technology Oct 1966, California Department of National Resources, Division of Mines.

Bishop, A.W. (1959). The principle of effective stress. *Teckniskk Ukebald,* 106(39): pp. 859–863.

Cameron, D.A. & Walsh, P.F. (1984). Damage to buildings on clay soils, Australian Council of National Trusts, Melbourne, Australia.

Chan, D. (2008), *Performance of water and gas pipes buried in reactive soil*, MSc thesis, Monash University, Australia.

Chan, D. (2013), *Study of pipe-soil-climate interaction of buried water and gas pipes*, PhD thesis, Monash University, Australia.

Gould, S. (2011), *A study of the failure of buried reticulation pipes in reactive soils*, PhD thesis, Monash University, Australia.

Gould, S., Kodikara, J., Rajeev, P., Zhao, X.-L. & Burn, S., 2011. A void ratio – water content – net stress model for environmentally stabilised expansive soils. *Canadian Geotechnical Journal*, 48(6): 867–877.

Peck, W.A., Neilson, J.L. & Olds, R.J. 1992. Engineering Geology of Melbourne: Proceedings of the Seminar on Engineering Geology of Melbourne, Melbourne, Victoria, Australia, 16 September 1992, A.A. Balkema.

Rajeev, P. & Kodikara, J (2011). Numerical analysis of an experimental pipe buried in swelling soil. *Computers and Geotechnics*, 38. pp. 897–904.

Terzaghi, K. (1931). The influence of elasticity and permeability on swelling of two-phase systems. *Colloid Chemistry*, 3: pp. 65–88.

Unsaturated Soil Mechanics—from Theory to Practice – Chen et al. (Eds)
© 2016 Taylor & Francis Group, London, ISBN 978-1-138-02921-7

Numerical study on expansive soil slope stability considering the cracks and coupling effects

S.C. Qi & S.K. Vanapalli
Department of Civil Engineering, University of Ottawa, Ottawa, Ontario, Canada

ABSTRACT: In conventional engineering practice, suction reduction associated with rainfall is considered to be the main cause of shallow slip failures in expansive soils slopes. Hydraulic analysis is usually used to interpret the expansive soil slope instability without considering cracks and coupling effects. In this study, expansive soil slope stability is numerically investigated using a typical representative slope in China. The hydraulic response (seepage analysis without considering coupling effect) and hydro-mechanical response (coupled analysis) of the slope are simulated using commercial software SEEP/W and SIGMA/W, respectively. The bimodal soil water characteristic curve and permeability function of a typical expansive soil from Zaoyang, Hubei, China, are used for considering the effect of cracks within the shallow layer. The factors of safety (FS) for shallow layer of unsaturated soil expansive slope are calculated using the two-dimensional modified Limit Equilibrium Method to incorporate effect of suction. The results of study summarized in this paper show that: (i) cracks significantly influence the hydraulic response and lower the FS; (ii) coupled analysis also results in lower FS in comparison to uncoupled analysis. Both the coupling behavior and cracks have adverse effects on the slope stability of expansive soils and hence should be taken into account in conventional engineering practice.

1 INTRODUCTION

Expansive soils, also known as black cotton soils, vertisol soils or shrink swell soils are considered to be problematic soils in the literature. These soils typically have high plasticity and are widely distributed around the world. There are several thousands of natural and engineered slopes consisting of expansive soils all over the world. Historical evidence shows that the failures of slopes, especially for the expansive soil slopes, are vulnerable to climatic factors, such as the rainfall infiltration. Thus, the instability of expansive soil slopes poses a great threat to safety of life and property nearby.

It is reported that, expansive soils are distributed in more than 20 different provinces of China, occupying approximately 600,000 km^2 of area (Shi et al. 2002). The rainfall-induced shallow failure of both natural and engineered slopes in these areas has been widely reported and discussed in the literature (Bao, 2003). These problems have become more pronounced with a significant increase in engineering infrastructure construction during the last two decades in China. For example, the water transfer canals in Northern China (e.g. Ningxia Province), and highway systems in Southern China (e.g. Yunnan and Guangxi Provinces) can be cited.

Recently, great efforts have been directed to better understand the sliding mechanisms of expansive soil slopes using various research methods, such as field studies (e.g. Ng et al. 2003, Zhan et al. 2007, Chen, 2006), model tests (e.g. Chen, 2007) centrifuge tests (e.g. Xu et al. 2006, Cheng et al. 2011) and laboratory tests (e.g. Zhan & Ng, 2007; Miao et al. 2002; Pineda et al. 2014). In addition, the numerical methods have also been widely used to simulate the response of expansive soils to rainfall infiltration, followed by calculating the Factor of Safety (FS) of slope under varying environmental factors using Finite Element Methods (e.g. Wei et al. 2010, Qi and Vanapalli, 2015), Limit Equilibrium Method (e.g. Yin et al. 2011) and Limit Analysis Method (e.g. Yin et al. 2009). Numerical analyses studies (Hamdhan & Schweiger (2013), Alonso et al. (2003); Rouainia et al. (2009)) show that the input soils properties, especially the hydraulic properties, have a significant influence on the predicted pore-water pressures (PWPs) and calculated FS. Several field studies (Ng et al. 2003, Zhan et al. 2007) suggest that the hydraulic properties of surficial expansive soil can be affected and altered by varying environmental factors through desiccation-induced fissures and cracks. Recent studies (Burger & Shackelford, 2001; Azam and Ito, 2011; Li et al. 2011; Li et al. 2014) suggest that bimodal soil-water characteristic curve (SWCC) and the bimodal permeability function can provide a more precise description in the variation of water content and permeability with respect to suction. In the present study, the behavior of a slope under water infiltration is numerically modeled based on expansive soil properties, from a field

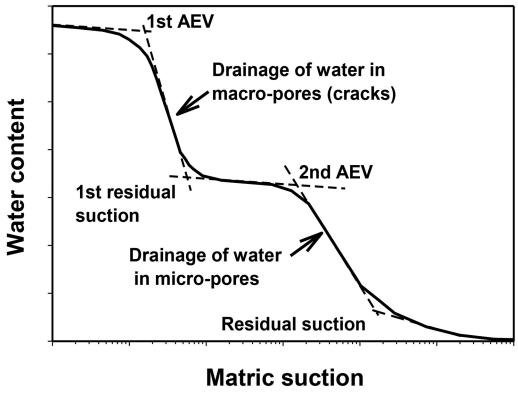


Figure 1. A typical bimodal SWCC.

study on cut slope in Zaoyang, Hubei, China (Ng et al. 2003). The bimodal SWCC and bimodal permeability function are used to account for the effect of fissures and cracks. The hydro-mechanical coupling effect on FS calculated using Limit Equilibrium Method is also discussed.

2 BIMODAL SWCC

The soil water characteristic curve (SWCC) describes the relationship between the water content and suction, which is a key function in analyzing water flow through unsaturated zone. In addition, the SWCC is often used as a tool to predict the unsaturated soil properties for a wider application of unsaturated soil mechanics, such as the unsaturated soil shear strength model (Vanapalli et al. 1996) for geotechnical engineering stability analysis, and unsaturated soil elasticity model (Oh et al. 2009; Vanapalli and Oh, 2010) for geotechnical engineering deformation analysis. Thus, a reliable SWCC model is important for the rational geotechnical engineering analysis extending unsaturated soil mechanics.

Many equations (e.g. van Genuchten, 1980; Fredlund and Xing 1994; Leong and Rahardjo, 1997) have been proposed in the literature to fit the experimental data of SWCC, most of these equations have a sigmoid form and are unimodal, however, there are an increasing number of experimental data sets showing a bimodal behaviour in the shape of SWCCs (Burger and Shackelford, 2001, Azam and Ito, 2011; Zhang and Chen, 2005; Li et al. 2011; Li et al. 2014; Rahardjo et al. 2012, etc.). The bimodal behavior of SWCC can be attributed to two distinct or bimodal pore-size distributions of soil with a dual porosity structure (Li et al. 2014), such as he compacted coarse colluvial soils, the gap-graded soils, residual soil mixed with sand. A typical bimodal SWCC is shown in Figure 1. Drainage of water with increasing suction can be generally divided into two stages: (i) the water stored in the macro-pores of soil starts to be drained out when increasing the suction from the first air-entry value (1st AEV) to the first residual suction, and (ii) the water stored in the micro-pores is then drained out when the suction is beyond the second air-entry value (2nd AEV). Some researchers (Fredlund et al. 2010; Li et al. 2011) suggested that the SWCC of cracked soil may also exhibit a bimodal behavior, because the cracks behave like macro-pores for a drainage process, which have a larger size than the micro-pores within the soil matrix. Several experimental studies conducted on cracked expansive soils (Azam and Ito, 2011; Elkady, 2014) exhibits a strong bimodal characteristic behavior. In other words, a bimodal SWCC is required to best-fit these data.

Therefore, for slope stability analysis in the present study, considering that surficial layer of slope can be highly desiccated by varying environmental factors, a bimodal SWCC and corresponding bimodal permeability function are used for the surficial layer of expansive soil slope.

3 SLOPE STABILITY ANALYSIS

The FS is the most intuitive and commonly used scalar for evaluating slope stability when using deterministic analyses methods. Various types of methods in the literature for solving FS have been developed based on different theories. For example, (i) the limit equilibrium methods based on force and (or) moment equilibrium analysis considering the failure mass as a rigid block; (ii) the limit analysis methods based on upper bound theorem in plasticity; (iii) finite element methods based on stress-deformation analysis (including the stress based finite element method, strength reduction finite element method and gravity increase based finite element method). All these methods have their individual strengths and limitations; a detailed discussion on this topic is beyond the scope of this study. However, the limit equilibrium methods are still the most preferable for practice applications mainly due to its simplicity. There are many variants of limit equilibrium methods proposed in the literature depending on different assumptions made about the unknowns and the satisfactory equilibrium conditions. In both these methods, the force and moment equilibrium conditions appear to be able to provide reliable FS (e.g. Morgenstern-Price Method (Morgenstern and Price, 1965); General Limit Equilibrium Method (Fredlund and Krahn 1977).

The FS in limit equilibrium methods is defined as (Duncan, 1996) a factor by which the shear strength of the soil would have to be divided to bring the slope such that it is barely in a state of stable equilibrium. Thus the mobilized shear force at the soil slice base can be written as follows for saturated soils:

$$S_m = \beta\left\{c' + \left(\sigma - u_w\right)\tan\phi'\right\} / FS \qquad (1)$$

where, S_m is the mobilized shear force at the base of a slice; and β is the base length of the slice, $c' =$ effective cohesion, $\phi' =$ internal friction angle at saturated condition, $\sigma =$ normal stress acting on the slip surface

under the failure mass, and u_w = PWP at the corresponding point on the slip surface. The total normal force on the base of slice can be expressed as:

$$N = \frac{\{W + (X_R - X_L) - [c' + u_w \tan\phi']\beta \sin\alpha / FS\}}{\cos\alpha + \sin\alpha \tan\phi' / FS} \quad (2)$$

where: X_L and X_R designates the vertical interslice normal forces the left and right sides of the slice, respectively; α = the angle between the tangent to the base of slice and the horizontal. The interslice shear force, X, are assumed to be related to the interslice normal force, E, by the interslice function $f(x)$, which is expressed as: $X = \lambda f(x)E$, where, λ is a constant that represents the percentage of the interslice function when the limit equilibrium condition is satisfied. The value of λ requires to be determined using an iterative procedure when solving the FS equation, the interslice function $f(x)$ is often assumed as a half sine function in both Morgenstern-Price Method and General Limit Equilibrium Method. The FS with respect to moment and force equilibriums can then be calculated by summing the moment and horizontal forces, respectively, their expressions are as follows:

$$(FS)_m = \frac{\sum [c'\beta R + (N - u_w\beta)R\tan\phi']}{\sum Wx - \sum Nf} \quad (3)$$

$$(FS)_f = \frac{\sum [c'\beta\cos\alpha + (N - u_w\beta)\tan\phi'\cos\alpha]}{\sum N\sin\alpha} \quad (4)$$

where: $(FS)_m$ is the factor of safety with respect to moment equilibrium; $(FS)_f$ is the factor of safety with respect to force equilibrium; W is the total weight of the slice; R is the radius of a circular slip surface or the moment arm associated with the mobilized shear force; f is the perpendicular offset of the normal force from the center of moments; and x is the horizontal distance from the center line of each slice to the center of moments. Obtaining solution to the above equations involves finding a value of λ which makes $(FS)_m$ equal to $(FS)_f$ Usually, an iterative technique, such as Newton-Raphson method or Rapid Solver method is required for obtaining this solution (GeoSlope International Ltd., 2007).

The above equations based on effective stress principle and are only applicable for saturated zones. For expansive soil slope stability problem considered in this study, a large portion of unsaturated zone may exist with the slope profile, and the strength contribution due to suction has to be considered. The classic Mohr-Coulomb criterion was extended by Fredlund et al. (1978) in two stress state variable space to consider the effect of suction on soil strength:

$$\tau_f = c' + (\sigma - u_a)\tan\phi' + (u_a - u_w)\tan\phi^b \quad (5)$$

where, τ_f is the soil shear strength, $(\sigma - u_a)$ is net normal stress, $(u_a - u_w)$ is suction, ϕ^b represents the rate of linear increase in shear strength relative to the matric suction. However, significant nonlinearity in variation of shear strength with respect to suction has been manifested by accumulated experimental data (Escario and Saez 1986; Fredlund et al. 1987). Based on the general relationship between the SWCC and the unsaturated shear strength curve a semi-empirical model was proposed by Vanapalli et al. (1996) to predict the unsaturated soil shear strength:

$$\tau_f = c' + (\sigma - u_a)\tan\phi' + (u_a - u_w)\left[\left(\frac{\theta_w - \theta_r}{\theta_s - \theta_r}\right)\tan\phi'\right] \quad (6)$$

where, θ_w is volumetric water content, θ_s is saturated volumetric water content, and θ_r is residual volumetric water content. In order incorporate the unsaturated shear strength into the FS equation, Eqs and can be rewritten as

$$\tau_f = c_a + (\sigma - u_a)\tan\phi' \quad (7)$$

where, $c_a = c' + (u_a - u_w)\tan\phi^b$ for Eq. (5) and $c_a = c' + (u_a - u_w)(\theta_w - \theta_r)/(\theta_s - \theta_r)\tan\phi'$ for Eq. (6).

Comparing Eq. (7) with Eq. (1), it is found that Eqs (2), (3) and (4) can also be used to compute the FS for unsaturated soil slopes, when the c' and u_w are replaced with c_a and u_a, respectively. The assumption $u_a = 0$ is often made and considered reasonable for most cases.

Based on above discussion, the FS for an unsaturated soil slope under various environmental conditions can be computed provided that the positive PWP within the saturated zone and (or) the negative PWP within the unsaturated zone are known. The PWP within a slope profile considering environmental variations can be obtained using either analytical or numerical methods. In this study, the commercial software SIGMA/W and SEEP/W are used to obtain the numerical solution to the PWP within a slope profile under rainfall condition. The swelling phenomenon and its influence on the hydraulic response of expansive soil to water infiltration is simulated using coupled hydro-mechanical finite element analysis in SIGMA/W. In SIGMA/W, the hydraulic analysis code in the SEEP/W is incorporated to solve the force equilibrium equations and water continuity equations, simultaneously. The interaction between flow and swelling behavior can be simulated; especially, the effect of swelling on pore water pressure variation can be captured. In SEEP/W, only the water continuity equation is solved using finite element method to model the water infiltration process ignoring the effect of any soil deformation. However, comparing the results from SIGMA/W and SEEP/W can provide us a better picture about the effect of soil swelling on the flow behavior as well as stability of expansive soil under infiltration condition.

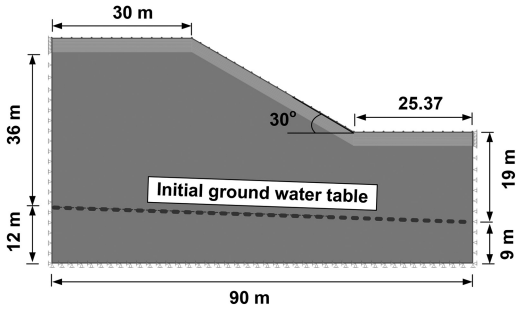


Figure 2. Model slope for numerical analysis.

Table 1. Soil mechanical properties.

Properties	Layer 1	Layer 2
Unit weight, γ (kN/m^3)	18*	18*
Effective cohesion, c' (kPa)	5–15	32
Effective internal friction angle, ϕ' (°)	17	21.3
Modulus of elasticity, E (MPa)	10*	10*
Poisson's ration, μ	0.33*	0.33*

*Assumed values

4 EVALUATING AN EXPANSIVE SOIL SLOPE

4.1 *Model slope and soil properties*

In this study, the response of a typical expansive soil slope to rainfall infiltration with respect to time is first modeled using SEEP/W (seepage analysis) and SIGMA/W (coupled hydro-mechanical analysis) software, followed by a slope stability analysis using SLOPE/W.

The established model slope shown in Figure 2 has a height of 20 m and an inclination of 30°, respectively. The model slope consists of two layers (i.e. the surficial cracked layer with a thickness of 3 m underlain by the intact expansive soil). For seepage analysis (SEEP/W), the initial ground water table is assigned to form the initial PWP condition as shown in Figure 2. The linear variation of suction or PWP along the lateral sides with reference to the ground water table is used as the side boundary condition, and zero flux boundary is assigned to the bottom side. A zero PWP is applied to the slope surface to model the rainfall infiltration greater than the saturated coefficient of permeability. The same hydraulic initial and boundary condition is used in coupled hydro-mechanical analysis (SIGMA/W). The in-situ analysis is carried out to form the initial stress condition. Fixed boundary conditions in both horizontal and vertical directions are used for the bottom side, and two side boundaries are restricted to move only in horizontal direction.

The mechanical properties for the two soil layers within the slope profile are summarized in Table 1. The saturated shear strength parameters for the layer 1 were suggested by Liu (1997) for cracked expansive soils, which were also used by Ng et al. (2003)

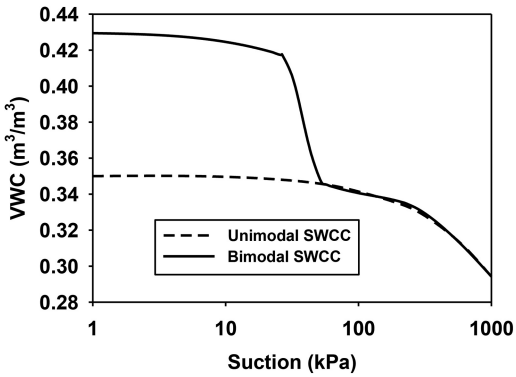


Figure 3. FS based on unimodal and bimodal SWCC.

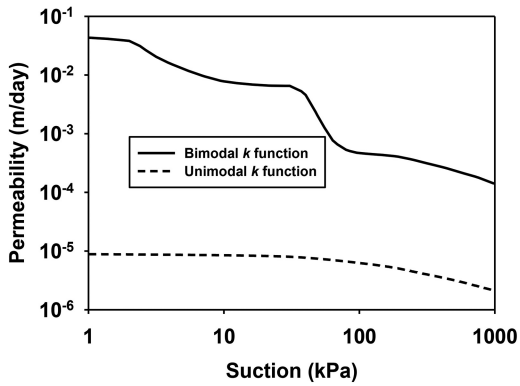


Figure 4. FS based on unimodal and bimodal SWCC.

for expansive soils located Zao-yang, Hubei, China. The saturated shear strength parameters for the layer 2 were measured on a compacted expansive soil from China by Miao (2002). The ϕ^b indicating the increasing rate of shear strength with respect to suction is assumed to be equal to $2\phi'/3$ for both layers. The unimodal and bimodal hydraulic properties (including SWCC and permeability function) used in this study is shown in Fig. 3 and Fig. 4. These hydraulic properties were back calculated by Adem (2015) for a case study of the hydraulic response of an expansive slope in Zao-yang, Hubei, China, in which, the bimodal SWCC and permeability functions were used for achieving a good match between the predicted and measured PWPs within this case slope.

4.2 *Modelling results*

In order to show the effect of bimodal SWCC on the slope stability, a preliminary analysis is first conducted using SEEP/W and SLOPE/W, which including two parallel analysis: (i) both layers are assigned with the unimodal SWCCs in SEEP/W; (ii) bimodal and unimodal SWCCs are used for layer 1 and layer 2, respectively. In the preliminary analysis, the effective cohesion is set to be 5 kPa for the surficial layer. Fig. 5

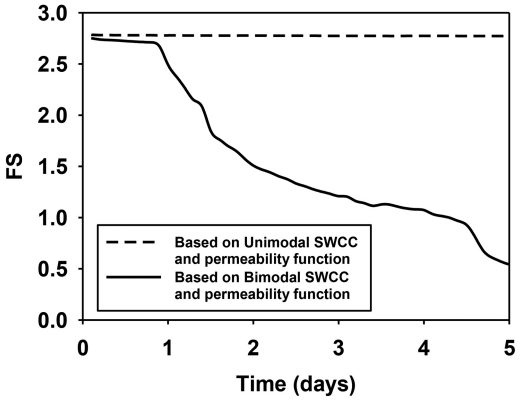


Figure 5. FS based on unimodal and bimodal SWCC.

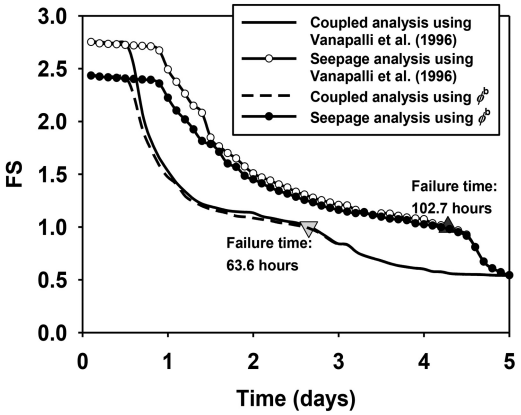


Figure 6. Comparison in FS from coupled and seepage analysis for effective cohesion of 5 kPa.

illustrates calculated FS at each elapsed time using General Limit Equilibrium Method based on nonlinear shear strength model (Vanapalli et al. 1996). No obvious decrease trend in FS with time can be observed when unimodal hydraulic properties are used for both layers. This is because the saturated coefficient of permeability is too low, such that the surface soil acts like an impermeable layer and suction within the slope profile can be maintained during the time period considered in this study. When bimodal hydraulic properties are used for the layer 1, the FS decreases significantly with time, this means the cracks of expansive soils have a considerable adverse effect on the slope stability under rainfall condition by significantly increasing the coefficient of permeability of soil layer 1 (i.e. the surficial layer). The effect of cracks can be considered using bimodal SWCC and permeability in numerical analysis. In the following analysis, only bimodal SWCC is used for layer 1.

The effect of hydro-mechanical coupling of expansive soils on slope stability is investigated by comparing FSs calculated based on PWPs from coupled analysis (SIGMA/W) and seepage analysis (SEEP/W). Three different effective cohesion (i.e. 5, 10, 15 kPa) in

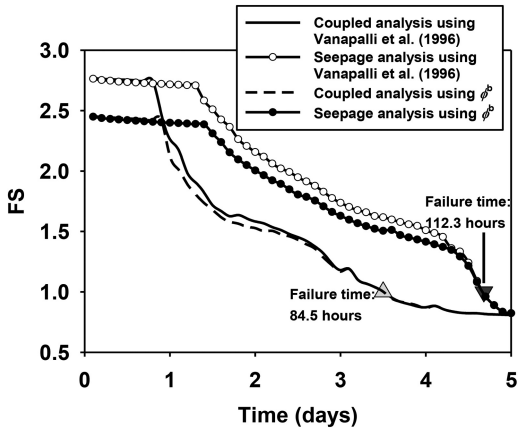


Figure 7. Comparison in FS from coupled and seepage analysis for effective cohesion of 10 kPa.

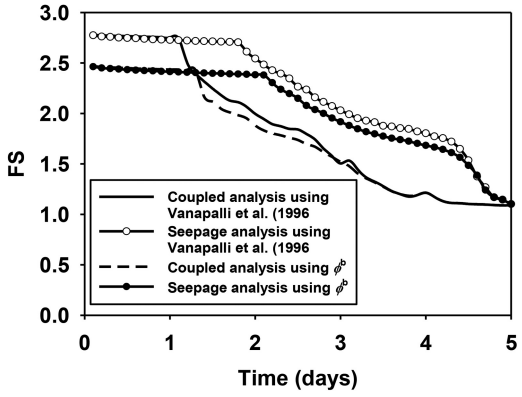


Figure 8. Comparison in FS from coupled and seepage analysis for effective cohesion of 15 kPa.

the range suggested by Liu (1997) was used for layer 1. The calculated FS variations with time are shown in Fig. 6, Fig. 7 and Fig. 8, respectively. It can be seen from these figures that the FS resulting from a coupled analysis decreases faster than those from seepage analysis for all cases (Fig. 6, 7 and 8). At the same elapsed time during the rainfall period, the FS based on coupled analysis is significantly lower than that from seepage analysis. As a consequence, the time to possible failures from coupled analysis is shorter than those predicted based on seepage analysis. This means hydro-mechanical coupling of expansive soils also have a negative influence on the slope stability under water infiltration condition.

5 CONCLUSIONS

Desiccation-induced cracks within the surface layer of expansive soil ground can significantly affect the hydraulic properties, and therefore have a considerable influence on the hydraulic response of expansive

soil to water infiltration. Selecting the appropriate hydraulic parameters plays a vital role in evaluating the stability of expansive soils under various environmental conditions. A detailed parametric analysis with respect to bimodal hydraulic property functions (Qi and Vanapalli, 2015) shows that, the saturated coefficient of permeability of bimodal function has a significant effect on the FS and time to failure of an expansive soil slope in Regina, Canada under snow.

In the present study, the stability of a typical slope from China, during a period of rainfall is numerically investigated. The bimodal SWCC and bimodal permeability function are used to describe the hydraulic properties of cracked expansive soil in the surface layer. The analysis results suggest that the stability of expansive soils is considerably deteriorated by cracks due to preferential flow channels. Furthermore, coupled hydro-mechanical analysis shows the adverse effect of coupling behavior induced by soil expansion and should be properly considered in engineering practice for reliable estimation of the FS.

ACKNOWLEDGMENTS

The first author gratefully acknowledges and appreciates the China Scholarship Council and the University of Ottawa, Canada for funding his PhD research program. The second author thanks the support from NSERC for his research programs.

REFERENCES

Adem, H.H. Modulus of elasticity based method for estimating the vertical movement of natural unsaturated expansive soils, PhD thesis, University of Ottawa, Ottawa, ON, Canada, 2014.

Alonso, E.E., Gens, A. & C.H. Delahaye. 2003. Influence of rainfall on the deformation and stability of a slope in overconsolidated clays: a case study. Hydrogeology Journal, 11(1): 74–192.

Azam, S. & M. Ito, 2011. Unsaturated soil properties of a fissured expansive clay. Proceedings, 64th Canadian Geotechnical Conference, Toronto, Canada. 313: 1–5.

Bao, C.G. 2003. On slope stability of expansive soil canal of Middle Route Project of S-N Water Transfer and counter measures. Yangtze iver, 34(5): 4–6. (in Chinese)

Burger, C.A. & C.D. Shackleford. Evaluating dual porosity of pelletized diatomaceous earth using bimodal soil-water characteristic curve functions. Canadian Geotechnical Journal, 38.1 (2001): 53–66.

Chen, J.B., Kong, L.W., Guo, A.G., Zhao, Y.L. & H.B. Lu. 2007. Deformation characteristics of expansive soil slopes under precipitation and evaporation. China civil engineering journal, 40(11): 70–77. (in Chinese)

Chen, X.G. In-situ test and stability analysis of Nanyou highway cut slope in expansive soils with cracks. Master thesis. Central South University, 2006. (in Chinese)

Cheng, Y.H., Cheng, Z.L. & Y.B. Zhang, 2011. Centrifugal model tests on expansive soil slope under rainfall. Chinese Journal of Geotechnical Engineering, 33(1): 409–414. (in Chinese)

Duncan, J.M. 1996. State of the art: limit equilibrium and finite-element analysis of slopes. Journal of Geotechnical engineering 122.7: 577–596.

Elkady, T.Y. Unsaturated characteristics of undisturbed expansive shale from Saudi Arabia. Arabian Journal of Geosciences 7.5 (2014): 2031–2040.

Escario, V. & Saez, J. 1986. The shear strength of partly saturated soils, Géotechnique. 36(3): 453–456.

Fredlund, D.G., Houston, S.L., Nguyen, Q. & M.D. Fredlund, 2010. Moisture movement through cracked clay soil profiles. Geotech. Geol. Eng., 28(6), 865–888.

Fredlund, D.G. & J. Krahn. 1977, Comparison of slope stability methods of analysis. Canadian Geotechnical Journal 14.3: 429–439.

Fredlund, D.G., A. Xing & S.Y. Huang. 1994. Predicting the permeability function for unsaturated soils using the soil-water characteristic curve. Canadian Geotechnical Journal 31.4: 533–546.

Fredlund, D.G., N.R. Morgenstern & R.A. Widger. 1978. The shear strength of unsaturated soils. Canadian Geotechnical Journal 15.3: 313–321.

Fredlund, D.G., Rahardjo, H. & J.K.-M. Gan, 1987. Nonlinearity of strength envelope for unsaturated soils. In Proceedings of the Sixth 624 International Conference on Expansive Soils, New Delhi, Vol. 1, pp. 49–54.

GeoSlope International Ltd., 2007a. Sigma/W User's Guide for Stress-Deformation Analysis. GEO-SLOPE International Ltd, Calgary, Alta.

GeoSlope International Ltd., 2007b. Seep/W User's Guide for Finite Element Seepage Analysis. GEO-SLOPE International Ltd, Calgary, Alta.

GeoSlope International Ltd., 2007c. Slope/W User's Guide for Slope Stability Analysis. GEO-SLOPE International Ltd, Calgary, Alta.

Hamdhan, I.N. & H.F. Schweiger, 2013. Finite element method-based analysis of an unsaturated soil slope subjected to rainfall infiltration. International Journal of Geomechanics, 13(5): 653–658. DOI:10.1061/(ASCE) GM.1943-5622.0000239.

Leong, E.C. & H. Rahardjo. 1997. Permeability functions for unsaturated soils. Journal of Geotechnical and Geoenvironmental Engineering, 123(12), 1118–1126.

Li, J.H., Zhang L.M. & X. Li. 2011. Soil-water characteristic curve and hydraulic conductivity function for unsaturated cracked soil. Canadian Geotechnical Journal, 48(7): 1010–1031. DOI:10.1139/t11-027.

Li, X., Li J.H. & L.M. Zhang. 2014. Predicting bimodal soil-water characteristic curves and hydraulic conductivity functions using physically based parameters. Computers and Geotechnics, 57: 85–96.

Liu, T.H. 1997. Problems of expansive soils in engineering construction. Architecture and Building Press of China, Beijing. (in Chinese)

Miao, L.C., Liu, S.Y. & Y.M. Lai. 2002. Research of soil–water characteristics and shear strength features of Nanyang expansive soil. Engineering Geology, 65.4: 261–267

Morgenstern, N.R. & V.E. Price, 1965. The analysis of the stability of general slip surfaces. Géotechnique, 15(1): 79–93. DOI:10.1680/geot.1965.15.1.79.

Ng, C.W.W., Zhan, L.T. Bao, C.G. Fredlund, D.G. & B.W. Gong, 2003. Performance of an unsaturated expansive soil slope subjected to artificial infiltration. Géotechnique, 53(2): 143–157.

Oh, W.T., Vanapalli, S.K. & A. Puppala. 2009. Semi-empirical model for the prediction of modulus of elasticity for unsaturated soils. Canadian Geotechnical Journal, 46(8): 903–914.

Pineda, J.A., Romero, E., Gracia, M.D. & D. Sheng, 2014. Shear strength degradation in claystones due to environmental effects. Géotechnique, 64(6): 493–501.

Qi, S.C. & S.K. Vanapalli. 2015. Stability Analysis of an Expansive Clay Slope: A Case Study of Infiltration Induced Shallow Failure of an Embankment in Regina, Canada. International Journal of Geohazards and Environment, 1(1): 7–19.

Rahardjo, H., Satyanaga, A., DAmore, G.A. & E. C. Leong, 2012. Soil-water characteristic curves of gap-graded soils. Engineering Geology, 125, 102–107.

Rouainia, M.O., Davies T.O. & S. Glendinning, 2009. Numerical modelling of climate effects on slope stability. Proceedings of the Institution of Civil Engineers Engineering Sustainability, 162(ES2): 81–89.

Shi, B. Jiang, H.T., Liu, Z.B. & H.Y. Fang. 2002. Engineering geological characteristics of expansive soils in China, Engineering Geology, 63–71.

van Genuchten, M. Th. 1980. A closed-form equation for predicting the hydraulic conductivity of unsaturated soils. Soil science society of America journal 44.5: 892–898.

Vanapalli, S.K., Fredlund, D.G., Pufahl, D.E. & A.W. Clifton. 1996. Model for the prediction of shear strength with respect to soil suction. Canadian Geotechnical Journal, 33(3): 379–392.

Vanapalli, S.K. & W.T. Oh. 2010. A model for predicting the modulus of elasticity of unsaturated soils using the soil-water characteristic curve. International Journal of Geotechnical Engineering, 4: 425–433.

Wei, L.D., Huang, W. & C.X. Chen, 2010. FEM for stability assessment of expansive soil slope under saturated-unsaturated seepage. Journal of water resources and architectural engineering, 8(4): 21–36. (in Chinese)

Xu, G.M., Wang, G.L., Gu, X.W. & Y.J. Zeng, 2006. Centrifuge modeling for instability of excavated slope in expansive soil due to water infiltration. Chinese Journal of Geotechnical Engineering, 28(2): 270–273. (in Chinese)

Yin, Z.Z. & B. Xu. Slope stability of expansive soil under fissure influence. Chinese Journal of Geotechnical Engineering, 2011, 33(3): 454–459. (in Chinese)

Yin, H.L., Xu, Q.J. & Z.K. Li. 2009. Effect of swelling deformation on stability of expansive soil slope. Rock and Soil Mechanics, 30(8): 2506–2510. (in Chinese)

Zhan, L.T., Ng, C.W.W. & D.G. Fredlund, 2007. Field study of rainfall infiltration into a grassed unsaturated expansive soil slope. Canadian Geotechnical Journal, 44(4): 392–408.

Zhan, T.L.T. & C.W.W. Ng. 2006. Shear strength characteristics of an unsaturated expansive clay. Canadian Geotechnical Journal 43.7: 751–763.

Zhang, L.M. & Q. Chen. 2005. Predicting bimodal soil–water characteristic curves. Journal of Geotechnical and Geoenvironmental Engineering 131.5: 666–670.

This page intentionally left blank

Unsaturated Soil Mechanics—from Theory to Practice – Chen et al. (Eds)
© 2016 Taylor & Francis Group, London, ISBN 978-1-138-02921-7

A numerical model for heat and moisture migration in unsaturated freezing soil

J. Teng, D. Sheng, S. Liang & S. Zhang
Department of Geotechnical Engineering, Central South University, Changsha, China

ABSTRACT: Taking the evaporation and condensation processes of water vapor into account, a new approach is put forward in this paper to model moisture and heat migration in unsaturated freezing soil. The predicted result of proposed model is compared with the experimental data of one-dimensional soil freezing test, it is shown that the proposed model is capable of effectively simulating the freezing process of unsaturated soil. Whereafter, parametric analysis is performed to clarify the role of vapor in soil freezing, the results show that vapor largely contributes to ice formation, occupying around 10%–60% of total water fluxes in an unsaturated and closed system. It is also shown that, total ice content and vapor flux percentage increases and decreases with the increase of initial water content, respectively. The higher the temperature gradient, the greater the vapor flux percentage, while the total ice content is insensitive to the temperature gradient. Peak values exist for the variations of total ice content and vapor flux against saturated hydraulic conductivity.

1 INTRODUCTION

The soil freezing process is a coupling movement of heat and pore water transfer. In the freezing process of a fully saturated soil with sufficient water supply, only the water increase in the frozen zone and consequently the total frost heave are of concern, and the problem can be solved by ignoring the effect of water content variation and skeletal deformation in unfroze zone (Zhou et al., 2014). When analyzing the freezing behavior of an unsaturated soil, however, the water migration is complicated due to temporal and spatial variations of water content and temperature in both frozen and unfrozen zone. As a result, aiming to simply and quickly solve the simultaneous equations of modelling heat-mass transfer in unsaturated freezing soil, most researcher preferred to neglect the process of vapor flow (Harlan, 1973; Hu et al., 1992; Zhou et al., 2014; etc.). As a matter of fact, water vapor flow can represent a major part of overall water flow especially in the case that temperature gradient is remarkable. The recent experimental evidences also proved that vapor flow in freezing soil could lead to large amount of ice formation, even dominate the moisture migration (Eigenbrod & Kennepohl, 1996; Guthrie et al., 2006; Wang et al., 2012). Additionally, water vapor flow significantly affects the movement of heat, since it drives a substantial amount of energy as the latent heat of vaporization (Sakai et al., 2006). Therefore, it is important to take vapor flow into account when modelling the process of soil freezing, and also, it is essential to clarify the role of vapor transfer in unsaturated freezing soil.

In theory of water-heat coupling movement in unsaturated soil, Philip and de Vries (1957), as the pioneer, developed mathematical model to describe coupled movement of liquid water and water vapor under nonisothermal conditions. Milly (1984) adopted a matric head based formation to modify the volumetric water content based Philip and de Vries (1957) model. Nassar and Horton (1989) further extended by including osmotic effects on liquid and water vapor movement. Sakai et al. (2009) presented a coupled model for water and vapor movement with condensation and evaporation under nonisothermal and low water content. Although numerical models of the simultaneous movement of liquid water, vapor, and heat in unsaturated soil have been proposed in the past, few simulations have been performed with considering soil freezing, that is to say, existing theories mainly demonstrate the limited situation of soil temperature over than 0, the coupling theory of heat and mass movement in unsaturated soil under both negative and positive temperature is not fully understood.

In this paper, a numerical model is presented to simulate the one-dimensional moisture-mass transfer in unsaturated freezing soil, which considers the processes of evaporation and condensation of water vapor, to evaluate its performance, one-dimensional soil freezing tests would be presented to compare with the predicted result. The role or contribution in freezing of unsaturated soil is therefore elucidated on basis of a parametric study.

2 THEORY

Some essential assumptions are stated as follows:

(a) The freezing front always locates at the depth where soil temperature is 0.
(b) The vapor evaporates and condenses in unfrozen part that is up to the freezing front, in the frozen zone only liquid water flows feeding the ice formation.
(c) The hysteresis in unsaturated soil is neglected.

2.1 *Liquid water and vapor flow*

For the unfrozen and frozen soil as a whole, the water flow is continuous. An improved Darcy's law as given by Philip and de Vries (1957) is adopted to describe the liquid water flux q_L, which considers both the flow driven by temperature gradient and pressure head gradient. Fick's law for vapor flux q_v, can also be separated into two (thermal and isothermal) components. Thus the liquid water and vapor flux in unsaturated soil can be given as follows,

$$q_L = q_{Lh} + q_{LT} = -K_{Lh}\left(\frac{\partial h}{\partial z} + 1\right) - K_{LT}\frac{\partial T}{\partial z} \tag{1a}$$

$$q_v = q_{vh} + q_{vT} = -K_{vh}\frac{\partial h}{\partial z} - K_{vT}\frac{\partial T}{\partial z} \tag{1b}$$

where q_{Lh} and q_{LT} are isothermal and thermal liquid water fluxes ($m\,s^{-1}$), respectively; q_{vh} and q_{vT} are isothermal and thermal vapor fluxes ($m\,s^{-1}$), respectively. h is the pressure head (m), T is the temperature (K), and z is the spatial coordinate positive upward (m). K_{Lh} ($m\,s^{-1}$) and K_{LT} ($m^2\,K^{-1}\,s^{-1}$) are the isothermal and thermal hydraulic conductivities for liquid water fluxes due to gradients in h and T, respectively; K_{vh} ($m\,s^{-1}$) and K_{vsT} ($m^2\,K^{-1}\,s^{-1}$) are the isothermal and thermal vapor hydraulic conductivities, respectively (Teng et al., 2013).

Supposing that the vapor evaporates in unfrozen soil, condenses into liquid water, and then flows and get frozen in frozen part, the volumetric water content here can be divided into three components accounting for liquid water, ice lensing and vapor content. Liquid water flow mainly results in the quantitative change of liquid water content and ice content, while vapor flow leads to the variation of vapor content. By using mass conservation law, the following expressions are given as:

$$\frac{\partial \theta_L}{\partial t} + \frac{\rho_i}{\rho_w}\frac{\partial \theta_i}{\partial t} = -\frac{\partial q_L}{\partial z} - E \tag{2a}$$

$$\frac{\partial \theta_v}{\partial t} = -\frac{\partial q_v}{\partial z} + E \tag{2b}$$

where θ_L, θ_i and θ_v are the liquid water content, pore ice content, and water vapor content (in form of an equivalent water content, $m^3\,m^{-3}$), respectively, and E represents the evaporation or condensation rate (s^{-1}), ρ_i and ρ_w are the densities of ice and liquid water, respectively, t is time (s).

Substituting Eqs. (1a) and (1b) into Eqs. (2a) and (2b) respectively and making combination, the governing equation for one-dimensional flow of liquid water and vapor in an unsaturated frozen soil can be obtained

$$\begin{aligned}\frac{\partial \theta}{\partial t} &= \frac{\partial \theta_L}{\partial t} + \frac{\partial \theta_v}{\partial t} + \frac{\rho_i}{\rho_w}\frac{\partial \theta_i}{\partial t} = -\frac{\partial q_L}{\partial z} - \frac{\partial q_v}{\partial z} \\ &= \frac{\partial}{\partial z}\left[K_{Lh}\left(\frac{\partial h}{\partial z} + 1\right) + K_{LT}\frac{\partial T}{\partial z} + K_{vh}\frac{\partial h}{\partial z} + K_{vT}\frac{\partial T}{\partial z}\right]\end{aligned} \tag{3}$$

where θ is total volumetric water content ($m^3\,m^{-3}$).

2.2 *Soil hydraulic properties*

Neglecting the hysteresis between drying and wetting curves, the van Genuchten model (van Genuchten, 1980) is adopted to simulate the Soil Water Retention Curve (SWRC), as follows:

$$\Theta = \left[1 + (-\alpha h)^n\right]^{-m} \tag{4}$$

where, Θ is the effective saturation (unitless), $\Theta = (\theta_L - \theta_r)/(\theta_s - \theta_r)$, θ_s and θ_r are the saturated and residual water content ($m^3\,m^{-3}$), respectively; α (m^{-1}), n (unitless), and m ($= 1 - 1/n$) are empirical shape parameters. Without considering the ice lens in frozen soil for obstructing the flow of remained liquid water, the isothermal unsaturated hydraulic conductivity of liquid water in both frozen and unfrozen soil is modeled following Mualem (1976):

$$K_{Lh} = K_s\Theta^l\left[1 - (1 - \Theta^{1/m})^m\right]^2 \tag{5}$$

where K_s is the saturated hydraulic conductivity ($m\,s^{-1}$), l is fitting parameter, which was suggested as 0.5 by Mualem (1976).

The definitions of thermal hydraulic conductivity of liquid water K_{LT}, and hydraulic conductivities of vapor due to temperature K_{vT}, and water head K_{vh} refers to Saito et al. (2006):

$$K_{LT} = K_{Lh}\left(hG_{wT}\frac{1}{\gamma_0}\frac{d\gamma}{dT}\right) \tag{6}$$

$$K_{vh} = \frac{D}{\rho_w}\left(\rho_{vs}\frac{Mg}{RT}H_r\right) \tag{7}$$

$$K_{vT} = \frac{D}{\rho_w}\eta H_r\left(\frac{d\rho_{vs}}{dT}\right) \tag{8}$$

respectively, in Eq. (6), G_{wT} is the gain factor, which amends the temperature dependence of the SWRC. γ is the surface tension of soil water ($J\,m^{-2}$), and γ_0 is the surface tension at 25°C ($= 71.89\,g\,s^{-2}$). In Eqs. (7) and (8), M is the molecular weight of water ($= 0.018\,kg\,mol^{-1}$), g is the gravitational acceleration (m/s^2), R is the universal gas constant ($= 8.341\,J\,mol^{-1}\,K^{-1}$), H_r is the relative humidity

Table 1. Computation of parameters in the mathematical model.

Parameter	Equation
Surface tension of liquid water γ (J m^{-2})	$\gamma = 75.6 - 0.1425T - 2.38 \times 10^{-4}T^2$
Saturated vapor density ρ_{vs} (kg m^{-3})	$\rho_{vs} = \exp(31.37 - 6014.79T^{-1} - 7.92 \times 10^{-3}T) \times 10^{-3}T^{-1}$
Enhancement factor η (unitless)	$\eta = 9.5 + 3\theta_L\theta_s^{-1} - 8.5(1/\exp(1 + 2.6(f_c)^{-0.5}\theta_L\theta_s^{-1})^4)$
Relative humidity H_r (unitless)	$H_r = \exp(hMg/RT)$
Vapor diffusivity in air D_a (m^2 s^{-1})	$D_a = 2.12 \times 10^{-5}(T/273.15)^2$
volumetric heat capacities of soil C_p (MJ m^{-3} K^{-1})	$C_p = C_n\theta_n + C_L\theta_L + C_v\theta_v + C_i\theta_i$
Latent heat of water vaporization L_w (J kg^{-1})	$L_w = 2.501 \times 10^6 - 2369.2T$

Note: f_c is the mass fraction of clay in the soil (dimensionless), θ_n is volumetric fraction of the solid phase (m^3 m^{-3}).

(unitless), η is an enhancement factor (unitless), ρ_{vs} is the saturated vapor density (kg m^{-3}). D is the vapor diffusivity in soil (m^2 s^{-1}), it can be derived from the diffusivity of water vapor in air, as follows,

$$D = \tau\theta_a D_a = \frac{\theta_a^{7/3}}{\theta_s^2}\theta_a D_a \tag{9}$$

where τ is the tortuosity factor, θ_a is the air-filled porosity (m^3 m^{-3}), D_a is the diffusivity of water vapor in air (m^2 s^{-1}). The definitions of the related parameters are presented in Table 1.

2.3 *Heat transport and soil thermal properties*

Considering vaporization, condensation, and freezing in unsaturated soil, the governing equation of heat conservation can be given as (de Veries, 1958; Nassar and Horton, 1992):

$$\begin{aligned} &C_p\frac{\partial T}{\partial t} + L_w\rho_w\frac{\partial\theta_v}{\partial t} - L_i\rho_i\frac{\partial\theta_i}{\partial t} \\ &= \frac{\partial}{\partial z}\left[\lambda(\theta)\frac{\partial T}{\partial z}\right] - C_L\frac{\partial q_L T}{\partial z} - L_w\rho_w\frac{\partial q_v}{\partial z} - C_v\frac{\partial q_v T}{\partial z} \end{aligned} \tag{10}$$

where, C_p is defined as the sum of the volumetric heat capacities of unsaturated soil (MJ m^{-3} K^{-1}), which equals to the solid C_n (= 1.92 MJ m^{-3} K^{-1}), liquid C_L (= 4.18 MJ m^{-3} K^{-1}), air C_v (= 6.3 KJ m^{-3} K^{-1}) and ice C_i (= 2.10 MJ m^{-3} K^{-1}) phases multiplied by their respective volumetric fractions (de Vries, 1958). L_w is the latent heat of water vaporization (J m^{-3}), the expressions of C_p and L_w are presented in Table 1. L_i is the latent heat of water freezing (= 334 kJ kg^{-1}). $\lambda(\theta)$ in Eq. (10) is the soil thermal conductivity (W m^{-1} K^{-1}), which can be defined by the following equation,

$$\lambda(\theta) = b_1 + b_2\theta_L + b_3\theta_L^{0.5} \tag{11}$$

where b_1 (= 0.228 W m^{-1} K^{-1}), b_2 (= −2.406 W m^{-1} K^{-1}), and b_3 (= 4.909 W m^{-1} K^{-1}) are empirical regression parameters. In Eq. (10), the three terms on the left-hand side represent energy changes in soil, the latent heat of the vapor phase, the heat generated during water freezing, the negative sign indicates the exothermic process for water freezing. The four terms on the right-hand side of Eq. (10) are soil heat flow by conduction, the convection of sensible heat with flowing water, the transfer of latent heat by vapor diffusion, and the transfer of sensible heat by vapor diffusion, respectively (Sakai et al., 2009).

It should be noted that four variables of θ_L, θ_v, θ_i and T exist in the two simultaneous equations of Eqs. (3) and (10) that governing the moisture and heat transport in unsaturated frozen soil, the other two equations is necessary to solve the simultaneous equations. The one is presented as follows,

$$\theta_L + \theta_v + \theta_i = \theta_s \tag{12}$$

To derive the second equation, the generalized Clapeyron equation is introduced to set up the relationship between pressure of unfrozen liquid water and that of pore ice when these two phase are in equilibrium in frozen soil, which is expressed as (Sheng, 2014),

$$du_w = du_i + \frac{L_i}{gT_0}dT \tag{13}$$

where u_w and u_i are the unfrozen water pressure (in unit of a water head, m) and pore ice pressure (m), T_0 is the freezing point of water (K), and noted that T in this equation is in unit of °C. Neglecting the overburden loading, u_i remains practically unchanged, that is to say, the first term on right hand of Eq. (13) changes into 0. Moreover, it has been validated that the pore water pressure in frozen soil equals to that in unsaturated soil with the same liquid water content (Harlan, 1973), thus u_w has the equivalent meaning with h in Eq. (4). Integrating both sides of Eq. (13) and then substituting into Eq. (4), one can get the function accounting for one-to-one correspondence between unfrozen liquid water content θ_L and soil temperature T in frozen soil, as follows,

$$\theta_L = (\theta_s - \theta_r)\left[1 + (-\alpha\frac{L_i T}{gT_0})^n\right]^{-m} + \theta_r \tag{14}$$

Eq. (14) above is also named as Soil Freezing Characteristic Curve (SFCC), and it is the additional information for solving the simultaneous equations.

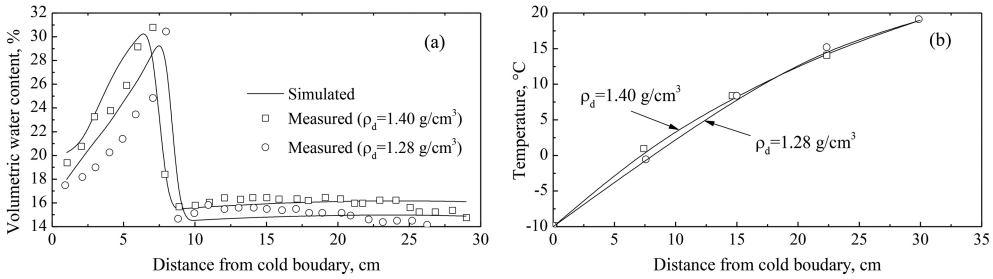


Figure 1. The computed and measured profiles of volumetric water content (a) and soil temperature (b), Case 1: the initial gravity water content is 13.6%, the freezing period is 7 days.

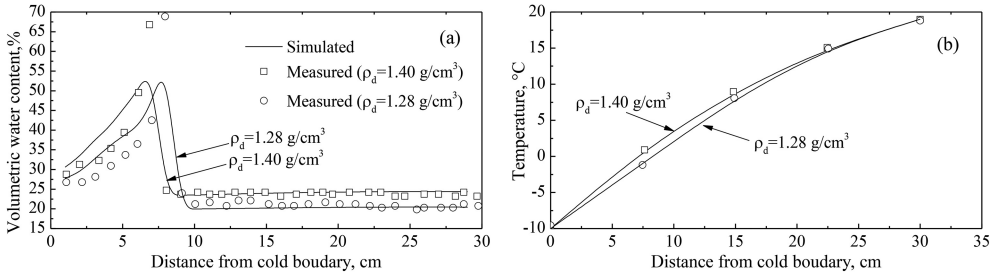


Figure 2. The computed and measured profiles of volumetric water content (a) and soil temperature (b), Case 2: the initial gravity water content is 20.8%, the freezing period is 7 days.

3 EXPERIMENTAL VALIDATION

The equations has been numerically solved based on the finite difference method, to evaluate the performance, the proposed model is used to analyze one example on basis of published experimental data.

Wang et al. (2012) performed a one-dimensional freezing experiment, during which a partially saturated soil column was frozen from the top to the bottom without an external water supply. The soil material was loess of Xi'an area in China, the liquid limit and plastic limit are 30.2% and 17.8%, respectively. The soil column was 30 cm in height and 7.5 cm in diameter, two kinds of initial water content were controlled in the measurement, 13.6% and 20.8% in gravity water content, for these two cases separately included two cases of controlling soil density ρ_d, 1.40 g/cm^3 and 1.28 g/cm^3, thus totally four conditions were carried out in this test. For each case, soil sample was subjected to a temperature gradient of top −10°C and bottom 19°C in 7 days. During the test, the side wall of the sample was adiabatic, the water content and temperature distributions were measured at the end of test.

Figure 1 illustrates the simulated profiles of water content (a) and soil temperature (b) with comparing with the measured result. It can be seen that the volumetric water content decreases in the unfrozen zone and increases in the frozen zone, it is because that no water was supplied during soil freezing, the liquid and vapor water was "sucked" from unsaturated zone. It can be observed that both the simulated result of water content and temperature agrees reasonable well with the experimental result. The predicted water content at the freezing front is somehow lower while at the frozen zone is slightly higher than the measured result, and it is due to the indeterminacy of hydraulic conductivity in frozen part.

Figure 2 simulated the test result of case 2 with a higher initial water content, and it shows that the increase in water content frozen region of small density loess is smaller than with the big density loess, and the freeze frontal water content increase in big density loess is relatively smaller than in small density loess. Comparing Fig. 1 (a) and Fig. 2 (a), it is found that the greater initial water content, the greater increase in the water content of freezing front. Same with case 1, an acceptable simulated result can be generated from the proposed model except for the water content at freezing front. In a word, the proposed model is capable of effectively simulating the freezing process of unsaturated soil.

4 PARAMETRIC ANALYSIS

In this section, we aim to evaluate the effects of relevant factors on soil freezing in an unsaturated soil, including initial water content, temperature gradient and saturated hydraulic conductivity. The control condition is designed as that a homogeneous soil column in height of 1 m is subjected to a temperature gradient of 20°C in 30 days, the top and bottom temperature are

Table 2. The soil hydraulic parameters in control case, the parameters originate from van Genuchten (1980) model.

Parameter	K_s (cm/d)	α (cm^{-1})	θ_r (m^3/m^3)	θ_s (m^3/m^3)	n (m)
Value	20.0	0.00546	0.065	0.49	2.32

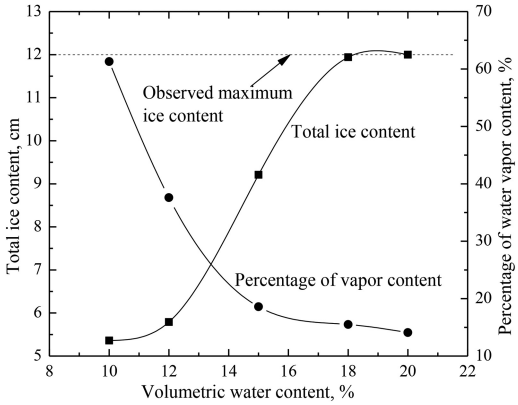


Figure 3. The effect of initial water content on freezing behavior of unsaturated soil, initial water contents are 10%, 12%, 15%, 18% and 20%.

−10°C and 10°C, respectively, the soil properties in the controlled case are given in Table 2, the initial profiles of water content and temperature are constantly 15% and 5°C, respectively. During soil freezing, no water flows at the lower boundary. Two indexes, total ice content Θ_i and percentage of vapor content θ_v/θ in unfrozen part, are chosen as assessment criteria. Here the Θ_i is defined as

$$\Theta_i = \int_0^{d_f} \theta_i \tag{15}$$

where d_f is the frost depth (cm), thus Θ_i represents the amount of ice in the magnitude of height, while θ_v/θ denotes the percentage of vapor flow in total water flow of the unfrozen part.

Figure 3 illustrates the total ice content and percentage of vapor content against the initial volumetric water content, the initial water content was assigned as five values from 10% to 20%. It can be observed that the total ice content Θ_i gradually increase with the increase of initial water content, it is easily imagine that much more water can migrate from the unfrozen part if the initial water content is higher. A maximum value of Θ_i, however, seems to appear at around 12 cm, which indicates the ice formation would terminate even if giving a high water content. It is deduced that the "sucking force" at freezing front affects the amount of water flowed into frozen part, which limits the increase of ice formation. Additionally, the percentage of vapor content θ_v/θ decreases with the increase of initial water content, the range is about from 60% to 15%, it implies that the vapor flux cannot be neglected

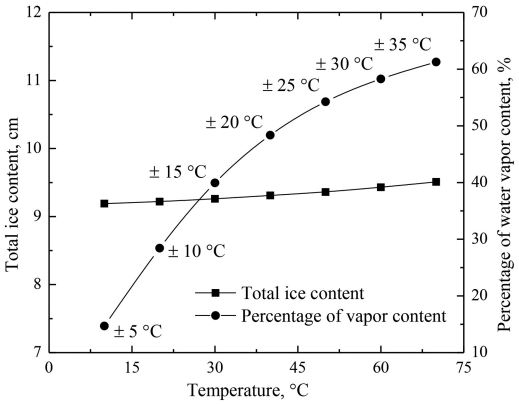


Figure 4. The effect of temperature gradient on freezing behavior of unsaturated soil, the temperature gradient are marked in the figure.

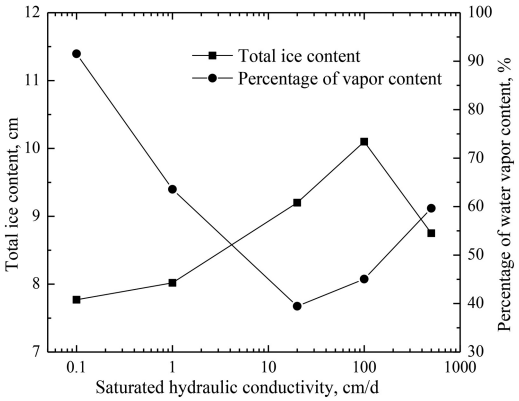


Figure 5. The effect of saturated hydraulic conductivity K_S on freezing behavior of unsaturated soil, the selected values of K_S are 0.1, 1, 20, 100 and 500 cm/d.

in an unsaturated soil with closed system, especially when the water content is low.

Figure 4 displays the variations of Θ_i and θ_v/θ against temperature. When adding a couple of equivalent temperature of positive and negative values on the bottom and top boundary of soils, respectively, the higher the temperature, the more the vapor flux generated in the soil. It can be demonstrated like that higher temperature increases the vaporization rate in soil body, and its higher gradient supplies greater driving force for vapor flow. It should be noted that the temperature gradient produces tiny influence on the total ice content, which smoothly increase in the range of 9.0–9.5 cm. The reason may be that the water content profile in unfrozen zone reaches to an equilibrium state, at the status, little water can be driven by the temperature.

Figure 5 shows the developments of Θ_i and θ_v/θ with saturated hydraulic conductivity K_s. Focusing on the total water content Θ_i, it can be seen that Θ_i firstly decreases and then increases with the increase of saturated hydraulic conductivity, an inflection point of

minimum value appears at around $K_s = 20$ cm/d. As to the variation of θ_v/θ, it initially increases with the increase K_s, a reduction occurs after a peak value of about $K_s = 100$ cm/d. it should be noted that there is an optimal value of K_s for the amount of ice formation and vapor flux, their relationship cannot be linear.

5 CONCLUSIONS

This paper presents a coupled model of heat, liquid water, and vapor movement in unsaturated freezing soil, the model of simultaneous equations consist of two equations governing mass and heat transfer, respectively, one equation for mass conservation, and one equation derived from Clapeyron equation. The advantages of this model are taking the vapor evaporation and condensation process into account, which was always neglected in previous researches. One example of soil freezing experiment from literature is presented to evaluate the performance of proposed model, the comparison between measured and predicted result shows that the proposed is capable of effectively simulating the freezing process of unsaturated soil.

Parametric analysis is carried out to clarify the role of vapor in moisture migration during freezing, the results show that vapor largely contributes to ice formation, occupying about 20%–60% of total water fluxes in an unsaturated and closed system under regular temperature gradient, it indicates the vapor flow in freezing soil cannot be neglected. The results also show that, total ice content and vapor flux increases and decreases with the increase of initial water content, respectively. The higher the temperature gradient, the greater the vapor flux percentage, while the total ice content is insensitive to the temperature gradient. Peak values exist both for the variations of total ice content and that of vapor flux against saturated hydraulic conductivity.

ACKNOWLEDGEMENTS

This research was supported by National Basic Research Program of China (2014CB047001).

REFERENCES

de Vries, D.A. 1958. Simultaneous transfer of heat and moisture in porous media. *Trans. Am. Geophys. Union* 39: 909–916.

Eigenbrod, K.D. and Kennepohl G.J.A. 1996. Moisture Accumulation and Pore Water Pressures at Base of Pavements. *Transportation Research Record* 1546: 151–161.

Guthrie, W. and Hermansson, Å. and Woffinden, K. 2006. Saturation of Granular Base Material Due to Water Vapor Flow during Freezing: Laboratory Experimentation and Numerical Modeling. *Cold Regions Engineering*: 1–12. doi:10.1061/40836(210)66

Harlan, R.L. 1973. Analysis of coupled heat-fluid transport in partially frozen soil. *Water Resources Research* 9(5): 1314–1323.

Hu, H., Yang, S. and Lei, Z. 1992. A numerical simulation for heat and moisture transfer during soil freezing. *Journal of Hydraulic Engineering* 7: 1–8 (in Chinese).

Milly, P.C.D. 1984. A simulation analysis of thermal effects on evaporation. *Water Resource Research* 20: 1087–1098.

Mualem, Y. 1976. A new model for predicting the hydraulic conductivity of unsaturated porous media. *Water Resources Research* 12: 513–522.

Nassar, I.N. and Horton. R. 1989. Water transport in unsaturated nonisothermal salty soil: II. Theoretical development. *Soil Science Society of America Journal* 53: 1330–1337.

Nassar, I.N. and Horton, R. 1992. Simultaneous transfer of heat, water, and solute in porous media: I. Theoretical development. *Soil Science Society of America Journal* 56: 1350–1356.

Philip, J.R. and de Vries, D.A. 1957. Moisture movement in porous materials under temperature gradient. *Trans. Am. Geophys. Union* 38: 222–232.

Sakai, M., Toride, N., Šimùnek, J. 2009. Water and vapor movement with condensation and evaporation in a sandy column. *Soil Science Society of America Journal* 73(3): 707–717.

Saito, H., Šimůnek, J. and Mohanty, B.P. 2006. Numerical analysis of coupled water, vapor, and heat transport in the vadose zone. *Vadose Zone Journal* 5: 784–800.

Sheng, D., Zhang, S., Niu, F. and Cheng, G. 2014. A potential new frost heave mechanism in high-speed railway embankments. *Géotechnique* 64(2): 144–154.

Teng, J.D., Yasufuku, N., Liu, Q. and Liu, S.Y. 2013. Analytical solution for soil water redistribution during evaporation process. *Water Science and Technology* 68(12): 2545–2551.

van Genuchten, M.Th. 1980. A closed-form equation for predicting hydraulic conductivity of unsaturated soils. *Soil Science Society of America Journal* 44: 892–898.

Wang, T., Wang, J. and Zhang, L. 2012. Experimental research on moisture migration in freezing unsaturated loess. *Journal of Xi'an University of Architecture & Technology (Natural Science Edition)* 44(1): 7–13 (In Chinese).

Zhou, J., Wei, C., Li, D. and Wei, H. 2014. A moving-pump model for water migration in unsaturated freezing soil. *Cold Regions Science and Technology* 104–105: 14–22.

Unsaturated Soil Mechanics—from Theory to Practice – Chen et al. (Eds)
© 2016 Taylor & Francis Group, London, ISBN 978-1-138-02921-7

Effective stress based numerical modelling of shallow foundations on unsaturated soil

Y. Tang & H.A. Taiebat
UNSW Australia, Sydney, Australia

ABSTRACT: Most shallow foundations are built on unsaturated soils. Evaluation of the bearing capacity of these foundations is one of the key issues in foundation design since the traditional bearing capacity equations for saturated/dry soil are not directly applicable to unsaturated soil. This paper presents an effective stress based finite element formulation that can be used to estimate the bearing capacity of shallow foundations on unsaturated soil. The formulation is validated by simulating experimental tests on unsaturated samples. The effect of uniform suction, developed in the soil due to partial saturation, on the bearing capacity of strip footings is presented. A series of analyses has also been performed to investigate the bearing capacity of footings on unsaturated soil with a varied suction profile. The results of these analyses show that the water table and suction profile have a great influence on the bearing capacity.

1 INTRODUCTION

In geotechnical engineering, the bearing capacity is a key parameter required when designing foundations. The theory of bearing capacity of shallow foundation on saturated/dry soil has been developed mainly in the last century (e.g. Terzaghi 1943, Meyerhof 1953, Vesic 1973). However, in reality, most of shallow foundations are typically located above the groundwater table. Due to the contribution of suction on the bearing capacity, overconservative estimations are obtained using the conventional bearing capacity equations.

Research on the bearing capacity of shallow foundation on unsaturated soil is relatively limited. Very few experimental studies on the bearing capacity of footings on unsaturated soil have been reported (Steensen-Bach et al. 1987, Costa et al. 2003, Mohamed and Vanapalli 2006). The bearing capacity was found to be significantly increased by suction developed within the soil. However, these results are not extendable to all boundary conditions and all unsaturated states of the soil. Limited investigation has also been carried out for footings on unsaturated soil using numerical methods (Sheng et al. 2003, Oh & Vanapalli 2008, Oh & Vanapalli 2011).

Finite element method which is widely used in numerical modelling of geotechnical problems has been proved to be an alternative tool that can be used to investigate the behaviour of unsaturated soil (Li et al. 1999, Sheng et al. 2003). Several attempts have been made to simulate the behaviour of unsaturated soil numerically using the effective stress principle (Khalili et al. 2000, Khalili et al. 2008, Khoshghalb & Khalili 2013). The effective stress principle can significantly simplify the deformation model and hence reduce many model parameters.

The main objective of this paper is to propose a robust finite element model to predict the bearing capacity of footings on unsaturated soil by implementing fully coupled flow-deformation governing equations based on the effective stress principle. The theoretical framework adopted here is based on the contributions of Khalili et al. (2008). The governing equations are implemented into a general finite element program, AFENA (Carter & Balaam 1995). The formulation is validated by simulating some experimental tests on samples of unsaturated soil. A series of analyses are performed to investigate the bearing capacity of strip footings on unsaturated soils with uniform suction profile using the elastic-perfectly plastic Mohr-Coulomb constitutive model. The results are compared with the values of bearing capacity calculated by the equation proposed by Vanapalli & Mohamed (2007). A bearing capacity equation is also proposed here that can be used to predict the bearing capacity of foundations on unsaturated soil assuming uniform suction in the soil. The proposed finite element model is also applied to investigate the bearing capacity of footings on unsaturated soil with varied suction profile and different levels of water table.

2 FINITE ELEMENT FORMULATION FOR FULLY COUPLED FLOW-DEFORMATION ANALYSES

2.1 *Effective stress principle*

Effective stress principle is the fundamental concept used in the conventional soil mechanics to describe the behaviour of soils. It was extended to unsaturated soils by Bishop (1959) and was expressed as:

$$\sigma' = (\sigma - p_a) + \chi(p_a - p_w) \tag{1}$$

where σ' is the effective stress and σ is the total stress. p_a and p_w are pore air and pore water pressures, respectively. χ is the effective stress parameter which can be evaluated by the equations proposed by Khalili & Khabbaz (1998) and extended by Khalili & Zargarbashi (2010):

$$\chi = \begin{cases} 1 & for\ \dfrac{s}{s_e} \le 1 \\ \left(\dfrac{s}{s_e}\right)^{-0.55} & for\ \dfrac{s}{s_e} > 1 \end{cases} \tag{2-a}$$

$$\chi = \begin{cases} \left(\dfrac{s_{rd}}{s_{ae}}\right)^{-0.55}\left(\dfrac{s}{s_{rd}}\right)^{\zeta} & for\ drying\ reversal \\ \left(\dfrac{s_{rw}}{s_{ex}}\right)^{-0.55}\left(\dfrac{s}{s_{rw}}\right)^{\zeta} & for\ wetting\ reversal \end{cases} \tag{2-b}$$

where s is the matric suction, s_e is the suction value marking the transition between saturated and unsaturated states. For wetting processes, $s_e = s_{ex}$, where s_{ex} is the air expulsion value; for drying processes, $s_e = s_{ae}$, where s_{ae} is the air entry value. ζ is the slope of the scanning curve between the main drying and wetting curves in a $\ln\chi \sim \ln s$ plane, and s_{rd} and s_{rw} are the points of suction reversal on the main drying and wetting curves, respectively.

The effective stress principle for unsaturated soil plays a central role in the present study: not only it describes the stress-strain relationship of soil skeleton, but also presents the coupling of flow and deformation models. Due to the strong nonlinearity of the elasto-plastic constitutive models, the effective stress equation is normally written in incremental format:

$$\dot{\sigma}' = (\dot{\sigma} - \dot{p}_a) + \psi(\dot{p}_a - \dot{p}_w) \tag{3}$$

where a superimposed dot indicates the rate of change, $\psi = \partial(\chi s)/\partial s$ is the incremental effective stress parameter which is used to couple the flow and deformation models.

The interrelation of hydraulic and mechanical behaviour in unsaturated soil is a subject of great interest in geotechnical engineering practice. Several flow and deformation models were developed for unsaturated soil (Lloret & Alonso 1980, Schrefler & Xiaoyong 1993, Gatmiri & Delage 1995), where the flow model and deformation model were separated. Khalili et al. (2008) proposed differential equations governing fully coupled flow and deformation in unsaturated porous medium. The flow models for water and air phases were derived based on momentum balance (Darcy's law) and mass balance. The deformation model was expressed using the linear momentum balance equation of a soil element. These models were fully coupled by two constitutive relationships: the volumetric deformations of water and air phases and the stress-strain relationship of the soil skeleton using the effective stress concept. The fundamental equations are presented as follows:

$$div\left[D(\nabla\dot{u}) - \psi\dot{p}_w\delta - (1-\psi)\dot{p}_a\delta\right] + \dot{F} = 0 \tag{4}$$

$$\begin{aligned} &div\left(\frac{k_{rw}k}{\mu_w}(\nabla p_w + \rho_w g)\right) \\ &= \psi div\dot{u} + a_{11}\dot{p}_w - a_{12}\dot{p}_a \end{aligned} \tag{5}$$

$$\begin{aligned} &div\left(\frac{k_{ra}k}{\mu_a}(\nabla p_a + \rho_a g)\right) \\ &= (1-\psi)div\dot{u} - a_{21}\dot{p}_w + a_{22}\dot{p}_a \end{aligned} \tag{6}$$

with

$$\begin{aligned} &a_{11} = c_w n_w + a_{12},\ a_{22} = a_{21} + c_a n_a \\ &a_{12} = a_{21} = -n\frac{\partial S_r}{\partial s} \end{aligned} \tag{7}$$

where ∇ is the spatial gradient and *div* is the divergence operator. D is the stiffness matrix of the soil, u is the displacement vector of the soil skeleton. δ is the Kronecker delta and F is the body forces per unit volume. k is the intrinsic permeability of the soil, k_{rw} and k_{ra} are the relative permeability with respect to water and air phases, respectively. μ_w and μ_a are the dynamic viscosities of water and air, respectively. ρ_w is the mass density of water, ρ_a is the mass density of air. g is the vector of gravitational acceleration. c_w and c_a are the coefficients of water and air compressibility. n_w and n_w are the volumetric water and air contents, respectively. a_{11}, a_{12}, a_{21}, and a_{22} are the constitutive coefficients ensuring the coupling of air and water phases. n is the porosity and S_r is the degree of saturation. $\partial Sr/\partial s$ is evaluated using the slope of the Soil Water Characteristic Curve (SWCC) for the specific volume of interest. In this paper, the SWCC equations proposed by Russell & Buzzi (2012) and Russell (2014) including the

effects of hysteresis and volume change are adopted. The equations of SWCC are defined as:

$$S_r = \begin{cases} 1 & for \ \dfrac{s}{s_e} \le 1 \\ \left(\dfrac{s}{s_e}\right)^{\alpha} & for \ \dfrac{s}{s_e} > 1 \end{cases} \tag{8-a}$$

$$S_r = \begin{cases} \left(\dfrac{s_{rd}}{s_{ae}}\right)^{\alpha}\left(\dfrac{s}{s_{rd}}\right)^{\beta} & for\ drying\ reversal \\ \left(\dfrac{s_{rw}}{s_{ex}}\right)^{\alpha}\left(\dfrac{s}{s_{rw}}\right)^{\beta} & for\ wetting\ reversal \end{cases} \tag{8-b}$$

where α is the slope of the main drying and wetting curves, β defines the slope of the scanning curves.

2.2 *Discretization of governing equations*

The spatial and temporal discretization of the governing equations is achieved using the Galerkin method and the implicit Eular backward interpolation scheme, respectively. The discretised governing equations may be written in a matrix form as:

$$\begin{bmatrix} K & -\psi L^T & -(1-\psi)L^T \\ -\psi L & -a_{11}M - \eta\Delta t H_w & a_{12}M \\ -(1-\psi)L & a_{21}M & -a_{22}M - \beta\Delta t H_a \end{bmatrix} \tag{9}$$

$$\begin{Bmatrix} \Delta u \\ \Delta p_w \\ \Delta p_a \end{Bmatrix} = \begin{Bmatrix} \Delta P \\ \Delta t H_w p_w^t \\ \Delta t H_a p_a^t \end{Bmatrix} + \eta\Delta t \begin{Bmatrix} 0 \\ Q_w^{t+\Delta t} \\ Q_a^{t+\Delta t} \end{Bmatrix}$$

where P is the vector of nodal forces, and Q_w and Q_a are the vectors of nodal fluxes for water and air phases, respectively. K, L, H_w, H_a and M are the global property matrices. η is a parameter which corresponds to the type of interpolation method used for time discretization. In the current study, a temporal integration with $\eta = 1$ (implicit Euler backward interpolation method) is used for all analyses. The vectors and matrices are evaluated as:

$$P = \int_V N^T F dV + \int_S N^T T dS \tag{10-a}$$

$$Q_w = \int_S N^T q_w dS \tag{10-b}$$

$$Q_a = \int_S N^T q_a dS \tag{10-c}$$

$$K = \int_V B_1^T D B_1 dV \tag{10-d}$$

$$L = \int_V B_2^T N dV \tag{10-e}$$

Table 1. Material properties of the tested samples.

	Khabbaz (1997)	Cui & Delage (1996)
E (MPa)	12.5	10
υ	0.3	0.25
n	0.492	0.38
S_r	0.974	0.77, 0.74, 0.68, 0.62
s (kPa)	150	200, 400, 800, 1500
s_{ae} (kPa)	200	58
s_{ex} (kPa)	20	5.8
α	−0.15	−0.147
β	−0.001	−0.074
ζ	−0.003	−0.28

$$M = \int_V N^T N dV \tag{10-f}$$

$$H_w = \int_V \frac{k_{rw}}{\mu_w} B_3^T k B_3 dV \tag{10-g}$$

$$H_a = \int_V \frac{k_{ra}}{\mu_a} B_3^T k B_3 dV \tag{10-h}$$

where N is the matrix of shape functions, V and S are the volume and surface boundary of the domain, q_w and q_a are the fluid and air fluxes across the boundary, B_1, B_2 and B_3 are matrices of derivation of shape functions, and T is the boundary traction.

3 VERIFICATION AND APPLICATION

To validate the fully coupled finite element formulation, two experimental tests on samples of unsaturated soil are simulated. Then a series of analyses is carried out on the bearing capacity of footings on unsaturated soils with uniform suction. The bearing capacity of unsaturated soil with varied suction profile and different levels of water table are also investigated.

3.1 *Sample tests on unsaturated soil*

Khabbaz (1997) performed laboratory tests on compacted kaolin to investigate the volume change behaviour of unsaturated soil. One of these tests, named U14, is simulated in this study. The laboratory test simulated a wetting process by increasing the pore water pressure at a constant net stress. The initial parameters of the sample are given in Table 1.

The water pressure increased from 250 kPa to 350 kPa and the change in the volume of water and soil sample with time were measured. Figure 1 compares the numerical results with the tests data. It can be seen that the volumes of water phase and soil skeleton increase due to the applied water pressure. Excellent agreement is obtained between the experimental and numerical results.

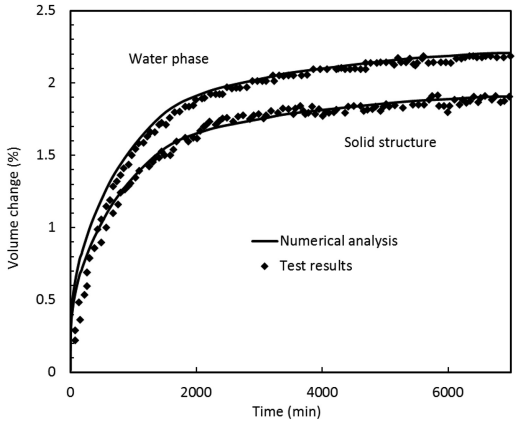


Figure 1. Comparison of the results of numerical analysis with test results of Khabbaz (1997).

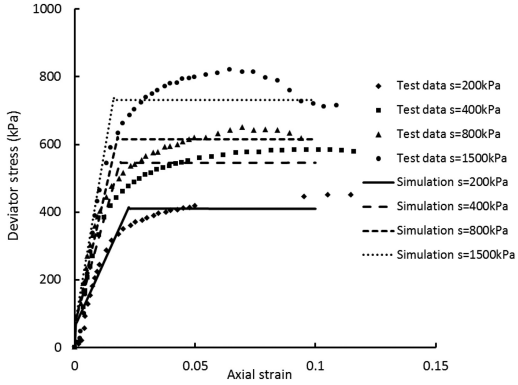


Figure 2. Comparison of the results of numerical analysis with test results of Cui & Delage (1996).

There are limited studies on the shearing resistance of unsaturated soil samples. Cui & Delage (1996) conducted a series of shear tests on unsaturated compacted silt. The tests were performed under constant cell pressure and different initial suctions. The stress-strain curves of the tests with cell pressure 100 kPa are simulated here. During the tests, suction was kept constant. The material parameters used in the simulations are summarized in Table 1. Friction angle is calculated to be $\phi' = 26°$. The parameters representing the SWCC were not available and had to be calibrated from the data presented by Cui & Delage (1996).

The numerical results are compared with the experimental data in Figure 2. The simple elastic-perfectly plastic Mohr-Coulomb constitutive model used in the current study cannot predict the gradual change in the stiffness of the soil under shear stress. However, the numerical simulation shows the deviatoric stress at failure increases dramatically with increasing suction and is in a reasonable agreement with the experimental data.

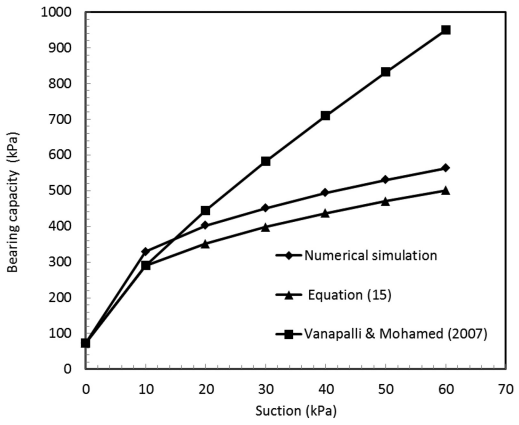


Figure 3. Comparison of the results of numerical simulations with those obtained by equation (15) and by the equation proposed by Vanapalli & Mohamed (2007).

3.2 *Bearing capacity of footings on unsaturated soil*

The robustness of the effective stress based fully coupled governing equations for bearing capacity problems is demonstrated by a series of analyses performed to predict the bearing capacity of strip footings on unsaturated soil with different suctions. Suction is assumed to be constant and uniformly distributed over the soil layer. The hydraulic hysteresis and the influence of volume change on the SWCC are considered in these analyses. The bearing capacity will be a function of the air entry and air expulsion values which are assumed to be 100 kPa and 10 kPa, respectively. The material parameters used in this analysis are $E = 10$ MPa, $\nu = 0.3$, $n = 0.5$, $\alpha = -0.15$, $\beta = -0.05$ and $\zeta = -0.183$. The initial hydraulic state is on the main wetting curve. For a specific friction angle of $\phi' = 30°$, the simulated bearing capacity for different suction values are shown in Figure 3 and compared with that obtained by the equation proposed by Vanapalli & Mohamed (2007) as:

$$q_u = \left\{c' + s_e \tan\phi' + (s - s_e) S_r^{\kappa} \tan\phi'\right\} N_c + 0.5\gamma B N_r \qquad (11)$$

In the above equation q_u is the ultimate bearing capacity, N_c and N_γ are the bearing capacity factors. c' is the effective cohesion, ϕ' is the effective frictional angle, γ is the unit weight of soil under the footing and B is the footing width. κ is a fitting parameter which increases with the plasticity index of the soil and assumed to be 1 here.

Also shown in Figure 3 is the bearing capacity under uniform suction obtained by a simplified equation derived as follows.

Based on the effective stress principle, Khalili and Khabbaz (1998) proposed an equation to estimate the shear strength of unsaturated soil:

$$\tau = c' + (\sigma + \chi s)\tan\phi' \qquad (12)$$

where τ is the shear strength of unsaturated soil. Equation (11) can be rewritten to be:

$$\tau = \left(c' + \chi s \tan\phi'\right) + \sigma \tan\phi' \tag{13}$$

This equation can be used in the traditional form of the bearing capacity equation, separating cohesion and suction components from the contribution of normal stress. By modifying the traditional Terzaghi's bearing capacity equation for strip footing, we have:

$$q_u = \left(c' + \chi s \tan\phi'\right) N_c + qN_q + 0.5\gamma BN_r \tag{14}$$

where N_q is the bearing capacity factor for overburden pressure, q.

For cohesionless soil without any overburden pressure, Equation (13) is simplified to:

$$q_u = \chi s \tan\phi' N_c + 0.5\gamma BN_r \tag{15}$$

Figure 3 compares the results of the finite element analysis with those obtained using Equation (15) and the one proposed by Vanapalli and Mohamed (2007). It shows that the bearing capacity increases with suction. The bearing capacity obtained by equation proposed by Vanapalli and Mohamed (2007) is larger than those predicted by the finite element analysis. However, reasonably good agreement is obtained between the results of the analysis and those obtained using equation (15). For saturated soil when suction is equal to 0, the numerical prediction is identical to the value calculated by the traditional bearing capacity equation. The rate of change in the bearing capacity reduces as the suction becomes larger than the air expulsion value. This is due mainly to the reduction in the magnitude of the effective stress parameter, χ.

In reality, suction in the soil varies with depth. In this paper, a simple assumption is made on linear variation of suction from water table to the soil surface. Five different depths of water table are considered from the top of the soil layer to a depth of 2B. For all cases, soil is assumed to be fully saturated below the water table with zero suction. Suction increases from zero at the water table with a rate of 20 kPa/m to its maximum value at the surface.

The bearing capacity of foundations predicted by the numerical analysis with different levels of water table is plotted in Figure 4. The effect of water table is often included in the traditional bearing capacity equations approximately by changing the effective unit weight of soil from submerged value to total value. Obviously this method cannot take into account the effect of suction developed in the unsaturated zone. The bearing capacity obtained by this method is also shown in Figure 4 for comparison. It can be seen that, in general, as the water table is lowered, a larger bearing capacity is expected. When the water table is on the soil surface, the soil is submerged and the bearing capacity predicted by the numerical analysis is the same as that obtained by the traditional method.

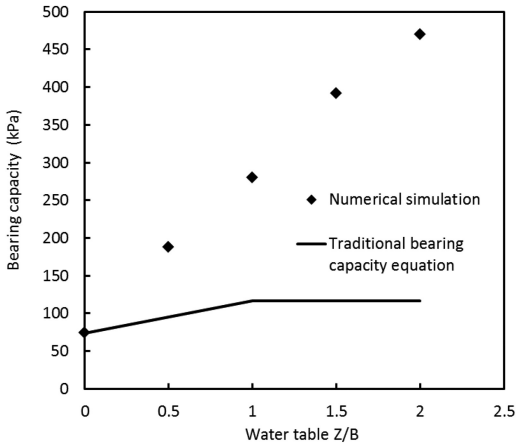


Figure 4. Effects of water table on bearing capacity of unsaturated soil.

However, The numerical analysis takes into account the effects of suction and shows a much larger change in the bearing capacity with lower water table. When the water table is lowered, a thicker layer of soil under the footing becomes unsaturated with larger suction at the surface, both increasing the bearing capacity of the footing.

4 CONCLUSION

A finite element model for fully coupled flow-deformation analysis of unsaturated soil was presented to estimate the bearing capacity of shallow foundation. The simple elastic-perfectly plastic Mohr-Coulomb criterion was used to describe failure. It was shown that the results predicted by this model are in a reasonable agreement with the experimental tests data on samples of unsaturated soil. The finite element model was applied to the bearing capacity problems for unsaturated soils. It was shown that suction has a profound effect on the bearing capacity. A simple equation was also derived, in the form of the traditional bearing capacity equation, to include the effect of uniform suction on the bearing capacity of strip footings. Good agreement was obtained between the numerical predictions and the bearing capacity obtained by this equation for a range of suctions. For a soil with linearly varying suction above water table, it was shown that a lower water table results in a larger bearing capacity and the capacity predicted by the numerical analysis is much larger than that predicted by the traditional method. Overall, this study provides a robust and useful tool that can be used to predict the bearing capacity of footings on unsaturated soil.

In this study, the Mohr-Coulomb failure criterion is used to simulate the mechanical response of unsaturated soils. A more complex constitutive model could have been used to better predict the response of unsaturated soil under loading. However, the Mohr-Coulomb model is often used to evaluate the bearing capacity of

foundations and to be able to compare the results with that of the traditional bearing capacity equations.

REFERENCES

Bishop, A.W. 1959. The principle of effective stress, *Teknisk Ukeblad* 106(39): 859–863.

Carter, J.P. & Balaam, N.P. 1995. AFENA users' manual. University of Sydney, Australia. Centre for Geotechnical Research.

Costa, Y.D. Cintra, J.C. & Zornberg, J.G. 2003. Influence of Matric Suction on the Results of Plate Load Tests Performed on a Lateritic Soil Deposit. *Geotechnical Testing Journal* 26(2): 219–226.

Cui, Y.J. & Delage, P. 1996. Yielding and plastic behaviour of an unsaturated compacted silt. *Geotechnique* 46: 291–311.

Gatmiri, B. & Delage, P. 1995. A new void ratio state surface formulation for the non-linear elastic constitutive modelling of unsaturated soil: Code U-Dam. *Proceedings, 1st International Conference on Unsaturated Soils*, Paris, France: 745–750.

Khabbaz, M.H. 1997. An effective stress based numerical model for flow and deformation in unsaturated soils. University of New South Wales, Sydney, Australia.

Khalili, N. Habte, M. & Zargargashi, S. 2008. A fully coupled flow deformation model for cyclic analysis of unsaturated soils including hydraulic and mechanical hysteresis. *Computers and Geotechnics* 35(6): 872–889.

Khalili, N. & Khabbaz, M.H. 1998. A unique relationship for the determination of the shear strength of unsaturated soils. *Geotechnique* 48(5): 681–687.

Khalili, N., Khabbaz, M.H.& Valliappan, S. 2000. An effective stress based numerical model for hydro-mechanical analysis in unsaturated porous media. *Computational Mechanics* 26: 174–184.

Khalili, N. & Zargarbashi, S. 2010. Influence of hydraulic hysteresis on effective stress in unsaturated soils. *Geotechnique* 60: 729–734.

Khoshghalb, A. & Khalili, N. 2013. A meshfree method for fully coupled analysis of flow and deformation in unsaturated porous media. Int J Numer Anal Methods Geomech 37(7): 716–743.

Li, X. Thomas, H.R. & Fan, Y. 1999. Finite element method and constitutive modelling and computation for unsaturated soils. *Computer methods in applied mechanics and engineering* 169: 135–159.

Lloret, A. & Alonso, E.E. 1980. Consolidation of unsaturated soils including swelling and collapse behavior. *Geotechnique* 30(4): 449–477.

Meyerhof, G.G. 1953. The bearing capacity of foundations under eccentric and inclined loads. *Proceedings, 3rd International Conference on Soil Mechanics and Foundation Engineering*, Zurich: 440–445.

Mohamed, F.M.O & Vanapalli, S.K. 2006. Laboratory Investigations for the Measurement of the Bearing Capacity of an Unsaturated Coarse-Grained Soil. *59th Canadian Geotechnical Conference*. BC, Vancouver.

Oh, W.T. & Vanapalli, S.K. 2008. Modelling the stress versus settlement behaviour of model footings in saturated and unsaturated sandy soils. *Proceedings, 12th International Conference of IACMAG*, Goa, India: 2126–2137.

Oh, W.T. & Vanapalli, S.K. 2011. Modeling the applied vertical stress and settlement relationship of shallow foundations in saturated and unsaturated sands. *Canadian Geotechnical Journal* 48: 425–438.

Russell, A.R. 2014. How water retention in fractal soils depends on particle and pore sizes, shapes, volumes and surface areas. *Geotechnique* 64(5): 379–390.

Russell, A.R. & Buzzi, O. 2012. A fractal basis for soil-water characteristics curves with hydraulic hysteresis. *Geotechnique* 62(3): 269–274.

Schrefler, B.A. & Xiaoyong Z. 1993. A fully coupled model for water flow and air flow in deformable porous media. *Water Resource Research* 29(1): 155–167.

Sheng, D., Sloan, S.W., Gens, A. & Smith, D.W. 2003. Finite element formulation and algorithms for unsaturated soils. Part I: theory. *Int J Numer Anal Methods Geomech* 27(9): 745–765.

Steensen-Bach, J.O. & Salinas, L.M. 1987. Capillary induced stresses – fact of fiction?. *Proc. 9th European conf. on Soil Mechanics and Foundation Engineering*, Budapest: 83–89.

Terzaghi, K. 1943. *Theoretical soil mechanics*. New York: John Wiley.

Vanapalli, S.K. & Mohamed, F.M.O. 2007. Bearing capacity of model footings in unsaturated soils. *Experimental Unsaturated Soil mechanics*, Springer, New York: 483–493.

Vesic, A.S. 1973. Analysis of ultimate loads of shallow foundations. *Journal of Soil Mechanics and Foundations Division* 99(1): 45–73.

Unsaturated Soil Mechanics—from Theory to Practice – Chen et al. (Eds)
© 2016 Taylor & Francis Group, London, ISBN 978-1-138-02921-7

Development of a fully coupled thermo-hydro-chemical simulator for gas hydrate extraction

W.T. Li, C.F. Wei & T.T. Ma
State Key Laboratory of Geomechanics and Geotechnical Engineering, Institute of Rock and Soil Mechanics, Chinese Academy of Sciences, Wuhan, China

ABSTRACT: A fully coupled thermo-hydraulic-chemical simulator PorousTH2C has been developed for the extraction of gas hydrate. Within this simulator, the phase change from hydrate to fluids, the flow of pore water and gas, and heat transfer can all be simultaneously solved. The numerical method is based on the finite element scheme with an adaptive relaxed Picard method. To verify the proposed simulator, the dissociation processes that occur in the heating and the depressurizing methods of gas hydrate production are analyzed. The numerical results are compared with the world's leading gas hydrate reservoir simulators: Tough+Hydrate, MH-21 and et al. An excellent agreement has proved that the simulator is both accurate and stable.

1 INTRODUCTION

The gas hydrates, which are made of water and natural gas and exist in giant quantity, are being considered as a potential source for natural gas production (Sloan Jr and Koh, 2007). However, the severe environmental conditions of gas hydrate reservoirs and the solid form of hydrates require extensive technological development and expertise before the commercial gas production becomes possible (Moridis et al., 2011). The technologies for recovering natural gas from hydrates are greatly challenging, which are still under development.

Numerical studies often give helpful information for predicting the potential and economic viability of a recovery process (Moridis, 2003, Narita, 2003). Simulation of gas hydrate reservoir production involves solution of a complex combination of highly coupled fluid, heat, and mass transport equations combined with the potential for formation and/or disappearance of multiple solid phases in the system. What's more, the physical and chemical properties of the multiphasic porous media are highly dependent on the amount of gas hydrate present in the system at any given time.

This paper presents a fully coupled finite element simulator named PorousTH2C for gas production from hydrate reservoirs. Firstly, the basic formulations based on the theory of porous media are derived, including intrinsic kinetics of hydrate decomposition, gas-water two-phase flow and conductive and convective heat transfer. Then, the nonlinear transient finite element formulation is developed for the fully coupled model. In order to effectively deal with the high nonlinearity, an adaptive relaxed Picard method (Li and Wei, 2015) is introduced.

The proposed simulator PorousTH2C is verified by solving the hydrate dissociation problems designed by the international code comparison project (Wilder et al., 2008). An excellent agreement with previously published results is obtained, implying that the simulator is accurate and stable.

2 FORMULATIONS

Based on the theory of porous media (Coussy, 2004, Lewis and Schrefler, 1998), formulations for coupled gas hydrate dissociation, two-phase fluid flow and heat transport are derived as follows.

2.1 *Gas hydrate dissociation*

The conservation equation of hydrate is given as

$$\frac{\partial\left(n\rho_h S_h\right)}{\partial t}-\dot{m}_h=0 \tag{1}$$

where n is the porosity of the hydrate bearing medium, ρ the density, S the saturation, which is defined as the fraction of the total pore volume, and $\dot{m}$ is the mass rate generated by hydrate dissociated per unit volume. Here the subscript "h" refers to the hydrate phase, so as "g" and "w" refer to the gas phase and the water phase respectively in the following.

The intrinsic rate of hydrate decomposition is computed by the Kim-Bishnoi model (Kim et al., 1987). Rates of gas and water production and rate of hydrate decomposition are then given by

$$\dot{m}_h=-K_d M_h A_{hs} n S_h\langle P_{eq}-P_g\rangle \tag{2}$$

$$\dot{m}_w=-\left(M_w/M_h\right)N_h\dot{m}_h \tag{3}$$

$$\dot{m}_g=-\left(M_g/M_h\right)\dot{m}_h \tag{4}$$

where K_d is the dissociation constant, N_h the hydrate number, M_h, M_w and M_g the molecular weight of hydrate, gas and water, respectively, P_g the gas pressure. $\langle\ \rangle$ are Macaulay brackets describing the ramp function. P_{eq} is the phase-equilibrium pressure depending on the temperature T, which is described by Moridis's model (Moridis, 2003) here.

2.2 *Two phase flow*

Considering temperature and pressures of fluids as the primary variables, the mass balance equations for gas and water flow through the porous media are

$$\left(\frac{nS_w}{K_w}-n\frac{\partial S_w}{\partial P_c}\right)\frac{\partial P_w}{\partial t}+n\frac{\partial S_w}{\partial P_c}\frac{\partial P_g}{\partial t}-nS_w\beta_w\frac{\partial T}{\partial t}$$
$$-\nabla\cdot\boldsymbol{w}_w=\frac{1}{\rho_w}\dot{m}_w-\frac{1}{\rho_h}\frac{\partial S_w}{\partial S_h}\dot{m}_h \tag{5}$$

$$n\frac{\partial S_w}{\partial P_c}\frac{\partial P_w}{\partial t}+\left(\frac{nS_g}{K_g}-n\frac{\partial S_w}{\partial P_c}\right)\frac{\partial P_g}{\partial t}-nS_g\beta_g\frac{\partial T}{\partial t}$$
$$-\nabla\cdot\boldsymbol{w}_g=\frac{1}{\rho_g}\dot{m}_g+\frac{1}{\rho_h}\dot{m}_h+\frac{1}{\rho_h}\frac{\partial S_w}{\partial S_h}\dot{m}_h \tag{6}$$

where K is the bulk modulus, and β is the thermal expanding coefficient. P_c represents the capillary pressure, defined as the pressure difference of the gas phase and the water phase.

According to generalized Darcy's law, Darcy velocities of the pore fluids can be written as

$$\boldsymbol{w}_f=\boldsymbol{k}k_f/\mu_f\left(\nabla P_f-\rho_f\boldsymbol{g}\right),\quad f=w,g \tag{7}$$

where μ is the dynamic viscosity, $\boldsymbol{g}$ the body force vector; $\boldsymbol{k}$ and k are the intrinsic and relative permeability, respectively.

2.3 *Heat transfer*

Hydrate dissociation is an endothermic process and the dissociation rate depends strongly upon the temperature. From the energy and the entropy conservation equations, the formulation of heat transfer can be expressed as

$$\varsigma\frac{\partial T}{\partial t}-nS_w\beta_wT\frac{\partial P_w}{\partial t}-nS_g\beta_gT\frac{\partial P_g}{\partial t}$$
$$+\left(\rho_wC_w\boldsymbol{w}_w+\rho_gC_g\boldsymbol{w}_g\right)\cdot\nabla T-\nabla\cdot\left(\chi\nabla T\right)=\frac{\Delta H}{M_h}\dot{m}_h \tag{9}$$

where $\varsigma=(1-n)\rho_sC_s+n(S_w\rho_wC_w+S_g\rho_gC_g+S_h\rho_hC_h)$; C is the heat capacity; ΔH is the enthalpy change in hydrate dissociation.

3 NONLINEAR TRANSIENT FINITE ELEMENT FORMULATION

3.1 *Spatial domain discretization*

Galerkin's method is employed to develop the finite element formulation of the model presented above. Consider a space domain Ω of porous media, with a boundary Γ. Let N_T be the shape function matrix for temperature and N_p for pore water pressure and pore gas pressure. After discretizing the weak form of the non-linear partial differential equations (5), (6) and (9) in the spatial domain, one obtains the following set of fully coupled algebraic equations

$$C\dot{X}+KX=F \tag{10}$$

where

$$C=\begin{bmatrix}P_{TT}&C_{Tw}&C_{Tg}\\C_{wT}&P_{ww}&C_{wg}\\C_{gT}&C_{gw}&P_{gg}\end{bmatrix},\quad K=\begin{bmatrix}H_{TT}&K_{Tw}&K_{Tg}\\0&H_{ww}&0\\0&0&H_{gg}\end{bmatrix},$$
$$F=\begin{Bmatrix}f_T\\f_w\\f_g\end{Bmatrix},\quad X=\begin{Bmatrix}T\\P_w\\P_g\end{Bmatrix},$$

in which the coefficient matrices are

$$P_{TT}=\int_\Omega N_T^T\left(\varsigma/T\right)N_Td\Omega$$
$$C_{Tw}=\int_\Omega N_T^TnS_w\beta_wN_pd\Omega$$
$$C_{Tg}=\int_\Omega N_T^TnS_g\beta_gN_pd\Omega$$
$$K_{Tw}=\int_\Omega\left(\nabla N_T\right)^T\rho_wC_w\boldsymbol{w}_wN_pd\Omega$$
$$K_{Tg}=\int_\Omega\left(\nabla N_T\right)^T\rho_gC_g\boldsymbol{w}_gN_pd\Omega$$
$$H_{TT}=\int_\Omega\left(\nabla N_T\right)^T\left(\chi/T\right)\nabla N_Td\Omega$$
$$f_T=\int_\Omega N_T^T\left(\Delta H/TM_h\right)\dot{m}_hd\Omega-\int_{\Gamma_T}N_T^T\left(\hat{q}_T/T\right)d\Gamma$$
$$C_{wT}=\int_\Omega N_p^TnS_w\beta_wN_Td\Omega$$
$$P_{ww}=\int_\Omega N_p^T\left(\frac{nS_w}{K_w}-n\frac{\partial S_w}{\partial P_c}\right)N_pd\Omega$$
$$C_{wg}=\int_\Omega N_p^Tn\frac{\partial S_w}{\partial P_c}N_pd\Omega$$
$$H_{ww}=\int_\Omega\left(\nabla N_p\right)^T\left(\boldsymbol{k}k_{rw}/\mu_w\right)\nabla N_pd\Omega$$
$$f_w=\int_\Omega\left(\nabla N_p\right)^T\left(\boldsymbol{k}k_{rw}/\mu_w\right)\rho_w\boldsymbol{g}d\Omega-\int_{\Gamma_{qw}}N_p^T\hat{q}_wd\Gamma$$
$$+\int_\Omega N_p^T\left(\frac{1}{\rho_w}\dot{m}_w-\frac{1}{\rho_h}\frac{\partial S_w}{\partial S_h}\dot{m}_h\right)d\Omega$$
$$C_{gw}=\int_\Omega N_p^Tn\frac{\partial S_w}{\partial P_c}N_pd\Omega$$
$$C_{gT}=\int_\Omega N_p^TnS_g\beta_gN_Td\Omega$$
$$P_{gg}=\int_\Omega N_p^T\left[\frac{n\left(1-S_w\right)}{K_g}-n\frac{\partial S_w}{\partial P_c}\right]N_pd\Omega$$
$$H_{gg}=\int_\Omega\left(\nabla N_p\right)^T\left(\boldsymbol{k}k_{rg}/\mu_g\right)\nabla N_pd\Omega$$
$$f_g=\int_\Omega\left(\nabla N_p\right)^T\left(\boldsymbol{k}k_{rg}/\mu_g\right)\rho_g\boldsymbol{g}d\Omega-\int_{\Gamma_{qg}}N_p^T\hat{q}_gd\Gamma$$
$$+\int_\Omega N_p^T\left[\frac{1}{\rho_g}\dot{m}_g+\frac{1}{\rho_h}\left(1+\frac{\partial S_w}{\partial S_h}\right)\dot{m}_h\right]d\Omega$$

Table 1. The basic material data for the simulations.

Parameter	Value
Porosity	0.3
Grain density	2600 kg/m^3
Water density	1000 kg/m^3
Gas density	$P_g M_g/(zRT)$, $z = 0.88$
Intrinsic permeability	3.0×10^{-13} m^2
Viscosity of water	$0.6612(T-229)^{-1.562}$
Viscosity of gas	$\mu_g = \mu_0(T_0+c)/(T+c)(T/T_0)^{1.5}$ $c = 198$ K, $T_0 = 288.15$ K, $\mu_0 = 1.59 \times 10^{-5}$ Pa · s
Water bulk modulus	2.0×10^{-9} m^2
Gas bulk modulus	$1/P_g$
Dissociation constant	$K_d = K_{d0} e^{-\Delta E/(RT)}$ $K_{d0} = 1.24 \times 10^5$ mol/(m^2 · Pa · s), $\Delta E = 7.8155 \times 10^4$ J/mol $R = 8.3144$ J/(mol · K)
Grain specific heat	1000 J/kg/K
Water specific heat	$4023.976 + 0.57736T$
Gas specific heat	$1238.79 + 3.1303T$
Hydrate specific heat	2080 J/kg/K
Thermal conductivity	$\chi = (\sqrt{S_h} + \sqrt{S_w})(\chi_{wet} - \chi_{dry}) + \chi_{dry}$ $\chi_{dry} = 2$ W/m/K, $\chi_{wet} = 2.18$ W/m/K
Enthalpy change	$\Delta H = a \cdot T + b$ $a = -16.744$ J/(mol · K), $b = 56599$ J/mol
Soil expansion	9×10^{-7}
Water expansion	6.3×10^{-6}
Gas expansion	$1/T$
Hydrate expansion	4.6×10^{-4}

3.2 *Time domain discretization*

The time discretization of Eq. (10) can be obtained by means of a finite difference scheme. Let

$$\dot{X} = \left(X^{i+1} - X^i\right)/\Delta t\,, \quad X = \theta X^{i+1} + (1-\theta) X^i \qquad (11)$$

It follows from Eq. (10) that

$$\left(C + \theta \Delta t K\right) X^{i+1} = \left[C - (1-\theta)\Delta t K\right] X^i + \Delta t F^{i+\theta} \quad (12)$$

where i is the time-step number, Δt the time-step size, θ an integral constant. As a general rule, central difference ($\theta = 0.5$) is more accurate than backward difference method ($\theta = 1$), but the latter shows better performance in terms of oscillation suppression. Here, backward difference method is adopted.

3.3 *Iterative scheme*

After finite element discretization, a set of nonlinear algebraic equations have to be solved at each time step. An adaptive relaxed Picard iteration method (Li and Wei, 2015) is introduced as following.

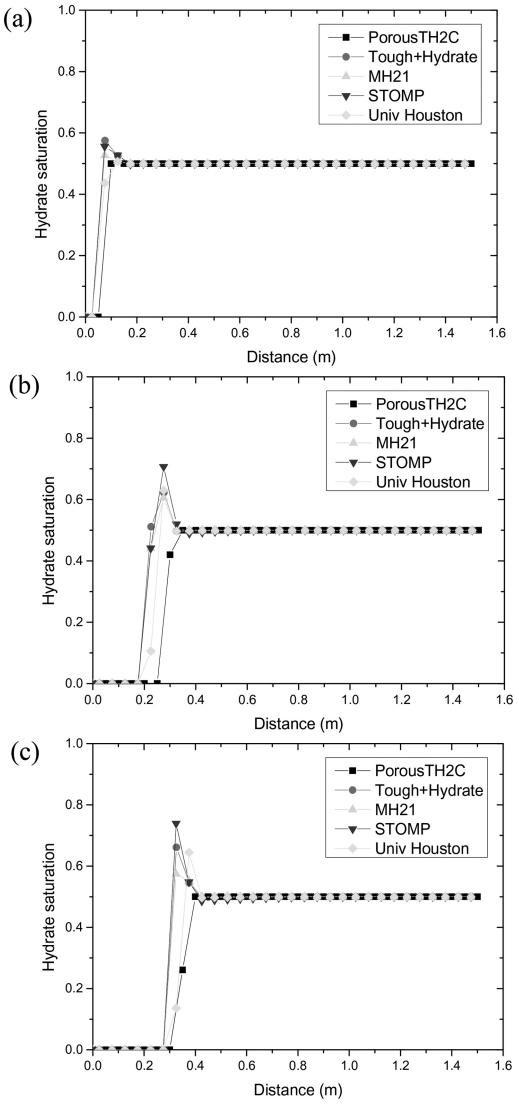


Figure 1. Distributions of hydrate saturation in the test case 1 at (a) 1 h, (b) 12 h and (c) 1 d.

At each time step, coefficient matrices C, K and F are nonlinear functions of X. Applying a Picard linearization scheme, one has

$$\left(C^{k,i+1} + \Delta t K^{k,i+1}\right) X^{k+1,i+1} = C^{k,i+1} X^i + \Delta t F^{k,i+1} \qquad (13)$$

superscript k represents the iterative step number.

In order to reduce oscillation and accelerate convergence, the adaptive relaxed method is adopted from the second iteration at each time step:

$$X^{k+1,i+1} \leftarrow X^{k,i+1} + \lambda^{k,i+1} \cdot \mathrm{d}X^{k,i+1}; \quad \lambda^{k,i+1} \in (0,1] \qquad (14)$$

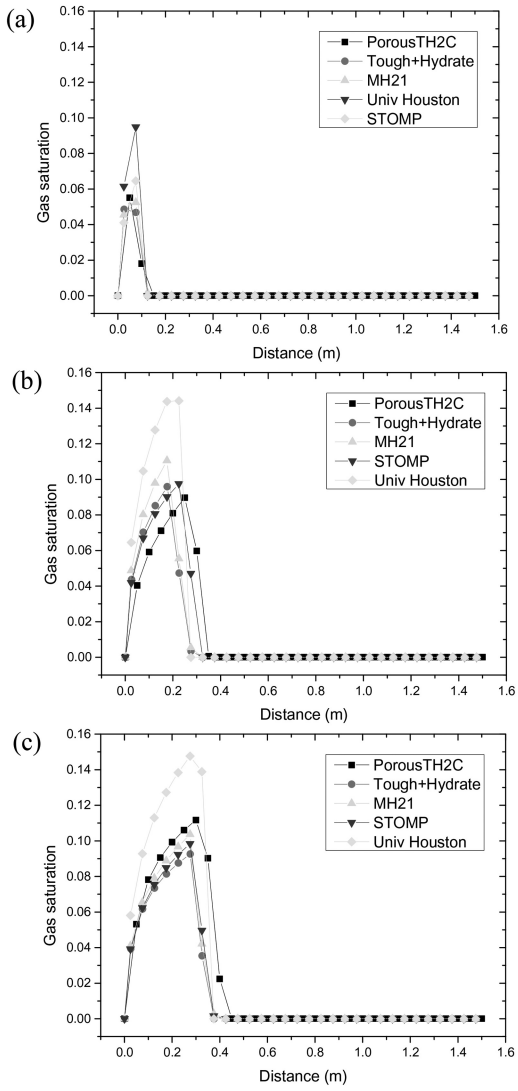


Figure 2. Distributions of gas saturation in the test case 1 at (a) 1 h, (b) 12 h and (c) 1 d.

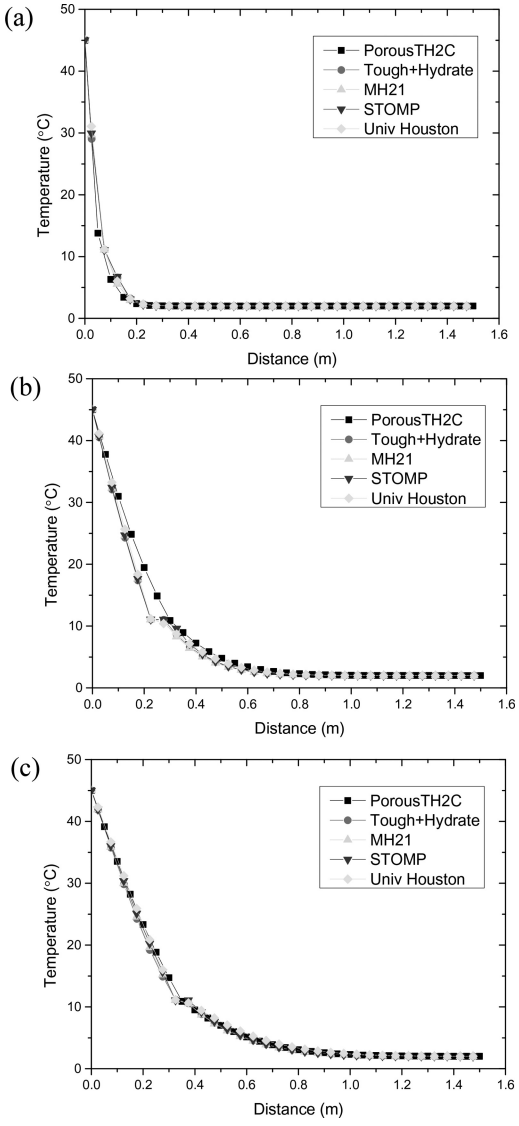


Figure 3. Distributions of temperature in the test case 1 at (a) 1 h, (b) 12 h and (c) 1 d.

where $\mathrm{d}X^{k,i+1}$ is the increment for iteration k and $\mathrm{d}X^{k,i+1} = X^{k+1,i+1} - X^{k,i+1}$; λ is the relaxation factor, the value of which is determined by the method proposed in the reference (Li and Wei, 2015).

With $X^{k,i+1}$, the material properties (e.g. saturation of each phase, bulk modulus, relative permeability coefficients and so on) are updated to execute the next iteration, until the relative error satisfies the given tolerance.

4 BENCHMARK AND TEST RESULTS

The formulations and the iterative algorithm described above have been implemented into a finite element program, called PorousTH2C. In the light of an international effort to compare different hydrate reservoir simulators (Wilder et al., 2008), two separate cases in Problem 3 designed by this effort were simulated and compared to verify the proposed simulator PorousTH2C: (1) dissociation due to thermal stimulation, (2) dissociation due to depressurization to a pressure above the quadruple point (ensuring that no ice forms in the reservoir).

4.1 *Problem description*

The domain modeled is a one-dimensional Cartesian system with $L = 1.5$ m and a discretization of 30

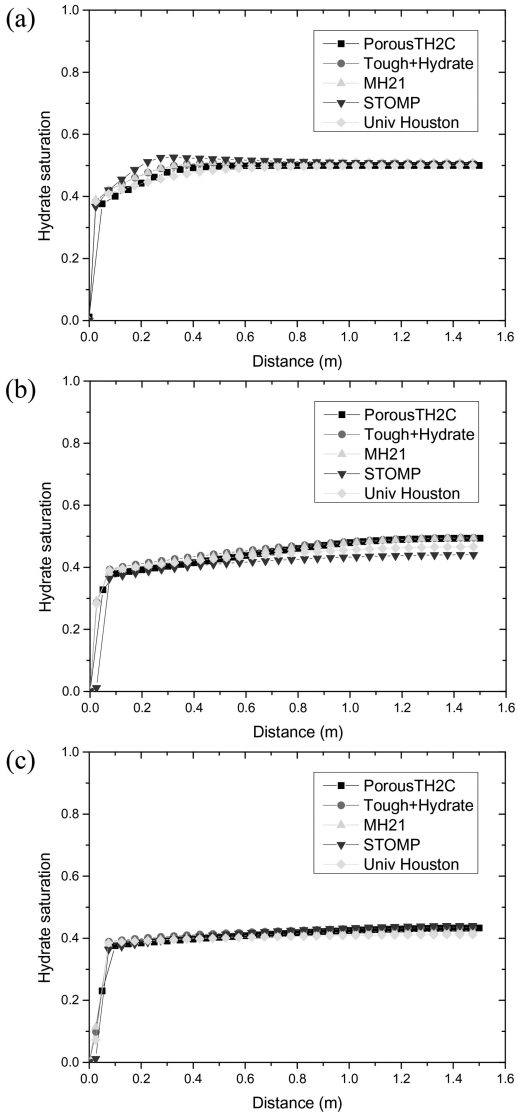


Figure 4. Distributions of hydrate saturation in the test case 2 at (a) 2 min, (b) 20 min, and (c) 1 h.

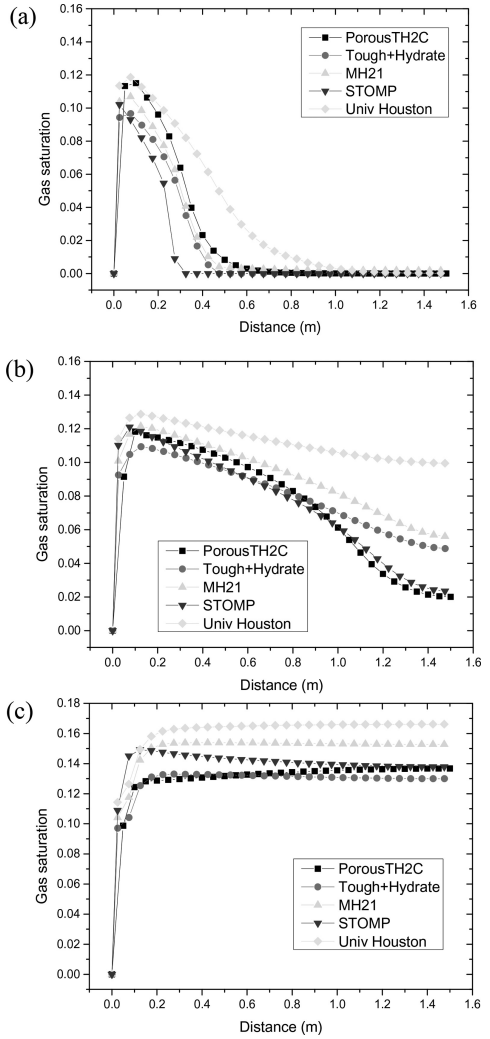


Figure 5. Distributions of gas saturation in the test case 2 at (a) 2 min, (b) 20 min, and (c) 1 h.

uniformly-sized gridblocks. The initial pressure of the domain was 8 MPa and the initial temperature was 2°C for the thermal stimulation case 1 and 6°C for the depressurization cases 2. The initial saturations for both cases were $S_h = 0.5$, $S_w = 0.5$, $S_g = 0.0$.

The specific flow, heat, and dissociation parameters involved in the simulations are summarized in Table 1. More details about the input values can be found in the original paper (Wilder et al., 2008).

4.2 *Boundary conditions*

The boundary conditions were specified for two different cases, each leading to different hydrate dissociation scenarios.

For both cases:
At $x = X_{max}$, no mass or heat flow; At $x = 0$, $S_w = 1.0$.
Case 1: Thermal stimulation
Constant $T = 45$°C; Constant $P_w = P_g = P_i = 8$ MPa.
Case 2: Depressurization
Constant $T_0 = T_i = 6$°C; Constant $P_w = P_g = 2.8$ MPa.

4.3 *Simulation results*

Figures 1–3 show the distributions of hydrate saturation, gas saturation and temperature at different times and also the comparisons of the proposed simulator to the other four leading simulators for the problem of thermal injection (Case 1). Similarly, Figures 4–6 show the distributions and the comparisons for the case of depressurization (Case 2). Four other simulators are Tough+Hydrate (Moridis, 2003), MH-21 HYDRES (Narita, 2003), STOMP-HYD (White et al., 2011) and one developed by University of Houston (Sun and

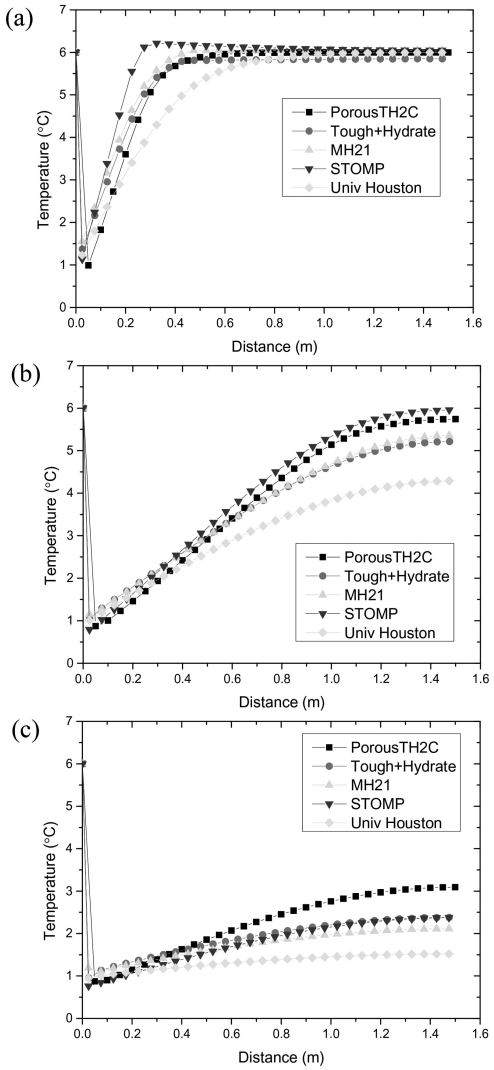


Figure 6. Distributions of temperature in the test case 2 at (a) 2 min, (b) 20 min, and (c) 1 h.

Mohanty, 2006). Their simulated results for the test problems can be found online[1].

For the case of thermal injection, Fig. 1–3 show that with the development of heat transfer, the temperature of the reservoir increases gradually, leading to the dissociation of the gas hydrate and the production of gas and water. Accompanied by the decrease of the hydrate saturation, the gas saturation slowly goes up.

All three figures show a good agreement between the results calculated by PorousTH2C and those obtained by other simulators. What's more, note that the unphysical abrupt rise of hydrate saturation at the dissociation front, which appears in the results of other simulators, does not show up in our simulation (Fig. 1). This reveals that PorousTH2C performs better in terms of numerical stability.

Figures 4–6 show a similar dissociation process in case 2 to Fig. 1–3, while the cause of gas hydrate dissociation is depressurization. The figures also show an excellent agreement between results calculated by PorousTH2C and those obtained by other simulators. As noted before, hydrate dissociation is an endothermic process, which results in absorption of heat. Fig. 6 shows that as the hydrate dissociates, heat is absorbed from the surrounding, which results in the decrease of the local temperature in the reservoir.

As can be seen from all the comparisons above, an excellent agreement exists between the proposed and the other simulators. This suggests that the simulator PorousTH2C is both accurate and stable in the entire process of modeling gas hydrate extraction.

5 CONCLUSION

A new hydrate simulator PorousTH2C is developed based on the fully coupled thermo-hydro-chemical model, by use of the Galerkin finite element method and the adaptive relaxed Picard iteration method. Within this simulator, the interacting phenomena of gas-water two-phase flow, heat transfer and gas hydrate dissociation during thermal stimulation and depressurization can all be simultaneously solved.

To verify the proposed simulator, dissociation process that occurs in the heating and depressurizing methods of gas hydrate production are analyzed in this study. The numerical results are compared with those obtained by the world's leading gas hydrate reservoir simulators: Tough+Hydrate, MH-21 and et al. An excellent agreement has proved that the simulator is both accurate and stable.

ACKNOWLEDGMENTS

The research was supported by the Natural Science Foundation of China (Grant no. 11372078) and the Guangxi Natural Science Foundation through grants 2012GXNSFGA060001, and the Major Projects of Guangxi Natural Science Foundation through grants 2012GXNSFEA053002.

REFERENCES

Coussy, O. 2004. *Poromechanics*, Wiley. com.

Kim, H. C., Bishnoi, P. R., Heidemann, R. A. & Rizvi, S. S. H. 1987. Kinetics of Methane Hydrate Decomposition. *Chemical Engineering Science,* 42, 1645–1653.

Lewis, R. W. & Schrefler, B. A. 1998. *The finite element method in the static and dynamic deformation and consolidation of porous media*, John Wiley.

Li, W. T. & Wei, C. F. 2015. An efficient finite element procedure for analyzing three-phase porous media based on the relaxed Picard method. *International Journal for Numerical Methods in Engineering,* 101, 825–846.

Moridis, G. J. 2003. Numerical studies of gas production from methane hydrates. *Spe Journal,* 8, 359–370.

[1] http://www.netl.doe.gov/research/oil-and-gas/methane-hydrates/mh-codecompare

Moridis, G. J., Collett, T. S., Pooladi-Darvish, M., Hancock, S., Santamarina, C., Boswell, R., Kneafsey, T., Rutqvist, J., Kowalsky, M. B., Reagan, M. T., Sloan, E. D., Sum, A. K. & Koh, C. A. 2011. Challenges, Uncertainties, and Issues Facing Gas Production From Gas-Hydrate Deposits. *Spe Reservoir Evaluation & Engineering,* 14, 76–112.

Narita, H. 2003. Introduction of MH21 (Research Consortium for methane hydrate resources in Japan) and current topics in production method & modeling of methane hydrate (invited paper). *Proceedings of the Fifth Isope Ocean Mining Symposium*, 7–11.

Sloan Jr, E. D. & Koh, C. 2007. *Clathrate hydrates of natural gases*, CRC press.

Sun, X. F. & Mohanty, K. K. 2006. Kinetic simulation of methane hydrate formation and dissociation in porous media. *Chemical Engineering Science,* 61, 3476–3495.

White, M. D., Wurstner, S. K. & McGrail, B. P. 2011. Numerical studies of methane production from Class 1 gas hydrate accumulations enhanced with carbon dioxide injection. *Marine and Petroleum Geology,* 28, 546–560.

This page intentionally left blank

Unsaturated Soil Mechanics—from Theory to Practice – Chen et al. (Eds)
© 2016 Taylor & Francis Group, London, ISBN 978-1-138-02921-7

Three-dimensional DEM simulation of constant-water-content triaxial tests on the unsaturated remolded loess

T. Li & M.J. Jiang
State Key Laboratory of Disaster Reduction in Civil Engineering, Tongji University, Shanghai, China
Department of Geotechnical Engineering, Tongji University, Shanghai, China
Key Laboratory of Geotechnical and Underground Engineering of Ministry of Education, Tongji University, Shanghai, China

ABSTRACT: To investigate the micro-mechanical performances of the unsaturated remolded loess, the Discrete Element Method (DEM) is applied to simulate the constant-water-content triaxial tests. In the simulation, a reasonable van der Waals' force and the inter-particle frictional coefficient were considered. An adhesive force is applied to the contacts in the DEM assembly to represent the capillary force which was related to matric suction. The matric suction was related to the effective degree of saturation by a representative soil-water characteristic curve. Based on the above relations, constant-water-content triaxial tests on unsaturated remolded loess were carried out and the macro- and micro-mechanical performances were analyzed. Microscopically, the average coordination numbers for samples with low water contents are nearly the same at the critical state which demonstrates that there is a lower limit of the average coordination number at the critical state. The deviator fabric at the critical state decreases with the decrease in water content.

1 INTRODUCTION

Silt-sized aeolian loess is widely located at the northwest China. Most of the loess soils are naturally unsaturated. Water from rain and irrigation is a considerable cause of the engineering problems such as slope and embankment instability and large settlement of foundations. Hence, many in-situ and laboratory tests on unsaturated loess have been carried out to study the shear strength (Cui and Delage, 1996, Chen et al., 1999) and soil-water characteristic curve (MuñOz-Castelblanco et al., 2012, Wang et al., 2008, Zhao, 2010).

These tests can demonstrate the macro-mechanical performances of unsaturated loess rather than the micro-mechanical characteristics which are considered to be essential to the macroscopic behaviors. For example, the volumetric behavior is related to the average coordination number and the mechanical anisotropy comes from the microscopic fabric anisotropy.

It is more and more accepted that the Discrete Element Method (DEM), which was originally proposed for dry sands by Cundall and Strack (1979), is an efficient tool to investigate the micro-mechanical behaviors of soils and to bridge the micro- and macro-mechanical behaviors (Jiang et al., 2011, 2014).

Many papers have been reported to simulate the unsaturated soils using the DEM. A theoretical work (Fisher, 1926) is commonly adopted to compute the capillary force. However, some simulations (Scholtès et al., 2009) using this method are limited to the pendular regime which denotes a situation that the degree of saturation is roughly smaller than 20%. To simulate the unsaturated soil in a large extent of degree of saturation, Jiang et al. (2004) proposed a method to consider the disappearance of menisci and air bubbles. Unfortunately, this method can only simulate the suction stress and capillary force qualitatively because Fisher's theory is ideal and the particle shape is simplified to sphere in three-dimensional. In the light of the above limits using Fisher's theory, some researchers (Liu and Sun, 2002) used inter-particle adhesive forces directly to represent the capillary force.

In the present study, to investigate the relationship between inter-particle capillary forces and the effective degree of saturation, the capillary forces were calculated by particle radii and the matric suction firstly, and then a representative soil-water characteristic curve (SWCC) was applied to relate the suction to the effective degree of saturation. Besides, a reasonable van der Waals' force was taken into account to sustain the open structure of the numerical loess sample. The influence of the effective degree of saturation on the inter-particle frictional coefficient was also considered. After parameter calibration, the constant-water-content triaxial tests on unsaturated remolded loess were simulated and the micro-mechanical performances such as the average coordination number and the contact normal fabric were analyzed.

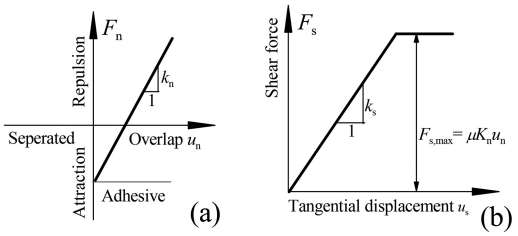


Figure 1. Mechanical performances in normal and tangential directions of a simple contact model with adhesive force.

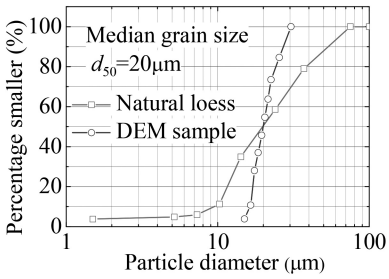


Figure 2. Particle distribution curves of the DEM sample and the loess from Jingyang, Shaanxi, China.

2 CONTACT MODEL AND SPECIMEN

2.1 *Adhesive force model*

A simple contact model with adhesive force between contacted spheres is employed, in which a linear elastic force-displacement law is adopted for both normal and tangential mechanical performances. When a pair of particles separate, the adhesive force is considered to be zero.

Figure 1 (a) presents the normal mechanical response expressed as

$$F_n = \begin{cases} k_n u_n - F_{ad} & u_n \geq 0 \\ 0 & u_n < 0 \end{cases} \tag{1}$$

where k_n is the normal contact stiffness and u_n is the overlap of a particle pair with a negative value denoting separation. Figure 1 (b) presents the perfectly tangential mechanical response. The tangential force F_s is incrementally calculated according to the incremental tangential displacement Δu_s as

$$F_s \leftarrow F_s - k_s \Delta u_s \tag{2}$$

where k_s is the tangential contact stiffness. The Mohr-Coulomb sliding criterion is adopted as

$$|F_s| \leq \mu k_n u_n = \mu(F_n + F_{ad}) \tag{3}$$

Tangential sliding would occur when the tangential force reaches the threshold controlled by the sliding criterion.

2.2 *Specimen preparation*

Spheres are used to represent the loess skeleton grains. As shown in Figure 2, compared to the natural loess at Jingyang, a narrower particle size extent is adopted to make homogenous numerical sample using small particle number to improve computing efficiency. The median grain size of the DEM assembly is 20 μm, which is the same to the natural loess at Jingyang which is near to Xi'an city.

A cubic sample composed of 40005 particles was prepared of the target void ratio of 0.84 in four layers using the Multi-layer Under-compaction Method (UCM) (Jiang et al., 2003). Then, a weak adhesive force with a magnitude of 1.6×10^{-6} N was applied to all the contacts to sustain the open structure of loess. The weak adhesive force is mainly van der Waals force for silt soils which is assumed to be recovered when two spheres come into contact. Finally, a vertical pressure of 12.5 kPa was applied to the top and bottom walls and the side walls were confined to reproduce the in-situ stress state. In the above preliminary compaction, the inter-particle frictional coefficient is taken as 0.7. After the preliminary compaction, the void ratio of the sample is 0.806.

The magnitude of the van der Waals force is estimated by the method presented by Jiang et al. (2013) which can calculate the van der Waals force between two contiguous particles with the same radius, as

$$F_{van} = \frac{H_a \beta^2 R^2}{24 h^3} \tag{4}$$

where H_a is the Hamaker coefficient which is taken as 6.5×10^{-20} J, R is the radius of the particle pair and is taken as half of the median grain size d_{50}, β is the shape parameter of the contact with a reasonable range of 0–1 and is taken as 0.4, and D is the micro-separation of the two spheres and is taken as 3×10^{-9} m.

3 PARAMETER CALIBRATION

The normal stiffness between both ball-ball and ball-wall contacts is 9.0×10^3 N/m and the ratio of tangential stiffness to the normal stiffness is 2/3. The frictional coefficient and capillary force between ball-wall contacts is zero. A smaller sample with 10000 particles was used to calibrate contact parameters.

3.1 *Calibration of the frictional coefficient*

The relationship between the inter-particle frictional coefficient and the effective degree of saturation can be derived from laboratory tests and the DEM simulation.

After investigation on several reported tests, Equation 5 is suggested by the authors to fit the relationship between the internal frictional angel and the effective degree of saturation.

$$\varphi = a_\mu \sqrt{S_e} + b_\mu \tag{5}$$

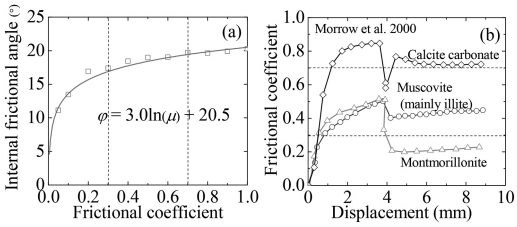


Figure 3. Calibration of the inter-particle frictional coefficient: (a) the relationship between the internal frictional angle and the frictional coefficient in the DEM simulation, (b) frictional coefficients for different dry and wet minerals.

where φ is the internal frictional angle defined in classical soil mechanics, S_e is the effective degree of saturation which is defined in Equation 6 (Barbour, 1998, Brooks and Corey, 1964) and a_μ, b_μ are two fitting parameters.

$$S_e = \frac{S_r - S_r^{res}}{S_r^0 - S_r^{res}} \tag{6}$$

where S_r is the degree of saturation, S_r^{res} is the residual degree of saturation and S_r^0 usually equals 1. For loess investigated in this paper, the residual degree of saturation is about 5%.

In the DEM simulation, the internal frictional angel increases with the inter-particle frictional coefficient, as shown in Figure 3 (a). Equation 7 can be used to fit the data.

$$\varphi = c_\mu \ln \mu + d_\mu \tag{7}$$

where μ is the inter-particle frictional coefficient and $c_\mu = 3.0$, $d_\mu = 20.5$ are two fitting parameters.

Hence, the relationship between the inter-particle frictional coefficient and the effective degree of saturation can be derived from Equations 5 and 7 as follows

$$\mu = \exp\left(\frac{a_\mu}{c_\mu}\sqrt{S_e} + \frac{b_\mu - d_\mu}{c_\mu}\right) = \exp\left(A_\mu\sqrt{S_e} + B_\mu\right) \tag{8}$$

There are two parameters A_μ and B_μ to determine. A reasonable extent of the internal frictional angle was obtained by a sliding experiments on different minerals (Morrow et al., 2000), see Figure 3 (b). The peak values are the frictional coefficients of dry minerals and the residual values are that of wet minerals. In general, the materials bond and coat the skeleton particles in natural loess are mainly clay minerals (mainly illite and montorillonite) and crystalline carbonate (Gao, 1996). The crystalline carbonate leached out when the loess is wetted. Thus, it is assumed that the inter-particle frictional coefficient for dry loess ($S_e = 0$) is 0.7, which is the average value of that of clay minerals and calcium carbonate, and the inter-particle frictional coefficient for wet loess ($S_e = 1$) is 0.3, which is the average value of that of illite and montmorillonite. Using this extent of the inter-particle frictional coefficient, the parameters can be obtained, $A_\mu = -0.84$ and $B_\mu = -0.37$.

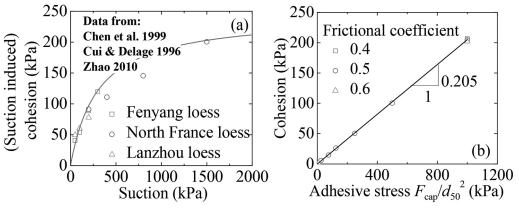


Figure 4. Calibration of the capillary force: (a) relationship between the cohesion and the suction in laboratory tests, (b) relationship between the cohesion and the adhesive force in the DEM simulation.

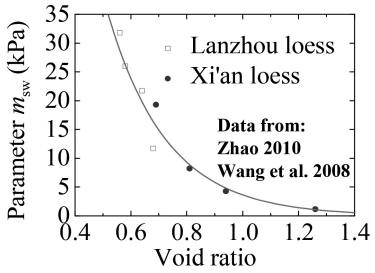


Figure 5. Relationship between the parameter m_{sw} in Equation 13 and the void ratio.

3.2 *Calibration of the capillary force*

The matric suction enhances the shear strength on unsaturated soil. Following Fredlund et al. (1978), the shear strength can be separated into three parts, i.e. effective cohesion for saturated states c', shear strength due to net normal stress τ_{nf} and the suction induced cohesion c_s.

$$\tau_f = c' + \tau_{nf} + c_s \tag{9}$$

Many equations have been proposed to describe the suction induced cohesion (Jiang et al., 2004, Vanapalli et al., 1996). Figure 4 (a) presents the relationships between the suction induced cohesion and the matric suction for Fenyang loess (Chen et al., 1999), north France loess (Cui and Delage, 1996) and Lanzhou loess (Zhao, 2010). The following equation is suggested by the authors to fit the relationship of the three kinds of loess.

$$c_s = \frac{s}{\left(1 + (s/m)^n\right)^{1-1/n}} \tag{10}$$

where s is the matric suction and $m = 52$ kPa and $n = 1.6$ are fitting parameters.

In the DEM simulation, the suction induced cohesion increases linearly (see Figure 5 (b)) with the inter-particle capillary force, as

$$c_s = \xi F_{cap} / d_{50}^2 \tag{11}$$

where F_{cap} is the capillary force, d_{50} is the median grain size and $\xi = 0.205$ is the fitting parameter.

Hence, the capillary force can be determined using Equations 10 and 11, as follows

$$F_{cap} = \frac{d_{50}^2 s}{\xi\left(1+(s/m)^n\right)^{1-1/n}} \tag{12}$$

3.3 *Soil-water characteristic curve (SWCC)*

A general soil-water characteristic curve which takes the void ratio into account was obtained based on some reported tests on unsaturated loess from North France (MuñOz-Castelblanco et al., 2012), Lanzhou (Zhao, 2010, Zhao and Wang, 2012) and Xi'an (Wang et al., 2008). A SWCC proposed by Van Genuchten (1980) (VG model) can fit the soil-water characteristics of loess well and has only two parameters, as follows

$$S_e = \frac{1}{\left(1+(s/m_{sw})^n\right)^{1-1/n}} \tag{13}$$

where S_e is the effective degree of saturation defined by Equation 6, s is the suction and m_{sw} and n are fitting parameters. For different kinds of loess, the variability of the parameter n is small, varying from 1.3 to 1.6. Following some researchers' opinion (Vanapalli et al., 1996), there should be some relationship between the shear strength and the SWCC for unsaturated soil. According to Equation 10, $n = 1.6$ is adopted here. On the contrary, the parameter m_{sw} decreases with the increase in the void ratio, as shown in Figure 5 (Wang et al., 2008, Zhao, 2010). The relationship between m_{sw} and the void ratio is suggested by the authors as follows

$$m_{sw} = m_1 \exp(m_2 e) \tag{14}$$

where e is the void ratio and $m_1 = 400$ kPa and $m_2 = -4.7$ are fitting parameters.

The SWCC can be obtained from Equations 13 and 14 as follows

$$S_e = \frac{1}{\left(1+\left(\frac{s}{m_1 \exp(m_2 e)}\right)^n\right)^{1-1/n}} \tag{15}$$

4 DEM RESULTS

In this simulation, a local damping coefficient of 0.7 was applied to each ball. The density of each ball is 2.7×10^3 kg/m^3. After preliminary compaction, the numerical specimen was isotropically compressed to several confining pressures, i.e. 50 kPa, 100 kPa, 200 kPa and 400 kPa. The suction was constant throughout the isotropical compression. Then, the deviator stress was applied by moving the top and bottom walls downward and upward respectively at an absolute strain velocity of 1.0%/ms with the side walls servo controlled. The ratio of the magnitude of the out-of-balance force acting on the particles and the magnitude of the average contact force is about 0.002, 0.0013, 0.001, 0.0007 when the confining pressure is 50 kPa, 100 kPa, 200 kPa and 400 kPa, respectively. Kuhn (2006) has suggested to try to keep this ratio below 0.005.

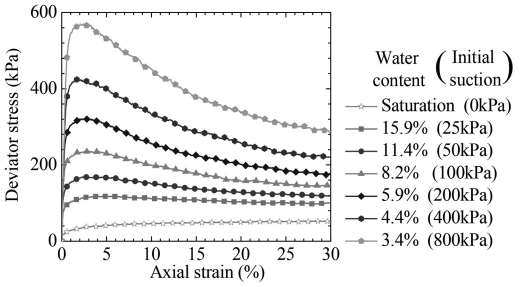


Figure 6. Stress-strain relationships of samples with the same confining pressure (50 kPa) and different initial suctions.

When applying the deviator stress, the water content was constant. The capillary force was determined by the water content as follows. The effective degree of saturation can be obtained through the water content and the void ratio. Then, the frictional coefficient was computed by Equation 8. The suction was calculated by the inverse function of Equation 15 and then the capillary force can be obtained by Equation 12. The frictional coefficient and the capillary force were updated every 100 steps. The simulation is hydro-mechanical coupled as the influence of the void ratio on the SWCC is considered.

4.1 *Deviator stress and matric suction*

Tests with the confining pressure of 50 kPa are chosen to demonstrate the results. Figure 6 shows the stress-strain relationships. For the saturated sample, the deviator stress increases with the axial strain. Weak strain softening occurs on samples with small initial suction while strong strain softening appears with large initial suction, which agrees with experimental observations generally. The deviator stresses tend to steady values for samples with different initial suctions at large axial strain which can be taken as the critical state. The deviator stress at the critical state increases with the decrease in water content.

Figure 7 shows the changes of suctions with the axial strain. Both the void ratio and SWCC change throughout the simulation which results in the variation of suction in the simulation.

4.2 *Void ratio and average coordination number*

Figure 8 shows the changes of void ratios with the axial strain. The saturated sample presents contraction while the unsaturated samples with different initial suctions present dilation. The void ratio at the critical state increases with the decrease in water content which demonstrates that large suction sustains a soil structure with large void ratio.

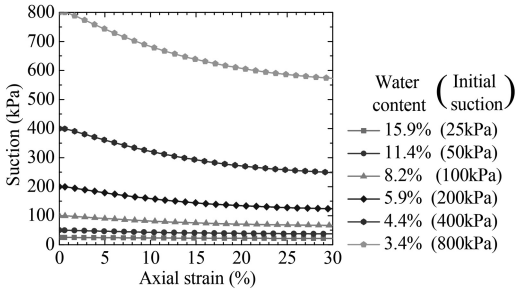


Figure 7. Changes of suctions of samples with the same confining pressure (50 kPa) and different initial suctions.

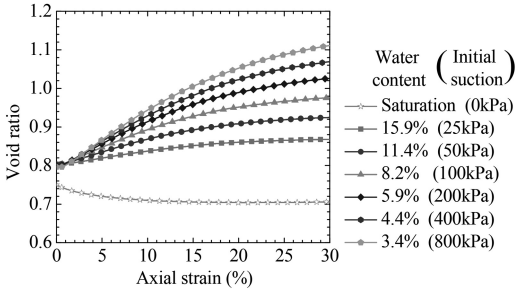


Figure 8. Volume-strain changes of samples with the same confining pressure (50 kPa) and different initial suctions.

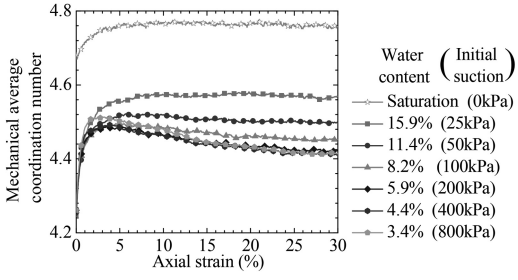


Figure 9. Changes of the average coordination numbers of samples with the same confining pressure (50 kPa) and different initial suctions.

Figure 9 shows the changes of the mechanical average coordination numbers (Thornton, 2000) throughout the tests. The average coordination number for saturated assembly is much greater than those for unsaturated assemblies. For unsaturated assemblies, the average coordination number increases rapidly at first and then increases or decreases slightly until the end of the tests. The average coordination number generally decreases with the decrease in the water content. Nevertheless, the average coordination numbers for samples with low water contents are nearly the same at the critical state which demonstrates that there is a lower limit of average coordination number at the critical state.

The limit should be related to the particle shapes.

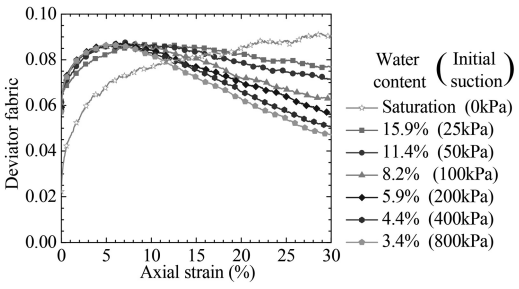


Figure 10. Changes of the deviator fabrics of samples with the same confining pressure (50 kPa) and different initial suctions.

4.3 *Deviator fabric of contact normal*

A fabric tensor F_{ij} (Satake, 1982, Oda et al., 1982) shown in Equation 16 can be used to describe microstructure orientation of granular materials.

$$F_{ij} = \frac{1}{N}\sum_{k=1}^{N} n_i^k n_j^k = < n_i n_j > \tag{16}$$

where N is the number of contacts, n_i are the direction cosines of the contact normals.

The deviator fabric of the fabric tensor F_{ij} can be expressed as

$$\Delta = \frac{1}{\sqrt{2}}\sqrt{(F_1 - F_2)^2 + (F_2 - F_3)^2 + (F_1 - F_3)^2} \tag{17}$$

where the F_1, F_2 and F_3 are principal fabrics of F_{ij}. The deviator fabric denotes the anisotropy of the contact normals in an assembly.

Figure 10 shows the changes of the deviator fabrics with the axial strain. For the saturated sample, the deviator fabric increases with the axial strain throughout the test. For the unsaturated samples, nevertheless, the deviator fabric increases rapidly to a peak value and then decreases gradually with the axial strain. The deviator fabric at the critical state decreases with the decrease in water content.

5 CONCLUSIONS

To simulate the unsaturated remolded loess using the Discrete Element Method (DEM), a reasonable van der Waals' force was taken into account to sustain the open structure of the numerical assembly. The influence of the effective degree of saturation (Se) on the inter-particle frictional coefficient was considered. An adhesive force was applied to each contact in the DEM assembly to represent the inter-particle capillary force. The magnitude of the adhesive force was determined by the matric suction. A representative soil-water characteristic curve which considers the hydro-mechanical effect was applied to relate the suction to the Se.

By simulating the constant-water-content triaxial tests on the unsaturated remolded loess, the following

conclusions can be drawn. In general, the DEM simulation can acquire similar stress-strain, suction-strain and volume-strain relationships in typical laboratory tests. Microscopically, the average coordination number increases rapidly at first and then increases or decreases slightly until the end of the tests. The average coordination numbers for samples with low water contents are nearly the same at the critical state. It demonstrates that there is a lower limit of average coordination number at the critical state. The deviator fabric increases rapidly to a peak value and then decreases gradually with the axial strain. The deviator fabric at the critical state decreases with the decrease in water content.

ACKNOWLEDGMENTS

The work reported here was supported by State Key Lab. of Disaster Reduction in Civil Engineering (Grant No. SLDRCE14-A-04) and the National Basic Research Program of China with Grant Nos. 2011CB013504 and 2014CB046901.

REFERENCES

Barbour, S. L. 1998. Nineteenth Canadian Geotechnical Colloquium: The soil-water characteristic curve: a historical perspective. *Canadian Geotechnical Journal,* 35, 873–894.

Brooks, R. H. & Corey, A. T. 1964. Hydraulic properties of porous media. *Colorado State University Hydrology Paper,* 27.

Chen, Z. H., Fredlund, D. G. & Gan, J. K. M. 1999. Overall volume change, water volume change, and yield associated with an unsaturated compacted loess. *Canadian Geotechnical Journal,* 36, 321–329.

Cui, Y. J. & Delage, P. 1996. Yielding and plastic behaviour of an unsaturated compacted silt. *Géotechnique,* 46, 291–311.

Cundall, P. A. & Strack, O. D. L. 1979. A discrete numerical model for granular assemblies. *Géotechnique,* 29, 47–65.

Fisher, R. A. 1926. On the capillary forces in an ideal soil. *Journal of Agricultural Science and Technology,* 16, 492–505.

Fredlund, D. G., Morgenstern, N. R. & Widger, R. A. 1978. The shear strength of unsaturated soils. *Canadian Geotechnical Journal,* 15, 313–321.

Gao, G. R. 1996. The distribution and geotechnical properties of loess soils, lateritic soils and clayey soils in China. *Engineering Geology,* 42, 95–104.

Jiang, M. J., Konrad, J. M. & Leroueil, S. 2003. An efficient technique for generating homogeneous specimens for DEM studies. *Computers and Geotechnics,* 30, 579–597.

Jiang, M. J., Leroueil, S. & Konrad, J. M. 2004. Insight into shear strength functions of unsaturated granulates by DEM analyses. *Computers and Geotechnics,* 31, 473–489.

Jiang, M. J., Li, T., Hu, H. J. & Thornton, C. 2014. DEM analyses of one-dimensional compression and collapse behaviour of unsaturated structural loess. *Computers and Geotechnics,* 60, 47–60.

Jiang, M. J., Shen, Z. F. & Thornton, C. 2013. Microscopic contact model of lunar regolith for high efficiency discrete element analyses. *Computers and Geotechnics,* 54, 104–116.

Jiang, M. J., Yan, H. B., Zhu, H. H. & Utili, S. 2011. Modeling shear behavior and strain localization in cemented sands by two-dimensional distinct element method analyses. *Computers and Geotechnics,* 38, 14–29.

Kuhn, M. R. 2006. OVAL and OVALPLOT: Programs for analyzing dense particle assemblies with the discrete element method. http://faculty.up.edu/kuhn/oval/doc/oval_0618.pdf.

Liu, S. H. & Sun, D. A. 2002. Simulating the collapse of unsaturated soil by DEM. *International Journal for Numerical and Analytical Methods in Geomechanics,* 26, 633–646.

Morrow, C., Moore, D. & Lockner, D. 2000. The effect of mineral bond strength and adsorbed water on fault gouge frictional strength. *Geophysical Research Letters,* 27, 815–818.

Mu Ozcastelblanco, J. A., Delage, P., Cui, Y. J. & Pereira, J. M. 2012. The water retention properties of a natural unsaturated loess from northern France. *Géotechnique,* 62, 95–106.

Oda, M., Nemat-Nasser, S. & Mehrabadi, M. M. 1982. A statistical study of fabric in a random assembly of spherical granules. *International Journal for Numerical and analytical methods in Geomechanics,* 6, 77–94.

Satake, M. 1982. Fabric tensor in granular materials. *Proceedings of IUTAM Symposium on Deformation and Failure of Granular materials.* Delft, Rotterdam.

Scholt, S. L., Chareyre, B., Nicot, F. & Darve, F. 2009. Micromechanics of granular materials with capillary effects. *International journal of engineering science,* 47, 64–75.

Thornton, C. 2000. Numerical simulations of deviatoric shear deformation of granular media. *Géotechnique,* 50, 43–53.

Van Genuchten, M. T. 1980. A closed-form equation for predicting the hydraulic conductivity of unsaturated soils. *Soil science society of America journal,* 44, 892–898.

Vanapalli, S. K., Fredlund, D. G., Pufahl, D. E. & Clifton, A. W. 1996. Model for the prediction of shear strength with respect to soil suction. *Canadian Geotechnical Journal,* 33, 379–392.

Wang, T. X., Lu, Q. & Yue, C. K. 2008. Soil-water characteristic curve for unsaturated loess considering temperature and density effect. *Rock and Soil Mechanics,* 29, 1–5. [in Chinese]

Zhao, T. Y. & Wang, J. F. 2012. Soil-water characteristic curve for unsaturated loess soil considering density and wetting-drying cycle effects. *Journal of Central South University (Science and Technology),* 43, 2445–2453. [in Chinese]

Zhao, Y. X. 2010. *Unsaturated soil mechanics characteristics of compacted loess moistening deformation.* PhD. thesis, Lanzhou University. [in Chinese]

Unsaturated Soil Mechanics—from Theory to Practice – Chen et al. (Eds)
© 2016 Taylor & Francis Group, London, ISBN 978-1-138-02921-7

Simulation of particle crushing using Discrete-Element Method (DEM)

Y. Xi & Y.F. Xu
School of Naval Architecture and Civil Engineering, Shanghai Jiao Tong University, Shanghai, China

ABSTRACT: This paper simulates the crushing test of rock by the discrete-element method. A rock sample is a synthetic material whose micro-properties can be chosen as to reproduce the relevant behaviors. The fractal dimension is obtained by analyzing particle size distributions. Derive a theoretical formula of crushing strength and survival probability based on the fractal model to predict the value of different sizes. Compare the predicted results with the numeral experimental data, and prove to be consistent. The fractal dimension increases with the porosity of rock decreasing.

1 INTRODUCTION

It is a fact that the constitutive behavior of a soil is largely determined by its particle size distribution (McDowell 2000), and it is necessary to do more research about mechanical property of a rock by exerting particle size distribution. The size effect on ice strength can be well predicted using the fractal dimension $D = 2.50$ of the ice fragment size distribution (Xu 2004).The tensile strength is not independent of the fragment size, but decreases with increasing size (Xu 2014).

A series of one-dimensional compression tests was performed to study the microscopic particle crushing (Hagerty 1992).The particle size distribution of crushing rock satisfies the fractal model and the fractal dimension is between 2 and 3. Zhang (2008) used a confined compression test to investigate the crushing behaviors of coarse quartz sand and fine gravel particles under high compressive stress, and their fractal crushing was studied based on the fractal concept and the measured data of particle-size distribution. It was shown that fractal crushing dimension has a close relationship with Hardin index of particle breakage. The fractal crushing dimension might be useful indicator for quantitative analysis of the particle breakage of granular materials.

Discrete-element method (Cundall & Strack 1979) is effective to describe the micro structure of the crushing rock. Ueda (2013) investigated the effects of particle shape on the compression behavior of granular materials. Jiang (2009) introduced a two-dimensional discrete element method to capture the roughness of particles and investigate the mechanical response of the material of different roughness. Agglomerates were made by bonding elementary spheres in 'crystallo-graphic' arrays to simulate crushable soils (Cheng 2003). McDowell (2013) used discrete-element modeling to investigate the micro mechanics of one-dimensional compression. Compression is related to the evolution of a fractal distribution of particles.

Crushing has generally been modeled using the Discrete-Element Method (DEM) via two alternative methods: replacing 'breaking' grains with new, smaller fragments; or by using agglomerates groups of bonded particles with finite bond strengths. Astrom & Herrmann (1998) showed that it was possible to model the fragmentation of grains in two dimensions using DEM. This work was supplemented by Tsoungui et al. (1999). Lobo-Guerrero & Vallejo (2005) developed a similar two-dimensional model of granular crushing, but in that model mass was not conserved. Ben-Nun & Einav (2010) and Ben-Nun et al. (2010) used their own two-dimensional model of grain fracture to explore the particle and force-chain topology, and the evolution of fractal distributions, and also used a distribution of particle strengths. In this paper, a rock were made by bonding elementary particles with diameters from 0.075 mm to 0.145 mm. Uniaxial compression tests of different sizes were performed to obtain the fractal dimension and analyze the crushing strength by the fractal model.

2 FRACTAL MODEL

A fractal is a shape consisting of parts similar to the whole (Kranenburg 1994), as shown in Figure 1. The fractal dimension is usually used to express the similarity between the parts and the entirety. The number of particles $N(d)$ displays scale invariance with a non-integer exponent. Let $\lambda = d/d_0$, where d_0 is the minimum size of the observation of scale invariance, and,

$$N(d) = N(\lambda d_0) = [N(d_0)d_0^D]d^{-D} \propto d^{-D} \quad (1)$$

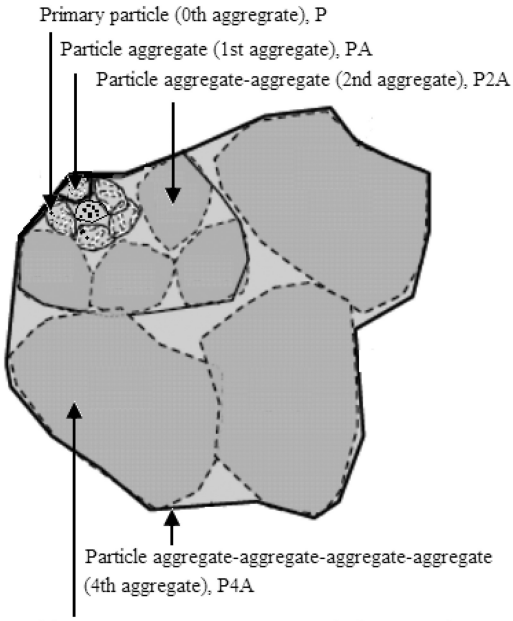


Figure 1. Conceptual model for aggregate order.

In Eq. (1), the fractal dimension D can be estimated from the slope of a straight line in the log–log plot.

3 UNIAXIAL ROCK COMPRESSION TEST SIMULATION

3.1 *Contact constitutive models*

The overall constitutive behavior of a rock is simulated by associating a simple constitutive model with each contact. The constitutive model provides an elastic relation between the contact force and relative displacement. The normal stiffness is a secant stiffness,

$$F_n = k_n U_n. \tag{2}$$

since it relates the total normal force to the total normal displacement. The shear stiffness is a tangent stiffness,

$$\Delta F_s = -k_s \Delta U_s. \tag{3}$$

since it relates the increment of shear force to the increment of shear displacement. The relation between stiffness and the modulus can be expressed as:

$$k = 2E_c t. \tag{4}$$

Particles are bonded together at contacts. The contact bond can be envisioned as a kind of glue joining the two particles, as shown in Figure 2.

A contact bond is defined by the following two parameters: normal contact bond strength F_c^n and shear

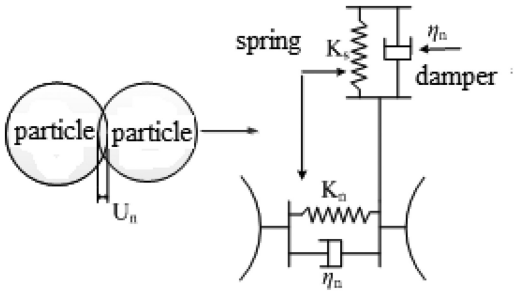


Figure 2. Particle contact constitutive models.

contact bond strength F_c^s. If the magnitude of the tensile normal contact force exceeds F_c^n, the bond breaks, and both the normal and shear contact forces are set to zero. If the magnitude of the shear contact force exceeds F_c^s, the bond breaks. However, if the normal force is compressive and the shear force does not exceed the friction limit, the contact forces are not altered. The friction limit is the maximum allowable shear contact force:

$$F_{\max}^s = \mu |F_n|. \tag{5}$$

3.2 *Test preparation and test method*

Generate a rectangular area surrounded by four walls, and the rock's diameter is the distance d between the vertical walls. The porosity is specified with 0.15, and create particles randomly in the area, whose diameter is ranging from 0.075 mm to 0.1245 mm. Then move the walls to apply the initial pressure to the particles so that the particles contact with the neighboring ones. The next step is to eliminate the floating ball which has less than three contacts in the assembly. After that, the particles are bonded to the neighboring ones and release the residual stress. In the end, delete the balls outside the circle with a diameter of d centered at the center of the rectangle. The rock sample is shown in Figure 3.

Discrete-element method parameters for simulation of rock are listed in Table 1. Six hundred rock compressing tests of different sizes were conducted and the diameter of a rock is ranging from 3.0 mm to 22.mm. After creating the rock sample according to the rock size, give walls velocity of 5 mm/s to compress the rock sample. During the compression process, the real-time data of force and displacement are recorded automatically. When the rock sample is crushed, stop loading for data analysis.

3.3 *Results and discussion*

The first peak value on the force-displacement compression curve in the rock crushing test is defined as the particle crushing force. The relationship between the rock compressing force and displacement is shown in Figure 4. There is an elastic relation between the contact force and relative displacement before the rock

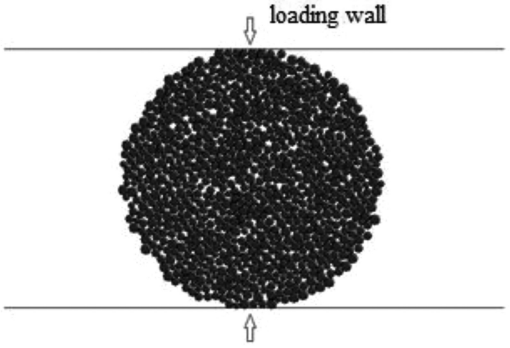


Figure 3. Single particle crushing test model.

Table 1. Parameter value of a single particle.

Input parameter	Value
Density, ρ/kg/m^3	2630
Particle friction coefficient, μ	0.5
Modulus, E_c/N/m^2	8.8×10^{10}
Wall friction coefficient, μ_{wall}	0.0
Wall's stiffness, k_{wall}	$1.1k_p$
Particle's stiffness, k_{n}	$2E_c t$
Normal contact bond strength, F_c^n/N	2×10^8
Shear contact bond strength, F_c^s/N	2×10^8

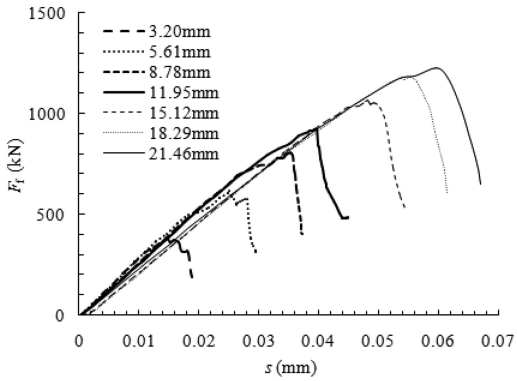


Figure 4. Load-displacement relationship.

crushing. Besides that, it can be seen that the rock crushing force grows as particle sizes.

The particle size distribution of the crushing rock is shown in Figure 5. The abscissa represents the particle size after crushing, and the ordinate represents the ratio of $N(d)$ to $N(d_0)$. It should be noted that the crushed particles demonstrate a linear distribution in log–log coordinates, the slope of which is approximately -2.73. Therefore, the fractal dimension is $D = 2.73$ according to Eq. (6).

$$P(\geq d) = \frac{N(\geq d)}{N(\geq d_0)} \propto d^{-D}. \tag{6}$$

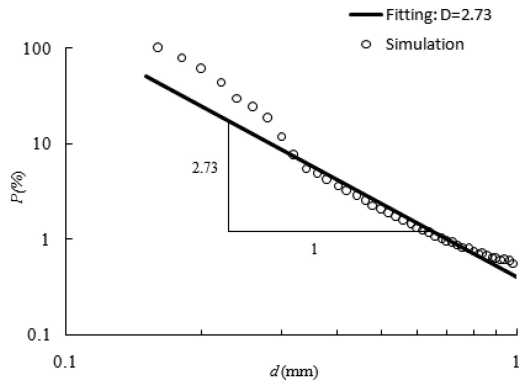


Figure 5. Particle size distribution of the crushing rock.

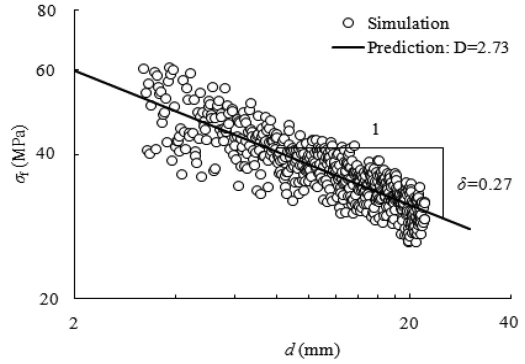


Figure 6. Comparisons of predictions with numeral experimental data for crushing strength.

4 ROCK CRUSHING STRENGTH

The apparent rock crushing strength is given by

$$\sigma_f = F_f / A_{app}. \tag{7}$$

where σ_f is the rock crushing strength and A_{app} is the apparent area of the section perpendicular to F_f. The apparent area of the rock is written as

$$A_{\text{app}} = k_1 d^2. \tag{8}$$

where d is the real diameter of the rock. The fractal dimension of the particles size distribution is D-1 in two dimensional planes as the fractal dimension of the particle size distribution is D in three dimensions. The real particle area in any section with size d is written as

$$A_{\text{real}} = k_2 d^{D-1}. \tag{9}$$

where A_{real} is the real section area of the rock. Intrinsic failure strength is a constant value that does not vary with rock size, which is written as

$$\sigma_f^* = \frac{F_f}{A_{\text{real}}}. \tag{10}$$

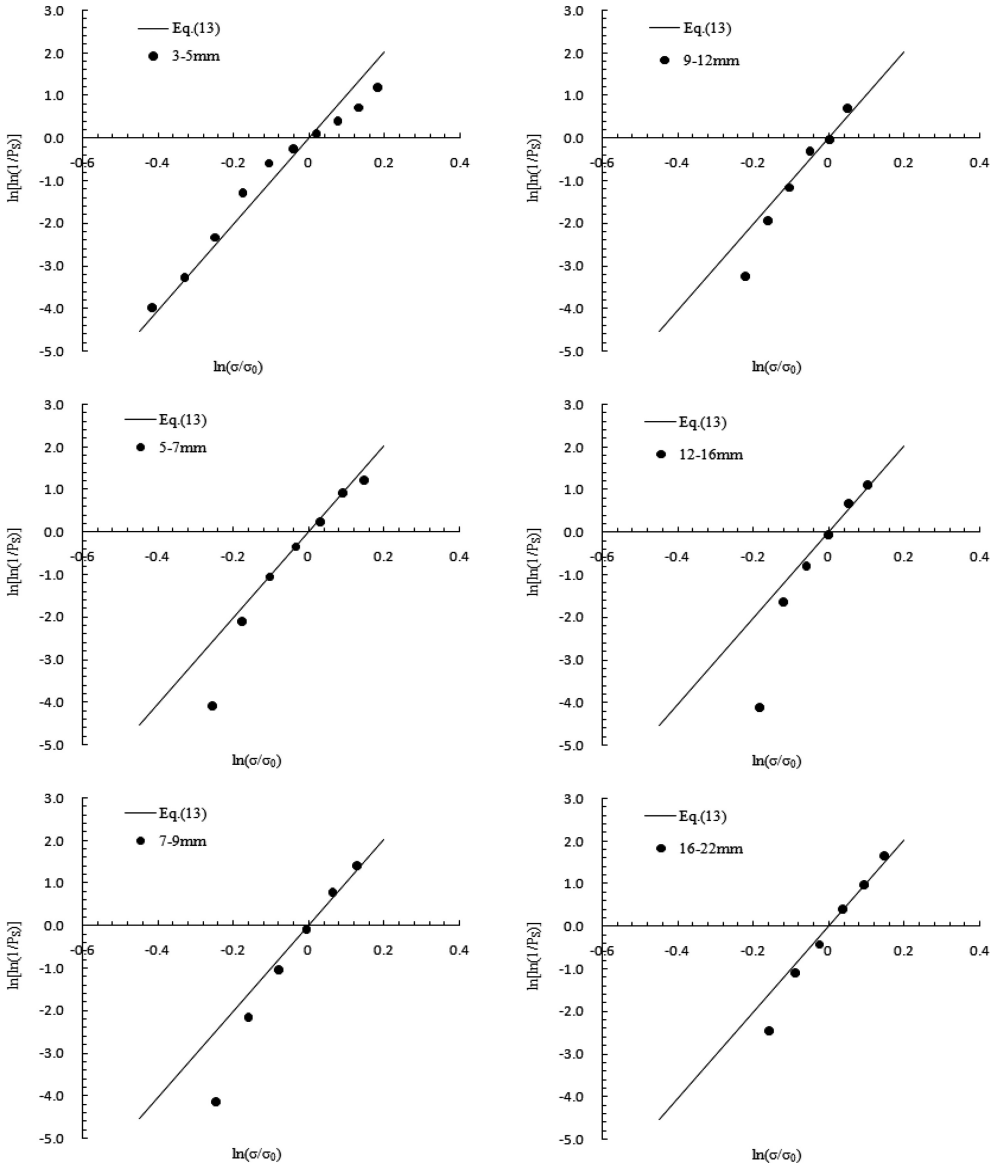


Figure 7. Comparisons of predictions using Eq. (13) with numeral experimental data of the relationship between the probability of survival and crushing strength.

From Eq. (8) Eq. (9) and Eq. (10), it is obtained that

$$\sigma_f = \sigma_f^* d^{D-3}. \tag{11}$$

$$\sigma_f^* = \frac{\sum_{i=1}^{n}\left(\frac{\sigma_{fi}}{d_i^{D-3}}\right)}{n}. \tag{12}$$

Figure 6 shows the particle crushing strength and diameter relationships in a log–log plot. The slope of the trend line determined from around 500 points is $K = -0.27$. According to Eq. (11) and the value of $D = 2.73$ measured in the previous section, K is equal to $D - 3$. The DEM numerical test results are in agreement with the crushing strength calculated by the fractal theory. It can also be seen a quite high discrete value of the crushing strength, which is mainly due to the irregularity of the construction. The probability of survival at a given crushing stress σ_f is defined as

$$P_s = \frac{\text{the amount of crushed particles at } \sigma > \sigma_f^*}{\text{total number of particles tested}} \times 100\% \tag{13}$$

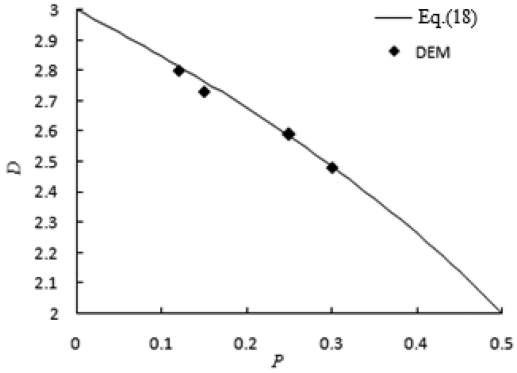


Figure 8. Relationship between fractal dimension and porosity.

Weibull (1951) proposed an equation for calculating the survival probability $P_s(\sigma, n)$ of block material

$$P_s(\sigma,n) = \exp\left[-n\left(\frac{\sigma}{\sigma_0}\right)^m\right] \tag{14}$$

where $P_s(\sigma, n)$ is the probability of survival of any particle subjected to a stress σ, σ_n is the characteristic stress at which 37% of particles survive, m is the Weibull modulus (Xu 2005),

$$m = \frac{D}{3-D} \tag{15}$$

$$n = \left(\frac{d}{d_0}\right)^D \tag{16}$$

Figure 7 shows comparisons of predictions using Eq. (14) with the numeral experimental data of the relationship between the probabilities of survival and crushing strength. Curves are presented for the particle size ranges of 3.0–5.0 mm, 5.0–7.0 mm, 7.0–9.0 mm, 9.0–12.0 mm, 12.0–16.0 mm and 16.0–22.0 mm, respectively.

It can be seen that there is a linear relationship between $\ln(\ln(1/P_s))$ and $\ln(\sigma/\sigma_0)$, as shown in Figure 7, and the slope is m. Taking the numeral experiment result $D = 2.73$ in Eq. (15), it can be calculated that $m = 10.11$. The predictions of Eq. (14) based on the use of a fractal dimension of 2.73 are also plotted in Figure 7. These predictions match well with the experimental data.

5 FACTORS OF FRACTAL DIMENSION

In the fractal model of crushing rock established by Sammis (1991), an Euclidean three-dimensional particle of size d crushed into 8 subordinate particles, whose size is half of the superordinate particle's. Assuming that the porosity of the particle is P, the particle crushed repeatedly in such way and the number of particles has a relationship with the particle size, which is written as

$$N(d_i) = (d_i)^{(3+\ln(1-P)/\ln 2)} \tag{17}$$

where $d_i = d/(2^i)$. The fractal dimension is then obtained that

$$D = 3 + \ln(1-P)/\ln 2 \tag{18}$$

Figure 8 shows the relationship between fractal dimension and porosity of the rock grain simulated. As Figure 8 shown, four different kinds of porosity are 0.12, 0.15, 0.25, 0.30 and the corresponding fractal dimension are 2.80, 2.73, 2.59, 2.48. The result obtained from the DEM simulation matches well with the Eq. (18). The fractal dimension increases with the porosity of rock decreasing.

6 CONCLUSIONS

A large number of rock crushing tests were conducted by discrete element method. The force-displacement curve is linear. The rock crushing force grows as the particle size increases.

The fractal dimension of the rock sample has a constant value of 2.73 obtained from the particle size distribution. The fractal theoretical model of crushing strength and probability of survival are proven consistent with the numerical experimental data so that the fractal theory is applicable for analysis of rock crushing.

Porosity is the dominant factor to affect the fractal dimension. The fractal dimension increases with the porosity decreasing.

ACKNOWLEDGEMENTS

The National Nature Science Foundation of China (Grant Nos. 41272318 and 41472251) is acknowledged for its financial support.

REFERENCES

Ben-Nun, O. & Einav, I. 2010. The role of self-organization during confined comminution of granular materials [J]. *Philosophical Transactions of the Royal Society A: Mathematical, Physical and Engineering Sciences* 368(1910): 231–247.

Ben-Nun, O., Einav, I. & Tordesillas, A. 2010. Force attractor in confined comminution of granular materials [J]. *Physical review letters* 104(9): 108001.

Cundall, P.A. & Strack, O.D.L. 1979. A discrete numerical model for granular assemblies. *Geotechnique* 29(1): 47–65.

Cheng, Y.P., Nakata, Y. & Bolton, M.D. 2003. Discrete element simulation of crushable soil. *Geotechnique* 53(7): 633–641.

Hagerty, M.M., Hite, D.R. & Ullrich, C.R. 1992. One-dimensional high-pressure compression of granular media [J]. *Soils Found* 32: 117–129.

Jiang, M., Leroueil, S. & Zhu, H. 2009. Two-dimensional discrete element theory for rough particles. *International Journal of Geomechanics* 9(1): 20–33.

Kranenburg, C. 1994. The fractal structure of cohesive sediment aggregates. *Estuarine, Coastal and Shelf Science* 39(5): 451–460.

McDowell, G.R. & Bolton, M.D. 2000. Effect of particle size distribution on pile tip resistance in calcareous sand in the geotechnical centrifuge. *Granular Matter* 2(4): 179–187.

McDowell, G.R. & de Bono, J.P. 2013. On the micro mechanics of one-dimensional normal compression. *Géotechnique* 63.

Steacy, S.J. & Sammis, C.G. 1991. An automaton for fractal patterns of fragmentation [J]. *Nature* 360: 250–252.

Ueda, T., Matsushima, T. & Yamada, Y. 2013. DEM simulation on the one-dimensional compression behavior of various shaped crushable granular materials. *Granular Matter* 15(5): 675–684.

Weibull, W. 1951. Wide applicability. *Journal of applied mechanics*.

Xu, Y. 2005. Explanation of scaling phenomenon based on fractal fragmentation. *Mechanics Research Communications* 32(2): 209–220.

Xu, Y., Xu, J. & Wang, J. 2004. Fractal model for size effect on ice failure strength. *Cold regions science and technology* 40(1): 135–144.

Xu, Y. & Wang, Y. 2014. Size effect on crushing of rock particles. *Journal of Engineering Geology* (6).

Zhang, J. & Zhu, J. 1992. Crushing and fractal behaviors of quartz sand-gravel particles under confined compression. *Chinese Journal of Geotechnical Engineering* 30(6): 783–789.

Unsaturated Soil Mechanics—from Theory to Practice – Chen et al. (Eds)
© 2016 Taylor & Francis Group, London, ISBN 978-1-138-02921-7

A new numerical method for one-dimensional compression test of crushable particles based on DEM

Y.D. Wang & Y. Xi
Department of Civil Engineering, Shanghai Jiao Tong University, Shanghai, China

ABSTRACT: The discrete element method is used to investigate the one-dimensional compression of a large number of particles. The method to simulate particle crushing is conducted through substituting the original particles for some small particles under certain principles, which avoid the use of agglomerates. The randomly chosen rule of the particles crushing is set for more realistic simulation. The Normal Compression Line (NCL) and Particle Size Distribution (PSD) are explored on the behaviour of the particles. The influence of the randomly crushing mechanism is also discussed.

1 INTRODUCTION

Crushing of rock particles, while a separate phenomenon, is commonly encountered in geotechnical engineering practice and largely affects the stress and strain behaviour of rocks. The degree of particle crushing is influenced principally by the strength of the grains and the effective stress state and a number of other factors such as size, shape, mineral features, etc. The effects of particle crushing are greatest at high pressures (Yamamuro & Lade 1997).

Discrete element modelling (DEM) is a numerical simulation technique that be used to study the mechanics of particle crushing only in recent years, because it is difficult to achieve an effective and realistic crushing mechanism. The DEM algorithm was originally described by Cundall & Strack (1979). The original application of this method was as a tool to perform research into the behavior of granular material; representative elements containing several hundred particles were tested numerically. DEM has often been used to simulate the uniaxial compression of agglomerates, particularly of soil particles (Cheng et al. 2003; Golchert et al. 2004; Robertson & Bolton 2001) and other materials (Antonyuk et al. 2011; Khanal et al. 2005; Samimi et al. 2005).

The traditional method for studying particle crushing with DEM was agglomerated many small spheres to simulate a particle, and the spheres are bonded together. The algorithm adopts a soft contact approach, so that the particles are modelled as rigid bodies which are permitted to overlap at the contact points to simulate compressive contact deformation. However, there is a prominent drawback with using agglomerates. A large number of elementary particles are required. It is inconvenient to consider the evolution of a particle size distribution during normal compression. Cheng et al. (2003) and Bolton et al. (2008) have investigated various stress paths in addition to isotropic compression, although again a limited number of agglomerates were used.

A new idea proposed and performed by Ben-Nun & Einav (2010), McDowel et al. (2013) and McDowell & de Bono (2013) for studying particle crushing with DEM is one elementary particle really represents one particle, the crushing is emerged by deleting broken sand particles and being replaced with new, smaller grains. When several forces acting on a particle satisfy the critical conditions, the particle can crush and be replaced by several fragments. As the system compacts, the volume of the sample decreases and the number and diameters of the particles change. The evolution of particle size distribution (PSD) would emerge. In this paper, we used the new method for simulating and gave an improvement. We considered three different forms of crushing, that is means when a particle will be crushed, it would break into two, three or four pieces randomly. The NCL and PSD was got and compared with existing experimental data.

2 METHOD

The traditional way of simulating particle crushing using discrete element method is aggregating elementary spheres to form a large particle, and the elementary spheres separate from the mother particle, when the crushing occurred. So no consideration was given to the complex distribution of loads on each particle at its multiple contacts of this method. The same crushing criteria and mechanism are used in the new simulation method, in which each basic sphere represents a real particle, and the elementary sphere is allowed to split into some new fragments (Figure 1), when it the crushing condition reached. Figure 1a

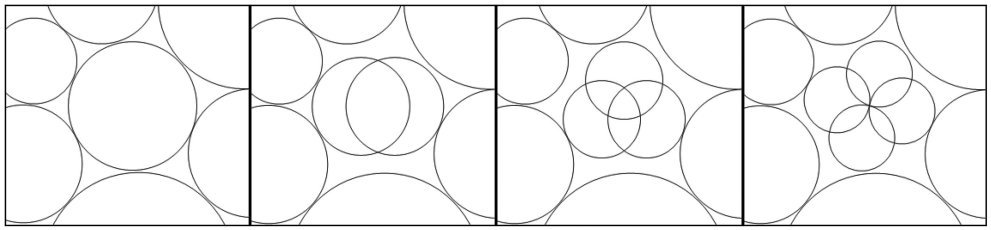


Figure 1. The crushing mechanisms of the particle.

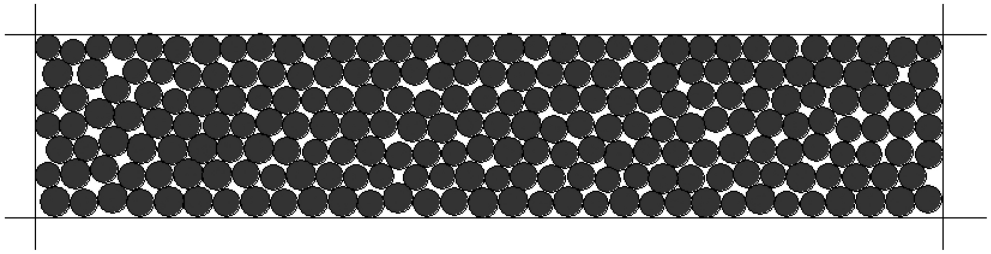


Figure 2. The images of the sample before compression.

shows the original particles (uncrushed), Figure 1b, 1c and 1d shows the crushed particles, respectively. The difference of the three is the number fragments formed after crushing, two fragments in Figure 1b, three fragments in Figure 1c, and four fragments in Figure 1d. In practice, we make a particle breakage, and it certainly will form small particles of different pieces. In this paper, three crushing cases are considered together. But under what conditions it will crush into two pieces, what will three and four? Randomly! When the value of particle stress is found to be greater or equal to its strength, the particle will crush as the above form. To obeying conservation of mass, the total volume of the new spheres is equal to that of the original parent sphere. To ensure sample stability, particle breakages are updated at once and to make the elastic energy release after a number of computational cycles equivalent.

The advantage of this method is simple and efficient for simulating particle crushing. In addition the particle size distribution can be obtained directly which played an important role in analysing the particle properties. Although it is impossible to simulate realistic fracture using this method; rather a best approach to investigate the effects of particle crushing.

3 NUMERICAL MODEL

A random sample composed of 225 spheres of diameter 1.2–1.4 mm. was created with diameter 50 mm and height 10 mm and the sample was loaded one dimensionally. The typical particle parameters are shown in Table 1. The linear contact model was used. The above panel pressed down, and the other three planes kept fixed. The simulations are strain controlled, for example, the top platen is accelerates slowly at the beginning, then loading at a constant speed, at last decelerated stopped when the increase in axial strain close to 20%. Figure 2 shows the images of the sample before compression.

Jaeger (1967) suggested that the tensile strength of grains could be expressed by diametric compression between platens as:

$$\sigma_f = \frac{F}{d^2} \tag{1}$$

where σ_f is the tensile stress at failure, F is the diametric compressive force applied by the platens and d is the diameter of the grain at failure.

For PFC^{2D}, if a sphere compressed diametrically between two walls, the value of stress q judging the particle whether fracture generated could be expressed as:

$$q = 0.9\frac{F}{d^2} \tag{2}$$

4 RESULT AND DISCUSSION

Figure 3 shows the images of the sample after compression. Large particles are in placed by small spheres when the stress reaches to its strength. Figure 4 shows the result of the normal compression line (NCL) of DEM in the e–log p space. The NCL for Nakata et al. (2001) is also shown in the same figure. It is clear that the two results are very consistent. The yield stress for the sample is about 14 MPa.

The evolution of the particle size distribution is also measured by the percentage of mass of particles smaller than a given size plotted against the logarithm

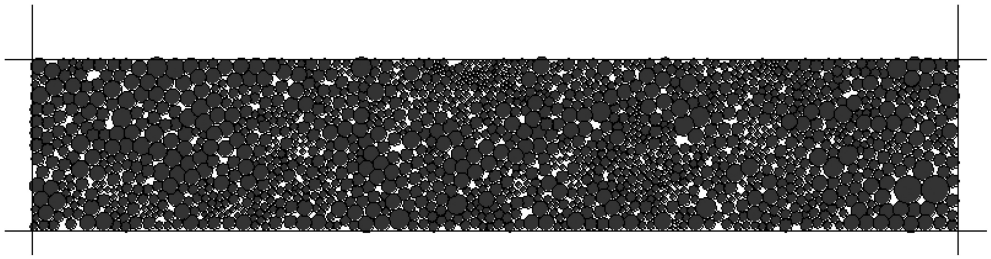


Figure 3. The images of the sample after compression.

Table 1. DEM parameters for simulations.

height × diameter (mm)	50 × 10
Particle diameter, d_0 (mm)	1.2–1.4
No. of particles	225
Particle friction coefficient	0.5
Contact model	Linear Contact Model
Elastic modulus (GPa)	70
Poisson's ratio, ν	0.25
Density (kg/m^3)	2650
Voids ratio, e_0	0.65

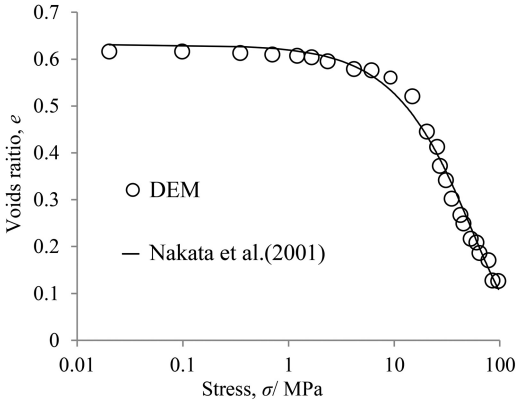


Figure 4. The normal compression line (NCL) compared DEM with Nakata et al. (2001).

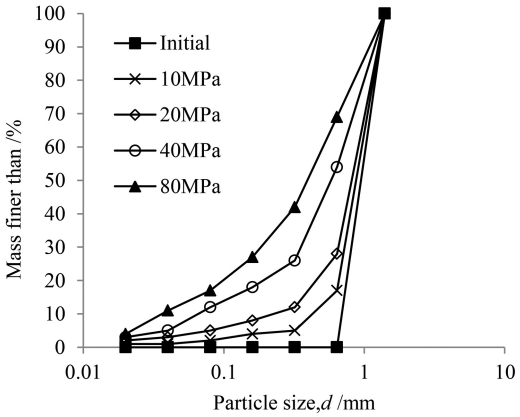


Figure 5. The particle size distributions (PSD).

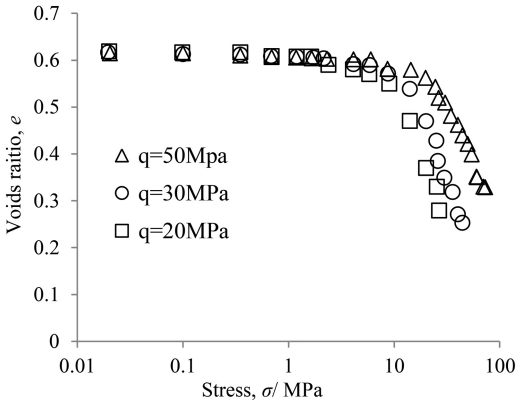


Figure 6. The NCL plots for various particle strengths.

of that size, in the traditional way as shown in Figure 5. With the development of particle crushing, the PSD line is close to an exponential curve. Einav (2007) has noted that the ultimate distribution of crushing particles will emerge a fractal distribution.

Figure 6 shows the effects of increasing the tensile strength from these simulations. When the stress small than 2 MPa, they have not yet yielded, no particle breakage and hence have the same grading curve as at the start of the simulations. Then, these three particles gradually start to crush, so the curves trend to different. The particles with large strength will crush at a high stress, but the slope of the compression curves almost the same.

As mentioned before, we make particles randomly crushing into different numbers. Does it make sense to do so? It is needed to discuss the influence induced by different crushing ways. Three extreme examples are shown in Figure 7. The three curves represent the particles only crushing into two, three or four pieces, respectively. From Figure 7, three curves is the same before the particle crushing, and they almost begin to crush in the same values (about 7 MPa). After crushing, the three curves showed different developments. The slopes of the compression curves are different.

We can quantitatively control the occurrence probability of every crushing way, this will show different results, the slopes of the compression curves ranging

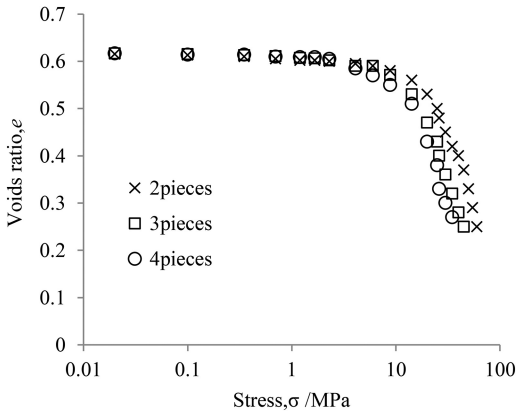


Figure 7. The NCL plots for various crushing mechanisms.

from between totally crushing into two pieces and four pieces. Any material should correspond to a certain crushing mechanism We will form a parameter with the crushing mechanism that can make the simulation of particle breakage problem become simple in future studies.

5 CONCLUSIONS

A new discrete element modelling has been used to investigate the mechanics of 1D normal compression. Particle crushing has been simulated using a very simple mechanism, replacing the crushing particle with new smaller particles while complying with the law of conservation of mass. The crushing particles are broken into two, three or four pieces randomly, which is more consistent with the real situation. This method is more efficient than agglomerates to simulate particle crushing during compression, because this does not need a very large number of initial particles and bonds.

Normal compression lines are observed and the results are consistent with the experimental data existing outcomes. The evolution of particle size distributions is emerged and the results show a fractal distribution of particle sizes.

In particular, we showed that the chosen rule of the particles crushing does affect the ultimate result.

The results of one-dimensional compression test on crushable particles using the new method are encouraging. This method is really efficient and worthy of promotion.

ACKNOWLEDGMENTS

The National Nature Science Foundation of China (Grant Nos. 41272318 and 41472251) is acknowledged for its financial support.

REFERENCES

Antonyuk, S., Palis, S. & Heinrich, S. 2011. Breakage behaveiour of agglomerates and crystals by static loading and impact. *Powder Technology* 206(1): 88–98.

Bolton, M., Nakata, Y. & Cheng, Y. 2008. Micro- and macro-mechanical behaviour of DEM crushable materials. *Geotechnique* 58(6):471–480.

Ben-Nun, O. & Einav, I. 2010. The role of self-organization during confined comminution of granular materials. *Philosophical Transactions of the Royal Society A: Math, Phy and Eng Sci* 368(1910): 231–247.

Cundall, P.A. & Strack, O.D. 1979. A discrete numerical model for granular assemblies. *Geotechnique* 29(1): 47–65.

Cheng, Y., Nakata, Y. & Bolton, M. 2003. Discrete element simulation of crushable soil. *Geotechnique* 53(7): 633–641.

Einav, I. 2007. Breakage mechanicspart I: theory. *J of the Mech and Phy of Solids* 55(6): 1274–1297.

Golchert, D., Moreno, R., Ghadiri, M. & Litster, J. 2004. Effect of granule morphology on breakage behaviour during compression. *Powder Technology* 143: 84–96.

Khanal, M., Schubert, W. & Tomas, J. 2005. DEM simulation of diametrical compression test on particle compounds. *Granular Matter* 7(2–3): 83–90.

McDowell, G.R., De Bono, J.P., Yue, P. & Yu, H.-S. 2013. Micro mechanics of isotropic normal compression. *Geotechnique Letters.* 3(October–December):166–172.

McDowell, G.R. & de Bono, J.P. 2013. On the micro mechanics of one-dimensional normal compression. *Geotechnique* 63:1–14.

Nakata, Y., Hyodo, M., Hyde, A.F.L., Kato, Y. & Murata, H. 2001. Microscopic particle crushing of sand subjected to high pressure one-dimensional compression. *Soils and Founs* 41(1): 69–82.

Robertson, D. & Bolton, M. 2001. DEM simulations of crushable grains and soils. *Powders and grains. Lisse. The Netherlands: Balkema*, pp. 623–626.

Samimi, A., Hassanpour, A. & Ghadiri, M. 2005. Single and bulk compressions of soft granules: experimental study and DEM evaluation. *Chem Eng Sci* 60(14): 3993–4004.

Yamamuro, J.A. & Lade, P.V. 1997 Drained sand behavior in axisymmetric tests at high pressures-Closure. *J of Geotech and Geoenvir Eng* 123(9): 887–887.

Unsaturated Soil Mechanics—from Theory to Practice – Chen et al. (Eds)
© 2016 Taylor & Francis Group, London, ISBN 978-1-138-02921-7

Sensitive THM coupled analysis of buffer-rock barriers for nuclear waste storage

Y.F. Qiao
Department of Geotechnical Engineering, Tongji University, Shanghai, China
Laboratory of Soil Mechanics, École Polytechnique Fédérale de Lausanne, EPFL, Lausanne, Switzerland

A. Ferrari & L. Laloui
Laboratory of Soil Mechanics, École Polytechnique Fédérale de Lausanne, EPFL, Lausanne, Switzerland

W.Q. Ding
Department of Geotechnical Engineering, Tongji University, Shanghai, China

ABSTRACT: The buffer-rock barriers system is widely proved to be one of the most promising options for isolating high-level radioactive waste from the human environment. To certify the efficiency and provide the additional development regarding design and assessment of this barriers system, it is essential to understand the complex Thermo-Hydro-Mechanical (THM) behavior of confining buffer under a variety of environmental conditions. To this end, a case of buffer-rock barriers system is studied using a THM finite element approach. The contributions of different processes, including the vapor diffusion process, the water saturation dependent thermal conductivity and specific heat capacity as well as the temperature dependent water properties, involved in the TH couplings are investigated in details. Based on all the simulation results, the key factors of design and assessment of buffer-rock barriers system are also analyzed.

1 INTRODUCTION

With more and more radioactive materials used in industries, medical applications and military, the treatment and disposal of high-level radioactive waste and spent fuel attract a high attention from nuclear application decision makers and government agencies. Among all disposal methods, the geological disposal is widely proved as the most promising and safest option to protect human beings and the environment for extremely long periods of time [1, 2]. The key component of this disposal method is the multi-layer barriers system, which consists of both nature barriers and man-made barriers. The clay formations are being widely investigated as host nature barrier, such as the Opalinus Clay in Switzerland and the Boom Clay in Belgium. The man-made barriers are the Engineered Barrier System (EBS), consisting of the canister that contains nuclear waste and the buffer materials that are used to back fill the space between canisters and the host rock. The bentonite is widely proposed as the buffer material due to its low permeability, high swelling property, suitable thermal conductivity and reasonable stability.

With the heat flux from the high-level radioactive waste and the water inflow from the host rock, the buffer system undergoes complex Thermo-Hydro-Mechanical (THM) coupling processes. To isolate the waste from the human environment efficiently, it is essential to understand the behaviour of this buffer system under such complex THM condition. The aim of this paper is to identify the various coupling processes evolved in this buffer material. Both the physical processes and the physical quantities are analyzed and the critical coupling processes are also highlighted.

To present the problem clearly, the THM processes that occur in the buffer are firstly described and presented in a schematic way. The corresponding equations to describe them are also introduced, following by an EBS synthetic case study. Five coupling cases are simulated with FEM method to investigate the most critical coupling processes. The main focuses are on the vapor diffusion process, the temperature dependent water properties and the hydraulic effects on temperature evolution. Finally, a further analysis regarding design, assessment and validation of the geological disposal concept is shown.

2 PROBLEM STATEMENT

2.1 *THM coupling problem identification*

The significant phenomena that affect the buffer system are the heating from canisters and hydration from the surrounding host rock. The hydration process

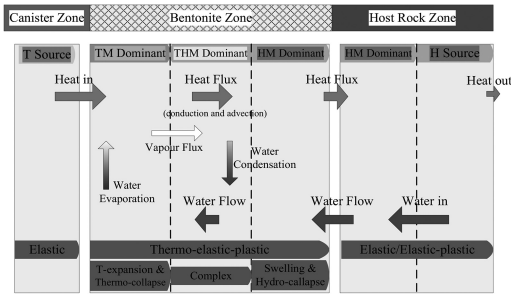


Figure 1. Driving processes in buffer systems.

occurs once the buffer system is constructed while the thermal effects only begin after the installation of the canisters containing the waste. Therefore, only Hydro-Mechanical (HM) couplings occur in the buffer system before the installation of canisters. Since the HM couplings are the simpler cases of THM coupling only the most complex THM couplings are identified in the Figure 1 in a schematic way.

Two driving forces dominate the THM couplings within the buffer system. The first one is the hydraulic gradient between the buffer system and the host rock, inducing the water movement from the host rock towards the buffer. This hydration process would lead to the full saturation of the buffer eventually. However, this saturation process can be very long due to the low permeability of the buffer material. The second driving force is the heat generated by the high-level radioactive waste inside the canister. The heat flows into the buffer system mainly via the conduction. A strong water evaporation would happen near the canister due to the high temperature developed in this region. This water vapor flux moves outwardly and condenses in the cooler zone. This vapor diffusion process makes the TH couplings much more complex. Note that the fluid viscosity decreases with temperature increases and this will further enhance the hydraulic flow. Such mutual influence would be investigated in details in the following sections.

Under aforementioned TH couplings condition, the mechanical response of the buffer system varies with temperature and suction. The mechanical changes such as the change of porosity and storage of deformation energy can also modify the thermal and hydraulic processes, which leads to a fully THM coupled interactions.

2.2 *THM coupling framework*

Both buffer material and host rock are porous media which is assumed to be composed of a solid matrix and voids filled with liquid and gas phase. The liquid phase contains two species: liquid water and dissolved air. While the gas phase is composed of dry air and water vapor. To describe the diffusive processes in such media, both the theory of mixtures [3] and compositional approach [4, 5] are adopted. Four primary state variables are required to describe the state of the material: gas pressure p_g, water pressure p_w, temperature T, and displacement vector $\boldsymbol{u}$.

The aforementioned THM phenomena and framework are available in the Lagamine FEM software. Details about the basic theories with the formulated governing equations are described references [5, 6, 7]. In the following, the balance equations and main constitutive equations are briefly presented. In the following equations, the subscripts l, g, w, da, a and v are related to the liquid phase, the gas phase, the liquid water, the dissolved air in water, the dry air, and the water vapor, respectively.

2.3 *Balance equations*

For a given mixture volume V, the mass balance equation is:

$$\frac{\partial \rho_s (1-n) V}{\partial t} = 0 \tag{1}$$

where ρ_s is the density of solid grains, n the soil porosity, and t the time.

The mass conservation equations for the water and air species are, respectively:

$$\underbrace{\frac{\partial}{\partial t}\left(\rho_w n S_r\right) + div\left(\rho_w \mathbf{f_l}\right) - Q_w}_{\text{Liquid water}} + \underbrace{\frac{\partial}{\partial t}\left(\rho_v n\left(1-S_r\right)\right) + div\left(\mathbf{i_v} + \rho_v \mathbf{f_g}\right) - Q_v}_{\text{Water vapour}} = 0 \tag{2}$$

$$\underbrace{\frac{\partial}{\partial t}\left(\rho_a n\left(1-S_r\right)\right) + div\left(\rho_a \mathbf{f_g} + \mathbf{i_a}\right) - Q_a}_{\text{Dry air in gas phase}} + \underbrace{\frac{\partial}{\partial t}\left(\rho_a H_s n S_r\right) + div\left(\rho_a H_s \mathbf{f_l}\right) - Q_{da}}_{\text{Dissolved air in water}} = 0 \tag{3}$$

where ρ_w, ρ_v, and ρ_a are the bulk density of liquid water, water vapor, and dry air. $\mathbf{f}_l$ and $\mathbf{f}_g$ are the macroscopic velocity of the liquid and gas phases, respectively. $\mathbf{i}_v$ and $\mathbf{i}_a$ are the non-advective flux of water vapor and dry air. S_r is the degree of saturation. The Henry's coefficient H_s, defining the proportion of dissolved air in the liquid phase, is taken equal to 0.017. Q_w, Q_v, Q_a, and Q_{da} are volume sources of liquid water, water vapor, dry air, and dissolved air in water, respectively.

The soil equilibrium equation is given by:

$$div(\boldsymbol{\sigma}) + \mathbf{b} = 0 \tag{4}$$

where $\boldsymbol{\sigma}$ is the total (Cauchy) stress tensor, with compressive stress taken as positive, and $\mathbf{b}$ is the body force vector which is equal to $\rho \boldsymbol{g}$ if the only body force is gravity.

The energy balance equation of the mixture has the following form:

$$\underbrace{\frac{\partial S_T}{\partial t}+L\frac{\partial}{\partial t}\left(\rho_v n\left(1-S_r\right)\right)}_{\text{Heat storage}}+ \underbrace{div\left(\mathbf{f_T}\right)+L\frac{\partial}{\partial t}\left(\mathbf{i}_\mathbf{v}+\rho_v\mathbf{f_g}\right)}_{\text{Heat transfer}}-Q_T=0 \tag{5}$$

where $\mathbf{f}_\mathrm{T}$ is the heat flow and Q_T is a volume heat source. L is the latent heat of water vaporisation. S_T is the enthalpy of the system.

2.4 *Constitutive equations*

With the main focuses of this paper in mind, only the related constitutive equations are introduced here. To describe the vapor diffusion, the Fick's Law in a tortuous medium is adopted. It reads:

$$\mathbf{i_v}=n\left(1-S_r\right)\tau D\mathbf{grad}\left(\rho_v\right) \tag{6}$$

where $\mathbf{i}_\mathrm{v}$ is vapor diffusion vector, D is the air diffusion coefficient and τ is the tortuosity of the material. ρ_v is vapor density expressed based on Kelvin-Laplace's Law as,

$$\rho_v=\exp\left(\frac{\left(p_w-p_g\right)M_v}{R\,T\rho_w}\right)\frac{p_{v,0}M_v}{R\,T} \tag{7}$$

where M_v is the vapor molar mass (=0.018 kg/mol), T is temperature expressed in Kelvin, and $p_{v,0}$ is the saturated vapor pressure given by an experimental expression depending on temperature [8, 9]

$$p_{v,0}=a\exp\left(-b/T\right) \tag{8}$$

with $a=1126589$ MPa and $b=5192.74$ K for the temperature range between 273 K and 373 K. Submitting Equation (7) and (8) to Equation (6), it is clearly shown that both suction gradient and temperature gradient can induce the water vapor flow.

Another element of TH coupling is the evolution of the water properties with temperature, such as the water density and water dynamic viscosity. In this paper, this coupling element is investigated in detail to analyze its contribution. When the temperature dependent water properties are not considered, both water density and water dynamic viscosity are assumed as constant values. While considering the temperature dependent water properties, the following equations are assumed:

$$\rho_w=\rho_{w0}\left(1+\chi_w\left(p_w-p_{w0}\right)-\beta_w'\left(T-T_0\right)\right) \tag{9}$$

$$\mu_w=0.6612\left(\mathrm{T}-229\right)^{-1.562} \tag{10}$$

where ρ_{w0}, p_{w0}, and T_0 are the initial values of water bulk density, pore water pressure, and temperature, respectively. χ_w is the water compressibility coefficient and the used value is 3.3×10^{-10} Pa^{-1}. β_w' is the volumetric water thermal expansion coefficient and the value of 3.3×10^{-4} K^{-1} is used in this work. μ_w is the dynamic viscosity of water.

The main hydraulic effects on material thermal properties are captured by the dependency of the thermal conductivity of the mixture, Γ, and the enthalpy, S_T, on the degree of water saturation. The following formulations are adopted:

$$\Gamma=1.3S_r+0.7\left(1-S_r\right) \tag{11}$$

$$\begin{aligned}S_T=&\left(nS_r\rho_w c_{p,w}+\left(1-n\right)\rho_s c_{p,s}+n\left(1-S_r\right)\rho_a c_{p,a}\right.\\&\left.+n\left(1-S_r\right)\rho_v c_{p,v}\right)\left(T-T_0\right)\end{aligned} \tag{12}$$

where n, S_r are porosity and the degree of saturation, respectively. ρ_s is the soil grain bulk density and ρ_a is the air density. λ_s, λ_w, and λ_a are the thermal conductivity of solid, liquid water, and gas phase, respectively. $c_{p,w}$, $c_{p,s}$, $c_{p,a}$, and $c_{p,v}$ are the specific heat of liquid water, solid, dry air, and water vapor respectively.

The stress-strain behavior of the host rock is modelled by the thermo-elastic constitutive law (Equation (13)) and the generalized effective stress theory (Equation (14)) is adopted.

$$d\boldsymbol{\varepsilon}=\mathbf{E}^{-1}d\boldsymbol{\sigma}'+\frac{\beta_s}{3}dT\mathbf{I} \tag{13}$$

$$\boldsymbol{\sigma}'=\boldsymbol{\sigma}-p_g\mathbf{I}+S_r\left(p_g-p_w\right)\mathbf{I} \tag{14}$$

where d$\boldsymbol{\varepsilon}$ is the total strain tensor increment, d$\boldsymbol{\sigma}'$ the effective stress increment, $\mathbf{E}$ the current non-linear elastic tensor, β_s the volumetric thermal expansion coefficient. $\boldsymbol{\sigma}'$ is the effective stress and $\boldsymbol{\sigma}$ is the total stress.

3 NUMERICAL ANALYSIS

3.1 *Model geometry and boundary conditions*

The assumed case study is based on the Swedish disposal concept for an EBS [10]. Figure 2 shows the numerical model and the boundary conditions. The model consists of a single canister, a buffer system and the host media. It is worth to note that the access tunnel and backfill material are not considered in the analysis. The boundary conditions are also presented in the figure. Two sections are investigated in the detail. One is the cool section which is away from the canister, including points P11, P12 and P13. The other one is the hot section which is closer to the canister, including points P21, P22 and P23.The canister emits heat according to the decay of a real high-level waste canister (Figure 3).

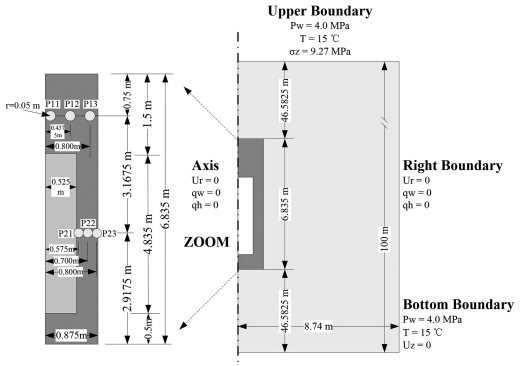


Figure 2. The geometry and boundary conditions of the numerical model.

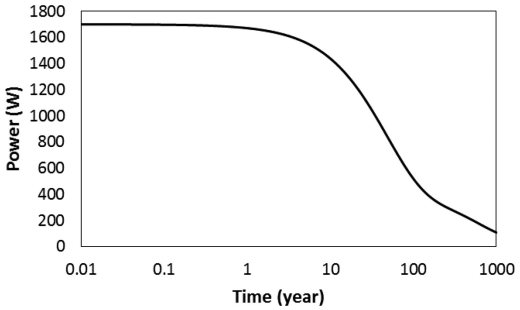


Figure 3. Heating power evolution of the canister.

3.2 *Materials properties*

The material parameters of the host rock and bentonite are summarized in Table 1. It is worth to note the values for density, heat conductivity and heat capacity are the values for the solid phase only. When the temperature dependent water properties are not considered, the density and viscosity of water are assumed as a constant value of 1000 kg/m^3 and 1.0×10^{-3} Pa·s respectively. Otherwise, Equation (9) and Equation (10) are used to calculate the density and viscosity. The heat conductivity and the specific heat capacity of water are 0.6 W/(m·K) and 4183 J/(kg·K), respectively.

In the present analysis, we would like to highlight the TH physical processes in the buffer system (bentonite). This is why the host rack is modeled with a thermos-elastic constitutive law while the bentonite is considered as a non-deformable medium. Note that the canister is modeled as an impermeable and non-deformable material.

3.3 *Simulation processes and cases*

The excavation of the EBS zone and a long enough ventilation process are simulated to generate a reliable initial conditions for the following TH coupling analysis of the EBS system as suggested by [11]. Five different coupling cases are summarized in Table 2.

Table 1. Parameter for the rock material and bentonite.

Parameter	Rock material	Bentonite
Particle density	2700 kg/m^3	2780 kg/m^3
Initial degree of saturation	1	0.61
Porosity	0.003	0.438
Retention curve s [MPa]	$S_r = \left(1 + \left(\frac{s}{1.74}\right)^{1/0.4}\right)^{-0.6}$	If s ≥ 3 MPa $S_r = 1 - \ln(s/3)/7$ If s < 3 MPa $S_r = 1$
Intrinsic permeability	1.0×10^{-17} m^2	6.4×10^{-21} m^2
Relative permeability	$\sqrt{S_r}\left(1 - \left(1 - S_r^{1/0.6}\right)^{0.6}\right)^2$	S_r^3
Tortuosity	1.0	1.0
Heat conductivity	2.4 W/(m.K)	Eqution 11
Specific heat capacity	770 J/(kg.K)	800 J/(kg.K)
Thermal expansion coefficient	7.2×10^{-6} K^{-1}	3.4×10^{-6} K^{-1}
Biot's coefficient	1.0	1.0
Young's modulus	62 GPa	–
Poisson ratio	0.24	0.2

Table 2. Different TH coupling cases.

Case	Description
1	T analysis without considering H effects
2	H analysis without considering T effects
3	TH coupling analysis without considering diffusion process and temperature dependent water properties
4	TH coupling analysis only considering diffusion process
5	TH coupling analysis considering diffusion process and temperature dependent water properties

4 RESULTS AND INTERPRETATION

4.1 *Temperature evolution*

The simulated temperature evolution results under different coupling cases are summarized in the Figure 4. At the beginning of heating, the temperature around the canister increases quickly due to a high heating power. The maximum temperature at the hot section is 81.4°C without considering the hydraulic effects, while the maximum temperature at the cool section is 59.9°C. Moreover, a temperature gradient along the radial direction is also generated during this process. It is clear that the temperature gradient at the cool section is quite small owing to its far distance to the canister. As showed in Figure 3, the heating power decreases quickly after 20 years. This induces the decrease of temperature but also the loss of the temperature gradients. There is almost no temperature gradient along the radial direction around 100 years. The temperature reaches the equilibrium around 1000 years. Therefore,

only the distance to canister and the heating power affect the evolution of temperature.

When considering the hydraulic effects, the maximum temperature at the hot section decreases to 78.4°C and that at the cool section decreases to 59.0°C. The reason is that the specific heat capacity of water is higher than that of bentonite. With the hydration process, the degree of water saturation at the buffer zone increases and this leads to an increase of the total specific heating capacity of the bentonite, see Equation 12. The increase of the water saturation also increases the thermal conductivity of the bentonite according to Equation 11, meaning faster to reach the maximum of temperature. However, these phenomena are not clearly shown in the Figure 4. The reason may be that the water saturation modification is very small owning to the low permeability of the bentonite. The temperature gradients along the radial direction also decrease while considering the hydration process. Comparing Figures 4b, 4c and 4d, it is noticeable that the vapor diffusion process and temperature dependent water properties have small effects on the temperature evolution of temperature at both the cool and the hot sections.

4.2 *Water pressure evolution*

The simulated water pressure evolutions under different coupling cases are summarized in the Figure 5. Without considering the temperature evolution and thermal effects, the section near the canister reaches the full saturation at first due to the short distance. For example, much more water at the point P13 flows into the inner part than that at P23. The P13 reaches the full saturation condition around 2.5 years, 0.8 years later than that at P23. The whole buffer zone reaches the full saturation condition around 8.5 years.

When considering the thermal evolution only, a minor change of hydration process is found in Figure 5b. However, the vapor diffusion process sees a great modification in Figure 5c. The water pressure at P21 decreases at the beginning of heating, and reaches the minimum value of −77.3 MPa around the 0.228 years. The reason is that with the high temperature generated at P21, a strong water evaporation happens at P21. This water vapor moves towards outside and condenses at a cooler zone, increasing the hydration rate in the middle part, see P22. Owning to the small thermal gradient at the cool section, considering the vapor diffusion process leads slight modification of hydration process.

Both the density and the dynamic viscosity of water decrease with the increase of the temperature. These physical phenomena are only considered in the case 5, and the corresponding results are showed in Figure 5d. Comparing to case 4, the major difference is that the hydration process is accelerated by the decrease of dynamic viscosity of water. The whole buffer system reaches the full saturation condition around 5 years, about 2 years faster than that under the case

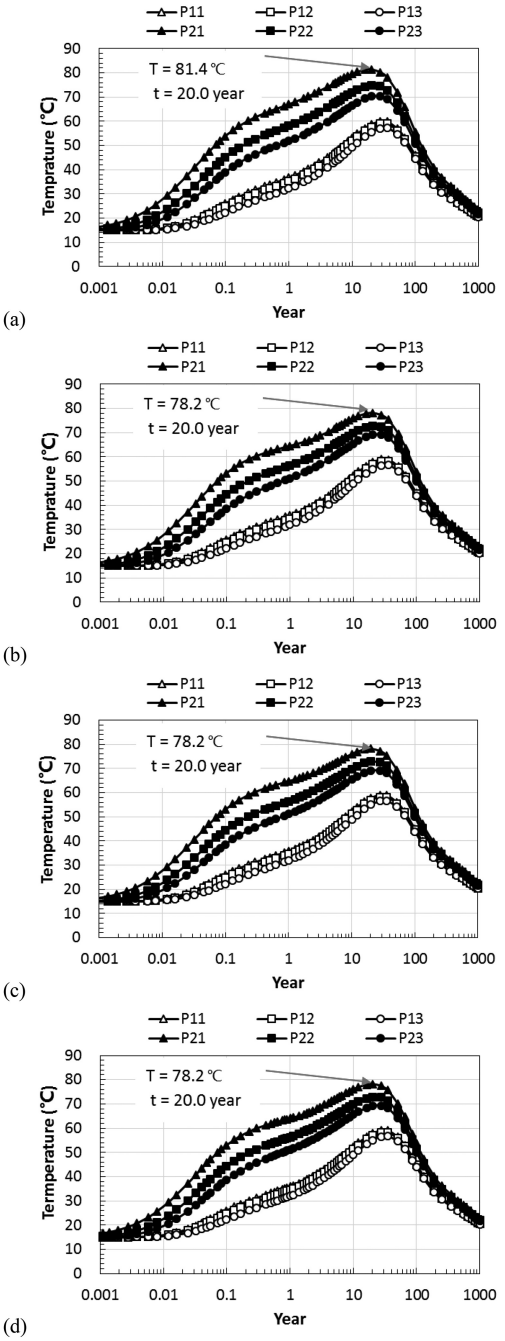


Figure 4. Temperature evolution at different coupled cases: (a) case 1; (b) case 3; (c) case 4; (d) case 5.

4. The decrease of the dynamic viscosity also counteracts the effects of the vapor diffusion. Taking P21 for example, the minimum water pressure increases from −77.3 MPa to −64.2 MPa and the time to reach this minimum water pressure decreases from 0.228 years to 0.163 years. The reason is that the water flow rate

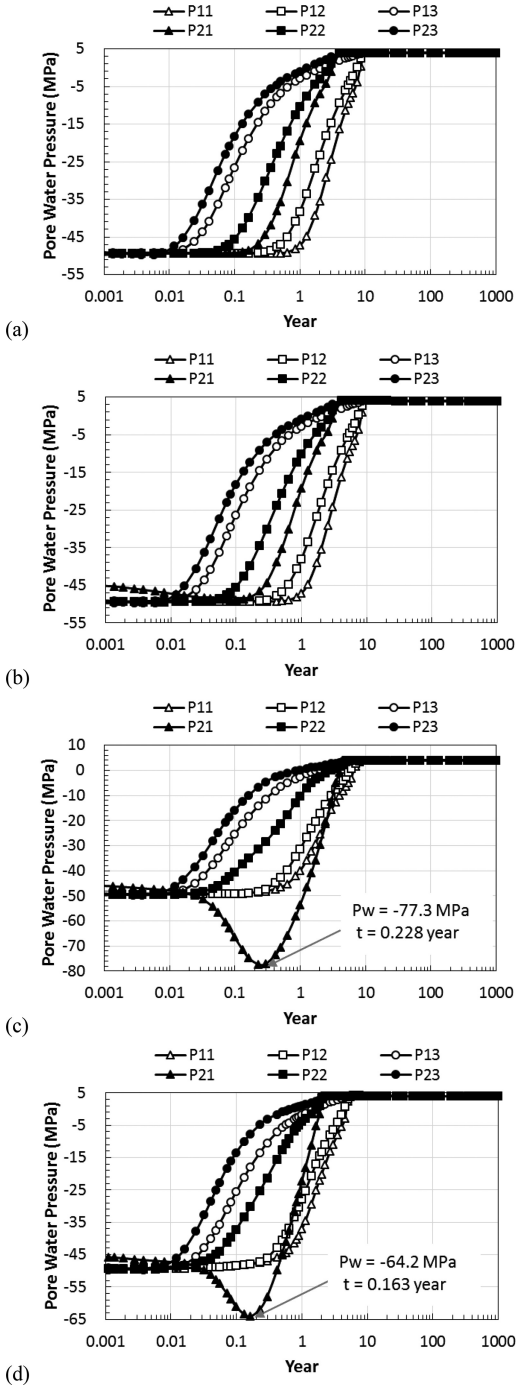


Figure 5. Pore water pressure evolution at different coupled cases: (a) case 2; (b) case 3; (c) case 4; (d) case 5.

increases due to the decrease of viscosity. Therefore, the vapor diffusion process and the temperature dependent water properties are the two main factors which dominate the thermal effect on the hydraulic processes.

5 CONCLUDING REMARKS

As the most feasible method to isolate the high-level radioactive waste from human environment, the geological disposal is widely accepted and adopted by many countries. To ensure the efficiency of this disposal method, the EBS should be chosen and investigated carefully due to the complex THM processes occurring in it. In this paper, the TH coupling processes are investigated in details and the following conclusions can be summarized:

1. The main influence factors of hydraulic processes on temperature evolution are the water saturation dependent thermal conductivity and specific heat capacity.
2. The main influence factors of thermal processes on the hydration are the vapor diffusion and the temperature dependent water properties.
3. The above two coupled factors are suggested to be taken into account in the design and the assessment of EBS system.

ACKNOWLEDGEMENT

The authors wish to thank NAGRA for its support and the Chinese Scholarship Council for its financial support to the first author.

REFERENCES

[1] IAEA, 1993. International Atomic Energy Agency: *Report on radioactive waste disposal*. Technical Reports Series No. 349.
[2] IAEA, 2006. International Atomic Energy Agency: *geological disposal of radioactive waste*. Safety Requirements, IAEA Safety Standards Series.
[3] Bowen R.M., 1982. Compressible porous media models by use of the theory of mixtures. *International Journal of Engineering Science* 20:697–735.
[4] Panday S. & Corapcioglu M.Y., 1989. Reservoir transport equations by compositional approach. *Transport in Porous Media* 4(4):369–393.
[5] Collin F., Li X.L., Radu J.P. & Charlier R., 2002. Thermo-hydro-mechanical coupling in clay barriers. *Engineering Geology* 64(2–3):179–193.
[6] Lagmine, 2012. *Lagamine Code User's Guide*. University of Liege.
[7] Dupray F., Francois B. & Laloui L., 2013. Analysis of the FEBEX multi-barrier system including thermo-plasticity of unsaturated bentonite. *International Journal for Numerical and Analytical Methods in Geomechanics* 37:399–422.
[8] Collin F., 2003. *Couplages thermo-hydro-mécaniques dans les sols et les roches tendres partiellement saturés*. PhD Thesis, Université de Liège in Department ArGEnCo, Liège, Belgium.
[9] Gerard P., Charlier R., Chambon R. & Collin F., 2008. Influence of evaporation and seepage on the convergence of a ventilated cavity. *Water Resources Research*, 44:W00C02.
[10] http://www.skb.se/Templates/Standard____24109.aspx.
[11] Qiao Y.F., Ferrari F. & Laloui L., 2015. THM modelling and analysis of FEBEX-DP project. *Technical report*, LMS, EPFL, Lausanne, p.29.

Engineering applications and case histories

Field testing

This page intentionally left blank

Unsaturated Soil Mechanics—from Theory to Practice – Chen et al. (Eds)
© 2016 Taylor & Francis Group, London, ISBN 978-1-138-02921-7

Monitoring of a suburban environment: Soil-plant-atmosphere and clay movements

D.A. Cameron, S.J. Vorwerk & G. Keppel
School NBE, University of South Australia, Mawson Lakes, Adelaide, Australia

ABSTRACT: Tree roots remove and re-distribute soil moisture. If the soil suffers seasonal unsaturation and is essentially clay, the ground will experience greater settlement than normal during the drying months. Of great concern to building authorities, engineers and the community is the potential damage to buildings and infrastructure that may ensue. The Australian Standard for construction of residential footings has, since 2011, incorporated some broad guidelines for estimating the additional drying settlement due to trees. These rules require extensive validation. This paper describes the establishment of a field site to study the interactions between the weather, the foundation soil and four species of trees (about 12 years old), planted in streets in a suburb of Adelaide, Australia. Selected initial monitoring data are presented, which concern initial potential reference evapotranspiration, soil suction profiles, soil moisture changes and soil movement near two Australian tree species; paperback and Queensland box. The ultimate aim of the research is to develop better numerical modelling of the impacts of trees on clay soils.

1 INTRODUCTION

The Standard in Australia for design and construction of residential footings, AS2870-2011, (Standards Australia 2011) presents a site classification process. This classification relies to an extent on the Thornthwaite Moisture Index (TMI) to provide the design depth of suction change. The TMI incorporates potential evapotranspiration, drainage and the water holding capacity of the soil (Leao & Osman-Schlegel, 2013). Yearly TMI is not a constant for a region; however long term average annual TMIs can reflect prevailing weather patterns. If the TMI is negative, then expansive soils are more likely to cause problems.

The design suction changes in the Standard are for normal site conditions, which do not include soil drying due to trees and shrubs. Tree roots are known to draw moisture from clay soil at depth in semiarid to temperate climates, resulting in deep shrinkage settlement (Cameron, 2001). Guidelines have since been provided in AS2870 for the extra suction changes due to drying of soils by trees, based on experience in South Australia using similar guidelines and limited investigations of house footing failures (Cameron and Beal, 2011). More data concerning different species and within different climates are needed to improve the guidelines (Standards Australia 2011). The prediction of the destabilisation, or stabilisation, of clay soils due to tree roots changing soil moisture requires better models from an improved understanding of the soil-plant-atmosphere continuum, or SPAC (Amabile et al., 2014). An excellent, but pessimistic, early treatise on SPAC modelling in agriculture was given by Philip (1966). Empirical to theoretical approaches have been used to predict the water use of crops, orchards and individual trees. For example, Pereira et al. (2006) related transpiration for irrigated orchard trees to potential reference evapotranspiration, ET_o, of short grass multiplied by the ratio of leaf area (m^2/tree) to the assumed leaf area index (LAI) of short grass (2.88 m^2/m^2). The relationship was strong for apple trees, walnut trees, olive trees and grapevines, but failed when applied to data from Kiwifruit vines.

Geotechnical engineers require simple but reliable SPAC models, combined with the ability to predict ground settlements. Fatahi et al. (2008) developed a numerical model in ABAQUS to predict transpiration, but did not deal with weather patterns well. For a single tree, the root formation geometry is needed and an estimate of soil matric suction at the wilting point. As water becomes less freely available, transpiration is affected and so the empirical relationship of Feddes et al. (1978) was applied to model this behaviour. An unsaturated effective stress law was adopted to translate suctions into stresses and hence permit estimation of soil deformation. Hemmati et al. (2012) developed a model that relied on a canopy coefficient, which may be derived from LAI and leaf conductance, to determine the proportion of potential evapotranspiration contributing to actual evapotranspiration. Therefore, knowledge of the root system is not required. Soil layers were characterized by SWCCs and shrinkage curves. These relatively simple models of a complex natural problem are not suited to

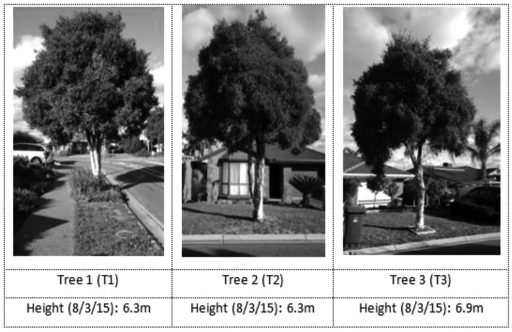


Figure 1. Prickly Paperbark trees at Site 1, Adelaide.



Figure 2. Site 1 layout.

suburban street trees which are influenced also by neighboring infrastructure.

In order to develop appropriate models for suburban street trees, collaborators at the University of Wollongong are developing the model by Fatahi et al. (2008). To assist this process, field data have been collected from the suburban area of Walkley Heights, Adelaide, in Australia, from late 2013 to early 2015. This paper presents the design of the field study and preliminary findings.

2 SUBURBAN STUDY SITE

The study area is located in the suburb of Walkley Heights, Adelaide, South Australia, within the City of Salisbury. In this 15 year old suburb, soil profiles of house sites are commonly classified as extremely reactive according to AS2870-2011. There is abundant evidence of cracking and distortion in roads, although masonry veneer houses on deep stiffened raft footings have generally performed well.

The study sites were chosen based on observed level of damage to pavements and the availability of specific street trees species; Chinese elm (Ulmus parvifolia), golden rain tree (Koelreuteria paniculata), ornamental pear (Pyrus ussuriensis), Queensland Box (Lophostemon confertus) and prickly paperbark (Melaleuca styphelioides). Of the seven study sites just two are



Figure 3. Queensland box trees at Site 2, Adelaide.



Figure 4. Site 2 layout.

detailed in this paper. Site 1 is part of a suburban street, planted with prickly paperbacks. Three replicate trees (T1, T2 and T3) have been selected as indicated in Fig. 1 and Fig. 2. Survey level points are indicated as points across the road. A similar setup has been implemented at Site 2, with a selection of Queensland box trees (T4, T5 and T6), as is shown in Fig. 3 and Fig. 4.

3 SITE SOIL PROPERTIES

Soil profiles at each site have been assessed, largely based on Atterberg Limits and shrink-swell indices, I_{ss} (Fityus et al., 2005). Figures 5 and 6 provide soil profiles near the target trees (T1 and T4), which indicate that calcareous soil overlies extremely reactive clay soil to a depth of 1.2 m. In this Figure, I_{ss} is the shrink-swell index with units of % strain/change in logarithm of total suction in kPa, while LL, PI and LS represent liquid limit, plastic index and linear shrinkage in percentages, respectively. The site classification parameter, y_s is indicated in the Figure captions. Both sites are highly reactive.

4 MONITORING METHODS

The Food and Agriculture Organisation's (FAO) potential reference evapotranspiration, ET_o, is based on weather data and fields with uniform crops (Walter

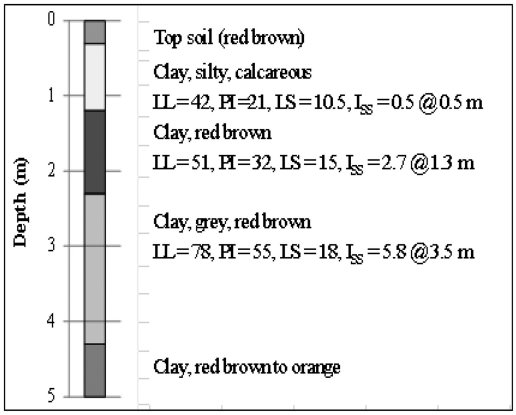


Figure 5. Soil profile description Site 1, $y_S = 61$ mm.

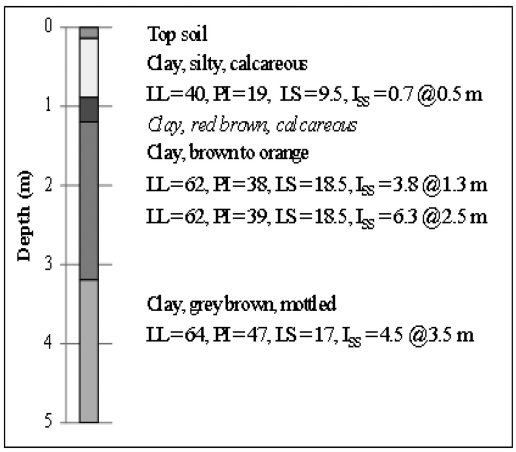


Figure 6. Soil profile description Site 2, $y_S = 65$ mm.

et al., 2005). Weather data (solar radiation, air temperature, humidity and wind speed) were obtained from a weather station at the University of South Australia, Mawson Lakes Campus, a 7 km drive away. The weather station is approximately 75 m closer to sea level than the field site.

The movement of moisture within clay soil has been investigated primarily through use of a neutron moisture meter (NMM) depth probe, lowered down access tubes, which have been established to an average depth of five metres. The layout of the sites (with regards to NMM boreholes), follows the pattern: near the primary-targeted tree, well away from the tree's influence and under the nearby asphalt pavement. NMM data are collected six times a year from 25 NMM boreholes.

Soil suction samples were collected during the installation of NMM access boreholes and occasionally at other times. Total suctions were determined in a controlled laboratory environment using Wescor dew point hygrometer chambers in accordance with Standards Australia AS2189 (Standards Australia, 1998). Solute suctions were estimated from electrical conductivity testing of soil-water solutions (1:5) The solute suction was increased in proportion to the field moisture content. Matric suction was taken as the difference between solute and total suction.

Ground movement is captured within each season through level surveys of steel road pins and concrete pads in the verge (Figs. 2 & 4). Surveying is aided by a the permanent survey mark, installed and maintained by the Australian Land Title Office, and four, 6 m deep bench marks (within the research area). For recording deeper-seated movement, access tubes for magnetic extensometer measurements have been established across all sites, next to at least one of each of the four main tree species. Data are collected over an average depth of 4 m at 0.5 m intervals.

Tree physiology is being monitored, which includes tree dimensions (circumference and height), leaf area index (LICOR LAI-2200), leaf water potential (Scholander device) and leaf conductance (DELTA T, AP4 porometer). The latter two plant properties have been shown to correlate strongly with transpiration (Cochard et al., 2002).

The measurements of tree physiology are taken once a month. However sap flow is measured continuously with sap flow meters (SFM1, ICT International) since December 2014 on four different tree species. These species-specific observations will enhance the strength of SPAC models (Manzoni et al., 2013).

5 EARLY INDICATIONS

5.1 *The atmosphere*

The potential reference evapotranspiration, ET_o, between November 2013 and May 2015 is presented in Figure 7 for a short crop (Walter et al., 2005). Three summer periods are indicated on this plot, however, for this paper the summer/autumn period of 2014–2015 is of most interest. In this period, ET_o peaked at about 8 mm/day.

5.2 *The soil*

Selected NMM data collected over 2014 at both study sites near the target trees (T1 & T4) are detailed in Figs. 8 and 9. Unfortunately the NMM depth probe required repair in early 2015, so the data are limited to that end time.

Higher NMM count ratios indicate wetter soil, and it can be seen that some wetting up is evident in the first 2 m between April and September 2014.

In April, the soil below the pavement was wetter than adjacent to the tree.

The differences in NMM count ratios at Site 1 are shown in Fig. 10 in autumn 2014. The trends are as expected; on the opposite side of the road away from the tree ("Away"), the soil was noticeably wetter than near the tree, while the profile below the road was a little wetter than near the tree. At site 2, the soil below the road was much wetter.

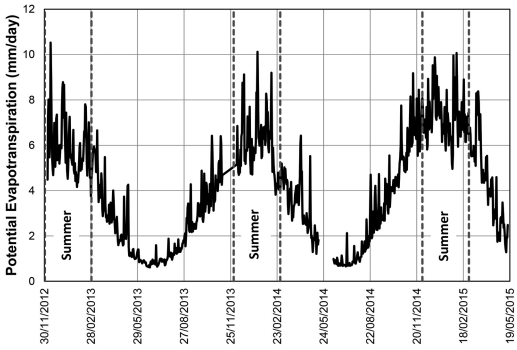


Figure 7. Potential evaporation from weather data.

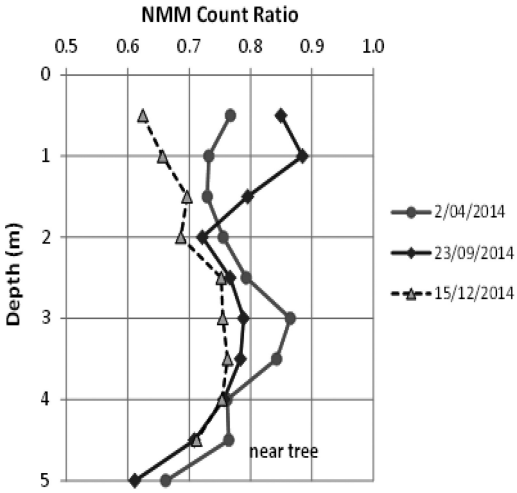


Figure 8. Site 1 Soil moisture NMM count ratios.

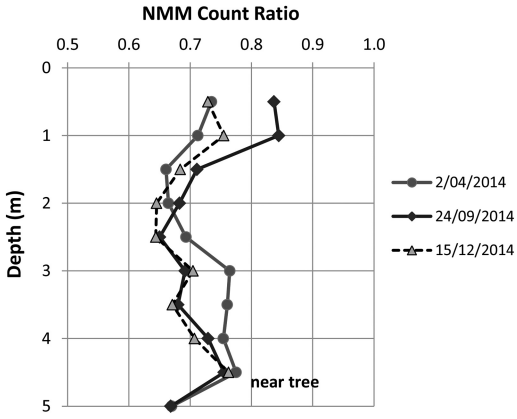


Figure 9. Site 2 Soil moisture NMM count ratios.

Total soil suction data are given in Figure 11 for Site 1, again in autumn 2014 for comparison with the NMM data in Fig. 10. The two Figs. agree quite well, with distinctly low suctions observed "Away".

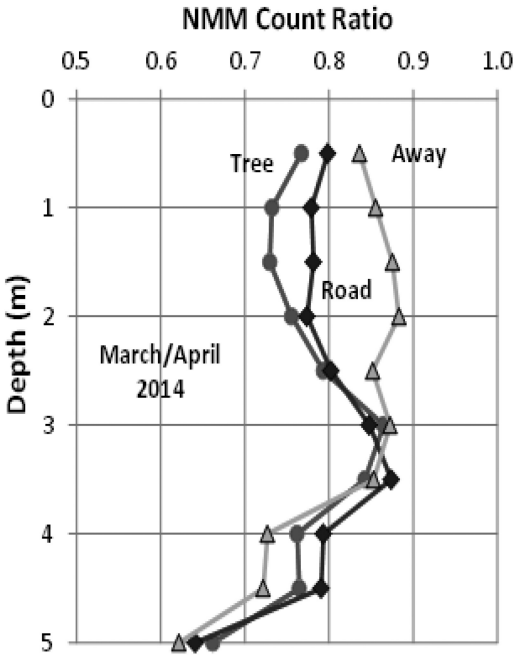


Figure 10. NMM count ratios, Site 1, 2nd April 2014.

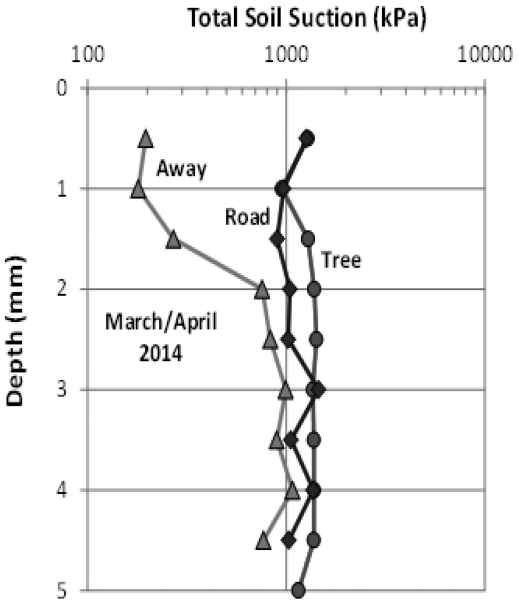


Figure 11. Total soil suction profiles, Site 1, March/April 2014.

Soil specimens from sampling for shrink-swell testing near the tree at both sites in October 2014 indicated that at a depth of 1.3 m at Site 1 and at 0.5 m at Site 2, the soil had matric suctions which were approximately zero, indicating soil saturation. The total suctions at this time were generally close to 1 MPa, ranging

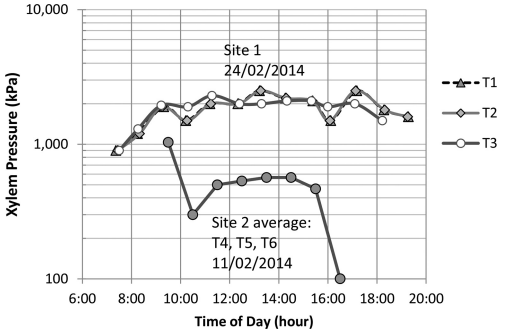


Figure 12. Daily xylem pressures, Feb 2014.

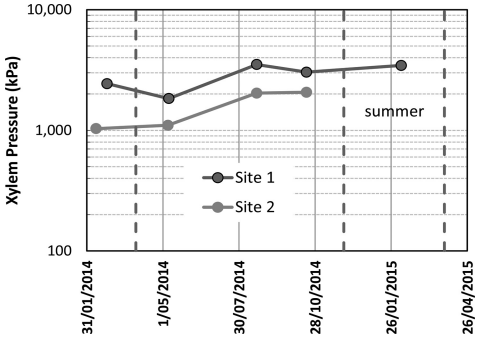


Figure 13. Site 1, xylem pressure average maximum values (Feb 2014 to Feb 2015).

between 400 and 1400 kPa. Further investigation into solute suction is being undertaken.

5.3 *The trees*

Leaf xylem pressures have been plotted in Figs. 12 and 13. The first Figure indicates the uniformity of readings during a day in February 2014 for the prickly paperbark at Site 1 (trees T1, T2 and T3). The Queensland box trees at Site 2 showed less agreement and so an average plot is given for all 3 specimens. The paperbark trees appear to be under significantly greater water stress than the Queensland box trees, suggesting greater water availability at Site 2.

Fig. 13 shows the variation of xylem pressures over one year. The maximum average values of xylem pressure reached were 2.1 and 3.5 MPa for the box trees and paperbarks, respectively. The Queensland box trees were consistently under less stress than the prickly paperbarks, although both species appeared healthy. Total soil suction profiles indicated similar moisture conditions near each of the target trees at both sites, however, below the road at Site 2, significant moisture seemed to be held to 2 m depth.

Measured daily sap flux (transpiration) for trees T1 and T4 at Sites 1 and 2, respectively, are plotted in Fig. 14 over the period of measurement of approximately 4 months. Measurements were taken on the north side of the tree. Checks on sap flow on the south

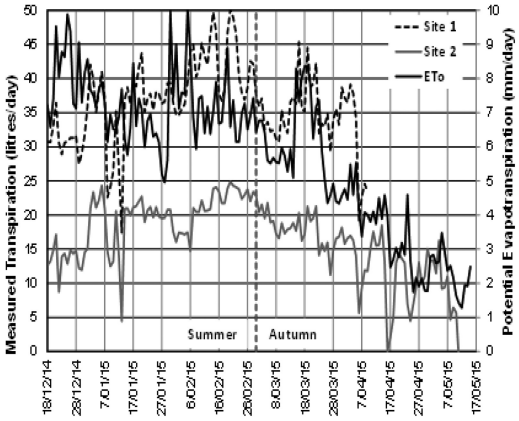


Figure 14. Daily sap flux and ET_o.

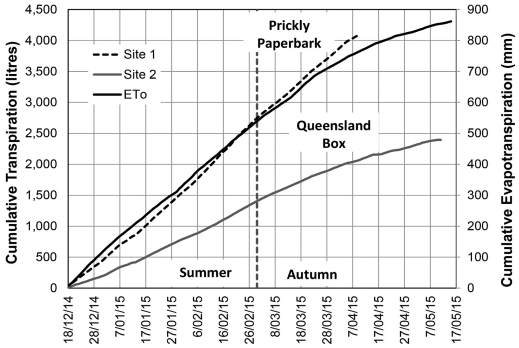


Figure 15. Cumulative transpiration and ET_o.

side have been made over shorter periods to correct the estimated flow for nonuniformity of flow across the trunk. Corrections have not been made to the data presented herein. It must also be noted that sap thickness has been estimated as a sixth of the xylem diameter, as cores have yet to be taken.

The prickly paperbark has used more water than the Queensland box tree and this is more evident in the cumulative transpiration plot in Fig. 15. From 18th December to 7th April, the paperbark had been estimated to have used 4 kL of water, while the estimate for the Queensland box tree was half of that value. Corresponding values of ET_o in mm/day or mm are provided in Figs. 14 and 15, using a secondary vertical axis. Daily sap flow showed some correspondence with ET_o, which will be investigated.

Trends of cumulative transpiration better match ET_o for both tree species. Assuming transpiration equalled ET_o at the end of summer, the transpiring area of each canopy may be estimated to be 4.9 m^2 and 2.5 m^2 for trees at Sites 1 and 2, respectively.

5.4 *Ground movement*

A level survey taken in February 2014 formed the set of datum levels for the two sites, which was well after the trees were established. The difference in reduced

level of the road next to tree T1 up until late April 2015 was 10 mm, while at Site 2 it was closer to 18 mm near tree T4.

6 DISCUSSION AND CONCLUSION

At the two sites reported on in this paper, ground movements have been modest. Considering the soil profiles, it is unlikely that water has yet to be taken from the deeper and more reactive soil layers. Confirmation of the soil water uptake zone will be sought in the next growth period in 2015/2016.

Initial estimates of cumulative water uptake by the trees showed an almost linear increase over time into early autumn, which matched the trend of cumulative ET_o, suggesting that soil drying has not been excessive.

A difference in species' water demand was noted, with the prickly paperbark estimated to use about twice as much water as the Queensland box tree.

Not all the field data have been able to be presented in this paper. However it has become clear that more rigorous monitoring over the next growth period will be needed to achieve the objective of a simple empirical SPAC model.

ACKNOWLEDGEMENTS

The research presented in this paper is supported by the Australian Research Council, the University of South Australia (School of Natural & Built Environments) and the City of Salisbury. The ARC project is in partnership with the University of Wollongong, which is leading the project.

REFERENCES

Amabile, A., Balzano, B., Caruso, M. & Tarantino, A. 2014. A conceptual model for root water extraction taking into account root depth, root density and vulnerability to xylem cavitation. 6th Int. Conf. Unsaturated Soils, Sydney, pp. 1047–1052.

Cameron, D.A. 2001, 'The Extent of Soil Desiccation near Trees in a Semi-Arid Environment', Geotechnical and Geological Engineering, vol. 19, pp. 357–370.

Cameron, D.A. & Beal, N.S. 2011. Estimation of foundation movement and design of footing systems on reactive soils for the effects of trees. Australian Geomechanics Journal, vol. 46, no. 3, pp. 97–113.

Cochard H., Coll L., Roux X. & Améglio, T. 2002. Unraveling the effects of plant hydraulics on stomatal closure during water stress in walnut. Plant Physiology, 128, Jan., pp. 282–290.

Fatahi, B., Indraratna, B. & Khabbaz, H. 2008. Conceptual development and numerical modelling of vegetation induced suction and implications on rail track stabilisation. 12th Conf. Int. Assocn. for Computer Methods and Advances in Geomechanics (IACMAG), Goa, India.

Feddes, R.A., Kowalik, P.J. & Zaradny, H. 1978. Simulation of field water use and crop yield. Pudoc for the Centre for Agricultural Publishing and Documentation, Wageningen.

Fityus, S.G., Cameron, D.A. & Walsh, P.F. 2005, The shrink swell test. ASTM Geotechnical Testing Journal, vol. 28, no. 1, pp 1–10.

Hemmati, S., Gatmiri, B., Cui, Y. & Vincent, M. 2012. Thermo-hydro-mechanical modelling of soil settlements induced by soil-vegetation-atmosphere interactions. Engineering Geology, vol. 139-140, pp. 1–16.

Hill, W. 1983. Tree root damage to low rise buildings. Structural Survey, vol. 1, no. 3, pp. 254–261.

Kalantari, B. 2012. Engineering significance of swelling soils. Research J. Applied Sciences, Engg. and Technology, vol. 4, no. 17, pp. 2874–2878.

Leao, S. & Osman-Schlegel, N.-Y. 2013. TMI for urban resilience: measuring and mapping long-term climate change effects on soil moisture. Proceedings 7th Australasian Housing Researchers' Conference, Fremantle, WA.

Manzoni, S., Vico, G., Porporato, A. & Katul, G. 2013. Biological constraints on water transport in the soil–plant–atmosphere system. Advances in Water Resources, vol.51, pp. 292–304.

Novák, V. 2012. The role of plants in transport processes in the soil-plant-atmosphere system. Evapotranspiration in the Soil-Plant-Atmosphere System, Springer, pp. 127–144.

Pereira, A.R., Green, S., Villa Nova, N.A., 2006. Penman-Monteith reference evapotranspiration adapted to estimate irrigated tree transpiration. Agricultural Water Management, 83(1–2), pp.153–161.

Richards, B.G., Peter, P. & Emerson, W.W. 1983. The effect of vegetation on the swelling and shrinking of soils in Australia. Geotechnique, vol. 33, pp. 39–127.

Philip, J.R. 1966. Plant water relations: some physical aspects. Annual Review of Plant Physiology, vol. 17, no. 1, pp. 245–268.

Standards Australia 1998. Soil Moisture Content Tests – Determination of the total suction of a soil – Standard Method. AS1289.2.2.1-1998. SAI Global.

Standards Australia 2011. Residential Slabs and Footings, AS 2870-2011. SAI Global.

Walter, I., Allen, R.G., Elliott, R., Itenfisu, D., Brown, P., Jensen, M.E., Mecham, B., Howell, T.A., Snyder, R., Eching, S., Spofford, T., Hattendorf, M., Marin, D., Cuenca, R.H. & Wright, J.L. 2005. The ASCE (American Society of Civil Engineers) Standardized Reference Evapotranspiration Equation. The Environmental and Water Resources Institute.

Unsaturated Soil Mechanics—from Theory to Practice – Chen et al. (Eds)
© 2016 Taylor & Francis Group, London, ISBN 978-1-138-02921-7

Field monitoring of suction distribution in Coarse-Grained and Fine-Grained residual soil

N. Gofar & H. Rahardjo
School of Civil and Environmental Engineering, Nanyang Technological University, Singapore

M.L. Lee
Faculty of Engineering and Science, Universiti Tunku Abdul Rahman, Kuala Lumpur, Malaysia

ABSTRACT: This paper compares the suction distribution monitored at two sites whereby the soil can be characterized by Coarse-Grained (CG) and Fine-Grained (FG) residual soils. The sites were located 2 km apart, thus similar rainfall characteristics could be expected. The rainfall was monitored by a rain-gauge while matric suctions were monitored for a period of one year using Jet fill tensiometers. Readings were taken three times a day to represent the daily cyclic suction variations. The field monitoring shows that the maximum suctions were 26 kPa and 74 kPa for CG and FG, respectively, while the minimum suction was zero. The range of suction obtained from the field monitoring data yields reasonably consistent results with those determined from the analysis of SWCC. The minimum suction was achieved in CG soil after a major rainfall with an intensity higher than its saturated permeability while the minimum suction in FG soil is achieved after a 7-day antecedent rainfall. The maximum suction was attained after 18 days without rain. Rainfall-runoff analysis shows that the amount of infiltration is controlled by saturated permeability, rainfall intensity, and antecedent rainfall.

1 INTRODUCTION

Negative pore-water pressure or suction has been recognized as the contributing factor in unsaturated slope stability. The magnitude of the suction is influenced by rainfall infiltration into soil. Field monitoring of suction response to rainfall infiltration has been adopted to study the mechanism of rainfall-induced slope failure. The field measurements show that the matric suctions could be lost during wet seasons, thus the shear strength of the soil decreases and the slope becomes more susceptible to failure.

Some studies on infiltration process have been performed based on field monitoring and several conclusions were derived from the study. For instance, Tsaparas et al. (2003) found that the changes in the pore water pressure were affected by both total rainfall and initial conditions of the slope. Li et al (2005) concluded that the propagation of wetting front was limited to the top 3 m of soil and the movements of wetting front were different depending on the rainfall pattern. Other studies (Pradel & Raad, 1993; Tsaparas et al., 2002; Cai and Ugai, 2004) inferred that permeability plays an important role on the effect of rainfall infiltration on slope stability. The slopes with low permeability failed after sufficient duration of rainfall, while the failure of slope with comparatively high permeability possibly took place during rainfall with a shorter duration and a greater intensity.

Further study by Gofar et al (2008) and Lee et al (2009) shows that the ratio of rainfall intensity to the saturated permeability of soil (q/k_t) can be used as an indication for determining the critical rainfall pattern. If the rainfall intensity is less than the saturated permeability, the rainfall with the highest intensity and shortest duration is critical. Otherwise, the long duration rainfall appears to be the critical rainfall pattern on soil with low saturated permeability. The duration of antecedent rainfall which establishes the initial condition is also an important factor. Besides the permeability, the amount of rainfall that infiltrates into the soil is also affected by the surface cover and the hydraulic properties of the soil. Some soils never reach fully saturated state while others never achieve a very high suction value under typical tropical climate.

In this paper, data obtained from field monitoring of suction distribution and factors affecting the resulting distribution were evaluated. Two types of soil were considered i.e. coarse-grained (CG) and fine-grained (FG). The SWCC and saturated permeability of the soils were obtained experimentally while the hydraulic conductivity function was estimated using the modified Fredlund & Xing (1994) equation. The actual amount of rainfall infiltration resulting from several rainfall events was evaluated on site and used for the estimation of the advancement of water front.

2 FIELD SETUP

The field study was conducted at two sites whereby the soil can be characterized by coarse-grained (CG) and

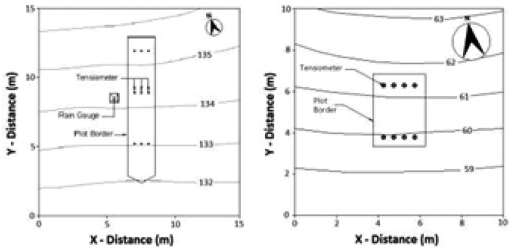


Figure 1. Configuration of field plot.



Figure 2. Runoff collector installed at Site 1.

fine-grained (FG) residual soils. The sites were located 2 km apart, thus similar rainfall characteristics could be expected. Site 1 plot was 2 m in width and 10 m long, poised a sloping angle of 21°, consisted of clayey gravel (GC) while Site 2 was 2.5 m in width and 4 m in length and inclined at an average angle of 30°, comprised sandy silt (MH). The details on the location of the sites can be found in Gofar et al (2008). The rainfall was monitored by a rain-gauge located at Site 1. Matric suctions were monitored using Jet fill tensiometers at depths of 0.5, 1.0 and 1.5 m in three rows (Site 1) and two rows (Site 2). Readings were taken three times a day i.e. at 7 a.m., 12 noon, and 7 p.m. to represent the daily cyclic suction variations. Suction monitoring was performed for one year. Site 1 was monitored from 12th September 2006 to 11th September 2007 while Site 2 was monitored from 1st January 2007 to 31st December 2007. Monitoring of Site 2 was delayed because the site was slightly impaired during the extreme rainfall on December 2006. In addition, a runoff collector was installed at the site with CG soil to determine the actual amount of rainfall infiltration. Figure 1 shows the configuration of the field plot while Figure 2 shows the runoff collector at Site 1.

3 SOIL PROPERTIES

Figure 2 shows the grain size distribution of the soil obtained at the sites. Following ASTM D2487, the coarse- and fine-grained soils can be classified as SC and MH. The fine-grained soil has liquid limit of 68% and plasticity index of 24%. The specific gravity of the CG and FG soils are 2.65 and 2.63, respectively.

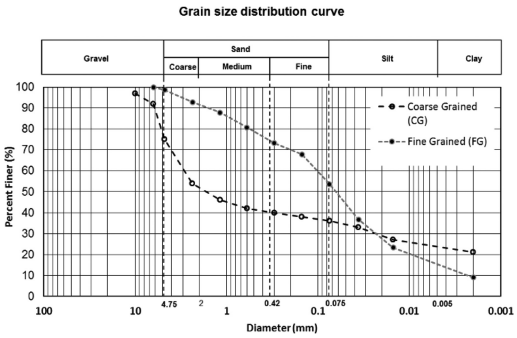


Figure 3. Grain size distribution of the soils found at site.

The samples for laboratory tests were prepared at dry unit weight of 90% relative density and water content at 70% saturation.

The SWCC was obtained experimentally by conducting pressure plate tests using the axis translation technique whereby the air pressure (u_a) inside the apparatus was increased while the pressure of the water phase (u_w) was maintained at the atmospheric level (Fredlund and Rahardjo, 1993). Due to the time required for equilibrium, only a few data in the lower suction range were obtained for each soil. Thus, fitting equation (Fredlund & Xing, 1994) for $C(\psi) = 1$ was used to construct the SWCC curves. Figure 4 shows the SWCC of the soils together with the properties derived from the curves.

Comparing the plotted SWCC in Figure 4, FG soil has a relatively higher AEV as compared to CG because the soil comprises a higher content of clay mineral (Fig. 3), and hence possesses a high water carrying capacity. On the other hand, CG is capable of dissipating water quickly, resulting in a lower AEV. At residual water content, FG requires a high suction to draw out water because of the role of stern layer in holding the water layer. The transition zone for FG covers a wider suction range of 0.9–76 kPa as compared to CG where the transition zone is only between 2.8 and 26 kPa. The transition zone for FG is significantly wider and the slope of the transition zone is less steep than that of the CG. These agree with the discussion in Fredlund & Rahardjo (1993).

The coefficients of saturated permeability of the CG and FG are 1.23×10^{-5} and 3.25×10^{-8} m/s respectively. Based on these values and the SWCC, the permeability function can be constructed following the Fredlund et al (1994) permeability function (Figure 5) based on SWCC.

4 RAINFALL-RUNOFF ANALYSIS

Not all rainfall contribute to infiltration. From the definitions, the rainfall may be separated into four components, i.e. runoff, infiltration, interception (rainfall

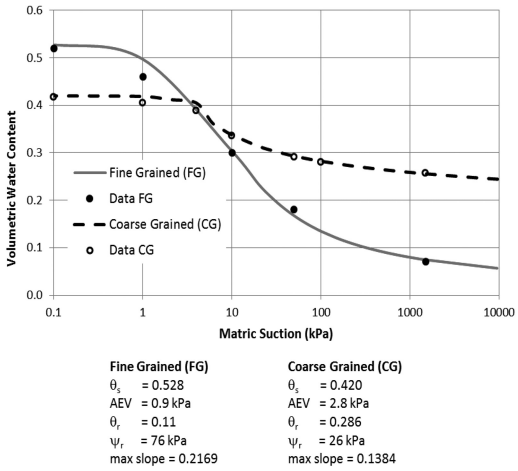


Figure 4. Soil water characteristic curves.

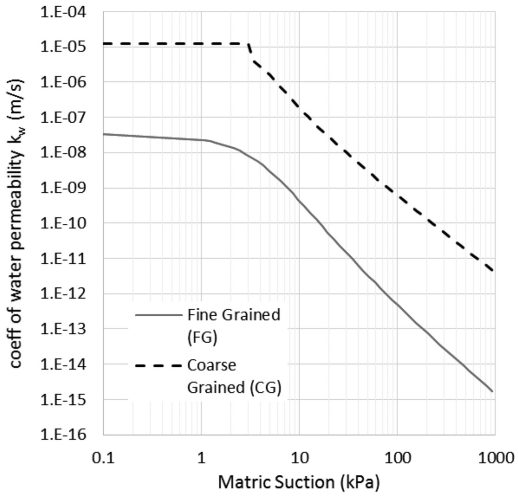


Figure 5. Permeability functions.

that is caught on the vegetation surfaces), and evapotranspiration (ET). Interception and ET are often disregarded when identifying rainfall components because they represent a small portion of the total rainfall (Joel et al. 2002). These simplifications leave the approximation of rainfall is nearly equal to the infiltration and runoff. Researchers used different assumptions on their study. Ng et al. (2003) considered that 40% of rainfall in Hong Kong as surface loss while Rahardjo et al. (2005) suggesting 60% of rainfall in Singapore contributes to the surface loss. In their study of extreme rainfalls in Malaysia, Gofar et al. (2009) used 30% surface loss which is quite conservative especially for high intensity rainfall.

In this study, runoff amounts for twenty rainfall events were collected from runoff collector installed at Site 1. Only the rainfall pattern was considered as the influencing parameter while other factors such as ground surface cover, slope angle, type of soil etc. were

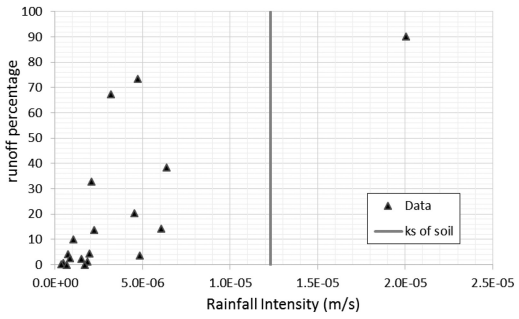


Figure 6. Runoff amount (as percentage of rainfall amount) vs. rainfall intensity and saturated permeability of soil.

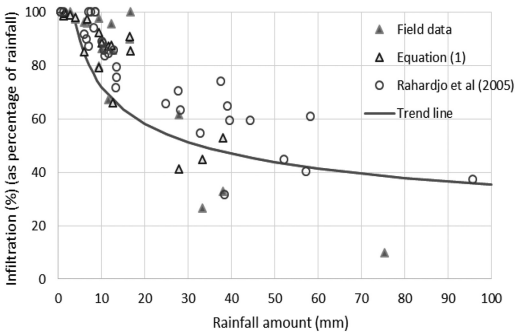


Figure 7. Infiltration as percentage of rainfall vs. rainfall amount.

considered constant. The data is presented as runoff percentage versus rainfall intensity in Figure 6. Analysis shows that the amount of infiltration is influenced by both rainfall intensity and duration. However, saturated permeability of the soil also plays an important role. Figure 6 indicates that under most typical rainfall conditions, the measured runoff amounts were lower than 40% of total rainfall, but for rainfall intensity higher than the saturated permeability of the soil, the runoff amount can be as high as 90% of total rainfall leaving only 10% of infiltration.

Empirical equation (Eq.1) was developed in this study for the estimation of the run-off percentage (R_f) as a function of rainfall intensity (q in mm/hr) and rainfall depth (P in mm) to take into account the rainfall duration.

$$R_f(\%) = 85.078\left[1 - \frac{1}{1.00013246^{(13.944 \times q \times P)}}\right] \quad (1)$$

In Figure 7, the infiltration amount (as the percentage of total rainfall) are plotted against rainfall amounts from the twenty events and values calculated from Equation (1). It appears that the percentage of infiltration to rainfall obtained in this study is a bit lower than those from Rahardjo et al (2005), however; the trend is similar. The data suggests that as long as the rainfall intensity is less than saturated permeability of soil, than the amount of infiltration is from 40 to 100%.

In addition, rainfall intensity of less than 10 mm/h will contribute to 100% infiltration.

5 ANALYSIS OF SUCTION RESPONSE

Figures 8 presents the maximum and minimum suctions measured at 0.5 m depth at Site 1 (CG) and Site 2 (FG), respectively. From the overall trend of suction distributions, it was obvious that the suctions recorded at Site 1 were generally more consistent and lower than those of Site 2. The minimum suction for both sites was 0 kPa which represented the saturated condition of the soils, while the maximum suctions for Site 1 and Site 2 were 26 kPa and 74 kPa, respectively. Apparently, Site 2 with FG soil displayed a wider range of suction variation than Site 1.

Observation of the field suction data indicates that zero suction or saturated condition was only recorded by tensiometers at depth of 0.5 m. In Green and Ampt's model of infiltration, water from precipitation is assumed to enter the soil as a sharp wetting front. The soil above the front is assumed to be saturated while the soil below of the front is assumed at some uniform initial moisture (Bouwer, 1966). Lee at al (2009) used the following formulas for the calculation of depth of wetting front (L_f) and the time required to reach a specified depth (t_p):

$$L_f = \frac{q \times t}{\theta_a - \theta_i} \tag{2}$$

$$t_p = \frac{\mu}{k_w}\left[L_f - S\ln\left(\frac{S + L_f}{S}\right)\right] \tag{3}$$

In Equation 2, q is rainfall infiltration, t is rainfall duration; θ_a and θ_i are the final and initial volumetric water content. If the rainfall intensity is higher than the saturated permeability of the soil, then q is replaced by k_s while θ_a is replaced by θ_s. In Equation 3, μ is the difference between the volumetric water content before and after wetting; k_w is water permeability of the wetted zone; and S is the wetting front capillary suction.

Assuming the initial condition was that of residual water content, the wetting front (L_f) reached the depth of 0.5 m after a rainfall infiltration of 67 mm and 209 mm for CG and FG soils, respectively. The time required to reach this depth (t_p) is about 20 minutes for CG soil and 7 days for FG soil.

A few points were selected where suction measurements at all depth were zero or greater than zero. Then the amount of rainfall (P) as well as the intensity (q) of major rainfall at the points were identified and analyzed. The results are presented in Figure 8. An interesting finding is that a high daily rainfall of 174 mm on January 12th 2007 had saturated the FG soil but not CG because of the low maximum hourly rainfall intensity of 25.6 mm. On the other hand, the slopes experienced the driest condition throughout the course of monitoring in February 2007 with

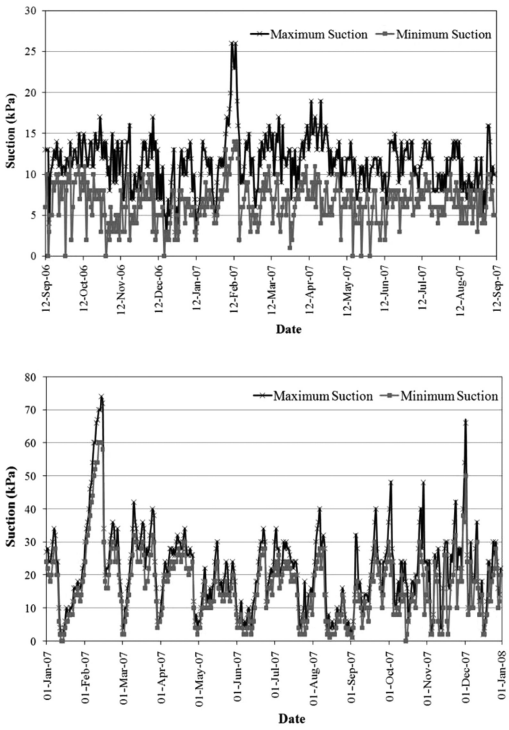


Figure 8. Suction measurements at Site 1 (CG) and Site 2 (FG).

continuous 18 days without rainfall. The highest suction recorded was 26 kPa on CG soil which was in close agreement with the residual suction from SWCC (26 kPa). Subsequently, a typical short and intense tropical rainfall occurred on 16 February 2007 (maximum intensity of 34 mm/h) caused the suction to drop dramatically to 2 kPa. However, FG soil maintained a high suction of 30 kPa on 16 February 2007 after reaching the highest suction of 74 kPa on the previous day because the amount of rainfall had not reached the amount required to wet the soil down to 0.5 m depth.

There are also few points where the rainfall intensity higher than 42 mm/h led to the saturation of CG soil down to 0.5 m but the initial condition was slightly wet and then the suction increased quickly as water drained out from the soil. Contrary to CG soil, few days of continuous daily rainfall were required to induce the minimum suction of 0 kPa for FG soil. Thus, it can be concluded that the suction distribution of fine-grained soil is more influenced by the prolonged rainfall. Saturated permeability of CG in mm/h (=40.59 mm/h) and FG in mm/7 day (=22.46 mm/7day) were considered suitable to define the limit where soil becomes saturated (Fig. 9).

6 CONCLUSIONS

This study explores some findings from one year suction monitoring on two sites whereby the soil can be

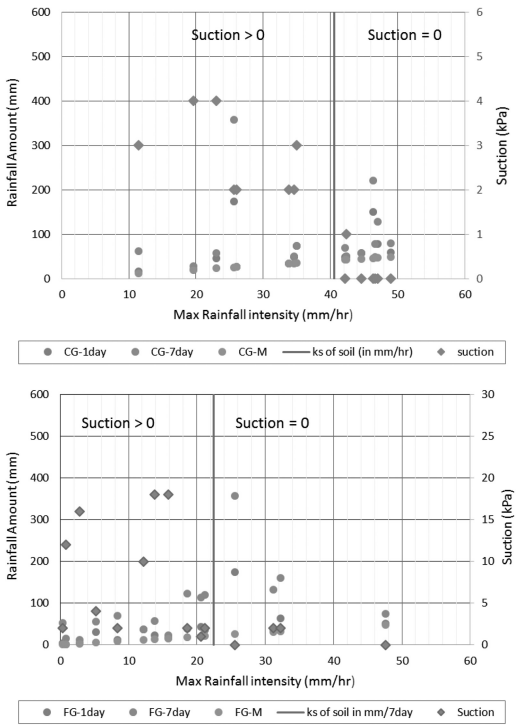


Figure 9. Rainfall amount and suction vs max rainfall intensity.

characterized as coarse-grained (CG) and fine-grained (FG). The monitoring data showed that the maximum suctions were 26 kPa and 74 kPa for Site 1 and Site 2, respectively while the minimum suction was zero. The ranges of suction obtained from the field monitoring data were reasonably consistent with those determined from the analyses of SWCC.

An equation was proposed to estimate the amount of rainfall that infiltrates into the soil based on rainfall intensity and rainfall amount. Under most typical rainfall conditions, the measured runoff amounts were between 40 and 100% of total rainfall, but for rainfall intensity higher than the saturated permeability of the soil, the runoff amount can be as high as 90% of total rainfall. In addition rainfall intensity less than 10 mm/h contributes to 100% infiltration (no runoff).

Zero suction or saturated condition was recorded by tensiometer at depth of 0.5 m only. Assuming the initial condition was the condition at residual water content, the wetting front reached this depth in CG soil after an infiltration amount of 67 mm with minimum time of 20 minutes and in FG soil after a rainfall amount of 209 mm with a duration of about 7 days.

The suction distribution of CG soil is influenced by short and intense rainfalls while that of FG soil is affected more by the prolonged rainfall. Saturated permeability of CG in mm/h and FG in mm/7 day were considered suitable to define the limit where soil becomes saturated

ACKNOWLEDGEMENT

Data used in this paper was obtained from research study at University Teknologi Malaysia funded by IRPA Grant No. 74179. The first author thanks Prof. N. Mokhtar for opportunity to join in this research.

REFERENCES

Bouwer, H. (1966). Rapid Field Measurement of Air Entry Value and Hydraulic Conductivity of Soil as Significant Parameters in Flow System Analysis. *Water Resources Research.* 2(4): 729–738.

Cai, F. & Ugai, K. 2004. Numerical Analysis of Rainfall Effects on Slope Stability. *International Journal of Geomechanics.* ASCE. 4(2): 69–78.

Fredlund, D. G. & Rahardjo, H. (1993). *Soil Mechanics for Unsaturated Soils*. New York: John Wiley & Sons, Inc.

Fredlund, D. G. & Xing, A. 1994. Equations for the Soil-Water Characteristic Curve. *Canadian Geotechnical Journal,* 31: 521–532.

Gofar N. & Lee, M.L. 2008. Extreme Rainfall Characteristics for Surface Slope Stability in the Malaysian Peninsular. *Georisk* 2(2): 65–78.

Fredlund, D.G., Xing, A. & Huang, S. 1994. Predicting the Permeability Function for Unsaturated Soils Using the Soil-Water Character Curve. *Canadian Geotechnical Journal*. 31(3): 533–546

Gofar N. Lee, M.L. & Kassim, A. 2008. Response of Suction Distribution to Rainfall Infiltration in Soil Slope. *Electronic Journal of Geotechnical Engineering*. 13(E): 1–13.

Joel, A., Messing, I., Seguel, O., & Casanova, M. 2002. Measurement of surface water runoff from plots of two different sizes. *Hydrological Processes*. 16(7): 1467–1478.

Lee, M.L. Gofar N. & Rahardjo H. 2009. A Simple Model for Preliminary Evaluation of Rainfall-Induced Slope Instability. *Engineering Geology* 108(3–4): 272–282.

Li, A.G., Tham, L.G., Yue, G.Q., Lee, C.F. & Law, K.T. 2005. Comparison of Field and Laboratory Soil-Water Characteristic Curves. *Journal of Geotechnical and Geoenvironmental Engineering, ASCE*. 131(9): 1176–1180.

Ng, C.W.W., Zhan, L.T., Bao, C.G., Fredlund, D.G., & Gong, B.W. 2003. Performance of Unsaturated Expansive Soil Slope Subjected to Artificial Rainfall Infiltration. *Géotechnique*. 53(2): 143–157.

Pradel, D. & Raad, G. 1993. Effect of Permeability on Surficial Stability of Homogeneous Slopes. *Journal of Geotechnical Engineering*, ASCE. 119(2): 315–332.

Rahardjo, H., Li X. W., Toll D. G. & Leong E. C. 2001. The Effect of Antecedent Rainfall on Slope Stability. *Journal of Geotechnical and Geological Engineering*. 19: 371–399.

Rahardjo, H. Lee, TT, Leong, EC. And Rezaur, RB. (2005) Response of a Residual Soil Slope to Rainfall. Canadian Geotechnical Journal. 42: 340–351.

Rahardjo, H. Satyanaga, A. Leong, EC. (2013) Effects of flux Boundary Conditions on Pore-water pressure Distribution in Slope. Engineering geology 163: 133–142.

Tsaparas, I., Rahardjo, H., Toll, D.G. & Leong E.C. 2003. Infiltration Characteristics of Two Instrumented Residual Soil Slopes. *Canadian Geotech. Journal*. 40: 1012–1032.

Tsaparas I., Rahardjo, H., Toll D.G. & Leong E.C. 2002. Controlling Parameters for Rainfall-Induced Landslides. *Computer & Geotechnics* 29: 1–27.

This page intentionally left blank

Unsaturated Soil Mechanics—from Theory to Practice – Chen et al. (Eds)
© 2016 Taylor & Francis Group, London, ISBN 978-1-138-02921-7

Determining volume of failed soil mass in a landslide from satellite images

B.J.M. Lim, E.C. Leong & K.S. Low
Satellite Research Centre, Nanyang Technological University, Singapore

ABSTRACT: Knowledge regarding the extent of landslides in terms of its volume is necessary to increase our understanding of its triggering factors and associated impacts. Yet, the volume of landslides is seldom quantified due to impracticalities of in-situ measurements as well as challenges encountered in conventional surveying. Various studies have been conducted to empirically relate volume (i.e. displaced material) of a landslide to its area. However, these empirical relationships may not be accurate and are approximations at best. In this paper, a mathematical explanation of the empirical relationships is provided. The empirical relationships are bounded by the volumes of an 'idealized' landslide where the décollement plane is either spherical or elliptical. Using this discovery, an alternative technique is proposed to compute the volume of a landslide from a single satellite image. Finally the technique is illustrated with a published case study.

1 INTRODUCTION

Landslides are serious natural hazards triggered typically by rainfall or earthquakes. They cause billions of dollars in damages and thousands of deaths and injuries each year (Schuster 1996, Kirschbaum et al. 2009). They result in widespread destruction in terms of property and environmental damages as well as fatalities (Nadim et al. 2006, Kjekstad & Highland 2009, Petley 2009). Hence, it is crucial to map the spatial distributions and capacity for damage of potential landslides. While the spatial extent of single or multiple landslides can be mapped either via land-based surveying or aerial/satellite imagery, it is not straightforward to determine the damage capacity of a landslide for two reasons: a) the rate of displacement or debris run-out distance is not known, and b) the amount of failed soil mass in any landslide is difficult to quantify.

According to Derron et al. (2005), the preliminary assessment of a landslide event should include geometry and volume of the sliding mass. The volume of a failed soil mass is one of the indicators for the magnitude of destruction of a landslide (Guzzetti et al. 2006, 2009, Malamud et al. 2004). Landslide volume is also one of the critical parameters controlling the amplitude of landslide-generated tsunamis (Murty 2003, Watts & Grilli, 2003, Geist et al. 2009). Martha et al. (2010) also stated that information regarding landslide failure volumes are essential for risk mapping (Flentje et al. 2007) and to enable more accurate understanding of landslide processes, such as travel distances and frequency-volume relationships (e.g. Okura et al. 2003, Dai & Lee 2001).

To compute the volume of a landslide, knowledge regarding its three-dimensional extents is necessary. However, it is recognised that accurate landslide volume estimates are hard to obtain (Urgeles et al. 1999, Guzzetti et al. 2009, Chen et al. 2014). Detailed monitoring of landslides relying on field investigations and instrumentations is time- and resource-consuming (Behling et al. 2014) and frequently not feasible due to inadequate scientific expertise, insufficient budgets for subsurface investigations or that the size of the monitored landslide is simply too large (Wieczorek & Snyder 2009, Martha et al. 2010). The advent of satellite technology has greatly facilitated observations of landslides via remote sensing, thus overcoming the limitations of conventional surveying. Planar dimensions of a landslide can be readily observed through two-dimensional imagery. However, it remains a challenging task to derive an accurate estimate of the volume of a landslide (Guthrie & Evans 2004), mostly due to the difficulty of quantifying the depth of the décollement plane. Therefore, the objective of this paper is to examine the empirical area to volume relationship and development of a landslide volume estimation method which optimizes both time and volumetric accuracy.

1.1 *Area-to-volume relationship*

Empirical landslide area-to-volume relationships (in the form of Equation 1) have been widely used to estimate volume of failed soil mass using landslide area. As shown in Table 1, the ranges of α and β values reported by various authors (e.g., Hovius et al. 1997, Hewitt 2002, Haflidason et al. 2005, Korup 2005, 2006, ten Brink et al. 2006, Chaytor et al. 2008, Guzzetti et al. 2008, Kalderon-Asael et al. 2008, Larsen et al. 2010, Parker et al. 2011, Tseng et al. 2013) fall within a narrow band. While the underlying

Table 1. Ranges of α and β values for empirical landslide area-to-volume relationships.

Parameter (s)	Minimum	Maximum
A	0.013	0.050
B	1.032	1.950
Landslide area (km^2)	3×10^{-12}	4×10^{4}

basis is unclear, it has been demonstrated that Equation 1 applies regardless of size, locations and trigger mechanism of the landslide (Guthrie & Evans 2004, Kalderon-Asael et al. 2008, Guzzetti et al. 2009).

$$V_L = \alpha A_L^{\beta} \quad (1)$$

where V_L = landslide volume; A_L = landslide surface area; α and β = empirical constants.

Various research has attempted to provide insights to Equation 1. To account for the variation in β values, Chaytor et al. (2009) stated that it is due to differences in the failed soil mass, landslide processes or presence of saturated or over-pressured sediments. More recently, Klar et al. (2011) pointed out that Equation 1 is independent of slope height, slope angle, physiographical settings and is a result of the self-affine nature of landslides. As opposed to self-affinity, self-similarity (or scale-invariance) indicates that the aspect ratio of a landslide remain the same at different scales. Thus, this implies that the dimensions of a smaller landslide could simply be stretched by an equal amount in all directions to replicate a larger landslide. As observed by the variability of β values in Table 1, deviations from the assumed self-similar behavior seems apparent, suggesting that the aspect ratios are not constant (i.e. larger landslides are relatively thinner compared to smaller landslides). This phenomenon was also discussed by Kalderon-Asael et al. (2008), where the transition of self-similar to self-affine nature of a landslide occurs to account for the different exponent values. In addition, it is generally agreed that the empirical area-to-volume relationships is largely a result of geometrical variations (Kalderon-Asael et al. 2008, Guzzetti et al. 2009). Hence, an implication of these findings is that there could be a possible link between a three-dimensional representation (i.e. geometry) of a landslide and its self-affine characteristic.

1.2 *Landslide volume estimation*

While the direct use of Equation 1 to estimate volume of a landslide is convenient, it appears to be error-prone and seems to yield inconsistent results (Brunetti et al. 2009, Guzzetti et al. 2009, Tseng et al. 2013, Wang et al. 2014).

Alternatively, a common geometrical method to calculate the volume of a landslide is to assume that the failed soil mass possess the shape of an ellipsoid (Cruden & Varnes 1996). Nikolaeva et al. (2014) accounted for a translational component by augmenting the ellipsoidal assumption using two planar constraints. However, in the absence of a 'truth' volume, they yielded approximately 50% volumetric error when compared to an empirical area-to-volume relationship.

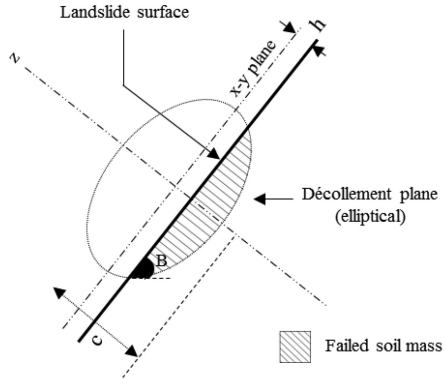


Figure 1. Ellipsoidal approximation for décollement plane.

Existing techniques used to compute landslide volume typically require information beyond those obtainable from satellite images. In the current study, an explanation is first provided to the empirical area-to-volume relationships based on three-dimensional geometrical and mathematical characteristics of landslides. Following this justification, a method that allows convenient computation of landslide volume from satellite images observing pre- and post-landslide images is developed. Finally, the method is validated using landslide case studies with reported volume estimates. The advantage of the proposed approach is a trade-off between speed and accuracy in volumetric estimation of the failed soil mass in landslides.

2 RATIONALIZING THE AREA-TO-VOLUME RELATIONSHIPS

In the current study, it is hypothesized that the upper and lower bounds of the various reported landslide area-to-volume relationships (Table 1) could possess underlying geometrical characteristics. First, the décollement plane of the failed soil mass in a landslide is assumed to lie between a spherical and oblate ellipsoidal surface. Figure 1 provides such an illustration for the case of an ellipsoidal décollement plane, where the surface of a landslide is at a distance h below the point of origin of the sphere, in an oblique plane (defined by the slope angle B). Therefore, the orientation of the sphere is aligned such that its horizontal axes (x-y plane) are parallel to the inclination of the slope surface.

Table 2. Parameters defined in the geometrical modelling approach.

Parameter	Description	Value(s)
h/c	Depth of cut-off plane	$0 \leq h/c < 1$ ($\Delta h/c = 0.1$)
k	Aspect ratio between planar and vertical dimensions (k: 1: 1)	1 (Spherical)
		$8 \leq k \leq 125$ (Ellipsoidal)
a	Length of semi-major axis	0.1 to 1.5 km ($\Delta a = 0.1$ km)

The volume of the displaced soil material in a landslide can be subsequently computed using Equation 2.

$$V_L = \frac{ab(c-h)^2(2c+h)\pi}{3c^2} \quad (2)$$

where a = semi-major axis; b, c = semi-minor axes; and h = depth from ellipsoid origin to landslide surface. For a spherical décollement plane, a = b = c.

A typical representation of V_L is denoted by the shaded region in Figure 1, where it is bounded by the surface of the landslide and the presumed ellipsoidal décollement plane. For a given landslide, the factors determining volume of the displaced material are the lengths of the principal axes (a, b, c) as well as the distance h (defined in terms of h/c). For the case of décollement plane modelling using a presumed spherical surface, semi-major axis a (or radius r) can be computed conveniently, since it is equal to semi-minor axes b and c. For an ellipsoid, the aspect ratio (A.R.) between its axes is not 1: 1: 1. In this study, the aspect ratios utilised for the ellipsoid varies according to k: 1: 1, where $8 \leq k \leq 125$. In this manner, the variability of the vertical dimension (i.e. depth of the décollement plane) is only dependent on the ratio h/c, where increasing values of h/c would correspondingly result in decreasing landslide volume. To obtain the geometries of the spheres and ellipsoids which bound the empirical area-to-volume relationships found in the literature, values between 0.1 to 1.5 km were assigned to the semi-major axis, covering approximately $0.01\,km^2 \leq A_L \leq 10\,km^2$. In addition, h/c values varied within $0 \leq h/c < 1$, where values greater than 1 are physically meaningless. The parameters for the geometrical modelling study are summarized in Table 2.

Figure 2 illustrates the results from the upper and lower bounds analysis of the area-to-volume relations reported in the literature. When the spherical décollement plane was assumed, it is able to encompass the upper limit of the empirical area-to-volume relationships using $h/c \leq 0.9$.

However, when h/c ratio of 0.9 was applied on the ellipsoidal décollement plane, the aspect ratio k, varies (depending on A_L) in order to cater to the lower bound of the literature data. As shown in Figure 3, the aspect

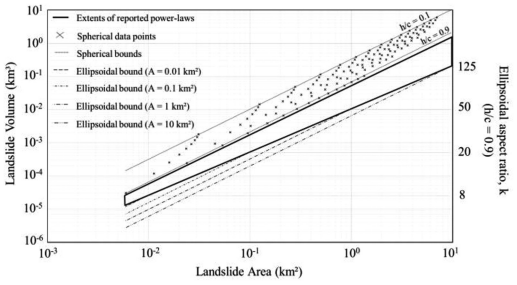


Figure 2. Upper and lower bounds of reported power laws.

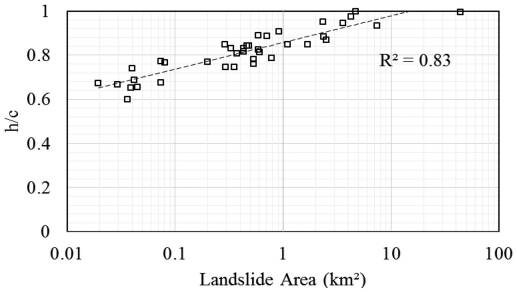


Figure 3. Results of h/c calibration.

ratios at $h/c = 0.9$ of the ellipsoids used to demarcate the lower bound of the empirical area-to-volume relationships are 8, 20, 50 and 125: 1: 1 corresponding to the landslide areas of 0.01, 0.1, 1 and 10 km^2 respectively.

Consequently, the results of the geometrical modelling approach clearly suggest that the empirical area-to-volume relationships observed by various authors could be explained by the inherent geometry of the failure mass, which takes on the shape between a spherical and ellipsoidal décollement plane.

3 NEW METHOD OF ESTIMATING LANDSLIDE VOLUME FROM SATELLITE IMAGES

As the décollement plane for any landslide may be modelled as a spherical or ellipsoidal surface, it is therefore possible to compute individual landslide volumes from satellite images without the use of DEMs. Landslide scars can first be delineated using either a single satellite image (e.g. RGB compositions) or via the change detection technique (e.g. Normalized Difference Vegetation Index) using multi-temporal satellite images (Tsai et al. 2010, Schlogel et al. 2011). With accurate geo-referencing or topographical scale, the identification of landslide scars allows both the surface area and ratio between the planar semi-major to semi-minor length of each landslide to be quantified. Once the semi-axes have been defined, the only parameter that remains is h/c. Since h/c is an adjustable

Table 3. Landslide case studies used for validation.

Reference (s)	Landslide	Location	Volume (km^3)
Agliardi et al. (2001)	Ruinon	Italy	0.013
Kokusho & Ishizawa (2005)	Higashi-Takezawa	Japan	0.0012
Bonzanigo et al. (2007)	Campo Vallemaggia	Italy	0.800
Schneider et al. (2011)	Hattian Bala	Pakistan	0.065
Oppikofer et al. (2012)	Punta Cola	Chile	0.00064

parameter, it is calibrated using a large set of landslide cases (n = 38) with reported area and volume measurements or estimates ('truth').

Global landslide morphometric datasets collected for calibration of h/c were obtained from single event mapping, multiple landslides inventories as well as reported statistics by geologists and relevant authorities, for example, United States Geological Survey (USGS). Among the 38 landslide case studies, about 40% of the case studies involved the use of digital elevation (DEM). Other approaches incorporated information from field investigations (e.g. boreholes), differential GPS (DGPS) measurements, seismic reflection profiles or multi-beam swath bathymetry data. Calibration of h/c allows the landslide décollement plane to be obtained on the basis of its area observable by satellite images. The ranges of A_L used in the calibration of h/c are between 0.01 km^2 and 100 km^2. The corresponding landslide volumes range from 0.0005 km^3 to 50 km^3. Results of the h/c calibration is presented in Figure 3 (R^2 ~0.83) with the dependency of h/c on A_L expressed in the form of Equation 3. From Figure 4, it is observed that h/c approaches unity when A_L is approximately 20 km^2 and thereafter appears to be insensitive to further increases in A_L.

$$\frac{h}{c} = 0.05 \ln A_L + 0.85 \quad for\ A_L \le 20km^2 \qquad (3)$$
$$= 1.0 \qquad for\ A_L > 20km^2$$

where a = semi-major length; b, c = semi-minor lengths; and h = depth from ellipsoid origin to landslide surface.

To validate computation of landslide volume using the proposed geometric approach, five separate landslide events (Table 3) with corresponding volume estimates were assembled. Using the h/c value for each landslide obtained from Equation 3, the predicted landslide volumes were computed and compared against the reported volumes.

As shown in Figure 4, the volumetric error obtained using the proposed method is within +/−20%, as a result of the 8% mean deviation of h/c values from the corresponding truth values (Fig. 5).

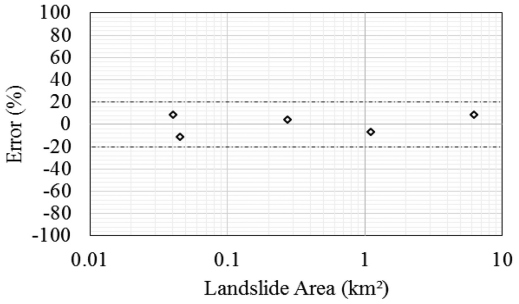


Figure 4. Volumetric error analysis on validation dataset.

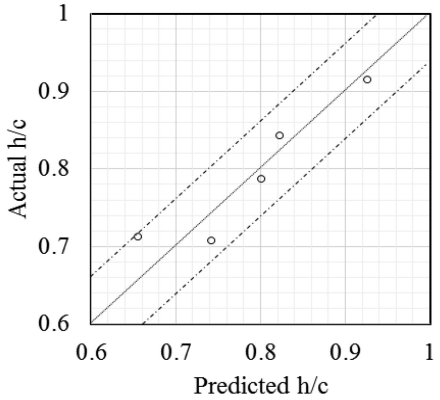


Figure 5. Actual versus predicted h/c values.

The proposed approach provides more consistent landslide volume estimates than regression-based area-to-volume power-law equations. The mean error obtained for the validation datasets was approximately 9% and is significantly less than the mean errors (>30%) obtained from empirical area-to-volume relations. In addition, as compared to the novel algorithm-based approach proposed by Wang et al. (2014) who obtained volumetric error of 25%, the proposed method fares marginally better.

4 CONCLUSION

Landslides constitute a significant proportion of natural hazards. They are triggered by different factors (e.g. rain or earthquake) and thus can occur in any part of the world. Frequently, they result in property and environmental damages and more importantly, the loss of lives. While remote sensing via satellite imagery has greatly facilitated the identification of landslide events, however the landslide volume remains a variable that is difficult to quantify.

In this study, a geometric method to estimate the volume of a landslide is introduced. The formulation of the proposed volume computation framework was initially derived to explain the empirical area-to-volume

relationships commonly used in the literature, where the upper and lower bounds of the empirical area-to-volume relationships could be obtained by assuming that the décollement plane of a landslide was either spherical or ellipsoidal.

Using this discovery, a general ellipsoidal assumption regarding the shape of the décollement plane was employed for landslide volume computation. The only information required is satellite images to provide planar measurements of the landslide scar dimensions. After obtaining the aspect ratio of the landslide, an adjustable parameter, h/c, was incorporated to vary the depth of the décollement plane. The dependency of h/c on landslide area was subsequently calibrated using 38 landslide cases with resulting $R^2 \sim 0.83$ and valid for $A_L \leq 20\,km^2$. Volume of a landslide can then be calculated based on the region bounded by the landslide surface and décollement plane. Finally, the proposed method was validated using five separate landslide events with resulting accuracy within +/−20% volumetric predictive error.

ACKNOWLEDGEMENTS

This study was supported by Nanyang Technological University – Satellite Research Centre (SaRC). The authors express sincere gratitude for the support.

REFERENCES

Agliardi, F., Crosta, G., & Zanchi, A. (2001). Structural constraints on deep seated slope deformation kinematics. *Engineering Geology, 59*, 83–102.

Behling, R., Roessner, S., Kaufmann, H., & Kleinschmit, B. (2014). Automated Spatiotemporal Landslide Mapping over Large Areas Using RapidEye Time Series Data. *Remote Sensing, 6*, 8026–8055.

Bonzanigo, L., Eberhardt, E., & Leow, S. (2007). Long-term investigation of a deep-seated creeping landslide in crystalline rock. Part I. Geological and hydromechanical factors controlling the Campo Vallemaggia landslide. *Canadian Geotechnical Journal*, 1157–1180.

Brunetti, M. T., Guzzetti, F., & Rossi, M. (2009). Probability distributions of landslide volumes. *Nonlinear Processes in Geophysics, 16*, 179–188.

Chaytor, J. D., ten Brink, U. S., Solow, A. R., & Andrews, B. D. (2009). Size distribution of submarine landslides along the U.S. Atlantic margin. *Marine Geology, 264*, 16–27.

Chen, Z., Zhang, B., Han, Y., Zuo, Z., & Zhang, X. (2014). Modeling Accumulated Volume of Landslides Using Remote Sensing and DTM Data. *Remote Sensing, 6*, 1514–1537.

Cruden, D. M., & Varnes, D. J. (1996). Landslides Types and Processes. In A. K. Turner, & L. R. Schuster (Eds.), *Landslides: Investigation and Mitigation* (pp. 36–75). Washington, United States: National Academy Press.

Dai, F. C., & Lee, C. F. (2001). Frequency-volume relation and prediction of rainfall-induced landslides. *Engineering Geology, 59*(3/4), 253–266.

Derron, M.-H., Jaboyedoff, M., & Blikra, L. H. (2005). Preliminary assessment of rockslide and rockfall hazards using a DEM (Oppstadhornet, Norway). *Natural Hazards and Earth System Sciences*, 285–292.

Flentje, P., Stirling, D., & Chowdhury, R. N. (2007). Landslide Susceptibility and Hazard derived from a Landslide Inventory using Data Mining – an Australian case study. Vail, Colorado: Landslides and Society : Integrated Science, Engineering, Management and Mitigation.

Geist, E. L., Lynett, P. J., & Chaytor, J. D. (2009). Hydrodynamic modeling of tsunamis from the Currituck Landslide. *Mar. Geo., 264*, 41–52.

Guthrie, R. H., & Evans, S. G. (2004). Analysis of landslide frequencies and characteristics in a natural system, coastal British Columbia. *Earth Surface Processes and Landforms, 29*, 1321–1339.

Guzzetti, F., Ardizzone, F., Cardinali, M., Galli, M., & Reichenbach, P. (2008). Distribution of landslides in the Upper Tiber River basin, central Italy. *Geomorphology, 96*, 105–122.

Guzzetti, F., Ardizzone, F., Cardinali, M., Galli, M., Rossi, M., & Valigi, D. (2009). Landslide volumes and landslide mobilization rates in Umbria, central Italy. *Earth and Planetary Science Letters, 279*, 222–229.

Guzzetti, F., Galli, M., Reichenbach, P., Ardizzone, F., & Cardinali, M. (2006). Landslide hazard assessment in the Collazone area, Umbria, Central Italy. *Natural Hazards and Earth System Sciences, 6*, 115–131.

Haflidason, H., Lien, R., Sejrup, H. P., Forsberg, C. F., & Bryn, P. (2005). The dating and morphometry of the Storegga slide. *Marine and Petroleum Geology*, 123–136.

Hewitt, K. (2002). Postglacial landform and sediment associations in a landslide-fragmented river system: The Transhimalayan Indus streams, Central Asia. In H. e. al., *Landscapes of Transition. Landform Assemblages and Transformations in Cold Regions* (pp. 63–91). New York: Springer.

Hovius, N., Stark, C. P., & Allen, P. A. (1997). Sediment flux from a mountain belt derived by landslide mapping. *Geology, 25*(3), 231–234.

Kalderon-Asael, B., Katz, O., Aharonov, E., & Marco, S. (2008). *Modeling the relation between area and volume of landslides.* Jerusalem, Israel: Steering Committee for Preprartion for Earthquakes.

Kirschbaum, D. B., Adler, R., Hong, Y., Hill, S., & Lerner-Lam, A. L. (2009). A global landslide catalog for hazard applications – Methods, Results and Limitations. *Journal of Natural Hazards, 52*(3), 561–575.

Kjekstad, O., & Highland, L. (2009). Economic and Social Impacts of Landslides. In K. Sassa, & P. Canuti, *Landslides – Disaster Risk Reduction.* Heidelberg: Springer.

Klar, A., Aharonov, E., Kalderon-Asael, B., & Katz, O. (2011). Analytical and observational relations between landslide volume and surface area. *Journal of Geophysical Research, 116*, 1–10.

Kokusho, T., & Ishizawa, T. (2005). Energy approach to slope failures and a case study during 2004 Niigata–ken Chuetsu earthquake. Osaka, Japan: Proceedings of Geotechnical Earthquake Engineering Satellite Conference.

Korup, O. (2005). Distribution of landslide in southwest New Zealand. *Landslides, 2*, 43–51.

Korup, O. (2006). Effects of large deep-seated landslides on hillslope morphology, western Southern Alps, New Zealand. *Journal of Geophysical Research: Earth Surface*, 1–18.

Larsen, I. J., Montgomery, D. R., & Korup, O. (2010). Landslide erosion controlled by hillslope material. *Nature Geoscience*, 247–251.

Malamud, B. D., Turcotte, D. L., Guzzetti, F., & Reichenbach, P. (2004). Landslide inventories and their statistical properties. *Earth Surface Processes and Landforms, 29*, 687–711.

Martha, T. R., Kerle, N., Jetten, V., van Westen, C. J., & Vinod Kumar, K. (2010). Landslide Volumetric Analysis Using Cartosat-1-Derived DEMs. *IEEE Geoscience and Remote Sensing Letters, 7*(3), 582–586.

Murty, T. S. (2003). Tsunami wave height dependence on landslide volume. *Pure and Applied Geophysics, 160*, 2147–2153.

Nadim, F., Kjekstad, O., Peduzzi, P., Herold, C., & Jaedicke, C. (2006). Global landslide and avalanche hotspots. *Landslides, 3*(2), 159–173.

Nikolaeva, E., Walter, T. R., Shirzaei, M., & Zschau, J. (2014). Landslide observation and volume estimation in central Georgia based on L-band InSAR. *Natural Hazards and Earth System Sciences, 14*, 675–688.

Okura, Y., Kitahara, H., Kawanami, A., & Kurokawa, U. (2003). Topography and volume effects on travel distance of surface failure. *Engineering Geology, 67*(3/4), 243–254.

Oppikofer, T., Hermanns, R. L., Redfield, T. F., Sepulveda, S. A., Duhart, P., & Bascunan, I. (2012). Morphologic description of the Punta Cola rock avalanche and associated minor rockslides caused by the 21 April 2007 Aysen earthquake (Patagonia, southern Chile). *Revista de la Asociación Geológica Argentina, 69*(3), 339–353.

Parker, R. N., Densmore, A. L., Rosser, N. J., de Michele, M., Li, Y., Huang, R., . . . Petley, D. N. (2011). Mass wasting triggered by the 2008 Wenchuan earthquake is greater than orogenic growth. *Nature Geoscience*, 449–452.

Petley, D. (2009). On the occurence of fatal landslides in 2008. *EGU general assembly conference abstracts*, (p. 9030).

Schlogel, R., Torgoev, I., De Marneffe, C., & Havenith, H.-B. (2011). Evidence of a changing size-frequency distribution of landslides in the Kyrgyz Tien Shan, Central Asia. *Earth Surface Processes and Landforms, 36*, 1658–1669.

Schneider, J. F., Gruber, F. E., & Mergili, M. (2011). Recent cases and geomorphic evidence of landslide-dammed lakes and related hazards in the mountains of Central Asia. Rome: Proceedings of the Second World Landslide Forum.

Schuster, R. L. (1996). Socioeconomic effects of landslides. In A. K. Turner, & R. L. Schuster (Eds.), *Landslide: Investigation and Mitigation.* National Research Council, Washington: National Academy Press.

ten Brink, U. S., Geist, E. L., & Andrews, B. D. (2006). Size distribution of submarine landslides and its implication to tsunami hazard in Puerto Rico. *Geophysical Research Letters*, 1–4.

Tsai, F., Hwang, J.-H., Chen, L.-C., & Lin, T.-H. (2010). Post-disaster assessment of landslides in southern Taiwan after 2009 Typhoon Morakot using remote sensing and spatial analysis. *Natural Hazards and Earth System Sciences, 10*, 2179–2190.

Tseng, C.-M., Lin, C.-W., Stark, C. P., Liu, J.-K., Fei, L.-Y., & Hsieh, Y.-C. (2013). Application of a multi-temporal, LIDAR-derived digital terrain model in a landslide-volume estimation. *Earth Surface Processes and Landforms, 38*, 1587–1601.

Urgeles, R., Masson, D. G., Canals, M., Watts, A. B., & Le Bas, T. (1999). Recurrent large-scale landsliding on the west flank of La Palma, Canary Islands. *Journal of Geophysical Research, 104*(B11), 331–25 248.

Wang, T.-S., Yu, T.-T., Lee, S.-T., Peng, W.-F., Lin, W.-L., & Li, P.-L. (2014). MATLAB code to estimate landslide volume from single remote sensed image using genetic algorithm and imagery similarity measurement. *Computers & Geosciences, 70*, 238–247.

Watts, P., & Grilli, S. T. (2003, May). Tsunami Generation by Deformable Underwater Landslides. *Proc. 13th Offshore and Polar Eng. Conf.*, pp. 364–371.

Wieczorek, G. F., & Snyder, J. B. (2009). Monitoring slope movements. In R. Young, & L. Norby, *Geological Monitoring* (pp. 245–271). U.S.A: The Geological Society of Ameria, Inc.

Unsaturated Soil Mechanics—from Theory to Practice – Chen et al. (Eds)
© 2016 Taylor & Francis Group, London, ISBN 978-1-138-02921-7

Field monitoring to study the effect of rainfall on tree stability

N. Amalia, H. Rahardjo, T.T. Lee & E.C. Leong
Nanyang Technological University, Singapore

Y.K. Fong
National Parks Boards, Singapore

ABSTRACT: Tree failure in Singapore commonly occurred during or after heavy rainfall. This incidence could cause economic losses and even serious casualties. However, the relationship between a rainfall event and a tree failure has not been well understood. This study presents details of a field monitoring program used to investigate the water flow characteristics in the soil around a tree during and after rainfall. The results of the study were then used for assessment of tree stability. Data from a specified period of field instrumentation were used for limit equilibrium analyses. The analyses showed that the matric suction in the soil decreased during rainfall and as a result, the shear strength of the soil decreased. The reduction in shear strength of soil led to a decrease in tree stability.

1 INTRODUCTION

As Singapore lies just north of the Equator (Latitude 1.5°N and Longitude 104°E), its geographical location and maritime exposure, leads to a climate that is characterized by uniform temperature and pressure, high humidity and abundant rainfall. Record showed that tree failing incidence commonly occurred during and after rainfall (Ow, et al., 2010).

Very few studies have been performed to investigate the relationship between rainfall and tree failure. Koizumi (1987) conducted several tree-pulling experiments and showed that stability of a tree after rainfall is lower than stability of a similar tree in soil without occurrence of rainfall. However, there is very limited explanation on the mechanism that leads to lower tree stability after rainfall.

The effect of rainfall on tree stability can be related to effect of rainfall on slope failure. The mechanism of rainfall induced slope failure is related to the loss of matric suction in the slope that reduces the shear strength of the soil (Brand, 1982). Several researchers (Rahardjo, et al., 2014; Lim et al., 1996; Evangelista et al., 2008) performed field measurements in order to study the development of pore-water pressure in the slope during rainfall. The data from the field measurements were then used for slope stability analyses.

Based on previous studies where field instrumentation were widely used to determine slope stability characteristics during rainfall, a comprehensive field monitoring involving various instruments was designed to investigate the effect of rainfall on tree stability. The objective of this paper is to describe the details of field monitoring conducted for a two-year study on the effect of rainfall on tree stability. The results were then used to validate numerical modeling. Some parameters required for the seepage modelling such as rainfall rate, evapotranspiration rate, ground water table, pore water pressure, and volumetric water content were obtained from instrumentations installed in the field. The results of seepage modeling were then used as input of the limit equilibrium tree stability analyses.

2 THEORY

2.1 *Water flow in unsaturated soil*

Darcy's law is commonly used to describe the flow of water in saturated and unsaturated soils. (Richards, 1931; Childs & Collis-George, 1950). Darcy's law states that the rate of water flow through a soil mass is proportional to the hydraulic head gradient as follows:

$$V_w = -k_w \frac{\partial h_w}{\partial y} \quad (1)$$

where v_w = flow rate of water; k_w = coefficient of permeability with respect to water phase; and $\partial h_w / \partial h_y$ = hydraulic head gradient in the y-direction, which can be designated as i_{wy}.

The relationship between the coefficient of permeability and water content is commonly described as a permeability function. One of the popular prediction methods of permeability functions was proposed by Childs and Collis-George (1950) where the permeability function is predicted from soil-water characteristic curves (SWCC). SWCC is the relationship between

water content or degree of saturation and matric suction. The theory and procedure of this method can be found in Fredlund & Rahardjo (1993).

2.2 *Shear strength of unsaturated soil*

The shear strength of an unsaturated soil can be formulated as follows (Fredlund et al. 1978):

$$\tau_{ff} = c' + (\sigma_f - u_a)_f \tan\phi' + (u_a - u_w)_f \tan\phi^b \qquad (2)$$

τ_{ff} = shear stress on the failure plane at failure (kPa); c' = intercept of the "extended" Mohr-Coulomb failure envelope on the shear stress axis where the net normal stress and the matric suction are equal to zero; it is also referred to as "effective cohesion" (kPa); $(\sigma_f - u_a)_f$ = net normal stress on the failure plane at failure (kPa); u_{af} = pore-air pressure on the failure plane at failure (kPa); ϕ' = angle of internal friction associated with the net normal stress state variable; $(u_a - u_w)_f$ = matric suction on the failure plane at failure (kPa); and ϕ^b = angle indicating the rate of increase in shear strength relative to the matric suction.

When a soil is saturated, the matric suction $(u_a - u_w)_f$ component of the shear strength equation is zero. When the soil is unsaturated, the matric suction component changes with the change in water content or degree of saturation. Therefore, in unsaturated soil mechanics, the shear strength of a soil is also affected by the changes in flux boundary conditions such as rain water infiltration and evapotranspiration.

2.3 *The soil water balance*

The soil water balance controls the state of moisture in the unsaturated zone of soil between the ground surface and the water table (Blight, 1997). It can be described by:

Water stored in soil = water input to soil - water output (3)

The water balance concept was used in the numerical modeling where rainfall acted as the water input whereas drainage and evapotranspiration acted as the water output. In contrast to rainfall intensity measurement, evapotranspiration intensity cannot be easily measured. There are several empirical methods to obtain evapotranspiration rate (ET). The most well-known and widely used technique to estimate ET is the one based on the K_c approach (Allen et al., 1998) where the evapotranspiration for certain species of vegetation (ET_c) is calculated by using standard agrometeorological variable and a crop-specific coefficient, the crop coefficient K_c (Lazzara & Rana, 2010). ET_c is calculated as follows:

$$ET_c = K_c \times ET_o \qquad (4)$$

Where K_c = crop coefficient.

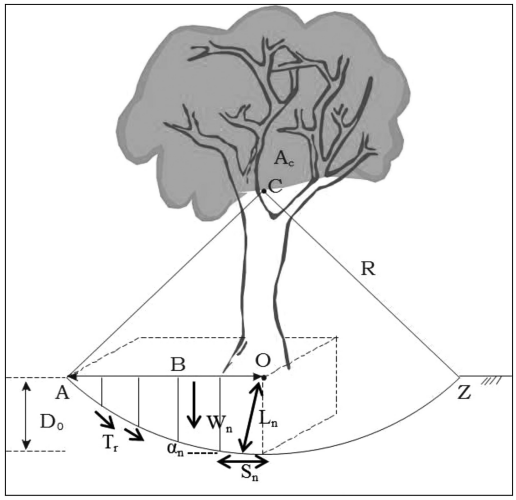


Figure 1. Tree stability analysis by the Ordinary method of slices (Rahardjo et. al., 2010).

Reference evapotranspiration (ET_o) is defined as the rate at which readily available soil water is vaporized from specified vegetated surface (Jensen et al., 1990). An updated Penman-Monteith Evapotranspiration (FAO-56 Method) was recommended by Allen et al. (1998) and Smith et al., (1992). The equation is as follows:

$$ET_o = \frac{0.408\Delta(R_n - G) + \gamma \frac{900}{T + 273} u_2 (e_s - e_a)}{\Delta + \gamma(1 + 0.34u_2)} \qquad (5)$$

Where T = mean air temperature (^oC), and u_2 = wind speed (m/s) at 2 m above the ground. The detailed calculation of this method can be found in Zotarelli et al. (2009).

2.4 *Tree stability*

The ordinary method of slices (Rahardjo, et al., 2010) was used to perform the tree stability analysis. This method was found to be suitable in analyzing the stability for a heart-rooted tree which is commonly found in tree's rooting system in Singapore (Ghani, et al., 2009; Rahardjo, et al., 2010). The failure mechanism of the heart root can be found in Mattheck & Breloer (1994). Figure 1 shows the parameters used to perform tree stability analysis using the ordinary method of slices.

The resisting shear force for a particular slice is T_n where:

$$T_n = \tau_n S_n \qquad (6)$$

$$\tau_n = c' + \left(\frac{W_n \cos\alpha_n}{S_n}\right) \tan\phi' + (u_a - u_w)\tan\phi^b \qquad (7)$$

And total resistive moment is

$$M_r = 2\sum T_n R \tag{8}$$

T_n = total shear resistance from the slice; R = Radius of the circle; W_n = weight of each slice; S_n = length of each base slice; ϕ' and ϕ^b = effective angle of internal friction and phi-b; c' = cohesion intercept; $(u_a - u_w)$ = matric suction.

3 MATERIAL AND METHODS

3.1 *Field instrumentations*

A road side tree located at Silat Avenue, Singapore was instrumented. The field instrumentation can be divided into two parts; the first part was weather instrumentation for climatic data measurement and the second part was soil instrumentation for pore-water pressure, volumetric water content, and ground water table measurements.

The weather instrumentation includes tipping bucket rain gauge (TB4, Campbell Scientific Corp) for rainfall intensity measurement, Pyranometer (CS300 Apogee Silicon Pyranometer, Campbell Scientific Corp) for solar radiation, wind monitor (model 05103, Young's Corp) for wind speed and direction and temperature cum relative humidity probe (HMP60, Campbell Scientific Corp). A 10 m high galvanized mast was erected on a concrete footing. On top of the mast, the wind monitor, the solar panel, the lightning protection rod and the pyranometer were installed. The other sensors were installed at a height of 1 m from the ground surface together with the data logger (CR1000, Campbell Scientific Corp).

The soil instrumentation was performed to measure pore-water pressure and volumetric water content (VWC) of the soil. The pore-water pressure was measured using a jet-fill tensiometer (model 2100F, Soil Moisture Corp) with an attached pressure transducer (Model GT3-15, ICT International Pty. Ltd). The volumetric water content was measured using a time-domain reflectometer (TDR) (CS650 reflectometer, Campbell Scientific Corp). There were six tensiometers and six VWC sensors installed at three different depths, of 0.5, 1 and 1.5 m at the site. In addition, the ground water table was also measured using a Casagrande piezometer. All the instruments were connected to the data logger (CR200X, Campbell Scientific Corp) and can be monitored real-time. The field monitoring schematic diagram is shown in Figure 2.

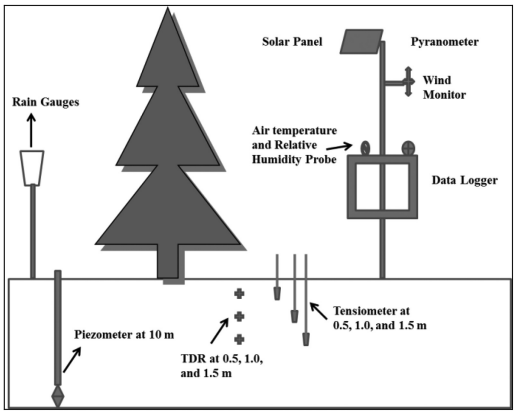


Figure 2. Field monitoring schematic.



Figure 3. Point cloud of *Syzygium grande.*

3.2 *Tree properties*

The properties of the tree that are required for the stability analyses are the tree height, the canopy area, the tree centroid and also the tree diameter at breast height (DBH). The properties were obtained through an imaging procedure using a laser scanning system. (Leica Scanstation C10). The results of the scanning system are shown in Figure 3.

The tree properties obtained from the result of laser scanning are summarized in Table 1. The tree species is *Syzygium grande.* The height of the tree was around 18 m. The centroid of the tree was 8.18 m from the ground surface. This is an important property as this is assumed as the location of the centre of the arc (tree stability analysis) and also the location of the wind force load. The crown area is also important for the tree stability analysis as the wind force magnitude is dependent on the crown area. Leaf Area Index (LAI) value estimation for *Syzygium grande* is 3 m^2/m^2 (source: Plant@NP; http://mobilearn.np.edu.sg/plantsnp/). This is a common LAI value for many mature crops which are ranges between 3–5 m^2/m^2 (Allen et al., 1998).

Table 1. Properties of the tree in Silat Avenue.

Silat Avenue *Syzygium grande*	
Height (m)	18.513
Canopy width (m)	6.2
Canopy area (m^2)	30.2
Centroid Z (m)	8.1859
Leaf Area Index (LAI) (m^2/m^2) (source : Plant@NP; http://mobilearn.np.edu.sg/plantsnp/)	3

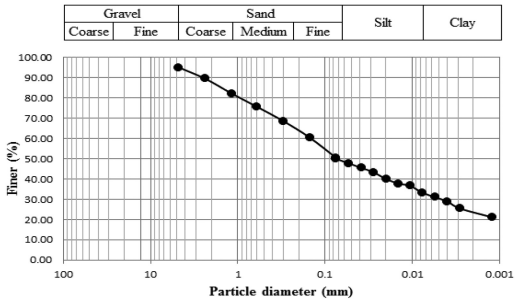


Figure 4. Grain size distribution of the soil in Silat Avenue Site.

3.3 *Soil properties*

The soil properties at the site were investigated by taking soil samples and performing laboratory tests on the samples. The basic properties investigated include specific gravity (ASTM D-854), grain size distribution and hydrometer test (ASTM D-1140, ASTM D-422), Atterberg limit (ASTM D-4318) and soil classification (ASTM D-2487). The saturated permeability of the soil was determined using the flexible wall saturated permeability test (ASTM D-5084). The saturated shear strength of the soil was determined using the triaxial consolidated-drained (CD) test (ASTM D7181). The unsaturated shear strength of the soil was determined using the unsaturated triaxial CD test. The procedure for unsaturated triaxial CD test is explained in more details in Fredlund and Rahardjo (1993).

The basic properties and grain size distribution of the soil from the site are presented in Figure 4 and Table 2, respectively. The material at the site is generally top soil which consists of a mixture between sands and residual soils. The grain size analyses show that about fifty percent of the material was clay. The unified soil classification system (USCS) categorized the soil to be SC-CL or sandy clays. The saturated permeability of the material was 10^{-6} m/s. The total density of the material was also quite high of around 1.95 Mg/m^3. The effective shear strength parameters of the soil were also quite high with an effective friction angle of 34° and effective cohesion of zero. The rate of increase in shear strength due to the increase in matric suction as described by ϕ^b angle is 34°.

Table 2. Basic soil properties of the soil in Silat Avenue Site.

Soil Properties Unified Soil Classification System	
Group name	Sandy Clays
Group symbol	SC-CL
Specific Gravity G_s	2.67
Total density, ρ (Mg/m^3)	1.95
% Gravel	4.9
% Sand	44.6
% Fines	50.5
Atterberg's Limits	
Liquid Limit, LL (%)	30
Plastic Limit, PL (%)	17
Plasticity Index (%)	13
Saturated Coefficient of Permeability, k (m/s)	10^{-6}
Effective Friction angle, Φ (°)	34
Effective cohesion, c′ (kPa)	0

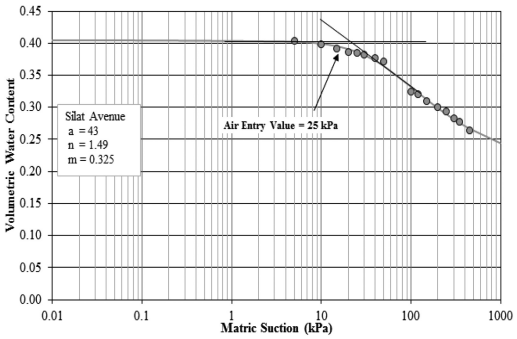


Figure 5. SWCC data point, fitting line and parameters of the soil at Silat Avenue Site.

The SWCC of the soil was measured using a Tempe pressure cell for air pressures lower than 80 kPa and using a pressure plate extractor for air pressures higher than 80 kPa (ASTM D-2325).

The SWCC fitted with the Fredlund & Xing (1994) SWCC equation with Leong & Rahardjo (1997) recommendation for the correction function is shown in Figure 5.

The permeability function was predicted from the SWCC curve using the method proposed by Childs and Collis-George (1950). The procedure for this method can be found in Fredlund and Rahardjo (1993). Figure 6 shows that the permeability starts to decrease at around 6 kPa, and as the matric suction increases the coefficient of permeability keeps decreasing.

3.4 *Numerical model*

A seepage numerical modeling was conducted using SEEP/W (Geo-slope international Ltd, 2012). The objective of the numerical modeling was to obtain the complete profile of pore-water pressure for the time

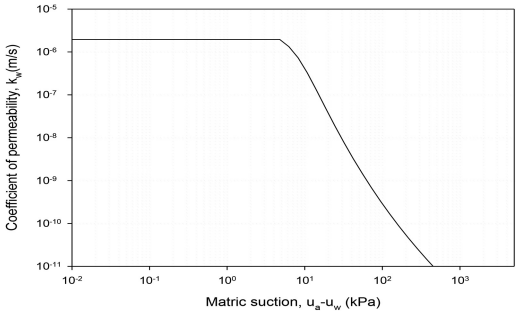


Figure 6. Permeability function of the soil at Silat Avenue Site.

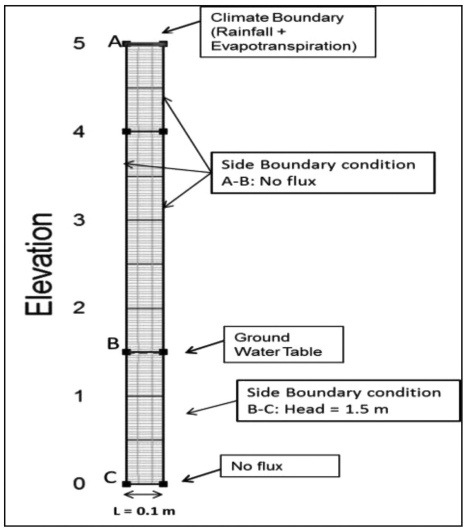


Figure 7. Numerical seepage models.

period of the field measurement. The results of the numerical model were then verified with data from the field measurements points. The results of the seepage analyses were then used as input for the tree stability analysis.

The model for the seepage analysis is shown in Figure 7. The seepage analysis was a two-dimensional (2-D) analysis with a height of 5 m. The SWCC and permeability function data were the main input data for the numerical modeling and the values were taken from the laboratory measurements shown in the previous section. The boundary condition used at the bottom of the model was total head being equal to the initial water table and at the top of the model was the flux boundary condition which includes rainfall and evapotranspiration. Measurement point at 0.5 m, similar to the field measurements point, was chosen from the model for the comparisons of the field and numerical results. The initial condition for the seepage model was water table at a depth of 3.5 m from the ground surface.

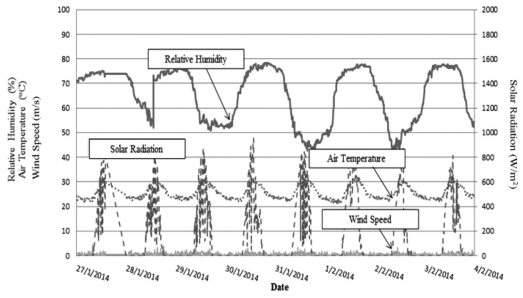


Figure 8. Typical climatic data from field instrumentations.

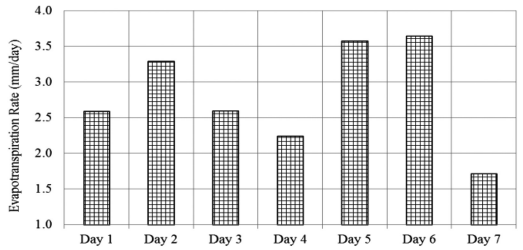


Figure 9. Evapotranspiration rate of *Syzygium grande* for one week period.

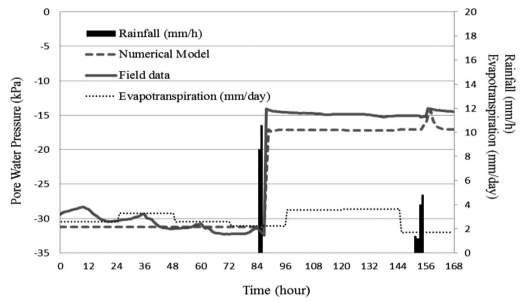


Figure 10. Numerical model verification.

4 RESULTS AND DISCUSSION

Typical climatic data (relative humidity, solar radiation, air temperature, and wind speed) obtained from field instrumentation are shown in Figure 8. These data together with tree properties then used as input for evapotranspiration calculation. Evapotranspiration rate for one week monitoring period are summarize in Figure 9. The evaporation rate ranges between 1.7 to 3.6 mm/day

Figure 10 shows the comparisons of pore-water pressure obtained from the field instrumentations and the numerical modeling. The result shows that the field instrumentation results agreed well with the results from the seepage modeling. Therefore, the numerical model was deemed to be able to represent the field condition for the tree stability analyses.

The pore-water pressure obtained from the seepage modeling was used as the input for the tree stability analyses. Figure 11 shows the changes in tree resisting

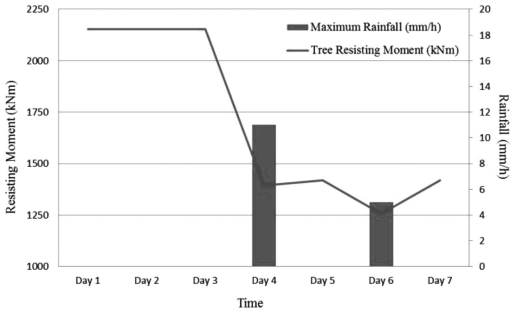


Figure 11. Change in tree resisting moment for one week period due to rainfall occurrences.

moment in one week period due to rainfall occurrences. In day 1 to day 3 when there was no rainfall occurrence, the tree resisting moment showed a stable value at 2153 kNm. However when rainfall occurred in day 4, the tree resisting moment decreased from 2153 kNm to 1394 kNm and started to increase to 1418 kNm on the next day when there was no rainfall. The results show that the event of rainfall decreased the stability of tree. The changes in tree resisting moments after rainfall occurrences provided an indication of the effect of rainfall on tree stability.

5 CONCLUSION

A comprehensive field measurement and monitoring including climatic data, soil properties, and tree properties provides reliable data as input for seepage modeling. The seepage modeling results showed a good agreement with the field instrumentation data. The tree stability analysis results show that rainfall decreased the tree resisting moment which contributed to tree failure.

ACKNOWLEDGEMENT

The study was carried out as a part of a research collaboration to study effect of rainfall on tree stability. The study was conducted by the Nanyang Technological University and National Parks Board, Singapore.

REFERENCES

Allen, R.G. et al. 1998. *Crop evapotranspiration: guidelines for computing crop water requirements Food and Agriculture Organization of the United Nation*, Rome.

Blight, G.E. 1997. *The "Active" Zone in Unsaturated Soil Mechanics*. 1st GRC Lecture, Nanyang Technological University, Singapore.

Brand,E.W. 1984. *Lanslides in Southeast Asia: A state-of-art report*. Proceedings, 4th International Symposiom on Landslides, Toronto, September 16–21, vol.1, pp. 17–59.

Childs, E.C. & Collis-George, G.N. 1950. *The permeability of porous materials*. Proceedings of the Royal Society of London 210A, 392–405.

Evangelista, A. et al. 2008. *Field investigation on triggering mechanisms of fast landslides in unsaturated pyroclastic soils*. 1st European Conference on Unsaturated Soils, Durham, UK, pp. 909–915.

Fredlund, D.G. & Xing, A., 1994, "Equations for the Soil-Water Characteristic Curve", *Canadian Geotech. J.*, Vol. 31, pp. 521–532.

Fredlund, D.G. et al. 1978. The Shear Strength of Unsaturated Soils. *Canadian Geotechnical Journal* 15, 313–321.

Fredlund, D.G. & Rahardjo, H. 1993. *Soil Mechanics for Unsaturated Soils*. John Wiley & Sons Inc., New York.

Geo-slope international Ltd. 2012. *Seep/W user's guide for finite element seepage analysis*. GEO-SLOPE International Ltd., Calgary, Alberta, Canada.

Ghani, M. A. et al. (2009). The effect of root archtecture and root loss through trenching on the anchorage of tropical urban trees (Eugenia grandis Wight). *Trees, 23*, 197–209. doi: 10.1007/s00468-008-0269-9

Plants@NP. 2014. *http://mobilearn.np.edu.sg/plantsnp/Mobile/Default.aspx*

Jensen, M.E. et al. 1990. Evapotranspiration and Irrigation Water Requirements. *ASCE manuals and Reports on engineering Practice* No.70. American Society of Civil engineers, New York.

Koizumi, A. 1987. Studies on the estimation of the mechanical properties of standing trees by non-destructive bending test (In Japanese with English Summary). *Journal of Toyama Forestry for Production Research Center* 14, 1–77.

Lazzara, P. & Rana, G. 2010. The use of crop coefficient approach to estimate actual evapotranspiration: a critical review for major crops under Mediterranean climate. *Italian Journal of Agrometeorology* 2, 25–39.

Leong, E.C. & Rahardjo, H. 1997a. Review of soil-water characteristic curve equations. *Journal of Geotechnical and Geoenvironmental Engineering*, ASCE, Vol. 123, No. 12, pp. 1106–1117.

Lim, T.T. et al. 1996. Effect of Rainfall on Matric Suction in a Residual Soil Slope. *Canadian Geotechnical Journal*, Vol.33, pp 618–628.

Ow, L. et al. 2010. Tree-pulling experiment: an analysis into the mechanical stability of rain trees. *Trees Structure and Function* 24, 1007–1015.

Rahardjo, H. et al. 2014. Comprehensive Instrumentation for Real Time Monitoring of Flux Boundary Conditions in Slope. Procedia Earth and Planetary Science 9, 23–43.

Rahardjo, H. et al. 2010. *Soil improvement for tree stability*. Research project report, Nanyang Technological University, Singapore.

Richards, L.A. 1931. Capillary conduction of liquids through porous medium. *Physics* 1, 318–333.

Smith, M. et al. 1992. *Report on the expert consultation on procedures for revision of FAO guidelines for prediction of crop water requirements*. Land and Water Development Division, United Nations Food and Agricultural Service, Rome, Italy.

Zotarelli, L. et al. 2009. *Step by step calculation of Penman-Monteith evapotranspiration (FAO-56 Method)*, University of Florida.

Unsaturated Soil Mechanics—from Theory to Practice – Chen et al. (Eds)
© 2016 Taylor & Francis Group, London, ISBN 978-1-138-02921-7

The impacts of climate change on expansive soil movements in Australia

X. Sun, J. Li, A.N. Zhou & G. Ren
School of Civil, Environmental and Chemical Engineering, RMIT University, Melbourne, Australia

ABSTRACT: The effect of climate change on expansive soil movement has long been the greatest global challenge for built infrastructures. Numerous lightly-loaded residential buildings constructed on expansive soils are subjected to distortions arising from differential ground movements due to seasonal soil moisture (suction) changes. Thornthwaite Moisture Index (TMI) has been widely employed by geotechnical engineers to quantify expansive soil movement resulted from climatic variation. It is difficult to estimate the patterns of future soil movement due to the inherently highly variable nature of Victorian (Australia) climate, but it is likely that with the collected precipitation and temperature data, the TMI can be derived to infer depth of design soil suction change (H_s) which allows the characteristic ground movement (y_s) to be estimated. This paper outlines an overview of residential footing design in Australia. Three TMI isopleth maps of Victoria are also developed for the convenience of TMI users to infer H_s.

1 INTRODUCTION

Expansive soils are also referred to reactive soils, volumetrically active soils, swelling and heaving soils. Expansive soil swells laterally as well as vertically and has the tendency of volume change, for example, shrink or dry-crack when water content decreases and swell when water content increases. Seasonal variation in climate is the dominate factor of expansive soil volume change and other factors such as tree root drying, underground pipe leaking and garden over-watering are also responsible for soil volume change.

Serious damage to the foundation of light structures may be caused by differential ground movements due to non-uniform moisture change of expansive clays. Structural damage caused by expansive soils has been widely reported in many countries such as Australia, China, India, Israel, South Africa, the United Kingdom and the United States of America (Li & Cameron 2002, Li et al. 2014). The problems are particularly significant in Australia as approximately 20% of the surface area in Australia (Richards et al. 1983) and 50% of the surface area in Victoria is covered by expansive soils (Mc Andrew 1965). Expansive soil associated problems such as foundation movement can strongly affect the function and performance of light structures and lead to serious damages or even failure of the structure. Consequently, much research in Australia has been dedicated to the foundation movement prediction to cope with long-term and seasonal change induced ground movement.

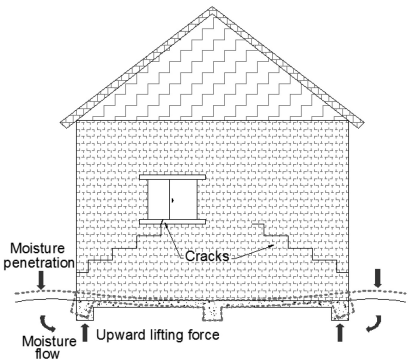


Figure 1. Typical edge heave for a slab footing.

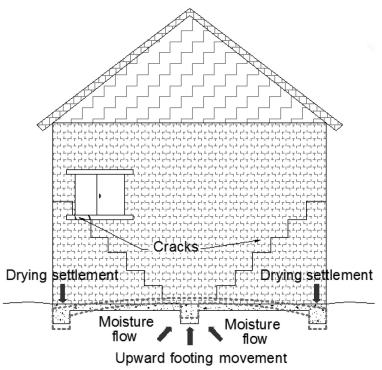


Figure 2. Typical centre heave for a slab footing.

2 OVERVIEW OF RESIDENTIAL FOOTING DESIGN UNDER AS2870

Research into expansive soil behaviour has been carried out in Australia since the late 1950's, the outcome of much of the Australian research was an Australian standard. The Australian Residential Slabs and Footings Standard AS2870 was first published in 1986 followed by two editions published in 1996 and 2011. Since 1986, Australian footing design and construction practices have been guided by AS2870.

During the process of residential footing design, the specifications of beams and reinforcements adopted are largely dependent on the site classification. Site classification according to AS2870, is determined based on the expected ground surface movement and the depth to which this movement extends. The design site where ground movement is prevailingly caused by soil reactivity under normal moisture condition, shall be categorized into 5 classes shown in Table 1. The equation outlined in AS2870 for characteristic surface movement y_s calculation is expressed in Equation 1.

$$y_s = \frac{1}{100} \sum_{n=1}^{N} \left(I_{pt} \, \overline{\Delta u} h \right)_n \quad (1)$$

I_{pt} is the instability index and can be derived from the shrinkage index I_{ps} which is determined from laboratory tests, namely shrink-swell, core shrinkage or loaded shrinkage test. It should be noted that a shrinkage index of 4%/pF would be regarded as a highly expansive soil, 6%/pF very highly expansive and 8%/pF, an extremely expansive soil (Li et al. 2014). Δu is the soil suction change averaged over the thickness of the layer under consideration, the maximum surface suction change Δu_s is 1.2pF. h is the thickness of layer and N is the number of layers within the design depth of suction change H_s. H_s is the depth below which no significant seasonal suction changes and hence no volume changes occur in response to climate (Figure 3). Values of H_s for various locations in Australia are summarized in AS2870 and for other locations, the standard recommend that by the use of the climate indictor TMI to estimate the depth of design soil suction change H_s based on the TMI – H_s correlation outlined in Table 2.

Soil suction profile was a representation of a state of physical balance between various processes operating to add or to subtract water at any part of the profile (Aitchison & Woodburn 1969). The simplified reverse triangular suction profile is shown in Figure 3, it assumes the reduction of suction change is linear with depth, however the reduction is usually more rapid in real suction behaviour.

Table 1. Site classification by characteristic ground movement (AS2870, 2011).

Characteristic surface movement (y_s) (m)	Site classification	Description
$0 < y_s \leq 20$	S	Slightly reactive
$20 < y_s \leq 40$	M	Moderately reactive
$40 < y_s \leq 60$	H1	Highly reactive
$60 < y_s \leq 75$	H2	Very highly reactive
$y_s > 75$	E	Extremely reactive

3 THORNTHWAITE MOISTURE INDEX

The climatically-controlled parameter Thornthwaite Moisture Index (TMI), developed by an American climatologist Charles Warren Thornthwaite (1948) has been widely accepted and used by many researchers in estimating climatic variations. This climatic parameter is dimensionless and is expressed in a number that can be used to indicate climatic condition for a particular location. Negative index present an arid climate with less moisture in soil while humid climate with higher soil moisture is expressed in positive index, zero index means there is no net soil moisture change for the study period.

3.1 *Equation for TMI calculation*

TMI is mainly a function of precipitation (P), temperature and potential evapotranspiration (PET). The original equation used to calculate TMI was developed by C. W. Thornthwaite in 1948. This equation is computationally intensive since numerous parameters are required. The original Thornthwaite equation was modified by Mather in 1974, it assumed that rainfall would not augment the depleted storage and there was no net change in soil water storage over long-term. The revised Thornthwaite equation leads to a major simplification with only monthly precipitation and temperature data required. It eliminates the need to carry out the water-balance approach which is required

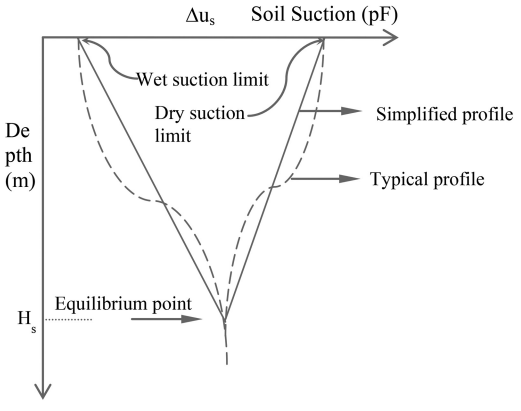


Figure 3. Typical soil suction profile.

in the original equation. The simplified Thornthwaite equation was expressed in Equation 2.

$$TMI = 100\ (\frac{P}{PET} - 1) \quad (2)$$

Where P = annual precipitation; PET = adjusted potential evapotranspiration.

Thornthwaite Moisture Index (TMI) in Equation 2 is defined as an annual index which is calculated by the use of monthly values of precipitation and potential evapotranspiration. Step by step TMI calculation procedures were given in McKeen & Johnson (1990). Metrological parameters required to calculate TMI using Equation 2 include (a) monthly precipitation (P), (b) mean monthly temperature (t_i) and (c) the day length correction factor (D_i) for a particular weather observation station.

Table 2. Relationship between TMI, H_S and climatic zone (AS2870, 2011).

Climatic Zone	Description	TMI	H_S (m)
1	Alpine/wet coastal	> +10	1.5
2	Wet temperate	−5 to +10	1.8
3	Temperate	−15 to −5	2.3
4	Dry temperate	−25 to −15	3.0
5	Semi-arid	−40 to −25	4.0
6	Arid	< −40	>4.0

3.2 *Correlation between TMI and H_s*

Ideally the depth of seasonal suction change, H_S should be determined from the field data on ground movements and soil suction variations with depth and seasons over a long period. Unfortunate such data is very rare. Reliable field data from which H_s can be inferred could take years even decades to collect and involve extensive field measurements.

A rationally-based TMI - H_s relationship (Table 2) introduced by AS2870-2011, enables users to estimate H_s for a particular site use the calculated TMI value. The standard suggested at least 25 continuous years of climate data are needed for the estimation of H_s. As shown in Table 2, it seems that TMI corresponds to a specific value of H_s. Large positive TMI (greater than 10 TMI units) leads to a shallow H_s depth in climate zone 1 while large negative TMI arising from climate zone 6 have a much deeper H_s of greater than 4 m.

It should be recognized that the theoretical basis for TMI-H_s relationship remains limited and the correlation introduced in AS2870 may has been based more on anecdotal evidence and empirical experience rather than quantitative research and scientific data. Therefore, further work needs to done to investigate a better correlation between TMI and H_s.

4 THORNTHWAITE MOISTURE INDEX ISOPLETH MAPS

The original Thornthwaite moisture index (TMI) based isopleth map of Victoria along with its climate zones was endorsed in AS2870, as shown in Figure 4. This



Figure 4. Victorian climate zones under AS2870.

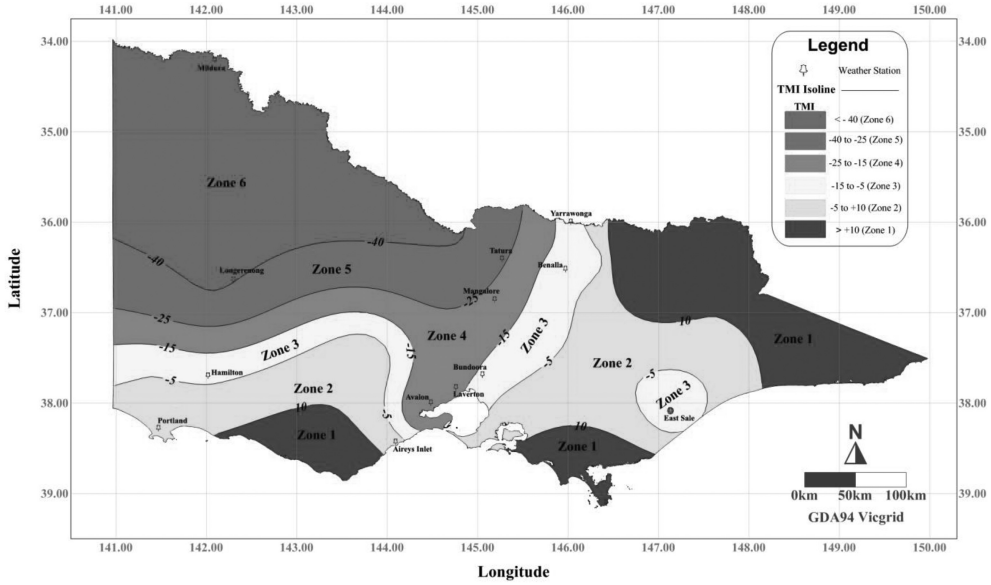


Figure 5. Mean TMI Contour Map for Victoria from 1954 to 1973.

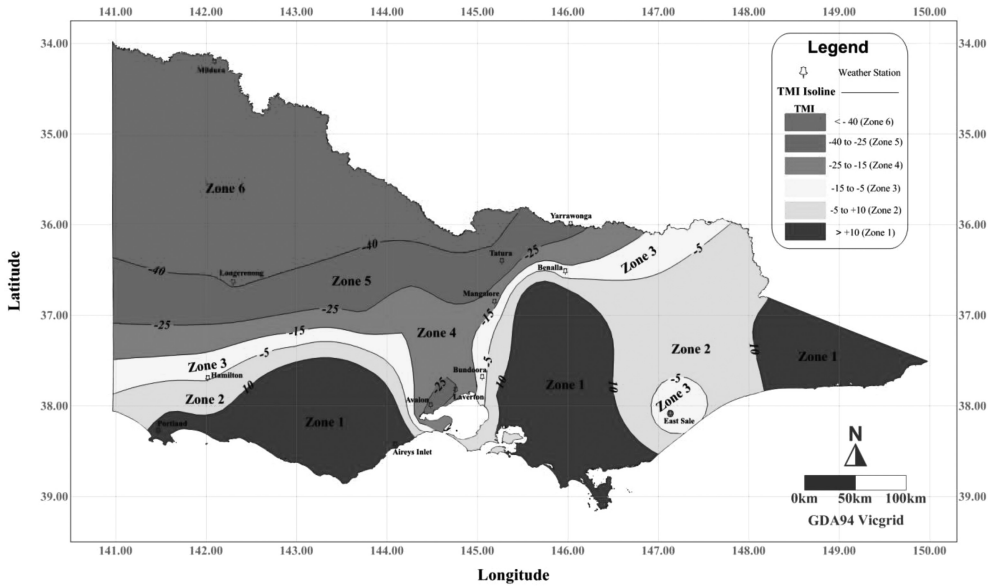


Figure 6. Mean TMI Contour Map for Victoria from 1974 to 1993.

map has been used as guidance for design engineers to infer the depth of design suction change H_s that is needed for estimate of characteristic surface movement y_s. Unfortunately, this map is out of date and may not be appropriate since it was produced using climate data over the 1940–1960 period (McManus et al. 2003) and thus cannot truly reflect the current climate conditions in Victoria.

A few different versions of TMI based contour map of Victoria have been published in the past decade. McManus et al. (2003) used the climatic data taken from 1960 to 1991 and Lopes & Osman (2010) calculated TMI from the 1948 to 2007 data. More recently, Simone (2014) produced a climate zone map of Victoria using the climatic data from 2001 to 2011.

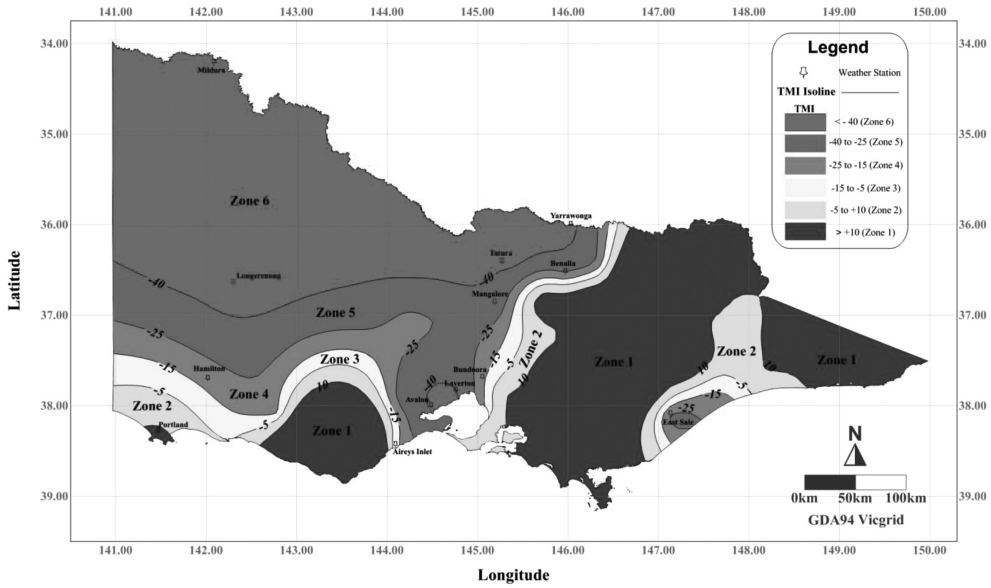


Figure 7. Mean TMI Contour Map for Victoria from 1994 to 2013.

Table 3. Shrinkage index I_{ps} values at different depth (Karunarathen et al. 2014).

Depth (m)	I_{ps} (%)
0.5–1.0	5.69
1.5–2.0	5.62
2.5–3.0	4.88

Table 4. The comparison of the estimated y_s values for Braybrook.

Study period	TMI	Interpolated H_s (m)	y_s (mm)	Site class
1954–1973	−12	2.2	35	M
1974–1993	−16	2.4	49	H1
1994–2013	−28	3.2	81	E-D

4.1 *The delineation of TMI isopleth maps of Victoria from 1954 to 2013*

In this paper, long term historical climate records (i.e. precipitation and temperature data) over 60 years (in 3 × 20 year periods, i.e. 1954–1973, 1974–1993 and 1994–2013) sourced from 70 weather stations of Victoria were used for TMI computation.

The TMI isolines were plotted to produce the isopleth maps for 3 × 20 periods (Figures 6–8) by the use of software Surfer®11 (2012). Climate zoning of Victoria which was classified based on Table 2, was also shown to present the climate change since 1954.

Figures 5–7 have confirmed the belief of many geotechnical engineers that Victorian soils have become drier over the past 60 years. Generally speaking, north to south part of the state become more arid where arid climate (zone 6) is spread out over north western while south and east part of Victoria is in zone 1 with wet coastal climate type. The changes in isolines in Figures 5–7 present the following:

- Soil in far north-west (e.g., Mildura areas) have been experienced the driest climate condition since 1954, leading to climate zone 6 (Arid climate) expanded to south and east to include the Longerenong, Yarrawonga, Tatura areas and Melbourne south-west suburbs (i.e. Avalon, Laverton).
- Climate zone 5 (Semi-arid climate) has expanded to further south and east and now include the Mangalore and most Melbourne Metropolitan areas.
- Climate zone 4 (Dry temperate climate) has moved east and south-west to include Bundoora, Benalla and Hamilton areas and has a marked shrinkage in south of the state whilst enlarged in East Sale areas.
- Climate zone 3 (Temperate climate) has shrank and moved south-west to include Aireys Inlet areas.
- Climate zone 2 (Wet temperate climate) has a noticeable shrinkage in south coastal and western inland areas whereas enlarged towards the north-east.
- Climte zone 1 (Wet coastal climate) has expanded to south-west coast to include Portland area while a significant growth in south east towards the north-east border.

5 CASE STUDY

To compare and evaluate the impact of climate change on residential footing design, a case study has been carried out in Braybrook, a western suburb

of Melbourne over 60 years (in 3×20 year periods, i.e. 1954–1973, 1974–1993 and 1994–2013). The Thornthwaite evapotranspiration equation is adopted for PET calculation and the simplified Thornthwaite Equation 2 is employed for TMI computation respectively. Meteorological parameters used to calculate TMI were extracted from Melbourne Regional Office (086071) weather observation station. Surface soil suction change Δu_s of 1.2 is used for the estimation of y_s by the use of Equation 1. Values of shrinkage index I_{ps} at various depths are taken from Karunarathen et al. (2014), as shown in Table 3.

From the calculated results in Table 4, it can be seen that Braybrook have experienced an increasing severity of the desiccation of soils over the past 60 years. It is noted that there is a marked decrease of the TMI value from −12 (the 1st 20 year period) to −16 during the 1974–1993 period, and then −28 in the last 20 years. Table 4 also shows the estimated potential ground movement y_s has increased by 46 mm (131%) from 1954–1973 period (i.e. 35 mm) to recent 20-year period (i.e. 81 mm), leading to the site class changed from M to E-D site. As the consequence of increased ground movement due to climatic variation, larger beams and extra reinforcements may be required to cater the future potential effects of climate change on residential footings.

6 CONCLUSIONS

Residential building constructed over expansive soils have long been a concern not only to house owners but also to design engineers. In this paper, the current Australian Standard of residential slabs and footing design was reviewed.

TMI as a climate indicator was employed to produce isopleth maps of Victoria over the past 60 years (in 3×20 year periods, i.e. 1954–1973, 1974–1993 and 1994–2013). These maps conformed that Victoria has experienced a drying climate since the early 1950's where the most noticeable aridity has occurred in recent 20-year period. This implies an increase in the severity of desiccation of the soil profile, which could potentially result in a higher incidence of soil moisture variation induced ground movement and the subsequent structural failure.

A case study has been conducted to compare and evaluate the impact of climate change on residential footing design. The calculated results show that climate change resulted in a more negative TMI along with time and hence the larger depth of design suction change, the greater ground surface movement and subsequently increased the financial cost for constructing residential footings.

REFERENCES

Aitchison, G.D. & Woodburn, J.A. 1969. Soil suction in foundation design. *Proceedings of 7th International Conference on Soil Mechanics and Foundation Engineering*, Mexico City: 1–8.

AS2870, 2011. Australian Standard: Residential Slabs and Footings. Standards Australia.

Karunarathne, A., Sivaner, S., Gad, E., Disfani, M., Rajeev, P., Wilson, J. & Li, J. 2014. Field and laboratory investigation of an expansive soil site in Melbourne. *Australian Geomechanics Journal*, 49(2): 85–93.

Li, J. & Cameron, D.A. 2002. A case study of a courtyard house damaged by expansive soils. *Journal of Performance of Constructed Facilities*, ASCE, 16(6): 169–175.

Li, J., Cameron, D.A. & Ren, G. 2014. Case study and back analysis of a residential building damaged by expansive soils. *Computers and Geotechnics*, 56: 89–99.

Lopes, D. & Osman, N.Y. 2010. Changes of Thornthwaite's total moisture indices in Victoria from 1948–2007 and the effect on seasonal foundation movement, *Australian Geomechanics*, 45(1): 37–48.

Mather, J.R. 1974. *Climatology: fundamentals and applications*. McGraw-Hill, New York, USA: 113–131.

Mc Andrew, J. 1965. The geological map of Victoria in geology of Australia ore deposits. *The 8th Commonwealth Mining & Metallurgical Congress*, Australia & New Zealand, Melbourne, AusIMM, 1, McAndrew J., Marsden M.A.H.(eds): 440–449.

McKeen, R.G. & Johnson, L.D. 1990. Climate-controlled soil design parameters for mat foundations. *J. Geotechnical Engineering*, 116(7): 1073–1094.

McManus, K.J., Lopes, D. & Osman, N.Y. 2003. The influence of drought cycles on the Thornthwaite Moisture Index contours in Victoria Australia. *An International Conference on Problematic Soils*, Nottingham, United Kingdom, CI-Premier, Singapore: 357.

Richards, B.G., Peter, P. & Emerson, W.W. 1983. The effects of vegetation on the swelling and shrinking of soils in Australia. *Geotechnique*, 33: 127–139.

Simone Leao, 2014. Mapping potential risk for housing damage from ground movement due to climate change. *International Journal of Environmental Science and Development*, 5(4): 387–392.

Surfer®11, 2012. Golden Software, LLC, Colorado: Golden. Available at: http://www.goldensoftware.com/.

Thornthwaite, C.W. 1948, An approach toward a rational classification of climate. *The Geographical Review*, 38(1): 55–94.

Unsaturated Soil Mechanics—from Theory to Practice – Chen et al. (Eds)
© 2016 Taylor & Francis Group, London, ISBN 978-1-138-02921-7

A study on the feasibility of using centrifugal model test to simulate in-situ soaking test on loess

S.L. Jin, Y.C. Xing & W.Q. Zhao
China Institute of Water Resources and Hydro-power Research, Beijing, China

A.J. Zhang
Northwest A&F University, Yangling, Shanxi, China

P. An
Chang'an University, Xi'an, Shanxi, China

ABSTRACT: Data was analyzed about the engineering practice for the foundation of the diversion canal which is in Yili region of Xinjiang Province. Tsinghua University geotechnical centrifuge was used to saturate the undisturbed loess (with a natural water content) and perform the centrifugal model test. The undisturbed loess becomes stabilized after the step-loading increased to 60 g and then becomes saturated at a constant acceleration. Thus collapsibility by single-line method was obtained. The differences of collapsibility between the saturated loess foundation and foundation with a natural water content with the same thickness were calculated to obtain collapsibility by double-line method. Results show that foundation collapsibility results calculated by single-line method and double-line method are similar, demonstrating that the two methods have little influences on collapse deformation. The collapsibility results obtained from centrifugal model test is close to the on-site results, validating the feasibility of using centrifugal model test to simulate in-situ soaking test on loess.

1 INTRODUCTION

Self-weight collapsible deformation of loess has been one of the major concerns to engineers in the past few years. The quantity of deformation is determined by engineers by indoor model test and in-situ soaking test (Luo & Wen 2004). With regard to indoor model test, though the expense is low, the efficiency is high and the modeling results are scattered to a large extent. Also the results don't agree well with the in-situ values. For in-situ soaking test, though the expense is high, the consumption of water is large, the modeling values agree well with the in-situ values (Huang et al. 2006, Huang et al. 2007, Cui et al. 2013).

In this study, geotechnical centrifuge is used to simulate in-situ soaking test on loess. During the simulation process, a model is made on a given scale using building materials. It was placed into a field with high centrifugal force generated by rotating and then self-weight body force of the model is magnified so that the model can undergo deformation and failure under a given stress which is similar to real condition. Therefore, the geotechnical centrifuge is, essentially, a physical simulation (Du 2010). Centrifugal model test is especially suitable for determining the deformation and failure caused by body force. Thus it is widely applied, both at home and abroad, in geotechnical engineering projects such as dam, slope, underground projects and soft ground. In the field of loess engineering, researches mainly focus on stability of loess slope and supporting effect, while studies on loess collapsibility is very rare (Gong 2010, Wang 2010, Hu 2000). Loess collapsibility can be investigated with centrifugal model test which is economic and efficient and has the advantages of laboratory test and in situ immersion test.

Data was analyzed about the engineering practice for the foundation of the diversion canal which is in Yili region of Xinjiang Province. Tsinghua University Geotechnical Centrifuge was used to saturate the undisturbed loess (with a natural water content) and perform the centrifugal model test for loess. Undisturbed loess model is stabilized, after the step loading increased to 60 g, and then saturated at a constant acceleration. Then collapsibility of the loess by single-line method and double-line method was obtained and compared with each other in order to demonstrate whether calculating methods have influences on results of collapsibility. Besides, collapsibility obtained from centrifugal model test and obtained on site is compared with each other to validate the feasibility of using centrifugal model test to simulate in-situ soaking test.

2 DESIGN OF THE MODEL

2.1 *Engineering background and in-situ soaking test*

The loess section accounts for 50% of the total length of the diversion canal line. Exploration results show that loess in the station has a thickness of more than 30 m and belongs to collapsible loess with high or medium self-weight. In order to obtain the measured value of self-weight collapsible foundation, large-scale in-situ immersion test was performed.

In the in-situ immersion test, we used two test pits: test pit 1# (a circular pit) and test pit 2# (a rectangular pit). Test pit 1# was 30 m in diameter. In this pit, penetrating wells was used to accelerate the soaking process of the foundation. The experimental duration was 190 days: water injection lasted for 7 days, and the observation lasted for 183 days. The experimental results showed that test pit 1# had a soaking depth of 30 m and the maximum collapsibility was 2.7 m.

Test pit 2# was 66 m in length and 44 m in width. Collapsibility under the natural state was determined, so penetrating wells are not used in this pit. The experimental duration was 184 days: water injection lasted for 15 days, and the observation lasted for 179 days. The experimental results showed that test pit 2# had a soaking depth of 16 m, and the maximum collapsibility occurring in the central position of the pit was 1.2 m.

2.2 *Samples and physical properties of loess*

In typical locations of the regions applied with the field immersion tests, soil samples at different depths were acquired by excavating pit artificially for all kinds of laboratory tests and the centrifugal model test. The soil samples include original loess samples and remolded loess samples. Maximum depth of the pit is 30 m and two original loess samples were acquired every one-meter depth of the pit. The size of the original loess samples is about 20 × 20 × 30 cm (h = 30 cm). Original loess samples were sealed immediately and placed in a cool and dry place after evacuation in order to maintain the natural structure and avoid evaporation.

Results of routine laboratory tests, including particle size analysis, water content limit analysis, and cutting ring test of soil samples at different depth, showed that particle composition, water content, dry density, and water content limit did not change much for loess at varying depth. Exploration found no presence of ancient soil. The above evidences indicated that loess in this area was homogeneous within a thickness of 30 m. Therefore, samples could be taken from the site soil when centrifuge model test was performed to simulate the stress and deformation of the foundation which is made up of undisturbed loess.

2.3 *Test equipment*

Test equipment used included a centrifuge, a model box, a rainfall soaking device and an image acquisition system. This experiment was carried out using the 50 g·t geotechnical centrifugal testing machine at Tsinghua University (see Fig. 1). The basic parameters of the centrifugal tests are as follows:

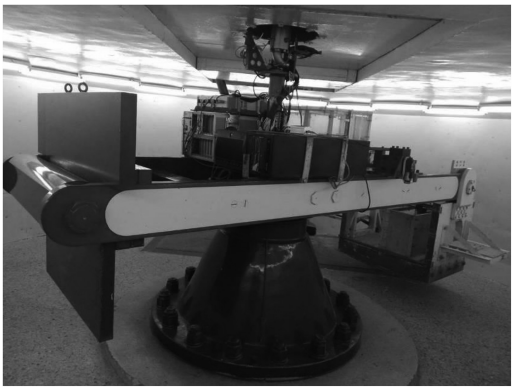


Figure 1. Centrifugal model test machine.

Effective radius of the turning arm, 2 m (from the loading center to the rotation center);
The largest centrifugal acceleration, 250 g.

The net size of the model box used in this experiment is 50 cm × 35 cm × 20 cm. One side of the model box is made of organic glass 5.8 cm thick, and the other three sides and the bottom side are all made of aluminum alloy.

The image acquisition system was a non-contact displacement measuring system. A camera was arranged at one side of the centrifuge and in alignment with the glass pane, so that the whole process of deformation and development of soil could be observed and recorded through the glass pane. Another camera was set at the top of the model box to observe the changes. Data about deformation observed and recorded were transmitted to the control room through a data transmission line. The rainfall soaking device was made up of water tanks supplying water, electromagnetic valves controlling water as well as water boxes. Two water tanks were placed on the arm of the centrifuge and each tank 18 cm × 20 cm × 36 cm in size had a water outlet. The water outlet was connected with the electromagnetic valve whose data line was linked to the control room through a sliding ring Thus, the soaking time and duration can be controlled in the centrifuge room.

2.4 *Testing scheme*

Two centrifugal models were designed: soil with a natural water content and saturated soil. Undisturbed soil from test pits was used to build loess foundation. Steps of making a centrifugal model were as follows (see Figure 2):

1. Soil sample was placed in the model box along the boundary. In order to reduce restriction effect of the model box on soil deformation, vaseline was

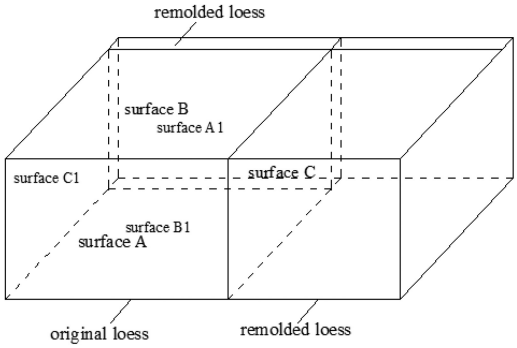


Figure 2. Model box of centrifugal model test.

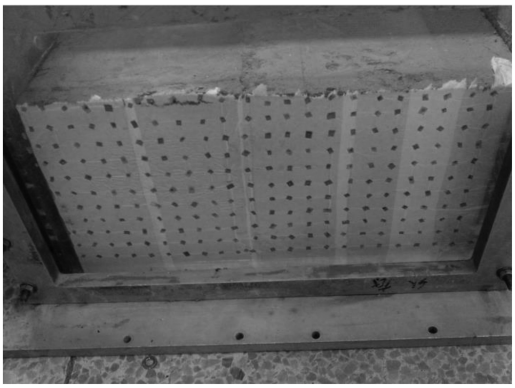


Figure 3. Displacement markers of sample.

smeared over the side wall of the model box in advance.

2. To make compaction easier, the remolded soil (from the test pit where the undisturbed soil sample was obtained) was crushed, mixed with water to the optimum moisture content, and sealed for at least 24 h.
3. In the left space of model box remolded soil was compacted to the same height as the undisturbed soil sample, in addition to the same dry density.
4. Soil samples were saturated with the method of low-pressure bottom-up soaking (for the saturated model only). The initial conditions of all models were shown in Table 1.

When the natural moisture content model was completed, the undisturbed soil sample was 26.5 m in height. In-situ soaking test (as mentioned before, the actual saturated soil was 16 m in depth) in the test pit 2# should be simulated to obtain loess collapsibility by single-line method. In light of this, the centrifugal acceleration of 60 g was determined (16 m/26.5 cm = 60) for the natural moisture content model. Considering the instability of image acquisition system in high-speed rotation, the centrifugal acceleration of 100 g was determined for the saturated model. It was obvious that the maximum simulated saturated soil was 100 × 27.5 cm = 27.5 m in depth.

2.5 *Displacement markers of sample*

Pins with a sheet of plastic were set at a distance of 2 cm along the vertical direction and horizontal direction on the surface of soil samples which were in contact with the model box as a marker of displacement change (see Figure 3) In the process of test, displacement of pins and nearby soil unit was analyzed, so as to give the vertical and lateral deformation.

2.6 *Displacement markers of sample*

Stepwise loading was adopted with a step interval of 10 g. Each-stage loading would not be imposed until the deformation caused by the previous stage loading was stable, i.e. no change of displacement of soil could be observed in the multiple discrete photos. The ultimate loading of the saturated soil was 100 g, and the natural moisture content model was 60 g. For the natural moisture content soil, when it reached a stable state after the acceleration of 60 g, the acceleration was kept constant. Then the electromagnetic valve was opened and the soil was soaked. In the process of soaking, we constantly looked at the screen till the water which was added before the test in the water tank was entirely discharged. The amount of the added water was calculated according to the volume of undisturbed and remolded soil, initial moisture content and saturated water content.

Water loss due to evaporation and other factors was also considered in the calculation. The centrifuge continued to run at an acceleration of 60 g even at the end of the soaking process, and was shut down till the soil deformation and collapsibility was stable.

3 TEST RESULTS AND ANALYSIS

3.1 *Calculating collapsibility of double-line method*

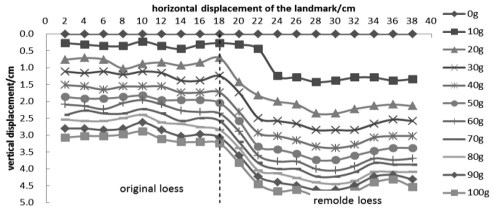
1 The total settlement deformation of a model.

Fig. 4 shows the total settlement deformation of the saturated soil and the natural water content soil at different acceleration. It can be seen from Fig. 4 that the total settlement deformation of each saturated model increases with the increase of centrifugal acceleration. Significant settlement was not observed when the acceleration increases from 1 g to 60 g, but was observed when the soil sample was saturated at the acceleration of 60 g.

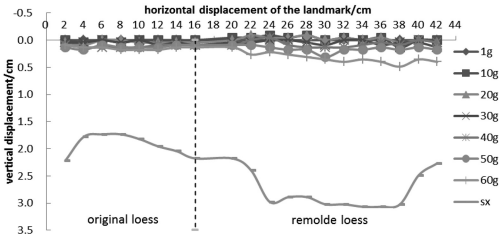
This is mainly caused by two reasons. Firstly, some or all of the soluble salt which plays a role of cementing between the skeleton particles dissolved when encountered with water, thus the coupling effects between the particles are weaken or even destroyed; Secondly, for loess with natural water content it is in non-saturated state and the inter-particle force caused by matric suction exists will quickly dissipate after the soil is saturated. Weakening of cementation and dissipation of matrix suction eventually led to reduction

Table 1. Initial conditions of the four models.

Model name	Sample depth	Sample size (length × width × height)	Initial water content	Initial dry density	Initial wet density	Specific gravity
	m	cm	%	g/cm^3	g/cm^3	
Saturation model	13.5–14	22.5 × 16.5 × 27.5	11.48	1.25	1.39	2.74
Natural moisture content model	8.5–9	21.5 × 17.5 × 26.5	9	1.25	1.36	2.71



(a) Low pressure saturation model



(b) Natural moisture content model

Figure 4. Total settlement of each model.

of inter-particle coupling strength and increase of soil deformation and finally led to loess collapse.

In addition, compared with the original loess, the settlement of the remolded soil increases significantly, reflecting the unique internal structure of the original loess. The phenomenon that the farther the distance to the left border of the model box, the greater the settlement of the remolded soil, reflects the constraint of the boundary of the model box on the soil deformation. Thus the displacement of the marks near the boundary of the remodeled soil is selected as the total deformation value of each model (shown in dotted lines in Fig. 4).

2 The settlement deformation of foundation.

The height and total settlement deformation of model at different acceleration was used to calculate the thickness of the foundation and the corresponding settlement deformation according to the similarity theorem (Du 2010). The result is shown in Figure 5. As can be seen, the total settlement deformation increases with the increase of thickness, and a quadric relationship could be established between them. For the foundation with the same thickness, settlement of saturated foundation was significantly larger than that of the natural water content foundation.

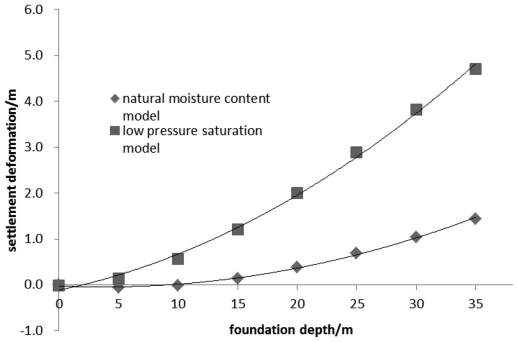


Figure 5. Relation curves between the settlement deformation and the foundation thickness.

The relationship between the thickness of the foundation with the natural water content and total settlement deformation can be well reflected by the polynomial curve:

$$h=0.0014H^2-0.0132H \quad (1)$$

The relationship between the thickness of saturated foundation and total settlement deformation can be well reflected by the polynomial curve,

$$h=0.0032H^2+0.0357H \quad (2)$$

where h is the total settlement deformation of foundation, m; H is the thickness of foundation, m.

(3) The collapsible deformation of foundation

Under the condition that foundation has the same thickness, the settlement deformation of natural moisture content foundation was subtracted from that of saturated foundation to give a curve which describes the relationship between the collapsible deformation and the thickness of foundation:

$$h=0.0018H^2+0.0489H \quad (3)$$

where h is the total settlement deformation of foundation, m; H is the thickness of foundation, m.

3.2 *Collapsibility by single-line method*

With regard to the centrifugal test of soil with the natural water content, the whole soaking process could

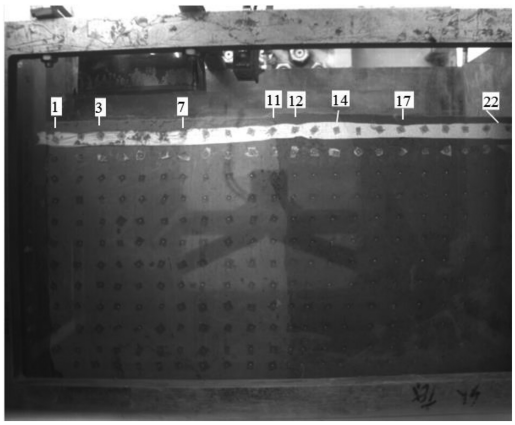


Figure 6. Numbering of displacement markers.

be observed and analyzed from the photos shot by the camera installed at the top of the model box. At the beginning of the soaking process, the water flowed along the slit between undisturbed soil and the left side of box model, and the crushed soil at the corner of the model box continuously, forming sinkholes. Then the water continuously flowed through contact with gaps and sinkholes to the bottom of model box and saturated the low-level soil. With the increase of saturation of the low soil, the water level of sinkholes and gaps rose and water started to saturate the soil in two directions (upward and downward). In order to analyze the soil's collapsible deformation, displacement markers at the top of the model were numbered from left to right, as shown in Fig. 6. The number of undisturbed soil ranged from 1 to 11, and that of remolded soil ranged from 12 to 22. For any marker, the stable vertical coordinate after deformation caused by acceleration of 60 g minus stable vertical coordinate after deformation caused by soaking was its collapse.

Collapsibility of undisturbed loess of different positions (where the markers are) in the top rows is shown in Table 2. As can be seen from Table 2, because of water erosion, collapsibility close to the boundary of model box was 21.33 mm, which is larger than that of other areas. In areas without water erosion, with the increase of the distance to the left boundary of model box, the markers' collapsibility gradually increases, which reflects the constraint effect of model box boundary on soil deformation. The maximum collapsibility was 20.44 mm. Collapsibility of number 11 marker near the remolded soil boundary was selected as the representative value of undisturbed soil. According to the similarity law, the test value was converted into real value, thus we obtained the total collapse of 1.23 m for foundation with a thickness of 16 m after soaking.

3.3 *Comparison between single-line method and double-line method*

The collapsible deformation by single-line method was 1.23 m for foundation with a thickness of 16 m, which was analyzed from results of the natural water content model test. The collapsible deformation by double-line method was 1.14 m for foundation with the same thickness, which was obtained by applying 16 m into formula (3). Foundation collapsibility by single-line method and double-line method is similar with a relative error of 7%, which demonstrates that calculating methods do not have significant effect on collapse deformation.

With single-line method soil samples are saturated by precipitation in high-speed rotation. The test process is complicated and the saturation degree of soil samples is difficult to control. In contrast, with double-line method soil samples are saturated before the imposition of the centrifugal acceleration. So the operation is simple, and two centrifugal model tests can result in collapsibility of foundation with different thickness. In light of this, double-line method will be the first choice.

Table 2. Displacement markers collapsibility of original loess.

Displacement markers number	Collapsibility mm
1	21.33
2	16.44
3	16.00
4	15.56
5	16.44
6	17.78
7	19.11
8	20.00
9	20.44
10	20.33
11	20.44

Table 3. Foundation collapse of different method.

	Geotechnical centrifugal model test		Field immersion test measured collapse
Foundation thickness	Single line method	Double line method	
m	m	m	m
16	1.23	1.14	1.20
30	\	2.98	2.70

4 COMPARISON BETWEEN CENTRIFUGAL MODEL TEST AND IN-SITU SOAKING TEST

As shown in Table 3, 16 m was applied into formula (3) to obtain the collapsibility by double-line method, which was 1.14 m and similar to the measured value of 1.20 m with a relative error of 5%; 30 m was applied

into formula (3) to obtain the collapsibility by double-line method, which was 2.98 m and similar to the measured value of 2.70 m with a relative error of 9.4%. The results verified that it is feasible to using centrifugal model test to simulate in-situ soaking test.

5 CONCLUSIONS

Research was conducted on collapsible deformation of loess foundation based on single-line method and double-line method. The test results show that:

(1) Foundation collapsibility by single-line method and double-line method is similar, which demonstrates that calculating methods have insignificant effect on collapse deformation. For single-line method, the test process is more complicated and the saturation degree of soil samples is more difficult to control than double-line method. Therefore double-line method is preferred.
(2) Collapsibility obtained from centrifugal model test is close to that obtained from in-situ soaking test, which validates the feasibility of using centrifugal model test to simulate in-situ soaking test on loess.
(3) Centrifugal model test is convenient and economic. The test cycle is short and the boundary conditions are easy to control. It serves as a new approach for the research on loess collapsibility. Because of differences of the physical properties of soil at different depth of the loess foundation, uneven properties of soil at different depth should be taken into consideration when conducting centrifuge model test.

ACKNOWLEDGEMENTS

Financial support from National Natural Science Foundation of China (Grant No. 51379220) is gratefully thanked.

REFERENCES

Cui, Z.Z., Zhu, N. & Wang, X.Y. 2013. Theoretical and experimental research on evaluation of loess collapsible under overburden pressure. *Journal of Lanzhou University of Technology* 39(6): 115–117.

Du, Y.L. & Han, L.B. 2010. Geotechnical centrifuge model test technology. Beijing: China's Water Conservancy and Hydropower Press.

Gong, C.M., Cheng, Q.G. & Liu, Z.P. 2010. Centrifuge model tests on excavation and reinforcement effect of loess slope. *Rock and Soil Mechanics* 31(11): 3481–3486.

Hu, Z.Q., Xie, D.Y. & Shen, Z.J. 2000. Centrifugal model test on unsaturated loess canal inundation deformation. *Journal of Xi'an University of Technology* 16(3): 244–247.

Huang, X.F., Chen, Z.H. & Ha, S. 2006. Large area field immersion tests on characteristics of deformation of self weight collapse loess under overburden pressure. *Chinese Journal of Geotechnical Engineering* 28(3): 382–389.

Huang, X.F., Chen, Z.H. & Fang, X.W. 2007. Study on foundation treatment thickness and treatment method for collapse loess with large thickness. *Chinese Journal of Rock Mechanics and Engineering* 26(2): 4332–4338.

Luo, Y.S. & Wen, J. 2004. Code for building construction in collapsible loess region (GB50025-2004). Beijing: Architecture & Building Press.

Wang, C.D., Wang, X. & Zhou, S.H. 2010. Centrifugal model tests on self-weight collapsible loess and negative skin friction of pile foundations. *Chinese Journal of Rock Mechanics and Engineering*. 29: 3101–3107.

Unsaturated Soil Mechanics—from Theory to Practice – Chen et al. (Eds)
© 2016 Taylor & Francis Group, London, ISBN 978-1-138-02921-7

Model test on lateral earth pressure of highly expansive soil

S.A. Khattab, M.K. Al-Shamam & K.A. Al-Juari
University of Mosul, Mosul, Iraq

ABSTRACT: The main objective of the study is to investigate the effect of expansive soil on the resulting horizontal stresses and deformations inflicted on a retaining wall. Laboratory physical model was designed with box of dimensions 950 × 900 × 600 mm. The main studied variables include; the magnitude of horizontal swelling pressure, suction along the depth of the wall, the vertical swelling during saturation, time as well as the surcharge weight. The surcharge and resulted settlement of the backfill soil was also measured during the test. The results showed that; at saturation stage, the lateral swelling pressure increased with time to a maximum value and then decreased gradually until reaching a constant value. The maximum values of lateral swelling pressure increased with the depth of the wall then decreased near the wall base. Total suction varied along the depth of the wall during saturation. At upper half, the total suction decreased and then dropped to zero with time increasing. However, near the wall base, the total suction decreased to a small value during saturation period. At loading stage, the maximum increase in lateral earth pressures under the applied vertical stresses were observed at the top of the wall and reached a maximum values at the depth 100 mm from the surface, then decreased to reach the minimum values at the depth 285 mm. The total suction varied between (0 to 12), (0 to10) and (10 to 0) kPa at depths of 100, 350 and 650 mm, respectively.

1 INTRODUCTION

Expansive soil could be found mainly in arid and semi arid regions. Swelling occurs when moisture content increases in soil and this causes volume increase. Expansive soil considered as a source of the problems that faced the geotechnical engineers due to damages in the light weight structures such as houses, commercial buildings, walks, parking areas, highways and streets.

During the past three decades, researches were directed to evaluate vertical soil swelling. Soil has anisotropic nature, thus it exerts swelling in all directions. Sometimes, the lateral swelling pressure could be more than the vertical swelling pressure. Where Andy (1989) founded that the lateral swelling pressure was twice the vertical swelling pressure. Also, Erguler & Ulusay (2003b) reported that the swell pressure ratios (lateral/vertical) for Ankara clay's samples were 1.46 and 2.75. (Clayton et al., Ertekin 1991, Thompson & McKeen 1995 and Ozer et al. 2012) mentioned that the lateral swelling pressure is more than the vertical swelling pressure and vertical applied stresses of their studied cases. This will cause large damages and distresses observed in the retaining wall and walls of the building (Marsh &Walsh 1996 and Ozer et al. 2012).

Many researchers adapted several techniques to evaluate swelling; (Ertekin 1991, Edil & Alanazy 1992, Erol & Ergun 1994, Windal & Shahrour 2002, Sapaz 2004, Sudjianto et al. 2009, Ozalp 2011, Hergul & Cokca 2012) studied the factors affecting the lateral swelling pressures using thin wall oedometer test. (Katti et al. 1983, Clayton et al. 1991, Mohamed et al. 2014 and Wang et al. 2015) constructed laboratory large physical models using expansive soil. They found that the lateral swelling pressure increased rapidly to a certain depth of the wall. (Robertson & Wagener 1975 and Mohamed et al. 2014) constructed field model test. Their results showed that the active earth pressure on retaining wall adjacent to the expansive soil was approximately seven times greater than the active earth pressure of soil without swelling pressure. Whereas, (Ahmed 2010, Papagiannakis et al. 2013) estimated the lateral swelling stresses of highly expansive soil exerted on tie-back and drilled shaft wall using numerical approach, after monitoring volumetric water content in the site of a wall built in San Antonio. The results showed that the lateral swelling pressure decreased with depth when moisture content decreased with depth.

This research work focused on the distribution of lateral swelling pressure for the saturated – unsaturated soil along the depth of the retaining wall. The studied parameters are suction, vertical swelling, time and overburden stress.

2 EXPERIMENTAL WORK AND TESTING PROGRAM

2.1 *Soil and methodology*

Undisturbed and disturbed soil samples of highly swelling potential are obtained from al-Majmoua district, Mosul city. The physical properties of the used



Figure 1. Large scale physical model.

Table 1. Engineering properties of the used soil.

Property		Value
Liquid Limit (%)		89
Plastic Limit (%)		39
Plasticity index (%)		50
Shrinkage limit (%)		12
Linear shrinkage (%)		20.75
Soil classification		CH
Specific gravity		2.8
Total soluble salts (%)		5.6
Organic matter (%)		1.8
Sulphate salts		0.45
Gypsum content (%)		5.12
Sand (%)		14
Silt (%)		34
Clay (%)		52
Max. dry unit weight (kN)/m^3	Standard compaction	14.4
Optimum moisture content OMC (%)	Standard compaction	27.4
Max. dry unit weight (kN)/m^3	Modified compaction	16.8
Optimum moisture content (%)	Modified compaction	13.8

soil with their specifications are shown in Table 1. The soil was classified (CH) according to unified classification system. The X-ray diffraction analysis of the soil showed that the major clay minerals are montmorillonite, palygorskite and kaolinite. Whereas, the minor clay minerals are chlorite and illite. The non-clay minerals are calcite and quartz.

The experimental setup was designed and built at the University of Mosul, is a steel structure which consists mainly of a box with dimensions of 900 mm in length, 600 mm in wide and 950 mm in height. Two sides of box were made of mild steel plate of 8 mm thickness, the third side was made of fiberglass plates with 20 mm thickness to allow observation of the clay deformation during testing. The forth side of the test box was a movable retaining wall with dimensions of 800 × 450 mm and thickness 8 mm. At the center line of the retaining wall, four circular openings with 50 mm diameter were made. The height of these openings from the top of the retaining wall are 100, 285, 470 and 655 mm which are used for the installation of the pressure cell transducers (PC). The setup was designed to enable lateral swelling pressure, at rest swelling pressure, active and passive earth pressures measurements.

Vertical load was applied to the soil by a mechanical hydraulic jack with capacity of 50 ton. In order to insure a uniformly distributed applied stresses on the surface of the soil, four rectangular steel plates with dimensions 786 × 468 mm, 600 × 350 mm, 450 × 250 mm and 250 × 150 mm with thickness 25 mm were used. Figure 1 presents the layout of the experimental setup used in this investigation.

2.2 *Preparation of soil in the model*

At the box bottom, a layer of gravel with thickness of 100 mm was used to permit a uniformly distribution of water below the bottom surface of the soil. Also, a layer of geogrid was put above the gravel layer to allow the water to pass through it easily.

In order to satisfy the plain strain conditions, sidewall friction between soil and the box sides must be reduced as low as possible. So, the sides of the box were lubricated with silicon grease. Also, plastic sheets of 70 mm height were placed on the silicon grease to cover over all height of the box's sides.

The soil was compacted in the box using static compaction method by electrical hydraulic press till reaching a dry unit weight of 14.4 kN/m^3 and optimum moisture content 27.4%. The compaction was achieved in the box in 14 layers. The thickness of each layer was 50 mm to reach overall depth of 700 mm. The compaction pressure was kept for two hours to prevent rebound of clay soil and insure that the top soil is on the required level. Three holes were bored by special hand auger with diameter 20 mm. These holes were bored on the left side and at the back of the box at depths of 100, 345 and 590 mm. These holes were used to install calibrated water probes to be used for measuring the total suction of the soil. Also, the probes were utilized to check the variation of total suction at different depths of soil as well as different locations on the same soil level.

After the compaction, a rectangular steel plate of dimensions 786 × 468 mm was placed at the top of the compacted soil surface, where the center line of the steel plate and soil surface was coincided. Then, all the equipments were installed in appropriate positions. So, three linear variable displacement transducers LVDTs were fitted on the longitudinal center line surface as shown in Figure 2. Beside that, four dial gauges were installed at each corner of the surface soil to measure the vertical deformation of the soil and to ensure uniform soil deformation. Four pressure cells were installed on the retaining wall. Finally, three LVDTs

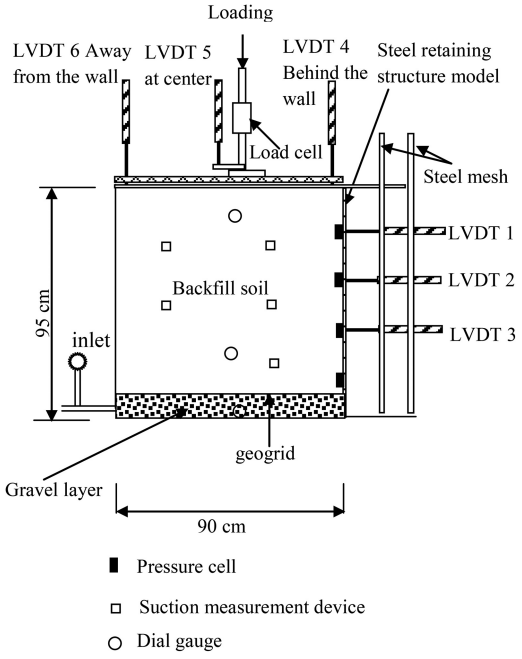


Figure 2. Schematic diagram of the model with their instrumentation devices.

were installed on a steel mesh which was placed in front of the retaining wall, the pointer of these LVDTs were localized on the pressure cells to measure the wall movement.

2.3 *Data acquisition system*

Computerized system was used in the test for automatically collecting, saving, displaying and test duration. So, two data loggers were utilized in the test obtaining both night and day drawing the output data. This feature helps for measurement according to the measurement interval and along the The cables of water probes were jointed to water mark monitor type (900 M) used for suction measurement. The water mark monitor was arranged with intervals of each 15 minutes for a period of 28 days. The readings were taken until the soil reached the equilibrium state. The output data were saved in the water mark monitor.

Data logger type (TDS-530) can be used for load, pressure, displacement measurement with different intervals according to the testing stage. The data were monitored, collected, recorded, displayed and drew by a computer.

2.4 *Soil saturation and load application systems*

Expansive soil could exerts a lateral pressures on retaining wall when suction changes at the top and at deeper depth due to rainfall and seasonal change of water table. Thus, the soil was saturated in this study from the top and the bottom. The saturation at the bottom was done by inlet water which was connected to water source. The water raised to the soil by capillarity. Beside that, the saturation of the top was done by a plastic pool which was put at the top of hydraulic press frame. Then, the plastic pool filled with water and used to distribute water on the soil surface. Consequently, water penetrate to the soil mass by gravity.

After saturation stage, the soil was prepared for the vertical load application, thus four plates with load cell and their circular disk were arranged. They were placed at the surface of the compacted soil. The center line of the mechanical hydraulic jack and load cell with their jointed plates were coincided with the center line of the top soil surface.

3 EXPERIMENTAL RESULTS AND DISCUSSION

The test was conducted in three stages, the out put data were collected and analyzed as shown below:

3.1 *First stage: Equilibrium time of water probes*

To measure the variation in total suction at different locations of the sample, five water probes were used. Three of them were inserted at depths 100, 345 and 590 mm at left side of the box, the other two water probes were placed at depths of 100 and 345 mm behind the box. Figure 3 shows the variation in total suction with elapsed time in which an increase in total suction with time can be observed for all the water probes. On the other hand, the total suction of the soil sample at depths 100 and 345 mm of the box was more than that at depth 590 mm. After 95, 151 and 133 hours, the total suction at the top, middle and bottom, reached the maximum reading capacity of the data logger which was 239 kPa. Therefore, filter paper method was used to measure the final total suction of the soil sample by taking soil samples at the same studied depths. Results showed that the total suction at the top, middle and bottom of the soil sample were 7904.2, 7446.8 and 5282.5 kPa, also the water content of the same samples after the equilibrium time (14 day) of the test were 23.32, 23.20 and 24.46%, respectively. It should be noted that, the total suction decreases with the depth of sample that is related to the increase of the water content of soil sample with the depth before the test which were 26.37, 26.6 and 27.08% at the top, middle and bottom of the soil sample, respectively due to dissipation of water from top to bottom of the soil sample with time.

3.2 *Second stage: Saturation stage*

3.2.1 *Effect of saturation on lateral swelling pressure of the soil*

This stage was continued for 34 days. Figure 4 shows the variation of lateral swelling pressure with elapsed time at four selected points located at different depths 100, 285, 470 and 655 mm on retaining wall. It is obvious that the lateral swelling pressure increased with

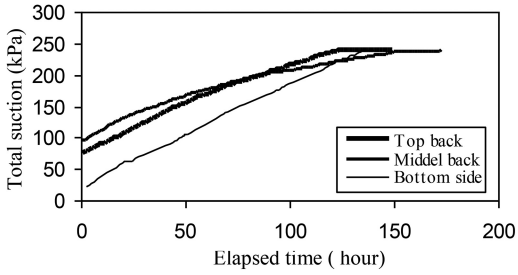


Figure 3. Equilibrium time of water probes.

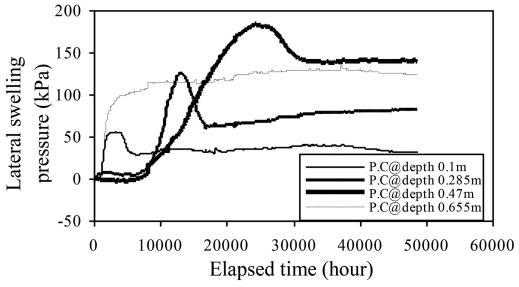


Figure 4. Lateral swelling pressure with elapsed time

time along the overall depths until reaching peak values then followed by a reduction to an ultimate value and then, remained approximately constant. Similar results were obtained by (Joshi & Katti 1980, Katti et al. 1983) in which large scale models under constant overburden stresses and free swell test were used. Clayton et al. (1991) used two types of London Clay by large scale model to investigate the lateral swelling pressure. They found that peak values of lateral swelling pressure can be obtained and followed by a reduction with time. Also, Ikizler et al. (2008) were developed a small scale model to study the lateral swelling pressure based on a mixed soil of highly expansive soil. They concluded that the lateral swelling pressures increased with time and reached the maximum values, then decreased and remained constant. It is important to mention that the time required to reach the maximum values of lateral swelling pressure were 3, 10, 17.5 and 30 days at depths 100, 285, 470 and 655 mm, respectively. This behavior is related to the type of soil (highly expansive soil) which has a very small coefficient of permeability. Moreover, the large size of the sample required long time to complete saturation.

It is also noted that the rate of increase in lateral swelling pressure with elapsed time increased with depth increasing. This may be attributed to that the water requires more time to penetrate the soil. It is worth mentioning that, the curve of the lateral swelling pressure with time at depth 655 mm reaches 95% of the maximum lateral swelling pressure in 6 days and remained constant in 13 days. Then, the maximum value was obtained at 30 days.

A rapid rate of increase in lateral swelling pressure was also noted at depths 100 and 650 mm through the first 3 days. After that, the lateral swelling pressure decreased. This could be explained by that the soil at depth 100 mm is near surface of the soil in which free vertical movement can be occurred. While, at depth 655 mm the lateral swelling pressure is continued to increase with very slow rate due to confinement of the overburden soil. Consequently, it is clear that the rate of decrease in lateral swelling pressure diminished with depth and required more time 2, 3.5, 4 and more than 5 days to reach the equilibrium state.

Figure 5 shows the daily variation of the lateral swelling pressures with depth of the wall. It is shown that the peak values of lateral swelling pressures increased with depth of the wall until reaching the maximum value of 184 kPa at depth 470 mm then decreased. This result coincided with that obtained by (Katti et al. 1983, Mohamed et al. 2014).

It is worth mentioning that, the maximum lateral swelling pressure 184 kPa at depth 470 mm was approximately equal to vertical swelling pressure 175 kPa obtained by constant volume test. The constant volume test was carried by an oedometer device for samples statically compacted at the same dry unit weight 14.4 kN/m^3 and OMC 27.4% of the model test.

3.2.2 *Effect of saturation on the vertical swelling of the soil*

The vertical swelling of highly expansive soil was measured in addition to the lateral swelling pressure exerted on the retaining wall during saturation stage of the soil. The vertical swelling of the soil was measured using three LVDTs located at the longitudinal center line of the surface soil. The positions of LVDTs are shown previously in Figure 2. Figure 6 shows the relationship between the vertical swelling % with elapsed time. The vertical swelling % increased with elapsed time until reaching an equilibrium state in 30 days. It should be noted that the vertical swelling increased with a slow rate at the first 15 hours of saturation stage and reached 1.030 mm. This can be attributed to two reasons: first, the soil at this time was saturated from the bottom of sample only (not at the top), the second reason is a large column of soil was located above the bottom layer of soil. This is caused the slow rate of vertical swelling due to movement restriction. Then the vertical swelling increased rapidly with a high rate to reach 18.79 mm in 114.58 hours when water was added at the top of the soil. This was followed by a small increase of vertical swelling of 31.99 mm in 192.5 hours. Also, the slightly increase in vertical swelling continued with time until reaching 58.950 mm in 714.15 hours. The final percentage of the vertical swelling was 8.54%. The decrease in the rate of the vertical swelling was related to the swelled soil at the top layers in which the voids between the particles decreased and prevented water to pass through them to the underlined layers. Hence, these layers depend on the humidity migration in order to reach saturation stage.

On the other hand, the percent of the vertical swelling obtained from the physical model was approximately equal to the percent of swelling

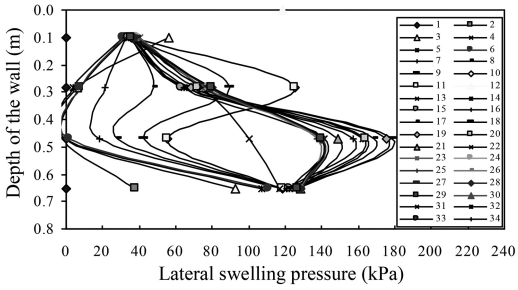


Figure 5. Daily variation of lateral swelling pressure with depth of the wall.

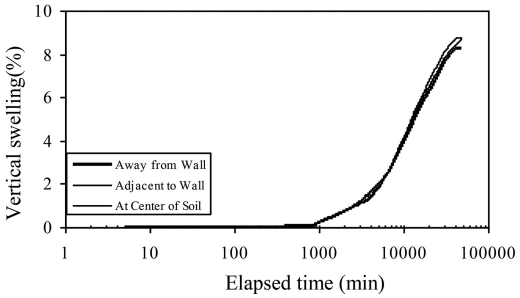


Figure 6. Percentage of vertical swelling of backfill soil.

obtained from the free swell test conducted by the oedometer apparatus (8.346) %. The maximum variation in vertical swelling measurements at behind, center and away from the wall were very small (±1.68) mm which is equal (error=2.86) % from the average value, that is refer to the uniform distribution and transportation of water above and through the soil layers.

3.2.3 *Effect of saturation on the variation of total suction with time*

The total suction was measured at different depths and locations of the soil sample during the test until the test was accomplished.

Results presented in Figure 7 showing the relationship between the total suction with elapsed time. Generally, the total suction decreased with time. The first water probe was sensitive to change in total suction which was located at the bottom side of the sample and at depth 590 mm. The decrease in total suction started after 4 days, and continued in decreasing until reaching 31 kPa in 11 days. Then the total suction continued to decrease but with a very slow rate within the next 23 days and reached (10) kPa at 34 days.

The total suction at depth 100 mm located at the top side and top back of the sample started to decrease after 6 days. The total suction was suddenly dropped during 6th and 7th days, then, reached values of 25 and 12 kPa at the top side and top back of the sample, respectively in 8 days. Then, the total suction dropped to zero within the next 2 and 4 days at the top back and side of the sample, respectively and remained constant (0 kPa) until the saturation stage was finished in 34 days.

It should be noted that the differences between total suction at the top side and top back of the soil sample were very small during the test. Thus, it could be concluded that changing the location of water probes at the same level of the sample had no effect on the total suction of soil sample. The rate of decrease in total suction at the top side and top back of the soil sample was more than that at the bottom of the soil sample.

It is worth mentioning that, the total suction at depth 340 mm at the middle back and middle side of the sample started to decrease in 15 days from the beginning of the test. The total suction decreased with time with a large rate to reach 24 and 32 kPa at the middle side and

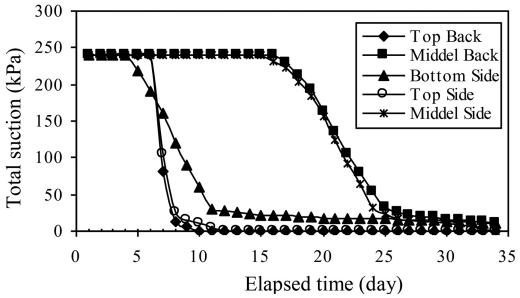


Figure 7. Varaition of total sution during saturation period.

middle back of the sample, respectively in 25 days. The rate of decrease reduced and the total suction reached (0 and 10) kPa at the middle side and middle back, respectively in 34 days. It should be noted that the differences in total suction at middle side and middle back of the soil sample were very small which was referred to the state of equilibrium of the total suction.

3.3 *Third stage: Loading stage*

3.3.1 *Effect of applied vertical stresses on the lateral earth pressure*

After the completion of the saturation stage, the vertical stresses were applied at the surface of the soil using mechanical hydraulic jack. The applied stresses were measured by load cell with a capacity 200 kN. The applied normal stresses were 13.39, 26.78, 53.57, 107.1, 160.7 and 214.3 kPa, which represent the surcharge load of each one meter height of the backfill soil.

The distributions of lateral stresses with depth of the wall were depicted in Figures 8 and 9. It should be noted that the lateral stresses increased with increasing the applied vertical stresses. Generally, the maximum lateral stresses were located at the top of the wall at depth 100 mm, then the lateral stresses decreased and approximately remained constant with the further depths of the wall at 470 and 655 mm. It could be noted that with the application of a low vertical stresses (13.39 kPa) there was a small increase in lateral stresses which is equal to 1.56 kPa at depths 100 and 285 mm. When the vertical applied stress

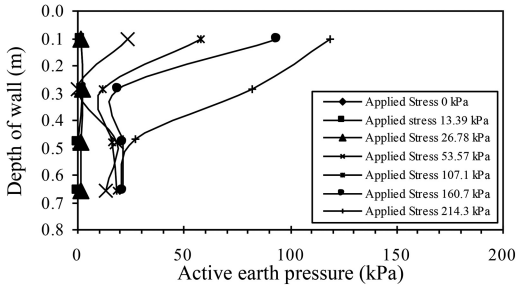


Figure 8. Distribution of active earth pressure along the depth of the wall.

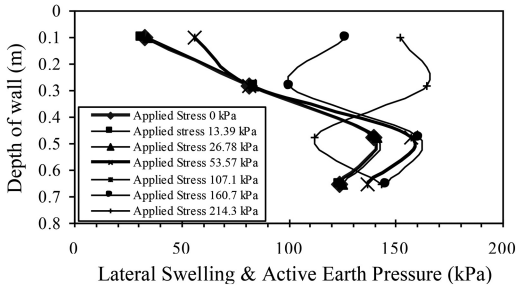


Figure 9. Distribution of latesr al swelling & active earth pressure along the depth of the wall.

increased to 26.78 kPa, the lateral stresses at depths 470 and 655 mm slightly increased. On the other hand, at a high level of applied vertical stresses 53.57, 107.1, 160.7 and 214.3 kPa, the lateral stresses increased to 23.4, 57.72, 93.6 and 119.04 kPa, respectively at depth 100 mm. Then, followed by a sudden decrease in lateral stresses occurred at a depth of 285 mm which had values of 0, 11.4, 19 and 82.3 kPa, respectively. Then, the lateral stresses remained approximately constant with further depth of the wall.

The ratios between the maximum lateral swelling pressures and the lateral stresses resulted from the applied vertical stresses at different depths were more than one, except at stress levels 160.7 an 214.3 kPa and at a depth 100 mm as shown Table 2. It is worth mentioning that, at low vertical stresses 13.39 and 26.78 kPa, the lateral swelling pressure was equal to 37–184 times the lateral stresses. Also, at high level of applied vertical stresses 53.57, 107.1, 160.7 and 214.3 kPa, the lateral swelling pressure was equal to 1.0–11.22 times the lateral stresses as depicted in Figure 10. Consequently, the lateral swelling pressure should be considered in the design of retaining wall when an expansive soil is the backfill material.

To conclude, the lateral stresses resulted from the applied vertical stresses were more effective on the top part of the wall than the bottom part. Also, the lateral swelling pressure was more effective than the lateral stresses resulted from the applied vertical stresses along the depth of the wall.

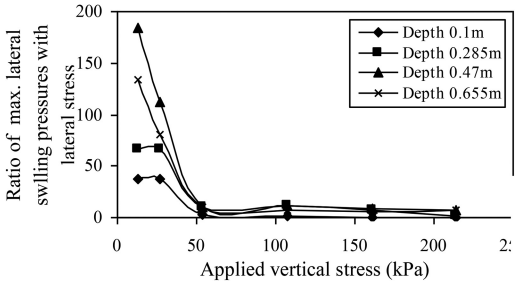


Figure 10. Relationship between Max. lateral swelling pressure & lateral earth pressure under applied normal stresses.

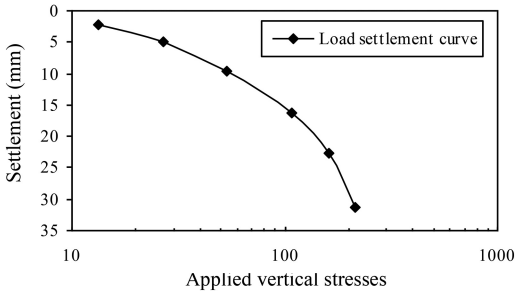


Figure 11. Settlement of backfill soil under vertical stresses.

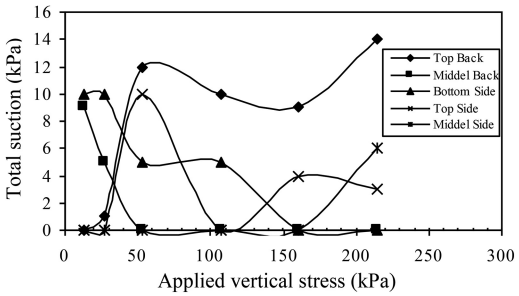


Figure 12. Varaition of total suction under applied stresses.

3.3.2 *Effect of applied vertical stresses on settlement*

The settlement of the backfill soil increased with increasing the applied vertical stresses as shown in Figure 11. Beside that, the rate of increase in settlement was augmented with the increase of the applied vertical stress.

3.3.3 *Effect of applied vertical stresses on the total suction*

The total suction at different depths and locations were measured by water probes at different times during application the vertical stresses. Figure 12 shows the relationship between the total suctions and the applied vertical stresses. It is clear that, the total suctions at the top layer of the soil increased with applied vertical stresses specially when the applied vertical stress

Table 2. Ratios between the maximum lateral swelling pressures and the lateral stresses due to applied vertical stresses.

Applied vertical stress (kPa)	13.39	26.78	53.57	107.1	160.7	214.3
Lateral stress at depth 0.1 m	1.56	1.56	23.4	57.72	93.6	119.04
Max. lateral swelling pressure (kPa) at depth 0.1 m			57.72			
Number of times of increase	37	37	2.467	1.0	0.617	0.485
Lateral Stress at depth 0.285 m	1.9	1.9	0	11.4	19	82.3
Max. lateral swelling pressure (kPa) at depth 0.285 m			125.4			
Number of times of increase	66	66	12.5	11.0	6.6	1.523
Lateral stress at depth 0.47 m	0	1.64	16.40	18.04	21.32	27.3
Max. lateral swelling pressure (kPa) at depth 0.47 m			184			
Number of times of increase	184	112.19	10.199	11.22	8.63	6.739
Lateral stress at depth 0.655 m	0	1.65	13.2	18.15	21.45	19.77
Max. lateral swelling pressure (kPa) at depth 0.655 m			133.65			
Number of times of increase	133.65	81	10.125	7.364	6.231	6.76

reached 53.57 kPa, and the total suction increased and reached 10 and 12 kPa at the top side and top back, respectively. This is related to the squeeze out the water from the voids and the diminishes of the size of the voids. Then, the total suction increased and reached 15 kPa at vertical stress 216 kPa at top back.

At middle layer of the soil, the total suction decreased with the applied vertical stresses from 10 to zero kPa at vertical stress 53.57 kPa. Also the total suction at the middle side remained zero along the time of the applied vertical stresses, this can be explained by the dissipation of water from the top to middle layer.

At the bottom layer, the total suction decreased under the application of the vertical stresses. A large decrease occurred from 10 to 5 kPa at 53.57 kPa, then the total suction dropped to zero at 160.7 kPa due to the dissipated water drawdown which caused decrease in total suction of the soil. This is similar to the behavior of the total suction at the middle back, but required an application of vertical stress more than that at middle back to drop the total suction to zero.

4 CONCLUSIONS

1. The lateral swelling pressure increased with depth of the wall until reaching a maximum value at a depth of the mid third layer of wall height then decreased.
2. The lateral swelling pressure continued to increase with time until reaching the maximum value after about 30 day, then decreased to the lowest value through the whole depth.
3. The maximum lateral swelling pressure, and the percent of the vertical swelling obtained from the model test, were approximately equal to the vertical swelling pressure and percentage of vertical swelling measured by conventional oedometer apparatus.
4. Total suction varied along the depth of the wall during saturation stage at the top and middle layers, then total suction decrease and drop to zero during the 10 and 34 day, respectively. However; at the bottom layer, the total suction decreased and remained constant 10 kPa during the saturation period.
5. The lateral stresses resulted from the applied vertical stresses were more effective than the lateral swelling pressures at the top part of the wall compared with the bottom part.
6. The lateral swelling pressure was more effective than the lateral stresses resulted from the applied vertical stresses along the depth of the wall. The lateral swelling pressure was equal to (0.485-184) times the lateral stresses obtained from the applied vertical stresses.
7. During the vertical stresses application, the total suction at the top part of the wall varied between (0 to 12) kPa, also at the middle part varied between (0–10) kPa. However, at the bottom part dropped from (10 to 0) kPa.

REFERENCES

Ahmed, M.N. 2010. Design of Drilled Shaft and Tied-Back Retaining Walls in High Plasticity Clays. *MSc. Thesis. The University of Texas at San Antonio.*

Andy, B.F. 1989. Laboratory Evaluation of Lateral Swelling Pressure. *Journal of Geotechnical Engineering*. *ASCE* 115(10): 1481–1486.

Clayton, C.R.I., Symons, I.F. & Hiedra-Cobo, J.C. 1991. The Pressure of Clay Backfill Against Retaining Structures. *Canadian Geotechnical Journal* 28: 282–297.

Edil, T.B. & Alanazy, A.S. 1992. Lateral Swelling Pressures. *Proceedings of the 7th International Conference on Expansive Soils*. Dallas, Texas. 227–232.

Erguler, Z.A. & Ulusay, R. 2003b. A Simple Test and Predictive Models for Assessing Swell Potential of Ankara (Turkey) Clay. *Engineering Geology* 67: 331–352.

Erol, A.O. & Ergun, U. 1994. Lateral Swell Pressures in Expansive Soils. *8th International Conference on Soil Mechanics and Foundation Engineering*. New Delhi, India. 1511–1514.

Hergul, T. & Cokca, E. 2012. Measurement of Lateral Swell Pressure by Thin Wall Oedometer. *10th International Congress on Advances in Civil Engineering.* Middle East Technical University, Ankara, Turkey.

Ertekin, Y. 1991. Measurement of Lateral Swell Pressure with Thin Wall Oedometer Technique. *MSc. Thesis, Middle East Technical University*.

Ikizler, B.S. & Aytekin, M. & Nas, E. 2008. Laboratory study of expanded polystyrene (EPS) geofoam used with expansive soils. *Geotextiles and Geomembranes* 26: 189–195.

Joshi, R.P. & Katti, R.K. 1980. Lateral Pressure Development under Surcharge. *Proceedings of the 4th International Conference on Expansive Soils*. Denver (1): 227–241.

Katti, R.K. Bhangale, E.S. & Moza, K.K. 1983. Lateral Pressure in Expansive Soil With and Without a Cohesive Non-Swelling Soil Layer, Application to Earth Pressures on Cross Drainage Structures in Canals and Key Walls in Dams. Final Report Part-I, Submitted to central Board of Irrigation and Power, New Delhi 110(21): pp. 1–303.

Marsh, E.T. & Walsh R.K. 1996. Common Causes of Retaining-Wall Distress: Case Study. *Journal of Performance of Constructed Facilities* 10(1): 35–38.

Mohamed, O.Z. & Taha, Y.K. & Abd El-Aziz, S.M. 2014. Experimental Study on the Effect of Lateral Swelling Pressure of Expansive Soil on Retaining Structure. *Journal of Engineering Sciences, Assuit University, Faculty of Engineering* 42(1): 84–92.

Mohamed, O.Z. & Taha, Y.K. & Abd El-Aziz, S.M. 2014. Field Study of the Distribution of Lateral Swelling Pressure of Expansive Soil on Retaining Structure. *Journal of Engineering Sciences, Assuit University, Faculty of Engineering* 42(2): 289–302.

Ozalp, H.K. 2011. Determination of lateral swelling pressure. *Ph.D. Thesis in Civil Engineering, Istanbul Technical University*.

Ozer, M. & Ulusay, R. & Isik, N.S. 2012. Evaluation of Damage to Light Structures Erected on a Fill Material Rich in Expansive Soil. *Bull Engineering Geological Environmental* 71: 21–36.

Papagiannakis, A.T. & Bin-Shafique, S. & Lytton, R.L. 2013. Retaining Structure in Expansive Clays. *Geotechnical and Geological Engineering Journal*. Springer 31(5).

Robertson, A.G. & Wagener, F.M. 1975. Lateral Swelling Pressures in Active Clay. *Sixth Regional Conference for Africa on Soil Mechanics and foundation Engineering*. Durban, South Africa.

Sapaz, B. 2004. Lateral Versus Vertical Swell Pressures In Expansive Soils. *MSc. Thesis. Middle East Technical University.*

Sudjianto, A.T. Suryolelono, K.B., Rifa'I, A. & Mochtar, I.B. 2009. Behavior of Expansive Clay of Ngawi Region (East Java) Under Water Content Variation. *Civil Engineering Dimension* 11(2): 100–105.

Thompson, R.W. & Mckeen, R.G. 1995. Heave Prediction Using Soil Suction a Case History. *Soil Suction Application in Geotechnical Engineering Practice, ASCE* (48): 1–13.

Wang, L.J. & Liu, S.H. & Zhou, B. 2015. Experimental Study on the Inclusion of Soil bags in Retaining Walls Constructed in Expansive Soils. *Geotextiles and Geomembranes Journal*. 43: 89–96.

Windal, T. & Shahrour, I. 2002. Study of the Behavior of Compacted Soil Using Flexible Oedometer. *Mechanics Research Communication.*

Unsaturated Soil Mechanics—from Theory to Practice – Chen et al. (Eds)
© 2016 Taylor & Francis Group, London, ISBN 978-1-138-02921-7

Experimental study on the saturation changes of dredged fills during vertical vacuum preloading

J.J. Ma, J. Wang, P. Wang, Y.Q. Cai & H.T. Fu
College of Architecture and Civil Engineering, Wenzhou University, Wenzhou, China

ABSTRACT: Vertical vacuum preloading is the most common method to consolidate dredged fills in most land reclamation projects on the coastal belts of southeastern China. However, most theoretical analysis overlooks the unsaturated state of dredged fills around the Prefabricated Vertical Drains (PVDs). Most engineers even pay no attention to this problem, thus leading to some insufficient improvement of soft soil foundations. This study presents an experimental investigation to gain some insights into the saturation state changes of dredged fill during vertical vacuum preloading. Several laboratory tests are conducted, and a number of key parameters are measured, including the vacuum suction pressure, pore pressure and water content changes along both the radial and vertical directions, and their relationship to the changes of void ratios. Experimental results demonstrate that saturation changes play a significant role in the formation of smear zone, thereby affecting the effects of improvement on dredge fills.

1 INTRODUCTION

In order to accommodate the rapid economy development and the booming population in Eastern China, more tideland has been planned to be reclaimed. The biggest tideland reclamation program in China is the Wenzhou Oufei Project (Fig. 1), which aims to reclaim a total area of 448 km2 along the Eastern Sea belt of China. However, due to the lack of gravel and sand materials around land reclamation projects, the dredged slurry has been utilized as the man fill. It is typically characterized by high water content, high compressibility, low undrained shear strength, low coefficient of consolidation, low penetrability (Chu et al., 2000, Yan et al., 2010). Thus, in most tideland reclamation projects, vertical vacuum preloading method has been served as the most common and effective approach to improve the extra soft dredged fill (Kjellman, 1952). The mechanism of vacuum preloading have been analyzed and discussed extensively in literature, i.e., Kjellman (1952), Holtz and Wager (1975) and Chu and Yan (2005). It is accepted that, the increase in effective stress is directly due to the suction (negative) pressure, while maintaining the same total stress (Chu & Yan, 2005).

However, most theoretical analysis overlooks the unsaturated state of dredged fills around the prefabricated vertical drains (PVDs) (Indraratna et al., 2005, Wu & Hu, 2012). Most engineers even pay no attention to this problem, thus leading to some insufficient improvement of soft soil foundations. This study presents an experimental investigation to gain some insights into the saturation state changes of dredged fill during vertical vacuum preloading. Several laboratory tests are conducted, and a number of key parameters are measured, including the vacuum suction pressure, pore pressure and water content changes along both the radial and vertical directions, and their relationship to the changes of consolidation effects.



Figure 1. Wenzhou Oufei Project.

2 EXPERIMENTAL PROCESS

The testing system (Fig. 2) consists of a testing bin and a vacuum preloading system. The dimension of the testing bin is 1.5 cm thick, 60 cm in inner diameter and 90 cm in height. The vacuum preloading system are composed of PVDs, vacuum pipes, a layer of geotextile, two layers of geo-membranes, water-air separation bottles and a vacuum pump. Details of the soil properties are summarized in Table 1. As the water content is over the liquid limit, the testing dredged fill is too soft with almost no shear strength.

Table 1. Summary of soil properties.

Water content (%)	109.5
Liquid limit (%)	56.8
Plastic limit (%)	27.3
Saturation (%)	99.8
Specific gravity, Gs	2.73
Vane shear Strength (kPa)	0
Density (KN/m^3)	14.4
Void Ratio e	3.12



Figure 2. The testing system.

Following is the testing process:

(1) filling two testing bins with the same amount of fresh dredged fill (around 80 cm deep) which is taken from Wenzhou Oufei project; one bin (No. 1) serves as the comparison, the other (No. 2) for vacuum preloading test.
(2) inserting PVDs in the center of the testing bin; placing one layer of geotextile and two layers of geo-membrane on the top of dredged fill; connecting PVDs with vacuum pipes and settling all connection between water-air separation bottles and the vacuum pump.
(3) installing all pore pressure (20 cm away from PVDs), vacuum suction (PVDs) sensors and the surface settlement plates (nearby PVDs) and dial gauges.
(4) sealing off the geo-membrane by keying it into the bottom of bins and placing/smearing some mud cake around the geo-membrane and bins.
(5) keeping vacuum pressure around −90 kPa for 2 weeks for one bin (No. 2), do nothing for the other bin (No. 1). The surface settlement, pore pressure and vacuum pressure has been monitored;
(6) after testing, soil samples (nearby PVDs, 10 cm and 20 cm away from PVDs) along depth are taken to measure the water content.

3 TESTING RESULTS AND DATA ANALYSIS

Due to the fact that almost no changes had been observed in NO. 1 bin, only the results from No. 2 bin are analyzed in this paper. During the vacuum process, both pore pressures, vacuum suction and surface settlement were measured; after test, water content in different depths had been tested.

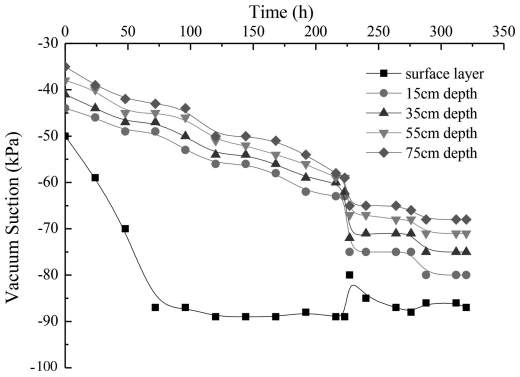


Figure 3. Variations of vacuum suction along the PVD with depths of 0 cm, 15 cm, 35 cm, 55 cm and 75 cm.

3.1 *Vacuum suction along PVDs*

During vacuum preloading, the variations of vacuum suction along the PVD with depth of 0 cm, 15 cm, 35 cm, 55 cm and 75 cm had been monitored, and relevant data is presented in Figure 3. As can be seen, the vacuum pressure observed on the surface later reached to a stable level after 3 days. Obviously, the vacuum suction in deep soils were lower than those observed in shallow layers; and the transition rates along depth were not so much different. After 220 hours, the testing system stopped for 4 hours to accommodate the transition of vacuum suction, it is found that only the surface vacuum pressure dropped back with a value of up to 10 KPa and these values along depth kept constant. Then reloading the vacuum suction, vacuum pressure increased dramatically in soils along depth, and the vacuum suction on surface layer got recovered. During the vacuum process, vacuum suction loss along depth had been clearly observed.

3.2 *Pore pressure changes*

In the process of vacuum preloading, the variations of pore pressure (20 cm away from PVDs) at depth of 15 cm and 75 cm had been recorded, as shown in Figure 4. As can be seen, with the vacuum preloading pore pressure kept dropping at two depths, changing from positive to negative. When the vacuum preloading stopped, the pore pressure rose back with a value of around 5 KPa. When the vacuum preloading continued, the pore pressure dropped again. During the vacuum preloading, pore pressure in deep soil layer was lower than that monitored in shallow layer. The negative pore pressures recorded in both shallow and deep soil layers also imply that the soil under vacuum preloading was under unsaturated state, which

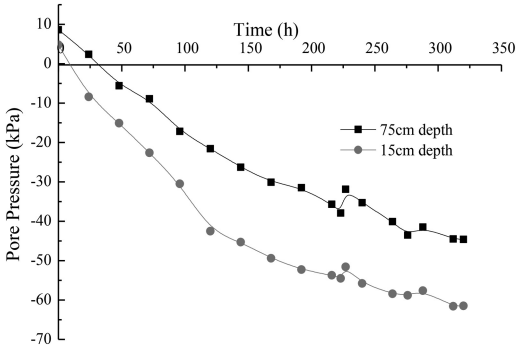


Figure 4. Variations of pore pressure with depths of 15 cm and 75 cm.

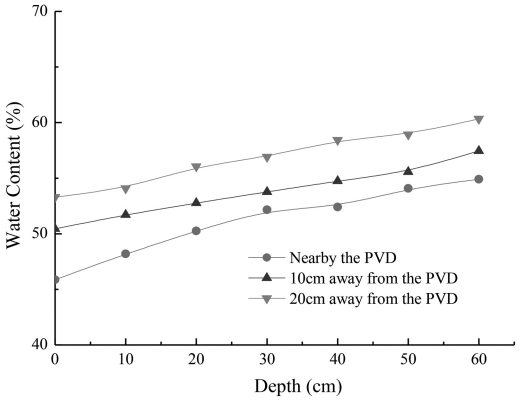


Figure 5. Variations of water contents with depth at distances of 0 cm, 10 cm and 20 cm from the PVD.

go against most analytical model with an assumption of fully saturated state for soils.

3.3 *Changes in water content and saturation degree*

After preloading, soil samples (nearby the PVD, 10 cm and 15 cm away from the PVD) at different depths were taken to measure the water contents (Figure 5) and the degree of saturation (Figure 6).

It can be seen that the water contents nearby the PVD along depth were lower than those measured at 10 cm and 20 cm away from the PVD, which demonstrates that the water contents inside the smear zone was less than those outside of it. Also, due to lower vacuum pressures transferred to deep soil layers, in which water contents were higher than those in shallow layers. The changes in degree of saturation comply with the trend in water contents changes along both the radial and vertical directions. The initial saturation degree of the whole soil was 99.8%, indicating that it was fully saturated before improvement. In two weeks' vacuum preloading, the values along two directions were lower than 80%. Inside the smear zone, the degree of saturation was lower than 75%, which was around 5% lower than those in the non-smear zones. Thus, the

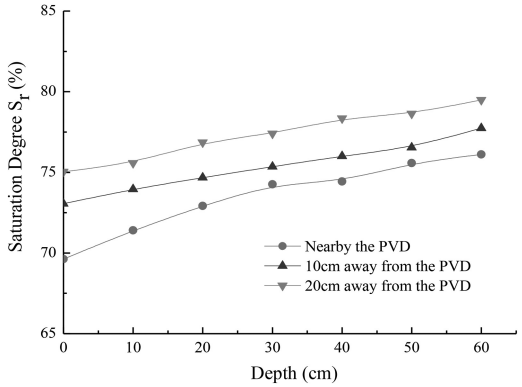


Figure 6. Variations of saturation degrees with depth at distances of 0 cm, 10 cm and 20 cm from the PVD.

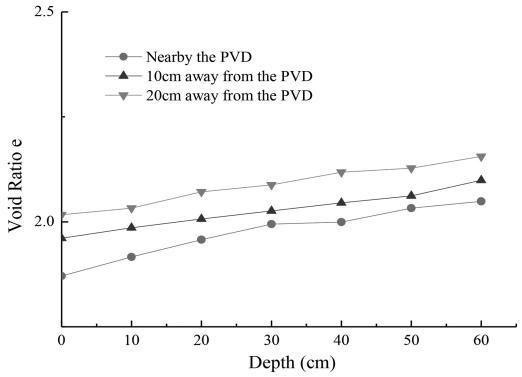


Figure 7. Variations of void ratios with depth at distances of 0 cm, 10 cm and 20 cm from the PVD.

changes in degree of saturation may be regarded as the indicator for formation of smear zone in vacuum preloading.

3.4 *Variations of void ratios*

The variations of void ratios nearby the PVD, 10 cm and 15 cm away from the PVD at different depths are presented in Figure 7. Obviously, the changes in void ratios comply with the changes in water contents and degree of saturation along both the radial and vertical directions. The initial void ratio of the whole soil was 3.12 before the soil improvement. After vacuum preloading, the values along two directions were lower than 2.2. Inside the smear zone, void ratios were less than 2.0; in shallow layers of the smear zone, the values were below 1.8. Thus, the consolidation effects or density achieved in the smear zone were superior than those in non-smear zones, which may indicate the formation of smear zone.

3.5 *Surface settlement*

Figure 8 shows the average ground settlement against time in this test. The surface settlement in the first

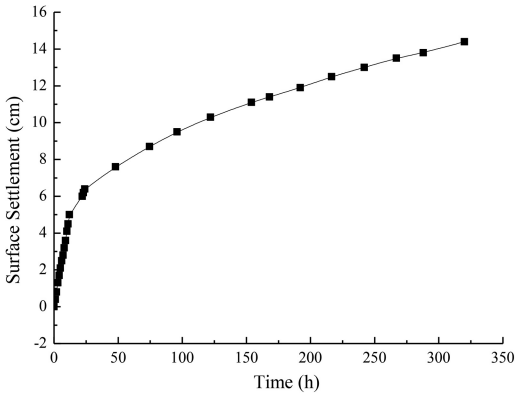


Figure 8. Surface settlement versus time.

25 hours was faster than that in the later stage. At the end of this test, about 15 cm in settlement was observed. And the settlement versus time curve was not flatter in the end, indicating that further settlement could be achieved if continuing the vacuum preloading.

4 DISCUSSION

Experimental results show that, better consolidation effects (water contents, void ratios and degree of saturation) were achieved in the smear zone than the non-smear zone in the radial direction. Also, along the depths for both smear and non-smear zones, better improvement were observed in shallow layers than deep layers. This is easy to understand, as the vacuum suctions transferred to areas far away from the PVD and in deep soil layers were lower compared with those nearby the PVD and in shallow soil layers. In most analytical models, the soil to be improved was supposed to be fully saturated for the ease of model simulation. This is not applicable when keeping an eye on the changes in degree of saturation during vacuum preloading. In particular, most engineers believe that the formation of smear zone was contributed solely by the soil squishing in the process of installing PVDs. This experiment work demonstrated that the soil was unsaturated when vacuum pressure transferred. Also, the soil nearby the PVD formed a smear zone which was featured with lower values in void ratio, water content, degree of saturation and higher value in vacuum suction. The higher the vacuum suction, the higher the effective stress and density, thus in turn forming the smear zone.

5 CONCLUSIONS

Several laboratory tests are conducted, and a number of key parameters are measured, including the pore pressure, vacuum suction, water content changes along both the radial and vertical directions, and their relationship to the changes of void ratios. Experimental results demonstrate that saturation changes play a significant role in the formation of smear zone, thereby affecting the effects of improvement on dredge fills.

ACKNOWLEDGEMENTS

The work presented is supported by the Science Foundation of Wenzhou (No. S20140011), Key Scientific and Technological Innovation Team of Zhejiang (No. 2011R50020), Key Scientific and Technological Innovation Team of Wenzhou (No. C20120006). These financial supports are acknowledged.

REFERENCES

Chu, J. & Yan, S.W. 2005. Application of the vacuum preloading method in soil improvement projects. *In:* BUDDHIMA, I. & JIAN, C. (eds.) *Ground Improvement – Case Histories.* Elsevier.

Chu, J., Yan, S.W. & Yang, H. 2000. Soil improvement by the vacuum preloading method for an oil storage station. *Geotechnique*, 50, 625–632.

Holtz, R.D. & Wager, O. 1975. Preloading by vacuum: current prospects. Washington D.C., Transportation Research Board.

Indraratna, B., Sathananthan, I., Rujikiatkamjorn, C. & Balasubramaniam, A. 2005. Analytical and Numerical Modeling of Soft Soil Stabilized by Prefabricated Vertical Drains Incorporating Vacuum Preloading. *International Journal of Geomechanics*, 5, 114–124.

Kjellman, W. Consolidation of clayey soils by atmospheric pressure. *Proc. conf. soil stab.*, *1952 MIT, Boston*. 258–263.

Wu, H. & Hu, L. 2012. Analytical and numerical solutions for vacuum preloading considering a radius related strain distribution. *Mechanics Research Communications,* 44, 9.

Yan, J., Wang, Q. & Zhang, J. Environmental influence of vacuum preloading dredging project. 2010. 1613–1621.

Unsaturated Soil Mechanics—from Theory to Practice – Chen et al. (Eds)
© 2016 Taylor & Francis Group, London, ISBN 978-1-138-02921-7

Stress evolution in THMC GMZ-bentonite China-Mock-up for geological disposal of high level radioactive waste in China

Y.M. Liu, S.F. Cao, J. Wang, J.L. Xie, L.K. Ma, X.G. Zhao & L. Chen
CNNC Key Laboratory on Geological Disposal of High-level Radioactive Waste, Beijing Research Institute of Uranium Geology (BRIUG), Beijing, R.P. China

ABSTRACT: In order to study the behavior of the GMZ-Na-bentonite under relevant HLW repository conditions, a mock-up facility, named China-Mock-up, was proposed based on a preliminary concept of HLW repository in China. Under THMC coupled condition, the stress evolution of the compacted bentonite may be influenced by several mechanisms, including the gravity, thermal expansion induced by high temperature, and the swelling pressure generated by bentonite saturation. With the bentonite gradually saturation as the water injection, the stress in the bentonite increased steadily, and a maximum value around 3.8 MPa is recorded at section VI within the inner ring after 1512 days. The vertical stress, radical stress and hoop stress distribution in China-Mock-up are gradually changing with the saturation. The experimental results and achievements obtained from the THMC experiments provide important references on investigating the behaviors of bentonite under simulative HLW repository conditions and the design of HLW repository.

1 INTRODUCTION

High-level Radioactive Waste (HLW) repositories are generally designed on the basis of a multiple barrier system concept, which is composed of engineered and natural barriers between the HLW and the biosphere. As the engineered barrier between the waste container and host rock, the buffer material is an important component in the engineered barrier system. The buffer material is essential to stabilize the disposal borehole under coupled thermal-hydro-mechanical-chemical (THMC) conditions, and to provide low permeability and long-term retardation of contaminant movement (Wang, 2010). Currently, bentonite is widely considered as a potential buffer/backfill material for the isolation of the HLW.

Therefore, to understand and guarantee the long-term safety of the engineered barrier, it is of importance to conduct research on coupled THMC behaviors of bentonite under simulative geological disposal conditions, and determine the property variation of the bentonite over a long period of time. In recent years, there has been an increasing interest internationally in the construction of large-scale mock-up experimental facilities in the laboratory and in situ. Among these investigations, the most representative ones include the Long Term Experiment of Buffer Material (LOT) series at the Äspö HRL in Sweden (Karnland et al. 2000), the Buffer Container Experiment (BCE) and the Isothermal Test (ITT) conducted at the URL in Canada (Dixon et al. 2002),FEBEX experiment in Spain and Switzerland (Alonso, et al. 2005; Gens, A et al. 2009; Sanchez, M et al. 2012), OPHELIE and PRACLAY heater experiments in Belgium (Li et al. 2006, 2010; Romero and Li, 2006) and Mock-Up-CZ experiment in Czech Republic (Pacovsky et al. 2007). The experimental results and achievements obtained from these large-scale experiments provide important references on investigating the behaviors of bentonite under simulative HLW disposal conditions.

The preliminary concept of HLW disposal in China is a shaft-tunnel structure, located in saturated zones in granites. The site characterization for nuclear waste disposal in China was started in 1985, and the Beishan area located in northwest China is currently considered as the most potential site for final disposal (Wang, 2010). The engineered barrier system (EBS) comprises the vitrified waste, waste canisters, buffer materials, backfill and seals. In China, the Gaomiaozi (GMZ) bentonite is currently considered as the candidate buffer and backfill material for the disposal project. Based on the extensive experimental investigations, favorable results have been obtained (Liu, 2003; Liu et al. 2007a; Ye et al. 2009a; Cui et al. 2011; Chen et al. 2006).

In order to further study the behavior of the GMZ-bentonite under relevant repository conditions, a mock-up facility, named China-Mock-up, was designed in accordance with the reference concept of HLW disposal in China. The experiment is intended

to demonstrate the technical feasibility, to evaluate THMC processes taking place within the compacted bentonite during the early phase of HLW disposal and to provide a reliable database for numerical modeling and further investigations. It is assumed that the duration of the China-Mock-up test will not be shorter than 4 years. Then, after a cooling period, the experiment will be dismantled and all the available results will be collected and evaluated.

In this paper, the stress evolution of the compacted bentonite under THMC coupled condition are presented and analyzed, including the variation of vertical stress, radical stress and hoop stress in 4 years. The experimental results and achievements obtained from the THMC experiments provide important references on investigating the behaviors of bentonite under simulative HLW repository conditions and the design of HLW repository.

2 CHINA-MOCK-UP TEST

2.1 *Description of the experimental infrastructure*

According to the reference concept of HLW disposal in China, the China-Mock-up is designed as a vertical cylindrical tank, and the main components of the experiment are designed as follows (Fig. 1): a steel tank ($\Phi 900 \times H2200$ mm) to simulate the vertical gallery; a central electrical heater ($\Phi 300 \times H1600$ mm, weight: 1 ton); a hydration system to simulate the water penetration; the engineered barrier composed of the compacted GMZ bentonite surrounding the heater; and a Data Acquisition System (DAS) (Liu et al. 2013). A layer of geotextile is placed between the tank and compacted GMZ bentonite. The gaps between the tank and the bentonite blocks are filled with crushed pellets.

In the hydration system, the water supply to the barrier is realized by the four vertical tubes ($\Phi 10$ mm) with small holes installed on the interior boundary of cylindrical tank. As presented in Figure 1, the water tank is connected to the injection tubes and an argon tank in the experiment. By controlling the gas pressure in the argon tank, the water is injected to the top of the four vertical tubes (Liu et al. 2014), then through the geotextile to the bentonite pellets and bentonite blocks. Simultaneously, the injection rate is measured by a mass flowmeter, and the water sample tank is weighted constantly by a mass balance to quantify the injected water mass. The used water is sampled at the depth of 524.24 m from BS05 in Beishan area. The main chemical compositions are SO_4^{2-} (718 mg/L), Cl^- (771 mg/L), Na^+ (798 mg/L), Ca^{2+} (177 mg/L).

The heater which substitutes the waste canister and corresponding temperature monitoring system are controlled by the computer automatically. According to the reference concept of HLW disposal in China, the canister is completely supported by the surrounding buffer material. Therefore, the mechanical performance of buffer material may influence the overall stability of the canister. The heater which could be

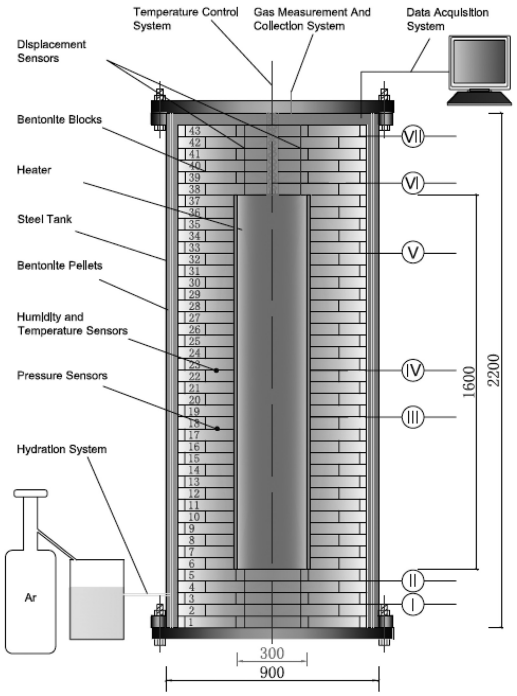


Figure 1. Sketch of the China-Mock-up facility (unit: mm).

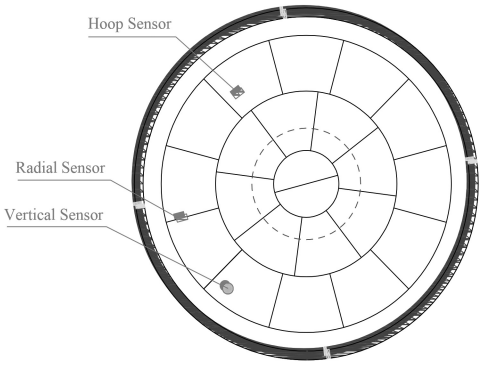


Figure 2. Stress sensors in the compacted bentonite.

vertical moved in the bentonite is specially installed. In order to evaluate this potential influence, six LVDT sensors are installed on the top and bottom of the heater to monitor its vertical displacement.

More than 160 sensors have been installed within the compacted bentonite blocks or in the surrounding pellets of the experiment to measure the important parameters, including the temperature, relative humidity, water injection pressure and the total pressure etc. 37 Total pressure sensors (CYG-1712, Wheatstone bridge) are distributed in 7 sections and the top of the bentonite in vertical direction. The sensors were placed within the grooves cut in the compacted bentonite blocks in three directions including vertical, radical and hoop (Fig. 2).

2.2 *Compacted bentonite blocks*

The GMZ-Na-bentonite is extracted from the northern Chinese Inner Mongolia autonomous region. According to the X-diffraction analysis, the clay mineralogy is dominated by montmorillonite ($75 \pm 1\%$) which is the essential mineral needed to ensure the sealing properties. The GMZ bentonite also contains variable quantities of quartz ($12 \pm 1\%$), cristobalite ($7 \pm 1\%$), feldspar ($4 \pm 1\%$) and kaolinite ($1 \pm 1\%$). The high content of montmorillonite results in a high cation exchange capacity (CEC = 77.30 meq/100 g), a large plasticity index ($I_p = 275$), and large specific surface area ($a_s = 570\ m^2/g$) (Liu, 2003). The major exchangeable cations are Na^+(43.6 meq/100 g), Ca^{2+}(29.1 meq/100 g) and Mg^{2+}(12.3 meq/100 g). The thermal conductivity of GMZ bentonite was found to increase as the dry density and water content increase. For the GMZ bentonite with a dry density of 1600 kg/m^3 and water content of 8.7%, the thermal conductivity is about 0.81 W/mk (Liu et al. 2007). A swelling pressure about 3.17 MPa was measured for the GMZ bentonite with dry density of 1600 kg/m^3 (Wen, 2006).

The blocks were manufactured by uniaxial compaction of the bentonite powder with average water content of 8.7% and dry density of 1710 kg/m^3. Totally, 5 types of compacted blocks were used in building the test. The installation space which is 5 cm width between the compacted bentonite and wall of the vertical tank, and 1 cm width between the heater and the compacted bentonite, was filled with the crushed pellets, with an averaged dry density of 1300 kg/cm^3. The total mass of bentonite used in the experiment is about 2.1 tons with an average dry density 1600 kg/m^3 (Chen et al. 2014).

2.3 *China-Mock-up operation*

The China-Mock-up experiment was assembled completely on 10th September 2010. After a pre-operational phase, the real-time data acquisition and monitoring system has recorded all the measurement data from 1st January 2011, and the data identified as "day 0" on the time scale.

The heater was switched on to reach a low temperature at 30°C from 19th January 2011 until 8th July 2011. The THMC experiment was commenced on 8th July 2011, then the power rises at 1°C/d to reach a maximum temperature at 90°C. Finally, the heating system was switched to the constant temperature control model automatically at 90°C. The heating phase with the time is illustrated in Figure 3. The temperature distribution in the China-Mock-up is shown in Figure 4.

The water injection started from 8th July, 2011. In order to avoid potential damage to the sensors by a rapid saturation process, the rate of water supply is limited in the initial stage. The hydration was controlled by a water injection rate which was increased gradually from 400 g/day to 1500 g/day in the first stage, and the injection was controlled by a constant pressure from

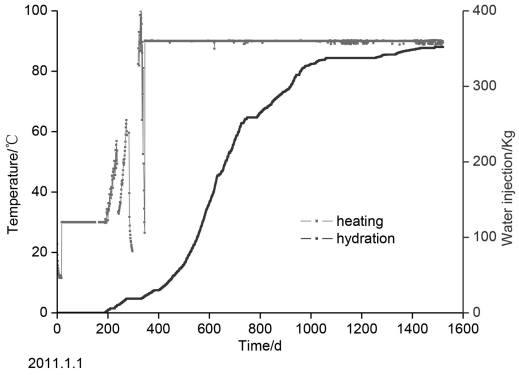


Figure 3. Temperature and water consumption with time.

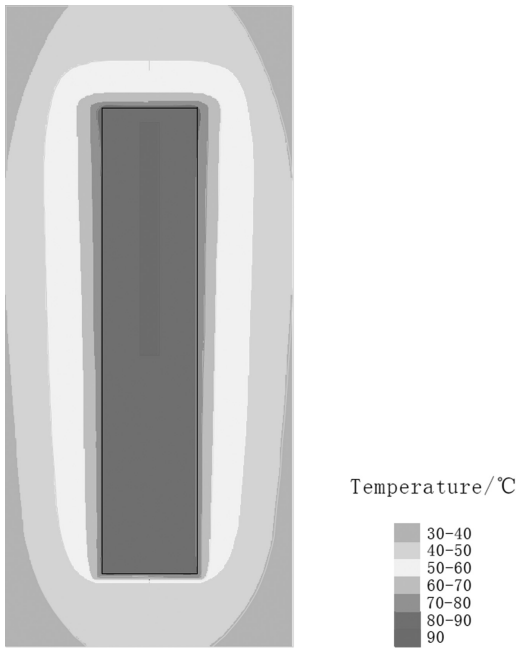


Figure 4. Temperature distribution in the China-Mock-Up.

0.2 MPa to 0.5 MPa since 25th August 2013. The water consuming with the time is illustrated in Figure 3. To mentioned here, the water injection was preformed artificially every day in the first stage, and the platforms illustrated in Figure 3 indicates no water supply during the corresponding period of time. As planned, a constant pressure of 2 MPa is to be applied when the pellets and the bentonite blocks near the water tubes become fully saturated.

3 STRESS EVOLUTION

3.1 *Total pressure evolution*

Under THMC coupled condition, the stress evolution of the compacted bentonite may be influenced by

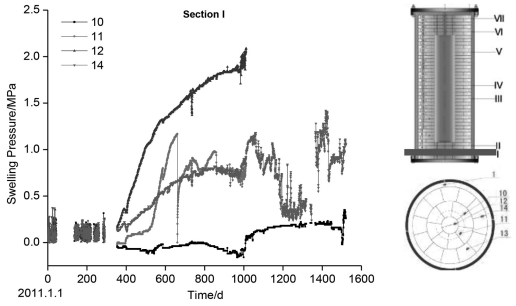


Figure 5. Stress evolution at section I of China-Mock-up.

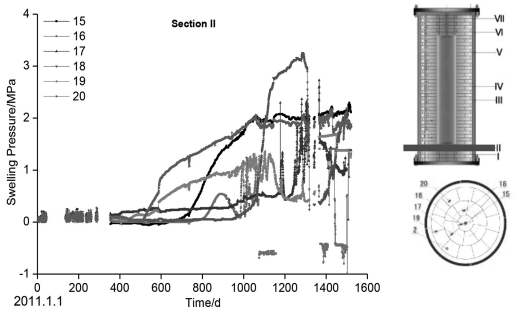


Figure 6. Stress evolution at section II of China-Mock-up.

several mechanisms, including the gravity, the thermal expansion induced by high temperature, and the swelling pressure generated by bentonite saturation with water penetration.

The water injection started from 8th July 2011, and the stress increase is noticed on 12th December 2011 due to the limited water supply at the beginning. In Figure 5, the stress evolution in section I is given. As shown in the figure, the total stress variation is rather limited or negligible in the initial stage which could be induced by the initial gaps between the gaps between the sensors and the blocks, and the bentonite blocks and pellets. After, the total stress increased steadily, and a maximum value 2.09 MPa is recorded by sensor 12 in radical direction within the inner ring after 1011 days. As mentioned in the former section, the water pressure at this moment is rather limited. Therefore, this value (2.1 MPa) can be considered as the swelling pressure which is lower compared to the swelling pressure values of the GMZ bentonite measured in the laboratory: 3.17 MPa for dry density of 1600 kg/m^3. This could be attributed to three reasons: the saturation process of whole barrier is not finished yet; stress releasing induced by the initial gaps between the bentonite blocks and pellets, the gaps between the sensors and the blocks, and also the upward displacement of the heater of 7.57 mm after 1287 days could be another reason.

In other sections, stress variation in compacted bentonite and pellets is recorded with the saturation in Figure 6–10. The data indicate the stress in the bentonite increased from the bottom to the top, and from

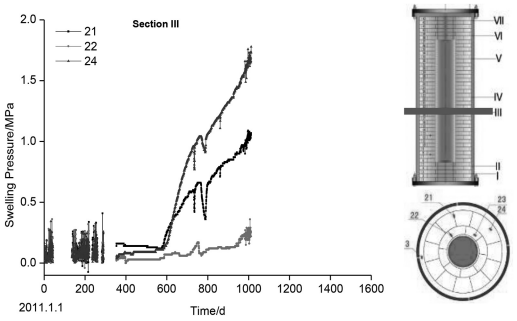


Figure 7. Stress evolution at section III of China-Mock-up.

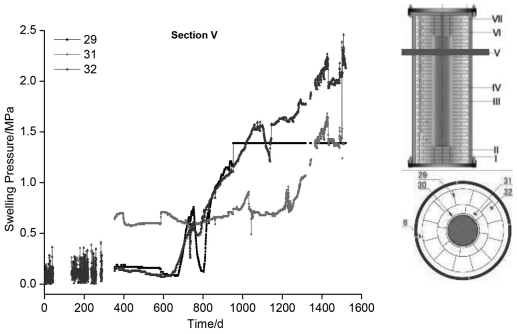


Figure 8. Stress evolution at section V of China-Mock-up.

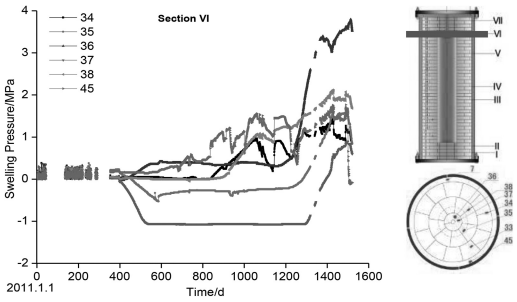


Figure 9. Stress evolution at section VI of China-Mock-up.

the place near the water tube to the inner gradually. After more than 2 years water injection, the stress in the inner part increased quickly, and is higher than the outer part gradually. That means the water penetrated to the inner part.

The highest vertical stress 3.8 MPa is recorded by sensor 36 in the middle of section VI located on the top of heater after 1512 days. At the bottom of the heater, the highest vertical stress 2.3 MPa is recorded by sensor 15 in section II on the same day after 1512 days. On the top of bentonite, the highest vertical stress 2.4 MPa is recorded by sensor 44 after 1403 days. The value (3.8 MPa) can be considered as the swelling pressure which is higher compared to the swelling pressure 3.17 MPa of the GMZ bentonite at dry density of 1600 kg/m^3. The main reason of the higher pressure could be caused by the upward displacement of

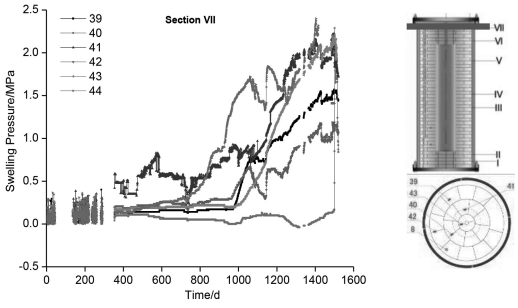


Figure 10. Stress evolution at section VII of China-Mock-up.

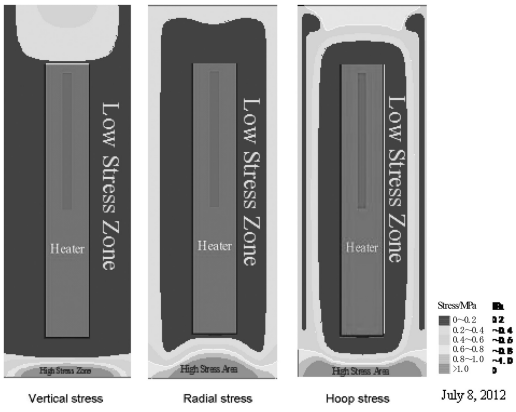


Figure 11. Stress distribution in the China-Mock-Up on July 8, 2012.

the heater of 7.57 mm after 1287 days which could decrease the gaps between the bentonite blocks and pellets, the gaps between the sensors and the blocks in the top of the heater. According to the stress evolution and the stress difference, the downward displacement of heater could be predicted.

The highest hoop stress 3.26 MPa is recorded by sensor 18 within the inner ring in section II located on the bottom of heater after 1284 days. It is higher than the swelling pressure 3.17 MPa of the GMZ bentonite at dry density of 1600 kg/m^3. The main reason could be the dry density 1710 kg/m^3 of the bentonite blocks because the swelling pressure increased with the dry density evidently. The sensor near the heater where the temperate is higher may be another reason.

The highest radical stress 2.73 MPa is recorded by sensor 17 within the inner ring in section II located on the bottom of heater after 1365 days. It is lower than the vertical stress and the hoop stress.

3.2 *Stress distribution*

According to the data of the stress sensor in three directions, the stress distribution after 1 year operation on July 8, 2012 is given in figure 11. After the water injection, water may concentrate on the bottom due to the gravity effect, and the initial gaps between bentonite

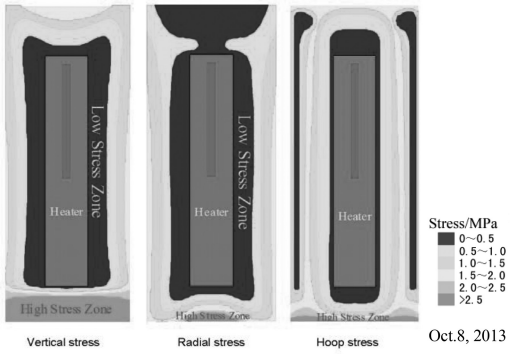


Figure 12. Stress distribution in the China-Mock-up on Oct 8, 2013.

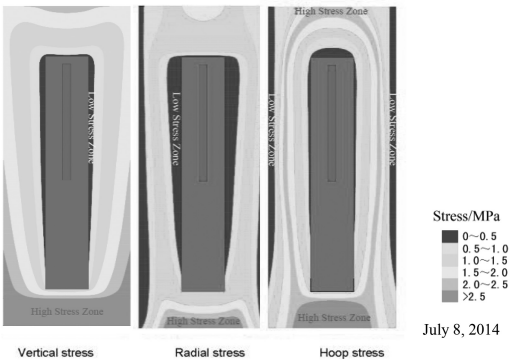


Figure 13. Stress distribution in the China-Mock-up on July 8, 2012.

and container and bentonite and heater, and the saturation process is vertically non-uniform which may cause difficulties to the definition of boundary condition in numerical studies. Because of the low hydration rate and inhomogeneous saturation process in vertical direction, the stress variation is relatively limited and inhomogeneous. The stress is higher at the bottom of heater which could be due to the gravity of heater. Because the mass of the heater is 1000 kg, the pressure under the heater by its weight is 1.24 MPa. The radical stress and hoop stress around the heater is lower which means that water has not penetrated to the inner part of the bentonite.

In Figure 12, the stress distribution after more than 2 years operation on October 8, 2013 is shown. The stress is higher at the bottom of heater due to the gravity of heater and higher saturation of bentonite at the bottom of heater. The stress around the heater is lower which could be attributed to the stress release induced by the initial gaps between the bentonite blocks and pellets with heater and steel tank, and also the gaps between the sensors and blocks. It also indicates that the water has not penetrated to the bentonite near the heater because that the bentonite has a very low permeability can make the arrival of water to the inner parts very slow.

The stress distribution after more than 3 years operation on July 8, 2014 is shown in Figure 13. It indicates that bentonite at the bottom of heater is nearly saturated. The stress is still higher at the bottom of heater due to the gravity of heater. The radical stress and hoop stress near the steel tank and heater is lower which could be attributed to the lower dry density of the bentonite pellets.

4 CONCLUSIONS

The China-Mock-Up as a large-scale mock-up facility to investigate the THMC behavior of GMZ bentonite, based on a preliminary concept of HLW repository in China, has worked well for more than 4 years. A lot of valuable data about the evolutions of compacted bentonite and experience about how to evaluate the suitability of buffer material in long-term under THMC coupled condition have been obtained for the first time.

The stress evolution in the compacted bentonite may be influenced by the gravity of heater and water, the thermal expansion induced by high temperature, the swelling pressure of bentonite generated by water penetration, stress releasing induced by the initial gaps between the bentonite blocks and pellets, the gaps between the sensors and the blocks, and also the upward displacement of the heater.

The highest vertical stress 3.8 MPa is recorded in the middle of section VI located on the top of heater after 1512 days. The highest hoop stress 3.26 MPa and radical stress 2.73 MPa are recorded within the inner ring in section II located at the bottom of heater after 1284 days and 1365 days separately.

Based on the analysis of the current experimental data, the China-Mock-up test is considered as a source of valuable data to improve the knowledge of the THMC process in the EBS, to establish the reliable numerical method to predict the THMC coupled behavior of EBS in long-term, and the design of HLW repository.

REFERENCES

Alonso, E.E., Alcoverro, J., Coste, F., Malinsky, L. et al. 2005. The FEBEX benchmark test: case definition and comparison of modeling approaches. *International Journal of Rock Mechanics & Mining Sciences* 45: 611–638.

Chen, B., Qian, L.X., Ye, W.M., et al. 2006. Soil-water characteristic curves of Gaomiaozi bentonite. *Chinese Journal of Rock Mechanics and Engineering* 25 (4): 1054–1058.

Chen, L., Liu Y.M., Wang J., Shao S.F., et al. 2014. Investigation of the thermal-hydro-mechanical (THM) behavior of GMZ bentonite in the China-Mock-up test. *Engineering geology* 172: 57–68.

Cui, Y.J., Tang, A., Qian, L.X., Ye, W.M., Chen, B. 2011. Thermal-mechanical behavior of Compacted GMZ bentonite. *Soils and Foundations* 51 (6): 1065–1074.

Dixon, D., Chandler, N., Graham, J., Gray, M.N. 2002. Two large-scale sealing test conducted at Atomic Energy of Canada's underground research laboratory: the buffer-container experiment and the isothermal test. *Can. Geotech. J.* 39: 503–518.

Gens, A., Sanchez, M., Guimaraes. L. do N., et al. 2009. A full-scale in situ heating test for high-level nuclear waste disposal: observations, analysis and interpretation. *Geotechnique* 59 (4): 377–399.

Karnland, O., Sandén T., Johannesson, Lars-Erik, et al. 2000. Long term experiment of buffer material, Final report on the pilot parcels. *SKB Technical Report*, TR-00-22.

Li, X.L., Frédéric, B., Johan, B. 2006. The Belgian HLW repository design and associated R&D on the THM behaviour of the host rock and EBS. *Chinese Journal of Rock Mechanics and Engineering* 25 (4): 682–692. (in Chinese)

Li, X.L., Bastiaens, P., VanMarcke, P, et al. 2010. Design and development of large-scale in-situ PRACLAY heater experiment and horizontal high-level radioactive waste disposal gallery seal experiment in Belgian HADES. *Journal of Rock Mechanics and Geotechnical Engineering* 2 (2): 103–110.

Liu, Y.M., Wen, Z.J. 2003. Study on clay-based materials for the repository of high level radioactive waste. *Journal of Mineralogy and Petrology* 23(4): 42–45. (in Chinese)

Liu, Y.M., Cai M.F. 2007. Thermal conductivity of buffer material for high-level waste diaposal. *Chinese Journal of Rock Mechanics and Engineering* 26(S1), 3891–3896. (in Chinese)

Liu, Y.M., Wang, J., Shao S.F., et al. 2013. A large-scale THMC experiment of buffer material for geological disposal of high level radioactive waste in China. *Rock and Soil Mechanics* 34(10): 2756–2762

Liu, Y.M., Ma, L.K., Ke, D., et al. 2014. Design and validation of the THMC China-Mock-Up test on buffer material for HLW disposal. *Journal of Rock Mechanics and Geotechnical Engineering,* vol. 6(2): 119–125.

Pacovsky, J., Svoboda, J., Zapletal, L., 2007a. Saturation development in the bentonite barrier of the Mock-Up-CZ geotechnical experiment. *Physics and Chemistry of the Earth* 32: 767–779.

Romero, E., Li, X.L., 2006. Thermo-hydro-mechanical characterization of OPHELIE backfill mixture. *Chinese Journal of Rock Mechanics and Engineering* 25 (4): 733–740.

Sanchez, M., Gens, A., Oliver, S., 2012. THM analysis of a large-scale heating test incorprating material fabric changes. Int. J. Numer. Anal. *Methods Geomech.* 36: 391–421.

Wang, J. 2010. High-level radioactive waste disposal in China: update 2010. *Journal of Rock Mechanics and Geotechnical Engineering* 2 (1): 1–11.

Wen Z.J. 2006. Physical property of china's buffer material for high-level radioactive waste repositories. *Chinese Journal of Rock Mechanics and Engineering* 25 (4): 794–800.

Ye, W.M., Cui, Y.J., Qian L.X., Chen, B. 2009. An experimental study of the water transfer through confined compacted GMZ-bentonite. *Engineering Geology* 108 (3-4): 169–176.

Unsaturated Soil Mechanics—from Theory to Practice – Chen et al. (Eds)
© 2016 Taylor & Francis Group, London, ISBN 978-1-138-02921-7

Selection and analysis of enclosure structure of deep foundation pit in Lanzhou metro

N. Guo
School of Civil Engineering, Lanzhou University of Technology, Lanzhou, China

Z.H. Chen
Department of Architectural Engineering, Logistical Engineering University of PLA, Chongqing, China

X.H. Yang
School of Civil Engineering, Lanzhou University of Technology, Lanzhou, China

ABSTRACT: In order to accumulate experience in design and construction of deep excavation of metro station in Lanzhou, fill the subway in Lanzhou the pile brace deep foundation pit supporting design, blank in Lanzhou subway deep foundation pit engineering of soil nail wall (composite soil nailing wall), underground continuous wall, pile and prestressed anchor support within four palisade scheme comparison, selected bored piles and steel pipe support scheme. According to monitoring results found that with increasing of excavation depth, the horizontal displacement and the depth of the excavation related to internal support and applying prestress, ring beam in the middle of pit has maximum lateral displacement; Deformation curve of retaining the gradually to the ")" shape and the maximum horizontal displacement down. During the construction process, in order to reduce the exposure time without support, it should be applied to internal support prestressing timely, speed up the bottom pouring, to prevent large displacement which caused by soil rheology, pouring the floor should be accelerated. The results show, pile brace support can effectively limit the lateral foundation, it can be extended in similar projects.

1 INTRODUCTION

Reasonable design of retaining structure of deep foundation pit of subway engineering not only affects the project quality and safety, but also has a direct impact on the difficulty of implementation, project duration, cost and construction period of the city residents life, economic activities and the surrounding environment will be affected. Therefore, how to achieve not only economic and reasonable, but also safe and reliable deep foundation pit supporting design, becoming the hot and difficult problems in geotechnical engineering research and engineering practice (Liu et al. 2009; Kong et al. 2011). The foundation pit of Lanzhou is simpler than coastal areas, soil nailing wall, composite soil nailing wall, prestressed bolting, and pile anchor supporting technology have gained some experiences (Zhou et al. 2007; Yang et al. 2014). But at present, the deep foundation still is in the stage of practice and exploration, the design theory of supporting structure is far behind than the engineering practice, the least aspect is leading to the conservative design of supporting structure, while the most aspect is that engineering accident of foundation pit will be caused (Zhu et al. 2010). At the same time, Lanzhou is a typical loess and collapsible loess area, the engineering and hydrology geological condition is complex, the wall rock of foundation pit is mainly loess soil, and the upper part has collapsibility, soft-flow plastic distributes near the water line, Some of side and bottom of foundation pit has thicker sand, The above conditions make it has differences when compared with of large cities at home and abroad which have constructed the excavation of the subway, the selection of deep foundation pit support and treatment measures of groundwater can't copy the successful experience of other regions(Industry standard editorial committee of the People's Republic of China 2012; Chen et al. 2009; Ren et al. 2009). Lanzhou experiences the subway construction for the first time, and lack of reference experience, so it is particularly urgent and important to carry out related research. This article conducts scheme selection for Lanzhou Metro Line 1#, reinforced concrete piles and steel tube bracing scheme is chosen firstly, according to the monitoring and analysis of foundation pit excavation, proving that the scheme is reasonable and feasible, so it is worthy to promote.

2 PROJECT OVERVIEW

Lanzhou rail transit network system includes 6 lines, having a total length of 207 km, the 1#, 2#, 3# as the center of the city line, their total length is 90 km, and have a total of 68 stations. 1# and 2# lines form the skeleton structure of wire netting, the lines run

through the center of the city, 3# is a auxiliary line of the network, connecting four groups of Chengguan, as shown in Figure 1. As the city lines, 4#, 5#, 6# lines respectively standard for Zhongchuan line, Yuzhong line and Qingshi line, having a total length of 117 km, which can strengthen the link of city center and the peripheral groups. For the deep foundation pit engineering of Lanzhou subway station, the standard depth is 14∼18 m; The pit depth of transfer nodes is 20∼24 m; The other ancillary facilities deepth ranging from 6∼10 m (Guo 2014).

The first phase project of 1# line, which from Chen Guanying to Donggang began to be constructed during 2012 and 2016, the total length approximately is 26.53 km, setting up a total of 20 stations, which are all underground stations, mainly using the open excavation method, involving a number of deep excavation engineering, and need support for the deep foundation pit. Lanzhou belongs to the typical loess and collapsible loess area, the terrain is long, the Yellow River Passes through the city, both sides of river are hillsides, the area can be used to construct in the urban is small, the construction density is big, the subway 1# line to be built is near to buildings and underground municipal pipelines, the difficulty of transfer station excavation technology lies in the protection of the surrounding undisturbed loess, prevention surface subsidence, reducing the impact on existing buildings. The supporting designers need to consider the selection of retaining structure, analysis, stress and deformation of the supporting structure of foundation pit excavation, the influence on the surrounding existing buildings and underground pipelines and the measure selection for groundwater treatment etc.

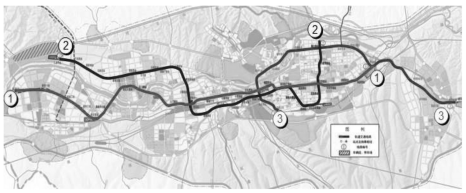


Figure 1. Subway network plan of Lanzhou.

3 RETAINING STRUCTURE SCHEME SELECTION

The loess layer of Lanzhou subway excavation is a special soil, its mechanical behavior in the foundation pit engineering is different from the common soil and the soft soil, because the natural loess itself has high strength, foundation pit supporting structure requirement of relatively low. But the loess high strength and its ability under erect conditions (flooding, disturbance, deformation) will weaken or lose the original structure, which is a hidden danger to the project, so the analysis for selection of deep foundation pit support is particularly important.

The local usually uses slope excavation and no-slope excavation. Slope excavation utilizes soil stability and suitable surface slope protection to form stable slope, the method can speed up the construction progress, and the cost is low, but large space need for the construction, so it is not suitable for Lanzhou foundation pit of subway construction, whose surrounding environment is restricted. Combined with the theoretical research and design practice of complex deep foundation pit engineering (Zhou et al. 2007; Yang et al. 2014; Zhu et al. 2010). The typical foundation pit engineering are shown in Table 1, the deep foundation pit of Lanzhou Metro must choose no-slope excavation and is constructed under the protection of enclosure structure, available retaining structure are summarized as follows.

Table 1. Typical examples retaining structures of Lanzhou area.

Project Title	Location	Foundation Overview m	Supporting Structure
Gansu Province, Chamber of Commerce Building Foundation	Chengguan District of Lanzhou City, the east side of the home district Yantan	Foundation depth-20 m, Excavation area 201.8*67.8 m^2	Row piles + three prestressed anchors
Comprehensive building foundation of Lanzhou TCM Traumatology Hospital	Yantan road of Chengguan District of Lanzhou City	Foundation depth −6 m, −10.8 m, −15 m	Adopting soil Nail Wall of Shallow foundation, For deep foundation The upper part of the concrete Wall The lower part of the pile anchor Retaining
Lanzhou Red House Times Square Foundation	Chengguan District of Lanzhou City, Cross the southeast corner of South Gate	Foundation depth −19.3 m, Excavation area 120*70 m^2	Row piles + three prestressed anchors
Lanzhou Real Estate Place Foundation	Supply and marketing Chengguan District of Lanzhou City, cooperatives west of Gansu Province	Foundation depth −15.8 m	The upper part of soil Nail Wall The lower part of the Pile Anchorage
Lanzhou, 7th land of Miaotanzi rotating lane Foundation	Jingyuan road of Lanzhou City, the north side of the police station	Foundation depth −15.6 m	Row piles + three prestressed anchors

3.1 *Retaining structure with soil nailing wall*

Soil nailing is a kind of in-situ reinforcement technology, by laying reinforcement in the soil and mechanical properties of the whole soil system can be improved, it is generally suitable for the 6 m∼12 m depth of foundation pit, the N value of soil is generally greater than 5 for sandy soil or N value of clay soil greater than 3. The natural state of loess has good independence and certain structural strength, soil nailing is suitable to support, and it has been widely used in Lanzhou; but for the pit of main body of subway station, the control of large displacement or groundwater influence is strict, so the soil nailing cannot be used. In addition, although the mechanical for construction of prestressed anchor rod is simple, and can make fully use of the shear strength of soil itself, can effectively maintain the stability of the structure, prevent dumping, displacement, and so on. But the surroundings are more restrictive, the risk of prestress loss is too big. Namely, the shallow pit of ancillary facilities can use this type of support structure or composite soil nailing wall. Because the main problem for the current soil nailing wall design is controlled by stability analysis, and has not yet developed to use deformation control stage, the stability analysis for soil nailing wall or composite soil nailing structure is not analyze deeply enough, often leading to engineering accident(Zhu et al. 2010; Zhang et al. 2014).

3.2 *Underground continuous wall enclosure structure*

The underground continuous wall uses mechanical construction method to pour reinforced concrete into the groove, then the wall will be formed, more and more domestic and foreign engineering combined with the design of supporting structure and main structure, bearing permanent horizontal and vertical load in normal use stage, known as the "two walls in one". It doesn't dewater outside the pit, can avoid settlement problem of the ground surface and construction site induced by dewatering, the pile stiffness is relative bigger, it is good to control the deformation of foundation pit excavation, and has good applicability for different soil layers. It is generally used for foundation pit against which has high requirements for penetration stringent and settlement of surrounding buildings. But the underground continuous wall is almost the most expensive taining structure, the application is not much in northwest area currently; Considering from the perspective of deformation, reinforced concrete piles can replace the underground continuous wall, considering the seepage, high pressure jet grouting piles can be constructed between support piles to solve this problem.

3.3 *Row piles with prestressed anchor retaining structure*

The local large-scale deep foundation pit is mainly used with pile anchor retaining structure (Yang et al. 2014), which effectively overcomes the traditional rigid retaining structure construction is slow, difficult construction, high cost, the disadvantage of displacement control and poor structural stability etc. But deep excavation pile anchor retaining structure includes many experience factors in the theoretical system, especially the focus of geotechnical engineering field for deep foundation pit has gradually shifted from the bearing capacity and stability analysis to design problems of displacement control, traditional limit state design method can't considering pit displacement changes or the effect of prestressing on the change of soil stress, not reflect positive effect of prestress, which is obviously not reasonable(Wang et al. 2014). At the same time, the single fulcrum supporting structure using equivalent beam method to determine the traditional embedded depth, the multiple fulcrum supporting structure according to overall stability conditions by simple arc slice method to determine the block design method of solid depth, the actual position and changes of excavation pile inflection point need to be verified by field measurement. Considering displacement control and the surrounding environment, the pile anchor retaining structure should not be used.

3.4 *Pile and inner bracing structure*

Because the reinforced concrete piles with inner supporting system is suitable for irregular and narrow plane shape foundation pit, and the steel support can be recycled, the cost can be reduced, structure state of steel support is simple, its stress state can be mastered easily, so pile support system has been applied widely in other subway station deep foundation pit support design (Chen et al. 2009; Ren et al. 2009). Reinforced concrete piles with internal bracing system, according to the mechanism of elastic foundation beam, pile foundation pit must rely on the insertion depth and inner support to balance the active earth pressure. The pile has bigger stiffness and control the deformation of foundation pit, the construction process is relatively simple, the pile body can be used as a part of the permanent structure, strong applicability (applicable to fill, general clay, loess and sand soil stratum). The theoretical calculation is relatively reliable, the calculation is generally divided into two parts, the first part is the stability verification of retaining structure based on the limit equilibrium theory, second part is the calculation of internal force and deformation of retaining structure.

The foundation pit excavation of Lanzhou metro has deep depth, and the requirements of surrounding environmental conditions are more stringent, bolting can provide a more open environment for excavation, but because of its relatively poor reliability, the deformation of foundation pit are not easy to control, and restricting to the underground pipeline, having a certain impact on the surrounding buildings and pipelines; According to the geological conditions, the subway station structure locates in the gravel layer, the bolt hole is difficult, it is not recommended to

use prestressed anchor supporting structure. From the point of security and stability view, the underground continuous wall has more advantages than reinforced concrete pile with prestressed anchor retaining structure and reinforced concrete piles with inner support, but under the premise of excavation safety, the latter two is more economic; Besides, the stiffness of steel pipe bracing is big, controlling the deformation of foundation pit is better, recycling, is the common form of subway station used to support. Therefore, the main structure uses the bored pile and steel tube bracing as a retaining structure.

4 THE FOUNDATION PIT CONSTRUCTION MONITORING

The main station structure is underground two layer, double column and three span (part of the section with three column span), the net length is 305.15 m, the standard section width is 21.60 m, the floor buried depth is about 17.19∼18.70 m, the overburden depth of roof structure is about 2.75∼3.49 m, the open cut construction practices is used to construct. According to the engineering experience and the calculation(Yang et al. 2014; Guo 2014), the main supporting structure uses Φ800@1400 diameter bored pile + three φ609 support (standard section), the length of the pile is 22.34 m the embedded depth is 5.0 m. First, the design of axial force for the first, second and third supporting are 750, 1380, 1216 kN, pre-axial force are 300, 552, 487 kN. The parameters of foundation pit supporting design are shown in Table 2. In order to test the design rationality, according to the requirements of informatization construction, the test section of support system and surrounding environment monitoring are conducted for Century Avenue station of Lanzhou Metro, the layout of foundation pit monitoring points are shown in Figure 2.

Table 2. Parameter table of foundation pit supporting design.

Geotechnical number	Geotechnical name	r (kN/m^3)	c (kPa)	φ (°)	k m/d
1-1	Miscellaneous fill	17.0	0	12	5∼8
2-1	loess soil	17.7	17	27	3∼5
2-10-3	grait	23.0	0	40	50∼60
2-10-4	grait	23.5	0	40	50∼60
3-11	grait	25.0	20	43	45∼55

The typical measuring point ZQT-12 of pile inclinometer results are shown in Figure 3, the positive value means that the pile moves towards the pit, while the negative value means that the pit deviates from the pit. The initial stage of excavation, the side displacement of pile is smaller, the value is basically negative. With the excavation, foundation pit retaining pile has lateral displacement in the direction of the pit, with the support is installed, the horizontal displacement is well controlled, the displacement becomes smaller. In this process, the deformation curve of the pile body gradually changes towards the “)” shape, the location

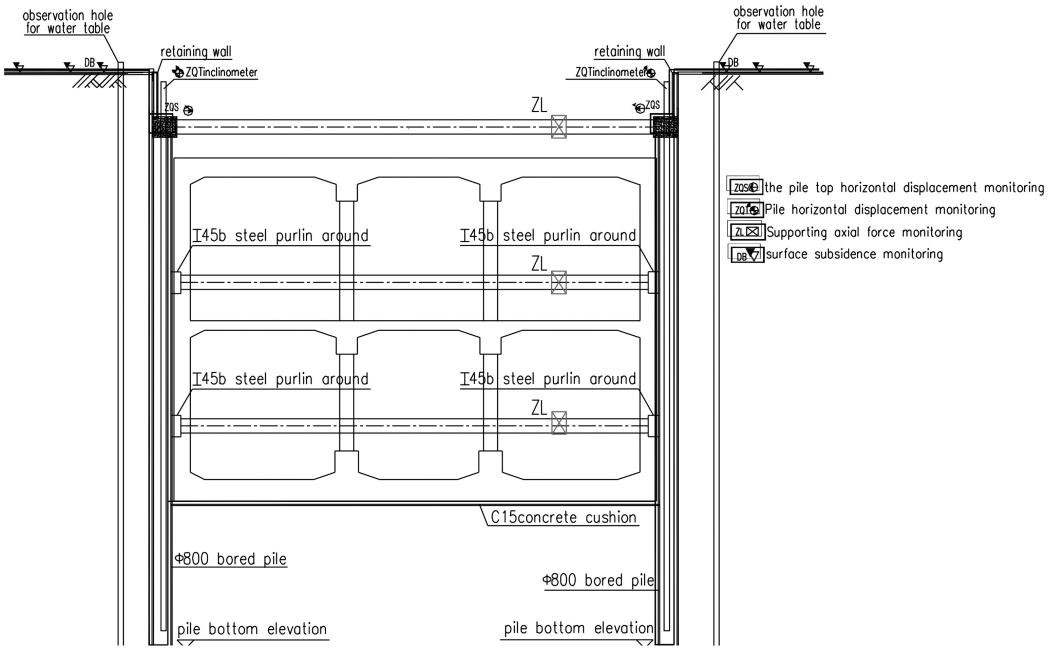


Figure 2. Section of monitoring points.

of the maximum horizontal displacement shift down, the horizontal displacement of top pile changes not large over the time, this correlates with steel support dig support scheme, timely prestressing along the steel support axial.

Based on the data analysis of pile top horizontal displacement, ground surface settlement, horizontal displacement of deep pile body and supporting axial force monitoring, found that the horizontal displacement of top pile increases with the increase of the depth of excavation, the horizontal displacement of excavation every stages correlates with depth change, inner support and adding prestress, soil displacement distribution along with the foundation pit is not uniform, the displacement of central pit beam is the biggest. The maximum value is lower than the standard value, indicating steel support has significant restraint on displacement of the top pile; During initial excavation, the foundation pit is shallow, lateral soil settlement is small, the surface settlement curve is basically unchanged. With the increase of the excavation depth, maximum surface settlement begin to move away from the edge of the pit, the soil around foundation experiences settlement-uplift-sedimentation-uplift-subsidence; With the excavation, retaining pile produces lateral displacement in the direction of foundation ditch, in this process, the deformation curve of the pile body gradually changes towards ")" shape, the occurrence location of biggest horizontal displacement moves the downward direction; The monitoring data of supporting axial force show that the support system can effectively restrict the lateral displacement of foundation pit; But because of uncertainty around the pit and the unforeseen external load effects of around the pit, making the envelope stress become more complex. But through the test section construction, overall, the retaining structure with supporting bored pile and steel pipe meets the requirements for displacement and deformation, showing that the original design scheme is reasonable.

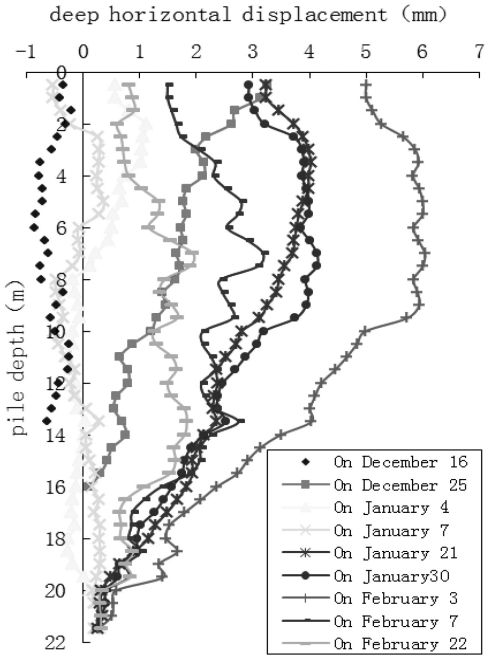


Figure 3. Variation of horizontal displacement curves.

5 CONCLUSIONS

(1) By comparing with the four kinds of retaining scheme: composite soil nailing wall, underground continuous wall, anchor pile and pile, based on the calculation and monitoring results of test section envelope, the bored pile and steel pipe support scheme of subway station foundation pit of Lanzhou controls the deformation of the foundation pit well, successfully solve the problem of deep foundation pit supporting of subway in collapsible loess area.

(2) Through the information construction, found the measured data of pile body displacement and the inner support axial force are all less than design value, it is shown that the original design scheme can be further optimized.

(3) The steel support uses with quick excavation and quick support scheme can well restrict the lateral displacement of foundation pit; during the process of foundation construction, Axial prestress should be exerted timely along with the steel support, reducing the exposure time with no support, speeding up the floor pouring, preventing larger displacement produced by rheology of soil.

REFERENCES

Liu J H & Hou X Y. 2009. Excavation engineering handbook (second edition). Beijing: China Building Industry Press.

Kong L W & Chen Z H. 2011. General report of research progress on special soil and slope. Proc. 11th National Conference on Soil Mechanics and Geotechnical Engineering.

Zhou Y & Zhu Y P. 2007. Inquiry into supporting technique of deep excavation in Lanzhou region. Journal of Lanzhou University of Technology 33(5): 109–113.

Yang X H, Zhu Y P & Guo N, et al. 2014. Optimization design and construction of large deep foundation pit groups in northwestern areas of China. Chinese Journal of Geotechnical Engineering 36(S2): 165–173.

Zhu Y P, Ye S H & Mo Y. 2010. Analysis and treatment of a deep foundation pit accident in Xining, Qinghai Province. Chinese Journal of Geotechnical Engineering 32(S1): 404–409.

Industry standard editorial committee of the People's Republic of China. 2012. Construction of foundation pit supporting technology discipline JGJ 120-2012. Beijing: China building industry press.

Chen Q N, Zhou G H & Zhang F, et al. 2009. Bracing design for deep foundation pit of subway in loess area. Journal of Hunan University of Science & Technology (Natural Science Edition) 24(1): 49–52.

Ren J X, Feng X G & Liu H, et al. 2009. Research on the deformation law of supporting structure for deep foundation pit of metro station. Journal of Railway Engineering Society 3(126): 89–92.

Guo N. 2014. Subway station in Lanzhou a pile brace deep foundation pit supporting structure construction monitoring and numerical simulation analysis. Lanzhou: Lanzhou university of technology.

Zhang Y C, Yang G H & Wu S J, et al. 2014. Discussion on relationship between deformation and stability of soil nailing structure. Rock and Soil Mechanics 35(1): 238–247.

Wang D Q & Zhu Y P. 2014. Additional stress apply to analyzing the stability of prestressed anchor support. Engineering mechanics 31(4): 196–202.

Unsaturated Soil Mechanics—from Theory to Practice – Chen et al. (Eds)
© 2016 Taylor & Francis Group, London, ISBN 978-1-138-02921-7

Design and installation of comprehensive instrumentation system of high-fill foundation in mountainous airport

Y.P. Zhu, X.H. Yang, Z.B. Shi, W.X. Cai & H.J. Jiang
Department of Civil Engineering, Lanzhou University of Technology, Lanzhou, China

ABSTRACT: In order to study some important issues of high-fill foundation traits in mountainous airport changing with time and space, we plan to rely on the high-fill foundation of Chengzhou airport in Longnan to expand space-time monitoring. The test used single point settlement meter, layered settlement meter, soil pressure box, TDR moisture meter, osmometer, inclinometer and other smart sensors, those of which are connected with data acquisition, making the first time the remote wireless instrumentation be come true through a wireless transmitter and a receiver. The research describes in detail the design and installation of the comprehensive automatic instrumentation system of instrumentation test, according to instrumentation results, the research deeply analysis after-work settlement component of the original foundation and filling body, and the causes of uneven settlement, analysis the filling height, filling velocity, comprehensive compaction of ground, effect on the high-fill foundation after-work of time and other factors, put forward some quality control suggestions. The results showed that reducing fill velocity, appropriately increasing the compaction of ground and reducing the filling height are all effective measures to reduce settlement, which can be a powerful guide similar high-fill engineering.

1 INTRODUCTION

With the acceleration of urbanization construction and the implementation of "One Belt and One Road" strategy, projects such as energy, airports, roads, railways will gradually be increased in newly-built intensity and expansion; "State Council on promoting the development of the civil aviation industry" pointed out that the central government continue focused on the central and western regional airport construction and operation, gave full play to the comparative advantages of civil aviation in remote areas and complex terrain transportation and emergency rescuing and so on. But limited by hilly terrain conditions, the contradiction between large quantity demand of civil aviation development construction and lack of available land resources in the mountain area increasingly stands out, "cut mountains fill ditches, build the airport up to mountain" becomes a feasible solution. Thereby forming large area, large amount of high-fill foundation and slope, brought a series of geotechnical problems (Liu et al. 2005).

Domestic System Study for high-fill foundation of mountainous area was less, literature can be found mainly in roads, railways, etc. The outcome was more scattered, less systematic, less deep enough. There has not been an uniform technical standards for the high-fill foundation (Cao 2011). From the use of high-fill foundation airport which has been completed, there are not only successful examples, but also occurred instability and excessive settlement project, such as Panzhihua airport construction and operation of the process, which has occurred landslide at least 10 times. Landslide, occurring on 12 June 2011, the total volume of landslide reached 510×10^4 m^3, led to the airport suspended for two years, spent about 200 million yuan for maintenance (LI T B et al. 2012), the main reason is that the theory of the unsaturated compacted soil did not unit with its practice (Bao & Zhan 2006; Chen 2014), and the lack of systematic instrumentation.

The most effective way to solve this problem is to monitor such data, during and after the construction carried out on the high-fill foundation, which are foundation settlement, horizontal displacement, soil pressure, pore water pressure, soil moisture. By the real-time instrumentation, it can effectively reduce the airport construction process of high-fill foundation the settlement after construction, high slope stability and groundwater environmental changes may lead to geological disasters geotechnical engineering problems. Geotechnical engineering began in the last century, 30 s∼40 s (Au 1998). In the early time, deformation, soil pressure and pore water pressure were usually monitored with simple mechanics and water equipment (Franks 1999); No matter in the produce practice or science study, geotechnical engineering instrumentation has been widely used in foreign countries (Cooper et al. 1998; Angeli et al. 2000; Corominas 2000; Bhasin et al. 2002); However, because the site intelligent instrumentation of high-fill foundation takes a long period, high cost, especially when doing in the process of construction, it is effected on the construction factors, and the document that is in the field instrumentation of high-fill foundation in

mountainous airport is short, partly in previous instrumentation on high slope (Li et al. 2003) has a different nature and the high-fill foundation and high fill slope. Therefore, relying on a state airport Longnan high-fill and being combined with the construction process in the test section, the body is buried at different depths filling a single point of settlement meter, layered settlement meter, soil pressure cells, TDR moisture meter, osmometer, measuring inclinometer smart sensors, which are connected with data acquisition, making the first time the remote wireless instrumentation be come true through a wireless transmitter and a receiver.

2 DESIGN OF MONITORING SYSTEM

2.1 *Site selection*

The proposed airport lies in the county in Gansu Luo ditch on the west side of the hilly area that has large changes in topography. To construct airport, the original site should be modified by digging and filling. Engineering geological condition of the site is complex, bedrock surface are of ups and downs, surface height difference, uneven thickness of overlying soil, especially in the construction field area, to some runways excavation area is located partly in the fill area, both surface silty clay and sandy mudstone large distribution, there are high steep natural slopes and rich groundwater, where the area is located in high intensity seismic zone meanwhile.

According to the design of filling and digging earth height, in term of the principle "the part which exists potential danger, the key part of engineering and the part whose geological conditions is poor, trying to save investment, shortening the construction period reasonably" in light of the actual topography condition airport layout and field areas, hydrological conditions, ground conditions and the structure of land acquisition and resettlement schedule, and select the first section of the western end of the field area and the groove area on both sides of the soil surface area is used to monitor the test section (general layout in P 95 + 10.0~P 103 + 20.0 above). The test section is located in the largest fill area of channel slot, where contains both cutting and filling filler ratio and large-scale construction of high slope encountered, dealing with the junction of digging and filling and other conditions. The construction method in this comparative test is more representative than those in the field instrumentation tests of typical guidance for subsequent construction.

2.2 *Site Engineering geology and hydrological conditions*

Depth investigation in this field, stratigraphic distribution from top to bottom are: ① fill soil layer (Q_4^{ml}), thickness of 0.10~2.30 m, with cultivated soil, a little wet, a little secret; ② silty clay layer (Q_4^{dl+pl}), depth of 0.10~2.30 m, thickness 0.20~29.40 m, local area at the top missing plastic – hard plastic, the local rich groundwater zone is soft plastic; ③ strong weathered bedrock (N_2), depth of 0.10 to 30.20 m, a thickness of 3.00~5.80 m, according to topography vary widely; easy to soften water; ④ weathered bedrock (N_2), depth of 4.00~34.00 m, reconnaissance thickness 1.20~46.80 m (not through), the mountain Potential from the foot to the top of the hill from deep shallow depth. Site groundwater depth 0.40~10.00 m, belong to Quaternary loose pore diving, in low-lying valley on both sides of the runway ridge are distributed locally to the upper surface water infiltration form of stagnant water and bedrock fissure water, the main aquifer silty clay layer.

2.3 *Filler ratio and compacting*

According to the survey report, the vast majority of the filling materials are weathered sandy mudstone and silty clay, sandy mudstone. Because the material gradation is so poor that it formed coarse gradation material which has high shear strength, high packing density, high carrying capacity advantages, but water softening disintegration characteristics, creep properties, strong permeability all need to rely on the viscosity of filling silty clay, clay content, the ratio between the thickness of the grain to improve. To reduce the after-work high-fill settlement, the first thing is compacting silty clay layers of different thicknesses with different levels; "the nearest materials, the nearest balance" based on the principle of filling body filler, based on a large number of heavy compaction test system, filler groove area silty clay and sandy mudstone chosen with the ratio of 2:8 mixture, the coefficient for compaction is not less than 0.95, the soil surface area using Rocky ratio of 4:6 mixture, the coefficient for compaction is not less than 0.90, during the construction fill the lower part of earth with strong punning, while the upper part of earth with vibration and compaction.

2.4 *The project design*

In order to grasp the dynamics of the original foundation, and the filling different thickness variation of soil condition during and after the construction work, the high-fill foundation instrumentation mainly contains layered settlement and total settlement, soil pressure, pore water pressure and moisture content changing with time and space; while high-fill foundation slope instrumentation mainly contains slope top settlement and displacement, horizontal displacement, slope temporal and spatial change of pore water pressure. Combining test section spring distribution, groundwater and blind ditch strike, the instrumentation test of filling body is taken in both typical and important area, along the deepest gully segments respectively groove area, the soil surface area and slope area, in the soil base choice 1# point (P: 4006, H: 4027.5), 2# point (P: 4006, H: 4071.5), 3# point (P: 4006, H: 4112.5), combined with construction fill, layered laid sensors, The first layer sensor starting position is in

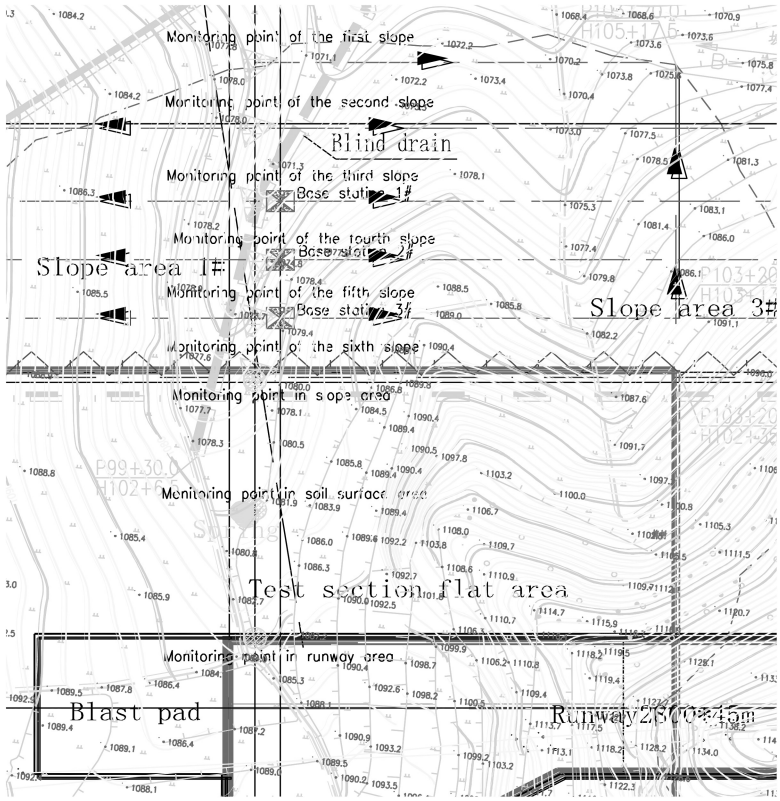


Figure 1. The plane arrangement map of instrumentation points.

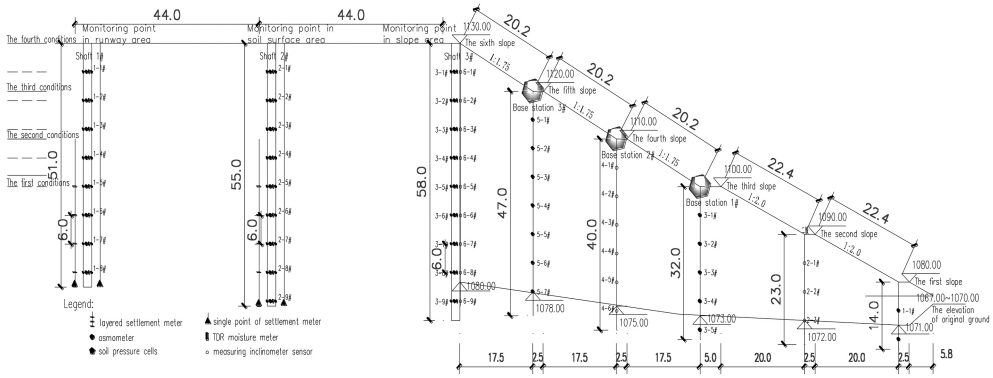


Figure 2. The profile arrangement map of instrumentation points.

the silty clay layer original foundation, sensor vertical spacing is approximately 6 meters. According to the construction condition, on a platform ranging from1 to 6 level slope, we respectively select the point (P: 4006, H: distance from the slope of the line about 1 m) drilled a vertical hole, buried sensors, sensor vertical distance is also about 6 m, where the level of first, third and fifth slope filling earth was conducted with pore water pressure instrumentation, the level of second, fourth and sixth filling earth was conducted with deep soil slope displacement instrumentation. When instrumentation began to construct, site construction fill elevation is about 1100.00 m, namely, on the third level platforms, in order to conveniently control construction, we regard the construction of level 1∼3 platforms as the first working condition, the following level are second, third, fourth working condition, instrumentation point layout is shown in Figure 1, the cross-sectional arrangement shown in Figure 2. After each level slope filling construction platform to design elevation, the inclinometer hole distance of about 15 m evenly arranged on both sides of settlement

displacement of two observation points, monitoring the situation of settlement platform slope deformation.

3 INSTRUMENTATION SYSTEM INSTALLATION

3.1 *Layered settlement construction*

In order to monitor the construction process in the different settlement of layered soil filling layer, we usually choose layered settlement gauge to conduct instrumentation. Using the electromagnetic induction principle inductance frequency-modulation displacement meter insert into solenoid coil with inserting magnetizer piston rod fixed in the subsidence so that it can move back and forth. Magnet coil inductance is related to the length of the piston rod inserted into the coil. The settling will cause the change of the coil inductance, inductance frequency modulation circuit alters the change of the coil inductance into frequency signal, displacement value can be obtained through reading meter.

The installation process: under good weather conditions, using Φ108 bit to drill, generally we need a deeper drill than the depth needed for installation. The principle is using 10 m + 0.5 m, 20 m + 1 m, etc. Don't take out bit immediately after the drilling to the desired location, there need to use the pump to irrigate water down until all of the mud water changes into clear water, then take out the bit and install. PVC pipe and stainless steel armor (displacement meter are built in), PVC connecting pipe and screw connection (irrigate water into the pipe when putting down the pipe if pipe buoyancy is too big) is used to connect PVC pipe and another PVC pipe, screw connection Firstly screw connect the end of tube and PVC pipe, and then connect stainless steel protecting tube (at both ends are equipped with PVC connecting pipe) and PVC pipe (the length and the number are according to the design requirement) should pay attention to the direction of the metal pipe installation, put the side with settlement ring slot toward orifice and the another side toward the bottom of the hole. Displacement meter wires should across through the PVC pipe and tube. After finishing all the pipe connection, groove at the last PVC pipe orifice and lead wire, and set on the protection pipe to protect the wire. Finally cover the cap, screw connection. Backfill materials is the coarse sand, backfill speed cannot too fast, in order to avoid blockage and gap, the best is to check it again after one or two days later, backfill after backfill materials sinking, add protective measures around pipe. Installation site is shown in Figure 3.

Found in construction that there is no guarantee to make sure the initial range is the minimum in the installation process of the settlement magnet ring of the layered settlement gauge, a large range is wasted Being limited by the PVC pipe of the instrument. when fill thickness is large, each hole can only place eight settlement magnetic rings, which is unable to meet the demand of more hierarchical collection;



Figure 3. Installation drawing of layered settlement meter.

When constructing in layer, the place around settlement gauge cannot be normally compacted so that the measured settlement value is not a of real settlement of soil compaction that design required. So the layered settlement meter constructed only in the first condition.

3.2 *Construction of single point settlement meter*

After finding out defects of layered settlement gauge, we use single point settlement meter to equivalent substitution the follow-up condition, namely along with the construction of the filling body, install more single point settlement meter. Total settlement of corresponding filling body can be measured and the difference also can reflect the layered settlement. Inductance frequency-modulation displacement meter used the electromagnetic induction principle and inserting magnetizer piston rod fixed in the subsidence ring into solenoid coil so that it can move back and forth. Magnet coil inductance is related to the length of the piston rod inserted into the coil. The settling will cause the change of the coil inductance, inductance frequency modulation circuit alters the change of the coil inductance into frequency signal, through reading meter displacement value can be obtained. The whole settlement gauges are buried, the underlying anchor head is anchored to the bedrock (relative to the fixed point), wire is leaded out from the side. When the foundation sink, settlement plate with sink too, relative sliding appears between the sensor and the rod, then the signal is output, the displacement is obtained, the goal of settlement observation is attained.

The process is as following: drilling, according to the depth of the hole calculating the length of the required bar, completely with fittings. Plugged install bar, pins (settlement measuring rod pulled up to a maximum), and the bottom anchor assembly (including the underlying anchor head, PVC pipe, rod) connecting with an extension rod section, and then for the inner PVC pipe filled with concrete slurry. Nylon rope (the length at least 3 m more than a specific hole) on one end of the rope attached to PVC pipe, then filling good pulp anchor assembly into the hole to the next section at the orifice connecting bar to continue the hole, and connect the next section extensions until all bars connected to a single point. Application installation tester for single-point settlement plan instrumentation entirely, in order to ensure a single point of settlement terms in the maximum range of the state. After the bottom of the anchor head is in place, pulled the Nylon rope, so that PVC pipe is pulled out of the hole bottom,



Figure 4. The installation drawing of single point of settlement meter.

and that concrete mortar sink hole bottom anchor bottom anchor head, then cut the nylon rope. Here it should be noted: First, when the installation compressive bar press the anchor head to the bottom of the hole, but it still higher than expected settlement plate measurement level, using brick, measuring the level of the soil between the original and getting the settlement plate gap filled, making sure settlement board level. The second, when the installation compressive bar is in the process of pressure force, the bottom anchor head has not been pressed into the bottom hole, while settlement plate touches measuring surface, the level of exposure has been unable to continue to press down, now soil under the settlement board should be removed until the bottom portion of the plate under the anchor head down to the bottom of the hole so far. Site construction drawing is shown in Figure 4.

3.3 *Soil pressure cells, osmometer, TDR moisture meter construction*

Consider that airport filler is coarse mixes, select double membrane intelligent memory type earth pressure cells to meet the high precision and high sensitivity requirements; At the same time for the accurate knowledge of the pore water pressure and water content of different filling height of the soil, Smart osmometer and TDR moisture meter should be buried at the corresponding position. Installation process: under good weather conditions, measure to determine the position of the sensor is embedded, the proposed position is about 400 mm deep, 400 mm diameter holes.

When installing the bottom of the filling 10 cm sand compaction pad level, the soil pressure cell membrane stress (pressure film) should be facing up, soil pressure cells will control the horizontal ruler soil pressure cells mounted horizontally, osmometer and TDR water meter vertical buried in sand, and the top cover around 30 cm thick sand compaction. Site installation is shown in Figure 5.

3.4 *Fixed inclinometer construction*

In order to monitor high-fill slope accurately at different depths of soil horizontal displacement until the slope reach the design elevation after filling in the trail to the original drilling ground following strong weathered shale, we should bury pipes fixed inclinometer (with pulley). Fixed inclinometer inside the angle sensor (axis tilt sensor), and intelligent electronic chips from a height of 35 mm diameter 70 mm metal cylinder



Figure 5. The installation drawing of smart sensors embedded memory.



Figure 6. The installation drawing of memory measuring inclinometer sensor.

package, placed on top of a rectangular metal plate of 5 mm thick; installation in Φ70 PVC inclinometer tube, pipe deformation occurs when the inclinometer, inclinometer measure the vertical direction with respect to the inclination of the axis of gravity, using the installation location of the geometry, we can calculate the horizontal inclinometer tube deformation, so as to measure the horizontal displacement of the structure embedded inclinometer tube purposes. Figure 6 is embedded site.

3.5 *Wire, station construction*

To achieve process instrumentation, to be combined with the construction processes fill sensor buried, and to collect in the case of data not affect the construction of the construction process is a major difficulty in this test. With the sensor layer construction, because different access station, we need to be embedded reasonable lead, according to the construction schedule and the time slot is wired, and TDR moisture meter and fixed inclinometer required to connect module I, and the remaining sensors required to connect module A, how to achieve the shortest each sensor wiring, to collect sensors data as soon as possible after construction, Therefore, after repeated comparison, calculations, combined with the construction process, optimized for different sensor points three stations access acquisition module, wireless remote instrumentation, data acquisition twice daily. Station measuring point wiring distribution is shown in Table 1, the scene of Figure 7.

4 SURVEY RESULTS AND ANALYSIS

4.1 *Analysis of two stage slope inclinometer*

Two stage slope's horizontal displacement change as shown in Figure 8, two stage slope has small changes

Table 1. Instrumentation point all location table station wiring condition.

	Condition & mode	Quantity	Observation station 1# 2*32A, 1*16I mode	Observation station 2# 1*8A, 1*32I mode	Observation station 3# 1*32A, 1*1A mode
Condition 1	Single point of settlement meter	2	2		
	layered settlement meter	8	8		
	osmometer	14	14		
	Soil pressure cells	23	23		
	TDR moisture meter	14	13	1	
	measuring inclinometer sensor	3	3		
	slope osmometer	7	7		
Condition 2	Single point of settlement meter	2	2		
	osmometer	3		3	
	soil pressure cells	5	5		
	TDR moisture meter	3		3	
	measuring inclinometer sensor	6		6	
Condition 3	Single point of settlement meter	2			2
	osmometer	6		1	5
	soil pressure cells	10		3	7
	TDR moisture meter	6		6	
	measuring inclinometer sensor	7			7
Condition 4	Single point of settlement meter	2			2
	osmometer	3			3
	soil pressure cells	5			5
	TDR moisture meter	3		3	
	measuring inclinometer sensor	9		9	
	Total	143	77	35	31

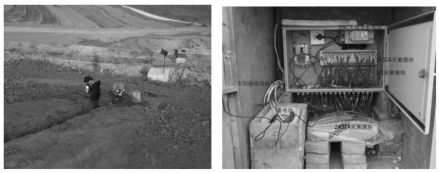


Figure 7. The base station of remote wireless instrumentation system.

in slope displacement, the overall is stable, the cumulative maximum displacement is about 2 mm. Since the impact of sand flowing which is used to fill of buried inclinometer inclinometer tube in the beginning, leading to the change of displacement haven't law in a few days, starting from September 18, 2014 became stable; the earlier stage have a larger displacement, the medium-term volatility is small, the current is stable; displacement values is within the range of 0.1∼0.2 mm. Surface appears linear increase is influenced to increasing of the upper filling material load weight; from a depth of 6 m, the accumulated displacement have small changes in a certain percent, or because of the impact of the one stage slope's construction and artificial mechanical disturbance; underlying change slightly, due to in the blind drainage ditch have water seepage cause impact of wet soil deformation. It should be noted that where a slope of pore water pressure increases with the filling height increases, and significant changes with the seasons, so blind drainage ditch should be strengthened, non toe ponding area.

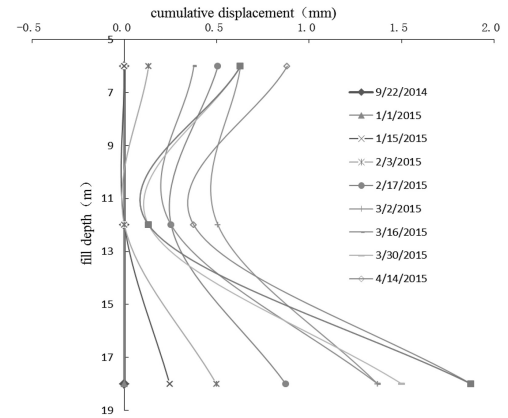


Figure 8. The variation graph of cumulative displacement in the second slope.

4.2 *Analysis of four stage slope inclinometer*

Four stage slope's body changes of horizontal displacement as shown in Figure 9, Currently four stage slope cumulative displacement trends overall slope stabilization, pre-change erratically, to a lesser extent the medium-term linear growth stabilized at the maximum displacement of 10 m and 17 m depth place, at 10 m depth place, the initial deformation is large, analyzing the reasons that believed to be buried inclinometer tube construction cause, that does not change the prelaw at a depth of 10 m has increased significantly since the beginning of buried inclinometer inclinometer tube

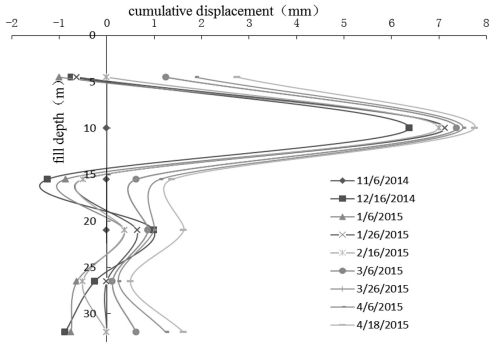


Figure 9. The variation graph of cumulative displacement in the fourth slope.

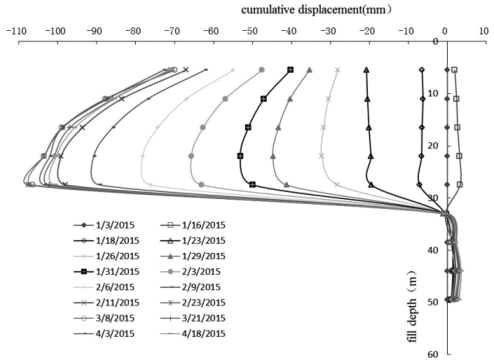


Figure 10. The variation graph of cumulative displacement in the sixth slope.

filling sand flow impact and the sensor has a settling time; but the overall trend will reflect distortion filling the upper fill soil load weight to increase the depth and Its effects affected. 27 m deep displacement is mainly due to the impact of blind ditch seepage water, the daily variation in the range of 0.1～0.2 mm, the overall slope stabilization. However, due to continued rainfall and spring loaded top cause deformation rate continued to increase slightly in 2015 after March 17.

4.3 *Analysis of six stage slope inclinometer*

Six stage slope's horizontal displacement of slope inclinometer analysis changes as shown in Figure 10. Since the beginning of the buried inclinometer measure the early impact of displacement swash pipeline filling sand used varies greatly, January 3, 2015 began to stabilize. Inclinometer change the basic shape is divided into two parts, under the depth of 30 m has little change, upper the depth of 30 m has more significant changes, the first to be noted that for 60 m fill, how to ensure that does not happen inclinometer buried crack, difficult; In addition, buried set inclinometer tube with a filling of sand flow affects the front four days displacement is no law.

Due to the influence of slope surface mechanical compaction and construction disturbance, the depth

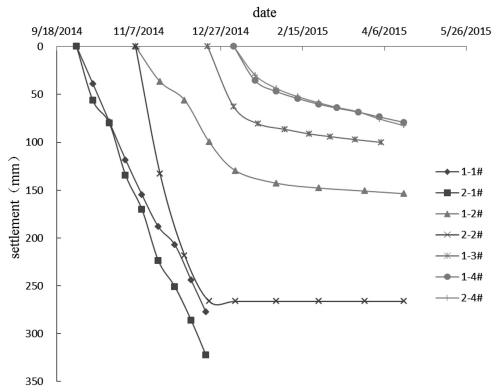


Figure 11. The variation graph of settlement of filling body.

of 5.5 m, 11 m, 16.5 m at a displacement rate changed significantly larger displacement of more than 32 m filling soil analysis reason to think: 30 m or less fill the soil longer, slower construction rate, starting from level four slope, filling construction significantly accelerated consolidation of the soil itself settling time is short, the larger the soil pore water pressure, ultra pore water pressure dissipation requires a period of time, so the soil deformation lag effect. In addition, the displacement of the upper filling a significant increase, the reason is because the surface mechanical compaction, construction disturbance and filling velocity was too fast in December 2014. Although the overall displacement tends to be stabilized, but top of the hill from loading and requires further observation. Spatial and temporal variations settlement.

4.4 *Embankment settlement law of space-time analysis*

Filling body vertical settlement changes of condition one to condition four in Figure 11.

Filling variation of settlement can be seen from Figure 11, from 30 September 2014 a single point of settlement meter 1-1# and 1-2# gauge buried after start, settlement is velocity uniform, basically appears linear trend. To 18 December 2014, reaching the maximum range of the settlement plan, the settlement total of 320 mm, the daily average settlement is about 4 mm. Single-point settlement plan 2-1# and 2-2# after the November 5th, 2014 buried completely, since the upper construction speed, load increased rapidly, settling velocity large, mid and late December 2nd, 2014, 2# settlement gauge reaches the maximum range, settling a total of 320 mm, the daily average settlement is about 8 mm. The 1-2# settlement meter sedimentation rate stabilized at the end of December, the rate from the previous day, 2.5 mm, reduced to less than a day 0.5 mm. Single-point settlement plan 1-3# (2-3# damaged during construction) from December 19th, 2014 buried, since the upper construction speed, load increased rapidly, settling velocity large, rapid settlement of 80 mm, daily average settlement is about 2.5 mm. Mid to late 2015, the construction close to

the winter break, filling slowed down, settling velocity decreases, the rate from the previous day, 2.5 mm, reduced to less than 0.5 mm a day, the settlement tended to be stabilized. Considering the level of displacement, it is recommended not to load the top, needs further observation analysis. Single-point settlement plan and after 1-4# and 2-4# from 3 January 2015 buried complete, single-point settlement plan since the top load increased rapidly, greater sedimentation rate, around January 16, 2015, Settlement of a total of 40 mm, the daily average settlement is about 4 mm. After settling meter mid to late sedimentation rate stabilized, the rate from the previous day, 4 mm, reduced to about 0.6 mm per day.

Combined with field of indoor and outdoor soil tests and displacement crest subsidence monitoring shows that about 50% to 60% of the original amount of the total settlement of foundation settlement, while filling body mainly consists of strongly weathered sandy mudstone and silty compacted clay whose compaction is 0.95, the basic control moisture content is between 13% to 18%, indicating that if the original ground handled in compentently, the loading initial of high fill will have a lot of settlement. According to the original topography filling body construction in different areas, it is impossible for design of filling height and degree of compaction to keep consistency, resulting in large differential filling settlement, slope displacement will also change unevenly; and the fill thickness every 10% increase, degree of compaction will be reduced by 1% to 3%, the settlement after construction is more than 10%, particularly apparent from Figure 11, the high-fill foundation soil or settlement after construction and filling soil velocity rate take on non-linear relationship, fill velocity rate increases 10%, post-construction settlement will increase more than 30%, some severe situation will lead to a large deformation, result in tension crack, and induce landslides.

5 CONCLUSIONS

For complex topography, large area and large cubic quantity of earth-rock fill, special soil conditions of project of high fill soil conditions, in order to fill the study blank of its deformation and stability, it is need to process in situ monitoring and longer-term monitoring, remote wireless monitoring system can be applied to all similar projects. The study found that: 1) the original foundation settlement amount is about 50%∼60% of total settlement, if the original foundation treatment is unqualified, high fill loading early will produce a large number of settlement. 2) fill body is construct in different regions according to the original terrain, filling height and degree of compaction are impossible to keep consistent with design, differential settlement caused by filling body itself is larger, the slope displacement also will result in a change to the uneven. 3) fill thickness, every 10% increase, compaction could reduce by 1%∼3%, post-construction settlement increases more than 10%; Fill rate increases by 10%, the post-construction settlement will increase more than 30%.

According to the remote wireless monitoring results, combined with the indoor and outdoor test, in view of the airport construction and operation safety, Suggestions: 1) the arrangement of horizontal vertical blind ditch at base of slope, strictly processing the rise of ground water caused by high fill; 2) hierarchical compaction backfill as strictly control water content, height of virtual filling and compaction, according to different slope, it can appropriately adding geotextile or reinforced belt; if vibration compaction cannot reach the requirements of the compactness, using 150 t.m compaction reinforcement, until qualified a layer of backfill layer; The rest fill each 6 m high with 200 t.m compaction reinforcement. 3) paying attention to the new and old lap surface processing, the overlap between construction blocks to ensure enough lap length, lap on the surface of the dynamic compaction must be deal with up to standard.

REFERENCES

Angeli M G, Pasuto A & Silvano S. 2000. A critical review of landslide monitoring experiences. *Q. J. Engineering Geology* 55(3): 133–147.

Au S W. 1998. Rain-induced slope instability in Hong Kong. *Q. J. Engineering Geology* 51(1): 1–36.

Bao C G & Zhan L T. 2006. Relationship between unsaturated soil behavior and engineering problems. *Chinese Journal of Geotechnical Engineering* 28(2): 129–136.

Bhasin G, Grimstad E. & Larsen J O, et al. 2002. landslide hazards and mitigation measures at Gangtok, Sikkim Himalaya. *Q. J. Engineering Geology* 64(4): 351–368.

Cao G X. 2011. Study on post-construction settlement of high fill foundation in mountains airport, Ph. D. Beijing: Tsinghua University.

Chen Z H. 2014. On basic theories of unsaturated soils and special soils. *Chinese Journal of Geotechnical Engineering* 36(2): 201–272.

Cooper M R, Bromhead E N & Petley D J, et al. 1998. The Selbome cutting stability experiment. *Geotechniqu*e 48(1): 83–101.

Corominas J. 2000. Measurement of landslide displacements using a wire extensometer. *Q. J. Engineering Geology* 55(3): 149–166.

Franks C A M. 1999. Characteristics of some rainfall-induced landslides on natural slopes, Lantau Island, Hong Kong. *Q. J. Engineering Geology* 32(3/4): 247–259.

Li A G, Yue Z Q & Tan G Q, et al. 2003. Design and installation of comprehensive instrumentation system for slope in Hong Kong. *Chinese Journal of Rock Mechanics and Engineering* 22(5): 790–796.

Li T B, Liu J & Ren Y, et al. 2012. Sliding mechanism of high-fill slope with pre-reinforced piles at Pan ZhiHua airport. *Journal of Engineering Geology* 20(5): 723–731.

Liu H, Li P F & Zhang Z Y. 2005. Prediction of the post-construction settlement of the high embankment of Jiuzhai-Huanglong airport. *Chinese Journal of Geotechnical Engineering* 27(1): 90–93.

Engineering applications

This page intentionally left blank

Unsaturated Soil Mechanics—from Theory to Practice – Chen et al. (Eds)
© 2016 Taylor & Francis Group, London, ISBN 978-1-138-02921-7

Comparisons between the measured and predicted resilient modulus of subgrade Red clay using a SWCC based model

W.L. Zou, J.F. Zhang & Y.L. Li
College of Civil Engineering, Wuhan University, Wuhan, China

S.K. Vanapalli & H.Y. Tu
Department of Civil Engineering, University of Ottawa, Ottawa, Ontario, Canada

J. Zhang
Wuhan Hanyang District Housing Security and Management Bureau, Wuhan, China

ABSTRACT: Red clays are widely distributed in mountainous regions of various provinces in China; namely, Yunan, Guizhou, Jiangxi, Hunan, and Guangdong. These clays are used as subgrade material for pavements in spite of their unfavorable properties because of lack of other favorable soils in these regions. In recent years, the resilient modulus, M_R of subgrade soil, which is a mechanistic property, has been used as key parameter in the rational design of pavement structures. Several studies in the literature established that the matric suction, ψ_m of unsaturated subgrade soil has a significant influence on the M_R. A series of dynamic triaxial compression tests are conducted on the compacted Red clay specimens from Chenzhou, Hunan Province, China to determine the various factors that influence the M_R. Based on the regression analyses on the testing data, a model has been proposed in this paper for predicting the variation of the M_R of Red clay with respect to ψ_m, using the Soil-Water Characteristic Curve (SWCC) as a tool taking account of the influence of stress state (i.e. confining stress σ_3, and deviator stress, σ_d).

1 INTRODUCTION

Resilient modulus, M_R is defined as the ratio of the applied deviator stress to the resilience or recoverable strain. The M_R value is calculated from the slope of stress-strain relationship during unloading stage, which represents instantaneous pulse loading that occurs as vehicles pass over a pavement. Seed et al. (1962) introduced this term and presented its relationship with fatigue damage in asphalt pavements. During the last two decades, M_R has used as a mechanistic material property in the structural analysis and design of pavements (AASHTO 1993, NCHRP 2004). According to the study results from Darter et al. (1992) the M_R has a significant influence on the thickness of the base course and asphalt layers of pavement structures.

In order to estimate reliable M_R values which are representative of field conditions, several investigators proposed interpretation methods or prediction models considering the influence of environmental factors, such as the changes of moisture content (MC) and/or matric suction, ψ_m. For example, Khoury & Zaman (2004) measured M_R value both for a sandy soil and a clayey soil and provided a 3–*D* plot to describe the relationships among M_R, MC and ψ_m. Yang et al. (2005) conducted several studies on a compacted residual lateritic soil to determine the variations of M_R with respect to suction (i.e. from 10 to 11000 kPa) in addition to studying the influence of MC, which changed from optimum moisture content (OMC) to equilibrium moisture content (EMC). Kung et al. (2006) studied the influence of ψ_m on the M_R and the plastic deformation by performing laboratory tests on the unsaturated soil specimens, which were compacted on the wet–side of the OMC. The results of all these studies suggest that the M_R non-linearly increases as ψ_m increases, while the plastic deformation dramatically decreases at the same time. Kim & Kim (2007) tested two different soils and Nazzal & Mohammad (2010) tested four subgrade soils from Louisiana, USA. The test results of both these studies suggest that the M_R was not only related to stress state of soils, but also related to the physical properties of soils; which include OMC, MC, moisture content ratio (MC/OMC), dry density, degree of saturation, % sand (percent sand in particle size distribution curve), % clay, liquid limit and plasticity index. Khoury et al. (2009) investigated the variation of M_R with respect to the soil suction for a sandy soil, of which the post-construction MC changed along different paths (i.e. drying, wetting, drying after wetting and wetting after drying) from different initial MC. Cary & Zapata (2011) suggested incorporating matric suction as an independent stress state variable to improve the performance of the universal M_R prediction model (NCHRP 2004). Oh et al. (2012) investigated the relationship between the M_R value and the ψ_m

Table 1. Physical properties of the Red clay from Chenzhou.

Plastic limit %	Liquid limit %	Specific gravity	Free swell strain %	Optimum moisture content %	Maximum dry density kg/m^3
39.4	84.1	2.84	25	30.0	1502

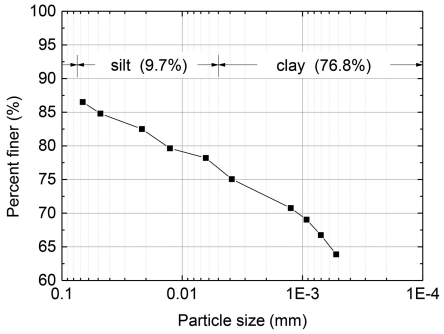


Figure 1. Grain-size distribution curve of Chenzhou Red clay.

(0–250 kPa) for the soil undergoing drying and/or wetting processes (soil specimens were compacted at OMC) and suggested a model for predicting the test results.

From the above investigations it can be seen that the recent research on the M_R has been directed to understand the influence of the physical properties of soils and the matric suction, ψ_m. One problem that affects the reliability of the proposed prediction models is that they were generally confined to the investigated soil types; therefore, these models have to be recalibrated or modified such that they would be valid for other soils. More recently, Han & Vanapalli (2015) proposed a simple model to predict the variation of M_R with respect to the soil suction, which was verified by 16 sets of data including 210 testing results and is promising for use in practice as it only requires conventional soil properties.

Red clays are widely distributed in mountainous regions in China, such as Yunan, Guizhou, Jiangxi, Hunan, and Guangdong Provinces. These soils typically exhibit high strength; however, they tend to soften due to their strong hydrophilic nature and crack when there is a decrease in the MC associated with shrinkage. Because of the unfavorable engineering properties, Red clay is considered to be a problematic soil for use in engineering practice. However, the Red clays or the modified Red clays with cement/lime/gravel have to be used as subgrade materials as other favorable soils are not available in these regions for using them as subgrade materials. In the present study, a series of repeated load triaxial compression tests were conducted to investigate the M_R of compacted Red clay, to better understand the pavement performance as several highways are being constructed in these regions. Based on the testing data, a model is proposed for predicting the M_R considering the influencing factors including ψ_m.

2 SOIL PROPERTIES

The typical soil properties of the Red clay from Chenzhou, Hunan Province, China that has been investigated for the present study are presented in Table 1. The grain-size distribution is presented in Figure 1. The color of this soil is maroon.

3 RESILIENT MODULUS TESTS

3.1 *Equipment*

The repeated load triaxial compression tests are conducted on the cylindrical Red clay specimens using a Dynamic/Stress-Path Soil Triaxial System manufactured by the American Geotechnical Consulting and Testing Systems (GCTS) Co. Ltd. The size of specimen is 70 mm in diameter and 140 mm in height.

The axial load was measured with a built-in 4.5 kN ±4.5 N load cell (model 2029 manufactured by American Tovey Co. Ltd) located between the cap and the chamber piston rod. This type of setup reduces the equipment compliance errors as well as the alignment errors. As the confining stresses, σ_3 applied for the M_R testing are low, air was used as the confining fluid to have a uniform control on the confining pressures instead of using a water head for confinement.

3.2 *Stress states/testing sequence*

Procedures laid out in AASHTO T292-91 were followed for conducting the repeated load triaxial compression tests. Before conducting the primary test sequence, stress conditioning at a given stress state had to be achieved to eliminate the irregularities on the top and bottom surfaces of the test specimen. This technique also assisted in minimizing the effects of initial imperfect contact between end platens and the test specimen. The conditioning process was performed by applying a repeated deviator stress, σ_d of 50 kPa on the specimens for 1000 loading cycles, along with application of a constant confining stress, σ_3 of 25 kPa. Once the plastic strain (i.e. axial permanent deformation) reached 5%, the stress conditioning was stopped.

Afterwards, four σ_d levels, namely, 35, 55, 75, and 105 kPa were sequentially applied on each specimen. For each σ_d, four σ_3 levels, namely, 60, 45, 30, and 15 kPa were applied in sequence. The cyclic loads (including σ_d and σ_3) for each loading sequence were repeated for 100 times.

The stress pulse shape was half-sine wave which was achieved using stress controlling mode. The loading duration for each repetition was 0.1 sec followed by 0.9 sec rest period leaving drainage valves open. The M_R values were calculated utilizing the average of the last 5 rebound strain values.

3.3 *Initial state of test specimens*

According to the Chinese Technical Specification for Construction of Highway Subgrade (CTSCHS, 2006),

Table 2. Predetermined initial states of the specimens.

Degree of compaction, K (%)	90	94	96	98
Moisture content, w_1 (%)	28	28	28	28
	30	30	30	30
	34	34	34	34
	36	36	36	36

the subgrade soils of a highway should be compacted at water contents close to their OMC and the degree of compaction, K should be between 90–96%, in the field depending on the grade of the highway and the locations of subgrade soils within the pavement structure. However, due to the influence of rainfall infiltration, groundwater flow and the changes associated with environmental factors, the MC of a clayey subgrade will gradually increase from OMC to EMC within 3–5 years after the highway is put into use. Typically, the EMC is about 20–30% greater than the plastic limit of the clayey soil. The MC between OMC and EMC is termed as the transition moisture content (TMC). The previous field investigations (Quintus & Killingsworth 1998) on 59 clayey subgrades, which have been in function for several years, indicated that the MCs of these clayey subgrades were located on the wet-side of OMC and ranged from OMC to OMC+7%, with most of the subgrades remaining in a state of unsaturated condition.

The K of the specimens used for this study were; 90, 94, 96 and 98%. The initial MC of the specimens, w_1, were OMC-2% (28%), OMC (30%), TMC (=OMC + 4% = 34%) and EMC (=OMC + 6% = 36%), respectively (see Table 2). When the M_R testing of each specimen was completed, its MC, w_2, was determined using three representative portions (top, middle, and bottom 45 mm of the specimen). The average of the MCs of the three values is used in the interpretation of the results.

4 TEST RESULTS AND ANALYSES

4.1 *Effect of σ_d and σ_3 on M_R*

Figure 2 shows the change of the relationship between the M_R and σ_d with the change of σ_3 under the same initial MC, $w_1 = 30\%$ with different K values ranging from 90 to 98%. The M_R increased as the σ_3 increased. For example, for the specimens with the K of 96%, at the four repeated σ_d levels, 35, 55, 75, 105 kPa, the increment of M_R was between 10.72 and 18.34% as the σ_3 increased from 15 to 60 kPa. While the M_R decreased with an increase in the cyclic loads, σ_d. For example, for the specimens with the K of 96%, at the four σ_3 levels, 60, 45, 30, 15 kPa, the decrease of the M_R was between 7.7 to 23.9% as the σ_d increased from 35 to 105 kPa.

4.2 *Effects of K and MC on M_R*

Figure 3 shows the change of the relationship betwe en the M_R and the w_2 with the change of K. The stress state

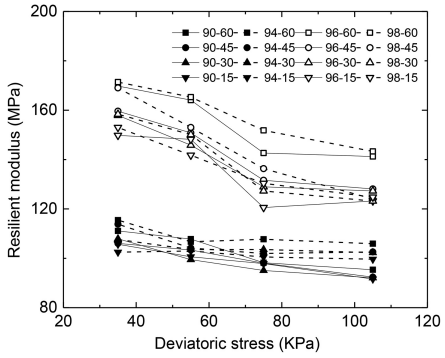


Figure 2. Relationships between M_R and σ_d (Note: in the marker "90–60", numbers 90 and 60 respectively denote the K of 90% and the σ_3 of 60 kPa).

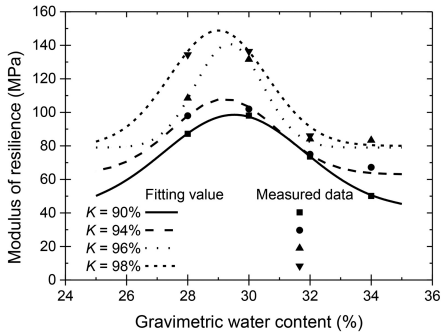


Figure 3. M_R with respect to gravimetric MC relationship.

of the specimens for all the tests was the same level (i.e. $\sigma_d = 75$ kPa and $\sigma_3 = 45$ kPa). It can be observed from Figure 3 that the M_R increased with an increase in the K. When the K increased from 94% to 96%, the M_R showed a significant increase; however for K values greater than 96%, the increase of M_R was not significant. For example, for the soil specimens with the $w_2 = 30.36\%$ (corresponding to the initial MC, w_1 = OMC = 30%), the M_R increased from 105 to 130 MPa as the K increased from 94% to 96%. However, the M_R only increased 5 MPa when the K increased from 96% to 98%. These results suggest a K value of 93%–94% is a better choice of Red clays subgrade.

It can be also seen that the specimens had the maximum M_R values at MCs close to 29%, which is on the dry side of the OMC and close to the OMC (30%). The specimens had the lowest M_R values at the lower ends of the dry and the wet sides of the OMC and the specimens had the intermediate M_R values at the OMC.

The Mechanistic Empirical Pavement Design Guide (NCHRP 2004) adopted the generalized M_R constitutive model shown in Equation (1).

$$\frac{M_R}{P_a} = k_1\left(\frac{\theta}{P_a}\right)^{k_2}\left(\frac{\tau_{oct}}{P_a}\right)^{k_3} \quad (1)$$

where, M_R = resilient modulus; θ = bulk stress; τ_{oct} = octahedral shear stress; P_a = normalizing stress equals to atmospheric stress, $P_a = 101.4$ kPa; and k_1, k_2, and k_3 = coefficients of the tested material.

The k_1 describes the stiffness of a material; the k_2 describes the hardening (higher modulus) of a material as the bulk stress increases; and k_3 describes the softening of a material (lower modulus) as the shear stress increases.

The M_R of subgrade soil does not represent its strength but stiffness. Equation (1) indicates for certain soil, when the stress states (σ_d, σ_3) is constant, the change of the k_1 will directly influence the M_R. The k_1 is proportional to the stiffness of a material. Therefore, both k_1 and M_R, will increase as the effective stress increases. The effective stress of unsaturated soils can be determined using the Bishop equation (Bishop 1959) shown in Equation (2).

$$\sigma' = \sigma - u_a + \chi(u_a - u_w) \tag{2}$$

where, σ' is effective stress; σ is total stress; u_a is pore-air pressure; u_w = is pore-water pressure; $(u_a - u_w)$ is matric suction; and χ is effective stress parameter.

In Equation (2), when the total stress is constant, the effective stress is determined by both the matric suction $(u_a - u_w)$ and the effective stress parameter χ. The two variables have different relations as MC increases. χ is zero for dry soils and increases to unity for saturated soils, which explains the low values of M_R obtained at the lower end of the dry side of OMC. While the matric suction is extremely high at the low MC, it decreases to zero for saturated soils, which results in a significant decrease in stiffness on the wet-side of OMC. Although the two variables have opposite trends, there exists a MC value at which their combined effect is maximum; consequently, at this value the stiffness peaks. This MC differs with the type of cohesive soils considered, but it occurs at the dry side of the OMC (Nazzal & Mohammad 2010).

5 A MODEL FOR PREDICTING THE RESILIENT MODULUS

The AASHTO testing procedure for determining the M_R is complex and is time-consuming. For this reason, testing procedures have not been widely implemented in practice. Many agencies prefer to use other approaches to estimate the M_R. For example, for small pavement projects, the California Bearing Ratio (CBR) test is performed and an empirical correlation is used to convert CBR to M_R (Kim & Kim 2007). CBR, however, is a property derived from static tests that cannot account for the actual response of the subgrade under the dynamic loads of moving vehicles. Therefore, a simple model that is capable of predicting M_R would be valuable for the design and analysis of a pavement structure.

The experimental results undertaken in the present study for Red clays suggest that many factors, including the σ_3, σ_d, K, and MC, have significant effects on the M_R. Therefore, these factors should be considered as variables to reliably predict the M_R. Since the soil-water characteristic curve (SWCC) represents the relationship between MC and ψ_m, the SWCC can be used as a tool for predicting the variation of M_R with respect to matric suction, ψ_m by taking account the influences of other parameters on the M_R. The SWCCs of Chenzhou Red clay specimens with different K, which were measured using a pressure plate apparatus and the filter paper method are presented in Figure 4a.

As discussed earlier, Red clay dramatically shrinks with a decrease in the MC. Based on the experimental data, Zou et al. (2012) pointed out that for a contractive soil, the volume shrinkage under dehydration path had noticeable influence on its SWCC expressed with volumetric moisture content, θ or degree of saturation, S_r. The comparison of SWCCs of Chenzhou Red clay specimens with different K between before and after considering the volume correction of the specimens are shown in Figure 4b.

According to the variation trend of the measured SWCC data of Chenzhou Red clay (see Fig. 4a), the V-G model (Eq. 3) can be used to fit these data.

$$\frac{w - w_r}{w_s - w_r} = \frac{1}{[1 + (a\psi_m)^n]^m} \tag{3}$$

where, w: actual moisture content; w_r: residual moisture content; w_s: saturated moisture content; ψ_m: matric suction; and a, m and n: fitting parameters.

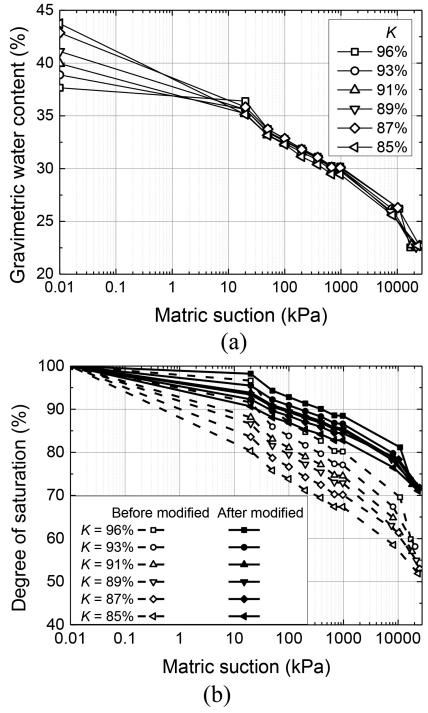


Figure 4. SWCCs of Chenzhou Red clay specimens with different K: (a) gravity MC vs ψ_m; (b) comparison between before and after volume correction.

Based on the measured w_2 value of each specimen after its M_R test had been completed, the fitting parameters (a, n, m) corresponding to the initial void ratio (e_0), the ψ_m of each specimen can be calculated by using Equation (3). Table 3 presents the back calculated values of ψ_m for the specimens with the same K of 96% (corresponding to the initial void ratio, $e_0 = 0.97$). With respect to the χ value in the Bishop's effective stress formula for unsaturated soils (Bishop 1959), the soil can be regarded as fully saturated when the ψ_m is less than the air entry value, ψ_e, and χ equals to 1, corresponding to the Terzaghi's effective stress formula. For unsaturated soil, Khalili & Khabbaz (1998) found that χ is closely related to (ψ_m/ψ_e); and proposed the Equation (4) based on the testing results of 14 different types of soils including silts, sandy clays and clays (Khalili et al. 2004).

$$\begin{cases} \chi = \left(\dfrac{\psi_m}{\psi_e}\right)^{-0.55}, & if \quad \psi_m > \psi_e \\ \chi = 1, & if \quad \psi_m < \psi_e \end{cases} \tag{4}$$

where: χ represents the contribution of a part of matric suction to effective stress; ψ_e can be determined from the SWCC of soil. In this study, the value of ψ_e for the Red clay specimen with the K of 96% is 52.67 kPa.

By observing the relationships between M_R and w_2 (see Figure 3), a Gaussian function was selected to fit these curves. This is achieved by combining Eqs (3) and (4), and a M_R prediction model for the Red clay with high liquid limit, which reflects the influence of ψ_m, can be presented in Equation (5).

$$M_R = A + Be^{\left[-\left(\frac{\ln(\chi\psi_m)-C}{D}\right)\right]} \tag{5}$$

where A, B, C and D are the fitting parameters depending upon the stress states of subgrade soils. According to the testing data of Chenzhou Red clay in this study, A and B can be expressed using Eqs. (6) and (7), respectively.

$$A = 100.40 + 0.17\sigma_3 - 0.42\sigma_d \tag{6}$$

$$B = 1.09\sigma_3 + 190.23 \tag{7}$$

The measured values of C only vary between 6.09 and 6.31, and those of D vary between 0.53 and 0.80. Thus, C and D take as the average of their respective measured data, i.e. 6.24 and 0.73, respectively. Based on the above analysis results, a M_R predictive model (Eq. 8) for Chenzhou Red clay can be obtained by substituting Equation (6), Equation (7), $C = 6.24$ and $D = 0.73$ into the Equation (5).

$$M_R = (100.40 + 0.17\sigma_3 - 0.42\sigma_d) + (1.09\sigma_3 + 190.23)e^{\left[-\left(\frac{\ln(\chi\psi_m)-6.24}{0.73}\right)\right]} \tag{8}$$

Figure 5 shows the reasonably good comparison between the measured values of M_R and the predictive curves obtained using Equation (8), with the R-square ranging from 0.962 to 0.998. As it can be observed from Figure 5, the M_R values of the Chenzhou Red clay at different stress states are predicted to reach the maximum values at $\ln(\chi\psi_m) \approx 6.25$, which corresponds to gravity moisture content of about 29%, a value consistent with one obtained from Figure 3 (refer to section 4.2). Since ψ_m can obtained from the MC using SWCC, the proposed M_R model, which introduces the ψ_m as a variable, can be effectively used to predict the variation of the M_R of Red clay with high liquid limit with respect to matric suction for subgrade soils.

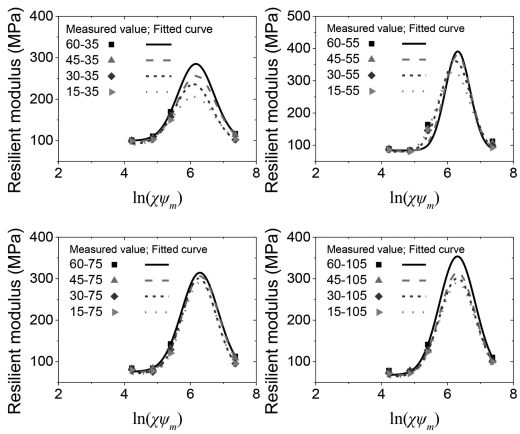


Figure 5. Comparison between the prediction and the measured values of M_R (Note: in the marker "60–35", numbers 60 and 35 respectively denote σ_3 of 60 kPa and repeated σ_d of 35 kPa).

Table 3. VG model parameters and matric suction of the Red clay with $K = 96\%$.

K (%)	w_1 (%)	w_2 (%)	e_0	w_r (%)	w_s (%)	Model parameters a	n	m	ψ_m (kPa)	χ
96	28	27.59	0.97	18.00	34.23	0.019	0.978	0.086	100639.48	0.0157
96	30	30.36	0.97	18.00	34.23	0.019	0.978	0.086	1281.96	0.1728
96	32	31.57	0.97	18.00	34.23	0.019	0.978	0.086	385.75	0.3345
96	34	33.88	0.97	18.00	34.23	0.019	0.978	0.086	93.22	0.7305

6 CONCLUSIONS

In the present study, a series of repeated load triaxial compression tests were conducted on several Red clay specimens to investigate the relationships between the M_R and the main influencing factors, namely, σ_d, σ_3, MC and K. By means of the SWCC of the Red clay, a M_R predictive model considering the influence of matric suction was proposed. The following can be drawn from this study.

(1) The M_R of the Red clay increased as the σ_3 increased, while decreased as σ_d increased.
(2) The M_R increased with an increase in the K. For the investigated Red clay specimens compacted on the dry side of OMC under the same K, the M_R increased with an increase in the MC. However, for specimens compacted on the wet side of OMC, the M_R decreased with an increase in the MC. However, the M_R of the specimens compacted on the dry side of OMC but close to the OMC shows increases due to the influence of the ψ_m on the effective stress of the unsaturated Red clay specimens.
(3) A M_R predictive model for Red clay with high liquid limit, which comprehensively takes into account of the influence of the matric suction and the stress state, was proposed. There is a good comparison between the measured values of M_R and the predicted curves obtained using the model with an average of R-square of 0.988. More research studies on the prediction model of M_R of the modified Red clays with cement/lime/gravel are required for the purpose of engineering practice applications.

ACKNOWLEDGMENTS

This research was funded by National Natural Science Foundation of China (NSFC, Grant No. 51479148) and the Western Traffic Science and Technology Project of Ministry of Transportation of China (Project No. 2011318785760). The authors would like to express their thanks to all who provided assistance to this project.

REFERENCES

AASHTO. 1993. AASHTO Guide for Design of Pavement Structures. *American Association of State Highway and Transportation Officials*, Washington, D.C.

AASHTO. 1992. Designation T292-91: *Standard Method of Test for Resilient Modulus of Subgrade Soils and Untreated Base/Sub-Base Materials.* American Association of State Highway and Transportation Officials. Washington, D.C.

Bishop, A.W. 1959. The principle of effective stress. *Teknisk Ukeblad* 106(39): 859–863.

Cary, C.E. & Zapata, C.E. 2011. Resilient modulus for unsaturated unbound materials. *Road Materials and Pavement Design* 12(3): 615–638.

CTSCHS. 2006. Chinese Technical Specification for Construction of Highway Subgrade. China Communication Press, Beijing.

Darter, M.I., Elliot, R.P., and Hall, K.T. 1992. Revision of AASHTO pavement overlay design procedures. Appendix: Documentation of design procedures. National Cooperative Highway Research Program Study Rep. No. 20-7, TRB, National Research Council, Washington, D.C.

Han, Z. & Vanapalli, S.K. 2015. Model for predicting the resilient modulus of unsaturated subgrade soil using the soil-water characteristic curve. *Canadian Geotechnical Journal* (in press).

Khoury, N.N. & Zaman, M.M. 2004. Correlation between resilient modulus, moisture variation, and soil suction for subgrade soils. *Transportation Research Record, 1874*. Transportation Research Board, Washington, D.C., 99–107.

Khoury, N., Brooks, R., Zaman, M.M. & Khoury, C.N. 2009. Variations of resilient modulus of subgrade soils with post-compaction moisture contents. *Transportation Research Record. 2101*. Transportation Research Board, Washington, D.C. 72–81.

Kim, D. & Kim, J.R. 2007. Resilient behavior of compacted subgrade soils under the repeated triaxial test. *Construction and Building Materials* 21(7): 1470–1479.

Khalili, N. & Khabbaz, M.H. 1998. A unique relationship of chi for the determination of the shear strength of unsaturated soils. *Geotechnique* 48(5): 681–687.

Khalili, N., Geiser, F., & Blight, G.E. 2004. Effective stress in unsaturated soils: review with new evidence. *International Journal of Geomechanics* 4(2): 115–126.

Kung, J.H.S, Lin, H.D., Yang, S.J., & Huang, W.H. 2006. Resilient modulus and plastic strain of unsaturated cohesive subgrade soils. *The 4th International Conference on Unsaturated Soils. ASCE, Arizona*, Vol. 1: 541–552.

Nazzal, M.D. & Mohammad, L.N. 2010. Estimation of Resilient Modulus of Subgrade Soils for Design of Pavement Structures. *Journal of Materials in Civil Engineering* 22(7): 726–734.

NCHRP. 2004. Guide for Mechanistic-empirical Design of New and Rehabilitated Pavement Structures. Final Rep. No. NCHRP 1-37A (submitted by ARA, Inc., ERES Consultants Division), National Research Council, Transportation Research Board, Washington, D. C., http://www.trb.org/mepdg/guide.htm (Jan. 2, 2008).

Oh, J.H., Fernando, E.G., Holzschuher, C., & Horhota, D. 2012. Comparison of resilient modulus values for Florida flexible mechanistic-empirical pavement design. *International Journal of Pavement Engineering* 13(5): 472–484.

Quintus, H.V., & Killingsworth, B. Analyses Relating to Pavement Material Characterizations and Their Effects on Pavement Performance. *Publication FHWA-RD-97-085*, FHWA, U S Department of Transportation, 1998.

Seed, H.B., Chan, C.K., & Lee, C.E. 1962. Resilience characteristics of subgrade soils and their relation to fatigue failures in asphalt pavements. *Proceedings of the International Conference on the Structural Design of Asphalt Pavements*, Michigan, USA, 611–636.

Yang, S.R., Huang, W.H., & Tai, Y.T. 2005. Variation of resilient modulus with soil suction for compacted subgrade soils. *Transportation Research Record. 1913*. Transportation Research Board, Washington, D.C., 99–106.

Zou, W.L., Zhang, J.F., & Wang, X.Q. 2012. Volume correction and soil-water characteristics of remodeling expansive soil under dehydration path. *Chinese Journal of Geotechnical Engineering* 34(12): 2213–2219. (in Chinese)

Unsaturated Soil Mechanics—from Theory to Practice – Chen et al. (Eds)
© 2016 Taylor & Francis Group, London, ISBN 978-1-138-02921-7

Application of MPK framework to interpret volume change behavior of compacted unsaturated soils

A. Abeyrathne, T. Islam, J. Kodikara & H. Bui
Monash University, Melbourne, Victoria, Australia

ABSTRACT: The attention for unsaturated soils has grown significantly over the last four decades as a result of numerous engineering problems encountered in field where the geotechnical engineering design based on classical saturated soil mechanics principles have proven to be difficult. As a result of the significant developments in theoretical analyses and experimental investigations, by now there are number of models which can define the unsaturated soil behavior reasonably satisfactorily. However, the applicability of most of the well-defined theoretical models in routine engineering practice is still problematic primarily due to difficulty in determining input properties. In contrast, new (MPK) framework introduced by Kodikara (2012) is based on the traditional compaction curve and relatively simple and practical in defining compacted unsaturated soil behavior. The current paper presents the application of this framework to interpret the volume change behavior of compacted unsaturated soils and its validation under different state path test results.

1 INTRODUCTION

More than one third of the earth's surface is arid or semi-arid where the soils near the surface are in dry condition, exhibiting varying characteristics in comparison to saturated soils. This condition of soil is usually referred to as unsaturated, where soil particles, air and water co-exist in one system. The presence of air and water as a mixture in void spaces affects both the mechanical and hydraulic behavior of unsaturated soils in such a way that the application of classical saturated soil mechanics principles based on the use of effective stress becomes challenging. Until very recently, the behavior of unsaturated soils was ignored in common engineering practice and they were treated as saturated soils. This is because unsaturated soil behavior is very complex, and the associated theoretical and experimental difficulties have significantly delayed the development of a good set of principles to explain unsaturated behavior.

However, with increasing opposition in engineering design to the assumption of full saturation even when the soil is unsaturated, research has been directed to modelling the mechanical behavior of unsaturated soils. Since the 1950s, significant developments have been made in understanding unsaturated soil behavior with varying degrees of success, and there are now a number of constitutive models capable of accurately predicting unsaturated soil behavior.

The common approach is to model unsaturated soil behavior in terms of four independent stress state variables: mean net stress, deviator stress, suction and specific volume. Alonso et al. (1990) proposed the first elasto-plastic constitutive model to define the mechanical behavior of unsaturated soils, known as the Barcelona Basic Model (BBM), in the net stress – suction space which was then followed by many subsequent researchers such as Wheeler and Sivakumar (1995). However, the choice of state variables varied with the progression of research, and different efforts were made to describe the behavior of unsaturated soils through alternative pairs of state variables. These deviations from most commonly used state variables attempted to address the imperfections with the existing models, such as difficulties in practical application. One such attempt is the new MPK framework introduced by Kodikara (2012) to model compacted unsaturated soil behavior in net stress – moisture ratio space.

The net stress and moisture ratio, which is the product of gravimetric moisture content and the specific gravity (giving the ratio of volume of water divided by volume of solids), have been identified as a potential pair of state variables, and the MPK framework for volumetric behavior has shown promising signs to date.

In this context, the present paper reviews the application of the MPK framework to interpret the volume change behavior of compacted unsaturated soils.

2 VOLUME CHANGE BEHAVIOUR OF COMPACTED UNSATURATED SOILS

The volume change behavior of unsaturated soils greatly depends on the method of formation, as the soil structure has a significant influence on its behavior. In practice, soils can be unsaturated when 1) the water table is considerably lower than the ground

level and evapo-transpiration exceeds the rainfall, 2) soils are compacted in unsaturated state for construction purposes such as embankments, behind retaining walls and beneath foundations and 3) gas is generated within the soil by biological activities. In addition, for compacted unsaturated soils the soil structure varies considerably, depending on the method of compaction, the amount of compaction and the compaction water content. Since many engineering problems encountered in practical situations are in some way related to compacted unsaturated soils, accurate prediction of compacted unsaturated soil behavior is of vital practical concern.

Usually, compacted unsaturated soils have high strength and low compressibility. However, under the influence of varying climate conditions, compacted unsaturated soils may suffer loss of strength and large deformations leading to catastrophic failures. One such example is the collapse settlement of the Beliche dam in Portugal, which resulted from one of the most distinctive features of unsaturated soil behavior, potential of swelling or collapse upon wetting (Alonso et al., 2005). Alonso et al. (1987) pointed out that most partially saturated soils may undergo either swelling or collapse upon wetting, if the confining stress is sufficiently low (swelling) or high (collapse).

In general, the mechanical behavior of unsaturated soils is strongly influenced by both pore air pressure (u_a) and pore water pressure (u_w), and the volume change is therefore defined by the changes in both stress and matric suction (the difference between pore air pressure and pore water pressure). The presence of matric suction in unsaturated soils makes its behavior complex and difficult to address by classical saturated soil mechanics principles, as the changes in suction do not have the same effect as changes in the applied stresses, especially at low saturations.

3 MPK FRAMEWORK

The basic concept of the MPK framework is that there exists a state boundary surface in void ratio (e), moisture ratio (e_w) and net stress (p) space, referred to as the Loading Wetting State Boundary Surface (LWSBS), depicting the loosest states that compacted unsaturated soil can take from loading and (or) wetting paths. This boundary surface can be produced by a family of compaction curves at different compaction stresses.

The LWSBS in (e, e_w, p) space is shown in Figure 1, where the constant net stress lines represent the compaction curves and the line joining the optima of each compaction curve is referred to as the Line Of Optimums (LOO). However, as shown in Figure 1, in the wet side of LOO the typical compaction curve characterizes the (water) undrained compression path in which it is hard to achieve full saturation. Therefore, in the construction of LWSBS for the wet side of LOO, curves corresponding to drained paths have been used. The intersection of LWSBS with the saturation

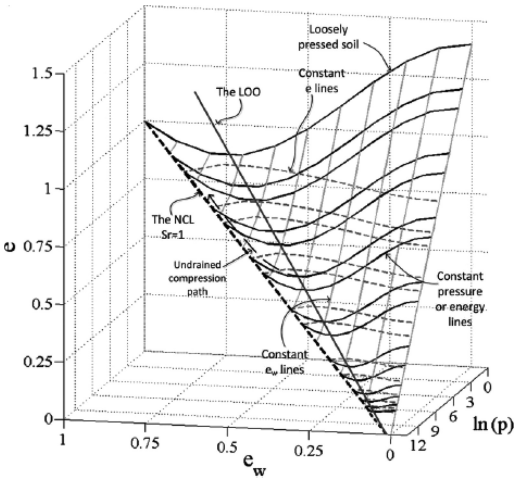


Figure 1. The LWSBS in $e-e_W-\ln(p)$ (adapted from Kodikara et al., 2012).

plane ($e = e_w$ plane) gives the normally consolidated line (NCL) for saturated soils.

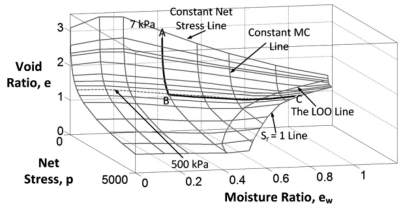
The LOO is one of the important features of the LWSBS concept, which demarcates the boundary of the continuous air phase. In the MPK framework it is postulated that on the dry side of LOO, the air phase is continuous and therefore air is free to drain during loading and wetting. In contrast, on the wet side of LOO air is trapped within the water menisci. In addition, it is considered that the effective stress principle is readily applicable in the region between the LOO and the NCL. The effective stress may be calculated from $p' = p + S_r s$, where s is the matric suction and S_r is the degree of saturation, which indicates that the void ratio would be a minimum at LOO corresponding to its maximum effective stress.

The LWSBS concept is capable of defining different volume change behaviors of compacted unsaturated soils under loading and/or wetting, including yielding due to loading, collapse and/or swelling due to wetting, dependence of collapse potential on operational stress, swelling pressure development, and change in yield pressure due to wetting. Some of these behaviors are validated using the MPK framework in Section 4.

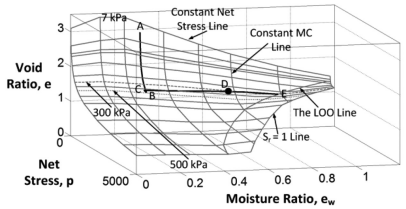
4 EXPERIMENTAL RESULTS

4.1 *Validation of the framework under one dimensional and isotropic compression*

Numerous laboratory experiments were carried out on kaolin soil under one-dimensional (K_o condition) and isotropic compression to develop the LWSBS. In addition, different state path validation tests were performed to examine whether the volumetric behavior follows the principles outlined by the framework. Kaolin, known by the trade name Ecalite, is commercially available white colored (china) lightly reactive



(a) 15.77% moisture content (e_w=0.418) loaded to 500 kPa and then wetted to 38.1% moisture content (e_w=1.01)



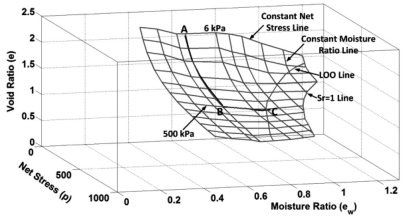
(b) 11.88% moisture content (e_w=0.315) loaded to 500 kPa and then unloaded to 300 kPa and then wetted to 34.951% moisture content (e_w=0.926)

Figure 2. Different state path validation tests on kaolin soil under one-dimensional (K_o condition) (Note that net stress is the vertical net stress).

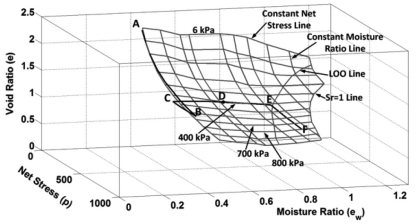
clay. The geotechnical properties of this soil are presented in Islam (2015). Four validation experimental results are presented here, two for K_o condition and two under isotropic condition. It should be noted that the LWSBS under isotropic compression is constructed only for the operational region of the moisture ratios, ranging between degrees of saturation of 20% to 100%.

Figures 2(a) and 2(b) show one-dimensional loading/wetting and loading/unloading/wetting state path validation test results, while Figures 3(a) and 3(b) present isotropic loading/wetting and loading/ unloading/wetting/loading state path validation test results. Figures 2(a) and 3(a) show state paths where the soil specimens were mixed to specific water contents from the dry state as for the compression tests, compressed to certain stress levels and then wetted at that stress level. According to the MPK framework, in these cases, the state paths should follow the constant moisture ratio line on the LWSBS from nominal stress to the compressed stress (the AB line in Figures 2(a) and 3(a)). Subsequently, during wetting, they should follow the constant net stress line on the LWSBS to the final moisture content (the BC line in Figures 2(a) and 3(a)). It is clear from Figures 2(a) and 3(a) that the loading/wetting state paths follow the path predicted by the MPK framework.

On the other hand, Figures 2(b) and 3(b) present state paths where specific moisture content soil specimens were compressed to certain stress levels and then unloaded to lower stress levels and then wetted at that stress level. It is evident that the state paths followed the constant moisture ratio lines on the LWSBS from nominal stress to the compressed stress and then moved to the unloading space inside the



(a) 25.0% moisture content (e_w=0.66) loaded to 500 kPa and then wetted to 33.2% moisture content (e_w=0.88)



(b) 17.1% moisture content (e_w=0.45) loaded to 700 kPa and then unloaded to 400 kPa and then wetted to 33.6% moisture content (e_w=0.88) and then loaded again to 800 kPa

Figure 3. Different state path validation tests on kaolin soil under isotropic condition (Note that the net stress is the all-round net stress).

LWSBS during unloading. Subsequently, during wetting, they swelled towards the previously compressed net stress contour of the LWSBS and then started to compress by following the LWSBS after intercepting it (point D in Figures 2(b) and 3(b)). Moreover, as Figure 3(b) shows, after following the LWSBS along the wetting path, the soil compressed again to the new stress level during the second loading stage following the new constant moisture ratio contour of the LWSBS. It is apparent that the loading/unloading/wetting state paths also followed the path, in agreement with the MPK framework.

The state path test results described above provide some evidence that the MPK framework can be used to define the volumetric behavior of compacted unsaturated soils under different loading, wetting or combination state paths with non-decreasing degrees of saturation. The results also verify some concepts of the framework under one-dimensional and isotropic loading conditions.

4.2 *Comparison of one-dimensional and isotropic LWSBSs*

Figure 4 shows the comparison of LWSBS constructed under one-dimensional compression and isotropic compression. As noted previously, since the LWSBS for isotropic compression has been generated only for a region of high practical concern, the comparison is limited to that region. It can be seen that the two LWSBSs are parallel, while the LWSBS for isotropic compression shown by dark color lines is located above the LWSBS for one-dimensional compression.

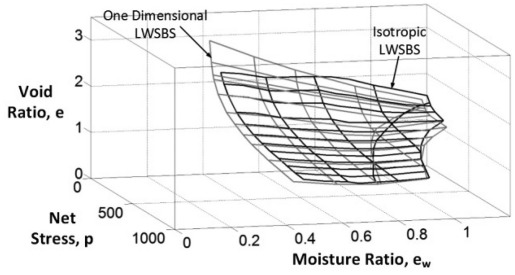


Figure 4. One-dimensional and isotropic LWSBSs in $e-e_w-p$ space.

All other features of the two LWSBSs are similar, both having approximately similar positions of the LOO.

This orientation of LWSBSs is acceptable, because for saturated soils the normal consolidation line (NCL) for isotropic compression will always lie above the NCL for one-dimensional compression, with both having a similar slope, and the same positioning of NCLs is evident in Figure 4 (Atkinson, 1978). Although $q'/p' = 0$ for isotropic compression, it is non-zero for one-dimensional compression, having the effect of deviator stress. Therefore, the soil will compress more under one-dimensional compression, achieving a lower void ratio when compared with an identical soil sample compressed at the same stress level under isotropic condition.

5 CONCLUSION

The results of different state path tests performed on compacted unsaturated kaolin indicate that the concept of LWSBS introduced in the MPK framework is capable of defining any volume change behavior resulting from loading and (or) wetting paths with non-decreasing degrees of saturation. LWSBSs constructed under different compression conditions, namely one-dimensional and isotropic, are in close agreement with the expected behavior with respect to saturated soils.

Since LWSBS can be constructed by simple constant moisture content compaction testing, which does not require specialized equipment or expertise for suction measurement and is common in engineering practice, the concept proposed by the MPK framework could significantly simplify the application of unsaturated soil mechanics in routine engineering practice. While the framework without suction can be applied to solve a number of practical problems, if the role of suction can be developed within the framework, it will complete the modelling framework, making it more general.

REFERENCES

Alonso, E., Gens, A. & Hight, D. Special problem soils. General report. *Proceedings of the 9th European Conference on Soil Mechanics and Foundation Engineering*, Dublin, 1987. 1087–1146.

Alonso, E. E., Gens, A. & Josa, A. 1990. A constitutive model for partially saturated soils. *Geotechnique,* 40, 405–430.

Alonso, E. E., Olivella, S. & Pinyol, N. M. 2005. A review of Beliche Dam. *Geotechnique,* 55, 267–285.

Atkinson, J. H. Bransby, P. L. 1978. *The mechanics of soils: an introduction to critical state soil mechanics,* London, McGraw-Hill Book Co.

Islam, T. 2015. *A study of volumetric behaviour of compacted clayey soils in the void ratio, moisture ratio and net stress space*, PhD thesis, Monash University, Australia.

Kodikara, J. 2012. New framework for volumetric constitutive behaviour of compacted unsaturated soils. *Canadian Geotechnical Journal,* 49, 1227–1243.

Wheeler, S. J. & Sivakumar, V. 1995. An elasto-plastic critical state framework for unsaturated soil. *Geotechnique,* 45, 35–53.

Unsaturated Soil Mechanics—from Theory to Practice – Chen et al. (Eds)
© 2016 Taylor & Francis Group, London, ISBN 978-1-138-02921-7

Behaviour of pipes subjected to fault movements in unsaturated soils using spring analysis

D.J. Robert
School of Civil, Environmental and Chemical Engineering, RMIT University, Melbourne, Australia

K. Soga
Department of Engineering, University of Cambridge, Cambridge, UK

ABSTRACT: The damage to pipelines caused by earthquake induced fault movement can be disastrous. Due to the fact that pipelines are generally spread over large geographical areas and exist in the form of a network, it is almost impossible to avoid active faults ruptures across which a huge body of soil can move relative to the pipe displacements during earthquakes. Recent large scale testing performed at Cornell University showed that significant amount of strains can be accumulated to fail the pipe at the intersection between the pipe and fault plane in the events of earthquake induced soil displacements. Pipes buried in unsaturated soils can enhance such risk of failure as the effect of suction could be detrimental in some sands as shown by Robert et al, 2010. In the current study, spring analyses were performed to investigate the behaviour of buried pipelines subjecting to strike-slip fault movements in dry as well as partially saturated soils. The spring model was first validated by comparing the computed results to the 3-D finite element analysis results as well as to the data produced from large scale experiments carried out at Cornell University, US. Analyses are further extended to investigate the effects of fault movements on pipes buried in partially saturated soils at different embedded depths in various soil types. The results revealed that spring analysis can predict realistic pipe deformation in dry and partially saturated soils when pipe does not possess excessive ovaling or buckling at the fault rupture.

1 INTRODUCTION

Pipelines for the transportation of water and fuels are very important for modern society. The vital role that they play in our present economy is reflected in the many thousands of kilometres of pipelines laid in onshore and offshore locations worldwide. They are often buried in the ground for protection and support, which also exposes them to ground movements that can induce unwanted loading and deformation. A pipeline network is often placed over large geographical areas, where it is difficult to avoid crossing faults. Past earthquakes such as those in Turkey (Kocaeli & Duzce, both in 1999) and Taiwan (Chi-Chi, 1999) offer numerous examples of pipe damage (Koseki et al., 1998; Takada et al., 2001). Case histories show that these pipes were subjected to significant deformations by earthquake-induced ground deformations, causing pipe failures either by buckling, wrinkling or joint failure/tensile cracking. Damage to even a minor part of a pipe can terminate the service of the entire pipeline network. Such disruption in services and operations can cause significant economic and social losses.

Several researchers have proposed methodologies to analyse a pipeline subjected to fault movements. Pioneering work was carried out by Newmark and Hall (1975), who proposed an approximate method to consider an underground pipeline that deforms in extension due to strike-slip fault displacement. This work was extended by Kennedy et al. (1977) to consider pipeline bending at constant curvature and non-uniform friction between the pipe and the surrounding soils. The proposed methodology was further enhanced by Wang and Yeh (1985), who considered pipe bending stiffness for assessing the pipe's ultimate bending capacity. An analytical methodology was also proposed by Karamitros et al. (2007) to compute axial and bending strains along the pipe with the aid of beam-on-elastic-foundation and elastic-beam-theories. More recently, Kokavessis and Anagnostidis (2006), Liu et al. (2008) and Vazouras et al. (2010) conducted numerical simulations to investigate pipeline responses under fault movements. For example, Kokavessis and Anagnostidis (2006) developed a finite element methodology to simulate buried pipe behaviour under permanent ground-induced actions, using contact elements to describe the soil–pipe interaction. Liu et al. (2008) conducted numerical simulations of pipelines crossing active faults through a shell finite element model to present distribution of axial

strains along the pipe, similar to a model developed by Karamitros et al. (2007). Vazouras et al. (2010) developed a simplified analytical model to illustrate the local buckling response of pipes using the behaviour from numerical simulations. Design guidelines (e.g., ASCE, 1984) recommend analyses of soil-pipe interaction by discrete springs specified in three directions (axial, horizontal and vertical directions).

In the current study, spring analyses were performed to investigate the behaviour of buried pipelines subjecting to strike-slip fault movements in dry as well as partially saturated soils. The spring model was first validated by comparing the computed results to the 3-D finite element analysis results as well as to the data produced from large scale experiments carried out at Cornell University, US. Analyses are further extended to investigate the effects of fault movements on pipes buried in partially saturated soils at different embedded depths in various soil types.

2 OVERVIEW OF LARGE SCALE TESTS

Large-scale soil-pipe interaction model experiments to investigate the behaviour of a buried pipe subjected to fault movement have been carried out at Cornell University (O'Rourke, 2007; O'Rourke et al., 2008). The experiments allowed the simulation of conditions similar to those in the field with detailed characterization and response measurements of the soil and pipe. The tests were performed mainly using high density polyethylene (HDPE) pipe, which was able to accommodate substantial abrupt ground displacements at strains and cross-sectional deformations well below those associated with pipe wall rupture and/or loss of serviceability. The soil used for the experiments was glacio-fluvial sand (referred to as Cornell sand in the present paper) with approximately 71% of siltstone by volume, fine-grained sandstone, shale, and limestone fragments, and 29% quartz grains. The mean grain size, of the soil was 0.67 mm, and the coefficient of uniformity, was 2.83. Figure 1 shows the split-box test basin used for the large scale testing.

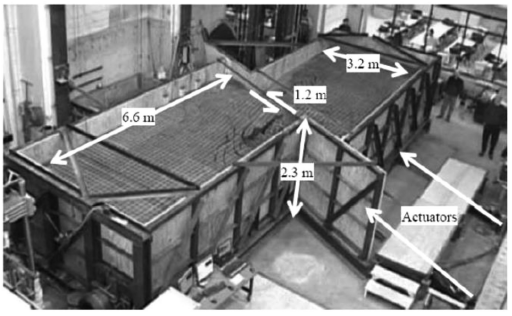


Figure 1. Large scale split box test basin at Cornell University (O'Rourke et al., 2008).

The results obtained from large scale tests revealed valuable findings. A zone of concentrated soil deformation was identified around the pipe. A significant passive rupture occurred adjacent to the front edges of the pipe along with the active zone formed by the collapse of the soil behind the pipe. The peak dimensionless loads were located in the same ASCE design curve, revealing that maximum load encountered during 3-D fault movement is similar to the peak load encountered in pipes subjected to lateral soil movement in 2-D.

3 FULL SCALE SPRING MODEL

3.1 *Spring modeling to simulate large scale experiments*

The spring analyses were conducted to simulate the large scale experiments of pipeline crossing strike-slip fault movements performed at Cornell University. The analysis considered large strain deformations, geometric non-linearity, non-linear soil-pipeline interaction forces (i.e soil-springs) and strain rate dependence of HDPE pipe material.

The spring model analysis employed a model which included transverse and longitudinal soil springs as recommended by the ASCE guidelines (ASCE, 1984). Figure 2 shows a schematic diagram of the pipeline (with attached springs) subjected to the strike-slip fault displacement. Displacements were applied to the far end of the springs in axial direction (δ_x) and lateral direction (δ_y) to induce the fault displacement of δ along the fault trace that is inclined at α to the alignment of the pipeline.

The pipe was represented using PIPE31 elements in ABAQUS (140 elements to represent 10.7 m of pipe length). Each node in the pipe is attached to transverse and longitudinal springs (SPRING2 elements in ABAQUS) for which stiffnesses are defined using 2-D bilinear spring models. The transverse soil spring model is derived from the FE results of lateral pipeline test conducted in unsaturated sand, and the axial spring model is obtained using ASCE guidelines (see Fig. 3 for the spring models used in the study).

The results of a series of large-scale tests con-ducted with a HDPE pipe subjected to 1.22 m of strike-slip displacement at a crossing angle of 65° are discussed

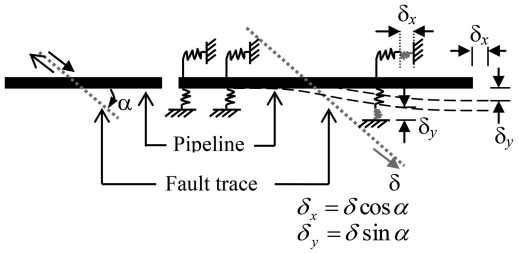
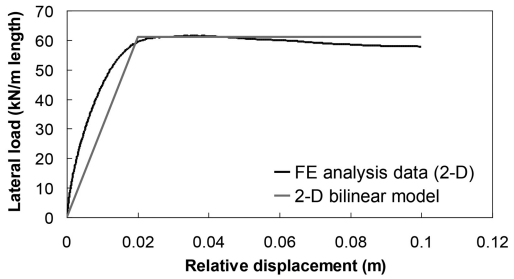


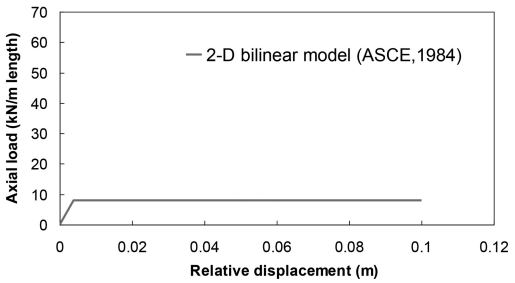
Figure 2. Pipeline subjected to strike-slip fault movement and associated spring model.

in validation of the spring model. A 400 mm diameter pipe was buried at an embedment depth of H/D = 2.8 (H = height from the ground sur-face to the centre of the pipe and D=diameter of the pipe). Cornell sand was compacted around the pipe, with 4% moisture content and 1.60 g/cm^3 of initial dry density.

Figure 4 shows the comparison of strain distribution of the HDPE pipeline obtained from the Cornell large scale experiments and the spring model analysis. As it can be seen, realistic axial and bending strains are predicted by the spring analyses compared to the experimental data. Hence, the spring model with the incorporation of properties as defined in Fig. 3,



(a) Lateral soil spring model



(b) Axial soil spring model

Figure 3. 2-D bilinear spring models used in (a) Lateral and (b) Axial soil springs.

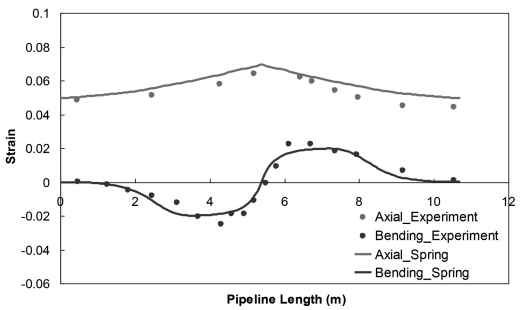


Figure 4. Comparison of strain distribution (axial and bending strains) along the pipeline between Cornell large scale experiments and spring analysis.

can effectively be used to simulate the behavior of pipe-lines subjecting to strike-slip fault displacements un-der unsaturated conditions.

3.2 *Spring modeling to simulate full scale 3D FE analysis*

A full scale three dimensional (3-D) finite element (FE) analysis was conducted to simulate the lateral pipeline test, and the results were compared with the spring model analysis. The objective of this study was to investigate the capability of proposed spring model for simulating full scale 3-D FE analysis. The FE analysis was carried out using ABAQUS (ABAQUS, 2007) to obtain the stress state and deformation of the pipe crossing a strike-slip fault. The behavior of HDPE pipe material was modeled using strain rate dependant von Mises plasticity. The behaviour of soil was modelled by (a) the Nor-sand model (e.g. Jefferies, 1993) and (b) the strain hardening/softening Mohr-Coulomb model (Robert, 2010). Both models have been modified to model the partial saturation effect (Robert, 2010). Figure 5 shows the geometry and mesh descritization of the FE model used in the analyses.

The comparison of strain distribution (axial and bending) along the pipeline obtained from 3-D FE analysis and the spring analysis are showed in Fig. 6 at the fault displacements of 300 mm, 600 mm and 900 mm. It can clearly be seen that the strain distribution (both axial and bending) using spring analysis closely predicts the full scale 3-D FE analysis at all fault displacements. Figure 7 shows the deformation shape of the pipeline from 3-D FE analysis at 900 mm fault displacement. As it can be seen, the pipe response from the spring model has good agreement with the results obtained from FE analysis.

4 PARAMETRIC STUDY

Further spring analyses were conducted to investigate the effects of fault movements on pipes buried in partially saturated soils at different embedded depths in various soil types. The results were also compared with the identical 3D FE analysis. Simulations were carried out for HDPE pipelines (D = 114.6 mm, t = 4.9 mm) subjected to lateral fault movements in coarser sand

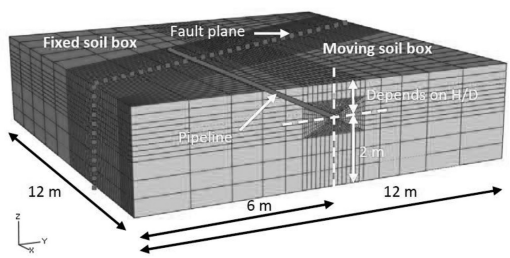
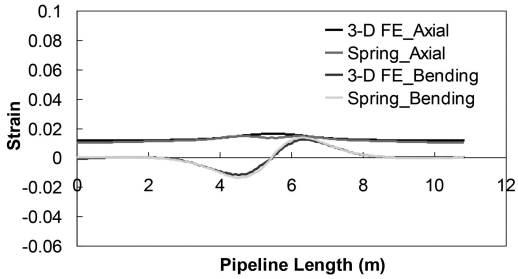
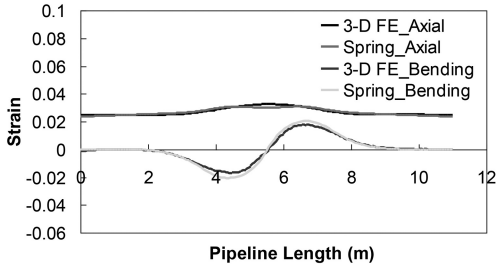


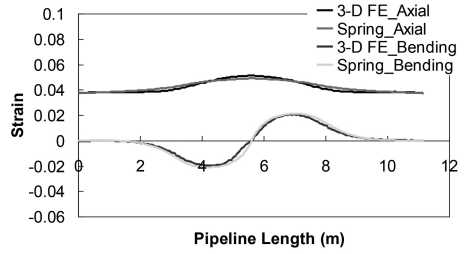
Figure 5. Full scale 3D FE mesh model for soil.



(a) 300mm fault displacement



(b) 600mm fault displacement



(c) 900mm fault displacement

Figure 6. Comparison of strain distribution (axial and bending strains) along the pipeline between full scale 3-D FE analysis and spring analysis at (a) 300 mm, (b) 600 mm & (c) 900 mm fault displacements.

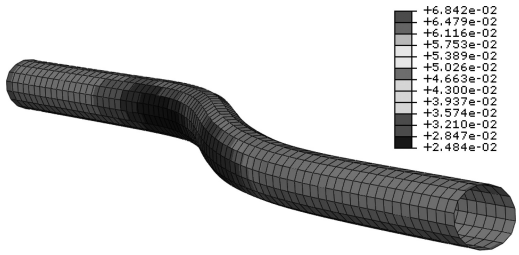
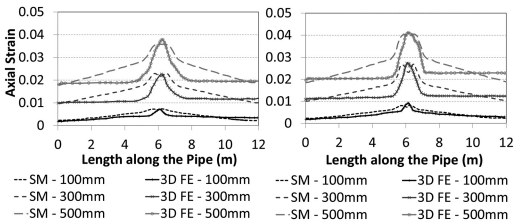


Figure 7. Pipeline deformation (axial strain is shown) of full scale 3-D FE analy-sis at 900 mm fault displacement.

(used in large scale testing discussed above) and finer sands at an initial relative dilatancy index of 0.1 (Bolton, 1986) under dry and unsaturated conditions. The relationships for the longitudinal springs were obtained based on the ASCE guidelines (ASCE, 1984)



(a) Dry sand (b) Wet sand

Figure 8. Axial strain distributions at different fault displacements, H/D = 5.7 (a) Cornell dry sand and (b) Cornell wet sands having.

and the of transverse springs were derived using the 2-D FE analyses results of pipelines subjected to lateral soil movements in dry and unsaturated sands (Robert, 2010).

4.1 *Pipe response under different moistures of soils*

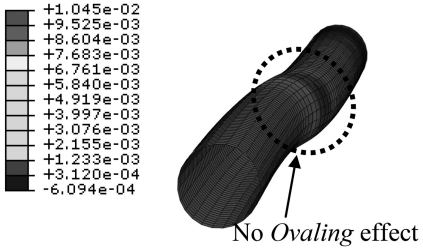
Spring analyses are conducted to investigate the behavior of buried pipes subjected to strike fault movements in dry and unsaturated conditions. Analyses were performed on the basis of HDPE pipeline buried at H/D = 5.7 in Cornell sand under dry condition and partially saturated condition (initial moisture content 4%).

The results from the analyses are showed in Fig. 8 in terms of pipe axial strains at different fault displacements. It can be seen that the maximum pipe strains in the modeled HDPE pipe increase linearly with the increase in fault displacements under both dry and wet conditions. The results also showed that the partial saturation of soil has more impact on pipe deformation compared to the deformations in dry soils. This is because the enhanced strength and stiffness of unsaturated sand by capillarity increase the pipe deformations in wet soil.

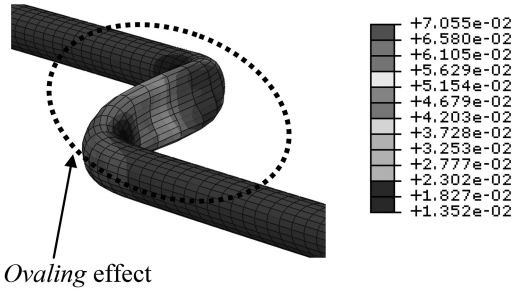
The maximum strain prediction from the spring analyses are in comparable with the results from 3-D FE analyses for both dry and wet conditions. However, once the fault displacement has exceeded about 100 mm, the pipeline strain distribution obtained in the 3-D FE analyses show more localised strains close to the fault rupture than that derived from the spring analyses. This is because the ovaling effects of the pipeline at larger fault displacements (see Fig. 9) and the spring analyses are not capable of capturing them. Hence the spring analysis can only predict the strain distribution at smaller fault displacements (<100 mm) when there is no squeezing and ovaling effects in the pipe cross section.

4.2 *Pipe response under different embedded depths*

Further spring analyses were conducted to investigate the response of HDPE pipes subjected to fault



(a) 100mm fault displacement



(b) 600mm fault displacement

Figure 9. Ovaling effect (legend-axial strains) of the HDPE pipeline buried in wet sand at H/D = 5.7 at the fault displacements of (a) 100 mm and (b) 600 mm.

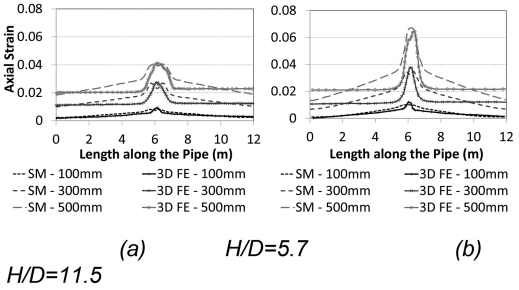


Figure 10. Axial strain distributions at different fault displacements, (a) H/D = 5.7 & (b) H/D = 11.5 in Cornell unsaturated sands.

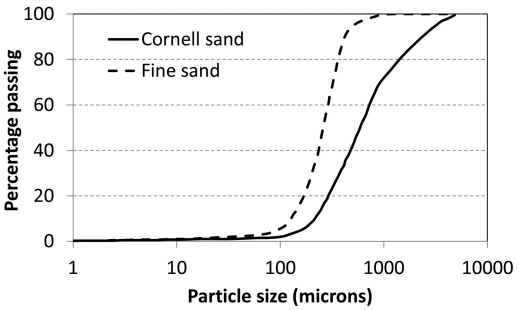


Figure 11. Description of the sand used in the study.

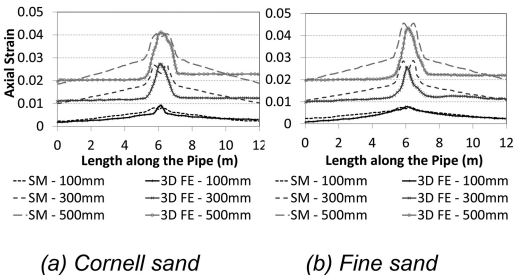


Figure 12. Axial strain distributions at different fault displacements, H/D = 5.7 (a) Cornell sand and fine sands.

movements when buried at different embedded depths in unsaturated Cornell sand (initial moisture 4%). The pipe deformation increases with the increase in pipe embedment depths (see Fig. 10). This is because the larger confining stresses at deeper level generated higher soil stresses, which acted on the pipes to produce larger strains. Further, similar to what was obtained in the analyses for different moisture contents, spring analyses are capable in capturing the maximum pipe strains under different confining stress levels. However, the strain distribution was not realistically predicted around the fault rupture as of incapability of spring models to capture the ovaling effects.

4.3 *Pipe response in different unsaturated sands*

Analyses were also conducted to examine the behaviour of HDPE pipe (H/D = 5.7) crossing active fault movements in different types of unsaturated sands; (a) coarse sand, i.e. Cornell sand (wet initial degree of saturation, S_r of 20%) and (b) fine sand, i.e. Chiba sand (wet initial degree of saturation, S_r of 60%). The particle size distributions of the two sands are showed in Fig. 11. The mechanical behavior of the sand can be found in Robert, 2010.

The results showed that the partial saturation of soil has more impact on pipes buried in fine sand compared to that in coarser sand (i.e. Cornell sand). This is because the enhanced strength and stiffness of fine sand by capillarity increase the pipe deformations in wet soil. The comparison between spring model and FE model results reveal that the distribution of strains is hardly captured by the spring model in both the sands, while showing a good agreement for peek strains between the models.

5 DISCUSSION AND CONCLUSION

This study investigates the behaviour of pipelines subjecting to lateral fault movements using spring analyses which were employed transverse and longitudinal soil springs as recommended by the ASCE guidelines (ASCE, 1984). The transverse soil spring model is derived from the FE results of lateral pipeline test conducted in dry and unsaturated sand, and the axial spring model is obtained using ASCE guidelines. The spring model was first validated by comparing the computed results to the 3-D finite element analysis results as well as to the data produced from large scale experiments carried out at Cornell University, US. Further spring analyses were conducted to examine the effects of moisture content, embedment depths and soil type on the pipe response during strike-slip fault movements.

The investigations showed that, at a given fault displacement, a pipe deforms more when buried in deeper embedment and partially saturated conditions. This is because the additional loading is generated due to enhanced strengths under higher confinements in the former case and suction effects in the latter case. The results also revealed that, partial saturation of soil has more impact on pipes buried in fine sand compared to that in coarser sand due to the enhanced strength and stiffness of fine sand from higher capillarity effects.

The current study further investigated that the spring modeling, with the incorporation of proper transverse and longitudinal soil springs, yield peak pipe strains similar to what obtained from 3-D FE analysis. Hence, such analysis can be effective in occasions where 3-D FE analysis are not capable for determining pipe response undergoing fault displacements. Traditional 3-D FE modeling demands substantial time, memory, storage and in some cases severe convergence problems due to non-linearity effects.

However, the spring analysis predicts realistic strain distributions only when the pipeline is not subjected to excessive ovaling or buckling at the fault rupture plane. Based on the results obtained from 400 mm and 114.6 mm diameter pipelines, it is noted that the ovaling and squeezing effects are more prominent in smaller diameter pipelines and hence the spring analysis will have difficulty in predicting the pipeline behaviour in such cases. In addition, the spring analysis will have difficulty in computing the strain distribution for pipelines at larger fault displacements and deeper embedment depths due to the excessive pipeline deformation (ovaling and squeezing of the cross section) under those circumstances.

REFERENCES

ABAQUS, Inc. 2007. ABAQUS V.6.7 User's Manual, *Providence, Rhode Island*.

ASCE-Guidelines. 1984. Guidelines for the seismic design of oil and gas pipeline systems, *Committee on Gas and Liquid Fuel Lifelines of the ASCE Technical Council on Lifeline Earthquake Engineering*, US.

Jefferies, M.G. 1993. Nor-Sand: a simple critical state model for sand, *Geotechnique*, 43(1):91–103.

Karamitros, D.K., Bouckovalas, G.D. & Kouretzis, G.P. 2007. Stress analysis of buried steel pipelines at strike-slip fault crossings, *Soil Dynamics and Earthquake Engineering*, 27:200–211.

Kennedy, R.P., Chow, A.W. & Williamson, R.A. 1977. Fault movement effects on buried oil pipelines, *Transport Engineering Journal of ASCE*, 103:617–633.

Kokavessis NK, & Anagnostidis GS. 2006. Finite element modelling of buried pipelines subjected to seismic loads: soil structure interaction using contact elements, *In: Proceedings, ASME PVP Conference*, Vancouver, BC, Canada.

Koseki, J., Matsuo, O. & Tanaka, S. 1998. Uplift of sewer pipes caused by earthquake-induced liquefaction of surrounding soil, *Soil and Foundations*, 38(3):75–87.

Liu M, Wang, Y-Y & Yu Z. 2008. Response of pipelines under fault crossing, In: Proceedings, *International Offshore and Polar Engineering Conference*, Vancouver, BC, Canada.

Newmark, N.M. & Hall, W.J. 1975. Pipeline design to resist large fault displacement, *Proceedings of the US National Conference on Earthquake Engineering*, University of Michigan:416–425.

O'Rourke, T. 2007. NEESR Annual Report, *Cornell University*, Rensselaer Polytechnic Institute and Sciencenter Discovery Centre.

O'Rourke, T.D., Jezerski, J.M., Oslon N.A., Bonneau, A.L., Palmer, M.C., Stewart, H.E., O'Rourke & M.J., Abdoun, T. 2008. Geotechnics of pipeline system response to earthquakes, *Proceedings of the Geotechnical Earthquake Engineering and Soil Dynamics iv Congress*.

Robert, D.J. 2010. Soil-pipeline interaction in unsaturated soils, *PhD Thesis*, University of Cambridge.

Takada, S., Hassani, N. &Fukuda, K. 2001. A new proposal for simplified design of buried steel pipes crossing active faults, *Journal of Earthquake Engineering and Structural Dynamics*, 30:1243–1257.

Vazouras, P., Karamanos, S. A., & Dakoulas, P. 2010. Finite Element Analysis of Buried Steel Pipelines Under Strike-Slip Fault Displacements, *Soil Dynamics and Earthquake Engineering* , 30(11):1361–1376.

Wang, L.R.L. & Yeh, Y.A. 1985. A refined seismic analysis and design of buried pipeline for fault movement, *Journal of Earthquake Engineering Structural Dynamics*, 13:75–96.

Unsaturated Soil Mechanics—from Theory to Practice – Chen et al. (Eds)
© 2016 Taylor & Francis Group, London, ISBN 978-1-138-02921-7

Engineering characteristics of granite residual soils of landslide in Wuzhou, Guangxi, China

Z.B. Wang
GuangXi Key Laboratory of New Energy and Building Energy Saving, Guilin University of Technology, Guilin, China

K. Li, C.F. Wei & Z.Q. Xu
Guilin University of Technology, Guilin, China

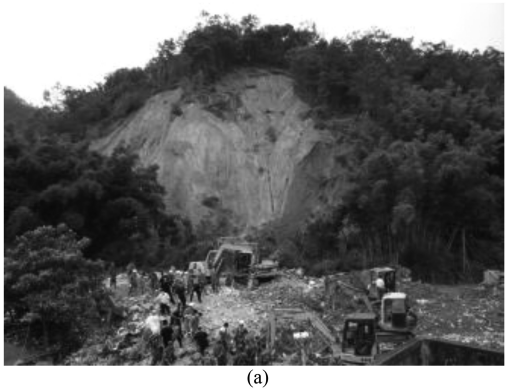
ABSTRACT: Residual soil of weathered granite under unsaturated conditions is probably one of the highest prone soils of rainfall-induced landslide. A large part of the region is covered by unsaturated residual soil subjected to rainfall-induced landslides in the southeast of Guangxi province, China. The properties of residual soil are a function of the degree of weathering. A series of physical and mechanical properties, thin section under the microscope, Scanning Electron Microscope (SEM), X-ray diffraction (XRD) and chemical analysis are performed on residual soils from granite profile of Chencun landslide in this region. The results indicate that the variation in weathering indices and engineering geological properties as well as the change of mineral components and microstructures of the granite residual soils with the degree of weathering. Feldspar and biotite gradually become kaolinite (halloysite) and illite, respectively, which increases the amount of pores and decreases the bonding strength of minerals with the increased degree of weathering. Direct shear tests between residual soil (completely weathered granite) and highly weathered granite show that the former is much more susceptive to water and disturbed factors than the latter, The reduction of shear strength parameters of the residual soil is much higher than completely weathered granite when the saturation of soil specimen increased, which is relation to the high clay content and the porous micro-structure in residual soils of granite.

1 INTRODUCTION

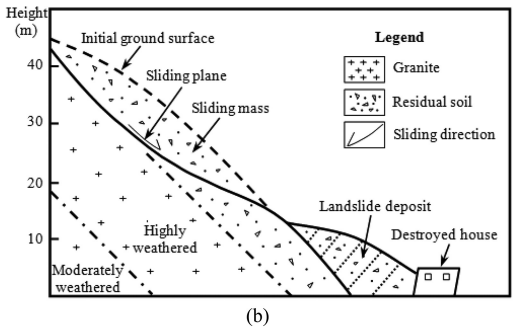
Most of landslides had occurred in weathered granite, in Wuzhou-Yulin Border Area of Guangxi province, China. The volumes of such landslides just reached hundreds or thousands of cubic meters and the depth of the slide zone is only several meters, and they belonged to shallow landslides according to Varnes classification of landslide (Varnes, 1978; Hungr, 2014). Although their small volumes, theycould cause severe casualties and property losses. It was important to study engineering geological properties of weathered rocks and soils to understand the mechanism of those landslides for preventing disasters and reducing damages (Bhattarai, 2007; Picarelli, 2008). Weathering led to physical and chemical alteration of granite, which undermined the physical and geotechnical properties by alteration of the chemical and mineral compositions of granite (Lan, 2003; Rahardjo, 2004; Wen, 2004; Da Fonseca, 2006). The main objective of this paper is to evaluate the effect of weathering on physical and mechanical properties of residual soil from a landslide area, and ultimately on the mechanism of instability of natural slopes of weathered granite.

2 DESCRIPTION OF THE STUDY AREA

Wuzhou-Yulin Border Area is a typical low mountainous and hilly area in Guangxi province of China, and a sub-tropical humid climate with an annual average temperature of 19.2–21.3°C and precipitation of 1450–2000 mm, slope gradient is 30 ~ 60°, the height difference is several tens of meters, max is 200 m. The slope is underlain by medium grained granite of Yanshan age. Weathering processes alter the mineralogical, Micro-structural and geotechnical characteristics of granite and its weathering products. Typical weathering granite profile is stratified stratums. There are 6 layers in typical weathering granite profile of the slopes: the topsoil, the residual soil layer (also named the completely weathered layer), the highly weathered granite layer, moderately weathered granite layer, the slightly weathered layer and the fresh layer. The topsoil, the residual soil layer, and the highly weathered granite layer nearly parallel to the soil surface. Depth of weathering in most granite profiles often reaches more than 30 m. The slide zone located nearby the interface between the residual soil layer and the highly weathered granite layer.



(a)



(b)

Figure 1. (a) Photograph of Chencun landslide (Liu, 2010) and (b) its schematic profile.

This Area experienced prolonged rainfall in June 1st–2nd, 2010, with cumulative precipitation values exceeding 300 mm. The maximum precipitation was 21 0mm from 1:00 am to 3:00 am, which caused the breaking out of several hundred shallow landslides in this region and caused 42 deaths. One of the most serious disasters was Chencun landslide with a volume of approximately 7000 m^3 (length is 70 m, width is 50 m, average depth is 2 m), which caused 11 deaths. For this study, Chencun landslide was selected, and specimens were collected from weathering profile cut by an excavator, in the study area (Fig 1).

In the upper part of slopes covered with thick Masson pines, the middle and bottom part with bamboo and farmland. Intense chemical weathering of granite bedrock produced very thick weathering layer over the mountainous terrain.

3 LABORATORY ANALYSIS

Engineering geological properties of weathered rocks and soils were often controlled by their chemical and mineral compositions. In order to compare the mineralogy and chemistry of the residual soils with that of the parent rocks with different weathering degree, Soil or rock samples from five weathering degrees were collected from granite residual soil slope of Chencun landslide, and analyzed by the following analysis program in this study.

Geological characteristics of granite residual soil and their host materials were determined by X-ray diffraction (XRD), scanning electron microscopic (SEM), thin section under the microscope and chemical analysis. XRD technique was employed to determine constituent mineral species of fine-grained soil in the samples. Scanning electron microscopy (SEM) was used to analyze the microstructure of the residual soil samples, and to reveal clay particles and their arrangements directly. The SEM technique could lead to a better understanding of the engineering geological properties and is especially useful for bonded soil. In this study, samples of the residual soil and severe weathering granite were analyzed by SEM.

Thin section under a petrographic microscope was illustrated the appearance of the rock-forming mineral and the secondary mineral, mean grain size, grain shape, type of grain contacts in the samples of the granite. Major element oxides were measured by chemical analysis of the granite samples with different weathering degree, which can be used to study the formation and evolution of the process of granite.

Plenty of samples of residual soil (completely weathered granite) and highly weathered granite were taken from weathering profile by soil ring sampler. Physical properties investigated included Particle size analysis, specific gravity, dry and saturated density, porosity, permeability coefficient and Atterberg limit tests were the main index property tests performed in accordance with Chinese Standard for Soil Test Method (1999). Direct shear tests were performed to determine the shear strength of the soils under different saturation kept in a constant-temperature-and-humidity test box.

4 RESULTS AND DISCUSSION

4.1 *Weathering profile characteristics*

4.1.1 *Micro-structure and mineralogy of the granite profile*

The micro-structural analysis is carried out for samples of highly weathered granite and residual soil using SEM, samples of moderately weathered, slightly weathered and fresh granite using thin section under the microscope. Electron photomicrograph of residual soil is illustrated in Figures 2a, b. The foremost characteristic of residual soil is laminated structure, and this kind of lamination is formed by well-formed six-sided plates looked a lot like book. The lateral dimensions of these plates are about tens of μms, but their thicknesses are difficult to determine by magnified 800 times. An electron photomicrograph of highly weathered granite is shown in Figure 2c. It mainly dominated by amorphous mass, micro grains and some crystals. The reticular structural minerals are illite and most of the others are kaolinite. Kaolinite formed in highly weathered granite has nearly hexagonal plates, the lateral

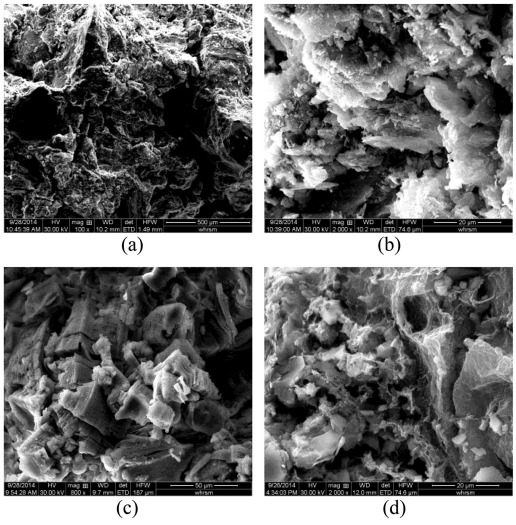


Figure 2. SEM photograph showing the microstructure of (a) Residual soil: The whole microstructure of the intact soil under lower magnification (100×); (b) Residual soil: the disorderly arrangement in the intact soil under higher magnification (2000×); (c) Highly weathered granite: a book-like minerals are kaolinte in the intact soil, magnification 800×. (d) Moderately weathered granite: a net-like minerals are illite and nearly hexagonal plate-like minerals are kaolinite (magnification 2000×).

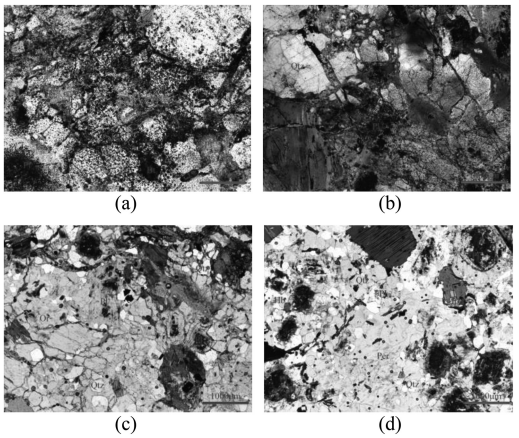


Figure 3. Polarizing microscope photographs of moderately weathered granite (a, b), slight weathered granite (c) and fresh granite (d).

dimensions of these plates range from about several tenths of 1 μm to several μm, and their thicknesses are from about several percents of 1 μm to 1 μm. The particle size of kaolinite in highly weathered granite is widely smaller than in residual soil.

The mineralogical and textural characteristics of the samples are examined by optical microscopy. All samples of fresh, slightly weathered and moderately weathered granite exhibited fine-grained granitic texture and the main minerals are plagioclase, orthoclase, quartz and biotite (Figs 3a–d). The dark minerals are biotite and amphibole. Apatite, magnetite and epidote (in some samples) are only accessories and the content of each is less than one hundredth. Plagioclase occurs as a hypidiomorphic-platy texture, the length of these plates range from 0.5 μm to 2.5 μm, and their width are from 0.1 μm to 1.5 μm. Orthoclase occurs as xenomorphic and irregular shape, Quartz occurs as xenomorphic granular aggregates 0.2–2.5 mm in diameter. There are hydromicazation and kaolinization during the weathering process of feldspar and orthoclase, and alteration for biotite stained by iron, and all three kinds of primary minerals are partly altered. Weathering cracks develop along the plane between both same and different minerals. The scale of mineral alteration and the amount of the weathering cracks increase with the increase degree of weathering.

The mineralogy is determined for the <0.075 mm fraction of the residual soil, highly weathered and moderately granites by X-ray diffractometry (XRD). The X-ray diffractograms of the residual soil highly weathered and moderately granites are plotted in Figure 4. The results show that the mineralogy of the residual soil is similar to that of its parent rock. The two diffractograms of residual soil and comletedly granite are all characterized by high amounts of kaolinites and illites, moderately granite was also characterized by kaolinites and illites, but it has a lot of primary mineral (feldspar) and another secondary mineral (montmorillonite). The kaolinite and illite content of the weathered granite increase at the expense of feldspar and biotite during the process of weathering.

The result of the XRD-analysis can be obtained from the kind of clay minerals, because it gives some general insights to the mechanical properties of the soil. The mineralogy of the moderately weathered granite is complex, showing severe weathering in this layer. Weathered soils with higher clay content are commonly less resistant and characterized by a lower material strength than soils with smaller clay content. The secondary minerals of weathered granite soils are dominated by kaolinite (halloysite) and illite, meaning the residual soils is a youthful soil. (Mitchell, 2005).

The X-ray diffractograms of the residual soil (Fig 4a) is similar as the completely weathered granite (Fig 4b), they have the same clay mineral types (kaolinite and illite), and there is a little difference between their diffraction intensity. The moderately weathered granite (Fig 4c) not only had more clay mineral types (kaolinite, illite and montmorillonite), but also the primary mineral type (feldspar), which indicate high susceptibility to further weathering.

4.1.2 *Chemistry of the granite profile*

The whole major element compositions are summarized in Table 1, and all the content of oxide and loss on ignition (LOI) are expressed in percentage. The ratio of Si/Al and SiO_2/R_2O_3 decreases with the process of weathering because of the loss of Si and the enrichment of Al, Fe. The CIA is proposed by

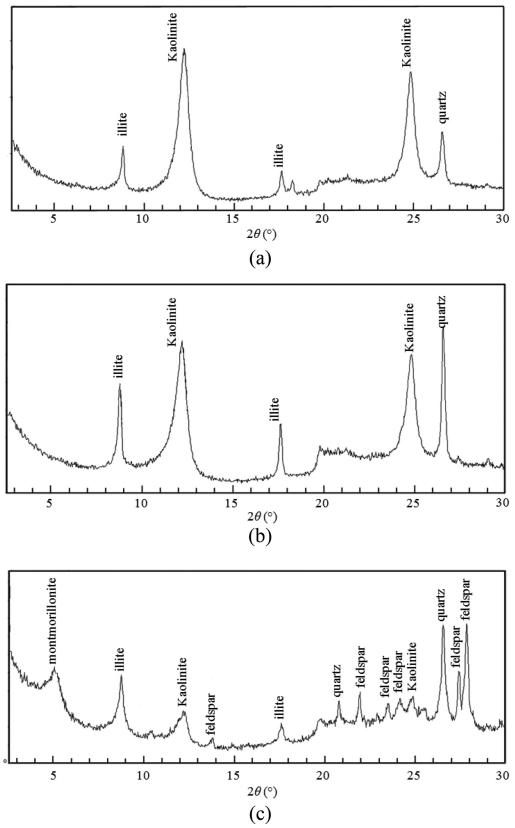


Figure 4. The X-ray diffractograms of showing the clay mineralogy of (a) the residual soils, (b) highly, (c) moderately weathered granites, both (a) and (b) are characterized by high amounts of Kaolinite and illite, (c) is characterized by kaolinites, illites, montmorillonite.

Nesbitt and Young (1982), can be defined as the ratio of Al_2O_3 and $(Al_2O_3 + CaO + Na_2O + K_2O)$ in molecular proportions. Higher values of chemical Index of Alteration (CIA) shows a higher degree of granite weathering. The Parker index (Wp) is expressed as $W_p = 2Na_2O/0.35 + MgO/0.9 + 2K_2O/0.25 + CaO/0.7$ and is proposed by Parker (1970). Values of W_p is considered to indicate susceptibility to further weathering, The values of Parker index decrease as the degree of weathering increases. All weathering indices show good relation with the degree of granite weathering.

The values of CIA decrease, while W_p increase with the depth of the weathered granite profile, which indicate that weathering intensity decrease gradually from the surface to the interior of granite slopes. Residual soil, the most weathered sample of granite, have the highest LOI content, which may relate with the highest halloysite content comparing with other low weathered granite samples. The content of CaO, MgO, Na_2O in residual soil are reduced by more than ninety percent than in fresh granite, however, the reduction percentage of K_2O is much less than of CaO, MgO, Na_2O in residual soil, which is relation to the formation and enrichment of illite in residual soil. Overall, Ca, Na, K and Si decrease, whereas Al, Fe and LOI increase with the process of granite weathering. The enrichment of Al, Fe are consistent with the formation and enrichment of kaolinite, halloysite and illite in residual soil.

4.2 *Physical properties*

Figure 4 shows the particle size distributions of residual soil, highly weathered, moderately weathered granite of Chencun landslide. Three distinct particle size distributions are observed from different degree

Table 1. Major chemical compositions of samples of granite profile and their weathering indices.

Weathering degree	Depth(m)	SiO_2	Al_2O_3	Fe_2O_3	FeO	K_2O	Na_2O	CaO	MgO	LOI	SiO_2/Al_2O_3	SiO_2/R_2O_3	CIA	W_p
V	0.8–1.0	60.96	21.98	4.66	0.41	1.83	0.035	0.013	0.21	8.93	2.77	2.29	92.13	15.09
	1.6–1.8	61.45	21.22	4.45	0.32	2.35	0.058	0.0047	0.2	8.51	2.90	2.39	89.79	19.36
	2.4–2.6	65.52	18.89	4.06	0.21	2.66	0.067	0.023	0.2	7.04	3.47	2.85	87.29	21.92
IV	6.4	68.28	16.36	3.07	1.14	4.31	0.23	0.032	0.65	4.97	4.17	3.51	89.74	36.56
III	18.2	71.91	13.93	2.77	0.22	3.35	2.70	2.07	0.64	1.47	5.16	4.31	78.16	45.90
II	32.4	70.21	14.47	1.93	1.22	2.80	3.05	2.92	1.13	1.02	4.85	4.28	63.17	45.26
I	38.0	69.52	14.23	1.01	2.04	2.86	3.02	3.11	1.29	1.77	4.89	4.56	62.26	46.01

Table 2. Physical parameters of residual soil and completely weathered granite.

Soil type	Natural water content (%)	Relative density	Natural density (g/cm^3)	Dry density (g/cm^3)	Saturate density (g/cm^3)	Void ratio	Porosity (%)	Liquid limit(%)	Plastic limit (%)	Plasticity index (%)
1	21	2.71	1.504	1.504	1.949	0.802	44.50	45.8	30.3	15.5
2	17	2.66	1.479	1.479	1.923	0.799	44.41	43.7	28.6	15.1

weathering granite (Fig 4). The residual soil (completely weathered) is named silty clay, because it has fines content ($d \leq 0.075$) of about 55.76% and its plasticity index is 15.1($<$17, Table 2). The coarse-grained fraction of highly weathered, moderately weathered granite are more than the fine-grained fraction (the fines content is less than 50%) and the soil type changed to silty sand and medium sand (Based on Chinese standard "Code for investigation of geotechnical engineering (GB50021-2001)"). This implies that the fines content decreases with depth as the degree of weathering decreases. Structure characteristics of weathering granite is more fines content in upper layer than lower layer, Conversely, lower layer has more coarse grains, which implies that the degree of weathering decreases with depth.

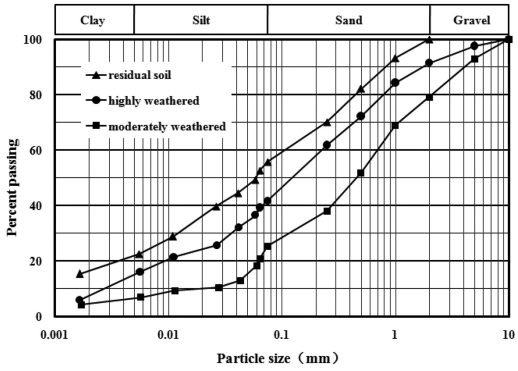


Figure 5. Particle size distributions of residual soil, highly weathered, moderately weathered granite of Chencun landslide.

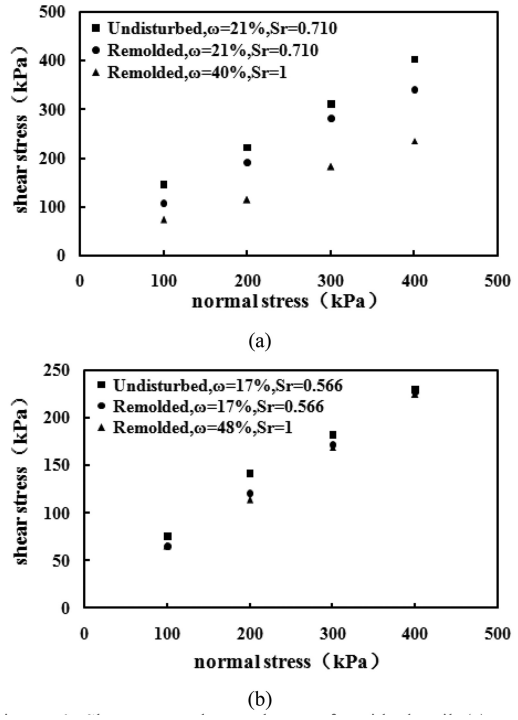


Figure 6. Shear strength envelopes of residual soil (a) and highly weathered granite (b) for undisturbed and remolded conditions.

4.3 *Mechanical properties*

The shearing resistance of a soil depends on many factors, such as the composition, the structure, the water content of soil (Fredlund, 1978; Rahardjo, 2004; Mitchell, 2005). The mechanical properties are analysed comparing data obtained from undisturbed and remoulded specimens under natural and saturated water content by direct shear tests. The saturation of natural residual soil is 0.71, and highly weathered granite is 0.566. Figure 6 illustrates the stress-strain curves of residual soil and highly weathered granite, all these curves showe a good linear relationship. Table 3 illustrates shear strength parameters of residual soil and completely weathered granite, and these shear strength parameters of soils are obtained according to Mohr-Coulomb rule (Mitchell, 2005).

The most significant reductions in shear strengths are the remoulded residual soil under saturated water content. The reduction of residual soil shear strengths between under undisturbed and remolded conditions is also significant. These reductions of highly weathered granite don't seem obvious in this study,which shows a significant decrease in shear strength with disturbance by rainfall or slope cutting, as a result of an increase in water content (Fredlund, 1978) and structure (or particle bonding) breaking (HuÈrlimann, 2001).

4.4 *Implications to shallow landslides*

Generally, rainfall-induced landslides of natural granite slopes in Wuzhou-Yulin Border Area are shallow landslides because of the decrease of the shear strength of the slide soil. Most of the sliding planes are located

Table 3. Shear strength parameters of the residual soil and highly weathered granite or undisturbed and remolded conditions.

Soil type	Specimen state	Saturation	c(kPa)	φ(°)
Residual soil	undisturbed	0.710	55.3	40.7
	remolded	0.710	32.8	38.4
		1	13.5	28.9
Completely	undisturbed	0.566	31.7	26.7
weathered	remolded	0.566	11.5	28.4
granite		1	9.7	28.1

in the residual soil by field investigation and analysis. Rainfall plays an important role in the process of landslide due to the friction angle and cohesion of the residual soil decreased by the increased water content. As showed in Table 3, shear strength parameters of the residual soil fall a lot when the residual soil is saturated and disturbed. The reduction of shear strength parameters of the residual soil is much higher than completely weathered granite. This is due to higher clay content and more cracks in residual soil. The residual soil is much more susceptive to water or other disturbed factors than completely weathered granite.

The weak shear strength of the residual soils strongly decreases once their saturation is increased. Although the test stress applied in soils is too high comparing to the real stress states because landslides often have shallow thickness (only 2–3 m), the difference of micro-structure and mineralogy between residual soil and completely weathered granite is still significant, and can be used to an indicator for the instability of weathered granite slopes.

5 CONCLUSIONS

The results of the analysis of physical and engineering properties, thin section under the microscope, XRD, SEM and chemical analysis indicate that the variation in the properties of the residual soils become worse with the degree of weathering. The process of weathering cause obvious deterioration in physical properties, micro-structure and mineralogy of granite. Water contents have a significant shear strength reduction effect on residual soil but less effect on completely weathered granite. Such reduction in shear strength has considerable impact on the stability of slopes in the residual soils.

ACKNOWLEDGEMENTS

This research was supported by the National Natural Science Foundation of China (No. 41302227), Guangxi Natural Science Foundation (No. 2012GXNSFBA053138, 2012GXNSFGA060001), and Scientific Research Foundation of the Higher Education Institutions of Guangxi, China (No. 201204LX179).

REFERENCES

Bhattarai P., Tiwari B. & Marui H. 2007. Variation of Soil Properties in Mudstone with Depth and its Effect on Slope Stability. *Embankments, Dams, and Slopes@ sLessons From the New Orleans Levee Failures and Other Current Issues*. ASCE: 1–10.

Da Fonseca A. V., Carvalho J., Ferreira C., et al. 2006. Characterization of a profile of residual soil from granite combining geological, geophysical and mechanical testing techniques. *Geotechnical & Geological Engineering* 24(5): 1307–1348.

Duzgoren-Aydin N. S., Aydin A. & Malpas J. 2002. Reassessment of chemical weathering indices: case study on pyroclastic rocks of Hong Kong. *Engineering Geology* 63(1): 99–119.

Fredlund D. G., Morgenstern N. R. & Widger R. A. 1978. The shear strength of unsaturated soils. *Canadian Geotechnical Journal* 15(3): 313–321.

Hürlimann M., Ledesma A. & Martı J. 2001. Characterisation of a volcanic residual soil and its implications for large landslide phenomena: application to Tenerife, Canary Islands. *Engineering Geology* 59(1): 115–132.

Mitchell J. K. & Soga K. 2005. Fundamentals of soil behavior (3rd edition). New York: Wiley.

Lan H. X., Hu R. L., Yue Z. Q., et al. 2003. Engineering and geological characteristics of granite weathering profiles in South China. *Journal of Asian Earth Sciences* 21(4): 353–364.

Parker A. 1970. An index of weathering for silicate rocks. *Geological Magazine*. 107(06): 501–504.

Picarelli L., Olivares L. & Avolio B. 2008. Zoning for flowslide and debris flow in pyroclastic soils of Campania Region based on "infinite slope" analysis. *Engineering Geology* 102(3): 132–141.

Rahardjo H., Aung K. K., Leong E. C., et al. 2004. Characteristics of residual soils in Singapore as formed by weathering. *Engineering geology* 73(1): 157–169.

Varnes D. J. 1978. Slope movement types and processes. In: Schuster RL, Krizek RJ (eds) Landslides, analysis and control, special report 176: Transportation research board, National Academy of Sciences, Washington, DC., 11–33.

Wen B. P., Duzgoren-Aydin N. S. & Aydin A. 2004. Geochemical characteristics of the slip zones of a landslide in granitic saprolite, Hong Kong: implications for their development and microenvironments. *Environmental Geology*, 47(1): 140–154.

Unsaturated Soil Mechanics—from Theory to Practice – Chen et al. (Eds)
© 2016 Taylor & Francis Group, London, ISBN 978-1-138-02921-7

Cavity expansion in unsaturated silty sand exhibiting hydraulic hysteresis for three drainage conditions

H. Yang
Department of Civil Engineering, The University of Hong Kong, Hong Kong

A.R. Russell
Centre for Infrastructure Engineering and Safety, School of Civil and Environmental Engineering, The University of New South Wales, Sydney, NSW, Australia

ABSTRACT: A cavity expansion analysis is presented for an unsaturated silty sand which exhibits significant hydraulic hysteresis. The cavity expansion problem is solved using the similarity technique in which soil stress-strain behavior is described by a bounding surface plasticity model. The influence of where the initial hydraulic state is located on the soil-water characteristic curve on the cavity wall pressure is investigated. Also, the dependence of the cavity wall pressure on three different drainage conditions (constant suction, constant moisture content and constant contribution of suction to the effective stress) is studied. It is found that the drainage condition in which the contribution of suction to the effective stress is constant offers a good approximation to the other two. Also, hydraulic hysteresis has negligible influence on the relationship between cavity wall pressure and initial effective stress. These findings may simplify interpretation of in situ tests.

1 INTRODUCTION

Cavity expansion in soil is of interest to geotechnical engineers, especially when interpreting in situ tests. For the cone penetration test (CPT) the penetration resistance (q_c) is related to the wall pressure of a spherical cavity. For the pressuremeter test (PMT) the expansion pressure—cavity strain relationship can be related to a cylindrical cavity expansion. Most cavity expansion studies have been for saturated soils under drained or undrained conditions. However, many CPTs and PMTs are performed in unsaturated soils. There have been only a few attempts to solve the cavity expansion problem in unsaturated soils (e.g. Russell & Khalili 2006a, Yang & Russell 2015). They showed suction may have a significant effect on the pressure required to expand a cavity. This is consistent with CPT results (e.g. Pournaghiazar et al. 2013) where suction has a pronounced affect on q_c. Many unsaturated soils exhibit hydraulic hysteresis which enables there to be many possible suction values for any combination of void ratio and moisture content. Never before has the effect of hydraulic hysteresis on cavity expansion been investigated. This is the focus of this paper.

2 SOIL-WATER CHARACTERISTIC CURVE

The relationship between void ratio (e), degree of saturation (S_r) and suction (s) is defined through a soil-water characteristic curve (SWCC). S_r on a main drying or wetting curve is (Russell & Buzzi 2012):

$$S_r = \begin{cases} 1 & \text{for} \quad s \le s_e \\ \left(\dfrac{s}{s_e}\right)^{\alpha} & \text{for} \quad s \ge s_e \end{cases} \tag{1}$$

where s_e is the s value separating saturated from unsaturated states. For a state on the main drying curve, $s_e = s_{ae}$, where s_{ae} is the air entry value. For a state on the main wetting curve, $s_e = s_{ex}$, where s_{ex} is the air expulsion value. α is a negative constant. For fractal soils $\alpha = D_p - 3$, where D_p is the fractal dimension of the pore size distribution. On scanning curves S_r is:

$$S_r = \begin{cases} \left(\dfrac{s_{ae}}{s_{rd}}\right)^{-\alpha}\left(\dfrac{s_{rd}}{s}\right)^{-\beta} & \text{for drying path reversal} \\ \left(\dfrac{s_{ex}}{s_{rw}}\right)^{-\alpha}\left(\dfrac{s_{rw}}{s}\right)^{-\beta} & \text{for wetting path reversal} \end{cases} \tag{2}$$

where β is the slope and s_{rd}, s_{rw} are the points of suction reversal on the main drying and wetting curves. s_{ae} depends on e through $s_{ae} = C_1 e^{-\gamma}$, in which C_1 is a positive constant with units of stress and γ is a constant. A fixed ratio between s_{ae} and s_{ex} is assumed, $s_{ex} = C_2 s_{ae}$, in which C_2 is a constant. For fractal soils $\gamma = D_s$, where D_s is the fractal dimension of the particle size distribution (Russell 2014).

3 CONSTITUTIVE MODEL

The model is based on that of Russell & Khalili (2006b), the only difference being that the isotropic compression lines and elastic unload-reload lines are linear in the ln $e \sim \ln p'$ plane, where $p\prime$ is the mean effective stress. Conventional $p' \sim q$ notation is used, where q is the deviator stress. The corresponding strain variables are the volumetric strain ε_p and shear strain ε_q. Compressive stresses and strains are assumed positive and ε_p is linked to specific volume v according to $\varepsilon_p = -\ln(v/v_0)$ and $\dot{\varepsilon}_p = -\dot{v}/v$, where $v = 1 + e$ and v_0 is the specific volume at the reference configuration. A superimposed dot indicates an increment. Elastic and plastic strain increments sum to give total strain increments and superscripts e and p denote the elastic and plastic components. The stresses and strains are written in vector form, $\sigma' = [p', q]^T$ and $\varepsilon = [\varepsilon_p, \varepsilon_q]^T$.

The effective stress is:

$$p' = p_{net} + \chi s \qquad \dot{p}' = \dot{p}_{net} + \psi \dot{s} \tag{3}$$

where $p_{net} = p - u_a$ is the net stress, $s = u_a - u_w$ (u_a and u_w are pore air and water pressures), χ is the effective stress parameter (having a value of 1 for saturated soils and 0 for dry soils) and $\psi = \mathrm{d}(\chi s)/\mathrm{d}s$. When the state is on a main wetting or drying curve χ is:

$$\chi = \begin{cases} 1 & \text{for } \dfrac{s}{s_e} \le 1 \\ \left(\dfrac{s}{s_e}\right)^{-\Omega} & \text{for } \dfrac{s}{s_e} \ge 1 \end{cases} \tag{4}$$

where Ω is a parameter with a best fit value of 0.55. When the hydraulic state is located on a scanning curve χ is defined as (Khalili & Zargarbashi 2010):

$$\chi = \begin{cases} \left(\dfrac{s_{rd}}{s_{ae}}\right)^{-\Omega}\left(\dfrac{s}{s_{rd}}\right)^{-\zeta} & \text{for drying path reversal} \\ \left(\dfrac{s_{rw}}{s_{ex}}\right)^{-\Omega}\left(\dfrac{s}{s_{rw}}\right)^{-\zeta} & \text{for wetting path reversal} \end{cases} \tag{5}$$

A simple isotropic elastic rule is adopted. K and G are defined as:

$$K = \frac{(1+e)p'}{e\kappa} \qquad G = \frac{3(1-2\mu)}{2(1+\mu)}K \tag{6}$$

where κ is a material constant and is the slope of the elastic unload-reload line in the ln $e \sim \ln p'$ plane and μ is Poisson's ratio. The incremental elastic deformation is given by $\dot{\varepsilon}_p^e = \dot{p}'/K$ and $\dot{\varepsilon}_q^e = \dot{q}'/3G$.

In bounding surface plasticity theory (Dafalias 1986) the current stress state (σ') lies on a loading surface. Plastic deformation occurs when σ' moves towards an image point ($\bar{\sigma}'$) located on a bounding surface. The hardening modulus is a decreasing function

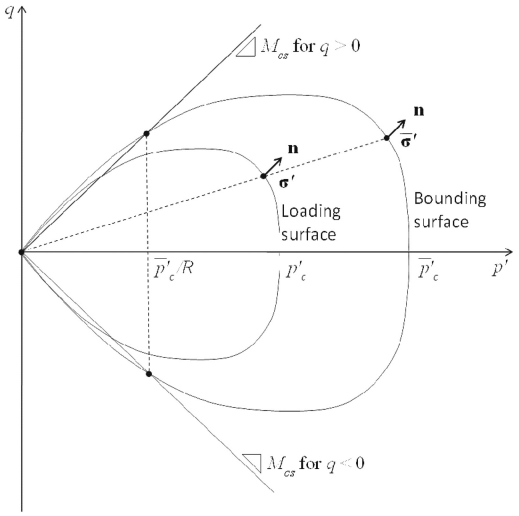


Figure 1. Illustration of the loading surface, bounding surface and mapping rule in the $q \sim p'$ plane.

of the distance between σ' and $\bar{\sigma}'$. The unit normal vectors at σ' and $\bar{\sigma}'$ are the same, denoted **n**. The bounding and loading surface functions are (Figure 1):

$$F = \bar{q} - M_{cs}\bar{p}'\left(\frac{\ln\left(\dfrac{\bar{p}'_c}{\bar{p}'}\right)}{\ln R}\right)^{\frac{1}{Q}} \qquad f = q - M_{cs}p'\left(\frac{\ln\left(\dfrac{\bar{p}'_c}{\bar{p}'}\right)}{\ln R}\right)^{\frac{1}{Q}} \tag{7}$$

The superimposed bar denotes stress conditions on the bounding surface. Q and R are constants. M_{cs} is the slope of the critical state line in the $p' \sim q$ plane.

Linear critical state lines (CSLs) and limiting isotropic compression lines (LICLs) are assumed in ln $e \sim \ln p'$ plane. The LICLs depend on suction:

$$\ln e_{LICL} = \ln N(s) - \lambda(s)\ln p' \tag{8}$$

where, for a given s, $N(s)$ is the value of e at $\ln p' = 0$ and $\lambda(s)$ is the slope.

The CSLs are deduced implicitly by an elastic shift from the LICLs along the κ line of magnitude $\kappa \ln R$. They are also suction dependent:

$$\ln e_{CSL} = \ln N(s) - \lambda(s)\ln(Rp') + \kappa \ln R \tag{9}$$

A non-associated flow rule is assumed:

$$d = \frac{\dot{\varepsilon}_p^p}{\dot{\varepsilon}_q^p} = A\left(M_{cs} - \frac{q}{p'}\right) \tag{10}$$

where d is dilatancy and A is a material constant.

The unit vector of plastic flow (**m**) at σ' is then:

$$\mathbf{m} = [m_p, m_q]^T = \left[\frac{d}{\sqrt{1+d^2}} \quad \frac{1}{\sqrt{1+d^2}}\right]^T \tag{11}$$

The hardening modulus h is divided into two components, $h = h_b + h_f$, where h_b is the modulus at $\bar{\sigma}'$ and h_f is an arbitrary modulus at σ' and depends on the distance between σ' and $\bar{\sigma}'$.

Imposing the consistency condition at the bounding surface and forcing $\bar{\sigma}'$ to remain on bounding surface under isotropic hardening leads to:

$$h_b = -\frac{\partial F}{\partial \bar{p}'_c}\left(\frac{\partial \bar{p}'_c}{\partial \varepsilon_p^p}+\frac{\partial \bar{p}'_c}{\partial s}\frac{\dot{s}}{\dot{\varepsilon}_p^p}\right)\frac{m_p}{\sqrt{\left(\frac{\partial F}{\partial p'}\right)^2+\left(\frac{\partial F}{\partial q}\right)^2}} \tag{12}$$

h_f used here is:

$$h_f = k_m\left(\frac{\partial \bar{p}'_c}{\partial \varepsilon_p^p}+\frac{\partial \bar{p}'_c}{\partial s}\frac{\dot{s}}{\dot{\varepsilon}_p^p}\right)\frac{p'}{\bar{p}'_c}\frac{\bar{p}'_c - p'_c}{p'_c}\left(\eta_b - \frac{q}{p'}\right) \tag{13}$$

where $\eta_b = (1-2\xi)M_{cs}$ controls the slope of the peak strength line in the $q \sim \varepsilon_q$ plane and ξ is the state parameter of Been and Jefferies (1985).

The relationship between $\bar{p}'_c$, s and e is:

$$\frac{\dot{e}}{e} = \frac{\dot{N}(s)}{N(s)} - \dot{\lambda}(s)\ln(\bar{p}'_c) - \lambda(s)\frac{\dot{\bar{p}}'_c}{\bar{p}'_c} \tag{14}$$

The rate form of the elastic volumetric strain is:

$$\dot{\varepsilon}_p^e = \frac{e}{1+e}\kappa\frac{\dot{p}'}{p'} \tag{15}$$

The rate form of $\bar{p}'_c$ is:

$$\dot{\bar{p}}'_c = \frac{\bar{p}'_c}{\lambda(s)-\kappa}\frac{v}{v-1}\dot{\varepsilon}_p^p + \frac{\bar{p}'_c}{\lambda(s)-\kappa}\left(\frac{1}{N(s)}\frac{\partial N(s)}{\partial s} - \ln(\bar{p}'_c)\frac{\partial \lambda(s)}{\partial s}\right)\dot{s} \tag{16}$$

A radial mapping rule is used to link σ' and $\bar{\sigma}'$. According to the rule σ' and $\bar{\sigma}'$ are on the same straight line passing through the origin.

n defines the direction of loading and is:

$$\mathbf{n} = [n_p, n_q]^T = \left[\frac{\frac{\partial F}{\partial p'}}{\sqrt{\left(\frac{\partial F}{\partial p'}\right)^2+\left(\frac{\partial F}{\partial q}\right)^2}}, \frac{\frac{\partial F}{\partial q}}{\sqrt{\left(\frac{\partial F}{\partial p'}\right)^2+\left(\frac{\partial F}{\partial q}\right)^2}}\right]^T \tag{17}$$

The final plastic stress-strain relationship is then:

$$\begin{bmatrix}\dot{\varepsilon}_p^p \\ \dot{\varepsilon}_q^p\end{bmatrix} = \frac{1}{h}\begin{bmatrix}n_p m_p & n_q m_p \\ n_p m_q & n_q m_q\end{bmatrix}\begin{bmatrix}\dot{p}' \\ \dot{q}\end{bmatrix} \tag{18}$$

The moisture content v_w can be written in an incremental form $\dot{v}_w = \dot{S}_r e + S_r \dot{e}$. It follows that:

$$\frac{\partial S_r}{\partial s}(v-1)\dot{s} + S_r(\alpha\gamma+1)\dot{v} = \dot{v}_w \tag{19}$$

where $\partial S_r/\partial s = \alpha S_r/s$ when the state is on main wetting or drying curves and $\partial S_r/\partial s = \beta S_r/s$ when the state is on a scanning curve.

The complete stress-strain relationship is:

$$\begin{bmatrix}\dot{\varepsilon}_p \\ \dot{\varepsilon}_q\end{bmatrix} = \begin{bmatrix}\frac{1}{K}+\frac{n_p m_p}{h} & \frac{n_q m_p}{h} \\ \frac{n_p m_q}{h} & \frac{1}{3G}+\frac{n_q m_q}{h}\end{bmatrix}\begin{bmatrix}\dot{p}' \\ \dot{q}\end{bmatrix} \tag{20}$$

To aid numerical implementation this can be rearranged to give:

$$\begin{bmatrix}\dot{\varepsilon}_p \\ \dot{\varepsilon}_q \\ \dot{v}_w\end{bmatrix} = \begin{bmatrix}D_{11} & D_{12} & D_{13} \\ D_{21} & D_{22} & D_{23} \\ D_{31} & D_{32} & D_{33}\end{bmatrix}\begin{bmatrix}\dot{p}' \\ \dot{q} \\ \dot{s}\end{bmatrix} \tag{21}$$

where

$$D_{11} = \frac{1}{K}+\frac{\hat{n}_p m_p}{\hat{h}} \quad D_{12} = \frac{\hat{n}_q m_p}{\hat{h}} \quad D_{13} = \frac{\hat{n}_s m_p}{\hat{h}}$$

$$D_{21} = \frac{\hat{n}_p m_q}{\hat{h}} \quad D_{22} = \frac{1}{3G}+\frac{\hat{n}_q m_q}{\hat{h}} \quad D_{23} = \frac{\hat{n}_s m_q}{\hat{h}}$$

$$D_{31} = -vS_r(\alpha\gamma+1)\left(\frac{1}{K}+\frac{\hat{n}_p m_p}{\hat{h}}\right) \quad D_{32} = -vS_r(\alpha\gamma+1)\frac{\hat{n}_q m_p}{\hat{h}}$$

$$D_{33} = -vS_r(\alpha\gamma+1)\left[\frac{\hat{n}_s m_p}{\hat{h}}+\frac{\partial S_r}{\partial s}(v-1)\right]$$

In the rearranged form the hardening modulus has become $\hat{h} = \hat{h}_b + \hat{h}_f$. **m** is unchanged. $\hat{n}$ is given by (Morvan et al. 2010) $\hat{n} = [\hat{n}_p, \hat{n}_q, \hat{n}_s]^T$. $\hat{h}_f$ and $\hat{h}_b$ are related to h_f and h_b. $\hat{h}_f$ and $\hat{h}_b$ are:

$$\hat{h}_f = \hat{k}_m\frac{\partial \bar{p}'_c}{\partial \varepsilon_p^p}\frac{p'}{\bar{p}'_c}\frac{\bar{p}'_c - p'_c}{p'_c}\left(\eta_b - \frac{q}{p'}\right) \tag{22}$$

$$\hat{h}_b = -\frac{\partial F}{\partial \bar{p}'_c}\frac{\partial \bar{p}'_c}{\partial \varepsilon_p^p}\frac{m_p}{\sqrt{\left(\frac{\partial F}{\partial p'}\right)^2+\left(\frac{\partial F}{\partial q}\right)^2+\left(\frac{\partial F}{\partial \bar{p}'_c}\frac{\partial \bar{p}'_c}{\partial s}\right)^2}} \tag{23}$$

4 CAVITY EXPANSION ANALYSIS

The expanding cavity is surrounded by soil in which deformation comprises a combination of elastic and plastic strains. The elastic-plastic region is surrounded by soil which deforms purely elastically. The radius of the expanding cavity is denoted c and the radius of the elastic-plastic boundary is denoted R. The radius of a particular soil element is denoted r. Only spherical cavities expanded from zero initial radius are considered here.

The radial stress (σ'_r) represents the major principal stress and the tangential stress (σ'_θ) represents the minor principal stress. p' and q are defined in terms of

σ'_r and σ'_θ. ε_p and ε_q are related to radial strain ε_r and tangential strain ε_θ.

$$p' = \frac{\sigma'_r + 2\sigma'_\theta}{3},\ q = \sigma'_r - \sigma'_\theta,\ \varepsilon_p = \varepsilon_r + 2\varepsilon_\theta,\ \varepsilon_q = \frac{2(\varepsilon_r - \varepsilon_\theta)}{3} \quad (24)$$

ε_r and ε_θ at r are defined in terms of radial displacement u of the soil element at r by $\varepsilon_r = -\partial u/\partial r$ and $\varepsilon_\theta = -u/r$. Stress or strains expressed in rate form using the symbol $(^\circ)$ denote the material time derivative. $(\dot{})$ denotes the local time derivative. These are related by $(^\circ) = (\dot{}) + w(\partial)/r$, where w is the radial velocity of the soil element at r. The radial and tangential strain rates at any instant are then defined in terms of w and r as $\mathring{\varepsilon}_r = -\partial w/\partial r\, \mathring{\varepsilon}_\theta = -w/r$.

The solution for displacement in an elastic region for $R \le r \le \infty$ is $u = \varepsilon_R (R/r)^2 R$, where ε_R is the tangential strain at the elastic-plastic boundary. For cavities expanded in soils of infinite radial extent, the elastic region has zero volumetric strain, thus p', K and G are constant throughout the entire elastic region. An expression for q then becomes $q = 6G\varepsilon_R (R/r)^3$. Then at the elastic-plastic boundary $\varepsilon_R = q_i/G_i/6$ (Carter et al. 1986).

Ten differential equations govern soil behavior in the elastic-plastic region. The ten equations involve ten variables and can be presented in differential form and solved as an initial value problem.

The stress equilibrium equation is:

$$\frac{\partial p'}{\partial r} + \frac{2}{3}\frac{\partial q}{\partial r} + \frac{2q}{r} - \left(\psi \frac{\partial s}{\partial r} + \chi \Omega \frac{s}{s_e} \frac{\partial s_e}{\partial r} \right) = 0 \quad (25)$$

in which $\psi = (1 - \Omega)\chi$ when the soil state is on main drying or wetting curves and $\psi = (1 - \zeta)\chi$ when on scanning curves.

The incremental forms of plastic strains come directly from the bounding surface model:

$$\mathring{\varepsilon}_p - \mathring{\varepsilon}_p^e = \frac{m_p}{\hat{h}} \left(\hat{n}_p \mathring{p}' + \hat{n}_q \mathring{q} + \hat{n}_s \mathring{s} \right) \quad (26)$$

$$\mathring{\varepsilon}_q - \mathring{\varepsilon}_q^e = \frac{m_q}{\hat{h}} \left(\hat{n}_p \mathring{p}' + \hat{n}_q \mathring{q} + \hat{n}_s \mathring{s} \right) \quad (27)$$

The rate forms for s_{ae} and s_{ex} are $\mathring{s}_{ae} + C_1 \gamma (v-1)^{-\gamma-1} \mathring{v} = 0$ and $C_2\, \mathring{s}_{ex} - \mathring{s}_{ae} = 0$.

Suction has a multiplicative effect on hardening:

$$\mathring{\bar{p}}'_c = -\frac{\bar{p}'_c}{\lambda(s) - \kappa} \mathring{v} - \frac{v}{K} \frac{\bar{p}'_c}{\lambda(s) - \kappa} \mathring{p}' + \frac{\bar{p}'_c}{\lambda(s) - \kappa} \left(\frac{1}{N(s)} \frac{\partial N(s)}{\partial s} - \ln \bar{p}'_c \frac{\partial \lambda(s)}{\partial s} \right) \mathring{s} \quad (28)$$

The consistency equation causes the stress state to remain on the loading surface so that:

$$\frac{\partial f}{\partial p'} \mathring{p}' + \frac{\partial f}{\partial q} \mathring{q} + \frac{\partial f}{\partial p'_c} \mathring{p}'_c = 0 \quad (29)$$

The continuity equation links the rate of volumetric change to the total strain rates ensuring the conservation of solid mass:

$$\frac{\mathring{v}}{v} = \frac{\partial w}{\partial r} + \frac{2w}{r} \quad (30)$$

Two drainage conditions were considered by Russell & Khalili (2006a), namely a constant s condition and a constant v_w condition, controlled by $\mathring{s} = 0$ and $\mathring{v}_w = 0$. Here a third condition is also considered, that is constant χs:

$$\mathring{\chi} s + s \mathring{\chi} = \mathring{s} \psi + \chi \Omega \frac{s}{s_e} \mathring{s}_e = 0 \quad (31)$$

In the elastic region the solution procedure is straightforward and involves using the above closed form expressions for stresses, strains and velocity in terms of r and R. In the elastic-plastic region the solution procedure is more complex and involves solving a set of differential equations as an initial-value problem. Of the ten variables some at the elastic-plastic boundary may be taken as being equal to the far-field values as no volume change occurs in the elastic region. These include p'_0, v_0, s_0, v_{w0}, s_{ae0} and s_{ex0}, where the subscript 0 denotes initial value. Initial values of the others require definition.

p'_c at the elastic-plastic boundary, which controls the size of the purely elastic region, satisfies:

$$p'_{c0} = \exp\left[\left(M_y / M_{cs} \right)^Q \ln R \right] p'_0 \quad (32)$$

with M_y being a constant slightly larger than zero, necessary to avoid a singularity at the initial condition. q_0 is associated with M_y through $q_0 = M_y p'_0$.

$\bar{p}'_c$ at the elastic-plastic boundary is:

$$\bar{p}'_{c0} = \exp\left(\frac{\ln N(s) - \ln e - \kappa \ln p'_0}{\lambda(s) - \kappa} \right) \quad (33)$$

The non-dimensional boundary velocity $\tilde{w}_0$ is:

$$\tilde{w}_0 = -\dot{u}/\dot{R} = q_0/2G_0 \quad (34)$$

The governing equations are expressed as functions of a dimensionless radial coordinate, η, defined as (Collins et al. 1992) $\eta = r/R = r/Wt$, where W is the velocity of the expansion at the elastic-plastic boundary. The variables can then be converted from a rate form to differential form using:

$$\left(\mathring{} \right) = \frac{W(\tilde{w} - \eta)}{R} \frac{\mathrm{d}}{\mathrm{d}\eta} \quad (35)$$

where $\tilde{w} = w/W$ is the non-dimensional radial velocity at r. Variables p', q, p'_c, $\bar{p}'_c$, v, w, s, v_w, s_{ex} and s_{ae} may then be determined for any particular value of η throughout the elastic-plastic region. Of interest is $\eta = \tilde{w}$ as it represents the state at the cavity wall, which is also at the critical state (Collins et al. 1992).

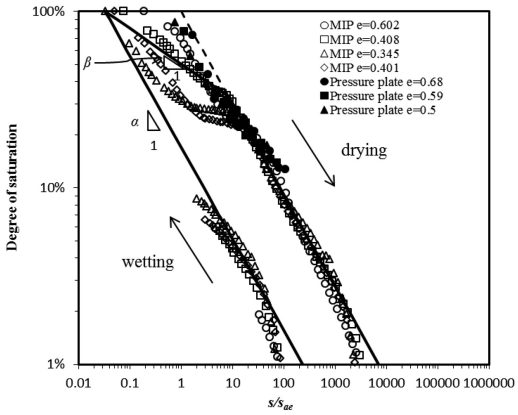


Figure 2. The SWCC inferred from results of mercury intrusion/extrusion (MPI) tests and pressure plate tests.

Table 1. Parameters $N(s)$ and $\lambda(s)$ defining LICLs.

s (kPa)	$s \le s_{ex}$	$s^* = 10$	100	300
$N(s)$	0.52	1.48	1.58	1.81
$\lambda(s)$	0.08	0.156	0.160	0.170

5 SOIL AND MODEL PARAMETERS

The soil is Lyell silty sand, a decomposed granite, which is predominantly coarse-grained but well-graded. The particle and pore size distributions are fractal with $D_s = 2.61$ and $D_p = 2.48$. Also, $C_1 = 1.5$ kPa, $C_2 = 30$, $\alpha = -0.52$, $\gamma = 2.61$ and $\beta = -0.2$, $s_{ae} = 1.5e^{-2.61}$ kPa and $s_{ae} = 30 s_{ex}$ describe the SWCC (Figure 2) (Russell 2014, Yang et al. 2014).

Model parameters were found by fitting simulations to experimental data from triaxial, oedometric compression and isotropic compression tests, performed on samples in saturated states under drained and undrained conditions and in unsaturated states. They include $\kappa = 0.012$, $\mu = 0.4$, $M_{cs} = 1.45$ (for both saturated and unsaturated conditions), $A = 1.2$, $Q = 3.0$ and $R = 2.30$. $\lambda(s)$ and $N(s)$ for different suction values are listed in Table 1. $\lambda(s)$ and $N(s)$ for intermediate suction values are found by linear interpolation. Wetting collapse for this soil commences in experiments when suction is between 13.8 kPa and 6.9 kPa, with an average of 10 kPa (denoted s^*). The suction values considered here all lie above well this value. $\hat{k}_m$ that fits the data well is:

$$\hat{k}_m = \frac{\langle \xi_0 + 0.33 \rangle 1.891 e^{-12.9\xi_0} - \langle -\xi_0 - 0.33 \rangle 0.949 e^{-0.08\xi_0}}{(\xi_0 + 0.33)} \quad (36)$$

where ξ_0 is the initial state parameter and $\langle x \rangle = x$ if $x > 0$ and $\langle x \rangle = 0$ if $x \le 0$.

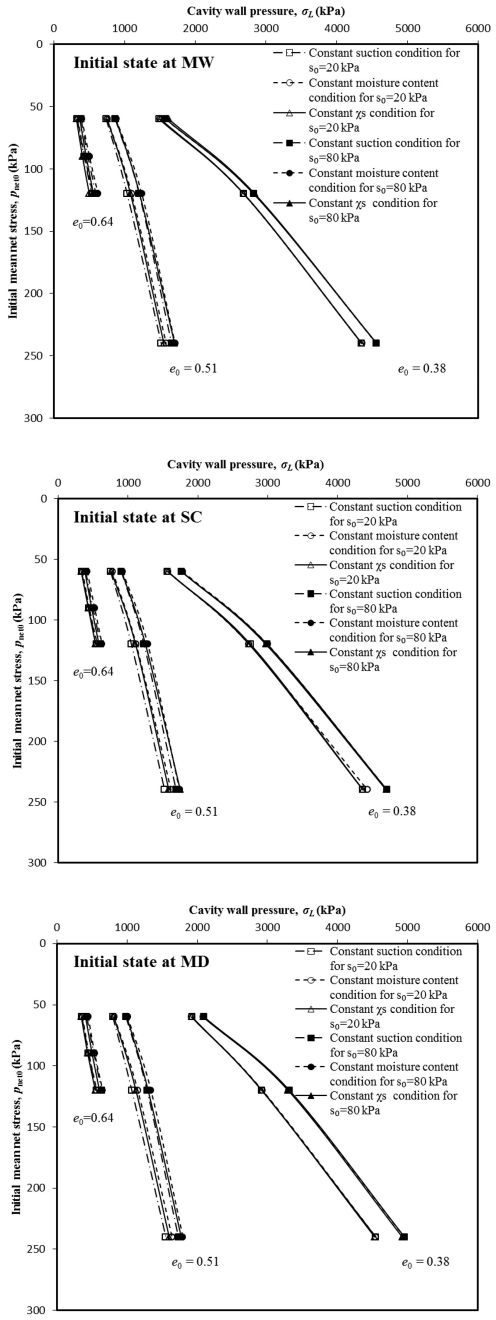


Figure 3. Cavity expansion results in the $p_{net0} \sim \sigma_L$ plane for $s_0 = 20$ kPa and 80 kPa; $e_0 = 0.64$, 0.51 and 0.38 under a constant s, constant v_w and constant χs conditions, for initial states on the main wetting (MW) and main drying (MD) curves and the midpoint of a scanning curve (SC).

6 CAVITY EXPANSION RESULTS

Cavity expansion results are generated for a range of initial states involving $p_{net0} = 60$ kPa, 90 kPa, 120 kPa or 240 kPa, $s_0 = 20$ kPa, 40 kPa and 80 kPa and

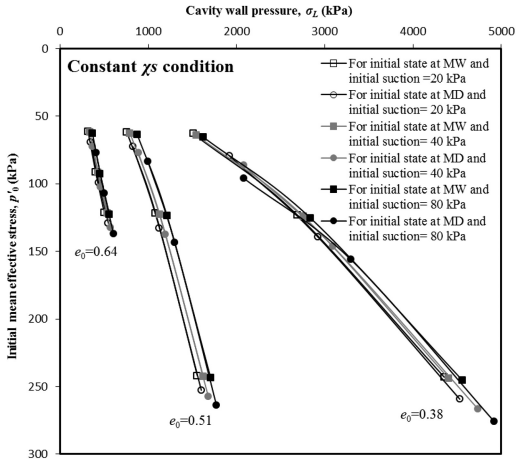


Figure 4. Cavity expansion results in the $p'_0 \sim \sigma_L$ plane for $s_0 = 20$ kPa, 40 kPa and 80 kPa; $e_0 = 0.64$, 0.51 and 0.38 for initial states at MW and MD under constant χs conditions.

$e_0 = 0.38$, 0.51 or 0.64 under constant s, constant v_w or constant χs conditions. Initial states on a main drying curve (MD), main wetting curve (MW) or at the midpoint of a scanning curve (SC) are also considered.

Values of the net radial stress at the cavity wall, denoted σ_L, are plotted against p_{net0} for a range of s_0, e_0 and drainage conditions in Figure 3. The effects of locations of initial states on the SWCC (MW, SC and MC), and drainage conditions can be observed.

The values of σ_L for the three initial hydraulic state locations are quite different. For a given s_0, σ_L for initial hydraulic states at MD are always larger than that for initial hydraulic states at MW. The differences between σ_L at MD and at MW become greater as s_0 increases. As s has a reduced affect on σ_L as p_{net0} increases the hydraulic hysteresis also has a reduced affect. The σ_L for a constant χs condition is a good approximation to the other two.

Figure 4 presents results for constant χs conditions. The results for initial hydraulic states SC are always between those for MD and MW. The results for SC are not shown to improve clarity. In this Figure σ_L is plotted against p'_0. For a given s_0 the results for MW and MD almost overlap. This indicates that the effect of hydraulic hysteresis is largely removed in plots of σ_L against p'_0. However, hysteresis and the location of the hydraulic state on the SWCC influences the determination of χs within p'_0. Evidently, as long as p'_0 is correctly determined, the hydraulic hysteresis influence on the subsequent cavity expansion results can be assumed negligible when results are viewed in the σ_L versus p'_0 plane.

7 CONCLUSION

For this soil the constant moisture content condition is associated with the largest cavity wall pressures whilst the constant suction condition is associated with the lowest. A constant χs condition produces cavity wall pressures in between those for the other two drainage conditions. Assuming a constant χs condition at all times would be associated with errors that are always less than 10%. Further, cavity wall pressures for different initial hydraulic state locations were indistinguishable when plotted against p'_0. Evidently, as long as p'_0 is correctly determined, the hydraulic hysteresis influence on the cavity expansion results can be assumed negligible. This may simplify interpretation of a CPT or PMT. Even when testing occurs quickly, meaning a constant moisture content condition prevails, a constant χs condition (being equal to the in situ value) can be assumed without loss of significant accuracy.

REFERENCES

Been, K. & Jefferies, M.G. 1985. A state parameter for sands. *Geotechnique* 35(2): 99–112.

Carter, J.P., Booker, J.R. & Yeung, S.K. 1986. Cavity expansion in cohesive frictional soils. *Geotechique* 36(3): 349–358.

Collins, I.F., Pender, M.J. & Wang Yan. 1992. Cavity expansion in sands under drained loading conditions. *Int. J. Num. Anal. Methods Geomech.* 16(1): 3–23.

Dafalias, Y.F. 1986. Bounding surface plasticity. I: Mathematical foundation and hypoplasticity. *Journal of Engineering Mechanics* 112(9): 966–987.

Khalili, N. & Zargarbashi, S. 2010. Influence of hydraulic hysteresis on effective stress in unsaturated soils. *Geotechnique* 60(9): 729–734.

Morvan, M., Wong, H. & Branque, D. 2010. An unsaturated soil model with minimal number of parameters based on bounding surface plasticity. *Int. J. Num. Anal. Methods Geomech.* 34(14): 1512–1537.

Pournaghiazar, M., Russell, A.R. & Khalili, N. 2013. The cone penetration test in unsaturated sands. *Geotechnique* 63(14): 1209–1220.

Russell, A.R. & Buzzi, O. 2012. A fractal basis for soil-water characteristics curves with hydraulic hysteresis. *Geotechnique* 62(3): 269–274.

Russell, A.R. & Khalili, N. 2006a. On the problem of cavity expansion in unsaturated soils. *Computational Mechanics* 37(4): 311–330.

Russell, A.R. & Khalili, N. 2006b. A unified bounding surface plasticity model for unsaturated soils. *Int. J. Num. Anal. Methods Geomech.* 30(3): 181–212.

Russell, A.R. 2014. How water retention in fractal soils depends on particle and pore sizes, shapes, volumes and surface areas. *Geotechnique* 64(5): 379–390.

Yang, H. & Russell, A.R. 2015. Cavity expansion in unsaturated soils exhibiting hydraulic hysteresis considering three drainage conditions. *Int. J. Num. Anal. Methods Geomech.* DOI: 10.1002/nag.2379.

Yang, H., Khoshghalb, A. & Russell, A.R. 2014. Fractal-based estimation of hydraulic conductivity from soil water characteristic curves considering hysteresis. *Geotechnique Letters* 4: 1–10.

Unsaturated Soil Mechanics—from Theory to Practice – Chen et al. (Eds)
© 2016 Taylor & Francis Group, London, ISBN 978-1-138-02921-7

Translational slip failures on slope incorporating unsaturated soil mechanics

W. Huang, E.C. Leong & H. Rahardjo
School of Civil and Environmental Engineering, Nanyang Technological University, Singapore

ABSTRACT: Many slopes experienced shallow translational slips due to rainwater infiltration. Infinite slope model has been widely used for such landslides in past decades. It is widely stated that infinite slope analysis is valid when the depth of the sliding mass is much smaller than its length, but how the depth/length ratio influences the accuracy of analysis was rarely investigated in the literature. By comparing the factor of safety obtained by infinite slope analysis and finite element analysis to slopes of finite length and with real boundary conditions, the influence of depth/length ratio on the accuracy of infinite slope analysis is investigated. The error caused by infinite slope analysis is found to be highly linear with respect to the depth/length ratio of the failing mass. It is important to consider the depth/length ratio in order to check the accuracy of the infinite slope model in translational slip analysis.

1 INTRODUCTION

Infinite slope model has two assumptions: First, strata of different strengths exist, and the sliding surface is more likely to pass through the stratum of lower shear strength (Craig, 2004; Duncan and Wright, 2005). Second, the depth of the sliding surface is much smaller than the length of slope, so that the boundary resistance can be neglected (Taylor 1948). Due to rainwater infiltration, the matric suction above the wetting front is greatly reduced and the wetted soil can be considered as a weak layer compared with the underlying unsaturated soil. Besides, most rainfall-induced landslides were reported to be shallow compared with its length. Hence, the two assumptions of infinite slope model are satisfied by most rainfall-induced landslides, which justify the wide use of the infinite slope model in the analysis (Pradel and Raad, 1993; Cho and Lee, 2002; Collins and Znidarcic, 2004; Lu and Godt, 2008; Cho, 2009; Godt et al., 2012).

Although it is widely known that infinite slope analysis is only valid when the depth of the sliding mass is much smaller than its length (e.g. Iverson, 2000; Collins and Znidarcic, 2004; Godt et al., 2012), the depth/length ratio was rarely reported and how the depth/length ratio influences the accuracy of analysis result was rarely investigated in the literature.

Griffiths et al. (2011) compared the factors of safety of slopes calculated by infinite slope analysis and finite element analysis. In the finite element analysis, the slopes were of finite length with boundary resistances. It was found that factors of safety obtained by infinite slope analysis were always conservative, and the infinite slope solutions approached the factors of safety estimated by the finite element analysis when the length of the slope is much larger than its depth. However, so far the relationship between depth/length ratio and the error caused by infinite slope analysis has not beendeveloped.

The purpose of this paper is to investigate how the depth/length ratio influences the accuracy of infinite slope analysis. By comparing the factors of safety obtained by finite element analysis and infinite slope analysis, the influence of depth/length ratio on the accuracy of infinite slope analysis is investigated, and the relationship between depth/length ratio and the error caused by the infinite slope analysis is constructed.

2 EQUATIONS OF INFINITE SLOPE MODEL

Figure 1 shows a shallow translational slip due to rainwater infiltration. The height of the slope is H, the slope angle is β, and the length of the slope is l which can be considered as the maximum length for a possible translational slip. The wetting front is parallel to the ground surface with vertical depth of z_w and normal depth of d. The groundwater table is assumed to be parallel to the ground surface with vertical distance of H_{wt}. The possible pore-water pressure profiles a, b and c in a residual soil slope as suggested by Rahardjo et al. (1995) are also illustrated in Figure 1. Under no infiltration condition the distribution of pore-water pressure is assumed to be hydrostatic and the pore-water pressure at ground surface is equal to $-\gamma_w H_{wt} \cos\beta^2$. Under rainwater infiltration condition, the pore-water pressure distributions are non-hydrostatic (profiles a, b and c). Profile a represents the situation where the matric suction is reduced to zero at the ground surface and the suction increases with depth until it reaches the hydrostatic

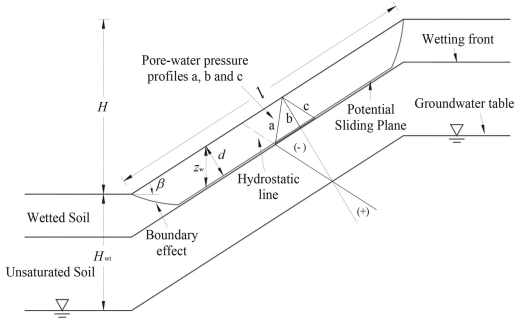


Figure 1. Model of shallow translational slip.

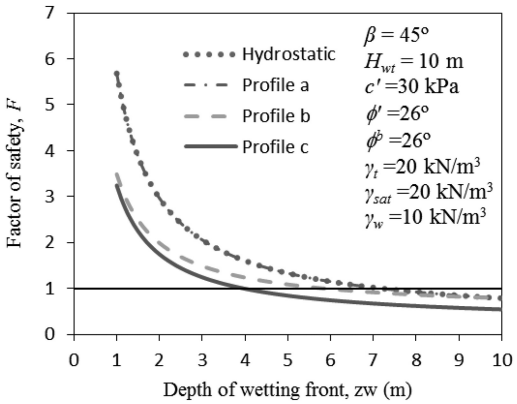


Figure 2. Factor of safety for various depths of wetting front under different pore-water pressure profiles.

line at z_w. Profile a tends to occur in fine-grained soils (Lee et al., 2009). Profile b represents the situation where the matric suction above wetting front is reduced to zero as suggested by Lumb (1962), and it tends to occur in coarse-grained soils (Lee et al., 2009). Profile c corresponds to the situation where positive pore-water pressure builds up and it is equal to $\gamma_w z_w \cos\beta^2$ at the wetting front. Profile c tends to happen in a layered soil system (Ng and Bruce, 2007).

If the depth/length ratio (d/l) is small, the boundary resistance is negligible, slope can be treated as "infinite" and limit equilibrium method using a modified Mohr-Coulomb failure criteria (Fredlund et al. 1978) can be applied to calculate the factor of safety.

Under no infiltration condition, the factor of safety can be expressed as,

$$F = \frac{c'}{\gamma_t z \sin\beta\cos\beta} + \frac{\tan\phi'}{\tan\beta} + \frac{\gamma_w}{\gamma_t}\left(\frac{H_{wt}}{z} - 1\right)\frac{\tan\phi^b}{\tan\beta} \quad (1)$$

where c' is effective cohesion, φ' is effective angle of internal friction, φ^b represents the rate of increase of shear strength due to matric suction, γ_t is total unit weight of the soil, γ_w is unit weight of water, z is vertical depth of the potential sliding plane.

Under infiltration condition with profile a, the unit weight of the soil above the wetting front is assumed to be equal to its saturated unit weight γ_{sat}. For sliding plane at vertical depth of z ($0 < z \le z_w$), the factor of safety can be expressed as,

$$F = \frac{c'}{\gamma_{sat} z \sin\beta\cos\beta} + \frac{\tan\phi'}{\tan\beta} + \frac{\gamma_w}{\gamma_{sat}}\left(\frac{H_{wt}}{z_w} - 1\right)\frac{\tan\phi^b}{\tan\beta} \quad (2)$$

From Equation (2), it can be easily shown that F is minimum when $z = z_w$ and $F_{\min}$ is equal to the F calculated by Equation (1) when $\gamma_t = \gamma_{sat}$ and $z = z_w$.

Under infiltration with profiles b and c, it is obvious that the most critical slip surface would be located at the wetting front $z = z_w$.

For profile b,

$$F = \frac{c'}{\gamma_{sat} z_w \sin\beta\cos\beta} + \frac{\tan\phi'}{\tan\beta} \quad (3)$$

For profile c,

$$F = \frac{c'}{\gamma_{sat} z_w \sin\beta\cos\beta} + \frac{\tan\phi'}{\tan\beta} - \frac{\gamma_w}{\gamma_{sat}}\frac{\tan\phi'}{\tan\beta} \quad (4)$$

For illustration, a residual soil slope of the Jurong Formation in Singapore is used. The typical soil properties of the residual soil of the Jurong Fromation in Singapore reported by Rahardjo et al. (1995) are: c' varies from 30 to 45 kPa, $\varphi^b \approx \varphi' = 26°$ for matric suction up to 400 kPa, $\gamma_t \approx \gamma_{sat} = 20\,\text{kN/m}^3$. For a slope with slope angle $\beta = 45°$ and depth of groundwater table $H_{wt} = 10$ m, the factors of safety for various depths of wetting front with different pore-water pressure profiles are shown in Figure 2. Since $\gamma_t = \gamma_{sat}$, F would be the same for same depths of wetting front under no infiltration hydrostatic condition and infiltration with profile a pore-water pressure distribution. For profiles a, b and c, F would fall below 1 when z_w is larger than 7.1 m, 5.8 m and 4 m, respectively. The above conclusions are valid when boundary resistances of the translational slips are negligible. However, for slope of fixed height H and length l, with the increase in z_w and therefore d ($=z_w \cos\beta$), depth/length ratio d/l would also increase and the boundary effects become more and more considerable. Thus, slopes reported to be unstable by infinite slope analysis may still be stable due to the contribution of the boundary resistances. In order to check the validity of infinite slope model, it is necessary to consider the length (height) of the slope, and this will be shown in the next section.

3 INFLUENCE OF d/l ON VALIDITY OF INFINITE SLOPE MODEL

The factor of safety of a translational slip which considers the boundary resistance can be calculated by using shear strength reduction finite element method (Griffiths et al., 2011). By comparing the factor of

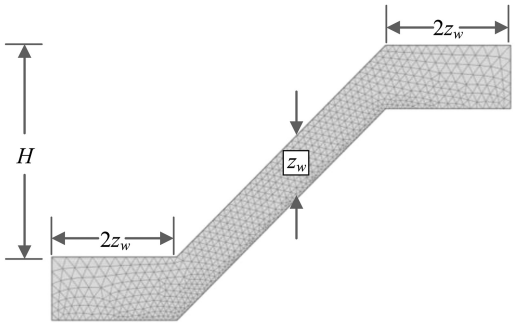


Figure 3. Finite element Mesh.

safety obtained by finite element analysis (FEA, considering the boundary effect) and infinite slope analysis (ISA, neglecting the boundary effect) to slopes of finite length and with real boundary conditions, the influence of depth/length ratio on the accuracy of infinite slope analysis can be investigated.

Plaxis 2D (2012) was used in this study. A typical finite element mesh used is shown in Figure 3. The global coarseness of the mesh was set to be "very fine", but the mesh near the bottom boundary was made finer. As suggested by Griffiths et al. (2011), the length of the left and right boundaries were two times the depth of the wetting front, the bottom boundaries were fixed, the left and right boundaries were constrained only in the horizontal direction.

The soil properties and geometry conditions listed in Figure 2 were adopted. The Young's modulus E, Poisson's ratio ν and dilation angle ψ have little influence on the stability predictions (Milledge et al., 2012) and were set to be 10^5 kPa, 0.3 and 0, respectively. Depth of wetting front z_w ranged from 1 m to 10 m with an interval of 1 m and $H = 10$ m, 20 m and 30 m were used for the parametric study.

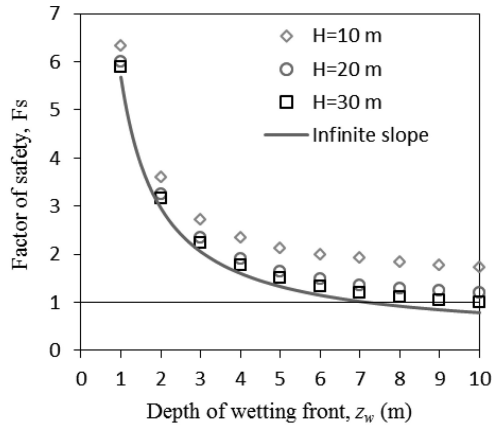
The results are shown in Figures 4 (a), (b) and (c). It is found that slopes that are predicted to be unstable ($F < 1$) by ISA may still be standing with $F \geq 1$ calculated by FEA. With the increase of H, F obtained by ISA approach the F obtained by FEA for the same depth of wetting front z_w.

Since FEA considered the boundary effects, the factors of safety obtained by FEA (F_{FEA}) were treated as "corrected". The factors of safety obtained by ISA (F_{ISA}) which neglect the boundary effects are treated as "estimated". According to Equation (5), d/l is related to z_w/H. The influence of d/l on the accuracy of ISA was assessed through Equation (6).

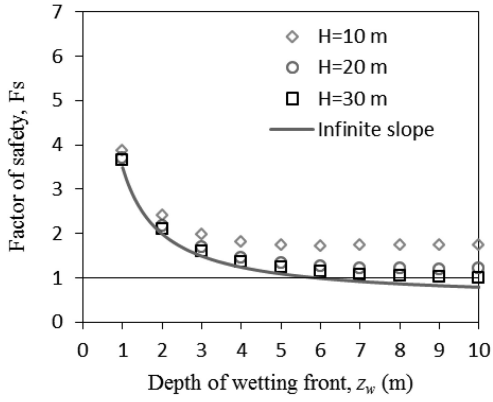
$$\frac{d}{l} = \frac{z_w}{H}\sin\beta\cos\beta \tag{5}$$

$$Error(\%) = \frac{F_{FE} - F_{IS}}{F_{IS}} \times 100\% \tag{6}$$

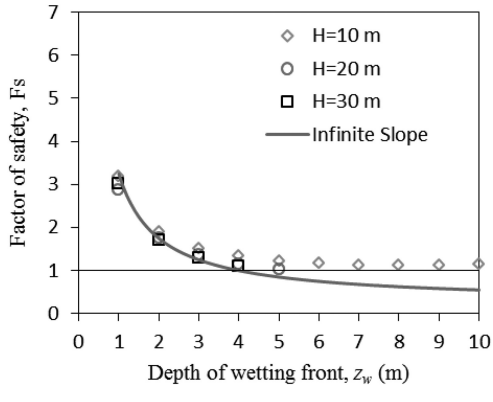
The errors for the results presented in Figure 4 were analyzed. Figure 5 shows the relationship between error (%) and d/l, in which a-10 means that the data



(a) Profile a



(b) Profile b



(c) Profile c

Figure 4. Comparison of factor of safety obtained by finite element analysis and infinite slope analysis.

were from profile a and $H = 10$ m and b-20 means that the data were from profile b and $H = 20$ m.

For profiles a and b, the values of F_{ISA} are always conservative and the errors are always positive. Most of

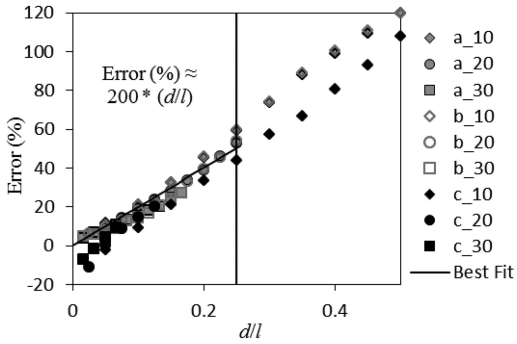
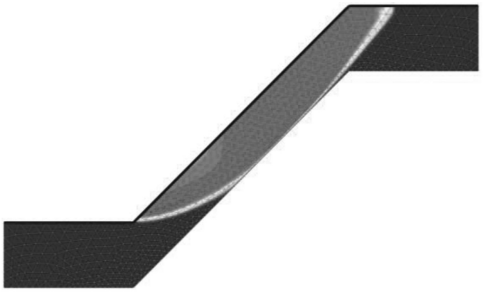
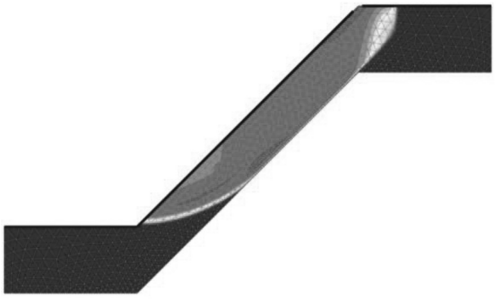


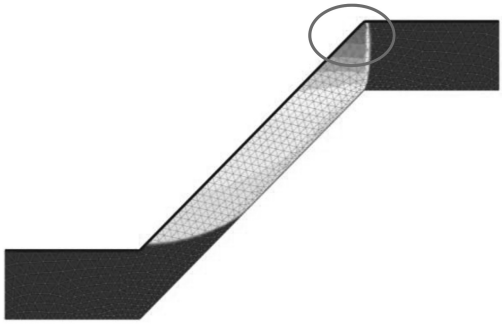
Figure 5. Relationship between Error (%) and d/l.



(a) Profile a

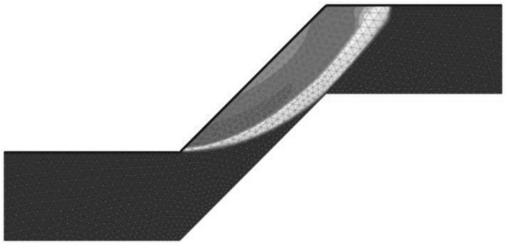


(b)Profile b

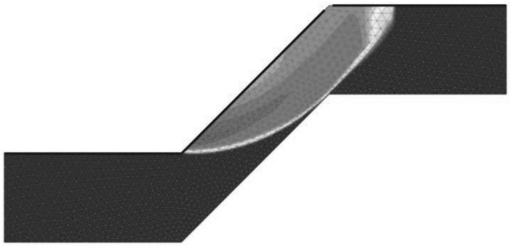


(c) Profile c

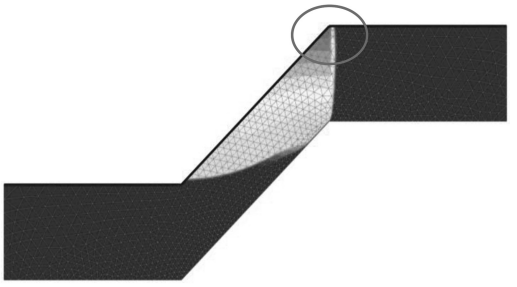
Figure 6. Failure mechanism under different pressure profiles ($z_w = 3$ m, $H = 10$ m, $d/l = 0.15$).



(a) Profile a



(b) Profile b



(c) Profile c

Figure 7. Failure mechanism under different pressure profiles ($z_w = 6$ m, $H = 10$ m, $d/l = 0.3$).

the critical slip surface would be tangential to the wetting front when $d/l \leq 0.1$. As d/l increase, boundary resistances become more and more considerable, as illustrated in Figures 6 (a) and (b) for $d/l = 0.15$. When $d/l > 0.25$, the failure mechanism obtained by FEA becomes rotational and the critical slip surface will not or only slightly be tangential to the wetting front, as shown in Figures 7 (a) and (b) for $d/l = 0.3$. In the latter situation, the comparison between FEA and ISA may not make sense, as the comparison is performed based on different failure mechanisms, rather than on the consideration of boundary effects. For $d/l \leq 0.25$, the errors caused by ISA can be estimated by Equation (7).

$$Error(\%) = 200\frac{d}{l} \tag{7}$$

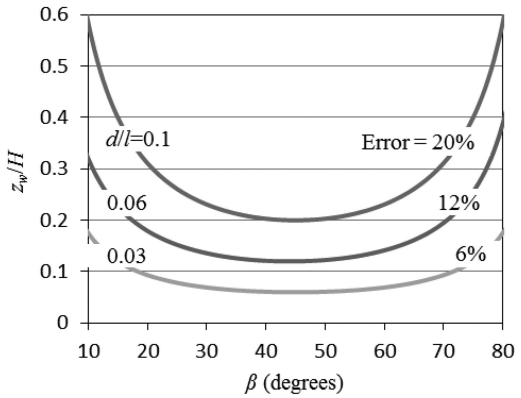


Figure 8. Relationship between z_w/H and d/l.

For profile c, F_{FEA} may be lower than F_{ISA}. The reason is that the weakest point searched by FEA is not on the wetting front, instead it is at the top corner of the slope, as indicated by the red eclipse in Figures 6 (c) and 7 (c). In this situation, the comparison between FEA and ISA may not be appropriate.

4 CONSIDERING d/l IN TRANSLATIONAL

The d/l of the shallow landslides reported by Skempton (1953) lie between the limits of 0.03 and 0.06. According to Equation (7), the error for $d/l = 0.03$ is around 6% and for $d/l = 0.06$ is around 12%. In order to limit the error caused by ISA in translational slip analysis, it is important to check the value of d/l. In order to know the value of d/l, length (l) or height ($H = l/\sin\beta$) of the slope must be known. The combination of Equations (5) and (7) can be plotted as Figure 8. It is shown that for a specific slope angle β and an allowable error (d/l), z_w/H must be limited within certain values. For example, for $\beta = 45°$, in order to ensure that the error is less than 20% ($d/l \leq 0.1$), z_w/H should be smaller than 0.2, which means that for the results shown in Figures 4(a) and (b), $z_w \leq 2$ m is required for $H = 10$ m, $z_w \leq 4$ m is required for $H = 20$ m, and $z_w \leq 6$ m is required for $H = 30$ m.

5 CONCLUSION

Infinite slope model was broadly used in rainfall-induced landslide analysis. Though it was widely stated that infinite slope model would be valid when the slip has a small depth/length (d/l) ratio, how the d/l influences the accuracy of analysis result was rarely investigated. By performing infinite slope analysis and finite element analysis to slopes of finite length and real boundary conditions, the influence of d/l on the accuracy of infinite slope analysis for translational slips under different pore-water conditions was investigated. It was found that the errors caused by infinite slope analysis are highly linear with respect to the value of d/l. In translational slip analysis, the height or length of the slope should be given in order to check the value of d/l and to judge the validity of the infinite slope model.

ACKNOWLEDGEMENT

The first author acknowledges the research scholarship provided by Nanyang Technological University, Singapore.

REFERENCES

Brinkgreve, R. B. J., Engin E. & Swolfs, W. M. 2012. Plaxis 2D 2012. *Manual*. Plaxis bv, the Netherlands.

Cho, S. E., & Lee, S. R. (2002). Evaluation of surficial stability for homogeneous slopes considering rainfall characteristics. *Journal of Geotechnical and Geoenvironmental Engineering*, 128(9), 756–763.

Cho, S. E. (2009). Infiltration analysis to evaluate the surficial stability of two-layered slopes considering rainfall characteristics. *Engineering Geology*, 105(1), 32–43.

Collins, B. D., & Znidarcic, D. (2004). Stability analyses of rainfall induced landslides. *Journal of Geotechnical and Geoenvironmental Engineering*, 130(4), 362–372.

Craig, R. F. (2004). *Craig's soil mechanics*. CRC Press. Page 347.

Duncan, J. M., & Wright, S. G. (2005). *Soil strength and slope stability*. Page 104–405.

Griffiths, D. V., Huang, J., & Dewolfe, G. F. (2011). Numerical and analytical observations on long and infinite slopes. *International Journal for Numerical and Analytical Methods in Geomechanics*, 35(5), 569–585.

Godt, J. W., Şener-Kaya, B., Lu, N., & Baum, R. L. (2012). Stability of infinite slopes under transient partially saturated seepage conditions. *Water Resources Research*, 48(5).

Fredlund, D. G., Morgenstern, N. R., and Widger, R. A. ~1978!. "The shear strength of unsaturated soils." *Can. Geotech. J.,* 15, 313–321.

Lee, L. M., Gofar, N., & Rahardjo, H. (2009). A simple model for preliminary evaluation of rainfall-induced slope instability. *Engineering Geology*, 108(3), 272–285.

Lumb, P.B.,1962. The Properties of Decomposed Granite. *Geotechnique*, vol.12, pp. 226–243.

Lu, N., & Godt, J. (2008). Infinite slope stability under steady unsaturated seepage conditions. *Water Resources Research*, 44(11).

Milledge, D. G., Griffiths, D. V., Lane, S. N., & Warburton, J. (2012). Limits on the validity of infinite length assumptions for modelling shallow landslides. *Earth Surface Processes and Landforms*, 37(11), 1158–1166.

Ng, C.W.W., Bruce, K.M., 2007. Advanced Unsaturated Soil Mechanics and Engineering. Taylor and Francis, Routledge.

Rahardjo, H., Lim, T.T., Chang, M.F., Fredlund, D.G.,1995. Shear strength characteristics of a residual soil. Canadian Geotechnical Journal 32, 60–77.

Skempton, A.W., 1953. Discussion. In: R. Glossop and G.C. Wilson (Editors), Soil Stability Problems in Road Engineering. *Proc. Inst. Civil Eng. Road Eng. Div. Meeting*, 2: 219–280.

Taylor, D. W. (1948). Fundamentals of soil mechanics. *Soil Science*, 66(2), 161. Page 418–431.

This page intentionally left blank

Unsaturated Soil Mechanics—from Theory to Practice – Chen et al. (Eds)
© 2016 Taylor & Francis Group, London, ISBN 978-1-138-02921-7

Investigation on the failure mechanisms of unsaturated high loess slope triggered by irrigation

X.T. Zhang, T.L. Li & W.H. Liu
Department of Geological Engineering, Chang'an University, Xi'an, Shaanxi, China

ABSTRACT: The loess platform to the south bank of The Jinghe River in Shaanxi province, China, is an irrigation farmland. Because of the river side erosion, a high loess slope had been formed in the northern side of the platform and a series of irrigation-induced landslides occurred in the side since 1980s. In this paper, the landslides at the high loess slope were investigated. The undisturbed loess samples were taken to determine the basic physical properties and particle components. The soil-water characteristic curve was estimated by the modified Kovacs method while the hydraulic conductivity function was determined by Van Genuchten method based on the loess physical indexes and particle size distribution. Then a model of the high slope was built up to simulate the irrigation and infiltration processes as well as the stability variation. The results show that, the groundwater level rises with the infiltration of irrigation water, and the pore water pressure in the slope increases. The slope stability is not decreased until irrigation water reaches the original groundwater level. When the water level rises to a certain extent, soil on potential sliding surface is almost saturated, and the landslide occurs.

1 INTRODUCTION

With development of agricultural irrigation systems and increase of irrigation quantity in the loess platform, the groundwater level rises, seriously affecting the stability of the high loess slope, and triggering a series of landslides. The landslides have occurred frequently and in large scale since the irrigation system began to work in 1970s. The typical zones where landslides concentrating include the sides of the Heifangtai loess platform in Yongjing county, Gansu province; south-west side (Baoji-Changxing) and north east side (Liquan-Jingyang) of the Weibei loess platform in the Guanzhong plain, Shaanxi province. The Hei-Fang platform is composed of two high flat lands with total irrigation area of 10 km^2. Loess landslides around the platform began to occur in 1983 after the irrigation system began to work in 1968. Investigation reveals that in the 27 years between 1983 and 2010, there are 72 landslides occurring at the sides of the platform causing 37 causalities and more than 100 injured (Zhao 2013). The south-west side of the Weibei loess platform has a 98 km long irrigation canal from Baoji to Changxing. The zone has occurred more than 110 landslides since the canal had been built up and utilized in 1971 (Zhang & Li 2011). Leakage of the canal is the main cause of landslides. The north-east side of the Weibei loess platform is a 28 km long high and steep loess slope from Liquan to Jingyang, Where is close to the south bank of The Jinghe River and the slope is formed by the river side erosion. The zone has occurred a large number of landslides since the irrigation system on the top of the platform began to work in 1976. The total sliding mass of the whole landslides is 1000×10^4 m^3, of which, more than 30 landslides is over 30,000 m^3 in size. The landslides have killed 30 persons, damaged 240 residential houses and 2.3 km^2 farmlands (Li 2012).

Due to the severe results, the landslides, triggered by irrigation in the sides of loess platforms have been attracting much attention of the researchers. For Hei-Fang platform irrigation area, Hu (2013) studied the changes of engineering geological properties of loess caused by irrigation, Zhao (2013) studied the failure mechanism of irrigation-induced loess slide-flow, and concluded that when irrigation water infiltrate from the loess layer, the soil is almost saturated, and matric suction decreases; Wang (2001) studied the mechanism for movement of irrigation-induced high-speed loess landslide, and proposed loess creeping liquefaction mechanism. For southern plateau of Jingyang on the south bank of The Jinghe River, Lei (1995) studied the hazards of loess landslides and the relationships with the channel water into field, and concluded that the groundwater table rise caused shearing strength much decreases, which accelerated formation of landslides; Sang (2007) studied on stability of table land slopes and causes for landslides on southern-bank of lower reaches of The Jinghe River, and concluded that the essential cause of landslide occurred was groundwater level rising; Jin (2007) studied the mechanism of irrigation-induced landslides of loess, and concluded that loess slope transformed from unsaturated state to saturated state under the condition of rainfall or irrigation infiltration, the soil on the potential sliding surface occurred shear shrinkage because of pore

water pressure increased, then the landslide occurred. Wang (2013) studied the mechanisms and simulation of the rapid long run-out loess landslide. Previous studies of landslides triggered by irrigation often focused on saturated soil, but in fact the intermittent irrigation water infiltration is an unsaturated seepage problem, and so far there has been little research on analyzing stability of unsaturated loess high slope under the condition of irrigation infiltration.

This research focused on the Dongfeng landslide which occurred in the southern plateau of Jingyang County, Shaanxi Province of China. Based on the field investigation and laboratory tests, obtained the water-soil characteristic curve and set up a model of the pre-failure slope to simulate the irrigation and infiltration process and change in stability of unsaturated loess high slope.

2 GEOLOGICAL CHARACTERS OF THE LANDSLIDE

There are some landslides triggered by irrigations scattering on the southern plateau of Jingyang, which is located at the south bank of The Jinghe River in Jingyang County (Fig. 1). The platform is 27.1 km in length from east to west, with a broad area of 70 km^2, and the terrain is high in the northwest and low in the southeast. The loess high slopes located at the bank of The Jinghe River, are controlled by tectonic movement and lateral erosion of The Jinghe River, with the slope height 70–90 m and the slope angle\varying in the range from 45° to 70°. The high-steep terrace of the slopes provides gravitational potential for the landslides occurrence.

The Dongfeng landslide occurring on July 7, 2003 is choosen as a study case. It's 500 m away from Dongfeng Country, Jingyang County, Shaanxi Province, China (Fig. 1). In-situ observations show that the front of the landslide is on the first terrace of The Jinghe River; the landslide has a length of 360 m from the back to the front, and the maximum width is 536 m. The slide terrain is not levelling, as the displaced mass moved forward from the back to the front of the landslide orienting to a wavy structure. The sliding mass has a depth of 10–30 m, covering an area of 86,734 m^2, with a volume of about 996,000 m^3. The maximum horizontal sliding distance is 252 m (Fig. 2). The slope height is 74 m, and its slope is 50°. There is a miniature diversion channel 38 m away from the edge of the loess tableland. The sliding mass separated from the slope and moved down, with high speed. Then it formed wide concave at the toe of the landslide, and the road in front of the landslide bulged about 2 m high. There were lots of tension cracks at the road surface in the lateral margin of the landslide.

The landslide section was measured in field, and pre-failure slope section was presumed according to the neighboring slope topography (Fig. 3). The outcropping strata are loess-paleosol sequences belonging to later (Q_3), middle (Q_2) to early (Q_1) Pleistocene

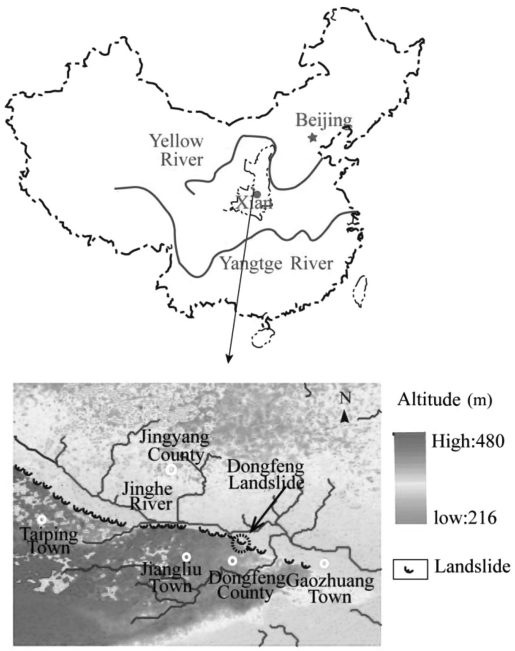


Figure 1. Location of Dongfeng landslide; The distribution of partial landslides along the The Jinghe River.

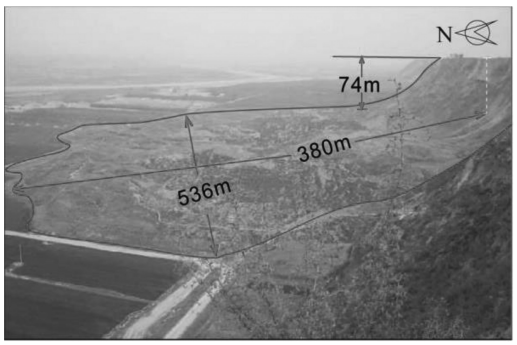


Figure 2. The landscape of Dongfeng landslide.

deposits. In-situ investigations suggest that the Q_3 loess layer on the top fails in form of tensile cracks, and it already lost its strength before the landslide occur. The Q_2 layer with 50 m thick in the middle and the Q_1 layer at the bottom are the control layers for the slope safety, and fail in form of shearing. Groundwater outcrop at the slope toe surface.

3 LOESS PHYSICAL AND MECHANICAL PARAMETERS

3.1 *The basic physical property indexes*

The physical and mechanical properties of three samples from Q_3, Q_2 and Q_1 layers respectively are

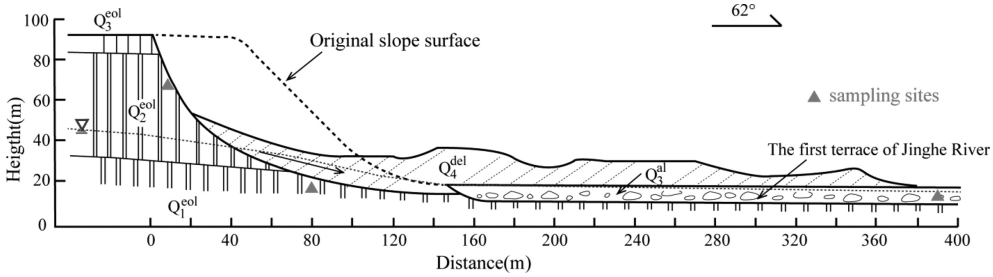


Figure 3. The profile of Dongfeng landslide.

Table 1. The physical and mechanical properties of the loess sample.

Loess layer	Specific gravity	Moisture content	Density	Dry density	Void ratio	Saturation	Liquid limit	Plastic limit	Plastic index	Grain size	Grain size
	Gs	*w*/ (%)	ρ/(g/cm^3)	ρ_d/(g/cm^3)	e_0	*Sr*/(%)	w_L/(%)	w_P/(%)	I_P	*D*10/mm	*D*60/mm
Q_3	2.71	16.8	1.48	1.25	1.165	29.1	28.5	17.4	11.1	0.0004	0.0195
Q_2	2.73	17.6	1.75	1.49	0.832	57.7	31.2	15.6	15.6	0.0003	0.0162
Q_1	2.73	18.9	2.03	1.71	0.596	86.5	33.3	18.6	14.7	0.0003	0.0146

Table 2. Parameters of physical and mechanical in landslide area.

Loess layer	Effective cohesion	Effective friction angle	Elastic module	Poisson's ratio	Saturated permeability
	c'/(kPa)	φ'/(°)	*E*/(kPa)	ν	*Ks*/(m/d)
Q_3	12.5	28.9	60000	0.33	0.61
Q_2	47.9	24.9	72000	0.32	0.12
Q_1	33.3	21.1	80000	0.30	0.01

displayed in Table 1. Specific gravity G_s was empirically determined. Natural densities were determined through the ratio of gravity and volume of soil columns with the cutting ring. Natural moisture content was determined by the oven drying method. Liquid limit W_L and plastic limit W_P were respectively measured by the dishing liquid limit instrument and the 3 mm rod formation, and the particle size distributions were determined by the laser particle size measurement with samples air-dried. Effective strength parameters were selected according to the triaxial test results of Q_2 and Q_3 loess by Yang (2014). Modulus of elasticity was approximately calculated by the segment slope of the stress-strain curve. Physical and mechanical parameters in landslide area were shown in Table 2. Saturated permeability coefficient was tested by the falling water head permeability test.

3.2 *Soil-water characteristic curve (SWCC) and hydraulic conductivity functions (HCF)*

The soil-water characteristic curve (SWCC) was estimated by the modified Kovacs method (2003). The method is composed with the degree of saturation for two main components. One contributes to the amount of water stored in soil by capillary forces. The other contributes to the volumetric moisture content function at large negative pore water pressures where the amount of water that exists in soil is primarily a function of adhesion.

The measured data were utilized to regress with the equation (1):

$$\Theta_w = n\left[S_c + S_a^*(1 - S_c)\right] \tag{1}$$

where Θ_w is the volumetric moisture content; n is the porosity; S_c is the degree of saturation due to capillary forces, which is determined by the equation (2); and S_a^* is the bounded degree of saturation due to adhesion, which is determined by the equation (3).

$$S_c = 1 + \left[\left(\frac{h_{co}}{\Psi}\right)^2 + 1\right]^m \exp\left[-m\left(\frac{h_{co}}{\Psi}\right)^2\right] \tag{2}$$

$$S_a^* = 2 - aC_\Psi \frac{\left(\frac{h_{co}}{\Psi_n}\right)^{2/3}}{e^{1/3}\left(\frac{\Psi}{\Psi_n}\right)^{1/6}} \tag{3}$$

where Ψ is the matric suction; m and a can both be regarded as constants with $m = 3 \times 10^{-5}$ and $a = 7 \times 10^{-4}$; Ψ_n is a matric suction term introduced to ensure dimensionless component; and $\Psi_n = 1$ kPa; h_{co} is the mean capillary rise (cm) determined by the equation (4); and C_Ψ is the correction coefficient determined by the equation (5).

$$h_{co} = \frac{0.75}{eD_{10}(1.17 \log C_u + 1)} \tag{4}$$

$$C_{\Psi} = 1 - \frac{\ln\left(1 + \frac{\Psi}{\Psi_r}\right)}{\ln\left(1 + \frac{\Psi_0}{\Psi_r}\right)} \tag{5}$$

where e is the void ratio; C_u is the coefficient of uniformity with $C_u = D_{60}/D_{10}$, which D_{60} and D_{10} are the particle diameter (cm) corresponding to 60% and 10% passing on a grain-size analysis, respectively; $\Psi_0 = 1 \times 10^6$ kPa; and Ψ_r is the matric suction corresponding to the residual moisture content.

Van Genuchten (1980) proposed the following equation to describe the hydraulic conductivity function of unsaturated soil:

$$k_w = k_s \frac{\left[1 - a\Psi^{n-1}\left(1 + \left(a\Psi^n\right)^{-m}\right)\right]^2}{\left(1 + a\Psi^n\right)^{\frac{m}{2}}} \tag{6}$$

where k_w is unsaturated hydraulic conductivity; k_s is saturated hydraulic conductivity; a, n and m are curve fitting parameters, $n = 1/(1-m)$, m is a parameter that controlled by the slope at the SWCC, and $a = \frac{1}{\Psi}(2^{1/m} - 1)^{1-m}$.

Soil water characteristic curves of Q_1, Q_2 and Q_3 layers are calculated based on the results of the physical index and grain-size analysis in Table 1 Results are shown in Fig. 4. The unsaturated hydraulic conductivity curve shown in Figure 5 can be obtained based on the SWCC (Fig. 4) and the saturated hydraulic conductivity (Table 2). A comparison of SWCC between the Q_2 and Q_3 loess indicates that there is a distinct difference between the two layers for suctions less than 30 kPa where the volumetric moisture content of Q_3 is higher than Q_2. Whereas the two curves tend to merge together when suction exceeds 30 kPa and then decrease greatly. For the Q_1 loess, it is clear that the volumetric moisture content is less than Q_2 and Q_3 for the suction less than 40 kPa and keeps relatively stable till the suction is 60 kPa. Then it decreases greatly in the following but the curve keeps higher than Q_2 and Q_3. The differences may be contributed to the distinctions of initial dry densities of the three layers. Figure 5 shows that the hydraulic conductivity of Q_1 loess is greater than Q_2 loess, but still less than Q_3 loess after the matric suction is more than 90 kPa. The reason may be that moisture content begins to reduce sharply when matric suction increases, and the function of adhesion begins to play an important role in moisture content and migration. Q_1 loess has properties of low porosity ratio and high clay content, and in unsaturated condition it has properties of high moisture content and good moisture migration performance and is easy to infiltrate.

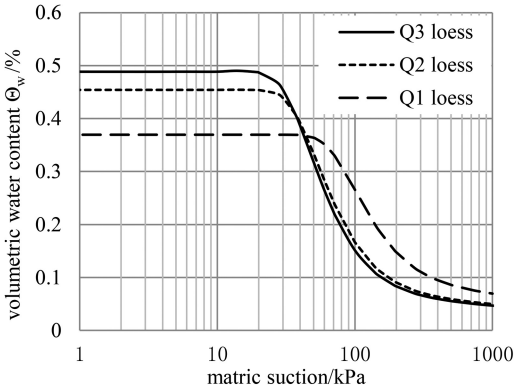


Figure 4. Soil-water characteristic curves.

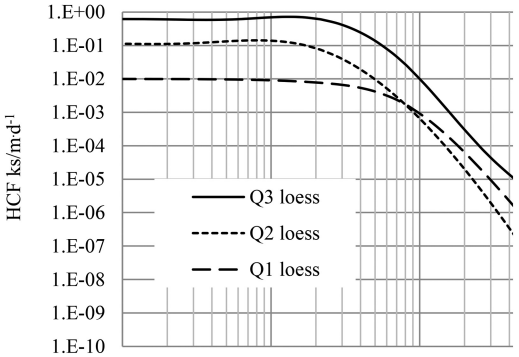


Figure 5. Hydraulic conductivity curves.

4 SEEPAGE SIMULATION

Utilize the finite element method to simulate the infiltration process of irrigation water in the slope. According to the measured profile, a model of three layers was built: the upper is Q_3 loess layer with thickness of 12 m, the middle is Q_2 loess layer with thickness of 50 m, and the underlying formation is Q_1 loess. The initial groundwater level table is slightly above the Q_1 loess layer. The gravel sand layer lies on the first terrace of The Jinghe River. The sliding surface is determined by in-situ investigation.

May and November are the main irrigation periods every year in the region. According to the irrigation amount measurement in November, the irrigation flow is about 400 mm/day. Therefore, in the seepage simulation, the irrigation amount is set for 400 mm/day in May and November every year. And seepage flow is set for 0 mm/day in other months. As shown in Figure 6, the irrigation boundary is set at the slope top. The slope surface is regarded as the potential seepage surface, allowing water to over-flow from the surface. The other boundary is zero pressure surface. Simulation processes are shown in Table 3. Calculate unsaturated soil stability coefficient utilizing Morgenstern-Price method, and terminate the simulation until the calculating stability coefficient is 1.0.

Table 3. Seepage Simulation and Stability Factor Calculation Step.

Calculation Step	Year	Month	Irrigation condition	Stability
0	Initial Seepage Field			Initial Stability factor
1	1976	5	irrigate	Stability factor
2		5-10	stop	
3		11	irrigate	
4		11-4	stop	
5	1977	5	irrigate	Stability factor
6		5-10	stop	
7		11	irrigate	
8		11-4	stop	
⋮				

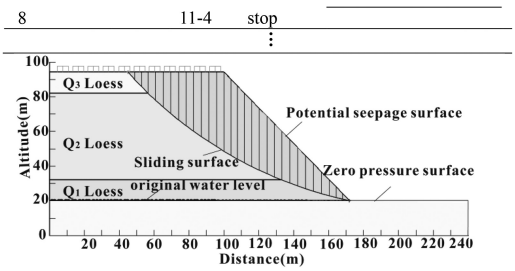


Figure 6. The initial model of Seepage field numerical simulation.

5 SEEPAGE SIMULATION ANALYSIS

The pore water pressure contours before autumn irrigation in 1980, 1990 and 2000 is shown in Figure 7. The groundwater table rises gradually with irrigation.

Take a vertical profile 5m away from the slope shoulder, and extract the pore water pressure. The relationship of water pressure versus elevation is shown in Figure 8. The permeability of loess layer has relatively great effect on pore water pressure distributions. The hydraulic conductivity of Q_2 loess is relatively lower than Q_3 loess, and Q_1 loess is lower than Q_2 loess. In the process of seepage, stratigraphic boundaries are regarded as the relative water-resisting layers. Moisture enriches in the stratigraphic boundaries and moisture content in the zone is relatively high, so the negative pore water pressure locally decreases and the curves turn to the direction of positive pore pressure. In the simulation of 2003, the pore water pressure increases from 0 kPa (water surface) to 206.8 kPa at the slope toe, and groundwater level rises about 23 m, which is relatively close to the height of groundwater level after the slope fails as shown in Figure 2. Q_3 loess only has a rapid growth of pore water pressure at the beginning of the irrigation, and there is no significant change in pore water pressure under the condition of irrigation for many years. Extract the pore water pressure value at the three points of 84 m, 57 m 20 m in the vertical profile in the entire simulation step, the relationship between pore water pressure and irrigation time is shown in Figure 9. It suggests that moisture content has an unsaturated stable state in the process of unsaturated seepage.

The first point of 84 m is 10 m away from the slope top. The pore water pressure rises to −139.4 kPa after irrigation for one year in 1977, and then slows down subsequently and keeps stable in −105.0 kPa three years later. Also, pore water pressure changes little in the following irrigation years.

The second point of 57 m is 37 m away from the slope top It is in the central position of the slope. The pore water pressure begins to rise significantly seven years later, namely, after irrigation in November 1982. This phenomenon illustrates that moisture migrates to the elevation of 57 m of the slope. Then the pore water pressure begins to rise rapidly to −127.3 kPa one year later. After that the increase slows down, and pore water pressure finally stables at about −90.0 kPa.

The third point of 20 m is 74 m away from the slope top. It is also the position of the slope toe and the initial groundwater elevation in the vertical profile. When pore water pressure is 0 kPa. The pore water pressure begins to rise after the autumn irrigation in 1987 which informs that moisture migrates to groundwater level 12 years later. Groundwater level rises and positive pore water pressure increases with the irrigation.

Li (2013) dips a well depth of 9 m (Q_3 Malan loess) in Gansu in-situ monitoring the soil moisture changes under rainfall and infiltration condition. The moisture content increases obviously in paleosol, even if the moisture content change is extremely little in the upper part of the loess, demonstrating that there exists unsaturated seepage or moisture migration in loess. Liu (2008) conducts an artificial rainfall test for 30 days on a loess slope in Guanzhong, Shaanxito monitor the moisture content and the settlement at the depth of 5 m. The infiltration influence depth is less than 2.7 m in the collapsible loess under rainfall, and the saturated depth is 20 cm.

Therefore, water infiltrates only several meters in loess. According to the irrigation simulation in Dongfeng landslide, unsaturated seepage field has the characteristics of stable moisture content. When the moisture content reaches to the stable moisture content, moisture content does not increase with water keeps downward migration. And when the excess water reaches the groundwater, the groundwater level rises, that is related to the slope stability. In this paper, the simulation initial conditions do not consider rainfall and evaporation process. In fact, groundwater, unsaturated moisture field and rainfall, evaporation should be in a state of equilibrium before irrigation started in 1976.

6 STABILITY ANALYSIS

Irrigation system began to run in Jingyang area in 1976, so the paper simulated the first irrigation in May

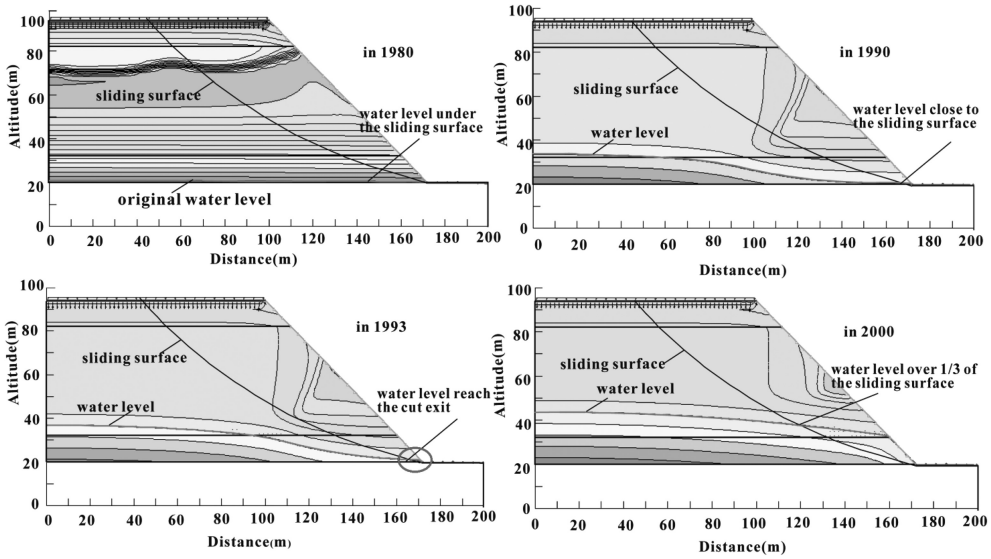


Figure 7. Pore water pressure contours before irrigation in 1980, 1990, 1993 and 2000.

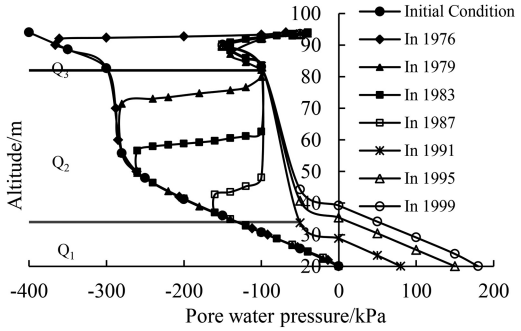


Figure 8. Pore water pressure changing with irrigation time (Profile position distance slope shoulder 5 m).

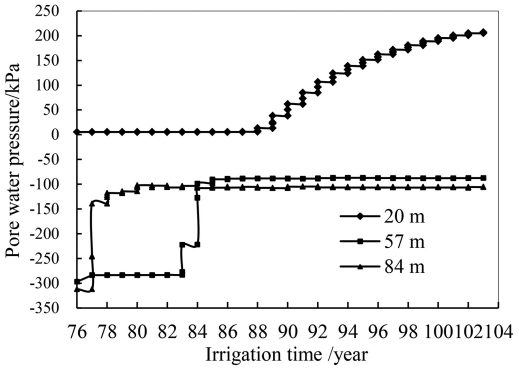


Figure 9. Pore water pressure changing with irrigation time of three points in profile.

1976. Analyze the slope stability after irrigation each year and find the relationship between stability factor and irrigation time (Fig. 10). Figure 10 shows that the initial factor of slope stability is just 1.11. Before 1990, the slope stability increases a little instead of decreases with the irrigation, and the stability coefficient increases only 0.015 for 15 years. The reason is that during this period the groundwater level rises but not reaches the sliding surface, the slope stability does not reduce accordingly. But after 1990, the factor of safety begins to decrease sharply, and it fall to 1.0 in 2001, a critical state. The landslide occurred in July 2003, which almost tallies with the simulation time of the model.

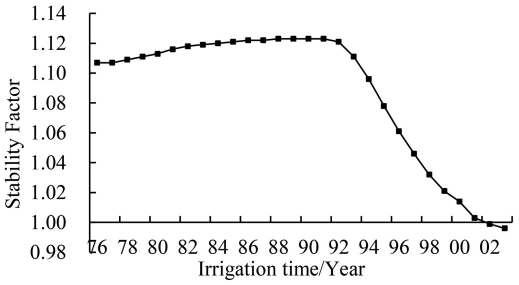


Figure 10. The Stability factor changing with irrigation time.

7 CONCLUSIONS

The research focuses on the Dongfeng landslide in Jingyang southern plateau. Measure the basic physical indexes, grain size analyze and saturated hydraulic conductivities of three loess layers. Estimate the soil water characteristic curve by modified Kavacs method, and determine the penetration equations by Van Genuchten method. Then simulate irrigation infiltration process and calculate the slope safety with the

M-P method. Results show that: Before Dongfeng landslide sliding, the slope has a height of 74 m, a slope of 45.8°, and the stability coefficient is 1.11. The slope stability is not reduced, even though negative pore water pressure increases before the irrigation water reaches to the groundwater level. Only when groundwater level gradually rises to the potential sliding surface, pore water pressure rises from negative to positive the slope stability begins to decrease fast until the slope fails.

REFERENCES

Aubertin M. Mbonimpa M. Bussiere B. & Chapuis R.P. 2003. A model to predict the water retention curve from basic geotechnical properties. *Canadian Geotechnical Journal* 40(6): 1104–1122.

Hu, W. Zhu L.F. & Zhang M.S. 2013. The changes of engineering geological properties of loess caused by irrigation. *Geological Bulletin of China* 32(6): 875–880.

Liu H.S., Ni W.K., Yang. H.Q. et al. 2008. Site test on infiltration of loess subgrade under rainfall circumstance. *Journal of Earth Sciences and Environment* 30(1): 60-63.

Jin Y.L. & Dai. F.C. 2007. The mechanism of irrigation-induced landslides of loess. *Chinese Journal of Geotechnical Engineering* 29(10): 1493–1499.

Li, T.L. 2012. Loess Deposit and Loess Landslides on the Chinese Loess Plateau. *Progress of Geo-Disaster Mitigation Technology in Asia*: 235–260.

Lei, X.Y. 1995. The Hazards of Loess Landslides in the Southern Tableland of Jingyang County, Shaanxi and the Relationships with the Channel Water into Field. *Journal of Engineering Geology* 3(1): 56–64.

Li, P. Li T.L. & Wang. A.D. 2013. In-situ test research on regularities of water migration in loess. *Rock and Soil Mechanics* 34(5): 1331–1339.

Sang G.S., Feng L.H. & Shang, L.H. 2007. Study on Stability of Table land Slopes and Causes for Landslides on Southern-Bank of Lower Reaches of The Jinghe River. *Journal of soil and water conservation* 21(5): 187–191.

Van Genuchten M Th. 1980. A closed-form equation for predicting the hydraulic conductivity of unsaturated soils. *Soil Science Society of America Journal* 44: 892–898.

Yang, F. Chang, W. Wang, F.W. et al. 2014. Motion Simulation of Rapid Long Run-out Loess Landslide at Dongfeng in Jingyang, Shaanxi. *Journal of Engineering Geology* 22(5): 890–895.

Wang, J.D. 1999. A Mechanism of High-speed Loess Landslides-saturated Loess Creeping Liquefaction. *Journal of Xibei University* 29(01): 79–82.

Wang, J.D. S.F. Xiao & Z.Y. Zhang, 2001. The Mechanism for Movement of Irrigation-indued High-speed Loess Landslide. *Journal of Engineering Geology* 9(3): 241–246.

Wang, P. 2013. The Mechanisms and Simulation of the Rapid Long Run-out Loess Landslide. Xi'an.

Zhao, J.F. 2013. The failure mechanism of irrigation-induced slide-flow on Heifangtai loess platform. Xi'an.

Zhang M.S. & Li. T.L. 2011. Triggering Factors and Forming Mechanism of Loess Landslides. *Hydrogeology & Engineering Geology* 19(4): 530–540.

This page intentionally left blank

Unsaturated Soil Mechanics—from Theory to Practice – Chen et al. (Eds)
© 2016 Taylor & Francis Group, London, ISBN 978-1-138-02921-7

Estimation of soil shrinkage curve

M. Wijaya & E.C. Leong
School of Civil and Environmental Engineering, Nanyang Technological University, Singapore

ABSTRACT: The relationship between water content and void ratio is given by the soil shrinkage curve. Such a curve is important to understand the volume change behavior of soils upon drying and it has a direct influence on other properties of an unsaturated soil such as soil-water characteristic curve and shear strength. However, the shrinkage curve is seldom determined as the volume change may not be uniform and cracks may appear during the test depending on the soil type and the method of determination. Therefore, an estimation of soil shrinkage curve will be necessary especially when time is a constraint. In this paper, several methods that have been proposed to estimate the soil shrinkage curve will be evaluated using data from extant literature.

1 INTRODUCTION

Moisture change of soils (wetting or drying) will change their matric suction and volume. Such changes are more pronounced for fine-grained soils (Wijaya et al., 2015) and therefore requires special attention. The shrinkage curve comes in handy to relate the moisture change of soils with change in their volume. The shrinkage curve can also be combined with the soil-water characteristic curve based on gravimetric water content w (SWCC-w) to estimate the soil-water characteristic curve based on degree of saturation Sr (SWCC-S) (Wijaya et al., 2015) or to infer the relationship between matric suction and void ratio (Fredlund et al., 2002, Wijaya et al., 2015).

Figure 1 shows the properties of a shrinkage curve. When the soil dries, the water content of the soil follows the loading line (line 2) and therefore the soil remains saturated until it reaches the air entry point which is indicated by the water content at air entry value (AEV) wAE in Figure 1. The soil will then follow the residual shrinkage with curvature k2 until it reached the zero shrinkage line (line 1) at the true shrinkage limit SL which is the commonly used definition of shrinkage limit in the soil sciences. The intersection between the loading line and zero shrinkage line SL' is the commonly used definition for shrinkage limit in geotechnical engineering as it is easier to be determined (Leong and Wijaya, 2015).

A number of equations has been proposed to estimate the shrinkage curve (Cornelis et al., 2006a, Leong and Wijaya, 2015).The parameters of the shrinkage curve are usually obtained by curve-fitting the shrinkage curve data obtained from measurement. Therefore, it is useful to extend the capability of curve-fitting type shrinkage curve equation into predictive type shrinkage curve equation as only a few parameters are required to estimate the shrinkage curve. The objective of this paper is to evaluate several equations that have been proposed to estimate the shrinkage curve. Data from the literature were used for the evaluation.

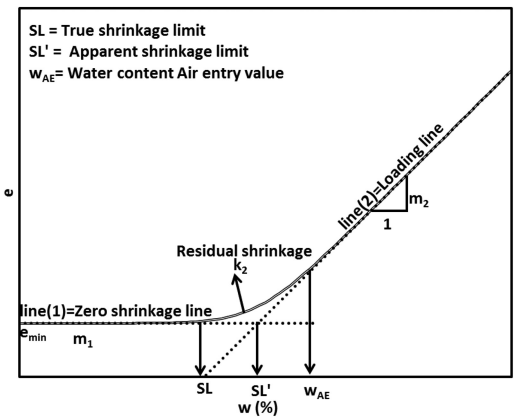


Figure 1. Properties of a typical two linear shrinkage curve.

2 SHRINKAGE CURVE EQUATIONS

Four shrinkage curve equations are evaluated in this paper. The choices for selecting these four shrinkage curve equations and their brief descriptions are given below. The four equations are summarised in Table 1.

2.1 *Braudeau et al. (1999) equation*

Braudeau et al. (1999) equation is a piecewise type equation where linear and non-linear parts of the shrinkage curve are modelled with different functions. Braudeau et al. (1999) equation is able to model shrinkage curve data quite well (Cornelis et al., 2006a; Leong and Wijaya, 2015). Another advantage of Braudeau

Table 1. Equations for shrinkage curve.

Reference	Equation	Notation
Braudeau et al. (1999)	$e = \begin{cases} e_{min};\ w \le SL \\ e_{SL} + (e_{AE} - e_{SL})\dfrac{f}{\exp(1) - 2};\ SL < w \le w_{AE} \\ e_s + (e_{AE} - e_s)\dfrac{w - w_{AE}}{w_s - w_{AE}};\ w > w_{AE} \end{cases}$ $f = \exp\left(\dfrac{w - SL}{w_{AE} - SL}\right) - \left(\dfrac{w - w_{SL}}{w_{AE} - SL}\right) - 1$	e_{min} = minimum void ratio w = gravimetric water content w_s = saturated water content at loading line SL = Shrinkage limit w_{AE} = water content at air entry value e_s = saturated void ratio at loading line e_{AE} = void ratio at air entry value e_{SL} = void ratio at shrinkage limit
Fredlund et al. (2002)	$e(w) = e_{min}\left(\dfrac{w^C}{SL'^C} + 1\right)^{1/C}$ $\dfrac{e_{min}}{SL'} = \dfrac{G_s}{S_0}$	SL' = apparent shrinkage limit G_s = specific gravity S_0 = initial degree of saturation c = the curvature of the shrinkage curve
Modified Cornelis et al. (2006b)	$e = e_{min} + \gamma\left[\exp\left(\dfrac{-\xi}{w^{\zeta}}\right)\right]$	$\gamma, \zeta, \xi =$ model parameter
Leong and Wijaya (2015)	$e(w) = e_{min} + \dfrac{G_S}{2S_0}\left\langle w + \dfrac{1}{k_2}\ln\left\{\dfrac{\cosh[k_2(w - SL')]}{\cosh(k_2 \cdot SL')}\right\}\right\rangle$ $k_2 = \dfrac{2}{SL - w_{AE}}$	k_2 = curvature parameter between linear segment 2 and linear segment 1

et al. (1999) equation is in its ability in modelling shrinkage curve with any number of linear segments. However, Braudeau et al. (1999) equation uses a number of parameters (Cornelis et al., 2006a) which are time-consuming to obtain. In Table 1, the Braudeau et al. (1999) equation has been simplified only for two linear segments shrinkage curve.

2.2 *Fredlund et al. (2002) equation*

Fredlund et al. (2002) equation is a continuous equation that was specifically formulated for a shrinkage curve with two linear segments. Most of the parameters are physically significant parameters except for the curvature parameter c. Leong and Wijaya (2015) showed that the c may affect the position of the intersection between the loading line and the zero shrinkage line especially when the c value is low. Typical values of c have been proposed by Fredlund et al. (2002). The value of c can be taken as 9.57 for undisturbed soil specimens, 25.31 for slurries and 8.47 for compacted soils. Wijaya et al. (2015) proposed that c can be assumed to be 9. Fixing the value of c gives a predictive ability to the Fredlund et al. (2002) equation as it is then no longer necessary to curve fit the equation.

2.3 *Cornelis et al. (2006b) equation*

Cornelis et al. (2006b) modified Groenevelt and Grant (2001) equation in order to model shrinkage curve with any number of linear segments. The Cornelis et al. (2006b) equation was formulated in term of moisture ratio instead of gravimetric water content. However, the moisture ratio can be converted into gravimetric water content without changing the form of equation as shown in Table 1. It is important to note that the empirical parameters of Cornelis et al. (2006b) equation are different when gravimetric water content was used instead of moisture ratio.

2.4 *Leong and Wijaya (2015) equation*

Leong and Wijaya (2015) proposed a universal shrinkage curve equation that can be applied to a shrinkage curve with any number of segments. The equation uses a transition function that can model any additional linear segment with a smooth transition. In Table 1, Leong and Wijaya (2015) universal shrinkage curve equation for two linear segments curve is given. The difference between the curvature parameters in Fredlund et al. (2002) equation and Leong and Wijaya (2015) equation is that the curvature parameter in the Leong and Wijaya (2015) equation can be directly determined from the shrinkage curve and therefore does not require curve fitting. The curvature parameter also does not affect the physical meaning of SL' which makes Leong and Wijaya (2015) equation more stable.

It is desirable to extend the Leong and Wijaya (2015) from a curve-fitting type equation into a predictive

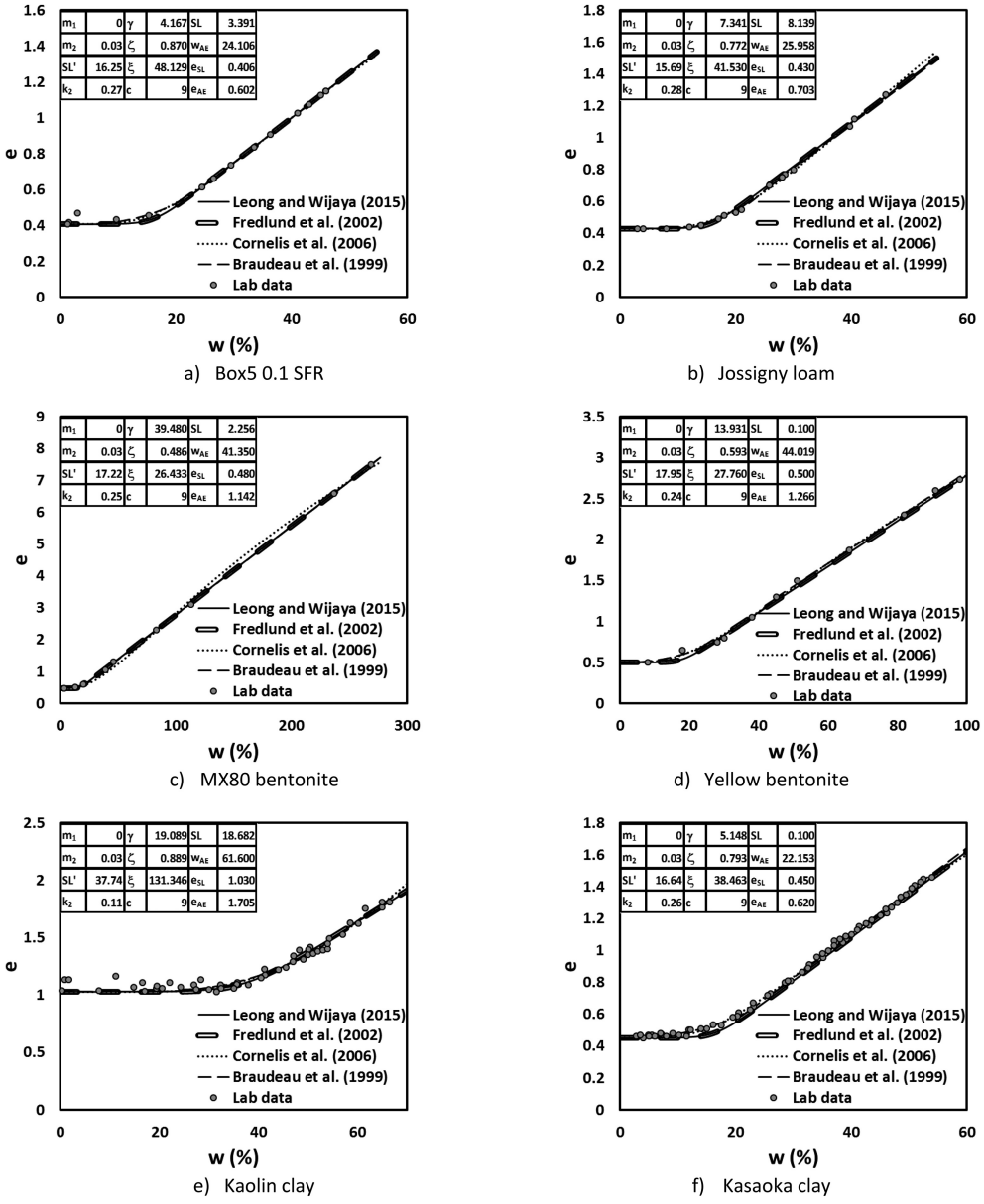


Figure 2. Comparison of the estimation method.

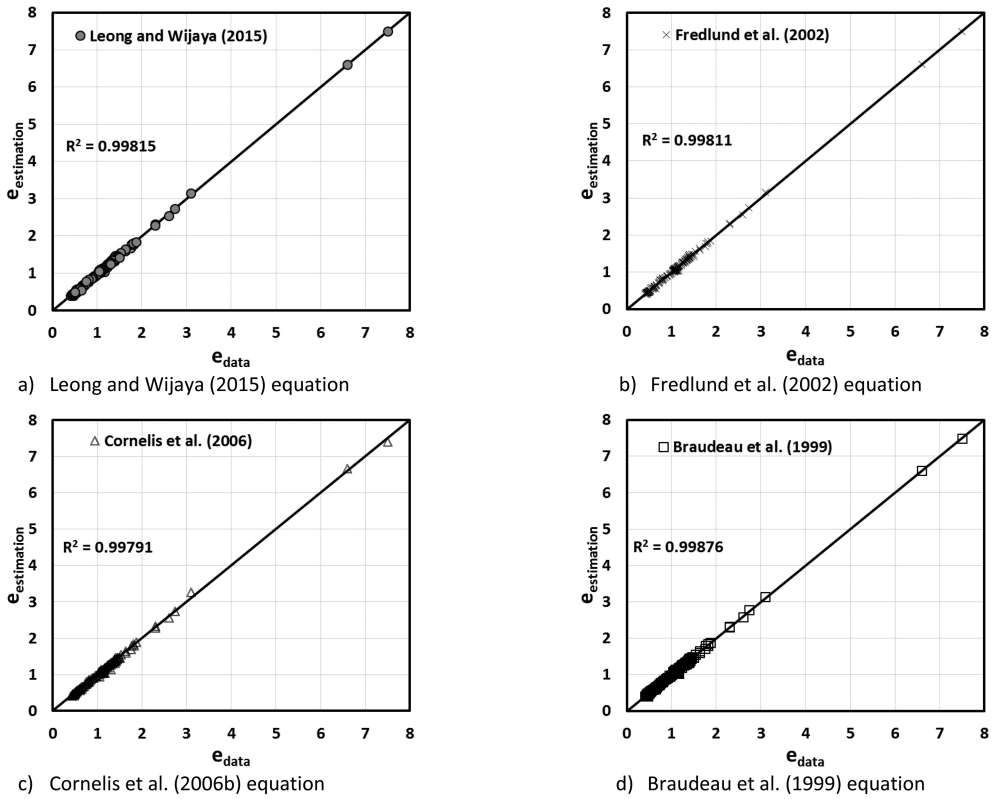
type equation. The predictive type equation can be obtained by comparing Fredlund et al. (2002) equation and Leong and Wijaya (2015) equation. Leong and Wijaya (2015) derived the transition function for Fredlund et al. (2002) equation T_F which is given as:

$$T_F = \frac{e_{min}}{SL'}\left[w^c + SL'^c\right]^{\frac{1}{c}} - e_{min} \tag{1}$$

where e_{min} is the minimum void ratio of the soil after drying. The second derivative of the transition function gives the Dirac delta function δ which is useful to evaluate the curvature parameter of Leong and Wijaya (2015) equation. The Dirac delta functions of Leong and Wijaya (2015) equation and Fredlund et al. (2002) are given, respectively as:

$$\delta(w, SL', k_i) = \frac{k_i}{2\cosh^2 k_i (w - SL')} \tag{2}$$

$$\delta_F(w, SL', c) = \frac{(c-1)\left(\frac{SL'}{w}\right)^c \left[\left(\frac{SL'}{w}\right)^c + 1\right]^{\frac{1}{c}-2}}{w} \tag{3}$$



a) Leong and Wijaya (2015) equation
b) Fredlund et al. (2002) equation
c) Cornelis et al. (2006b) equation
d) Braudeau et al. (1999) equation

Figure 3. Comparison of estimated void ratio with measured void ratio.

The maximum inflection point is given when $w = SL'$. Therefore, substituting $w = SL'$, the equivalent curvature parameter k_2 in Leong and Wijaya (2015) equation for $c = 9$ in Fredlund et al. (2002) is given as:

$$k_2 = \frac{4.32}{SL'} = \frac{4.32G_s}{S_0 e_{min}} \quad (4)$$

By using Equation (4), Leong and Wijaya (2015) equation becomes a predictive type shrinkage curve equation.

3 COMPARISON OF SHRINKAGE CURVE EQUATIONS

Six soils were collated from the literature in order to evaluate the shrinkage curve equations. One soil from Fredlund et al. (2011) which is Box 5-0.1 SFR, one soil from Fleureau et al. (2002) which is Jossigny loam, two soils from Tripathy et al. (2014) which are American MX 80 bentonite and Greek yellow bentonite and two soils from Umezaki and Kawamura (2013) which are Kaolin clay and Kasaoka clay. Cornelis et al. (2006b) equation and Braudeau et al. (1999) equation are considered as curve-fitting type equations while Leong and Wijaya (2015) equation and Fredlund et al. (2002) equation are considered as predictive type equations.

Figure 2 shows the estimated shrinkage curves for the four equations along with their parameters. The accuracy of an equation can be evaluated by using either sum of residual error SS_{res}, root mean square error RMSE, and coefficient of determination R^2. The SS_{res}, RMSE and R^2 are given in Tables 2 and 3 for the curve fitted type and predictive type equation, respectively. The comparison of the estimated and measured void ratio is given in Figure 3.

The four equations performed very well with R^2 value greater than 0.95. It appears that the Cornelis et al. (2006b) equation gives the worst performance compare to the other equations in modelling shrinkage curve with two linear segments. Therefore, it is not recommended to use Cornelis et al. (2006b) equation to model shrinkage curve with two linear segments. The predictive type equations give slightly less accuracy compare to the Braudeau et al. (1999) equations with Leong and Wijaya (2015) equation performing slightly better than the Fredlund et al. (2002) equation for Kaolin clay specimen while it performed equally good for the other specimens. Figure 3 shows that the measured and estimated void ratios is very close to the 1:1 line with the overall R^2 values of about 0.998 for all of the equations.

Based on this observation, it appears that using predictive type equation for shrinkage curve is more beneficial as there is negligible loss in accuracy but it can significantly reduce the amount of test measurement.

Table 2. Accuracy of the curve fitting type shrinkage curve equation.

	Braudeau et al. (1999)			Cornelis et al. (2006)		
	SSres	RMSE	R2	SSres	RMSE	R2
Box5-0.1 SFR	0.004	0.017	0.996	0.005	0.017	0.996
Jossigny loam	0.001	0.009	0.999	0.002	0.012	0.998
MX80 bentonite	0.003	0.017	1.000	0.084	0.092	0.999
Greek yellow bentonite	0.008	0.027	0.999	0.015	0.036	0.998
Kaolin clay	0.105	0.046	0.958	0.105	0.046	0.958
Kasaoka clay	0.012	0.014	0.998	0.013	0.014	0.998

Table 3. Accuracy of the predictive type shrinkage curve equation.

	Fredlund et al. (2002)			Leong and Wijaya (2015)		
	SS_{res}	RMSE	R^2	SS_{res}	RMSE	R^2
Box5-0.1 SFR	0.005	0.019	0.995	0.005	0.019	0.995
Jossigny loam	0.003	0.014	0.997	0.003	0.013	0.997
MX80 bentonite	0.006	0.024	1.000	0.006	0.024	1.000
Greek yellow bentonite	0.028	0.051	0.996	0.028	0.051	0.996
Kaolin clay	0.112	0.048	0.955	0.109	0.047	0.956
Kasaoka clay	0.048	0.027	0.993	0.048	0.027	0.993

4 CONCLUSION

In this paper, two curve fitting type equations and two predictive type equations were evaluated. The curve fitting equations were Braudeau et al. (1999) equation and Cornelis et al. (2006b) equation. The predictive type equations were Fredlund et al. (2002) equation and Leong and Wijaya (2015) equation. The evaluation was performed by using six shrinkage curve data from the literature and it was shown that the predictive type equations were able to estimate the shrinkage curve with negligible loss in accuracy compared to curve-fitting type shrinkage curve equations. Therefore, it is recommended to estimate the shrinkage curve by using predictive type equations.

ACKNOWLEDGEMENT

The first author acknowledges the research scholarship from Nanyang Technological University.

REFERENCES

Braudeau, E., Costantini, J. M., Bellier, G., and Colleuille, H. (1999). New Device and Method for Soil Shrinkage Curve Measurement and Characterization. *Soil Sci. Soc. Am. J.*, 63(3): 525–535.

Cornelis, W. M., Corluy, J., Medina, H., Diaz, J., Hartmann, R., Van Meirvenne, M., and Ruiz, M. E. (2006). Measuring and modelling the soil shrinkage characteristic curve. *Geoderma*, 137(1–2): 179–191.

Cornelis, W. M., Corluy, J., Medina, H., Hartmann, R., Van Meirvenne, M., and Ruiz, M. E. (2006). A simplified parametric model to describe the magnitude and geometry of soil shrinkage. *Eur. J. Soil. Sci.*, 57: 258–268.

Fleureau, J. M., Verbrugge, J. C., Huergo, P. J., Correia, A. G., and Kheirbek-Saoud, S. (2002). Aspects of the behaviour of compacted clayey soils on drying and wetting paths. *Canadian Geotechnical Journal of Agricultural Science*, 39(6): 1341–1357.

Fredlund, D. G., Stone, J., and Stianson, J. (2011). Obtaining unsaturated soil properties for high volume change oil sands material. In A. Jotisankasa, A. Sawangsuriya, S. Soralump, & W. Mairaing (eds), *Proceedings of the 5th Asia Pacific conference on unsaturated soils, Pattaya, Thailand*, 1, 415–420.

Fredlund, M. D., Wilson, G. W., and Fredlund, D. G. (2002). "Representation and estimation of the shrinkage curve." *3rd International Conference on Unsaturated Soils, UNSAT 2002,* Recife, Brazil, 145–149.

Groenevelt, P. H., and Grant, C. D. (2001). Re-evaluation of the structural properties of some British swelling soils. *European Journal of Soil Science*, 52(3): 469–477.

Leong, E. C., and Wijaya, M. (2015). Universal soil shrinkage curve equation. *Geoderma*, 237–238(0): 78–87.

Tripathy, S., Tadza, M. Y. M., and Thomas, H. R. (2014). Soil-water characteristic curves of clays. *Canadian Geotechnical Journal*, 51(8): 869–883.

Umezaki, T., and Kawamura, T. (2013). Shrinkage and desaturation properties during desiccation of reconstituted cohesive soil. *Soils and Foundations*, 53(1): 47–63.

Wijaya, M., Leong, E. C., and Rahardjo, H. (2015). Effect of shrinkage on air-entry value of soils. *Soils and Foundations*, 55(1):4 166–180.

This page intentionally left blank

Unsaturated Soil Mechanics—from Theory to Practice – Chen et al. (Eds)
© 2016 Taylor & Francis Group, London, ISBN 978-1-138-02921-7

Effect of infiltration characteristics of soil on tree stability

A. Rahimi, H. Rahardjo, E.C. Leong, T.T. Lee & A.W.K. Law
Nanyang Technological University, Singapore

Y.K. Fong
National Parks Boards, Singapore

ABSTRACT: Tree failures are often catastrophic to public and infrastructure of a densely populated urban environment like Singapore. Soil properties, rainfall condition, wind condition and green wood properties are main factors that contribute to tree stability. In this paper, the effect of infiltration characteristics of soil on tree stability is investigated through numerical modelling. A typical residual soil of Singapore was subjected to different rainfall conditions to study its infiltration characteristics and its effect on tree stability. The results of the analyses show that hydraulic properties of the soil have significant effects on infiltration characteristics of the soil and consequently on tree stability.

1 INTRODUCTION

Tree failures during rain storm have been reported worldwide, including Singapore. The tropical climatic condition of Singapore results in abundance of rainfall. In 2010, NParks reported approximately 1400 cases of tree failure in Singapore (NParks, 2011). These events have caused economic losses and even serious injuries and deaths (Straits Times, April 2013). Therefore, it is important to identify the cause of tree failures and ways to prevent them. The soil used for tree planting is usually well above the ground water table and is usually in an unsaturated condition. The shear strength of the unsaturated soil is governed by two independent stress-state variables, matric suction (negative pore-water pressure) and net normal stress (Fredlund and Rahardjo, 1993). Infiltration of rainwater into the soil reduces the negative pore-water pressure which in turn reduces the shear strength of the soil. This would result in a reduction in resistance of the tree against uprooting. Infiltration of rainwater into the soil depends on the hydraulic properties of the soil. Limited studies have been conducted to investigate the relationship between rainfall and tree failure. Koizumi (1987) conducted several tree-pulling experiments and showed that stability of a tree after rainfall is lower than stability of a similar tree in soil without occurrence of rainfall. However, limited studies investigated the effect of infiltration characteristic of soil on tree stability. Therefore, it is essential to understand the stability of trees planted in different soils with different infiltration characteristics.

2 METHODOLOGY

In order to investigate the effect of infiltration characteristics of soil on tree stability, two different soil types were selected to represent good drainage (GD) and poor drainage (PD) residual soils of Singapore. The GD and PD soils were subjected to a rainfall of 1×10^{-6} m/s for a duration of 24 hours. Seepage analysis was performed to compute the pore-water pressure changes due to the rainfall. The computed pore-water pressures were then used as initial condition to conduct load/deformation analysis in order to assess the stability of a tree subjected to wind load. A wind load of 150 kN was used in the load/deformation analyses. The pore-water pressures at initial time before the rainfall; at time equal to 12 hours and at time equal to 24 hours (i.e., end of the rainfall) were imported in load/deformation analyses as initial pore-water pressures. The induced strain in the root plate and soil was observed and compared at different times during the rainfall. Tree instability or failure was assumed to have occurred when the soil experienced more than 15% strain (ASTM D4767-11, 2011) or the tree or root plate experienced more than 5% strain at its extreme fibers (Lee, 2015).

3 NUMERICAL MODELING

Seepage analyses were conducted using a numerical model of simplified tree-root-soil model using SEEP/W (Geo-slope International, 2012a) software.

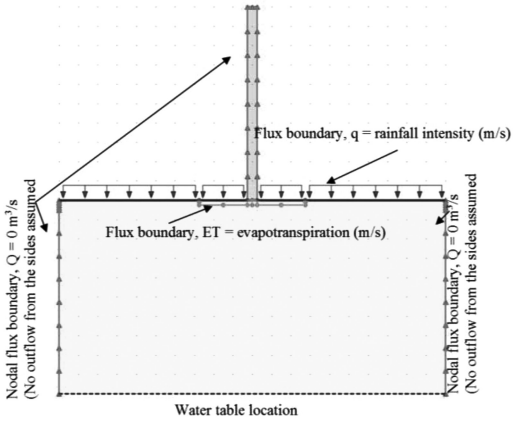


Figure 1. Finite element model and initial condition for the tree-root-soil model.

A tree of 10 m height and 0.5 m width with a root plate of 0.25 m thickness and diameter of 5.5 m surrounded by a soil block of 20 m width and 10 m height was considered for the analyses as shown in Figure 1. The dimensions of tree and root plate were selected based on the recommendation by NParks (2009). The infiltration process of the rainwater into the soil was conducted using a saturated-unsaturated, finite element seepage analysis. The boundary conditions applied to the tree-root-soil model are also shown in Figure 1. A boundary flux, q, equal to rainfall intensity, Ir = 10^{-6} m/s was applied to the surface of the model. The nodal flux, Q, equal to zero was applied along the sides of the soil to simulate no flow zone. The water table was assumed to be at the bottom of the model (i.e., 10 m depth). A boundary flux, ET, equal to evapotranspiration was applied to the root plate boundaries.

Soil-water characteristic curve (SWCC) and permeability functions are two primary soil properties used in the seepage analysis as shown in Figure 2 for both of GD and PD soils.

The saturated coefficient of permeability of GD soil, k_s, was equal to 10^{-4} m/s and SWCC parameters of the soil were a = 10 kPa, m = 0.5 and n = 1. The saturated coefficient of permeability of PD soil was equal to 10^{-6} m/s. SWCC parameters of PD soil were a = 300 kPa, m = 1 and n = 1. The detailed explanation of the two selected soils can be found in Rahimi et al. (2010).

The water-flow governing equation used in the software for solving a transient and two dimensional seepage analysis is as follows:

$$m_w^2 \gamma_w \frac{\partial h_w}{\partial t} = \frac{\partial}{\partial x}\left(-k_{wx}\frac{\partial h_w}{\partial x}\right) + \frac{\partial}{\partial y}\left(-k_{wy}\frac{\partial h_w}{\partial y}\right) + q \qquad (1)$$

where m_w^2 = slope of soil-water characteristic curve; γ_w = unit weight of water; h_w = hydraulic head or total head; t = time; k_{wx} = coefficient of permeability with respect to water as a function of matric

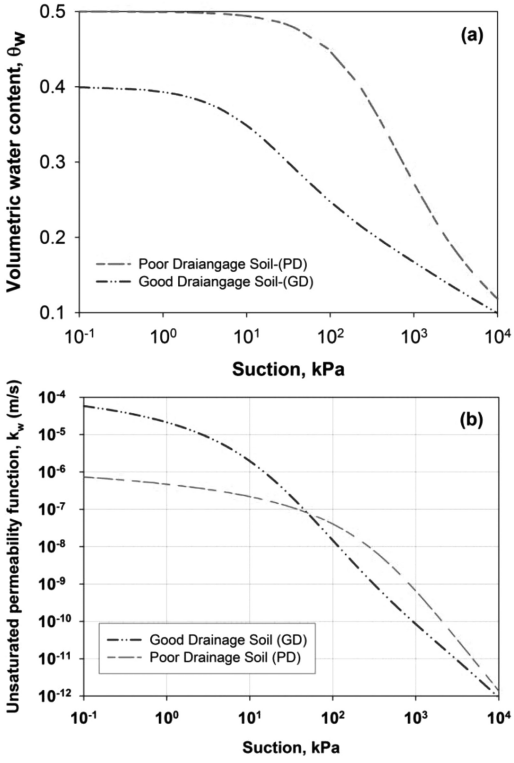


Figure 2. Soil hydraulic properties of GD and PD soils used in numerical modelling: (a) soil-water characteristic curve, (b) unsaturated permeability function.

sucion in x-direction; k_{wy} = coefficient of permeability with respect to water as a function of matric suction in y-direction; and q = applied flux at the boundary. The pore-water pressures was computed by seepage analyses and used as initial pore-water pressures for load/deformation analyses. SIGMA/W (Geo-slope International, 2012b) software was used for the load/deformation modelling of the tree stability. The model was a two-dimensional plane strain model. The mesh of the root and the surrounding soil consists of rectangular elements. Friction between soil and root was ignored. The boundary conditions of the tree-root-soil model are shown in Figure 3. Horizontal displacement was fixed on both vertical boundaries, and displacements in both directions were fixed on the bottom boundary of the model as shown in Figure 3.

For load/deformation analyses, the soil was modelled as an elastic–plastic material. The elastic part was governed by modulus of elasticity, E, and Poisson's ratio, μ, of the soil. Typical values of 10000 kPa and 0.4 were assumed for the modulus of elasticity and Poisson's ratio of the soil, respectively. Root-plate material was considered as a linear-elastic material with a modulus of elasticity of 1200000 kPa and a Poisson's ratio of 0.3 (Lee, 2015). Typical shear strength properties of Singapore residual soils (Rahardjo et al., 2007) were selected for both GD and PD soils. An effective cohesion, c′ = 10 kPa, effective angle of internal friction,

$\phi' = 26$ degrees, and unit weight of soil, $\gamma = 20\,\text{kN/m}^3$ were used in the analyses. Table 1 shows the soil properties and Table 2 shows the root plate and tree properties used in the study.

4 RESULTS AND DISSCUSSION

The results of seepage analyses for t = 0, t = 12 h and t = 24 h were used as initial pore-water pressures in load/deformation analyses. The induced strains in the tree, root and soil due to the applied wind load on the tree were observed and presented below.

The strain profiles are shown at three locations, namely trunk base, root plate base and soil as shown in Figure 4.

The resulting strains at the trunk base for GD and PD soils are shown in Figure 5 at different times during the rainfall. As shown in the figure, the windward side of the trunk base experienced tension and the leeward side of the trunk base experienced compression as reflected by the positive and negative values of strains, respectively for both of GD and PD soils. The maximum magnitude of the tension strain and compression strain at the trunk base was 2.3% (t = 0 h) and −3.2% (at t = 24 h), respectively, for both of GD and PD soils. The tree and root plate properties were the same for both of PD and GD soils. In addition the pore-water pressure changes due to the applied rainfall did not affect the tree and root plate properties. As a result, the strains at the trunk base were more or less the same during the rainfall and they were similar in both soils. The change in the strain due to the applied rainfall was negligible and it remained under 5% at all times. Therefore, it can be concluded that the tree trunk did not experience any failure at all times.

The resulting strains at the root plate base for GD and PD soils are shown in Figure 6 at different times during the rainfall. As shown in the figure, the windward side of the root plate base experienced tension and the leeward side of the root plate base experienced compression as reflected by the positive and negative values of strains, respectively, for both of GD and PD soils. As shown in the figure, the tension strain increased significantly due to the applied rainfall, while the compression strain increased marginally for both of GD and PD soils. The maximum magnitude of the compression strain at the root plate base was −2.1% (t = 24 h) for GD soil and −2.1% (t = 12 h) for PD soil which remained under 5% at all times. However, the tension strains increased from 2.5% (t = 0 h) to 4.7% (t = 24 h) near the trunk and from 0.8% (t = 0 h) to 10.8% (t = 12 h) and 14% (t = 24 h) at the edge of the root plate for GD soil. On the other hand, the tension strains increased from 2.5% (t = 0 h) to 5.6% (t = 24 h) near the trunk and from 0.8% (t = 0 h) to 12% (t = 12 h) and 17% (t = 24 h) at

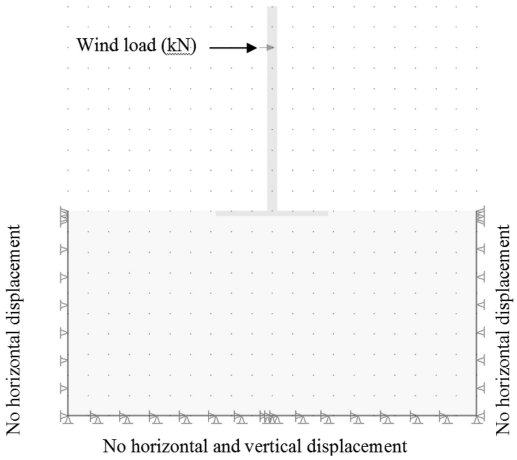


Figure 3. Boundary condition and schematic diagram of tree-root-soil model used in load/deformation analyses.

Table 1. Soil properties.

	E modulus (kPa)	Unit weight (kN/m^3)	Poisson's ratio	Friction angle (°)	Cohesion (kPa)
Soil	10000	20	0.4	26	10

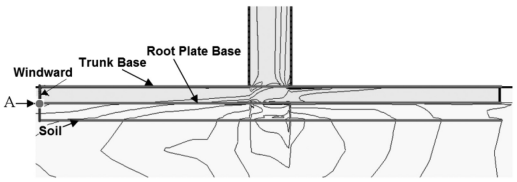


Figure 4. Location of the observed strains in the trunk base, root plate base and soil.

Table 2. Root plate and tree properties.

	E modulus (kPa)	Unit weight (kN/m^3)	Poisson's ratio	Height (m)	Trunk diameter (m)	Root plate tickness (m)	Root plate diameter (m)
Root plate and Tree	1200000	10	0.3	10	0.5	0.25	5.5

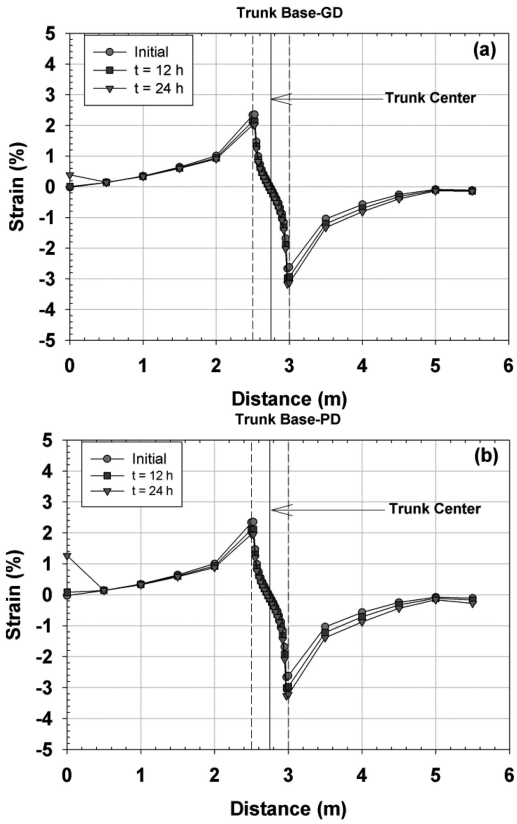


Figure 5. Strains profile in the trunk base: (a) GD soil, (b) PD soil.

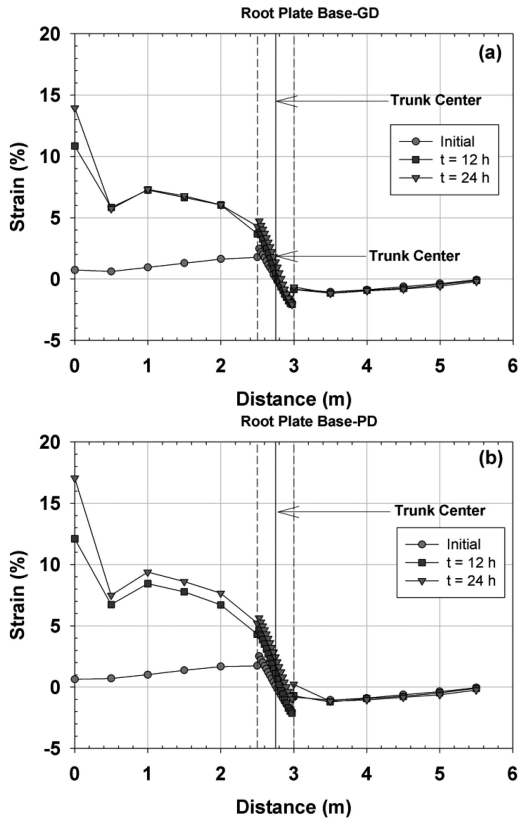


Figure 6. Strains profile in the root plate base: (a) GD soil, (b) PD soil.

the edge of the root plate for PD soil. The significant increase in tension strain at the base of the root plate (i.e., larger than 5%) reflected the failure of the tension roots due to the presence of rainfall. It can be seen that the increase in strains inroot plate base due to the rainfall was larger in PD soil as compared to that in GD soil. This was due to the higher permeability of GD soil which resulted in a faster infiltration of rainwater into the soil. As a result, the increase in pore-water pressures in GD soil was less as compared to that of PD soil. For instance, the pore-water pressure at point A (see Figure 4) increased from −94.6 kPa (t = 0 h) to −48 kPa (t = 12 h) and −30 kPa (t = 24 h) in GD soil whereas it increased from −93 kPa (t = 0 h) to −38 kPa (t = 0 h) and −11 kPa (t = 0 h) in PD soil. As a result, the decrease in the shear strength of the soil was less in GD soil as compared to that of PD soil. Therefore, the induced tension strains in GD soil were smaller than that of PD soil.

The resulting strains at the soil (see Figure 4) for GD and PD soils are shown in Figure 7 at different times during the rainfall. As shown in the figure, the windward side of the soil experienced tension and the leeward side of the soil experienced compression as reflected by the positive and negative values of strains, respectively, for both of GD and PD soils. As shown in the figure, the tension strain increased significantly due to the applied rainfall, while the compression strain increased slightly. The magnitude of tension strains in the soil increased as the distance from the trunk increased significantly due to the presence of rainfall. For instance, the tension strain in the soil underneath the edge of the root plate increased from 0.8% (t = 0 h) to 11.1% (t = 12 h) and 17.4% (t = 24 h) in GD soil. On the other hand, the tension strain in the soil underneath the edge of the root plate increased from 0.7% (t = 0 h) to 12.7% (t = 12 h) and 22.5% (t = 24 h) in PD soil. The significant increase in the tension strains reflected the failure of the soil at windward side. Therefore, if any root existed at that location it may experience tension failure as well which potentially could cause the failure of the tree due to root break.

5 CONCLUSIONS

Based on the seepage and load/deformation analyses of the tree-root-soil model subjected to rainfall of 1×10^{-6} m/s and wind load of 150 kN, it was found that the presence of rainfall significantly increased the tension strains which resulted in tree failure. The lower

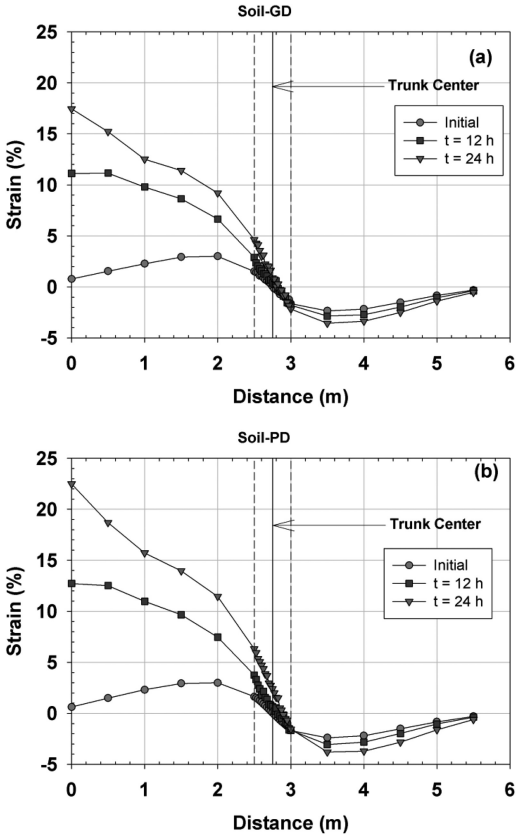


Figure 7. Strains profile in the soil: (a) GD soil, (b) PD soil.

permeability of PD soil resulted in a slower infiltration of rainwater into the soil. As a result, the increase in pore-water pressures in PD soil was larger as compared to that of GD soil. Therefore, the increase in tension strain was higher in PD soil as compared to GD soil.

ACKNOWLEDGEMENT

The study was carried out as a part of a research collaboration to study effect of rainfall on tree stability. The study was conducted by the Nanyang Technological University and National Parks Board, Singapore with some financial supports from DHI-NTU.

REFERENCES

ASTM D4767-11. 2011. Standard Test Method for Consolidated Undrained Triaxial Compression Test for Cohesive Soils.

Fredlund, D. G. and Rahardjo, H., 1993. Soil mechanics for unsaturated soils. Wiley, New York.

Geo-slope International, 2012. SEEP/W for finite element seepage analysis, user's guide. Calgary, Alta., Canada.

Koizumi, A., Motoyama, J., Sawata, K., Sasaki, Y., & Hirai, T., 2010. Evaluation of drag coefficients of poplar-tree crowns by a field test method. The Japan Wood Research Society, 56: 189–193.

Lee, T. T., 2015. Effect of rainfall on tree stability. PhD Thesis under examination. Nanyang Technological University, Singapore.

National Parks Board., 2011. Conservation of Trees /Plants.

Rahardjo, H., Ong, T.H., Rezaur, R.B. and Leong E.C., 2007. Factors controlling instability of homogeneous soil slopes under rainfall. Journal of Geotechnical and Geoenvironmental Engineering, ASCE, 133(12): 1532–1543.

Rahimi, A., Rahardjo, H., and Leong, E.C. 2010. Effect of antecedent rainfall patterns on rainfall-induced slope failure. Journal of Geotechnical and Geoenvironmental Engineering, 137(5): 483–491.

This page intentionally left blank

Unsaturated Soil Mechanics—from Theory to Practice – Chen et al. (Eds)
© 2016 Taylor & Francis Group, London, ISBN 978-1-138-02921-7

An analysis of plain strain deformation and strength characteristics of loess with vertical structure

Y. Zhang & S.J. Shao
Institute of Geotechnical Engineering, Xi'an University of Technology, Xi'an, China
Shaanxi Key Laboratory of Loess Mechanics and Engineering, Xi'an, China

L.J. Wang
School of Civil Engineering and Architecture, Xi'an Technology University, Xi'an, China

ABSTRACT: In this paper, by using the true triaxial apparatus of Xi'an University of Technology, plane strain tests of different moisture content loess with vertical structure are conducted under different confining pressure and vertical loading in order to study the relationship of intact loess strength, deformation characteristics and intermediate principal stress. The result shows that loess with low moisture content tends to be in brittle failure state and its stress-strain relationship curve is softening in the condition of low confining pressure. However, it change to be hardening with the confining pressure increasing. The result also reveals that the lateral deformation of loess has a non-linear relationship with its vertical one, and the volume deformation is of shrinkage in the process of shearing. With the development of vertical loading deformation, the principal stress in the direction of plane strain transforms from minor principle stress to intermediate one, and the coefficient of which stops decreasing and starts increasing gradually, ranging from 0.15 to 0.35. In brief, the failure strength of loess is closely related to moisture content, confining stress and even normal stress state. With the moisture content increasing, cohesion effect reduces obviously, while the internal friction angle decreases slightly.

1 INTRODUCTION

Loess is distributed widely in the world, accounting for about one-tenth of the world's land area. And China has the world's most widely distribution loess, thickness of which is also maximum. Because of its specially deposition, loess has the characteristics of loose fabric, large pores, vertical joint structure, soluble salt content, and collapsibility etc. (Liu 2001). Strength and deformation of loess are the key issues in the construction of the loess area. In practical engineering, the common embankment, soil dam, retaining wall, slope, foundations, tunnel and other projects are constructed in the soil which is approximately in the plane strain state. Therefore, the plane strain state is one of the common stress states in geotechnical engineering. In fact, there are some differences between plane strain state of the soil and the stress state as well as stress path of the sample in the triaxial test. It is quite unreasonable to adopt the strength index obtained by the conventional triaxial test applying to practical engineering. Shao and other scholars (Shao et al. 2013; Shao et al. 2008, Chen et al. 2013) have tested the structural strength characteristics of intact loess with the true triaxial test. The soil strength under plane strain state are mainly explored on the basis of theoretical analysis and numerical simulation (Chen et al. 2013, Zhang et al. 2011, Shi et al. 2001, Qian et al. 2009, Luo et al. 2001), and the change law of intermediate principal stress under the plane strain state is done in the sand soil and soft clay etc. (Li et al. 2006, Jiang et al. 2004 Ma et al. 2006, Li et al. 2004, Deng et al. 2008, Shi et al. 2001). Although many scholars have done much research on the strength of the soil in plane strain conditions and achieved a lot, little research is done on the deformation and intermediate principal stress variation of intact loess in plane strain condition. Therefore, to carry out a comprehensive analysis on such aspects is particularly important. In this paper, the author made corresponding plane strain transformation of the true triaxial loading mechanism made independently by Xi'an Technology of University, Institute of Geotechnical Engineering, and carried out test studies on vertical loading of intact loess under plane strain state.

2 TEST PROGRAM

2.1 *Materials and preparation*

The test soil was taken from a scarp in Xi'an Bailu Plateau at a depth of 6–8.0 m in accordance with the soil testing requirements. In order to ensure uniformity of moisture content, the sample was taken by hand inward the existed scarp at the depth of about 1 meter.

It was generally taken as a large rectangular block, wrapped tightly by black plastic film and tape paper, avoiding moisture dissipation, and finally transported back to the lab, packed. Soil sample was brown, with more tuberculosis in certain part which would form silt occasionally, worm holes. It is named as silty clay or Q_3 loess. To ensure the integrity of the soil samples, the tested specimens were cut directly by the intact loess block from site. The specimen is 7 cm × 7 cm × 14 cm in the preparation process to minimize disturbance on soil structure.

The basic physical properties of testing soil are dry density 1.46 g/cm^3, natural moisture content 15.8%, liquid limit 32.82%, plastic limit 21.58%, plasticity index 11.25, saturation 27.3%, Specific gravity 2.7. The plane strain tests of intact loess are completed at five moisture content (24%, 21%, 17%, 13%, 9%) and four confining pressure (50 kPa, 100 kPa, 200 kPa, 300 kPa). The soil samples with different moisture content were made by air-drying and titration. When you make a soil specimen with large water content was prepared by placing samples into a moist cylinder more than 24 hours to allow water to spread freely and evenly.

2.2 *Test equipment*

The plane strain tests of loess are conducted by the true triaxial apparatus (Shao et al. 2009) developed independently by the Institute of Geotechnical Engineering, Xi'an University of Technology. After confining the strain developing in the direction of intermediate principle stress by installing a pair of steel plates, the author carried out some tests to explore the soil strength and deformation characteristics under plane strain condition. The working principle of instrument reconstruction is basically the same with the original true triaxial test apparatus. A set of glossy rigid plates made of steel was installed on the baffle plates to simulate plane strain state in a direction of true triaxial pressure chamber, and a soil pressure gauge was installed on the rigid plates to determine the principal stress in the shearing process. True triaxial rigid plate in the chamber is shown in Figure 1; the glossy rigid plate along plane strain condition and pressure gauge are shown in Figure 2; the plane strain pressure chamber after loading mechanism transformation is shown in Figure 3; a plane pressure chamber after the contingency loading with a load of soil samples is shown in Figure 4.

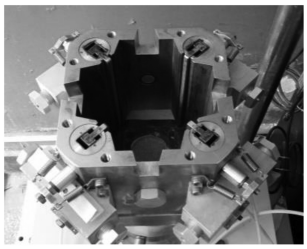


Figure 1. Pressure chamber of true triaxial.



Figure 2. The rigid plate and pressure gauge.

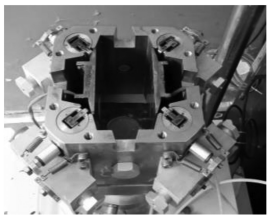


Figure 3. Pressure chamber after Transforming.

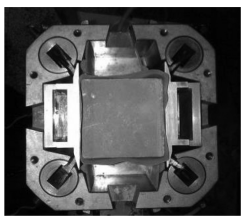


Figure 4. Pressure chamber after into the soil.

2.3 *Test methods*

For a certain moisture content intact loess, confining pressure is exerted on the vertical and lateral sides of the specimens. After the consolidation, maintaining lateral confining pressure, controlling the draining shear rate under loading along vertical structure of loess, deformation and stress variation of intact loess were measured during loading in three directions, and the plane strain test was done. According to the field conditions of Bai Lu Plateau, the test took the level deposition surface as a sample of major principal stress loading surface, maintained the vertical position of the sample and simulated soil vertical load. Collection frequency of data acquisition system in Xi'an University true triaxial is 5s. The system sets a strain controlling condition for the testing end. That is if the vertical stress strain reaches 12%, the test ends, and the specimen is damaged. The whole process took about six hours, getting various types of curves based on the collected data points.

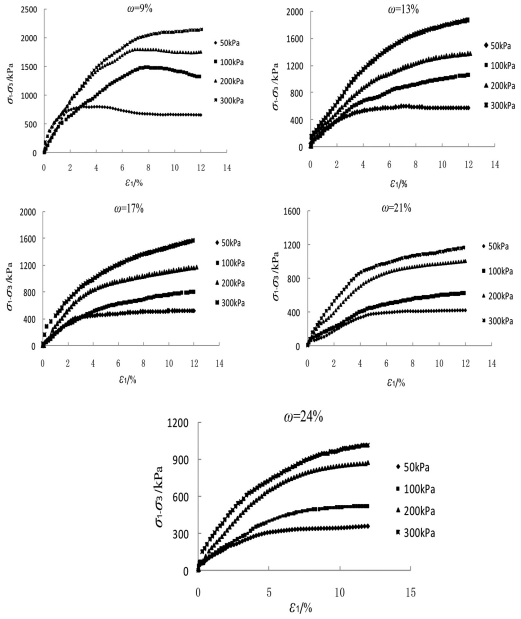


Figure 5. The stress-strain curves of intact loess at different confining pressures.

2.4 *Test loading conditions*

Sample confining pressure was 50 kPa, 100 kPa, 200 kPa, 300 kPa respectively. The same pressure from the lateral and vertical direction was exerted and the sample was consolidated under drained condition for six hours. After the consolidation, shear tests under the provisions of vertical loading effect were carried out in accordance with the required rate.

3 STRESS STRAIN RELATION OF INTACT LOESS UNDER PLANE STRAIN STATE

3.1 *Effect of moisture content and confining pressure on strain-stress relation of loess*

Intact loess has certain structure strength, and its stress strain curve can be classified as three types and five forms according to the state of the loess, strained condition, and the formation time. They are brittle failure (strong softening, weak softening), plastic collapse (strong hardening, weak hardening) and perfect plasticity (Liu, 2001). Figures 5 and 6 have showed the relationship between strain and stress of the intact loess Q_3 under the plane strain state.

3.1.1 *Effect of confining pressure on strain-stress relation of intact loess*

To the intact loess of the same moisture content, Figure 5 has showed the different stress-strain curves of intact loess at different confining pressure in the plane strain tests.

Figure 5 shows the curve which illustrates the relation between two deviator stress and vertical principal strain, underside is the same situation. We can know from fig.5 that during the vertical principal stress loading, the stress-strain relationship curve of the intact loess with higher moisture content under the higher confining pressure is the hardening type, and the principal stress difference increases with the increase of vertical principal strain, which accords with the hyperbolic-type. Another stress and strain curve of the sample loess with low moisture content ($\omega = 9\%$) under low confining pressure ($\sigma_{3c} = 50$ kPa, 100 kPa, 200 kPa) is softening type. This is because low moisture content and low confining pressure are not sure enough to destroy the structure of loess, and the shear strength of the intact loess decreases sharply as the structure is destructed by the shearing force, which results to a softening type of stress and strain curve. As the increase of moisture content and the confining pressure, if the confining consolidation pressure exceeds the structure strength of the intact loess, the effect will cause structure failure. The strength of loess is mainly provided by the strength of friction resisting shear and the structure strength of its inside part of cementation. Under this condition, the stress and strain curve of the intact loess will become hardening type. Therefore, under the condition of low moisture content, the curve shifts from strong softening and weak softening of brittle failure to weak hardening and hard hardening; when the moisture content is above 13%, the curve will transit from weak hardening to strong hardening with the increase of the consolidation confining pressure.

On the occasion of the same moisture content, as the confining pressure increases, it has a greater effect on the enhancement of loess structure; and the bigger initial tangential modulus is, the higher strength of the loess will be when it's totally disrupted. As the axial strain develops, the tangent slope of the curves decreases, and the trend is universal. During the loading process, the high constitutive property loess will also soften because the destruction force of the primary structure exceeds that of the secondary structure. On the contrary, the weak structure loess will be hardened because the destruction force of secondary structure exceeds that of the primary structure.

3.1.2 *Effect of moisture content to stress-strain relation of intact loess*

Figure 6 shows us the stress and strain curves of the intact loess with different moisture contents under the same confining pressure. Figure 6 shows that: during the vertical loading process, the stress and strain curves will transfer to hardening types, except the example under the condition of low moisture content ($\omega = 9\%$). In that case it will transfer to softening type. With the increase of moisture content, the curve transforms from weak hardening to strong hardening.

Under the same confining pressure, the higher moisture content is, the lower position the curve of the stress and strain will be, the lower initial tangent slope will be, as well as the principal stress difference needed to get the same vertical strain, and the weaker

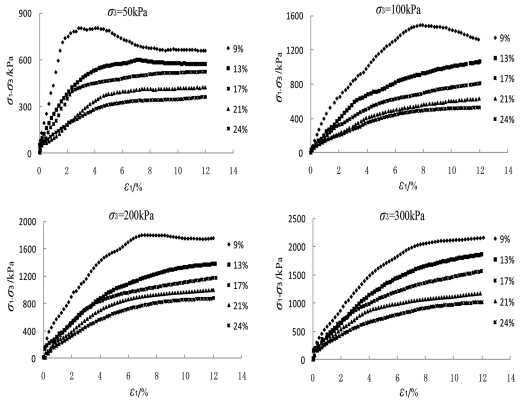


Figure 6. The stress-strain curves of intact loess at different moisture contents.

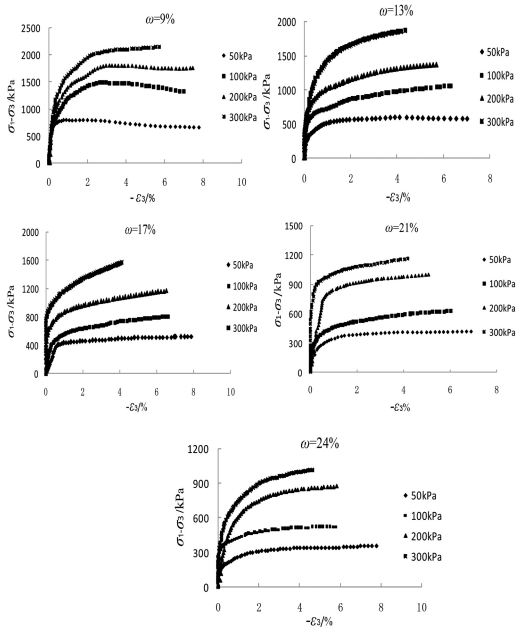


Figure 7. The stress-strain curves of intact loess at different confining pressures.

the intact loess strength will be. The effect of moisture content on the strength of the loess is negative. The higher moisture content is, the more obvious effect it will work on the strength. It is because: as the moisture content increases, water film between the granular will be thicker, partial agglutinate dissolves, and cementation working among the granular fades. As a result: the ability of agglutinating is weakened; the curvature of the shrinkage film of the soil skeleton's pore decreases; suction will also decrease. Since the water film in the soil particle becomes thicker, this can lubricate the soil particles, the bite frictional resistance decreases as well as the function of double electric layer. Considering these factors, it can be concluded that the strength of loess will decrease as the moisture content increases.

From Fig. 5 and Fig. 6 we can know the intact loess of low moisture content under low confining pressure are more likely to evoke brittle collapse; and the intact loess of high moisture content under high confining pressure are more likely to evoke plastic collapse. Confining pressure and moisture content are two main factors to affect the strength of intact loess as well as the strain during shearing process. Specifically speaking, when the strain is not that much, its development will dramatically damage the structure of the loess. On the contrary, the damage will become weaker and weaker. So does the effect of confining pressure and moisture content on the loess structure which tends to be stable gradually.

Under the experiment condition, the consolidation stress in the plane strain direction is less than that of the deformation plane. So at the primary stage, the development of vertical strain is greater than that in the triaxial test under the same confining pressure. During the shearing process, the principal stress in the direction of plane strain gradually increases, going through the transform from minor principal stress to intermediate principal stress. At the primary stage of shearing, the principal stress in the plane strain direction is actually minor principal stress. At this time, principal stress difference $(\sigma_1 - \sigma_3)$ is actually major, intermediate principal stress difference, and until the principal stress in the direction of plain strain increases as intermediate one, principal stress difference $(\sigma_1 - \sigma_3)$ is the major, minor principal stress difference. However, in the conventional triaxial test, principal stress difference $(\sigma_1 - \sigma_3)$ is always the major (minor principal stress difference. As a result, under the condition of plane strain and the process of shearing, at primary stages the primary tangent slope of the strain and stress curve in the shearing process is smaller than that in the corresponding conventional triaxial test.

3.2 *Lateral deformation characteristics of loess*

3.2.1 *Analysis of relationship between deviatoric stress and lateral strain*

In this paper, the deviatoric stress $(\sigma_1 - \sigma_3)$ and lateral strain $(-\varepsilon_3)$ of the intact loess with different moisture content are tested under different confining pressure. Figures 7 and 8 have shown us the relationship curve between them. As it can be seen from Figures 7 and 8, the relationship curves are similar. Except for that the curve of low moisture content loess under low confining pressure is softening, the curves under other conditions are all hardening. With the confining pressure and moisture content increasing, the curve develops into strong hardening from weak type; When the confining pressure is big and the water content is low, the initial tangent curve slope is high as well as the soil strength. However, the initial tangent slope of the $\sigma_1 - \sigma_3 \sim -\varepsilon_3$ curve is larger than $\sigma_1 - \sigma_3 \sim \varepsilon_1$, when the principal stress difference to a certain level, the lateral strain begins to develop and more obvious turning point will appear. Because of the primary

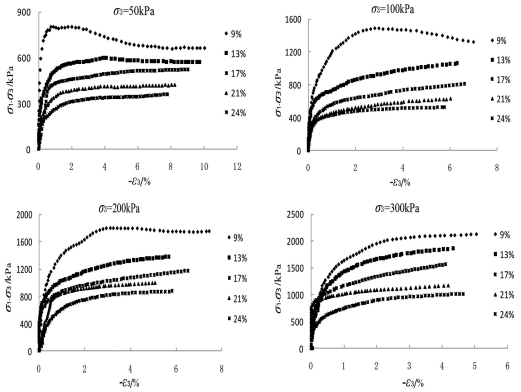


Figure 8. The stress-strain curves of intact loess at different moisture contents.

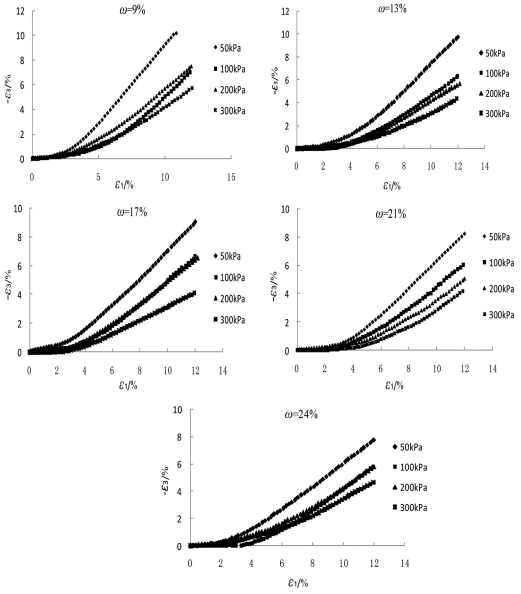


Figure 9. $-\varepsilon_3 \sim \varepsilon_1$ curves of intact loess at different confining pressures.

structure of intact loess, the concretion stress in the plane strain direction is less than confining pressure. At the initial stages of shearing, when the shear stress is less than the initial structural strength of loess in the plane strain direction, the stress will develop rapidly and the principal stress will increase in the plain stress direction. But no lateral deformation will occur for the primary structure of loess and minor principal stress of plane strain direction. The vertical stress is taken by the initial structure of loess. When the stress gradually becomes greater than the initial structural strength, the primary structure of loess will be damaged with a small increase of stress and the secondary structure will gradually form, which is shown by the increasing lateral strain.

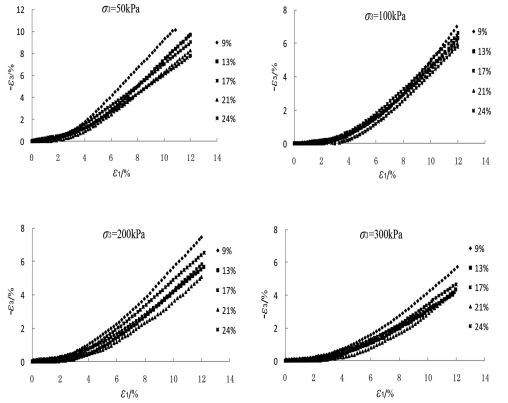


Figure 10. The $-\varepsilon_3 \sim \varepsilon_1$ curves of intact loess at different moisture contents.

3.2.2 *Lateral deformation analysis*

The relationship curve between the vertical strain (ε_1) and the lateral strain ($-\varepsilon_3$) of loess with different moisture content under different confining pressure is shown in Figures 9 and 10.

As it can be seen from Figure 9, 10, the relationship curve between the vertical strain (ε_1) and the lateral strain ($-\varepsilon_3$) of loess with different moisture content under different confining pressure is nonlinear; With the development of the vertical strain, lateral strain evolves too. When the vertical strain less than 2%, lateral strain is very small, almost zero; when the vertical strain is between 2% and 4%, the slope of the curve increases, the lateral deformation begins to develop obviously; when the vertical strain is larger than 4%, the slope stabilizes, then the lateral and vertical strain develop in a linear relationship way.

According to Figure 9, we know the larger the confining pressure is, the smaller the soil lateral deformation becomes. All lateral deformations under different confining pressures are less than the amount of vertical deformation. As the confining pressure increases, the lateral compression of the soil specimen grows, the macro performance of which is smaller side expansion deformation. Figure 10 shows that with the increase of moisture content, the lateral deformation corresponding to the same axial strain becomes smaller, and the regularity of the curve is weaker. Meanwhile the development rate of the vertical deformation is much higher than the side bulging deformation, and the bigger the moisture content is, the faster the development of vertical deformation will become. Therefore, the side expansion strain corresponding to the same vertical strain under higher moisture condition would be less than that under low moisture content. Both confining pressure and moisture content have great effect on the lateral deformation of the intact loess.

3.3 *Volumetric strain characteristics of loess*

In order to analyze the volume change characteristics of the intact loess during the shear process, volume strain (ε_v) and vertical strain (ε_1) of loess with different

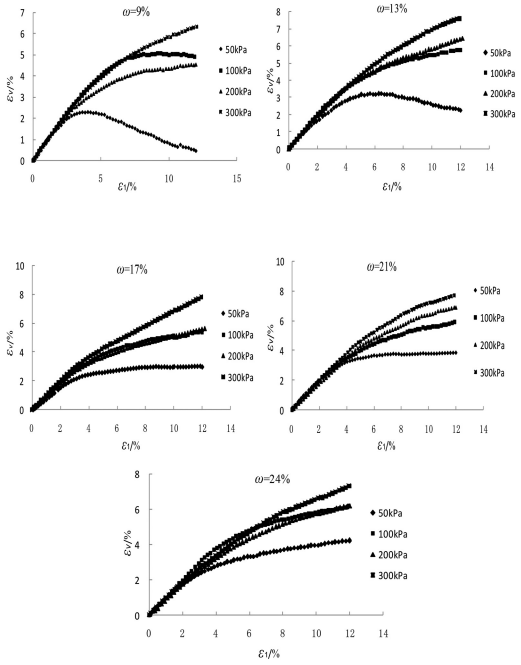


Figure 11. $\varepsilon_v \sim \varepsilon_1$ curves of intact loess at different confining pressures.

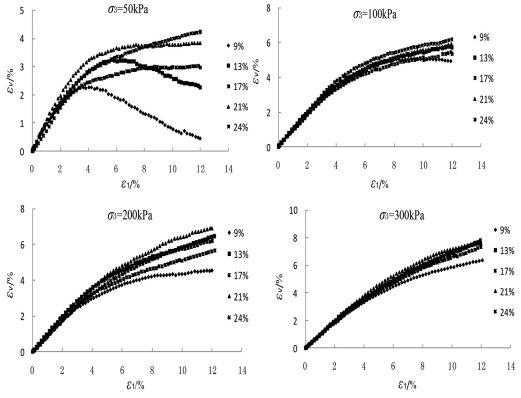


Figure 12. $\varepsilon_v \sim \varepsilon_1$ curves of intact loess atdifferent moisture contents.

moisture content under different confining pressure are tested. And based on the result, the relationship between volume strain (ε_v) and vertical strain (ε_1) can be concluded from Figures 11 and 12.

The intact loess during the shear process will be shear shrink except for that under the condition of low moisture content and low confining pressure ($\omega = 9\%$, $\sigma_{3c} = 50$ kPa, 100 kPa) ($\omega = 13\%$, $\sigma_{3c} = 50$ kPa), the intact loess during the shear process will be converted to dilatancy, which is contributed by the strong structure of low moisture content. When the concretion confining pressure was not sufficient to cause structural compression damage, the loess can resist the

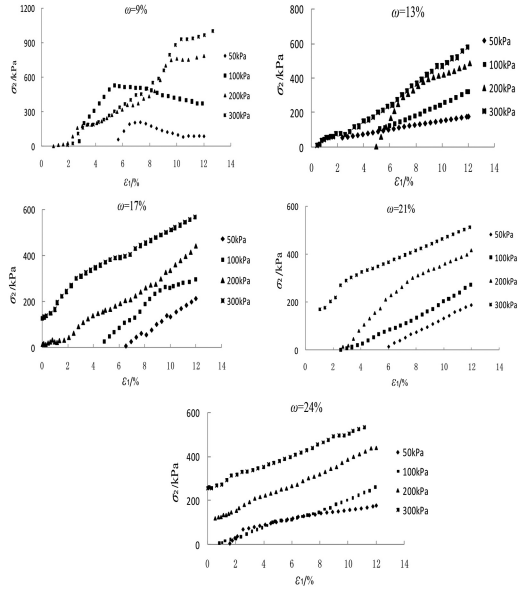


Figure 13. $\sigma_2 \sim \varepsilon_1$ curves of intact loess at different confining pressures.

initial effect of vertical load and side expansion deformation and the volume contraction is mainly vertical compression. With the development of vertical compressive deformation, the structure of loess would be destroyed progressively, and side expansion became more and more conspicuous, and finally ran into volume swelling deformation. The structure of the loess with high moisture content is weak. The confining pressure has already damaged partial even the whole structure of the loess. Therefore, when the vertical compression load is apparently greater than the side expansion deformation, volume shrink will occur.

3.4 *Variation rules analysis of principal stress in the plane strain direction*

Several researches have shown that the strength of the loess under plane strain condition is greater than axial symmetry state. The fundamental reason is that the principal stress in the plane strain direction will enhance the loess strength. Therefore, it's particularly important to study the variation rules of the principal stress in the plane strain direction during the shearing process.

3.4.1 *Analysis of the changing characteristics of the principal stress in the plane strain direction*

The relationship curves of Fig. 13 (Fig. 14 are concluded from tests of the principal stress (σ_2) in the plane strain direction and vertical strain (ε_1) which was under different moisture content and confining pressures.

What can be seen from Fig. 13 (Fig. 14 is that with the development of the vertical strain, the principal stress increases first and then decreases in the direction

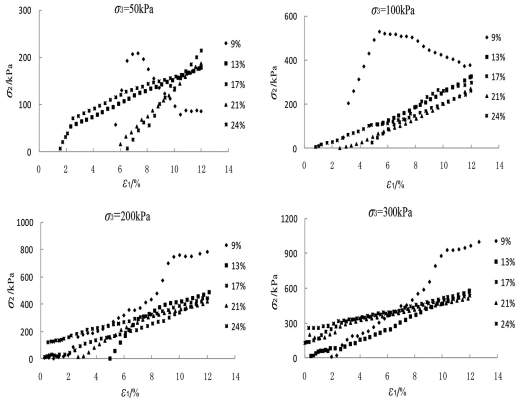


Figure 14. $\sigma_2 \sim \varepsilon_1$ curves of intact loess at different moisture contents.

of plane strain under the condition of low confining pressure and low moisture content. In other conditions, the principal stress of plane strain direction increases with the increase of vertical strain. The strength of the loess grew quickly until the peak with the development of shearing deformation in the process of softening stress-strain development of the loess under low moisture content and confining pressure and the principal stress in the plane strain direction was on fast growth during the period. The principal stress of plane strain direction is correspondingly reduced and the principal stress increases first and then decreases at last when the strength goes down and gradually tends to be stable. The principal stress of the plane strain direction would be increased as well as the shear strength in the process of hardening stress-strain of the loess with high moisture content or confining pressure; the greater the confining pressure is, the greater principal stress of the same plane direction will be, so will the regularity. While the higher the moisture content is, the smaller the corresponding principal stress will be as well as the regularity. Confining pressure has a great effect on the principal stress of the plane strain direction than moisture content in the process of shearing.

3.4.2 *Characteristics analysis of the intermediate principal stress coefficient changes*

Consider the principal stress in the plane strain direction changes between minor principal stress and intermediate principal stress in the process of shearing. The relationship curves between the intermediate principal stress coefficient (b) and vertical strain (ε_1) of loess under different moisture content and different confining pressure is shown in Figures 15 and 16.

Figures 15 and 16 show that under different confining pressure and moisture content condition, the $b \sim \varepsilon_1$ curve changes as follows: First, when $\sigma_2 < \sigma_3$, σ_3 is the Intermediate principal stress. As ε_1 increases and σ_3 remains stable, σ_1 and σ_2 are both gradually increasing, so b decreases with ε_1 increasing, and until $\sigma_2 = \sigma_3$, $b = 0$, the soil reaches the plane strain stress. Second, when σ_2 is the Intermediate principal stress, the soil

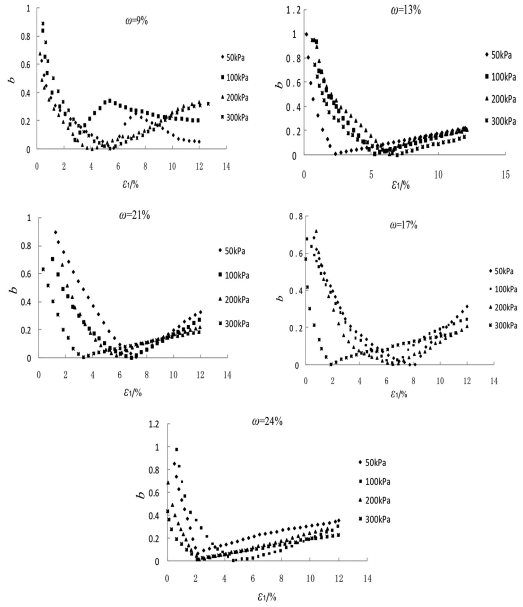


Figure 15. $b \sim \varepsilon_1$ curves of intact loess at different confining pressures.

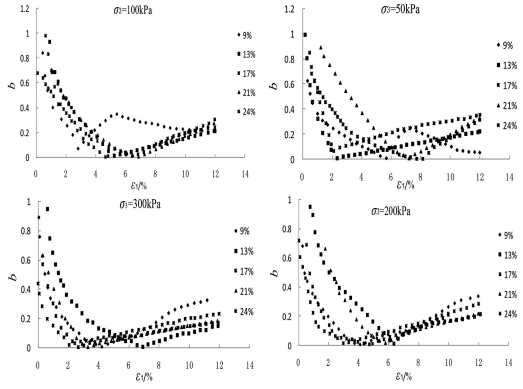


Figure 16. The $b \sim \varepsilon_1$ curves of intact loess at different moisture contents.

is in plane strain stress state, and with the development of deformation, σ_1 and σ_2 continue increasing; b keeps growing until the sample is destroyed. At low confining pressure and low moisture content, the Intermediate principal stress coefficient b increases and then decreases with axial strain. The reason is the same to the changing rules of the principal stress in plane strain direction. Both the confining pressure and moisture content can affect b during shear process; when confining pressure and moisture content become greater, the loess is in plane strain state. So, in the initial stages of shear, the stress in the direction of plane strain stress is minor principal stress and it is converted to the intermediate principal stress with the development of the shearing process.

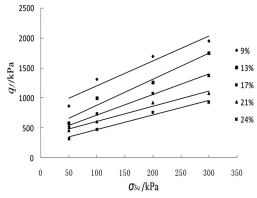


Figure 17. q_f vs σ_{3c} relation

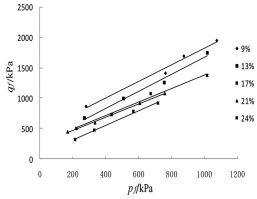


Figure 18. q_f and p_f relation.

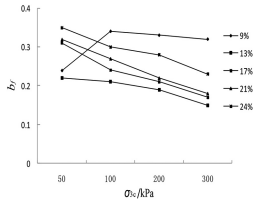


Figure 19. b_f vs σ_{3c}.

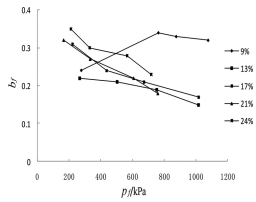


Figure 20. b_f vs p_f.

3.5 *Analysis of strength properties*

In this part, for softening stress-strain curve, peak stress is taken as the destruction stress; for hardening curve, the stress of vertical strain at 10% is taken as the destruction stress. And damage generalized shear stress q_f intermediate principal stress coefficient b_f and average normal stress p_f under different confining pressure and moisture content are analyzed to reveal the strength properties of the intact loess under plane strain condition.

3.5.1 *Stress conditions analysis of strength destruction state*

The relationship curves of $q_f \sim \sigma_{3c}$, $q_f \sim p_f$, $b_f \sim \sigma_{3c}$, and $b_f \sim p_f$ are shown respectively in Figures 17, 18, 19 and 20.

As can be seen from Figure 17 and 18, with the confining pressure and average normal stress increasing, the generalized shear stress at failure also increases,

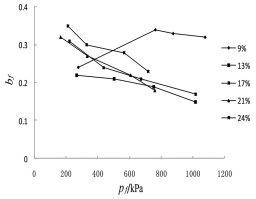


Figure 21. σ_{2f} vs σ_{3c}.

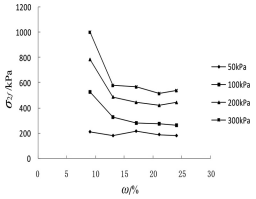


Figure 22. σ_{2f} vs w.

and this can be approximately described as a linear relationship; moisture content affects shear stress at failure significantly. The higher the moisture content is, the smaller the shear stress at failure will be and water immersion reduces the strength of intact loess. Analysis of Figures 19 and 20 shows that when the moisture content reaches 9%, the destroyed intermediate principal stress coefficient first increases and then decreases with confining pressure and average normal stress. Except for the situation mentioned above, the destroyed intermediate principal stress coefficient all decreases with the increase of confining pressure and average normal stress under other moisture content conditions. And the regularity is obvious. The strength characteristics of intact loess destroyed is closely related to its confining pressure, moisture content, and the average normal stress state.

3.5.2 *Analysis of intermediate principal stress at failure*

The relationship between intermediate principal stress at failure and confining pressure as well as moisture content is Figures 21 and 22.

As can be seen from Figure 21 and 22, the intermediate principal stress at failure state increases with the increase of the confining pressure, and the regularity is obvious; the greater the confining pressure is, the greater the shrinkage reduction of soil will be, and the greater the strength at failure is, the higher degree the increase of the intermediate principal stress will be. When moisture content increases from 9% to 13%, the destruction intermediate principal stress decreases significantly. When moisture content is above 13%, the intermediate principal stress decreases slightly.

3.5.3 *Analysis of intermediate principal stress coefficient at failure*

The $b_f \sim \omega$ curve is shown in Figure 23, and the $b_f \sim \sigma_{3c}$ curve is shown in Figure 19.

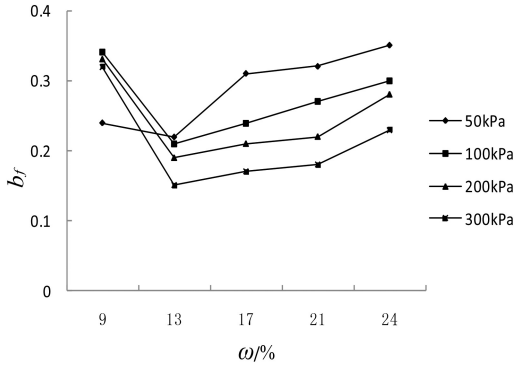


Figure 23. The change law between b_f and w.

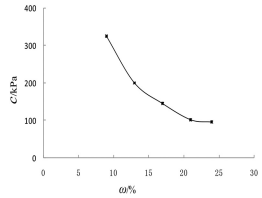


Figure 24. c vs w.

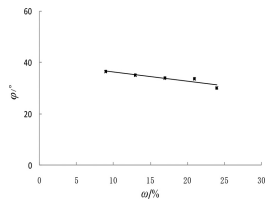


Figure 25. φ vs w.

As can be seen from Figures 19 and 23, both confining pressure and moisture content will affect the intermediate principal stress coefficient at failure. With the increase of moisture content, intermediate principal stress coefficient first increases and then decreases, and the regularity is obvious. Under plane strain conditions, the intermediate principal stress coefficient b_f at failure state is between 0.15 and 0.35 for the intact loess.

3.5.4 *The variation regularity analysis of strength parameters*

Based on the strength envelope under the condition of plane strain, we can get the strength indexes of cohesive force c and internal friction angle φ values of intact loess with different moisture content. Strength index curves along with different moisture content are shown in figure 24 and 25.

As can be seen from Figure 24, cohesive force decreases with the increase of moisture content. When moisture content is less than 21% (close to the moisture content of the plastic limit), the cohesive force decreases fast along with the increase of moisture content. When moisture content is more than 21%, the cohesive force decreases tends to be stable. The increase of moisture content leads to soil particles of water membrane thickening, suction of which will decrease, and when the structure is damaged, the cohesive force is becoming small. When the moisture content reaches the plastic limit, soil water film can connect and adapt to soil particles slip and the cohesive force of soil becomes stable under the condition of consolidation complete. The analysis of diagram 25 shows that with the increase of moisture content, the internal friction angle decreases in a small degree under plane strain condition. This is mainly because with the increase of moisture content and the wedging of water film, the water film among soil particles becomes thick, which will make the particle contact smooth and reduce the friction between the soil particles. So the internal friction angle of soil tends to decrease.

4 CONCLUSIONS

(1) Stress-strain relationship curve of the intact loess with low moisture content and low confining pressure under plane strain state is softening and the rest were hardening type. The change of moisture content and confining pressure significantly affect the strength of loess. The greater the confining pressure is, the higher the strength will be. And the higher the moisture content is, the lower the strength will be.

(2) During the process of shearing, the lateral strain of the intact loess increases with the development of vertical strain and the relationship between them is nonlinear. Lateral strain in the initial shear stage is almost zero. Then, the rate of lateral strain growth increases gradually. The vertical strain is larger, and has a linear relationship with lateral strain growth until the sample is damaged. The bigger the consolidation confining pressure is, the smaller the lateral deformation of soil will be. The influence rule of moisture content on the lateral deformation is weak.

(3) Under low confining pressure, during vertical loading, the intact loess with low moisture content first shows reduction and then dilatancy, and volume strain shows a peak with vertical strain development; under high confining pressure, the intact loess of high moisture content shows shear reduction, volume shrinkage strain shows non-linear monotonic increasing with vertical strain.

(4) During the shearing, the intermediate principal stress σ_2 on the plane strain direction increases with increasing vertical strain ε_1; b is divided into two stages with development of ε_1: When $\sigma_2 < \sigma_3$, σ_3 is the intermediate principal stress, and b decreases with ε_1 increasing; when σ_2 is the intermediate principal stress, with the development of the deformation, σ_1 and σ_2 continues increasing, and b grows until the sample is destroyed. The principal stress of the plane stress direction

is minor principle at the initial stage, and it will be gradually converted to the intermediate principal stress with the development of the shearing process.

(5) When the strength of the intact loess is at failure, generalized shear increases with the increase of average normal stress and confining pressure, and they show a linear relationship; the smaller the moisture content is, the greater the generalized shear stress at failure will be. The intermediate principal stress coefficient at failure shows approximately linearly decrease with the increase of the average normal stress and the confining pressure, intermediate principal stress coefficient decreases and then increases with the increase of the moisture content, and the intermediate principal stress coefficient at failure is between 0.15 and 0.35.

(6) With the increase of moisture content, cohesion continues decreasing as well as the decreasing rate. The cohesion tends to be stable when the moisture content is above a certain degree (plastic limit moisture content). The internal friction angle decreases linearly, but its attenuation is small.

REFERENCES

Chen, C.L., Shao, S.J., Luo, A.Z. and Fang, J. 2013. The structural effects of intact loess strength under the true triaxial test. Chinese Journal of Geotechnical Engineering, 35(12): 2322–2327.

Cheng, T., Wang, J.T. and Yan, K.Q. 2007. Decoupling analysis of elastoplastic plane strain consolidation. Huazhong Univ. of Sci. & Tech. (Nature Science Edition), 35(3): 113–122.

Deng, C.J., Zheng, Y.R. and Zhu, J.K. 2008. Formula of intermediate principal stress at failure for Mohr-Coulomb material in plane strain state. Rock and Soil Mechanics, 29(2): 310–314.

Jiang, G., Qiu, J.Y. and Wang, Z. 2004. Character of undisturbed unsaturated expensive soil under plane-strain test. Engineering Journal of Wuhan University, 37(6): 117–120.

Li, G.X., Zhang, Q.G. and Huang, Y.N. 2006. Study on transforming of principal stresses in constant stress ratio plane strain tests. Rock and Soil Mechanics, 27(11): 1867–1872.

Li, G., Xie, Y. and Chen, Z.H. 2004, Formula of intermediate principal stress at failure for coherent soil in plane strain state [J]. Chinese Journal of Rock Mechanics and Engineering, 23(18): 3174–3177.

Liu, Z.D. 1997. Mechanics and Engineering of Loess. Shaanxi Science and Technology Press, Xi'an: 1–5.

Luo, T., Yao, Y.P. and Matsuoka, H. 2001. Soil strength equation in plane strain based on SMP. Rock and Soil Mechanics, 21(4): 390–393.

Ma, X.F., Akitoshi, M. and Wen, Y.J. 2006. Chinese Journal of Rock Mechanics and Engineering, 25(9): 1745–1753.

Qian, J.G., Lü, X.L. & Huang, M.S. 2009. Softening characteristics of soils and constitutive modeling under plane strain condition. Rock and Soil Mechanics, 29(3): 617–622.

Shao, S.J., Xu, P. and Chen, C.L. 2013 Several shear spatially mobilized planes and anisotropic strength criteria of soils Chinese Journal of Geotechnical Engineering 35(3): 422–435.

Shao, S.J. and Deng, G.H. 2008. The strength characteristics of loess with different structures and its application in analyzing the earth pressure on loess tunnel, China Civil Engineering Journal, 41(11): 93–98.

Shao, S.J., Luo, A.Z. and Deng, G.H. 2009. Development of a new true triaxial apparatus. Chinese Journal of Geotechnical Engineering, 31(8): 1172–1179.

Shi, H.Y. and Liu, B.J. 2001. An empirical formula determining intermediate principal stress of cohesionless soil under plane strain condition. Journal of Xi'an Highway University, 21(1): 19–22.

Shi, H.Y., Xie, D.Y., and Wang, W.S. 2001, Failure criterion for cohesionless soil under plane strain condition. China Civil Engineering Journal, 34(1): 79–83.

Zhang, C.G., Hu, Y.S. and Zhao, J.H. 2011. Unified solution of shear strength for unsaturated soil under plane strain condition and its application. Chinese Journal of Geotechnical Engineering, 33(1): 32–37.

Unsaturated Soil Mechanics—from Theory to Practice – Chen et al. (Eds)
© 2016 Taylor & Francis Group, London, ISBN 978-1-138-02921-7

Engineering properties of lead contaminated expansive soil

X.Q. Zhang, F.S. Zha, J.J. Liu & K.R. Cui
School of Resource and Environmental Engineering, Hefei University of Technology, Hefei, China

ABSTRACT: Heavy metals contamination could change the engineering properties of expansive soils. Therefore, a series of laboratory experimental studies were performed on the Pb-contaminated soils, such as grain size distribution, atterberg limits, free swell rate, direct shear strength and unconfined compressive strength test. The experimental data supplied by the tests showed that the presence of lead caused the reduction in the clay particles content, liquid limits, plasticity index and free swell rate. Moreover, unconfined compressive strength and shear strength decreased with Pb^{2+} concentration increased as well. It was concluded that the presence of Pb^{2+} had detrimental effects on mechanical properties of expansive soils, while the expansibility could be weakened.

1 INTRODUCTION

With the development of industrial society and frequently activities of human beings, the phenomenon of heavy metal contaminated soils has been a more and more serious problem. Contaminants existed in the soils not only threaten the health of human beings but also have some complicated negative influences on the natural soils engineering properties. Therefore, a large quantity of studies have been performed on the heavy metal contaminated soils (Ratnaweera et al. 2006, Pachecoe Silva et al. 2005, Maaitah et al. 2005, Singh et al. 2008, Meegoda et al. 2001, Rajasekaran et al. 2001).

Li et al. (2015) investigated the effects of Pb^{2+} on the mechanical behaviors through a series of laboratory tests. The results presented that liquid limits and plasticity index, clay particles content and expansion ratio decreased, while the shear strength increased with the increase of Pb^{2+} concentration. Shackelford et al. (2000) indicated that increasing Pb^{2+} concentration caused a smaller individual granule of clay due to compression of interlayer region. Thereby, the expansion ratio of lead contaminated soils increased. The increasing content of inorganic salt in the soils, such as NH_4Cl, $FeSO_4$, $CuSO_4$ and KCl and so on, leads to the increase of liquid limits and plastic limits (Arasan & Yetimoglu 2008). Yong et al. (2001) argued that the reduction in consistency limits of the lead contaminated soils was attributed to the decreased pH due to the additional Pb^{2+}. Moreover, Dermatas et al. (Dermatas et al. 2003, Moon et al. 2006) indicated that Pb^{2+} and Cr^{3+} could adsorb on the surface of clay soils effectively, and the content of clay particles primarily governed the leaching properties and immobilization of Pb^{2+} and Cr^{3+}. At present, a large amount of studies focused on the influence of acid and contaminants on the compressibility and strength characteristics of foundation soils in China (Zhu et al. 2007, 2008, 2011, Qi et al. 1999, Li et al. 2004). However, it is rarely seen that studies revealed the mechanical properties of the soil contaminated with heavy metals as well as the interaction mechanism between heavy metal ions and soil particles.

Expansive soils distribute extensively in Hefei, China. Variations in environment would lead to a serious change of expansive soils (Chen 2013, Wu & Yuan 2013, Tang & Shi 2011). The paper intends to determine the effects of heavy metals contamination on the basic physical and mechanical properties of the expansive soils. Therefore, a series of laboratory tests, such as grain size distribution test, atterberg limits test, free swell ratio test, expansibility test, direct shear strength test and unconfined compressive strength test, were conducted on the specimens contaminated by lead with different concentrations.

2 MATERIALS AND METHODS

2.1 *Materials*

Expansive soil used was obtained from the intersection of Baohe Road and Meihe Road, Hefei City, with a 3.0–3.5 m depth, hard plastic. The basic physical properties were given in Table 1.

$Pb(NO_3)_2$ was chosen as the contaminant due to its high solubility The lead pollution sources used in this study were $PbNO_3$, because it has a high solubility and cation activity (Boardman 1999). The Pb^{2+} concentrations were designed as 0, 0.1, 0.5, 1.0, 2.0 and 3.0% by mass of dry soils.

2.2 *Methods*

2.2.1 *Product preparation*

The soil sample was oven-dried under 105°C, and then pulverized, passed through 2 mm sieves. Dissolving

Table 1. Physical properties of tested expansive soil.

Water content/%	Density/ $g \cdot cm^{-3}$	Specific gravity G_s	Liquid limit/%	Plastic limit/%	Optimum moisture content/%	Maximum dry density/ $g \cdot cm^{-3}$
18	1.545	2.669	49.6	24.0	21.2	1.663

$Pb(NO_3)_2$ with a certain quantity of de-ionized water based on the optimum moisture content. And then mixing the soil sample and $Pb(NO_3)_2$ solution thoroughly. Finally, casting the mixture into the cylindrical moulds and cutting rings depended on the 95% of the maximum dry density. The size of specimens is Φ 5 cm × H5 mm and Φ6.18 cm × H2 cm, respectively. After remolded of the specimens, wrapped with plastic bags and curing for 24 hours in the standard curing room (temperature 20 ± 2°C, humidity 95% ± 2%).

2.2.2 *Tested methods*

The specimens after cured in the curing room, were oven-dried, pulverized and sieved with 2 mm sieves again for atterberg limits test and free swell test. Unconfined compressive strength test and direct shear strength were performed on the cylindrical specimens and cutting ring specimens, respectively. The broken specimens could be used for grain size distribution analysis.

All the test methods referenced to the *Road test procedures* (JTGE40-2007).

3 TEST RESULTS AND ANALYSIS

3.1 *Physical properties of contaminated expansive soils*

3.1.1 *Grain size distribution*

The grain size distribution curves of specimens contaminated with different Pb^{2+} concentrations are presented in Figure 1. It can be seen that increasing the Pb^{2+} concentrations results in the increase of silt particle content and reduction of clay particle content. While the Pb^{2+} concentrations reach at 1.0%, increasing the Pb^{2+} concentration has insignificant effects on both clay and silt particle contents.

3.1.2 *Atterberg limits*

Considering that the atterberg limits could be used as a specific parameter associated with engineering properties, the variations of liquid limits, plastic limits and plasticity indexes with different Pb^{2+} concentrations were obtained by the paper as shown in Fig. 2. It is concluded that the liquid limits and plasticity decrease with increasing of Pb^{2+} concentrations. While the plastic limits are insignificantly influenced by the variation of Pb^{2+} concentrations.

Mitchell et al. (1993) suggested that the liquid limit was directly governed by the thickness of the double diffusion layer surrounding the clay particles. Rao et al. (2013) reported that an increase in the ions concentration on the surface of soil particles attributed to the cation exchange reaction between the Pb^{2+} and Na^+/K^+ would lead to a reduction in the thickness of the double diffusion layer. Liquid limits and plastic limits decrease due to the thinning bound water membrane. The results are consistent with the conclusions proposed by Li et al. (2015).

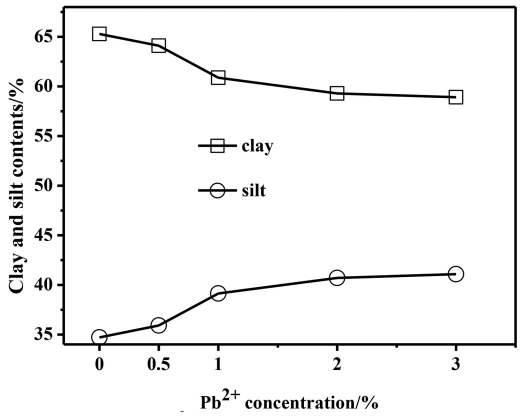


Figure 1. Effect of Pb^{2+} concentrations on clay and silt contents.

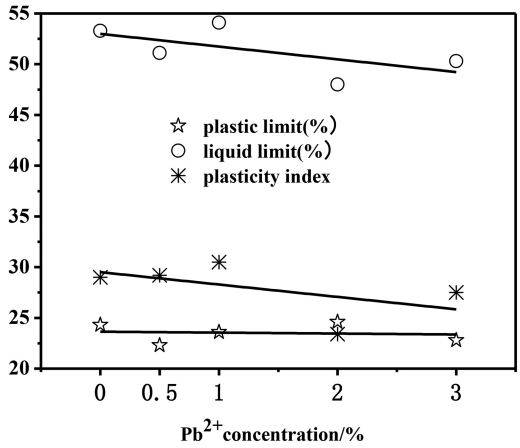


Figure 2. Effects of Pb^{2+} concentration on atterberg limits.

3.1.3 *Free swell rate*

Free swell rate is one of the most important indexes that reflecting the characteristics of expansive soil. And it is correlated to the mineral compositions, colloidal particles content and the chemical composition in the soils.

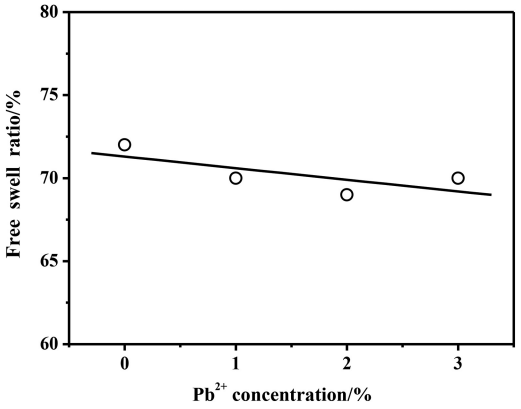


Figure 3. Effects of Pb^{2+} concentration on the free swell rate.

The effects of Pb^{2+} concentration on the free swell rate were investigated in the paper. As presented in Fig. 3, the Pb-contaminated soil exhibit a lower expansibility than that of specimens without Pb^{2+} and free swell rate decreases with Pb^{2+} concentration increases. Due to the permeation of Pb^{2+}, the thickness of diffusion double layer decreases. Attraction between soil particles increase, thus free swell rate decreases.

3.2 *Mechanical properties*

3.2.1 *Shear strength*

Direct shear test was conducted on the specimens contaminated with different concentrations of Pb^{2+}. As presented in Figure 4, the cohesion *c* decreases apparently with increase of Pb^{2+} concentrations, the angle of internal friction φ appears nearly stable as the Pb^{2+} concentrations add from 0.1% to 1.0%.

Cho et al. (2006) proposed that the geometric arrangement and soil particles shape significantly and mainly dominated the variations of angle of internal friction. Addition of Pb^{2+} may change the soil particles arrangement and shape, forming a little more heterogeneous fabric that leads to a slightly increase in the angle of internal friction. The presence of Pb^{2+} weakens the cementation between clay particles and hinders the formation of aggregates. Therefore, result in a reduction in cohesion. In general, increasing Pb^{2+} concentration would lower the shear strength of the soils. A similar conclusion was obtained by Zha et al. (2012).

3.2.2 *Unconfined compressive strength*

As shown in Figure 5, the relationships between Pb^{2+} concentration and unconfined compressive strength were investigated. It is suggested that an obviously reduction in strength attributed to the addition of Pb^{2+} is observed under a lower concentration (lower than 0.5%). It is well known that the compositions, agglutination between particles and micro-structure characteristics of soils predominantly control the strength properties. The added Pb^{2+} decreases the clay content,

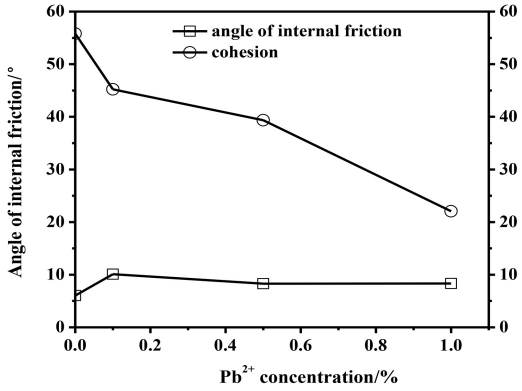


Figure 4. Relationships between Pb^{2+} concentrations and shear strength.

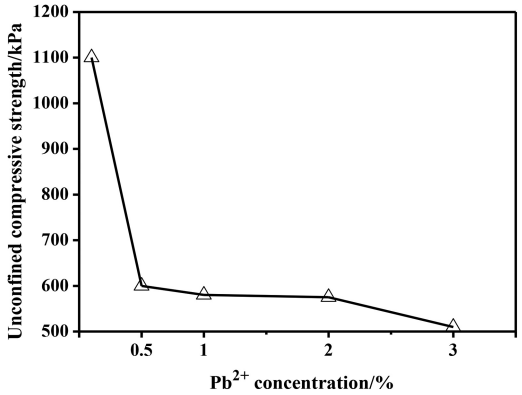


Figure 5. Effect of the concentration of Pb^{2+} on the unconfined compressive strength of expansive soil specimens.

which weakens the aggregation between soil particles. And the decreasing of double diffusion layer aroused by the presence of Pb^{2+} would accelerate the formation of flocculation. As a result, some large pores appear. Therefore, the unconfined compressive strength of the specimens decreased extensively. However, as the Pb^{2+} content added from 0.5% to 2.0%, the reduction rates of strength of the contaminated soils tend to decrease apparently. It may due to the recrystallization the excessive Pb^{2+}. Some stiffer crystals contain Pb^{2+} produced by the recrystallization could fill in the pores and improve the micro-structure of the soil. Thereby, decrease the unconfined compressive strength reduction rate.

4 CONCLUSION

The paper studied the effects of Pb^{2+} concentration on the physical and mechanical properties of expansive soils. The results were concluded as follows:

1) Increasing the Pb^{2+} concentration could cause a reduction in clay particle content and an increase in silt particle content.

2) With the increase of Pb^{2+} concentration, the liquid limits, plasticity index and free swell rate decrease due to the decrease of diffusion double layer thickness.
3) The additional Pb^{2+} lead to the reduction in shear strength and unconfined compressive strength.

ACKNOWLEDGEMENTS

This study is financially supported by Natural Science Foundation of China (NSFC) (Grant No. 41372281, 41172273).

REFERENCES

Arasan, S. & Yetimoglu, T. 2008. Effect of inorganic salt solution on the consistency limits of two clays. *Turk. J. Environ. Sci* 32: 107–115.

Boardman, D.J. 1999. *Lime stabilization: clay-metal-lime interactions*. Loughborough: Loughborough University.

Chen, Y.L. 2013. Microstructure of expansive soil from Yunnan Province. *Chinese Journal of Geotechnical Engineering* 7(35): 334–339.

Cho, G.G., Dodds, J.S. & Santamarina, J.C. 2006. Particle shape effects on packing density, stiffness and strength-natural and crushed sands. *Geotech. Geoenviron* 132(5): 591–602.

Dermatas, D. & Meng, X. 2003.Utilization of fly ash for stabilization/solidification of heavy metal contaminated soils. *Engineering Geology* 70(3): 377–394.

Li, J.S., Xue, Q., Wang, P. & et al. 2015. Effect of lead(II) on the mechanical behavior and microstructure development of a Chinese clay. *Applied clay science* 105–106:192–199.

Li, Q., Shi, B. & Wang, Y.C. 1999. Environmental-Geotechnical Properties of Soils Contaminated by Waste Alkaline. *Environmental Pollution & Control* 19(5): 16–18.

Li, X.R., Yao, Z.X. & Cao, Z.B. 2004. Study on physical and mechanical property variation of polluted erosive foundation soils in typical district of Jinan. *Rock and Soil Mechanics* 25(8): 1229–1233.

Maaitah, O.N. & Al-Hamaiedeh, H.D. 2005. Effect of Treated and Raw Waste water on the Behavior of Unsaturated Soil. *Electronic Journal of Geotechnical Engineering*.

Meegoda, N.J. & Rajapakse R.A. 1993. Short-Term and Long-Term Permeabilities of Contaminated Clays. *Journal of Environmental Engineering* 119(4): 725–743.

Mitchell, J.K. 1993. *Fundamentals of Soil Behavior*. NewYork: Wiley & Sons.

Moon, D.H. & Dermatas, D. 2006. *The effectiveness of quicklime-based stabilization/solidification (S/S) on lead(Pb) contaminated soils*. 5th ICEG Environmental Geotechnics london, 221–228.

Pachecoe Silva, D., Esquivel, E.R., Giacheti, H.L. & et al. 2005. Copper Chloride Contamination Influence on the Shear Strength of Soils, Tarauneh Used as Liners. *Solos e Rochas* 28(3): 283–294.

Rajasekaran, G. & Rao, S.N. 2001. Effect of Pollutants on the Physical and Engineering Behavior of Lime-Treated Marine Clay. *Marine Georesources and Geotechnology* 19(1): 17–35.

Rao, W.G., Ma, F.R., Chen, R.G. & et al. 2013. Experimental research on the effect of the heavy metal pollutants on soil compactness and shear strength. *Industrial Construction* 43(4): 92–97.

Ratnaweera, P. & Meegoda, J. 2006. Shear Strength and Stress-Strain Behavior of Contaminated Soils. *Geotechnical Testing Journal* 29(2): 133–140.

Shacheford, C.D., Benson, C.H., Katsumi, T., Edil, T.B. & Lin, L. 2000. Evaluation the hydraulic conductivity of GCLs permeated with non-standard liquids. *Geotextiles and Geomembranes* 18:(2–4): 133–161.

Singh, S.K., Srivastava, R.K. & Siby, J. 2008. Settlement Characteristics of Clayey Soils Contaminated with Petroleum Hydrocarbons. *Soil and Sediment Contamination* 17(3): 290–300.

Tang, C.S. & Shi, B. 2011. Swelling and shrinkage behaviour of expansive soil during wetting-drying cycles. *Chinese Journal of Geotechnical Engineering* 9(33): 1376–1384.

Wu, J.H. & Yuan, J.H. 2013. Field tests on expansive soil during wetting-drying cycles using large shear apparatus. *Chinese Journal of Geotechnical Engineering* 7(35): 103–107.

Yong, R.N. 2001. *Geoenvironmental engineering, contaminated soils, pollutant fate and mitigation*. Boca Raton: CRC Press.

Zha, F.S., Liu, J.J., Cui, K.R. & et al. 2012. Engineering properties of solidified and stabilized heavy metal contaminated soils with cement. *Industrial construction* 42(11): 74–77.

Zhu, C.P. & Liu, H.L. 2007. Study on engineering properties of polluted soil. *Rock and Soil Mechanics* 28(3): 625–630.

Zhu, C.P., Liu, H.L. & Zhang, X.L. 2008. Laboratory tests on compression characteristics of soil polluted by acid and alkali. *Chinese Journal of Geotechnical Engineering* 30(10): 1477–1483.

Zhu, C.P., Liu, H.L. & Shen, Y. 2011. Laboratory tests on shear strength properties of soil polluted by acid and alkali. *Chinese Journal of Geotechnical Engineering* 33(7): 1146–1152.

Unsaturated Soil Mechanics—from Theory to Practice – Chen et al. (Eds)
© 2016 Taylor & Francis Group, London, ISBN 978-1-138-02921-7

Feasibility investigation of a local weathered soil as final cover material for a landfill in south China

J. Liu & R. Chen
Shenzhen Key Laboratory of Urban and Civil Engineering for Disaster Prevention and Mitigation, Shenzhen Graduate School, Harbin Institute of Technology, Shenzhen, China

T.L.T. Zhan
MOE Key Laboratory of Soft Soils and Geoenvironmental Engineering, Zhejiang University, China

Z.Q. Li
Shenzhen Xiaping Solid Waste Landfill, Shenzhen China

C.W.W. Ng
The Hong Kong University of Science and Technology, HKSAR, Hong Kong

ABSTRACT: Local soil materials are generally preferred for the construction of final landfill covers due to their low costs. In the southern parts of China, weathered soils can be found readily. In this study, the feasibility of a local weathered soil to be used as a landfill final cover material is investigated as a potential material for the final cover system at the municipal solid waste site at Xiaping in Shenzhen. A series of tests are first carried out to obtain physical and hydraulic properties of the candidate cover material. Subsequently, water balance analysis is conducted to study the performance of covers built using this soil in humid climate in the southern part of China. Finally, some suggestions are made to optimize the design of final cover using the local weathered soil at the Xiaping Landfill site.

1 INTRODUCTION

One of the most important functions of a landfill cover is to limit the production of leachate into underlying waste by minimizing percolation of water through the cover (Koermer & Daniel 1997). A hydraulic barrier layer must be designed in a landfill cover. Typical hydraulic barrier layer is composed of a composite liner or a compacted clay liner. For the former, however, its smooth and texture surfaces are unavoidable. The shear resistance between the interface of the composite liner and overlying soil is usually lower than that of soil-soil interfaces (Daniel 1994). There have been notorious cases of landfill instability failures caused by weak composite interfaces (Feng & Gao 2012; Stark et al. 2012). Moreover, thin composite liners are more susceptible to construction damage and puncture failure. Due to the shortcoming of the composite liner, the cover with compacted clay liner is widely used, especially in steep side slopes. However, the clay is not readily available in the southern parts of China, e.g., Shenzhen and Hong Kong. In these cities, long-distance transportation for the clay must be at high cost and thus unrealistic.

In the southern parts of China, local weathered soil (e.g., completely decomposed granite (CDG)) can be found readily. The local soil is the rock that has been weathered to the point that it completely fractures into smaller pieces or chunks of weak rock, generally composing of gravel, sand, silt and clay (Kim 2007). Due to the existence of the coarse-grained soil (i.e., gravel and sand), the saturated coefficient of permeability of the local weathered soil with the relative compaction (RC) of 100% is about 1×10^{-8} m/s (Yin 2009). Assuming that the soil is saturated and its hydraulic gradient maintains 1 all over the year, the percolation through the local weathered soil is larger than 30 mm/year (the percolation criteria proposed by CJJ112-2007). It suggests the relatively high risks for the local weathered soils as the cover soil. Therefore, a feasibility study on water balance is necessary for the local weathered soils at the municipal solid waste site at Xiaping in Shenzhen.

In this study, based on the measured WRCs, water balance analysis is conducted to study the performance of covers built using this soil in humid climate in the southern part of China. Subsequently, some suggestions are made to optimize the design of final cover

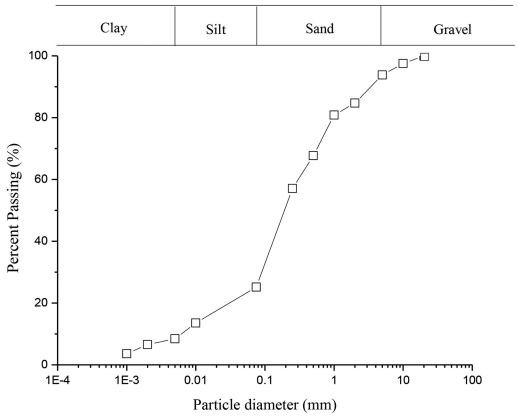


Figure 1. Particle size distribution curve of local weathered soil.

Table 1. Summary of basic physical properties of local weathering soil.

Particle size distribution	
Gravel (%)	7.1
Sand (%)	67.3
Silt (%)	16.8
Sand (%)	8.8
D_{10} (mm)	0.006
D_{30} (mm)	0.091
D_{60} (mm)	0.31
C_u	51.7
C_c	4.5
Plastic limit, ω_p (%)	18.7
Liquid limit, ω_L (%)	31.9
Specific gravity, G_s	2.6
Optimum moisture content, ω_{ovt} (%)	19.1
Maximum dry density, $\rho_{d,max}$ (g/cm^3)	1.82
Coefficient of permeability at $\rho_{d,max}$ (m/s)	4.2×10^{-8}

using the local weathered soil at the Xiaping Landfill site.

2 PHYSICAL AND HYDRAULIC PROPERTIES OF LOCAL WEATHERED SOIL

2.1 *Basic physical properties*

Basic physical property tests are performed in accordance with Chinese Standard (GB/T 50123-1999), which include specific gravity tests, standard proctor compaction tests, atterberg limit tests, tests for determination of particle-size distribution and saturated permeability tests. The results of particle-size distribution are shown in Figure 1, whereas the basic parameters from the tests are summarized in Table 1.

Based on the basic properties, this local weathered soil is described as silty sand (SM). It is noted that the saturated coefficient of permeability at the maximum dry density is close to the results measured by Yin (2009).

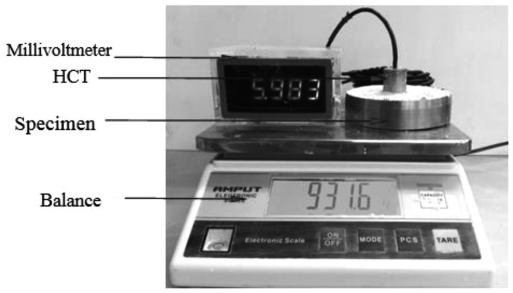


Figure 2. Instruments for measuring WRC (Chen et al. 2015).

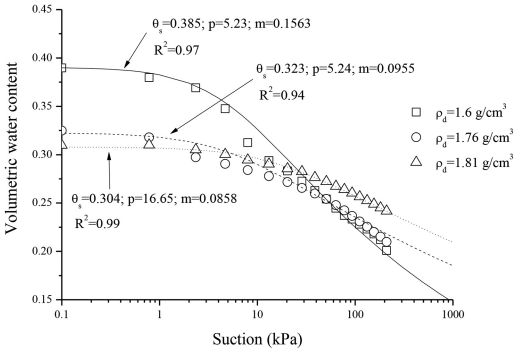


Figure 3. Measured WRCs of soil with three dry densities.

2.2 *Hydraulic properties of unsaturated soil*

Figure 2 shows the setup for measuring the water retention curve (WRC) consists of a soil specimen, an electronic balance and an integrated high-capacity tensiometer (HCT). The HCT developed by Chen et al. (2013) is used to measure the suction of soil. Its highest suction of soil measured by this HCT was 500 kPa. The mass of the soil is monitored using an electronic balance, whereas the suction of the soil specimen is monitored using the integrated HCT and the digital millivoltmeter. The readings of the balance and the millivoltmeter can be automatically captured using a webcam during the continuous drying process. Based on the change in the water content and suction, a WRC can be plotted using the data of the water content and suction during continuous drying. More details on the integrated HCT for WRCs are described in Chen et al. (2015).

Figure 3 shows the WRCs of the local weathered soil with the dry densities of 1.6, 1.76 and 1.81 g/cm^3. These WRCs are measured using the integrated proposed by Chen et al. (2015). As expected, the volumetric water contents of three WRCs all decrease as suction increases. When the suction is below 1 kPa (the soil is almost saturated), the larger the dry density, the smaller the volumetric water content. As the suction increases from 0 to 20 kPa, the curves begin to approach each other until a cross. The large the dry

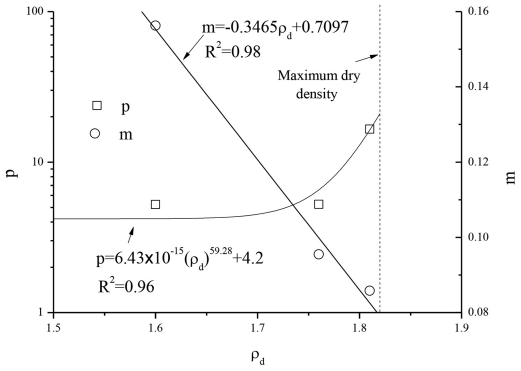


Figure 4. Effect of dry density on fitting parameters p and m in van Genuchten (1980) equation.

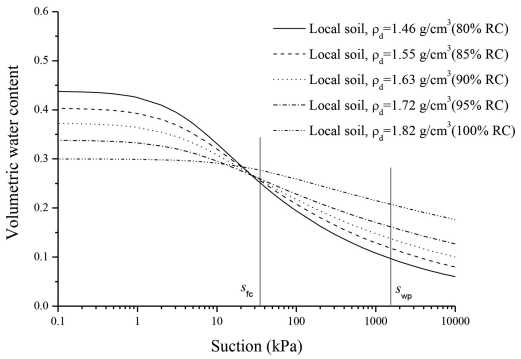


Figure 5. Calculated WRCs based on fitting parameters.

density, the steeper the WRC. It may be due to the large pore size for the small dry density. After the cross, the curves move far away from each other. The largest volumetric water content occurs in the dry density of 1.81 g/cm^3, then 1.76 g/cm^3 and 1.6 g/cm^3.

Based on van Genuchten's (1980) equation, Figure 4 shows the relationship between dry density and the fitted parameters p and m. As the dry density increases, p increases in function of power whereas m decreases linearly. Based on these relationships, WRCs for various dry densities using van Genuchten's (1980) equation can be drawn as follows:

$$\theta_w = \left(1-\frac{\rho_d}{\rho_w G_r}\right)\left[1+\left(\frac{s}{6.43\times10^{-15}\left(\rho_d\right)^{59.28}+4.2}\right)^{\frac{1}{0.3465\rho_d+0.2903}}\right]^{(0.3465\rho_d-0.7097)} \quad (1)$$

Based on Eq. (1), five dry densities from 1.46 g/cm^3 to 1.82 g/cm^3 (i.e., 1.46, 1.55, 1.63, 1.72 and 1.82 g/cm^3, corresponding to RC of 80%, 85%, 90%, 95% and 100%, respectively) are chosen. Their WRCs of local weathered soil are estimated as shown in Figure 5.

3 WATER BALANCE ANALYSIS

3.1 *Methods*

Water balance analysis can describe the relationship between water input and output. The input of water is precipitation whereas output is runoff (or lateral drainage) and percolation. Within a cover, water can be stored, or returned to the atmospheres via evapotranspiration. The relationship between these components of water balance are described as follows:

$$P = R + AET + CWS + PERC \quad (2)$$

where P is precipitation, R is runoff, AET is actual evapotranspiration, CWS is change in water storage and $PERC$ is percolation.

(1) Precipitation

P can fall on the cover in the form of either rain or snow. Because P varies from year to year even in a city, an average monthly P is used in order to estimate the long-term behavior of landfill cover. In this study, P is obtained from the average monthly precipitation (1981–2010) according to Meteorological Bureau of Shenzhen Municipality (2015).

(2) Runoff

Rain that reaches the surface of the cover can either run off or infiltrate into the cover. Runoff is calculated from P:

$$R = \max(cP, P - k_s \cos\varphi) \quad (3)$$

where k_s is saturated permeability of the cover soil, φ in slope angle and c is runoff coefficient. c is the most difficult parameters to determine accurately because very little information is available on actual runoff rates from landfill covers. One simple approach is used based on the type of soil and average angle of the slope (Fenn et al., 1975). It should be noted that R must consider the state of cover soil. If $k_s \cos\varphi$ is smaller than P, its differences would occur as sheet flow over the surface and thus R is $P - k_s \cos\varphi$.

(3) Actual evapotranspiration

When water infiltrates into the cover, the water can evaporate directly to the atmosphere near the ground surface. AET can be estimated by temperature, duration of sunshine, water stored in cover (P-R) and volumetric water content of cover soil (Koerner & Daniel, 1997). Similar to precipitation, the average monthly temperature and sunshine duration (1981–2010) are obtained from Meteorological Bureau of Shenzhen Municipality (2015).

(4) Change in water storage

The change in water stored is the water stored in the calculated period (typically month) minus the water stored in the previous period:

$$CWS = \left(WS\right)_t - \left(WS\right)_{t-1} \quad (4)$$

where $(WS)_t$ and $(WS)_{t-1}$ are the amount of water stored in the cover soil in this month and last month, respectively. It is noted that *CWS* is negative if the cover soil is losing water and positive if it is gaining water. *WS* is calculated as follows:

$$WS = \theta_a H \tag{5}$$

where H is the thickness of cover soil for *WS*, θ_a is available storage capacity. θ_a is estimated based on the WRCs of the soil.

$$\theta_a = \theta_{fc} - \theta_{wp} \tag{6}$$

where θ_{wp} is the water content at wilting point (suction = 1500 kPa), θ_{fc} is the water content at filed capacity (suction = 33 kPa). θ_{fc} and θ_{wp} can be obtained from the WRCs of cover soil (see Fig. 5).

(5) Percolation

PERC is the amount of water draining into the underlying waste and is calculated as follows:

$$\begin{cases} PERC = 0 & WSP - R - AET \le 0 \\ PERC = P - R - AET - C & WSP - R - AET > 0 \end{cases} \tag{7}$$

(6) Minimum thickness

Based on the storage capacity of the cover soil, the minimum thickness of the cover soil can be estimated as follows:

$$L = \frac{CWS_{\max}}{\theta_a} \tag{8}$$

where L is the minimum thickness, CWS_{max} is maximum change in water storage.

3.2 *Water balance analysis*

Figure 6 shows the calculated monthly *R*, *AET, CWS* and *PERC* for the dry density of 1.82 g/cm^3 (RC of 100%). As expected, the development of *R* is similar to that of *P*, but not completely proportional to *P*. It is mainly due to the insufficient permeability of the cover soil ($P > k_s \cos\varphi$). *AET* increases from Jan. to Jul. but decrease after Jul. At Jul., the maximum of about 165 mm is obtained. It is mainly because the temperature is the highest at Jul. and lowest at Jan. in Shenzhen. *CWS* is positive (gaining water) from Feb. to Mar. and negative (losing water) from Apr. to Jan. of the next year. It is due to the insufficient permeability and thus not enough water for evaporation. In this water balance condition, *PERC* maintain zero all over the year.

Similar to 1.82 g/cm^3, the water balance for other four dry densities are estimated, as shown in Figure 7. As the dry density increases *R* increases from 348 mm to 1061 mm. It is due to the decrease in the permeability and thus less water flows into the cover soil. Similarly, CWS is positive for the region of small dry densities (i.e., 1.46, 1.55, 163 g/cm^3) and negative for the region of large dry density (i.e., 1.72, 1.82 g/cm^3). However, almost constant *AET* for different dry densities. It is due to the same temperature for these five cases. Based on this relationship of water balance, *PERC* decreases with the dry density. It should be noted *PERC* is small than 30 mm/year (the percolation criteria proposed by CJJ112-2007) as the dry density is not smaller than 1.72 g/cm^3 (i.e., RC of 95%).

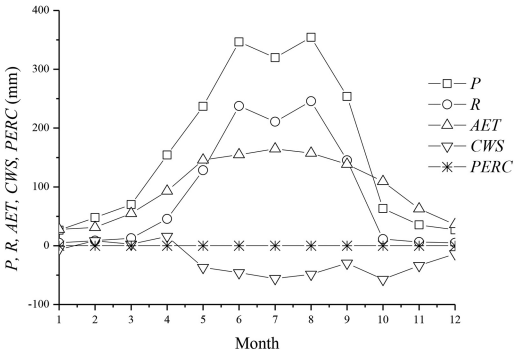


Figure 6. Calculated monthly water balance for the dry density of 1.82 g/cm^3 under Shenzhen's climate.

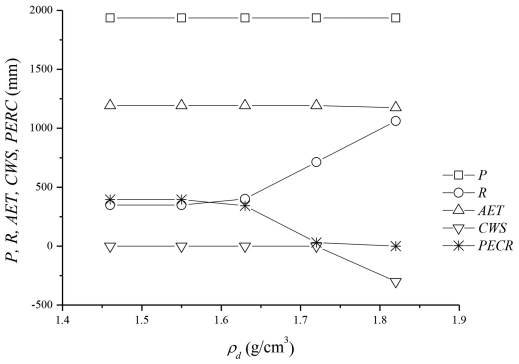


Figure 7. Calculated annual water balance for various dry densities.

3.3 *Calculated thickness for hydraulic barrier*

Figure 8 shows the calculated minimum thickness of soil cover for various dry densities. The calculated thickness increases with the dry density when dry density is relatively small. When the dry density is 1.72 g/cm^3, its thickness is maximum, about 1.2 m. Over this dry density, the thickness begins to decrease from 1.2 m to 0.3 m. It is due to the complex change of $CWS_{\max}$ and θ_a, as described by Eq. 8. As previously analyzed, as the dry density increases, $CWS_{\max}$ is almost constant at the relatively small dry density but largely decreased at the relative large dry density(see Fig. 7). Meanwhile, θ_a decreases as the dry density increases (see Fig. 5).

Based on pervious results, the dry density of 1.82 g/cm^3 has smallest thickness of soil cover with

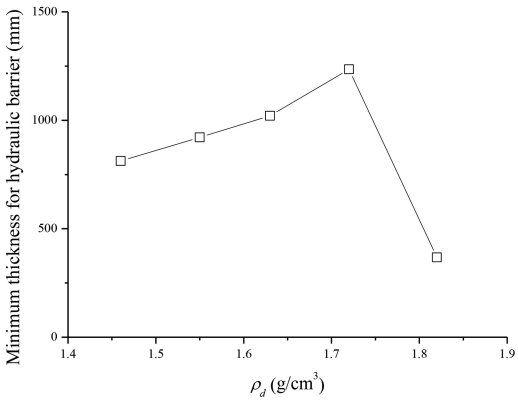


Figure 8. Calculated minimum thickness for hydraulic barrier.

the least percolation. However, it is difficult for the cover soil to reach the RC of 100% in particle engineer. Dwyer et al. (2007) pointed out that an acceptable zone of RC for landfill cover is 85%–95%. For the local weathered soil, therefore, the dry density is suggested to be not smaller than 1.72 g/cm^3 (i.e., RC of 95%) and the thickness to be thicker than 1.2 m. To further verify the effectiveness of local weathered soil on water infiltration, finite element method, flume and field model tests must be conducted in the future.

Recently, Ng et al. (2015a; 2015b; 2015c) proposed an alternative three-layer capillary barrier system for humid climatic conditions, such as Shenzhen, Hong Kong and Singapore, where an annual rainfall of over 2000 mm is expected. This alternative system consists of a fine-grained soil layer overlaying a coarse-grained layer, which in turn overlies another fine-grained soil. For Xiaping landfill, this new alternative soil cover gives more choice to prevent water percolation.

4 CONCLUSIONS

A series of tests are first carried out to obtain the basic and hydraulic properties of the local weathered soil for the final cover system at Xiaping in Shenzhen. Based on the measured WRCs, water balance analysis are subsequently conducted to investigate the influence of dry density on the water balance and soil cover thickness in humid climate in the southern part of China. Based on the measured and calculated results, the following conclusions may be drawn:

(1) Based on the method for water balance, it is found that as the dry density increases, *R* increases whereas *PERC* decreases. It is due to the decrease of permeability and thus less water flows into the cover soil.
(2) For the local weathered soil, the dry density is suggested to be not smaller than 1.72 g/cm^3 (i.e., RC of 95%) and the maximum thickness to be thicker than 1.2 m.
(3) To further verify the effectiveness of local weathered soil on water infiltration, finite element method, flume and field model tests must be conducted in the future.

ACKNOWLEDGEMENTS

The authors would like to acknowledge the research grant 2012CB719805 of 2012CB719800 provided by the Ministry of Science and Technology of the People's Republic of China through the National Basic Research Program (973 project), the financial support provided by the Research Grants Council of the Hong Kong Special Administrative Region for the research grant HKUST6/CRF/12R and the research grant (No. 50909030) provided by the National Science Foundation of China.

REFERENCES

Chen, R., Chen, Z.K., Zhang, M. & Deng, G. 2013. Applications of a high-capacity tensiometer for direct measurement of suction. *Journal of Hydraulic Engineering* 44(6): 743–747.

Chen, R., Liu, J., Li J.H. & Ng, C.W.W. 2015. An integrated high-capacity tensiometer for measuring water retention curves continuously. *Soil Science Society of America Journal* 79(2): 943–947.

CJJ112-2007. 2007. Technical Code for Municipal Solid Waste Sanitary Landfill Closure. Ministry of Construction of China.

Daniel, D.E. 1994. Surface barriers: problems, solutions, and future needs. Proc 33rd Sym on Health and the Environment Columbus Ohio 1: 441–487.

Dwyer, S.F., Rager. R.E. & Hopkins, J. 2007. Cover system design guidance and requirements document. EP2006-0667, Los Alamos National Laboratories, Los Alamos, New Mexico, USA.

Feng, S.J. & Gao, L.Y. 2012. Seismic stability analyses for landfill cover systems under different seepage buildup conditions. *Environmental Earth Sciences* 66: 381–391.

Fenn, D.G., Hanley, K.J. & De Geare, T.V. 1975. Use of the water balance method for predicting leachate generation from solid waste disposal sites. U.S. Environmental Protection Agency, EPA/530/SW-168, Washington, D.C., 40.

GB/T 50123-1999. 1999. Standard for soil test method. Ministry of Water Resources of the People's Republic of China.

Kim, T.M. 2007. Influence of stress states on soil-water characteristics, conjunctive surface-subsurface flow modelling and stability analysis. Master Thesis, The Hong Kong University of Science and Technilogy.

Koerner, R.M. & Daniel, D.E. 1997. Final covers for solid waste landfills and abandoned dumps, ASCE, Press (Reston Virginia) and Thomas Telford (London, UK).

Meteorological Bureau of Shenzhen Municipality. 2015. The climate of Shenzhen. Retrieved Apr. 6, 2015, from http://www.szmb.gov.cn/article/QiHouYeWu/qihouxinxigongxiang/qhgxtezheng.html.

Ng, C.W.W., Liu, J., Chen, R. & Xu, J. 2015a. Physical and numerical modeling of an inclined three-layer (silt/gravelly sand/clay) capillary barrier cover system under extreme rainfall. *Waste Management* 38: 210–221.

Ng, C.W.W., Liu, J. & Chen, R. 2015b. Numerical investigation on gas emission of three landfill earthen covers under dry weather conditions. *Vadose Zone Journal.* Publish online.

Ng, C.W.W., Liu, J., Chen, R. & Coo, L. J. 2015c. Numerical parametric study of an alternative three-layer capillary barrier cover system. *Environmental Earth Sciences*. Publish online.

Stark, T.D., Choi, H., Lee, C. & Queen, B. 2012. Compacted soil liner interface strength importance. *J Geotech Geoenviron Eng* 138(3): 544–550.

van Genuchten, M.T. 1980. A closed form equation for predicting the hydraulic conductivity of unsaturated soils. *Soil Science Society of America Journal* 44(5): 892–898.

Yin, J.H. 2009. Influence of relative compaction on the hydraulic conductivity of completely decomposed granite in Hong Kong. *Canadian Geotechnical Journal* 46(10): 1229–123.

Unsaturated Soil Mechanics—from Theory to Practice – Chen et al. (Eds)
© 2016 Taylor & Francis Group, London, ISBN 978-1-138-02921-7

Modelling of transport and erosion of bentonite in the fracture

T. Chen & Y.F. Xu
Department of Civil Engineering, Shanghai Jiao Tong University, Shanghai, China

ABSTRACT: Compacted bentonite in the buffer will penetrate into open fractures of surrounding rock when in contact with water, and form a gel with the seeping water. Under appropriate conditions, the gel can transform into a sol that can release colloids which then are carried away by the water. The sol can even flow downstream along with water when the viscosity of gel/sol is reduced enough with the particle concentration to permit to flow. The process is modelled that the bentonite gel expands into a fracture and is exposed to the combined erosion of colloid diffusion and water flow. The model is solved using a numerical code.A series of water flow velocities are tested in the simulations, different ionic concentrations are adopted to estimate the influence of the sodium concentration both in seeping water and pore water of bentonite.

Keywords: Bentonite gel; Transport; Erosion; flow

1 INTRODUCTION

With the increasing use of nuclear energy, a large number of high-level nuclear waste have been generated inevitably, and how to deal with this waste becomes an urgent problem. Several countries such as France, Sweden and China have adopted the method of deep geological disposal, nuclear waste sealed in underground repository emplaced 500–1000 m deep below the surface (Liu, 2013). The function of buffer material is to separate the radioactive waste from surrounding environment to prevent radionuclide migrating and leaking from the canister containing the high-level nuclear waste to the extent of 10000 years or even more. As a result of its high swelling potential, low permeability, good self-sealing ability, compacted bentonite is chosen as buffer and backfill material of the deep geological repository, set as engineered barrier (Pusch, 1983). So a lot of researches have been conducted on swelling characteristics of different types of bentonite (Komine et al., 2004; Alawaji, 1999, Xu et al., 2014).

Once connecting with water, bentonite swells filling up pores of itself, creating an impermeable zone around the canister. But at the same time of swelling, bentonite also forms a gel which will penetrate into open fractures of surrounding rock. Under appropriate conditions, the gel can transform into a sol that can release colloids which then flow downstream along with the water. Therefore, it's necessary to evaluate how much bentonite could be lost by erosion of flow and colloid diffusion, which may cause a significant influent to the stability and functionality of repository in the long term.

When the concentration of counterions is above the critical coagulation concentration, CCC, the clay gel will expand to a density, at which point attractive and repulsive forces between bentonite particles become balanced. After this, the gel is stable and cohesive, releasing very little or no colloid to the seeping water. Conversely, if the concentration of counterions is blow CCC, the repulsive forces between the particles dominate over the attractive forces over all density. As a result, at any densities, the gel will turn into sol and release colloids which could be carried away by flow (Moreno et al., 2011). The CCC of monovalent cations is much larger than of divalent cations. In this paper, we only take a migrating monovalent cation, sodium into account, since little data about the rheological properties of calcium dominated bentonite is available (Missana et al., 2011).

To estimate the erosion rate to bentonite caused by colloid diffusion and flow, Borrelli and Ahn (2008) used a planar model to study the transport of bentonite and radionuclide. We also establish a simplified model to describe the intrusion of bentonite and the erosion by flow in the fracture of rock. However, comparison with these experimental results is not possible since our calculations were done for the steady state. The results are as follow.

2 SIMPLIFIED MODEL

The model includes three parts: the diffusion of cation, the expansion of bentonite, and the flow of seepage. Because the latter two take place in vertical directions, a two-dimensional model is established.

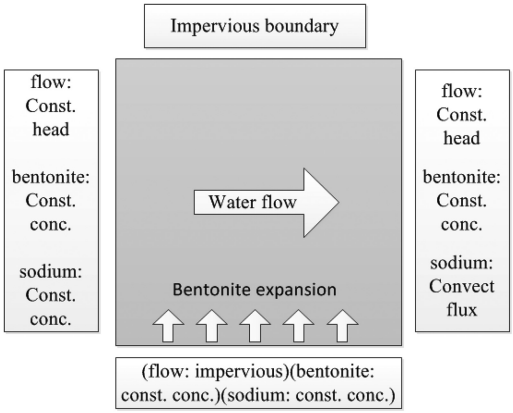


Figure 1. Boundary condition of simplified model.

The intersection between buffer and the fracture is simplified to a horizontal and straight line.

2.1 *Boundary conditions*

The fracture size in the model is a length of 6 m square. The seeping water flows from the left to the right. The depth perpendicular to the flow is chosen 6 m to be large enough to minimize the marginal effect on the consequents. The fracture aperture is 1 mm.

The boundary conditions of the model are illustrated as Figure 1. At both the left and right boundary a constant hydraulic head is set to create a steam flow from the left to the right and the difference is 0.6 m. The sodium concentration and the volume fraction of bentonite are imposed constant at the fracture mouth, i.e. the lower boundary. The bentonite volume fraction at the fracture mouth is 0.40. A constant sodium constration and no bentonite are available at the left boundary. At the right boundary both the sodium and bentonite are allowed only convective flux leaving the system. The top boundary is impervious and closed.

2.2 *Governing equations*

The Darcy equation we used here is the most common equation to model the flow of the fluid containing gel/sol and water, written in detail:

$$\vec{u}=\frac{T\nabla hg}{a} \tag{1}$$

where $\vec{u}$ (m/s) is the velocity field, and a (m) the fracture aperture. hg (m) is the hydraulic head of the fluid, conforming to the relation (Todd and Mays, 2005)

$$S_s\frac{\partial hg}{\partial t}=\nabla\cdot(\frac{T}{a}\nabla hg) \tag{2}$$

where t(s) is time. T (m^2/s) is the transmissivity of the fracture, which depends on the fluid viscosity. When the viscosity of the fluid is low, the transmissivity is large leading to that the fluid flows quick and vice-versa. The relationship between the transmissivity and the viscosity can be written as

$$T=T_w\frac{\eta_w}{\eta} \tag{3}$$

η (N $\cdot$ s/m^2) is the fluid viscosity and the subscript w stands for the water. η is strongly related to the volume fraction of bentonite and the concentration of sodium. Neretnieks et al. (2009) fitting vast experimental data, gave an empirical formula:

$$\frac{\eta}{\eta_w}=1+1.022\varphi_{\text{cov}}+1.358\varphi_{\text{cov}}^3 \tag{4}$$

where φ_{cov} is co-volume fraction, defined as

$$\varphi_{\text{cov}}=\frac{2}{3}\frac{(D_p+2m\kappa^{-1})^3}{D_p\delta_p}\varphi \tag{5}$$

where φ is the volume fraction of bentonite, and the Debye length κ^{-1} given by

$$\kappa^{-1}=\left(\frac{\varepsilon_0\varepsilon_r RT}{2F^2cz^2}\right)^{\frac{1}{2}} \tag{6}$$

ε_o (F/m) stands for the permittivity in vacuum, ε_r is the relative permittivity, R(J/K $\cdot$ mol) denotes the gas constant, T(K) is the absolute temperature, F(C/mol) is the Faraday constant, z is the valence, and c(mol/L) is the sodium concentration.

Sodium migration in the fluid is modelled by the advection-diffusion equation, which is given by

$$\frac{\partial c}{\partial t}=-\vec{u}\cdot\nabla c+\nabla\cdot(D\nabla c) \tag{7}$$

where D(m^2/s) is the diffusion coefficient, also dependent on the volume fraction of bentonite, and is written by Archies (1942)

$$\frac{D}{D_0}=(1-\varphi)^{1.6} \tag{8}$$

The value of D_0 is taken by 2×10^{-9} m^2/s.

According to the mass balance of bentonite Liu et al. (2008) deduce a bentonite expansion equation similar to the advection-diffusion equation which can be written as

$$\frac{\partial\varphi}{\partial t}=\vec{F}_s\cdot\nabla(\frac{\varphi}{f})-\vec{u}\cdot\nabla\varphi+\nabla\cdot(\frac{\zeta}{f}\nabla\varphi) \tag{9}$$

F_s(N) stands for the resultant force of the gravitational force and the buoyant force. $f=f_{fr}/(1-\varphi)$ where f_{fr} (N $\cdot$ s/m) is the friction coefficient between bentonite particles and water, given by

$$f_{fr}=6\pi\eta_w r_{eq}+V_p k_0\tau^2 S_p^2\eta_w\frac{\varphi}{(1-\varphi)^2} \tag{10}$$

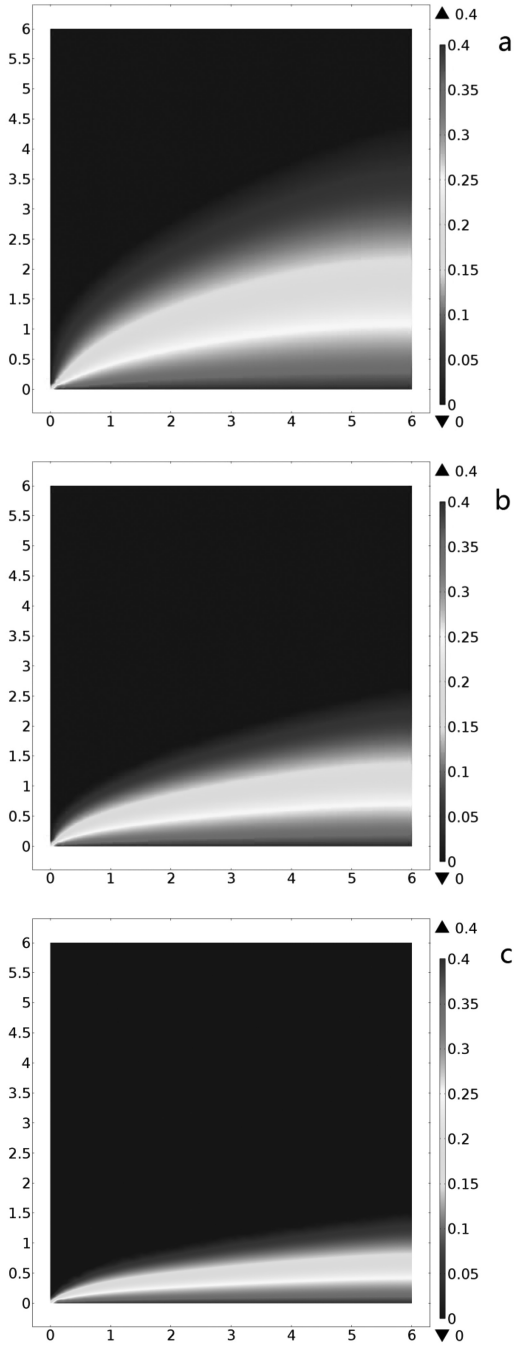


Figure 2. Bentonite volume fraction with different flow velocities (a) 3.15 m/year, (b) 9.45 m/year, (c) 31.5 m/year.

where r_{eq} (m) is the equivalent radius of particles. k_0 is the pore shape factor, τ denotes the tortuosity of the flow channels in the gel, V_p (m^3) is the volume of the particles and S_p (m^2/m^3) the specific surface area per volume of particles.

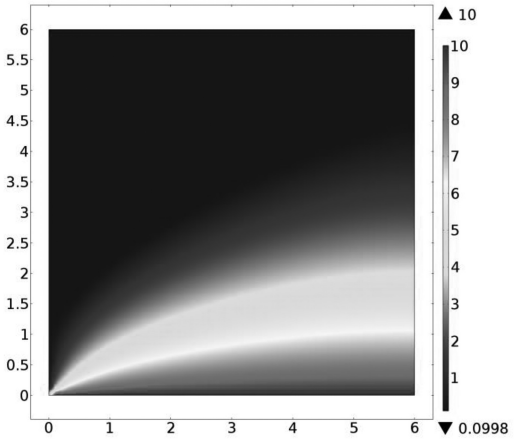


Figure 3. Sodium concentration distribution with a flow velocity 3.15 m/year.

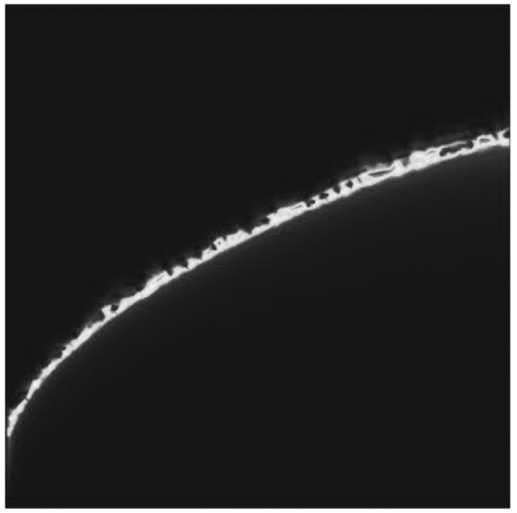


Figure 4. Convective flux of bentonite.

The ratio ζ (J) to f could be regarded as a diffusivity. The term ζ is the sum of the energy of the particles consist of the energy from the thermal motion and the energy result from the electrostatic and the van der Waars force. It is given by

$$\zeta = k_B T + \left(h + h_p\right)^2 \left(\frac{\partial F_A}{\partial h} - \frac{\partial F_R}{\partial h}\right) \tag{11}$$

where k_B (J/K) is the Boltzmann constant, h(m) is the layer spacing between the flat particles and h_p (m) is the particle thickness. F_A (N) and F_R (N) represent the van der Waar *attractive* force and the electrical double layer repulsive force respectively, based on the DLVO theory. Their specific expressions can be found in Verwey et al. (1999).

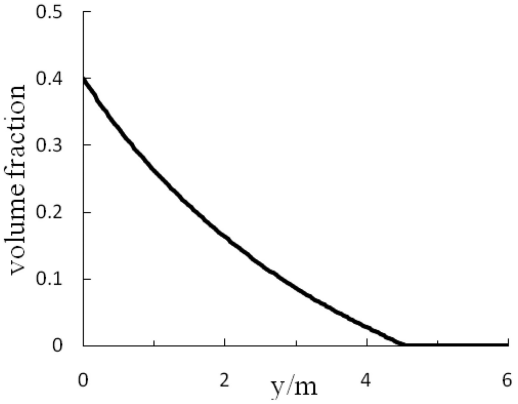


Figure 5. Bentonite volume fraction at right boundary.

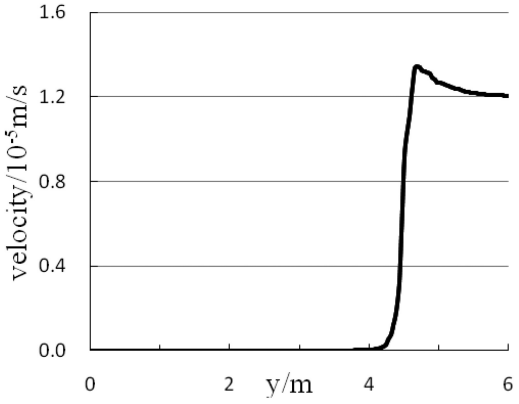


Figure 6. Fluid velocity at right boundary.

3 RESULTS AND DISCUSSION

The model is calculated by Comsol Multiphysics software. For the first set of calculation, the sodium concentration is 10 mmol/L at the fracture mouth, and it is 0.1 mmol/L in the coming seeping water. The fracture aperture is 1 mm and transmissivity is varied from $1 \cdot 10^{-9}$ to $1 \cdot 10^{-7}$ m^2/s, inducing the undisturbed water flow velocity varied from 3.15 to 315 m/year. Figure 2 illustrates the distribution of bentonite volume fraction with different flow velocities.

Obviously with the increasing of water flow velocity, the penetration depth decreases rapidly. It can be expected due to the gel can't expand further but be carried away by the water with a raising rate. The sodium concentration distribution is shown in Figure 3 for the smallest water velocity 3.15 m/year. It deserves to note that the bentonite volume and sodium concentration distribution are almost in the same shape for the same simulation.

Figure 4, the convective flux of bentonite in the model, shows that almost all the bentonite transport occurs along the gel/water interface. (Although it's a gradual transition from gel to sol, we use the term gel/water for simplified description.) And the transport is concentrated in a very narrow ribbon region. Figure 5 and Figure 6 show the bentonite volume fraction and the fluid velocity at the right boundary under the flow velocity of 3.15 m/year, respectively. It can be seen that the fluid velocity promptly becomes negligible when the volume faction of bentonite is upon 2%, which exactly explains why the transport almost takes place at the gel/water interface.

3.1 *Influence of the water flow velocity*

The statistics for the erosion rate and penetration depth of bentonite are listed in Table 1 under different water flow velocities, corresponding to different fracture transmissivities. The relationship between the erosion rate and the water velocity in double logarithm coordinate is shown in Figure 7, as well as the relationship between the penetrate depth and the water velocity in Figure 8. It excites us that both the relationships have a strong linear relationship in log-log plot. The erosion rate to bentonite increases with the water velocity with an exponent of 0.33, while the penetration depth decreases with the water velocity with an exponent of 0.48.

Table 1. Erosion rate and penetration depth with different water velocities.

Water velocity m/year	Erosion rate kg/year	Penetration depth m
3.15	0.048	4.52
9.45	0.060	2.67
31.5	0.085	1.55
94.5	0.143	0.91
315	0.205	0.47

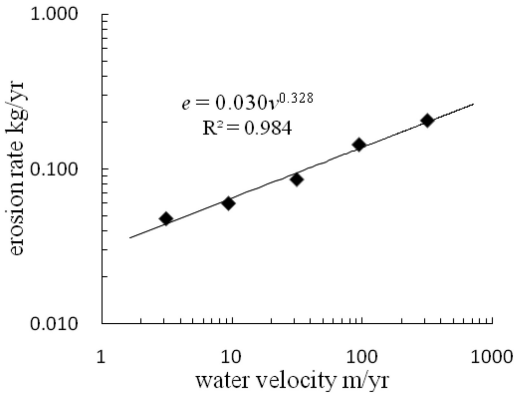


Figure 7. The relationship between the erosion rate and the water velocity.

3.2 *Influence of the sodium concentration*

The sodium concentration is unaltered in the calculations above. To estimate the influence of the sodium

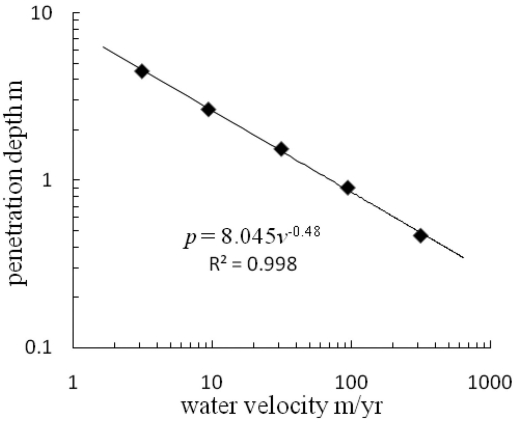


Figure 8. The relationship between the penetration depth and the water velocity.

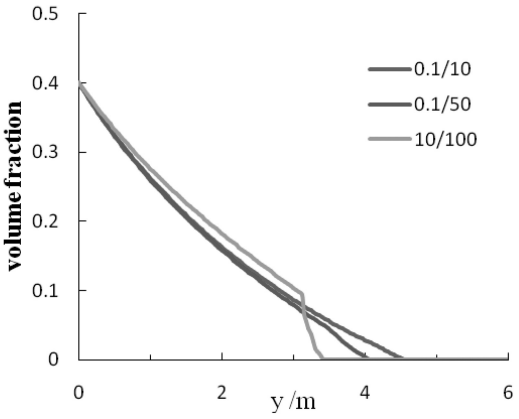


Figure 9. Bentonite volume fraction for different sodium concentrations at right boundary.

concentration both in seeping water and pore water of bentonite, different concentrations are adopted in follow simulations. In some calculation the sodium concentration was increased to 100 mmol/L above the CCC, which is about 50 mmol/L in the model.

Based on the model with the water velocity of 3.15 m/year, when the sodium concentration in the bentonite porewater increases to 50 mmol/L, the erosion rate to bentonite decreases by 6%. Furthermore, if the sodium concentration is 100 mmol/L in the pore water and 10 mmol/L in the seeping water, the erosion rate will decrease by about 18%.

Figure 9 shows the bentonite volume fraction distribution at right boundary in several kinds of simulation with the concentrations above. From Figure, it can be seen that the penetrate depth diminishes with a increasing sodium concentration in the pore water. And the larger sodium concentration in the seeping water result in that the bentonite volume fraction drop more sharply at the front of gel/sol. It's in expectation because the electrical double layer repulsive force decreases with an increasing sodium concentration and is dominated by the van der Waar attractive force preventing the gel from expand further.

4 CONCLUSIONS

Compacted bentonite in the buffer will penetrate into open fractures of surrounding rock when in contact with water. The swelling characteristics of bentonite is controlled by various forces mainly consist of the electrical double layer repulsive force and the van der Waar attractive force. Bentonite forms a gel with the seeping water in the fracture, and if the ionic concentration is below the critical coagulation concentration, the gel can transform into a sol that can release colloids which then are carried away by the water. The sol can even flow downstream along with water when the viscosity of gel/sol is reduced enough with the particle concentration to permit to flow. The viscosity grows rapidly with the volume fraction of bentonite, and suffers from the impact of ionic concentration simultaneously.

The process is modelled that the bentonite gel expands into a fracture and is exposed to the combined erosion of colloid diffusion and water flow. The simulations show that almost all the bentonite transport occurs along the gel/water interface, a very narrow ribbon region, and that the fluid velocity promptly becomes negligible when the volume faction of bentonite is upon 2%.

A series of water flow velocities are tested in the simulations. The results suggest there is a strong linear relationship in double logarithm coordinate to the erosion rate and the water velocity, as well as to the penetrate depth and the water velocity. The erosion rate could reach about 0.2 kg/year with the largest water flow velocity.

To estimate the influence of the sodium concentration both in seeping water and pore water of bentonite, different concentrations are adopted. As expected, the larger the sodium concentrations become, the nearer the gel can penetrate and the more the erosion rate decreases.

It should be noticed that the model we established here is simplified, overlooking many factors. Such as the non-swelling minerals in the bentonite which may be left behind retard smectite particles diffusion like a filter during the expansion. So the result could be conservative and the model will be improved to some extent in our future work.

REFERENCES

Alawaji, H. A. 1999. Swell and compressibility characteristics of sand–bentonite mixtures inundated with liquids. *Applied Clay Science*, *15*(3), 411–430.

Archie, G.E., 1942. The electrical resistivity log as an aid in determining some reservoir characteristics. *Trans. AIME* 146, 56–62.

Borrelli, R. A., & Ahn, J. 2008. Numerical modeling of bentonite extrusion and radionuclide migration in a saturated

planar fracture. *Physics and Chemistry of the Earth, Parts A/B/C*, *33*, S131–S141.

Liu, L. 2013. Prediction of swelling pressures of different types of bentonite in dilute solutions. *Colloids and Surfaces A: Physicochemical and Engineering Aspects*, 434, 303–318.

Liu, L., Moreno, L., & Neretnieks, I. 2008. A dynamic force balance model for colloidal expansion and its DLVO-based application. *Langmuir*, *25*(2), 679–687.

Missana, T., Alonso, U., Albarran, N., García-Gutiérrez, M., & Cormenzana, J. L. 2011. Analysis of colloids erosion from the bentonite barrier of a high level radioactive waste repository and implications in safety assessment. *Physics and Chemistry of the Earth, Parts A/B/C*, *36*(17), 1607–1615.

Moreno, L., Liu, L., & Neretnieks, I. 2011. Erosion of sodium bentonite by flow and colloid diffusion. *Physics and Chemistry of the Earth, Parts A/B/C*, *36*(17), 1600–1606.

Neretnieks, I., Liu, L., & Moreno, L. 2009. *Mechanisms and models for bentonite erosion*. Swedish Nuclear Fuel and Waste Management Co., Stockholm (Sweden).

Komine, H., & Ogata, N. 2004. Predicting swelling characteristics of bentonites. *Journal of Geotechnical and Geoenvironmental engineering*, *130*(8), 818–829.

Pusch, R. 1983. Use of clays as buffers in radioactive repositories. *Svensk Kaernbraenslefoersoerjning* AB, Stockholm.

Todd, D. K., & Mays, L. W. 2005. *Groundwater hydrology edition*. Wiley, New Jersey.

Verwey, E. J. W. & Overbeek, J. T. G. 1999. *Theory of the stability of lyophobic colloids*. Courier Corporation.

Xu, Y., Xiang, G., Jiang, H., Chen, T., & Chu, F. 2014. Role of osmotic suction in volume change of clays in salt solution. *Applied Clay Science*, *101*, 354–361.

Unsaturated Soil Mechanics—from Theory to Practice – Chen et al. (Eds)
© 2016 Taylor & Francis Group, London, ISBN 978-1-138-02921-7

Water-rock interaction for marly rocks of Badong group in the Three Gorges Reservoir Area

X.J. Chen, L.L. Xia, Z.Y. Zhao & Y. Song
Guilin University of Technology, Guilin, Guangxi, China

B. Chai
China University of Geosciences, Wuhan, Hubei, China

J. Tong
Hunan Insititute of Geological Survey, Changsha, Hunan, China

B. Jiang
Hunan Insititute of Geological Sciences, Changsha, Hunan, China

ABSTRACT: Characterization of water-rock interaction plays an important role in Rock Engineering. Since the Three Gorges Reservoir was put into operation, a long-term soak and drying-wetting cycles have occurred in the hydro-fluctuation belt, which introduce complex water-rock interaction and change the mechanical properties of the rock. This in turn affects the slope stability of reservoir bank. In this paper two monitoring boreholes cores were sampled from Baitupo bank at Badong new city, and the mineral composition and microstructure characteristics of rock mass were investigated. Through water-rock leaching experiments and rock soaking experiments, the interaction between the rock and water is characterized, and the effects of water-rock interaction on the slope stability are discussed.

1 INTRODUCTION

Water-Rock Interaction (WRI), either physical or chemical, mainly refers to the mechanical, physical and/or chemical actions between water (surface water, groundwater and snow water) and rock or soil media. The effect of the water-rock interaction include swelling, disintegration, erosion, long-term seepage water pressure variation and slope stability (Liu et al. 2012). The construction of the Three Gorges Reservoir Area had brought great benefits to coastal residents. At the same time, however, because of the water storage and drainage of the reservoir, a series of ion exchange, adsorption, corrosion and other physical and chemical effects between water and rock media occur. Long-term WRI can change the chemical properties and microstructure of rock, and pose serious threat to the stability of slope, resulting in landslide and other environmental geological problems.

Badong county is located on marly rocks of Trias Badong group. The lithology of Badong group layer is mainly argillaceous limestone, marl and calcium mudstone (totally called marly rocks). The third paragraph of Badong group, the focus of this study, is composed of gray, green gray marl mainly. Marl combines some features of both limestone and mudstone. For limestone, because of containing calcium carbonate, it is prone to karstification. Then rocks have voids and fissures and rock skeleton changes, weakening rock mechanical properties. As for mudstone, which is prone to weathering and plastic deformation, it can cause landslide, collapse, debris flow, etc. In this paper two monitoring boreholes cores were sampled from Baitupo bank at Badong new city, and the mineral composition and microstructure characteristics of rock mass were investigated. By water-rock leaching experiments and rock soaking experiments, the interaction between the rock and water is characterized, and the effects of water-rock interaction on the slope stability are discussed.

2 EXPERIMENTAL METHODS

2.1 *Core selection and rock properties test*

The original rock of Badong third (T_2b^3) comprises mainly dark grey argillaceous limestone and marl, and three deep borehole BQX01, BQX02, BQX03 of Baitupo bank of New Badong County in Three Gorges Reservoir area reveal Badong marl stratum (Chai, 2008). This paper mainly used BQX02 and BQX03 to obtain the full set third sections of marly rocks of Badong group with different clay content and gray matter content rates, to carry out the relevant research work. Before and after experiment, we get

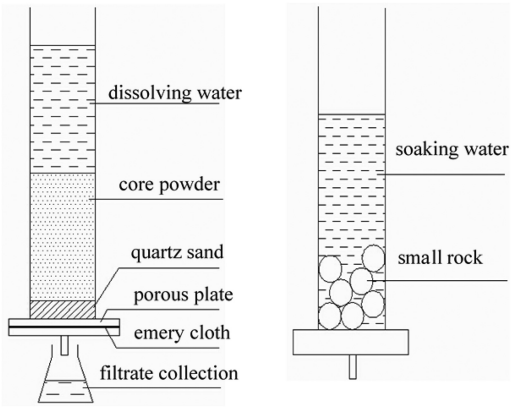


Figure 1. Device of water-rock leaching experiments and device of rock soaking experiments.

rock mineral composition and micro structure indicators through the X mineral composition, cation and anion diffraction test, electronic microscope scanning.

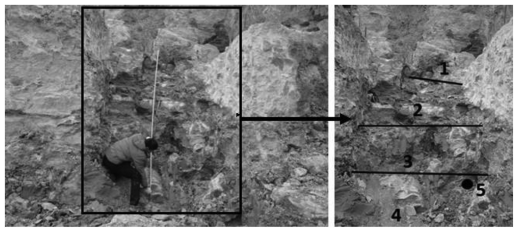
2.2 *Indoor water-rock interaction experiments*

Water-rock leaching experiments: according to the study results of Liu Jiawei (Liu, 2012), when using the river water and tap water to carry out saturation experiment, the change trend of various ion concentration is more consistent and the ion concentrations in numerical is relatively close. So paper used tap water instead of river water in the experiment under normal temperature. Because water-rock reaction is slow, we grind rock core to powder to speed up reaction period. Water-rock volume ratio is 1:1. The water supply part experimental device adopts the open type structure to ensure that the water and air participate in water-rock interaction experiments at the same time. The experiment used two sets of parallel experiment to verify each other with regular sampling test. Total weight of core powder is 1.5 kg. Core powder is put into A, B pipe respectively, with powder column height 145 mm. We use the underlay filter paper, 300 mesh gauze and 20 mm thick quartz sand To prevent the loss of the powder particles (See Figure 1).

Rock soaking experiments: cut the core segments into small rock pieces soaked in tap water. Because water-rock reaction is slow, we soak rock pieces for two days and then slowly turn on the water for one day. And then continue to soak , drain, repeating the above process with cumulative experiment for 120 days. Carry out scanning electronic microscopy (SEM) and test mineral composition of rock samples before and after experiment (See Figure 1).

2.3 *Field sampling verification*

Paper takes one profile due to construction near Baitupo of new Badong county as research object. Original profile rock is argillaceous limestone of T_2b^3. Sample rocks and soils to obtain wild indicators,



*1-Brown full regolith; 2-Brown-red argillaceous limestone; 3-Gray-green marl; 4-Gray argillaceous limestone; 5-Red-brown clay sampling point.

Figure 2. Baitupo field sampling profile.

Table 1. Mineral diffraction results of undisturbed drilled cores (mineral relative content/%).

Number	Y1	Y2	Y3	Y4	Y5	Y6	Y7	Y8	Y9	Y10
Calcite	20	42	50	36	62	30	44	63	62	80
Quartz	30	23	15	24	15	25	26	12	15	10
Illite	15	15	10	15	5	15	10	5	10	5
Chlorite	30	20	20	20	15	25	15	5	10	5
Dolomite	3	0	3	2	3	2	0	15	0	0
Feldspar	2	0	2	3	0	3	5	0	3	0

Table 2. Mineral diffraction results of excavation profile rocks of Baitupo (mineral relative content/%).

Number	B0*	B1*	B2*	B3*	B4*
Calcite	3	0	77	56	81
Quartz	52	51	8	12	8
Illite	19	15	6	13	6
Chlorite	3	6	0	5	5
Montmorillonite	23	28	9	14	0

*B0 represents the brownred clay marked by black point in Figure 2. B1, B2, B3, B4 in turn represents the first layer, second layer, third and fourth layer.

such as mineral composition and microstructure with X mineral composition, micro diffraction scanning electron microscope etc. Compare these results with indoor experiment results.

3 EXPLORATION OF CHEMICAL REACTION RULES OF WATER-ROCK INTERACTION

Results are as follows in Table 1, 2 & 3.

Potential major chemical reaction of water-rock interaction in water-rock interaction in Table 4.

From Table 1, minerals in rocks are mainly composed of original minerals, clay minerals and organic matter. The original minerals include calcite, quartz, feldspar and dolomite. The clay minerals include illite, chlorite. The minerals in field profile samples are mainly composed of clay minerals (chlorite, illite and montmorillonite), quartz and calcite.

Table 3. Ion composition of leaching water after WRI.

Item	K^+	Na^+	Ca^{2+}	Mg^{2+}	Cl^-	SO_4^{2-}
1d	65.16	29.69	63.73	27.07	31.35	238.87
3d	73.75	32.65	95.67	43.23	29.96	459.35
6d	62.78	27.5	74.65	33.27	22.92	343.28
10d	41.08	24.7	60.71	22.13	19.91	106.99
18d	37.41	17.48	54.64	17.38	19.66	119.27
30d	37.56	21.59	44.32	22.26	19.69	103.12
45d	32.73	18.07	37.61	22.03	20.75	29.89
60d	30.78	16.99	28.37	21.85	20.99	20.79
TW*	2.65	12.95	46.53	11.02	16.81	34.18

*TW: Tap water.

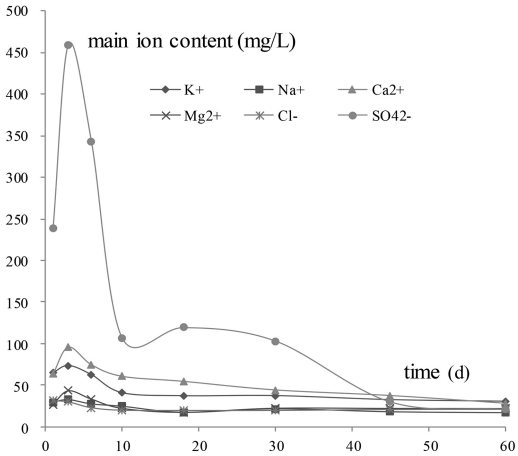


Figure 3. Variation curve of each ion.

Table 4. Solubility and dissolution (Liu et al. 2012).

Mineral	Chemical reaction formula
Quartz	$SiO_2 + 2H_2O \rightarrow H_4SiO_4$
Dolomite	$CaMg(CO_3)_2 + 2CO_2 + 2H_2O \rightarrow Ca^{2+} + Mg^{2+} + 4HCO_3^-$
Calcite	$CaCO_3 + CO_2 + H_2O \rightarrow Ca^{2+} + 2HCO_3^-$
Illite	$KAl_3Si_3O_{10}(OH)_2 + H^+ + 2.5H_2O \rightarrow 1.5Al_2Si_2O_5(OH)_4 + K^+$
Montmorillonite	$Al_2Si_2O_5(OH)_4 + 6H^+ \rightarrow 2H_4SiO_4 + 2Al^{3+} + H_2O$
Potassium feldspar	$KAlSi_3O_8 + CO_2 + 5.5H_2O \rightarrow 0.5Al_2Si_2O_5(OH)_4 + K^+ + 2H_4SiO_4 + HCO_3^-$
Albite	$NaAlSi_3O_8 + CO_2 + 5.5H_2O \rightarrow 0.5A_{l2}Si_2O_5(OH)_4 + Na^+ + 2H_4SiO_4 + HCO_3^-$
Organic matter	$CH_2O + 0.5SO_4^{2-} = 0.5H^+ + HCO_3^- + 0.5HS^-$

From See Table 3 and Figure 4, K^+, Ca^{2+} and SO_4^{2-} content in solution increased and then decreased. They peaked in the third leaching day, and then decreased gradually. Na^+, Mg^{2+} content increased first and then decreased and then increased and finally decreases to a stable, with larger fluctuation. Cl^- content was relatively stable in the late. The increase of ion content in early experiment mainly dued to dissolution.

Table 5. Ion exchange (Liu et al. 2012).

Item	Ion exchange reaction formula
1	$Ca^{2+} + 2KX(s) \rightarrow CaX(s) + 2K^+$
2	$Mg^{2+} + 2KX(s) \rightarrow MgX(s) + 2K^+$
3	$Ca^{2+} + 2NaX(s) \rightarrow CaX(s) + 2Na^+$
4	$Mg^{2+} + 2NaX(s) \rightarrow MgX(s) + 2Na^+$

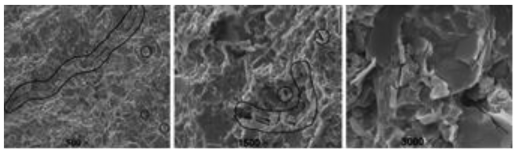


Figure 4. SEM of undisturbed drilled rock samples Y04.

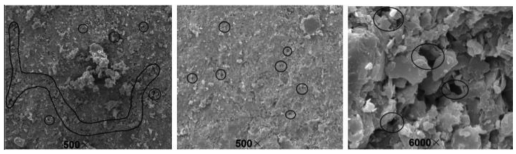


Figure 5. SEM of soaked rock samples Y4.

From Table 1 and Table 2, calcite content decreased more, showing that corrosion effect of water-rock interaction on calcite is particularly significant. Illite and montmorillonite content increased, showing that rock content turned to illite and montmorillonite direction. Water-rock interaction gave first place to leaching effect in early days so that each ion content increased. K^+ concentration in water increased. The reason is that chlorite, illite, feldspar and other clay minerals tend to have a high surface energy, hydrophilic, swelling and other properties and are easily hydrolyzed into illite and montmorillonite clay minerals in water. Rock and soil adsorb K^+ easily due to dissolution of dolomite, transformation of illite to montmorillonite and the presence of illite. H^+ in groundwater can replace K^+ in potassium feldspar. After initial stage, ion exchange played the role.

4 WATER-ROCK INTERACTION INFLUENCE ON MICROSTRUCTURE

Micro fracture is directional. The particles are closely arranged, and they are directed. Micro fracture and pores have good integrity. Mineral particle edges are significant (See Figure 4). Micro cracks are filled with crushed minerals. Granular structure is broken with poor integrity. Orientation is not obvious. Mineral particles are flake (See Figure 5).

Mineral particle integrity is poorer than undisturbed cores. Detrital minerals and flake minerals increase

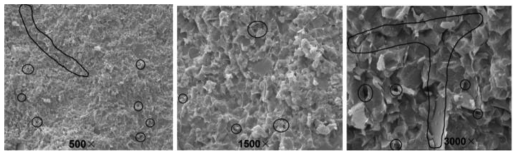


Figure 6. SEM of Baitupo profiles deep rock samples B4.

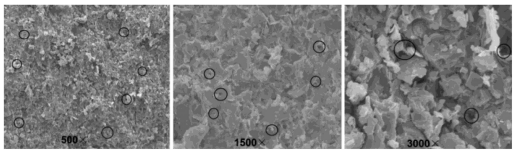


Figure 7. SEM of Baitupo profiles shallow rock samples B3.

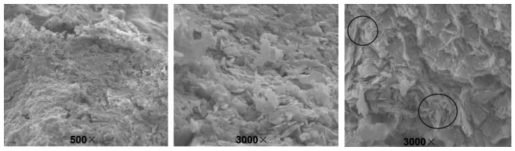


Figure 8. SEM of Baitupo profiles red-brown clay B0.

(See Figure 6). Part of the pores are filled with mineral debris with broken loose structure and tanglesome mineral arrangement. Mineral particles are abrasive and dissolution pores appeared. Tiny pores increased (See Figure 7). Minerals are flake or pinnate with lots of holes and cracks and loose structure. Corrosion degree is more serious and frizzy illite-montmorillonite mixed clay minerals appeared (See Figure 8).

As shown above, water rock interaction made the rock under erosion, and rock integrity was damaged. Micro pores and fractures in rocks increased, rock structure becoming loose and fragile.

When using SEM images to calculate mineral particles and porosity parameters, its value is closely linked with the magnification. There is a big difference in mineral particles and porosity parameters under different magnification. It has been shown that mineral particles and porosity parameters are most accurate in 1500 times condition (Liu et al. 2010). So choose SEM images in 1500 times conditions as study objects. (1) Porosity: turn TIF format of original SEM images into jpg format with Photoshop. Adjust the appropriate grayscale to turn SEM imagines to binary images by MATLAB program. Then smooth the imagines. After that, there are only black and white left in image. The white areas represent particles and black areas represent voids. Derive porosity by pixels occupied by the black and white areas. (2) Fractal dimension: fractal dimension D values quantitatively cluster extent, concentration trends, uneven or irregular extent, the degree of structural complexity and roughness of the object, etc. (Yu et al. 2011). Pore distribution fractal dimension reflects flat distribution of pores. Generally

Table 6. Rock particles and pore parameters table.

Rock samples	Number	Particle pixels	Pore pixels	Porosity	D
Undisturbed rocks	Y4-1	808001	157631	0.1632	1.4386
	Y4-2	819401	146231	0.1514	1.5023
	Y4-3	808331	157301	0.1629	1.4737
	Y4-4	803865	161767	0.1675	1.4975
	Mean	809900	155733	0.1613	1.4780
Rocks soaked for 120 days	Y4-1	774437	191195	0.1980	1.5391
	Y4-2	774498	191134	0.1979	1.5203
	Y4-3	790233	175399	0.1816	1.4612
	Y4-4	785382	180250	0.1867	1.5486
	Mean	781138	184495	0.1911	1.5173
Deep profile rocks	B4-1	795672	169960	0.176	1.5308
	B4-2	788347	177285	0.1836	1.5130
	B4-3	796234	169398	0.1754	1.5170
	Mean	793418	172214	0.1783	1.5202
Shallow profile rocks	B3-1	771840	193792	0.2007	1.4867
	B3-2	780964	184668	0.1912	1.5479
	B3-3	777156	188476	0.1952	1.546
	Mean	776653	188979	0.1957	1.5269
Weathered soil samples	B0-1	757458	208174	0.2156	1.6285
	B0-2	751052	214580	0.2222	1.5574
	B0-3	721125	244507	0.2532	1.6533
	B0-4	727687	237945	0.2464	1.5741
	Mean	739330	226302	0.2344	1.6033

speaking, the larger pore distribution fractal dimension is, the more porosity develops. The more complex pore structure is, the higher the degree of dispersion on the plane is. In this paper, use the box method to obtain the D value based on the MATLAB software (See Table 6).

Porosity variation: after drilling rock soaking experiment, rock porosity increased compared to undisturbed rocks. The average porosity increased from 0.1623 to 0.1911, showing that the particles were gradually eroded and void content in rocks increased through dissolution and ion exchange reaction of mineral composition in rock soaking experiment. Porosity of Baitupo profile rock samples at different depths is different. Average porosity of deep rock samples is 0.1783, which is slightly larger than undisturbed bore rock porosity. It showed that it suffered some water-rock interaction, but it's not obvious. Porosity of shallow rock samples increased to 0.1957 compared to porosity of deep rock samples, showing that the water rock interaction in shallow rocks is stronger than that in deep rocks. This is consistent with the results of indoor water-rock soaking experiment. Finally, argillaceous limestone formed reddish-brown clay after weathering. Its porosity reached 0.2344, further validating that rock mineral composition was reacted and rock structure became more loose after water-rock interaction.

Pore fractal dimension variation: after drilling rock soaking experiment, pore distribution fractal dimension changed from 1.4780 to 1.5173. The increase of D value showed that pore distribution area became large, pore structure became complex and dispersion degree was high. Agglomerated particles broke down and rock

samples become loose. Compared with different field rock samples, pore distribution fractal dimension of deep rock samples, shallow rock samples and clay after weathering were respectively 1.5202, 1.5269, 1.6033. Results of laboratory tests and field rock sample data are consistent. Fractal dimension of pore distribution increased with the time and intensity of water saturation. There are two factors that determine the D value: one is pore area, and the other is the pore distribution in the plane. With the ongoing of water saturation, large pores were partly filled with loosely and crushed mineral particles (As shown in Figure 5 and Figure 7). But on the whole, as dissolution proceeded, pore area would become increasingly larger and larger. New pore would also appear making the pore distribution dispersion increase in the plane, thus resulting in the increase of D value. Particles of completely weathered reddish brown clay were corroded seriously and the corrosion degree was of heterogeneity. This lead to complex pore distribution and big difference, and it's not conducive to the stability of rock and soil of slope.

5 CONCLUSION

(1) In initial stage, water-rock interaction gave first place to leaching effect. It mainly dissolved calcite. After that, water-rock interaction gave first place to ion exchange. Rock converted to illite and montmorillonite direction. (2) Water-rock interaction made the rock under erosion. Micro pores and fractures in rocks increased, rock porosity increasing and rock structure becoming loose and fragile. Pore distribution discrete in the plane increased, resulting in the increase of D value. This lead to complex pore distribution and big difference, and it's not conducive to the stability of slope.

ACKNOWLEDGMENT

This work was supported by the National Natural Science Fund of China (No. 41262011), Key Laboratory Program of Guangxi Geotechnical Mechanics and Engineering (No. 11-kf-02 & No. 11-CX-01 & No. 12-A-01-02), Science and Technology Research Project of Guangxi University (No. KY2015YB119).

REFERENCES

B. Chai. 2008. Systematic Research on Rock Mass Structure of Three Gorges Reservior Shoreline Slope in the New Badong County [D]. *Dissertation Submitted to China University of Geosciences for the Doctor Degree of Phiosophy*, (in Chinese).

J.W. Liu, 2012. Experimental Study on Micro Structure of the Soil and the Influence of Shear Strength of Hydration [D]. *Dissertation Submitted to China University of Geosciences for the Master Degree of Phiosophy*, (in Chinese).

J.W. Jiang, W. Xiang, W. Zeng, J. Rohn, Y. Yao. 2012, Water-rock (soil) interaction mechanism of Huangtupo riverside landslide in Three Gorges Reservoir [J]. Chinese Journal of Geotechnical Engineering 34(7):1209–1216, (in Chinese).

L. Yu, X.L. Wang, B. Zhao. 2011. the Fractal Dimension Characteristics of Element Abundance of the Granitoid in China [J]. *Earth Science Frontiers* 18(3): 293–301, (in Chinese).

L.S. Tang, S.M. Wang, P.C. Zhang, C. Tang. 1999. Water-rock Chemical Interaction and Hazard Control [J]. The Chinese Journal of Geological Hazard And Control 10(3): 61–69, (in Chinese).

X.Q. Liu, S.L. Zhou, M.F. Shang, Y. Li. 2012. Analysis on Mechanical Properties of Rock Based on Water-Rock Interaction[J]. *Journal of Chongqing Jiaotong University (Natural Science)* 31(2): 268–313, (in Chinese).

Y. Liu, H.C. Liang, Z.H. Tang, H.S. Cai, J.W. Liu, 2012. Reverse Simulation of Ca^{2+} Geochemical Behavior in Watersoil Interaction System of Landslide [J]. *Hydrogeology & Engineering Geology* 39(2): 106–110, (in Chinese).

Z. Liu, H.C. Liang 2010. The SEM analysis of rock-soil mini-structure after saturation. Soil Behavior and Geo-Micromechanics Proceedings of the 2010 Geo-shanghai International Conference [J]. *Geotechnical Special Publication*: 275–280, (in English).

Z.L. Yi, X. Liang, F.M. Li, Q. Yuan, T. Peng. 2007, ERDAS Apply in Quantified Analysis of Soil Microstructure [J]. *Hydrogeology & Engineering* (1): 113–119 (in Chinese).

Z.H. Pan. 2007. Study of Water-Rock Interaction in Chencun Dam-site [D]. *Dissertation Submitted to HoHai University Infulfllment of the Requirement for the Degree of Master of Engineering*, (in Chinese).

This page intentionally left blank

Unsaturated Soil Mechanics—from Theory to Practice – Chen et al. (Eds)
© 2016 Taylor & Francis Group, London, ISBN 978-1-138-02921-7

Feasibility analysis of electromagnetic field in geotechnical engineering research

B.X. Shi, S.S. Chen & G.R. Zhang
Geotechnical Engineering Department, Nanjing Hydraulic Research Institute, Nanjing, China

C. Zhou
Sichuan University, Chengdu, China

ABSTRACT: Indoor model test, with its less time-consuming and better repeatability, is an indispensable tool in indoor geotechnical study. Its advantages become more prominent when the in-situ test can not be carried due to special conditions. Starting from the field similarity of the heavy force field, analyze the distinction and similarity between various fields. Making use of the similarity between the magnetic and gravity fields, adopting the dimensional analysis method, it turns out that in electromagnetic force field a similar criterion can be obtained in which the time t and the geometric dimension l will be reduced by n times, the acceleration of gravity g will expand by n times, while the similarity ratios of the material's other basic physical and mechanical parameters are all 1. An electromagnetic force model test method is discussed in which magnetic materials are mixed in rock body, so that it is effected by the magnetic force in a magnetic field to simulate ng gravity field, thus to improve the model test material's stress level. The generation of a uniform magnetic field and the preparation method of model material are both introduced briefly.

1 INTRODUCTION

People continue to explore the laws of nature, and some direct experimental methods are gradually developed to solve some visual phenomenon, but what is got is often only the regular relationships between some special discrete amounts, it's hard to find or seize the essence of the phenomenon. Thus a new theory — "the similarity theory" — for guiding natural law study has emerged at the right moment through long-term practice and summarization. It combines the mathematical analytical method with the test method to study and solve problems in production and engineering. From 1960s, some scholars carried out research work with the geomechanical model according to the similarity theory (Fumagalli 1968, Baumgarter & Stimpson 1979, Stewart et al. 1994). Conventional model test is a simulation test which is carried out in a gravity field, where the prototype is reduced by n times according to the geometric similarity. In brittle materials (concrete rock) simulation study, the model is similar to the prototype (Li & Lu 2003, Li et al. 2004, Ma et al. 2004).

The method is often used in studying the soil material's deformation, strength, permeability and mechanism, and relevant research results have been obtained, but because the geological environment was usually complex when the earth mass came into being, meanwhile the earth itself is crumbling, nonlinear deformed material, it's harder to maintain its original physical and mechanical properties, therefore its geostatic stress level is transformed into l/n, that's why the model test can only partially meet the geometric similarity and mechanical similarity between the physical model and the prototype, it can not really reflect the overall characteristics of the prototype (Yuan 1998).

Geotechnical centrifuge model test is a test that uses the centrifugal force provided by centrifugal machine to simulate gravity centrifuge, the geometry of the prototype is reduced according to the similar criteria, so that the stress at various points in the model will be consistent with that in the prototype. There is some essential differences between the centrifuge model and the conventional model tests, geotechnical centrifuge model test method is widely used in the world (Huang & Wang 1998, Bai & Zhou 2000), but its acceleration varies due to different rotation wheelbase, the simulated force line direction is not parallel to force line of the gravity field (Bao & Rao 1998), It is expected that we can overcome the shortcomings of centrifugal model tests and find out a new model test method to study civil engineering problems by adding magnetic powder to rock and earth mass to simulate *ng* gravity field.

2 THE ELECTROMAGNETIC FIELD AND THE GRAVITY FIELD

Because of insurmountable difficulties in geotechnical centrifugal technology and the urgent need for practical engineering research, we start from the principle

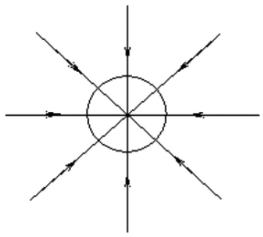


Figure 1. Gravitational field around the earth.

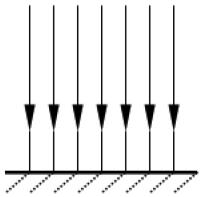


Figure 2. Gravitational field near the ground.

of using the external force field to simulate the gravity field, making use of the field similarity theory to carry out research on model test technology, to seek other analog technology so as to achieve gravitational field simulations. There is field similarity between the electromagnetic and gravitational fields, now we begin to compare and analyze the differences and connections between the two kinds of fields. The electric and magnetic fields can inspire each other through movement; some certain coordinate system conversion relationship is adaptable to them. The ordinary electric and magnetic fields can be seen as a form of electromagnetic field in a specific coordinate system, which will not be further explained in detail.

2.1 *Shape of the field*

The shape of the Earth's gravitational field around is radial; its direction is identical with the direction of gravity acting on objects, pointing to the earth's core, as shown in Figure 1. Gravitational field near the ground can be considered as parallel lines of uniform distribution, whose direction is horizontal to the ground, as shown in Figure 2.

Electric field around the point charge is radial, it has the same direction with the positive charge's electric force at that point (Fig. 3), and density of the electric field lines can embody strength of field density. When two or more point charges can interact with each other, the shape of the electric field around them is as shown in Figure 4, the electric field lines start from the positive charge and ends at the negative charge.

Electric field between parallel metal plates with heterogeneous charge may be considered as uniform parallel lines, the direction pointing from the positive electrode plate to the negative electrode plate, as shown in Figure 5. Therefore, both the gravitational field near the ground and the electric field between dotted metal plates can be considered as uniform parallel lines, that

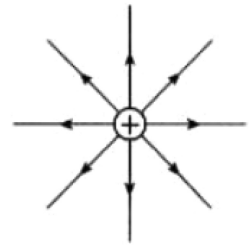


Figure 3. Single electric charge.

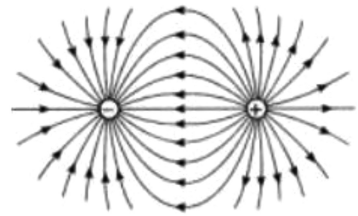


Figure 4. Two electric charge.

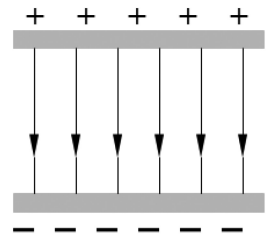


Figure 5. Multipoint electric charge between parallel plates.

is to say, electromagnetic fields at any space between the plates have the same strength.

2.2 *Field strength*

In the gravitational field, the ratio of the gravity G suffered by an object and its mass m is the gravitational field strength, i.e. $g = G/m$, which is suitable for the gravity field of any shape. The gravitational field strength around the earth (or object that can be seen as a particle) is: $g = G \cdot M/r^2$, while the uniform gravitational field strength near the ground is: $g = W/mh$.

Electric field strength is expressed as testing the ratio of electric field force $\boldsymbol{F}$ the charge suffered at some point of the electric field and the charge q, i.e. $E = F/q$, which is suitable for the electric field of any shape. For the electric field around a point charge, its field strength is $E = k \cdot q/r^2$, the field strength formula which is suitable for uniform electric field is $E = U/d$. For the field strength, besides the differences in coefficient, the uniform electric field intensity and the uniform gravitational field strength have the same basic meaning.

2.3 *Field energy*

What determines the size of an object's energy is the location it is in the gravitational field, when it moves from a to b, the gravity acting on the object is equal to its gravitational potential incremental negative value, that is $E_{pb} - E_{pa} = -W$. The gravity near the ground can be approximately seen as uniform gravitational field, gravitational potential energy is $E_p = mgh$. Potential energy of any space around the earth is $E_p = -(G \cdot M/r)m$.

The charge in the electric field also has a similar nature. When a point charge moves from a to b, the electric force and gravity acting the same on the object, which is equal to its electrical potential incremental negative value, that is $E_{pb} - E_{pa} = -W$. Uniform electric field's electric potential is adaptable to the equation of $W = qEd = Ud$.

The non-uniform electric field potential around a point charge can be expressed by the formulas of $E = (k \cdot M/r)q$ (positive charge) and $E = -(k \cdot M/r)q$ (negative charge). Therefore, when an object is at the same position of the uniform gravitational field or the electromagnetic field, its potential energy formulas are basically the same, only with differences in the coefficient or direction.

By comparing and analyzing the field shape, field strength and field energy of the gravity field and electromagnetic field, it can be known that the electromagnetic and gravitational fields are both specific substances in existence, both of them have strength properties and energy properties, and have similar relationships of defined physical quantity. Both he gravitational field near the ground and electromagnetic fields generated between dotted metal plates can be considered as uniformly distributed parallel lines. And uniform field strength almost have the same meaning with uniform field energy, with differences that the gravitational field is associated with the mass of the substance, whereas the electric field is closely linked with the electricity quantity of the charge. Therefore, the electromagnetic field and gravitational field are similar, if appropriate amount of magnetic powder is added to the rock and earth mass, making it suffer magnetic force magnetic field generated by electric power, defining the field strength and field energy coefficients if simulated gravity, improving the model test material's stress levels, then the goal of simulating *ng* gravitational field can be achieved (Luo, X.Q. et al. 2009, Tang, K. et al. 2010).

3 FEASIBILITY ANALYSIS OF ELECTROMAGNETIC FIELD SIMULATING GRAVITY FIELD

3.1 *Several concepts for electromagnetic field*

1) Electromagnetic force: one of the four fundamental forces of nature is the general name for the force that the charge and current suffer in the electromagnetic field. Sometimes the force the current-carrying conductor suffers in a magnetic field is called the electromagnetic force, whereas the force the static charge suffers in an electrostatic field is called static electricity.
2) Magnetic flux density B: the number of magnetic force line per unit area that is perpendicular to the direction of magnetic field, which is also called magnetic flux B, $B = F/IL$. Its unit is T or Gs, $1T = 10^4 Gs$. It's the fundamental physical quantity to describe the magnetic field properties, reflecting the moving charge's properties in a magnetic field.
3) Magnetic flux: is the total number of magnetic lines getting through some specific sectional area, represented by Φ, whose unit is Weber, with the symbol of W_b. The expression for magnetic flux through the coil is: $\Phi = BS$ (where B is the magnetic flux density, S is area of that coil.) $1W_b = 1\ Tm^2$.
4) Permeability: a physical quantity that represents the magnetic medium's permeable properties in a magnetic field. Its unit is H/m. The permeability of vacuum is constant, i.e. $\mu = 47\pi \times 10^{-7}$. Permeability of other media is generally expressed with μ_r in multiples of the vacuum.
5) Magnetic field strength H: In any magnetic medium, the ratio of the magnetic induction intensity of a point in the magnetic field with the permeability of the same point is called the magnetic field strength, that is $H = B/\mu$.
6) Suction Maxwell: If the magnetic field lines distribute uniformly along the area, such as: the magnetic lines of two parallel planes poles in close proximity can be considered to distribute uniformly, then the suction of Maxwell is: $F_d = B^2 S/2\mu_0$, where F_d is the suction strength, B is the magnetic field intensity, μ_0 is the vacuum permeability, and S is the flux area.

3.2 *Electromagnetic and gravitational fields' similarity theory*

It is known from the above-mentioned formulas of electromagnetic field strength and Maxwell suction that, in a uniform gradient magnetic field, such as the area between magnetic plates of parallel planes can be regarded as a uniform gradient magnetic field, a constant current will maintain an unchanged magnetic field strength. At this moment, the magnetic field strength B, the magnetic flux area S, and the vacuum magnetic permeability are all constant, then the Maxwell suction F_d is of a constant value.

Let $n'g = B^2 S/2\mu_0$, then the suction is n' times of the gravitational acceleration, the object whose mass is m will suffer a magnetic electromagnetic force of:

$$F_c = m \bullet B^2 S/2\mu_0 = mn'g \tag{1}$$

And because in the gravitational field the objects suffer a gravity of:

$$F_g = mg \tag{2}$$

Comparing the above formulas (1) and (2), it can be known that if the electromagnetic field is distributed uniformly, the electromagnetic force F_c will be similar to the gravity F_g, both of them can be expressed as the product of mass m and acceleration. If the electromagnetic force F_c suffered by an object has the same direction with the gravity F_g, then what the magnetic material suffers in the magnetic field will be the joint-force of both:

$$F=F_g+F_c=mg+mn'g=mg(1+n') \tag{3}$$

The joint-force has the direction of with the gravitational force.

Then in the magnetic environment, the vertical stress an object suffers in the electromagnetic field:

$$\sigma=\rho(n+1)gh \tag{4}$$

where ρ the density of the test material, h is the depth from the object surface, $(n+1)g$ is the gravity acceleration of the material which is caused by the joint-roles of the electromagnetic and gravitational fields.

Obviously, in the magnetic model test, what is added to the model test material is a volume force, acting the same force on any point of the model and with the same direction, which is different from nature of natural gravity field. The stress level of the test material can be increased by adding magnetic force additional; meanwhile deficiencies existing in the up-mentioned centrifuge model tests can be overcome, so the technology will have its unique advantages when it is used in geomechanical model test.

It can be known form the formula (3) that, gravity increases multiples is: $n=1+n'$, which can also be understood like this: the gravitational acceleration increases from g in the natural state to ng, if the object itself suffers a uniform electromagnetic force, it is like that the body force with the acceleration of $n'g$ is added to the object besides its original gravity, as a result, its stress level will be increased.

3.3 *Dimensional analysis of field similarity*

Both the electromagnetic force field and the centrifugal force field are model test theories starting from field similarities, namely with the help of electromagnetic force or centrifugal force, making the weight of the materials of which the model is composed increase by n times, so as to simulate prototype works whose geometries shrink by n times. The following is about the theoretical basis of establishing electromagnetic field simulation by dimensional analysis of field similarity.

The physical quantities and units that may be involved in the test are: the elastic modulus E(Pa), the strain ε, the poison ratio μ, time t (s), length l (m), force F (N), the stress σ (Pa), the shearing stress τ (Pa), the displacement u (m), the cohesion c (Pa), the internal friction angle φ (^{0}), the lateral pressure p (Pa), the density ρ (kg/m^3), the permeability coefficient k(m/s), the flow velocity υ (m/s), rainfall intensity q (m/s) and the gravitational acceleration g (m/s^2). Let X' be the similarity ratio (affinity constant), $X'=X_y/X_m$, or in other words, the ratio of the prototype parameter X_y and the model parameter X_m, with a total of 18, which is same with the number of similarity ratios. On the basis of the second theorem of the Three Similarity theorems, the relevant parameters are classified according to dimension.

$$F(\sigma,E,u,t,\mu,\varphi,c,g,p,k,\nu,q,l)=0 \tag{5}$$

In Formula (5), φ, μ and ε are dimensionless quantities; σ, E, c and p have the same dimension; k,υ and q have the same dimension; $L$and $u$also have the same dimension, according to the similarity theory it is known that: similarity ratio of the dimensionless quantity is 1, the same dimension have the same similarity ratio. In addition, according to the π similarity theorem, σ, g, μ are selected to be the independent variable under the same dimension, then the three above-mentioned mutually independent dimensions can be expressed as a function of among the similarity criterions of π_1,π_2,π_3:

π_1,π_2,π_3:

$$F(\pi_1,\pi_2,\pi_3)=0 \tag{6}$$

of which,

$$\pi_1=\rho gu/\sigma,\ \pi_2=t\sqrt{g/u},\ \pi_3=k/\sqrt{gu} \tag{7}$$

Supposing three independent variables, $\sigma_m=1$, $\mu_m=n$, $g_m=1/n$, because the similarity ratio of dimensionless quantity is 1, then the similarity ratios of other parameters are: $p_m=\sigma_m=E_m=C_m=1$, $L_m=\mu_m=n$, $K_m=V_m=q_m=1$, $t_m=n$, $\rho_m=1$, $g_m=1/n$.

The similarity criteria of the parameters can be seen from the above-mentioned dimensional analysis: In the simulation test that is conducted in the electromagnetic field, both the time and geometry reduce by n times, but gravity acceleration g is expanded by n times, the similarity ratio of all the other basic physical parameters is 1. That is to say, it is entirely feasible in theory to carry out mechanical model test in electromagnetic force field by using the prototype material and making its geometry shrinks by n times. Meanwhile the test efficiency is greatly improved and the model test difficulty is greatly reduced when time and geometry shrink by n times.

4 ELECTROMAGNETIC FORCE FIELD MODEL'S REALIZATION

The electromagnetic force field model test is a brand-new model test method that is set up by making use of the similarity theory of electromagnetic and gravitational fields. To make the material suffer a constant magnetic force, the electromagnetic field needs to

meet certain conditions, and to ensure that adding and subtracting magnetic force is consistent with magnetic force variation of the test material.

4.1 *Generation of a uniform and stable electromagnetic field*

The force that the permeability materials or the current-carrying conductor suffer in a magnetic field is called the magnetic force. The methods to obtain magnetic force mainly include the permanent magnets or the electromagnets. The permanent magnet is a magnet that is made from a material of broad hysteresis loop, high coercivity and remanence, which will maintain constantly magnetic once magnetized. Magnetic force that is generated by the permanent magnet is permanent, and can not be changed or adjusted, can not be used for the electromagnetic force field test. The electromagnet is a device that can generate magnetic force by electricity, it is a non-permanent magnet, whose magnetism can easily be started or eliminated. Twine electricity-conducting coils around the iron core whose power matches each other, so that a uniform magnetic field will be generated around the wire when electric current passes through. Supposing the ferromagnetic material is placed into the center a solenoid, it will be magnetized and will greatly enhance the magnetic field. An electromagnet is usually made from soft iron or silicon steel that has the characteristic of quicker demagnetization to ensure immediate degaussing after power-off, the electromagnet can also control magnetic strength by controlling the current intensity.

A uniform magnetic field can be formed around the wire after the alternating current of a steady current going through the electromagnet, which is formed by the winding of homogeneous coils. According to the law of energy conservation, when the coil is energized for a long time, the magnetic force will be reduced due to the heat of the wire. Therefore in order to ensure the uniformity of a high-strength magnetic field, it's necessary to study the electromagnet's thermal stability when it is in long-term operation, to determine by experiment the coil's heat production and magnetic attenuation laws, to develop automatic measurement control system so as to cooling coil heat as soon as possible and regulate uniformity of the high-strength magnetic field.

4.2 *Preparations of similar materials*

The physical and mechanical property of the soil performed in the electromagnetic field is closely related with the physical composition of the rock and earth mass. The main component of the rock and soil earth mass is clay minerals, and clay minerals in different rock and earth mass have different particle diameter distribution and shows different specific surface properties. There is electric double layer on the surface of clayey soil particle, and the particles are surrounded by water film, the charge on the surface of soil particle changes in the electromagnetic field magnetization, resulting in an dynamic potential shift of the electric double layer, affecting clay aggregation or particles segregation between the soil colloidal particles, and resulting in the changes in soil's meso-structure and structural intensity.

Soil pore water exists inside the rock and earth mass in different ways, according to the influence degree of the electric double layer on the soil surface it can be divided into: combining water, viscous water and free water. As we all know, the magnetic field's magnetization may increase the activity of water, and the roles of water in studying geotechnical engineering problems can not be ignored, in theory, the activity of water does not produce significant impact on mechanical property and overall penetrating quality of the soil mass. (Luo et al. 2009) shows us by tests that the magnetic force water suffers in magnetic field is very small, the impact of magnetic force on the water is negligible, but its impact on infiltration path and pore water pressure deserves our great attention.

In the electromagnetic model test, both time and geometry reduce by n times, the gravity acceleration expands by n times, and the similarity ratio of all the other basic physical parameters is 1. Magnetic material needs to be added in order to make the test material's gravity acceleration increase by n times. Geomaterials itself contains a lot of iron, whose content differs in different types of soil, therefore mixing magnetic materials with the rock and earth mass will inevitably change the soil composition, and as a result, physical and mechanical properties of the rock and earth mass will be influenced. The coarse particle material in the rock and earth mass is replaced by particle or powder magnetic materials, namely, the "equivalent replacement" of the powder materials in the model test. According to different test purposes, adjust appropriately the ratio of materials or add other materials, so as to compound geotechnical materials of similar magnetism which meets similar conditions and physical and mechanical properties required by the rock and earth mass. The mechanical properties, the generated gravity n value, and the magnetic particle size distribution, etc.

5 CONCLUSION

The experimental technique of using the electromagnetic force model to simulate centrifugation is a model test technology that making use of the increasing magnetic force to improve the test material's stress level. The technique starts from the theory of field similarities, compares and analyzes the centrifugal model test, comprehensively applies the model test theory, the magnetic physics, the magnetic field design theory, rock mechanics and other multi-disciplinary knowledge to analyze its feasibility.

1) Both the electromagnetic force field and the centrifugal force field are model test theory

starting from the field similarity, namely the actual work that makes the model test material's weight increase uniformly by n times and geometry reduces by n times through electromagnetic force or centrifugal force. Defects of the centrifugal model test may be overcome by making use of the similarity between magnetic field and gravity field and adding powder magnetic material to the rock and earth mass so as to simulate the *ng* gravitational field, which has become a new model test method in the applications of geotechnical engineering field.

2) It is know from dimensional analysis that, in simulation test that is carried out in an electromagnetic field model, both time and geometry reduce by *n* times, the gravity acceleration expands by *n* times, and the similarity ratio of all the other basic physical parameters is 1. This indicates that when similar materials are used and when geometry shrinks by n times, mechanical model test of *ng* gravitational field is entirely feasible. Meanwhile, when the time scale reduces by n times, the test efficiency can be greatly improved and the difficulty of model tests can be reduced.
3) The electromagnetic force field model test is a brand-new model test method that is set up by making use of the similarity theory of electromagnetic and gravitational fields. The increase of the test material's stress level is caused by mixing magnetic material with the test materials, and the stress of the test material is generated by composition of the gravity and the electromagnetic force. To make the material suffer a constant magnetic force, the electromagnetic field needs to meet certain conditions, and to ensure that adding and subtracting magnetic force is consistent with magnetic force variation of the test material.

Applying the electromagnetic force field theory to the geotechnical engineering field still belongs to the frontier of an interdiscipline, there are still many issues to be further studied, such as: how to ensure the generation of a uniform and stable magnetic field in normal pressure and temperature, the stability control technology after consumption of electromagnetic energy and the generation of heat, similarity problem of the model materials and the prototype materials, the diamagnetic and automatic control technologies of various measurement equipments in the electromagnetic force field, magnetization of the free water in the model material and the formation of the *n* times gravitational field. The settlement of all these problems needs collaborative research of experts in fields of magnetic physics, similarity theory and geotechnical engineering.

ACKNOWLEDGEMENT

Financial supported by the National Natural Science Foundation of China (No. 51009097) and the Hebei Science Foundation (No. E2012402049).

REFERENCES

Bai, B. & Zhou, J. 2000. Some advances on geotechnical centrifuge model test technology. *West-China Exploration Engineering* 65(4):8–11.

Bao, C.G. & Rao, X.B. 1998. Principle of the geotechnical centrifuge model test. *Journal of Yangtze River Scientific Research Institute* 15(2):2–7.

Baumgarter, P. & Stimpson, B. 1979. Development of a bitable base friction frame for kinematics studies of caving at various depths. *International Journal of Rock Mechanics and Mining Sciences and Geomechanics Abstracts*, 16(4):265–267.

Fumagalli, E. 1968. Model simulation of rock mechanics problem. *Rock mechanics in engineering practice*. London: 125–147.

Huang, Z.Q. & Wang, S.J. 1998. A survey of application of centrifugal model testing in China. *Chinese Journal of Rock Mechanics and Engineering* 17(2):199–203.

Li, Z.K. & Lu, D.R. 2003. Development and application of new technology for 3D geomechanics model test of large underground houses. *Chinese Journal of Rock Mechanics and Engineering* 22(9):1430–1436.

Li, Z.K., Xu, Q.J. & Luo, G.F. 2004. 3D geotechnical model test for large-scale underground hydropower station. *Journal of Hydraulic Engineering* 23(2):181–186.

Luo. X.Q., Ge, X.R. & Cheng, S.G. 2009. Study of magnetic material property of geomechanical model test in electromagnet field. *Chinese Journal of Rock Mechanics and Engineering* (S2):3801–3807.

Ma, F.P., Li, Z.K. & Luo, G.F. 2004. NIOS model material and its use in geotechnical similarity model test. *Journal of Hydroelectric Engineering* 23(1):48–51.

Stewart, D. P., Adhikary, D. P. & Jewell, R. J. 1994. Study on the stability of model rock slope// *Proceedings of the Int. Conf. Centrifuge 94.* Singapore: [s.n.]: 629–634.

Tang, K., Luo, X.Q. & Zhang, Z.H. 2010. Study of Magnetic Field Gradient in Geomechanical Model Test. *Journal of China Three Gorges University (Natural Sciences)* (1): 56–58.

Unsaturated Soil Mechanics—from Theory to Practice – Chen et al. (Eds)
© 2016 Taylor & Francis Group, London, ISBN 978-1-138-02921-7

Improvement of soil stability along rail corridors through native vegetation

M. Pallewattha, B. Indraratna & C. Rujikiatkamjorn
School of Civil, Mining and Environmental Engineering, University of Wollongong, Wollongong City, Australia

ABSTRACT: Field studies have revealed the effective utilization of native trees as an economical and environmental friendly method of soil stabilization along railway lines in Australia. Native trees grown along rail corridors are capable of providing mechanical strength to the subgrade soil through the root network and the additional cohesive increment provided by the osmotic suction generated at the hair roots. Moreover matric suction generation due to evapo-transpiration of the tree canopy has significant influence on shear strength of soil underneath the railway lines. Therefore the true effect of vegetation should be evaluated considering the mechanical root reinforcement effect, evapo-transpiration induced matric suction development and in addition the alteration of potential failure conditions in the soil-root system from a saturated to an unsaturated domain. This paper will discuss the requirement of a shear strength model that combines the root reinforcement effect with both osmotic and matric suction components generated in the soil through naturally coupled osmotic evapo-transpiration phenomenon.

1 INTRODUCTION

1.1 *Concept of green corridor*

The concept of a green corridor is an expedient method for most geotechnical engineering projects provided its subsequent effects have been thoroughly quantified, because in this concept, tree roots and their spatial distribution are the most important part. Furthermore the spatial distribution of a tree root system varies according to the environmental factors (Kramer 1995).

Even though native vegetation is still not commonly used as a ground improvement technique, field studies have already shown its potential for stabilising slopes and controlling erosion. For instance, Potter (2006) conducted extensive field studies to evaluate the true effect of vegetation and the associated development of matric suction underneath the railway lines in Miram, Horsham, and WalWal in Australia. He reported that the variations in total suction underneath a railway track in non-vegetated and vegetated conditions were distinct, with the latter typically exhibiting larger values of suction. Moreover Docker & Hubble (2008) conducted extensive number of in-situ shear test on eucalyptus root systems and proved the potential increase of shear strength of soil with respect to the root system is high.

1.2 *Root systems and soil strength*

The root system of a tree can be broadly categorised into two sub root systems known as the active root system and the main root system. Small (active) roots contribute to the uptake of water and nutrients while main roots help to stabilise the tree. These two root systems provide mechanical strengthening to the soil by means of anchoring and increments of cohesion (Fatahi 2007). Moreover, tree roots also improve the matric suction of soil by means of the root water uptake in conjunction with the evapotranspiration of the tree (Fatahi 2007). This means the true effect of vegetation on the stability of soil consists of mechanical strengthening and suction improvement, including the influence of suction on mechanical strengthening (Kramer 1995).

In ground improvement the total generation of shear strength in terms of mechanical strengthening and suction induced by root water uptake, is mainly governed by the spatial distribution of the root system. Therefore, a comprehensive understanding of the root system is vital for an in depth study of the effect of suction on soil stabilisation.

The spatial distribution of root systems varies according to environmental factors such as species, soil conditions, temperature, wind speed, rainfall and humidity. Common variations in shapes of root systems influenced by environmental factors such as soil bulk density, temperature and rainfall amount are illustrated in Figures 1–3.

However, bioengineering techniques can be used in hill slopes where there are risks of landslides, as well as for other improvement processes (Bache et al. 1989; Docker & Hubble 2001; Potter 2006; Fatahi 2007).

2 SUCTION EFFECT

The root water uptake of a tree increases the matric suction of the adjacent soil due to the subsequent reduction in the moisture content. This can be very significant

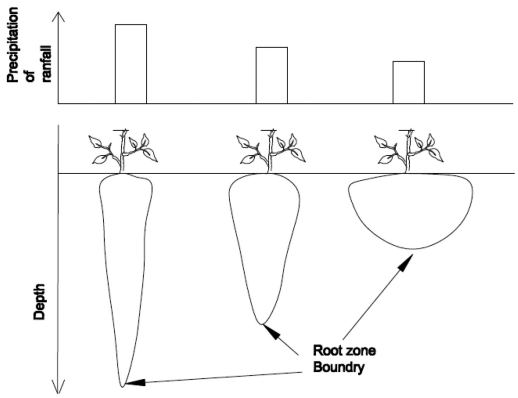


Figure 1. Schematic diagram of the effect of the amount of rainfall on the depth of rooting of winter wheat (very fine sandy loam – silty loam in the Great Plains) (modified after Sattelmacher et al. 1990).

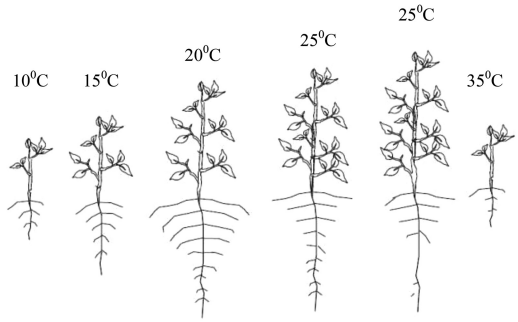


Figure 2. Influence of root zone temperature on root morphology and shoot growth of potato seedlings (modified after Sattelmacher et al. 1990).

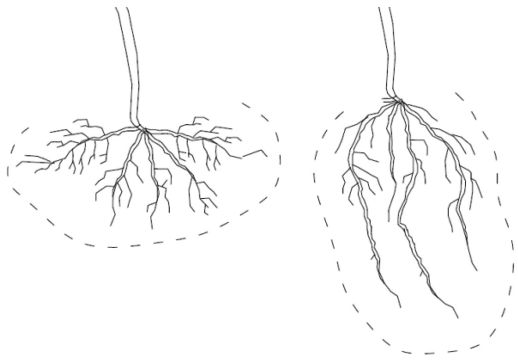


Figure 3. Root system of young barley plants grown in the field in soils with different bulk densities (Left) 1.35 g cm^{-3}; (right) 1.50 g cm^{-3} (modified after Gilmen 1980).

because trees such as Pinus radiata can absorb amounts of water equal to its own weight per day, and most mature trees can generate up to 30 MPa of suction in their soil-root systems. The main factor that affects the root water uptake is the rate of transpiration of a tree because the volume of water consumed by plant cells for metabolism is negligible compared to the total root water uptake (Radcliffe et al. 1980).

2.1 *Rate of root water uptake and transpiration*

Only active roots uptake water through the process of osmosis, but the rate of uptake in a given time varies from point to point in a root system according to the spatial distribution of the active roots. The rate of root water uptake has been described considering the hydraulic conductivity of leaves and water potential differences between root and soil (e.g. Gardner 1960; Whisler et al. 1968; Molz & Remson 1970; Feddes et al. 1974; Hillel et al. 1976). Furthermore, recently Fatahi (2007) developed a more comprehensive approach to evaluate the rate of root water uptake considering transpiration of tree canopy (Eq. 1).

$$S(x,y,z,t) = f(\psi)G(\beta)F(T_P) \tag{1}$$

where, F(T_p) is a factor related to the potential transpiration model developed by Nimah & Hanks (1973) which can be described according to Eq. 2.

$$F(T_P) = \frac{T_P(1 + k_4 z_{max} + k_4 z)}{\int_{v(t)} G(\beta)(1 + k_4 z_{max} + k_4 z)dv} \tag{2}$$

where G(β) is the root density which depends directly on species of tree and condition of the soil, and k_4 is an experimental coefficient (Fatahi et al. 2010). The coefficient k_4 depends on the rate of transpiration, which is directly affected by the environmental factors such as the humidity, temperature, and wind speed, as well as soil moisture (soil water potential) and physiology of the tree, and f(ψ) is the factor related to the soil moisture condition. The soil water potential inversely affects the root water uptake, while the soil suction relates to the soil moisture content through the soil water characteristic curve. Therefore, the soil reduction factor is a function of the moisture content of soil (Indraratna et al. 2008; Fatahi et al. 2009).

The flow equation related to the unsaturated soil incorporating the root water uptake as a sink term is as follows:

$$\frac{\partial \theta}{\partial t} = \nabla.(k\nabla\psi) - \frac{\partial k}{\partial z} - S(x,y,z,t) \tag{3}$$

3 MECHANICAL STRENGTHENING

The effect of root reinforcement with regards to the bioengineering aspects of controlling slope stabilisation and erosion has been widely discussed over the past few decades. Waldron (1977) and Wu et al. (1979) developed a simple root model for vertical root, and then Gray & Leiser (1982) modified the model for an inclined root.

Waldron (1977) defined three different increments of shear strength (ΔS) related to the three different

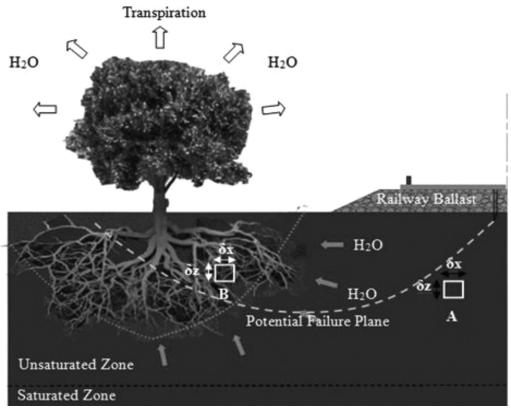


Figure 4. Schematic diagram of root water uptake process and root reinforcement.

failure patterns known as stretching, slipping, and breaking. According to Waldron (1981), an increment of the shear strength (ΔS) can be added directly to the coulomb equation because there is no change in the friction.

$$\tau = c + \Delta S + \sigma_N \tan\phi \tag{4}$$

Docker & Hublle (2009) carried out many in-situ direct shear tests of root permeated saturated soil for four Australian tree species, and then introduced an emperical equation (eq. 5) for the shear strength increments that were mainly based on the Root Area Ratio (RAR).

$$\Delta S = B.(RAR) + C \tag{5}$$

In equation 5, 'C' and 'B' are experimental coefficients related to the different tree species.

4 DISCUSSION

As stated in the introduction, most sub soil structures remain in a partially saturated state where it is certain that the depth and degree of saturation of the vadose zone increases in that part of the soil structure which interacts with mature trees. As a result, the parameters developed for mechanical strengthening in a saturated condition are not realistic, and therefore a combined effect must be included, and the parameters should be defined accordingly.

Figure 4 gives a general understanding of an improvement in the subsoil structure due to this combined effect. Soil element A in Figure 1 is directly under the Railway ballast and Soil element B is in the area of the root zone.

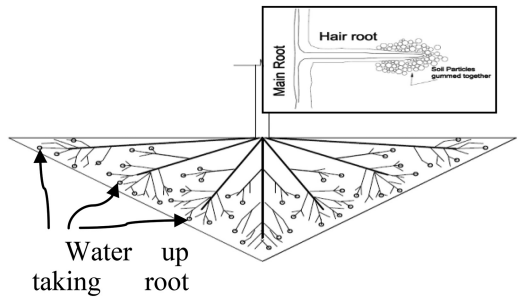


Figure 5. Schematic diagram of root system with distribution of water up-taking active root tips, (b) Enlarged root tip.

General unsaturated soil mechanics theories are valid for soil element A and therefore Vanapalli, Fredlund et al. 1996 equation can be used.

$$\tau = c' + (\sigma_n - u_a)\tan\phi' + (u_a - u_w)\,[\tan\phi'\left(\frac{\theta - \theta_r}{\theta_s - \theta_r}\right)] \tag{6}$$

In this equation u_a and u_w are the pore air and water pressures, θ_s, θ_r, and θ are the saturated, residual, and instant volumetric water contents, and all the other symbols have their usual meaning.

The value of θ in this equation changes with time due to the root water uptake, so the following equation can be stated by considering Fatahi's 2007 equation and Reynolds differential transport theorem.

$$\frac{\partial\theta}{\partial t} = \nabla.(k\nabla\psi) - \theta\frac{\partial k}{\partial z} - dS(x,y,z,t) + dI(x,y,z,t) \tag{7}$$

In this equation 'S' is the Root water uptake sink term and 'I' is the irrigation source term, ∇ is the volumetric moisture content, k is the hydraulic conductivity, and θ is the matric suction. At the same time the usual soil water characteristic curve can be used for element 'A'.

Element 'B' has a significant effect from the root suction and root reinforcement because it is in the root zone of the tree, and therefore the usual unsaturated soil mechanics theories cannot be directly used for element 'B'. However, the stiffness of the root zone increases the shear strength of the soil around element A, so it can be defined as a "shear capacity" of the root area zone which acts as an external stiffener with help from the root reinforcement and suction.

Figure 5(a) shows a schematic diagram of the root zone and water uptake points. According to the enlarged view of the root tip shown in Figure 2(b), and according to the classical botanical understanding, osmosis at the root tip binds the soil matrix together, and therefore the failure patterns described in section 3 may be altered such that it is governed by osmosis at the root tip. The suction changes the bond strength between the root and the soil, and also alters the material properties of the root. In this case the failure of the root system due to slipping, stretching, breaking, or

pulling out with the soil annulus were greatly affected by suction induced by the tree roots, as well as the adjacent soil suction.

Computing the effects from root reinforcement and suction separately and then superimposing them may not give a realistic answer because the suction influences the root reinforcement. Suction changes the bond strength between the root and the soil and also alters the material properties of the root. In this case the failure of the root system due to slipping, stretching, breaking, or pulling out with soil annulus were greatly affected by suction induced by the tree roots, as well as the adjacent soil suction.

5 CONCLUSIONS

Tree roots can be used economically to improve the subgrade after the subsequent affects have been analysed. Previous models that were developed to compute the root based suction and root reinforcement effect have contributed to improvements in the sub grade, but as described in this paper, a comprehensive model consisting of mechanical strengthening and root based suction is needed to obtain more realistic results. Moreover, most trees are unable to improve the sub soil because of their shallow root system and deciduous behaviour. Therefore it is essential to select plants with a good root system and which are evergreen.

ACKNOWLEDGEMENTS

The authors acknowledge funding from the Australian Research Council; industry partners GHD, City of Salisbury and Transport Construction Authority and a number of past PhD students.

REFERENCES

B. Bache, D. H., Coppin, N. J. and Casebowk, A. J. (1989). Vegetation In Civil Engineering Construction: Role And Uses. I*CE Proceedings* 86(1): 247–249.

Docker, B. B. and Hubble, T. T. C. (2001). Strength and stability of Casuarina glauca roots in relation to slope stability. *14th Southeast Asian Geotechnical Conference*. Lisse: 745–749.

Docker, B. B. and Hubble, T. T. C. (2008). Quantify root-reinforcement of river bank soils by four Austrailian tree species. *Science Direct* 100 (2008): 401–418.

Docker, B. B. and Hubble, T. T. C. (2009). Modelling the distribution of enhanced soil shaer strength beneath riparian trees of south-eastern Australia. *Ecological engineering* 35 (2009): 921–924.

Fatahi, B. (2007). Modelling of Influence of Matric suction induced by Native vegetation on sub-soil Improvement. *PhD Thesis, University of Wollongong.*

Fatahi, B., Indraratna, B. and Khabbaz, M. (2007) Soft soil improvement induced by tree root suction, *Australian Geomechanics Journal*, 42(4), 2007, 13–18.

Fatahi, B., Khabbaz, H. and Indraratna, B. (2008). Analysis of Matric Suction Effects Induced by Tree Roots on Rail Track Subgrade. *The Core of Integrated Transport Conference Proceeding Conference on Railway Engineering*, Perth, Railway Technical Society of Australasia: Engineers Australia.

Feddes, R. A., Bresler, E., Neuman, S.P. (1974). Field Test of Modified Numerical Model for Water Uptake by Root System. *Water Resources and Research*. 10(6): 1199–1206.

Fredlund, D. G., Rahardjo, H. and Fredlund, M. D. (2012). *Unsaturated soil mechanics in engineering practice*. Hoboken, N.J., Wiley-Blackwell.

Gardner, W. R. (1960). Dynamic Aspects Of Water Availability To Plants. *Soil Science* 89(2): 63–73.

Gilmen, E. F. (1980). *An Illustrated Guide to Pruning, Environmental Horticulture Department*, IFAS, University of Florida.

Hillel, D., Talpaz, H. and Van Keulen, H. (1976). A Macroscopic Sacle model for water uptake by anon uniform root system and of water and salt movement in the soil profile. *Soil Science Society of America Proceedings* 121: 242–255.

Indraratna, B., Khabbaz, H. & Fatahi, B. (2008). Conceptual Development and Numerical Modelling of Vegetation Induced Suction and implications on Rail Track Stabilisation, *Proceedings of the 12th International Conference of International Association for Computer Methods and Advances in Geomechanics* (IACMAG), Indian Institute of Technology, Bombay, Mumbai, India, 4335–4344.

Molz, F. J. and Remson, I. (1970). Extraction term models of soil moisture use by transpiring plants. *Water Resources Research* 6(5): 1346–1356.

Nimah, M. H. and Hanks, R. J. (1973). Model for estimating soil water, plant and atmospheric inter relations. *Soil Science Society of America* 37(4): 522–527.

Nobel, P. S. (1991). Physiochemical and envi-ronmental plant physiology. *Academic Press New York*.

Operstain, V. and Frydman, S. (2000). The Influence of Vegetation on Soil Strength. *Ground Improvemen*t 4: 81–89.

Potter, W. (2006). The feasibility of improving rail infrastructure by using native vegetation on clay soils *M.Sc. Thesis*, University of South Australia.

Radcliffe, D., Hayden, T., Watson, K., Crowley, P. and Phillips, R. E. (1980). Simulation of Soil Water within the Root Zone of a Corn Crop 1. *Agronomy Journal* 72(1): 19–24.

Sattelmacher, B., Marschner, H. and Kuhne, R. (1990). Effects of the Temperature of The Rooting Zone on The Growth and Development of Roots of Potato (Solanum-Tuberosum). *Annals Of Botany* 65(1): 27–36.

Waldron, L. J. (1977). The Shear Resistance of Root-Permeated Homogeneous and Stratified Soil1. *Soil Science Society of America.* 41(5): 843–849.

Waldron, L. J. and Dakessian, S. (1981). Soil Reinforcement By Roots: Calculation of Increased Soil Shear Resistance From Root Properties. *Soil Science* 132: 427–435.

Whisler, F. D., Klute, A. and Milliongton, R. J. (1968). Analysis of steady state evapotranspiration from a soil column. *Soil Science Society of America Proceedings* 32(167–174).

Unsaturated Soil Mechanics—from Theory to Practice – Chen et al. (Eds)
© 2016 Taylor & Francis Group, London, ISBN 978-1-138-02921-7

Mechanism of new anchored reinforced vegetation system for strengthening swelling rock and soil slope

Y. Xu, S. Xian & S. Pei
Guangxi Key Laboratory of Disaster Prevention and Engineering Safety, College of Civil and Architectural Engineering, Guangxi University, Nanning, Guangxi, China

ABSTRACT: Anchored Reinforced Vegetation System (ARVS) is a new vegetation protection system for surface slope stabilization to resist shallow plane instability. It is composed of High Performance Turf Reinforcement Mats (HPTRM) and Percussion Driven Earth Anchor (PDEA). It is very important to study the strengthening effect of ARVS on swelling rock and soil slope. The swelling rock and soil in Nanning, China was used for the micro deformation of swelling force test and model test, and the effect of HPTRM on the swelling rock and soil was simulated. The relationship between expansion force and micro deformation was fitted. Test results show that HPTRM has high tensile strength and low elongation and is suitable for constraining the deformation of swelling rock and soil. The results of model test and numerical simulation prove that AVRS has good constraining effect to swelling rock and soil.

1 INTRODUCTION

The surface protection of swelling rock and soil slope is very important. There are many swelling rock and soil slope problems in engineering construction due to its swell- shrink, fissured and over-consolidated characteristics (Bao 2004). Especially, its swell- shrink characteristic often leads to progressive the failure of shallow swelling rock slope. There are many studies about swelling rock and soil slope protection technologies availbale (Da & Wang 1998, Zeng 2005, Tan 2006, Yang & Zheng 2009), but constraining swelling rock slope deformation research by geonet reinforced vegetation technology is limited. The anchored reinforced vegetation system (ARVS) is a kind of advanced flexible armoring technology available for the surface slope stabilization to resist shallow plane instability. The ARVS consists of woven three-dimensional high performance turf reinforcement mat (HPTRM) and percussion driven earth anchors (PDEA). Mechanism of ARVS (HPTRM without grass) to constrain swelling rock and soil is analyzed in this paper.

2 HPTRM PERFORMANCE TEST

High performance turf reinforcement mat (HPTRM) is a three-dimensional, lofty, woven polypropylene geotextile (Clifton 2010). The HPTRM made in China was tested according to the geosynthetic material test standard (GB/T 18744_2002). As contrast, another two kinds of three-dimensional geonet mats Enkamat R30 and EM5 were tested at the same time. Enkamat R30 is a kind of HPTRM made in America (Colbond Inc.) and EM5 is a kind of normal three-dimensional geonet mat (TRM) made in China. The test results of the physical and mechanical properties are shown in Table 1.

Table 1. Mechanical properties testing results.

Mechanical properties	Units	Chinese HPTRM	Enkamat R30	EM5
Thickness	mm	4.2	10.2	6.8
Mass per unit area	$g{\cdot}m^{-2}$	455	455	360
Tensile strength	$kN{\cdot}m^{-1}$	57 × 39	29 × 26	3.1 × 1.4
Average elongation	%	18.3 × 14.6	15 × 17.3	48.3 × 15.3

The test results show that the tensile performance of the Chinese HPTRM is very good. Chinese HPTRM's vertical and horizontal average elongation is close to that of Enkamat R30 and is only 1/3 of EM5. Chinese HPTRM's vertical and horizontal tensile strength is also greater than that of America-made HPTRM and is more than 10 times of the EM5. Chinese HPTRM is suitable for constraining swelling rock and soil slope. So the Chinese HPTRM material was adopted in this project.

3 MECHANICAL ANALYSIS OF AVRS CONSTRAINING SWELLING ROCK AND SOIL

3.1 *Deformation analysis of HPTRM*

In ARVS installation, HPTRM is unrolled down the swelling rock slope first, and then is fixed by earth

percussion anchors (EPA). The profile of ARVS is shown in Figure 1.

Swelling rock and soil expands after absorbing water, and its expansion force can be released freely in the free slope. When ARVS is used to control swelling rock and soil slope, HPTRM can constrain swelling rock and soil's deformation effectively due to its high tensile strength and low elongation, and the HPTRM's property of tensile elongation allows the deformation of swelling rock to release some expansion force.

HPTRM adheres to the slope surface of swelling rock closely and deforms along with the deformation of swelling rock and soil. There is no deformation at the point of EPA. When the swelling rock expands upon imbibing water between two anchors, its deformation is constrained by HPTRM. The closer to the anchor, the less the deformation of HPTRM is, and the more HPTRM constraint to the swelling rock is. Conversely, the farther away from the anchor, the more deformation of HPTRM is, and the less HPTRM constraint to the swelling rock is. Therefore, swelling rock and soil releases different expansion force with different distance from anchor. Accordingly, HPTRM will bear different expansion force due to different distance from anchor. The HPTRM between two anchors can be considered as simply supported beam, as shown in Figure 2. The deformation of beam is greater in midspan and less near the supporting seat under the action of expansive force. The more deformation of swelling rock is, the more expansion force is released and the less expansion force HPTRM bear. Therefore, HPTRM bears less expansion force in the midspan, while bearing more expansion force near the anchor.

The relationship between HPTRM deformation and its expansion force need be studied by tiny deformation test.

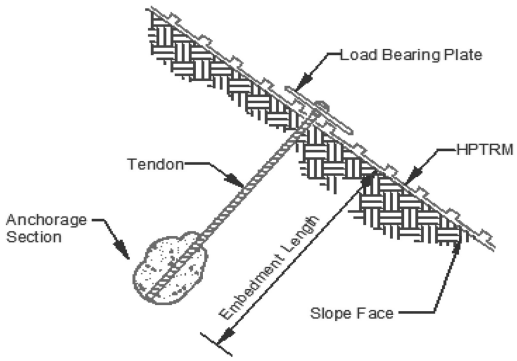


Figure 1. Profile of ARVS.

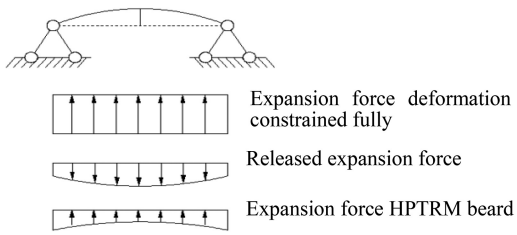


Figure 2. Diagram of expansion force HPTRM beard.

3.2 *Experiment relationship between expansion force and micro deformation*

In order to study the relationship between the expansion force and micro deformation, micro deformation test was carried out adopting swelling rock in Nanning East Station. Physical parameters of swelling rock and soil sample are shown in Table 2. The free expansion rate of the soil sample is 70%, so its expansive potential is medium. According to Specification of Soil Test (SL237-1999), the light compaction test was conducted. The optimal rate of water content is 17% and the maximum dry density is 1.73 g/cm^3. The compaction degree of the sample was set to be 90%, so its dry density is 1.557 g/cm^3 and its initial water content was set to be 14% in this test.

WG consolidation apparatus of Nanjing Soil Instrument Factory is used for the micro deformation test. Micro deformation rates were 1.0%, 2.5% and 5.0%, respectively, and each deformation rate chooses 3 samples. The test results are shown in Table 3.

According to the test results and Tang's work (Tang 2013), the relationship between expansion force and deformation rate of expansion soil sample was fitted with initial water content 14% and dry density 1.557 g/cm^3 :

$$P/P_0 = 0.843e^{-0.26\varepsilon} \quad (R^2=0.937) \qquad (1)$$

where P_0 = expansion force when deformation is 0, kPa. If vertical deformation of HPTRM is known, the expansion force can be deduced.

Table 3. Test Results of Micro Deformation vs. Expansion Force.

Deformation Rate ε/%	Expansion Force P /kPa		
0	48.55	64.50	43.25
1	42.17	19.55	24.45
2.5	17.85	16.77	27.17
5	10.89	15.17	11.25

Table 2. Physical parameter of swelling rock and soil sample.

Density g·cm^{-3}	Dry Density g·cm^{-3}	Water Content %	Liquid Limit %	Plastic Limit %	Free Expansion Rate %	<5 μm Clay Content %
2.07	1.78	16.5	58.91	23.46	70	53.74

4 MODEL TEST OF HPTRM REINFORCING SWELLING ROCK AND SOIL

4.1 *Model test setup*

According to the idea of indoor expansion force test, a round model test apparatus was designed to test the ability of HPTRM constraining swelling rock and soil. The main body of test apparatus is a height of 200 mm and radius of 500 mm round steel plate with baseboard on a rigid table, as shown in Figure 3. An active rigid anchor bolt is designed in the center of the plate with a diameter of 100 mm anchor plate under the anchor head to press the sample surface. The anchor bolt is connected to the load device through the round plate and rigid table. A hoop is set at the top of the round steel plate to fasten HPTRM, as shown in Figure 4. The swelling rock and soil is filled in the round plate. Perforated PVC tube filled with coarse sand is placed evenly in the plate to ensure the imbibition of swelling rock and soil. The support is set above the round plate to lay dial indicator every 10 cm along the direction of the radius to measure the vertical deformation of swelling soil.

4.2 *Test schemes and test process*

Swelling rock and soil specimens with HPTRM and without HPTRM were tested. Testing values include the vertical expansion deformation in different positions and the load value of anchor bolt.



Figure 3. Internal diagram of steel ring.



Figure 4. Model test.

Soil samples were filled into the round plate layer by layer (5cm/layer) with dry density 1.557 g/cm^3 and initial water content 14%. When the soil was filled to the surface of the steel ring, the HPTRM was placed and fixed with the anchor board. The anchor bolt was connected with the HPTRM through anchor plate. The dial indicator was set every 10 cm on the support along the two diameters directions to measure the vertical deformation value of the samples. A dial indicator was set at the anchor plate to control the displacement of the anchor head. In the process of swelling rock and soil deformation, load of anchor was added to keep the anchor head no deformation. After the layout was completed, water is injected into the soil to make it expand, and the readings of the dial indicator were recorded during the whole deformation process. To keep the anchor head non-deformation, loads were added to the loading device gradually.

4.3 *Results and discussion*

4.3.1 *Swelling rock and soil's vertical deformation*

The vertical deformations of the two models were tested in different radius respectively. The final vertical deformations of the two models are shown in Figure 5. Results show that in HPTRM model there is no deformation at the point of anchorage and around the hoop. The farther from the fixed support (such as anchorage and hoop), the more deformation. With the effect the side wall of the round plate and the anchor head plate, the similar results were obtained for the model without HPTRM. The vertical deformation for the model without HPTRM is much higher than that in HPTRM model at the same position. The maximum vertical deformation in HPTRM model is 17.32 mm and it is 20.69 mm for the model without HPTRM. Comparing the two models, the deformation of the sample with HPTRM restriction is obviously less than the deformation under free condition. HPTRM plays a good constraining effect. What's more, the elongation of HPTRM is small, totally within the allowed range.

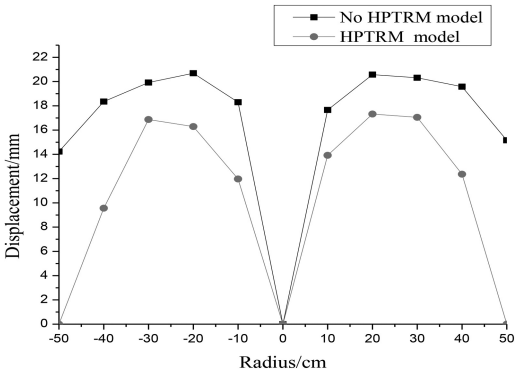


Figure 5. Final vertical deformation of swelling rock and soil.

4.3.2 *Anchor bolt force*

In this model test, the anchor bolt force is the load added in the loading device, which is connected to the anchor bolt. The anchor head keeps immobile when the anchor bolt works, though swelling rock and soil expands after sucking water. If the expansion deformation is constrained by the HPTRM, then the expansion force is caused by HPTRM constraint and the anchor bolt bears the force that HPTRM passes to. In HPTRM model, with the swelling rock and soil expanding when sucking water, the load in the loading device was gradually adjusted to balance the loading value and the expansion force to ensure no deformation of the anchor head.

There's no vertical deformation constrained by the anchor head plate. In the model without HPTRM, the final load value is equal to the vertical expansion force in the anchor head plate area. In the model with HPTRM, HPTRM is under the anchor head plate. The anchor head plate is not only subjected to the vertical expansion force, but also to the vertical component of HPTRM tension produced when HPTRM constraining swelling rock. Therefore, the anchor bolt force is composed of the vertical expansion force the anchor head born by swelling rock and the vertical component of HPTRM tension.

When adding water continually in the process of the model test, the values of anchor bolt force were recorded constantly until the dial indicator reading tends to be stable and the final stable load value was recorded too. After 33 days the deformation of the model without HPTRM tended to be stable, and the anchor bolt force was 82 kg. After 21 days the deformation of the HPTRM model tended to be stable, and the anchor bolt force was 106 kg. The deformation difference between the two models was the vertical component of HPTRM tension.

5 NUMERICAL MODELING METHODOLOGY

5.1 *Model establishment and parameters selection*

In this study, finite element program, ANSYS, is used to analyze how the HPTRM restricts the swelling rock and soil. According to the size of the model test, HPTRM was simplified to be a thin shell with the inner diameter of 0.05 m, external diameter of 0.5 m and thickness of 0.004 m. And Shell63 element was selected to simulate HPTRM material. The model was meshed by mapping grid with totally 960 units and 1040 nodes. The physical parameters of the model were set in table 4. Displacement boundary condition of the model was fixed constraint to the inner and outer circle boundary, and force boundary condition was vertical expansion force on HTPRM.

5.2 *Simulation process and discussion*

In order to simulate the actual condition, the expansion force was added to the HPTRM by using the relationship between expansion force and micro deformation as Formula (1). Firstly, an even expansion force was added and the first deformation of every node was calculated, and then iterative calculation was done with the last deformation value to get expansion force of each node, then the expansion force of each node was added again to get the new deformation value. Iterative calculation was done repeatedly to get the expansion force needed when the variation of iterated expansion force was small enough.

Table 4. Physical parameters of HPTRM.

Thickness m	Modulus of elasticity MPa	Poisson ratio	Density $kg \cdot m^{-3}$
0.004	1000	0.4	108

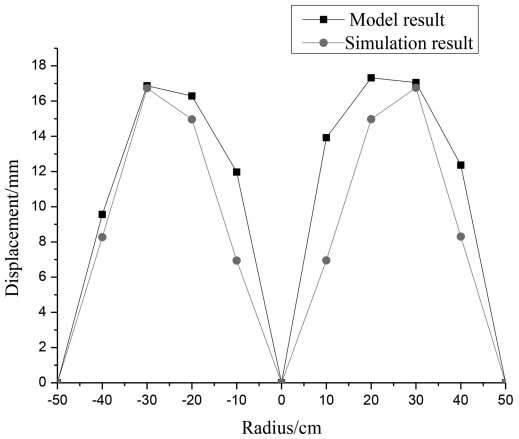


Figure 6. Comparison of the vertical displacement of nodes along the radial direction.

The expansion force was determined by Formula (1). The thickness of the expansion soil in the model test is 0.2 m. Formula (1) can be changed into

$$P/P_0 = 0.843e^{-130\delta} \quad (2)$$

where $\delta =$ deformation value, m.

According to the simulation results, the vertical displacement of each node was gotten along diameter direction and compared it with the model test result, as shown in Figure 6. Simulation results show that the farther from fitted support it is, the more the vertical deformation is, which is just the same tendency as the model test's results. The deformation of HPTRM is close to parabolic symmetric distribution. In 30 cm away from the center, the vertical deformation value of HPTRM is 16.76 cm, the result of the model test is 17.32 mm. So the results of numerical simulation and the model test have a good coincidence.

The sum of the vertical constraining reaction force of the inner ring boundary is 224 N, which force can be regarded as the force the anchor bolt to HPTRM. In

the model test, when the deformation is 0 in the center, the vertical tension of HPTRM to anchor bolt is 240 N. The above two results are very close. It is clear that, the numerical simulation can back calculate the model test well. It is feasible to conduct numerical simulation with the relationship between the expansion force and the micro deformation value and this method can be applied to actual engineering simulation.

6 CONCLUSIONS

The study has led to the following conclusions:

(1) In ARVS system, the new-type material HPTRM has the ability of high tensile force and resistance to deformation. It is suitable for constraining the deformation of swelling rock and soil.
(2) The fitting formula between the expansion force of the swelling rock and soil and the micro deformation can reflect the change process of the expansion force when the swelling rock and soil was sucked with water fully and expand.
(3) Both the model test and the numerical simulation results prove that HPTRM allow certain deformation of swelling rock and soil but restrain it. So HPTRM can bear certain expansion force and release part. AVRS has good constraining effect to swelling rock and soil. The anchor bolt bears the tension from HPTRM and swelling rock and soil. In shallow protection engineering to the swelling rock and soil slope, AVRS has a broad application prospect.

ACKNOWLEDGMENTS

This research was supported by National Natural Science Foundation of China (NSFC) (No. 51178124) and the Systematic Project of Guangxi Key Laboratory of Disaster Prevention and Structural Safety (No. 2013ZDX12).

REFERENCES

Bao, C. 2004. Behavior of unsaturated soil and stability of expansive soil slope. *Chinese Journal of Geotechnical Engineering* 26(1): 1–15 (in Chinese).

Clifton D. H. 2010. *Full-scale testing of three innovative levee strengthening systems under overtopping condition*. Thesis (Master). Jackson State University.

Da Z. & Wang X. 1998. Swelling rock slope disease and its protection. *Subgrade Engineering* (4): 58–63 (in Chinese).

Tan B. 2006. *Research on cut slope stability analysis of Ning-ming expansive soil and treatment technology of flexible supporting structure*. Thesis (Master). Changsha University of Science & Technology.

Tang Y. 2013. *Study on the interaction of Nanning expansive rock and subway shield segment*. Thesis (Doctor). Guangxi University.

Yang H. & Zheng J. 2009. *Expansive Soil Engineering of Highway*. Beijing: China Communications Press.

Zeng J. 2005. *Research on the stability of expansive rock slope in the Nanning basin*. Thesis (Master). Guangxi University.

This page intentionally left blank

Unsaturated Soil Mechanics—from Theory to Practice – Chen et al. (Eds)
© 2016 Taylor & Francis Group, London, ISBN 978-1-138-02921-7

Research on the electrical resistivity of early solidified soil composing of dredged clays

F.Z. Cheng, X.W. Lei & Y.S. Liao
College of Urban Construction, Wuhan University of Science and Technology, Wuhan, China

Q.S. Meng
State Key Laboratory of Geomechanics and Geotechnical Engineering, Institute of Rock and Soil Mechanics, Chinese Academy of Sciences, Wuhan, China

J. Chen
College of Urban Construction, Wuhan University of Science and Technology, Wuhan, China
Zhongkai University of Agriculture and Engineering, Guangzhou, China

ABSTRACT: The electrical resistivities ρ(t) within 72 hours of solidified soil composing of dredged clays are measured in a non-contacting electrical resistivity measurement device. And the changing characteristics of the resistivity of solidified soil are analyzed from the angle of the reaction of the curing materials cement, trying to interpret the microscopic reaction mechanism of solidified soil from the perspective of resistivity. And the XRD diffraction intensity of 3d stabilized soil is tested. The results show that according to the resistivity development of the solidified soil, the solidified soil reaction process can be divided into three stages: wrap dissolving period, setting period, hardening period. Chemical reaction speed of silt solidified soil is relatively a lot slower than cement paste and concrete. XRD tests find that the middle of the cement hydration product Ca $(OH)_2$ generated $CaCO_3$ in the reaction.

1 INTRODUCTION

Like the soil index of unconfined compressive strength, soil resistivity is another inherent property of soil which can be used to characterize the state of soil. Chemical solidification silt treatment has high strength, good effect, no pollution, energy saving and many other advantages, becoming an important method of dealing with silt. The microscopic reaction mechanism of solidified soil has always been the hot problem in scientific research. At present research in this area is likely to use the methods of XRD, SEM, etc, and from the angle of resistivity continuously changing on the early reaction of solidified soil research article is less. While the existing research showed that the late silt solidified soil properties, such as mechanical properties, have a direct relationship with the early reactions in solidified soil, early reaction of silt solidified soil research is very important. Soil resistivity testing methods have Wenner method, two-phase electrode method (Han et al. 2006, 2009), four electrodes method (Sun et al. 2010), ohmmeter method (Jia et al. 2014), voltammetry method (Dong et al. 2007) and many other methods. There is contact resistance problem in both dc resistivity method and ac electrode method, influencing the accuracy of the measurement results. And these methods cannot collect real-time data in response to the interior reactions of the solidified soil. Dong X.Q. tested the resistivity of cement-soil mixed with NaOH (Dong et al. 2007), $NaSO_4$ (Dong et al. 2011) and soaked by sewage (Dong et al. 2014) at specific age. Sun et al. (2010) tested the resistivity of clay mixed with lime on different factors such as dosage of lime, moisture content, saturation, soil structure and soil particle size. These methods didn't continuous test the resistivity which may reflect the internal reactions of the solidified soil. While non-contacting resistivity measurement method can not only well solve the contact resistance problem in traditional methods but also continuously collect data. So non-contacting resistivity tester is used to test the resistivity of solidified soil over time, gaining the characteristic curve $\rho(t)$-t, analyzing the relationships between the cement hydration process and the resistivity of silt solidified soil. At the same time XRD diffraction intensity at the age of 3d is used to seek the hydration information of cement solidified soil.

2 THE PRINCIPLE OF NON-CONTACTING ELECTRICAL RESISTIVITY MEASUREMENT DEVICE

The principle of non-contacting electrical resistivity meter is shown in Figure 1.The frequency of the alternating current will increase from 50 Hz to 1000 Hz by

a signal generator, and then the amplifier will amplify the alternating current, meanwhile a transformer is used to change the ac voltage in the circuit. The transformer primary coil is made up of some turns of coil, and a circular mould is equal to the secondary coil, thus placing the ring voltage V on the sample. After pouring new mixed solidified soil into the mold, the computer will measure and record the ring current I through a small current sensor, and then the corresponding resistivity ρ is finally calculated.

3 TEST METHOD

3.1 *Test materials*

The dredging silt in tests is taken from Wuhan East Lake, and the main physical property index of the silt is shown in Table 1. The cement in test is 42.5# ordinary Portland cement of "Chang Ge" brand of Hubei Junshan Cement co, LTD.

3.2 *Test method*

The initial moisture content of the silt is 100%, and the cement dosage is set to three groups of 15%, 20% and 25%. The cement dosage is the ratio of cement weight and wet silt weight. First mix water and air dry silt soil and stir them well to simulate silt environment, and then add in curing material cement. Stir the mixture for 1 min by hand first, and then stir them slowly in cement mortar mixer for 6 minutes. After the completion, pour the mixture into the ring-shaped plastic mould (1.67 L) of the resistivity meter quickly, and then oscillate the mould slightly a few times to eliminate the air bubbles, and at last add the lid and seal immediately. At the same time the resistivity of mud solidified soil is tested by CCR-2 non-contacting electrical resistivity measurement device manufactured by Hong Kong Brilliant Concept Technologies. The data is automatically recorded by a computer up to 4320 min and the sampling interval is 1 min. The data is calibrated by the height of the solidified soil after demoulding. Grind the solidified soil of 3 d age and then sift by a 0.080 mm square hole sieve. Take 5 g solidified soil powder, and then fill in a slot of flat glass. A certain pressure is put on the sample to paste them well, and at the same time pay attention to the grain direction to make them randomly distributed. Analyze the phase of mud solidified soil by the production transfer target X-ray diffraction manufactured by Japan Science Company. The starting Angle is 3° and termination Angle is 70°.

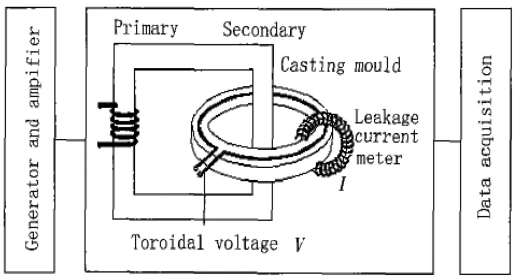


Figure 1. Schematic of non-contacting resistivity meter (Wei et al. 2004).

4 TEST RESULTS AND ANALYSIS

4.1 *Characteristic of resistivity ρ(t) of solidified soil changing with time t curve*

Resistivity under three different dosages of cement solidified soil along with time curve is shown in Figure 2. From Figure 2, resistivity curve trends under different cement dosage is overall the same when cement dealing with dredging silt. Resistivity curve declines rapidly first, and then decline slowly, obtaining an inflection point. The curves pass through the inflection point and then continue to fall to the lowest points and then rises slowly.

When cement dosage is 15%, the resistivity of the solidified soil drops quickly first, and then declines slowly, getting to a singular minimum point after 6.5 hours and the resistivity dropping to 2.71 Ωm. Then the resistivity slowly rises to 2.80 Ωm and the time is 9.4 h. Then the resistivity slowly drops to the minimum point 2.51 Ωm after 8.5 hours, and the time t is 27.1 h. And then after 21 hours' approximate level development, the resistivity begins to grow. When the dosage of cement is 20%, the resistivity of silt solidified soil drops quickly first, at around 7.8 h declines at a slower pace, passes through an inflection point and then continues to fall to the minimum point 2.17 Ωm with the time being 26.2 h, and then begins to rise slowly. When the cement dosage increases to 25%, the resistivity of silt solidified soil falls rapidly first. When the time is 12.0 h, it passes through an inflection point rapidly and continues to fall to the minimum point 2.09 Ωm, and the time is 16.7 h. Then it begins to rise rapidly, but the rate of the growth slows down. And the resistivity finally maintains a certain growth rate. In short, the resistivity curve falling fast first, and after an inflection point it reaches to the lowest point, and then increases, and meanwhile the curve rises. Comparing the minimum resistivity points of the three dosages of cement, it is found that the bigger the dosage of cement is, the smaller the low resistivity is, and the shorter the time it cost to the lowest point is. But the shortest time is

Table 1. Physical properties of test soil.

Moisture content/%	Liquid limit/%	Silt content/%	Clay content/%	Relative density	Plasticity index	PH	Organic content/%
85.5–89.7	65.3	43.0	57	1.2	13–15	5.7	1.1

16.7 h, is much longer than cement paste's 0.58 h (Wei et al. 2004), and concrete's 1 h (Xiao et al. 2005, Wei et al. 2013).

4.2 *Division of three stages of cement solidified silt soil*

According to the characteristic resistivity curve of the cement solidified soil, the reaction process of the cement solidified soil is divided into the following three stages.

(1) Wrap dissolving period. The period from adding cement into the silt soil to inflection point A is the wrap dissolving period. When adding solidification material cement, K^+, Na^+ and SO_4^{2-} will dissolve in silt from sulfate and cement particle. Ca^{2+}, OH^-, aluminum and silicate ions from minerals such as the free CaO, silicate dicalcium, silicate tricalcium and aluminate tricalcium calcium dissolve out (Wei et al. 2013), reducing the liquid resistivity, so as to make the system resistivity of the solidified soil decrease. This period costs more than 6.5 hours, far greater than the dissolution of cement paste and concrete, showing that the dissolution of the cement particles in silt soil is slower. The possible reason is the cement particles is wrapped by mud particles, causing cement particles dissolving at a slower pace, and making the time the follow-up reactions such as the hydration of cement and ion exchanges between soil particles and the ion of cement hydration. This maximizes the curing time to achieve the cement- soil strength required and makes the maintenance time longer than concrete. Silt particles also hinder the ions from transferring and electric conduction in the system. This may also be a reason the resistivity of silt solidified soil declined at a slower pace.

(2) The induction period. The period from inflection point A to the lowest point and keep rising at the approximate level rate to B is the induction period. In the period the resistivity of a curve drops rapidly to a singular minimum point, and then rises slowly to a maximum point and falls to the lowest point. Then keep rising at a approximate level rate for a period of time. The reason for the slow rise of resistivity may is that reactions such as adsorptions of organic and soil particle to ions happens in the process of ions dissolving slowly. b curve passes through an inflection point slowly, while c curve passes through the inflection point rapidly. The reason is that the adsorption (Zhu et al. 2008) of organic existing in the silt soil to conductive ion Ca^{2+} reduces the ion concentration in the pore solution, increasing the resistivity. And the organic content in soil is limited. When the cement dosage is very large, the organic ion adsorption capacity will soon be met, and the cement particles continue to dissolve ions. After passing through the inflection point, the resistivity begins to decline acceleratedly. The ion adsorption exchange (Pu 2011) of high metal ions like Ca^{2+} and low metal ions on the surface of soil particles such as Na^+, K^+ is equivalent on the amount of charge, having a little effect on the resistivity. Therefore the process of ion exchange cannot be reflected by the change of resistivity.

(3) Hardening period. When the cement particles dissolved, and ion exchanges on the surface of soil particles and adsorptions of organic to ions finished, after the resistivity decreasing to point B, the hydrations of cement clinkers C_3S, C_2S, C_3A and C_4AF accelerate, consuming the ions in the pore solution to make the electrical resistivity of liquid phase increase. Meanwhile the hydration products will fill the clearance between soil particles to decrease the porosity of the solidified soil. These two reasons make the resistivity rise in hardening period.

4.3 *The XRD diffraction intensity*

The Figure 3 illustrates that the existence of ettringite shows that after adding cement to silt, cement

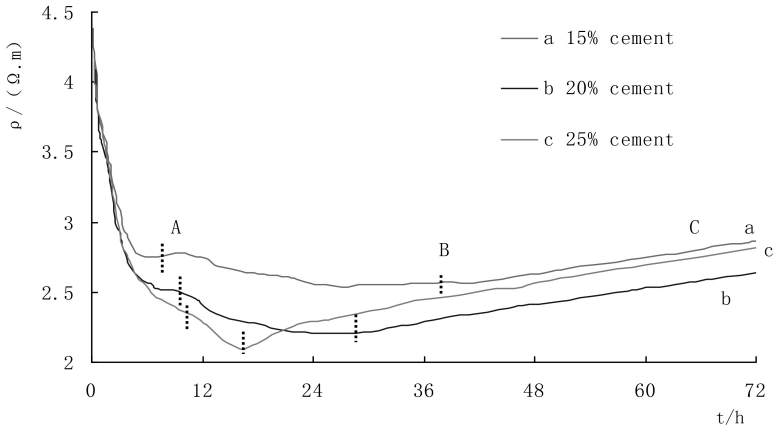


Figure 2. Electrical resistivity curves of stabilized soil with different dosage of cement.

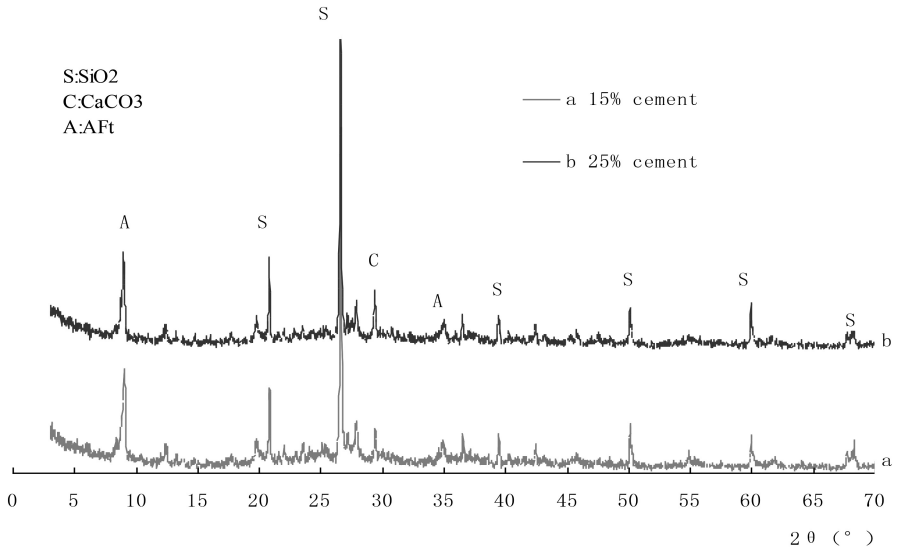


Figure 3. X-ray diffraction of cemented soil samples at 3 d.

hydrates, for ettringite is one of the products of the clinker C_3A. But hydration products $Ca(OH)_2$ continues to participate in other reactions to generate $CaCO_3$. From Figure 3 we can see that when the cement dosage is 25% $CaCO_3$ diffraction intensity is obvious stronger than 15%, suggesting that there is the formation of $CaCO_3$ to fill the clearance. Crystallization is better and crystal grain size is bigger.

5 CONCLUSIONS

(1) Chemical reaction speed of silt solidified soil is relatively a lot slower than cement paste and concrete. Cement particles is wrapped by silt soil and dissolves slowly, affecting the chemical reaction rate of the solidified soil from silt, and slowing down the chemical reaction rate of the solidified soil.
(2) Non-contacting electrical resistivity method can be used to reflect early internal microscopic reaction in the silt solidified soil. The resistivity-time curve of cement solidified silt soil first falls and then rises. The chemical reactions in solidified soil can be divided into three stages: wrap dissolving period, setting period, and hardening period according to the resistivity – time curve.
(3) The XRD tests find that the early product $Ca(OH)_2$ of cement in solidified soil will generates $CaCO_3$ to fill soil particle clearance, enlarging the compactness of solidified soil, thereby increasing the resistivity of solidified soil.

REFERENCES

Dong, X.Q., Bai, X.H., Zhao, Y.Q. & etc. 2007. Study on electrical resistivity of soil-cement polluted by NaOH. Chinese Journal of Geotechnical Engineering 11:1715–1719.

Dong, X.Q., Bai, X.H. & Lu, Y.K. 2011. Study on the electrical resistivity and strength of cemented soil contaminated by sodium sulfate. China Civil Engineering Journal S2: 186–189.

Dong, X.Q., Su, N.N., Huang, X.N. & etc. 2014. Effect of sewage on electrical resistivity and strength of cemented soil. Rock and Soil Mechanics 35(7):1862–1870.

Han, L.H., Liu, S.Y. & Du, Y.J. 2006. New method for testing contaminated soil-electrical resistivity method. Chinese Journal of Geotechnical Engineering 28(8):1028–1032.

Han, L.H. & Liu, S.Y. 2009. Experimental study on the electrical resistivity of contaminated soil-cement. Journal of Safety and Environment 9(4):135–139.

Jia H.J., Li, S.Q. & Shang, J. 2014. Study of Relationship between Electrical Resistivity and Saturation Degree of Soils. Journal of Tianjin Chengjian University 20(4): 87–90.

Pu, F. 2011. Research on the Srength and Deformation Characteristics of Solidified Tide-land Sludge. Zhejiang University.

Sun, S.L., Li, F. & Chen, J. 2010. Electrical resistivity measurement for lime-stabilized silt soil. Rock and Soil Mechanics 31(1):51–55.

Wei, X.S., Xiao, L.Z. & Li, Z.J. 2004. Study On Hydration Of Portland Cement Using an Electrical Resistivity Method. Journal of the Chinese Ceramic Society 01:34–38.

Wei, X.S. & Xiao, L.Z. 2013. Determination and Kinetics Parameters of Structure Formation Periods of Concrete by Electrical Resistivity Measurement. Journal of the Chinese Ceramic Society 02:171–179.

Xiao, L.Z., Li, Z.J. & Wei, X.S. 2005. Early Setting And Hardening Process Of Young Concrete Using the Resistivity Measurement. Journal of the Chinese Ceramic Society 10:96–100.

Zhu, W., Zeng, K.L. & Zhang, C.L. 2008. Influence of organic matter component on solidification of dredged sediment. Rock and Soil Mechanics 29(1):33–36.

Unsaturated Soil Mechanics—from Theory to Practice – Chen et al. (Eds)
© 2016 Taylor & Francis Group, London, ISBN 978-1-138-02921-7

The hydrological mechanism of a residual soil slope underwent deformations during rainfall

C.C. Fan & S.H. Liu
National Kaohsiung First University of Science and Technology, Taiwan

ABSTRACT: This paper investigates the hydrological behavior of a residual soil slope undergoing deformations during rainfall. An automatic logging system is installed at the site to measure the soil moisture content at various depths and at different elevations. The behavior of rainfall induced infiltration in the slope and development of wetting front in the slope are investigated through the response of soil moisture content with time at various depths in the slope in a rainfall event. The time (Ts) when the wetting front takes place at a given depth is identified during a rainfall event. Major findings drawn from the research are: (1) Tension cracks developed on the slope considerably affect the behavior of subsurface flow during rainfall; (2) Wetting fronts may take place at greater depths where cracks and shear zone in the slope are developed, whereas it may not take place at shallow depths; (3) Tension cracks in the slope may accelerate the rainfall-induced infiltration to greater depths; (4) Ts values at a given depth in the slope with noticeable tension cracks are lower than that free of tension cracks on the slope.

1 INTRODUCTION

Slope failures are common natural disasters in mountainous regions all around the world during rainfall season, especially when climate change causes frequent occurrence of high-intensity rainfall. The government budget on the rehabilitations of infrastructures in the area prone to slope failures is considerable. Occurrence of slope failures depends on a number of factors. Slope topography, mechanical and hydrological properties of the geological formation, vegetation cover, human activities, and climatic impact, etc, are major factors governing the incidence of slope failures in the area frequently subjected to intensive rainfall. Few slope failures are attributed by a single cause. The hydrological mechanism, however, is considered one of the most important factors affecting the stability of slopes (Dai et al, 2001). Rainfall-induced infiltration in the slope results in an increase in the soil moisture content and reduces the soil shear strength, which in turn lessening the stability of the slope. Rainfalls are considered the major cause blamed for the slope failures all around the world.

The response of soil moisture content with time during rainfall has been investigated in the laboratory (Huang et al, 2008; Orense et al, 2004; Uchimura et al, 2010) and in the field (Towhata et al, 2005). Towhata et al (2005) suggested that the time when the soil moisture content at a given depth in a slope starts to increase during rainfall can be used as a precursor of soil movements in a slope, and Huang et al (2008) summarized a similar observation. However, researches on the hydrological mechanism of slopes undergoing soil deformations are limited. This topic is involved with the process how slopes fail from the onset of the soil deformation to the collapse.

This study carried out a field study on the hydrological behavior of a slope undergoing soil deformations. An instrumentation project for measuring variation of soil moisture contents with time in the slope is carried out in this study, and the data are analyzed in the aspect of time factor. The effect of tension cracks in the slope on the hydrological behavior of the slope is investigated and discussed. The study carried out herein can be helpful in the precaution of occurrence of large soil deformations (collapses) in the slope which may potentially fail.

2 MATERIALS AND METHODS

2.1 *Experimental site and soil properties*

The experimental site is located in Jiasian district in Kaohsiung Taiwan. The experimental slope dips southeastward and is covered with mixed woods. Photo of the experimental slope is shown in Figure 1. The average precipitation in the region is about 2800 mm/yr for the past 30 years. Typhoon in this region occurs quite often in the summer time and brings considerable amount of precipitations. Soil erosion and shallow landslides are commonly seen in this region. The average slope gradient at the experimental site is about 30°. The topography of the slope is shown in Figure 2 The slope is mostly covered with residual soils, formed from weathered shale. Thickness of the residual soil



Figure 1. Photo of the experimental site.

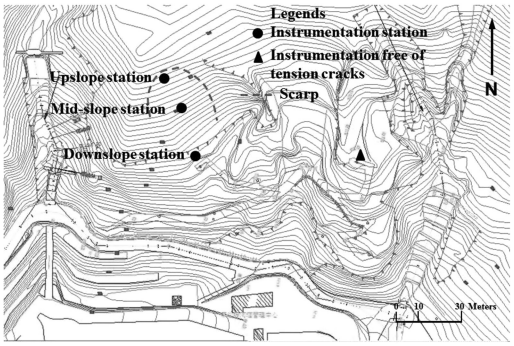


Figure 2. Topography and instrumentation station at the experimental slope.

ranges from 3 to 4 m. Rock fragments are occasionally seen at the experimental site. In addition, the experimental slope has been undergoing deformations and surface subsidence since June, 2012. Tension cracks can be clearly identified on the slope. Figures 3 and 4 show tension cracks and scarps of the experimental slope, respectively, and the location of the scarp is shown in Fig. 2. Subsidence at the scarp of the slope was first observed in June, 2012, and it continued to develop in the year of 2012 and 2013 due to rainfall The subsidence at the scarp in August, 2014 was 18 m.

Soil samples at depths of 0.15 m, 0.5 m, 1 m, 1.5 m, and 2 m were collected using a soil auger. Physical properties of the soil were acquired at the laboratory. Specific gravity of the soil ranges from 2.66 to 2.7. Liquid limit of the soil ranges from 30 to 32, and plastic index ranges from 18 to 23. Soils at the site are classified as CL based on unified soil classification system. Figure 5 shows soil particle distribution curves at the upslope station.

2.2 *Instrumentations*

Sensors manufactured by Decagon Inc. were used to measure the soil moisture content, and a rain gauge was installed at the site. Soil moisture sensors were installed at three different elevations, namely upslope station, mid-slope station and downslope station (as shown in Figure 2), and sensors were installed at 0.15 m, 0.5 m, 1 m, 1.5 m, and 2 m below the ground surface at each instrumentation station The upslope



Figure 3. Tension cracks (0.2∼0.25 m wide) adjacent to the mid-slope station.



Figure 4. Scarp of the slope.

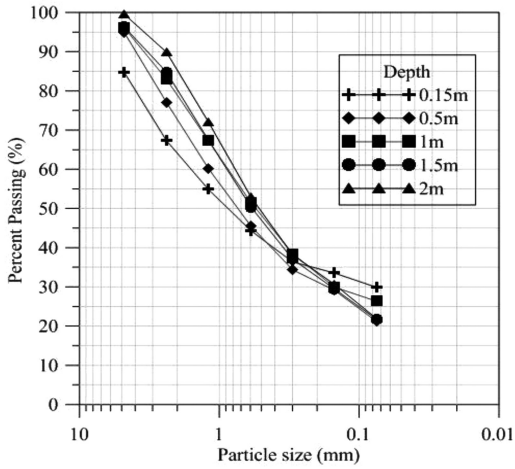


Figure 5. Soil particle distribution curves at various depths at the upslope station of the experimental slope.

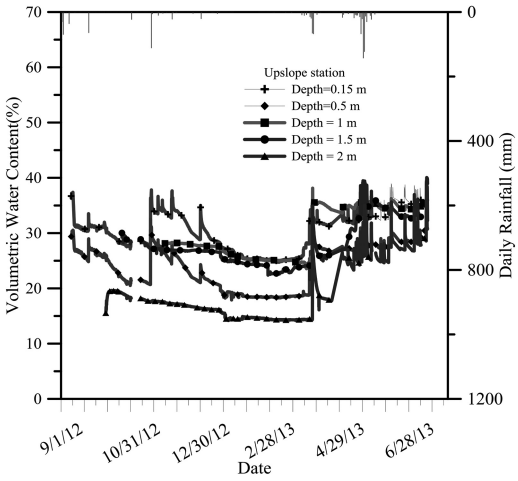


Figure 6. Variation of the soil moisture content with time at the upslope station.

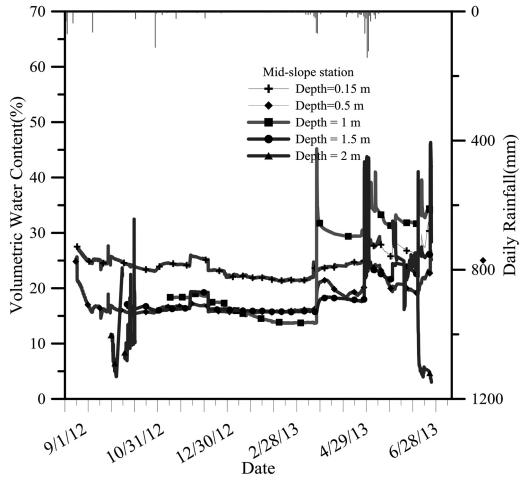


Figure 7. Variation of the soil moisture content with time at the mid-slope station.

station is near the scarp of the sliding slope. The distance between the instrumentation stations is about 15–25 m. An automatic data logging system was set up at the site, and data at the site can be transmitted to the workstation at the office through the Global System for Mobile Communications (GSM). Data were automatically recorded every 60 minutes.

3 RESULTS AND DISCUSSION

3.1 *Time history of soil moisture contents*

Figures 6, 7 and 8 shows the variation of soil moisture contents with time from September 2012 thru July 2013 at the upslope, mid-slope, and downslope station, respectively. The daily rainfall data is also illustrated in the top x-axis of the figures. Rainfall results in an increase in the soil moisture content for some of the depths at different instrumentation stations, installed at different elevations of the experimental slope. The soil moisture content at depth of 0.15 m and 0.5 m at upslope station increases noticeably during rainfall event in Sep. and Nov. of 2012, and the soil moisture contents at various depths remain nearly unchanged during the period of Jan. thru March of 2013, which is normally a dry season. However, the soil moisture content at the shallow depths at the md-slope and downslope stations have slight response with the rainfall in Sep. and Nov. of 2012. Additionally, soil moisture contents at various depths at different stations respond with severe rainfall in April and May of 2013.

Furthermore, the soil moisture content at the depth of 2 m at the upslope and mid-slope stations increases considerably compared with that at shallow depths during rainfall event in March and April of 2013. Analysis of the soil moisture content at different depths and at different stations for selected rainfall events will be further discussed in the next section.

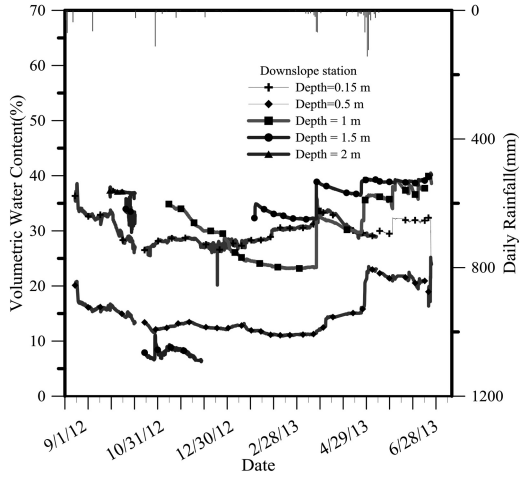


Figure 8. Variation of the soil moisture content with time at the downslope station.

3.2 *Variation of soil moisture contents with time during rainfall events*

Shown in Figure 9 is variation of soil moisture contents with time at various depths at the upslope station for the rainfall event on April 5, 2013. The rainfall event on April 5, 2013 lasted for 17 hours, and the accumulated precipitation was 127 mm. The maximum rainfall intensity was 12.4 mm/hr for this rainfall event. A noticeable increase in the soil moisture content at depths of 0.5 m, 1.0 m, 1.5 m, and 2 m at the upslope station can be observed at a certain time following the onset of the rainfall, and the soil moisture content continues to increase until a nearly stable value is reached. The soil moisture content, however, at the depth of 0.15 m remains minor variations during the rainfall. In addition Figures 10 and 11 illustrate variations of soil moisture contents with time at various

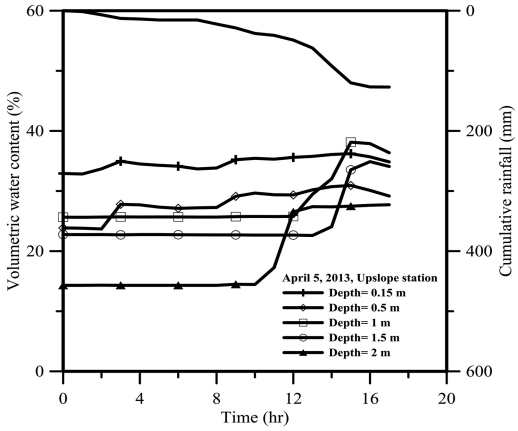


Figure 9. Variation of soil moisture contents with time at the upslope station for the rainfall event on April 5, 2013.

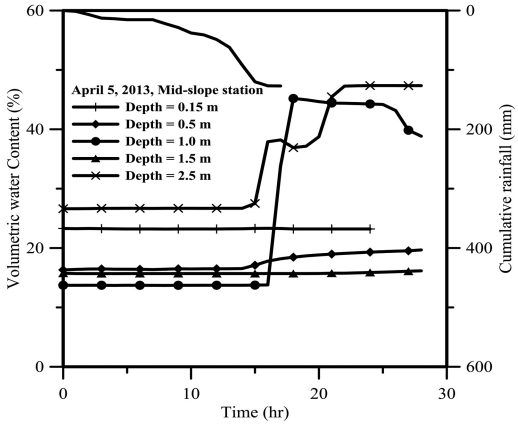


Figure 10. Variation of soil moisture contents with time at the mid-slope station for the rainfall event on April 5, 2013.

depths at the mid-slope and downslope stations for the rainfall event on April 5, 2013. At the mid-slope station, the soil moisture content at depths of 1.0 m and 2.5 m shows a noticeable increase during rainfall compared with other depths, and the soil moisture content at depth of 0.5 m illustrates a slight increase. The soil moisture content at the depth of 0.15 m and 1.5 m at the mid-slope station remain unchanged during the rainfall. At the downslope station, the soil moisture content at the depth of 1.0 m and 1.5 m shows a noticeable increase during rainfall, and that at the depth of 0.15 m and 0.5 m remains constant during the rainfall.

Typical variation of soil moisture content with time for some of the depths experiencing an increase in the soil moisture content during rainfall can be illustrated in Fig. 12. Two key times, Ts and Te, are identified in the relationship. Ts values denote the time when the soil moisture content at a given depth starts to increase after the onset of the rainfall, and it can represent the time when the wetting front at a given depth takes place during rainfall. Ts values also refer to the time that

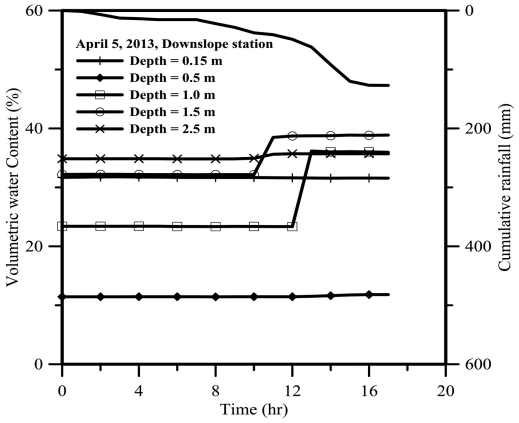


Figure 11. Variation of soil moisture contents with time at the downslope station for the rainfall event on April 5, 2013.

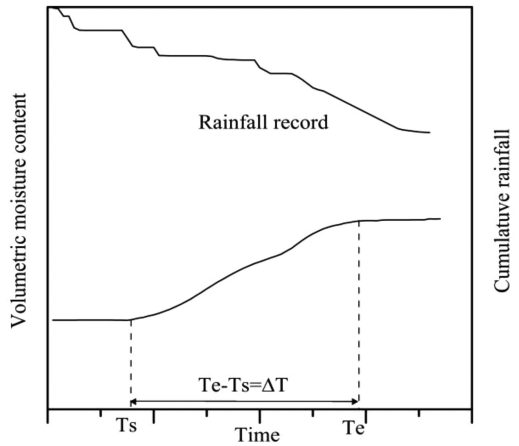


Figure 12. Typical relationship of soil moisture content vs. time during rainfall at a given depth (Fan & Chen, 2013).

shear strength of the unsaturated soil starts to decrease during the rainfall activity. Te values refer to the time when the soil moisture content reaches a stable value after an increase in an approximately constant rate, and it implies that the soil shear strength contributed by the unsaturated part of the soil reaches to the lowest value during rainfall. It is of interest to note that the wetting front at a certain depth in the slope occurs faster than that at the shallow depth for the slope undergoing displacements. The data measured at the instrumentation stations at different elevations show similar findings. It is believed that tension cracks on the slope provide major passage for seepage in the slope during rainfall.

3.3 *Time factors in the relationship between soil moisture content and time*

The time (Ts) when the wetting front takes place at a given depth and Te values, referring to the time when the soil shear strength contributed by the unsaturated part of the soil reaches to the lowest value

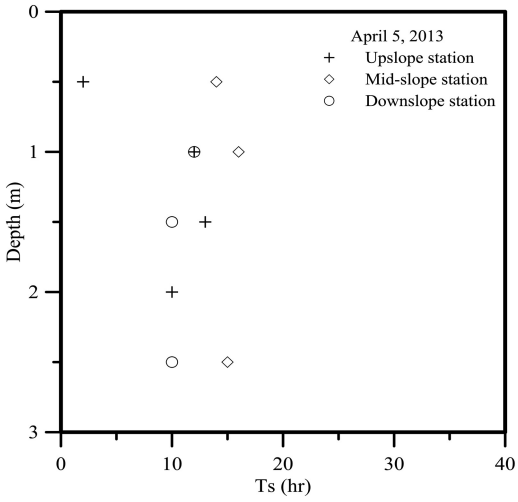


Figure 13. Distribution of Ts values with depth for rainfall event on April 5, 2013.

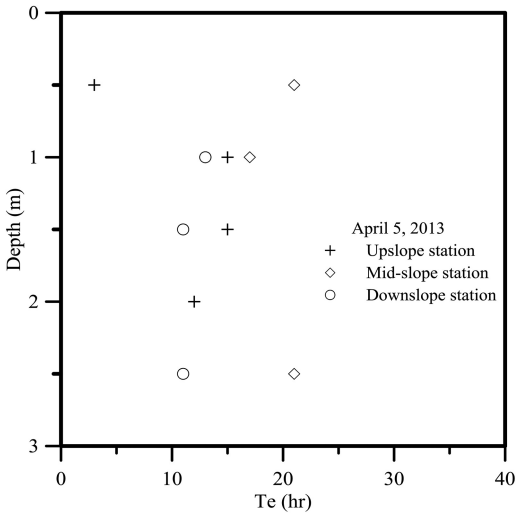


Figure 14. Distribution of Te values with depth for rainfall event on April 5, 2013.

during rainfall, can be used as an indicator to investigate the hydrological behavior of the slope undergoing deformations. The soil moisture contents measured in the rainfall event on April 5, 2013 are analyzed in this study to obtain Ts and Te values for each instrumentation station.

Figure 13 shows the distribution of Ts values with depth, respectively, for the rainfall event on April 5, 2013. Ts values are 2, 12, 13, and 10 hrs, at the depth of 0.5 m, 1 m, 1.5 m, and 2 m, respectively, at the upslope station. At the mid-slope station, Ts values are 14, 16, and 15 hrs at the depth of 0.5 m, 1 m, and 2.5 m, respectively. At the downslope station, Ts values are 12, 10, and 10 hrs at depth of 1 m, 1.5 m, and 2.5 m, respectively. It is of interest to note that the wetting front at the depth less than 0.5 m does not take place for the upslope and mid-slope stations, and the wetting front at the depth less than 1.0 m at the downslope station does not occur. The fastest wetting front for the upslope, mid-slope, and downslope stations takes place at the depth of 0.5 m, 0.5m, and 1.5 m, respectively. In addition, the Ts value at the depth of 2 m at the upslope station and that at the depth of 1.5 m and 2.5 m at the downslope station are less than that at its shallower depth. It implies that surface runoff during rainfall does not uniformly infiltrate the slope from the ground surface. Tension cracks provide passage for the runoff to reach deeper depths in the slope. In addition, Fig. 14 shows the distribution of Te values with depth for the instrumentation stations. The behavior of Te values with depth is similar to that of Ts values. Te values are 3, 15, 15, and 12 hrs, at depth of 0.5 m, 1 m, 1.5 m, and 2 m, respectively, at the upslope station. At the mid-slope station, Te values are 21, 17, and 21 hrs at the depth of 0.5 m, 1 m, and 2.5 m, respectively. At the downslope station, Te values are 13, 11, and 11 hrs at depth of 1 m, 1.5 m, and 2.5 m, respectively. Most of the difference between Ts and Te values are 1–3 hrs

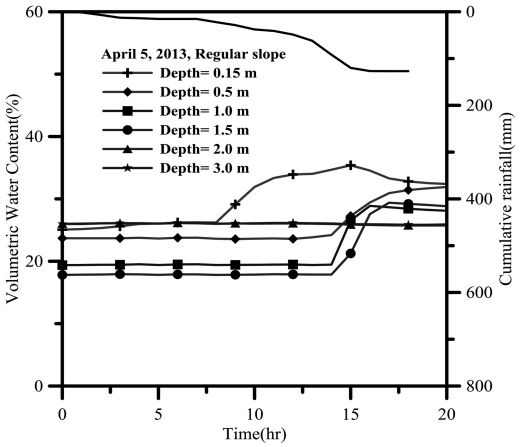


Figure 15. Variation of soil moisture contents with time at the area free of tension cracks on the slope for the rainfall event on April 5, 2013.

except that it is 7 and 6 hrs at the depth of 0.5 m and 2.5 m, respectively, at the mid-slope station.

To investigate the effect of tension cracks on the propagation of wetting front in the slope during rainfall, the Ts values measured at the slope area without tension cracks, as shown in Fig. 2, are recorded. Figure 15 shows the variation of soil moisture contents with time at the area free of tension cracks on the slope for the rainfall event on April 5, 2013. The soil moisture contents at the depth of 0.15 m thru 1.5 m illustrate a noticeable increase during the rainfall, and the soil at the depth greater than 1.5 m shows no response in the moisture content during the rainfall. The distribution of Ts and Te values with depth for the slope area free of tension cracks at the rainfall event on April 5, 2013 is illustrated in Fig. 16. Ts values are 7, 14, 14, and

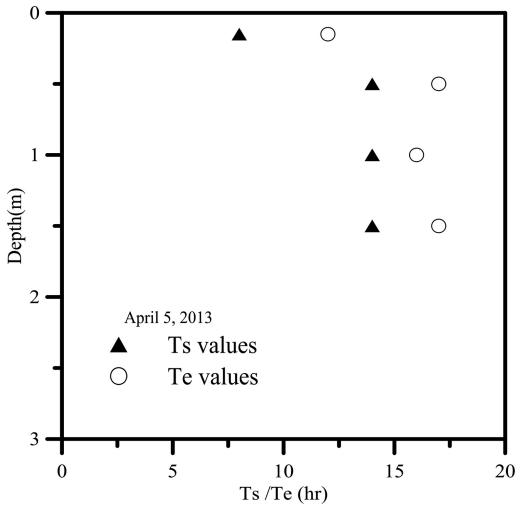


Figure 16. Distribution of Ts and Te values with depth at the area free of tension cracks on the slope for the rainfall event on April 5, 2013.

14 hrs at the depth of 0.15 m, 0.5 m, 1 m, and 1.5 m, respectively, and Te values are 12, 17, 16, and 17 hrs at the depth of 0.15 m, 0.5 m, 1 m, and 1.5 m, respectively. The soil moisture contents at a depth less than 1.5 m show noticeable increase during the rainfall, and Ts and Te values at the depth of 0.15 m (the shallowest sensor in this study) is considerably less than that at greater depths. These results implied that wetting front at the shallow depth takes place faster than that at greater depths. In addition, the Ts value at a given depth in the slope free of tension cracks is greater than that with tension cracks on the slope. Tension cracks on the slope provide passage for rainfall-induced runoff to infiltrate the soil, and the seepage may flow through the sliding plane instead of infiltrating from the ground surface of the slope. Consequently, the slope may move once the soil moisture content in the sliding plane reaches a certain level.

The occurrence of tension cracks in the slope may accelerate the rainfall-induced infiltration to greater depth in the slope. The subsidence around the scarp area of the instrumented slope reaches a value of 1.8 m in August, 2014 since the first identification of the cracks in June, 2012. A noticeable bulge in the geometry of the slope can be clearly identified in the field. Thus, occurrence of tension cracks in the slope may accelerate and exaggerate the soil movement in the slope during rainfall.

4 CONCLUSIONS

This paper presents the hydrological behavior of the soil in a residual soil slope where tension cracks are identified and soil deformations are noticeable. Variation of soil moisture contents with time and the arrival time of wetting fronts at various depths are measured. Major findings summarized from this study are as follows.

(1) Tension cracks on the slope provide major passage for subsurface flow in the slope during rainfall. For a slope with tension cracks on the surface, soil moisture contents at shallow depths may remain unchanged during rainfall whereas wetting front may take place at greater depths where shear planes may develop.
(2) Ts values at a given depth in the slope with noticeable tension cracks are lower than that free of tension cracks on the slope.
(3) Tension cracks in the slope may accelerate the rainfall-induced infiltration to greater depths, and it may speed up and exaggerate the soil movement in the slope during rainfall.
(4) The arrival time of wetting fronts at various depths in the slope undergoing deformations can be used to identify the distribution of shear planes in the soil if the Ts value at a given depth is noticeably low compared with that at shallower depths.

ACKNOWLEDGEMENTS

This study was sponsored by the National Science Council in Taiwan under Grant No. NSC 100-2625-M-327-003

REFERENCES

Dai, F.C., Lee, C.F., Li, J. and Xu, Z.W. 2001. Assessment of landslide susceptibility on the natural terrain of Lantau Island, Hong Kong, Environmental Geology, 40(3): 381–391.

Fan, Chia-Cheng and Chen, Hau-Juh. 2013. Time effect on the failure mechanism of unsaturated soil slopes subjected to rainfall. In Leung, Goh & Shen (eds). *Proceeding of 18th Southeast Asia Geotechnical Conference*. *Singapore, 29–31 May*: Research Publishing.

Huang C.-C., Lo C.-L., Jang J.-S. and Hwu L.-K. 2008. Internal soil moisture response to rainfall-induced slope failures and debris discharge. Engineering Geology, 101: 134145.

Orense R.P., Shimoma S., Maeda K. and Towhata I. 2004. Instrumented model slope failure due to water seepage. Journal of Natural Disaster Science, 26:15–26.

Towhata I., Uchimura T., Gallage C.P.K. 2005. On early detection and warning against rainfall-induced landslide. Proc. of the First General Assembly and The Fourth Session of Board of Representatives of the International Consortium on Landslides (ICL). Springer, Washington, DC, 133–139.

Uchimura, T., Towhata, I., Anh T.T.L., Fukuda, J., Bautista, C.J.B., Wang, L., Seko, I., Uchida, T., Matsuoka, A., Ito, Y., Onda, Y., Iwagami, S., Kim, Min-Seok, Sakai, N., 2010. Simple monitoring method for precaution of landslides watching tilting and water contents on slopes surface. Landslides, 7:351–357.

Unsaturated Soil Mechanics—from Theory to Practice – Chen et al. (Eds)
© 2016 Taylor & Francis Group, London, ISBN 978-1-138-02921-7

Comparative analysis on flexible supporting technology of different types of expansive soil cutting slope in the south and the north of China

H.P. Yang, J.S. Lin & J. Xiao
Changsha University of Science and Technology, Changsha, Hunan, China

ABSTRACT: The problem of collapse and sliding of expansive soil cutting slope in the expressway of Nanning to Youyiguan and Baise to Longlin in the Guangxi Zhuang Autonomous Region and West Sixth Ring in Beijing municipality has been successfully treated by geogrid reinforced flexible supporting technology. These treated projects have been experienced for six to eleven years. The actual cases of different expansive rock (soil) cutting slopes treated by this technology in the south and the north of China are reviewed and summarized. Three aspects, i.e. the engineering geology and soil characteristics, the forms and characteristics of slope failure, the design plan of treatment considering the impact of soil (rock) properties and climatic environment are compared specifically. The universal validity of using flexible supporting technology to treat expansive soil cutting slope with the characteristic of shallow damage has been verified. The technology needs to be supplemented, modified and perfected based on the actual conditions, and then the world technical problem that different types of expansive rock (soil) subgrade in different areas will be slippery while in cutting can be effectively solved.

1 INTRODUCTION

Expansive soils rich in strong hydrophilic clay minerals, are unsaturated special soils that can expand or contract in volume, as well as attenuate in intensity under alternating wet and dry conditions (Zheng & Yang 2009). Shallow slumping of the cutting slope resulted from the wet and dry cycle effect is becoming the largest engineering geological disaster of road construction in expansive soil areas (Zheng & Yang 2004). To overcome this technical problem, in 2002 the Ministry of Transportation built project to investigate technologies expansive land area road construction. Through lots of field testing and investigation, they found out the destruction rules and causes of the cutting slope destruction, and established geogrid reinforced Flexible Support Technology. This technology has solved 14 cases of expansive soil cut slope slumping in Ningming, southwestern Guangxi (Yang et al. 2005), 3 cases in Baise, Western Guangxi (Yang & Ni (2010)) and expansive shale problem on the both sides of West Sixth Ring Road Cutting Slope in Fengtai, Beijing (Xiao et al. 2010). After 6 to 11 years of testing of these projects, it shows that this technology is effective in both north and south parts of China where there are different climates and soil properties. This paper mainly describes 3 successful cases of expensive soil treatment in Guangxi and Beijing by comparison and summarizing their experience, for the purpose of better application of the technology and thus overcoming the puzzles of expansive rock (soil) cutting slope slumping by an economic, environmental friendly and effective way.

2 COMPARATIVE ANALYSIS OF ENGINEERING GEOLOGICAL PROPERITIES

Expansive soils are widely distributed in southern China, for example Guangxi where there are frequent disasters of expansive soil cutting slope slumping; and the causes are belong to, a residual type. This type of expansive soil, e.g. Ningming and Baise, is highly affected by humid subtropical climate. However, the expansive soil in Beijing Fengtai is influenced by a typical warm temperate semi-humid continental monsoon climate. Analyzing and comparing the engineering geological properties of expansive rock (soil) in different climates conditions is of great importance for choosing supporting techniques.

2.1 *Material composition*

To obtain the components of the expansive soil (rock) in Fengtai, Ningming and Baise, quantitative analyses of the samples were carried on by the Association of the Chinese Academy of Geological. The test results are shown in Table 1. It is found that the components of the two expansion (rock) soil are different. The soils of Ningming and Baise are mainly montmorillonite/illite mixed-layer minerals (mixed-layer ratio of 65% and 45%), while the expansive mudstone of Beijing Fengtai is single mine montmorillonite. The soil content of montmorillonite of Beijing was more than twice as high as that in Guangxi. The main components of the expansion soil in Guangxi are fine granular with sticky granular component of more than 40%,

Table 1. Mineral composition of expansive rock (soil).

Soil Samples	Sampling Sites	Depth/m	Montmorillonite/%	Surface Area/ (m^2/g)	Granularity Composition/mm.%				Ratio of Mixed-layer/%	Relative Content of Clay Minerals/%				
					>0.075	0.075–0.005	<0.005	<0.002		S	I/S	I	K	C
1	Beijing	2	45.23	331.22	0.13	46.31	53.56	48.00	–	97	–	2	1	–
2	Beijing	10	38.89	280.27	0.04	48.64	51.32	39.12	–	96	–	3	1	–
3	Ningming	1.5∼1.8	21.65	175.46	1.48	56.04	42.48	40.12	65	–	54	21	17	8
4	Ningming	3.5∼3.8	19.07	170.90	8.55	41.37	50.08	47.12	65	–	59	19	15	7
5	Baise	6	16.58	130.77	0.10	52.02	47.88	45.20	45	–	54	22	24	1

Table 2. Basic engineering properties of expansive rock (soil).

Soil Samples	Sampling Sites	Depth/m	Density/ g·cm^{-3}	Moisture Content/ %	Dry Density/ g·cm^{-3}	Void Ratio	Liquid Limit/%	Plastic Limit/%	Plasticity Index /%	Consistency/°	Bulk Shrinkage/ %	Free Expansion Ratio/%	Expansibility/ Kpa
1	Beijing	4	2.03	22.99	1.65	0.98	57.32	32.03	25.29	1.36	17.62	42	103
2	Beijing	10	1.93	29.31	1.49	0.98	63.91	32.87	31.04	1.11	16.10	32	84
3	Ningming	1.5∼1.8	1.88	35.34	1.39	0.99	52.9	27.46	25.45	0.69	14.58	45	125
4	Ningming	3.5∼3.8	1.96	31.38	1.49	0.86	58.0	30.40	27.61	0.96	15.14	44	125
5	Baise	6	2.093	20.65	1.735	0.59	60.24	21.83	38.41	1.03	9.13	82	400
6	Baise	7	2.117	20.33	1.759	0.57	58.89	22.46	36.41	1.06	9.50	87	350

while the surface area of the expansive soil in Beijing is far larger than those of Ningming and Baise. Based on the comparison of the components of the expansive soils in these two provinces, we proposed that the expansive mudstone in Fengtai, Beijing has larger expansive potential than the soil in Ningming and Baise, Guangxi.

2.2 *Basic engineering properties*

The geological properties of Guangxi and Beijing are different, leading to a variety of the basic engineering properties of expansive (rock)soil. Experiments to find out the engineering properties of the soils in Beijing and Guangxi were carried and the results are listed in table 2. It shows that expanded shale has large porosity, indicating its poor cementation. It also shows that the expansive soil natural consistency in Beijing and Baise are greater than 1, indicating that both of them can be used as embankment filling; however, the natural state of soil in Ningming cannot be used as roadbed filling. The contraction of the expansive soil in Beijing is larger than that in Guangxi, but its free expansion and the expansion force are smaller than that in Guangxi, indicating that it changes mainly by contraction, which may give the reason why it is a sedimentary type of expansive rocks.

3 COMPARING ON FAILURE MODE OF EXPANSIVE SOIL CUTTING SLOPE IN THE TWO PLACES

The stability of expansive rock (soil) cutting slopes is affected by geotechnical properties, engineering geological condition, climatic and environment, human factor, etc., and it leads that the distribution of geological hazards in expansive rock (soil) has distinct regional characteristics. In order to provide basis and reference on the treatment technology of expansive rock(soil) cutting slope, the cutting slope failure mode of sedimentary expansive rock(soil) in the north of China and residual expansive rock(soil) in the south of China is compared, and its similarities and differences were analyzed.

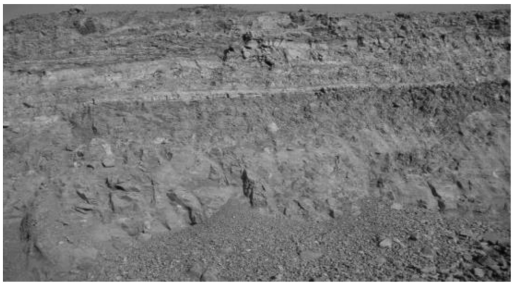


Figure 1. Exfoliation and Slough in the east slope of the K10+430 in the expressway of the West Sixth Ring in Beijing.

3.1 *Analysis of cutting slope failure mode in the two places*

3.1.1 *Expansive mudstone cutting slope in Beijing*

(1) Exfoliation and slough

Exfoliation and slough is a widespread phenomenon in the expansive mudstone cutting slope of 1.2 kilometer (shown in Fig. 1). Through field investigation and laboratory test, the reason caused this phenomenon is obtained, which is poor weather resistance and strong contractibility of soil in slope, slope surface untreated in time, and a steep slope, etc.



Figure 2. Collapse in the west slope of the K10+260 to K10+300 in the West Sixth Ring expressway.



Figure 3. Sliding in the west slope of the K10+525 to K10+623 in the West Sixth Ring expressway.

(2) Collapses

Due to the mechanics equilibrium and rock mass structure of original strata was damaged during slope excavation, and the upper soil of slope was slide down under the action of atmospheric weathering and gravity, the collapse was formed. The larger collapse in the west sixth ring in Beijing municipality was found in the west slope (shown in Fig. 2). The presence of secondary normal fault and the fragmentation of the upper soft rock mass fracture in this slope collapse was found, and it was presented a shape of "∧".

(3) Sliding

There were four slopes sliding in the expansive mudstone cutting slope of 1.2 kilometer in the west sixth ring in Beijing municipality. The biggest sliding was occur in the K10+500~K10+650 of the west slope, and its earth volume was about 7200 m^3 (shown in Fig. 3). The four cutting slope sliding were all slide at one time without gradual traction. The sliding scale was controlled by geological structure and the interface of weathered layer and rock layer. The slope sliding was often occurring in the mudstone or shale layer, and its surface was smooth and had significant scratches.

3.1.2 *Expansive soil cutting slope in Guangxi*

Through the tracking investigation and analysis to the expansive soil cutting slope failure in the expressway of Nanning to Youyiguan and Baise to Longlin, the four primary slope failures, erosion, swelling in the middle of slope, surface collapse, landslide, were summarized.



Figure 4. Slope-surface-erosion in the expansive cutting slope.



Figure 5. The phenomenon of Swelling in the Middle of Slope in the expansive cutting slope.



Figure 6. Surface collapse in the slope of ramp K176 in the in the expressway of Baise to Longlin in Guangxi.

(1) Slope-surface-erosion

The Slope-surface-erosion in the expansive rock (soil) mainly occurs in the slope surface failed to protection in time after slope excavation, and it was caused by the effect of wetting-drying cycle and erosion under surface runoff.

(2) Swelling in the middle of slope

The phenomenon of swelling in the middle of slope was formed by the swell in the middle of expansive slope after rainfall and water suction. It was likely to relate to high free swell ratio and large expansibility

of expansive soil in the Guangxi Zhuang Autonomous Region. The loose of slope surface soil caused by swelling, and it was creating conditions for the slope failure.

(3) Surface collapses

The surface collapse hadn't direct relation with the slope rate, and was likely to occur in a gentle slope. The original structure damaged and fracture grown significantly under the effect of wetting-drying cycle and the soil strength attenuation after soil saturated under the condition of rainfall were the main reason to generate the surface collapse caused by the effect of gravity and seepage pressure.

(4) Landslides

The expansive soil cutting slope in the expressway of Nanning to Youyiguan in Guangxiall has found sliding after experiencing a rainy season. Through the investigation and analysis to the slide slope, the sliding surface was mainly exists in two forms, one was formed by the weak intercalated layer existed in the interface of rock and earth, the another was formed by weak structural plane in the weathered residual expansive soil. The landslide of expansive soil cutting slope was not only in a single slope, but also in groups. The landslide failure hadn't direct relation with the slope height, slope rate.

3.2 *Similarities and differences on the slope in the two places*

3.2.1 *Similarities*

The landslide of cutting slope in sedimentary expansive soft rock in the West Sixth Ring in Beijing and residual expansive soil in Guangxi all had the characteristic of shallow damage, and the depth of sliding surface rarely had more than 6 m; The sliding surface was often a composite sliding surface and controlled by structural plane. The landslide was taken place in the slope suffered the repeated construction vehicle load.

3.2.2 *Differences*

As can be seen from the form of slope failure, the exfoliation and slough was a unique feature in the West Sixth Ring in Beijing municipality, the slope-surface-erosion and swelling in the middle of slope were exist in the Guangxi Zhuang Autonomous Region. Although both had slope failure, different geological structure generated different slope sliding, the landslide in the West Sixth Ring in Beijing municipality was a single slope and not exist in gradual traction and slide repeatedly. Due to the characteristic of dual structure strata in the Guangxi Zhuang Autonomous Region, the landslide mass often presented continuous and slide repeatedly.

3.3 *Analyze on the reason of differences*

Based on comparative analysis of the characteristics and laws of cutting slope failure in two places, and compared with the expansive rock (soil) slope in Beijing, it can be seen that the numbers of form of residual expansive rock (soil) slope failure in Guangxi were more, and its damage scale was larger and slope failure had the characteristics of repetition. The reason on the different characteristics of cutting slope failure between the Guangxi and the Beijing was that on one hand, the slope in the West Sixth Ring in Beijing had horizontal bedding structure, which had adverse to slide, but the slope in Guangxi had the structure of bedding; on the other hand, the rainfall capacity and the effect of wetting-drying cycle in Guangxi was more than in Beijing, and the decrease of soil shear strength in Guangxi was faster than in Beijing. In a word, geological structure, engineering properties and climatic environment was the main reason that formed the different cutting slope failure in the two places.

4 COMPARATIVE ANALYSIS ON TREATMENT TECHNOLOGY

The slope failure between the sedimentary expansive rock(soil) in Beijing and residual expansive soil(rock) in Guangxi had similarities and differences. The geogrid reinforced flexible supporting treatment technology was been applied to treat the slope by research group, but it was been modified and perfected correspondingly according to the actual working condition in the two places. The practical project case in the two places compared and analyzed, the reasonable design scheme under different conditions was summarized.

4.1 *Treatment concepts of flexible supporting technology*

The flexible supporting technology was mainly use geogrid reinforced to treat slope and combined with other necessary comprehensive treatment measures. Its characteristic is not only can bear the earth pressure, but also allow deformation in soil in some extent, it can absorb the expansion energy generated by stress release caused by over-consolidation and the change of moisture content in the soil of slope, and then prevent the slope failure.

The design scheme in the south and north of China were slightly different, but the overall thought of treatment was consistent. The basic steps of treating slope in expansive rock-soil were shown in figure 7.

4.2 *Design scheme of flexible supporting technology in the two places*

On the basis of the basic concepts of flexible supporting treatment technology, the engineering geological properties, the mode of slope failure, the construction conditions and the climatic environment of the cutting slope in the two places has been considered, and then the design scheme conformed the actual conditions was put forward.

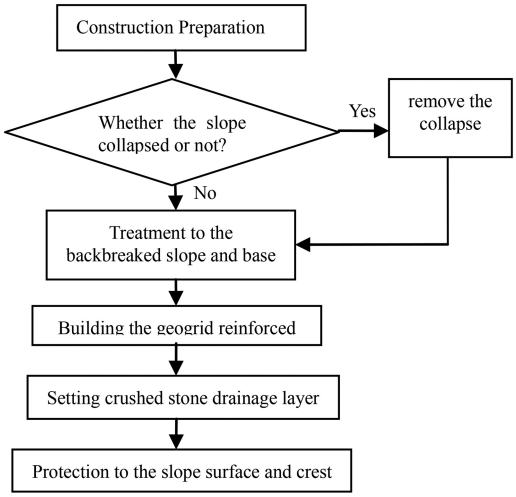


Figure 7. Basic steps in the treatment to expansive cutting slope.

4.2.1 *Design scheme in Guangxi*

The cutting slope in the expressway of Nanning to Youyiguan in Guangxi was untreated in time after excavation, and all of the slope was almost taken place landslide in some extent under the effect of consecutive rainfall. On the basis of the different height and destructiveness of cutting slope, the scheme of expansive soil cutting slope treated by geogrid reinforced flexible supporting technology was designed by research group. The space in this paper Limited, the treatment scheme of cutting slop in the expressway of Nanning to Youyiguan K133+970 to K134+120 in Guangxiwas only given(show in figure 8).The depth of slope collapse was 8 meters, the thickness and height of the flexible supporting was 3.5 meters and 9.8 meters respectively, Two sewers was designed below the flexible supporting, The measures of planting grass in the slope surface and laying "two geotextiles and one geomembrane" in the slope crest were taken.

4.2.2 *Design scheme in the Beijing Municipality*

There were a 1200 meters deep cutting slope of expansive rock(soil) in the expressway of West Sixth Ring in Beijing municipality, the slope height in both sides was in the range of 3 to 18 meters. Due to the treatment scale in Beijing was larger than in the Guangxi Zhuang Autonomous Region, and the destructiveness of slope in Beijing was smaller than in the Guangxi Zhuang Autonomous Region, so the design had slightly different, but followed the core concepts of flexible supporting technology in general. In view of the cutting slope height, the five treatment schemes of the section flexible support were designed. One of the treatment schemes on the west slope of H≥10 m was shown in figure 9. There were two cases for specific treatment scheme on the east slope: ①2 m≤H < 5 m, the treated thickness (horizontal direction, the same below) was 3 m

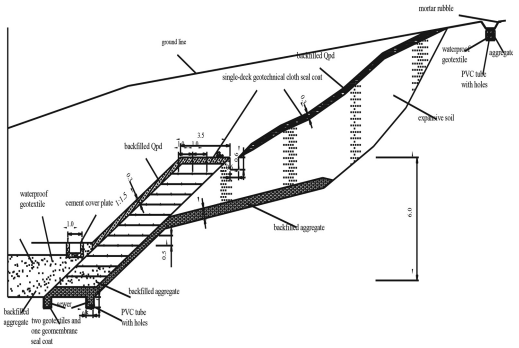


Figure 8. Treatment scheme of the K133+970 to K134+120 in the expressway of Nanning to Youyiguan in Guangxi.

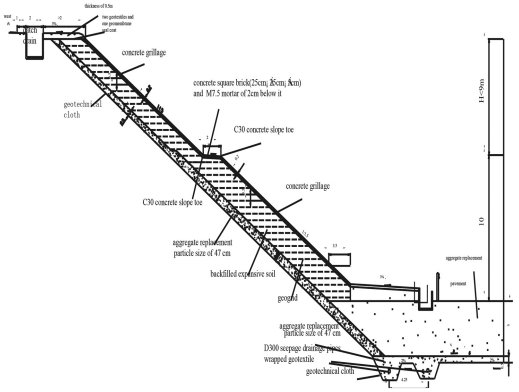


Figure 9. Treatment scheme of the west cutting slope (H ≥ 10 m) in the expressway of the West Sixth Ring in Beijing.

(0.5 + 2.3 + 0.2 = 3), ②H ≥ 5 m, the treated thickness was 3.5 m (0.5 + 2.8 + 0.2 = 3.5); There were three cases on the west slope: ①2 m ≤ H < 5 m, the treated thickness in horizontal direction had the same as the east. ②5 m≤H < 10 m, the treated thickness was 4 m (0.5 + 3.3 + 0.2 = 4), ③H ≥ 10 m, in view of the security, a 2 m wide platform in the slope height of 10 m was designed, the treated thickness above and below the platform was 4 m (0.5 + 3.3 + 0.2 = 4) and 6 m (0.8 + 5.0 + 0.2 = 6) respectively; The 0.5 m and 0.8 m is the thickness of drainage blanket, the 2.3 m, 2.8 m, 3.3 m, and 5.0 m is the width of geogrid-reinforced, the 0.2 m is the thickness of concrete grillage and backfill.

4.3 *Similarities and differences on the scheme of flexible support in the two places*

The main differences of design scheme between the two places were the width of geogrid-reinforced, the drainage facilities, the treated height of flexible support, the protective measure of slope surface and so on. The similarities and differences on the scheme in the Two Places were compared as follow:

4.3.1 *Width of geogrid-reinforced*
On the basis of the local geological conditions, failure forms, construction machinery and the influence depth of wetting-drying cycle and so on, the width of geogrid-reinforced in Guangxiwas designed with 3.5 m, but it was designed with 2.3 m, 3.3 m, 5.0 m in Beijing, according to the actual conditions. The enough geogrid-reinforced width can effectively prevent the slope failure.

4.3.2 *Treated height of flexible support*
The treated height of flexible support in Guangxiwas about two-thirds of the slope generally, the untreated slope surface was lay geotechnical tile, backfill cultivated soil, the slope crest was closed by the two geotextiles and one geomembrane. The planting in slope surface was grow rapidly under the hot and humid climate in the south of China, it played an important role in protecting slope; Due to the planting in the slope surface in the Beijing municipality wasn't easy to grow rapidly under the dry climate, all the slope surface was taken measure of geogrid-reinforced, which can effectively prevent the slope failure.

4.3.3 *Drainage facilities*
The catchment area of the east slope in the expressway of West Sixth Ring in Beijing was low, the sewer wasn't designed below the flexible support, and the crushed stone drainage layer with a vertical slope of 3% was filled in the bottom of the roadbed; the longitudinal sewer was designed below the flexible support with the lower slope height and catchment area in the west slope, and the crushed stone drainage layer with the thickness of 0.5 m was also designed behind the wall. the two longitudinal sewers was designed in the slope with the higher slope height, the larger slope failure scale, andthe existence of permeable sandstone layer, the thickness of crushed stone drainage layer behind the wall was also increased to 0.8 m. To meeting the requirements of the drainage, the two sewers was designed below all the flexible support with the reason of the larger rainfall in the summer of Guangxi Zhuang Autonomous Region, the crushed stone drainage layer with the thickness of 0.5 m was designed behind the wall, and the intercepting ditch was set at the slope crest.

4.3.4 *Protective measure of slope surface*
Due to the influence of climate, the plant in Beijing was grow slower than in the Guangxi Zhuang Autonomous Region, therefore, the protective measure of slope surface in Guangxiwas all taken by growing plant, but the protective measure of slope surface in Beijing was taken by the concrete grillage wall to prevent the scour of rain, and then the parthenocissus quinquefolia was planted in the slope surface to reduce the adverse impact under the effect of wetting-drying cycle.

4.3.5 *Special setting of flexible support in Beijing*
To prevent the direct erosion of the slope crest surface during a heavy rain, the hornblock made by concrete in the slope crest was increased to the design scheme of the Beijing municipality. Furthermore, due to the height of the concrete grille in the slope surface was high, the concrete stage for heaping debris in the slope toe was set to reinforce the toe.

5 CONCLUSIONS

The geogrid reinforced flexible supporting technology was created by the research group of expansive soil in Changsha University of Science and Technology at 2004. It has successfully treated dozens of different expansive rock (soil) slope. In spite of basic technical concept on flexible support adopted by the south and the north of China was consistent completely, in order to achieve the objective of treatment prospectively, the supporting scheme was modified, replenished, and perfected correspondingly according to the geotechnical cause, engineering characteristic, geological structure, climatic environment, and construction conditions in the actual working conditions, and the feasible, safe and economic of this technology will be realized truly to ensure strength and stability of the treated slope for a long time.

REFERENCES

Xiao, J., Yang, H.P., Ni, X., 2010. Flexible supporting treatment technology of cutting slope in the expansive rock (soil) in the expressway of West Sixth Ring in Beijing municipality. *Journal of China and Foreign Highway*, 30(3): 38–41.

Yang, H.P., Zheng J.L., Wu, X.H., 2005. Engineering treatment technology in subgrade of expansive Soil in the expressway of Nanning to Youyiguan in the Guangxi Zhuang Autonomous Region. *Conference Proceedings in the Academic Conference of 2005 in China Highway and Transportation Society*.

Yang, H.P., Ni, X., 2010. A construction case of ramps located on expansive soil for expressway interchange. *Highway*, 1: 9–1.

Zheng, J.L., Yang, H.P., 2004. *Engineering problems, current research state and future prospect of highway expansive soil in China:Theory and Practice of Expansive Soil Treatment Technology*. Beijing: China Communication Press

Zheng, J.L, Yang, H.P., 2009. *Expansive soil in road engineering*. Beijing:China Communication Press.

Unsaturated Soil Mechanics—from Theory to Practice – Chen et al. (Eds)
© 2016 Taylor & Francis Group, London, ISBN 978-1-138-02921-7

Effect of sodium chloride solution on adsorbed water content of clays

Xiaolong Xia, Changfu Wei, Tiantian Ma & Huihui Tian
State Key Laboratory of Geomechanics and Geotechnical Engineering, Institute of Rock and Soil Mechanics, Chinese Academy of Sciences, Wuhan, Hubei, P. R. China

ABSTRACT: In this paper the influence of NaCl solutions on the adsorbed water content and hydraulic conductivity of clays has been investigated. The adsorbed water content of two kinds of natural clays treated with NaCl solutions at various concentrations is measured using the NMR technique. It is shown that the adsorbed water content decreases with the increment of NaCl concentration. Furthermore, comparison of hydraulic conductivity for different NaCl solutions shows that the hydraulic conductivity increases with increasing NaCl concentration. A quantitative explanation for the changes that occur in the adsorbed water content and hydraulic conductivity of these clays as a result of NaCl solutions treatment is provided. This explanation relates the changes in adsorbed water content to changes in the diffuse double layer thickness. It is suggested that NaCl solutions affect the behavior of adsorbed water in clays and, through that, many other clay properties.

1 INTRODUCTION

Due to the charged surface of clay minerals and the existence of physicochemical effects, water is strongly attracted to clay mineral surfaces. It has been well recognized that adsorbed water properties form a vital link to the understanding of shear strength, compression, and the apparently anomalous fluid flow behavior of clay soils (Martin, 1960; Cui et al., 2010; Jaeger et al., 2010; Tian & Wei, 2014). Several authors (e.g., Dolinar & Trauner, 2003; Sridharan, 2014) have shown that the undrained shear strength of saturated montmorillonitic soils is dependent on the quantity of adsorbed water and the cohesion is related to the viscous nature of the adsorbed layer of water. The environmental loads, namely temperature, changes in water chemistry, irradiation, and chemical loads from hazardous wastes, may affect the behavior of adsorbed water in clays and, through that, many other geotechnical properties of clays (Hueckel, 1992). Thus, studies of the influence of pore fluid chemistry on the quantity and characteristics of adsorbed water are of great significance in understanding the chemomechanical behavior of clays. The study presented here is limited to the investigation of the effect of the change in pore solution concentration on the adsorbed water content and thus on the hydraulic conductivity of two kinds of saturated clays.

The objective of the study presented here is to conduct a systematic investigation of the change in the adsorbed water content during the treatment of the soil samples with NaCl solutions at different concentrations. To this end, a newly proposed method to calculate the adsorbed water content based on the NMR technique by Tian et al. (2014) is adopted. A possible cause of the changes in adsorbed water content of the clays is presented, with some supporting physicochemical analyses.

Table 1. Physical properties of the clay samples.

Properties	Low plasticity clay	Expansive clay
Liquid limit (%)	32.9	57.4
Plastic limit (%)	19.1	26.5
Specific gravity	2.71	2.73
Specific surface area (m^2/g)	22.63	52.87

2 MATERIALS AND METHODS

Two reconstituted clays were used for the experiments. A low plasticity clay from Wuhan City and an expansive clay from Nanyang City have been used as delivered. The physical parameters are listed in Table 1. The grain size distribution curves of the two clays are shown in Figure 1.

The experimental procedure for the calculation of the adsorbed water content is very similar to the one adopted by Tian et al. (2014). Many concepts will consequently only be briefly recalled here, while a more detailed description can be found in Tian et al. (2014). A NMR apparatus developed by Niumag Corporation, Suzhou, China and a cool bath were used in the experiments.

All of the tested soil samples were first compacted statically to the required dry density of 1.5 g/cm^3 in a Teflon cylinder and then put in a sealed chamber for complete saturation using the vacuum method. After the samples were saturated with distilled water,

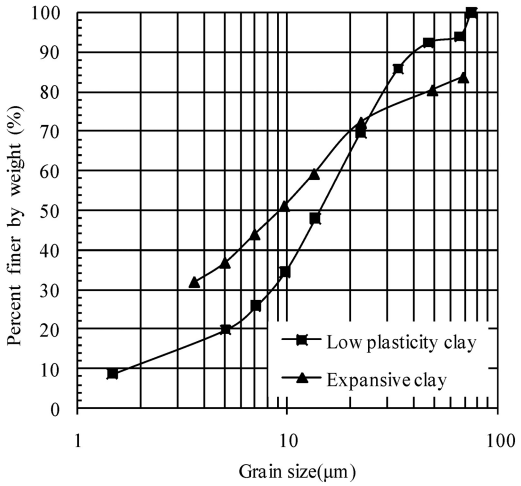


Figure 1. Grain size distribution of the clays.

a cool bath was used to cool the samples. The temperature was slowly decreased from 27.9°C to 0.43°C step by step for the low plasticity clay samples, while for the expansive clay samples, the temperature was decreased from 30.00°C to 0.79°C. In each step, the samples were moved out to the NMR sample tube for NMR measurements after thermal equilibrium was reached. The measured data were analyzed by an inversion software provided by the NMR apparatus.

To compare the adsorbed water content of clay samples treated with NaCl solutions at different concentrations, the expansive clay samples were immersed in distilled water and in NaCl solution at various concentrations for 7 days after saturated with distilled water, while the low plasticity clay samples were mixed with distilled water and NaCl solution at various concentrations. Then the samples were moved out to the NMR tube for NMR measurements.

Additionally, several hydraulic conductivity tests according to the Chinese National Standards (CNS) GB/T50123-1999 were performed. The samples were first saturated with distilled water based on the vacuum method. They were subsequently immersed in distilled water and NaCl solutions at various concentrations for 7 days. The hydraulic conductivity tests were conducted in the falling head permeameters. Distilled water and NaCl solutions used to treat the samples were chosen as the permeant liquid. The hydraulic head and corresponding time was recorded during the experiments.

3 EXPERIMENTAL RESULTS AND DISCUSSIONS

3.1 *The threshold value of T_2 for defining the adsorbed water*

The relaxation time T_2 is linearly proportional to the pore size and the T_2 distribution curve represents

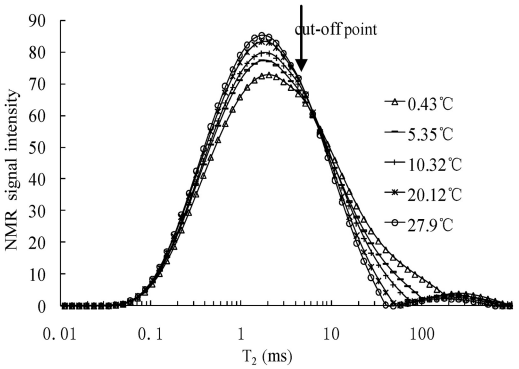


Figure 2. T_2 distribution curves for low plasticity clay samples.

qualitatively the size distribution of pores saturated with water (Tian et al., 2014). Figure 2 shows the T_2 distribution curves for low plasticity clay samples under different temperature conditions. Generally, it is assumed that the adsorbed water resides mainly within smaller pores while the free water is located in larger pores. That is to say, there may be a threshold value of T_2 in Figure 2 for defining the adsorbed water. To explore this idea and indentify the threshold value of T_2, the temperature effects on the adsorbed water content are discussed. It has been well documented in the literature that adsorbed water content of the clays is strongly influenced by temperature. Several authors have found that the adsorbed water content increases with increasing temperature (e.g., Yong, 1962; Morin, 1984). The analytical approach followed here is very similar to the one followed by Tian et al. (2014). However, an opposite suggestion was made here that, as temperature increases, the amount of adsorbed water in smaller pores increases, leading to an increase in the peak of signal intensity to the left of the cut-off point and an decrease in the peak of signal intensity to the right of the cut-off point (i.e., a decrease in the amount of the adsorbed water). Thus, the threshold value of T_2 of the low plasticity clay is assumed to be 5.8 ms according to Figure 2. Figure 3 reports the T_2 distribution curves for expansive clay samples under different temperature conditions. The same threshold value of T_2 (5.8 ms) can be found for the expansive clay samples.

3.2 *Variation in the adsorbed water content of tested clays treated with different NaCl solutions*

The adsorbed water content is defined as the ratio of the area under the T2 distribution curve below 5.8 ms to the total area under the T2 distribution curve. Figure 3 reports the variation of the adsorbed water content of two kinds of tested clays with various NaCl concentrations. It can be observed that for both clays, the adsorbed water content decreases with increasing NaCl concentration. This decrease can be attributed

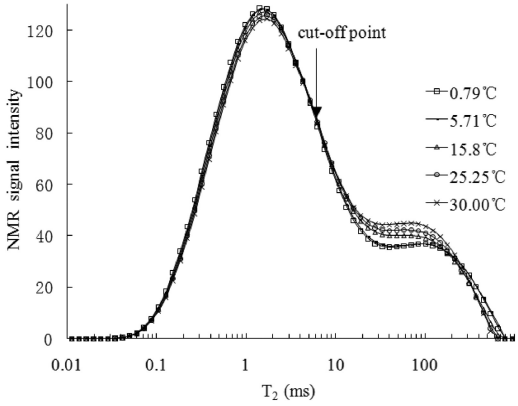


Figure 3. T_2 distribution curves for expansive clay samples.

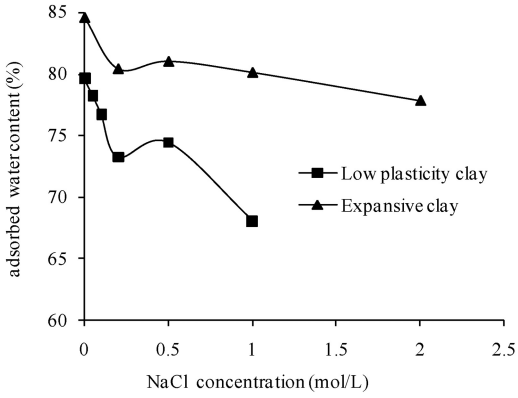


Figure 4. Effect of NaCl concentration on adsorbed water content.

to a decrement in diffuse double layer thickness. The layer of adsorbed water can be considered as the inner layer of the diffuse double layer (Sridharan, 2014). Hence, it is shown that, a relationship exists between the adsorbed water content and the double-layer thickness. Generally, the adsorbed water content decreases with decreasing double-layer thickness.

Figure 4 also shows that the low plasticity clay seems to be more sensitive to the NaCl solution concentration than the expansive clay. This is probably due to the different sample preparation methods for the two tested clays. As stated above, 7 days are chosen as the immersion time of the expansive clay samples, which may be too short to establish chemical equilibrium.

3.3 *Variation in the hydraulic conductivity of tested clays treated with different NaCl solutions*

Figure 5 shows that, for the tested expansive clay, a change in NaCl concentration from 0(distilled water) to 1 mol/L results in a significant increase in the coefficient of permeability, but a further increase in NaCl solution concentration leads to a decrease of the coefficient of permeability. A similar trend was found for

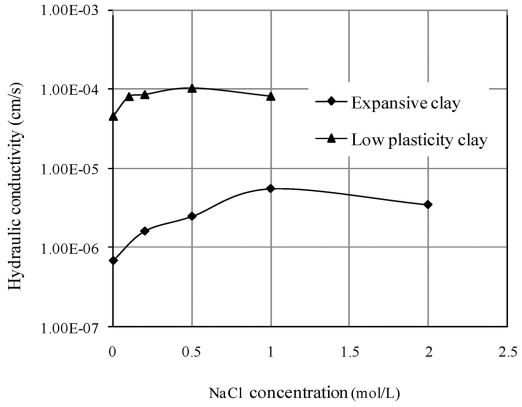


Figure 5. Effect of NaCl concentration on coefficient of permeability.

the low plasticity clay as shown in Figure 5. Adsorbed water is bound to the external and internal (i.e., interlayer) mineral surfaces by strong electrical forces, and is believed to be an extension of the solid surface (Hueckel, 1992; Kolstad, 2004). When the quantity of adsorbed water increases, the interparticle flow paths for free water become more constricted and tortuous (Kolstad, 2004). Jo et al. (2005) proposed that the increase in hydraulic conductivity can be attributed to the shrinkage of clay aggregates and formation of larger interaggregate pores (i.e., the pores conducting flow) due to the decreases of the amount of adsorbed water. Thus, it seems reasonable to hypothesize that the decrease of adsorbed water content of the tested clay as a result of NaCl solution treatment is responsible for the increase in the coefficient of permeability. The various NaCl concentrations influence on the adsorbed water content and thence on the hydraulic conductivity of the tested clays.

It is noted that the coefficient of permeability of the tested clay decreases with increasing concentration in the high NaCl concentration range, indicating factors other than adsorbed water content (i.e. double layer thickness) should be involved. It is suggested that the high viscosity of the NaCl solution at high concentration may be the main cause of the decrease in the coefficient of permeability. According to the research findings (Liu, et al., 2002), the viscosity of NaCl solution increases by a factor of 1.23 when the NaCl solution concentration increases from 1 mol/L to 2 mol/L at a given temperature. This variation of the viscosity may result in significant change in the coefficient of permeability.

4 CONCLUSIONS

This work presents experimental results of adsorbed water content and hydraulic conductivity of low plasticity clays and expansive clays. Different clay samples were tested with distilled water and NaCl solutions at

various concentrations in order to evaluate the influence of NaCl solution concentration on adsorbed water content and thence on the relevant clay properties such as hydraulic conductivity. The main conclusions of this work can be summarized as follows:

(1) The two kinds of clay samples respond in a similar way but with a different magnitude.
(2) The adsorbed water content decreases with increasing NaCl solution concentration. This change of the adsorbed water content can be related to the change of double layer thickness.
(3) NaCl solution concentration exerts great influence on the hydraulic conductivity through their influence on adsorbed water content and dispersion or aggregation of the clay aggregates.
(4) According to hydraulic conductivity tests, the coefficient of permeability of the samples decreases at high NaCl solution concentration conditions. This decrease may be related to the high viscosity of the NaCl solution due to the high concentration.

ACKNOWLEDGMENTS

The research was supported by the Natural Science Foundation of China (Grant no. 11372078) and the Guangxi Natural Science Foundation through grants 2012GXNSFGA060001, and the Major Projects of Guangxi Natural Science Foundation through grants 2012GXNSFEA053002.

REFERENCES

Cui, D.S., Xiang, W., Cao, L.J., Liu, B.B. 2010. Experimental study on reducing thickness of adsorbed water layer for red clay particles treated by ionic soil stabilizer. *Chinese journal of Geotechnical Engineering*, 32(6):944–949.

Dolinar, B. & Trauner, L. 2003. Undrained shear strength in dependence on the quantity of free water and firmly adsorbed water in fully saturated clays. Academic open internet journal [Online ed.], iss. 10 http://www.acadjournal.com/2002/v8/part8/pl/index.html.

Hueckel, T. 1992. Water-mineral interaction in hygromechanics of clays exposed to environmental loads: a mixture-theory approach. *Canadian Geotechnical Journal*, 29(6): 1071–1086.

Jaeger, F., Shchegolikhina, A., As, H.V., Schaumann, G.E. 2010. Proton NMR relaxometry as a useful tool to evaluate swelling processes in peat soils. Open Magn. Reson. J. 3, 27–45.

Jo, H.Y., Benson, C.H., Shackelford, C.D., Lee, J.M., Edil, T.B. 2005. Long-Term hydraulic conductivity of a geosynthetic clay liner permeated with inorganic salt solutions. *Journal of Geotechnical and Geo- environmental Engineering,* 131(4):405–417.

Kolstad, D.C., Benson, C.H., Edil, T.B. 2004. Hydraulic conductivity and swell of nonprehydrated GCLs permeated with multispecies inorganic solutions. *Journal of Geotechnical and Geo- environmental Engineering* 130(12):1236–1249.

Liu, G.Q., Ma, L.X., Xing, Z.Y. 2002. Handbook of nomographic charts for the physical properties in chemical engineering. Beijing: Chemical Industry Press.

Martin, R.T. 1960. Adsorbed water on clay: A review. Clays and clay minerals 9(1):28–70.

Morin, R. & Silva, A.J. 1984. The effects of high pressure and high temperature on some physical properties of ocean sediments. *Journal of Geophysical Research* 89(B1): 511–526.

Sridharan, A. 2014. Soil clay mineralogy and physical-chemical mechanisms governing the fine-grained soil behavior. *Indian Geotechnical Journal* 44(4):371–399.

Tian, H.H. & Wei, C.F. 2014. A NMR-based testing and analysis of adsorbed water content. *Science China* 44(3): 295–305.

Tian, H.H., Wei, C.F., Wei, H.Z., Zhou, J.Z. 2014. Freezing and thawing characteristics of frozen soils: Bound water content and hysteresis phenomenon. *Cold regions science and technology 103*:74–81.

Yong, R.T., Taylor, L.O., Warkentin, B.P., 1962. Swelling pressures of sodium montmorillonite at depressed temperature. *Proceeding of the 11th National Conference on, Clays and Clay Minerals*, pp. 268–281.

Unsaturated Soil Mechanics—from Theory to Practice – Chen et al. (Eds)
© 2016 Taylor & Francis Group, London, ISBN 978-1-138-02921-7

Swelling of GMZ bentonite with saline solutions and its prediction

L. Zhang & D.A. Sun
Department of Civil Engineering, Shanghai University, Shanghai, China

Y.M. Liu
Beijing Research Institute of Uranium Geology, Beijing, China

ABSTRACT: A series of one-dimensional constant-volume and constant-stress tests on two GMZ Na-bentonites saturated with distilled water and saline solutions were performed in this study. Based on the concept of the montmorillonite void ratio, the relationships of the montmorillonite void ratio versus the swelling pressure can be represented by a series of straight lines in the double logarithmic coordinator system and these lines (corresponding to different concentrations of saline solution) were parallel or superposition to each other. The test results also showed that the swelling pressure on a logarithmic scale changed linearly with the saline concentration but the variation is up to the initial density of the sample. Furthermore, a new simple method with different decay factors was proposed to describe the variation in the montmorillonite void ratio of GMZ bentonite with different saline solutions under the same stress.

1 INTRODUCTION

The deep geological disposal concept has been accepted by many countries to isolate the high level radioactive waste (HLW) from the biosphere. In this multi-barrier system of the disposal repository, bentonite is regarded appropriate to be buffer/backfill materials for its low hydraulic conductivity, high swelling property, good self-sealing capacities and high absorption of radionuclide. In China, Gaomiaozi (GMZ) bentonite has been identified as a potential buffer/backfill material for the national repository (Liu and Chen 2001).

Swelling property is one of the main reasons for using the bentonite clay as buffer material in the repository for the high level radioactive waste (Pusch & Bergström 1980). When the bentonite confined by the bedrock (it is the granite in Beishan area, where was considered the best candidate area for a national repository for HLW in China) in the disposal system is immersed in underground water, the swelling pressure from the bentonite (buffer material) will be applied on the bedrock and the nuclear waste container, while the low hydraulic conductivity of bentonite contributes to efficient sealing of the volume. Therefore, the swelling characteristic of the bentonite is an important technical issue for the deep geological disposal method. Moreover, the biological environment of the deep geological repository is so complex that various elements affected the swelling property of the bentonite.

In China, around the multiple-barrier of HLW disposal system in the Beishan area, there are various chemical elements dissolved in the ground water, which may influence the swelling capacity of the bentonite. Therefore, it is necessary to study the swelling characteristics of bentonite in chemical solutions with different total dissolved solid (TDS). As a consequence, extensive studies have been performed over the years on different bentonites or bentonite–aggregate mixtures in both distilled water and saline solutions (Alawaj 1999, Di Maio 1996; Zhu *et al*., 2013; etc.). On the other hand, some research works have focused on the insights into the mechanisms governing the bentonite swelling (Komine & Ogata, 1994). As a whole, the swelling pressures were deemed to depend largely on the final dry density of bentonites, the nature of exchangeable cations, and the salinity of pore-water (Xu *et al*. 2003, Zhu *et al*. 2013).

The present paper is focused on the swelling characteristics of two GMZ Na-bentonites when saturated with distilled water and saline solutions with different TDS concentrations and the prediction of the swelling pressure. Considering that the concentration of TDS in the underground water and the final dry density of GMZ bentonite used in the engineering practice have not been determined specifically, a prediction method based on the concept of montmorillonite void ratio is proposed in this research to predict the swelling pressure of the GMZ Na-bentonite with various final dry densities and TDS concentrations.

2 MATERIALS

Two GMZ Na-bentonites (briefly called GMZ001 and GMZ07 Na-bentonite) used in this research work

Table 1. Main mineral composition and physical property of GMZ Na-bentonites.

Type	Mt content (%)	Quartz (%)	Feldspar (%)	Illite (%)	Christobalite (%)	Specific gravity
GMZ001	74	12∼18	6.7	1	9	2.71
GMZ07	70.8	12.4	10.6	–	6.2	2.76

Mt = montmorillonite

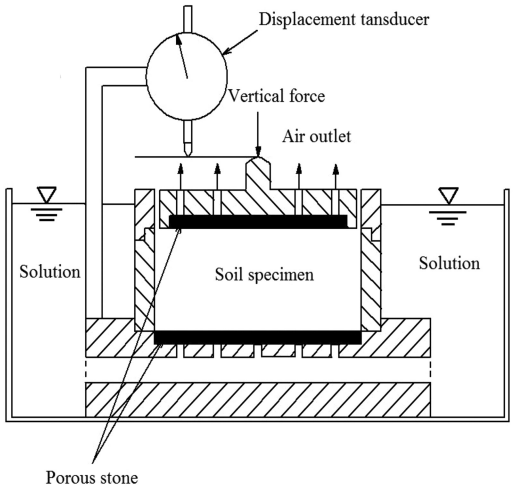


Figure 1. Oedometer used for testing.

consisted mainly of montmorillonite, together with the associated minerals such as quartz, calcite and feldspar. The main mineralogical composition and physical parameters of GMZ Na-bentonite are presented in Table 1. A study conducted by Guo *et al*. (2001) showed that in the Beishan area Na^+ is the predominant positive ion in the underground water, while the predominant negative ions are Cl^- and SO_4^{2-}. Therefore NaCl and Na_2SO_4 (mass ratio 2 : 1) were chosen as the dissolved solids in this study to simulate the main chemical components of underground water in the Beishan area.

An oedometer (Fig. 1) was used in the laboratory tests. The oedometer ring has an internal diameter of 50 mm and a height of 20 mm.

In order to prevent the specimen from expanding out of the oedometer ring and spilling over when swelling upon water uptake at low vertical pressure, the initial height of specimens was chosen to be 15 mm, which were achieved by adding a spacer with a thickness of 5 mm into the oedometer ring. Specimens were statically compacted at the different pressures using a hydraulic jack to achieve the specified dry density. In order to realistically represent the field conditions, the initial water contents of 14% and 9% were adopted for GMZ001 and GMZ07 Na-bentonite specimens, respectively.

Table 2. Physical indexes of two GMZ-Na bentonites specimens and TDS for the tests.

Type	Initial dry density ρ_{d0} (g/cm^3)	*TDS*(g/l) 0.3	3	12.3
GMZ001	1.10			√
	1.11		√	
	1.34	√	√	√
	1.45		√	
	1.46			√
	1.51	√	√	√
	1.60	√	√	√
	1.63		√	
	1.63			√
	1.64	√	√	√
	1.65			√
	1.66		√	
GMZ07	1.20	√	√	√
	1.30	√	√	√
	1.41	√	√	√
	1.46	√	√	√
	1.50	√	√	√
	1.62	√	√	√
	1.70	√	√	√

3 TESTING METHOD

A series of the constant-volume tests and constant-stress tests were performed to study the swelling characteristics of two GMZ bentonites due to saturation with distilled water and TDS solutions. The tests were carried out on the compacted two GMZ bentonites with different initial dry densities under different TDS concentrations. The initial dry density of specimens and the TDS concentrations used in each test are listed in Table 2.

The in situ investigation indicated that the TDS concentration of the underground water in the Beishan area varied from 0.3 to 12.3 g/l (Guo et al., 2001). For this reason, the TDS concentrations used in the tests were chosen as 0.3, 3.0 and 12.3 g/l, respectively.

The testing method adopted in the constant-volume tests on bentonites saturated with solutions was the load balance method. In this method, the specimen was placed in a consolidation apparatus and the TDS solution was then poured into the testing container, which allowed the specimen to absorb the solution from the bottom. When the specimen began to swell

(i.e., the displacement meter pointer began to move), the vertical pressure was adjusted to bring the pointer back to the initial readings and to keep the specimen height change within ±0.01 mm. If the reading of the displacement meter had not changed within 24 hours under an applied load, it was considered that the specimen had reached a stable state. At this time, the applied vertical load σ_v was taken as the swelling pressure p_s.

For the constant stress test, a constant vertical pressure σ_v was first applied on the specimen and after consolidation is completed the water was then supplied from the specimen bottom. Water uptake leads to the development of swelling deformation of the specimen. With the growth of swelling deformation, the swelling potential decreases. In general, when the swelling pressure has grown to be equivalent to the vertical pressure σ_v and the swelling deformation tends to a stable state. The deformation is considered finished when the variation in the indicator on the displacement transducer is less than 0.01 mm after an interval of 24 hours.

4 TEST RESULTS AND PREDICTION OF SWELLING PRESSURE

4.1 *Test results*

The initial and final states of GMZ Na-bentonite specimens and the TDS concentrations are listed in Table 2. A total of 19 tests were carried out using distilled water and the solutions with different TDS concentrations.

The results of tests indicated that the swelling pressure decreased from 3350 kPa to 2900 kPa for GMZ001 bentonite and from 2475 kPa to 2075 kPa for GMZ00 bentonite as the concentration of saline solution increased from 0.3 g/l to 12.3 g/l (Fig. 2a and Fig. 2b).

Figure 3 presents the variation in the swelling deformation as the concentration of saline solution increased at the pressure of 2400 kPa. This result is consistent with the results reported by different researchers (Alawaji, 1999; Zhu et al., 2013) and can be explained by the double electric layer theory of montmorillonite structure (DI Maio, 1996), which showed that the electric layer thickness is inversely proportional to the ion concentration.

4.2 *Prediction of swelling pressure for GMZ Na-bentonite*

Based on the test results on two Na-bentonites, a fitted linear regression model was used to describe the relationships between the vertical swelling pressures and corresponding void ratios (Fig. 4). Figure 4 presents the relationships of swelling pressure and void ratio for the two GMZ Na-bentonites. Obviously, the test results make a large distinction between these two GMZ Na-bentonites.

Sun *et al*. (2009) put forward the concept of the montmorillonite void ratio based on the study of swelling characteristics of mixtures of sand and

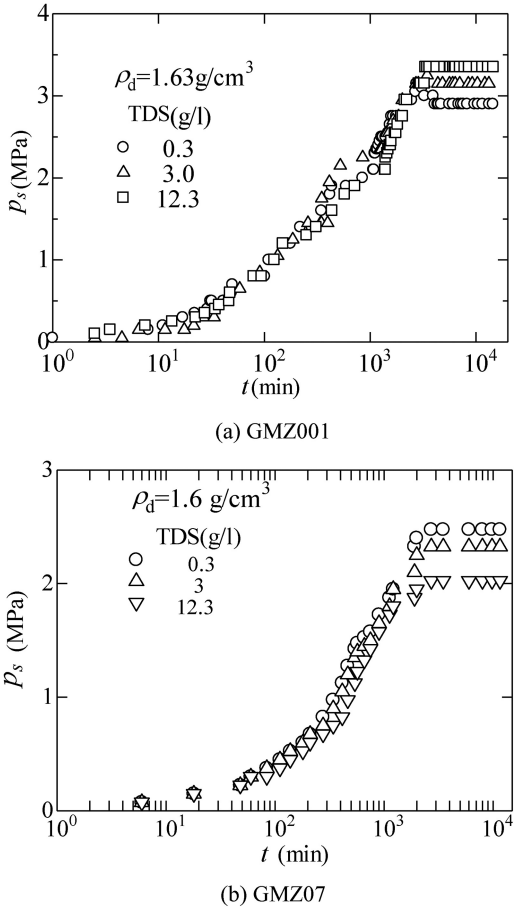


Figure 2. Change in swelling pressure with time for GMZ Na-bentonites.

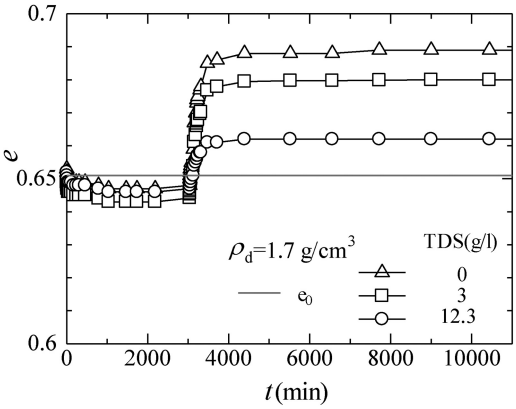


Figure 3. Change in swelling deformation with time for GMZ07 Na-bentonite.

Japanese Kunigel-V1 sodium bentonite when it was saturated with distilled water. The swelling deformation of bentonite can be attributed mainly to the

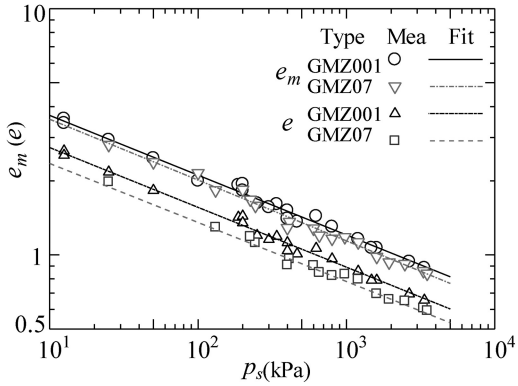


Figure 4. Montmorillonite void ratios (e_m) and void ratios (e) *vs* swelling pressures (p_s) for two GMZ Na-bentonites.

swelling of montmorillonite when it absorbs the solution. Here the montmorillonite void ratio e_m is defined as a ratio of the solution volume (V_w) to the volume of the montmorillonite solid particle (V_m) at full saturation. e_m can characterize the volume of the solution that is absorbed by per unit volume of montmorillonite when the swelling deformation becomes stable, namely:

$$e_m = \frac{V_w}{V_m} = e\frac{\rho_m}{\rho_s \alpha \beta} \tag{1}$$

where e is a void ratio at full saturation, ρ_m the grain density of montmorillonite, ρ_s the soil grain density of the mixture, α the bentonite content in the mass in the mixture, β the montmorillonite content in the mass in bentonite.

Based on the concept of the montmorillonite void ratio, Figure 4 presents that the two fitting lines are almost superposition in the double logarithmic plots of the vertical pressure (i.e., the swelling pressure) versus montmorillonite void ratio. The test results reveals that the relationship between the swelling pressure and void ratio for two GMZ Na-bentonites depends mainly on their montmorillonite contents.

In order to consider the effect of TDS concentration in saline solution on the swelling capacity, the linear fitting of the data in distilled water is extended to the data obtained from GMZ Na-bentonites in the saline solutions with the TDS concentration of 12.3 g/l.

The relationships for Na-bentonite saturated with distilled water and the solution with TDS concentration of 12.3 g/l can be expressed as

$$\log e_m^i = a_i - b_i \log p_s \quad (i = 0,\ 12 \tag{2}$$

where the unit of p_s is kPa, and e_m^i ($i = 0$ and 12.3) are the montmorillonite void ratios of GMZ Na-bentonites saturated with distilled water and the solutions with TDS concentration of 12.3 g/l, respectively. a_i and b_i ($i = 0$ and 12.3) are the parameters of the fitting lines, as listed in Table 3.

Table 3. Parameters used in the model prediction for GMZ Na-bentonites.

Parameter	GMZ001	GMZ07
a_0	0.810	0.799
$a_{12.3}$	0.761	0.750
b_0	0.245	0.247
$b_{12.3}$	0.236	0.239
$\gamma_{12.3}$	0.893	0.893
α	1.000	1.000
β	0.740	0.708
G_s	2.71	2.76

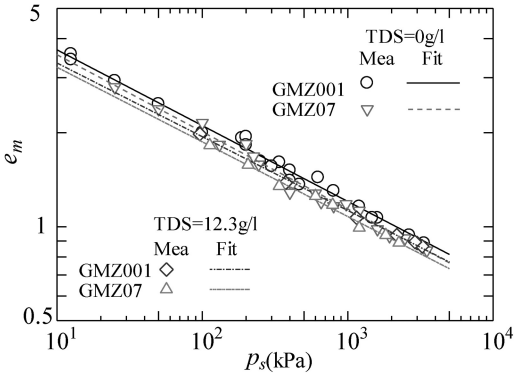


Figure 5. Montmorillonite void ratios (e_m) *vs* swelling pressures (p_s) for two GMZ Na-bentonites in saline solution.

Since montmorillonite was the sole component of the mixture responsible for water intake and swelling processes, it is also convenient to use the montmorillonite void ratio to describe the final state of bentonites saturated by the saline solutions. In that way, the decay factor γ_{TDS} was used to describe the variation in the montmorillonite void ratio (e_m^{TDS}) in different saline solutions under the same vertical pressure.

$$e_m^{TDS} = \gamma_{TDS} e_m \tag{3}$$

Substituting p_s from Eq. (2) with $i = 0$ into $i = 12.3$, and taking Eq. (3) into consideration give:

$$\gamma_{12.3} = \frac{1}{e_m} \times \left[e_m \times 10^{b_0/b_{12.3} \times a_{12.3} - a_0} \right]^{b_0/b_{12.3}} \tag{4}$$

where $\gamma_{12.3}$ is a decay factor for TDS concentration of 12.3 g/l.

The fitting lines for test data in distilled water and the solution with TDS concentration of 12.3 g/l are almost parallel in the double logarithmic plots of the vertical pressure versus montmorillonite void ratio, as shown in Figure 5, and thus $b_0 = b_{12.3}$. Inserting $b_0 = b_{12.3}$ into Eq. (4) gives

$$\gamma_{12.3} = 10^{a_{12.3} - a_0} \tag{5}$$

Substituting Eq. (1) into Eqs. (2) and (3), and taking the identical equation ($e = G_s \rho_w / \rho_d - 1$) between

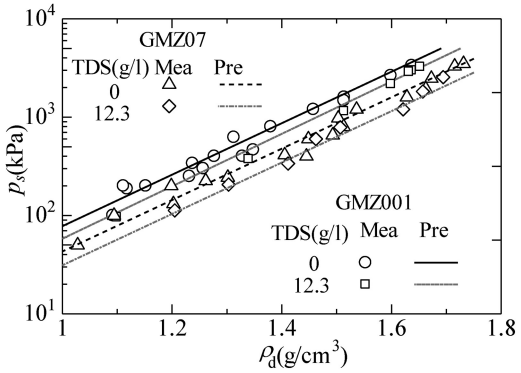


Figure 6. Measured and predicted swelling pressures at full swelling of two GMZ Na-bentonites.

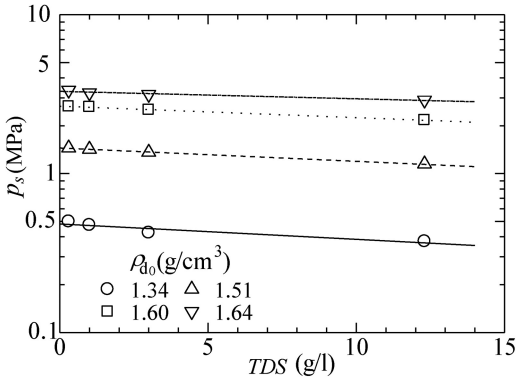


Figure 7. Total dissolved solids (TDS) *vs* swelling pressures (p_s) relation with different initial densities.

void ratio e and the dry density lead to the following $\rho_d - p_s$ relations:

$$\log p_{si} = \frac{a_0}{b_0} - \frac{1}{b_0}\log\frac{\rho_m}{\gamma_i \rho_s \alpha\beta}\left(\frac{G_s\rho_w}{\rho_d} - 1\right) \quad (i = 0, 12.3) \tag{6}$$

where, $p_{si}(i = 0$ and $12.3)$ are the swelling pressures of Na-bentonite saturated with distilled water and the solution with TDS = 12.3 g/l, respectively. G_s and ρ_d are specific gravity and dry density of bentonite, and ρ_w is the water density. γ_i $(i = 0$ and $12.3)$ are decay factors of bentonite saturated with distilled water and TDS concentration of 12.3 g/l.

Eq. (6) was depicted in Figure 6 in the log p_s-ρ_d plane. The two straight lines are almost parallel and the logarithmic value of the pressure (p_s) changed linearly with TDS at a given dry density (Fig. 7). Therefore, *TDS* was introduced as a variable to link Eq. (6) with $i = 0$ and 12.3:

$$\log p_s = \frac{a_0}{b_0} - \frac{1}{b_0}\log\frac{12.3\rho_m}{[12.3 - (1-\gamma_{12.3})TDS]\rho_s\alpha\beta}\left(\frac{G_s\rho_w}{\rho_d} - 1\right) \tag{7}$$

where the unit of TDS concentration is g/l.

Once the TDS concentration and dry density are known, Eq. (7) can be used to predict the swelling pressure when the TDS concentration ranges between 0 to 12.3 g/l. The comparison of the predicted swelling pressures with actually measured value is listed in Tables 4 and 5, indicating that the difference between predicted and measured swelling pressure is less than 10%, which is within the acceptable range of engineering practice.

Table 4. Measured and predicted swelling pressure for GMZ001 Na-bentonite.

Mt void ratio e_m	Initial dry density (g/cm^3)	*TDS* (g/l)	Measured pressure (kPa)	Predicted Pressure (kPa)
1.98	1.100	12.3	96	79
1.96	1.105	3.0	106	116
1.38	1.340	0.3	500	535
1.38	1.340	3.0	450	486
1.38	1.340	12.3	375	341
1.18	1.445	3.0	1100	915
1.16	1.457	12.3	1050	891
1.07	1.513	0.3	1450	1524
1.07	1.513	3.0	1362	1383
1.07	1.513	12.3	1150	1072
0.94	1.598	0.3	2650	2573
0.94	1.598	3.0	2525	2335
0.94	1.598	12.3	2175	1941
0.90	1.625	3.0	3050	2765
0.89	1.632	12.3	2950	2630
0.89	1.637	0.3	3350	3285
0.89	1.637	3.0	3150	2981
0.89	1.637	12.3	2900	2695
0.87	1.652	12.3	3250	2903
0.84	1.672	3.0	3850	3721

Note: Mt = montmorillonite

Table 5. Measured and predicted swelling pressure for GMZ07 Na-bentonite.

Mt void ratio e_m	Initial dry density (g/cm^3)	*TDS* (g/l)	Measured pressure (kPa)	Predicted Pressure (kPa)
2.08	1.20	12.3	112.5	92.8
2.09	1.20	3.0	129.3	131.8
2.09	1.20	0.3	131.3	145.1
1.80	1.30	12.3	206.3	167.7
1.81	1.30	3.0	220.0	238.3
1.81	1.30	0.3	243.8	262.4
1.54	1.41	12.3	337.5	320.0
1.55	1.41	3.0	398.3	454.6
1.55	1.41	0.3	412.5	500.6
1.43	1.48	12.3	600.0	497.5
1.46	1.45	3.0	600.0	575.0
1.46	1.45	0.3	600.0	633.3
1.34	1.50	12.3	787.5	543.6
1.35	1.50	3.0	812.5	772.2
1.35	1.50	0.3	975.0	850.4
1.01	1.69	12.3	2550	2007.4
0.98	1.71	3.0	2950	2745.9
0.98	1.71	0.3	3300	3024.0

Note: Mt = montmorillonite

5 CONCLUSIONS

The swelling characteristics of two GMZ Na-bentonites immersed in distilled water and saline solutions with different TDS concentrations were studied through the constant-volume tests and constant-stress tests. The test results showed that when GMZ bentonites were saturated with different TDS solutions, the relationship between the montmorillonite void ratio and swelling pressure was almost a straight line in double logarithmic plots for a given TDS concentration and was independent of the initial dry density. A predicted equation between the swelling pressure and dry density was obtained based on the linear relationship of the montmorillonite void ratio and swelling pressure.

The test results reveals that the relationship between the swelling pressure and void ratio for two GMZ Na-bentonites depends mainly on their montmorillonite contents. The TDS concentration was introduced in the prediction equation, from which the swelling pressure can be finally obtained for a given TDS concentration and dry density. A comparison of predicted and experimental swelling pressures showed that the discrepancy was within 10%.

ACKNOWLEDGEMENT

The authors express their gratitude for the grants provided by the National Natural Science Foundation of China (No.11272194).

REFERENCES

Alawaji H A (1999): Swell and compressibility characteristics of sand–bentonite mixtures inundated with liquids. *Applied Clay Science*, 15(3–4): 411–430.

Di Maio C (1996): Exposure of bentonite to salt solution: osmotic and mechanical effects. *Geotechnique*, 46: 695–707.

Guo Y H, Yang T X & Liu F S (2001): Hydrogeological characteristics of Beishan preselected area, Gansu province for China's high-level radioactive waste repository. *Uranium Geology*, 17(3): 184–189.

Komine H & Ogata N (1994): Experimental study on swelling characteristics of compacted bentonite. *Canadian Geotechnical Journal*, 31: 478–490.

Liu Y M & Chen Z R (2001): Bentonite from Gaomiaozi, Inner Mongolia as an ideal buffer/ backfilling material in handling highly radioactive wastes- a feasibility study. *Acta Mineral Sinica*, 21(3): 541–543.

Pusch R & Bergström A (1980): Highly compacted bentonite for borehole and shaft plugging. In: Proceedings of the Workshop on Borehole and Shaft Plugging, Columbus, OH, May 7–9, Organization for Economic Co-operation and Development, Paris pp: 161–168

Sun D A, Cui H B & Sun W J (2009): Swelling of compacted sand–bentonite mixtures. *Applied Clay Science*, 43: 485–492.

Xu Y F, Matsuoka H & Sun D A (2003): Swelling characteristics of fractal-textured bentonite and its mixtures. *Applied Clay Science*, 22: 197–209.

Zhu C M, Ye W M, Chen Y G, Chen B & Cui Y J (2013): Influence of salt solutions on the swelling pressure and hydraulic conductivity of compacted GMZ001 bentonite. *Engineering Geology*, 166: 74–80.

Unsaturated Soil Mechanics—from Theory to Practice – Chen et al. (Eds)
© 2016 Taylor & Francis Group, London, ISBN 978-1-138-02921-7

Geo-Barrier System as a retaining structure

H. Rahardjo, Q. Zhai, A. Satyanaga & E.C. Leong
School of Civil and Environmental Engineering, Nanyang Technological University

C.L. Wang & L.H. Wong
Building Research Institute, Housing and Development Board, HDB Hub, Singapore

ABSTRACT: Capillary Barrier System (CBS) is a cover system that can be used to control rainfall infiltration into a slope and improves the stability of the slope. The use of a capillary barrier system as part of a retaining structure for steep slopes has never been investigated. In this paper, the results of a study on the application of capillary barrier to a retaining structure using Geo-bags, named as a Geo-Barrier System (GBS) are presented. In addition, the use of recycled materials (e.g. recycled concrete aggregates and road asphalt) in forming the Geo-Barrier System is explored in this study as part of sustainable infrastructure development. Results of characterization of unsaturated properties of the recycled materials are also presented in this paper. The study shows that the Geo-Barrier System can be used effectively as a retaining structure and offers slope protection from rainfall-induced failures.

1 INTRODUCTION

Many cases of rainfall-induced failure were reported in tropical areas (Brand 1992; Gasmo et al. 2000; and Tsaparas et al. 2002). Soil above the ground water table in tropical areas generally consists of residual soils that have negative pore-water pressure (or matric suction). The matric suction in the residual soil increases the shear strength of the soil and therefore, increases the factor of safety of the residual soil slope. However, the matric suction in the soil would be reduced due to rainwater infiltration and the factor of safety of the residual soil slope would be decreased. Numerous researchers (Toll et al. 1999; Gasmo et al. 2000; Tsaparas et al. 2003; Rahardjo et al. 2005, 2006, 2007, 2010, 2011) studied the importance of rainfall infiltration on slope instabilities in tropical regions.

Capillary barrier system (CBS) which utilizes a fine-grained layer overlying a coarse-grained layer was first proposed for controlling rainfall infiltration and enhancing slope stability (Rahardjo et al. 2013). However, CBS is a cover system and does not act as a soil retaining structure. Singapore has limited land area with scarcity of natural resources. Creation of space to expand Singapore's land capacity and creating highly-livable and compact model towns become a high priority for her increasing population. A system that can prevent rainwater infiltration and also works as a soil retaining structure for steep slopes is needed. A Geo-barrier system which combines the capillary barrier system and Geo-bag is proposed in this project. It was proven numerically to work effectively for prevention of rainfall infiltration and improving slope stability.

2 LITERATURE REVIEW

Rahardjo et al. (2011) instrumented residual soil slopes in Singapore to study the effect of rainfall on the stability of slope. It was observed that the infiltration of rainwater would reduce the matric suction within the unsaturated zone and in turn, reduce the shear strength of soil. The reduction in shear strength might in turn cause slopes to become unstable and prone to failure. The schematic diagram of a capillary barrier system is illustrated in Figure 1. Rahardjo et al. (2013) indicated that the effective capillary barrier, a two-layer cover system, is minimizing infiltration dependent on the distinctly different hydraulic properties between a fine-grained layer and a coarse-grained layer of soil. Rahardjo et al. (2007) carried out parametric studies on three capillary barrier models and suggested the ratio of ψ_w, which defines the ratio between the water-entry values of the fine-grained layer and coarse-grained layer, to be greater than 10. In addition, two other controlling parameters that have to be considered in the material selection of CBSs are (1) the water-entry value, ψ_w of the coarse-grained layer and (2) the coefficient of saturated permeability of the fine-grained layer.

Geo-bag was produced by sewing a few sheets of geo-textile together, filled with soil and stacked in certain patterns. Geo-bags were normally used for coastal structures (Heerten et al. 2000, Saathoff et al. 2007, Oberhagemann et al. 2004, JMREM 2006, Jackson et al. 2006). With construction of an open channel hydraulic flume using Geo-bag, Akter et al. (2009) presented three failure models (i.e. piping, local vortices and overtopping) in the Geo-bag structure. Geo-bag

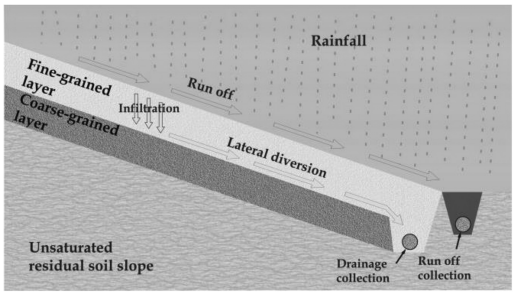


Figure 1. Schematic diagram of capillary barrier system (after Rahardjo et al. 2013).

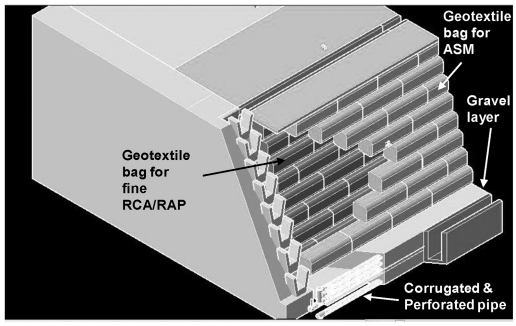


Figure 2. Schematic diagram of Geo-barrier system.

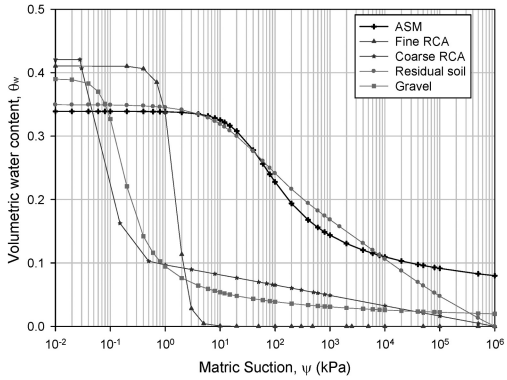
is an effective system for a retaining structure but it has never been designed for minimizing rainfall infiltration. A Geo-barrier system which was developed from capillary barrier system and Geo-bag structure can be used to minimize the rainwater infiltration and to increase slope stability using the principles of unsaturated soil mechanics.

3 GEO-BARRIER SYSTEM (GBS)

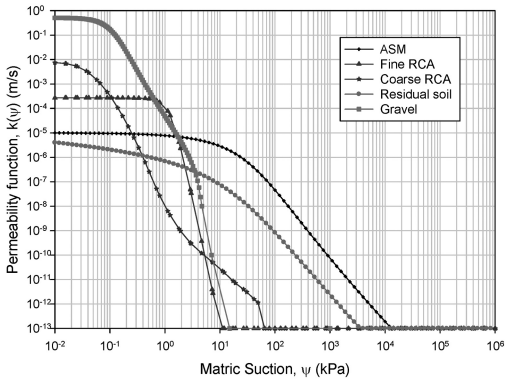
Figure 2 shows a schematic diagram of a GBS that will be constructed on a residual soil from Bukit Timah Granite in Singapore. The GBS consists of 2 layers, fine-grained material overlying coarse-grained material. In this study, fine recycled concrete aggregate (RCA) will be used as fine-grained material that will be placed inside Geo-bag within GBS whereas coarse RCA will be used as coarse-grained material within GBS. In order to facilitate the vegetation/plantation above GBS, the approved soil mixture (ASM) will be placed inside Geo-bag and located on top of Geo-bag. Gravel layer will be placed at the bottom of GBS to drain out the water from GBS into the main surface drainage. The GBS will be constructed with 75 degrees of slope angle and 4 meters of slope height.

The RCA used in this study was obtained from a recycling plant in Singapore. RCA was produced by feeding large pieces of construction and demolition waste into a jaw crusher. Laboratory tests for determination of saturated and unsaturated properties of RCA, approved soil mixture and residual soil from Bukit Timah Granite were carried out based on American Standards of Testing Methods (ASTM). The unsaturated properties which include the soil-water characteristic curves and permeability functions of fine and coarse RCA, approved soil mixture and residual soil are presented in Figure 3.

The site consists of a slope with an angle of 45 degrees and a height of 4 meters. The ground water table is observed at a depth of 1.86 meters and 4.54 meters below ground surface on the top and bottom of the slope, respectively, as illustrated in Figure 4(a). Four models were simulated using Seep/W and Slope/W as illustrated in Figure 4(a).



(a) SWCC of the soils used in the models

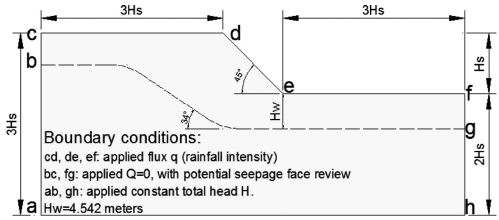


(b) Permeability functions of the soils used in the models

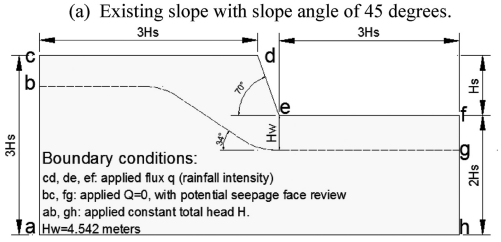
Figure 3. SWCCs and permeability functions of RCA, approved soil mixture (ASM) and residual soil from Bukit Timah Granite.

4 NUMERICAL SIMULATION

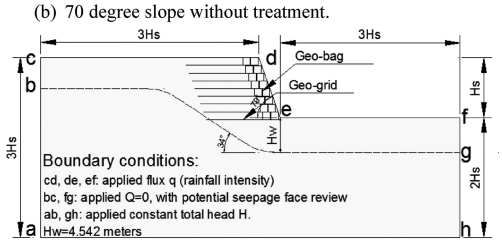
Two-dimensional seepage analyses were carried out using finite element software, SEEP/W (GEO-SLOPE International Pte Ltd., 2007a) and slope stability analyses were conducted using SLOPE/W (GEO-SLOPE International Pte. Ltd., 2007b). The boundary conditions applied to the finite element model are illustrated in Figure 4. The distance between the slope and the side



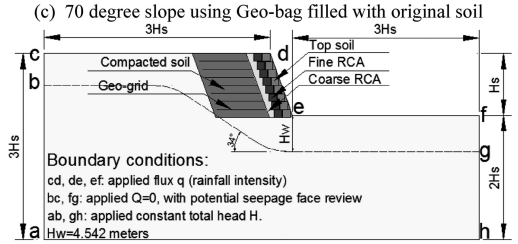
(a) Existing slope with slope angle of 45 degrees.



(b) 70 degree slope without treatment.



(c) 70 degree slope using Geo-bag filled with original soil



(d) 70 degree slope using Geo-barrier system (GBS)

Figure 4. Geometries and boundary conditions of four models.

of the slope model was set to three times the height of the slope to avoid the influence of the side boundary conditions. No flow boundaries were simulated by assigning a nodal flux, Q, equal to zero at the bottom and along the sides of the slope model above the groundwater table. A constant total head, h_w, on each side was applied as the boundary along the sides of the slope model below the groundwater table. Rainfall was applied to the slope surface as a flux boundary, q. Ponding was not allowed to occur on the slope surface. This meant that when a flux greater than the permeability of the soil was applied to the top boundary, the seepage model would not allow pore-water pressures at the ground surface greater than 0 kPa to build up. This simulated the actual field conditions where the excess rainfall at the slope surface is removed as runoff. The initial condition of the slope was taken based on the position of groundwater table in the field. The finite element model within the CBS and residual soil layer

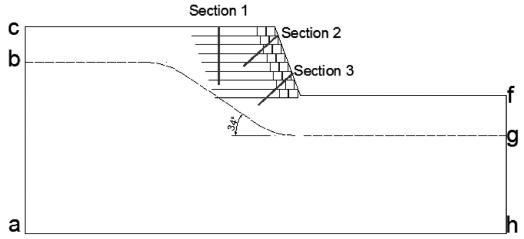


Figure 5. Illustration of sections for monitoring of pore-water pressure profiles.

Table 1. Parameters of material and Geo-grid used for slope stability analyses.

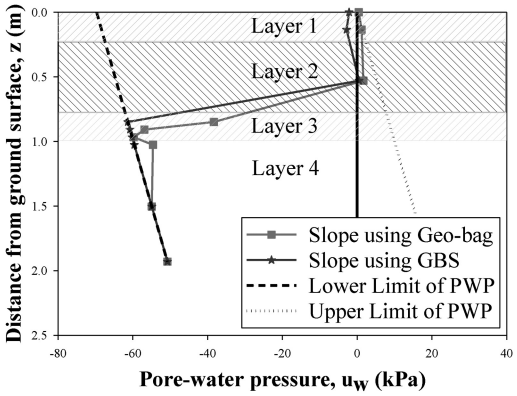
Soil Description	γ' (kN/m^3)	c′ (kPa)	ϕ' (degree)	ϕ^b (degree)
Approved soil mixture	18	2	30	15
Fine RCA	20	0	34	17
Coarse RCA	21	0	35	17
Residual soil	18	5	28	14
Gravel	21	0	34	17

Geo-grid	Fabric Capacity (kPa)	Interface ϕ (degree)	Length L (m)
	28	19	2.3

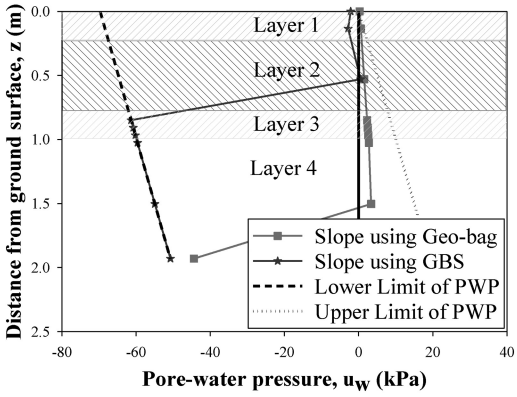
down to 5 m below the slope surface had a mesh size of approximately 0.5 m, smaller than elements in other parts of the slope, in order to obtain accurate results within the infiltration zone.

The site investigation results indicated that the ground water table is located at a depth of 1.86 m and 4.54 m below the ground surface on the top and bottom of the designated slope, respectively (Figure 4a). The SWCCs and permeability functions of residual soil from Bukit Timah Granite, coarse RCA, fine RCA, gravel and approved soil mixture as shown in Figure 3 were used in the seepage analyses. The rainfall intensity of 22 mm/h with 24 hours duration was applied to the slope for the seepage analyses. Four cases of seepage analyses were carried out in this study to investigate the behavior of slope without GBS with 45° slope angle (Figure 4a), the behavior of slope without GBS with 75° slope angle (Figure 4b), the behavior of slope covered with Geo-bag filled with the residual soil from Bukit Timah Granite (Figure 4c) and the behavior of slope covered with GBS (Figure 4d).

In case 3 (Figure 4c), the properties of the residual soil from Bukit Timah Granite was assigned to the material inside the Geo-bags while in case 4 (Figure 4d) the properties of the approved soil mixture, fine RCA and coarse RCA were assigned to the materials inside the Geo-bags. Figure 5 indicates three sections

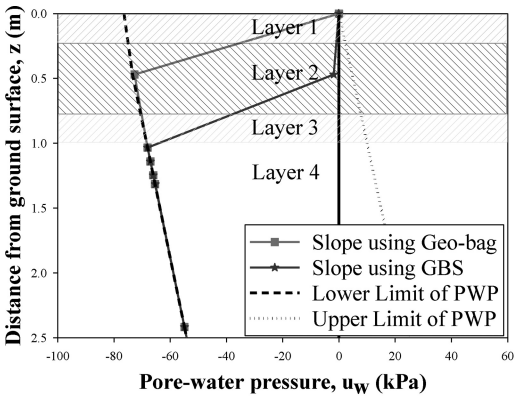


(a) After 12 hours of rainfall.

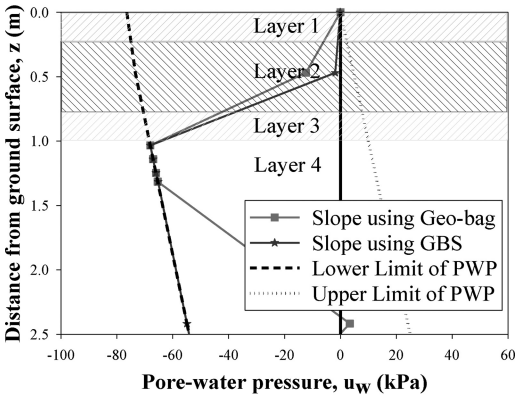


(b) After 24 hours of rainfall.

Figure 6. Pore water pressure profiles on Section 1.



(a) After 12 hours of rainfall.



(b) After 24 hours of rainfall.

Figure 7. Pore water pressure profiles on Section 2.

that were observed during seepage analyses of cases 3 and 4.

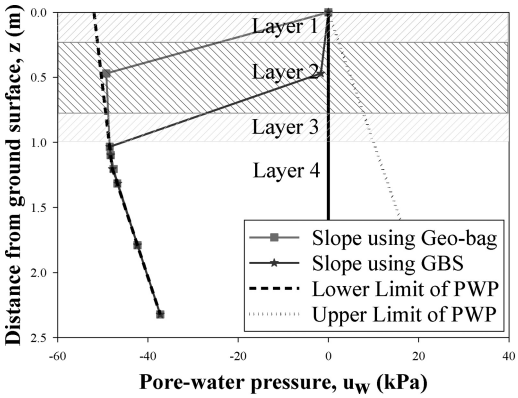
Stability analyses in this study were performed using Slope/W by incorporating the pore-water pressure from seepage analyses. The variation in factor of safety obtained from the four models of slope stability analyses were calculated using Bishop's simplified method of slices. For case 4, stability analyses of slope covered with GBS, Geo-grid was incorporated in the analysis. The Geo-grid was designed and connected to the Geo-bag to work as a tie-back system since the Geo-bag is insufficient for a retaining structure of 4 m high slope. The parameters of materials and geo-grid used in the slope stability analyses are summarized in Table 1.

5 RESULTS AND DISCUSSIONS

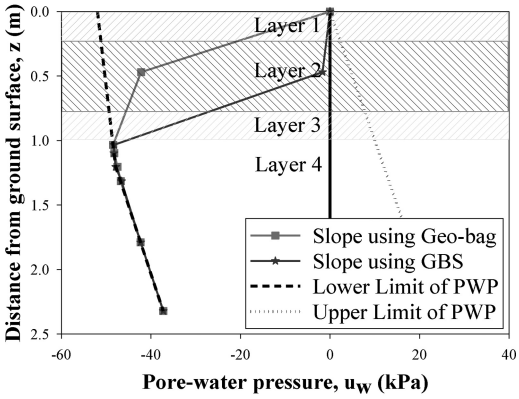
The pore water pressure profiles within sections 1, 2 and 3 (see Figure 5) from the seepage analyses of case 3 (slope using Geo-bag) and case 4 (slope using GBS) are shown in Figures 6 to 8. The upper limit of PWP represented the possible maximum PWP when the GWT reached ground surface while the lower limit of PWP represented the possible maximum matric suction as calculated from the original GWT under hydrostatic condition. Figures 6 and 7 indicate that rainfall infiltration could be controlled using GBS (i.e. rainwater could only flow within the layer of fine RCA and top soil) while the normal Geo-bag could not control the rainwater infiltration. As the slope was very steep and most of the rainfall became run-off on the slope, there was no significant difference in pore-water pressures on Section 3 for both models as illustrated in Figure 8.

The factors of safety (FOS) computed using Slope/W for these three models are illustrated in Figure 9 and the comparison of factor of safety for the three models is illustrated in Figure 10. As the computed FOS for the model with a 70° slope was less than 1 (i.e. between 0.78 and 0.76), meaning that the slope should have failed, the FOS is not plotted in Figures 9 and 10.

Figure 10 indicates that factor of safety (FOS) dropped by about 38% (i.e. decreases from 1.23 to 0.76) by changing the slope angle from 45° to 705°. In other words, the slope would not be able to stand at an angle of 70°. The FOS of the slope at 70° could be



(a) After 12 hours of rainfall.



(b) After 24 hours of rainfall.

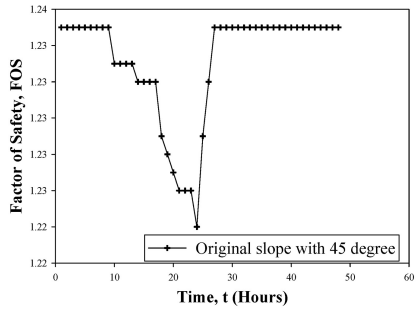
Figure 8. Pore water pressure profiles on Section 3.

increased to 1.87 when Geo-bags filled with residual soil were used. However, PWP could build up behind the Geo-bags due to rainfall infiltration as shown in Figures 6 to 8. As a result, the value of FOS would be further reduced from 1.87 to 1.25 because of the reduction in matric suction due to rainwater infiltration.

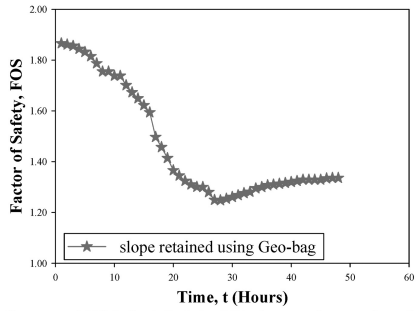
On the other hand, GBS could enhance slope stability by increasing FOS from 0.76 to 1.92. Figures 6 to 8 indicate that PWP behind GBS was well controlled during the heavy rainfall period due to the capillary barrier mechanism of the GBS (i.e. minimizes rainfall infiltration into the soils behind GBS). As a result FOS only decreased from 1.92 to 1.75 due to the heavy rainfall applied. In addition, there was no further reduction in FOS (i.e. remained constant at 1.75) after the rainfall had stopped.

6 CONCLUSIONS

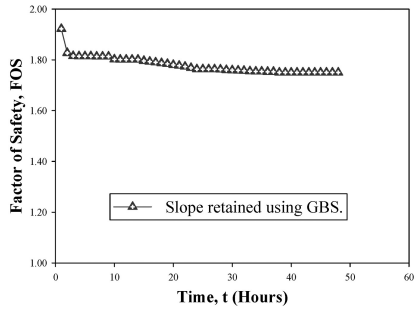
A new slope protection system named as Geo-barrier system (GBS) is proposed. The GBS can be used as a retaining structure that utilizes capillary barrier mechanism for controlling rainfall infiltration into the



(a) Computed FOS for Model of existing slope with slope angle of 45°



(b) Computed FOS for Model of 70 degree slope using Geo-bag filled with original soil.



(c) Computed FOS for Model of 70 degree slope using Geo-barrier system (GBS)

Figure 9. Computed FOSs for three models.

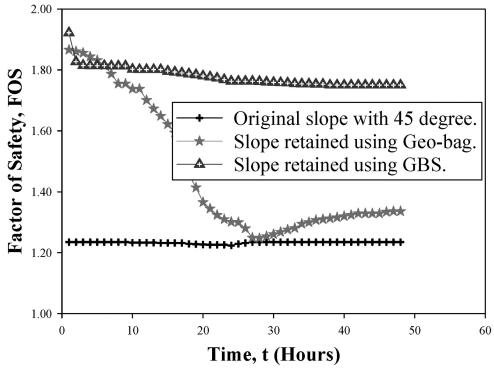


Figure 10. Comparison of FOSs for three Models.

original soil behind the retaining structure. The results of the numerical analyses illustrated that GBS is an effective method for a retaining structure and slope stabilization.

ACKNOWLEDGEMENT

The work described in this paper was supported by the Ministry of National Development (MND), Housing and Development Board (HDB) and Nanyang Technological University, Singapore.

REFERENCES

Akter, A., Wright, G., Crapper, M., & Pender, G., (2009) "*Failure Mechanics in Geo-bag structure.*" Proceedings of the 4th IASME/WSEAS Int. Conference on WATER RESOURCES, HYDRAULICS & HYDROLOGY (WHH'09).

Gasmo, J. M., Rahardjo, H. & Leong, E. C. (2000) "*Infiltration effects on stability of* residual soil slope." Computers and Geotechnics 26, 145–165.

Heerten, G., Jackson, L.A., Restall S. & Stelljes K. (2000) "*Environmental Benefits of Sand Filled Geotextile Structures for Coastal Applications*", GeoEng 2000, Melbourne, Australia.

Jackson, L.A., Corbett, B.B. & Restall, S. (2006) "*Failure Modes and Stability Modelling for Design of Sand Filled Geosynthetic Units in Coastal Structures*', 30th International Conference on Coastal Engineering, San Diego,

JMREM (2006), "*Jamuna-Meghna River Erosion Mitigation Project Part B*", Special Report 21, Site Data and Details of Work, Government of the People's Republic of Bangladesh, Asian Development Bank and Bangladesh Water Development Board, Vol. I.

Oberhagemann K. & Kamal M.S. (2004) "*Geobag Protection in Bangladesh*", 4th international Conference on filters and Drainage in Geotechnical and Environmental Engineering, Geofilters, pp. 205–216.

Rahardjo, H., Lee, T. T., Leong, E. C. & Rezaur, R. B. (2005) "*Response of a residual soil slope to rainfall.*" Can. Geotech. J., 42(2), 340–351.

Rahardjo, H., Lee, T. T., Leong, E. C. & Rezaur, R. B. (2006) "Reply to Discussion by Londono A. C. on "Respsonse of a residual soil slope to rainfall." by Rahardjo, H., Lee, T. T., Leong, E. C. and Rezaur, R. B. [Can. Geotech. J., 42: 340–351 (2005)]." Can Geotech. J., 43, 979–984.

Rahardjo, H., Ong, T. H., Rezaur, R.B. & Leong, E. C. (2007) "*Factors controlling instability of homogeneous soil slopes under rainfall loading.*" ASCE J. of Geotechnical and Geoenvironmental Eng. 133 (12), 1532–1543.

Rahardjo, H., Ong, T. H., Rezaur, R.B., Leong, E. C. & Fredlund, D. G. (2010) "*Response parameters for characterization of infiltration.*" Environmental Earth Science, 60(7), 1369–1380.

Rahardjo, H., Santoso, V. A., Leong, E. C., Ng, Y. S. & Hua, C. J. (2011) "*Numerical analysis and monitoring performance of residual soil slopes.*" Soils and Foundations Vol. 51, No.3, 471–482.

Rahardjo, H., Santoso, V. A., Leong, E. C., Ng, Y. S., Tam C.P.H. & Satyanaga A. (2013) "*Use of recycled crushed concrete and Secudrain in capillary barriers for slope* stabilization." Canadian Geotechnical Journal 50: 1–12.

Saathoff, F., Oumeraci, H & Restall, S.,(2007) "*Australian and German experiences on the use of Geotextile Containers.*" Geotextiles and Geomembranes, Vol. 25, No. 4–5, pp. 251–263.

Tsaparas, I., Rahardjo, H., Toll, D.G. & Leong, E. C. (2002) "Controlling parameters for rainfall-induced landslides." Computer and Geotechnics, 29(1), 1–27.

Unsaturated Soil Mechanics—from Theory to Practice – Chen et al. (Eds)
© 2016 Taylor & Francis Group, London, ISBN 978-1-138-02921-7

Numerical stimulation of geogrid reinforced flexible supporting treating expansive soil cut slope

J. Xiao, H.P. Yang & S.Y. Zhu
School of Traffic and Transportation Engineering, Special Soil Engineering Research Institute, Changsha University of Science and Technology, Changsha, China

ABSTRACT: The influence of different interface strength parameters, various reinforcement spacing, enveloping with or without geogrid on flexible supporting reinforced expansive soil cut slope was researched by numerical stimulation considering the decay of shear strength of expansive soil in combination with shear strength parameters determined by laboratory measured expansive soil nonlinear strength envelope. The results show that the geogrid can effectively restrain the slope horizontal displacement, decrease soil expansion softening effect to a certain extent; the maximum axial force changes along the height for different geogrid reinforcement spacing is basically the same; expansive soil slope stability is greatly influenced by the reinforcement spacing. The smaller the spacing, the better the slope stability; the enveloped geogrid can improve its resistance to erosion and the integrity of the slope.

1 INTRODUCTION

The strength of expansive soils is particularly sensitive to the surrounding environment due to containing hydrophilic minerals such as smectite. The failure of expansive soil slope is one of the most serious geological disasters (Liao 1984; Li et al. 1992; Qu et al. 2000; Qu et al. 2002; Yang and Zheng 2004). There is no economical reasonable and effective measures treating the failure of expansive soil slope before the research group of expansive soil at Changsha University of Science & Technology initiated and implemented geogrid reinforced flexible supporting technology which has successfully treated the failure of expansive soil slope in Ningming basin at Nanning-Youyiguan expressway in 2004. Fourteen expansive soil failure slope treated by this measure are still stable for more than 10 years. In recent years, Xu et al. (2007), Cai et al. (2008), Ding (2014) and other individuals carried out numerical simulation of geogrid reinforced slope canal of expansion soil and got some meaningful results. Xiao et al (2014) also found some valuable conclusions by the contrast model test of expansive soil slope reinforced by geogrid or not. But the real working mechanism of expansive soil cut slope reinforced by geogrid is not very clear.

This paper considered rainfall, evaporation and other long-term weathering resulting in the attenuation of expansive soil shear strength and applied nonlinear strength line of measured expansive soil to select the shear strength parameters. By using the finite difference software FLAC 2D to analyze the changes in the relationship between stress and strain, the interaction characteristics of geogrid and expansive soil caused by the expansion of surficial weathered soil during rainfall. The impact of different strength parameters on the soil interaction interface, reinforced layer spacing slope enveloped or not and the other factors are made further study on the mechanism of geogrid reinforced flexible supporting treatment on expansive soil slope and found the inhibitory effect of geogrid on shallow failure of slope.

2 NUMERICAL CALCULATION MODEL

The construction schematic design of expansive soil cut slope treated by geogrid reinforced flexible supporting are shown in the Figure 1.

According to the actual construction plans, simplified numerical model is established in Fig. 2. For the calculating slope model, the height is 6.0 m, the slope rate is 1:1.5 and the total grid units are 1014. The width of horizontal reinforcement is 3.5 m, which is in agreement with the vertical depth in 2.32 m of weathered layer. Based on the degree of weathering, the soil is divided into four layers of 0.5 m, 0.5 m, 0.66 m and 0.66 m. Left and right boundaries are rolling constraint, the bottom is fixed constraint.

3 SELECTION OF CALCULATION MODEL PARAMETERS

A lot of cracks occurs in the reinforced expansive soil slope due to wet and dry cycles resulting in the continually decay of shear strength. The shear strength envelope with the increase in normal stress

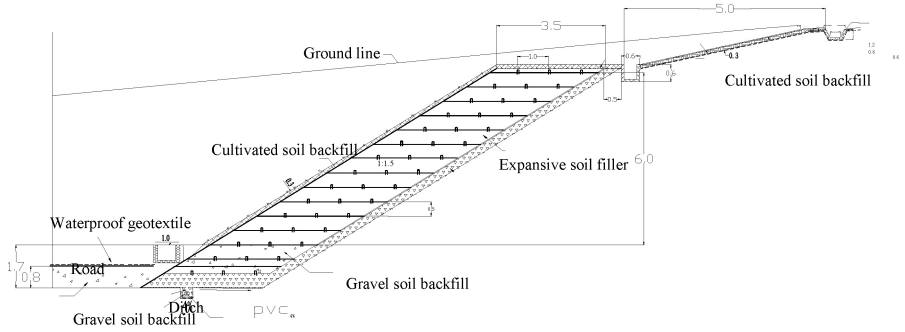


Figure 1. Schematic diagram geogrid reinforced expansive soil slope.

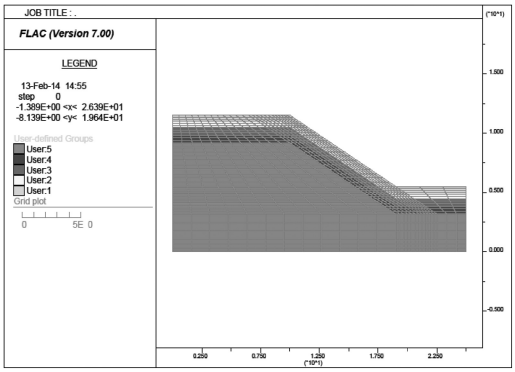


Figure 2. Numerical model diagram.

is nonlinear, which can be fitted well by generalized power function (Xiao et al. 2014), as Eq. (1).

$$\tau = S_{NL}\left(\sigma\middle|A,n,T\right) \equiv P_a A\left(\frac{\sigma}{P_a}+T\right)^n \tag{1}$$

Where: P_a is atmospheric pressure; $\{A, n, T\}$ are dimensionless strength parameters; $S_{NL}(\sigma|A, n, T)$ is nonlinear strength function.

By Eq. (1), the effective friction angle, ϕ_t, as shown in Eq. (2):

$$\varphi_t' = \tan^{-1}\left(\frac{An}{\left(\sigma/P_a+T\right)^{(1-n)}}\right) \tag{2}$$

Combination of Eq. (1) and (2), the effective cohesion c_t can be obtained as the following Eq. (3):

$$\begin{aligned} c_t' &= P_a A\left(\frac{\sigma}{P_a}+T\right)^n - \sigma\times\frac{An}{\left(\sigma/P_a+T\right)^{(1-n)}} \\ &= \frac{A\left[(1-n)\sigma+P_aT\right]}{\left(\sigma/P_a+T\right)^{(1-n)}} \end{aligned} \tag{3}$$

When the limit equilibrium method is used to analyze the slope stability, it is very easy to calculate normal stress at the bottom surface of sliding soil slices. Thus, the nonlinear strength function can only be directly used to analyze the slope stability firstly assuming the sliding surface. But using FLAC 2D to analyze slope stability, it is found that this method could not be directly applied because the slip surface is unable to be determined in advance.

Under six wet and dry cycles with loading for the compacted expansive soils, A, T and n of nonlinear saturation drained shear strength are 0.4691, 0.0352 and 0.8352, respectively. The corresponding cohesion and friction angle determined by the normal stresses of 5 kPa, 10 kPa, 20 kPa and 50 kPa are (3.1 kPa, 30.5°), (3.4 kPa, 28.6°), (4.1 kPa, 26.5°) and (6.2 kPa, 23.5°) to approximately replace the nonlinear drained shear strength parameters of the soil of 1–4 four layers of 3.5 m reinforced body. In general, it is assumed that the undisturbed soil at the rear of 3.5 m reinforced body is nearly influenced by wet and dry cycles. Therefore, the cohesion and friction angle of conventional linear fitting saturated drained shear strength obtained from unweathered undisturbed soil under no wet and dry cycles for the 5th soil are 30.4 kPa and 28.5° (Xiao et al. 2014).

It is supposed that the dry density, saturation and porosity for the initial state of the model are the same of 1700 kg/m^3, 54% and 0.40, respectively. The saturated permeability coefficient of the top two layers (1 and 2), the middle two layers (3 and 4) and the innermost layer (5) are 2.3e^{-6} m/s, 2.3e^{-7} m/s and 2.3e^{-8} m/s, respectively.

The basic characteristic parameters of expansive soil are shown in Table 1.

Simulation of geogrid unit is used the Cable built-in FLAC 2D. Parameters of geogrid and reinforcement interface are shown in Table 2.

4 RESULTS AND ANALYSIS

4.1 *Comparative analysis of reinforced effect*

First of all, numerical simulation on reinforced and unreinforced expansive soil slope is carried out to investigate the effect of reinforcement. Among them, the reinforced slope has no enveloped, the spacing of geogrid reinforcement is 0.5 m, its length is 3.5 m,

Table 1. Expansive soil basic characteristic parameters.

Number of soil	Dry density/ ρ (kg/m^3)	Bulk modulus/ K(MPa)	Shear modulus/ G(MPa)	Thermal expansion coefficient/α(m/K)	Strength parameters	
					Cohesion/c (kPa)	Internal friction angle/ϕ(°)
1	1700	8.710	2.394	2.34e^{-5}	3.1	30.5
2					3.5	29.6
3					5.7	27.7
4					8.5	26.3
5					30.4	28.5

Table 2. Parameters of geogrid and reinforcement interface.

Geogrid models	Thickness/(m)	Elastic Modulus/(Mpa)	Interfacial shear stiffness/(kN/m)	Geogrid spacing/m	Interfacial cohesion/(kPa)	Interface friction angle/(°)
RS 35PP	5e-4	450	4.7e^3	0.5	5	5
				0.25	10	10
				0.5		
				0.75		
				1.0		
				0.5	15	15
				0.5	20	20

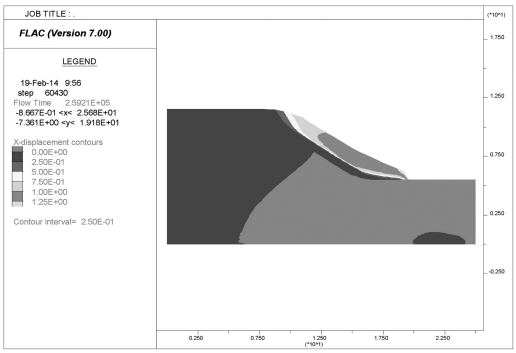


Figure 3. Horizontal displacement of unreinforced slope.

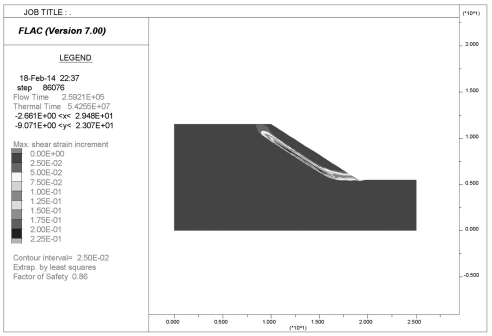


Figure 4. Maximum shear strain increment and safety factor of unreinforced slope.

the interface cohesion and friction angle are 10 kPa and 10°.

Figure 3 is a horizontal displacement of calculated unreinforced slope. Figure 4 is the maximum shear strain increment and the safety factor schematic after the strength reduction. It can be seen that the maximum horizontal displacement of unreinforced slope reaches 1.25 m, the safety factor is 0.86 and the depth of slip surface is 1.5 m. It indicates that unreinforced slope in the role of wet-dry cycle with the shear strength of expansion soil decreasing, and the shallow failure of expansive soil slope will occur in case of continuous rainfall.

Figure 5 to Figure 7 are the geogrid axial force of reinforced slope, horizontal displacement of slope, and maximum shear strain increment and safety factor of reinforced slope. It can be seen that the maximum axial force of geogrid increases with height increasing. Its value increases firstly and then decreases, the maximum of which is 2.545 kN in the sixth layer.

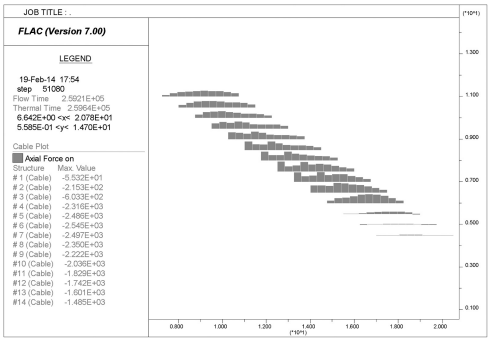


Figure 5. Axial force of reinforced slope.

The location of the maximum axial force of horizontal geogrid is basically the same to the sliding surface position of unreinforced slope about 2/3 width of the distance to the slope surface. The maximum horizontal displacement of reinforced slope slopes is only

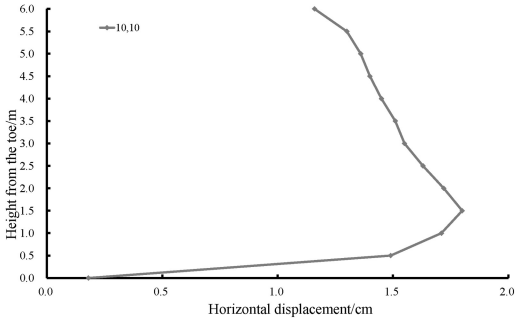


Figure 6. Horizontal displacement of reinforced slope.

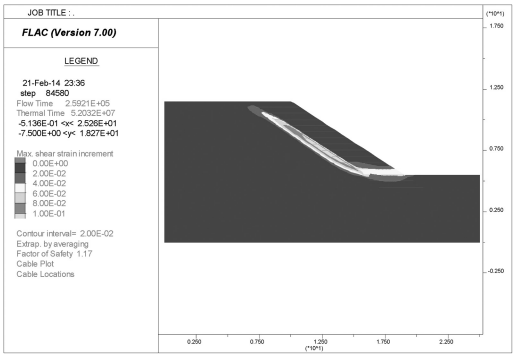


Figure 7. Maximum shear strain increment and safety factor of reinforced slope.

1.80 cm at the 1.5 m height from the toe of slope, which significantly reduced with comparison of unreinforced slope. The safety factor of reinforced slope is 1.17, but the location of the most dangerous sliding surface moved to from shallow to the rear of reinforced body. Therefore, the interactions between geogrid and reinforced soil effectively restricted the horizontal displacement of the slope.

4.2 *Effects of different interface parameters*

Figure 8 shows the horizontal displacement of the reinforced slope with different interface parameters.

For comparison, the maximum axial force changes in height for various interface parameters is shown in Figure 9. It is easy to know that when the interfacial strength parameters change from small to large, the maximum axial forces of geogrid are 2.768 kN, 2.545 kN, 2.545 kN and 2.499 kN, which appear at the 4th layer (the height is 0.5 m), 6th layer (the height is 1.5 m), 6th layer (the height is 1.5 m) and 7th layer (the height is 2.0 m), respectively. The difference between the maximum and minimum is only 0.269 kN, and the change curve of the geogrid maximum axial force along the height coincides basically (except the smallest). The maximum horizontal displacement of the slope are 2.19 cm, 1.80 cm, 1.80 cm and 1.75 cm, the positions of which are all located at a height of about 1.5 m. The change curve of horizontal displacement

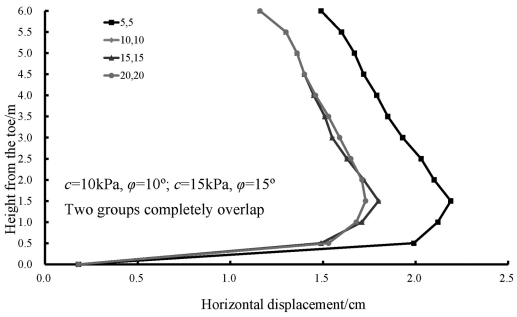


Figure 8. Horizontal displacement of reinforced slope for various interface parameters.

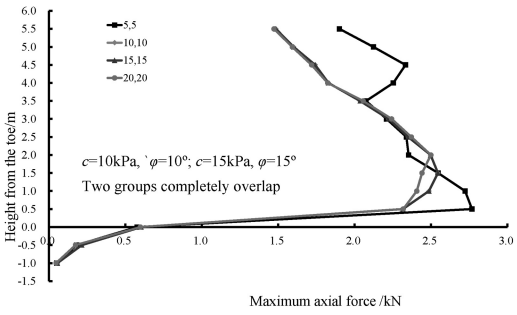


Figure 9. Maximum axial force change in height for various interface parameters.

along the height coincides basically (Except the smallest). The safety factors are 1.08, 1.17, 1.24 and 1.31, but the most dangerous sliding surface is at the same location. Substantially, as the effective shear stress distribution, the maximum of about 20 kPa appeared at the toe of slope. It can be seen that the changes of maximum axial force of geogrid have a small impact on the stress of reinforced geogrid, stress field in the body of reinforced soil and the displacement of slope when the interfacial strength parameter greater than a certain value, but the safety factor will continually increase with the interface strength increasing. It is noteworthy that even when the apparent cohesion and apparent friction angle of the interface parameters between soil and geogrid are 5 kPa and 5° in the case of three days heavy rainfall and without the strengthen role of geogrid for permeability and strength of soil, the safety factor is also 1.08 still greater than 1.0. It is not in a limited equilibrium state which indicates the presence of geogrid can significantly improve the stability.

4.3 *Effects of different reinforced spacing*

Fig. 10 and Fig. 11 are horizontal displacement of reinforced slope for various reinforced spacing and maximum axial force change in height for various reinforced spacing.

It is easy to know that under the conditions of different geogrid spacing, the maximum axial forces of each layer are the same in variation along the height,

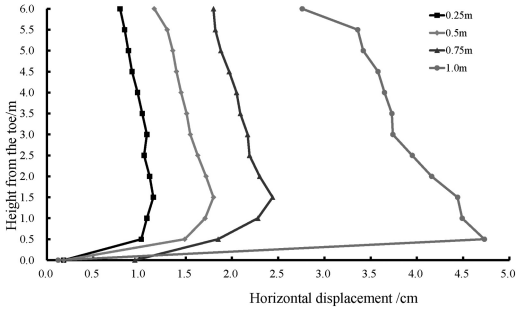


Figure 10. Horizontal displacement of reinforced slope for various reinforced spacing.

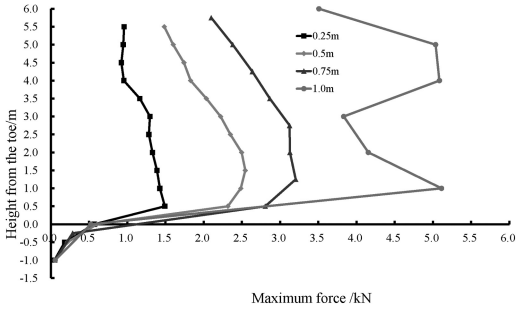


Figure 11. Maximum axial force change in height for various reinforced spacing.

which decreases firstly and then increases. The smaller geogrid spacing, the smaller the maximum value. Such as the four kinds of slope geogrid of reinforced spacing are 0.25 m, 0.5 m, 0.75 m and 1.0 m, the maximum axial force are 1.499 kN, 2.545 kN, 3.235 kN and 5.3 kN. The horizontal displacement of slope increases with height firstly and then decreases. When the geogrid spacing changes from 0.25 m to 0.75 m, the difference between the two displacements is more consistent, but when the geogrid spacing increases from 0.75 m to 1.0 m, the displacement difference changes large. The differences of maximum reinforced spacing are 1.17 cm, 1.80 cm, 2.43 cm and 4.75 cm. The safety factors of 1.33, 1.17, 1.11 and 1.06 decreased with the reinforced spacing increasing and the critical sliding surface position is consistent. Thus, geogrid spacing has greater impact on slope stability of expansive soils. The smaller the geogrid spacing, the higher the slope stability. Therefore, the reason is probably the smaller geogrid spacing, the more layers slope divided which result in the smaller thickness of the reinforced soil and the smaller moisture expansion softening effect of soil. On the other hand, with the increase in the number of geogrid, the ability to limit soil horizontal distortion is enhanced. However, in terms of the actual project, the geogrid spacing is not the smaller the better, which need to combine practical engineering properties, construction of operability and economic and other factors to determine the geogrid spacing.

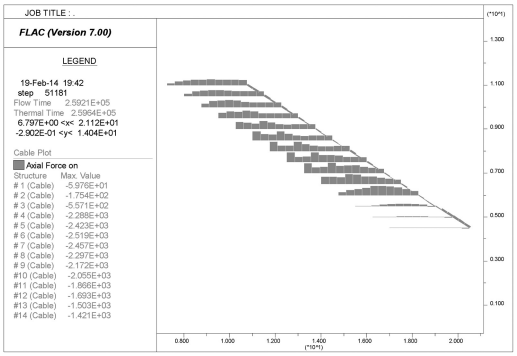


Figure 12. Axial force of geogrid enveloped reinforced slope.

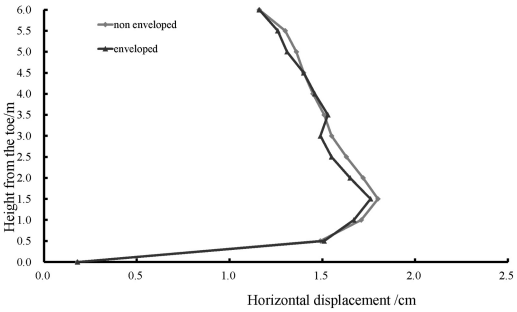


Figure 13. Horizontal displacement of enveloped and enveloped slope.

5 IMPACT OF GEOGRID ENVELOPED OR NOT

Due to the construction of reinforced expansion soil slope making the geogrid enveloped layer by layer, each layer set aside a certain length of geogrid and then connected with the upper geogrid by a connecting rod, and used staples of "U" shaped to fix the geogrid at the end, so that the reinforcement formed an integral to play a role. But the mechanical response of enveloped geogrid also needs to study. Therefore, the strength parameters cohesion and friction angle of the reinforcement and soil interaction are 10 kPa and 10°, the geogrid spacing is 0.5 m. A numerical simulation of slope enveloped by geogrid and a comparative analysis with that enveloped without geogrid is made to study the effects.

The axis force distribution of the horizontal reinforcement grid in the enveloped slope is in the Fig. 12. Fig. 13 shows the horizontal displacement of enveloped and no enveloped reinforced slope.

The maximum axial forces of each layer are the same in variation along the height, the maximum value appears in the 6th layer with value of 2.519 kN. It is slightly less than 2.545 kN obtained from that without enveloped. The maximum axial force of enveloped geogrid is 0.514 kN that appears at the toe of the slope, which makes the axial force of horizontal geogrid near the slope become larger. However, the maximum axial

force decreases slightly. The maximum horizontal displacement is at the same position, but the value is slightly smaller (1.75 cm), and the safety factors are also the same as 1.17. Thus, it is almost no effect on the safety factor of the slope compared without geogrid enveloped. Although the axial force of horizontal geogrid near the slope surface increased slightly and the horizontal displacement of slope decreased slightly. The reason must be that the critical sliding surface of the slope has been moved to the rear of reinforcement from the shallow after horizontal geogrid stiffened. The reinforced body can be seen as a whole. Enveloped geogrid changes the stress state of horizontal geogrid and soil, which make a more holistic in reinforced body and ensure the stability of the reinforced body. In fact, the strength of the soil behind reinforcement is become a decisive role for slope stability. But on the other hand, the enveloped geogrid has a protective role of effectively reducing the impact of the role of wet-dry cycle by rainfall and evaporation for the reinforced soil. And when the surface soil expansion, the ability to limit the level of expansion is slightly stronger than the slope without enveloped geogrid.

6 PRINCIPLE OF FLEXIBLE SUPPORTING

The shallow failure of expansive soil slope often occurred under the wet and dry cycles, which can be treated successfully using the treatment of geogrid reinforced flexible supporting technologies. On the one hand, reinforced geogrid made an effective segmentation of the slope, and the development depth of fissure in slope is limited after reinforced. The deepest of each crack is only the distance of reinforcement spacing due to the presence of geogrid restraining further expansion of cracks. Therefore, the cracking of reinforced soil will not develop as natural slope or expansive soil slope under the role of wet-dry cycle, and cannot reach to the interface of weak weathered and unweathered layer. In addition, the reinforcement became a very thick supporting body due to the geogrid considerably limited the expansion of the soil and prevent its disintegration in a certain. The supporting body can guarantee not destroy itself because of the slope rate is general gentler. Supporting body has a certain weight equivalent to exert a certain amount of additional pressure on the slope soil, which limit expansion of the soil to effectively maintain its strength. Therefore, geogrid reinforced flexible support can effectively solve the shallow failure of expansive soil slope.

7 CONCLUSIONS

(1) The interactions between geogrid and reinforced soil restricted the horizontal displacement of the slope effectively. This reduced the expansion softening effect of soil and improved its strength indirectly, which made the critical sliding surface transfer to a deep slope.
(2) The maximum axial force of geogrid is minor influenced by the soil interface parameters. The changes of maximum axial force of geogrid have a small impact on the stress of reinforced geogrid, stress field in the body of reinforced soil and the displacement of slope. The safety factor will continually increase with the intensity of interface increasing. The slope stability can be significantly improved by adding the geogrid even the apparent soil interface parameters small.
(3) The maximum axial force of each layer is the same in variation of height with different geogrid spacing. Geogrid spacing have a greater impact on the stability of expansive soil slope, the smaller the spacing, the higher the slope stability.
(4) The enveloped geogrid can improve the resistance to erosion of slope and integrity of the slope, and can make the axial force of horizontal geogrid near slope slightly increased and horizontal displacement of slope slightly decreased.

REFERENCES

Cai, J.T., Wang, M.Y. & Zhou, X.W. et al. 2008. Analysis of expansive soil slope stability reinforced by geogrid under the condition of moisture absorption. Yangtze River 39(11):84–88.

Ding, J.H. 2014. Research on failure mechanism of shallow instability of expansive soil slope and geogrid-confined effect on swelling deformation. Zhejiang University.

Liao, S.W. 1984. Expansive Soil and Railway Engineering. Beijing: China Railway Publishing House.

Li, S.L., Qin, S.J, & Bo, Z.Z. et al. 1992. Chinese expansive soil engineering geological studies. Nanjing: Jiangsu Science and Technology Publishing House.

Qu, Y.X., Zhang, Y.S. & Yang, J.F. et al. 2000. Theory and practice of classification of rock soil engineering geology, the integration of the expansion Chinese. Fifty years for chinese engineering geology. Beijing: Seismological Press: 140–164.

Qu, Y.X., Feng, Y.Y. & Zhang, Y.S. 2002. Discuss on some basic problems in studying the expansive rock (soil) of Nanning Kunming railway. Chinese Geological Scientific Research Institute of Geological Engineering Center.

Xiao, J., Yang, H.P. & Fu, H. et al. 2014. Comparison model test on effect of geogrid reinforcement for expansive soil slope. C*hina Journal of Highway and Transport* 27(7): 24–31.

Xiao, J., Yang, H.P. & Wang, X.Z. et al. 2014. Analysis of nonlinear characteristics of shear strength of Nanning expansive soil and its influencing factors. *China Journal of Highway and Transport* 27(10):1–8.

Xu, H., Wang, M.Y. & Huang, B. et al. 2007. Numerical stimulation research on canal slope of expansive soil strengthened by geogrid. *Rock and Soil Mechanics* 28(S1):599–603.

Yang, H.P. & Zheng, P. 2004. Geological investigation and reflection on the expansive soil in Nanning-Youyiguan highway. *Journal of Changsha University of Science and Technology (Natural Science)* 1(1): 14–19.

Unsaturated Soil Mechanics—from Theory to Practice – Chen et al. (Eds)
© 2016 Taylor & Francis Group, London, ISBN 978-1-138-02921-7

The effect of traffic loading to buried water mains in partially saturated soils

C. Randeniya, D.J. Robert & C.Q. Li
School of Civil, Environmental and Chemical Engineering, RMIT University, Melbourne, Australia

ABSTRACT: Most of the water pipelines are buried in unsaturated soils. However, the design considerations and analytical solutions for buried water mains assume that the soil is either dry or fully saturated. In unsaturated soils, such assumption often leads to incorrect estimation of induced deformation/stress on buried water pipes by external loads such as from traffic loading. These different anticipated loads are generated because the water meniscus between soil particles creates an additional normal force due to suction, which in turn makes the soil stiffer and stronger. Such stiff soil could contribute to absorb external energy induced by traffic loading (i.e. less pipe mobilize), while providing additional support to the pipe by restraining its deformation. In the current study, FE analyses are conducted to investigate the effects of traffic loading on the stress distribution of water mains buried in non-dry soil conditions using advanced constitutive soil models. Results showed that the impact of traffic loads on pipes buried in partially saturated soils is substantially different than that result in dry or fully saturated soils. The effects of soil plasticity on buried pipelines subjected to traffic loading are also discussed in comparison with the predictions from the analytical models. These findings are useful to include in current buried pipe design practices by accounting the effect of unsaturated soil behaviour.

1 INTRODUCTION

Pipelines used for water and other services are very important lifelines in the current economy and modern society. The vital role that they play in our present economy is reflected in the many kilometres of pipelines laid in worldwide. The ever increasing needs of the socio-economic aspects demand more use of the pipelines in present days. They are often buried in the ground which provides protection and support, but, these buried pipes are subjected to significant stresses due to external (traffic and earth) and internal (water pressure) loads.

The internal and external loading to buried pipes can cause pipeline failures as many of these pipelines have been laid sometime in the last century or earlier (i.e. highly corroded). The failures can be highly disruptive to both water utilities and to the society in general. Such failures can cause significant consequences in terms of economic loss to water utilities, public safety, damage to property and also have an adverse effect on the overall performance of their assets.

The knowledge of the stresses to which pipes are subjected is an essential to understand the in-service pipe failures. The condition of the soil significantly affects the generated stress in the pipe as it acts as the medium of protection from external traffic load and internal water pressure. The pipe can be failed when the generated stress due to internal/external loading exceeds the nominal material strength or when the stress intensity generated at a critical defect (such as in pitting corrosion) exceeds the material toughness of the material, or possibly as a combination of both.

There are various analytical and empirical models available at present to estimate buried pipe stress. Methods developed by Spangler (1941), Watkins and Spangler (1958) are widely used to estimate the stresses of the buried pipelines due to internal and external loading. However, the provisions are not made in such models to account the most essential properties of soil such as plasticity and moisture content. Neglecting to account for important factors can lead to inaccurate predictions of pipe stresses, thus leading to false designs.

Most of the water pipelines are buried at shallower depths (Petersen and Melchers, 2012) in which the soil condition would be partially saturated. The stress state in unsaturated soil is fundamentally different from stress state in dry or fully saturated soil. Because dry or saturated soils are two-phase systems which are comprised with soil particles and pore air (in dry condition) or pore water (in saturated condition), but unsaturated soils are three phase systems comprising soil particles, pore water and pore air. As a result, depending on the relative amounts and corresponding pressures of the pore water and pore air in unsaturated soil, it affects the macroscopic mechanical behaviour (shear resistance and volume change) of the soil mass (Robert, 2010). The recent laboratory experiments performed at Pipeline Engineering Research Laboratory (PERL) of Tokyo Gas showed that the pipeline loading resulted in partially saturated soil can be significantly different

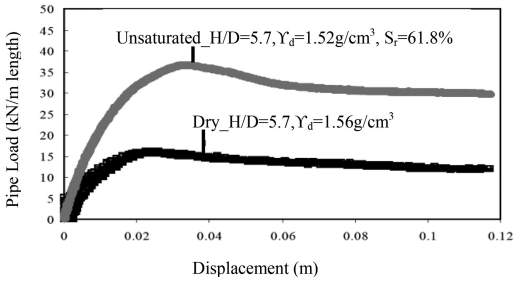


Figure 1. PERL experiment results (Robert & Soga, 2013).

when compared to the loading from dry soils (Fig. 1). Such results indicate that the behavior of pipes buried in non-dry soil conditions are fundamentally different and needs further investigations (Robert and Soga, 2013).

In the current study, FE analyses are conducted to investigate the effects of traffic loading on the stress distribution of water mains buried in non-dry soil conditions using advanced constitutive soil models. Results showed that the impact of traffic loads on pipes buried in partially saturated soils is substantially different than that result in dry or fully saturated soils. The predictions from analytical models for pipe stresses are also compared with the findings from numerical analyses. These findings are useful to include in current buried pipe design practices by accounting the effect of soil plasticity and unsaturated soil behavior.

The presence of road pavement is ignored in the current study, and it is considered that a single effective modulus representing the pavement and soil could be used to represent the condition of backfill. Such pipe setting may also be approximately applicable to other scenarios including that of pipes subjected to loading from construction machinery during pipe lay or road renewal and where pipe is laid in a non-traffic area, but subjected to only soil loads and nominal traffic loads.

2 METHODOLOGY

2.1 *Analytical models*

Several analytical models were considered in the current study to compare the pipe stress predictions due to traffic loading. The modified Spangler formula proposed by Warman et al. (2007), elastic ring and modified elastic ring (can be derived from Watkins and Anderson (1999)) models are showed below in Eq. 1, 2 & 3 respectively to calculate maximum pipe stress.

$$\sigma = \frac{6 \cdot K_b \cdot W_{vertical} \cdot E \cdot t \cdot r}{E \cdot t^3 + 24 \cdot K_z \cdot P \cdot r^3 + 0.732 \cdot E' \cdot r^3} \quad (1)$$

where K_b and K_z are bending moment and deflection parameters respectively and those are depending on bedding angle, values for K_b and K_z can be found in Moser and Folkman (2008). $W_{vertical}$ is the vertical load due to backfill and surface loads including an impact factor, E' is the modulus of passive soil resistance, E is the pipe modulus of elasticity and P is the internal pressure, r is the pipe radius and t is the pipe thickness. Analyses conducted in current study assume $K_b = 0.157$, $K_z = 0.096$ and $E' = 80.25$ MPa (McGrath and Timothy, 1998). Marston load theory (Marston and Anderson, 1913) was used in the current study to calculate the soil load due to over burden stresses.

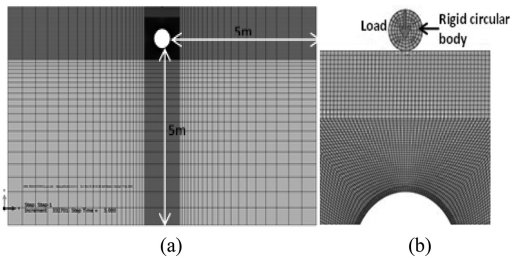


Figure 2. (a) Mesh discretization and model dimensions of finite element model, (b) Traffic load application in FE model.

$$\sigma = \frac{1.5 \cdot q \cdot D^2}{4 \cdot t^2} \quad (2)$$

where q is the uniform vertical stress due to soil and traffic loadings and D is the pipe diameter.

$$\sigma = \frac{k \cdot q \cdot D}{2 \cdot t} + 1.5 \cdot (1-k) \cdot \frac{q \cdot D^2}{4 \cdot t^2} \quad (3)$$

where k (0.35 used in the current study) is the lateral earth pressure coefficient and q is the uniform vertical stress due to soil and traffic loadings.

In all models, Boussinesq solution is used to calculate soil stress due to traffic loads.

2.2 *Finite element model*

FE analyses were carried out using ABAQUS/EXPLICIT with geometric non-linearity and large strain formulation. The non-linear geometry option (NLGEOM) in ABAQUS/EXPLICIT considers the changes in geometry during the analysis, and thus the dynamic equilibrium is achieved using the current configuration (i.e. current nodal position) of the model.

All the analyses were performed under plane strain conditions and the model uses soil and pipe elements with 4-noded bilinear, plane strain, reduced integration with hourglass control elements (CPE4R). Figure 2 shows the geometry and the mesh discretisation of the FE model used to simulate the effects of traffic loading on buried pipelines. The wall boundaries were assumed to be smooth and supported only in the normal direction. The pipe was set free to move during the application of traffic loading. Adaptive meshing has been incorporated in the analyses to control the

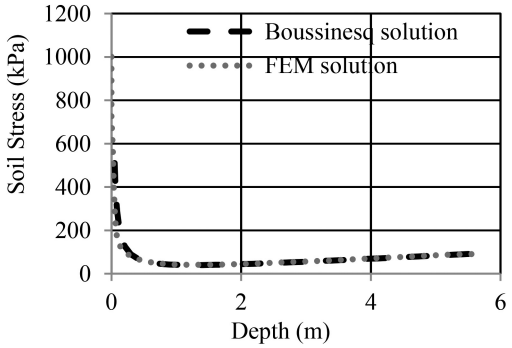


Figure 3. Comparison of analytical and FE model soil stress variation with depth.

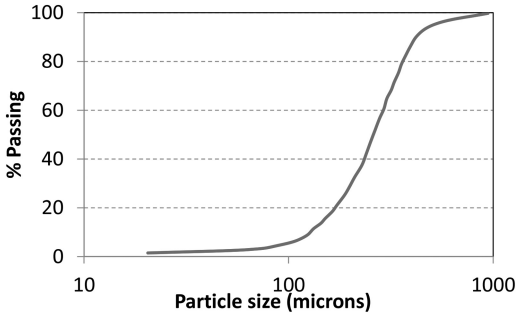


Figure 4. Particle size distribution of the soil used in the current study.

mesh distortions that result from large deformations of the soil caused by lateral pipe displacements.

The traffic load was applied to soil via a rigid body (Fig. 2b), as a concentrated load on soil creates severe mesh distortions (especially in yielded soil) causing to terminate the analyses. The comparison of the soil stress distribution from the FE model for 40 kN traffic load shows similar stress prediction by *Boussinesq* solution (Boussinesq, 1885) at the same level of loading as showed in Fig. 3.

2.3 *Soil type*

The particle size distribution of the soil used in the current study is showed in Fig. 4. The grain sizes of the soil are uniformly distributed within the range of 0.9 mm to 0.08 mm (Cc = 1.06, Cu = 2.1). This soil has been fully characterized in past by Robert (2010), using triaxial tests under both dry and unsaturated conditions.

2.4 *Soil models*

The behavior of the soil surrounding the pipe was modeled using elastic as well as elasto-plastic constitutive models. The plasticity of the soil has been modelled by (a) Mohr-Coulomb model and (a) Nor-sand model (Jefferies, 1993).

Table 1. Soil properties for Mohr Coulomb model.

Degree of saturation (%)	Cover height (m)	Friction angle (deg)	Maximum dilation angle (deg)	E (MPa)	Cohesion (MPa)
0 (Dry)	0.6	47.5	15.04	3	0.5
	1.5	47.5	14.47	5.7	0.5
20	0.6	45	25	15	0.5
	1.5	45	19	18.5	0.5
60	0.6	45	22	6.6	0.5
	1.5	45	17	11.1	0.5

2.4.1 *Mohr Coulomb model*

Soil behaviour was initially modeled using Mohr-Coulomb constitutive model. The model was chosen considering its simplicity, easiness to use, CPU time and higher community understanding of the model. Also the Mohr-Coulomb model only demands few parameters which can be easily determined through direct shear tests, unlike other models which demand their parameters through proper controlled triaxial testing. Further, Mohr-Coulomb model is widely popular in the community for modelling the behaviour of soils due to its relative simplicity and the need of popular soil properties (such as friction and dilation of soils).

The properties of the Mohr-Coulomb model used in the current analyses are showed in Table 1 for dry and unsaturated sands.

2.4.2 *Nor-Sand model*

Nor-Sand model (NS) was also used in the current study, as the model requires single set of input parameters for a particular sand type irrespective of its initial state. Nor-Sand model is a generalised Cambridge-Type constitutive model for sand, developed on the basis of the critical state theory. It uses the state parameter concept (Been and Jefferies, 1985) and attempts to accurately reproduce dilation and softening on the dry side of the critical state. This is achieved by postulating infinite isotropic Normal Consolidation Loci (NCL), which allows a separation of the intrinsic state from the over-consolidation state. A main feature of Nor-Sand model is the use of rate-based hardening using the state parameter, to size the yield surface. The original Nor-Sand model was proposed by Jefferies (1993) and was implemented into STANDARD finite elements by Dasari and Soga (2000). In order to enhance the model performance, three modifications were made by Cheong (2006). They include (i) a new definition for the critical state, (ii) lode angle dependency on the critical state parameter and (iii) the evolution of yield surface with respect to plastic shear strain. Nor-Sand code was implemented into explicit finite elements by Robert (2010) in order to be benefited by explicit simulations.

The model has been modified in conjunction with the Bishop's effective stress framework to incorporate the behaviour of unsaturated soils (Robert, 2010). The modification includes capturing the effects of

Table 2. Soil properties for Nor-Sand model.

Parameters	Unsaturated sand	Dry sand
Shear Modulus constant	850	300
Pressure exponent	0.5	0.5
Poisson's ratio	0.35	0.35
Void ratio constant	0.9	–
Water saturation constant	0.6	–
'N' value in flow rule	0.33	0.33
Hardening parameter	400	300
Maximum dilatancy coefficient	3.5	2.5
Critical state ratio	1.33	1.33
Maximum void ratio	0.946	0.946
Minimum void ratio	0.5	0.5
Switch to use constant or exp H	0.0	0.0
Dilatancy enhancement constants;		–
A_d	10	
k_1	1.5	
S_{w1}	0.25	
S_{w2}	0.3	
Cohesion enhancement constants;		–
A_s	5	
k_2	1.7	
$S_{w\max}$	0.55	
S_{w3}	0.5	

increasing apparent tensile strength by water meniscus at particle contacts as well as increased dilation when the material is unsaturated. Apparent tensile strength captures the cohesion enhancement while the dilation enhancement is included in preconsolidation pressure which used to define the double hardening mechanism (i.e. hardening based on saturation and plastic strains). These two hardening effects (Cohesion and Dilation) as well as the classical plastic hardening effect make the proposed model a triple-hardening model. The properties of the Nor-Sand model are showed in Table 2 for both dry and unsaturated sands. The calibration and validation of the model based on triaxial compression data, as well as mesh sensitivity effects can be found in Robert (2010).

2.5 *Pipe models*

The behavior of the pipe has been assumed as elastic steel material for all the analyses conducted in the current study. A Young's modulus of 204 GPa and a Poisson's ratio of 0.3 have been assumed for steel (ASTM A 36). The nominal diameter and thickness of the pipe considered in this study are 610 mm and 24.61 mm respectively. The burial depths of the pipe are at H/D of 1 & 2.5.

2.6 *Analysis plan*

Several analyses were performed to investigate the behavior of steel pipe subjected to external traffic loading. Firstly, FE analyses were conducted to compare the predictions from the analytical models with numerical model results (case 1). Secondly, analyses were performed to investigate the effect of different soil plasticity for pipe behaviour under traffic loading (case 2). Further simulations were performed to explore the effect of partial saturation in soil for pipes undergoing external loading. Table 3 summarizes the analyses plan for the three cases considered in the current study.

Table 3. Analysis plan.

Cases	Model	Degree of saturation (%)	Cover height (m)	Traffic load (kN)
1	FE-Elastic	0 (Dry)	0.6, 1.5	0,20,40
	Ring	0 (Dry)	0.6, 1.5	0,20,40
	Modified ring	0 (Dry)	0.6, 1.5	0,20,40
	Modified Spangler	0 (Dry)	0.6, 1.5	0,20,40
2	FE-Elastic	0 (Dry)	0.6, 1.5	0,20,40
	FE-Mohr coulomb	0 (Dry)	0.6, 1.5	0,20,40
	FE-Nor Sand	0 (Dry)	0.6, 1.6	0,20,40
3	FE-Nor Sand	0,20,60	0.6, 1.5	0,20,40

3 RESULTS

3.1 *Comparison of FE results with analytical models (case 1)*

The results from the FE analyses (elastic soil) conducted to investigate the effect of traffic loads on pipes are compared with the predictions from analytical models in Fig. 5. It can be seen that pipe stress derived from Modified Spangler model predicts similar pipe stress compared to FE analysis in shallow and deep embedded pipes.

The pipe stress predictions from Modified Ring model under-estimate the maximum pipe stress especially for shallow embedded pipes (upto $\sim$ 45%). This is because the modified Ring model is not incorporated with realistic soil stiffness which controls the pipe deformation during the application of traffic loads. The under-estimation of the pipe stress for deep embedded pipes (upto $\sim$ 15%) was over-shadowed by larger confining stress effects in deeper depths. The predictions from Ring model are always higher than the predictions from Modified Ring model, due to disregard of the lateral soil support in derivation of Ring model. Hence, only the analytical models, such as Modified Spangler predicts comparable pipe stresses to FE modeling with elastic soil.

3.2 *FE analysis of soil plasticity effect under traffic loading (case 2)*

The effect of soil plasticity on buried pipes subjected to traffic loading was studied considering two elasto-plastic soil models; Mohr-Coulomb and Nor-Sand.

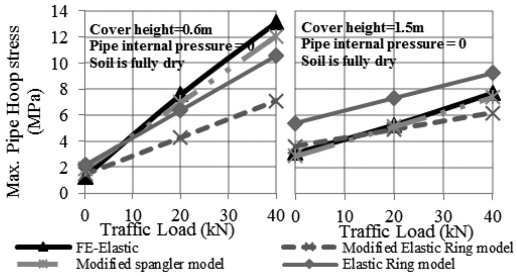


Figure 5. FE results and analytical results.

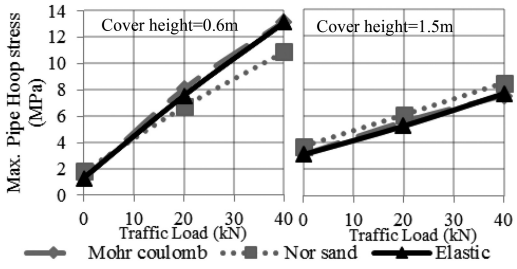


Figure 6. Elastic and plastic behavior of soil.

The maximum pipe stress induced by traffic loading obtained from different soil plasticity is showed in Fig. 6 in comparison with the results from elastic soil models.

The results showed that there is no substantial soil plasticity effect on pipe stresses simulated using Mohr-Coulomb soil model, but considerable effect (10–15%) has been observed from Nor-Sand soil plasticity for pipes buried at shallower depths. Within the Mohr-Coulomb frame work, soil behaves elastically and obeys Hooke's law until the onset of yielding which is determined by the Mohr-Coulomb yield criterion. Further, it models the soils as an isotropic dilatant elastic-perfectly plastic material, which is lack of strain softening/hardening during soil deformation. However, Nor-Sand model predicts the realistic deformation of soils due to the use of state parameter based hardening approach (Cheong, 2006) which can capture hardening/softening of soils during traffic loading. The effect of soil plasticity becomes insignificant for pipes buried in deeper depths.

3.3 *Effect of unsaturated behavior under traffic loading (case 3)*

The results of the analyses conducted to investigate the effect of partial saturation on buried pipes are showed in Fig. 7 for various traffic loading. The resulted maximum pipe stresses are substantially affected by the degree of saturation in soils. i.e. pipe stresses are lowered by 10–80% when compared to the response in dry soils. This is because the enhanced stiffness induced by suction in wet soil resists pipe mobilization and hence its deformations during traffic loading. The load-displacement plot obtained for pipes buried

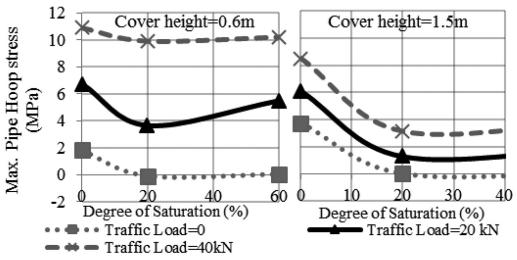


Figure 7. Maximum hoop stress of pipe variation with degree of saturation of soil.

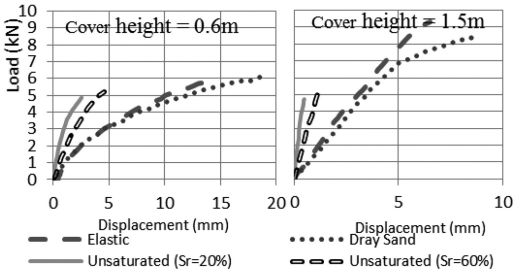


Figure 8. Load displacement curves for pipe.

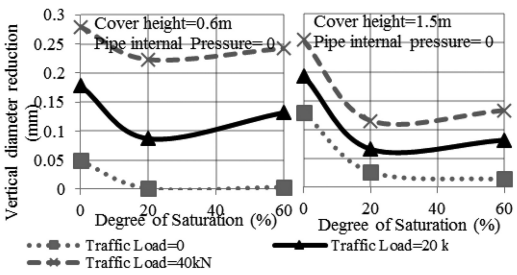


Figure 9. Pipe vertical diameter reduction with degree of saturation.

in different soil conditions revealed higher stiffness response for pipes buried in wet soils compared to that in dry condition (Fig. 8). However, pipes are subjected to less mobilization displacements and hence the imposed pipe loads are smaller when compared to pipes buried in dry soils. The lower loads imposed on pipes buried in wet soil have resulted less pipe deformation (Fig. 9), which caused to induce lower stresses on pipes under unsaturated condition at a given traffic loading.

The results further revealed that the pipe stresses increase with the change in degree of saturation from 20% to 60%. Similar progression is reflected in the change in pipe deformation with saturation degree (Fig. 9). This behavior of pipe stress is due to the suction induced apparent cohesion effect which possessed a similar trend as was obtained from the triaxial test data for this sand (Robert, 2010).

4 CONCLUSION

In the current study, FE analyses are conducted to investigate the effects of traffic loading on the maximum induced stress of pipelines buried in non-dry soil conditions using advanced constitutive soil models. Results showed that the impact of traffic loads on pipes buried in partially saturated soils is substantially affected by the degree of saturation in soils. The pipe stresses are lowered by 10–80% when buried in non-dry soils when compared to the response in dry soils for the tested pipe conditions. This is because the enhanced stiffness induced by suction in wet soil resists pipe mobilization and hence its deformations during traffic loading.

The predictions from analytical models for pipe stresses are also compared with the findings from numerical analyses. It was found that the current methods generally over-predict the pipe stresses to varying magnitudes, due to the use of simplifying assumptions for making it solvable as a statically determinate problem. In general, Sprangler model predicts similar pipe stresses as observed from FE model results. The predictions from the Ring model are over-estimating the pipe stresses at deeper embedded depths when compared to the predictions from modified Sprangler model and FE models. On the other hand, the predictions from modified Ring model which incorporates the lateral soil support effect predicts comparable stresses when buried at deeper depths. Therefore, the analytical models, such as Ring and modified Ring should be used with care as they predict realistic response only under certain conditions.

The results from the current study further revealed that there is substantial soil plasticity effect for pipe stress response, especially when buried at shallower depths. However, traditional soil plasticity models such as linear elastic-perfectly plastic Mohr Coulomb, are unable to capture this effect due to lack of strain softening/hardening during soil deformation. The use of advanced soil plasticity models, such as Nor-Sand can effectively capture the realistic deformation of soils during traffic loading.

The findings from the current research work can be useful to include in current buried pipe design practices by accounting the effect of soil plasticity and unsaturated soil behavior. This research work is currently being extended to quantify these effects within an analytical framework.

ACKNOWLEDGEMENT

This research work is supported under Australian Research Council's Discovery Projects funding scheme (DP140101547).

REFERENCES

Abaqus (Inc. 2011) ABAQUS V.6.11 User's Manual. *Providence, Rhode Island*.

Been, K. & Jefferies, M. G. (1985) STATE PARAMETER FOR SANDS. *Geotechnique* 35(2):99–112.

Boussinesq, J. (1885) Application des Potentiels a I'Etude de I'Equilibre et du Mouvement des Solides Elastiques.

Cheong, T. P. (2006) Numerical modelling of soil-pipeline interaction.) Phd Thesis, University of Cambridge.

Dasari, G. R. & Soga, K. (2000) *A guide book for soil models and soil-pipe analysis using ABAQUS*. Tokyo, Japan.

Jefferies, M. G. (1993) Nor-Sand: a simple cricital state model for sand. *Geotechnique* 43(1):91–103.

Marston, A. & Anderson, A. O. (1913) The theory of loads on pipes in ditches and tests of cement and clay drain tile and sewer pipe. *Bulletin 31.Ames: Iowa Engineering Experiment Station*.

Mcgrath & Timothy, J. (1998) Replacing E' with the constrained modulus in flexible pipe design. In *Proceedings of the 1998 Pipeline Division Conference*.) ASCE, Reston, VA, United States, pp. 28–40.

Moser, A. P. & Folkman, S. (2008) *Buried Pipe Design*. The McGraw-Hill Companies.

Petersen, R. B. & Melchers, R. E. (2012) Long-term corrosion of cast iron cement lined pipes In *Proceedings of Annual Conference of the Australasian Corrosion Association 2012*. Australian Corrosion Association vol. 1.

Robert, D. J. (2010) Soil-Pipeline Interaction in Unsaturated Soils. In *Churchill College*.) PhD Thesis, University of Cambridge.

Robert, D. J. & Soga, K. (2013) Soil-Pipeline Interaction in Unsaturated Soils. In *Mechanics of Unsaturated Geomaterials*.) John Wiley and Sons, pp. 303–325.

Spangler, M. G. (1941) *The structural design of flexible pipe culverts*. Ames,Iowa.

Warman, D. J., Chorney, J., Reed, M. & Hart, J. D. (2007) Development of a pipeline surface loading screening process. In *2006 6th International Pipeline Conference, IPC 2006*.), Calgary, AB, vol. 1, pp. 803–814.

Watkins, R. K. & Anderson, L. R. (1999) *Structural Mechanics of Buried Pipes.* CRC Press.

Watkins, R. K. & Spangler, M. G. (1958) Some characteristics of the modulus of passive resistance of soil-a study in simlitude. *Highway research board proceedings* 37: 576–583.

Unsaturated Soil Mechanics—from Theory to Practice – Chen et al. (Eds)
© 2016 Taylor & Francis Group, London, ISBN 978-1-138-02921-7

Effect of water content on long-term cyclic behaviour of railway track-bed materials

F. Lamas-Lopez, Y.J. Cui, J.C. Dupla, A.M. Tang & J. Canou
Ecole des Ponts ParisTech, Laboratoire Navier/CERMES, Marne-la-Vallée, France

N. Calon
SNCF, Direction Projet Systèmes, Ingénierie. Département Ligne, Voie et Environnement. La Plaine Saint-Denis, France

S. Costa D'Aguiar
SNCF, Direction Innovation & Recherche. Paris, France

ABSTRACT: The 'Interlayer' soil in the French conventional railways track-beds, a coarse grain soil with low permeability, was studied at different hydric conditions: $w = 4\%$ (OPM) and $w = 10\%$ (Saturated) using a large-scale triaxial ($ø = 300$ mm) cell. For each test, 5 different cyclic loading levels has been considered (from $\Delta q = 10$ kPa to $\Delta q = 30$ kPa per cycle). The loading levels simulate the real loading at the interlayer depth in a real railway track-bed. The results clearly show the influence of the non-saturation on the evolution of elastic modulus and damping ratio. When the loading level is increased, the elastic modulus decreases and the damping ratio increases. The accumulation of plastic strains after 90000 cycles was also analyzed for both hydric conditions, showing that the initial moisture content and the elastic modulus greatly affect the accumulative strains.

1 INTRODUCTION

In order to improve the service of transportation and to optimize the use of the conventional railway lines, it is necessary to increase the load and the speed of trains. This can cause accelerated degradation of track-bed materials, and thus more frequent maintenance operations would be needed. In France, the conventional lines represent 94% of the whole network and the high-speed lines represent 6% only. The main difference between the conventional line and the new line is the existence of a layer namely Interlayer (ITL) that was naturally formed by the interpenetration of ballast and subgrade (Cui et al. 2013; Fortunato et al. 2010; Tennakoon et al. 2012; Trinh et al. 2012; Duong et al. 2013).

When trains increase their speed, dynamic amplification of load occurs (Xu et al. 2013; Chen et al. 2013; Bian et al. 2014). This amplification is more notable in shallower layers where the amplitude of loads is larger. If the axle weight of a train is increased while the train speed does not change, an amplification of load is also expected in track-bed materials. Thus, the amplification of load is the result of the increase of train speed or the increase of train weight. This increase of load could result in an increase of deformation of materials. Thus, a degradation of the elastic modulus of track-bed materials may be the result of the increase of strain induced by trains (Alves Costa et al. 2010; Menq 2003). Furthermore, the damping ratio of soil could increase with the increase of strain. The stress amplitude of cyclic loading induced by trains at the interlayer depth ($d = -0.9$ m below the rail surface) is about $\Delta q = 15$ kPa (Bian et al. 2014). This cyclic stress amplitude can be amplified if the train speed or the axle weight is increased. For clayey soft soils, this amplification could reach 70% of the static amplitude (Chen et al. 2013). The long-term behavior will also be influenced by the cyclic loading amplitude (Gidel 2001). The permanent deformations depend also on the mechanical conditions (initial dry density, confining pressure and moisture content) (Gidel 2001; Trinh 2011). To the authors' knowledge, the effect of moisture content on the long-term behavior of ITL soil have not been carried out yet under simulated railway cyclic loadings.

In this study, the effects of the amplitude of cyclic loading and moisture content on the mechanical behavior of an ITL soil is analyzed. First, an analysis of the results with isolated cycles is performed to highlight the effect of different loadings and moisture contents on the dynamic properties of soil. Secondly, a long-term behavior analysis is performed to compare the accumulative permanent deformations for different initial conditions and loadings. The applied cyclic loading simulates the passage of train bogies. The applied stress amplitudes simulates the real loading to the ITL soil and their amplifications when the train speeds are increased or the axle weight is modified.

Table 1. ITL soil state parameters.

w_L [%]	PI [%]	w_{OPM} [%]	$\gamma_{d\text{-}OPM}$ [Mg/m^3]	d_{50} [mm]	c (kPa)	ø (°)
43.7	26.4	4.3	2.2	10	72	33

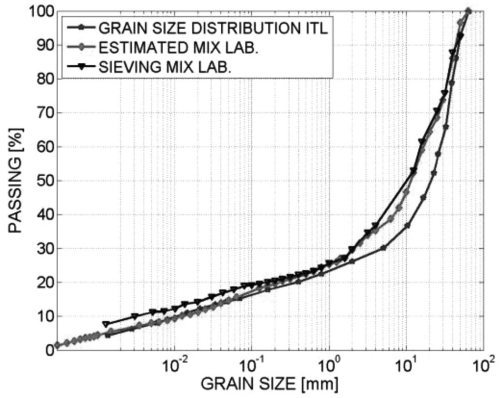


Figure 1. Grain Size distributions of Interlayer soil (blue), of the mix of the 13 materials obtained by estimation (red) and by sieving (black).

2 MATERIAL & METHOD

2.1 *Material used*

The mechanical behavior of ITL was studied by Cui et al. (2013), Duong et al. (2013) and Trinh et al. (2012). Even though the ITL nature is dependant on the site, it was found that the grain size distribution is similar for all the ITL soils. This layer is created naturally over time, forming a 'transition layer' between the ballast and the subgrade. The ITL soil used in this study was fabricated in the laboratory. To prepare a laboratory ITL soil, 13 different materials were used: from ballast grains (maximal diameter = 63 mm) to speswhite clay (maximal diameter = 10 µm). The fines of the fabricated ITL were adapted to obtain a similar plasticity (Table 1) to the natural ITL soil (Trinh et al. 2012). The grain size distribution (Fig. 1) of the ITL created in the laboratory follows the same distribution as the real ITL one. The fabricated ITL has the same volumetric fraction of ballast grains inclusions ($f_v = 28\%$). This volumetric fraction of inclusions is a key factor for the mechanical behavior (Pedro et al. 2005; Seif-el-Dine 2007). The fines percentage content is the same for both soils.

2.2 *Equipment*

Cyclic triaxial tests were performed to analyze the mechanical behavior of the ITL soil. As the ITL has ballast size grains up to 63 mm, and the diameter of the triaxial cell has to be at least 5 times bigger (Indraratna et al. 2010), a ø = 300 mm triaxial cell was used in this study. The height of the sample is h = 600 mm. The range of loading amplitudes are: confining pressures from $\sigma_3 = 15$ kPa to $\sigma_3 = 2000$ kPa; axial loads up to 500 kN corresponding to $\sigma_1 = 7000$ kPa; and frequency up to 20 Hz.

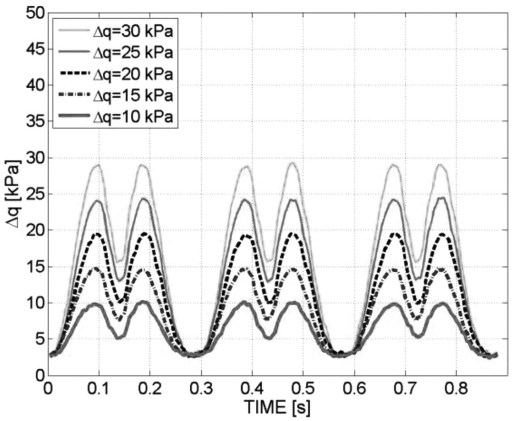


Figure 2. Three bogies load with five different loading amplitudes.

2.3 *Sample preparation*

The sample was compacted at optimum moisture content (w = 4%) using a hydraulic hammer in 5 layers of 12.5 cm each. To reach a dry density of $\rho_d = 2.01$ Mg/m^3, 17.75 kg of ITL soil was mixed with 0.7 kg of water and then compacted by layer. The specimen was compacted in a cylindrical steel mold composed of a base and 4 semicircular identical parts of 30 cm height.

2.4 *Test procedure*

After the preparation and installation of the sample in the triaxial cell, the initial confining and axial pressures were applied ($\sigma_3 = 30$ kPa, $\sigma_1 = 30$ kPa) in steps of 5 kPa every 2 minutes. Thus, the initial mean pressure was $p_0 = 30$ kPa and the initial deviator stress was $q_0 = 0$ Kpa. The tests were drained and the evolution of pore water pressure was thus not measured. For saturated ITL soils, once the sample was compacted and installed in the triaxial cell, saturation was conducted for 48 h. Prior to the introduction of de-aired water into the specimen, carbon dioxide was applied under 15 kPa pressure for 5 min to obtain a better saturation. After 2 days of saturation, the Skempton ratio was 0.8, higher than th value of 0.6 obtained by Trinh et al. (2012). The back pressure applied was 100 kPa. The initial confining pressure applied on saturated samples to compensate the back pressure was $\sigma_3 = 130$ kPa. Once the initial test conditions wer applied to the specimen, cyclic loading started. In this study, each simulated bogie passage was considered as a cycle. Figure 2 presents the applied loads to the specimen simulating real train bogies (2 axles

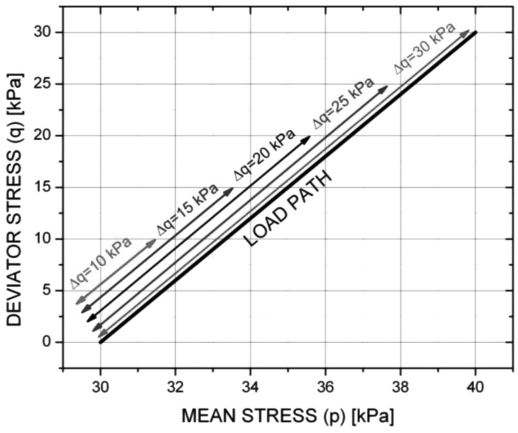


Figure 3. Loading paths in p-q plane for each considered loading amplitude.

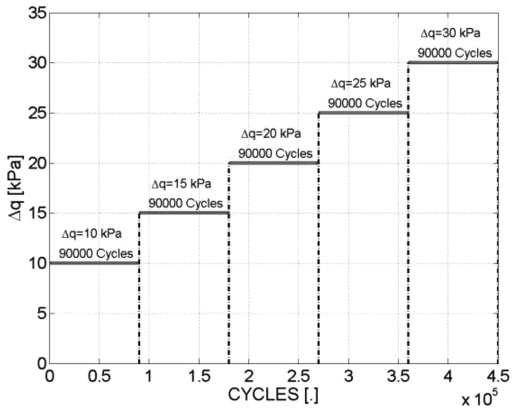


Figure 4. Scheme of cyclic loadings in each test.

per bogie). Three 'bogie' passages for 5 different axial stress amplitudes were presented, from $\Delta q = 10$ kPa to $\Delta q = 30$ kPa.

Figure 3 presents the load path for each applied loading cycle in p-q plan. The maximum deviator stress reached is 30 kPa and the maximum total mean stress applied is 40 kPa. Each cyclic loading can be divided into 4 steps:

- 1st increase until the maximum of the considered load amplitude (simulating the 1st bogie's axle).
- Decrease step until 50% of the total amplitude (simulating the middle part of a bogie, the part between both axles of a bogie). This condition was better achieved in the case of low frequencies. When the loading frequencies are high, it is more complicated to follow the commanded signal with the load jack control system, and thus the decreasing level did not reach the 50% decreased amplitude).
- 2nd increase until the maximum load amplitude (simulating the 2nd bogie's axle).
- Decrease until the initial deviator stress level (the initial Δq_0 was not 'zero' to always conserve the sample under compression).

Figure 4 shows a test loading scheme. There are 5 stages, from $\Delta q = 10$ kPa to $\Delta q = 30$ kPa. For each load amplitude, 90000 'bogie' cycles were applied, totalizing 450000 cycles in each test. Note that all tests were carried out by following the fatigue test method applied by Gidel (2001).

2.5 *Test program*

Two tests were performed, one on an ITL sample at the OPM moisture content ($w = 4\%$) and another on a saturated saturated after installation in the triaxial cell ($w = 10\%$).

3 RESULTS & DISCUSSION

3.1 *Cycle analysis*

The cyclic behavior is analyzed by considering one of the last 100 cycles for each loading amplitude. Figure 5 presents the 'stress – strain' cycles of (a) the unsaturated and (b) the saturated samples. In the saturated case, the area of the hysteresis cycle seems a little larger than in the unsaturated case, suggesting that the damping ratio could be higher in the former. The difference between resilient modulus (slope of strain-stress cycle) for both hydric cases is easily recognizable in Figure 5. The resilient modulus can be determined using Equation 1.

$$M_r = \frac{\Delta q}{\Delta \varepsilon_1} \tag{1}$$

The damping ratio can calculated for each cycle using Equation 2.

$$D_R = \frac{E_{loop}}{4 \cdot \pi \cdot E_d} \tag{2}$$

Figure 6 presents an example of how damping ratio was calculated from one experimental cycle. The transferred energy to the system (E_{loop}) corresponds to the surface of the hysteresis loop in the 'stress – strain' diagram. The dissipated energy (E_d) by soil deformation is related to the surface of the triangle formed by the deviator stress amplitude at the maximal strain of the first hysteresis cycle, the value of this maximal strain and the origin, as described in Equation 3.

$$E_d = \frac{\left(\Delta q_{\max \varepsilon_1} \cdot \max \Delta \varepsilon_1\right)}{2} \tag{3}$$

Figure 7 shows the trend of (a) the resilient modulus (M_r) and (b) the damping ratio at the end of each loading stage. It can be noted that the resilient modulus decreases in a similar way for both hydric

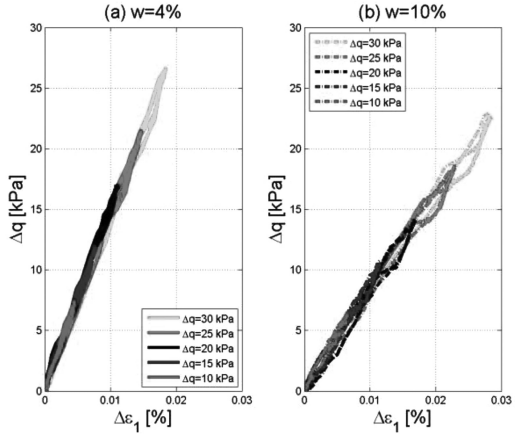


Figure 5. Stress – strain ($\Delta q - \varepsilon 1$) cycles for each loading amplitude for (a) the non-saturated and (b) the saturated samples.

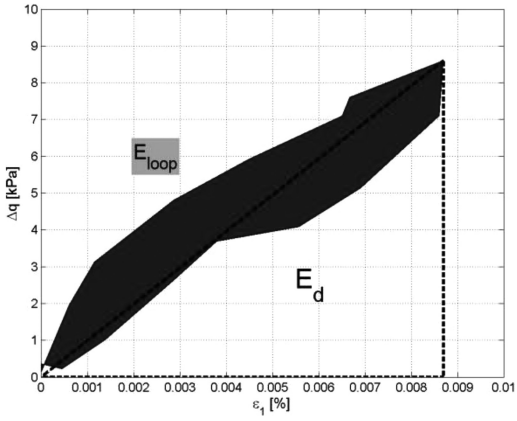


Figure 6. Areas of the provided energy (E_{loop}) and the dissipated energy (E_d) from stress – strain ($\Delta q - \varepsilon 1$) cycles, used in calculating the 'Damping ratio'.

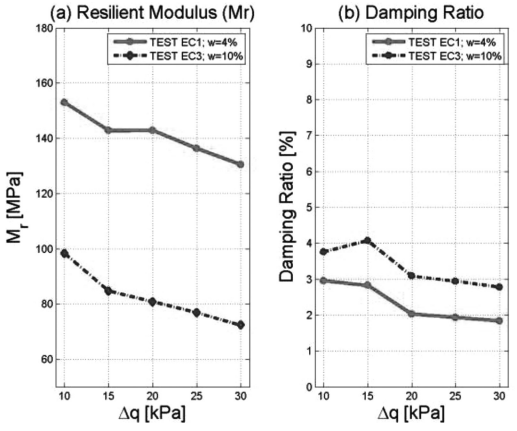


Figure 7. Evolutions of the resilient modulus (a) and the damping ratio (b) for both samples at each loading amplitude.

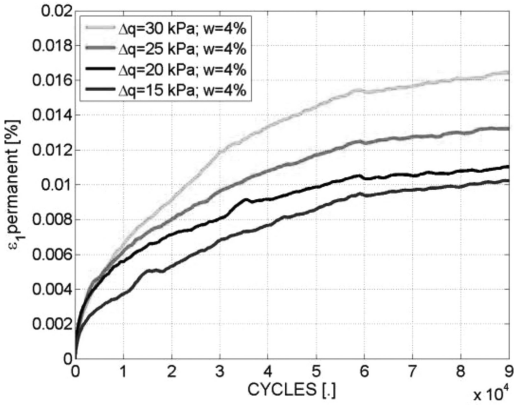


Figure 8. Accumulation of axial permanent deformations for different loading amplitudes on a sample at OPM moisture content (w = 4%).

conditions when the loading amplitude increases. Consequently, the resilient modulus decreases by 1 MPa for 1 kPa increase of loading amplitude. In conclusion, the hydric conditions have great effect on the soil resilient modulus. There are about 60 MPa of difference between the resilient modulus in both cases. Regarding the damping ratio, it decreases from 3% to 2% for the 5 loading amplitudes in the unsaturated case. However, in the saturated case, it decreases from 4% to 3% when the loading amplitude is increased from $\Delta q = 10$ kPa to $\Delta q = 30$ kPa. Moreover, the damping ratio is larger for the saturated sample under the same loading conditions.

3.2 *Long-term behavior analysis*

The long-term behavior was analyzed based on the results after application of 90000 simulated 'bogie' cycles for each loading amplitude. While cyclic loading was imposed, the permanent deformation developed. The cyclic resilient deformation is stable for each loading amplitude. The resilient part of the deformation can be appreciated in Figure 5. In the following figures, only permanent deformation is presented, the resilient deformation part being removed.

Figure 8 shows that the permanent deformation increases for each loading amplitude in the unsaturated case. For the purpose of comparison, a translation to origin was performed to each curve section from their initial permanent deformation. Furthermore, the first stage of $\Delta q = 10$ kPa is not comparable with the other 4 loading stages, because the first loading stage usually gives rise to larger permanent deformation. Each line represents the added permanent deformation to the material if the loading amplitude is increased from the previous level to a new one. For the increment of $\Delta q = 5$ kPa, the added permanent deformation to the soil after 90000 cycles is about 0.012%. It can be also appreciated that the increase of permanent deformations is non-linear depending on the previous loading levels.

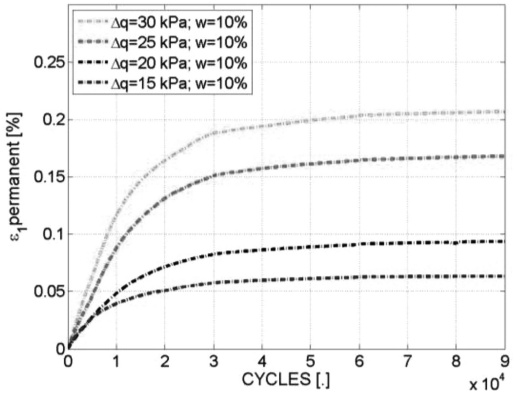


Figure 9. Accumulation of axial permanent deformations of the saturated sample (w = 10%) for different loading amplitudes.

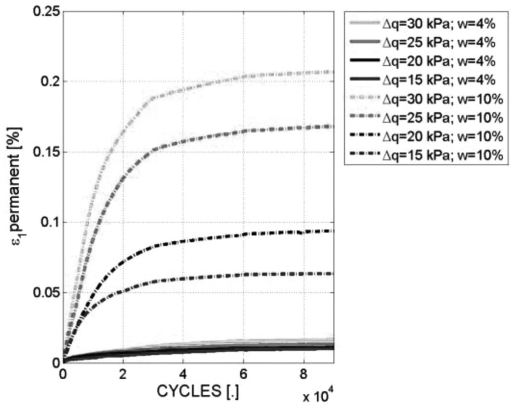


Figure 10. Comparison between axial permanent deformations after 90000 loading cycles on saturated (w = 10%) and unsaturated (w = 4%) samples at different loading amplitudes.

Figure 9 shows the permanent deformation of the saturated soil. In this case, it can be noted that the increase of permanent deformation is more non-linear than in the case of non-saturated sample. The added permanent deformation is about 0.05% for an increase of loading amplitude from $\Delta q = 10$ to $\Delta q = 15$ kPa. The same increment is 0.2% for an increase of loading amplitude from $\Delta q = 25$ to $\Delta q = 30$ kPa.

Figure 10 presents a comparison between the evolution of permanent deformations on the saturated (continuous lines) and non-saturated (dotted lines) samples. When the loading amplitude is increased from $\Delta q = 10$ to $\Delta q = 15$ kPa the increment of permanent deformation is 6 times larger for the saturated ITL sample. Moreover, when the loading amplitude is increased from $\Delta q = 25$ to $\Delta q = 30$ kPa the increment of permanent deformation is 12.5 times larger for a saturated ITL sample.

It is also possible to appreciate the normalized permanent strain evolution with respect to the maximum

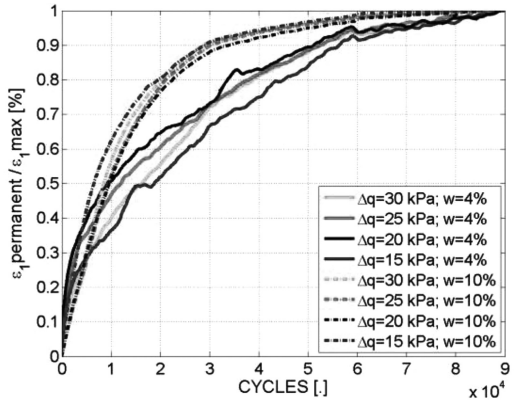


Figure 11. Evolution of the normalized axial permanent deformations on saturated (w = 10%) and unsaturated (w = 4%) samples.

strain at 90000 cycles for both saturated and unsaturated samples (Fig. 11). It appears that the shape of accumulative permanent strain curve depends strongly on the moisture content. For the saturated sample, 80% permanent deformations developed in the first 20000 cycles while for the unsaturated sample, 80% of permanent deformations developed after 40000 loading cycles.

4 CONCLUSIONS

It can be concluded that the influence of moisture content is a key factor in the long-term cyclic behavior of an ITL soil. Saturated ITL soils had lower resilient moduli than unsaturated ITL soils (about 60 MPa lower on average). The effect of increasing the cyclic loading amplitude, from $\Delta q = 10$ to $\Delta q = 30$ kPa had the same effect on resilient modulus evolution for both hydric conditions. Damping ratio depended on the moisture content and the cyclic loading amplitude. Moreover, the accumulative permanent deformations were larger for saturated soils, and depended on the cyclic loading amplitude because of the non-linearity of the soil. The permanent deformation of saturated soils was about 12 times larger that that of unsaturated soils, in the range of tested loading amplitudes. The saturated soils accumulated 80% of permanent deformations in the first 20000 cycles, twice faster than the unsaturated soils.

REFERENCES

Alves Costa, P., Calçada, R., Silva Cardoso, A., & Bodare, A. (2010). Influence of soil non-linearity on the dynamic response of high-speed railway tracks. Soil Dynamics and Earthquake Engineering, 30(4), 221–235. doi:10.1016/j.soildyn.2009.11.002

Bian, X., Jiang, H., Cheng, C., Chen, Y., Chen, R., & Jiang, J. (2014). Full-scale model testing on a ballastless high-speed railway under simulated train moving loads. Soil

Dynamics and Earthquake Engineering, 66, 368–384. doi:10.1016/j.soildyn.2014.08.003

Chen, R. P., Zhao, X., Bian, X. C., & Chen, Y. M. (2013). Dynamic soil pressure and velocity of slab track subgrade in High-Speed railway. In Advances in Environmental Vibration; Sixth International Symposium on Environmental Vibration: Prediction, Monitoring, Mitigation and Evaluation. Shanghai.

Chen, R., Zhao, X., Wang, Z., Jiang, H., & Bian, X. (2013). Experimental study on dynamic load magnification factor for ballastless track-subgrade of high-speed railway. Journal of Rock Mechanics and Geotechnical Engineering, 5(4), 306–311. doi:10.1016/j.jrmge.2013.04.004

Cui, Y., Duong, T. V., Tang, A. M., Dupla, J.-C., Calon, N., & Robinet, A. (2013). Investigation of the hydro-mechanical behaviour of fouled ballast. Journal of Zhejiang University SCIENCE A, 14(4), 244–255. doi:10.1631/jzus.A1200337

Duong, T.-V., Tang, A.-M., Cui, Y., Trinh, V.-N., Dupla, J.-C., Calon, N., ... Robinet, A. (2013). Effects of fines and water contents on the mechanical behavior of interlayer soil in ancient railway sub-structure. Soils and Foundations, 53(6), 868–878.

Fortunato, E., Pinelo, A., & Matos Fernandes, M. (2010). Characterization of the fouled ballast layer in the substructure of a 19th century railway track under renewal. Soils and Foundations, 50(1), 55–62.

Gidel, G. (2001). Comportement et valorisation des graves non traitées calcaires utilisées pour les assises de chaussées souples. Retrieved from http://www.theses.fr/2001BOR12366

Indraratna, B., Thakur, P. K., & Vinod, J. S. (2010). Experimental and Numerical Study of Railway Ballast Behavior under Cyclic Loading. International Journal of Geomechanics, 10(August), 136–144.

Menq, F.-Y. (2003). Dynamic Properties of Sandy and Gravelly Soils. The University of Texas at Austin.

Pedro, L. S., Dupla, J.-C., & Canou, J. (2005). Comportement mecanique d'un sol grossier. Revue Française de Geotechnique, 112, 35–42.

Seif-el-Dine, B. (2007). Etude du comportement mécanique de sols grossiers à matrice. Ecole Nationale des Ponts et Chaussées (Marne la Vallée).

Tennakoon, N., Indraratna, B., Rujikiatkamjorn, C., Nimbalkar, S., & Neville, T. (2012). The Role of Ballast-Fouling Characteristics on the Drainage Capacity of Rail Substructure. Geotechnical Testing Journal, 35(4), 104107. doi:10.1520/GTJ104107

Trinh, V.-N. (2011). Comportement hydromécanique des matériaux constitutifs de plateformes ferroviaires anciennes. Université Paris-Est (Marne la Vallée).

Trinh, V.-N., Tang, A., Cui, Y., Dupla, J., Canou, J., Calon, N., ... Schoen, O. (2012). Mechanical characterisation of the fouled ballast in ancient railway track substructure by large-scale triaxial tests. Soils and Foundations, 52(3), 511–523. doi:10.1016/j.sandf.2012.05.009

Xu, X., Jiang, H. G., Bian, X. C., & Chen, Y. M. (2013). Accumulative settlement of saturated silt subgrade under cyclic traffic-loading. In Advances in Environmental Vibration; Sixth International Symposium on Environmental Vibration: Prediction, Monitoring, Mitigation and Evaluation (pp. 493–501). Shanghai.

Unsaturated Soil Mechanics—from Theory to Practice – Chen et al. (Eds)
© 2016 Taylor & Francis Group, London, ISBN 978-1-138-02921-7

Analogy study on surface deterioration of earthen monuments

Y. Chen
School of Civil Engineering and Mechanics, Lanzhou University, China

J.F. Wang
Key Laboratory of Western China's Environment Systems of Ministry of Education, Lanzhou University, China

H.Y. Zhang
Key Laboratory of Mechanics on Disaster and Environment in Western China of Ministry of Education, Lanzhou University, China

Y.X. Gai
School of Civil Engineering and Mechanics, Lanzhou University, China

ABSTRACT: Surface fracturing is the primary cause responsible for earthen monuments deterioration. The mechanism of surface deterioration keeps unknown because of the longevity and complexity in weathering. This paper selects the road cuts in loess soil deposits exposed to natural weathering for many years as an analogy to investigate the effects of sun radiation direction, soluble salts and grain size on earthen monument deterioration. Scanning Electron Microscope (SEM) shows that surface particles with lamelliform were arranged in an imbricate pattern. Mercury Intrusion Porosimetry (MIP) results indicate that pore diameters of the weathered surface soil show a distinctly bimodal distribution, while the unweathered soil shows an unimodal distribution in pore diameter. This means that one part of the pore diameters become larger while some others become smaller than the unweathered soil. The former can be attributed to the leaching out of soluble salts in surface soil by rain, whereas the latter can be attributed to the sedimentation of atmospheric dust into the pores of surface soil. The evolution model of soil pore structures under weathered condition provides another explanation to the surface deterioration of earthen monuments.

1 INTRODUCTION

Soil has been used as construction materials for a long time. For example, rammed earth structures are still well preserved. These earthen structures are suffered from natural weathering for centuries and the most famous example of them is the Great Wall of China. In northwest China, the Great Wall was built with the local material: rammed earth, stones, even sand and gravels. It is reported that silty clay from a nearby site was used for the rammed earth wall (Bui et al. 2009). Compared to the rock material, rammed earth is more sensitive to the environmental impact; therefore, the protection of earthen monuments exposed in the open air becomes a new challenge. Because of the effect of temperature varieties, raining, wind erosion and dissolution and crystallization of soluble salts, earthen monuments are suffered from many types of diseases. One of which is surface fracturing, the most common disease responsible for rammed earth deterioration. Generally, the deterioration of rammed earth is derived from the damage of soil structure during natural weathering, leading to the quality loss and strength decrease.

Until now, many researches have been concentrated to the protection of stone cultural relics (Rossi-Manaresi et al. 1991). For example, laboratory simulation tests and field observations show that severe temperature changes and salt participation play an important role in the surface weathering of stone cultural relics. Contrarily, few studies have been conducted on the deterioration of rammed earth. Available tests were conducted on the remoulded samples with accelerated aging simulation in laboratory. In fact, natural weathering occurs for a long time and is an uncontrolled environment conditions. This means that the deterioration of rammed earth is a result of multi-field coupling. It is reported that the erosion of rammed earth is nonlinear with time and the surface deterioration is much more complex from crust forming to peeling off. Thus it is reasonable to observe the earthen monument deterioration from a long-term in natural conditions.

Filed observation provides an analogy study from the perspective of Engineering Geology. This work takes the loess road cuts exposed for different years to natural weathering in situ as samples, and field surveying and laboratory tests were conducted to gain an

insight into the evolution of microstructure during the deterioration progress of rammed earth. For this aim, Scanning Electronic Microscope (SEM) and Mercury Intrusion Porosimetry (MIP) tests were conducted to survey the microstructure change of loess soil. These results can be used to explain the deterioration progress of rammed earth as influenced by factors such as solar radiation, soluble salt content and grain size.

2 MATERIALS AND TESTS

2.1 *Field sampling*

Most earthen monuments were constructed with silty clay rammed layer-by-layer vertically from the ground. Compared to the rammed earth walls, loess road cuts are characterized with a flat and nearly vertical façade and a uniform property. The analogy specimens were sampled from the in-situ loess road cuts along the National Road 312 (G312) from Lanzhou to Dingxi, China. The loess from these road cuts all belong to the Late Quaternary. In addition, the geological environment and weather conditions are similar to that of monument in the distribution area. According to the field survey and historical documents, the routine of this G312 was dated as early as the Late Qing Dynasty. Around 1920s, bus stations were set up along the routine. In 1953, this road was widened and covered with asphalt. Since 2000, part of the road line has been straight in the mountain area. The abandoned road cuts, seldom disturbed by human being since they were built, provide good chance to observe the influences of natural weathering to soil deterioration in different years.

Table 1 lists the basic properties of loess soil sampled at two road cuts. To compare the difference between the surface deterioration and the unweathered soil under surface, road cuts were sampled at two depths. As indicated in Table 1, A_1 and B_1 stand for the samples at cut surface, representing a weathering effect, while A_2 and B_2 represent unweathered conditions. To ensure not to be disturbed, samples were cut carefully into the loess with complete surface. At 30 cm depth of the same point, interior loess soil was sampled similarly. All the block samples were put into plastic containers and the free space of the container were filled with the sample soil and sealed.

2.2 *Microstructure investigation*

MIP and SEM tests were conduced to the field samples which were dehydrated with freeze-drying technique in laboratory. A SU-1500 SEM was employed for microstructure observation of samples. And the MIP apparatus in this study was the PoreMaster 60 MIP device with the intrusion pressure ranging from 1.5 kPa minimum to 420 MPa maximum.

It has been recognized that different viewing angle can give differing SEM images (Chen Y et al. 1980). In this study, the representative SEM observations on the horizontal plane for the surface and fresh samples were chosen to interpret the structural characterization. A small piece from the central part of sample was severed carefully, and then fitted on the top of the microscope stub with a thin layer of gold covering. The prepared sample was put into the SEM device. A series of horizontal photograph were taken at magnification of 400 times.

An introduction on the procedures for the measurement of pore size distribution is presented here in detail: first, a set of small soil blocks, of only around 1 g in weight, was taken from the surface and fresh soil of each sample. Then, the soil blocks were freeze-dried to remove all the pore fluid and vapors while the original soil micro-structure was preserved for testing in the MIP tests (Delage et al., 1982). Finally, the freeze-dried samples were placed inside the porosimeter and a vacuum was first applied. Mercury was then allowed to enter the chamber containing the samples, and the pressure in the mercury was subsequently increased in steps. This caused the mercury to progressively penetrate the voids, from the larger to the smaller in size (Jiang M et al., 2014). The volume of mercury entering the samples during each pressure-increment was continuously monitored, and the cumulative volume of mercury, identical to the cumulative pore volume, can be easily obtained.

3 RESULTS AND ANALYSES

Figure 1 presents the pore size density function of the surface and inner soil from different samples. By comparing the density curves, Figure 1 shows that all of samples present two peaks except for sample B_1, but the peak intensity is apparently different. The first pore family of inter-aggregate type with a dominant macro-pore diameter is about 10 μm in all samples. While the second pore family of intra-aggregate type with a dominant micro-pore diameter is 2 μm in sample A_1, 0.05 μm in sample A_2 and 0.013 μm in sample B_1, respectively.

By comparing the curves from sample A_1 and B_1, it can be found that the dominant macro-pore population and peak intensity of sample A_1 is much larger than that of sample B_1. Contrarily, the dominant micro-pore population and peak intensity of sample A_1 is much smaller than that of sample B_1. This indicates that more large pores turn into smaller pores in the surface soil as weathering time increase. Similarly, compared the

Table 1. Basic property of loess samples at road cuts.

Sample	Location	Weathering Time (year)	Moisture content (%)	Natural density (g/cm^3)
A_1	Surface	2	0.8	1.57
A_2	30 cm depth	2	1.3	1.54
B_1	Surface	13	1.1	1.68
B_2	30 cm depth	13	3.4	1.49

curves from inner soil, sample B_2 has only one peak and wider distribution in pore size though its peak intensity is smaller than sample A_2, implying that pores in the inner soil keep almost homogeneous even with weathering time increasing. Logically, sample A_2, A_1 and B_1 establish a framework for understanding the soil surface deterioration with weathering time: A_2 is the interior soil with no weathering, while A_1 and B_1 are surface soils weathered for 2 and 13 years respectively. It seems that soil deterioration progress can be divided into two stages with weathering time. At the initial stage as indicated from A_2 to A_1, the macro-pore population and its peak intensity in the surface soil become larger but the pore diameter becomes smaller while the micro-pore population and its intensity become smaller and the pore diameter becomes lager, that is, the two dominant peaks become closer to each other than which in the inner soil (comparing curves A_1 and A_2). This indicates that the pores become uniform and can be attributed to the destruction of the original structures in soil mass. At the second stage as indicated from A_1 to B_1, the macro-pore population and its intensity decrease but the pore diameter remains the same and the extra peak appears in the micro-pore distribution area which means a new structure type different from the inner soil forms in the surface part.

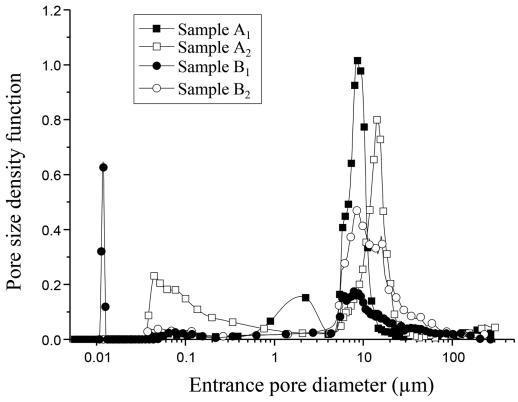


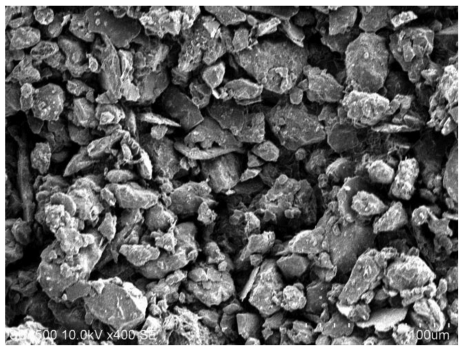
Figure 1. MIP results of different samples.

Fig. 2 presents the observations conducted to the field samples. It shows that there is a distinct structure with a preferential orientation of the particles for the surface and inner soil.

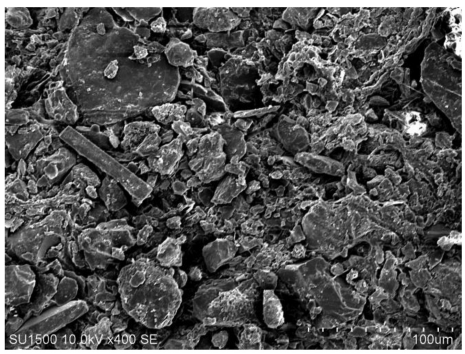
Compared to the inner part, the particles in the surface soil (A_1 and B_1) take the shape of lamelliform and arrange more densely. On the other hand, the samples have a more diversity of pore size and more small pores than those from inner soil. In addition, with weathering time increasing, the differences between the surface soil samples become more obvious in structure while the inner part resembles nearly the same for A_2 and



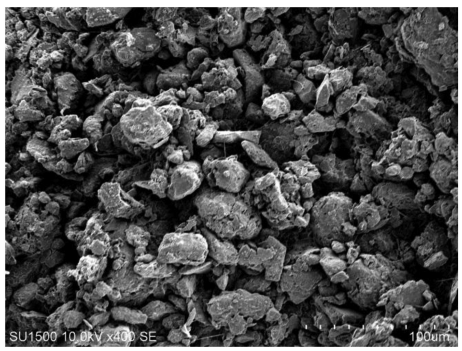
(a) Sample A_1



(b) Sample A_2



(c) Sample B_1



(d) Sample B_2

Figure 2. SEM photos of different filed samples.

B_2. These observations are consistent with the MIP test results in Fig. 1.

It has been demonstrated that the grain content with smaller than 0.02 mm in the surface crust is higher than which in the original soil. That is, the surface soil is with smaller particles and pores. It is in agreement with the test results in this paper. Thus the deterioration pattern of surface soil can be described as follows. Firstly, rain water makes the soil surface saturated, result in the dispersion of surface soil. The dynamic impact of rain drop s compact the soil surface and soil particles come to be closer than before. The original structure is destroyed and the pores in the soil become smaller. While the water permeate into the soil, the salt is dissolved and thus part of the volume occupied by the salt becomes extra, this makes some pores become lager though the volume of which is negligibly small to the whole. This explains why the two peaks in sample A_1 become closer in the initial state. It can be defined as the "Zero Point" in the deterioration progress. And with weathering time going by, the sun radiation vaporizes the water in soil and shrinkage makes the pores become much smaller. Thus, a new structure called "Rural Crust" forms on the surface of soil. When the rural crust shrinks to crack, the wind blown sand erodes the interface with lower connection between the surface and inner part. Moreover, the severe temperature difference aggravates this progress. Finally, the rural crust peels off from the soil mass. And the next circulation of deterioration begins.

4 CONCLUDING REMARKS

This paper investigates the deterioration progress of rammed earth with analogy study method. The loess cuts exposed for different years to natural weathering were chosen as analogy models and MIP and SEM techniques were used to research the microstructure in the field samples in situ. The following conclusions can be drawn based on the results obtained.

(1) The microstructure is different between the surface and inner soil. And the difference is more obvious in the surface soil with weathering time increasing. In general, the pores tend to be smaller in the surface soil and homogeneous in the inner soil. Besides, the particles arrange more densely in the surface part.

(2) The deterioration progress can be divided into two phases represented by the change of pore diameter. Firstly, most of pores become smaller with the destruction caused by raining impaction while the few part becomes lager attributed to the dissolution of salt in the soil. Secondly, the shrinkage of soil affected by the sun radiation makes the pores much smaller.

(3) The deterioration of the soil is a circulation progress. The exterior part peels off gradually under the insisting weathering conditions and it makes mass loss of the soil. Thus to prevent the earthen monuments from suffering natural weathering, methods on surface protection should be developed. Generally, surface soil particles tend to be arranged in a dense microstructures with smaller pore size compared with the homogeneous interior soil after being weathered for 2 to 13 years.

ACKNOWLEDGEMENT

The present work has been sponsored by the Foundation of Key Laboratory of Mechanics on Disaster and Environment in Western China (Lanzhou University), Ministry of Education (No. 201405).

REFERENCES

Bui Q B, Morel J C, Reddy B V V, et al. 2009. Durability of rammed earth walls exposed for 20 years to natural weathering. *Building and Environment*, 44(5): 912–919.

Chen Y, Tarchitzky J, Brouwer J, et al. 1980. Scanning electron microscope observations on soil crusts and their formation. *Soil Science*, 130(1): 49–55.

Delage P, Tessier D, Marcel-Audiguier M. 1982. Use of the Cryoscan apparatus for observation of freeze-fractured planes of a sensitive Quebec clay in scanning electron microscopy. *Canadian Geotechnical Journal*, 19(1): 111–114.

Jiang M, Zhang F, Hu H, et al. 2014. Structural characterization of natural loess and remolded loess under triaxial tests. *Engineering Geology*, 181: 249–260.

Rossi-Manaresi R, Tucci A. 1991. Pore structure and the disruptive or cementing effect of salt crystallization in various types of stone. *Studies in Conservation*, 36(1): 53–58.

Unsaturated Soil Mechanics—from Theory to Practice – Chen et al. (Eds)
© 2016 Taylor & Francis Group, London, ISBN 978-1-138-02921-7

Analysis of the failure of a polluted red clay foundation in the north Guilin karst area

C.M. Mu, K.L. Han & Y. Liu
Guilin University of Technology, Guilin, Guangxi, China

ABSTRACT: This paper mainly research on the problem of polluted red clay foundation treatment failure of a project in Guilin karst area. Because of a thick layer of soft plastic-like organic red clay on the upper part of engineering site, the cement stirring pile body appeared severe stress softening phenomenon, at the same time, the bearing capacity characteristic value of composite foundation is far to meet the design requirements, so we have to take reinforcement measures. After conducting the gravel pile and grouting treatment around each original mixing pile again, with the using of root pile to reinforce in local area, the problem was solved. The study of this problem can not only provide scientific theory basis for foundation design, foundation reinforcement treatment, and subgrade filling of polluted red clay in north Guilin karst area, but also has been of great practical significance for the foundation stability evaluation and the prevention of geological disaster in Karst area.

1 INTRODUCTION

North Guangxi karst area (mainly referring to the urban area of Guilin city) is one of the typical karst development zone in our country, where the distribution of red clay formation is very extensive. The problems of the natural foundation treatment occur frequently in many engineering construction sites of red clay[1-3] in the beginning Train station located in the north of Guilin, the eastern Jin Jiling, the southern high-tech zone, and the bamboo river area. It mainly caused by following 2 aspects: (1) the natural foundation shows a good bearing capacity, but the local deformation is large, especially continuous subsidence deformation after the construction of buildings, resulting in the crack of the wall body; (2) because of the composite foundation of red clay reinforced by cement mixing pile, of which the pile strength reduced in different degree, and the extent of the strength decrease of pile body in the same construction site is different, the bearing capacity characteristic value of composite foundation is far less than the design requirements, and the single pile bearing capacity of some piles is far from meeting the design requirements. The reasons of the above problems include deteriorating of environmental conditions and engineering geological conditions in recent years, and for the wet natural climate conditions of Guilin, which cause red clay contamination in large area, mainly embodied in that the pollutants would increased the content of contaminants in the red clay in different levels through various channels such as waste discharge, artificial fertilization, building construction, as well as the contaminated surface water and groundwater flow. These pollution sources pass pollutants to the red clay in different degrees through different ways, which result in chemical and physical effect on the red clay and lead to changes in the composition and the structure of red clay, then exerting an important influence on engineering characteristics (deformation and strength) of red clay. Red clay itself is a kind of special soil. When polluted, its composition, structure, physical and mechanical properties will undergo a fundamental change, forming a new kind of special soil-polluted red clay. If the project is built on polluted red clay ground, we must be very careful about the foundation design, foundation treatment, embankment dam engineering design, the selection of roadbed filler and so on, otherwise there would be continuous subsidence deformation and a large number of "Problematic and failure foundations". This impacts the project schedule, cost or social aspects and so on in varying degrees.

2 PHYSICAL AND MECHANICAL PROPERTIES OF CONTAMINATED RED CLAY

The project site of the research was located in the Development Zone of south Guilin, which has 8 new commercial and residential buildings with 8 to 12 floors. The site where the original building had been demolished was filled with a lot of construction waste and garbage. The site topography takes on gently sloping shape with partial terrain undulating; the ground elevation is approximately 158～163 m; the landform belongs to level III terrace on the left bank of the Li River. There is a large thickness (1.5 m to 2.0 m) of red clay polluted by organic in the upper part of

Table 1. Statistics of physical and mechanical properties of red clay being polluted by organic matter in Guilin areas.

Contaminants	0 (Uncontaminated a)	1–8 (contaminated b)	Amplitude*
MC(W_u/%)*	26–53	46–78	11.8
Void ratio(e)	0.8–1.5	1.2–1.6	6.58
Density(ρ/g/cm^3)	1.22–1.95	1.03–1.62	5.08
Liquid Limit(%)	49–96	66–98	29.8
Plastic limit(%)	23–54	44–65	60.6
Plastic Index(I_P)	23–42	22–33	12.5
CC(a_{1-2}/Mpa^{-1})*	0.24–0.67	0.39–0.84	18.96
CM(E_s/Mpa)*	6.3–17.8	5.4–12.6	23.2
Cohesion(c/Kpa)	21–61	12–43	34.8
Friction angle(°)	21–61	5–11	42.8

* MC: Moisture content CM: Compression modulus CC: Compression coefficient Amplitude: $\left|\frac{a-b}{a}\right|$%

the site. No prior test for the content and component and other related issues for organic red clay are carried out, leading to a total of 4 times of the foundation treatment was carried out to reach the design value of foundation bearing capacity finally in the site. Through field investigation on foundation treatment failure of the engineering site, combined with information collected from geotechnical investigation, in-site testing and foundation handling data, we carried out comparative study of the composition, structure and the physical mechanics properties on the natural or contaminated red clay, in order to re-make the geotechnical engineering evaluation in this site. The basic physical-mechanical properties index of natural or contaminated red clay and the changes of the basic physical-mechanical properties index are shown in beneath Table 1.

As it shown in the indicators of the first and second rows of Table 1, because of contamination of organic matter, physical and mechanical properties of red clay exhibited different changes. Compared with natural red clay that is not polluted by organic matter its moisture content and initial void ratio increased, and the density reduced; the liquid limit and plastic limit increased significantly, while the plasticity index reduced. In mechanics index, compression modulus, cohesion and internal friction angle all reduced in different degree, by the value of the plasticity index knowing that the clay content is higher in the red clay not contaminated.

By the third row of table 1 we can also see that due to the presence of organic matter, the physical and mechanical properties of red clay changed, but the amplitude of indicators presented at different levels. The degree of liquid limit and plastic limit amplitude is large, so is the mechanical index. Bush and Keller (1981)[4-5] found that liquid limit and plastic limit of soil will increase with the addition of organic matter content in soil by the experiment on basic properties of the different organic matter content soil. Booth and Dahl (1986)[5-6]and others through further study found that only when the soil reaches a certain amount of organic matter content, will the liquid limit and plastic limit of soil increase with the increase of the organic matter content, and the minimum content of organic matter is 3–4% which has significant effect on liquid limit and plastic limit.

3 ANALYSIS OF THE CAUSES AND TREATMENT MEASURES

3.1 *Failure analysis*

A large number of red clay is distributed in Guilin Karst region, because of the invasion of contaminant substances, the red clay which was originally a special soil occur significant variation in its composition, structure and properties, resulting in the foundation soil swelling or collapse, causing the building foundation sinking or wall cracking, affecting the normal use of the building seriously. After a field investigation we knew that the red clay of the site is contaminated with wide range and local extremely depth features, due to the different distances from the pollution sources, distribution of red clay in the site being uneven, thus also resulting in the complex distribution of the pile quality of cement mixing pile, some body of which presented mechanical softening phenomenon very seriously, and a small part of the piles basically reached the strength of the design.

Neither did they know that the red clay in the accident site had been polluted when dealt with the foundation, nor tested if the soil body was polluted or got the data to analysis the nature and content of the pollutants when exploration, only treating the red clay with cement mixing pile composite foundation as the original red clay in normal situation. After piling, when testing the quality and bearing capacity of a pile body, we found that strength softening phenomenon of the pile was serious, at the same time many piles didn't consolidate completely and blew into blocks falling after gently hammering. By situ test, sampling to conduct a comprehensive analysis and detection in indoor test, we found that the red clay was polluted in different degrees in this area, so that the strength of the red

Table 2. Statistics of the parameters of four ground treatment methods.

Parameters Solid type	Pile layout pattern	Replacement rate/%	Pile diameter/ mm	Piles or pitch/m	Row spacing/m	Spacing/m
Cement mixing pile	Equilateral triangle layout	25	600		1.15	1.00
Gravel pile	Evenly around the mixing pile arrangement 3 root, two of which are shared, grid-like layout	20	200		1.15	1.00
Chemical grouting	Each mixing pile added a grouting hole, the plum flower form layout		Diffusion radius 600–800	1.15	1.00	
Root pile(straight pile)	Evenly arrange 3 root around each mixing pile, equilateral triangle layout	8.3	200	0.72		

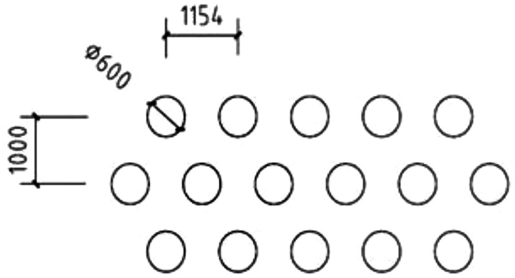


Figure 1. Cement mixing pile, the pile diameter D = 600 mm, spacing 1000 mm, row spacing 1154 mm.

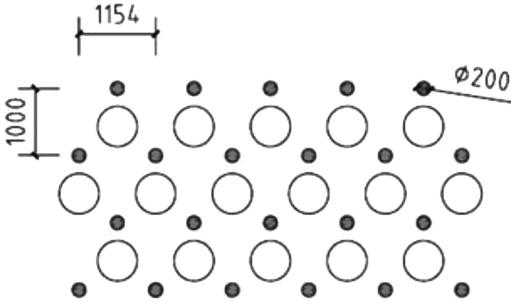


Figure 2. Around the cement mixing pile setting gravel pile, the pile diameter D = 200 mm.

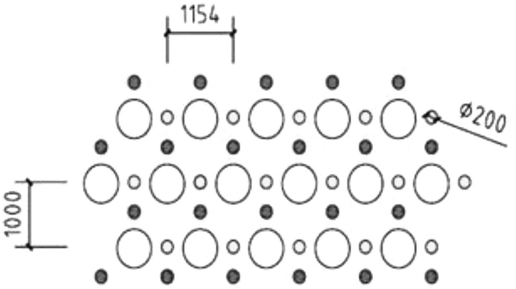


Figure 3. On the basis of the 2 deploy the grouting hole, diffusion radius D = 200 mm, spacing 1000 mm, row spacing 1150 mm.

clay foundation reinforced by mixing cement pile presented reduction in different degrees, and pile of partial section was not curing, but going into the shape of the fragments. Composite foundation treatment processed by cement mixing pile of entire site failed. Later, we re-explored and redesign the foundation of this area.

To sum up, it would effect on the design and construction if they didn't pay attention to the exploration or spend little money; and it would be bound to an accident if they dealt with the foundation where they did not know the specific circumstances of the geotechnical engineering in the site. This problem should be taken seriously by all parties, especially the prospecting units. Particularly, it is important to note that if the site is contaminated, the nature of pollutants, the scope and the depth of contamination, during geotechnical engineering exploration on the originally existed buildings field surrounding urban areas when removing old buildings and reconstruction where the waste discharge, artificial fertilization, and building operations were misconducted. There is a very important practical significance in selecting the foundation design, foundation reinforcement, earth-rock dam engineering design and the selection of Roadbed filler.

3.2 *The specific implementation of reprocessing foundation*

The site had been re-treated gravel pile reinforcement. According to the design, each mixing pile added 3 root gravel pile, while the bearing capacity characteristic value in static load test still not reached the design requirements, and according to each mixing pile adding one grouting holes (seeing figure 1) we also conducted a chemical grouting treatment on the treated soil between piles in the upper part of the construction site. After testing, we found that bearing capacity characteristic value of the local area composite foundation still didn't meet the design requirements of 180 kPa. We had to reinforce the drill exploration designated area by root pile on the basis of the original, seeing the composite foundation dealt with by mixing pile, crushed stone pile, pressure grouting as the soil around the pile. After being reinforced by

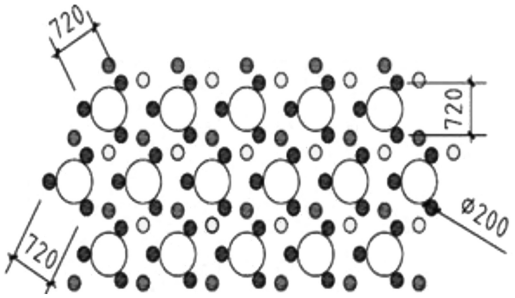


Figure 4. On the basis of the 3 around the mixing pile evenly layout three root pile, the pile diameter D = 200 mm, the aperture 720 mm.

root pile which can be viewed as the enhancers of the composite foundation and tested the bearing capacity characteristic value of composite foundation that reached 200 kPa, thus the issue resolved finally. A total of 4 kinds of treatment measures used during the foundation treatment, they were cement mixing piles, gravel pile, pressure grouting, and root pile, taking a lot of manpower and material resources, and not only caused serious economic losses, but also delayed the construction period, resulting in adverse social impact.

4 CONCLUSION

The commercial and residential building would be constructed in local large fluctuation place where the original building had been demolished and filled with much living garbage and construction waste. In the early exploration, the determination of the pollutants' nature and content for the soft soil layer in the site were not conducted, so that the contaminated red clay foundation reinforced by cement mixing piles failed.

Surrounding each failed cement mixing pile, 3 gravel piles were arranged uniformly for strengthening treatment. But the characteristic value of bearing capacity could not reach the design requirements. Then chemical grouting was conducted to reinforce the soft soil, while the value still could not meet requirements. Eventually, the composite foundation formed by mixing pile, crushed stone pile and pressure grouting was seen as the soil around the piles, using root pile to reinforce the composite foundation, so the characteristic value of bearing capacity reached the design requirements.

Because of the loss of detailed experimental research on soil in advance, the soil had been treated for 4 times totally, including the foundation of deep mixing pile reinforcement, the gravel pile foundation reinforcement, the chemical pressure grouting foundation reinforcement and the foundation root pile's partial treatment. It not only caused the delays of the project and enormous economic losses, but also brought great influence on society.

ACKNOWLEDGMENT

This research was supported by Guangxi Education Department (#KY2015ZD055, the Natural Science Foundation of Guangxi (#2012GXNSFEA053002), and the National Science Foundation of China (#51169004).

REFERENCES

[1] Liu Baochen and Chun-mei Mu. The organic matter pollution red clay foundation reinforcement effect analysis of the mechanical effects [J]. Industrial building, 2010, 40(2):128–131 (in Chinese).
[2] Chun-mei Mu and Li Baifeng. The analysis of effect of organic matter content on the mechanical properties of soft soil [J]. Hydrogeology and Engineering Geology, 2008, 25(3):42–46 (in Chinese).
[3] Chen Xianhua and Tang Hui-ming. Research Status and Prospect of contaminated soil [J]. Geological and prospecting, 2003, 39(1):77–80 (in Chinese).
[4] Bush, W.H., and Keller, G.H. 1981. The Physical properties of Peru-Chile continental margin sediments- the influence of coastal upwelling on sediment properties. Journal of Sedimentary Petrology, 51:705–719.
[5] Fan Shaoping, The influence of organic matter in sludge solidification mechanism and the research on countermeasures [D]. Master's thesis in Hohai University, 2004. 390 (in Chinese).
[6] Booth, J. S., and Dahl, A. G. 1986. A note on the relationships between organic matter and some geotechnical properties of marine sediment. Marine Geotechnology, 6(3):281–297.

This page intentionally left blank

In the past decades advances have been made in the research and practice on unsaturated soil mechanics. In 2000 the first Asia-Pacific Conferences on Unsaturated Soils was organized in Singapore. Since then, four conferences have been held under the continued support of the Technical Committee on Unsaturated Soils (TC106) of the International Society of Soil Mechanics and Geotechnical Engineering (ISSMGE). The conferences provided an excellent forum for researchers and practitioners in the region and beyond to present the latest developments and to exchange ideas on the subjects related to unsaturated soils.

Unsaturated Soil Mechanics - from Theory to Practice collects more than 140 technical papers, and 10 invited and keynote lectures presented at the sixth Asia-Pacific Conference on Unsaturated Soils (Guilin, China, 23-26 October 2015). The first Asia-Pacific distinguished lecture, launched at the conference, is also included. The contributions address the fundamental behavior of unsaturated soils, and present theoretical and numerical modeling and engineering applications. The topics of concern span the full spectrum from theory to practice, with strong relevance to the problems in the region and beyond such as collapse/swelling, freezing/thawing, desiccation shrinkage, rainfall-induced slope failure, contaminant transport, shale gas extraction and so on, largely representing the latest developments in unsaturated soil mechanics.



CRC Press
Taylor & Francis Group
an informa business
www.crcpress.com

6000 Broken Sound Parkway, NW
Suite 300, Boca Raton, FL 33487
Schipholweg 107C
2316 XC Leiden, NL
2 Park Square, Milton Park
Abingdon, Oxon OX14 4RN, UK

ISBN 978-1-138-02921-7

an informa business